COHERENCE OF E-BEAM RADIATION SOURCES AND FELS – A THEORETICAL OVERVIEW

Avi Gover, Egor Dyunin, Tel-Aviv University, Ramat Aviv, Israel.

GENERAL FORMULATION FOR RADIATION EMISSION FROM MICROSCOPIC CHARGES

This publication is mostly tutorial. It presents a general time-frequency modal-expansion linear formulation for radiation excitation from charges. This, however, can be employed to analyze front-line FEL research problems. Starting from description of synchrotron undulator radiation, the model is extended to describe the coherence characteristics of stimulated emission devices (FEL amplifiers and oscillators), and then further extended to the SASE regime. It is then employed to point out directions for development of coherent X-UV FEL sources.

The starting point of our formulation is the general Maxwell Equations driven by particulate point charge sources (the source dimension is smaller than the emission wavelength):

$$\begin{aligned}\nabla\times\mathbf{E} &= -\mu\frac{\partial\mathbf{H}}{\partial t}-\mu_0\frac{\partial\mathbf{M}}{\partial t}\\ \nabla\times\mathbf{H} &= \varepsilon\frac{\partial\mathbf{E}}{\partial t}+\mathbf{J}+\frac{\partial\mathbf{P}}{\partial t}\end{aligned} \qquad (1)$$

where in general the point sources may be free electrons, atomic electric dipoles or atomic magnetic dipoles and spins [1]:

$$\begin{aligned}\mathbf{J} &= \sum_{j=1}^{N}-e\mathbf{v}_j\delta\left(\mathbf{r}-\mathbf{r}_j(t)\right)\\ \mathbf{P} &= \sum_{j=1}^{N}\mathbf{p}_j\delta\left(\mathbf{r}-\mathbf{r}_j(t)\right)\\ \mathbf{M} &= \sum_{j=1}^{N}\boldsymbol{\mu}_j\delta\left(\mathbf{r}-\mathbf{r}_j(t)\right)\end{aligned} \qquad (2)$$

In this article we focus on free electrons.

Maxwell Equations can be exceedingly simplified in the frequency domain. In the frequency domain it is possible in many structures to expand the radiation field in terms of a complete set of eigenmodes $\{\tilde{\mathbf{E}}_q\}$:

$$\tilde{\mathbf{E}}(\mathbf{r},\omega)=\sum_q C_q(z,\omega)\tilde{\mathbf{E}}_q(\mathbf{r}) \qquad (3)$$

This certainly can be done in a waveguide, but also in free-space, where one can use a discrete set of modes like Hermit-Gaussian modes, commonly used in laser physics, or continuous modes – like plane waves. In this latter case the summation of q degenerates into integration over transverse wave numbers.

After modal expansion it is possible to simplify Maxwell's set of 3-D differential equations into a simple infinite set of first order ordinary differential equations for the complex amplitudes $C_q(z,\omega)$ [2,3]. These can be solved for each mode at steady state, if the initial condition $C_q^{in}(\omega)$ (the complex amplitudes at the entrance to the interaction region) is given (see Fig.1). The formal solution for the increment of the complex amplitudes in the case of *free electron* microscopic charges is:

$$\begin{aligned}C_q^{out}(\omega)-C_q^{in}(\omega) &= \sum_{j=1}^{N}\Delta C_{qj} =\\ &= -\frac{1}{4}\sum_{j=1}^{N}\left\{-e\int_{-\infty}^{\infty}\mathbf{v}_j(t)\cdot\tilde{\mathbf{E}}_q{}^{*}\left(\mathbf{r}_j(t)\right)\mathrm{e}^{i\omega t}\,dt\right\}\end{aligned} \qquad (4)$$

For any charges in the interaction volume the output amplitudes C_q^{out} can be calculated. Thus the entire output radiation field can be calculated then by substituting $\{C_q^{out}\}$ back into the expansion series (3), or using it otherwise to calculate optical parameters.

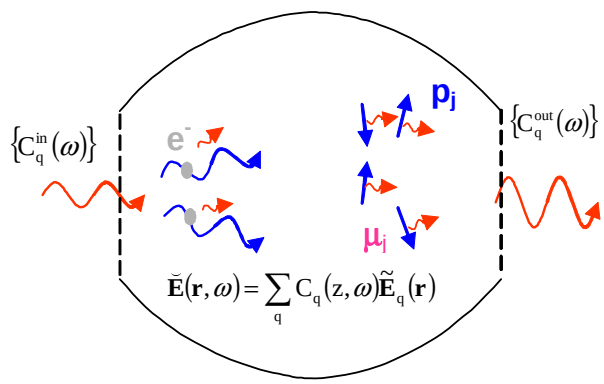

Fig.1: Excitation of radiation modes by particulate charges (Frequency Domain).

This suggests the following picture for modal excitation: the field amplitude increment of each mode is composed of the sum of contributions from the individual electrons, which correspond to the "wavepackets" emitted by the individual electrons. To calculate the increment to the radiation mode amplitude, one must solve a contour integral along the trajectory of each electron and sum up the wavepacket contributions.

In principle, the trajectories can be expanded in series in terms of the field amplitudes C_q. To zero order, the trajectories of the electrons are not modified by the radiation field and we know them explicitly. In this case the contour integrals can be performed straightforwardly. If all the electrons have the same trajectories (a narrow beam), then their wavepacket amplitudes are identical, except for a "start oscillation" or "entrance time" phase factor [3]:

$$C_q^{out}(\omega) = C_q^{in}(\omega) + \Delta C_{qe}^{(0)}(\omega)\sum_{j=1}^{N} e^{i\omega t_{oj}} + \sum_{j=1}^{N} \Delta C_{qj}^{st} \qquad (5)$$

The contribution of the electrons to the total field depends to *zero order* in the fields on the phase relation between the wavepackets. These contributions (second term in (5)) give rise to the *spontaneous* or *superradiant* emission of the electron beam [3]. At higher order of expansion in terms of the fields, the modification of the electron trajectories by the fields, gives rise to *stimulated emission* or *stimulated absorption*, represented by the last term of (5).

Once one calculated the mode amplitudes (5) it is possible to substitute them in (3) to find the total field. Alternatively, one can use them to calculate optical parameters as radiation mode power or spectral energy (both are quadratic forms of C_q):

$$P_q = \left|C_q^{out}(\omega)\right|^2 \quad \text{or} \quad \frac{dW_q}{d\omega} = \frac{2}{\pi}\left|C_q^{out}(\omega)\right|^2 \qquad (6)$$

Several physical situations can be distinguished, corresponding to the manner the amplitudes in (5) combine in the complex $C_q(\omega)$ plane to produce the total radiation field. These are shown graphically in Fig.2 [3]. Let us now neglect the stimulated emission terms, and assume no input field $C_q^{in}(\omega) = 0$. When one absolute value square the second term in (5) and then average over the electron phases j, one can distinguish two cases, corresponding to two different emission processes:

(1) The electron entrance times are random (Fig.2a). In this case only the non-mixed terms in the square of the sum do not average down to zero ($\left\langle \sum_{j=1;\, j\neq i}^{N} e^{i\omega t_{oj}} \cdot e^{i\omega t_{oi}} \right\rangle_j = 0$), consequently the spectral energy is proportional to the number of particles N. This process is referred to as *spontaneous emission* or *shot noise emission*, and radiation spectral energy (6) is proportional to:

$$\left\langle \left| \sum_{j=1}^{N} e^{i\omega t_{oj}} \right|^2 \right\rangle_j = N \qquad (7)$$

(2) The electron entrance times are correlated (Fig.2b): either they enter in a bunch of duration shorter than the radiation period, or periodically at the radiation frequency. In these cases the wavepackets emitted by the individual electrons interfere in phase with each other, and the spectral power is proportional to N^2:

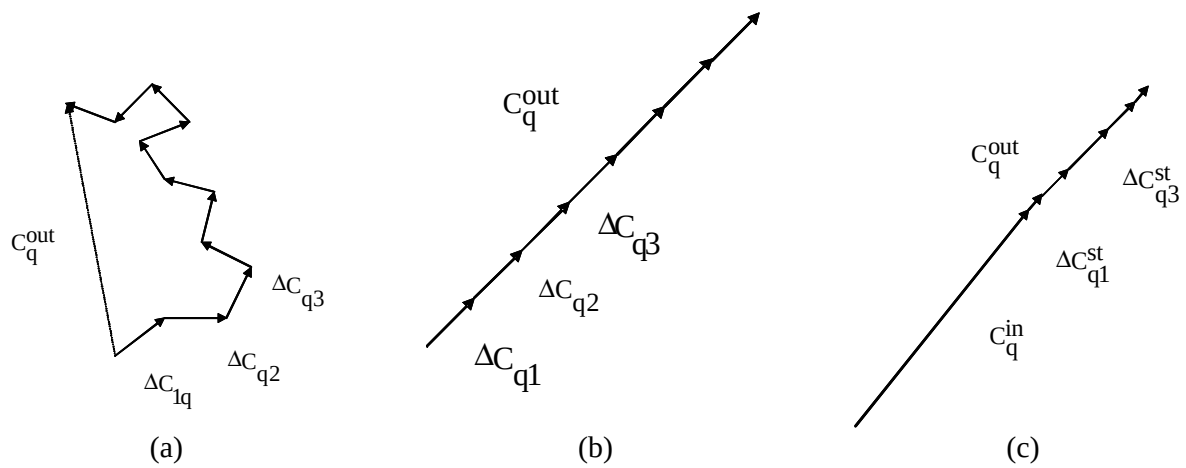

Fig.2: Superposition of mode wavepacket amplitudes of electrons C_{qj} in the complex plane: a) spontaneous emission, b) superradiant emission, c) stimulated emission.

$$\left\langle \left| \sum_{j=1}^{N} e^{i\omega t_{oj}} \right|^2 \right\rangle_j = N^2 \qquad (8)$$

We term this emission process "superradiance", following Dicke [4], who analyzed this case for an ensemble of molecules having electric or magnetic dipoles, employing a full quantum formulation (note though that the superradiance effect is classical even in Dicke's problem [1]). Superradiant emission is also termed *coherent emission*, as in CSR [5].

(3) When the mode field amplitudes at entrance do not equal to zero ($C_q^{in} \neq 0$) (Fig.2c), the electron trajectories may be modified by the presence of the radiation field, and the integral (4) will result in, beyond the zero order expansion approximation, a field-dependent radiation term (third term in (5)). This is the *stimulated Emission* term. In first order expansion in the fields (linear regime), neglecting inter-mode scattering, and this term is proportional to the mode field amplitude:

$$\sum_{j=1}^{N} \Delta C_{qj}^{st} \propto C_q$$

and therefore produces radiation wavepackets in phase with the incoming wave of amplitude C_q^{in}, and the total radiation is coherent.

UNDULATOR RADIATION OF A SINGLE ELECTRON

The formalism and classification described in the previous section can be applied to any kind of radiation mechanism: undulator, synchrotron, Smith-Purcell etc. [3, 6]. We now concentrate on the case of radiative emission in an undulator. Expressing the radiation field both in frequency domain and time domain, helps to understand the coherence characteristics of undulator radiation and FEL devices. We therefore will employ on occasions inverse Fourier transform on the radiation expressions which are generally derived in this formulation in the frequency domain.

The frequency domain amplitude of a wavepacket emitted into transverse mode q by a single electron traversing through an undulator is calculated from (4):

$$C_q^{out}(\omega) = -\frac{1}{4}\left\{ -e \int_{-\infty}^{\infty} \mathbf{v}_j(t) \cdot \tilde{\mathbf{E}}_q^{\,*}\left(\mathbf{r}_j(t)\right) e^{i\omega t}\, dt \right\} \qquad (9)$$

$$\mathbf{v}_j(t) = \mathrm{Re}\left\{ \tilde{\mathbf{v}}_w e^{-ik_w z_j(t)} \right\} + v_z \hat{\mathbf{e}}_z$$

The result is:

$$C_{qj}^{out}(\omega) = e \frac{\mathbf{v}_w \cdot \mathbf{E}_q^*(\mathrm{r}_{\perp 0})}{8 v_z} L\, \mathrm{sinc}(\theta(\omega)L/2)\, e^{i\theta(\omega)L/2}\, e^{i\omega t_{0j}} \qquad (10)$$

where $\theta(\omega)L \equiv \left(\frac{\omega}{v_z} - k_z(\omega) - k_w \right) L = (\omega - \omega_0) t_{sl}$ is the detuning parameter); $t_{sl} = \frac{2\pi}{\Delta\omega} = \frac{L}{v_z} - \frac{L}{v_g}$ is the slippage time, and ω_0, the synchronism frequency, is defined from $\theta(\omega_0) = 0$. Substituted in (6), this is a resonant emission linewidth function, centered on the synchronism frequency, and having a frequency bandwidth equal to the inverse of the slippage time (Fig.3):

Note that the amplitudes (10) of the wavepackets C_{qj}^{out} of different electrons differ only by a phase factor (as in (5))!

One can describe the wavepacket field in the time domain by performing an inverse Fourier transform over the complex amplitude function (10):

$$\mathbf{E}(\mathbf{r},t) = \mathbf{F}^{-1}\left\{ C_q(z,\omega)\mathbf{E}_q(\mathbf{r}_\perp) e^{ik_z(\omega)z} \right\} =$$

$$= \sum_{i=1}^{2} A_i \mathbf{E}_q(\mathbf{r}_\perp) \cos(k_z(\omega_i)z - \omega_i t)\, \mathrm{rect}\left[\frac{t - z/v_z + t_{sl_i}/2}{|t_{sl_i}|} \right] \qquad (11)$$

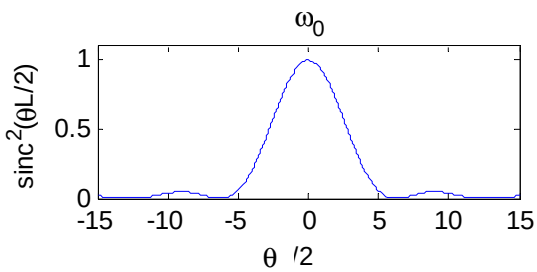

Fig.3 The spectral emission curve of undulator radiation of single electron emission.

In the time domain, the wavepacket is composed of two simple truncated sinusoidal waveforms (Fig.4). The *high frequency* radiation wavepacket of slippage time duration t_{sl1} arrives first after a retardation time L/v_{g1}; then the electron arrives after time L/v_z and at the end the *low frequency* wavepacket, corresponding to backward emission in the electron rest-frame, arrives with a radiation (back-slippage) time L/v_{g2} [7]. Here v_{g1}, v_{g2} are the group velocities of the waves propagation in a waveguide enclosure [7]. In free space $v_{g1} = c$, $v_{g2} = -c$ and the low frequency wavepacket is actually emitted backward also in the lab frame. In any case this low frequency wavepacket is not important for the present discussion and will be neglected in the subsequent discussion.

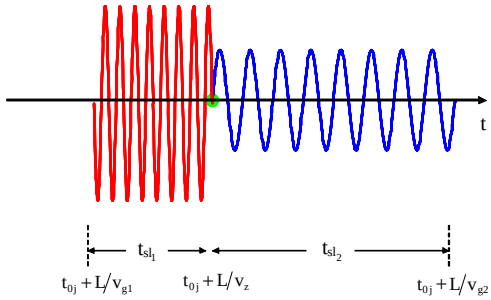

Fig.4: Time domain waveform of a single electron emission wavepacket.

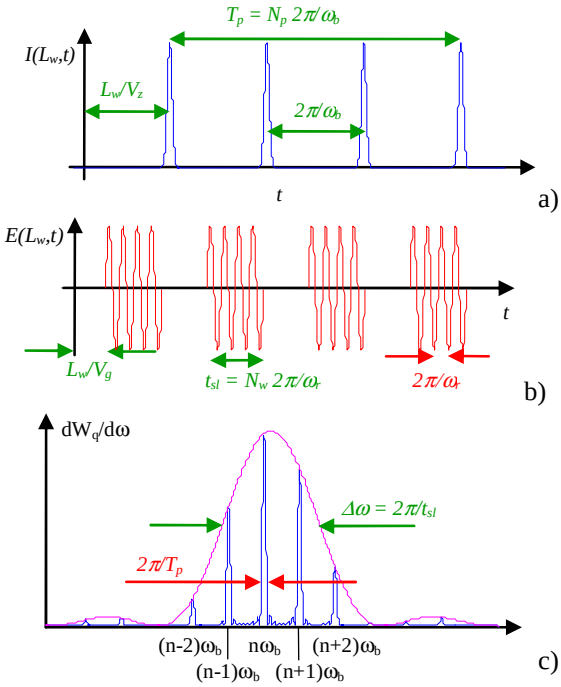

Fig.5: Superradiant (coherent) radiative emission from a macropulse train of e-beam bunches:
a) current waveform; b) time domain picture of the train of phase coherent radiation wavepackets;
c) spectral power of the radiation field waveform (b).

UNDULATOR RADIATIVE EMISSION OF A BUNCH OF ELECTRONS

If we consider now emission from a bunch of N electrons, its resultant radiative emission field will be composed of a superposition of wavepackets like the one in Fig.4 [3]. In the frequency domain the emission amplitude from all electrons (10) is the same except for a phase factor. Therefore the spectral emission curve is the same function as of a single electron (Fig.3). It is multiplied by N in the case of spontaneous emission (when t_{0j} is random - see Eq.7) or by N^2 in the case of superradiant emission (when $|t_{0j}\text{-}t_0| < 2\pi/\omega$ - see Eq.8).

EMISSION OF A PERIODIC TRAIN OF ELECTRON BUNCHES

Examine now superradianat radiative emission from a train of electron bunches, for example a macro pulse of an RF accelerator (Fig.5a).

The periodic bunches radiate independently of each other. The resultant radiation waveform (Fig.5b) is a temporal periodic sequence of the single bunch wavepackets of Fig.4 (only the high frequency wavepackets are considered). The duration of the electron beam macropulse is $T_p = N_p{*}2\pi/\omega_b$: the number of electron bunches N_p times the bunching period. The duration of the wavepacket is $t_{sl} = N_w{*}2\pi/\omega_r$: the number of wiggles N_w times the optical radiation period. The Fourier transform of the wave is dominated by these two time constants. Fig.5c displays the spectral power of this waveform (frequency domain) for the common case where $t_{sl} << 2\pi/\omega_b$. In this case there is no overlap between the wavepackets, and consequently there are several harmonics under the emission curve.

In the frequency domain, the macropulse spectral emission curve is the product of the single electron emission curve (the absolute value square of (10) – Fig.3) and the macropulse "form factor" [3]:

$$M_M(\omega) = \left[\frac{\sin\left(N_P \pi\omega / \omega_b\right)}{N_P \sin\left(\pi\omega / \omega_b\right)}\right]^2 \qquad (12)$$

The emission is wide band ($2\pi/t_{sl}$), but if one can filter out one harmonic, or if $\omega_b > \Delta\omega_{sl}$, it will have a narrow linewidth corresponding to the macropulse duration (under the condition of *stability* of the bunching frequency during the entire macropulse duration). This observation will be important also for the later discussion on the case of FEL oscillator and SASE.

A nice verification of this concept was demonstrated by the MIT research group [8] who measured superradiant Smith-Purcell coherent emission using an RF Linac beam. Carefully filtering out the radiation emission at the 14th harmonic of the microbunch repetition rate within the macropulse by *heterodyne* detection *techniques*, they measured the exceedingly narrow linewidth of the total waveform of the macropoulse radiation. It was indeed $2\pi/T_p$, corresponding to the duration T_p of the e-beam macropulse.

If the electron bunch has a finite duration t_b, then the expression for radiation spectral energy includes also a "bunch–form factor"

$$\left|M_B(\omega)\right|^2 = \left|\frac{1}{Q}\int_{-\pi/\omega_b}^{\pi/\omega_b} I(t) e^{i\omega t}\, dt\right|^2 \qquad (13)$$

(which is equal to unity as long as $t_b << 2\pi/\omega$).
This, in practice, limits the harmonic number n_H, that can have appreciable amplitude out of the infinite numbers of harmonics that the macropulse form factor (12) admits, to

$$n_H << 2\pi/\omega t_b \qquad (14)$$

If the waveform of the electron-beam current does not contain high harmonics (e.g. it is sinusoidally modulated) then there will be no harmonics under the spectral energy curve in Fig.5b except the fundamental ($n_H=1$), and its amplitude will be appreciable only within the bandwidth of the single electron emission spectrum $(\omega-\omega_b) < \Delta\omega = 2\pi/t_{sl}$. The narrow linewidth ($\delta\omega \sim 2\pi/T_p$) radiation of the prebunched FEL follows the detuning curve of Fig.3 as demonstrated experimentally in [22].

Single harmonic radiative emission can take place also at high harmonic n_H of the bunching frequency ω_b. This will happen (under the condition (14)) if the spacing between the harmonics exceeds the emission bandwidth:

$$\omega_b > \Delta\omega_{sl} = 2\pi/t_{sl}$$
$$\text{or} \quad n_H < 2\pi/\omega_0 t_{sl} \cong N_w \qquad (15)$$

In this case, the wavepackets train of Fig.5b merges into an harmonic wave of the macropulse duration T_p.

FEL AMPLIFIER

Our main interest is in stimulated emission. Many of the spectral features of superradiant emission discussed above apply quite closely also to stimulated emission in an amplifier configuration. The derivation of the increments ΔC_q^{st} in the wavepacket amplitudes (third term in Eq.5) in the amplifier case is more involved, since it requires the calculation of the modification of the electron trajectories by the input radiation field. When this is done, it is found that also in this case the electron beam is bunched. The classical stimulated emission from an electron beam, always involves electron beam density bunching. Contrary to superradiance the bunching is not set *ab-initio*, before entrance into the interaction region, but it is created by the input radiation signal, at the signal frequency, in the first part of the wiggler.

As well known, in a CW (or long pulse) FEL amplifier the single mode (1-D) incremental power gain is given in the linear (small signal) small gain regime by (see Fig.6) [6, 16]:

$$\frac{\Delta P}{P} = \bar{Q}\frac{d}{d\bar{\theta}}\mathrm{sinc}^2\left(\bar{\theta}(\omega)/2\right) \qquad (16)$$

The frequency ω of the electron bunching and the consequent radiation is determined by the input radiation signal. Thus the bandwidth of emitted radiation is determined by the bandwidth of the input signal, and if it is monochromatic then the output radiation is temporally coherent (except for admixture of noise (spontaneous undulator radiation) power emitted in the wiggler. Note however that the gain curve (16) (Fig.6, which is the derivative of the spontaneous emission spectral curve Fig.3) is quite wide still – about one half the width of the spontaneous emission curve $\Delta\omega_{st} = \pi/t_{sl}$.

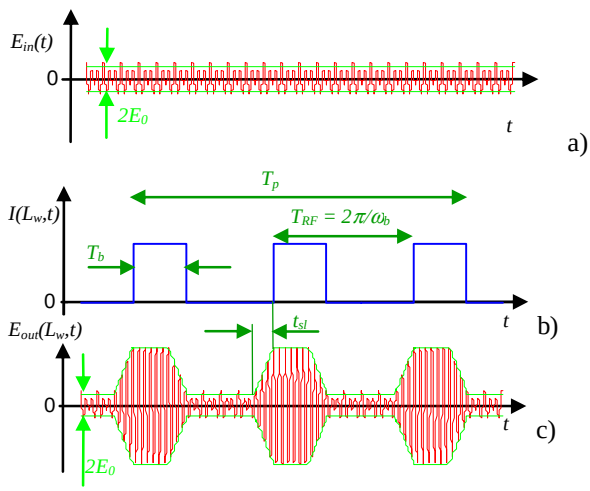

Fig.7: RF-Linac FEL Amplifier in the time domain.
a) multi-frquency coherent input signal
b) Electron beam macropulse current waveform
c) Amplified signal.

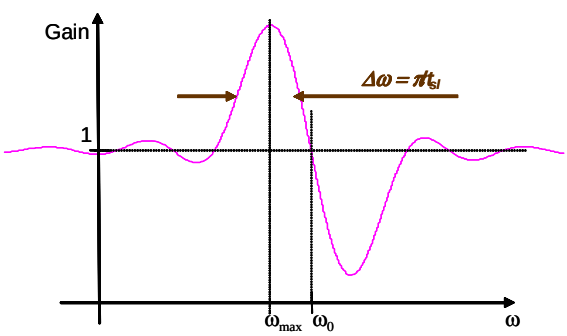

Fig.6: The FEL Linear regime small-gain curve.

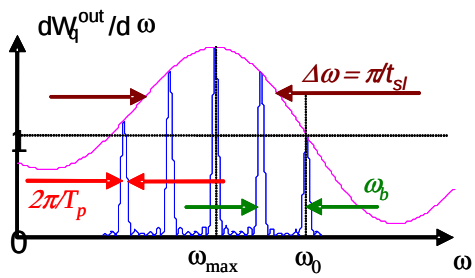

Fig.8: Spectral power of the amplifier output radiation waveform of Fig.7c.

If the electron beam is not continuous, of course, its temporal wave-form will modify the spectrum of the amplifier radiation output. Let us consider an FEL amplifier fed by a train of electron beam pulses (microbunches) from a continuously operating RF-LINAC (see Fig.7b). The electron macropulse duration, micropulse duration and repetition period are typically $T_p = 10$ μs, $T_b \sim$ ps, $T_{RF} \sim$ ns respectively. The radiation signal period (say is the visible spectral region) $2\pi/\omega_0 \sim$ fs and the slippage time $N_w 2\pi/\omega_0 \sim 10 - 100$ fs, are both much shorter than the pulse duration T_b.

Fig.7 depicts this case in the time domain. For didactic reasons we assume that the input radiation (Fig.7a) is a *coherent* multi-frequency wide spectrum signal, wider than the gain bandwidth of the FEL ($\Delta\omega_{st} \sim \pi/t_{sl}$). The output signal (Fig.7c) is time gated by the waveform of the electron beam (Fig.7b) and also frequency filtered by the gain bandwidth of the FEL during the pulse duration.

The same case is displayed in the frquency domain in Fig.8. Only radiation frequencies within the gain bandwidth π/t_{sl} of the gain curve Fig.6 are amplified. Among the amplified frqeuncies only the ones which are harmonics of the bunching frequency ω_b, within a

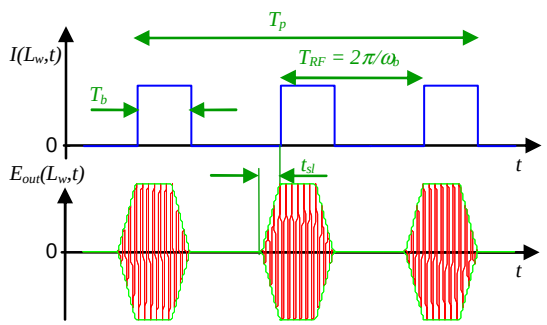

Fig.9: The time domain waveform of the radiation wavepackets emitted at saturation by an RF-Linac FEL oscillator during the electron beam macropulse.

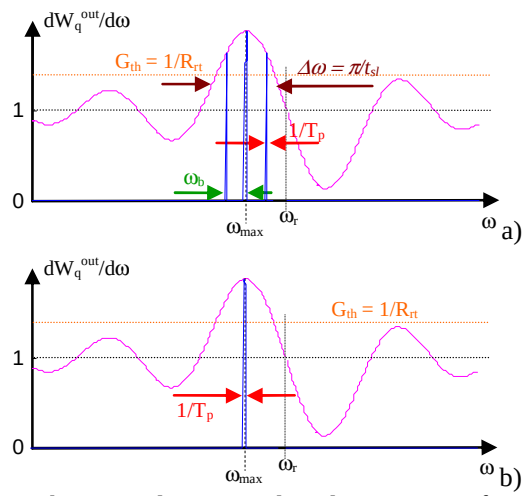

Fig.10: The spectral power and modes structure of saturated FEL oscillator – a)multiple modes, coherently mode-locked in an RF-Linac FEL, b) Single mode operation in a quasi-CW or long pulse (electrostatic accelerator) FEL.

frqeuncy deviation $\Delta\omega \sim 2\pi/T_p$ will contribute coherently to a Fourier transformation of the waveform in Fig.7c (carried out over the entire macropulse). Consequently the amplified signal spectrum will contain harmonics of ω_b of linewidth $2\pi/T_p$.

RF – LINAC FEL OSCILLATOR

In laser physics it is customary to present an oscillator as an amplifier with feedback. In each round-trip a radiation wave-packet synchronous with an overlapping e-beam bunch gets amplified and is reflected back by mirrors into the entrance to the interaction region. It is assumed that the bunching frequency is commensurate with the round-trip frequency of the resonator: a new e-beam bunch arrives together with the radiation pulse, and the amplification process continues up to steady state saturation.

How does the saturation of an RF Linac FEL look in the time domain? Fig.9 displays the steady state waveform of the oscillator radiation in the time domain. It displays radiation pulses emitted synchronously with the RF bunches, somewhat modified by the slippage effect (as in the amplifier case – compare to Fig.7c).

In the frequency domain (Fig.10a), the single path gain curve is the same as in the amplifier (Fig.8), and the RF frequency of the e-beam bunches is synchronized (by cavity length detuning) with the round-trip frequency of the radiation pulses – namely the longitudinal modes of the resonator. In addition, in the oscillator there is a gain threshold condition: $P_{out}/P_{in} > 1/R_{rt}$. In the oscillation build-up process all modes (harmonics) are initially excited. But at saturation only modes with gain higher than the threshold are filtered in, and have a chance to survive the oscillation build-up process (Fig.10a).

The steady state output is as in the superradiant emission case (Fig.5) a finite coherent sum of longitudinal modes that lie within the gain bandwidth π/t_{sl} of the FEL. This finite sum of harmonic frequencies looks in the time domain as a periodic train of radiation pulses synchronous and with good overlap with the macropulses of e-beam bunches train that provides the gain. This is an exact analogue of an actively locked conventional *"mode locked laser"*. Also in this case, if the RF frequency is stable over the macropulse, the coherence of the harmonics is very high (if they are filtered out), and is determined by the duration of the macropulse $\Delta\omega \sim 2\pi/T_p$. Namely, the consecutive radiation wavepackets are coherent with each other throughout the macropulse (assuming a single bunch per round-trip).

It is worth noting that high coherence between the radiation wavepackets emitted by consecutive microbunches was measured in a long-wavelength FEL oscillator [19]. This was measured both for the spontaneous and stimulated emission of the FEL. It is remarkable that this coherence was observed when there are several microbunches in the resonator at the same time (RF bunching period shorter than the cavity round-trip time). This is explained there as the result of high

stability of the e-beam RF frequency and the microbunches envelop shapes. It is argued that in the parameters regime of the FELIX FEL [19], the microbunch formfactor (16) is appreciable of the emission frequency, and the superradiant (coherent) undulaotr radiation related to the stable shape of the micropulse current waveform dominates the random shot noise radiation, and consequently determines the phase of all wavepackets. This happened both under conditions of saturated stimulated emission (oscillator lasing) and absence of stimulated emission (no overlap of the recirculating wavepackets).

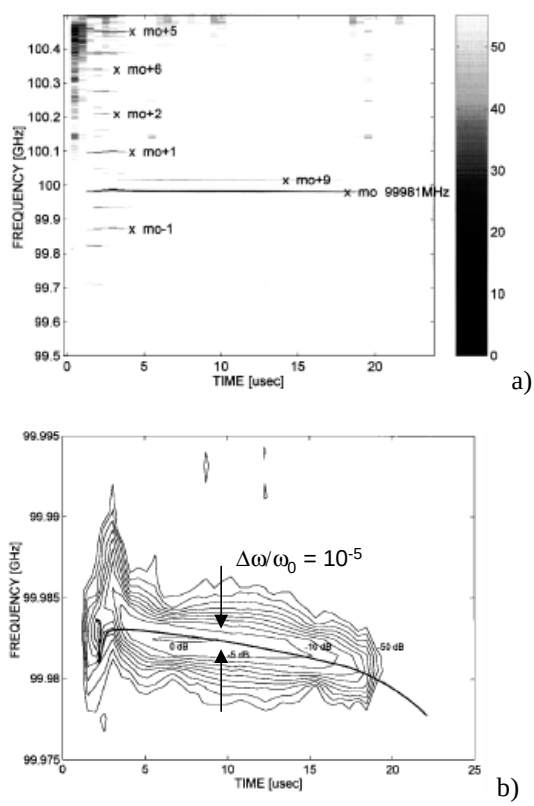

Fig.11: Spectrogram of the radiation output from an electrostatic accelerator FEL oscillator [9].

a) Multimode spectrum evolving into single mode operation during the oscillation build-up periods.

b) Fourier transform limited spectrum of the surviving single mode.

Table 1: Intrinsic Linewidth Conditions		
Maser	$\Delta\nu_{maser} = 2\pi kT\dfrac{(\Delta\nu_{sp})^2}{P_{gen}}$	Gordon, Zeiger, Townes [11]
Laser	$\Delta\nu_{laser} = 2\pi h\nu\dfrac{(\Delta\nu_{1/2})^2}{P_{gen}}$	Schawlow, Townes [12]
FEL	$\Delta\nu_{FEL} = \dfrac{(\Delta\nu_{1/2})^2}{I_0/e}$	Gover, Amir, Elias [13]

CW (ELECTROSTATIC ACCELERATOR) FEL OSCILLATOR

What would happen in a CW or a long pulse FEL oscillator (like an electrostatic accelerator FEL)? In this case, there are longitudinal modes due to the round-trip periodicity, but there is no active mode locking. In principle, many longitudinal modes can co-exist within the gain bandwidth, and there is no external que that can phase-lock them.

The oscillation build-up stage involves in this case a mode competition process, which arises when the oscillator approaches saturation and arrives to the non-linear regime. In the FEL, as in other "homogenously broadened lasers", this process ends with single mode operation (see Fig.10b). The single mode laser radiation linewidth is very narrow corresponding to the pulse duration. It is given by the Fourier transform limit $\Delta\omega_{line} \sim 2\pi/T_p$, and it tends to zero as $Tp \to \infty$ (CW operation). An experimental confirmation for the mode competition process and the Fourier transform limited linewidth of the single-surviving mode in an Electrostatic Accelerator FEL was provided in the Israeli FEL [9] (see Fig.11). In [9] a relative linewidth $\Delta\omega_{line}/\omega_0 = 10^{-6}$ was measured at frequency f_0 = 100 GHz corresponding to a pulse duration $T_p \sim 10$ μs.

What determines the linewidth in the limit $Tp \to \infty$? This fundamental problem was addressed already in the early days of conventional masers [11] and lasers [12]. In principle the oscillator line breadth is determined by a process of admixture of incoherent radiation with the coherent stored radiation field in the cavity. This process leads to random phase drift of the radiation mode amplitude C_q at the saturation stage (the amplitude is locked by the saturation process). In a maser the intrinsic linewidth results in from incoherent black body radiation emission into the cavity [11]. In a conventional laser, the limiting factor is the quantum spontaneous emission [12]. In the FEL the limiting factor is the spontaneous undulator radiation emission (or the electron beam shot noise) [9, 13]. The three intrinsic linewidth expressions are listed in Table 1.

HIGH GAIN FEL AMPLIFIER

Our analysis of the FEL in the linear regime is based on the Pierce TWT model for TWT [14, 6]. It is found that the amplitude of the radiation mode $C_q(L)$ in an FEL amplifier of interaction length L, depends on the input field amplitude $C_q(0)$ (regular FEL), but also on the amplitudes of the e-beam velocity and current (density) pre-modulation [15, 16]:

$$C_q(L,\omega) = H^E(\omega)C_q(\omega,0) + H^v(\omega)v(\omega,0) + H^I(\omega)I(\omega,0) \tag{17}$$

where the transfer functions are:

$$H^{E}(\omega)=\sum_{j=1}^{3}\mathrm{Res}\left(\frac{(\delta k_j-i\theta)^2+{\theta_{pr}}^2}{\Delta}\right)\mathrm{e}^{i(k_{zq}+\delta k_j)L} \quad (18.1)$$

$$H^{v}(\omega)=\sum_{j=1}^{3}\mathrm{Res}\left(\frac{ik_zL/v_{0z}\cdot {P_b}^{1/2}}{\Delta}\right)\mathrm{e}^{i(k_{zq}+\delta k_j)L} \quad (18.2)$$

$$H^{I}(\omega)=\sum_{j=1}^{3}\mathrm{Res}\left(\frac{(\delta k-i\theta)\cdot {P_b}^{1/2}/I_b}{\Delta}\right)\mathrm{e}^{i(k_{zq}+\delta k_j)L} \quad (18.3)$$

$$P_b=\frac{{I_b}^2\sqrt{\mu_0/\varepsilon_0}}{32}\cdot\left(\frac{a_w}{\gamma\beta_z}\right)^2\cdot\frac{L^2}{A_{em}} \quad (18.4)$$

$$\Delta=\delta k(\delta k-\theta-\theta_{pr})(\delta k-\theta+\theta_{pr})+\Gamma^3 \quad (18.5)$$

In these formulas we use the "conventional" parameters: θ - detuning parameter; Γ – gain parameter; θ_{pr} – space-charge parameter with reduction factor; L – interaction length; I_b – electron beam current, A_{em} – effective mode area. Here $\delta k = k_z - k_{zq}$ is the modification to the wavenumber of mode q (at fixed frequency ω) due to the interaction. Solution of the Pierce cubic dispersion equation 18.5 and substitution into (17, 18.1-18.3) results in the output radiation field amplitude for all gain regimes and any initial conditions.

In the high gain tenuous beam regime ($\Gamma^3 >> \theta, \theta_{pr}, 1$) one gets for an FEL amplifier:

$$P_q(L,\omega)=\left|\tilde{H}^{FEL}\right|^2\cdot\left|\tilde{C}_q(0,\omega)\right|^2=\left|\tilde{H}^{FEL}\right|^2P_q(0,\omega) \quad (19.1)$$

for a current (density) pre-bunched FEL:

$$P^{pb-I}(L,\omega)=\left|\tilde{H}^{FEL}\right|^2\cdot P_b\left(\frac{1}{I_b\Gamma L}\right)^2\left|\tilde{I}(0,\omega)\right|^2 \quad (19.2)$$

for a velocity pre-bunched FEL:

$$P^{pb-v}(L,\omega)=\left|\tilde{H}^{FEL}\right|^2\cdot P_b\left(\frac{k_zL}{v_{0z}(\Gamma L)^2}\right)^2\left|\tilde{v}_z(0,\omega)\right|^2 \quad (19.3)$$

Here

$$\left|\tilde{H}^{FEL}\right|^2=\frac{1}{9}\mathrm{e}^{\sqrt{3}\Gamma L}\cdot\mathrm{e}^{-(\omega-\omega_0)^2/(\Delta\omega_{HG})^2} \quad (19.4)$$

is the power transfer function of the high gain FEL, and

$$\Delta\omega_{HG}=\frac{3^{3/4}}{2\pi}\lambda_w\sqrt{\frac{\Gamma}{L}}\omega_0 \quad (19.5)$$

is the full width of 1/e of maximum of the high gain FEL gain curve and

SASE FEL

The current and velocity modulation amplitudes in (19.2, 19.3) may be deterministic (prebunching) or random (noise). The video presentation in the transparencies demonstrates the meaning and significance of the current and velocity coherent modulation and noise processes.

The SASE FEL is based on amplification of electron beam noise in the FEL high gain regime. To analyze this case it is proper to calculate spectral energy and spectral power parameters instead of the single frequency gain and radiative power parameters (19.1-19.3):

$$\frac{dW_q}{d\omega}=\frac{2}{\pi}\left\langle\left|\breve{C}_q(\omega)\right|^2\right\rangle \quad (20.1)$$

$$\frac{dP_q}{d\omega}=\frac{1}{T}\left\langle\frac{dW_q}{d\omega}\right\rangle \quad (20.2)$$

where the averaging is over the electrons random entrance times and T is an averaging time duration longer than the slippage time t_{sl}.

The SASE FEL is nothing but a single path high gain FEL with an effective beam-prebuncing input signal due to current shot noise and velocity shot noise. Near the synchronism frequency its spectral power is a sum of the amplified current and velocity shot noise sources:

$$\frac{dP_q{}^I}{d\omega}=\frac{2}{\pi}H^{FEL}\cdot P_b\left(\frac{1}{I_b\Gamma L}\right)^2\frac{\left\langle\left|\breve{I}(0,\omega)\right|^2\right\rangle}{T} \quad (21.1)$$

$$\frac{dP_q^{\ v}}{d\omega} = \frac{2}{\pi} H^{FEL} \cdot P_b \left(\frac{k_z L}{v_{0z} (\Gamma L)^2} \right)^2 \frac{\left\langle \left| \breve{v}_z (0,\omega) \right|^2 \right\rangle}{T} \tag{21.2}$$

where

$$\frac{\left\langle \left| \breve{I}(0,\omega) \right|^2 \right\rangle}{T} = eI_b \tag{22.1}$$

$$\frac{\left\langle \left| \breve{v}_z (0,\omega) \right|^2 \right\rangle}{T} = \frac{e}{I_b} \left| \delta v_z \right|^2 \tag{22.2}$$

Here δv_z is the axial velocity spread of the electron beam.

Usually the current shot noise is considered the main source for SASE input power and the velocity noise is neglected. This is not self evident. For this assumption to be valid (21.1) should exceed (21.2). Considering (22.1, 22.2) this leads to the condition

$$\frac{\delta v_z}{v_{oz}} < \frac{\Gamma}{k_z} \tag{23}$$

SPIKING IN SASE-FEL AND THE IMPULSE RESPONSE FUNCTION

Since the SASE-FEL is a wide band amplifier of a wide band incoherent signal (the shot noise), it is no wonder that the spectrum of its radiation output is relatively wide and its temporal waveform is characterized by a random sharp structure (spiky). Fig.12 [10, 17] displays the typical spectrum of a single SASE radiation pulse (Fig.12a), the averaged spectrum over many pulses (Fig.12b) and the spiky time-domain waveform of a single radiation pulse (Fig.12c). One should note that the relatively high bandwidth of the averaged radiation spectrum ($1/T_{coh}$) is related to the characteristic duration of the spikes (T_{coh}). It is also noteworthy, that the single pulse spectrum contains spectral lines that are very narrow ($1/T_b$) – corresponding to the duration of the e-beam micro bunch - but appear at random centre frequencies.

Since the shot noise spectrum is uniform, the average spectrum of the SASE is determined merely by the transfer functions (18.2, 18.3). Consider now only the current shot noise. It is useful to expand the logarithm of the exponentially growing term in (18.3) (including the phase, namely the imaginary part) to second order in terms of frequency ω around the *synchronism* frequency ω_0. In the high gain (tenuous beam limit) this results in:

$$\begin{aligned} \tilde{H}^I(z,\omega) &\cong \frac{P_b}{3 I_b \Gamma z} e^{-i\pi/12} \, e^{\left(\sqrt{3}+i\right)\Gamma z/2} \times \\ &\times e^{-\left(1+i/\sqrt{3}\right)(\omega-\omega_0)^2/2(\Delta\omega_{HG})^2} \, e^{ikz} \end{aligned} \tag{24}$$

where $\Delta\omega_{HG}$ is the width of the high gain FEL gain curve. Indeed this spectral width is the linewidth $\Delta\omega_{HG} \sim 1/T_{coh}$ of the SASE average spectrum shown in Fig.12b.

It is instructive now to calculate the "impulse response function" corresponding to the complex transfer function (24). This is straightforwardly found by applying an inverse Fourier transformation on (24):

$$\begin{aligned} E(z,t) = \mathrm{Re}\{ &\left(P_b \Delta\omega_{HG} / 3^{3/4} \sqrt{2\pi\left(i+\sqrt{3}\right)} I_b \Gamma z \right) \cdot \\ &\exp\left[-i\pi/12 + (\sqrt{3}+i)\Gamma z/2 \right] \cdot \\ &\exp\left[+i\left(\omega_0 \left(t - \tfrac{z}{c} - t_0 \right) - (\Delta\omega_{HG})^2 \left(t - \tfrac{z}{c} - t_0 \right)^2 / 8 \right) \right] \cdot \\ &\exp\left[-(\Delta\omega_{HG})^2 \left(t - \tfrac{z}{c} - t_0 \right)^2 / 8 \right] \} \end{aligned} \tag{25}$$

This function is displayed in Fig.13. It depicts (within the quadratic expansion approximation a Gaussian wave form envelope of width $T_{coh} \sim 1/\Delta\omega_{HG}$. It also reveals an

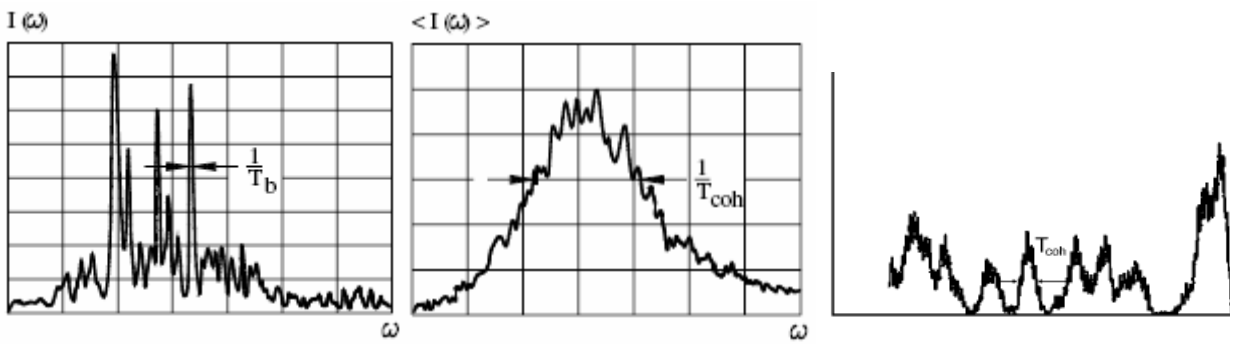

(a) (b) (c)

Fig.12: Simulation data of SASE radiative emission [9, 16]:
a) Single pulse spectral power, b) Spectral power averaged over many pulses, c) Time domain "Spiky" intensity distribution of a single pulse.

inherent (negative) chirp of the centre frequency

$$\frac{d\omega}{dt} = \frac{d^2\varphi}{dt^2} = -(\Delta\omega_{HG}/2)^2 \qquad (26)$$

The impulse response function (25) is the coherent field wave-form created by an impulse of charge (of duration much shorter than the radiation wavelength), which is superimposed at entrance over a uniform e-beam current I_b. it is quite natural to identify it with the spikes phenomenon shown in Fig.12c. The physical picture of the phenomenon is based on appearance of random electron bunches (current fluctuation) on the electron beam current entering the interaction region. This current is uniform on the average, but fluctuates because of the randomness of electrons generation in the cathode ("shot noise"). The random electron bunches start radiating *superradiantly* right at start, and their radiation wavepackets dominate over the spontaneous radiative emission from the other uniformly (but randomly) injected electrons. Due to the forward slippage effect of the radiation wavepacket and the high gain stimulated emission process, the random electrons, that are flowing within a cooperation length $v_z T_{coh}$ ahead of the initial radiating random bunch, are induced to emit at the same frequency and phase (except for the inevitable chirp effect), and consequently a coherent wavepacket (Fig.13) is emitted. The output wavepacket duration $T_{coh} = \pi/\Delta\omega_{HG}$ (determined by the high gain FEL bandwidth 19.4) is the minimal width of the spike. Spikes that are excited by random bunches in time always shorter than T_{coh} merge into one spike. Assuming there are always enough random bunches to negate presence of long "silent" spaces between the spikes; one can estimate that the average number of spikes in a bunch of duration T_b is T_b/T_{coh} [10]. Fig.14a displays the spikes waveforms of this physical model. It should be compared to the simulation spiky pattern of Fig.12c. If $T_b \cong T_{coh}$ then there is only one spike in the macropulse duration [17]. In this case the SASE radiation is as coherent as can be (Fourier transform limited). Its spectral width is $\cong \pi/T_{coh} = \pi/T_b$. It can be narrowed down only if pulse stretching techniques can be employed.

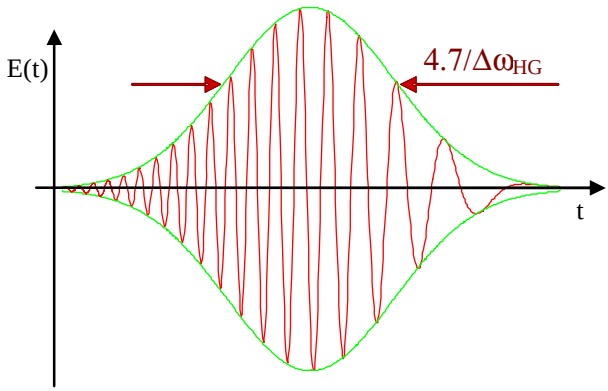

Fig.13: The time domain charge-impulse response function of an FEL in the high gain regime (Eq. 20).

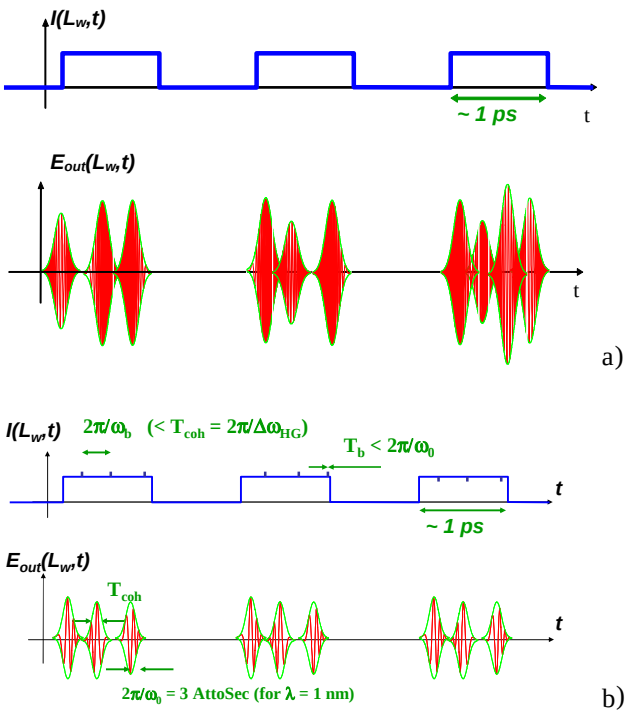

Fig.14: Spikes emission in SASE FEL within the micropulses duration: a) Random emission
b) Phase-locked coherent spikes emission initiated by subharmonic current prebunching.
Prebunching can be produced by a train of superimposed positive or negative current impulses or any stable periodic current waveform of high harmonic contents.

CONDITIONS FOR COHERENT X-UV FEL

It is well known that the radiation output of SASE FEL is spatially coherent (due to the optical guiding effect). This is the reason why SASE FELs can be so much brighter than any other existing radiation source in this spectral regime. However there will be even greater interest in this source if it would be also temporally coherent and stable (pulse to pulse). How can a SASE FEL be turned into a coherent radiation source?

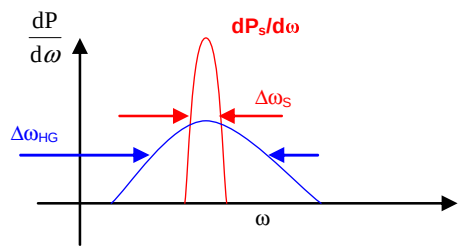

Fig.15: Spectral power of the coherent radiation output of the FEL amplifier (red) and the SASE (shot noise) radiation (blue).

Realizing that the SASE-FEL is an amplifier of noise, it is evident that what is required is a coherent input signal. The input signal can be a coherent radiation wave (this is sometimes called seed radiation injection), and there has been intensive studies of developing an appropriate coherent seed radiation sources based on high harmonic multiplication of intense laser pulses in gas. Another scheme is based on filtering the undulator synchrotron radiation after a few sections of the undulator, and reinjecting the narrower bandwidth radiation into the undulator for high gain amplification.

Another approach for attaining coherent emission from SASE-FEL is based on coherent prebunching of the electron beam (within the duration of its pSec microbunches) at the radiative emission frequency of a high power optical laser or its subharmonics. This process can be repeated in several steps, in which the bunched radiation is amplified at high gain, and then high harmonics of the electron bunching are filtered out and amplified again, and so on (High Gain High Harmonic Generation – HGHG [21]).

In all of these schemes the condition for attaining coherent high power output radiation is that the coherent input signal will be significantly larger than the noise. In the first case of *seed radiation injection* (coherent amplification) a simple criterion can be inferred by comparing (19.2) to (21.1-22.2). Assuming the current shot noise is dominant, this condition is:

$$P_s(0) >> P_b \frac{e}{I_b (IL)^2} \Delta\omega \qquad (27.1)$$

Here $\Delta\omega$ is the frequency bandwidth of the detection system in which inevitable (now undesirable) SASE radiation is collected. If there are no means of filtering available, then $\Delta\omega = \Delta\omega_{\mathrm{HG}}$ - the SASE radiation bandwidth. In any case $\Delta\omega_s$, $\pi/T_b < \Delta\omega < \Delta\omega_{HG}$, where $\Delta\omega_s$ is the linewidth of the injected input radiation and π/T_b is the Fourier limited bandwidth of the finite pulse. Similar condition can be derived for the required prebunching current required to dominate the current shot-noise by comparing (19.2) to (21.1, 22.1):

$$\left|\tilde{I}(0,\omega)\right|^2 >> \frac{2}{\pi} e I_b \Delta\omega \qquad (27.2)$$

PHASE LOCKING THE SPIKES

If sufficient coherent seed radiation input power is attainable it makes the output power of the FEL amplifier coherent as well. But other aspects of the *seed radiation injection* approach, as tunability and operating wavelengths range still need to be addressed. The *current prebunching* approach may provide more options of frequency tunability and short wavelengths availability. But its realization requires more intricate conceptual schemes.

Much insight into this problem may be gained from the physical description of the radiation processes in the previous section. In particular it is worth noting the striking correspondence between the emission of single mode undulator radiation wavepackets by a single electron (or single bunch) (10) (in the frequency domain) and (11) (in the time domain) and the corresponding expressions of spectral transfer function (24) and impulse response function (25) in the case of FEL in the high gain regime. In the first case the wavepackets emission process is spontaneous (or superradiant in the case of a bunch) and no supporting medium is required for the wavepacket emission. In this case Eq.11 (Fig.4) is the explicit time-domain expression of the wavepacket emitted in the undulator from a particulate charge of *one electron* (e). In the second case, (Eq.25) (Fig.13) is the radiation wavepacket emitted by a *current impulse of a unit charge*, and the excitation of this wavepacket is conditioned on the presence of an electron beam medium (assumed uniform) in front of the beam current impulse. Its emission process involves stimulated emission and bunching of the e-beam, in contrast to the first case.

In both cases the coherence of the total radiation of the e-beam depends on the phase relation between the emitted respective wavepackets by the charged particles or by the bunches. In the first case, when the electrons enter into the undulator at random, the superposition of the radiation wavepackets (11) in (5) produces incoherent radiation (or more correctly - partially coherent radiation with coherence time t_{sl}). Analogously, in the SASE case, the superposition of the impulse response waveforms (23) from random bunches (the "spikes") produces partially coherent radiation of coherence length $T_{coh} \sim 1/\Delta\omega_{HG}$.

How can we turn the SASE radiation to be coherent? In analogy to the case of superradiant emission from a periodic train of bunches it is suggested that periodic superposition of current impulses on top the uniform current of the microbunch will phase-lock the spikes into a coherent train of wavepackets with distinct phase relation of the "carrier" radiation waves along the entire microbunch (see Fig.14b as opposed to Fig.14a). This situation is analogous to the one described by Fig.5.

How to create the sub optical period current impulses is still an open challenge. It is important to note that the current perturbation does not have to be positive (see third pulse in Fig.15b). It can be of any shape, as long as it is kept periodic along the pulse with accuracy (stability) better than one optical period (which may be AttoSeconds in the X-UV regime!), and as long as it is "sharp" enough to produce significant current amplitude of Fourier harmonics to satisfy (27.2).

It is noteworthy that the prebunching frequency does not need to be equal to the radiation emission frequency and it can be a high sub-harmonic of this frequency. In this case the coherent spectrum may contain several harmonics as in Fig.5c, however as discussed in that context, each harmonic would be coherent throughout the

entire duration of the pulse, and its linewidth is Fourier transform limited ($2\pi/T_p$). In principle the harmonics can be filtered out by physical means or by numerical processing of the data acquired by a coherent detection system data in a spectroscopic application.

Note that if single harmonic operation is desired it is not necessary that the prebunching frequency be equal to the radiation frequency. It is only required that the bunching frequency ω_b (sub-harmonic n_H of the radiation frequency ω_0) will be larger than the FEL high gain bandwidth (compare to (15)):

$$\omega_b = \frac{\omega_0}{n_H} > \Delta\omega_{HG} = \frac{3^{3/4}}{2\pi}\lambda_w\sqrt{\frac{\Gamma}{L}}\omega_0 \qquad (28)$$

$$\text{or } n_H < \frac{2\pi}{3^{3/4}}\sqrt{\frac{\Gamma}{L}}\Big/\lambda_w$$

The spectrum will look then as in Fig.5b, but with a single harmonic frequency of linewidth $2\pi/T_p$ under the amplifier gain curve. In time domain the radiation waveform will look then as in Fig.14, without spacing between the overlapping phase locked spikes. In the extreme limit of (25) the waveform would be a single coherent wavepacket along the entire pulse (microbunch) duration T_p.

As mentioned above, realization of the high harmonic bunching schemes is still a challenge. We examine in principle (Fig.16) a scheme of optical laser bunching, employed on a uniform electron beam, which is trapped by the ponderomotive wave of a wiggler and an external coherent bunching laser. Fig.16a displays the θ-ψ phase-space electron distribution of one pondermotive period exactly after one quarter period of synchrotron oscillation [16]. The current distribution along one bunching period is shown in Fig.16b and its Fourier harmonic amplitudes are shown in Fig.16c. Notice that significant amplitudes can be attained even at very high harmonics. However, in practice realizing the sharp current waveform structure of Fig.16b may be difficult, because of the electron beam energy spread and finite emittance. One should also bear in mind that in this scheme also velocity (energy) modulation of the beam is generated collaterally, and this contribution of to the radiation power (18.2) should be taken into account, including the consideration of the relative phase between the velocity and the current modulation.

A third scheme that should be considered for phase locking and increasing the coherence of the radiation in a SASE FEL consists of imposing periodic perturbation on the wiggler (e.g. periodic dispersive sections) [20]. The filtering effect of the periodic structure may be viewed as the analogue of linewidth narrowing of radiation emitted in a Fabri-Perot resonator. It is speculated (but needs further study) that if the SASE FEL in such a structure arrives to saturation within the wiggler length, nonlinear process of mode competition between the filtered spikes will lead to further increase of coherence and stability in analogy to the CW FEL oscillator case discussed previous.

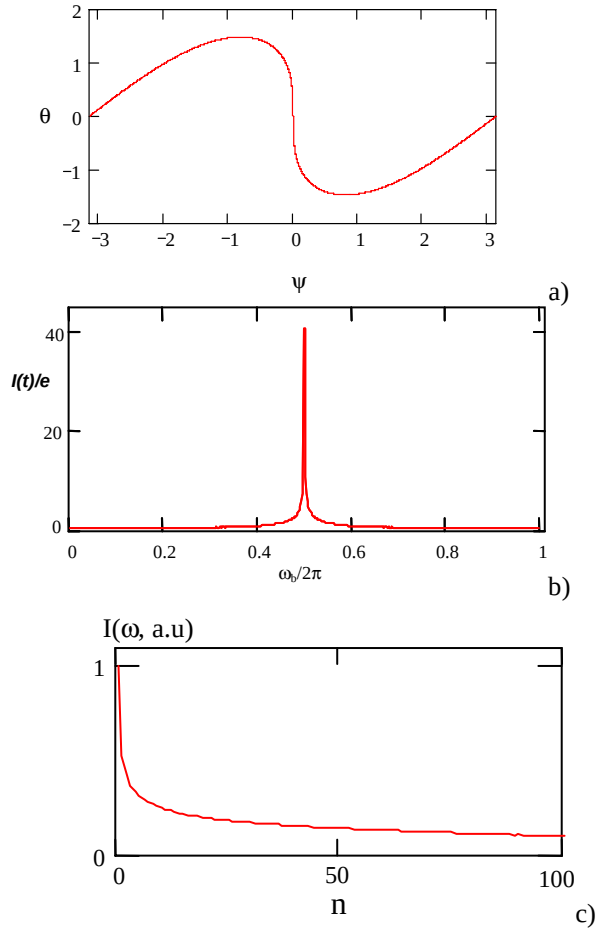

Fig.16: Bunching of a cold beam by the pondermotive wave (pendulum equation model [15]):
a) Electron detuning phase distribution in one period after one quarter period of synchrotron oscillation
b) Corresponding current waveform in one bunching period
c) Fourier harmonic amplitude of the waveform in (b).

Acknowledgement: This presentation was dedicated to the memory of Josef and Sofia Pietrowski (Yad-Vashem Righteous among Nations awardees) who saved the life of the parents of A.Gover during the Hollocaust.

REFERENCE

1. A. Gover, PRL, 96, 124801 (2006); A. Gover, Phys.Rev ST-AB, 9, 060703, (2006).
2. A.A. Barybin, "*Modern electrodynamics and coupled-mode theory: application to guided-wave optics*", Rinton Press, (2002).
3. A. Gover, Phys.Rev. ST–AB, 8, 030701 (2005).
4. R.H. Dicke, Phys.Rev., 93, 99 (1954).
5. G.L. Carr et al, Nature, 420, 153 (2002).
6. A.Gover, P. Sprangle, QE-17, 1196 (1981).
7. A. Gover et al, Phys.Rev.Lett., 72 1192 (1994).

8. S.E. Korbly et al, PRL, 94, 054803/1 (2005).
9. A. Abramovich et al, Phys.Rev.Lett., 82, 5257 (1999).
10. S. Krinski and R.L. Gluckstern, Phys.Rev. ST-AB, 6, 050701, (2003).
11. Gordon, Zeiger, Townes, Phys.Rev., 99, 1264 (1955).
12. Schawlow and Townes Phys.Rev., 112, 1490 (1958).
13. A. Gover A. Amir, L. Elias, Phys.Rev.-A, 35, 164 (1987).
14. J.R. Pierce, "*Traveling-Wave tubes*", Toronto,Van Nostrand, (1950).
15. I. Schnitzer, A. Gover, NIMPR A237, 124 (1985).
16. A. Gover, "Lasers: Free Electron Lasers" *Encyclopedia of Modern Optics*, Ed. R. D. Guenther, D. G. Steel and L. Bayvel, Elsevier, Oxford (2005).
17. R. Bonifacio et al, PRL, 73, 70 (1994).
18. E. L. Saldin, E. A. Schneidmiller, and M.V. Yurkov, *The Physics of Free Electron Lasers,* Chap. 6 (Springer-Verlag, Berlin, 2000).
19. H.H. Weits, D. Oepts, IEEE QE, 35, 15, 1999.
20. Y.C. Huang – private communication.
21. L.H. Yu et al, Phys.Rev.Lett., 91, p 74801/1, 2003.
22. M. Arbel et al, Nucl.Inst.Meth.Phys.Res., A445, 247 (2000).

EVOLUTION OF FELS OVER THE LAST 34 YEARS

W.B. Colson, NPS, Monterey, California

Abstract

The concept of the free electron laser (FEL) started 34 years ago with Madey's 1972 paper. The basic mechanism which employs a beam of free electrons to amplify co-propagating light has remained essentially the same as further developments have demonstrated high peak power, high average power, high gain, optical guiding, continuous tunability and reliability. FELs have operated at wavelengths from the far infrared, infrared, visible and down to the ultraviolet. The realization of high gain has lead to the generation of soft x-rays and soon hard x-rays where there are no mirrors. About a hundred FELs and user facilities are distributed around the world, and in many ways the FEL has become a "perfect" source of coherent electromagnetic radiation. FELs are in encyclopedias, in laser textbooks, with several textbooks specifically on FELs, and have clarified several physical principles for stimulated emission and laser physics. Today a Google search on "free electron lasers" produces nearly 13 million hits. The accomplishments during this time have been many, but none so important as establishing a community. Prospects for future directions are also briefly considered.

PAPER NOT AVAILABLE

LASING AT 13 NM OF THE SASE FEL AT FLASH

E. Schneidmiller, M.V. Yurkov, DESY, Hamburg

Abstract

We present the recent result from FLASH (VUV FEL at DESY): lasing at 13 nm, the shortest wavelength ever generated in free electron lasers.

PAPER NOT AVAILABLE

FIRST LASING AT SCSS

Tsumoru Shintake# and SCSS Team
RIKEN/JASRI/SPring-8, Hyogo 679-5148 Japan.

Abstract

On 20 June, the first lasing was observed at 49 nm in SCSS prototype accelerator for Japanese XFEL project. A challenging approach: 500 kV gun using CeB_6 single crystal thermionic cathode generates low emittance beam from 500 kV gun, followed by velocity bunching, and magnetic chicane bunch compression, the measured emittance at 50 MeV was 3 π.mm.mrad normalized. When we firstly closed undulator, we observed narrow spectrum of amplified SASE signal. Radiation energy per pulse is around 1 μJ/pulse at moment.

INTRODUCTION

Unique combination of three key technologies: the in-vacuum short period undulator, the C-band high gradient accelerator and low emittance injector using thermionic electron source make possible to realize SASE-FEL at 1 Å within available site length at SPring-8 less than 800 m. It was named as SCSS: SPring-8 Compact SASE Source [1]. From year of 2001, we have been carrying out R&D on the key components: the electron gun, injector, C-band klystron modulator with oil-filled compact design, high resolution beam position monitor, digital rf signal processing system, etc.

TEST ACCELERATOR

In order to test this challenging scheme, and check all hardware components developed in our R&D [2], we constructed prototype accelerator in 2004-2005 as shown in Fig. 1. Beam line layout is shown in Fig. 4. We use four C-band accelerating structures, 1.8 m long each, energy gain 32 MV/m maximum. With maximum beam energy of 250 MeV, the shortest wavelength of VUV-radiation at 50 nm can be obtained.

We commissioned beam operation in November 2005 and spent a few months to repair some hardware and software. From May 2006, we started dedicated beam tuning to demonstrate first lasing.

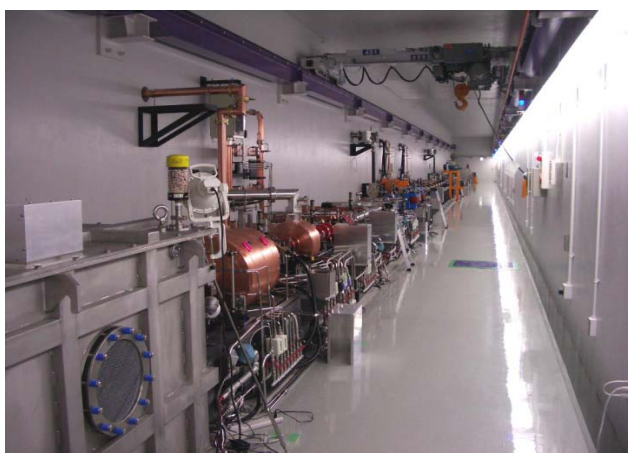

Fig. 1 Tunnel view in SCSS prototype accelerator.

FIRST LASING EVENT

Two in-vacuum undulators were installed, whose undulator period is 15 mm, minimum gap is 3.5 mm, nominal K value is 1.3 and one undulator length is 4.5 m. In the beam tuning, we firstly opened the gap to 20 mm and passed the e-beam through gap and transported into the beam dump. We tuned the beam optics upstream of the undulator. We setup the optics, in coming beta-matching and focusing Q-magnet in between two undulators.

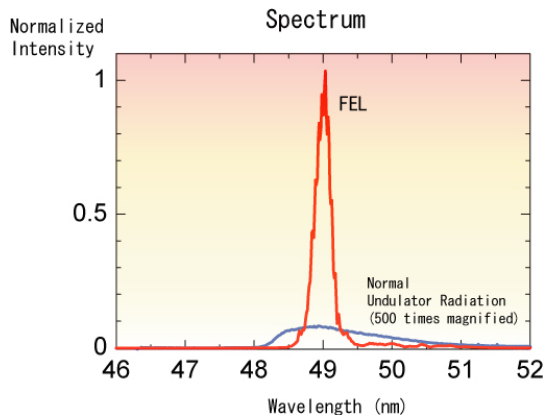

Fig. 2 Radiation spectrum at the lasing condition, 0.25 nC per bunch and 250 MeV. Peak at 49 nm is the coherently amplified signal (6000 times) from the spontaneous undulator radiation (blue line).

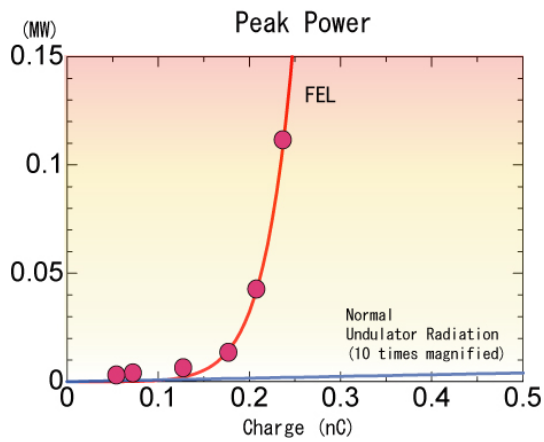

Fig. 3 Peak output power v.s. bunch charge. Using photo diode, peak height was detected from averaged pulses.

#shintake@spring8.or.jp

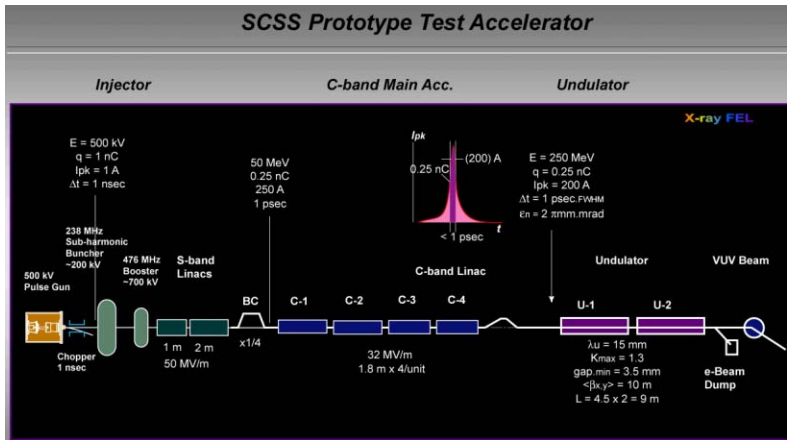

Fig. 4 SCSS prototype accelerator, two undulators of 15 mm pitch, 250 MeV e-beam, generates VUV-radiation.

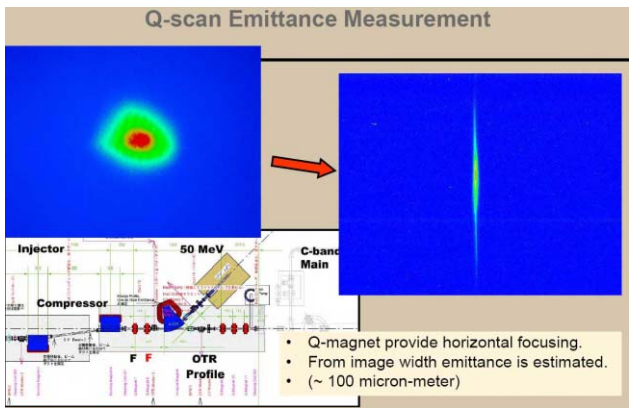

Fig. 5 Beam profile during Q-san emittance measurement. Transition radiation from Au coating of optical mirror was monitored by CCD camera.

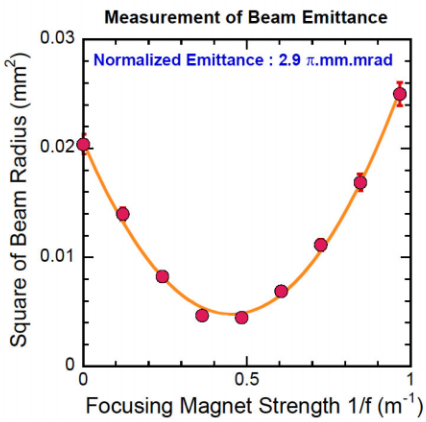

Fig. 6 Beam width as a function of focusing power. At beam energy 50 MeV, charge 0.25 nC, length <1 psec.

On 15 June, evening, we firstly closed the gap in the upstream undulator, and measured radiation spectrum, where the spectrum width was already quite narrow peaked at 49 nm, and totally different from the natural spontaneous radiation, as shown in Fig. 2. The spectrum width is around 1% FWHM, which is much narrower than the spontaneous undulator radiation, while it is dominated by e-beam energy fluctuation, at moment.

As shown in Fig. 3, when we varied the bunch charge, the lasing power drastically changed. This threshold phenomenon indicates high FEL amplification. The power has not yet reached the saturation. Further tuning is required. Detail analysis is now undertaken.

EMITTANCE MEASUREMENT

At the injector end, the velocity bunching and chicane bunch compression have been completed, where the beam energy reaches to 50 MeV, bunch charge is 0.25 nC and the bunch length is 1 psec or less, which depending on operation condition, specifically phase & amplitude tuning of 238 MHz and 476 MHz cavities.

We measured projected emittance right before the C-band accelerators, using Q-scan method. By reversing polarity of one of the Q-magnets to provided strong focusing in X- and Y-direction, and measured the minimum beam width. By varying focusing power, the beam width response was measured as Fig. 5. By fitting the beam size data as a function of the Q-magnet focusing strength as shown in Fig. 6, we found the normalized projected emittance of around 3 π.mm.mrad for both X- and Y- directions. The slice emittance was also measured at 50 MeV beam dump, it was 2 π.mm.mrad, where the measurement was limited by spatial available resolution of profile monitor. Probably, the slice emittance is still lower than 1 π.mm.mrad [3], but we do not have instrument to measure it at moment.

We repeated many measurements in this kind, always observed emittance around 3~4 π.mm.mrad. This experimental data indicates that the velocity bunching in our system does not largely deteriorate the projected emittance for compression ratio exceeding 100 times.

CONCLUSION & SCHEDULE

We measured the e-beam emittance and observed first lasing in the SCS prototype accelerator. From this experiment, superior performance of the thermionic gun and injector system has been demonstrated.

Analysing the experimental data carefully, we refine hardware design, and start XFEL construction this year.

REFERENCES

[1] T. Shintake, et. al, "SPring-8 Compact SASE Source", SPIE2001, San Diego, USA, June 2001.

[2] T. Shintake, Status of SCSS Project, 3rd Asian Particle Accelerator Conference, APAC2004, Gyeongju, Korea, March 2004.

[3] K. Togawa et.al., "Emittance Measurerment on the CeB6 Electron Gun for the SPring-8 Compact SASE Source", FEL2004, Trieste Italy.

THE FIRST LASING OF 193 NM SASE, 4TH HARMONIC HGHG AND ESASE AT THE NSLS SDL*

X.J. Wang, Y. Shen, T. Watanabe, J.B. Murphy, J. Rose and T. Tsang, BNL, Upton, NY 11973, USA

Abstract

The first lasing of three types of single-pass high-gain FELs, SASE at 193 nm, 4th harmonic HGHG at 199 nm and ESASE at the Source Development Lab (SDL) of Brookhaven National Laboratory (BNL) is reported. The saturation of 4th harmonic HGHG and ESASE FELs was observed. We also observed the spectral broadening and instability of the 4th harmonic HGHG.

INTRODUCTION

After the successfully experimental demonstration of Self-Amplified Spontaneous Emission (SASE) and High-Gain Harmonic Generation (HGHG) around the world[1-4], great progress was made recently in reducing the SASE wavelength [5-6]. We present recent progress in both SASE and HGHG at the the National Synchrotron Light (NSLS) Source Development Lab (SDL). The new lasing of three types of the single-pass high-gain FELs at the NSLS SDL, SASE at the 193 nm, the first lasing of the 4th harmonic HGHG and ESASE is reported in this paper.

After a short description of the SDL facility, we will present the preliminary experimental characterization of new lasing of three types of single-pass high-gain FELs. We will first discuss the experimental characterization of the new lasing of a SASE FEL at 193 nm. The first lasing and saturation of the 4th harmonic HGHG at 199 nm with a 795 nm seed laser is presented. With the same experimental setup of the 4th harmonic HGHG, we observed first lasing of the laser enhanced SASE at 210 nm after detuning the electron beam energy. The first successful demonstration of ESASE [7-8] not only will open a new avenue to improve the performance of a SASE FEL, but will also greatly expand the HGHG tunability.

THE NSLS SDL

The SDL is a laser linac facility dedicated for linac based light source technology R&D and applications. The main components of the SDL are a high-brightness electron accelerator, an RF synchronized Ti:Sapphire laser system, a High Gain Harmonic Generation (HGHG) FEL, together with sophisticated electron and photon beam instrumentation. The accelerator system of the SDL consists of a 1.6 cell BNL photo-injector driven by the Ti:Sapphire laser system and a S-band traveling wave linac. After the recent electron beam energy upgrade [9], the maximum electron beam at the SDL is about 250 MeV. The magnetic chicane bunch compressor at the SDL produces sub-ps long electron bunches with a peak current of a few hundred amperes. The high brightness electron beam transits the three magnets used for the HGHG and laser seeded FEL amplifier (Fig.1): a modulator undulator, a dispersion magnet and the 10 m long radiator undulator (named NISUS) (Table 1).

One of the unique features of the SDL laser system is that it was designed in such a way that a single laser system is used to drive both the photocathode RF gun and to provide a seed laser pulse. This setup make it possible to achieve sub-ps timing jitter between the seed laser and the electron beam. The seed laser used for the experiment has a bandwidth of 7 nm (FWHM), the pulse length can be adjusted from 100 fs to 6 ps (FWHM). Table 1 lists the undulators, seed laser and electron beam parameters used for the single-pass high-gain FELs presented here. The matching optics for the seed laser focuses the seed laser into the HGHG modulator on axis while a mini-chicane is used to manipulate the electron beam to by-pass the seed laser mirror. There are 16 beam profile monitors (BPM) uniformly distributed along the NISUS and they have been used both for e-beam matching and trajectory studies. There is a dipole magnet after the NISUS undulator which bends the electron beam to the beam dump. The beam profile monitor in front of the beam dump was used to monitor the electron beam energy and energy modulation. The FEL radiation can also be transported by a periscope to the diagnostic station for characterization. The diagnostics station allows us to characterize the FEL output.

Table 1: the SDL accelerator, seed laser and HGHG magnet parameters.

e-beam Energy (MeV)	180 - 210
e-beam peak current (A)	300 - 400
e-beam bunch length (FWHM, ps)	~ 1
Emittance (rms, mm-mrad)	2 - 4
Seed laser wavelength (nm)	795
Seed laser pulse length (FWHM, ps)	~ 2 - 3
HGHG modulator period (cm)	8
HGHG modulator length (m)	0.8
HGHG modulator K	1.67 -3.02
HGHG dispersion magnet R_{56} (mm)	0 - 5
HGHG radiator period (cm)	3.89
HGHG radiator length (m)	10
Undulator parameter of the radiator	1.1

#xwang@bnl.gov

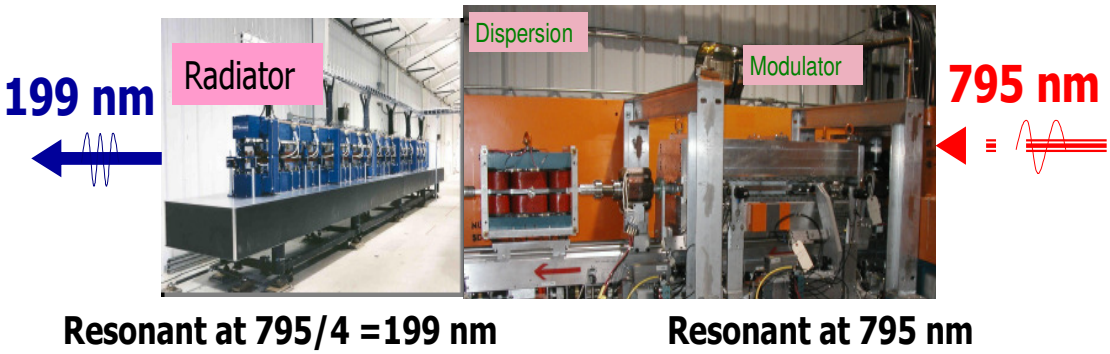

Figure 1: The SDL HGHG magnets and schematic of the 4th harmonic HGHG.

FEL CHARACTERIZATION

The major steps of the single-pass FEL experiment are electron beam and trajectory optimization, seed laser and e-beam synchronization, and FEL output characterization.

193 nm SASE Characterization

We first present the experimental characterization of a SASE FEL generated by the HGHG radiator – NISUS undulator. SASE was first used to optimize the electron beam and its trajectory inside the NISUS undulator. For the NISUS undulator, the shortest SASE FEL wavelength at the SDL should be about 150 nm when the electron beam energy chirped is taken into consideration. The UV Ocean Optics spectrometer and joulemeter used for characterizing the FEL are in the open air, which limits the minimum observable SASE wavelength to about 193 nm. Fig.2 is the shortest single-shot SASE spectrum obtained. The spectrometer resolution is about 0.7 nm. The maximum SASE energy is about 1 μJ when 5% transmission is assumed.

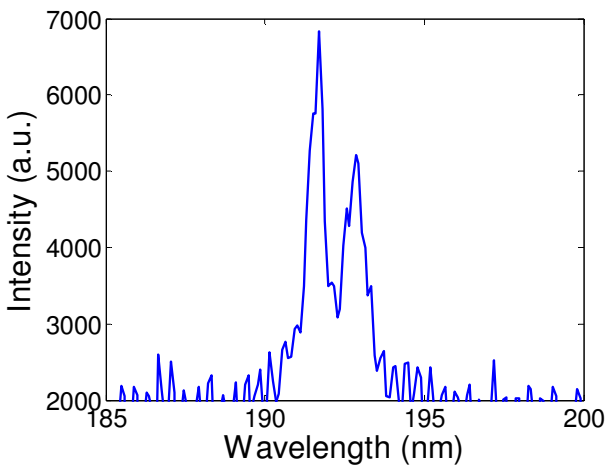

Figure 2: The shortest SASE spectrum at the SDL.

The First Lasing of the 4th Harmonic HGHG

To improve the performance of the SASE FEL, BNL has been performing R&D on laser seeded and HGHG FELs. Prior to April 2006, the shortest wavelength achieved is the 3rd harmonic HGHG at 266 nm [4].

As part of the recent electron beam energy upgrade [9], extensive modification of the HGHG modulator was done to make it possible to achieve HGHG at harmonics as high as seven . A new vacuum chamber and a stronger motor drive were installed. After the successful lasing of SASE at 193 nm, the electron beam energy was tuned to 202.5 MeV for the 4th harmonic HGHG with the seed laser at 795 nm. The synchronization of the seed laser and electron beam was realized in two steps. First we observed the SASE and seed laser using a fast photo-diode at the diagnostics station to make the two of them within 100 ps. The final synchronization was realized by observing the electron beam energy modulation while adjusting the seed laser delay line. With the seed laser pulse length at about 2 ps (FWHM) and a peak power of 50-100 MW, we successfully observed the first lasing of the 4th harmonic HGHG at 199 nm (Fig. 3). The slight difference of the measured central spectrum from the 199 nm could be explained by the seed laser bandwidth, and that will be discussed in more detail later.

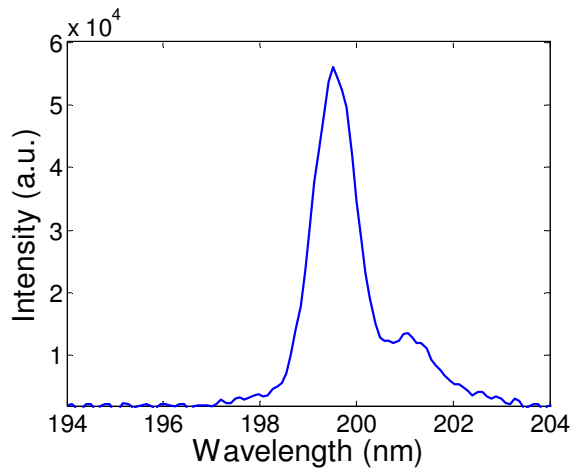

Figure 3: The 4th harmonic HGHG spectrum.

The HGHG dispersion magnet was adjusted to optimize the output of the 4th harmonic HGHG. The HGHG energy was measured at the diagnostics station while the electron beam was steered off the trajectory along the NISUS undulator. Fig. 4 plots the maximum energy of the 4th harmonic HGHG along the NISUS using the techniques just described. It can be clearly seen that the energy growth of the HGHG deviates from the exponential

growth which indicates the saturation of the 4th harmonic HGHG.

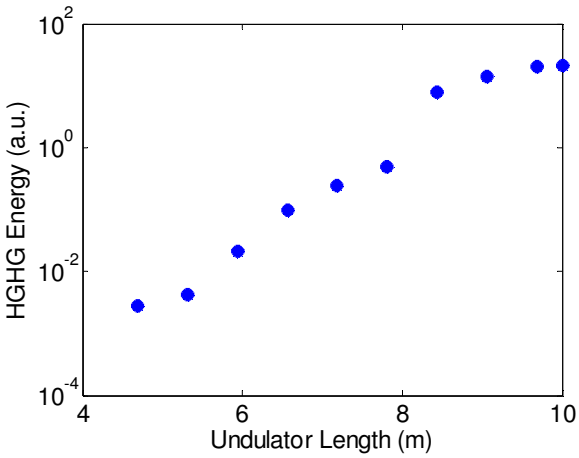

Figure 4: The log plot of the 4th harmonic HGHG energy along the NISUS undulator.

Experimental Characterization of the HGHG Spectrum Broadening and Instability

As we pointed out earlier, the HGHG spectra stability and width are not as stable and narrow as we expected. We decided to explore this more by taking hundreds of single-shot HGHG spectra using the UV spectrometer with 0.7 nm resolution. Fig. 5 plots four of the typical HGHG spectrums obtained. The electron beam energy stability is one of the first considerations for the source of this instability. We measured the shot-to-shot electron beam energy fluctuation to be about 0.2% (Full width), which could contribute to about 0.4% fluctuation in the HGHG spectrum. But we observed as large as a 2% fluctuation of the HGHG spectrum. After carefully analyzing the data, we concluded that the dominant source of the HGHG spectrum fluctuation is the seed laser bandwidth.

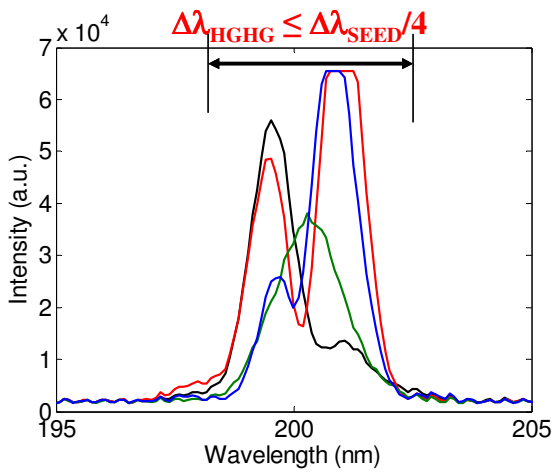

Figure 5: The 4th harmonic HGHG spectra.

In all of the previous HGHG experiments [4], the seed laser pulse length is much longer than the electron beam bunch length. The effective seed laser bandwidth sampled by the electron beam is much narrower than the seed laser bandwidth. So the HGHG bandwidth observed in earlier experiments is dominated by the electron beam bunch length. In our 4th harmonic HGHG experiment, to increase the seed laser power, the seed laser pulse length employed is comparable to the electron beam bunch length (2 ps vs. 1 ps). When timing jitter and drifting are taken into consideration, the electron beam will sample the full range of the seed laser bandwidth. Fig. 5 shows the HGHG spectral fluctuation is about 2%, which is comparable to the seed laser bandwidth. The spectral broadening shown in Fig. 5 is well above the spectrometer resolution, which could be explained by the electron beam distribution and mismatch between the electron beam energy and the seed laser [10].

The First Lasing of ESASE at 210 nm

We also explore the tuning range of the HGHG modulator undulator. For this study the seed laser wavelength and power were kept constant while the electron beam energy was adjusted. We observed no significant change in electron beam energy modulation as the electron beam energy was adjusted from 190 MeV to 208 MeV. This corresponds to ± 5% energy tuning. Since our modulator has only 10 periods, the observed tuning range is well within our expectation.

Taking advantage of the large tuning range of the HGHG modulator, we moved the electron beam energy to 197 MeV to demonstrate ESASE [7-8]. The resonance wavelength of the HGHG radiator at 197 MeV is about 210 nm, which is beyond the seed laser bandwidth. We successfully observed first lasing of a laser enhanced SASE FEL at the 210 nm (Fig. 6) using the same HGHG arrangement. The intensity of the ESASE is a couple orders of magnitude stronger than SASE without the seed laser.

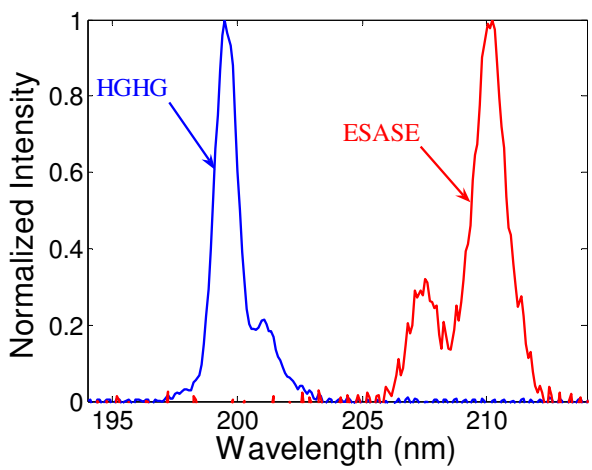

Figure 6: ESASE Spectrum vs. 4th harmonic HGHG.

SUMMARY AND ACKNOWLEDGMENT

We present the new lasing of a SASE FEL at 193 nm, and the first ever lasing of the 4th harmonic HGHG and ESASE. We have experimentally investigated the spectral instability and broadening of the HGHG FEL; the bandwidth of the seed laser is one of the major sources of the HGHG spectral instability. This observation could have important implications for a future X-ray FEL based on a cascaded HGHG concept, where a short broad band seed laser will be employed. By taking advantage of the large tuning range of the HGHG modulator we have successfully demonstrated the first lasing of the so called ESASE. Our experiment shows that ESASE not only will open a new avenue to improve the performance of a SASE FEL, but will also greatly expand the HGHG tunability. More detailed analysis and simulation of the experiments presented here will publish in the future.

We are grateful for support from the NSLS and its staff, and this work is partially supported by the Office of Naval Research (ONR) and U.S. Department of Energy under contract No. DE-AC02-98CH1-886.

REFERENCES

[1] S. Milton et al., Science **292**, 2037 (2001).
[2] A. Tremaine et al., Phys. Rev. Lett. **88**, 204801-1 (2002).
[3] V. Ayvazyan, et al., Phys. Rev. Lett. **88**, 104802-1(2002).
[4] L.H. Yu, et al, Phys. Rev. Lett. 91, 074801-1 (2003).
[5] E. Schneidmiller, et al, "Lasing of FLASH at 13 nm", this proceedings.
[6] T. Shintake, "First Lasing at SCSS", this proceedings.
[7] Y. Liu et al, Phys. Rev. Lett. **80**, 4418 (1998).
[8] A.A. Zholents, Phys. Rev. ST Accel. Beams **8**, 040701 (2005).
[9] X. J. Wang et al, Proceeding of the 2004 FEL conf., Trieste, Italy, 209-211 (2004).
[10] W. Fawley, "Output Bandwidth Effects in Seeded Harmonic Cascaded FELs", this proceedings.

STATUS OF THE LINAC COHERENT LIGHT SOURCE

D. Dowell, SLAC, Menlo Park, California

Abstract

The world's first x-ray free electron laser, the Linac Coherent Light Source (LCLS), is currently under construction at the Stanford Linear Accelerator Center (SLAC). This facility uses the last kilometer of the SLAC 3 km Linac to produce 1.5 to 15 angstrom photons in a 100 meter long undulator with up to 15 GeV electrons. The production of the high-brightness electron beam requires the construction of a new RF photocathode gun and a 135 MeV injector at the 2/3 point of the SLAC Linac. In addition, two stages of chicane compressors will be installed for compressing the electrons to a 22 micron bunch length, boosting the peak current to 3.5 kiloamperes. The bright, dense electron bunches then radiation via the SASE process in the long undulator. The coherent x-ray beam propagates through a gas attenuator and various diagnostics, before delivery to the experimental stations in the Far Hall. The design features and status of this novel facility will be presented.

PAPER NOT AVAILABLE

RESULTS AND LESSONS FROM FLASH

B. Faatz, DESY, Hamburg

Abstract

Since first lasing beginning of 2005, we have continuously extended the wavelength range and improve the performance of FLASH. With regular blocks of accelerator and FEL studies and user beam time, we have now covered a wavelength range between 13 and 45 nm, at power levels between 5 and 50 μJ. Depending on user demands, we have delivered single bunch or multiply bunches at repetition rates of 1 MHz or 250 kHz. The latest results of the machine performance will be shown. In addition, the specific problems that have been encountered and our solutions during the past 18 months will be discussed. Finally, future plans for FLASH will be presented.

PAPER NOT AVAILABLE

THE EUROPEAN XFEL PROJECT

R. Brinkmann, Deutsches Elektronen-Synchrotron (DESY), D-22607 Hamburg, Germany
for the XFEL Team

Abstract

The European X-ray Free Electron Laser XFEL is a 4th generation synchrotron radiation facility based on the SASE FEL concept and the superconducting TESLA technology for the linear accelerator. This multi-user facility will provide photon beams in a wavelength regime from 0.1nm to 5nm in three FEL beam lines and hard X-rays in two spontaneous radiation beam lines, serving in total 10 experimental stations in the first stage. The project is in an advanced planning and technical preparation stage and its construction as a European/International facility near DESY in Hamburg will start in 2007. This talk gives an overview of the overall layout and parameters of the facility, with emphasis on the accelerator design, technology and physics.

INTRODUCTION

The XFEL was originally proposed as part of the TESLA facility, first in a version integrated with the linear collider using the same linac [1,2], in a later version with its own separate linac [3]. In February 2003 the German Government announced the decision that the XFEL should be realized as a European project, with 60% of the funding provided by Germany (Bund and Länder Hamburg and Schleswig-Holstein) and 40% requested from partner countries. In mid-2003 an XFEL project group was established at DESY which, together with partner institutes, pushed forward the preparation work necessary to achieve the status of readiness for start of construction by 2006. Besides the optimization of the overall design, main objectives in this phase are preparations for the site and civil construction (including the legal procedure for construction permission), industrialization of major technical components and detailed studies of beam physics and the FEL process. The XFEL has a strong link to the FLASH (VUV-FEL) facility at DESY [4 – 6], which is in nearly all respects (accelerator technology, FEL operation, photon beam lines and user experiments) truly a pilot facility for the future project.

The project organization at the international level is supervised by a steering committee (ISC) with members from all countries interested in participating in the project. Up to date, 13 countries (Figure 1) have signed the XFEL Memorandum of Understanding for the preparation phase.

The ISC is supported by two working groups: STI for scientific and funding issues and AFI for administrative and funding issues. In 2005 ISC nominated a European Project Team (EPT), with the main charge to deliver the technical and administrative documents required for the process of negotiations and decisions at the political level towards achieving the final go-ahead for the project.

CH CN DE DK ES FR GB GR HU IT PL RU S

Figure 1: Signature countries of the European XFEL MoU as of August 2006.

In July 2006, an updated Technical Design Report (TDR) was completed [7] and delivered to ISC. The report had previously been reviewed and endorsed by STI and additional experts from the international scientific community. In addition, the administrative documents have been essentially completed and reviewed by AFI.

LAYOUT AND PARAMETERS

The main components of the XFEL Facility are the injector, the linear accelerator, the beam distribution system, the undulators, the photon beam lines, and the instruments in the Experiments Hall (see Figure 2).

These components are distributed along an essentially linear geometry, 3.4 km long, starting on the DESY campus in the northwest part of the city of Hamburg, and ending in the neighbouring Federal State of Schleswig-Holstein, south of the city of Schenefeld, where the Experimental Hall is located. Permission for construction and operation on this site was recently (July 2006) obtained (concluding a so-called Plan Approval Procedure) and publicly announced by the authority in charge *(LBEG Clausthal-Zellerfeld)*.

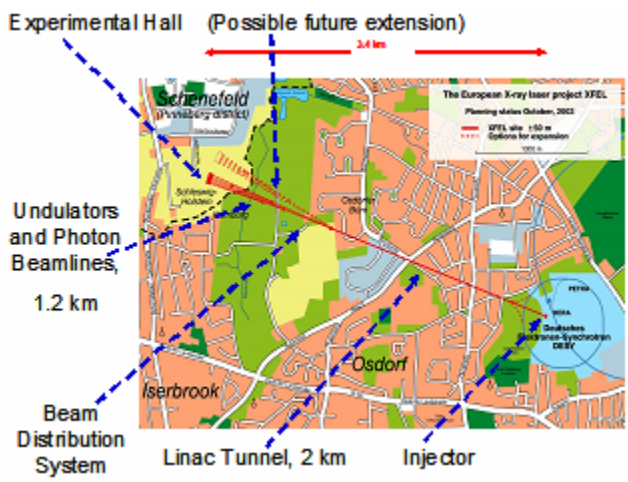

Figure 2: Site and schematic layout of the European XFEL Facility.

The basic functions of the main components are schematically described in the following: In the injector, electron bunches are extracted from a solid cathode by a laser beam, accelerated by an electron RF gun and directed towards the linear accelerator with an exit energy of 120 MeV. In the linear accelerator, consisting of a 1.6 km long sequence of superconducting accelerating modules, magnets for beam steering and focusing, and diagnostic equipment, the electrons are accelerated to energies of up to 20 GeV (17.5 GeV is the energy foreseen for the standard mode of operation of the XFEL facility at 0.1nm FEL wavelength). Along the accelerator, two stages of bunch compression are located, to produce the short and very dense electron bunches required to achieve saturation in the SASE process. At the end of the linac follows a beam transport section with collimation, stabilization feedback and diagnostics systems, after which the individual electron bunches are fed into one or the other of two electron beam lines by the beam distribution system. The linac and beam transport line are housed in a 2.1 km long underground tunnel (Figure 3).

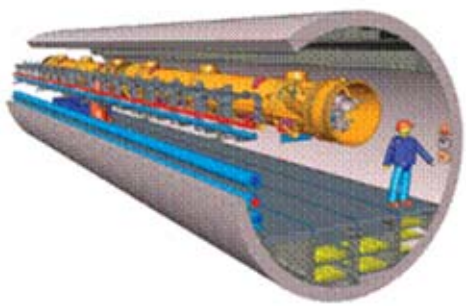

Figure 3: Layout of the 5.2 m diameter linac tunnel.

In the initial configuration the user facility has 3 SASE-FEL and two spontaneous radiation undulator beam lines (Figure 4) with in total 10 experimental stations. The site layout permits a later extension of the facility by another 5 beam lines. Independent wavelength tuning by undulator gap variation is foreseen and, together with electron beam energy variation, a total wavelength range of 0.1 – 5 nm (FEL) and 0.014 – 0.2 nm (spontaneous radiation) can be covered. The peak brilliance of FEL radiation (Figure 5) is in the range 10^{32} - $5{\cdot}10^{33}$ photons/0.1%bw/s/mm^2/mrad^2. The baseline operating point for 0.1nm wavelength (SASE1) at 17.5 GeV electron energy has been chosen on the basis of extensive studies of the FEL process with a relatively conservative assumption on the minimum undulator gap (10mm). At the design electron beam emittance (ε_N = 1.4 mrad·mm, see below) very good transverse coherence of the FEL radiation is predicted [8]. The magnetic lengths of the undulators (105 – 210 m) include a safety margin of at least 20% w.r.t. the calculated saturation lengths.

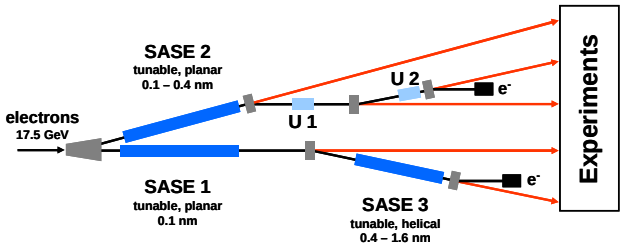

Figure 4: Schematic layout of the beam lines in the user facility.

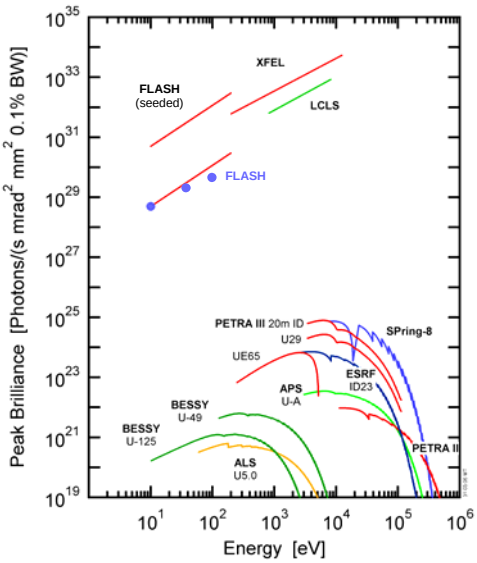

Figure 5: Peak brilliance of X-ray FELs versus 3rd generation SR light sources. Blue spots show experimental performance of the FLASH facility.

ACCELERATOR COMPLEX

The layout of the accelerator is schematically shown in Figure 6 and its main parameters are summarized in Table 1. The beam energy required for 0.1 nm photon wavelength in the SASE1 and SASE2 beam lines is 17.5 GeV. The linac design energy of 20 GeV thus already includes the potential to reach a lower wavelength of about 0.08 nm. The required peak power per RF station is well below the limit of the 10 MW multibeam klystrons. This de-rated mode is beneficial for highly reliable operation on one hand and for an upgrade potential regarding beam energy or duty cycle on the other. Likewise, the cryogenic system is laid out with an overhead of 50% with similar operational benefits.

The electron beam is generated in a laser-driven photocathode RF gun and pre-accelerated in a single superconducting accelerator module. The injector is housed in an underground enclosure separate from the linac tunnel, so that it can be commissioned at an early stage, well before installation work in the linac tunnel is

completed. Furthermore, there is space foreseen for a completely separate and radiation-shielded second injector, which can be constructed, commissioned and maintained independently from the operation of the first injector.

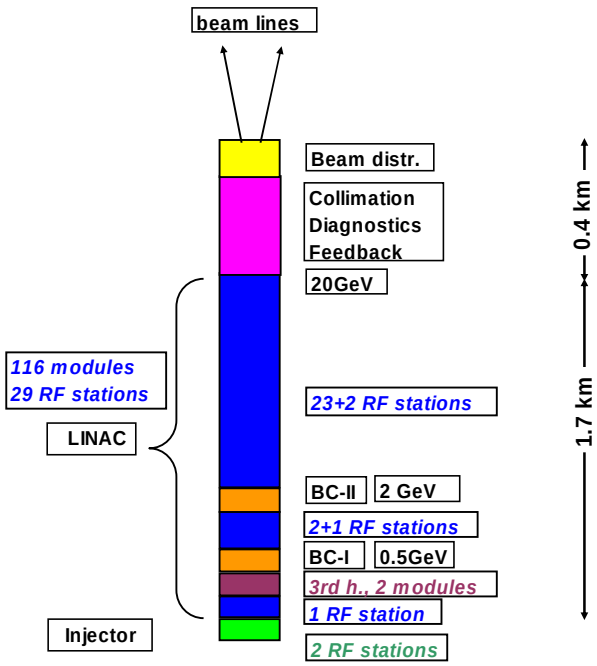

Figure 6: Schematic layout of the accelerator.

Table 1: Main parameters of the XFEL accelerator.

Energy for 0.1 nm wavelength	17.5 GeV
(max. design energy)	*(20 GeV)*
# of installed accelerator modules	116
# of cavities	928
Acc. Gradient (104 act. mod.) at 20 GeV	23.6 MV/m
# of installed RF stations	29
Klystron peak power (26 active stations)	5.2 MW
Loaded quality factor Q_{ext}	4.6×10^6
RF pulse length	1.4 ms
Beam pulse length	0.65ms
Repetition rate	10 Hz
Max. average Beam power	600 kW
Unloaded cavity quality factor Q_0	10^{10}
2K cryo load (incl. transfer line losses)	1.7 kW
Max. # of bunches per pulse *(at 20 GeV)*	3,250 *(3,000)*
Min. bunch spacing	200 ns
Bunch charge	1 nC
Bunch peak current	5 kA
Emittance (slice) at undulator	1.4 mm×mrad
Energy spread (slice) at undulator	1 MeV

The results from simulation studies of the RF gun show that a normalized beam emittance below 1mrad·mm at the design RF field of 60MV/m on the cathode is achievable, even if the thermal emittance is somewhat larger than originally expected, as measurements performed at the PITZ facility (DESY-Zeuthen) indicated [9]. A high priority of the future program [10] at PITZ will be on the verification of the XFEL gun design parameters, with improvements expected from higher cathode field and optimized laser profile.

After transfer to the main accelerator tunnel (see the layout sketched in Figure 7), the beam is further accelerated by one linac unit (4 accelerator modules with 8 cavities each, driven by one RF station) to an energy of 0.5 GeV before entering the first bunch compression stage. A third harmonic (3.9 GHz) RF system is foreseen to optimize the longitudinal phase space properties. After acceleration to 2 GeV with three linac units the beam enters the second (final) compression stage, after which the 1nC bunch peak current has increased to 5 kA (σ_z = 23μm for a 1nC bunch), a factor of 100 higher than the initial peak current from the RF gun. Considerable attention has been paid to foresee beam diagnostics stations in order to assess the beam phase space properties after the compression process in great detail [11]. Beam simulation studies of the compression system (see [12] for a recent overview of simulation code developments) show that the slice emittance growth due to space charge and CSR effects can be kept at a low level and there is room for further parameter optimization beyond the nominal design bunch parameters [13].

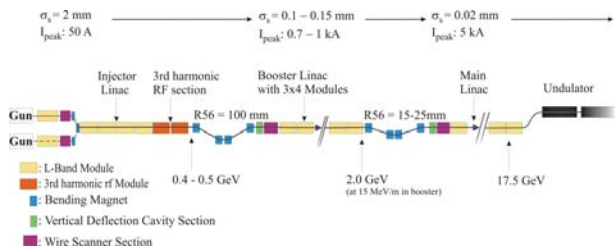

Figure 7: Layout of the XFEL bunch compression system.

The large compression factor and resulting short bunches (70fs rms) require timing, synchronization and diagnostics devices at the fs level. A considerable R&D program is ongoing in this field, see e.g. [14 – 16] for recent developments. Furthermore, extremely accurate RF control is required in the low-energy part of the accelerator [17].

Final acceleration to a nominal maximum beam energy of 20 GeV takes place in the main part of the linac, consisting of 25 RF stations and 100 accelerator modules in total. Downstream from the linac follows a conventional beam line for installation of the beam collimation and trajectory feedback systems, as well as providing distribution of the beam into the different undulator beam lines, including the connection to a future upgrade of the user facility with more beam lines. A combination of slow and fast switching devices permits to generate bunch trains of different time patterns for

different experiments without having to generate and accelerate bunch trains with strongly varying transient beam loading. A fraction of each bunch train will be used to accurately stabilize the following bunches in position and energy by means of a fast feedback system [18]. After having passed through the undulators, the "spent" beam is stopped in radiation shielded solid absorbers. An additional beam dump is installed in the beam distribution shaft XS1, just upstream from the undulator beam lines. It allows to commission or to operate the accelerator while installation or maintenance work is ongoing in the undulator tunnels.

The layout of the linac includes precautions for energy management in case of RF component failure. The section between the two bunch compression stages consists of three RF units with four accelerator modules each, out of which only two have to be active to accelerate the beam to 2 GeV at the design gradient. Likewise, the main section of the linac (from 2 to 20 GeV) has an overhead of two RF stations. This guarantees that in case of an RF unit failure there is sufficient energy reserve to maintain both the beam energy at the second bunch compressor stage as well as at the end of the linac. Tunnel access for repair of RF stations during scheduled operation time can thus be safely avoided. In practice, the reserve stations will not be left idle when not needed. Instead, all available stations will be operated with reduced gradient and in case a station fails the gradient will be increased in the other sections such as to keep the beam energy constant.

Operational Flexibility

The single set of basic reference parameters in Table 1 does not cover the full range of operational flexibility of the linac. There is, within certain limits, a considerable flexibility regarding operation parameters, based on built-in performance reserves of its technical components. Operation at lower beam energy, thus extending the photon wavelength range to softer X-rays, is an obvious possibility. On the other hand, based on the experience gained with the superconducting TESLA cavities, it can be realistically expected that the linac can be operated at an accelerating gradient somewhat above the specified design value of 23.6 MV/m at 20 GeV. An increase of the gradient to about 28 MV/m would permit a maximum beam energy of 24 GeV, thus significantly extending the photon wavelength range to harder X-rays, provided that simultaneously also an improved injector beam quality becomes available to be able to maintain saturation of the SASE FEL process. In addition to the possibility of higher beam energies, the available reserve in the RF and cryogenic systems can also be used for increasing the linac repetition rate and thus the duty cycle of the pulsed linac. At sufficiently low beam energy, a 100% duty cycle, i.e. continuous wave (CW), mode of operation is conceivable, an option which is only possible with a superconducting linac. This option is viewed as not being part of the first stage of the XFEL facility but is considered as a future option. A preliminary set of possible parameters for CW operation is shown in Table 2.

Table 2: Sketch of possible parameters for a future option of operating the linac in CW mode.

Beam energy	7 GeV
Accelerating Gradient	7.5 MV/m
# of CW RF stations	116
RF power per accelerator module	≈20 kW
Beam current	0.18 mA
Loaded quality factor Q_{ext}	2×10^7
Bunch frequency	180 kHz
Unloaded quality factor Q_0	$2 \cdot 10^{10}$
2K cryogenic load	≈3.5 kW

PROJECT COST AND SCHEDULE

An in-depth re-evaluation of project construction costs has been performed as part of the project preparation work (see the TDR [7] for more details). In year 2005 prices, the construction costs are 986 M€, out of which 736 M€ are capital investment and 250 M€ personnel costs (including overhead). A breakdown of the construction costs is shown in Figure 8 and the budget time profile in Figure 9.

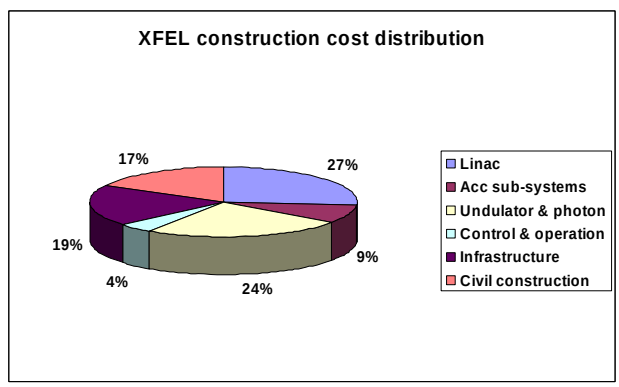

Figure 8: XFEL construction cost distribution.

The project schedule assumed for the profile of Figure 9 is based on an expected project go-ahead decision in the beginning of 2007. After a construction period of 6.5 years, beam through the linac and the first beam line (SASE1) is scheduled for 2013 and first user operation for 2014. There will be a transition phase until end of 2015, during which operation of beam lines takes place in parallel with completion of construction and commissioning of others. By 2016 the entire facility will be operational. The yearly operation budget (in 2005 prices) has been estimated at 83 M€, including administrative overhead and user support.

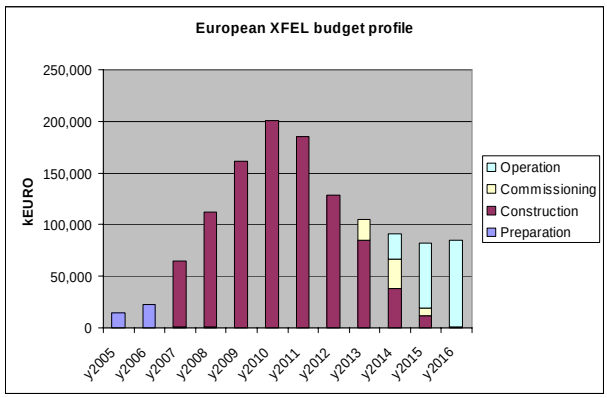

Figure 9: XFEL budget profile, including preparation phase and transition from construction to operation.

ACKNOWLEDGEMENT

The paper presented here is based on the recently published XFEL Technical Design Report. The author would like to express his thanks to the co-editors and co-authors of the TDR, who contributed and shaped a vast amount of material for that comprehensive report, of which this paper can be viewed as a short summary.

REFERENCES

[1] R. Brinkmann, et al., “An X-Ray FEL Laboratory as Part of a Linear Collider Design”, Nucl. Instr. Meth A393, (1997) 86-92.
[2] R. Brinkmann et al. (eds.), ”TESLA Technical Design Report”, DESY-2001-011, March 2001.
[3] R. Brinkmann et al. (eds.), “TESLA XFEL Technical Design report – Supplement”, DESY-2002-167, Oct. 2002.
[4] J. Roßbach, “Results from the VUV-FEL”, Proc. EPAC, Edinburgh 2006.
[5] H. Weise, “The TTF/VUV-FEL (FLASH) as the Prototype for the European XFEL Project”, Int. Linac conf., Knoxville 2006.
[6] B. Faatz, “Results and Lessons from FLASH”, This conference MOBAU02.
[7] “XFEL Technical Design Report”, DESY 2006-097, http://xfel.desy.de.
[8] E. Saldin et al., “Transverse and Longitudinal Coherence Properties of the Radiation from X-ray SASE FELs”, this conference MOPPH069 .
[9] J. H. Han et al., “Emission Mechanisms in a Photocathode RF Gun”, Proc. PAC, Knoxville 2005.
[10] A. Oppelt et al., “Upgrade of the PITZ Facility and First Beam Measurements”, this conference THPPH022 .
[11] C. Gerth, “Layout of the Diagnostic Sections for Emittance and Energy Spread Measurements at the European XFEL”, this conference THPPH010.
[12] M. Dohlus, “Modeling of Space Charge and CSR Effects in Bunch Compressor Systems”. Proc. EPAC, Edinburgh 2006.
[13] T. Limberg et al., “Optimized Bunch Compression System for the European XFEL”, Proc. PAC, Knoxville 2005.
[14] A. Winter et al., “High Precision Master Oscillator for Optical Timing Distribution Systems”. Proc. EPAC, Edinburgh 2006.
[15] J.-W. Kim, “Femtosecond Synchronization and Stabilization Techniques”, this conference TUBAU02.
[16] B. Schmidt, “Overview on Diagnostics for X- and VUV-FELs”, this conference THCAU01.
[17] F. Ludwig et al., “Phase Stability of the Next Generation RF Field Control for VUV- and X-ray Free Electron Lasers”, Proc. EPAC, Edinburgh 2006.
[18] V. Schlott et al., “An Intra Bunch Train Feedback System for the European XFEL”, Proc. EPAC, Edinburgh 2006.

OPTICAL KLYSTRON ENHANCEMENT TO SASE X-RAY FELS

Yuantao Ding*, Paul Emma, Zhirong Huang†, SLAC,Menlo Park, CA 94025, USA
Vinit Kumar‡, ANL, Argonne, IL 60439, USA.

Abstract

The optical klystron enhancement to self-amplified spontaneous emission (SASE) free electron lasers (FELs) is studied in theory and in simulations. In contrast to a seeded FEL, the optical klystron gain in a SASE FEL is not sensitive to any phase mismatch between the radiation and the microbunched electron beam. The FEL performance with the addition of four optical klystrons located at the undulator long breaks in the Linac Coherent Light Source (LCLS) shows significant improvement if the uncorrelated energy spread at the undulator entrance can be controlled to a very small level. In addition, FEL saturation at shorter x-ray wavelengths (around 1.0 Å) within the LCLS undulator length becomes possible. We also discuss the application of the optical klystron in a compact x-ray FEL design that employs relatively low electron beam energy together with a shorter-period undulator.

INTRODUCTION

An x-ray free electron laser (FEL) operated in the self-amplified spontaneous emission (SASE) mode is the primary candidate for the next-generation light source and is under active development around the world [1, 2, 3]. In such a device, based on the achievable electron beam qualities such as peak current and transverse emittances, the total length of the undulator required to reach the x-ray intensity saturation usually exceeds 100 m. The electron beam energy spread is typically too small to affect the SASE performance.

To enhance the FEL gain, the optical klystron concept has been invented by Vinokurov and Skrinsky [4] and has been successfully implemented in many FEL oscillator facilities such as the Duke FEL [5]. An optical klystron consists of two undulators, separated by a dispersive section (a magnetic chicane). The dispersive section converts beam energy modulation into density modulation and hence speeds up the gain process. Theoretical studies of the optical klystron in high gain FEL amplifiers show that its performance depends critically on the electron beam energy spread [6, 7, 8]. More recently, Neil and Freund [9] have studied a distributed optical klystron configuration using the LCLS parameters. Based on the FEL amplifier simulations that start with a coherent seed, they point out that the performance of the optical klystron for short-wavelength FELs is very sensitive to the exact slippage of the electron beam relative to the radiation in the dispersive section. Thus, the magnetic fields of the chicane must be carefully designed and controlled to very high precision.

Motivated by the very small uncorrelated energy spread of the electron beam that has been measured in a photocathode RF gun [10], we study the possible optical klystron enhancement to SASE x-ray FELs. We show that a SASE optical klystron is not sensitive to the relative phase of the electron beam to the radiation as long as the electron slippage length in the dispersive section is much longer than the coherence length of the radiation. Based on extensive SASE simulations, we illustrate the gain enhancement of the optical klystron to the LCLS and a compact x-ray FEL scheme.

ONE-DIMENSIONAL ANALYSIS

In this section, we analyze an optical klystron configuration with a magnetic chicane between two high-gain FEL undulators and extend the previous theoretical treatments [6, 7, 8] to the high-gain SASE operating mode. A detailed description may be found in [11].

A magnetic chicane introduces an energy-dependent longitudinal delay of the electron relative to the radiation, which can be expressed as a change of the radiation phase "seen" by the electron:

$$\Delta\theta = -\frac{k_r R_{56}}{2} + k_r R_{56}\delta \tag{1}$$

Here $\lambda_r = 2\pi/k_r = 2\pi c/\omega_r$ is the FEL resonant wavelength, R_{56} is the momentum compaction of the chicane, and $\delta = (\gamma - \gamma_0)/\gamma_0$ is the relative energy deviation. The first term in Eq. (1) describes the overall phase slippage between the FEL radiation and the reference electron having the energy $\gamma_0 mc^2$, and the second term describes the relative phase change for an electron with a slightly different energy. Following the one-dimensional (1D) theory of Kim [8] but keep the overall phase slippage, we write down the optical klystron (OK) enhancement factor to the radiation field E_ν at the scaled frequency $\nu = \omega/\omega_r$:

$$\begin{aligned} R(\nu) \equiv & \frac{E_\nu^{\mathrm{OK}}}{E_\nu^{\mathrm{no\ OK}}} \\ = & \frac{1 - \int d\xi \frac{dV(\xi)/(d\xi)}{(\mu-\xi)^2} e^{-i\rho k_r \nu R_{56}\xi} e^{ik_r \nu R_{56}/2}}{1 + 2\int d\xi \frac{V(\xi)}{(\mu-\xi)^3}} \end{aligned} \tag{2}$$

where $\xi = \delta/\rho$ is the normalized energy variable, ρ is the FEL Pierce parameter [12], μ is the complex growth rate of the radiation field in each undulator, $\mu = (-1 + i\sqrt{3})/2$ for a beam with a vanishing energy spread, and $V(\xi)$ is the

* Electronic address: ding@slac.stanford.edu. On leave from IHIP, Peking University, Beijing, China.
† Electronic address: zrh@slac.stanford.edu.
‡ Current address: G-20, ADL Building, Raja Ramanna Centre for Advanced Technology, Indore-452013, INDIA.

energy distribution of the electron beam with the normalization $\int V(\xi)d\xi = 1$.

The first term in the numerator of Eq.(2) represents the contribution from the radiation in the first undulator, while the second term in the numerator represents the contribution of the microbunched electron beam. For a seeded FEL with $\nu = 1$, $k_r R_{56}/2 = 2\pi n (n = 1, 2, 3, \ldots)$ yields a nearly matched phase (i.e., constructive interference between two terms). The optical klystron is then optimized for a matched phase. However, in the hard x-ray wavelength range, changing R_{56} of the chicane by a fraction of 1 Angstrom can result in a complete phase mismatch. Thus, there can be large fluctuations in the radiation power due to small fluctuations in the magnetic fields as observed in Ref. [9]. Even when the magnetic fields are held constant, a small energy jitter (on the order of 10^{-4}) can also mismatch the phase.

Nevertheless, SASE FELs start from shot noise and have a relatively wide bandwidth. For a given value of R_{56}, the phase may be mismatched for one particular wavelength but may be properly matched for another wavelength within the SASE bandwidth. Thus, we should integrate over the SASE spectrum $S(\nu)$ to obtain the optical klystron power gain factor as:

$$G = \int d\nu |R(\nu)|^2 S(\nu) \tag{3}$$

For an electron beam with a Gaussian energy distribution of rms width $\sigma_\delta \ll \rho$ (i.e., $\sigma_\xi \ll 1$), we can integrate Eq. (1) over energy and Eq. (3) over frequency (assuming a Gaussian average SASE spectrum) to obtain

$$\begin{aligned} G = \frac{1}{9}\Bigg[& 5 + D^2 \exp(-D^2 {\sigma_\xi}^2) + 2\sqrt{3} D \exp\left(-\frac{D^2 {\sigma_\xi}^2}{2}\right) \\ & + \left(4 + \sqrt{3} D \exp\left(\frac{-D^2 {\sigma_\xi}^2}{2}\right) \cos\left(\frac{D}{2\rho}\right)\right. \\ & \left. - D \exp\left(\frac{-D^2 {\sigma_\xi}^2}{2}\right) \sin\left(\frac{D}{2\rho}\right)\right) \exp\left(\frac{-D^2 {\sigma_\nu}^2}{8\rho^2}\right) \Bigg] \end{aligned} \tag{4}$$

where $D = k_r R_{56} \rho$. The power gain factor G as a function of the chicane strength R_{56} is shown in Fig. 1 for two typical values of the rms energy spread σ_δ, assuming a typical rms SASE bandwidth $\sigma_\nu = \rho$.

When R_{56} is very small, the optical klystron operates as a phase shifter, and the FEL power is oscillatory depending on the relative phase between the radiation and the electron beam. As $k_r R_{56} \sigma_\delta \to 1$, the optical klystron gain peaks and starts to decay exponentially due to the smearing effect of the intrinsic energy spread. Thus, the phase matching is no longer important when the optical klystron is near its peak performance.

A simple physical picture emerges in the time domain. The path length difference between the SASE radiation and the electron beam passing the dispersive section is about $R_{56}/2 \approx 1/(2k_r\sigma_\delta) = \lambda_r/(4\pi\sigma_\delta)$ at the optimal chicane setting. Since the typical SASE coherence length is on the order of $\lambda_r/(4\pi\rho)$ [13, 14], it is much smaller than the path length difference introduced by the chicane when the beam energy spread $\sigma_\delta \ll \rho$ (a necessary condition for the operation of the high-gain optical klystron). Therefore, there is no place for the electron beam to match the radiation phase after the beam is slipped from the SASE radiation more than a few temporal spikes. The radiation power averaged over many statistically independent spikes is then not sensitive to the exact slippage introduced by the chicane.

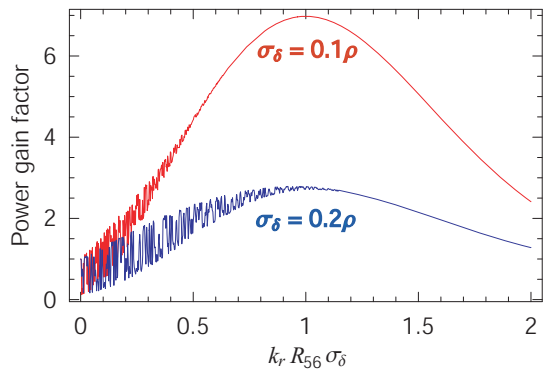

Figure 1: (color) 1D power gain factor with relative energy spread $\sigma_\delta = 0.1\rho$ (red line) and $\sigma_\delta = 0.2\rho$ (blue line)

UNCORRELATED ENERGY SPREAD

Since the uncorrelated energy spread plays a crucial role for the gain enhancement of the optical klystron, we analyze here two main sources of energy spread. One is from the gun and the linac, which forms the initial energy spread at the entrance of the FEL undulator; while the other is the quantum diffusion due to spontaneous radiation along the undulator, which leads to an increase of energy spread after the electron beam is injected into the undulator. The uncorrelated energy spread of electron beams generated from a photocathode rf gun can be extremely small, at an rms value of 3 to 4 keV from both measurements [10] and simulations. Nevertheless, a microbunching instability driven by longitudinal space charge and coherent synchrotron radiation in the accelerator system may be large enough to significantly degrade the beam qualities including the energy spread [15, 16]. This microbunching instability occurs at much longer wavelengths than the FEL microbunching and requires much larger R56 (from bunch compressor chicanes) than the optical klystron chicanes. To maintain a relatively small energy spread after compression and acceleration, a laser heater [15, 16] will be used in the LCLS injector to increase the rms energy spread from 3 to 40 keV. After a total compression factor of about 30, the slice rms energy spread at the undulator entrance can be controlled to 1×10^{-4} at 14 GeV, which is tolerable for the SASE FEL at 1.5 Å. However, considering the gain enhancement of the optical klystron (see Fig.1), a smaller energy spread (e.g., 5×10^{-5} or 0.1ρ) is desirable. This may be achiev-

able by dropping the heater-induced energy spread to 20 keV at the expense of the increased microbunching instability gain. For a smooth enough photocathode drive laser profile, this higher instability gain may still be tolerable after acceleration and bunch compression. Thus, the final slice energy spread at the undulator entrance may be kept at 5×10^{-5} for the LCLS.

The energy diffusion due to spontaneous radiation along the undulator was discussed by Saldin et al [17]. This energy diffusion rate increases with γ^4 and K^3 for $K^2 \gg 1$. For the LCLS at $\lambda_r = 1.5$ Å and $K = 3.5$, the rms energy spread increases from initial value of 5×10^{-5} to 1×10^{-4}at the undulator position of 40 m due to the spontaneous radiation. We will include this effect in the FEL simulations to be discussed below.

THREE DIMENSIONAL SIMULATIONS

Three-dimensional (3D) simulation code Genesis 1.3 [18] is used to explore the LCLS gain enhancement with a distributed optical klystron configuration for two different radiation wavelengths of 1.5 Å and 1.0 Å and a very compact x-ray FEL at 1.5 Å.

We place four 4-dipole chicanes in the first four long breaks between LCLS undulator sections (at 12, 24, 36, and 48 m) to form a distributed optical klystron configuration. For each chicane, the optimal gain enhancement is obtained by scanning the chicane dipole magnetic field strength. Two initial rms energy spread values of 1×10^{-5} and 5×10^{-5} at the entrance of the undulator are used in the 3D simulations. While we consider the energy spread of 5×10^{-5} may be achievable in the LCLS with a reasonably smooth drive-laser profile or with the low-charge option [19], the energy spread of 1×10^{-5} requires to switch off the laser heater completely and is probably not allowed by the microbunching instability in the linac. It is still included in the simulations in order to study the best possible optical klystron performance and the influence of spontaneous energy diffusion in the undulator.

Fig. 2 shows the FEL power gain along the undulator with and without optical klystrons at the resonant wavelength of 1.5 Å for K = 3.5 (the current LCLS design parameters), with an electron peak current of 3.4kA and normalized rms emittance of 1.2 μm. The saturation length is shortened by 13 m using these optical klystrons with an initial energy spread of 5×10^{-5} and R_{56} of the chicanes at around 0.25μ m (with a small variation for each chicane). Note that a 10% variation of the chicane R_{56} values does not make a visible difference for the FEL output power.

To allow for the LCLS to reach 1.0 Å without increasing the beam energy, the undulator gap may be increased by 2 mm to reduce the undulator parameter to K= 2.7. The 3D simulation results are presented in Fig. 3, using a peak current of 3.4kA and normalized rms emittance of 1.2 μm. Without any optical klystron, the nominal LCLS beam cannot reach SASE saturation at this wavelength. With the addition of four optical klystrons as described here, the saturation distance is shortened by about 26 m and is well within the LCLS total undulator length. At this K value and using a lower beam energy (11.0 GeV), simulations also show the FEL at 1.5 Å approximately save 25 m of saturation length compared to that without any optical klystron.

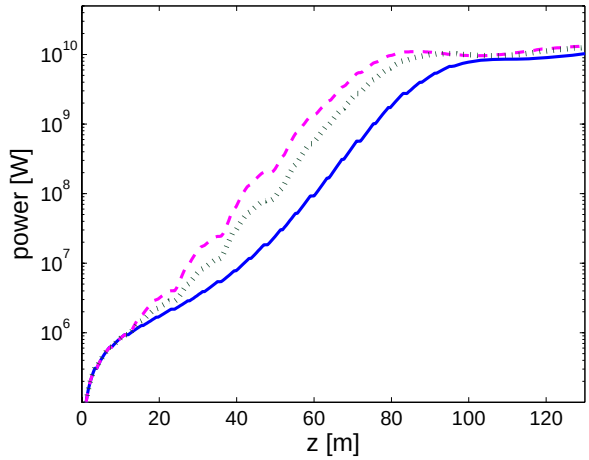

Figure 2: (color) SASE FEL power along the undulator without any optical klystron (blue solid curve), and with 4 optical klystrons for the initial rms energy spread of 1×10^{-5} (magenta dashed curve) and 5×10^{-5} (green dotted curve). The FEL wavelength is 1.5 Å, and the undulator parameter $K = 3.5$.

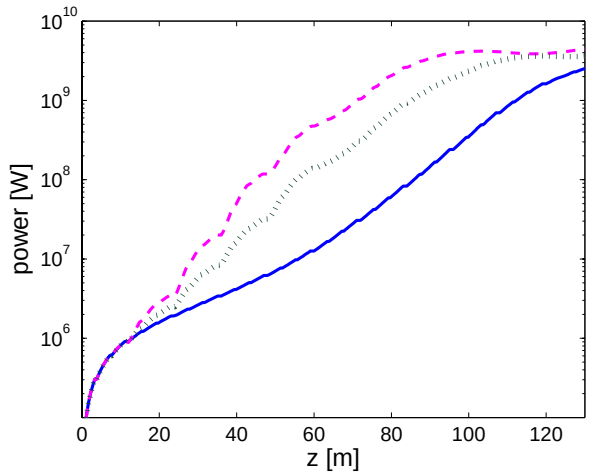

Figure 3: (color) SASE FEL power along the undulator without any optical klystron (blue solid curve), and with 4 optical klystrons for the rms energy spread of 1×10^{-5} (magenta dashed curve) and 5×10^{-5} (green dotted curve). The FEL wavelength is 1.0Å, and the undulator parameter $K = 2.7$.

It is clear from these numerical examples that a simultaneous reduction in beam energy and undulator parameter for the same radiation wavelength is beneficial for the optical klystron enhancement, where the energy diffusion due

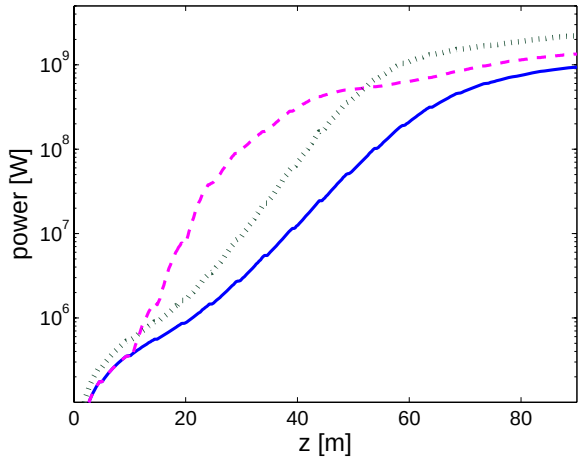

Figure 4: (color) SASE FEL power along the undulator at a peak current of 2kA without any optical klystron (blue solid curve) and with 4 optical klystrons (magenta dashed curve), and at peak current of 3kA without any optical klystron (green dotted curve). The FEL wavelength is 1.5 Å and the undulator parameter $K = 1.3$.

to spontaneous radiation in the undulator is much reduced. Inspired by the Spring-8 Compact SASE Source (SCSS) design [3], we study the possibility of using a relatively low energy electron beam together with a short-period undulator to drive a compact x-ray FEL with the aid of the distributed optical klystrons. A 1.5-cm period in-vacuum undulator with $K = 1.3$ is used according to the design parameters in SCSS. To produce 1.5-Å FEL radiation, the necessary electron energy is about 5 GeV. Rather than a standard peak current of 3 kA as described in Ref. [3], we assume a lower peak current of 2 kA and an rms energy spread of 100 keV (or 2×10^{-5}) at the undulator entrance. A smaller peak current allows for a smaller energy spread and may also help reduce the microbunching instability gain in the accelerator, as well as any wakefield effect in the small gap, in-vacuum undulator. Fig. 4 shows the simulation results for the SASE mode without any optical klystron (for both 3-kA and 2-kA bunches) and with four optical klystrons (for a 2-kA bunch). The latter saturates at around 50 m of the undulator distance, which is still about 10 m shorter than the higher-current case without any optical klystron.

SUMMARY

The small, experimentally measured uncorrelated energy spread from RF guns offers the opportunity to consider applications of optical klystrons in x-ray FELs. In contrast to a seeded FEL, our study shows that the optical klystron gain is not sensitive to the relative phase between the SASE radiation and the electron beam, and that the radiation power is very stable with a relatively large tuning range of optical klystrons. 3D simulations of the LCLS with a distributed optical klystron configuration show significant gain enhancement if the slice energy spread at the undulator entrance can be controlled to a very small level. The improved performance can be used to obtain the FEL saturation at shorter x-ray wavelengths for a fixed undulator length or to relax the stringent requirement on the beam emittance. The exploration of optical klystrons in a very compact x-ray FEL also indicates promising results. Therefore, we think that the optical klystron configuration can be an easy "add-on" to SASE x-ray FELs provided that electron beams with very small energy spreads are obtainable at the final beam energy.

We thank J. Wu and S. Reiche for useful discussions, J. Galayda and R. Ruth for their encouragement on this work. This work was supported by Department of Energy Contracts No. DE-AC02-76SF00515.

REFERENCES

[1] Linac Coherent Light Source (LCLS) Conceptual Design Report, SLAC Report No. SLAC-R-593, 2002.

[2] Technical Design Report, DESY TESLA-FEL Report, 2002.

[3] SCSS X-FEL conceptual design report, RIKEN, 2002.

[4] N.A. Vinokurov and A.N. Skrinsky, Preprint of INP 77-59, Novosibirsk, (1977).

[5] Y. K. Wu *et al.*, Phys. Rev. Lett. 96, 224801 (2006).

[6] R. Bonifacio, R. Corsini, and P. Pierini, Phys. Rev. A 45, 4091 (1992).

[7] N.A. Vinokurov, Nucl. Instrum. Methods Phys. Res. A 375, 264 (1996).

[8] K.J. Kim, Nucl. Instrum. Methods Phys. Res. A 407, 126 (1998).

[9] G.R. Neil and H.P. Freund, Nucl. Instrum. Methods Phys. Res. Sec. A 475, 381 (2001).

[10] M. Huning and H. Schlarb, in Proceedings of the 2003 Particle Accelerator Conference, Portland, 2074 (2003).

[11] Y. Ding, P. Emma, Z. Huang, V. Kummar, Phys. Rev ST Accel. Beams 9, 070702 (2006).

[12] R. Bonifacio, C. Pellegrini, and L.M. Narducci, Opt. Commun. 50, 373 (1984).

[13] R. Bonifacio, L. De Salvo, P. Pierini, N. Piovella, and C. Pellegrini, Phys. Rev. Lett. 73, 70 (1994).

[14] E.L. Saldin, E.A. Schneidmiller, and M.V. Yurkov, Opt. Commun. 148, 383 (1998).

[15] E. Saldin, E. Schneidmiller, and M. Yurkov, TESLA-FEL-2003-02, DESY (2003).

[16] Z. Huang *et al.*, Phys. Rev. ST Accel. Beams 7, 074401 (2004).

[17] E.L. Saldin, E.A. Schneidmiller, and M.V. Yurkov, Nucl. Instrum. Methods Phys. Res. A 381, 545 (1996).

[18] S. Reiche, Nucl. Instrum. Methods Phys. Res. A 429, 243 (1999).

[19] P. Emma *et al.*, the Proceedings of 2005 Particle Accelerator Conference, Tennessee, 344, (2005).

STATUS OF JAPANESE XFEL PROJECT AND SCSS TEST ACCELERATOR

Tsumoru Shintake# and SCSS Team
RIKEN/JASRI/SPring-8, Hyogo 679-5148 Japan.

Abstract

On 20 June, the first lasing has been observed at 49 nm in SCSS test accelerator, which is prototype machine for Japanese XFEL project. A challenging approach is employed in injector system: a low density electron beam is generated from 500 kV gun using thermionic cathode, followed by velocity bunch compression by factor of a few 100 times, and magnetic chicane bunch compression. The injector created high quality and high density electron bunch, whose measured emittance was 3 π.mm.mrad normalized with 800 A peak current and 1 psec pulse width or less. When we firstly closed the gap in one undulator in 15th June, we observed the SASE signal at 49 nm. Using two undulators, the signal amplification gain reached 10^5, which is close to the saturation level. The average radiation energy is 1 micro-J/pulse at moment, we need more beam tuning.

The XFEL project aiming at generating 1 Å coherent intense X-ray laser based on SASE using 8 GeV normal-conducting accelerator has been funded. The construction is scheduled 2006-2010, and beam operation will start in 2011.

INTRODUCTION

SCSS project has started in 2001 [1]. Unique combination of three key technologies: the in-vacuum short period undulator, the C-band high gradient accelerator and low emittance injector using thermionic electron source make possible to realize SASE-FEL at 1 Å within available site length at SPring-8 less than 800 m as shown in Fig. 1. It was named as SCSS: SPring-8 Compact SASE Source because of this reason. From year of 2001, we have been carrying out R&D for key components: the electron gun, injector, C-band klystron modulator with oil-filled compact design, high resolution beam position monitor, digital rf signal processing system, etc [2]. In order to check performance of developed hardware components and verify system performance, especially the low emittance electron injector, we constructed prototype accelerator for XFEL in 2004-2005 as shown in Fig. 2. The tunnel length is 60 m long, the maximum electron beam energy is 250 MeV, the shortest lasing wavelength is around 50 nm. From May 2006, we started dedicated beam tuning to demonstrate first lasing.

In 2006, the Japanese MEXT: Ministry of Education, Culture, Sports, Science and Technology has decided construction of XFEL at SPring-8 site. The project is aiming at generating 1 Å coherent intense X-ray laser, which is based on SASE using 8 GeV normal-conducting accelerator. Figure 2 shows the computer image of the facility, the XFEL will be constructed right next to the 1 km beam line. The construction is scheduled 2006-2010.

One big benefit to have XFEL at SPring-8 site is to share human resources and sample preparation facilities in the existing 8 GeV synchrotron light source.

CHOICE OF ACCELERATOR TECHNOLOGY

We have decided to use normal conducting linear accelerator technology at C-band frequency (5712 MHz). It is "warm" technology, not super conducting "cold" technology. The reason why we chose this technology is

(1) Since C-band accelerator can generate high

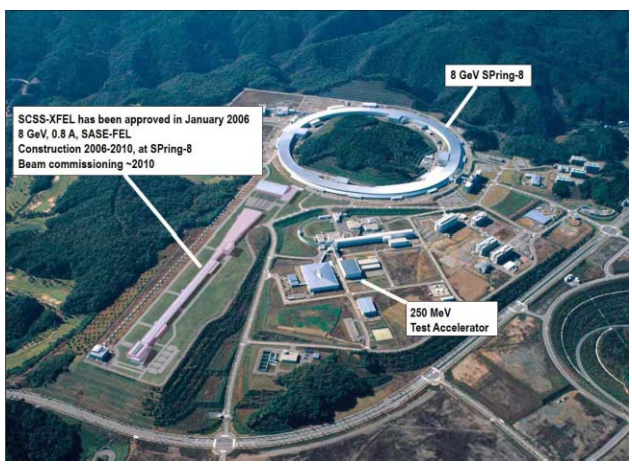

Fig. 1: The XFEL will be build at SPring-8 site.

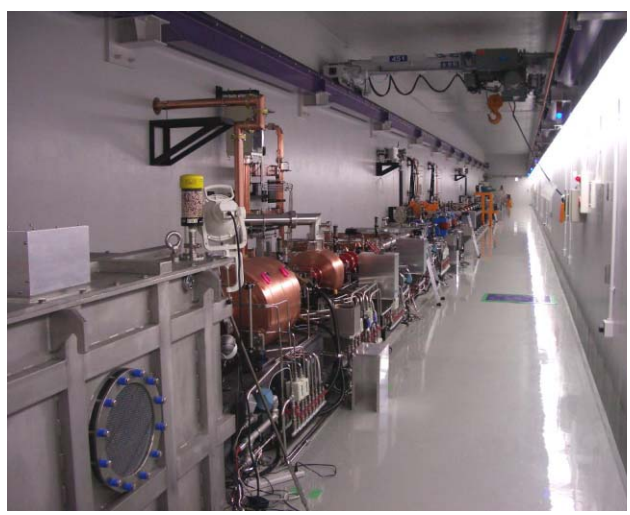

Fig. 2: Tunnel view in SCSS test accelerator.

#shintake@spring8.or.jp

gradient, as high as 35 MV/m, with reasonable cost. Technology is available right now.

(2) Pulse repetition frequency of C-band accelerator is limited to 60 pps maximum, and average flux becomes quite lower (about 1/100 times) than the case of super conducting machine. The special feature of XFEL radiation is extremely high peak power (~ 2 GW) and short pulse duration (~30 femot-sec), and most of all scientific case to make use these features does not request high average flux. The existing SPring-8 3rd generation light source provides high average flux, thus XFEL and SPring-8 are complementary facilities in the same site.

CHOICE OF ELECTRON SOURCE

The SASE-FEL at 1 Å wavelength region requires high quality electron beam of extreme parameter: peak current > 2 kA, low slice emittance ~ 1 π.mm.mrad, and low slice energy spread < 10^{-4}. Additionally, it requires fairly long undulator line, near 100 m long, where the beam trajectory has to be guided in a straight line within small error < 10 μm. In this alignment, we use high resolution e-beam position monitors, and relay on beam-based-alignment. To perform this alignment, the electron beam has to be very stable, and also the beam hallow component and dark-current must be negligibly small (clean beam).

The transverse electron beam size at the undulator section is order of 30 μm, from this beam the X-ray is radiated with diffraction limited condition, thus the X-ray beam spot is also quite small, which is order of 100 μm at the sample located 30 m or 100 m downstream from the undulator. Pointing of the radiated X-ray beam follows e-beam trajectory, therefore, e-beam trajectory angle has to be fairly stable, such as, 3 μrad, and otherwise X-ray does not hit small samples.

In order to make such a stable and clean beam, first of all, the initial condition of electron beam trajectory, or the emission condition of the electron from the source has to be very stable. One candidate to meet this requirement is the thermionic cathode.

The LaB_6 or CeB_6 have been widely used in the scanning electron microscope, because of its high brightness and superior performance of quick recovery from contaminations [3]. Since they operate at high temperature near 1800 K, no any residual gases can condensed on the cathode surface. Additionally, there is constant rate of cathode material evaporation from the surface, which provides continuous activation, and also self-cleaning process. If we use a high quality single crystal, a very flat surface is formed in a single atomic layer after evaporation, which provides very uniform emission density and ensures no emittance break associated with rough cathode surface or non-uniform emission density sometimes observed in Ba-oxide cathode materials.

It should be noted that the pin-shaped cathode is commonly used in electron micro scope, since it provides extremely high brightness, i.e., small emission area provides small emittance while high current density, which meets imaging optics in microscope. However, it can emit fairly low current beam, typically less than 1 μA. In contrast, the SASE-FEL requires a few Ampere beam from the cathode, thus we use a flat surface. We chose CeB_6 rather than LaB_6, because of longer life time. At 1700 K operation temperature, expected lifetime is 20,000 hours for 100 μm material loss due to evaporation.

We use rod shape CeB_6 of 3 mm in diameter as shown in Fig. 3. We extract 1 A beam via 10 MV/m acceleration field in the gun (500 kV/5cm), which is in the temperature limited condition. The theoretical normalized emittance due to thermal motion at the cathode is 0.4 π.mm.mrad. The emittance was carefully measured at the gun using double slits, it was 1.1 π.mm.mrad including tail component for 1 A beam current. Eliminating tail components from the data, we estimated the net emittance of core beam as 0.6 π.mm.mrad [3].

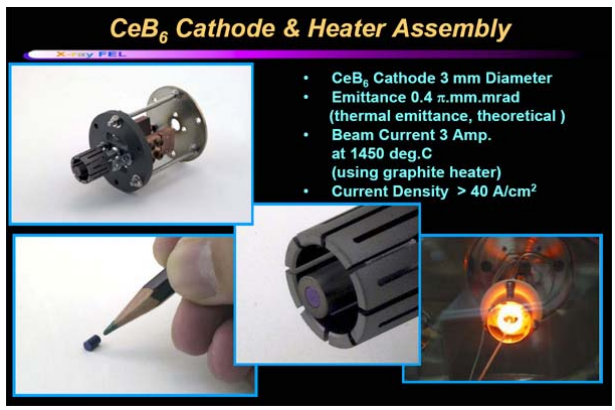

Fig. 3: CeB_6 single crystal thermionic cathode for low emittance electron source.

BUNCH COMPRESSION

In the X-ray FEL for 1 Å wavelength, very high peak current is required for e-beam to obtain high SASE-FEL gain. Nominal beam current value of 3 kA is required in our design. We can not generate such beam from any kind of electron sources, therefore we compress the bunch length in longitudinal direction by means of velocity bunching in injector and magnetic chicane bunch compressor. We designed the compression factor as 20, 18, 8 in velocity bunching at injector, the first and second bunch compression system, respectively. Big question is how we maintain low emittance value from the gun to undulator through these compressions.

In the injector and bunch compressors, if the following conditions are satisfied, the slice emittance can be conserved.

(1) Radiation damping or excitation through synchrotron radiation is small.

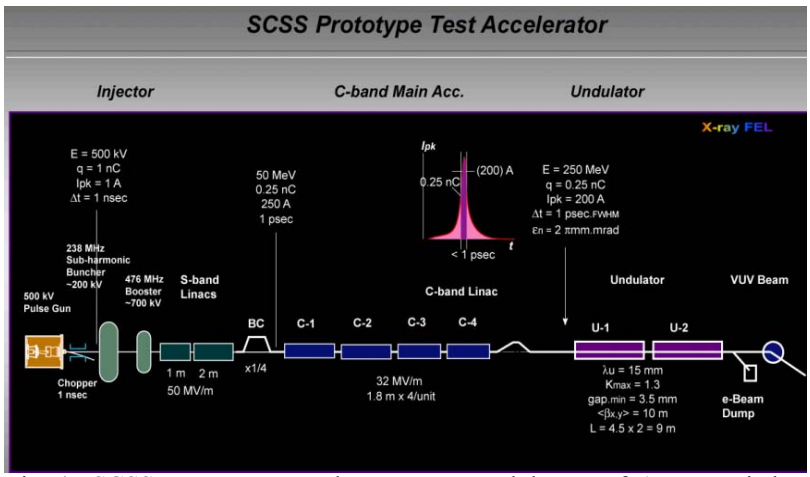

Fig. 4: SCSS prototype accelerator, two undulators of 15 mm pitch, 250 MeV e-beam, generates VUV-radiation.

(2) There is no highly nonlinear optics, which mix particle in radial direction, resulting in non laminar flow.

(3) There is no over-bunching process, which mixes and overlaps two or more slice components from different z-positions.

To satisfy above condition, we designed the injector system based on "adiabatic compression" scheme: the gun with beam chopper generate 1 A x 1 nsec x 500 kV beam, then velocity modulation by 238 MHz sub-harmonic buncher cavity, followed by velocity bunching along a drift section, then the space charge effect becomes severe as raising peak current, then 476 MHz booster cavity accelerates beam energy to 1 MeV, relativistic effect lowers the space charge effect, followed by velocity bunching, and inject into the S-band standing wave accelerator, and capture single bunch.

In order to test this challenging scheme, and check all hardware components developed in our R&D [4], we constructed prototype accelerator in 2004-2005 as shown in Fig. 2. Beam line layout is shown in Fig. 4. We use four C-band accelerating structures, 1.8 m long each, energy gain 32 MV/m maximum. With maximum beam energy of 250 MeV, the shortest wavelength of VUV-radiation at 50 nm can be obtained.

EMITTANCE MEASUREMENT

At the injector end, the velocity bunching and chicane bunch compression complete, where the beam energy reaches to 50 MeV, bunch charge is 0.25 nC and the bunch length is 1 psec or less, which depending on operation condition, specifically phase & amplitude tuning of 238 MHz and 476 MHz cavities.

We measured projected emittance right before the C-band accelerators, using Q-scan method. By reversing polarity of one of the Q-magnets to provided strong focusing in X- and Y-direction, and measured the minimum beam width. By varying focusing power, the beam width response was measured as Fig. 5 and 6. We found the normalized projected emittance of around 3 π.mm.mrad for both X- and Y-directions. The slice emittance was also measured at 50 MeV beam dump, it was 2 π.mm.mrad, where the measurement was limited by spatial available resolution of profile monitor.

We repeated many measurements in this kind, always observed emittance around 3~4 π.mm.mrad. This experimental data indicates that the velocity bunching in our system does not largely deteriorate the projected emittance for compression ratio exceeding 100 times. For more detail, refer the report by H. Tanaka [6].

FIRST LASING EVENT

Two in-vacuum undulators were installed, whose undulator period is 15 mm, minimum gap is 3.5 mm, nominal K value is 1.3 and one undulator length is 4.5 m. In the beam tuning, we firstly opened the gap to 20 mm and passed the e-beam through gap and transported into the beam dump. We tuned the beam optics upstream of the undulator. We setup the optics, in coming beta-matching and focusing Q-magnet in between two undulators.

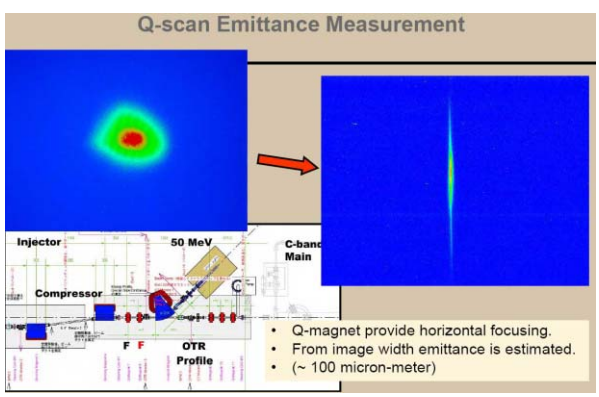

Fig. 5: Beam profile during Q-san emittance measurement. Transition radiation from Au coating of optical mirror was monitored by CCD camera.

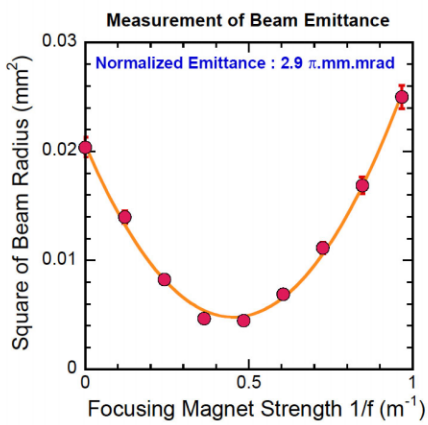

Fig. 6: Beam width as a function of focusing power. At beam energy 50 MeV, charge 0.25 nC, length < 1 psec.

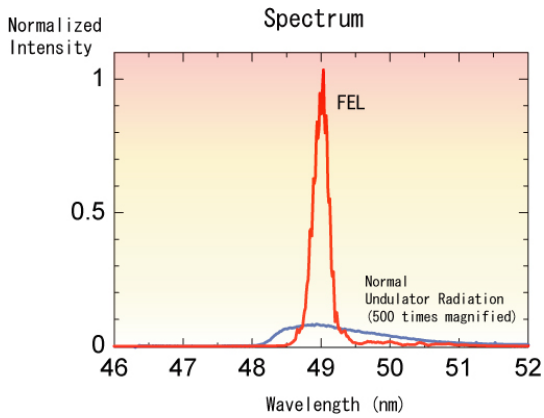

Fig. 7: Radiation spectrum at the lasing condition, 0.25 nC per bunch and 250 MeV. Peak at 49 nm is the coherently amplified signal (6000 times) from the spontaneous undulator radiation (blue line).

On 15th June evening, we firstly closed the gap in the upstream undulator, and measured radiation spectrum, where the spectrum width was already quite narrow, peaked at 49 nm, and totally different from the natural spontaneous radiation, as shown in Fig. 7. The spectrum width is around 1% FWHM, which is much narrower than the spontaneous undulator radiation, while it is dominated by e-beam energy fluctuation, at moment.

As shown in Fig. 8, when we varied the bunch charge, the lasing power drastically changed. This threshold phenomenon indicates high FEL gain. The power has not yet reached the saturation.

By varying K-value of undulator, response of the power gain was measured. Comparing to numerical simulation we determined the electron beam brightness as 270 ~ 310 $A/(\pi.mm.mrad)^2$ in the undulator.

FROM TEST ACCELERATOR TO XFEL

To obtain enough FEL-gain at 1 Å, we need ten times higher brightness than the test accelerator case, i.e., 3 kA at 1 π.mm.mrad. This will be easily obtained by the second stage bunch compressor at high energy (designed compression factor is x 8, at 1.8 GeV).

On the other hand, about the X-ray energy, we need improvement. The lasing pulse energy in the test accelerator is 1 micro-J/pulse average, which is about ten times lower than theoretically predicted value for 0.25 nC charge. This is partly due to the fact that the second undulator field is not perfectly matched with requirement, and may be also due to non-uniform charge distribution in electron bunch [6]. While we do not have enough data to determine amount of charge contributed to lasing, it may be 10% or less.

In XFEL machine, to raise fraction of charge for lasing and increase total charge, we improve injector design as follows.

(1) Run the electron gun at 2 A beam current (twice higher than test accelerator case). The cathode and gun handle this beam without loosing cathode lifetime and breaking emittance.

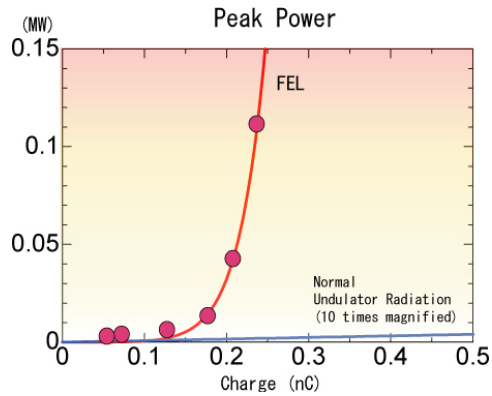

Fig. 8: Peak output power v.s. bunch charge. Using photo diode, peak height was detected from averaged pulses.

(2) Use L-band accelerator instead of S-band at the buncher cavity, which makes beam acceptance 8-times larger. In the test accelerator, acceptance is limited upstream end of the S-band standing-wave buncher. Lowering frequency twice, all structure dimensions will scale twice larger, resulting in larger acceptance in x, y, z-directions.

(3) Flat-topping cavities will be used in the injector. Since we use rf-field to compress bunch, the non-linear curve associated with cosine-function creates non-uniform charge distribution after bunching. Applying higher harmonic cavity, we can obtain a linear response function. This technique is well known as "flat-topping cavity" in traditional cyclotrons.

With this improvement, we will be able to generate bunch to drive FEL with 1 nC charge, with emittance 1 π.mm.mrad and with uniform charge distribution.

CONCLUSION & SCHEDULE

We measured the e-beam emittance and observed first lasing in the SCSS prototype accelerator. From this experiment, superior performance of the thermionic gun and injector system has been demonstrated.

Analysing the experimental data carefully, we refine hardware design, and start XFEL construction this year.

REFERENCES

[1] T. Shintake *et al.*, "SPring-8 Compact SASE Source", SPIE2001, San Diego, USA, June 2001.
[2] http://www-xfel.spring8.or.jp
[3] http://www.feibeamtech.com
[4] K. Togawa *et al.*, "Emittance Measurerment on the CeB6 Electron Gun for the SPring-8 Compact SASE Source", FEL2004, Trieste Italy, August 2004.
[5] T. Shintake, Status of SCSS Project, 3rd Asian Particle Accelerator Conference, APAC2004, Gyeongju, Korea, March 2004.
[6] H. Tanaka *et al.*, "Low Emittance Injector at SCSS", FEL2006 conference, Berlin, August, 2006.

COHERENT HARMONIC GENERATION EXPERIMENT ON UVSOR-II STORAGE RING

M. Labat, CEA, Saclay, France
G. Lambert, CEA, Saclay, France, RIKEN SPring-8 Harima, Hyogo, Japan
M.E. Couprie, Synchrotron Soleil, Saint-Aubin, France
D. Nutarelli, LAC, Orsay, France
M. Hosaka, A. Mochihashi, J. Yamazaki, M. Shimada, M. Katoh, IMS, Okazaki, Japan
Y. Takashima, Nagoya University, Nagoya, Japan
T. Hara, RIKEN SPring-8 Harima, Hyogo, Japan.

Abstract

In the Coherent Harmonic Generation Free Electron Laser configuration, an external seed signal, a commercial laser source, is focused inside the first undulator. The interaction between the electron beam and this seed leads to a more coherent light emission. Such devices are very promising for short wavelength operation with a rather compact facility. Experiments have been performed on the UVSOR-II Storage Ring (Okazaki, Japan) with electrons stored at 600 MeV, and using a 2.5 mJ Ti:Sa laser at 800 nm wavelength, 1 kHz repetition rate, and 150 fs up to 2 ps pulse duration, allowing emission at 266 nm. This third harmonic has been characterised versus various parameters. Optimizations have been realized on the electron beam and laser synchronisation. The dependency of the harmonic signal on the gain (undulator gap, magnetic functions) has also been studied. Theory is compared to experiment using analytical model. These encouraging results make UVSOR-II storage ring an active test facility for Coherent Harmonic Generation scheme, as well as a potential VUV source for users experiments.

INTRODUCTION

Recent Free Electron Lasers aim at reducing the radiated wavelength to the X-ray domain, the time duration to the femto-second domain, and at improving the coherence of the source. FELs based on linear accelerators are mainly experimenting SASE [1], HGHG, and seeded configurations. Coherent Harmonic Generation (CHG) is a seeded FEL configuration based on storage ring [2, 3]. The seed can be either the own spontaneous emission of the electrons as demonstrated on DUKE [4] and ELETTRA [5] storage rings, or an external source [6] such as a commercial laser. This paper presents the successful generation of the third coherent harmonic of a Ti:Sa laser in USOR-II.

In the Coherent Harmonic Generation configuration, the laser is focused in the modulator [7], and synchronized with the circulating electron bunch. The electron beam is micro bunched at fundamental and sub harmonic wavelengths of the seeded laser. The light emission of the electrons is then enhanced in the radiator at the third harmonic of the seed, i.e. 266 nm. Figure 1 presents the general scheme of the experiment.

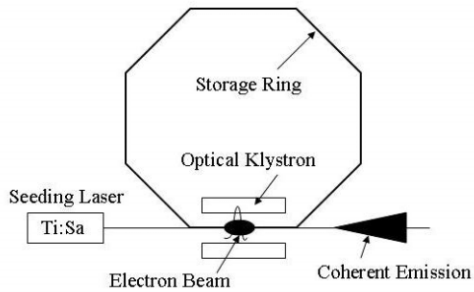

Figure 1: Coherent Harmonic Generation scheme on a storage ring

The seeding laser used for the CHG experiment was initially optimized for Slicing and Coherent Synchrotron Radiation experiments (CSR) [8], requiring high repetition rate (1 kHz) and short pulse duration (150 fs), and therefore not perfectly adapted for generation of the third harmonic. UVSOR-II facility can now provide coherent, short duration and intense light in the far infra red (using CSR) and in the VUV range (using CHG) simultaneously, using one single high power laser. Figure 2 illustrates a burst of CSR emission observed in CHG operation.

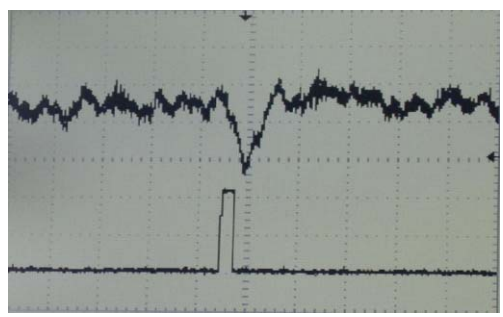

Figure 2: Oscilloscope trace of CSR signal detected by a bolometer observed in CHG operation.

Throught out this paper, an analytical model for CHG will be reminded, followed by a description of the components of the experiment. The first results and optimisation on the third harmonic are finally presented.

ANALYTICAL MODEL FOR CHG

In 1982, R. Coïsson and F. De Martini [9] proposed an analytical model to describe the Coherent Harmonic Generation process in an optical klystron. The intensity of the light emitted by a relativistic electron bunch in an optical klystron can be expressed as the sum of an incoherent and a coherent term. The coherent term equals zero for randomly distributed electronic phases. In the case of CHG process, and assuming that the energy modulation only occurs in the first undulator, the interaction between the electric field E_L and the electrons induces an additional energy spread given by:

$$\Delta\gamma = \frac{eKNE_L\lambda_0}{2\gamma^2 mc^2}(J_0(\xi) - J_1(\xi)), \quad (1)$$

where J are Bessel functions, depending of $\xi = \frac{K^2}{4(1+K^2/2)}$. K is the undulator deflexion parameter, λ_0 the spatial period, N the number of periods, c the velocity of light, e the electrons charge, m their mass, and γ their normalized energy. This energy spread results into an additional phase difference at the exit of the dispersive section, equal at its maximum to: $\Delta\alpha = 4\pi(N + N_d)\Delta\gamma$. N_d is the number of equivalent periods of the dispersive section. The intensity of the coherent emission no longer averages to zero, and is given by the following expression:

$$\frac{\delta W_{coh}}{\delta w \delta\Omega} = \frac{n^2e^2N_e^2f_n^2J_n^2(n\Delta\alpha)}{16\pi\epsilon_0 c\lambda_L^2}(\frac{KN\lambda_0}{\gamma})^2A_n^2. \quad (2)$$

n is the harmonic number, N_e the number of electrons in the bunch, f_n the modulation rate, λ_L the seeded laser wavelength, and:

$$A_n = 1/2(J_{n+1}(n\xi) - J_{n-1}(n\xi)). \quad (3)$$

The intensity of the incoherent emission is given by:

$$\frac{\delta W_{incoh}}{\delta w \delta\Omega} = \frac{n^2e^2N_e}{16\pi\epsilon_0 c\lambda_L^2}(1 + f_n)(\frac{KN\lambda_0}{\gamma})^2A_n^2. \quad (4)$$

This model, already used for ACO [2] and Super-ACO [3] storage rings configurations, allows apprehending Coherent Harmonic Generation process and its dependency to electron beam and seeded laser parameters. In addition, calculations performed before the experimental sessions provided with reasonable expectations on the generation of the third coherent harmonic with UVSOR-II storage ring, and its laser parameters.

CHARACTERISTICS OF THE EXPERIMENTAL COMPONENTS

Electron Beam

For CHG experiment, UVSOR-II [10] facility (see Figure 3) was used in single bunch mode. The characteristics of the electron beam delivered are given in Table 1. Experiments have been performed with beam current up to 40 mA, since no beam instability occurs below this value. The modulator and radiator of UVSOR-II's optical klystron [11] are identical and made up of 9 periods of 11 cm, separated by a 33 cm long dispersive section.

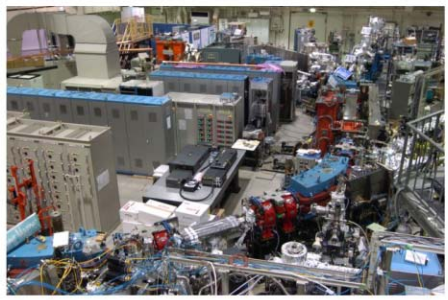

Figure 3: UVSOR-II storage ring

Table 1: Characteristics of the electron beam on UVSOR-II Storage Ring for CHG operation.

Parameter (Unit)	Symbol	Value
Energy (MeV)	E	600
Circumference of the Ring (m)	C	53.2
Cavity voltage (kV)	V_{RF}	100
RF Frequency (MHz)	f_{RF}	90.1
Harmonic number	n_H	16
Number of bunches stored	n_b	1
Period of revolution (ns)	T_0	178
Momentum compaction	α	0.028
Synchrotron frequency (kHz)	f_S	19.4
Current (mA)	I	0 - 40
Natural Energy spread	σ_γ	0.00034

Beam diagnostics

Four different diagnostics have been used to characterize the output radiation of the radiator (which includes electron beam radiations, and IR laser), and therefore the coherent emission. For spectral selection, the light is sent to an interferometric filter (CVI-F25-265), centered at 266 nm with 25 nm bandwidth. The detection of the UV light is then performed using a solar blind PhotoMultiplier (PM, Hamamatsu, R759). In order to observe the coherent emission at 1 kHz, among incoherent emission at 5.6 MHz, the PM signal is observed on an oscilloscope, triggered by the laser timing system. A streak camera (Hamamatsu, C5680) has also been used. It allows to follow the longitudinal distribution of the electron bunch, and to measure relative position in the time domain between laser pulse and electron bunch. The light was spectrally characterised using a spectrometer for spontaneous emission, and a monochromator followed by the photomultiplier for the coherent emission.

Seeding Laser

The characteristics of the seeding laser system used are given in Table 2. This system includes a mode-locked titanium-sapphire (Ti:Sa) laser oscillator (Coherent, Mira 900-F) and a regenerative amplifier (Coherent, Legend HE) driven by a Q switched pump laser, which delivers high intense femto-second pulses. Those elements are shown in Figure 4.

Table 2: Seeded Laser characteristics

Parameter	Value	Unit
Wavelength	800	nm
Spectral width	12	nm
Repetition rate	1	kHz
Pulse duration (Δt)	0.15 to 2	ps
Average Power (P_L)	1.8	W
Diameter	11.5	mm
Gaussian quality factor	1.25	
Polarization	Horizontal	

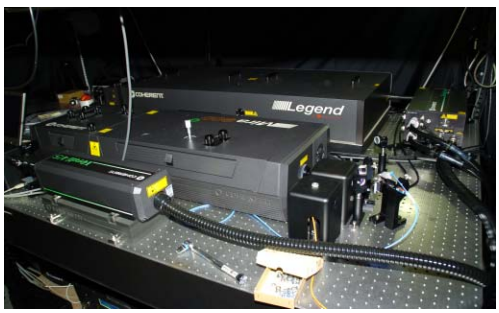

Figure 4: Photograph of the laser system used for CHG experiment.

Synchronisation

The overlap in the modulator for the micro bunching of the electronic distribution, requires a precise synchronisation of the laser pulse and the electron bunch, and therefore a specific timing system for UVSOR-II facility [12] organized as following. The mode-locked Ti:Sa laser is synchronised with the RF signal (f_{RF}) of the storage ring. In addition, the repetition frequency f_Q of the Q switched laser is based on the sub-harmonics of the revolution frequency of the bunches f_{rev}=f_{RF}/n_H=5.6 MHz, leading to f_Q=f_{rev}/5632=1kHz. To select and fix the electron bunch with the laser pulse cuts, an RF bucket selector is used for making the Q switching trigger signal. The timing of the laser pulse within the bunch spacing time is adjusted using a phase shifter modifying the phase of the RF signal. The condition of synchronisation is observed using in first stage a photodiode, receiving both laser pulses and synchrotron radiation (SR). More accurate tuning is further performed using the streak camera, which temporal resolution reaches 10 ps.

Alignment

Spatial overlap is an other key step in Coherent Harmonic Generation. An accurate alignment of the IR laser on the electrons trajectory has to be performed in the modulator. The electronic orbit of the FEL oscillator at 800 nm has been selected for this trajectory. Auto collimation was then used to mark the seeded laser path from the laser hutch through out the FEL cavity. Three periscopes made of two flat mirrors at 45^o incidence allowed the transport of the IR and a 5 m long focal lens its focusing inside the modulator. This allows to optimize the overlapping with the e-beam and to increase the local energy. Both beams have horizontal polarization. Figure 5 illustrates the experimental setup for transport and alignment of the seeding laser.

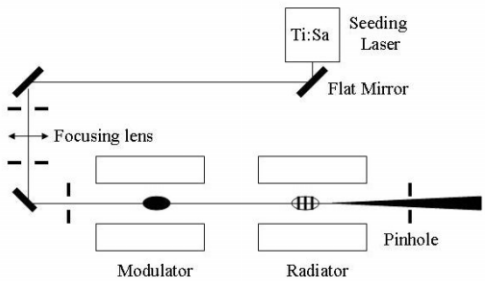

Figure 5: Setup of the laser transport to the FEL cavity.

OBSERVATION OF THE THIRD COHERENT HARMONIC

A picture of the oscilloscope screen is presented in Figure 6, illustrating the output radiation of the undulators. Central peak corresponds to the radiation of the laser heated electron bunch. The intensity at 266 nm is dramatically enhanced thanks to the coherent emission at the third harmonic of the seeding laser.

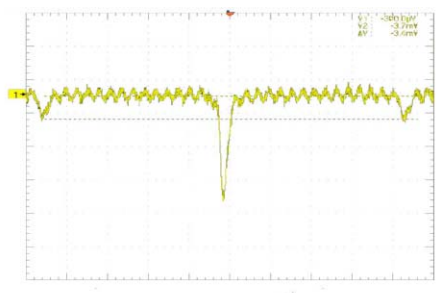

Figure 6: Oscilloscope trace of of the optical klystron out put radiation. Central peak corresponds to the laser heated bunch emission, and edged peaks to unheated bunch emission. P_L=1.78 W, Δt= 1.12 ps, I=4.29mA. Time scale: 40 ns/division.

Figure 7 shows the streak camera image of CHG signal. This diagnostic confirms the enhancement of the intensity at 266 nm radiated by the heated electron bunches (see

bright blue spots). In addition, the vertical axis of the image allows to evaluate the duration of the heated bunch radiation: it is much shorter than unheated one's, and measurment of the pulse duration is limited by the streak camera resolution. The temporal coherence achieved with Coherent Harmonic Generation allows to expect pulse durations below 2 ps.

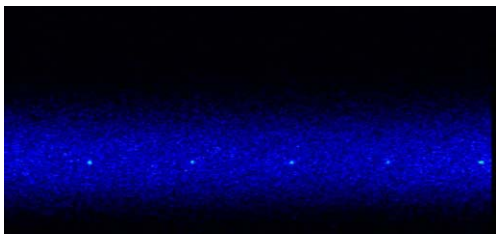

Figure 7: Photograph of the streak camera image. The bright spots correspond to laser heated bunch emission (coherent emission). Full scales are 85 ms for the horizontal and 700 ps for the vertical axis.

Once the Coherent Harmonic Generation systematic and reproducible, the harmonic radiation was studied as a function of various parameters.

According to the analytical model previously mentioned, the number of coherent photons produced is proportional to the square of the number of electrons heated by the laser, linearly related to the peak current, assuming that the electron bunch duration is much wider than the laser pulse duration (by two orders of magnitude). First results seem to confirm the expected quadratic behaviour.

The third harmonic has then been studied versus synchronisation. Using a 3 mA beam current, the laser pulse position in time was shifted back and forth by 200 ps from its initial position: where maximum UV intensity is recorded. Coherent emission could be detected over 360 ps, with total disapearing for delays longer than 200 ps, giving an rms width of 70 ps. This result is in good agreement with the rms bunch length measured at this current: 85 ps. Indeed, since the coherent emission is linked to the electronic density, maximum emission is obtained when the seeding laser heats the centre of the bunch, and a scan with the laser pulse in the time domain gives back the longitudinal distribution of the bunch.

The undulator gap has also been studied as a varying parameter. CHG process is based on the amplification by the radiator of the sub harmonics of the seeding laser wavelength. To be properly amplified, this sub harmonic wavelength must correspond to a resonant wavelength of the optical klystron, defined by the undulator parameter K, and therefore by its gap. Consequently, a detuning of this parameter might kill the radiation at 266 nm. Indeed, CHG emission is maximum for an undulator gap of 40.8 mm and the signal vanishes for gaps of 39.7 and 42.5 mm.

CONCLUSION

Using a 1 kHz Ti:Sa laser, a Coherent Harmonic Generation FEL configuration has been successfully set up at UVSOR-II facility. Short (below 2 ps), UV (266 nm), coherent laser pulses are delivered. In addition, both CHG and CSR can be operated in parallel, using the same laser system and experimental setup: an important step in the development of the fourth generation light sources.

More Coherent Harmonic Generation experiments on UVSOR-II are to be performed in order to study the influence of the seeding laser characteristics: energy, diameter, pulse duration, as well as shaping inside the modulator. Observation of the fifth harmonic is also foreseen.

ACKNOWLEDGMENTS

We would like to thank all the UVSOR-II staff for its help during experimental sessions. This work was supported by International Collaboration program of IMS.

REFERENCES

[1] F. Ciocci et al., IEEE Jour. Quant. Elec. 31 (1995) 1242.

[2] R. Prazeres, J.M. Ortega, C. Bazin, M. Bergher, M. Billardon, M.E. Couprie, M. Velgue and Y. Petroff, Nucl. Inst. Meth. A 272 (1988) 68-72.

[3] R. Prazeres, P. Guyot-Sionnest, J. M. Ortega, D. Jaroszynski, M. Billardon, M. E. Couprie, M. Velghe and Y. Petroff, Nucl. Inst. Meth. A 304 (1991) 72-76.

[4] V. Litvinenko, Nucl. Inst. Meth. A 507, 265 (2003).

[5] G. De Ninno, M. B. Danailov, B. Diviacco, M. Ferianis and M. Trovo, FEL'04, August 2004, p. 237-240.

[6] P.L. Csonka, Part.accele. 8, 225 (1978).

[7] N.A. Vinokurov and A.N. Skrinsky, Preprint 77-59, Nuclear Physics Institute of Novossibirsk (1977).

[8] M. Katoh, M. Hosaka, S. Kimura, A. Mochihashi, M. Shimada, T. Takahashi, Y. Takashima and T. Hara, to be published in the Proceedings of EPAC'06, THPLS041.

[9] R. Coïsson, F. De Martini, Phys. of Quant. Electron., 9, p. 939, Addison-Wesley (1982).

[10] M. Katoh, M. Hosaka, A. Mochihashi, J. Yamazaki, K. Hayashi,Y. Hori,T. Honda, K. Haga, Y. Takashima, T. Koseki, S. Koda, H. Kitamura, T. Hara, T. Tanaka, AIP'04, 2004, (708) p. 49-52.

[11] H. Hama, K. Kimura, M. Hosaka, J. Yamazaki and T. Kinishita, Nucl. Instr. and Meth. A393 (1997) 23.

[12] A. Mochihashi, M. Hosaka, M. Katoh and Y. Takashima, UVSOR ACTIVITY REPORT 2005 (2006).

GENERATION REGIMES OF FEL WITH VOLUME DISTRIBUTED FEEDBACK*

K. Batrakov†, S. Sytova‡, INP BSU, Minsk, Belarus.

Abstract

This paper discusses different generation regimes of Volume Free Electron Lasers (VFELs) which utilize Volume distributed feedback (VDFB). Dependence of VFEL operation on VDFB parameters is studied.

INTRODUCTION

VDFB significantly extends operation possibilities of Free Electron Lasers (FELs). It was shown in [1] that properly parameters choice of VDFB geometry lowered down the threshold current magnitude of generation. VDFB can solve the problem of mode discrimination at great electromagnetic power generation in oversized systems. The beam cross section in such systems significantly exceeds wavelength. Large sizes of electron beam cross section allow to distribute power and to lower local load of system elements. However, standard oversized system suffers from excitation of great number of parasitic undesired modes. As a result, the destructive interference takes place, the coherence of radiation degrades and the generation efficiency significantly reduces. So, analysis of electron beam dynamics dependence on VDFB parameters is of great importance. Partly, threshold parameters of electron beam instability in VFEL can be investigated by using linear theory. For example, the first threshold point j_1 corresponds to beginning of the electron beam instability. At this point the first radiating mode appears. Instability stage corresponding to regenerative amplification is in the range of parameters $j_1 < j < j_2$ when generating mode is already appeared, but the radiation gain of this mode is less than radiation losses of the coupled feedback mode. Such system can amplify incident wave. Parameters at which radiation gain becomes equal to absorption correspond to the second threshold point. When magnitude of beam current exceeds the second threshold value, generation process occurs without incident wave. For current density j in the range $j_2 < j < j_3$ the beam instability in short period of time changes into the stationary nonlinear saturation regime. If current exceeds the third threshold value $j > j_3$, the nonlinear stage becomes non-stationary. The threshold currents mentioned above depend on parameters of VDFB. So, variation of VDFB can change the type of generation. For providing VFEL experiments and their interpretation it is necessary to have theoretical description and numerical simulation of effects considered. Here some such theoretical results are presented.

* Work supported by Belarus Foundation for Fundamental Research, Grant F06R-101.

† batrakov@inp.minsk.by ‡ sytova@inp.minsk.by

ENERGY TRANSFER IN VDFB SYSTEMS

Let's study energy exchange between electron beam and radiation in the system with VDFB. Electromagnetic field in this case can be expressed as

$$\mathbf{E} = \sum_{\alpha} a_\alpha \exp\{i\mathbf{k}_\alpha \mathbf{r} - i\omega t\}\{\mathbf{e} + .. + \mathbf{e}_i s_i \exp[i\tau_i \mathbf{r}] + ..\}, \quad (1)$$

where τ_i are the set of reciprocal vectors, $\mathbf{e}_i$ are unit polarization vectors, s_i are coupling coefficients between waves, a_α are mode amplitudes which are determined from initial and boundary conditions. Using the equation of electron motion in the electromagnetic field and averaging over initial electron phases the following expression for mean electron energy can be obtained

$$\Delta\gamma = -\frac{e^2(\mathbf{ue})^2}{2m^2u^3c^2\gamma}\left(\frac{k^2}{\omega} - \frac{\mathbf{ku}}{c^2}\right)L_*^3 F, \quad (2)$$

where L_* is the length of interaction region,

$$F = \mathrm{Im}\left[\sum_{\alpha\beta} a_\alpha a_\beta^* \left(\frac{\exp\{i(\nu_\beta - \nu_\alpha)\} - 1}{(\nu_\beta - \nu_\alpha)\nu_\beta^2} + \frac{\exp[-i\nu_\alpha] - 1}{\nu_\alpha \nu_\beta^2} + \frac{\exp[-i\nu_\alpha](i\nu_\alpha + 1) - 1}{i\nu_\alpha^2 \nu_\beta}\right)\right],$$

$\nu_i = (\omega - \mathbf{k}_i\mathbf{u})L_*/u$ are parameters of detuning from synchronism.

Control of Emission Line Shape by VDFB

Generally in the case of n-wave VDFB the energy transfer (2) between electron and electromagnetic field depends on n detuning parameters. This gives additional possibilities to regulate the shape of emission line in comparison with one-wave synchronism case.

Shapes of one-wave and different two-wave synchronism lines is illustrated in Fig. 1. It is seen that corresponding selection of parameter $a = \nu_1 - \nu_2$ increases the width of amplification region by two times (compare the curves "one-wave" and "a=7"). Due to this fact, electron beam will be synchronous with electromagnetic wave for a longer time. So, more energy is transferred to electromagnetic wave that raises the laser efficiency. On the other hand emission line can be narrowed by properly choice of detuning parameters.

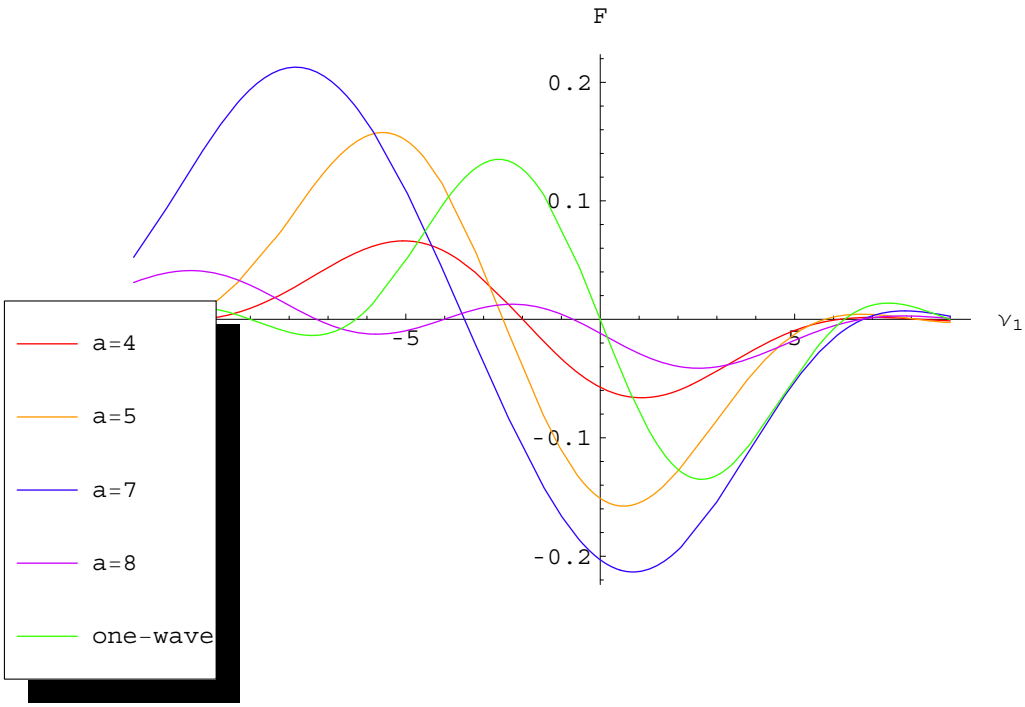

Figure 1: Emission line dependence on the relation between detuning parameters $a = \nu_1 - \nu_2$ for one and two-wave synchronism.

REGENERATIVE AMPLIFICATION (LINEAR STAGE)

Eigenmodes for two-wave VDFB are obtained from the dispersion equation [1]

$$(\omega - \mathbf{ku})^2 \left\{ \left(k^2c^2 - \omega^2\varepsilon_0\right)\left(k_\tau^2c^2 - \omega^2\varepsilon_0\right) - \omega^4 r \right\} = -\frac{\omega_L^2 (\mathbf{ue})^2}{\gamma}\left(k^2c^2 - \omega^2\right)\left(k_\tau^2c^2 - \omega^2\varepsilon_0\right). \quad (3)$$

Here $\mathbf{k}_\tau = \mathbf{k} + \tau$, $\varepsilon_0 = 1 + \chi_0$, $r = \chi_\tau\chi_{-\tau}$, χ_0 and χ_τ are polarizabilities of periodical structure with VDFB which appear in the expansion of permeability:

$$\varepsilon(r,\omega) = 1 + \sum_\tau \chi_\tau \exp\{-i\tau\mathbf{r}\}. \quad (4)$$

Representing solutions of (3) as $\mathbf{k} = \mathbf{k}_0 + \mathbf{n}\delta\omega/c$, where $\mathbf{k}_0$ satisfies to the condition $\omega - \mathbf{k}_0\mathbf{u} = 0$ the following boundary conditions for mode amplitudes a_i can be written:

$$\begin{aligned} \sum_i a_i &= a, \quad \sum_i s_i a_i \exp\{ik\delta_i L\} = b, \\ \sum_i \frac{a_i}{\delta_i} &= 0, \quad \sum_i \frac{a_i}{\delta_i^2} = 0. \end{aligned} \quad (5)$$

The first and the second equalities in (5) correspond to the continuity of electromagnetic field at the input ($z = 0$) and the output ($z = L$) of VDFB structure, a and b are amplitudes of incident waves. The third and the fourth equations correspond to the density and current density continuity of unperturbed at the input electron beam. Solving system (5) one can obtain the following expression for intensity of output electromagnetic waves:

$$\begin{aligned} \frac{I}{I_0} &= \frac{\gamma_0 |\mathbf{E}_0|^2 + \gamma_1 |\mathbf{E}_\tau|^2}{\gamma_0 |a|^2 + \gamma_1 |b|^2} = \\ &= \left(\frac{\gamma_0 c}{\mathbf{nu}}\right)^3 \frac{16\pi^2 n^2}{-\beta (k\chi_\tau L_*)^2 (\Gamma_{th} - \Gamma)}, \end{aligned} \quad (6)$$

where

$$\Gamma_{th} = \frac{\left(\frac{\gamma_0 c}{\mathbf{nu}}\right)^3 16\pi^2 n^2}{-\beta (k\chi_\tau L_*)^2 kL_*} + \mathrm{Im}\chi_0 \left(1 - \beta \pm \frac{\mathrm{Im}r}{\chi_\tau \mathrm{Im}\chi_0}\right)$$

$$\Gamma = \frac{\pi^2 n^2}{4\gamma}\left(\frac{\omega_L}{\omega}\right)^2 k^2 L_*^2 \left(\chi_0 \pm \sqrt{-\beta}\,|\chi_\tau| - \gamma^{-2}\right) \cdot$$

$$\cdot \left(\chi_0 \pm \sqrt{-\beta}\,|\chi_\tau|\right) f(y),$$

$$f(y) = \sin y \frac{(2y + \pi n)\sin y - y(y + \pi n)\cos y}{y^3 (y + \pi n)^3}.$$

$I_0 = \gamma_0 |\mathbf{E}_0|^2 + \gamma_1 |\mathbf{E}_\tau|^2$ is the intensity of incident waves. $y = \nu_1/2$, β is diffraction asymmetry factor, γ_0 and γ_1 are diffraction cosines. Expression (6) is derived in the low gain approximation.

It follows from (6) that $I/I_0 > 1$ when $\Gamma > \mathrm{Im}\chi_0 \left(1 - \beta \pm \mathrm{Im}r/\left(\chi_\tau Im\chi_0\right)\right)$ ($j > j_1$ is the first threshold point) and the amplification process starts. Fig. 2

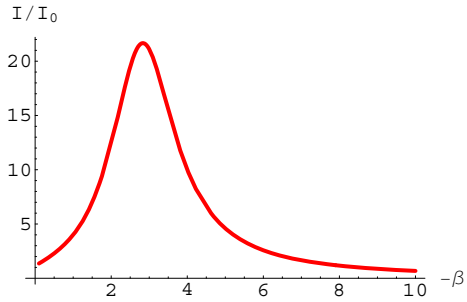

Figure 2: Dependence of regenerative amplification coefficient on asymmetry factor β of VDFB.

demonstrates amplification dependence on VDFB geometry factor β. So, VDFB can control amplification process. When current reaches some critical value $j > j_2$ the oscillation regime develops. Dependence of the second threshold current on VDFB asymmetry is illustrated in Fig. 3. It is seen that VDFB allows to control the second thresh-

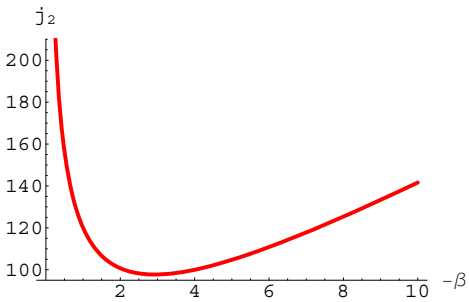

Figure 3: Dependence of the second threshold current j_2 on asymmetry factor β of VDFB.

old current too. Regenerative amplification ($j_1 < j < j_2$) is stationary and can occur in linear or nonlinear regime depending on magnitudes of I (nonlinear regime will be discussed bellow). In contrary, oscillation regime has the non-stationary character and the linear stage rapidly transfers to the nonlinear one. To study nonlinear regime the numerical simulation of VFELs must be carried out.

NUMERICAL SIMULATION OF THE SYSTEM WITH VDFB

For n-wave VDFB from Maxwell equations in the approximation of slow varied amplitudes the system of n equations for n strong coupled waves can be obtained Here we restrict ourselves by considering three-wave VDFB. The system for n-wave VDFB can be written by evident generalization. So, using the field representation in the form $\mathbf{E} = \sum_{\tau_i} \mathbf{e}_i E_i \exp\{i\mathbf{k}_{\tau_i}\mathbf{r} - \omega t\}$, $i = 0, 1, 2$ we obtain the following nonlinear equations:

$$\frac{\partial E_0}{\partial(\omega t)} + \gamma_0 \frac{\partial E_0}{\partial(kz)} + \tfrac{1}{2} l E_0 - \tfrac{1}{2}\chi_1 E_1 - \tfrac{1}{2}\chi_2 E_2$$

$$= 2\pi j \Phi/\omega \int_0^{2\pi} \tfrac{2\pi - p}{8\pi^2} \left(\exp(-i\Theta(t,z,p)) + \right.$$

$$\left. \exp(-i\Theta(t,z,-p))\right) dp,$$

$$\frac{\partial E_1}{\partial(\omega t)} + \gamma_1 \frac{\partial E_1}{\partial(kz)} - \tfrac{1}{2}\chi_{-1} E_0 + \tfrac{1}{2} l_1 E_1 - \qquad (7)$$

$$\tfrac{1}{2}\chi_{2-1} E_2 = 0,$$

$$\frac{\partial E_2}{\partial(\omega t)} + \gamma_2 \frac{\partial E_2}{\partial(kz)} - \tfrac{1}{2}\chi_{-2} E_0 - \tfrac{1}{2}\chi_{1-2} E_1$$

$$+ \tfrac{1}{2} l_2 E_2 = 0.$$

Here $l_i = \left(k_{\tau_i}^2 c^2 - \omega^2 \varepsilon_0\right)/\omega^2$. $\gamma_0,\ \gamma_1,\ \gamma_2$ are three VDFB cosines.

System (7) must be supplemented with equations for the phase dynamics:

$$\frac{d^2\Theta(t,z,p)}{dz^2} = \frac{e\Phi}{m\gamma^3\omega^2}\left(k_z - \tfrac{d\Theta(t,z,p)}{dz}\right)^3 \cdot$$

$$\cdot \mathrm{Re}\left(E_0 \exp(i\Theta(t,z,p))\right), \qquad (8)$$

$$\frac{d\Theta(t,0,p)}{dz} = k_z - \omega/u, \quad \Theta(t,0,p) = p.$$

In (8) it was proposed that the electron beam is synchronous with the wave $\mathbf{E}_0$ only. The integral form of beam current in the right hand side of (7) is obtained by averaging over the following initial phases of electrons in the beam: entrance time of electron in interaction zone ωt_0 and transverse coordinate of entrance point in interaction zone $\mathbf{k}_\perp \mathbf{r}_\perp$.

Equation (8) depends on these two initial phases only in combination $\mathbf{k}_\perp \mathbf{r}_\perp - \omega t_0$ (that appears in initial condition for phase at $z = 0$). Therefore, in the mean field approximation double integration over two initial phases can be reduced to the single integration. As the result, the averaged current in right hand side of the first equation of (7) differs from expressions frequently used in literature (in which the current is used in the form $\int_0^{2\pi} d\Theta_0 \exp\{-i\Theta\}$).

Regimes of VFEL Generation (Nonlinear Stage)

VFEL dynamics simulated on the basis of the system (7) and (8) is illustrated in Fig. 4 - 7. In the Fig. 4 the regimes of regenerative amplification and stationary generation are presented. It follows from this Fig., that the region of regenerative amplification is rather narrow. This region $j_1 < j < j_2$ is marked by two dotted lines. Therefore, the idea to control amplification by regulating VDFB parameter β (and other VDFB parameters) seems to be very useful. Let's note, that the region of regenerative amplification by corresponding choice of VDFB parameters can be

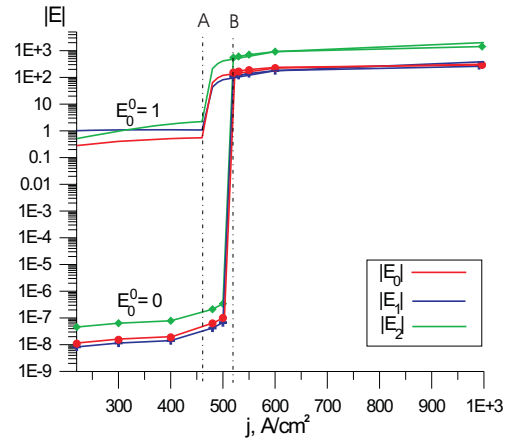

Figure 4: Amplification and oscillation regimes for three-wave VDFB. Vertical dotted lines (A and B) shows positions of the first and the second threshold currents.

increased for three-wave VDFB in comparison with two-wave VDFB ([2]).

When electron beam current increases, generation remains stationary up to the third threshold current j_3. Then at $j > j_3$ non-stationary periodic regime of generation starts. Fig. 5 demonstrates temporal dynamics of generation in this region ($j > j_3$).

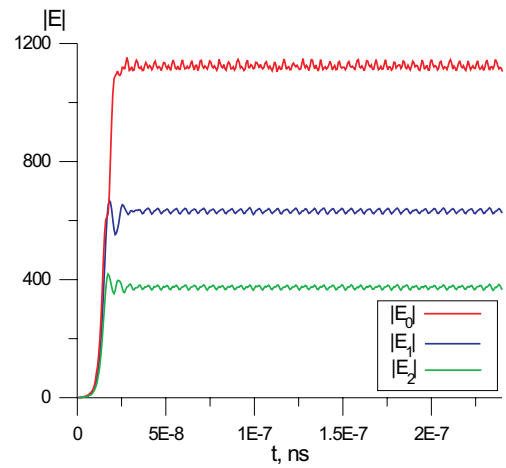

Figure 5: Current exceeds third threshold value ($j > j_3$). Periodic regime of oscillation for three-wave VDFB.

Oscillations appear at discrete number of frequencies at further current increase.

At some current value dynamics becomes chaotic and the regions with continuous frequency spectrum appears (Fig. 6 and Fig. 7).

CONCLUSION

In the paper presented it was shown that VDFB allows to regulate the generation regime. Changing VDFB parameters at given current value can transfer generation process

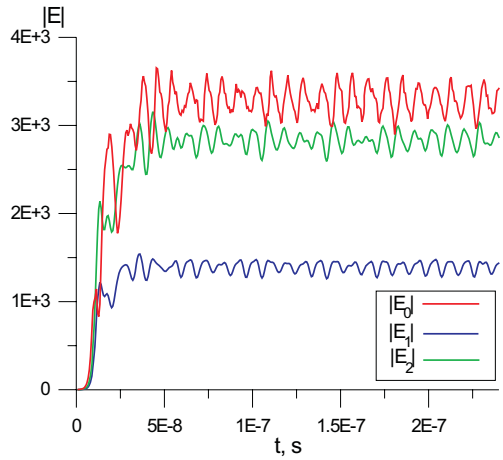

Figure 6: Chaotic oscillation regime.

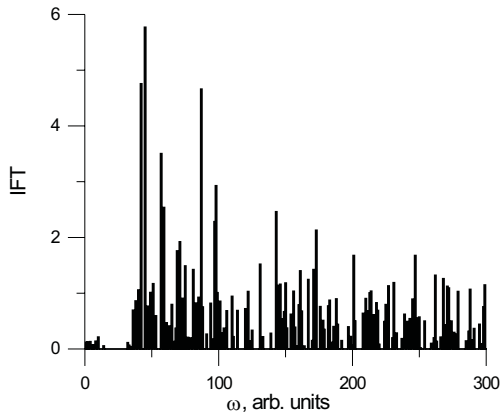

Figure 7: Fourier transform of $\mathbf{E}_0$ corresponding to chaotic generation in Fig. 6 .

between different regimes. In addition n-wave VDFB allows to discriminate parasitic modes at generation of great power in large volume. First experiments with VFEL generation was presented in [3, 4] and the following papers. So, VFEL has great future prospect.

REFERENCES

[1] V. Baryshevsky, K. Batrakov, I. Dubovskaya, J. Phys. D. 24 (1991) 1250.

[2] K. Batrakov, S. Sytova, Nonlinear Phenomena in Complex Systems, 8 (2005) 359.

[3] V. Baryshevsky, K. Batrakov, A. Gurinovich et al., NIM 483A (2002) 21.

[4] V. Baryshevsky, K. Batrakov, N. Belous et al., LANL archive, physics/0409125 (2004), http://arxiv.org/pdf/physics/0409125, 3 p.

EXTRACTING INFORMATION FROM SMITH-PURCELL FEL SIMULATIONS

J.T. Donohue, Centre d'Etudes Nucléaires de Bordeaux-Gradignan, BP 120, 33175 Gradignan, France
J. Gardelle, CEA CESTA, BP 2, F-33114 Le Barp, France

Abstract

Simulations of coherent Smith-Purcell radiation using 2D particle-in-cell codes have provided insight into the nature of the process, and have generally provided support to the viewpoint of the Vanderbilt University FEL group. However, if one is interested in terahertz frequencies, the need for small meshes and short time intervals makes the calculations exceedingly long. In particular, the S-P correlation between frequency and angle is only valid at distances large compared to the grating size, and may not be apparent if the simulation area is too small. With the help of the multipole expansion, we show how simulation data obtained with a small area may be extended to an area of arbitrary size. This enables us to confirm the presence of coherent higher order S-P peaks at the appropriate angles. We also isolate the forward and backward surface Floquet waves. Evidence for the presence of unsuspected components is presented.

INTRODUCTION

In attempting to simulate Smith-Purcell (S-P) radiation at terahertz frequencies with a 2D particle-in-cell code, one is confronted with problems of time and memory, at least if the simulation is performed on a PC. The reasons are easy to understand. Typical wavelengths are hundreds of μm, which means that mesh sizes must be tens of μm. The time step is tied to the mesh size Δ through stability conditions, and is, typically Δ/c, where c denotes the speed of light. Finally, the overall size of the simulation area is determined by the experimental circumstances. For example, the Dartmouth College experiment[1]using a low energy continuous electron beam has a grating about 12.7 mm long, and we perform our simulation in an area of approximately 20 mm $\times$ 5 mm, with Δ = 10 μm. To follow the system through one ns takes about 10 hours of calculation with the commercially available code we use, MAGIC[2]. In contrast the MIT experiment using a 15 MeV pre-bunched beam[3](at 17.1 GHz) had a grating 10 cm long, which means that our simulation area must be considerably larger than for the Dartmouth set-up. However, two ns are all that is needed to get a satisfactory simulation, since the beam is already bunched. At FEL 2005,[4]we reported our first attempts to simulate coherent S-P radiation in these two experiments. While we did find some interesting results, we used an unrealistically large current in the Dartmouth case, which led to copious emission of radiation from the ends of the grating at a frequency less than any allowed S-P frequency. This corresponded to the evanescent surface wave predicted by the theory of Andrews and Brau (AB)[5] but it obscured the true S-P signal that we sought. In the MIT simulation, we found that there remained a substantial emission of radiation even when we removed the grating. Furthermore, although we observed up to 20 harmonics of the bunching frequency, we didn't see the usual S-P relation between wavelength and angle. This is given by $\lambda = L(1/\beta - \cos\phi)/n$, where λ is the wavelength, L the grating period, β the relative velocity (in a plane parallel to the grating and perpendicular to the direction of the grooves), ϕ the angle of emission (with respect to the beam direction), and the integer n denotes the order. While this relation is true, it only holds precisely when the radiation is observed at distances large compared to both the wavelength and the grating size. Given the constraints of small mesh size, it is impractical to simulate in an area large enough to see the wavelength-angle correlation.

Another problem we encountered was the presence on the grating surface of two distinct surface waves. One of these, according to the AB theory, is in resonance with the electron beam, while the other, of the same frequency but propagating in the opposite direction, is generated by reflection at the grating ends. It is of some interest to isolate these two Floquet waves, in order to obtain a direct verification of the AB theory, and to determine the reflection coefficient when such a wave reaches the grating end. This coefficient may be used in a refinement of the AB theory proposed by Andrew, Boulware, Brau and Jarvis[6]in order to estimate the start current needed to produce coherent S-P radiation in the Dartmouth experiment. In reference 6 an estimate of 50 A/m was made, while Kumar and Kwang-Je Kim[7] obtained a slightly smaller value of 36.5 A/m.

In this paper we describe two methods we have developed to address these problems. The first method we call the Small Box→Big Box transformation, since it allows us to simulate in a small area and extrapolate to a much larger area, so as to see the S-P wavelength-angle correlation. While the near-to-far-field transformation is the subject of a chapter of Taflove's monograph[8],our simple method uses Finite Fourier Transforms (FFT) and fitting procedures readily available in such high-level programs as *Mathematica* and MAPLE, and thus involves relatively little effort on the part of the user. The second

method has been developed to extract from a simulation the two oppositely moving Floquet evanescent waves, which are important only in the neighborhood of the grating. Again, the FFT and fitting capacities of *Mathematica* or MAPLE may be used to execute the task.

In Section II we describe the Small Box→Big Box transformation as applied to a MIT simulation. In Section III we show how to separate the Floquet components from a simulation of the Dartmouth set-up. The anomalies observed in our fitting procedure reveal an unsuspected presence of higher temporal harmonics in the field, as well as incipient coherent S-P radiation. Our conclusions are given in Section IV.

SMALL BOX→BIG BOX TRANSFORMATION

In a source-free half-plane region extending to infinity, the magnetic field in the z-direction may be written as

$$B_z(\rho,\phi,t)=\Re\int_0^\infty d\omega e^{-i\omega t}\sum_{m=1}^{\infty}\sin(m\phi)H_m^1\left(\frac{\omega\rho}{c}\right)b_m(\omega),$$

where the standard Hankel functions H_m^1 are used and the complex quantities $b_m(\omega)$ are the coefficients of the multipole field. They may be written as

$$b_m(\omega)=\frac{2}{\pi^2 H_m^1\left(\frac{\omega\rho_0}{c}\right)}\int_{-\infty}^{\infty}dt e^{i\omega t}\int_0^{\pi}d\phi\sin(m\phi)B_z(\rho_0,\phi,t).$$

The azimuthal component of the electric field (cgs units) may then be written as

$$E_\phi(\rho,\phi,t)=-\Re\int_0^\infty d\omega e^{-i\omega t}\sum_{m=1}^{\infty}i\sin(m\phi)H_m^{1\prime}\left(\frac{\omega\rho}{c}\right)b_m(\omega)$$

The total energy/cm radiated across a semicircle of radius ρ is then

$$\frac{dW}{dz}=\left(\frac{c\rho}{4\pi}\right)\int_{-\infty}^{\infty}dtE_\phi(\rho,\phi,t)B_z(\rho,\phi,t)$$

which reduces, after some manipulations involving the Wronskian, to

$$\frac{dW}{dz}=\frac{c^2}{4}\int_0^\infty d\omega\sum_{m=1}^{\infty}\frac{|b_m(\omega)|^2}{\omega},$$

which is independent of the radius.

In the context of our simulation, we calculate $B_z(\rho_0,\phi_k,t_r)$, with $\phi_k=(2k-1)\pi/180,\ 1\le k\le 90$ and $t_r=t_1+(r-1)T/N,\ 1\le r\le N$, where the time step T/N is chosen by MAGIC. Accordingly, we use FFT rather than continuous Fourier transforms, and we perform a FFT at each of the 90 angles, obtaining $\tilde{b}(s,\phi_k)=\mathrm{FFT}(B_z(\rho_0,\phi_k,t_r))$, where $\omega\to 2\pi(s-1)/T$. Then at fixed *s*, we write

$$\tilde{b}(s,\phi_k)=\sum_{m=1}^{85}\tilde{b}_m(s)\sin(m\phi_k)$$

and we apply a fitting procedure to determine the $\tilde{b}_m(s)$ for $1\le m\le 85$. Finally we introduce the normalized multipole coefficients $\hat{b}_m(s)$,

$$\hat{b}_m(s)=\tilde{b}_m(s)/H_m^1(2\pi(s-1)\rho_0/cT).$$

We may now calculate the magnetic field and the azimuthal component of the electric field at any point in the source-free region by taking the Inverse FFT of the sequence of sums

$$B_z(\rho,\phi,t)=\mathrm{IFFT}(\left\{\sum_{m=1}^{85}\hat{b}_m(s)\sin(m\phi)H_m^1(2\pi(s-1)\rho/cT)\right\})$$

$$E_\phi(\rho,\phi,t)=\mathrm{IFFT}(\left\{\sum_{m=1}^{85}-i\hat{b}_m(s)\sin(m\phi)H_m^{1\prime}(2\pi(s-1)\rho/cT)\right\})$$

It is often desirable to examine the fields in a given frequency range, and this may be accomplished by introducing a filter in the Inverse FFT. We should point out that since the FFT assumes a periodic function, the time behavior we obtain at an arbitrary point may violate causality. However, an *ad hoc* translation in time allows one to find the true pulse shape at the new radius.

The energy radiated during the interval of time *T* is given by (ergs/cm if $\hat{b}_m(s)$ is in Gauss)

$$\frac{dW}{dz}=\left(\frac{c^2T^2}{4\pi^2N}\right)\sum_{s=2}^{N}\left(\left(\sum_{m=1}^{85}\left|\hat{b}_m(s)\right|^2\right)/(s-1)\right).$$

To illustrate this procedure, we plot in Figure (1) our simulated $B_z(t)$ (for the MIT set-up) *vs. t* at a distance 5.5 cm from the center of the grating, and at angle 89°, with its FFT.

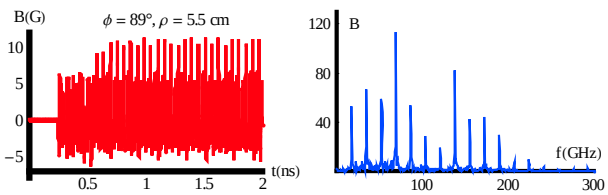

Figure 1. $B_z(t)$ *vs. t* and its FFT, $\phi = 89°$, $\rho = 5.5$cm.

After performing the operations indicated above, we obtain the extrapolated function $B_z(t)$ *vs. t* at a distance 50 cm from the center, again with its FFT, which are shown in Figure (2).

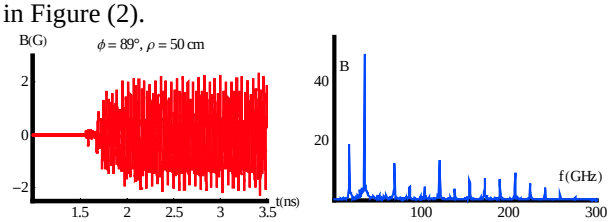

Figure 2. $B_z(t)$ *vs. t* and its FFT, $\phi = 89°$, $\rho = 50$ cm.

The reconstructed signal is smaller than the original, as expected, since the fields decrease asymptotically as $\rho^{-1/2}$. Even taking into account the overall reduction in size, the reconstructed FFT is quite different from that at small radius. This must be attributed to the fact that for the

second harmonic, there is a broad S-P first order peak at 82°, close enough to our angle of 89° to favor the frequency near 34 GHz.

To indicate how the small box → big box transformation affects the angular distribution of energy, we show in Figure (3) the energy radiated during our 2 ns pulse as a function of angle for a band of frequencies centered around the sixth harmonic, near 103 GHz.

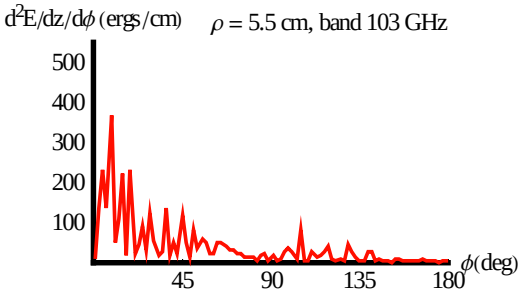

Figure 3. The angular distribution of energy at 5.5 cm in a frequency band centered at 103 GHz.

For comparison we show in Figure (4) the reconstructed distribution of energy as predicted by our small box → big box transformation with ρ = 50 cm. The angles at which coherent S-P radiation is expected in the MIT experiment at this frequency are indicated. For both distributions we find the same total energy radiated

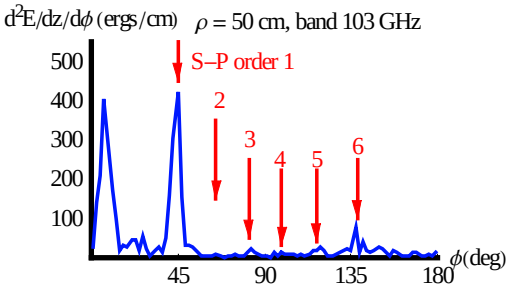

Figure 4. The reconstructed angular distribution of energy at 50 cm in a frequency band centered at 103 GHz.

119.3 ergs/cm, calculated by numerical integration. This in good agreement with the direct formula for the energy radiated in that band. Results similar to these were obtained for the first 20 harmonics. The prominent peak at small angles (8° here) is not S-P radiation but is associated with the appearance and disappearance of short current pulses, even in the absence of a grating.

ISOLATING FLOQUET WAVES

In the AB approach the electron beam interacts with a component of an evanescent Floquet wave. In the Dartmouth configuration, the wave has a negative group velocity, and the mechanism is that of a Backward Wave Oscillator. Upon reaching the end of the grating, the wave is partly reflected, and some of its energy is emitted as free radiation. The magnetic field in the neighborhood of the grating is then a sum of two Floquet evanescent waves propagating in opposite directions, and one may write,

$$B_z(x,y,t) = \Re \sum_{p=-\infty}^{\infty} e^{-\alpha_p y}\left\{B_p e^{i((k_F+pK)x-\omega t)} + B'_p e^{i((-k_F-pK)x-\omega t)}\right\}$$

where $\alpha_p = \sqrt{(k_F + pK)^2 + (\omega/c)^2}$.

The reflected wave is not in resonance with the beam, and essentially traverses the grating without change, until it is also reflected at the other end, again emitting radiation. To better understand this, we have developed a simple method for isolating the Floquet waves. We use the "range" command of MAGIC, which measures a component of the electromagnetic field along some straight line in space (along the *x*-direction here), at a fixed time. An example is shown in Figure (5).

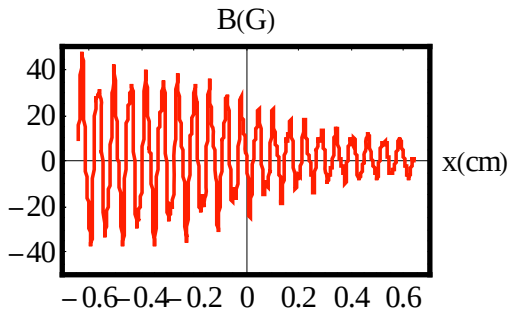

Figure 5. B_z *vs. x* at fixed *t* and *y*. Dartmouth Grating.

By performing three ranges separated by short time intervals, obtaining the spatial FFTs and fitting the three complex amplitudes for each wave number *k* to an assumed form $\alpha_k e^{-i\omega t} + \beta_k e^{i\omega t}$, we can empirically determine the coefficients α_k and β_k. An FFT is shown in

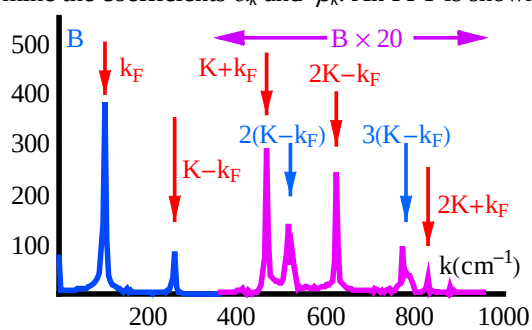

Figure 6. FFT of signal in Figure 5.

Figure (6). The prominent peaks are indicated by red arrows, and the right-hand side of the figure has been multiplied by 20 to make details visible. The blue arrows indicate second and third harmonics of K-k_F, the component resonant with the beam. Here the frequency ω is known ($2\pi f$, with f = 432 GHz). By comparing with the general expression for B_z, we see that the components of the Forward Floquet wave have peaks at $k_F + pK$, while the Backward Floquet wave has support at pK-k_F. If we multiply the α_k by a filter that includes only the peaks at $k_F + pK$, and perform the Inverse FFT, we obtain the

Forward Floquet waves at each of the three instants. Similarly, by filtering around pK-k_F, we find the backward wave, and both are shown in Figure (7).

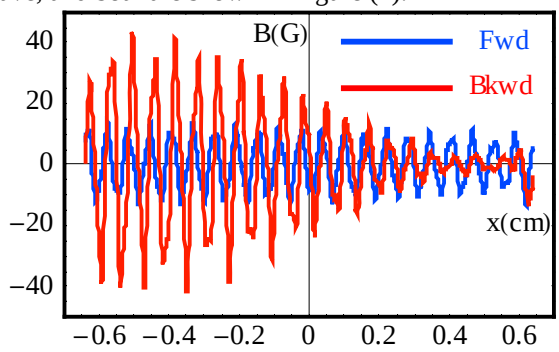

Figure 7. Forward (blue) and backward (red) Floquet waves extracted from signal in Figure 5.

It is clear from this figure that the forward Floquet wave shows little or no growth across the grating, while the backward wave shows considerable growth, indicating an imaginary part of k of order 4 cm^{-1}. We note also that at both ends of the grating the ratio of the incident to the reflected wave is approximately 3:1.

As a check on our empirical method, which uses a least-square method to fit all the FFT components, we attempted to see whether the fit is adequate. This led to a somewhat serendipitous discovery that we now discuss. If we define

$$\Delta B_k(t) = \mathrm{FFT}_k(t) - \alpha_k e^{-i\omega t} - \beta_k e^{i\omega t},$$

the complex number that is a measure of the validity of our fit, we may plot its absolute value as a function of wave number. The results are shown in Figure (8). The

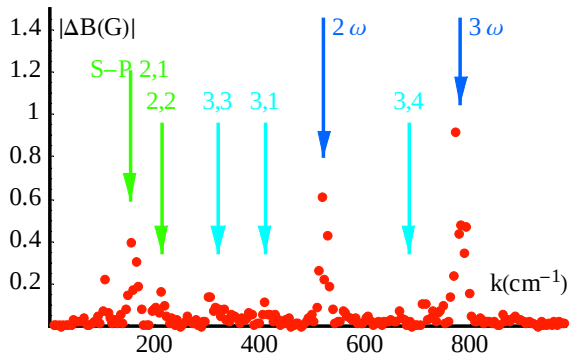

Figure 8. Discrepancy ΔB *vs.* wave number k.

major anomalies occur at 520 and 780 cm^{-1}, which are just the second and third harmonics, respectively, of the resonant wave number, 260 cm^{-1}. They appear also in Figure (6). Upon examining the data, we found that these anomalies disappear if we fit using 2ω and 3ω instead of ω in our fitting procedure. That means that there are components of the form $e^{im((K-k_F)x-\omega t)}$, with m = 2, 3, etc. Such components are readily found in the FFT analysis of the current, and they follow from the non-linear nature of the bunching phenomenon. By an argument based on Ampère's law, modulation of the current must appear as modulation in the magnetic field, and that is what we see. Aside from these two major anomalies, there appear to be several smaller ones. We attribute these to the presence, in small amounts, of the coherent S-P signal corresponding to various harmonics and orders. From the S-P relation and the fact that all coherent radiation will occur at a multiple of the frequency of the evanescent wave, one may derive the following expression,

$$k = m\omega/\beta c - 2\pi n/L,$$

where n denotes the order, m the harmonic, the period L is 173 μm, and $\omega = 2\pi \times 4.32\times10^{11}$ s^{-1}. Using it we have drawn arrows to indicate the wave numbers associated with some pairs m, n. It must be noted that our FFT is symmetric, and peaks that should occur for negative k values are shown at positive values.

CONCLUSIONS

We have presented results concerning our attempts to extract information from simulations of coherent Smith-Purcell Radiation, using a 2-D PIC code. Two distinct methods have been discussed. One permits results obtained in a small area to be extended to a larger area. In doing so, we see more clearly the coherent S-P radiation produced in the MIT experiment with a high-energy pre-bunched beam. The second method involves fitting the FFT data at three closely spaced times, in order to separate the forward and backward Floquet surface waves postulated in the approach of Andrews and Brau. As a by-product, the presence of second and third harmonics of the fundamental bunching component were demonstrated, and evidence for tiny amounts of coherent S-P radiation was provided.

REFERENCES

[1] A. Bakhtyari, J. E. Walsh, and J. H. Brownell, Phys. Rev. E **65**, 066503 (2002).
[2] MAGIC, Mission Research Corporation.
[3] S.E. Corbly, A. S. Kesar, J. R. Sirigiri, and R. J. Temkin, Phys. Rev. Lett. **94**, 054803 (2005).
[4] JT. Donohue and J. Gardelle, *Proceedings of the 2005 FEL Conference, Stanford,California USA* p. 262 (http://www.JACoW.org).
[5] H.L. Andrews and C.A. Brau, Phys. Rev. ST Accel. Beams **7**, 070701 (2004).
[6] H.L.Andrews, C. H. Boulware, C. A. Brau and J. D. Jarvis, , Phys. Rev. ST Accel. Beams **8**, 050703 (2005).
[7] Vinit Kumar and Kwang-Je Kim, Phys. Rev. E **73**, 026501 (2006).
[8] A.Taflove, *Computational Electrodynamics*, (Artech House, Boston, 1995), p. 203.

SIMULATION OF SMITH-PURCELL FELS AT TERAHERTZ FREQUENCIES

J.T. Donohue, Centre d'Etudes Nucléaires de Bordeaux-Gradignan, BP 120, 33175 Gradignan, France
J. Gardelle, CEA CESTA, BP 2, 33114 Le Barp, France

Abstract

Our previous work on the 2D simulation of a coherent Smith-Purcell FEL operating in the terahertz domain is extended to a systematic study of the dependence on various parameters. The important question of the starting current required to produce coherent radiation is addressed, and our new results are presented. As in our previous work we concentrate on two configurations, one similar to the Dartmouth S-P FEL, with a low energy continuous beam, and the other similar to the MIT experiment that used a pre-bunched 15 MeV beam.

INTRODUCTION

At FEL 2005[1]we reported on simulations of coherent Smith-Purcell (S-P) radiation at terahertz (THz) frequencies using a two-dimensional (2D) particle-in-cell code, MAGIC. Two quite different experimental set-ups were considered; one similar to the long-running Dartmouth College experiments initiated by Walsh[2], while the other was similar to the MIT experiment that used a pre-bunched 15 MeV electron beam[3].The results we presented were rather preliminary and a fuller account has recently appeared[4].We remind the reader of the S-P relation, $\lambda = L(1/\beta - \cos\phi)/n$, where λ is the wavelength, L the grating period, β the relative velocity (in a plane parallel to the grating and perpendicular to the direction of the grooves), ϕ the angle of emission (with respect to the beam direction), and the integer n denotes the order. One of our aims was to verify the analytical model proposed by Andrews and Brau[5](AB) and subsequently extended by Andrews, Boulware, Brau and Jarvis[6]to explain coherent Smith-Purcell radiation. Our results did indeed support the viewpoint of Brau and co-workers, that the mechanism for coherent radiation is the bunching of the initially continuous beam by an evanescent wave that is significant only in the vicinity of the grating. The frequency of this wave is always less than the minimum allowed S-P frequency. The process is unstable in the sense that the wave bunches the beam, the beam drives the wave and growth occurs, both in time and along the grating. Our simulation of the Dartmouth set-up found that this is indeed what happens. In particular, the frequency and axial wave number (in the first Brillouin zone) of the simulated grating wave were very close to what the model predicts. Since the bunching is inherently non-linear, once it becomes significant the current is modulated at harmonics of the fundamental frequency, and these may correspond to allowed S-P frequencies. The radiation emitted then shows both intrabunch (since the bunches are small compared to a wavelength) and interbunch (since the fields of all bunches over the grating add up) coherence. Consequently, the coherent radiation occurs only at integer multiples of the fundamental, and only at the corresponding S-P angles. However, the simulation also revealed a major unexpected effect, namely the copious emission of radiation at the fundamental frequency. Indeed, this unforeseen radiation made the direct observation of the S-P radiation quite difficult. Our simulated grating has a finite length. When the evanescent wave reaches the end of the grating, part of its energy is emitted as free radiation of the same frequency, and part of it is reflected back in the opposite direction. The result is that there are two evanescent waves on the grating, which propagate with equal and opposite wave numbers. Only one of these waves is resonant with the electron beam, and since the beam-wave instability is absolute in the Dartmouth configuration, it displays growth both in space and time. The other Floquet wave grows in time only (through reflections), but not in space. In a companion paper we show how both of these Floquet waves may be extracted from the simulation data.

For the MIT experiment, since the beam was already bunched, the bunching mechanism referred to played no role, and the simulation was expected to be straightforward. However, the simulation failed to display unambiguous S-P radiation. In fact, there were two distinct problems, first the emission of considerable radiation even when no grating was present, and secondly, the expected frequency-angle correlation was not apparent. The former has been understood to be a consequence of standard electrodynamics. It is associated with the appearance and disappearance of a relativistic short bunch of electrons. The latter was caused by the fact that the S-P relation is valid only at distances large compared to the grating size. Since the MIT grating was 10 cm long, S-P radiation can be seen clearly only at distances of order 40 cm or more from the center of the grating. Since we are dealing with radiation whose wavelength is a few hundred μm, the mesh size in the simulation must be kept on the order of tens of μm. Under such circumstances, the computing time and memory needed become unreasonable, at least for a PC-based simulation. In the companion paper we outline a simple method we call the Small Box→Big Box transformation, which enables us to circumvent this difficulty. While techniques for passing from the near

zone fields to the far zone based on Green's theorem are well known[7],our method appears to work quite well. It makes use of Finite Fourier Transforms (FFT) and fitting tools available with symbolic manipulation programs such as *Mathematica* or MAPLE. Once this transformation is performed, we see clearly the expected coherent S-P radiation at a large number of angles and frequencies.

Since the last FEL conference, other work on coherent S-P radiation has appeared, notably by Dashi Li and collaborators[8],who also use MAGIC for simulations, and by Kumar and Kwang-Je Kim[9]. In their simulations Li and co-workers studied the effects both of a single short bunch and a periodic train of such bunches passing over a grating of the Dartmouth type. The former showed intrabunch coherent S-P radiation, followed by the emptying of the evanescent wave from the grating after the passage of the bunch. The latter illustrated interbunch coherence, since the second harmonic of the imposed bunch frequency was S-P allowed and indeed emerged at the expected angle. The extensive analysis of Kumar and Kim, based on the traditional approach of diffraction by the grating of the incident electron's field, yielded a dispersion relation quite similar to that obtained by Andrews and Brau. The analysis included a treatment of coherent S-P radiation similar to that of a Backward Wave Oscillator (BWO), for which a start current is known to exist. Using both numerical and analytical methods, they estimated a start current (minimum current needed to produce the instability) of 36.5 A/m for a sheet beam 10 μm above the grating. This is similar to the estimate of 50 A/m found in reference 6.

Our attempt to find the start current for the Dartmouth configuration is discussed in the second Section, and some results on our simulation of the MIT set-up are presented in the third Section. Simulation parameters are shown in the Table 1.

Table 1. Parameters of the Simulations

Parameters	Dartmouth	MIT
beam energy	35 keV	15 MeV
Current (peak for MIT)	variable	25 kA/m
Beam thickness	δ = 10 μm	1 mm
Beam-grating distance	e = 10 μm	0.7 mm
Grating period	L = 173 μm	1 cm
Max. wave number	K = 363 cm^{-1}	2π cm^{-1}
Grating groove depth	H = 100 μm	echelette
Grating groove width	A = 62 μm	
Number of periods	N = 74	10
External magnetic field	B_x = 2 T	0
Mesh size	8.65 × 8 μm^2	(100μm)^2

START CURRENT FOR DARTMOUTH

In Figure (1) we show a contour map of the magnetic field B_z in the area of our MAGIC simulation. The beam appears as a red line, and one sees cylindrical waves of wavelength ≈ 700 μm radiating from the grating ends. This is the evanescent wave, predicted by AB.

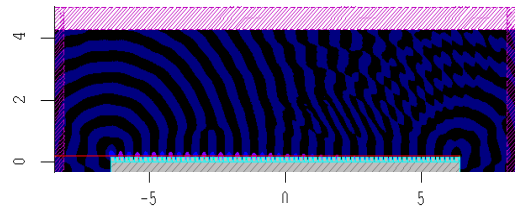

Figure 1. Contour map of B_z.

In contrast to our earlier simulations, we have raised the grating slightly. This is more consistent with the physical situation, where the grating is not flush with a ground plane. Upon doing so, we found that the height of the grating plays a significant role in the reflection at the ends of the grating. In the Dartmouth set-up the system behaves like a BWO, with two Floquet waves proceeding in opposite directions. The backward wave has a component in resonance with the beam, and it displays an absolute instability, with growth both in time and in space. The forward wave shows no growth in space, but since it is fed by reflection at the upstream end, it does grow in time. We found this to be the case in our earliest simulations, with a very large current. In fact, more sophisticated analyses, such as those of references 6 and 9 point out that the boundary conditions at the grating ends play an important role in determining the start current. In our companion paper[10],we separate the two Floquet waves, and we see that the forward wave is essentially constant across the grating, while the backward wave grows strongly in the negative x-direction. However, this was for a current of 175 A/m, which reached saturation in about 1 ns. In order for the BWO mechanism to work, the gain must be sufficient to allow the ratio of the backward wave to forward wave be small at the downstream end and large at the upstream end. The greater the reflection the less is the gain needed to close the loop, and in principle the smaller the starting current.

In order to estimate the start current, we monitor the variation with time of the current at the middle of the grating. We filter the signal, and then estimate the gain by fitting a logarithmic plot of the summits. We also note the time required to reach saturation, t_{sat}, defined by the first maximum of the bunched current. Finally we note the ratio of the peak current at saturation to the direct current, I_{sat}/I. Once the details of the simulation have been fixed, such as mesh size, beam width, beam height above grating, kinetic energy, we then repeat the simulations for various currents. To our surprise, we obtained the curves shown below.

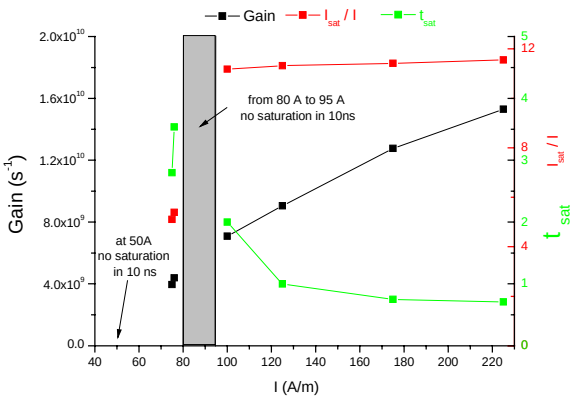

Figure 2. Gain, t_{sat} and I_{sat}/I *vs.* current I.

In the shaded region running from 80 to 95 A/m, and including three runs at 80, 90 and 95 A/m, no instability was observed, even for times of 10 ns. In contrast for currents > 100 A/m, the system always saturated in just a few ns. More astonishingly, at 75 and 76 A/m, the system reached saturation. However, at 50 A/m, it again failed. We are unable to understand these results, but clearly more work is needed. As additional evidence, we show the MAGIC phase space densities (kinetic energy-x) for the 76, 95 and 100 A/m runs.

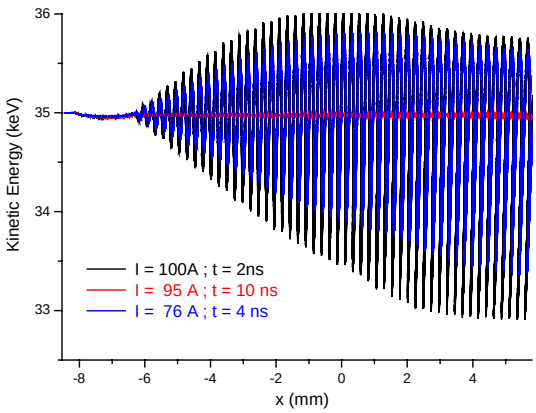

Figure 3. Phase space density plots in the Kinetic Energy-*x* plane, for 76 (blue), 95 red and 100 (black) A/m.

The oscillations correspond to an axial wave number of 260 cm^{-1}, which is what the AB theory suggests. For the 76 and 100 A/m runs, the average energy losses are roughly 0.5 and 0.8 keV, respectively, while the red curve shows neither oscillation nor energy loss. Again, we can only express our surprise at this result.

MIT SIMULATION

In our first simulation of the MIT experiment, we encountered a major difficulty in trying to identify the coherent S-P radiation that was produced. The beam consisted of short pulses (1 ps) produced by a linear accelerator functioning at 17.14 GHz. Consequently, the only frequencies allowed are integer multiples of that frequency. Since the beam energy was 15 MeV, and the grating period was 1 cm, it is straightforward to compute the frequencies predicted by the standard S-P relation. If we keep only the first six orders, and concentrate on angles in the forward direction, we find the curves shown in Figure (4). The harmonics are shown as horizontal lines, and each intersection of any of them with any of the curves marked "order" corresponds to coherent S-P radiation at the angle shown. Clearly there are a great number of possibilities, and for some angles like 49, 65 and 82 degrees, several frequencies may occur. The problem of observing S-P radiation is thus quite complex.

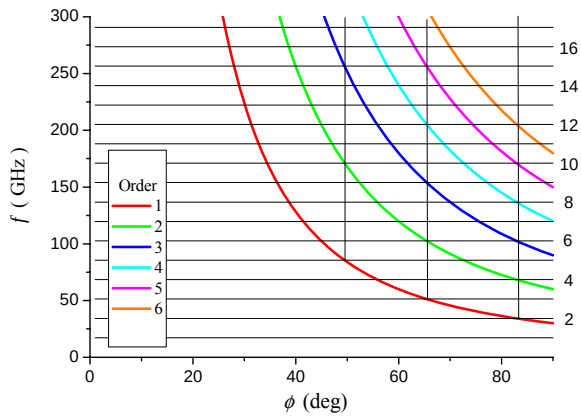

Figure 4. Intersections of the harmonics of 17.14 GHz with the first six S-P orders.

The situation was complicated further when we found that even if we removed the grating, we still observed substantial radiation. This was clearly not S-P radiation but it was present in our simulation. As we indicated in reference 4, the radiation we observed without grating may be calculated exactly using classical electrodynamics, at least for a sheet beam of infinitesimal width. We show in Figure (5) the results of such a calculation. The contour map of B_z in a 120 mm ×100 mm region of the x-y plane bears a strong resemblance to the results of our simulation without grating. A «plume» in which the magnetic field is mainly concentrated accompanies each bunch. The tiny red dots visible beneath each bunch indicate a large positive magnetic field between the beam and the ground plane. This component is an important contribution even when a grating is present, and no attempt to understand our simulation can avoid taking it into account.

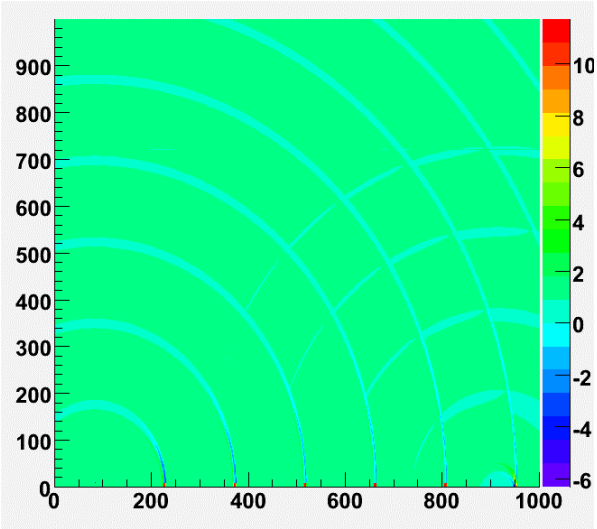

Figure 5. Contour map of B_z following the predictions of classical electrodynamics. The area shown corresponds to 12 cm in x, and 10 cm in the y direction.

In order to illustrate the difficulty of interpreting the simulation directly, we show in Figure (6) the Finite Fourier Transform (FFT) of $B_z(t)$ as observed directly in our simulation, which was made in a relatively small area, 12×6 cm^2. The observation point is at 5.5 cm from the center of the grating, and placed at 65°. The most prominent lines in the spectrum are the forth, sixth and eighth harmonics, but only the sixth is an S-P frequency at this angle.

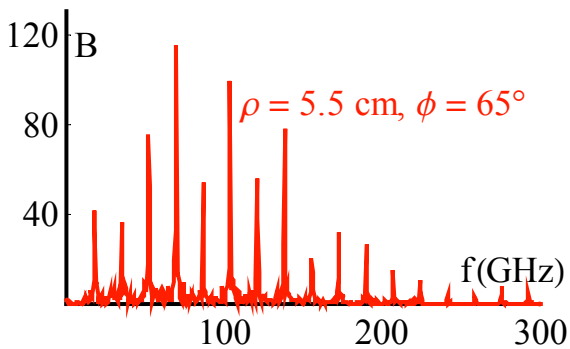

Figure 6. FFT of B_z at position indicated.

As outlined in reference 10, we have developed a procedure for extrapolating the results of our simulation to larger distances from the grating. Shown in Figure 7 is the result of applying our procedure to the data obtained in the small area simulation, after extrapolation to a larger distance from the center, but at the same angle.

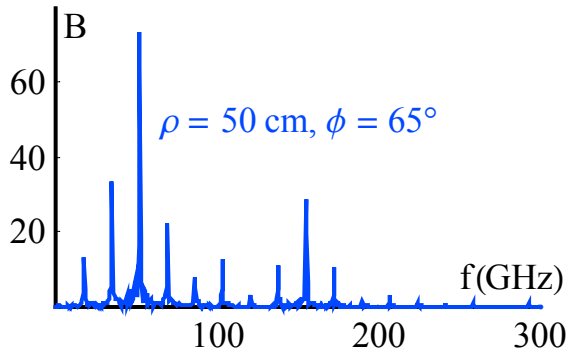

Figure 7. FFT of B_z following extrapolation. Third, sixth and ninth harmonics are more apparent.

It is clear that the relative importance of the third, sixth, ninth and twelfth harmonics, all of which are S-P allowed at this angle, has increased.

REFERENCES

[1] J.T.Donohue and J. Gardelle, *Proceedings of the 2005 FEL Conference, Stanford, California USA,* p. 262 (http://www.JACoW.org).
[2] A. Bakhtyari, J.E. Walsh, and J. H. Brownell, Phys. Rev. E **65**, 066503 (2002).
[3] S.E. Corbly, A. S. Kesar, J. R. Sirigiri, and R. J. Temkin, Phys. Rev. Lett. **94**, 054803 (2005).
[4] J.T. Donohue and J. Gardelle, Phys. Rev. ST Accel. Beams **9**, 060701 (2006).
[5] H.L. Andrews and C. A. Brau, Phys. Rev. ST Accel. Beams **7**, 070701 (2004).
[6] H.L. Andrews, C. H. Boulware, C. A. Brau and J. D. Jarvis, , Phys. Rev. ST Accel. Beams **8**, 050703 (2005).
[7] A.Taflove, *Computational Electrodynamics*, (Artech House, Boston, 1995), p. 203.
[8] Dashi Li, Z.Yang, K. Imasaki and Gun-sik Park, Phys. Rev. ST Accel. Beams **9**, 040701 (2006).
[9] Vinit Kumar and Kwang-Je Kim, Phys.Rev. E **73**, 026501 (2006).
[10] J. T. Donohue and J. Gardelle, these Proceedings.

A BEAM SHAPER FOR THE OPTICAL BEAMLINE OF RF PHOTOINJECTORS

G. Klemz#, I. Will, Max-Born-Institute, D-12489 Berlin, Germany.

Abstract

The paper reports on first results on beam shaper for the generation of a flat-top beam profile in the ultraviolett (UV). The shaper can be integrated into the optical beamline of the PITZ facility [1]. This will improve the efficiency of the optical beamline significantly.

INTRODUCTION

A high performance of SASE FELs requires a low emittance of the electron bunches that emerge from the photoinjector. This in turn can be favoured by irradiating the cathode by a laser beam with a spatial and temporal flat-top profile [2]. A simple way to illuminate the photocathode with a uniform beam profile is to strongly expand the laser beam with a telescope and select the very central region of the magnified beam by means of a small "beam shaping aperture". This method which is presently implemented at PITZ, inherently gives rise to a large loss of the incident UV-laser power. At PITZ the transmission amounts to approximately 20%, and 80% of the UV laser radiation are lost at the beam shaping aperture.

Thus, a more efficient technique for optical beam-shaping is desirable.

BEAM SHAPING TECHNIQUES

Conceivable technical solutions can be associated with one of the following methods:

Field mapping: The input beam is transformed into the desired output beam by refraction at appropriately designed aspherical surfaces in a prescribed manner. This technique works well for diffraction-limited beams and can be nearly lossless. A plane wavefront, i.e. a collimated beam can be generated at the ouptut of the shaper by adding a second aspherical lens. Both, the temporal shape of the pulse and the coherence of the laser beam are maintained, which is particularly important for the optical beamline of photoinjectors. Field mapping permits to precisely control the final intensity profile. For these reasons it is the method of choice for our beam shaper compared to the alternatives outlined below.

We suggest the setup of Fig. 1 for integration of the beam shaper into the optical beamline. Two magnifying telescopes are used to match the beam diameter to the requirements of the individual components. The former beamshaping aperture remains in place. It is needed to increase the edge steepness in the wings of the flat-top.

Another alternative are **beam integrators** which split the input beam by a lens array into a large number of facets. Subsequently, the energy within each facet is dispersed over the cross section of the desired output beam. The output profile is the sum of the diffraction patterns of each individual aperture of the lens array. That's why the output beam exhibits strong, small-scale intensity modulations (speckles) and the beam integrators work satisfactory only for multimode beams. They are lossless as well.

However, due to their principle of operation they destroy the spatial coherence of the laser beam. There is also no condition of constant optical path, so some temporal broadening of the pulse duration results.

A third medthod is the **radial intensity filter** (RIF) [3]. This filter can be realized based on birefringent crystals with a curved surface that provides a radial variation of polarization retardation. One or more such radial birefringent elements in combination with polarizers form a RIF. They are lossy due the absorption of light in the polarizers. As a further disadvantage, flattening of the nearly Gaussian infrafred (IR) laser beam can only approximately be obtained due to limited degrees of freedom in its design parameters.

Beam shaping elements based on by **internal conical refraction** are commercially available [4]. These systems require depolarized or circular polarized monochromatic radiation and contain a biaxial/trigonal crystal. The crystal

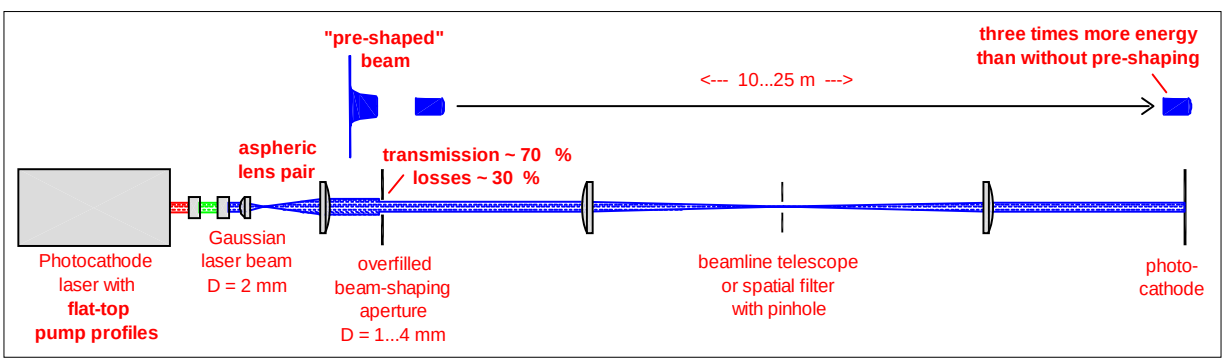

Figure 1: Proposed scheme of an optical beamline for the rf-photoinjector at PITZ that integrates a refractive beam shaper.

#klemz@mbi-berlin.de

length has to be adapted to wavelength and diameter of the input beam. Since no polarizers are needed, this system can be highly transmissive. Unfortunately, there are no suitable biaxial birefingent crystals available for the UV at present. That's why the technique cannot be used in the UV beamline of a photocathode laser.

EXPERIMENT

We have designed a beam shaper that consists of a Galilean telescope made of two refractive aspherical lenses. Fig. 2 shows how the input rays from the laser system are redirected into a uniform distribution within a Galilean telescope. The Fig. 3 shows our measured beam profiles at the input, in the middle and the exit of the lens pair when using a HeNe-laser. The absence of a focus between the aspheres is important for application at the PITZ beamline, since this excludes possible optical breakthrough due to high UV peak powers.

Our beam shaper is presently designed for 4 mm diameter (FWHM) of the flat-top and 2.8 mm ($1/e^2$) diameter of the Gaussian input. The aspheres are 100 mm apart. There diameters were chosen for a nominal power transmission of 99.9%. Following [5], a smooth Fermi-dirac profile instead of a step function was chosen to represent the flat-top profile, since this reduces diffraction effects along the propagation path of the output profile.

Sensitivity against beam size fluctuations

For application of the shaper in a beamline of a photocathode laser, the beam profile at the cathode should be stable as far as possible, even if the diameter of the input beam varies slightly. That's why we have carefully examined the sensitivity of of the otput beam against a 10% fluctuation of the input beam diameter for our spherical lens pair. The results are depicted in Fig. 4.

The amount of the deviations on the edge of the flat-top depends approximately linear on the dimensionless shape parameter ß of the Fermi-dirac profile. ß represents the ratio of the radius of the flat-top and the total width of the soft transition region where the intensity returns to zero [5]. With increasing ß the profile becomes gradually flat and square, approaching a step function as $ß \rightarrow \infty$. In the example shown in Fig. 4 the overshoot amounts to 15%.

We conclude from our experience with the current beam shaper that a design tolerant against fluctuation of the input beam diameter is more important than an almost perfectly flattened output profile with steep edges. This means that ß should be reduced considerably, a future value of ß = 6 seams to be suitable for our application.

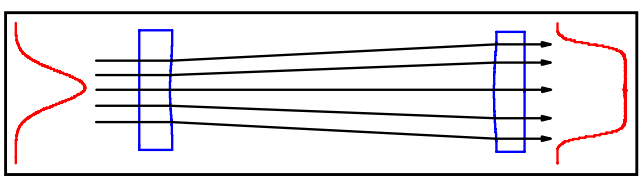

Figure 2: Basic scheme of the refractive field mapping beamshaper (Galilean design)

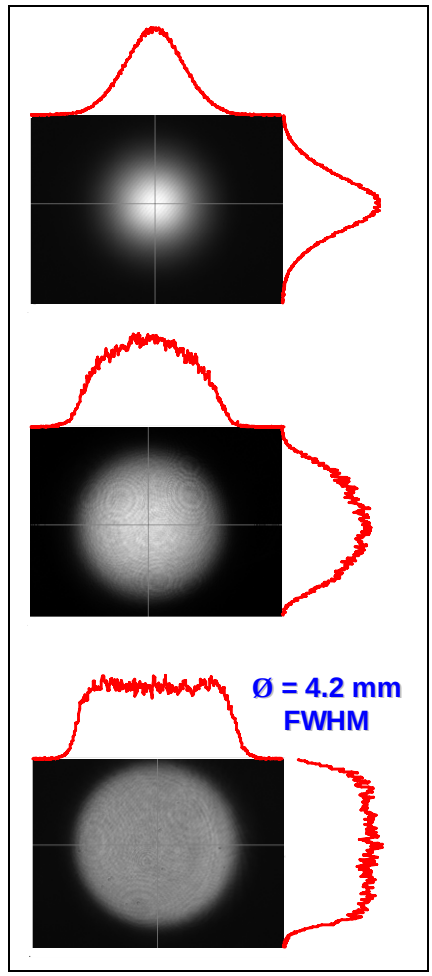

Figure 3: Mesasured beam profiles at the entrance, midway and at the exit of the beam shaper

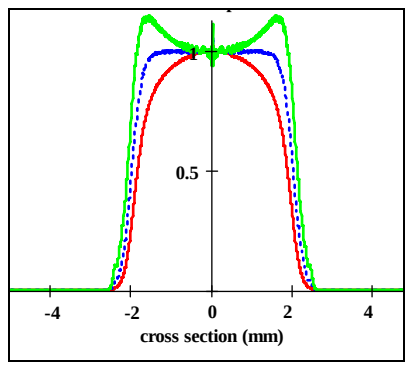

Figure 4: Output profile for varying beam radius w at the input (shape parameter $\beta = 16$): $w = 0.9 \cdot w_0$ (red), $w = w_0$ (blue), $w = 1.1 \cdot w_0$ (green), design value: $w_0 = 1.422$ mm ($1/e^2$)

With the additional option of a spatial light modulator that might preceed the aspherical lens pair the remaining error at the edges as well as some remaining radial variation of the intensity might be corrected.

Propagation of the UV beam

Fig. 5 shows the beam profile produced by the refractive beam shaper in a matched UV beam (left). The present realization of the nonlinear frequency conversion produces a slight elliptical beam in the UV. Its horizontal cross section is slightly larger than in the vertical direction. This is responsible for the observed overshoot in the horizontal cross section at the output plane of the aspherical lens pair. The beam profile was reasonable preserved by relay imaging over a distance of about 1 m, see Fig. 5 (right).

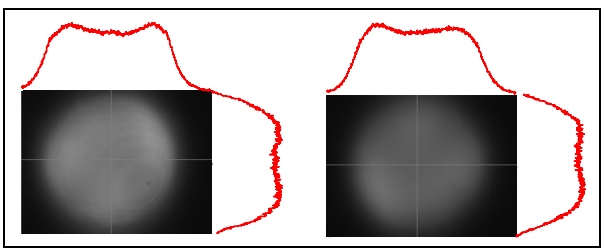

Figure 5: Output beam profile of the aspherical lens pair at 262 nm wavelength (left) and its relay image in a distance of approx. 1 m with (right).

CONCLUSION AND OUTLOOK

The suggested integration of a refractive beam-shaper into the optical beamline of the PITZ photocthode laser has the potential to form a flat-top beam profile and simultaneously improve the energy efficiency of the complete beam-line. Consequently, the application of an appropriately designed beam shaping system can lead to a significant reduction of the overall costs of the laser due to its reduced power requirements.

ACKNOWLEDGEMENT

This work is in part supported by the European Community, Sixth Framework Programme, Research Infrastructure Actions EUROFEL Design Study, contract number 011935. Further support comes from the German ministry of Education and Research (BMBF), contract number 05ES4 BR1/8.

REFERENCES

[1] J. Bähr et al., “Upgrades of the laser Beam-Line at PITZ”,Proc. FEL2005, JaCoW/eConf C0508213, p.110-113.

[2] M.Krasilnikov, “Experimental Characterization and Numerical Simulation of the Electron Source at PITZ”, ICAP2004, St. Petersburg.

[3] M. Yun et al., “Transformation of Gaussian to uniform or annular beams by radial birefringent filters”, Proc. of SPIE 5525 (2004), p.182-187.

[4] “Laser beam sahping with only one element”, OLE (October 2004), p. 18, http://www.vct-ag.de.

[5] J.A. Hoffnagle and C.M. Jefferson, “Design and performance of a refractive optical system that converts a Gaussian to a flattop beam”, Appl. Opt. 39 (2000), p.5488-5499.

Beam Dynamics Experiments and Analysis on CSR Effects at FLASH

Bolko Beutner, Winfried Decking, Martin Dohlus, Torsten Limberg
and Michael Röhrs,
Deutsches Elektronen-Synchrotron DESY, D-22603 Hamburg, Germany.

Abstract

The Free Electron Laser in Hamburg (FLASH) is a linac driven SASE-FEL in the vacuum-ultra-violet (VUV) wavelength range [1]. High peak currents are produced using magnetic bunch compressor chicanes. In these magnetic chicanes, the energy distribution along an electron bunch is changed by the emission of Coherent Synchrotron Radiation (CSR). Energy changes in dispersive sections lead to transverse displacements along the bunch. Measurements of CSR induced transverse displacements are presented and compared with simulations.

INTRODUCTION

The peak current of an electron bunch emitted by an rf gun is about 50-100 A. For SASE operation at FLASH, the necessary peak currents of 1-3 kA are reached using longitudinal bunch compression. A two stage bunch compression system with the magnetic chicanes BC2 and BC3 is employed (see Fig.1).

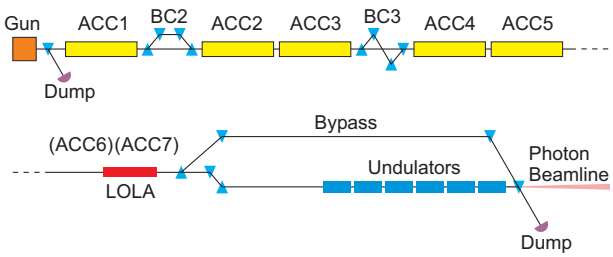

Figure 1: Sketch of FLASH. The blue triangles indicate dipole magnets, the yellow boxes TESLA acceleration modules.

A transverse deflecting rf-structure (LOLA) [2] is used to take "top view" pictures of the bunch - the projection into the longitudinal-horizontal plane. Thus, centroid shifts along the bunch, for instance caused by CSR fields, can be observed.

However, other forces like space charge cause transverse shifts of beam centroids as well. For an undisturbed measurement of CSR effects, space charge effects have to be reduced. To that purpose, we over-compress the bunch. The longitudinal energy correlation (chirp) introduced in the module ACC1 is chosen to reach minimum bunch length and a peak current beyond 2 kA towards the end of the second magnet in the BC2 chicane. The bunch will exit the chicane roughly with its incoming length of about 2 mm, corresponding to about 50 A peak current. The integrated effect of space charge from the exit of BC2 to LOLA is then small compared to the centroid offsets caused by CSR.

MEASUREMENTS AND ANALYSIS

For our measurements, we vary the ACC1 phase and keep ACC2/3 on crest. The expected CSR effects are created during over-compression in BC2. Downstream, the transverse deflecting rf structure is passed at the zero-crossing phase. The particles are kicked transversely with a strength proportional to their longitudinal offset to the bunch center. The bunch is thus tilted and its longitudinal-transverse projection is observed on a screen.

Fig.2 shows a LOLA measurement. The red curve shows the longitudinal beam profile, the white dashed lines indicate the fwhm points.

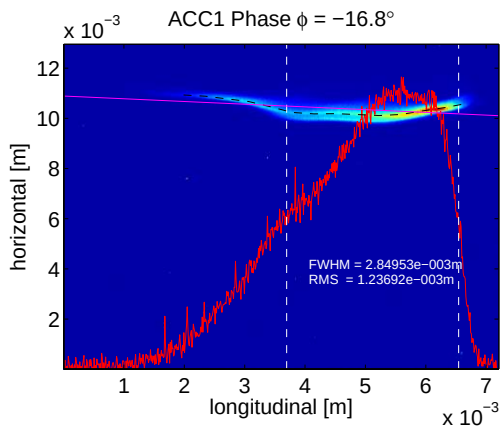

Figure 2: An example of a LOLA measurement. Longitudinal charge profile (red line), fwhm and rms bunch length are shown.

Fig.3 shows measured bunch length at LOLA as a function of the ACC1 phase as well as simulation results. The measured bunch length agrees well with the simulation downstream of BC3, as it should. The calculated bunch length downstream of BC2 (green line) is, for small phase offsets, longer, since the bunch is further compressed in BC3. At about 12 degrees, the bunch is fully compressed in BC2. Above 12 degrees, the bunch is over-compressed, the chirp changes its sign and the BC2 bunch length is shorter.

Fig.4 shows measured longitudinal-horizontal projections of the bunch for different compression scenarios. In the uppermost picture, the ACC1 phase is on crest, no com-

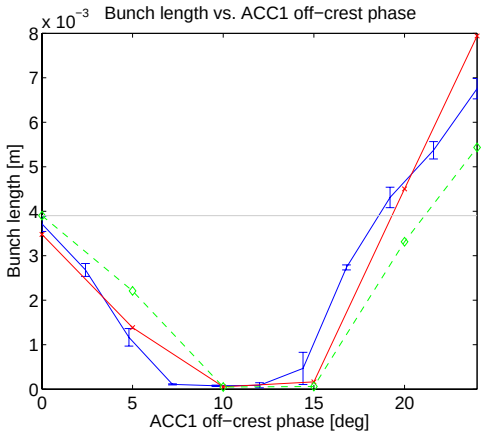

Figure 3: Measured fwhm bunch length at LOLA (blue line) are compared with simulations. Red line: calculated bunch length at LOLA. Green line: calculated bunch length after BC2.

pression occurs and the horizontal centroid positions line up straight. Close to full compression (middle picture), the beam is heavily distorted by CSR and space charge effects. This is understood and simulated [3], but would be very challenging as a starting point for quantitative CSR studies.

The bottom picture shows the over-compressed case, where the space charge effects are negligible and strong CSR occurs only in BC2. The beam centroids are still on a smooth line. Its shape and sag will be compared with simulations in the next paragraph.

Fig.5 reflects the bunch shape changes described above in plotting the peak to peak bunch centroid shift as a function of ACC1 phase offset.

Comparison with Simulations

Tracking calculations were done to simulate longitudinal-horizontal beam projections at LOLA. Beam transport through ACC1 was calculated with the space charge tracking code ASTRA [4]. After ACC1, wake fields are applied as a discrete effective kick [5]. The tracking code CSRTrack [6] is used to simulate CSR effects in BC2. The 1D projected model is used [7]. The long bunch length after BC2 in the over-compression case allows the simulation of the beam transport to LOLA by a first order matrix.

To compare the simulated longitudinal slice centroid positions with the measurements these data have to be extracted from the measured distributions. In a first step each distribution is divided into slices along the longitudinal axis. The horizontal charge profiles of these slices are then calculated. Gaussian fits are used to determine the center of each profile. An example for the resulting centroid curve is the dashed black line in Fig.2.

At big ACC1 phase offsets, the bunches start to be tilted

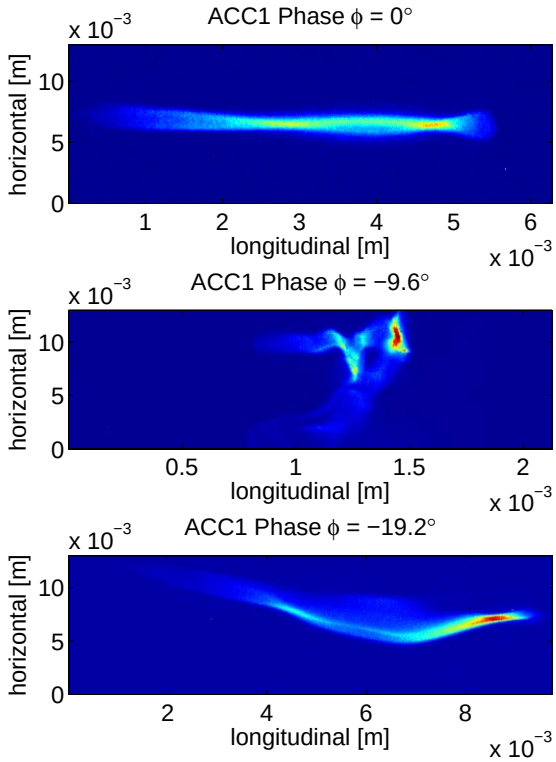

Figure 4: Measured top view for different ACC1 phase offsets. Top: no compression. Middle: near full compression. Bottom: over-compression.

on the screen. The cause of this is under investigation. The linear correlation as indicated by the magenta line in Fig.2 is subtracted from the centroid curve.

For error analysis, a series of pictures is taken for each ACC1 phase setting. The different centroid curves are

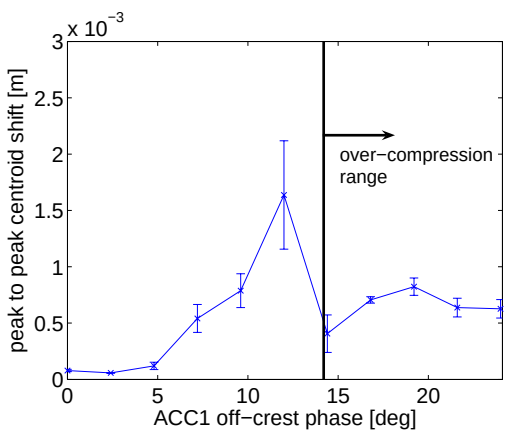

Figure 5: The peak to peak centroid shift along the bunch is plotted vs. the phase offset in ACC1. Phase range used for the experiment: 14 to 24 degrees.

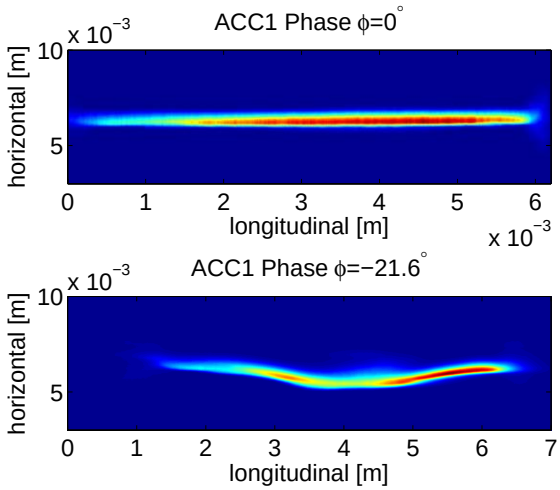

Figure 6: Simulated top view after BC2 for different ACC1 phase offsets. Top: no compression. Bottom: over-compression.

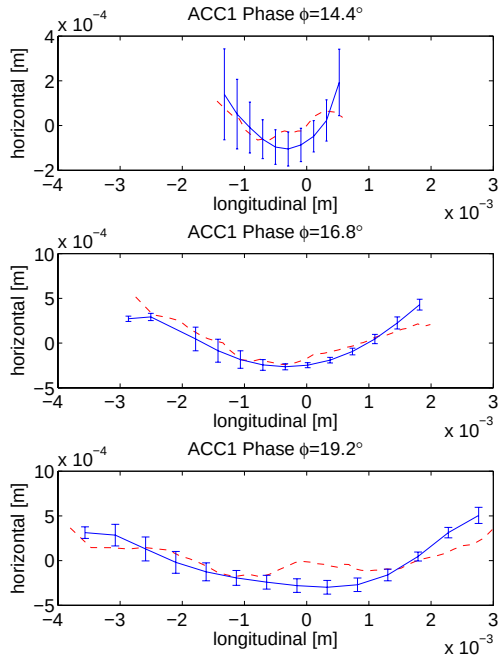

Figure 7: Experimental centroid curves are compared with simulated data. The blue lines represent the data taken with LOLA and the dashed red curves represent the results of simulations. Linear correlations are subtracted.

aligned to their individual centre of mass. The curves are then fitted with a polynomial and their mean value and rms spread are calculated for different longitudinal positions. In Fig.7, these results are compared with the tracking calculations.

CONCLUSION AND OUTLOOK

CSR effects in the first bunch compressor chicane in FLASH were observed using the transverse deflecting rf-structure LOLA.

The offsets of the centers of the longitudinal bunch slices for different over-compression scenarios were measured and compared with simulation calculations.

Next steps in the experimental program are studies of slice emittance growth due to CSR effects and dependences on bunch charge and beam optics in the chicanes [8].

The observed beam tilt will be investigated to improve both SASE operation and CSR measurements.

REFERENCES

[1] E. Schneidmiller and M. Yurkov: ”Lasing at 13 nm of the SASE FEL at FLASH”, this conference.

[2] M. Röhrs et. al.: ”Investigations of the Longitudinal Electron Bunch Structure at the FLASH Linac with a Transverse Deflecting RF-Waveguide”, this conference.

[3] M. Dohlus: ”CSR Calculation for TTF-II”, 2005, http://www.desy.de/xfel-beam/talks_a.html#dohlus.

[4] K. Flöttmann: ”ASTRA user manual”, http://www.desy.de/mpyflo/Astra_dokumentation.

[5] I. Zagorodnov: private communication.

[6] M. Dohlus, T. Limberg: ”CSRtrack: Faster Calculation of 3D CSR effects”, FEL 2004, 2004.

[7] M. Dohlus: ”Two Methods for the calculation of CSR Fields”,TESLA-FEL-2003-05.

[8] M.Dohlus, T. Limberg: ”Impact of Optics on CSR-related Emittance Growth in Bunch Compressor Chicanes”, PAC 2005, 2005.

FELO: A ONE-DIMENSIONAL TIME-DEPENDENT FEL OSCILLATOR CODE

B.W.J. M[c]Neil, G.R.M. Robb, SUPA, Department of Physics, University of Strathclyde, Glasgow, UK
D. Dunning and N.R. Thompson, ASTeC, CCLRC Daresbury Laboratory, UK.

Abstract

A one-dimensional, SDDS compliant time-dependent FEL oscillator code has been developed in Fortran 90. The code, FELO, solves universally-scaled FEL equations to simulate oscillator FELs operating from the low to high gain regime. The code can simulate start-up from shot noise, different electron pulse current distributions, the effects of cavity length detuning and temporal jitter between electron bunches. Cavity detuning curves for both the low-gain IR-FEL and the regenerative amplifier VUV-FEL of the 4th Generation Light Source (4GLS) proposal at Daresbury Laboratory are modelled. The code predictions for the VUV-FEL output are compared with simulations performed with the parallel implementation of Genesis 1.3 and are found to be in good agreement.

INTRODUCTION

Several computational codes are available to the FEL community to aid with the simulation and design of FEL amplifiers e.g. Genesis 1.3 [1]. The authors have developed a simulation package containing FEL simulation code and pre and post-processors that models a FEL with cavity feedback. The code, called FELO, solves a one-dimensional spatio-temporal set of equations which are able to model much of the physics relevant to such FELs. The design of two of the UK 4GLS project FELs were aided by FELO and examples from the 4GLS Conceptal Design Report [2] are presented.

THEORETICAL MODEL

The 1D equations governing the spatio-temporal evolution of the pulsed FEL interaction are well known and in the the universal scaling of [3, 4] may be written:

$$\frac{d\theta_j}{d\bar{z}} = p_j \quad (1)$$

$$\frac{dp_j}{d\bar{z}} = -\left(A\left(\bar{z},\bar{z}_1\right)\exp\left(i\theta_j\right)+c.c.\right) \quad (2)$$

$$\left(\frac{\partial}{\partial\bar{z}} + \frac{\partial}{\partial\bar{z}_1}\right)A\left(\bar{z},\bar{z}_1\right) = \chi\left(\bar{z}_1\right)b\left(\bar{z},\bar{z}_1\right) \quad (3)$$

where $\theta_j = \left(k+k_u\right)z - \omega t_j$ is the phase of the jth electron with respect to the particular ponderomotive potential well in which it evolves and $p_j = \left(\gamma_j-\gamma_r\right)/\rho\gamma_r$ is its scaled energy, $b\left(\bar{z},\bar{z}_1\right) \equiv \left\langle e^{-i\theta(\bar{z})}\right\rangle\Big|_{\bar{z}_1}$ is the bunching factor and is the average over the electrons contained within the ponderomotive well centred at $\bar{z}_1$ at distance through the interaction region $\bar{z}$. The weight factor $\chi\left(\bar{z}_1\right) = I\left(\bar{z}=0,\bar{z}_1\right)/I_{pk}$ where $I\left(\bar{z}=0,\bar{z}_1\right)$ describes the electron pulse current distribution of peak value I_{pk} at the entrance to the FEL interaction region and $A\left(\bar{z},\bar{z}_1\right)$ is the scaled complex radiation field envelope with magnitude defined by the radiation and electron beam powers as $|A|^2 = P_{rad}/\rho P_{beam}$.

The scaled independent variables may be written [4]:

$$\bar{z} = \frac{z}{l_g} = 2\rho k_u z \quad (4)$$

$$\bar{z}_1 = \frac{z-c\bar{\beta}_z t}{l_g\left(1-\bar{\beta}_z\right)}. \quad (5)$$

where $l_g = \lambda_u/4\pi\rho$ is the nominal gain length of the FEL interaction, the initial z-component of the mean electron velocity within the interaction region is $c\bar{\beta}_z = \langle v_{z0}\rangle$ and ρ is the fundamental FEL, or Pierce, parameter [3]. The latter may be written in practical units for a planar undulator as $\rho \approx 5.7\times10^{-3}\gamma_r^{-1}\left(I\bar{a}_u^2\lambda_u^2 f_B^2/\sigma_b^2\right)^{1/3}$ where f_B is the usual difference of Bessel function factor associated with planar undulators and σ_b is the RMS electron beaM radius which for an electron beam of normalised emittance ϵ_n in a focussing channel of beta-function β is given by $\sigma_b = \sqrt{\epsilon_n\beta/\gamma_r}$.

For the case of small gain FELs typical to those encountered in high-Q cavity FELs, previous studies [5] have shown that the effects of emittance and energy spread, electron/radiation pulse slippage effects and the relative transverse overlap between electron beam and cavity modes may be accounted for in correction factors to the expressions for the FEL gain. A small signal gain coefficient was defined which in the universal scaling of the above equations may be written:

$$g_0 = \frac{\bar{z}^3}{\pi}. \quad (6)$$

The maximum single pass gain is then approximated by the fitting formula:

$$G_{max} = g_0F\left(0.85+g_0F\left(0.19+4.12\times10^{-3}g_0F\right)\right)$$

where the factor $F = F_{inh}F_fF_c$ is a product of correction factors that that respectively account for the effects of inhomogeneous broadenning due to emittance and energy spread; a filling factor for the transverse overlap; and the effects of relative slippage between the radiation and electron pulses. The inhomogeneous broadening factor is given by:

$$F_{inh} = \frac{1}{\left(1+1.7\mu_\gamma^2\right)\left(1+\mu_\epsilon^2\right)} \quad (7)$$

where $\mu_\gamma = 4N_u\sigma_\gamma/\gamma$ and $\mu_\epsilon = 2N_u\epsilon_n\bar{a}_u/\lambda_u\left(1+\bar{a}_u^2\right)$. The filling factor is given by:

$$F_f = \frac{1}{1+\bar{w}^2/4\sigma_b^2} \tag{8}$$

where $\bar{w}$ is the mean optical mode size, defined by the radius at which the intensity drops to $1/e^2$ of its on-axis value, averaged over the length of the undulator.

Noting from (4 & 6) that $g_0 \propto \rho^3$ and that the expression for G_{max} contains only factors $g_0 F$ allows the inhomogeneous fitting factor F_{inh} and that for the filling factor F_f to be incorporated into the definition of an effective FEL parameter

$$\rho_{eff} \equiv \left(F_{inh}F_f\right)^{1/3}\rho \tag{9}$$

to replace that of ρ in the definitions and working equations of (2..5). Note that the factor that accounts for slippage effects, F_c, is not used in the definition of ρ_{eff} as slippage is directly modelled by the partial derivatives of the wave equation (3). It is interesting to note that from the definitions of g_0 and the filling factor F_f that the product g_0F_f , can be expressed as

$$g_0F_f \propto \frac{1}{\sigma_b^2+\bar{w}^2/4}.$$

Hence, if the electron beam radius $\sigma_b \ll \bar{w}$, as for example in a long wavelength FEL, the gain is independent of the electron beam radius.

When used with the ρ_{eff} scaling the above equations (2..3) will then estimate the effects of inhomogeneous broadening due to electron energy spread and emittance, and also the effects of transverse electron-radiation coupling, without the need for increased number of computational particles required in 2-D and 3-D models. The FELO code which uses these equations is therefore significantly faster to run than these codes and yet, as will be shown in the following work, gives results which are in good agreement with 3-D simulations.

COMPUTATIONAL MODEL

The working equations (2..3) are solved using the method of characteristics as described in [6] using a code written in Fortran-90. The metod of characteristice allows the resultant equations to be integrated via a 4th order Runge-Kutte method with slippage effects between electrons and radiation modelled using simple array shifts. Because the effects of electron energy spread, emittance and transverse coupling are simply accounted for in the modified FEL parameter ρ_{eff}, no electron macroparticle distribution in the scaled energy parameter p is required and $p_j = 0 \ \forall \ j$ to describe a resonant FEL interaction. Thus, only a relatively small number of macroparticles are required per ponderomotive well (typically $\sim$ 100) distributed uniformly in θ. The option to include shot-noise effects is included using the method of [7]. Although other shot-noise models more correctly describe the physics [8], the method of [7] is sufficient here. The FEL cavity length can be varied to allow investigation of cavity detuning effects and the effects of a random temporal jitter in the electron arrival into the cavity can be simulated by introducing a small random variation about the mean cavity length [9].

The FELO source code is written in Fortran-90 and is freely available [10]. The code has been tested using the open-source g95 compiler [11]. A parameter spreadsheet is available to assist the user in preparing the relatively simple input file for the code. Output from the code is written into SDDS formated files [12]. Post-processing and plotting routines are provided using both SDDS toolkit functions in Tcl script files and MATLAB and are described in more detail in the user-manual provided for the code.

EXAMPLE SIMULATIONS

The FELO code has been used in the design of two of the three FELs of the UK 4GLS project [2]. Both the IR-FEL and the VUV-FEL are cavity FELs. The IR-FEL is designed to operate in the wavelength range 2.5-200 μm. It has a relatively low gain and needs a relatively high Q cavity to lase. The VUV-FEL is designed to generate photon energies of 3-10 eV and will operate in the intermediate gain regime ($\bar{z} \sim 4$) where the FEL interaction evolves exponentially but cannot achieve saturation withou seeding in a single pass. Saturation is made possible by introducing a small amount of feedback via a low Q cavity [13]. This also has the advantage of cleaning up the spectral quality of the output over that of SASE [14]. FELO simulations for both of these designs are presented and, in the case of the VUV-FEL, comparison is made with the results of the 3-D code Genesis 1.3 [1]. No such comparison is available for the IR-FEL due to the large number of cavity round-trips required to achieve saturation and the prohibitively long simulation time this would require.

4GLS IR-FEL

The IR-FEL simulations presented are for 2.5 μm operation of the IR-FEL. From the detailed specifications of [2], with an electron energy of 60 MeV, charge 200 pC and RMS duration of 2 ps the IR-FEL operates at 2.5 μm. The undulator has 50 periods, so that the approximate efficiency $\eta \approx 1/4N_u$ gives a peak power output at saturation of $P_{pk} \approx 12$ MW. A more detailed estimate of the efficiency that accounts for passive cavity losses due to mirror reflectivity and all diffraction losses has been derived and reduces the efficiency from that above [2]. Including these effects gives the optimised power estimate for operation of the IR-FEL from 2.5-25 μm as shown in Fig. 1. A FELO simulation at 2.5 μm operation with cavity length detuning of $\delta_c = 9$ μm, so that the output pulse width is close to its maximum, gives good agreement with these estimates as shown in Fig. 2. (Note that positive values of δ_c correspond to a shortened cavity length.) Fig. 3 plots the results of FELO simulations for both the peak power and FWHM

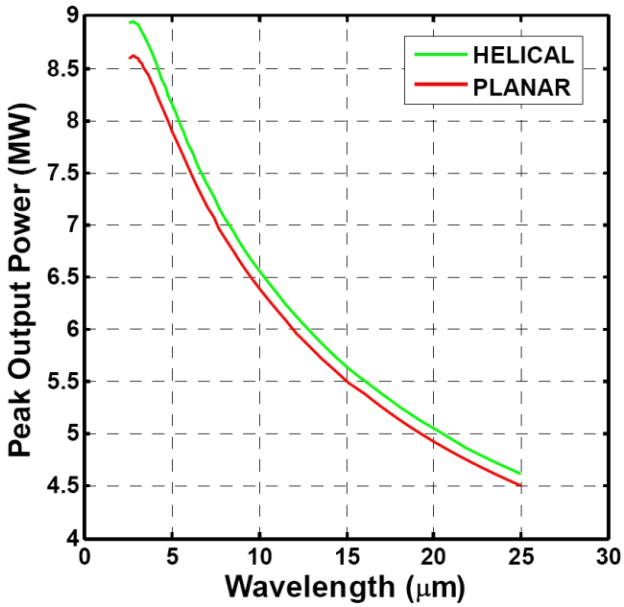

Figure 1: The peak output power for the 4GLS IR-FEL, assuming 2 ps RMS electron pulses and an outcoupling fraction optimised for every wavelength to give the maximum output power. Calculations for helical and planar mode are shown in green and red respectively.

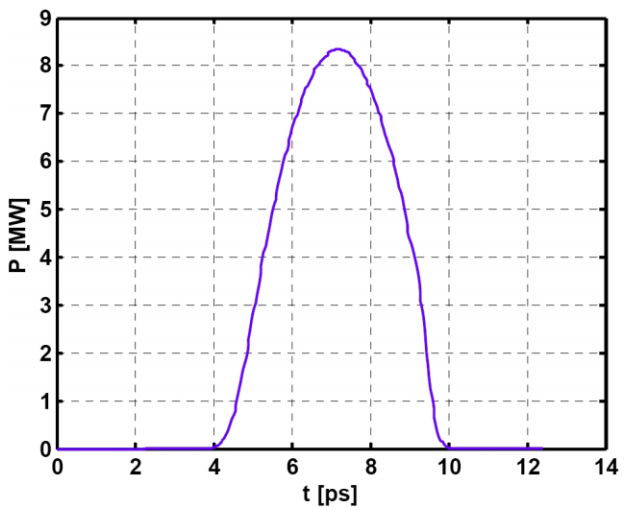

Figure 2: 4GLS IR-FEL pulse power as a function of time for 2.5 μm operation with a cavity length detuning of 9 μm.

pulse width for 2.5 μm operation as a function of cavity detuning δ_c. As cavity resonance is approached at $\delta_c = 0$ it is seen that the peak output power increases and pulse width decreases, typical of superradiant behaviour in an FEL cavity [15].

4GLS VUV-FEL

FELO simulations have also been used in the conceptual design of the 4GLS VUV-FEL. This FEL operates with an intermediate gain of $\bar{z} \sim 4$ and uses a low Q cavity.

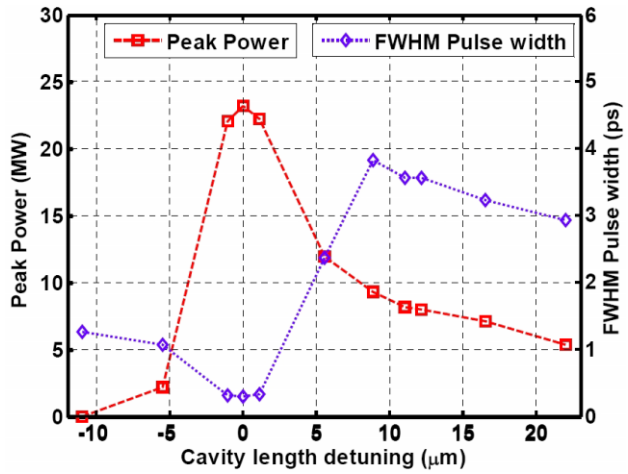

Figure 3: Peak power and FWHM pulse width as a function of cavity length detuning, for the 4GLS IR-FEL at 2.5 μm with 2 ps electron bunches.

Saturation then occurs after only a few cavity passes, typically $\sim$ 10, which allows multi-pass simulation to saturation using the 3-D code Genesis. For 10 eV operation in a planar undulator, the VUV-FEL conceptual design uses a 600 MeV, 300A peak current electron beam and gives an FEL parameter of $\rho \approx 1.5 \times 10^{-3}$. Although utilising cavity feedback, the VUV-FEL still saturates as a high-gain FEL [13] so that the efficiency is $\eta \approx \rho$. Hence, the saturated power can be approximated as $P_{sat} \approx \rho P_{beam} \approx 270$ MW. Fig. 4 plots the results of FELO simulations for both the peak power and FWHM pulse width for 10 eV photon energy operation as a function of cavity detuning δ_c. There are clear similarities with the IR-FEL cavity detuning curve of Fig. 3. As with the IR-FEL, assuming the greatest pulse width approximates most closely to the steady-state, the saturated power for cavity length detuning of $\delta_c \approx 18$ μm agrees well with the saturated power estimate of ≈ 270 MW of above. The plot of Fig. 5 shows a comparison of the pulse power as the VUV-FEL pulse energy saturates for the case of a FELO (blue) and Genesis (red) simulation for a cavity detuning of 12 μm. The number of cavity passes for the Genesis simulation was 8 while that for the FELO was 30. Although the FELO simulation approached pulse energy saturation after 8 caivity passes, the shape of the pulse power underwent a transition from a narrower, higher peak power pulse to that shown. This accounts for the higher peak power and narrower pulse width of Fig. 4 where $\tau_{FWHM} \approx 65$ fs $\Rightarrow$ $s \approx 20$ μm in the units of Fig. 5. This effect of higher peak power and narrower pulse width of the FELO simulation appears to be a transiatory superradiant phase. It is not thought that the Genesis simulations show this behaviour, although this will need to be investigated further. As cavity resonance is approached, the radiation pulse width shortens to approximately an order of magnitude less than the electron pulse width of 250 fs FWHM (75 μm). Also, pulse

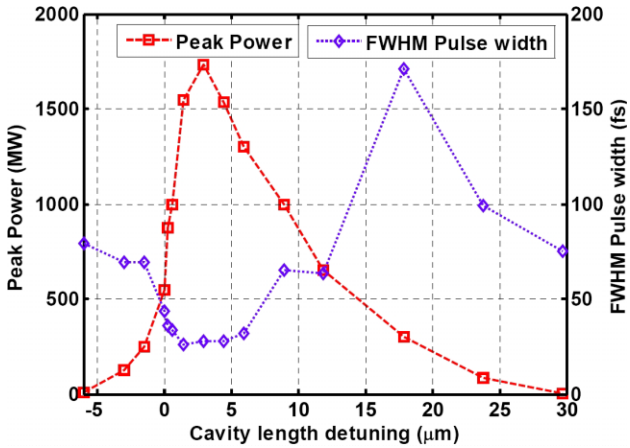

Figure 4: Peak power (red) and FWHM pulse width (blue) as a function of VUV-FEL cavity detuning. The parameters are for 10 eV photon output.

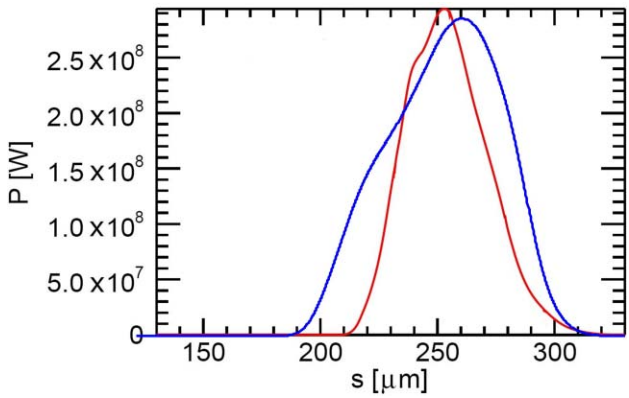

Figure 5: Comparison between FELO radiation power output pulse (blue) with that of a Genesis simulation (red) approaching saturation of the output energy. The parameters are for 10 eV photon output.

peak powers are significantly greater than the predicted by the steady-state simulations [2]. A plot of the shape of the pulse output close to cavity resonance is shown in Fig. 6. This pulse shape is typical of superradiant radiation with a narrow, high peak power spike followed by secondary pulses or ringing [15].

CONCLUSIONS

The FELO code package has been developed to allow reasonably quick and accurate simulations of cavity FELs operating from the low to high gain. The package has been used succesfully in the development of the design of two cavity FELs for the UK 4GLS project. Some of these simulation results were presented. The code including manual is freely available for general use [10].

REFERENCES

[1] S. Reiche, Nucl. Inst. and Meth. A **429**, 243 (1999)

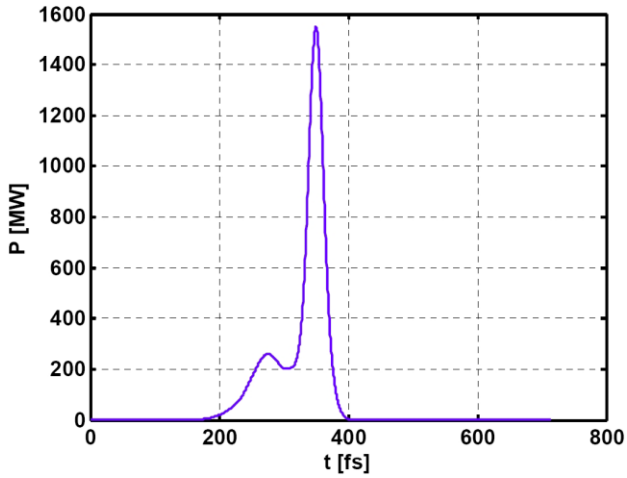

Figure 6: FELO simulation showing the 10 eV radiation power at saturation as a function of time for near-zero cavity detuning. The pulse shape demonstrates a spiking behaviour typical to FEL superradiance.

[2] *4GLS Conceptual Design Report*, Council for the Central Laboratory of the Research Councils, UK, http://www.4gls.ac.uk/documents.htm#CDR (2006)

[3] R. Bonifacio, C. Pelligrini and L.M. Narducci, Opt. Commun. **50**, 373 (1984)

[4] R. Bonifacio and B.W.J. M^{c}Neil, Nucl. Instrum. Methods A **272**, 280 (1988)

[5] F. Ciocci, A. Torre, G. Dattoli and A. Renieri, *Insertion Devices for Synchrotron Radiation and Free Electron Lasers*, World Scientific Publishing, Singapore (2000)

[6] R. Bonifacio, B.W.J. M^{c}Neil and P. Pierini, Phys. Rev. A **40**, 4467 (1989)

[7] C. Penman and B.W. J. M^{c}Neil, Opt. Commun. **90**, 82 (1992)

[8] B.W.J. M^{c}Neil, M.W. Poole, and G.R.M. Robb, Phys. Rev. ST Accel. Beams **6**, 070701 (2003)

[9] D. Dunning et al., *First Tolerance Studies for the 4GLS FEL Sources*, *ibid.*

[10] Currently available from http://www.astec.ac.uk/id_mag/ID-Mag_Software.htm

[11] Currently available from http://www.g95.org/

[12] M. Borland, L. Emery, H. Shang and R. Soliday, Proceedings of the IEEE 2003 Particle Accelerator Conference 2003, Portland, Oregon

[13] B.W.J. M^{c}Neil, IEEE Journal of Quantum Electronics **26**, 1124 (1990)

[14] N.R. Thompson, B.W.J. M^{c}Neil and M.W. Poole, *A VUV-FEL for 4GLS:Design Concept and Simulation Results*, Proceedings of the 27th International Free Electron Laser Conference, Stanford (2005)

[15] D.A. Jaroszynski et al., Phys. Rev. Lett. **78**, 1699 (1997)

THE CONCEPTUAL DESIGN OF THE 4GLS XUV-FEL

B.W.J. M^{c}Neil, SUPA, Department of Physics, University of Strathclyde, Glasgow, UK
N.R. Thompson, ASTeC, CCLRC Daresbury Laboratory, UK
B. Sheehy, Sheehy Scientific Consulting, New York, USA.

Abstract

The Conceptual Design Report for the 4th Generation Light Source (4GLS) at Daresbury Laboratory in the UK was published in Spring 2006 [1]. A key component of the proposal is an XUV-FEL amplifier directly seeded by a High Harmonic source and operating in the photon energy range 8-100eV. Numerical modelling shows the FEL may generate 50fs (FWHM) pulses of variably-polarised, temporally-coherent radiation with peak powers in the range 2-8 GW.

INTRODUCTION

Synchronised free-electron laser (FEL) sources which operate in the XUV, VUV and IR regions of the spectrum are fundamental components of the 4GLS design. These sources will deliver ultra-short pulses of temporally coherent photons with peak brightness at least 10^8 greater than that available from the best 3rd-generation light sources. 4GLS is intended to be a beyond state-of-the-art facility that must operate over extended periods, generating stable, synchronous and reproducible radiation pulses over the wide spectral range to end-user stations. In the conceptual design of 4GLS, therefore, the aim has been to create a robust design that does not overly stretch the specification of its individual components. This mildly cautious approach should minimise the risk in proceeding to the future design phase and enable further, more advanced, designs to be incorporated as technological progress permits. Here details mainly relating to the choice of undulator and electron focussing specifications and their relation to the FEL output are presented for the conceptual design of the XUV-FEL covering the 8-10eV photon energy range of the spectrum. The effects of FEL seeding by High Harmonic pulses are discussed in [2, 3] and the temporal seed/electron pulse offset due to jitter is discussed in [4].

GENERAL SPECIFICATION

The XUV-FEL baseline design will generate short, tunable, high-brightness pulses of 8-100 eV photons from an undulator system directly seeded by an external laser source. The radiation output will have good temporal and transverse coherence and also have variable polarisation. These specifications are expected to satisfy a wide range of current user requirements and also open up many new areas of science for exploration. It is also possible to utilise the exhaust electrons of the XUV-FEL in a spontaneous spent-beam undulator source, before the electron beam is dumped. The radiation from this source is then guaranteed to be synchronous with the XUV-FEL output for pump-probe type experiments. A schematic of the conceptual design for the 4GLS XUV-FEL is given in [3] of these conference proceedings.

Photon energy tuning in the XUV-FEL will be achieved by a combination of both undulator gap tuning and energy tuning of the electron bunches between 750 and 950 MeV. The electron bunches are assumed to have a rep-rate of 1-10 kHz, to be Gaussian of width $\sigma_t = 266$ fs and total charge of 1 nC giving a peak current of 1.5 kA, and with normalised emittance $\epsilon_n = 2$ mm mrad and fractional RMS energy spread of 0.1%. The FEL undulator will consist of a lattice of individual undulator modules allowing electron beam focusing elements and diagnostics to be placed in between. The final undulator modules of the FEL will be of APPLE-II design that will enable the generation of variable elliptically polarised radiation. Existing HHG laser systems can provide seed energies of 10 - 100 nJ with pulse widths of 30 fs FWHM over the photon energy range [2, 3]. The quality of XUV-FEL output can be expected to be similar to that of the input seed pulse which has a high degree of both spatial and temporal coherence [5]. The amplified pulse widths will also be only slightly longer than the seed pulse.

UNDULATOR AND FOCUSSING LATTICE

The design for the XUV-FEL undulator consists of a lattice of undulator modules containing both planar and variable polarisation undulator modules. For the planar undulators a relatively simple pure permanent magnet (PPM) was chosen and an APPLE-II design was chosen for the variable polarisation undulators. Each type of module will have a fixed period and a variable magnetic gap, g, that allows tuning of the RMS undulator parameter $\bar{a}_u$ via the undulator magnetic field. A minimum undulator magnetic gap is assumed for the design of both planar and variable undulators. Note that the gap between the vacuum vessel walls will be $(g - 3)$ mm, the 3 mm reduction from the magnetic gap being the estimated thickness of the vacuum vessel walls and the clearance between magnets and vacuum vessel. A schematic giving further detail of the undulator lattice and incorporating BPMs, phase matching devices and the focussing quadrupoles is shown in Fig. 1. The variable polarisation undulator sections, VU1..VU5, ensure that variably polarised photons may be generated across the full design spectrum. In practice, operation at higher photon energies will require a longer undulator

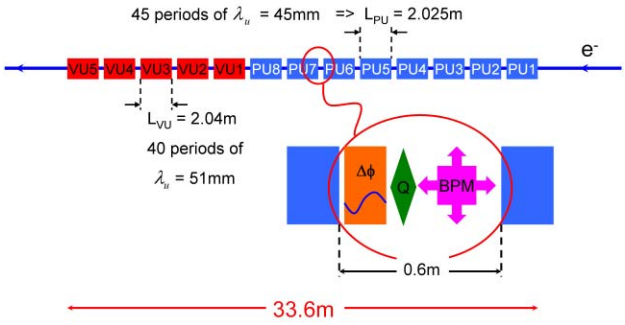

Figure 1: Schematic of the modular undulator system of the XUV-FEL. Undulator modules PU1..8 (blue) are planar undulators; VU1..5 (red) are variable polarisation undulators. The gap between undulator sections may contain a beam position monitor, quadrupole and radiation/electron phase matching unit.

length to achieve saturation. The effective undulator length may be varied by opening the magnetic gaps of individual undulator modules to their maximum. Those modules that have maximum magnetic gap generate only small on-axis magnetic fields and are effectively switched off for the purpose of the FEL interaction. For example, when operating for 100eV photon energy generation all undulator modules PU1..VU5 would be functional to achieve saturation, whereas for 50 eV operation only modules PU5..VU5 would need to be functional to achieve saturation, with PU1..PU4 gaps fully opened. This method of operation should allow a tapered vacuum vessel to be used along the undulator modules which will assist with reducing diffraction effects of HHG seed injection at lower photon energies [1, 3]. The minimum undulator parameter due to undulator gap tuning is taken to be $\bar{a}_u \approx 1$ to ensure sufficient FEL coupling. With this constraint then for a beam energy of 950 MeV the maximum planar undulator period that can achieve 100 eV FEL resonance is $\lambda_u \approx 45$ mm with a gap of $g \approx 28$ mm. At the lower beam energy of 750 MeV and for $\lambda_u \approx 45$ mm, the resonant photon energy is ≈ 10 eV for the minimum magnetic gap of $g \approx 10$ mm. The period of $\lambda_u \approx 45$ mm is then the optimum for the beam energy, magnetic gap and photon tuning range. A similar analysis for the variable polarisation APPLE-II undulators gives them an optimum period $\lambda_u \approx 51$ mm

A FODO focussing lattice has been chosen for the conceptual design. Other systems based upon quadrupole doublet and triplet focussing were investigated [5] and rejected. Although these latter designs allow longer, and therefore fewer, undulator modules of up to 4-5 m in length to be used, the quadrupole field strengths must be significantly greater by a factor of 3-4 than those required for a FODO lattice distributed between more modules. Tighter quadrupole alignment tolerances would therefore be required for the doublet and triplet positioning [6]. Monitoring of the electron beam transverse position, critical to the FEL interaction, would also be limited as would the ability to step-vary the full undulator length by opening the individual module gaps. For these reasons a simpler FODO focussing lattice of module length ≈ 2 m is the chosen design option.

In order to investigate the effect of β-function variation due to the discrete focussing quadrupoles of the FODO lattice, the 3-D code Genesis 1.3 [7] was used to determine both the saturation length L_{sat} and power P_{sat} as a function of average β-function. This was carried out for a planar undulator system of module length ≈ 2 m. The respective results are shown in Fig. 2. It is seen that $\beta \approx 3.5$ m minimises the saturation length whereas $\beta \approx 5.5$ m maximises the output power. The nominal value of the β-function is chosen to be that which gives the maximum output power: β = 5.5 m. This is motivated by the fact that the planar modules PU1-PU8 produce a seed pulse (and prebunched beam) which will be amplified to saturation in the APPLE-II modules VU1-VU5, so maximising the power of the seed into the VU modules reduces the required length of the more technologically challenging APPLE-II modules. For the parameters used here a β-function of 5.5 m is satisfied by quadrupoles of magnetic length 0.09 m and of strength =13 T/m. The RMS electron beam radius may be calculated as $\sigma_b = \sqrt{\epsilon_n \beta/\gamma}$ = 77 μm for beam energy 950 MeV and the design normalised emittance $\epsilon_n = 2$ mm mrad.

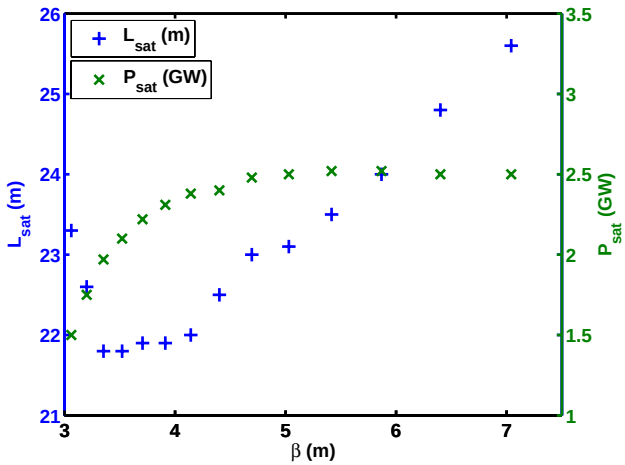

Figure 2: Genesis simulation of the saturation length, L_{sat}, and power, P_{sat}, as a function of the β-function in a FODO lattice for 100 eV operation.

UNDULATOR MODULE & GAP LENGTH

The modular construction of the combined undulator and FODO focussing lattice requires choice of the length of each undulator module, L_{PU} for planar and L_{VU} for variable undulators, and L_{gap} the spacing between modules. The FEL performance has a functional dependence on these parameters so optimisation is needed. The energy dispersion induced into the electron beam by the FEL interaction, and the natural homogeneous energy spread, are trans-

formed into a spatial dispersion in proportion to the gap between undulator sections, L_{gap} which may disrupt the FEL bunching process. Furthermore, it is seen from Fig. 1 that the undulator module length and gap define the FODO focussing lattice period, $\lambda_{FODO} = 2(L_{PU} + L_{gap})$. In a FODO lattice, the β-function varies about its mean value by $\pm\lambda_{FODO}/2$ so affecting the electron beam radius via the relation above for σ_b. Thus if λ_{FODO} is too large (as determined principally by the module length) the electron beam radius variation may also adversely affect the FEL coupling. Alignment of the electron beam through the undulators is of critical importance to maintain the electron-radiation coupling. This requires both beam alignment between undulator modules and careful construction of the undulators to ensure that the beam wander due to magnetic field errors and pole alignment are minimised. Ideally, beam wander off the optical axis should be no greater than 20% of the electron/radiation beam radius.

Genesis 3-D simulations were carried out to simulate the FEL operating at 100 eV. Only the planar undulator modules were used with the nominal design parameters. Fig. 3 plots the results of Genesis steady-state simulations for the saturation power, P_{sat}, as a function of the gap between undulator modules, L_{gap}, for three different module lengths, L_{PU}. It is seen that the saturation power is nearly independent of the undulator module length and decreases almost linearly with the undulator gap. A gap of $L_{gap} = 0.6$ m is chosen for the design specification. This is the estimated minimum length into which the quadrupoles, BPMs and phase matching units can fit.

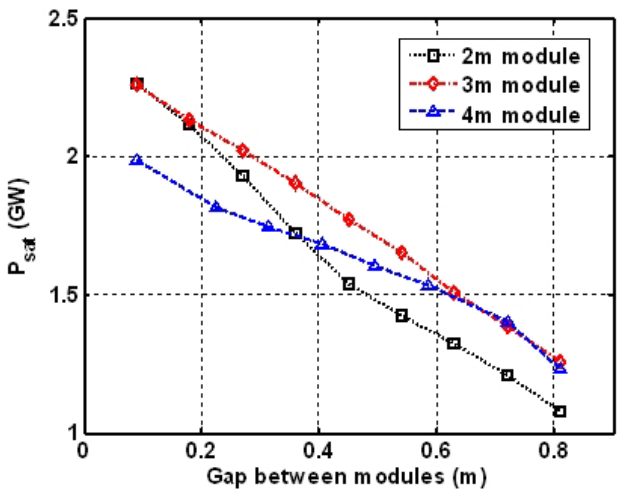

Figure 3: Simulation of the saturation power, P_{sat}, for XUV-FEL planar undulator operation at 100 eV as a function of the gap between undulator modules. The results are plotted for three module lengths: L_{PU}=2, 3 and 4 m.

Simulations of the saturation length L_{sat} of a seeded amplifier interaction, starting from a seed power of 30 kW at 100 eV, are shown in Fig. 4. For each length of undulator module L_{sat} is seen to increase with the module gap. However, there is a significant difference between each undulator module length, with the 4 m module having a saturation length longer than that of the 2 m module. This is attributed to the greater variation in the β-function for the longer module as discussed above. For this reason, and the greater opportunities for beam monitoring and control afforded by the greater number of undulator modules, the module lengths for the design specification are chosen to be $L_{VU} \approx L_{PU} \approx 2$ m. Hence, for the baseline design for 8 - 100 eV operation, each planar PPM undulator will have 45 periods of 45 mm giving a module length L_{PU} = 2.025 m and each variable undulator APPLE-II undulator will have 40 periods of 51 mm giving a length L_{VU} = 2.04 m.

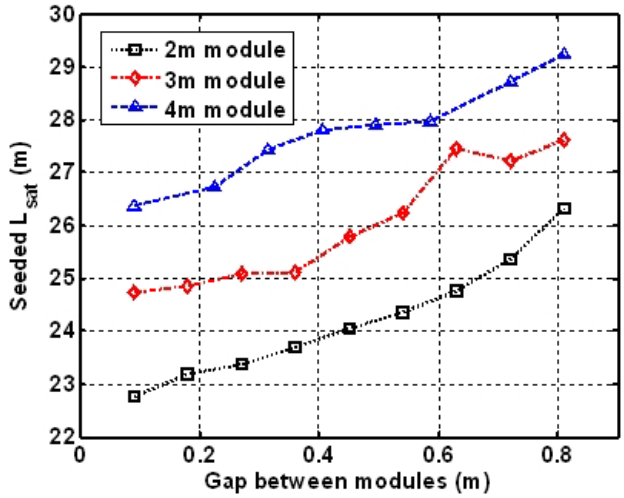

Figure 4: Simulation of the saturation length L_{sat} for XUV-FEL planar undulator operation at 100 eV as a function of the undulator module gap, L_{gap} for three module lengths: L_{PU}=2, 3 and 4 m. (The saturation length is the undulator length only: gaps between modules are not included.

3D STEADY-STATE SIMULATIONS

The design choices and optimisations discussed may be summarised by plotting both the saturation powers and lengths across the operating spectrum of the XUV-FEL. It has been assumed that the XUV-FEL is operating in an amplifier mode with a seed power equal to 10% of the peak power currently available from seed pulses as described in [2, 3]. The reduction in seed power by a factor of approximately ten conservatively estimates the power available following transmission and focussing losses from the seed laser into the undulator. The seed is focussed to the centre of the first in-use undulator module with Rayleigh length equal to half the module length. For seed pulses of 30 fs FWHM and of energy 3 nJ for 10 to 40 eV photons and 1 nJ for 40 to 100 eV give corresponding approximate peak powers of 100 kW and 30 kW. The saturation power over the operational spectral range as calculated by both Genesis (in steady state mode) and Xie formulae [8] are shown

in Fig. 5. Both planar and helical mode results are shown.

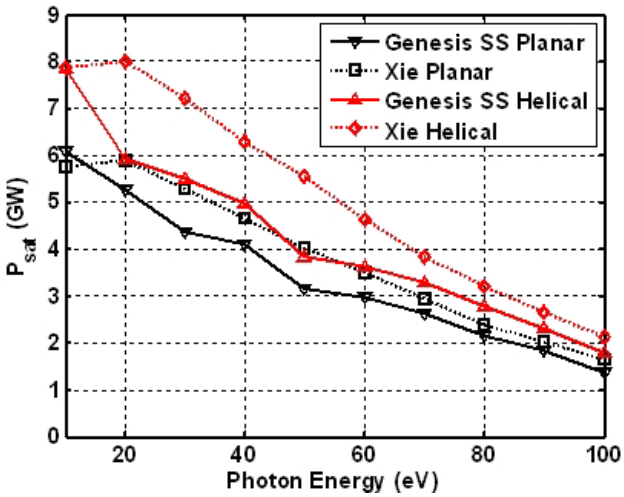

Figure 5: Summary of saturation power estimates for the XUV-FEL across its spectral operating range. 3-D Genesis steady-state (SS) simulations and the Xie formulae are in excellent agreement.

Note that the Xie design formulae cannot take into account mixed planar/helical undulators, so the 'Xie Helical' estimates assume a helical-only undulator for the equivalent length of the planar-helical combination. The Xie estimates also do not include the effects of gaps between undulator modules. These differences account for the small discrepancy of the 'Xie Helical' estimates from the other simulations, in the slightly higher saturation power estimation. Notwithstanding this, the 3-D numerical and Xie estimates are in excellent agreement. In Fig. 6, the length of undulator required for saturation is plotted as a function of photon energy. Note that the gaps between undulator modules are not included in this length and must be added on to obtain the total length of the combined undulator-focussing lattice.

CONCLUSIONS

A robust conceptual design for the XUV-FEL has been developed. Established FEL theory and state-of-the-art simulation codes predict this free-electron laser will generate 8-100 eV photon energies at giga-watt power levels and, as shown elsewhere [3], in pulses of duration 40-60 fs FWHM. The pulses will have very good temporal and spatial coherence with time-bandwidth products close to the Fourier transform limit for a Gaussian pulse [3, 5]. Unlike the SASE mode of operation, which effectively self-starts from intrinsic noise, the FEL interaction here is truly acting as a simple, bandwidth limited amplifier. So long as the radiation input seed pulses have sufficient spectral purity, the output radiation is very nearly a simple amplified version of the input. Recent advances in the High Harmonic seed sources of choice ensure that the seed requirements for the XUV-FEL already exist [2, 3]. Research in the next design phase will require full start-to-end simulations from the electron gun through to the end of the undulator. This will allow the modelling of the FEL interaction with more realistic electron pulses than that used here which assume a Gaussian variation of most variables. Investigation of tolerances, for example in quadrupole position and undulator field errors, will also be required, as will a more detailed study of the effects of relative electron-seed pulse jitter than the initial results presented at this conference [4]. Extension of the operational range down to 6eV photons may be possible and will be investigated further in the next design phase.

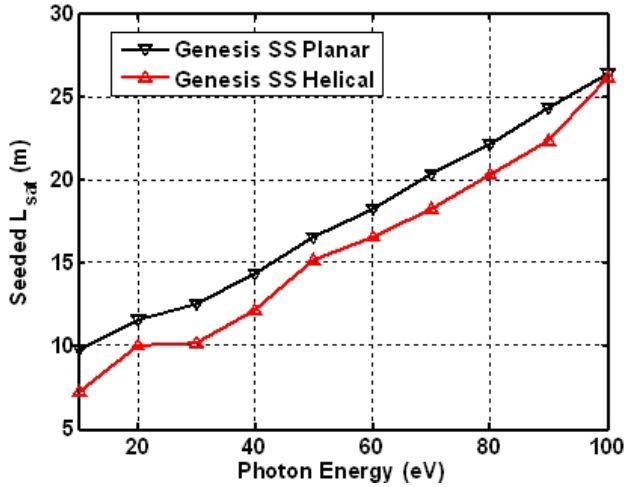

Figure 6: Summary of steady-state 3-D Genesis simulation estimates for the XUV-FEL undulator saturation length across the spectral operating range.

REFERENCES

[1] *4GLS Conceptual Design Report*, Council for the Central Laboratory of the Research Councils, UK, http://www.4gls.ac.uk/documents.htm#CDR (2006)

[2] B. Sheehy *et al.*, *High harmonic seeding and the 4GLS XUV-FEL*, 37th ICFA Advanced Beam Dynamics Workshop on Future Light Sources, Hamburg, Germany (2006)

[3] B.W.J. M^{c}Neil, *The Use of HHG at 4GLS, (ibid.)* (2006)

[4] D. Dunning, *First Tolerance Studies for the 4GLS FEL Sources, (ibid.)* (2006)

[5] B.W.J. M^{c}Neil *et al.*, *Design considerations for the 4GLS XUV-FEL*, Proceedings of the 27th International Free Electron Laser Conference, Stanford, USA (2005)

[6] B. Faatz and J. Pflger, Nucl. Inst. Meth. Phys. Res. A, **475**, 603 (2001)

[7] S. Reiche, Nucl. Inst. Meth. Phys. Res. A, **429**, 243, (1999)

[8] Ming Xie, Proc. Of 1995 Part. Accel. Conf., 183 (1996)

OPTIMIZATION OF PARAMETERS OF SMITH-PURCELL BWO *

Vinit Kumar†,RRCAT, Indore, M.P. 452013,INDIA
Kwang-Je Kim, ANL, Argonne, IL 60439,USA.

Abstract

We study the dependence of start current in Smith-Purcell backward wave oscillator (SP-BWO) on grating parameters and electron beam parameters. The attenuation due to finite conductivity of the grating material is taken into account and three-dimensional effects are included in an approximate way in the analysis. We find that the start current can be significantly reduced by optimizing the grating parameters.

INTRODUCTION

The Smith-Purcell free-electron laser (FEL) is a backward wave oscillator (BWO) for low energy electron beam [1,2]. In a BWO, like any oscillator system, the electron beam current needs to be higher than a threshold value, known as the start current, in order to produce coherent electromagnetic oscillation. In a recent paper [2], we have performed a calculation of start current for the case of sheet electron beam skimming over the grating surface in a SP-BWO. The attenuation of the backward wave due to finite conductivity of the grating was not taken into account in this calculation. The issue of attenuation becomes important while optimizing the parameters of SP-BWO. Recently, Andrews et al. [3] have discussed the calculation of attenuation coefficient for the backward wave supported by the grating. They have also studied the dependence of gain and attenuation in SP-BWO as a function of group velocity as the energy of the co-propagating electron beam is varied, keeping the grating parameter fixed. In this way, they have calculated the net gain. However, gain does not have a straightforward meaning in a BWO. In this paper, we therefore present a calculation of start current taking into account the effect due to attenuation. We use this calculation to study the dependence of start current on grating parameters as well as electron beam parameters.

START CURRENT CALCULATION

In a SP-BWO, the electron beam interacts with the co-propagating surface electromagnetic mode supported by the grating. The co-propagating surface mode has a group velocity in the direction opposite to the electron beam. We consider a sheet electron beam in the (y, z) plane propagating at a height b from the grating top surface along the z-axis. The grating grooves are in the y-direction and perpendicular to the grating is in the x-direction. Due to the finite conductivity of the material of the grating, the surface electromagnetic mode suffers attenuation. The attenuation coefficient can be calculated as per the prescription given by Andrews et al. in Ref. 3. Attenuation occurs in the direction in which the energy is flowing. Here, the phase velocity of the resonant surface mode is along the positive z-axis and the group velocity v_g is along the negative z-axis. Let the longitudinal component of the the electric field of the backward wave be given by $E(z,t)\exp(ik_0z - i\omega t)$. Including attenuation in the analysis, the equation for the evolution of the amplitude $E(z,t)$ of the backward wave described in Ref. 2 gets modified to

$$\frac{\partial E}{\partial z} - \frac{1}{v_g}\frac{\partial E}{\partial t} = \frac{IZ_0\chi}{2\beta\gamma\Delta y}e^{-2\Gamma_0 b}\langle e^{-i\psi}\rangle + \alpha E, \quad (1)$$

where α is the complex attenuation coefficient having positive real part. Note that we are here closely following the notations and derivations given in Ref. 2. Here, I is the electron beam current, Δy is the beam width in the y-direction assumed to be so large that two-dimensional approximation is valid, β is the electron velocity in the unit of speed of light c, γ is the electron energy in unit of rest energy, Z_0 = 377 Ω is the characteristic impedence of free space, $\Gamma_0 = k_0/\gamma$, ψ is the electron phase and χ is the residue of the singularity associated with the surface mode as defined in Ref. 2. Converting to dimensionless variables, this equation can be transformed to the following form

$$\frac{\partial \mathcal{E}}{\partial \tau} - \frac{\partial \mathcal{E}}{\partial \zeta} = -\mathcal{J}\langle e^{-i\psi}\rangle - \alpha L\mathcal{E}, \quad (2)$$

where L is the length of the grating, $\mathcal{E}$ is the dimensionless electric field, $\mathcal{J}$ is the dimensionless beam current, τ is the dimensionless time and $\zeta = z/L$ is the normalised distance along the grating [2]. The second term in the right hand side of the above equation is the contribution due to attenuation. The above equation for the evolution of surface mode electric field will be coupled to equations for the electron beam dynamics as discussed in Ref. 2. We then linearise the equations and look for the solution for the electric field growing as $e^{\nu\tau}$. For a given value of $\mathcal{J}$ and αL, we can obtain the complex growth rate ν by simultaneously solving the following set of two equations

$$\kappa^3 - (\nu + \alpha L)\kappa^2 + i\mathcal{J} = 0. \quad (3)$$

$$\kappa_1^2(\kappa_2 - \kappa_3)e^{\kappa_1} + \kappa_2^2(\kappa_3 - \kappa_1)e^{\kappa_2} + \kappa_3^2(\kappa_1 - \kappa_2)e^{\kappa_3} = 0. \quad (4)$$

Note that we have ignored the space charge parameter Q defined in Ref. 2, and assumed Q = 0. Here, κ_1, κ_2 and κ_3 are three solutions for κ in Eq. (3). For a particular

* Work supported by U.S. Department of Energy, Office of Basic Energy Sciences, under Contract No. W-31-109-ENG-38.
† vinit@cat.ernet.in

value of αL, by solving these equations numerically, we can find out the minimum value of $\mathcal{J}$ for which the real part of ν is positive. Let us call this as dimensionless start current denoted by $\mathcal{J}_s$, which is a function of αL. For the case when there is no attenuation ($\alpha L = 0$), we had earlier obtained that $\mathcal{J}_s$ =7.68 [2]. Here, by numerically solving Eqs. (3) and (4), we obtain the dependence of $\mathcal{J}_s$ on αL. This is shown in Fig. 1. Note that $\mathcal{J}_s$ depends only on the real part of αL.

The expression for the start current density dI_s/dy is given by

$$\frac{dI_s}{dy} = \mathcal{J}_s(\alpha L)\frac{I_A}{2\pi\chi}\frac{\beta^4\gamma^4}{kL^3}e^{2\Gamma_0 b}, \qquad (5)$$

where I_A = 17 kA is the Alfvén current. Here, $k = \omega/c = 2\pi/\lambda$ and λ is the free space wavelength of the surface mode. In the next section, we use the above formula to calculate and optimize the start current.

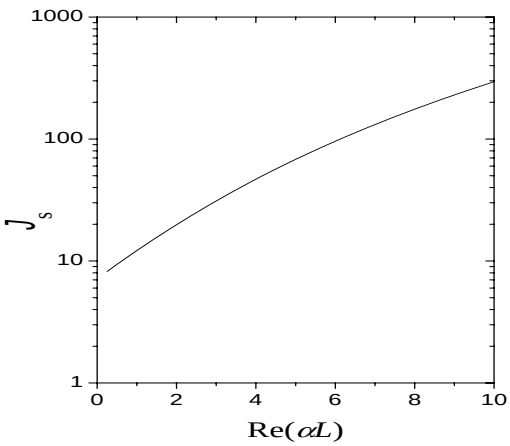

Figure 1: Plot of threshold dimensionless current $\mathcal{J}_s$ as a function of the real part of the attenuation coefficient αL.

OPTIMIZATION OF GRATING PARAMETERS

In the past, many authors [1-5] have used the parameters corresponding to the Dartmouth experiment [6] for studying the performance of SP-BWO. For the Dartmouth experiment, the grating parameters and the electron beam parameters are given in Table 1. Note that we interpret the electron beam radius in Table 1 as the parameter b in our model. Using the formula derived in the previous section, we optimize the grating parameters for this case to minimise the start current.

Table 1: Parameters for the Dartmouth experiment

Groove width (w)	62 μm
Groove depth (d)	100 μm
Period (λ_g)	173 μm
Grating length (L)	12.7 mm
Electron beam radius (b)	10 μm
Electron beam energy	35 keV

First, we calculate the attenuation coefficient for different values of groove depth d and groove width w. For w = 62 μm, we vary the groove depth d and find out the attenuation coefficient α for each groove depth. This is shown in Fig. 2(a). Note that for the calculation of the attenuation coefficient, we have chosen Aluminum as the material of the grating and used the prescription given by Andrews et al. in Ref. 3. Then, keeping w = 62 μm, we calculate χ for different values of d as shown in Fig. 2(b). For the calculation of χ, we have used the prescription given in our earlier paper [2]. Next, knowing the value of α and χ, we use Eq. (5) to obtain the start current density as a function of groove depth for w = 62 μm. As the groove depth increases from 100 μm, the χ parameter increases, which means that the start current density decreases. However, as the groove depth is increased beyond 100 μm, the attenuation also increases, which tends to reduce the start current

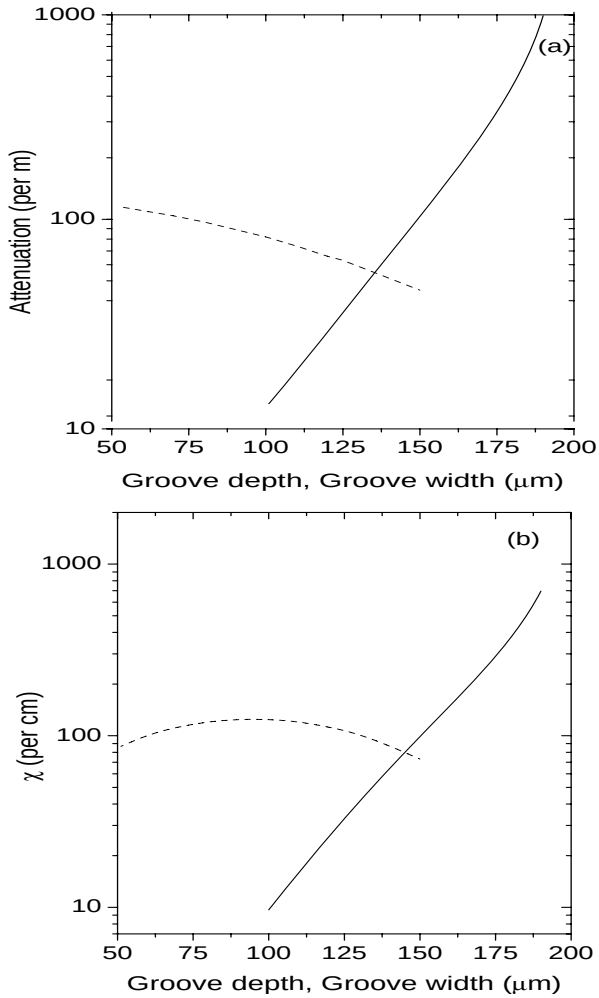

Figure 2: Plot of the real part of attenuation coefficient α (a), and the χ parameter (b) as a function of groove depth (solid curves) for groove width = 62 μm, and as a function of groove width (dashed curves) for groove depth = 150 μm.

density. Consequently, there is an optimum groove depth at which dI_s/dy is minimum. As we find in Fig. 3, the start current density is minimum for d = 150 mm. The value of dI_s/dy reduces from 40 mA/mm to 7.7 mA/mm when the groove depth is changed from 100 μm to 150 μm.

After optimizing the groove depth, we next optimize the groove width. Keeping d = 150 μm, we vary w from 50 μm to 150 μm and obtain the attenuation coefficient and the χ-parameter as shown in Fig. 2. Then, using Eq. (5), we obtain the value of dI_s/dy for different values of groove width, keeping groove depth fixed at 150 μm. This is shown in by the dotted curve in Fig. 3. We find that the optimum value of groove width is 110 μm for which the start current density is 5.6 mA/mm.

Hence, we find that the parameters for the Dartmouth experiment are not optimized for the minimum value of the start current. The optimized value of the groove depth and the groove width are 150 μm and 110 μm respectively. For these parameters, the start current density is 5.6 mA/mm, which is a substantial reduction compared to start current density of 40 mA/mm corresponding to the parameters given in Table 1.

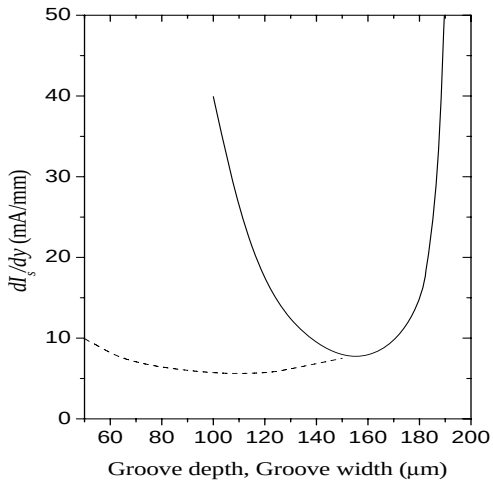

Figure 3: Plot of the start current density dI_s/dy with groove depth (solid line) as well as groove width (dashed line). For the solid line, we have kept groove width fixed at 62 μm. For the dashed line, the groove depth is fixed at 150 μm.

In the above calculations, when we change the groove width and the groove depth, the resonant wavelength λ of the surface mode also changes. The value of λ can be obtained by finding out the location of the singularity of the reflection matrix associated with the surface mode, as discussed in Ref. 2. Fig. 4 shows the variation of the resonant wavelength. We find that for w = 110 μm and d = 150 μm, for which the start current is minimum, the resonant wavelength is 819 μm. Note that for the calculation of dI_s/dy, one needs to put the value of the free-space resonant wavelength λ of the surface mode in Eq. (5), which has been taken from Fig. 4.

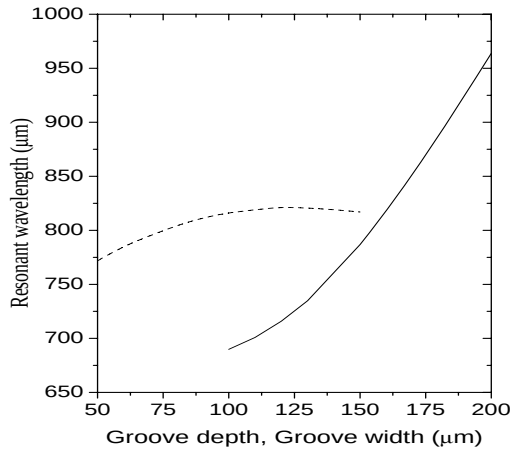

Figure 4: Plot of the free-space resonant wavelength λ with groove depth (solid line) as well as groove width (dashed line). For the solid line, we have kept grove width = 62 μm. For the dashed line, groove depth = 150 μm.

DISCUSSIONS

We would now like to discuss the dependence of the start current on the length of the grating. It is important to include three-dimensional effects for such an analysis [7]. A fully three-dimensional analysis of SP-BWO does not exist yet. However, we will attempt an approximate analysis here. The surface mode in the (y, z) plane is expected to diffract freely as an optical packet of wavelength $\beta\lambda$ since the grating is open in y-direction. The minimum average rms beam size of the optical beam over the length L due to diffraction effects is given by $\sqrt{\beta\lambda L/4\pi}$. In order to maximize the overlap between the electron beam and the optical beam, the rms electron beam size σ_y in the y-direction should be chosen equal to this. Putting the electron beam size in the y-direction in Eq. (5), we obtain that the start current I_s should be proportional to $\mathcal{J}_s(\alpha L)/L^{5/2}$. As we increase the length, the start current increases due to increase in $\mathcal{J}_s$. This is however counterbalanced by the $L^{5/2}$ factor in the denominator. For $\alpha L < 1$, $\mathcal{J}_s$ can be assumed to be slowly varying. Hence, the start current should decrease as $1/L^{5/2}$. For the larger values of αL, the attenuation effects will be dominating since $\mathcal{J}_s$ becomes exponential as shown in Fig. 1. In this case, the start current increases with grating length.

One of the important requirements for the operation of SP-BWO is that the electron beam should be sufficiently close to the grating surface. As the electron beam size in the x-direction increases, the start current increases exponentially due to the $\exp(2\Gamma_0 b)$ factor in Eq. (5). Hence, the rms electron beam size σ_x in the x-direction should be around $1/4\Gamma_0$. In order that the electron beam size in the

x–direction is maintained around this value over a length L, we need that the normalised electron beam emittance ϵ_x is less than $\beta\gamma/L(4\Gamma_0)^2$. We therefore notice that although the start current reduces by increasing the grating length, the requirement on electron beam emittance in the x-direction becomes more stringent.

One should also confirm that the space charge effect does not blow up the emittance. For this to be valid, the space charge term in the envelope equation should be less than the emittance term. This leads to the following condition in the x-direction [7]

$$\frac{4}{\beta\gamma}\frac{I}{I_A}\frac{\sigma_x^3}{(\sigma_x+\sigma_y)\epsilon_x^2} < 1. \qquad (6)$$

It is important to point out here that for the Dartmouth parameters given in Table 1, the above inequality is not satisfied. After optimizing the grating parameters, the start current is reduced and then the above inequality is satisfied.

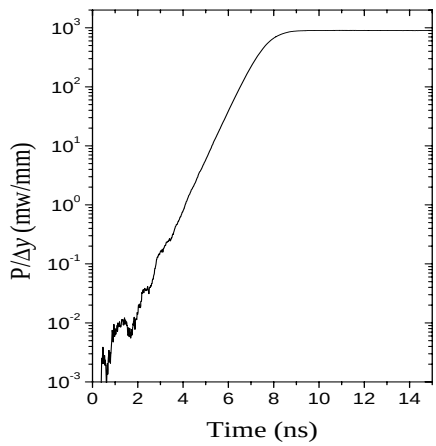

Figure 5: Plot of power per unit beam width in the surface mode as a function of time at the entrance of the grating for the optimized grating prameters.

We would like to point out that for the optimized grating parameters that we discussed, although the start current is reduced significantly compared to the grating parameters in Table 1, the attenuation is increased as seen in Fig. 2. This means that the heat loss in the grating will be more for the optimized parameters, which implies that the power conversion efficiency of SP-BWO will be reduced. For example, for the optimized grating parameters that we discussed, $I_s/\Delta y$ = 5.6 mA/mm. For this case, if we take $I/\Delta y$ = 7 mA/mm, we obtain $P/\Delta y$ = 900 mW/mm at saturation as shown in Fig. 5. This translates to a power conversion efficiency of 0.37%. Note that this calculation is performed by numerically solving the coupled Maxwell-Lorentz equations as discussed in Ref. 8. On the other hand, for the Dartmouth parameters, we have $I_s/\Delta y$ = 40 mA/mm. For this case, if we take $I/\Delta y$ = 50 mA/mm, we obtain $P/\Delta y$ = 14.3 W/mm at saturation. This translates to a power conversion efficiency of 0.56%.

CONCLUSIONS

We have derived a simple formula for the start current density in a SP-BWO taking the attenuation due to finite conductivity of the grating material into account. This formula has been used to optimize the parameters of the grating. We find that for the parameters corresponding to the Dartmouth experiment, the start current can be reduced by six times by optimizing the grating parameters.

ACKNOWLEDGMENTS

It is a pleasure to thank Charlie Brau for many helpful discussions.

REFERENCES

[1] H. L. Andrews and C. A. Brau, Phys. Rev. ST Accel. Beams, 7 (2004) 070701.

[2] V. Kumar and K.-J. Kim, Phys. Rev. E 73 (2006) 026501.

[3] H. L. Andrews et al., Phys. Rev. ST Accel. Beams, 8 (2005) 050703.

[4] J. T. Donohue and J. Gardelle, Phys. Rev. ST Accel. Beams, 9 (2005) 060701.

[5] D. Li et al., Phys. Rev. ST Accel. Beams, 9 (2005) 040701.

[6] J. Urata et al., Phys. Rev. Lett. 80 (1998) 516.

[7] K.-J. Kim and V. Kumar, under preparation.

[8] V. Kumar and K.-J. Kim, these proceedings.

ANALYSIS OF SMITH-PURCELL BWO WITH END REFLECTIONS *

Vinit Kumar†,RRCAT, Indore, M.P. 452013,INDIA
Kwang-Je Kim, ANL, Argonne, IL 60439,USA.

Abstract

We present a one-dimensional time-dependent analysis and simulation of Smith-Purcell (SP) backward wave oscillator (BWO) taking end reflections and attenuation into account. In the linear regime, we obtain an analytic solution and calculate the start current. The dependence of start current on end reflections is studied taking the attenuation due to finite conductivity into account.

INTRODUCTION

The Smith-Purcell (SP) free-electron laser in the terahertz (THz) regime using a low energy electron beam is a backward wave oscillator (BWO) [1,2]. Previous analyses of SP-BWO [1-3] have ignored the reflection at the ends of the grating. However, there will in general be some reflection at the end of the grating due to discontinuity in the medium. One can, if desired, also add external mirrors to enhance reflection. In the presence of reflection, the start current, which is defined as the minimum value of the electron beam current needed to produce coherent electromagnetic oscillations, can be reduced. In this paper, we present a self consistent nonlinear analysis of SP-BWO including end reflections and attenuation. We set up Maxwell-Lorentz equations equations and develop a computer code to solve these equations. We present the results of numerical simulation and discuss the evolution of power. In the linear regime, we solve the coupled Maxwell-Lorentz equations analytically and calculate the start current taking end reflection and attenuation into account.

MAXWELL-LORENTZ EQUATIONS

In a SP-BWO, the electron beam interacts with the backward surface wave co-propagating with the electron beam. We assume that the electron beam is in the form of a thin sheet moving along the z-axis above a metal grating with rectangular grooves, the direction of the grooves is along the y-axis and the outward normal to the grating surface is along the x-axis. The plane of the sheet electron beam is at x = 0, and the top surface of the grating is at $x = -b$. We have earlier studied the interaction between the electron beam and the backward surface mode using Maxwell-Lorentz equations where we ignored the reflection at the end of the grating [2]. The backward surface mode supported by the grating is a linear combination of infinite number of Floquet-Bloch harmonics having the z-component of propagation vectors differing from each other by an integral multiple of k_g, where $k_g = 2\pi/\lambda_g$ and λ_g is the period of the grating. The y-component H_y of the magnetic field of the backward surface mode can be written as $\sum A_n \exp(ik_0 z + ink_g z - \Gamma_n x - i\omega t)$, where the summation is implied over all n from -∞ to +∞ [2]. Here, ω is the frequency, k_0 is the propagation vector of the backward surface mode, $\Gamma_n = \sqrt{(k_0 + nk_g)^2 - \omega^2/c^2}$ and c is the speed of light. The zeroth-order component of this mode has the longitudinal electric field given by $E_-(z,t)\exp(ik_0 z - i\omega t)$ at $x = 0$. The amplitude of all other components of the backward surface mode have to maintain a fixed ratio with the amplitude of the zeroth-order component such that the electromagnetic field satisfies the required boundary conditions. Hence, as the zeroth-order component of the surface mode evolves due to interaction with co-propagating electron beam, the amplitude of all other components also evolve proportionately. One can calculate the group velocity, which is $d\omega/dk$, from the dispersion relation of the backward surface mode. For low energy electron beam, the group velocity of the co-propagating surface mode having $\omega/k_0 = \beta c$ is along the negative z-axis [1,2]. Let us denoted the magnitude of the group velocity by v_g. Here, βc is the velocity of electrons.

For a grating with rectangular grooves considered here, a wave going along the positive z-axis will see the same boundary as the wave going along the negative z-axis. Hence, if we construct a mode having H_y given by $\sum A_n \exp(-ik_0 z - ink_g z - \Gamma_n x - i\omega t)$, it will satisfy the Maxwell equations and the required boundary condition for the reflection grating. This is actually the forward surface mode supported by the grating. This has the propagation vector -k_0 and the group velocity v_g along the positive z-axis. Hence, the grating supports forward as well as backward surface mode. However, none of the components of the forward surface mode co-propagate with the electron beam. Consequently, the forward surface mode does not interact with the electron beam. It however arises due to reflection of the backward wave at the end of the grating. As the backward surface mode extracts energy from the electron beam and grows, it gets reflected at the end to the forward surface mode and consequently the forward surface mode also grows. Let us denote the zeroth-order component of the forward surface mode as $E_+(z,t)\exp(-ik_0 z - i\omega t)$ at the location of sheet electron beam.

In our previous work [2], we had set up Maxwell equation for the backward wave, which is coupled to Lorentz equations for the beam dynamics. We will now add the Maxwell equation for the forward wave to this set of equa-

* Work supported by U.S. Department of Energy, Office of Basic Energy Sciences, under Contract No. W-31-109-ENG-38.
† vinit@cat.ernet.in

tions. We will be following notations used in Ref. 2. The energy flows along the negative z-axis for the backward wave and hence, it gets attenuated along the negative z-axis. Similarly, for the forward wave, the energy flows along the positive z-axis and it gets attenuated along the positive z-axis. The complex attenuation coefficient α for the backward wave supported by a rectangular reflection grating can be obtained as per the prescription given in Ref. 3. For the forward wave, the complex attenuation coefficient will be simply $-\alpha$. Taking the attenuation into account, the equation for the evolution of the amplitude E_+ of the forward wave becomes

$$\frac{\partial E_+}{\partial z} + \frac{1}{v_g}\frac{\partial E_+}{\partial t} = -\alpha E_+. \quad (1)$$

The equation for the evolution of the amplitude E_- of the backward wave as derived earlier is given by [2,4]

$$\frac{\partial E_-}{\partial z} - \frac{1}{v_g}\frac{\partial E_-}{\partial t} = \frac{IZ_0\chi}{2\beta\gamma\Delta y}e^{-2\Gamma_0 b}\langle e^{-i\psi}\rangle + \alpha E_-, \quad (2)$$

where I is the electron beam current, Z_0 = 377 Ω is the characteristic impedence of free space, χ is the residue of the singularity associated with the surface mode as defined in Ref. 2, γ is the energy of the electron beam in unit of rest energy, ψ is the electron phase and Δy is the width of the sheet electron beam in the y-direction. Both these equations are coupled through boundary condition at the end of the grating. Let ρ_0 and ρ_L be the complex reflection coefficient at the entrance and exit end of the grating. The boundary conditions will then given by $E_+(z = 0) = \rho_0 E_-(z = 0)$, and $E_-(z = L)e^{ik_0 L} = \rho_L E_+(z = L)e^{-ik_0 L}$, where L is the length of the grating. The entrance and the exit of the grating are at z = 0 and $z = L$ respectively.

In order to further simplify the analysis, we define a new amplitude of the forward wave given by $E_+ = -\rho_0\tilde{E}_+$. The boundary conditions, in term of this definition can then be written as $\tilde{E}_+(z = 0) = -E(z = 0)$ and $E_-(z = L) = \mathcal{R}e^{-i2k_0 L}\tilde{E}_+(Z = L)$, where $\mathcal{R} = -\rho_0\rho_L$. As discussed in Ref. 2, we can define dimensionless variables and make a transformation from (z, t) to (ζ, τ) to simplify the analysis. Here, $\zeta = z/L$ is the normalised length and τ is the dimensionless time defined in Ref. 2. We define dimensionless amplitude of the forward and the backward wave denoted by $\mathcal{E}_+$ and $\mathcal{E}_-$ respectively as

$$\mathcal{E}_\pm = \frac{4\pi}{I_A Z_0}\frac{k_0 L^2}{\beta^2\gamma^3}\tilde{E}_\pm\ , \quad (3)$$

where I_A = 17 kA is the Alfvén current and $\tilde{E}_- = E_-$. After making these transformations, the equation for evolution of $\mathcal{E}_+$ and $\mathcal{E}_-$ are given by

$$\frac{\partial\mathcal{E}_-}{\partial\tau} - \frac{\partial\mathcal{E}_-}{\partial\zeta} = -\mathcal{J}\langle e^{-i\psi}\rangle - \alpha L\mathcal{E}_-, \quad (4)$$

$$\frac{\partial\mathcal{E}_+}{\partial\tau} + d_1\frac{\partial\mathcal{E}_+}{\partial\zeta} = -d_1\alpha L\mathcal{E}_+, \quad (5)$$

where $d_1 = (v_p + v_g)/(v_p - v_g)$. The boundary conditions now become $\mathcal{E}_+(\zeta = 0) = -\mathcal{E}_-(\zeta = 0)$ and $\mathcal{E}_-(\zeta = 1) = \mathcal{R}e^{-i2k_0 L}\mathcal{E}_+(\zeta = 1)$. These equations are coupled to the electron beam dynamics equations

$$\frac{\partial\eta_i}{\partial\zeta} = (\mathcal{E}_- + \mathcal{E}_{sc})e^{i\psi_i} + c.c., \quad (6)$$

$$\frac{\partial\psi_i}{\partial\zeta} = \eta_i, \quad (7)$$

where the $\mathcal{E}_{sc}$ is the dimensionless longitudinal electric field due to space charge given by $\mathcal{E}_{sc} = iQ\langle e^{-i\psi}\rangle$, and $Q = (\mathcal{J}/\chi L)(\chi_1 - e^{2\Gamma_0 b})$. The χ_1-parameter appears in the analysis of singularity associated with the surface mode and can be calculated as per prescription discussed in Ref. 2. Here the subscript i stands for i^{th} electron and $\eta_i = (\gamma_i - \gamma)/\gamma$ is the relative energy deviation of the i^{th} electron. Eqs. (4-7) along with the boundary conditions form the complete set of differential equations needed to describe the one-dimensional time-dependent behavior of SP-BWO with end reflections and attenuation. In the next section, we discuss the analytic solution of these equations in the linear regime.

LINEAR ANALYSIS

We can linearize Eqs. (4-7) around an equilibrium solution and perform a stability analysis to find out the parameter regime in which the instability for exchange of energy from electron beam to electromagnetic oscillation can be excited. For simplicity, let us assume that the injected beam is monoenergetic, and η_i = 0 for all the electrons at ζ = 0. Further, we assume that the injected beam is unbunched, i.e., $\langle e^{-i\psi_0}\rangle$ = 0, where $\psi_{0,i}$ is the phase of the i^{th} particle at ζ = 0. An equilibrium solution of the system of Eqs. (4-7) is obviously $\mathcal{E}_- = 0, \mathcal{E}_+ = 0, \eta_i = 0$, and $\psi_i = \psi_{0,i}$. Let us define the perturbative solution by $\mathcal{E}_-$ = $\tilde{\epsilon}_-$, $\mathcal{E}_+ = \tilde{\epsilon}_+$, $\eta_i = \delta\eta_i$, and $\psi_i = \psi_{0,i} + \delta\psi_i$. We introduce the following collective variables as done by Bonifacio et al. [5] for conventional FELs:

$$\tilde{x} = \langle\delta\psi e^{-i\psi_0}\rangle, \qquad \tilde{y} = \langle\delta\eta e^{-i\psi_0}\rangle. \quad (8)$$

In terms of these variables, Eqs. (4-7) can be linearized and written as

$$\frac{\partial\tilde{\epsilon}_-}{\partial\tau} - \frac{\partial\tilde{\epsilon}_-}{\partial\zeta} = i\mathcal{J}\tilde{x} - \alpha L\tilde{\epsilon}_-, \quad (9)$$

$$\frac{\partial\tilde{\epsilon}_+}{\partial\tau} + d_1\frac{\partial\tilde{\epsilon}_+}{\partial\zeta} = -d_1\alpha L\tilde{\epsilon}_+, \quad (10)$$

$$\frac{\partial\tilde{x}}{\partial\zeta} = \tilde{y}, \quad (11)$$

$$\frac{\partial\tilde{y}}{\partial\zeta} = \tilde{\epsilon}_- + Q\tilde{x}. \quad (12)$$

The boundary conditions for these equations are: (1) $\tilde{x} = 0$ at ζ = 0 at all τ since the injected beam has no phase modulation, i.e., it is injected unbunched. (2) $\tilde{y} = 0$ at ζ =

0 at all τ since the injected beam has no energy modulation, i.e., it is injected monoenergetically. (3) $\tilde{\epsilon}_+ = -\tilde{\epsilon}_-$ at $\zeta = 0$ for all τ, and $\tilde{\epsilon}_- = \mathcal{R}e^{-i2k_0L}\tilde{\epsilon}_+$ at $\zeta = 1$ for all τ. Assuming a solution of the type $e^{\nu\tau}$, we can find out the growth rate ν for the above linearised equations with the boundary conditions. In order to find out the growth rate ν, one has to first solve the following cubic equation

$$\kappa^3 - (\nu + \alpha L)\kappa^2 - Q\kappa + \nu Q + i\mathcal{J} = 0. \qquad (13)$$

Then, the three roots of the above cubic equation κ_1, κ_2 and κ_3 should satisfy the following transcendental equation

$$\begin{aligned}\mathcal{R}e^{-\alpha L}e^{-i(2k_0L - i\frac{\nu}{d_1})}[(\kappa_1^2 - Q)(\kappa_2 - \kappa_3)\\ +(\kappa_2^2 - Q)(\kappa_3 - \kappa_1) + (\kappa_3^2 - Q)(\kappa_1 - \kappa_2)]\\ +(\kappa_1^2 - Q)(\kappa_2 - \kappa_3)e^{\kappa_1} + (\kappa_2^2 - Q)(\kappa_3 - \kappa_1)e^{\kappa_2}\\ +(\kappa_3^2 - Q)(\kappa_1 - \kappa_2)e^{\kappa_3} = 0. \qquad (14)\end{aligned}$$

By solving the above two equations, we can find out the minimum value of $\mathcal{J}$, called the dimensionless start current $\mathcal{J}_s$ for a given Q, $\mathcal{R}$, α and L, for which the real part of the complex growth rate ν is positive.

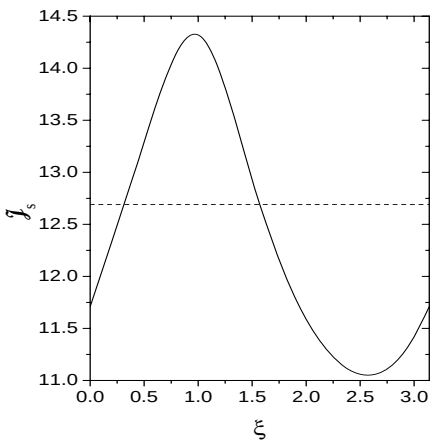

Figure 1: Variation in the dimensionless start current with ξ for $\mathcal{R}$ = 0.8 (solid curve) and $\mathcal{R}$ = 0 (dashed curve).

Next, we use Eqs. (13-14) for the calculation of start current. In a companion paper [4], we have optimized the parameters corresponding to Dartmouth experiment [6] taking attenuation into account, but excluding end reflection. We use those parameters for calculation of start current here. For the grating, we use groove depth d = 150 μm, groove width w = 110 μm, period λ_g = 173 μm and length L = 12.7 mm. For the 35 keV sheet electron beam, we use b = 10 μm. From our calculation [2], for these parameters, we obtain the free-space wavelength λ = 819 μm, χ = 120 per cm, χ_1 = 3.9, $\alpha L = 0.94(1 - i)$ and v_g/c = 0.0925. Note that in Eq. (14), for a given grating length, when we change the electron beam energy, the value of k_0 will change, which will change the phase factor term e^{-2ik_0L}. Let us define ξ = mod(k_0L, π). Hence, for a given set of parameters, if we make a slight change in the electron beam energy, the value of ξ changes accordingly and affects the value of start current. For our parameters, Q is very small, and we take Q = 0. Figure 1 shows the variation of dimensionless start current $\mathcal{J}_s$ with ξ for $\mathcal{R}$ = 0.8. We find that that the value of $\mathcal{J}_s$ oscillates between 11.1 and 14.2. Note that the start current density corresponding to $\mathcal{J}$ = 11.1 is 4.7 mA/mm. The value of $\mathcal{J}_s$ is 12.7, when we neglect end reflection. When the attenuation is smaller, the effect of end reflection is more pronounced.

NUMERICAL SIMULATION

For numerically solving Eqs. (4-7), we use the approach used by Ginzburg et al. [7] and later also by Levush et al. [8] for BWO. The electron dynamics equations for a given field distribution along the interaction region are solved by the predictor-corrector method. Then, knowing the modified electron distribution in phase space, the field distribution at the next time step is obtained by solving the partial differential equations (Eqs. 4-5) by the finite difference method. The method is stable for $\Delta\tau < \Delta\zeta$ for the backward wave and for $\Delta\tau < (1/d_1)\Delta\zeta$ for the forward wave. Here, $\Delta\tau$ and $\Delta\zeta$ are the step sizes in τ and ζ respectively, used in the finite difference method.

For initializing the electron beam in phase space, we simulate the shot noise using the algorithm given by Penman and McNeil [9], which is commonly used in FEL codes.

We performed a couple of tests on the code we developed. We first checked for the convergence of the solution by increasing the number of particles and also by reducing the step size. Based on this convergence test, we chose the number of particles to be used in the simulation as 1024 and the step sizes as $\Delta\tau$ = 0.01 and $\Delta\zeta$ = 0.02. We also confirmed that the energy conservation equation along with the damping term due to attenuation is satisfied in the code at each integration step.

Figure 2 shows the evolution of power in the backward wave at the entrance of the grating for $\mathcal{J}$ = 11.6 and $\mathcal{J}$ = 10.6. The parameters used in the calculation are same as mentioned in the last section. We have chosen ξ = 2.5 for which $\mathcal{J}_s$ is minimum as shown in Fig. 1. For these parameters, $\mathcal{J}_s$ = 11.1 and hence for the case $\mathcal{J}$ = 10.6, there is no build-up of power, whereas for the case $\mathcal{J}$ = 11.6, we find that the power grows exponentially and saturates. Note that $I/\Delta y$ = 4.9 mA/mm for $\mathcal{J}$ = 11.6. After saturation, the variation of the amplitude of electric field for the forward as well as the backward wave along the length of the grating is shown in Fig. 3.

Let us now discuss the calculation of outcoupled power. Power in the backward and the forward surface mode denoted by P_- and P_+ respectively can be obtained by the following expression

$$\frac{P}{\Delta y} = 2\frac{\beta\gamma}{Z_0\chi}\left(\frac{mc^2\beta^3\gamma^3}{ek_0L^2}\right)^2 e^{2\Gamma_0 b}|\mathcal{E}|^2, \qquad (15)$$

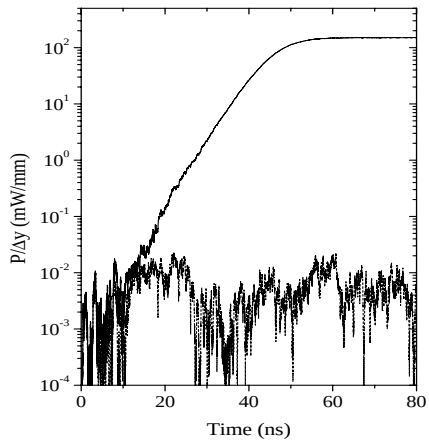

Figure 2: Evolution of power in the backward wave at the entrance of the undulator for $\mathcal{J}$ = 11.6 (solid curve), and $\mathcal{J}$ = 10.6 (dashed curve). We have used $\mathcal{R}$ = 0.8 and ξ = 2.5 in the calculation.

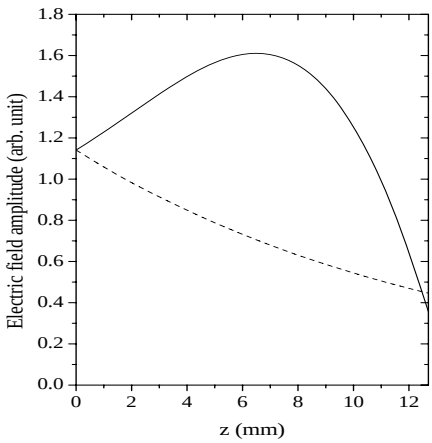

Figure 3: Variation of the amplitide $|\mathcal{E}_-|$ of the backward wave (solid curve) and the amplitude $|\mathcal{E}_+|$ of the forward wave (dashed curve) along the length of the grating for $\mathcal{J}$ = 11.6. Other parameters are same as those used in Fig. 2.

where $P = P_-$ for $\mathcal{E} = \mathcal{E}_-$ and $P = P_+$ for $\mathcal{E} = \rho_0\mathcal{E}_+$. The outcoupled power P_0 at the entrance of the grating is given by $P_-(z = 0) - P_+(z = 0)$ and at the exit, the outcoupled power P_1 is given by $P_+(z = L) - P_-(z = L)$. If we assume $\rho_L = 1$, the power will be outcoupled only at the entrance of the grating. For the case of Fig. 3, the outcoupled power is calculated to be 54 mW for Δy = 1 mm. The total power in the electron beam for this case is 171.5 W for 35 keV, 4.9 mA electron beam current. Hence, the overall efficiency is only 0.03%. Such a low efficiency is there beacuse we have chosen the electron beam current very close to the start current and also the heat loss occurring in the grating due to attenuation deteriorates the efficiency. We have checked that the efficiency is improved at higher value of beam current. Our emphasis here is to show that including reflection, it is possible to reduce the start current surface density to as low as 4.7 mA/mm.

In our calculation, we have not calculated the value of reflectivity, instead we have assumed a value for reflectivity. In a realistic situation, there will be some reflectivity at the end of the grating due to change of boundary, which needs to be calculated. However, we can put an external mirror and the reflectivity $\mathcal{R}$ can be adjusted to a desired value. By introducing a reflectivity, the start current is reduced, but the outcoupled power may not be optimized. Using our calculation in the saturation regime, one can optimize the parameters to obtain optimum combination of start current and outcoupled power.

CONCLUSIONS

In this paper, we have set up Maxwell-Lorentz equations for the one-dimensional time-dependent analysis of SP-BWO including end reflection and attenuation due to finite conductivity. We have obtained a solution in the linear regime and extended the analysis to the nonlinear regime by solving the Maxwell-Lorentz equations numerically. Our analysis can be used for detailed optimization of outcoupled power and start current in SP-BWO taking end reflection and attenuation into account.

REFERENCES

[1] H. L. Andrews and C. A. Brau, Phys. Rev. ST Accel. Beams, 7 (2004) 070701.

[2] V. Kumar and K.-J. Kim, Phys. Rev. E 73 (2006) 026501.

[3] H. L. Andrews et al., Phys. Rev. ST Accel. Beams, 8 (2005) 050703.

[4] V. Kumar and K.-J. Kim, these proceedings

[5] R. Bonifacio, C. Pelligrini, and L. M. Narducci, Opt. Commun. **40** 373 (1984).

[6] J. Urata et al., Phys. Rev. Lett. 80 (1998) 516.

[7] N. S. Gingburg, S. P. Kuznetov, and T. N. Fedoseeva, Sov. Radiophys. Electron., 21 (1979) 728.

[8] B. Levush et al., IEEE Trans. Plasma Sci. 20, (1992) 263.

[9] C. Penman and B. W. J. McNeil, Opt. Commun. 90 (1992) 82.

MODE COUPLINGS IN A RAMAN FREE-ELECTRON LASER WITH ION-CHANNEL GUIDING

B. Maraghechi[a,b,*], T. Mohsenpour[a]
[a] Department of Physics, Amirkabir University of Technology, Tehran, Iran
[b] Institute for Studies in Theoretical Physics and Mathematics (IPM),
P.O. Box 19395-5531, Tehran, Iran.

Abstract

The free-electron laser (FEL) theory in the collective or Raman regime relies on the unstable coupling between the radiation and the negative-energy space-charge wave. Due to the high density and low energy of electron beam a focusing mechanism like an axial magnetic field is usually required to guide the beam. It is found that the wiggler has direct effect on the right and left waves and the wiggler effect on their dispersion relations are of the second order in the wiggler amplitude. Due to the fully relativistic treatment the dispersion relation is to fourth order in wiggler amplitude and it can be used to study new couplings between the negative and positive-energy space-charge waves as well as between the right and left circularly polarized electromagnetic waves.

INTRODUCTION

Relativistic electron bean injected into an ionized plasma channel ejects plasma electrons leaving a positive ion core which attracts and confines the beam electron. There are important applications in this subject such as advanced accelerators [1] and free-electron lasers (FELs) [2,3]. Ion-channel guiding as an alternative to the conventional axial magnetic-filed guiding, was first proposed for use in FELs by Takayama and Hiramatsu [4]. Experimental results of a FEL with ion-channel guiding have been reported by Ozaki at al. [5] Also, Yu et al. [6] have reported that the combination of ion focusing and beam conditioning would lead to high gain FEL operation in the soft x-ray regime. Jha and Wurtele [7] developed a three-dimensional code for FEL simulation that allows for the effects of an ion channel. The theoretical studies of this problem with a helical wiggler are carried out in the low-gain [8] and high-gain [9,10] regimes. In Ref 10, the relativistic Raman backscattering theory is used to find the FEL dispersion relation with ion-channel guiding, in the beam frame of electrons, with the left circularly polarized backscattered wave neglected. This DR was used to find the growth rate of the FEL resonance due to the coupling of radiation with the slow space-charge wave.

The purpose of the present investigation is to obtain the dispersion relation (DR) for the interaction of all possible waves in a relativistic electron bean that passes through a one-dimensional helical wiggler magnetic field with ion-channel guiding. The motion of a relativistic electron through the wiggler is analyzed. Three coupled equations are derived and a formula for the general DR is obtained.

* Electronic mail: behrouz@aut.ac.ir

ELECTRON MOTION

Consider a relativistic electron moving along the z axis of an idealized helical wiggler magnetic field described by

$$\mathbf{B} = B_w\left(\hat{\mathbf{x}}\cos k_w z + \hat{\mathbf{y}}\sin k_w z\right), \tag{1}$$

where B_w denotes the wiggler amplitude, and $k_w\left(=2\pi/\lambda_w\right)$ is wiggler wave number. In the presence of an ion channel, with its axis coincident with the wiggler axis, the following transverse electrostatic field is acted on the electron beam

$$\mathbf{E}_i = 2\pi e n_i\left(x\,\hat{\mathbf{x}} + y\,\hat{\mathbf{y}}\right), \tag{2}$$

where n_i is the number density of positive ions with charge e. The steady-state motion of an electron in the above field consists of an axis centred helical motion, with radius $R_0 = v_w/k_w v_\parallel$, given by Eq. (16) with [8,11]

$$v_w = \frac{\Omega_w k_w v_\parallel^2}{\omega_i^2 - k_w^2 v_\parallel^2}, \tag{3}$$

where $\Omega_w \equiv eB_w/\gamma mc$, $\omega_i^2 = 2\pi n_i e^2/\gamma m$, m is the electron rest mass, e is the magnitude of the charge of an electron, and c is the speed of light in vacuum. This velocity is related to the axial velocity $v_\parallel$ through

$$\gamma_0^{-2} = 1 - \frac{v_w^2}{c^2} - \frac{v_\parallel^2}{c^2}. \tag{4}$$

Equation (4) is cubic in $v_\parallel^2/c^2$ and describes two classes of trajectories propagating along the positive z axis of the FEL.

DISPERSION RELATION

An analysis of the propagation of electromagnetic/electrostatic waves in the electron beam may be based on the continuity equation,

$$\frac{\partial n}{\partial t} + \nabla\cdot\left(n\mathbf{v}\right) = 0, \tag{5}$$

the relativistic momentum equation

$$\frac{d\,\mathbf{v}}{d\,t} = -\frac{e}{\gamma m_0}\left(\mathbf{E} - \frac{1}{c^2}\mathbf{v}\,\mathbf{v}\cdot\mathbf{E} + \frac{1}{c}\mathbf{v}\times\mathbf{B}\right), \tag{6}$$

and the wave equation

$$\nabla\times\left(\nabla\times\mathbf{E}\right)+\frac{1}{c^2}\frac{\partial^2\mathbf{E}}{\partial t^2}=\frac{\partial}{\partial t}\frac{4\pi e n\mathbf{v}}{c^2}. \quad (7)$$

Here n is the electron density, $\mathbf{v}$ is the electron velocity, γ is the Lorentz factor corresponding to $\mathbf{v}$, $\mathbf{E}$ is the electric field, and $\mathbf{B}$ is the magnetic field. With the unperturbed electron density n_0 taken to be independent of position and time and the self-fields of the unperturbed state neglected, the electron and field variables may be expressed in the form

$$n=n_0+\delta n, \quad (8)$$

$$\mathbf{v}=\mathbf{v}_0+\delta\mathbf{v}, \quad (9)$$

$$\mathbf{E}=\mathbf{E}_i+\delta\mathbf{E}, \quad (10)$$

$$\mathbf{B}=\mathbf{B}_w+\delta\mathbf{B}, \quad (11)$$

$$\mathbf{R}=\mathbf{R}_0+\delta\mathbf{R} \quad (12)$$

The linearized equations for the continuity equation, the relativistic momentum equation, and the wave equation may be derived as

$$\frac{\partial\delta n}{\partial t}+n_0\nabla\cdot\delta\mathbf{v}+\mathbf{v}_0\cdot\nabla\delta n=0, \quad (13)$$

$$\frac{\partial\delta\mathbf{v}}{\partial t}+\mathbf{v}_0\cdot\nabla\delta\mathbf{v}+\delta\mathbf{v}\cdot\nabla\mathbf{v}_0=-\frac{e}{\gamma_0 m_0}\left[\delta\mathbf{E}-\frac{1}{c^2}\mathbf{v}_0\mathbf{v}_0\cdot\delta\mathbf{E}\right.$$
$$-\frac{1}{c^2}\mathbf{v}_0\delta\mathbf{v}\cdot\mathbf{E}_i-\frac{1}{c^2}\delta\mathbf{v}\mathbf{v}_0\cdot\mathbf{E}_i+\frac{1}{c}\delta\mathbf{v}\times\mathbf{B}_w+\frac{1}{c}\mathbf{v}_0\times\delta\mathbf{B}$$
$$\left.-\frac{\gamma_0^2}{c^2}\left(\mathbf{E}_i+\frac{1}{c}\mathbf{v}_0\times\mathbf{B}_w-\frac{1}{c^2}\mathbf{v}_0\mathbf{v}_0\cdot\mathbf{E}_i\right)\left(\mathbf{v}_0\cdot\delta\mathbf{v}\right)\right], \quad (14)$$

$$\nabla\times\left(\nabla\times\delta\mathbf{E}\right)+\frac{1}{c^2}\frac{\partial^2\delta\mathbf{E}}{\partial t^2}=\frac{\partial}{\partial t}\frac{4\pi e}{c^2}\left(\delta n\mathbf{v}_0+n_0\delta\mathbf{v}\right). \quad (15)$$

By introducing a new set of basis vectors $\hat{\mathbf{e}}=\left(\hat{\mathbf{x}}+i\hat{\mathbf{y}}\right)/\sqrt{2}$, $\hat{\mathbf{e}}^*=\left(\hat{\mathbf{x}}-i\hat{\mathbf{y}}\right)/\sqrt{2}$, and $\hat{\mathbf{e}}=\hat{\mathbf{z}}$, the unperturbed magnetic field, electron density, and transverse electrostatic field can be written as

$$\mathbf{B}_w=\left(B_w/\sqrt{2}\right)\exp(-ik_w z)\hat{\mathbf{e}}+\left(B_w/\sqrt{2}\right)\exp(ik_w z)\hat{\mathbf{e}}^*, \quad (16)$$

$$\mathbf{v}_0=\left(v_w/\sqrt{2}\right)\exp(-ik_w z)\hat{\mathbf{e}}+\left(v_w/\sqrt{2}\right)\exp(ik_w z)\hat{\mathbf{e}}^*+v_\parallel\hat{\mathbf{e}}_z, \quad (17)$$

$$\mathbf{E}_i=i\sqrt{2}\,\pi e n_i R_0\left(\exp(-ik_w z)\hat{\mathbf{e}}+\exp(ik_w z)\hat{\mathbf{e}}^*\right), \quad (18)$$

The perturbed state is assumed to consist of a longitudinal space-charge wave and right and left circularly polarized electromagnetic waves, referred here as radiation, with all perturbed waves propagating in the positive z direction. Accordingly, solution of the system of equations (13)-(15) may be assumed as

$$\delta\mathbf{v}=\delta v_R\hat{\mathbf{e}}+\delta v_L\hat{\mathbf{e}}^*+\delta v_Z\hat{\mathbf{e}}_z, \quad (19)$$

$$\delta\mathbf{E}=\left(2\pi e n_i\delta R_R+\delta E_R\right)\hat{\mathbf{e}}+\left(2\pi e n_i\delta R_L+\delta E_L\right)\hat{\mathbf{e}}^*+\delta E_Z\hat{\mathbf{e}}_z, \quad (20)$$

$$\delta\mathbf{B}=\delta B_R\hat{\mathbf{e}}+\delta B_L\hat{\mathbf{e}}^*, \quad (21)$$

$$\delta\mathbf{R}=\delta R_R\hat{\mathbf{e}}+\delta R_L\hat{\mathbf{e}}^* \quad (22)$$

$$\delta n=\tilde{n}\exp[i(kz-\omega t)], \quad (23)$$

$$\delta v_R=\tilde{v}_R\exp[i(k_R z-\omega t)], \quad (24)$$

$$\delta v_L=\tilde{v}_L\exp[i(k_L z-\omega t)], \quad (25)$$

δv_z and δE_z are analogous to δn; δE_R, δR_R, and δB_R are analogous to δv_R; δE_L, δR_L, and δB_L are analogous to δv_L; the wave numbers are related to by

$$k_R=k-k_w, \quad (26)$$

$$k_L=k+k_w. \quad (27)$$

The linearized wave equation yield

$$\left(k_R^2c^2-\omega^2\right)\tilde{E}_R=-4\pi ie\omega\left(\tilde{n}\frac{v_w}{\sqrt{2}}+n_0\tilde{v}_R\right), \quad (28)$$

$$\left(k_L^2c^2-\omega^2\right)\tilde{E}_L=-4\pi ie\omega\left(\tilde{n}\frac{v_w}{\sqrt{2}}+n_0\tilde{v}_L\right), \quad (29)$$

$$-\omega^2\tilde{E}_z=-4\pi ie\omega\left(\tilde{n}v_\parallel+n_0\tilde{v}_z\right). \quad (30)$$

Similarly, the linearized continuity and momentum equations yield

$$\tilde{n}\left(\omega-kv_\parallel\right)=n_0k\tilde{v}_z, \quad (31)$$

$$\left[\omega-k_Rv_\parallel-\frac{\omega_i^2}{\omega-k_Rv_\parallel}\left(1-\frac{v_w^2}{2c^2}\right)-\frac{\omega_i^2}{k_wv_\parallel}\frac{v_w^2}{2c^2}+A_1\right]\tilde{v}_R$$
$$+\left[\frac{\omega_i^2}{k_wv_\parallel}\frac{v_w^2}{2c^2}+\frac{\omega_i^2}{\omega-k_Lv_\parallel}\frac{v_w^2}{2c^2}+A_1\right]\tilde{v}_L+\frac{ie}{\gamma_0m_0}\left[\left(1\right.\right.$$
$$\left.\left.-\frac{v_w^2}{2c^2}\right)-\frac{k_Rv_\parallel}{\omega}\right]\tilde{E}_R-\frac{ie}{\gamma_0m_0}\frac{v_w^2}{2c^2}\tilde{E}_L-\frac{ie}{\gamma_0m_0}\frac{v_wv_\parallel}{\sqrt{2}c^2}\tilde{E}_z$$
$$+A_2\tilde{v}_z=0, \quad (32)$$

$$\left[\omega-k_Lv_\parallel-\frac{\omega_i^2}{\omega-k_Lv_\parallel}\left(1-\frac{v_w^2}{2c^2}\right)+\frac{\omega_i^2}{k_wv_\parallel}\frac{v_w^2}{2c^2}-A_1\right]\tilde{v}_L$$
$$+\left[-\frac{\omega_i^2}{k_wv_\parallel}\frac{v_w^2}{2c^2}+\frac{\omega_i^2}{\omega-k_Rv_\parallel}\frac{v_w^2}{2c^2}-A_1\right]\tilde{v}_R+\frac{ie}{\gamma_0m_0}\left[\left(1\right.\right.$$
$$\left.\left.-\frac{v_w^2}{2c^2}\right)-\frac{k_Lv_\parallel}{\omega}\right]\tilde{E}_L-\frac{ie}{\gamma_0m_0}\frac{v_w^2}{2c^2}\tilde{E}_R-\frac{ie}{\gamma_0m_0}\frac{v_wv_\parallel}{\sqrt{2}c^2}\tilde{E}_z$$
$$-A_2\tilde{v}_z=0, \quad (33)$$

$$-i\left(\omega-kv_\parallel\right)\tilde{v}_z+\frac{e}{\gamma_0m_0}\left(1-\frac{v_\parallel^2}{c^2}\right)\tilde{E}_z+\frac{e}{\gamma_0m_0}\left[-\frac{v_wv_\parallel}{\sqrt{2}c^2}\right.$$
$$\left.+\frac{k_Rc}{\omega}\frac{v_w}{\sqrt{2}c}\right]\tilde{E}_R+\frac{e}{\gamma_0m_0}\left[-\frac{v_wv_\parallel}{\sqrt{2}c^2}+\frac{k_Lc}{\omega}\frac{v_w}{\sqrt{2}c}\right]\tilde{E}_L$$
$$+i\left[\left(\frac{\omega_i^2}{k_wv_\parallel}-\frac{\omega_i^2}{\omega-k_Rv_\parallel}\right)\frac{v_wv_\parallel}{\sqrt{2}c^2}-\frac{\Omega_w}{\sqrt{2}}\right]\tilde{v}_R$$
$$+i\left[\left(-\frac{\omega_i^2}{k_wv_\parallel}-\frac{\omega_i^2}{\omega-k_Lv_\parallel}\right)\frac{v_wv_\parallel}{\sqrt{2}c^2}+\frac{\Omega_w}{\sqrt{2}}\right]\tilde{v}_L=0, \quad (34)$$

where

$$\gamma_{\|}^{-2} = 1 - \frac{v_{\|}^2}{c^2}, \tag{35}$$

$$A_L = k_L^2 c^2 - \omega^2, \tag{36}$$

$$A_R = k_R^2 c^2 - \omega^2, \tag{37}$$

$$A_1 = \left(\frac{1}{2}\right)\gamma_0^2 \frac{v_w}{c}\left(\frac{v_w}{c}\frac{\omega_i^2}{k_w v_{\|}} - \frac{v_{\|}}{c}\Omega_w\right), \tag{38}$$

$$A_2 = \left(\frac{1}{\sqrt{2}}\right)\left(k_w v_w + \Omega_w\right) + \left(\frac{1}{\sqrt{2}}\right)\gamma_0^2 \frac{v_{\|}}{c}\left(\frac{v_w}{c}\frac{\omega_i^2}{k_w v_{\|}} - \frac{v_{\|}}{c}\Omega_w\right). \tag{39}$$

The electron density $\tilde{n}$ may be eliminated in (30) by use of (29) to obtain

$$\tilde{v}_z = -i\frac{\omega - k v_{\|}}{4\pi e n_0}\tilde{E}_z. \tag{40}$$

with the use of Eqs. (28)-(31) and (40), $\tilde{v}_R$, $\tilde{v}_L$ and $\tilde{v}_z$ may be eliminated in the three components of the momentum equation (32)-(34) to obtain

$$\left[D_R^0 + \psi_R^+ v_w^2/c^2\right]\tilde{E}_R + \left[\psi_L^- v_w^2/c^2\right]\tilde{E}_L + \left[\xi_{R1} v_w/c + M^+ v_w^3/c^3\right]\tilde{E}_z = 0, \tag{41}$$

$$\psi_R^-\left(v_w^2/c^2\right)\tilde{E}_R + \left[D_L^0 + \psi_L^+ v_w^2/c^2\right]\tilde{E}_L + \left[\xi_{L1} v_w/c + M^- v_w^3/c^3\right]\tilde{E}_z = 0, \tag{42}$$

$$\xi_{R2}\left(\frac{v_w}{c}\right)\tilde{E}_R + \xi_{L2}\left(\frac{v_w}{c}\right)\tilde{E}_L - \omega\left[\varepsilon^0 + k v_{\|}\left(\frac{\omega_i^2}{\omega - k_L v_{\|}} + \frac{\omega_i^2}{\omega - k_R v_{\|}}\right)\frac{v_w^2}{2c^2}\right]\tilde{E}_z = 0, \tag{43}$$

where D_R^0, D_L^0, $\psi_R^{\pm}$, $\psi_L^{\pm}$, $M^{\pm}$, ξ_{R1}, ξ_{R2}, ξ_{L1}, ξ_{L2}, ε^0 are defined in the appendix. Here, D_R^0, D_L^0, and ε^0 are the uncoupled dispersion relations, i.e., in the absence of the wiggler, for the right and left circularly polarized electromagnetic waves, and the space-charge wave, respectively. Equations (41) and (42) show that the DR for the right and left waves, alone, in the absence of the other two waves, are

$$D_R = D_R^0 + \psi_R^+\left(v_w^2/c^2\right) = 0, \tag{44}$$

$$D_L = D_L^0 + \psi_L^+\left(v_w^2/c^2\right) = 0, \tag{45}$$

which indicate that the wiggler has direct effect on the right and left waves and the wiggler effect on their DRs are of the second order in the wiggler amplitude. On the other hand, Eq. (43) Shows that the DR for the space-charge wave in the absence of the right and left wave is $\varepsilon^0 = 0$, which indicates that the wiggler has no direct effect on the space-charge wave. The reason is that the transverse helical motion of electrons, due to the wiggler, has no effect on the longitudinal oscillations of the space-charge wave. Therefore, if the electromagnetic waves are removed the wiggler effect on the space-charge wave will also be removed and the space-charge wave will be unaffected by the wiggler in the absence of the transverse electromagnetic waves.

The necessary and sufficient condition for a nontrivial solution consists of the determinant of coefficients in Eqs. (41)-(43) equated to zero. Imposing this condition yields the dispersion relation

$$\omega\left[\varepsilon^0 + \omega k v_{\|}\left(\frac{\omega_i^2}{\omega - k_L v_{\|}} + \frac{\omega_i^2}{\omega - k_R v_{\|}}\right)\right]D_R D_L = -\left[D_R \xi_{L2}\left(\xi_{L1} + M^- \frac{v_w^2}{c^2}\right) + D_L \xi_{R2}\left(\xi_{R1} + M^+ \frac{v_w^2}{c^2}\right)\right]\frac{v_w^2}{c^2} + \left[\psi_L^- \xi_{R2}\left(\xi_{L1} + M^- \frac{v_w^2}{c^2}\right) + \psi_R^- \xi_{L2}\left(\xi_{R1} + M^+ \frac{v_w^2}{c^2}\right) + \omega\varepsilon^0 \psi_L^- \psi_R^- + \psi_L^- \psi_R^- \omega k v_{\|}\left(\frac{\omega_i^2}{\omega - k_L v_{\|}} + \frac{\omega_i^2}{\omega - k_R v_{\|}}\right)\right]\frac{v_w^4}{c^4}. \tag{46}$$

Equation (46) is the DR for coupled electrostatic and electromagnetic waves propagating along a relativistic electron beam in the presence of a wiggler magnetic field and an axial guide magnetic field. A numerical analysis of the general dispersion relation can be used to study interactions among all possible waves. In group II orbits, with relatively large wiggler induced velocities, new couplings between the negative and positive-energy space-charge waves as well as between the right and left circularly polarized electromagnetic waves are expected to be found. These instabilities are distinct from the usual FEL resonance.

APPENDIX: DEFINITION OF QUANTITIES

The following quantities are used in equations (41)-(43)

$$D_R^0 = \left(\omega - k_R v_{\|} - \frac{\omega_i^2}{\omega - k_R v_{\|}}\right)A_R + \omega_p^2(\omega - k_R v_{\|}),$$

$$D_L^0 = \left(\omega - k_L v_{\|} - \frac{\omega_i^2}{\omega - k_L v_{\|}}\right)A_L + \omega_p^2(\omega - k_L v_{\|}),$$

$$\psi_R^{\pm} = \left(\frac{1}{2}\right)\left[\left(\frac{\omega_i^2}{\omega - k_R v_{\|}} - \frac{\omega_i^2}{k_w v_{\|}} \pm \gamma_0^2 k_w v_{\|}\right)A_R - \omega\omega_p^2\right],$$

$$\psi_L^{\pm} = \left(\frac{1}{2}\right)\left[\left(\frac{\omega_i^2}{\omega - k_L v_{\|}} + \frac{\omega_i^2}{k_w v_{\|}}\frac{\omega_i^2}{\omega - k_L v_{\|}} \mp \gamma_0^2 k_w v_{\|}\right)A_L - \omega\omega_p^2\right]$$

$$M^{\pm} = \left(\frac{\omega k c}{2\sqrt{2}}\right)\left(\frac{\omega_i^2}{\omega - k_R v_{\|}} + \frac{\omega_i^2}{\omega - k_L v_{\|}} \pm 2\gamma_0^2 k_w v_{\|}\right),$$

$$\xi_{R1} = \left(\frac{\omega}{\sqrt{2}}\right)\left[kc\left(\omega - k_R v_{\|} - \frac{\omega_i^2}{\omega - k_R v_{\|}}\right) - \omega_p^2 \frac{v_{\|}}{c}\right.$$

$$-\left(\frac{\omega_i^2 c}{k_w v_\parallel^2}+\frac{\gamma_0^2 k_w v_\parallel}{c}\right)\left(\omega-kv_\parallel\right)\Bigg],$$

$$\xi_{L1}=\left(\frac{\omega}{\sqrt{2}}\right)\Bigg[kc\left(\omega-k_L v_\parallel-\frac{\omega_i^2}{\omega-k_L v_\parallel}\right)-\omega_p^2\,\frac{v_\parallel}{c}$$

$$+\left(\frac{\omega_i^2 c}{k_w v_\parallel^2}+\frac{\gamma_0^2 k_w v_\parallel}{c}\right)\left(\omega-kv_\parallel\right)\Bigg],$$

$$\xi_{R2}=\left(\frac{1}{\sqrt{2}}\right)\Bigg[-A_R\left(\frac{\omega_i^2}{k_w c}-\frac{\omega_i^2 c}{k_w v_\parallel^2}+k_w c-\frac{\omega_i^2}{\omega-k_R v_\parallel}\right)$$

$$+\omega_p^2\left(k_R c-\omega v_\parallel/c\right)\Bigg],$$

$$\xi_{L2}=\left(\frac{1}{2}\right)\Bigg[-A_L\left(-\frac{\omega_i^2}{k_w c}+\frac{\omega_i^2 c}{k_w v_\parallel^2}-k_w c-\frac{\omega_i^2}{\omega-k_L v_\parallel}\right)$$

$$+\omega_p^2(k_L c-\omega v_\parallel/c)\Bigg],$$

$$\varepsilon^0=(\omega-kv_\parallel)^2-\omega_p^2/\gamma_\parallel^2\ .$$

REFERENCES

[1] E. Esarey, P. sprangle, J. Krall, and A. Ting, IEEE Trans. Plasma Sci. **24** (1996) 252.

[2] D.H. Whittum, A.M. Sessler, and J.M. Dawson, Phys. Rev. Lett. **64** (1990) 2511.

[3] S. Wang, C.E. Clayton, B.E. Blue *et al*., Phys. Rev. Lett. **88** (2002) 135004.

[4] K. Takayama and S. Hiramatsu, Phys. Rev. A **37** (1988) 173 .

[5] T. Ozaki, K. Ebihara, S. Hiramatsu, Y. Kimura, J. Kishuro, T. Monaka, K. Takayama, and D.H. Whittum, Nucl. Instrum. Methds Phys. Res. A **318** (1992) 101.

[6] L.H. Yu, A.M. Sessler, and D.H. Whittum, Nucl. Instrum. Methods Phys. Res. A **318** (1992) 721.

[7] P. Jha and J.S. Wurtele, Nucl. Instrum. Methods Phys. Res. A **331** (1993) 477.

[8] P. Jha and P. Kumar, IEEE Trans. Plasma Sci. **24** (1996) 1359.

[9] P. Jha and P. Kumar, Phys. Rev. E **57** (1998) 2256.

[10] A.A. Kordbacheh, B. Maraghechi, B. Farokhi, and J.E. Willett, Phys. Plasmas **12** (2005) 113106.

[11] S. Mirzanejhad, P. Maraghechi, and B. Maraghechi, Phys. Plasmas **11** (2004) 3047.

ENHANCEMENT OF A COHERENT (SUPER-RADIANT) EMISSION IN FEL BY MEANS OF ENERGY MODULATION OF AN EMITTING SHORT ELECTRON BUNCH

Yu. Lurie* and Y. Pinhasi, The College of Judea and Samaria, Ariel, Israel
A. Gover, Tel-Aviv University, Tel-Aviv, Israel

Abstract

Super-radiant emission from a wiggling short electron bunch, is strongly suppressed at high frequencies in comparison with radiation, obtained in a FEL if an ultra-short e-beam pulse of the same total charge is available. However, radiation intensity of a wiggling short electron bunch can be greatly enhanced by means of energy modulation. In this way, a super-radiant FEL source driven by short electron bunches and operating in the Tera-Hertz regime can be realized. Analytical evaluations and numerical simulations utilizing a space-frequency 3D model show, that a linear energy modulation enables one to increase the power of super-radiant emission by few orders of magnitude. Possible limitations in application of this method are also discussed, as well as a spectral purity of enhanced radiation.

INTRODUCTION

Development of experimental set-ups utilizing mechanism of short bunching of relativistic electron beams enables construction of high-power free-electron lasers (FELs) operated by a single short pulse or by a train of such pulses. Optimal efficiency of such radiation sources may be achieved with ultra-short beam pulses, when a super-radiant (SR) emission occurs (see [1, 2] and references therein).

Unfortunately, a beam pulse duration obtained in practice is still relatively long, leading to a dramatic reduction in SR emission at high frequencies. For example, in a case of Gaussian electron pulse, the super-radiant to spontaneous emission ratio at a synchronism frequency f_s is decreases with the beam duration as fast as the Gauss function [1]:

$$\mathrm{SNR} \equiv \frac{dP_q^{sr}(z)/df}{dP_q^{sp}(z)/df} = \overline{k} \cdot e^{-(2\pi f_s T)^2} \qquad (1)$$

(here $\overline{k}$ is a number of electrons in the bunch and T is the standard deviation of the electron Gauss distribution, which corresponds to the bunch duration $\Delta T \approx 2T$). It means that to provide an intense high frequency SR emission, ultra-short electron bunches of time duration $\Delta T << 1/f_s$ have only to be applied. For example, with ultra-short femtoseconds bunches, intense SR emission may be obtained at radiation frequencies up to approximately 100 THz only.

* e-mail: ylurie@yosh.ac.il

It was suggested that emission of a short electron bunch of some finite duration may be greatly enhanced by means of its proper energy modulation [3]. In this work, the effect of energy modulation on SR emission of a wiggling short electron bunch is analyzed in a space-frequency 3D approach and demonstrated by numerical simulations carried out using WB3D code [4].

ANALYTICAL EVALUATIONS

The total electromagnetic field emitted by a wiggling electron bunch may be found in the frequency domain in terms of expansion over transverse eigenmodes of the medium (free-space or waveguide) in which the radiation is excited and propagates [5]:

$$\vec{E}(\vec{r},t) = \sum_q \Re\left\{ \int_0^\infty \widetilde{C}_q(z,f)\ \widetilde{\mathcal{E}}_q(x,y)\ e^{+jk_{zq}(f)z}\ df \right\} \qquad (2)$$

where $\widetilde{\mathcal{E}}_q(x,y)$ is the transverse profile (Hermitte-Gaussian free-space mode or waveguide mode) of the mode q and $k_{zq}(f)$ is its wavenumber. (Although the form of mode presentation given in Eq. (2) is not valid in the far-field free-space propagation, it is still applicable to most electron devices in which the interaction takes place within a Rayliegh length of the Hermitte-Gaussian modes, where the diffraction is small). $\widetilde{C}_q(z,f)$ is the propagating mode amplitude, which may be found from the excitation equation (see [4, 5] for details).

Neglecting the influence of the emitted electromagnetic field on the emitting electrons, the mode expansion coefficients $\widetilde{C}_q(z,f)$ of electromagnetic field emitted by *a single wiggling electron* may be found in the following simple analytical form:

$$\widetilde{C}_q(L_w,f) = \mathcal{A}_q\ \mathrm{sinc}\left(\tfrac{1}{2}\,\theta_q\,L_w\right)\ e^{j\left(2\pi f t_0 + \frac{1}{2}\theta_q L_w\right)} \qquad (3)$$

where $\mathcal{A}_q$ is some normalization coefficient, $\mathrm{sinc}(\alpha) \equiv \sin(\alpha)/\alpha$, t_0 is the time that the electron enters into the interaction region, L_w is the length of the interaction region, and

$$\theta_q \equiv \frac{2\pi f}{v_z} - (k_{zq} + k_w) \qquad (4)$$

is the detuning parameter (k_w is the wiggler wave number and v_z is the electron longitudinal velocity in z-direction).

In the low-gain regime, electromagnetic field emitted by a bunch of N electrons may be given in the terms of a summation of (3) over all the electrons in the bunch:

$$\widetilde{C}_q(L_w, f) = \mathcal{A}_q \sum_{p=1}^{N} \mathrm{sinc}\left(\frac{1}{2}\,\theta_{q_p}\,L_w\right)\, e^{j\left(2\pi f t_{0_p} + \frac{1}{2}\theta_{q_p} L_w\right)} \tag{5}$$

here the coefficient $\mathcal{A}_q$ is supposed to be approximately a constant for all the electrons in the bunch. At some synchronism frequency f_s, a coherent summation in (5) may only be obtained when $\mathrm{sinc}\left(\frac{1}{2}\,\theta_{q_p}\,L_w\right) \approx 1$ (or $\theta_{q_p} \approx 0$, what defines the synchronism frequency f_s), and the phase matching condition $2\pi f t_{0_p} + \frac{1}{2}\theta_{q_p} L_w \approx 0$ is satisfied. A SR emission from a single ultra-short ($\Delta T << 1/f_s$) bunch takes place in this situation, when the radiated field is simply proportional to a number of the electrons in the bunch (to the total charge of the driving bunch): $\widetilde{C}_q \approx \mathcal{A}_q \cdot N$, and energy flux spectral density of the emitted radiation may be given as

$$\frac{d\,W}{d\,f} \sim \left|\widetilde{C}_q\right|^2 \sim \mathcal{A}_q^2 \cdot N^2$$

As mentioned above, this energy flux is drastically reduced if the driving bunch duration is increasing compared with period $1/f_s$ of the emitted radiation. But also in this case of "finite-duration" beam bunches, the summation in (5) may still remain a partly coherent in the vicinity of synchronism frequency f_s, if the previous conditions are fulfilled in a bit modified form:

- The most part of sinc-functions in (5) save their sign: $\mathrm{sinc}\left(\frac{1}{2}\,\theta_{q_p}\,L_w\right) > 0$, to prevent the terms compensation in the summation; and
- The phase shifts $2\pi f_s t_{0_p} + \frac{1}{2}\theta_{q_p} L_w$ remains constant.

The first condition means, that:

$$\left|\frac{2\pi f_s}{v_{z_p}} - \left(k_{z_q} + k_w\right)\right| \lesssim \frac{2\pi}{L_w}$$

Introducing

$$k_{z_q} + k_w \equiv \frac{2\pi f_s}{\overline{\beta_z}\,c} \tag{6}$$

where $\overline{\beta_z}\ c$ is some bunch mean longitudinal velocity in z-direction, the previous equation may be rewritten as:

$$\left|\frac{1}{\beta_{z_p}} - \frac{1}{\overline{\beta_z}}\right| < \frac{\lambda_s}{L_w} \tag{7}$$

here λ_s is the radiation wave length and $\beta_{z_p} = v_{z_p}/c$. The phase-matching condition may only be satisfied, if the driving electron bunch is *pre-modulated* so that the longitudinal velocities of the electrons are distributed as follows:

$$\beta_z(t) = \overline{\beta_z}\,\frac{L_w}{L_w - 2\overline{\beta_z} c t} \tag{8}$$

where we assume that $\beta_z(t=0) = \overline{\beta_z}$. Substitution of (8) into (7) provides the following limitation on the maximal bunch duration:

$$|t| < \frac{1}{2 f_s} \tag{9}$$

Therefore the considered enhancement of SR emission may be obtained with as long as $\Delta T \approx 1/f_s$ beam bunches.

Condition (8) actually requires an *energy modulation* of the driving electron bunch as follows:

$$E_k(t) = m_0 c^2\ \left\{\sqrt{\frac{1+a_w^2}{1-\overline{\beta_z}^2/\left(1-2\overline{\beta_z}\,c\,t/L_w\right)^2}}\ -\ 1\right\} \tag{10}$$

here $a_w = eB_w/(k_w m_e c)$ is the wiggler parameter. Because

$$\left(\frac{2\overline{\beta_z}c}{L_w}\right)|t| \ < \ \left(\frac{2\overline{\beta_z}c}{L_w}\right)\frac{1}{2f_s} = \overline{\beta_z}\frac{\lambda_s}{L_w} \ << 1$$

the distribution (10) may be linearized:

$$E_k(t) \approx E_k(t=0)\ +\ \left(\frac{d\,E_k}{d\,t}\right)\Big|_{t=0} \cdot t \tag{11}$$

where

$$E_k(t=0) \equiv m_e c^2\ \left\{\sqrt{\frac{1+a_w^2}{1-\overline{\beta_z}^2}}\ -\ 1\right\} \tag{12}$$

and the modulation rate is

$$\left(\frac{d\,E_k}{d\,t}\right)\Big|_{t=0} \approx m_e c^2\ \left(\frac{2\overline{\gamma}\,\overline{\beta_z}^3}{1-\overline{\beta_z}^2}\right)\frac{c}{L_w} \tag{13}$$

here

$$\overline{\gamma} = \frac{m_e c^2 + E_k(t=0)}{m_e c^2} = \sqrt{1 - \frac{1+a_w^2}{\overline{\beta_z}^2}} \tag{14}$$

So, energy modulation of a wiggling electron bunch according (10) or (11) may considerably enhance its SR emission, even if the driving bunch is as long as $\Delta T \approx 1/f_s$.

Obviously, energy modulation of the beam reduces the spectral purity of the emitted radiation in comparison with that of SR emission, emitted by an unmodulated ultra-short electron bunch. The reason is that the synchronism frequencies of radiation emitted by individual electrons are different due to difference in there kinetic energies. Therefore a bandwidth of radiation, emitted by energy modulated bunch is supposed to be more wide by a factor of $\Delta f \approx |f_s(+T) - f_s(-T)|$, so that the radiation band width may be evaluated by

$$BW \approx \frac{f_s}{N_w} + \underbrace{\frac{df_s}{dE_k}\left(\frac{dE_k}{dt}\right)\Delta T}_{\Delta f} \tag{15}$$

revealing a linear growth with the energy chirp rate dE_k/dt.

NUMERICAL SIMULATIONS

To demonstrate the effect, a number of numerical simulations with the code WB3D [4] were carried out for a THz-regime free-electron laser with operational parameters given in the table 1. Simulations demonstrate, that extremely short electron bunches ($f_s \Delta T \lesssim 2\%$) have to be applied in order to produce a strong super-radiant emission. With such ultrashort bunches, the total energy flux of super-radiant emission may be as large as $W_{SR} = 22.5$ nJ. With a longer unmodulated bunches, the total energy flux of emitted radiation is drastically reduced and it is just about $W = 4.9$ pJ when $\Delta T \approx 1.0$ pSec unmodulated bunches are applied. In accordance with analytical evaluations, a linear energy modulation (11) of the electron bunch enables one to enhance this radiation by more than a three orders of magnitude, as demonstrated in the figure 1. It is evident, that the energy modulation causes the emitted total energy flux to increase rapidly, saturating at the energy chirp rate $d E_k/d t$ of about 0.12 MeV/pSec (resulting in the energy flux of $W_{SR} \approx 9$ nJ) and slowly reducing for a higher values of the energy chirp rates. Note, that equation (13) provides the value of $d E_k/d t \approx 0.17$ MeV/pSec. With a longer bunches ($\Delta T \approx 2.0$ pSec, $f_s T \approx 1.0$), the obtained effect is even more strong (circle symbols at the picture).

Energy spectrums of the radiation emitted by energy modulated ΔT=1.0 pSec bunches are given in the figure 2, comparing to that emitted by an unmodulated ultrashort bunch (solid line) and by unmodulated ΔT=1.0 pSec bunch. A spectral purity of the emitted radiation is obviously reduced if the driving electron bunch is energy modulated. At high energy chirp rates, the radiation band width grows linearly with $d E_k/d t$, as demonstrated at the figure 3, in accordance with above evaluation (15). It's interesting to note some non-linear dependence near the "optimal" value of the energy chirp rate $d E_k/d t$=0.12 MeV/pSec, when a high-power radiation is emitted.

To explain the effect, a microscopic analysis of trajectories of emitting electrons was carried out (see figure 4). As easily seen from the picture, a non-modulated bunch propagates through the undulator saving its initial temporal duration. Initial energy modulation of the driving bunch

Table 1: Operational parameters for THz FEL.

Accelerator	
Electron beam energy:	E_k=2.8 MeV
Total charge:	$Q = I_0 \cdot \Delta T = 10$ pCl
Wiggler	
Magnetic induction:	B_w=3 kGauss ($a_w \approx 0.56$)
Period:	λ_w=20 mm
Number of periods:	N_w=20
Waveguide	
Rectangular waveguide:	5×5 mm

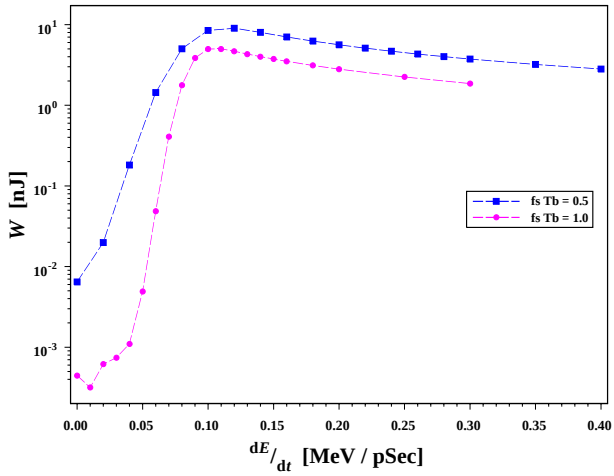

Figure 1: Total energy flux emitted by $\Delta T = 1.0$ pSec (box symbols) and $\Delta T = 2.0$ pSec (circle symbols) bunches as a function of the energy chirp rate $d E_k/d t$.

develops while propagating in the wiggler to a density compression and the e-beam pulse becomes an ultra-short one, generating a strong super-radiant emission. At this moment, the most intensive radiation is emitted, as may be seen from the time-domain dependence of electric component of the emitted field given in figure 5.

CONCLUSIONS

In a practical case of FEL driven by a single short bunch or by a train of such bunches, a super-radiant emission is strongly suppressed at high frequencies. It was shown that it can be greatly enhanced by means of a proper energy modulation of the driving beam. The effect is studied in the framework of space-frequency model and is explained in a

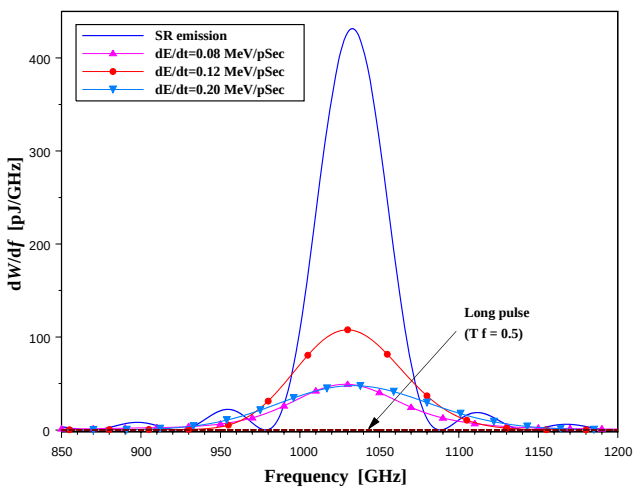

Figure 2: Total energy flux emitted by $\Delta T = 1.0$ pSec bunch as a function of the energy chirp rate $d E_k/d t$.

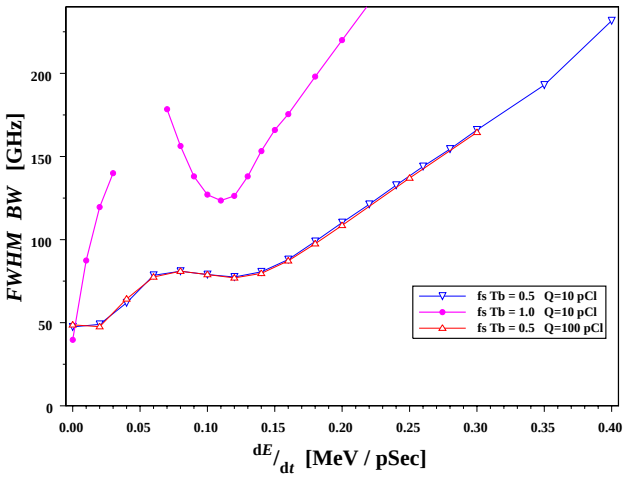

Figure 3: Full-width half-maximum radiation bandwidth as function of the energy chirp rate $d\,E_k/d\,t$.

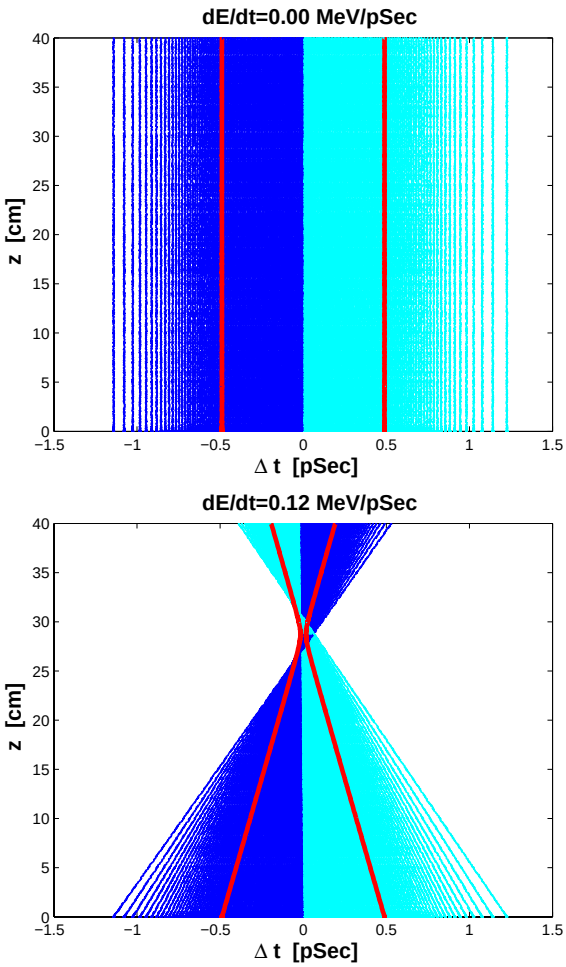

Figure 4: Trajectories of the emitting electrons in unmodulated (top) and energy modulated with $d\,E_k/d\,t$=0.12 MeV/pSec (bottom) bunches.

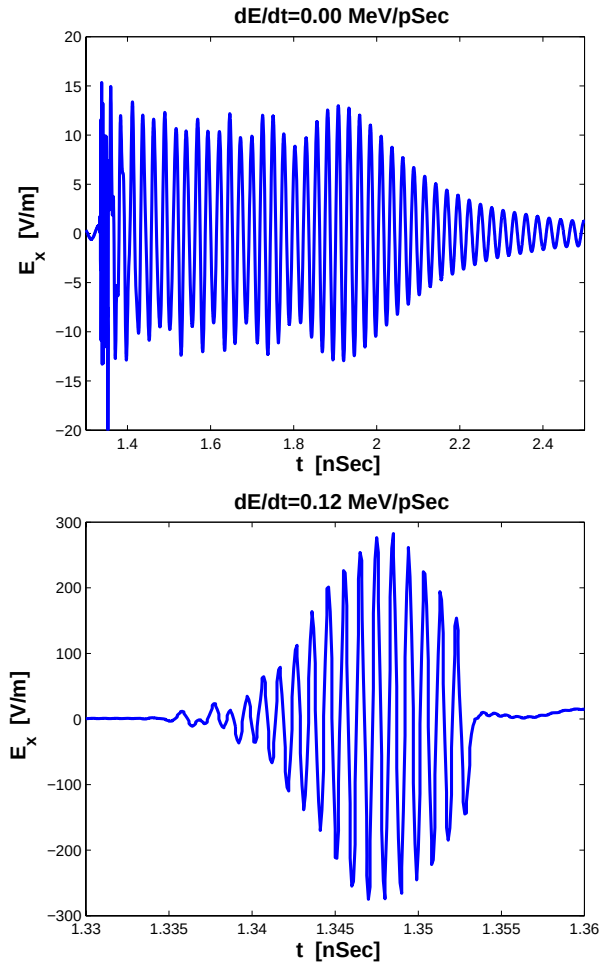

Figure 5: Time-domain electromagnetic field, emitted by unmodulated (top) and by energy modulated ($d\,E_k/d\,t$=0.12 MeV/pSec, bottom) bunches.

simple analytical approach as well as by numerical simulations with WB3D code. The considered principal scheme may be realized in a construction of a pulsed FEL, which enables to provide intensive high-frequency radiation with a reasonable spectral quality.

REFERENCES

[1] Y. Pinhasi, and Yu. Lurie, Phys. Rev. E **65**, 026501 (2002).

[2] A. Gover, Phys. Rev. ST Accel. Beams. **8**, 030701 (2005).

[3] A.Doria et al., PRL **80**, 2841 (1998).

[4] Y. Pinhasi, Yu. Lurie and A. Yahalom, Nucl. Instr. and Meth. in Phys. Res. A, **475**, 147 (2001).

[5] Y. Pinhasi and A. Gover, Phys. Rev. E **51**, 2472 (1995).

CONTROL OF THE INTENSITY OF A WAVE INTERACTING WITH CHARGED PARTICLES

R. Bachelard, C. Chandre, X. Leoncini, M. Vittot
CNRS Luminy, Case 907, F-13288 Marseille Cedex 9, France
A. Antoniazzi, D. Fanelli*
Dipartimento di Energetica and CSDC, Universitá di Firenze, INFN, Italy

Abstract

The interaction of a wave with a beam of particles is of paramount importance in a great number of physical applications. We here focus on the case of a Free Electron Laser and review two control strategies aimed at re-shaping the inner topology of the single-particle phase-space to stabilize the oscillations of the laser intensity in the deep saturated regime.

INTRODUCTION

The interaction between a wave and a bunch of charged particles plays a central role in many branches of applied physics ranging from particle accelerators to laser physics. Generically, this self-consistent interaction leads to an exponential increase of the intensity of the wave, followed by an oscillating saturation. Oscillations are generated by the rotations in phase space of a clustered bunch of particles.

The wave-particle interaction can be cast in a Hamiltonian form with $N+M$ degrees of freedom, where N and M are respectively the number of charged particles and electromagnetic waves. Examples include the so called electron beam-plasma instability, a phenomenon of paramount importance in the wide realm of kinetic plasma turbulence, and single-pass high-gain Free Electron Lasers (FELs). In the following we shall refer to the latter case, focusing in particular on seeding schemes where a small laser signal is injected at the entrance of the undulator and guides the subsequent amplification process [1]. Basic features of the system dynamics are successfully captured within a simplified one-dimensional framework discussed in the pioneering work by Bonifacio and collaborators [2]. The Hamiltonian reads:

$$H = \sum_{j=1}^{N} \frac{p_j^2}{2} - \delta I + 2\sqrt{\frac{I}{N}} \sum_{j=1}^{N} \sin(\theta_j - \varphi), \qquad (1)$$

where I and φ stands respectively for the intensity and phase of the wave, while the N conjugated pairs (p_j, θ_j) refer to the electrons. The detuning parameter δ measures the average relative deviation from the resonance condition.

As previously anticipated, the theory predicts a linear exponential instability and a late oscillating saturation for the amplitude of the radiation field, Fig. 1. Inspection of the asymptotic phase-space, see Fig 2, suggests that a bunch of particles gets trapped in the resonance and forms a clump that evolves as a single macro-particle localized in space. The remaining particles are almost uniformly distributed between two oscillating boundaries, and populate the so called *chaotic sea* [3].

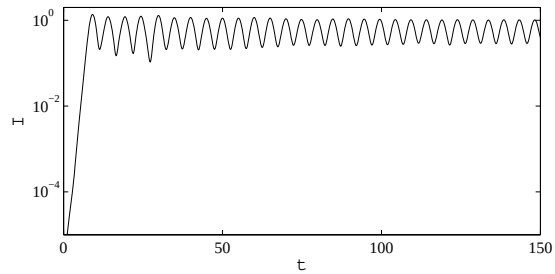

Figure 1: Normalized intensity calculated from the dynamics of Hamiltonian (1).

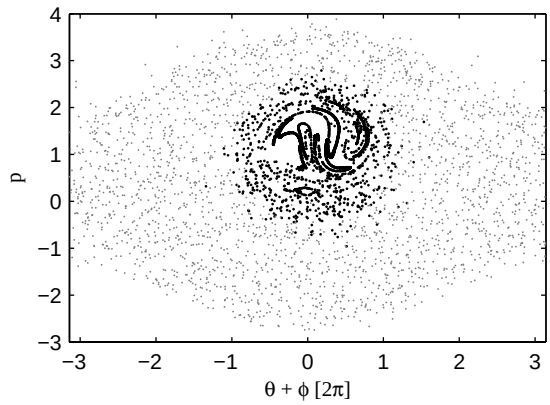

Figure 2: Snapshot of the N particles at $t = 1000$, with $N = 10^4$. The grey points correspond to the chaotic particles, the dark ones refer to the macro-particle

The macro-particle rotates around a well defined fixed point and this *microscopic* dynamics is shown to be responsible for the *macroscopic* oscillations observed at the intensity level. Qualitatively similar observations have been reported for the case of a Travelling Wave Tube (TWT)[4], a specially designed apparatus that mimics the plasma in-

* duccio.fanelli@ki.se

stability and enables to accurately investigate the non linear regime of the self-consistent wave-particles interaction. Given the above, it is an interesting problem to define dedicated strategies aiming at regularizing the saturated dynamics that could eventually contribute to improve the performance of the aforementioned devices.

The goal of this paper is to show that it is indeed possible to influence by an external perturbation the dynamics of the particles and enhance the stability of the system. To this end we shall consider a mean field type of approach which constitutes the natural reduction of the original N-body formulation (1). According to this simplified picture, the conjugated variables (ϕ, I) are replaced by two functions of time $\phi(t)$ and $I(t)$, the latter being obtained from direct simultations of the self-consistent dynamics. This in turn amounts to formally neglecting the action of the electrons on the field, an assumption that holds true in the late saturated regime.

The N-body Hamiltonian (1) can therefore be reduced to

$$\tilde{H_N} = \sum_{i=1}^{N} H_{1p}(\theta_i, p_i, t), \qquad (2)$$

where

$$H_{1p}(\theta, p, t) = \frac{p^2}{2} - 2\sqrt{\frac{I(t)}{N}}\cos(\theta + \phi(t)). \qquad (3)$$

In conclusion, the dynamics of a FEL can be adressed by monitoring the evolution of a *test particle*, obeying the Hamiltonian (3) where the functions $I(t)$ and $\phi(t)$ act as external fields and are here imposed by assuming their simplified asymptotic behaviour as obtained by a frequency analysis [5] :

$$2\sqrt{\frac{I(t)}{N}}e^{i\phi(t)} \approx F - \epsilon\sum_{k=1}^{K} W_k e^{i\omega_k t}, \qquad (4)$$

in the reference frame of the wave.

TOWARD STABILIZATION: TWO ALTERNATIVE APPROACHES

Two different control strategies are here shortly discussed and shown to produce beneficial effects on stability of the system at saturation. For a detailed account on the techniques and an extensive report of the main findings, the interested reader may refer to [6] and [7].

Hamiltonian control of a test particle

First let us consider a Hamiltonian control technique. The method is based on the introduction of a small and apt modification of the potential that enables to recreate (alternatively destroy) invariant (KAM) tori in phase space. The Hamiltonian control addresses systems which are close to integrable, i.e. whose Hamiltonian can be written as $H = H_0 + V$, where H_0 is integrable and V a perturbation of order ϵ (compared to H_0). The results we use here have been proven rigorously [8, 9]. In practice, it can be shown that a suitable *control term* f of order ϵ^2 exists such that $H_0 + V + f$ has an invariant torus at a given frequency ω_0. In the present case, and focusing on the late saturated regime, the perturbation term is associated with the oscillating part of the intensity.

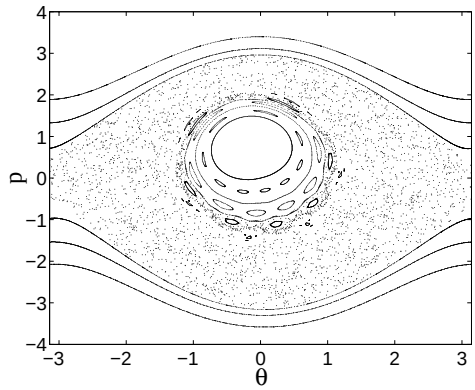

Figure 3: Poincaré sections of a test-particle of Hamiltonian $H_{1p}(\theta, p, t)$.

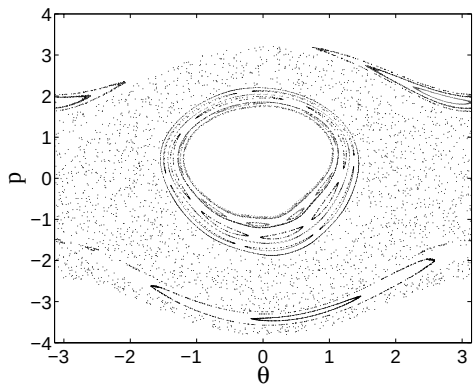

Figure 4: Poincaré sections of a *controlled* test-particle of Hamiltonian $H_{1p}(\theta, p, t) + \tilde{f}(\theta, p, t)$ (right).

The calculation of the control term [6] is carried on into action-angle variables (φ, J) and the derivation is not esplicitly reported here due to space limitations [1]. Instead, we shall present results of numerical experiments which clearly demonstrate (see Figs.3 and 4), that, in (θ, p) variables the analytical control term derived in [6] is successful in reconstructing some invariant tori around the macro-particle. In other words, it enlarges the macro-particle which in turn corresponds to enhancing the bunching factor, a quantity of paramount importance in FEL context. Finally, it is worth emphasising that according to this approach the form of the control term is derived and not imposed a priori.

[1] As a side remark, note that the exact change of variables from (φ, J) to (θ, p) presents a singularity at the pendulum separatrices. In order to implement our control on the whole space, a simplified, but regular, change of variables is used which mimics the exact one in the region of the invariant torus predicted by the control

The residue method

An alternative strategy can be elaborated that enables to modifying the intrinsic characteristics of the macro-particle. Contrary to the above technique, a (generic) parametrized perturbation is here a priori introduced, which allows to modify the topology of phase-space, by tuning appropriately the parameters. The residue method [10, 11, 12, 13] is used to predict the resulting local bifurcations, by an analysis of linear stability of periodic orbits. Information on the nature of these orbits (elliptic, hyperbolic or parabolic) is provided using e.g. an indicator like Greene's residue [10, 14], to monitor local changes of stability in a system subjected to an external perturbation [11, 12, 13, 15]. As we shall see, this approach enables one to tune the size, gyration radius and internal structure of the macroparticle, thus resulting in an effective tool for the stabilization of the intensity.

Consider an autonomous Hamiltonian flow with two degrees of freedom which depends on a set of parameters[2] $\boldsymbol{\lambda} \in \mathbb{R}^m$:

$$\dot{z} = \mathbb{J}\nabla H(z;\boldsymbol{\lambda}),$$

where $z = (p, E, \theta, t) \in \mathbb{R}^4$ and $\mathbb{J} = \begin{pmatrix} 0 & -\mathbb{I}_2 \\ \mathbb{I}_2 & 0 \end{pmatrix}$, and $\mathbb{I}_2$ being the two-dimensional identity matrix. In order to analyze the linear stability properties of the associated periodic orbits, we also consider the tangent flow written as

$$\frac{d}{dt}J^t(z) = \mathbb{J}\nabla^2 H(z;\boldsymbol{\lambda})J^t,$$

where $J^0 = \mathbb{I}_4$ and $\nabla^2 H$ is the Hessian matrix (composed of second derivatives of H with respect to its canonical variables). For a given periodic orbit with period T, the linear stability properties are given by the spectrum of the monodromy matrix J^T. These properties can be synthetically enclosed in the definition of Greene's residue :

$$R = \frac{4 - \mathrm{tr}J^T}{4}.$$

In particular, if $R \in]0,1[$, the periodic orbit is elliptic; if $R < 0$ or $R > 1$ it is hyperbolic; and if $R = 0$ and $R = 1$, it is parabolic.

Since the periodic orbit and its stability depend on the set of parameters $\boldsymbol{\lambda}$, the features of the dynamics will change under apposite variations of such parameters. Generically, stability od periodic orbits is robust to small changes of parameters, except at specific values when bifurcations occur. The residue method [11, 12, 13] detects these rare events thus allowing one to calculate the appropriate values of the parameters leading to the prescribed behaviour in the dynamics. This method yield reduction as well as enhancement of chaos.

To illustrate the potentiality of method we shall introduce a parametrized perturbation, in the form [7]:

[2] At this level $\boldsymbol{\lambda}$ represents any generic family of parameters that influence the dynamics of the system

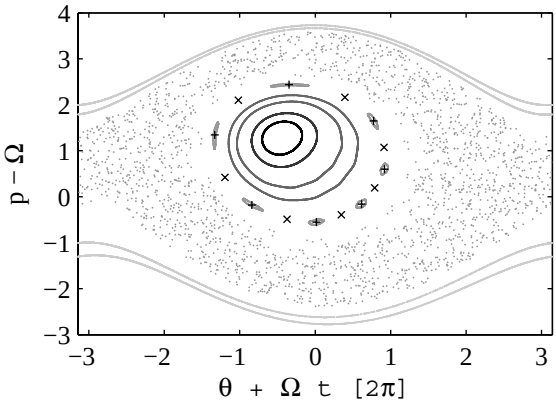

Figure 5: Poincaré section of a test-particle, described by Hamiltonian (3). The periodic orbits with r.n. 7 are marked by plus (elliptic orbit) and crosses (hyperbolic orbit). Ω stands for the wave velocity.

$$H^c_{1p}(\theta, p, t; \lambda) = H_{1p}(\theta, p, t) - 2\lambda\sqrt{\frac{I(t)}{N}}\cos(2\theta + \phi(t)). \quad (5)$$

Here λ controls the amplitude of the injected wave. Focus then on $\lambda = 0$, which corresponds to the original Hamiltonian H_{1p}, and consider two coupled Birkhoff periodic orbits, i.e. orbits having the same action but different angles in the integrable case and having the same rotation number (r.n.) on the Poincaré section, one elliptic $\mathcal{O}_e$ and one hyperbolic $\mathcal{O}_h$ (see Fig. 5) [3].

Call R_e and R_h the residues of these orbits: We have $R_e(0) > 0$ and $R_h(0) < 0$. We then modify the parameter λ until the following condition is matched :

$$R_e(\lambda_c) = R_h(\lambda_c) = 0, \quad (6)$$

at $\lambda_c = -0.0370$ [7]. Bifurcation (6) is associated with the creation of an invariant torus [13]. This diagnostic is confirmed by the Poincar section (see Fig.6) of the *controlled* Hamiltonian (5), at $\lambda = \lambda_c$: The elliptic islands with r.n. 7 have been replaced by a set of invariant tori, leading to an enlargement of the macro-particle. Note that elliptic islands with r.n. 6 are now present around the regular core.

The associated couple of elliptic/hyperbolic orbits can be treated similarly as those of r.n. 7, in order to gain further enlargement of the macro-particle (not reported here).

The control is naturally introduced in the self-consistent dynamics as :

$$H^c_N(I, \phi, p_i, \theta_i, \lambda) = H_N(I, \phi, p_i, \theta_i) - 2\lambda\sqrt{\frac{I}{N}}\sum_i \cos(2\theta_i + \phi) \quad (7)$$

[3] Let us recall that the rotation number (or winding number) of a periodic orbit is the number of times it crosses the Poincaré section before closing back on itself

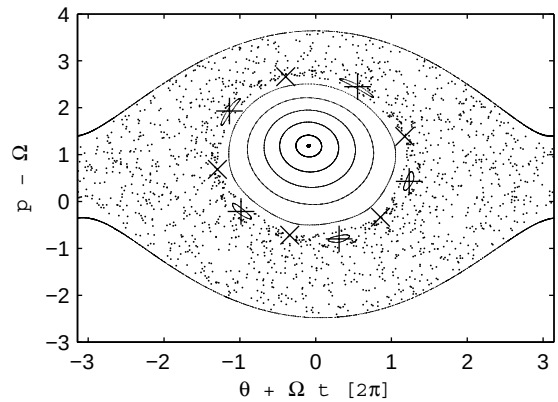

Figure 6: Poincaré section of a controlled test-particle of Hamiltonian (5), with $\lambda = \lambda_c \approx -0.0370$. The periodic orbits with r.n. 6 are marked by plus (elliptic orbit) and crosses (hyperbolic orbit). Ω stands for the wave velocity.

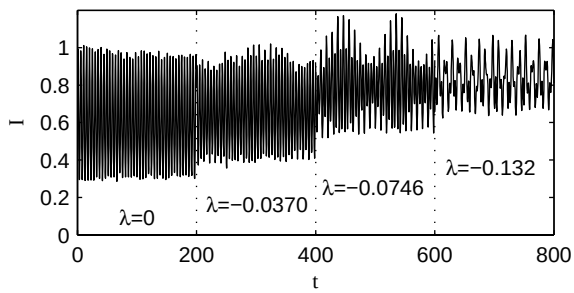

Figure 7: Intensity of the wave at saturation, in the four regimes : $\lambda = 0, -0.037, -0.0746$ and -0.1321 . Further improvements over this condition are discussed in [7]

where H_N is given by Eq. 1. The behaviour of the system is investigated in correspondence of the critical values $(\lambda_c, \lambda_c', \lambda_c'')$ which have been calculated in the framework of the test-particle model, and identifying successive corrections as outlined in the precedding discussion. Importantly, the macro-particle is shown to increase also when operating within the relevant self-consistent context. As concerns the wave, the control results in a stabilization of its intensity (see Fig.7) [7].

CONCLUSIONS

In this paper, we focus on the physics of the wave-particle interaction and consider in particular the case of a FEL. Control techniques are developed in the framework of a simplified mean-field description aiming at stabilizing the laser behavior at saturation. In both cases, the size of the macro-particle is shown to be increased by adding a small pertubation to the system. These procedures result in a low–cost correction in term of energy[4]. Both approaches are utterly general and could be eventually considered to define innovative strategies aimed at adjusting the size of the macro-particle, and consequentely enhancing the bunching factor. In this respect, it is worth stressing that an experimental test of the Hamiltonian control method on a modified Travelling Wave Tube has been performed [16] in absence of self-consistency. Exploring the possibility of experimentally implementing the above control terms in both FEL and TWT contexts will be addressed in future research.

[4] As concerns the method of residues, the fact that the applied corrections are indeed small is confirmed by the values of λ that are calculated for the various setting considered above.

REFERENCES

[1] L.H. Yu et al., Science **292**, 2037 (2003).

[2] R. Bonifacio, *et al.*, Rivista del Nuovo Cimento **3**, 1 (1990).

[3] A. Antoniazzi, Y. Elskens, D. Fanelli and S. Ruffo, Europ. Phys. J. B, *in press* (2006).

[4] Y. Elskens, D. Escande, *Microscopic Dynamics of Plasmas and Chaos* IoP Publishing, Bristol (2003).

[5] J. Laskar, *Proc. of NATO ASI Hamiltonian Systems with Three or More Degrees of Freedom*, (C. Simò Ed, Kluwer) 134 (1999).

[6] R. Bachelard, A. Antoniazzi, C. Chandre, D. Fanelli, M. Vittot, Comm. in Nonlinear Sci. and Num. Simu. *in press* (2006).

[7] R. Bachelard, A. Antoniazzi, C. Chandre, D. Fanelli, X. Leoncini, M. Vittot, preprint nlin/0609030 (2006).

[8] Vittot, M. (2004). Perturbation theory and control in classical or quantum mechanics by an inversion formula. *J. Phys. A: Math. Gen.*, **37**, pp. 6337-6357.

[9] Chandre C., M. Vittot, G. Ciraolo, Ph. Ghendrih, R. Lima (2006). Control of stochasticity in magnetic field lines. *Nuclear Fusion*, **46**, pp. 33-45.

[10] J.M. Greene, J. Math. Phys. **20**, 1183 (1979).

[11] J. Cary, J.D. Hanson, Phys. Fluids **29**(8), 2464 (1986).

[12] J.D. Hanson, J. Cary, Phys. Fluids **27**(4) 767 (1984).

[13] R. Bachelard, C. Chandre, X. Leoncini, Chaos **16** 023104 (2006).

[14] R.S. MacKay, Nonlinearity **5** 161 (1992).

[15] J.E. Howard, R.S. MacKay, J. Math. Phys. *28* 1036 (1987).

[16] Chandre, C., G. Ciraolo, F. Doveil, R. Lima, A. Macor and M. Vittot (2005). Channeling chaos by building barriers. *Phys. Rev. Lett.*, **74**, 074101.

FREE ELECTRON LASER AS A PARADIGMATIC EXAMPLE OF SYSTEMS WITH LONG-RANGE INTERACTIONS

A. Antoniazzi, D. Fanelli, S.Ruffo
Dipartimento di Energetica and CSDC, Universitá di Firenze, INFN, Italy
J. Barré, T. Dauxois, ENS, Lyon, France
G. De Ninno, Sincrotrone Trieste, Trieste, Italy

Abstract

We here shortly review the field of long-range interactions and presents selected issues of fundamental interest for statistical mechanics and dynamical systems theory. Applications to the case of a Single-Pass Free Electron Laser are discussed.

INTRODUCTION

Physical systems are constituted by interacting elements, point particles or atoms. In presence of short-range couplings, every element is solely sensitive to the adjacent environment, being therefore uniquely subjected to the interaction with local neighbors. Conversely, when long-range forces are to be considered, the direct coupling of each element to every other element in the system must be taken into account (the system is dominated by *mean-field* effects). This crucial distinction is responsible for the enhanced degree of complexity in the treatment of long-range systems when compared to short-range ones.

Moreover, basic concepts in physics, notably in the framework of equilibrium statistical mechanics, have been developed only for short range interactions. The potential interest of such tools is however very broad since for all fundamental interactions in nature (with the exception of gravity), screening mechanisms manifest, resulting in effective short-range couplings. For this reason, it has essentially only been in the context of astrophysics and cosmology that the very specific and difficult features of long-range interactions have been tackled. Recently, however, a growing number of physical laboratory systems have emerged in which the interactions are truly long-range, e.g. unscreened Coulomb interactions, vortices in two-dimensional fluid mechanics, wave-particle systems relevant to plasma physics and Free-Electron Lasers (FELs). These developments gave new impetus [1] to attempts aiming at describing the peculiar behaviour of long-range interacting systems, in a context where, in contrast to astrophysics, laboratory experiments are possible. Moreover, a number of " toy models" have been proposed that provide the ideal ground for theoretical investigations. Among others, the Hamiltonian Mean Field (HMF) model [2] is nowadays widely analyzed for pedagogical reasons, because of its intrinsic simplicity.

In presence of long-range interactions, physics is in fact very peculiar and a wide range of striking and curious phenomena appears. Importantly, energy is non additive, hence the system under scrutiny cannot be divided into independent macroscopic parts, as it is usually the case for short-range interactions. This fact leads to unexpected consequences when performing the analysis in terms of statistical mechanics.

Single-pass FELs constitute an example of systems with long-range interactions, where the interplay between collective (wave) and individual (particles) degrees of freedom is well known to be central. This interplay being essentially non dissipative, its prototype is described by a self-consistent Hamiltonian [3], which provides a clear and intuitive picture of the basic mechanisms that drive the process of light amplification and saturation. In this respect, FELs provides a very general experimental ground to investigate the universal features that characterize systems with long range interactions.

In this paper we shall present a short review of recent progress in this field of research by focusing in particular on the relevant case of a Single Pass FEL. A wider overview on long range systems can be found in Ref. [1].

DEFINITION OF LONG-RANGE SYSTEMS

Let us consider the potential energy U of a given particle positioned in the center of a sphere of radius R. Assume that the matter is homogeneously distributed with density ρ and introduce a lower cut-off $\varepsilon << R$, as depicted in Fig. 1. Focusing on the case where the interaction potential decays at large distances with a power-law with exponent α, one gets:

$$\begin{aligned} U &= \int_{\varepsilon}^{R} \rho \left[\frac{1}{r^{\alpha}}\right] 4\pi r^2 dr = \\ &= 4\pi\rho \int_{\varepsilon}^{R} r^{2-\alpha} dr \propto \left[r^{3-\alpha}\right]_{\varepsilon}^{R} \sim R^{3-\alpha}\,, \end{aligned}$$

Clearly, the above energy diverges with R *if the exponent* α *is smaller than* 3, which in turn corresponds to the dimension of the physical space where the interaction is embedded.

This argument holds true in any dimension d, implying that similar divergences are found when $\alpha \leq d$. We hence *define* the interaction to be *long-range* if $\alpha \leq 3$ (resp. $\alpha \leq d$). Equivalently, it can be said that the contribution to the

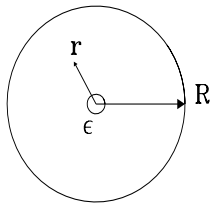

Figure 1: The energy in a sphere of radius R diverges as $R^{3-\alpha}$ if the interaction is long-range and $\alpha \leq 3$.

energy due to the surface of the sphere with respect to the bulk can be safetly neglected *only if* $\alpha > 3$. In the latter case, the interaction is of the *short-range* type.

As anticipated in the preceding discussion, long-range forces arise in many different contexts. Few physical examples of broad relevance are listed below:

- **Gravity**: $\alpha = 1, d = 3$. In addition to the long range nature of the interaction, the system displays a singularity at the origin that needs to be carefully tackled by involving dedicated regularization schemes.
- **Coulomb interactions**: $\alpha = 1, d = 3$.
- **Dipolar interactions**: $\alpha = 3, d = 3$. The shape-dependence phenomenon is found, which makes the energy dependent on the form of the sample.
- **Onsager's 2D vortex systems** or **2D Coulomb systems**. Here $\alpha = 0$, because the interaction decays logarithmically, and $d = 2$.
- **Mean-Field**: $\alpha = 0$, due to the infinite-range interaction, and any d. This latter cathegory does not reflect a pure physical example, but rather a useful (and common) approximation to which one resorts when treating complex problems. In fact, it provides the ideal setting to gain insight into a number of different physical problems and eventually enables to perform analytical calculations. As we shall see, Single Pass FELs can be effectively described by resorting to a mean-field type of approach .

THE PROBLEM OF ADDITIVITY

The long range nature of the interaction reflects in a number of peculiar phenomena which will be shortly reviewed in the forthcoming sections. Such curious behaviours are intrinsically connected to the *non additivity* of the system, a crucial concept that one can illustrate with reference to a specific case, namely the Curie-Weiss model of magnetism. Consider the following Hamiltonian:

$$H = -\frac{J}{2N}\sum_{i,j} S_i S_j, \qquad (1)$$

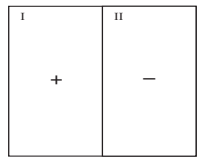

Figure 2: A microscopic configuration with total zero magnetization, illustrating the lack of additivity in the Curie-Weiss model.

where $S_i = \pm 1$ labels a spin variable, J is the ferromagnetic coupling and the sum extends over all pairs spins, N being their total number. Note that Hamiltonian (1) is *extensive*, since $H \propto N$, but, as we shall see, *not additive*.

Refer, in fact, to the situation schematized in Fig. 2 where all the spins in the left portion of the space are equal to 1, whereas the ones in the right are assumed to be -1. Under this conditions the energy of the two regions reads $E_I = E_{II} = -(J/8)N \neq 0$. Conversely, when computing the total energy, one finds $E = -J/(2N)(N/2 - N - 2)^2 = 0$. The relation $E = E_I + E_{II}$ does not hold, and consequently the system is not additive. The underlying reason is that the above Hamiltonian is long range, since every spin interacts with all the others. This in turn implies that the energy at the interface cannot be neglected, the latter being of the same order of the energies in the two bulks. As a side remark, we shall note that the lack of additivity affects dramatically the usual construction of the canonical ensemble, and therefore peculiar behaviours are to be expected for a long-range system in contact with a thermal reservoir. Next paragraph is devoted to a short account on this topic.

THERMODYNAMICS PECULARITIES

As previosuly pointed out, the non-additivity issue is responsible for a number of important and non trivial consequences. As soon as first order phase transitions are present, "convex intruders" in the microcanonical entropy appear [4, 5]. A typical situation is displayed in Fig 3. Only if interactions are short-range and, hence, the additivity property holds, the states in the convex entropy region $\epsilon_1 < \epsilon < \epsilon_2$ of Fig 3a are unstable, when compared to those obtained by combining, in appropriate portions, the two limiting states with energies ϵ_1 and ϵ_2. This is not the case if long-range interactions are to be considered and additivity is violated. The presence of stable, non-concave, entropy regions implies the appearance of *negative specific heat* in the microcanonical ensemble. As an immediate consequence *statistical ensembles are not equivalent*, since the specific heat is always positive in the canonical ensemble. Note that, *large deviation techniques* allow one to solve, both in the microcanonical and in the canonical ensemble, a large class of mean-field models and constitute therefore a powerful tool to detect possible discrepancies.

Another intriguing effect is related to temperature jumps, as depicted in Fig. 3b. In this case, two branches of the

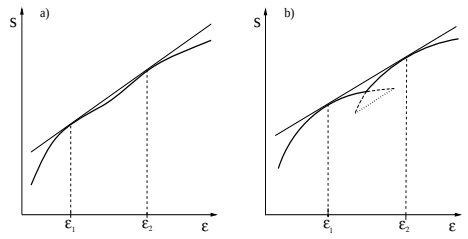

Figure 3: (a) Entropy $s(\epsilon)$ can be non-concave in the microcanonical ensemble, giving rise to negative specific heat. (b) In the non-concave region, entropy can develop kinks in the slope, creating temperature jumps.

entropy exist, respectively a high and a low energy ones. When crossing each other, they generically form an angle: this sets the origin of the temperature jumps, the derivative of the entropy with respect to energy being different on the two sides of the intersection point.

NON-LINEAR DYNAMICAL ASPECTS

In this Section we shall shortly report about a selection of peculiar dynamical features, which are generically encountered when dealing with long-range interacting systems. First, the existence of *quasi-stationary states* has been often discussed in the literature with reference to various test models. Particularly important is the case of the so called Hamiltonian Mean Field (HMF) model [2], which describes the motion of N coupled rotators and is characterized by the following Hamiltonian

$$H = \frac{1}{2}\sum_{j=1}^{N} p_j^2 + \frac{1}{2N}\sum_{i,j=1}^{N}[1-\cos(\theta_j-\theta_i)] \qquad (2)$$

where θ_j represents the orientation of the j-th rotor and p_j is its conjugate momentum. Note that the HMF model correpsonds to the XY model with $J=1, K=0$. To monitor the evolution of the system, it is customary to introduce the magnetization, a global order parameter defined as $M = |\mathbf{M}| = |\sum \mathbf{m}_i|/N$, where $\mathbf{m}_i = (\cos\theta_i, \sin\theta_i)$ is the local magnetization vector. A second order phase transition is found at $\epsilon_c = E_c/N = 0.25$ ($T_c = 0.5$). For energy close to the transition value, the finite N system can remain trapped in *quasi-stationary* states whose life-time increases with a power of N. An example of the evolution of magnetization from an initial homogeneous (non-magnetized) water-bag state to the final maximum entropy state is displayed in Fig. 4. As N is increased the lifetime of the non-equilibrium quasi-stationary state increases: curves with growing N go from left to right. Importantly, in this intermediate regime, the magnetization is lower than predicted by the Boltzmann–Gibbs equilibrium and the system apparently displays non Gaussian velocity distributions. The above phenomena can be successfully interpreted in the framework of the statistical theory of the Vlasov equation [6], a wide general approach originally introduced in the astrophysical and 2D Euler turbulence contexts [7, 8].

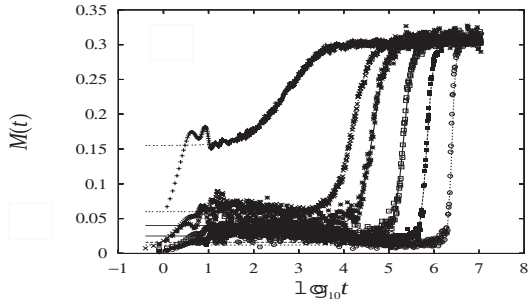

Figure 4: Temporal evolution of the magnetization $M(t)$ for different particles numbers: $N = 10^2(10^3)$, $10^3(10^2)$, $2.10^3(8)$, $5.10^3(8)$, $10^4(8)$ and $2.10^4(4)$ from left to right (the number between brackets corresponding to the number of samples).

Finally, let us mention that recently [9], in analyzing a Ising model with both short and long-range interactions on a ring, it has been realized that the accessible region of extensive parameters (energy, magnetization, etc.) may be non convex. This implies that *broken ergodicity* can appear, due to the fact that the accessible magnetization states at a given energy can be disconnected.

THE CASE OF A SINGLE-PASS FEL

For Single-Pass FEL amplifiers, the Colson-Bonifacio [3] model applies:

$$\frac{d\theta_j}{d\bar{z}} = p_j \qquad (3)$$

$$\frac{dp_j}{d\bar{z}} = -\mathbf{A}e^{i\theta_j} - \mathbf{A}^* e^{-i\theta_j} \qquad (4)$$

$$\frac{d\mathbf{A}}{d\bar{z}} = i\delta\mathbf{A} + \frac{1}{N}\sum_j e^{-i\theta_j} \qquad (5)$$

The complex field amplitude $\mathbf{A}$ is the degree of freedom associated to the wave, while θ_i, p_i are the conjugate variables related to the electron position and "momentum". $\bar{z}$ is the (rescaled) longitudinal position along the undulator, N is the number of electrons and δ stands for the so-called detuning parameter. The above model can be derived from the *mean-field* Hamiltonian

$$H_N = \sum_{j=1}^{N}\frac{p_j^2}{2} - N\delta I^2 + 2I\sum_{j=1}^{N}\sin(\theta_j-\varphi)\,, \qquad (6)$$

where $\mathbf{A} = I\exp(-i\varphi)$. In this respect, FELs fall naturally in the realm of systems with long-range interactions.

The microcanonical equilibrium entropy of this model can be obtained using large deviation techniques [10]. Ensembles are equivalent, no negative specific heat or temperature jump appears. However, the evolution towards the maximum entropy equilibrium state is highly non trivial, as shown in Fig. 5, and shares many similarities with

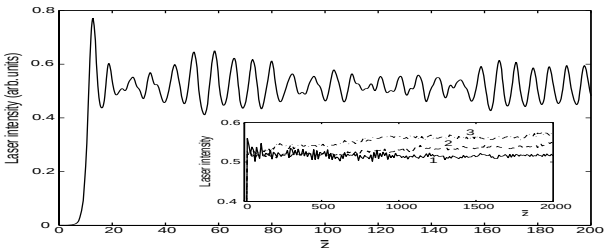

Figure 5: Typical evolution of the radiation intensity using Hamiltonian (6). The detuning δ is set to 0, the energy per electron $H/N = 0.2$ and $N = 10^4$ electrons are simulated. The inset presents averaged simulations on longer times for different values of N: $5 \cdot 10^3$ (curve 1), 400 (curve 2) and 100 (curve 3).

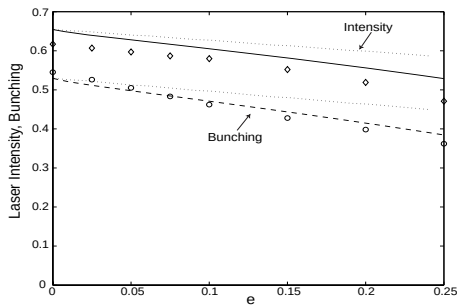

Figure 6: Comparison between theory (solid and long-dashed lines) and simulations (symbols) for a non monoenergetic beam when the energy (e) characterizing the initial velocity dispersion of the initial electron beam, is varied. The dotted lines represent the intensity and bunching ($b = |\sum_j e^{i\theta_j}|/N$) predicted by the full (Boltzmann-Gibbs) statistical equilibrium, not very appropriate here, whereas the solid line and long-dashed lines refer to the Vlasov equilibrium [10]. The discrepancy between theory and numerical experiments is small over the whole range of explored energies.

the case of the HMF. After the initial exponential growth, the system converges to a *quasi-stationary state* that gets more pronounced when increasing the number of simulated electrons N. Finally it relaxes to the Boltzmann-Gibbs equilibrium, driven by granularity. The intermediate quasi-stationary state is indeed the only experimentally relevant regime, due to the finite extension of the undulators. As already pointed out, the latter state, is a *Vlasov equilibrium*, sufficiently well described by Lynden-Bell's Fermi-like distribution arising from "violent relaxation" (constrained maximum entropy principle) [7, 8, 10, 11]. Results reported in Fig. 6 provide a clear support to this conclusion.

CONCLUSIONS

In this paper, we discussed the concept of long-range interactions and shortly reviewed the fundamental properties of such systems. In particular, microcanonical and canonical ensembles disagree for long range interactions at canonical first order transitions. Negative specific heat and temperature jumps are typical signatures of this ensemble inequivalence. Dynamical non equilibrium features arise, and more specifically, *quasi-stationary* states, where the system gets trapped for long times. Their life-time increases in fact with the system size N. Moreover, as an indirect signature of non-additivity, broken ergodicity manifests as a generic feature of systems with long-range interactions.

Further we focused on a simple model of the Free Electron Laser dynamics, which shares many similarities with the so called Hamiltonian Mean Field model, a paradigmatic toy-model often referred to for theoretical applications. For the case of the FEL, we have shown that collective phenomena for wave-particle interactions can be succesfully interpreted through a constrained maximum entropy principles of the associate Vlasov system. Given the above, it is here anticipated that FELs will constitute a promising experimental set up to investigate the universal pecularities that characterize systems with long range interactions.

REFERENCES

[1] T. Dauxois, S. Ruffo, E. Arimondo and M. Wilkens (eds), *Dynamics and thermodynamics of systems with long-range interactions*, Lecture Notes in Physics 602 (Springer, Berlin, 2002).

[2] M. Antoni and S. Ruffo, *Phys. Rev. E* **52** (1995) 2361.

[3] W. B. Colson, Phys. Lett. A **59**, 187 (1976); R. Bonifacio et al., Opt. Comm **50**, 373 (1984).

[4] J. Barré, D. Mukamel and S. Ruffo, *Phys. Rev. Lett.* **87** (2001) 030601.

[5] D. H. E. Gross, *Microcanonical Thermodynamics: Phase Transitions in Small Systems*, Lecture Note in Physics, **66**, World Scientific, Singapore (2001).

[6] A. Antoniazzi, D. Fanelli, J. Barré, P.H. Chavanis, T. Dauxois, S. Ruffo, submitted to *Phys. Rev. Lett.*, cond-mat/0603813 (2006)

[7] D. Lynden-Bell, *Monthly Notices of the Royal Astronomical Society* **136**, 101 (1967).

[8] P.H. Chavanis, J. Sommeria, R. Robert, *Astrophys. J.*, **471**, 385 (1996).

[9] D. Mukamel, S. Ruffo and N. Schreiber, *Phys. Rev. Lett.*. **95**, 240604 (2005)

[10] J. Barré, T. Dauxois, G. De Ninno, D. Fanelli, S. Ruffo, *Phys. Rev. E*, Rapid Comm. **69** (2004) 045501.

[11] F. Curbis, A. Antoniazzi, G. De Ninno, D. Fanelli, submitted to *Phys. Rev. E* (2006)

OVERVIEW OF PERSEO, A SYSTEM FOR SIMULATING FEL DYNAMICS IN MATHCAD

L. Giannessi, ENEA C. R. Frascati, Via E. Fermi 45, 00044 Frascati (Rome) Italy.

Abstract

Perseo is a library of functions devoted to the simulation of FEL dynamics in the *Mathcad* environment. Functions for the generation of phase space variables, for the solution of the pendulum-like equation and for manipulating the phase space in a number of devices are available. These function can be combined in order to model more complicated situations as time dependent simulations, 3D simulations, oscillator FEL configurations, optical klystron, cascaded FELs …

INTRODUCTION

Mathematical computer aided scratchpads which integrate standard mathematical notation, text, graphs and programming capabilities in worksheets as *Mathcad* or *Mathematica* and *Matlab*, are widespread tools in the scientific community. Nowadays computers are fast enough to execute interactively from start-up to saturation an FEL simulation involving a few thousands macro-particles. This suggested to develop a set of basic functions which can be called from within the *Mathcad* environment, devoted to solve FEL dynamics related problems. The result is *Perseo*[1], a flexible tool that can be simply programmed to set up FEL simulations in a wide variety of configurations.

THE FEL MODEL IN *PERSEO*

The core of the library consists of a routine solving the pendulum-like FEL equations coupled with the field equations which govern the FEL longitudinal dynamics [2,3]. This routine includes self consistently the field variables for the higher order harmonics. In this picture the field is the superposition of slowly varying complex amplitudes $a_n = |a_n| e^{i\varphi_n}$ for each harmonic *n*, $E(z,t) = \sum_n \tilde{E}_n |a_n| e^{i(k_n z - \omega_n t + \varphi_n)}$. The parameters $\tilde{E}_n$ link the dimensionless field amplitude a_n to the field at the harmonic *n*. They may be defined in terms of the saturation intensity [4] as $\tilde{E}_n = \sqrt{z_0 I_s(n)/4\pi}$ where z_0 is the vacuum impedance. In a linear undulator the n^{th} harmonic saturation intensity is defined as $I_s(n) = 1/(4\pi)(m_0 c^3/r_0)(\gamma/N)^4 (\lambda_u K f_b(n,\xi))^{-2}$ where γ is the beam energy in $m_0 c^2$ units, λ_u is the undulator period, *N* is the number of undulator periods, *K* is the undulator parameter. The function $f_b(n,\xi) = J_{(n-1)/2}(\xi) - J_{(n+1)/2}(\xi)$ where $\xi = K^2/4(1+K^2/2)$, is the Bessel factor arising from the average over the longitudinal fast motion typical of linear undulators. The evolution of the amplitudes a_n is governed by the equations:

$$\begin{aligned} \frac{\partial \mathrm{Re}(a_n(\tau))}{\partial \tau} &= -2\pi g_n \langle \cos(in\vartheta_i(\tau)) \rangle_i \\ \frac{\partial \mathrm{Im}(a_n(\tau))}{\partial \tau} &= 2\pi g_n \langle \sin(in\vartheta_i(\tau)) \rangle_i \end{aligned} \qquad (1)$$

where the variable $\tau = \beta_z ct/L_u$ is a dimensionless interaction time, $L_u = N\lambda_u$ is the undulator length and $c\beta_z$ is the longitudinal beam velocity. The phase $\vartheta_i = (k_L + k_u) z_i - \omega_L t$ is the electron phase in the ponderomotive bucket corresponding to the first harmonic field (*n=1*, $k_L = \omega_L/c = k_1 = 2\pi/\lambda_1$ is the wave-vector corresponding to the first harmonic and $k_u = 2\pi/\lambda_u$ is the wave-vector associated to the undulator period). The coupling coefficients at the odd harmonics g_n are given by [3]

$$g_n = 2\pi \left(\frac{N}{\gamma}\right)^3 [\lambda_u K f_b(n,\xi)]^2 \frac{I_{peak}}{I_A \Sigma_b} \qquad (2)$$

where I_{peak}/Σ_b is the electron current density and I_A is the Alfven current . The i[th] particle motion is governed by pendulum-like equations:

$$\begin{aligned} \frac{d\vartheta_i}{d\tau} &= \nu_i \\ \frac{d\nu_i}{d\tau} &= \sum_n \cos(n\vartheta_i)\mathrm{Re}(a_n) - \sin(n\vartheta_i)\mathrm{Im}(a_n) \end{aligned} \qquad (3)$$

where $\nu_i = 2\pi N(\omega_i - \omega_L)/\omega_i$ represents the frequency shift of the i[th] particle resonance $\omega_i/c = 2\gamma_i^2 k_u/(1+K^2/2)$ from the reference frequency ω_L. Note that the above choice for the coefficients $(\tilde{E}_n, g_n)$ leads to the expression (3) for the particles dynamics, where all the harmonics in the expression of $d\nu_i/d\tau$ have the same weight factor. Analogous expressions for the helical undulator are easily obtained by substituting $f_b(n=1,\xi) = 1$, $K \to K_{helical} = \sqrt{2}K$ in (2) and in the definition of $I_s(n)$, and neglecting the higher order harmonic coupling ($f_b(n \neq 1,\xi) = 0$) in (2).

In the following we will analyze the subset of functions that are necessary for setting up a simple FEL simulation

in the *Mathcad* environment. Some knowledge of the basic *Mathcad* language is assumed [5].

The function FELPendulum_h

In *Perseo* the coupled equations (2) and (3) are solved by calling the function:

$$PHSP_{new} := FELPendulum_h(PHSP_{old}, g, \tau_0, \tau_1, tol) \quad (4)$$

This function integrates the coupled system of equations (2) and (3) with the coupling coefficients g (g is indeed an array with number of components equal to the number of simulated harmonics) advancing the system from τ_0 to τ_1 with tolerance *tol*. The variables $PHSP_{new}$ and $PHSP_{old}$ represent the status of the system before and after the integration and are defined as:

$$PHSP = \begin{pmatrix} n_h & not\ used \\ \mathrm{Re}(a_1) & \mathrm{Im}(a_1) \\ \vdots & \vdots \\ \mathrm{Re}(a_{n_h}) & \mathrm{Im}(a_{n_h}) \\ \nu_1 & \vartheta_1 \\ \vdots & \vdots \\ \nu_{n_p} & \vartheta_{n_p} \end{pmatrix} \quad (5)$$

The first line contains the number of harmonics n_h, then n_h lines contain the real and imaginary part of the field at each harmonic, followed by the coordinates (ν, ϑ) of an arbitrary number of simulated particles n_p.

The function FELquietstart_h

The variable *PHSP* may be prepared by filling the matrix with the desired field values and particles coordinates, but a more convenient way is that of using the function

$$PHSP := FELquietstart_h(\nu_0, \sigma_\nu, n_\nu, \vartheta_0, \vartheta_1, n_\vartheta, a) \quad (6)$$

that fills the variable *PHSP* with $n_p = n_\nu \cdot n_\vartheta$ particles, n_ν particles in the ν space, over a Gaussian centred in ν_0 with r.m.s. σ_ν, and n_ϑ particles distributed uniformly in the interval (ϑ_0, ϑ_1).

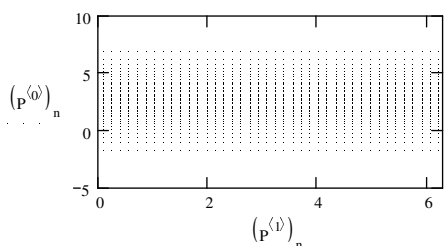

Figure 1: Phase space distribution obtained by calling the function *FELquietstart_h* with ν_0=2.6, σ_ν=2, n_ν=40, ϑ_0 =0, ϑ_1 =2π, n_ϑ =40.

A quiet start distribution is obtained by setting $\vartheta_1 = \vartheta_0 + 2n\pi$ with n integer (normally ϑ_0, ϑ_1 =0, 2π).

An example of the phase space distribution as returned by *FELquietstart_h* is shown in Fig. 1.

A simple simulation

A simple simulation is realized by the *Mathcad* sequence in Fig. 2

$\nu_0 := 2.6 \quad \sigma_\nu := 2 \quad n_\nu := 40$

$n_\theta := 40 \quad \theta_0 := 0 \quad \theta_1 := 2 \cdot \pi \quad a := \begin{pmatrix} 1 + 3i \\ 0 \\ 0 \end{pmatrix}$

$P := FELquietstart_h\left(\nu_0, \sigma_\nu, n_\nu, \theta_0, \theta_1, n_\theta, a\right)$

$g_0 := \begin{pmatrix} 10 \\ 0 \\ 0 \end{pmatrix}$

$P := FELpendulum_h\left(P, g_0, 0, 1, TOL\right)$

Figure 2: Mathcad sequence integrating the pendulum-like equation coupled to the field equations with coupling coefficient *g=10* on the first harmonic and *0* on the higher harmonics.

The phase space in P is integrated over the undulator length with the coupling coefficient *g=10* on the first harmonic and *0* on the higher harmonics. The resulting phase space is plotted in Fig.3.

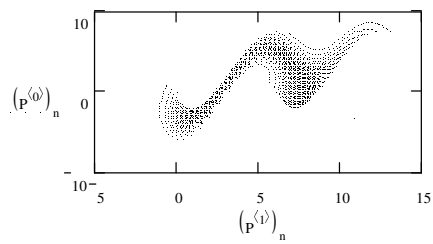

Figure 3: Phase space distribution at the end of the simulation with the parameters listed in Fig. 2.

After the FEL interaction the phase space is distributed in an interval longer than *(0, 2π)*. The periodicity in ϑ of the system of equations (2) and (3) can be imposed to the phase space variables with the function *P := FELBox_h(P, ϑ_0, ϑ_1)*. By calling this function with *(ϑ_0, ϑ_1)=(0, 2π)* we obtain the phase space distribution of Fig. 4.

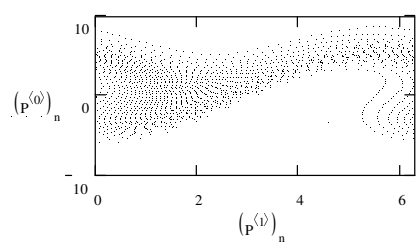

Figure 4: Phase space distribution after imposing a periodicity condition in the interval *(0, 2π)*.

Start-up from e-beam shot noise

Startup from shot noise may be simulated by using the function *FELquasiquietstart_h(*ν_0, σ_ν, $n_\nu, \vartheta_0, \vartheta_1$, n_ϑ, ϕ_{ns}, *a) w*hich is analogous to the function *FELquietstart_h* except for the additional argument ϕ_n which is used to displace the particles according to the function

$$\vartheta_i = \arg(\phi_{ns}) + (1 - |\phi_{ns}|)\left[\left(\frac{\vartheta_1 - \vartheta_0}{n_\vartheta}\right)\left(i - \frac{n_\vartheta - 1}{2}\right)\right] \qquad (7)$$

In the limit of small perturbation ($|\phi_{ns}| \to 0$) and sufficiently large number of particles n_ϑ the distribution has Fourier coefficients $b_n \cong \phi_{ns}$ (bunching coefficients at the harmonic *n*) almost independent from *n* (see ref. [1]). The coefficient b_1 can be estimated in a steady state simulation using the procedure of ref.[6].

Inhomogeneous broadenings and three dimensional effects

The variable $\nu_i = 2\pi N(\omega_i - \omega_L)/\omega_i$ represents the relative shift of the resonance of the ith particle from a given reference frequency ω_L. According to the definition of the resonant frequency of the ith particle $\omega_i = 2\gamma_i^2 ck_u / \left(1 + K(x_i, y_i)^2/2 + \gamma_i^2\left(\theta_{x,i}^2 + \theta_{y,i}^2\right)\right)$, where we have included the dependence on the angle between the average particle trajectory and the undulator axis $\theta_{xy,i} = \beta_{xy}/\beta_z$ (we use the notation $\theta_{xy,i} = \theta_{x,i}, \theta_{x,i}$) and the dependence of the undulator K parameter on the transverse coordinates, the particles distribution in energy and transverse phase space may be converted in a distribution in the detuning parameter space ν. At the lowest order in x_i, y_i and $\theta_{xy,i}$ we have [7]

$$\begin{aligned}
\sigma_{x,y} &= \sqrt{2}\pi N h_{x,y} \frac{2\gamma^2}{1 + K^2/2}\left(\frac{\pi K}{\gamma\lambda_u}\right)^2\left(\frac{\beta_{x,y}\varepsilon_{n,xy}}{\gamma}\right) \\
\sigma'_{x,y} &= \sqrt{2}\pi N \frac{2\gamma^2}{1 + K^2/2}\left(\frac{\pi K}{\gamma\lambda_u}\right)^2\left(\frac{\varepsilon_{n,xy}}{\beta_{x,y}\gamma}\right) \\
\sigma_e &= 4\pi N \frac{\sigma_\gamma}{\gamma}
\end{aligned} \qquad (8)$$

where $h_{x,y}$ are the undulator focusing parameters (with $h_x + h_y = 2$), $\varepsilon_{n,xy}$ and $\beta_{x,y}$ are the normalized emittances and the β Twiss coefficients in the *x* and *y* planes respectively. An approximated expression for standard deviation in the ν space is obtained by combining quadratically the standard deviations (8)

$$\sigma_\nu \cong \sqrt{\sigma_x^2 + \sigma_y^2 + \sigma_x'^2 + \sigma_y'^2 + \sigma_e^2} \qquad (9)$$

In an oscillator FEL or in a seeded FEL and in general, when the transverse properties of the radiation may be considered as a constraint of the problem, the coupling coefficients (2) have to be corrected by a proper filling factor. In general when the radiation size is the result of the balance between diffraction and focusing induced by the gain, as in a single pass FEL, a filling factor coefficient may be derived from the Xie scaling laws [8] by calculating the ratio between the Xie factor with and without diffraction effects. In a similar way a coefficient correcting the coupling factor *g* may be derived from the semi-analytical model in [9].

TIME DEPENDENT SIMULATIONS

Mathcad programming may be used to set up FEL simulations in a wide variety of conditions. As an example we analyse the case of 1D FEL simulations including pulse propagation effects. The field is governed by the evolution equation

$$\left(\frac{\partial}{\partial\tau} + \Delta\frac{\partial}{\partial\zeta}\right)a_n(\tau,\zeta) = -2\pi g_n \mathrm{I}(\zeta)\left\langle \exp(in\vartheta_i(\tau,\zeta))\right\rangle_\zeta \qquad (10)$$

where $\Delta = N\lambda_l$ is the slippage length, ζ is the longitudinal coordinate in the frame moving with the electron bunch and $\mathrm{I}(\zeta)$ is the normalized current shape. The average on the r.h.s. of (10) is intended in a region λ_l at the position ζ. The solution of this equation is obtained by defining an array of variables of the type of *PHSP* in (5), representing the sampling of both the field and the beam phase space variables along the coordinate ζ at the positions $\boldsymbol{\zeta} = \zeta_0, \zeta_1, \ldots, \zeta_{nb-1}$. The phase space beamlets are defined as

$$\boldsymbol{P} = (P_0, P_1, \ldots, P_{nb-1}) \qquad (11)$$

The undulator is divided in time steps such that the step length $\Delta\tau$ is related to the spatial sampling $\Delta\zeta$ by the condition $\Delta\zeta = \Delta/\Delta\tau$. With such a choice, at each time step the field variables at the ith position in the $\boldsymbol{P}$ array have to slip to the next position: ith⇒ ith+1. For this purpose the function in Fig. 5 is defined.

```
FELSlipField(P1, P2) := | for n ∈ 1..P1[0,0]
                        |     P1[n,0] ← P2[n,0]
                        |     P1[n,1] ← P2[n,1]
                        | P1
```

Figure 5: Function *FELSlipField* loading the field data from beamlet *P2* to *P1*. Fields in *P2* are overwritten.

The simulation of a single pass FEL in time dependent mode is then simply obtained with the function shown in Fig. 6. The first loop over the *nb* beamlets loads the initial phase space array ***P,*** generating each beamlet with a

different shot noise coefficient $\phi_{n,i}$. The initial field amplitude a_0 is multiplied by a modulating coefficient se_i which can be defined in order to simulate the ζ dependence of an input seed. The second loop over the variable n_τ takes care of the integration of the phase space beamlets P along the undulator. At each time step of length $\Delta\tau$ the array of beamlets ***P*** is stored in the matrix ***OUT***, particles and fields are advanced by the *FELpendulum_h* and the slippage is applied by the *FELSlipField* procedure defined in Fig. 5. Each column of the matrix ***OUT*** contains the array ***P*** at time $\Delta\tau n_\tau$. As an example of a simulation obtained with the routine in Fig. 6, we have considered the case of a SASE FEL with the resonance at 200 nm, a FEL parameter $\rho \approx 4\text{x}10^{-3}$ and gain length of about 0.3 m. In Fig. 7 the longitudinal phase space at saturation is shown. The beamlets at the same time frame have been joined together in the same plot. The horizontal axis represents the beamlets position along ζ. The phase space variable ϑ in each beamlet is expanded by the factor $\Delta\zeta/2\pi$ in order to give the impression of a continuous beam. The ζ window is large enough to contain two spikes, the red line represents indeed the separatrix of the motion and is proportional to the root of the field.

```
FELTimedep := | for i ∈ 0..nb − 1
              |   P_i ← FELquasiquietstart_h(v_0, σ_v, n_v, 0.0, 2·π, n_θ, φ_{n,i}, a_0·se_i)
              | τ ← 0
              | for n_τ ∈ 0..n_T
              |   for i ∈ 0..nb − 1
              |     OUT_{n_τ, i} ← P_i
              |     P_i ← FELpendulum_h(P_i, g·I_i, τ, τ + Δτ, TOL)
              |   for n ∈ n_b − 1..0
              |     PT ← FELSlipField(P_i, P_{if(i=0, nb−1, i−1)})
              |     P_i ← FELbox_h(PT, 0, 2·π)
              |   τ ← τ + Δτ
              | OUT
```

Figure 6: Function simulating the longitudinal dynamics of a single pass FEL in time dependent mode. The result returned by the matrix ***OUT*** contains the beamlets phase spaces composing the beam at the n_T time steps.

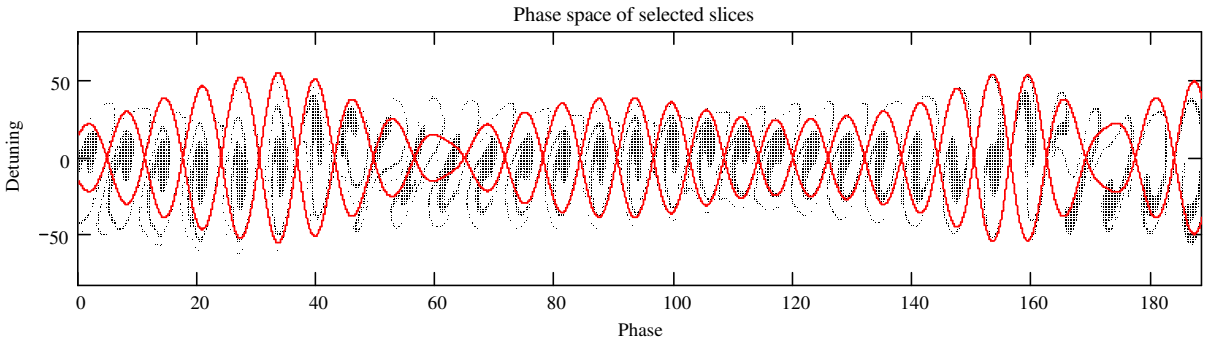

Figure 7: The beamlets resulting after a SASE FEL simulation at saturation have been joined together in the same plot. The horizontal axis represents the beamlets position along ζ. The phase space variable ϑ in each beamlet is expanded by the factor $\Delta\zeta/2\pi$ in order to give the impression of a continuous beam. The red line represent the separatrix of the motion and is proportional to the root of the field.

CONCLUSIONS

We have provided a brief overview of the physical model implemented in *Perseo*. The main functions required for setting up a simple simulation have been analysed and the algorithm for implementing time dependent simulation has been explained. With a similar procedure fully 3D simulations can be implemented but the cpu and memory requirements becomes excessive for an interactive execution.

For additional information and further insight in *Perseo* capabilities the reader is addressed to the web page [1] and to the Perseo Electronic Handbook included in the installation package.

REFERENCES

[1] See www.perseo.enea.it

[2] W. B. Colson, Laser Handbook vol 6, *Classical Free Electron Laser Theory*, 301 North-Holland, Amsterdam, 1990.

[3] W. B. Colson, G. Dattoli, F. Ciocci, Phys. Rev. A 31, 828 , 1985.

[4] G. Dattoli, S. Cabrini, L. Giannessi, Phys. Rev. A 44, 8433 , 1991.

[5] Mathcad Help files – see also www.mathsoft.com

[6] L. Giannessi, in Proc. of the 26th FEL conference, Trieste 2004 , p. 37.

[7] G. Dattoli, A. Renieri, Laser Handbook vol. 4 ed. by M.L.Stich and M.S. Bass , North Holland Amsterdam 1985.

[8] M. Xie, in Proceedings of the 1995 Particle Accelerator Conference, Dallas, Texas, 1–5 May 1995, IEEE, Piscataway, NJ, 1996 , p. 183.

[9] G. Dattoli et al., Journal of Appl. Phys. 95, 3206 2004.

FUTURE SEEDING EXPERIMENTS AT SPARC

L. Poletto, G. Tondello, Università di Padova, Padova, Italy
S. De Silvestri, M. Nisoli, G. Sansone, S. Stagira, Politecnico di Milano, Milano, Italy
P. Musumeci, M. Petrarca, M. Mattioli, INFN Sez. Roma I, Rome, Italy
M. Labat, O. Tcherbakoff, M. Bougeard, B. Carré, D. Garzella, G. Lambert, H. Merdji, P. Salières, Service des Photons Atomes et Molécules, CEA Saclay, DSM/DRECAM, France.
M. E. Couprie, SOLEIL, Sant-Aubin, Gif-sur-Yvette CEDEX, France
D. Alesini, M. Biagini, R. Boni, M. Castellano, A. Clozza, A. Drago, M. Ferrario, V. Fusco, A. Gallo, A. Ghigo, M. Migliorati, L. Palumbo, C. Sanelli, F. Sgamma, B. Spataro, S. Tomassini, C. Vaccarezza, C. Vicario, INFN-LNF, Frascati, Italy
L. Serafini, INFN, Milano, Italy
S. Ambrogio, F. Ciocci, G. Dattoli, A. Doria, G. P. Gallerano, L. Giannessi, E. Giovenale, I. Spassovsky, M. Quattromini, A. Renieri, C. Ronsivalle, ENEA C. R. Frascati, Rome, Italy
P.L. Ottaviani, S. Pagnutti, M. Rosetti, ENEA C.R. Bologna, Italy
A. Dipace, E. Sabia, ENEA C. R. Portici, Napoli, Italy.

Abstract

This communication describes the research work plan that is under implementation at the SPARC FEL facility in the framework of the DS4 EUROFEL programme. The main goal of the collaboration is to study and test the amplification and the FEL harmonic generation process of an input seed signal obtained as higher order harmonics generated both in crystals (400 nm and 266 nm) and in gases (266 nm, 160 nm, 114 nm). The SPARC FEL can be configured to test several cascaded FEL layouts that will be briefly analysed.

INTRODUCTION

The SPARC FEL experiment is based on two main components, a high brightness photoinjector that is expected to provide a high quality beam at energies between 150 and 200 MeV (see Tab.I and ref.[1]) and a single pass FEL, whose undulator beam-line is composed by six undulator sections of 77 periods each, with a period length of 2.8 cm and a gap ranging from 6 to 25 mm[2].

The FEL will operate in self amplified spontaneous emission (SASE) mode at a wavelength of about 500 nm with an expected saturation length of about 10-12 m, according to the beam parameters listed in table 1. The flexibility offered by the variable gap configuration of the SPARC undulator and the natural synchronization of the electron beam with the laser driving the photoinjector, makes the SPARC layout particularly suited for a number of experiments where the FEL amplifier is seeded by an external laser source. The seed laser is driven by the same oscillator initiating the laser cascade which is used to run the photocathode and consists in a regenerative amplifier delivering 2.5mJ at 800 nm with a pulse duration shorter than 120 fs.

Table 1. List of the main SPARC beam parameters

Beam energy	155-200 MeV
Bunch Charge	1.1 nC
Rep. Rate	1 – 10 Hz
Peak current (>50% bunch)	100 A
Norm. emittances (integrated)	2 mm-mrad
Norm. emitt. (slice len. 300μm)	< 1 mm-mrad
Total correlated energy spread	0.2 %
Total uncorrelated energy spread	0.06 %
e-bunch duration (rms)	~ 4 ps

Different schemes of non-linear harmonic generation are then implemented to generate the shorter wavelength radiation for seeding the FEL. Second and third harmonic generation in LBO crystals will provide the powerful pulses required to reach saturation and study the non-linear pulse propagation in FELs and FEL cascades in superradiant regime, at 400nm and 266nm [3], [4]. The other method considered for the frequency up-conversion of the Ti:Sa fundamental wavelength, is based on the non-linear higher order harmonics generation of the Ti:Sa laser in a gas-jet or in a gas-cell [5]. While at SPARC we plan to seed the FEL with the harmonics up to the 9^{th} of the Ti:Sa [6], the harmonic generation in gas allows to extend the seed source spectral range down to the EUV region of the spectrum and represents a promising technique to seed FEL amplifiers at shorter wavelengths.

In the following we will review some of the planned experiments with the two different seed sources.

SEEDING WITH HIGH HARMONICS GENERATED IN GAS

The experiment of seeding high harmonics generated in gas at SPARC is based on the installation of a gas jet interaction chamber and an in vacuum optical system which matches the transverse optical mode of the harmonic to that of the e-beam in the first undulator section [6]. The UV pulse is injected into the SPARC undulator by means of a periscope and a magnetic chicane deflecting the e-beam from the straight path. High-order odd harmonics of the Ti:Sa laser may be generated at the wavelengths 266nm, 160nm, and 114nm. The undulator resonance condition is tuned at these wavelengths by varying the beam energy and undulator strength K according to the plot shown in Fig. 1.

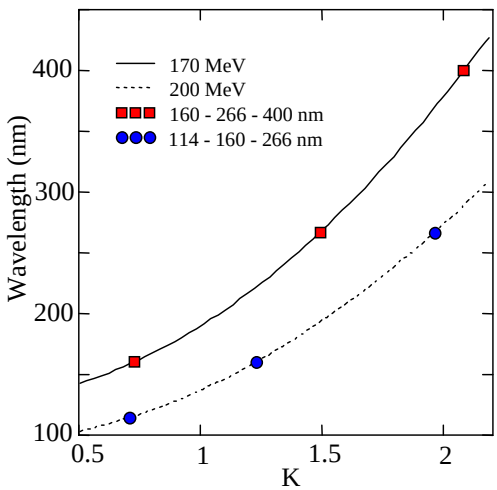

Figure 1: Seeded SPARC FEL operation wavelengths.

The high order harmonics result from the strong non-linear polarisation induced on the rare gases atoms, such as *Ar*, *Xe*, *Ne* and *He*, by the focused intense electromagnetic field of the "pump" laser. The emitted pulse is composed by a sequence of short bursts separated by one half of the fundamental laser period (400nm) and the spectrum contains the odd harmonics of the original laser. A simulation of the amplification of a pulse at 160nm with the typical time structure of harmonics generated in gas has been done with *Perseo*[7]. The laser pulse shape vs. the longitudinal coordinate is shown in Fig. 2 at different positions along the undulator. The radiation spectrum is also shown in Fig.2 and the effect of the spectral "cleaning" associated with the limited FEL bandwidth (FEL parameter $\rho \approx 4 \cdot 10^{-3}$) is evident. An analogous behaviour is observed at the third harmonic generated by the non-linear FEL dynamics. More detailed simulations based on an accurate model of the seed fields distribution and including transverse effects are under study.

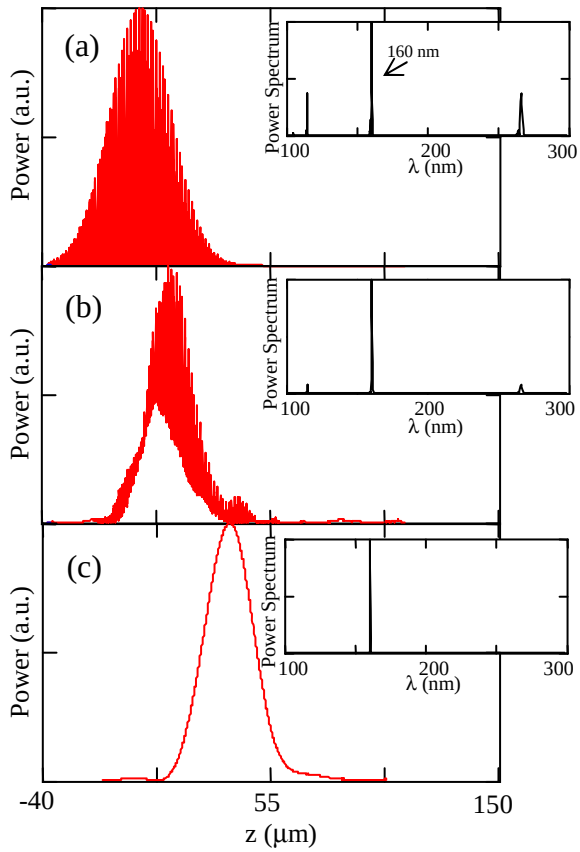

Figure 2 Power and spectrum of the radiation at different positions in the undulator for the SPARC FEL seeded at 160nm. Seed signal (a), after the first undulator section (b), at the end of the undulator (c). Beam energy 200 MeV, K=1.226, the other beam parameters as in Table 1.

SEEDING WITH 2ND AND 3RD HARMONICS OF TI:SA GENERATED IN CRYSTAL

The six SPARC undulators may be configured in order to set up a single stage cascaded FEL based on a modulator – radiator configuration, similar to the one tested at BNL [8]. The layout of this configuration is shown in Fig.3.

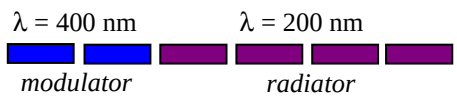

Figure 3 Single stage cascaded FEL layout.

The number of sections of the modulator and of the radiator may be tuned depending on the intensity of the laser seed. The availability of intense short pulses from the seed laser allows to test the superradiant cascade concept [4]. The seed laser power is indeed sufficient to bring at saturation a modulator made by a single undulator segment tuned at 400 nm. The pulse generated in these conditions propagates with the typical signature of superradiance in the following radiator composed by the re-

maining five sections. The feasibility of this experiment was studied in[9].

A second interesting configuration consists in the experimental test of the fresh-bunch injection technique [10]. The layout is shown in Fig.4. In this case the first two undulators (A and B) represent the modulator and radiator sections of single stage cascade, the following two undulators (C and D) are tuned off resonance with the seed wavelength and its higher order harmonics. These undulators play the role of the dispersive section where the radiation exiting the first radiator at 200 nm (B) is longitudinally separated from the electron beam part where the high quality beam has been heated in the previous sections, by the FEL interaction with the seed.

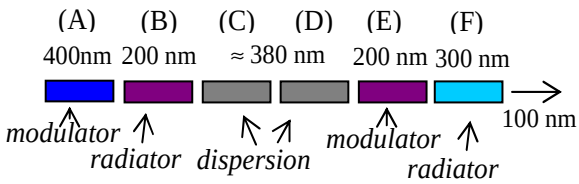

Figure 4 Fresh bunch injection technique layout.

Section (E) is the modulator of the second stage cascade and section (F) is the radiator that is tuned in order to match the resonance of its third harmonic with the second harmonic of the radiator (E). This is necessary since the K parameter excursion of the undulator is not sufficient to span the 1st to 3rd harmonic range and coupling on the higher order odd harmonics in a linear undulator based FEL has been considered [11].

The last configuration considered in this overview consists in the harmonic FEL cascade [12]. As in the last stage of the previous configuration, the two undulators are tuned at different, not-harmonic fundamental frequencies, but have instead one of their higher order harmonics in common. According to the SPARC FEL undulator properties, this scheme may be tested in configurations where the fourth of the sixth harmonic of the 266nm signal used as seed of the first section, are amplified as the third or fifth harmonics in the second section. This configuration has been analysed with numerical simulations in time dependent mode. Both the codes *Perseo* and a modified version of the code *Genesis 1.3* [13-14] which includes the self consistend dynamics of the higher order harmonics have been used. In the example considered in Fig. 5, we show the result obtained with *Perseo*. The cascade is driven by a seed of 2 MW peak power at a wavelength corresponding to the third harmonic of the Ti:Sa drive laser. The first undulator has the fundamental resonance at 266nm and the second section is tuned at 222nm. The two undulators have a common resonance at 44nm, corresponding to the 6th harmonic of the first section and the 5th of the second.

Figure 5 FEL Harmonic cascade FEL configuration.

The energy of the radiation pulse at the wavelength of 44nm vs the longitudinal coordinate in the radiator is shown in Fig. 6.

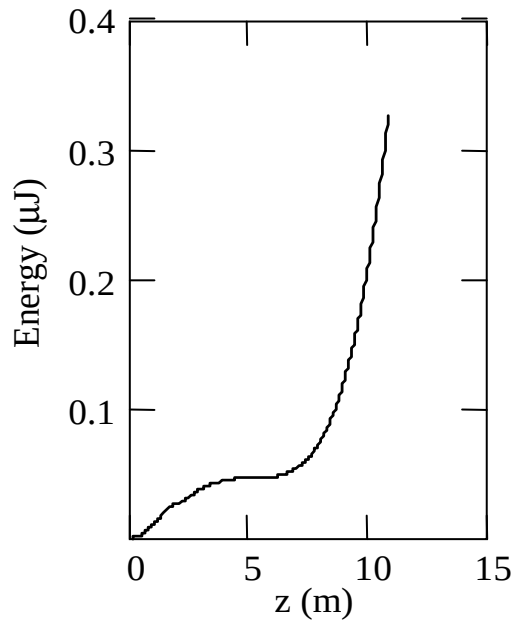

Fig. 6 Pulse energy vs. the longitudinal coordinate in the radiator.

A transition to superradiance where the pulse energy grows as $z^{3/2}$ occurs after about five meters of the radiator section.

The pulse shape is shown in Fig. 7 and the relevant spectrum is shown in Fig. 8.

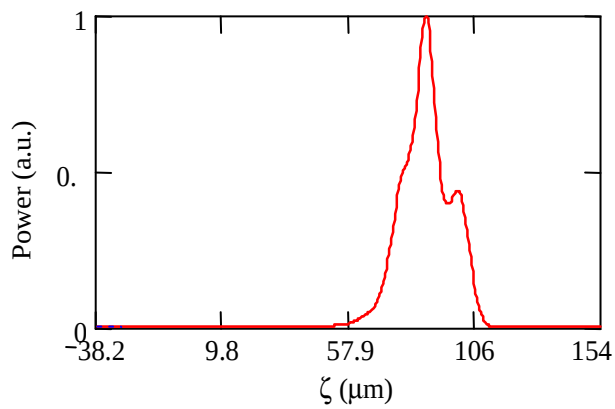

Fig. 7. Longitudinal profile of the radiation power at the end of the second undulator.

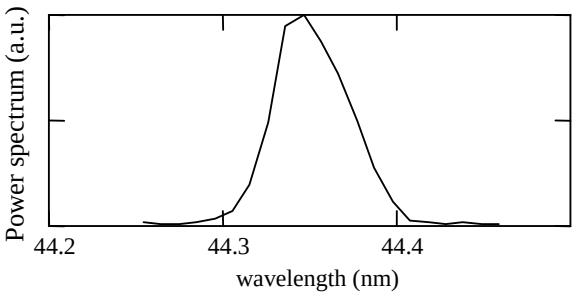

Fig. 8 Power spectrum of the radiation pulse as shown in Fig. 7.

CONCLUSIONS

We have given a brief overview of some of the experiments that will be implemented at SPARC thanks to the flexibility of the SPARC configuration and of the variable gap undulator. Seeding the FEL with harmonics generated in gas and testing schemes as the fresh bunch injection technique and the harmonic FEL cascade are among the capabilities of the SPARC hardware. The harmonic cascaded FEL scheme is in particular a promising scheme to extend to the short wavelength the operation range of a Free Electron Laser. A wavelength of 44nm was obtained in simulations with a beam energy of only 200 MeV.

The opportunities provided by the SPARC experiment of a deeper understanding of the amplification process and of experimentally testing and of the FEL dynamics through a whole cascade, may affect in the future the design of the foreseen FEL facilities aiming at the generation of radiation in the VUV-EUV region of the spectrum.

ACKNOWLEDGMENTS

Work partially supported by the EU Commission in the sixth framework programme, contract no. 011935 – EUROFEL.

REFERENCES

[1] SPARC Collaboration, Nucl. Instr. & Meth. A507 (2003) 345-349, see also http://www.sparc.it and these proceedings.
[2] A. Renieri et al. Status report on SPARC project, in Proc. of the 26th FEL conference, Trieste 2004 JACoW (Joint Accelerator Conference Website) at http://www.JACoW.org, p. 163 (2004).
[3] R. Bonifacio, L.De Salvo Souza, P.Pierini, and N. Piovella, Nucl.Instrum. & Meth. A 296, 358 (1990)
[4] L. Giannessi, P. Musumeci, S. Spampinati, J. Appl. Phys. 98, 043110 (2005).
[5] T. Brabec, F. Krausz, Rev. Mod. Phys. 72, 545 (2000).
[6] M. Labat et al., Seeding SPARC Facility with Harmonic Generation in Gases, MOPPH047 these proceedings.
[7] L. Giannessi, *Perseo* see http://www.perseo.enea.it
[8] L. H. Yu et al. Phys. Rev. Lett. 91, 074801 (2003).
[9] L. Giannessi, P. Musumeci, in Proc. of the 27th FEL conference, JACoW (Joint Accelerator Conference Website) at http://www.JACoW.org, p. 210 (2005).
[10] I. Ben-Zvi, K.M. Yang, L. H. Yu, Nucl. Instrum. & Meth. A 318, 726 (1992).
[11] W. B.Colson, G. Dattoli and F. Ciocci, Phys. Rev. A 31, 828 (1985).
[12] L. Giannessi and P. Musumeci, in proc. of 46th workshop on the Physics and applications of high brightness electron beams, Erice (Tr), 9 - 14 October 2005.
[13] S. Reiche, Nuclear Instrum. & Meth. A429, 243 (1999).
[14] L. Giannessi and P. Musumeci, The Free Electron Laser Harmonic Cascade" submitted to New Journal of Physics, June 2006.

X-RAYS GENERATION WITH A FEL BASED ON AN OPTICAL WIGGLER

A. Bacci, C. Maroli, L. Serafini, *INFN*-Sezione di Milano, 20133 Milano (Italy)
V. Petrillo , Dipartimento di Fisica dell'Università di Milano-INFN Sezione di Milano, 20133 Milano (Italy)
M.Ferrario , INFN-LNF, 00044 Frascati, Roma, Italy.

Abstract

The interaction between high-brilliance electron beams and counter-propagating laser pulses produces X rays via Thomson back-scattering. If the laser source is long and intense enough, the electrons of the beam can bunch and a regime of collective effects can be established. In the case of dominating collective effects, the FEL instability can develop and the system behaves like a free-electron laser based on an optical undulator. Coherent X-rays can be irradiated, with a bandwidth very much thinner than that of the corresponding incoherent emission. The main quantities that limit the brilliance of the X-rays are emittance, mean radius, current and energy spread of the electron beam, and the distribution and intensity of the laser beam. In this work we discuss first some ideal examples. Secondly we present the preparation of the electron beam by means of the use of a genetic code that optimizes the output of the code ASTRA. The electron beam obtained is analysed in slices and the best one is used in the 3-D radiation code.

INTRODUCTION

A Thomson back-scattering set-up can be considered in principle as a source of intense X-ray pulses which is at the same time easily tunable and highly monochromatic. Due to recent technological developments in the production of high brilliance electron beams and high power CPA laser pulses, it is now even conceivable to make steps toward their practical realisation.

The radiation generated in the Thomson back-scattering is usually considered incoherent and calculated by summing at the collector the intensities of the fields produced in single processes by each electron. If the laser pulse is long enough, however, collective effects can establish and become dominant. The system in this range of parameters behaves therefore like a free-electron laser, where the static wiggler is substituted by the optical laser pulse.

From the point of view of the theoretical description of the process, it is convenient to start with the same set of one-dimensional equations that are used in the theory of high-gain free-electron laser amplifier [1,2]. To take into account the many aspects of the process connected with the finite transverse geometry of the electron beam and of the laser and radiation pulses it is necessary to consider 3D equations [3].

A set of numerical results based on ideal electron beams is first presented. Secondly we present a genetic code that permits the optimization of the outputs of the beam dynamics code ASTRA, in order to obtain an electron beam with suitable characteristics. The electron beam obtained is analysed in slices and the best slice is used in the computation of the X-ray radiation under the effect of the laser. A short discussion of the importance of the data will be given at the end of the paper.

MODEL EQUATIONS AND IDEAL EXAMPLES

We start from the Maxwell-Lorentz equations that describe both laser and collective electromagnetic fields and from the relativistic equations of motion for the electrons of the beam. The laser and collective fields are given in terms of the corresponding scalar and vector potentials in the Coulomb gauge.

We assume that the laser is circularly polarised with the following form of the vector potential $\mathbf{A}_L$ (the laser pulse propagates along the z-axis in the negative direction):

$$\mathbf{A}_L(\mathbf{r},t) = \frac{a_{L0}}{\sqrt{2}}(g(\mathbf{r},t)e^{-i(k_L z+\omega_L t)}\hat{\mathbf{e}} + cc) + O(\frac{\lambda_L}{w_0}) \qquad (1)$$

where $\lambda_L = 2\pi/k_L$ is the laser wavelength, w_0 the laser spot size, $\omega_L=ck_L$ the angular frequency and $\hat{\mathbf{e}} = (\mathbf{e}_x + i\mathbf{e}_y)/\sqrt{2}$. The envelope g(**r**,t) is considered to be a slowly varying function of all variables xyz and t and is defined as a complex number with $|g(\mathbf{r},t)|\leq 1$. In the case of a laser pulse with a Gaussian transverse shape, the envelope has the form

$$g(\underline{r},t) = \Phi(z+ct)\frac{1+i\frac{z}{z_0}}{1+\frac{z^2}{z_0^2}}\exp\left[-4\frac{x^2+y^2}{w_0^2(1+\frac{z^2}{z_0^2})} - 4i\frac{x^2+y^2}{w_0^2(\frac{z}{z_0}+\frac{z_0}{z})}\right] \qquad (2)$$

where $z_0 = \pi w_0^2/4\lambda_L$ is the Rayleigh length and the form of the (real) function Φ (with $0\leq\Phi(z)\leq 1$) depends on the shape of the pulse along the z-axis. In the case of a guided laser pulse the quantity g(r,t) is a step function. We suppose that $\varphi(\mathbf{r},t)$ and $\mathbf{A}(\mathbf{r},t)$ have a slow dependence on x and y, i.e., that they vary on a transverse scale L_T much greater than the radiation wavelength $\lambda=2\pi/k$ and write, accordingly to the single-mode hypothesis frequently used in 1D treatments

$$\begin{aligned}\mathbf{A}(\mathbf{r},t) &= M(\mathbf{r},t)\hat{\mathbf{e}} + cc + O(\lambda/L_T) \\ &= A(\mathbf{r},t)e^{i(kz-\omega t)}\hat{\mathbf{e}} + cc + O(\lambda/L_T)\end{aligned} \qquad (3)$$

where $M(\mathbf{r},t) = A(\mathbf{r},t)e^{i(kz-\omega t)}$ and $\omega=ck$ is the radiation angular frequency. In the three-dimensional equation of

the model derived in details in Ref [3] a critical role is played by the FEL parameter $\rho = \frac{1}{\gamma_0}\left(\frac{\omega_b^2 a_{L0}^2}{16\omega_L^2}\right)^{\frac{1}{3}}$.

The resonant frequency is at $\omega \approx \frac{4\gamma_0^2\omega_L}{1+a_{L0}^2}$. The fact that the quantum effects are negligible is guaranteed by taking the quantum parameter $q = \frac{\hbar k}{\rho mc < \gamma >} < 1$.

First, we have solved our model equations in the following case: the laser has a wavelength λ_L=10 micron and the parameter a_{L0} = 0.3. The diameter of the laser focal spot w_0 has been assumed 50 μm, the length of the pulse 70-100 psec, for a total power of 40-100 GW and a total energy of 4-10 J. The bunch of electrons has been chosen with an average value of γ, <γ>=60, corresponding to an energy of 30 MeV. This value of <γ> leads to a resonant wavelength λ=7.56 Angstrom. The quantum parameter q =0.2 and the classical model is expected to be fully valid. The collective effects appear and saturate after 7 gain lengths which in our case correspond to times of the order of 60-70 ps (each gain length corresponds to Lg=1 mm), i.e., of the same order of the duration of the laser pulse.

The electron beam has a mean radius σ_0=25 micron , a total charge of 1-5 nC and a length L_b= 1 mm, so that the Pierce parameter is $\rho = 2.8 \cdot 10^{-4}$. Its energy spread $\Delta\gamma/\gamma$ ranges from 0 to $1.5 \cdot 10^{-4}$ and the initial normalized transverse emittance ε_n has been varied up to 1.

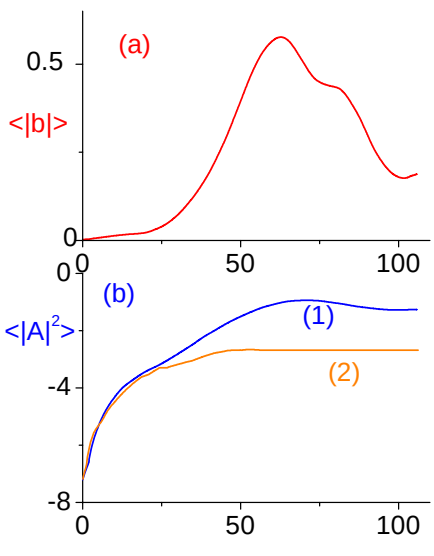

Figure 1 (a) |b| averaged on the transverse section *vs* t in psec and (b), (1) coherent value of $|A|^2(z_m)$ (b),(2) incoherent value for w_0= 50 μm, ε_n=0,6 mm mrad

Fig 1 shows the typical growth of the bunching factor in time (a), as well as the collective potential (b) curve 1 and the incoherent potential (b) curve 2. The amplitude of the vector potential $|A|^2$ has been calculated in the middle of the electron bunch at the position z_m =<z> and averaged on the transverse plane. The peak number of X coherent photons is $2.5 \cdot 10^{10}$, while the incoherent process provides $2 \cdot 10^{8}$ photons.

In this case w_0= 50 micron, ε_n=0,6 mm mrad, Q=3 nC, I=0.9 KA and the signal saturates at t=70 psec.

Figure 2 gives the first peak value of $<|A|^2>$ versus $\Delta\omega/(\omega\rho)$, representing the spectrum of the signal. As can be seen the width of the spectrum is few times ρ. In Fig 3 the peak value of $<|A|^2>$ is given as function of the transverse emittance, showing a depletion of the emission for emittances larger than 0.6-0.7 mm mrad.

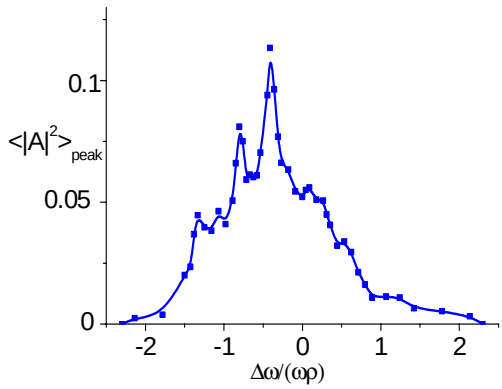

Figure 2: First peak value of $<|A|^2>$ versus $\Delta\omega/(\omega\rho)$ for the same parameters as Fig 1

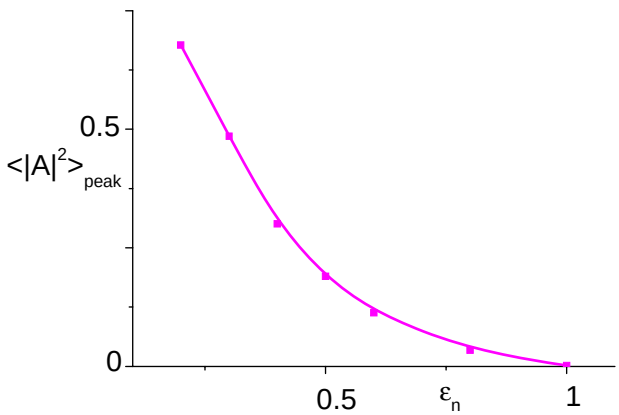

Figure 3: $<|A|^2>_{peak}$ versus ε_n evaluated in micron for the same case of Fig 1 and with $\Delta\omega/\omega = -10^{-4}$, w_0=50 micron, a_{L0}=0.3, $\Delta\gamma/\gamma = 10^{-4}$.

In Figures 4,5,6,7 a different case is shown. The laser wavelength in this case is 0,8 μm.The electron beam has <γ>=30, for a Pierce parameter $\rho = 4{,}38 \cdot 10^{-4}$. Other parameters of the beam are: a mean radius σ_0=10 micron, a total charge of 1 nC, a length L_b= 200 micron, corresponding to a beam current of I=1.5 KA.

In Fig 4 the bunching (a) and the collective (b) (1) and

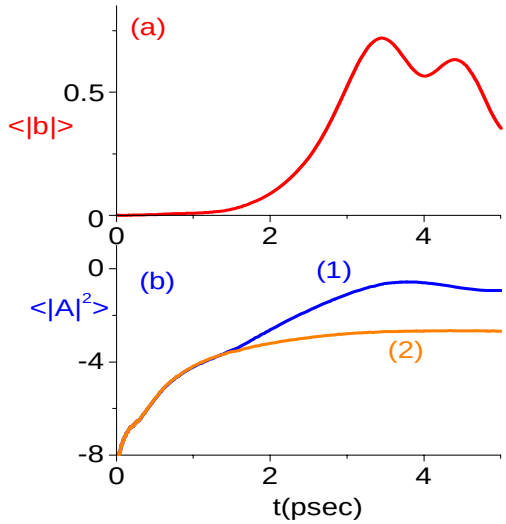

Figure 4: Bunching (a) and log of the radiation intensity (b) vs t in the coherent (1) and incoherent (2) case for: λ_L=0.8 μm, a_{L0}=0.8, $\Delta\gamma/\gamma=10^{-4}$,$\Delta\omega/\omega=-2\cdot10^{-4}$, ε_n=0.88.

incoherent (b) (2) potential amplitude are shown versus time. Furthermore, we have assumed a focal spot of radius w_0 of about 50 μm with a laser parameter of a_{L0}=0.8 so that the radiation turns out to have λ= 3,64 Angstrom. With these values the gain length corresponds to about 145 micron, the appearance and the saturation of the collective effects (taking place in 7-12 gain lengths) being contained in 5 picoseconds, a time of the same order of the duration of the laser pulse. The quantum parameter q is 0.5.

The energy spread $\Delta\gamma/\gamma$ of the electron beam has been chosen 1. 10^{-4} and the initial normalized transverse emittance has been varied from 0 up to 2.

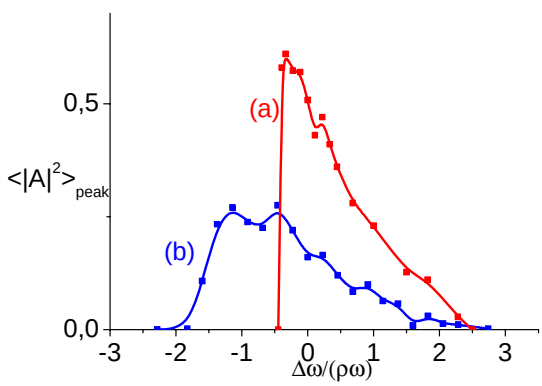

Figure 5: $\langle|A|^2\rangle_{peak}$ versus $\Delta\omega/(\omega\rho)$ for the case of fig 5 and (a) ε_n=0,44 μm and (b) ε_n=0,88 μm.

The saturation level of the radiation is reached at t=4 psec at $\langle|A|^2\rangle_{peak}$=0,275, with a total number of photons of 1,86 10^{10}, against the 2 10^8 provided by the incoherent process.

In Fig. 5 the spectrum of the radiation is presented, while in Fig. 6 the dependence of the maximum of $\langle|A|^2\rangle$ on the transverse normalized emittance is shown. Curve (a) is relevant to the situation of flat laser pulse with w_0=50 micron, while curve (b) shows the more critical situation where a Gaussian profile for the laser has been assumed. In this case the quantity σ_L has been taken equal to 106 μm with a_{L0}=0.8, increasing consequently the laser power.

We must note that we have considerable emission also in violation of the Pellegrini criterion for a static wiggler. In fact, the emittances considered exceed largely the value $\gamma\lambda/4\pi$, which in this case is $9\cdot10^{-4}$ μm. On the other hand, on the fact that $Z_R/Lg=1.2\cdot10^4$, the criterion of Pellegrini can be rewritten in a generalized form for both static and optical undulators as $\varepsilon_n \le \alpha\sqrt{Z_R/L_g}\lambda_R\gamma/4\pi$ [5] where $\alpha=\sqrt{d\omega/(\omega\rho)}\approx 2$, giving the more relaxed limit ε_n<0,3μ.

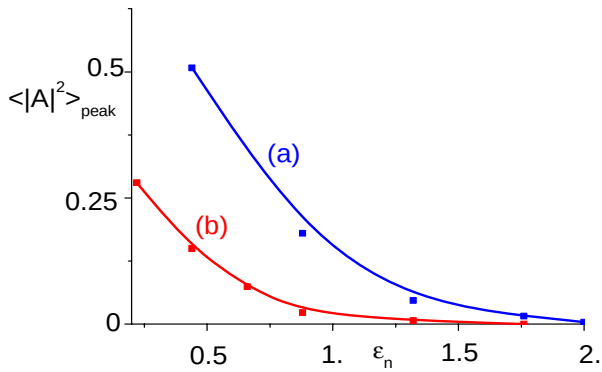

Figure 6: $\langle|A|^2\rangle_{peak}$ ves ε_n, with $\Delta\omega/\omega$=0. and: (a) flat laser profile with w_0=50 μm and a_{L0}=0.8 and (b) Gaussian laser profile with a_{L0}=0.8 and σ_L=106 μm.

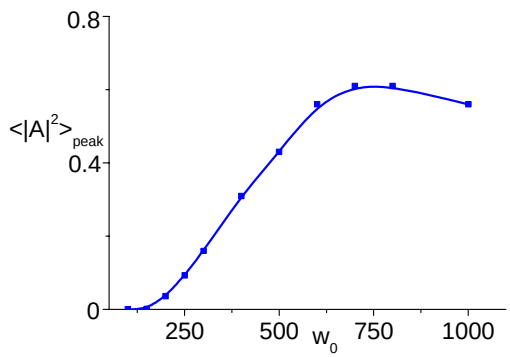

Figure 7 $\langle|A|^2\rangle_{peak}$ vs w_0 for a Gaussian laser for ε_n=0,44 μm, $\Delta\omega/\omega=-1\cdot10^{-4}$, a_{L0}=0.8.

Fig 7 shows the dependence of the growth of the signal on the transverse energy distribution of the laser in the case of a Gaussian pulse for ε_n=0,44 μm, $\Delta\omega/\omega=-1\cdot10^{-4}$, a_{L0}=0.8. In fact, in this case, a spot size with a radius smaller than 75 micron does not permit the instauration of the instability. The collective signal in this condition, therefore, does not grow.

REALISTIC EXAMPLE OBTAINED BY MEANS OF A GENETIC ALGORITHM

A realistic electron beam has been generated using the beam dynamic code ASTRA. The sequence of the accelerating and focalization elements in the beam line is shown in Fig 8, where the RF section works in the velocity bunching configuration.

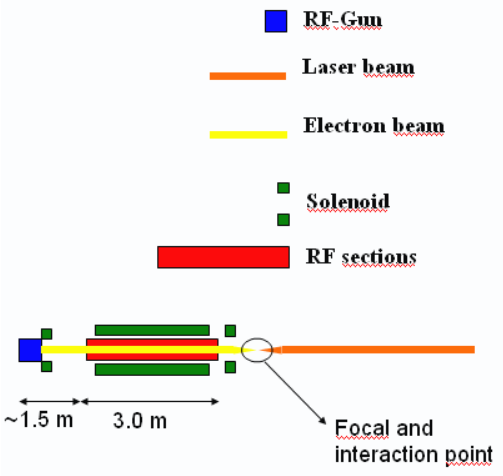

Figure 8: Beam line lay-out.

However, the optimization of the output is very difficult due to the high number of parameters which have to be fixed and to the non linear correlations existing between them. To circumvent this difficulty we have developed a genetic code that manages to fix the values of the parameters. The optimization is made by maximizing the following fitness function:

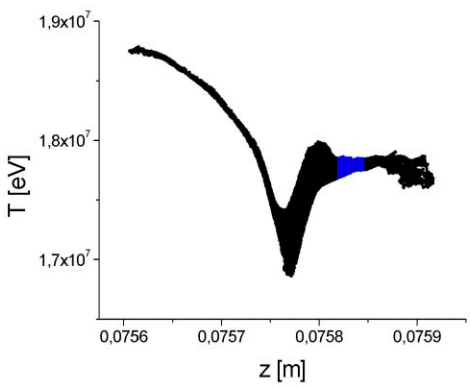

Figure 9: Bunch phase space and slice used (in blue).

$$F_{fitness} = \frac{I^{3.5}}{\varepsilon_{n-x,y} \cdot \sigma_{x,y} \cdot \sqrt{\left(\frac{\Delta\gamma}{\gamma}\right)}}$$

as function of the following genes defining the beam line: 1) Phase of the gun radiofrequency ϕ_{rf}. 2) Acceleration gradient in the bunching structure g_a. 3) Injection phase in the bunching structure ϕ_b. 4) Position of the bunching structure l_b. 5) Intensity of the first solenoid field B_1, used to control the envelope in the emittance compensation layout. 6) Intensity of the second solenoid field B_2, used to control the envelope. 7) Position of the second solenoid l_{s2}.

The convergence is reached in 500 generations on an electron beam configuration whose best slice has an emittance of 0,56 mm mrad, a radius of 15 micron, a length of 15 micron with a charge Q=0.05 nC. The genis values for the final configuration are: ϕ_{rf} =9.77°, g_a = 17.68 MV/m, ϕ_b =-91.57°, l_b =1.3868 m, B_1 =0.256 T B_2=0.0532 T, l_{s2} =1.3685m. The energy spread of the slice $\Delta\gamma/\gamma$ is 0.15 %. The growth of the signal is shown in fig 10, while the spectrum is in Fig 11. The saturation occurs in 6 psec, the focal spot size is w_0=30 μm, a_{L0}=0.8, for a total laser power of W=9.77 TW.

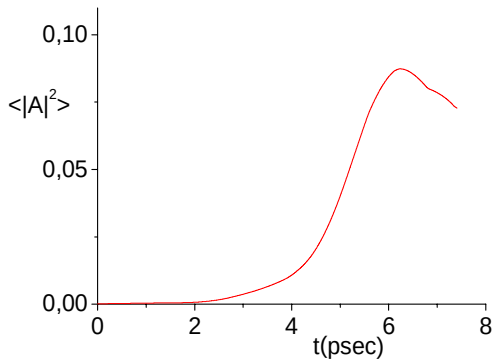

Figure 10: Growth of the signal.

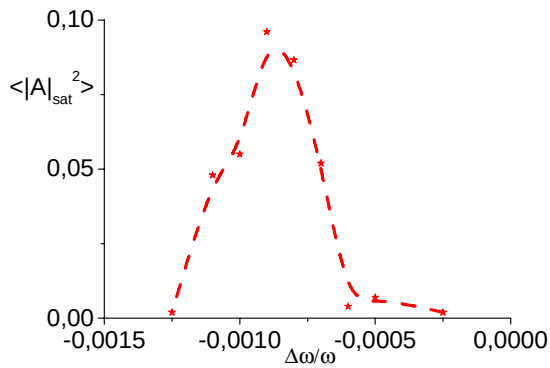

Figure 11: Spectrum of the signal.

REFERENCES

[1] W.B. Colson, Phys.Lett. 59A,187,(1976). R. Bonifacio, C. Pellegrini, L. Narducci Opt. Commun. 50 (1984) 313

[2] A.Bacci, C.Maroli, V.Petrillo, L.Serafini:"Collective effects in the Thomson back-scattering between a laser pulse and a relativistic electron beam" EPJAP (in print)

[3] A.Bacci, M.Ferrario, C. Maroli, V. Petrillo, L. Serafini PRST-AB 9 (2006) 060704

THE SATURATED REGIME OF A SEEDED SINGLE-PASS FREE ELECTRON LASER: A THEORETICAL INVESTIGATION THROUGH THE STATISTICAL MECHANICS OF THE VLASOV EQUATION

F. Curbis*, University of Trieste & Elettra, Basovizza, Trieste, Italy,
A. Antoniazzi, Dipartimento di Energetica, Università di Firenze, Italy
G. De Ninno, Elettra, Basovizza, Trieste, Italy,
D. Fanelli, Dipartimento di Energetica, Università di Firenze, Italy.

Abstract

The quasi-stationary state characterizing the saturation of a single-pass free-electron laser is governed by the Vlasov equation obtained by performing the continuum limit of the Colson-Bonifacio model. By means of a statistical treatment, this approach allows to predict analytically the saturated laser intensity as well as the final electron-beam energy distribution. In this paper we consider the case of coherent harmonic generation obtained from a seeded free-electron laser and present predictions for the first stage of the project FERMI@Elettra project at Sincrotrone Trieste.

INTRODUCTION

In a single-pass FEL, the physical mechanism responsible for the light emission and amplification is the interaction between a relativistic electron beam, a magnetostatic periodic field generated by an undulator and an optical wave co-propagating with electrons. Two different schemes can be distinguished, depending on the origin of the optical wave which is used to initiate the process. In the SASE configuration, the initial seed is provided by the spontaneous emission of the electron beam which is forced by the undulator field to follow a curved trajectory. The seed is then amplified all along the undulator until the laser effect is reached. The SASE radiation produces tunable signal at short (x-ray) wavelengths with several GW peak power and excellent spatial mode. An alternate approach to SASE is Coherent Harmonic Generation (CHG) [1], which is capable of producing temporally coherent pulses. A schematic layout of CHG is shown in Figure 1.

In this case, the initial seed is produced by an external light source, e.g. a laser. The light-electron interaction in a short undulator, called modulator, imposes an energy modulation on the electron beam. The modulator is tuned to the seed wavelength λ. The energy modulation is then converted into a spatial density modulation as the electron beam transverses a magnetic dispersion. Figure 2 shows the evolution of the electron-beam phase space (i.e. energy vs. electrons' phase in the undulator plus radiator field) from the entrance of the modulator to the exit of the dispersive section. Finally, in a second undulator, called radiator and tuned at the n-th harmonic of the seed frequency, the micro-bunched electron beam emits coherent radiation at the harmonic wavelength λ/n. Such a radiation is then amplified until saturation is reached.

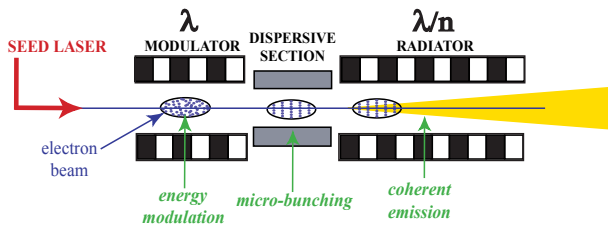

Figure 1: Schematic layout of the CHG scheme.

Importantly, it shall be noticed that Single-pass FELs represent an example of systems with long-range interactions [2]. When long-range forces are to be considered, a global network of connections between individual constituting elements is active, and $mean - field$ effects are dominant. Surprisingly, within the realm of long range interacting systems, a wide number of striking phenomena appear including ensemble inequivalence, negative specific heat and emergence of Quasi–Stationary States (QSS), i.e., long–living states where the system gets eventually trapped before relaxing to its final statistical equilibrium. This latter remarkable non equilibrium feature is also reported for

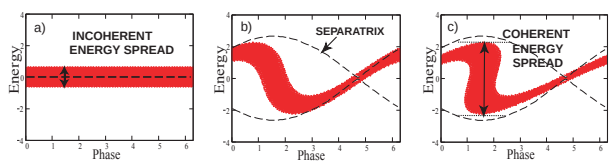

Figure 2: Electron-beam phase space at the entrance a) and at the exit b) of the modulator; c) phase space at the exit of the dispersive section. In a), the thickness of the distribution corresponds to the (initial) incoherent energy spread of the electron beam. In c) the gap between the boundaries of the separatrix corresponds to the energy modulation induced by the seed-electron interaction (see Figure 1).

* francesca.curbis@elettra.trieste.it

FELs, where it plays a central role, being the only state experimentally accessible in real devices. In this respect, FELs provide a general experimental ground to investigate the universal characteristics of systems with long range interactions.

Motivated by this analogy, we shall apply a maximum entropy principle, inspired to Lynden-Bell's theory of "violent relaxation" [3]–[6] for the Vlasov equation and analytically predict the characteristics of the laser signal at saturation. More specifically, the above theoretical interpretative framework will enable us to estimate the expected intensity for the case of FERMI@Elettra [7], a future user-facility based on CHG, without resorting to direct numerical simulations. Our results will be shown to correlate well with Genesis-based [8] estimates.

FROM THE MEAN-FIELD MODEL TO THE LYNDEN–BELL PREDICTION

In this section we will introduce the model that is customarily employed to investigate the time evolution of a single-pass FEL, both in SASE and CHG configurations. By putting forward the hypothesis of one-dimensional (longitudinal) motion and monochromatic radiation, the steady-state dynamics of a single-pass FEL is described by the following set of equations:

$$\frac{\mathrm{d}\theta_j}{\mathrm{d}\bar{z}} = p_j \quad , \tag{1}$$

$$\frac{\mathrm{d}p_j}{\mathrm{d}\bar{z}} = -Ae^{i\theta_j} - A^* e^{-i\theta_j} \quad , \tag{2}$$

$$\frac{\mathrm{d}A}{\mathrm{d}\bar{z}} = i\delta A + \frac{1}{N}\sum_j e^{-i\theta_j} \quad , \tag{3}$$

where $\bar{z} = 2k_u\rho z\gamma_r^2/\langle\gamma_0\rangle^2$ is the re-scaled longitudinal coordinate, which plays the role of time. Here, $\rho = (a_w\omega_p/4ck_u)^{2/3}/\gamma_r$ is the so-called Pierce parameter, γ_r the resonant energy, $\langle\gamma_0\rangle$ the mean energy of the electrons at the undulator's entrance, k_u the wave vector of the undulator, $\omega_p = (e^2\bar{n}/m\varepsilon_0)^{1/2}$ the plasma frequency, $\bar{n}$ being the electron number density, c the speed of light, e and m respectively the charge and mass of one electron. Further, $a_w = eB_w/(k_u mc^2)$, where B_w is the rms undulator field. Introducing the wavenumber k of the FEL radiation, the phase θ is defined by $\theta = (k+k_u)z - 2\delta\rho k_u z\gamma_r^2/\langle\gamma_0\rangle^2$; its conjugate momentum reads $p = (\gamma - \langle\gamma_0\rangle)/(\rho\langle\gamma_0\rangle)$. The complex amplitude $A = A_x + iA_y$ represents the scaled field, transversal to z. Finally, the detuning parameter is given by $\delta = (\langle\gamma_0\rangle^2 - \gamma_r^2)/(2\rho\gamma_r^2)$, and measures the average relative deviation from the resonance condition. The above system of equations (N being the number of electrons) can be deduced by the Hamiltonian:

$$H = \sum_{j=1}^{N}\frac{p_j^2}{2} - \delta I + 2\sqrt{\frac{I}{N}}\sum_{j=1}^{N}\sin(\theta_j - \varphi), \tag{4}$$

where the intensity I and the phase φ of the wave are defined by $A = \sqrt{I/N}\exp(-i\varphi)$. Here, the canonically conjugated variables are (p_j, θ_j) for $1 \le j \le N$ and (I, φ). Besides the "energy" H, the total momentum $P = \sum_j p_j + I$ is also a conserved quantity. Let us finally define the bunching parameter as $b(t) = \sum\exp(i\theta_i(t))/N := \langle\exp(i\theta(t))\rangle$. The latter provides a quantitative measure of the degree of spatial compactness of the particles distribution.

Numerical simulations based on the above system of equations show that the amplification of the wave occurs in several subsequent steps. First, an initial exponential growth takes place, which is successfully captured by a linear analysis. Then, as previously anticipated, the system attains a QSS, where the wave intensity displays oscillations around a well-defined plateau. As predicted by the Boltzmann-Gibbs statistics, for longer times a slow evolution toward the final equilibrium is found. The process is driven by granularity and the relaxation time diverges with the system size N. Hence, due to the constraint imposed by the typical length of an undulator, the QSS is the only regime experimentally accessible in the case of single-pass FELs.

When performing the thermodynamics limit, i.e., $N \to \infty$, one gets to the following Vlasov–wave picture:

$$\frac{\partial f}{\partial \bar{z}} = -p\frac{\partial f}{\partial\theta} + 2(A_x\cos\theta - A_y\sin\theta)\frac{\partial f}{\partial p} \quad , \tag{5}$$

$$\frac{dA_x}{d\bar{z}} = -\delta A_y + \int f\cos\theta\,\mathrm{d}\theta\,\mathrm{d}p \quad , \tag{6}$$

$$\frac{dA_y}{d\bar{z}} = \delta A_x - \int f\sin\theta\,\mathrm{d}\theta\,\mathrm{d}p \quad . \tag{7}$$

which can be shown to govern the initial growth and relaxation towards the QSS. The latter conserves the pseudo-energy per particle

$$h(f,A) = \int\frac{p^2}{2}f(\theta,p)\,\mathrm{d}\theta\,\mathrm{d}p - \delta(A_x^2 + A_y^2) + \int(A_x\sin\theta + A_y\cos\theta)f(\theta,p)\,\mathrm{d}\theta\,\mathrm{d}p \tag{8}$$

and the momentum per particle

$$\sigma(f,A) = \int pf(\theta,p)\,\mathrm{d}\theta\,\mathrm{d}p + (A_x^2 + A_y^2). \tag{9}$$

In ref. [4] it was shown that the average statistical parameters of the laser (intensity and the bunching in the QSS) are accurately predicted by a statistical mechanics treatment of the Vlasov equation, according to prescriptions of the seminal work by Lynden-Bell [5]. The analysis developed in [4] was limited to the case of spatially homogeneous initial conditions (i.e., initial zero bunching). In [9], we extended the analysis by including initially bunched distributions. In the remaining part of this section we will review the foundation of the analytical method and presented select numerical results.

The basic idea of Lynden–Bell "violent relaxation" theory [4, 6] is to coarse-grain the microscopic single-particle distribution function $f(\theta, p, t)$, which is filamented and stirred by the dynamics. An entropy is then associated to the coarse-grained function $\bar{f}$, which essentially counts the number of microscopic configurations giving rise to it.

Starting with an initial centered water-bag distribution, which corresponds to a rectangle uniformly occupied in the phase space (θ, p) with $-p_0 < p < p_0$ and $-\theta_0 < \theta < \theta_0$, the normalization condition reads $f_0 = 1/(4\theta_0 p_0)$.

The entropy can be expressed as [5, 6]:

$$s(\bar{f}) = -\int \left[\frac{\bar{f}}{f_0}\ln\frac{\bar{f}}{f_0} + \left(1-\frac{\bar{f}}{f_0}\right)\ln\left(1-\frac{\bar{f}}{f_0}\right)\right] \mathrm{d}\theta\,\mathrm{d}p. \tag{10}$$

The equilibrium is computed by maximizing this entropy:

$$\max_{\bar{f}, A_x, A_y} \left(s(\bar{f})\right), \tag{11}$$

while imposing the dynamical constraints:

$$h(\bar{f}, A_x, A_y) = h_0, \tag{12}$$

$$\sigma(\bar{f}, A_x, A_y) = \sigma_0, \tag{13}$$

$$\int f(\theta, p)\,\mathrm{d}\theta\,\mathrm{d}p = 1, \tag{14}$$

where h_0 and σ_0 stand, respectively, for the energy and momentum (per particle) of the system. Performing the analytical calculation and introducing the rescaled Lagrange multipliers for the energy, momentum and normalization constraints (β/f_0, λ/f_0 and μ/f_0) one obtains the typical Fermi-Dirac distribution:

$$\bar{f} = f_0 \frac{e^{-\beta(p^2/2 + 2A\sin\theta) - \lambda p - \mu}}{1 + e^{-\beta(p^2/2 + 2A\sin\theta) - \lambda p - \mu}} \tag{15}$$

$$A = \sqrt{A_x^2 + A_y^2} = \frac{\beta}{\beta\delta - \lambda}\int \sin(\theta)\bar{f}(\theta, p)\,\mathrm{d}\theta\,\mathrm{d}p.$$

The three constraints (12)–(14) are then imposed by making use of the above expression for $f(\theta, p)$ and A, and the obtained equations numerically solved to provide an estimate of the multipliers as functions of energy h_0 and momentum σ_0 of the system. Ones β, γ, μ are calculated, one can in turn estimate the value of the intensity I and the bunching parameter b of the QSS.

To validate our findings, we performed numerical simulation for a water-bag initial distribution as specified above, where $\theta_0 < \pi$. Further, label with $|b_0|$ the initial bunching, i.e., the positive quantity given by $|b_0| = |\langle \exp(i\theta(0))\rangle|$. Numerical calculations are performed based on the discrete system (1–3). In Figure 3 the average intensity at saturation is reported as function of $|b_0|$, for different values of the initial kinetic energy. Results are compared with the analytical estimate obtained above. Analogous plots for the average value of the bunching parameter at saturation are reported in Figure 4. A direct inspection of the figures confirms the adequacy of the proposed theoretical framework: predictions based on the Vlasov theory correlate well with numerical curves. In the next section, starting from these results, we will elaborate a strategy to gain insight into the non–linear evolution of a CGH scheme without resorting to direct numerical investigations. In particular, we will focus on the case of the FERMI@Elettra project.

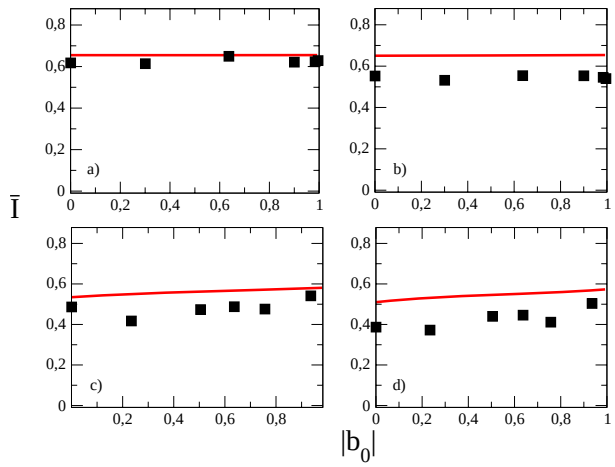

Figure 3: Average intensity $\bar{I}$ at undulator exit as function of the initial bunching $|b_0|$ for different values of the initial average kinetic energy, respectively a) $h_0 = 0.01$ b) $h_0 = 0.16$ c) $h_0 = 0.21$ d) $h_0 = 0.315$). The continuous lines correspond to the Lynden–Bell theoretical prediction, while symbols represent numerical results obtained averaging intensity fluctuations in the saturated regime over ten different realizations of the initial conditions resting on the same values of θ_0 and p_0.

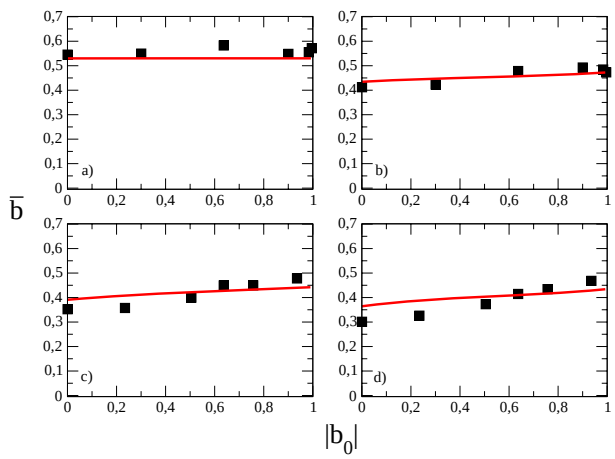

Figure 4: Average values of the bunching parameter $|\bar{b_0}|$ at the undulator exit as function of $|b_0|$. Same choice of parameters as in Figure 3.

CHARACTERIZING THE SATURATION OF CHG FELS

The seed-electron interaction in the first undulator of a CHG scheme induces a coherent modulation, $\Delta\gamma$, of the electron-beam energy, which superimposes to the initial incoherent energy spread σ_γ. Inside the dispersive section, the energy modulation is converted into a spatial density modulation. Performing a Fourier analysis of the spatial beam distribution at the end of the dispersive section one finds the following bunching parameters:

$$|b_0| \simeq J_n(n)/\exp(1/2), \tag{16}$$

where J_n stands for the n-th order Bessel function [1].

On the other hand, the total energy spread $\sigma_{\gamma,tot}$ at the entrance of the second undulator reads:

$$\sigma_{\gamma,tot} = \sqrt{\sigma_\gamma^2 + \frac{(\Delta\gamma)^2}{2}} \simeq \sigma_\gamma \sqrt{1 + \frac{n^2}{2}}, \tag{17}$$

where n is the harmonic number. Moreover, in term of the rescaled variables used in the formulation of the above one-dimensional model, the associated energy profile can be ideally schematized as a water-bag distribution, where

$$p_0 = \frac{\sigma_{\gamma,tot}}{\gamma\rho}. \tag{18}$$

Taking full advantage of the above theoretical analysis, we are therefore in a position to quantify the saturated (QSS) behaviour of a CHG device. In particular, we shall focus on the case of the project FERMI@Elettra [7] and assume the experimental setting relative to the output wavelength 100 nm. In this case, $n = 3$ (i.e., the initial seed wavelength is 100 nm), γ = 2348, $\sigma_\gamma = 150$ KeV and $\rho = 3 \cdot 10^{-3}$. Direct numerical simulations are performed using GENESIS [8], a three dimensional code that explicitly accounts for the coupling between the transverse and longitudinal dimensions. Assuming a radiator length of 16 m, a horizontal and vertical (normalized) beam emittance of 1.5 μ m and on optical waist of $w \simeq 300$ μm, simulations give an output power of about 3 GW.

Independently, one can calculated the value of $|b_0|$ and p_0 by inserting the nominal values of the relevant parameters in equations 18 16. Then, Lynden–Bell theory enables us to predict the QSS value for the intensity which are shown to correlate extremely well with Genesis based calculation, the disagreement being quantified in at most $10\,\%$ [9] .

CONCLUSIONS

The theoretical approach outlined in this paper constitutes a novel strategy to predict the intensity at saturation for a CHG setting, provided the value of the incoherent energy spread is assigned and without involving to direct numerical investigations.

The short recipe goes as follows: by knowing σ_γ one can calculate $\sigma_{\gamma,tot}$ by means of eq.(17) and consequently estimate both $|b_0|$ and p_0, based on eqs.(16)–(18). The spatial width, θ_0, of the initial water-bag distribution (here assumed to mimick the more natural Gaussian profile) is eventually obtained upon inversion of relation $|b_0| = \sin(\theta_0)/\theta_0$. Once the values of θ_0 and p_0 are given, the theory of the violent relaxation allows to quantitatively predict the saturated state of the system.

Finally let us stress that the applicability of the method we have developed is currently limited to situations in which transverse effects are neglected. This in turn entails the possibility of assuming the electron-beam geometrical emittance smaller than the radiation wavelength, the beam relative energy spread smaller than ρ and the Rayleigh length of emitted radiation much longer than the radiator length. These conditions apply for instance to the case of the whole spectral range that is to be covered by the FERMI@Elettra FEL (100-10 nm).

[1] Note that in deriving equation (16) an optimization scheme for the bunching parameter has been put forward according to the standard experimental procedure. A detailed account on the approximations involved is presented in [9] starting from the usual expression given in [1]

REFERENCES

[1] L. H. Yu, *Phys. Rev. A* **44** 5178 (1991).

[2] T. Dauxois, S. Ruffo, E. Arimondo, M. Wilkens (Eds), Lecture Notes in Physics 602, Springer *Dynamics and Thermodynamics of Systems with Long Range Interactions* (2002).

[3] A. Antoniazzi, D. Fanelli, J. Barré, P. H. Chavanis, T. Dauxois, S. Ruffo, submitted to *Phys. Rev. Lett.* (2006).

[4] J. Barré *et al.*, *Phys. Rev. E* **69** 045501 (2004).

[5] D. Lynden-Bell, *Mon. Not. R. Astron. Soc.* **136**, 101 (1967).

[6] P. H. Chavanis, J. Sommeria, R. Robert, *Astrophys. J.* **471**, 385 (1996).

[7] See http://www.elettra.trieste.it/FERMI/.

[8] http://pbpl.physics.ucla.edu/ reiche/.

[9] F. Curbis, A. Antoniazzi, G. De Ninno, D. Fanelli, preprint submitted to *Phys. Rev. E* (2006).

ANALYSIS OF FEL OSCILLATIONS IN A PERFECTLY SYNCHRONIZED OPTICAL CAVITY

N. Nishimori*, JAEA, Ibaraki, Japan.

Abstract

We analyze free-electron-laser (FEL) oscillations in a perfectly synchronized optical cavity by solving the one-dimensional FEL equations. The radiation stored in the cavity can finally evolve into an intense few-cycle optical pulse in the high-gain and low-loss regime. The evolution of the leading slope of the optical pulse, which is defined from the front edge toward the primary peak, is found to play an important role in generating the intense few-cycle pulse. The phase space evolution of electrons on the second pass which interact with the leading slope of a SASE output pulse is obtained in a perturbation method similar to that used in our previous study for a SASE FEL. The resulting analytical solution of the leading slope in the second pass is shown to be approximated by that of a SASE FEL with FEL parameter greater than ρ. The same perturbation method can thus be used to the subsequent passes.

INTRODUCTION

The FEL dynamics is affected by the slippage that is caused by the velocity difference between the electron bunch and the optical pulse inside an undulator. The group velocity of the optical pulse becomes slightly slower than the vacuum speed of light, since the trailing slope of the optical pulse is mainly amplified due to the slippage. This phenomenon, called the laser lethargy (see Ref. [1] and references therein), can be compensated in oscillators by slightly shortening the optical cavity length from the perfect synchronism ($\delta L = 0$), where the cavity length exactly matches with the injection period of the electron bunches. The FEL dynamics of the oscillators with shorter cavity length ($\delta L < 0$) has been studied extensively [2, 3]. At $\delta L = 0$, the optical pulse centroid continues to be retarded on successive passes through the undulator, and the optical pulse finally dissipates, as shown in theoretical studies [4, 5, 6].

An experiment of a high-power FEL driven by a superconducting linac in the Japan Atomic Energy Research Institute (JAERI) FEL facility has however showed that an intense, ultrashort optical pulse is generated at δL = 0.0 $\pm$ 0.1 μm despite the lethargy [7, 8]. The optical power curve measured with respect to δL is well reproduced by the time-dependent simulation code based on one-dimensional (1D) FEL equations [9], if shot-noise effect is included in every fresh electron bunch. A few theoretical studies have attempted to explain the FEL oscillations at $\delta L = 0$, proposing that sideband instability [10] or superradiance in short-pulse FELs [11] is the fundamental physics responsible for the lasing at $\delta L = 0$. Nevertheless, the underlying physics responsible for the FEL oscillations at $\delta L = 0$ has not been clearly explained yet.

In this paper, we investigate the FEL evolution at $\delta L = 0$ by analytically solving the 1D FEL equations. A set of nondimensional parameters and the 1D FEL equations used in Ref. [12] are employed for the present study. The optical pulse on the first pass, which is equivalent to the output of a self-amplified spontaneous-emission (SASE) FEL and represented by the solution of the cubic equation [14, 15, 16], is reflected back into the undulator for subsequent amplifications in FEL oscillators. The phase space evolution of electrons on the second pass which interact with the leading slope of the FEL pulse, which is defined from the front edge toward the primary peak amplitude in the present paper, is obtained in a perturbation method similar to that used in our previous work for the phase space evolution of electrons in a SASE FEL [12]. Consequently, an analytical solution for the optical growth of the leading slope during the second pass is derived. The leading slope of the output pulse is shown to be approximated by that of a SASE FEL with FEL parameter greater than ρ. The same process can thus be applied to pass numbers greater than $n = 2$ and the evolution of the leading slope with respect to n is obtained analytically. The output field similar to that of a SASE FEL accounts for the exponential increase of the field amplitude in the leading slope from the front edge toward the primary peak, and the amplitude gradient with respect to the longitudinal position is shown to increase with n. With the increasing gradient, the field gain per pass decreases down to the level of optical cavity loss α, and a self-similar radiation pulse is generated at saturation. The evolution of the leading slope leads to sustained FEL oscillations at $\delta L = 0$ and thus disappearance of the lethargy effect. More details are described in Ref. [13].

1D FEL EQUATIONS

The dimensionless 1D FEL equations of Colson are used in the present study under the slowly varying envelope approximation [17], while the variables used here are similar to Bonifacio's variables [16]. The simplest situation is considered in the present study. The electron beam energy is given by $\gamma_0 mc^2$ with small energy spread. The initial electron bunch has a rectangular shape with density of n_e and a uniform distribution in phase. The fundamental FEL parameter in MKSA units is given by

$$\rho = \frac{1}{\gamma_0}[ea_w F\sqrt{n_e/(\varepsilon_0 m)}/(4ck_w)]^{2/3}. \qquad (1)$$

Here $\lambda_w = 2\pi/k_w$ is the period of the undulator, a_w is the undulator parameter, and F is unity for a helical undulator

* nishimori.nobuyuki@jaea.go.jp

or Bessel function $[JJ]$ for a planar undulator [16]. The dimensionless time is defined by $\tau = 4\pi\rho ct/\lambda_w$, so that $\delta\tau = 1$ corresponds to the transit time of light through one gain length of $\lambda_w/(4\pi\rho)$. The longitudinal position of the ith electron is defined by $\zeta_i(\tau) = 4\pi\rho[z_i(t) - ct]/\lambda_r$, so that $\delta\zeta = 1$ corresponds to the cooperation length defined by $L_c = \lambda_r/(4\pi\rho)$. Here $\lambda_r = \lambda_w(1 + a_w^2)/(2\gamma_0^2)$ is the resonant wavelength. The dimensionless field envelope is defined by

$$a(\zeta,\tau) = \frac{2\pi e a_w \lambda_w F}{(4\pi\rho)^2 {\gamma_0}^2 mc^2} E(\zeta,\tau)\exp[i\phi(\zeta,\tau)], \quad (2)$$

with phase $\phi(\zeta,\tau)$, which is equivalent to Bonifacio's envelope [16]. Here $E(\zeta,\tau)$ is the rms optical field strength. The dimensionless energy and phase of the ith electron are respectively defined by $\mu_i(\tau) = [\gamma_i(t) - \gamma_0]/(\rho\gamma_0)$ and $\psi_i(\tau) = (k_w + k_r)z_i(t) - \omega_r t$, where $k_r = 2\pi/\lambda_r$ is the wave number of the resonant wavelength λ_r. The dimensionless energy $\mu_i(\tau)$ also means the dimensionless energy change at τ from $\tau = 0$, since the energy spread of the initial electron beam is assumed to be small, i.e., $\mu_i(0) = 0$.

In the present definition, the evolutions of the field envelope $a(\zeta,\tau)$, the energy $\mu_i(\tau)$ and phase $\psi_i(\tau)$ of the ith electron during FEL interaction are respectively given by [5]

$$\frac{d\mu_i(\tau)}{d\tau} = a[\zeta_i(\tau),\tau]\exp[i\psi_i(\tau)] + \text{c.c.}, \quad (3)$$

$$\frac{d\psi_i(\tau)}{d\tau} = \mu_i(\tau), \quad (4)$$

$$\frac{\partial a(\zeta,\tau)}{\partial\tau} = -\langle\exp[-i\psi_i(\tau)]\rangle_{\zeta_i(\tau)=\zeta}. \quad (5)$$

The angular bracket indicates the average of all the electrons in the volume V around ζ.

EVOLUTION OF SASE FEL PULSE

The optical field and electron phase space evolutions on the first pass, which are equivalent to those in a SASE FEL, are presented in our previous work [12]. The startup process known as spectrum narrowing [18] or as longitudinal phase mixing [19] leads to a uniform field in time and space. The phase of the field $\phi(0)$ is almost uniform over the length $N\lambda_r$ along the propagation direction when the incident electron beam passes through N undulator periods [5, 19]. In the present study, the initial uniform field is assumed to be given by $|a(0)|e^{i\phi(0)}$ for simplicity. The initial field evolves through electric interaction with undulating electrons as it passes through the undulator. The incident electron beam is assumed to be uniformly distributed in phase $\psi_i(0)$ with resonant energy $\mu_i(0) = 0$ and interacts with the SASE FEL field in the steady-state region due to the slippage [16]. The evolution of the uniform field as a function of time is derived from Eqs. (3), (4), and (5), as described by Colson *et al.* in Ref. [15].

The electron phase can be expressed as $\psi_i(\tau) = \psi_i(0) + \Delta\psi_i(\tau)$ where $\Delta\psi_i(\tau)$ is the first-order perturbation in $a(\tau)$. The field at time τ for the steady-state region where $\zeta < -\tau$ is given by

$$a(\tau) = a(0) + i\int_0^\tau \langle e^{-i\psi_i(0)}\Delta\psi_i(\tau')\rangle_{\zeta_i(\tau)=\zeta} d\tau'. \quad (6)$$

The ith electron interacts with the field in the steady-state region due to the slippage, and the energy modulation at τ' during $\delta\tau'$ is given from Eq. (3) by $\delta\mu_i(\tau') = [a(\tau')e^{i\psi_i(0)} + \text{c.c.}]\delta\tau'$. The energy change of the ith electron at time τ, $\mu_i(\tau)$, is given by the sum of those modulations during τ:

$$\mu_i(\tau) = \int_0^\tau \{a(\tau')e^{i\psi_i(0)} + \text{c.c.}\}d\tau'. \quad (7)$$

The electron phase perturbation is given from Eq. (4) by

$$\Delta\psi_i(\tau) = \int_0^\tau \mu_i(\tau')d\tau' \quad (8)$$

$$= \int_0^\tau d\tau' \int_0^{\tau'} \{a(\tau'')\exp[i\psi_i(0)] + \text{c.c.}\}d\tau'' \quad (9)$$

Substitution of Eq. (9) into Eq. (6) leads to

$$a(\tau) = a(0) + i\int_0^\tau d\tau' \int_0^{\tau'} d\tau'' \int_0^{\tau''} a(\tau''')d\tau'''. \quad (10)$$

The integral equation (10) can be written in a differential form by taking successive derivatives. The solution is expressed in the form $a(\tau) = \sum_{n=1}^{3} a_n \exp(\alpha_n\tau)$ where the α_n are three complex roots of the cubic equation $\alpha^3 = i$ [14, 15, 16]. When the initial conditions $\dot{a}(0) = \ddot{a}(0) = 0$, the field at time τ for the steady-state region where $\zeta < -\tau$ is given by

$$a(\tau) = \frac{|a(0)|e^{i\phi(0)}}{3}\left(e^{\tau e^{i\pi/6}} + e^{-\tau e^{-i\pi/6}} + e^{\tau e^{-i\pi/2}}\right). \quad (11)$$

Equation (11) is valid in the linear regime before saturation when the incident electron beam is resonant.

EVOLUTION OF OSCILLATOR FEL PULSE

We first study the optical field and electron phase space evolutions on the second pass ($n = 2$) in an analytical way and then show that the analytical method can be applied to the nth pass with reasonable approximations. At first the notation n is thus used for $n = 2$.

FEL evolution on the second pass

The input field for the second pass, $a_n(\zeta) = a_n(\zeta,0)$, is the same as the output of a SASE FEL with FEL parameter ρ except for a decrease of the amplitude due to the cavity loss α. The leading slope of the input field for the second pass is therefore given as a function of ζ by

$$a_n(\zeta) = (|a_n(0)|e^{i\phi_n(0)}/3)(e^{-\rho_n\zeta e^{i\pi/6}} + e^{\rho_n\zeta e^{-i\pi/6}} + e^{-\rho_n\zeta e^{-i\pi/2}}), \quad (12)$$

where $\rho_2 = 1$ and $|a_2(0)| \approx (1-\alpha/2)|a(0)|$. Equation (12) can be used where $|\zeta| < L_s$ and $|\zeta| < L_b$ before the field reaches saturation. Here L_b is the incident electron bunch length in units of L_c and $L_s = 4\pi\rho N_w$ is the slippage distance. The phase space evolution of electrons during interaction with the leading slope given by Eq. (12) is quite similar to that of a SASE FEL. The perturbation method used in Ref. [12] can be applied to a study of the optical growth during the second pass, as long as the growth is small and the field $a_n(\zeta)$ remains almost unchanged during the FEL interaction. The electron phase can be expressed as $\psi_i(\tau) = \psi_i(0) + \Delta\psi_i(\tau)$ where $\Delta\psi_i(\tau)$ is the first-order perturbation in $a_n[\zeta_i(\tau)]/\rho_n^2$, since the field in the leading slope divided by ρ_n^2 is weak even after saturation except for a narrow range near ζ_p. When the ith electron is modulated in energy by interacting with the leading slope, the energy modulation at τ' during $\delta\tau'$ is expressed from Eq. (3) by $\delta\mu_i(\tau') = \{a_n[\zeta_i(\tau')]e^{i\psi_i(0)} + \text{c.c.}\}\delta\tau'$. The energy change of the ith electron at time τ, $\mu_i(\tau)$, is given by the sum of those modulations during τ:

$$\mu_i(\tau) = \int_0^\tau \{a_n[\zeta_i(\tau')]\exp[i\psi_i(0)] + \text{c.c.}\}d\tau'. \quad (13)$$

The integration of Eq. (13) after substitution of Eq. (12) yields

$$\begin{aligned}
&\mu_i(\tau) = [2|a_n(0)|/3\rho_n] \times \\
&\{e^{-\sqrt{3}\rho_n\zeta_i(\tau)/2}\cos[\psi_i(0)+\phi_n(0)-\rho_n\zeta_i(\tau)/2-\pi/6] \\
&-e^{-\sqrt{3}\rho_n\zeta_i(0)/2}\cos[\psi_i(0)+\phi_n(0)-\rho_n\zeta_i(0)/2-\pi/6] \\
&-e^{\sqrt{3}\rho_n\zeta_i(\tau)/2}\cos[\psi_i(0)+\phi_n(0)-\rho_n\zeta_i(\tau)/2+\pi/6] \\
&+e^{\sqrt{3}\rho_n\zeta_i(0)/2}\cos[\psi_i(0)+\phi_n(0)-\rho_n\zeta_i(0)/2+\pi/6] \\
&+\cos[\psi_i(0)+\phi_n(0)+\rho_n\zeta_i(\tau)+\pi/2] \\
&-\cos[\psi_i(0)+\phi_n(0)+\rho_n\zeta_i(0)+\pi/2]\}. \quad (14)
\end{aligned}$$

The integration of Eq. (8) after substitution of Eq. (14) yields

$$\begin{aligned}
&\Delta\psi_i(\tau) = [2|a_n(0)|/3\rho_n^2] \times \\
&\{e^{-\sqrt{3}\rho_n\zeta_i(\tau)/2}\cos[\psi_i(0)+\phi_n(0)-\rho_n\zeta_i(\tau)/2-\pi/3] \\
&-e^{-\sqrt{3}\rho_n\zeta_i(0)/2}\cos[\psi_i(0)+\phi_n(0)-\rho_n\zeta_i(0)/2-\pi/3] \\
&-\rho_n\tau e^{-\sqrt{3}\rho_n\zeta_i(0)/2}\cos[\psi_i(0)+\phi_n(0)-\rho_n\zeta_i(0)/2-\pi/6] \\
&+e^{\sqrt{3}\rho_n\zeta_i(\tau)/2}\cos[\psi_i(0)+\phi_n(0)-\rho_n\zeta_i(\tau)/2+\pi/3] \\
&-e^{\sqrt{3}\rho_n\zeta_i(0)/2}\cos[\psi_i(0)+\phi_n(0)-\rho_n\zeta_i(0)/2+\pi/3] \\
&+\rho_n\tau e^{\sqrt{3}\rho_n\zeta_i(0)/2}\cos[\psi_i(0)+\phi_n(0)-\rho_n\zeta_i(0)/2+\pi/6] \\
&-\cos[\psi_i(0)+\phi_n(0)+\rho_n\zeta_i(\tau)] \\
&+\cos[\psi_i(0)+\phi_n(0)+\rho_n\zeta_i(0)] \\
&-\rho_n\tau\cos[\psi_i(0)+\phi_n(0)+\rho_n\zeta_i(0)+\pi/2]\}, \quad (15)
\end{aligned}$$

where $\zeta_i(\tau) = \zeta_i(0) - \tau$ is used, which is valid as long as the electron energy change $\mu_i(\tau)$ is small and $d\zeta_i(\tau)/d\tau = -1$ holds. Equations (14) and (15) represent the phase space evolution of the ith electron during the second pass.

The field gain $da_n(\zeta)/d\tau$ caused by the electron microbunch in units of λ_r whose initial position is $\zeta_i(0) = \zeta + \tau$ is derived from substitution of $\psi_i(\tau) = \psi_i(0) + \Delta\psi_i(\tau)$ into Eq. (5) as follows:

$$\begin{aligned}
&da_n(\zeta)/d\tau = (|a_n(0)|e^{i\phi_n(0)}/3\rho_n^2) \quad (16)\\
&\times\{e^{(-\rho_n\zeta e^{i\pi/6}+i\pi/6)}[1-e^{-\rho_n\tau e^{i\pi/6}}(1+\rho_n\tau e^{i\pi/6})] \\
&-e^{(\rho_n\zeta e^{-i\pi/6}-i\pi/6)}[1-e^{\rho_n\tau e^{-i\pi/6}}(1-\rho_n\tau e^{-i\pi/6})] \\
&+e^{(-\rho_n\zeta e^{-i\pi/2}-i\pi/2)}[1-e^{-\rho_n\tau e^{-i\pi/2}}(1+\rho_n\tau e^{-i\pi/2})]\},
\end{aligned}$$

when $|\Delta\psi_i(\tau)| \ll 1$.

The field $a_n(\zeta)$ is sequentially amplified from $\tau = 0$ to $\tau = -\zeta$ by the electron microbunches whose initial position are $\zeta_i(0) = \zeta + \tau$ as it passes through the undulator. The field gain per pass is given by

$$\begin{aligned}
&da_n(\zeta)/dn = [|a_n(0)|e^{i\phi_n(0)}/3\rho_n^3] \\
&\times\{-\rho_n\zeta[e^{(-\rho_n\zeta e^{i\pi/6}+i\pi/6)} - e^{(\rho_n\zeta e^{-i\pi/6}-i\pi/6)} \\
&+e^{(-\rho_n\zeta e^{-i\pi/2}-i\pi/2)}] - 2[e^{(-\rho_n\zeta e^{i\pi/6})} + e^{(\rho_n\zeta e^{-i\pi/6})} \\
&+e^{(-\rho_n\zeta e^{-i\pi/2})}] + 6\}. \quad (17)
\end{aligned}$$

The leading slope of the output field for the second pass is thus given by

$$\begin{aligned}
&a_n(\zeta) + da_n(\zeta)/dn = [|a_n(0)|e^{i\phi_n(0)}/3\rho_n^3] \\
&\times\{-\rho_n\zeta[e^{(-\rho_n\zeta e^{i\pi/6}+i\pi/6)} - e^{(\rho_n\zeta e^{-i\pi/6}-i\pi/6)} \\
&+e^{(-\rho_n\zeta e^{-i\pi/2}-i\pi/2)}] + (\rho_n^3-2)[e^{(-\rho_n\zeta e^{i\pi/6})} \\
&+e^{(\rho_n\zeta e^{-i\pi/6})} + e^{(-\rho_n\zeta e^{-i\pi/2})}] + 6\}. \quad (18)
\end{aligned}$$

The amplitude and phase of the output field given by Eq. (18) are plotted as solid circles in Figs. 1(a) and 1(b), respectively, as a function of ζ. The solid line shows the output field of the second pass obtained in a time-dependent numerical calculation, which solves Eqs. (3)−(5) with an input field given by Eq. (12) with $\rho_n = 1$ and represented by the dotted line. In the calculation, the shot-noise effect is neglected. One can see that the field given by Eq. (18) agrees well with the numerical calculation where $|\zeta| < 3.5$ but the phase gradually deviates from the calculation where $|\zeta| \geq 3.5$. This is because the assumption that the field remains almost unchanged during the passage through an undulator does no longer hold where $|\zeta| \geq 3.5$ for the second pass.

FEL evolution on pass numbers greater than 2

The output field of the second pass is equivalent to the input field for the third pass except for amplitude decrease due to the optical cavity loss α. If the input field for the third pass is found to be approximated by Eq. (12), the same procedure described in the previous subsection can be used for a study of the optical growth during the third pass. The dash-dotted line in Fig. 1 shows the field given by Eq. (12) with $\rho_n = 1.28$. The amplitude of this field is different from that obtained in a numerical calculation

(solid line) by only 10% to −20% where $|\zeta| < 5$, and the phase is different from the numerical calculation by only ± 0.17 rad. These results suggest that the input field for the third pass can be approximated by Eq. (12) with $\rho_3 = 1.28$. In a similar way, one can obtain ρ_n of the input field for pass numbers greater than $n = 3$ as well. For example$\rho_4 = 1.52$, $\rho_5 = 1.73$, $\rho_6 = 1.90$, and $\rho_7 = 2.05$.

As ρ_n increases, $\rho_n^3 - 2 \sim \rho_n^3$ and Eq. (18) asymptotically approaches

$$a_n(\zeta) + da_n(\zeta)/dn \sim a_n(\zeta) + [|a_n(0)|e^{i\phi_n(0)}/3\rho_n^3] \times\{-\rho_n\zeta[e^{(-\rho_n\zeta e^{i\pi/6}+i\pi/6)} - e^{(\rho_n\zeta e^{-i\pi/6}-i\pi/6)} + e^{(-\rho_n\zeta e^{-i\pi/2}-i\pi/2)}]\}, \quad (19)$$

The field evolution per pass can also be obtained by differentiation of Eq. (12) with respect to the pass number n under the assumption that ρ_n is independent of ζ as follows:

$$da_n(\zeta)/dn = (|a_n(0)|e^{i\phi_n(0)}/3)(d\rho_n/dn) \times\{-\zeta[e^{(-\rho_n\zeta e^{i\pi/6}+i\pi/6)} - e^{(\rho_n\zeta e^{-i\pi/6}-i\pi/6)} + e^{(-\rho_n\zeta e^{-i\pi/2}-i\pi/2)}]\}. \quad (20)$$

Equation (20) should be equal to Eq. (19) subtracted by $a_n(\zeta)$ as long as the gain is much higher than the optical cavity loss and ρ_n is large enough for Eq. (19) to hold. This yields

$$d\rho_n/dn = 1/\rho_n^2. \quad (21)$$

When we assume that Eq. (19) holds when $\rho_n > 2$, Eq. (21) gives

$$\rho_n \approx (3n - 12)^{1/3} \quad (22)$$

for $n \geq 7$. Substitution of Eq. (22) into Eq. (20) yields

$$(1/|a_n(\zeta)|)(d|a_n(\zeta)|/dn) \approx -(\sqrt{3}/2)\zeta(3n - 12)^{-2/3}, \quad (23)$$

when $\exp(-\sqrt{3}\rho_n\zeta/2) \gg 1$. Equation (23) shows that the gain per pass decreases with increasing pass number n. Please see Ref. [13] for further discussions.

ACKNOWLEDGEMENTS

The author would like to acknowledge valuable discussions with T. Shizuma at JAERI, S. Hiramatsu at KEK, and H. Hama at Tohoku University.

REFERENCES

[1] G. Dattoli and A. Renieri, in *Laser Handbook*, edited by M.L. Stitch and M. Bass (North Holland, Amsterdam, 1985), Vol.4, p.75.

[2] N. Piovella et al., PRE **52**, 5470 (1995); P. Chaix et al., PRE **59**, 1136 (1999).

[3] G. Dattoli and A. Renieri, Nuovo Cimento B **59**, 1 (1980); G. Dattoli et al., Opt. Comm. **35**, 407 (1980).

[4] H. Al-Abawi et al., Opt. Comm. **30**, 235 (1979); J. G. Kuper et al., Opt. Comm. **34**, 117 (1980).

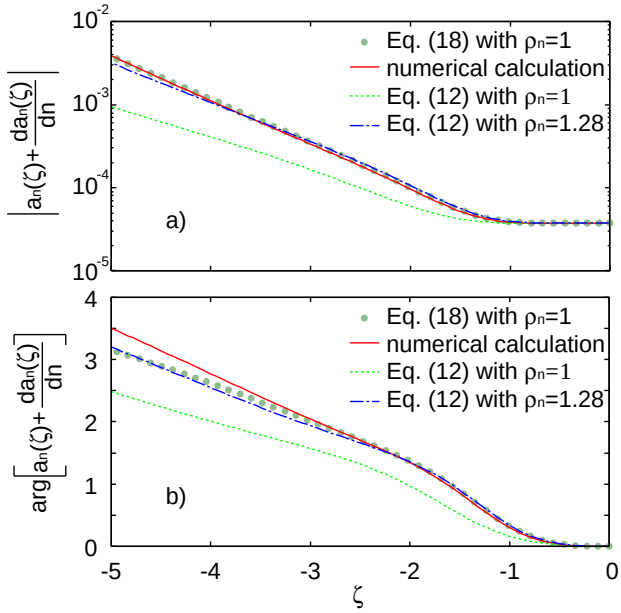

Figure 1: The amplitude (a) and phase (b) of the output field $a_n(\zeta) + \frac{da_n(\zeta)}{d\zeta}$ as a function of ζ. The solid circles stand for the output field of the second pass given by Eq. (18) with $\rho_n = 1$, and the solid line is that obtained from a numerical calculation where Eq. (12) with $\rho_n = 1$, which is represented by the dotted line, is used as an input field envelope. The dash-dotted line expresses an approximated output field of the second pass given by Eq. (12) with $\rho_n = 1.28$. The amplitude of the front edge $|a_n(0)| = 3.7\times10^{-5}$ is used.

[5] W.B. Colson, in *Laser Handbook*, edited by W.B. Colson, C. Pellegrini, and A. Renieri (North Holland, Amsterdam, 1990), Vol.6, pp. 115–193.

[6] Nicola Piovella, PRE **51**, 5147 (1995).

[7] N. Nishimori et al., PRL **86**, 5707 (2001); NIM A **483**, 134 (2002).

[8] R. Nagai et al., NIM A **483**, 129 (2002).

[9] R. Hajima et al., NIM A **475**, 270 (2001); *ibid*. **483**, 113 (2002).

[10] Z.-W. Dong et al., NIM A **483**, 553 (2002).

[11] Ryoichi Hajima and Ryoji Nagai, PRL **91**, 024801 (2003).

[12] Nobuyuki Nishimori, PRST AB **8**, 100701 (2005).

[13] Nobuyuki Nishimori, accepted for publication in PRE.

[14] Norman M. Kroll and Wayne A. McMullin, PRA **17**, 300 (1978).

[15] W. B. Colson et al., PRA **34**, 4875 (1986).

[16] R. Bonifacio et al., Riv. Nuovo Cimento **13**, 9 (1990).

[17] W.B. Colson and S.K. Ride, Phys. Lett. **76**A, 379 (1980).

[18] Kwang-Je Kim, PRL **57**, 1871 (1986); NIM A **250**, 396 (1986).

[19] N. Nishimori, R. Hajima, R. Nagai and E.J. Minehara, NIM A **507**, 79 (2003).

TWO-STREAM SMITH-PURCELL FREE-ELECTRON LASER USING A DUAL-GRATING: LINEAR ANALYSIS*

Wenxin Liu[1#], Zheng Liang [1], Ziqiang Yang[1], D. Li[2], K. Imasaki[2]
[1]Institute of High Energy Electronics, University of Electronic Science and Technology of China, Sichuan Chengdu, 610054, P. R. China
[2]Institute for Laser Technology, 2-6 yamada-oka, suita, Osaka 565-0871, Japan

Abstract

A linear theory of two-stream Smith-Purcell Free-Electron Laser (SP-FEL) using a dual-grating has been given in this paper. A rectangular dual-grating is considered to be driven by two admixed electron beams with velocity separation. The linear dispersion equations for even and odd modes are derived with the help of fluid theory and the beam-wave interaction is analyzed through the numerical solutions. The considerable enhancement of growth rate is demonstrated due to the presence of two-stream instability. An example of THz-band two-stream SP-FEL is discussed.

INTROUCTION

It is well known that Smith-Purcell (SP) radiation is emitted when an electron passes near the surface of grating [1].At present, an intense interest has been raised in SP radiation since J.Urata *et al* observed the super-radiance in the THz regime from the experiment at Dartmouth college [2,3]. The superradiance is regarded as the result of periodic electron bunching, which is produced by the interaction between the electron beam and the fields above the grating. Some theories [4,5] have been proposed to understand the physical mechanism of beam-wave interaction. Recently, D.Li and Z.Yang [6,7], J.T.Donohue and J.Gardelle[8] have performed the simulations of SP-FEL in the THz regime with PIC code.

The THz sources, a currently flourish research area, are of importance in varieties of applications in far-infrared spectroscopy, imaging, ranging and biomedical [9]. In order to improve the performance of such kind of device, it is necessary to find an efficient mechanism for the beam-wave interaction. The two-stream instability is an important physical mechanism, which has been successfully applied to some high power microwave sources [10-12].

In this paper, we present a two-stream Smith-Purcell Free-Electron Laser using a dual-grating, as shown in Fig.1. The two admixed electron beams are symmetric about *z* axial and guided by an infinite magnetic field. For simplicity, we assume that the system is uniform in the *y* direction which is parallel to the slots of grating.

DISPERSION EQUATION

The system of beam-wave interaction is illustrated in Fig.1. Two admixed beams with thickness 2*b* are located above the rectangular grating, which drift in the *z* direction at a constant velocity v_1 and v_2, respectively. The quantities *D, H, d, a* denote the rectangular grating period, groove depth, slot width, the distance between *z* axial and grating surface, respectively. For convenience, the operation area is divided into five regions: $-a \le x < -b$ is region Ⅰ, $b < x \le a$ is region Ⅱ, $-b \le x \le b$ is region Ⅲ, Region Ⅳ and Ⅴ is the lower groove $-a-h \le x < -a$ and upper groove $a < x \le a+h$. In the following analyses, we focus on the TM waves.

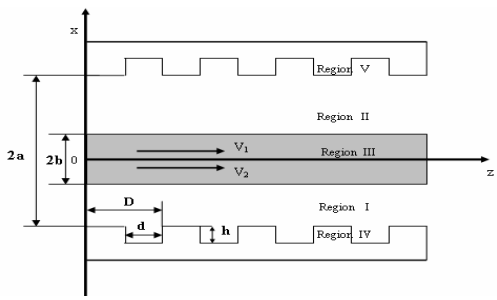

Fig.1 Schematic illustration of two admixed beams propagating over the dual-grating

We assume that (i)the externally applied magnetic field is so strong that perturbed electron motions are restricted in the *z* direction; (ii)the effect of beams self static fields are negligible; and (iii)the perturbations are uniform along the *y* direction. Maxwell's equations and relativistic hydrodynamic equations for two cold electron beams are employed to describe this system as follows:

$$\nabla \times \vec{E} + \frac{1}{c}\frac{\partial \vec{B}}{\partial t} = 0 \tag{1}$$

$$\nabla \times \vec{B} + \frac{1}{c}\frac{\partial \vec{E}}{\partial t} = \frac{4\pi}{c}\sum_{i=1}^{2} J_i \tag{2}$$

$$(\frac{\partial}{\partial t} + v_{i0}\frac{\partial}{\partial z})\delta v_{i1} = -\frac{e}{\gamma_i^3 m_0}E_z \tag{3}$$

$$(\frac{\partial}{\partial t} + v_{i0}\frac{\partial}{\partial z})\delta n_{i1} = -n_{i0}\frac{\partial}{\partial z}\delta v_{i1} \tag{4}$$

Here, subscript $i = 1,2$ represents the first and second electron beam, respectively. $\vec{E}$ and $\vec{B}$ are the electric and

*Work supported by National Nature Science Foundation of P. R. China (60571020),#liuwenxin76@163.com

magnetic field vectors. $\gamma_i = 1 + eV_i / m_0 c^2$ is the relativistic mass factor, c is the speed of light ,V_i is the ith beam voltage, the voltage ratio of two electron beams is $v_r = V_2 / V_1$,and $v_{i0} = c \cdot [(\gamma_i^2 - 1)^2 / \gamma_i^2]^{1/2}$ is the unperturbed velocity of ith beam. $-e$, m_0, n_{i0}, δn_{i1}, δv_{i1} are the electron charge, the electron rest mass , the unperturbed density , perturbed density and perturbed velocity of ith beam, respectively. $J_i = -e(n_{i0}\delta v_{i1} + \delta n_{i1} v_{i0})$ is perturbed current density. The relative density factor α is n_{20} / n_{10} .To obtain the dispersion equation, we expand $n_i = n_{i0} + \delta n_{i1}$, $v_i = v_{i0} + \delta v_{i1}$, $\vec{E} = \delta \vec{E}_z$, $\vec{B} = \delta \vec{B}_y$ and solve for the perturbed variables. Using Floquet's theorem, all the fields and beam parameters can be written as a sum of space harmonics which have the periodicity of the grating [13],

$$f(x,z) = \sum_{n=-\infty}^{\infty} f_n(x) \exp(jk_n z - j\omega t) \qquad (5)$$

where $k_n = k_0 + 2\pi n / D$, k_0 is wave number, ω is the angular frequency, n is an integer.

From Eqs.1, 2, 3, 4 and expression (5), the wave equation for the nth space harmonic of axial electric field is given and the transverse components of electric and magnetic fields can be expressed in terms of the axial electric field as follows[14]:

$$[\frac{\partial^2}{\partial x^2} + \varepsilon_{l,n}(\frac{\omega^2}{c^2} - k_n^2)]\delta\hat{E}_{z,n,l}(x) = 0 \quad , \quad l=1,2,3 \qquad (6)$$

$$\delta\hat{E}_{x,n,l} = \frac{jk_n}{\kappa_n^2}\frac{\partial}{\partial x}\delta\hat{E}_{z,n,l} \qquad (7)$$

$$\delta\hat{B}_{y,n,l} = \frac{j\omega}{c\kappa_n^2}\frac{\partial}{\partial x}\delta\hat{E}_{z,n,l} \qquad (8)$$

$$\varepsilon_{3,n} = 1 - \sum_{i=1}^{2}\frac{\omega_{pi}^2}{\gamma_i^3(\omega - k_n v_i)^2} \quad , \quad \varepsilon_{1,n} = \varepsilon_{2,n} = 1 \qquad (9)$$

where $\omega_{pi} = (e^2 n_{i0} / m_0 \varepsilon_0)^{1/2}$ is the beam-plasma angular frequency, $\varepsilon_{l,n}$ is the dielectric function, $\kappa_n = [(\omega/c)^2 - k_n^2]^{1/2}$ is the transverse wave number. $l = 1,2,3$ represents the region Ⅰ, Ⅱ, Ⅲ, respectively.

Components of electromagnetic fields in each region [13]

Employed the wave Eq.6 and expressions (7) and (8), the components of electromagnetic fields in the three regions can be treated as follows:

The fields in Region Ⅰ $-a \le x < -b$ and Ⅱ $b < x \le a$ can be expressed in terms of two coefficients, respectively:

$$\delta\hat{E}_{z,n,l_0} = A_n^{l_0}\sin\kappa_n x + B_n^{l_0}\cos\kappa_n x \qquad (10)$$

$$\delta\hat{E}_{x,n,l_0} = \frac{jk_n}{\kappa_n}(A_n^{l_0}\cos\kappa_n x - B_n^{l_0}\sin\kappa_n x) \qquad (11)$$

$$\delta\hat{B}_{y,n,l_0} = \frac{j\omega}{c\kappa_n}(A_n^{l_0}\cos\kappa_n x - B_n^{l_0}\sin\kappa_n x) \qquad (12)$$

where superscript $l_0 = 1,2$ respects the region Ⅰ and region Ⅱ, respectively.

Region Ⅲ($-b \le x \le b$)

$$\delta\hat{E}_{z,n,3} = C_n\sin\beta_n x + D_n\cos\beta_n x \qquad (13)$$

$$\delta\hat{B}_{y,n,3} = \frac{j\omega\beta_n}{c\kappa_n^2}(C_n\cos\beta_n x - D_n\sin\beta_n x) \qquad (14)$$

where $\beta_n = \sqrt{\varepsilon_{3,n}}\kappa_n$.

Region Ⅳ and Ⅴ is the lower groove $-a-h \le x < -a$ and upper groove $a < x \le a+h$, respectively. As the grating period is less than the free-space wavelength, we represent the fields inside the 1^{th} groove using the form of TEM standing wave modes as follows:

$$\delta\hat{E}_z = S_{\pm a}\sin[\frac{\omega}{c}(x \mp (a+h)]\exp(ik_0 D) \qquad (15)$$

$$\delta\hat{B}_y = jS_{\pm a}\cos[\frac{\omega}{c}(x \mp (a+h)]\exp(ik_0 D) \qquad (16)$$

where the "$\mp$" denotes the upper interface $x=a$ and the lower face $x=-a$, respectively. The $A_n^{l_0}$, $B_n^{l_0}$, C_n, D_n, $S_{\pm a}$ mean unknown coefficients, which are depended on the boundary conditions.

Dispersion equation

Applying the boundary conditions at the grating surfaces $x = \pm a$,the beam surfaces $x = \pm b$,solving simultaneously Eqs.10-16 and then eliminating the coefficients of $A_n^{l_0}$, $B_n^{l_0}$, C_n, D_n, $S_{\pm a}$,the odd mode and even modes dispersion equation is obtained as follows, respectively.

$$\frac{D}{d}\cot(\frac{\omega h}{c})+\sum_{n=-\infty}^{\infty}\frac{\omega}{c\kappa_n}\mathrm{sinc}^2(\frac{k_n d}{2})\frac{Q_n-R_n/\varepsilon_{3,n}^{1/2}}{\varepsilon_{3,n}^{1/2}+T_n}=0$$

(17)

is the dispersion equation for the odd modes, and

$$\frac{D}{d}\cot(\frac{\omega h}{c})-\sum_{n=-\infty}^{\infty}\frac{\omega}{c\kappa_n}\mathrm{sinc}^2(\frac{k_n d}{2})\frac{1+T_n\varepsilon_{3,n}^{1/2}}{Q_n/\varepsilon_{3,n}^{1/2}-R_n}=0$$

(18)

is the dispersion equation of the even modes, where $Q_n=\varepsilon_{3,n}^{1/2}\cot[\kappa_n(a-b)]$, $R_n=\varepsilon_{3,n}^{1/2}\cdot\tan\beta_n b$, $T_n=\tan\beta_n b\cdot\cot[\kappa_n(a-b)]$ .The Eqs.17and 18 is the similar to Ref.[13] when the voltages of two electron beams are the same. In the absence of beams, the dispersion equations of odd modes and even modes can be reduced to:

$$\frac{D}{d}\cot(\frac{\omega h}{c})+\sum_{n=-\infty}^{\infty}\frac{\omega}{c\kappa_n}\mathrm{sinc}^2(\frac{k_n d}{2})\cot\kappa_n a=0$$

(19)

is the dispersion equation for the odd modes, and

$$\frac{D}{d}\cot(\frac{\omega h}{c})-\sum_{n=-\infty}^{\infty}\frac{\omega}{c\kappa_n}\mathrm{sinc}^2(\frac{k_n d}{2})\tan\kappa_n a=0$$

(20)

is the dispersion equation for the even modes.

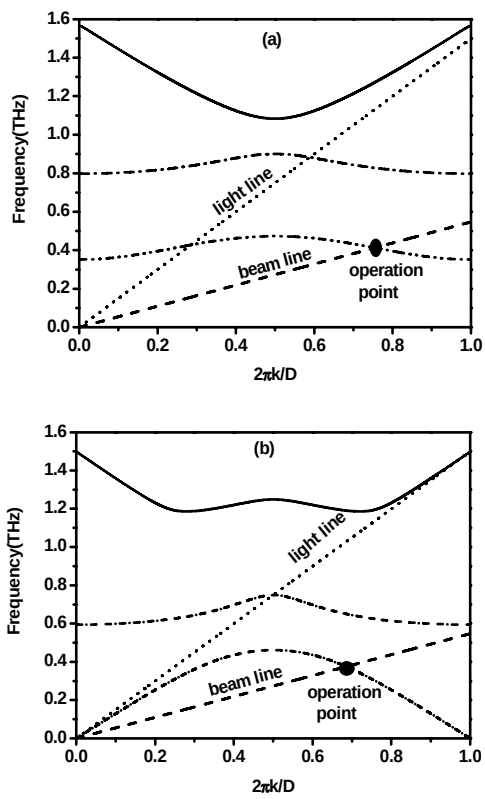

Fig2. Dispersion curves of (a) even mode and (b) odd mode. The parameters are period *D=0.2mm*, slot width *d=0.1mm*, slot depth *h=0.1mm* and the distance of two-gratings *2a=0.3mm*

NUMERICAL SOLUTIONS

In this section, we focus on the characteristics of dispersion equation through the numerical solutions.

The dispersion curves without beams for the even modes are found by the solutions of Eq.20, which are shown in Fig.2 (a). The beam line with voltage 40kv is plotted for reference. It is observed that the lowest order mode has a cutoff frequency of 0.345THz and has a maximum frequency 0.475THz. There is a stop band between the two lowest order modes extending from 0.475THz to 0.8THz.

Similarly, the dispersion curves without beams for the odd modes are obtained by the solutions of Eq.19, which are shown in Fig.2 (b). The band gap is evident extending from 0.46THz to 0.6THz. Obviously, the band gap of even modes and the frequency of operation point (solid dot) which is the intersection point of beam-wave are greater than that of the lowest odd mode.

The two admixed beams are turned into a single beam when the beam voltages are the same. The dispersion curves of single beam for the even mode found by the solution of Eq.18 are shown in Fig.3, where the left

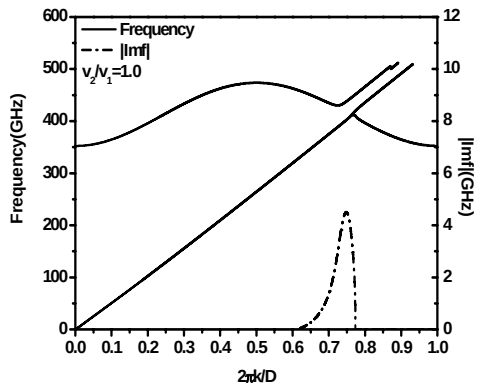

Fig3. Dispersion curves showing the real and imaginary components of the frequency for the lowest-order even mode, the parameters of grating are the same as that of in Fig.2. The beam voltage is *40*kv, electron beam density is $n_0=5.97\times10^{18}$ m^{-3}

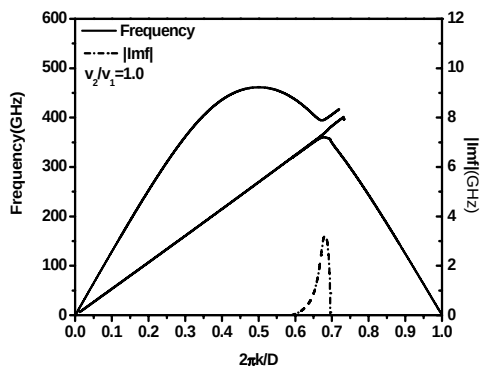

Fig4. Dispersion curves showing the real and imaginary components of frequency for the lowest-order odd mode, the parameters are the same as in Fig.3

axis is the real component of frequency and the right axis is the growth rate. Seen from Fig.3, the growth rate is found at the vicinity where the slow-wave and electron beam are synchronous, which occurs at a frequency near 0.41 THz. The peak growth about 4.5GHz is found at a frequency of 0.403THz. Similarly, the dispersion curves of single beam for the odd modes are shown in Fig.4. The peak growth rate about 3.24GHz is found at the normalized wave number of 0.68, which occurs at a frequency of 0.371THz.Obviously, the peak growth rate of the lowest order even mode are greater than that of odd mode.

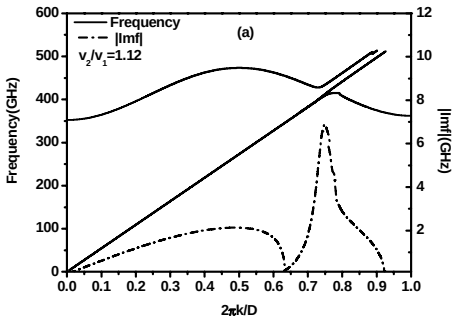

Fig5. Dispersion curves showing the real and imaginary components of the frequency for the lowest-order even mode, the parameters of grating are the same as that of in Fig.2. The beam voltage is *40*kv, electron beam density is $n_0=5.97\times10^{18}$ m-3,the voltage ratio is v_r=1.12

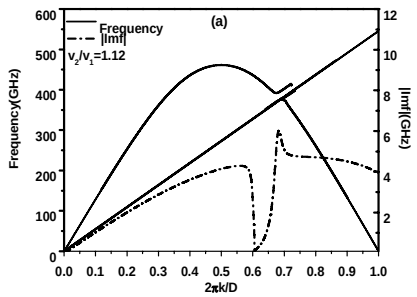

Fig6. Dispersion curves showing the real and imaginary components of the frequency for the lowest-order odd mode. The parameters of grating are the same as that of in Fig.2. The beam voltage is *40*kv, electron beam density is $n_0=5.97\times10^{18}$ m^{-3}, and the voltage ratio is v_r=1.12

The dispersion curves of two-stream for the lowest-order even mode obtained by the solution of Eq.18 are shown in Fig.5. Obviously, the growth rate is remarkably different from that of single beam, the cambered growth rate is produced by the TSI, and the growth rate is remarkably enhanced when the TSI wave is synchronous with the slow-wave. The peak growth rate about 6.91GHz is found at the frequency of 0.412THz, which is enhanced by a factor of 2 than that of single beam. Outside the synchronous range of TSI and electro-magnetic wave, the growth rate is still existed, which is thought to be yielded by the TSI

Similarly, the dispersion curves of two-stream for the lowest-order odd mode solved the Eq.29 are shown in Fig.6. The peak growth rate about 6.04GHz is found at the frequency of 0.375THz, which is enhanced by a factor 2. We may note from Figs.3, 4, 5and 6 that the even mode could be an operation mode for which the growth rate is greater than that of odd mode. To obtain the higher operation frequency, we should make the even mode as an operation mode.

CONCLUSIONS

In this paper, we have studied the two-stream Smith-Purcell Free-Electron Laser with a dual-grating. The linear dispersion equations for the even modes and odd modes are derived by making use of fluid theory, and those of characteristics are analyzed through the numerical solutions. We find that the peak growth rate is enhanced by a factor of 2 than that of single beam when the TSI wave is synchronous with the electromagnetic wave. The nonlinear effect is under consideration, which will be reported in the future.

ACKNOWLEDGEMENT

This work is supported by National Natural Science Foundation of P. R. China (60571020, 60178011).

REFERENCES

[1]S.J.Smith, E.M.Purcell, "Visual light from localized surface charges moving across a grating", *Phys. Rev.* ***92***,1069,1953

[2]J.Urata,M.Goldstein,M.F.Kimmitt,A.Naumov,C.Platt. andJ.E.Walsh,"Superradiant Smith- Purcell Radiation", Phys.Rev.Lett.80,(1998)516

[3]A.Bakhtyari,J.E.Walsh,andJ.H.Brownell,"Amplified-spontaneous-emission power oscillation in a beam-wave interaction"Phys.Rev.E.65,066503(2002)

[4]K.J.Kim,and S.B.Song, "Self-amplified spontaneous in Smith-Purcell free electron lasers", *Nucl. Instrum.,Methods Phys. Res., Sect. A* **475**,158 (2001)

[5]H.L.Andrews and C.A.Brau. "Gain of a Smith-Purcell free-electron laser",*PRSTAB* **7**, 070701 (2004)

[6]D.Li, K. Imasaki, Z.Yang and Gun-Sik Park, "Three-dimensional simulation of super-radiant Smith-Purcell radiation", Appl.Phys.Lett. **88** (201501), 2006

[7]D.Li and Z.Yang, K. Imasaki,and Gun-Sik Park "Particle-in-cell simulation of coherent and super-radiant Smith-Purcell radiation",*Phys Rev. ST. Accel. Beams*, **9**, (2006)040701,

[8]J.T.Donohue and J.Gardelle "Simulation of Smith-Purcell terahertz radiation using a particle-in-cell code" *Phys Rev.ST.Accel.Beams*,**9**,060701,2006

[9]P.H Siegel, "Terahertz technology", IEEE Trans, Microwave and Tech., **50**, (2002)910,

[10]J. R. Pierce, *et al* "A new type of high frequency amplifier," *Bell Syst.Tech* ,*J*.**28**. (1949) 33

[11]V.V. Kulish, A.V. Lysenko, V.I. Savchenko. Two-stream free electron lasers. General properties. *Int. J. Infrared Millim. Waves*, vol. **24**, (2003)129

[12]H.P. Freund, *et al.*, "Multiple-beam free-electron laser", *Nucl. Inst. Method A***507**, (2003)373

[13]H.P. Freund and T.M.Abu-Elfadl.,"Linearized Field Theory of a Smith-Purcell Traveling Wave Tube", *IEEE, Plasma Science* **32,**1015,2004

[14]K. Mehrany and B. Rshidaian, "Dispersion and Gain Investigation of a Cerenkov Grating Amplifier", *IEEE Trans. On Electron Devices*, **50**,1562, 2003.

PRODUCTION OF 'GIANT' PULSES OF SCATTERED RADIATION FROM PUMP WAVE SPOT RUNING OVER THE ELECTRON BEAM*

V. Baryshev, N. Ginzburg#, A. Sergeev, I. Zotova IAP RAS, Nizhny Novgorod, Russia.

Abstract

To generate ultrashort electromagnetic pulses it is suggested to scan a spot formed by pump wave along an electron beam. When pump spot velocity is equal to the group velocity of scattered radiation the short 'giant' pulse of scattered radiation with amplitude increasing proportional to interaction distance will be produced. The running spot of pump wave can be realized after reflection of frequency chirped laser beam from echelette grating.

INTRODUCTION

In [1] the generation of millimetre wave superradiance (SR) pulses have been observed in the process of stimulated backscattering of relatively long pump wave pulse by extended electron bunch with the length restricted by cooperative length (the distance of the scattered wave propagation during the time of instability growth up). Under such conditions the scattered radiation represented a single pulse with peak power strongly exceeding the level of spontaneous emission.

In this paper we study the alternative method of generation superradiance type pulses in the process of stimulated scattering when the relatively short spot illuminated by pump wave runs over the quasi-continuous electron beam. Obviously scattering and beam modulation take place only in area illuminated by pump wave. In the case when the pump spot moves with group velocity of scattered radiation the pulse of scattered radiation propagating along electron beam will be amplified continually by fresh (unmodulated) electrons due to difference between signal wave group velocity c and electron translational velocity $v_{||}$. As a result the peak amplitude of scattered pulse increases proportionally to shifting distance. The running spot of pump wave can be realized after passing (reflection) of frequency chirped laser pulse from frequency depended refraction system like prism or echelette grating (see Fig. 1). It should be noted that the shifting direction and velocity of the pump wave spot are not correlated with the phase and group velocities of this wave. For our purpose to obtain the large frequency conversion the direction of spot shifting should be approximately opposite to the group velocity vector.

In the case of scattering of laser radiation by a moderately relativistic electron beam with energy ~1-3 MeV above process can be used to produce intense SR pulses either at UV band (up frequency conversion), at terahertz band (down frequency conversion) or bands depending on direction of scattered wave propagation with respect to electron beam. Correspondingly at the first case illuminated spot should run together with scattered wave in the direction of electron motion while in the second case this spot together with scattered wave should run at opposite direction.

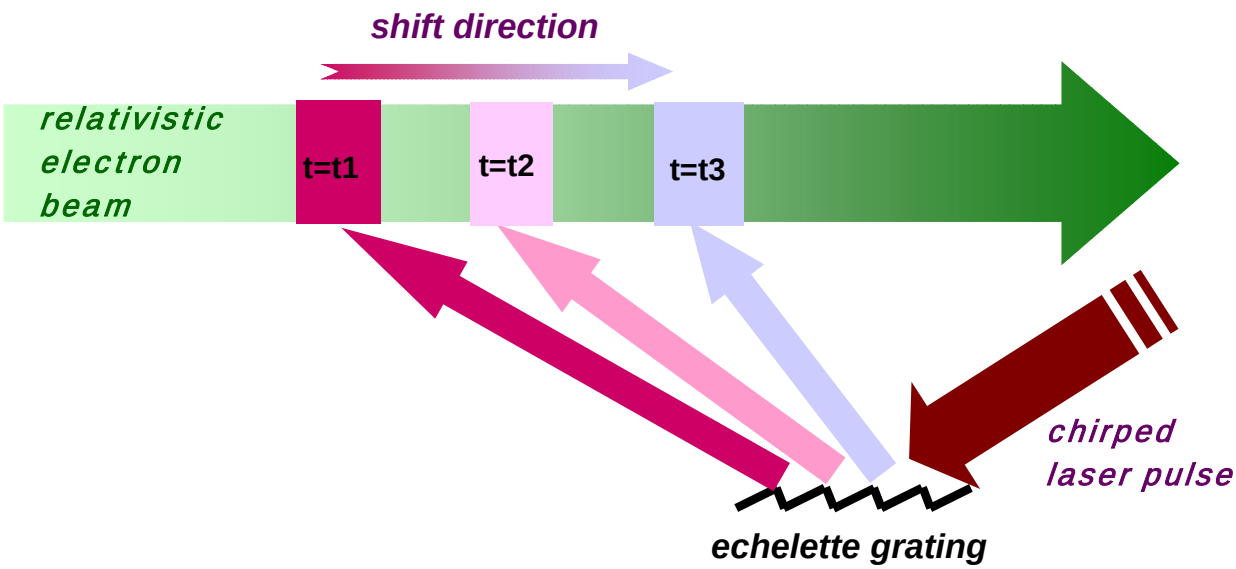

Figure 1: Echelette scheme of scanning of pump field spot using frequency chirped laser pulse.

*Work supported by … Russian Fund for Fundamental Researches, grant 05-02-17553
#ginzburg@appl.sci-nnov.ru

MODEL AND BASIC EQUATIONS

Let us consider the process of stimulated scattering in situation when the spot illuminated by a pump wave runs along electron beam with velocity u in the direction of electron motion. In this case due to the Doppler effect the frequency of scattered radiation ω_s essentially exceeds the frequency of pump wave ω_i. Neglecting pump wave exhaustion the generation of pulses of scattered radiation in the above process can be described by the system of equations including the nonstationary equation for scattering signal amplitude and the averaged electron motion equations [2]:

$$\left(\frac{\partial}{\partial z}+\frac{1}{c}\frac{\partial}{\partial t}\right)a_s = i\chi(t-z/u)k_c a_i I\,\frac{1}{\pi}\int_0^{2\pi} e^{-i\theta}d\theta_0$$
$$\left(\frac{\partial}{\partial z}+\frac{1}{v_{||}}\frac{\partial}{\partial t}\right)^2\theta = \mu k_c^2\chi(t-z/u)\,Im\left\{a_s a_i^* e^{i\theta}\right\} \qquad (1)$$

Here $a_{i,s}=eA_{i,s}/m_0\gamma_0 c^2$ is the dimensionless amplitude of scattered and pump waves, $\theta=\omega_c t-k_c z$ is the electron phase respect to the combination wave, $\omega_c=\omega_s-\omega_i$, $k_c=\omega_c/c-\omega_i/c$, $\mu=\gamma_0^{-2}\beta_{||}^{-3}$, I is the dimensionless parameter which is proportional to the beam current. Function $\chi(t-z/u)$ describes the profile of the spot illuminated by pump filed. Introducing the new independent variables

$$Z=C\frac{\omega_c}{c}z,\quad \tau=C\frac{\omega_c c(t-z/v_{||})}{1/c-1/v_{||}} \qquad (2)$$

and assuming that the velocity of pump spot is equal to the group velocity of scattered signal (u=c) Eqs. (2) can be presented in the form

$$\frac{\partial a}{\partial Z}+\frac{\partial a}{\partial \tau}=-\frac{i}{\pi}\chi(\tau-Z)\int_0^{2\pi}e^{-i\theta}d\theta_0$$
$$\frac{\partial^2\theta}{\partial Z^2}=\chi(\tau-Z)\,Im\left\{ae^{-i\theta}\right\} \qquad (4)$$

where $a=\mu a_s a_i^* C^{-2}$, $C=\left(\omega_p^2|a_i|^2\right)^{1/3}$ is the gain (Pierce) parameter. Under assumption that the development of instability starts from the small perturbation of electron beam density the initial and boundary conditions can be

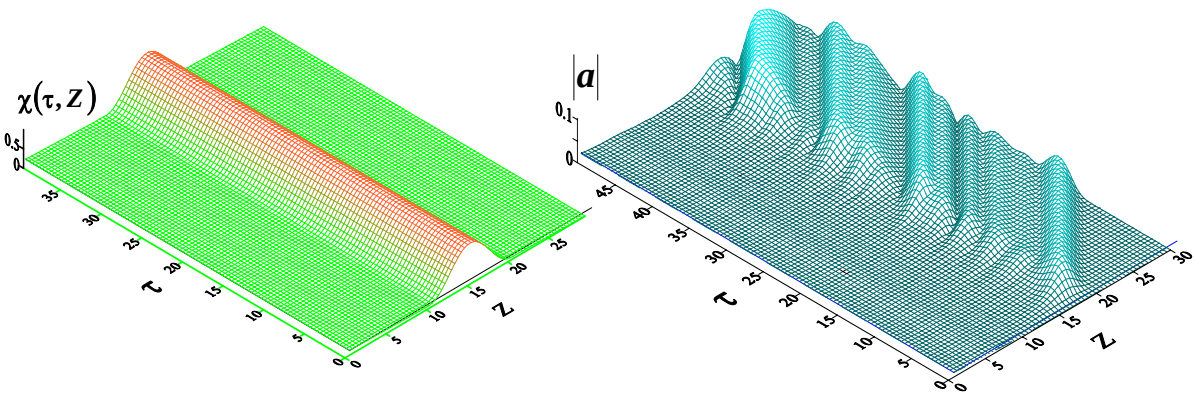

Figure 2: Production of the SASE signal in the case of standing pump field spot.

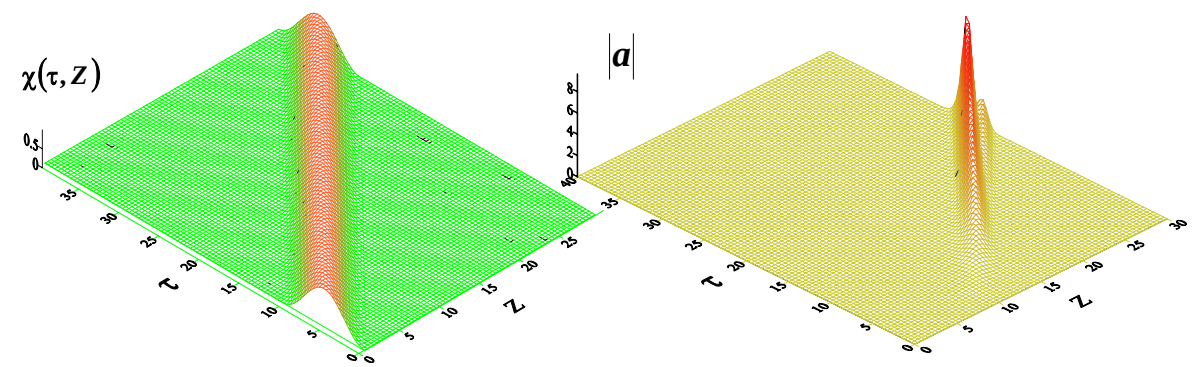

Figure 3: Production of 'giant' single pulse in the case of moving pump field spot.

written in the form

$$\theta|_{Z=0} = \theta_0 + r\cos(\theta_0 + \varphi(\tau)),\ \ \theta_0 \in [0,2\pi],\ \ r << 1$$
$$\left.\frac{\partial\theta}{\partial Z}\right|_{Z=0} = 0,\ \ a|_{Z=0} = 0 \qquad (5)$$

where $\varphi(\tau)$ is the random function.

SIMULATION RESULTS

Let's consider at first the traditional situation with the unmovable $u = 0$ bell-shaped pump spot: (see Fig. 2a). In this case, due to the slippage, radiation escapes from pump spot. As a result the well-known multi-spikes regime of SASE [3,4] is realized (Fig. 2b) when different parts of beam radiate practically independently.

The totally different situation takes place when the pump spot moves along the electron beam together with scattered signal: $u = c$ (Fig. 3a). But because electron velocity $v_{||}$ is slightly less than c. the interaction (scattering) spot slips along beam and the pulse of scattered radiation formed at initially stage of interaction propagates through the unmodulated electrons being effectively amplified (see Fig. 3b). As a result the scattered radiation represents the single short pulse with amplitude essentially exceeding the amplitude of spikes in the SASE regime (compare with Fig. 2b). In the ideal situation the amplitude of above 'giant' pulse growths proportionally to the interaction distance L (see Fig. 4).

It is important to note that due to short lifetime of individual electrons in the interaction spot above process is less sensitive to the spread of beam parameters in comparison with traditional steady state regime (see Fig. 5).

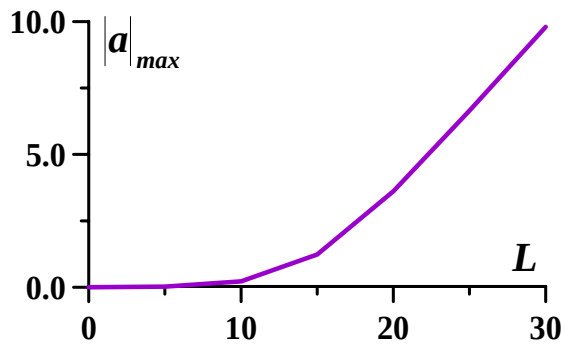

Figure 4: Dependence of pulse peak amplitude on the shifting distance.

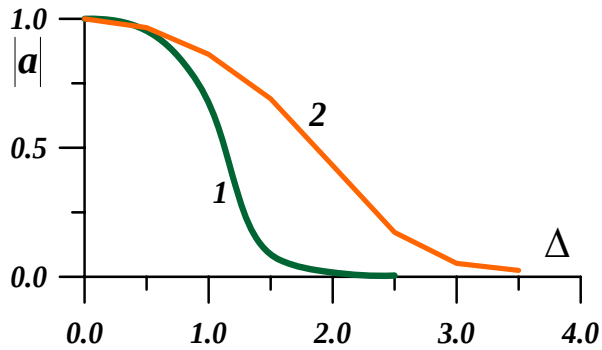

Figure 5: Dependence of radiation peak amplitude on electron velocity spread Δ for steady state regime (1) and 'giant' pulse regime (2).

CONCLUSION

In conclusion lets make preliminary estimations of possible experiments on backscattering of 10 μ CO_2 laser radiation by high current () relativistic electron beam. For electron energy 3 MeV scattered wavelength ~200 nm will belong to UV bands. For laser pump pulse with duration 1 ns the shift of pump spot will be about 30 cm. For power density of pump wave ~150 GW/cm^2 and current density 30 kA/cm^2 the gain parameter is $C \approx 6.3 \cdot 10^{-5}$. As a result for initial perturbation $r = 0.001$ the maximal power density of scattered radiation can achieved ~1 GW/cm.

REFERENCES

[1] A. Reutova, M. Ulmaskulov, A. Sharypov, V. Shpak, S. Shunailov, M. Yalandin, V. Belousov, G. Denisov, N. Ginzburg, A. Sergeev and I. Zotova JETP Lett. 82(5) 295.

[2] V. Bratman, N. Ginzburg, M. Petelin JETP 76(3) (1979) 930.

[3] R.H. Bonifacio, N. Piovella and B.W.J. McNeil, Phys. Rev. A, 44, (1991) 3441.

[4] C.Pelegrini "High power femtosecond pulses from an X-ray SASE-FEL", FEL'1999, Hamburg, Germany August 1999, p.124.

INFLUENCE OF LINER FLUCTUATIONS ON LOW- AND HIGH-GAIN CHERENKOV FELS

I. de la Fuente*, P.J.M. van der Slot, K.-J. Boller
Laser Physics and Non-Linear Optics Group, University of Twente
PO Box 217, 7500 AE Enschede, The Netherlands.

Abstract

Imperfections in the dielectric liner of a Cherenkov Free-Electron Laser (CFEL) result in fluctuations in the phase velocity of a radiation wave when it propagates through the lined waveguide. Random fluctuations in the phase velocity reduce the bunching of the electrons and consequently lower the gain of CFELs. Here we theoretically investigate the influence of these liner-induced phase fluctuations in the radiation field on the saturated power of low to high gain CFELs. To obtain different gain regimes, we keep the electron beam radius constant and vary the current density. As an example, we study a 50 GHz CFEL and quantify the reduction in the single-pass saturated power for different rms liner fluctuations when the CFEL is driven by an electron beam with current densities varying from 1 A/cm^2 (average gain of 0.43 dB/cm) to 25 A/cm^2 (average gain of 1.39 dB/cm).

INTRODUCTION

The increasing number of microwave applications in both research and industry [1, 2] has increased the interest in tuneable high-power microwave sources. The Cherenkov Free-Electron Laser (CFEL) is a promising candidate as a compact high-power microwave source for various applications. CFELs have been operated at 100 kW peak power level at 1 mm wavelengths, at 200 MW peak power level at 8 cm wavelengths and at wavelengths as short as in the far infrared [3]. The simplicity of its construction, the high efficiency and an affordable compact design have made the CFEL attractive for applications where high microwave frequencies and high powers are needed. However, simple imperfections in either the electron beam or the lined waveguide section, that are used to generate the laser gain, can seriously degrade the performance of the device [4].

In a CFEL, accelerated electrons are injected through a wave-guiding structure that slows the phase velocity of the electromagnetic wave to a sub-luminous value. An example is a metallic, cylindrical tube lined with a dielectric material, e.g., quartz. By choosing appropriate dimensions for the waveguide, i.e., the inner diameter for the tube, the thickness and dielectric constant of the liner, the phase velocity of EM waves can be matched to the velocity of the injected electron beam for a desired wave frequency [5]. A transversely magnetic (TM) wave can decelerate or accelerate co-propagating electrons. A net deceleration of electrons in the pump beam and, correspondingly, a net amplification of the wave, occurs only if the electrons are forming bunches, if these bunches travel with the phase velocity of the radiation wave, and if the bunches are located within a certain phase range of the radiation wave (when seen from the frame of that wave). A fluctuating phase velocity of the wave in the waveguide would appear as a fluctuating relative phase of the bunches; it could bring bunches out of the optimum driving phase, and this would reduce the amplification. Likewise, a spread in longitudinal electron velocities results in a spread in relative phases between wave and the electrons. This results in a reduced bunching within the electron beam and consequently in a lower amplification of the wave [3].

Although the variations in the phase velocity can have different origins, we will model only one type of imperfection, namely, fluctuations in the inner radius of the liner. Other types of fluctuations, such as a spatial inhomogeneity of the liner's dielectric constant, are not treated separately because we expect widely analogous results. In a previous study we have shown that in a low current CFEL, a typical manufacturing tolerance in the inner radius of the liner of 5 % can reduce the saturated power by a factor of 2 [4]. In this paper, we investigate the sensitivity of the CFEL to small random liner imperfections for different gain regimes. We therefore consider a 50 GHz CFEL with a fixed liner geometry, electron beam energy, and electron beam radius. The different gain regimes are obtained by varying the electron beam current density from 1 A/cm^2 to 25 A/cm^2.

In the remainder of this paper we first present a summary of the theoretical model that describes the dynamics of the CFEL in the presence of radii fluctuations. Next, we will show the numerical results for a CFEL system operating in different gain regimes. We end with a discussion and conclusions.

THEORETICAL MODEL

The theoretical model describing the dynamics of a CFEL in the presence of small and random fluctuations of the liner inner radius is presented in previous work [4] and here we present a summary.

The standard CFEL dynamical model [3, 6] assumes that the electromagnetic wave co-propagating with the electron beam can be described by a superposition of empty (i.e., without the electron beam) waveguide eigenmodes with amplitudes that vary slowly with longitudinal distance z. Using the power orthogonality property of the eigenmodes,

* i.delafuentevalentin@utwente.nl

and applying the slowly varying amplitude and phase approximation to Maxwell's equations, the dynamical equation for the mode amplitudes are derived. The system is closed by the Newton-Lorentz equations, that describe the motion of the electrons under influence of the electromagnetic wave.

The effect of a small random fluctuation in the inner radius $r_d(z)$ of the liner that varies slowly along its length is twofold. First, it varies the phase velocity of the wave. Second, it modifies, in principle, the transverse mode profile. However, our analysis shows that the liner fluctuations mainly affect the phase velocity of the wave and that the transverse mode profile remains approximately unchanged [4]. In our model, we allow the wave number to vary slowly along the length of the liner, and write for the longitudinal component of the electric field $E_{z,n}$ for mode TM_{0n}:

$$E_{z,n}(r,z,t) = a_{0n}(z)\frac{f_n(r)}{\sqrt{k_n(z)}} exp\left(i\int_0^z k_n(z')dz' - \omega t\right), \quad (1)$$

where $f_n(r)$ is the transverse mode profile of an empty lined waveguide [7], $a_{0n}(z)$ the slowly varying mode amplitude, and the slowly varying longitudinal wave number $k_n(z)$ is given by:

$$k_n(z) = k_{0n} + \int_0^z \frac{dk_n}{dz'}dz' \approx k_{0n} + \left.\frac{\partial k_n}{\partial r_d}\right|_{r_{d0}} \int_0^z \frac{dr_d}{dz'}dz', \quad (2)$$

where, for convenience, the inner radius of the liner at $z = 0$ is taken equal to the mean radius r_{d0} and k_{0n} is the wave number corresponding to a homogeneous waveguide with $r_d = r_{d0}$. The evolution of the normalized field amplitude $a'_{0n}(z) = \frac{e}{mc}a_{0n}(z)$ for the TM_{0n} modes is:

$$2\sqrt{k_n(z)}(1 - \frac{\kappa_n^2}{k_{0n}^2})\frac{\partial a'_{0n}}{\partial z} = -4\frac{\omega_p^2}{c_0^2}\frac{\beta_{z0}}{A_n r_{d0}^2}\times$$
$$\int_0^{r_{d0}} drr\left[iI_1(\kappa_n r)\langle\frac{\beta_r}{|\beta_z|}e^{i\alpha_n}\rangle + \frac{\kappa_n}{k_{0n}}I_0(\kappa_n r)\langle e^{-i\alpha_n}\rangle\right] \quad (3)$$

Here A_n is a normalization constant, ω_p is the plasma frequency, β is the electrons velocity normalized to the speed of light in vacuum, I_0 and I_1 are the Bessel functions of second kind, and κ_n is the transverse wave number. The symbol $\langle \ldots \rangle$ represents an average over all electrons within one radiation wavelength. Undefined symbols are described in [4].

DESCRIPTION OF THE CFEL

This model has been applied to a particular design for a Cherenkov free-electron laser that can be operated with both low and high electron beam currents. In this analysis we choose Al_2O_3 with a dielectric constant of ϵ=9.8 as the liner material, and keep the geometry constant. Likewise, the outer radius of the cylindrically shaped electron beam is fixed at r_b=5 mm. However, to vary the single-pass gain and saturated power of this device, we consider different total beam currents I_b ranging from 0.8 A to 20 A. The remaining geometrical parameters are: an average inner liner radius of r_{d0}=5.5 mm and an average liner thickness of d=0.57 mm. This system requires an electron beam energy of 84.2 keV to operate at 50 GHz. We integrate the dynamic CFEL equation (eq. 3) up to the point where the laser saturates. Using a constant inner radius equal to r_{d0} and an initial seed power of 10 mW, these electron currents produce a saturated power P_0 of about 200 W at a distance z_0 of 100 cm and 20.8 kW at a distance of 45 cm for I_b=0.8 A and 20 A, respectively. The corresponding average gain is 0.43 dB/cm and 1.39 dB/cm, respectively.

The variation in the inner liner radius is modeled using a random fluctuation superimposed on the average radius r_{d0}. A spatial low-pass filter with cut-off distance z_c is used to remove fast fluctuations from the random distribution. Further, the fluctuations are scaled to obtain a certain standard deviation σ_{rd} of the distribution. For each particular realization of a fluctuating liner radius we numerically calculate the saturated power P_{sat} and the position z_{sat} at which this power is obtained. To obtain also statistical information on the output as a function of the experimental parameters, we generate 100 different realizations of liner fluctuations for each combination of the rms amplitude σ_{rd} and cut-off distance z_c. For each combination we determine the ensemble average $\overline{P_{sat}}$ and standard variation σ_p and corresponding values for the distance to saturation z_{sat}.

RESULTS AND DISCUSSION

First, we numerically study the sensitivity of this particular CFEL to an increasing amplitude of the random fluctuations in the liner inner radius while the spatial filter is kept constant at z_c=10 cm, corresponding to approximately 16 times the free-space wavelength. The ensemble average of the saturated power, $\overline{P_{sat}}$, normalized to the saturated power in absence of fluctuations, P_0, is shown in Figs. 1a and 1b as a function of the standard deviation of the fluctuations in the inner liner radius, σ_{rd}, for the two beam currents of 0.8 A and 20 A, respectively. Corresponding values for the distance to saturation z_{sat} are shown in Fig. 2. Fig. 1 shows that for this particular CFEL and a beam current of 0.8 A, a small rms liner fluctuation of 2.5 μm (=0.05 % of r_{d0}) is sufficient to reduce the saturated power by a factor of 2 on average. The rms liner fluctuation increases to 25 μm (=0.5 % of r_{d0}) to obtain a similar reduction when the CFEL is driven by a beam current of 20 A. At the same time we observe that the relative spread $\sigma_p/\overline{P_{sat}}$ is much larger for the 0.8 A beam current compared to the 20 A beam current. The variation of the distance to saturation with the rms liner amplitude (see Fig. 2) shows a different behavior for the two beam currents. For the 0.8 A current, the distance increase quickly from 100 cm to close to 150 cm and then remains approximately constant. The ob-

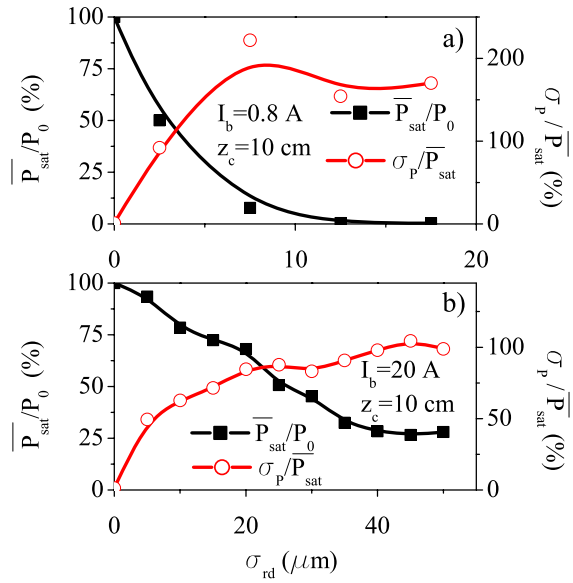

Figure 1: Normalized saturated power ($\overline{P_{sat}}/P_0$) and normalized standard deviation ($\sigma_p/\overline{P_{sat}}$) as a function of the standard deviation of the liner fluctuations σ_{rd} for a current of 0.8 A (a) and 20 A (b).

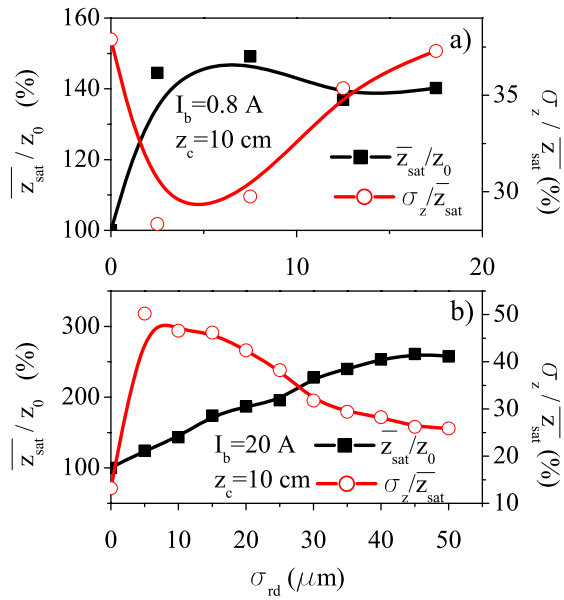

Figure 2: Normalized distance to saturation ($\overline{z_{sat}}/z_0$) and normalized standard deviation of z_sat ($\sigma_z/\overline{z_{sat}}$) as a function of the standard deviation of the liner fluctuations σ_{rd} for a current of 0.8 A (a) and 20 A (b).

served spread in z_{sat} remains approximately constant. On the other hand, for the 20 A current the distance to saturation increases approximately linearly with σ_{rd}, while the relative spread is slightly reduced.

These findings indicate that this particular CFEL is far more sensitive to fluctuations in the inner liner radius than the system studied in our previous study [4]. In that study we also considered a CFEL operating at 50 GHz. However, that system used a 0.8 A electron beam with a 1 mm radius (25 A/cm^2 current density) to drive the CFEL. We found that an rms fluctuation of about 5 % was required to reduce the saturated power by a factor of 2. For the device of this work, this is 0.5 % and 0.05 % for the same current density and total beam current respectively. To allow the CFEL of this work to be driven by a higher total current, we have increased the beam radius. As a consequence, the transverse dimensions of the CFEL have increased and we have chosen a different liner material. This leads to a larger variation of k_n with inner liner radius r_d (see eq. 2): $\partial k_n/\partial r_d$ is -4.6 10^6 m^{-2} for the device in this work, while it equals -0.46 10^6 m^{-2} for the device in our previous study. It is therefore not surprising that the current system is more sensitive to liner imperfections than the system considered in our previous study.

Second, we have investigated the influence of spatial distribution of the liner imperfections by varying the cut-off distance z_c of the low pass filter applied to the randomly generated liner fluctuations. The normalized ensemble average $\overline{P_{sat}}/P_0$ and the normalized spread $\sigma_p/\overline{P_{sat}}$ are shown in Fig. 3 for I_b=0.8 A and 20 A, and the corresponding values for z_{sat} are shown in Fig. 4. These figures show that both the saturated power P_{sat} and the distance to saturation z_{sat} vary only weakly with increasing z_c if z_c is sufficiently large ($z_c >> \lambda = c/f$). Note, that the latter condition is anyhow implicit in the approximations used in deriving the dynamical CFEL equation (eq. 3).

Last, we compare the sensitivity of this system to liner imperfections as a function of the total beam current I_b for a fixed σ_{r_d} =15 μm and a fixed cut-off distance z_c=10 cm. Fig. 5a shows the normalized ensemble average $\overline{P_{sat}}/\overline{P_0}$ and spread $\sigma_p/\overline{P_{sat}}$ as a function of I_b and Fig. 5b shows the corresponding values for z_{sat}. These figures show that I_b must be larger than 30 A to keep the reduction in $\overline{P_{sat}}$ to less than 15 %. We also observe that the relative spread $\sigma_p/\overline{P_{sat}}$ reduces with increasing beam current, while the spread $\sigma_z/\overline{z_{sat}}$ shows a slight increase.

CONCLUSION

We have studied the sensitivity to imperfections in the liner of a particular CFEL operating at 50 GHz as a function of total beam current. The system studied in this work is based on a previously studied system with increased transverse dimensions and a different liner. The increased dimensions allow a larger total current to pass through the lined waveguide and study the system in different gain regimes. As a consequence, the variation of longitudinal wave number with inner radius increased by a factor of 10 compared to the system we used in a previous study, that also operated at 50 GHz. Taking this difference into ac-

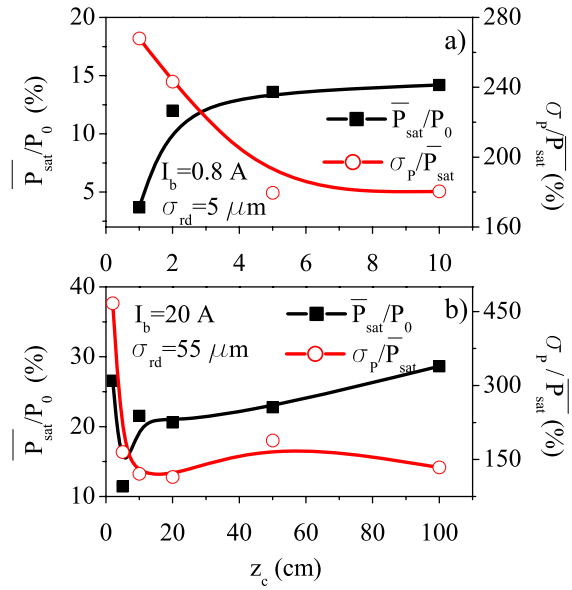

Figure 3: Normalized saturated power ($\overline{P_{sat}}/P_0$) and normalized standard deviation ($\sigma_p/\overline{P_{sat}}$) as a function of the cut-off distance z_c for a current of 0.8 A (a) and 20 A (b).

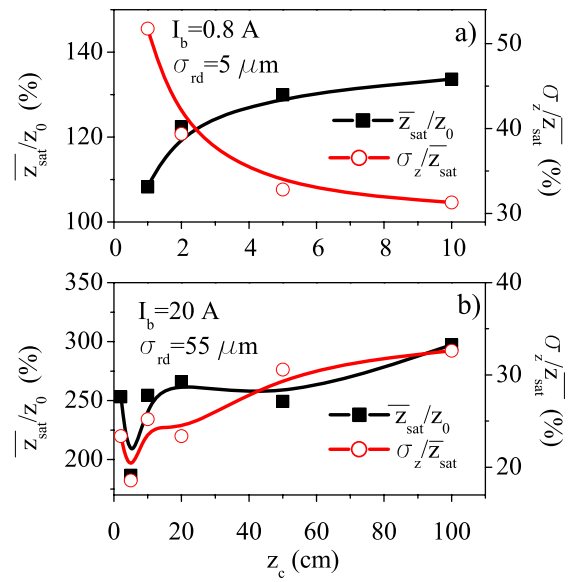

Figure 4: Normalized distance to saturation ($\overline{z_{sat}}/z_0$) and normalized standard deviation of z_sat ($\sigma_z/\overline{z_{sat}}$) as a function of the cut-off distance z_c for a current of 0.8 A (a) and 20 A (b).

count, we find that both systems show similar sensitivity to liner imperfections when the CFELs are driven by electron beams having the same current density of 25 A/cm^2. For the current system we find that a total current of at least 30 A is required to keep the reduction in ensemble average $\overline{P_{sat}}$ to less than ∼15 % of P_0 (for σ_{rd}=15 μm). The same

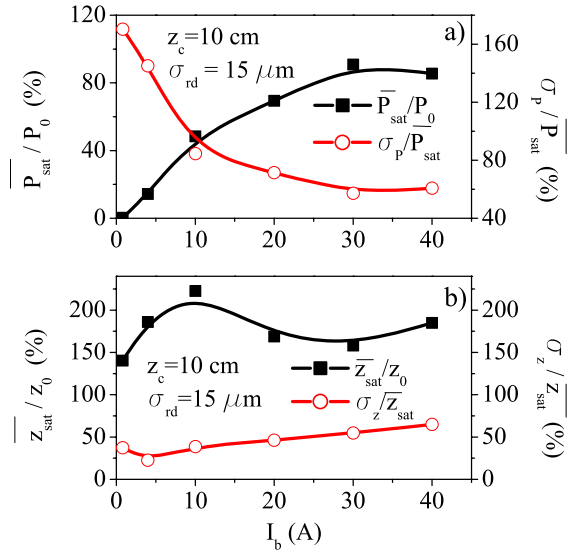

Figure 5: Normalized saturated power ($\overline{P_{sat}}/P_0$) and normalized standard deviation ($\sigma_p/\overline{P_{sat}}$) (a) and corresponding values for z_{sat} (b) as a function of the electron beam current for $\sigma_{rd} = 15$ μm and z_c=10 cm.

rms liner fluctuation reduces $\overline{P_{sat}}$ to less than 20 % of P_0 for I_b <5 A. A high gain also reduces the relative spread in P_{sat} for an ensemble of similar imperfections, while at the same time the relative spread in z_{sat} increases slightly. These findings show that systems with high gain are less sensitive to liner imperfections compared to systems with low gain. However, the actual allowable rms fluctuation depends both on the gain and on the particular geometry of the lined waveguide of the Cherenkov FEL.

REFERENCES

[1] W.K. Gwarek, M. Celuch-Marcysiak, A review of microwave power applications in industry and research, 15th International Conference on Microwaves, Radar and Wireless Communications, MIKON, p 843-848 (2004).

[2] D.A. Jones, T.P. Lelyveld, S.D. Mavrofidis, S.W. Kingman and N.J. Miles, Microwave heating applications in environmental engineering–a review, Resources, Conservation and Recycling, **34**, 2, 75-90 (2002).

[3] H.P. Freund,'Nonlinear Analysis of High-Power Cherenkov Masers',*Phys. Rev. Lett.*, **65**, p.2993 (1990).

[4] I. de la Fuente, P.J.M. van der Slot, and K.-J. Boller, 'Phase velocity fluctuations and gain in Cherenkov free-electron lasers', *J. Appl. Phys.* (accepted for publication).

[5] J.E. Walsh and J.B. Murphy, Tunable Cerenkov Lasers, *IEEE J. Quant. Electr.*, **QE-18**, 1259 (1982).

[6] H.P. Freund and A.K. Ganguly, Nonlinear analysis of the Cerenkov maser, *Phys. Fluids*, **B2**, 2506 (1990).

[7] R.A. Waldron, Theory of guided electromagnetic waves, Van Nostrand Reinhold Company, London (1970).

THEORY OF RADIATION OF ELECTRONS IN THE FIELD OF A LINEAR POLARIZED STATIONARY ELECTROMAGNETIC WAVE

Drebot I.V., Grigoryev Y.N., Zelinsky A.Y., NSC KPTI, Kharkov, Ukraine

Abstract

In the paper the results of exact integration of Lorentz equation for a free electron in the field of a linear polarized standing electro-magnetic wave are presented. Standing wave is considered as a sum of two running in opposite directions linear polarized waves. Projections of equations on coordinate axes can be integrated once. It allows us to reduce the task to solution of nonlinear equation of the second order for electron coordinate. The axis of projection coincides with a wave line. For approximate integration of the second order equation the expansion on two small parameters are used. Velocity and coordinate of electron in parametric form are presented in the paper. It is shown that under interaction of a relativistic electron with stationary wave there is a motion, which has of beating character. The amplitude and period of the beating were calculated.

INTRODUCTION

The theory of the electron interaction with a standing light wave originates in description of the Kapiza-Dirac effect [1]. The physical sense of the effect is stipulated radiation of electrons in the field of a stationary wave. After that sufficiently large amount of papers were devoted to the theoretical investigations of electron radiation in the field of a light wave.

The interest to the subject has been revived lately due to huge progress in intense laser technique. The latest works use both quantum and classical electrodynamics approach.

The main difficulty in using of classical electrodynamics approach is determination of solution of equations of electron motions in the form which will be convenient for analytical calculations of the radiation spectrum and for estimations of the electron velocity and coordinate evolutions. For example, in basic works [2,3] the solving of motion equations is reduced to the solving of the equation system of the two first order equations. But in this case one can find only approximate solution and the solution can be formulate as a function of intrinsic time of the electron. Such approach makes calculations of the radiation spectrum and other characteristics quite difficult. In the paper [4] an electron trajectory in the field of a standing linear polarized electromagnetic wave was reduced to the solving of nonlinear differential equation system with time dependent coefficients. After linearization of the system the Hill equations has to be solved.

In the presented paper, the approximate solutions of the Lorenz equation for an electron in the field of linear polarized standing wave are presented. The standing wave is considered as a sum of two running in opposite directions waves with the same polarizations.

Two projections of the Lorenz equation can be integrated once [4]. It allows to reduce the task to the solving of a second order nonlinear equation. For the approximate solution the expanding on two small parameters was used.

In the work the expressions for velocity and coordinates of an electron were derived in a form of parametrical functions of time. Using [5] and with the help of derived formulas one can calculate radiation spectrum of an electron in the field of standing linear polarized electromagnetic wave.

As one can see from the derived solutions, the electron motion in the standing wave has beating character and can lead to electron grouping in the propagation direction. The period and amplitude of the beatings were calculated.

MOTION EQUATIONS

An electron motion in the field of standing wave can be described with Lorenz equation:

$$\frac{d}{dt}\frac{m_0\vec{v}}{\left(1-\beta^2\right)^{1/2}} = c\vec{E} + \frac{e}{c}\left[\vec{v}\vec{H}\right], \qquad (1)$$

where, $\beta = v/c$, m_0 the rest mass of the electron, c is the velocity of light, e is the electron charge, $\vec{v} = \frac{\partial \vec{r}}{\partial t}$ is the vector of an electron velocity, $\vec{r} = \vec{i}x + \vec{j}y + \vec{k}z$, t is time, $\vec{E}, \vec{H}$ are vectors electrical and magnetic field.

We will consider the standing wave as a sum of two linear polarized running in opposite direction waves:.

$$\vec{E}=\vec{E}_1+\vec{E}_2;\ \vec{E}_1=\vec{k}E_{1z};\ \vec{E}_2=\vec{k}E_{2z};$$
$$E_{1x}=0;\ E_{1y}=0;\ E_{2x}=0;\ E_{2y}=0; \qquad (2)$$
$$\vec{H}=\vec{H}_1+\vec{H}_2;\quad \vec{H}_1=[\vec{i};\vec{E}_1]=-\vec{j}E_{1z};$$
$$\vec{H}_2=[-\vec{i};\vec{E}_1]=\vec{j}E_{1z}; \qquad (3)$$
$$H_{1z}=0;\ H_{1x}=0;\ H_{2z}=0;\quad H_{2x}=0;$$
$$\vec{E}_1 = \vec{k}E_{01}\cos\left[2\pi\nu_1\left(t-\frac{x}{c}\right)+\delta_1\right];$$
$$\vec{E}_2 = \vec{k}E_{02}\cos\left[2\pi\nu_2\left(t+\frac{x}{c}\right)+\delta_2\right]; \qquad (4)$$

Substituting (4) in (2) and (3) one can get:

$$\vec{E} = \vec{k}\left(E_{01}\cos\left[2\pi\nu_1\left(t-\frac{x}{c}\right)+\delta_1\right]+ \right.$$
$$\left. + E_{02}\cos\left[2\pi\nu_2\left(t+\frac{x}{c}\right)+\delta_2\right]\right); \quad (5)$$

$$\vec{H} = -\vec{j}\left(E_{01}\cos\left[2\pi\nu_1\left(t-\frac{x}{c}\right)+\delta_1\right]- \right.$$
$$\left. - E_{02}\cos\left[2\pi\nu_2\left(t+\frac{x}{c}\right)+\delta_2\right]\right); \quad (6)$$

Using expression: $mc/\left(1-\beta^2\right)^{1/2} = \xi$ (where ξ - is electron energy), and expressions (5),(6) we project equation (1) on coordinate axes:

$$\frac{1}{c}\frac{d}{dt}(\xi\beta_z) = e(1-\beta_x)E_{01}\cos\left[2\pi\nu_1\left(t-\frac{x}{c}\right)+\delta_1\right]+$$
$$+ e(1+\beta_x)E_{02}\cos\left[2\pi\nu_2\left(t+\frac{x}{c}\right)+\delta_2\right] \quad (7)$$

$$\frac{1}{c}\frac{d}{dt}(\xi\beta_y) = 0 \quad (8)$$

$$\frac{1}{c}\frac{d}{dt}(\xi\beta_x) = e\beta_z\left(E_{01}\cos\left[2\pi\nu_1\left(t-\frac{x}{c}\right)+\delta_1\right]- \right.$$
$$\left. - E_{02}\cos\left[2\pi\nu_2\left(t+\frac{x}{c}\right)+\delta_2\right]\right) \quad (9)$$

where $\beta_x = \frac{1}{c}\frac{dx}{dt}$, $\beta_z = \frac{1}{c}\frac{dz}{dt}$, $\beta_y = \frac{1}{c}\frac{dy}{dt}$.

Equations (7,8) can be integrated once. As a results the following expressions can be derived:

$$\beta_z/\sqrt{1-\beta^2} = \psi \quad (10)$$

$$\beta_y/\sqrt{1-\beta^2} = A \quad (11)$$

where $\psi = PF + \xi_z$ (12)

$$F = \left(Sin\left[2\pi\nu_1\left(t-\frac{x}{c}\right)+\delta_1\right]+Sin\left[2\pi\nu_2\left(t+\frac{x}{c}\right)+\delta_2\right]\right)-$$
$$\left(Sin\left[2\pi\nu_1\left(t_0-\frac{x(t_0)}{c}\right)+\delta_1\right]+Sin\left[2\pi\nu_2\left(t_0+\frac{x(t_0)}{c}\right)+\delta_2\right]\right); \quad (13)$$

$$P = \frac{eE_0}{mc(2\pi\nu)};\ \begin{matrix}\xi_z = \gamma(t_0)\beta_z(t_0);\\ A = \gamma(t_0)\beta_y(t_0)\end{matrix} \quad (14)$$

t_0 is initial time; $\vec{E}_0 = \vec{E}_{01} = \vec{E}_{02}$.

With use of two integrals (10) and (11) one can express, β_z, β_y, ξ through β_x, ψ, A

$$\beta_z^2 = \psi^2(1-\beta_x^2)/(1+\psi^2+A^2) \quad (14)$$

$$\beta_y^2 = A^2(1-\beta_x^2)/(1+\psi^2+A^2) \quad (15)$$

$$\xi = m_0c^2(1+\psi^2+A^2)^{1/2}/(1-\beta_x^2)^{1/2} \quad (16)$$

Substituting (14-16) to (9) and using expression:

$$\frac{d\xi}{dt} = e(\vec{v}\vec{E}), \quad (17)$$

one can derive the second order equation for electron coordinate x.

$$\frac{\dot{\beta}_x}{1-\beta_x^2} = \frac{eE_0}{m_0c}\frac{\psi}{(1+\psi^2+A^2)}\left((1-\beta_x)\right.$$
$$Cos\left[2\pi\nu_1\left(t-\frac{x}{c}\right)+\delta_1\right]-$$
$$-(1-\beta_x)Cos\left[2\pi\nu_1\left(t-\frac{x}{c}\right)+\delta_1\right]- \quad (18)$$
$$\left.-(1+\beta_x)Cos\left[2\pi\nu_2\left(t+\frac{x}{c}\right)+\delta_2\right]\right)$$

where $\dot{\beta}_x = \frac{d}{dt}\beta_x = \frac{1}{c}\frac{d^2x}{dt^2}$.

Integrating (18), we derive:

$$\ln\frac{1+\beta_x}{1-\beta_x} = \frac{2eE_0}{m_0c}\int_{t_0}^{t}\frac{\psi}{(1+\psi^2+A^2)}\left\{(1-\beta_x)Cos[\varphi_-]-\right.$$
$$\left.-(1+\beta_x)Cos[\varphi_+]\right\}dt + C_2 \quad (19)$$

$$C_2 = \ln\frac{1+\beta_x(t_0)}{1-\beta_x(t_0)}.$$

For standing wave we can set:

$\vec{E}_0 = \vec{E}_{01} = \vec{E}_{02}$; $\delta_1 = \delta_2 = 0$; $\nu_1 = \nu_2 = \nu$.

Than $\varphi_- = 2\pi\nu\left(t-\frac{x}{c}\right)$; $\varphi_+ = 2\pi\nu\left(t+\frac{x}{c}\right)$.

As it follows from (19):

$$\frac{1+\beta_x}{1-\beta_x} = \frac{1+\beta_x(t_0)}{1-\beta_x(t_0)}e^{\Phi(t)} \quad (20)$$

where

$$\Phi(t) = \frac{2eE_0}{m_0c}\int_{t_0}^{t}\frac{\psi}{(1+\psi^2+A^2)}\left\{(1-\beta_x)Cos[\varphi_-]-(1+\beta_x)Cos[\varphi_+]\right\}dt$$

APPROXIMATE SOLUTION

Assuming $P << 1$, $\xi_z << 1$, $\Phi(t) << 1$ and $e^{-\Phi(t)} \approx 1-\Phi(t)+O\frac{\Phi(t)^2}{2}$

one can get from (20):

$$\beta_x(t) \approx \beta_x(t_0) + \frac{1}{2}(1-\beta_x^2(t_0))\Phi(t) \quad (21)$$

$$\Phi(t) \approx P^2\Phi_1 + P\xi_z\Phi_2 + P^2\xi_z\Phi_2 \quad (22)$$

where

$$\Phi_1 \approx \Gamma^{-2}\{(-\frac{1}{2})(Cos[2\varphi_-]-Cos[2\varphi_+]) - 2(Sin[\varphi_-(t_0)]+$$
$$+ Sin[\varphi_+(t_0)])(Sin[\varphi_-]-Sin[\varphi_+]) \quad (23)$$
$$-\frac{1}{2}(Cos[2\varphi_-(t_0)]-Cos[2\varphi_+(t_0)])\}$$

$$\Phi_2 \approx 2\Gamma^{-2}\{(Sin[\varphi_-]-Sin[\varphi_+])- \\ -(Sin[\varphi_-(t_0)]+Sin[\varphi_+(t_0)])\} \quad (24)$$

$$\Phi_3 = 2(2\pi\nu)\Gamma^{-2}\left\{\int_{t_0}^{t} Sin\left[4\pi\nu\frac{x}{c}\right]dt - \right. \\ \left. -\int_{t_0}^{t}\beta_x(t)Sin[4\pi\nu t]dt\right\} \quad (25)$$

and $\Gamma^{-2} = 1+\gamma^2(t_0)(\beta^2(t_0)-\beta_x^2(t_0))$.

The approximate solution of (21) we will find in the form:

$$\frac{x}{c} = \beta_x(t_0)(t-t_0)+\alpha_1^m(\alpha_1 x_1+\alpha_2 x_2) \quad (26)$$

$$\beta_x = \beta_x(t_0)+\alpha_1^m(\alpha_1\dot{x}_1+\alpha_2\dot{x}_2) \quad (26)$$

$\dot{x}_1 = \frac{dx_1}{dt}$; $\dot{x}_2 = \frac{dx_2}{dt}$; $\alpha_1 << 1$; $\alpha_2 << 1$;

Substituting (26,27) to (21) one can get $m=1$; $\alpha_1 = P$; $\alpha_2 = \xi_z$;

$$\frac{\dot{x}_1}{c} \approx \frac{1}{2}(1-\beta_x^2(t_0))(\tilde{\Phi}_1-\tilde{\Phi}_3) \quad (28)$$

$$\frac{\dot{x}_2}{c} \approx \frac{1}{2}(1-\beta_x^2(t_0))\tilde{\Phi}_2 \quad (29)$$

$$\beta_x = \beta_x(t_0)+P^2\dot{x}_1+P\xi_z\dot{x}_2;$$

$$\frac{x}{c} = \beta_x(t_0)(t-t_0)+P^2x_1+P\xi_z x_2 \quad (30)$$

Expressions for $\tilde{\Phi}_1$, $\tilde{\Phi}_2$ one can produce from the corresponding expressions for Φ_1, Φ_2 by substitution of φ_-, φ_+, to $x = c\beta(t_0)(t-t_0)$, and change $\varphi_- \to \tilde{\varphi}_-, \varphi_+ \to \tilde{\varphi}_+$.

$$\tilde{\varphi}_- = 2\pi\nu\left((1-\beta_x(t_0))+\eta_0\right)$$

$$\tilde{\varphi}_+ = 2\pi\nu\left((1+\beta_x(t_0))-\eta_0\right)$$

where $\eta_0 = 2\pi\nu\beta_x(t_0)t_0$

$\tilde{\Phi}_3$ And after approximate integration (25) is equal to:

$$\tilde{\Phi}_3 = \Gamma^{-2}\left\{\left(\frac{1}{\beta_x(t_0)}\right)(1-Cos[2\pi\nu\beta_x(t)t-2\eta_0])+ \right. \\ \left. +\beta_x(t_0)[Cos[2\pi\nu t]-Cos[2\pi\nu t_0]]\right\} \quad (31)$$

Integrating (28) and (29) one can get for x_1, x_2

$$\frac{x_1}{c} = \frac{1}{2}(1-\beta_x^2(t_0))\Gamma^{-2}\frac{1}{2\pi\nu}\left\{\left(-\frac{1}{4}\right)\left[\frac{Sin2\tilde{\varphi}_-}{(1-\beta_x(t_0))}-\frac{Sin2\tilde{\varphi}_+}{(1+\beta_x(t_0))}\right]\right. \\ +4Sin[2\pi\nu t_0]\left[\frac{Cos2\tilde{\varphi}_-}{(1-\beta_x(t_0))}-\frac{Cos2\tilde{\varphi}_+}{(1+\beta_x(t_0))}\right]-\frac{7}{2}Sin[4\pi\nu t_0] \quad (32) \\ +\left[\frac{1}{\beta_x(t_0)}-\beta_x(t_0)Cos[4\pi\nu t_0]\right]2\pi\nu(t-t_0)-\frac{\beta_x(t_0)}{2}Sin[4\pi\nu t_0] \\ \left.-\frac{1}{2}\frac{1}{\beta_x^2(t_0)}Sin[2\pi\nu\beta_x(t)t-2\eta_0]+\frac{1}{2}\beta_x(t_0)Sin[2\pi\nu t]\right\}$$

$$\frac{x_2}{c} = (1-\beta_x^2(t_0))\Gamma^{-2}\frac{1}{2\pi\nu}\left\{\left[\frac{Sin\tilde{\varphi}_-}{(1-\beta_x(t_0))}-\frac{Sin\tilde{\varphi}_+}{(1+\beta_x(t_0))}\right]+ \right. \\ \left. +\frac{\beta_x(t_0)}{1-\beta_x^2(t_0)}Cos[2\pi\nu t_0]\right\} \quad (33)$$

As it is followed from expressions (2-3), at $\beta_x \approx 1$ running in the initial propagation direction wave exits electron oscillations with larger amplitude than the wave running in opposite direction.

Two last items in (32):

$$\frac{1}{2}(1-\beta_x^2(t_0))\Gamma^{-2}\frac{1}{2\pi\nu}\left\{-\frac{1}{2}\frac{1}{\beta_x^2(t_0)}Sin[2\pi\nu\beta_x t-2\eta_0]+ \right. \\ \left. +\frac{1}{2}\beta_x(t_0)Sin[2\pi\nu t]\right\}$$

At $\beta_x \approx 1$ an electron motion, which has beating character [7] with period *T*:

$$T = \frac{1}{2\pi\nu(1-\beta_x(t_0))} \quad (34)$$

The $A_{\max}$ maximum and $A_{\min}$ minimum beating amplitude can be described with following expressions

$$A_{\min} = \frac{p^2c(1-\beta_x^2(t_0))}{8\pi\nu\Gamma^2}\frac{(1-|\beta_x(t_0)|^3)}{\beta_x^2(t_0)} \quad (35)$$

$$A_{\max} = \frac{p^2c(1-\beta_x^2(t_0))}{8\pi\nu\Gamma^2}\frac{(1+|\beta_x(t_0)|^3)}{\beta_x^2(t_0)} \quad (36)$$

Substituting expressions for β_x and x from (30) to (14) and keeping items of the second order on p and ε_z one can derive approximate expression for β_z

$$\beta_z = \Gamma^{-1}(1-\beta_x^2(t_0))^{1/2}(PF_0+\xi_z)+0P^3$$

where

$$F_0 = Sin[2\pi\nu(1-\beta_x(t))t+\eta_0]+ \\ +Cos[2\pi\nu(1-\beta_x(t_0))t-\eta_0]+2Sin[2\pi\nu t_0]$$

In the same way, substituting expressions for β_x and x from (30) to (15) and keeping items of the second order on p and ε_z we can produce approximate expression for β_y:

$$\beta_y = \frac{A}{\Gamma^2}(1-\beta_x^2(t_0))^{1/2}\left[1-P^2\frac{\beta_x(t_0)}{1-\beta_x^2(t_0)}\dot{x}_1- \right. \\ \left. -P\xi_z\frac{\beta_x(t_0)}{1-\beta_x^2(t_0)}\dot{x}_2-\frac{P^2}{2\Gamma^2}F_0^2-\frac{P\xi_z}{\Gamma^2}F_0^2\right]+0P^3 \quad (38)$$

Integrating (37) and (38) we derive dependence coordinates z and y on time t

$$z = \sqrt{c}\Gamma^{-1}(1-\beta_x^2(t_0))^{1/2}\left\{\frac{P(-1)}{2\pi\nu}*\right.$$
$$\left[\frac{Cos[2\pi\nu(1-\beta_x(t_0))t+\eta_0]}{(1-\beta_x(t_0))}+\frac{Cos[2\pi\nu(1-\beta_x(t_0))t-\eta_0]}{(1+\beta_x(t_0))}\right]+ \quad (39)$$
$$\left.+\frac{P}{2\pi\nu}\frac{2Cos[2\pi\nu t_0]}{(1-\beta_x^2(t_0))}+(\xi_Z+2Sin[2\pi\nu t_0])(t-t_0)\right\}+z_0(t_0)$$

$$y = \frac{A}{\Gamma^2}(1-\beta_x^2(t_0))^{1/2}\left[(t-t_0)-P^2\frac{\beta_x(t_0)}{1-\beta_x^2(t_0)}x_1-\right.$$
$$\left.-P\xi_z\frac{\beta_x(t_0)}{1-\beta_x^2(t_0)}x_2-\frac{P^2}{2\Gamma^2}\int_{t_0}^{t}F_0^2dt-\frac{P\xi_z}{\Gamma^2}\int_{t_0}^{t}F_0^2dt\right]+y_0(t_0) \quad (40)$$

CONCLUSION

The expressions derived above, describe the electron motion in the field of standing linear polarized light wave and allows to calculate spectrum of electron radiation with use of methods described in [5,6].

Today, it is supposed to use interaction of relativistic electron with intense laser beams accumulated in an optical cavity for generation of shirt wave radiation. The transversal sizes of the beams in the interaction point are equal of about several tens of micrometers. For this reason, the evaluation of transversal sizes of the electron beam during interaction is very actual task. It necessary to note, that the largest increasing of the electron beam transversal size is produced with the wave running in the direction of electron beam propagation and not the wave which generates the shirt wave radiation.

REFERENCES

[1] P.L. Kapitze and P.A.M. Dirac, Proc. Combridge Phys. Sos, 29, 287 (1933).

[2] V.I Ritus, «Quantum effects of interactions elementary particles with intense electro magnetic fields», Proceedings Physics Institute of Lebedev. 5-151 ст. (1979).

[3] A. Ts. Amatuni, Yerevan 375036 Republic of Armenia. I.V. Pogorelsky, Brookhaven National Laboratory, 725 C, Upton, New York 11973, (034001-034001-8) pp, (1998)

[4]. A. F. Kurin, Letters JTP, 2005, vol 31. issue 13

[5] Landau & Lifshic, «Theoru of field»

[6] A.N. Krilov, «Proceedings of academian A.N. Krilov», vol. 3, mathematics, part two, Publishers of Academy USSR, 481p. (1949)

TRANSVERSE COHERENCE PROPERTIES OF THE LCLS X-RAY BEAM*

S. Reiche†, UCLA, Los Angeles, CA 90095, USA.

Abstract

Self-amplifying spontaneous radiation free-electron lasers, such as the LCLS or the European X-FEL, rely on the incoherent, spontaneous radiation as the seed for the amplifying process. Though this method overcomes the need for an external seed source one drawback is the incoherence of the effective seed signal. The FEL process allows for a natural growth of the coherence because the radiation phase information is spread out within the bunch due to slippage and diffraction of the radiation field. However, at short wavelengths this spreading is not sufficient to achieve complete coherence. In this presentation we report on the results of numerical simulations of the LCLS X-ray FEL. From the obtained radiation field distribution the coherence properties are extracted to help to characterize the FEL as a light source.

INTRODUCTION

Self-Amplified Spontaneous Emission Free-Electron Lasers (SASE FEL) [1] allow to overcome the restriction in wavelength imposed by existing seeding sources and to explore new wavelength regimes. A particular interest is in the Ångstrom wavelength regime which opens entire new classes of experiments such the 3D imaging of individual molecules or the analysis of chemical reaction on the femtosecond scale. Supported by the successful demonstration of SASE FELs at wavelength down to 14 nm [2], several X-ray FELs are currently under construction such as the Linac Coherent Light Source (LCLS) [3] or the European X-FEL [4].

The drawback of any SASE FEL is that it uses the spontaneous undulator radiation as its seed signal, which is intrinsically broadband and incoherent. Though the FEL process increases the longitudinal and transverse coherence by slippage and diffraction over the length of the undulator it never reaches the coherence level of a seeded FEL amplifier. In particular at short wavelength diffraction – the main method to the build-up transverse coherence – is ineffective and under certain circumstances the FEL can reach saturation before obtaining transverse coherence [5].

For the design of the optical transport line and diagnostic as well as proposed experiments it is of importance to characterize the radiation properties of the SASE FEL as a light source in advance. For that simulations were conducted and the results are presented here. The work was done in context of the LCLS (Tab.1 list the main parameters of LCLS). The main radiation properties have been presented elsewhere [6] and this presentation focusses solely on the fluctuation in the spot size at the detector locations (expressed by divergence and effective source location of the FEL beam) and the degree of coherence of the FEL signal.

Table 1: LCLS Design Parameters

Beam Energy	13.4 GeV
Beam Current	3.4 kV
Undulator Period	3 cm
Undulator Parameter	3.5
Undulator Length	130 m
Radiation Wavelength	1.5 Å

RADIATION SIZE AND DIVERGENCE

Because a SASE FEL has no well-defined input to be amplified, the output is of stochastic nature and varies from shot to shot. For the purpose of designing the X-ray beamline the evolution of the FEL pulse along the optical beam line is of importance to know. In particular the divergence and beam size determine the design of apertures and target sizes.

The easiest quantities to extract from the results of FEL simulations are the rms sizes of the radiation pulse in the near and far field. To these values the envelope equation of a fundamental Gauss-Hermite mode [7]

$$w(z) = w_0\sqrt{1+\left(\frac{z-z_0}{z_r}\right)^2} \qquad (1)$$

is matched. Although Eq. 1 has three unknown parameter – the waist size w_0, the waist position z_0 and Rayleigh length z_r – the system is fully deterministic because w_0 and z_r are related to each other by the radiation wavelength, which is a fixed parameter for our calculation.

Higher mode content obscures the results because the mode number becomes an additional unknown parameter. Due to the similarity of the Gauss-Hermite modes to the solution of the two-dimensional harmonic oscillator in quantum mechanics [8] and the fact that the calculation of the rms size is equivalent to the energy eigenvalue of the harmonic oscillator the waist size w_0 has to be corrected to

* Work supported by the U.S. Department of Energy contract DE-AC02-76F00515

† reiche@ucla.edu

$w_0 \rightarrow w_0(1+n+m)$, where n and m are the mode numbers of the Gauss-Hermite mode. In the far field zone ($z \ll z_0$) it can be also viewed as a reduction in the Rayleigh length $z_r \rightarrow z_r/(1+n+m)$ for a given and fixed waist size w_0.

The motivation for this work is to estimate the radiation size of the FEL pulse at any detector position in the far field zone. With that assumption we treat the entire higher-mode content as a single fundamental mode, defined by its Rayleigh length and waist position. This will yield wrong results at the source position by a mismatch in the actually waist size and the assumed one, however that information is irrelevant for the design process of the X-ray beam beamline and diagnostics.

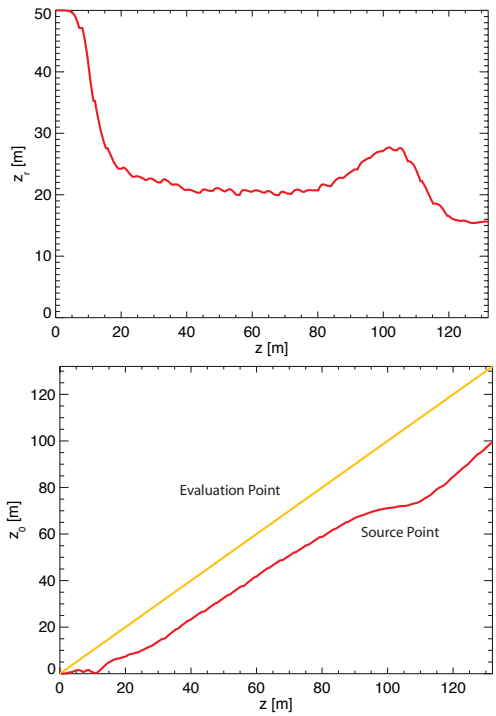

Figure 1: Effective Rayleigh length and waist position (top and bottom plot, respectively) along the undulator for an FEL amplifier.

As the initial step we analyze z_r and z_0 for the case of a seeded FEL with LCLS like parameters. The results are shown in Fig.1. The FEL is seeded with a radiation field ($z_r = 50$ m) larger than the electron beam size but after a few gain length the FEL-eigenmode is dominating. Because the mode size becomes smaller the Rayleigh length is reduced to about 20 m. In the lethargy regime of the FEL the radiation field remains almost unaffected and follows free-space diffraction as is seen by the almost constant waist position over the first 10 m. The FEL eigenmode has an intrinsic phase front curvature enhancing the diffraction and putting the source point behind the point where the field distribution is evaluated. At saturation gain-guiding vanishes and the phase front curvature straightens out as indicated by the growth in the Rayleigh length and a semi-constant waist position. However in deep saturation electrons gain some energy back while the radiation field has spread out by diffraction. This causes a disruption in the phase front at the electron location, coupling higher mode to the field distribution. As a result the diffraction is enhanced and the Rayleigh length becomes shorter.

SASE Simulations, using the LCLS design parameters, yield a radiation pulse with about 200 spikes at the undulator exit. Each spike is analyzed and the effective source position and Rayleigh length are extracted. To avoid that the analysis is obscured by the incoherent part of the radiation pulse (namely the area between spikes) only spikes are considered which have a peak power of at least 20 % of the maximum power in the pulse. Also we assume that over a single spike the phase fronts are very similar and thus can be treated as a single sample point.

As it can be expected from the intrinsic stochastic nature of the SASE FEL process there is fluctuation in both waist position and Rayleigh length. The distributions are shown in Fig. 2. The effective waist position is in average 38 m within the undulator from the undulator exit and has a rms fluctuation of 4.8 m. The average Rayleight length of 32 m is actually larger than the steady-state case. The rms variation is 4 m. The reason for a longer Rayleigh length is the deep saturation behavior of an SASE FEL, where the radiation further gains power in this super-radiant regime. The phase fronts are not as disrupted as in the seeded FEL case (see above). No significant correlation between Rayleight length and waist position has been observed.

Start-end simulations yield a different electron distribution than specified in the design case. Most notable is that only the electron bunch as a whole is aligned and match to the undulator axis while each slice has a certain degree of mismatch and misalignment. In addition wakefields are included which alter the energy of the electron along the undulator and thus disrupt the FEL process. While the statistic of the waist position remains almost unchanged ($< z_0 >= 37$ m with an rms fluctuation of 5.7 m) the Rayleigh length is significantly shorter with 7.8 m and a rms variation of 2 m. Though some asymmetry in the electron distribution and the mismatch of the beta-function yield a coupling of higher modes to the emission the main reason is the centroid motion of the electron slices. In the saturation regime most electron slices undergo a turning point of their betatron oscillation. The strong focusing lattice provides a rather sawtooth-like trajectory, typical for any alternating-gradient focusing system, and the electron beam slice emits predominantly in two directions. Instead of once central distribution in the far field there are two overlapping distributions, left and right of the axis. The resulting distribution is significantly broader than for the aligned case, which is reflected by the shorter Rayleigh length in the statistic.

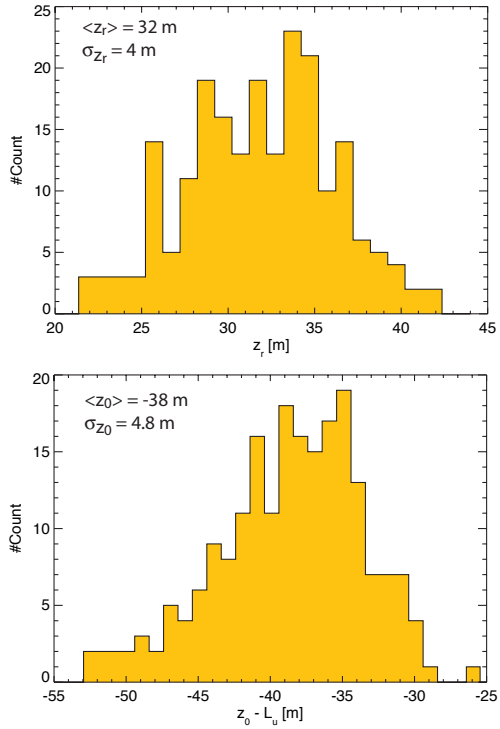

Figure 2: Histogram of Rayleigh length and waist position (top and bottom plot, respectively) for an SASE FEL pulse, evaluated at the undulator exit.

COHERENCE

In the previous section we expressed the quality of the SASE FEL radiation pulse by the fluctuation in the divergence and effected source position for all longitudinal modes (spikes in the radiation power profile). With the extracted Rayleigh length the size of a corresponding fundamental Gauss-Hermite can be calculated and be compared to the radiation size of the FEL mode as an indication for the higher mode content. However higher modes are not necessarily an indication for poor transverse coherence. In the case that the phase relation between all modes remains constant from shot to shot corresponds actually to a fully transverse coherent pulse.

Coherence is a statistical property of a radiation source and refers to how much you can extrapolate the radiation phase information in time and space for any given measurement. Mathematically it is expressed by the mutual coherence function [9]:

$$\Gamma_{12}(\tau) = \left\langle \vec{E}(\vec{r}_1, t)\vec{E}(\vec{r}_2, t+\tau) \right\rangle \qquad (2)$$

While the temporal coherence function is easy to define ($\Gamma_{11}(\tau)$) any experiment which relies on spatial coherence (e.g. diffraction on a grating) will always include some temporal information due to the difference in the path length to the detector. For sake of simplicity we assume that the signal $\vec{E}(\vec{r}, t)$ is quasi-monochromatic so that the time delay due to the path length difference from $\vec{r}_1$ and $\vec{r}_2$ falls within the temporal coherence of the signal and thus the time dependence in the mutual coherence function can be neglected. The mutual coherence function becomes then the mutual intensity $J_{12} \equiv \Gamma_{12}(0)$. In analogy to the temporal coherence function, the mutual intensity function is normalized as

$$\mu_{12} = \frac{J_{12}}{\sqrt{J_{11}J_{22}}} \qquad (3)$$

to yield values between zero and one. It is referred to also as the complex coherence factor. A zero value refers to no correlation in phase between the observed field at the two postions $\vec{r}_1$ and $\vec{r}_2$ while a value of one means that the phase remains constant over time.

The complex coherence factor compares two fixed points in the transverse plane. If we allow both points to be free parameter μ_{12} would yield a four dimensional distribution. For sake of simplicity we restrict one point to be on the undulator axis. In analogy to the temporal coherence time [10] the coherence area is defined as

$$A_c = \int \mu_{12} dA \qquad (4)$$

and reflects the size of a usable target area for experiments, relying on coherence, without the need to enforce coherence (e.g. with a pin hole). The optimum case would be when the coherence area is much larger than the actual spot size. Note that for a fully coherent signal the coherence area is infinite.

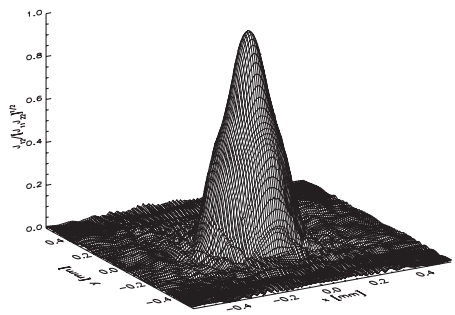

Figure 3: Complex coherence factor for LCLS design case at the undulator exit.

The entire field information of a time-dependent simulation for the LCLS design case was saved and used to evaluate the mutual intensity function and complex coherence factor. The resulting distribution for μ_{12} is shown in Fig. 3. The coherence area, as defined in Eq. 4, is 0.071 mm^2, about five times larger than the spot size Σ. This indicates sufficient transverse coherence over the entire spotsize and that the FEL pulse can be used for diffraction experiments without the requirement to enhance coherence by a pin hole aperture. The growth in the transverse coherence can be seen in Fig. 4 which is a monotonically increasing function along the undulator. On the other hand

the radiation diffracts faster than the build up in the coherence area within the first tens of meter. However, at around 70 m gain guiding is dominant and the spotsize remains constant till saturation where the spot grows again due to diffraction. At around 60 m, the coherence area becomes larger than the spot size though it does not necessarily indicate good transverse coherence. For that the ratio between A_c and Σ must be much larger than one.

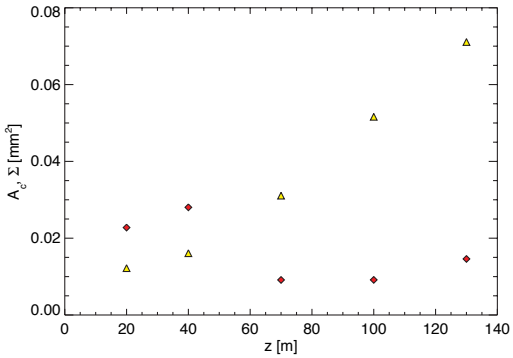

Figure 4: Evolution of the coherence area A_c and spotsize Σ (triangle and diamond shape, respectively) along the undulator.

For LCLS the FEL pulse has to propagate at least 115 m till it reaches the first user station. The coherence area is further increase and in the case of the LCLS design case the value becomes 0.32 mm^2 while the spot size is 0.044 mm^2. The reason is that noise consists typically of higher modes which diffracts stronger than the FEL pulse itself, clearing up the signal at the detector location. This becomes more apparent in the case of the start-end simulation where the electron beam slices are not aligned and matched to the focusing lattice (see previous section). The complex coherence factor is shown in Fig. 5 and the resulting coherence area is 0.27 mm^2 while the spotsize is 0.057 mm^2. The ratio indicates that the coherence is still sufficient.

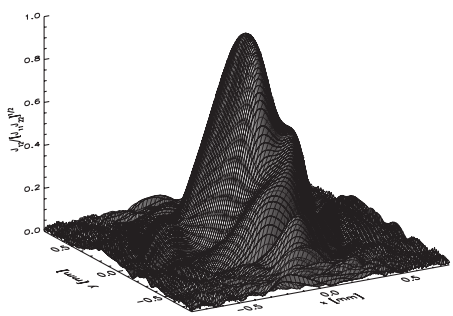

Figure 5: Complex coherence factor for LCLS for the start-end simulation, evaluated 115 m downstream of the undulator exit.

CONCLUSION

Simulations have been conducted to study the radiation properties of the LCLS pulse, namely the variation in the beam size at the detector location and the degree of coherence. A fundamental Gauss-Hermite has been matched to each spike in the radiation profile to describe the divergence by an effective Rayleigh length and source position. The average source position is about 35 m within the undulator before the undulator exit and fluctuate by about 5 m. The Rayleigh length depends strongly on the underlying model of the simulation and shows significantly smaller values for start-end simulation. It is caused by centroid misalignment of the individual electron slice of the LCLS electron bunch. The build-up of transverse coherence during the FEL amplification process is sufficient to spread throughout the entire bunch. For the LCLS case The effective coherence area, within which the field amplitude and phase have a significant correlation to each other, is about 5 times larger than the spot size when evaluated at the first experimental location 115 m downstream the undulator.

REFERENCES

[1] R. Bonofacio *et al*, Opt. Comm. **50** (1984) 373.

[2] A list can be found e.g. W.B. Colson, *Proc. of the FEL 2004 Conference* (2004) 706.

[3] *LCLS CDR*, SLAC Report No. SLAC-R-593, 2002.

[4] A.S. Schwarz, *Proc. of the FEL2004 Conference* (2004) 85.

[5] E.L. Saldin, E.A. Schneidmiller and M.V. Yurkov, Opt. Comm. **97** (1993) 272.

[6] S. Reiche *et al*, Nucl. Inst. & Meth. **A483** (2002) 70.

[7] A.E. Siegman, Lasers (University Science Book, Mill Valley, CA, 1986).

[8] S. Reiche, /it Numerical Studies for Single Pass HighGain Free-Electron Laser, Ph. D. Thesis, DESY report: DESY-Thesis-2000-012 (2000).

[9] J. Goodman, Statistical Optics (John Wiley and Sons, New York, 1985).

[10] E.L. Saldin, E.A. Schneidmiller and M.V. Yurkov, Nucl. Inst. & Meth. **A407** (1998) 291.

AN ANALYSIS OF SHOT NOISE PROPAGATION AND AMPLIFICATION IN HARMONIC CASCADE FELs

Zhirong Huang*
Stanford Linear Accelerator Center, Stanford, CA 94309, USA.

Abstract

The harmonic generation process in a harmonic cascade (HC) FEL is subject to noise degradation which is proportional to the square of the total harmonic order [1]. In this paper, we study the shot noise evolution in the first-stage modulator and radiator of a HC FEL that produces the dominant noise contributions. We derive the effective input noise for a modulator operating in the low-gain regime, and analyze the radiator noise for a density-modulated beam. The significance of these noise sources in different harmonic cascade designs is also discussed.

INTRODUCTION

Harmonic cascade (HC) FELs are envisioned to generate fully coherent x-ray pulses [2] and are currently under active development for several VUV and soft x-ray projects (see, e.g., Refs. [3, 4]). It was pointed out in Ref. [1] that electron shot noise can be amplified by at least the square of the total harmonic order in this process, much like a frequency multiplication chain in radar communications [5]. Thus, it is important to understand the shot noise contributions in the harmonic generation process which may be the limiting factors in determining the temporal coherence or the final wavelength reach of these seeded FELs.

In a self-amplified spontaneous emission (SASE) FEL, the one-dimensional (1D) shot noise power spectrum is $\rho\gamma mc^2/(2\pi)$ [6], where ρ is the FEL Pierce parameter [7] and γmc^2 is the electron energy. The shot noise power spectrum can be identified to be about the forward-direction spontaneous undulator radiation in the first two power gain lengths [8]. The three-dimensional (3D) correction to this simple 1D result including effects of energy spread and emittance is given in Refs. [9, 10]. If the first undulator of a HC FEL operates in the high-gain regime (i.e., much longer than the gain length), the SASE noise power (integrated over the gain bandwidth) may be used to estimate its noise contribution to a HC FEL. However, due to the availability of high-power seed laser, the typical design of the first undulator of a HC FEL is a short (energy) modulator that operates in the low-gain (or even no-gain) regime [3, 4, 11]. Thus, the shot noise content of this modulator can be different from a high-gain undulator. After the dispersion section, the density-modulated electron beam entering the radiator generates additional shot noise. In this paper, we analyze the shot noise evolution in the first-stage modulator and radiator of a HC FEL that produces the dominant noise contributions. We also discuss the significance of these noise sources in different harmonic cascade designs.

* zrh@slac.stanford.edu

ANALYSIS

To illustrate this noise degradation process, we consider a seed signal at the fundamental wavelength $\lambda_1 = 2\pi/k_1 = 2\pi c/\omega_1$:

$$E_1 = (E_0+\Delta E)e^{i\theta+i\Delta\theta} \approx (E_0+\Delta E)e^{i\theta}(1+i\Delta\theta)\,. \quad (1)$$

Here E_0 and $\theta = -\omega_1 t$ are the amplitude and the phase of the signal, ΔE and $\Delta\theta$ represent any small amplitude and phase noises (such as caused by the electron shot noise and/or any noise carried by the seed laser). After a total of $N_h = h_1 h_2 ...$ frequency multiplication, the electric field at the output harmonic is

$$\begin{aligned} E_{N_h} =& G(E_0+\Delta E)\exp\left(iN_h\theta + iN_h\Delta\theta\right) \\ \approx& G(E_0+\Delta E)e^{iN_h\theta}\left(1+iN_h\Delta\theta\right)\,, \end{aligned} \quad (2)$$

where we have assumed that $N_h\Delta\theta \ll 1$ (otherwise the effect is rather large), and G is an arbitrary function of the field amplitude (such as the Bessel function bunching factor). Thus, the noise-to-signal ratio at the final harmonic radiation is [1, 5]

$$\left(\frac{P_n}{P_s}\right)_{N_h} = {N_h}^2\left(\frac{P_n}{P_s}\right)_1\,. \quad (3)$$

N_h can be a very large number (a few hundred to a few thousand when harmonic cascading a UV laser to an x-ray FEL). $(P_n)_1$ is the initial noise power which includes both the intrinsic laser noise and the electron shot noise. Suppose that the seed laser noise is controlled to a tolerable level, the shot noise fluctuations of the electron beam provide the essential contributions, which will be studied here.

We focus our analysis on the first-stage of a harmonic cascade that includes a modulator, a dispersion section and a radiator (tuned to the h^{th} harmonic of the seed wavelength) as shown in Fig. 1. This first stage has the largest total harmonic conversion factor and hence produces the dominate noise sources. The initial longitudinal phase space distribution function is

$$F(\theta_0,\eta_0) = \frac{k_1}{\chi}\sum_{j=1}^{N_e}\delta(\theta_0-\theta_j)\delta(\eta_0-\eta_j)\,, \quad (4)$$

where $\theta_0 = -ck_1t_0$ describes the electron phase relative to the EM wave (i.e., input laser field), η_0 describe the initial relative energy deviation, and $\chi = N_e/l_b$ is the line density of the electron bunch with N_e electrons and l_b bunch

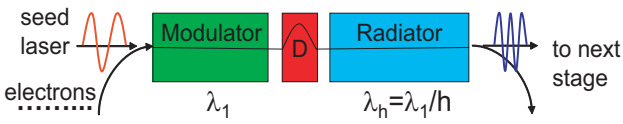

Figure 1: Schematic of the first-stage HC FEL.

length. The normalization in Eq. (4) is chosen so that the ensemble average

$$\left\langle \int F(\theta_0,\eta_0)d\eta_0 \right\rangle = 1 \tag{5}$$

for a constant current profile.

In typical HC FEL designs [3, 4, 11], the first undulator is relatively short and is mainly an energy modulator, then we have

$$\eta_1 = \eta_0 + \eta_s \sin\theta_0 + \eta_n(\theta_0)\,, \tag{6}$$

where η_s is the energy modulation amplitude induced by the seed laser field, and η_n is the energy modulation induced by the noisy spontaneous undulator radiation.

A dispersion section immediately after the modulator can convert the beam energy modulation into a density modulation. This is accompanied by a magnetic chicane that changes the phase of the electron according to its energy deviation:

$$\theta_1 = \theta_0 + k_1 R_{56}\eta_1 = \theta_0 + D\eta_1\,. \tag{7}$$

Here R_{56} is the net momentum compaction of the chicane together with the first undulator (modulator), and $D = k_1 R_{56}$. The harmonic bunching near the h^{th} harmonic (when $\nu \sim h$) can be found as

$$\begin{aligned} b_\nu &= \int \frac{d\theta_1}{k_1 l_b} d\eta_1 e^{-i\nu\theta_1} F(\theta_1,\eta_1) \\ &= \int \frac{d\theta_0}{k_1 l_b} d\eta_0 e^{-i\nu[\theta_0 + D(\eta_0+\eta_s\sin\theta_0+\eta_n)]} F(\theta_0,\eta_0)\,. \end{aligned} \tag{8}$$

Here we have assumed the laser pulse length is at least as long as the electron bunch length. If the laser pulse only overlaps a fraction of the electron bunch, l_b should be taken to be the laser pulse length instead of the electron pulse length, then N_e represents number of electrons within l_b. Let us also assume that the modulated part of the electron bunch is long compared to the laser wavelength (i.e., $k_1 l_b \gg 1$), and that the electron energy distribution is Gaussian with a slice rms energy spread σ_η, we expand Eq. (8) in Bessel series of η_s and to the first-order in η_n (as $|hD\eta_n| \ll 1$) to obtain

$$\begin{aligned} b_\nu &= \int \frac{d\theta_0}{k_1 l_b} \int d\eta_0 \sum_{p=-\infty}^{\infty} J_p(-hD\eta_s) e^{i(p-\nu)\theta_0} e^{-i\nu D\eta_0} \\ &\quad \times (1 - ihD\eta_n) F(\theta_0,\eta_0) \\ &= \sum_{p=-\infty}^{\infty} J_p(-hD\eta_s) \left[\frac{1}{N_e} \sum_{j=1}^{N_e} e^{i(p-\nu)\theta_j} e^{-i\nu D\eta_j} \right. \\ &\quad \left. - ihD \exp\left(-\frac{h^2D^2\sigma_\eta^2}{2}\right) \int \frac{d\theta_0}{k_1 l_b} e^{i(p-\nu)\theta_0} \eta_n(\theta_0) \right], \end{aligned} \tag{9}$$

where we have applied the smooth distribution function in the second term of the bracket as η_n is treated as a small perturbation.

When $\nu = p = h$, the first term in the bracket produces the desired harmonic bunching signal as

$$\begin{aligned} b_h &= \frac{J_h(-hD\eta_s)}{N_e} \sum_{j=1}^{N_e} e^{-ihD\eta_j} \\ &= J_h(-hD\eta_s) \exp\left(-\frac{h^2D^2\sigma_\eta^2}{2}\right). \end{aligned} \tag{10}$$

When $\nu \neq h$, the first term produces the noise bunching in the radiator as the ensemble average

$$\langle |b_\nu^r|^2 \rangle = \frac{1}{N_e} \sum_{p=-\infty}^{\infty} J_p^2(-hD\eta_s) = \frac{1}{N_e}\,. \tag{11}$$

Thus, the modulated bunch generates the same amount of the shot noise bunching in the radiator as a fresh electron bunch.

The second term in the bracket of Eq. (9) is the noise bunching originated from the modulator. As η_n is nearly a sinusoidal function of θ_0, it can be written as

$$\begin{aligned} b_\nu^m &= \exp\left(-\frac{h^2D^2\sigma_\eta^2}{2}\right) \left[-ihDJ_{h+1}(-hD\eta_s)\eta_n^+(\Delta\nu) \right. \\ &\quad \left. - ihDJ_{h-1}(-hD\eta_s)\eta_n^-(\Delta\nu) \right], \end{aligned} \tag{12}$$

where $\Delta\nu = \nu - h$ and

$$\eta_n^\pm(\Delta\nu) = \int \frac{d\theta_0}{k_1 l_b} e^{i(\pm 1 - \Delta\nu)\theta_0} \eta_n(\theta_0) \tag{13}$$

is the Fourier component of η_n near the first undulator (modulator) resonant frequency ck_1.

If $x = hD\eta_s \ll 1$, we can expand $J_h(x) \sim (x/2)^h/h!$; If the dispersion strength is optimized to yield the maximum $|b_h|$ at $hD\eta_s \sim h$ or $D \sim 1/\eta_s$, then $J_h \sim J_{h\pm1} \sim 0.3$. In either case, we can approximate the bunching ratio as

$$\left|\frac{b_\nu^m}{b_h}\right|^2 \approx 4h^2 \frac{|\eta_n^\pm(\Delta\nu)|^2}{\eta_s^2}\,. \tag{14}$$

The power spectrum $dP/d\omega$ in the radiator is proportional to $|b|^2$. Integrating over their respective bandwidths in the radiator, we obtain the modulator noise-to-signal power ratio as

$$\left(\frac{P_n^m}{P_s}\right)_h = 4h^2 \frac{\Delta\omega_n^m \langle|\eta_n^{\pm}(\Delta\nu)|^2\rangle}{\Delta\omega_s \eta_s^2}\,, \tag{15}$$

where $\Delta\omega_s = 2\pi c/l_b$ is the Fourier transform limited bandwidth for the signal, and $\Delta\omega_n^m$ is the bandwidth of the modulator noise. For simplicity, we assume that the full modulator bandwidth is much smaller than the full radiator bandwidth centered around a much higher frequency (i.e., $\Delta\omega_m = \Delta\nu_m\omega_1 < \Delta\omega_r = \Delta\nu_r\omega_h$), then we have $\Delta\omega_n^m = \Delta\omega_m = \Delta\nu_m\omega_1$ without convoluting the bandwidths of the modulator and the radiator.

The laser-induced energy modulation amplitude can be estimated as

$$\eta_s^2 = K_1^2[\mathrm{JJ}]^2 \frac{L_{u1}^2}{\gamma^4\sigma_L^2}\frac{P_L}{P_0}\,, \tag{16}$$

where $P_0 = I_A mc^2/e \approx 8.7$ GW. Using the one-dimensional FEL theory, we find that the Fourier component of the shot-noise-induced energy modulation is

$$\eta_n^{\pm}(\Delta\nu) = \frac{1}{8\gamma^3}\frac{I}{I_A}\left(\frac{\lambda_{u1}K_1[\mathrm{JJ}]}{\sigma_x}\right)^2 N_{u1}^2 f(\bar{\nu}) \times \frac{1}{N_e}\sum_{j=1}^{N_e} e^{i(\pm 1+\Delta\nu)\theta_j}\,, \tag{17}$$

where $\bar{\nu} = \pi\Delta\nu N_{u1}$ is the scaled detune in the first undulator with N_{u1} period, and

$$f(\bar{\nu}) = \left[\frac{e^{-i\bar{\nu}}\sin(\bar{\nu})/\bar{\nu} - 1}{i\bar{\nu}}\right] \tag{18}$$

describes the energy modulation bandwidth due to the shot noise with a relative bandwidth given by $\Delta\nu_m = 1/N_{u1}$ for $N_{u1} \gg 1$. Inserting Eq. (16) and (17) into Eq. (15), we obtain finally

$$\left(\frac{P_n^m}{P_s}\right)_h = h^2 \frac{\lambda_{u1}N_{u1}r_e\sigma_L^2}{8\sigma_x^4}\frac{K_1^2[\mathrm{JJ}]^2}{1+K_1^2/2}\frac{(mc^2/e)\,I}{P_L} = h^2\left(\frac{P_n^m}{P_L}\right)_1\,. \tag{19}$$

Thus, the effective modulator noise is

$$P_n^m = \frac{\lambda_u N_{u1} r_e \sigma_L^2}{8\sigma_x^4}\frac{K_1^2[\mathrm{JJ}]^2}{1+K_1^2/2}\frac{mc^2}{e}I\,. \tag{20}$$

For efficient laser-beam interaction in the modulator, the laser spot size is usually chosen to be $\sigma_L = \sqrt{\lambda_1\lambda_{u1}N_{u1}/8\pi}$ (i.e., the Rayleigh length is one half the undulator length with the laser waist located at the middle of the undulator). When the electron beam matches the laser spot (i.e., $\sigma_x \approx \sigma_L$), we have

$$P_n^m \approx \frac{\lambda_{u1}N_{u1}r_e}{8\sigma_x^2}\frac{K_1^2[\mathrm{JJ}]^2}{1+K_1^2/2}\frac{mc^2}{e}I \tag{21}$$

$$\approx \frac{\pi r_e}{\lambda_1}\frac{mc^2}{e}I\,. \tag{22}$$

Equation (21) can be shown to be the spontaneous undulator radiation in the forward direction (within a solid angle $\lambda_1^2/(2\pi\sigma_x^2)$ and a full bandwidth ω_1/N_{u1}). Equation (22) holds for $K_1^2 \gg 1$ and can be used for a quick estimation of modulator noise power. If the modulator length is much shorter than two power gain lengths, then the modulator noise power is much smaller than the usual SASE noise power as discussed in the introduction.

As shown in Eq. (11), the density-modulated beam generates the same shot noise bunching. The additional radiator noise-to-signal ratio can be estimated as

$$\left(\frac{P_n^r}{P_s}\right)_h = \frac{\Delta\omega_n^r\langle|b_\nu^r|^2\rangle}{\Delta\omega_s b_h^2} = \frac{\Delta\omega_n^r/N_e}{\Delta\omega_s J_h^2(hD\eta_s)e^{-h^2D^2\sigma_\eta^2}}\,, \tag{23}$$

where $\Delta\omega_n^r = \Delta\omega_r = \Delta\nu_r\omega_h$ is the noise bandwidth in the radiator. If the radiator is also a low-gain device, then $\Delta\nu_r \approx 1/N_{u2}$. If the radiator is a high-gain device, then $\Delta\nu_r \approx 2\rho$. In either case we can write

$$\left(\frac{P_n^r}{P_s}\right)_h = \frac{1/N_{lc}}{b_h^2} = \frac{1/N_{lc}}{J_h^2(hD\eta_s)e^{-h^2D^2\sigma_\eta^2}}\,, \tag{24}$$

where $N_{lc} = N_e l_c/l_b$ is the number of electrons within the radiator coherence length $l_c = \lambda_h/(\Delta\nu_r)$. Note that the radiator noise-to-signal ratio is independent of the signal laser power P_L, but depends strongly on the harmonic bunching strength. This has implications on different designs of HC FELs to be discussed below.

NUMERICAL EXAMPLES AND DISCUSSIONS

Equations (20), (22), and (24) are the main results of this paper and may be used to estimate the shot-noise-to-signal ratio of a HC FEL using a high-power seed laser in a short modulator. Let us take some numerical examples to illustrate the significance of various noise contributions. Consider the BESSY HC FEL design at the final radiation wavelength $\lambda_f = 1.24$ nm [3]. For $I = 1.75$ kA and $\lambda_1 = 297.50$ nm, the modulator noise power according to Eq. (22) is 26 W. If the laser power is 100 MW, then the modulator noise-to-signal ratio at the final wavelength after the total harmonic number $N_h = 297.50/1.24 = 240$ is

$$\left(\frac{P_n^m}{P_s}\right)_{N_h} = N_h^2 \times \frac{26}{100\times 10^6} \approx 1.5\%\,. \tag{25}$$

Thus, the modulator noise contribution is noticeable but still small. In passing, we note the bandwidth of the modu-

lator noise is about ω_1/N_{u1}, hence the final relative bandwidth of the first-stage modulator noise is

$$\frac{\Delta\omega_n^m}{\omega_f} = \frac{1}{N_h N_{u1}} \,. \tag{26}$$

This may still be a small relative bandwidth than a SASE FEL at 1 nm. For example, , $N_h = 240$, $N_{u1} = 18$ in the BESSY FEL, and $\Delta\omega_n^m/\omega_f \sim 2\times 10^{-4}$. Thus, even when the final noise level due to the first modulator is comparable to the signal strength, the temporal coherence of the HC FEL is still improved as any noisy structure within the slippage length $\lambda_1 N_{u1}$ of the first modulator is naturally smoothed. This noise filtering effect was observed in the LUX HC FEL simulations [11].

Let us now consider the radiator noise. First, we take $I = 1.75$ kA, $N_{u2} = 40$, and $\lambda_h = 297.50/5 = 59.50$ nm, then we have $N_{lc} = N_e N_{u2}\lambda_h/l_b \sim 10^8$ in Eq. (24). The BESSY FEL employs a fresh bunch approach that shifts the output radiation to a fresh part of the bunch for the next-stage interaction and hence allows for a large energy modulation to be induced in the part of the electron bunch that overlaps with a very short laser signal [12]. In this approach, the harmonic bunching is usually maximized by choosing $D \sim 1/\eta_s$. If $hD\sigma_\eta \ll 1$, we have $b_h^2 \sim 0.1$. The increase of the energy spread due to the large energy modulation is not an issue as the next stage interaction occurs at a fresh part of the bunch with the same initial energy spread. In this case, the radiator noise-to-signal ratio given by Eq. (24) is extremely small, at the 10^{-7} level. Even after another harmonic conversion factor of 48 (from the radiator wavelength $\lambda_h = 59.50$ nm to the final wavelength $\lambda_f = 1.24$ nm), the contribution from the radiator noise is still small.

Nevertheless, the fresh bunch technique requires a tight timing control between the short laser pulse and the electron bunch. In addition, experiments demanding most photons in a narrow bandwidth may benefit from using a laser pulse longer than the electron bunch length to seed the whole bunch. In this case, the induced energy modulation must be controlled to a small level in order not to degrade the beam energy spread (i.e., $\eta_s < \sigma_\eta$). In view of Eq. (10), the harmonic bunching cannot be maximized as $hD\eta_s < hD\sigma_\eta < 1$, then the radiator noise-to-signal ratio can increase dramatically. For example, in the whole-bunch seeding example described in Ref. [1], the second-harmonic bunching at the radiation wavelength 130 nm is only $b_2^2 \sim 0.25\times 10^{-4}$ in order to avoid a significant increase in the energy spread. Thus, the radiator noise-to-signal ratio given by Eq. (24) can be much larger ($\sim 10^{-3}$). An additional harmonic conversion factor of 16 (to the final wavelength at 8 nm) will amplify this radiator noise-to-signal ratio to 25%. Therefore, the shot noise contribution, especially in the radiator section, may limit the temporal coherence of such a harmonic cascade.

ACKNOWLEDGMENTS

The author wishes to thank W. Fawley, W. Graves, K.-J. Kim, L.-H. Yu, and J. Wu for many useful discussions. This work was supported by the U.S. Department of Energy contract No. DE-AC02-76SF00515.

REFERENCES

[1] E.L. Saldin, E.A. Schneidmiller, and M.Y. Yurkov, *Opt. Commun.* **202**, 169 (2002).

[2] L.-H. Yu and J.H. Wu, *Nucl. Instrum. Methods Phys. Res., Sect. A* **483**, 493 (2002).

[3] BESSY FEL Technical Design Report, http://www.bessy.de/publicRelations/publications/files/TDR_WEB.pdf.

[4] C. J. Bocchetta et al, In *Proceedings of the 2005 Free Electron Laser Conference*, Stanford, CA, USA, 2005.

[5] W. Robins, *Phase noise in signal sources*. Peter Peregrinus Ltd., London, 1982.

[6] K.-J. Kim, *Phys. Rev. Lett.* **57**, 1871 (1986).

[7] R. Bonifacio, C. Pellegrini, and L.M. Narducci, *Opt. Commun.* **50**, 373 (1984).

[8] L.-H. Yu and S. Krinsky, *Nucl. Instrum. Methods Phys. Res., Sect. A* **285**, 119 (1989).

[9] M. Xie, *Nucl. Instrum. Methods Phys. Res., Sect. A* **475**, 51 (2001).

[10] Z. Huang and K.-J. Kim, *Nucl. Instrum. Methods Phys. Res., Sect. A* **475**, 59 (2001).

[11] W. Fawley, W. Barletta, J. Corlett, and A. Zholents, In *2003 Particle Accelerator Conference*, Portland, OR, USA, 2003.

[12] I. Ben-Zvi, K. Yang, and L.-H. Yu, *Nucl. Instrum. Methods Phys. Res. Sec. A* **318**, 726 (1992).

OPTICAL BEAM QUALITY IN FREE-ELECTRON LASERS*

P.A. Sprangle#, Naval Research Laboratory, Washington, DC, 20375, U.S.A.

H.P. Freund, Science Applications International Corp., McLean, VA 22102, U.S.A.

J. Peñano, Naval Research Laboratory, Washington, DC, 20375, U.S.A.

B. Hafizi, Icarus Research Inc., P.O. Box 30780, Bethesda, MD 20824-0780, U.S.A.

Abstract

It is widely known that the mode quality of the output of free-electron lasers (FELs) is near the diffraction limit. In this paper, we analyze the optical mode quality in FELs using the M^2 parameter, which is an optical analogue of the emittance for particle beams and measures the divergence of the optical mode. For a perfect Gaussian beam M^2 = 1 and increases as the mode quality deteriorates (*i.e.*, the divergence angle and the higher order mode content increase). Thus, the optical mode is often described as M^2 times diffraction limited in the far field. We show how M^2 may be calculated in two ways: (1) by a direct integration over the transverse mode structure, and (2) by allowing the mode to expand beyond the wiggler and analyzing the divergence. We then simulate a forthcoming experiment at Brookhaven National Laboratory using the MEDUSA simulation code and show that M^2, as expected, is near unity at saturation.

INTRODUCTION

It widely known that the mode quality of the output of free-electron lasers (FEL) is near the diffraction limit [1-3]. The question of mode quality is relevant to atmospheric propagation of high power FELs [4,5]. Numerical analysis has shown that the mode content in oscillators is predominantly in the TEM_{00} mode by solution of the paraxial wave equation for a fixed electron beam profile and the subsequent decomposition into Gaussian optical modes [1]. The optical mode quality was observed in the Los Alamos FEL oscillator [2,3] where the mode was shown to be near the diffraction limit. The mode quality in this experiment was characterized by a measurement of the Strehl ratio, which is defined as the ratio of the on-axis intensity at the mode waist to the intensity of a pure Gaussian mode (TEM_{00}) with the same spot size at the lens plane. However, the Strehl ratio is difficult to determine for optical modes that differ appreciably from a Gaussian. Higher order mode content is likely to be more important in single-pass FELs, such as Master Oscillator Power Amplifiers (MOPA) or Self-Amplified Spontaneous Emission (SASE) configurations that are operated past saturation. Hence, an alternate and less ambiguous measure of beam quality is desirable.

In this paper, we quantify beam quality by means of the M^2 parameter, which is an optical analog of the emittance for particle beams and provides a measure of the divergence of the optical mode [6-8]. It is equal to unity for a perfect Gaussian beam (pure TEM_{00}) and increases as the mode quality deteriorates (*i.e.*, the divergence angle of the mode and the higher order mode content increase). Thus, the optical mode is often described as M^2 times diffraction limited in the far field. The M^2 parameter, as well as optical mode distortion due to mirror heating was measured in the FEL oscillator experiment at Thomas Jefferson National Accelerator Facility [9]. This experiment produced average powers in excess of 2 kW at a wavelength of 3.1 microns. Measurements indicated beam quality near the diffraction limit with M^2 = 1.1 at the output mirror for powers up to about 350 W. As the power increased beyond 350 W, M^2 increased and reached values of about 2 for powers of 500 W. However, much of the increase in M^2 that occurred at higher power increased was attributed to mirror distortions and not the wave-particle interaction in the FEL. As a result, the mode quality may be improved in high-power oscillators using mirrors that compensate for distortions. Note that the mode quality in high-power amplifiers is governed solely by the FEL interaction.

In this paper we determine M^2 in two ways: (1) by a direct integration over the transverse mode structure, and (2) by allowing the mode to expand beyond the wiggler and analyzing the mode divergence. This is discussed in Sec. II. In Sec. III we study M^2 in FEL amplifiers using the MEDUSA simulation code [10,11] and then simulate a forthcoming experiment at the Source Development Laboratory at Brookhaven National Laboratory. A summary and discussion is given in Sec. IV.

THE M^2 PARAMETER

A perfect Gaussian beam experiences parabolic expansion in which the spot size increases on either side of the waist via [12]

$$w^2(z) = w_0^2 + \frac{\lambda^2}{\pi^2 w_0^2}\left(z - z_0\right)^2, \qquad (1)$$

where $w(z)$ is the spot size, w_0 is the minimum spot size (*i.e.*, at the waist), λ is the wavelength, and z_0 is the location of the waist. Note that the Rayleigh range is given by $z_R = \pi w_0^2/\lambda$ so that $w^2(z_0 \pm z_R) = 2w_0^2$ and the optical mode area increases by a factor of two over the course of the Rayleigh range. The asymptotic diffraction angle is given by $\tan\theta_D = \lambda/\pi w_0 = w_0/z_R$. Since the waist size is, typically, much less than the Rayleigh range, this means that $\theta_D \approx \lambda/\pi w_0$.

*Work supported by the JTO and ONR
#sprangle@ppd.nrl.navy.mil

A similar expression describing parabolic expansion also holds for a more general optical beam that includes higher order modes and can be written as [6-8]

$$W^2(z) = W_0^2 + M^4 \frac{\lambda^2}{\pi^2 W_0^2}\left(z - z_0\right)^2 , \qquad (2)$$

where the upper case W_0 corresponds to the average waist size for the overall optical beam, and

$$W^2(z) = 2\,\frac{\iint dxdyr^2 I(x,y,z)}{\iint dxdyI(x,y,z)} , \qquad (3)$$

denotes the spot size of the overall optical mode where $I(x,y,z)$ is the average (over a wave period) intensity. Observe that in the limit of a purely Gaussian optical beam, $W(z) = w(z)$ and $M^2 = 1$. As such M^2 (≥ 1) is a measure of the optical beam quality and is the optical analogue of the emittance for particle beams. Note also that this definition of M^2 can unambiguously deal with optical modes that differ markedly from a pure Gaussian, unlike the definition of the Strehl ratio. This asymptotic divergence angle θ_D is given by

$$\tan\,\theta_D = M^2\,\frac{\lambda}{\pi W_0} , \qquad (4)$$

so that $\theta_D \approx M^2\lambda/\pi W_0$ for small divergence angles. This is shown schematically in Fig. 1.

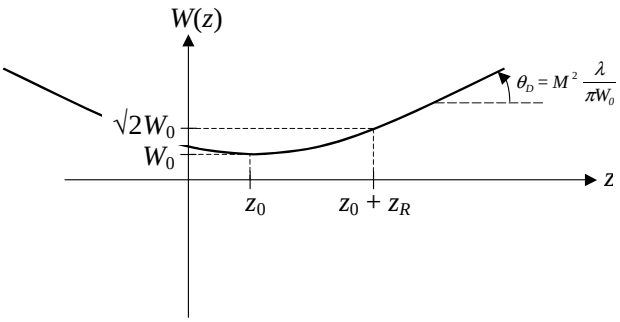

Figure 1: Schematic illustration of parabolic mode expansion

In general, the optical mode may be expressed as a superposition of Gauss-Hermite modes and we can write

$$\delta\mathbf{A}(\boldsymbol{x},t) = \hat{\boldsymbol{e}}_x \sum_{l,n} e_{l,n}(x,y)\left[\delta A_{l,n}^{(1)}\cos\,\varphi(x,t) + \delta A_{l,n}^{(2)}\sin\,\varphi(x,t)\right], \qquad (5)$$

where $e_{l,n}(x,y) = \exp[-r^2/w(z)^2]H_l[\sqrt{2}x/w(z)]H_n[\sqrt{2}y/w(z)]$, H_l is the Hermite polynomial of order l, $\varphi(\mathbf{x},t) = k_0 z - \omega t + \alpha(z)r^2/w(z)^2$ for wavenumber k_0 ($= \omega/c$) and angular frequency ω, and $\alpha(z)$ describes the curvature of the phase front. For propagation *in vacuo*, the amplitudes $\delta A^{(1,2)}$ are constant, φ is the overall phase, and the spot size and curvature vary as $w(z) = w_0[1 + (z - z_0)^2/z_R^2]^{1/2}$ and $\alpha(z) = (z - z_0)/z_R$. However, the optical mode in an FEL is both amplified and guided by the interaction with the electron beam so that the amplitudes, spot size and curvature will vary in a more complex way along the length of the wiggler. Nevertheless, it may be shown that the overall spot size is given in terms of this representation by

$$W^2(z) = w^2(z)\,\frac{S_2}{S_1} . \qquad (6)$$

where

$$S_1 = \sum_{l,n} 2^{l+n} l!n!\,\delta A_{l,n}^2 , \qquad (7)$$

$$S_2 = \sum_{l,n} 2^{l+n} l!n!\Big[(l+n+1)\delta A_{l,n}^2 + 2(l+1)(l+2)\left(\delta A_{l,n}^{(1)}\delta A_{l+2,n}^{(1)} + \delta A_{l,n}^{(2)}\delta A_{l+2,n}^{(2)}\right) + 2(n+1)(n+2)\left(\delta A_{l,n}^{(1)}\delta A_{l,n+2}^{(1)} + \delta A_{l,n}^{(2)}\delta A_{l,n+2}^{(2)}\right)\Big], \qquad (8)$$

and $\delta A_{l,n}^2 = \delta A_{l,n}^{(1)2} + \delta A_{l,n}^{(2)2}$. Observe that $S_1 = S_2$ for a pure Gaussian Mode (TEM_{00}) and we recover $W(z) = w(z)$.

We now discuss the calculation of the M^2 parameter. If we express the overall field in the form $\delta\mathbf{A}(\mathbf{x},t) = A(\mathbf{x})\hat{\boldsymbol{e}}_x\cos[k_0 z - \omega t + \theta(\mathbf{x})]$, then it may be shown that

$$M^2 = \left[\iint dxdyI\right]^{-1} \times \left\{\left(\iint dxdyr^2 I\right)\left(\iint dxdy\left[\left(\frac{\partial I^{1/2}}{\partial r}\right)^2 + I\left(\frac{\partial\theta}{\partial r}\right)^2\right]\right) - \left(\iint dxdyrI\,\frac{\partial\theta}{\partial r}\right)^2\right\}^{1/2}, \qquad (9)$$

where the intensity is $I = (\omega k_0/8\pi)A^2$. As a result, it can be shown that

$$M^2 = \frac{W^2(z)}{w^2(z)}\left[\frac{2w^2(z)}{W^2(z)} - 1 - \frac{S_3^2}{S_2^2} + \frac{S_4}{S_2}\right]^{1/2} , \qquad (10)$$

where

$$S_3 = 2\sum_{l,n} 2^{l+n} l!n!\Big[(l+1)(l+2)\left(\delta A_{l,n}^{(2)}\delta A_{l+2,n}^{(1)} - \delta A_{l,n}^{(1)}\delta A_{l+2,n}^{(2)}\right) + (n+1)(n+2)\left(\delta A_{l,n+2}^{(2)}\delta A_{l,n}^{(1)} - \delta A_{l,n}^{(2)}\delta A_{l,n+2}^{(1)}\right)\Big], \qquad (11)$$

$$S_4 = \sum_{l,l',n,n'} F_{l,l',n,n'}\left(\delta A_{l,n}^{(1)}\delta A_{l',n'}^{(1)} - \delta A_{l,n}^{(2)}\delta A_{l',n'}^{(2)}\right) , \qquad (12)$$

and

$$F_{l,l',n,n'} = \frac{1}{\pi}\int_0^{2\pi} d\theta \int_0^{\infty} d\rho\rho\exp\left(-\rho^2\right) \times\left[\cos\theta H_l'(\rho\cos\theta)H_n(\rho\sin\theta) + \sin\theta H_l(\rho\cos\theta)H_n'(\rho\sin\theta)\right] \times\left[\cos\theta H_{l'}'(\rho\cos\theta)H_{n'}(\rho\sin\theta) + \sin\theta H_{l'}(\rho\cos\theta)H_{n'}'(\rho\sin\theta)\right] , \qquad (13)$$

is a coefficient that depends only on the mode indices. In the limit of a purely Gaussian mode $S_1 = S_2$, $W(z) = w(z)$, and $S_3 = S_4 = 0$ so that Eq. (10) yields $M^2 = 1$ as expected.

In principle, if we know the modal decomposition at the exit from the wiggler in an FEL (including the mode amplitudes, the spot size w and the curvature α), then M^2 can be calculated for the output optical mode using the above method. However, if there is significant higher order mode content, then it can prove numerically arduous to evaluate the $F_{l,l',n,n'}$ coefficients. Therefore, it is useful to have an alternate technique for obtaining M^2. One such technique makes use of the expansion of the optical mode. If the spot size is known at three different locations beyond the end of the wiggler, then the three equations $W_i^2 = W_0^2 + M^4\theta_0^2(z_i - z_0)^2$ for $i = 1$–3 can be solved for M^2 where $\theta_0 = \pi W_0/\lambda$. Thus,

$$M^2 = \frac{\lambda}{\pi |z_i - z_0|} \sqrt{\frac{W_i^2}{W_0^2} - 1} \quad , \qquad (14)$$

for any choice of i, where

$$z_0 = \frac{z_3 + 2z_1 + z_2}{4} + \frac{z_3 - z_2}{4} \frac{(z_3 - z_1)(W_2^2 - W_1^2) + (z_2 - z_1)(W_3^2 - W_1^2)}{(z_3 - z_1)(W_2^2 - W_1^2) - (z_2 - z_1)(W_3^2 - W_1^2)} \quad , \qquad (15)$$

and

$$W_0 = \sqrt{W_1^2 + (z_1 - z_0)^2 \frac{(z_3 - z_1)(W_2^2 - W_1^2) - (z_2 - z_1)(W_3^2 - W_1^2)}{(z_3 - z_1)(z_3 - z_2)(z_2 - z_1)}} \qquad (16)$$

This technique can be applied either in experiment or simulation. When used in simulation (experiment), the optical mode must be allowed to propagate into free space and the overall spot size [(3) or (6)] must be calculated (measured) at three such points.

NUMERICAL ANALYSIS

For simulation purposes, we use the 3-D FEL simulation code MEDUSA [10,11] which can model planar or helical wiggler geometry and treats the electromagnetic field as a superposition of Gaussian modes (Hermite or Laguerre) and uses an adaptive eigenmode algorithm called the Source-Dependent Expansion [13] to self-consistently describe the guiding of the optical mode through the wiggler and which reproduces free-space diffraction in the absence of the wiggler. The field equations are integrated simultaneously with the 3-D Lorentz force equations for an ensemble of electrons. No wiggler-average orbit approximation is used, and MEDUSA can propagate the electron beam through a complex wiggler/transport line including multiple wiggler sections, quadrupole and dipole corrector magnets, FODO lattices, and magnetic chicanes.

The example under consideration is that of a seeded amplifier experiment to be conducted at the Source Development Laboratory at Brookhaven National Laboratory [14] that will operate at a wavelength of 0.8 microns using the VISA wiggler [15]. The electron beam will have an energy of about 72.3 MeV and a peak current of 300 A. The emittance and rms energy spread are 2.0 mm-mrad and 0.01% respectively. The VISA wiggler is a Halbach design using NdFeB magnets and incorporates a FODO lattice for stronger beam focusing. The wiggler period is 1.8 cm and the maximum on-axis field strength is 7.5 kG with a field error of 0.4% and a gap of 6.0 mm. The FODO cells have a length of 24.75 cm and each quadrupole has a length of 9.0 cm and a focusing gradient of 33.3 T/m. Hence, the separation between quadrupoles is 12.375 cm. The VISA wiggler was built in segments, and the wiggler to be used in the experiment will have 110 periods of uniform field strength. The photo-cathode drive laser is also used to provide the seed for the amplifier and can provide up to several tens of MW; however, this is larger than needed for the experiment that will use about 10-100 kW of seed power for saturation to be achieved within the length of the wiggler.

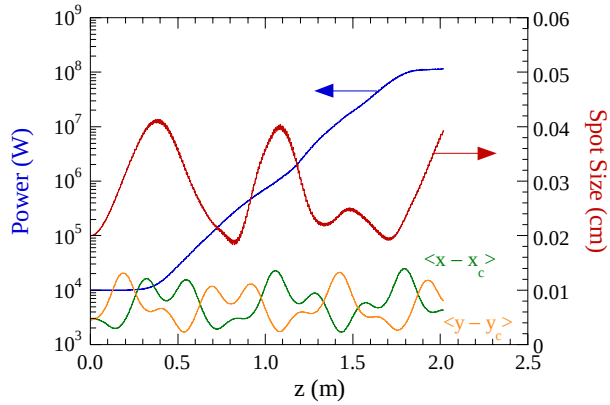

Figure 2: Evolution of the power, spot size and beam envelopes in the *x*- and *y*-directions.

The first case we consider makes use of 34 Gauss-Hermite modes and assumes a seed power of 10 kW. This yields saturation at the end of the wiggler at a power level of 115 MW. The evolution of the power, overall spot size of the optical mode, and the beam envelopes in the *x*- and *y*-directions is shown in Fig. 2. Observe that the beam is not perfectly matched into the wiggler/FODO lattice since the beam envelopes in the *x*- and *y*-directions vary in the FODO lattice and that the overall mode spot size expands and contracts with the beam envelope showing the optical guiding of the radiation; however, the guiding is not strong enough for the optical mode to follow all the variations in the beam envelope.

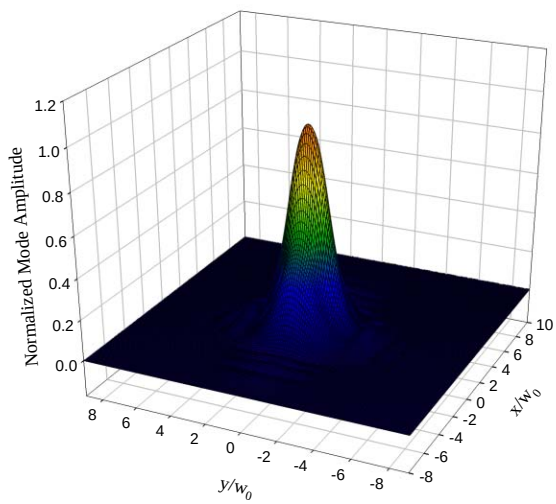

Figure 3: Transverse mode pattern at the wiggler exit for a seed power of 10 kW.

The use of 34 modes in the simulation means that very high order modes are included. Because of this the

method for calculating M^2 based on integration over the transverse mode profile is numerically arduous, and we choose rather to allow the mode to propagate beyond the end of the wiggler and use the three-point solution given in Eq. (14). This can be accomplished easily in simulation simply by terminating the wiggler, after which the Source-Dependent Expansion reproduces free-space propagation when the resonant wave-particle interaction ceases. The result of this calculation shows that $M^2 = 1.45$ for the optical mode at the wiggler exit. This is close to the diffraction limit as expected in FELs and corresponds to a near-Gaussian mode pattern as shown in a normalized transverse mode pattern in Fig. 3.

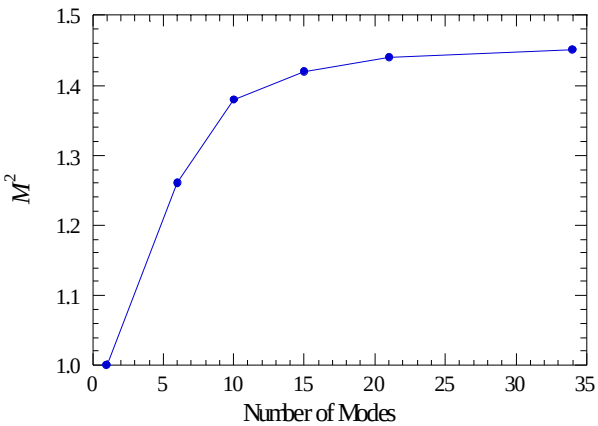

Figure 4: Variation in M^2 versus the number of modes included in the simulation showing convergence after about 20 modes.

An important issue in modeling the beam quality in FELs is the convergence of the simulation with respect to the number of modes in the superposition. The number of modes required to obtain reasonable values for the saturated power is generally smaller than that required to obtain an accurate determination of the optical mode quality as measured by M^2. For example, simulation using 6 Gauss-Hermite modes also yields a saturated power of 115 MW but the exponentiation length is somewhat shorter and $M^2 = 1.26$. Hence, it is important to determine the number of modes required to reach convergence. This is shown in Fig. 4 for these parameters where we plot M^2 versus the number of Gauss-Hermite modes in the superposition. It is clear from the figure that convergence is achieved using about 20-25 modes for $M^2 = 1.45$. It is important to bear in mind, however, that the number of modes required for convergence will vary with the specific parameters of interest. In particular, for optical guiding to be effective the exponentiation length must be shorter than the Rayleigh range. In general, the smaller the ratio between the exponentiation length and the Rayleigh range, the fewer the number of modes that will be needed to achieve convergence.

SUMMARY AND DISCUSSION

In summary, we have discussed the determination of M^2 in FELs by two methods. One is a direct calculation based upon the mode decomposition at any point within the wiggler, and the other relies on a three-point fit to the optical mode spot size as it propagates beyond the end of the wiggler. These techniques have been applied to an example that corresponds to an amplifier experiment at Brookhaven National Laboratory. We found that the simulation required a relatively large number of higher order modes to achieve convergence in the determination of M^2. While MEDUSA employs a Gaussian modal representation of the electromagnetic field, it is likely that this implies that alternate techniques using a transverse field solver will require a relatively fine mesh to achieve the same result. Further, the results indicate that the beam quality to be expected is near-diffraction limited when the wiggler length is comparable to the saturation length.

REFERENCES

[1] D.C. Qiumby and J. Slater, IEEE J. Quantum Electron. QE-19 (1983) 800.

[2] B.E. Newnam *et al.*, IEEE J. Quantum Electron. QE-21 (1985) 867.

[3] B.E. Newnam *et al.*, Nucl. Instrum. Meth. A237 (1985) 187.

[4] P.A. Sprangle, B. Hafizi, and J.R. Peñano, IEEE J. Quantum Electron. 40 (2004) 1739.

[5] P.A. Sprangle, J.R. Peñano, and B. Hafizi, J. Directed Energy (to appear 2006).

[6] A.E. Siegman, Proc. Soc. Photo-Opt. Instrum. Eng. 1224 (1990) 2.

[7] T.F. Johnson, Jr., Laser Focus World 26 (1990) 173.

[8] A.E. Siegman, IEEE J. Quantum Electron. 27 (1991) 1146.

[9] S.V. Benson, J. Gubeli, and M. Shinn, Nucl. Instrum. Meth. A483 (2002) 434.

[10] H.P. Freund *et a*l., IEEE J. Quantum Electron. 36 (2000) 275.

[11] H.P. Freund, Phys. Rev. ST-AB 8 (2005) 110701.

[12] A.E. Siegman, *Lasers* (University Science Books, Mill Valley, CA, 1986).

[13] P.A. Sprangle, A. Ting, and C.M. Tang, Phys. Rev. A 36 (1987) 2773.

[14] T. Watanbe *et al.*, "Design study of a compact megawatt class FEL amplifier based on the VISA undulator," presented at the 27th Int'l. Free Electron Laser Conference, Stanford, CA, 21-26 August 2005.

[15] R. Carr *et al.*, Phys. Rev. ST-AB, 4 (2001) 122402.

SEEDING THE FEL OF THE SCSS PROTOTYPE ACCELERATOR WITH HARMONICS OF A TI: SA LASER PRODUCED IN GAS.

G. Lambert, M. Bougeard, W. Boutu, B. Carre, D. Garzella, M. Labat, CEA, Saclay, France
M.E. Couprie, O. Chubar, Synchrotron Soleil, Saint-Aubin, France
G. Lambert, T. Hara, H. Kitamura, T. Shintake SPring-8/RIKEN Harima Institute, Hyogo, Japan.

Abstract

A particular seeded configuration will be tested in 2006 on the SCSS prototype accelerator (SPring-8 Compact Sase Source, Japan). This facility is based on a thermionic cathode electron gun (1 nC), a C-band LINAC (5712 MHz, 35 MV/m) and an in-vacuum undulator (15 mm of period. 2 sections of 4.5 m length). The maximum electron beam energy is 250 MeV and the SASE emission from visible to 60 nm can be obtained. The external source, coming from the High order Harmonic Generation (HHG) process, can be tuned from the 3rd (266 nm) to the 13th harmonic (60 nm) of a Ti: Sa laser generated in a gas cell. The experiment contains a first chamber, dedicated to harmonic generation and a second one for harmonic beam diagnostics and adaptation of the harmonic waist in the first undulator section. The tests have been performed in Saclay (15 mJ, 10 Hz, 50 fs). An energy of 2 μJ with a high stability for the 3rd harmonic and a good transversal shape with an optimized energy level and a high stability for the 13th harmonic have been obtained at the first undulator center place. The performances using analytical formulas, GENESIS and SRW have been updated. The chambers will be installed on the SCSS prototype accelerator in the beginning of October for the seeding tests.

INTRODUCTION

These last years, most of the new FEL sources were dedicated to the so-called Self Amplified Spontaneous Emission (SASE) [1], which provides with a very high brightness photon beam at short wavelength but with limited temporal coherence. Consequently, a few FEL facilities, like ARC-EN-CIEL (Accelerator Radiation Complex for Enhanced Coherent Intense Extended Light) a French proposal for a 4th generation light source [2], have adopted a new configuration: a seeding configuration, in which High order Harmonics of a laser Generated in gas (HHG) are injected into a FEL, giving its full coherence property to the emitted radiation. It also reduces the saturation lengths allowing a more compact source [3]. In addition, other SASE projects have decided to implement it on their facility: SCSS prototype accelerator (SPring-8 Compact Sase Source) [4] and SPARC (Sorgente Pulsata e Amplificata di Radiazione Coerente) [5]. Recently such a seeding experiment with high harmonics produced in gases was performed in an X-ray laser [6]. It is proposed here to seed the FEL of the SCSS prototype accelerator at a 60 nm radiation, corresponding to the 13th harmonic of a Ti: Sa laser (H13) generated in a gas cell. June, the first lasing of the SCSS prototype accelerator FEL [7] has been observed at 49 nm. The characteristics of the electron beam, undulators, laser and harmonics come from ref. [8] and the basic layout is given in Figure 1.

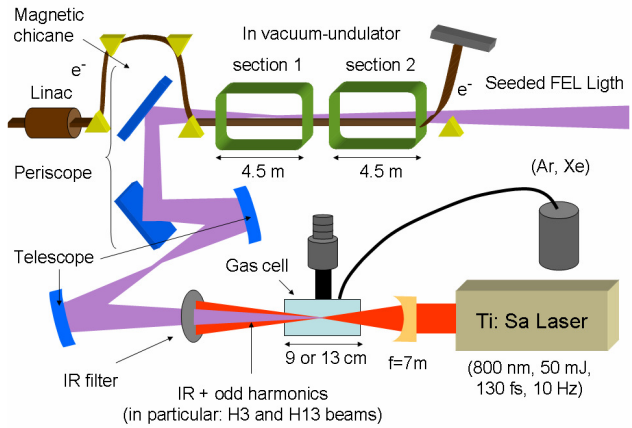

Figure 1: General layout of the seeding experiment with harmonics generated in a gas cell.

HHG SYSTEM

The harmonic generation in gas results from the strong non linear polarization induced on the rare gases atoms, such as Ar, Xe, Ne and He, by the focused intense electromagnetic field E_{Laser} of a "pump" laser [9]. In our case, a 7 m focal length lens focuses a Ti: Sa laser in a cell (Figure 2) filled with Xe or Ar gases, which are well-adapted for the generation of 60 nm radiation. The laser passes through the cell and is aligned by means of two pinholes of 1 mm of diameter, made on Tantalus plates, which create a constant leak of gas.

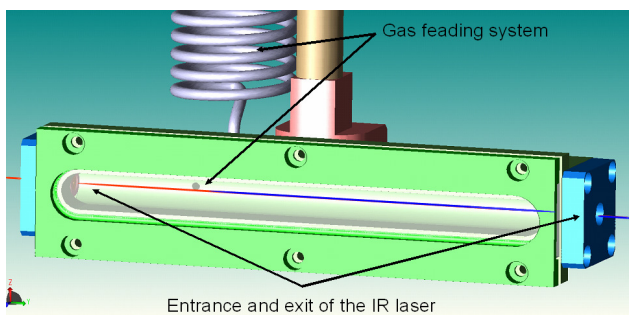

Figure 2: Gas cell system producing HHG light.

The general experiment is based on a system of two chambers (Figure 3).

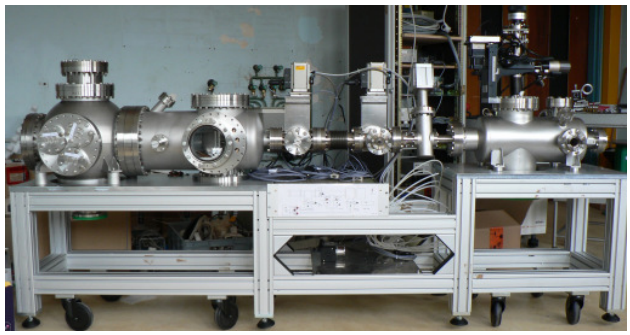

Figure 3: General layout of the HHG system.

The first one is dedicated to the HHG production (Figure 4). The cell position is motorized for accurate alignment of the IR laser and optimization of the harmonic production rate.

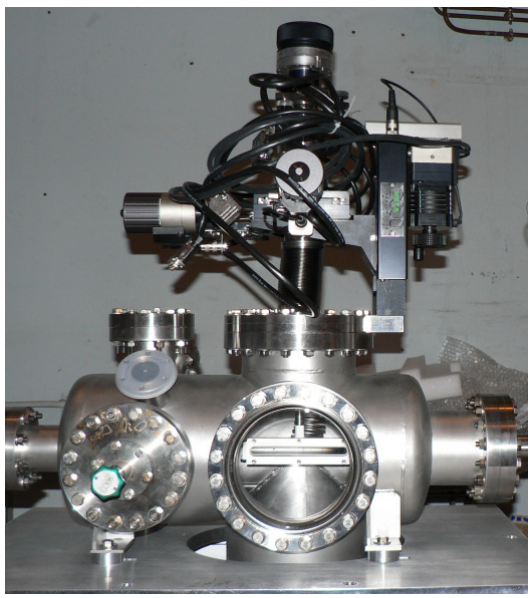

Figure 4: HHG chamber with gas cell and motorization system.

The second one (Figure 5) has been designed for adjusting the harmonic beam at the focusing point in the first undulator section by means of two SiC spherical mirrors. A periscope system is used to align the harmonic beam with the e-beam.

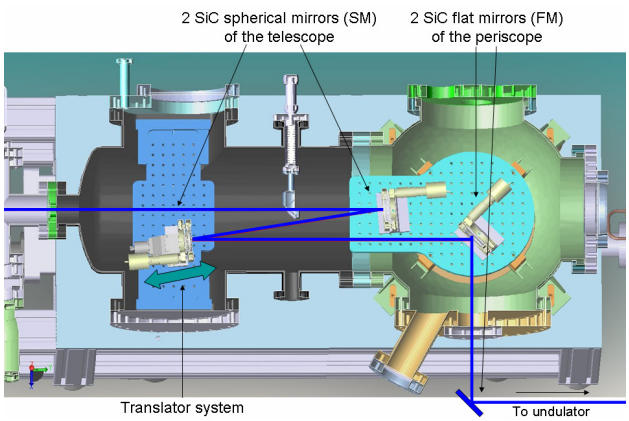

Figure 5: Refocusing system and periscope.

FIRST HHG TESTS IN SACLAY

The first tests have been performed in Saclay with the LUCA laser beam (1 to 15 mJ, 20 Hz, 50 fs, 5 m long of focal lens). In the starting phase of tests, the seeding wavelength was the 3rd harmonic (H_3, 266 nm), which is a more intense and easily useable source (can be propagated outside vacuum, and detected with a VUV photomultiplier). The behavior of the harmonics (Figure 6 for the 3rd harmonic) in operation is mainly optimized with the IR beam diameter (a), power, focusing position in the cell and the gas pressure (b). The respective optimal values, in the test configuration, are 20.8 mm, 115 mW, 4 cm before the cell center and 5 10^{-3} mbar in the first chamber.

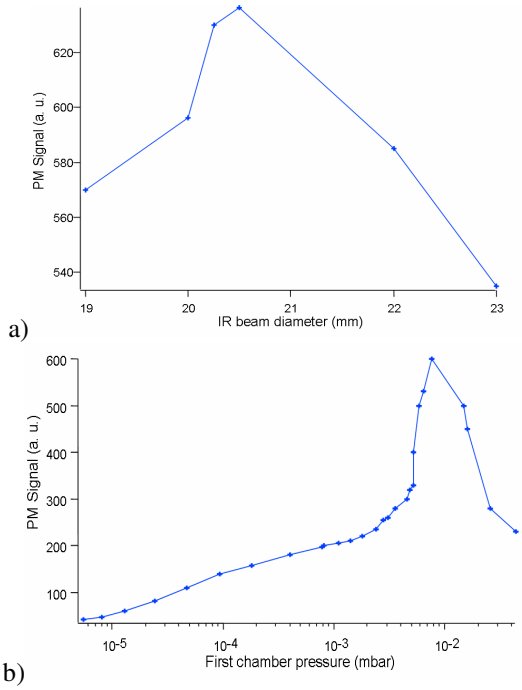

Figure 6: Optimization of the 3rd harmonic flux, generated in a 9 cm cell filled with Ar gas, with the Hamamatsu PM R759, as function of the IR beam diameter (a) and of the gas pressure in the first chamber (b).

The transverse profiles (Figure 7) of the 3rd harmonic, observed with a VUV CCD camera (COHU solid state camera) are quit similar to a Gaussian fit.

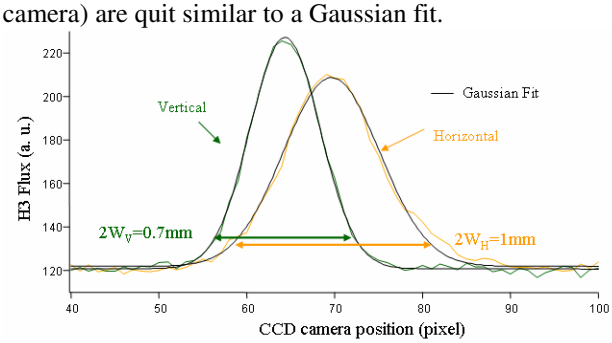

Figure 7: Horizontal and vertical profiles of the 3rd harmonic, at the theoretical focusing point in the first undulator section.

Figure 8 shows the influence of the gas pressure on the optimum of the flux on the two different harmonics.

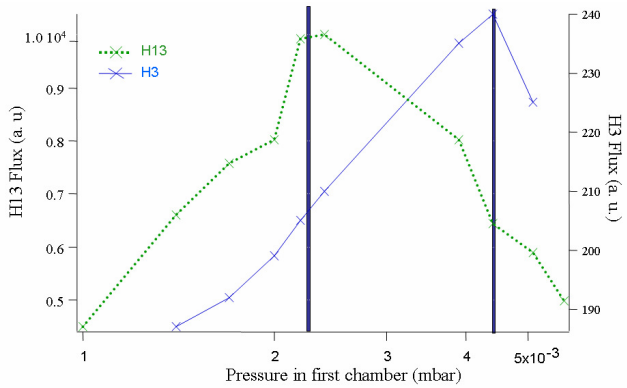

Figure 8: Comparison between optimization of 3rd and 13th harmonics (resp. H3 and H13) as function of the pressure inside the gas cell (proportional to the first chamber pressure)

The shape of the 13th harmonic can be observed (Figures 9 a and b), 3 m after the cell corresponding to 8 m before the theoretical focusing point in the first undulator section. A Micro-Channel Plate (MCP, Hamamatsu F2221) was used with a phosphor screen (P43) associated to a CCD camera and placed after a Sn filter (eliminating the IR laser and selecting especially the 13th harmonic). The beam section presents some light aberrations particularly visible in the horizontal profile. These latter must be really more important in the first undulator section, where the interaction occurs with the e-beam (the overlapping can be decreased of 15%), but can be compensated using a toroidal mirror.

a)

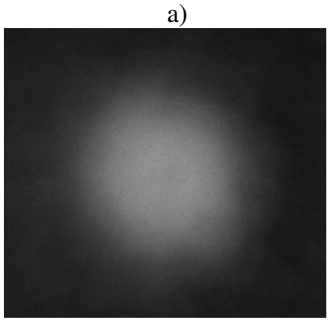

b)

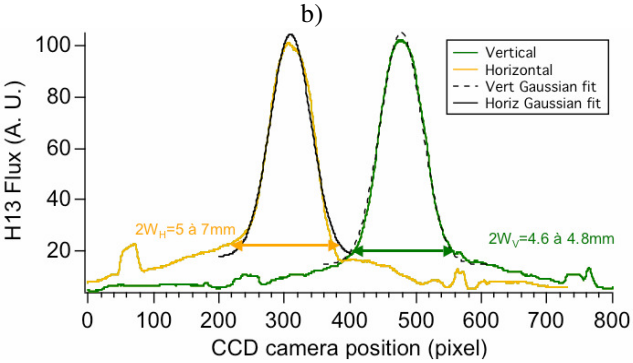

Figures 9 a and b: Transverse section (a) and profiles (b) of the 13th harmonic, 3 m after the cell but 8 m before the theoretical focusing point in the first undulator.

IMPLANTATION ON THE SCSS PROTOTYPE ACCELERATOR

The harmonic generation experiment will be located in the SCSS prototype accelerator tunnel, together with the accelerator and the undulator sections, between the chicane and the shielding wall (Figure 10). The focusing of an intense IR laser comes from the laser hutch, on the opposite side of the shielding wall. The Ti: Sa laser is based on a Tsunami mode-locked oscillator, a Spitfire regenerative chirped-pulse amplifier and a Coherent multipass amplifier and delivers more than 50 mJ at 100 fs. On an optical table, the IR beam is adapted for harmonic generation optimization and synchronized with the e-beam.

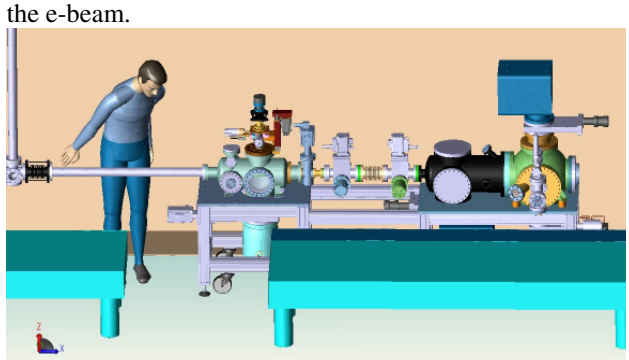

Figure 10: Location for the HHG experiment on the SCSS prototype accelerator.

The laser waist propagation in horizontal (x) and vertical (y) (W_{ox} and W_{oy}) has been calculated [10] to evaluate the geometrical aberrations caused by the two spherical mirrors at the theoretical focusing point in the first part of the first undulator section. Correlated to the e-beam transverse sections, the filling factor (measuring the overlapping of the two beams) can be calculated and is then implemented in our simulation codes (see next section). Figures 11 a and b present the focusing of the IR beam and the 13th harmonic vertical and horizontal propagations, which are quite similar until the focusing part, where the geometrical aberrations lead to a difference of 35 cm in the focusing position between the vertical and horizontal propagations. (b) is a zoom of (a) with the implementation of the e-beam dimensions [8].

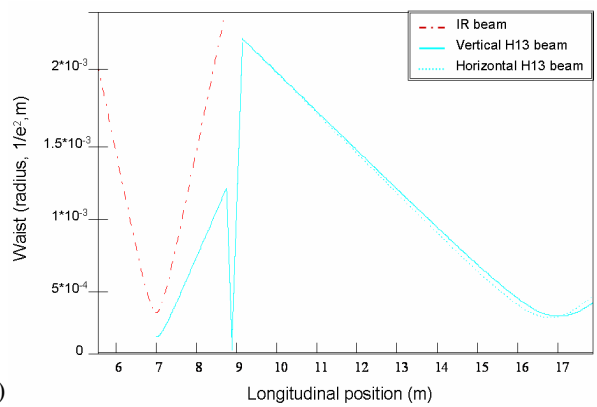

a)

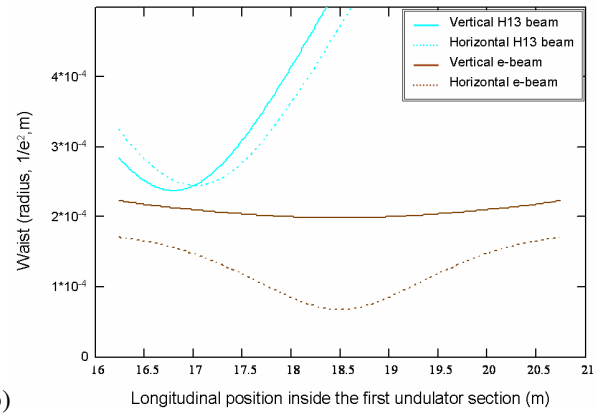

b)

Figure 11: a) propagation of focused IR laser and the 13th harmonic, b) focusing inside the first undulator section and overlapping with the e-beam.

SIMULATIONS

New calculations (with ref. [8] characteristics) with SRW [11], analytical expressions from G. Dattoli [12] and Genesis [13] (respectively Figures 12 a, b and c), have been performed for comparing the SASE and the seeding configuration, with 20 kW of seed (corresponding to a slightly pessimistic value of what can be expected). The different simulations converge very well to a similar evolution. First, the saturation peak power levels are very similar (10^8 W). Second, the saturation length for the SASE case is about 10.5 m (10^7 W at 9 m) for all the simulations but varies from 6m to 7.5 m in the seeding case.

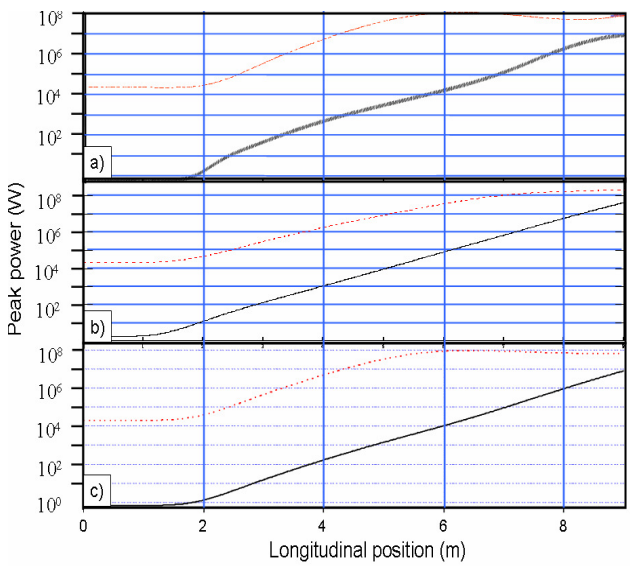

Figures 12 a, b and c: Comparison between SASE (black plain line) and seeding configuration (red dash line) with a) SRW b) analytical expressions and c) Genesis.

CONCLUSIONS

Using state-of-the-art High Order Harmonics in gas for seeding a FEL appears very interesting, because the seed radiation is fully coherent and tunable in the VUV-XUV range. Moreover, it reduces the saturation lengths in a more compact source. From the HHG part, the experiment has been perfectly designed and optimized for producing harmonics and especially the 13th. New tests will be performed in situ (near SCSS area in September) with a more performing vacuum system, a more powerful laser system and with different optical characteristics, allowing to still increase the harmonic production and to completely test remote control system before installing it inside the accelerator tunnel for the seeding experiment (October).

REFERENCES

[1] F. Ciocci et al, IEEE Jour. Quant. Elec. 31 (1995) 1242.
[2] G. Lambert et al., Proceedings SPIE 2005, San Diego, USA, 31 July-4 August 2005.
[3] G. Lambert et al., Proceedings FEL 2004, 155-158, Trieste, Italy, 29 August-3 September 2004.
[4] http:\\www-xfel.spring8.or.jp
[5] L. Giannessi et al., Proceedings EPAC 2006, 95-98, Edinburgh, 26-30 June 2006.
[6] Ph. Zeitoun et al., Nature 431, 426-429 (23 Sep 2004). Letters to nature.
[7] T. Shintake, Proceedings EPAC 2006, 2741-2743, Edinburgh, 26-30 June 2006.
[8] G. Lambert et al., Proceedings EPAC 2006, 44-47, Edinburgh, 26-30 June 2006.
[9] P. B. Corkum, Phys. Rev. Lett. **71** (1993) 1994.
[10] G. Lambert et al., Proceedings FEL 2005, San Francisco, USA, 20 –26 August 2005.
[11] O. Chubar and P. Elleaume, http://www.esrf.fr/Accelerators/Groups/InsertionDevices/Software/SRW
[12] G. Dattoli, P. L. Ottaviani and S. Pagnutti, J. Appl. Phys. 97, 113102 (2005).
[13] Sven Reiche, http://pbpl.physics.ucla.edu/~reiche/

SEEDING THE SPARC TEST FACILITY WITH HARMONIC GENERATION IN GASES: PRELIMINARY TESTS OF THE HARMONIC GENERATION IN GAS CHAMBER

O. Tcherbakoff, M. Labat, G. Lambert, D. Garzella, M. Bougeard, P. Breger,
P. Monchicourt, H. Merdji, P. Salières, B. Carré, CEA, DSM/SPAM, 91191 Gif-sur-Yvette, France
M.E. Couprie, SOLEIL, 91192 Gif-sur-Yvette, France
A. Doria, L. Giannessi , ENEA C.R. Frascati, Italy.

Abstract

A coherent short wavelength source can be realised with a Free Electron Laser by using High Gain Harmonic Generation configuration. The injection of an external light source in the first part of an undulator results in a coherent light emission in its second part. The SPARC FEL (Frascati, Italy), delivering an electron beam at 200 MeV passing through an undulator of 6 sections, can be configured to test such schemes. We propose to use High order Harmonic Generation (HOHG) in gases process as the seed. HOHG produces a coherent XUV source by focusing an intense laser pulse into a gas medium. This beam, composed of odd harmonics of the fundamental laser, is then shaped using a telescope of two spherical mirrors, allowing the focusing at a given position, in the SPARC undulator. Appropriate tuning of the undulator gaps will amplify the 3rd and 5th harmonics seeded, and non-linear harmonics of those wavelengths, allowing the perspective of producing VUV coherent radiation. The chambers for harmonic generation and shaping have been realised and tested at the CEA (Saclay, France). We present these tests.

INTRODUCTION

Along the last few years, other Free Electron (FEL) schemes than the common Self Amplified S neous Emission (SASE) [1] have been proposed to ge intense and short pulse duration in XUV domain. I Gain Harmonic Generation (HGHG) configuration an external seed, a laser source, induces energy modu of the relativistic electrons in the modulator, leadir coherent emission of the microbunched electron be the radiator at the n^{th} harmonics of the laser funda wavelength. The harmonic radiated is selected tuni undulator gap. The properties of the output radiati determined by the seed laser and can thus inherit degree of temporal coherence. Seeded FEL amplifi eration in combination with harmonic generation ha demonstred experimentally in midinfrared and VU main [4, 5].

A way to reach shorter wavelengths is to use a seed laser in VUV domain. Development in femtosecond laser technology have made possible to imagine new coherent short wavelength sources. One of these sources, called High Order Harmonics Generation (HOHG), is based on the interaction between the laser beam and a gas target [6, 7]. Microjoule energies can be obtained at wavelengths down to 50 nm [8, 9]. It has been proposed to use HOHG as seed to inject an undulator, either in the amplifier or in the HGHG configuration [10]. HOHG seem to be a very good candidate to seed FEL cascade, to extend the operating wavelength of FELs down to sub nm. The SPARC configuration will allow the study of the problems related to the injection of an external radiation seed in a single pass FEL and the analysis of the coupling efficiency of the electron-photon beams in terms of the input parameters [11].

EXPERIMENTAL SETUP FOR THE HARMONIC CHAMBERS

SPARC undulator is composed of 6 sections of 75 periods each. The e-beam energy may be varied up to 150-200 MeV. A Coherent femtosecond laser which delivers 120 fs, 2.5 mJ pulse with a central wavelength at 800 nm and a modified repetition rate of 10 Hz, generates HOHG in a gas jet. The VUV radiation is then injected into the undulator by means of a magnetic chicane. Electron and photon

the undula-

llow to test

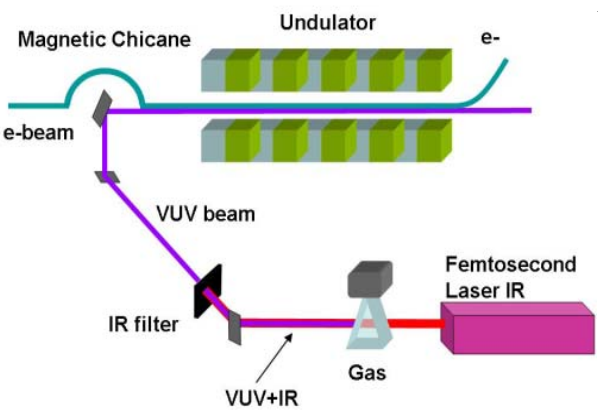

Figure 1: Experimental layout to seed harmonics generated in gas into FEL.

HIGH ORDER HARMONIC GENERATION

HOHG is obtained by focusing an intense laser pulse into a rare gas medium. The atoms of the gas medium are irradiated and ionized by the strong laser field, releasing free electrons with no kinetic energy. Those electrons are then accelerated by the laser electric field. When the electric field sign changes, the electrons can be driven back in the vicinity of the parent ions, and if a collision occurs, the extra-energy of the ion-electron recombination is released by emitting a photon. New frequencies are created and, after the gas medium, one can observe odd high order harmonics of the fundamental frequency co-propagating with the fundamental laser beam. This VUV radiation also exhibits an excellent spatial and temporal coherence [14, 15, 16]. The coherence properties of the harmonics are similar to those of the fundamental laser beam which make them suitable for seeding experiment.

The setup for the production of the harmonics in gas is mainly composed of two chambers. The laser is focussed by a plano-convex lens (f=2 m) and delivered through an antireflecting coated 790 nm window in the first chamber where HOHG occurs. Then, 1.5 meters downwards, the second chamber is used to adapt the waist, i.e. the harmonic beam mode in the middle of the first undulator for a correct overlap with the e-beam. This shaping is performed using two spherical mirrors reflecting nearly at normal incidence, both equipped with motorized mounts, and an additional translation stage under the second mirror, for the adaptation of the focusing point in the undulator. The distance between the gas jet and the middle of the first undulator is about 8 m. A scheme of the experimental setup is given in Figure 2.

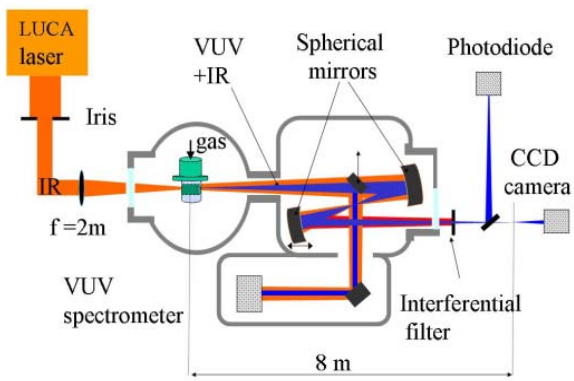

Figure 2: Experimental setup

CHARACTERISATION OF THE HHG PRODUCED IN CEA-SACLAY

In order to prepare the seeding experiment on SPARC facility, the chambers for harmonic generation have been tested during two months at the CEA-Saclay (see Figure 3). The radiation generated in the chambers passes through an interferometric filter centred at 266 nm (H3) eliminating IR beam as well as other harmonics. The 266 nm radiation is then detected with a calibrated VUV photodiode blinded for diffused IR light.

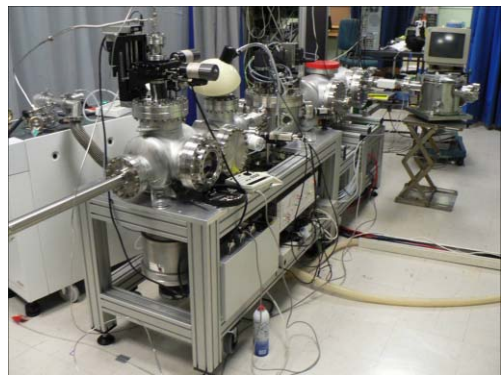

Figure 3: Picture of the chambers being tested at CEA-Saclay.

The femtosecond laser system (LUCA) of the Saclay Laser-matter Interaction Center (SLIC) has been used as fundamental source for the tests. The characteristics of this laser based on 2 TW, 20 Hz CPA Titanium:Sapphire System [17] are given in Table . Both duration and energy of the laser pulse were tunable: several tests were performed using a 2.5 mJ - 120 fs laser pulse in order to work in similar conditions as the one expected on SPARC facility.

Table 1: Characteristics of the laser system LUCA used for the tests. The pulse duration was measured using autocorrelator, assuming a gaussian profile.

Laser characteristics	Value	Unit
Wavelength	800	nm
Spectral width	20	nm
Pulse duration	56.8	fs
Energy	50	mJ
Beam diameter	35	mm

The initial configuration foreseen for harmonic generation, a simple gas jet with an aperture of 0.5 mm and no additional nozzle, allowed a very small amount of UV photons to be produced. To reach a better conversion factor, the geometry was improved through out the testing of four different configurations: Jet and vertical guide, Jet and horizontal guide, Static Cell and finally Pulsed Cell. The increasing performances are summarized in Figure 4. In the Pulsed Cell configuration, the gas is injected in a 1 cm long-windowless cell by bursts of 1.3 μs through an electromagnetic valve synchronized with the incoming laser pulses. A conversion factor of 10^{-3} was obtained as regularly acheived in recent experiments. A good stability was also reached, as well as a nearly perfectly gaussian harmonic beam.

The first step to optimize the harmonic yield was to con-

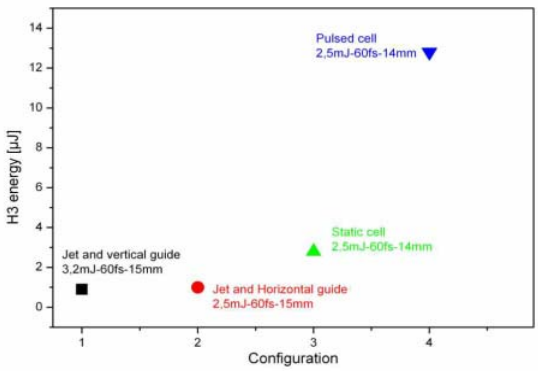

Figure 4: Energy obtained on the third harmonic using different interaction medium configurations.

trol the laser aperture and the cell focus position[18, 19]. Closing an iris placed before the lens means decreasing the energy laser and increasing the focal spot size, therefore decreasing the focal intensity. As illustrated in Figure 5 with 2.5 mJ laser energy in Argon gas, a larger aperture is needed in case of a long pulse duration: 14 mm (resp. 18 mm) for 60 fs pulse (resp. 120 fs chirped laser pulse). The energy contained in each pulse remains unchanged, and fixed to 2.5 mJ. The optimum at 60 fs corresponds to a focal spot diameter of 340 μm, and at 120 fs of 279 μm; both leading to an intensity of $2 \times 10^{14}\ W/cm^2$. The reduced spot diameter at 120 fs involves less medium in the laser-matter interaction, resulting into a lower energy emission (less photons are produced).

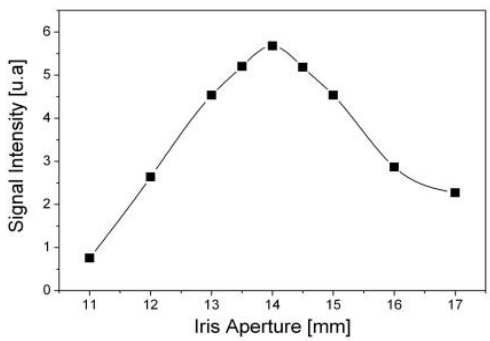

Figure 5: Aperture size dependence of H3 in Argon with 2.5 mJ laser energy for two pulse durations.

Figure 6 illustrates the third harmonic dependency in the cell position. The maximum efficiency has been reached when the focusing point of the laser beam was 1.5 cm after the cell.

Figure 7 illustrates the influence of the pressure on the 3rd harmonic signal. The amount of UV photons produced increases with the backing pressure. No optimum could be reached, since the electromagnetic valve was limiting the available pressure in the cell.

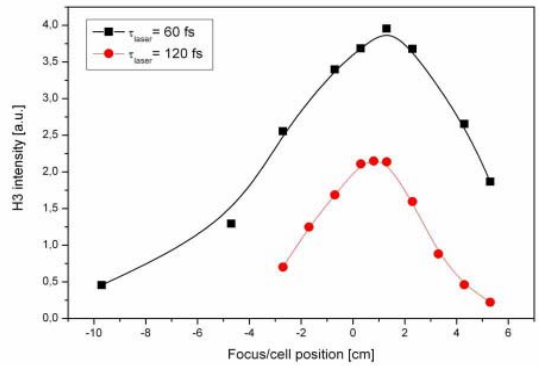

Figure 6: Cell position dependence of H3 in Argon with 2.5 mJ laser energy, for two pulse durations.

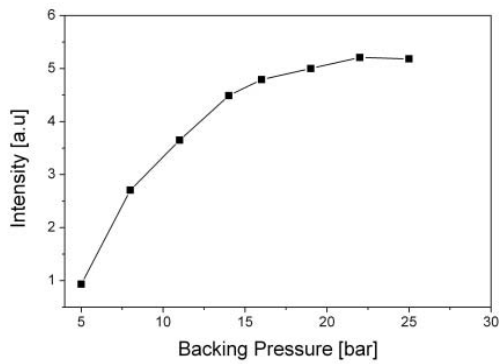

Figure 7: Pressure dependence of H3 in Argon.

The number of 3rd harmonic photons generated in the optimized conditions with 60 fs pulse is 1.3×10^{13} (9,7 μJ) and the corresponding conversion efficiency reaches 4×10^{-3}. In the same conditions, when 3rd harmonic is generated by a chirped 120 fs pulse, the number of photons decreases by factor 4.

We used a VUV spectrometer composed of a LiF prism and a photomultiplier to measure H3 and H5 with an entrance pinhole of 5 mm. Scanning on the prism angle being manual, we only measured maximum signal at one position of the prism angle for H3 and H5 allowing the coarse comparison of the relative contribution of each harmonic, as illustrated in Figure 8.

The harmonic beam propagation has also been studied. It is crucial for evaluating the overlap between the light wave and the electron bunch in the undulator. The harmonic beam is shaped using two concave mirrors optimized for 266 nm wavelength with respectively a focal length of 200 mm and 150 mm. The distance between the two mirrors is about 38 cm. The incidence angle of 2° induces small geometric aberrations. The total transmission for 3rd harmonic is 90 %. The spatial profile of the 3rd harmonics has been measured using a CDD camera. Figure 9 shows the evolution of H3 from the exit of the chambers through out the undulator, and Figure10 shows the transverse pro-

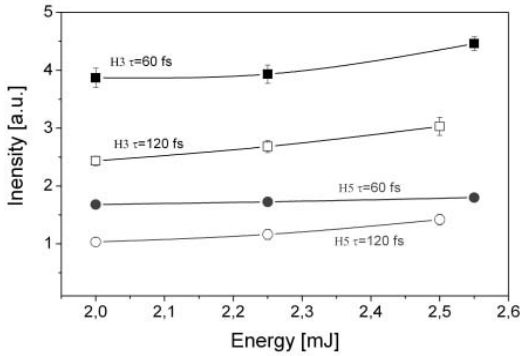

Figure 8: 3rd and 5th harmonics in argon as function of energy laser for two pulse widths.

file of the harmonic at focusing point. The focal spot size is about 940 μm. The theoretical fit with a quasi-gaussian beam [20] gives a M^2 value of 1.6 and a 3rd harmonic size of 220 μm at generation point . With these measurements, we will able to determine the filling factor which takes into account the interaction between electrons and photons.

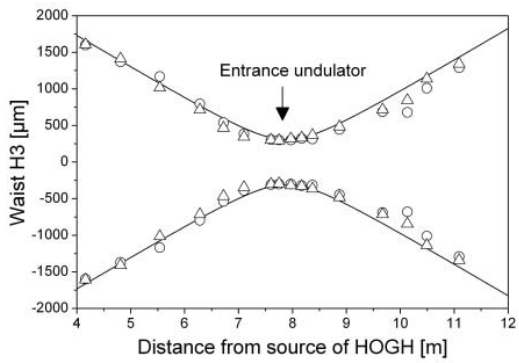

Figure 9: Longitudinal evolution of the beam waist of the 3rd harmonic in vertical (△) and horizontal (○) direction. In solid line indicate the quasi-gaussian beam fit.

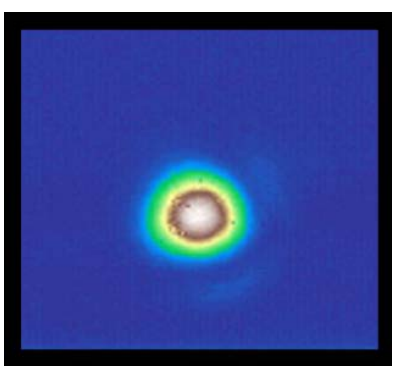

Figure 10: Transverse profile of the 3rd harmonic at focusing point

CONCLUSION

The results of the preliminary tests performed at CEA-Saclay on the chambers are encouraging. An efficient geometric configuration has been defined for the generating medium. According to those first measures, the laser system foreseen at SPARC (120 fs, 2.5 mJ) should be adapted for generation of both 3rd and 5th harmonics with HOHG. We expect more than 4μJ on the 3rd harmonic in Argon. The telescope system focuses the 3rd harmonic beam, which is slightly astigmatic, at the estimated entrance of the first undulator with a focus waist size of 300 μm.

The peak power of this coherent VUV light was estimated to be 19 MW. Calculations with PERSEO and with GENESIS 1.3 code have shown that saturation can be reached with SPARC undulator, using a 266 and 160nm wavelength seed with only a few kW power [11].

The harmonic chambers should be transported to SPARC facility by the end of January 2007. After implementation on the linear accelerator modules, in spring 2007, first seeding experiments of SPARC FEL with this scheme should start.

ACKNOWLEDGMENTS

This work was supported by the EU Commission in the Sixth Framework Program, Contract No. 011935-EUROFEL.

REFERENCES

[1] S.V. Milton *et al.*, Science **92**, 2037 (2001).

[2] L.H. Yu, P.R.A. **44**, 5178 (1991).

[3] I. Ben-Zvi *et al.*, Nucl. Instrum. Methods Phys. Res. Sect. A **304**, 181 (1991).

[4] L.H. Yu, Science. **289**, 932 (2000).

[5] L.H. Yu *et al.*, P.R.L. **91**, 074801 (2003).

[6] M. Ferray *et al.*, J. Phys. B: At. Mol. Opt. Phys. **21**, L31 (1988).

[7] A. McPherson *et al.*, J. Opt. Soc. Am. B **4**, 595 (1987).

[8] J.F. Hergott *et al.*, Phys. Rev. A **66**, 21801 (2002).

[9] E. Takahashi, N. Y., and M. K., Opt. Lett. **27**, 1920 (2002).

[10] D. Garzella *et al.*, Nucl. Instrum. Methods Phys. Res. Sect. A **528**, 502 (2004).

[11] L. Poletto *et al.*, FEL Conference, 63 (2005).

[12] L. Giannessi *et al.*, www.sparc.it ref:SPARC-FEL-05/004.

[13] L. Poletto *et al.*, proceedings EPAC 2006 (unpublished).

[14] T. Ditmire *et al.*, Phys. Rev. Lett. **77**, 4756 (1996).

[15] L. Le Déroff *et al.*, Phys. Rev. A **61**, 43802 (2000).

[16] L. Bellini *et al.*, Phys. Rev. Lett. **81**, 297 (1998).

[17] http://www-femtodrecam.cea.fr/slic/luca/luca1.htm.

[18] P. Balcou *et al.*, J. Phys. B **25**, 4467 (1992).

[19] T. Ditmire *et al.*, Phys. Rev. A **51**, R902 (1995).

[20] A. E. Siegmann, "Lasers", University Science Books.

THE ARC-EN-CIEL FEL PROPOSAL

M. E. Couprie, C. Bruni, O. Chubar, J.M. Filhol, A. Loulergue, L. Nahon, Synchrotron SOLEIL, Saint-Aubin, France
B. Carré, D. Garzella, O. Gobert, P. Hollander, M. Labat, G. Lambert, P. Monot, O. Tcherbakoff, CEA-DSM-DRECAM Service de Photons, Atomes et Molécules, Gif-sur-Yvette, France
G. Petite, CEA-DSM-DRECAM Service des Solides Irradiés, Gif-sur-Yvette, France
P. Bosland, G. Devanz, M. Jablonka, M. Luong, F. Méot, A. Mosnier, B. Visentin, CEA-DSM-DAPNIA Service de Accélérateurs de la Cryogénie et du Magnétisme, Gif-sur-Yvette, France
J. R. Marquès, Lab. d'Utilisation des Lasers Intenses, École Polytechnique, Palaiseau, France
J. M. Ortega, H. Monard, Laboratoire de Chimie-Physique, Univ. Paris-Sud, Orsay, France
A. Rousse, Laboratoire d'Optique Appliquée, École Polytechnique, France.

Abstract

ARC-EN-CIEL (Accelerator-Radiation for Enhanced Coherent Intense Extended Light) aims at providing the user community with coherent femtosecond light pulses covering from UV to soft X ray in France. It is based on a CW 1.3 GHz superconducting linear accelerator delivering high charge, subpicosecond, low emittance electron bunches at high repetition rate. Phase 1 exploits the different sources of seeding with 220 MeV at 1 kHz, in particular High order Harmonic generation in Gas (HHG), to improve the longitudinal coherence and shorten the output radiation wavelength in a rather compact device. Phase 2 is based on a CW 10 KHz 1 GeV superconducting linear accelerator for HHG seeded High Gain Harmonic Generation (HGHG) extending to 1 nm. In phase 3, fs undulator sources in the IR, VUV and X ray and a FEL oscillator in the 10 nm range will be implemented on two ERL beam loops for beam current or energy enhancement.

INTRODUCTION

France is now equipped with a third generation synchrotron light source under commissioning [1] at Saint-Aubin, close to Paris. The Storage Ring consists in a 357 m circumference ring, with 16 cells and 24 straight sections, out of which up to 21 will house insertion devices (ID). High brilliance radiation, from the VUV up to the hard X ray domain will be provided to external users in 2007 with the low emittance (3.7 nm.rad) beam at the 2.75 GeV. Innovative ID's are under construction to provide the best possible performances in a wide energy range (5 eV to 50 keV) [2].

Prospects concerning the Fourth Generation Light Source in France are based on the ARC-EN-CIEL project [3], following a long tradition in FEL in France, in particular in storage ring based FELs (ACO [4], Super-ACO [5]) and on infra-red LINAC based FELs (CLIO [6], ELSA [7]). After considering the installation of an FEL in the VUV on SOLEIL in the oscillator or coherent harmonic generation configurations, it was decided to propose an independent LINAC based dedicated facility providing coherent radiation down to 1 nm, for easier access of the users. The possible implementation of the first and potentially second phase of ARC-EN-CIEL in the former tunnel of the Accélérateur Linéaire de Saclay, at l'Orme des Merisiers, next to SOLEIL, would make a very attractive acclerator based light source complex.

From the beginning, the project aims at developing a strong synergy between the FEL and the laser communities, leading to couple the electron beam and lasers. The innovative choice of seeding the FEL with High order Harmonic produced in Gas, at a high repetition rate leads to a significant shortening of the wavelength of the seed, in addition to the advantages of seeding with respect to SASE (pulse to pulse intensity stability, reduction of jitter, compactness, enhanced longitudinal coherence). Indeed, more than 70% of the users intend to perform pump-probe experiments and a high stability is requested, confirming the choices of seeding and High Gain Harmonic Generation, as discussed in the frame of the user workshop "Applications of VUV X fs tunable sources combining accelerators and laser: "slicing" at SOLEIL and the ARC-EN-CIEL project" (Feb. 3-4 2004, Orsay). Besides, propositions of plasma acceleration and Thomson scattering emerged from the laser-electron beam combination.

The request of high repetition rate (1-10 kHz) in order to couple as efficiently as possible the electron beam with the high harmonics produced in gas led to the choice of a superconducting type of Linear Accelerator. Expertise exits in DAPNIA in CEA and in SOLEIL with the superconducting RF cavity. A high repetition rate of the photon source is also desirable for users. A 100 fs pulse corresponds to the typical demand.

ARC-EN-CIEL is planned into three phases: a first phase reaching an energy of 220 MeV for HGHG sources in the VUV, a phase 2 at 1 GeV with HGHG sources down to 1 nm using High Harmonics produced in gas, and a phase 3 including two recirculation loops, for Energy Recovery or energy enhancement where undulators (12 m long, period 30 and 20 mm) are installed, providing subpicosecond radiation in the VUV and X ray ranges (5.10^{12} phot/s/0.1%bw for 0.1 mA average current). In addition, a 0.1-1 kW average power, 0.1-1 % bandwidth FEL oscillator, installed in the first loop, could cover the 120-10 nm, thanks to recent development of multilayer

mirrors for lithography, and SiC mirrors in normal incidence. Harmonics can also be produced from the FEL oscillator, with 500 MW at 4.5 nm and 10 MW at 2.7 nm. The beam at 2 GeV from the loop will allow shortening further the radiation wavelength down to 0.4 nm with an additional undulator section. Expected radiation from ARC-EN-CIEL is illustrated in figure 1, comparing radiation of its three phases with respect to the insertion devices of SOLEIL. THz radiation will also be provided. The present work, part from the detailed analysis of the components of the project, is concentrating on the progress on several key elements.

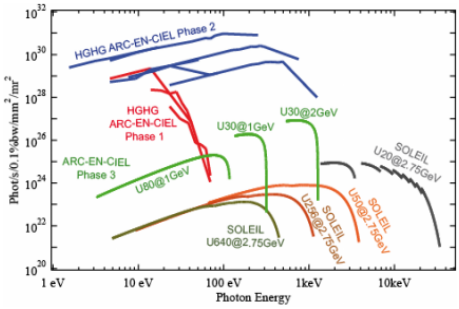

Figure 1 : Peak brilliance. Phase 1 : HGHG radiation + seeding wavelength, P_{seed} = 100 kW for HHG harmonics n°7-9, 600 kW for n°3-5. 1 kA, F= 0.1. Phase 2 :HGHG radiation 1.5 kA, 1.35 π mm.mrad, 0.0004% slice energy spread, 200 fs, beta=2 m, F = 0.088. Phase 3 : spontaneous emission of undulators of period 30 and 80 mm calculated with SRW. Undulator period length in mm in ID name.

THE ACCELERATOR

The gun

The choice of the gun is not completely defined. It should provide 1 nC for 2πmm.mrad total emittance ε. At the beginning, we have considered a Zeuthen photo-injector [8], with a CsTe cathode, to be modified for operation at 1 KHz. This requires a coupler modification with respect to the present design. The active removal of the power can be performed via a phase inversion during falling time. A longer term system is based on a superconducting gun, as presently developed by Rossendorf [9], where emittance compensation and reliability can still be an issue. We also thought about the adaptation of the CeB6 thermo-ionic gun developed at RIKEN for the SCCS project, and the recent very spectacular results in terms of beam stability and emittance [10] bring us to go further in the analysis of this solution for ARC-EN-CIEL. Besides, R&D is going on the cathode materials in LSI (Polytechnique) with the use of Carbon nanotubes.

The cryomodules

ARC-EN-CIEL is based on TESLA type cavities at 1.3 GHz, to be operated in CW mode. The elliptical 9-cell cavities routinely provide 25 MV/m accelerating gradient, while recent advances in the cavity design and integration procedures indicate the possibility of pushing the gradient to 35 MV/m, which is a target parameter for the International Linear Collider. The design of the cryomodule may be revisited for a better cryogenic efficiency accounting for the CW operation.

Studies concerning the compensation of the microphonics are presently under way at CEA-DAPNIA and BESSY [11]. The microphonics have been analysed with appropriate techniques and different compensation schemes are elaborated using active piezoelectric tuners. However, the large number of the transverse mechanical eigen-modes of the cavity represents a strong limitation for the compensation. A passive damping of these modes by a careful design and mounting of the cavity-tuner system in the cryomodule would alleviate the complexity of the active compensation scheme and improve its efficiency.

The electron beam dynamics

Calculations performed for ARC-EN-CIEL phase 1 accelerator consider an RF gun, a first cryomodule bringing the energy to 100 MeV, a third harmonic cavity compensating the non linearity of the longitudinal phase space, a S-chicane compressor, and a second cryomodule raising the energy to 220 MeV. 6 additional modules are included in phase 2. ASTRA [12] is used to simulate the RF gun and the cavity modules, and CSRTrack code [13] for the compression scheme, taking into account Coherent Synchrotron Radiation in the chicane.

Figure 2a presents the evolution of the different emittances along the bunch compressor. The total emittance is raised to 2.7 πmm.mrad in the compression process through the chicane (from 2.1 to 0.1 mm/ 300 fs rms). With an adequate electron beam optics [14], the slice emittances along the bunch remain almost unchanged (ranging from 0.7 to 1.1) with a small mismatch from slice to slice. The compressor creates a correlated emittance that reaches 0.18 π mm.mrad, betraying a spread of the slices in the transverse phase space. It is the main contribution to the total emittance increase by strong mismatching.

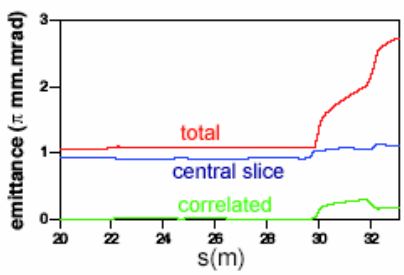

Figure 2 : Evolution of the emittance along the chicane. Chicane parameters: total length: 10 m, R56=0.15 m, dipole length : 0.3 m. First dipole at s=23 m.

The influence of the laser pulse length on the optimization of the different emittances while keeping a constant space charge density was also investigated. A longer laser pulse is favorable in the compressor, for avoiding emittance degradation due to coherent synchrotron radiation, the longitudinal wake function being proportional to $\sigma_l^{-4/3}$, with σ_l the beam length.

Although the output bunch is also compressed down to 300 fs, its mean length through the chicane is longer and the emittance is smaller. In order to avoid beam degradation due to non linear part of the R_{566} coefficient, the voltage of the harmonic cavity has to be increased to give an invert sign of the non linear component. For longer laser pulse and longer electron beam length before the chicane, the energy variation is more important and the deformation of phase space is larger (see fig. 3). Systematic simulations done for different pulse lengths (20-40 ps range) and harmonic cavity voltages (20-25 MV/m range), keeping the final bunch length constant at 0.1 mm bring to a minimum of the total emittance for E_H=22 MV/m. In Fig. 4, one finds at the end of the S-chicane, a minimum total emitance at 2.1 π mm.mrad for the laser pulse length σ_l=25 ps. The total emittance globally increases with the laser pulse length apart for σ_l=20 ps, for which it is higher. The central slice emittance decreases with the laser pulse length (radial laser spot reduction). Further studies concern the pre-injection in the case of the thermo-ionic gun (SCSS type) will be studied, calculations for the phase 2, including the second bunch compressor and for phase 3 with ERL loops.

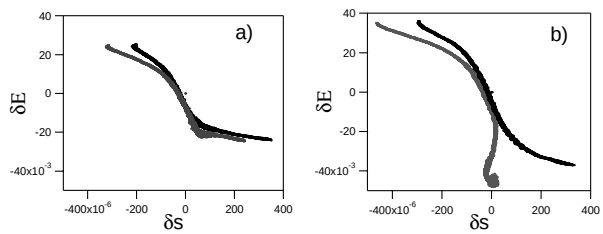

Figure 3 : Longitudinal phase space representation for a laser pulse length of a) 20ps, b) 40 ps for different voltages of the harmonic cavity. Black (resp. grey): E_H=22 (resp. 20)MV/m.

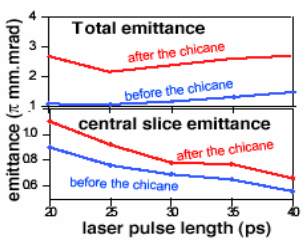

Figure 4 : Emittance evolution versus the laser pulse length.

THE LASER SYSTEM AND SYNCHRONISATION

The laser system

One passive mode locked Ti:Sa based oscillator is foreseen, delivering 1 W at 76 MHz repetition rate (around 13 nJ /pulse). This will feed three independent high power, multiple repetition rate, laser systems.

The first system, devoted to the photo-injector should provide ~50-100 µJ pulse energy in the UV (266 nm), producing a 1 nC electron beam following interaction with a photocathode with 1 % quantum efficiency. Special attention will be paid to the laser beam transverse features (dimensions and shape) for preventing the electron beam emittance increase [15]. A laser amplifier delivering at least 1 mJ in the IR (800 nm), followed by a regenerative amplifier and single pass preamplifier, both pumped by a 15 W Q-switched solid state laser can be adopted. Very highly efficient third harmonic generation will be performed with an ultra short pulse (~50 fs) on a sufficiently thin nonlinear crystal (BBO), in order to reduce pulse distortion. A prism or gratings based UV stretcher will bring the duarton up to 20 ps.. Transverse and longitudinal measurement as well as shaping of the laser pulse call for a complete setup including a DAZZLER system [16] in the IR, spectral interferometric techniques (either self-referencing, like SPIDER [17] or not), a beam transverse filter and deformable mirror with high dynamics. Such approaches are under study on the CEA-SLIC servers LUCA (20 Hz) and PLFA (1 kHz) [18]. Recent promising developments by FASTLITE [19] of a Dazzler operating in the UV domain Dazzler, should allow a direct shaping of the laser beam issued by THG process. Otherwise, we intend to develop brand new solutions for a dedicated UV regenerative amplifier, based on the amplification and Kerr properties of crystals like Ce^{3+}:$LiCaAlF_6$ [20].

The second one, a broadband system, includes non linear processes like Optical Parametric Amplification, Third and Fourth Harmonic Generation (THG, FHG) and HHG, for two color pump-probe based experiments. It is based on Chirped Pulse Amplification (CPA) technique, on a basis of a 10 mJ, kHz or multi-kHz system, in which a 4-pass amplifier is injected with the beam issued a first regenerative amplifier. The first two systems will operate at a multi-kHz rate, while the third will be limited to few Hz (eventually few tens of Hz).

The third laser system will deliver high energy (1 J), short duration pulses and will be mainly devoted to plasma acceleration and Thomson scattering.

The synchronisation

The synchronisation of the RF and the master clock in respect to the femtosecond time scale taking into account the natural pulse-to-pulse jitter for a Ti:Sa oscillator of a few tens of fs lead to adopt a frequency-stabilized laser oscillator. Care will be devoted to minimize the intrinsic jitter encountered by the e- beam through its travel in the accelerator to the wiggler. The jitter between the different laser branches distributed on relatively long distance (~ 100 m) should also be reduced and environmental contributions such as slow thermal drift should be lowered. Moreover, unlike the accelerator beneficing of the vacuum technique, inherent jitter sources along the complex laser system (stretcher /compressor pair, regenerative /multipass amplifiers, thermal lensing…) is under study in CEA-SPAM. Measurement of the synchronisation between the laser pulse and the electron is a key issue, the development of the electro-optical measurement has been set-up on the ELYSE gun at LCI (Orsay). The first step of measurements leads to a resolution of 250 fs.

THE LIGHT SOURCES

The undulators

ARC-EN-CIEL phase 1 plans to use a 20 mm period in-vacuum hybrid undulator as a modulator (50 periods), and a 30 mm Apple-II undulator as a radiator (400 periods). Identical sections of modulator and radiator will be added for the second phase of ARC-EN-CIEL (4 to 8 m for the modulator, and 4 sections of 4 m for the radiator). Such undulators are currently developed for SOLEIL third generation facility.

The choice of such radiator type undulators follows estimations of magnetic performance of an Apple-II type undulator with a small period based on magnetostatic calculations performed using the Radia computer code [21]. The expected horizontal and vertical peak fields of an Apple-II at 30 mm period and 6 mm vertical gap are Bx = Bz ≈ 0.63 T; corresponding to the effective deflection parameter K ≈ 2.5 (see fig. 5).

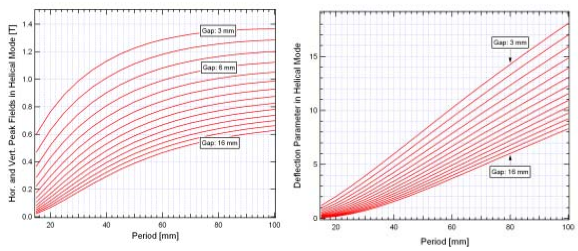

Figure 5. Peak magnetic fields (left) and deflection parameters (right) as functions of period of an Apple-II undulator in helical mode at different vertical gaps. Calculations done for NdFeB magnet blocks with remnant magnetization of 1.22 T and transverse dimensions 30 mm x 30 mm, horizontal gap between movable and fixed magnet arrays : 1 mm.

Seeding with High Harmonics generated in gas

Collaborations have been set up for demonstrating the feasibility to seed a LINAC based FEL with HHG on SCSS phase 1 in Japan [22] and on SPARC in Italy [23]. Tests of the chambers and of the optical transport have been performed this year with the Luca laser, and seeding will be performed at SCSS on fall 2006 and in summer 2007 on SPARC. This will provide an experimental demonstration of the concept for ARC-EN-CIEL. FEL radiation based on analogous systems for ARC-EN-CIEL is calculated using PERSEO 1D code [24] with a gain reduction due to the filling factor [25] and recently compared with GENESIS1.3 [26] integrated in a new test version of SRW [27] allowing the wavefront to be transported in the beamline to the user sample (see fig. 6).

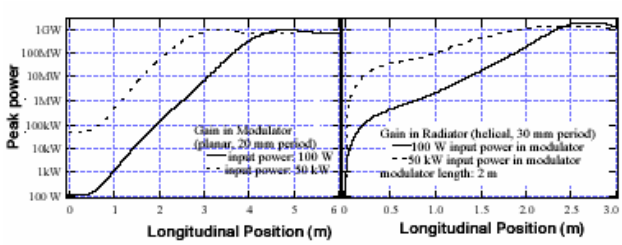

Figure 6: Steady-state GENESIS simulations for ArcEnCiel phase 1, 1 – 1 HGHG scheme, 266 nm seed: a) gain in modulator, b) gain in radiator (30 mm period helical mode).

ACKNOWLEDGMENTS

The support given by EUROFEL contract No 011935 is acknowledged, and to ANR. The authors thank L. Giannessi for fruitful discussions.

REFERENCES

[1] J. M. Filhol et al, JACoW, EPAC'06, Edinburg, June 2006, p. 2723, http://www.jacow.org.
[2] F. Briquez et al, JACoW, EPAC'06, Edinburg, June 2006, p. 3556.
[3] M. E. Couprie et al, JACoW, FEL'05, Stanford, August 2005; M.E. Couprie et al, Proceed. SRI 06, Daegu, May 2006, M. E. Couprie et al, JACoW, EPAC'06, Glasgow, June 2006, p. 53, M.E. Couprie et al, EPAC 04, 55.
[4] M. Billardon et al, Phys. Rev. Lett. 51, (1983) 1652.
[5] M. E. Couprie et al., Phys. Rev. A . 44(2), (1991) 1301.
[6] R.Prazeres et al Phys. Rev. Lett. 78(11), 2124-2127 (1997).
[7] P. Guimbal et al, Nucl. Inst. Meth. A 341 (1994) 43.
[8] D. Dwersteg et al , NIM. A393, 93 (1997).
[9] R. Xiang et al, PAC 2005.
[10] T. Shintake et al, EPAC'06, Edinburg, p 2741 ; Togawa et al, APAC2004, Gyeongju, Koera, March 2004.
[11] M. Loung et al., JACoW, EPAC'06, Edinburg, June 2006, p. 3167, Kugeler et Neumann, EPAC06, p. 408, G. Devanz et al., EPAC'06, p. 378.
[12] K. Flottman, "ASTRA, a space charge tracking algorithm", http://www.desy.de/~mpyflo
[13] M. Dohlus, T. Limberg, "CSRtrack", http://www.desy.de/xfel-beam/csrtrack/index.html
[14] M. Dohlus and T. Limberg,. PAC 2005, p 1015.
[15] C. Limborg and P. Bolton, NIMA 557 (2006), pp 106-116.
[16] F. Verluise et al., JOSAB, n° 17 (2000), pp. 138-145).
[17] C. Iaconis and I.A. Walmsley, IEEE Jour. Quant. Elec. 15 (4), April 1999 pp. 501-509.
[18] D. Garzella et al., this conference.
[19] N. Forget et al., "Direct Pulse shaping of ultraviolet pulses by an AOPDF", presented at CLEO/QELS 2006.
[20] Liu et al., Opt. Lett, Vol.26 n°5 (2001), pp. 301-303.
[21] P. Elleaume, O. Chubar, J. Chavanne, "Computing 3D Magnetic Field from Insertion Devices", PAC97 1997, 3509.
[22] G. Lambert, this conference.
[23] O. Tcherbakoff, this conference.
[24] Luca Giannessi, PERSEO, www.perseo.enea.it
[25] W. Colson P. Elleaume Appl. Phys. B 29, (1982)10.
[26] GENESIS 1.3, http://pbpl.physics.ucla.edu/~reiche/
[27] SRW, ESRF-SOLEIL collaboration http://www-sources.synchrotron-soleil.fr:8002/mid.software

THE PROPERTIES OF THE FEL OUTPUT FOR SELF SEEDING

J. Bahrdt, BESSY, Berlin, Bart Faatz, Rolf Treusch, Deutsches Elektronen-Synchrotron (DESY), Hamburg, Velizar Miltchev, Hamburg University (Uni HH) Institut fuer Experimentalphysik, Ruben Reininger, ruben@sas-rr.com.

Abstract

Several seeding schemes, like self seeding for FLASH or seeded HGHG cascades for BESSY soft X-ray FEL, are proposed for existing or planned free electron laser facilities. The simulation of these schemes requires the detailed knowledge of the properties of the seeding radiation and the implementation of these properties in the codes. Time dependent simulations with the 3D code GENESIS calculate the electric field distribution in and at the end of the undulator. The physical optics code PHASE permits the propagation of wave fronts across grazing incidence optics. Using the combination GENESIS PHASE GENESIS, the properties of the FEL output for different seeding schemes can be obtained. For example, the radiation quality of a SASE FEL can be improved in a self seeding scheme. Here, the radiation is monochromatized after a first undulator section and seeded to the second undulator modules. We present simulation studies for the self seeding option of FLASH.

INTRODUCTION

Synchrotron radiation beamlines at 3rd generation storage rings are generally optimized with ray tracing codes which are based on geometrical optics. This is justified as long as the radiation is incoherent. Coherent radiation has to be propagated with physical optic codes which describe the coherent properties of the light. FELs, the 4th generation light sources, are built to produce transversally and longitudinally coherent radiation in the wavelength regime down to 1Å.

X-ray FEL facilities based on the SASE principle are under construction at various places [1-3]. Since the SASE is a random process the longitudinal distribution of the light pulse as well as the spectrum is spiky.

Using a coherent seed pulse the FEL output can hence significantly be improved. The cascaded HGHG FEL scheme uses the coherent properties of the seed laser and transforms these properties through several stages to the required wavelength regime where no seeding laser is available [4,5]. The radiation properties degrade with the number of stages involved. Therefore, it is advantageous to start with a rather short seeding wavelength which can be produced by high harmonic generation (HHG) [6] in order to reduce the number of stages.

Self seeding is another approach to improve the spectral properties of the FEL [7]. The SASE radiation is passed through a monochromator which filters out the central frequency. This radiation is used as a seed for the following undulators.

It has also been shown that the output power of a cascaded HGHG FEL can be enhanced if the radiation of the first stage is monochromatized before transportation to the next one [8].

These examples demonstrate that there is no strict separation between FEL undulators and monochromators. They have to be described in a closed form, instead. In this paper we demonstrate for the example of the self seeding option of FLASH the necessity for a three dimensional and time dependent description of the propagating coherent radiation within the undulators and the monochromators.

THE PHYSICAL OPTICS CODE PHASE

The propagation of wavefronts in free space is usually done using Fourier optics techniques [9]. Depending on the geometry one of three propagators can be applied:

i) In the near field approximation the electric field distribution is expanded in plane waves, the plane waves are propagated by multiplication with a complex factor and the result is back transformed to real space.

ii) In the far field approximation the image distribution is composed of the contributions from individual point sources.

iii) In the very far field the field distribution equals the angle distribution in the source plane (apart from a constant factor).

Optical elements can be introduced into this formalism in the following way: The electric field is propagated to the center of the optical element with Fourier optics. Then, the wavefront is propagated over the optical element using a ray tracing technique which takes into account the phase differences. Then, the wavefront is further propagated with Fourier optics methods (ZEMAX, GLAD [10,11]).

The code PHASE, written at BESSY, is based on another technique, the stationary phase approximation [12] which will be briefly explained.

The following equation correlates the electric fields in the source and the image plane.

$$\vec{E}(\vec{a}') = \int h(\vec{a}', \vec{a}) \cdot \vec{E}(\vec{a}) \cdot d\vec{a}$$

The integration is done over the source plane and the propagator $\vec{h}$ has the form:

$$h(\vec{a}', \vec{a}) = \frac{1}{\lambda^2} \int_{Surface} \frac{\exp(ik(r+r'))}{rr'} \cdot b(w,l) \cdot \cos(\alpha) \cdot dw \cdot dl$$

r, r' are the distances between the source / image plane and the optical element, b is the obliquity factor

and the integration extends over the optical element surface. Each point in the image plane requires the evaluation of a four dimensional integral. Each additional optical element adds another two dimensions in the integral and it is obvious that the expressions can not be evaluated within reasonable time without certain assumptions. The stationary phase approximation uses the fact that the optical path length changes quadratically with the optical element coordinates in a region close to the principle rays (extremum of the optical path). The integration over the optical element coordinates can be done analytically if the beam is not scraped at that element and hence, the dimensions of the integral can be reduced from six to four.

All expressions (coordinates, path length, scaling factors etc.) are expanded up to fourth order in the coordinates and angles of the initial plane. Using these expansions the transformation of cross products of coordinates and angles can be derived as well. Using these cross terms the transformation over one element can be expressed via a 70x70 matrix. The combination of several optical elements is done simply by the multiplication of the individual matrices.

In principle the complete beamline can be described with one single matrix for each term as long as the photon beam does not hit an aperture. In case of a monochromator at least two runs are required: i) propagation from the initial plane to the exit slit and ii) propagation from the exit slit to the image plane.

Monochromatic light is assumed during the propagation. For time dependent simulations, the input data have to be Fourier transformed and the individual frequencies have to be propagated one after the other. The results are again Fourier transformed yielding the time dependent fields at the exit of the monochromator.

All equations have been derived with the algebraic code REDUCE [13] and the basic code has been produced automatically. For more details on the algorithm we refer to [12].

THE SELF SEEDING OPTION OF FLASH

The basic setup of the self seeding option is illustrated in Figure 1. It consists of two undulator stages separated by a magnetic chicane and a monochromator. The first undulator operates as a SASE FEL in the linear regime. After it the electrons are separated from the SASE radiation. The electron beam passes through the magnetic bypass that is used to remove the longitudinal charge density modulation (micro bunching). The radiation pulse is spectrally filtered in a high resolution grating monochromator and afterwards is superimposed with the electron beam at the entrance of the second undulator. Thus the monochromatic photon beam serves as a coherent radiation seed, which is amplified up to saturation in the second undulator. The self seeding technique increases the spectral brilliance significantly i.e. the output power of the seeded FEL is concentrated in a single line which is orders of magnitude narrower than the spectrum of the conventional SASE FEL. The concept of the self seeding has the advantage that it is independent of any external radiation source and the seed is naturally synchronized with the electron bunch.

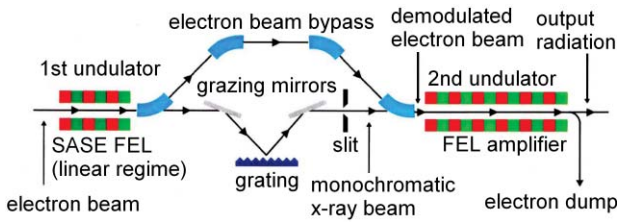

Figure 1: Schematic layout of the self seeding setup.

THE MONCHROMATOR

The seeding requirements for energy resolution, unity magnification, and only vertical deflections have been addressed [14] with a beamline (Figure 2) based on a spherical varied-line spacing grating (SVLSG).

The monochromator includes a plane mirror and three SVLSG (in the same spherical substrate) covering the energy range 6-64 nm. The plane mirror illuminates the grating at the correct angle of incidence such that the monochromator magnification is close to unity. In addition, each grating is designed to perfectly focus the beam along the dispersion (vertical) direction at the exit slit at two energies in its range, and to zero the coma aberration at one energy.

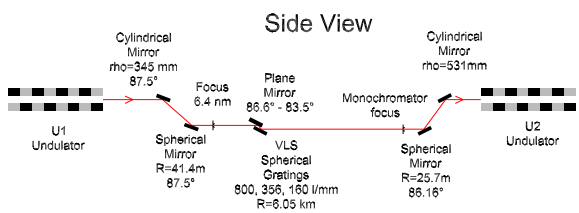

Figure 2: Seeding monochromator.

The pre and post focusing optics include four optical elements. The first and last optical components are two sagittally focusing cylinders that provide the unity magnification along the horizontal direction. The demagnification along the dispersion direction onto the entrance slit is performed with a spherical mirror. A spherical mirror after the exit slit magnifies the entrance slit width such that the size and divergence at the entrance of the second undulator overlaps with the electron beam for maximum amplification.

SIMULATIONS

Time dependent simulations for the first undulator at a carrier frequency of 60nm have been performed using GENESIS [15]. The standard FLASH undulator geometry has been assumed, where the electron beam is kicked in order to avoid saturation within the 15m undulator length which is required for shorter

wavelengths [16]. The total length over which the SASE interaction takes place is about 6.5 m, which is enough to reach a power level of about 0.2 GW. This value is well below saturation, but high enough to guarantee that after monochromatization the power is several orders of magnitude above shot noise. Electric fields for 560 slices (121x121 grid points) separated by 540nm provide the full information of the radiation pulse. The frequency resolution after Fourier transformation is determined by the length of the total pulse to be transformed. For a reasonable resolution the pulse length has been enlarged to 4096 slices by adding slices with no intensity.

After Fourier transformation the frequency slice for the central frequency (60nm) has been propagated upstream to find the beam waist. For this specific case the waist is located 1000mm upstream of the undulator exit.

The PHASE propagation has been limited to 40 frequencies. The other frequencies are diffracted by the grating to large angles such that they are blocked by the exit slit. The wavefronts corresponding to the 40 frequencies have been propagated to a plane close to the first element which is the initial plane for the subsequent PHASE propagation. The PHASE simulations have been done in two steps. First, the electric fields in the exit slit plane have been evaluated on a grid with 51x51 data points. The sizes of the slit aperture was chosen to be 2mm horizontally and 40µm, 200µm and 400mµ vertically. These data have then been used in a second PHASE run from the exit plane to the center of the second undulator (2500mm downstream of the undulator entrance).

These 40 frequency slices plus the other 4096-40 frequency slices (the latter ones with no intensity) have been Fourier transformed to time space to be used in further GENESIS simulations through the second undulator. For this a modified version of GENESIS is used in order to include the full 6x6 matrix to describe the electron bypass that debunches the electron beam. The electric fields behind the monochromator have been scaled such that the intensity at the central frequency has dropped to 11 percent corresponding to the theoretical beamline transmission.

Figure 3 shows the temporal and spectral power of the initial pulse and the pulses behind the monochromator. Though the line width behind the monochromator shrinks with the slit width, the pulse duration does not increase.

The reason is the correlation between the wavelength and the spot location in the dispersion plane of the grating which is imaged to the center of the second undulator. The bandwidth at a certain grid point does not scale with the slit width because only a small frequency interval contributes to the intensity at that point.

For the simulation of the second undulator, the particle distribution of the first undulator is taken, which is debunched, using the full 6x6 matrix which has been simulated with ELEGANT. The field used as a seed is the one as calculated by PHASE. The total interaction

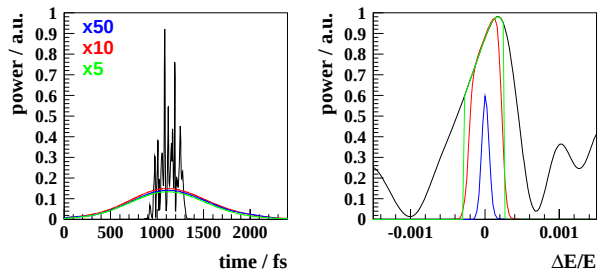

Figure 3: Relative power versus time (left) and frequency (right) for the initial pulse at the exit of the first undulator (black) and behind the monochromator for exit slits of 40µm (blue), 200µm (red) and 400µm (green). The monochromator transmission is not yet included.

length simulated is about 4.3 m, after which maximum peak brilliance has been reached.

RESULTS

The simulations for the three different slits show similar results. The main difference is that the seed power is different at the entrance of the second undulator. However, in all cases it is well above shotnoise and only influences the position at which saturation is achieved. In Figures 4 and 5, the results for a 400 µm slit are shown.

Wider monochromator slits increase the total power which is, however, not completely passed to the electron beam because the transverse beam size acts as further slit. The spectral power increases by a factor of 2.5 going from 40 to 200µm slit width and does not increase further at 400µm.

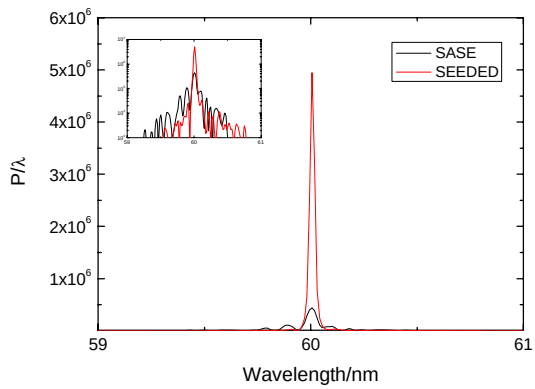

Figure 4: Comparison of the power spectrum for SASE (black curve) and a seeded pulse (red curve) for a slit of 400 µm. The small graph in the top left corner shows the same spectrum on a logarithmic scale. Note that the central frequency of 60 nm for the seeded pulse is about an order of magnitude higher compared to SASE, whereas the other peaks are about a factor of 5 lower.

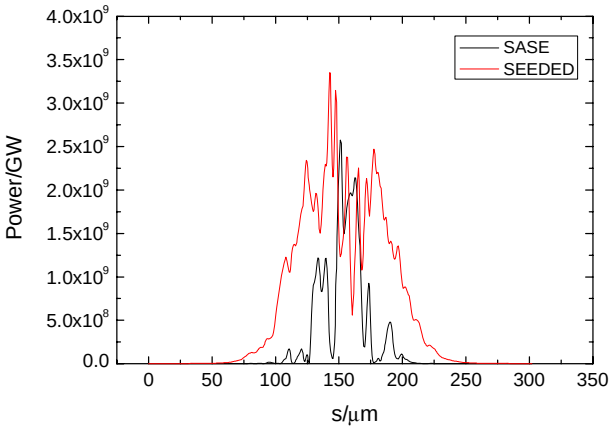

Figure 5: Power along the bunch for a SASE pulse (black curve) and the seeded pulse (red curve). Note that the seeded pulse is much smoother. The remaining spikes are at least partially due to the fact that the bunching is not fully suppressed in the simulation due to the limited number of particles used.

CONCLUSION

We presented for the first time combined time dependent FEL simulations and physical optics wavefront propagations using the codes GENESIS and PHASE. The wavefronts generated in a time dependent simulation of GENESIS have been propagated with the physical optics code PHASE and the result has been used as a seed for a further GENESIS run. It has been demonstrated that the self seeding scheme significantly improves the spectral performance of FLASH. The line width becomes narrower, the power increases and the temporal structure is smoother.

ACKNOWLEDGEMENT

We thank A. Meseck for adapting the code GENESIS and for many fruitful discussions.

REFERENCES

[1] TESLA-Technical Design Report, TESLA X-FEL, Technical Design Report, 2002-9, 2002.

[2] Linac Coherent Light Source (LCLS), Conceptual Design Report, SLAC-R-593, 2002.

[3] T. Shintake, Nucl. Instr. and Meth., A507 (2003) 382-397.

[4] L. H. Yu, NIM A, 483 (2002) pp493-498.

[5] X. J. Wang et al., DUV, Proceedings of the 26th International FEL Conference, Trieste, Italy, 2004, pp 209-211.
C. Bochetta et al., FERMI, Proceedings of the 27th International FEL Conference, Stanford, CA, 2005, pp 632-685.
The BESSY Soft X-ray Free Electron Laser, Technical Design Report March 2004, eds.: D. Krämer, E. Jaeschke, W. Eberhardt, ISBN 3-9809534-08, BESSY, Berlin (2004).
M.-E. Cuprie et al., ARC-EN-CIEL, Proceedings of the 27th International FEL Conference, Stanford, CA, 2005, pp.55-58.
A. Andersson et al., MAX IV, Proceedings of the 26th International FEL Conference, Trieste, Italy, 2004, pp 190-192.
D. Wang et al., MIT, Proceedings of 2005 PAC, Knoxville, Tennessee, pp1961-1963.
J. Wu, Z. Huang, LCLS, Proceedings of the 27th International FEL Conference, Stanford, CA, 2005.
Gullens et al., LBNL, Proceedings of the EPAC 2006, Edinburgh, Scotland, pp 142-144.
J. Qi-ka et al., SDUV, Proceedings of the 26th International FEL Conference, Trieste, Italy, 2004, pp 494-497.

[6] O. Tscherbakoff et al., Proceedings of the EPAC 2006, SPARC, Edinburgh, Scotland, pp 47-49.
G. Lambert et al., SCSS, Proceedings of the EPAC 2006, Edinburgh, Scotland, pp 44-46.
J. A. Clarke, 4GLS, Proceedings of the EPAC 2006, Edinburgh, Scotland, pp 181-183.

[7] J. Feldhaus et.al., Opt. Commun., 140 (1997), 341.

[8] K. Goldammer et al, Proceedings of the 27th International FEL Conference, Stanford, CA, 2005, pp.23-26.
M. Abo-Bakr et al., Proceedings of the 27th International FEL Conference, Stanford, CA, 2005, pp.19-22.

[9] J. W. Goodman, "Introduction to Fourier Optics", McGraw-Hill Physical and Quantum Electronics Series, New York, 1968.

[10] GLAD, Theory Manual, Applied Optics Research, 1087 Lewis River Road, 217 Woodland, WA, 2004.

[11] ZEMAX, Optical Design Program, User's Manual, ZEMAX Development Corporation, November 2005.

[12] J. Bahrdt, Applied Optics, 34 (1995) 114-127.
J. Bahrdt, Applied Optics, 36 (1997) 4367-4381.
J. Bahrdt, Proceedings of the 27th International FEL Conference, Stanford, CA, 2005, pp694-701.

[13] A. C. Hearn, "REDUCE 3.5, A General Purpose Algebra System" [RAND, Santa Monica, Calif. 90407-2138 (reduce@rand.org), 1993].

[14] R. Reininger, J. Feldhaus, P. Gürtler, and J. Bahrdt, Nucl. Instr. Methods A, **467**, 38-41, 2001

[15] S. Reiche, GENESIS 1.3, Nucl. Instr. Meth. A 429 (1999) 243.

[16] V. Miltchev, "Simulation studies on the self seeding option at FLASH", presented at this conference.

DEVELOPMENT AND APPLICATION OF FIGURES OF MERIT TO EVALUATE THE OUTPUT OF HGHG FEL CASCADES*

B. Kuske †, R. Follath, A. Meseck, BESSY, Berlin, Germany

Abstract

In the design of Free Electron Lasers (FEL), parameters like the peak power and the spectral power were established as figures of merit to evaluate the FEL's output quality. However, spectra obtained with studies using bunches from start-to-end simulations including errors show that it is not sufficient to optimise these simple parameters. To establish a stable and reliable user facility, parameters like pulse reproducibility, stability of the source point or signal to background ratio have to be considered and optimised. This paper suggests different criteria and parameters to describe and compare the output of different FEL schemes with respect to a regular user operation. As these criteria are not readily available from common FEL codes a post processing IDL code has been written, that extracts the relevant information from a standard GENESIS output. The code is used to reevaluate start-to-end simulations for the BESSY low energy FEL [1].

INTRODUCTION

A growing number of proposals for FEL projects plan to use High Gain Harmonic Generation (HGHG) structures in order to exploit the advantages that arise from seeding the FEL process, at wavelengths much shorter than what is available today with conventional seed lasers [2]. As the efficiency in the generation of higher harmonics declines rapidly with the harmonic number, a multi step harmonic generation in cascaded structures can be used to extend the wavelength range of this concept down to a few nanometers. Cascaded structures require an overall bunch length of the electron beam in the order of some hundred femtoseconds, because for each stage an unspoiled part of the bunch must be used (fresh-bunch technique). These long bunches usually exhibit parameter profiles at the end of the linac that are far from being constant. For example, an energy chirp is needed for bunch compression, the current is not constant and the emittance and energy spread vary for different slices. As a result, the temporal and spectral power functions are not as smooth as known from theoretical studies. Fig. 1 shows the power spectra of three different simulations including errors of the BESSY low energy FEL. The spectra are not Gaussian anymore, and they vary considerably for each set of errors. Although the peak power varies by less than 20% the pulse energy differs significantly.

The result of start-to-end simulations including phase and amplitude errors in the gun and in the linac and charge and timing errors of the photo cathode laser, for the two stage low energy FEL line have been published in [3]. Those 24 cases are reevaluated in the current paper incorporating aspects that are relevant for the users of the FEL radiation.

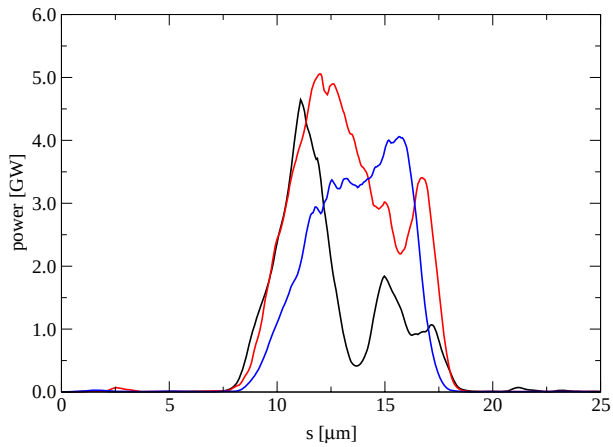

Figure 1: Power emitted by the final amplifier of the BESSY low energy FEL-line for three different sets of errors in the gun and the linac. The pulses are not Gaussian.

The BESSY soft X-ray FEL is designed as a user facility and hence the quality of the radiation will be judged at the position of the experiment. For the passage through the beam line, three radiation parameters are of major importance, namely the transverse and longitudinal position of the source point and its size. Vertical offsets give rise to energy fluctuations behind the monochromator. Horizontal offsets lead to intensity fluctuations behind horizontal slits. Both offsets should not exceed 20% of the radiation size. Variations in the size or the location of the source point degrade the energy resolution. Location fluctuations should not exceed one Rayleigh length. The signal to background ratio and the pulse energy within a selected bandwidth are further figures of great interest to the experimenters and beam line designers. Most of these criteria are indirectly supplied by FEL codes like GENESIS [5], but not easily accessible, especially when a larger number of runs are considered, as in tolerance studies. Therefore, a small evaluation program has been written using IDL [6] in combination with the original GENESIS output interpretation routines. The given figures of merit as well as the limits set for stability, result from discussions with the BESSY

* Funded by the Bundesministerium fr Bildung und Forschung (BMBF), the State of Berlin and the Zukunftsfond Berlin

† Bettina.Kuske@bessy.de

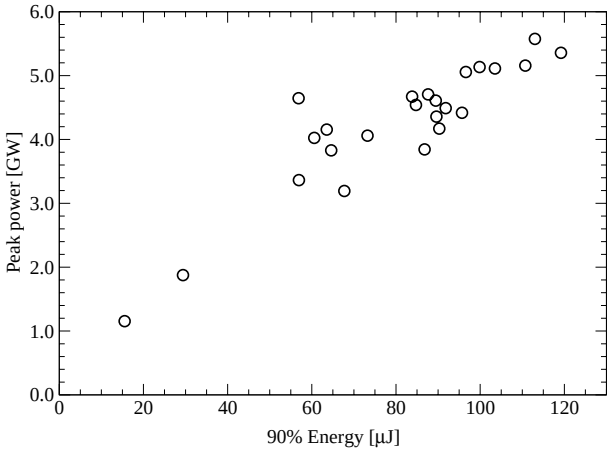

Figure 2: Peak power versus 90% energy for 24 pulses in the BESSY low energy FEL final amplifier. The spread in pulse energy can be considerable for similar peak power.

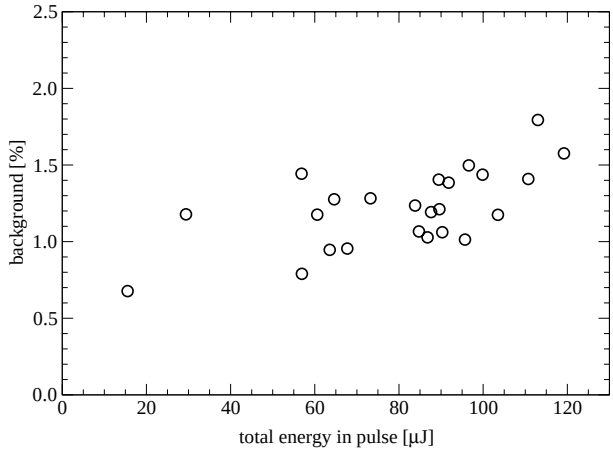

Figure 3: The background signal of the lasing part of the bunch in percent of the total pulse energy.

experimental group.

PULSE ENERGY AND BACKGROUND

In order to describe the FEL pulse, the FWHM of the pulse is determined as well as the width of the pulse at 10% of the peak power, called the 10%-width. For a Gaussian pulse, the ratio of the two is ≈ 1.8. 75% of the 24 investigated cases have a ratio around 1.2, indicating a pulse shape with steep flanks, only one case showed a wide profile with a ratio bigger than three.

The integral of the power inside the 10%-width is called the 90% pulse energy. Fig. 2 shows the peak power versus the 90% energy for the 24 runs. Especially around peak powers of 4 GW, where most pulses lie, the spread in pulse energy, which is the figure of interest for the experiment is considerable, due to the different pulse shapes. Therefore the peak power is not well suited as a figure of merit.

Any power outside the 10%-width is considered to be background. The signal to background ratio is important for the quality of the experiments. The background is computed in percent of the total pulse energy, see Fig. 3. It is below 2% in all cases.

It must be mentioned, that in order to reduce the computation time only short parts of the complete 700 fs bunch are simulated in the studies. The calculation of the background at this point includes power emitted outside the 10%-width of the 100 fs long bunch part tracked through the final amplifier. Contributions of the two parts seeded in upstream stages will approximately double the shown background, while the contribution of unseeded parts is negligible.

SOURCE POINT CHARACTERISATION

In seeded devices, the determination of the radiation size is not straightforward. At the beginning, the radiation is dominated by the seed. While the seeding radiation diverges, bunching builds up in the seeded part of the electron bunch and power is emitted, increasing exponentially. The radiation size calculated by FEL codes thus usually increases in the initial part of seeded FEL amplifiers due to the diverging seed and only later decreases due to the build up of coherent FEL radiation.

FEL codes usually calculate the radiation size for each slice of the bunch. For seeded devices though, averaging over all bunch slices will yield wrong results, as the radiation size at the location of the seed's interaction is much smaller than in the rest of the bunch, where the little power emitted is independent of the seeded process.

The radiation size and divergence of each slice provided by GENESIS has to be weighted with the power emitted by the slice. The result follows the behaviour described earlier. The radiation size has a maximum inside the final amplifier, where the divergence slightly decreases. In order to calculate the phase space volume, the radiation size and divergence at the end of the final amplifier are used. Note that from [7] it is known, that the beam waist, when calculated exactly by back tracking the radiation, lies a couple of meters upstream and is smaller than at the end of the device. Thus, the data plotted in Fig. 4 is an upper limit, and the phase space volume is expected to be up to 50% smaller. Still most points lie close to the line indicating twice the diffraction limit. As the waist location will jitter from shot to shot, this conservative estimate seems adequate.

SOURCE POINT STABILITY

Transverse Stability

As mentioned earlier, transverse jitter of the source point reduces the energy resolution of the beam line. It is desired to reduce the transverse fluctuations to less than 20% of the rms radiation size.

Rather than first locating the source point, and then com-

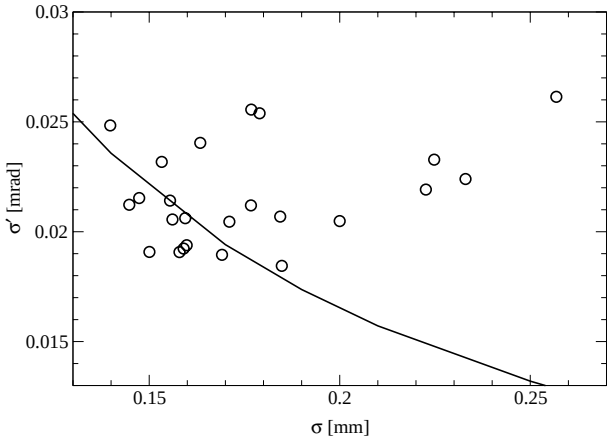

Figure 4: The size and divergence of the radiation field at the end of the final amplifier. The black line indicates twice the diffraction limit. The beam waist will in reality lie a few meters upstream the end of the undulator and will be up to 50% smaller, on the other hand jitter of the waist location has to be taken into account.

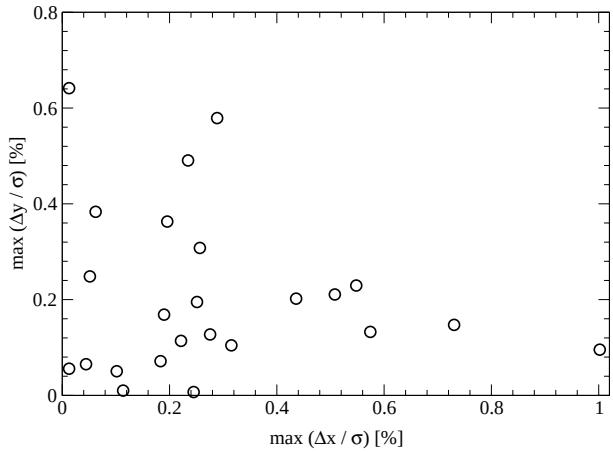

Figure 5: The maximum of the vertical and horizontal transverse offsets in the final amplifier in percent of the radiation size, when errors in the gun and the linac are included in the start-to-end calculations. To include effects of quadrupole offsets, the data can be linearly scaled.

paring the beam offsets at this point to the radiation size, the ratio between the transverse offsets and the radiation size is computed at each point in final amplifier. The maximum of each of the resulting curves for the 24 runs is depicted in Fig. 5. These results only show shot-to-shot fluctuations, that are due to phase and amplitude errors in the gun and in the linac. The amplitudes at the beginning of the cascades amounted to $< 1\mu$m rms in the horizontal and $< 0.5\mu$m rms in the vertical plan.

The major source for beam steering, though, are quadrupole jitters, e.g. due to ground vibrations. All time independent beam offsets will be corrected by the steering magnets. Start-to-end calculations assuming a Gaussian rms quadrupole jitter of 300 nm, resulted in rms beam offsets at the beginning of the HGHG cascades as listed in Tab. 1.

Table 1: Transverse jitter (rms) at the end of the linac, due to random quadrupole vibrations with 300 nm offsets (rms).

	offset [μm]	angle [μrad]
horizontal	27.5	1.55
vertical	10.0	1.57

For an estimate of their effect, bunches where started on the phase space ellipse described in Tab. 1 and tracked through the final amplifier. The largest transverse offsets in the undulator where reached for large initial horizontal amplitudes, the maximum reached was 28μm. The minimal radiation size of all investigated cases is 140μm, Fig. 4, therefore the 20% criterion is fulfilled throughout the final amplifier for all runs. Alternative optics, taking the larger horizontal trajectory jitter into account, could even improve on the results.

Longitudinal Stability

The longitudinal location of the source point is difficult to determine. It does not coincide with the saturation point. Furthermore, in start-to-end calculations including errors, each bunch is populated differently and is seeded at varying locations due to timing jitter, so that the source point moves from shot to shot.

In [7], an exact, but time consuming procedure is introduced to locate the position and size of the radiation waist. It is pointed out that the waist lies over 5m upstream of the end of the undulator for the investigated cases. Furthermore, the horizontal and vertical waist position do not necessarily coincide.

A shot-to-shot jitter in the location of the source point or a variation in its size, leads to a degradation of the energy resolution. The criterion for longitudinal stability has been set to fluctuations in the beam radius of less than a factor of $\sqrt{2}$, which for Gaussian beams corresponds to variations of the source point location of less than one Rayleigh length.

It can be extracted from [7] that the distance, in which the beam radius increases by $\sqrt{2}$ is $>$ 5m and thus much larger than the theoretical Rayleigh length. With a total length of the final amplifier of 7.5 m, the longitudinal stability criteria is fulfilled as long as the beam waist location lies well inside the final amplifier.

SPECTRUM

Due to the energy chirp on the electron bunch and the jitter between the arrival time of the bunch and the seeding laser, the average energy of the electrons interacting with

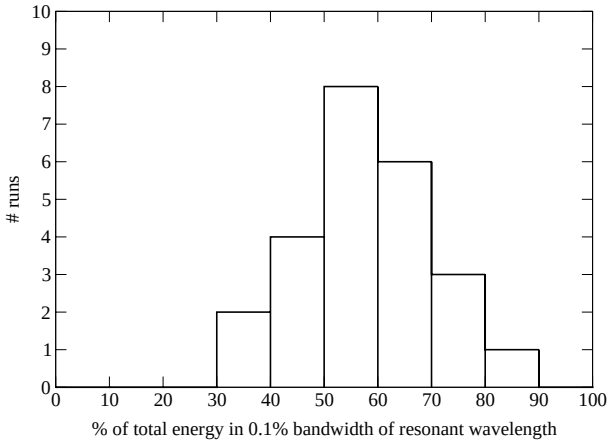

Figure 6: Histogram over the percent of total pulse energy in 0.1% bandwidth around the central frequency of each pulse. High temporal resolution experiments usually work without monochromator.

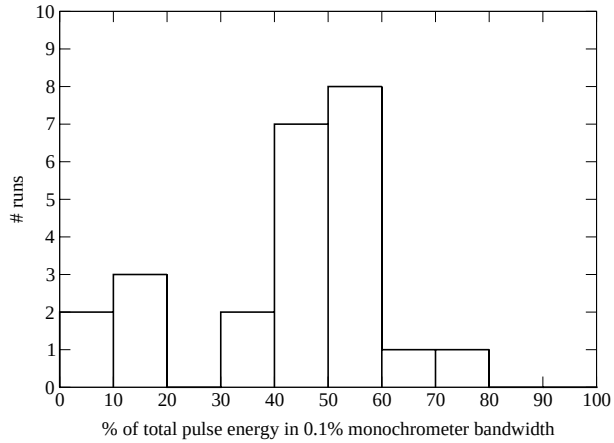

Figure 7: Histogram over the percent of total pulse energy in 0.1% bandwidth of a given (monochromator) frequency. The figure is important for high energy resolution experiments.

the seeding radiation varies, which results in a fluctuation of the central wavelength of the HGHG spectrum.

In order to evaluate spectral properties, the routines supplied by the post processing IDL-code XGENESIS are used on the Fairfield power on axis. The fraction of the energy in 0.1% bandwidth is calculated and compared to the total energy in the spectrum. The bandwidth can be either taken around a given frequency for all runs, or for the central frequency of the individual spectra.

Different experiments are interested in different spectral qualities. Experiments depending on high temporal resolution will usually work without monochromator and depend on the energy in a certain bandwidth around the resonant wavelength of each pulse. This case is depicted in Fig. 6, where 75% of the runs hold more than half and up to 90% of their power in 0.1% of the bandwidth of their resonant frequency, amounting to 50 μJ on average.

High energy resolution experiments need a large fraction of the total pulse energy close to the central frequency of the monochromator, Fig. 7. 70% of the runs would still deliver above 40% of their total pulse energy within the given bandwidth. These experiments usually average over many shots.

CONCLUSION

FEL codes deliver information about the development of the radiation inside the amplifying devices during the interaction between the electrons and the electro magnetic field. The quality of the produced radiation is judged much further down the beam line at the experimental station. Figures of merit have been proposed to evaluate the FEL output in view of the beam line and experimental demands. All quantities can be deduced from the output provided by, e.g. GENESIS. A post processing code for GENESIS has been introduced. It has been used to evaluate the results of 24 complete start-to-end runs including errors in the gun and the linac of the BESSY low energy FEL line. The given criteria for the radiation quality could be met. Despite the immense computing effort it would be desirable to improve on the statistics.

ACKNOWLEDGEMENT

I would like to thank my colleges Johannes Bahrdt and Michael Scheer of the BESSY experimental groups for the helpful discussions.

REFERENCES

[1] ”The BESSY Soft X-ray Free Electron Laser, Technical Design Report”, March 2004, eds.: D. Krmer, E. Jaeschke, W. Eberhardt, ISBN 3-9809534-0-8, BESSY, BERLIN (2004)

[2] ”VUV/Soft X-ray FELs on the Horizon”, Rene Bakker, http://leg.web.psi.ch/public/publications/TOAB001_Talk.pdf

[3] ”Start-To-End Simulations for the BESSY Low and Medium Energy FEL Line Including Errors”, B. Kuske, M. Abo-Bakr, K. Goldammer, A. Meseck, BESSY, Berlin, Germany, FEL2005, proc.

[4] ”Impact of Realistic Bunch Profiles and Timing Jitter on the Output of the BESSY Low Energy FEL Line”, B. Kuske, M. Abo-Bakr, A. Meseck, BESSY, Berlin, Germany, FEL2005, proc.

[5] ”GENESIS 1.3: A Full 3D Time Dependent FEL Simulation Code”, S. Reiche, Nuclear Instruments and Methods A429 (1999) p. 243

[6] Interactive Data Language, http://www.ittvis.com/idl/

[7] ”Source Characterisation of the BESSY Soft X-Ray FEL ” A. Meseck, M. Abo-Bakr, J. Bahrdt, B. Kuske, BESSY, Berlin, Germany, FEL2005, proc.

STUDY OF A DEFLECTING DISPERSIVE CHICANE FOR THE BESSY SOFT X-RAY FEL*

A. Meseck†, G. Wüstefeld‡
BESSY GMbH, Albert-Einstein-Str.15, Berlin, Germany.

Abstract

High power, short pulse length and full coherence are the main parameters of the second generation free electron lasers like the BESSY Soft X-ray FEL. To provide radiation with these properties, BESSY proposed a seeded FEL facility based on high-gain harmonic-generation (HGHG) scheme [1]. This scheme uses cascaded stages each consisting of undulator/dispersive chicane/undulator section to up-convert the seeding frequency.

The transverse separation of the seeding radiation and electron beam after the first undulator is desirable, as not only the output of the following undulators improves but also the seeding radiation itself can be used for diagnostics.

Based on an exact linear model, a dispersive chicane is designed for the BESSY FEL, which deflects the electron beam providing the separation without coupling and spoiling effects [2]. The linear model and the deflecting chicane will be presented and the properties of the chicane will be discussed by means of simulation results.

INTRODUCTION

The BESSY Soft X-Ray FEL is designed as a multi-user facility consisting of three independent FEL lines. Each line is seeded by a tunable laser covering the spectral range of 230 nm to 460 nm. The target wavelength ranges from 51 nm to 1.24 nm with peak powers up to a few GWs and pulse lengths less than 20 fs (rms). The polarization of the fully coherent radiation will be variable.

Cascades of two to four HGHG stages are planned to reduce the existing laser wavelength to the target range of the BESSY-FEL. In the first undulator of such an HGHG stage, the modulator, an energy modulation is imprinted on the electron beam by the seeding radiation. The following dispersive chicane converts this energy modulation to a spatial modulation which is optimized for a particular harmonic. The second undulator, the radiator, is resonant to this harmonic and generates radiation at the higher harmonic, which serves as seed for the next stage. The last HGHG-stage is followed by the so-called final amplifier. It is seeded at the desired wavelength and the amplification process is brought to saturation.

The quality of the FEL output radiation depends strongly on the quality of the frequency up-conversion procedure, which again depends on the quality of the spatial modulation (bunching) and on the quality of the seeding radiation. Although in an HGHG stage, the radiator is resonant to a harmonic of the seeding radiation, short interactions between the seeding radiation and the electron beam are still possible. During such an interaction the phase correlation between the seeding radiation and the electron beam is good enough to permit an energy exchange. These interactions are short as the resonance condition is not fulfilled for the seeding radiation, but due to the high intensity of the radiation, the electron beam quality degrades, and thus the radiator output quality suffers. Separating the seeding radiation and the electron beam after the energy modulation would avoid these undesired interactions. In addition, the separation offers the possibility to use the radiation - seeding radiation as well as the spontaneous undulator radiation- for diagnostics.

In principle, the separation can take place before, inside or after the dispersive chicane, but it has not to affect the spatial modulation. Also other effects like residual dispersion, coupling or increased beam size have to be avoided. Each of the dispersive chicanes planned for the BESSY FEL consist of four dipoles providing a closed bump. Generally, the dispersion strength, which is necessary to convert the energy modulation to the spatial modulation, is not high. Hence the bump amplitudes are not large enough to install mirrors or other optical elements to deflect the radiation. A separation of the radiation and electrons can only take place by an additional bending of the electron beam. A simple bending, with an additional dipole or due to a mismatch of the four bump dipoles, causes residual dispersion, coupling between transverse and longitudinal motion and spoils the bunching. Thus it deteriorates the radiator output strongly.

However, an exact linear model offers the possibility to design an optimal dispersive section, which allows the separation of the electron beam and seeding radiation without any coupling and spoiling effect. In this paper we present the dispersive section which is designed based on this model. Comparisons of simulation results of an HGHG stage using the four dipole chicane and the deflecting dispersive section respectively, demonstrate that the new dispersive section meets all demands.

THE DEFLECTING DISPERSIVE CHICANE

The dispersive chicane, which converts the energy modulation of the bunch to a spatial density modulation is optimized for a particular harmonic of the seed. This spatial modulation results when the energy modulated beam passes through a dispersive chicane, which is described by

* Work funded by the Bundesministerium für Bildung und Forschung and the Land Berlin
† meseck@bessy.de
‡ wuestefeld@bessy.de

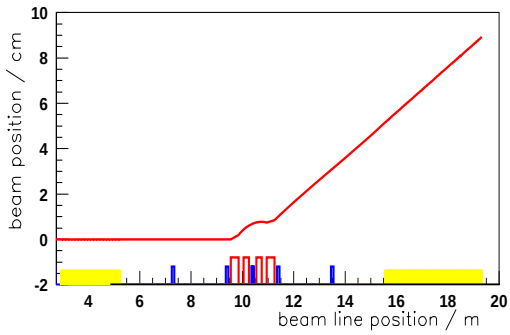

Figure 1: Horizontal trajectory of the electron beam as a function of beam line position. The red line shows the trajectory for the deflecting chicane (dipoles in red, quadrupoles in blue and undulators in yellow colours).

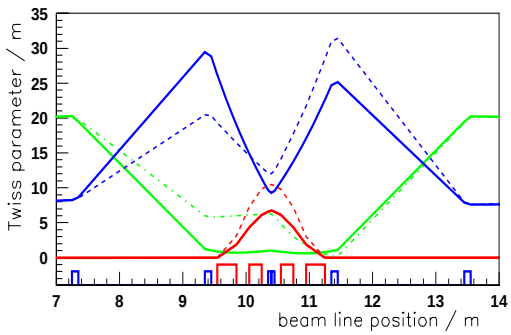

Figure 2: Horizontal (blue) and vertical (green) beta functions and dispersion (1000 times enhanced, red) of the deflecting chicane. The value of m_{56} is tuned to $6.5 \cdot 10^{-5}$ (solid line) and $26 \cdot 10^{-5}$ (dots), colours of magnets as described in fig. 1.

a properly chosen matrix element m_{56}. The energy modulated electrons must be shifted by $\lambda/4$ in the longitudinal position within the dispersion section for the optimal radiator output. For BESSY FEL seeding wavelength, this translates to a distance of 60 nm to 120 nm. Note, the factor two in the distance tuning-range is given by the spectral range of the seeding radiation.

The necessary density modulation is commonly achieved by a simple four dipole bump of zero integrated dipole field strength. By a scaled field strength change of the four dipoles, m_{56} can be varied.

Instead of the simple 2 m long bump, we propose a more elaborate optics, which deflects the beam by a fixed angle of 10 mrad, see Fig. 1 and 2. In addition, the value of m_{56} can be varied by a factor of four, twice as much as required. This deflecting chicane consists of two dipole families and one quadrupole, tuned as an achromatic bend with variable m_{56} value. The integrated dipole fields are kept constant to define the deflection angle. One family is excited opposite to the other one, the difference between the integrated fields of both family yields the value of m_{56}. The quadrupole tunes the dispersion outside of the chicane to zero. At the entrance and exit side of the chicane an optical matching section is required, consisting of one quadrupole doublet on each side. For the full optical line m_{56}=$6.5 \cdot 10^{-5}$, the same tuning as for the simple bump. Different settings of the dipoles leads to different orbits inside the quadrupole, this steering has to be taken into account.

This optics is 10 m long and has the advantage of separating the electron and photon beams, and delivering the necessary m_{56}. In addition it avoids the coupling between different planes of the electron motion as described below. The separation can be used for easier diagnostics purposes and eliminates further unwanted interaction of the photon beam with the electrons.

The linear matrix theory can be used, to discuss the coupling of the horizontal (x, x') and longitudinal (z, z') particle oscillations [2]. Effects of the vertical plane have to be treated similarly, but are presently not discussed. A general transfer matrix m_{ij} describes the chicane plus matching sections. The longitudinal elements m_{51} and m_{52} are not independent. They are coupled to the horizontal plane, described by

$$m_{51} = m_{16}m_{21} - m_{11}m_{26}$$

and

$$m_{52} = m_{16}m_{22} - m_{12}m_{26}.$$

The coupling depends on the dispersive terms m_{16} and m_{26}. If dispersion is produced and m_{16} and m_{26} are nonzero, for example by a single dipole kick, one gets a dependency of the longitudinal position z on the horizontal plan (x, x'). Even a single dipole kick of 5 mrad generates dispersion and in turn coupling. Using the BESSY FEL parameters of a horizontal beam emittance of $0.9 \cdot 10^{-9}$ m rad one obtains a longitudinal spread of 280 nm as a result of the final beam diameter. This can not be tolerated for a proper seeding process. With the presented chicane, this coupling is cancelled, i.e. the matrix elements m_{51} and m_{52} are zero.

As the transverse beam amplitudes and the accumulated spread in chromatic phase errors stay sufficiently small, the layout of this section is done without any higher order correcting multi poles. The comparison between the simple dipole bump and this deflecting chicane shows very good agreement, as shown in the next section. For the comparison, the deflecting chicane has the same Twiss parameters β and α as the four bump chicane at the start and end points. Both sections have a m_{56} value of $6.5 \cdot 10^{-5}$. In this case the rms-beam dimensions are equal (within the numerical uncertainties due to limited number of macroparticle in the

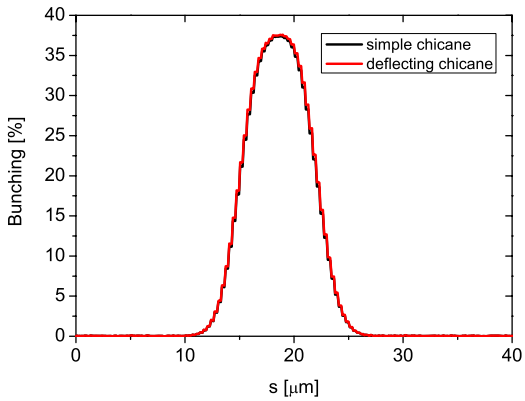

Figure 3: The bunching at the entrance of the first radiator of medium-energy FEL along the bunch for both dispersive sections. Both dispersive sections produces the optimal density modulation for the given energy modulation.

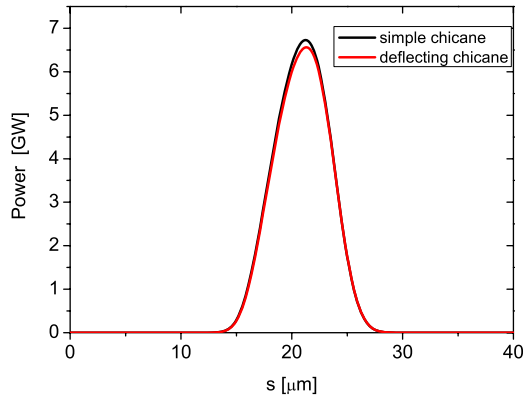

Figure 4: The radiator output power of the first stage of the medium-energy FEL for both dispersive sections. There exists a small difference between both cases, which is negligible concerning the seeding of the next section.

simulations) for both solutions, independent of the different phase advances obtained from the different approaches.

This chicane is similar to the optics of the NewSUBARU storage ring [3, 4]. It was recognized in this ring, that even a very small power supply ripple of the dipole families could limit the isochronous tuning of the optics [5]. However, this seems not to be a problem for our parameters. A deflection error of 10^{-3} in one of the dipole families leads to a two times larger error of m_{56}, which is negligible.

PERFORMANCE SIMULATION OF BOTH DISPERSIVE SECTIONS

In order to compare the performance of the new deflecting dispersive chicane with the simple four dipole chicane, the first stage of the medium-energy FEL-line of the BESSY FEL [1] was simulated for both cases. The simulations were carried out using a modified version of the simulation code GENESIS 1.3 [6] which includes a transfer matrix routine. This routine was used to model both dispersive sections at the entrance of the radiator.

The bunching at the entrance of the radiator is shown in Fig. 3 for both cases. For the given energy modulation, both dispersive sections produce the optimal spatial modulation. Fig. 4 displays the temporal power distribution at the exit of the first radiator. This radiation will be used as a seed for the next section. The difference in maximum power between both cases is negligible concerning the seeding.

The development of the horizontal and vertical electron beam size (rms) along the first radiator is shown in Fig. 5 and 6 for both dispersive sections. Because of the limited number of macroparticles that can be simulated, numerical deviations of the rms beam size of order 0.5% are expected. Therefore any deviation in beam sizes less than 0.5 % can be neglected. Obviously, there exist a small difference in

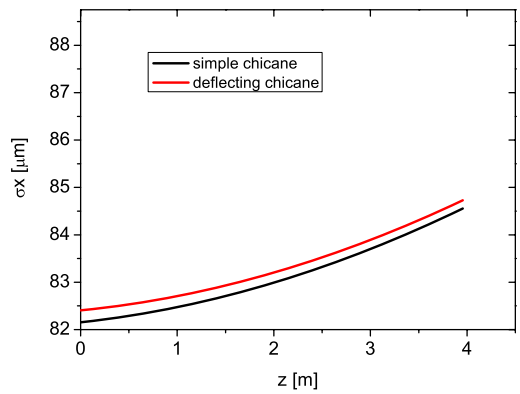

Figure 5: The development of the horizontal electron beam size (rms) along the first radiator for both dispersive sections. The difference between the beam sizes is less than 0.5 % and can be neglected.

vertical divergence for both cases of about 0.4 μ rad. This difference might also indicate small tuning differences of the two chicanes.

The above simulations were done for constant average energy along the bunch. In order to exclude undesired effects due to the energy chirp of the electron beam needed for the bunch compression [7], the simulations of both dispersive sections were repeated with an energy chirped beam. The bunching and radiator output are almost the same for both dispersive sections. The spectral purity is conserved for both dispersive sections, see Fig. 7. Due to the energy chirp, there is a shift in the wavelength [7], which is independent of the choice of the dispersive section.

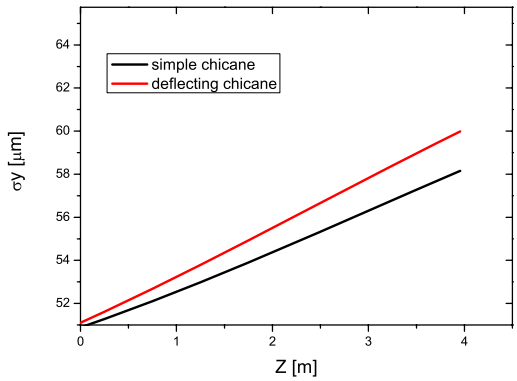

Figure 6: The development of the vertical electron beam size(rms) along the first radiator for both dispersive sections.

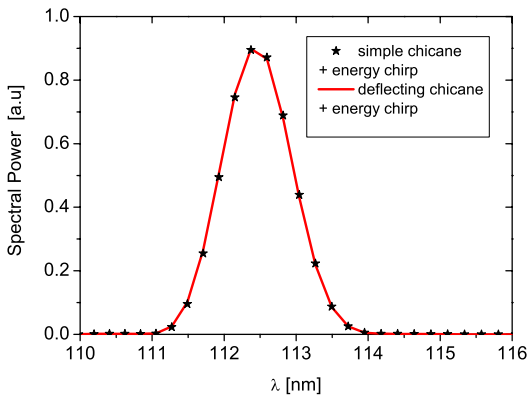

Figure 7: Spectrum of the output radiation for both dispersive sections. There is a shift in the wavelength due to the energy chirp. This is independent of the dispersive section.

CONCLUSION

Using an exact linear model an optimized dispersive section is designed for the medium-energy FEL-line, which allows the separation of the electron beam and seeding radiation without any coupling and spoiling effect. Based on the linear coupling matrix, a deflecting dispersive chicane is introduced. The comparison of the simulation results of an HGHG stage shows that the new dispersive section meets all demands.

REFERENCES

[1] The BESSY Soft X-ray Free Electron Laser, Technical Design Report March 2004, eds.: D.Krämer, E. Jaeschke, W. Eberhardt, ISBN 3-9809534-08, BESSY, Berlin (2004).

[2] G. Wüstefeld, "Horizontal-longitudinal coupling in the FEL beam line," BESSY (Berlin) Technical Report TB 227/05, 2005.

[3] A. Ando, S. Amano, S. Hashimoto, H. Kinosita, S. Miyamoto, T. Mochizuki, M. Niibe, Y. Shoji, M. Terasawa, T. Watanabe and N. Kumagai, "Isochronous storage ring of the New SUBARU project," J. Synchrotron Rad. (1998). 5, 342-344.

[4] A. Amiry, C. Pellegrini, E. Forest, D. Robin, "Study of magnetic lattice for a quasi-isochronous ring," Particle Accelerators, Vol. 44, Num. 2, p.65, 1994.

[5] Y. Shoji, Y. Hisaoka, T. Matsubara, T. Mitsui, "Longitudinal Coherent Oscillation Induced in Quasi-isochronous Ring," proceedings EPAC 2006, Edinburgh (UK).

[6] S. Reiche, GENESIS 1.3, Nucl. Instr. Meth. A 429 (1999) 243.

[7] B. Kuske, M. Abo-Bakr, A. Meseck, "Impact of Realistic Bunch Profiles and Timing Jitter on the Output of the BESSY Low Energy FEL Line," proceedings FEL 2005, Stanford USA.

SIMULATION STUDIES ON THE SELF-SEEDING OPTION AT FLASH*

V. Miltchev†, J. Rossbach, Hamburg University, 22761 Hamburg, Germany
B. Faatz, R. Treusch, DESY, 22603 Hamburg, Germany.

Abstract

In order to improve the temporal coherence of the radiation generated by the Free-electron LASer in Hamburg (FLASH), a two-stage seeding scheme [1] is presently under construction. It consists of two undulator stages separated by a magnetic chicane and a monochromator. In this contribution we investigate various configurations of the electron optics of the seeding set-up. The optimization of the lattice in the first (seeding) stage and the parameters of the magnetic chicane will be discussed. Simulation results for the performance of the second (seeded) stage of the FEL will be presented.

INTRODUCTION

The basic setup of the self-seeding option [1, 2] is illustrated in Fig.1. It consists of two undulator stages separated by a magnetic chicane and a monochromator. The first undulator operates as a SASE FEL in the linear regime. After it, the electrons are separated from the SASE radiation. The

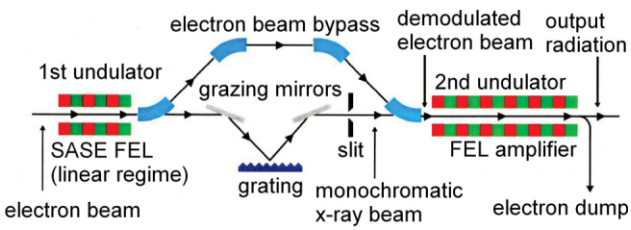

Figure 1: Schematic layout of the self-seeding setup.

electron beam passes through the magnetic bypass, that is used to remove the longitudinal charge density modulation (micro bunching). The radiation pulse is spectrally filtered in a high resolution grating monochromator [3] and afterwards is superimposed with the electron beam at the entrance of the second undulator. Thus the monochromatic photon beam serves as a coherent radiation seed, which is amplified up to saturation in the second undulator. The seeding increases the spectral brilliance by about a factor of 100, i.e. the output power of the seeded FEL is concentrated in a single line which is about a hundred times narrower than the spectrum of the conventional SASE FEL. The concept of the self-seeding has the advantage that it is independent of any external radiation source and the seed is naturally synchronized with the electron bunch. An additional advantage is that the seeding wavelength is continuously tunable. The monochromator optics, to be installed at FLASH, is designed for operation in the 6-60 nm range [2]. It is important to note, that the gain in the first undulator section is essential for the effective operation of the self-seeded FEL. The output power level should be sufficiently low (about two-three orders of magnitude below saturation) in order to preserve the energy spread and the emittance of the electron beam. On the other hand the power of the seed, obtained from the first stage, should be much higher than the power of the shot noise in the second undulator.

* This work has been partially supported by the EU Commission in the Sixth Framework Program, Contract No. 011935-EUROFEL
† velizar.miltchev@desy.de

ELECTRON OPTICS

Undulator stages

The undulator stages for the self-seeding option are subdivided into segments of about 4.5 m length. The first and the second undulator consist of three and six such segments respectively. A separated focusing system for the undulator stages is used at FLASH [4]. The focusing is accomplished by quadrupole doublets placed in-between two neighbouring undulator segments. The main feature of such focusing scheme, relevant to the implementation of the self-seeding, is the variable quadrupole strength. The total length of the first undulator (about 14.5 m) is optimized for operation at a wavelength in the order of 6 nm. The minimum average β-function for this case is about 4.5 m. As mentioned above, the power gain in the first undulator is crucial for the performance of the self-seeded FEL. Therefore, in order to compensate the scaling of the gain with the wavelength, one can vary the quadrupoles strength i.e. tune the average β-function accordingly.

Electron bypass

The bypass has to meet various requirements in order to ensure the proper operation of the self-seeding. The most essential of them are summarized in the following:

- Generation of an additional path length for the electrons, which is equal to the extra path length of the photons in the monochromator.
- Reduction of the micro bunching generated by the SASE process along the first undulator section. The micro bunching after the bypass is reduced by a factor of $\exp\left(-\frac{1}{2}\sigma_\delta^2 R_{56}^2 k_L^2\right)$ [5]. Here σ_δ is the fractional momentum spread, R_{56} is the momentum compaction factor of the bypass and k_L the radiation wavenumber.
- Adjustment of the electron optics to the optics of the two undulator sections for radiation wavelengths in the range 6-60 nm.

- Correction of the first and second order dispersion, minimization of the degradation of beam quality due to coherent synchrotron radiation effects.

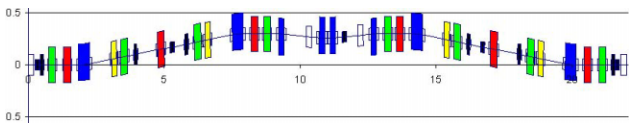

Figure 2: Final magnet layout of the electron bypass for the Seeding Option (side view). *black*: steerer, *blue*: dipole, *green*: quadrupole, vertical focusing, *red*: quadrupole, horizontal focusing, *yellow*: sextupole.

In contrast to the simplified scheme shown in Fig. 1, the final design of the electron bypass optics [2], as sketched in Fig. 2, consists of a total 37 magnets.

SIMULATION TECHNIQUES

The simulation studies presented in this paper divide into two groups: studies on the performance of the self-seeded FEL and investigations of the impact of the coherent synchrotron radiation (CSR), emitted in the electron bypass, on the output brilliance.

Performance of the self-seeded FEL

The performance of the self-seeded FEL has been simulated with the 3-D time dependent FEL-code GENESIS [6]. The simulation is split into two runs - the first undulator operating as a SASE FEL and then simulation of the electron bypass together with the second undulator. The complete particle distribution at the end of the first undulator is extracted and then is used in the next simulation step. The electron bypass is implemented in GENESIS by the means of a 6×6 transfer matrix. In the second step, the particle distribution extracted from the first part of the simulation is transformed with the help of the bypass matrix and then tracked through the second undulator section. A certain wavelength λ_{seed} and average power P_{seed} is assumed for the external seed, which should be obtained at the output of the monochromator beamline. In the presented studies the two extreme cases $\lambda_{seed} \approx 6\,\mathrm{nm}$ and $\lambda_{seed} \approx 60\,\mathrm{nm}$ are considered. It is helpful to remind that the seed power should fulfill the requirement $P_{seed} \gg P_{shot}$, where P_{shot} is the effective shot noise power. Since P_{shot} $\leq$100 W, a seed of P_{seed} $\approx$10 kW has been assumed in all cases. The code ELEGANT [7] has been used for the calculations of the electron optics, to find the electron beam matching conditions and for the calculation of the transfer matrix of the bypass. The electron beam parameters, which have been assumed in the simulations, are summarized in Table 1

Studies on CSR effects

These investigations follow a similar scheme as the one described above. However, in order to include CSR effects in the numerical calculations, the bypass has been simulated together with the first undulator section with the ELEGANT code. The program incorporates 1-D CSR algorithm [8] for dipoles and drift spaces. The produced particle distribution file is afterwards analyzed and converted into averaged slice information, which is used by GENESIS to simulate the interaction between the electrons and the radiation field along the second undulator section. In order to quantify the influence of the emitted synchrotron radiation, the described procedure has been repeated twice. Once including the CSR effects and second time with the CSR algorithm switched off. The average spectral flux has been considered as a figure of merit to compare the radiation quality for the two cases.

Table 1: Nominal electron beam parameters for operation at 6 nm

Energy, E_0	1000 MeV
Peak current, I_0	2500 A
rms energy spread	0.2 MeV
Normalized rms emittance, ϵ_n	2 mm mrad
rms bunch length, σ_z	50 μm

SELF-SEEDING PERFORMANCE

As it is pointed out in [4], one of the main advantages of the separate focusing is that the number of quadrupoles in-between the undulator segments can be reduced, what

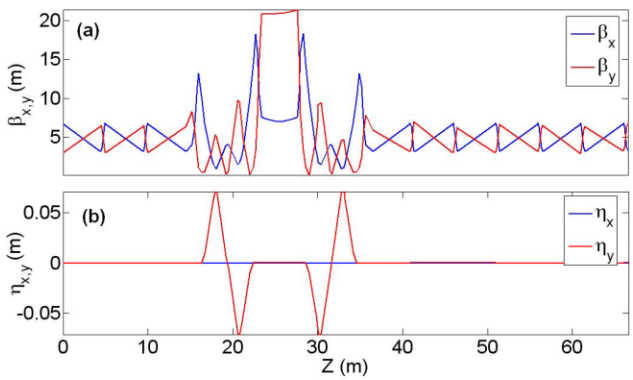

Figure 3: β-function (a) and dispersion (b) along the self-seeding electron beamline.

results however in an increase of the minimum average beta function $\langle\beta\rangle$. For the case of electron energy E_0=1000 MeV, corresponding to a wavelength $\lambda \approx 6\,\mathrm{nm}$, an average β-function of about 4.5 m is used. As shown in Fig.3, the design of the electron optics allows operation with the same $\langle\beta\rangle$ at the both sides of the magnetic chicane. For such setup the first stage works in the linear regime (see Fig. 4) with an average power of the output radiation of about 5 MW. Again in Fig. 4 it is shown the evolution of the micro bunching along the undulator. The kinks around Z=10 m and Z=5 m (less pronounced) are due

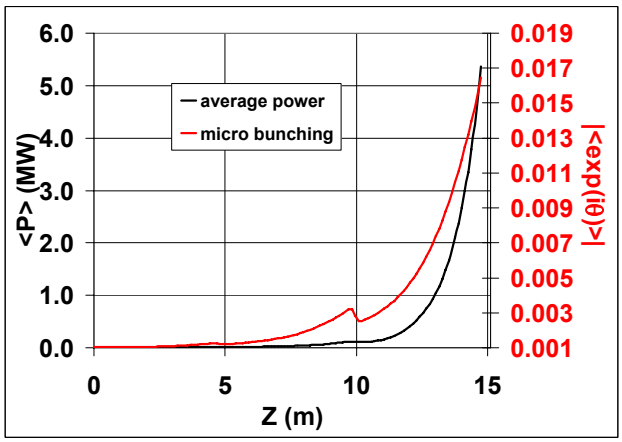

Figure 4: Average radiation power and micro bunching (right axis) along the first undulator.

to debunching taking place in the quadrupole doublet intersections [4]. Figure 5 shows the radiation power and

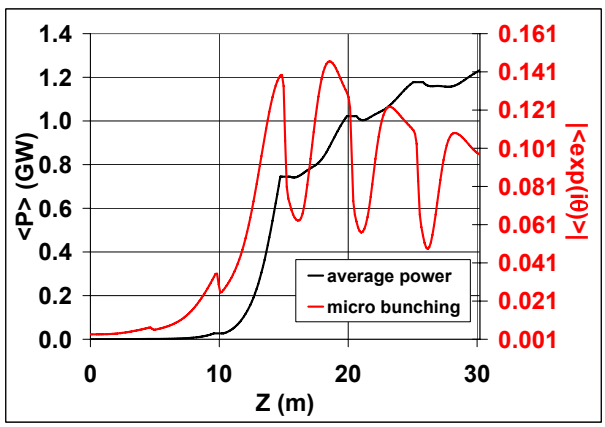

Figure 5: Radiation power and micro bunching (right axis) along the second undulator. Seeding wavelength $\lambda_{seed} \approx 6.31\,\mathrm{nm}$.

bunching as a function of the length of the second undulator. A comparison between the graphs in Fig.4 and Fig.5 demonstrates that the momentum compaction factor of the bypass $R_{56} \approx 0.73\,\mathrm{mm}$ is sufficient for the reduction of the micro bunching induced in the first undulator.

For operation at electron beam energy of 325 MeV, corresponding to a resonant wavelength of about 60 nm, one has to consider modifications in the electron optics of the first undulator section and the chicane. These changes are necessary because of the scaling of the FEL gain with the wavelength. The electron optics designed for 6 nm, with $\langle\beta\rangle \approx 4.5$ m (see Fig.3), provides saturation length in the order of 20 m for SASE mode. For the 60 nm case, however, the saturation length is only about 9 m, which is significantly shorter than the first undulator (14.5 m) and therefore not acceptable from the point of view of the self-seeding option. One possible solution, as confirmed by simulations, is to increase $\langle\beta\rangle$ in the first stage to a value in the order of 25 m, corresponding to the desired low gain of about three orders of magnitude below saturation.

Variation of the seeding wavelength

The monochromator design gives the possibility for variation of the wavelength of the seed across the full bandwidth of the FEL amplifier. Therefore it is interesting to investigate the influence of the seeding wavelength on the power and the spectrum of the output radiation. In Fig. 6 the spectral flux along the second undulator is presented for various seeding wavelengths. The simulations show a maximum at Z ≈ 15.5 m for λ_{seed} = 6.305 nm. One has to

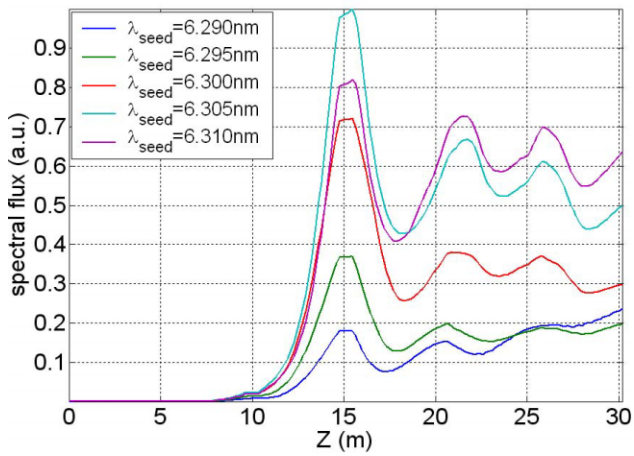

Figure 6: Spectral flux as a function of the undulator length for different λ_{seed} and constant seeding power.

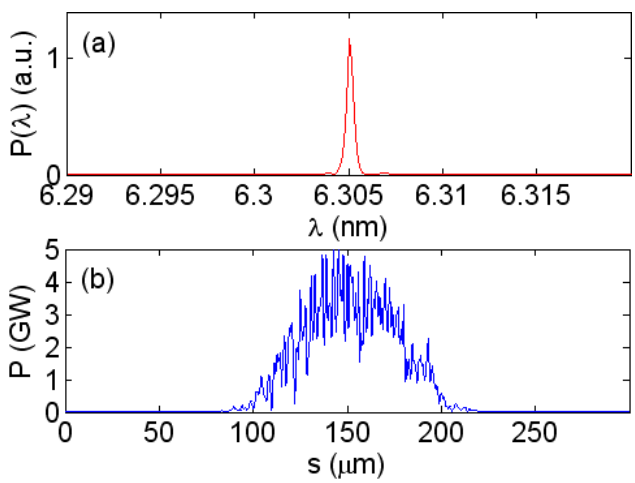

Figure 7: Spectrum (a) and power along the radiation pulse (b) in the second (seeded) section at Z=15.5 m.

mention that the position of the maximum of the spectral flux is related to the onset of the nonlinear regime (see Fig. 5). Further increase of the output power is coupled with a spectral broadening and in consequence with reduction of the spectral flux. As studied in [9], the length of the second

undulator can be optimized in order to compensate the large fluctuations of the seed intensity after the monochromator. The simulation results plotted in Fig. 7 demonstrate the effect of the self-seeding on the spectrum and the power of the output radiation. The two graphs in Fig. 7 correspond to the maximum of the spectral flux.

CSR effects

The electron bunches entering the magnetic chicane are of rms length $\sigma_z \approx 50\,\mu$m and high peak current $I_0 \approx 2.5$ kA. Therefore, despite the small bending angle $\theta = 3\,^\circ$,

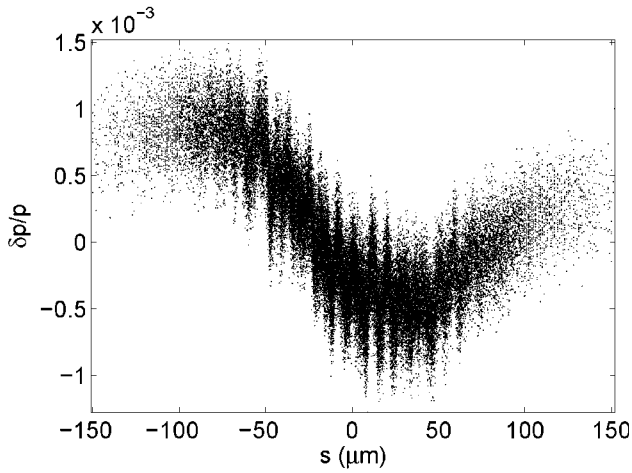

Figure 8: Distortion of the longitudinal phase space due to synchrotron radiation produced in the bypass dipoles.

the coherent component of synchrotron radiation, generated in the bypass dipoles, can be significant and might dilute the electron beam quality. Simulations of the CSR-induced emittance dilution have been made using the ELEGANT code, which result in a projected emittance growth in the order of a percent. The slice emittance is, however, almost unchanged. A much more significant impact on the longitudinal phase space is expected, as presented in Fig.8. The total relative energy spread has increased from 2×10^{-4} up to about 5×10^{-4}. The growth of the energy spread is due to the correlation in the longitudinal phase space created by the synchrotron radiation, but on the other hand the slice energy spread is practically unaltered. The increased energy spread will drive more particles outside of the amplifier bandwidth and as a result one anticipates a reduction of the gain. Moreover the correlation in the phase space produces side bands in the spectrum or in other words spectral broadening. Fig. 9 shows that there is about a factor of two decrease in spectral flux due to CSR effects. It is important to note that we have considered the worst case scenario i.e. the bypass optics and electron beam parameters have not been tuned to mitigate the impact of CSR.

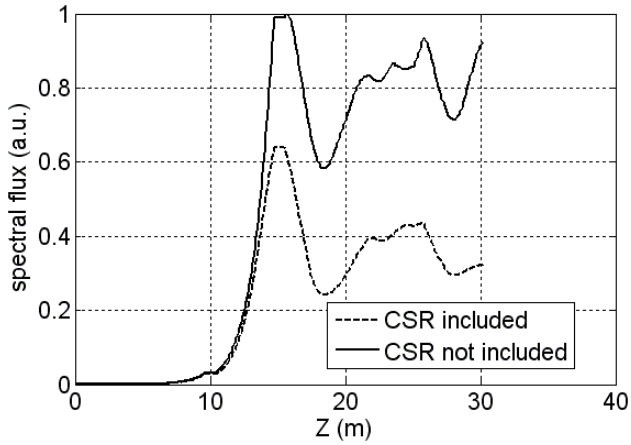

Figure 9: Demonstration of the impact of CSR effects - the spectral flux as a function of the undulator length.

CONCLUSIONS AND OUTLOOK

The operation of the two stage FEL has been studied, taking into account all the details in the design of the electron optics. Simulation results demonstrate a feasible operation in a wide range of electron energies and wavelengths. Investigated is also the possibility to fine tune the seeding wavelength, accomplished using the monochromator beamline settings. The impact of the coherent synchrotron radiation emitted in the bypass dipoles was studied. The simulations predict about a factor of two reduction of the spectral flux due to CSR. Further studies including wave front propagation through the monochromator beamline are ongoing [10]. As a next step the tolerances of the electron beam parameters, the accuracy of magnets alignment and the impact of the magnetic field errors will be analyzed.

ACKNOWLEDGEMENTS

We thank A. Meseck for the modifications of the code GENESIS and for many fruitful discussions.

REFERENCES

[1] J. Feldhaus et. al., Opt. Commun., 140 (1997), 341.

[2] R. Treusch et. al. "The Seeding Project for the FEL in TTF Phase II", HASYLAB Annual Report 2001.

[3] R. Reininger et. al., Nucl. Instr. and Meth. A (2001) 467-468, 38.

[4] B. Faatz et. al., Nucl. Instr. and Meth. A 475 (2001), 603.

[5] E.L. Saldin et al., Nucl. Instr. and Meth. A 539 (2001), 499.

[6] S. Reiche, Nucl. Instr. and Meth. A 429 (1999), 243.

[7] M. Borland, "elegant: A Flexible SDDS-Compliant Code for Accelerator Simulation," Advanced Photon Source LS-287, September 2000.

[8] M. Borland, Phys. Rev. ST Accel. Beams 4, 070701 (2001).

[9] E.L. Saldin et al., Nucl. Instr. and Meth. A 445 (2000), 178.

[10] Johannes Bahrdt et.al., "The Properties of the FEL Output for Self Seeding", these proceedings.

FERMI@ELETTRA: A SEEDED FEL FACILITY FOR EUV AND SOFT X-RAYS

E. Allaria, C.J. Bocchetta, D. Bulfone, F. Cargnello, D. Cocco, M. Cornacchia, P. Craievich, G. D'Auria, M.B. Danailov, G. De Ninno, S. Di Mitri, B. Diviacco, M. Ferianis, A. Galimberti, A. Gambitta, M. Giannini, F. Iazzourene, E. Karantzoulis, M. Lonza, F. Mazzolini, F. Parmigiani, G. Penco, L. Rumiz, S. Spampinati, M. Stefanutti, G. Tromba, M. Trovo', A. Vascotto, M. Veronese, M. Zangrando, Sincrotrone Trieste, Trieste, Italy
J.N. Corlett, L.R. Doolittle, W.M. Fawley, S.M. Lidia, G. Penn, I.V. Pogorelov, J. Qiang, A. Ratti, J.W. Staples, R.B. Wilcox, A. Zholents, LBNL, Berkeley, CA, USA
P. Emma, Z. Huang, J. Wu, SLAC, Stanford, CA, USA
W. Graves, F.X. Kaertner, D. Wang, MIT, Cambridge, MA, USA

Abstract

We describe the conceptual design and major performance parameters for the FERMI@Elettra Free Electron Laser (FEL) project funded for construction at Sincrotrone Trieste, Italy. This user facility complements the existing storage ring light source at Sincrotrone Trieste, and will be the first facility to be based on seeded harmonic cascade FELs. Seeded FELs provide high peak power pulses, with controlled temporal duration of the coherent output allowing tailored x-ray output for time domain explorations with short pulses of 100 fs or less, and high resolution with output bandwidths of the order of meV. The facility uses the existing 1.2 GeV S-band linac, driven by electron beam from a new high-brightness RF photocathode gun, and will provide tunable output over a range from ~100 nm to ~10 nm, and APPLE undulator radiators allow control of x-ray polarization. Initially, two FEL cascades are planned, a single-stage harmonic generation to operate over ~100 nm to ~40 nm, and a two-stage cascade operating from ~40 nm to ~10 nm or shorter wavelengh, each with spatially and temporally coherent output, and peak power in the GW range.

INTRODUCTION

The single-pass seeded FEL project FERMI@Elettra will be a User facility providing quality photons in the EUV to soft X-ray range. Photon production will be based on harmonic generation. The concept design has been studied and optimised towards a detailed engineering phase [1]. All major parameters and systems have been studied and an overview is presented here. Comprehensive studies including collective effects from space charge, coherent synchrotron radiation and wakefields as well as nonlinear dynamics from RF waveforms and bunch compressors have been performed to determine the optimum electron beam parameters for the facility. The studies have included error tolerances and beam jitter sensitivities in start-to-end computations.

The project covers the lower energy region of the XUV-X ray spectrum. With a peak brightness of more than ten orders of magnitude greater than 3rd generation sources, full transverse coherence, transform limited bandwidth, choice of pulse lengths of the order of a ps or less, variable polarization and energy tuneability, the FERMI source represents a powerful tool of scientific exploration in a large field of research. The coherence properties will provide single-shot imaging, allowing the study of chemical reactions as they happen. The high peak power will allow the study of non-linear multi-photon processes in a regime never explored before. The short time properties will allow the visualisation of ultra-short nuclear and electronic dynamics. The facility will enable the study of dilute samples of paramount importance in atmospheric, astrophysical and environmental physics, as well as in the characterization of nano-size materials. The applications extend from chemical reaction dynamics to biological systems, materials and surfaces, nano-structures and superconductors. The nature of harmonic generation schemes, with an external laser driving the FEL process, is particularly suitable for pump/probe synchronization at the ps time scale or less.

Figure 1 shows the layout of the facility. The accelerator and FEL complex is housed below ground and is composed of the following parts: (a) A photo-injector and two short linac sections, where a bright electron beam is generated and accelerated to ~100 MeV. (b) The main linear accelerator, where the electron beam is time-compressed and accelerated to a final energy of ~1.2 GeV. (c) A beam transport system to the undulators. (d) The undulator chains where the FEL radiation is generated. (e) The undulator to experimental area transport lines. (f) The experimental area. The new constructions include pushing back by ~ 80 m the linac tunnel and surface klystron gallery to make room for the photo-injector, accelerating sections and the first bunch compressor. At the downstream end, the klystron gallery is extended by ~30 m to power more accelerating sections. A FEL hall will be constructed below ground at the exit of the linac with transverse dimensions for the installation of up to four undulators side-by-side. Finally, an experimental hall, also below ground, will be constructed to house the FEL radiation transport optics and the experimental hutches. The facility will be provided with new support laboratories and office spaces.

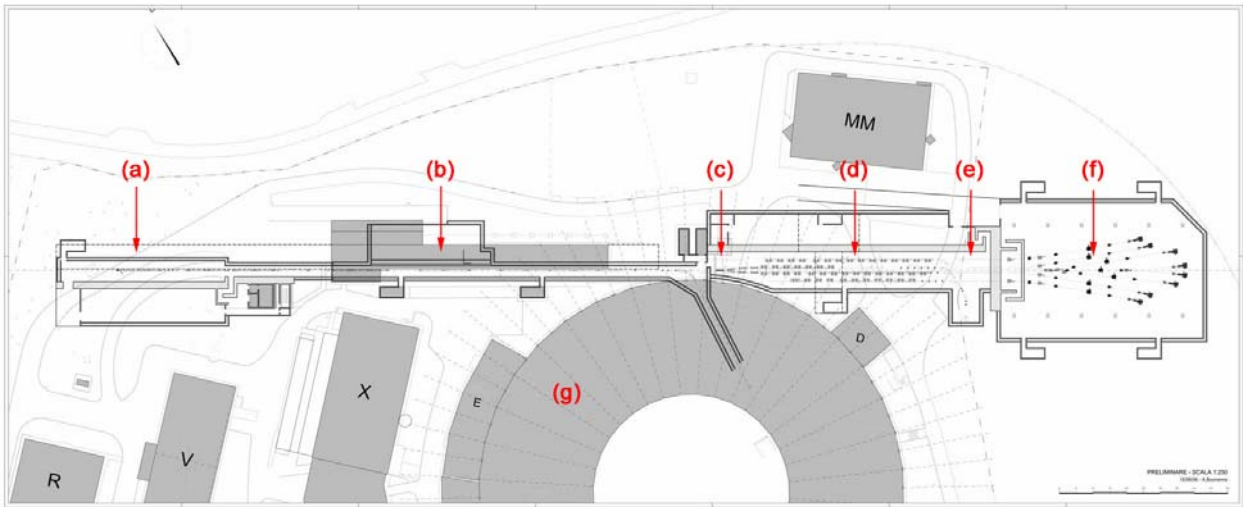

Figure 1: Schematic FERMI layout beside the ELETTRA storage ring building (g). See text for details.

THE PHOTO-INJECTOR

The photo-injector [2] is based on the proven 1.6 cell electron gun developed at BNL/SLAC/UCLA and adopted by the Linac Coherent Light Source (LCLS). The RF gun will provide a peak-accelerating gradient of 110 MV/m and an exit beam energy of around 5 MeV from a 10 MW peak input pulse (2.8 μsec). The injector will produce a 10ps long pulse with 0.8-1 nC charge and a rms normalized transverse emittance of 1.2 mm-mrad at 100 MeV. The initial repetition rate of 10 Hz will later be increased to 50 Hz following a modified gun design. The design includes a solenoid for emittance compensation, an off-axis diagnostic line and acceleration to 100 MeV with two booster S-band rf sections. These sections, named S0A and S0B, are part of the present Elettra injection system. Their on-axis, iris coupled cells resonate at 2.998 GHz in the 2π/3 mode, and provide peak accelerating gradients of ~18 MV/m, for a total energy gain of ~45 MeV (with operational 10% energy margin). The booster modules include solenoid magnets to provide transverse focusing, to assist with emittance compensation, and to match the optical functions at the input to the main linac.

A laser pulse provides temporal and spatial shaping of the electron bunch. To compensate wakefield effects in the main linac sections [3], the electron bunch should ideally have a linear ramped peak current distribution at the exit of the injector rather than a flat top [4]. Studies have showed that such a profile at the start of acceleration produces a more uniform energy and current profile at the entrance to the undulators. The FERMI photo-injector addresses this novel concept by using a laser profile that has a quadratic ramp. Space charge forces subsequently transform this distribution to a linear ramped current shape at the exit of the injector, i.e. a profile where the current in the bunch increases approximately linearly with time. The photo-injector laser system [5] includes two amplifier stages, a regenerative one followed by a multipass, and reaches pulse energy of 20 mJ in the IR. Pulse shaping is done partially in the IR, by an acoustic optic dispersive filter (DAZZLER), and completed in UV in a transmission grating based stretcher or Fourier-system. Beam shaping is done either in the IR or in the UV by an aspheric shaper. A small part ~400 μJ of the IR beam is split away and transported for use by the laser heater.

Beam dynamics in the injector system have been extensively modelled from photocathode emission to the exit of the booster accelerator modules using 2D and 3D space-charge tracking codes (GPT and ASTRA). Simulations confirm that electron beam performance objectives for injection into the main linac at ~ 100 MeV are reachable. The timing and charge stability are both challenging, 0.5 ps and 1% respectively, but have been shown to be within present state of the art techniques.

ACCELERATION, COMPRESSION AND BEAM TRANSPORT

The accelerator is shown schematically in Figure 2 [6]. It consists of four linacs, two bunch compressors, a laser heater and a beam transport system (spreader) to the undulators. The function of this system is to accelerate the electron beam to the FEL energy of ~1.2 GeV and to compress the ~10 ps long pulse from the photo-injector to the final lengths and peak current. Two FEL layouts are envisaged. FEL-1 will provide photons with wavelengths in the range 100-40 nm. Depending on the experiments, electron bunch lengths of 200 fs and a peak current of 800 A or higher can be provided (in this case with shorter bunch lengths). For those experiment where small time jitter is important, and to account for a predicted jitter of up to 400 fs, an electron bunch of 600 fs (“medium bunch”) has been designed. Including the inevitable inefficiency of the compression system, the obtainable peak current is ~800 A with 0.8 nC of charge from the photo-injector. FEL-2 will cover the wavelength range 40-10 nm and will make use of a ~1 ps long pulse to provide close to Fourier-transform-limited radiation and

or a ~200 fs high brightness FEL radiation using the fresh-bunch technique. In both cases a "long bunch" of 1.5 ps is required from the accelerator. With 1 nC charge from the injector, the attainable peak current is ~ 500 A.

For both FELs the final energy and charge distributions correlated with the distance along the electron bunch should be as flat as possible in order not to broaden the FEL bandwidth. The aim is to produce an energy variation no greater than 1-2 x 10^{-4} along the useable part of the bunch and a peak current variation no greater than ~100 A. In transverse space, the horizontal and vertical normalized emittances at the end of the linac, 1.2 GeV, will not be greater than 1.5 mm-mrad in order to meet the desired photon throughput. This represents a ~30% increase from the photo-injector simulation results and includes a safety margin against emittance dilution effects. The emittance value of 1.5 mm-mrad is a condition of the shortest wavelength and accelerator performance is aimed at satisfying this most stringent requirement. This specification may be relaxed for longer photon wavelengths.

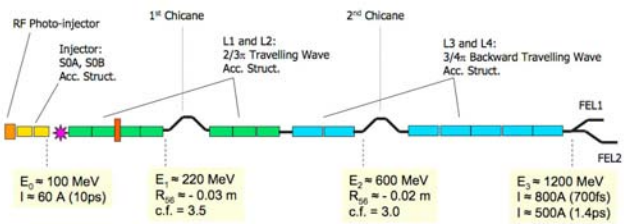

Figure 2: Schematic layout of the accelerator. The star indicates the position of the laser heater, while the red section the X-band accelerator.

At the exit of the photo-injector the electrons enter the L1 linac where they are accelerated to ~250 MeV. Acceleration occurs off-crest to provide correlated energy spread along the bunch that will compress it in the first compressor BC1. An RF structure tuned at the 4th harmonic of the main s-band sections, ie at X-band frequency, is placed half-way in L1. The function of the X-band linac is to provide the non-linear quadratic and, when operated off-crest, cubic corrections of the correlated momentum distribution along the bunch in the presence of the non-linearities of the photo-injector, the magnetic compressors and the non-linear effects of the longitudinal wakefields.

The linac structures L2 and L3 between the first and second bunch compressors accelerate the beam from ~ 250 MeV to ~650 MeV. They also provide the residual momentum chirp for the second compressor, BC2. After BC2 the beam is further accelerated to its final energy in the L4 structure. The phases of the linac after BC1 are chosen to provide the necessary momentum spread for compression and also to cancel the linear part of the longitudinal wakefields. The non-linear correlated momentum spread at the end of the linac is fine-tuned with the amplitude and phase of the X-band structure. The focusing structure of the linac is designed to minimize transverse emittance dilution due to transverse wakefields, momentum dispersion and coherent synchrotron radiation in bending magnets. Exhaustive computations with codes LiTRACK and "elegant" were performed to optimise beam parameters and to simulate expected jitter and parameter sensitivities. The computed electron distributions were further used in the FEL simulation studies.

The electron beam is transported from the end of the linac to the FELs by a FODO spreader channel. It is designed for diagnostics and parallel separation of the two FELs. The spreader has been designed to preserve electron beam emittance. This is done in two ways: by using a lattice with a small "curly-*H*" function in the magnets and by employing a scheme of self emittance compensation. Quadrupoles in the deflecting arcs, located near the positive and negative peaks of the dispersion function, are separated by a unit transfer matrix and. This allows simultaneous change of their gradients and the production of a dispersion bump localized between the quadrupoles. Control of this bump regulates R56 within the spreader allowing it to be exactly zero or any other reasonable value. It is in fact kept slightly positive in some cases to disperse the electrons in the spikes of the peak current.

THE UNDULATORS AND THE FEL PROCESS

FEL configurations are based on harmonic generation schemes seeded by an external laser. FEL-1 will utilise one stage (modulator, dispersion section and radiator) while for FEL-2 two stages will be used in a fresh part of the bunch seeding scheme. A whole bunch seeding scheme was also studied for FEL-2 and requires a larger number of undulators and a higher quality electron beam.

FEL-1 and FEL-2 are required to have continuously tuneable output polarizations at all wavelengths, ranging from linear-horizontal to circular to linear-vertical. For this reason, the FEL-1 radiator and the final radiator in FEL-2 have been chosen to have APPLE-II configurations with pure permanent magnets. For the modulator a simple, linearly-polarized configuration, is optimal both due to its simplicity and because the input radiation seed can be linearly polarized. The tuning of the wavelength will be done by changing the gap of the undulator while keeping the electron beam energy constant. The magnetic lengths of the undulators segments are 2.34 m (containing 36 periods) for the FEL-1 and 1st FEL-2 radiators and 2.40 m (48 periods) for the 2nd FEL-2 radiator. FEL-1 and 2 consist of 6 and 10 segments respectively. The intra-segment spools contain electromagnetic quadrupoles, high quality beam position monitors and quadrupole movers to steer the electron trajectory.

Theoretical and computational studies led to a selection of the accelerator and FEL parameters. An exhaustive study through start-to-end simulations, that included the use of FEL codes GENESIS and GINGER, was performed [7]. The simulations took into account

perturbations in the accelerator and FEL parameters. In particular parameter sensitivity and time dependent jitter studies were carried out for both FELs. Studies of the variation of mean energy, energy spread, peak current, emittance and seed input power were done both for single and multi-parameter variations. Methods, such as undulator tapering, to reduce the sensitivity to variations, were also examined. Table 1 gives the expected performance parameters for the two FELs.

The seed laser will provide tuneable UV radiation in two pulse duration schemes: 100 fs and 1 ps. A dual pulse duration regenerative amplifier will be used. In the 100 fs case the amplifier directly pumps a travelling wave parametric amplifier (TOPAS) followed by harmonic conversion stages. In the 1 ps case this output is further amplified in a two pass stage to the 10 mJ level that then pumps a ps TOPAS. Timing and synchronization [8] of RF, laser and diagnostic systems will be guaranteed to sub 50 fs levels by an integrated system handling both CW and pulsed transmission schemes. A central clock system generating stable timing signals for the whole facility will be used. The signals will be distributed over distances exceeding 300 m by optical fibres in a star configuration. Timing information is transmitted using either RF modulated CW light mainly for the RF systems or pulsed light mainly for the laser systems.

The consequence of orbit displacements from the ideal trajectory in the undulators were simulated. The FEL process at the shortest wavelength, 10 nm, requires the straightness of the electron orbit in the undulators to be within 10 μm (rms value over the undulators length). Although this is beyond state-of-the art mechanical alignment techniques, realistic simulations show that a combination of the latter and of beam-based-alignment (tested at the Stanford Linear Collider and proposed for the LCLS) will achieve the desired performance.

Table 1: Principal FEL output parameters

Parameter	**FEL-1**	**FEL-2**
Wavelength range [nm]	100 to 40	40 to 10
Output pulse length (rms) [fs]	< 100	> 200
Bandwidth (rms) [meV]	17 (at 40 nm)	5 (at 10 nm)
Polarization	variable	Variable
Repetition rate [Hz]	50	50
Peak power [GW]	1 to >5	0.5 to 1
Harmonic peak power (% of fundamental)	~2	~0.2 (at 10 nm)
Photons per pulse	10^{14} (at 40 nm)	10^{12} (at 10 nm)
Pulse-to-pulse stability	≤ 30 %	~50 %
Pointing stability [μrad]	< 20	< 20
Virtual waist size [μm]	250 (at 40 nm)	120
Divergence (rms, intensity) [μrad]	50 (at 40 nm)	15 (at 10 nm)

PHOTON BEAM TRANSPORT AND EXPERIMENTAL AREAS

After leaving the undulators the electron beam, carrying an average power of 75 W (at 50 Hz) will be dumped into a shielding block by a sequence of bending magnets, while the FEL radiation will be transported to the experimental areas. The transport optics is designed to handle the high power density (up 10 GW) in a very short temporal interval. In order to handle the high peak photon energy density, the beam line optics operate at low grazing incidence angles with low Z-materials and the radiation intensity can be controlled by a gas absorption cell. The vacuum system is windowless with differential pumping sections. Pulse length preservation, mono-chromatization, energy resolution, source shift compensation, focusing in the experimental chamber and beam splitting are all included in the design of the FEL radiation transport system.

REFERENCES

[1] FERMI@Elettra Conceptual Design Report, 2006, to be published.

[2] M. Trovo', et al., "Further Studies in the FERMI@Elettra Photoinjector Optimisation", this conference.

[3] S. Di Mitri, "How to obtain high quality electron bunches in the presence of normal conducting wakefields", this conference.

[4] G. Penco, et al., "Ramping longitudinal distribution studies for the FERMI@Elettra injector", this conference.

[5] M. Danailov, et al., "Design of a two stage laser pulse shaping system for FEL photoinjectors", this conference.

[6] G. D'Auria, "Linac design for the FERMi Project", LINAC conference, 2006, Knoxville, Tennessee, USA.

[7] G. De Ninno, et al., "Design and optimisation of the FERMI@Elettra FEL" and "Start to end time-dependent study of FEL output sensitivity to electron beam jitters for the first stage of FERMI@Elettra project", this conference.

[8] M. Ferianis, "Timing and Synchronization in Large-Scale Linear Accelerators", LINAC conference, 2006, Knoxville, Tennessee, USA.

COHERENT HARMONIC EMISSION OF THE ELETTRA STORAGE RING FREE ELECTRON LASER IN SINGLE PASS CONFIGURATION: A NUMERICAL STUDY FOR DIFFERENT UNDULATOR POLARIZATIONS

F. Curbis*, University of Trieste & Elettra, Basovizza, Trieste, Italy,
H.P. Freund, Science Applications International Corporation (SAIC),
G. De Ninno, Elettra, Basovizza, Trieste, Italy.

Abstract

The optical klystron installed on the Elettra storage-ring is normally used as interaction region for an oscillator free-electron laser, but, removing the optical cavity and using an external seed laser, one obtains an effective scheme for single-pass harmonic generation. In this configuration the high-power external laser is synchronized with the electron beam entering the first undulator of the optical klystron. The laser-electron beam interaction produces a spatial partition of electrons in micro-bunches separated by the seed wavelength. The micro-bunching is then exploited in the second undulator to produce coherent light at the harmonics of the seed wavelength. The Elettra radiator is an APPLE type undulator and this allows to explore different configurations of polarization. We present here numerical results obtained using the code Medusa for both planar and helical configurations. We also draw a comparison with predictions of the numerical code Genesis.

INTRODUCTION

Coherent Harmonic Generation (CHG) can be implemented in a storage ring using two undulators as a cascade. The first undulator (called modulator) is tuned at the wavelength of an external high-power laser and the second undulator (called radiator) at a higher harmonic of the seed. Between the undulators there is a region, i.e., dispersive section, with a strong magnetic field, which, in single-pass configuration, converts the energy modulation, occurred in the modulator, in spatial modulation (usually referred as "bunching"). The Elettra storage-ring FEL is presently operating in oscillator configuration [1, 2], but, with minor modification, the optical klystron will be used as interaction region for CHG in single-pass configuration. In the new configuration (see Figure 1) the optical cavity will be removed and a conventional laser will be focused into the modulator and synchronized with the electron beam. The main difference between conventional single-pass seeded FEL and storage-ring harmonic generation is that in the latter case the electron beam is re-circulated and not renewed each pass through the optical klystron. This peculiarity determines the maximum repetition rate for this configuration, because the electrons need few synchrotron damping times (order of ten of milliseconds) to cool down after each interaction with the seed laser. Preliminary simulations [3] have been done using Genesis [4] for different working points, i.e. different machine (electron-beam energy, Twiss parameters, emittance, strength of the dispersive section) and the seed laser (power and duration) parameters. The work reported in this paper characterizes the emission of the Elettra APPLE-type undulator, operated in both linear and helical configurations. Numerical results are obtained using Medusa and Genesis. Medusa provides the possibility to calculate the harmonic power at the end of the radiator. This means that the radiator is tuned at the third harmonic of the seed laser (i.e. the fundamental in the modulator) and Medusa is able to calculate any desired harmonics besides the fundamental. This will allow to investigate if wavelengths shorter than the fundamental will be detectable. The external seed laser [5] is be a titanium-sapphire (Ti:Sa) with a very high peak power (2.5 GW) and very short pulse duration (variable between 100 and 250 fs (RMS)). The repetition rate will be initially 10Hz. Using this frequency, the contribution from incoherent synchrotron emission, provided by electrons circulating in the storage ring but not interacting with the seed laser, may spoil the signal-to-noise ratio. Possible strategies will be explored in the aim of increasing the repetition rate, therefore improving the signal quality. The first undulator is tuned at the fundamental of the seed laser (240 nm), while the second undulator at the third harmonic (80 nm).

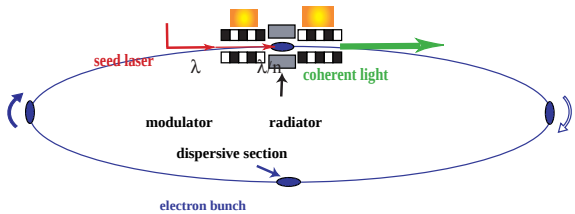

Figure 1: Layout of the Elettra storage-ring FEL after removing the optical cavity and using an external seed laser.

OPTIMIZATION FOR MEDUSA SIMULATIONS

In this section we report some studies performed in time-independent mode in order to optimize the parameters before the introduction of the slippage, e.g. time-dependent simulation. The main run parameters used in Medusa simulations are reported in Table 1 [5, 6]. With respect to the

* francesca.curbis@elettra.trieste.it

values used in Genesis simulations, there are some minor differences: the pulse shape of the electron bunch and the seed laser is parabolic instead of Gaussian, the seed duration is 250 fs FWHM instead of 140 fs and the number of periods for both undulators is 22 instead of 20, because Medusa needs one period more at the entrance and exit of the undulator to properly model the simulation. The variation of the radiator output power versus the dipole field strength in the chicane is shown in Figure 2 for the case of a planar radiator. We have found from Genesis simulation that the energy spread induced by the seed laser is so high that the beam needs only a drift to transform the energy modulation in spatial modulation (bunching). In Medusa simulation instead, the power level when the chicane field vanishes is 1.06 MW (and this is very close to the time-dependent result), but a little more power (about 1.36 MW) could get using a chicane field of about 0.5 kG. However, in order to compare the results of these two codes, we have chosen to set to zero the chicane field also in this case. The same power optimization with respect to the magnetic field has been performed tuning the radiator at the third harmonic (see Figure 3). The output power at 80 nm is about 1.7 MW which is almost a factor two over the value found for the planar undulator. The second harmonic (40 nm) power is not very sensitive to the variation of the chicane field and is about 200 W when the chicane field is set to zero. These results have been confirmed by time dependent simulations. The same behavior has been found for a helical undulator tuned at the second harmonic (120 nm) of the seed laser. The result, shown in Figure 4, looks similar to previous case: the highest power is found when the chicane field is set to zero and the power is about 4.7 MW at 120 nm and 5.7 kW at 60 nm. As before, while the power at the fundamental (120 nm) drops fast with increasing chicane field, the harmonic power (60 nm) doesn't drop so much. An other important issue to be considered when using numerical codes is the number of simulated particles which is needed in order to guarantee a correct modelization of the process. For the CHG in helical configuration, we found that a larger number of particles is needed with respect to planar configuration. The case for zero energy-spread is reported in Figure 5. We can argue from the results that to do this kind of simulation about 60000 particles per slice are needed without energy spread and, including the energy spread, an order of magnitude more particles is required. In the latter case, the power level will be of course smaller. To conclude, in order to treat the energy spread and the additional harmonics, the following runs used 1210104 particles.

Table 1: Run parameters used in Medusa simulations

Electron beam	
Energy	0.9 GeV
Peak current	77 A
x-Emittance	2.46 mm-mrad
y-Emittance	0.246 mm-mrad
Energy-spread	0.12%
Bunch length	27 ps
Bunch charge	1.38 nC
Bunch shape	parabolic
Twiss parameters	
α_x = 0.24	β_x = 8.986
α_y = 0.89	β_y = 4.695 m
Modulator	
Magnitude	5.62kG
Period	10.0 cm
Length	22 periods
Radiator	
Magnitude	3.00kG
Period	10.0 cm
Length	22 periods
Undulator-to-undulator gap	0.9 m
Seed laser	
Wavelength	240 nm
Seed power	2.5 GW
Seed duration	0.25 ps
Seed shape	parabolic

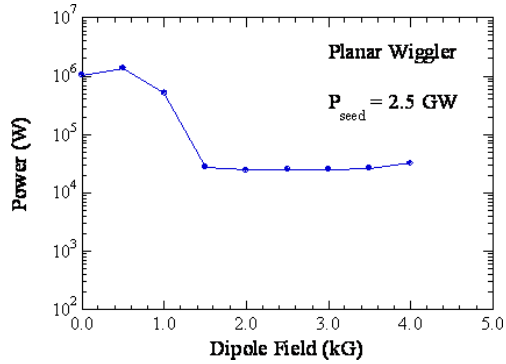

Figure 2: Output power versus dipole field strength at 80 nm for planar radiator.

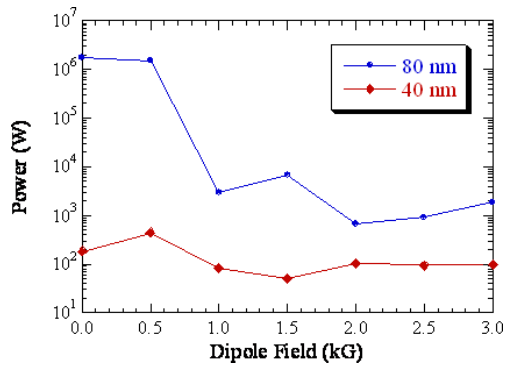

Figure 3: Output power versus dipole field strength for helical undulator tuned at at 80 nm and second harmonic (40 nm) power.

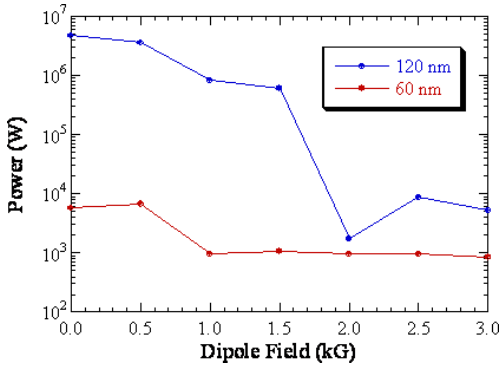

Figure 4: Output power versus dipole field strength for helical undulator tuned at 120 nm and second harmonic (60 nm) power.

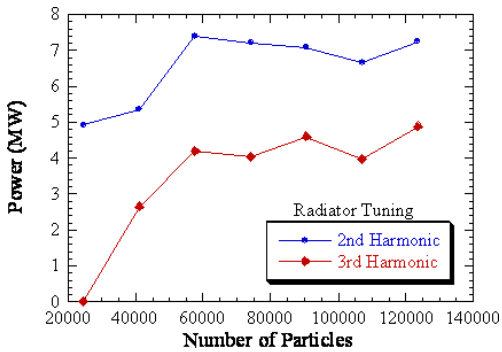

Figure 5: Output power versus number of simulated particles for helical undulator tuned at the second and the third harmonic of 240 nm.

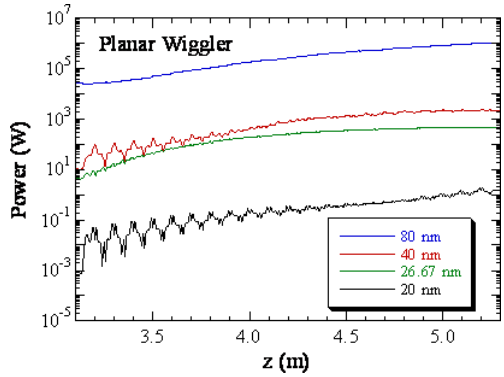

Figure 6: Evolution of the 80 nm radiation and its first three harmonics in planar configuration.

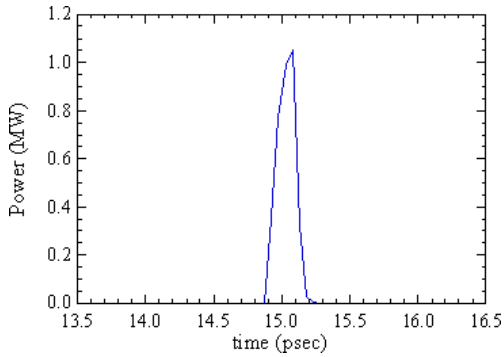

Figure 7: Power versus time of the 80 nm pulse at the end of the radiator in planar configuration.

MEDUSA PERFORMANCE

Planar undulator

In time-dependent mode, we firstly looked at the harmonics of the 80 nm wavelength, using 2.5 GW seed power and zero magnetic field inside the dispersive section. The evolution along the undulator of the fundamental (80 nm) and the first three harmonics of that wavelength are shown in Figure 6. The second harmonic (40 nm) reaches a power level of about 2 kW, the third harmonic (26.67 nm) a power level of about 500 W and the fourth harmonic (20 nm) a power of 2 W. While in the steady-state simulations we looked exclusively at the evolution of the power along the radiator, in time-dependent simulations the output temporal profile (see Figure 7) and the harmonic spectrum (see Figure 8) can be displayed. The electron bunch is two order of magnitude longer than the seed laser (27 ps versus 250 fs) and the total slippage, considering 80 nm wavelength and 44-periods undulator, is much smaller than the bunch-length, thus the differences between steady-state and time-dependent simulations are expected to be small. Indeed, the observed peak power is about 1MW in both cases. The shortness of the laser pulse may lead to numerical problems because one should increase the number of slices in order to resolve the FEL pulse structure and an adequate number of particles must be holden in each slice. In our case, the simulation includes 600 slices, with 17496 particles per slice, but only about 10 slices across the seed pulse. This is the reason why the output spectrum in Figure 8 is not smooth and displays a spiky behavior. If one believes the problem is the lack of resolution, the envelope could be considered as the spectral shape. Considering the Fourier

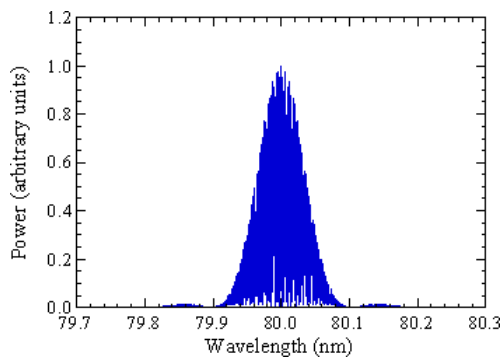

Figure 8: Fourier transform of the output spectrum at 80 nm (planar configuration).

limit, given by the equation:

$$\frac{c \cdot \Delta t[FWHM]\Delta\lambda[FWHM]}{\lambda^2} = 0.441 \qquad (1)$$

where c is the speed of light, Δt is the $FWHM$ duration of the output pulse, $\Delta\lambda$ is the $FWHM$ of the output spectrum and λ is the emission wavelength, the results presented here give a quantity that is 1.7 times above the limit. This value indicates that the emitted light have an high level of coherence.

Helical undulator

As already reported before, the steady-state simulation could give enough information about the power level of the 80 nm signal and the first two harmonics of that. For this reason, the simulation of the helical configuration has been obtained in time-independent mode. In Figure 9 the evolution of the signal power along the radiator is displayed. One can observe that the 40 nm harmonic is still about 1 kW as in planar configuration, but the 26.67 nm harmonic has a much lower power than for the planar undulator.

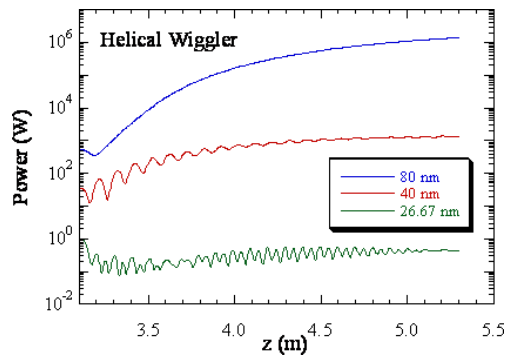

Figure 9: Evolution of the 80 nm radiation and its first two harmonics in helical configuration.

Comparison with Genesis simulation

The campaign of simulation has been completed exploring the helical polarization in Genesis. The power level founded at 80 nm for each configuration is very close between Genesis and Medusa and between planar and helical configuration the differences are lower than one order of magnitude. All Genesis simulation has been performed in time-dependent domain, but, to limit the computing time, just a portion of the electron bunch around the seed pulse has been simulated, with the implicit assumption that the slippage doesn't not affect too much the emission.

The evolution of the output power along the radiator is shown in Figure 10 for both planar and helical configuration. In comparison with Medusa, Genesis results don't exhibit a big difference between planar and helical power. The value found is about 1.1 MW in both cases, as shown also in Figure 11, where the power is plotted as a function of time at the end of the radiator.

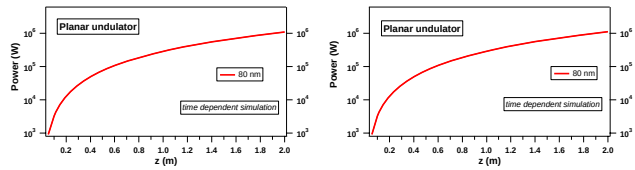

Figure 10: Harmonic power for planar undulator (at left) and helical undulator (at right) obtained tuning the radiator at 80 nm.

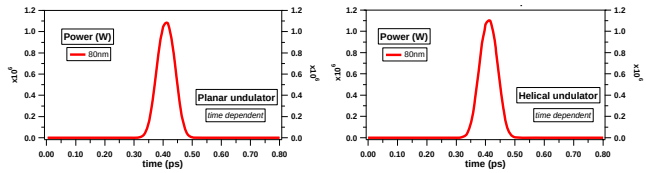

Figure 11: Temporal profile for planar undulator (at left) and helical undulator (at right) obtained tuning the radiator at 80 nm.

The Fourier transform of the output spectrum is reported in Figure 12. Using the Equation 1, we found a value that is 1.6 times above the limit. Also in this case, the radiation emitted shows an high degree of coherence.

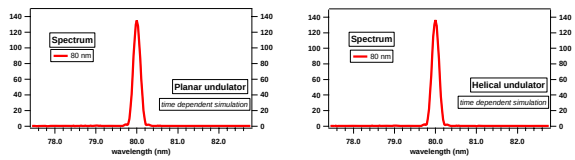

Figure 12: Harmonic spectrum for planar undulator (at left) and helical undulator (at right) obtained tuning the radiator at 80 nm.

CONCLUSION

The Medusa simulations confirmed in general the results already obtained by Genesis, with a good agreement in both planar and helical configuration. Some differences should be longer investigated, i.e., the higher power level found in planar configuration when the dispersive section is 0.5 kG and the factor two more power found in helical radiator.

REFERENCES

[1] R. P. Walker, Proc. EPAC'99, 93.

[2] G. De Ninno et al., *Nucl. Instrum. and Meth. A* **483** (2002) 177.

[3] F. Curbis, G. De Ninno, Proc. FEL'05.

[4] S. Reiche, *Nucl. Instrum. and Meth. A* **429** (1999) 243.

[5] M. Danailov, Private Communication.

[6] F. Iazzourene, Private Communication.

DESIGN AND PERFORMANCE OF THE FERMI AT ELETTRA FEL

G. De Ninno, E. Allaria, Sincrotrone Trieste, 34012 Trieste, Italy;

W. Fawley, G. Penn, LBNL, Berkeley, CA 94720-8211 USA.

Abstract

The FERMI at ELETTRA project will be comprised of two FELs, each based on the principle of seeded harmonic generation. The first undulator line, FEL-1, will operate in the 40-100 nm wavelength range relying upon one stage of harmonic up-conversion. The second undulator line, FEL-2, extends the output spectral domain to the 10-40 nm wavelength range and will use two harmonic stages operating as a cascade. We review the FEL studies that have led to the final design and present results of numerical simulations with GENESIS and GINGER codes including predicted output bandwidths and the effects of shot-to-shot fluctuations in multiple input parameters.

INTRODUCTION

The FERMI@ELETTRA project is based on the harmonic up-shifting of an initial radiation "seed" signal in a single-pass FEL amplifier employing multiple undulators. The basic principles which underlie this approach are: energy modulation of the electron beam via the resonant interaction with an external laser seed in a first undulator (modulator); use of a chromatic dispersive section to then develop a strong density modulation with large harmonic overtones; production of coherent radiation by the microbunched beam in a downstream undulator (radiator). The first stage of the project, FEL-1, aims at generating coherent output radiation in the 40-100 nm spectral range. For these wavelengths, users require short (< 100 fs) pulses with adjustable polarization together with high temporal and spatial reproducibility. The project's second stage, FEL-2, will extend the spectral range down to 10 nm. Present users' requirements for FEL-2 point to long (narrow-bandwidth) pulses with high peak brilliance and adjustable polarization. FEL-1 relies upon a single-stage scheme (i.e., modulator-dispersive section-radiator), similar to the one already operational at Brookhaven [1]. As for FEL-2, a two-stage harmonic cascade is necessary for reaching short wavelengths. The selected configuration is based on the so-called "fresh bunch" approach [2], in which the output radiation from the first radiator is used to energy-modulate in a subsequent modulator a part of the electron beam that did not interact in the first stage with the external seed.

In this paper we review the FEL studies that have led to the final design of FEL-1 and FEL-2 and present results of both time-independent and time-dependent numerical simulations with GENESIS and GINGER.

BASIC FEL OUTPUT REQUIREMENTS AND RELATED ISSUES

Table 1 summarizes the basic FEL output requirements for FEL-1 and FEL-2. At all wavelengths, both FEL-1 and FEL-2 are to have continuously tuneable output polarizations ranging from linear-horizontal to circular to linear-vertical. Consequently, the FEL-1 radiator and final radiator in FEL-2 have an APPLE-type configuration. Both FELs will operate at the accelerator repetition rate of 10-50 Hz.

At present it is believed that the major application for FEL-1 will involve time-domain experiments such as pump-probe interactions and possibly nonlinear phenomena. Consequently, the requirements for FEL-1 are more related to total photon number per pulse (*i.e.,* 0.4 – 2×10^{14}) and pulse duration (20-100 fs) than they are to spectral bandwidth. A critical parameter affecting the needed electron beam duration is the timing jitter in the beam relative to that of the seed laser. In order that there be reasonably overlap between the seed and the electrons, the duration of the electron beam must be bigger than the duration of the seed pulse plus two times the RMS timing jitter. The expected RMS timing jitter from the accelerator is of order 130 fs [3], and therefore an electron-beam pulse duration of at least 600 fs is needed for 100-fs seed pulses. This timing jitter requirement may be one of the more difficult to satisfy in terms of the injector and accelerator subsystems.

Another important parameter associated with FEL-1 time domain experiments is shot-to-shot repeatability. Ideally, for nonlinear phenomena experiments, shot-to-shot RMS jitter in normalized photon number should be 5% or less. As reported in [3], we do not at present believe that such a low value is obtainable with the expected accelerator and injector parameters. Many FEL-1 experiments will be able to deal (via recording individual shot photon number for later post-processing) with values as high as 25% or greater.

In contrast to FEL-1 users, for whom timing and photon number jitter are critical parameters, most FEL-2 users are (presently) interested in the frequency domain experiments where longitudinal coherence and narrow bandwidth are crucial. The most important output goal for FEL-2 is $\geq 10^{12}$ photons/pulse/meV. Consequently, FEL-2 requirements favor long output pulses (≥ 200 fs) whose spectral properties are as close as possible to the transform limit. Although the total photon jitter is not critical for most experiments in the frequency domain, shot-to-shot central wavelength jitter is of concern. Consequently, in order not to increase the effective time-

averaged, output bandwidth as seen by the user, the wavelength jitter needs to be less than the individual shot bandwidth.

UNDULATOR DESIGN

In the FERMI case, wavelength tuning in the undulators will be done by changing the gap (and thus a_w) and not by changing the electron beam energy.

The FEL-1 undulator layout is shown in Fig. 1.

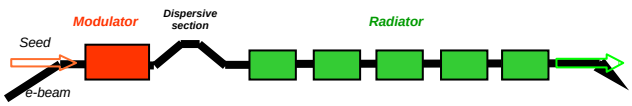

Fig. 1: FEL-1 undulator layout

For the first modulator which must satisfy FEL resonance over a nominal wavelength range of 240 to 360 nm, an undulator wavelength of 16 cm has been adopted. The modulator will be a standard planar undulator about 3-m long. In order to reach saturation over the whole spectral range, the necessary active radiator length for FEL-1 is about 16 m. For many reasons (e.g., magnetic forces, alignment, external focusing and diagnostic needs, possible tapering), this is far too long to construct as one continuous magnetic structure. Consequently, the radiators will be subdivided into six modules, each consisting of an active undulator segment (with a period of 6.5 cm and a length of about 2.3 m) and a break segment (about 1 m long), with the latter containing a number of items such as quadrupoles, a longitudinal phase shifter, beam position monitors, dipole correctors, and diagnostics. In order to produce light with variable polarization, the radiator modules will be APPLE-type. The FERMI design includes external quadrupole focusing to produce an average value of 10 m for the Twiss beta function in each plane.

Following the modulator is a break section (about 1 m long) that contains a magnetic chicane whose chromatic dispersion is used to develop a strong coherent microbunching from the energy modulation impressed upon the electron beam by the FEL interaction in the modulator. The undulator layout for FEL-2 is shown in Fig. 2.

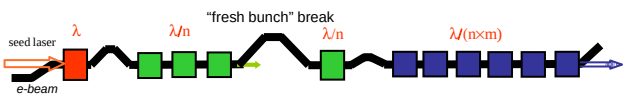

Fig. 2: FEL-2 undulator layout

The selected configuration is based on the so-called "fresh bunch" approach [2], in which the radiation from the first radiator is used to energy-modulate in a subsequent modulator a "fresh" part of the electron beam that did not interact with the external seed. The core design for the first stage of fresh-bunch FEL-2 is extremely similar to that described earlier for FEL-1.

Where the design for FEL-2 fresh bunch layout begins to differ significantly is that the first stage radiator is relatively short (i.e., 2-3 segments) and only brings the radiation to a sufficient level to provide adequate coherent energy modulation in the following undulator. The basic parameters for the second stage modulator are the same as for the first stage radiator (i.e., 6.5-cm period; 2.3-m segment length). In general, the choice has been made to keep the first stage as short as possible, both for cost reasons and to minimize SASE growth which can increase the incoherent energy spread of the "fresh" portion of the e-beam to be used in the second stage modulator and radiator. The second-stage radiator has a shorter period (5 cm) and is subdivided into 2-m long active APPLE-type undulator segments separated by 1-m breaks. These breaks contain a quadrupole singlet for focusing, a phase shifter, dipole correctors, and diagnostics. The length of the final radiator is somewhat arbitrary; in general it has been presumed for the fresh bunch approach one would want sufficient length for power saturation, i.e., 6 segments at 10-nm wavelength. However, one could certainly increase the output power by adding more radiator segments and possibly also taper the undulator strength.

FEL-1 PERFORMANCE

Figure 3 displays the growth of power at 40-, 60-, and 100-nm wavelengths as predicted by the GENESIS and GINGER codes (each operated in time-independent mode). Electron-beam and seed parameters are reported in the figure caption.

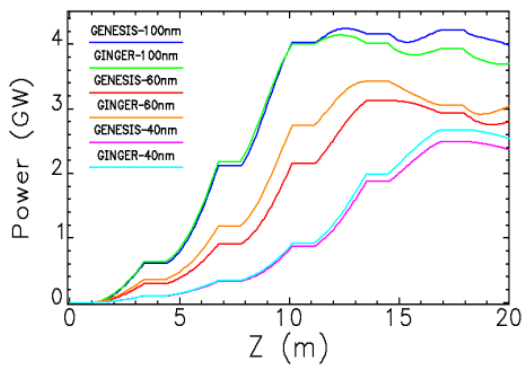

Fig. 3: Power growth as a function of radiator distance for FEL-1 tuned at 100-, 60-, and 40 nm, as predicted by Genesis and Ginger. Electron-beam parameters utilized for the simulation are: energy = 1.2 GeV; current = 800 A; incoherent energy spread (RMS) = 150 keV; normalized emittance = 1.5 mm mrad; input seed power = 100 MW; input seed wavelength = 240-300 nm.

As can be seen in Fig. 3, at the longer wavelengths power saturation is reached well before the end of the sixth section. The simulations show good basic agreement between the GENESIS and GINGER predictions. A factor of about two in output power can be gained by properly tapering the six radiator segments.

In order to get an estimate of output power sensitivity to electron beam and laser parameters, an extensive set of GENESIS and GINGER simulations has been performed varying single parameters at a time.

Parameter	FEL-1	FEL-2
Wavelength range [nm]	100 to 40	40 to 10
Output pulse length (rms) [fs]	≤ 100	> 200
Bandwidth (rms) [meV]	17 (at 40 nm)	5 (at 10 nm)
Polarization	Variable	Variable
Repetition rate [Hz]	50	50
Peak power [GW]	1 to >5	0.5 to 1
Harmonic peak power (% of fundamental)	~ 2	~ 0.2 (at 10 nm)
Photons per pulse	10^{14} (at 40 nm)	10^{12} (at 10 nm)
Pulse-to-pulse stability	≤ 30 %	~50 %
Pointing stability [μrad]	< 20	< 20
Virtual waist size [μm]	250 (at 40 nm)	120
Divergence (rms, intensity) [μrad]	50 (at 40 nm)	15 (at 10 nm)

Table1: FEL-1 and FEL-2 expected performance

We present here time-independent calculations in which the input laser seed power and various electron beam quantities were allowed to vary independently around their individual design values (see Table 1) following Gaussian distributions characterized by the following RMS values: mean electron energy: 0.1%; current: 8%; emittance: 10%; energy spread: 10%; input seed power: 5%. Expected output fluctuations are about 22 % (see Fig. 4). The most limiting factor to output stability is represented by the 0.1% input energy fluctuation. Detailed time-dependent start-to-end simulations, including the impact on output stability of seed-bunch time jitter and beam distribution homogeneity, are reported in [3].

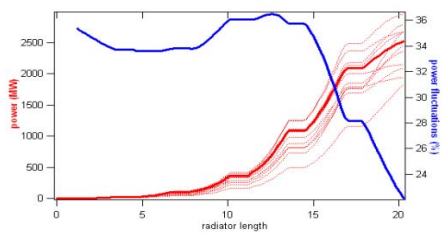

Fig. 4: Power growth for different initial random conditions (red curves, left vertical scale) and associated power fluctuation (blue curve, right vertical scale) vs. radiator distance.

A campaign of time-dependent start-to-end simulations has been performed making use of various electron-beam distributions provided by the FERMI gun and linac groups [4]. Figure 5 shows the GENESIS-predicted output temporal and spectrum profiles at 40-nm wavelength for an optimized (i.e., flat in both energy and current) input electron-beam distribution. The input seed was a 40-fs (RMS) Gaussian at a peak power of 100 MW.

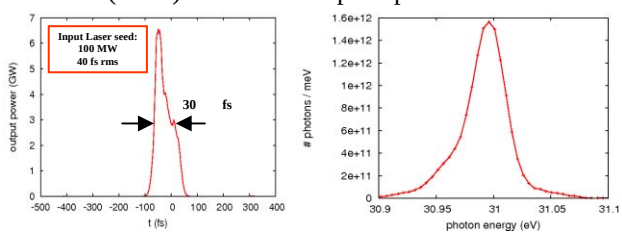

Fig. 5: FEL-1 temporal and spectrum profiles resulting from a GENESIS simulation in time-dependent mode.

The output number of photons per pulse is about $9 \cdot 10^{13}$ with ~80% in single transverse mode. The output pulse length is 30 fs and the spectral bandwidth 17 meV, about a factor of 2.5 above the transform limit

FEL-2 PERFORMANCE

Figure 6 displays the growth of power at 40-, 20-, and 10-nm wavelengths as predicted by the GENESIS and GINGER codes operated in time-independent mode. For a final radiator of six modules (see Fig. 2) deep saturation is reached only at 40 and 20 nm. At 10 nm, the output peak power is 1 GW for 800-A current and 0.35 GW for 500-A beam current (data not shown).

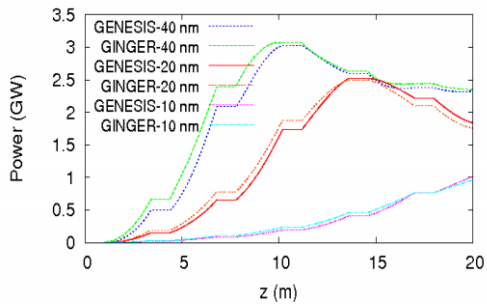

Fig. 6: GENESIS and GINGER time-independent simulations for the FEL-2 radiation power at various wavelengths versus radiator distance in the final radiator for the fresh bunch approach. These runs were done with 800-A beam current and 200-keV initial incoherent energy spread (for the other parameters see caption of Fig. 3).

FEL-2 is typically more sensitive to variations in input parameters than is FEL-1. This is largely due to the shorter wavelengths targeted for FEL-2, which leads to similar displacement errors translating into larger longitudinal phase errors, and there is the additional complexity of having two rather than one stage of harmonic conversion. Furthermore, at shorter wavelengths radiation diffraction is less important, which renders the FEL more sensitive to deviations in the electron orbit and to misalignments. However, it is presently believed that most applications for FEL-2 output will be in the spectral domain where reproducibility is less important and there is a premium for obtaining narrow bandwidth. Consequently, most of

our work on FEL-2 has concentrated utilizing a relatively long (~1 ps) electron-beam pulse with a moderate (~500 A) current. For the fresh bunch approach, such a long pulse is nearly essential given the practicalities of temporal jitter between the electron beam and input radiation seed. As discussed in [5], flatness of electron-beam phase space and homogeneity of current and energy spread distributions at undulator entrance are essential for obtaining the best output spectral resolution and shot-to-shot stability. An example of output temporal and spectrum profiles at 10 nm based on an optimized input electron-beam is shown in Fig. 7. The obtained number of photons per pulse is about 10^{13} (93% in single transverse mode). The output pulse length is 110 fs (rms) and the bandwidth 5 meV, about a factor of 1.5 above the transform limit. The peak brightness is about 10^{32} photons /mm^2/mrad^2 /sec/ 0.1% bandwidth.

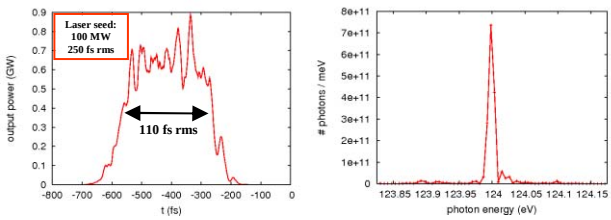

Fig. 7: FEL-2 temporal and spectrum profiles for fresh-bunch scheme resulting from a GENESIS simulation in time-dependent mode.

An alternative scheme we are considering for the FEL-2 is based on the so-called "whole-bunch" approach. Here, the entire electron beam pulse is energy-modulated by the external laser seed and, following the first radiator, there is neither a temporal delay section nor a second modulator. Instead, the electron beam immediately enters a weak dispersive section followed by a second radiator whose FEL resonant wavelength is tuned to an integer harmonic of the first radiator. Due to the relatively small harmonic microbunching at this new wavelength, this second radiator must operate deep in the exponential gain regime. Thus, to keep the exponential gain length and power saturation lengths acceptably small, the energy modulation produced by the first (and only) modulator must be relatively small compared to $\rho_2 \gamma$ where ρ_2 is the FEL parameter for the second radiator (generally ~ 1×10^{-3}). This small energy modulation means that at entrance to the first radiator the e-beam will have a smaller microbunching level relative to that of the fresh bunch scheme.

Consequently, the whole bunch approach can essentially fail (in terms of the needed second radiator undulator length for saturation) if the initial energy spread becomes too large. Moreover, because the microbunching level is small at the beginnings of both the first and second radiator, the relative strength of the shot noise microbunching is much higher and the final SASE strength can be 2 or more orders of magnitude greater in the whole bunch approach than in the fresh bunch approach. The main advantage of such a scheme is that it is less sensitive to shot-to-shot fluctuations of the relative timing between the e-beam and external seed laser. The output temporal profile and spectrum obtained at 10 nm using the whole bunch configuration are shown in fig. 8. The initial electron beam distribution is the same as for the fresh-bunch scheme (see Fig. 7).

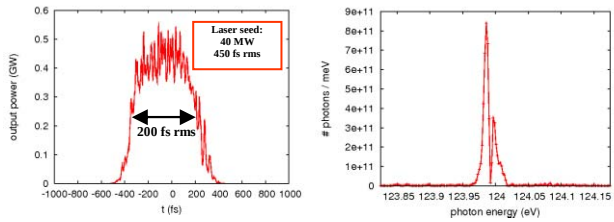

Fig. 8: FEL-2 temporal and spectrum profiles for whole-bunch scheme resulting from a GENESIS simulation in time-dependent mode.

In this case the obtained number of photons per pulse is about 10^{13} (93% in single transverse mode). The output pulse length is 200 fs (rms) and the bandwidth 4 meV. This gives a result which is a factor about 2.5 above the transform limit.

CONCLUSIONS

We have presented the current design configurations for both FELs of the FERMI@Elettra project. Design optimization has been driven by users' requests (see table 1), i.e. short pulse and low shot-to-shot power fluctuations for FEL-1, and high energy resolution for FEL-2. We also give results derived from both time-independent and time-dependent simulations, using reference parameters and electron-bunch distributions as provided by the FERMI start-to-end group.

REFERENCES

[1] L. H. Yu *et al.*, *Phys. Rev. Lett.* ***91***, 074801 (2003).
[2] I. Ben-Zvi, K.M. Yang, and L.H. Yu, Nucl. Inst. Meth. A **318**, 726 (1992).
[3] E. Allaria, G. De Ninno, M. Trovo, these proceedings, Paper MOPPH058.
[4] S. Dimitri et al.,these proceedings, Paper THBAU03.
[5] W. Fawley, G. Penn, and A. Zholents, these proceedings, Paper THAAU01.

START-TO-END TIME-DEPENDENT STUDY OF FEL OUTPUT SENSITIVITY TO ELECTRON-BEAM JITTERS FOR THE FIRST STAGE OF THE FERMI@ELETTRA PROJECT

E. Allaria, G. De Ninno, M. Trovó, Sincrotrone Trieste, 34012 Trieste, Italy.

Abstract

Sensitivity of the output laser pulse to electron-beam jitters is one of the major issues affecting the expected performance of both SASE and seeded FELs. Focusing on the first stage of the FERMI@Elettra project, in this paper we present results of time-dependent numerical simulations in which the codes GENESIS and GINGER have been used to run a large number of electron-beam distributions generated at the gun by the code GPT and propagated through the linac using the code ELEGANT.

INTRODUCTION

The FERMI@ELETTRA project is dedicated to the development of a FEL facility based on the principle of harmonic up shifting of an initial "seed" signal in a single pass [1]. The first stage of the project will be a single harmonic cascade tuneable in the 40-100 nm range. At present, it is believed that the major application for FEL-1 will involve time-domain experiments such as pump-probe interactions and possibly nonlinear phenomena. Consequently, the requirements for FEL-1 are more related to total photon number per pulse (*i.e.*, $0.4 - 2 \times 10^{14}$) and pulse duration (20-100fs) than they are to spectral bandwidth. Another important parameter associated with FEL-1 time-domain experiments is shot-to-shot repeatability [1]. Time-independent simulations of the FEL process based on the Fermi layout show a strong sensitivity of the output power with respect to many electron-beam parameters [2]. Jitter studies performed using jitter of input parameters as estimated by the linac group of the Fermi project provided fluctuation on the output power that can be greater that 20% for the radiation at 40nm. However, while time-independent simulations can give just an indication of the FEL performance, more accurate investigations should rely on "start-to-end" (S2E) simulations, that begin at the emitting cathode and end at the undulator exit.

In collaboration with the injector and linac groups of the Fermi project, dedicated simulations have been performed considering fluctuations on main machine parameters [3]. To examine the effects of injector and accelerator jitters upon the shot-to-shot, time-resolved properties of the output FEL-1 radiation, 100 individual files of 1M macroparticles were propagated starting from the injector (GPT code) through the linac (Elegant code). Nominal beam parameters are reported in the following table [3,4].

Table1: Nominal electron-beam parameters for the first stage (FEL-1) of the FERMI project

Parameter	*Value*	*Units*
Input Seed power	100	MW
Electron Beam Energy	1.2	GeV
Peak current	800	A
Uncorrelated energy spread ("slice" value)	150	KeV
Norm. Transverse Emittance ("slice" value)	1.5	mm-mrad
Electron Bunch Length (flat portion)	0.6	ps

Each file included the effects of random jitter in the individual injector and accelerator cell voltages. The jitter follows Gaussian distributions with variances set by the budget allowances allocated by the gun and linac groups.

GINGER and GENESIS time-dependent simulations for the FEL-1 lattice tuned at 40 nm were performed over a large time window with high resolution. For each jittered file, simulations where done using artificial macroparticles created from the time-dependent envelope quantities previously determined by the *elegant2genesis* code and also using directly the ELEGANT particles.

It is important to note that we here only consider the effect of the jitter on the electron bunches, without taking into account any jitter source on the seed laser.

ANALYSIS OF ELEGANT JITTERED FILES

The 100 jittered files have been produced starting from 100 GPT files that consider the possible jitter sources in the gun. Those files have been propagated through the linac with ELEGANT. Output distributions have been pre-processed in order to evaluate the resulting jitter in bunch arrival times (Fig.1).

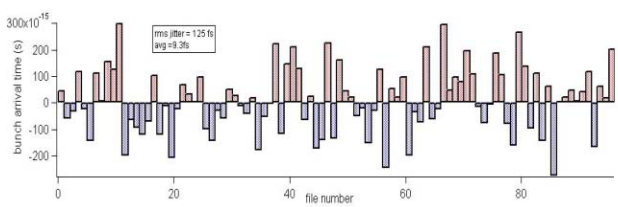

Figure 1: Arrival time jitter of the 100 elegant files with respect to the arrival time of the nominal file.

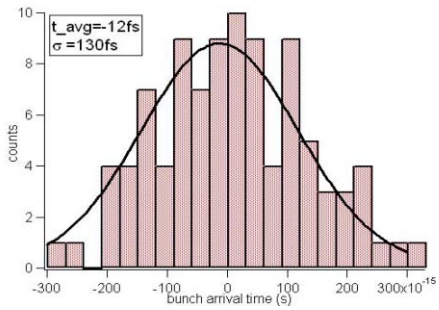

Figure 2: Distribution of the arrival time jitter reported in Fig.1; data can be fitted with a Gaussian distribution, whose sigma is about 130fs.

The analysis shows a distribution with an rms jitter of about 130 fs, which is close to the one predicted by LiTrack simulations [4]. These data can be fit with a Gaussian distribution (Fig.2).

By plotting the electron energy and current profiles of the 100 bunches taking into account of the arrival time (figs.3-6) it is evident that it exists a time window of the order of 400fs where the fluctuations of electron parameters due to the jitter arrival time are small. This is the "useful" part of the bunches to be used for the FEL process. We also report the analysis of the electron beam properties (electron energy, current, emittance, energy spread) on that window.

The electron mean energy, γ, in the useful part of the bunch (from -200fs to 200fs, see fig. 3,4,5) presents a distribution with an rms of 0.09%, in agreement with the values predicted by the linac group.

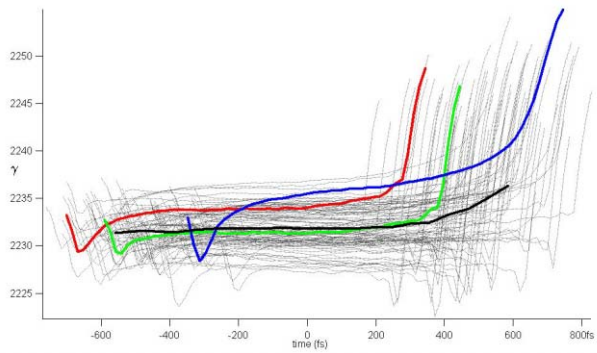

Figure 3: Temporal profile of the electron beam mean energy of the 100 jittered ELEGANT files.

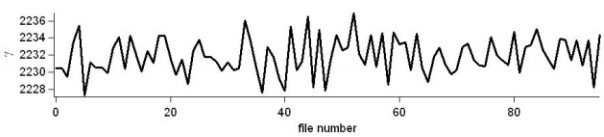

Figure 4: Average of the electron mean energy of the jittered electron bunch calculated in the useful time window (-200fs; 200fs).

The current distribution shows an rms value (6.6%) that is slightly lower than the one predicted by the linac group (8%).

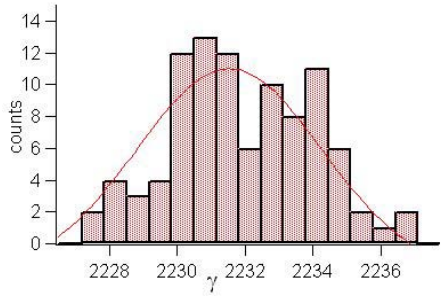

Figure 5: Distribution of the average electron mean energy of the useful part of the jittered bunches; data can be fitted with a Gaussian distribution whose sigma is 0.09%.

Similar analysis have been performed for other electron beam properties, (emittance, energy spread, ..). As for emittance, data show a distribution with an rms value which is close to the one predicted (about 12%). The energy spread, instead, is slightly affected by the temporal jitter of bunches and the rms distribution shows a larger value (almost 20% instead of 10%). Calculated electron-beam average values and corresponding standard deviations are reported in Table 2.

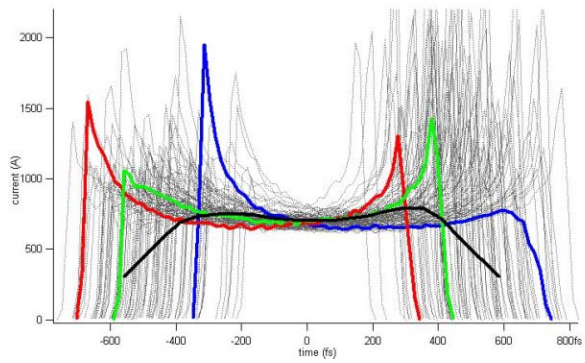

Figure 6: Temporal profile for current of the 100 jittered files.

Table 2: Average values and corresponding standard deviations for the main electron beam parameters extracted from time-dependent simulations.

Quantity	Mean Value	Std. Dev.
Gamma	2231.9	0.09%
Current (A)	718	6.6%
Incoherent energy spread	0.33	19.5%
Normalized emittance	1.35	12.4%

TIME-DEPENDENT FEL SIMULATIONS OF JITTERED FILES

For the FEL simulation we used the nominal setup of FEL1 [1] that has been optimized in terms of aw and R56 in order to maximize the output power extracted from an

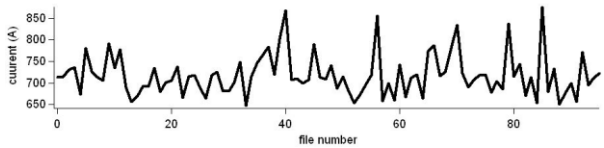

Figure 7: Average of the electron bunch current calculated on the useful part of the jittered files (from -200fs to 200 fs).

ideal bunch, whose parameters are equal to the average values reported in Table 2.

Time-dependent simulations using this optimized setup for the jittered files show a quite high sensitivity to beam jitters (e.g., about 50% of fluctuation in the output power), which is far from what it is predicted by time-independent simulations [2].

A new optimization has been necessary in order to find a setup that minimizes the effect of the beam jitters. In order to reduce the sensitivity of the FEL output power we slightly changed the tuning of the radiator, setting a smaller value of aw.

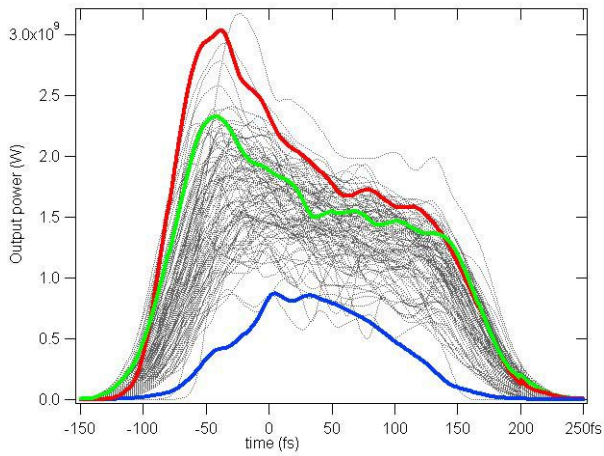

Figure 8: Temporal profiles for the FEL output radiation at 40 nm obtained from GINGER simulations using the jittered ELEGANT files; Red, Green and Blue curve refer to bunches reported with the same colors in figs. 3-6.

The setup utilized for simulations is the following: a seed laser of 100MW with a Gaussian temporal profile (100fs rms), the modulator tuned at 240nm, the dispersive section set with a R56=19e-6 and the radiator tuned at 40 nm.

Figure 8 displays the output power profiles obtained from the 100 jitter bunches, while Fig.10 shows the corresponding output spectra. Red, Green and Blue traces

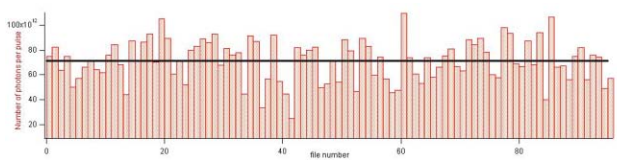

Figure 9: Number of photons per pulse obtained from the FEL simulation at 40 nm. Data show an average number of photons of the order of 70e12 with an rms fluctuation of about 23%.

in Fig.8,10 refers to the electron bunches reported in Red, Green, Blue in Figs. 3-6.

The analysis of the FEL output power has been performed by integrating the pulse profile in order to calculate the number of photons of each FEL pulse. Figure 9 report the number of photons of FEL output pulses for each of the 100 jittered electrons bunches. The statistical analysis of data shows a distribution which is close to a Gaussian centered at 70e12 photons per pulse with a standard deviation of about 23%.

By looking at the output spectra of the FEL pulses, one can see that the jitter of the input electron-beam parameters induces a fluctuation of the central wavelength. However, such a fluctuation is about a factor 3 smaller than the average bandwidth and, as a consequence, is not affecting too much the FEL performance (see Fig.10 and Tab.3). Considering the equation for the undulator resonance $\lambda = L_w \cdot \frac{(1+a_w)}{2\gamma^2}$ we can derive that, if the emission wavelength is defined by the resonance wavelength of the radiator, the jitter in wavelength, λ, should be two times that associated to the jitter in electron mean energy, γ. This is not true in a seeded FEL where the emission wavelength is defined by the seeding laser and only partially by the undulator resonance wavelength.

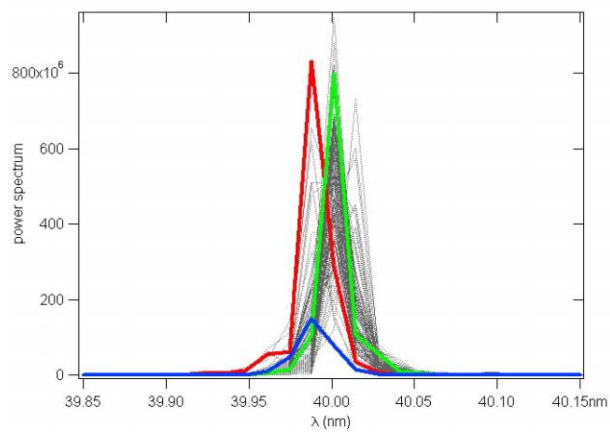

Figure 10: Output power spectra obtained from the FEL simulations of the jittered files.

Our results are in agreement with predictions and the obtained fluctuation for the wavelength is very lower compared to the fluctuation of the mean energy of the input jittered bunches.

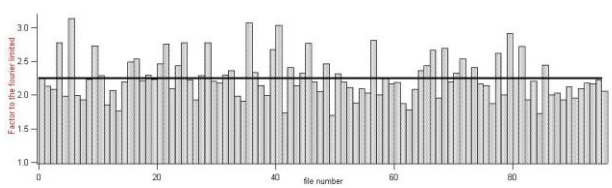

Figure 11: Factor to the Fourier transform limit of the FEL output pulses for the jittered ELEGANT files.

We also characterized the FEL output pulses in terms of how close they are to the Fourier limit. In Fig. 11 we report the distance of each FEL output pulse with respect to the Fourier limit for the 100 simulated jittered files. The average Fourier factor for the simulated data is 2.2 and the standard deviation of the distribution is about 13%.

Table 3: Statistics of the 100 FEL pulses.

Quantity	Mean Value	Std. Dev.
Average pulse width (fs)	73.2	
Average photon number	7.1e+13	23.3%
Average central wavelength (nm)	40.0019	0.013%
Average bandwidth	0.033%	
Fourier factor	2.2	13%

In order to verify the prediction of time independent simulations, which indicate the jitter in the mean electron energy as the most limiting factor for achieving a good output stability, in Fig. 12 we plot the number of photons per pulse *vs* the average electron-beam energy.

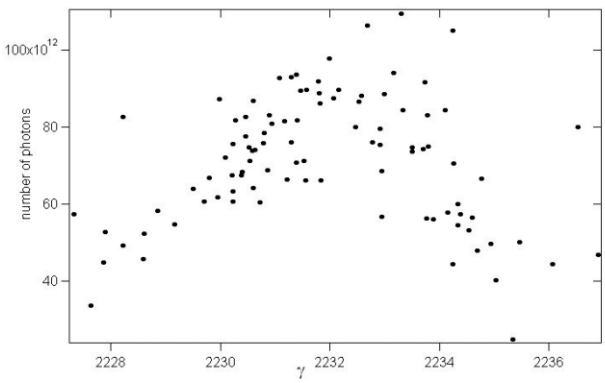

Figure 12: Number of photons per pulse vs the average electron mean energy of the corresponding electron bunch.

The good correlation between the two quantities clearly confirms the high sensitivity of the FEL output to the electron mean energy.

CONCLUSIONS

An extensive campaign of start-to-end simulations for the first stage of the FERMI@Elettra project has been presented. Results show a quite strong sensitivity of FEL characteristics to shot-to-shot jitters of electron-beam parameters.

The effect of the proposed strategies for the reduction of the output power fluctuation by means of sophisticated radiator configuration (tapering) or linear chirping of the electron bunches will be considered in a forthcoming work.

REFERENCES

[1] C. Bocchetta *et al.*, MOPPH054 proceedings of this conference.
[2] W. Fawley et al., Sincrotrone Trieste tech. note, ST/F-TN-06/16.
[3] P. Craievich, S. Dimitri, G. Penco, private communication.
[4] M. Cornacchia *et al.*, Sincrotrone Trieste tech. note, ST/F-TN-06/15.

THE TEST FACILITY FOR HARMONIC GENERATION AT THE MAX-LAB INJECTOR LINAC *

Mathias Brandin, Tue Hansen, Sara Thorin, Sverker Werin, MAX-lab, Lund
Michael Abo-Bakr, Johannes Bahrdt, Kathrin Goldammer, BESSY GmbH, Berlin
Jörgen Larsson, Anne L'Huillier, Anders Persson, Claes-Göran Wahlström, Department of Physics, Lund University.

Abstract

A test facility for harmonic generation is being built at MAX-lab. The third and fifth harmonic, at 90 and 53 nm respectively, will be created using a fs seed laser at 266 nm. The MAX-lab injector will be operated at 400+ MeV with a photo RF gun and the optics will be retuned to achieve compression. An optical klystron will be installed comprising of two undulators and a chicane.

OVERVIEW AND SCOPE

The BESSY FEL project [1] and the MAX IV proposal [2] are both focused on seeded FEL sources as part of the facilities. In the aim of improving the designs a decision was made to build a test facility for harmonic generation at MAX-lab.

The MAX injector system [3] is a recirculated linac with energy capabilities up to 500 MeV. Few other locations have this linac energy available for a test facility. The joint effort includes simulations, a new electron source, laser systems, an optical klystron and experimental activities.

The test facility is intended to use an electron beam of at least 400 MeV with an emittance of 3 μmRad and a bunch length around 500 fs. It will be injected into an optical klystron consisting of a modulator undulator, a chicane and a radiator undulator. A fs seed laser at 266 nm will be used and harmonic generation at 90 nm and later 53 nm will be studied.

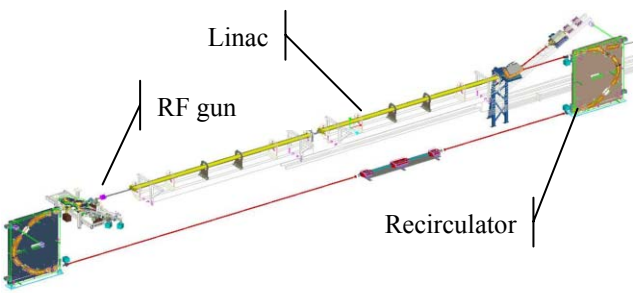

Fig 1. The MAX injector.

The FEL Principle

The FEL section consists of an Optical Klystron where in the first undulator, called modulator, the electron beam co-propagates with a strong seed laser of 266 nm wavelength and is modulated in energy. The particles then pass through the magnetic chicane which serves as a dispersive element. It consists of four dipole magnets and introduces an energy-dependant longitudinal delay of the electrons: the unmodulated particles are bent into a longer trajectory than the higher energy particles so that the beam is redistributed longitudinally. The process is referred to as "(micro)bunching". The bunching is tunable to achieve a maximal Fourier component at either the resonant frequency of the modulator or at higher harmonics. In the MAX-lab FEL experiment, the third harmonic will be used, thus efficiently shortening the output wavelength of the FEL to 88 nm. In the second undulator, called radiator, the bunched beam will then emit intense, coherent radiation at the shorter wavelength with an output power in the megawatt-range. Substantial development of this method, HGHG, has been done at BNL [4].

* This work has been partially supported by the Swedish Research Council and by the European Commission in the Sixth Framework Program, Contract No. 011935 – EUROFEL.

THE ACCELERATORS

While most of the accelerator systems are already at hand at MAX-lab some additions and alterations are necessary. These mainly regard a new photo cathode RF gun [5] and finding a new optics [6] which creates compression and transports the bunch to the optical klystron.

The Gun Pre Injector

In order to produce a transversely and energetically collimated electron beam, the electrons will be generated in a low emittance photocathode gun. The gun is a 3 GHz 1.6-cell cavity, mounted slightly off axis, with a copper cathode illuminated by a ten ps long laser pulse at 266 nm. This produces bunches with a total charge of 0.5 - 1 nC. The beam parameters at the exit from the gun can be seen in table 1.

Table 1: Beam parameters after the gun (simulated)

Energy	3.7 MeV
Energy spread	3 %
Normalized emittance ε_N	3 mm mrad
Charge	0.5 nC
Pulse length	11 ps
Peak current	45 A

The emittance compensation scheme adopted is similar to the LCLS [7]. Results of the tracking are shown in fig 2.

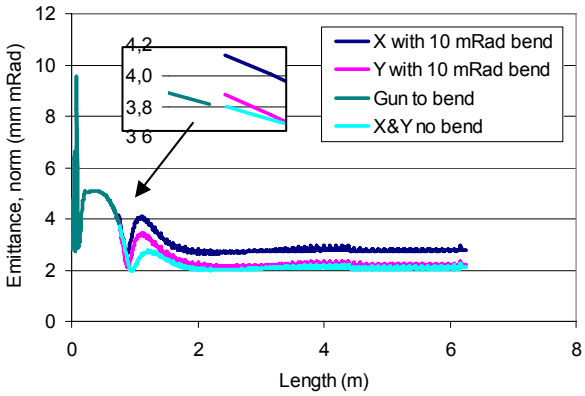

Figure 2: Emittance (normalised) (1 nC, 3.7 MeV, 10ps). off axis compensation (10mR) at 0.75 m and linac from 1m.

Linac and Recirculator

The linacs and recirculator system in the MAX-injector have been in operation for several years. They routinely deliver 380 MeV as injector for MAX I and II. They are currently being conditioned above 400 MeV.

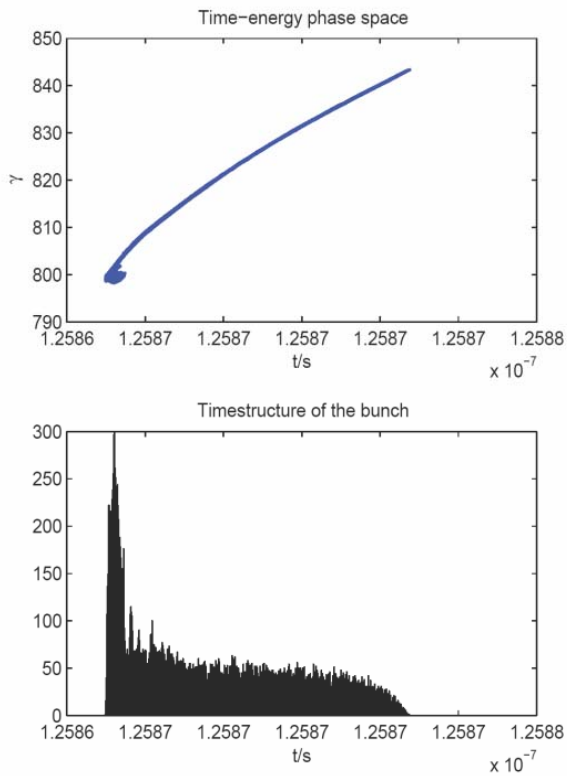

Figure 3: Electron bunch after the recirculator.

Since a high peak current is important for FEL efficiency, the electron bunches have to be compressed after the gun. Bunch compression is achieved using the linacs and the magnetic optics in the recirculator. The electric field in the linac is given such a phase that an energy chirp is induced in the electron pulses. Through the quadrupoles and dipoles in the recirculator block, this chirp can then be rotated time wise to result in a very short pulse. Because of the sinusoidal shape of the accelerating field, the energy spread will not be completely linear but some second order effects will occur. These second order effects can be compensated by the use of sextupole magnets which introduce second order corrections and straighten the energy chirp up to a line. In the MAX-injector sextupoles are incorporated in some of the quadrupoles in the recirculation blocks and are not separately tuneable. They can thus not be used to completely linearize the second order effects, but they do contribute a bit towards higher peak brilliances. With separately tunable sextupoles linearization more corresponding to that of a higher order cavity can be done.

Approximately 25% of the bunch charge can be confined within the usable part of the bunch. This way bunch lengths shorter than 300 fs and peak currents of 300 A can be obtained. Table 2 and figure 3 show the beam at the exit of the recirculator.

Table 2: Beam parameters after the recirculator

Energy	400 MeV
Energy spread	0.1 %
Normalized emittance ε_{Nx}, ε_{Ny}	3 mm mrad, 8 mm mrad
Bunch charge in peak	0.12 nC
Pulse length	400 fs
Peak current	300 A

Transport

The transport from the injector to the undulator section is about 40 m and includes a vertical lift of the beam from the cellar to the ground floor. This lift is done with an achromatic dogleg [8] consisting of two 15 degree bends with 5 quadrupoles in between. The middle quad is used to control the beta-function while the two outer ones are used to close dispersion after the second bend. To avoid space charge effects in the centre of the dogleg, where the beta function can hit a very low minimum, the two quads on either side of the middle are used for modification of the beta function.

THE OPTICAL KLYSTRON

Existing magnet structures will be used to build the undulators. A pure permanent magnet (PPM) structure has been loaned from the ESRF to be used in the modulator. The radiator will be equipped with the APPLE structure of the BESSY UE56-1. The parameters are summarized in table 3.

Table3: Parameters of the undulators and the chicane

Modulator	
Period length	48 mm
Number of periods	30
Minimum gap	10 mm
Maximum K-parameter	4.3
Radiator	
Period length	56 mm
Number of periods	30
Minimum gap	12 mm
Maximum K-parameter	4.3
Chicane	
Number of magnets	4
Type of magnet	H-frame, electromagnet
Gap	15 mm
Maximum field	0.2 T
Distance between magnets	400 mm

Both undulators will have a motorized gap drive. The radiator provides also a motorized phase variation for polarization control. The modulator is moved only in case of an electron energy change whereas the radiator has to be tuned also when the harmonic number of the radiation or the state of polarization is changed.

The Chicane

The magnetic chicane converts the energy modulation of the electron beam into a spatial modulation. Optimum bunching is achieved if the energy modulation dominates the energy spread times the harmonic number n:

$$\Delta\gamma/\gamma \geq n \cdot \sigma_\gamma$$

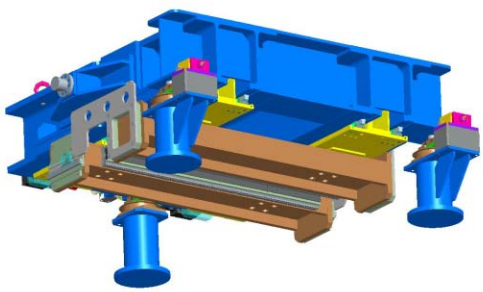

Figure 4: Modulator in operating position.

With a relative energy spread of $\sigma_\gamma = 5 \cdot 10^{-4}$ an energy modulation of at least $\Delta\gamma/\gamma = 1.5(2.5) \cdot 10^{-3}$ is needed to operate on the third (fifth) harmonic. This defines the laser power.

The maximum bunching appears for a path length difference of $\Delta L = \lambda_{photon}/4$ between modulated and non modulated electrons. The chicane is optimized such that $\Delta L = \lambda^{1st}_{photon}/4 = 67nm$ can be reached with 500MeV electrons and an energy modulation of $\Delta\gamma/\gamma = 1.0 \cdot 10^{-3}$.

For higher harmonics (shorter wavelengths) $\Delta L \geq \lambda_{photon}/2$ can be produced and overbunchig effects can be studied.

Mechanical Layout

The electron beam height at the HGHG-FEL is only 400 mm and conventional undulator carriages cannot be used. Therefore, a new carriage has been developed which can cope with this geometry (figure 4). The same structure is used for both undulators.

The two undulators will be measured and shimmed at the existing measurement bench at BESSY. For this purpose the undulators have to be flipped into upright orientation (figure 5). At MAX-lab the final magnetic measurements will be performed in the operating position using a pulsed wire system.

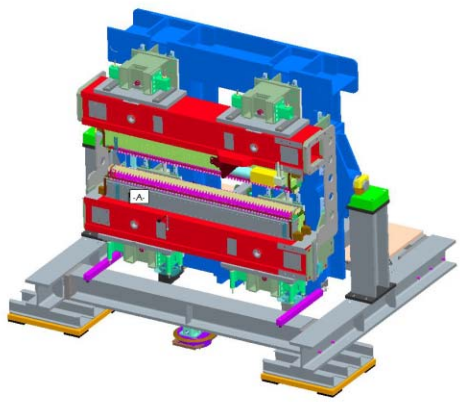

Figure 5: Radiator in measurement position.

LASER SYSTEMS

A combined laser system for the gun and the seeding of the HG-FEL has recently been sent out with an invitation to tender. We foresee a common system locked to the RF of the accelerators to better than 1 ps. The system should deliver 500 µJ in a 10 ps pulse at 266 nm to the RF gun and 100 µJ in a 300 fs pulse at 266 nm to the seeding. The solution is up to the supplier while the basic thought is a centrally located oscillator locked to the accelerator RF-system and an optical distribution to the amplifiers. (Due to the commercial actions the information is minimized. Please contact the authors for more information: sverker.werin@maxlab.lu.se)

DIAGNOSTICS

The diagnostics have two main duties. The first is to control the electron beam performance and the second to assure overlap in time and space of the laser and electrons. Table 4 shows the intended methods to be used to approach the different areas.

In a resent test set-up the uncompressed bunch length at the MAX injector was measured to σ = 2.3 ps. The technique used was detecting coherent transition radiation with an interferometer [9]. This set up will now be finalized to be able to diagnose sub ps pulses.

Table 4. Diagnostics

Feature	Method
Energy spread	Dispersive section
Emittance	Q scans
Bunch length	CTR and interferometer
Current/charge	Beam transformers, Faraday cage
X and y positions	YAG/OTR screens
Alignment	Apertures for spontaneous and laser beams
Synchronization/time	Electro-optical methods Energy spread
Beam loss	Cherenkov fibre

THE FEL SIMULATION

For realistic simulation of the FEL, the particles were tracked all the way through gun, linac, beam transport and the undulator section using ASTRA [10], elegant [11] and GENESIS [12]. In order to study time-dependant effects of FEL interaction, the 6-dimensional phase space file from elegant was converted into a GENESIS input file by cutting out the seeded part of the beam +/-50fs and split it up into a collection of temporal slices. For each slice, the relevant beam parameters were calculated externally and delivered to a GENESIS compatible input file.

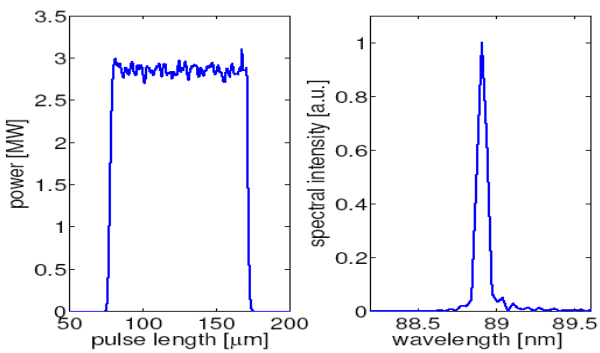

Figure 6: Temporal and spectral power distributions of FEL pulse at exit of radiator.

Simulation Results

Due to the fact that the simulation work is still ongoing, the results for the FEL section presented in this section were achieved without a formal start-to-end-transport of the original input bunch from ASTRA to GENESIS. However, the beam parameters gained by the slice analysis were used to perform fully time-dependant simulations taking into acount the seed laser beam temporal profile. A 95%-emittance of 3 mm mrad (normalized) was assumed. The parameters used to model the undulator section and the magnetic chicane are listed in table 3.

Using a seed laser of 150 MW peak power and a FWHM flat top length of 300 fs, the necessary energy modulation can reliably be established within the modulator. When optimizing the magnetic chicane for maximal bunching at the third harmonic, the radiator lases at 88 nm with a power level in the range of 1-10 MW. Figure 6 shows the temporal and spectral power distribution at the end of the radiator.

SUMMARY

A test facility for FEL and HGHG is currently being built at MAX-lab. The coming year will be spent on installation of undulators, the new pre injector, build up of the laser systems and finalizing the diagnostics. The aim of the facility is to test and develop the techniques, but also to already at an early stage of the BESSY FEL and MAX IV projects practically address the processes.

Simulations and development of beam optics are also part of this process.

An important side effect of this project is to start the process of joining forces between the accelerator and laser science. The future of accelerators lies in many ways in starting to use lasers as natural parts of accelerator installations.

The capabilities of this installation are also such that new ideas and a continuation after the initial generation of the 3rd harmonic are a natural continuation.

REFERENCES

[1] BESSY TDR, D. Kraemer et al., 2004.
[2] MAX IV Conceptual Design report, MAX-lab, 2006.
[3] S.Werin et al., Commissioning of the 500 MeV Injector for MAX-lab, EPAC 2004
[4] L. H. Yu, J. Wu, Nucl. Instr. and Meth. in Nucl. Res. A 483 (2002) 493.
[5] S. Werin et al, “Design of a New Preinjector for the MAX Recirculator to be used in EUROFEL”, EPAC 2006
[6] S. Thorin et al, “Simulations for the FEL Test Facility at MAX-lab within EUROFEL”, EPAC 2006
[7] R. Boyce, D.H. Dowell, J. Hodgson, J.F. Schmerge, N. Yu, Design Considerations for the LCLS RF Gun, LCLS TN 04-4 (2004)
[8] J. England et al., Sextupoles Correction of the Longitudinal Transport of Relativistic Beams in Dispersionless translating sections, Phys. Rev. ST Accel. Beams 8, 012801 (2005) .
[9] M. Brandin, B. Nelander, S. Werin, Measurement and diagnostics on the MAX recirculaor, EPAC 2006
[10] K. Flöttman “ASTRA User Manual”, September 18, 2000, www.desy.de/~mpyflo
[11] M. Borland, "elegant: A Flexible SDDS-Compliant Code for Accelerator Simulation" Advanced Photon Source LS-287, September 2000.
[12] S. Reiche, “Numerical Studies for a Single Pass High Gain Free-Electron Laser”, PhD Thesis, Uni Hamburg, corona.physics.ucla.edu/~reiche/links.html

COHERENT X-RAY PRODUCTION BY CASCADING STAGES OF HIGH GAIN HARMONIC GENERATION FREE ELECTRON LASERS SEEDED BY IR LASER DRIVEN HIGH-ORDER HARMONIC GENERATION*

Juhao Wu† and Paul R. Bolton, SLAC, Menlo Park, CA 94025, USA.

Abstract

Coherent x-ray production achieved by a seeded free electron laser (FEL) with cascaded high gain harmonic generation (HGHG) is important for next generation development of synchrotron light sources. We examine the feasibility and some features of FEL emission seeded by a high order harmonic of an intense infrared conventional laser source (HHG). In addition to the intrinsic FEL chirp phenomenon, the longitudinal profile and spectral bandwidth of the HHG seed are modified significantly by the FEL interaction well before saturation occurs. This smears out original attosecond pulselet structure. As an example, we describe a cascaded HGHG scheme for coherent x-ray FEL generation that is seeded by the twenty-seventh harmonic of an ultrashort 800 nm laser pulse with 10 fs rms duration. By cascading two stages of HGHG, 15 GW peak power FEL emission at 0.3 nm can be produced with 90 MW peak power radiation at 0.1 nm via the non-linear harmonic generation.

INTRODUCTION

Short-wavelength Free-electron Lasers (FELs) are perceived as the next generation synchrotron light sources. Self-Amplified Spontaneous Emission (SASE) [1, 2, 3, 4], is the dominating approach to produce an x-ray FEL (XFEL). While it has good transverse coherence, the SASE FEL pulses are composed of a series of ultrashort spikes due to a short longitudinal coherent length. To improve the longitudinal coherence, various approaches have been proposed. Among them, a cascaded high gain harmonic generation (HGHG) FEL [5, 6, 7, 8, 9, 10] looks promising by invoking high order harmonic generation of an infrared (ir) laser (HHG) as the seed. In this paper, we study an HHG seeded FEL. This is of particular interest [11], since HHG can provide a uv to soft x-ray seed, making a coherent hard XFEL feasible.

HHG SEEDED HGHG FELS AT LCLS

HHG Seed: Attosecond Structure and Smearing Effect

HHG generates an electric field comprised of multiple harmonic orders, s and multiple time pulselets, n expressed as the following double summation [12, 13]:

$$E_{\rm HHG}(t,z) = \sum_s E_{s,0} e^{i(k_s z-\omega_s t)} e^{-i\mathcal{B}_s\omega_s^2 t^2} \times \sum_{n=-N}^{N} e^{-\frac{t_n^2}{4\sigma_{t,0}^2}} e^{-\alpha_s\omega_s^2[(t-t_n)-z/c]^2}, \quad (1)$$

where for each order, s we sum over the temporal sequence of $2N+1$ pulselets for which $n \in [-N, N]$. Because of temporal coherence of a group of harmonic orders, the pulselets can exhibit attosecond structure (with periodicity of $\tau/2$), limited by the relative amplitudes and phases of the different harmonic orders. The order dependent parameter, $\mathcal{B}_s$ accounts for the small intrinsic chirp that characterizes each harmonic order [14]. In Eq. (1), $t_n = n\tau/2$ with τ being the period of the unchirped ir pulse (2.67 fs at 800 nm); $\sigma_{t,0}$ is the ir pulse rms duration; k_s and ω_s are the wavenumber and angular frequency of the s^{th} harmonic; and $\alpha_s = (4\sigma_{t,s}^2\omega_s^2)^{-1}$ with $\sigma_{t,s}$ being the rms duration of each pulselet in the HHG pulse. Typically $\sigma_{t,0} \approx 10$ fs and $\tau/20 \le \sigma_{t,s} \le \tau/2$ for a single pulselet, where the lower limit assumes relative phase synchronization of a harmonics group [12, 15]. In this paper, we consider only a single harmonic order, s as the carrier frequency and for simplicity, we negelect the harmonic chirp ($\mathcal{B}_s \approx 0$). The HHG field expression then simplifies to:

$$E(t,z) = E_{s,0} e^{i(k_s z-\omega_s t)} \sum_{n=-N}^{N} e^{-\frac{t_n^2}{4\sigma_{t,0}^2}} \times e^{-\alpha_s\omega_s^2[(t-t_n)-z/c]^2}, \quad (2)$$

which represents an attosecond pulselet train (APT) derived from the amplitude modulation of carrier frequency, ω_s. We use $\sigma_{t,0} = 10$ fs and $\sigma_{t,s} = \tau/8 \approx 334$ attosecond in the Fourier-transform limit. In this case, it is important to note that, although the central carrier frequency of the seed is a single harmonic, the transform limited seed spectrum also includes components from several neighboring harmonic orders [16]. A multi-pulselet HHG seed is the sum of many single pulselets. We address the single pulselet at $t_n = 0$ for $n = 0$ so that $E_s(t, z=0) = E_{s,0}\exp(-i\omega_s t - \alpha_s\omega_s^2 t^2)$, assuming for simplicity that the single harmonic pulselet is transform-limited, *i. e.*, $\sigma_{t,s}\sigma_{\omega,s} = 1/2$, so that the rms bandwidth $\sigma_{\omega,s} = \sqrt{\alpha_s}\omega_s$. Since each pulselet is ultra short, the spectral bandwidth is broad. The seeded FEL solution reads [17]

$$E_{\rm FEL}(t,z) = E_{0,\rm FEL} e^{\rho(\sqrt{3}+i)k_w z} \quad (3)$$

* The work was supported by the US Department of Energy under contract DE-AC02-76SF00515.

† jhwu@SLAC.Stanford.EDU

$$\times \quad e^{i(k_s z-\omega_s t)} e^{-[\alpha_{s,f}(z)+i\beta_{s,f}(z)]\omega_s^2(t-z/v_g)^2}, \tag{3}$$

where $v_g = \omega_s/(k_s + 2/3k_w)$ is the group velocity of the FEL light,

$$\alpha_{s,f}(z) = \frac{1}{4\sigma_{t,s,f}^2(z)\omega_s^2}, \tag{4}$$

and

$$\beta_{s,f}(z)^2 = \alpha_{s,f}(z)\frac{\sigma_{\omega,s,f}^2(z)}{\omega_s^2} - \alpha_{s,f}(z)^2 \tag{5}$$

with

$$\begin{cases} \sigma_{t,s,f}(z) = \sigma_{t,s}\sqrt{\frac{3+6R(z)^2+4R(z)^4}{3[1+R(z)^2]}} \\ \sigma_{\omega,s,f}(z) = \frac{\sigma_{\omega,s}}{\sqrt{1+R(z)^2}} \end{cases}, \tag{6}$$

with

$$R(z) \equiv \frac{\sigma_{\omega,s}}{\sigma_{\omega,\mathrm{GF}}(z)}, \tag{7}$$

and

$$\sigma_{\omega,\mathrm{GF}}(z) \equiv \sqrt{\frac{3\sqrt{3}\rho\omega_s^2}{k_w z}}. \tag{8}$$

Here $\sigma_{\omega,\mathrm{GF}}(z)$ is the rms bandwidth of the FEL Green function for a coasting electron beam with ρ being the Pierce parameter [1]. The transform limit also means that $\alpha_{s,f}(0) = \alpha_s$, $\beta_{s,f}(0) = \beta_s = 0$, $\sigma_{t,s,f}(0) = \sigma_{t,s}$, and $\sigma_{\omega,s,f}(0) = \sigma_{\omega,s}$. The FEL-interaction intrinsically generates a chirped FEL waveform,

$$\langle(t-\langle t\rangle)(\omega-\langle\omega\rangle)\rangle = \frac{\beta_{s,f}(z)}{2\alpha_{s,f}(z)} = \frac{R(z)^2}{2\sqrt{3}[1+R(z)^2]}. \tag{9}$$

The emittance of the FEL light at any position, z, is conserved, $\varepsilon \equiv \{\langle(t-\langle t\rangle)^2\rangle\langle(\omega-\langle\omega\rangle)^2\rangle - \langle(t-\langle t\rangle)(\omega-\langle\omega\rangle)\rangle^2\}^{1/2} = 1/2$, indicating that the FEL emission is fully coherent longitudinally [17].

We introduce the critical location, z_c, where the FEL Green function bandwidth reduces to the pulselet initial bandwidth, *i.e.*, $R(z_c) = 1$. Recall that, the power gain length $L_\mathrm{G} = \lambda_w/(4\sqrt{3}\pi\rho)$, hence, if $\sigma_{\omega,s}/\omega_s > 3\sqrt{2}\rho$, then $z_c < L_\mathrm{G}$. For large enough z, where $R(z) \gg 1$, the FEL has

$$\begin{cases} \sigma_{t,s,f}(z) & \rightarrow & \frac{1}{\sqrt{3}\sigma_{\omega,\mathrm{GF}}(z)} \\ \sigma_{\omega,s,f}(z) & \rightarrow & \sigma_{\omega,\mathrm{GF}}(z) \\ \langle(t-\langle t\rangle)(\omega-\langle\omega\rangle)\rangle & \rightarrow & \frac{1}{2\sqrt{3}} \end{cases}, \tag{10}$$

i.e., the final characteristics are determined by the FEL interaction. In accordance with Eq. (6), the FEL interaction rapidly reduces the seed pulselet bandwidth, extending its duration [16].

HHG-HGHG FELs at LCLS

Considering the feasibility of an HHG seeded HGHG XFEL, we use an ir laser at 800 nm with $\sigma_{t,0} = 10$ fs. We choose the 27^{th} harmonic as the seed to interact with an LCLS-type high brightness electron bunch [18]. The initial pulselet is assumed to have $\sigma_{t,s} = \tau/8$. Assuming a Fourier-transform limited single harmonic pulselet, we have $\sigma_{\omega,s} = 1/(2\sigma_{t,s})$. The relative rms bandwidth is $\sigma_{\omega,s}/\omega_s \approx 2.4$ %. Due to the FEL interaction, according to Eq. (7), the FEL bandwidth decreases. For the scheme shown in Fig. 1 with parameters in Table 1, we have $\rho = 0.54$ % and $\lambda_w = 0.2$ m, we have $z_c \approx 1.6$ m. Considering that the first modulator is 25 m long and the power gain length is about 3 m, attosecond structure is smeared out within a short distance [16]. Consequently, the HHG seed resembles a conventional harmonic seed generated via wave-mixing in a solid such that we can ignore initial attosecond structure, at least as a good approximation.

In Fig. 1, we show the generic configuration of an HHG seeded cascaded HGHG FEL. It has the following features.

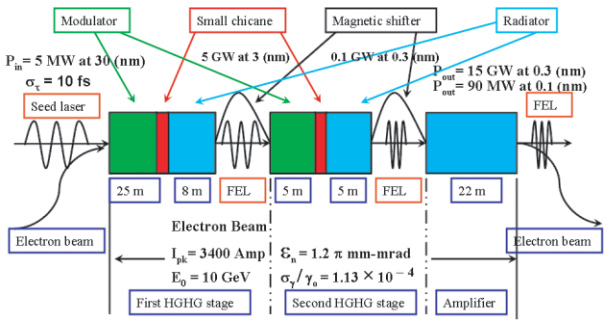

Figure 1: Schematics of an HHG seeded cascaded HGHG FEL. In this scheme an HHG seed of 30 nm is used. After two stages of HGHG and a final amplifier, we obtain 15 GW at 0.3 nm, and 90 MW at 0.1 nm.

1. We need multiple stages. During each stage the nth harmonic of the seed laser will be produced at the end of the radiator, and then this harmonic will be used as the seed for the next stage. In reality, n cannot be too large due to that stability consideration [7, 9]. In our paper we use $n = 10$ to achieve stable performance, and we need only two stages.

2. Conceptually, the device is composed of two parts: a converter [19] and an amplifier. The converter, consisting of several stages, converts the seed laser to the designed wavelength step by step. Then at the end, an amplifier exponentially amplifies the radiation obtained from the last stage to saturation.

3. Except for the first modulator and the last amplifier, each stage only converts the light to its n^{th} harmonic. Exponential growth is not required as long as the harmonic power is high enough to be used as the seed for the next stage.

4. The phase mixing induced by the emittance in the dispersion section is much smaller than that in an undulator. For an HGHG FEL, bunching is produced mainly in the dispersion section; while for a SASE FEL, bunching is produced in the undulator. Therefore, the emittance effect turns out to be less important in an HGHG FEL than in a SASE FEL [10].

5. Since we need to cascade several stages of HGHG, we need some extra components. Each stage will consist of one modulator, a dispersion section (a small chicane), and one radiator. The physics process in each stage will be the same as in Refs. [5, 6]. During the process, the output radiation has disturbed the coincident part of the e-bunch. Therefore, to achieve the best efficiency in the next stage of HGHG, we need use a fresh region of the e-bunch. To do this, the laser (i.e., the output radiation from the previous HGHG stage) is shifted to the front part of the same e-bunch, so that the laser will interact with a fresh part of the same e-bunch. *i.e.*, we use a magnetic shifter to relatively delay the electron bunch.

As mentioned above, this conceptual design uses the 27^{th} harmonic of the 800 nm ir pulse with $\sigma_{t,0} = 10$ fs. Assuming the input seed peak power of 5 MW, with two stages of HGHG and a final amplifier, we obtain a 15 GW FEL at 0.3 nm, and 90 MW at 0.1 nm via nonlinear harmonic generation [20, 21]. In this example, the 27^{th} harmonic pulselet interacts with an LCLS-type electron beam [18] (normalized emittance $\varepsilon_n = 1.2\ \pi$ mm-mrad, relative energy spread $\sigma_\gamma/\gamma_0 = 1.13\times10^{-4}$, energy $E_0 = 10$ GeV, and peak current $I_{pk} = 3,400$ Amp). In the 25 m modulator of the first HGHG stage, the HHG seed is amplified, and simultaneously modulates the electron beam energy. A small chicane then converts the energy modulation into density microbunching at 30 nm. This microbunched electron beam then traverses the 8 m radiator which is resonant at 3 nm (the 10^{th} harmonic of the original 30 nm seed). This microbunched electron beam first coherently radiates at 3 nm and then exponentially amplifies this 3 nm radiation to a peak power of 5 GW, which is used to seed the next HGHG stage. In the second stage, the 5 GW, 3 nm seed energy modulates the electron beam in the 5 m modulator. The energy modulation is converted into density microbunching at 3 nm via a second small chicane. This density modulated electron beam initially radiates coherently in the 5 m radiator, resonant at 0.3 nm (the 10^{th} harmonic of the 3 nm seed). At the end of the 5 m radiator, the 0.3 nm radiation is amplified to 0.1 GW, which is further amplified in the 22 m final amplifier, resonant at 0.3 nm. At the amplifier exit, the FEL is well into saturation, and the system finally produces 15 GW, 0.3 nm radiation. Due to the microbunching at 0.3 nm, there are substantial harmonics. The third harmonic emission at 0.1 nm has a peak power of 90 MW.

As shown in Fig. 1, we consider an HHG seed with a wavelength of 30 nm, and a peak power of $P_{\rm in} = 5$ MW. As we will discuss later, the corresponding start-up shot-noise power is only about $P_{\rm noise} \approx 70$ W. Thus the input seed laser power dominates the shot-noise power. This dominance is necessary, because even though there is only negligible noise power in the initial stage, the signal-to-noise ratio of the final radiation at 0.3 nm can be degraded [22]. A simple estimate shows that the noise-to-signal (NTS) ratio at the seed will be amplified by $n_{\rm tot}^2$ times for the $n_{\rm tot}^{th}$ harmonic generation. In this case, the two stage approach has an overall $n_{\rm tot} = 100$, hence, the NTS ratio will be amplified by 10^4 times. Hence for the final radiation at 0.3 nm, the NTS ratio will be about 14 %.

Table 1: Parameters for the undulator, the dispersive section and the electron bunch.

	1^{st} stage		2^{nd} stage		Amplifier
λ_r (nm)	30	3	3	0.3	0.3
λ_w (cm)	20	6	6	3	3
$\frac{d\psi}{d\gamma}$	0.2		0.4		
$\frac{\sigma_\gamma}{\gamma_0}$	1.13×10^{-4}				
L_w (m)	25	8	5	5	22
L_G (m)	3	2	2	3	3

After two HGHG stages, we have generated 0.3 nm radiation, and this 0.3 nm radiation is amplified to saturation with a peak power near 15 GW in a final amplifier stage. The parameters for the electron beam and the radiation are given in Fig. 1. The number in the first row stands for the output power and wavelength of the radiation of each stage. The output power of one stage is the input power of the next stage, though diffraction has been taken into consideration in the simulation. The e-beam parameters are printed below the schematic device. The relative local energy spread σ_γ/γ_0 given in Fig. 1 is the initial relative local energy spread before the e-beam enters the first modulator. This is increased by spontaneous radiation [23]. We take this into account in the simulation [21].

In Table 1, the first row gives the radiation wavelength λ_r; the second row, the undulator period λ_w, and the third row the dispersion strength $d\psi/(d\gamma)$ with ψ being the ponderomotive phase in the radiator. The fourth row gives the initial relative local energy spread σ_γ/γ_0. In our simulation, quantum diffusion [23] has been taken into account [21]. The fifth row gives the length of the undulators (modulators, radiators, and the amplifier) L_w. For example, the last amplifier has a length of 22 m. The sixth row gives the power gain length L_G in each undulator without energy modulation. The table has three boxes; the first two boxes are for the two convertor stages and the last one is for the amplifier. For the two convertor stages, the left column gives the parameters for the modulator and the right column those for the radiator; the numbers in the middle stand for the dispersion strength $d\psi/(d\gamma)$. For example, the left column in the second box stands for the modulator of the second stage. The table shows that in the modulator the resonant radiation has a wavelength of 3 nm, the modulator has a period of 6 cm, the length of the modulator is 5 m, and the corresponding power e-folding length without energy modulation is 2 m. The right column shows that the radiation in the radiator has a wavelength of 0.3 nm, the radiator has a period of 3 cm, the length of the radiator is 5 m, and the corresponding power e-folding length is 3 m. In the middle, i.e. 0.4, stands for the dispersion strength $d\psi/(d\gamma)$.

Start-up Noise Issue

First, we need to compute the effective start-up noise power for the fundamental SASE guiding mode [24, 9]

$$P_{\rm SASE}^{\rm Start-up} = C_1 \frac{2L_G}{L_w}\pi\left(\frac{2\lambda_r}{L_w}\right)\sqrt{\frac{3\sqrt{3}\rho}{N_w}} \times \frac{eZ_0 I_{pk}}{4\pi}N_w^2\gamma^2\frac{K^2}{\left(1+\frac{K^2}{2}\right)^2}[JJ]^2\omega_r, \quad (11)$$

where the coupling factor is found to be [24],

$$C_m(a) \approx \frac{\sqrt{3}}{\pi a^2}\exp\left[-\frac{1}{a\sqrt{1+a^2}}\left(\beta_{m,0}+\beta_{m,1}\frac{1}{a^2}\right)\right], \quad (12)$$

where, m is the index referring to a certain mode being excited; $a = \sqrt{4\rho k_w k_r}R_0$ is the scaled beam size with $k_w = 2\pi/\lambda_w$, $k_r = 2\pi/\lambda_r$, and R_0 the hard edge of an electron beam. The above formula is a good approximation, when $a > 0.25$. Within such range, $\beta_{m,0} = 1.093$, and $\beta_{m,1} = -0.02$ for the fundamental guiding mode. In Eq. (11), L_G is the power gain length; L_w the undulator length; λ_r the radiation wavelength; N_w the number of undulator period; Z_0 the vacuum impedance; I_{pk} the peak current; $\omega_r (= c2\pi/\lambda_r)$ the radiation angular frequency with c the speed of light in vacuum. The Bessel factor $[JJ] = J_0\left[\frac{a_w^2}{2(1+a_w^2)}\right] - J_1\left[\frac{a_w^2}{2(1+a_w^2)}\right]$, with $a_w = K/\sqrt{2}$, and J_0 and J_1 are the zeroth order and first order Bessel function, respectively. Approximately, $K \approx 93.4 B_w\lambda_w$ is the undulator parameter with B_w the peak field of the undulator in units of Tesla and λ_w in units of meter.

In the above SASE calculation, the bandwidth of the fundamental guided mode is $\sigma_{\omega,\rm GF}$ for $z = 2L_G$ according to Eq. (8). However, the seeded FEL has a different bandwidth of $\sigma_{\omega,s,f}(z = 2L_G)$ according to Eq. (6). Hence, the true start-up noise power in the seeded FEL bandwidth is

$$P_{\rm Seeded}^{\rm Start-up} = P_{\rm SASE}^{\rm Start-up}\frac{\sigma_{\omega,s,f}(z=2L_G)}{\sigma_{\omega,\rm GF}(z=2L_G)}. \quad (13)$$

Considering the first modulator, the Pierce parameter is $\rho \approx 5.4\times10^{-3}$; the scaled beam size is $a \approx 0.8$, which gives the coupling coefficient to be $C_1 \approx 0.3$. The SASE effective start-up noise power in the fundamental guided mode is $P_{\rm SASE}^{\rm Start-up} \approx 400$ W; however, since $\sigma_{\omega,s,f}(z = 2L_G) \approx 2.0\times10^{-3}$ and $\sigma_{\omega,\rm GF}(z = 2L_G) \approx 1.2$ %, the true start-up noise power in the seeded FEL bandwidth is only about $P_{\rm Seeded}^{\rm Start-up} \approx 70$ W.

DISCUSSION

In this paper, we explored the details of an HHG seeded FEL. For simplicity, the HHG seed is modelled as an attosecond pulselet train (APT). Bandwidth reduction, intrinsic to the FEL interaction, smears out the initial attosecond structure of the seed within a very short distance, $z < L_G$. The seeded FEL remains coherent, if we do not consider the accompanied noise power and electron beam non-uniformity [10]. The true start-up noise power in the seeded FEL bandwidth, $P_{\rm Seeded}^{\rm Start-up}$ is only about 70 W. Since the HHG seed has a power of $P_{\rm in} = 5$ MW, the noise-to-signal ratio at the final radiation $\lambda_r = 0.3$ nm is still only about 14 %, even though it has $n_{\rm tot}^2 = 10^4$ ($n_{\rm tot} = 100$) times amplification, *i.e.*, the effective noise level is increased from the initial 70 W to 0.7 MW.

REFERENCES

[1] R. Bonifacio, C. Pellegrini, L.M. Narducci, Opt. Commun., **50**, 373 (1984).

[2] J.-M. Wang and L.-H. Yu, Nucl. Instr. and Meth., **A 250**, 484 (1986).

[3] K.-J. Kim, Nucl. Instr. and Meth., **A 250**, 396 (1986); Phys. Rev. Lett. **57**, 1871 (1986); Lawrence Berkeley National Loboratory Report No. 40672 (1997).

[4] S. Krinsky and Z. Huang, Phys. Rev. ST Accel. Beams **6**, 050702 (2003); E.L. Saldin *et al.*, *Proc., 2005 Int. FEL Conf.*, p.258.

[5] L.H. Yu, *Phys. Rev. A* **44**, 5178(1991).

[6] L.-H. Yu, *et al.*, *Science*, **289**, 932(2000).

[7] J. Wu and L.H. Yu, Nucl. Instr. and Meth., **A 475**, 104 (2001).

[8] L.H. Yu and J. Wu, Nucl. Instr. and Meth., **A 483**, 493 (2002).

[9] J. Wu and L.H. Yu, Stanford Linear Acclerator Center Report No. SLAC-PUB-10494 (2004).

[10] J. Wu and L.H. Yu, Stanford Linear Acclerator Center Report No. SLAC-PUB-10495 (2004).

[11] M.-E. Couprie *et al.*, *Proc., 2005 Int. FEL Conf.*, p.55.

[12] R. López-Martens, Phys. Rev. Lett. **94**, 033001 (2005).

[13] E.A. Gibson *et al.*, IEEE J. of Selected Topics in Quant. Elec. **10**, 1339 (2004).

[14] J. Mauritsson *et al.*, Phys. Rev. A **70**, 021801(R) (2004).

[15] P.M. Paul *et al.*, Science **292**, 1689 (2001).

[16] J. Wu, P.R. Bolton, J.B. Murphy, and X. Zhong, Stanford Linear Acclerator Center Report No. SLAC-PUB-11891 (2006).

[17] J.B. Murphy *et al.*, Brookhaven National Laboratory Report No. BNL-75807-2006-JA, and Stanford Linear Acclerator Center Report No. SLAC-PUB-11852 (2006); J. Wu *et al.*, Stanford Linear Acclerator Center Report No. SLAC-PUB-11985 (2006).

[18] J. Arthur *et al.*, Stanford Linear Acclerator Center Report No. SLAC-R-593 (2002).

[19] I. Boscolo and V. Stagno, *Nuovo Cimento B* **56**, 219(1980).

[20] Z. Huang and K.J. Kim, Phys. Rev. E **62**, 7295 (2000).

[21] J. Wu, *Proc., 2003 Particle Accel. Conf.*, p. 1035.

[22] E.L. Saldin, E.A. Schneidmiller, and M.V. Yurkov, *Opt. commun.* **202**, 169 (2002).

[23] E.L. Saldin, E.A. Schneidmiller, and M.V. Yurkov, *Nucl. Instrum. Methods Phys. Res. A* **381**, 545(1996).

[24] L.H. Yu, *Phys. Rev. E* **58**, 4991(1998).

THE FIRST EXPERIMENTAL OBSERVATION OF FEL AMPLIFIER EFFICIENCY IMPROVEMENT USING ELECTRON BEAM ENERGY DETUNING AT THE NSLS SDL

T. Watanabe*, J.B. Murphy, J. Rose, Y. Shen, T. Tsang, X.J. Wang, BNL, Upton, NY 11973, USA
H.P. Freund, Science Applications International Corporation, McLean, VA 22102, USA

Abstract

The first experimental observation of efficiency enhancement using electron energy detuning in a single-pass laser seeded Free-Electron Laser (FEL) amplifier is reported. Our experiments show that it is possible to double the FEL efficiency by increasing the electron energy by +0.7 % relative to the resonance energy. The measurement of the laser seeded FEL spectra versus energy detuning shows that the peak wavelength of the FEL radiation is determined by the seed laser. The experimental results are discussed using FEL theory and a three-dimensional simulation code GENESIS1.3 [1].

INTRODUCTION

One of the advantages of the FEL is the ability to produce high power laser light without the conventional thermal issues associated with other laser systems [2]. In addition, the operating wavelength of the FEL can be adjusted according to the application. Because of the advantages, the FEL has been regarded as one of the promising approaches to generate Megawatt (MW) average power laser at 1 μm wavelength. Such an application is called directed energy application [3, 4].

In order for the FEL to realize the MW average power output, it is required to optimize the efficiency of the FEL process. Supposed that the interaction between the electron beam and the radiation is strong enough in the undulator, the radiation power grows exponentially as the electron beam goes through the undulator. According to the steady-state theory of a single-pass FEL, the radiation is saturated at ρP_e due to the deposition of the electron energy to the radiation. Here, ρ is the Pierce parameter and P_e is the input electron power. After the saturation, the electrons with lower energy no more resonate with the radiation as it does in the exponential gain regime. Instead, the mutual energy deposition between electrons and radiation is repeated.

To overcome the saturation, several schemes have been proposed and tested. One is to taper an undulator, in which the field strength of the undulator is gradually decreased after the saturation so that the electrons with lower energy can maintain the resonance with the radiation [5, 6]. Another is to detune the electron energy, in which the input electrons with slightly higher energy can resonate with the radiation longer than the normal (resonant) case [3]. The detuning effect had been theoretically and numerically studied [7, 8, 9, 10]. The study indicates that the growth rate is deteriorated by the detuning, while the saturation power can be enhanced by optimizing the detuning. It is an advantage of the detuning scheme that the scheme does not require any modification of the experimental setup; only the requirement is to change electron beam energy. As far as authors know, however, the detuning effect in a single-pass FEL had not been experimentally verified.

In a self-amplified spontaneous emission (SASE) FEL, in which no external seed laser is supplied, the radiation wavelength is shifted when the electron energy is changed. Thus, the wavelength of the output radiation is inevitably resonated with the incident electron energy and no enhancement of FEL efficiency due to the detuning should be expected. In a seeded FEL, where an external laser is injected and then amplified via interaction with electrons, the wavelength of the radiation may be affected by both electron energy and the seed laser. Eventually, it may enhance the efficiency of the amplification to detune electron energy in terms of the wavelength of the seed laser.

In the paper, the experimental demonstrations of efficiency enhancement by the electron energy detuning is reported. The experimental results are compared with the numerical simulation and interpreted by FEL theory.

DETUNING EXPERIMENT

The experiments were conducted at the Source Development Laboratory (SDL) of National Synchrotron Light Source (NSLS), Brookhaven National Laboratory (BNL). The picosecond (ps) electron pulse generated by a photoinjector is compressed to 1.5 ps by a chicane-type bunch compressor. The compressed e-beam passes through a 10 m long planar undulator, of which period is 3.89 cm and the undulator parameter is K=1.1. The seed laser generated by a Ti:Sapphire laser system is compressed to 6 ps, with the frequency chirp being slightly negative. Passing through a bandpass filter, the seed laser has the central wavelength of 795 nm and the bandwidth of 1.5 nm at Full Width at Half Maximum (FWHM). The major experimental parameter are summarized in Table. 1.

* twatanabe@bnl.gov

Table 1: Major experimental parameters

Undulator parameter K	1.1
Undulator period	3.89 cm
Undulator length	10 m
Electron energy	98 - 102 MeV
Peak current	380 A
Electron bunch duration (FWHM)	1.5 ps
Energy spread (rms)	0.1 %
Normalized emittance	2-4 mm.mrad
Seed laser wavelength	795 nm
Seed laser bandwidth (FWHM)	1.5 nm
Seed laser pulse duration (FWHM)	6 ps
Seed laser energy	4 kW

Efficiency measurement

For a planar undulator, the wavelength of the FEL radiation, λ_r, is written as,

$$\lambda_r = \frac{\lambda_u(1 + K^2/2)}{2\gamma^2}, \quad (1)$$

where λ_u is the undulator period and γ is the electron energy normalized with its rest mass. In general seeded FEL experiments, the electron energy is adjusted to satisfy Eq.(1) for a given wavelength. In what follows, such an energy is called the energy on resonance. In our experiment, the energy on resonance was determined by measuring SASE spectrum without the seed laser.

In Fig. 1, the energy gains in the undulator on resonance and with two detuning cases are plotted; one is 0.7 % higher (+0.7 % detuning) and another is 0.5 % lower (-0.5 % detuning) relative to the energy on resonance. All the three data are shown with root-mean-squared (rms) error bars, but at most of points, the error bars are overlapped with the dots. In -0.5 % detuning case, the seed laser energy is dominant until 7.8 m, because both transversely and longitudinally the seed laser size is larger than the electron beam. The simulation results on resonance and with detuning were also presented in Fig. 1. The gain curve on resonance is shown by the solid curve, and those with +0.5 and -0.5 % detuning are respectively shown by dotted and dashed curves.

It is obvious in both experiment and simulation that the gains with detuning are asymmetric between positive and negative detuning; the negative detuning degrades the gain by more than one order of magnitude, while the positive detuning enhances it by factor of two. To interpret it, we recall one-dimensional steady-state theory [7, 8, 9, 10]. First, at the early stage of amplification, small-signal gain theory indicates that the direction of energy deposition between electrons and radiation is opposite depending on the direction of detuning. In Fig. 1, the radiation energy with negative detuning is deposited to electrons once, while that with positive detuning immediately gains energy from electrons. On resonance, there is no energy deposition, which is also presented by the theory. Next, in a high gain regime, a cubic equation for time-dependent gain of FEL radiation in the form $exp(i\lambda\tau)$ is written as,

$$\lambda^3 - \delta\lambda + 1 = 0, \quad (2)$$

where λ is an eigenvalue, of which negative imaginary part gives the growth rate, and δ is the normalized energy detuning $\delta = (\gamma^2 - \gamma_R^2)/2\gamma_R^2\rho$. In Eq.(2), the efficiency parameter is assumed to be small, $\rho \sim 0$. The preferable instability exists only when the detuning is smaller than the threshold, i.e., $\delta < \delta_{th} \sim 1.89$, where two of the three eigenvalues in Eq.(2) have imaginary part. The maximum growth rate, $Im\lambda = \sqrt{3}/2$, occurs at no detuning, $\delta = 0$. It has also been shown with the aid of numerical simulation that as the electron energy goes higher, the saturation energy becomes higher until it reaches the threshold, $\delta \sim \delta_{th}$. Since the efficiency parameter ρ of the experiment is in the range of 0.003 through 0.004, the threshold corresponds to the electron energy detuning of +0.55 to +0.75 % (shown grey in Fig.1). One can see in Fig. 1 that both experiment and numerical simulation represent the characteristics predicted by the theory and numerical simulation; the positive detuning in the range of threshold enhances the output energy, whereas the same amount of detuning but in negative direction just degrades the gain due to the combination of energy deposition to the electrons in small-signal gain regime and degraded gain in high gain regime.

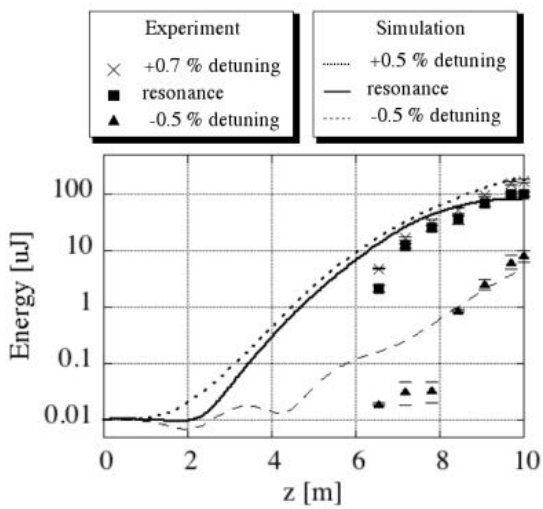

Figure 1: Gain curves on resonance and with detuning.

To see the detuning effect more clearly, the output energy of FEL radiation was plotted as a function of the electron energy in Fig. 2. The dots with peak-to-peak error bars are experimental data and the solid line is evaluated by the time-dependent simulation under the same condition as the experiment. The output radiation energies are normalized with those on resonance in both experiment and simulation results. The energy on resonance is 102 and 82 μJ respectively for the experimental and the numerical results. In

Fig. 2, the asymmetry between positive and negative detuning is again clearly observed. The negative detuning of 0.5 % deteriorates the FEL gain by one order of magnitude, while the positive detuning of 0.7 % enhances the gain by 70%. In addition, further detuning by a half percent in a positive direction, i.e., total detuning of +1.2 %, does no more enhance the gain, but suppresses it. It is because the detuning goes beyond the threshold δ_{th} (grey in Fig. 2). The experimental result agrees with the simulation result except for two things in detail; the enhancement of the energy in the experiment is lower than that of by simulation, and the amount of the detuning that gives the enhancement is +0.7 % in experiment and +0.5% in simulation. It is because there was an electron energy jitter in the experiment, so the energy enhancement at the detuning was smoothed out by taking the average. In fact, the maximum energy given at the +0.7 % detuning was 206 μJ, which is more than 2 times higher than the average energy on resonance.

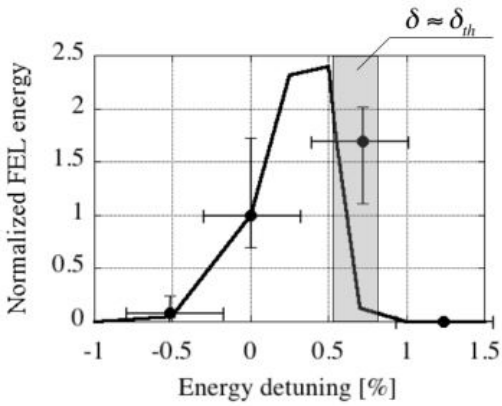

Figure 2: FEL output energy vs electron energy detuning. Solid line is simulation and dots are experimental result.

Spectral measurement

The spectra of the seeded FEL pulse were also measured. Figure 3 represents the example spectra of seeded FEL on resonance (solid line) and with the positive detuning at the threshold $\delta \sim \delta_{th}$ (dashed). The positive detuning in the experiment (Fig. 3 (a)) is +0.7 %, and that in the numerical simulation by GENESIS1.3 (Fig. 3 (b)) is +0.5 %.

It is both experimentally and numerically verified in Fig. 3 that the peak wavelength of output seeded FEL pulse is not notably shifted by detuning electron energy. In both cases, the difference of the peak wavelength between on resonance and with the positive detuning is much less than 1 nm. It follows that the seeded FEL spectrum with detuning is dominated by the seed laser, so the detuning scheme does not induce the undesirable frequency shift in the output pulse. Note that the detuning of +0.7 % in electron energy corresponds to the down-shift of SASE spectrum by as much as 11 nm.

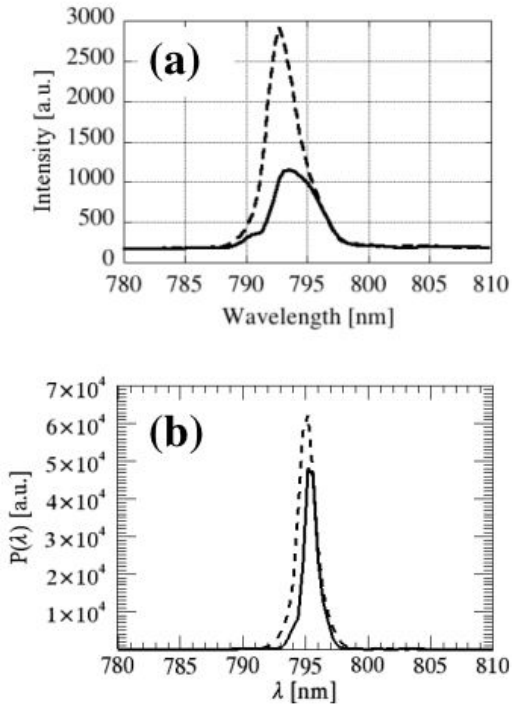

Figure 3: Spectra of laser seeded FEL on resonance (solid line) and with positive detuning at the threshold $\delta \sim \delta_{th}$ (dashed). (a) experiment and (b) GENESIS calculation.

CONCLUSION

We experimentally observed the efficiency enhancement by the electron energy detuning. By applying the energy detuning of +0.7 %, the efficiency was doubled. Both the further detuning and the opposite detuning significantly degrades the efficiency. The results were well consistent with one-dimensional steady-state theory as well as the three dimensional numerical simulation.

The spectra of seeded FEL pulses on resonance and with detuning were also measured. It was verified that the peak wavelength of seeded FEL with detuning was almost same as that on resonance both by the experimental result and the numerical simulation. It indicates that the detuning scheme works without modifying the seeded FEL spectrum substantially.

The study gives fundamental knowledge for implementing seeded FEL experiments as well as designing the high power FEL such as a directed energy application.

ACKNOWLEDGMENTS

We are grateful for support from the NSLS and BNL director's office and this work is supported by the Office of Naval Research and U.S. Department of Energy under contract No. DE-AC02-98CH1-886. The authors are pleased to acknowledge valuable technical contribution from Boyzie Singh.

REFERENCES

[1] S. Reiche, Nucl. Instrum. Methods Phys. Res. A **429**, 243 (1999).

[2] C.W. Roberson and P. Sprangle, *A review of free-electron lasers*, Phys. Fluides, **429**, 3, Jan. 1989.

[3] P. Sprangle et al., IEEE J. Quantum Electronics, **40**, 1793 (2004).

[4] T. Watanabe et al., Proc. of FEL2005, p.320 (2005).

[5] T.J. Orzechowski et al., Phys. Rev. Lett. **57** 2172 (1986).

[6] D.A. Jaroszynski et al., Phys. Rev. Lett. **74**, 2224 (1995).

[7] P. Sprangle et al., Phys. Rev. A. **21**, 302 (1980).

[8] R. Bonifacio et al., Opt. Commun. **50**, 373 (1984).

[9] J.B. Murphy and C. Pellegrini, J. Opt. Soc. Am. B **2**, 259 (1985). J.B. Murphy and C. Pellegrini, NIM A **237**, 159 (1985).

[10] J.B. Murphy and C. Pellegrini, *Laser Handbook Volume 6*, (Elsevier Science Pub., North-Holland, 1990), Chap. 2.

CHIRPED PULSE AMPLIFICATION EXPERIMENT AT 800 nm

L.H. Yu, T. Shaftan, D. Liu, T. Tsang, J. Rose, X.J. Wang, T. Watanabe
NSLS, BNL, Upton, NY 11973, USA.

Abstract

We report the chirped pulse amplification (CPA) experiment carried out using 800 nm direct seeding and NISUS undulator as free electron laser amplifier at SDL of BNL. The experiment indicated that due to saturation in the center part of the chirped electron bunch the output pulse shape has a dip in the middle, as result the edge of the bunch has higher power than the center. Hence the output spectrum also showed a dip in the center, resulting in a larger FWHM bandwidth than the seed. An interesting result is that the 800 nm chirped FEL output was compressed down to a pulse length shorter than what the seed pulse itself can be compressed to.

INTRODUCTION

Chirped pulse amplification (CPA) [1-4, 8] can be used to generate short high intensity pulse in FEL, and it has been shown theoretically possible to generate pulse shorter than what the seed can be used to generate [2]. Initial CPA experiment has been carried out in HGHG process at 266 nm but without the final compression of the pulse [5]. The experiment showed that by matching the electron bunch energy chirp with that of the seed pulse properly we were able to maximize the bandwidth of the output pulse while maintaining coherence. First SPIDER traces were measured and quadratic optical phase dependence along the pulse was obtained [7]. However, due to limited beam time, we were unable to finish the compression of the output pulse at 266 nm so far. In this paper, we report our preliminary result on the CPA at 800 nm with direct seeding.

EXPERIMENT SETUP AND CPA EXPERIMENT

A schematic diagram of the 788 nm experiment is shown in figure 1. The 788 nm seed pulse with pulse length of 2.5 ps and bandwidth of about 6 nm is chirped with the head of the pulse at longer wavelength. The 103 MeV electron bunch with charge of 500 pC is compressed down to about 2.5 ps and chirped using the last section of the linac to about 0.5% of projected energy spread with head at lower energy. During the experiment the chirp is adjusted to maximize the output bandwidth. The seed and the electron beam are sent into the FEL undulator NISUS and aligned to overlap in the first section of the undulator. The seed has a Rayleigh range of 1.95 m. We used first two pop-in monitors inside the NISUS undulator to carry out the alignment. Since the seed table where the seed is injected into the undulator beam line by a 45° mirror is 7 meters away from the entrance of the NISUS undulator, the physical limitation of the system made it impossible to match the seed beam size to the electron beam size at the beam waist of the seed, which is about 0.6 m inside of the entrance. As a result the laser beam size is much larger than the electron beam. This is illustrated in figure 2

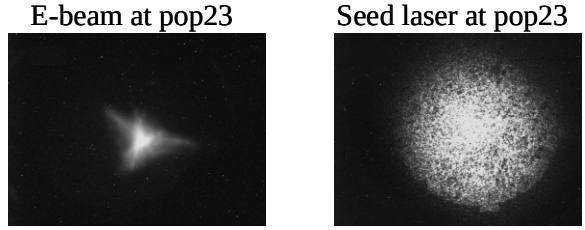

Figure 2: Images of the beam (left) and seed laser (right)

where we show the images of the seed and electron beam at the first pop in monitor in the NISUS. Thus this FEL amplifier setup is not very efficient. But it is sufficient to be used for a demonstration of the CPA process. The NISUS undulator has a period of 3.9cm with K=1.126.

The electron bunch length is measured by the zero-

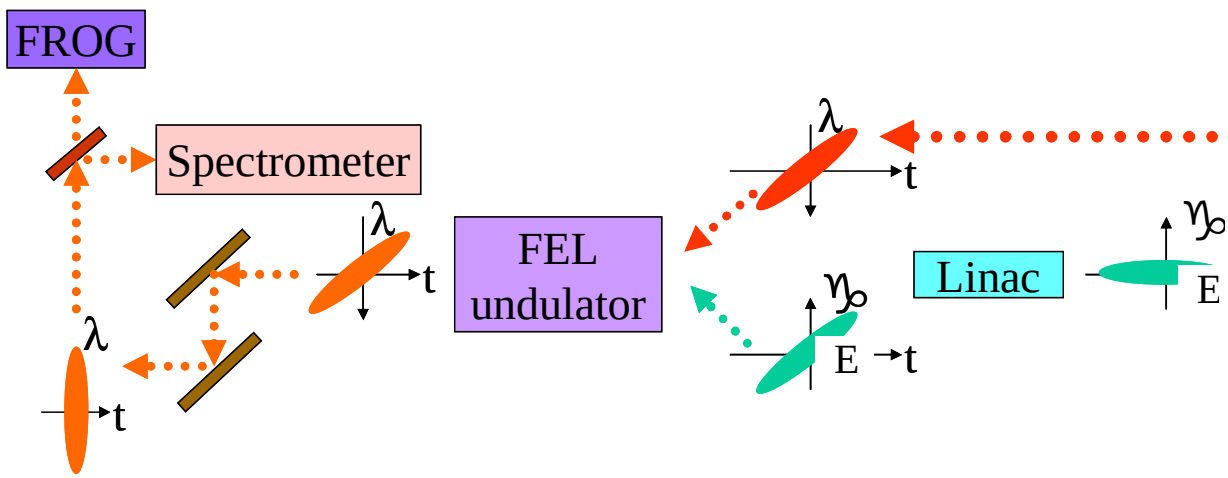

Figure 1: Layout of the experimental set-up.

phasing method using the dipole right after the last linac section as the energy spectrometer. The images of the measurement at 90 and -90 degree of the RF phase are shown in figure 3.

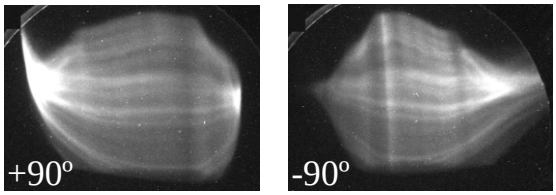

Figure 3: Measurement of bunch length

The synchronization between the electron bunch and the seed laser pulse is realized by observing the significant increase of energy spread when they temporally overlap. The energy spread is measured using the monitor after the beam passes through the undulator and the last dipole. This is shown in figure 4. The upper picture shows that the energy spread is adjusted to about 0.5% when the seed laser is turned off (the full screen corresponds to 1.5% of energy spread). When we turn on the seed laser and change the seed pulse time delay by an optical trombone so it overlaps with the electron bunch, the energy spread is increased significantly and hence the image of the electron beam occupies the full screen.

The seed laser pulse energy is 13.4 μJ before sent into the NISUS undulator during the CPA experiment. To ease the synchronization procedure before we achieve the overlap between the seed and the electron bunch, we remove the attenuation (which is 10 when the pulse energy is 13.4 μJ) so the energy spread increase will be more visible even when the tail of the electron bunch overlaps with the seed. This helps to increase the step size that we used to move the optical trombone and complete the synchronization procedure faster.

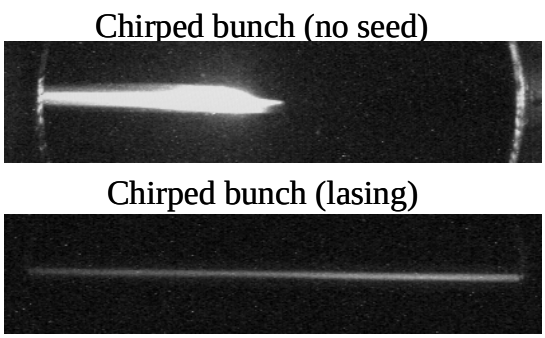

Figure 4: Electron beam energy spectra before (upper plot) and after (lower plot) interaction with electron beam

Due to energy and phase jitter and drift of the electron bunch (energy jitter is about 0.2% rms, time jitter about 140 fs rms), during the scan for synchronization for each trombone position we also scan energy within about 0.5% range then move to next position about 100 μm apart. Once the synchronization is found, we send the amplified FEL output to the spectrometer to fine tune the synchronization. Since the seed laser is chirped, and the output wavelength is determined by the seed, if the tail of the electron bunch overlaps with the head of the laser pulse the output pulse wavelength is centered at longer wavelength of around 795 nm. When the head of the electron bunch overlaps with the tail of the seed, the wavelength moves to shorter wavelength of around 785 nm. This helps us to determine which direction and how much we should move the trombone to maximize the overlap. In figure 5 we show the measured FEL output spectrum at different positions of the optical trombone micrometer. The center of the spectrum is at 790 nm.

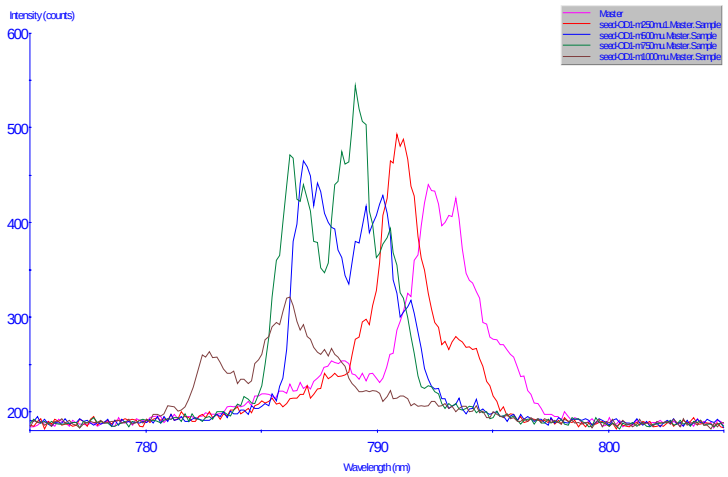

Figure 5: Measured FEL spectra

During the scan the FEL pulse central wavelength is also measured and plotted against the micrometer position, as shown in figure 6.

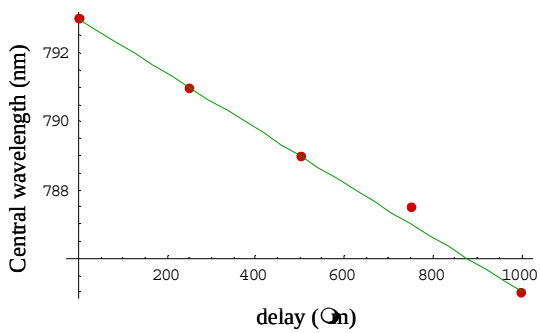

Figure 6 Central FEL wavelength for different delays between seed and electron bunch

The figure 6 shows the wavelength has a linear dependence on the delay of electron bunch relative to the seed laser, as determined by the micrometer position. The slop of the curve (2.6 nm/ps) is the measured chirp of the

seed by FEL process. This is to be compared with the chirp setup by the seed laser compressor-stretcher system, which is 6 nm/2.5 ps=2.4 nm/ps, providing with a reasonable agreement.

The gain length of the FEL process is measured using SASE output pulse energy as function of distance in the NISUS by kicking the electron beam away from axis sequentially at different longitudinal locations inside the NISUS undulator with the horizontal trajectory correctors. The result is shown in figure 7. Considering the spacing between the monitor is 0.62 m, the power gain length is obtained from this plot as 1m.

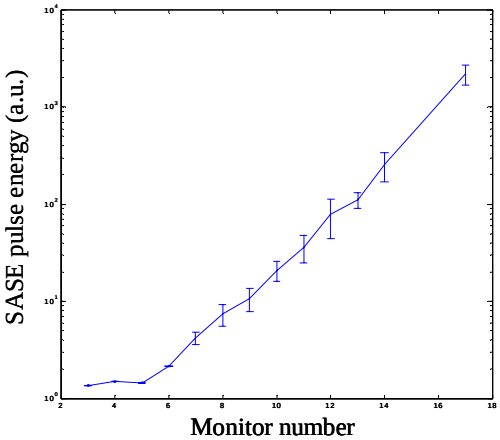

Figure 7: SASE gain length measurement

The normalized emittance was measured to be 6 mm-mrad by fitting with the beam profile measurement in the NISUS undulator. Once the synchronization is achieved, we tune electron beam chirp by adjusting the last linac section to vary the energy spread and observing the bandwidth of the FEL output until we reach the maximum bandwidth. When the chirp is optimized and when the seed laser is turned off, the image of the energy spread is shown in the top of the figure 4.

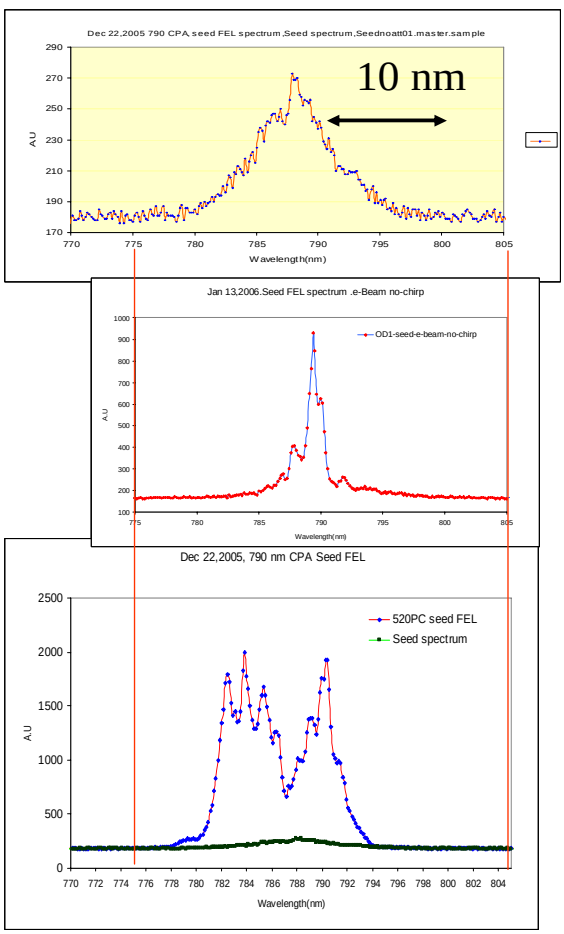

Figure 8: Measurements of seed (upper), unchirped FEL (middle) and FEL output with matched chirp (lower plot)

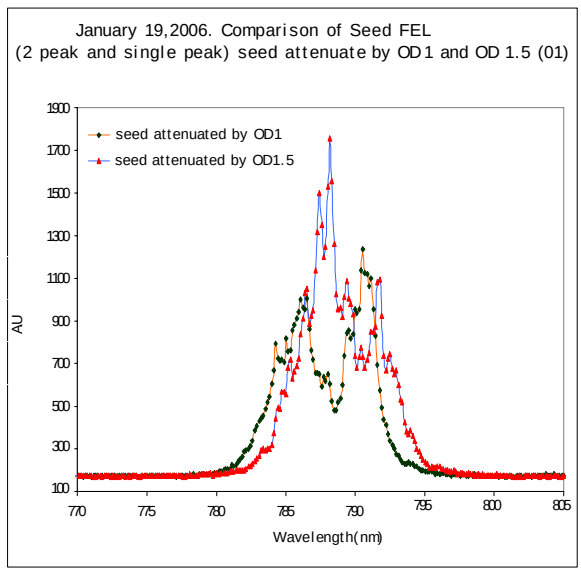

Figure 9: Spectra of the seeded FEL output for two values of attenuation 10 (OD1) and 30 (OD1.5)

In the top plot of figure 8 we show the measurement of the seed spectrum. The middle plot of the same figure is the spectrum of the FEL output when the electron bunch is not chirped (when energy spread is minimized with the seed laser turned off). Lower plot shows the FEL radiation spectrum for the case when the chirp of the electron bunch is optimized. To be able to compare the bandwidth, we align the three plots vertically so that they use the same horizontal scale. It is seen that when the electron bunch is not chirped, the output bandwidth is narrower than the seed, showing that only the part of the seed pulse with the wavelength in resonance with the electron beam energy is amplified, and the width of the line is clearly determined by the bandwidth of the amplifier.

It is interesting to remark here that figure 8 shows when the energy chirped to match the seed chirp, the bandwidth increases to about 10 nm, significantly larger than the seed bandwidth of about 6 nm. And in particular there is a pronounced dip near the center of the FEL output spectrum. This can be explained by deep saturation in the

central part of the electron bunch. If the current at the central part of the electron bunch is and since the central part of the seed is also at peak, the FEL amplifier can be oversaturated so that power is lower than at the edge of the bunch where the FEL is just reaching saturation, thus creating a dip in the spectrum because due to linear chirp, the spectrum corresponds to time.

To further test this interpretation, we expect that when the seed power is lowered properly so that the central part of the bunch just reach saturation, the dip in the central part of the pulse will disappear, and hence the double peaks in the spectrum should be replaced by a single peak. And indeed, when we increase the attenuation from 10 to 30, we did observe that the double peaks are replaced by a single peak. This is shown in figure 9.

Because of the output bandwidth is larger than the seed bandwidth we expect that when compressed, the final pulse width can have a smaller pulse length than the fourier-transform-limited seed pulse length. This has been confirmed by our next step of the experiment, the compression and measurement of the compressed pulse.

MEASUREMENT OF THE COMPRESSED PULSE BY FROG

As shown in figure 1, the output FEL pulse is sent through a compressor, compressed and sent to a FROG (Frequency-Resolved Optical Gating) device [6]. This device is designed to measure spectral and temporal distribution of short laser pulse simultaneously, and generate the amplitude and phase as function of time for the pulse. It is compact and, in particular, easy to align. The schematic diagram of the arrangement of compressor, spectrometer and FROG is shown in figure 10. In figure 11, we show the FROG result of compressed chirped FEL output pulse. In the picture, the upper right one is the measured FROG image while the upper left one is the retrieved image from the reconstructed pulse shape, the agreement between these two pictures testifies the correctness of the FROG result. The lower left is the reconstructed temporal pulse while the lower right one is the reconstructed spectrum.

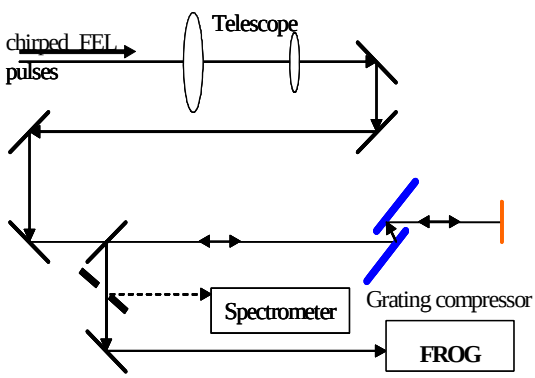

Figure 10: Time- and spectrum measurements set-up.

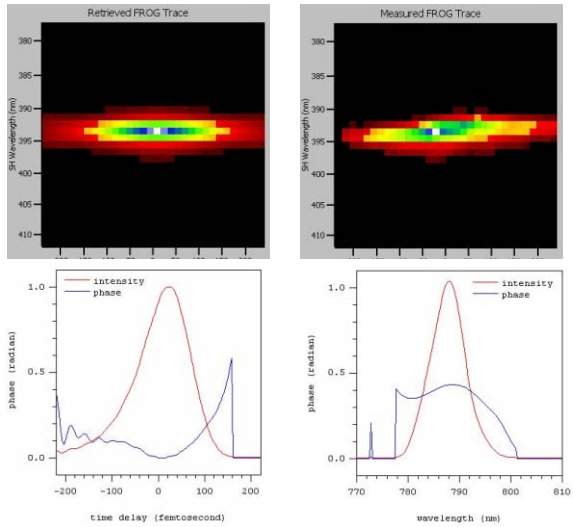

Figure 11: FROG traces of the compressed FEL pulse.

The result shows that pulse length is 122 fs FWHM. We remark that resolution of the spectrum obtained from the FROG is not as good as that of the spectrometer we used, so that in the reconstructed spectrum we could not see the double peaks feature as shown in figure 8 and 9.

This is to be compared with a fourier-transform-limited compressed seed. With the seed bandwidth of 6 nm at 800 nm, assuming minimum wave packet of Gaussian shape, the FWHM pulse length and FWHM bandwidth product is Log(2)/π*0.8 μm/(0.3 μm/fs) = 1.17. So the pulse FWHM length should be 1.17*800 nm/6 nm =156 fs. Hence even if the seed is fourier-transform-limited, it is still significantly longer than the CPA result.

In conclusion, we carried compressed CPA from FEL output at 800nm and obtained shorter pulse than what can be obtained from compressed seed. The result can be explained by the deep saturation of the FEL output. This illustrated the potential in the future to generate short pulse using CPA process in an FEL device.

REFERENCES

[1] G..T. Moore, Nucl. Instrum. Methods in Phys. Res. A 272, p. 302 (1988).
[2] L.H. Yu *et al.*, Phys. Rev. E 49, 5, p. 4480 (1994).
[3] C. Pellegrini, Nucl. Instrum. Methods in Phys. Res. A 445, p. 124 (2000).
[4] G. Andonian *et al.*, Phys. Rev. Lett. **95**, 054801 (2005).
[5] A. Doyuran *et al.*, Nucl. Instrum. Methods in Phys. Res. A 528, p. 467 (2004).
[6] R. Trebino *et al.*, Lithuanian Journal of Physics, v. 33, p. 247-252.
[7] Z. Wu et al., in Proc. of FEL-2004.
[8] E. Saldin et al., Phys. Rev. ST-SB, 9, 050702 (2006).

ISSUES IN HIGH HARMONIC SEEDING OF THE 4GLS XUV-FEL

B. Sheehy, Sheehy Scientific Consulting, New York, USA; J.A. Clarke, D. J. Dunning, N. R. Thompson, CCLRC, ASTeC, Daresbury Laboratory, Warrington, UK; B. W. J. McNeil, SUPA, Department of Physics, University of Strathclyde, Glasgow, UK

Abstract

Using High Harmonics (HH) as a seed for free electron lasers is currently under consideration in a number of proposed facilities. An HH seed source is independent of machine dynamics, and allows for extensive manipulation of the seed pulse using well-established techniques of ultrafast laser physics. These allow for rapid tuning, and may enable the extension of chirped pulse amplification and even pulse shaping for coherent control to short wavelengths. In addition, there are advantages in terms of noise and synchronization. There are a number of issues involved in the implementation of HH seeding: energy, tunability, coherence, temporal structure, etc. We discuss these issues and their application in the 4GLS XUV-FEL.

INTRODUCTION

The limitations of spontaneous sources have motivated a great deal of development in short-wavelength FEL design. For reasons of stability, coherence and bandwidth, SASE sources are disadvantageous relative to coherent alternatives. A number of seeding methods have been proposed, including high-gain harmonic generation, several self-seeding techniques, and using high harmonic generation to produce sufficient radiation at the fundamental resonant wavelength of the radiator to directly seed the FEL.

The attraction of seeding with high harmonics is that a great deal of control over the seed radiation can be had by using well-known ultrafast laser techniques to control the fundamental that drives the HH generation. Harmonic pulses can be made extremely short, down to a few femtoseconds, and tuning is relatively simple. Demands on timing and synchronization with the electron bunch are less stringent than in other techniques. Also, the coherent transfer of phase information from the HH pump to the harmonics opens the possibility of creating a chirped HH seed and performing chirped pulse amplification [1] in the FEL to achieve higher output energies, or even of pursuing more elaborate pulse shaping.

The efficiency of HH generation is currently too low for FEL seeding at soft X-ray energies. However, in the wavelength range planned for the 4GLS XUV-FEL (8-100 eV), available sources could provide sufficient energy for seeding at kHz repetition rates, and the available energy will increase with coming improvements in ultrafast laser technology.

A number of other issues must also be addressed. Tunability is required, and must be provided in a way that minimizes downtime and perturbations to timing and synchronization. Other spectral and temporal properties have also been raised as issues. We address these issues and discuss the implementation of seeding in the 4GLS XUV-FEL.

ENERGY AND TUNABILITY

The 4GLS XUV-FEL will operate between 8-100 eV. We have simulated the XUV-FEL [2], using GENESIS 1.3 [3], using 100 kW peak seed power for output photon energies below 30 eV, and 30 kW for energies between 30 eV and 100 eV. For 30 fsec pulses, this is equivalent to 3 nJ and 1 nJ pulse energies respectively. This is three orders of magnitude above the spontaneous power generated in the first gain length due to intrinsic density fluctuations in the electron bunch, and, in simulations produces an output pulse with good contrast [2].

A number of groups have measured harmonic yields from Ti:Sapphire based systems, and we show a scaled synopsis of recent results [4-6] in Fig. 1. The experimental results represented here (unconnected points on the plot) were obtained using fundamental pulse energies from 3-50 mJ, and we have scaled the results to an energy of 14 mJ – the energy of the Ti:Sapphire system described below. These scaled yields exceed our requirements by over three orders of magnitude at the low energy end of the XUVFEL operating range, and by a factor of six at the high energy end.

The scaling energy of 14 millijoules was chosen because such a laser system has been demonstrated at kHz repetition rates [7]. This is conservative, as ultrafast laser technology is developing very rapidly, and extension to higher powers is not constrained by a fundamental limit. A number of recent developments, eg the use of optical parametric chirped pulse amplification [8], high power Yb:YAG lasers [9], and enhancement cavities [10-12], offer new opportunities for larger systems. Several 100-Watt kilohertz system designs have been proposed [13], and are likely to be demonstrated soon.

There is also considerable effort in the community focused on extending the wavelength range and yield of harmonics. Recent experiments [6] using two-color fields demonstrated an enhancement of over 2 orders of magnitude in the harmonic yield in Helium, producing 150 nanojoules in the 38th harmonic (59 eV), using only 2.8 mJ in the pump laser. Fig. 1 also shows the results of that experiment (scaled from the experimental energy of 2.8 mJ to 14 mJ). Since Helium is the least efficient of the rare gas targets used, it is reasonable to expect that when these techniques are extended to other gases and longer

pump wavelengths, available seed energies over the XUV-FEL operating range will increase substantially.

The simplest and most versatile way to tune between the harmonic orders is through control of the amplitude and phase of the fundamental. This can be as simple as a chirp [14-16], but more general adaptive pulse shaping [17-20] allows greater tuning range and greater control over the harmonic pulse width. This method presents minimal impact on synchronization during tuning, and is rapid once the system has been calibrated. The tuning range is of the order of $q\Delta\nu$, where q is the harmonic order and $\Delta\nu$ is the bandwidth of the fundamental, so the method does not work well at low harmonic orders. Reitze et al [18] demonstrated complete tunability (i.e. a tuning range exceeding the separation of adjacent harmonics) down to 40 eV in Argon using 28 fsec, 800 nm pulses, a tuning range of $2.2q\Delta\nu$. At some energy below 40 eV, complete tunability will be lost. For this reason in the current design, a tunable fundamental is used for the low-energy end of the XUV-FEL energy range.

Using a tunable fundamental entails a double loss, from the frequency conversion losses as well as the drop in harmonic efficiency at longer wavelengths [21]. Conversion to wavelengths shorter then 800 nm, where the harmonic efficiency is higher, is possible, but then the harmonic orders used to reach the very low end of the tuning range are smaller, and complete tunability cannot be obtained there. For an infrared source tunable from 1200 nm to 1475 nm, complete tunability would be obtained. Conversion efficiencies for commercial noncollinear phase-matched optical parametric amplifier (NOPA) systems in this range, pumped by a Ti:Sapphire system, are typically ~10%, while laboratory systems have reported efficiencies of 20% [22]. The harmonic efficiency drops as λ^{-3} [21,23,24], so it is 15-30% of the harmonic efficiency at 800 nm. Harmonic efficiencies are high enough at these lower energies that sufficient seed power can still be produced. Fig. 1 shows the projected range of the tunable source's harmonic yields in Xenon using the expected wavelength scaling of the harmonic efficiency, and assuming 15% conversion efficiency in the NOPA. Above 40 eV, tuning is done using adaptive control of the Ti:Sapphire fundamental

Developments in laser technology will probably make this two-track system unnecessary in the near future, as new high-power kilohertz ultrafast sources in the 1-2 micron wavelength range are developed [13]. Because the high energy cutoff of harmonic production increases with λ^2 [25], at longer wavelength, gases with higher harmonic efficiency can be used to generate higher photon energies, offsetting some of the wavelength-dependent drop in efficiency. A longer fundamental wavelength also increases the wavelength range over which adaptive tuning may be used, since the harmonic order q for a given wavelength increases and the harmonic spacing decreases. For example, assuming an adaptive tuning range of $2q\Delta\nu$, a source with a fixed wavelength of 1.8 microns and 20 fsec pulse width could cover the entire XUV-FEL energy range using only adaptive tuning.

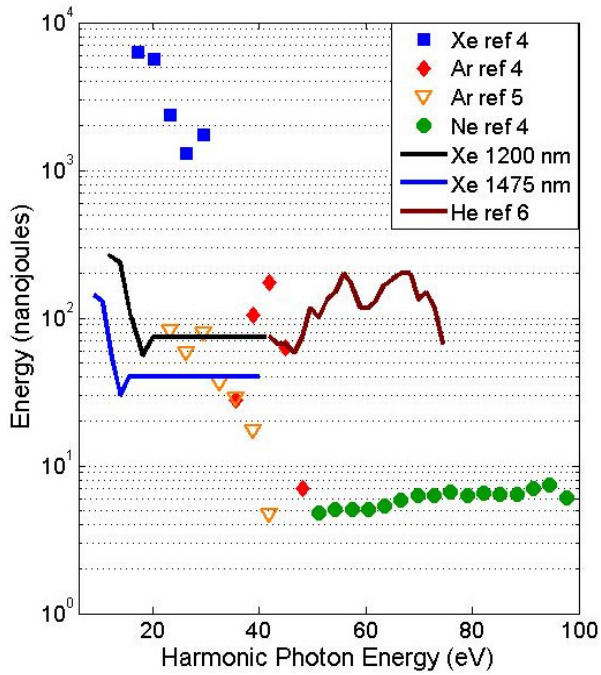

Figure 1. Recent high harmonic generation experimental results scaled by energy and wavelength. The unconnected points were taken with an 800 nm fundamental, and are scaled here to a pulse energy of 14 mJ. The solid Xe curves show the projected range of harmonic yields for the NOPA (2 mJ pulse energy), tuning between 1200 and 1475 nm. The solid He curve shows the results of a two-color experiment using 800 and 400 nm fundamentals, scaled to a 14 mJ pump energy. The minimum energy for seeding the XUV-FEL with a 30 fs pulse is 1 nJ.

COHERENCE, STRUCTURE AND CONTRAST

Other spectral and temporal qualities of the harmonics must also be considered. Over the design range of the XUV-FEL, the gain bandwidth of the FEL radiator is both larger than the bandwidth of individual harmonics, and much smaller than the separation between harmonics. This allows for efficient seeding without requiring the separation of harmonic orders in the seeding optics. The transverse spatial coherence of harmonics depends sensitively on the generation geometry, but very high coherent flux has been measured [26]. This concerns primarily the seeding efficiency, as the spatial coherence increases dramatically as the pulse is amplified to saturation.

Because harmonics are used to generate attosecond pulses, there is some question whether subfemtosecond temporal structure could affect seeding. There are, however, fundamental reasons for expecting little effect from this structure. Sub-femtosecond structure arises from the coherent superposition of multiple harmonics; it

is essentially an interference effect. Since the FEL radiator's bandwidth is restricted to a single harmonic order (the harmonic separation is ~3 eV, while the FWHM gain bandwidth of the radiator lies in the range of .04-.4 eV) it effectively acts as a filter, and the time profile of an individual harmonic, which is smooth [27], is the relevant temporal shape. Furthermore, the period of any sub-femtosecond structure is quite short – half of the fundamental optical cycle – so that, even if multiple harmonics could be amplified, slippage would tend to smooth out any short scale structure. We have considered the attosecond structure issue in our simulations however, and it is discussed in greater detail in Ref. [28].

An issue in all seeding techniques is the achievable contrast between the coherent output pulse and any incoherent background. This is of particular concern in experiments involving nonlinear interactions, as lower-order interactions with the background pedestal surrounding the main pulse can alter the target's initial state before the main pulse arrives or the product state after the main pulse is over, so that both the height of the background and the length of the window over which it persists are important. Our simulations [2,28] show that, for the minimal seed power, we obtain, over the XUV-FEL energy range, contrasts of 10^{-2} to 10^{-3} immediately beneath the main pulse, dropping to 10^{-5} to 10^{-7} within a picosecond on either side of the pulse.

The background consists of SASE evolving in the unseeded part of the bunch, and so the context of these numbers should also be considered carefully. First, the contrast improves with increasing seed power, as the length to saturation decreases and the ratio of the coherent seed power to spontaneous power in the wings of the pulse increases. The feasibility simulations were done with minimal seed power but, depending on the energy and tunability required, orders of magnitude more may be available. The simulations were also done with a Gaussian longitudinal electron bunch distribution with a FWHM pulse width of 625 fs; more sharply peaked distributions would also improve contrast, as the gain in the wings would drop accordingly. The full parameter space has not yet been explored with respect to contrast, and these aspects will be investigated further in future design work. A more detailed discussion and simulation results may be found in Ref [2].

IMPLEMENTATION

The current design for implementing HH seeding in the 4GLS XUV-FEL is shown schematically in Fig. 2. An ultrafast Titanium Sapphire oscillator producing 30 fsec, 800 nm pulses is synchronized at a subharmonic of the accelerator RF frequency. Pulses are selected at 1 kHz and amplified to 14 mJ. Amplifier chains capable of this power presently exist [7], and systems with higher output are expected to appear soon.

After amplification, the pulse is switched into one of two paths, depending on the FEL photon energy. For low

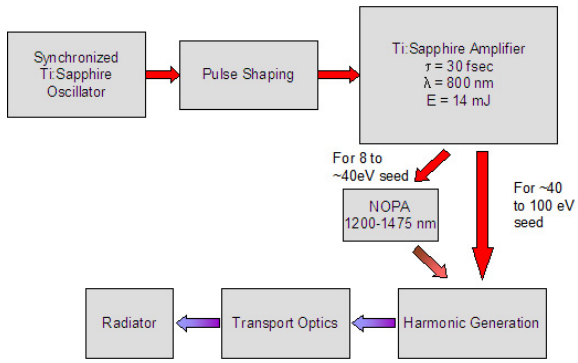

Figure 2. Block diagram of high harmonic seeding for the 4GLS XUV-FEL.

energies (8 to approximately 40 eV), a tunable pump pulse is generated using a noncollinear optical parametric amplifier (NOPA) operating between 1200-1475 nm. At higher energies (40 - 100 eV), the 800 nm light is used for HH generation, and adaptive tuning is used. Pulse shaping for the adaptive tuning can be done either before the amplifier, as shown here, or afterwards.

The geometry for the HH generation is still under study. A loose focusing geometry in a variable length cell is the simplest to implement over the entire range of the XUV-FEL and is equivalent to waveguide geometries at sufficiently high power [29]. Waveguide geometries [30] may be beneficial for the low photon energies, where the pump pulse energy is lower, Modulated waveguide geometries [31] may provide greater efficiency, but it may be difficult to implement multiple configurations to cover the entire wavelength range. Efficient materials (eg SiC) for grazing incidence optics are available for the optics coupling the HH seed into the radiator.

SUMMARY

We have developed a design to establish the feasibility of seeding the 4GLS XUV-FEL with high harmonics. Currently available technology is capable of supplying sufficient seed energy, and tuning may be accomplished with a tunable fundamental at the low-energy end of the XUV-FEL operating range, and with pulse shaping of a fixed-frequency fundamental at higher energies. Technological improvements are expected to increase the available power and simplify the implementation. Spectral and temporal properties of the harmonics appear to be commensurate with the requirements for seeding.

REFERENCES

[1] L. H. Yu et al., Physical Review E 49 (1994) 4480.
[2] *4GLS Conceptual Design Report*. (Council for the Central Laboratory of the Research Councils, UK, http://www.4gls.ac.uk/, 2006)

[3] S. Reiche, Nuclear Instruments and Methods A 429 (1999) 243.
[4] E. J. Takahashi et al., IEEE Journal of Selected Topics in Quantum Electronics 10 (2004) 1315.
[5] J. F. Hergott et al., Physical Review A 66 (2002) 021801.
[6] I. Jong Kim et al., Physical Review Letters 94 (2005) 243901.
[7] Y. Nabekawa et al., Optics Letters 23 (1998) 1384.
[8] A. Dubietis et al., Optics Communications 88 (1992) 437.
[9] D. J. Ripin et al., IEEE Journal of Quantum Electronics 41 (2005) 1274.
[10] R. Jones and J. Ye, Optics Letters 27 (2002) 1848.
[11] R. Jones and J. Ye, Optics Letters 29 (2004) 2812.
[12] F. Ö. Ilday and F. X. Kärtner, "Cavity-Enhanced Optical Parametric Chirped-Pulse Amplification," Joint Conference on Ultrafast Optics V and Applications of High Field and Short Wavelength Sources XI, Nara, Japan, 2005,
[13] F. X. Kärtner et al., "Experiments in Laser Seed Generation," MIT Workshop on the Physics of Seeded FELs, Boston, MA, June 2004,
[14] J. Zhou et al., Physical Review Letters 76 (1996) 752.
[15] D. G. Lee et al., Physical Review Letters 87 (2001) 243902.
[16] H. T. Kim et al., Physical Review A 67 (2003) 051801.
[17] R. Bartels et al., Nature 406 (2000) 164.
[18] D. H. Reitze et al., Optics Letters 29 (2004) 86.
[19] T. Pfeifer et al., Optics Letters 30 (2005) 1497.
[20] T. Pfeifer et al., Appl Physical B 80 (2005) 277.
[21] M. Lewenstein et al., Physical Review A 49 (1994) 2117.
[22] V. Yakovlev, B. Kohler, and K. Wilson, Optics Letters 19 (1994) 2000.
[23] B. Shan and Z. Chang, Physical Review A 65 (2002) 011804.
[24] A. Gordon and F. X. Kärtner, Optics Exp 13 (2005) 2941.
[25] J. L. Krause, K. J. Schafer, and K. C. Kulander, Physical Review Letters, 68 (1992) 3535.
[26] L. Le Deroff et al., Physical Review A 61 (2000) 043802.
[27] I. P. Christov, M. M. Murnane, and H. C. Kapteyn, Physical Review Letters 78 (1997), 1251.
[28] B. W. J. McNeil et al. “The Use of HHG at 4GLS”, These proceedings MOCAU03
[29] S. Kazamias et al., Physical Review Letters 90 (2003) 193901.
[30] C. G. Durfee III et al., Physical Review Letters 83 (1999) 2187.
[31] A. Paul et al., Nature 421 (2003) 51.

ATTOSECOND PULSES FROM X-RAY FEL WITH AN ENERGY-CHIRPED ELECTRON BEAM AND A TAPERED UNDULATOR

E.L. Saldin, E.A. Schneidmiller, and M.V. Yurkov
Deutsches Elektronen-Synchrotron (DESY), Hamburg, Germany.

Abstract

We present a new scheme for generation of attosecond pulses in X-ray SASE FEL. A short slice in the electron beam is strongly modulated in energy by a few-cycle laser pulse in a short undulator, placed in front of the main undulator. Gain degradation within this slice is compensated by an appropriate undulator taper while the rest of the bunch suffers from this taper and does not lase. Three-dimensional simulations with the code FAST predict that short (200 attoseconds) high-power (up to 100 GW) pulses can be produced in Angstrom wavelength range with a high degree of contrast. A possibility to reduce pulse duration to sub-100 attosecond scale is discussed.

INTRODUCTION

Generation of attosecond pulses would significantly increase scientific potential of future hard X-ray FELs such as European XFEL [1] and Linac Coherent Light Source [2]. Up to now several schemes for generation of attosecond pulses from X-ray SASE FELs have been proposed [3, 4, 5, 6, 7, 8]. In this paper we study a new scheme making use of energy chirp in the electron beam and a tapered undulator. The impact of energy chirp on SASE FEL performance was studied in details in [9]. It was found that FEL gain degradation can be perfectly compensated by undulator tapering. An application of the compensation effect for generation of attosecond pulses from X-ray FELs was conceptually proposed in [9]. In this paper we present the results of numerical simulations demonstrating that the scheme works very well in a realistic situation. We also discuss a possible extension of this scheme that can allow to generate high-power, high-contrast hard X-ray pulses with a duration in 10-100 attosecond range.

ENERGY CHIRP AND UNDULATOR TAPERING

The energy chirp parameter [9]

$$\hat{\alpha} = -\frac{d\gamma}{dt}\frac{1}{\gamma_0\omega_0\rho^2} \qquad (1)$$

is defined such that, for positive sign of $\hat{\alpha}$, particles in the head of the bunch have larger energy than those in the tail. Here $\rho = \lambda_{\rm w}\Gamma/(4\pi)$ is the efficiency parameter, $\Gamma^3 = \pi j_0 K^2 A_{JJ}^2/(I_A\lambda_{\rm w}\gamma_0^3)$, j_0 is the beam current density, $I_A = mc^3/e \simeq 17$ kA, γ_0 is relativistic factor, $K = e\lambda_{\rm w}H_{\rm w}/(2\sqrt{2}\pi mc^2)$ is rms undulator parameter, $A_{JJ} = J_0(Q) - J_1(Q)$ is the Bessel function factor, $Q = K^2/[2(1+K^2)]$, Relativistic factor γ_0 and reference frequency ω_0 are connected by the FEL resonance condition: $\omega_0 = 2ck_w\gamma_0^2/(1+K^2)$. It is also useful to define normalized detuning [11]: $\hat{C} = [k_w - \omega(1+K^2)/2c\gamma_0^2]/\Gamma$.

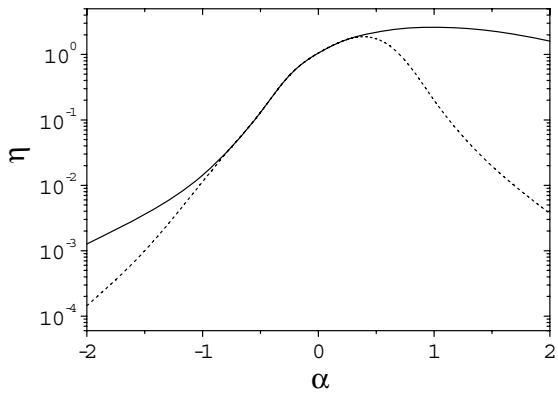

Figure 1: Normalized output power versus parameter $\hat{\alpha}$. Solid: $\hat{z} = \hat{z}_{\rm sat}(\hat{\alpha})$; dash: $\hat{z} = \hat{z}_{\rm sat}(0) = 13$.

A high-gain linear regime of a chirped SASE FEL operation was studied in [10, 9]. The main results of the simulations of the nonlinear regime [9] with 1-D version of the code FAST [11, 12] are presented in Fig. 1. Saturation length and power are functions of two parameters, $\hat{\alpha}$ and $N_{\rm c}$. For our simulations we have chosen $N_{\rm c} = 3\times10^7$ - a typical value for VUV SASE FELs. Note, however, that the results, presented in Fig. 1, very weakly depend on $N_{\rm c}$. In Fig. 1 the output power is plotted versus chirp parameter for two cases: when undulator length is equal to a saturation length for a given $\hat{\alpha}$ and when it is equal to the saturation length for the unchirped beam case ($\hat{z} = 13$). One can see sharp reduction of power for negative $\hat{\alpha}$ while a mild positive chirp ($\hat{\alpha} < 0.5$) is beneficial for SASE.

Let us consider now the case when there is no energy chirp ($\hat{\alpha} = 0$) and the detuning parameter changes linearly along the undulator [11]: $\hat{C}(\hat{z}) = \hat{b}_1\hat{z}$. This change can be due to variation of undulator parameters ($K(\hat{z})$ and/or $k_{\rm w}(\hat{z})$), or due to an energy change $\gamma_0(\hat{z})$.[1] We have found from numerical simulations [9] that in such case the effect on FEL gain is exactly the same as in the case of energy chirp and no taper if $\hat{\alpha} = 2\hat{b}_1$ for any value of $\hat{\alpha}$ (Figure 2 shows an example).

A symmetry between two considered effects (energy chirp and undulator tapering) can be understood as follows.

[1] An effect of undulator tapering (or energy change along the undulator) on FEL gain was studied in [13] in the limit $\hat{b}_1 \ll 1$.

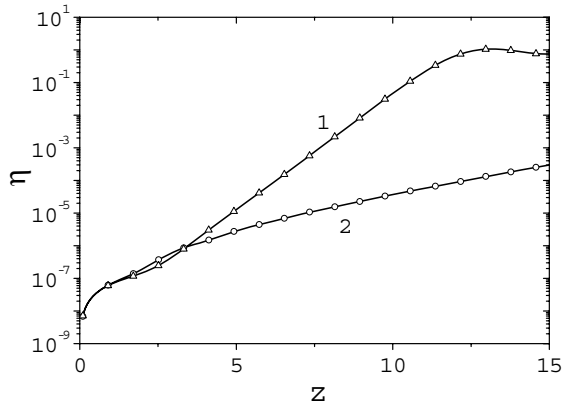

Figure 2: Normalized power versus undulator length. Solid line 1: $\hat{\alpha} = 0$, $\hat{b}_1 = 0$; triangles: $\hat{\alpha} = 4$, $\hat{b}_1 = -2$; solid line 2: $\hat{\alpha} = 4$, $\hat{b}_1 = 0$; circles: $\hat{\alpha} = 0$, $\hat{b}_1 = 2$.

If we look at the radiation field acting on some test electron from an electron behind it, this field was emitted at a retarded time. In the first case a back electron has a detuning due to an energy offset, in the second case it has the same detuning because undulator parameters were different at a retarded time. The question arises: can these two effects compensate each other? We give a positive answer based on numerical simulations (see Fig. 2 as an example): by setting $\hat{b}_1 = -\hat{\alpha}/2$ we get rid of gain degradation, and FEL power at any point along the undulator is the same as in the case of unchirped beam and untapered undulator. This holds for any value of $\hat{\alpha}$. For instance, if one linearly changes magnetic field H_w of the undulator, the compensation condition can be written as follows (nominal values of parameters are marked with subscript '0'):

$$\frac{1}{H_{\rm w0}}\frac{dH_{\rm w}}{dz} = -\frac{1}{2}\frac{(1+K_0^2)^2}{K_0^2}\frac{1}{\gamma_0^3}\frac{d\gamma}{cdt} \qquad (2)$$

Of course, in such a case we get frequency chirped SASE pulse. Since compensation of gain degradation is possible also for large values of $\hat{\alpha}$ (there is no theoretical limit on the value of chirp parameter, except for above mentioned condition $\rho\hat{\alpha} \ll 1$), one can, in principle, organize a regime when a frequency chirp within an intensity spike is much larger than the natural FEL bandwidth (given by $\rho\omega_0$).

GENERATION OF ATTOSECOND PULSES

A new scheme looks similar to those considered in [5, 6] making use of energy modulation of a short slice in the electron bunch by a high-power few-cycle optical pulse in a two-period undulator. Due to energy modulation the frequency of SASE radiation in X-ray undulator is correlated to the longitudinal position within the few-cycle-driven slice of the electron beam. The largest frequency offset corresponds to a single-spike pulse in time domain (about

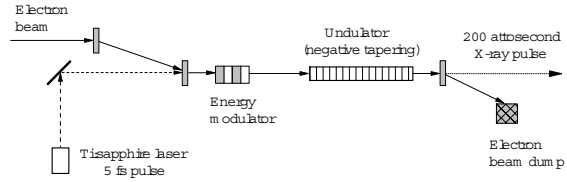

Figure 3: Schematic diagram of attosecond X-ray source. Energy modulator performs slice energy modulation of the electron bunch (see Fig. 5). Undulator tapering leads to complete suppression of the amplification process in the most fraction of the electron bunch, and output X-ray pulse has 200 attosecond pulse duration.

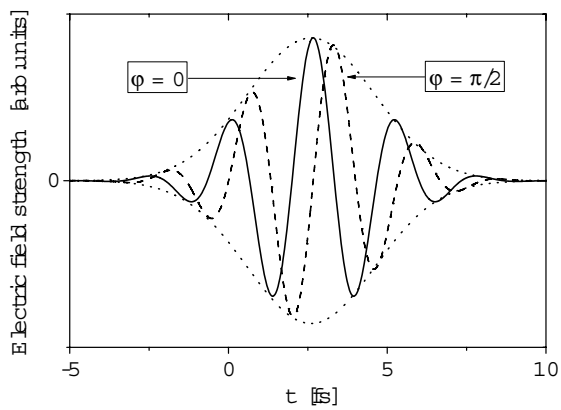

Figure 4: Possible evolutions of the electric field in the 5-fs pulse. carried at a wavelength 800 nm for two different pulse phases ($\phi = 0, \pi/2$)

300 attoseconds). The selection of single-spike pulses is achieved by using a crystal monochromator after the X-ray undulator [5], or with the help of the other undulator tuned to the offset frequency [6].

In this paper we consider a new scheme (see Fig. 3) that makes use of the compensation effect, described in the previous Section. Indeed, there is a strong energy chirp around zero-crossing of energy modulation. If one uses appropriate undulator taper then only a short slice around zero-crossing produces powerful FEL pulse. The main part of the bunch is unmodulated and suffers from strong negative undulator tapering (see Fig. 1). One should also note that for large negative taper the SASE FEL gain is very sensitive to longitudinal velocity spread. Therefore, a high-contrast attosecond pulse is directly produced in the undulator.

Operation of attosecond SASE FEL is illustrated for the parameters close to those of the European XFEL operating at the wavelength 0.15 nm [1]. The parameters of the electron beam are: energy 15 GeV, charge 1 nC, rms pulse

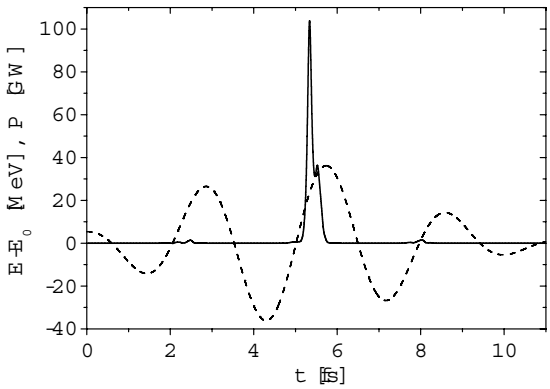

Figure 5: Energy modulation of the electron beam at the exit of the modulator undulator (dotted line) and a profile of the radiation pulse at the undulator length 100 m

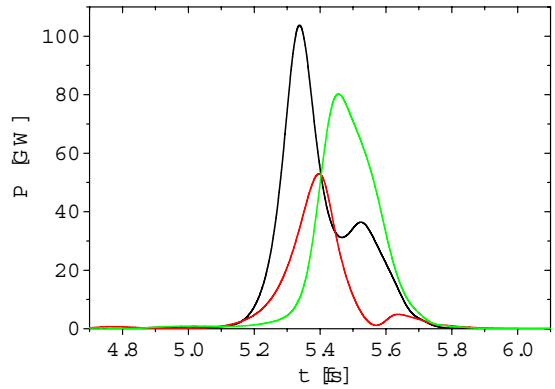

Figure 6: Temporal structure of the radiation pulse (three different shots) at the undulator length 100 m.

length 25 μm, rms normalized emittance 1.4 mm-mrad, rms energy spread 1 MeV. Undulator period is 3.65 cm, and the rms K-value is 2.5.

The parameters of the seed laser are: wavelength 800 nm, energy in the laser pulse 3 mJ, and FWHM pulse duration 5 fs (see Fig. 4). The laser beam is focused onto the electron beam in a short undulator resonant at the optical wavelength of 800 nm. Optimal conditions of the focusing correspond to the positioning of the laser beam waist in the center of the modulator undulator. It is assumed that the phase of laser field corresponds to "sine" mode (dashed line with $\varphi = \pi/2$, see Fig. 4). Parameters of the modulator undulator are: period length 50 cm, peak field 1.6 T, number of periods 2. The interaction with the laser light in the undulator produces a time-dependent electron energy modulation as it is shown in Fig. 5. This modulation corresponds to the energy chirp parameter $\hat{\alpha} \simeq 2$ at zero crossing ($t = 5$ fs in Fig. 5).

Optimization of the attosecond SASE FEL has been performed with the three-dimensional, time dependent code FAST [12] taking into account all physical effects influencing the SASE FEL operation (diffraction effects, energy spread, emittance, slippage effect, etc.). Three-dimensional simulations confirmed the predictions of the one-dimensional model: the energy chirp and the undulator tapering compensate each other, there is strong suppression of the amplification in the case of uncompensated negative taper.

Undulator tapering is performed by changing the gap of undulator modules [1] such that magnetic field increases linearly along the undulator length ($\hat{b}_1 < 0$). We performed the scan of tapering depth $\hat{b}_1$ in order to maximize the power in the main peak on one hand, and to minimize contribution of the background, on the other hand. We ended up with the value of taper which is about 20 % smaller than that required for a perfect compensation of chirp at $t = 5$ fs. Note that the chirp is not linear in the region of interest. In addition, a mild net positive chirp is beneficial for SASE, as it was discussed above (see Fig. 1).

A typical radiation pulse at the undulator length 100 m is shown in Fig. 5. One can see a high-power spike in the region where the energy chirp is well compensated by the taper and two weak side peaks at $t \simeq 2$ fs and $t \simeq 8$ fs where the net effect is negative taper. In the rest of the bunch a large negative taper together with velocity spread and 3-D effects completely suppresses amplification. In Fig. 6 we present three different shots illustrating the properties of the main peak. Typical pulse duration is about 200 attoseconds (FWHM) and peak power ranges from several tens up to hundred GW. To estimate the contrast (which we define as the ratio of energy in the main peak to the total radiated energy at the experiment) we assume that an angular collimation is used in order to reduce spontaneous emission background. A collimator with half-angle 3 μrad allows the entire intensity in the main peak to be transmitted. The contrast is influenced by SASE intensity in two side peaks and by spontaneous emission in the first harmonic from the rest of the bunch. For the charge of 1 nC, as in our numerical example, the contrast is about 95 %. Higher harmonics of undulator radiation (if they disturb an experiment) can be cut, for instance, by a multilayer monochromator with a bandwidth of the order of 1 %.

BEYOND "FUNDAMENTAL LIMIT"

It is generally accepted that the shortest pulse, that can be obtained from a SASE FEL, is given by a duration of intensity spike in time domain, i.e. it is defined by inverse FEL bandwidth $(\rho\omega_0)^{-1}$. However, the fact that a SASE FEL can operate with a strong chirp parameter (in combination with undulator tapering) without gain degradation, opens up a possibility of a conceptual breakthrough: one can get from SASE FEL a radiation pulse which is much

shorter than the inverse FEL bandwidth. Indeed, in the case of $\hat{\alpha} \gg 1$, the frequency chirp inside an intensity spike is much larger than FEL bandwidth. Thus, one can use a monochromator to reduce pulse duration. By an appropriate choice of the monochromator bandwidth one can select an X-ray pulse that is shorter by a factor of $\sqrt{2\hat{\alpha}}$ than the inverse FEL bandwidth. The only theoretical limit in this case is given by the condition $\rho\hat{\alpha} \ll 1$. Note that for hard X-ray FELs the parameter ρ is in the range $10^{-4} - 10^{-3}$.

To illustrate a possible technical realization of this idea, we can suppose that the energy modulation by a few-cycle optical pulse is increased by a factor 3 so that $\hat{\alpha} \simeq 6$. In combination with undulator tapering and a monochromator, this would allow to obtain sub-100-GW coherent X-ray pulses with a duration below 100 attoseconds and a contrast above 90 %. Note that the contrast remains high because the spectrum of spontaneous emission from the rest of the bunch gets broader due to the stronger taper.

REFERENCES

[1] M. Altarelli et al. (Eds.): XFEL: The European X-Ray Free-Electron Laser. Technical Design Report, Preprint DESY 2006-097, DESY, Hamburg, 2006.

[2] J. Arthur et al.: Linac Cherent Light Source (LCLS). Conceptual Design Report, SLAC- R593, Stanford, 2002.

[3] E.L. Saldin and E.A. Schneidmiller and M.V. Yurkov, Opt. Commun. **212**(2002)377.

[4] A.A. Zholents and W.M. Fawley, Phys. Rev. Lett. **92**(2004)224801.

[5] E.L. Saldin, E.A. Schneidmiller, M.V. Yurkov, Opt. Comm. **237**(2004)153.

[6] E.L. Saldin, E.A. Schneidmiller, M.V. Yurkov, Opt. Comm. **239**(2004)161.

[7] P. Emma, Z. Huang and M. Borland, Proc. of the 2004 FEL Conference, p. 333.

[8] A.A. Zholents and G. Penn, Phys. Rev. ST Accel. Beams **8**(2005)050704.

[9] E.L. Saldin, E.A. Schneidmiller, M.V. Yurkov, Proc. of the 2005 FEL Conference, p. 258.

[10] S. Krinsky, Z. Huang, Phys. Rev. ST Accel. Beams **8**(2003)050702.

[11] E.L. Saldin, E.A. Schneidmiller, M.V. Yurkov, *The Physics of Free Electron Lasers* (Springer-Verlag, Berlin, 1999).

[12] E.L. Saldin, E.A. Schneidmiller, M.V. Yurkov, Nucl. Instr. and Methods **A 429**(1999)233.

[13] Z. Huang and G. Stupakov, Phys. Rev. ST Accel. Beams **8**(2005)040702.

TRANSVERSE AND LONGITUDINAL COHERENCE PROPERTIES OF THE RADIATION FROM X-RAY SASE FELS

E.L. Saldin, E.A. Schneidmiller, and M.V. Yurkov
Deutsches Elektronen-Synchrotron (DESY), Hamburg, Germany

Abstract

We present a comprehensive analysis of coherence properties of the radiation from X-ray free electron laser (XFEL). We consider practically important case when XFEL is optimized for maximum gain. Such an optimization allows to reduce significantly parameter space. Application of similarity techniques to the results of numerical simulations allows to present all output characteristics of the optimized XFEL as functions of the only parameter, ratio of the emittance to the radiation wavelength, $\hat{\epsilon} = 2\pi\epsilon/\lambda$. our studies show that optimum performance of the XFEL in terms of transverse coherence is achieved at the value of the parameter $\hat{\epsilon}$ of about unity. At smaller values of $\hat{\epsilon}$ the degree of transverse coherence is reduced due to strong influence of poor longitudinal coherence on a transverse one. At large values of the emittance the degree of transverse coherence degrades due to poor mode selection. Comparative analysis of existing XFEL projects, European XFEL, LCLS, and SCSS is presented as well.

INTRODUCTION

In the X-ray FEL the radiation is produced by the electron beam during single-pass of the undulator [1]. The amplification process starts from the shot noise in the electron beam. Any random fluctuations in the beam current correspond to an intensity modulation of the beam current at all frequencies simultaneously. When the electron beam enters the undulator, the presence of the beam modulation at frequencies close to the resonance frequency initiates the process of radiation. The FEL collective instability in the electron beam produces an exponential growth (along the undulator) of the modulation of the electron density on the scale of undulator radiation wavelength. The fluctuations of current density in the electron beam are uncorrelated not only in time but in space, too. Thus, a large number of transverse radiation modes are excited when the electron beam enters the undulator. These radiation modes have different gain. As undulator length progresses, the high gain modes start to predominate more and more. For enough long undulator, the emission will emerge in a high degree of transverse coherence.

The first analysis of the problem of transverse coherence has been performed in [2]. It has been found that even after finishing the transverse mode selection process the degree of transverse coherence of the radiation from SASE FEL visibly differs from the unity. This is consequence of the interdependence of the longitudinal and transverse coherence. First studies of the evolution of transverse coherence in the nonlinear regime of SASE FEL operation have been performed in [3]. It has been found that the degree of transverse coherence reaches maximum value in the end of the linear regime. Further increase of the undulator length leads to its decrease. Despite output power of the SASE FEL grows continuously in the nonlinear regime, maximum brilliance of the radiation is achieved in the very beginning of the nonlinear regime. Due to limited computing power available at that time we limited our study with a specific numerical example just illustrating the general features of coherence properties of the radiation produced by the SASE FEL operating in the nonlinear regime.

In this paper we present general analysis of the coherence properties (longitudinal and transverse) of the radiation from SASE FEL. The results have been obtained with time-dependent, three-dimensional FEL simulation code FAST [4] performing simulation of the FEL process with actual number of electrons in the beam. Using similarity techniques we present universal dependencies for the main characteristics of the SASE FEL covering all practical range of X-ray FELs.

BASIC RELATIONS

Design of the focusing system of XFEL assumes nearly uniform focusing of the electron beam in the undulator, so we consider axisymmetric model of the electron beam. It is assumed that transverse distribution function of the electron beam is Gaussian, so rms transverse size of matched beam is $\sigma = \sqrt{\epsilon\beta}$,where $\epsilon = \epsilon_{\rm n}/\gamma$ is rms beam emittance and β is focusing beta-function. In the case of negligibly small effects of the space charge and energy spread, operation of the FEL amplifier is described by the diffraction parameter B and the betatron motion parameter $\hat{k}_\beta$: [5]:

$$B = 2\Gamma\sigma^2\omega/c\,, \qquad \hat{k}_\beta = 1/(\beta\Gamma)\,, \tag{1}$$

where $\Gamma = \left[I\omega^2\theta_{\rm s}^2 A_{\rm JJ}^2/(I_{\rm A}c^2\gamma_{\rm z}^2\gamma)\right]^{1/2}$ is the gain parameter. When describing shot noise in the electron beam, one more parameter appears, the number of electrons in the volume of coherence: $N_{\rm c} = I/(e\omega\rho)$, where $\rho = c\gamma_{\rm z}^2\Gamma/\omega$ is the efiiciency parameter. The following notations are used here: I is the beam current, $\omega = 2\pi c/\lambda$ is the frequency of the electromagnetic wave, $\theta_{\rm s} = K_{\rm rms}/\gamma$, $K_{\rm rms}$ is the rms

undulator parameter, γ is relativistic factor, $\gamma_z^{-2} = \gamma^{-2} + \theta_s^2$, $k_w = 2\pi/\lambda_w$ is the undulator wavenumber, $I_A = 17$ kA is the Alfven current, $A_{JJ} = 1$ for helical undulator and $A_{JJ} = J_0(K_{rms}^2/2(1+K_{rms}^2)) - J_1(K_{rms}^2/2(1+K_{rms}^2))$ for planar undulator. Here J_0 and J_1 are the Bessel functions of the first kind.

Target value of interest for XFEL optimization is the field gain length of the fundamental mode. For this practically important case the solution of the eigenvalue equation for the field gain length of the fundamental mode and optimum beta function are rather accurately approximated by [6]:

$$L_g = 1.67 \left(\frac{I_A}{I}\right)^{1/2} \frac{(\epsilon_n \lambda_w)^{5/6}}{\lambda^{2/3}} \frac{(1+K^2)^{1/3}}{K A_{JJ}}$$
$$\beta_{opt} \simeq 11.2 \left(\frac{I_A}{I}\right)^{1/2} \frac{\epsilon_n^{3/2} \lambda_w^{1/2}}{\lambda K A_{JJ}}, \quad (2)$$

Accuracy of this fit is better than 5% in the range of parameter $\hat{\epsilon} = 2\pi\epsilon/\lambda$ from 1 to 5. It follows from (1) and (2) that diffraction parameter B and parameter of betatron oscillations, $\hat{k}_\beta$ are functions of the only parameter $\hat{\epsilon}$. FEL equations written down in the dimensionless form involve an additional parameter N_c defining the initial conditions for the start-up from the shot noise. Note that the dependence of output characteristics of the SASE FEL operating in saturation is slow, in fact logarithmic in terms of N_c.

SIMULATION ALGORITHM

Rigorous studies of the nonlinear stage of amplification is possible only with numerical simulation code. Typically FEL codes use an artificial ensemble of macroparticles for simulating of the FEL process when one macroparticle represents large number of real electrons. Thus, a natural question arises if macroparticle phase space distributions are identical to those of actual electron beam at all stages of amplification. Let us trace typical procedure for preparation of an artificial ensemble [7, 8]. The first step of particle loading consists in a quasi-uniform distribution of the macroparticles in the phase space. At this stage an ensemble of particles with random distribution is generated which occupies a fraction of the phase space. Then this ensemble is copied on the other parts of the phase space to provide pseudo-uniform loading of the phase space. Pseudo-uniformity means that initial microbunching at the fundamental harmonic (or for several harmonics) is equal to zero. Also, phase positions of the mirrored particles are correlated such that microbunching does not appear due to betatron oscillations, or due to the energy spread. Finally, artificial displacements of the macroparticles are applied to provide desired (in our case gaussian) statistics of microbunching at the undultor entrance. We note that it is not evident that such an artificial ensemble reflects actual physical situation for a short wavelength SASE FEL. Let us consider an example of the SASE FEL operating at the radiation wavelength of 0.1 nm. With the peak current of 5 kA we find that the number of electrons per wavelength is about 10^4. On the other hand, it is well known that properties of an artificial ensemble (even at the first step of pseudo-uniform loading) converge very slowly to the model of continuous media. In fact, even with the number of macroparticles per radiation wavelength 6.4×10^4 the FEL gain still visibly deviates from the target value. Introducing of an artificial noise makes situation with the quality of an ensemble preparation even more problematic. The only way to test the quality of an artificial ensemble is to perform numerical simulations with actual number of electrons in the beam. We constructed such a version of three-dimensional, time-dependent FEL simulation code FAST [4]. Comparison of the results with direct simulations of the electron beam and with an artificial distributions has shown that artificial ensembles are not adequate to the problem. Artificial effects are pronouncing especially when calculating such fine features as transverse correlation functions. Thus, all the simulations presented in this paper have been performed with code FAST using actual number of electrons in the beam.

GENERAL DEFINITIONS

The first-order transverse correlation function is defined as

$$\gamma_1(\vec{r}_\perp, \vec{r}\prime_\perp, z, t) = \frac{\langle \tilde{E}(\vec{r}_\perp, z, t) \tilde{E}^*(\vec{r}\prime_\perp, z, t) \rangle}{\left[\langle |\tilde{E}(\vec{r}_\perp, z, t)|^2 \rangle \langle |\tilde{E}(\vec{r}\prime_\perp, z, t)|^2 \rangle \right]^{1/2}},$$

where $\tilde{E}$ is the slowly varying amplitude of the amplified wave. For a stationary random process γ_1 does not depend on time, and the degree of transverse is:

$$\zeta = \frac{\int |\gamma_1(\vec{r}_\perp, \vec{r}\prime_\perp)|^2 I(\vec{r}_\perp) I(\vec{r}\prime_\perp) \, \mathrm{d}\vec{r}_\perp \, \mathrm{d}\vec{r}\prime_\perp}{[\int I(\vec{r}_\perp) \, \mathrm{d}\vec{r}_\perp]^2}, \quad (3)$$

where $I(\vec{r}_\perp) = \langle |\tilde{E}(\vec{r}_\perp)|^2 \rangle$. The first order time correlation function, $g_1(t, t')$, is calculated in accordance with the definition:

$$g_1(\vec{r}, t - t') = \frac{\langle \tilde{E}(\vec{r}, t) \tilde{E}^*(\vec{r}, t') \rangle}{\left[\langle |\, \tilde{E}(\vec{r}, t)\, |^2 \rangle \langle |\, \tilde{E}(\vec{r}, t')\, |^2 \rangle \right]^{1/2}}, \quad (4)$$

For a stationary random process time correlation functions are functions of the only argument, $\tau = t - t\prime$. The coherence time is defined as

$$\tau_c = \int_{-\infty}^{\infty} |g_1(\tau)|^2 \, \mathrm{d}\tau. \quad (5)$$

If one traces evolution of the brilliance of the radiation along the undulator length there is always the point, which we define as the saturation point, where the brilliance reaches maximum value [9]. In the following we present characteristics of the radiation at the saturation point which

are universal functions of the only parameter, $\hat{\epsilon}$. In fact, the brilliance is proportional to the degeneracy parameter δ, i.e. the number of photons in a single pulse which are transversely and longitudinally coherent. We introduce a notion of normalized degeneracy parameter

$$\hat{\delta} = \hat{\eta}\hat{\zeta}\hat{\tau}_{\rm c} \, .$$

Here normalized FEL efficiency is defined as $\hat{\eta} = P/(\rho W_{\rm b})$ where P is radiation power, and $W_{\rm b} = \gamma mc^2 I/e$ is electron beam power. Normalized coherence time is defined as $\hat{\tau}_{\rm c} = \rho\omega\tau_{\rm c}$. Parameter $\hat{\delta}$ and the degeneracy parameter δ are simply related as:

$$\delta = \frac{W_{\rm b}}{\hbar\omega^2}\hat{\delta} = 2.7\times 10^7 \times \lambda[\mathring{A}\,] \times I[{\rm kA}] \times E[{\rm GeV}] \times \hat{\delta} \, .$$

PROPERTIES OF THE RADIATION

Simulations of the FEL process have been performed for the case of a long bunch with uniform axial profile of the beam current. Such a model provides rather accurate predictions for the coherence properties of the XFEL, since typical radiation pulse from the XFEL is much longer than the coherence time. Calculations has been performed with FEL simulation code FAST using actual number of electrons in the beam. The value of parameter $N_{\rm c} = 8\times 10^5$ corresponds to the parameter range of XFEL operating at the radiation wavelength about 0.1 nm.

A series of simulation runs have been performed in the range of the parameter $\hat{\epsilon} = 0.25\ldots 4.5$. Application of similarity techniques described above allowed us to extract universal parametric dependencies of the main characteristics of the optimized XFEL operating in the saturation (see Figs. 1-3).

Figure 1 shows the dependence of the saturation length $\hat{z}_{\rm sat} = \Gamma z_{\rm sat}$ on parameter $\hat{\epsilon}$. Analysis of the curve shows that the saturation length scales as $\hat{z}_{\rm sat} \propto \hat{\epsilon}^{5/6}$. Such dependence directly follows from the optimization procedure of the gain length given by (2). The normalized coherence

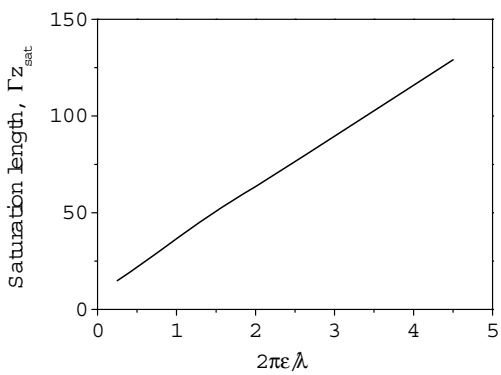

Figure 1: Saturation length $\Gamma z_{\rm sat}$ versus parameter $\hat{\epsilon}$.

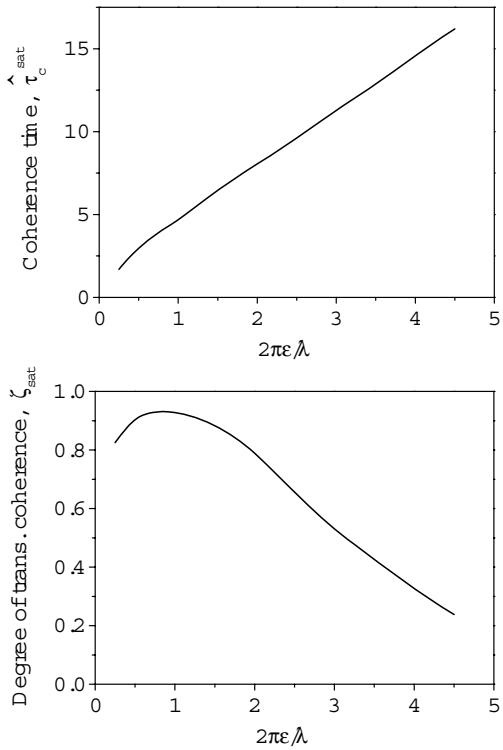

Figure 2: Degree of transverse coherence, $\zeta_{\rm sat}$, and normalized coherence time, $\hat{\tau}_{\rm c}^{\rm sat}$ in saturation versus parameter $\hat{\epsilon}$.

time in the saturation, $\hat{\tau}_{\rm c}^{\rm sat}$ is also proportional to $\hat{\epsilon}^{5/6}$ (see Fig. 2).

The dependence of the degree of transverse coherence in the saturation on the parameter $\hat{\epsilon}$ exhibits rather complicated behavior (see Fig. 2). It reaches maximum value in the range of $\hat{\epsilon}$ values about of unity, and drops at small and large values of $\hat{\epsilon}$. Actually, the degree of transverse coherence is formed due to two effects. The first effect takes place due to interdependence of the poor longitudinal coherence and transverse coherence [2]. Due to the start-up from shot noise every radiation mode is excited within finite spectral bandwidth. Actually this means that in the high gain linear regime the radiation of the SASE FEL is formed by many fundamental $\rm TEM_{00}$ modes with different frequencies. The transverse distribution of the radiation field of the mode is also different for different frequencies. Smaller value of the diffraction parameter (i.e. smaller value of $\hat{\epsilon}$) corresponds to larger deviation of the radiation mode from the plane wave. This explains a decrease of the transverse coherence at small values of $\hat{\epsilon}$. When the parameter $\hat{\epsilon}$ increases, the diffraction parameter increases as well thus leading to the degeneration of the radiation modes. Amplification process in the SASE FEL passes limited number of the field gain lengths, and starting from some value of $\hat{\epsilon}$ the linear stage of amplification becomes too short to provide mode selection process. When amplification process enters nonlinear stage, the mode content of

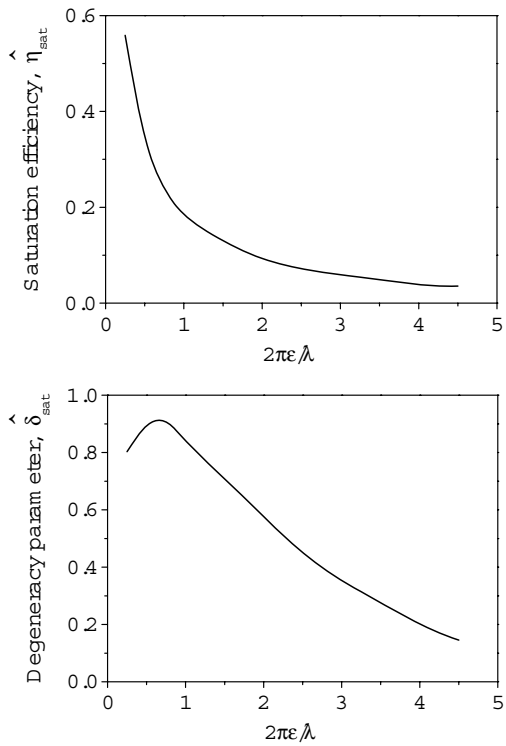

Figure 3: Efficiency, $\langle\hat{\eta}_{\rm sat}\rangle$, and normalized degeneracy parameter, $\hat{\delta}_{\rm sat}$, in the saturation versus parameter $\hat{\epsilon}$.

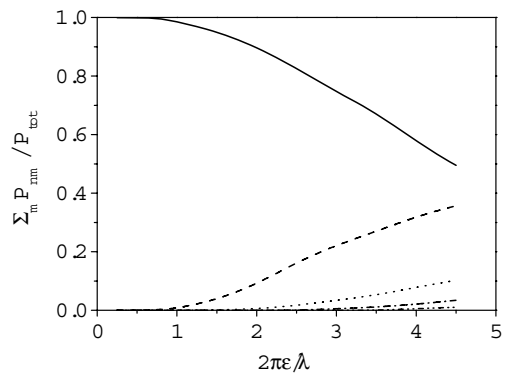

Figure 4: Partial contributions of the modes with azimuthal index $m = 0 \ldots 4$ into the total power versus parameter $\hat{\epsilon}$. SASE FEL operates in the saturation.

the radiation becomes even more rich due to independent growth of the radiation modes in the nonlinear medium (see Fig. 4). Thus, at large values of $\hat{\epsilon}$ the degree of transverse coherence is limited by poor mode selection. Analytical estimations presented in [9] show that in the limit of large emittance, $\hat{\epsilon} \gg 1$, the degree of transverse coherence scales as $1/\hat{\epsilon}^2$.

We present in Fig. 3 the plots for normalized efficiency and degeneracy parameter for optimized XFEL. Normalized efficiency in saturation has simple scaling, it falls inversely proportional to the parameter $\hat{\epsilon}$. Taking into account that the value of the coherence time $\hat{\tau}_{\rm c}^{\rm sat}$ scales proportional to $\hat{\epsilon}^{5/6}$, we find that the normalized degeneracy parameter of the radiation is nearly proportional to the degree of transverse coherence, $\hat{\delta} \propto \zeta/\hat{\epsilon}^{1/6}$.

Table 1: Parameter space of XFEL projects

	European XFEL		LCLS	SCSS
	SASE1	SASE2		
λ, nm	0.1	0.15	0.15	0.1
E, GeV	17.5	17.5	14.35	6.135
ϵ_n, mm-mrad	1.4	1.4	1.2	0.85
$\hat{\epsilon}$	2.6	1.7	1.8	4.5
ζ	0.65	0.85	0.83	0.24

Finally, in Table 1 we present comparison of existing XFEL projects, the European XFEL, LCLS and SCSS in terms of degree of transverse coherence [10–12]. We see that the European XFEL and LCLS are in the same range of parameter space. These projects assume conservative value of the emittance, and relatively high degree of transverse coherence is achieved by increasing the energy of the driving accelerator. Project SCSS assumes much smaller energy of the driving accelerator. However, despite much smaller value of the normalized emittance it falls in the range of parameters for the output radiation with poor transverse coherence.

REFERENCES

[1] Ya.S. Derbenev, A.M. Kondratenko and E.L. Saldin, Nucl. Instrum. and Methods **193**(1982)415.

[2] E.L. Saldin, E.A. Schneidmiller, and M.V. Yurkov, Opt. Commun. **186**(2000)185.

[3] E.L. Saldin, E.A. Schneidmiller, and M.V. Yurkov, Nucl. Instrum. and Methods **A 507**(2003)106.

[4] E.L. Saldin, E.A. Schneidmiller, and M.V. Yurkov, Nucl. Instrum. and Methods **A 429**(1999)233.

[5] E.L. Saldin, E.A. Schneidmiller and M.V. Yurkov, Nucl. Instrum. and Methods **A475**(2001)86.

[6] E.L. Saldin, E. A. Schneidmiller, and M.V. Yurkov, Opt. Commun. 235(2004)415.

[7] W.M. Fawley, Phys. Rev. STAB 5(2002)070701.

[8] S. Reiche, Nucl. Instrum. and Methods **A429**(1999)243.

[9] E.L. Saldin, E.A. Schneidmiller and M.V. Yurkov, Preprint DESY 06-137, Hamburg, 2006.

[10] M. Altarelli et al. (Eds.), XFEL: The European X-Ray Free-Electron Laser. Technical Design Report, Preprint DESY 2006-097, DESY, Hamburg, 2006 (see also http://xfel.desy.de).

[11] J. Arthur et al., Linac Cherent Light Source (LCLS). Conceptual Design Report, SLAC- R593, Stanford, 2002 (see also http://www-ssrl.slac.stanford.edu/lcls/cdr.

[12] SCSS X-FEL: Conceptual design report, RIKEN, Japan, May 2005. (see also http://www-xfel.spring8.or.jp).

DESIGN STATUS OF PAL-XFEL*

T.-Y. Lee†, Y. S. Bae, J. Choi J. Y. Huang, H. S. Kang, C. B. Kim, D. E. Kim, M. G. Kim,
Y. J. Kim[a], I. S. Ko, J. S. Oh, Y. W. Parc, and J. H. Park
Pohang Accelerator Laboratory, San 31, Hyoja-dong, Pohang, Kyungbuk 790-784, KOREA
[a]Free Electron Laser Laboratory, Duke University, N.C. 27708-0319, USA

Abstract

Pohang Accelerator Laboratory has a plan to build an X-ray FEL machine. This new machine will utilize the existing 2.5 GeV injection linac to the storage ring by upgrading its energy up to 3.7 GeV or more. The target wavelength will be 3-4.5 Å and its third harmonic 1-1.5 Å will also be used. The project will proceed in two stages: In the first stage, a VUV SASE machine with 320 MeV will be constructed and tested for the proof-of-principle. The full X-ray machine will be constructed in the next stage.

INTRODUCTION

PAL-XFEL is the name of new project of Pohang Accelerator Laboratory (PAL) to build a new X-ray FEL machine based on SASE (self amplified spontaneous emission) scheme. This new machine will utilize the existing 2.5 GeV electron linac by increasing its energy to 3.7 GeV and upgrading the performance. The linac is currently used for injection to the 2.5 GeV storage ring of Pohang Light Source (PLS). The new linac energy will be 3.7 GeV. The overview of the PAL-XFEL project was reported previously [1]. For readers unfamiliar with the project, fundamental parameters of PAL-XFEL are listed in Table 1 and the machine layout is displayed in Fig. 1. At the moment, detailed design study and machine R& D are going on. In the figure, K2,...,K12 denote the currently used accelerating columns and X1,...,X9 denote the new accelerating columns that will be added to the existing linac. X3X denotes the X-band high harmonic cavity. We are going to build the new part of PAL-XFEL while still running PLS.

However, there have been a few modifications in the PAL-XFEL project. The first important modification is the target wavelength that will be used mainly. The X-ray community, which is the biggest synchrotron user community in Korea, has demanded that the target wavelength be in 1-1.5 Å range, which put quite a challenge for the PAL-XFEL design. Since the available linac energy of PAL is limited, we decided to utilize the high harmonic radiation of SASE. It is well known that the high harmonic radiations are also amplified to FEL by the so called nonlinear harmonic generation [2, 3]. The existence and usefulness of SASE higher harmonic radiation was verified experimentally in VUV-FEL at DESY [4]. According to calculation based on [5], the third harmonic radiation power is approximately 1% of the fundamental one.

* Work supported by Korean Ministry of Science and Technology
† tylee@postech.ac.kr

The fundamental wavelength of PAL-XFEL was determined to be 3 Å in which case the third harmonic becomes 1 Å. These wavelengths are achieved by using an in-vacuum undulator of 4 mm gap. Recently, we are considering an alternative choice in which the fundamental wavelength is 4.5 Å and the third harmonic wavelength is 1.5 Å. In this case, wider undulator period and gap (and thus out-vacuum undulator) are allowed and the undulator wakefield is smaller. Currently, we are estimating the two designs and the final decision is not made yet. Below, comparison of the two choices is given briefly.

Another important modification is the procedure of PAL-XFEL construction. The PAL-XFEL project will proceed in two stages. In the first stage, only a small 320 MeV SASE machine will be constructed. The purpose of this machine is to test and prove the design strategy of PAL-XFEL. Hence, this test machine (TM) will use the same undulator as PAL-XFEL. Only in the second stage, the full PAL-XFEL will be constructed. The design of TM is under active study. Brief introduction to the TM design will be given below. This status report will describe major modifications of the PAL-XFEL design briefly. The PAL-XFEL photo-injector status has been prepared separately [6, 7].

ALTERNATIVE UNDULATOR DESIGN

The point of the alternative undulator design is to relax the original design slightly and make the whole scheme safer. For the purpose, the fundamental radiation wavelength is changed from 3 Å to 4.5 Å, which makes the third harmonic wavelength 1.5 Å. This change makes some difference. The comparison of the two undulator designs is given in Table 2.

What advantages do we get from this alternative design over the original one? First of all, the undulator gap is relaxed from 4 mm to 7.8 mm, which is wide enough to allow an out-vacuum undulator. With out-vacuum undulator, the chamber inner gap would be 6.8 mm which gives wakefield 40 % smaller. The longitudinal wakefield induces relative energy spread in the bunch, which is inversely proportional to the electron energy E. The relatively low energy, 3.7 GeV, of PAL-XFEL as a hard X-ray FEL machine may make the undulator wakefield particularly serious. Hence 40% reduction of wakefield is not negligible.

Another advantage is related to the transversal coherence of the SASE radiation and explained by a number B=gain length/Rayleigh length. B measures how fast the transversal higher modes diffract out of the electron beam. One of the advantages of the SASE FEL radiation is the transver-

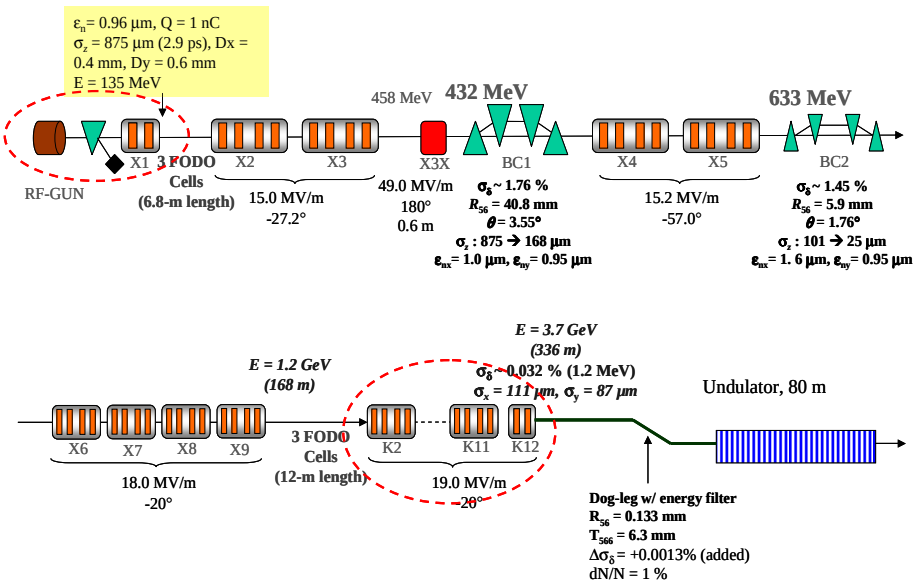

Figure 1: Layout of the PAL-XFEL injector and linac. K2,...,K12 denote the currently used accelerating columns and X1,...,X9 denote the new accelerating columns that will be added.

Table 1: Parameters of PAL-XFEL

Beam Parameters	**Value**	**Unit**
Electron energy	3.7	GeV
Peak current	3	kA
Normalized slice emittance	1	mm mrad
RMS slice energy spread	0.01 %	
Full bunch length	270	fs
Undulator Parameters		
Undulator period	1.5	cm
Segment length	4.5	m
Full undulator length	80	m
Peak undulator field	1.19	T
Undulator parameter, K	1.49	
Undulator gap	4	mm
Average β-function	10	m
FEL Parameters		
Radiation wavelength	3	Å
FEL parameter, ρ	5.7×10^{-4}	
Peak brightness	5×10^{31}	*
Peak coherent power	1	GW
Pulse repetition rate (Max.)	60	Hz
1D gain length	1.2	m
Saturation length, L_{sat}	45	m

* photon/(sec mm^2 mrad^2 0.1%BW)

Table 2: Comparison of the two undulator designs

Design	**Original**	**Alternative**
Wavelength	3 Å	4.5 Å
Third harmonic	1 Å	1.5 Å
Undulator	in-vacuum	out-vacuum
Undulator period	1.5 cm	2.2 cm
Undulator gap	4 mm	7.8 mm
Undulator parameter, K	1.49	1.52
FEL parameter	5.8×10^{-4}	6.6×10^{-4}
1-D gain length	1.2 m	1.5 m
Gain Length/Rayligh length	0.04	0.07
Saturation length	45 m	48 m
Peak power	2 GW	4 GW

sal coherence. However, the transversal coherence is not an intrinsic property of the undulator radiation but acquired by the amplification process in which all the transversal higher modes diffract out oh the beam while only the fundamental mode keeps growing. The bigger B is, the faster the higher modes diffract. It is true that B values of both the original design and the alternative design are not big enough compared with other machines such as LCLS. Figure 2 shows the power gain of the original design, while Fig. 3 shows that of the alternative design.

It is hard but possible to see that the power gain in Fig. 2 is not in a straight line but slightly over it. This indicates that the transversal higher modes do not diffract out fast enough and thus a small portion of it might remain at the final stage. Figure 3 shows a better case.

The third advantage of the alternative design is that its radiation power is bigger than that of the original design. As shown in Figs. 2 and 3, the peak radiation power of the original design is almost 2 GW while that of the alternative design is almost 4 GW.

The disadvantage of the alternative design compared with the original design is that its third harmonic radiation is 1.5 Å not 1 Å that is preferred by scientists working on organic samples. Those scientists include material scientists, biologists, organic chemists, and the number grows rapidly. The alternative design can provide 0.9 Å radiation

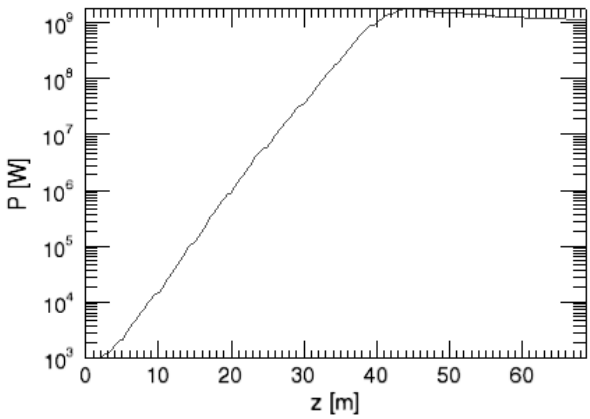

Figure 2: Power gain of the original undulator design.

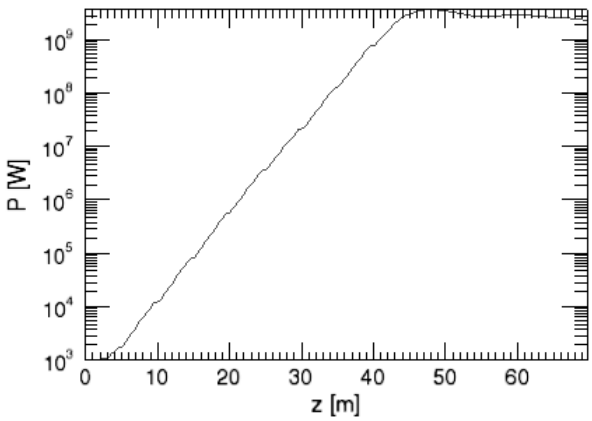

Figure 3: Power gain of the alternative undulator design.

as a fifth harmonic but its power is approximately 1/10 of the third harmonic radiation.

BUNCH COMPRESSOR DESIGN

The bunch compressor design is not fixed yet. There are a few issues still to be examined. One of the issues is the space charge in the bunch compressors. The ELEGANT code that is used in the linac design does not include the space charge effect and thus the space charge effect has not been checked seriously. It has been suggested that the second bunch compressor be in the higher energy region to make the space charge effect unimportant. A simulation study to estimate the space charge effect in the bunch compressors is going on.

Another important issue is the coherent synchrotron radiation (CSR). According to simulation, the electron distribution in the phase space is shifted slightly in the x, x' direction by CSR. This has to be fixed for the successful SASE FEL. A start to end simulation from the gun to the undulator was carried out. In case the CSR effect is off, the final radiation profile is very good as shown in Fig. 4, which was obtained with the alternative undulator design.

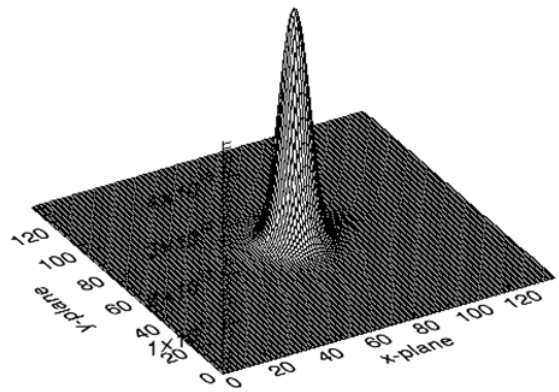

Figure 4: Radiation beam profile obtained from start to end simulation.

TEST MACHINE

The purpose of TM is to prove, in the low energy, that PAL-XFEL is achievable. It will not be used as a user facility. The reason why we need TM is that PAL-XFEL is challenging. It is challenging to generate hard X-ray (3 - 4.5 Å) SASE radiation with 3.7 GeV electron beam. The validity of the PAL-XFEL scheme will be proved by TM. TM will have a low energy of 320 Mev, lower than a tenth of PAL-XFEL energy, but the undulator will be the same as in PAL-XFEL except the total length. It will still adopt a pair of bunch compressors, but X-band higher harmonic cavity is not planned to be used at the moment. Beam parameters are chosen to give comparable magnitude of energy spread to the PAL-XFEL case. The optimal average β function of the undulator lattice is reduced from 10 m of PAl-XFEL to 5 m. A few fundamental parameters of TM are shown in Table 2.

Table 3: Parameters of the test machine

Parameters	**Value**	**Unit**
Electron energy	0.32	GeV
Peak current	0.7	kA
Normalized slice emittance	0.8	mm mrad
RMS slice energy spread	0.01 %	
Full undulator length	8	m
Average β-function	5	m
Radiation wavelength	28	nm
FEL parameter, ρ	3.4×10^{-3}	
1D gain length	0.2	m
Saturation length, L_{sat}	6	m

Since the high harmonic cavity is not used, the compressed bunch has a different shape from the PAL-XFEL case. The layout of TM is displayed in Fig. 5 and Fig. 6 shows the current distribution in a bunch at the test linac end.

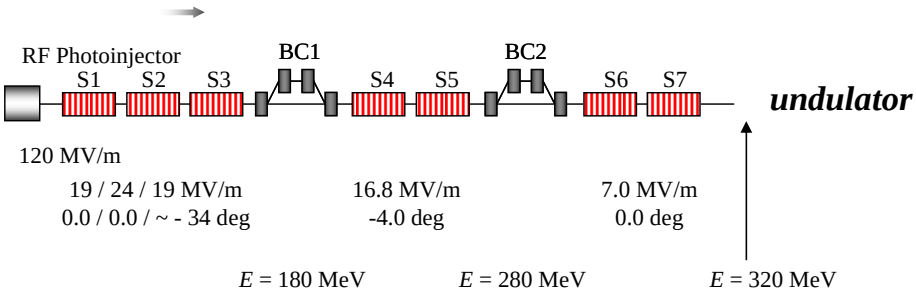

Figure 5: Layout of the test machine.

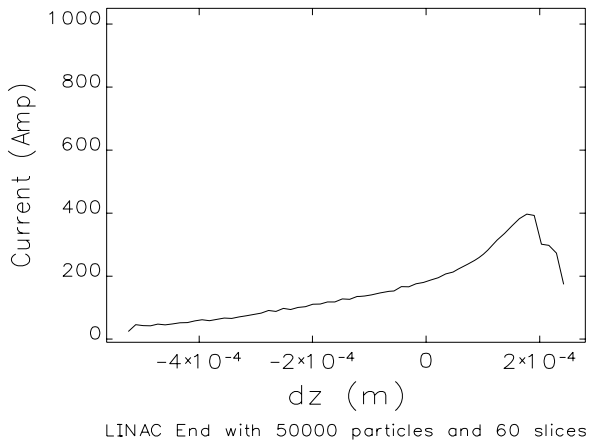

Figure 6: Current distribution in the linac end of the test machine.

SUMMARY

The progress of the PAL-XFEL design since the previous report [1] has been described. The bunch compressor design needs to be examined further with respect to the CSR and space charge effect. As for the undulator design, an alternative design has been described in comparison with the original design. The alternative design gives 4.5 Å fundamental radiation and 1.5 Å third harmonic, while the original design gives 3 Å fundamental and 1 Å third harmonic. The final decision for the undulator is not made yet. Also, an important change of the PAL-XFEL construction plan has been described. PAL-XFEL will be constructed in two stages. In the first stage, 320 MeV test machine will be constructed and the full 3.7 GeV machine will be constructed only in the second stage.

REFERENCES

[1] I. S. Ko, Proceedings of the 27th International Free Electron Laser Conference, SLAC, USA (2005) 216.

[2] R. Bonifacio, L. D. Salvo, and P. Pierini, Nucl. Instrum. Methods Phys. Res. A 293 (1990) 627.

[3] Z. Huang and K.-J. Kim, Phys. Rev. E 62 (2000) 7295.

[4] S. Schreiber, Proceedings of the 27th International Free Electron Laser Conference, SLAC, USA (2005) 12.

[5] E. L. Saldin, E. A. Schneidmiller, and M. V. Yurkov, Phys. Rev. ST Accel. Beams, 9 (2006) 030702.

[6] Y. W. Parc et al., In this proceedings.

[7] J. H. Park et al., In this proceedings.

ULTRA HIGH BRIGHTNESS ACCELERATOR DESIGN

R.J. Bakker, A. Adelmann, A. Anghel, M. Dehler, R. Ganter, S. Leemann, K. Li, M. Pedrozzi, J-Y. Raguin, L. Rivkin, V. Schlott, F. Wei, A. Wrulich
Paul Scherrer Institut, Villigen CH 5232, Switzerland.

Abstract

The PSI FEL Project at the Paul Scherrer Institute in Switzerland incorporates the development of a low emittance gun as a driver for a cost-effective X-ray free-electron laser user facility ($\lambda_s \geq 0.1$ nm, $\hbar\omega_s \leq 12.4$ keV). We investigate sources based on field-emitter technology and photoemission, followed by high gradient ($\Gamma \geq 0.25$ GV/m) acceleration up to 1 MeV. We present a concept to preserve the emittance in the acceleration process where the first 250 MeV of acceleration is the most delicate. Experimentally we intend to verify the validity of ultra-high brightness acceleration over this energy range in the period 2008-2011.

INTRODUCTION

In a free-electron laser (FEL) the resonant wavelength (λ_s) is given by:

$$\lambda_s = \frac{\lambda_u}{2\gamma^2}\left(1 + K^2\right), \quad (1)$$

where λ_u is the undulator period, γ the Lorenz factor corresponding to the beam energy (γ = E [Mev]/0.511), and K the dimensionless undulator strength ($K \approx 0.66\ \lambda_u \cdot B_u$ [cm] [T]). It follows that the X-ray regime (0.1 nm) is accessible with conventional undulator technology ($\lambda_u \geq 0.8$ cm) and a beam-energy as low as 4 GeV. Lasing at such a wavelength is more restrictive, however, since it is fundamental to control the transverse emittance (ε), the energy spread (σ_γ) and the current (I) of the electron-beam. An estimate for the critical wavelength limit λ_{cr} for sufficient gain in the FEL is [1]:

$$\lambda_{cr} \cong 18\pi\varepsilon_n \frac{\sigma_\gamma}{\gamma}\sqrt{\frac{1}{\gamma}\frac{I_A}{I}}, \quad (2)$$

where ε_n, σ_γ/γ, and I_A are the normalized emittance, the relative energy-spread, and the Alfèn current (≈ 17 kA) respectively. For typical electron beam parameters for short wavelength operation (Q = 1 nC, $\varepsilon_n \approx 1$ mm mrad) λ_{cr} is then reduced by increasing beam-energy combined with an increased undulator period and length.

As a future alternative, the PSI-FEL project at the Paul Scherrer Institute in Switzerland attempts to develop an electron source with a significantly lower transverse emittance as a basis to develop a cost-effective X-ray FEL user facility [2] by pushing the beam-energy as low as technological possible. That is, for the case with $\varepsilon_n \leq 0.1$ mm mrad, parameter studies [2] suggest that the beam energy and peak current may be limited to 6 GeV and 1.5 kA, respectively.

In this paper we present a concept for an ultra-high brilliance 6-GeV accelerator. Starting point is the performance expectations of the Low Emittance Gun (LEG) [3], which is under construction at PSI. The first 250 MeV deserves special attention since emittance preservation proves to be most challenging in this part of the machine. It is our intention to test the concept of emittance conservation in this part of the machine experimentally. If successful, it should then serve as an injector for a linac that feeds a cost-effective X-FEL. An outlook follows at the end of this paper.

Table 1. Electron Source Parameters for the PSI FEL.

Peak current	I	≥ 5	A
Bunch charge	Q	0.2	nC
Bunch length (full width)	τ	≤ 40	ps
Bunch shape	-	uniform	-
Normalized emittance*	ε_n	≤ 0.05	mm mrad
Repetition rate#	f	10	Hz

* Slice parameter of a field-emitter at E=1 MeV and a slice-charge of 1 pC, i.e., the charge in the FEL-corporation length [2].
\# Limited by high-gradient pulser technology.

THE ELECTRON SOURCE

In a linac the emittance is limited by the intrinsic emittance at the electron source, which can be expressed as [4]:

$$\varepsilon_n = \frac{R}{2}\sqrt{\frac{2}{3}\frac{E_{kin}}{mc^2}} \quad (3)$$

where R is the beam radius in the case of a uniform radial distribution and E_{kin} is the mean kinetic energy of emitted electrons. With Eq. (3) in mind two strategies are persued: laser assisted Field Emission and photo-emission. Both technologies rely on laser-illumination to shape the temporal profile of the pulse.

With field emission electrons are drawn from sharp tips that are exposed to high gradient electric fields ($\Gamma \approx 6$ GV/m). Normally the emitting radius is small ($R \leq 5$ μm) and the field-emission process keeps the kinetic energy of the emitted electrons low ($E_{kin} \approx .0.15$ eV), which suggests a normalized emittance below 10^{-3} mm mrad. However, with increasing current the required electrical field-strength goes up followed by increased space-charge forces. This makes the combination of high-current and low-emittance challenging, both from technological and operational point of view. To reach ultra-low emittance two types of field emitters (FE) are under investigation: (*i*) a macroscopic single-tip FE and (*ii*) Field-Emitter Arrays (FEA). Construction of the former is technologically less demanding but the latter permits a reduction of the current density and most likely a lower

emittance. The status and performance are discussed in detail in [3]. Target specifications are summarized in Tab. 1, where the emittance refers to the slice-value after acceleration up to 1 MeV.

The transverse emittance of a photo-cathode for a 1 nC electron bunch typically is $\varepsilon_n \approx 1$ mm mrad. This value may become smaller with a reduced bunch-charge, a reduced peak-current, combined with an appropriate choice of cathode material. Optimizations based on Eq. (3) suggest that the slice emittance can reach $\varepsilon_n \leq 0.1$ mm mrad for a Cu cathode with beam parameters as quoted in Tab. 1 and an initial transverse radius $R = 0.25$ mm.

Since the fabrication and operation of a photo-cathode is less challenging then field emission, we anticipate commencing with a photo-cathode. A second stage based on field emission should then permit a lower initial emittance, which should permit a final value of 0.1 at the entrance of the undulator section of the FEL. Note that we have chosen the beam parameters identical for both types of cathodes such that the choice of cathode does not affect the design of the following accelerator structure.

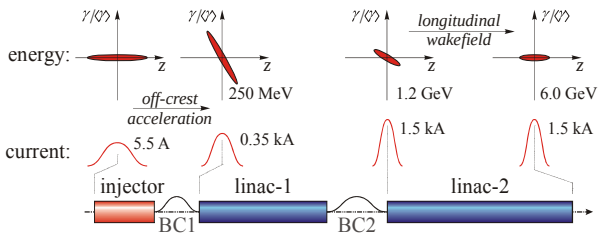

Figure 1. Functional layout of a low-emittance linac for an X-FEL. See text for details on the longitudinal shaping of the electron bunch.

ACCELERATOR CONCEPT

The performance parameters specified in Tab. 1 have, compared to more conventional RF photo-cathode designs, a low beam current and bunch charge at the cathode. This is beneficial to reduce the initial emittance and its dilution due to space charge in the region where the electron beam is sub-relativistic. The obvious drawback is the increased bunch compression ratio, which is required to obtain sufficient current for lasing. E.g., the LCLS [5] and the European X-FEL at DESY [6] have a total compression ratio of 70 and 100, respectively. The PSI-FEL aims for a ratio of 270.

The concept shown in Fig. 1 enables the increased compression ratio as it focuses on the control of the longitudinal phase-space. This is possible because we do not expect a significant emittance dilution in the bunch-compressors BC1 and BC2 [7]. Hence, the difficulties related to the emittance preservation are transferred to the design of the injector, which follows in the next section.

In terms of functionality the injector and BC1 accommodate most of the shaping of the longitudinal phase-space (γ,z). Similar to the design of the LCLS [5], linac-1 and linac-2 serve to boost the energy and allow of adiabatic damping of the emittance and relative energy spread. Deformation of the longitudinal phase-space, caused by wakefields in the linac structures, is controlled by off-crest acceleration in the injector and linac-1. In the present design both linac sections consist of 3-GHz room temperature (RT) traveling wave structures. We did not consider super-conducting technology because of the low repetition rate of the injector. Higher frequency RT will be considered later as an option to reduce the accelerator length.

THE INJECTOR

Fig. 2 shows a schematic of the injector. Details of the low-energy section are presented in Fig. 3.

Low Energy Acceleration

To minimize the initial blow-up of the emittance by space-charge, the cathode is positioned in a high-gradient field. The necessity of such a field is illustrated in Fig. 4, which shows a CAPONE [9] simulation of the slice-emittance of an ideal uniform beam with parameters as presented in Tab. 1. To obtain the gradient, the cathode is followed by a pulsed diode configuration as illustrated in Fig. 3. A 500 kV pulser has been constructed, which allows for initial tests with gradients up to 125 MV/m (top curve in Fig. 4). After sufficient operational experience the pulser will be upgraded to 1 MV to reach gradients up to 250 MV/m.

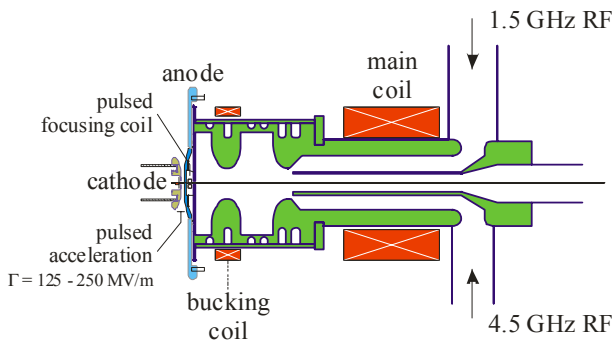

Figure 3. Layout of the high-gradient accelerating section followed by the initial RF acceleration [8].

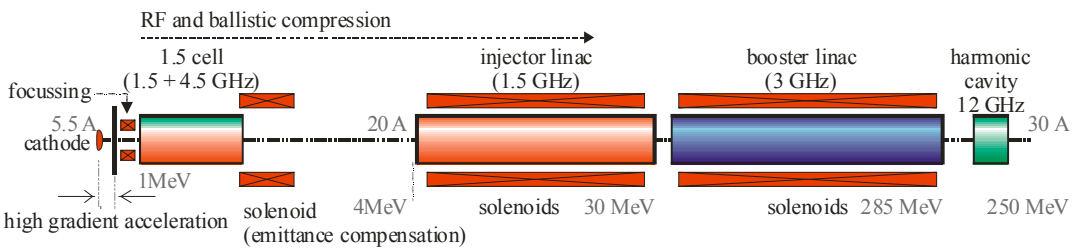

Figure 2. Schematic layout of the injector.

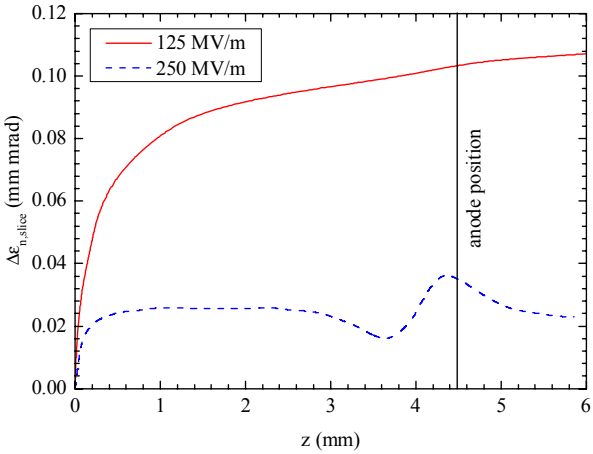

Figure 4. CAPONE [9] simulation of the slice emittance growth of a uniform electron bunch (Tab. 1) in a DC accelerator field (1 pC slice with an initial radius of 0.25 mm).

For further acceleration we have chosen an initial RF frequency of 1.5 GHz as a compromise between a high accelerating gradient (≥ 40 MV/m) and a large acceptance window to collect sufficient charge in a single bunch. A specially designed double-frequency 1.5-cell cavity [8] behind the diode further increases acceptance, see Fig. 3. Additional advantages of the double-frequency are: (*i*) a reduction of the emittance dilution caused by non-linear RF fields [8] and (*ii*) optimized RF compression. The latter is incorporated to reduce the bunch-length, see Fig. 2. We note that RF-compression is, in this part of the machine, the preferred choice as compared to magnetic compression since it maintains the cylindrical symmetry of the beam. That is, it avoids a break-up of the horizontal and vertical beam-optics in the space-charge dominated regime. For the similar reasons there are no quadrupoles included in the injector design.

During RF acceleration, it is important to control the transverse beam size since non-linear off-axis fields in the RF cavity may dilude the emittance otherwise. This is especially true in the first RF-structures where the beam-size may be blown up by a strong defocusing field as the beam passes the anode. For this reason, we plan to install a pulsed coil behind the anode to control the beam-size. We note that the pulsed technology has the advantage that the eddy-currents in the anode naturally shield the magnetic field from the cathode area.

Energy Booster

The RF compression is finalized in a 3-m long 1.5 GHz traveling wave structure. As soon as the electron bunches are short enough they enter a 3-GHz structures. A 12-GHz harmonic cavity at the end of the booster linearizes the longitudinal phase-space before further compression. All linac structures require additional focusing to control the electron beam-size. The final energy is 250 MeV. At this energy, the influence of space charge on the beam-optics is sufficiently reduced to permit the use of a chicane to reduce the bunch length.

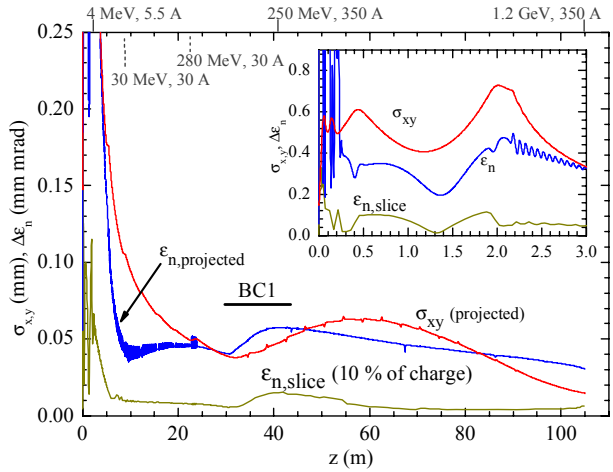

Figure 5. HOMDYN [10] simulation of the beam envelope and emittance dilution for the PSI FEL linac up to BC2, see Fig. 1. The inset is a zoom of the first 3 m.

Performance

As a first step, the emittance dilution has been tracked over the initial 1 GeV of acceleration (up to BC2) with HOMDYN [10], see Fig. 5. Initial conditions were an electron beam with the parameters presented in Tab. 1 with zero emittance at the cathode. It follows that a low emittance can be maintained during compression and acceleration. Verification of these results with more sophisticated codes is still in progress. Here we use MAFIA [11] to simulate the configuration presented in Fig. 3. Calculations are complemented with PARMELA [12] and GPT [13] simulations for tracking of the electron beam behind the diode. As a next step we will use IMPACT [14] for more elaborate calculations and tolerance studies.

Figure 6. Installation of the 500-kV pulser in the test-bunker OBLA.

STATUS AND OUTLOOK

The status of the field emitter development and the associated test stands are reported in [3]. As a first step towards the preservation of the emittance a 500 kV, 200-

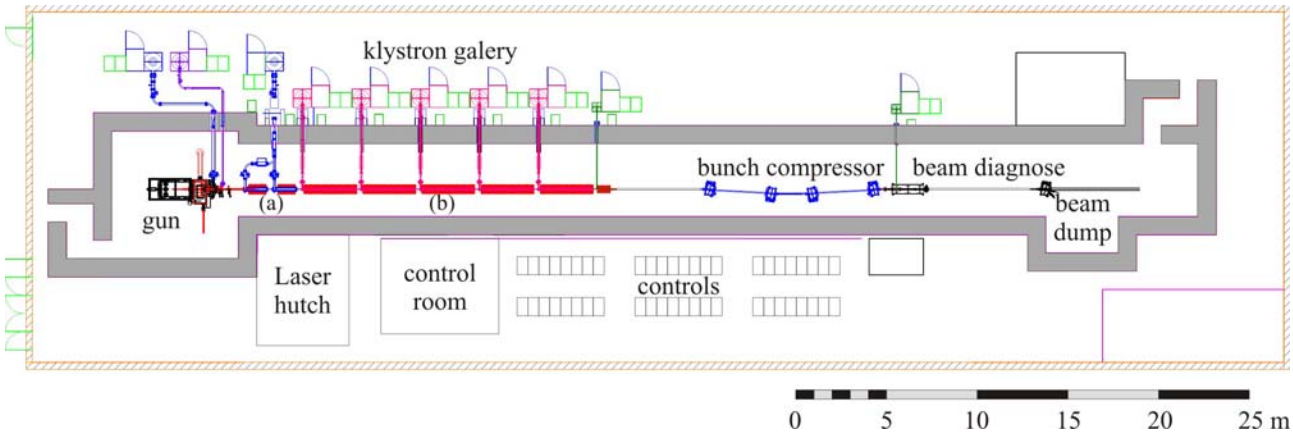

Figure 7. Layout of the 250 MeV test injector. The areas (a) and (b) mark the injector linac and booster linac as depicted in Fig. 2. The designed tunnel is sufficiently long to house the first bunch compressor (BC1 in Fig. 1).

ns pulser has been installed in a bunker at the PSI. It permits the operation of a diode configuration with a variable gap from 30 mm to 2 mm. A photo of the pulser is shown in Fig. 6. In fall of 2006 the pulser will be complemented with a diagnostic station for current and emittance measurements. First tests with pure field emitters (without laser illumination) are then foreseen for the end of the same year. In 2007 the experimental setup will be upgraded to permit laser assisted field emission and photo-emission combined with 1.5 cell RF cavity as depicted in Fig. 3. We note here the different laser systems. Laser assisted field emission has a high quantum efficiency (≈ 1) and requires a photon energy below the work function ($\lambda > 400$ nm). This can be a sub-system of the laser required for photo-emission, which typically has to deal with a low quantum efficiency at a wavelength of 266 nm.

In parallel surface cleaning techniques are studied to optimize the operation at high gradient and to minimize the occurrence of breakdowns in the high-gradient accelerator structure.

We plan to extend the experimental capabilities to a 250 MeV accelerator in the period 2008-2011. This linac should demonstrate low-emittance acceleration and bunch compression to reach a beam current of 350 A. In addition, it should serve as a test environment for the development of diagnose for an X-FEL. A possible layout is presented in Fig. 7. It includes the injector sketched schematically in Fig. 2 as well as the first bunch compressor, which is shown in Fig. 1.

REFERENCES

[1] J. Rossbach, E.L. Saldin, E.A. Schneidmiller, M.V. Yurkov, "Interdependence of parameters of an X-ray FEL", Nucl. Instr. Meth. In Physics Research, A374, 401 (1996)

[2] http://leg.web.psi.ch/public/publications/2005/ESFRI 20PSI-FEL.pdf

[3] R. Ganter, R.J. Bakker, M. Dehler, J. Gobrecht, C. Gough, E. Kirk, S.C. Leemann, K. Li, M. Paraliev, M. Pedrozzi, F. Le Pimpec, J.-Y. Raguin, L. Rivkin, V. Schlott, H. Sehr, S. Tsujino, "High Current Electron Emission from Microscopic Tips", THCAU04, this conference

[4] S. Humphries, Charged Particle Beams (John Wiley & Sons, 1990).

[5] LCLS CDR, SLAC Report No. SLAC-R-593, 2002.

[6] TESLA TDR, DESY Report No. DESY-2001-011, 2001.

[7] K. Li, A. Adelmann, A. Anghel, R.J. Bakker, A. Candel, M. Dehler, R. Ganter, G. Ingold, S. Leemann, M. Pedrozzi, J-Y. Raguin, L. Rivkin, V. Schlott, A. Streun, A. Wrulich, "Low Emittance X-FEL Development", Proc. of the 27th FEL Conf., Stanford (CA), USA , p. 483 (2005).

[8] J. -Y. Raguin, R. J. Bakker, K. Li, M. Pedrozzi, "A Two-Frequency RF Cavity for the PSI Low Emittance Gun", Proc. of the 27th FEL Conf., Stanford (CA), USA , p. 324 (2005).

[9] A.E. Candel, M.M. Dehler, S.C. Leemann, "Electron Beam Dynamics Simulations for the Low Emittance Gun", Proc. of EPAC2004, Lucerne, Switzerland, p. 2505 (2004)

[10] M. Ferrario, J.E. Clendenin, D.T. Palmer, J.B. Rosenzweig, L. Serafini, "HOMDYN study for the LCLS photoinjector", SLAC-PUB-8400 (2000).

[11] CST GmbH, Bad Nauheimer Strasse 19, D-64289 Darmstadt, http://www.cst.com

[12] L.Young, PARMELA, LA-UR-96-1835, LANL (1996)

[13] Pulsar Physics, De Bongerd 23, NL-3762 XA Soest, http://www.pulsar.nl/

[14] J. Qiang , S. Lidia, R. Ryne, C. Limborg, "A 3D Parallel Beam Dynamics Code for Modeling High Brightness Beams in Photoinjectors", Proc. of the 2005 Particle Accelerator Conference, Knoxville, USA, p. 3316 (2005)

AN ENHANCED GINGER SIMULATION CODE WITH HARMONIC EMISSION and HDF5 IO CAPABILITIES*

William M. Fawley†, LBNL, Berkeley, CA 94720, USA

Abstract

GINGER [1] is an axisymmetric, polychromatic $(r-z-t)$ FEL simulation code originally developed in the mid-1980's to model the performance of single-pass amplifiers. Over the past 15 years GINGER 's capabilities have been extended to include more complicated configurations such as undulators with drift spaces, dispersive sections, and vacuum chamber wakefield effects; multi-pass oscillators; and multi-stage harmonic cascades. Its coding base has been tuned to permit running effectively on platforms ranging from desktop PC's to massively parallel processors such as the IBM-SP. Recently, we have made significant changes to GINGER by replacing the original predictor-corrector field solver with a new direct implicit algorithm, adding harmonic emission capability, and switching to the HDF5 IO library [2] for output diagnostics. In this paper, we discuss some details regarding these changes and also present simulation results for LCLS SASE emission at λ =0.15 nm and higher harmonics.

INTRODUCTION

Over the past 25 years, there has been a steady advance in the use of numerical simulation codes to explore FEL physics, analyze experimental results, and to help design elaborate and expensive projects such as the LCLS. As the underlying computer hardware has grown both faster and often more complex (*i.e.,* massively parallel environments), FEL codes have similarly become more complex both in terms of the underlying physical phenomena they model (*e.g.,* wakefield losses) and the more realistic forms of simulation they attempt (*e.g.,* importation of massive macroparticle files for start-to-end tracking runs). Moreover, the amount of information the codes utilize and produce has increased by several orders of magnitude with multi-GB output and/or particle restart files becoming necessary for full time-dependent simulations of x-ray FEL's and multi-stage harmonic cascades.

This paper present recent changes to the GINGER simulation code[1] which originally was designed in the mid-1980's to study sideband growth in single-pass FEL amplifiers and which has steadily evolved since to study more and more elaborate configurations such as SASE devices, harmonic cascades and oscillators. The Fortran90 base currently underlying GINGER has proven very useful both in terms of modularization and in the number of useful language features (*e.g.,* array syntax and built-in operators, type definitions, memory management). The code structure has proven very amenable to efficient multiprocessing in which the different longitudinal slices are assigned to different processors with MPI [3] handling the necessary interprocessor communication. In the past year, we have replaced the original predictor-corrector field solver by a new implicit solver and also have extended the code to calculate radiation emission at multiple harmonics; the next section gives details on these changes. We then present results from a GINGER calculation for predicted harmonic emission from the LCLS.

With the addition of calculations of harmonic emission, typical GINGER output file sizes doubled or more. Based upon file compactness, IO speed, and flexibility in data layout, the output file format was changed from simple ASCII to HDF5[2]. In part because we believe that the FEL simulation community should become aware of the usefulness of HDF5 IO, the last section of this paper gives details concerning its implementation into GINGER .

THE NEW FIELD SOLVER AND IMPLEMENTATION OF HARMONICS

Adopting the slowly-varying envelope approximation (SVEA) with $E(r,z,t) \equiv \tilde{E}(r,z,t) \times \exp i(k_o z - \omega_o t)$, the field equation becomes

$$2ik_s \frac{\partial \tilde{E}}{\partial Z} = -\nabla_\perp^2 \tilde{E} - \left(\frac{\omega_0}{c^2} - k_o^2\right)\tilde{E} - \frac{4\pi i}{c^2}\,\omega_0 J_\perp \quad (1)$$

where $\partial/\partial Z$ is the Lagrangian derivative in the forward (*i.e.,* positive z) direction, and $J_\perp$ is the microbunched transverse current at angular frequency ω_0. The original GINGER field solver used a Gear predictor-corrector scheme [4] which automatically controlled step size to maximize computational speed for a given error allowance, but had negative aspects regarding algorithmic complexity and non-trivial coding difficulties with regards to adding additional dimensions such as harmonics and (eventually) non-axisymmetric modes. Consequently, we developed a completely new field solver based upon a backward-biased, implicit solution of the heat flow equation ("Case 5" in table 8.1 of [5]). This solution is always stable for arbitrary step size ΔZ and the chosen default bias factor makes the scheme equivalent to the Crank and Nicholson algorithm with errors scaling as Δr^2 and ΔZ^2. Tests of simple vacuum Gaussian mode propagation over multiple Rayleigh ranges show normalized energy conservation to better than 10^{-3} for $\Delta r/R_0 \leq 0.1$ where R_0 is the mode waist size.

* Work performed in support of the LCLS project at SLAC under US DOE Contract DE-AC02-76SF00515 (SLAC) and also supported under Contract DE-AC02-05CH11231 (LBNL).

† WMFawley@lbl.gov

Sec. 8.5 of Ref. [5] gives an elegant (and simple to code) solution method based upon a Gaussian elimination procedure where one first sweeps outward in r and then back to the axis Extension of the field solver to include higher harmonics is simple with (k_o, ω_0) being replaced by (hk_o, $h\omega_o$) and use of the appropriate current source term. For the latter, GINGER uses wiggler-period averaging and follows the standard formulation (see, *e.g.*, [6]) for odd harmonic emission that depends only upon the local harmonic microbunching amplitude (and ignores even harmonic emission arising from transverse gradients in the electron beam density). Tests by Z. Huang comparing the predicted 3rd harmonic power from nonlinear microbunching with that computed by GINGER for a simple $\lambda_0 = 0.15\,\mathrm{nm}$, steady-state amplifier with LCLS parameters show excellent agreement (*e.g.*, 10% or better) for sufficient macroparticle number (*e.g.*, $\geq$ 65K per slice). Use of smaller macroparticle number tends to lead to an overestimation of the harmonic power, perhaps because the longer Rayleigh length (and thus less radial smoothing in Z) at $0.05\,\mathrm{nm}$ makes the effective source term "grid noise" (*i.e.*, in higher radial modes) much worse than that corresponding to the fundamental (for which 8K macroparticles appear more to be than sufficient).

The original macroparticle longitudinal mover also used a Gear-scheme (which was extreme computational overkill given the slow evolution of particle phase and energy) and was replaced by a simple second-order Runge-Kutta solver in which only the fundamental radiation field acts back upon the particles. Within this limitation one can study nonlinear harmonic generation (the dominant emission term for most SASE and harmonic cascade devices) but not linear amplification. As shown in Ref. [7], ignoring the harmonic emission feedback is an extremely good approximation for SASE x-ray FELs and essentially all FELs in which gain at the fundamental wavelength is much larger than that at the harmonics, as is the usual case.

In fall 2006 we expect to add the harmonic field feedback terms to the mover and also a fourth-order Runge-Kutta scheme as an option. Lastly, we note that Eq. (1) is separable by azimuthal mode and thus the new field solver can be easily extended (as is hopefully planned for 2007) to solve for $\tilde{E}(r, \varphi, z, t)$.

AN EXAMPLE LCLS HARMONIC EMISSION CALCULATION

Nonlinear harmonic emission from the LCLS is potentially extremely useful, both for experimentalists and as a diagnostic of FEL performance. Adopting design parameters (3.4 kA, $\gamma = 26693$, 1.2 mm-mrad, $B_w = 1.25\,\mathrm{T}$, $\sigma_\gamma/\gamma = 10^{-4}$), and a quad FODO focusing lattice that produces an average Twiss β-function of 28 m, we simulated a LCLS 9.2-fs segment at 6-attosecond temporal resolution with 32768 macroparticles per slice. The calculation was run on 128-POWER 5 (1.9 GHZ) processors of the "BASSI" IBM p575 system at NERSC and required $\approx$ 40 minutes of wall-clock time. Figure 1 plots the power at the fundamental wavelength of 0.15 nm and also the 3rd and 5th harmonics as functions of z. One sees that the plateau region (on this semi-log plot) for small z where spontaneous emission dominates the coherent FEL component lasts much longer for the harmonics than the fundamental; in reality the plateau region would extend even further because these calculation do not include non-axisymmetric spontaneous emission. While the third harmonic grows more rapidly with z than the fundamental in the region $60 \leq z \leq 85\,\mathrm{m}$, it saturates at a low ($\sim 1\%$) relative power level.

Comparing the behavior of the on-axis far-field power (not displayed) with the total near-field power (Fig. 1) reveals that the plateau region is much smaller for the fundamental but there is essentially no change for the harmonics. This is likely related both to the short gain length for the

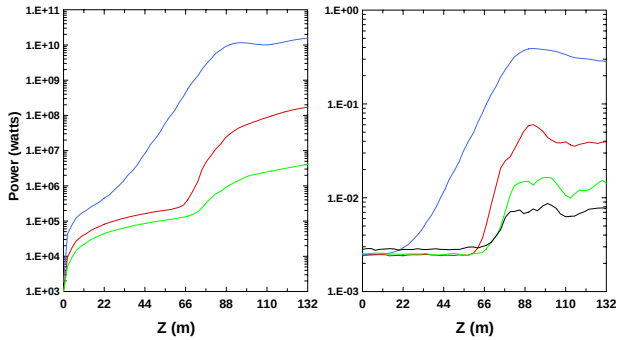

Figure 1: Time-averaged SASE power (left) and microbunching fraction (right) vs. z for an LCLS pulse at the 0.15-nm fundamental (blue curve) and also the 3rd, 5th, and 7th harmonics (bunching only) (red, green, black curves).

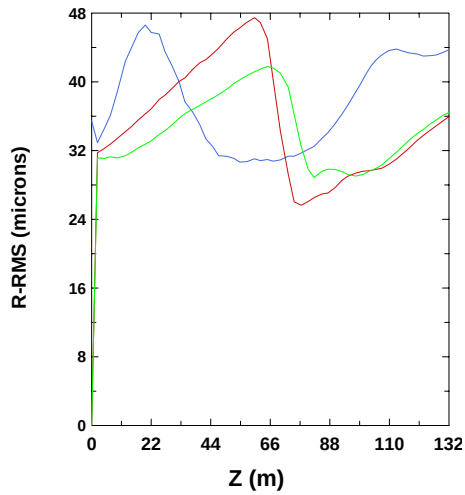

Figure 2: RMS transverse size vs. z for SASE emission from an LCLS pulse at the 0.15-nm fundamental wavelength (blue curve) and also the 3rd and 5th harmonics (red and green curves).

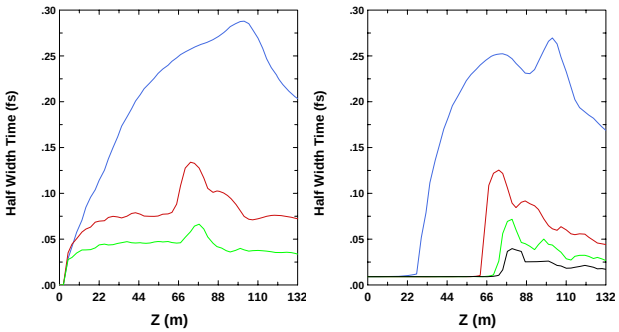

Figure 3: Plots of $C_{1/2}(\tau)$ for the on-axis far field emission (left) and microbunching (right) for the fundamental and harmonics (same color scheme as Fig. 1).

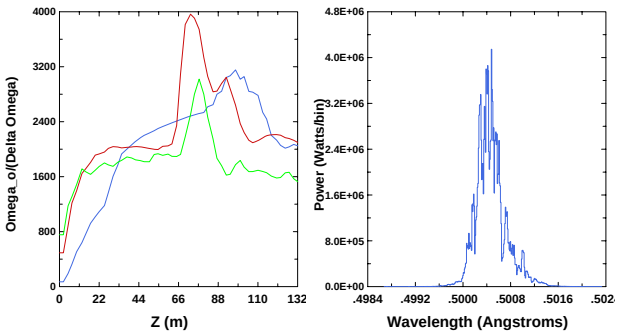

Figure 4: Plots of RMS spectral width for on-axis far field emission at the fundamental and harmonics (left) and the 3rd harmonic output (near-field) spectrum (smoothed with a 5-bin average) (right).

harmonics $L_{g,h} \approx L_{g,1}/h$ and the smaller mode size (see Fig. 2) for the coherent harmonic emission which reduces some of the far-field contrast *vis-a-vis* the spontaneous harmonic emission. Near power saturation, the RMS transverse sizes of the 3rd and 5th harmonic emission are ∼20% smaller than that of the fundamental (Fig. 2). However, after saturation, they also grow with z despite a greater Rayleigh range, indicating perhaps that optical guiding effects are far more important for the fundamental.

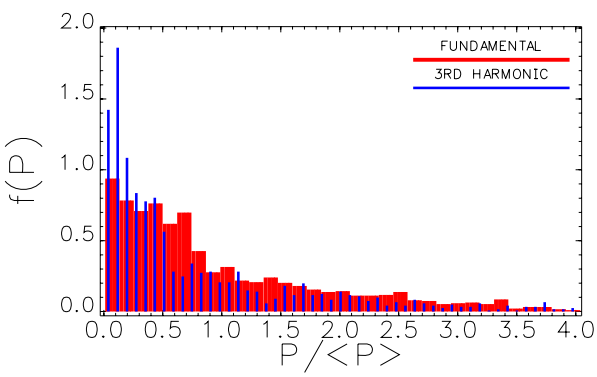

Figure 5: Histogram of the probability distribution of $P(t)/ < P >$ at the fundamental and 3rd harmonic at the undulator exit.

Standard SASE theory (*e.g.*, Ref. [8]) predicts that the inverse spectral bandwidth $\omega/\Delta\omega$ and autocorrelation time $C_{1/2}(\tau)$ (the point at which the temporal autocorrelation function drops to 0.5) for FEL radiation increase as $z^{1/2}$. Such behavior is demonstrated by radiation at the fundamental (blue curves in Fig. 3. For the harmonics, the coherent component of $C_{1/2}(\tau)$ suddenly dominates over the spontaneous emission (for the radiation) and shot noise (for the microbunching) at two-thirds of a saturation length, reaches a maximum within a gain length, and then begins declining with z, in contrast to the fundamental which reaches a maximum somewhat later in z (right plot in Fig. 1) and only drops in the last 20-m or so. Presumably, debunching due to the development of a large energy spread is responsible for the greater sensitivity of the harmonics.

An autocorrelation function and power spectrum can be similarly calculated for microbunching by using the complex average computed over the macroparticles corresponding to each longitudinal electron beam slice. In contrast to the radiation quantities, the microbunching $C_{1/2}(\tau)$ (right plot in Fig. 3) has a slow but steady linear decay from its maximum which is perhaps associated with the temporal variation of Ω_{syn} over the individual microspikes. Ideally, in a near time-steady situation with essentially no variation in radiation eikonal phase, $C_{1/2}(\tau)$ would be constant with harmonic. However, in the SASE regime, Saldin *et al.* [7] have predicted from 1-D numerical studies that $C_{1/2}^{h=3}(\tau)/C_{1/2}^{fund.}(\tau) \approx 0.65$; the GINGER LCLS results show a ratio $\simeq 0.5$, a reduction attributable perhaps to nonzero emittance effects not included in the 1-D study.

Figure 4 plots the inverse spectra width versus z together with the output spectrum at the third harmonic. Another diagnostic of radiation field correlation, the ratio $[\omega/\Delta\omega]/[1.18\omega C_{1/2}(\tau)]$ ($\equiv 1$ for a Gaussian power spectrum), is 0.76 for the fundamental and drops to to 0.69 and 0.65 for the third and fifth harmonics at the position of maximum inverse bandwidth.

Another apparent difference with the Saldin *et al.* 1-D results concerns the probability distribution for $P(t)$. In Fig. 5 we plot the normalized histogram for the fundamental and third harmonic ofthe output (near-field) radiation. One sees that in accord with the earlier study, the third harmonic emission is more peaked toward $P = 0$. However, the peak is more extreme and the first order moment is much smaller, evidently because of large temporal regions of relatively low harmonic power. The probability distribution for the fundamental is also more peaked toward $P = 0$ whereas Ref. [7] found a peak near $P =< P >$. Because our data is taken somewhat deeper in saturation than the z point chosen by Saldin *et al.*, it is possible (albeit unlikely) that the distribution function reverts back to a negative exponential corresponding to the exponential gain regime. or-that this particular SASE run does not have sufficient statistics in terms of slice number to clearly resolve the distribution shape. However, it may also be possible that inclusion of true transverse effects actually change the nature of

the distribution function in the saturation regime. Consequently, this topic may warrant some additional study.

IMPLEMENTATION OF HDF5 IO

As is true for most large-scale simulation tools, an FEL code must have numerous IO capabilities. On the input side, the user must be able to specify a number of beam and run parameters. Depending upon the run complexity, additional input might be required, *e.g.,* 6D macroparticle phase space information from a tracking particle output file or a "restart" file from a previous FEL code run (as might be true for a harmonic cascade); a time-dependent input radiation field; an undulator "lattice" including $a_w(z)$, possible pole error field and dipole corrector information, and possible vacuum chamber longitudinal wake field input. Output information can be very extensive: spatially- and temporally-resolved radiation field information including harmonics; 5D macroparticle phase space snapshots at different $z-$ and $t-$ locations for later use in scatterplots; $z-$ and $t-$ resolved "scalar" information such as total radiation power and macroparticle microbunching (at multiple harmonics), energy spread, on-axis far field complex amplitude; and possible full 6D macroparticle and/or 2D (r, t) radiation field information for a subsequent downstream undulator run. As the raw binary size of this information can exceed 100 MB for fields and 1 GB for particles, simple ASCII formats are unattractive both due to their size ($\sim$3X larger than pure binary) and slow IO transfer speed. Moreover, unless one designs a very clever and robust self-describing data structure and/or divides the heterogeneous output into many separate files per run, it is difficult to have an output file system that is reasonably easy to analyze (and which maintains good backward compatibility as the simulation code inevitably evolves in complexity).

In answer to the above requirements and problems, the HDF5[2] IO system offers a strong set of attractive features: (1) self-describing data format, including optional dataset attributes (2) Unix-like directory trees including soft links (3) compact data storage with little additional overhead relative to binary (4) multiplatform data file portability (*e.g.,* little- to big-endian, 32- to 64-bit native) (5) a rich class of native data types range from simple strings to 1-D integer arrays to many dimensional real arrays (6) user-definable data types (7) MPI-based parallel IO on platforms such as the IBM-SP. The HDF5 development group also provides a set of useful tools for HDF5 file data visualization and data dumping of individual structures. Many projects in the high performance computing community have embraced HDF5 as well as a number of 3rd party visualization tools venders (*e.g.,* IDL). I note that the GENESIS code [9] also has a growing HDF5 IO capability and would suggest that other FEL and tracking code developers consider this option.

Currently, the GINGER HDF5 output file has 5 main top directories: /base_param to pass simulation run variables such as the central wavelength, number of slices, etc.; /grids which have the r- and z- locations of grid points; /input which has the complete ASCII input and template files for the run; /radiation which contains all scalar and vector radiation field information; and /particles which has all particle-derived information including scatterplot dumps, if any. Separately, particle restart files can also be written in HDF5 format and the extension to radiation restart files (as is needed for multistage harmonic cascades) will be done in the near future. Knowledge of the exact "path" of a given data set (*e.g.,* /radiation/scalar_data/...) is completely sufficient for a HDF5 utility (and GINGER post-processor) to access the data set; the exact disk address within the HDF5 file is not needed by external programs but is provided by a low-level look-up table in the HDF5 file. This massively simplifies data access With the migration to HDF5 format, we believe it will be relatively straight-forward and painless to extend the GINGER output file to handle fully "3D" field information (*i.e.,* $[r, z, t] \rightarrow [r, \varphi, z, t]$) and variable spatial resolution (*e.g.,* relative finely z-resolved scalar quantities such a radiation power and microbunching but coarser resolution of vector quantities such as $E(r, z, t)$) as needed by future code upgrades.

ACKNOWLEDGEMENTS

I am pleased to acknowledge many useful discussions with numerous individuals including A. Adelmann, E. Allaria, M. Borland, W. Graves, Z. Huang, H.-D. Nuhn, G. Penn, E. Pourmal (HDF5 group/NCSA), and S. Reiche. I also thank the LCLS project office at SLAC for financially supporting much of the work presented here and also the US DOE National Energy Supercomputer Center for providing Computational resources.

REFERENCES

[1] W.M. Fawley, "A User Manual for GINGER ...", LBNL-49625-Rev. 1 (2004); see also http://www-ssrl.slac.stanford.edu/lcls/lcls_tech_notes.html/LCLS-TN-04-3.pdf .

[2] National Center for Supercomputing Applications (U. Ill.), "HDF5 Home Page", http://hdf.ncsa.uiuc.edu/HDF5/

[3] Message Passing Interface Forum, "MPI: A Message-Passing Interface standard", Int. J. Supercomputer Applications and High Perf. Comp. **8** (1994); see also: http://www.mpi-forum.org/docs/docs.html .

[4] C.W. Gear, Comm. ACM **14**, 176 (1971).

[5] R.D. Richtmeyer and K.W, Morton, "Difference Methods for Initial-Value Problems", (Interscience, New York), 2nd. Ed., 1967.

[6] Z. Huang and K.-J. Kim, Phys. Rev. E **62**, 7295 (2000).

[7] E.L. Saldin, E.A. Schneidmiller, and M.V. Yurkov, *Proc. 27th Int. FEL Conf.* (2005, Stanford, CA), 51.

[8] K.-J. Kim, Phys. Rev. Lett. **57**, 1871 (1986).

[9] S. Reiche, Nucl. Inst. Meth. Phys. Res. A **429**, 243 (1999).

SIMULATIONS OF HIGH POWER-FEL AMPLIFIERS*

J. Blau, D. Burggraff, T.Y. Voughs and W.B. Colson
Physics Department, Naval Postgraduate School
333 Dyer Road, Monterey, CA 93943.

Abstract

FEL amplifier simulations have been updated and parallelized, and system vibration effects have been added. The simulations are used to study proposed high-power amplifier FELs at LANL and BNL. We look at the single-pass gain and output power, including the effects of wiggler tapering, electron beam pinching, and shifting and tilting of the electron beam.

INTRODUCTION

At the Naval Postgraduate School over the past several years, we have made significant changes to our simulations of FEL oscillators, including an improved light propagation method using expanding coordinates [1], cavity and electron beam stability effects [2], better diagnostics such as optical mode analysis [3], and parallelizing the codes to run on a cluster computer. These same improvements have now been incorporated into our FEL amplifier simulations. In this paper, we discuss the results of using these simulations to study several existing and proposed high-power FEL amplifiers at Brookhaven and Los Alamos National Labs. We look at the effects of tapering the undulator, as well as shifting, tilting, and focusing of the electron beam. We consider how each of these affect the single-pass gain, energy extraction, and optical beam quality.

SIMULATION METHOD

We represent the optical field using a Cartesian coordinate system, following the amplitude and phase at each (x, y) grid point as it evolves through the undulator. The initial field has a Gaussian transverse profile, focused at the beginning of the undulator. The electron and optical pulse lengths are assumed to be much longer than the slippage distance $N\lambda$, where N is the number of undulator periods and λ is the optical wavelength. We use a large number of sample electrons, with an initial position and angular distribution determined by the transverse emittance, and an initial energy spread determined by the longitudinal emittance. To study stability effects we can include an initial shift or tilt in the electron beam, and we can also adjust the beam focus position along the undulator.

At each time step within the undulator, the electrons evolve according to the Lorentz force equation, including betatron focusing. The optical field evolves self-consistently according to Maxwell's wave equation. At the end of the undulator, the field is propagated to the first optical element using an expanding coordinate system [1] to handle the large scale change due to diffraction.

In our simulations, we use dimensionless parameters, with longitudinal lengths normalized to the undulator length L, transverse lengths normalized to $\sqrt{L\lambda/\pi}$, and time normalized to L/c, where c is the speed of light. Graphical output from the simulations shows the evolution of the optical field, bunching of the electrons in phase space, and the structure of the optical wavefront at the end of the undulator and at the first optical element.

SIMULATION RESULTS

Brookhaven SDL FEL

At the Source Development Lab (SDL) at Brookhaven National Lab (BNL), they have an FEL amplifier based on the NISUS undulator [4], with $N = 256$ periods, each $\lambda_0 = 3.9$ cm long, for a total length $L = N\lambda_0 \approx 10$ m. The undulator parameter is $K_{rms} = 0.78$. The electron beam has an energy of 102 MeV, with a bunch length of 1 ps and a bunch charge of 0.35 nC. The optical wavelength is $\lambda = 0.79$ μm, and the distance to the first optic is 20 m.

Figure 1 shows results from a simulation of this FEL. On the top, a cross-section of the dimensionless optical field amplitude $|a(y)|$ is represented as it evolves from the be-

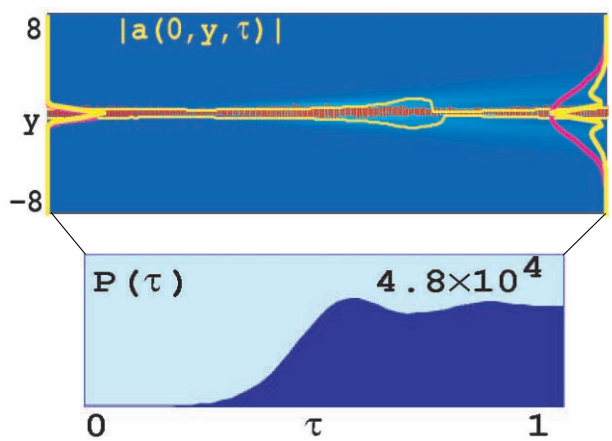

Figure 1: Simulation results for the SDL FEL with no taper. On the top is the evolution of the amplitude profile $|a(y)|$, as described in the text. On the bottom is the evolution of the dimensionless optical power $P(\tau)$ from the beginning ($\tau = 0$) to the end ($\tau = 1$) of the undulator. The maximum value of the power is indicated in arbitrary units.

* Work supported by JTO, ONR, and NAVSEA.

ginning (dimensionless time $\tau = 0$) to the end ($\tau = 1$) of the undulator. The narrow yellow contour line marks the $1/e$ value of the field amplitude at each time step, while the bold yellow curves on the left and right plot the field profile at $\tau = 0$ and $\tau = 1$. A few sample electrons are shown in red. The simulation predicts high gain, $G \approx 1000$, which leads to optical mode distortion and guiding [5]. Without the gain medium, the field would maintain a Gaussian profile and diffract out to a large radius, as shown in purple on the right; the actual field profile shown in bold yellow is much narrower and distorted. The simulation predicts an extraction of $\eta = 0.6\%$ (extraction is defined as the ratio of the output optical power to the input electron beam power). In the actual experiment, an extraction of about 0.4% was measured. The difference is likely due to pulse slippage effects, which are not included in the simulation.

The lower half of Fig. 1 shows the power saturating about halfway down the undulator, so we consider tapering the magnetic field to enhance the extraction. Figure 2 shows the simulation results with a linear taper rate $\Delta K/K \approx -5\%$ over the last 2.4 m of the undulator. Now the power continues growing, and the extraction is increased to $\eta = 1.2\%$. The final electron phase space on the lower left shows about half of the electrons trapped in closed orbits [5]. The electron phase ζ roughly corresponds to the position of an electron within an optical wavelength, while $\nu = d\zeta/d\tau$ is the phase velocity. The induced spread in phase velocities $\Delta\nu$ translates to an electron beam energy spread $\Delta E/E = \Delta\nu/4\pi N = 3.7\%$, compared to 2.5% for the untapered case. The final optical wavefront $|a(x, y)|$ at the output mirror is shown in the lower right.

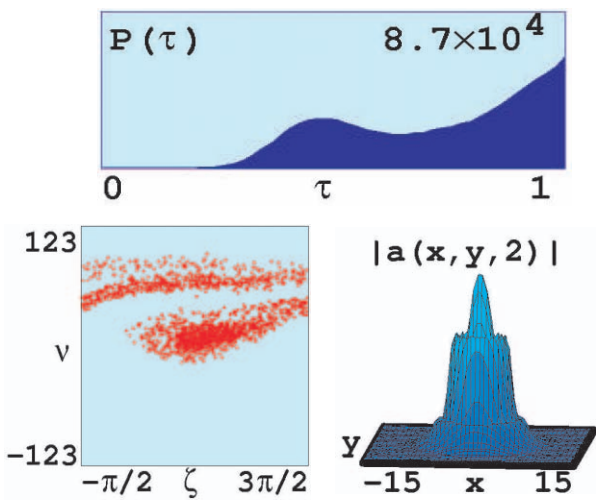

Figure 2: Simulation results for the SDL FEL with a -5% taper rate over the last 2.4 m of the undulator. On the top is the evolution of the optical power, $P(\tau)$. On the lower left is the final electron phase space as described in the text, with sample electrons shown in red. On the lower right is the final optical wavefront, $|a(x, y)|$, at the output mirror.

Another factor of two improvement in extraction could be achieved by starting the taper earlier at $\tau_s = 0.5$, near the onset of saturation for the untapered FEL. Figure 3 shows the results of many simulations, plotting extraction η versus phase acceleration δ for this latter case. The phase acceleration [5] is related to the undulator taper rate by

$$\delta = -4\pi N \frac{K^2}{1+K^2} \frac{(\Delta K/K)}{1-\tau_s}. \quad (1)$$

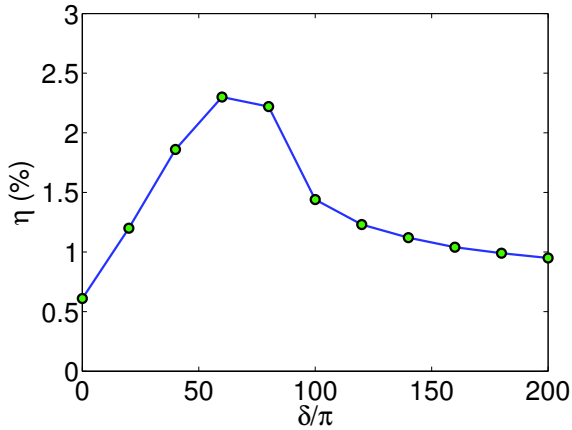

Figure 3: Extraction η versus phase acceleration δ for the SDL FEL, with a linear taper over the last 5 m of the undulator. The maximum extraction $\eta = 2.3\%$ is achieved for $\delta = 60\pi$, which corresponds to $\Delta K/K \approx -7\%$.

Figure 4 shows the results of simulating the SDL FEL with a taper rate of -7% over the last 5 m of the undulator, corresponding to the peak extraction value of 2.3% in Fig. 3. The optical power $P(\tau)$ grows significantly in the second half of the undulator, and the phase space plot shows good bunching. The induced energy spread is 5%.

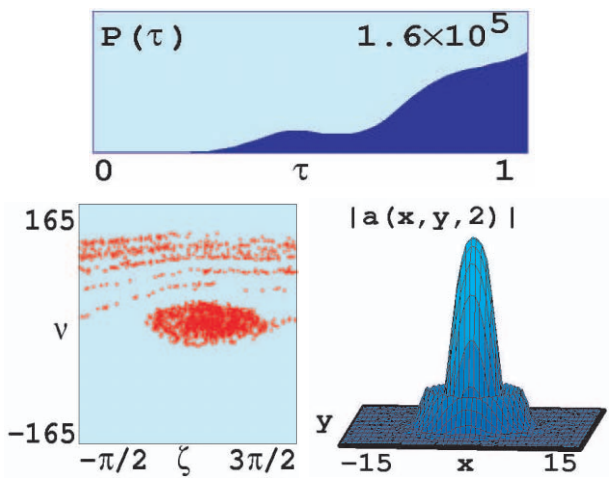

Figure 4: Simulation results for the SDL FEL, with a -7% taper rate over the last 5 m of the undulator.

Brookhaven proposed FEL

Another high-power amplifier FEL has been proposed at BNL [6]. This system would use an 80 MeV electron beam with a bunch length of 2.8 ps and a bunch charge of 1.4 nC. The undulator would have $N = 120$ periods, each $\lambda_0 = 3.25$ cm long, for a total length $L = 390$ cm, with $K_{rms} = 0.7$. The optical wavelength would be $\lambda = 1$ μm, with the first optic at a distance of 27 m.

Figure 5 shows simulation results for this FEL. Again we see guiding of the optical field (top), and the power is near saturation at the end of the undulator (center). The simulation predicts gain $G \approx 800$ and corresponding extraction $\eta \approx 1\%$; the design goal for this system is $\eta = 0.25\%$. In the lower left, the electron phase space shows bunching, and an induced electron beam energy spread of 3.5%. In the lower right, the final optical wavefront has a nearly top-hat shape.

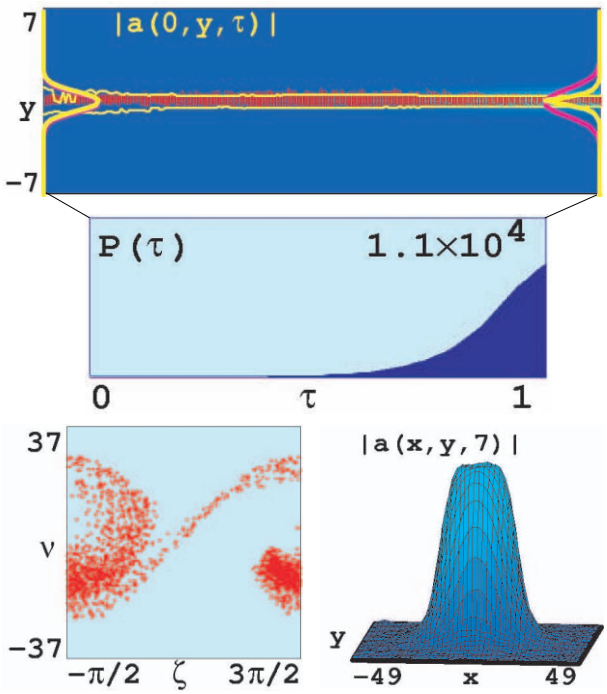

Figure 5: Simulation results for the proposed BNL FEL.

We also studied electron beam stability effects for this system. Figure 6 shows the results of many simulations, with the electron beam shifted off-axis in the plane of the undulator magnetic field. The extraction drops as the beam is shifted, but the design goal of $\eta = 0.25\%$ is still achieved for $y_0 < 1.2$ mm, about 5 times the electron beam radius ($r_b = 0.25$ mm, indicated on the graph). Figure 7 shows how guiding enables the optical mode to follow the shifted electron beam over about half of a betatron oscillation, for a beam shift of $y_0 = 1$ mm.

Figure 8 shows the effect of tilting the electron beam about the center of the undulator. The simulations predict that the system can tolerate a beam tilt of $\theta_y \approx 0.9$ mrad, well beyond the beam angular spread of $\Delta\theta = 0.1$ mrad.

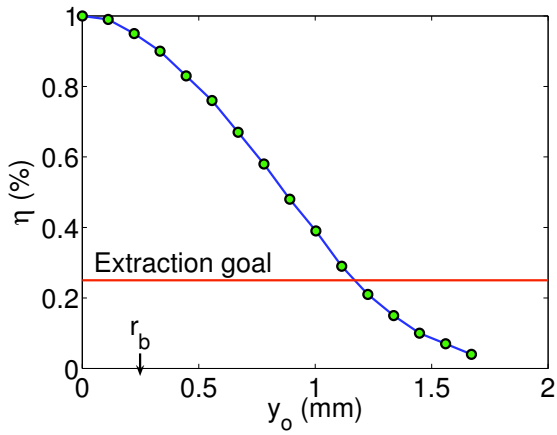

Figure 6: Extraction η vs. electron beam shift y_0 for the proposed BNL FEL. The extraction goal is exceeded for all values of $y_0 < 1.2$ mm, well beyond a typical experimental tolerance of ≈ 50 μm, and much greater than the electron beam radius $r_b = 0.25$ mm.

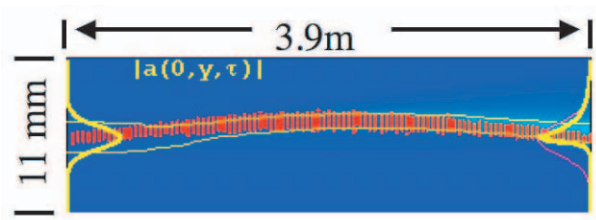

Figure 7: Optical field evolution for the proposed BNL FEL. Initial conditions are chosen so that the electron beam (shown in red) is shifted off-axis by $y_0 = 1$ mm at the center of the undulator. Betatron focusing bends the beam back towards the axis at the ends of the undulator. The horizontal and vertical axis scales are quite different, as indicated. Notice how guiding enables the optical mode (narrow contour line) to follow the electron beam as it shifts off axis.

Again, this is due to the guiding effect, as shown in Fig. 9. Our simulations predict good extraction for electron beam shifts x20 and tilts x100 greater than the experimental tolerance of existing FELs [7].

Los Alamos proposed FEL

At Los Alamos National Lab (LANL), they have proposed a somewhat different design for a high-power FEL amplifier [8]. This system would use an 81 MeV electron beam with a bunch length of 1 ps and a bunch charge of 1 nC. The undulator would have $N = 110$ periods, each $\lambda_0 = 2.18$ cm long, for a total length of $L = 240$ cm, with $K_{rms} = 1.2$. The optical wavelength would be $\lambda = 1.05$ μm, with the first optic at a distance of 24 m.

Our simulations of this design predict that it would achieve a gain of $G \approx 240$, corresponding to extraction of $\eta = 0.74\%$, with induced energy spread of about 5%.

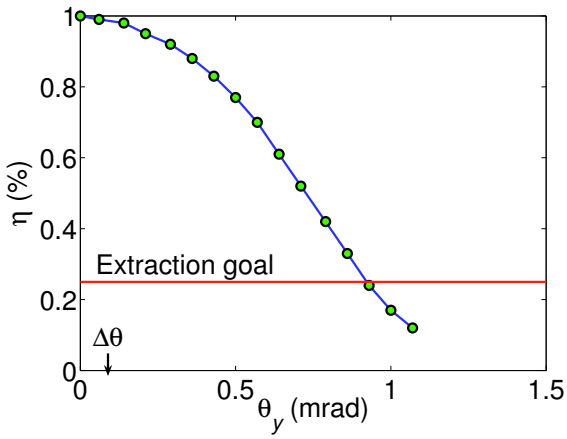

Figure 8: Extraction η vs. electron beam tilt θ_y for the proposed BNL FEL. The extraction goal is obtained for all values of $\theta_y < 0.9$ mrad, well beyond a typical experimental tolerance of 10 μrad, and much greater than the electron beam angular spread, $\Delta\theta = 0.1$ mrad.

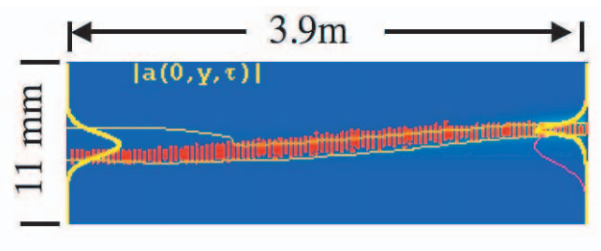

Figure 9: Optical field evolution for the proposed BNL FEL. Initial conditions are chosen so that the electron beam is tilted by $\theta_y = 0.9$ mrad at the center of the undulator. The tilt appears exaggerated due to the different horizontal and vertical scales. Notice that the optical mode (narrow yellow contour line) follows the tilted electron beam (red).

However, the design goal for this system is $\eta = 1.2\%$. We find that by tapering the undulator, $\Delta K/K \approx -18\%$ over the last 40 undulator periods, they could increase the gain to $G \approx 500$ and the extraction to $\eta = 1.7\%$, while only inducing an energy spread of about 6%.

We studied stability effects for the LANL amplifier design; our simulations predict that it will still achieve the desired extraction with beam shifts up to 0.4 mm, or beam tilts up to 0.4 mrad. These results are again well beyond the experimental tolerance of existing FELs.

We also tried varying the electron beam focus for this FEL. Figure 10 is a plot of the extraction versus the beam focus position, τ_β. The peak extraction $\eta \approx 1.9\%$ is at $\tau_\beta = 0.15$ or 0.75, rather than at $\tau_\beta = 0.5$ as one might expect. This is due to the betatron motion of the electrons, in both cases focusing the beam near the end of the undulator, where the tapering enhances the extraction. This "scalloped" shape of the electron beam, as seen in the inset plots in Fig. 10, leads to focusing of the optical wavefront at the undulator exit, thus allowing it to rapidly diffract afterwards, which should reduce the intensity at the first optic.

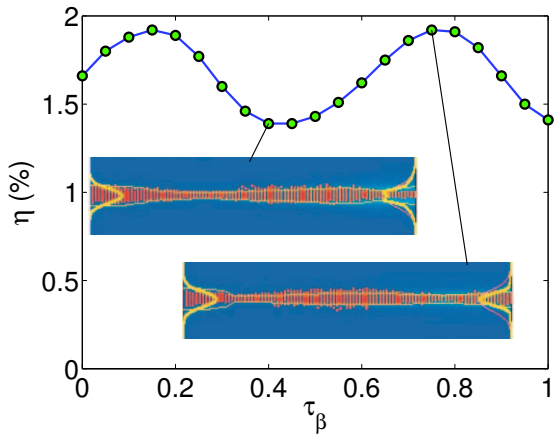

Figure 10: Extraction η vs. electron beam focus position τ_β for the proposed LANL FEL. The inset plots show the evolution of the electron beam and the optical mode at $\tau_\beta = 0.4$ (top) and $\tau_\beta = 0.75$ (bottom).

REFERENCES

[1] R.L. Armstead, J. Blau, and W.B. Colson, "Short Rayleigh length free electron laser simulations in expanding coordinates", Proceedings of the 26th International Free Electron Laser Conference (2004), p. 274. http://www.JACoW.org.

[2] P.P. Crooker, J. Blau, and W.B. Colson, "Stability of a short-Rayleigh length laser resonator", Phys. Rev. ST-AB, 8, 040703 (2005).

[3] R. Vigil, "Hermite-Gaussian modes and mirror distortions in the free electron laser", M.S. Thesis, Naval Postgraduate School, June 2006.

[4] T. Watanabe, et. al., "An experimental test of superradiance in a single pass seeded FEL", Proceedings of the 27th International Free Electron Laser Conference (2005), p. 526, http://www.JACoW.org.

[5] W.B. Colson, C. Pellegrini, A. Renieri (Eds.), Free Electron Laser Handbook, North-Holland Physics, Elsevier Science Publishing Co. Inc., The Netherlands, 1990 (Chapter 5).

[6] I. Ben-Zvi, D. Kayran and V. Litvinenko, "High average power optical FEL amplifiers", Proceedings of the 27th International Free Electron Laser Conference (2005), p. 232, http://www.JACoW.org.

[7] S. Benson, priv. comm.

[8] D. C. Nguyen, W. B. Colson and H. Freund, "Scalloped electron beam FEL", Proceedings of the 28th International Free Electron Laser Conference (2006), p. xxx, http://www.JACoW.org.

THE BESSY SOFT X-RAY FEL: A SEEDED HGHG FEL*

A. Meseck† for the BESSY FEL team
BESSY GmbH, Albert-Einstein-Str.15, Berlin, Germany.

Abstract

Reproducibility, high power and short pulse length combined with variable polarization and tunable wavelength are required to open new frontiers for the soft X-ray users. To provide radiation with such extraordinary properties, BESSY has been designing a seeded FEL based on the high-gain harmonic-generation (HGHG) concept [1]. The seeding with an external tunable laser ensures the reproducibility of the full-coherent radiation. The combination of so-called HGHG stages, used to down-convert the seed wavelength, and a final amplifier provides for the high power and superior spectral properties. Furthermore, the HGHG concept and the fresh bunch technique planned for the BESSY FEL mitigate the effects of parameter variation along the bunch which are expected from realistic assumptions of the Gun and LINAC structure. The design concept of the BESSY soft X-ray FEL will be presented and the stabilizing effect of HGHG stages and the benefits from the fresh bunch technique and the final amplifier will be discussed.

INTRODUCTION

The BESSY Soft X-Ray FEL is designed as a multi-user facility consisting of three independent FEL lines based on HGHG-concept. Each line is seeded by a tunable laser covering the spectral range of 230 nm to 460 nm. The target wavelength ranges from 51 nm to 1.24 nm with peak powers up to a few GWs and pulse lengths less than 20 fs (rms). The polarization of the fully coherent radiation will be variable.

In the HGHG-FEL approach the light output is derived from a coherent subharmonic seed field. Consequently the optical properties of the HGHG-FEL output reflect the characteristics of the high-quality seed. The benefit is a pulse with selectable short duration, a high degree of stability and control of the central wavelength and bandwidth. Cascades of two to four HGHG stages are planned to reduce the existing laser wavelength to the target range of the BESSY-FEL. The planned "fresh bunch" technique [2] prevents the final output from the electron beam heating effect of FEL interaction in the upstream stages, ensuring the high output power and the spectral quality.

The optimization of an HGHG-line includes the proper choice of the seeding radiation, the electron beam parameters, the harmonic cascade, the undulator parameters and the strength of the dispersive section. In the following the steps taken during the optimization process will be described.

All calculations have been performed with the time-dependent 3D simulation code GENESIS [3].

THE HIGH-GAIN-HARMONIC GENERATION

Several HGHG stages are necessary to reduce the seed laser wavelengths availabel today to the desired spectral range. Each stage consists of an undulator - dispersion - undulator structure. In the first undulator, the so called modulator, the interaction with a radiation field (e.g. provided by an external laser) leads to an energy modulation of the electron beam with the period of the seeding wavelength. The following dispersive section converts this energy modulation into a spatial modulation, or bunching, that includes bunching on higher harmonics of the seeding frequency. The fundamental of the second undulator, the so called radiator, is set in resonance with the chosen harmonic. The prebunched beam then radiates at the harmonic wavelength with high efficiency. The radiator output is used as the seed for the next stage. The last radiator is followed by the so called final amplifier. It is seeded at the desired wavelength and the amplification process is brought to saturation.

In a cascaded HGHG scheme the necessary seeding power for each stage is produced by adjusting the output power of the previous stage. The output power of the radiator is proportional to the square of the bunching factor, b_n, of the entering electron beam [4]:

$$p_{out} \sim b_n^2.$$

The bunching factor for the n^{th} harmonic of the seed laser is given by:

$$b_n = \langle \exp\left(i\, n\, \theta_j\right) \rangle^2$$

$$= \exp\left(\frac{-1}{2} n^2 \sigma_\gamma^2 \left(\frac{d\theta}{d\gamma}\right)^2\right) J_n\left(n \Delta\gamma \frac{d\theta}{d\gamma}\right)$$

$$= \exp\left(\frac{-1}{2} \sigma_\gamma^2 \left(\frac{d\psi}{d\gamma}\right)^2\right) J_n\left(\Delta\gamma \frac{d\psi}{d\gamma}\right),$$

where θ is the ponderomotive phase of the electron beam in the modulator, $\psi = n\theta$ is the phase in the radiator, $\Delta\gamma$ is the maximum energy modulation generated in the modulator, σ_γ is the energy spread of the electron beam, $\frac{d\theta}{d\gamma}$ is the strength of the dispersive section and J_n is the n^{th} order Bessel function.

* Work funded by the Bundesministerium für Bildung und Forschung and the Land Berlin

† meseck@bessy.de

Large bunching factors can be achieved when the energy modulation impressed by the seed dominates the energy spread of the electron beam. Hence, for a reasonable performance of an HGHG stage the energy modulation induced by the seed should fulfill the following inequality [4]:

$$\Delta\gamma \geq n\sigma_\gamma. \quad (1)$$

When the radiation size at the entrance of the modulator and the transverse size of the electron beam are matched, the energy modulation of the electron beam scales with the seed power, p_{seed}, seed wavelength, λ_s, the modulator length, L_{mod}, the electron beam energy, γ, and the undulator parameter, K, as [4]:

$$\Delta\gamma \sim \frac{K}{\gamma} L_{mod} \sqrt{\frac{p_{seed}}{\lambda_s}}. \quad (2)$$

The modulator length should not exceed twice its power gain length in order to avoid an increase in energy spread due to the spontaneous radiation. For given electron beam energy and seed wavelength, and a fixed modulator length, the energy modulation, $\Delta\gamma$, can be controlled by the undulator parameter, or the seeding power, p_{seed}, both of which have their technical limits. The dispersive section has to be adjusted according to the energy modulation, reached in the modulator, taking the effective dispersion in the modulator and radiator into account. The total dispersive strength is given by [4, 5]:

$$\frac{d\psi}{d\gamma} \approx -\frac{n\,2\pi L_{mod}}{\lambda_{um}\gamma} + \left(\frac{d\psi}{d\gamma}\right)_{dis.sec.} - \frac{4\,\pi L_{rad}}{\lambda_{ur}\gamma}, \quad (3)$$

where λ_{um} and λ_{ur} are the modulator and radiator period length, and L_{rad} is the length of the radiator.

Due to the interaction of the electron beam with the seed, the effective energy spread of the electron beam entering the radiator is given by

$$\sigma_{\gamma eff} = \sqrt{\sigma_\gamma^2 + \frac{(\Delta\gamma)^2}{2}}. \quad (4)$$

An increased energy spread causes an enhanced gain length and therefore extends the necessary length of the radiator. The "fresh bunch" technique is employed to limit the growth of energy spread from stage to stage in a cascaded HGHG FEL. In this approach the seeding pulse is significantly shorter than the electron bunch. As a result the harmonic generation process, and with it the enlargement of the energy spread applies only to a fraction of the bunch. After passing the first HGHG-stage the resulting radiation is shifted to a "fresh" part of the bunch which was not affected by the seed. A theoretical treatment of the HGHG-scheme can be found in [4, 5].

SEEDING RADIATION AND ELECTRON BEAM PROPERTIES

Contrary to a continuous seed pulse as used for the DUV-FEL [6, 7], in the case of a Gaussian-shaped pulse the electrons do not experience the seed peak power during the whole transition through the modulator. Since the integrated power experienced by electrons should be in the same order of magnitude to induce the same amount of bunching, the Gaussian-shaped seed pulse needs a higher peak power. For example, the $30\,MW$ continuous power with a wavelength of $800\,nm$ used for the DUV-FEL where the modulator has 10 periods, corresponds, according to equation 2, to a seed power of $90\,MW$ for a seed wavelength of $266\,nm$, and the same number of modulator periods. A Gaussian-shaped seed with $266\,nm$ wavelength and $15\,fs$ rms pulse duration would require a peak power of $1.3\,GW$ in a 10 periods modulator to induce the same bunching. Since the modulator can be chosen longer for the $266\,nm$ seed radiation, using a proper modulator of 18 periods a peak power of $400\,MW$ is sufficient. Note, to suppress the noise degradation effects [8] a higher peak power should be preferred.

The wavelength of the seed radiation within the range provided by the laser is deduced from the desired final wavelength and the harmonic cascade. Out of the several combinations of harmonics that can be used to provide the desired wavelength range in each particular HGHG-line, the one requiring the minimal number of stages is chosen. The accessible harmonic content in the bunching dropps off with rising harmonic numbers and photon energies, limiting the usable harmonics to the first five. The fifth harmonic is used in the early stages, where, due to the long wavelength, enough power and thus bunching can be obtained with acceptably short radiator lengths. Later stages use the third harmonics. The harmonic combination can change when the gaps are moved and the resonant wavelengths vary.

The planned tunable seed laser covers the spectral range of $230\,nm$ to $460\,nm$ with a Gaussian profile, a peak power of $500\,MW$ and a pulse length of about $15\,fs$ (rms), for more details see [1].

The energy of the electron beam has to fulfill the resonance condition, equation 5, for the whole HGHG-line with the minimum possible gain length. The nominal values of the electron beam parameters, extracted from start-to-end simulations, are listed in Table 1. The electron beam at the entrance of the HGHG-lines has a normalized transverse emittance of $1.5\,mm\,mrad$, a relative energy spread less then 0.02%, and an average current of about $2\,kA$ at the "flat top". The duration of the flat top amounts to $730\,fs$. For the presented calculation an electron bunch with transverse Gaussian distributions is assumed.

OPTIMIZATION OF UNDULATOR PARAMETERS

The resulting resonant wavelength of the FEL, λ, depends on the undulator period length, λ_U, the K-value and the electron beam energy γ in units of the electron's rest

Parameter	High-energy	Medium-energy	Low-energy
ϵ_n [mm mrad]	1.5	1.5	1.5
I_{peak} [kA]	1.75	1.75	1.75
E [GeV]	1.63-2.3	2.3	1.02
Δ E/E [%]	0.01-0.014	0.01	0.02
Δt [fs]	730	730	730

Table 1: The nominal electron beam parameters at the entrance of the first modulator used in the simulation studies.

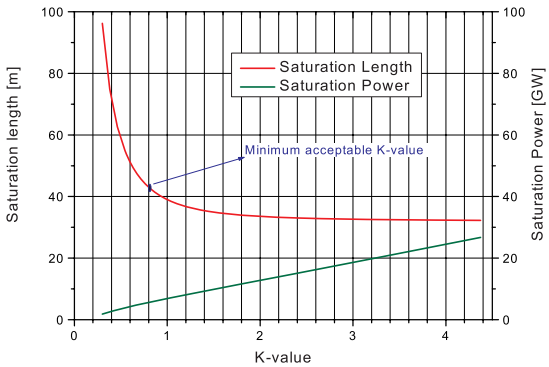

Figure 1: Saturation length and power as functions of the K-value for the final amplifier of the medium-energy HGHG-FEL. The FEL performace deteriorates with decreasing K-value.

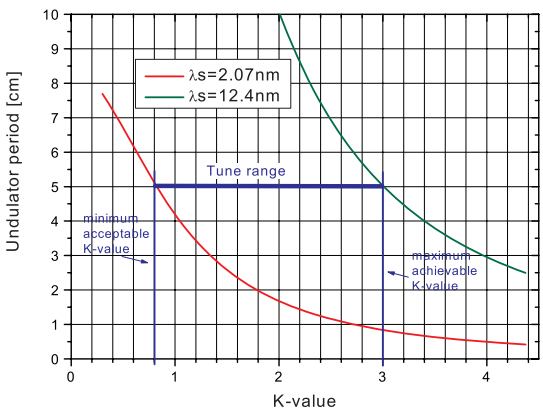

Figure 2: The undulator period as function of K-value for the final amplifier of the medium-energy HGHG-FEL. The tune range is limited by the minimum acceptable and maximum achievable K-value. With an undulator period of $5\,cm$ the desired wavelength range can be covered by gap variation.

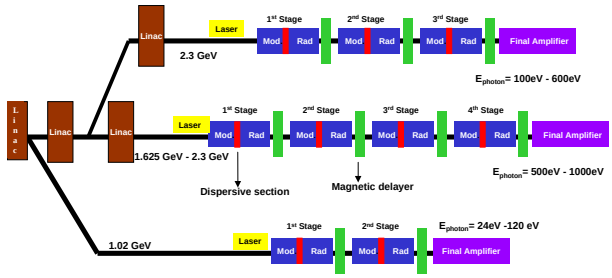

Figure 3: The BESSY HGHG multi user FEL-facility will consist of three HGHG-lines to cover the target wavelength range.

mass:

$$\lambda = \frac{1}{2\,\gamma^2}\,\lambda_U\,(1+K^2). \qquad (5)$$

The maximum achievable K-value is limited by the permanent magnet undulator technology. The minimal gap is set to $10.4\,mm$ according to impedance considerations.

The minimum acceptable K-value is set to 0.8 as the interaction between the radiation field and the electron beam suffers from too small K-values. Figure 1 shows the saturation length and power as functions of the K-value for the final amplifier of the medium-energy HGHG-FEL. The deterioration of the FEL performance with decreasing K-parameter is obvious.

The undulator period length is chosen such, that the desired wavelength range can be completely covered within the given range of K-parameter. Figure 2 shows the tune range for the medium-energy HGHG-FEL as an example. With an undulator period of $5\,cm$ the desired wavelength range can be covered. Once the period length, λ_U, is fixed, the resonant wavelength can be altered by adjusting the gap of the undulator.

LAYOUT OF THE HGHG UNDULATOR SECTION

The BESSY HGHG multi user FEL-facility will consist of three undulator-lines to cover the target photon energy range from $24\,eV$ to $1\,keV$ ($51\,nm \geq \lambda \geq 1.2\,nm$). The "low-energy" HGHG-FEL operates in two stages at a beam energy of $1.02\,GeV$ delivering photons in a spectral range of $24\,eV$ to $120\,eV$. An energy of $2.30\,GeV$ is chosen for the "medium-energy" HGHG-FEL. A cascade of three stages covers the energy range of $100\,eV$ to $600\,eV$. The "high-energy" HGHG-FEL operates at variable electron beam energies of $1.625\,GeV$ to $2.30\,GeV$. It delivers in four stages photon energy ranges from to $500\,eV$ to $1000\,eV$. Figure 3 shows a schematic view of the BESSY HGHG multi user FEL-facility. A description of the electron source, linac and compressor scheme providing electron beams with the required properties can be found in [1].

Each of the three HGHG-lines consist of several stages and a final amplifier. In order to optimize an HGHG-stage

Table 2: High Energy HGHG-FEL

Stage	*MODULATOR*			*RADIATOR*		
	λ_U $[mm]$	P #	L [m]	λ_U $[mm]$	P #	L [m]
1	122	18	2.196	92	40	3.680
2	92	22	2.024	70	86	6.020
3	70	30	2.100	50	180	9.000
4	50	69	3.450	28.5	225	6.413
Final				28.5	630	17.955

Table 3: Medium Energy HGHG-FEL

Stage	*MODULATOR*			*RADIATOR*		
	λ_U $[mm]$	P #	L [m]	λ_U $[mm]$	P #	L [m]
1	122	18	2.196	92	40	3.680
2	92	22	2.024	70	104	7.280
3	70	30	2.100	50	231	11.550
Final				50.	393	19.650

Table 4: Low Energy HGHG-FEL

Stage	*MODULATOR*			*RADIATOR*		
	λ_U $[mm]$	P #	L [m]	λ_U $[mm]$	P #	L [m]
1	80	20	1.600	62	56	3.472
2	62	26	1.612	50	69	3.450
Final				50	162	8.100

the lengths of the modulator und radiator as well as the strength of the dispersion section has to be adjusted. The modulator has to be long enough to imprint the necessary energy modulation according to the equation 1. The strength of the dispersion has to be adjusted according to the energy modulation with respect to the total dispersion given in equation 3. The radiator length has to be chosen suitable to deliver the required power for the next stage. Note, that the effective energy spread generated in the modulator determines the efficient of the radiator according to equation 4. The main parameter of the modulators and radiators for each HGHG-line are listed in tables 2, 3 and 4. Listed are undulator period length, λ_u, number of periods, P, and undulator length, L.

Magnetic delayers shift the electron bunch with respect to the radiation field between the HGHG stages and ensure that the radiation field interacts always with a undistrubed part of the bunch in the modulator. Quadrupoles and phase shifters are planned between the stages as well as between the undulator segments of the radiators and the final amplifier to focus and match the electron beam.

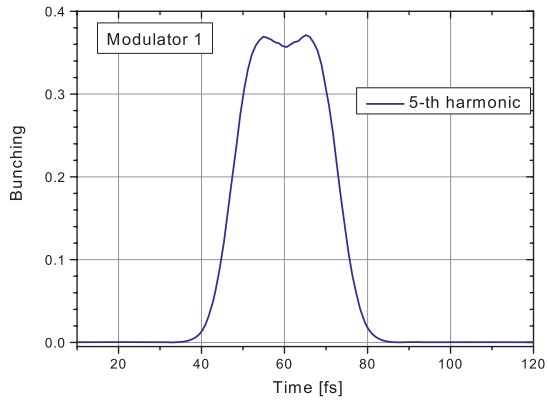

Figure 4: Bunching on the fifth harmonic after the first dispersion section for the high energy HGHG

POWER AND SPECTRUM OPTIMIZATION

For the optimization of the HGHG-FEL performance, the adjustment of the bunching, by setting the modulator length and the dispersion strength, is of major importance. The laser seed interacts with electrons at the rear of the bunch. Due to the slippage effect only a part of the interacting electrons experience the full power of the Gaussian shaped seed. Optimizing the modulator length and dispersive section to a somewhat reduced power level the output of the following radiator can be maximised. In this case the electrons at the center, which experience the full power sufficiently long are somewhat overbunched.

Figure 4 shows the bunching after the first dispersion section for the high energy HGHG. The overbunching causes a power dip in the radiation pulse provided by the first radiator, as shown in figure 5a. Figure 5b shows the corresponding radiation spectrum. The overbunched electrons fulfill synchrotron oscillations in the ponderomotive bucket. The resulting modulation of the emitted radiation frequency causes the side spikes (sidebands) [9].

The more electrons are overbunched the stronger is the growth of the sidebands. This effect is repeated in the following stages, where the slippage shifts the sidebands to one side. In this way the number of sidebands in the spectrum adds up from stage to stage. The higher the harmonic numbers in the cascade the stronger are the sidebands. For example in the case of the medium-energy HGHG-FEL the sidebands for $\lambda_s = 2.07\,nm$ with harmonic numbers $5\times5\times5$, figure 7, are much stronger than for $\lambda_s = 12.4\,nm$ with harmonic numbers $3 \times 3 \times 3$, see figure 6.

The side spikes can be avoided by optimizing the stages for the seed peak power. In this case the output of the following radiator is reduced. The bunching is of more Gaussian shape. The resulting radiation power and pulse length are reduced compared to the overbunched case. An example of such a spectrum purity optimized case is shown in

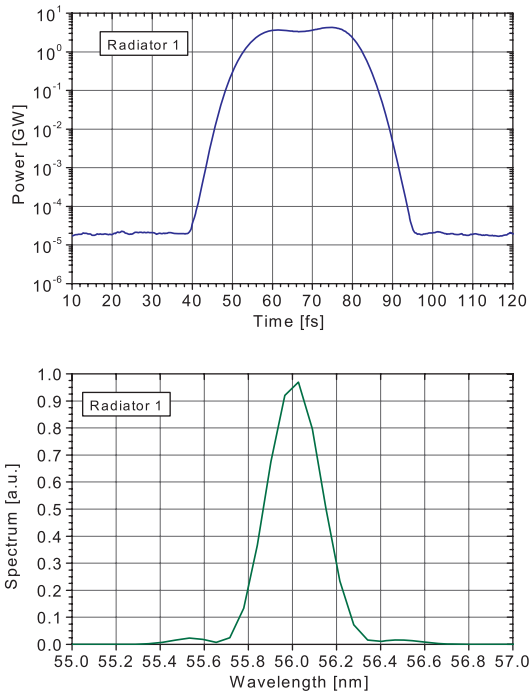

Figure 5: Simulation results for the first radiator of the high-energy HGHG-FEL a)the time resolved power distribution (top) and b) the spectral power distribution (bottom).

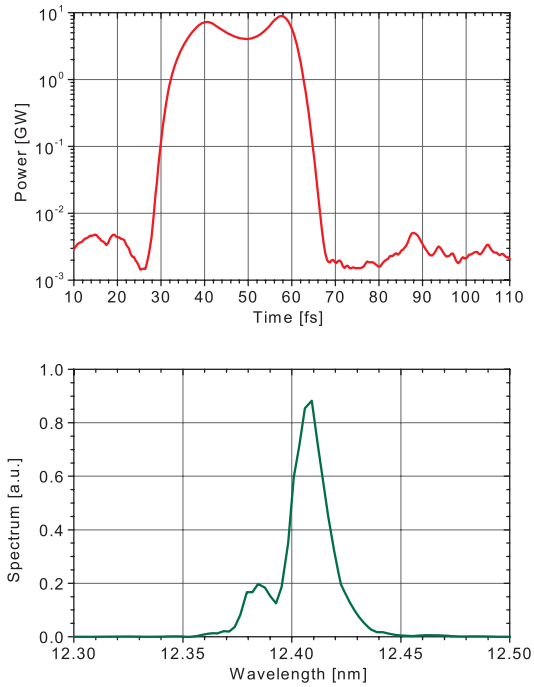

Figure 6: Simulation results for the medium-energy HGHG-FEL, $\lambda_s = 12.4\,nm$ the time resolved power distribution (top) and the spectral power distribution (bottom) are calculated.

figure 8, where the power and spectral distribution of a purity optimized and a power optimized case are displayed in the same graph for comparison.

The details of the cascades for the boundary wavelengths of each HGHG-line are summarised in [1].

PERFORMANCE CALCULATIONS

For the performance calculations the seeding radiation properties and electron beam parameters are chosen according to the considerations of the previous sections.

In order to obtain reliable results, the slippage effects in the undulators and the radiation diffraction in the fresh bunch sections have to be taken into account. The first effect lengthens the pulse, whereas the second one reduces the power density on axis which is relevant for the energy modulation in the following modulator. The time-dependent mode of GENESIS [3] used for the simulation allows an adequate treatment of this effects.

In spite of the short lengths of the modulators and radiators, see Tables 2-4, the degradation of the unseeded part of the bunch due to the emission of incoherent radiation can not be neglected. The resulting increase of the energy spread and decrease in the central energy from stage to stage are shown in figure 9 for the high-energy case.

The relative increase of the energy spread at the entrance of the second modulator is only 0.2%, but it increases to

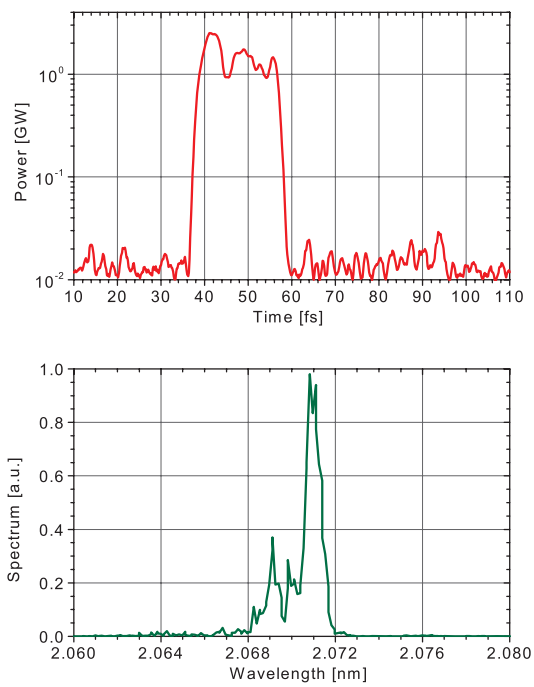

Figure 7: Simulation results for the medium-energy HGHG-FEL, $\lambda_s = 2.07\,nm$ the time resolved power distribution (top) and the spectral power distribution (bottom) are calculated.

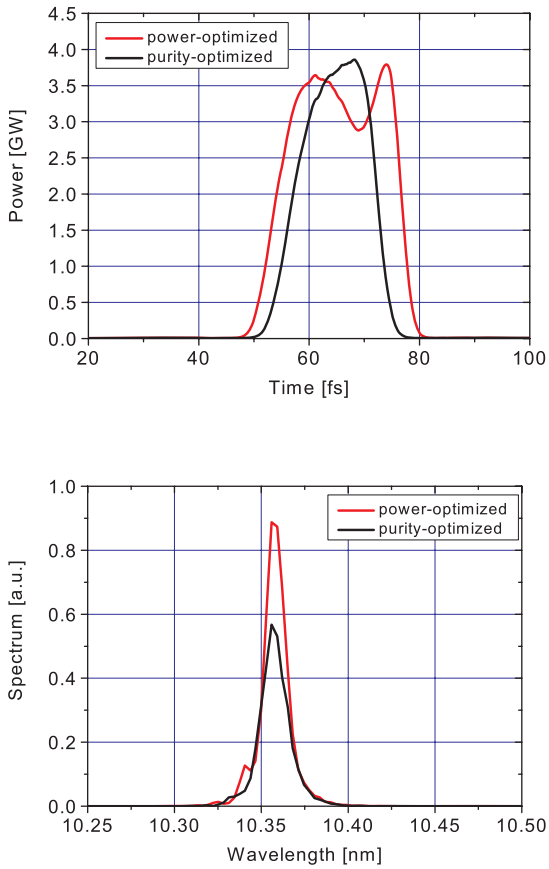

Figure 8: Simulation results for the low-energy HGHG-FEL, the power and spectral distributions of a purity-optimized case and a power-optimized case.

Table 5: The performance of the three HGHG-line for the boundary wavelengths

	LE-FEL		*ME-FEL*		*HE-FEL*	
λ $[nm]$	10.33	51.00	12.40	2.07	2.48	1.24
$Power$ $[GW]$	3.5	14.0	9.0	1.5	1.3	1.5

4% at the fourth modulator. The loss in the central energy at the entrance of the fourth modulator is about 0.45% which is larger than the bandwidth of about 0.2% of the fourth radiator and the final amplifier. This means that the following radiator and amplifier have to be readjusted to meet the resonance condition for the lower central energy.

This loss of the electron beam quality causes a reduction in the maximum bunching and a deterioration of the spectral properties of the radiation. Tracking the electrons through all the previous undulators, this effect has been taken into account. The performance of the three HGHG-lines for the boundary wavelengths are summarised in the

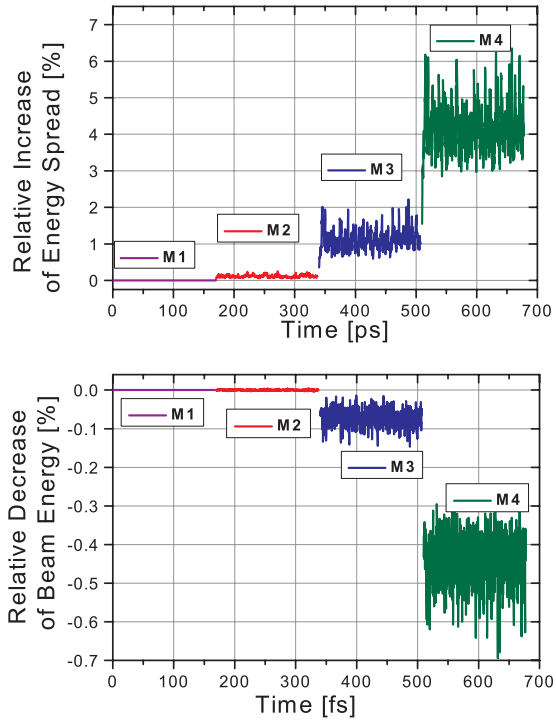

Figure 9: Degradation of the unseeded part of the bunch for the high-energy HGHG-FEL, the relative changes in energy spread (top) and the central energy (bottom) at the entrace of modulators, M1 to M4, are shown.

Table 5.

S2E BUNCHS AND SELF-STABILIZING

Start-to-end simulations for the BESSY FEL show variation of the electron beam parameter along the bunch [10]. The possibility to adjust the undulator gaps and the strengths of the dispersive sections independently, mitigates the effects of the parameter variations [11]. Each stage can be optimized according to the particular parameters of the interacting part.

Furthermore, the concept of the final amplifier allows to use the asymmetry of the detuning curve to reduce the output degradation due to the combination of the energy chirp and the arrival-time jitter of the bunch [12]. The energy chirp, induced for the bunch compression, combined with the arrival-time jitter, due to gun and LINAC errors, causes a mismatch between the central energy of the interacting part of the bunch and the resonance energy. This leads to a fluctuation of the FEL output power. Adjusting the final amplifier to a somewhat reduced K-value, stabilizes the output power, as the average energy of the interacting electrons is somewhat higher then the resonance energy.

CONCLUSION

BESSY has been designing a seeded FEL based on a cascaded high-gain harmonic-generation concept. Simulations with start-to-end bunchs including all relavant effects show that the BESSY FEL meets the user requirements with respect to pulse duration, tunability, spectral purity and power. Furthermore, simulation studies including errors in the gun and LINAC attest to the advantages of the HGHG concept planned for the BESSY FEL.

REFERENCES

[1] The BESSY Soft X-ray Free Electron Laser, Technical Design Report March 2004, eds.: D.Krämer, E. Jaeschke, W. Eberhardt, ISBN 3-9809534-08, BESSY, Berlin (2004).

[2] L. Yu, "High-gain harmonic generation of soft X-ray with the "fresh bunch" technique", NIM A 393 (1997) 96.

[3] S. Reiche, GENESIS 1.3, NIM A 429(1999) 243.

[4] L. Yu, "Theory of high gain harmonic generation: an analytical estimate", NIM A 483 (2002) 493.

[5] J. Wu, "Coherent X-ray production by cascading stages of a high-gain harmonic generation free electron laser", Thesis, May 2002.

[6] L.H. Yu, L. DiMauro, A.Doyuran,W. Graves, R. Heese, E.D. Johnson, S. Krinsky, H. Loos, J.B. Murphy, G. Rakowsky, J. Rose, T. Shaftan, B. Sheehy, Y. Shen, J. Skaritka, X.J. Wang, Z. Wang, "First Ultraviolet High-Gain Harmonic-Generation Free-Electron Laser", Phys. Rev. Lett. 91, 074801 (2003).

[7] A.Doyuran, L. DiMauro, W. Graves, R. Heese, E.D. Johnson, S. Krinsky, H. Loos, J.B. Murphy, G.Rakowsky, J. Rose, T. Shaftan, B. Sheehy, Y. Shen, J. Skaritka, X.J. Wang, Z. Wang, L.H. Yu, "Saturation of the NSLS DUV-FEL at BNL", PAC 2003, Proceedings.

[8] E.L. Saldin et al.,"Study of a noise degradiation of amplification process in a mulistage HGHG FEL", Opt. Commun. 202. (2002) 169.

[9] E.L. Saldin, E.A. Schneidmiller, M.V. Yurkov, The physics of free electron lasers, Springer-Verlag Berlin Heidelberg.

[10] M. Abo-Bakr et al., "Start to end simulations the for BESSY FEL", Proceeding of the FEL 2003 Conference, Japan, published in NIM-A, **258** (2004), 476.

[11] B. Kuske, M. Abo-Bakr, A. Meseck, "Impact of Realistic Bunch Profiles and Timing Jitter on the Output of the BESSY Low Energy FEL Line", Proceedings of the FEL 2005, Stanford, USA.

[12] B. Kuske, M. Abo-Bakr, A. Meseck, "Start-to-End Simulations for the BESSY Low and Medium Energy FEL Line Including Errors", proceedings of the FEL 2005, Stanford, USA.

THE CHALLENGES OF SEEDED FELS

G. De Ninno, ELETTRA, Basovizza, Trieste

Abstract

Basic users' expectations for the light produced by next generation FELs are:

- much higher peak brilliance than conventional synchrotron radiation and complete tunability in the VUV/X-ray spectral range;
- full transverse and longitudinal coherence of the radiation pulse;
- possibility of controlling pulse duration and spectral bandwidth;
- high shot-to-shot reproducibility, i.e. low power fluctuations, good pointing stability and reduced temporal jitter.

Seeded schemes appear nowadays as a way to satisfy all the above mentioned requirements. However, this achievement relies on the solution of several open technological and physical issues. In this paper we give a review of some of these challenges and discuss the expected performance of future seed-based FELs.

PAPER NOT AVAILABLE

THE USE OF HHG AT 4GLS

B.W.J. M^{c}Neil, SUPA, Department of Physics, University of Strathclyde, Glasgow, UK
D. Dunning and N.R. Thompson, ASTeC, CCLRC Daresbury Laboratory, UK
B. Sheehy, Sheehy Scientific Consulting, New York, USA.

Abstract

4GLS is a facility proposed for the Daresbury Laboratory in the UK which will offer users a suite of high brightness synchronised sources from THz frequencies into the XUV [1]. In the current design, photon energies from 8-100eV will be generated in a variable polarisation FEL amplifier directly seeded by a High Harmonic Gain system. The reasoning behind this choice will be discussed and characterisation of the sources based on the present design presented.

INTRODUCTION

The Conceptual Design Report for the 4GLS project to be based at UK's Daresbury Laboratory has been published [1]. A suite of synchronised coherent variably polarised radiation sources covering the spectrum from THz frequencies to photons energies of $\sim$ 100 eV will provide the scientific community with a tool that will enable new windows of scientific exploration to be opened and thereafter exploited. Initially, the major themes of the 4GLS science programme will lie in time-resolved measurements and nanoscience. Details of the science case driving the need for 4GLS were first published in [2] and more recently updated in [1].

A major component of 4GLS will be the XUV-FEL. The current design for this component is for a seeded FEL amplifier that operates in the 8-100 eV photon energy range to provide peak powers between approximately 1-10 GW allowing very high field intensities of up to 10^{17} W/cm^2 to be achieved. In order to tune over the spectral range both the electron beam energy and the undulator magnetic field are variable. Because the FEL acts as an amplifier the seed sources also need to be continuously tunable.

There are several potential benefits in operating an FEL as an amplifier of an injected seed as opposed to allowing the FEL to self-seed from inherent noise to generate Self Amplified Spontaneous Emission. An important benefit is the potential improvement in the temporal coherence of the FEL output over that of SASE. This increases the spectral brightness. Shot-to-shot reproducability and stability are also improved. The amplified pulse width, being determined by that of the seed, may be significantly shorter than that of the electron pulse, and indeed there is the potential to amplify more exotic pulses for post-amplification manipulation. Finally, the length of FEL interaction required to achieve saturation may be shortened, thereby reducing space requirements and ultimately costs. All of these benefits require that the seed power be significantly greater than the spontaneous power due to the inherent noise.

XUV-FEL OVERVIEW

The design of the 4GLS XUV-FEL has undergone several iterations [3]..[6]. The XUV-FEL branch of the 4GLS conceptual design is shown in schematic form in Fig. 1. Typical operating parameters and specification for the conceptual design are given in Table 1.

Table 1: XUV-FEL conceptual design parameters

General	
FEL design	High Gain Amplifier
Seeding mechanism	HHG source
Photon output	
Tuning Range	$\sim$ 8 - 100 eV
Peak Power	$\sim$ 8 - 2 GW
Repetition rate	$\sim$ 1 kHz
Polarisation	Variable elliptical
Min Pulse length FWHM	$<$ 50 fs
Typical $\Delta f \Delta t$	$\sim$ 0.6
Max pulse energy	400 μJ
Electron beam parameters	
Energy	750 - 950 MeV
Bunch Charge	1 nC
RMS bunch length	266 fs
Normalised emittance	2 π mm mrad
RMS energy spread	0.1%
Undulator parameters	
Undulator Type	PPM & APPLE-II
No of Modules	8 & 5
Module lengths	$\sim$ 2 m
Period	45 mm & 51 mm
Focusing	FODO
Minimum magnetic gap	$\sim$ 10 mm

The work of [6] describes some detail of the undulator and focusing lattice choices based upon studies using the design formulae of Xie [7] and steady state 3-D simulations using Genesis [8]. Undulator module lengths of $\approx$2 m were chosen with a simple FODO quadrupole focusing lattice inserted between modules along with BPMs and phase matching units. This solution requires a shorter total undulator length to achieve saturation than the longer module options considered in [5], which require a more complex quadrupole doublet or triplet focusing system. However,

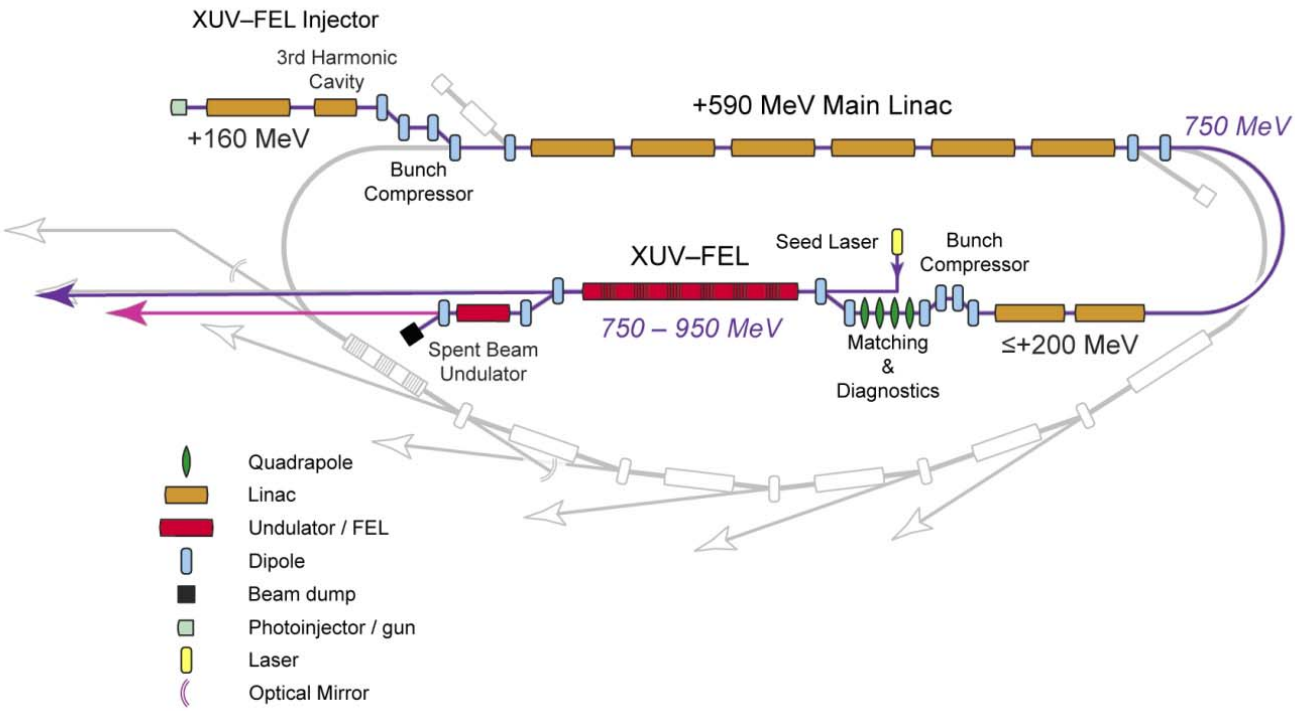

Figure 1: Schematic layout of the XUV-FEL conceptual design.

when gaps between modules are included, the total overall length of modules plus gaps is slightly longer for the shorter module option. The ability to monitor and optimise the electron beam transverse position at regular intervals to ensure optimal radiation-electron beam coupling throughout the FEL and the relative simplicity of the design ensured the shorter 2 m module length with FODO focusing was chosen.

A schematic for the undulator/focusing lattice is shown in Fig. 2. Also shown are the injected radiation seed fields focused to the beginning of the first resonant undulator module, for each of the cases. The undulator length is therefore controlled so that saturation always occurs in the final variable undulator module VU5. In this way, variable polarised photons may be generated across the full operational range of the FEL and it acts as a fixed source simplifying the optical transport system of the output to the final user experimental areas.

It can be seen from Fig. 2 that planar undulator module PU1 is only required to ensure saturation at $\sim$ 100 eV and that its magnetic gap will be at the operational maximum of $\sim$ 28 mm. This module will not be required to operate at gaps very much smaller than this, and therefore the vacuum vessel aperture containing both electron beam and radiation seed can be relatively large at this point. Similar considerations show that module PU2 will operate with minimum magnetic gap slightly smaller again, and so on for the rest of the modules PU3..PU8. Use of a step-tapered vacuum vessel has therefore been proposed that gradually decreases in aperture from module to module. The two advantages of this approach are that firstly resistive wall and surface roughness wakefields are much reduced compared to a constant minimum aperture, and secondly, as discussed later, the tapered internal aperture allows optimal focusing of the seed pulse across the whole wavelength range.

HIGH HARMONIC GENERATION SOURCES

Peak pulse powers due to intrinsic noise at the beginning of the FEL interaction for the XUV-FEL parameters of Table 1 are typically 30..50 W across the photon energy range 10..100 eV. Any seed source for the XUV-FEL must therefore generate significantly greater power than this if it is to dominate the evolution of the noise to saturation. In addition, these seed sources must be continuously tunable over 10-100 eV. Fortunately, High Harmonic Generation (HHG) sources now exist that meet these seed requirements, or are readily foreseeable within the very near future [1]. Indeed, it can be expected that the rapid advances in this field will be able to easily surpass present 4GLS design requirements for seed sources over the next few years, so this is an area of research that must be closely observed and the XUV-FEL design modified accordingly. Here the method of HHG generation is summarised and the properties of the HHG seed fields described to enable simulation by the 3-D FEL

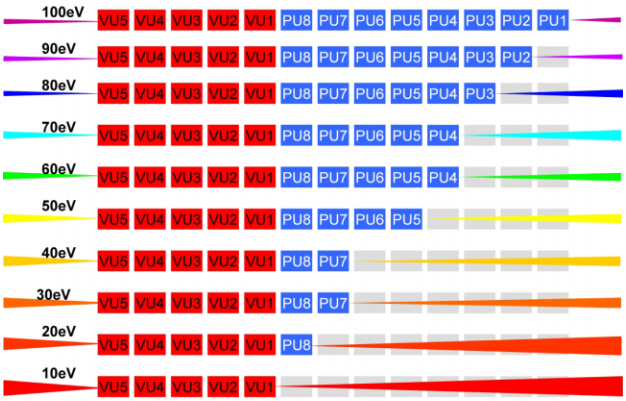

Figure 2: Schematic of the modular undulator system and focusing lattice of the XUV-FEL demonstrating the different modes of operation across the photon energy range 10-100 eV. Electron beam transport is right to left. Undulator modules marked in grey have large magnetic gaps $\bar{a}_u \approx 0$ and are effectively absent for the purposes of the FEL interaction. The minimum required undulator gap (and vacuum vessel internal aperture) decrease in gradual steps from 28 mm (25 mm) for PU1 down to 10 mm (7 mm) for PU8 and the variable polarisation modules VU1-VU5. Radiation beam waists of the seed and output are shown from 100 eV (violet)..10 eV (red).

code Genesis [8]. Further detail and references regarding the HHG sources systems may be obtained from [1, 9].

The HHG sources are based upon samples of Noble gases driven by a high-energy drive laser [10]. A typical drive laser is a linearly polarised Ti:Sapphire system operating at $\sim$ 800 nm generating several to tens of mJ per pulse of FWHM duration of a few tens of fs. For the 4GLS conceptual design, 14 mJ pulses of width 30 fs FWHM are assumed. The high fields generated by such lasers is the key to harmonic generation. The process can be understood semiclassically at the atomic level in terms of ionization and recombination steps occurring within an optical cycle, with the energy gained by the electron from the laser field between these steps going into the harmonics [11, 12], and the phase of the harmonics being related to the trajectories in the field between steps. By macroscopic phase matching, single trajectory lengths for each harmonic can be selected, and a coherent output, with well-defined phases between the harmonics obtained.

The experimentally observed shape of the HHG yield curve is of a rapid decline of the lower order harmonics followed by a plateau-region, in which the harmonic yield falls relatively slowly. An intensity dependent cut-off harmonic is then reached, beyond which the yield drops quickly to zero [13]. This model is used to construct an HHG field to simulate seed injection into the XUV-FEL in the simulations of later sections - see Fig. 4.

Tuning of the HHG sources may be achieved by suitably modifying the drive laser, for example by introducing a chirp or more generally by adaptive pulse shaping. Continuous tuning between adjacent harmonics is possible above about the 25th harmonic or a photon energy of $\sim$ 40 eV (31 nm). Below this photon energy it is proposed to introduce an intermediate noncollinear phase-matched optical parametric amplifier (NOPA) between Ti:Sapphire laser and the gas, which will give continuously tunable output between 1200 nm to 1475 nm. For the 14 mJ specification of the Ti:Sapphire laser this gives $\sim$ 2 mJ output from the NOPA. Although introducing this further efficiency loss, the system will enable more than sufficient continuously tunable power for XUV-FEL seeding for 8-40 eV operation.

Summarising, the powers available from HHG sources exceed 4GLS requirements. In the XUV-FEL modelling that follows, for 10 eV (100 eV) operation a Gaussian input seed of peak power $P_{pk} = 100$ kW (30 kW) in 30 fs FWHM pulses are assumed. The repetition rate of $\sim$ 1 kHz is well matched to the XUV-FEL seed requirements.

MODELLING SEEDING OF THE XUV-FEL

Seed injection

For effective seeding, the seed pulse should be injected coincident with the electron pulse at the start of the undulator and focused to a waist, w_0, of approximately the same transverse dimensions as the electron pulse. (The waist minimum w_0 is defined as the radius at which the radiation power is $1/e^2$ of its peak value.) Focusing should not be so tight that the seed diffracts rapidly within a gain length at the start of the FEL interaction (i.e. when the Rayleigh length $Z_R = \pi w_0^2/\lambda \ll L_g$.) The relation for the radiation waist size

$$w(z) = w_0 \sqrt{1 + \left(\frac{z - z_0}{Z_R} \right)^2},$$

where z_0 is the position of the focus along the axis of the undulator lattice, restricts the minimum aperture size of the vacuum vessel that will allow transmission of the seed to its focus. As the focal size is determined by the electron beam radius, which is nearly constant for all seed wavelengths, the vacuum vessel's minimum transverse dimensions are determined by the longest wavelength seed (10 eV photons) which must be focused furthest from the FEL entrance as shown in Fig. 2. As the minimum operational undulator gap decreases with undulator module PU1..PU8, as discussed for Fig. 2, the vacuum vessel may be tapered to accommodate the focusing of the 10 eV photon energy seed. This is demonstrated in Fig. 3, where the seed field is injected at the entrance of undulator module PU1 and focused to the optimal waist (as shown in following simulations) of $w_0 = 200$ μm at the entrance of module VU1 approximately 21 m downstream. It is seen that the vacuum vessel inner wall dimension at $z = 0$ is 25 mm to accommodate wall thickness and clearance for the 28 mm undulator magnetic gap. The walls are at least two beam

waists away from the peak power on axis at all positions up to the start of the FEL interaction region at $z \approx 21$ m. Thus the tapered vacuum vessel should provide sufficient clearance for injection of this (worst case) 10 eV seed injection.

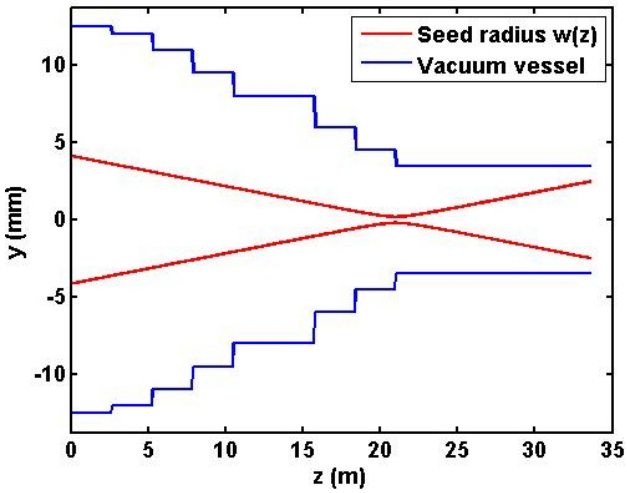

Figure 3: Plot of the dimension of the inner vacuum vessel wall (blue) which has been step-tapered to enable the undulator module tuning ranges of Fig. 2. The waist size $w(z)$ (red) for a 10 eV seed is also shown, focused at the entrance to VU1 at $z = 21$ m.

Seed with full harmonic content

The method of seed generation and specification across the XUV-FEL spectral range is summarised in the previous section and described in more detail in [1, 9]. The HHG seed has interesting spectral and temporal properties, being composed of a large number of narrow, phase-coherent odd harmonics of a fundamental drive laser. This forms a comb structure in frequency-space. Such a phase correlated comb in frequency space has a similar comb-like structure in the temporal domain, resulting in a series of atto-second pulse structures each separated by one half the drive laser period. For a drive laser such as the Ti:Sapphire laser with wavelength of $\sim$ 800 nm, the 65th harmonic corresponds to the maximum XUV-FEL photon energy of 100eV. If the complete frequency content of a HHG pulse were to be injected into the XUV-FEL it would be preferable if only one of the harmonics, say the nth harmonic, interact resonantly with the electrons. The HWHM gain bandwidth $\Delta\lambda/\lambda \approx \rho$ should then be less than the spacing between harmonics. This gives the condition $\rho < 1/n$. A typical value of $\rho \approx 2 - 3 \times 10^{-3}$ for 100 eV operation so that $\rho < 1/65 \approx 1.5 \times 10^{-2}$ is easily satisfied. Thus, it should be possible to inject all of the seed radiation, including all non-resonant harmonics, into the XUV-FEL without the need for band-pass pre-filtering of the seed, as all non-resonant harmonics will simply become negligible relative to the resonant harmonic as the FEL interaction proceeds through the undulator. For the purposes of investigating the effects a typical HHG radiation field was generated for use with the 3-D code Genesis. The full HHG spectral power is shown in Fig. 4. However, Genesis is a time-averaged code with a minimum interval between sample points of the field of one radiation period so the sampling rate is $\Delta t_s = f_r^{-1}$, the inverse of the resonant frequency. The Nyquist frequency, $f_N = 1/2\Delta t_s$ determines the bandwidth of frequencies that the field can contain without the effects of aliasing. Hence the range of frequencies that can be simulated by Genesis without aliasing effects is $f_r/2 < f_r < 3f_r/2$. Thus from Fig. 4 it is seen that if simulating 100 eV photon energy generation in the XUV-FEL, only the 50-100 eV components of the HHG spectrum should contribute to the Genesis input file using its 'RADFILE' option.

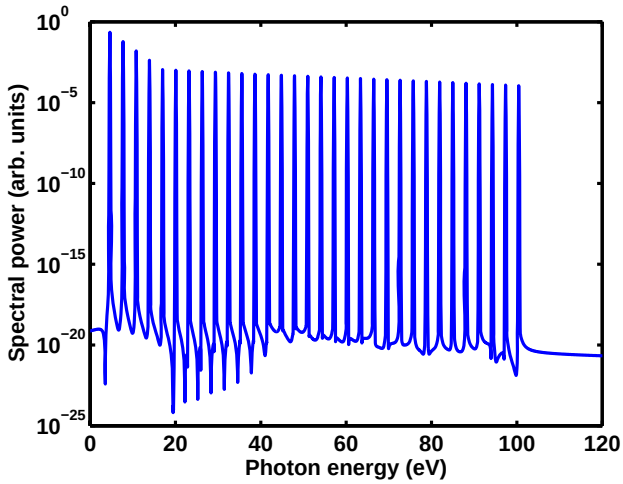

Figure 4: Simulated power spectrum from an HHG source.

A Genesis simulation was performed for 100 eV operation with the limited spectral range HHG seed pulse as described above. A uniform current of 1.5 kA was assumed. Due to the relatively short slippage experienced at these photon energies, this is very close to that experienced by a short pulse coincident with the Gaussian peak current of the XUV-FEL. All 13 undulator modules were assumed to be the planar type modules PU1..8. The seed at the beginning of the FEL interaction at $z = 0$, the entrance to PU1, is plotted in Fig. 5. Both the atto-second structure in the pulse power and the comb of odd-harmonic wavelengths (inset) are clearly visible. The peak power of the resonant 100 eV ($\sim$ 12.3 nm) component is approximately 22 kW.

On propagating through the amplifier to $z = 16.2$ m, Fig. 6 shows that the fine atto-second structure is beginning to be 'washed out' due to the selective amplification of the resonant wavelength at 12.3 nm (inset). All non-resonant harmonics of the seed appear unaffected by the resonant FEL interaction. This is further confirmed by Fig. 7 which shows the output at saturation at $z = 32.4$m, the end of the interaction region. The radiation pulse shows none of the atto-second structure of the input seed and the spectral power density shows a single high power emission at

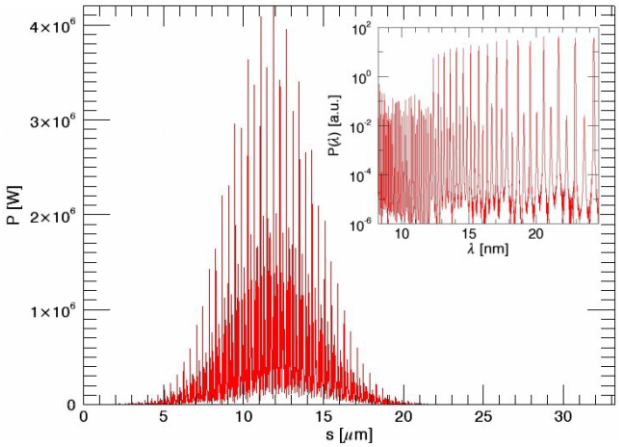

Figure 5: Radiation seed power at the beginning of the amplifier $z = 0$ m as a function of local distance, s. The spectral power content of this pulse is shown as a function of radiation wavelength in the inset.

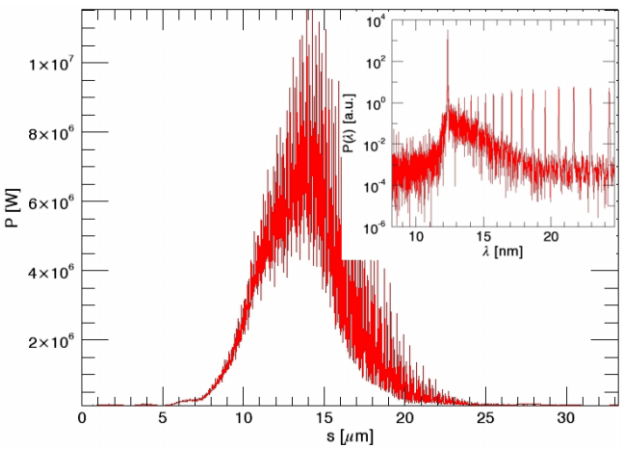

Figure 6: Radiation power as a function of local distance, s, at $z = 16.2$ m through the amplifier. The spectral power content of this pulse is shown as a function of radiation wavelength in the inset.

the resonant wavelength 12.3 nm. It is concluded that, at least for these three-dimensional simulations, the injection of the (Nyquist limited) harmonic content of the HHG seed appears to have no adverse effects in the FEL evolution, or in the saturated emission. The same conclusion may be drawn for lower photon energy XUV-FEL operation where the condition to enable neglect of non-resonant HHG content, $\rho < 1/n$, is more easily satisfied. Thus in all subsequent simulations only the resonant harmonic of the HHG seed content is used in the simulation input.

XUV-FEL 100eV simulations

A complete simulation of the design for the XUV-FEL operating at 100 eV is now demonstrated, using the parameters as given in Table 1. Full details of all parameters may be obtained in [1]. The system modelled is that of Fig. 2

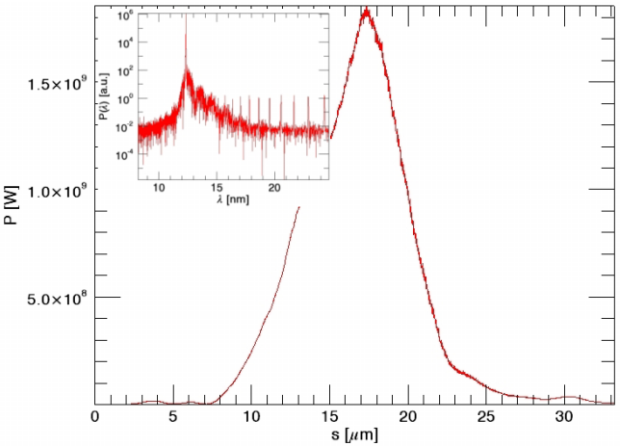

Figure 7: Radiation power as a function of local distance, s, at the end of the amplifier, $z = 32.4$ m. The spectral power content of this pulse is shown as a function of radiation wavelength in the inset.

which, for 100 eV operation, uses the full set of planar and variable undulator modules with the FODO lattice incorporated between modules. The variable APPLE-II undulator modules VU1..5 are set to helical mode so that circularly polarised radiation is generated. The radiation power is plotted in a spatial window that travels along the undulator axis at the speed of light. Fig. 8 plots the power distribution of the seed pulse of peak power $P_{pk} = 30$ kW and duration 30 fs FWHM at the entrance to the first undulator section, PU1. The seed is assumed to have only the resonant har-

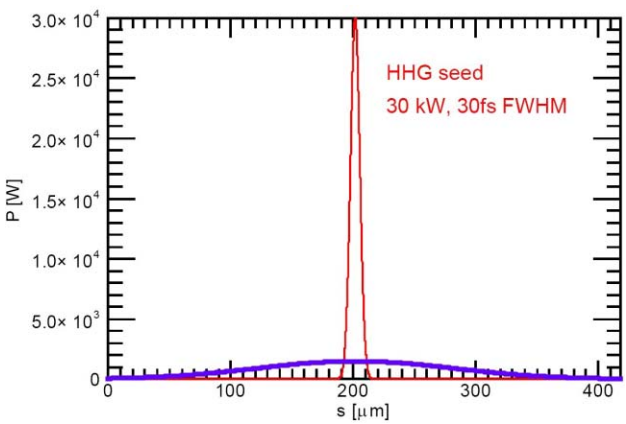

Figure 8: Input radiation seed power (red) to PU1 as a function of local distance, s. The electron beam current profile (blue) is also shown against the same numerical scale.

monic component so that none of the atto-second structure discussed above is present. Also plotted to scale is the electron beam current, here assumed Gaussian, of peak current $I_{pk} = 1.5$ kA and duration 626 fs FWHM. At the exit of the planar undulator modules, it can be seen from Fig. 9 that the peak radiation power has increased to ≈ 70 MW with little change in the pulse structure or width. This pulse

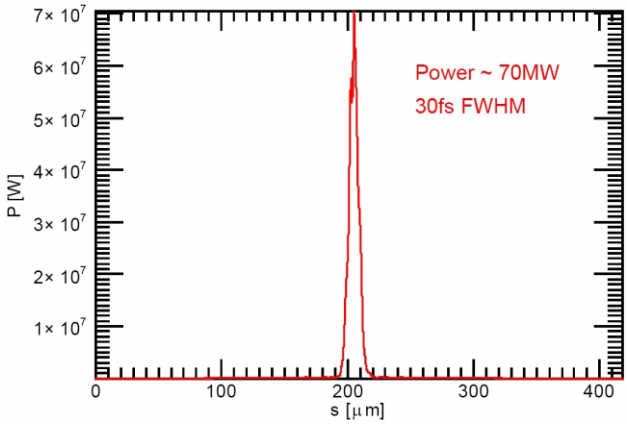

Figure 9: The radiation power at the exit of PU8 as a function of local distance, s.

and the co-propagating electrons are then injected into the set of APPLE-II undulators, VU1 to VU5. By the end of this set of undulator modules, it is seen from Fig. 10 that the FEL interaction has saturated, achieving a peak power of $P_{pk} \approx 2.5$ GW and of duration $\Delta t \approx 60$ fs FWHM. Fourier analysis gives the bandwidth of the spectrum as

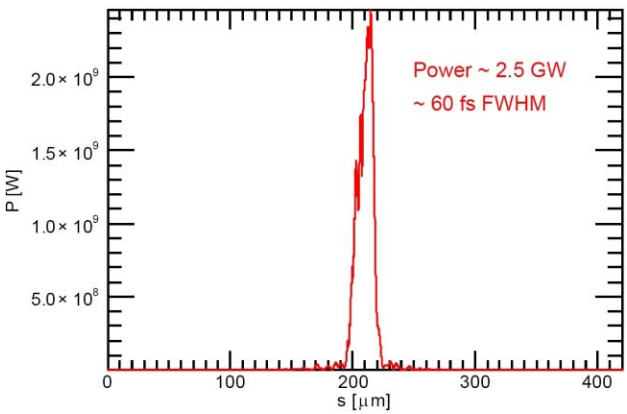

Figure 10: The radiation power at the exit of VU5 as a function of local distance, s.

$\Delta\nu/\nu \approx 5.6\times10^{-4}$ which gives a time-bandwidth product of $\Delta f\Delta t \approx 0.8$ which compares favourably with that for a transform limited Gaussian pulse of $\Delta f\Delta t \approx 0.44$. A log-plot of the same data clearly shows in Fig. 11 the relatively clean central seeded region upon a noisier pedestal. This pedestal is the amplified SASE radiation which remains well below saturation because of the smaller initial spontaneous noise radiation (typically a few tens of watts), compared with the initial peak seed power of 30 kW. The shape of the saturated pulse power envelope is not quite as Gaussian as may be expected which suggests that the FEL interaction may have progressed just past saturation. Taking the output power at the end of the previous undulator module, VU4, and plotting it in a similar log plot in Fig. 12, a cleaner Gaussian shape can be seen, with a slightly reduced peak power of $P_{pk} \approx 1.5$ GW. The improved pulse

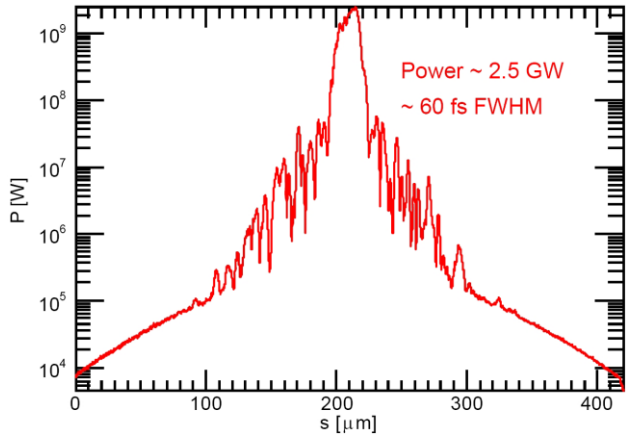

Figure 11: A log-plot of the radiation power at the exit of VU5 as a function of local distance, s.

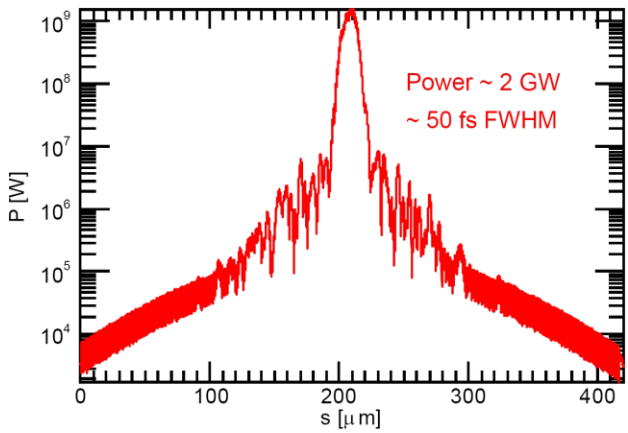

Figure 12: A Log-plot of the radiation power at the exit of VU4 as a function of local distance, s.

shape is confirmed from the pulse duration of $\Delta t \approx 43$ fs FWHM and spectral bandwidth of $\Delta\nu/\nu \approx 6\times10^{-4}$ giving an improved time-bandwidth product of $\Delta f\Delta t \approx 0.63$. An improved contrast between the peak power and that of the SASE pedestal is also evident.

XUV-FEL 10eV simulations

Similar simulations to those at 100 eV were carried out for the case of 10 eV operation of the XUV-FEL. Now only the APPLE-II undulator modules VU1 to VU5 are required to achieve saturation as shown schematically in Fig. 2. The input seed power is Gaussian with a peak power $P_{pk} = 100$ kW and duration 30 fs FWHM. The electron pulse current will have the same Gaussian distribution as that for the 100 eV case of Fig. 8.

Radiation power output at the end of undulator module VU5 is shown in Fig. 13 using a log scale. Pulse quality is very good with a peak power of ≈ 6 GW and pulse time-bandwidth product very close to that of a transform-limited Gaussian ($\Delta t\Delta f \approx 0.44$). If the radiation is instead extracted at the end of undulator VU4, the radia-

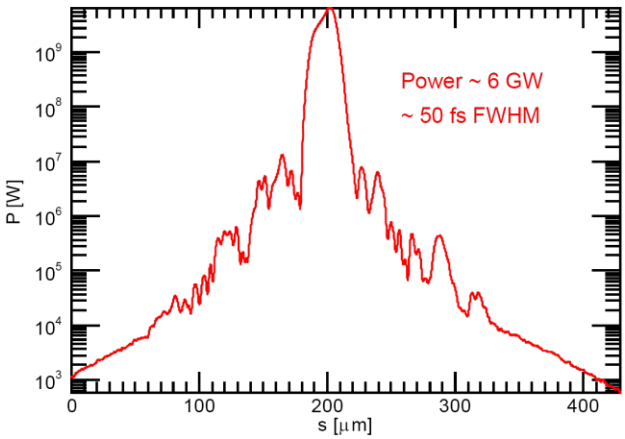

Figure 13: Log-plot of the radiation power for 10 eV operation at the end of undulator module VU5, as a function of local distance, s.

tion power output is shown in Fig. 14. A better contrast

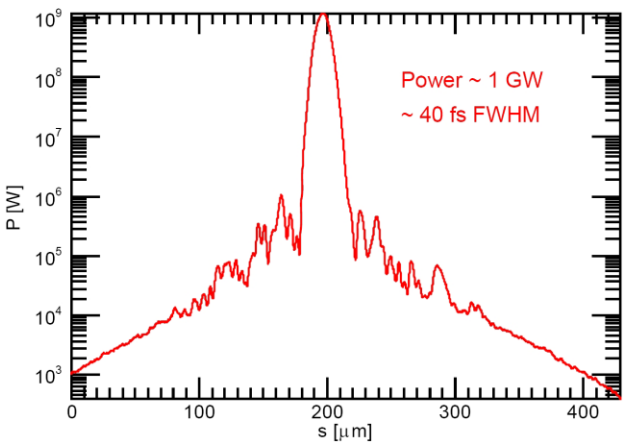

Figure 14: Log-plot of the radiation power for 10 eV operation at the end of undulator module VU4, as a function of local distance, s.

between the peak power of $P_{pk} \approx 1$ GW and the SASE pedestal power is seen from the case of Fig. 13, indicating that the FEL had already saturated before the end of VU5. The time-bandwidth product is approximately the same at $\Delta t \Delta f \approx 0.48$.

Time dependent Genesis 1.3 simulations have also been used to assess the sensitivity of the XUV-FEL output power to the seeding geometry. It is assumed that the most difficult photon energy to achieve optimum geometry will be 10 eV because of the relatively long distance of ≈ 21 m between the seed injection point (before PU1) and the first operational undulator (VU1). The peak seed power of 100 kW was focused to a waist at the beginning of VU1. Fig. 15 shows the effect of varying the size of the focal point waist. An optimum waist of ≈ 200 μm yields a peak output power of $P_{pk} \approx 7.5$ GW. The corresponding Rayleigh length for this focus is ≈ 1.0 m. The Xie formulae [7] estimate the

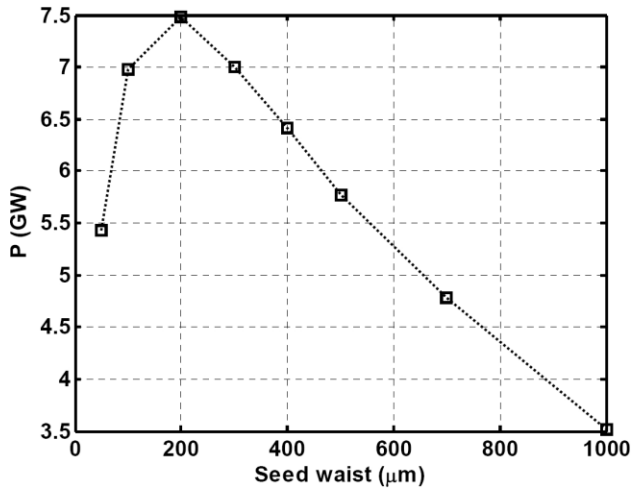

Figure 15: Radiation peak power for 10 eV operation at the end of undulator module VU5, as a function of seed beam waist at the entrance to VU1.

gain length at 10 eV for these parameters to be ≈ 0.5 m. The optimum Rayleigh length for a seed focused at the undulator entrance is therefore found to be $Z_{R\,opt} \approx 2L_g$. For this optimum focusing the seed beam waist at the injection point, $z = 0$ (beginning of PU1), is 4.1 mm. If it is assumed that a full aperture at the injection point of six times the beam radius is required to minimise diffraction effects, then a vacuum vessel aperture of ≈ 25 mm (magnetic gap minus 3mm) is sufficient. This is achieved with the step-tapered vacuum vessel design, as discussed above.

The above results show that the output power at the end of VU5 reduces as the seed waist size at the entrance to VU1 increases. (Consequently the seed radius at the injection point also decreases.) The reduced coupling between radiation and electrons with increasing radiation waist means that saturation is not achieved in the fixed undulator length. Nevertheless, it may be beneficial to use a larger seed waist size than the optimum value of 200 μm and compensate for the increased saturation length by focusing the seed into the previous module PU8 for example. (This will have no effect on the saturation power which is independent of seed.) A larger waist size will reduce output power fluctuation due to seed source pointing stability. While this will be investigated further in future design work, the current conclusion shows that the optimum seed focusing geometry may be obtained with the use of the proposed step-tapered vacuum vessel.

Variable polarisation

As has been noted above, the HHG seed sources are linearly polarised. However, this should not present problems in generating variable polarisation. When the HHG seed is injected into a planar undulator it causes the electrons to bunch in the axial ($\hat{\mathbf{z}}$) direction. The polarisation of the radiation emitted is determined by the electron trajectory. Hence, if the electron bunching is initiated in a planar

undulator and subsequently transfered into an elliptically polarised undulator, the electrons will emit elliptically polarised radiation and progress via the FEL interaction to saturation. If the linearly polarised HHG seed is injected with the electrons directly into an elliptically polarised undulator then coupling between seed and electrons will occur in the plane of the radiation electric field and will begin to bunch the electrons. The bunching electrons will then emit with the elliptical polarisation determined by the undulator. Optimal coupling will occur when the major axis of the elliptically polarised undulator is co-incident with that of the electric field polarisation of the seed.

Timing

Detailed discussion of synchronisation and timing jitter effects between the seed and electron pulse at the entrance to the XUV-FEL are summarised here and presented in more detail in [1, 14]. A relation between a timing offset Δt and the peak electron current has been used with the Xie formulae [7] to estimate the effects of timing offset upon the saturation length and saturation power of the XUV-FEL operating at 100 eV. From these estimates a 50 fs offset increases the saturation length by $\sim 1.3\%$, and decreases the saturation power by $\sim 4\%$. A 100 fs offset increases the saturation length by $\sim 5\%$, and decreases the saturation power by $\sim 13\%$. Genesis simulations have also been used to investigate the effect of timing offset and are in very good agreement. While timing jitters of ~ 100 fs should be readily achievable, it is projected that this figure may be reduced to the low tens of femto-second level. It may be possible to offset the effect of the increase in saturation length by allowing the amplifier sufficient length to oversaturate. In this way the saturated power will nearly always be attained. This area is the subject of future design and research effort.

CONCLUSIONS

The main use of HHG in 4GLS is to act as a seed source for the XUV-FEL. These sources have enabled a robust conceptual design for the XUV-FEL to be developed. Established theory and simulation codes predict this FEL will generate photons of giga-watt power levels in pulses of duration 40-60 fs FWHM. The design specification presented here is optimised for 10-100 eV operation but it has been demonstrated [1] that extension to a revised photon energy range of 8-100 eV requires only small parameter changes. The quality and tunability of the HHG seed ensures the FEL remains continuously tunable generating pulses that will have very good temporal and spatial coherence with time-bandwidth products close to the Fourier transform limit for a Gaussian pulse. The XUV-FEL interaction here is acting as a simple, bandwidth limited amplifier - so long as the radiation input seed pulses have sufficient spectral purity, the output radiation is very nearly a simple amplified version of the input.

HHG sources have also been included in the 4GLS conceptual design as user sources in their own right. This has not been discussed, but is of significant importance to the overall concept of 4GLS as a facility providing multi-colour synchronised sources to the user.

It has been demonstrated that the multi-harmonic content of the HHG seed need not be filtered before injection as the gain-bandwidth of the FEL interaction ensures that only the resonant harmonic affects the FEL output.

The most critical aspect to ensuring the success of the XUV-FEL design is in the spatio-temporal synchronisation between electron pulses and HHG seed at the beginning of the FEL interaction region. While initial study suggests this is feasible, this and other aspects will now be the subject of greater scrutiny as the 4GLS project enters the technical design phase.

REFERENCES

[1] *4GLS Conceptual Design Report*, Council for the Central Laboratory of the Research Councils, UK (2006), available from: http://www.4gls.ac.uk/documents.htm#CDR

[2] *The Science Case for 4GLS* (2001), available from: http://www.4gls.ac.uk/Documents/EPSRC-Dec2001/Science_Case.pdf

[3] M.W. Poole and B.W.J. M^{c}Neil, Nucl. Inst. Meth. Phys. Res. A **507**, 489 (2003)

[4] M.W. Poole and B.W.J. M^{c}Neil, Proceedings of the 25th International Free Electron Laser Conference, Tsukuba, Japan (2003)

[5] B.W.J. M^{c}Neil, G.R.M. Robb, N.R. Thompson, J. Jones, M.W. Poole and C.K.M. Gerth, Proceedings of the 27th International Free Electron Laser Conference, Stanford, JACoW / eConf C0508213 (2005)

[6] B.W.J. M^{c}Neil, N.R. Thompson, and B. Sheehy, *The Conceptual Design of the 4GLS XUV-FEL, ibid.*

[7] Ming Xie, Proc. Of 1995 Part. Accel. Conf., 183 (1996)

[8] S. Reiche, Nucl. Inst. Meth. Phys. Res. A, **429**, 243, (1999)

[9] B. Sheehy, J.A. Clarke, D.J. Dunning, N.R. Thompson, and B.W.J. M^{c}Neil, Proceedings of the 37th ICFA Advanced Beam Dynamics Workshop on Future Light Sources, Hamburg, Germany (2006)

[10] See e.g. Eiji J. Takahashi et al., IEEE Journal of Selected Topics in Quantum Electronics **10**, 1315 (2004)

[11] K.J. Schafer, B. Yang, L.F. DiMauro, and K.C. Kulander, Phys. Rev. Lett. **70**, 1599 (1993)

[12] P.B. Corkum, Phys. Rev. Lett. **71**, 1994 (1993)

[13] See e.g. Pascal Salieres, Anne LHuillier, Philippe Antoine and Maciej Lewenstein, Adv. At. Mol. Opt. Phys. **41**, 83 (1999)

[14] D. Dunning et al., *First Tolerance Studies for the 4GLS FEL Sources, ibid.*

FOCAL POINT LASER-FIELD AS OPTICAL SEEDER

Tsumoru Shintake, RIKEN/SPring-8, 679-5148 Japan.

Abstract

Focusing laser beam in wavelength size, passing electron beam at focal point in normal direction to the laser axis, we may apply periodic velocity modulation on the electron beam at optical wavelength. With energy chirp, the electron bunch is longitudinally compressed in the magnetic chicane. With appropriate depth of optical modulation and energy chirp, we may obtain micro-bunching at compressed wavelength after the chicane. If the slice energy spread of incoming electron beam is very low, we may compress the optical modulation down to X-ray wavelength, in principle. For example, using 2nd harmonic YAG-laser at 532 nm (green), the resulting optical modulation becomes 266 nm, then compressing bunch length by 1/60 and 1/30 in two stage bunch compressors, we may obtain 1 Å. The energy chirp will be compensated due to single bunch wake field in the linear accelerator. Sending the beam into undulator line, the density modulation will provide seeding, which will be strongly amplified and create single longitudinal mode with full coherence. If we use femto-second laser, such as TiSa in the optical modulator, we can obtain atto-second pulse of X-ray after the compression.

MOTIVATION

SASE-FEL: Self-amplified Spontaneous Emission Free Electron Laser, as it was named the spontaneous radiation (noise power) is amplified along with long undulator line, and reaches to saturation level. Since its power level is extremely higher than conventional X-ray sources, even higher than 3rd generation light sources, many new scientific applications are expected. Also the short pulse feature in femto-sec range is expected to be an important feature for analysing fast chemical and physical properties of condensed matter.

However, since SASE-FEL process starts from the spontaneous radiation at upstream undulator, the resulting saturated radiation power varies by shot-to-shot. And most importantly, there are many longitudinal modes, same as ruby laser does, temporal profile has many spikes, thus longitudinal coherence is quite limited.

If we seed a coherent signal from upstream undulator, whose power level has to be higher than spontaneous radiation, only the seeding signal will be amplified and saturated, thus it becomes (1) fully coherent, (2) temporally single-mode, and (3) stable energy in pulse-to-pulse. These features are favourable to all kind of scientific applications. Therefore, various proposals have been made on seeding schemes, including HGHG, HHG and wavelength shift [1, 2, 3]. They are promising approach to generate coherent radiation at VUV and also X-ray region. All of them use non-linear higher harmonic generation in high gain FEL, which requests high density electron beam.

In this paper, the author will propose a new approach: seeding density modulation at optical wavelength using conventional laser, and compress the bunch length together with wavelength of optical modulation down to X-ray wavelength. It does not rely on higher harmonic generation. Operational principle is simple. But there are many technical difficulties. However, the author believes that with extensive R&D efforts, in near future using this scheme we will be able to reach the X-ray wavelength with clean seeding signal after compressing bunch by factor of 1000 times. What we do is writing wave or coding signal on the electron beam, and transfer to the X-ray world.

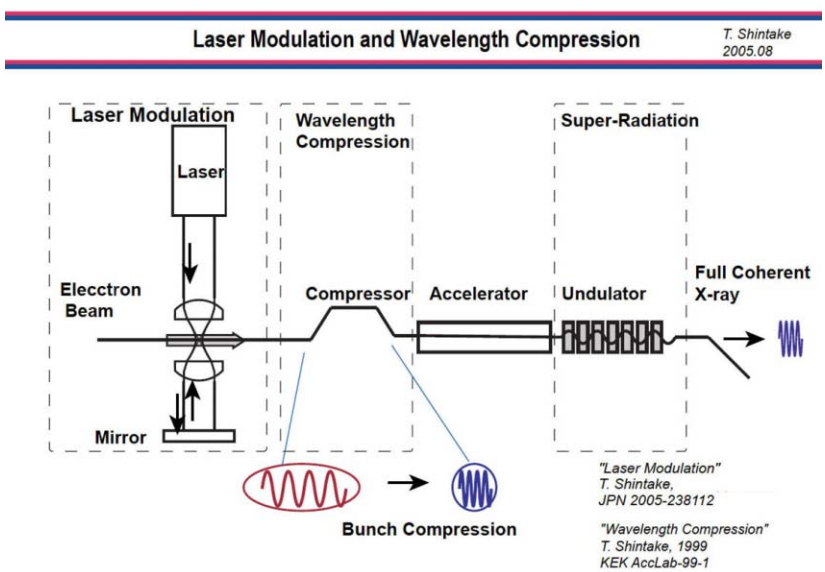

Fig. 1 Laser optical modulation and wavelength compression. Energy chirp after the compressor can be corrected by single bunch wake field and off crest acceleration in the linear accelerator.

BASIC CONFIGURATION

Figure 1 shows the basic configuration of this seeding scheme. We apply energy chirp on the incoming electron bunch, and add energy modulation at optical wavelength in the laser modulator, then compress the bunch length in the magnetic chicane. At the same time the velocity modulation is converted into density modulation at compressed short wavelength. The compression factors for the bunch length and the modulation wavelength are exactly same. After accelerating the beam up to higher energy, and sending into undulator, the bunch will radiate coherent signal. If the

#shintake@spring8.or.jp

wavelength of undulator radiation meets with the density modulation on the bunch, the undulator will radiate coherent radiation at super radiant mode.

In case of SASE-FEL of X-ray wavelength, we need 1/1000 times compression. Any kind of non-linear effect in magnetic chicane or wake-field will smear the optical modulation. However, if the residual density modulation exceeds the Schottky noise level, which is usually a few kW level only, the density modulation will provide coherent seeding signal to the SAS-FEL.

Similar approach was discussed independently by T. Shaftan and experimentally demonstrated using DUV FEL at BNL [3], where the tuning range that can be achieved is full range through a 10% tuning around each harmonic and switching between different harmonics.

APPLYING LASER MODULATION ON THE CATHODE

We may apply laser field directly on the cathode and create modulation on electron beam. If the electric field intensity of the laser field is strong enough, the accelerating field initially applied on the electron gun will be controlled, thus the current flow can be switch ON-OFF at the speed of the optical frequency. However, the thermal motion of electron erases the modulation at optical wavelength during acceleration as discussed below.

Fig. 2 shows electron trajectory in a constant accelerating field of E. The kinetic energy increases along its trajectory as

$$W_k(z) = eE_z \cdot z + W_{th} \qquad (1)$$

Where W_{th} is the initial kinetic energy on the cathode, which is given by the thermal energy,

$$\left\langle \frac{1}{2} m_e v_z^2 \right\rangle = \frac{1}{2} kT \qquad (2)$$

Solving eq. (1) under initial condition of eq. (2), we can compute thermal effect on the trajectory. Here we graphically estimate the thermal effect, refer Fig. 2. An electron starts from the cathode with zero initial energy, which follows curved line **A**, and reaches to the final position z_f at time t_f, where the velocity is very close to the speed of light. If the electron starts from the cathode with finite initial velocity, it follows trajectory **B**, at time t_f it runs more Δz, which smears out the modulation. This effect can be graphically estimated as follows. In the trajectory **A**, near the cathode, electron reaches to the point (t_1, z_1) where the kinetic energy becomes equal to the initial energy of trajectory **B**:

$$ct_1 = \frac{m_0 c^2}{eE_z}\sqrt{\frac{2W_i}{m_0 c^2}}, \quad z_1 = \frac{W_i}{E_z}, \qquad (3)$$

Trajectory **B** is exactly same as **A** if we shift the point (t_1, z_1) to origin (0, 0). Assuming the final energy is relativistic, the distance Δz is given by

$$\Delta z = ct_1 - z_1 \qquad (4)$$

As an example, we assume accelerating field of 10 MV/m, and thermionic cathode operating at 1800 K, thermal energy in z-direction is 74 meV, and we find:

$$t_1 = 61 \text{ femto-sec.}$$
$$z_1 = 7.4 \text{ nm} \qquad (5)$$
$$ct_1 = 19\ \mu\text{m}$$
$$\Delta z = 19\ \mu\text{m}$$

Δz is much longer than the optical wavelength, thus the modulation will be totally smeared out.

In case of RF-gun, the cathode temperature is room temperature, and cathode field is much higher, thus thermal diffusion becomes smaller. Assuming a very high acceleration field such as 100 MV/m, the diffusion distance becomes $\Delta z = 1.1\ \mu$m. They are summarized in Table 1. If we use CO_2 laser at 10 μm wavelength, the modulation will remain. Tuneable infrared radiation from OPO (Optical Parametric Oscillator) will also be a candidate.

Table 1: Thermal diffusion effect for electrons starting from the cathode

Physical Parameter	Thermionic Gun	Photo-cathode rf-gun
Field Gradient: E	10 (MV/m)	100 (MV/m)
Temperature: T	1800 (K)	300 (K)
Thermal energy: W_{th}	74 (meV)	12 (meV)
Equivalent point: t_1 z_1 ct_1	61 fs 7.4 nm 19 μm	3.8 fs 0.12 nm 1.1 μm
Diffusion length: Δz	19 μm	1.1 μm

In case of the photo-cathode rf-gun, the laser beam is introduced on the cathode from normal direction, and the electric field of the laser is oriented paralleled to the cathode surface, which takes minimum on the cathode

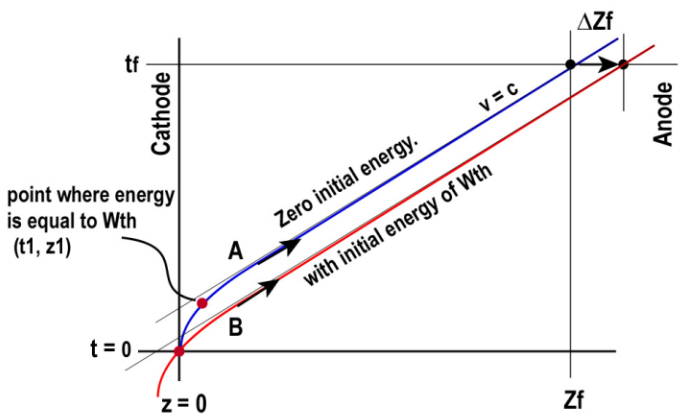

Fig. 2 The electron trajectory in the constant acceleration field. Starting from the cathode (z = 0), reaches to final position z_f at the time of t_f. With initial energy, the electron runs more: Δz, which smears out the modulation.

because the cathode is electric conductor, thus the laser field does not directly modulate velocity of emitting electron. However, in case of pulsed laser, if it is not seeded with coherent beam there are multi-modes in longitudinal direction, resulting in temporal variation. If the period of this variation is longer than ΔZ, the produced electron bunch from the rf-gun will contain density modulation. This will be a possible source of CSR instability in the magnetic chicane. Tiny density fluctuation on electron beam is amplified due to negative slope of energy (energy loss at bunch head, opposite to the wake-fields), which is amplified through dispersion in the bunch compressor, results in higher CSR radiation and positively feedbacks to the energy modulation on the electron bunch, cause CSR instability.

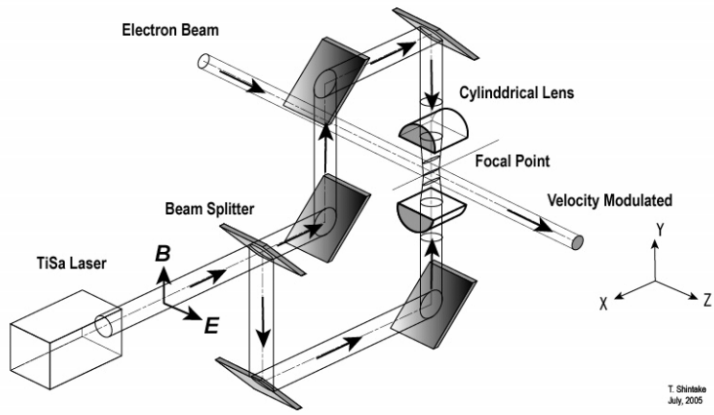

Fig. 3 Laser modulation, using focal point field in the standing wave of the laser beam. To make interaction area wider, the cylindrical lens is employed rather than spherical lens. Polarization is chosen as to make the electric field being oriented to the electron path.

THRESHOLD ENERGY

Reason why such a small thermal energy causes diffusion on accelerating electron in high gradient is that the electron remains near the cathode when the speed is not high enough. It can be shown by the following equations.

$$v = \sqrt{\frac{2eE_z}{m_0} \cdot z} \qquad (6)$$

$$dt = \frac{1}{v} dz \propto \frac{1}{\sqrt{z}} \cdot dz \qquad (7)$$

Near the cathode, z is small, thus it takes long time to travel. Once the electron departs from the cathode and increases speed, the travelling time for unit distance becomes shorter, and it becomes independent from initial thermal energy.

The diffusion distance during acceleration between point-1 and point-2 is given by

$$\Delta z_{th} = \frac{\Delta\gamma_{th}}{\gamma'}\left(\frac{1}{\beta_1} - \frac{1}{\beta_2}\right)$$

$$\gamma' = eE_z / m_0c^2 \qquad (8)$$

$$\Delta\gamma_{th} = kT / 2m_0c^2$$

For example, to accelerate beam up to 8 GeV (β_2 = 1) on 20 MV/m field gradient (γ' = 39.1/m), assuming thermionic gun (74 meV, $\Delta\gamma_{th}$ = 1.4 x 10^{-7}), to make the diffusion distance being lower than quarter wavelength of 4th harmonic of YAG: ΔZ<60 nm, we fined

$$\frac{1}{\beta_1} - 1 > 16.7 \qquad (9)$$

Thus, β_1 > 0.056, or the beam energy has to be higher than 810 eV. If we apply the laser modulation at this energy or at higher energy, the modulation will be kept up to relativistic energy.

At high energy, eq. (8) becomes

$$\Delta z_{th} = \frac{\Delta\gamma_{th}}{\gamma'} \cdot \frac{1}{2\gamma_1^2}\left[1 - \left(\frac{\gamma_1}{\gamma_2}\right)^2\right]. \qquad (10)$$

For example, if we compress the bunch into 1 Å at 1 GeV and accelerate to 10 GeV with 30 MV/m accelerating gradient, the diffusion due to thermal energy becomes ΔZ = 0.3 femto-meter, this is much smaller than 1 Å, thus the modulation will be kept.

The betatron oscillation of each electron inside the bunch causes path difference and smearing effect. Average path difference can be estimated by

$$\Delta z_\beta = \frac{2\varepsilon_n}{\pi^2\gamma} \cdot \frac{L}{\langle\beta\rangle} \qquad (11),$$

Assuming, $\varepsilon_n = 1\times10^{-6}\,\pi mm \cdot mrad$, L = 300m, β = 30 m, the path difference becomes 2 Å. Therefore, simple betatron oscillation contributes to erase micro bunching. But inside the bunch, near the core, betatron oscillation amplitude is lower, thus the modulation pattern will remain. This is ideal case, there is only accelerating static field, and no magnetic component which will create dispersion and cause path length difference inside the bunch and will smear the modulation patter. Further careful study is required.

LASER MODULATION

When an electron beam passes through a laser beam in free space, usually there is no energy transfer with relativistic electron beam. This is because the laser field is transverse electro-magnetic field, and no longitudinal electric field exists. "The laser acceleration" technology uses dispersive media, such as gas or plasma, to obtain longitudinal electric field propagating with speed of electron.

When we pass an electron in an undulator, the electron transversely oscillates. We inject laser beam from behind of the electron, where longitudinal drift velocity of electron is slower than speed of light even in relativistic case due to transverse velocity component, and the electron delays from laser beam. With optimum tuning condition, for each one period of undulation, the electron delays one wavelength on laser field, thus recover phase and continue to exchange energy through $v_t \cdot E_t$ coupling.

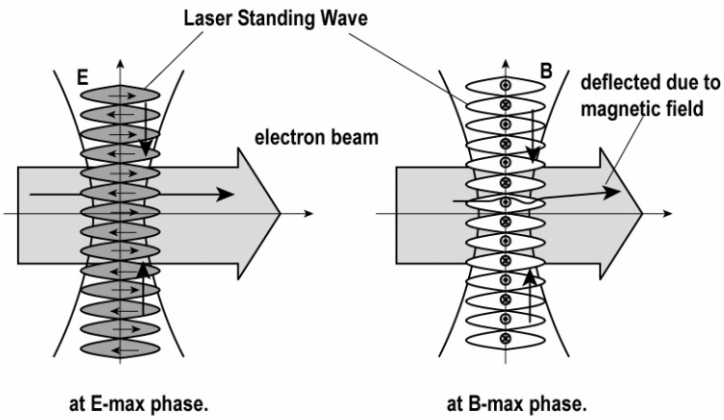

Fig. 4 Overlapping two laser beams create standing wave. At the electric field maximum location, electron receives velocity modulation. In between these maximums, the magnetic field deflects beam, which deteriorate beam emittance, also cause Compton scattering with laser photon and generate gamma-ray, which contributes to energy spread.

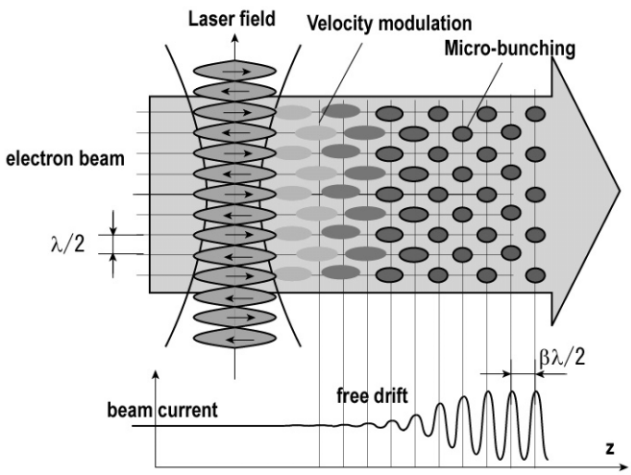

Fig. 5 Standing wave laser beam adopts velocity modulation and generate density modulation pattern at double frequency.

This type of laser modulator is so called "inverse FEL", and experimentally demonstrated elsewhere. However the system becomes complicated.

Here we introduce new scheme, which uses transverse electric field at focal point as illustrated in Fig. 3. This scheme uses same configuration as the spot size monitor tested at FFTB SLAC [4], but in this case we utilize the electric field. Since two leaser beam overlap at the focal point, the standing wave is created. By choosing polarization of the laser beam as the electric field being oriented to the electron beam path at the focal point, the electron beam receives energy modulation through $v_z \cdot E_z$ coupling at each electric field maximum points with $\lambda/2$ apart as Fig.4 left. In between them, there are magnetic field maximum points, where electron receives transverse kick from the magnetic field as shown in Fig. 4 right. This transverse coupling provides Compton scattering of laser photon, which causes increase of energy spread.

If the spot depth is much larger than laser wavelength, $v_z \cdot E_z$ oscillates along its trajectory and integration becomes zero, thus the electron does not receive energy gain. If we focus the laser beam into very small spot, the integral becomes non zero.

Here we assume Gaussian laser beam, and focus into a long elliptical spot using cylindrical lens as shown in Fig. 3. Here we define the coupling coefficient as follows.

$$T = \frac{\int_{-\infty}^{+\infty} E_z(z, t = z/c) \cdot dz}{\int_{-\infty}^{+\infty} E_z(z, t = 0) \cdot dz} = \mathrm{e}^{-(k\sigma_z)^2/4}. \quad (12)$$

Function T is plotted in Fig. 6. To obtain substantial coupling, we need to focus the laser spot very small close to the laser wavelength. From Fig. 6 we find that in order to obtain coupling of 0.1 or higher we have to focus the spot size $\sigma_z < 0.5\lambda$.

Can we focus the laser into such a small spot? The answer is yes. The CD player uses photo-pickup, where a short focal lens is used to focus laser beam into small spot in wavelength dimension to fit with the micron-size pits, and read out the reflection from those. The relation between the lens aperture, focal length and minimum spot size is given by

$$\sigma_z = \frac{\lambda}{\pi\theta}$$
$$NA = n \cdot \sin\theta \quad (13),$$
$$F = \frac{f}{D} \approx \frac{1}{2NA}$$

Where *NA* is called "Numerical Aperture" and higher *NA* provides smaller spot size, but it technically limited less than 1. One of the most advanced lens system is employed in the lithography system in Si-process, for example, NA of 0.85 has been realized in 157 nm F_2-laser lithography and 70-nm line width has been achieved[5].

From eq. (13), in order to obtain $\sigma_z < 0.5\lambda$, we need $\theta = 2/\pi = 0.64$, and *NA* = 0.59. There are commercially available products of cylindrical lenses having NA value 0.5 or even higher.

Using pulsed laser of 2nd harmonic of YAG-laser at 532 nm, assuming 1 mJ pulse and 10 nsec duration, this is small class laser oscillator in commercial production line, we may obtain 170 MV/m of peak electric field at the focal point, and 16 eV of modulation energy. This is quite enough for our purpose.

Table-2: Example laser system and modulation energy.

YAG-Laser 2nd			
wavelength	λ	532	nm
Output power	100 kW, 10 nsec, 1 mJ		
Focusing	Cylindrical lens		
Focusing length	f	5	mm
Numerical aperture	*NA*	0.6	
Matched laser beam size	$\sigma \sim 0.5D$	3	mm
Focused spot size	σ_{z0}	266	nm
Transverse width	σ_{x0}	3	mm
Field intensity	E_{z0}	170	MV/m
Modulation period	λ_{mod}	266	nm
Coupling Constant	T	0.1	
Modulation Energy		16	eV

REQUIRED ENERGY CHIRP AND OPTIMUM MODULATION

In the magnetic chicane, the bunch length is compressed according to its initial energy chirp: bunch head is lower energy and higher at tail, so that head part delays and tail catches up, results in compressing bunch length. If the optical modulation system is located upstream of the bunch compressor, the energy modulation will overlap with the linear energy chirp. After bunching,

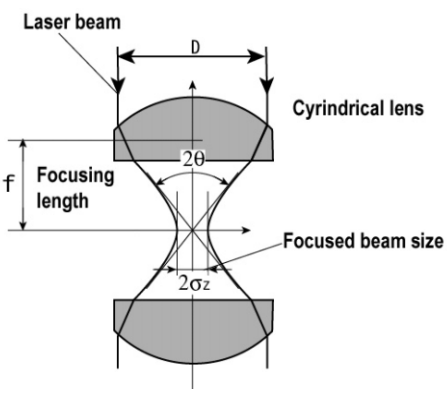

Fig. 7 High-NA focusing optics.

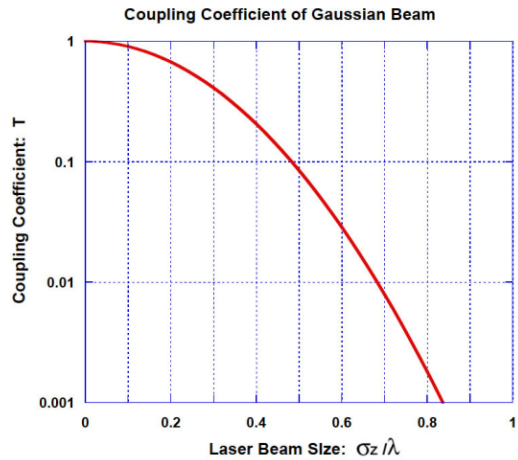

Fig. 6. Coupling coefficient as a function of the laser beam spot size.

the energy modulation will be converted into density modulation with shorter wavelength. If the energy modulation is too strong, the micro bunching will be over compressed and modulation contrast becomes lower. Thus there is certain relation between linear energy chirp and micro energy modulation. As shown in Fig. 8 left, there are three energy components: the initial energy chirp, optical modulation and energy spread:

$$E = E_0 - V_{I.RF} \cdot k_{RF} z - V_{\mathrm{mod}} \sin(2\pi z / \lambda_{\mathrm{mod}}) + \sigma_e , \qquad (13)$$

Where $V_{I.RF}$, k_{RF} is the RF cavity voltage to produce energy chirp (off crest component), V_{mod} is the optical modulation voltage, λ_{mod} is modulation wavelength before compression and σ_e is the energy spread. In the chicane, the bunch length is compressed according to $z_f = z_i + R_{56}\delta_i$. Optimum bunching condition is illustrated in Fig. 8 right, where the longitudinal spread of bunched beam becomes minimum, which is given by the following condition. Note the no space charge effect is considered in this discussion.

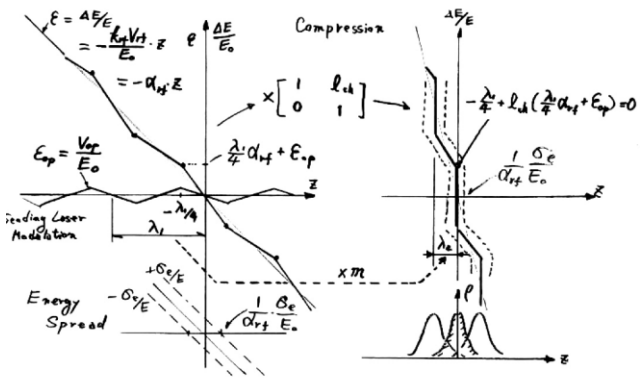

Fig. 8. Phase diagram of electron bunch before and after the compression.

$$\left.\frac{\partial z_2}{\partial \delta_2}\right|_{z=0} = 0, \quad (14)$$

$$\frac{V_{I.RF}}{E_0} k_{RF} + \frac{V_{\mathrm{mod}}}{E_0} k_{\mathrm{mod}} = R_{56}^{-1}, \quad (15)$$

The bunch compression factor is

$$m = \sigma_{zf} / \sigma_{zi} = 1 - \frac{V_{I.RF}}{E_0} k_{RF} R_{56} \quad (16)$$

At high compression ratio, i.e., we can approximate

$$\frac{V_{I.RF}}{E_0} = \left(k_{RF} R_{56}\right)^{-1} \quad (17)$$

For the optical modulation the optimum condition is,

$$\frac{V_{\mathrm{mod}}}{E_0} = m \cdot \left(k_{\mathrm{mod}} R_{56}\right)^{-1}. \quad (18)$$

For example, if we compress bunch length by 1000 times at 3 GeV, m = 0.001, with R_{56} = 40 mm, and λ_{mod} = 266 nm, the required modulation becomes $V_{\mathrm{mod}} = 1 \times 10^{-9} E_0$, that is optical velocity modulation becomes 3 eV. This value will be easily provided by the laser modulation as shown in Table 2.

If the energy spread is large, the modulation pattern will be smeared out. The energy spread has to be smaller than modulation energy. If the electron energy spread is still as low as the thermal energy: 74 meV, the modulation will be kept through the bunch compression process. The wavelength of the micro-bunching after the compressor becomes $\lambda = m \cdot \lambda_{\mathrm{mod}}$. If we use 532 nm wavelength, the modulation period becomes 266 nm, then, after the compression with m = 0.001, the modulation wavelength becomes 0.27 nm.

If we use femot-second laser, such as TiSa to optical modulator, we will be able to obtain atto-second pulse of X-ray after the compression.

CONCLUSIONS

New optical modulation scheme has been proposed in this paper. If we apply velocity modulation at optical wavelength, and compress it with bunch length, we will have density modulation at X-ray wavelength range. At least in an ideal case, mathematics shows possible parameter set. If we assume 1000 times compression ratio, we will have direct seeding source at X-ray wavelength.

Further studies will be required on non-linear field in bunch compressor, non uniform velocity distribution in bunch, energy spread due to radiation excitation, etc.

In year of 2007, we will install a laser modulator in our test accelerator to demonstrate velocity modulation, and compress the wavelength by ten times in bunch compression to seed FEL at 50 nm range.

REFERENCES

[1] L.-H. Yu, Phys. Rev. A44 (1991) 5178.

[2] Timur Shaftan and Li Hua Yu, "High-gain harmonic generation free-electron laser with variable wavelength", Phys. Rev. E 71, 046501 (2005).

[3] Timur Shaftan et al., "Experimental Demonstration of Wavelength Tuning in High Gain Harmonic Generation Free Electron Laser", Proc. FEL 2004, pp. 282-284, Trieste Italy.

[4] T. Shintake, “Proposal of nano-meter beam size monitor for e+e- linear colliders”, NIM A311, (1992) pp. 453-464.

[5] Toshiro Itani et al., "Effect of high numerical aperature lens on lighographic performance in 157 nm lithography", J. Vac. Sci. Technol. B 20(6), Nov/Dec 2002.

ANALYSIS OF THE PROCESS OF AMPLIFICATION IN A SINGLE PASS FEL OF HIGH ORDER HARMONICS GENERATED IN A GAS JET

L. Giannessi, M. Quattromini, ENEA C.R. Frascati, Frascati (Roma) Italy
P. Musumeci, INFN Sez. Roma I, Roma, Italy
G. Sansone, S. Stagira, M. Nisoli, S. De Silvestri, Politecnico di Milano, Milano, Italy.

Abstract

We have studied the amplification of high harmonics generated by a short infrared pulse in a gas jet, injected in a free electron laser amplifier. The high-order harmonic spectra have been simulated using a 3D non-adiabatic model that includes both the single atom response and the effect of the propagation of the XUV field inside the gas jet. The response of a single atom to the IR field is calculated in the framework of the Strong Field Approximation (SFA); The nonlinear polarization associated to this process is evaluated as the acceleration of the nonlinear dipole moment. This term is used as source term in the propagation of the harmonic field inside the gas jet. The propagation effect are extremely relevant for the temporal structure of the XUV field as the coherent interference of the dipole emission of the different atoms leads to the selection of only one XUV pulse for each semi-cycle of the driving IR field. The amplification in the free electron laser has been simulated with GENESIS 1.3. The effects of filtering the seed spectrum have been analyzed and the coherence properties of the light are considered.

INTRODUCTION

The FEL amplification in the SASE regime [1] leads to a longitudinal pulse shape and amplitude governed by the stochastic properties of the electron beam shot noise. The result is a reduced longitudinal coherence and intrinsic pulse to pulse energy fluctuations [2]. A single pass FEL, seeded with an external source, shows a number of advantages with respect to SASE, as the control over the pulse shape better coherence properties which are determined by the seed [3,4]. Intense seed sources are available in the visible and UV region of the spectrum based on reliable solid state laser technology. The FEL operating range may be extended to shorter wavelengths with cascaded schemes, i.e. taking advantage of the harmonic generation process in the FEL dynamics[5]. On the other hand high harmonic multiplication factors in a multi-stage cascade FEL are limited by the energy spread induced in each stage by the FEL process and these configurations are affected by stability issues associated to the fluctuation of one or more of the large number of parameters defining the configuration [6,7]. An alternative to a multi-stage cascade with a high harmonic multiplication factor is that of seeding the FEL amplifier directly at short wavelengths with the high order harmonics of an intense Ti:Sa laser pulse generated in a Gas Jet [8]. Such a possibility is considered in the scheme of several proposed facilities [9,10,11] and experiments are planned in the next future [12,13]. The high frequency field produced in the interaction with the gas jet has some very peculiar features. The pulse has a spiky structure, with attosecond pulses separated by half of the drive laser wavelength [14]. The spectrum contains the odd harmonics of the Ti:Sa drive laser and extends to short wavelengths with a cut-off depending on the nature of the gas used. The energy per pulse drops rapidly at the shortest wavelengths, where the combination of this seed source with an FEL amplifier would be more appealing. We are the interested in understanding what is the minimum energy required by an FEL amplifier in order to overcome the electron beam shot noise and amplify the harmonic pulse. A threshold intensity was obtained in the case of a seed constituted by a uniform plane wave [15], but it is not clear whether that threshold remains valid when the pulse has the time/spectral structure of the harmonics produced in gas and whether filtering the input seed is required despite of the fact that the FEL has a limited bandwidth proportional to the FEL parameter ρ [1,2]. Start to end simulations of the electron beam dynamics in a single pass FEL have been widely used to understand the dynamics of the coupled system of electrons and fields undergoing the FEL process. In order to answer the previous questions we have implemented a start-to-end simulation from the radiation point of view, starting with the process of harmonic generation in the gas jet and injecting the field distribution in a widespread and reliable FEL simulation code as GENESIS 1.3 [16]. The paper is organized as follows: in the next section we study the generation of the high harmonics field in the gas jet. In the last section we select the field at the target wavelength of 29.6 nm corresponding to the 27^{th} harmonic of the Ti:Sa and we analyse the results of simulations of the seeded FEL amplifier.

HIGH ORDER HARMONICS IN GAS

The high-order harmonic spectra have been simulated using a 3D non-adiabatic model that includes both the single atom response and the effect of the propagation of the XUV field inside the gas jet. The response of a single atom to the IR field is calculated in the framework of the Strong Field Approximation (SFA); in this model the atom is ionized via tunnelling by the IR field and the freed electron is then accelerated by the electric field of the driving pulse. For particular emission instant the

electron can be driven back to the parent ion and can recombine with the ground state emitting the exceeding energy as a photon in the extreme ultraviolet region or soft x ray region. The nonlinear polarizability associated to this process is evaluated as the acceleration of the nonlinear dipole moment:

$$d_{nl}(t) = 2\,\mathrm{Re}\left\{ i\int_{-\infty}^{t} dt' \left\{ \left(\frac{\pi}{\varepsilon + i(t-t')/2} \right)^{3/2} \exp\left[-iS_{st}(t,t') \right] \right.\right. \\ \left.\left. E(t') d^{*}\left(p_{st}(t,t') - A(t) \right) d\left(p_{st}(t,t') - A(t') \right) \right\} \right\} \\ * \exp\left(-\int_{-\infty}^{t} w(t')dt' \right) \quad (1)$$

In this equation $E(t)$ and $A(t)$ are respectively the electric field and the vector potential of the driving field; $p_{st}(t,t')$ is the stationary value of the momentum of the freed electron, $S_{st}(t,t')$ is the phase accumulated by the electron wave packet, $d(p)$ and $d^{*}(p)$ are the dipole matrix element for transitions from the ground state to a continuum state characterized by momentum p. The last term of equation (1) takes into account ground state depletion through the term ionization rate $w(t)$ calculated using the ADK model. The nonlinear dipole moment is used as source term in the propagation of the harmonic field inside the gas jet. The wave propagation equations for the driving and the harmonic field are solved in cylindrical symmetry in the framework of the paraxial approximation. The harmonic power spectrum is obtained integrating over the radial profile the harmonic electric field at the output of the gas jet.

Propagation effects are extremely relevant for a correct simulation of the time structure of the harmonic radiation. Indeed usually the single atom response is characterized by a complex time structure (usually two attosecond pulses for each half optical cycle), whereas the macroscopic time structure of the XUV radiation is characterized by a single attosecond pulse for each semi optical cycle. The origin of this difference is related to the phase matching mechanism operating during the propagation of the XUV field inside the gas jet.

In the process of high order harmonic generation, the electron can follow two different paths in order to recombine with the parent ion. These two paths are usually referred to as the "short" and the "long" path, as they are characterized by different times spent by the electron in the continuum of energy states. For the short path this time is usually less than half the optical period T_0, while for the long paths this time is typically of the order of the laser period. The coherent superposition of the contributions of these two paths leads to the generation of two attosecond pulses for each half optical cycle of the driving laser field. The coherent interference of the dipole emission of the different atoms inside the gas jet leads to different phase-matching conditions for the two paths. The relative contribution of the two paths to the harmonic spectra can be enhanced or reduced changing the relative position of the gas jet with respect the laser focus. The phase-matching condition in the HHG process are indeed determined by the geometric phase of the driving pulse and by the phase accumulated by the electron wave packet during his motion. In particular conditions, gas jet positioned few millimeters after the laser focus, it is possible to efficiently select on the contribution of the short path, leading to the selection of only one XUV pulse for each semi cycle of the driving IR field[17].

In other experimental condition (gas jet before or close to the laser focus), the contribution of the long paths increases and therefore also the time structure of the generated XUV radiation is more complex.

For our simulation we considered a Gaussian beam with a beam waist of $w_0 = 50\mu m$ (in the focus), and focused 3mm before a Neon gas jet with a thickness of 1mm. The pulse duration is FWHM=30 fs with a peak intensity in the focus of $1x10^{14} W/cm^2$. The high frequency portion of the spectrum, in the range 20 nm – 60 nm of the on axis radiation is shown in Fig. 1. The spectrum contains the odd harmonics of the Ti:Sa resonant wavelength (800 nm).

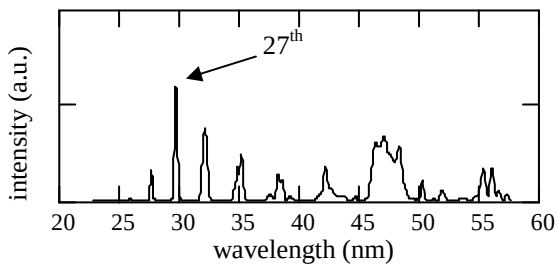

Fig. 1 Short wavelength spectrum of the HHG seed field.

The slowly varying envelope approximation (SVEA) has not been used in the model, but the FEL dynamics studied with GENESIS 1.3 rely on this approximation.

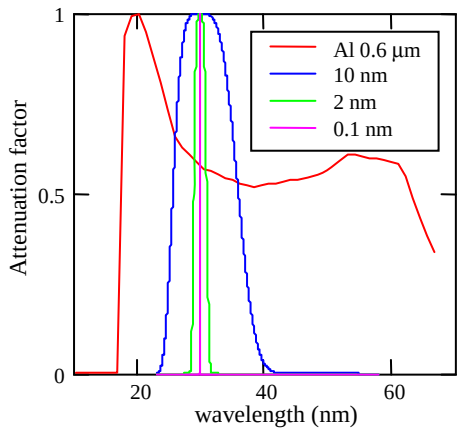

Fig. 2 Attenuation factor as a function of the wavelength of the different filters used in the simulations. The red line correspond to 600 nm layer of Aluminium.

For this reason we have to limit the bandwidth of the input signal by filtering the seed field and define the

slowly varying field as $\tilde{E}(z) = E(z)\exp(-ik_0 z)$ where k_0 is the FEL central resonant wave vector. In our example we consider filtering with different bandwidth as shown in Fig.2 centered at the resonant wavelength $\lambda_0 = 2\pi/k_0 = 29.66nm$ corresponding to the 27^{th} harmonic of the Ti:Sa (Fig.1).

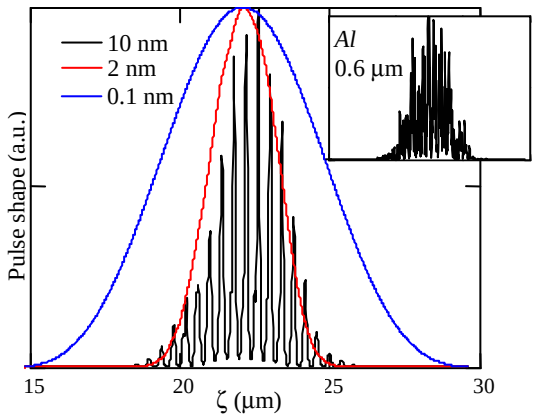

Fig. 3 Longitudinal pulse profile of the input seed after filtering. The plot in the upper right corner is the pulse shape filtered only with the Al broadband filter.

The effect of filtering on the seed temporal profile is shown in Fig. 3. The 10nm bandwidth is wide enough to preserve the attosecond structure of the input field. At 2nm the bandwidth preserves the pulse envelope, but overrides the fine structure. The 0.1nm filter induces an increase of the pulse length.

THE FEL SIMULATION

The FEL configuration considered is based on the parameters shown in Tab. 1. The FEL parameter is $\rho \sim 10^{-3}$ and an estimate of the seed intensity necessary to override the e-beam shot noise as calculated in ref.[15] is about $I_0 \approx 0.3 MW/cm^2$.

Table 1:FEL configuration parameters

Beam Energy (GeV)	1
Peak current (A)	1000
Energy Spread (%)	0.06
Emittance (mm-mrad)	1
Average β_T (m)	6
Undulator period (cm)	4.2
K (peak)	2.97
Periods per section	58
Sections	7

The field spot size and divergence have been matched to the e-beam optical functions by propagation through a drift+lens+drift optical system. The field phase and amplitude at the undulator entrance are shown in Fig.4.

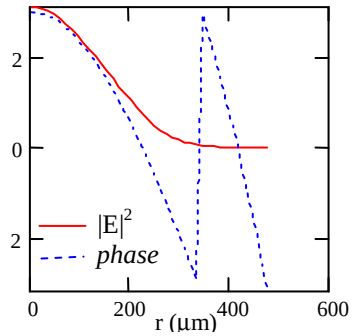

Fig. 4 Transverse field at the undulator entrance averaged over z.

The radiation power as a function of the longitudinal coordinate in the electron beam frame (horizontal) and position along the undulator at the coordinate z (vertical) is shown in Fig.5. The power is normalized at each z. The plots have been obtained by different filtering of the seed. The input seed energies, 2.5nJ@10nm, 1nJ@2nm and 0.5nJ@0.1nm have been chosen in order the energy in a bandwidth 2ρ to be roughly the same (0.5nJ) in the three cases.

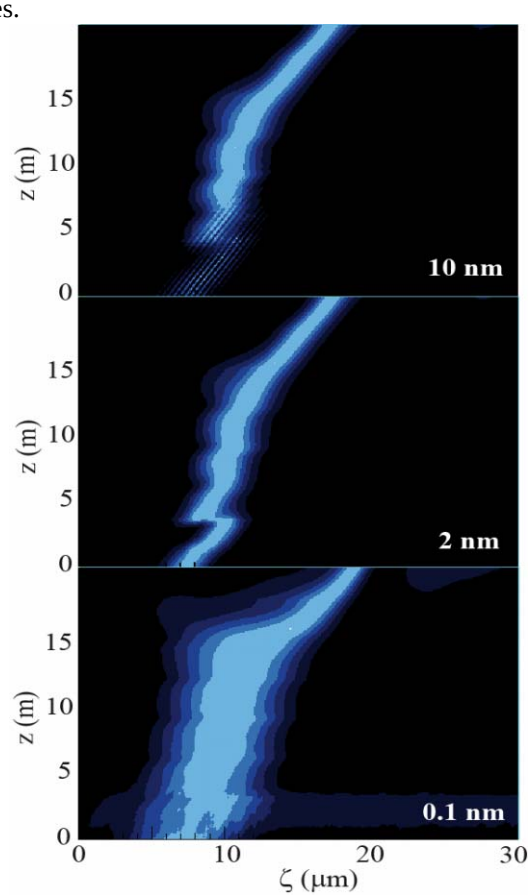

Fig. 5 Normalized longitudinal profile of the radiation power as a function of the longitudinal coordinate in the electron beam frame as it evolves along the undulator with coordinate z. The seed has been filtered at different bandwidths.

The fine structure present in the 10nm case is wiped out by the finite bandwidth of the FEL. The different filtering

affects the pulse shape only before saturation, which occurs at about 15m in all cases. Thereafter the pulse enters the superradiant regime where the pulse length is related to the peak power and is the same in all cases. The

The input seed intensity is 15MW/cm^2@10nm, 8.5 MW/cm^2@2nm, and 4 MW/cm^2@0.1nm averaged over z, always much larger than I_0. In Fig. 6, the simulation corresponding to 0.1nm has been repeated with input energies 0.05nJ and 0.01nJ, corresponding to intensities slightly above and below the threshold I_0 respectively. In both cases SASE is clearly visible at the beginning. In the latter case a structure in the pulse with loss of longitudinal coherence is present and SASE spikes compete with the seeded signal until saturation.

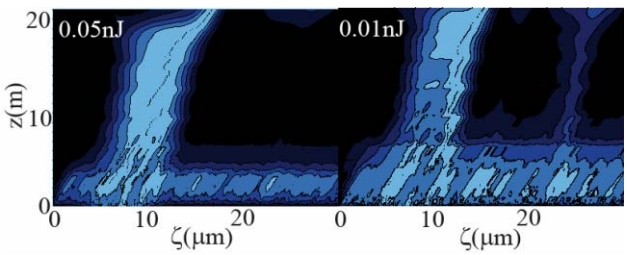

Fig. 6 Same as in Fig.5, case with 0.1nm BW above (left) and below (right) the threshold I_0.

The input energy levels considered are however very conservative. In fact recent results [18] have demonstrated the feasibility of pulses with energies up to several hundreds nanojoules at the considered photon wavelength. In Fig. 7 the power vs. ζ and z as in Figs. 5 and 6 (left) and the spectrum (right) are shown for the 100nJ@10nm case. Saturation is reached after only 8m. The splitting of the spectrum typical of the superradiant regime is clearly visible at the end of the undulator.

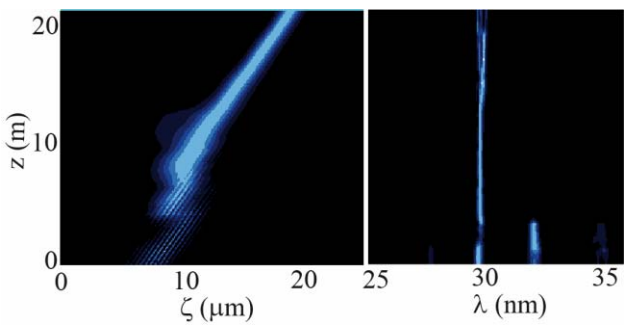

Fig. 7 Normalized longitudinal profile of the radiation power as a function of the longitudinal coordinate in the electron beam frame as it evolves along the undulator with coordinate z (upper plot). Corresponding wavelength spectrum as a function of z.

CONCLUSIONS

In this paper we have presented an analysis of the dynamics of a FEL seeded with the high order harmonics generated in gas. The minimum seed energy has been estimated in a specific FEL configuration with the resonance at the 27th harmonic of the Ti:Sa drive laser. The results are in reasonable agreement with the threshold estimation in [15]. Currently available sources in the XUV appears to be sufficiently intense to implement such a scheme. The analysis in the frequency domain, suggests that filtering the seed it is not necessary unless a line-width smaller than the natural FEL line-width is required.

This work was partially supported by the EU Commission in the Sixth Framework Programme, Contract No. 011935-EUROFEL.

REFERENCES

[1] R. Bonifacio, C. Pellegrini, and L. M. Narducci, Opt. Commun. 50, 373 (1984)
[2] E. L. Saldin, E. A. Schneidmiller, M. V. Yurkov, Opt. Commun. 148, 383 (1998)
[3] L. H. Yu et al., Science 289, 932 (2000)
[4] L. H. Yu et al. Phys. Rev. Lett. 91, 074801 (2003)
[5] G. Dattoli et al. Journal of Appl. Phys. 97, 113102 (2005)
[6] B. Kuske et al. Development of Figures of Merit to Evaluate the Output of FEL HGHG Cascades, MOPPH051, these proceedings
[7] G. De Ninno et al. Start-to-end Time-Dependent Study of FEL Output Sensitivity to Electron-beam Jitters for the First Stage of the FERMI@Elettra Project, MOPPH058, these proceedings
[8] D. Garzella *et al.*, Nucl. Instrum. Methods Phys. Res. Sect. A 528, 502 (2004).
[9] C. Bruni, The Arc En Ciel FEL proposal, MOPPH048, these proceedings
[10] B. McNeil et al, The Conceptual Design of the 4GLS XUV-FEL, MOPPH012, these proceedings
[11] C. Vaccarezza et al., Status of the SPARX FEL project , MOPCH028 in procs. of the 2006 EPAC conference (2006).
[12] G. Lambert, Seeding the FEL of the SCSS Phase I Facility, MOPPH046 these proceedings
[13] O. Tcherbakoff et al, MOPPH047 these proceedings, see also L. Giannessi, Future seeding experiments at SPARC, MOPPH028 these proceedings
[14] P. Salieres, M. Lewenstein, Meas. Sci. Technol. 12, 1818 (2001)
[15] L. Giannessi, Harmonic generation and linewidth narrowing in seeded FEL, in Proc. of the 26th FEL conference, Trieste 2004 JACoW (Joint Accelerator Conference Website) at http://www.JACoW.org, p. 37 (2004)
[16] S. Reiche, Nuclear Instrum. & Meth. A429, 243 (1999)
[17] P. Salières, B. Carré, L. Le Déroff, F. Grasbon, G. G. Paulus, H. Walther, R. Kopold, W. Becker, D. B. Milosevic, A. Sanpera, M. Lewenstein, Science 292, 902 (2001).
[18] E.J. Takahashi et al. IEEE J. of Sel. Topics in Q.Elec. 10, 1315 (2004)

PERFORMANCE ACHIEVEMENTS AND CHALLENGES FOR FELS BASED ON ENERGY RECOVERED LINACS*

G. A. Krafft, Jefferson Lab, Newport News, VA 23060, U.S.A.

Abstract

During the past decade several groups have assembled free electron lasers (FELs) based on energy recovered linacs (ERLs). Such devices have been built to obtain high average power electron and photon beams, by using high repetition rate beam pulses driving FEL oscillators. In this paper the performance of many existing and several proposed facilities from around the world are reviewed. Going forward, many questions must be addressed to achieve still better performance including: higher average current injectors, better optimized accelerating cavities, higher energy acceptance and lower loss beam recirculation systems, and better optical cavity designs for dealing with the optical beam power circulating in the ERL FELs. This paper presents some of the current thinking on each of these issues.

INTRODUCTION

The basic idea in same cell beam energy recovery is fairly straightforward to understand and has been discussed in great detail in recent reviews [1,2]. In a front-to-back recirculated linac the recirculation path length is chosen to be approximately an integer plus ½ RF wavelengths, and if the beam current does not change much in the time it takes for a complete circuit of the recirculation loop to be made, then energy can be transferred directly from the decelerating higher-energy beam to the accelerating first-pass beam, without the need for power to be provided by the RF systems attached to the cavities. This opportunity allows one to construct recirculated linacs, particularly those consisting of superconducting cavities, with energy transfer efficiencies approaching those in storage rings. This fact, in turn, allows one to build linacs that can transport and accelerate beam average currents approaching those in storage rings.

The energy transfer efficiency is nicely quantified by the power multiplication factor

$$k = P_{b,ave} / P_{RF} \tag{1}$$

where $P_{b,ave}$ is the average beam power and P_{RF} is the RF power needed to accelerate the beam. For normal conducting recirculators k is much less than 1, for present day ERL FELs k is of order 10, for advanced ERL light sources k is of order 100, and for typical storage rings k is of order 1000. It is straightforward to show that in the limit the optical cavity losses are small compared to the outcoupled radiation power, the transfer efficiency from RF power to photons is equal to ζk, where ζ is the fraction of beam energy converted to photons per pass in an optical cavity oscillator FEL.

The first superconducting linac to demonstrate same cell energy recovery was the Stanford University Superconducting Accelerator as reported at this conference twenty years ago [3]. In an experiment, the recirculation path length was set to allow energy recovery to proceed. Nearly all of the beam energy was recovered as indicated by the absence of RF power being needed to drive the beam load in the superconducting cavities of the accelerator. However, in this early experiment there was no optical cavity inside the recirculation loop.

PRESENT STATUS

Presently, there are three ERL-based free electron lasers in existence and a fourth being rapidly assembled as a prototype project for an advanced fourth generation light source suite. Two of the existing FELs, at Jefferson Lab and the Japan Atomic Energy Agency (JAEA), are based on superconducting RF (SRF) cavities, and the third, at the Budker Institute for Nuclear Physics (BINP), is based on CW normal conducting RF cavities. In all the devices, an optical cavity FEL is placed inside the beam recirculation loop.

Jefferson Lab Free Electron Laser

A group at Jefferson Laboratory has spent the last decade building and improving many increasingly capable free electron lasers based on energy recovery, including the first ERL to have an FEL inside the energy recovery loop [4]. This demonstration device has been upgraded in order to achieve higher average electron beam and optical beam powers. Some recent electron beam parameters are summarized in Table 1. Beam starts from a DC photocathode source, is accelerated to 10 MeV using two standard CEBAF superconducting cavities, injected onto a beamline containing an energy recovered linac that can achieve up to 150 MeV. The beam is recirculated with two Bates bend beam recirculation systems specially designed to contain and transport the large energy spread generated by the FEL in the electron beam.

Recent work at Jefferson Lab has concentrated on extending high power CW operations at the 10 kW level from 6 microns down in wavelength. Over the last year the average power has increased from about 4 kW to 6.7 kW at 2.8 microns, from 1 kW to 5.4 kW at 1.6 microns, and from 1 kW to 2.2 kW at 1 micron. The short wavelength performance of the FEL has improved as low absorption dielectric coatings have been developed for the high power optical systems. The group expects a considerable improvement of the high power performance

*Authored by Jefferson Science Associates, LLC under U.S. DOE Contract No. DE-AC05-06OR23177.

of the FEL when cryogenically cooled optical cavity mirrors are deployed to help deal with mirror distortion in the optical cavities at high power.

Table 1: Electron Beam Parameters for ERL FELs

PROJECT	**JLAB**	**JAEA**	**BINP**
Frequency (MHz)	1500	500	180 NC
Energy (MeV)	130	17	13
Current (mA)	10	8	20
Bunch Charge (pC)	130	400	500
Rep. Rate (MHz)	75	83	11.2
Normalized Emittance (mm mrad)	8	20	30

A user program has developed at the FEL. Because of the short bunch length at the FEL, copious amounts of wideband THz radiation are produced in the bend magnets of the chicanes surrounding the wiggler through the coherent synchrotron radiation emission. The THz radiation has been taken up to a user lab and is now routinely used for electron beam diagnostic purposes. Other experiments are performed with the FEL radiation extending from studies in condensed matter physics, to studies of fundamental optical physics using the FEL light to make far off resonance traps, all the way to fundamental particle physics in dark matter candidate searches.

JAEA Free Electron Laser

The JAEA FEL injector consists of a 230 keV thermionic gun, and 83 MHz subharmonic buncher, and two single-cell 500 MHz superconducting cavities that accelerate the beam to about 2.5 MeV. The injected beam is merged onto the axis of a linac that consists of two 5-cell superconducting cavities that boost the beam energy to 17 MeV. Beam is recirculated with three-bend achromats, and the undulator and optical cavity of the FEL are just upstream of the return achromat. As seen in Table 1, the lower cavity frequency allows higher charge per bunch in the beam to be accelerated efficiently.

Recent work has focused on doubling the electron bunch repetition rate by upgrading the gun grid pulser and the RF power for the non energy recovered 2.5 MeV accelerating cavities, increasing the energy acceptance of the achromats by reworking quad magnets and beam pipes in the achromats, and investigating and optimizing the achromat settings for increasing the FEL efficiency. Recently, the FEL extraction efficiency has been measured and the peak efficiency reaches 2.8%, and the group has achieved 0.7 kW output at 22 micron from an 8 mA beam during a 230 microsecond macropulse. A more complete summary of recent work has been given by N. Nishimori at this conference [5].

BINP THz FEL

The Budker Institute THz FEL is based on a normal conducting CW linear accelerator. Beam originates in a thermionic electron gun, is accelerated to 2 MeV through two 180 MHz cavities, injected on the main linac axis and accelerated up to 13 MeV by 16 180 MHz cavities. The beam drives an FEL oscillator which produces radiation in the THz band, and the beam energy is recovered in the second pass through the linac. This device is the highest average power source of narrowband THz radiation. Because of the low frequency and hence large aperture of the accelerating cavities, this device is able to handle much higher average current than the superconducting ERL FELs, achieving 20 mA average current now and planned to achieve 150 mA average current after an injector upgrade. This device has energy recovered the highest average beam current to date, and is unique in that the recirculation loop is oriented vertically.

There are plans to upgrade this device with two higher energy FELs that will produce radiation at 20-100 μm and 3-20 μm, in optical cavity oscillators. The 20-100 μm optical klystron will sit after a second pass of beam recirculated acceleration for a beam energy greater than 20 MeV, and the shorter wavelength optical klystron will sit after four beam passes up to about 40 MeV. The recirculation loops for this device will be oriented horizontally to the existing linac, which does not need to be upgraded substantially. When completed, the BINP FELs will be unique among energy recovered FELs in that a large number of passes will be accommodated, as the other existing ERL FELs are two pass machines. The multipass “energy recuperator” free electron lasers will be assembled throughout 2007 and commissioning is anticipated to begin towards the end of 2007. A more complete summary of recent work has been given by N. Vinokurov at this conference [6].

4GLS

The British 4GLS project is to produce a suite of three superconducting linac based free electron lasers in addition to an energy recovered high average current recirculated linac light source, to be located at Daresbury Laboratory. The IR FEL and the XUV-FEL in this project are not energy recovered, the IR FEL operating at a MHz-scale repetition rate and the XUV-FEL operating at a repetition rate of 1 kHz, ambitious for a SASE or a seeded source. The UV FEL source, based on a regenerative amplifier, is located in the high average current energy recovered recirculation loop. It is anticipated to operate this FEL simultaneously with the high average current ring.

In order to start the process of building the full 4GLS, which is based on 1.3 GHz superconducting cavities, a 35 MeV energy recovered FEL, ERLP, is being built [7]. Just prior to the conference, beam was extracted from the DC photocathode source of ERLP for the first time. The accelerator consists of two two-cavity cryostats, one inside and one outside the beam recirculation loop. These have now been assembled, as well as the three bend

achromat recirculation optics systems. Cold commissioning of the linac, in its planned location is scheduled for the month of October 2006, with the machine completely installed by the end of 2006. Machine studies, including beam energy recovery, are to be completed in the spring of 2007 and there should be a "first lasing" contribution by ERLP at the next FEL conference. A more complete summary has been given by J. Clarke at this conference [8].

High Average Power X-FELs

Perhaps the ultimate light source, i. e., one that could produce both high peak power and high average power X-ray beams, would consist of an energy recovered X-FEL. A superconducting linac as a driver for such an FEL has many inherent advantages: greater potential efficiency and the possibility of high gradient CW operation, the possibility to achieve repetition rates at the MHz or higher level, and the ability to transport cleanly high bunch charges because of the low transverse impedance of the accelerating structures [9]. Such a scheme has been studied in detail as a follow on project for the TTF FEL [10]. A major concern is achieving a high repetition rate injector. As discussed more thoroughly below, this injector would seem to require an SRF gun electron source.

FUTURE DEVELOPMENTS

In order to achieve another order of magnitude in electron and photon beam power many improvements must be made to the existing devices. The present photocathode injectors must be upgraded to produce higher average current. The accelerator design optics must be stable to the higher average recirculated beam current in the more ambitious designs. The optical cavities must be able to handle the increased recirculating beam power. High order mode (HOM) cooling becomes more problematic at higher average currents. Finally, non-invasive electron beam diagnostics should be developed to help monitor the beam during CW operations.

Electron Photocathode Sources

In order to increase the average beam current in the next generation FELs by an order of magnitude, it seems that the easiest method is to increase the bunch repetition rate until every accelerating (and decelerating!) phase in the RF waves are filled. This can be done with little change to the bunch charge presently obtained. This approach has been adopted by Cornell for the first energy recovered recirculated linac light source, which must achieve beam emittances much smaller than is typical for the long wavelength ERL FELs. Because of the higher average current in the non energy recovered portions of such accelerators, it is expected that the injection energy will be reduced and the number of superconducting cavities increased in order to deal with the increased beam power in the non-recovered portions of the accelerator [11]. Also, larger beam dumps may be needed to dissipate the non-recovered beam energy.

In the further future, one anticipates that SRF photocathode sources will be developed to produce electron beams at high energy and high levels of average current. The group at Rossendorf, who have been leaders in developing SRF guns, hope to achieve 1 mA average current from a 10 MV 3.5 cell gun in construction now, and Brookhaven National Laboratory have been developing guns in the 100 mA-1 A class for electon cooling applications [12]. The main benefit of marrying the SRF and photocathode source technology is the possibility to have high CW accelerating gradient on the photocathodes, which may lead to superior emittance in CW high repetition rate applications.

Drive Lasers

In the high average current applications of photocathode electron sources there is a need to develop drive lasers of sufficient power to extract the needed average current. Roughly an order of magnitude in laser power is needed beyond present experience for the DC photocathode sources presently used. In addition to the power requirement, to get the best beam parameters out of photocathode guns laser pulse shaping is needed. Cornell University is developing a fiber based system with 20 W capabilities untilizing transverse shaping and longitudinal pulse stacking in order to obtain a uniform laser pulse longitudinally. Jefferson Lab is also developing a system that should be able to deliver 32 W [13], about 5 times more than the present drive laser for the Jefferson Lab FEL.

Similar high average power lasers with high repetition rate may be quite useful in seeding applications in high repetition rate X-FELs.

Beam Breakup and Advanced Beam Optics

Recent work at Jefferson Lab has allowed direct quantification of the multipass beam breakup instability, as in some electron beam optical conditions the FEL beam is unstable. A recent review of the subject has been performed [14], including discussions of utilizing special electron beam optics to suppress the instability. The methods studied are likely sufficient for stabilizing the instability in future FELs, but simulation evidence exists indicating that some of the intended solutions may not apply to larger scale accelerators [15]. Significantly, many of the BBU simulation codes have now been properly benchmarked against experimental instability data.

Driven by the desire to operate the ERL FELs at higher energy extraction, advanced beamline designs for beam recirculation with energy spreads of 10% or more have been developed [16]. These designs feature magnet shapes and edges chosen to automatically yield nearly isochronous beam recirculation due to the shape choices. It is anticipated that such designs will become increasingly important as higher average power ERL FELs are built.

High Power Optical Cavities

In designing the next generation of optical cavities the following aspects of the problem must be understood [13]:

- One must minimize the absorptive loss which can quickly lead to mirror distortion and low output.
- Scatter loss should be minimized to control subsequent absorption on components causing pressure rise and drift.
- Mirror coatings and substrates must be chosen to mitigate the effects of any power loading from out-of-band radiation which may be incident on the mirrors.

Optical cavities and beam transport lines must be designed with these effects in mind.

HOM Power

Superconducting RF cavities have been used in storage ring applications for many years at beam average currents of 100 mA and above. Because the power deposited into HOMs can be substantially larger than the heat deposited in the cavity walls when the cavity is operated at gradient, it is particularly important to couple the HOM power out of the cavity volume to be absorbed at locations with higher temperature to reduce cooling requirements on the He refrigerator. Recent storage ring HOM absorbers consist of ferrite absorbers located upstream and downstream of the SRF cavities mounted on the beam pipe wall with a separate cooling loop to deal with the HOM power.

Similar solutions will be needed to absorb the HOM power in 100 mA-scale ERLs, and there is an additional complication. The bunch durations in ERLs can be up to two orders of magnitude smaller than in storage rings and now there is bunch spectrum available to excite HOMs at much higher frequencies than in rings. Thus, the overall power excited increases and the operational range of the HOM absorber must be much broader in frequency to handle the wider range of frequencies excited. This problem afflicts advanced ERL light source designs, and already a group has investigated material which is highly absorbing at frequencies up to 40 GHz at a temperature of 80 K [17]. Also, it is anticipated that advanced HOM absorbers will include several different materials absorbing in different frequency bands [18].

Electron and Photon Beam Diagnostics

Because the average current of next-generation ERLs is approaching that in storage rings, one would expect that the more standard electron beam diagnostics, e.g. beam position monitors, beam profile monitors, and current monitors, would follow the techniques previously developed for storage ring applications. The beam attributes unique to ERLs and ERL FEL sources are the need to diagnose and control short bunches, the need to deal with low average power tune up beam diagnostic modes, and the need to deal with high average beam power. Many longitudinal techniques are being investigated in X-FEL projects. Mainly they are highly disruptive and might not be technically useful in the higher average beam power regimes we are pushing into.

Real time measurements of bunch longitudinal distribution and phase space based on electro-optic methods or based on coherent synchrotron, edge, or undulater radiation, may provide correct approaches for non-invasive monitors. Presently, there seems to be a lack of a universal method yet demonstrated that is unambiguous in the results it reports [19]. Achieving such a universal longitudinal measurement will be at least as important for future ERL development as the development of good profile monitoring was in storage rings.

For photon beams, the key near-term developments need to occur in the shaping, both longitudinally and transversely, of the higher average power drive laser beams for electron production on the photocathodes. The production methods will be need to be diagnosed to some level with techniques suitable for power levels of several tens of W needed in the next generation electron sources. In the further future it will perhaps be required by the users of high average power FELs that the emerging high power optical pulses display customized and controlled characteristics. Very little is known about this subject now.

CONCLUSIONS

- The field of ERL-based FELs continues to grow and the performance of devices continues to improve.
- Upgrade paths for at least an order of magnitude in both electron beam and photon beam power, though not trivial, have been identified.
- Many new ideas are being explored, some in conjunction with recent work on Energy Recovered Linac light sources.
- The field seems to be thriving and there is no shortage of interesting problems to work on.

REFERENCES

[1] L. Merminga, D. R. Douglas, and G. A. Krafft, Ann. Rev. Nucl. Part. Sci., 53 (2003) 387.
[2] G. A. Krafft, “Recirculated and Energy Recovered Linacs”, Joint Accelerator School 2002, Long Beach, CA, USA, p. 301.
[3] T. I. Smith, H. A. Schwettman, R. Rohatgi, Y. Lapierre, and J. Edighoffer, Nucl. Inst. and Methods A 259 (1987) 1.
[4] G. Niel, et al., Phys. Rev. Lett. 84 (2000) 662.
[5] N. Vinokurov, these proceedings.
[6] N. Nishimori, these proceedings.
[7] D. J. Holder, et. al., “Status of the Daresbury Energy Recovery Prototype Project”, EPAC’06, http://www.jacow.org
[8] J. Clarke, these proceedings.
[9] G. A. Krafft, and J. J. Bisognano, “On Using a Superconducting Linac to Drive a Short Wavelength FEL”, PAC’89, Chicago, IL, USA, p. 1256, http://www.jacow.org

[10] J. Sekutowicz, et al., Phys. Rev. ST-AB 8 (2005) 010701.
[11] I. V. Bazarov and C. K. Sinclair, Phys. Rev. ST-AB 8 (2005) 034202.
[12] I. Ben-Zvi, private communication.
[13] M. Shinn, private communication.
[14] E. Pozdeyev, et al., "Multipass Beam Breakup in Energy Recovery Linacs", ERL 2005, Newport News, VA, USA, Nucl. Inst. and Methods A 557 (2005) 176.
[15] G. A. Krafft, and J. J. Bisognano, "Two Dimensional Simulations of Multipass Beam Breakup", PAC'87, Washington,DC,USA, p. 1356, http://www.jacow.org
[16] D. Douglas, private communication.
[17] V. Shemelin, M. Liepe, and H. Padamsee, "Measurements of Epsilon and Mu of Lossy Materials for the Cryogenic HOM Load", PAC'05, Knoxville, TN, USA, p. 3452, http://www.jacow.org
[18] M. Liepe and J. Knobloch, "Superconducting RF for energy-recovery linacs", ERL 2005, Newport News, VA, USA, Nucl. Inst. and Methods A 557 (2005) 354.
[19] G. A. Krafft and J.-C. Denard, "Diagnostics for Recirculated and Energy Recovered Linacs", BIW'02, Upton, NY, USA, AIP Conf. Proc. 648. p. 118.

FUTURE LIGHT SOURCES: INTEGRATION OF LASERS, FELS AND ACCELERATORS AT 4GLS

J. A. Clarke, CCLRC Daresbury Laboratory, Warrington, UK, on behalf of the 4GLS Design Team.

Abstract

4GLS is a novel next generation proposal for a UK national light source to be sited at Daresbury Laboratory, based on a superconducting energy recovery linac (ERL) with both high average flux photon sources (undulators and bending magnets) and three high peak brightness free electron lasers. Key features are a high gain, seeded FEL amplifier to generate XUV radiation and the prospect of advanced research arising from unique combinations of sources with femtosecond pulse structure. The conceptual design is now completed and a CDR recently published [1]. The 4GLS concept will be summarised, highlighting how the significant design challenges have been addressed, and the project status and plans explained.

INTRODUCTION

The 4GLS project design takes advantage of the very latest advances in accelerator science and technology incorporated in a unique scheme to provide state-of-the-art research facilities. This will enable a broad range of outstanding science to be undertaken by the UK and international communities.

4GLS will enable the study of real time molecular processes and reactions on timescales down to tens of femtoseconds in short-lived, nano-structured or ultra-dilute systems. The emphasis is on molecular and device function, rather than the largely 'static' structural focus of work on 3rd generation synchrotron radiation sources and X-ray FELs. Key areas where 4GLS will make unique contributions are in:

- understanding the function of single biomolecules in living systems and membrane transport;
- determining reaction pathways in areas as diverse as enzyme processes, reactions contributing to atmospheric pollution or reactions occurring in the interstellar medium;
- studies of electron motion in atoms/molecules and developing 'coherent control' of reactions and intense laser-matter interaction leading to new physics;
- developing new nano-scale devices through understanding electron charge and spin transport; and
- development of new dynamic imaging techniques to improve early diagnosis of conditions such as cancer and prion based diseases.

The major themes of the science case are time-resolved measurements in the life sciences and nanoscience. Particular areas of strength are high resolution pump-probe spectroscopy of atoms, molecules and clusters, including high field dynamics, dynamics at surfaces and interfaces, many-body problems in condensed matter, and studies of the dynamics of biomolecules in 'real' environments.

The science requirement is for an ultra-high brightness facility that allows the use of short pulsed sources in combination, and where the energy range is optimised to allow the extraction of electronic and vibrational information. The 4GLS suite of synchronised sources, operating from the THz to the soft X-ray range is designed to meet this science need.

The 4GLS facility is planned from the outset to be a multi-source, multi-user facility. This is achieved by superconducting radio-frequency (SCRF) accelerator technology, operating using energy recovery, to provide short pulse spontaneous radiation with pulse length variable from ps to < 100 fs. At long wavelengths this allows the condition for coherent synchrotron radiation (CSR) production to be met, with the result that 4GLS will provide enormously bright THz radiation. The high quality low emittance electron beam provided by the photoinjectors additionally provides an ideal source with which to operate free electron lasers (FELs). In the 4GLS conceptual design these are embedded within the facility, delivering ultra-high brightness short-pulse radiation in the IR, VUV and XUV energy ranges, with pulse lengths as short as 50 fs FWHM. In world terms, this gives a unique suite of synchrotron radiation (SR) and FEL sources covering the THz to the soft X-ray range. Many of the light pulses originate from the same electron bunch, thus offering potential levels of internal synchronization at the tens of femtoseconds level. All the 4GLS sources are offered with variable polarization, while the flexibility of SCRF technology allows the repetition rates of the sources to be varied. The peak brightness of the 4GLS sources is given in Figure 1. There is a typical enhancement of eight orders of magnitude when compared with 3rd generation light sources.

The 4GLS accelerator design concept consists of three inter-related accelerator systems [2, 3]. The high average current loop uses energy recovery as an essential element to deliver a 600 MeV electron beam of 77 pC bunches at repetition rates of up to 1.3 GHz. Distributed bunch compression allows for SR pulse lengths from a few ps to approximately 100 fs (RMS) to be delivered according to user requirements. A low-Q cavity VUV-FEL device is incorporated at the end of this loop. The most challenging area of accelerator design for 4GLS is in transporting and accelerating an extremely high quality high-average current (100 mA) beam to this loop, while simultaneously providing extremely high peak current (1.5 kA) at 750 – 950 MeV for the second accelerator system, the XUV-FEL branch. This beam is derived from 1 nC bunches

produced by a normal conducting RF photoinjector operating at 1 kHz and it is dumped after traversing a final spontaneous undulator source. The XUV-FEL uses an HHG (high harmonic generation) seed, offering considerable advantages in pulse quality over a SASE (self-amplification of spontaneous emission) design. The third accelerator system is required for the IR-FEL. SCRF linac technology is used to accelerate electrons to 25 – 60 MeV to provide a fully integrated and synchronized IR-FEL facility.

Significant aspects of the 4GLS design have been informed by experience gained on the 4GLS Energy Recovery Linac Prototype (ERLP) currently approaching completion at CCLRC Daresbury Laboratory [4, 5]. In considering detailed 4GLS design decisions considerable attention has been given to ensuring that future upgrade options are not designed out at this early stage. These possibilities include various routes to higher energy operation, increased repetition rate for the XUV-FEL and decreased photon pulse lengths.

4GLS is thus the leading energy recovery proposal in Europe and the most comprehensive in terms of utilisation of combined sources. In terms of multi-user capability it is currently the most advanced energy recovery linac (ERL) proposal in the world. 4GLS is complementary to XFEL, to table-top lasers and to 3rd generation sources.

The unique advantages of 4GLS are:

- Combinations of sources. The fully integrated capability to utilize both short pulse SR(ERL) and the FEL sources for pump-probe and two colour dynamics experiments. This results in both experimental flexibility and cost effective delivery.
- Intense, tuneable, variable polarisation FEL sources optimized for spectroscopy and imaging in the frequency ranges of XUV, VUV and IR-THz.
- Energy recovery linac spontaneous light sources available from soft X-ray to THz. This gives short pulse, high repetition rate operation, the capability to 'pulse tailor', and low probability of sample damage.
- Europe's most intense broadband source of coherent THz radiation.

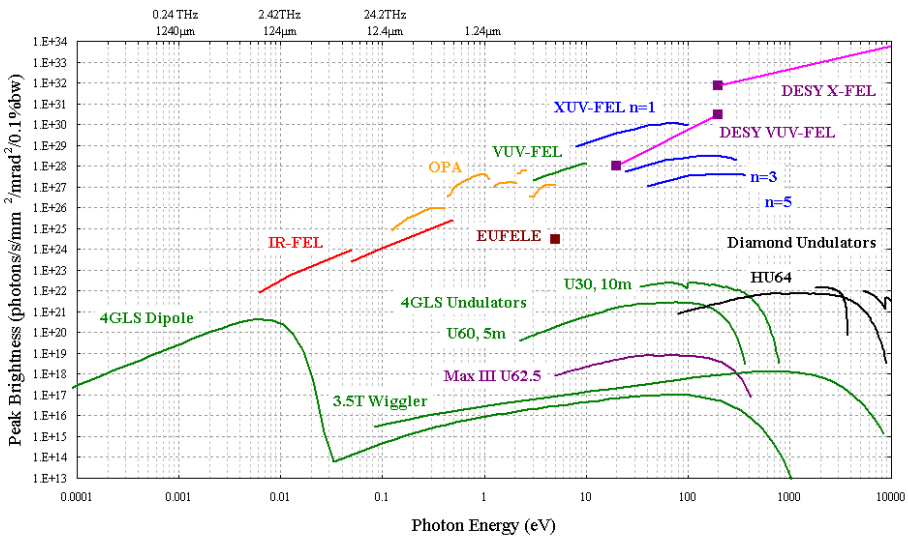

Figure 1. Peak brightness for 4GLS FELs, undulators, wiggler, OPA and dipoles compared with EUFELE, XFEL, Diamond and Max III undulators.

OVERVIEW

The 4GLS project design takes advantage of the very latest advances in accelerator science and technology incorporated in a unique scheme to provide state-of-the-art facilities. This has been made possible by a number of parallel developments at leading international laboratories, including successful demonstrations of technical solutions. The proposed design builds on current world achievements and in some cases extrapolates beyond them. In the most challenging areas an active R&D programme is already underway world-wide and the 4GLS team has augmented this, not least because to do so enhances the necessary skill base for detailed design, construction and operations.

The provision of high intensity electron beams has been revolutionised in the last decade by the successful development of a new variant of accelerator: the Energy Recovery Linac (ERL). Traditionally beam currents in linear accelerators can have high instantaneous values but are restricted to pulses with low repetition rates because the average power dissipation must be kept to manageable levels. For a light source high average flux emission is highly desirable and this output has been possible so far only by the widespread application of the electron storage

ring (e.g. Diamond and other 3rd generation sources) that achieves average currents of hundreds of milliamperes by recirculating the same electrons many times (and for many hours). This solution has serious drawbacks, in particular the ring defines the beam properties and they are dominated by the very emission of synchrotron radiation that the ring is built to deliver. If long-term storage of the electron beam can be avoided then greatly superior properties can be provided and this is one of the principal features of the ERL.

The ERL delivers high average currents without beam storage, since electrons are injected, accelerated and circulated only once before the system recovers their energy, dumps them and replaces them with new electrons. This means that if the beam is injected with superior brightness properties it maintains these during its radiation emission phase. The 4GLS project has an ERL at its heart in a generational leap from storage ring sources. Globally, pioneering work on ERLs has been undertaken at the Jefferson Laboratory in the USA where a low energy proof-of-principle ERL has been successfully demonstrated.

4GLS is best thought of in terms of three inter-related accelerator systems (see Figure 2). The first is the high average current loop. In this a 600 MeV beam of 77 pC bunches is delivered at repetition rates of up to 1.3 GHz and energy recovery is an essential element. Progressive compression of the electron bunches in this loop allows for photon pulse lengths from a few ps to approximately 100 fs (RMS). The VUV-FEL is placed towards the end of the high-average current loop.

The second major accelerator system is the XUV-FEL branch. The XUV-FEL requires a peak current of ~ 1.5 kA at beam energies from 750 to 950 MeV. This beam is derived from 1 nC bunches produced by a normal conducting RF photo injector operating at 1 kHz. At this repetition rate the 1 kW of beam can be safely dumped after traversing a final spontaneous undulator source.

Although the XUV-FEL beam and the high average-current beam discussed above are derived from separate electron sources after suitable low energy acceleration they are merged and accelerated in a single superconducting linac. The two beams are then separated using magnetic, energy dispersion for delivery to their respective devices.

The third accelerator system is that required for the IR-FEL. The same linac technology is used to accelerate electrons to between 25 and 60 MeV to provide a fully integrated and synchronised IR-FEL facility. The main electron beam parameters for 4GLS are given in Table 1.

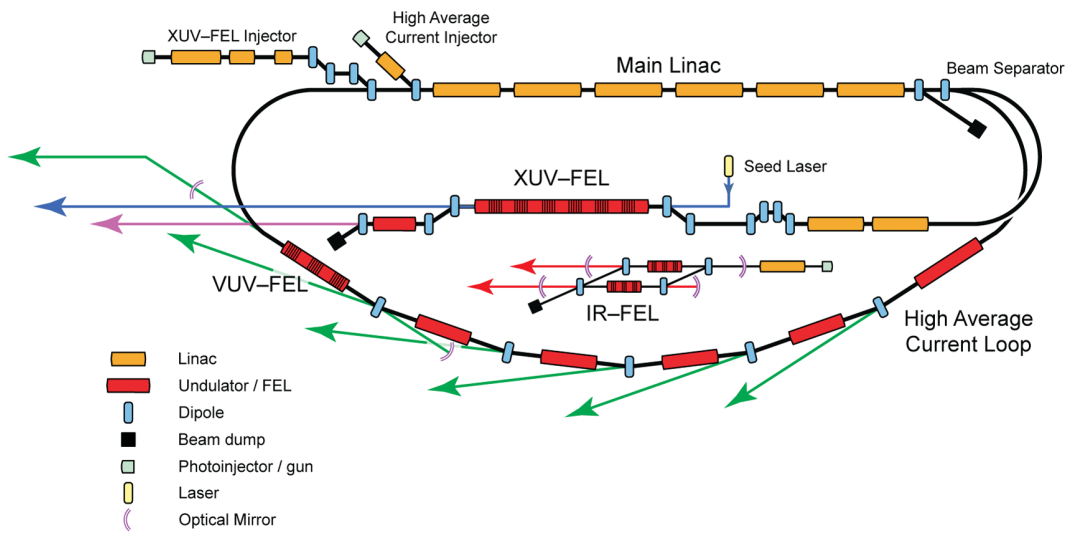

Figure 2. The conceptual layout of 4GLS.

Table 1. Main electron beam parameters of 4GLS

Bunch Parameter	*XUV-FEL*	*100 mA HACL Operation*	*VUV-FEL HACL Operation*	*IR-FEL*
Electron Energy	750 to 950 MeV	600 MeV	600 MeV	25 to 60 MeV
Normalised Emittance	2 mm mrad	2 mm mrad	2 mm mrad	10 mm mrad
RMS Projected Energy Spread	0.1 %	0.1 %	0.1 %	0.1 %
RMS Bunch Length	< 270 fs	100 to 900 fs	100 fs	1 to 10 ps
Bunch Charge	1 nC	77 pC	77 pC	200 pC
Bunch Repetition Rate	1 kHz	1.3 GHz	n x 4.33 MHz	13 MHz
Electron Beam Average Power	1 kW	60 MW	n x 200 kW	156 kW

SUPERCONDUCTING LINACS

The 4GLS design utilises superconducting linacs to accelerate and manipulate the three beams required to drive the photon sources. The accelerating structures are all based on a fundamental RF frequency of 1.3 GHz and a modified TESLA type cavity design operating at 2 K or below [6, 7]. The chosen RF frequency takes advantage of extensive development and operating experience of such systems (including the fact that industrialisation of the production and processing of such cavities is already well underway in preparation for the international linear collider ILC and superconducting XFEL).

Importantly the 4GLS design team at Daresbury are currently close to completing construction of an energy recovery prototype, ERLP, based on commercially procured linac modules incorporating TESLA 9-cell cavities which will provide a valuable test bed for the critical cavity and module developments required to produce linacs capable of operating in CW mode with the high-average beam currents.

For the high average current injector linac the major challenge is the delivery of the beam power required to accelerate a beam of up to 100 mA to 10 MeV without energy recovery. A cavity and coupler scheme similar to the two-cell geometry with symmetric couplers currently being developed at Cornell for the Cornell ERL prototype will be adopted for 4GLS. Two modules consisting of five of these two-cell cavities will suffice to provide the requirements of the ~ 10 MeV high average current injector system.

The main linac will be made up of six cryomodules each containing eight, seven-cell cavities which are currently under development within an international collaboration that includes CCLRC. This development is designed to meet the extreme demands of CW high-average current operation. The choice of six accelerating modules for the main linac is a balance between capital and operating costs which also provides a reasonable overhead in accelerating voltage. Another five similar accelerating modules are required within the accelerator system, two within the XUV-FEL injector system, two for the XUV-FEL linac to take this beam from 750 MeV to 950 MeV and one to give the 60 MeV requirement for the IR-FEL. Development and verification of this challenging module design will be a major activity during the technical design phase of 4GLS. A prototype 2 cavity cryomodule is currently being developed at Daresbury Laboratory [8].

INJECTORS

For linac-based light sources the injectors are an essential element in the delivery of high performance, high quality beams. The requirements for the three injectors proposed for 4GLS come directly from the challenging demands of the FEL and spontaneous sources. Unlike storage rings light sources where the beam properties are essentially decoupled from the properties of the injector beam, the performance of ERL-based sources are directly dependent on the quality of the electron beam as produced by the injector and preserved during transport and acceleration.

The IR-FEL of 4GLS makes relatively modest demands of the injector and the source envisaged requires 200 pC, 1 ps electron bunches with a normalised emittance of around 10 mm mrad. This can be delivered in a cost-effective and reliable way by mature thermionic gun technology. In contrast, the proposed injectors for both the high-average current loop and the high brightness XUV-FEL branch are based on developments of existing injectors.

The XUV-FEL injector source is required to deliver 1.5 kA peak current at 1 kHz repetition rate, the normalised emittance required to drive the device is 2 mm mrad. Normal conducting RF photoinjectors today already exceed the bunch charge (1 nC) and emittance requirements and are a proven mature technology but they are typically low duty-cycle systems operating at a few Hz and require development to meet the 4GLS target repetition rate. Development of the PITZ gun is already underway that would increase the demonstrated 0.9 % duty cycle to 2.5 %, a slightly higher duty cycle than that required for 1 kHz operation of the XUV-FEL. Simulations using well developed particle codes have shown that a normalised emittance of 1.7 mm mrad can still be delivered whilst using relatively modest accelerating gradients, producing acceptable thermal loads in a gun engineered to supply additional cooling. This design is an effective starting point for the technical design of the XUV-FEL gun-cavity.

The photoinjector chosen for the high average current loop is required to deliver an unprecedented 100 mA beam with an emittance of 2 mm mrad. With such a high current demand an optimal choice of cathode material is a high quantum efficiency semiconductor which limits the laser power required to reasonable levels. From the experience of the JLAB DC photo-injector, that has been utilised on the ERLP photo-injector, caesiated gallium arsenide may provide a suitable option for the cathode material. To meet the 4GLS requirements this gun will be driven by a simple stable 160 W, Yb-doped fibre laser operating at 1.3 GHz. Whilst the TJNAF DC and ERLP photo-injectors are already designed to achieve the 77 pC bunch charge required, the emittance of these guns is limited to around 5 – 10 mm mrad and the maximum, average current achieved at JLAB is only 9.1 mA. Further development is clearly required to meet the requirements of 4GLS and verification of such performance goes beyond the scope and capability of the current ERLP. Evolving from JLAB DC photoinjector developments, Cornell University is currently building a prototype injector which will produce a 100 mA beam of 77pC bunches. Extensive simulations of this gun based on the use of particle tracking codes predict that the emittance requirements for 4GLS would be fully met by this design.

BEAM DYNAMICS

The most challenging area of accelerator design for 4GLS is in meeting the requirements of extremely high peak current, (1.5 kA) for the XUV-FEL branch whilst simultaneously transporting and accelerating very high quality high-average current (100 mA) beam to the energy recovery loop. The conceptual solutions to the dynamics challenges for delivering the two most challenging beams are discussed below.

These two beams originate from separate photo-injectors, a high brightness RF photoinjector operating at 1 kHz delivering 2 mm mrad normalised emittance, 1 nC bunches for the XUV-FEL and a low emittance 100 mA, normal conducting DC injector. At relatively low injector energies these high quality beams are susceptible to intense space charge effects. Within the RF gun, the 1 nC beam undergoes rapid acceleration to a few MeV and is then injected into a superconducting linac which quickly boosts the energy to 220 MeV. Rapid acceleration of the 100 mA beam is achieved through the use of a high DC voltage followed closely by two superconducting booster modules delivering the ~1 MW power required to accelerate the beam to 10 MeV.

The bunches within both of these beams have to undergo a significant amount of compression to deliver the required peak currents to drive the XUV- and VUV-FELs and to meet the requirements of the science case for different pulse lengths from undulators in the high-average current loop. An innovative, integrated acceleration and compression scheme is proposed which meets the unique requirements for each of the two beams whilst using the same main superconducting accelerator [9]. By defining appropriate accelerating phases within the linacs, the high compression demands of the XUV-FEL are met using a two-stage compression scheme including a higher harmonic RF system for flexible non-linear correction, whilst progressive compression through the undulator arc delivers the high peak current in the 77pC bunches required to drive the VUV-FEL. An important part of this design is the optimisation of the scheme to maintain a high quality beam throughout the transport. Wakefield effects in the accelerator are reduced by performing the final compression stage at full energy so that the bunches around the arcs are kept relatively long to control the disruptive effects of coherent synchrotron radiation (CSR) emission which if uncontrolled can produce unacceptable energy loss and emittance growth. Acceleration of a 100 mA beam is very challenging; to accelerate and decelerate such a beam requires that the linac transport design is tailored to give a high threshold for the disruptive beam break-up instability. This is achieved through a combination of techniques including substantial damping of HOMs in an advanced design of RF cavity, tight control of beam focussing throughout the linac and optimisation of coupling and overall transport properties in the energy recovery loop [10, 11].

For the 4GLS XUV- and VUV-FELs, very high peak current is demanded simultaneously with narrow magnet gaps. These high peak currents are vulnerable to disruption by associated strong wakefields in nearby metallic chamber walls. This wakefield interaction and its undesirable consequences will be controlled through the use of appropriate vacuum materials and an optimisation of the FEL design which maintains vessel apertures that are compatible with delivering the required high quality beam.

FREE ELECTRON LASERS

The characteristics of 4GLS and its central ERL will be optimally exploited by the inclusion of three FELs, each covering a distinct photon energy range matched to the science needs of the UK and each offering excellent performance levels. The three designs are all state-of-the-art with key advantages over other designs being proposed elsewhere.

XUV-FEL

A simple yet robust seeded design for the XUV-FEL is proposed to ensure that ultra-high quality, reproducible, tunable radiation is available in the 8 to 100 eV photon range [12, 13].

A tunable laser seed pulse from a High Harmonic Generation source, that covers the full photon energy range, is amplified within the FEL. The FEL undulator consists of a lattice of individual undulator modules allowing electron beam focusing elements and diagnostics to be placed in between. The final undulator modules of the FEL will be of APPLE-II design that will enable the generation of variable elliptically polarised radiation. Figure 3 shows a schematic layout for the undulator modules and illustrates that for the low energy photons only the APPLE-II modules are in use whilst at high energy all of the modules are required.

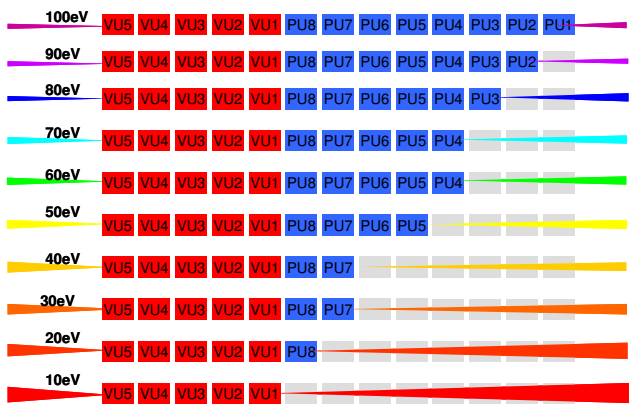

Figure 3. Schematic of the modular undulator system of the XUV-FEL demonstrating the different modes of operation across the photon energy range 10-100 eV. Electron beam transport is right to left. The minimum required undulator gap decreases in gradual steps from 28 mm for PU1 down to 10 mm for PU8 and the variable polarisation modules VU1-VU5.

The output pulses will have selectable polarisation and a pulse repetition rate of 1 kHz is set by the seed laser and the electron beam. Established FEL theory and state-of-the-art simulation codes predict this FEL will generate photon energies at multi giga-watt power levels in pulses of duration 40 - 60 fs FWHM. The pulses will have excellent temporal and spatial coherence with time-bandwidth products close to the Fourier transform limit for a Gaussian pulse. Unlike the self amplified spontaneous emission mode of operation, which effectively self-starts from intrinsic noise, the FEL interaction here is acting as a true amplifier. The high quality spectral properties of the radiation input seed pulses are maintained by the amplified output radiation pulses, as illustrated in Figure 4. Recent advances in High Harmonic Generation seed sources mean that the seed requirements for the XUV-FEL already exist and clearly future advances in conventional lasers can be readily harnessed. Further details on the issues raised by the use of HHG seeding can be found in [14].

The 4GLS design also incorporates an undulator after the XUV-FEL which enables the generation of spontaneous SR light with natural synchronisation to the XUV-FEL radiation

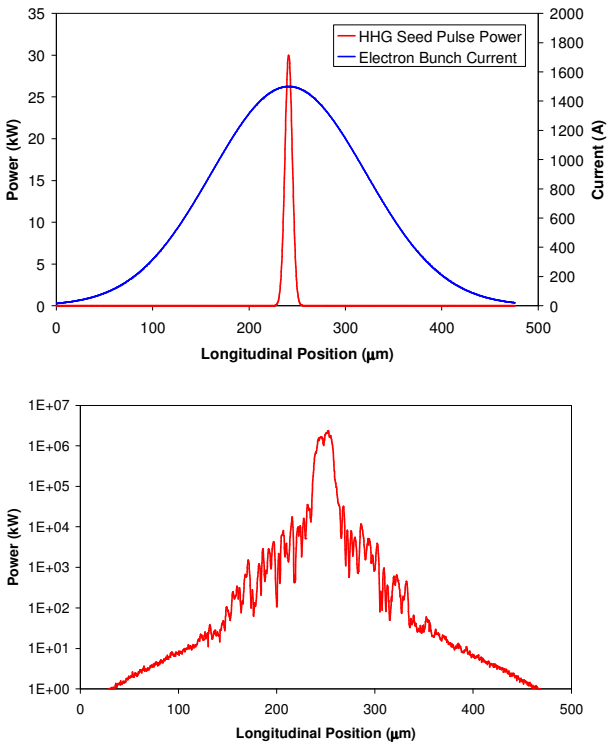

Figure 4. (a) Input HHG seed power (FWHM 30 fs) and electron bunch current as a function of longitudinal position (linear scale) and (b) radiation power (FWHM ~50 fs) at the exit of the XUV-FEL (log scale).

VUV-FEL

The VUV-FEL will be a Regenerative Amplifier FEL (RAFEL) which is a high gain system that is of insufficient length to achieve saturation in SASE mode. A small fraction of the radiation emitted by an electron pulse at the end of the undulator is fed back to the beginning of the undulator to act as a seed field to a subsequent electron pulse. The radiation feedback may readily be achieved by placing the undulator into a low-Q cavity. This self-seeding process rapidly builds up and allows the RAFEL to achieve saturation after only a few electron pulses have propagated through the undulator. Figure 5 shows the intracavity pulse power for a cavity length detuning of ~ 12 μm after the first and eighth pass. After the first pass, the pulse power has a noisy profile characteristic of SASE. However, after only eight passes saturation occurs and the intracavity peak power is 290 MW, equivalent to an output power of 218 MW. The corresponding spectrum, also shown in Figure 5, is seen to be noisy after the first pass. On subsequent passes however the spectrum narrows about a single wavelength. At saturation the spectrum has FWHM bandwidth of 0.26% giving a time-bandwidth product of ~1.0. This is just over a factor two greater than a Fourier transform limited gaussian pulse and indicative of excellent longitudinal coherence.

The FEL will offer high repetition rates (multiples of 4.33 MHz) with giga-watt peak power and > 100 W average power [15]. Here advantage is taken of mirrors (with hole out-coupling) that are able to operate over the photon energy range of 3 to 10 eV. Photon pulse lengths of ~ 170 fs (FWHM) will be obtained in standard mode and simulations suggest that pulses as short as ~ 25 fs will be generated in a super-radiant mode. The output pulses will have selectable polarisation and be fully tunable.

By using a pair of mirrors to reflect light emitted by the FEL back to the entrance of the device it becomes, in effect, self-seeding and no external conventional laser system is required. Hence high quality, stable light is ensured through a rather simple optical feedback loop. A particular feature of this FEL when compared with similar designs covering the same wavelength range is the tolerance to low mirror reflectivity. Extensive simulations have shown that mirror reflectivities in the range 40 to 60 % are acceptable for this design [16].

Detailed modelling has been used to study the effect of timing jitter in the electron bunch arrival time [17]. Figure 6 shows the build up of saturation with no timing jitter and with a jitter of ±80 fs, calculated using the 1D time dependent code FELO [18]. Statistical analysis of the peak output power during saturation suggests that the RMS variation in the peak output power increases from 2.5% for the no jitter case to 8% for a jitter of ±80 fs.

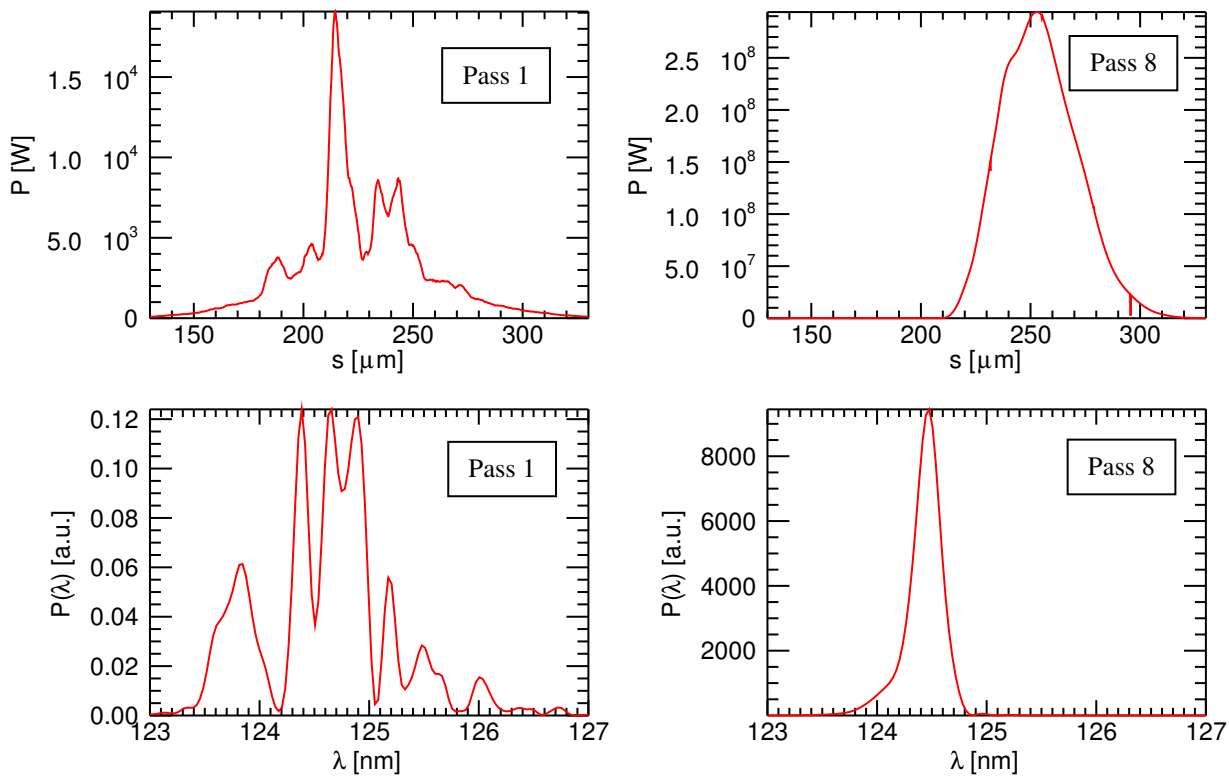

Figure 5. Genesis 1.3 [19] simulation of the radiation pulse power and the radiation spectrum after one and eight passes through the VUV-FEL for a cavity detune of 12μm.

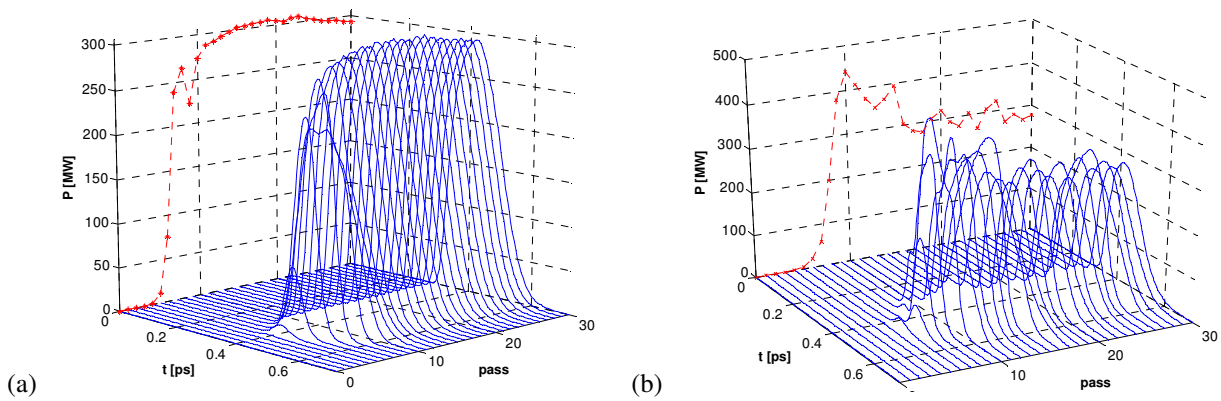

Figure 6. FELO simulation of the VUV-FEL at 10eV and cavity length detuning of 18μm with (a) zero electron bunch arrival time jitter and (b) jitter of ±80 fs. The red points show the peak intensity of the pulse at each pass.

IR-FEL

The IR-FEL has been designed to produce high intensity, spatially and temporally coherent radiation with variable pulse lengths, flexible output pulse patterns and variable polarisation over the wavelength range 2.5 - 200 μm. The high-Q cavity-based design employs two undulators in parallel and hence can serve two user experiments simultaneously. The provision of short electron bunches offers the potential to operate the FEL in super-radiant mode to produce shorter FEL pulses with higher peak intensities than available in normal operation: simulations predict FWHM pulse lengths of only a few optical cycles can be produced in this way. The implementation of a superconducting RF linac with the IR-FEL will offer highly stable operation and also high average powers (> 100 W) though the option of running in modes that reduce the average power for sensitive samples will also be available.

SPONTANEOUS SOURCES

There are six insertion device straights in the high average current loop, one of which is allocated to the VUV-FEL. The remaining five will be used to generate spontaneous radiation. To maximise the potential of the spontaneous sources three different undulator straight

lengths have been chosen; two 14 m straights; two 10 m straights and two 8 m straights. Thus the total space available for undulators is ~ 64 m, which exceeds all other existing low energy 3rd generation light sources. More than one insertion device can be placed in each straight with a small corrector magnet between them so as to angularly separate the photon output. Distributed pulse compression will be employed in the high average current loop in order to deliver to users pulse lengths optimised for their experiments ranging from a few ps down to 100 fs (RMS).

It is well known that electrons in a bunch radiate coherently at wavelengths of the order of, and longer than, the bunch length. Since 4GLS has very short bunch lengths this so-called Coherent Synchrotron Radiation (CSR) is emitted over a broad wavelength range. Calculations indicate that the onset of the CSR for 4GLS is at around 40 μm and hence it will be an extremely intense source THz radiation.

TABLE TOP LASERS

In order to make full use of 4GLS it is important to allow integration of its sources with conventional lasers. Continuous coverage of the visible and near-IR parts of the spectrum is provided by the spontaneous sources as illustrated in Figure 1. However, there are currently no plans to provide FEL radiation in the spectral range from 0.5 – 3 eV, as this is covered more cost-effectively by tabletop laser systems. These wavelengths will be made available by using continuously tuneable mid-infrared laser systems, such as mid-infrared Optical Parametric Oscillator and Optical Parametric Amplifier systems, Difference Frequency Generators and diode lasers. Ability to synchronise the additional lasers to within the temporal profile of the 4GLS sources is required. Current synchronisation is achievable to within < 100 fs, and is the subject of a vigorous worldwide research and development programme.

STATUS

The conceptual design of 4GLS is now complete and reported in [1]. The project is now entering the technical design phase which includes a substantial R & D element. The Energy Recovery Linac Prototype at Daresbury Laboratory is presently being commissioned and the results from this will be fed into the technical design of 4GLS. In addition to this a superconducting RF linac module prototype is under construction that will be capable of operating CW at a high average beam current of 100mA. It is intended that this will be installed into ERLP at a later date for electron beam trials. In addition to this a high current photoinjector project is being initiated at Daresbury Laboratory to ensure that the target current of 100 mA can be delivered with the required electron beam parameters.

REFERENCES

[1] 4GLS Conceptual Design Report 2006, available from www.4gls.ac.uk
[2] M. W. Poole and E. A. Seddon, '4GLS and the Energy Recovery Linac Prototype Project at Daresbury Laboratory', PAC 05, Knoxville, p431.
[3] J. A. Clarke, 'The Conceptual Design of 4GLS at Daresbury Laboratory', EPAC 06, Edinburgh, p181.
[4] D. J. Holder et al, 'The Status of the Daresbury Energy Recovery Prototype Project', EPAC 06, Edinburgh, p187.
[5] S. L. Smith, 'A Review of ERL Prototype Experience and Light Source Design Challenges', EPAC 06, Edinburgh, p39.
[6] P. A. McIntosh et al, 'RF Requirements for the 4GLS LINAC Systems', EPAC 06, Edinburgh, p439.
[7] S. Pattalwar et al, 'Key Cryogenics Challenges in the Development of the 4GLS', EPAC 06, Edinburgh, p499.
[8] P. A. McIntosh et al, 'Development of a Prototype Superconducting CW Cavity and Cryomodule for Energy Recovery', EPAC 06, Edinburgh, p436.
[9] B. D. Muratori et al, 'Lattice Design for the Fourth Generation Light Source at Daresbury Laboratory', EPAC 06, Edinburgh, p184.
[10] E. Wooldridge and B. D. Muratori, 'Linac Focusing and Beam Break Up for 4GLS', EPAC 06, Edinburgh, p2871.
[11] E. Wooldridge, 'Alternate Cavity Designs to Reduce BBU', EPAC 06, Edinburgh, p2874.
[12] B. W. J. McNeil et al, 'Design Considerations for the 4GLS XUV-FEL', FEL 2005, p506.
[13] B. W. J. McNeil et al, 'The Conceptual Design of the 4GLS XUV-FEL', these proc.
[14] B. Sheehy et al, 'Issues in High Harmonic Seeding of the 4GLS XUV-FEL', these proc.
[15] N. Thompson et al, 'A VUV-FEL for 4GLS: Design Concept and Simulation Results', FEL 2005, p79.
[16] N. R. Thompson et al, 'A 3D Model of the 4GLS VUV-FEL Conceptual Design Including Improved Modelling of the Optical Feedback Cavity', these proc.
[17] D. J. Dunning et al, 'First Tolerance Studies for the 4GLS FEL Sources', these proc.
[18] B. W. J. McNeil et al, 'FELO: A One-Dimensional Time-Dependent FEL Oscillator Code', these proc.
[19] S Reiche, Nucl. Instrum. Methods, A 429 (1999) p243.

FEL OSCILLATION WITH A HIGH EXTRACTION EFFICIENCY AT JAEA ERL FEL

N. Nishimori*, R. Hajima, H. Iijima, N. Kikuzawa, E. Minehara, R. Nagai, T. Nishitani, M. Sawamura, JAEA, Ibaraki, Japan.

Abstract

One of challenges that high-power FEL oscillators driven by energy recovery linac (ERL) are facing is to increase the extraction FEL efficiency as high as possible. The high-efficiency oscillation relaxes the total beam current needed for high-power lasing and makes the optical micropulse length shorter, which is useful for various applications. Two triple bend achromatic arcs have been used in a recovery loop for an ERL FEL at Japan Atomic Energy Agency (JAEA). The return arc after an undulator has an energy acceptance of 15%, which is large enough to recover the electron beam used for high-efficiency FEL oscillation. Recently we have achieved the efficiency exceeding 2%, which accompanies large energy spread, by doubling the electron bunch repetition rate. The FEL efficiency has been measured from the horizontal profiles of the exhausted electron beam with a wire scanner installed at a dispersive point in the return arc. The other arc placed upstream of the undulator has been found to work as a bunch compressor for the high-efficiency FEL oscillation.

INTRODUCTION

One of challenges that high-power FEL oscillators driven by energy recovery linac (ERL) are facing is to increase the extraction FEL efficiency as high as possible. The high-efficiency oscillation saves the total beam current needed for high-power lasing, which decreases the beam load to various accelerator components and increases the wall-plug efficiency. The high-efficiency oscillation is also appropriate for producing broadband ultrashort optical pulses, and makes the optical micropulse length shorter, which is useful for various applications [1].

In a high-power ERL FEL at Jefferson Lab, a high-efficiency FEL oscillation has been achieved at near IR wavelength region [2, 3, 4]. The exhausted beam is transported to accelerators through a Bates type recovery loop with energy acceptance of 15%, and full energy recovery has been successfully established [5]. A recovery loop which consists of two triple bend achromatic arcs has been used for an ERL FEL at Japan Atomic Energy Agency (JAEA) [6]. The energy acceptance of the return arc after an undulator was 7% before June 2006 [7, 6]. Recently we have achieved the efficiency exceeding 2%, which accompanies large energy spread beyond the energy acceptance of the arc, by doubling the electron bunch repetition rate [8]. The optical pulse can now interact with a fresh electron bunch every round trip, while it overlapped with an injected electron bunch every two round trips before the doubling.

In this paper, first we give brief description of the configuration and recent upgrade of JAEA ERL for a high-power FEL oscillation with the doubled beam current. Then our recent experimental results on the FEL efficiency and the beam dynamics through the energy recovery loop are reported in details. The FEL efficiency has been measured with a wire scanner installed at a dispersive point in the return arc, which can serve as a monitor of the energy distribution of the exhausted electron beam. The wire scanners have been also installed at other dispersive points for study of the beam dynamics through the triple bend achromatic arcs. A measurement of the energy distributions at the first arc, which is placed upstream of the undulator, as a function of the accelerator phase has revealed that magnetic bunch compression in the first arc is indispensable for a high-power FEL oscillation at the JAEA ERL. Finally, applications planned in JAEA FEL are presented.

CONFIGURATION OF JAEA ERL

The JAEA FEL facility has been developed as a high-power FEL at wavelength in far infrared region around 20 μm. The laser output power exceeded 1 kW within 500 μs macropulse duration without energy-recovery in 2000 [9]. In order to increase the FEL output power higher than 10 kW and demonstrate the technology and commercial profit of high-power FELs for industrial applications, we have developed an ERL FEL as an extension of the original superconducting accelerator [10].

The layout of the JAEA ERL is shown in Fig. 1. An injector, main super-conducting accelerator (SCA) modules, an undulator, and the first arc are from the original FEL. An injection merger, a half chicane before the undulator, and the return arc were installed for the ERL. The injector consists of 230 kV electron gun with a thermionic cathode, 83.3 MHz subharmonic buncher (SHB), and two cryomodules, each of which has a single cell SCA cavity driven at 499.8 MHz. An electron bunch of 0.5 nC with full width half maximum (FWHM) length of 600 ps is generated by a grid pulser at a 10.4 MHz repetition rate, that is 5 mA average current, and compressed by the SHB followed by a 4.5-m drift. The electron bunch is accelerated to 2.5 MeV by two single cells, and further compressed by ballistic bunching through a 9-m drift. A two-step staircase is used for the injection merger, because this configuration fulfills the design requirements, achromaticity and small emittance

* nishimori.nobuyuki@jaea.go.jp

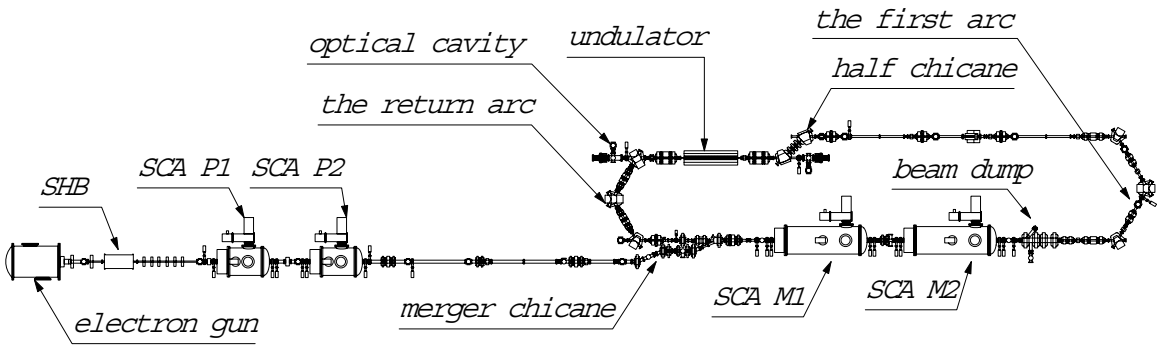

Figure 1: The layout of JAEA Energy-Recovery Linac. An electron bunch generated by 230 kV electron gun is accelerated to 2.5 MeV and injected into the energy-recovery loop. The electron bunch is accelerated to 17 MeV by main superconducting cavities and transported to the FEL undulator. The electron bunch is, then, re-injected to the main cavities and decelerated down to 2.5 MeV and collected by a beam dump.

growth, and fits in the existing space. The achromaticity of the merger is realized by setting three quadrupole magnets to the appropriate strengths. An electron bunch injected to two main cryomodules, each of which has five cell SCA cavities driven at 499.8 MHz, is accelerated up to 17 MeV and transported to the undulator through the first arc and the half chicane. After the FEL interaction, the electron bunch is re-injected into the main cryomodules at a deceleration phase for the energy recovery. The re-injection phase can be controlled by changing the recirculation path length. The return arc has been placed on movable tables for this purpose. Both arcs used in the recirculation loop have two families of quadrupole magnets which enable one to vary M_{56} while maintaining achromaticity. This variable M_{56} can be used for bunch compression in the first arc and for energy compression in the return arc. The return arc also has two families of sextupole magnets to compensate second-order aberrations T_{166}, T_{266}, T_{566} arising from the large energy spread due to the FEL interaction.

The JAEA ERL-FEL has been operated in pulsed mode of 1 ms macropulse length in maximum and 10 Hz repetition rate, because of the following reasons. 1) The cooling power of the refrigerator system for the SCA modules is not sufficient enough to operate in CW mode. 2) The shield of the building for the linac is not thick enough for the radiation protection.

UPGRADE OF JAEA ERL

Gun Grid Pulser and Injector RF sources

Increasing the injector beam current is a straightforward approach to increase the FEL power by taking full advantage of the energy-recovery. The JAEA gun has a thermionic cathode driven by a grid pulser. In the original configuration, the gun was designed to produce 0.5 nC electron bunches at 10.4 MHz repetition. We installed a new grid pulser working at 20.8 MHz, doubled repetition of the original one, and a 10 mA beam is now available [11]. The new grid pulser is designed at Budker Institute of Nuclear Physics and can be operated in CW-mode as well as pulsed mode [12]. The electron beam properties with the new grid pulser keep similar performance to the original one. The pulse width and the normalized rms emittance at the gun are 590 ps (FWHM) and 20 πmm·mrad, respectively [11].

Two single-cell cavities of the injector were driven by 8 kW solid state amplifier for each, enough capacity for 5 mA operation. The solid state amplifier was replaced by an IOT-klystrode of 50 kW, which enables one to inject a 40 mA beam into the ERL [13].

RF low-level controllers

Stable operation of an FEL relies much on the stability of an accelerator. An RF low-level controller for a SCA is one of the key components for achieving good stability. The original JAEA FEL was equipped with a low-level controller, which kept phase flatness at ± 1 degree within a 1 ms macropulse. The low-level controller was replaced by new one, which provides the following functions for the better stability: the feedback gain and bandwidth can be varied during operation to obtain good flatness of RF phase and amplitude, and all the circuits are contained in boxes with temperature stabilization. The new controller is installed in the vicinity of the SCA cavity to make the cable length between the controller and the SCA as short as possible. Furthermore the cables between the controller and the cavities are contained in a temperature-controlled pipe to suppress the temperature drift. After these upgrade, the accuracy and stability of accelerating RF has been improved. The flatness of RF phase and amplitude within a 1 ms macropulse are 0.06 deg. rms and 0.013% rms, respectively, while those for the old system were 0.20 deg. and 0.013% [14]. Phase and amplitude fluctuations for 5 minutes in the new system are measured as 0.15 deg. and

0.015%, respectively.

Increased energy acceptance of the arcs

The doubled beam current has enabled us to operate the JAEA ERL FEL with efficiency higher than 2%. The resulting large energy spread of the exhausted electron beam exceeded the energy acceptance of the return arc, which caused a radiation problem when the FEL was operated for a long time period at a macropulse length longer than 250 μs. We made minor modification of the return arc to increase the beam energy acceptance. The bore of quadrupole magnets of the return arc was enlarged from 64 mm to 102 mm. The beam pipe diameter was enlarged from 55 mm to 100 mm. The energy acceptance of the return arc has been increased from 7% to 15%. The quadrupole magnets in the first arc were also replaced with those used in the return arc. The energy acceptance of the first arc has been increased from 3.5% to 4.3%.

FEL EFFICIENCY

The FEL wavelength at the JAEA FEL is around 20 μm and a holed mirror is used to couple FEL out of the optical cavity. The coupling efficiency of the holed mirror is estimated to be around 30% [15]. It is however difficult to exactly determine the FEL efficiency from the measured FEL power only. The FEL efficiency can be obtained from a measurement of the beam centroid shift of the exhausted beam from the position without lasing at a dispersive point. A non-destructive method is indispensable for the energy analyzer, since the exhausted beam has to be recovered under an ERL operation. A synchrotron radiation (SR) monitor allows for continuous monitoring of the energy spectrum of the beam for an ERL operated even at a full power [16, 5]. The SR wavelength at the JAEA ERL is however longer than 20 μm, where no monitor camera is available. A beam position monitor is also a promising candidate for measuring the shift of the beam centroid [17]. It does not however provide information about the energy distribution of the exhausted beam, which is also important for beam energy recovery. We decided to use a wire scanner, which is appropriate for measuring profiles of pulsed or low-current-CW beams, although it is a partially intercepting device.

Wire Scanners

A wire scanner consists of a thin wire that is moved across the beam path. The local density of the electrons traversing the wire is detected by measuring such secondary particles as secondary electrons and bremsstrahlung photons produced by the interaction of the electron beam with the wire. Detection of the secondary particles allows one to measure the beam profile, and wire scanners are widely used as beam profile monitors. Detecting bremsstrahlung photons with a scintillator and a photomultiplier placed downstream of the wire has enabled one to measure large dynamic range beam profile in an ERL where small beam loss like beam halo represents significant amount of beam power [18]. A wire array based on secondary electron emission current is used to provide time resolved electron spectrum, which is useful to study the evolution of the energy spectrum from a narrow to a broad spectrum as a result of the FEL interaction [19, 20].

The wire scanner used in the present study is based on a linear movement of a copper wire in 0.6 mm diameter through the beam at a speed of 0.39 mm/s by 100 mm-stroke. The copper wire is mounted on an aluminium fork with a gap of 26 mm and electrically floated from the ground. The secondary electron emission current is measured with a current meter (TR8641 electronic picoammeter, ADVANTEST). The wire position is measured with a linear potentiometer and is recorded in an ADC (WE7272 isolated digitizer, YOKOGAWA) together with the secondary electron current.

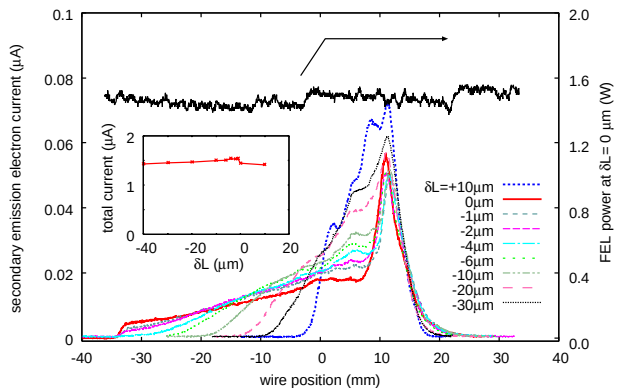

Figure 2: Horizontal beam profiles for various cavity detuning lengths measured with a wire scanner (WIRE #1) placed in the middle of the drift space between two quadrupole magnets just after the first bending magnet in the return arc, where horizontal dispersion is measured to be η = 0.376 m. The vertical axis shows secondary electron emission current and horizontal axis shows wire position. The total secondary emission electron current integrated along the wire position is plotted with respect to optical cavity detuning length in the inset. The FEL power at δL = 0 μm during a wire scan is represented by a black solid line.

Electron energy distributions and FEL efficiency

Figure 2 shows horizontal beam profiles measured for various detuning lengths (δLs) of an optical cavity with the wire scanner, which is installed in the middle between two quadrupole magnets placed just after the first bending magnet in the return arc. This wire is called WIRE #1 in the present paper. The horizontal dispersion at the wire scanner is measured to be η = 0.376 m from the shift of the beam centroid with respect to the magnetic field of the first bending magnet. This is similar to the value of η =

0.41 m calculated from a first-order matrix of beam transport (see Fig. 5). The vertical axis shows secondary emission electron current from the wire scanner and horizontal axis shows wire position. The polarity of the secondary electron current is positive. The inset shows the total secondary emission current integrated along the wire position as a function of δL. The total secondary current is 1.5 μA, which is almost independent of δL. The secondary electron production rate for 17 MeV electron on our wire scanner is estimated to be 8%, since the incident electron beam current during the measurement was 18.5 μA. The production rate is similar to that for for 30 MeV electron on carbon, which is measured to be 3% [21]. The peak secondary electron current measured by the wire is less than 0.07 μA (see Fig. 2), indicating that the beam loss due to the presence of the wire is small (less than 5%). This explains our observation that the FEL power at δL = 0 μm remains unchanged during the wire scan, which is shown by a black solid line in Fig. 2,

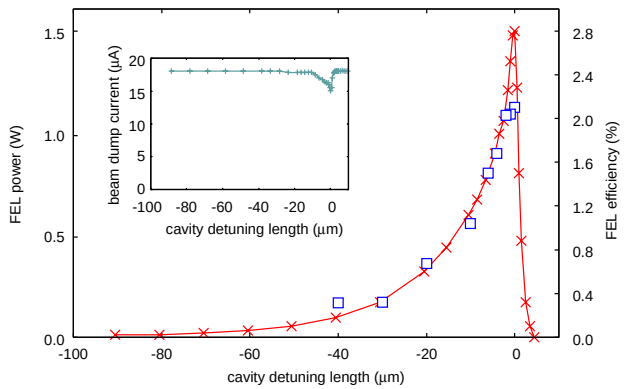

Figure 3: FEL power measured as a function of δL at macropulse length of 230 μs. FEL efficiencies obtained from the energy distributions of the exhausted electron beam are shown by open squares. The efficiencies near zero detuning length cannot be measured with our energy analyzer due to the limited energy acceptance, and they are determined from measured FEL power. The inset shows the beam dump current with respect to δL.

The FEL power changes as a function of δL, as shown in Fig. 3, and the energy distributions of the exhausted electron beam changes as well (see Fig. 2). The shift of the beam centroid from the position without lasing yields the FEL efficiency together with the dispersion η = 0.376 m. The measured FEL efficiencies are plotted as open squares in Fig. 3. The efficiency higher than 2% cannot be measured with our present wire scanner, since the scanner is placed downstream of the focusing quadrupole magnet where the dispersion is maximum of η = 0.6 m. The sharp edge of the beam profiles seen around the wire position of -34 mm in Fig. 2 represents the beam loss in the lower energy side at the first quadrupole. The amount of the beam loss is considered to be small, since the total secondary electron current is almost constant with respect to δL (see inset of Fig. 2). The maximum FEL efficiency is estimated to be 2.8%, as shown in Fig. 3.

Table 1: JAEA ERL FEL parameters

Parameter	Measured
Beam energy at undulator	17 MeV
Average current at undulator	8 mA
Bunch charge at undulator	0.4 nC
Bunch length at undulator	12 ps (FWHM)
Peak current	35 A
Energy spread before undulator	1.5% (FWHM)
after undulator	$>$ 15% (full)
Normalized emittance (rms)	40 mm mr
Bunch repetition	20.8250 MHz
Macropulse	1 ms $\times$ 10 Hz
Undulator period	3.3 cm
Number of undulator periods	52
Undulator parameter (rms)	0.7
Optical cavity length	7.2 m
Rayleigh range	1.00 m
Mirror radii	6 cm
Output wavelength	22 μm
FEL extraction efficiency	$>$ 2.5%

The coupling efficiency of the holed mirror is obtained from the present efficiency measurement. The measured FEL power is 1.5 W for macropulse length of 230 μs. The FEL power during the macropulse is estimated to be 0.75 kW, since the FEL power for the first 30 μs is negligibly small. The FEL is extracted through a KRS5 window, that has the transmittance of 70% in normal incidence. The beam current measured at the beam dump is 18.5 μA corresponding to the average beam current of 8 mA. From those experimental results, the coupling efficiency of the holed mirror is estimated to be 28% and agrees well with the calculated value of 30% [15]. The JAEA ERL FEL parameters are listed in Table 1.

Thermal effect on the wire scanner

Heating of the wire might be a concern when attempting to measure the profile of high average power electron beams [22]. The stopping power for 17 MeV electrons in copper is 2.5 MeV cm^2/g. [23], and the specific gravity of copper is 8.94 g/cm^3. We assume that the copper wire in 0.6 mm diameter is regarded as a foil with width of 0.532 mm and depth of 0.532 mm. The energy loss of 17 MeV electron in the copper wire is estimated to be 1.2 MeV. The total charge struck by the electron beam during a wire scan is measured to be less than 25 μC when macropulse length is 230 μs, and the maximum power deposited on the wire during the scan is 30 J. The specific heat of copper is 0.385 J/g/K at 25°C. Thus the temperature rise of the wire can be estimated to be 15000 K in maximum when we assume that the heat accumulates in the wire within a vertical distance of 2 mm, which is similar to the vertical beam size.

However we need to take thermal radiation power, thermal conductivity of copper, power of secondary emission particles, and others which can alleviate the temperature rise of the wire, into account. Although the wire scanner can be used as an energy analyzer as long as heating is not a problem, we need to study this thermal effect in details.

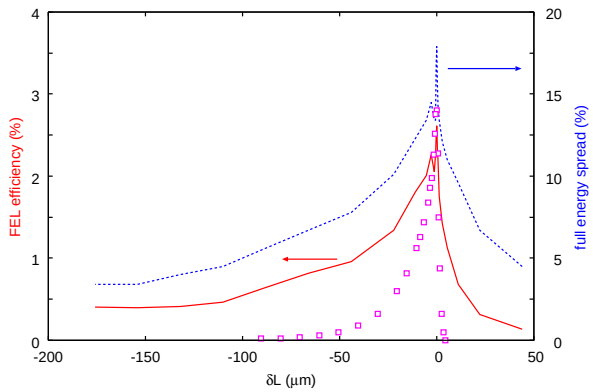

Figure 4: FEL efficiencies as a function of δL obtained from a one-dimensional time-dependent FEL simulation (solid line) and corresponding beam energy spread (dotted line). Measured FEL efficiencies are also plotted as open squares for comparison.

FEL simulation

We have conducted an FEL simulation for comparison with the experimental result. We use one-dimensional time-dependent FEL simulation code, which was used in our previous studies [24] and agrees well with experimental results obtained without energy recovery. The electron bunch length measured at the undulator center is 12 ps (FWHM). The electron bunch shape used in the simulation is assumed to be triangular with the peak Colson's dimensionless beam current of j_0 = 25. A mono energetic electron beam is assumed in the simulation, since the peak FEL efficiency depends little on initial energy spread [24]. The optical cavity loss is measured to be 4.2% from a cavity ring down of the FEL pulse with a Ge:Cu detector. Figure 4 shows calculated FEL efficiency and full energy spread of an electron bunch as a function of δL. The measured FEL efficiencies are much smaller than those obtained in the simulation at large detuning lengths. This may be due to the large energy spread of the incident electron beam.

BEAM TRANSPORT IN THE RETURN ARC

Transverse and longitudinal beam dynamics through the return arc for JAEA ERL has been already studied to find a matched beam envelope from the undulator to the beam dump [7]. In order to roughly estimate dispersion and M_{56} in the return arc, we calculate the beam envelope

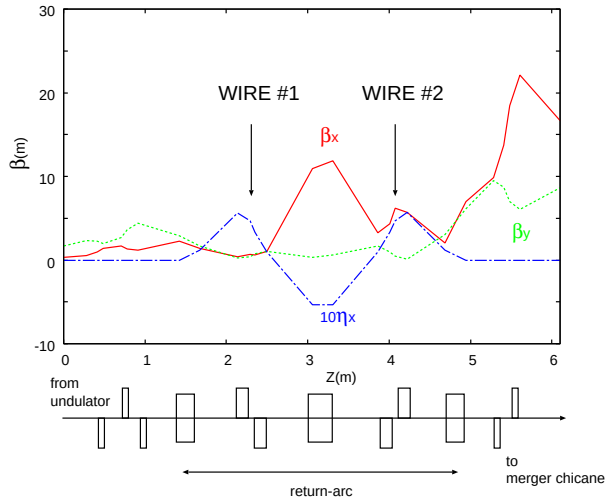

Figure 5: Beam envelopes from the undulator exit through the return arc to the merger chicane calculated from a first-order matrix of beam transport. The positions of wire scanners are indicated by arrows.

from the undulator to the entrance of main SCA modules based on magnet parameters used for actual beam transport. Courant-Snyder parameters at the exit of the undulator are given from the matched beam condition for the undulator, α_x = 0; β_x = 0.33 m; α_y =−1; β_y = 1.7 m. Figure 5 shows obtained betatron functions for the beam envelope, where M_{56} = −0.56 m from the undulator to the entrance of the merger chicane.

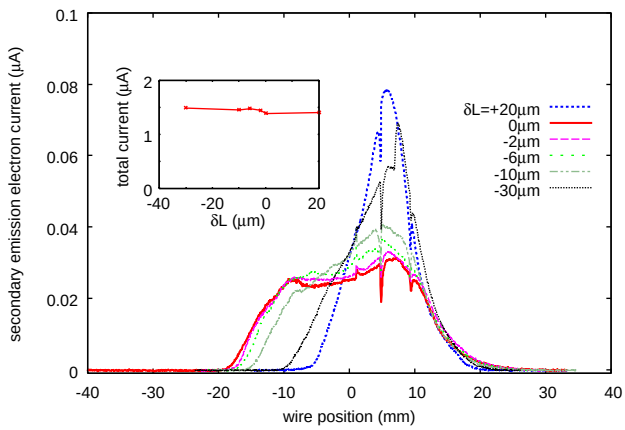

Figure 6: Horizontal beam profiles for various cavity detuning lengths measured with a wire scanner (WIRE #2) placed in the middle of the drift space between two quadrupole magnets just after the second bending magnet in the return arc, where horizontal dispersion should be the same as that of WIRE #1, η = 0.376 m, when the return arc is achromatic. The inset shows the total secondary emission electron current integrated along the wire position with respect to δL.

A drawback of a triple bend achromatic arc is that quadrupole magnets have to be properly set not only to adjust M_{56} for energy compression, but also to establish achromaticity in the arc. This is in contrast to the Bates type end loop where a pair of quadrupole magnets and a pair of sextupole magnets are used just to control M_{56}, T_{566}, respectively, since the end loop is intrinsically achromatic [5]. Therefore achromaticity has to be carefully checked in a triple bend achromatic arc. We have measured horizontal beam profiles downstream of the second bending magnet in the return arc with a wire scanner (see Fig. 6). This wire scanner is called WIRE #2 in the present paper and has been installed in the middle of the drift space between two quadrupole magnets after the second bending magnet and should have the same dispersion function as WIRE #1 when the return arc is achromatic. However, the beam profiles shown in Fig. 6 are similar to those in Fig. 2 only when the FEL efficiency is less than 1%, and they are quite different from each other when the efficiency is higher than 1%, requiring chromaticity correction. The total secondary electron current measured with WIRE #2, which is shown in the inset of Fig. 6, is almost the same as that with WIRE #1. The beam loss is thus expected to be small in the return arc. In the measurement shown in Fig. 6, sextupole magnets are not used to compensate second order aberrations T_{166}, T_{266}, T_{566} arising from the large energy spread due to the FEL interaction. We will perform a systematic measurement of the horizontal beam profiles with various parameter sets of sextupole magents soon.

A current transformer placed downstream of the return arc, which picks up an induction current, is also used as a beam loss monitor for the return arc. The current transformer signal remains almost the same when the FEL efficiency is low, but some beam loss is observed for the efficiency higher than 2%. The beam dump current with respect to δL should be constant when the full energy recovery is established. However the beam current gradually drops as the efficiency increases over 2%, as shown in the inset of Fig. 3. One possible reason is that the energy spread of the recovered beam is beyond the energy acceptance of the beam dump. Although the dump can collect the beam with four times different momentum, the energy spread of the recovered beam can exceed the acceptance under high-efficiency FEL oscillation. Without sufficient energy spread compression, the energy spread can remain 2.5 MeV, which corresponds to 15% of 17 MeV beam, while the mean energy of the recovered beam is lower than 2.5 MeV. We need to study carefully how much beam is recovered through the main SCA modules and how much of the recovered beam is collected by the beam dump.

MAGNETIC BUNCH COMPRESSION IN THE FIRST ARC

A high peak current electron beam, which can be accomplished by means of magnetic, ballistic, or velocity bunch compression, is indispensable to realize a high-efficiency

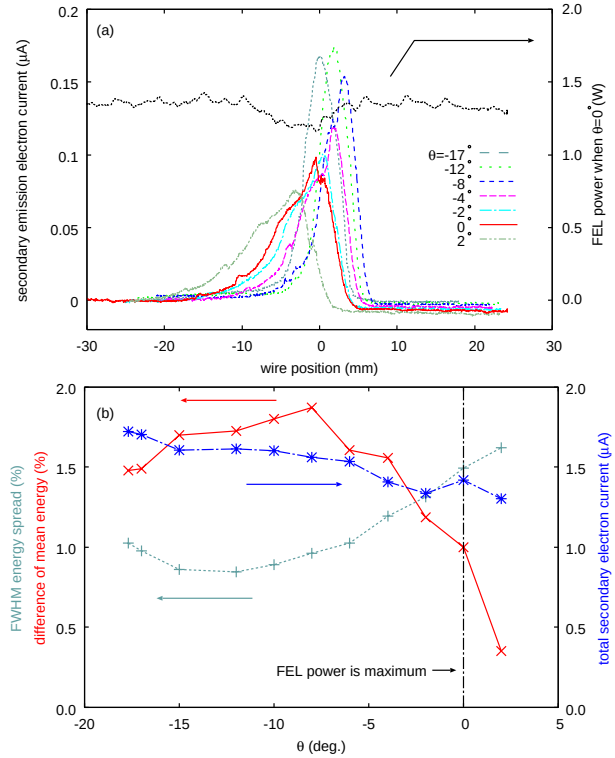

Figure 7: The top figure (a) shows horizontal beam profiles measured with a wire scanner placed just after the first bending magnet in the first arc, where horizontal dispersion is calculated as η = 0.50 m, with respect to the RF phase of the last SCA module M2 defined as θ. The black dotted line shows measured FEL power during a wire scan when $\theta = 0^\circ$, where the FEL power is maximum. The bottom figure (b) shows relative difference of the beam centroid energies (solid line), FWHM energy spreads (dotted line), and the total secondary emission electron current from the wire scanner as a function of θ. Those data are obtained from the top figure (a).

FEL oscillation. At the JAEA ERL, ballistic bunching, which is performed before the main SCA modules, had been considered to play a major role in the bunch compression [25]. Recently we measured powers of coherent synchrotron radiation (CSR) generated from three bending magnets in the first arc and found that the CSR power at the last magnet is much stronger than the remaining two. This indicates that another bunch compression occurs in the first arc. In order to confirm this magnetic bunch compression, we measured horizontal beam profiles with a wire scanner at a dispersive point as a function of the RF phase of the last SCA module (SCA M2). Hereafter we use θ as the RF phase of SCA M2. The horizontal dispersion at the wire scanner located just after the first bending magnet is estimated to be η = 0.50 m from the first-order matrix calculation. The measured beam profiles are shown in Fig. 7(a). Here we set $\theta = 0^\circ$ where the FEL power is maximum. The

black dotted line shows FEL power with respect to the wire position when $\theta = 0°$. The power decreases by 10% when the wire passes the beam centroid. The ratio of FEL power loss is consistent with the ratio of beam loss due to the presence of the wire scanner, which is calculated from the peak secondary current of 0.1 μA divided by the total secondary current of 1.4 μA.

Figure 7(b) shows difference of the mean energy, FWHM energy spread, and total secondary electron current with respect to θ. The energy spread is 1.5% when $\theta = 0°$, but it decreases down to 0.8% as θ decreases to $-12°$. The energy of beam centroid shifts toward higher energy side with decreasing phase and reaches maximum around $\theta = -10°$. The energy difference between $\theta = 0°$ and $\theta = -10°$ is 0.8% corresponding to 0.14 MeV for 17 MeV electron. Since the energy gain for each main SCA module is roughly 7.5 MeV, 11 degree off-crest acceleration yields the same amount of energy difference. From these results, we can conclude that $\theta = 0°$ is about 10 degree off-crest of the SCA M2 phase. The total secondary electron current gradually increases with decreasing θ, and the ratio of the current increases by 20% when $\theta = -17°$. The similar amount of beam loss is observed in another experiment. We have measured beam currents with a Faraday cup both in the straight section along the main SCAs and after the first arc, and observed that the beam loss through the first arc amounts to roughly 20% when the RF phase is adjusted for the FEL power to become maximum. This indicates that the lower energy side of the electron beam arising from the off-crest acceleration is lost at the beam duct of the first bending magnet in the first arc. We have a plan to replace the beam duct with one having larger bore and repeat the same measurement to study the energy spectra of the accelerated electron beam with respect to θ in more details.

We have also measured temporal beam profiles at the undulator center as a function of θ with a synchroscan streak camera (M1954-10, Hamamatsu) at macropulse length of 30 μs, as shown in Fig. 8(a). The centroid of beam profiles changes as a function of θ, since the beam arrival time shifts due to M_{56} from the SCA M2 to the undulator. The shift of arrival time and rms bunch length are shown in Fig. 8(b). The shortest FWHM bunch length of 12 ps is obtained when $\theta = 0°$, indicating that high peak current is indispensable for the high-efficiency FEL oscillation. The arrival time difference between $\theta = 0°$ and $\theta = -10°$ is 10 ps, and the corresponding momentum difference between the two acceleration phases is 0.8% from Fig. 7(b). This leads to M_{56} = 0.38 m, where the sign of M_{56} is determined from first-order matrix calculation of the first arc based on the magnet parameters used for actual operation. The calculation yields M_{56} = 0.6 for the first arc and M_{56} = 0.07 for the half chicane.

We will perform the same measurement somewhere downstream of the second arc to obtain M_{56} from the undulator center to the entrance to the main SCA modules. The value of M_{56} in the return arc should be the same as that to

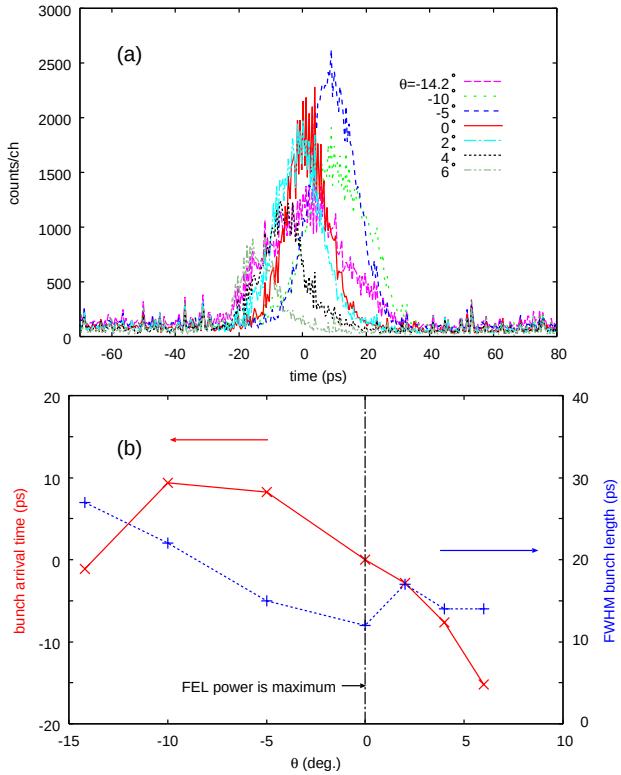

Figure 8: The top figure (a) shows temporal beam profiles measured with a synchroscan streak camera at the undulator center with respect to the RF phase of the SCA M2 (θ). The bottom figure (b) shows relative difference of the beam arrival time (solid line), and FWHM bunch length (dotted line). Those data are obtained from the top figure (a).

the undulator from the exit of SCA M2 except for its sign, if the energy compression in the return arc is properly executed. It is worth to mention that such a longitudinal phase space manipulation using magnetic bunch compression and decompression is performed in JLab FEL in an elegant way [5], where $M_{56} = -0.3$ m from the exit of SCA modules to the undulator for the bunch compression and M_{56} = 0.3 m from the undulator to the entrance of SCA modules for the energy compression.

APPLICATION

A laser-beam transport line has been built to deliver FEL pulses to an experiment room. We have upgraded an optical beam expander, which consists of two elliptic mirrors, at the end of FEL optical cavity to convert a diverging beam from a center-hole on a FEL cavity mirror into a parallel beam. The expanded beam is transported to the experimental room through a 24 m-long evacuated pipe. FEL transport efficiency 50% has been achieved [1].

For FEL applications, we investigate material processing using ultrashort FEL pulses. By using FEL pulse shorter than pico-second, it is possible to avoid thermally induced

stress and debris generation, which has been unavoidable in material processing with Q-switched YAG lasers or CO2 lasers [26]. Recently we found that non-thermal surface peeling of stainless steel by ultrashort laser pulses can be adopted to eliminate stress-corrosion-cracking (SCC), which is a critical problem in nuclear power plants [27]. A pilot experiment using Ti:sapphire laser showed that we can remove the residual stress and SCC susceptibility of cold-worked and hardened stainless steel by the laser peeling. Application of self-chirped FEL pulses is also studied. We reported that frequency chirp is induced in an FEL pulse, when the FEL oscillator has large gain and is operated at perfectly synchronized cavity length [28]. We demonstrated generation of an FEL pulse with frequency chirp of 14% and duration of 320 fs. A laser pulse with such large frequency chirp can be used for quantum control of chemical reaction: the resonant excitation of atomic or molecular systems, which have an anharmonic potential ladder [29].

REFERENCES

[1] H. Iijima et al.," Development of frequency-resolved optical gating for measurement of correlation between time and frequency of chirped FEL", in these proceedings.

[2] S. Benson et al.,"High power lasing in the IR Upgrade FEL at Jefferson Lab", Prof of the FEL-2004, 229 (2004).

[3] S. Benson,"Design challenges in high power free-electron laser oscillators", abstract of the FEL-2005, (2005).

[4] G.R. Neil et al.,"The JLab high power ERL light source", NIM A **557**, 9 (2006).

[5] D. Douglas,"The Jefferson Lab 1kW IR FEL", Prof of the LINAC-2000, 716 (2000).

[6] R. Hajima et al.,"First demonstration of energy-recovery operation in the JAERI superconducting linac for a high-power free-electron laser", NIM A **507**, 115 (2003).

[7] R. Hajima, E.J. Minehara,"Electron beam dynamics through a return-arc and a deceleration path of the JAERI energy-recovery linac", NIM A **507**, 141 (2003).

[8] R. Nagai et al.,"Beam current doubling of JAEA ERL-FEL", in these proceedings.

[9] N. Nishimori et al.,"High extraction efficiency observed at the JAERI free-electron laser", NIM A **475**, 266 (2001).

[10] R. Hajima et al.,"Design of energy-recovery transport for the JAERI FEL driven by a superconducting linac", NIM A **445**, 384 (2000); T. Shizuma et al.,"Simulated performance of the energy-recovery transport system for JAERI-FEL", *ibid* **475**, 569 (2001).

[11] N. Nishimori et al.,"20.8 MHz electron gun system for an energy recovery linac FEL at JAERI", Proc. of the APAC-2004, 625 (2004).

[12] V.P. Bolotin et al.,"Status of the Novosibirsk energy recovery linac", NIM A **557**, 23 (2006).

[13] M. Sawamura et al., "Status and development for the JAERI ERL-FEL for high-power and long-pulse operation", Prof of the EPAC-2004, 1723 (2004); Masaru Sawamura and Ryoji Nagai, "Status of RF system for the JAERI energy-recovery linac FEL", NIM A **557**, 287 (2006).

[14] R. Nagai et al.,"Improvement of RF low-level controller for JAERI ERL-FEL", Prof of the 1st annual meeting of Part. Acc. Soc. of Japan, 293 (2004) (in Japanese).

[15] R. Nagai et al., "Optical resonator optimization of JAERI ERL-FEL", NIM A **528**, 231 (2004).

[16] P. Chevtsov et al., "Non-invasive energy spread monitoring for the JLAB experimental program via synchrotron light interferometers", NIM A **557**, 324 (2006).

[17] A.P. Freyberger and G.A. Krafft, "Summary report on synchronization, diagnostics and instrumentation", NIM A **557**, 370 (2006).

[18] A.P. Freyberger, "Large dynamic range beam profile measurements", Proc of the DIPAC-2005, 12 (2005).

[19] T.I. Smith et al., "Status of the SCA-FEL", NIM A **296**, 33 (1990).

[20] W.A. Gillespie et al.,"Time-resolved electron spectrum measurement on the FELIX facility", NIM A **331**, 786 (1993).

[21] R.I. Cutler et al., "Performance of wire scanner beam profile monitors to determine the emittance and position of high power CW electron beams of the NBS-Los Alamos racetrack microtron", Proc of the PAC-1987, 625 (1987); M.A. Wilson et al., "Performance of the 5 MeV injector for the NBS-Los Alamos racetrack microtron", *ibid*, 322 (1987); D.B. Barlow et al.,"Prototype flying-wire beam-profile monitor", Proc of the PAC-1993, 2480 (1993).

[22] J. Camas et al.,"Observation of thermal effects on the LEP wire scanners", Proc of the PAC-1995, 2649 (1995).

[23] http://www.physics.nist.gov/PhysRefData/Star/Text/contents.html

[24] R. Hajima et al.,"Analyses of superradiance and spiking-mode lasing observed at JAERI-FEL", NIM A **475**, 270 (2001).

[25] R. Hajima et al.,"Development of an energy-recovery linac for a high-power FEL at JAERI", Proc. of the APAC-2004, 245 (2004).

[26] A. Nishimura et al., "Demonstration of material processing using JAERI-FEL", Proc of the FEL-2003, II-57 (2003).

[27] E.J. Minehara et al., "Preparation femtosecond laser prevention for the cold-worked stress corrosion crackings on reactor grade low carbon stainless steel", Prof of the FEL-2004, 665 (2004); E.J. Minehara et al., "JAERI 10kW high power ERL-FEL and its applications in nuclear energy industries", Prof of the FEL-2005, 305 (2005).

[28] Ryoichi Hajima and Ryoji Nagai, "Generation of a self-chirped few-cycle optical pulse in a FEL oscillator", PRL **91**, 024801 (2003).

[29] S. Chelkowski et al.,"Efficient molecular dissociation by a chirped ultrashort infrared laser pulse", PRL **65**, 2355 (1990).

ON THE DESIGN IMPLICATIONS OF INCORPORATING AN FEL IN AN ERL

G. R. Neil, S. V. Benson, D. Douglas, P. Evtushenko, and T. Powers
Thomas Jefferson National Accelerator Facility, Newport News VA 23606 USA.

Abstract

Encouraged by the successful operation of the JLab Demo in 1998, many high current ERLs are now being designed with not only short pulse synchrotron beamlines but also FELs. Such inclusion has major implications on magnet quality, rf feedback requirements, wiggler design, srf cavity Q_L, halo, etc.

Measurements on the JLab ERL FEL have identified new challenges. The JLab Upgrade was designed with a 160 MeV beam of 10 mA in 75 MHz, 300 fs bunches. FEL designers set transverse emittance and longitudinal bunching requirements, but to accommodate an FEL in our ERL also means setting stringent phase stability requirements of ($<6\text{x}10^{-9}/f_m$ *rms*) based on a desired FEL detuning tolerance of 1.2 microns. Recovered beam RF loading on the subsequent accelerated beam complicates satisfying these requirements. Gain in the rf feedback limits the accuracy of energy stability when loaded Qs are ~10^7. Energy recovery to <10 MeV sets magnetic field tolerances at 10^{-4}. We present measurements on the JLab ERL showing how to set system requirements to tolerate such FEL lasing.

BACKGROUND

Given the rising interest in Energy Recovered Light Sources incorporating Free Electron Lasers [1], it is helpful to review what specifications of the light source may need revision in order to accommodate the strict demands of the FEL. The discussion below should not be viewed as inclusive but rather is a starting point for further analyses based on experience to date. We give examples of specific criteria based primarily on our experience with the JLab IR Upgrade machine, which has proven to be a great learning tool in the path toward the next generation ERLs. Key areas for discussion include:

1) impact of longitudinal phase space manipulation on rf phase and amplitude control and srf cavity specifications
2) magnetic field quality, higher order term management for transverse and longitudinal acceptance
3) wakefields and resistive wall effects

LONGITUDINAL PHASE SPACE

For an FEL ERL it is generally desirable to let the bunch length remain long during initial acceleration to minimize longitudinal emittance growth. By operating off crest, a correlated energy spread in imposed on the beam that can be used to compress the beam to high peak current at the wiggler. The FEL then imposes an energy spread during lasing with a full width on the order of 6 times the extraction efficiency. This large energy spread must be transported to the dump during energy recovery. In addition the centroid of the distribution loses energy according to the FEL efficiency. If an appropriate M_{56} and path delay in the transport is applied before deceleration the energy spread of the beam can be compressed as the beam decelerates so that the ultimate energy spread as a fraction of the energy is not much larger than the FEL-imposed spread. The offset deceleration angle must be chosen to be sufficient to handle the full energy spread of the beam or successful transport to the beam dump will not be possible (Figure 1). Given the large energy spread of the decelerating beam it is also necessary to match the higher order terms of the magnetics. The Upgrade FEL utilizes sextupoles to help match the rf curvature and minimize dE/E at the dump [2-4].

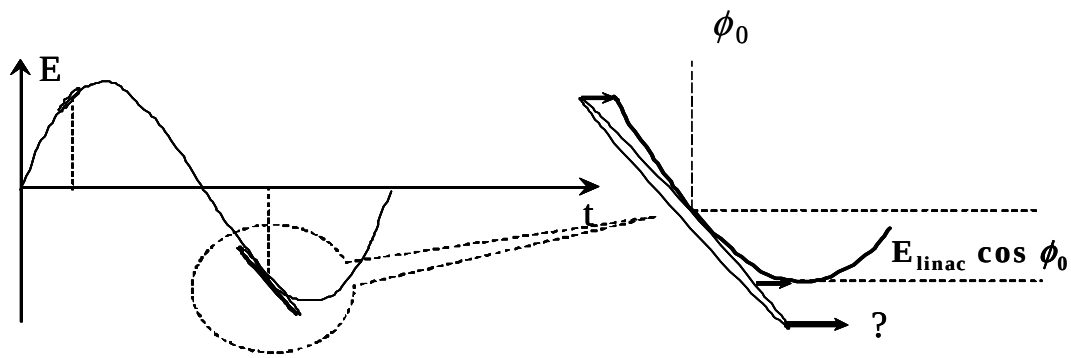

Figure 1. Electron distribution on the acceleration and deceleration rf phase. If the energy spread of the beam exceeds $(\Delta E/E)_{FEL}/2 < E_{linac} \cos \phi_0$ then there is not sufficient rf gradient to decelerate those electrons.

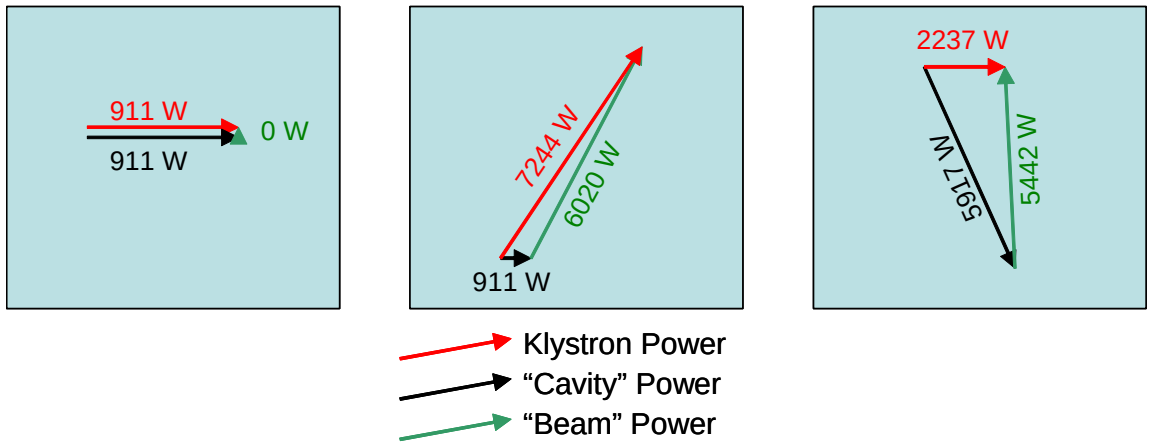

Figure 2. Loading of the rf with a) perfectly matched acceleration and deceleration, b) when the FEL turns on and instantaneously shifts in phase, c) after the srf cavity tunes its resonance to minimize power draw.

A practical rf control system must be able to manage transients associated with the FEL turning on and off. Figure 2 illustrates the beam load phasors in a typical rf cavity with the accelerated and decelerated beam initially perfectly canceling. For the example parameters, when the FEL turns on a phase shift of 7.2 degrees results and initially the rf power draw goes from 911 W at zero degrees to 7244 W at 50 degrees in the rise time of the laser: ~ 10 microseconds. Given time the srf cavity can retune to minimize the power draw (Figure 2c, 3). The resultant is then 2237 W at zero degrees. The energy of the accelerated beam must not change substantially during this transient or a relaxation instability between the FEL and accelerator can be initiated. It is important to note that although an ERL with perfectly opposed accelerating and decelerating beams can operate in principle with a very high loaded Q >> 10^7 such an arrangement makes this turn on and management of the FEL much more difficult. In practice, it may be more practical to trade the high CW power draw for ease of operation by having a lower Q_L [5].

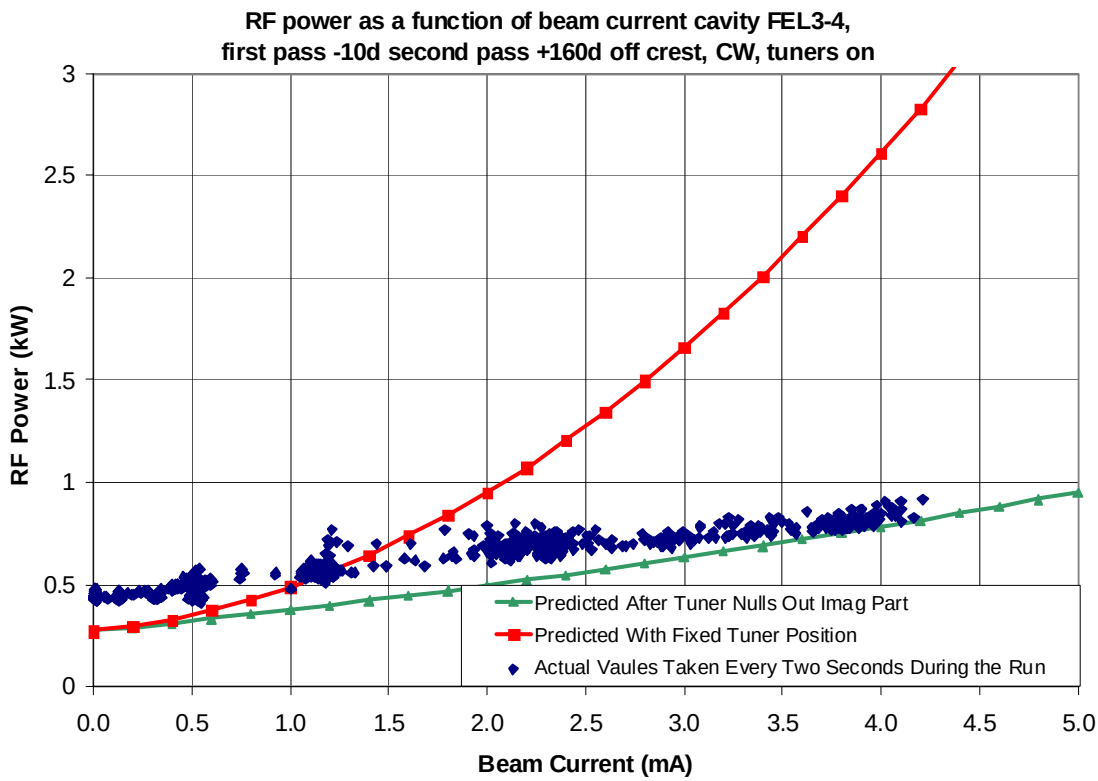

Figure 3. Measured and calculated RF power draw during lasing with cavity tuning for rf power minimum.

Having excess power available to stabilize fluctuations is crucial. The optical cavity must have its round trip travel time precisely matched to the arrival time of the electron bunches for stable lasing. To keep the peak-to-peak fluctuations smaller than 10% it is necessary to keep the cavity length stable to less than $0.05GN\lambda$. For example, in the JLab IR Upgrade for G of 0.5, a N of 32, and λ at 1.5 μm one must keep the cavity length constant to <1.2 μm peak to peak. The micropulse arrival time must be kept constant to the same precision:

$$\frac{\delta\omega}{\omega} < \frac{\delta L}{L} < \frac{1.2\times10^{-6}}{32} = 3.8\times10^{-8} \qquad (1)$$

From the frequency modulation constraint you get a timing jitter constraint of $\delta\tau < 6\text{x}10^{-9}/f_m$. Note that the FEL is fairly tolerant of slow timing jitter since the optical cavity can follow this.

FIELD QUALITY

Since the FEL and energy recovery is sensitive to the phase of the rf it goes without saying that magnetic field quality affects the path that any electron takes and therefore must have tight tolerances. A transverse variation in field ΔB leads to an erroneous angular spread across the beam of magnitude $\delta x' = \Delta Bl/B\rho \sim \Delta Bl/(33.3$ kG-m/GeV * $E_{linac})$. This evolves, via M_{52} a path length spread δl, which differential path length spread in turn translates to a final energy spread ΔE_{dump} which equals $2\pi \sin\phi_0 M_{52}(\Delta Bl/33.36$ kG-m)/λ_{RF} (GeV). From this one can conclude that the allowed error field integral ΔBl is *independent* of linac length/energy gain. In other words the tolerable relative field error falls as energy (required field) goes up. Higher energy ERLs will have increasing difficulty meeting this requirement. For the JLab Upgrade the tolerances are of order $\Delta E_{dump} \sim 3400$ MeV * ($\Delta B/B$) and ~ 0.16 keV/G-cm * (ΔBl); thus a 10^{-4} relative field error budget leads to a remnant momentum spread of 340 keV after energy recovery. This has led to the necessity of careful design, mapping, and hysteresis control of the magnets in the Upgrade. Major dipoles must be spectrometer grade with dB/B of 10^{-4} (see Figure 4 for an example of one of our IR Upgrade magnets).

A substantial amount of effort has gone into making the IR Upgrade FEL transport have the ability to linearize and control higher order transport terms so as to achieve the shortest possible bunch length at the wiggler and successfully transport beam energy spreads of up to 15% all the way to the beam dump with current losses less than 10^{-4}. A full discussion of this system is beyond the scope of this paper. We refer the reader to [3].

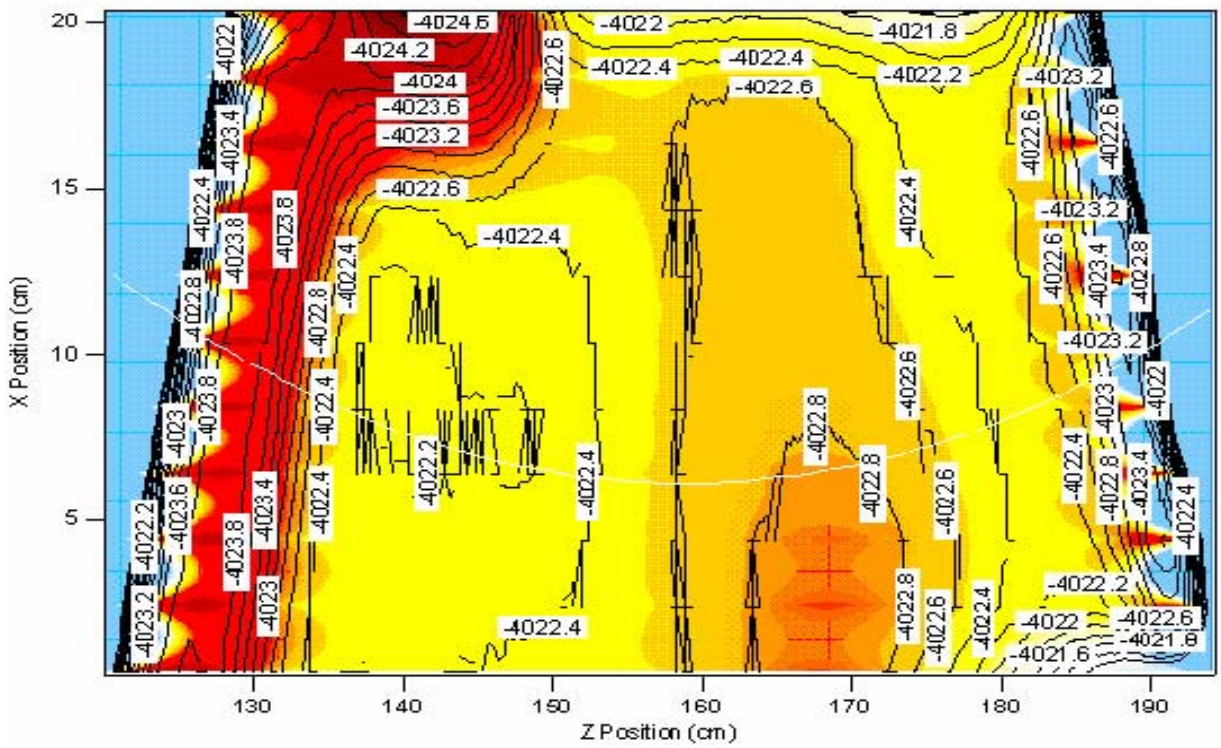

Figure 4. Measured field contours of a GX dipole at 0.4 G resolution. Precision measurements such as these must be made at all desired operating points (or ranges) and B• dl calculated for high order transport.

WAKEFIELDS

The wakefield produced by relativistic particles is an issue often dealt with in storage rings so techniques to address this are well known in the community. The issues with an ERL can be more severe than with such storage rings because of the short bunch lengths required at the FEL itself. This causes the high frequency collective emission cutoff to move to much higher frequencies, a benefit if one is looking for THz emission but a detriment in terms of resistive wall heating and excitation of unintended cavities along the beam pipe. Transitions between different size and shape chambers must be engineered to minimize wakefield problems or significant heating of the electron beam can result.

In addition, the narrow chamber required for wigglers exacerbates the problem since the longitudinal wake goes inversely with the square of the pipe diameter. Such effects can have dramatic consequences even at the modest currents (5 to 10 mA) of our first generation ERLs (Figure 5).

SUMMARY

We have illustrated a number of ways in which the demands of high longitudinal brightness at the input of the FEL, and large energy spread at the output of the FEL can drive tight specifications for the magnetic transport system and its apertures. In addition the need for output stability and the impact of laser transients sets additional strict requirements on the RF control system, and phase and timing stability of the beam. While existing engineered solutions meet the need of first generation machines, improvements will be needed to extend the performance to systems presently in the planning stage.

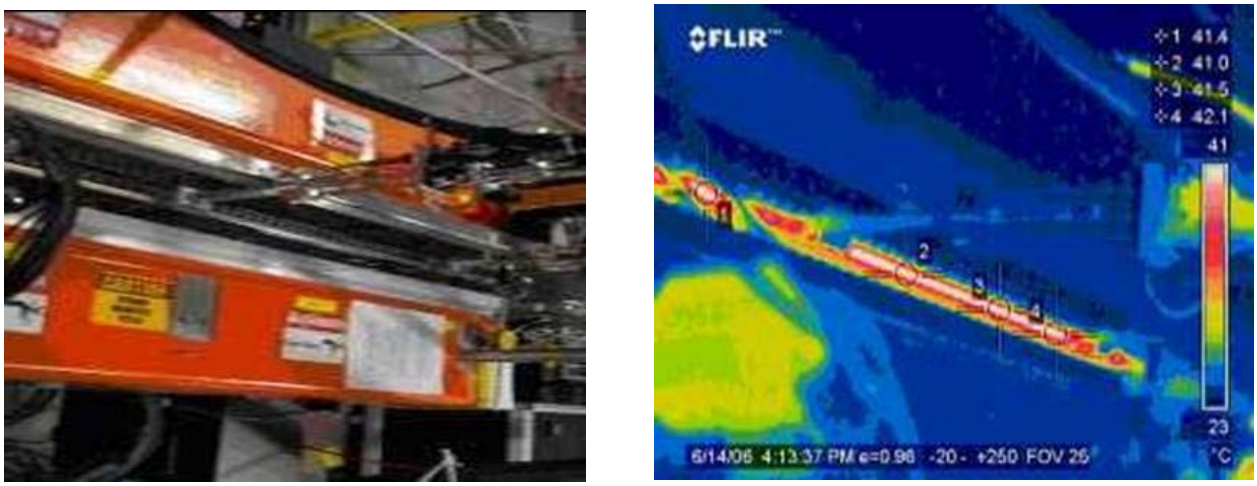

Figure 5. An image of the IR Upgrade wiggler chamber in the visible and infrared during 4.6 mA of beam. Heating is estimated at 35 W/m with the chamber reaching 42°C on top and 100°C at midplane.

ACKNOWLEDGEMENTS

We had the support of the entire FEL team in developing this work. We especially appreciate the help of Rui Li and Eduard Pozdeyev of CASA in analyzing the wakefield effects. This work was supported by U.S. DOE Contract No. DE-AC05-84-ER40150, the Office of Naval Research, the Air Force Research Laboratory, the Army Night Vision Laboratory, the Commonwealth of Virginia and the Laser Processing Consortium.

REFERENCES

[1] G.R. Neil, et al., *Nucl. Inst. And Meth. In Phys. Res.* **A557**, 9-15(2006).
[2] D. R. Douglas, et al., Proc. Linac 2000, Monterey, August 21-25, 2000.
[3] D. R. Douglas, JLab Technical Note JLABTN02002, (2002).
[4] S. Benson, *Nucl. Inst. And Meth. In Phys. Res.*, **A507,** 40-43 (2003).
[5] A.M. Vetter, *Nucl. Inst. And Meth. In Phys. Res* **A429,** 52-57(1999).

OPTICAL DESIGN OF THE ENERGY RECOVERY LINAC FEL AT PEKING UNIVERSITY*

Zhenchao Liu#, Kexin Liu+, Xiangyang Lu, Shengwen Quan, Guimei Wang, Baocheng Zhang, Jiankui Hao, Kui Zhao, Jiaer Chen

Institute of Heavy Ion Physics & MOE laboratory of Heavy Ion Physics, Peking University, Beijing, 100871, China.

Abstract

Peking University is currently designing an Energy Recovery Linac FEL (PKU-ERL-FEL). The system is consisted of a DC-SC photocathode injector, a superconducting linac which is composed of two nine cell TESLA-type cavities, an undulator and beam transport system. The objectives of the PKU-ERL-FEL are providing infrared FEL and building a test-bed for the study of beam dynamics and accelerator technology for energy recovery. In this paper the main parameters of the PKU-ERL-FEL are described and the optical design for the beam transport of PKU-ERL-FEL is presented. The simulation is carried out using the typical particle tracking codes such as *elegant*.

INTRODUCTION

Energy Recovery Linac (ERL) for FEL was approved in Jlab [1]. It is an economical operation mode for widely use in scientific research, industrial and other areas. As the benefit of reducing most of the energy loss, ERL would make it possible to construct large accelerators which need huge power and increase the beam current to a very high level that seems difficult nowadays. Recently many laboratories are developing ERL technology and some facilities are under constructing such as ERLP in Daresbury Laboratory [2][3][4]. Peking University also plan to build an Energy Recovery Linac FEL (PKU-ERL-FEL) based on the research work of RF superconducting technology. This facility will not only provide infrared FEL (IR-FEL) for users but also be used as a test-bed for the study of beam dynamics and superconducting linac techniques for energy recovery. In this paper we mainly discuss the optical issues of the PKU-ERL-FEL.

DISCRIPTION OF PKU-ERL-FEL

Similar with other facilities, PKU-ERL-FEL consists of a DC-SC photocathode injector, a superconducting linac which is composed of two nine cell TESLA-type cavities, an undulator with mirrors in each side and beam transport system. PKU-ERL-FEL is under design and the general parameters are determined. Figure 1 shows the layout and table 1 gives the main parameters of the PKU-ERL-FEL.

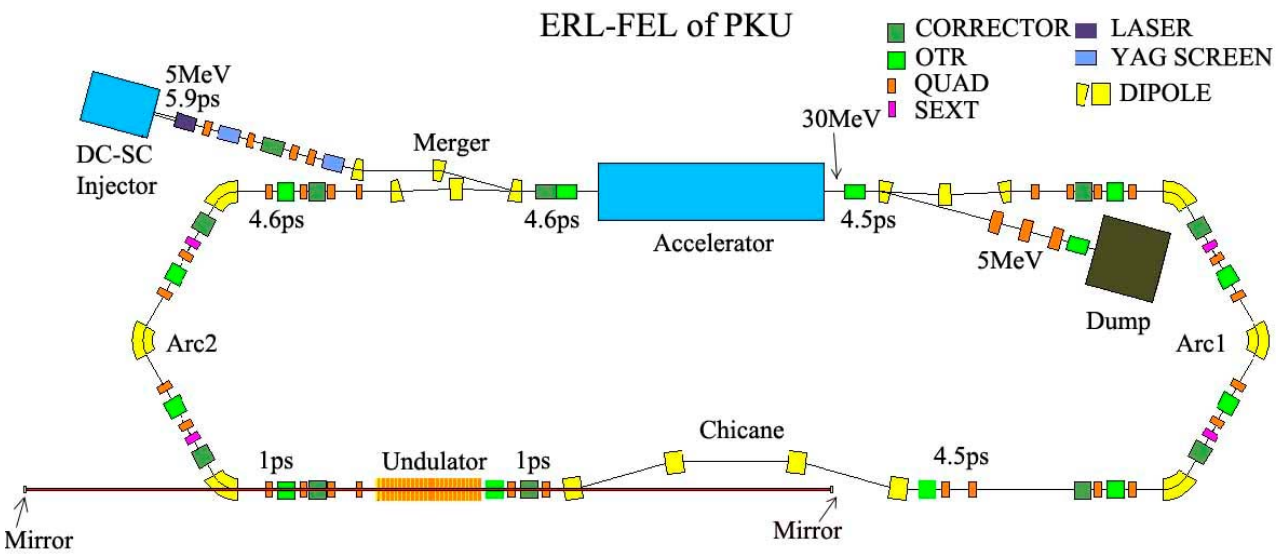

Figure 1: Layout of PKU-ERL-FEL.

*Work supported by National Basic Research Project
#lzhchao@pku.edu.cn
+kxliu@pku.edu.cn

Table 1: Main parameters of the PKU-ERL-FEL

Injection Energy	5MeV
Maximum Energy	30MeV
Bunch Frequency	26MHz
Bunch Charge	~60pC
Bunch length at Entrance of Undulator	~1ps
Macro Pulse Length	2ms
Rep. Frequency of Macro Pulse	10Hz
Energy Spread (rms)	0.24%
Transverse Emittance （rms, n.）	~3μm
Length of Undulator	1.5m
λ_u of Undulator	3cm
K of Undulator	0.5-1.4
Optical Cavity Length	11.52m
Wavelength of FEL	4.7-8.3μm

Injector

The injector is a three and half cell DC-SC photocathode injector working at 2K with a frequency of 1.3GHz. DC-SC photocathode injector has been studied at Peking University since 1999 and demonstrated with a one and half cell model [5]. The accelerating gradient of this three and half cell DC-SC photocathode injector will reach 15MV/m and the transverse emittance of the beam from the photocathode is less than 3.0μm.

Linac

The linac is composed of two nine cell TESLA-type cavities also working at 2K. Electron will be accelerated to 30 MeV from 5 MeV at a gradient of about 13MV/m. Then it goes through the whole loop and back to the linac to be decelerated to 5MeV at 180° phase shift which is exactly achieved by adjusting the length of the whole loop. The linac will be operated in pulse mode due to the limitation of the capability of the cryogenic system.

Undulator

The undulator is 1.5m long and with 50 periods. The wave length of the IR-FEL produced by the undulator is from 4.7μm to 8.3μm. As the bunch frequency is 26MHz, the length of the cavity is currently set at 11.52m. Before the undulator is a magnet compressor to compress the bunch length to about 1.0ps. The bunch length has to be lengthened for effective deceleration. There are two ways to lengthen the bunch after undulator, one is using a decompressing chicane and another is adjusting the R_{56} of return arc. We adopt the second way for saving cost and space. Therefore the undulator is put close to the second arc to make one mirror in the chicane and the other in the outside of the first bending dipole of the second arc.

Transport system

Considering the limited space, the transport loop should be at a smaller scale. The length between the outer side of the outward arc and return arc is near 17 meters and the width of the trajectories is about 4.2 meters. 3 bend merger is adopted for beam injecting to the linac. Following the linac is the extraction chicane which bends the decelerated beam to the dump. After the first arc which contains three 60° bending magnets the beam will be turned 180° to the opposite direction. Then the beam goes through the chicane with a bending angle of 15° and the undulator. The beam comes out from the second arc and goes back to linac through the merger chicane. The energy is recycled and the exhausted electron beam goes to the dump with an energy of about 5MeV.

DESIGN CONSIDERATION

It is well known that the lattice of an ERL-FEL system should be achromatic and the whole loop should be isochronous. Keeping the matrix elements

$$R_{16} = R_{26} = 0 \tag{1}$$

in each section is necessary to ensure the lattice to be achromatic. Keeping the matrix element

$$R_{56} = 0 \tag{2}$$

will make the whole loop isochronous. Because we will use the return arc to lengthen bunches, the R_{56} of the second arc should compensate the R_{56} coming from the compression chicane and other parts:

$$R_{56,arc2} = -(R_{56,chicane} + R_{56,other}) \tag{3}$$

The waist of the beta function should be removable and the beta function should match with the requirements of the undulator.

Energy spread is another important parameter to realize FEL and energy recovery successfully. The beam energy spread is determined by [6]

$$\delta < \frac{1}{4N} \tag{4}$$

N is the undulator period. The undulator in PKU-ERL-FEL has 50 periods so that the beam energy spread should be less than 0.5%.

Space Charge and Coherent Synchrotron Radiation (CSR) can cause the increase of beam emittance. Therefore they should be taken into account in our design.

In the optical design we also need to consider the second order matrix terms of T_{166}, T_{266} and T_{566}. Sextupoles should be used in the two arcs to reduce the value of second order matrix terms to a tolerable degree.

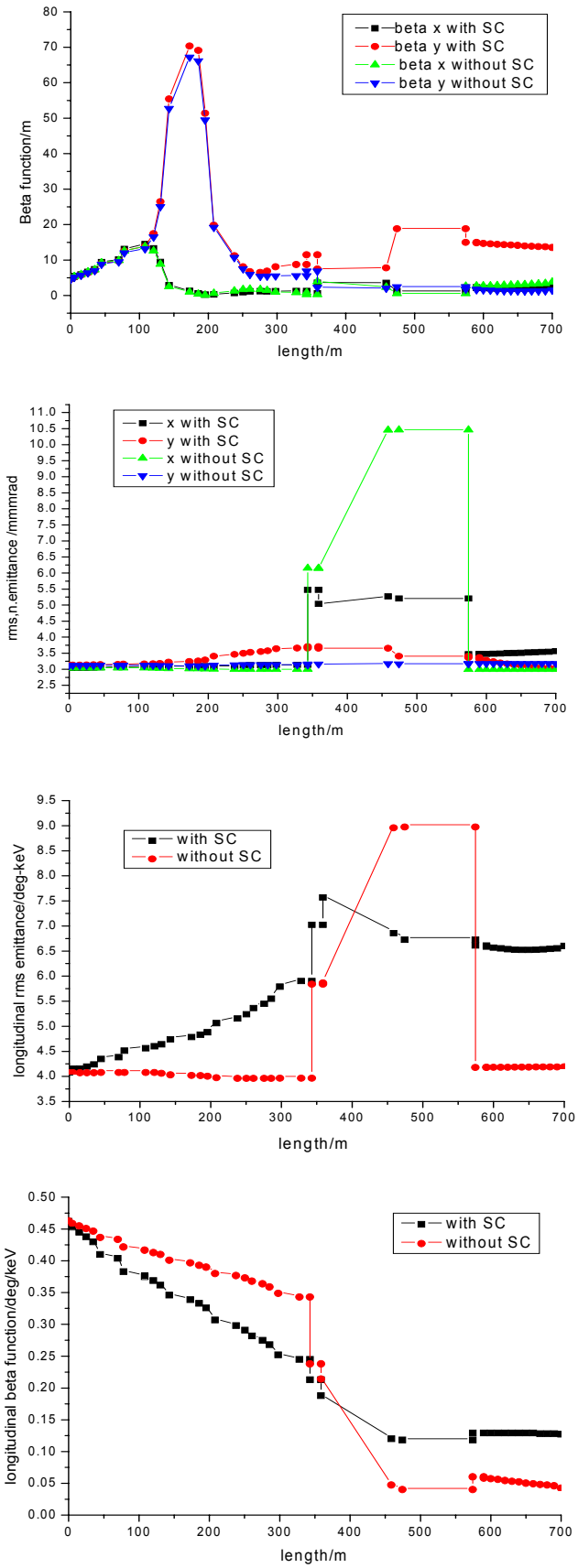

Figure 2: Beta functions and emittance from the injector to the linac

OPTICAL LAYOUT

Injector to linac

Considering the space charge, we have optimized the beam transmission with *parmela* in the injection line. Simulation has been carried out with and without space charge. The result shows that space charge takes little influence on beta function and emittance in x plane. In y plane, the emittance also doesn't change a lot but beta function changes obviously with and without space charge. Figure 2 shows the beta functions from the injector to the linac.

A waist of the transverse beta function has been made at the entrance of the linac but this requirement is not very strict. Simulation shows that the beta function does not change a lot in the exit of the accelerator when the waist is at different positions around the entrance of the linac.

Arc1 to arc2

In the first arc the beta function is symmetric but in the second arc is not. The beta function in x plane makes a waist in the middle of the undulator and keeps small within the undulator for higher radiation power gain. The energy spread is 0.24% (rms) at the entrance of the undulator which fulfills the requirement of lasing. The emittance and energy spread will increase greatly after undulator. We assume that the second arc has an acceptance of 30μm in emittance and 7% full width in energy spread according to the experiences of Jlab and JAERI [7]. The radius of beam envelope is up to 3.5cm in the outer quadrupole of the second arc due to this increase

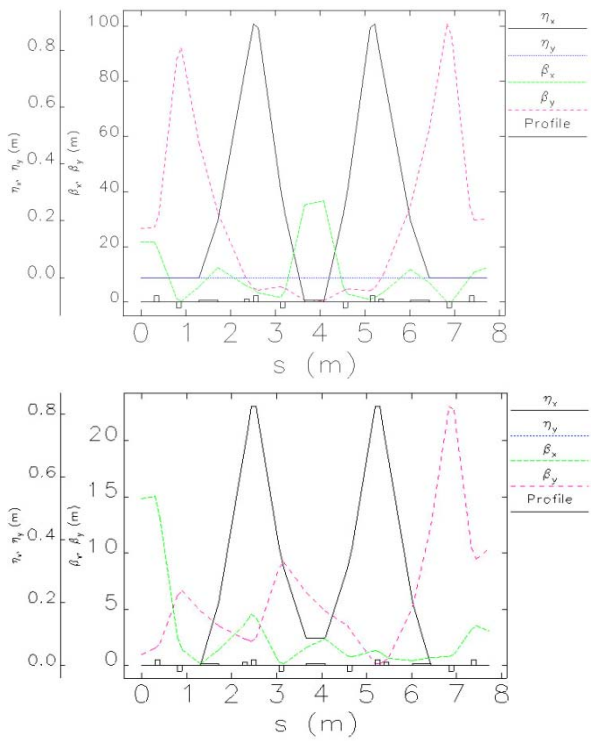

Figure 3: Twiss parameters in the two arcs (Top one is the first arc and bottom one is the second arc)

of emittance and energy spread. The diameter of the aperture of this quadrupole should be ~10cm for completely acceptance of the beam. Figure 3 shows the beta function and the dispersion in the two arcs.

CSR effect is taken into account from the first arc to the second arc in our simulation and it takes little influence on the emittance of the beam.

The second order matrix terms of T_{166} , T_{266} and T_{566} are decreased by using sextupoles in the two arcs. T_{166} and T_{266} are less than 0.02m and T_{566} is less than 1m after optimization.

Arc2 to linac and dump

The beta function of this section is well behaved in our design. The beta function of the beam from the second arc is adjusted by four quadrupoles and goes through the linac. After extraction it goes to the dump and the envelope is controlled well by three quadrupoles.

SUMMARY

The preliminary optical design of the PKU-ERL-FEL is carried out and the beta function of whole loop has been obtained. The result will be checked by further careful simulation with different particle tracking codes before the construction of the beam line of the PKU-ERL-FEL.

REFERENCES

[1] Lia Merminga, David R. Douglas, “HIGH-CURRENT ENERGY-RECOVERING ELECTRON LINACS”, Annu. Rev. Nucl. Part. Sci. 2003. 53:387–429.

[2] R. Hajima , M. Sawamura, “JAERI ERL-FEL: status and future plans”, The 14th Symposium on Accelerator Science and Technology, Tsukuba, Japan, November 2003.

[3] M.W. Poole, E.A. Seddon, “4GLS and the Prototype Energy Recovery Linac Project at Daresbury”, EPAC’04, Lucerne, July 2004.

[4] G. H. Hoffstaetter, I.V. Bazarov, “Status of a Plan for an ERL Extension to CESR”, Prodeedings PAC05, Knoxville/TN (2005), ERL-05-02.

[5] K. Zhao, et al, NIM, A475 (2001) 564.

[6] W. Colson, R. Freedman, “Oscillator evolution in free-electron lasers”, Phy. Rev. A, V.27 N.3, 1983.

[7] R. Hajima, T. Shizuma, “First Demonstration of Energy-Recovery Operation in the JAERI Superconducting Linac for a High-Power Free-Electron Laser”, FEL 2002, presentation.

PROSPECTS OF CASCADED HARMONIC GENERATION FELS*

G. Penn, Lawrence Berkeley National Laboratory, Berkeley, CA, USA

Abstract

Harmonic generation in Free Electron Lasers (FELs) encompasses many techniques for using an input seed laser to produce FEL radiation at a frequency that is multiples above that of the seed laser itself. This allows for the advantages of seeded FELs to be preserved, while extending the reach of these FELs to photon energies far above those produced by conventional laser sources. Many new projects are underway to make use of these methods, including the FERMI@Elettra [1] facility which envisions the use of two harmonic generation stages to reach photon energies above 100 eV. Different methods of harmonic generation are discussed, as well as the technical challenges to overcome in attempting to chain together multiple harmonic stages in an FEL.

INTRODUCTION

Harmonic generation in an FEL [2] is a promising technique for achieving high-intensity photon sources at short wavelengths. Among the benefits of this design is that the output is seeded by a laser signal, allowing for excellent frequency and timing control. The resulting output has the potential of being a transform-limited pulse, and the output power is not limited by the input power but instead by the saturation level of the FEL itself. In addition, the FEL output is at a harmonic of the laser signal, so that the required laser wavelength is longer than the desired output wavelength.

Multiple stages of harmonic generation can be combined into a cascade, where the output from each stage is used as the input seed for the next stage. A harmonic cascade allows conventional laser sources to be used to produce photons at extremely high energies. There are several facilities which plan to use a harmonic cascade as a source for experiments. Among these are FERMI@Elettra, which is to consist of two FELs, one with a single harmonic stage producing radiation in the 100 – 40 nm range, and one with two harmonic stages producing radiation in the 40 – 10 nm range. BESSY [3] is developing an FEL with up to four stages of harmonic generation, yielding wavelengths ranging from 50 nm down to as low as 1.2 nm. Both of these facilities plan to use conventional laser sources. An additional possibility is seeding with a High-Harmonic Generation (HHG) signal [4], which uses a short, intense laser pulse passing through a gas jet to generate many high harmonics of the initial laser. Such sources would drastically reduce the total harmonic conversion required in an FEL, but much work remains to be done to ascertain their suitability for use in this way.

This paper will begin with the FERMI@Elettra design to illustrate the harmonic generation process and to show some of the fundamental issues which need to be considered for a harmonic cascade. Sources of noise can degrade the FEL output, and phase noise is particularly important to consider for large harmonics. Simplified models are used to characterize the major constraints which must be considered for a harmonic cascade. Future prospects are

FERMI@ELETTRA SIMULATIONS

The electron beam parameters for FERMI@Elettra are: 1.2 GeV energy, 1.5 micron emittance, and depending on the beam compression the current can range from 400 A to 1 kA and the energy spread can range from 100 to 200 keV. The seed laser is tunable in the range 240 – 360 nm, has a peak power of 100 MW, and the pulse duration can be up to 1 ps. The first modulator has a period of 16 cm and is 3.04 m long. At the first harmonic, the undulators have a period of 6.5 cm and are in sections of 2.34 m length. The final radiator for the second harmonic has a period of 5 cm and is in sections of 2.4 m length. The initial modulator produces an energy oscillation in the electron beam with the same period as the wavelength of the seed laser, as the relative phase between the undulator field and the laser field when they both overlap the electrons determines the energy transfer. A dispersive chicane follows this modulator, converting the energy modulation into bunching at the wavelength of the seed laser. When this bunching is sufficiently strong, there are significant components at harmonics of the fundamental wavelength. Subsequently, the electron beam passes through undulators tuned to a harmonic of the seed laser, and radiates at that harmonic.

For the two-stage FEL, termed FEL-2, there are then two possibilities, as shown in Fig. 1. In the "fresh-bunch" approach, the radiation produced at the end of the first stage is made to overlap the electron beam in another modulating undulator after passing through a delay chicane. As a result, the radiation pulse produces an energy modulation in a region of the electron beam closer towards the head of the bunch, which was relatively unperturbed by the first stage of the FEL. The second stage produces a harmonic of the output from the first stage in the same way as the first stage generates a harmonic of the seed laser. In the "whole-bunch" approach, the first stage is continued until there is sufficient energy modulation at the harmonic to continue to the next stage. The electron beam is then passed through a dispersive chicane to enhance the bunching at the desired final harmonic. In the final radiator, the same section of

* This work was supported by the Director, Office of Science, High Energy Physics, U.S. Department of Energy under Contract No. DE-AC02-05CH11231.

electron beam radiates at this higher harmonic.

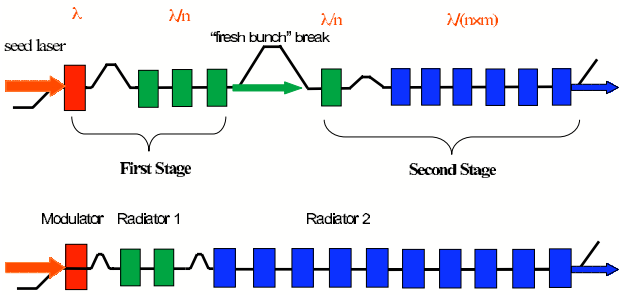

Figure 1: Two possible configurations for the FEL-2 line of the FERMI@Elettra facility: fresh-bunch (top) and whole-bunch (bottom).

An example from the FERMI@Elettra optimization study will motivate the topics discussed below. A realistic longitudinal beam distribution from accelerator studies is shown in Fig. 2. The central current is roughly 500 A. Note that there is a strong parabolic shape to the slice energy as a function of longitudinal position. More recent designs have advanced far towards removing this feature, but it serves as a useful reference. A whole-bunch configuration starting with a 240-nm seed laser with 1 ps duration FWHM produces 10 nm output with 0.1 mJ per pulse, and with peak power of 400 MW. The output power and phase (modulo 2π) resulting predicted by simulations using GENESIS [5] are shown in Fig. 3. The phase shows a strong quadratic dependence which mirrors the energy variation, and which leads to a broad, fluctuating spectrum as shown in Fig. 4. Applying an appropriate linear chirp to the seed laser is quite effective at cancelling the phase variation, resulting in the sharp spectrum shown on the same figure. While this demonstrates that a parabolic energy profile can be cancelled with a linear frequency chirp in the seed laser, proper tuning may be challenging and more complex phase space distributions will not be amenable to this type of a fix. Avoiding such features in the beam profile therefore becomes a high priority when high longitudinal coherence and spectral brightness are desired.

ENERGY AND PHASE ERRORS

A simplified view of harmonic generation in an FEL serves as a useful starting point for considering the challenges faced in designing a harmonic cascade FEL, as touched on above. In Fig. 5, a slice of the electron beam is modelled as a collection of mono-energetic beamlets, each one with a uniform distribution in longitudinal position (here expressed as phase). Note that phase increases towards the head of the bunch. After the modulator and dispersive chicane, the phase space distribution is folded over to produce significant bunching centered at the zero phase.

The spread in energies for the original beam results in a finite width for the microbunch, as a consequence of the

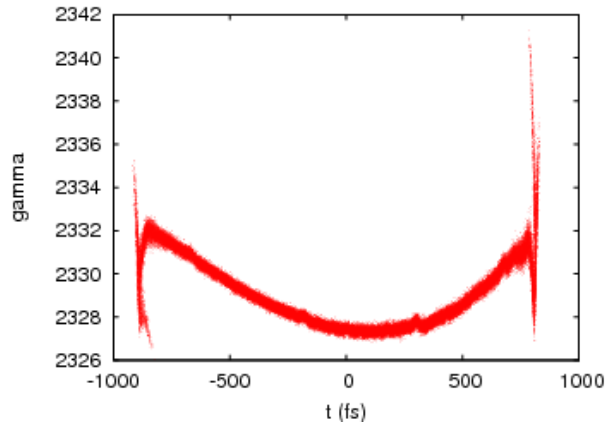

Figure 2: Preliminary phase space distribution from FERMI@Elettra study.

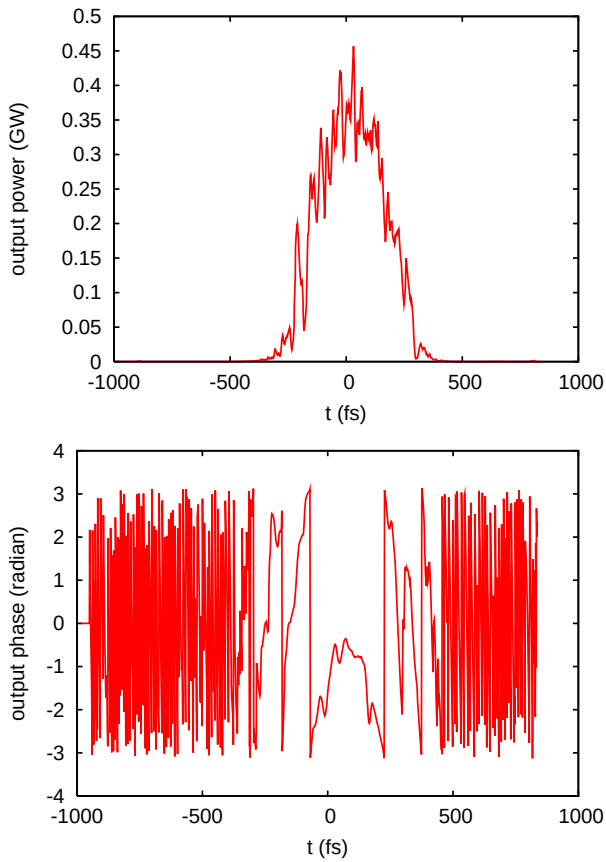

Figure 3: Output power and phase at 10 nm using whole-bunch approach.

conservation of phase space. There are more subtle issues which can be understood with this picture, however. Effective bunching, especially at higher harmonics, requires an energy modulation much larger than the initial energy spread. Roughly, this requires that the energy modulation, γ_M, satisfy

$$\gamma_M \geq (n-1)\sigma_\gamma, \quad (1)$$

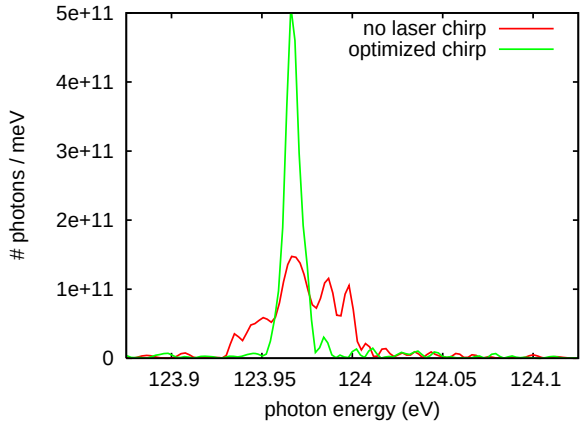

Figure 4: Output spectrum using laser seed with no chirp (red) and with optimized chirp (green).

where n is the harmonic number and σ_γ is the energy spread. The degree of bunching generated at the harmonic will be sensitive to the slice energy spread. Furthermore, because each energy value corresponds to a different phase for the microbunching, longitudinal variations in the average beam energy will lead to offsets in the timing of the microbunches. As the microbunches are separated by n wavelengths in terms of the harmonic output, these fractional timing offsets can have a large effect on the coherence of the output radiation.

To further understand the effect of longitudinal energy variation in the beam, we consider a similar effect where phase offsets are introduced within the seed laser itself. In Fig. 6, the bunching produced by a seed laser with a linear frequency chirp is compared to that produced by a seed laser with no chirp, but for an electron beam with a quadratic energy chirp. Both variations are greatly exaggerated compared to that which would be encountered in practice. The vertical bars indicate the phases of successive microbunches. It is apparent that a chirped seed laser can produce the same changes in timing structure as a chirp in the electron beam energy. This explains how a linear chirp in the seed laser can fix the output from an electron beam having a parabolic energy profile. Note that a linear energy chirp would simply produce a uniform offset in output wavelength. This is generated as the modulated electron beam passes through the dispersive chicane, where it is either compressed or stretched depending on the sign of the energy variation. Curvature in the energy profile leads to more complicated perturbations, as some sections of the beam are compressed and others are stretched. This can lead to sidebands in the spectrum or broadening, which would degrade the output radiation to be no longer transform-limited. This effect is made worse at high harmonics, as seen in Fig. 7. Here, an arbitrary small phase error is introduced to a pure Gaussian pulse. The effect is barely visible in the spectrum of the fundamental, but at the 24th harmonic the spectrum is drastically altered. At the fundamental, the signal is still transform limited, but

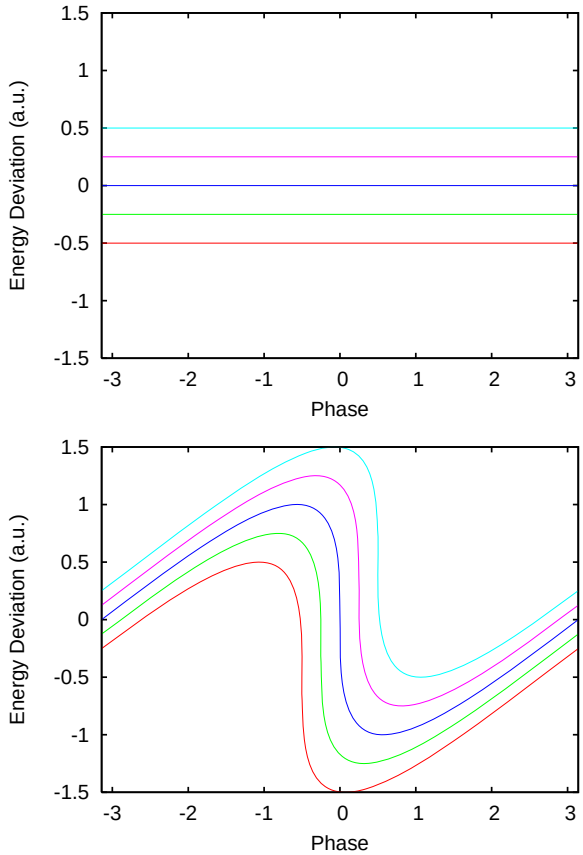

Figure 5: Illustration of bunching process as it affects electrons having different energies.

the pulse is still unsuitable for harmonic generation beyond a certain limit. This introduces added complexity to the design of the seed laser, as the constraints are more stringent than usual and are not a typical part of the vocabulatory of laser sources. In particular, even short pulses (i.e., a small number of wavelengths) will require a clock-like regularity of the field oscillation in order to function optimally as an FEL seed.

Macroparticle Noise

Because electrons at different energies are bunched at different phases, there are additional concerns for the proper simulation of harmonic generation. Typically, macroparticle noise in FEL simulations are controlled by starting with pseudorandom particle distributions, and using subsets of particles uniformly spaced in phase. Deviations from this uniform spacing are chosen to mimic the expected statistical fluctuations. However, an efficient bunching process will put most particles of a given energy at a single phase, so the final phase distribution will only depend on the initial energy distribution. In the example above, there will only be five bunches centered about the zero phase. Different choices of modelling the energy distribution will thus lead to different bunching pa-

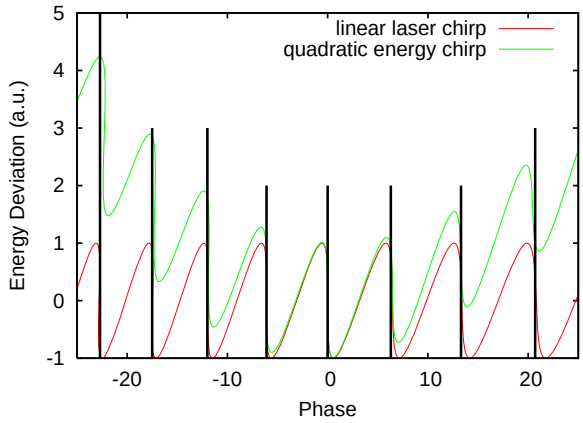

Figure 6: Comparison of bunching process for a flat beam seeded by a chirped laser, versus a beam with quadratic energy variation and no laser chirp. Vertical bars indicate the phases of successive microbunches.

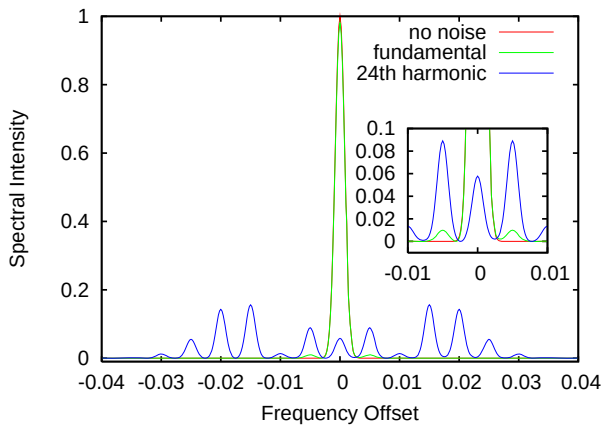

Figure 7: Spectra of Gaussian pulse with oscillating phase error, at original frequency and at 24th harmonic.

rameters. Furthermore, especially for large energy spread and harmonic number, the discrete nature of the bunching will lead to noise in the bunching parameter as the gaps between energy levels become resolved. The macroparticle noise for an optimally bunched beam will be given by $n\sigma_\gamma/N_\gamma\gamma_M$, where N_γ is the number of energies sampled by the distribution. Sampling more phases will not reduce this macroparticle noise, and may even make the problem worse if it is done at the expense of the number of discrete energies sampled. There is as of yet no known robust method to control this effect in simulations. It becomes increasingly difficult to get simulation results to converge as the initial energy spread in the electron beam is increased, especially when the nominal seeded bunching is already low.

POWER FLUCTUATIONS AND ENERGY OFFSETS

While phase distortions can reduce the longitudinal coherence of the FEL output, power fluctuations are also a major concern. There are many possible sources of power fluctuations, but typically the most important one is energy offsets in the beam. Note that while phase errors accumulate due to longitudinal variation of the slice beam energy, it is the difference between the slice energy and resonant energy which determines the output power. Shot-to-shot jitter in beam energy is thus a significant concern for output power flucuations. The sensitivity of the FEL to relative energy offsets is typically the larger of $1/N_U$ or the FEL parameter [6], $\rho_{\rm FEL} = \lambda_U/L_G$. Here, N_U is the number of undulator periods, λ_U is the undulator period, and L_G is the exponential gain length, all for the final undulator where the gain length is longest and the number of undulator periods is largest.

Reducing the sensitivity of the FEL involves a trade-off with trying to optimize the peak output power. One method is simply to reduce the number of undulator periods, at the cost of greatly reduced average power. A more efficient method is to introduce either variations in the magnetic field strength of the undulator, or phase offsets between undulator sections. Examples are shown in Figs. 8 and 10; the latter example is from a pseudorandom variation in the undulator field strength which drastically reduces the dependence on beam energy and reduces the peak power by a factor of 30. The evolution of the power and bunching for the example labelled “phase 3” are shown in Fig. 9. Note that the configuration is specific to the given length of undulator, at which point the various beam energies come close to each other in performance, but after passing through different dynamics.

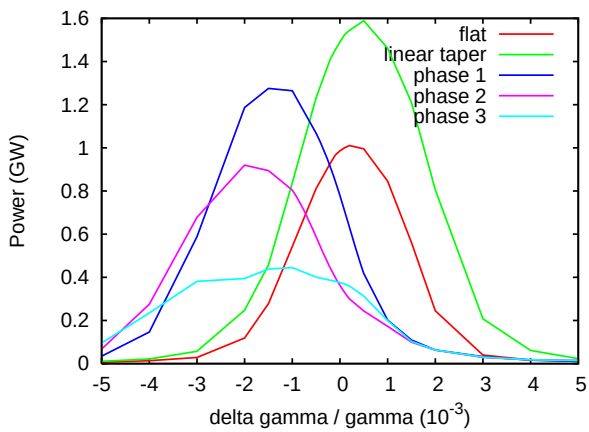

Figure 8: Sensitivity of FEL output power to beam energy offsets, for variations of the fine tuning.

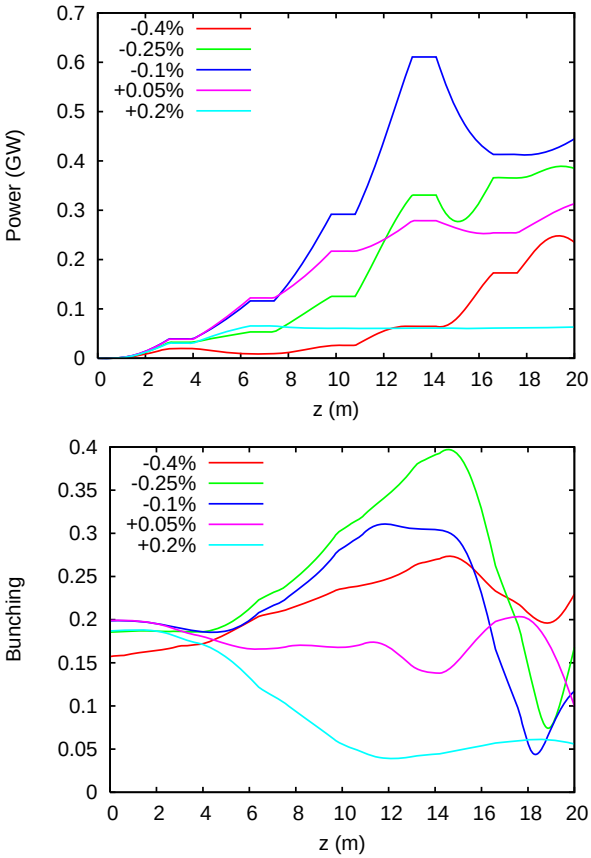

Figure 9: Power and bunching evolution in the FEL, for different electron beam energies, using the "phase 3" example in the previous figure.

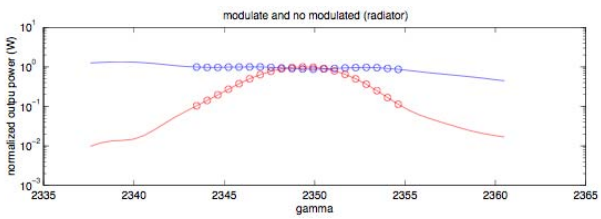

Figure 10: An example of extreme reduction in the sensitivity of FEL output to electron beam energy through pseudo-random tapering. Peak power in the tapered example (blue) is a factor of 30 below that in the nominal case (red), but is stable to much larger energy variations. Courtesy of G. De Ninno and E. Allaria.

CHALLENGES FOR HARMONIC CASCADES

The desire for even shorter wavelengths leads one to consider more ambitious harmonic cascade FEL designs, as in the BESSY multi-stage FEL. As the goal is moved to shorter wavelengths, the tendency is to consider more energetic electron beams. One motivation is the reduced effectiveness of the FEL when the normalized emittance is much larger than $\lambda_r/4\pi\gamma$, where λ_r is the radiation wavelength and γ is the relativistic factor of the beam. This is due to a combination of reduced electron density and increased spread in longitudinal velocities. Another is the challenge of satisfying the resonance condition,

$$\lambda_U = \frac{2\gamma^2}{1+a_U^2}\lambda_r, \qquad (2)$$

where a_U is the normalized strength of the undulator field. The FEL parameter also tends to drop drastically as the beam energy is reduced, which further constrains tolerances on energy jitter and energy spread.

The high harmonic numbers involved also introduce complications. Attempting to take a single, large harmonic jump becomes very impractical, as the required energy modulation must be extremely large or the energy spread must be very low in order to satisfy Eq. 1. This leads to an additional problem, that for larger energy modulations the beam will debunch more rapidly. If the gain length is longer than the debunching length, the electrons will not be trapped in the ponderomotive well and the FEL will not reach saturation. A rough requirement to reach saturation is

$$\gamma_M \leq \gamma\lambda_U/16L_G. \qquad (3)$$

Together with Eq. 1, this limits the range of acceptable energy modulations, and also imposes a maximum allowed energy spread.

Ultimately, many smaller harmonic stages become required. This adds to the complexity, and does not eliminate the sensitivity to phase noise and energy variations which depend on the total harmonic multiplication factor. The noise-to-signal power ratio within a given bandwidth can be expected to grow as the square of the total harmonic power through the harmonic generation process. The seeded FEL process must also compete with spontaneous FEL emission which may amplify the noise along the FEL, as well as spontaneous growth in energy spread.

As the energy modulation itself increases the slice energy spread with each harmonic multiplication stage, fresh-bunch delays between stages will ultimately be required. Each delay to an unseeded section of the electron beam introduces constraints on synchronization and reduces the maximum duration of the output pulse for a given electron distribution. While it may be possible to alternate between fresh-bunch and whole-bunch stages, these considerations lead to challenging electron source and acceleration requirements. Numerical simulations also require more resources and care when large harmonics are desired.

One attractive option is to take advantage of rapid advances in HHG sources, and seed the FEL at much shorter wavelengths than conventional lasers can achieve. There has been much recent activity studying the feasibility of HHG sources as an FEL seed [7, 8, 9]. While further characterization of these sources is clearly needed to make reliable predictions, some facts are already apparent. First, the typically low peak power in these signals is not an obstacle to their use. In particular, amplifying a signal is

much less difficult than conversion to a harmonic (hence the $(n-1)$ factor in Eq. 1). In addition, the HHG sources typically have durations of less than 100 fs, which favors experiments based on timing rather than spectral widths, and slippage between the radiation and the electrons will smooth out some phase noise components. Ultimately, HHG sources could be used to seed X-ray FELs which use only a single stage of harmonic generation.

While the challenges for developing cascaded harmonic FELs are daunting, they link together a large range of technologies; small improvements on many fronts may open up new horizons for seeded FELs in the future. It is clear that the lasers used as seeds for the FEL require more detailed characterization. In addition to improved or novel sources for seeding, advances in electron sources, acceleration, undulator design, and optics will enable more ambitious projects in the future. In the meantime, current facilities on the horizon will offer experience and testing grounds for new ideas, as well as provide opportunities for performing advanced scientific research.

ACKNOWLEDGMENTS

This paper discusses work performed in collaboration with many individuals, and much of this work came out of the collaboration to produce the FERMI@Elettra technical optimization study. The author would like to express his gratitude to Bill Fawley, Jonathan Wurtele and Sasha Zholents for their guidance in FEL studies, and John Corlett and Bill Barletta for their support and encouragement.

REFERENCES

[1] C. Bocchetta et al., Proceedings of the 2005 FEL Conference, (2005) 682.

[2] L.-H. Yu et al., Science **289** (2000), 932–934.

[3] The BESSY Soft X-ray Free Electron Laser, TDR BESSY March 2004, eds.: D.Krämer, E. Jaeschke, W. Eberhardt, ISBN 3-9809534-08, BESSY, BERLIN (2004).

[4] H.C. Kapteyn, M.M. Murnane, and I.P. Christov, Physics Today (March 2005) 39–44.

[5] S. Reiche, Nucl. Instr. Methods A **429** (1999), 243–248.

[6] R. Bonifacio, R. Corsini, and P. Pierini, Physical Review A **45** (1992), 4091–4096.

[7] G. Lambert et al., Proceedings of the 26th International Free Electron Laser Conference (FEL04), Trieste, Italy (2004), paper MOPOS21.

[8] B. Sheehy et al., Proceedings of the FLS 2006 Workshop, WG333.

[9] M. Gullans, J. Wurtele, G. Penn, Z. Zholents, submitted to Phys. Rev. ST:AB.

FEMTOSECOND SYNCHRONIZATION AND STABILIZATION TECHNIQUES*

J. Kim†, F. Ludwig‡, J. Chen, Z. Zhang§ and F. X. Kärtner, MIT, Cambridge, MA 02139, USA.

Abstract

High-precision synchronization and stabilization techniques are crucial for future advances in next generation light sources, seeded x-ray free electron lasers. In this paper, we present long-term stable femtosecond-precision optical-to-RF and optical-to-optical synchronization and stabilization techniques. For optical-to-RF synchronization, we demonstrate an optical-microwave phase detector that is capable of extracting an RF-signal from an optical pulse train in a long-term drift-free way. Extraction of an RF-signal with 3-fs in-loop timing jitter, integrated from 1 Hz to 10 MHz, from an optical pulse train is demonstrated. Optical-to-optical synchronization of two femtosecond lasers with sub-femtosecond precision over 12 hours is demonstrated. We also discuss how to use optically stabilized fiber links for timing distribution. Together with low-noise mode-locked lasers, a flexible femtosecond timing system can be constructed.

INTRODUCTION

Seeding of free electron lasers operating in the x-ray regime with radiation generated from ultrafast laser sources, either directly, via nonlinear crystals, or via high harmonics from noble gases, may result in a fully coherent x-ray laser. For seeding of such large-scale facilities spanning over several hundreds meters to a few kilometers, it is critical to synchronize low-level RF-systems, photo-injector lasers, seed radiation and potential probe lasers with low timing jitter, preferably in sub-10-femtosecond range, in a long-term stable arrangement [1].

Figure 1 shows the schematic of the envisioned timing distribution and synchronization system for the future next generation light sources, seeded x-ray free electron lasers (XFELs). The pulse repetition rate of an optical master oscillator implemented as a mode-locked laser is stabilized to an optical and/or microwave frequency standard. The pulse train is distributed to all critical subsystems, i.e., the pulsed klystron, the photo-injector laser, the low-level RF systems for linear accelerator, the seed laser as well as probe lasers, by use of timing stabilized fiber links. Finally, low-jitter, drift-free optical-to-RF and optical-to-optical synchronization between the distributed timing pulse trains and the remote RF- or optical subsystems will result in a tightly synchronized timing system over the large-scale accelerator facility.

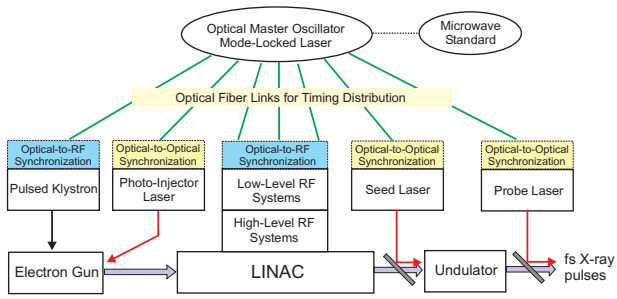

Figure 1: Schematic outline of timing distribution and synchronization for seeded X-ray free electron laser (XFEL) facilities.

Currently, the most promising candidates for ultra-low jitter optical master oscillators are passively mode-locked Er-doped fiber lasers [2], Yb-doped fiber lasers [3] and Er/Yb-glass lasers [4, 5]. Erbium and Ytterbium gain materials have long upper-state lifetime in the ms-range, and therefore, the high frequency fluctuations of the laser output in amplitude and timing are quantum noise limited [6]. Thus the timing jitter of mode-locked lasers is superior to that of conventional microwave oscillators in the high frequency range.

The crucial performance indicator for the optical master oscillator is the phase noise or timing jitter in the high frequency range. The bandwidth of optical/microwave reference locking is typically limited to tens of kHz range, and the high-frequency noise beyond locking bandwidth follows that of the free-running master oscillator. In addition, timing stabilization of fiber links based on the cross-correlation of the back-reflected pulse from fiber end with the fresh pulse also has a bandwidth limitation from the travel time of the reflected pulse. These limitations assure that a very low jitter mode-locked laser is a prerequisite for a high-precision timing system.

In Refs. [7] and [8], the timing jitter is characterized by measuring the phase noise of one harmonic (at 1.3 GHz) of the microwave signal obtained by direct photodetection of the pulse train. For standard Er-doped stretched pulse fiber lasers, the integrated timing jitter from 1 kHz to 22 MHz (Nyquist bandwidth) is measured on the order of 10 fs, which is already better than most commercial high-quality microwave signal generators (for example, Marconi 2041 signal generator). Note that the measurements are often limited in precision by the amplitude-to-phase (AM-to-PM) conversion from direct photodetection. A more detailed discussion on this conversion will be given in the next section. In theory, the high frequency timing jitter of pulse trains from mode-locked lasers can be below one femtosec-

* Supported by ONR, AFOSR, and EUROFEL.
† jungwon@mit.edu
‡ Permanent address: DESY, Hamburg, Germany
§ Permanent address: Peking University, Beijing, China

ond.

Once a timing signal in form of an optical pulse train is generated from a master oscillator, it should be distributed to the remote RF- or optical-subsystems that we aim to synchronize with minimal excess noise. Precise transfer of timing signals through fiber links for timing information dissemination has been demonstrated recently [7, 9, 10, 11] for short time spans, typically less than a minute. If the fiber length is L, we assume that no length fluctuations are faster than 2L/c, where c is the speed of light in the fiber. Relative fiber expansion by temperature change is typically on the order of 10^{-7}/K, which can be compensated by a fiber length control loop by referencing the back reflected pulse from the fiber end with the later pulse from the mode-locked laser. Recently, the demonstration of timing distribution over 500 meters in an accelerator environment was done with pure RF-techniques [7]. When the feedback loop is open, the jitter integrated from 0.1 Hz to 5 kHz is 66 fs; when the loop is closed, the in-loop jitter is suppressed down to 12 fs. More detailed information on this timing distribution experiment can be found in Ref. [7].

Although a short-term stabilization on the order of few tens of femtoseconds can be achieved with RF-techniques only, for long-term stabilization of fiber links with sub-10 fs accuracy over hours, balanced cross-correlation techniques [12] can be employed, as discussed later in this paper. Work is in progress to demonstrate long-term stable fiber links.

OPTICAL-TO-RF SYNCHRONIZATION

Once precise timing information encoded as an optical pulse train arrives at each remote location, the next task is to synchronize it with, for example, RF-subsystems. It is crucial to convert this optical signal into a low-jitter, drift-free RF-signal with a satisfactory power level in a long-term stable way. Recently, it has been shown that the extraction of an RF-signal from an optical pulse train using direct photodetection is limited in precision by excess phase noise [13]. The major contribution to this excess noise was identified to be the amplitude-to-phase (AM-to-PM) conversion in the photodetector. The intensity noise of the laser can be converted into a significant amount of phase noise and phase drift by this process. In Refs. [8] and [14], the AM-to-PM conversion factor was measured and it typically ranges 1 to 10 ps/mW depending on the bias and the bandwidth of the photodetector. The intensity noise of the delivered pulse train can be converted into a significant amount of excess timing jitter by this process. For a 12-GHz InGaAs photodetector at 6 V reverse bias that we tested, the AM-to-PM conversion factor was measured as 1.6 ps/mW [8]. For an Er-doped fiber laser with 0.03 $\%_{\mathrm{rms}}$ relative intensity noise (RIN), this may already result in 5-fs excess jitter when 10 mW of power is applied to the photodetector. In addition, direct photodetection has a limited extractable RF-power and signal-to-noise ratio (SNR) due to the damage threshold for the input optical power to the photodetector. Moreover, phase drifts in the diode due to temperature change as well as post-amplification to reach the required signal level can prevent a long-term stable regeneration of RF-signals.

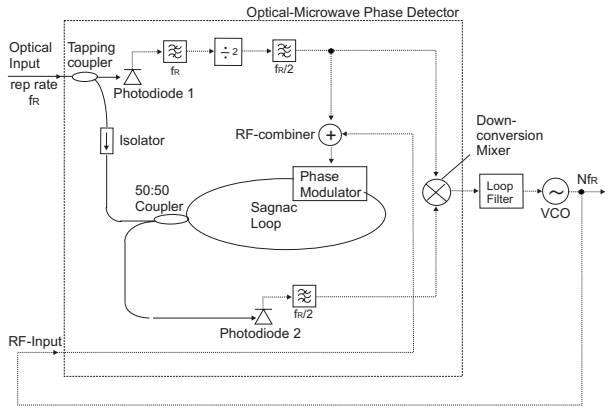

Figure 2: Schamatic of a balanced optical-microwave phase detector and its use for RF-signal regeneration from an optical pulse train. VCO, voltage-controlled oscillator.

Therefore, it is highly desirable to develop a phase-locked loop between an optical pulse train and a high-quality RF voltage-controlled oscillator (VCO) to prevent those undesired AM-to-PM conversion and drifts due to the photodetection process. In addition, one can leverage the fly-wheel effect of VCO. In doing so, the key issue is the development of drift-free, low-jitter phase detector which compares the relative phase between pulse trains and RF-signals in the optical domain before the photodetection is involved. Previously, we proposed and demonstrated a scheme to avoid the excess noise from direct photodetection by transfer of timing information in the optical domain [15]. However, due to acoustic vibrations and poor phase noise properties of the free-running VCO, the relative jitter was limited to 60-fs measured from 100 Hz to 10 MHz.

For the extraction of low-jitter, high-power, and drift-free RF-signals from optical pulse trains, a balanced optical-microwave phase detector is proposed and demonstrated. This phase detector is still based on the timing information transfer in the optical domain. The timing information transfer in the optical domain is implemented by use of a differentially-biased Sagnac fiber-loop and synchronous detection. We used the phase error signal from this balanced optical-microwave phase detector, which is robust against drifts and photodetector nonlinearities, to regenerate low-jitter RF-signals from optical pulse trains.

Figure 2 shows the schematic of the balanced optical-microwave phase detector. Part of the input pulse train is tapped off by Photodiode 1. This photodiode is used to generate a synchronous detection signal at half the repetition rate ($f_R/2$) of the optical pulse source. This signal is applied to both the phase modulator and the down-conversion mixer. The rest of the input pulse train is sent to

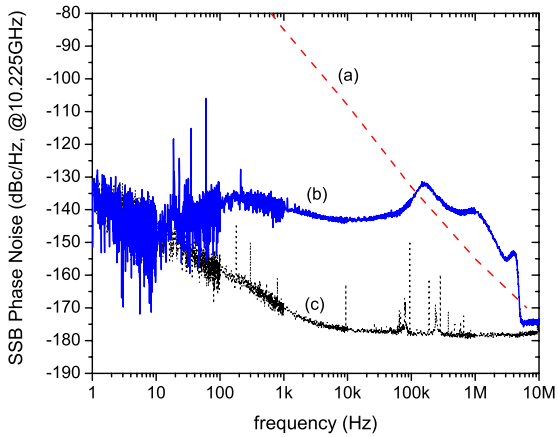

Figure 3: The single-sideband (SSB) phase noise spectra at 10.225 GHz. (a) Free-running VCO. (b) In-loop phase noise when it is locked. (c) Signal analyzer noise floor.

the Sagnac-loop with a phase modulator. The phase modulation in the Sagnac loop is converted into an amplitude modulated signal at $f_R/2$ at the output of the Sagnac-loop. The amplitude of this signal is, to the first order, proportional to the phase error between the optical pulse train and the RF-signal (which is, the output from the VCO). The detected signal at Photodiode 2 is band-pass filtered at $f_R/2$ and down-converted to the baseband by mixing with the reference signal. This error signal is filtered and controls the low-noise VCO to close the phase-locked loop.

For the demonstration experiment, a standard stretched-pulse Er-doped fiber laser [2] (repetition rate f_R = 44.26 MHz) is used as the optical pulse source. All optical components in the phase detector are implemented using commercial 1550-nm optical fiber and components. In the experimental implementation, we generated a signal with the frequency $10.5 f_R$ for the phase modulation in the Sagnac-loop in parallel with $f_R/2$ component to reduce the necessary fiber loop length. By closing the loop with a 10.225-GHz (231st harmonic of the fundamental repetition rate) VCO (PSI DRO-10.225), a long-term stable locking between the laser and the VCO is achieved.

Figure 3 shows the measured in-loop phase noise spectra at the output of down-conversion mixer. The voltage signal from the phase detector was amplified with a low-noise amplifier (G=10 non-inverting amplifier with AD797) and measured with a low-noise vector signal analyzer (Agilent 89410A), and converted into single-sideband (SSB) phase noise at 10.225 GHz. This measurement shows that the integrated in-loop jitter is 3.0 fs $\pm$ 0.2 fs integrated from 1 Hz to 10 MHz when it is locked. Currently, the system is limited by the thermal noise from electronic amplifiers and has not yet reached shot noise limited performance yet. We are currently pursuing to further suppress the timing jitter to below 1 fs by increasing optical and RF power levels as well as optimizing loop characteristics. In addition, the construction of a second loop is in progress to perform long-term out-of-loop measurements by mixing two VCO outputs in quadrature.

OPTICAL-TO-OPTICAL SYNCHRONIZATION

Tight synchronization is necessary not only between optical and RF-subsystems but also between different optical systems, for example, the photo-injector laser, the seed laser and the probe lasers as shown in Fig. 1. Conventional timing synchronization between two mode-locked lasers based on microwave mixers [16] suffers from high residual jitter and thermal drifts in the electronic amplifiers and mixers. To overcome this limitations, a balanced optical cross-correlator [12] can be used for the long-term optical-to-optical synchronization. This technique uses nonlinear optical processes for an extremely sensitive detection of timing differences between optical pulses.

Figure 4 shows the schematic of the balanced cross-correlator. The combined pulses from two mode-locked lasers with different spectra, denoted as wavelengths λ_1 and λ_2, are splitted by a broadband 50:50 beam splitter. The two beam paths have a different group delay (GD), for example, by inserting a glass plate in one of the arms. This group delay offsets the relative position between two pulses. Each combined pulse is focused into a nonlinear crystal to generate a sum-frequency component at $\frac{1}{\lambda_{SFG}} = \frac{1}{\lambda_1} + \frac{1}{\lambda_2}$. After bandpass filtering the sum-frequency generation (SFG) components, a balanced detector measures the intensity imbalance. For small timing differences (within the range of the group delay of the GD element), the output from the balanced detector is nearly proportional to the time difference between the two pulses. At the zero-crossing of the balanced detector output, the amplitude noise from each laser is balanced and does not affect the detected error signal. The signal from the balanced detector is used to lock the repetition rates of the two lasers by controlling the cavity length of one laser with cavity mirrors mounted on piezo-electric transducers (PZTs). This finally closes the loop. This method enables a drift-free and temperature-independent synchronization between two independent lasers.

The long-term timing synchronization performance using balanced optical cross-correlation is demonstrated using a 5-fs Ti:sapphire laser (centered at 830 nm) and a 30-fs Cr:forsterite laser (centered at 1250 nm). The pulses are combined and splitted by use of a broadband 50:50 beam splitter with matched group delay dispersion. LBO crystals with 1-mm thickness are used for SFG at 499 nm (1/830nm + 1/1250nm = 1/499nm). To generate a group delay offset of 45 fs between 830 nm and 1250 nm, a 3-mm thick fused silica plate is used.

Figure 5 shows the out-of-loop cross correrlation result for a timing jitter measurement between the Ti:sapphire and Cr:forsterite lasers. The black line shows the cross-

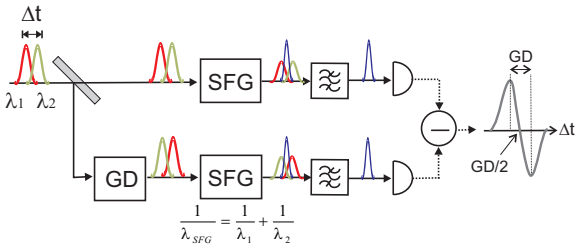

Figure 4: Schematic of a balanced cross-correlator. GD: group-delay element between two color pulses. SFG: sum-frequency generation.

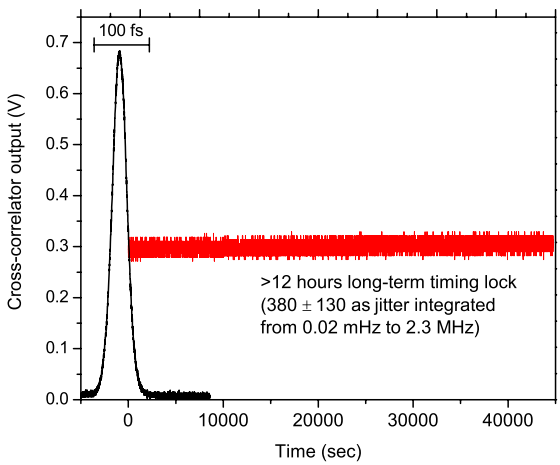

Figure 5: Long-term optical-to-optical synchronization result between Ti:sapphire and Cr:forsterite lasers. Drift-free sub-femtosecond synchronization over 12 hours were measured.

correlation trace when two lasers are not locked. The red line shows the cross-correlation trace when two lasers are locked adjacent to each other so that timing fluctuations are transferred into intensity fluctuations in the cross-correlation signal [16]. The pulse trains from the two lasers are locked with 380 attoseconds rms timing jitter over 12 hours without thermal drift in the bandwidth from 0.02 mHz to 2.3 MHz. Note that the duration of 12 hours does not constitute a limit to the locking scheme but was merely the duration of the experiment. In principle, as long as the lasers stay mode-locked, the timing lock can be maintained if the mechanical perturbations to the system are below a certain threshold value.

CONCLUSION

In summary, we reported on the progress toward a long-term stable and scalable timing distribution and synchronization system for future accelerator and seeded x-ray free electron laser facilities proposed in Ref. [1]. In particular, we demonstrated high-precision optical-to-RF and optical-to-optical synchronization techniques. We proposed and demonstrated the use of a balanced optical-microwave phase detector and balanced optical cross-correlator. By use of optical techniques, we could achieve a long-term femtosecond and sub-femtosecond accuracies which was not achievable with conventional pure RF-techniques.

REFERENCES

[1] J. Kim, F. Ö. Ilday, F. X. Kärtner, O. D. Mücke, M. H. Perrott, W. S. Graves, D. E. Moncton, T. Zwart, "Large-Scale Timing Distribution and RF-Synchronization for FEL Facilities," Proceedings of Free Electron Laser Conference 2004, p. 329, August 2004.

[2] G. Lenz, K. Tamura, H. A. Haus and E. P. Ippen, Opt. Lett. **20**, 1289 (1995).

[3] F. Ö. Ilday, J. R. Buckley, H. Lim, F. W. Wise and W. G. Clark, Opt. Lett. **28**, 1365 (2003).

[4] J. B. Schlager, B. E. Callicoatt, R. P. Mirin, N. A. Sanford, D. J. Jones and J. Ye, Opt. Lett. **28**, 2411 (2003).

[5] S. C. Zeller, L. Krainer, G. J. Spuhler, R. Paschotta, M. Golling, D. Ebling, K. J. Weingarten and U. Keller, Electron. Lett. **40**, 875 (2004).

[6] S. Namiki and H. A. Haus, IEEE J. Quantum Electron. **33**, 649 (1997).

[7] A. Winter, P. Schmüsser, H. Schlarb, F. Ö. Ilday, J. Kim, J. Chen, F. X. Kärtner, D. Cheever, T. Zwart, D. Wang, "High-Precision Optical Synchronization Systems for X-Ray Free Electron Lasers," Proceedings of Free Electron Laser 2005, p. 676, August 2005.

[8] F. X. Kärtner, F. Ö. Ilday, J. Kim, A. Winter, F. Grawert, H. Byun, J. Chen, "Progress in Large-Scale Femtosecond Timing Distribution and RF-Synchronization," Proceedings of 2005 Particle Accelerator Conference, p. 284, May 2005.

[9] J. Ye, J. Peng, R.J. Jones, K.W. Holman, J.L. Hall, D.J. Jones, S.A. Diddams, J. Kitching, S. Bize, J.C. Bergquist, L.W. Hollberg, L. Robertsson, and L. Ma, J. Opt. Soc. Am. B **20**, 1459 (2003).

[10] K. W. Holman, D. J. Jones, D. D. Hudson, J. Ye, Opt. Lett. **29**, 1554 (2004).

[11] D. D. Hudson, S. M. Foreman, S. T. Cundiff and J. Ye, Opt. Lett. **31**, 1951 (2006).

[12] T. R. Schibli, J. Kim, O. Kuzucu, J. Gopinath, S. N. Tandon, G. S. Petrich, L. A. Kolodziejski, J. G. Fujimoto, E. P. Ippen, and F. X. Kärtner, Opt. Lett. **28**, 947 (2003).

[13] E. N. Ivanov, S. A. Diddams and L. Hollberg, IEEE J. Sel. Top. Quantum Electron. **9**, 1059 (2003).

[14] A. Bartels, S. A. Diddams, C. W. Oates, G. Wilpers, J. C. Bergquist, W. H. Oskay and L. Hollberg, Opt. Lett. **30**, 667 (2005).

[15] J. Kim, F. X. Kärtner, and M. H. Perrott, Opt. Lett. **29**, 2076 (2004).

[16] R. K. Shelton, S. M. Foreman, L. Ma, J. L. Hall, H. C. Kapteyn, M. M. Murnane, M. Notcutt and J. Ye, Opt. Lett. **27**, 312 (2002).

CROSS-CORRELATION BETWEEN A VUV-FEL AND AN OPTICAL LASER

Theophilos Maltezopoulos, Ulrike Fruehling, Elke Plönjes, DESY, Hamburg;
Markus Drescher, Roland Kalms, Maria Krikunova, Marek Wieland, Uni HH, Hamburg;
Stefan Cunovic, Norbert Müller, Universität Bielefeld, Bielefeld

Abstract

At the Free Electron Laser in Hamburg (FLASH) a synchronized 800 nm optical laser is available for time-resolved VUV/vis pump-probe experiments. We crossed both femtosecond pulses in a Kr gas target and imaged the created photoelectrons with an energy-dispersive electron spectrometer. In the region where both pulses overlap in space and time, the photoelectrons are energetically shifted and form spectral sidebands. The imaging electron spectrometer projects the spectral- into an intensity modulation, thus, mapping time into space. This way, the technique delivers information about the relative timing between VUV- and visible pulse and is non invasive for both pulses. While observation of the cross-correlation signal currently requires data-averaging, with proper focussing single shot capability shall be reached, thereby enabling pulse-to-pulse jitter measurements.

PAPER NOT AVAILABLE

INVERSE FREE ELECTRON LASERS FOR ADVANCED LIGHT SOURCES

P. Musumeci, F. Germoni, M. Serluca, M. Mattioli
INFN-Roma1, P.le Aldo Moro 2, 00100, Rome, Italy.

Abstract

Laser accelerators hold the promise for high gradient acceleration and production of ultra short electron bunches. Among these, the inverse free-electron laser has recently demonstrated to be a mature and reliable scheme ready to step up from successful proof-of-principle experiments to cutting-edge applications. The very high gradient and the multi kAmp peak current of the output beam make it an attractive option in the hundreds of MeV to few GeV energy region. We examine the feasibility of using an IFEL driven by an high power Ti:Sa laser source to generate soft x-rays by FEL interaction in an undulator. A control of the slippage of the radiation over the ultrashort spikes of the IFEL-microbunched beam current is implemented to increase the gain and maintain the 200 as-long pulse structure in the radiation profile.

INTRODUCTION

While the wall plug efficiency of laser based accelerators still falls short of the requirements needed to cost-effectively build a high energy physics linear collider, high-gradient, short-wavelength advanced accelerator schemes are an attractive option to produce electron beams suitable to drive 4th generation x-ray lasers where one can choose peak brightness over average brightness. The small transverse emittances and high peak currents of current conventional radiofrequency based designs [1, 2] are within the reach of advanced state-of-the-art laser based accelerators. The requirements on the beam relative energy spread (less than few thousandths) could be tougher to satisfy but the progress in the experimental results in these last few years [3] brings closer to reality an advanced accelerator driven x-ray laser with an attractive reduction of the footprint and henceforth of the costs of such machines.

Among the various advanced accelerator schemes, the inverse free-electron laser (IFEL) is one of the most promising and well understood in terms of control of longitudinal phase space, trapping efficiency and final energy spread [4]. Using a high power laser and a properly designed undulator the IFEL has recently demonstrated accelerating gradients superior to conventional rf accelerators and very high energy gains [5]. Moreover, the IFEL is a far-field vacuum acceleration scheme which preserves the beam emittance through acceleration and it is in principle free of optics damage threshold limitations. Finally, the energy transfer mechanism, just the inverse of the well known FEL principle at the basis of the last generation light source facilities, is very efficient and one can design undulators able to transfer more than 75 % of optical power to beam power [6]. The final efficiency is in fact only limited by the wall-plug to optical conversion efficiency which for common high power laser systems is still quite low (below 1 %).

Even though many limitations arise when one considers the IFEL for multi-GeV energies mostly due to the synchrotron radiation losses from the wiggling electron trajectories, the tremendous progress and commercial availability of ultrahigh power laser sources makes the IFEL scheme a very feasible and convenient choice in the hundreds of MeV to few GeV energy, which is just the energy region for x-ray FEL drivers.

The detailed control over the electron beam longitudinal phase space obtainable with the interaction of a powerful laser and relativistic electrons passing through an undulator has already captured the interest of FEL physicists. In fact the IFEL mechanism in its not-accelerating prebunching version has been already proposed to be used at LCLS to enhance the SASE characteristics (ESASE). The short high current spikes obtained converting the IFEL-induced energy modulation into density modulation at the scale of the optical wavelength are foreseen to shorten the undulator distance needed to reach saturation and to produce sub femtosecond X-ray pulses [7].

In this paper we conjugate the advantages of using an IFEL as a prebuncher with its high gradient capabilities to design a soft X-ray source based on an IFEL accelerator. The design aims at producing coherent radiation in the so called water window region of the electromagnetic spectrum (λ = 3-4 nm) and it is tailored on the SPARC linac which is a state-of-the-art injector delivering a high brightness electron beam at 200 MeV energy in its final stage of construction at Frascati [8].

IFEL DESIGN

In Table 1 we report the input parameters considered for the IFEL design.

The electron beam input parameters like energy, energy spread and peak current are the nominal values of the SPARC linac [9]. In this design exercise we have considered to use a portion (20 TW out of 100 TW) of the high power laser foreseen to be installed in the same experimental area of the high brightness injector [10]. The ratio between the laser rayleigh range and the undulator length has been set to maximize the integrated gradient and so the final energy gain [11]. The choice for the IFEL coupling is

Table 1: IFEL input parameters

parameter	fixed value
Energy	210 MeV
Energy spread	0.5 %
Current	1 kA
Wavelength	800 nm
Peak Power	20 TW
Wiggler length	2 m
wiggler gap	7 mm
Rayleigh range	0.2 m
Waist position	1 m

a permanent magnet helical undulator. The particle transverse velocity is always different than zero and parallel to the electric field of a circularly polarized laser (easily obtainable from a linearly polarized pulse, using a high power quarterwave plate) so that the energy transfer mechanism between photons and electrons is always turned on. The undulator gap is set to 7 mm in order to be able to propagate without clipping along the undulator length both the laser and the electron beam. To ensure feasibility of the undulator construction, the Halbach relation

$$B_{max} = 1.79 e^{-\lambda_w / g} [Tesla] \quad (1)$$

which yields the maximum attainable magnetic field amplitude for a given gap g and period λ_w has been used as an upper bound for the magnetic field. [12]. The optimized variations for period and field amplitude are reported in Fig. 1a. The resulting resonant energy

$$\gamma_r = \sqrt{\frac{\lambda_w (1 + K^2)}{2\lambda}} \quad (2)$$

along the helical undulator is also shown (Fig. 1b). In (2) K is the normalized peak magnetic field amplitude and λ is the driving laser wavelength.

In order to guarantee an high quality final longitudinal phase space for the accelerated beam the ponderomotive resonant phase is varied along the undulator. In Fig. 2 we show the longitudinal phase space and its projection on the energy and time axis obtained tracking particles through the undulator and laser electromagnetic fields with the 3D IFEL code TREDI[13]. At the beginning the resonant phase is close to zero to improve capture efficiency while later in the undulator after the particles have been already captured and bunched its value grows to $\pi/3$ to maximize the accelerating gradient and reduce the final energy spread. The latter in particular is one of the most sensitive parameters for a 4th generation light source driver. The stable accelerating region of phasespace formed by the ponderomotive IFEL potential ensures that small variations in driving laser power and time/spatial jitter only affect the capture efficiency reducing slightly the final peak current and not the other parameters of the accelerator like final energy and

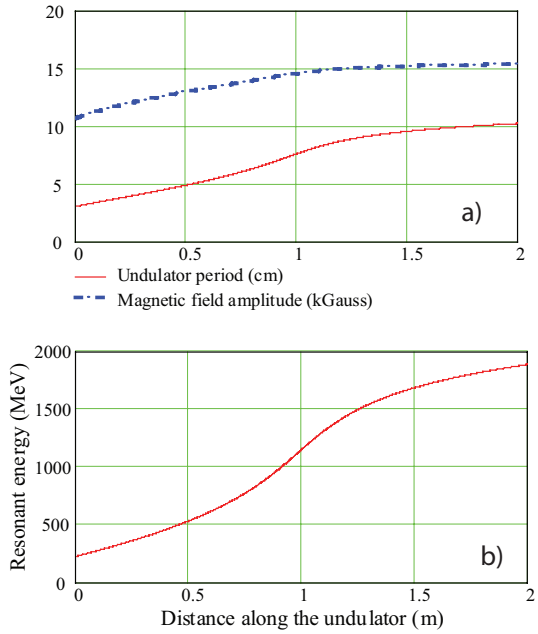

Figure 1: Variation of period and magnetic field amplitude along the undulator (a). The resonant energy is also shown (b).

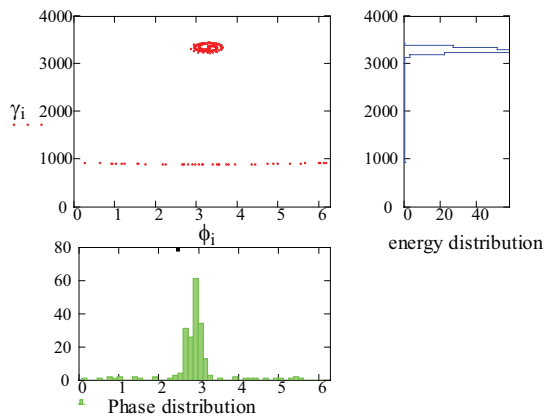

Figure 2: Simulated longitudinal phase space of the electron beam at the exit of the IFEL accelerator.

energy spread [13]. The output accelerator parameters are summarized in Table 2.

The average gradient obtained in this design is quite large, more than one order of magnitude larger than conventional rf-based designs. A length of just 2 m of undulator is sufficient to reach an energy of 1.5 GeV suitable to drive a x-ray laser at the water window wavelength (3 nm) which is the goal of our design exercise. The high peak current results from the bunching at the optical wavelength that takes place in the IFEL (see Fig. 3).

SLIPPAGE DOMINATED FEL

The undulator magnet envisioned to be used to generate the soft x-ray radiation is the same of the one being built

Table 2: IFEL output parameters

Energy	1.7 GeV
Energy spread	$< 0.5\,\%$
microbunch length	250 as
Peak current	6 kAmp
Avg. gradient	750 MeV/m

and installed for the SPARC project. The FEL parameters are reported in Table 3.

Start-to-end simulations of the entire system are performed using the output phase space from TREDI as the starting distribution in Genesis 1.3 [14]. Even though the physical mechanism of the interaction is the same along the system, it is required to use a different code to model the IFEL interaction since due to the strong tapering the period-averaged classical FEL approximation is not valid anymore, and the explicit 3d Lorentz-force equation solver is used for the particle dynamics in the simulation of the IFEL with TREDI. At the same time for the light generation section of the system, TREDI does not take into account the evolution of the electromagnetic field which has to be calculated using Genesis. The longitudinal phase space is periodic with period equal to the driving laser wavelength. The FEL simulation is performed over a window including a portion of the accelerated beam of a length such to include 6 to 8 periods of 800 nm. In Fig. 3 we show the beam parameters along the electron bunch coordinate inside the simulation window. The energy spread at the peak of the current is almost as large as the FEL ρ parameter and this degrades the interaction. Further work is needed in the optimization of the last section of the IFEL accelerator in order to minimize this effect.

The Genesis simulation result is shown in Fig. 4. The final peak power is limited to only few MW and in the longitudinal profile of the newborn radiation there is no trace of the attractive sub-fs structure of the incoming electron beam.

To explain these results, we must keep in mind that the the duration of the current spikes is only 1/10th of the optical wavelength, that is 250 attoseconds or ~ 90 nm. Considering the fact that in the undulator the radiation slips one radiation wavelength each undulator period, after only 30 periods of undulator the radiation has slipped over the peak

Table 3: FEL parameters

Radiation wavelength	3 nm
Undulator period	2.8 cm
Undulator K	1.65
Periods per section	77
Number of sections	6
ρ parameter	$4.5 \cdot 10^{-3}$

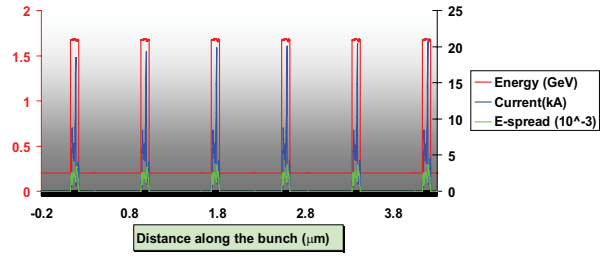

Figure 3: Electron beam current along the bunch. The current spikes are very short (250 as) and distant an optical period 2 fs between eachother.

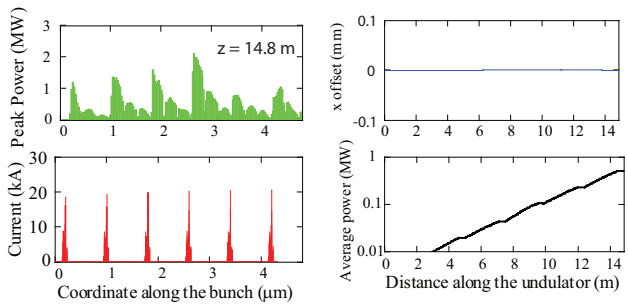

Figure 4: Output of the SASE simulation.

of its gain medium. An FEL driven by such beam would operate in a strongly slippage dominated regime. Clearly the problem is reduced if the IFEL accelerates the electron beam to higher energies enabling the production of shorter wavelength radiation. In this case in fact the length of each current spike would be the same, being fixed by the IFEL driver wavelength) and the shorter wavelength FEL radiation would experience a high gain for a larger number of undulator periods before slipping away of the high peak current region. Unfortunately the IFEL accelerator design gets more complicate for higher final energies since it requires a larger laser power and it also involves staging of two different IFEL modules. Moreover the planned extension of the SPARC photoinjector, SPARX [15], is foreseen to deliver coherent soft X-rays and user and diagnostics availability make attractive the few nm region of the electromagnetic spectrum.

One possible solution to the slippage problem is to take advantage of the microbunch train structure of the electron beam. In principle one could retard the charged particles inserting a magnetic path length between different undulator sections so that the radiation would slip faster over the electrons and take over the next high current spike at the beginning of the next undulator section. A cartoon illustration of this scheme is shown in Fig. 5. The advantage in this configuration is twofold: i) the FEL radiation only experience high gain and is amplified over the entire undulator length and ii) the magnetic chicane inserted to delay the electrons between undulator sections is a positive R_{56} element which helps the conversion of energy modulation into

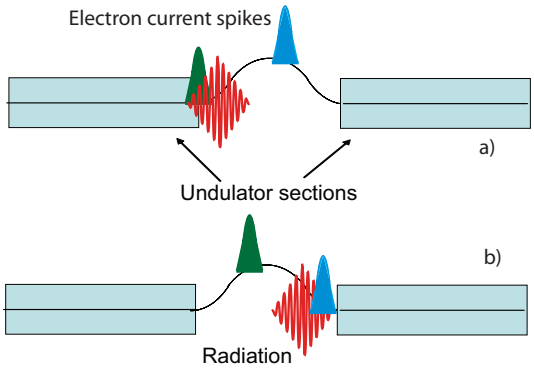

Figure 5: Schematics of chicane to compensate slippage inserted between undulator sections.

density modulation and so accelerates the microbunching process enhancing the FEL instability in a optical-klystron like configuration [16].

Without a coherent seed over all the electron bunch, on the other hand, the enhancement of the FEL interaction will not take place since the phase of the electromagnetic field and of the induced bunching starting in the different high gain high current regions is completely random being determined by the shot-noise in the electron beam. Suitable seeds at these short wavelengths are of course lacking at this time, but the strong progress in high harmonic generation in gas [17] could help in this regard. In Fig. 6 we show the results of the GENESIS simulation obtained introducing a coherent seed over the entire macrobunch length so that there is a definite phase relationship between the radiation and the bunching in the different current spikes and the FEL interaction can start constructively at the beginning of each undulator section. In the upper right corner the x-trajectory of the electron beam is represented. The bumps represent the magnetic chicanes located in between different undulator sections. The final peak power is > 1 GW and the radiation is composed by a train of sub-fs spikes locked with the 800 nm IFEL drive laser phase.

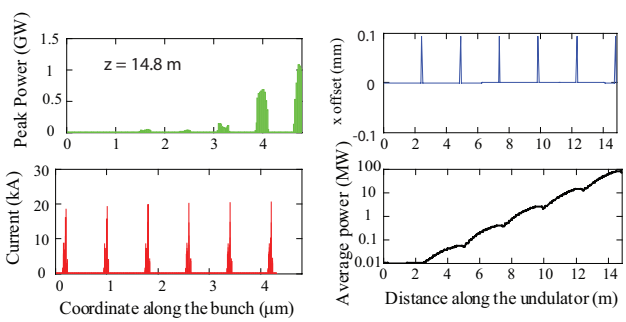

Figure 6: Output of the GENESIS1.3 simulation with a seed and with the magnetic chicanes between the undulator sections.

CONCLUSIONS

We propose the use of an inverse free electron laser to drive a 4th generation light source in the soft X-ray region of the electromagnetic spectrum. Taking advantage of the high gradient and of the precise control over the longitudinal electron beam phase space, the inverse free electron laser accelerator delivers a high current, high energy electron beam. The sub-fs structure on the current induces strong limitations due to the slippage on the FEL dynamics. If one wants to preserve the structure and increase the final power, some special precautions have to be taken. It is worthwhile to note that even if in this paper we considered the inverse free-electron laser as the advanced accelerator scheme to generate the electron beam, a similar output beam structure is likely to be found using other laser and/or plasma based accelerators. The considerations and the solutions discussed here are applicable to those cases also. Another benefit of the proposed laser driven source is the synchronization and phase-locking of the x-ray pulse with an external high power laser for pump-probe experiments.

REFERENCES

[1] J. Galayda et al. Linac Coherent Light Source Conceptual Design Report, SLAC-R-593, 2002.

[2] TESLA Technical Design Report TESLA-FEL-2002-9, DESY-2002-167, 2002.

[3] C. G. R. Geddes et al. *Nature*, 431:538, 2004.

[4] W. Kimura et al. *Phys. Rev. Lett.*, 92:054801, 2004.

[5] P. Musumeci et al. *Phys. Rev. Lett.*, 94:154801, 2005.

[6] P. Musumeci. *Proc. of 2006 Advanced Accelerator Concepts, Lake Geneva, WI*, 2006.

[7] A. A. Zholents and W. M. Fawley. *Phys. Rev. Lett.*, 92:224801, 2004.

[8] M. Bellaveglia. In *these proceedings*, 2006.

[9] D. Alesini et al. *Nuclear Instruments and Methods in Physics Research A*, 507:345, 2003.

[10] L. Serafini et al. In *Proc. of 2006 EPAC Conference*, 2006.

[11] W. Kimura et al. In *AIP Conf. Proc.*, volume 737, page 251, 2004.

[12] K. Halbach. *Journal de Physique*, C1:211, 1983.

[13] P. Musumeci et al. In *Proc. of 2001 Particle Accelerator Conference, Chicago, Illinois*, page 4008, 2001.

[14] S. Reiche. *Nuclear Instruments and Methods in Physics Research A*, 429:243–248, 1999.

[15] C. Vaccarezza et al. In *Proc. of 2006 EPAC Conference, Edinburh, Scotland*, 2006.

[16] Y. Ding et al. *PRSTAB*, 9:070702, 2006.

[17] J. Seres et al. *Nature*, 433:596, 2005.

TECHNICAL ASPECTS OF THE INTEGRATION OF THE OPTICAL REPLICA SYNTHESISER FOR THE DIAGNOSTICS OF ULTRA-SHORT BUNCHES INTO FLASH AT DESY*

P. van der Meulen, N. Javahiraly, M. Larsson, Department of Physics, AlbaNova, Stockholm University, Stockholm, Sweden
V. Ziemann, Department of Nulcear and Particle Physics, Uppsala University, Uppsala, Sweden
H. Schlarb, A. Winter, E. Saldin, E. Schneidmiller, M. Yurkov, DESY, Hamburg, Germany.

Abstract

In this paper we present an overview of current status of the Optical Replica Synthesiser at DESY. The method is based on producing an "optical copy" of the electron bunch with its subsequent analysis with optical techniques [1]. To this end, a near-IR laser beam is superimposed on the electron beam in the first undulated of an optical klystron. In the following dispersive section the laser-induced energy modulation is transformed into a density modulation. The modulated electron bunch then produces a strong optical pulse in the second undulator. Analysis of this near-IR pulse (the optical copy) then provides information about the profile, the slice emittance and the slice energy spread of the electron bunch. We discuss the implementation of such a measurement set-up at the FLASH facility at DESY and investigate the influence of various parameters on the performance of the device. Topics we address include the dispersive chicane, as well as the requirements for the seed laser pulses and the detection and analysis of the near-IR pulse.

INTRODUCTION

Monitoring and tuning the bunch properties are essential for the reliable operation of linac-based SASE free-electron lasers such as FLASH [2], XFEL [3], and LCLS [4]. This need has triggered the development of new diagnostic methods based on a transversely deflecting cavity [5] or electro-optical sampling [6]. The Optical Replica Synthesiser (ORS), a complementary scheme that was introduced in reference 1, is similar to an optical klystron FEL seeded by an infrared laser as is shown in figure 1. In the modulator the interaction of the laser with the transversely oscillating electrons causes an energy modulation. A dispersive section turns this energy modulation into a density modulation at the wavelength of the light. In a following radiator undulator the micro-bunched beam radiates coherently and the emitted light pulse has the same longitudinal profile as the electron beam. Hence the name optical replica synthesiser.

The optical replica pulse is analysed in a FROG (frequency resolved optical gating) device [7], which is based on recording the spectrally resolved signal of the auto-correlation. Subsequent application of a pulse retrieval algorithm reveals both amplitude and phase of the incident electric field and thus of the longitudinal profile of the electron bunch. A very compact second harmonic FROG device, Grenouille [8], which performs the analysis, is available commercially.

Following up on the signing of a letter of intent by DESY and the vice-chancellors of three Swedish universities in Uppsala and Stockholm the recently established SU-KTH-UU Free Electron Laser Centre has entered a collaboration with DESY to design and implement a prototype of the ORS in FLASH in order to establish the feasibility of the device for the X-FEL. In this note we present the status of the project as of August 2006.

SPACE AND TIME

The ORS will be installed in the beam line of FLASH between the collimating dog-leg and the VUV-undulator. The seed laser will be coupled in into the beam line just downstream of the dog-leg where a vacuum window is available. The modulator will be located about 10 m downstream of the vacuum window. The magnets will fit into 1.5m long unoccupied sections between quadrupoles and other equipment and the magnet gap of 40mm is sufficiently large to allow installation without modifying the existing beam pipe. The chicane consisting of four standard dipole magnets will also fit in between consecutive quadrupoles and can be mounted without breaking the vacuum. The housing of the extraction coupling mirror and some extra diagnostic for beam size measurements and alignment of laser and electron beam will require some vacuum intervention.

The distance between the modulator and the radiator will be on the order of 15m and it should indeed be short, because collective effects such a plasma oscillations [9] perturb the micro-bunching, caused by modulator, before it can generate the optical replica pulse in the radiator. The replica pulse in this case would not be a faithful replica of the electron bunch profile.

The laser system will be placed outside the linac tunnel with the shortest possible laser transfer line. For that an additional tunnel into the beam-tunnel will be drilled near the dog-leg. The installation of the ORS in the beam line is foreseen for a shutdown during spring 2007 which will be followed by commissioning and operating until the self-seeding option for FLASH will be installed in the beam line between the collimating dog-leg and the undulator.

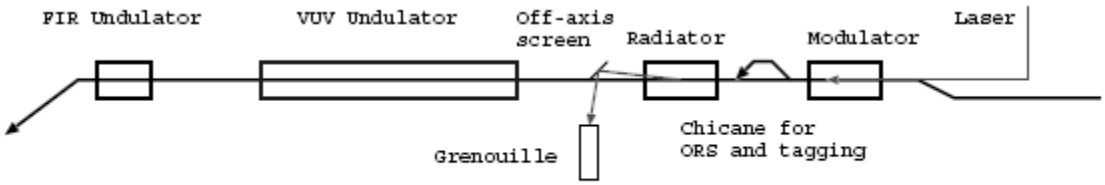

Figure 1: Schematic view of the Optical Replica Synthesiser.

SEED LASER

The seed laser will be based on an 1550 nm Erbium fiber oscillator that can be synchronised to the RF system of the linear accelerator. This oscillator has recently been constructed and the first, preliminary tests show that it is functioning properly. Stable mode locking is achieved and the pulse has the desired characteristics regarding pulse energy and spectral width. A schematic diagram of the Erbium fiber laser is shown in figure 2. As a next step the pulses will be compressed and frequency doubled. Subsequently the active synchronisation will be implemented and its effect on the laser operation will be tested.

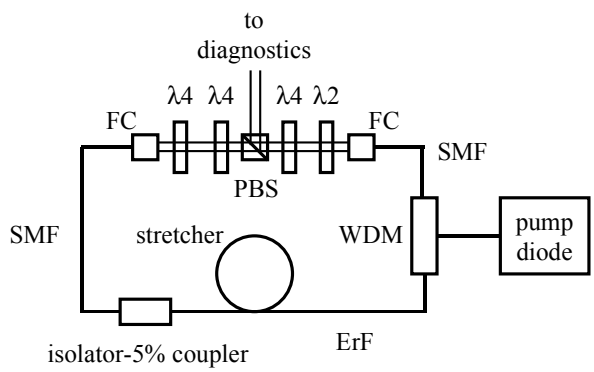

Figure 2: Schematic view of the Erbium fiber oscillator. FC: fiber coupler; SMF: single mode fiber; ErF: Erbium doped fiber, PBS: polarising beam splitter, WDM: wavelength division multiplexer, λ4: quarter lambda plate, λ2: half lambda plate.

As an amplifier we will use an existing Clark-MXR CPA2001 Ti:Sapphire laser from Stockholm University. The interfacing of the home-built oscillator and the amplifier will start soon. The choice for this amplifier is mainly motivated by budgetary reasons, as the CPA2001 is a highly compact laser system that is not easily adapted to this particular application. On the other hand, it has performed very reliably in our lab, with little maintenance and without major malfunctions for many years. The doubled output pulses of the Erbium fiber oscillator will be stretched before injection into the Ti:Sapphire amplifier cavity. We will attempt to use the stretcher currently installed inside the CPA2001. This means that we will have to separate the two layers of the CPA2001 in order to gain access to the lower level. No modifications of the amplifier cavity or the compressor are envisaged and only slight changes of control electronics are necessary, predominantly in the Pockels cell driver. The normal operating frequency of the CPA2001 is 1 kHz, but it can easily be reduced to 1-10 Hz to match the frequency of FLASH.

A seed laser intensity of about 4.5 GW/cm^2 is necessary to achieve required energy modulation of the electron bunch in a five period modulator undulator [1]. If we account for reflection losses during transport, the estimated maximum pulse energy of the modified CPA2001 laser system will be approximately 700 μJ inside the accelerator vacuum tube. The pulse length will be set to about 2 ps to attain a stable temporal overlap between the laser pulse and the electron bunch. This is achieved by deliberately misaligning the compressor of the CPA2001. The resulting longitudinal chirp on the laser pulse is not expected to influence the operation of the ORS significantly.

In order to estimate the beam diameter inside the modulator undulator we have performed a straightforward calculation using Gaussian optics. The results of this calculation, in which the beam is focussed by a Galilean telescope consisting of two achromatic lenses with focal lengths of 1.0 m and -0.8 m separated by 0.26 m, are shown in figure 3. The beam from the CPA2001 was assumed to be diffraction limited with an initial diameter of 6 mm (FWHM). From figure 3 we can see that a beam diameter of about 0.8 mm (FWHM) can be expected at the position of the modulator undulator located about 10 m downstream from the second telescope lens. This leads to a laser peak intensity of about 45 GW/cm^2 a factor of ten in excess compared to what should be required. A more realistic simulation that takes into account the transversal mode structure of the femtosecond pulses is under way using commercial beam propagation software. This simulation will also address the transport form the CPA2001 laser system to the focussing telescope.

In principle even higher laser intensities could be reached by focussing tighter, but here we are limited by the requirement that the intensity is essentially constant over the entire length (ca. 1.5 m) of the modulator and by the dimensions of the input vacuum window (16 mm diameter). Furthermore, the laser beam should easily accommodate the whole electron bunch, which has a diameter of 0.1-0.2 mm (FWHM), even while it is performing its oscillatory motion in the modulator, and by making the diameter of the seed laser beam too small we

may simply become too sensitive to the pointing stability of the laser system. In any case, the distance between the laser and the modulator is so large that probably active beam position stabilisers are required to maintain spatial overlap between the laser and the electron beam for extended periods of time. Existing beam position monitors and screens will be used to monitor the spatial overlap between the laser and the electron beams. Diagnostic stations to monitor the laser before the vacuum window as well as after the radiator undulator are foreseen, but not yet finalised.

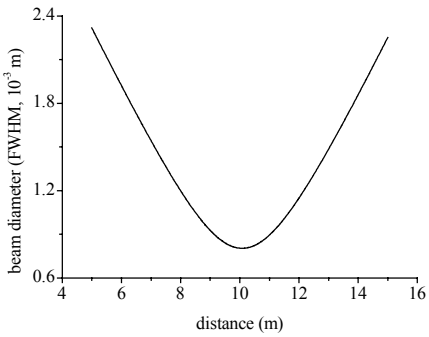

Figure 3: Seed laser beam diameter as a function of the distance to the focussing telescope showing a focus of 0.8 mm diameter (FWHM) inside the modulator.

One point of concern is the presence of a spatial chirp and / or a tilted wavefront on the CPA2001 seed laser pulse. At the moment it is not entirely clear how this will affect the detailed micro-bunching process or the subsequent analysis of the radiator pulse using the Grenouille FROG apparatus. We will perhaps be forced to take steps to correct the seed laser pulse for these imperfections.

UNDULATOR AND CHICANE

The undulators for the modulator and radiator with period l_0 and $K=93.4B_0l_0$ must fulfil the FEL resonance condition $\lambda=l_0(1+K^2/2)/2\gamma^2$ with an IR laser operating at λ = 780 nm and beam energies $E = \gamma mc^2$ between 500 and 1000 MeV. Together with the constraint to be shorter than 1.5 m we arrive at electromagnetic magnets that have 5 full periods plus two extra periods to zero the field-integrals with a period of 20 cm and a peak field B_0 below 0.5 T. In order to allow separating the high power seed laser from the weaker replica pulse by a polariser we will have one horizontal and one vertically polarised undulator. Both magnets are now ordered from Scanditronix in Sweden and will be delivered to DESY in spring 2007. The support structure for the undulators to move them in and out of the beam line will be designed by staff at DESY.

The standard steering dipoles with a peak excitation of $33x10^{-3}$ Tm are sufficient for chicane to provide an R_{56} of up to 0.3 mm. The transverse offset (ca. 10 mm) of the beam in the chicane can also be used to insert a mirror and extract a major portion of the seed laser pulse to avoid irradiating downstream equipment and disturbing the weak replica pulse.

LASER DIAGNOSTICS

Once the replica pulse is generated in the radiator undulator it has to be extracted from the beam pipe and transported to the diagnostic section with the Grenouille. Presently we are discussing several options to extract the light, either by pointing the radiator undulator at a downstream off-axis mirror. This option, however, would introduce significant wavefront distortion and is not favoured. In another option we add a second chicane downstream of the radiator with steering magnets to steer around an off axis screen. A third option would be to insert a mirror with a hole into the beam pipe such that the electron beam can pass the mirror, but the IR pulse is deflected out. These options will be scrutinised in the coming months.

The placement of the Grenouille either in the accelerator tunnel or in the new laser housing has not been decided yet. Placement of the Grenouille inside the tunnel has the advantage of a shorter beam path for the replica pulse as well as easier alignment and construction, but access to the tunnel during accelerator operation is impossible and parasitic operation without impeding other activities is, of course, much favoured.

CONCLUSIONS AND PROSPECTS

We have taken the first steps towards implementing the ORS in FLASH at DESY. Ordering the magnets which have a long lead time was the first major step and building the laser will be the next, together with solving all the other issues that we only mentioned in passing.

The infrastructure of lasers and undulators created for the ORS provides a fertile ground for further experiments with beams and lasers, especially regarding synchronisation. For example, using the FIR-undulator that will be installed downstream of the VUV-undulator as the radiator instead of the original radiator will allow to generate a coherent light pulse at the wavelength of the seeding laser close to the experimental hall where it can be cross-correlated with an external laser used for pump probe experiments. This will yield information about the relative timing of the external laser and the bunch arrival time, which also caused the VUV-pulse. In this way the relative timing between VUV-pulse and external laser can be determined.

Furthermore, passing the micro-bunched electron beam after the chicane through an optical transition radiation screen, will yield information about the bunching and this signal can be used for tuning.

REFERENCES

[1] E. Saldin, E. Schneidmiller, M. Yurkov, ``A simple method for the determination of the structure of ultrashort relativistic electron bunches," Nucl. Inst. and Methods A 539 (2005) 499.
[2] J. Rossbach, Nucl. Inst. Meth. A475 (2001) 13.
[3] P. Audebert, et.al., ``TESLA XFEL: The first stage of the X-ray laser laboratory - Technical Design Report," DESY 2002-167.
[4] The LCLS Design Study Group, ``LCLS Design Study Report'', SLAC-R-593, 2002.
[5] O. Grimm et al., ``Longitudinal bunch shape diagnostics with coherent radiation an a transverse deflecting cavity in TTF2", Proceedings of the 2004 FEL conference, 395.
[6] G. Berden, et al., ``Electro-Optic Technique with Improved Time Resolution for Real-Time, Nondestructive, Single-Shot Measurements of Femtosecond Electron Bunch Profiles," Phys. Rev. Lett. 93 (2004) 114802.
[7] R. Trebino, ``Frequency Resolved Optical Gating", Kluwer Academic, Boston, 2000.
[8] www.swanoptics.com
[9] G. Geloni, E. Saldin, E. Schneidmiller, M. Yurkov, ``Theory of space-charge waves on gradient-profile relativistic electron beam: An analysis in propagating eigenmodes," Nucl. Inst. and Methods A 554 (2005) 20.

INVESTIGATIONS OF THE LONGITUDINAL ELECTRON BUNCH STRUCTURE AT THE FLASH LINAC WITH A TRANSVERSE DEFLECTING RF-STRUCTURE

Michael Röhrs*, Christopher Gerth, Holger Schlarb
Deutsches Elektronen-Synchrotron DESY, D-22603 Hamburg, Germany.

Abstract

In the single-pass Free-Electron Laser FLASH, Self-Amplification of Spontaneous Emission (SASE) occurs in a small fraction of an electron bunch with a length in the order of micrometers. As a consequence, there is a need for bunch diagnostics with a time resolution in the femtosecond regime for understanding and improving the machine performance. At FLASH, a vertically deflecting structure (LOLA) is used to measure the longitudinal charge density profile and phase space distribution of single bunches with high time resolution. The horizontal slice emittance can be determined by additionally using quadrupole scan techiques. In this paper, we present results of measurements under conditions close to SASE operation at 13.7 nm. We reached a RMS resolution of 20 fs for the longitudinal profile measurements, and resolved the longitudinal phase space distribution and slice emittance with 50 fs and 60 fs, respectively. Strong indications for a substructure within the horizontal phase space distribution of the peak current region have been found.

INTRODUCTION

At the Free electron LASer in Hamburg (FLASH), electron bunches with peak currents of 1-3 kA are produced by longitudinal bunch compression in two magnetic chicanes. This results in a narrow high current region at the front of the bunch ("spike") with a width of less than 100 fs (FWHM) and a long trailing tail. The SASE process may be initiated within the spike, if transverse slice emittance and slice energy width are sufficiently small. However, these parameters are significantly degraded by coherent synchrotron radiation (CSR) effects in the dipoles of the magnetic chicanes, and by space charge forces along the linac. The SASE signal with a duration in the order of 10 fs suggests that only a fraction of the charge in the spike contributes to the lasing process. To resolve the longitudinal structure, bunch diagnostics with an appropriate time resolution is necessary.

The most powerful and multifunctional tools for this purpose are currently transverse deflecting rf-structures called LOLA [1, 2, 3]. LOLA structures operate in a hybrid mode (a superposition of a TM_{110} and a TE_{110} mode), which propagates with a phase velocity equal to the speed of light. A passing relativistic electron is subject to a deflecting force in vertical direction, which is independent of the transverse position of the electron within the structure and constant in time. The force sensitively depends on the phase of the fields at the arrival time due to a high frequency time variation at 2.856 GHz. Injection of a bunch at zero crossing of the deflecting force results in a shearing or "streaking" of the bunch without centroid deflection. As a consequence, the vertical positions of the bunch electrons downstream of the structure are linearly correlated with their longitudinal coordinates. Standard OTR screens then allow for measurements of the particle distribution in the longitudinal-horizontal plane. Alongside the measurement of the longitudinal charge density profile, this technique permits to determine the horizontal slice emittance by scanning quadrupoles upstream of LOLA [4]. Furthermore, the longitudinal phase space distribution can be obtained in a single shot measurement at locations with significant horizontal dispersion. An estimate for the time resolution is given by the vertical size of the bunches at the screen location without streak, i.e. with LOLA being switched off. Parameters of the LOLA structure are listed in Table 1 [3].

Table 1: Properties of LOLA [3]

Length	3.64 m
Frequency	2.856 GHz
Max. operating power	25 MW
Deflecting voltage at 20 MW	26 MV
Filling time	0.645 μs
Aperture	44.88 mm

EXPERIMENTAL SETUP

A schematic of the FLASH linac and the sections used for the measurements is shown in Fig. 1. Electron bunches are generated in an rf photocathode (gun) and accelerated in five superconducting modules ACC1 to ACC5. The bunches are longitudinally compressed in two magnetic chicanes BC2 and BC3 at energies of typically 127 MeV and 360 MeV, respectively. A dispersive section (dogleg) is used to collimate the beam before it enters the undulator section. For the presented measurements, the linac was operated with a bunch charge of 0.5 nC and a final energy of 677 MeV to produce a SASE signal at 13.7 nm wavelength. We obtained an average radiation energy of 5 μJ per electron bunch. The phase of module ACC1 was set to -7.6° from minimum energy width operation, which is 4.4 ° above the phase for maximum peak current (-12 °). The

* michael.roehrs@desy.de

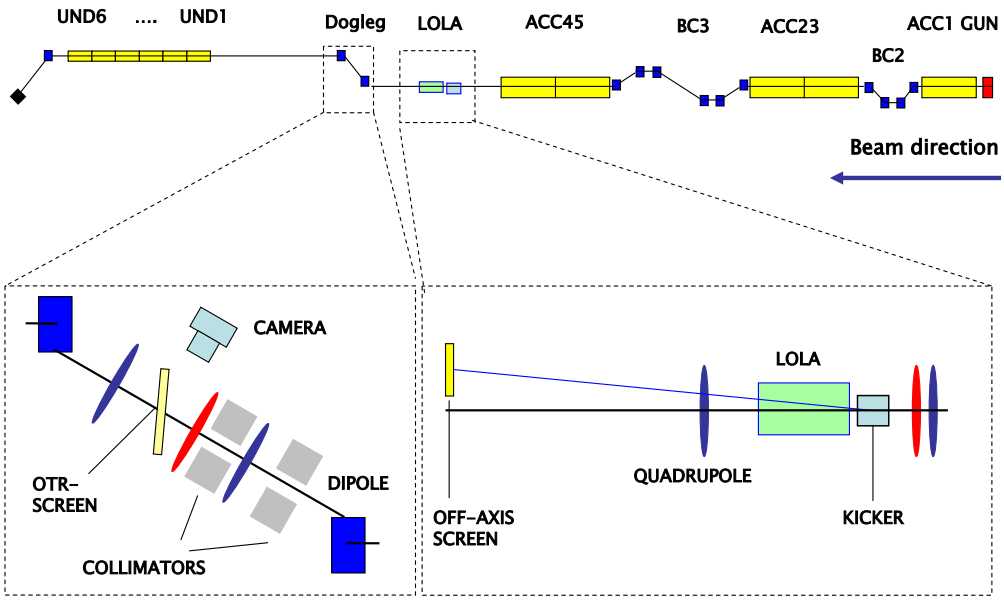

Figure 1: Schematic of the FLASH beamline and a zoom into the regions used for the measurements. Longitudinal profile and slice emittance have been measured on an off-axis screen (bottom right), the distribution in longitudinal phase space with a screen in the dogleg section (bottom left).

phases of modules ACC23 and ACC45 were set to -25° and 0°, respectively.

LOLA is located at the end of the linac. An off-axis screen with a hight of 17 mm has been used in combination with a horizontal kicker preceding LOLA to measure the longitudinal profiles. The time scale on the vertical axis of the screen has been calibrated by measuring the vertical bunch position while varying the phase of LOLA around zero crossing. The calibration constant or "streak strength" was 4.9 mm/ps in case of the density profile measurement. The input power of LOLA has been adjusted to observe entire bunches on the screen, including the long tails. In this way additional quantities may be infered, e.g. the charge portion within the spike, whereas the time resolution is slightly degraded. The horizontal slice emittance has been measured by varying quadrupoles upstream of LOLA. Several quadrupoles had to be scanned simultaneously in order to minimize the changes in time resolution (vertical beam size with LOLA switched off) while the phase advance in horizontal direction was varied.

An OTR screen in the horizontally dispersive dogleg section has been used for measuring the longitudinal phase space distribution. The dispersion generated by the upstream dipole has been determined to be 233 mm by measuring the horizontal beam position on the screen for different dipole currents.

Before the measurements, the optics downstream of BC3 had been modified in order to improve the resolution of the measurements. However, we expect only a negligible modification of the longitudinal bunch properties and the horizontal emittance. In case of longitudinal phase space measurements, also the optics upstream of BC3 had to be modified slightly, which may have altered CSR effects in the dipoles of BC3.

RESULTS

LONGITUDINAL PROFILE

Fig. 2 shows the measured longitudinal charge density profile of a single bunch. It consists of a sharp leading spike and a long tail. The width of the spike is ∼70 fs (FWHM). The time resolution is ∼50 fs FWHM and ∼20 fs RMS. The properties of the spike change slightly from bunch to bunch most likely due to phase and / or amplitude fluctuations of the first acccelerating module. An analysis for 100 successive bunches reveals a nearly gaussian-shaped distribution of the spike width with a mean of 74 fs and a sigma of 9 fs. The same applies to the charge in the spike defined by the coloured area in Fig. 2 and the corresponding current, which are 0.13 ± 0.01 nC (25 ± 1 % of the total bunch charge) and 1.7 ± 0.1 kA.

LONGITUDINAL PHASE SPACE

The particle distribution of a single bunch in longitudinal phase space, which is directly obtained from an OTR image of a streaked bunch in the dispersive dogleg section, is presented in Fig. 3 (top). It shows the expected overall

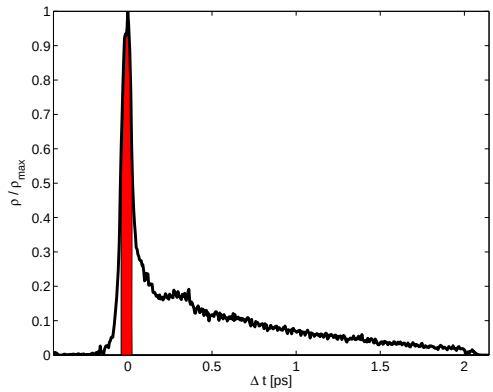

Figure 2: Normalized longitudinal charge density profile measured with LOLA. The width of the coloured region is equal to the width of the spike (FWHM). The specified charge fraction in the spike refers to this area.

correlation, which is characterized by a rapid energy variation at the head of the bunch leading to the observed sharp spike in the longitudinal profile, and an increasing energy along the tail due to off-crest acceleration. Within the high density region, there are deviations from the ideal shape in terms of spikes in time and energy direction. Tracking calculations with ASTRA [5] and CSR-Track [6] are in qualitative agreement with these results [7]. Some distinct distortion patterns are mostly related to longitudinal space charge (LSC) forces: On the way from BC3 to the screen, LSC causes an increase in energy width, which can clearly be seen in Fig. 3. The spike at the very front of the bunch in time direction is due to energy spread generated by LSC during the passage from BC2 to BC3, which is then sheared in longitudinal phase space in BC3.

The slice energy widths and the longitudinal density profile calculated from the measured phase space distribution are shown in the bottom plot in Fig. 3. The chosen slice widths is equal to the RMS resolution of 50 fs. The slice energy spread reaches a maximum value of $\sim$0.26 % or $\sim$1.8 MeV at the bunch head and decreases to $\sim$ 0.06 % ($\sim$406 keV) in the tail. Here, the values are limited by the residual transverse beam size without dispersion and provide an estimate for the energy resolution of the measurement.

The increase in energy width at the front is largely due to a non-gaussian energy distribution. Within this region, two local maxima of the energy profile can be observed (Fig. 4). This structure may arise from both, LSC and CSR, but we expect the LSC effects to be dominant. By dividing the phase space distribution between the two maxima as indicated by the dashed line in Fig. 4, the longitudinal density profile in the high current region can be considered seperately for the two regions, revealing a separation of the charge density maxima in time by $\sim$50 fs (see Fig. 4). It may be speculated that this is a true substructure of the spike in the longitudinal density profile, which could not be resolved here.

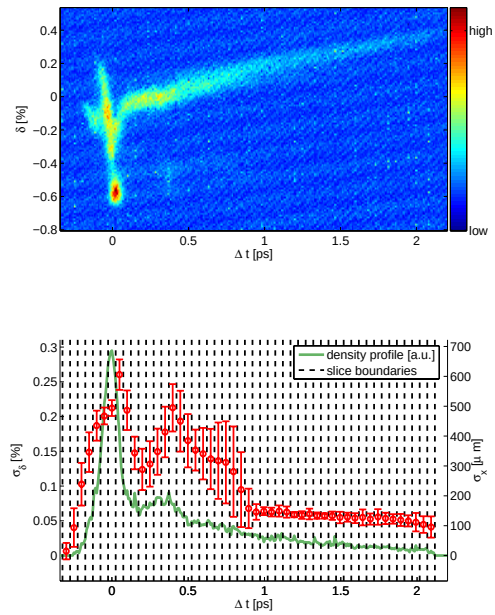

Figure 3: Longitudinal phase space distribution for a single bunch (top) and corresponding RMS slice energy width σ_δ (bottom). In the bottom image, the slice boundaries and the density profile are drawn in.

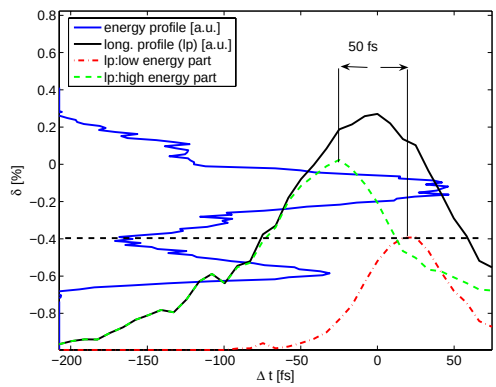

Figure 4: Projections of the longitudinal phase space distribution within the peak current region (Fig. 3) onto the time and energy axis. The longitudinal profile is splitted into two parts, as is indicated by the dashed horizontal line: The one for the low energy part and the one for the high energy part. The maximas of the profiles are seperated in time by $\sim$50 fs.

SLICE EMITTANCE

Figure (5) shows the measured horizontal 1σ slice emittance (normalized) along the bunch (bottom) with a resolution of 60 fs, and an OTR image of a bunch during the scan (top). Within the bunch tail the slice emittance ranges from 2 μrad to 3 μrad. There is a dramatic increase in slice emittance at the front of the bunch with a value of $\sim$16 μrad within the density spike, which is significantly larger than expected for SASE operation. Assuming an RMS energy

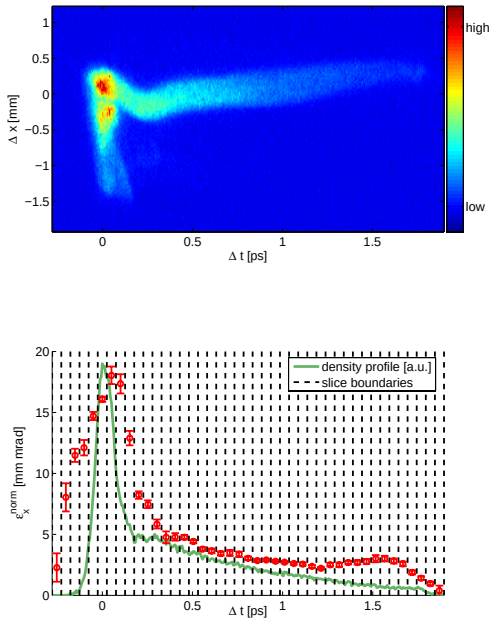

Figure 5: OTR image of a bunch during the quadrupole scan (top) and 1σ slice emittance along the bunch (bottom). In the bottom image, the slice boundaries and the density profile are drawn in.

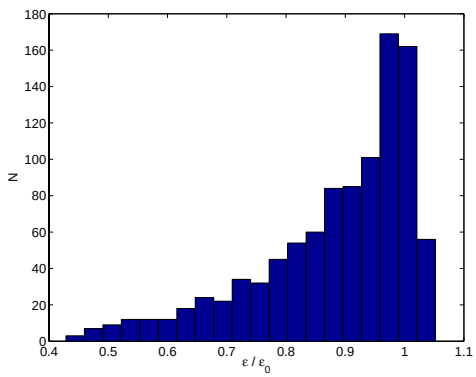

Figure 6: Result of a Monte Carlo simulation with 1000 seeds for the relative emittance error assuming 3 % peak to peak quadrupole gradient errors.

width of $\sim$0.2 % as measured in the spike, the emittance would have to be about $\sim$5 μrad to obtain the observed SASE power [8].

One contribution to this increase in slice emittance is due to a substructure in the horizontal profile of slices in the high current region. For certain quadrupole settings, two separate density maxima appear, as can be seen on the bunch image in Fig. 5. This suggests that there are two islands with high charge density in the horizontal phase space distribution, each for its own having a smaller emittance. Assuming that these density maxima correspond to the observed maxima in the energy profile of the head, the horizontal displacement of the two density maxima may be explained by dispersion in the order of 50 mm, which is a possible value at this location. The dispersion caused by the kicker amounts only to $\sim$10 mm and does therefore not explain this behaviour. In case CSR forces significantly contribute to the separation of the energy maxima, this would lead to a horizontal displacement as well. However, we have no proof yet that there is a connection between the observed structures in the energy profile and the horizontal profile.

Another contribution may come from a systematic error of the absolute emittance values. The accuracy is mainly determined by quadrupole gradient errors, since six quadrupoles have been used for the scan. Figure (6) shows the result of a Monte Carlo simulation for 3 % peak to peak errors of all quadrupole gradients (independently), which is a rather pessimistic assumption. The probability of having an error larger than 30 % is accordingly 15 %. The ratios of the given slice emittance values are not affected by gradient errors.

The shown results for the slice emittance suggest that a reasonable analysis of the emittance in the high current region can, at least for the time resolution given here, only be done by reconstructing the transverse phase space distribution. A main goal for the future is therefore to apply phase space tomography methods. Moreover, quantitative comparisons with simulations using ASTRA and CSR-Track will be done.

ACKNOWLEDGEMENTS

We would like to thank the FLASH team, in particular B. Faatz, M. Hüning and B. Beutner, for their support.

REFERENCES

[1] P. Emma *et al*, "A Transvers RF Deflecting Structure for Bunch Length and Phase Space Diagnostics", SLAC-PUB-8864, August 2000.

[2] M. Hüning *et al*,"Observation of femtosecond bunch length using a transverse deflecting structure", FEL Conference 2005, Stanford, August 2005.

[3] A. Bolzmann, "Investigations of the Longitudinal Charge Distribution of Electron Bunches at the VUV-FEL using the Tranverse Deflecting Cavity LOLA", Diploma thesis, Universität Würzburg,2005.

[4] M. Röhrs *at al*, "Measurement of Slice-Emittance using a Transvers Deflecting Structure", FEL Conference 2005, Stanford, August 2005.

[5] K. Flöttmann,"ASTRA - A Space ChargeTracking Algorithm" 2006, http://www.desy.de/ mpyflo/Astra dokumentation/

[6] M. Dohlus , "Two Methods for the calculation of CSR Fields", TESLA-FEL-2003-05.

[7] M. Dohlus, "Modelling of Space Charge and CSR Effects in Bunch Compression Systems", EPAC 2006, Edinburgh.

[8] B. Faatz, private communication.

A 3D MODEL OF THE 4GLS VUV-FEL CONCEPTUAL DESIGN INCLUDING IMPROVED MODELLING OF THE OPTICAL CAVITY

N. R. Thompson and D. J. Dunning, ASTeC, Daresbury Laboratory, Warrington WA4 4AD, UK*
B. W. J. M^{c}Neil, SUPA, University of Strathclyde, Glasgow G4 0NG, UK
J. G. Karssenberg, P. J. M. van der Slot and K.-J. Boller, Twente University, Enschede, Netherlands.

Abstract

The Conceptual Design Report (CDR) for the 4th Generation Light Source (4GLS) at Daresbury Laboratory in the UK was published in Spring 2006. The proposal includes a low-Q cavity (also called a regenerative amplifier) FEL to generate variably-polarised, temporally-coherent radiation in the photon energy range 3-10eV. A new simulation code has been developed that incorporates the 3D FEL code Genesis 1.3 and which simulates in 3D the optical components and radiation propagation within the non-amplifying sections of an optical cavity. This code is used to estimate the optimum low-Q cavity design and characterise the output from the 4GLS VUV-FEL.

INTRODUCTION

4GLS is a 4th Generation Light Source [1] proposed by CCLRC Daresbury Laboratory to meet the needs of the 'low photon energy' community. The Conceptual Design Report (CDR) was published in 2006 [2]. 4GLS will comprise synchrotron radiation sources, free-electron lasers and conventional lasers which will be combined synchronously to allow innovative pump-probe experiments.

A 600MeV high average current branch operating in energy recovery mode (80pC bunches at up to 1.3GHz) will feed spontaneous sources and a VUV-FEL. A 750-950MeV high peak current branch (1nC bunches at 1-10kHz) will feed a XUV-FEL[3]. There will also be an IR-FEL operating over 2.5–200μm.

This paper first summarises the VUV-FEL CDR design. The proposal is a low-Q cavity FEL, or Regenerative Amplifier FEL [4, 5], in which the high gain allows saturation to be reached in a few passes with mirrors of low reflectivity. It has been shown from 1D simulations [6] that the optimum outcoupling fraction is $\sim 75\%$ for mirrors of 60% reflectivity, using a hole for outcoupling. This fraction gives a near maximum output power but is a stable working point, such that the output power is relatively insensitive to small changes in outcoupling fraction or mirror reflectivity.

The next section presents 3D simulations of the CDR design, using Genesis 1.3 [7] and a new 3D optics simulation code developed at Twente University [8]. These simulations confirm the validity of the CDR design and the earlier 1D simulations which investigated the parameter space. The last section presents simulations to optimise the resonator.

* n.r.thompson@dl.ac.uk

Table 1: Baseline VUV-FEL parameters, as presented in the 4GLS CDR.

UNDULATOR	
Undulator Period λ_w	60 mm
Periods per module	37
Number of modules	5
ELECTRON BEAM	
Electron Beam Energy	600 MeV
Relative Energy Spread (rms)	0.1%
Bunch Charge	80 pC
Peak Current	300 A
Normalised emittance	2 mm-mrad
OPTICAL CAVITY	
Cavity length L_{cav}	34.6 m
Upstream ROC r_1	12.85 m
Downstream ROC r_2	22.75 m
Rayleigh length z_r	2.8 m
Fundamental mode waist w_0	0.34 mm
Waist position (measured from US mirror)	12.2 m
Outcoupling hole radius	2 mm
Cavity stability $g_1 \times g_2$	0.88

CDR PARAMETERS

The VUV-FEL will produce radiation of variable polarisation using APPLE-II undulator modules. The minimum gap is 10mm and the undulator period 60mm. The photon energy range 3–10eV is covered by gap tuning from 10–19mm in helical mode and 12–25mm in planar mode. For high enough gain for RAFEL operation, the undulator length, expressed in the universal scaling of [9], must give $\bar{z} \equiv 4\pi\rho N_u \geq 4$ over all wavelengths and polarisations. The required length is then 11m, achieved with five 2.2m modules of 37 periods. The intermodule gap is 0.6m to allow space for a quadrupole, BPM and phase matching unit. A FODO lattice is used with quadrupoles of length 0.12m and strength 9T/m. The electron beam parameters have been derived using the FEL design formulae of Ming Xie [10].

The resonator parameters are derived from simple assumptions, with the expectation they will be revised after 3D optics modelling. The fundamental cold cavity mode is focussed to maximise the overlap between radiation and electron beam over the first two undulator modules. This is done with a waist at the end of the first module, 12m from the upstream (US) mirror as shown in Fig.1. The *optimum* Rayleigh length z_R (for maximum overlap) is then approximately one third the total length of the two modules plus

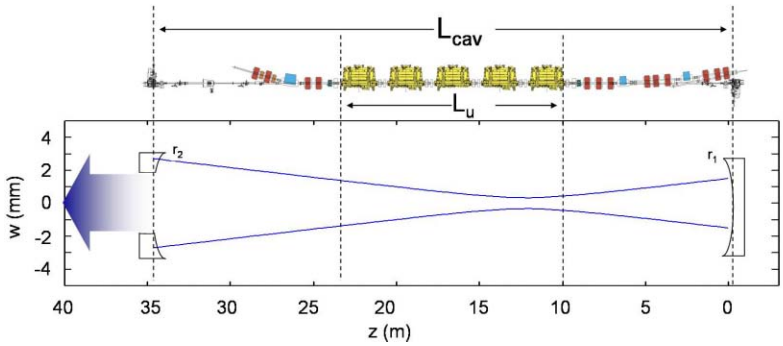

Figure 1: A schematic of the 4GLS VUV-FEL with the baseline CDR parameters. The fundamental cavity mode is shown on the same longitudinal scale as the engineering representation. The electron beam direction is right to left.

gap, i.e. around 1.7m. However, this z_R pushes the cavity geometry close to instability and gives an excessive spot size at the downstream mirror and some diffraction losses on the undulator aperture for the longer wavelengths. In addition the hole size on the downstream mirror is larger than the spot size of the spontaneous radiation emitted on the first pass and does not allow sufficient feedback. The Rayleigh length is therefore chosen so that the spot size of the fundamental cavity mode is the same as the estimated spot size of the spontaneous emission. This gives a Rayleigh length of 2.8m, somewhat larger than the value for maximum overlap.

The hole size is such that the outcoupling fraction of the fundamental cold cavity mode is 65%. This is slightly less than the optimum value (from 1D simulations) of 75% but the high gain FEL interaction is expected to guide the radiation reducing the spot size and increasing the outcoupling fraction towards its optimum value. The mirror material is protected aluminium with a reflectivity of 60% at 10eV. The CDR parameters are given in Table 1 and a schematic shown in Fig.1 where the fundamental cold cavity mode is shown on the same longitudinal scale as the machine layout.

3D SIMULATIONS

A new simulation code has been developed at Twente University that incorporates the 3D FEL code Genesis 1.3 and which simulates in 3D the optical components and radiation propagation within the non-amplifying sections of the optical cavity. Full details of the code are given elsewhere [8]. The code has been used to model the 4GLS VUV-FEL using Genesis 1.3 in steady-state mode. All the simulations presented here are for 10eV operation. Simulation results for 3eV will be presented in a later work.

Simulations of baseline design

The CDR parameters have been used for the initial simulations. The growth of output power and the measured outcoupling fraction, both as a function of pass number, are shown in Fig. 2. At saturation the output power is 350MW with a measured outcoupling fraction of 68%. The

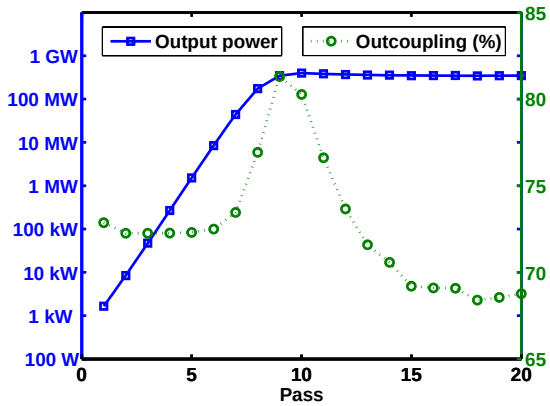

Figure 2: The growth of output power and the measured outcoupling fraction, both as a function of pass number, for the CDR parameters.

normalised power profiles at saturation, for different points within the optical cavity, are shown in Fig.3. A modal expansion algorithm is under development and will calculate the power distribution between the fundamental and higher order modes. It is clear however from Fig.3 that there is significant transverse HOM content in the radiation field. It is interesting to note that although the on-axis power of the radiation reflected from the downstream (DS) outcoupling mirror is zero, due to the large hole, by the time the radiation is reflected back off the upstream (US) mirror and back into the undulator the power is concentrated on-axis allowing good coupling with the electron beam for the next pass.

Cavity optimisation

Fig.4 shows the effect of varying the radius of the outcoupling hole and the mirror reflectivity on the output power after 20 passes (by which time the FEL has reached saturation for almost all parameter sets used here). The results show that the CDR working point (hole radius 2mm, reflectivity 60%) is satisfactory and stable—the output power is near optimum, yet small changes in hole size or reflectivity have a correspondingly small effect on the

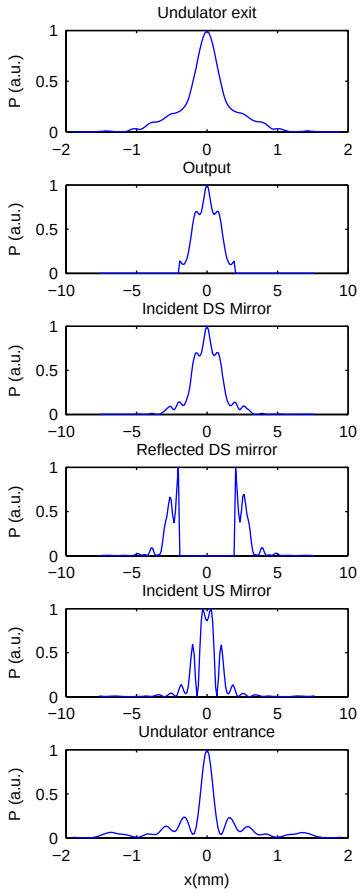

Figure 3: The normalised intensity cross sections at saturation, for different points within the optical cavity. The parameters are the CDR values (waist position 12 m, waist radius 0.34mm).

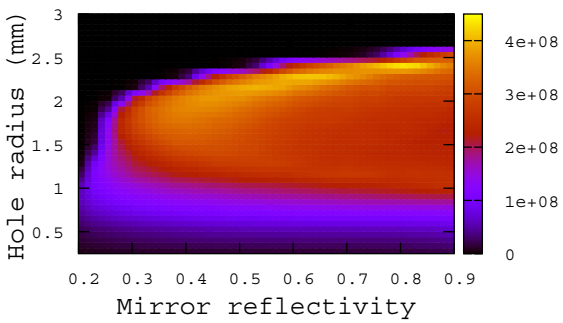

Figure 4: Output power (W) as a function of hole radius and mirror reflectivity. The CDR hole radius is 2mm and mirror reflectivity is 60%.

output power. In fact a reduction in reflectivity would cause a small increase in output power, as predicted by the earlier 1D simulations.

Different cavity configuration have been investigated by changing the ROC of the mirrors such that either waist size or waist position of the lowest order cold-cavity mode is kept constant and the other is varied. The dependence

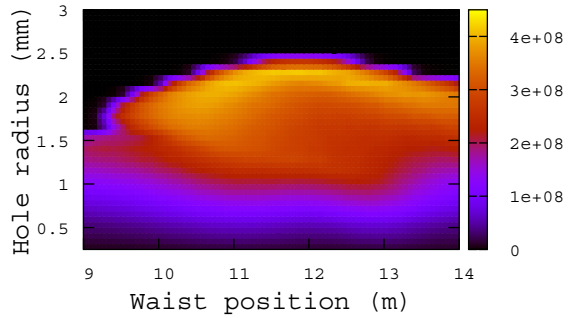

Figure 5: Output power (W) as a function of hole radius and waist position.

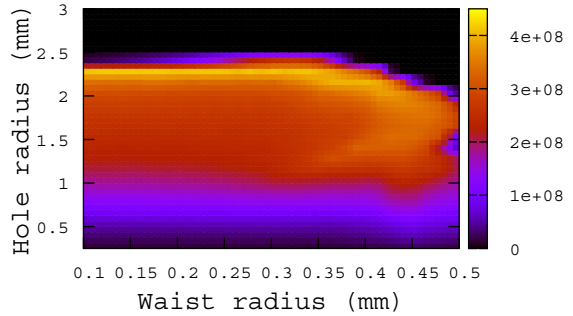

Figure 6: Output power (W) as a function of hole radius and waist size, for waist position 12.19m.

of the output power on hole radius and waist position is shown in Fig.5. It appears that moving the waist back 1m towards the undulator entrance (from 12m to 11m from the upstream mirror), i.e. to the centre of the first undulator module, gives a working point in a broader region of near maximum output power which would be beneficial.

The results of varying the waist radius from its CDR value of 0.34mm are shown in Fig.6 for a waist position of 12m where it is seen there is little dependence on waist radius even when the waist radius is 0.1mm which represents a cavity on the boundary of instability with $g_1 g_2 = 1.00$. Extensions of geometry into unstable resonator configurations will be investigated in the future. Similar results have been obtained for a waist position of 10.5m. These results demonstrate that considerations of cold cavity resonator modes are not very relevant to this design—the gain guiding of the high-gain FEL interaction strongly dominates.

This interpretation is supported by simulations investigating the effect of changes in waist position on the radiation profiles at different cavity positions. Shown in Fig. 7 are the far field intensity cross sections (calculated at 14m beyond the outcoupling hole, this being the position of the VUV-FEL optical diagnostic bench) and at the undulator entrance. The cross sections are displayed in arbitrary units. Again, the dependence on waist position is weak.

It is noted that the far field cross section in Fig.7 displays clear higher order transverse mode structure, with a

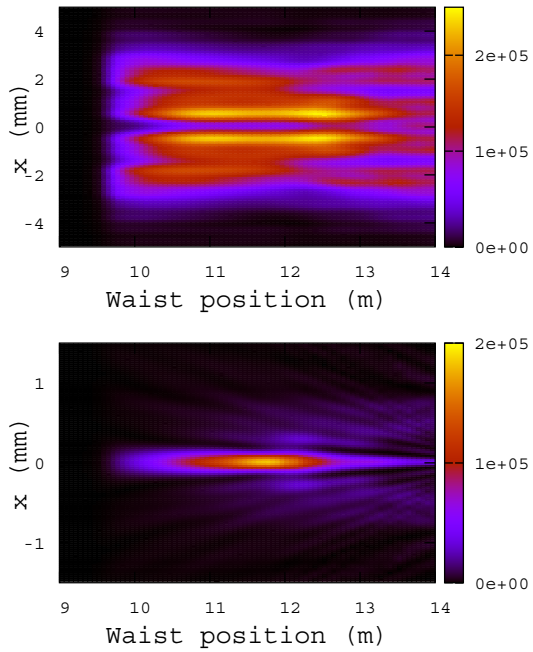

Figure 7: Intensity (a. u.) cross sections in the far field (top) and at the undulator entrance (bottom) as a function of the waist position of the cold-cavity fundamental mode of the resonator. The hole radius is 2mm.

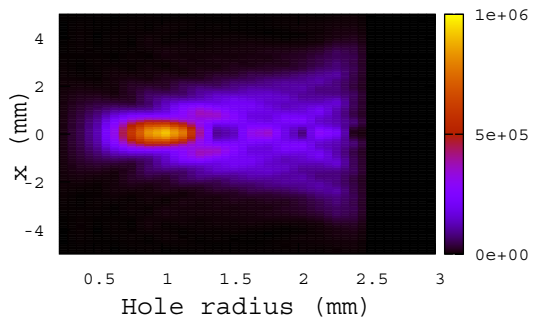

Figure 8: Intensity (a. u.) cross section in the far field as a function of hole radius, for waist position 12.19m.

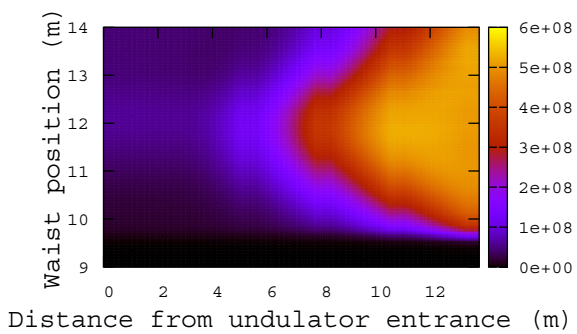

Figure 9: Power (W) growth along undulator as a function of waist position. The vertical bands are due to the gaps between the undulator sections.

minimum intensity on axis. A scan of the effect of hole radius on far-field cross section is shown in Fig.8 where it is seen that the far field cross section can be improved (i.e. brought closer to a fundamental gaussion mode) by reducing the hole radius. Further optimisation will now be done to maximise the output power while maintaining the optimum far-field cross section, including investigation of unstable resonators.

Finally, the total power within the undulator as a function of waist position is shown in Fig.9. The baseline waist position of 12m gives the strongest power growth.

CONCLUSION

Full 3D modelling of the VUV-FEL has been made possible with the new optics simulation package. The main conclusions are:

- The CDR parameters are close to the optimum values found with steady state simulations;
- The far field cross-section and total output power depend on hole radius but, for each hole radius, are otherwise relatively insensitive to the resonator configuration over a large range of ROC's around the CDR values;
- The high gain of the FEL ensures that optical guiding within the undulator and hole size are far more dominant in defining the radiation profile than the ROC of the mirrors.

These conclusions demonstrate that the VUV-FEL should be treated as a self-seeding amplifier FEL rather than as an oscillator FEL.

After 3eV simulations are complete it is expected that 3 mirror sets will be specified, one optimised for 10eV output, one for 3eV output and one for scanning over the full range.

REFERENCES

[1] M. W. Poole and E. A. Seddon, *4GLS and the ERLP Project at Daresbury Laboratory*, PAC05 Proceedings, (2005)

[2] *4GLS Conceptual Design Report*, CCLRC, `http://www.4gls.ac.uk/documents.htm#CDR`, (2006)

[3] B. W. J. McNeil *et al*, *The Conceptual Design of the 4GLS XUV-FEL*, (*ibid*), (2006)

[4] B. W. J. McNeil, IEEE Journal of Quantum Electronics, 26, 6, 1990, p1124

[5] D. C. Nguyen *et al*, *Regenerative Amplifier FEL*, Proceedings of the XX International Linac Conference, p731 (2000)

[6] N. R. Thompson *et al*, *A VUV-FEL for 4GLS*, Proc. 27th FEL Conf., Stanford (2005)

[7] `http://corona.physics.ucla.edu/~reiche/`

[8] J. G. Karssenberg *et al*, *FEL-Oscillator Simulations with Genesis 1.3*, (*ibid*), (2006)

[9] R. Bonifacio *et al*, Opt. Commun. 50, p373 (1984)

[10] Ming Xie, PAC Proceedings 1995, p183.

DEVELOPMENT OF FREQUENCY-RESOLVED OPTICAL GATING FOR MEASUREMENT OF CORRELATION BETWEEN TIME AND FREQUENCY OF CHIRPED FEL

H. Iijima, R. Hajima, E. J. Minehara, R. Nagai and N. Nishimori, Japan Atomic Energy Agency, 2-4 Shirakata-Shirane, Tokai, Naka, Ibaraki, Japan.

Abstract

A femtosecond infrared-chirped free-electron laser (FEL) is an effective tool of dissociating molecules without the intramolecular vibrational redistribution. The ultrashort FEL pulse with the broadband spectrum is achieved operating the long-pulse electron beam from an energy recovry linac at Japan Atomic Energy Agency. Until now, the broadband spectrum of ultrashort pulse was measured to be $\Delta\omega / \omega_0$ = 14% with the central wavelength of 23 μm and the pulse duration of 320 fs at FWHM by an autocorrelation of fringe-resolved second harmonic generation. However the information of pulse shape and variation of frequency depending on the time during the pulse were not obtained. Since it is essential to know both information in the pulse for the dissociation of the molecule, we will measure them by frequency-resolved optical gating (FROG).

INTRODUCTION

A femtosecond infrared-chirped free-electron laser (FEL) is an effective tool of dissociating polyatomic molecules without the intramolecular vibrational redistribution [1,2]. Coherent vibrational climbing proceeds from exciting a molecular vibration transitions by the ultrashort infrared pulse with the broadband spectrum which encompasses several vibrational transitions of the molecule. Indeed, these transition energies become smaller and smaller with climbing the ladder because of molecular anharmonicity. Therefore, the climbing efficiency can be increased dramatically when using a negatively chirped pulse so that its high-frequency components which resonant with the lower transitions of the ladder precede its low-frequency components which resonant with the upper transitions of the ladder. Coherent vibrational climbing can be viewed also as a rapid adiabatic passage leading to efficient excitation of the upper vibrational states with an efficiency that in theory can be close to 100% because of the coherent nature of the interaction.

At Japan Atomic Energy Agency (JAEA), an energy recovery linac (ERL) driven by superconducting accelerators has been constructed to produce a high-power far-infrared FEL(~20μm) [3,4]. Operating this device, it succeeds in generating ultrashort pulses with the broadband spectrum using a long macro pulse of electron beam by JAEA-ERL.

Until now, the broadband spectrum was measured to be $\Delta\omega / \omega_0$ = 14% at the central wavelength of 23 μm and the pulse width of 320 fs at FWHM by an autocorrelation of fringe-resolved second harmonic generation (FRSHG) [3]. However the intensity and the variation of frequency depending on the time during the FEL pulse were not obtained. Since it is essential to know both of the intensity and the variation of frequency in the pulse for the dissociation of the molecule, we will measure them by frequency-resolved optical gating (FROG) [5].

FREQUENCY-RESOLVED OPTICAL GATING

Principle of FROG

FROG is a technique to completely determine the intensity and phase versus time or frequency. The apparatus of FROG is only an autocorrelator followed by a spectrometer. In the autocorrelation and related techniques, the ultrashort pulse is measured purely in the time domain (autocorrelator), or in the frequency domain (spectrometer). In all these measurements, detectors can only measure the intensity of the signal. As a result, it is inevitable to lose the phase information, if the measurement is taken only in one domain. The measurement of FROG trace is taken in a hybrid domain: time-frequency domain. As time and frequency are two reciprocal domains connected by Fourier transform, the phase information in time domain is encoded into the intensity information in frequency domain, and vise versa. Therefore FROG trace contains the information of both intensity and phase of ultrashort FEL pulse by doing only intensity measurement in time-frequency domain.

As the time-dependent component of the pulse can be written in

$$E(t) = \mathrm{Re}\left\{\sqrt{I(t)}\exp(i\omega_0 t - i\varphi(t))\right\}, \qquad (1)$$

where $I(t)$ and $\varphi(t)$ are the time-dependent intensity and the variation of frequency, and ω_0 is a carrier frequency, FROG trace is described as

$$I_{FROG}(\omega,\tau) = \left|\int_{-\infty}^{\infty} E_{sig}(t,\tau)\exp(-i\omega t)dt\right|^2, \qquad (2)$$

where a quantity $E_{sig}(t,\tau)$ is a signal field defined by $E(t)g(t-\tau)$. The function $g(t-\tau)$ is a gate function with respect to the gate delay τ. Now, consider the Fourier transform of $E_{sig}(t,\tau)$ with respect to τ, Eq. (2) is transformed to

$$I_{FROG}(\omega,\tau)=\left|\int_{-\infty}^{\infty}\hat{E}_{sig}(t,\Omega)\exp(-i\omega t-i\Omega\tau)dtd\Omega\right|^2 \quad (3)$$

Since Eq. (3) is the 2-dimensional Fourier transform with respect to t and Ω, the signal field $E_{sig}(t)$ implementing I_{FROG} is determined uniquely due to the fundamental theorem of algebra. As a result, the information of $I(t)$ and $\varphi(t)$ in Eq. (1) are obtained from the quantity $I_{FROG}(\omega,\tau)$.

Various non-linearities such as second-harmonic generation (SHG), third-harmonic generation, self-diffraction and polarized-gate are well known as the gate function [6]. In our measurement, SHG autocorrelation is used as the gate for FROG trace.

Simulation of SHG-FROG

In the SHG-FROG geometry, the pulse is split into two pulses which are then spatially overlapped in a piece of frequency-doubling crystal. In the frequency-doubling crystal, the two pulses induce a second harmonic due to the second-order optical non-linearity. Hence the signal field for SHG-FROG is given by $E_{sig}(t,\tau) = E(t)E(t-\tau)$. The main advantage of SHG-FROG is sensitivity: it involves only the second-order nonlinearity. Consequently, for a given amount of input pulse energy, SHG-FROG will yield more signal pulse energy.

In order to evaluate retrieval of the intensity $I(t)$ and phase $\varphi(t)$ of the ultrashort pulse from SHG-FROG trace, a numerical simulation for SHG-FROG was carried out using the JAEA-FEL parameters. As a temporal profile of input intensity, the previous simulation result was used [7]. The carrier frequency ω_0 was determined by an experimental measurement of λ_0 = 21μm. Three types of input variation of frequency were assumed for the simulation.

The simulation results are shown in Fig. 1, in which the top row shows false-color FROG trace for each phase; red means high intensity and violet means low intensity. The images of FROG trace in Fig. 1 are cropped, but the simulation was achieved in double range. The bottom row shows retrieval results of FEL pulse, where red closed (open) circle indicates the retrieval intensity (phase) respectively, and blue lines mean the input shape of FEL pulse. The each column indicates the difference of the

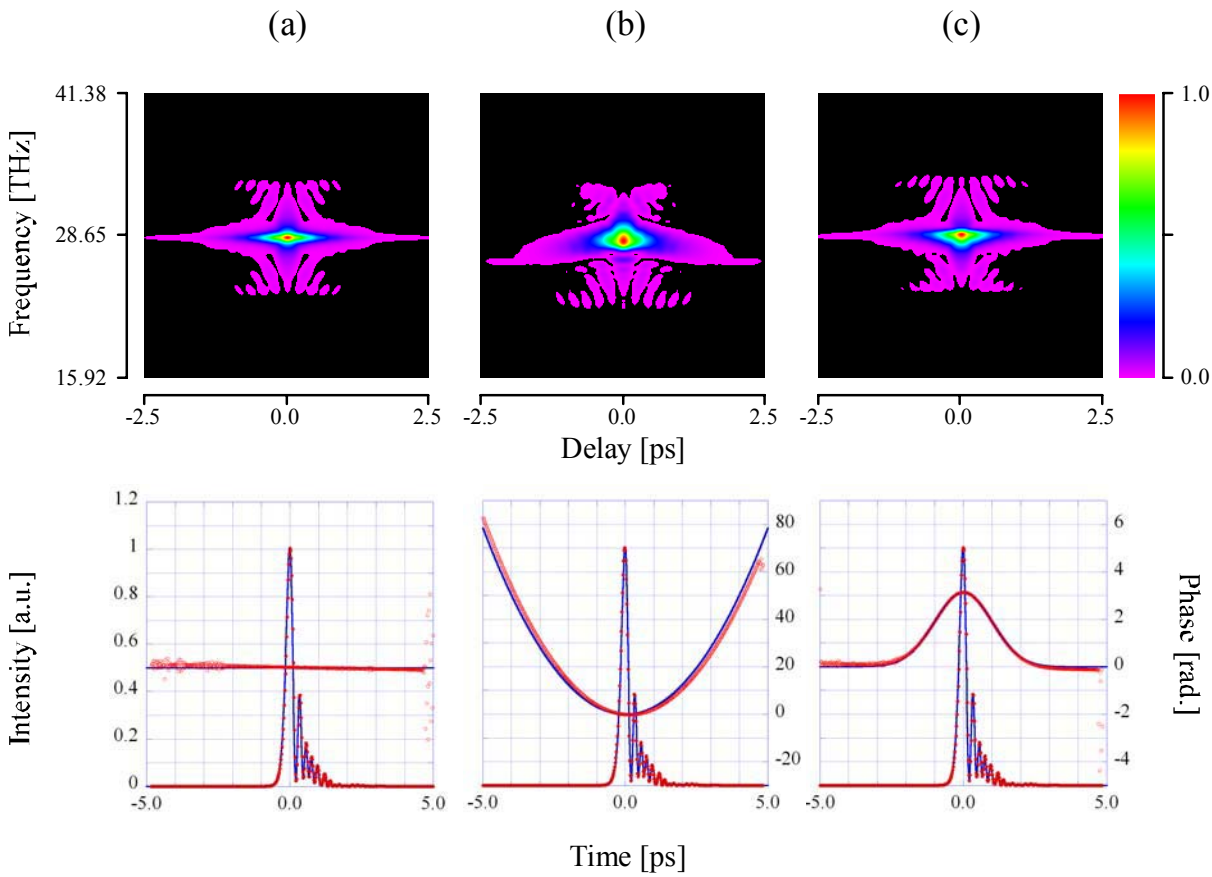

Figure 1: The top row shows false-color FROG trace for each phase; red means high intensity and purple means low intensity. The bottom row shows the retrieval result, where red closed (open) circle indicates the retrieval intensity (phase) and blue line indicates the initial parameter. The each column (a), (b), (c) indicates Fourier transformer-limited, negative chirp, self-phase modulated pulse respectively.

variation of frequency; (a) is a Fourier transformer-limited, (b) is a negative chirp, and (c) is a self-phase modulated pulse respectively. The retrieval intensity and phase were good agreement with the input intensity and phase.

MEASUERMENT SETUP

Focus and transport system

Since the FEL pulse is diverged by optical diffraction due to a ϕ2-mm pinhole on an output coupler mirror of FEL optical cavity, a pair of Au-coated elliptical mirrors is used to parallelize the FEL pulse with large beam size (approximately 5 cm in diameter). This optical focusing system is located near the output coupler. In an experimental room, the transported FEL is focused again by a pair of Au-coated parabolic mirrors. The whole set-up is mounted in vacuum boxes, which are evacuated up to 10^{-7} Torr, in order to avoid distortion of the FEL pulse due to absorption of the infrared radiation by ambient water vapour, and is connected to the 24-m FEL transport ducts. The optics design was determined to be close to 100% optical transport efficiency by a numerical simulation code GRAD [8].

Experimental setup of SHG-FROG

Figure 2 shows a schematic view of SHG FROG apparatus constructed now. As shown in Fig. 2, the incoming FEL pulse is split by a polyethylene terephthalate (PET) film, whose thickness is 23μm, into two beams. One of them is delayed by a movable retro reflector; the other has a fixed path length. The movable reflector can be achieved by a stepper-motor-driven linear stage on which the retro reflector is mounted. A parabolic mirror focuses both pulses onto the frequency doubling crystal consisting of 2mm thickness Tellurium (Te). The second harmonic generated in the crystal when both pulses have a temporal and spatial overlap propagates through a slit to the spectrometer. Finally a mercury-cadmium telluride (MCT) detector detects the intensity of signal.

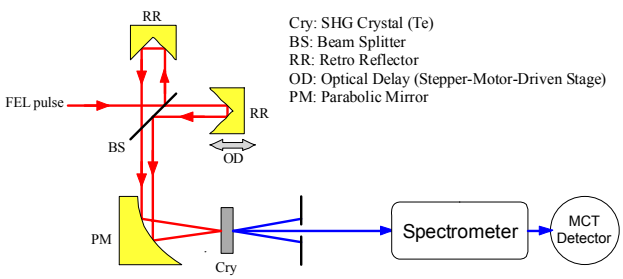

Figure 2: The schematic view of the SHG-FROG setup.

STATUS OF MEASUREMENTS

Spectrum of FEL pulse

Now, the whole optics is being adjusted precisely to provide the SHG signal from the Te crystal, therefore the focus, transport, and measurement system are in atmosphere. The atmospheric transport efficiency was measured to be 40 ~ 50 % due to the absorption by the ambient water vapour, and the average power of FEL pulses was measured to be 500 mW, typically.

Figure 3 shows a spectrum of the FEL pulse measured by a spectrometer. One can find the absorption by the ambient water vapour at 21.1, 21.8 and 22.6 μm.

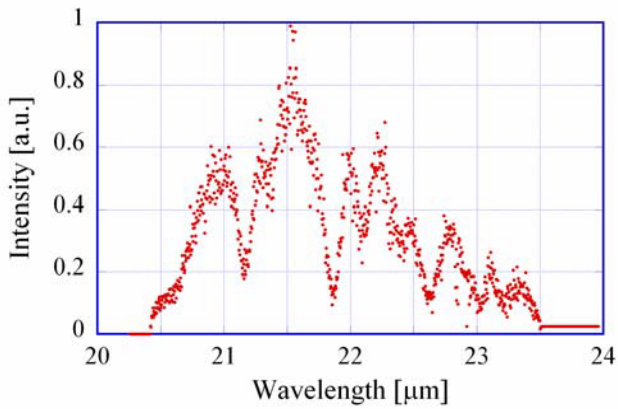

Figure 3: The spectrum of FEL pulse. The absorption of the infrared radiation by the water vapour can be seen at 21.1, 21.8 and 22.6 μm.

Polarization

High efficiency SHG is one of important points to perform SHG-FROG trace. The efficiency depends on an angle between a Te crystal orientation and a polarizing plane, and an input power of the FEL pulse dominantly. On the other hand, the surface of Te crystal is damaged if the pulse is strongly focused to generate the second harmonic. Therefore the angle between the Te crystal orientation and the polarizing plane of FEL pulse should be adjusted precisely.

Figure 4 shows a measurement result of polarizing angle of the FEL pulse at position of Te surface. The measurement was done using a polarizer. In this figure, zero degree corresponds to the horizontal direction. In our case, the FEL pulse has a vertical polarization at the output coupler. At the surface of Te crystal, the polarizing direction rotates to 133 degree due to the refractions via the mirrors in the transport system. The measurement value is good agreement with the designed value.

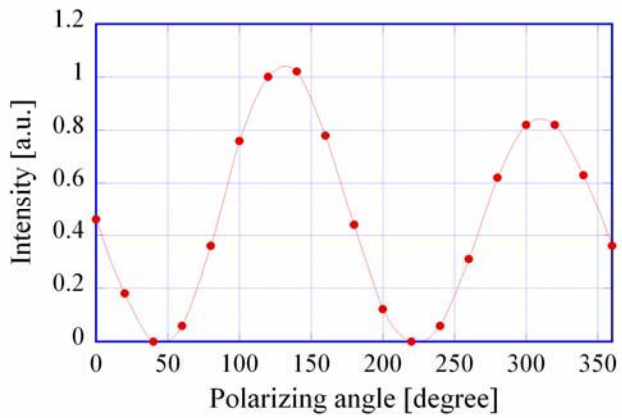

Figure 4: Polarizing angle on the surface of the doubling crystal.

SUMMARY

The femtosecond infrared-chirped FEL is the effective tool of dissociating molecules without the intramolecular vibrational redistribution. JAEA ERL-FEL has been constracted to provide a high-power far-infrared FEL. The ultrashort FEL pulse with the broadband spectrum is achieved operating the long-pulse electron beam from JAEA ERL-FEL. Since it is essential to know both of the intensity and the variation of frequency in the pulse for the high-efficiecny dissociation of the molecule, we consider to measure them by SHG FROG. The numerical simulation of SHG FROG using the FEL parameters can completely retrieves the intensity and phase of the pulse. In the following, we have start to develop the apparatus of SHG FROG. Now we are measuring basic parameters of the FEL pulse (beam size, power, wavelength, polarization and so on) in the experimental room.

ACKNOWLEDGEMENTS

This research is partially supported by MEXT KAKENHI 18740265.

REFERENCES

[1] S. Chelkowski, et al., Phys. Rev. Let., 65 (1990) 2355.
[2] Y. Fujimura, O plus E, No. 176, p. 102.
[3] R. Hajima and R. Nagai, Phys. Rev. Let., 91 (2003) 024801.
[4] N. Nishimori, et al., Nucl. Instrum. and Meth. A, 475 (2001) 266.
[5] R. Trebino, et al., Rev. Sci. Instrum., 68 (1997) 3277.
[6] B. A. Richman, et al., Opt. Lett., 22(1997)721.
[7] R. Hajima, et al., Nucl. Instrum. and Meth. A, 475 (2001) 270.
[8] GRAD; General Laser Analysis and Design program (Applied Optical Research, AOR).

BEAM CURRENT DOUBLING OF JAEA ERL-FEL

R. Nagai#, R. Hajima, H. Iijima, N. Kikuzawa,
E. Minehara, N. Nishimori, T. Nishitani, M. Sawamura,
Japan Atomic Energy Agency, Tokai, Ibaraki, Japan

Abstract

An energy-recovery linac (ERL) R&D program for a high-power free-electron laser (FEL) is in progress at Japan Atomic Energy Agency (JAEA; formerly JAERI and JNC). The first energy-recovery operation and FEL lasing was demonstrated in 2002 by remodeling the superconducting linac of the JAERI-FEL driver. In the first demonstration, the accelerated beam current was same as the original linac. One of the advantages of an ERL is that the accelerating beam current can be increased by only changing micro-pulse repetition rate without increasing the RF power of the main linac. The advantage of an ERL has been demonstrated by the current doubling.

INTRODUCTION

For the high-power free-electron laser (FEL), the FEL extraction efficiency or the drive beam power should be increased. Increasing of the drive beam power is more effective than increasing of the FEL extraction efficiency because the FEL extraction efficiency is limited in several percent. For the beam power increasing in a usual linac, there are some problems as follows: high-power RF source and coupler corresponding with the beam power are needed, high-power and high-energy beam should be dumped, radiation shield at the beam dump is very tough. A high-power beam can be accelerated by small RF power in an energy-recovery linac (ERL) because the beam power not extracted to the FEL light is recovered and used to the acceleration. The radiation shield and thermal design of the beam dump becomes easy because the dumped beam power and energy is reduced by the deceleration at the linac. Using an ERL as an FEL driver therefore solves the problems for the beam power increasing.

An ERL-FEL R&D program is in progress at Japan Atomic Energy Agency (JAEA; formerly JAERI and JNC). The first energy-recovery operation and FEL lasing was demonstrated [1] in 2002 by remodeling the superconducting linac of the JAERI-FEL [2]. In the first demonstration, the accelerated beam current was same as the original linac. One of the advantages of the ERL is that the accelerating beam current can be increased by only changing micro-pulse repetition rate without increasing the RF power of the main linac. To demonstrate the advantage, the e-gun, the injector RF source, the low-level RF (LLRF) controller, and the operation system have been improved. As a result of the improvement, the doubled beam acceleration and the FEL power improvement have been successfully achieved.

IMPROVEMENT OF THE JAEA ERL-FEL

The layout of JAEA ERL-FEL is shown in Fig. 1. The injector consists of a DC electron gun with thermionic cathode driven by a grid pulser, an 83.3 MHz sub-hermonic buncher, and two 499.8 MHz 1-cell superconducting modules. The merger is a two-step staircase type that consists of four bending magnets and three quadrupole magnets. The main linac consists of two 499.8 MHz 5-cell superconducting modules. The beam transport system to the undulator consists of a triple-bend achromatic (TBA) arc and a half-chicane achromatic system. The undulator is a hybrid type with period

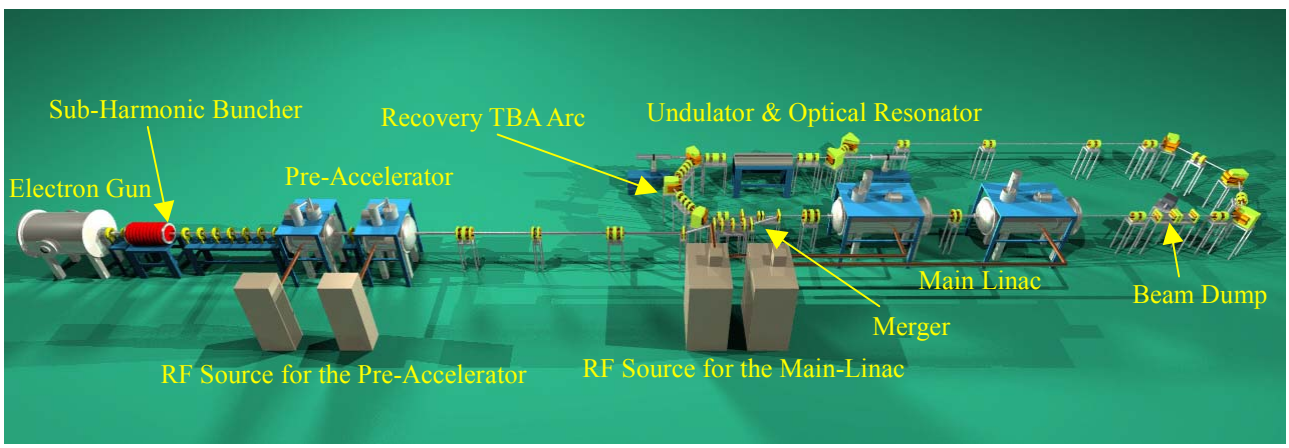

Figure 1: Layout of JAEA-ERL.

#Email: nagai.ryoji@jaea.go.jp

number of 52 and period length of 33 mm. The optical resonator is a near-concentric Fabry-Perot type that consists of two gold-coated mirrors with center-hole output coupler. The recovery beam transport system is a TBA arc.

In the original linac, the electron beam was accelerated in burst mode with 10 Hz macro-pulse and 10.4125 MHz micro-pulse repetitions. The macro-pulse average current was 5 mA that was mainly limited by the RF power sources and the grid pulser. To demonstrate that the higher beam current than the RF source capacity of the main linac can be accelerated, the ERL has been improved.

The electron gun is equipped with a thermionic cathode and operated at 230kV DC voltage. A train of electron bunch is generated by the grid pulser. To generate 20.825 MHz bunch train, doubled repetition of original one, a main-circuit of the grid pulser was replaced to new circuit [3]. The bunch length and timing jitter of the electron beam at the electron gun are 590 ps-FWHM and 12.8 ps-rms, respectively. The bunch length and timing jitter are compressed into about 1/100 through the beam transport system to the undulator.

In the original linac without energy-recovery, two 1-cell superconducting modules were driven by two 8 kW solid-state amplifiers for each, enough capacity for 5 mA operation. The solid-state amplifiers were replaced by two IOT of 50 kW [4], which is enough capacity for 40 mA operation.

Stable operation of an FEL depends much on the stability of an accelerator. In a superconducting accelerator, a LLRF controller is one of the key components for achieving good stability. The original LLRF controller was designed for phase flatness at ±1 deg. within a 1 ms macro-pulse. This LLRF controller contributed to the 10-year operation of JAERI-FEL. After the remodeling into the ERL, however, the original LLRF controller performance was insufficient for the ERL operation. The LLRF controller was replaced by new one. The new controller is based on analog phase and amplitude control of the cavity RF field coupled with a tuner controller, which is same as the original controller. In the new controller, the following functions were introduced for the better stability: the feedback gain, time constant and loop phase offset can be varied during operation to obtain good flatness of RF phase and amplitude within a macro-pulse, all the circuits are contained in a temperature regulated oven [5]. By the new controller, the phase and amplitude stabilities at the beam acceleration are 0.07 %-rms and 0.07 deg-rms, respectively. The original controller was placed at the control room, and the feedback loop involved 50 m cables to connect the controllers and the RF cavities. These long cables have large phase drift due to the temperature dependence of the electrical length. The new controller are installed just beside the cavities to make the cable length as short as possible. Furthermore the cables between the controllers and the cavities are contained in a temperature-regulated pipe to suppress the effect of the changing of the room temperature [6]. The phase stability in any season has been achieved less than 0.1 deg-rms by the temperature-regulated cable system.

The electron motion in the longitudinal and transversal phase space is very complex because the injector has long drift spaces before and after the pre-accelerator. The achromaticity of the merger and the bunch length of the electron beam are sensitive to the quadrupole magnets parameter. Therefore, the beam transport parameter adjustment of the injector and the merger is not easy. To support systematic parameter search, the accelerator operation system of the JAEA-ERL is equipped with a data-logging system and database services [7]. The initial parameter set of the injector was decided by the numerical optimization [8]. In the result, the electron bunch length of less than 10 ps has been achieved at the undulator.

The length of the optical resonator was changed along with remodeling to the ERL. The optical resonator geometry was optimized by a Fox-Li procedure utilized simulation code[9]. In the optimization, the center-hole thickness was not taking into account. The center-hole thickness causes additive loss. If the center-hole thickness is taking into account, the radius should be enlarged more than the ideal case. The center-hole radius of 1.0 mm was adopted in consideration of the loss by the center-hole thickness because the optimum radius was 0.8 mm in the ideal case. The misalignment tolerance of the resonator was estimated by the Fox-Li simulation code [10]. The offset and tilt tolerance for the FEL power fluctuation of 1% are 0.1 mm and 40 μrad, respectively. The vibration of the floor is less than 1 μm. The accuracy of the He-Ne alignment system of the optical resonator is less than 20 μrad. The offset and tilt tolerance of the optical resonator is therefore sufficiently large for the FEL power fluctuation of less than 1%.

ERL AND FEL DEMONSTRATIONS

In the adjustment of the beam transport, the higher current beam than the RF source capacity cannot be accelerated because the energy-recovery is not enough. The energy-recovery acceleration and beam transport have been adjusted in the condition of original micro-pulse repetition of 10.4125 MHz. Under the micro-pulse repetition in 10.4125 MHz, because the beam lost is allowed, the screen monitor can be used for the beam transport adjustment. After the adjustment, doubled beam in the repetition frequency of 20.825 MHz has been accelerated only changing of the micro-pulse repetition. The current increase only by changing the micro-pulse repetition is scalable. The successful current doubling shows that the current can be increased easily up to 40 mA corresponding with the repetition of the SHB frequency. Typical signal of the current monitor at the entrance of the main linac is shown in Fig. 2. These signals are the injection beam to the main linac and the re-circulated beam from the recovery beam transport system in the repetition of 20.4125 MHz. The amplitudes of the

injection and the re-circulated beam signal are the almost same.

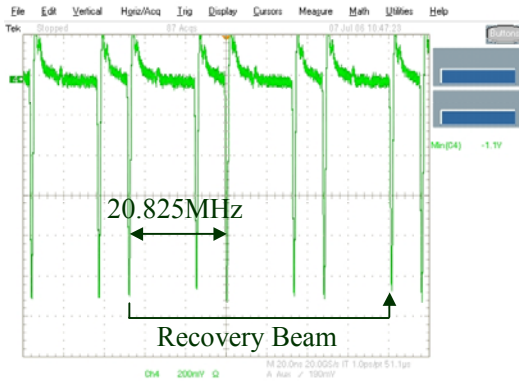

Figure 2: Typical signal of the current monitor at the entrance of the main linac.

Typical signal of output power of the main linac RF source is shown in Fig. 3. The RF source is operated in the pulse mode in the repetition of 10 pps and the pulse width of 2 ms. The electron beam has been accelerated with 1ms in the latter half. In the case of Fig. 3, the macro-pulse width of the electron beam is 230 μs. The RF output power with and without the electron beam are the almost same because the RF power is recovered by the decelerated electron beam. As shown in Fig. 3, the high-current electron beam can be accelerated if there is an RF power only of the amount of exciting the acceleration field. The spike at the edge of the electron beam macro-pulse is caused by the feedback of the RF low-level controller. In the pulse mode, the RF power to compensate the disturbance such as the edge of the electron beam macro-pulse is needed as shown in Fig. 3.

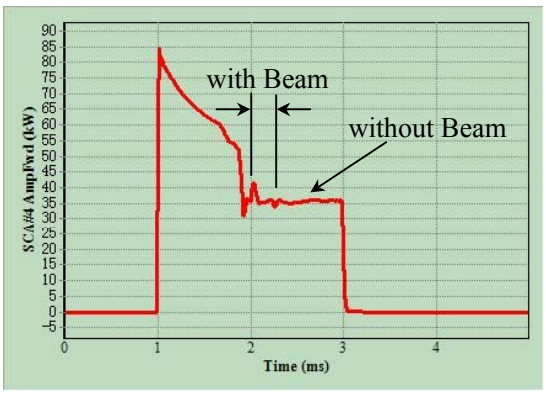

Figure 3: Typical signal of output power of the main linac RF source.

After the energy-recovery acceleration, the FEL lasing is successfully achieved by adjusting the length and the beam position of the optical resonator. The beam position is adjusted while monitoring the stored spontaneous emission with a liquid-nitrogen-cooled HgCdTe detector. The FEL extraction efficiency is obtained by measuring the energy loss of the electron beam. The energy loss and energy spectrum of the electron beam is measured by a wire-monitor set up on the way of the recovery TBA arc. The amount of the beam lost by the wire monitor is less than the RF power source capacity. The detune curve of the FEL extraction efficiency is shown in Fig. 4. The Maximum efficiency and power are 2.7 % and 0.7 kW, respectively. The output efficiency of the optical resonator is about 30 %. The output efficiency of the optical resonator is about 37 % in the numerical simulation. The difference of the measured value and calculated one is caused by the thickness of the output center-hole, and misalignment of the resonator.

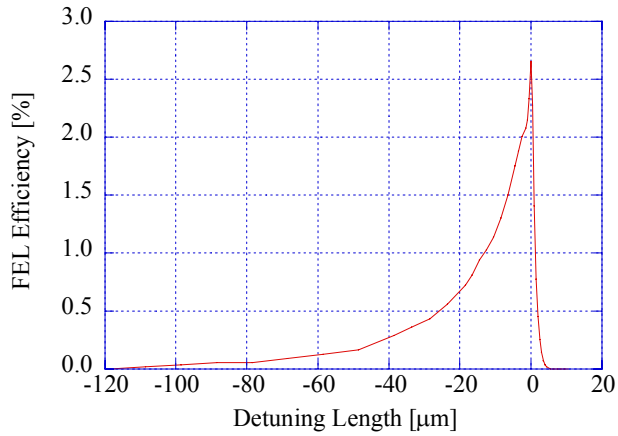

Figure 4: Detune curve of the FEL extraction efficiency.

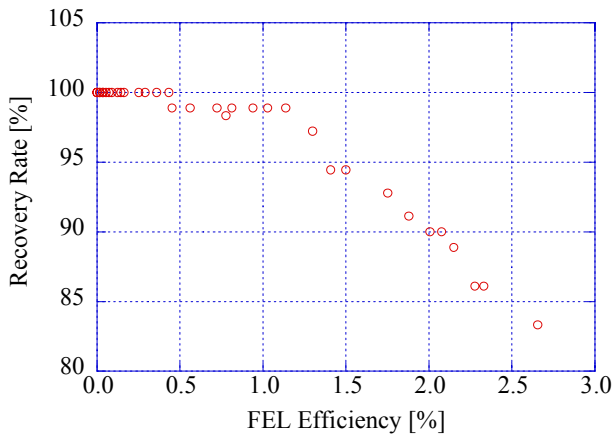

Figure 5: Recovery rate of the electron beam at the beam dump.

The recovery transport system with a large energy acceptance is necessary because after lasing the electron beam has large energy spread. The energy spread is about 5 times of the extraction efficiency. The recovery rate of electron beam at the beam dump is shown in Fig. 5. The electron beam is almost recovered up to the extraction efficiency about 1 %. Under the present condition, the beam loss at the FEL lasing is less than the RF source capacity. To increase the beam current, the recovery rate should be close to 100 %. Measured energy spread at the maximum output power is about 13.5 % (tail to tail). The energy acceptance of the recovery TBA arc is about 16 % in the calculation, and almost electron beam can be transported. There is actually little bremsstrahlung radiation in the arc part. The beam is therefore lost mainly in deceleration at the main linac. To recover the

almost electron beam, after lasing the energy spread of the electron beam should be compressed because it is too large into the energy after decelerating [11]. Therefore, R56 of the recovery TBA arc and deceleration phase should be optimized to achieve fully recovery. The optimization of the energy compression is in progress.

CONCLUSION

One of the advantages of an ERL is that the high beam current over the RF source capacity of the main linac can be accelerated. The advantage of an ERL has been successfully demonstrated by the current doubling with only changing of the micro-pulse repetition rate. The current increase only by changing the micro-pulse repetition is scalable. The successful current doubling shows that the current can be increased easily up to 40 mA corresponding with the repetition of the SHB frequency.

To achieve in the future the 10 kW class high-power FEL, the beam current will be increased by solving the problem of the recovery rate and increasing the repetition of micro-pulse up to the SHB frequency of 83.3 MHz. The RF sources of the pre-accelerators are ready for 40 mA beam. For the 83.3 MHz operation, the drive frequency of the grid pulser should be improved up to 83.3 MHz. Design of a grid pulser for the higher repetition rate is under investigation. A photo cathode electron gun driven by a laser as another option for the 83.3 MHz operation is under investigation also.

REFERENCES

[1] N. Nishimori, et al., Nucl. Instr. and Meth. **A475** (2001) 266-269.
[2] R. Hajima, et al., Nucl. Instr. and Meth. **A507** (2003) 115-119.
[3] N. Nishimori, et al., Proc. of the APAC2004 (2004) 625-627.
[4] M.Sawamura, et al., Nucl. Instr. and Meth. **A557** (2006) 287-289.
[5] R. Nagai, et al., Proc. of the Annual Meeting of Part. Acc. Soc. (2004) 293-295.
[6] R. Nagai, et al., Proc. of the 14th Symposium on Acc. Sci. and Tech. (2003) 362-363.
[7] N. Kikuzawa, Proc of the FEL2003 (2004) II-5.
[8] R. Nagai, et al., Proc. of the Annual Meeting of Part. Acc. Soc. (2004) 420-422.
[9] R. Nagai, et al., Nucl. Instr. and Meth. **A528** (2004) 231-234.
[10] R. Nagai, et al., Proc. of the FEL2004 (2004) 255-257.
[11] R. Hajima, E. Minehara, Nucl. Instr. and Meth. **A507** (2003) 141-145.

PERFORMANCE OF A CONVENTIONAL ANALOG Φ-A TYPE LOW-LEVEL RF CONTROLLER

R. Nagai[#], R. Hajima, H. Iijima, N. Kikuzawa,
E. Minehara, N. Nishimori, T. Nishitani, M. Sawamura,
Japan Atomic Energy Agency, Tokai, Ibaraki, Japan

Abstract

For a free-electron laser application and energy-recovery linac based light source, high-stability of accelerator RF amplitude and phase is required. A low-level RF controller of the JAEA-ERL has been improved to ensure high-stability accelerating RF field. The controller is a conventional analog Φ-A type controller. The controller performance is evaluated with a 499.8 MHz superconducting cavity and a 1300 MHz copper cavity. The phase and amplitude stabilities of the 499.8 MHz superconducting cavity within latter half of an RF pulse are 0.0055 deg-rms and 7.64×10^{-5}, respectively. For the 1300 MHz copper cavity, the performance of pulse and CW modes are evaluated. In the case of pulse mode, the phase and amplitude stabilities are 0.011 deg-rms and 7.64×10^{-5}, respectively. In the case of CW mode, the phase and amplitude stabilities are 0.011 deg-rms and 6.68×10^{-5}, respectively. Therefore, the performance of the analog Φ-A type low-level RF controller is sufficient for a free-electron laser stable operation and an energy-recovery linac based light source.

INTRODUCTION

Stable operation of a free-electron laser (FEL) and performance of an energy-recovery linac (ERL) based light source depend much on the stability of an accelerator. In a superconducting accelerator, a low-level RF (LLRF) controller is one of the key components for achieving good stability. An ERL R&D program for a high-power FEL is in progress at Japan Atomic Energy Agency (JAEA; formerly JAERI and JNC). A LLRF controller based on analog phase and amplitude feedback system was improved in the R&D program. An analog Φ–A system has the faster response than a digital feedback system because there is no delay caused by the computation. There is however the following disadvantages: the feedback parameters are not adjustable easily, the temperature coefficient of the circuit parts are larger than the digital feedback system. To solve the disadvantages, the following functions were introduced: the feedback gain, filter time constant and phase-lock loop (PLL) offset phase can be varied during operation, all the circuits are contained in a temperature regulated oven. As a result of the improvement, the accelerator phase stability of 0.06 deg-rms was achieved within latter half of an RF pulse [1].

The feedback filter of the LLRF controller is a low-pass filter of a single-pole RC circuit type. Only the resistance can be varied to change the time constant. The operation frequency of the PLL is 499.8 MHz, which is the same frequency of the superconducting cavity. To satisfy the requirements of the ERL based next generation light source, the following functions are added: the filter time constant can be varied by changing the resistance and capacitor, the frequency converter and band-pass filter can be added for the various frequency operation.

The improved controller performance is evaluated with a 499.8 MHz superconducting cavity and a 1300 MHz copper cavity. The stabilities are measured by the error signal of the controller. For the 499.8 MHz superconducting cavity, the RF mode is a pulse mode which is the same mode with the JAEA-ERL usual operation mode. For the 1300 MHz copper cavity, the phase and amplitude stabilities are measured in the pulse and CW modes. In the CW mode, the phase stability is estimated by also the phase noise measurement.

STABILITY MEASUREMENTS

Stability of the 499.8 MHz Superconducting Cavity

The RF field stability is measured for the 499.8 MHz superconducting cavity used as a pre-accelerator of the JAEA-ERL. The JAEA-ERL is operated by pulsed RF mode in the width of 2 ms and the repetition of 10 pps. The stability in the part of latter half used to accelerate the electron beam is measured in the setup as shown in Fig. 1. The setup is similar to the usual operation of the JAEA-ERL. The signal of 499.8 MHz from the master oscillator (Hewlett-Packerd 8665A) is input to the controller as a reference signal. The output of the controller is amplified with 400 W pre-amplifier (THAMWAY T145-56AAA) and 50 kW IOT (CPI CHK2500W5508) [2], and input to the superconducting cavity. The monitor signal of the superconducting cavity is returned to the controller for the feedback loop. The signals of the phase and amplitude of the cavity are output from the controller and measured by a signal monitor. The signal monitor consists of a digitizer (Yokogawa WE7000) and a computer. The signals of the phase and amplitude from the controller are digitized and acquired to the computer. The phase and amplitude stabilities are calculated with real-time from the digitized data. The feedback gain, filter time constant and PLL offset phase of the controller are adjusted in real-time monitoring of the stabilities.

Typical signal of the phase and amplitude within a pulse is shown in Fig. 2. The phase and amplitude stabilities within latter half of an RF pulse are 0.0055 deg-

[#]Email: nagai.ryoji@jaea.go.jp

rms and 7.64×10^{-5} rms, respectively. The accelerating gradient and loaded Q of the superconducting cavity are 5.2 MV/m and 1.3×10^{6}, respectively. In this case, main disturbance is an RF shaking due to the pulse operation.

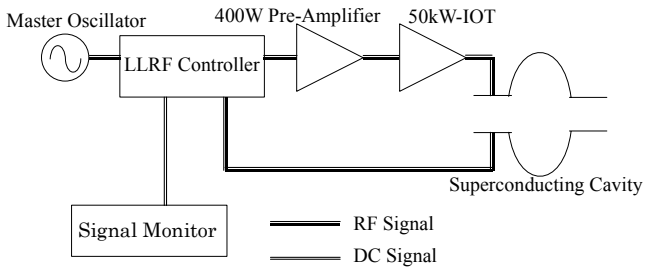

Figure 1: Stability measurement setup for the 499.8 MHz superconducting cavity.

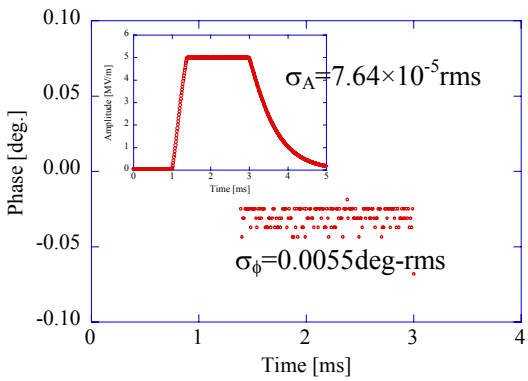

Figure 2: Typical result of the phase and amplitude (inset) within a pulse for the 499.8 MHz superconducting cavity.

Stability of the 1300 MHz Copper Cavity

To evaluate the performance of the LLRF controller at the 1300 MHz operation, the phase and amplitude stabilities are measured using a copper cavity in the pulse and CW modes. The loaded Q of the copper cavity is about 5800. The measurement setup is shown in Fig. 3. The signal of 1300 MHz from the master oscillator (Hewlett-Packerd 8341B) is input to the controller as a reference signal. The signal of 800.2 MHz from the local oscillator (Agilent 8662A) is input to the controller for a frequency conversion. The output of the controller is amplified with +28 dBm amplifier (Mini-Circuits ZHL-4240W), and input to the copper cavity. The monitor signal of the copper cavity is returned to the controller for the feedback loop. A part of the returned signal is input to a spectrum analyser (Tektronix RSA230) for the phase noise measurement in the CW mode. The master oscillator, local oscillator and spectrum analyzer are synchronized with the local signal of the master oscillator.

For the pulse mode measurement, the phase and amplitude stabilities are measured with the width of 3 ms and the repetition of 10 pps. The feedback parameters are adjusted according to the similar procedure of the superconducting cavity case. Typical signal of the phase and amplitude within a pulse is shown in Fig. 4. The phase and amplitude stabilities within latter half of an RF pulse are 0.011 deg-rms and 7.64×10^{-5} rms, respectively. For the CW mode measurement, the feedback parameters are re-adjusted. The phase and amplitude stabilities are 0.011 deg-rms and 6.68×10^{-5} rms, respectively.

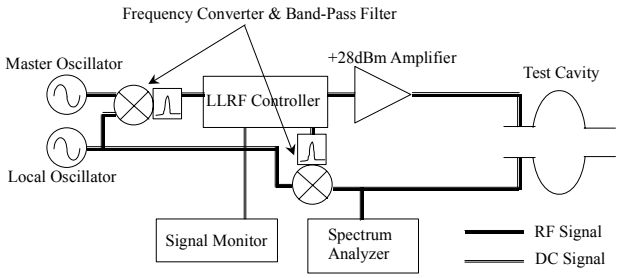

Figure 3: Stability measurement setup for the 1300 MHz copper cavity.

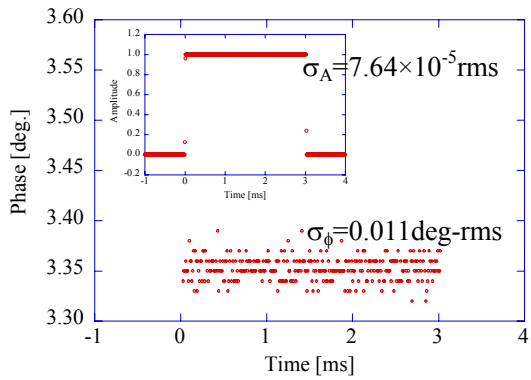

Figure 4: Typical result of the phase and amplitude (inset) within a pulse for the 1300 MHz copper cavity.

For the CW mode, the phase stability is estimated by also the phase noise measurement. The phase fluctuation (phase stability), σ_φ over a frequency range from f_1 to f_2 is given by

$$\sigma_\varphi = \left(\int_{f_1}^{f_2} 2L(f)\, df \right)^{1/2} \quad [rad], \qquad (1)$$

where $L(f)$ is a single sideband (SSB) phase noise [3]. In this measurement, the frequency range is 2 Hz to 10 kHz. The measurement accuracy of the spectrum analyzer used for this measurement is about -100 dBc/Hz. The phase noise of the master oscillator is not negligible small. The phase stability of the cavity is therefore estimated by

$$\sigma_\varphi = \left(\sigma_{\varphi m}^2 - \sigma_{\varphi 0}^2 \right)^{1/2}, \qquad (2)$$

where $\sigma_{\varphi m}$ is measured phase stability and $\sigma_{\varphi 0}$ is phase fluctuation of the oscillator and spectrum analyzer. The measured SSB phase noise against offset from the carrier frequency (offset frequency) is shown in Fig. 5. The inset is a phase noise of the oscillator and the spectrum analyzer. The phase stability is 0.013 deg-rms as a result of the measurement. Even if two phase noises in Fig. 5 are compared, the difference is hardly seen. The phase noise of the spectrum analyzer and the oscillator is not small enough to measure such a very high stability (less than 0.01deg-rms). The high-accuracy measurement of the phase noise by a low-noise measurement system is under arranging.

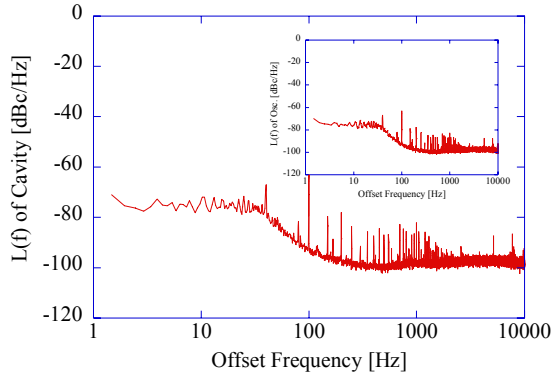

Figure 5: SSB phase noise of the copper cavity and the oscillator (inset).

The main disturbance of the ERL is a minute vibration of the acceleration cavity which is called microphonic [4,5]. To evaluate the microphonic disturbance, the phase noise is measured with the mechanical vibrated cavity. The phase and amplitude stabilities measured by the error signal of the controller are 0.014 deg-rms and 7.60×10^{-5}, respectively. The measured phase noise is shown in Fig. 6. The large phase noise (-37 dBc/Hz) due to the mechanical vibration is observed around 25 Hz without the feedback. When feedback is on, the phase noise is almost the same as the background level (-75 dBc/Hz). Therefore, the feedback gain of the phase around this frequency is 38 dB or more. The phase stability estimated from the phase noise is 0.034 deg-rms. The estimated value differs from the measured by the error signal due to the accuracy of the measurement system in this condition.

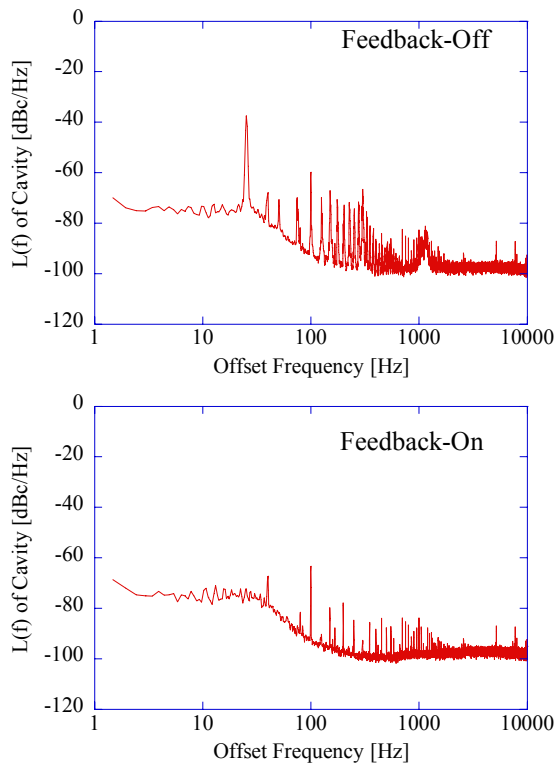

Figure 6: SSB phase noise with mechanical vibration.

CONCLUSION

The phase and amplitude stability requirements for an ERL based light source are 0.06 deg-rms and 3×10^{-4} rms, respectively [5]. The performance of the conventional analog Φ-A type LLRF controller is sufficient for the ERL-FEL stable operation and the ERL based light source as a result of the stability measurement.

The measurement of the SSB phase noise is useful for the performance evaluation of the controller with frequency resolved disturbance analysis.

REFERENCES

[1] R. Nagai, et al., Proc. of the Annual Meeting of Part. Acc. Soc. (2004) 293-295.
[2] M. Sawamura, R. Nagai, Nucl. Instr. and Meth. **A557** (2006) 287-289.
[3] E. Ezura, 'Characterization and Measurement of Frequency Stability' KEK Report 2000-6.
[4] C. Hovater, et al., Proc of the 20th Linac Conf. (2000) 518-520.
[5] M. Liepe, et al., Proc. of the PAC2003 (2003) 1329-1331.

JAEA PHOTOCATHODE DC-GUN FOR AN ERL INJECTOR

T. Nishitani, R. Hajima, H. Iijima, R. Nagai, M. Sawamura, N. Kikuzawa, N. Nishimori, E. Minehara, Japan Atomic Energy Agency, Tokai, Ibaraki, Japan
M. Tabuchi, Y. Noritake, H. Hayashitani, Y. Takeda, Nagoya Univ., Nagoya, Aichi, Japan.

Abstract

An ERL-based next-generation synchrotron light source and free electron laser require an electron beam of large current and small emittance. In order to realize an electron gun satisfying such requirements, we are developing an NEA-GaAs photocathode DC-gun. The gun is based on an existing DC-gun of Japan Atomic Energy Agency (JAEA) ERL-FEL and designed to provide a beam with energy of 250 keV and average current of 50 mA. Conditioning of a high voltage power supply has been completed up to design the target voltage of 250 kV. We have also decided to use superlattice semiconductor as a new type of photocathode with higher performance than an existing technology. We fabricated bulk-AlGaAs photocathode samples by molecular beam epitaxy in order to optimize the superlattice structure. We measured quantum efficiency and lifetime of the samples and achieved twice QE of a bulk-GaAs photocathode and longer NEA surface life than that of the bulk-GaAs photocathode.

INTRODUCTION

NEA-GaAs photocathodes have played very important roles as polarized electron sources in several fields of fundamental science [1]- [5], because polarized electrons is generated from an NEA-GaAs photocathode can be through the excitation of electrons by polarized photons tuned to the band-gap energy.

Now, an NEA-GaAs photocathode is also expected as a high-brightness electron source for ERL-based next-generation synchrotron X-ray light sources (ERL-LS). Ultimately high-brightness electron beam is required to realize the ERL-LS [6]. In order to realize such a high-brightness electron source, we need to control initial momentum spread of electrons as small as possible. An NEA photocathode can generate electron beam with such small initial momentum spread by excitation energy corresponding to the band-gap.

However, a conventional NEA-GaAs photocathode using a bulk type of GaAs semiconductor (bulk-GaAs) has serious problems, small quantum efficiency (QE) and short lifetime of the NEA surface.

In JAEA, we are developing a high-brightness electron gun for future ERL LS and FEL. In this study, we have decided to use a superlattice semiconductor for a high-brightness photocathode to fulfill the requirement of future ERL LSs. In the design of superlattice structure, we can optimize its electron affinity, band-gap energy and quantum confinement effect to improve the photocathode performance: higher QE, smaller momentum spread and longer lifetime.

DEVELOPMENTAL STATUS OF THE JAEA PHOTOCATHODE DC-GUN

An NEA photocathode has a fragile surface consisting of thin layer of cesium-atoms attached to gallium-atoms, which form electric dipole field to pull down the vacuum potential barrier. The NEA surface is easy to destroy by ion back-bombardment, which is ion generation by collision of extracted electrons and residual gas molecules followed by acceleration of the ions toward the cathode surface. Therefore, extreme high vacuum is essential to make an NEA surface of good quality and preserve it for long time.

A field emitting electrons also causes the ion back-bombardment. The field emission current can be suppressed using titanium and molybdenum as electrode materials [7] and isolating gun chamber from NEA activation chamber to prevent cesium contamination to the electrode.

The JAEA photocathode DC-gun consists of the gun chamber, the NEA surface preparation chamber and the load-lock system for transporting photocathode between these chambers. The preparation chamber is equipped with 200l/s NEG pump modules and a 500l/s ion pump. The gun chamber is equipped with 2000l/s NEG pump modules and two ion pumps, 500l/s and 200 l/s.

We have decided to use titanium alloy for the electrodes and these chambers. The titanium alloy shows out-gassing rate of 6×10^{-13} Pa m/s, which is much lower than that of standard vacuum materials by three orders of magnitude [8]. In our estimation of the ultimate pressure using the pumping speed and the out-gassing rate, the chambers is expected to be below 5×10^{-10}Pa

The ceramic insulator of the gun and the high voltage stack of the 250kV-50mA power supply are located side-by-side in a pressure vessel filled with SF6 gas of 2kgf/cm^2.

Figure 1 shows the gun chamber and the high voltage power supply.

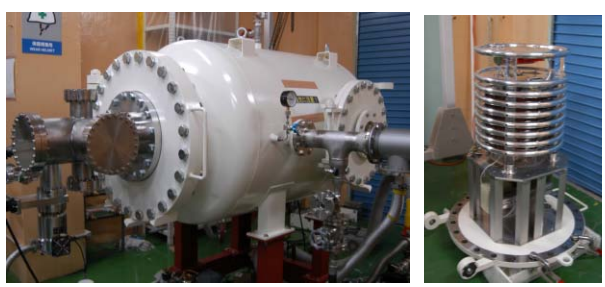

Figure 1 : JAEA photocathode DC-gun.

Conditioning of the high voltage power supply has been completed up to the design voltage of 250kV. Figure 2 shows leakage current of high-voltage terminal as a function of applied voltage. We confirmed the linear relationship between leakage current and supplying voltage without severe corona discharge.

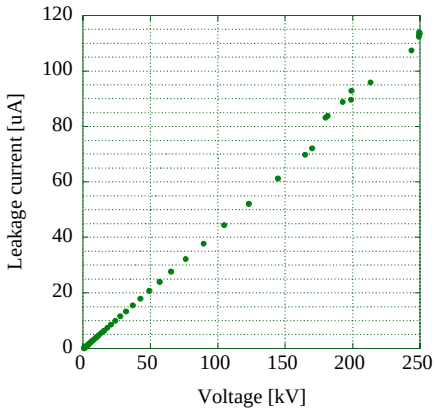

Figure 2: Leakage current of the high-voltage terminal as a function of applied.

STRATEGY OF A NEW TYPE OF PHOTOCATHODE

Superlattice photocathode

We have decided to use a superlattice photocathode as a new type of photocathode with higher performance than the existing technology [9]. A superlattice structure has periodically interchanging solid layers, well-layer and barrier-layer, thickness of which is less than 10nm. By selecting appropriate semiconductor for a each layer, a superlattice is possible to have larger band-gap energy and smaller electron affinity than that of a bulk-GaAs.

We consider the superlattice has intrinsic advantages in realization of higher QE, smaller initial momentum spread of photoelectrons and a longer lifetime of the NEA surface than those of a bulk-GaAs photocathode due to the following two reasons.

(1) Larger band-gap and smaller electron affinity than those of a GaAs is possible by optimization of a superlattice structure.

Experimental results of polarized electron sources have suggested that larger band-gap photocathode is more suitable for higher QE photocathode [10]. Moreover, we predict smaller electron affinity is more suitable for longer NEA life. Because a semiconductor with smaller electron affinity has lower vacuum level when the surface is NEA-activated.

(2) Electron density of state (DOS) for a superlattice is a step function of excitation photon energy because of quantum confinement effect.

In a semiconductor photocathode, QE is proportional to its DOS integrated from the band-gap energy to the excitation photon energy. A bulk GaAs, which has a monotonically increasing DOS function, requires rather higher energy photons to achieve high-QE operation at the expense of large momentum spread of electrons. A superlattice photocathode, on the other hand, enable one to achieve high-QE and small momentum spread simultaneously by choosing a photon energy just above the step energy of DOS [11].

NEA-ALGAAS PHOTOCATHODE

Advantages of bulk-AlGaAs in a high QE and a longer lifetime

In order to confirm the effect of band-gap energy and electron affinity on the photocathode performance, we have measured QE and lifetime of different materials: bulk GaAs and bulk AlGaAs, which has larger band-gap energy and smaller electron affinity than GaAs. It is known that the AlAs semiconductor has larger band-gap energy and smaller electron affinity than the GaAs semiconductor [12].

The measurement of the QE and the NEA surface lifetime as a function of band-gap energy and electron affinity is essential for optimization of the material fraction in the barrier layer of a superlattice structure. The bulk AlGaAs cathode is also expected to be a higher QE and a longer lifetime in comparison with a conventional GaAs photocathode.

Fabrication of crystal samples

We fabricated bulk-GaAs and bulk-AlGaAs samples with various Al fractions (=0.10, 0.17. 0.28). These samples have the same active-layer thickness for the photoelectron generation. Figure 3 shows samples fabricated by Molecular Beam Epitaxy at Nagoya University.

Exposure of a cathode surface to atmosphere results in adsorption of impurities such as oxide and carbide, which are harmful for NEA activation and hard to remove by heat cleaning. The samples have, therefore, covered by arsenide film in their preparation at the MBE chamber. The film is removed by heating in a vacuum chamber just before the NEA activation.

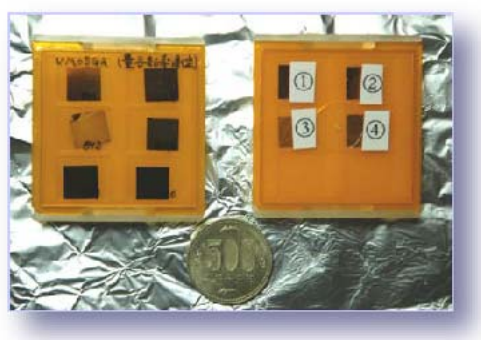

Figure 3: Photocathode samples: bulk-GaAs and bulk-AlGaAs.

Experimental setup

The measurements of QE and life time for GaAs and AlGaAs have been made at a test bench as shown in Figure 4.

The main chamber keeps extreme high vacuum of 3×10^{-9} Pa using the combination of a 500 l/s ion pump and a 1300 l/s NEG pump. The surface of samples is cleaned by radiation heating using a tungsten heater. The NEA surface is activated by alternatively adsorption of cesium and oxygen (yo-yo method).

Ti:Sapphire laser (720-870nm), He-Ne laser (633nm) and laser diode (690nm and 670nm) is used as a excitation laser.

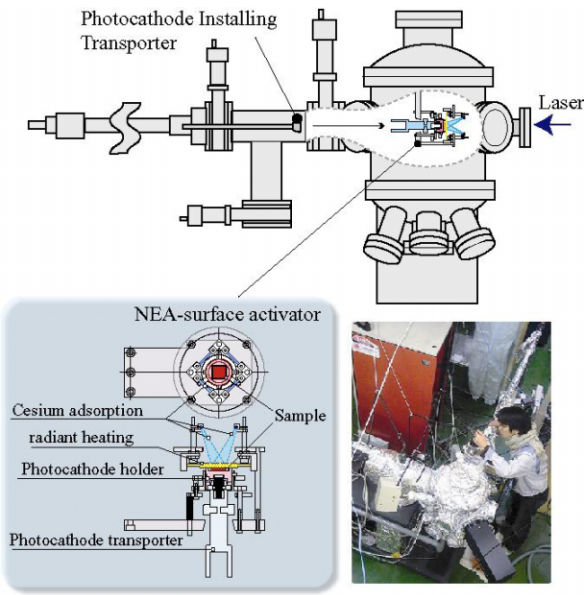

Figure 4: Experimental set up.

Quantum efficiency measurement

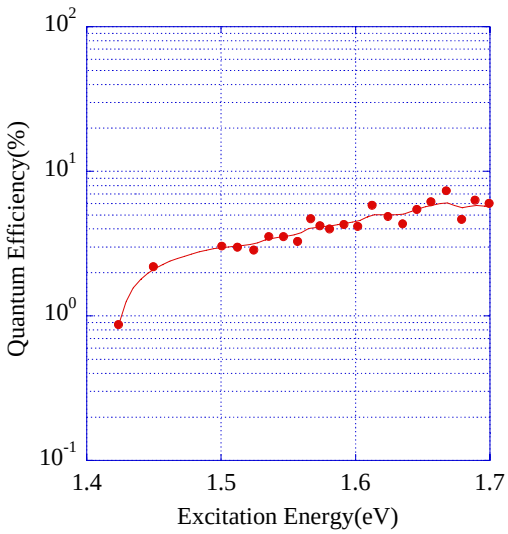

Figure 5: Quantum efficiency of the bulk-GaAs sample

Figure 5 shows measured QE spectrum of the bulk-GaAs sample. We can see a threshold around the band-gap energy (1.42eV) and QE of 2~3% from the band-gap energy to 0.1eV above the band-gap energy. These results are consistent with previous experiments [13].

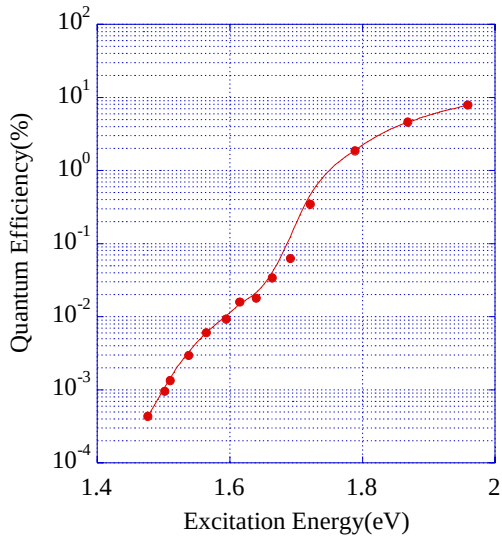

Figure 6: Quantum efficiency of the bulk-AlGaAs sample.

Figure 6 shows QE spectrum of the bulk AlGaAs sample. We can also see a threshold around the band-gap energy (1.79eV) calculated from the content of aluminum.. The QE from the band-gap energy to 0.1eV above the band-gap energy is 5~8%, which is two times higher than that of the bulk-GaAs sample.

NEA-surface life measurement

Figure 7 shows measurement results of NEA surface lifetime of samples, where laser photon energy was chosen at 0.1 eV above the band-gap for each sample. Photocurrent was below 100 nA and applied voltage was as low as 200 V to avoid NEA surface degeneration by ion back bombardment.

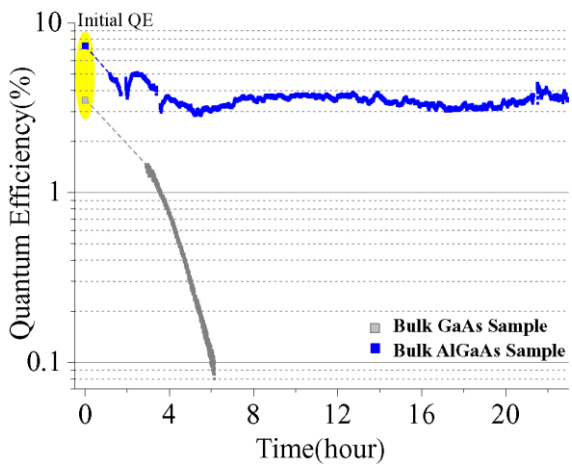

Figure 7: NEA-surface lifetime of bulk-GaAs (laser wavelength of 804nm) and bulk-AlGaAs (laser wavelength of 633nm).

In the case of the bulk-GaAs, QE, initially 3.5%, decreases below 1% 4hours after the NEA activation and the photocurrent ceases after 6 hours. In the case of the bulk-AlGaAs, QE shows initial drop from its initial value of 8% to 3% during 5 hours, but keeps 3% QE more than 26 hours.

From these results, we have found the bulk-AlGaAs has a longer lifetime of NEA surface than the bulk-GaAs. These results agree with our prediction that smaller electron affinity is suitable for longer NEA life.

SUMMARY

In JAEA, we are developing an electron gun for future ERL X-ray light sources and FELs. Fabrication of a DC gun and study on a photocathode for small emittance and high average current are in progress. We have proposed novel approaches, titanium alloy for the DC gun chambers and superlattice for the photocathode. The superlattice produces electrons with small initial momentum spread due to its quantum confinement effect, and realizes high QE, small emittance and long life time by optimizing well- and barrier-layers so that it has large band-gap and small electron affinity. Preliminary results from the measurements of QE and lifetime for the bulk GaAs and the AlGaAs photocathodes support our strategy. We will measure QE and NEA surface of samples with various fraction of aluminum to optimize the superlattice structure

ACKNOWLEDGEMENT

This work has been supported in part by Grant-in-Aid for Scientific Research for Ministry of Education, Culture, Sports, Science and Technology (Nos. 18740253).

REFERENCE

[1] D.T. Pierce et al., Appl. Phys. Lett. 26 (1975) 670.
[2] C.Y. Prescott et al., Phys. Lett. 77B (1978) 347.
[3] M. Meyerho¤ et al., Phys. Lett. B 327 (1994) 201.
[4] SLD Collaboration, Phys. Rev. Lett. 74 (1995) 2880.
[5] S. Mayer, J. Kessler, Phys. Rev. Lett. 74 (1995) 4803.
[6] Sol M. Gruner, et al., Review of Scientific Instruments, Vol. 73 Issue 3 pp. 1402-1406, 2002
[7] F. Furuta et al., NIM A 538 (2005) pp. 33–44
[8] H. Kurisu, et al., J. Vac. Sci Technol. A21 (2003) L10
[9] T. Rao, et al., Nuclear Instruments and Methods in Physics Research A557 pp.124–130, 2006
[10] T. Nakanishi, et al., AIP Conference Proceedings 421, (1998) pp. 300-310
[11] T. Nishitani et al. J. Appl. Phys. 97 (2005) 094907
[12] Sadao Adachi, J. Appl. Phys. 58 (3), (1985) pp. R1-R12
[13] T. Maruyama, et al., Appl. Phys. Lett. Vol82, 23, (2003) pp.4184-4186

HARMONIC LASING CHARACTERIZATION AT JEFFERSON LAB

S. V. Benson and M. D. Shinn, Jefferson Lab, Newport News VA 23606.

Abstract

Harmonic lasing is normally suppressed because of lasing at the fundamental wavelength. It can, however, be achieved using any of several methods that suppress fundamental lasing. In this paper we discuss two methods used at Jefferson Lab. The first is to use the characteristics of dielectric coatings to allow harmonic lasing at cavity lengths longer than the synchronous length for the fundamental. The second is to use a dielectric coating that has little reflectivity at the fundamental. This allows us to directly compare fundamental and harmonic lasing with the same optical resonator and electron beam. We present measurement carried out at Jefferson Lab using the IR Upgrade FEL operating at 0.53, 0.94, 1.04, 1.6, and 2.8 microns in which both schemes are used to produce lasing at both the 3rd and 5th harmonic of the fundamental.

INTRODUCTION

Harmonic lasing was predicted in 1980[1][2] and third harmonic lasing was demonstrated at Stanford and Los Alamos [3][4] in 1988. Since then many groups have demonstrated 3rd harmonic lasing and Jefferson Lab has demonstrated 2nd and 5th harmonic lasing as well [5][6]. In all cases the challenge has been two-fold: produce a sufficiently bright electron beam with high gain at harmonic wavelengths, and somehow suppress fundamental lasing. Photocathode injectors now routinely produce electron beams bright enough to lase well at harmonics. There are also several techniques that are available to suppress the fundamental. The first harmonic lasing demonstrations used a dispersive element to force the harmonic lasing to a longer cavity length or an aperture to preferentially diffract away the fundamental. Another way, more appropriate for a high power system, is to use dielectric mirrors to provide a high resonator Q at the harmonic and little or no Q at the fundamental. This is how lasing at the second and fifth harmonic were achieved at Jefferson Lab. In either case the gain was quite low so two high reflectors were used to produce lasing.

In this paper dielectric mirrors were used to produce harmonic lasing with relatively high gain at the third and fifth harmonic and a new mechanism was discovered that produces harmonic lasing using a resonator with high Q at the fundamental.

FEATURES OF DIELECTRIC MIRRORS RELATED TO HARMONIC LASING

Most high power resonator mirrors consist of a stack of layer pairs. The layers alternate between high and low refractive index materials, for example silicon dioxide/hafnium dioxide or thorium fluoride/zinc selenide. The thickness of each layer is one quarter of the center wavelength, or $\lambda/4n$ where n is the refractive index of the coating. The peak reflectivity is a function of the ratio of the refractive indices and the number of layer pairs. The spectral width of the reflectivity band is proportional to the square root of the ratio of the refractive indices. Note that the third harmonic center wavelength is not exactly one third of the fundamental wavelength because the refractive indices vary with wavelength, however in practice, if a quarter wave stack has good reflectivity for one wavelength, it will have similar reflectivity at the third harmonic of that wavelength.

As for the laser cavity, if a resonator has a high resonator Q at the fundamental wavelength, then it usually has high resonator Q for the third harmonic and possibly the fifth harmonic if the fundamental is a long wavelength. In our case the resonator Q is actually slightly higher for the third harmonic than for the fundamental. Since the gain at the fundamental wavelength is typically much higher than the third and fifth harmonic gain, the laser will almost always lase at the fundamental with a quarter wave stack. If the wiggler is set to a wavelength 5/3 as long as the center wavelength of the quarter wave stack coating, the third harmonic of the coating will be coincident with the fifth harmonic of the FEL. There is very little resonator Q at 5/3 of the center wavelength or at 5/9 of the resonator wavelength where the third harmonic is resonant. The laser then lases at the fifth harmonic of the FEL and the third harmonic of the coating. Note that it is also possible to lase at the fundamental of the FEL with the third harmonic of the coating.

CASE 1. LASING AT HARMONICS AT A FIXED WAVELENGTH

The first measurements were performed with the same resonator and center wavelength, while varying the wiggler strength. The resonant wavelength of the wiggler was set to 1.02 microns, 3.06 microns, and 5.1 microns. All three settings produced strong lasing. The detuning curves for the three settings are show in figure 1. It is very interesting to note that the fundamental, which has the highest gain of the three, has the shortest detuning curve. According to G. Dattoli's formulas [7], the detuning curve length should be proportional to $GhN_W\lambda$. where G is the small signal gain, h is the harmonic number, N_W is the number of wiggler periods and λ is the laser wavelength. The ratio of the detuning curve lengths using the measured gain should be 3.5:6.0:5.7 according to the formula. The third and fifth are a bit shorter than this would indicate but they are also closer to threshold, which shortens the detuning curve.

Table 1 shows a comparison of measured and predicted gain and power, where predicted values were obtained using Dattoli's formulas. The measured gain was inferred from the minimum turn-on time in the detuning

curve. Simulations indicate that the turn-on time to half power is 22.5 e-foldings and direct measurements of the gain support this observation. The power was measured using a high power laser power meter accurate to 5%. The gain and power are in good agreement for the fundamental and fifth harmonic but the experimental gain is lower and power is much larger than predicted for the third harmonic. This may have been due to differences in accelerator setup though no single accelerator parameter can explain the discrepancy.

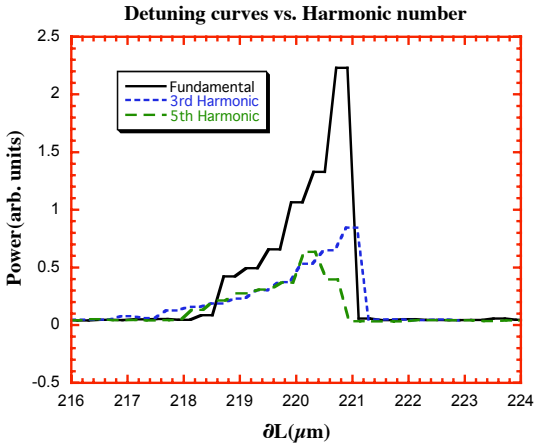

Figure 1. Power vs. cavity length for lasing at the fundamental, third, and fifth harmonic, with fundamental wavelength ~1.04 μm.

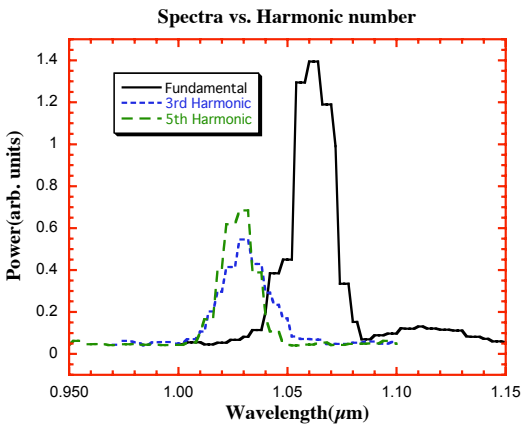

Figure 2. Spectra while lasing with 1.06 micron mirrors with the resonant wavelength equal to 1.02, 3.06, and 5.1 microns. The resonator losses were 3.5%/pass. Note the movement towards 1.02 microns as the harmonic number is increased.

Table 1. Measured and predicted gain and power when lasing at harmonics at ~1.04 microns.

h	Meas. Gain	Calc. Gain	Meas. Power(W)	Calc. Power (W)
1	48%	48%	700	885
3	20.4%	24%	275	180
5	11.6%	11%	63	65

Spectra for these three cases are shown in Figure 2. Note that the wavelengths are not the same. Simulations indicate that the lasing wavelength is typically a fraction $1/hN_W$ longer than the resonant wavelength. Since h is changing but the resonant wavelength is not, one expects the laser wavelength to get closer to the resonant wavelength. The fundamental is shifted further from the resonant wavelength because it is lasing harder than the harmonics, as is evident from the weak sideband at 1.11 μm.

CASE 2: LASING ON THE FIFTH HARMONIC OF THE LASER AND THE THIRD HARMONIC OF THE COATING

For both the 2.8 and 1.6 micron mirrors, it was possible to lase at the third harmonic of the laser coating and the fifth harmonic of the laser. For the 2.8 micron mirrors the wiggler was set to 4.65 microns and lased at 0.935 microns. For the 1.6 micron mirrors the wiggler was set to 2.74 microns and lased at 0.53 microns. In both cases the lasing was quite robust. Note that both mirror sets have higher reflectivity at the third harmonic than at the fundamental. The detuning curve at 0.53 μm was as long as 5 microns, which is comparable to the fundamental lasing curve. Dattoli's formula noted above, implies that the 5th harmonic gain is 3/5 of the fundamental gain. The gain inferred from the turn-on time and losses is about 1/3 the fundamental gain. Direct gain measurements will be necessary to resolve these discrepancies. The efficiency was not as good as the 1.06 micron lasing but we did obtain 35 W of CW light in the green.

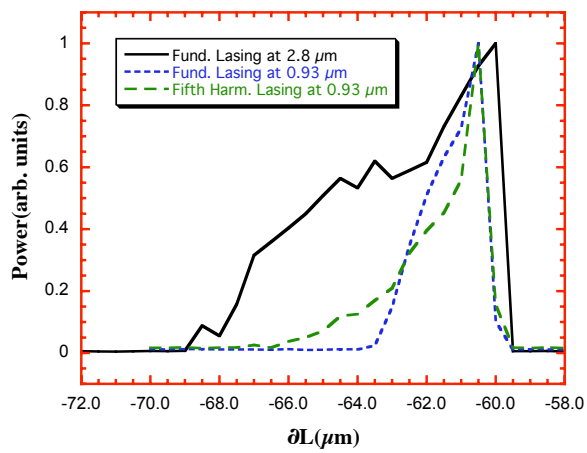

Figure 3. Detuning curves for three different configurations using the 2.8 micron mirrors.

In figure 3 we show the detuning curves while lasing at the fundamental using both the 2.8 μm and 0.935 μm reflectivity peaks. The detuning curves for the fundamental have a three to one ratio. Dattoli's formula then would indicate similar gain. In fact the gain at 2.8 microns is about 50% larger than at 0.935 microns. This apparent discrepancy has been seen before when varying the electron beam repetition rate [8]. Both curves have a convex shape (negative second derivative), which is common when the gain is well above threshold. The fifth harmonic curve at 0.935 μm should be five times as long as

the fundamental if the gain is similar. In fact it is only twice as long indicating a gain 40% of the fundamental. It also has a concave shape, which is typical for lasing close to threshold. The ratio between the fifth harmonic gain and fundamental gain is extremely sensitive to the energy spread. The ratio is 0.4:1 for an energy spread of 0.3%. This is a typical value for our machine, though the spread was not measured the day of these measurements.

CASE 3: A NEW WAY TO LASE AT THE THIRD HARMONIC

When the laser is very well tuned and the wavelength is very close to or slightly longer than the center wavelength of the mirror coatings, we see a very interesting phenomenon. The laser starts to lase sporadically at the third harmonic when the cavity length is very close to the synchronous cavity length where the round trip time in the resonator matches the arrival time of the electron bunches. This occurs for both the 1.6 micron and 2.8 micron mirrors. We sometimes use this as a measure of how well the laser is optimized. If the laser optimization is poor, harmonic lasing will not occur.

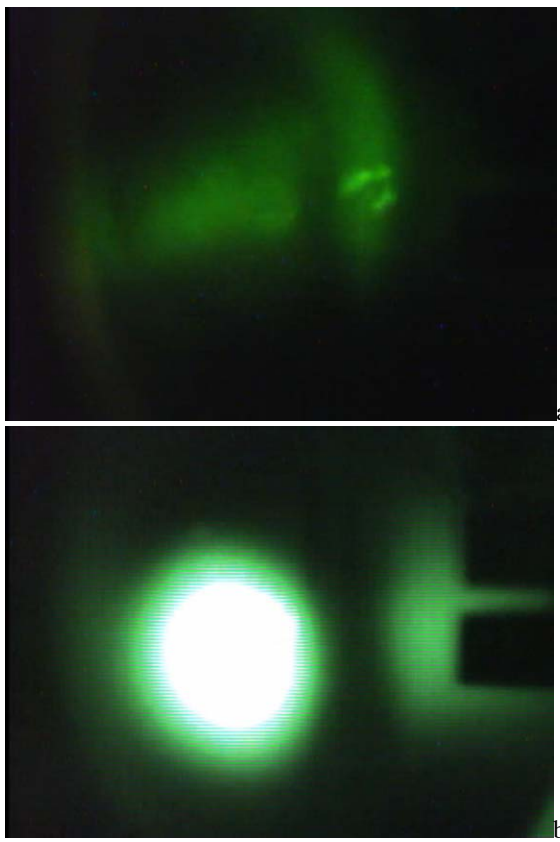

Figure 4. (a) coherent harmonics emitted during fundamental lasing on the output coupler of the laser. (b) Harmonic lasing at 0.53 microns obtained by lengthening the optical cavity by a fraction of a micron.

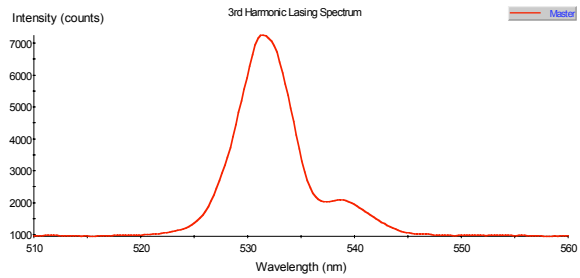

Figure 5. Lasing spectrum using an Ocean Optics visible spectrometer array. This is a single macropulse shot.

This behavior is shown in figure 4. In figure 4a we see the pattern of coherent spontaneous radiation that is always present when lasing at 1.6 microns. In figure 4b we have lengthened the optical cavity by a fraction of a micron and see very strong green emission with a TEM_{00} profile. The image here completely saturates the CCD camera. The spectrum of the third harmonic lasing is shown in Figure 5. This signal at 530 nm is not present when the cavity is tuned for strong fundamental lasing.

With the 2.8 μm mirrors the lasing can occur over a larger range of detuning and can be quite stable. In figure 6 we show a detuning curve obtained using a spectrometer at 0.935 microns. The detector did not show any signal when lasing at the fundamental but showed a strong signal when lasing at the 3rd harmonic.

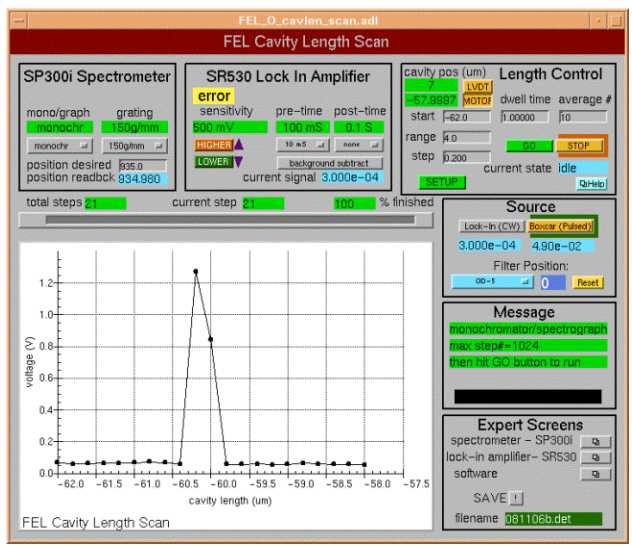

Figure 6. Detuning curve taken through a spectrometer set to 935 nm. The lasing occurs over about 0.5 microns in cavity length. The fundamental is not lasing over this range.

We do not understand exactly how this new lasing phenemonan works. It seems as though the round trip time in the resonator is less for the third harmonic than for the fundamental. This suggests that the fundamental light penetrates more deeply into the coating than the third harmonic light. The interference that produces the outgoing wave should be the same for the third harmonic as for the fundamental. The different penetration depth may

be related to the higher reflectivity of the coating at the third harmonic. Future experiments will study the wavelength dependence of the harmonic lasing and compare with reflectivity models of the coating.

CONCLUSIONS

The availability of a high brightness electron beam and a wiggler with large tuning range has opened up an interesting diagnostic device for free-electron lasers. Since the harmonic lasing is far more sensitive to beam parameters than the fundamental it allows one to more carefully optimize the laser. The presence of lasing at harmonics greatly restricts the laser modeling since the model must fit both the fundamental and harmonic lasing with the same optical resonator and electron beam.

In the future we plan to try to lase with an electron beam with half the energy spread of the one now used. This reduces the fundamental gain but greatly increases the harmonic gain. We should have a situation where the harmonic gain actually exceeds the fundamental gain. This should also allow lasing at the seventh and possibly the ninth harmonic.

ACKNOWLEDGEMENTS

George Neil was quite helpful in setting up the laser to take data. Shukui Zhang operated the Ocean Optics spectrometer to get the visible spectrum. This work was supported by U.S. DOE Contract No. DE-AC05-84-ER40150, the Office of Naval Research, the Air Force Research Laboratory, the Army Night Vision Laboratory, the Commonwealth of Virginia and the Laser Processing Consortium.

REFERENCES

[1] J. M. J. Madey, R. C. Taber, "Equations of Motion for a Free-electron Laser with a Transverse Gradient", In *Free-electron generators of coherent radiation*, **7,** Addison-Wesley (1979) 741.

[2] W. B. Colson, IEEE J. of Quant. Elec**. QE-17**, (1981) 1417.

[3] S. V. Benson, J. M. J. Madey, *Phys. Rev*. **A39**, (1989) 1579–1581.

[4] R. W. Warren, L. C. Haynes, D. W. Feldman, W. E. Stein, S. J. Gitomer, *Nucl. Inst. and Meth*. **A296** (1990) 84–88.

[5] George R. Neil, S. V. Benson, G. Biallas, J. Gubeli, K. Jordan, S. Myers, and M. D. Shinn, “Second Harmonic FEL Oscillation, Phys. Rev. Lett. **87**, (2001) 084801.

[6] S. Benson, M. Shinn, G. R. Neil, and T. Siggins, “First Demonstration of 5th Harmonic Lasing in a FEL”, presented at the 21st International FEL Conference, Hamburg Germany, August 1999.

[7] G. Dattoli, S. Cabrini, L. Gianessi, V. Loreto, and C. Mari, *Nucl. Inst. and Meth.* **A318** (1992) 495.

[8] S. Benson et al., *Nucl. Inst. and Meth.* **A429** (1999) 27–32.

A DESIGN STUDY OF A FIR/THZ FEL FOR HIGH MAGNETIC FIELD RESEARCH

M. Tecimer, L.C. Brunel, J. van Tol, NHMFL / FSU, Tallahassee, FL 32310, USA,
G. Neil, TJNAF, Newport News, VA 23606, USA.

Abstract

Presently a conceptual design for a NIR-FIR FEL system at the National High Magnetic Field Lab. - Florida State University (NHMFL-FSU) is being undertaken in collaboration with the FEL group at the Thomas Jefferson Laboratory. The system is expected to combine high magnetic field research with an intense, tuneable photon source spanning the spectral region ~ 2 - 1100 microns. Here, a design study involving the FIR/THz part of the NHMFL-FEL design proposal is presented. The suggested long-wavelength FEL encompasses in the first phase a thermionic injector with a ~2 mA average current and a ~10 MeV superconducting rf linac module operating at 1.3 GHz. The broadband outcoupling over the envisaged FIR/THz spectral range (100 - 1100 microns) can be accomplished by adopting a variable-outcoupler scheme in a waveguided cavity. Besides the performance predictions of the suggested long wave-length FEL, techniques for the generation of high peak power, nanoseconds long THz pulses (for magnetic resonance applications) are also briefly discussed.

Table 1:FIR FEL Specifications

PARAMETER	FIR FEL	UNITS
Wavelength	*100 to 1100*	μm
Micropulse Energy	*1 to 3*	μJ
Micropulse-width	*~ 5 to 60*	ps
Fract. bandwidth	*~ 0.3 - 5%*	
Resonator	*pp- waveguide, ~ 5.8*	m
Outcoupling	*Variable (others?)*	
Pulse rep. rate	*26 (13)*	MHz
Macropulse-width	*100μs to CW*	
Beam energy	*10 - 11*	MeV
Wiggler period	*70 (hybrid.)*	mm
Wiggler K	*0.6-3.5*	
Periods	*40*	

INTRODUCTION

In the framework of the NHMFL FEL initiative the design efforts for the construction of FIR/THz FEL radiation sources are twofold; the main effort is directed towards the generation of high peak power micropulses for time resolved measurements in the (tens of) picoseconds range. The planned rf-linac based system relies on relatively mature technologies developed at FELIX (FOM), Stanford, Jefferson Lab. and FZ-Rossendorf. The use of superconductive rf-linac cavities enables quasi-cw operation with the associated higher average THz radiation power levels (tens of Watts) and offers the possibility of an extension to an energy recovery linac (ERL) system (considered for the NIR-MIR FELs) as well. The second part of the FEL effort focuses on the development of techniques in producing relatively long ((sub-) nanoseconds), kW - level tuneable (sub-)millimetre wave pulses, in order to generate spin excitations at high magnetic fields and for possible pulsed magnetic resonance applications. While it has been shown that the FIR-FEL technology developed by the TeraHertz Center at UCSB with an electrostatic accelerator (EA) [1,2], this long wavelength range at the envisioned power levels have not yet been achieved with a rf linac system.

Here, we give an overview of the studied outcoupler design options and report on the simulated performance of a rf-linac driven waveguide FIR-FEL based on specified system settings. Finally, we discuss briefly on the current status of search for methods that would allow us to extend the inherently short pulse durations in the studied sc rf linac driven FIR FEL configuration into the ns range.

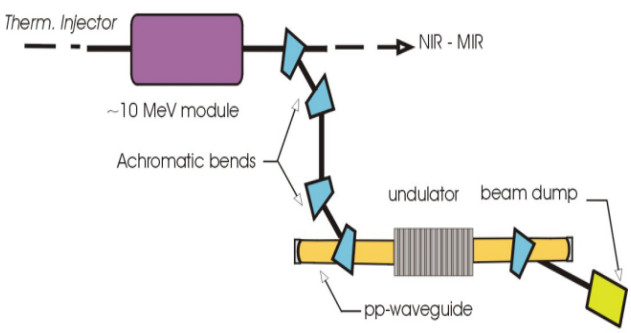

Figure 1: Layout of the FIR-FEL beamline option.

RF LINAC-FIR FEL DESIGN ISSUES

In the current design , the beam energy for the FIR FEL is provided by the first cryomodule (~10 MeV, operating at 1.3 GHz) which constitutes, along with the thermionic injector, the injector section of the NIR-MIR FELs. The thermionic injector system (a grid modulated DC gun followed by subharmonic and fundamental

mtecimer@magnet.fsu.edu

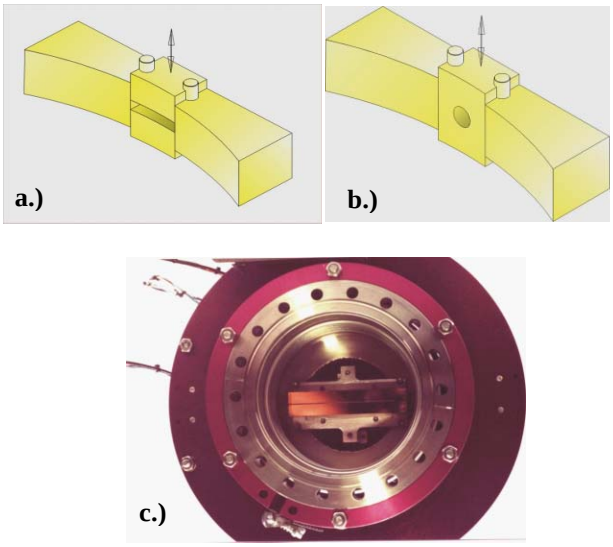

Figure 2 a-c: The lateral dimension of the outcoupler mirrors shown in a.) , b.) amounts to ~14 cm. The radius of curvature is ~3.5 m. The outcoupler mirror shown in c.) is constructed for an FIR FEL operating at ~230-650 μm.

bunchers) [3] is similar to the ones in use at FZ-Rossendorf and Stanford University. It is planned to provide ~2 mA average current at 26 MHz repetition rate. The NHMFL FIR-FEL is being designed to cover a large portion of the THz spectrum while employing a single wiggler, (possibly) a single cylindrical outcoupler mirror along with a waveguide structure that extends over the entire cavity (~5.8 meters). The latter option reduces the diffraction losses inherent in this long wavelength spectral region and avoids oversized cavity mirrors and mirror vacuum chambers. It requires the injection of the beam into the parallel-plate waveguide cavity (gap:10 mm) prior matching the beam into the undulator. After leaving the interaction section, the spent beam is directed into a beam dump. The design specifications along with the major system parameters are listed in Table 1.

The continuous tunability offered by the FEL over the envisaged large spectral range ideally would incorporate a broad-band feedback/outcoupling which can be accomplished by adopting a variable outcoupler scheme on one of the cylindrical metal-mirrors. The outcoupler option illustrated in Fig. 2a is a modified version of the variable height outcoupler (Fig. 2c) studied and realized in [4,5]. Adjusting the slot aperture in the vertical dimension between 0. – 3.0 mm continuously, the power output can be optimised over the entire 100 - 1100 microns. Hereby, the use of inserts with different lateral sizes (1.5mm, 3.0mm) allows one to keep the ratio of horizontal to vertical dimensions of the aperture < ~1.5 , at any slot aperture/wavelength configuration. In the second option, depicted in Fig. 2b, the middle insert (thus the centre of the hole aperture) is displaced in the vertical, sampling different areas of the hybrid waveguide mode on the mirror surface. The latter scheme covers the targeted wavelength range using max. three different hole apertures (or, alternatively, three cylindrical mirrors that could be moved up and down in the vertical, each having a different hole aperture). The optical beam transport accounts for the small (max. ~ 2 - 3 mm) off-axis displacement of the optical beam centre behind the outcoupler. Other variable outcoupler options such as FPI-meshes are being considered (as far as they remain operational at cw multi-kW level intracavity power), particularly for wavelengths above 500 microns.

The performance modelling of the FIR-FEL system is based on electron beam parameters (bunch charge, norm. transverse emittance, longitudinal emittance, energy spread) that are similar to those implemented at FZ-Rossendorf FEL, with the exception of an increase in the electron bunch repetition frequency up to 26 MHz, the latter being relevant in determining the resonator length and the average radiation power. Using the waveguide FEL code described in [5,6], that models the physics of a rf-linac driven, highly slippage dominated short pulse THz-FEL oscillator, the FEL performance for various

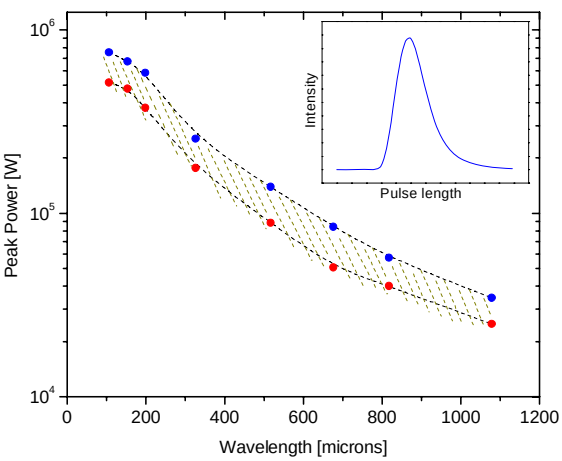

Figure 3: The upper peak power values (blue dots) are obtained at the peak of the detuning curve whereas the lower data points at cav. Detuning ~ -0.4·λ.

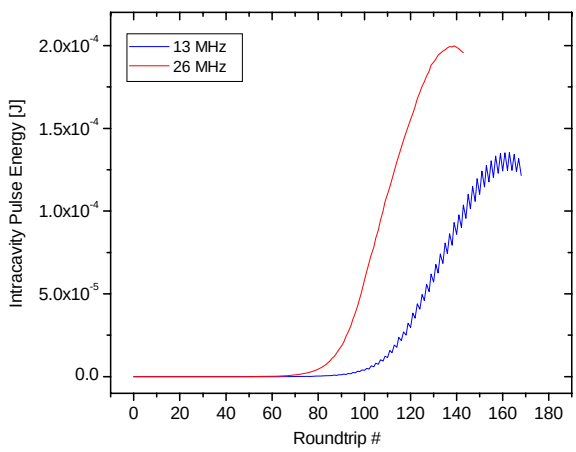

Figure 4: FEL operation at 13 MHz and 26 MHz pulse rep. rates with ~5.8 m cavity length , λ ~ 155 μm.

wavelength/wiggler settings (assuming a FEL operating at a fixed beam energy of 10.8 MeV) and outcoupling ratios (optimised by using the transmission characteristics of the scheme shown in Fig. 2a) are studied. An aspect that affects strongly the intracavity radiation build-up process and the evolution of the optical pulse structure is the use of ps-short electron bunches for the generation of (for rf-linac based systems unusually) long wavelength radiation in a waveguided propagation medium. Fig.3 shows the predicted (approximate) peak power levels achievable in the generated THz micropulses. The inset illustrates the simulated pulse shape whose leading edge exhibits a distinct exponential decay deviating from the Gaussian.

Another possible operational mode is driving the FIR FEL with 13 MHz rep. rate (limiting the average current to ~1mA), while keeping the waveguide resonator length 5.8 meters. In this case, the optical pulse interacts with the electron beam every other roundtrip, thus experiencing nearly twice as much cavity losses for each amplifying pass. The simulated evolution of the intracavity micropulse energy up to the saturation is shown in Fig. 4 at 155 microns (as an example) for both, 13 MHz and 26 MHz rep. rates. In the '13 MHz case' the outcoupling ratio is set to ~ 0.6 % (optimised to obtain the highest pulse energy coupled out), while the '26 MHz case' employs ~ 3.0 %. The calculated outcoupled pulse energies at different wavelengths indicate that 13 MHz rep. rate in combination with 5.8 m resonator length does not lead to a satisfying FEL operation. It results in a significant reduction in the pulse energies obtained. In addition, the micropulse energy fluctuations in subsequent roundtrips (by an amount defined by the cavity losses) may not be tolerable in many applications. In the following, simulated pulse energies are given for the '13 MHz and 26 MHz repetition rates' at two different wavelengths, 155 microns and 1080 microns respectively:

- '13 MHz 'case:

- outcoupled max. pulse energy ~0.7 μJ (@155 μm)
- outcoupled max. pulse energy ~0.3 μJ (@1080 μm)

- '26 MHz' case:

- outcoupled max. pulse energy ~3.1 μJ (@ ~155 μm)
- outcoupled max. pulse energy ~1.6 μJ (@ ~1080 μm)

GENERATION OF (SUB-) NS PULSES

For pulsed magnetic resonance excitations, the pulse length condition is given by $\gamma B_1 \tau \approx 0.5$ in which γ is 28 GHz/Tesla, B_1 is the amplitude of the oscillating magnetic field, and τ is the FIR pulse length. For the envisioned time resolution and the available power, the pulse length is of the order of 1 ns. At the present design stage, having optical pulse rep. rates of max. 26 MHz, the planned superconductive rf-linac FIR FEL configuration is not suitable for the implementation of interpulse phase-locking techniques described in [7] to generate narrow bandwidth, ns - long pulses. On the other hand, the flexibility offered by the variation of cavity desynchronization on modifying the pulse durations (thus the Fourier transform limited spectral bandwidth) falls short of providing the pulse lengthening effect that would be necessary to meet the requirements posed on the pulse durations and the associated spectral bandwidths. A possible (standard-) solution to lengthen the (rf-linac generated) picoseconds long optical pulses with sufficiently broad bandwidths is the use of grating stretchers [8], ending up with frequency chirped pulses of ns-duration. However, due to the introduced time frequency correlation within the pulse and the still existent broad bandwidth (not Fourier transform limited pulses), frequency chirped pulses remain restricted in their applications in the area of pulsed magnetic resonance experiments. Table 2 illustrates the parameters of a grating stretcher and the stretching factors achievable upon application of the device on the outcoupled FIR FEL pulses specified in Table 1. In Table 2, parameters *d*, *m*, *Z* denote the groove spacing of the blazed grating, the order at which the grating is used and the variable distance between the grating and the telescope mirror used in the setup, respectively.

Table 2: Grating Stretcher specifications

λ [μm]	*d* [μm]	*m*	*Z* [m]	*Initial* [ps]	*Final* [ns]
100	80	1	3.0	5.0	1.5
100	80	3	1.34	5.0	3.1
500	400	1	3.0	25.0	1.6
500	400	3	0.57	25.0	3.1
1000	800	1	3.0	65.0	1.2
1000	800	3	0.78	65.0	3.1

ACKNOWLEDGMENTS

We thank G. Ramian for helpful discussions. One of the authors (M.T.) acknowledges the input provided by P. Michel and J. Teichert regarding the sc rf-linac system at FZR-ELBE. This work has been supported by the NSF under grant no DMR-0520481.

REFERENCES

[1] G. Ramian, Nucl. Inst. and Meth. A 318, (1992) 225.

[2] Doty et al., Rev. Sci. Instrum., Vol.75, (2004) 2920.

[3] http://www.FZ-Rossendorf.de/ELBE

[4] M. Tecimer et al., Nucl. Instr. and Meth. A 528, (2004) 146.

[5] http://www2.hawaii.edu/~mtecimer

[6] M. Tecimer et al., Nucl. Instr. and Meth. A 528, (2004) 139.

[7] D. Oepts and W.B. Colson, IEEE QE-26, (1990) 723.

[8] E.B. Tracy and A.J. DeMaria, Phys. Lett., Vol. 29 A, 369.

EXPERIMENTAL STUDY OF A VOLUME FREE ELECTRON LASER WITH A "GRID" RESONATOR

V.G. Baryshevsky *, N.A.Belous, A.A.Gurinovich, A.S.Lobko, P.V.Molchanov, V.I.Stolyarsky,
Research Institute for Nuclear Problems, 11 Bobryiskaya str., 220050, Minsk, Belarus

Abstract

Operation of Volume Free Electron Laser with a "grid" photonic crystal, built from periodically strained metallic threads, was studied in the backward wave regime. Generation threshold was observed for different "grid" photonic crystals. Dependence of the generation threshold on the resonator length was investigated.

INTRODUCTION

Generators using radiation from an electron beam in a periodic slow-wave circuit (travelling wave tubes, backward wave oscillators, free electron lasers) are now widespread [1].

Diffraction radiation [2] in periodical structures is in the basis of operation of travelling wave tubes (TWT) [3, 4], backward wave oscillators (BWO) and such devices as Smith-Purcell lasers [5, 6, 7] and volume FELs using two- or three-dimensional distributed feedback [8, 9, 10, 11].

A challenge of precise electron beam guiding over the slowing structure (the electron beam should pass at the distance $\delta \leq \frac{\lambda\beta\gamma}{4\pi}$ over the diffraction grating, here δ is the so-called beam impact parameter, λ is the radiation wavelength, $\beta = v/c$, v is the electron beam velocity, γ is the electron Lorentz-factor) restricts application of Smith-Purcell lasers and the similar devices. Electrical endurance of resonator limits radiation power and current of acceptable electron beam. Conventional waveguide systems are essentially restricted by the requirement for transverse dimensions of resonator, which should not significantly exceed radiation wavelength.

The most of the above problems can be overcome in VFEL [8, 9, 10, 11, 12]. In VFEL the greater part of electron beam interacts with the electromagnetic wave due to volume distributed interaction. Transverse dimensions of VFEL resonator could significantly exceed radiation wavelength $D \gg \lambda$. In addition, electron beam and radiation power are distributed over the whole volume that is beneficial for electrical endurance of the system. One of the VFEL types uses a "grid" volume resonator ("grid" photonic crystal) that is formed by a periodically strained either dielectric or metallic threads.

The "grid" structure of dielectric threads was experimentally studied in [13], where it was shown that such "grid" photonic crystals have sufficiently high Q factors ($10^4 - 10^6$).

Theoretical analysis [14, 16] showed that periodic metal grid does not absorb electromagnetic radiation and the "grid" photonic crystal of metal threads is almost transparent for the electromagnetic waves in the wavelength range, where the skin-depth is less then the thread radius. The conclusions of [14] declared possibility of development of VFEL with the "grid" photonic crystal of metal threads.

First lasing of the volume FEL with a "grid" volume resonator, which was formed by the periodic set of metal threads inside a rectangular waveguide, was observed in the proof-of-principle experiment [15] and completely confirmed conclusions of [14].

In the present paper dependence of the generation intensity as a function of the grid photonic crystal length is studied for the backward wave oscillation regime.

THE CONCEPT

Waves propagation through photonic crystals is the subject for numerous studies both theoretical and experimental [17, 18, 19, 20].

Challenges, which appears when considering interaction of an electromagnetic wave with such a photonic crystal, are as follows: It is well known that a metal grid reflects electromagnetic waves perfectly. Therefore, the question arises as to whether a wave penetrate deep into resonator, especially since resonator contains a set of grids. Theoretical analysis [14, 16] showed that periodic metal grid does not absorb electromagnetic radiation and the "grid" photonic crystal, made of metal threads, is almost transparent for the electromagnetic waves in the frequency range from GHz to THz. In this range the skin depth δ is about 1 micron or less for the most of metals (for example, for 10 GHz $\delta_{Cu} = 0.66$ μm, $\delta_{Al} = 0.8$ μm, $\delta_W = 1.16$ μm and so on). Thus, in this frequency range the metallic threads can be considered as perfect conducting.

According to [14, 16] the refraction index for the "grid" photonic crystal, can be expressed as:

$$n^2_{\parallel(\perp)} = 1 + \frac{\eta_{\parallel(\perp)}}{k^2}, \tag{1}$$

where

$$\eta_{\parallel(\perp)} = \frac{4\pi}{\Omega_2} \frac{A_0}{1 + i\pi A_0 - 2CA_0}, \tag{2}$$

$n_\parallel$ and $n_\perp$ are the refraction indices for the waves with polarization parallel and perpendicular to the thread axis, respectively, $k = 2\pi/\lambda$ is the wave number, R is the thread radius, $\Omega_2 = d_y \cdot d_z$, where d_y and d_z are the photonic crystal periods along the axis y and z, respectively, $C = 0.5772$ is the Eiler constant. The values $A_{0(\parallel)}$ and $A_{0(\perp)}$ for perfectly conducting threads are defined as [15, 16]:

$$A_{0(\parallel)} = \frac{1}{\pi} \frac{J_0(kR) N_0(kR)}{J_0^2(kR) + N_0^2(kR)} + \frac{i}{\pi} \frac{J_0^2(kR)}{J_0^2(kR) + N_0^2(kR)},$$

* bar@inp.minsk.by

$$A_{0(\perp)}=\frac{1}{\pi}\frac{J_0'(kR)\,N_0'(kR)}{J_0'^2(kR)+N_0'^2(kR)}+\frac{i}{\pi}\frac{J_0'^2(kR)}{J_0'^2(kR)+N_0'^2(kR)}\,, \quad (3)$$

where J_0, N_0, J_0' and N_0' are the Bessel and Neumann functions and their derivatives, respectively.

To consider threads with finite conductivity one should use the following expressions:

$$A_{0(\parallel)}=\frac{i}{\pi}\frac{J_0(k_tR)J_0'(kR)-\sqrt{\varepsilon_t}J_0'(k_tR)J_0(kR)}{J_0(k_tR)H_0^{(1)\prime}(kR)-\sqrt{\varepsilon_t}J_0'(k_tR)H_0^{(1)}(kR)}, \quad (4)$$

$$A_{0(\perp)}=\frac{i}{\pi}\frac{J_0(k_tR)J_0'(kR)-\frac{1}{\sqrt{\varepsilon_t}}J_0'(k_tR)J_0(kR)}{J_0(k_tR)H_0^{(1)\prime}(kR)-\frac{1}{\sqrt{\varepsilon_t}}J_0'(k_tR)H_0^{(1)}(kR)}\,,$$

where ε_t is the dielectric permittivity of the thread material, $k_t=\sqrt{\varepsilon_t}k$, $H_0^{(1)}$ is the Hankel function of the zero order. The expressions (3) can be obtained from (4) considering $\varepsilon_t \to \infty$.

Difference in the refraction indices for different wave polarizations ($n_\parallel \neq n_\perp$) indicates that the system owns optical anisotropy (i.e. possesses birefringence and dichroism). To escape this anisotropy we can alternate the treads position in the grid: threads in each layer are orthogonal to those in the previous and following layers.

Smith - Purcell (diffraction) radiation in photonic crystal for an electron beam with the velocity $\vec{v}$ passing through the "grid"arises when the radiation condition is fulfilled:

$$\omega-\vec{k}n(k)\vec{v}=\vec{\tau}\vec{v}\,, \quad (5)$$

where $\vec{\tau}$ is the reciprocal lattice vector and $n(k)$ is the refraction index (see (1)). Suppose the electron beam velocity is directed along the axis OZ, then (5) can be presented in the form:

$$k-\tau_z\beta=k\,n(k)\,\beta\cos\theta, \quad (6)$$

where $\beta=\frac{v}{c}$, the angle between $\vec{k}$ and the electron beam velocity is denoted by θ and $\tau_z=\frac{2\pi m_h}{d_z}$, where $m_h=1,2,...$ is the number of harmonic. The roots of this equation give the spectrum of frequencies of diffraction (Smith-Purcell) radiation, which is induced by a particle moving in the above "grid" photonic crystal.

Diffraction radiation in a metal waveguide of the rectangular cross-section with the "grid" photonic crystal placed inside it is shown in [14, 16] to be described by the equation similar to (6):

$$\left(\frac{\omega-\tau_z v}{v}\right)^2=\left(\frac{\omega}{c}\right)^2-(\kappa_{mn}^2-\eta), \quad (7)$$

where η is determined by (2) and the eigenvalues κ_{mn} are determined by the waveguide transverse dimensions (width a and height b):

$$\kappa_{mn}^2=\left(\frac{\pi m}{a}\right)^2+\left(\frac{\pi n}{b}\right)^2\,. \quad (8)$$

The roots of equation (7) for $\frac{\eta}{\tau_z^2\beta^2}\ll 1$ can be obtained as:

$$\omega_1(m,n)=\frac{\tau_z v}{1-\beta^2}\left(1-\beta\sqrt{1-\frac{(\kappa_{mn}^2-\eta)}{\tau_z^2}\frac{1-\beta^2}{\beta^2}}\right), \quad (9)$$

$$\omega_2(m,n)=\frac{\tau_z v}{1-\beta^2}\left(1+\beta\sqrt{1-\frac{(\kappa_{mn}^2-\eta)}{\tau_z^2}\frac{1-\beta^2}{\beta^2}}\right).$$

It should be reminded here that $\tau_z=\frac{2\pi m_h}{d_z}$, where $m_h=1,2,...$ is the number of harmonic. From (9) it follows that higher harmonics provide for getting radiation with higher frequencies. For example, for the electron beam with the energy 200 keV, considering $\theta\sim 20^\circ$ and $d_z=1.6$ cm, the first harmonic ($m_h=1$) gives radiation frequencies ~ 10 GHz and ~ 40 GHz for the roots 1 and 2 of the equation (7), respectively, the 30-th harmonic ($m_h=30$) provides ~ 230 GHz and ~ 1 THz.

EXPERIMENTAL SETUP

The "grid" photonic crystal is built from tungsten threads with the diameter 0.1 mm strained inside the rectangular waveguide with the transversal dimensions $a=35$ mm, $b=35$ mm and length 300 mm (see Fig.1). The distance between the threads along the axis OZ is $d_z=12.5$ mm. A pencil-like electron beam with the diameter 32 mm, energy ~200 keV and current ~2kA passes through the above structure. The magnetic field guiding the electron beam is $\sim 1.55-1.6$ tesla. Period of grating is chosen to provide radiation frequency ~ 8.4 GHz. The "grid" structure

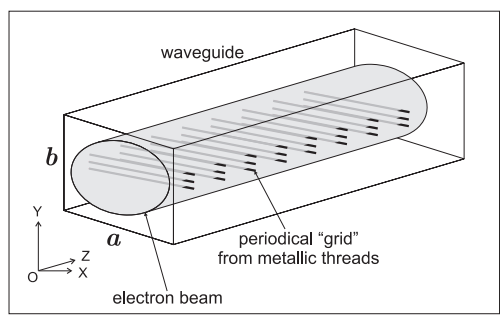

Figure 1: The "grid" diffraction grating placed inside the waveguide.

is made of separate frames each containing the layer of 1, 3 or 5 parallel threads with the distance between the next threads $d_y=6$ mm). Frames are joined to get the "grid" structure with the distance d_z between layers.

Frequency range was evaluated by means of tunable waveguide filters, which were tuned in the band 7.8 - 12.4 GHz with passbands 0.25 GHz, 0.5 GHz and 1 GHz. Attenuation of radiation in the suppressed band of this filter is ~ -25 dB.

EXPERIMENTAL RESULTS

The objective of the experiment is to study dependence of the generated radiation intensity on the "grid" photonic crystal length.

The maximal radiation power of VFEL generator in the this experiment was about 1.5 kiloWatt for one thread in the frame, 5 kiloWatts for three threads in the frame and 10 kiloWatt for five threads in the frame.

The sample oscillogram is shown in Fig.2, where signals marked 1 and 2 are the signals obtained from microwave detectors. Other two curves are the electron gun voltage and electron beam current. Time scale is 80 ns.

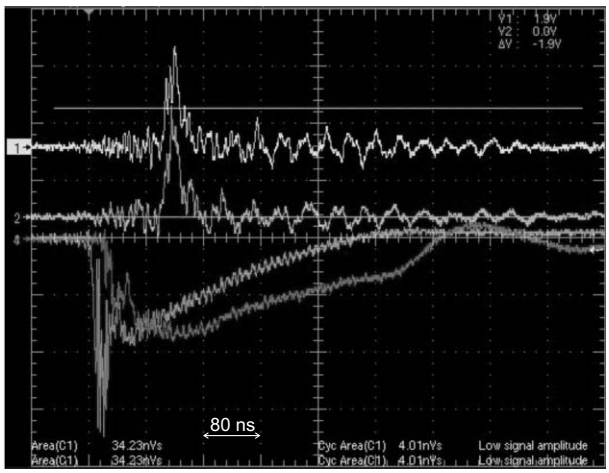

Figure 2: The sample oscillogram.

Two types of experiments are reported.

1. The radiation power was measured for photonic crystal with 4, 8, 10 and 24 frames each containing one thread equidistant from waveguide top and bottom walls (see Fig.3). The result of these measurements is presented in Fig.4, where the radiation power is normalized to the maximal detected power (1.5 kiloWatt).

2. The radiation power is measured for photonic crystal with 4, 6, 10, 12, 14 and 22 frames each containing five threads distant $d_y = 6$ mm each from other (see Fig.5).

The result of these measurements is presented in Fig.6, where the radiation power is also normalized to the maximal detected power (10 kiloWatt). The solid curve in this figure shows the numerically simulated radiation power, which also normalized.

CONCLUSION

Operation of Volume Free Electron Laser with a "grid" photonic crystal, built from periodically strained metallic threads, was studied in the backward wave regime. Generation threshold was observed for different "grid" photonic crystals. Dependence of the generation threshold on the resonator length was investigated. Use of volume resonators of the described type provides to weaken requirements for the electron beam shape and guiding precision, because the electron beam passes directly through the photonic crystal.

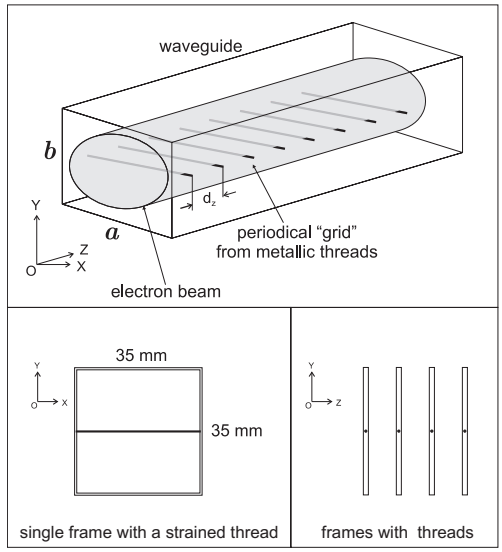

Figure 3: Photonic crystal with frames each containing one thread equidistant from waveguide top and bottom walls.

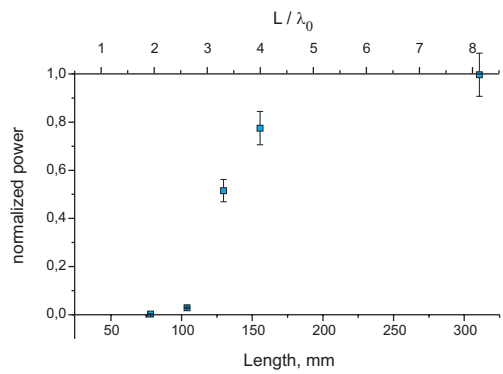

Figure 4: Dependence of the generation intensity on the length of the "grid" photonic crystal with one thread in the frame, the upper scale show the resonator length in the number of wavelength L/λ_0, where $\lambda_0 = 3.6$ cm.

REFERENCES

[1] V.L.Granatstein, R.K.Parker and C.M.Armstrong, Proceedings of the IEEE **87**, no.5 (1999).

[2] B.M.Bolotovskii and G.V.Voskresenskii, Usp. Fiz. Nauk. **88**, 209 (1966) (Sov. Phys. Usp. **9**, 73 (1966)).

[3] R.Kompfner, Wireless World **52**, 369 (1946).

[4] R.Pierce, Proc. IRE **35**, 111 (1947).

[5] S.J.Smith and E.M.Purcell, Phys. Rev. **92**, 1069 (1953).

[6] W.W.Salisbury, US Patent 2,634,372 (1953); J.Opt. Soc.Am. **60**, 1279 (1970).

[7] G.Doucas, J.H.Mulvey, M.Omori, J.Walsh and M.F.Kimmit, Phys.Rev.Lett. **69**, 1761 (1992); John E. Walsh US Patent 5,790,585 (1996).

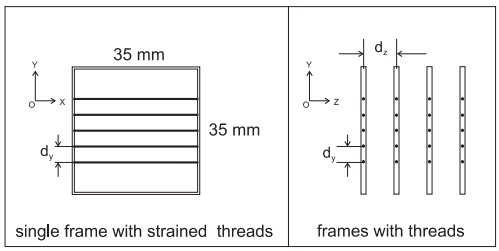

Figure 5: Photonic crystal with frames each containing five threads distant $d_y = 6$ mm each from other

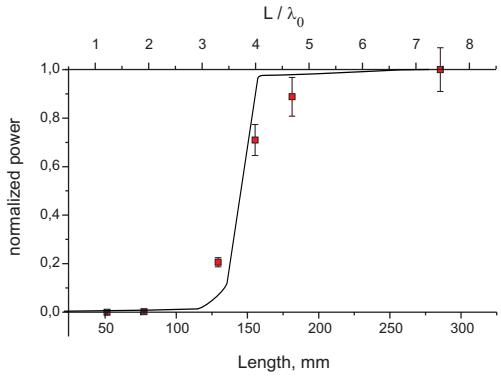

Figure 6: Dependence of the generation intensity on the length of the "grid" photonic crystal with 5 threads in the frame marked with squares and numerically simulated dependence of the wave amplitude on the "grid" photonic crystal length for the electron beam with the energy ∼200 keV and current density ∼ 2 kA/cm^2

[8] V.G.Baryshevsky, NIM **445A**, 281 (2000); LANL e-print archive physics/9806039.

[9] V.G.Baryshevsky, K.G.Batrakov, A.A.Gurinovich et al., NIM **483A**, 21 (2002).

[10] V.G.Baryshevsky, K.G.Batrakov, A.A.Gurinovich et al., NIM **507A**, 137 (2003).

[11] V.G.Baryshevsky et al., Eurasian Patent no. 004665.

[12] V.G.Baryshevsky, I.D.Feranchuk, Phys.Lett. **102A**, 141 (1984).

[13] V.G.Baryshevsky,K.G.Batrakov,I.Ya.Dubovskaya,V.A.Karpovich, V.M.Rodionova, NIM **393A**, 71 (1997).

[14] V.G.Baryshevsky, A.A.Gurinovich LANL e-print archive: physics/0409107

[15] V.G. Baryshevsky, K.G. Batrakov, N.A. Belous, A.A. Gurinovich, A.S. Lobko, P.V. Molchanov, P.F. Sofronov, V.I. Stolyarsky, LANL e-print archive: physics/0409125.

[16] V.G.Baryshevsky, A.A.Gurinovich, to be published in NIM B, Topical Issue RC2005.

[17] A. L. Pokrovsky and A. L. Efros, Phys. Rev. **B 65**, 045110 (2002).

[18] A. L. Pokrovsky, Phys. Rev. **B 69**, 195108 (2004).

[19] E. I. Smirnova, C. Chen, M. A. Shapiro et al., J. Appl.Phys. **91**(3), 960 (2002).

[20] E. I. Smirnova and C. Chen, M. A., J. Appl.Phys. **93**(10), 5859 (2003).

[21] R.W. James, *The Optical Principles of Diffraction of X-Rays* (Ox Bow Press, 1982).

[22] Shih-Lin Chang, *Multiple diffraction of x-rays in crystals* (Springer-Verlag, 1984).

[23] V.V. Nikolsky , Electrodynamics and propagation of radiowave (Nauka, 1978)

ELECTRODYNAMICAL PROPERTIES OF A VOLUME FREE ELECTRON LASER WITH A "GRID" RESONATOR

V.G. Baryshevsky, A.A.Gurinovich *
Research Institute for Nuclear Problems, 11 Bobryiskaya str., 220050, Minsk, Belarus.

Abstract

The electrodynamic properties and lasing in Volume Free Electron Laser with a "grid" resonator ("grid" photonic crystal) with changing in space parameters are considered. The equations describing lasing of VFEL with such a resonator are obtained. It is shown that use of diffraction gratings (photonic crystal) with variable period increases radiation intensity and provide to create the dynamical wiggler with variable period. This makes possible to develop a double-cascaded FEL with variable parameters, which efficiency can be significantly higher then that of conventional system.

INTRODUCTION

Diffraction radiation [1] in periodical structures is in the basis of operation of travelling wave tubes (TWT) [2, 3], backward wave oscillators (BWO) and such devices as Smith-Purcell lasers [4, 5, 6] and volume Free Electron Lasers [7, 8, 9] (see also [10]).

Volume Free Electron Laser (VFEL) is a radiation generator using non-one-dimensional distributed feedback, which is created with the aid of Bragg diffraction gratings or photonic crystals.

One of the VFEL types uses a "grid" volume resonator ("grid" photonic crystal) that is formed by a periodically strained either dielectric [11] or metallic threads [12, 13, 14, 15].

In the present paper the electrodynamic properties and lasing in Volume Free Electron Laser with a "grid" resonator ("grid" photonic crystal) with changing in space parameters are considered. The equations describing lasing of VFEL with such a resonator are obtained. It is shown that use of diffraction gratings (photonic crystal) with variable period provide to create the dynamical wiggler with variable period. This makes possible to develop a double-cascaded FEL with variable parameters changing, which efficiency can be significantly higher that of conventional system.

THEORY OF LASING FOR VFEL WITH A "GRID" PHOTONIC CRYSTAL WITH VARIABLE PERIOD

To obtain equations, which describe VFEL lasing in the "grid" photonic crystal (see Fig.1), the Maxwell equations and motion equations for a particle in an electromagnetic field should be considered:

$$\mathrm{rot}\vec{H} = \frac{1}{c}\frac{\partial \vec{D}}{\partial t} + \frac{4\pi}{c}\vec{j},\ \mathrm{rot}\vec{E} = -\frac{1}{c}\frac{\partial \vec{H}}{\partial t},$$
$$\mathrm{div}\vec{D} = 4\pi\rho,\ \frac{\partial \rho}{\partial t} + \mathrm{div}\vec{j} = 0, \qquad (1)$$

here $\vec{E}$ and $\vec{H}$ are the electric and magnetic fields, $\vec{j}$ and ρ are the current and charge densities, the electromagnetic induction $D_i(\vec{r},t') = \int \varepsilon_{il}(\vec{r},t-t')E_l(\vec{r},t')dt'$ and, therefore, $D_i(\vec{r},\omega) = \varepsilon_{il}(\vec{r},\omega)E_l(\vec{r},\omega)$, the indices $i,l = 1,2,3$ correspond to the axes x,y,z, respectively. The current and charge densities are respectively defined as:

$$\vec{j}(\vec{r},t) = e\sum_\alpha \vec{v}_\alpha(t)\delta(\vec{r}-\vec{r}_\alpha(t)),\ \rho(\vec{r},t) = e\sum_\alpha \delta(\vec{r}-\vec{r}_\alpha(t)),$$

where e is the electron charge, $\vec{v}_\alpha$ is the velocity of the particle α (α numerates the beam particles),

$$\frac{d\vec{v}_\alpha}{dt} = \frac{e}{m\gamma_\alpha}\left\{\vec{E}(\vec{r}_\alpha,t) + \frac{1}{c}[\vec{v}_\alpha \times \vec{H}(\vec{r}_\alpha,t)] - \frac{\vec{v}_\alpha}{c^2}(\vec{v}_\alpha\vec{E}(\vec{r}_\alpha,t))\right\},$$

here $\gamma_\alpha = (1-\frac{v_\alpha^2}{c^2})^{-\frac{1}{2}}$ is the Lorentz-factor, $\vec{E}(\vec{r}_\alpha,t)$ and $\vec{H}(\vec{r}_\alpha,t)$ are the electric and magnetic field in the point of location $\vec{r}_\alpha = \vec{r}_\alpha(t)$ of the particle α.

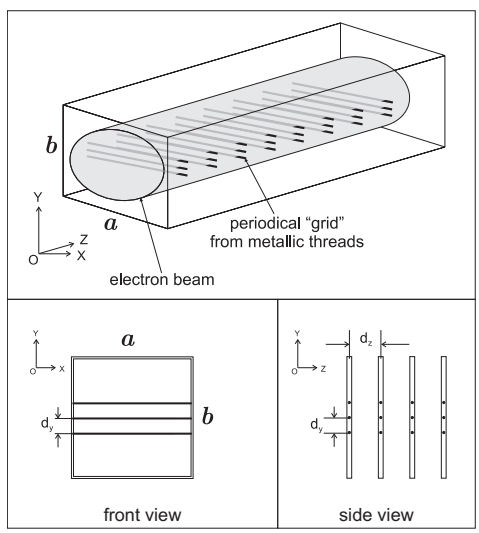

Figure 1: A "grid" photonic crystal.

The dielectric permittivity tensor can be expressed as $\hat{\varepsilon}(\vec{r}) = 1 + \hat{\chi}(\vec{r})$, where $\hat{\chi}(\vec{r})$ is the dielectric susceptibility.

* gur@inp.minsk.by

When $\hat{\chi} \ll 1$ the system (1) can be rewritten as:

$$\Delta\vec{E}(\vec{r},t) - \frac{1}{c^2}\frac{\partial^2}{\partial t^2}\int \hat{\varepsilon}(\vec{r},t-t')\vec{E}(\vec{r},t')dt' = \quad (2)$$
$$= 4\pi\left(\frac{1}{c^2}\frac{\partial\vec{j}(\vec{r},t)}{\partial t} + \vec{\nabla}\rho(\vec{r},t)\right).$$

When the grating is ideal $\hat{\chi}(\vec{r}) = \sum_\tau \hat{\chi}_\tau(\vec{r})e^{i\vec{\tau}\vec{r}}$, where $\vec{\tau}$ is the reciprocal lattice vector [16, 17].

Let the diffraction grating (photonic crystal) period is smoothly varied with distance, which is much greater then the diffraction grating (ptotonic crystal lattice) period. It is convenient in this case to present the susceptibility $\hat{\chi}(\vec{r})$ in the form, typical for theory of X-ray diffraction in crystals with lattice distortion [18]:

$$\hat{\chi}(\vec{r}) = \sum_\tau e^{i\Phi_\tau(\vec{r})}\hat{\chi}_\tau(\vec{r}), \quad (3)$$

where $\Phi_\tau(\vec{r}) = \int\vec{\tau}(\vec{r}')d\vec{l}'$, $\vec{\tau}(\vec{r}')$ is the reciprocal lattice vector in the vicinity of the point $\vec{r}'$. The expressions for $\hat{\chi}$ for the "grid" photonic crystal were obtained in [12, 14]:

$$\chi_{\parallel(\perp)} = \frac{4\pi}{\Omega_2 k^2}\frac{A_{0\parallel(\perp)}}{1 + i\pi A_{0\parallel(\perp)} - 2CA_{0\parallel(\perp)}}, \quad (4)$$

the symbols $\parallel$ and $\perp$ indicate the waves with polarization parallel and perpendicular to the thread axis, respectively, $k = 2\pi/\lambda$ is the wave number, R is the thread radius, $C = 0.5772$ is the Eiler constant, $\Omega_2 = d_y \cdot d_z$, where d_y and d_z are the photonic crystal periods along the axis y and z, respectively. The values $A_{0(\parallel)}$ and $A_{0(\perp)}$ for the threads with finite conductivity are defined as[14]:

$$A_{0(\parallel)} = \frac{i}{\pi}\frac{J_0(k_tR)J_0'(kR) - \sqrt{\varepsilon_t}J_0'(k_tR)J_0(kR)}{J_0(k_tR)H_0^{(1)\prime}(kR) - \sqrt{\varepsilon_t}J_0'(k_tR)H_0^{(1)}(kR)},$$
$$A_{0(\perp)} = \frac{i}{\pi}\frac{J_0(k_tR)J_0'(kR) - \frac{1}{\sqrt{\varepsilon_t}}J_0'(k_tR)J_0(kR)}{J_0(k_tR)H_0^{(1)\prime}(kR) - \frac{1}{\sqrt{\varepsilon_t}}J_0'(k_tR)H_0^{(1)}(kR)},$$

where ε_t is the dielectric permittivity of the thread material, $k_t = \sqrt{\varepsilon_t}k$, $H_0^{(1)}$ is the Hankel function of the zero order, J_0 and J_0' are the Bessel functions and their derivatives, respectively.

In contrast to the theory of X-rays diffraction, in the case under consideration $\hat{\chi}_\tau$ depends on $\vec{r}$. It is to the fact that $\hat{\chi}_\tau$ depends on the volume of the lattice unit cell Ω_2, which can be significantly varied for diffraction gratings (photonic crystals), as distinct from natural crystals.

It should be reminded that for an ideal crystal without lattice distortions, the wave, which propagates in crystal can be presented as a superposition of the plane waves:

$$\vec{E}(\vec{r},t) = \sum_{\vec{\tau}=0}^{\infty}\vec{A}_{\vec{\tau}}e^{i(\vec{k}_\tau\vec{r}-\omega t)}, \quad (5)$$

where $\vec{k}_\tau = \vec{k} + \vec{\tau}$.

In the case under consideration the solution of (2) can be written in the form (compare with [18]):

$$\vec{E}(\vec{r},t) = \mathrm{Re}\left\{\sum_{\vec{\tau}=0}^{\infty}\vec{A}_{\vec{\tau}}e^{i(\phi_\tau(\vec{r})-\omega t)}\right\}, \quad (6)$$

where $\phi_\tau(\vec{r}) = \int_0^{\vec{r}} k(\vec{r})d\vec{l} + \Phi_\tau(\vec{r})$ and $k(\vec{r})$ can be found as solution of the dispersion equation in the vicinity of the point with the coordinate vector $\vec{r}$, integration is done over the quasiclassical trajectory, which describes motion of the wavepacket in the photonic crystal with lattice distortion.

Let us consider now case when all the waves participating in the diffraction process lays in a plane (coupled wave diffraction, multiple-wave diffraction [17, 16]) i.e. all the reciprocal lattice vectors $\vec{\tau}$ lie in one plane. Suppose the wave polarization vector is orthogonal to the plane of diffraction.

Let us rewrite (6) in the form $\vec{E}(\vec{r},t) = \vec{e}\,E(\vec{r},t)$, where

$$E(\vec{r},t) = \mathrm{Re}\left\{\vec{A}_1e^{i(\phi_1(\vec{r})-\omega t)} + \vec{A}_2e^{i(\phi_2(\vec{r})-\omega t)} + ..\right\}, \quad (7)$$

$$\phi_1(\vec{r}) = \int_0^{\vec{r}}\vec{k}_1(\vec{r}')d\vec{l}, \quad (8)$$

$$\phi_2(\vec{r}) = \int_0^{\vec{r}}\vec{k}_1(\vec{r}')d\vec{l} + \int_0^{\vec{r}}\vec{\tau}(\vec{r}')d\vec{l}. \quad (9)$$

Then multiplying (2) by $\vec{e}$ one can get:

$$\Delta E(\vec{r},t) - \frac{1}{c^2}\frac{\partial^2}{\partial t^2}\int\hat{\varepsilon}(\vec{r},t-t')E(\vec{r},t')dt' = \quad (10)$$
$$= 4\pi\vec{e}\left(\frac{1}{c^2}\frac{\partial\vec{j}(\vec{r},t)}{\partial t} + \vec{\nabla}\rho(\vec{r},t)\right). \quad (11)$$

Substitution of (7) to (11) gives the following system:

$$\frac{1}{2}e^{i(\phi_1(\vec{r})-\omega t)}[2i\vec{k}_1(\vec{r})\vec{\nabla}A_1 + i\vec{\nabla}\vec{k}_1(\vec{r})A_1 - k_1^2(\vec{r})A_1 +$$
$$+\frac{\omega^2}{c^2}\varepsilon_0(\omega,\vec{r})A_1 + i\frac{1}{c^2}\frac{\partial\omega^2\varepsilon_0(\omega,\vec{r})}{\partial\omega}\frac{\partial A_1}{\partial t} + \frac{\omega}{c^2}^2\varepsilon_{-\tau}(\omega,\vec{r})A_2 +$$
$$+i\frac{1}{c^2}\frac{\partial\omega^2\varepsilon_{-\tau}(\omega,\vec{r})}{\partial\omega}\frac{\partial A_2}{\partial t}] + \text{ conjugated terms } =$$
$$= 4\pi\vec{e}\left(\frac{1}{c^2}\frac{\partial\vec{j}(\vec{r},t)}{\partial t} + \vec{\nabla}\rho(\vec{r},t)\right), \quad (12)$$
$$\frac{1}{2}e^{i(\phi_2(\vec{r})-\omega t)}[2i\vec{k}_2(\vec{r})\vec{\nabla}A_2 + i\vec{\nabla}\vec{k}_2(\vec{r})A_2 - k_2^2(\vec{r})A_2 +$$
$$+\frac{\omega^2}{c^2}\varepsilon_0(\omega,\vec{r})A_2 + i\frac{1}{c^2}\frac{\partial\omega^2\varepsilon_0(\omega,\vec{r})}{\partial\omega}\frac{\partial A_2}{\partial t} + \frac{\omega^2}{c^2}\varepsilon_\tau\,(\omega,\vec{r})A_1 +$$
$$+i\frac{1}{c^2}\frac{\partial\omega^2\varepsilon_\tau(\omega,\vec{r})}{\partial\omega}\frac{\partial A_1}{\partial t}] + \text{ conjugated terms } =$$
$$= 4\pi\vec{e}\left(\frac{1}{c^2}\frac{\partial\vec{j}(\vec{r},t)}{\partial t} + \vec{\nabla}\rho(\vec{r},t)\right),$$

where the vector $\vec{k}_2(\vec{r}) = \vec{k}_1(\vec{r}) + \vec{\tau}$, $\varepsilon_0(\omega,\vec{r}) = 1 + \chi_0(\vec{r})$, here notation $\chi_0(\vec{r}) = \chi_{\tau=0}(\vec{r})$ is used, $\varepsilon_\tau(\omega,\vec{r}) = \chi_\tau(\vec{r})$. Note here that for numerical analysis of (12), if $\chi_0 \ll 0$, it is convenient to take the vector $\vec{k}_1(\vec{r})$ in the form $\vec{k}_1(\vec{r}) = \vec{n}\sqrt{k^2 + \frac{\omega^2}{c^2}\chi_0(\vec{r})}$.

For better understanding let us suppose that the diffraction grating (photonic crystal lattice) period changes along one direction and define this direction as axis z.

Considering the right part of (2) let us take into account that microscopic currents and densities are the sums of terms, containing delta-functions, therefore, the right part can be rewritten as:

$$e^{-i(\vec{k}_\perp\vec{r}_\perp+\phi_{1z}(z)-\omega t)}4\pi\vec{e}\left(\frac{1}{c^2}\frac{\partial\vec{j}(\vec{r},t)}{\partial t}+\vec{\nabla}\rho(\vec{r},t)\right)=$$
$$=-\frac{4\pi i\omega e}{c^2}\vec{e}\sum_\alpha\vec{v}_\alpha(t)\delta(\vec{r}-\vec{r}_\alpha(t))e^{-i(\vec{k}_\perp\vec{r}_\perp+\phi_{1z}(z)-\omega t)}\times$$
$$\times\theta(t-t_\alpha)\,\theta(T_\alpha-t), \qquad (13)$$

here t_α is the time of entrance of particle α to the resonator, T_α is the time of particle leaving from the resonator, $\theta-$functions in (13) image the fact that for time moments preceding t_α and following T_α the particle α does not contribute in process.

Let us suppose now that a strong magnetic field is applied for beam guiding though the generation area. Thus, the problem appears one-dimensional (components v_x and v_y are suppressed). Averaging the right part of (13) over the particle positions inside the beam, points of particle entrance to the resonator $r_{\perp0\alpha}$ and time of particle entrance to the resonator t_α we can obtain:

$$e^{-i(\vec{k}_\perp\vec{r}_\perp+\phi_{1z}(z)-\omega t)}4\pi\vec{e}\left(\frac{1}{c^2}\frac{\partial\vec{j}(\vec{r},t)}{\partial t}+\vec{\nabla}\rho(\vec{r},t)\right)=$$
$$=-\frac{4\pi i\omega\rho\,\vartheta_1\,u(t)\,e}{c^2}\frac{1}{S}\int d^2\vec{r}_{\perp0}\frac{1}{T}\times \qquad (14)$$
$$\times\int_0^t e^{-i(\phi_1(\vec{r},\vec{r}_\perp,t,t_0)+\vec{k}_\perp\vec{r}_{\perp0}-\omega t)}dt_0=$$
$$=-\frac{4\pi i\omega\rho\,\vartheta_1\,u(t)\,e}{c^2}\langle\langle e^{-i(\phi_1(\vec{r},\vec{r}_\perp,t,t_0)+\vec{k}_\perp\vec{r}_{\perp0}-\omega t)}dt_0\rangle\rangle,$$

where ρ is the electron beam density , $u(t)$ is the mean electron beam velocity, which depends on time due to energy losses, $\vartheta_1=\sqrt{1-\frac{\omega^2}{\beta^2k_1^2c^2}}$, $\beta^2=1-\frac{1}{\gamma^2}$, $\langle\langle\ \rangle\rangle$ indicates averaging over transversal coordinate of point of particle entrance to the resonator $r_{\perp0\alpha}$ and time of particle entrance to the resonator t_α.

According to [19] averaging procedure in (14) can be simplified, when consider that random phases, appearing due to random transversal coordinate and time of entrance, presents in (14) as differences. Therefore, double integration over $d^2\vec{r}_{\perp0}\,dt_0$ can be replaced by single integration [19].

The system (12) in this case converts to:

$$2ik_{1z}(z)\frac{\partial A_1}{\partial z}+i\frac{\partial k_{1z}(z)}{\partial z}A_1-(k_\perp^2+k_{1z}^2(z))A_1+$$
$$+\frac{\omega^2}{c^2}\varepsilon_0(\omega,z)A_1+i\frac{1}{c^2}\frac{\partial\omega^2\varepsilon_0(\omega,z)}{\partial\omega}\frac{\partial A_1}{\partial t}+$$
$$+\frac{\omega^2}{c^2}\varepsilon_{-\tau}(\omega,z)A_2+i\frac{1}{c^2}\frac{\partial\omega^2\varepsilon_{-\tau}(\omega,z)}{\partial\omega}\frac{\partial A_2}{\partial t}=$$
$$=i\frac{2\omega}{c^2}J_1(k_{1z}(z)), \qquad (15)$$

$$2ik_{2z}(z)\frac{\partial A_2}{\partial z}+i\frac{\partial k_{2z}(z)}{\partial z}A_2-(k_\perp^2+k_{2z}^2(z))A_2+$$
$$+\frac{\omega^2}{c^2}\varepsilon_0(\omega,z)A_2+i\frac{1}{c^2}\frac{\partial\omega^2\varepsilon_0(\omega,z)}{\partial\omega}\frac{\partial A_2}{\partial t}+$$
$$+\frac{\omega^2}{c^2}\varepsilon_\tau(\omega,z)A_1+i\frac{1}{c^2}\frac{\partial\omega^2\varepsilon_\tau(\omega,z)}{\partial\omega}\frac{\partial A_1}{\partial t}=$$
$$=i\frac{2\omega}{c^2}J_2(k_{2z}(z)),$$

where the currents J_1, J_2 are determined by the expression

$$J_m=2\pi j\vartheta_m\int_0^{2\pi}\frac{2\pi-p}{8\pi^2}(e^{-i\phi_m(t,z,p)}+e^{-i\phi_m(t,z,-p)})dp,$$
$$\vartheta_m=\sqrt{1-\frac{\omega^2}{\beta^2k_m^2c^2}},\ m=1,2,\ \beta^2=1-\frac{1}{\gamma^2}\,, \qquad (16)$$

$j=en_0v$ is the current density, $A_1\equiv A_{\tau=0}$, $A_2\equiv A_\tau$, $\vec{k}_1=\vec{k}_{\tau=0}$, $\vec{k}_2=\vec{k}_1+\vec{\tau}$. The expressions for J_1 for k_1 independent on z was obtained in [19].

When more than two waves participate in diffraction process, the system (15) should be supplemented with equations for waves A_m, which are similar to those for A_1 and A_2.

Now we can find the equation for phase. From the expressions (8,9) it follows that

$$\frac{d^2\phi_m}{dz^2}+\frac{1}{v}\frac{dv}{dz}\frac{d\phi_m}{dz}=\frac{dk_m}{dz}+\frac{k_m}{v^2}\frac{d^2z}{dt^2}, \qquad (17)$$

Let us introduce new function $C(z)$ az follows:

$$\frac{d\phi_m}{dz}=C_m(z)e^{-\int_0^z\frac{1}{v}\frac{dv}{dz'}dz'}=\frac{v_0}{v(z)}C_m(z), \qquad (18)$$
$$\phi_m(z)=\phi_m(0)+\int_0^z\frac{v_0}{v(z')}C_m(z')dz'$$

Therefore,

$$\frac{dC_m(z)}{dz}=\frac{v(z)}{v_0}\left(\frac{dk_m}{dz}+\frac{k_m}{v^2}\frac{d^2z}{dt^2}\right). \qquad (19)$$

In the one-dimensional case the motion equation can be written as:

$$\frac{d^2z_\alpha}{dt^2}=\frac{e\vartheta}{m\gamma(z_\alpha,t,p)}\mathrm{Re}E(z_\alpha,t), \qquad (20)$$

therefore,

$$\frac{dC_m(z)}{dz}=\frac{v(z)}{v_0}\frac{dk_m}{dz}+ \qquad (21)$$
$$+\frac{k_m}{v_0v(z)}\frac{e\vartheta_m}{m\gamma^3(z,t(z),p)}Re\{A_m(z,t(z))e^{i\phi_m(z,t(z),p)}\},$$
$$\frac{d\phi_m(t,z,p)}{dz}|_{z=0}=k_{mz}-\frac{\omega}{v},\ \phi_m(t,z,p)|_{z=0}=p,$$
$$A_1|_{z=L}=E_1^0,\ A_2|_{z=L}=E_2^0,\ A_m|_{t=0}=0,\ m=1,2,$$
$$t>0,\ z\in[0,L],\ p\in[-2\pi,2\pi],$$

L is the length of the photonic crystal.

These equations should be supplied with the equations for $\gamma(z,p)$. It is well-known that

$$mc^2\frac{d\gamma}{dt} = e\vec{v}\vec{E}. \qquad (22)$$

Therefore,

$$\frac{d\gamma(z,t(z),p)}{dz} = \sum_l \frac{e\vartheta_l}{mc^2}\mathrm{Re}\{\sum_l A_l(z,t(z))e^{i\phi_l(z,t(z),p)}\}.$$

The above obtained equations (15,18,21,22) provide to describe generation process in FEL with varied parameters of diffraction grating (photonic crystal). Analysis of the system (21) can be simplified by replacement of the $\gamma(z,t(z),p)$ with its averaged by the initial phase value

$$\langle\gamma(z,t(z))\rangle = \frac{1}{2\pi}\int_0^{2\pi}\gamma(z,t(z),p)\,dp.$$

Note that the law of parameters change can be both smooth and stepped.

Analysis of such a system shows that its efficiency significantly exceeds efficiency of a system with constant parameters. Use of photonic crystals provide to develop different VFEL arrangements (see Fig.2). It should be noted

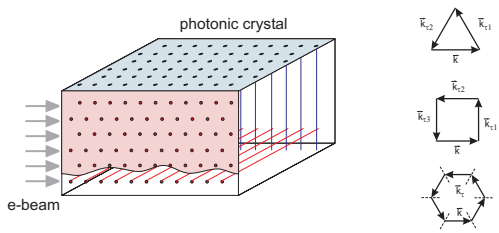

Figure 2: An example of photonic crystal with the thread arrangement providing multi-wave volume distributed feedback. Threads are arranged to couple several waves (three, four, six and so on), which appear due to diffraction in such a structure, in both the vertical and horizontal planes. The electronic beam takes the whole volume of photonic crystal.

that, for example, in the FEL (TWT,BWO) resonator with changing in space parameters of grating (photonic crystal) the electromagnetic wave with depending on z spatial period is formed (see eq. (6)). This means that the dynamical undulator with depending on z period appears along the whole resonator length i. e. tapering dynamical wiggler becomes settled. It is well known that tapering wiggler can significantly increase efficiency of the undulator FEL. The dynamical wiggler with varied period, which is proposed, can be used for development of double-cascaded FEL with parameters changing in space. The efficiency of such system can be significantly higher that of conventional system. Moreover, the period of dynamical wiggler can be done much shorter than that available for wigglers using static magnetic fields. It should be also noted that, due to dependence of the phase velocity of the electromagnetic wave on time, compression of the radiation pulse is possible in such a system.

CONCLUSION

The electrodynamic properties and lasing in Volume Free Electron Laser with a "grid" resonator ("grid" photonic crystal) with changing in space parameters are considered. The equations describing lasing of VFEL with such a resonator are obtained. It is shown that use of diffraction gratings (photonic crystal) with variable period increases radiation intensity and provide to create the dynamical wiggler with variable period. This makes possible to develop a double-cascaded FEL with variable parameters, which efficiency can be significantly higher then that of conventional system.

REFERENCES

[1] B.M.Bolotovskii and G.V.Voskresenskii, Usp. Fiz. Nauk. **88**, 209 (1966) (Sov. Phys. Usp. **9**, 73 (1966)).

[2] R.Kompfner, Wireless World **52**, 369 (1946).

[3] R.Pierce, Proc. IRE **35**, 111 (1947).

[4] S.J.Smith and E.M.Purcell, Phys. Rev. **92**, 1069 (1953).

[5] W.W.Salisbury, US Patent 2,634,372 (1953); J.Opt. Soc.Am. **60**, 1279 (1970).

[6] G.Doucas, J.H.Mulvey, M.Omori et al., Phys.Rev.Lett. **69**, 1761 (1992); John E. Walsh US Patent 5,790,585 (1996).

[7] V.G.Baryshevsky, NIM **445A**, 281 (2000); LANL e-print archive physics/9806039.

[8] V.G.Baryshevsky, K.G.Batrakov, A.A.Gurinovich et al., NIM **483A**, 21 (2002).

[9] V.G.Baryshevsky, K.G.Batrakov, A.A.Gurinovich et al., NIM **507A**, 137 (2003).

[10] V.L.Granatstein, R.K.Parker and C.M.Armstrong, Proceedings of the IEEE **87**, no.5 (1999).

[11] V.G.Baryshevsky, K.G.Batrakov, I.Ya.Dubovskaya, et al., NIM **393A**, 71 (1997).

[12] V.G.Baryshevsky, A.A.Gurinovich, LANL e-print archive: physics/0409107.

[13] V.G.Baryshevsky, K.G.Batrakov, N.A.Belous et al., LANL e-print archive: physics/0409125.

[14] V.G.Baryshevsky, A.A.Gurinovich, to be published in NIM B, Topical Issue RC2005.

[15] V.G. Baryshevsky, N.A. Belous, V.A. Evdokimov et al., LANL e-print arXiv: physics/0605122.

[16] R.W. James, *The Optical Principles of Diffraction of X-Rays* (Ox Bow Press, 1982).

[17] Shih-Lin Chang, *Multiple diffraction of x-rays in crystals* (Springer-Verlag, 1984).

[18] S.Takagi, Acta Crystall. **15**, 1311 (1962).

[19] K.G.Batrakov and S.N.Sytova, Computational Mathematics and Mathematical Physics **45**, No.4, 666 (2005).

LASER GAIN AND INTRA-CAVITY LOSSES OF THE ELBE MID-IR FEL

U. Lehnert, P. Michel, W. Seidel, J. Teichert, R.Wünsch
Forschungszentrum Rossendorf, PF 510119, 01328 Dresden, Germany.

Abstract

The U27-FEL of the ELBE radiation source allows to choose between five mirrors with different outcoupling holes. This allows to adapt the optical resonator to the required wavelength range to ensure the needed laser gain and to optimize the outcoupled laser power.

Another parameter which influences the achievable laser gain and output power is the detuning length of the optical cavity. While for CW operation often the minimum detuning point is choosen which maximizes the outcoupled power, for pulsed-mode operation about one wavelength of cavity detuning maximizes the laser gain and yields best stability of the laser.

To gain some insight into the behavior of the optical resonator we have measured the round-trip losses and the net laser gain and compared both to calulations. We have used a fast-readout MCT detector to measure the decay and rise-time of the outcoupled infrared beam caused by a 10 μs break in the electron beam micro-pulse train. We show gain and loss for 5, 10 and 20 μm wavelength with the typical detuning curves of an FEL.

INTRODUCTION

The U27 mid-IR FEL of the ELBE radiation source was designed to cover a wavelength range from 3 to 20 μm. The optical resonator is equipped with two spherical mirrors with a free propagating optical mode of fixed Rayleigh length. Therefore, the optical mode size at the mirrors shows a big variation over the whole wavelength range. To achieve a suitable outcoupling different sizes of the outcoupling hole are required. The mirror chamber containing the outcoupling mirror was designed with a mirror wheel which allows to choose between 5 different mirrors. At present outcoupling holes from 1.5 to 4 mm are available. Now, the fraction of outcoupling can be adjusted to ensure the needed laser gain and to optimize the outcoupled laser power.

GAIN AND LOSS MEASUREMENTS

For measurements of the laser gain and round-trip losses of the optical cavity we switch off the electron beam for a 10 μs period. An MCT detector with a fast readout electronics is used to measure the decay and rise of the optical power (see Fig. 1). The decay can easily be fitted by a single exponential giving the optical losses per round-trip.

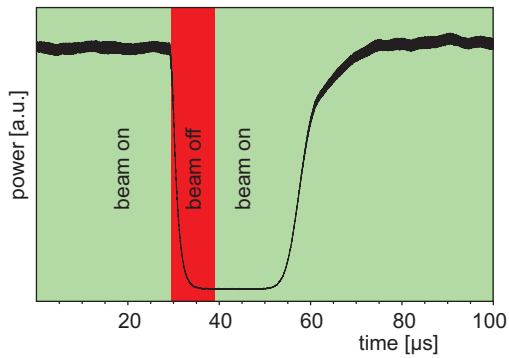

Figure 1: Decay and rise of the optical power caused by a 10 μs break of the electron beam.

ROUND-TRIP LOSSES

Round-trip losses inside the optical cavity were computed using the GLAD [1] code (see Fig. 2). The computation (totals shown with red triangles) includes the outcoupling of optical power (blue circles) as well as diffraction losses due to the aperture limits of the optical beam path in

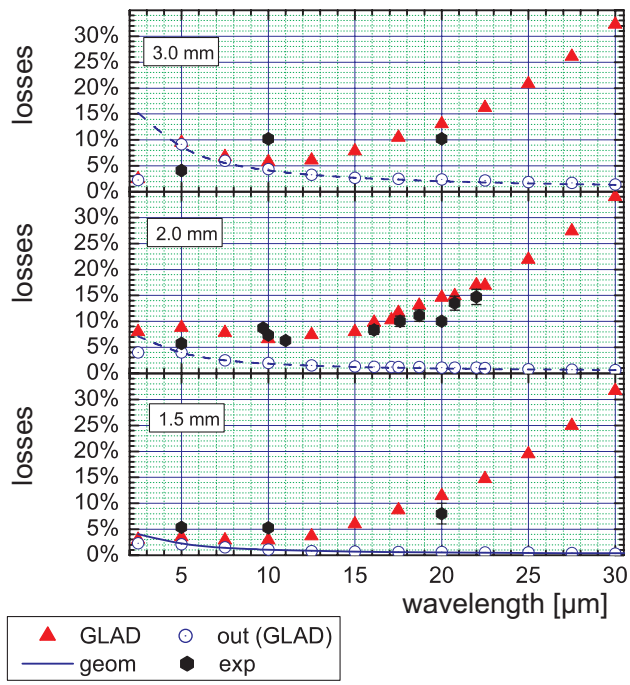

Figure 2: Comparison of measured and computed values of the round-trip losses inside the FEL resonator.

Table 1: Parameters of the optical resonator of the U27 FEL measured at 10 μm wavelength for different sizes of the outcoupling hole. The intra-cavity power is estimated using the computed fraction of outcoupling. To scale it to the saturation power a pulse length of 2 ps was assumed which was previously measured for a minimum-detuning setting of the optical resonator.

out-coupling hole size	1.5 mm	2.0 mm	3.0 mm
measured average power	16.8 W	24.8 W	13.9 W
measured round-trip losses	5.25 $\pm$ 0.25 %	7.25 $\pm$ 0.25 %	10.0 $\pm$ 0.6 %
computed round-trip losses	2.9 %	6.6 %	5.8 %
out-coupled fraction	1.1 %	2.0 %	4.4 %
average intra-cavity power	1600 W	1300 W	330 W
intra-cavity saturated power	62 MW	50 MW	13 MW

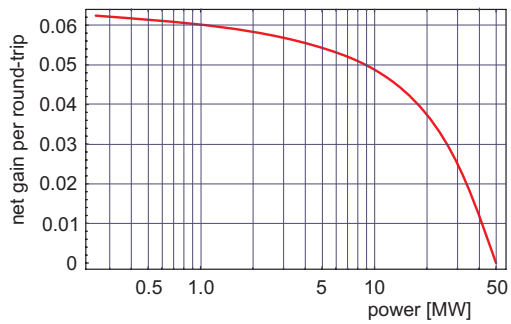

Figure 3: Analytical model of the gain drop at high laser powers approaching saturation.

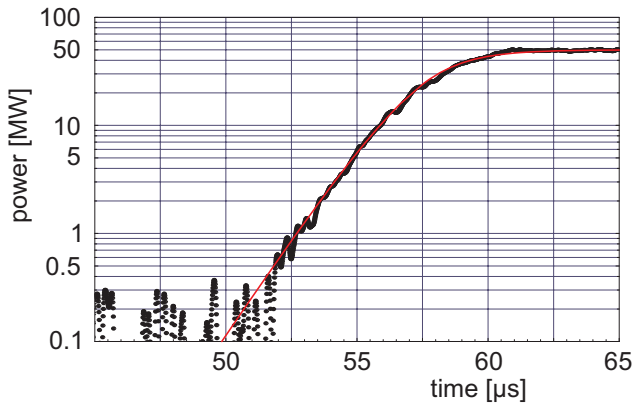

Figure 4: The rise of the optical power computed from the model in Fig. 3 very well fits the measured power data.

particular inside the undulator. The amount of outcoupling very well agrees with a simple geometrical model (blue line) except for very short wavelengths where the optical mode has a tendency to avoid the outcoupling hole. The latter effect was seen experimentally as well. At 5 μm wavelength the measured losses were significanly smaller when using the 3 mm outcoupling hole than with the 1.5 mm or 2 mm holes. In general, the measured round-trip losses show a quite reasonable agreement with the computation.

LASER GAIN AND POWER

The rise of the optical power is determined by the net laser gain. However, the rise curves shown in Fig. 1 need a more involved analysis as the gain itself depends on the optical power. We use a simple analytical model (see Fig. 3) to simulate the gain drop at high powers caused by overbunching and wave-breaking effects. This model very well fits the measured curves of the laser turn-on as shown in Fig. 4. In the example shown we have a 6% small-signal gain over 7% round-trip losses. The laser saturates at 50 MW optical power. At this point the gain has dropped to just match the losses.

THE OPTIMAL OUTCOUPLING

The measurements performed at 10 μm wavelength demonstrate that there exists an optimal outcoupling hole for a given cavity and beam setup. The data shown in Table 1 were measured with a 22 MeV electron beam with 50 pC bunch charge. The round-trip losses roughly correspond to the computed ones considering that the losses at the mirror surfaces are not included in the calculations. Going from 1.5 mm to 2 mm outcoupling hole size one sees the expected rise of the losses (approx. 2%) due to the outcoupling and the increased diffraction losses at the hole. At this power level the gain changes quite rapidly with the power. So the needed 2% higher gain translates only into a small drop of the intra-cavity power. The outcoupled power is increased. But when going further to 3 mm hole size the increased losses yield a much lower saturation power inside the cavity. Despite the higher outcoupling fraction the outcoupled power drops. The measured power levels again roughly confirm the gain model shown in Fig. 3.

REFERENCES

[1] GLAD, Applied Optics Research, Woodland, WA 98674, USA.

REMOTE CONTROLLED IR-DIAGNOSTIC STATION FOR THE FEL AT ROSSENDORF

W. Seidel, S. Friebel, R. Jainsch, M. Justus, K.-W. Leege, D. Proehl, D. Stehr, H. Weigelt, S. Winnerl, D. Wohlfarth
Forschungszentrum Rossendorf, Dresden, Germany

Abstract

The remote controlled diagnostic station delivers a small amount of the IR radiation by means of a system of relocatable mirrors, scraper mirrors and beam splitters to the spectrometer and to various power detectors working in different power ranges. Furthermore, a long wavelength MCT detector is integrated in the diagnostic station for gain and loss measurement in the whole wavelength range of the U27-FEL. The average FEL power for the users can be reduced by a remote controlled attenuator. We have built a non-collinear background-free autocorrelator as a part of the diagnostic station to characterize the optical micropulse duration. By using a CdTe single-crystal for second-harmonic generation a broad wavelength coverage is obtained. In order to decrease the average radiation power of the Rossendorf FEL, as required for certain experiments, the repetition rate can be reduced from 13 MHz to 1 kHz. For that aim a semiconductor plasma switch excited by a synchronized Nd:YAG amplifier is under commissioning and first results will be presented.

INTRODUCTION

The Radiation Source ELBE [1] at the Forschungszentrum Rossendorf in Dresden is centered around a superconducting Electron Linear accelerator of high Brilliance and low Emittance (ELBE), constructed to produce CW electron beams up to 1 mA beam current at 40 MeV. The electron beam is used to generate various kinds of secondary radiation, mainly to drive free-electron lasers in the infrared region (3-150 μm). Starting in the summer 2005, beam time is offered to external users in the frame of the EC funded "Integrating Activity on Synchrotron and Free Electron Laser Science" (FELBE project [2]). It is of great importance for routine user operation at ELBE that after changing the beam path or after beam interruptions stable operation in all wavelength ranges can be provided within a very short time (some minutes). Extensive diagnostics for the optical components of the FEL are very important to achieve fast availability.

DIAGNOSTIC STATION

Remote Controlled Power and Wavelength Measurement

We have developed an optical beam diagnostic system (see Fig. 1) to properly characterize and adapt the output of the two FELs (U27 and U100). The present system is

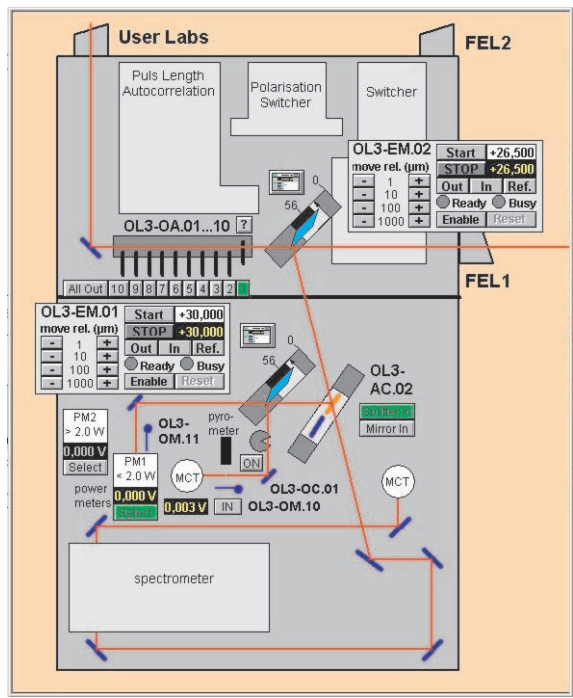

Figure 2: Interface of the remote controlled part of the IR-diagnostic station. One attenuator, two scraper mirrors on stepper controlled stages, one mirror and one beam splitter on a common pneumatic stage, spectrometer and different power meters are indicated. The red lines show different paths for the radiation when both scraper mirrors are not entirely within the beam.

compatible with a tuning range from 3 μm to 150μm, and can be extended beyond 150 μm, if necessary.

The FEL beam from each undulator will be transported separately from the resonator to the diagnostic area through beam pipes using reflective optics. Both lines will be merged on the diagnostic table, which may be purged with dry nitrogen to avoid absorption in air, if necessary. From here both the beams follow the same path. From the main beam, approximately 1-5 percent of the total power will be separated by a scraper mirror on a translation stage for wavelength measurement and power monitoring. The transmitted beam passes an attenuator and can be delivered to 6 optical laboratories. In this attenuator precisely fabricated metal grids diffract a calibrated (3,5, and 3 $\times$ 10 dB) percentage of power out of the beam. The rejected power is absorbed in the walls of the housing. The mode structure and other properties of the transmitted beam in-

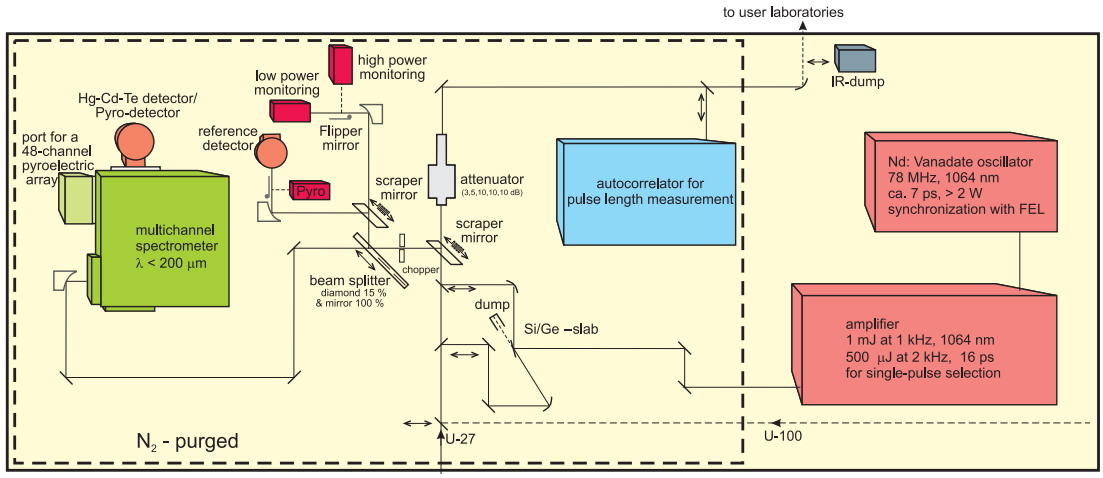

Figure 1: Arrangement of the different optical components and devices on the table.

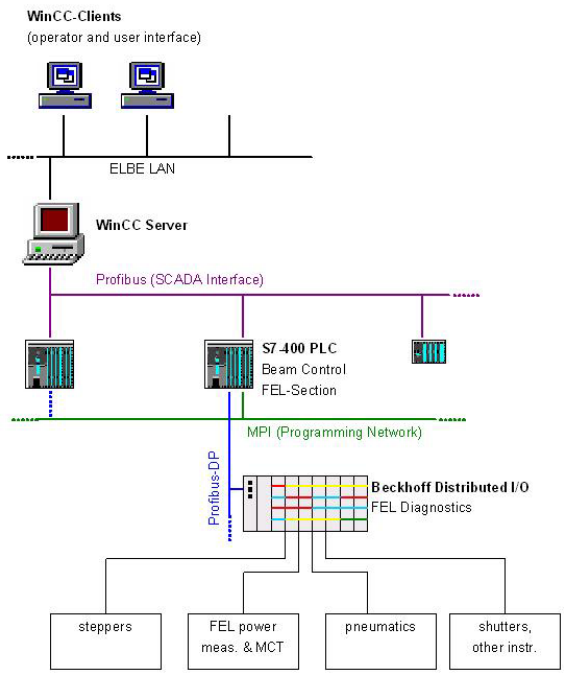

Figure 3: The existing Programmable Logic Control (PLC) and Human-Machine-Interface (HMI) environment of ELBE with the integrated FEL diagnostics instrumentation.

cluding the divergence and the M^2 parameters are fully preserved, the polarisation as well. The deflected part of the power goes through a synchronized chopper for measurement in CW-mode. Next to this the outcoupled beam is deflected by a mirror or a diamond beam splitter (350 μm thick, under 45 degrees, deflection 15 %) at a pneumatic translation stage. The beam transmitted through the diamond beam splitter (85 %) is transported to the spectrometer. The spectrum is measured with a Czerny-Turner type spectrometer which contains a turret with three different gratings to cover the whole wavelength range from 3 μm to about 200 μm. The monochromator will be equipped in near future with a 48-channel pyroelectric linear array detector. We use the second side exit slit equipped with a single Hg-Cd-Te or Ge-Ga detector for measurements with higher sensitivity. The part reflected from the pneumatic device is distributed with an other scraper mirror and two flipper mirrors to different power meters and reference detectors for monitoring the lasing process (see Fig. 2). The FEL diagnostic instrumentation has been integrated into the existing Programmable Logic Control (PLC) and Human-Machine-Interface (HMI) environment of ELBE (see Fig. 3). It ensures the access both for operators and users of the FEL. The basic technologies used are the WinCC server/client system, the SIMATIK PLC system and distributed I/O by Beckhoff Automation for control of pneumatic components (i.e. attenuators), analogue data logging (FEL power, MCT) and other instrumentation. The stepper control drivers for the scraper mirrors are integrated system components, whereby using (expensive) separate controllers could be avoided.

Characterization of the Optical Pulse

The optical pulse length can sensitively be tuned by varying the resonator length with respect to the nominal length resulting from the electron bunch repetition rate. At minimum detuning one yields the highest saturated power and the shortest optical pulse length. By detuning the resonator the spectral width can be decreased simultaneously increasing the pulse length. To characterize the ultrashort pulses generated by the FEL we built a non-collinear background-free autocorrelator system. We used a CdTe crystal as SHG medium [3], since it is transparent for a wide wavelength range in the FIR. We measured the autocorrelation function at maximum power in the detuning curve at a wavelength of 11.09 μm (see Fig. 4, upper part). We deduced a pulse duration of 0.89 ps (FWHM), assuming a Gaussian temporal pulse shape. The measured FWHM of the spectrum is approx. 176 nm. The cal-

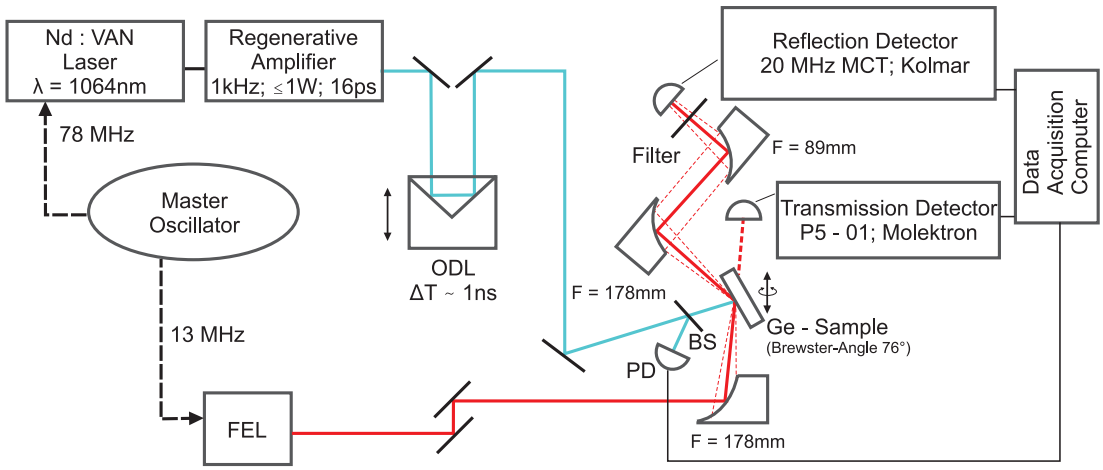

Figure 5: Setup for the plasma switch (see below).

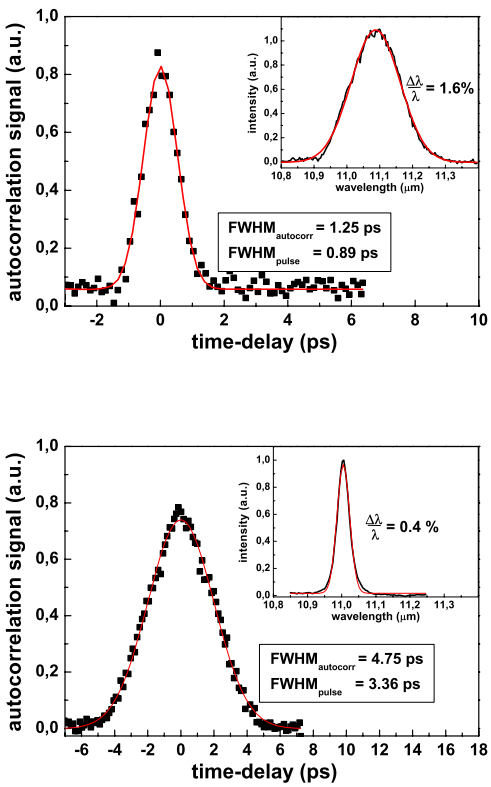

Figure 4: Pulse duration and the corresponding FWHM of the wavelength of 11 μm at maximum of the detuning curve (upper part) and from a detuned resonator (lower part).

culated time-bandwidth product is about 0.4 which indicates Fourier-transform limited operation. Long IR pulses with narrow bandwidth can be obtained from a detuned resonator (see Fig. 4, lower part).

Extraction of Single FEL Radiation Pulses Using a Laser-Activated Plasma Switch

In order to decrease the average radiation power of the Rossendorf free-electron laser FELBE, as required for certain experiments (high pulse energies but moderate or low average power), the FEL repetition rate can be reduced from 13 MHz to 1 kHz. To this end, plasma switching of FEL radiation pulses was demonstrated. The plasma switch bases on the principle of photo-induced reflectivity by an optically excited electron-hole plasma [4, 5]. Germanium serves as semiconductor material for the switch. The semiconductor was illuminated by a Nd:YAG laser amplifier system (1 kHz, λ = 1064 nm, $\tau \sim 16$ ps, $\leq$1 Watt), generating an electron-hole plasma on the front surface of the semiconductor. The generation of sufficient plasma density leads to a variation of the optical semiconductor properties for the infrared FEL-radiation (strongly focused and under Brewster's angle). For realizing the pulse selection the frequencies of both laser sources (FEL and Nd:YAG) were synchronised with RF electronics. For the exact timing of both laser pulses, when they hit the semiconductor, they were detected with a photon-drag detector or a fast pyroelectric detector (FEL) and a photo diode (Nd:YAG) and were adjusted on each other with cables, phase-shifter (trombone) and through moving a precision linear stage. Fig. 5 shows the experimental set-up. A gold mirror served as a reference for determining the reflectivity of the Germanium. The selected FEL pulses were detected by a fast MCT detector with a bandwidth of 20 MHz. Fig. 6 shows the switched pulse in two amplitude scales. The signal from the switch laser (photo diode) is shown in red. From the comparison of the black and blue curves we obtained an amount of dark pulses in the switched beam of about 0.5 % due to the angle of beam spread from the focussing. The time-resolved measurement of the reflectivity yields an exponential decay with a time constant of 590 ps. For the highest value of the Nd:YAG laser amplifier peak fluence of 25 mJ/cm^2, a reflectivity of Ge for FEL radi-

ation ($\lambda = 11\mu m$) of 100 % was achieved (see Fig. 7). We thus succeeded to extract single FEL radiation pulses out of the 13 MHz pulse train, indicating that this plasma switch is most suitable for the Rossendorf FEL. Further examinations will concentrate on achieving similar results for shorter wavelength. To integrate this plasma-switch into the existing diagnostic station we have to build an additional by-pass to the Germanium or Silicon slab which is under Brewster's angle (see Fig. 1). The selcted micro pulse will be refocused to the waist parameters outside of the by-pass line and transported to the user stations.

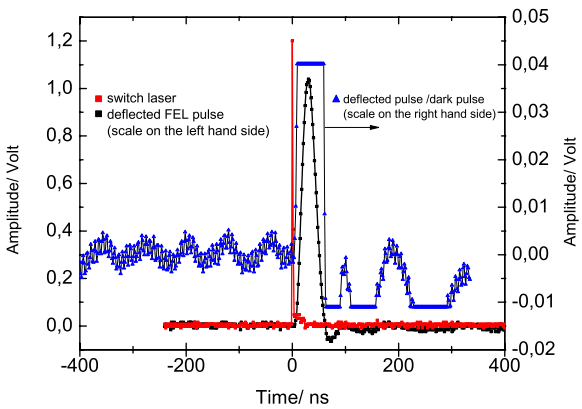

Figure 6: The switched FEL pulse at 11 μm in two different amplitude scales is measured by a fast MCT detector with a bandwidth of 20 MHz. The signal from the switch laser (photo diode) is shown in red. From the comparison of the black and blue curves we obtain an amount of dark pulse in the switched beam of about 0.5 %.

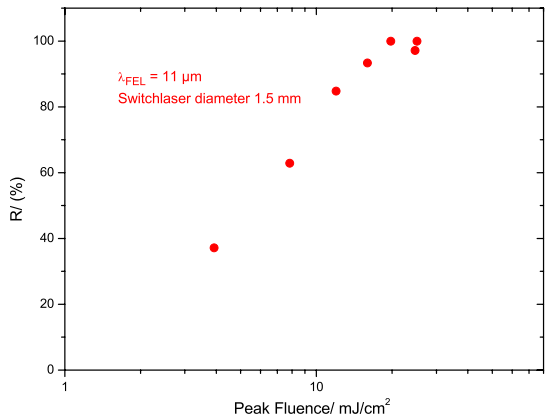

Figure 7: Dependence of reflectivity on the pump-laser peak fluence.

REFERENCES

[1] P. Michel et al., Proceedings of the 2004 FEL Conference, p. 8-13, Trieste, Italy

[2] www.fz-rossendorf.de/felbe

[3] J. Xu, G.M. Knippels, D. Oepts, and A.F.G. van der Meer, Opt. Comm. 197 (2001) 379-383

[4] P. Haar, Ph.D. thesis, Standford University (1996)

[5] E.H. Haselhoff et al., Nucl. Instr. and Meth. A358 (1995) ABS28

THE PARTIAL-WAVEGUIDE RESONATOR OF THE U100-FEL AT FZ ROSSENDORF

M. Freitag, R. Schlenk, W. Seidel, U. Willkommen, D. Wohlfarth, R. Wuensch, B. Wustmann,
FZ Rossendorf, Dresden, Germany.

THE U100-FEL

At the radiation source ELBE [1] an FEL with a permanent magnet undulator (U100) [2] has been constructed to extend the wavelength range to above 150 μm. Its lowest wavelength (20 μm) overlaps with the existing U27-FEL (Fig. 1). There is a first experimental evidence that wavelengths below 20 μm, maybe down to 15 μm, can also be reached.

The undulator is composed of 38 magnetic periods, each 100 mm long. The hybrid structure consists of SmCo magnets and soft-iron poles. It guarantees a sufficiently high

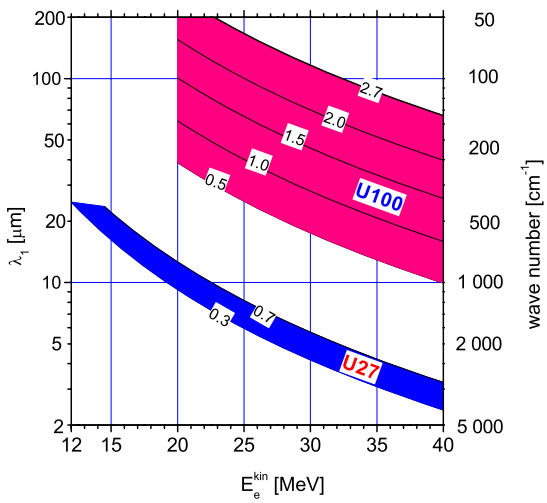

Figure 1: Wavelength λ_1 (fundamental harmonic) of the U27- and U-100 FELs as a function of the kinetic electron energy $E_e^{\rm kin}$ calculated for the indicated undulator parameters $K_{\rm rms}$.

magnetic field at a reasonable undulator gap, and a high radiation resistance. Increasing the gap from 24 to 85 mm the undulator parameter $K_{\rm rms}$ varies from 2.7 to 0.3.

A waveguide was installed to fit the optical resonator mode into the undulator gap. It is 10 mm high and spans over 7.92 m from the undulator entrance to the resonator mirror M2 on the opposite side of the resonator (Fig. 2). The waveguide consists of two parallel plates, each 5 mm thick and divided into three pieces made out of non-magnetic stainless steel. In the horizontal direction the waveguide is wide enough to allow a free propagation of the optical beam. On the upstream side of the electron

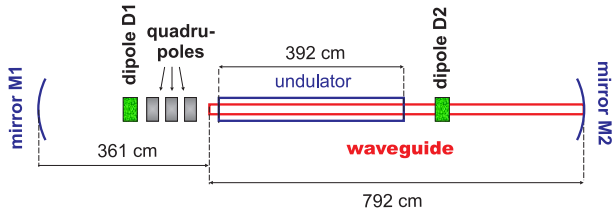

Figure 2: Scheme of the U100 resonator with partial waveguide. The electron beam enters the resonator at the dipole magnet D1 and leaves it at D2.

beam the optical beam propagates freely - both horizontally and vertically - through quadrupole and dipole magnets up to the toroidal mirror M1 with an outcoupling hole in the center.

The partial waveguide causes a series of problems which are not present in the case of an open resonator. The mirrors must have different curvatures in horizontal and vertical direction. Although embedded in the waveguide, the downstream mirror M2 must be movable to adjust beam direction and resonator length. The narrow waveguide complicates the entering of screens and mirrors for beam diagnostics, and impedes the evacuation of the vacuum chamber.

RESONATOR MIRRORS

In the horizontal direction the infrared beam has a Gaussian shape. The curvature of the resonator mirrors corresponds to a Rayleigh length of 180 cm with a waist in the center of the undulator. Within the waveguide the vertical propagation is confined by the upper and lower plate of the waveguide. The downstream mirror M2 is cylindrical and focuses the beam only in horizontal direction. On the opposite side the vertical beam size increases rapidly behind the exit of the waveguide. The size of the beam at the surface of mirror M1 depends strongly on the wavelength. This is illustrated in Fig. 3. The size of the mirrors (black rectangle) covers more than 99% of the beam intensity even at 150 μm.

At the entrance into the waveguide, the optical mode must be converted from a freely propagating one into a waveguide mode and vice versa. This conversion causes optical losses which reduces the net gain of the laser. In general, the curvature of mirror M1 which minimizes the mode conversion losses depends on the wavelength. In our case, the waveguide is sufficiently far away from M1 and we can use a common radius of curvature for all wave-

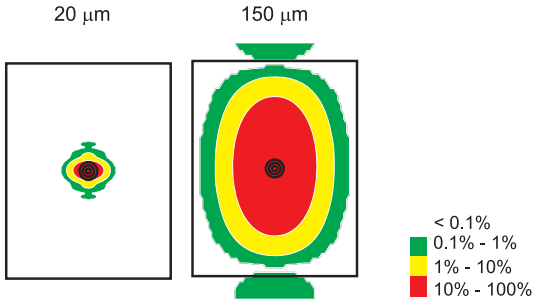

Figure 3: Transverse distribution of the light intensity at the surface of the outcoupling mirror M1 in comparison with the mirror size (black rectangle) calculated for the shortest (20 μm) and the longest wavelength (150 μm). The various colors represent the relative intensity in percent while the small circles in the center indicate the various outcoupling holes.

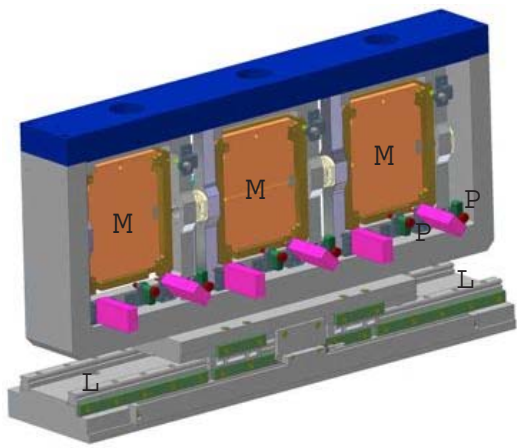

Figure 4: Support for the three mirrors M1. M: mirror, P: piezoelectric drives, L: linear translation stage,

lengths of the operating range of the U100-FEL. Above 35 μm the calculated coupling losses per round trip are below 5% [2]. Only at wavelengths below 25 μm they exceed 10% (simulations by means of the code GLAD [3]).

The beam is outcoupled through a circular hole in the center of mirror M1. Because of the large variation of the beam radius (factor 3) and of the expected laser gain (factor 5) in the operational range of the U100-FEL we need outcoupling holes of different size. We chose a set of 3 mirrors with the same curvature and holes with a diameter of 2, 4.5 and 7 mm. They are mounted on a support (Fig. 4). Using a linear translation stage the appropriate mirror can be shifted into the right position. The mirrors are gold-coated copper mirrors and cooled by water. They can be tilted horizontally and vertically by means of piezoelectric drives.

MIRROR ALIGNMENT AND CONTROL SYSTEM

Fig. 5 shows the scheme of the resonator alignment control system. It is similar to the system developed and used for the U27-FEL [4]. The correct location of the resonator axis is checked by means of two HeNe laser beams introduced into the resonator by auxiliary and pop-in mirrors.

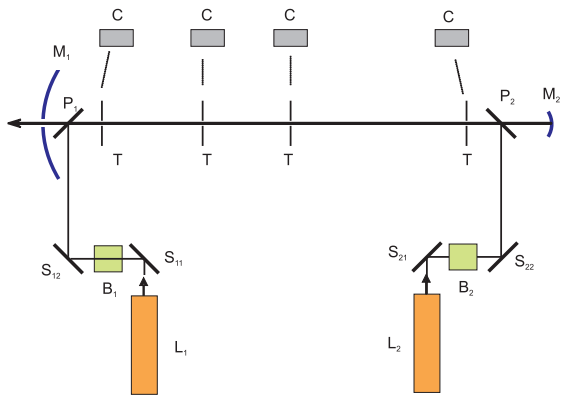

Figure 5: Schematic view of the resonator alignment system. $M_{1,2}$: resonator mirrors, $L_{1,2}$: HeNe alignment lasers, $B_{1,2}$: beam expander, $S_{11,12,21,22}$: steering mirrors, $P_{1,2}$: pop-in mirrors, T: adjustment apertures, C: monitoring cameras

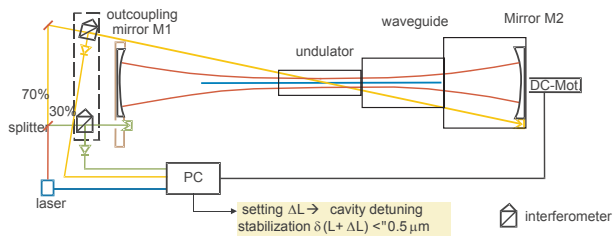

Figure 6: Schematic view of the resonator length control system.

A Hewlett-Packard interferometer system [5] is used for monitoring the resonator length (Fig. 6). It has also been taken from the U27-FEL.

The resonator has to be set and stabilized to a certain length and its axis has to be aligned to the electron beam. For that aim the mirrors are gimbal-mounted and can be tilted horizontally and vertically by means of piezoelectric (M1) and DC drives (M2). They allow the mirrors to be tilted up to 15 mrad in steps of 1 μrad. Moreover the cylindrical mirror M2 can be shifted along the resonator axis by 3.6 mm in steps of 100 nm (hysteresis 2 μm) by means of remote controlled DC drives (Fig. 7). Steps and hysteresis can additionally be reduced by a factor of about 30 by means of a beam in bending. Fig. 8 shows the opened mirror chamber M2.

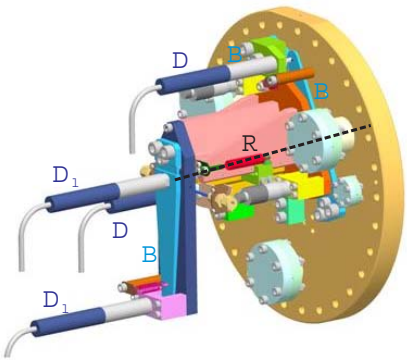

Figure 7: Back side of the flange of mirror chamber M2 with control elements. The mirror is mounted on the center of the front side. Schematic view with DC drives (D) for mirror tilting and shifting (D_l). The broken line (R) indicates the hidden driving rod, which transfers the motion onto the mirror on the front side. The beams in bending are labelled by B.

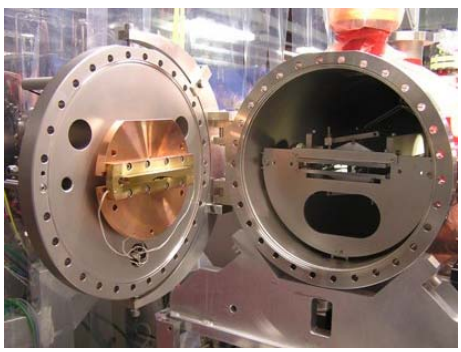

Figure 8: Open mirror chamber M2 with the rectangular cylindrical mirror (left side) and the end of the waveguide (right side).

BEAM DIAGNOSTICS

There is an extensive beam diagnostics system within the resonator region consisting of 20 view screens, markers and auxiliary mirrors. Most of them have to be inserted into the waveguide. They are not allowed to touch the polished surface of the waveguide, which is only 10 mm high. Fig. 9 shows the scheme of an auxiliary mirror with the corresponding insertion unit. The mirror is mounted at the end of a rod extending into the waveguide. The rod can be shifted into the waveguide by means of a pneumatic cylinder. It can precisely be moved along and perpendicular to the resonator axis, and allows an additional torsion of the rod which leads to a controlled and extremely sensitive tilting of the mirror at its head. The accuracy is 30 μm and 5μrad, respectively. Similar insertion units are used for OTR screens (7 mm high) made of beryllium with a 1 mm hole, foil screens consisting of a stretched aluminum foil, and markers (8 mm high) with a hole for the alignment and interferometer lasers. Among them are the pop-in mirrors and apertures used for the resonator alignment system (Fig. 5). CCD cameras in lead housings are used for observing the screens and markers through the viewports (Fig. 9).

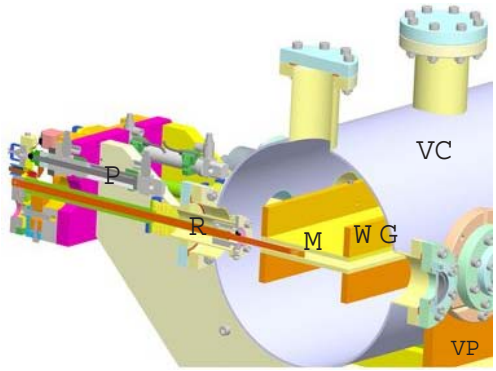

Figure 9: Diagnostic mirror for resonator axis tuning insertable into the waveguide. M: mirror, R: rod, P: pneumatic cylinder, VC: vacuum chamber, WG: waveguide, VP: view port.

Beam positioning monitors with an aperture of 75 mm have been developed for the online measurement of the electron beam position. One of them is located in front of the waveguide entrance.

VACUUM MANIFOLD

The presence of the waveguide does not allow to place the getter pumps directly below the beam line. A vacuum manifold with 6 getter pumps and 7 ports (Fig. 10) is installed below the waveguide instead. Their total throughput amounts to 520 l/s. An additional getter pump with 350 l/s throughput is fixed below each mirror chamber. The electron beam line can be separated by vacuum valves upstream and downstream the resonator. Another valve separates the mirror chamber M1 with the outcoupling window. Additionally, four powerful turbomolecular pumps

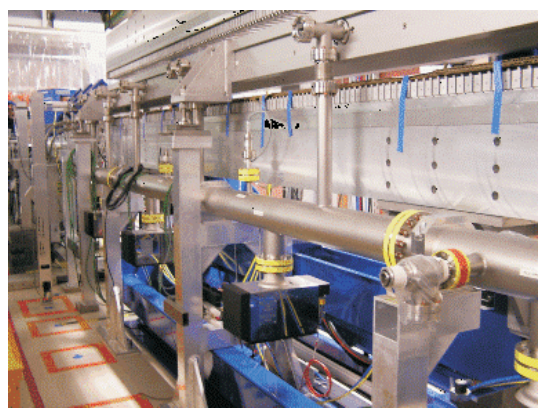

Figure 10: Collective vacuum line with getter pumps and connectors to the waveguide.

are linked to the manifold and to both mirror chamber as

well. They ensure to hold the vacuum in the whole system in the case of a local rise in pressure. Membrane pumps serve as fore-vacuum pumps. In stand-by mode the turbo- and membrane pumps can be switched off.

The system can be vented by means of needle valves with dry and particle-free nitrogen gas. A mass spectrometer allows to analyze the residual gas. The pressure in the vacuum line and in the mirror chambers is measured by means of Penning and Pirani vacuum gage heads.

SUMMARY

At the radiation source ELBE, another free-electron laser has started to produce light in the far infrared region. It is capable of producing IR radiation between 20 and 200 μm. Its resonator was equipped with a partial waveguide to allow a small undulator gap. Curvature and size of the resonator mirrors were adapted to minimimum optical losses. To optimize the outcoupled laser power three mirrors with circular holes of different size were installed on a linear translation stage. The resonator was equipped with a control and alignment laser system which allows to adjust and stabilize the resonator length and to align the resonator mirrors. Special beam diagnostic elements, which can be inserted into the waveguide, and a vacuum manifold were developed to fix the beam position and to ensure an extreme vacuum within the narrow waveguide.

REFERENCES

[1] http://www.FZ-Rossendorf.de/ELBE

[2] E. Grosse et al., FEL'05, Aug. 2005, SLAC, TUPP031, http://www.JACoW.org

[3] GLAD, Applied Optics Research, Woodland, WA 98674, USA.

[4] U. Lehnert et al., FEL'05, Aug. 2005, SLAC, MOPP032, http://www.JACoW.org

[5] U. Lehnert et al., FEL'05, Aug. 2005, SLAC, TUPP030, http://www.JACoW.org

NEW RESONATOR FOR THE ISRAELI FEL

A. Faingersh, Y. Socol, E. Dyunin, J. Dadoun, Kh. Garb, A.Gover[#],
Dept. of Physical Electronics - Faculty of Engineering, Tel-Aviv University,
Tel-Aviv, Israel

M. Einat, B. Litvak, B. Kapilevich, Y. Pinhasi, A. Yahalom,
Dept. of Electrical and Electronic Engineering - The College of Judea and Samaria, Ariel, Israel

G. Denisov, M. Shmelev,
Institute of Applied Physics, Nizhniy Novgorod, Russia

Abstract

The Israeli FEL resonator (W-band 75-110 GHz) was re-designed in order to reduce the overall round-trip losses and to control the radiation out-coupling.

In its new configuration, the resonator consists of an overmoded corrugated rectangular waveguide and two radiation mode splitters, separating the high-energy e-beam from the mm-wave radiation. The electron input splitter is based on Talbot effect in an overmoded rectangular waveguide. The radiation out-coupling takes place in the output splitter. The splitter is based on a novel design. It combines Talbot effect between two parallel plates with free space propagation and with focusing by two curved cylindrical mirrors in a confocal imaging scheme.

The waveguide and the splitters were tested, showing improved performance in comparison with the former resonator. The measured unloaded Q-factor of the new resonator is increased by a factor of ~3, up to Q=25,000. Accordingly, the round-trip losses are ~23%. Rotating grids control the radiation out-coupling, allowing optimization of the radiation power and the extraction efficiency. The design layout and the testing results are presented.

NEW RESONATOR DESIGN

The Israeli FEL with Curved Parallel Plate (CPP) waveguide-based resonator was reported earlier [1-2]. Only a small part (~5%) of the generated RF energy was coupled out in these configuration. In order to minimize the total round-trip losses of the resonator, it was re-designed. The previously used CPP waveguide was substituted by a two-corrugated-walls rectangular waveguide. To separate the laser RF radiation from the electron beam and to out-couple the desired part of the RF energy, the beam output confocal splitter was also designed.

General Layout

The resonator consists of several waveguide sections of different profiles. It is integrated into

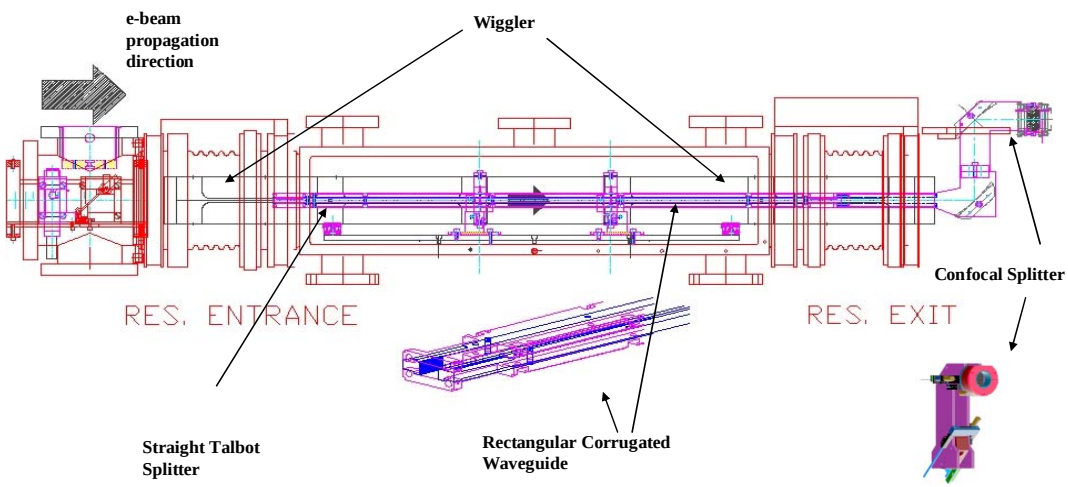

Fig. 1. The resonator lay-out and the scheme of installation of the resonator into the wiggler system.

[#] Corresponding author. Email: gover@eng.tau.ac.il

the wiggler system, so that the interaction between the electron beam and the wiggler magnetic field of takes place inside the waveguide cavity - rectangular corrugated waveguide. The latter is assembled from 4 separate walls, 2 smooth and 2 mill-machined corrugated. This waveguide was designed in such a way that the electron beam at the design energy (1.4 MeV) can interact only with the fundamental mode TE_{01} according to the dispersion relation. The resonator layout installed into the wiggler system is schematically shown in Fig. 1.

In order to obtain positive feedback from the resonator mirrors, two wave splitters were placed at both terminations of the corrugated waveguide. These splitters are reflectors, based on overmoded rectangular waveguides shorted with a mirror at one end.

Confocal Splitter

The confocal splitter is a quasi-optical mm-wave component that based on a novel design. The splitter consists of an overmoded rectangular waveguide and two curved metallic mirrors. The splitter scheme provides the continuous waveguide propagation and Talbot effect in one dimension, and free-space propagation of the radiation in the other dimension (both orthogonal to the direction of propagation). The two parabolic (shaped in the plane of free space propagation) mirrors provide the dispersion-free focusing. The splitter prototype design and the manufactured model photo are shown at fig. 2. Computer simulation of the radiation propagation through the confocal splitter was also performed. The round-trip losses in the splitter were theoretically estimated as 12%, and later measured experimentally to be about 15 %.

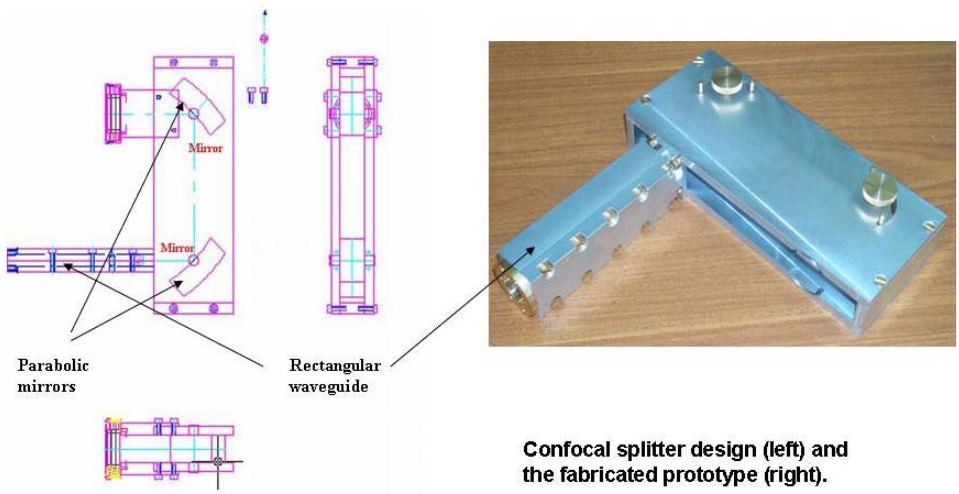

Fig. 2. Confocal splitter design (left) and the fabricated prototype (right).

The length of the input splitter equals to half of the Talbot-effect-optical-imaging length. At this distance, the overmoded (oversized) rectangular waveguide provides splitting of the original field distribution at the termination plane of the waveguide, where the reflecting mirror is placed. This effect allows to make a hole in the metallic mirror (as there is no field in the center), therefore to pass the electron beam through this hole.

The output confocal splitter is of the Talbot-effect-optical-imaging length and it provides the fundamental mode's field reconstruction at the plane of coupling grids that terminate the resonator.

MEASUREMENTS RESULT

After manufacturing of the resonator components, the whole resonator was assembled in the laboratory in order to enable experimental investigation outside the FEL tank. The round-trip reflectivity of the resonator was measured using excitation by special designed corrugated horn mode exciter through the 3-grid tuneable coupler system. In this experiment, the reflected signal from the excited resonator cavity was measured directly and the round trip reflectivity was calculated according to the theory presented in [2], [3].

Calculation of the round trip reflectivity

The algorithm of the round trip reflectivity is based on measurement of the reflection coefficient resonance curve and uses "optical" formulation. The reflection coefficient of the shorted Fabri-Perot resonator is

$$\Gamma = 1 - \frac{\left(R_1 - R_{rt}\right)\left(1 - R_1\right)/R_1}{\left(1 - \sqrt{R_{rt}}\right)^2 + 4\sqrt{R_{rt}}\sin^2\left(\delta/2\right)} \qquad (1)$$

were Γ is the power reflection coefficient, R_1 – reflection of the entering mirror (coupling condition), R_{rt} is the total round trip reflectivity and δ is a phase. On the other hand, choosing the Q factor definition as the ratio between the frequency f_0 (resonant wavelength λ_0) and bandwidth of the resonator mode $\delta f_{1/2}$ (or $\delta\lambda_{1/2}$):

$$Q = \frac{f_0}{\delta f_{1/2}} = \frac{\delta\lambda_{1/2}}{\lambda_0} \qquad (2)$$

As it shown in [2], one can derive:

$$Q = \frac{2\pi L}{\lambda}\frac{\sqrt[4]{R_{rt}}}{1 - \sqrt{R_{rt}}} \qquad (3)$$

were L is the resonator length and λ is wavelength. It should be noted that in Eq. 3 above, Q is the loaded Q-factor since both internal and external (coupling mirror) losses are included. Finally, the round trip reflectivity (or total losses, since R_{rt} = 1-Loss) can be found in terms of Q_{loaded} or directly in terms of FWHM ($\delta f_{1/2}$) of the measured resonator peaks:

$$R_{rt} = \left[-\frac{2\pi L}{\lambda_g Q_{loaded}} + \sqrt{\left(\frac{2\pi L}{\lambda_g Q_{loaded}}\right)^2 + 1}\right]^4 \qquad (4)$$

$$= \left[-\frac{2\pi L\delta f_{1/2}}{v_g} + \sqrt{\left(\frac{2\pi L\delta f_{1/2}}{v_g}\right)^2 + 1}\right]^4$$

were λ_g and v_g are the wavelength and velocity of wave propagation inside the resonator accordingly. The total round-trip reflectivity R_{rt} of the FEL resonator was calculated in the present work based on Eq. 4 and the direct measurement of the FWHM linewidth $\delta f_{1/2}$ of the resonant peaks. This linewidth was obtained from measurement of the power spectral reflection pattern.

CONCLUSIONS

The Israeli FEL resonator was re-designed in order to decrease the internal round-trip losses and thus to achieve threshold current reduction. The novel reflector and splitter based on the quasi-optical confocal scheme, were designed, manufactured and characterized. The round trip losses of the confocal splitter are about 15% (in good agreement with the theoretical limit estimation of 12%). The round trip losses of the overmoded corrugated waveguide and straight Talbot section were measured to be about 8 % for both waveguides. The total losses of the whole resonator system are therefore about 23%.

REFERENCES

[1] A. Faingersh, A. Gover, A. Eliran, and B.Kapilevich "Concluding report: measurements and calculation of round-trip reflectivity in the FEL waveguide resonator before and after modification and estimate of threshold current improvement", Internal report of the FEL group, 25-Aug-06, Tel-Aviv University.

[2] A. Gover, A. Faingersh, at al. "Radiation measurements in the new tandem accelerator FEL", Nuclear Instr. And Methods In Physics Research, A 528 (2004), pp. 23-27.

[3] B. Kapilevich, A. Faingersh, and A. Gover, **"**Accurate determination of Q-factor of a quasi-optical resonator", Microwave and Opt. Tech. Lett., vol.36, No.4, (2003).

PRESENT STATUS OF THE ISRAELI FEL: INCREASING FEL POWER BY ELECTRON BEAM ENERGY BOOSTING

E. Dyunin, M. Volshonok, A.Gover[#],
Dept. of Physical Electronics - Faculty of Engineering, Tel Aviv University, Tel-Aviv, Israel
M. Einat, Y. Lurie, Y. Pinhasi, Y. Socol, A. Yahalom,
Dept. of Electrical and Electronic Engineering – The College of Judea and Samaria, Ariel, Israel

Abstract

The status of a R&D work aimed on increasing the FEL power by boosting the electron beam energy after the radiation build-up is reported. A fine control of the electron beam energy during the radiation pulse is designed to compensate the small energy degradation during the pulse. Also, a controlled ramp (up or down) in the electron energy during the pulse will be applicable.

Theoretical estimations of the output power in the presence of an electron energy change during the pulse are presented. Two models, showing agreement between them are compared: Analytical model based on the pendulum equation, and, Rigorous 3D FEL interaction model solved numerically.

Another expected result of the design is to further extend the pulse duration with stable conditions and to obtain improved coherency.

The electrical and mechanical lay-outs of the high-voltage boosting (leading to electron beam energy boosting) are also presented.

INTRODUCTION

Electrostatic accelerator based FEL's (EA-FEL) are characterised by long pulse operation. Unlike RF-linac FEL's having a pulse width limited by the RF part, the EA-FEL's pulse width is incomparably longer and practically limited by the capability of the power supply to support the system with the required energy. In principle, an ideal power supply can support a CW operation of the FEL. Calculations of a long pulse operation of an FEL, show a saturation regime obtained at the end of the energy build up process, were the output power of the FEL is stable at its maximum. This maximum is related to the FEL characteristics and the operation conditions (such as electron-energy) which are kept constant.

In this paper the possibility of changing the electron energy during the pulse, after the radiation build-up, is considered. Calculations are made in two different methods to estimate the variations in the EA-FEL output power in saturation as a result of change in the electron energy during the pulse. Schematic of a high voltage boost system that supports a change in the electrons energy during the pulse is presented. This system allows a controlled ramp of the electron energy (up or down). This ramp can also be used to compensate the small degradation in the high voltage during the pulse to practically obtain constant electron energy for longer periods. That will lead to improvement of the coherency in the FEL radiation in view of the long pulse operation in constant conditions. In the following sections the two different models are presented and the results are given. Also the designed experimental setup to support the energy variations during the pulse is described.

THE FEL 3-D MODEL

The calculations were carried out in the framework of steady-state, three-dimensional, space-frequency approach, described in more details in [1]. In the approach, the total electromagnetic field oscillated at signal frequency f_s is presented in the frequency domain as an expansion in terms of transverse eigen-modes $\boldsymbol{\varepsilon}_q(x,y)$ of the cavity, in which the field is excited and propagates:

$$\tilde{\mathbf{E}}(\mathbf{r}) = \sum_q C_q(z)\,\boldsymbol{\varepsilon}_q(x,y)\,e^{-j\,k_{zq}\,z} \tag{1}$$

Here the time-domain field is

$$\mathbf{E}(\mathbf{r},t) = \mathrm{Re}\left\{\tilde{\mathbf{E}}(\mathbf{r})\,e^{+j\,2\pi\,f_s\,t}\right\} \tag{2}$$

and $C_q(z)$ is an amplitude coefficient of the mode *q*, which could be found from the excitation equation:

$$\frac{d}{dz}C_q(z) = -\frac{1}{2N_q}e^{+j\,k_{zq}\,z}\iint \tilde{\mathbf{J}}(\mathbf{r})\cdot\boldsymbol{\varepsilon}_q^{\,*}(x,y)\,dx\,dy \tag{3}$$

The power of the electromagnetic field emitted up to the point *z* can be found as follows:

$$P_{EM}(z) = \sum_q |C(z)|^2\,\frac{1}{2}\mathrm{Re}\{N_q\} \tag{4}$$

here N_q is the mode normalization power of the mode *q*.

* Work supported by the Israeli Ministry of Defence
# Corresponding author. E-mail: gover@eng.tau.ac.il

As usually accepted we consider the electron beam as consisting of a number of electron clusters or charged quasi-particles, distributed over the beam. Therefore the excitation current can be given in such a form:

$$\mathbf{J}(\mathbf{r},t) = -\sum_i q_i \mathbf{v}_i \, \delta(x-x_i)\delta(y-y_i)\,\delta[z-z_i(t)] \quad (5)$$

or in the frequency domain:

$$\tilde{\mathbf{J}}(\mathbf{r}) = -2\sum_i q_i \frac{\mathbf{v}_i}{v_{zi}} \delta(x-x_i)\delta(y-y_i)\, e^{-j\,2\pi\, f_s\, t_i(z)} \quad (6)$$

Substitution of the excitation current (6) into the excitation equation (3) enables one to re-write the last as follows:

$$\frac{d}{dz}C_q(z) = \frac{1}{N_q}\sum_i \frac{q_i}{v_{zi}} \mathbf{v}_i \cdot \boldsymbol{\varepsilon}_q^{\,*}(x_i,y_i)\, e^{+j\left[k_{zq} z - 2\pi\, f_s\, t_i(z)\right]} \quad (7)$$

In Eq. (5)-(7) q_i, $\mathbf{v}_i$ and $\mathbf{r}_i \equiv \{x_i, y_i, z_i\}$ are the charge, the velocity and the coordinates of the particle with a number *i*, and

$$t_i(z) = t_{0_i} + \int_0^z \frac{1}{v_{zi}(z')} dz' \quad (8)$$

is the moment when the particle number *i* comes to the point *z*.

With a known field, a next phase-space position of the particles can be found from the equations of motion:

$$\frac{d\mathbf{v}_i}{dz} = -\frac{1}{\gamma_i}\left\{\frac{e}{m}\frac{1}{v_{zi}}\left[\mathbf{E}(\mathbf{r}_i,t) + \mathbf{v}_i \times \mathbf{B}(\mathbf{r}_i,t) + \mathbf{v}_i \frac{d\gamma_i}{dz}\right]\right\} \quad (9)$$

$$\frac{d\gamma_i}{dz} = -\frac{e}{mc^2}\frac{1}{v_{zi}}\mathbf{v}_i \cdot \mathbf{E}(\mathbf{r}_i,t) \quad (10)$$

Figure 1 demonstrates schematically an FEL operated in oscillator regime. In that case some part of the radiation emitted by the beam is reflected by mirrors and returned to the interaction region, been forced to interact with a new portion of the driving current. Then the total electromagnetic field, emitted after *N* round-trips of the radiation in the resonator, may be found by:

$$\tilde{\mathbf{E}}_{tot}(\mathbf{r}) = \sum_q C_q^{tot}(z)\, \boldsymbol{\varepsilon}_q(x,y)\, e^{-j\,k_{zq}\,z} \quad (11)$$

Here the expansion coefficient of the total field is

$$C_q^{tot}(z) = \sum_{n=1}^{N} C_q^{(n)}(z) \quad (12)$$

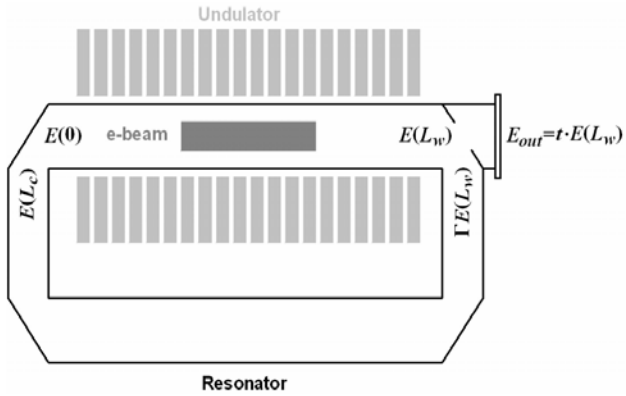

Figure 1: Principal scheme of FEL in an oscillator regime.

and the coefficients of the field emitted after *n* round trips of the radiation are defined by the recursion relation:

$$C_q^{(n+1)}(z=0) = \Gamma\, C_q^{(n)}(z=L_w)\, e^{-j\,k_{zq}\,L_c} \quad (13)$$

The above equations form a closed set of non-linear equations, which enables one to calculate the both radiated field and the beam trajectory. The model was realized in FEL3D numerical code and applied for the calculations considered in the next section.

THE "PARAMETRIC" PENDULUM EQUATION MODEL

The oscillation build-up and saturation process of the FEL oscillator were analyzed numerically in Ref. [3,4]. At saturation the radiation field inside the cavity is built up, and the small signal assumptions are not valid. The electron dynamics is described in the combined wiggler and radiation wave fields (the ponderomotive wave) in terms of the pendulum model [5]:

$$\frac{d^2\Psi}{dz^2} = -K_s^{\,2} \sin\Psi \quad (14)$$

$$\theta = \frac{d\Psi}{dz} \quad (15)$$

where $\Psi(z)$ is the phase of the electron relative to the ponderomotive wave: $\Psi(z) = \int_0^z \theta(\omega,z')dz' + \Psi_0$, and the detuning parameter is $\theta(\omega,z) = \frac{\omega}{v_z(z)} - k_{zq}(\omega) - k_w$. $k_{zq}(\omega)$ is the axial wavenumber of mode q, and $k_w = 2\pi/\lambda_w$ is the wiggler wavenumber. The Synchrotron oscillation wavenumber K_s is given by

$$P = A_p \overline{K}_s^4 \tag{16}$$

$$A_p = \frac{1}{2\pi^2} \cdot \frac{\left(\gamma_0 \gamma_z \beta_z^2\right)^4}{a_w^2} \cdot \frac{A_{em}\lambda^2}{L^4} \cdot \frac{\left(mc^2/e\right)^2}{Z_q} \tag{17}$$

where **E** and P are the circulating radiation field and power in the saturating oscillator cavity (we assume high round-trip resonator reflectivity, and therefore constant power -P along the resonator).

As well known, the pendulum equation (14) can be integrated once, resulting in a picture of open and closed trajectories in $\theta - \Psi$ phase-space (Fig. 2). This picture can also be viewed as a display of electron energy vs. phase trajectories, if one uses the differential linear relation between γ and θ near the synchronism energy γ_0 (Fig. 3).

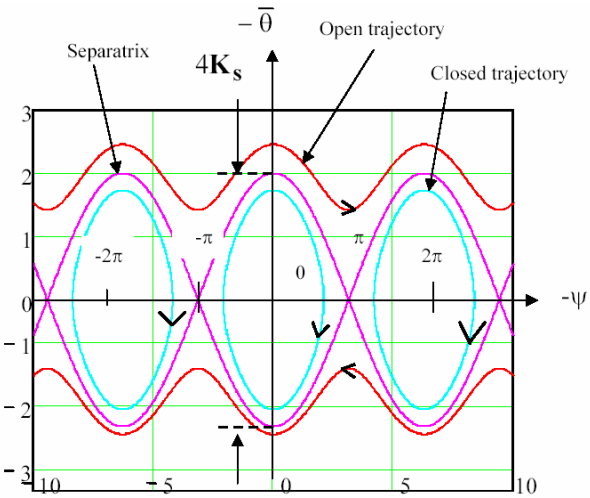

Figure 2: Phase-Space Trajectories of the Pendulum Equation.

OSCILLATION BUILD-UP EA-FEL

The oscillation build-up dynamics as a result of the two models are presented in Fig. 4. all the calculations are made for a single frequency. The result for a constant electron energy (1.42 MeV)) is shown in green. This calculation is done by the pendulum equation model. For the same frequency, a case with a step in the electron energy is calculated (red curve). The initial voltage is 1.4 MV and saturation is obtained. Than a voltage step is applied to 1.42 MV. As a result a new saturation level is obtained which is higher that the former level of a stable voltage. Thus, for the same final (i.e 1.42 MV) conditions two saturation levels are possible.

A verification of the red curve behaviour is obtained by the FEL 3D model (violet curve). Although different levels of saturation are obtained, the behavior is similar, where a jump in the saturation level is obtained. The differences between the models can be related to the differences in the assumptions in the models.

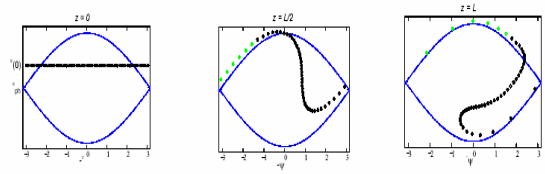

Fig. 3: Dynamics of electron beam trapping and synchrotron oscillation at steady state saturation stage of an FEL oscillator.

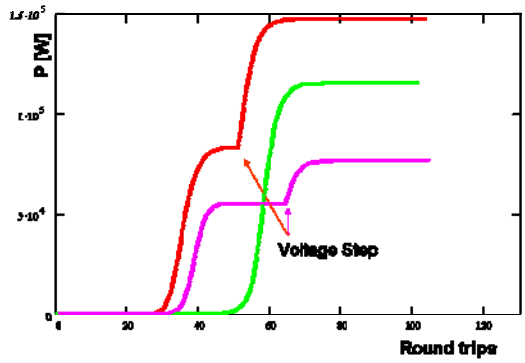

Fig. 4: The oscillations build-up in EA-FEL with constant electron energy and with a step in the energy during the pulse after saturation:
Constant Terminal Voltage 1.42 MV (PE) – Green,
Voltage Step from 1.4 to 1.42 MV (PE) – Red,
Voltage Step from 1.4 to 1.42 MV (FEL3D) – Violet.

ENERGY BOOST SYSTEM

Since the EA-FEL is capable of a long pulse operation, a coherent operation in high power is applicable [6]. Still. A practical experimental difficulty is the electrons the hit the terminal parts and reduce the voltage. These electrons can be related to non-ideal transport conditions and to returning electrons that could not reach the collector. This phenomena cause a drift in radiation frequency that is related to the drift in the voltage drop. Correcting this voltage drop was one of the motivations to the work presented here. But, if a correction system is designed, it can be used to more than a voltage correction but also to voltage control in a desired manner such as a ramp.

The voltage ramp control system is presented in Fig. 5. it is placed in the high voltage terminal and its output is added to the terminal voltage. A capacitor is charged to voltage of up to 30 kV. During the pulse it is partly discharge through a selected resistor to the terminal. Therefore the voltage of the terminal is raised. By selecting the resistor and voltage the rate of the voltage raise can be determined. Therefore a compensation to the electrons hitting the terminal can be achieved in order to stabilize the voltage conditions and as a result the frequency as well.

Also a ramp (positive or negative) in the voltage can be applied in order to enhance the saturation level as predicted by the theory.

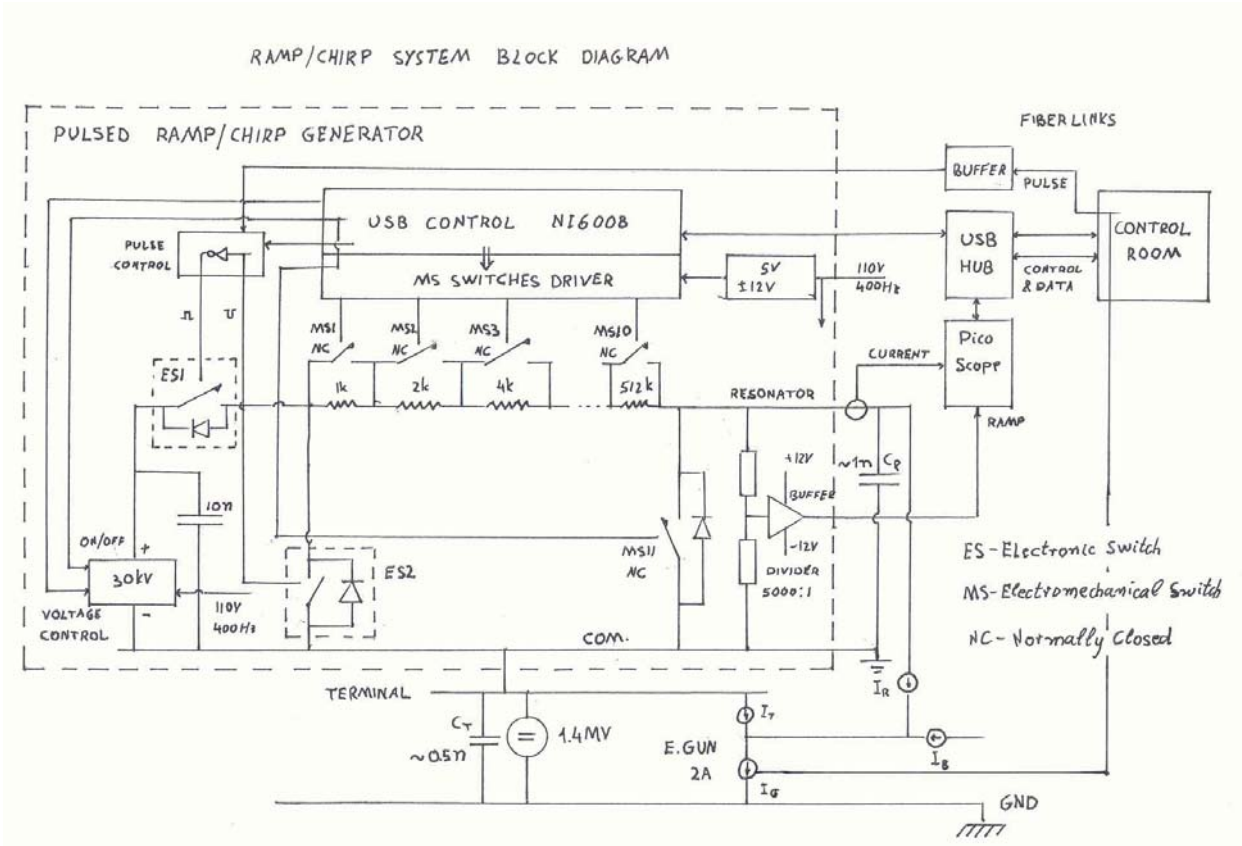

Fig. 5: The voltage ramp control circuit.

CONCLUSION

The possibility to achieve higher extraction efficiency and therefore higher operation power of the EA-FEL by electron energy step is theoretically possible.

Bi-stable saturation conditions are obtained for different initial conditions. An experimental setup is under construction in order to demonstrate the effect

REFERENCES

[1] Y. Pinhasi, A. Gover, and V. Shterngartz, Phys. Rev. E **54**, 6774 (1996)

[3] M.V. Krongaus, Y. Pinhasi, M. Tecimer, A. Gover, Nucl. Inst. and Meth .Phys. Res. A445, 28 (2000).

[4] M.V. Krongauz, Y. Pinhasi, A. Gover, "Dynamics and control of power build-up in a pre-bunched FEL", unpublished.

[5] A. Gover, E. Dyunin, Y. Lurie, Y. Pinhasi, M. V. Krongauz, "Superradiant and stimulated superradiant emission in prebunched electron-beam radiators - part II : Radiation enhancement schemes", Phys. Rev. ST – Acc. Beams Vol. 8, 030702 (2005).

[6] Y. Socol, A. Gover, A. Eliran, M. Volshonok, Y. Pinhasi, B. Kapilevich, A. Yahalom, Y. Lurie, M. Kanter, M. Einat, and B. Litvak, "Coherence limits and chirp control in long pulse free electron laser oscillator", Phys. Rev. ST – Acc. Beams Vol. 8, 080701, (2005).

DYNAMICS CONTROL OF THE ELETTRA STORAGE RING FREE-ELECTRON LASER WITH DIGITAL FEEDBACKS

E. Allaria#, G. De Ninno, Sincrotrone Trieste, 34012 Trieste, Italy
A. Antoniazzi, D. Fanelli, Dept. of Energetics, University of Florence, Florence Italy.

Abstract

The laser dynamics of a storage-ring free-electron laser has two main sources of instabilities. First of all, dynamical instabilities are developed as the free electron laser is moved away from the exact tuning between the period of the electron bunch(es) circulating into the ring and that of the photon pulse stored in the optical cavity. In addition, external (low-frequency) noise sources have a strong influence on the dynamical behavior of the system and can perturb its dynamics. Different feedback techniques have been proposed in order to control dynamical instabilities and stabilize the laser output. We present here a numerical and experimental investigation on the control of the Elettra storage ring free electron laser dynamics using different feedbacks techniques that can be experimentally implemented by means of a Field Programmable Gate Array.

INTRODUCTION

In a storage ring free electron laser (SRFEL) the electron bunch interacts with photons when passing through the optical klystron (Fig.1). The photons are stored in an optical cavity characterized by a traveling time ΔT and bounded by the two mirrors. The electron bunch, circulating in the storage ring, is characterized by the revolution period ΔT+ε which is determined by the storage ring radiofrequency.

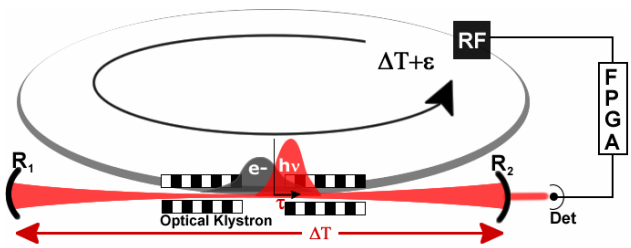

Figure 1: Layout of the storage-ring free-electron laser. The photon pulse (red) stored in the optical cavity interacts with the electron bunch (gray), circulating in the storage ring. The light intensity is acquired using an optical detector (Det). The resulting signal can be elaborated by an FPGA and used for slightly changing the electron revolution period (from ΔT to ΔT+ε) by varying the phase of the radio-frequency cavity (RF) of the ring.

Due to the impulsive character of the laser medium the laser intensity of a SRFEL is characterized by a sequence of micropulses whose duration is of the order of tens of picoseconds. Moreover its repetition rate is that of bunches in the ring (some MHz).

On a "slow" time scale (ms), the SRFEL behavior is strongly related to the temporal superposition of the photon and electron bunches inside the optical klystron. More precisely, the laser envelope displays a steady state regime for a perfect electron-photon tuning (ε=0 in Fig.1). Small light-electron detuning is sufficient to induce intensity oscillations on a slow time scale (Fig.2).

Due to these instabilities the quality of the laser temporal evolution is usually rather poor. Besides temporal detuning, the environmental noise (which is usually related to a residual 50Hz modulation coming from the power network) also perturbs the system and can strongly affect the SRFEL dynamics (Fig.2,5).

A simple model based on a recurrence map [1,2] can be used in order to describe the slow time-scale evolution of a SRFEL:

$$I_j(\tau) = R^2 I_{j-1}(\tau-\varepsilon)\cdot\left[1+g_{j-1}(\tau)\right]+i_s(\tau) \quad (1)$$

$$g_j(\tau) = g_0\frac{\sigma_0}{\sigma_j}e^{\left(-\frac{\sigma_j^2-\sigma_0^2}{2\sigma_0^2}\right)}e^{\left(-\frac{\tau^2}{2\sigma_{t,j}}\right)} \quad (2)$$

$$\sigma_{j+1}^2 = \sigma_j^2 + \frac{2\Delta T}{\tau_s}\left(\gamma_j + \sigma_0^2 - \sigma_j^2\right) \quad (3)$$

$$\varepsilon = \varepsilon + F(t) \quad (4)$$

$$F(t) = A\cdot\left[\frac{dI(t)}{dt}\right] \quad (5)$$

$$F(t) = A_1\cdot\left[I(t)-I(t-T_{d1})\right]+A_2\cdot\left[I(t)-I(t-T_{d2})\right] \quad (6)$$

Eq.1 describes the laser intensity at the j^{th} passage where τ is the temporal position with respect to the centroid of the electron bunch, R is the cavity mirror reflectivity, i_s stands for the spontaneous emission of the optical klystron, ε accounts for the detuning. The gain $g_j(\tau)$ is described by Eq.2 where g_0 and σ_0 respectively stand for the initial peak gain and energy spread respectively, $\sigma_{t,j}$ is the bunch length of the j^{th} interaction. The energy spread σ_j is described by Eq.3 where γ is the difference between equilibrium and initial energy spread, I_j the normalized laser intensity, ΔT the revolution period of electrons on the ring and τ_s the synchrotron damping time. For a more exhaustive description of the model we refer to Ref. [3].

Eqs.5,6 refers to the control signal $F(t)$ for the case of derivative and delayed feedbacks. Those signals are used to modulate the detuning (ε) according to Eq. (4) where $t = j\Delta T$.

#enrico.allaria@elettra.trieste.it

Table 1: Parameters used for the simulations of the Elettra SRFEL.

$\Omega = 16 \quad kHz$	$\sigma_{\tau,j} = \frac{\alpha}{\Omega}\sigma_j$	$R = R_1 \cdot R_2 = 0.96$
$\Delta T = 216 \quad ns$	$\alpha = 1.6 \cdot 10^{-3}$	$\gamma = \sigma_e^2 - \sigma_0^2 \quad {}^{\sigma_e}\!/_{\sigma_0} \approx 1.3$
$i_s = 4.3 \cdot 10^{-7}$	$\tau_s = 86 \quad ms$	$\varepsilon = \varepsilon_0 + \delta\varepsilon \cdot \sin(2\pi\nu t) \quad \nu = 50Hz$

The above model provides an ideal setting to investigate possible strategies for the stabilization of the SRFEL dynamics. The signal proportional to the laser output intensity extracted from the optical detector (Det in Fig.1) can be instrumental to the control of the system through dedicated feedback algorithms (Eqs. 4-6). More precisely, this signal can be used *ad hoc* to modify the electron revolution period (from ΔT to ΔT+ε) through the RF cavity of the ring (Fig.1).

Detuning and noise effects on SRFEL dynamics

By using the above model one can investigate the role of both the detuning and the external periodic noise modulation on the SRFEL dynamics.

Here we numerically simulate the Elettra SRFEL by using the model (Eq.1-3) assuming the values reported in Tab.1. We first assume an ideal case and neglect the external noise modulation at 50 Hz. In order to characterize the effect of a simple detuning ε_0 on the SRFEL dynamics, the bifurcations diagram of the laser output intensity (*I*) *vs* the detuning value (ε_0) has been reconstructed. Bifurcation diagrams are obtained by plotting the values of the laser intensity maxima and minima when dynamically varying the value of the photon-bunch detuning ε_0. In order to free our results from hysteresis effect we perform the scan both increasing and decreasing the values of ε_0.

Fig.2 (black curve) displays the results for the case of a non modulated detuning ε_0.

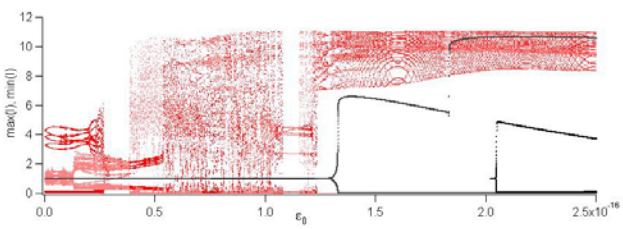

Figure 2: Bifurcation diagram of SRFEL intensity with respect of the detuning parameter ε_0. Black curve refers to the case without external perturbation of the detuning parameter ($\delta\varepsilon = 0$, see table 1). Red points refers to the case where also an external periodic perturbation is present ($\delta\varepsilon = 0.18$fs).

Results clearly show the presence of a steady state regime up to a detuning value of about 0.12fs where the transition to a pulsed regime occurs. Starting from $\varepsilon_0 =$ 0.12fs, the laser is characterized by high-intensity short pulses followed by long periods where the laser is off. If the detuning is further increased, the peak of the laser intensity decreases up to a second transition point ($\varepsilon_0 =$ 0.18fs). For larger detuning values the SRFEL achieves again a stable regime which falls outside the region considered in the subsequent analysis [4].

Results are instead different if one accounts for the presence of the external periodic noise signal. In Fig.2 (red curve) we report the bifurcation diagram of the SRFEL intensity *vs* the detuning value (ε_0) for a choice of the parameters which corresponds to the case of the Elettra SRFEL, i.e. $\delta\varepsilon_0 =$ 0.18fs [3]. The used value for the noise strength is sufficient to destroy the initial (i.e. small detuning) steady state region and the bifurcation diagram now shows a cascade of transitions between periodic and chaotic behaviors. However, depending on the detuning value, there exists regions where the laser is always turned on.

In the following we shall consider the Elettra SRFEL to be represented by the model of Eq.s1-3 with ε_0 and $\delta\varepsilon$ respectively equal to 0.5fs and 0.18fs [10].

CONTROL ALGORITHMS

The sensitivity of the system to the detuning ε can be exploited to implement a feedback system. A signal proportional to the laser can be used as an input in a feedback loop in order to control the system. To this aim an appropriate change to the electron revolution period is applied through the RF cavity of the ring (Fig.1, Eqs.1-6).

Recently, encouraging experimental results have been reported for a derivative feedback based on a low-pass filter [5]. In the near future we plan to implement a more sophisticated feedback system, exploiting the intrinsic flexibility of a FPGA to design innovative control algorithm. In the following we shall provide a first theoretical insight into this issue by comparing a digital derivative feedback (Fig.3,4) and a digital delayed feedback.

Derivative feedback

A derivative feedback enables to reduce the chaotic oscillations of the SRFEL dynamics.

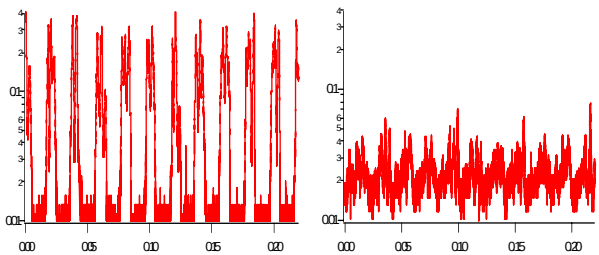

Figure 3: Time trace of the Elettra SRFEL showing the effect of the digital derivative feedback. a) Unstable behavior of the Elettra SRFEL. b) Controlled regime.

As appear evident from inspection of the experimental data reported in Fig.3, the digital derivative feedback control is able to prevent the laser to turn off. However, a small residual modulation at 50Hz is still present together with higher frequencies spurious contribution. In figure 4 we characterize the transition from the unstable pulsed

regime to the controlled one as a function of the strength of the control loop.

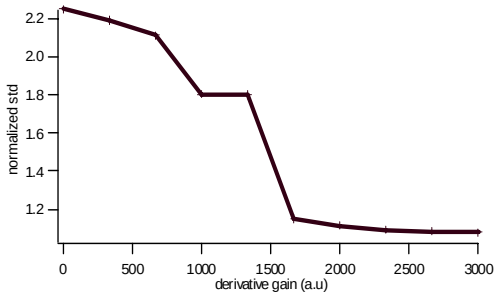

Figure 4: Transition from uncontrolled (Fig.3a) to controlled (Fig.3b) regimes: the normalized standard deviation of the SRFEL signal is reported as a function of the strength of the control signal.

One of the limitations of the derivative feedback is the fact that the sign of the controlling signal necessary for the stabilization of the SRFEL depends on the sign of the detuning [3]. For that reason in cases where the detuning (ε_0) is smaller or comparable to the perturbation of the external noise signal ($\delta\varepsilon$), a strong control signal cannot be employed. Otherwise, the control signal can induce detuning with the wrong sign and move the system away from the stability.

Delayed feedback

Delay control feedback can avoid the aforementioned problem because it involves a low correlation between the values of the laser intensities used for the calculation of the control signal.

Such a method consists in applying to the system a control signal *F(t)* described by Eq. (6): the loop gain A and the delay times $T_{d1,2}$ are the parameters to be set in order to stabilize the laser evolution.

Delayed feedbacks have been originally proposed for the stabilization of unstable periodic orbits of chaotic oscillators [6]. Recently two different incommensurable delays has been proposed to be used to obtain the stabilization of a steady state [7]. We further showed the possibility of using such a strategy in a SRFEL [8]. We are here interested in testing the robustness of the method to small fluctuations of SRFEL and/or algorithm parameters.

Figure 5 analyzes the performances of the method as a function of the two delay times. Results clearly show the existence of a region (blue) where the standard deviation of the signal has been strongly reduced (<0.5) thus pointing to the stabilization of the SRFEL signal. It is important to emphasize that those regions are located out from the diagonal which in turn enables one to conclude that at least two delays are necessary for the method to effectively work.

The possibility, and advantages, of using additional delay times should be addressed [9]. The robustness of the proposed method has been verified with respect of the variation of several input parameters.

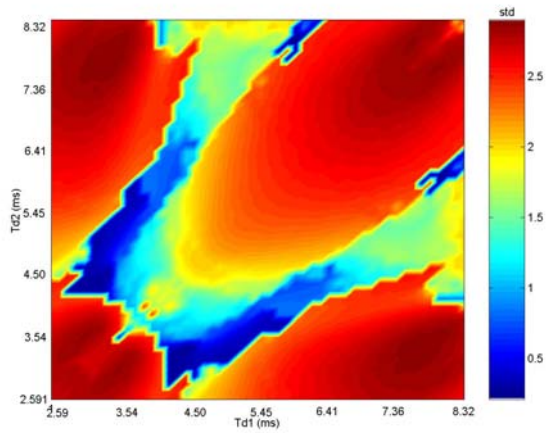

Figure 5: Color-scale plot of the standard deviation of the SRFEL output as a function of the delays used in the two delay lines of the control algorithm (A=1.9e-6). The plots clearly show the advantage of using two delays with respect to one (diagonal).

Numerical simulations indicate that the stable region (blue in Fig.4) is maintained when the input parameters (loop gain A, noise frequency and amplitude, electron-photons detuning …) are changed, as one would expect to occur in experimental conditions. This is a crucial observation in view of possible experimental realizations.

COMPARISON BETWEEN DERIVATIVE AND DELAYED FEEDBACK

In order to compare the performance of the delayed control algorithm and the derivative one we numerically tested both methods as a function of the strength of the external noise signal.

Figure 6 show the behavior of the SRFEL with ε_0=0.05fs as a function of the noise strength ($\delta\varepsilon$). The pulsed chaotic dynamics, which is usual for the Elettra SRFEL, is evident from the large range of fluctuation of the laser maxima for $\delta\varepsilon$ in the range 0.15-0.20fs.

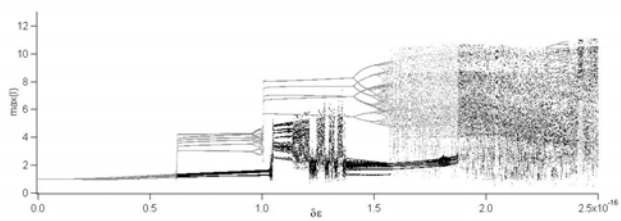

Figure 6: Bifurcation diagram of the SRFEL intensity as a function of the external noise modulation strength ($\delta\varepsilon$).

A proper setting of the derivative feedback [3] allows to stabilize the dynamics of the SRFEL in the region of $\delta\varepsilon \in$ (0.15-0.20fs) which is characteristic of the Elettra SRFEL. However, for larger values of $\delta\varepsilon$ the dynamics remains chaotic (Fig.7).

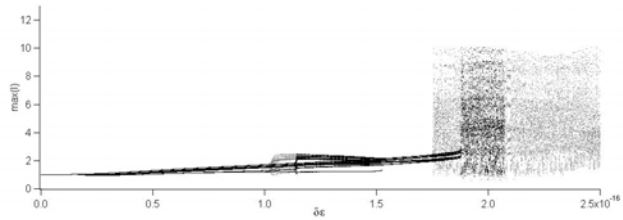

Figure 7: Bifurcation diagram of the SRFEL intensity with the use of the derivative feedback set for the stabilization (A=3.0e-2) of the unstable oscillations around the $\delta\varepsilon$ = 0.18fs case.

As clearly shown in figures 6,7,8 a dual delay algorithm results in a better stabilization of the SRFEL dynamics over a larger range of $\delta\varepsilon$.

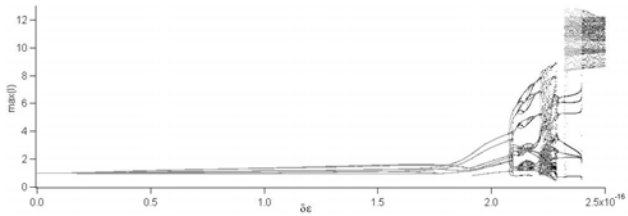

Figure 8: Bifurcation diagram of the SRFEL intensity with the use of the dual delay feedback set for the stabilization (A=1.9e-6, T_{d1}= 3.11ms, T_{d2}=4.24 ms) of the unstable oscillations around the $\delta\varepsilon$ = 0.18fs case.

Although the ultimate goal of obtaining a perfect steady state regime is beyond current possibilities, both methods are capable to stabilize the laser intensity for a large window of values of the noise strength $\delta\varepsilon$, a crucial quantity responsible for undesidered oscillations arising in the uncontrolled case (Fig. 6). A comparison between the proposed two methods in terms of extension of the allowed range of the noise strengthshow that the approach based on the multidelay performs better. This conclusion applies also as concerns the amplitude of the residual oscillations.

As previously anticipated, the reason for the above success is to be ascribed to the fact that the low correlation between delayed values in the case of chaotic signal allows us to implement a strong control term without facing the risk of producing opposite effects, reported instead for the case of the derivative feedback.

CONCLUSIONS

We presented a reliable model for the investigation of both detuned and noisy regimes in a SRFEL. The model has been applied to testing possible feedback algorithm to be developed with a FPGA. Preliminary experimental results have been reported concerning the stabilization of the Elettra SRFEL trough a digital derivative feedback. A proposed feedback method based on delayed signal has been presented and numerically investigated. The comparison of the delayed method with the derivative one shows the advantages of the former in terms of achieved stability and robustness to noise.

On the basis of these encouraging results, the experimental implementation of the delayed feedback control on the Elettra SRFEL is planned for the near future.

REFERENCES

[1] M. Billardon *et al.*, Phys. Rev. Lett. **69**, 2368 (1992).
[2] S. Bielawski *et al.*, Phys. Rev. **A**, **47**, 3276 (1993).
[3] G. De Ninno *et al.*, Phys. Rev. E **71**, 066504 (2005)
[4] M.E. Couprie *et al.*, Phys. Rev. E. **53**, 1871 (1996).
[5] S. Bielawski *et al.*, Phys. Rev. **E**, **69**, 045502 (2004).
[6] K. Pyragas, Physics Letters A, **170**, 421-428 (1992).
[7] A. Ahlborn and U. Parlitz, Phys. Rev. Lett. **93**, 264101 (2004).
[8] E. Allaria *et al.*, FEL05, JACoW/eConf C0508213, THPP005 (2005)
[9] Work in preparation.
[10] In the case of Elettra a detuning of 0.4fs correspond to a variation of 1Hz of the 500MHz RF frequency which is the limit of the accuracy of the instrument. Moreover to the time jitter of the master oscillator, that depending of the working conditions can be of the order of 1ps, can be associated a detuning of 0.02fs if we simplify the jitter to a 50Hz signal.

Q-SWITCH TECHNIQUES IMPLEMENTED AT THE ELETTRA STORAGE-RING FREE-ELECTRON LASER

F. Curbis*, M. B. Danailov, B. Diviacco, L. Romanzin, M. Trovò, G. De Ninno
Elettra, Basovizza, Trieste, Italy.

Abstract

In a Storage-Ring Free-Electron Laser (SRFEL) giant pulses can be produced by the interaction between the light stored in the optical cavity and an electron beam with low energy-spread (cold beam). This interplay produces the heating of the beam. After the generation of a single giant pulse the overlap between electrons and radiation is periodically prevented for a time necessary to dump the energy spread and recover the cold-beam condition. Two different methods are now implemented at Elettra for giant pulse generation. In the first, by modifying the radio-frequency of the ring, a change of the revolution time of electrons is induced. This avoids the temporal overlap between the electron beam and the optical field in the mirror cavity. The second method relies on a mechanical gating (chopper) which intercepts the light produced during previous interactions, inducing a periodic depletion of the optical cavity. The giant-pulses repetition rate is determined by the periodicity of the radio-frequency changes and the rotating velocity of the chopper, respectively. In this paper we compare the different techniques mentioned above for the case of the Elettra SRFEL.

INTRODUCTION

The customary layout of a Free-Electron Laser (FEL) in oscillator configuration takes advantage of an optical klystron. This magnetic structure is made up of two undulators and a dispersive section in between (see Figure 1). In the small gain case [1], which is indeed the oscillator case, the strong magnetic field of the dispersive section induces a delay between the radiation emitted in the first and in the second undulator. In comparison to the light the electrons spend longer time to pass through a magnetic chicane and, once in the the second undulator, their emission will have a different phase with respect to the light emitted formerly. This delay produces a constructive interference of radiation, changing the optical klystron spectrum in a more spiky structure and enhances the FEL process because its gain is proportional to the derivative of this interference structure. The other main component of an oscillator FEL is the optical cavity, composed by two mirrors on axis with the two undulators and the dispersive section, as depicted in Figure 1.

In the normal operational mode of a storage-ring FEL in oscillator configuration, the light emitted has a temporal structure depending on the ring filling and each pulse has a quite low power. When the electron beam interacts with the light stored in the optical cavity, emitting coherently, its energy spread grows up. This effect, called beam "heating", limits the maximum power achievable, because the gain is proportional to the electron density. Between the generation of two consecutive giant pulses it is necessary to wait few synchrotron damping times, this allows to restore the cold beam condition. In this period of time, in fact, if the light-electron interaction is prevented, the beam energy spread decreases to the initial value.

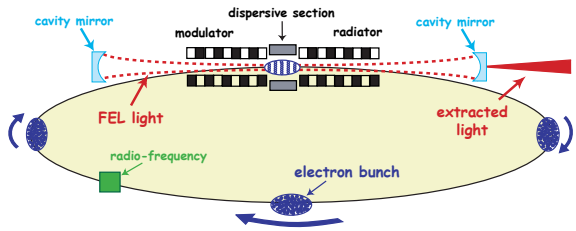

Figure 1: Layout of the Elettra storage-ring FEL in oscillator configuration.

Several methods have been studied and applied in oscillator FELs [2, 3, 4, 5] to create "giant pulses". There are basically three techniques that have been implemented:

- the gain modulation [6];
- the modulation of RF frequency [4, 5];
- the mechanical gating (chopper).

The first method is presently employed at Duke, where a dedicated magnet steers the electron beam orbit in the transverse direction. When the electron beam orbit is off-axis with respect to the optical cavity, the lasing is stopped and the electron beam can cool down. Once the electron beam orbit returns on-axis, a new giant pulse starts. The RF frequency modulation has been used in Super-ACO and is currently implemented at Elettra and UVSOR. This technique may excite synchrotron oscillations of the electron beam, or enhance them if already present. The induced oscillations can reduce the net gain at the laser start. While the first two techniques can be considered equivalent for generating giant pulses (as demonstrated for Duke in [7]), the mechanical gating is still under investigation.

The purpose of the Q-switch technique is twofold: to concentrate the average power of storage-ring FEL in a series of giant-pulses and to have a regular temporal dynamics of the light. This allows to use the light emitted for experiments, for example synchronizing an external trigger which drives the giant pulse repetition rate [8]. Besides, it

* francesca.curbis@elettra.trieste.it

is well known that the FEL light at the fundamental wavelength, which is reflected by the mirrors of the optical cavity, produces higher harmonics [9]. These harmonics survive just for a single pass in the optical cavity, because the mirrors do not reflect light with their wavelength. In normal operation mode the power of higher harmonics, which depends on the fundamental power, is too low to be detected. Giant pulse production is therefore a suitable way to enhance the fundamental power and accordingly the higher harmonic power. One example of harmonic generation in cavity is reported in Figure 2.

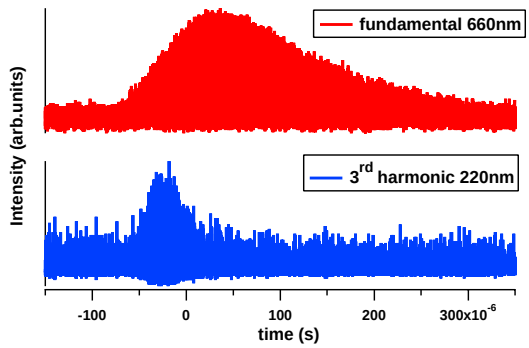

Figure 2: The fundamental (660 nm) and the third harmonic (220 nm) giant pulses. The harmonic signal is about a factor 25 above spontaneous emission.

The giant-pulse risetime provides also an estimation of the initial FEL gain. Between each pulse the electron beam is restored and when the giant pulse starts the only negative effect is due to the optical cavity losses. This allows to calculate the net gain of the FEL process, if the mirror reflectivity is known.

TWO DIFFERENT EXPERIMENTAL TECHNIQUES

In this section, we concentrate on the two techniques used at Elettra for the giant pulse generation, i.e., the RF frequency modulation and the Q-switch with the chopper.

RF frequency modulation

In a storage-ring FEL, in order to obtain the synchronization between the electron beam and the light stored in the optical cavity, the mirrors are placed at inter-bunch distance. Stepper or piezo-electric motors provide the fine tuning of the mirror position along the undulator axis. If the RF frequency of the storage ring changes the revolution time of electrons changes as well, causing the loss of synchronization with the optical filed in the cavity. Without temporal overlap the electrons do not interact with the radiation stored in the optical cavity and then the energy spread of the beam can decrease. The RF frequency modulation is based on a periodic detuning between the electron beam and the radiation stored into the optical cavity. When the system is detuned the lasing process is stopped. An external signal source induces the detuning and modifies the slope and the amplitude of the RF frequency jump. The detuned condition is maintained for few synchrotron damping times to allow the electron beam to cool down and the gain of the amplification process to recover its initial (i.e. laser-off) maximum value. Once this situation is reached, the system is led back to the perfect tuning condition which is maintained for a long enough time (order of dozens of milliseconds) to induce the onset of the laser giant pulse. Then the system is detuned again and the process repeated.

The main advantage of this technique is the fast transition time. The RF modulation is driven by a signal generator, therefore one can choose the slope of the signal to reach the maximum power. The unfavorable aspect is the beam perturbation caused by the RF modulation. The damping is regulated by the synchrotron frequency. Figure 3 shows a streak camera image of the synchrotron radiation and the FEL signal.

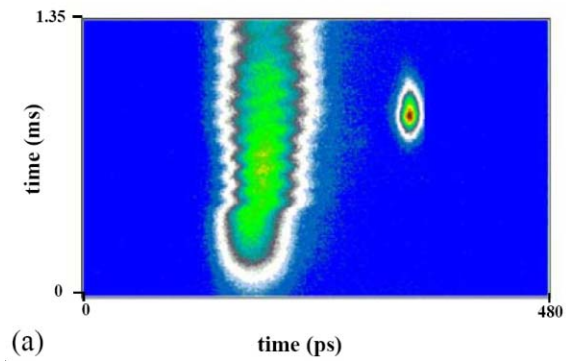

Figure 3: Streak-camera image of the electron beam (left trace) and of the FEL pulse (right trace) in Q-switch operation mode.

Along the vertical axis of the picture, the evolution in time of the distribution profile is reported and one can also see the excitation of synchrotron oscillation starting before the laser. The analysis in Figure 4 also shows the electron beam heating that begins before the giant pulse start.

Q-switch with chopper

In the Elettra storage-ring FEL a mechanical gating has been recently introduced in the optical cavity. This object, called chopper, is a molybdenum disc with a 115 mm radius with a little aperture positioned close to the border (see Figures 5). When the aperture is on-axis with the optical cavity the light stored can pass, otherwise the radiation is intercepted by the disc. The chopper is placed near the back mirror (see Figure 6) and rotates at constant speed, moved by a PHYTRON UHV stepper motor.

The rotating velocity determines the repetition rate of the Q-switch.

Generally speaking, when the electron beam interacts with the laser pulse (stored into the cavity) its longitudi-

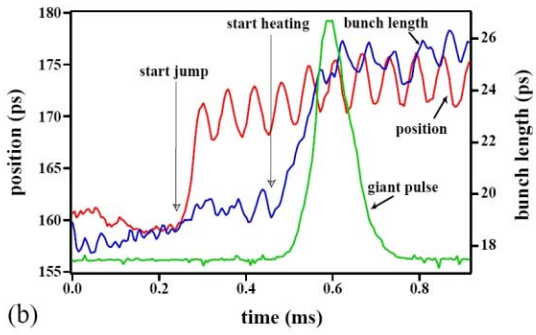

Figure 4: Analysis of the streak camera image in Figure 3. The longitudinal distributions are obtained by means of a horizontal cut of the picture.

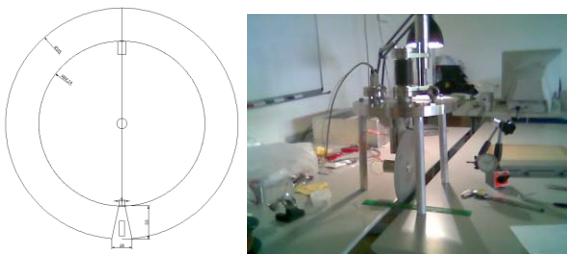

Figure 5: Left: schematic design of the metallic disc. Right: Preliminary studies in air.

nal dimensions grow up and the resulting energy spread reduces the FEL gain. The chopper allows the giant pulse creation because it prevents the electron-light interaction for a suitable time so that the energy spread reduces. This method does not generate beam perturbations and, as a consequence, higher power in the giant pulses is expected.

At the present the chopper technique can achieve only a limited repetition rate if compared to the RF modulation. Nevetheless we expect in the near future to operate the chopper at frequencies of 5 Hz or more. Furthermore, since the chopper Q-switch does not involve the RF frequency,

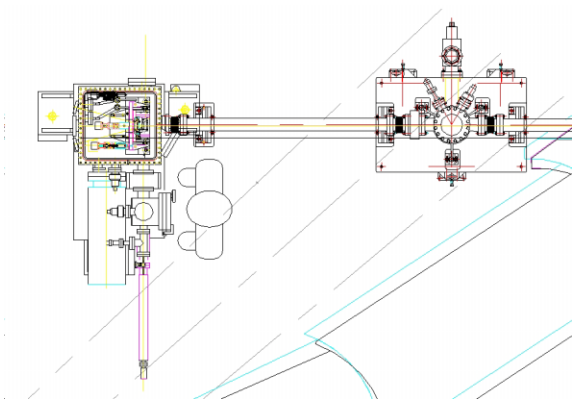

Figure 6: Schematic layout of the chopper chamber (at right), near the mirror chamber (at left).

Figure 7: Pictures of the chopper during the installation.

the latter can be used as a clock for cross-correlation measurement in order to characterize the harmonic signal.

A summary of the peculiarities of both methods is reported in Table 1.

Table 1: Chopper versus RF modulation

chopper advantages	**RF advantages**
no beam perturbation	fast transition time
chopper disadvantages	**RF disadvantages**
longer transition time	beam perturbation

Measurements and results

To compare the RF frequency modulation and the chopper Q-switch techniques, a campaign of measurement has been recently carried out using the Elettra SRFEL. Figure 8 and Figure 9 show preliminary risetime measurements for the RF modulation and the chopper case, respectively. The pictures report a train of giant pulses obtained at the same current and repetition rate. While the RF modulation method displays a quite constant level of the signal, the chopper exhibits an irregular behaviour. The reason is still under investigation.

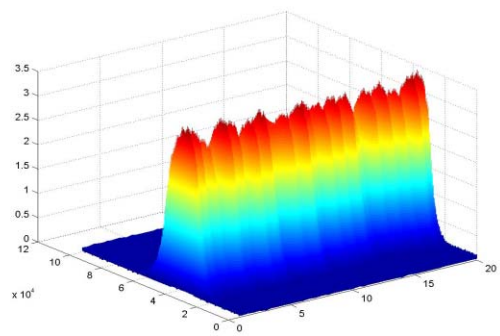

Figure 8: Sequence of 20 giant pulses, acquired by a fast photodiode, generated using the RF modulation. The electron beam current is about 10 mA and the repetition rate is 1.5 Hz

In Figure 10 we compare the two techniques for the 3 Hz case: the giant pulse risetime, calculated as a mean of 20 signals, is displayed as function of the total beam current.

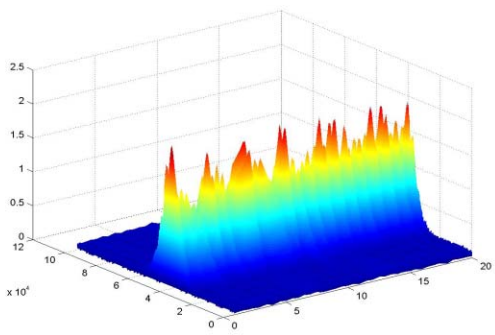

Figure 9: Sequence of 20 giant pulses, acquired by a fast photodiode, generated using the chopper Q-switch. The electron beam current is about 10 mA and the repetition rate is 1.5 Hz

For high currents the chopper and RF modulation seem comparable, while at medium-currents the chopper risetime is quite longer.

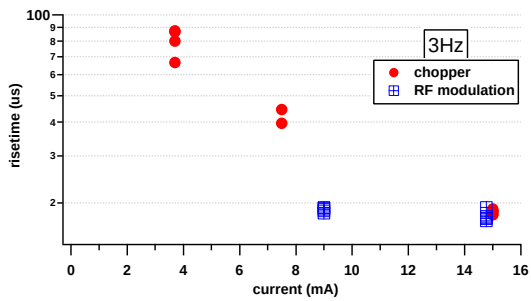

Figure 10: Comparison between chopper and RF modulation techniques, showing the risetime as a function of the total current at the same operational frequency (3Hz).

Figure 11 and Figure 12 report the risetime versus current for the RF modulation and for the chopper technique respectively. These data do not show any strong dependence of the risetime on the repetition rate.

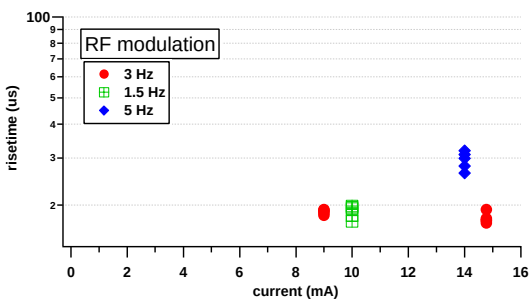

Figure 11: Efficiency of the Q-switch at different repetition rates using RF frequency modulation.

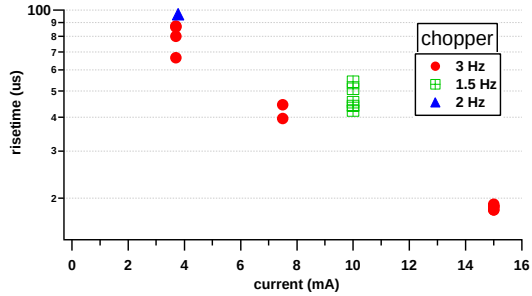

Figure 12: Efficiency of the Q-switch at different repetition rates using chopper.

CONCLUSIONS

The preliminary results presented here show the capability of the chopper method to generate giant pulses. This technique, although promising, needs more development in order to reach, and hopefully improve, the performance of the RF modulation method in terms of reproducibility and higher repetition rate.

REFERENCES

[1] J. M. J. Madey, J. Appl. Phys. **42**, 1906 (1971).

[2] G. N. Kulipanov, et al., *Nucl. Instr. and Meth. A* **296** (1990) 1.

[3] V. N. Litvinenko, et al., *Nucl. Instr. and Meth. A* **429** (1999) 151.

[4] T. Hara, et al., *Nucl. Instr. and Meth. A* **431** (1994) 21.

[5] G. De Ninno, et al., *Nucl. Instr. and Meth. A* **528** (2004) 278.

[6] I. V. Pinayev, et al., *Nucl. Instr. and Meth. A* **475** (2001) 222.

[7] G. De Ninno, et al., Elettra Internal Note.

[8] M. Amati, et al., these proceedings.

[9] V. N. Litvinenko, *Nucl. Instr. and Meth. A* **507** (2003) 265.

DEVELOPMENT OF A COMPACT CHERENKOV FREE-ELECTRON LASER IN TERAHERTZ SPECTRAL RANGE

M. R. Asakawa*[1], K. Nakao[2], N. Miyabe[1], M. Kusaba[2] and Y. Tsunawaki[2],
[1]Kansai University, Suita, Osaka, Japan,
[2]Osaka Sangyo University, Daito, Osaka, Japan.

Abstract

A Cherenkov free-electron laser (CFEL) generating terahertz radiation is now being developed under the joint research of Osaka Sangyo university and Kansai university. The main feature of the CFEL is its compactness. Microbeamlets from Spindt-type field emitter array are accelerated up to 50 keV and then injected into a silicon resonator with a path of 50 to 150 μ m spacing through which electrons propagate. Omitting the evacuation system and power supply, the size of CFEL section, including electron gun and resonator, is about $1 \times 1 \times 4$ cm^3. For the generation and the transport of the electron beam few μm in diameter, we investigated characteristics of the Spindt cathode, beam focusing by electrode and the magnetic field. A carbon nanotube field emitter was also tested for future application.

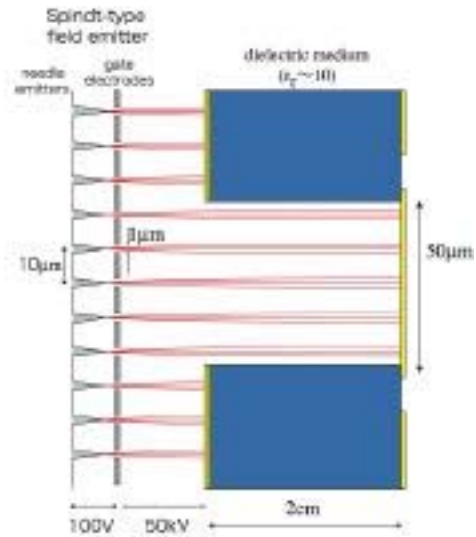

Figure 1: Schematic view of compact CFEL.

INTRODUCTION

Cherenkov free-electron lasers (CFELs) are one of the great candidates for compact tunable radiation sources. A pioneer work had demonstrated CFEL in 100 GHz frequency range using an electron beam with 35 to 75 keV acceleration energy [1]. In order to increase the operation frequency to terahertz frequency range, it is straightforward to scale down the optical resonator of CFEL. Fig. 1 shows a schematic view of a compact CFEL. Electron beamlets several μm in diameter are accelerated to 50 keV and then injected into a dielectric resonator. Electron beamlets passing through a channel bored in the dielectric resonator excite the Cherenkov radiation and interact with the evanescent part of that radiation.

The resonant frequency is determined principally by the radius of the channel: the resonant wavelength coms to severalfold of the channel radius. The dispersion curve of the evanescent wave in a circular dielectric waveguide is shown in fig. 2 with the dispersion of the light in vacuum and a beam-mode for 40 keV electron [2]. Because electrons moving along the channel transfer its kinetic energy to the radiation field via the interaction with the longitudinal component of the radiation field, the TM-mode which has that field component is important in such CFEL. Thus the dispersion relation for the TM_{01}-mode is shown in the figure. For the case of R_d=25 μm, the resonant frequency is 1.6THz. Note that the dispersion relations are scalable with the channel radius, thus the resonant frequency increases with decreasing the channel radius. CFELs are, therefore, capable to be operated in mid-infrared to sub-millimeter spectral range.

Our research aims a compact, more ambitiously, palmtop CFEL that can generate the radiation over the infrared spectral area. As the first step, we are developing the electron beam source which can produce μm beamlets. In following section, a CFEL test bench and experimental studies of the beam focusing will be described.

CFEL TEST BENCH

To produce the electron beam whose radius is order of micrometer, we used a Spindt cathode,[3] which contains 100,000 pairs of ultrasmall needles and gate electrodes in a 1 mm diameter array. Each pair of needle and electrode generate electron beamlet with diameter around 1 μm, and these tiny electron guns are arrayed with a spacing of 10 μm. Due to the needle-gate configuration and the high operation current density, Spindt cathode generates a diverging beam as shown in fig. 3. Therefore, the beam transport is the critical issue.

Figure 4 and fig.5 show the schematic view and the picture of a developing CFEL test bench, respectively. This system employs the magnetic field for the beam focusing. Main components, such as Spindt cathode, collector electrode and a optical resonator, are installed inside the bore

* asakawa@ipcku.kansai-u.ac.jp

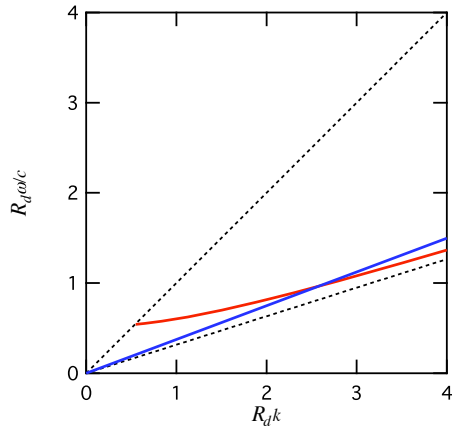

Figure 2: Dispersion relations of the evanescent wave for TM_{01} mode. The relative dielectric constant of the medium is 10.(red) Both axes are multiplied by the channel radius (R_d=25 μm) for the normalization. The blue solid line shows the dispersion of 40 keV beam mode. Upper and lower dashed lines denote the dispersion of the light in vacuum and the light in the dielectric medium, respectively.

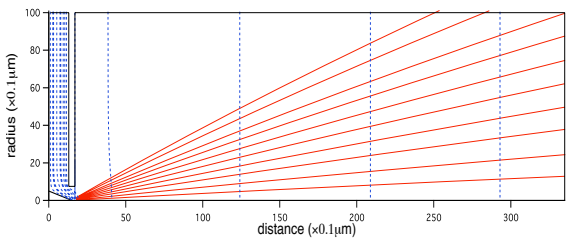

Figure 3: Calculated trajectories of electrons emitted by Spindt cathode. Red lines show the electron trajectories and Blue lines represent the equipotential lines. E-gun code was used for the calculation.

of a super conducting coil, which can produce magnetic flux density up to 5 T. The footprint of the whole system including the compressor unit for super conducting magnet is about 1 $\times$1 m^2.

Electron beamlets generated at the grounded Spindt cathode needles are accelerated toward the collector electrode, which is followed by the optical resonator. The resonator consists of a pair of silicon slabs gapped by thin spacers with thickness of 50, 100 or 150 μm. The resonant frequency increases from several hundreds GHz to few THz as decreasing the gap spacing. The end edges of slabs facing to the cathode are coated with Al and work as both the collector electrode and resonator mirror, while the other edges are left uncoated to extract Cherenkov radiation. One side of the gap between the slabs facing to cathode is opened for the beam injection, while the other side is blocked by the spacer for beam dumping and reflecting back of a part of radiation. The length of the laser interaction region is 2 cm.

Figure 6 shows the time trace of the gate voltage and the beam current. Pulsed voltage up to 100 V is applied to the gate electrode of Spindt cathode to generate a few

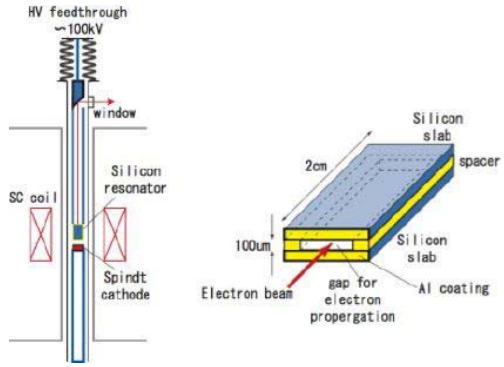

Figure 4: Schematic view of the CFEL test bench and the resonator. The left and right figures show the schematic view of the whole system and the detailed view of the resonator, respectively.

Figure 5: Picture of the CFEL test bench. The high voltage feedthrough, the 2-axis manipulator for resonator alignment and cryostat of the super conducting coil can be seen. The height and footprint of the device are 1.9 m (including a 0.7 m-height pedestal) and 0.7$\times$0.7 m^2, respectively.

milli-amperes beam current. The raise time of 50 μs was determined by the capacitance of the power feed cable and 100 kΩ resistance for current monitoring, and will be shorten by reducing the resistance in the laser experiments that higher beam current will be required. For the operation above the beam current shown in the figure, we suffered from the serious degassing and the following brake down. Such undesirable events were remarkable especially when the magnetic field was applied. This system is under aging process.

FOCUSING ELECTRODE

Because the magnetic focusing requires a large and expensive magnet, we also explored beam focusing using mid-electrode. A mid-electrode was located at a distance of 13 mm from the cathode. The spacing between the mid-

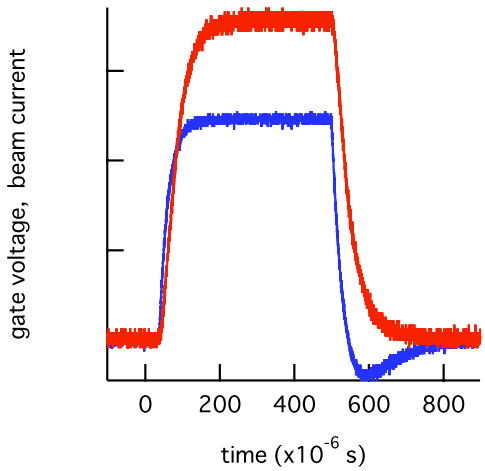

Figure 6: Time trace of the gate voltage (red) and the beam current (blue). Peak voltage is 50 V and peak current is 81 μA.

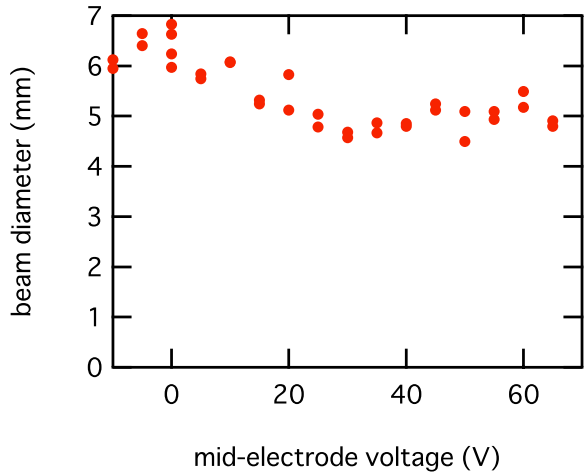

Figure 7: Beam diameter as a function of the mid-electrode voltage. During experiment, the collector voltage was held at 10 kV and pulsed 65 V voltage was applied to the gate electrode of Spindt cathode.

electrode and the collector electrode was set to 30 mm. Mid-electrode had a hole 5 mm in diameter through which the electrons pass through. The beam spot size at the collector electrode was evaluated from the fluorescence image on a phosphor screen placed at collector electrode. Figure 7 shows the beam diameters as a function of the mid-electrode voltage. The collector electrode voltage was held at 10 kV during the experiment. The gate voltage was set to 65 V and the pulse width was 10 ms to obtain luminance enough to observe. Note that these results show the diameter of the whole beam emitted from 100,000 tiny needles: the fine structure formed by each beamlet was smoothed out due to poor resolution of the measurement system. It is seen that the beam diameter decreases with mid-electrode voltage up to 30 V and then slightly increases with the voltage. It is inferred that the beam is over focused with the mid-electrode voltage above 30 V. This result indicates that the beam focusing by the focusing electrode is not enough to produce the electron beam with micrometer diameter. We are on the way to design optimal electrode configuration combined with the magnetic field configuration to find the reasonable focusing system.

CARBON NANOTUBE CATHODE

To develop the brighter electron beam source, we also tested a carbon nanotube cathode. As this test is a preliminary one: powdered carbon nanotubes were smeared over a 0.5 mm diameter plate of stainless steel and the gate electrode was not installed. Due to the lack of the gate electrode, the spacing between the cathode and the collector electrode was set to 0.2 mm to produce electric field enough for the field emission. Figure 8 shows the beam current vs. the collector electrode voltage. Electron emission stars at a voltage of 2.2kV and the current reaches to 2.4mA at 4.4 kV. Above 4.4 kV acceleration voltage, serious outgassing degraded the vacuum condition, thus we limited the supply voltage to this extent. It is worth to mention that the beam current was stable for long period of these experiment in spite of D.C. operation. Taking into account the fact that operation of Spindt cathode with D.C. 1 mA leads serious damage on Spindt cathode, we conclude that carbon nanotube cathodes are capable of generating denser electron beam. Installation of the gate electrode is the key issue for practical application.

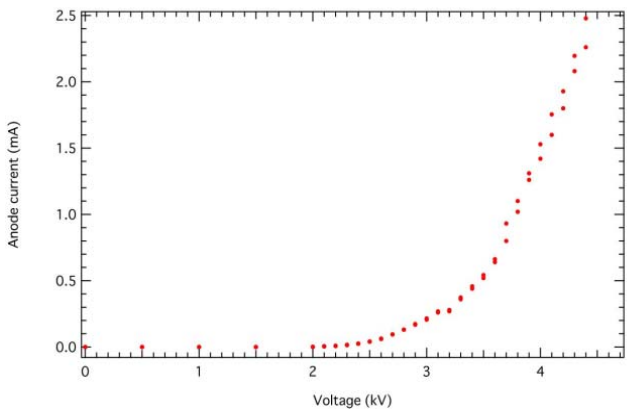

Figure 8: V-I curve for carbon nanotube cathode. D.C. voltage up to 4.4 kV was applied to the collector electrode.

SUMMARY AND RESEARCH PLAN

A compact THz CFEL driven by 50 keV electron beam is under development. Use of Spindt cathode and focusing of the electron beam are key technologies of this device. A CFEL test bench using super conducting coil for beam focusing was commissioned and is under conditioning. Beam focusing by mid-electrode was also studied. To

find the reasonable focusing system, we are investigating the beam focusing by the combination of the magnetic field and mid-electrode. First CFEL test will be started using high magnetic field up to 5 T after the aging conditioning of the test bench. The output frequency will be gradually increased from several hundreds GHz to few THz by reducing the gap spacing of the resonator. It is also planned to study Smith-Percell FEL and Cyclotron radiator on the test bench.

REFERENCES

[1] E. E. Fisch and J. E. Walsh: "Operation of the sapphire Cerenkov laser", Applied Physics Letter, Vol.60, No.11, pp.1298-1300 (1992).

[2] H.P. Freund and A. K. Ganguly: "Nonlinear analysis of the Cherenkov maser", Physics of Fluids B2, No.10, pp.2506-2515 (1990)

[3] K. Mima, S. Nakai, T. Taguchi, N. Ohigashi, Y. Tsunawaki, K. Imasaki , C. Yamanaka and M. Shiho: "A new FEL concept driven by a vacuum microfielf emitter", Nuclear Instruments and Methods in Physics Research SectionA, vol.331, pp.550-553 (1993).

HIGH POWER DEEP UV LASING ON THE UVSOR-II STORAGE RING FEL

M. Hosaka, M. Katoh, A. Mochihashi, M. Shimada, UVSOR Facility, Institute for Molecular Science, 38 Myodaiji-cho, Okazaki, Aichi 444-8585, Japan
Y. Takashima, Graduate School of Engineering, Nagoya University,Furo-cho, Chikusa, Nagoya, Aichi 464-8603, Japan
T. Hara, RIKEN/SPring8 1-1-1 Kouto, Mikazuki, Hyogo 679-5148, Japan

Abstract

Thanks to a recent upgrade of the UVSOR-II storage ring (lower beam emittance and higher peak current), an FEL gain has been enhanced much and we have succeeded in high power lasing in deep UV region. The highest extracted CW power so far is 0.25 W at wavelength of 215 nm and 1.1 W at 230 nm. Because of its variable wavelength even in deep UV region, high power and good coherence, the UVSOR-II FEL has come to be recognized as a useful tool by users inside and outside Institute for Molecular Science. Now UVSOR-II FEL has four users groups (solid state physics, surface physics, bio-moleculer science). Three different kinds of experiments have been successfully carried out in this year.

INTRODUCTION

On the UVSOR storage ring, a free electron laser has been developed as a new light source since early 1990s. In 1996, a helical optical klystron was installed and the performance of the FEL was improved much because of a smaller degradation of cavity mirrors and a higher FEL gain. Then the shortest wavelength (239 nm) of the storage ring FEL at that time was achieved [1].

Recently the storage ring was upgraded and the quality of the electron beam was much improved. With the increased FEL gain, a FEL lasing in shorter wavelength was expected, where more potential users exist. Here we report on an FEL experiment in the deep UV region at UVSOR-II aiming users application. The FEL should have enough power in addition to a good optical quality for application experiments. We also report recent upgrade of an rf accelerating cavity system, which plays an important role in the short wavelength lasing.

.

UPGRADE OF RF CAVITY SYSTEM

In 2003, the UVSOR storage ring was reconstructed toward a lower emittance ring; we call it “UVSOR-II” after the reconstruction [2]. The chief aim of this upgrade is to provide users with brighter synchrotron radiation. We still continue the upgrade of the ring. We replaced rf accelerating cavity system in 2005 [3]. The aim is to improve lifetime of the electron beam with higher accelerating voltage. At the UVSOR, 90.1 MHz rf cavity had been operated with a 20 kW transmitter but the rf accelerating voltage (55 kV at maximum) was limited by low shunt impedance (1 MΩ) of the former cavity.

Table 1: Basic parameters of previous/present rf cavity

	Previous	Present
Frequency	90.1 MHz	90.1 MHz
Cavity voltage	55 kV	150 kV
Shunt impedance	1 MΩ	2.45 MΩ
Unloaded Q	8370	20300
Coupling	1.75	1.34
Structure	Re-entrant ×1	Re-entrant×1
Inner diameter	1000 mm	964 mm
Bore radius	50 mm	55 mm
Material	SUS + Cu	Cu (OFHC)
Tuner	Plunge×1	Plunger ×2

Hence the new rf cavity was designed to have higher shunt impedance. Table 1 shows basic parameters of previous/present rf cavity. The new cavity was installed in the spring of 2005 and the high cavity voltage of 150 kV was achieved. With the new cavity system, observed Touschek beam lifetime was increased by a factor of 3. This upgrade is also favourable to the FEL because higher accelerating voltage leads to shorter electron bunch and higher peak current.

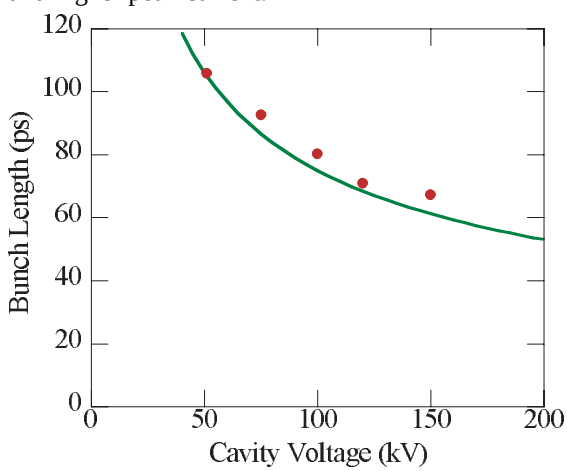

Figure 1: Natural bunch length in various rf voltage. The data points are measured values and the solid line is calculated bunch length.

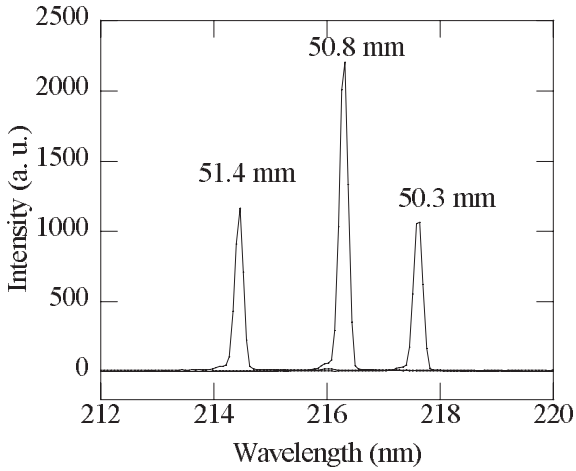

Figure 2: Typical FEL line spectra measured by changing gap width of the optical klystron. The resolution of the spectra is limited by that of the monochrometer used in the measurement.

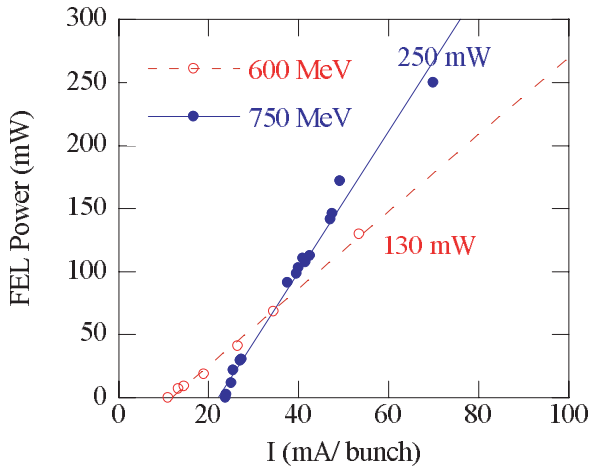

Figure 3: Measured extracted FEL power as a function of beam current at energy of 600 MeV and 750 MeV. The lines are guides to eyes.

Fig. 1 shows measured bunch length by using a streak camera after installing the new rf cavity. The bunch length at a cavity voltage of 150 kV is 67 psec; this value is 60 % of the previous one (110 psec). In this case FEL gain increased by a factor of 1.6 is expected. This leads the FEL lasing in the deep UV region where higher FEL gain is needed.

LASING AROUND 215 nm

We have planned an FEL lasing around 215 nm basically aiming to an user experiment. In the experiment, samples of bio-molecules are irradiated by a laser with the wavelength around 215 nm, where the absorption spectrum of the sample has a peak. The laser should have enough power in order to proceed the irradiation experiment quickly; otherwise the sample may be easily effected by bacteria.

In former UV lasing experiments at the UVSOR, multi-layers of HfO_2/SiO_2 had been employed for cavity mirrors. In a lasing experiment around 215 nm, the multi-layer can not be employed because the band gap energy of HfO_2 is about 5.6 eV (220 nm in a light wavelength) and a strong absorption is expected. Then we chose multi-layers of Al_2O_3/SiO_2; the band gap energy of Al_2O_3 is well above the laser photon energy requested. Since refraction index of Al_2O_3 is smaller than HfO_2, number of layers should be increased to attain reflectivity sufficiently high for lasing. On the other hand, transmission of a mirror becomes smaller and a less power is extracted through the mirror as increasing number of layers. Compromising reflectivity and transmission, we chose number of layer of 49 for downstream mirror and 37 for upstream mirror from which an FEL power is extracted. The expected round-trip reflectivity of the optical cavity is 99.3 % and the transmission of the upstream mirror is 0.5 %. Preparatory to the lasing experiment, we measured the round-trip reflectivity of the mirrors by ring-down method with a low electron beam current (~ 0.1 mA). The measured value was around 97.8 %, which was much smaller than the expected one. We suppose that the low reflectivity came from a degradation of the mirrors due to synchrotron radiation during reflectivity measurement. The mirrors degradation, however, seemed to stop after the first irradiation by synchrotron radiation. Even after exposure to SR of more than 1000 mA h during the lasing experiment, we did not observe the essential change of the reflectivity.

The lasing experiment was started with an electron energy of 600 MeV, with which UVSOR FEL experiment had been made so far. The storage ring was operated in two bunch mode with equal bunch spacing. As seen in Fig. 2. lasing from 214 nm to 218 nm was successfully obtained changing a gap width of the helical optical klystron. In Fig. 3, extracted laser power is plotted as a function of a stored beam current in the storage ring. The threshold beam current for lasing was 11 mA/bunch. The calculated FEL gain at a beam current of 11 mA/bunch is about 2.3 %. This value is very consistent with the measured cavity loss of 2.2 %.

As a next step of the lasing experiment, we raised the electron energy from 600 MeV to 750 MeV, with which the storage ring is operated for SR use. According to the Renieri limit [4], the extracted FEL power is proportional to the total synchrotron radiation power per turn from electron beam. Since the total radiation power is proportional to the 4th power of the electron energy, higher extracted laser power is expected at 750 MeV. Storing a rather high beam current in the storage ring, we have obtained successful lasing at this electron energy for the first time on UVSOR-FEL. The measured threshold current for lasing is about 2 times higher than that in the case of 600 MeV. But a higher laser power is extracted as is expected. The extracted FEL power at 750 MeV is about 1.6 times of that at 600 MeV at a beam current of 70 mA/bunch, that is well above the threshold current. This relation is consistent with that of synchrotron radiation power; the total synchrotron radiation power

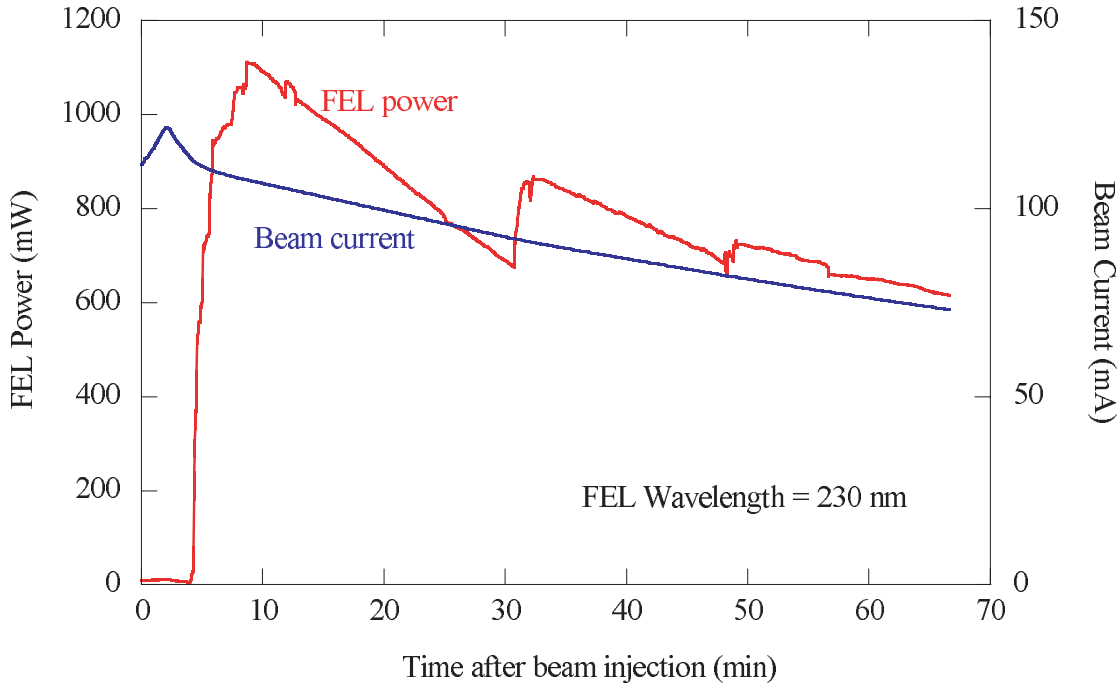

Figure 4: Extracted FEL power and beam current as a function of time. The FEL wavelength is around 230 nm. The maximum FEL power was 1.1 W.

from an electron at 750 MeV is about 2.4 times of that at 600 MeV. The higher electron energy has another advantage. The higher operating energy suppress Touschek effect, by which electron beam lifetime of UVSOR-II is limited. In the experiment at 750 MeV, we observed about three times longer lifetime, which resulted in longer lasing time for users experiment.

LASING AROUND 230 nm

Similar to the case of 215 nm-FEL, the lasing around 230 nm was planned oriented to users experiments. In the lasing experiment, multi-layers of Al_2O_3/SiO_2 were also employed for cavity mirrors. Measured round-trip reflectivity and transmission were 98.8 % and 0.8%, respectively. Therefore the optical characteristics of mirrors is advantageous for the FEL lasing as compared with mirror of 215 nm. The lasing experiment was carried out with an electron energy of 750 MeV. Fig 3 shows the extracted FEL power and the stored electron beam current as a function of time after the electron beam is stored. As is expected, higher extracted laser power was obtained and the observed maximum power reached 1.1 W at a beam current of 100 mA/bunch. During the experiment, drift of the laser power was observed especially at a high beam current as shown in the figure. The power could be recovered by adjusting the alignment with downstream mirror once again. Therefore the power drift can be explained by deformation of the cavity mirror due to heat-load from synchrotron radiation and from the FEL. The laser, however, became almost stable after about one hour exposure of synchrotron radiation.

The FEL around 230 nm was applied to two experiments on surface physics and photo-electron spectroscopy. The FEL extracted from the upstream mirror was transported to the experimental stations by using aluminium mirrors and was focused on samples by lenses. In the experiments, they started the measurement after the laser became stable. The FEL power around 0.5 ~ 0.2 W was actually applied. Although the experiments were made in limited machine time, the users succeeded in obtaining primary results.

CONCLUSION

We have succeeded in high power FEL lasing in deep UV around 215 nm and 230 nm. Users experiments of the FEL were carried out and primary results were obtained. The stability of the laser at the source position and also at the experimental station should be improved. Suppression of the thermal deformation of the cavity mirror and stability of the laser transport system are critical issues. We are going to lasing below 200 nm in near future. The shorter wavelength FEL is desired for the photo-electron spectroscopy experiment.

REFERENCES

[1] H. Hama et. al., Free Electron laser and its Applications in Asia, (1997) 17.
[2] M. Katoh et. al. Nucl. Instru. and Meth. A467 (2001) 68.
[3] A. Mochihasi et. al., UVSOR Activity Report 2004 (2005) 35. A. Mochihashi et. al., UVSOR Acitivity Report 2005 (2006) 37.
[4] A. Renieri, Nuovo Cimento, 53 (1979) 160.

SUPER COHERENT THZ LIGHT SOURCE BASED ON AN ISOCHRONOUS RING WITH VERY SHORT ELECTRON BUNCHES*

T. Tanaka#, T. Muto, F. Hinode, M. Kawai, K. Nanbu, K. Kasamsook, K. Akiyama, M. Yasuda and H. Hama, Laboratory of Nuclear Science, Tohoku University, 1-2-1 Mikamine, Taihaku-ku, Sendai, 982-0826, Japan
H. Tanaka, JASRI/Spring-8, 1-1-1 Koto, Sayo-cho Sayo-gun, Hyogo- pref. 679-5198, Japan

Abstract

A project to develop a coherent Teraherz (THz) light source has been progressed at Laboratory of Nuclear Science, Tohoku University. The coherent synchrotron light in the THz region is emitted from electron bunches with very short bunch less than 100 fs (rms) created by a thermionic RF gun and a sophisticated bunch compressor. The beam can circulate through the nearly complete isochronous ring for many turns, so that the average radiation power may be considerably enhanced. As an injector of this ring, we have developed an independently tunable cells (ITC) RF gun, which consists of two independent cavities to manipulate the longitudinal phase space. In order to generate short bunch with a significant bunch charge, a magnetic compressor is needed at downstream of ITC-RF gun. Two kinds of bunch compressor have been studied. This paper presents the isochronous THz ring design and describes ITC-RF gun, the magnetic bunch compressor and results of simulations. From simulation of the bunch compressor, we got a very short bunch length about 42 fs (rms).

INTRODUCTION

In these years, the coherent radiation in THz region has been observed in some 3rd generation light sources like BESSY-II [1]. However, it seems to be difficult on the storage ring to realize and/or maintain the short bunch with a significant beam current against bunch lengthening or other instabilities. On the other hand, when we focus on the condition of an isochronous beam transport, there is another possibility to generate the coherent radiation [2]. A very short electron bunch length around 100 fs is required to generate coherent THz radiation. To realize a coherent THz source based on the isochronous ring, total technologies of accelerators are required.

In this paper, a design study of an electron source and the bunch compressor for a novel coherent THz radiation source are described.

COHERENT THZ LIGHT SOURCE

Design of Isochronous Ring

The isochronous ring is the one of the candidates of the light source of coherent THz light [3]. Since this isochronous ring must keep a very short bunch length less than 100 fs (rms) from an injector in every place, it has been designed to have very small dispersion function. To keep bunch length for many turns at everywhere, the path difference for one turn should be much smaller than the bunch length. So that, the momentum spread of the injection beam must be order of 10^{-4} taking into account the momentum compaction factor which is designed as 0.0002. This ring has advantages; (1) multiple beam lines can be utilized, (2) a high average power of THz light can be generated since the electron beam can circulate ring for many turns. However, a betatron initial phase difference affects on the bunch lengthening larger than the effect of momentum compaction factor relatively. In order to reduce this bunch lengthening, an appropriate design of the phase advance in arcs is required [3]. We have designed the lattice of isochronous THz ring, then the effect of bunch lengthening in the bending arc has been calculated, and it is less than 40 fs which satisfies a condition to generate a coherent THz light. The major designed parameters of the isochronous ring are as follows. Tentative design parameters of this ring are shown in Table 1.

Table 1. Tentative design parameters of isochronous THz ring.

Circumference	C	45.691 m
Beam energy	E	200 MeV
Lattice type	-	Racetrack modified FODO
Bending radius	ρ	3 m (normal cell), 2 m (dispersion suppressor)
Momentum compaction factor	α	< 0.0002
Emittance of injection beam	ε_{rms}	5 π nmrad
Momentum spread of injection beam	$\Delta p/p$	2×10^{-4}

Coherent Synchrotron Radiation

The peak power of a coherent radiation from this ring has been calculated, and then it becomes about 100 kW with the bunch length of 100 fs (rms). This peak power of THz light is larger than other THz light sources (ex. FEL, other Lasers). This ring also has high performance in the average power of THz light. Radiation power of THz light sources is summarized in Table 2.

*Work supported by the Grants-in-Aid of Japan Society for the Promotion of Science, contract No. 17360035.
#takumi@lns.tohoku.ac.jp

Table 2. Radiation power from different THz light sources.

Source	Peak power (Micropulse length)	Average power
p-Ge Laser	1 W (10 ms)	100 mW
YAG + NOE	300 mW (4 ns)	60 nW
FEL	10 kW (1 ps)	10 mW
Isochronous THz ring	100 kW (250 fs)	350 mW

GENERATION OF VERY SHORT BUNCH

Design of a Thermionic RF Gun

As an injector of the isochronous ring, it is required to generate an electron beam with a very short bunch length less than 100 fs (rms) and with a very small normalized rms emittance less than 2 π mm mrad. To achieve high average power of coherent radiation, macropulse duration of the injector should be about 1.5 μs taking into account the circumference of the isochronous ring. In addition, the bunch charge should be as large as possible. To gather high bunch charge, the injector should have a large acceptance of momentum deviation. An acceptable momentum deviation is limited by acceptance of coherent THz ring. The coherent THz ring requires a momentum spread of the order of 10^{-4} for the injection beam. Because the beam is accelerated from 2 MeV to 200 MeV in the Linac, $\Delta p/p$ is limited to the order of 10^{-2} at the injector. To realize above parameters, a thermionic RF gun has been adopted for the injector. As a cathode material, a small single crystal of LaB_6 with a diameter 1.75 mm has been chosen. This cathode has a higher current density than conventional dispenser cathode. The normalized emittance can achieve a small value because of the small diameter. To reduce back-bombardment effect [4], this small diameter may be effective. In order to control a distribution of a longitudinal phase space at the exit of this RF gun, we employed independent two cells which don't couple with each other [5]. Parameters of ITC-RF gun are listed in Table 3.

Table 3. Design parameters of ITC-RF gun.

RF frequency	2,856 MHz (S-band)
Cathode material	LaB_6
Current density @ cathode	100 A/cm^2
Cathode diameter	1.75 mm
Number of cells	2
Feeding total power	～5 MW
E_{total} @ exit of gun	～2 MeV
Bunch length (rms)	～100 fs
Bunch charge	～several tens pC
$\varepsilon_{norm.\ rms}$	< 2 π mm mrad
$\Delta p/p$	< 2 %
Macropulse duration	1.5 μs

3D FDTD Simulation of ITC-RF Gun

In order to study the beam dynamics in ITC-RF gun and to design this geometry, we have used a 3D FDTD simulation code [6]. This code can include effects of the beam wakefield and of the space charge self-consistently. We have to design an appropriate distance between the cells and the strength of the accelerating field in each cell, because the longitudinal phase space strongly depends on these parameters. Since it is difficult for 3D FDTD code to calculate a precise geometry because of the mesh size, a 2D code: SUPERFISH [7] has been used to decide the precise geometry for manufacturing of ITC-RF gun. Because the RF coupling is a very small, accelerating fields are independent from each other. The prototype of ITC-RF gun is shown in Fig. 1.

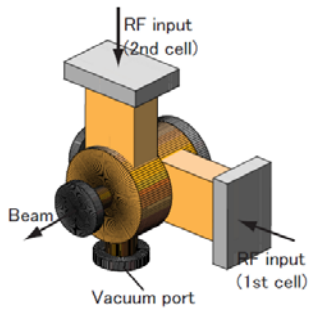

Figure 1. The prototype of ITC-RF gun. The RF input port is separated each other. This is now under manufacturing.

ITC-RF gun is designed to drive at π-mode basically. Peak accelerating fields of 1st cell E_1 [MV/m], 2nd cell E_2 [MV/m] and relative phase between cells Δθ are three degrees of freedom to control this gun. So as to compress the bunch length easier at the downstream of the gun, we have searched an optimum operating point of the gun to generate a beam with a linear dependence in the longitudinal phase space. At the optimization, the bunch charge from the gun should be as large as possible. The strength of E_1 was fixed around 25 MV/m in this gun, because the head of emitted electrons from a cathode must arrive at the middle point of between cells in time of a half RF cycle. With applying some suitable parameters (E_1, E_2) = (25, 50) MV/m and $\Delta p/p_{max}$ = 2 %, longitudinal and transverse phase spaces at exit of this gun are shown in Fig. 2 and Fig. 3 respectively.

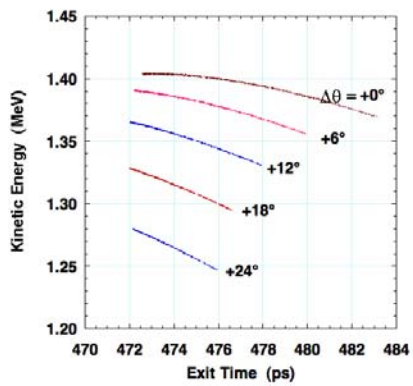

Figure 2. longitudinal phase space. Δθ is a variable in this simulation. (E_1, E_2) = (25, 50) MV/m.

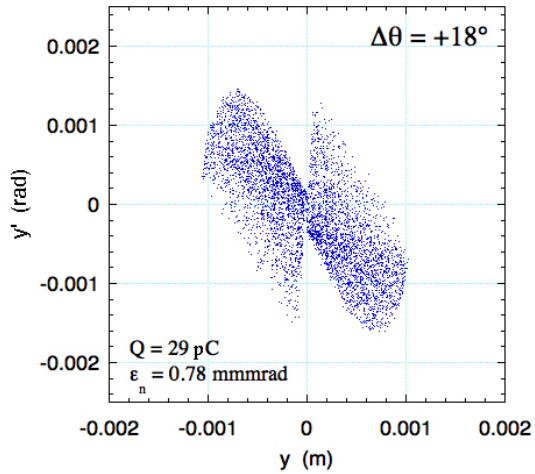

Figure 3. transverse phase space. (E_1, E_2) = (25, 50) MV/m, Δθ = +18 degree.

As shown in Fig. 2, a linearity of momentum distributions depends on the Δθ. From Fig. 3, the normalized rms emittance $\varepsilon_{norm.\ rms}$ = 0.78 π mm mrad satisfy the design value < 2 π mm mrad. Normalized rms emittances in other conditions also satisfy the design value. On the other hand, the bunch charge of this beam with momentum deviation $\Delta p/p$ = 2 % is about 30 pC which almost satisfy the design value. However the bunch lengths of these beams are far from the design value, so that the beams must be compressed at the downstream of the gun.

Magnetic Bunch Compressor

To compress the rms bunch length from several ps to less than 100 fs, a magnetic bunch compressor is needed. Magnetic bunch compression uses a difference of time of flight (TOF) for particles of different momenta p_0 and p_1 where these particles move from s_1 to s_2 along the beam axis. For these particles, the difference of TOF can be written as

$$\begin{aligned}\Delta t &= t_1 - t_0 \\ &= \frac{L_1}{c\beta_1} - \frac{L_0}{c\beta_0} \\ &= \frac{L_1}{c\beta_0\beta_1}\{-L_0(\Delta\beta) + \beta_0(\Delta L)\}\ , \qquad (1)\end{aligned}$$

where t is TOF from s_1 to s_2, L is a path length from s_1 to s_2, β is a relative velocity, index: 0, 1 represent particles with p_0 and p_1 respectively, $\Delta\beta = \beta_1 - \beta_0$ and $\Delta L = L_1 - L_0$. When we assume $p_0 < p_1$ and the longitudinal distribution in Fig. 2, a condition of the bunch compression leads $\Delta t > 0$. The first term of eq. (1) represents a difference of TOF caused by a difference of each particle velocity, and become negligible small when β goes to unity. The second term is caused by a difference of path lengths. In case of ITC-RF gun, the effect of the first term can not be negligible. When a total beam energy is 2 MeV, $s_2 - s_1$ = 1 m and p_1/p_0 = 1.02, the first term becomes about -5 ps. ΔL of the second term can be represented as

$$\begin{aligned}\Delta L &= \Delta L_{\Delta p/p} + \Delta L_{\beta} \\ &= \left\{\int \frac{\eta(s)}{\rho(s)} ds\right\}\frac{\Delta p}{p} + \int \frac{x_{\beta}(s)}{\rho(s)} ds\ . \qquad (2)\end{aligned}$$

The first term of eq. (2) means a path difference produced by an energy dispersion at bending section, and this term can be used for bunch compression. The second term of eq. (2) represents a path difference which comes from a different value of initial phase of a betatron motion, and this term can be suppressed by reducing the beta function and designing appropriate phase advances along lattice.

We have considered two kinds of magnetic compressor. The first is an α-magnet [8], and the second is a triple-bend achromat (TBA) lattice. An advantage of α-magnet is that this system has a larger energy acceptance, and has a possibility to gather larger bunch charge for a large $\Delta p/p$. An advantage of TBA lattice is that this system has a possibility to manipulate the higher order term of $\Delta p/p$ by adjusting optics. Each magnetic bunch compressor can apply different slopes of $(\Delta p/p)/\Delta t$ in longitudinal phase space. In case of TBA lattice, this system can vary the R_{56} by changing a dispersion function of the 2nd benging magnet without changing its reference orbit. When the α-magnet changes the field strength, reference orbit in it is changed correspondingly. Each system can be an achromat for the beam energy. At manufacturing the magnet of each system, it is easier for TBA lattice than α-magnet to design magnets. In order to select the method of a suitable bunch compression, studies have been continued. In the following, basic studies are shown.

In order to estimate a bunch compression, particle distributions in Fig. 2 and Fig. 3 have been used for both methods. The operating conditions of the gun are (E_1, E_2) = (25, 50) MV/m and Δθ = +18 degree. In case of α-magnet method, a beam tracking simulation has been done. In case of TBA lattice method, a design of optics and tracking simulations have been done by using SAD [9]. Since the bending angle of dipole magnets of TBA lattice are the same angle 60 degree, TBA lattice is 180 degree bending transport system totally. In addition, TBA lattice has four families of quadrupole which are used for two purposes mainly. The dispersion function in the 2nd bending magnet is controlled by quadrupole magnets between bending magnets to change the R_{56}. The other quadrupole magnets are used for matching of horizontal and vertical Twiss parameters at exit and reducing the beta function in bending magnets. One example of the TBA optics is shown in Fig. 4.

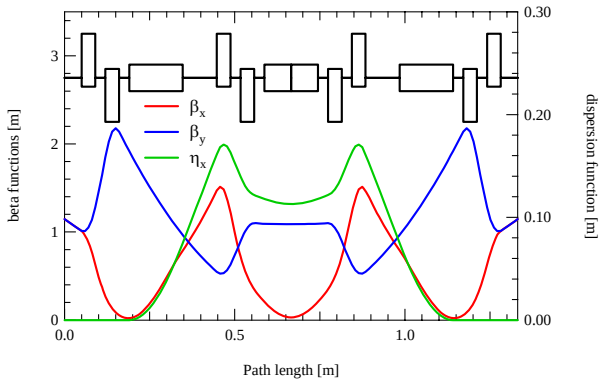

Figure 4. TBA optics. Left axis is for beta functions. Right axis is for dispersion function.

In case of an α-magnet, the first term of eq. (2) can be calculated by using following equation

$$\Delta L_{\Delta p/p} = \left\{ \int \frac{\eta(s)}{\rho(s)} ds \right\} \frac{\Delta p}{p}$$

$$= \frac{K_\alpha}{2} \sqrt{\frac{\beta\gamma}{g}} \frac{\Delta p}{p} \quad , \qquad (3)$$

where K_α = 191.655 Gauss$^{1/2}$cm$^{1/2}$ and g is the field gradient of α-magnet in Gauss/cm. The path length in α-magnet can be represented as $K_\alpha \sqrt{\beta\gamma / g}$. In order to estimate a difference of TOF in an α-magnet, the first term of eq. (1) and eq. (3) should be calculated, and then we can find the field gradient of an α-magnet for a suitable bunch compression. After optimizations of each bunch compressor, the longitudinal phase spaces and the particle time distributions are shown in Fig. 5.

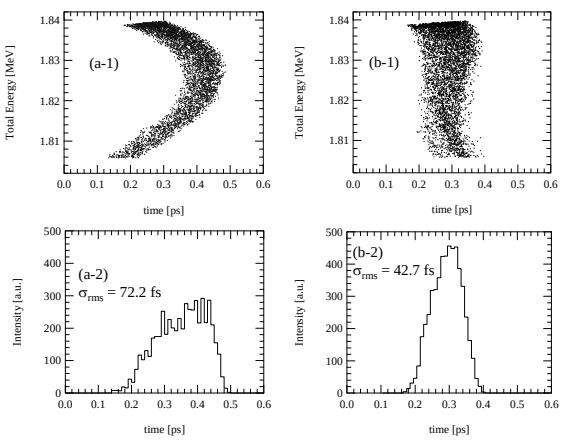

Figure 5. longitudinal phase space distributions and time distributions after bunch compression. (a-1), (a-2) α-magnet case, (b-1), (b-2) TBA lattice case.

As shown in Fig. 5, the compressed bunch lengths are 72.2 fs (rms) for the α-magnet system and 42.7 (rms) fs for the TBA lattice respectively. Both bunch compressors can achieve less than 100 (rms). TBA lattice can achieve shorter bunch length in this case, but more studies are needed for selecting a more suitable method.

SUMMARY

We have proposed the coherent THz light source by employing an isochronous THz ring and an injector which can generate a very short electron beam. From numerical calculations and simulations, the radiation power from the isochronous THz ring may achieve higher than other light sources of THz region. In order to generate the required short bunch beam for this ring, we have designed the injector which consists of ITC-RF gun and the magnetic bunch compressor. ITC-RF gun can generate a small normalized rms emittance value which satisfies the design parameter. For generating very short bunch, a magnetic compressor is needed at the downstream of ITC-RF gun. We have studied two kinds of bunch compressor: α-magnet transport and TBA lattice transport. Both of bunch compressors can achieve design bunch length less than 100 fs (rms). At a glance, TBA lattice seems to be better than α-magnet. However, we have continued to studied more detail about them including effect of the higher order momentum dependences and betatron initial phase difference.

REFERENCES

[1] M. Abo-Bakr, et al., Phys. Rev. Lett. 90 (2003) 94801.
[2] T. Nakazato, et al., Phys. Rev. Lett. 63 (1989) 1245.
[3] H. Hama, et al., Proc. of the 27th International FEL Conf., Stanford, California U.S.A., pp. 1.
[4] C.B. McKee and J.M.J. Madey, Nucl. Instr. and Meth. A 296 (1990) 716.
[5] T. Tanaka, et al., Proc. of the 27th International FEL Conf., Stanford, California U.S.A., pp. 142.
[6] H. Hama, et al., Nucl. Instr. and Meth. A 528 (2004) 371.
[7] http://laacg1.lanl.gov/laacg/services/download_sf.phtml
[8] H.A. Enge, Rev. Sci. Instr. 34 (1963) 385; M. Borland, Ph.D. Thesis, Stanford University, 1991.
[9] http://acc-physics.kek.jp/SAD/sad.html

RECENT EXPERIMENTS AND PROSPECT ON THE NIJI-IV VUV/IR FEL

H. Ogawa#, K. Yamada, N. Sei, M. Yasumoto, K. Yagi-Watanabe
Research Institute of Instrumentation, National Institute of Advanced Industrial Science and Technology (AIST), 1-1-1 Umezono, Tsukuba, Ibaraki 305-8568, Japan

Abstract

The NIJI-IV free electron laser (FEL) is being developed as a compact light source with very good optical quality and ultra-wideband tunability from the VUV to the IR. To obtain lasing at shorter wavelengths in the VUV region, continuous efforts to improve the cavity-mirror performance have been made, so that the original loss of mirrors was recently decreased around 195nm. A new optical cavity system, composed of two sets of a heavy granite base and a stable mirror manipulator, was installed to stabilize the lasing and also to extend the tuning range. As for the IR FEL, modification of the beam transport system to make space for installation of the optical cavity was completed.

INTORODUCTION

Storage ring FELs (SRFELs) are unique source and have advantages such as good spectral resolution, high repetition rate, and natural synchronisation with synchrotron radiation from insertion devices or bending magnets. These features of SRFELs are suitable for pump-probe experiments and observing a continuous change of a phenomenon without giving sample damage. Indeed, the use of SRFELs for the real-time surface observation has been investigated in combination with a photoemission electron microscopy (PEEM) at DUKE [1,2] and AIST [3,4]. Many efforts to shorten the wavelength in SRFELs have been made [5-7] for such applications. At AIST, an FEL research has been performed using the compact storage ring NIJI-IV and the FEL lasing down to 198nm was achieved [7]. The NIJI-IV is a racetrack-type storage ring whose circumference is 29.6m. The ring has two straight sections of 7.25 m and 4.1 m in length and a 6.3-m optical klystron ETLOK-II [8] is equipped in the longer straight section for the UV/VUV FEL experiments as shown in Fig.1. In 2004, a 3.6-m optical klystron ETLOK-III [9] was installed into the other straight section and the construction for lasing in the IR region is going on [10]. The optical klystron parameters are summarized in Table 1. Here we report recent progress in the NIJI-IV FEL.

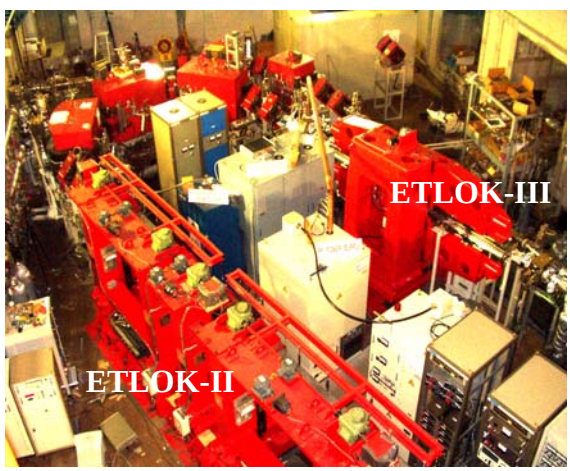

Figure 1: NIJI-IV FEL system.

Table 1: Parameters of optical klystron ETLOK-II and III

	ETLOK-II	ETLOK-III
Total length [m]	6.288	3.55
Magnetic period		
Undulator section [mm]	72	200
Dispersive section[mm]	216	720
Number of period N_u	42×2	7×2
Deflection factor K	<2.29	<10.04
Wavelength [μm]	0.198-0.595	(0.4-12)

DEVELOPMENT OF THE VUV/IR FEL

VUV FEL Mirror

To shorten the FEL wavelength, we have been upgrading the NIJI-IV FEL system. The replacement of NIJI-IV vacuum chambers as well as installation of thin sextupole magnets has been performed in order to increase FEL gain. As for the laser cavity, Al_2O_3/SiO_2 dielectric multilayer mirrors were adopted for the wavelength below 220 nm. In a previous study, we tried FEL oscillations below 195 nm with two kinds of Al_2O_3/SiO_2 mirrors but failed to obtain the oscillation. The original losses of the cavity composed of two mirrors around 195nm were small as 1.9%-2.6%, while the losses after irradiated by the undulator radiation from ETLOK-II were rapidly increased through degradation of dielectric multilayer mirrors as shown in Fig.2, so that the oscillation could not be realized [10]. To improve the mirror performance, the Al_2O_3/SiO_2 mirrors were manufactured again by tuning the dielectric coating condition. As a result, the original loss of the cavity was presently obtained to be down to 1.2%, which was sufficient to realize the lasing around 195nm. After measuring an evolution of degradation of the mirrors, we are planning to perform the FEL oscillation experiments below 195nm.

#ogawa.h@aist.go.jp

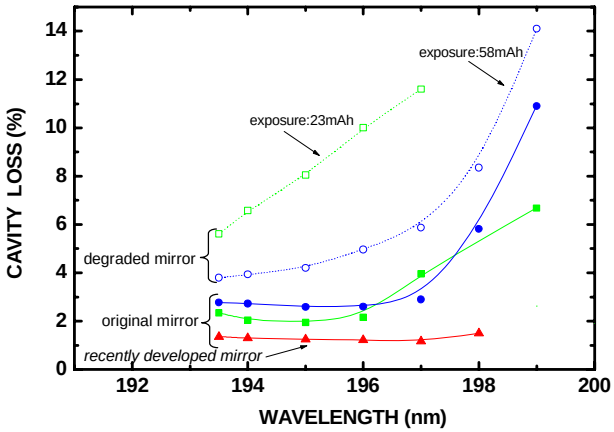

Figure 2: Wavelength dependence of the cavity loss of Al_2O_3/SiO_2 multilayer mirrors. The losses of mirrors manufactured in the previous work are shown by squares and circles, while the loss in the present work is represented by triangles.

Optical cavity system

It was observed that the intensity of the NIJI-IV FEL was modulated with a few to 10 ms period near the best cavity tuning condition and the lasing mode was not fixed at a stable CW mode [11]. Although its origin has never been identified, it is probably caused by a mechanical vibration of the mirror vacuum chamber, because the base of our mirror holders had a slender structure whose weight was only 20-30 kg. Therefore new optical cavity system has been made for the stabilization of the FEL oscillation, which is needed for FEL application research such as a photoemission electron microscopy. Figure 3 shows a photograph of the new system which was installed into an upstream side of ETLOK-II in this year. We chose heavy granite stone, whose weight was about 2 ton, as the base of the cavity, so that the vibration of the base in an optical axis was dumped below 0.1 mm, which was measured with a vibration sensor under frequency of 200 Hz. The mirror chamber is remotely manipulated by five-axis stage with gimbal optical mount and three linear stages (Newport SL20AN, M-MTM100PP.1, M-ILS50PP and M-MVN80 with precision motorized actuators LTA-HL). The cavity length and mirrors can be adjustable with resolutions of 0.1 mm and 0.8 mrad, respectively. In addition, a novel feature is that the chamber has two in-vacuum mirrors that are interchangeable with reproducible adjustment. This will enable us to extend FEL tuning range restricted by a narrow reflection bandwidth of dielectric multilayer mirrors. We will measure the stability of the FEL oscillation with the optical cavity system after commissioning of new beam transport system as described in the following subsection.

Figure 3: New optical cavity system.

Beam transport system

In order to extend lasing range toward a long-wavelength region, we have been developing the NIJI-IV FEL in the infrared (IR) region using ETLOK-III. The FEL gain in the visible and near-IR regions was evaluated to be over 2% from observed spectra of a spontaneous emission from the ETLOK-III [10]. The realization of FEL lasing can be expected in the visible and near-IR regions since high-reflection mirrors of 99.8% or more are available. We are preparing to make an optical cavity system for the IR FEL and its mirror diameter would be 50mm, which is larger than that for the UV/VUV FEL of 30mm, by considering diffraction loss.

However, there was no space to install the upstream cavity system for the IR FEL because a beam transport line was too close to the storage ring. Therefore we decided to modify the transport system to make a space for the cavity. The detail of design for new beam transport system was written in [10]. We have constructed the new transport system, as shown in Fig.4, which is 2.48m away from the former one and the beam commissioning has been started. The beam was transported from LINAC to

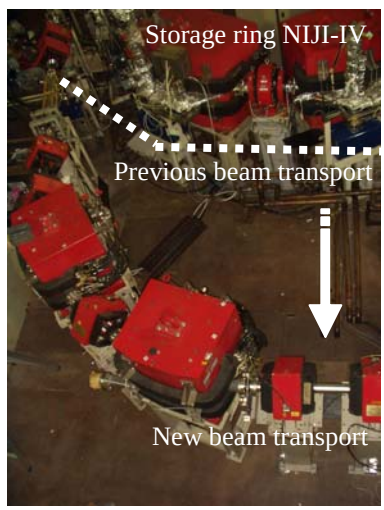

Figure 4: Photograph of a part of new beam transport system. The place where previous beam transport located is indicated by dashed line.

an entrance of the storage ring and focused into a septum chamber of NIJI-IV. The final tuning of beam parameter is now in progress.

DUV FEL APPLICATION

Recently, performance of the NIJI-IV FEL was improved at the deep UV (DUV) around 200 nm by both optimizing the transmittance of the output coupler and increasing stored electron-beam energy [3]. Thus we can make real-time observation of chemical reactions on a transition metal surface using a photoelectron emission microscopy (PEEM). The metal surface was irradiated by an FEL or spontaneous emission from ETLOK-II at a wavelength of 202 nm, and the catalytic CO-oxidation ($2CO + O_2 \rightarrow 2CO_2$) on a Pd(111) single crystal surface has been investigated by introducing CO and O_2 gases at a pressure of $\sim 10^{-5}$ Pa [4]. Figure 5 shows the setup for FEL-PEEM measurement. The PEEM system (STAIB Instrumente, type 350) is only applicable at pressures below $\sim 10^{-5}$ Pa, since a micro channel plate (MCP) image intensifier equipped in the system requires a vacuum of better than $\sim 10^{-5}$ Pa during operation. A differential pumping is necessary for observation of chemical reaction under higher pressure. Therefore we prepared a turbo molecular pump (Varian Turbo-V70LP) that is being added to a differential pumping port close to MCP. We are planning to observe chemical reactions on the transition metal surfaces at higher pressure of $\sim 10^{-3}$ Pa.

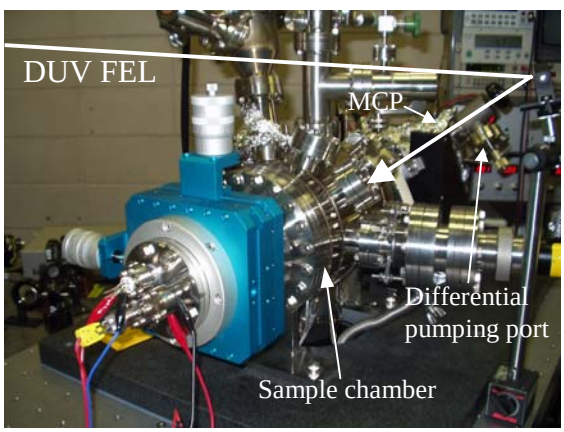

Figure 5: Photograph of the FEL-PEEM system.

SUMMARY

An FEL with wide wavelength range from the VUV to IR has been studied based on compact storage ring NIJI-IV. To shorten the lasing wavelength, Al_2O_3/SiO_2 multilayer mirrors optimized at 195nm were improved and the cavity loss of the original mirrors was successfully reduced by 30%, compared with that of previous ones. The preparation for the lasing in the IR region is also proceeding. The beam transport system in NIJI-IV has been modified to make space for the optical cavity of the IR FEL. Furthermore, in order to stabilize the FEL oscillations in the UV/VUV regions, new optical cavity system holding two in-vacuum interchangeable mirrors has been installed, which was composed of heavy granite base and five-axis manipulators. This will enable us to carry out reproducible FEL application experiments, such as real-time observation of surface chemical reactions.

ACKNOWLEDGEMENTS

This study was financially supported by the Budget for Nuclear Research of the Ministry of Education, Culture, Sports, Science and Technology, based on the screening and counseling by the Atomic Energy Commission of Japan.

REFERENCES

[1] W.-C. Yang et al., J. Appl. Phys. 94 (2003) 5720.
[2] W.-C. Yang et al., Phys. Rev. Lett. 90 (2003) 136102.
[3] K. Yamada et al., Proceedings of the 26th Free Electron Laser Conference, August 2004, Trieste, p.311.
[4] H. Ogawa et al., Proceedings of the 27th International Free Electron Laser Conference, August 2005, Stanford, p.467.
[5] F. Curbis et al., Proceedings of the 27th International Free Electron Laser Conference, August 2005, Stanford, p.473.
[6] V.N. Litvinenko et al., Nucl. Instr. and Meth. A470 (2001) 66.
[7] K. Yamada et al., Nucl. Instr. and Meth. A528 (2004) 268.
[8] T. Yamazaki et al., Nucl. Instr. and Meth. A331 (1993) 27.
[9] N. Sei et al., Jpn. J. Appl. Phys. 41 (2002) 1595.
[10] N. Sei et al., Proceedings of the 27th International Free Electron Laser Conference, August 2005, p.469.
[11] K. Yamada et al., Nucl. Instr. and Meth. A475 (2001) 205.

DISPERSION EFFECTS IN SHORT PULSE WAVEGUIDE FEL

N. S. Ginzburg, E. R. Kocharovskaya, A. S. Sergeev IAP RAS, Russia.

Abstract

The influence of waveguide dispersion on the FEL operation driven by short electron bunches is studied. Under the assumption of a high quality resonator, a parabolic equation for the evolution of the profile of electromagnetic pulse is derived. The condition of self-excitation are found by means of an analytical theory describing a structure of supermodes as the sum of resonator eigenmodes with locked phases. It is demonstrated that due to waveguide dispersion FEL is able to generate not only for positive but also for negative cavity detuning. The transient and nonlinear stages of the free-electron laser operation are analyzed by the computer simulation, and the optimal mismatches of group and cavity synchronism conditions are found.

INTRODUCTION

The mode-locking regime is typical for free-electron lasers (FEL) driven by a train of short electron bunches. In this regime, the electromagnetic radiation consists of micropulses with a duration nearly equal to that of the electron bunches. Both pulses (electron and electromagnetic) travel together through the resonator, but shift slightly away from each other due the difference between the wave group velocity and the electron velocity. Once they reach the right-hand mirror, the electron pulse escapes from the resonator, while the electromagnetic pulse reflects and comes back to the left-hand mirror at the time when the next current pulse arrives.

In short wavelength (optical, infrared) FEL experiments [1-4], the group velocity of electromagnetic pulses exceeds the velocity of electron bunches. To provide generation under such conditions, a specific mismatch between a period of electromagnetic pulse round trip over a resonator and a period of bunch injection was used. However, in some experimental investigations of long wavelength FELs [5-8], a waveguide may be used, so that the specific waveguide dispersion allows one to realize "zero-slippage" condition, for which the group velocity of electromagnetic pulse is equal to the longitudinal velocity of electrons. Under such conditions, mutual synchronization of radiation from different parts of electron bunches occurs due to dispersive spreading of the electromagnetic field, whereas localization of radiation near electron bunches is caused by its guiding properties [9,10].

In the present paper, a theoretical model of waveguide FEL is developed which takes into account the waveguide dispersion. Under the assumption of a high quality resonator, a parabolic equation for the evolution of the profile of electromagnetic pulse is derived. The linear, transient and nonlinear stages of the FEL operation are investigated, both analytically and numerically, and the optimal conditions are found.

THE MODEL AND BASIC EQUATIONS

Let us suggest that the radiation pulse propagating through a waveguide circulates between two mirrors (with reflection coefficients $R_{1,2}$), which are placed at some distance, L_0. Let FEL be fed by short electron pulses of duration τ_p, which is essentially less than both the round-trip of the radiation in the cavity $T_R = 2L_0 / v_{gr}$, and the repetition period of an electron bunch injection, T_i. During n-the pass through a resonator, the field can be represented as

$$A = \mathrm{Re}\left[E_s(r_\perp) \begin{Bmatrix} A_n^+(z,t)\exp(i(\omega_0 t - h_0 z)) + \\ A_n^-(z,t)\exp(i(\omega_0 t + h_0 z)) \end{Bmatrix} \right],$$

where E_S is a function, describing the profile of a given transverse waveguide eigenmode, ω_0 is the reference frequency, and $h_0 = h(\omega_0)$ the longitudinal wave number. Resonant electron-wave interaction takes place under the synchronism condition, $\omega_0 - h_0 v_\parallel \simeq \Omega_\perp$, where $\Omega_\perp = h_u v_\parallel$ is the bounce frequency, $h_u = 2\pi / \lambda_u$, λ_u the undulator period. We will consider the excitation of a resonator by a train of short electron bunches under the following conditions:

- the reflection coefficients are close to unity, $R_{1,2} \simeq 1$ and the changes of the wave amplitude during one pass are very small;
- dispersion spreading of the electromagnetic pulse during one pass over the resonator is small as well.

Under these approximations, we can replace the discrete variable n (pass number through the resonator) by a slow time τ with the period of one round trip, T_R taken as a time unit. Evolution of the pulse profile along the resonator can be described by the parabolic equation (for details see [9]):

$$\frac{\partial \alpha}{\partial \hat{\tau}} + \frac{\omega_0}{2Q}\alpha - \hat{\varepsilon}\frac{\partial \alpha}{\partial y} + i\frac{\hat{\nu} V_{gr}}{2}\frac{\partial^2 \alpha}{\partial y^2} = \frac{e\pi I_0 V_{gr}\kappa}{2m_e c^3 \gamma N_S h_0 l}\int_0^l f(y - z/V_{gr}) I_\omega dz, \qquad (1)$$

where $I_\omega = \frac{1}{\pi}\int_0^{2\pi} e^{-i\Theta} d\Theta_0$ is the synchronous harmonic of the beam current, $V_{gr} = \partial\omega / \partial h$ the wave group velocity, $\hat{\nu} = |\partial^2 h / \partial \omega^2|$ the wave dispersion parameter,

$Q = \omega_0 l / V_{gr}(1 - R_1 R_2)$ the resonator Q-factor, I_0 the peak current of electron bunch, $\gamma = 1/\sqrt{1-\beta^2}$ the relativistic Lorentz factor, n_s the norm of the operating mode, κ the electron-wave coupling coefficient, $f(y)$ a function, describing the electron pulse profile, $\alpha = eA_n/(m_e c\gamma)$ the dimensionless wave amplitude. Taking into account the cavity detuning $\hat{\varepsilon} = (T_i - T_R)/T_R$, we use an independent time variable, $y = t - z/V_{gr} - \hat{\varepsilon}\hat{\tau}$.

Under assumptions described above, we can relay upon the periodical boundary conditions:

$$\alpha(\hat{\tau}, y) = \alpha(\hat{\tau}, y + T_R) \tag{2}$$

and expand the field and the beam current into Fourier series:

$$\alpha(\hat{\tau}, y) = \sum_{m=-\infty}^{\infty} a_m(\hat{\tau}) \exp(i2\pi m y / T_R),$$
$$I_\omega = \sum_{m=-\infty}^{\infty} J_m(\hat{\tau}) \exp(i2\pi m y / T_R). \tag{3}$$

An amplitude of each harmonic a_m, can be treated as an amplitude of cavity eigenmode with the longitudinal index m.

Assuming a small variation of electron energy $E = m_e c^2 \gamma$ and neglecting the Coulomb interaction, the electron motion equation can be presented in the form

$$\left(\frac{\partial}{\partial z} + \left(\frac{1}{V_\parallel} - \frac{1}{V_{gr}}\right)\frac{\partial}{\partial y}\right)^2 \Theta = \left(\frac{\omega_0}{c}\right)^2 \mu\kappa \,\mathrm{Re}\left(\alpha e^{i\Theta}\right) \tag{4}$$

with the boundary conditions:

$$\left(\frac{\partial}{\partial z} + \left(\frac{1}{V_\parallel} - \frac{1}{V_{gr}}\right)\frac{\partial}{\partial y}\right)\Theta\Big|_{z=0} = \Delta,\ \Theta\Big|_{z=0} = \Theta_0 \in [0, 2\pi],$$

where $\Delta = (\omega_0 - h_0 V_\parallel - \Omega_\perp)/V_\parallel$ is the initial mismatch of synchronism at the reference frequency, $\mu \simeq \gamma^{-2}$ the inertial bunching parameter. With the use of normalized variables,

$$\xi = \frac{\omega_0 y}{\chi} P,\ \tau = \frac{\omega_0 \hat{\tau}}{2Q},\ \zeta = z\frac{\omega_0}{c} P,$$
$$P = \left(\frac{4\pi e I_0 \mu\kappa^2 \beta_{gr} Q}{m_e c\gamma d b N_s h_0 l \omega_0^2}\right)^{1/3},$$

equations (1), (4) can be transformed to the following form:

$$\frac{\partial a}{\partial \tau} + a - \varepsilon\frac{\partial a}{\partial \xi} + i\nu\frac{\partial^2 a}{\partial \xi^2} = \int_0^L F(\xi - \zeta) I_\omega d\zeta, \quad (a)$$
$$\left(\frac{\partial}{\partial \zeta} + \frac{\partial}{\partial \xi}\right)^2 \Theta = \mathrm{Re}\left(a e^{i\Theta}\right), \quad (b) \tag{5}$$

with boundary conditions:

$$a(\tau, \xi) = a(\tau, \xi + T),$$
$$\Theta\Big|_{\zeta=0} = \Theta_0 \in [0, 2\pi],\ \left(\frac{\partial}{\partial \zeta} + \frac{\partial}{\partial \xi}\right)\Theta\Big|_{\zeta=0} = \delta,$$

where

$$a = \frac{\alpha\kappa\mu}{P^2},\quad T = \frac{T_R \omega_0 P}{\chi},$$
$$\nu = \left|\frac{\partial^2 h}{\partial \omega^2}\right| \frac{V_{gr}\omega_0 Q P^2}{\chi^2},\ \varepsilon = \frac{(T_i - T_R)}{T_R}\frac{2QP}{\chi},\ \delta = \Delta\frac{c}{\omega_0 P}.$$

$L = l\omega_0 P/c$ is the normalized interaction length, $F(\xi)$ the function describing electron-pulse profile, $\chi = \beta_\parallel^{-1} - \beta_{gr}^{-1}$ is the relative value of the detuning of "zero-slippage" condition. The normalized energy stored in electromagnetic pulse is give by relation

$$W = \frac{1}{T_c}\int_0^T |a|^2 d\xi.$$

THE LINEAR THEORY

Linearizing the equation of electron motion (see Eq. 5b), we obtain an equation for the electron current:

$$\left(\frac{\partial}{\partial \zeta} + \frac{\partial}{\partial \xi}\right)^2 I_\omega = -ia \tag{6}$$

Using the expressions (3) we find all harmonics of current

$$J_m = \left[\frac{i}{k_m^2} + \frac{\zeta e^{-ik_m\zeta}}{k_m} - \frac{ie^{-ik_m\zeta}}{k_m^2}\right] a_m, \tag{7}$$
$$k_m = 2\pi m/T + \delta.$$

As a result for the amplitude of each mode a_m from (5a) taken into account (7) we obtain

$$\left[\frac{d}{d\tau} + 1 - i\varepsilon\frac{2\pi m}{T} - i\nu\left(\frac{2\pi m}{T}\right)^2\right] a_m = \sum_{n=-\infty}^{\infty} C_n^m a_n, \tag{8}$$

where

$$C_n^m = \int_0^T\int_0^L \left[\frac{i\left(1 - e^{-ik_n\zeta}\right)}{k_n^2} + \frac{\zeta e^{-ik_n\zeta}}{k_n}\right]\frac{F(\xi - \zeta)e^{i\xi(k_n - k_m)}}{T} d\zeta d\xi.$$

Obviously the diagonal elements of the matrix C_n^m coincide with the expression for a complex electron permittivity found in [9, 10].

Representing the solution of Eq. 8 in the form $a_m = e^{i\Omega\tau}\hat{a}_m$ where Ω is a complex frequency, we get the algebraic equations for the supermodes of the resonator excited by a train of electron bunches:

$$i\Omega\hat{a}_m = \sum_{n=-\infty}^{\infty} D_n^m \hat{a}_n, \tag{9}$$

where $D_n^m = C_n^m - 1 + i\varepsilon(2\pi m/T) + i\nu(2\pi m/T)^2$.

Assumed for simplicity that the electron pulse has the

rectangular form with normalized duration $T_c = \tau_c \omega_0 P / \chi$, we obtain the following expression for the elements of the matrix D_n^m:

$$D_n^m = \frac{\left(e^{i(k_n-k_m)T_c/2} - e^{-i(k_n-k_m)T_c/2}\right)}{T} \frac{e^{-ik_m T_c/2}}{(k_n-k_m)^2} \times$$

$$\left[\frac{ie^{ik_m L}}{k_m^2} - \frac{ie^{ik_n L}}{k_n^2} - \frac{i}{k_m^2} + \frac{i}{k_n^2} + \frac{L}{k_m} - \frac{L}{k_n}\right] +$$

$$i\varepsilon\frac{2\pi m}{T} + i\nu\left(\frac{2\pi m}{T}\right)^2 - 1.$$

The starting condition of generation corresponds to the equality

$$\mathrm{Im}[\Omega] = 0. \qquad (10)$$

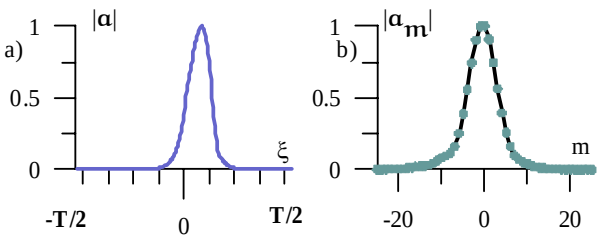

Figure 1: Normalized profile (a) and spectrum (b) of the supermode for the dimensionless parameters: $T_c = 4$, $\varepsilon = 1$, $L = 2.3$, $\nu = .3$. Resonator eigenmodes amplitudes are shown by blue dotes.

A spatial structure of supermodes calculated via eigen vectors of the matrix D_n^m is shown in Fig. 1a; it is a superposition of longitudinal resonator eigenmodes.

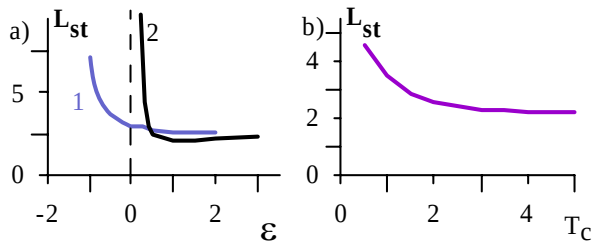

Figure 2: Dependence of the starting length, L_{st} a) on the cavity detuning ε: 1 for dispersive parameter $\nu = .3$, and 2 for the absence of dispersion and b) on the dimensionless electron bunch duration T_c.

Note that wave dispersion, playing a part of feedback, allows FEL to generate even in the case of negative values of the cavity detuning ($\varepsilon < 0$, see Fig. 2a, curve 1), for which the resonator can not be excited in the absence of dispersion (see Fig. 2a, curve 2). The increasing of the electron bunch duration leads to the decrease of the generation threshold (see Fig. 2b). For long electron bunch duration T_c this value as well as the cavity detuning does not practically influence the generation threshold.

COMPUTER SIMULATION OF THE NONLINEAR STAGE

The nonlinear stage of the electron-wave interaction was analyzed on the basis of computer simulation of Eqs. 5. The electron bunch profile has a rectangular form with normalized duration T_c. Three basic regimes of the FEL generation have been observed when the value of current exceeds the generation threshold: a) stationary regime (see Fig. 3), b) periodic self-modulation (see Fig. 4a), c) chaotic self-modulation (see Fig. 4b).

At a small excess over the generation threshold, a profile of the field and its spatial spectrum are closed to those found from the linear analysis (see Fig.1). The dynamics of electromagnetic pulse profile become more complicated with increasing the dimensionless resonator length, L (see Fig.3).

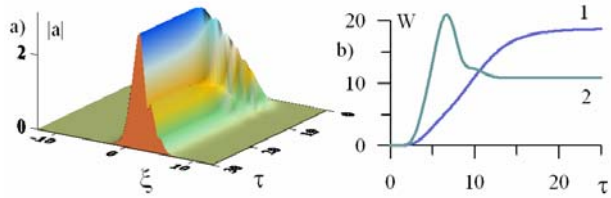

Figure 3: Regime of the stationary generation: $L = 4.4$, T=25.6, $\varepsilon = 0.5$, $T_c = 4$, $\nu = 0.3$,: a) time–space evolution of an envelope of the electromagnetic pulse; b) time dependence of the electromagnetic pulse energy W: for comparison the case of the absence of dispersion is shown by curve 2.

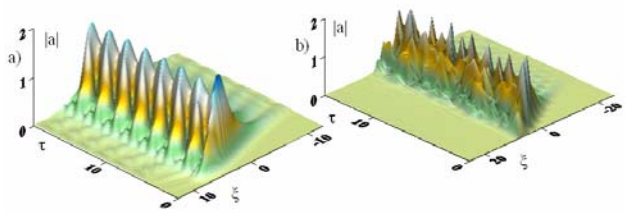

Figure 4:Time–space evolutions of an envelope of electromagnetic pulse in the regime of periodical (a) ($L = 4.4$, T=25.6, $\varepsilon = 4$, $T_c = 4$, $\nu = 1$) and chaotic self-modulation (b) ($L = 10$, T=51.2, $\varepsilon = 1$, $T_c = 6$, $\nu = 1$).

The self-modulation regime may be reached by two ways: via increasing the dimensionless length L and/or via enlarging the cavity detuning ε. Possible quasi-periodical behavior is demonstrated in Fig. 4a.

At large excess over the generation threshold, the chaotic regime of generation takes place (see Fig. 4b). At extremely large excess over the generation threshold, the pulse envelope evolves in a complicated stochastic manner, so that the generated radiation is distributed quasi-homogeneously over very wide spectral range of the resonator eigenmodes. According to estimates all these regimes are reasonable for the waveguide FEL to provide variety of applications (see Fig.5).

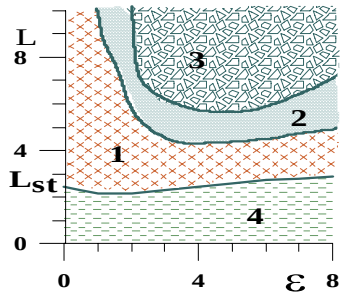

Figure 5: Zones of stationary (1), periodical (2) and chaotic (3) generation on the plane of dimensionless length L and cavity detuning ε for $\nu = 1$, $T_c = 4$, $T = 51.2$. Zone (4) is absence of generation.

The stationary regime, when one supermode is generated, has been investigated in detail for various parameters of dispersion, the detuning of "zero-slippage" conditions and cavity detuning. At the limit $\chi \to 0$ and $\varepsilon \to 0$ the equations (5) transform into the equations for the case of group synchronism [5, 6, 10]. Numerical simulation of the equations (5) at small values of the parameter ε, allows us to determine an optimal relation between all FEL parameters, χ, L, T_C and ν, which gives the maximum field amplitude, i.e., provides the most effective interaction between the electromagnetic pulse and the electron bunches.

Note also that a superradiant (nonstationary) type of operation regime [11] can be realized for small negative cavity detuning ε (see Fig. 6).

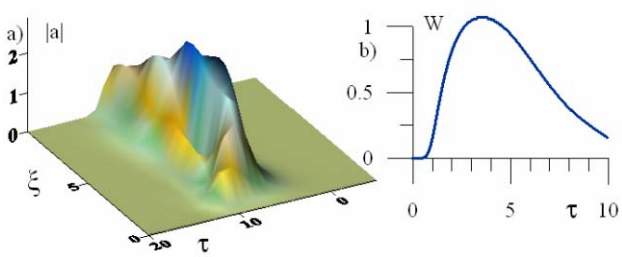

Figure 6: Superradiant operation regime: $L = 4.4$, T=51.2, $\varepsilon = -0.5$, $T_c = 16$, $\nu = 0.3$,: a) time–space evolution of an envelope of the electromagnetic pulse; b) time dependence of the field energy.

CONCLUSION

In conclusion, we develop both linear and nonlinear theory to describe regimes of operation of the waveguide FELs with finite detuning of "zero-slippage" condition and cavity detuning.

On the base carried out theoretical analyze it were estimated parameters of generated radiation for KAERI THz FEL ($\lambda = 100 \mu m$) [7, 8]. The experiments were done for an electron bunche of duration $\tau_p \simeq 30$ ps, an electron current ~ 0.5 A, particle energy ~ 6.5 MeV, the undulator period $\lambda_u = 25$ mm, the undulator length –2 m, amplitude of undulator field ~ 6 kG, transverse sizes of the plane waveguide $d = 30$ mm, $b = 2$ mm, resonator losses ~ 10% Above physical parameters corresponds to dimensionless ones of length of interaction $L = 7$. From simulations the duration of electromagnetic micropulse is ~ 20 ps (relative spectrum width ~ 1.5%) and peak power 30kW. The value of spectrum width corresponds to experimental date, but experimental value of peak power is much less the theoretical limit that in particular can be explained by the parameter spread in the real electron bunches.

This research was supported by the grant RFBR-05-02-17553.

REFERENCES

[1] D.A.G. Deacon et al., Phys. Rev. Lett. 38 (1977) 892.

[2] D. Oepts et al., Phys. Rev. Lett. 68 (1992) 3543.

[3] D. C. Ngueyn et al., Nucl. Instr.&Meth. in Phys. Res. A 358 (1995) 27.

[4] V.P. Bolotin et al., "Status of the Novosibirsk High Power Free Electron Laser," IRMMW'2004, Karlsruhe, September 2004, p.55.

[5] F. Ciocci et al., Phys. Rev. Lett. 70 (1993) 928.

[6] A.J. Doria et al., IEEE J. Quantum Electron. 29 (1993) 1428.

[7] Y.U. Jeong et al., Nucl. Instr.&Meth. in Phys. Res., A 483 (2002) 195.

[8] Y.U. Jeong et al., "THZ imaging by a wide-band compact FEL", FEL'2004, Trieste, Italy 2004, p.667.

[9] N.S. Ginzburg and M.I. Petelin, Int. J. Electronics 59 (1985) 291.

[10] N.S. Ginzburg et al., Nucl. Instr.&Meth. in Phys. Res. A 407 (1998) 64.

[11] N. Piovella, Phys. Rev. E. 51 (1995) 5147.

THE EXPERIMENTAL RESEARCH OF THE SR-FEL CAVITY MIRRORS AT 355nm AND 248nm*

GAO Huailin#, WANG Donglei, WANG Yong, TAN Rongqing, WU Jin, Institute of Electronics, CAS, P.O. Box 2702-45, Beijing100080, CHINA

WANG Naiyan, China Institute of Atomic Energy, P.O. Box 275-7, Beijing 102413, CHINA.

Abstract

The cavity mirrors of the SR-FEL at 355nm and 248nm central wavelengths are developed experimentally with the fused silica substrate and "HfO2/SiO2+Al2O3/SiO2+M-SiO2" optical coatings. The electron-beam evaporation and ion-beams sputtering are used as the deposition technologies. After heating condition at 400°C×4hrs, the absolute reflectance and wavelength-tunable range is measured with VARIAN-Cary-5000 spectrophotometer. The experimental results show that R=99.45% and Δλ(R≥99.00%) =75nm at 355nm for the broadband mirror. For the mirror with the dual-central wavelength at 355nm/248nm, R= 99.69% and Δλ(R≥99.00%)=59nm at 355nm, and R=98.21%, Δλ(R≥99.00%)=9nm and Δλ (R≥98.00%) =51nm at 248nm.

INTRODUCTION

Storage-Ring Free-Electron Laser (SR-FEL) is a wavelength-tunable, high power, short pulse light source. With the optical resonator, SR-FEL will generate a laser radiation with the best spatial and temporal coherences, tunable wavelength and harmonic radiations, simultaneously [1-3]. It is also the best seed light for generating HGHG, X-ray laser and γ-ray laser with new FEL schemes [1-11]. All of these light sources have a potential application in the nuclear physics, atomic physics, molecular physics, bioscience and medicine. But the high power UV/DUV free electron laser and the synchrotron radiation will induce the mirror reflectance degradation or direct damage. These will limit the laser gain and the development of the SR-FEL toward to the shorter wavelength, shorter pulse and higher power in the UV/DUV region [1-3,8,12-13]. Thus, it's very important to develop the resonator mirror with the lowest absorption, highest absolute reflectance, needed wide wavelength-tunable range, highest damage threshold and the best resistance to reflectance degradation [1-13]. In this paper, report the progress on the experimental research of the SR-FEL resonator mirrors at 355nm and at 355nm/248nm.

PHYSICAL DESIGN TO MIRROR COATING

The physical design of the mirror coatings is based on the experimental results in the Inertial Confinement Fusion (ICF) driven by high energy laser and Storage-Ring Free Electron Laser (SR-FEL) researches from 1982 to 2006, so that it can integrate the all advantages of different physical designs, deposition technologies, film-growing parameters, post-deposition conditions, and so on. Here, a compound mirror coating is designed for the broadband mirror coating at 355nm central wavelength and the dual-band mirror coatings at 355nm and 248nm central wavelengths. It is "HfO2/SiO2+Al2O3/SiO2+M-SiO2", where Sub is the material of the mirror substrate, fused silica is chosen because of its stable physical characteristics. HfO2/SiO2 and Al2O3/SiO2 are two coating stacks, M=6 the layer number of the SiO2 top layers. Because the HfO2/SiO2 coatings has the largest bandwidth and Al2O3/SiO2 coatings has the highest damage threshold in the UV/DUV region, as found by LANL, LLNL, CIAE scientists in the research of ICF driven by high-energy laser [13-18]. And the top-layer SiO2 has an evident effect to increase the damage threshold of the mirror coating as found by above researchers [13-18], and to resist the reflectance degradation induced by the synchrotron radiation and the UV/DUV FEL as found by the ELETTRA scientists [8,12]. The theoretical design are listed in table.1, where H is HfO2, H` is Al2O3, L and L` are SiO2. Since the damage threshold of the Al2O3/SiO2 mirror coatings is higher than that of the HfO2/SiO2, the absorption coefficient of Al2O3 material is lower than that of HfO2 materials, and the laser intensity of the coherent standing-wave electric field in the topmost layers of mirror coating is higher than that in the inner. Thus, the Al2O3/SiO2 coating stack is set above the HfO2/SiO2, the top-layers SiO2 is put on the HfO2/SiO2 coating stack. The basic structures of the mirror coatings are "Sub.-LL-(0.5H-L-0.5H)[12-pair]/ 355nm-(0.5H`-L-0.5H`)[25-pair]-LL-4L`/320nm" for the broadband mirror at 355nm and "Sub.-LL-(HL)[11-pair] /355nm-H-(LH)[11-pair]/248nm-H`-(LH`)[20-pair]-LL-4L/212nm" for the dual-band mirror at 355nm/248nm.

DEPOSITION TECHNOLOGY AND PARAMETER

The past experiment research has shown that, for an optimized mirror coating design, the deposition technology and parameters have a strong and direct affection to the realization of the physical design. As found by LLNL scientists in ICF research, a mirror coatings will have a higher damage threshold when

* Work supported by NSFC, Grant No. 10475081.
# Corresponding author, Prof. GAO Huailin, email: gao.hl@mail.china

deposited by electron-beams evaporation (EBE) than by ion-beams sputtering (IBS) deposition [14]. But, as found by ELETTRA scientists in the SR-FEL research [8,12], when deposited by IBS technology, the oxide coating of the resonator mirror will have resistance to the reflectance degradation induced by FEL and synchrotron radiation. Thus, in our experimental research, the "HfO2/SiO2+Al2O3/SiO2+2-SiO2" part of the mirror coatings is deposited by EBE technology with LEYBOLD-APS-1104 machine; the rest 4-SiO2 film layers are deposited by IBS technology with VECCO-SPECTRA-IBS machine, so that these cavity mirror will have high damage threshold to laser radiation and resistance to synchrotron radiation, simultaneously. The deposition parameters are listed in table 2.

In Table 1, the leaked oxygen is used to re-oxide the dissociated oxygen molecular to increase the damage threshold of coatings further, as found by IECAS scientists in ICF and FEL researches [13]. Finally, the fresh sample is conditioned at 400°C×4hrs to decrease the absorption of the mirror coating and increase the absolute reflectance and damage threshold together. The step-size of temperature increase is 70°C/1hr. After 4-hour continuous treatment, the mirror sample will cool down naturally to room temperature. Then, they are measured.

Table 1: deposition technology and parameters for SR-FEL mirror coatings.

Deposition technology	Deposition parameter	
Electron-beams evaporation	V(HfO2)	0.5nm/s
	V(Al2O3)	0.5nm/s
	V(SiO2)	0.6nm/s
	T	185°C
	P(O2)	1.5×10[-4]mbar
Ion-beams sputtering	V(M-SiO2)	0.3nm/s
	T	120°C
	P(O2)	4.0×10[-4]mbar
Heating condition	400°C×4hrs	

EXPERIMENTAL RESULT AND DISCUSSION

The spectral performance of the SR-FEL mirror coatings is measured with the spectrophotometer VARIAN-Cary-5000. The parameters include the absolute reflectance at the central wavelength and the bandwidth corresponding to the absolute reflectance higher than 99.00%, i.e., the top width of the reflectance spectrum.

Broadband Mirror Coatings at 355nm

In Fig.1 was shown the spectra of the absolute reflectance for the broadband mirror coatings at 355nm before and after heating condition. The top width with the reflectance higher than 99.00% is listed in Table2. From Fig.1 and Tab.2, it shows, after heating condition, that the absolute reflectance at 355nm central wavelength is R(355nm)=99.45%, the wavelength-tunable range is from 406nm to 331nm, i.e., Δλ(R≥99.00%)=75nm. Relative to the R` and Δλ` of the fresh mirror sample without heating treatment, the average increases of the absolute reflectance and the wavelength-tunable range in the top region are ΔR= 0.39% and Δλ*=7nm, where ΔR and Δλ* are defined as

$$\Delta R = \frac{1}{N}\sum_{j=1}^{N}\left(R(\lambda_j) - R`(\lambda_j)\right)$$

$$\Delta\lambda^* = \Delta\lambda - \Delta\lambda`$$

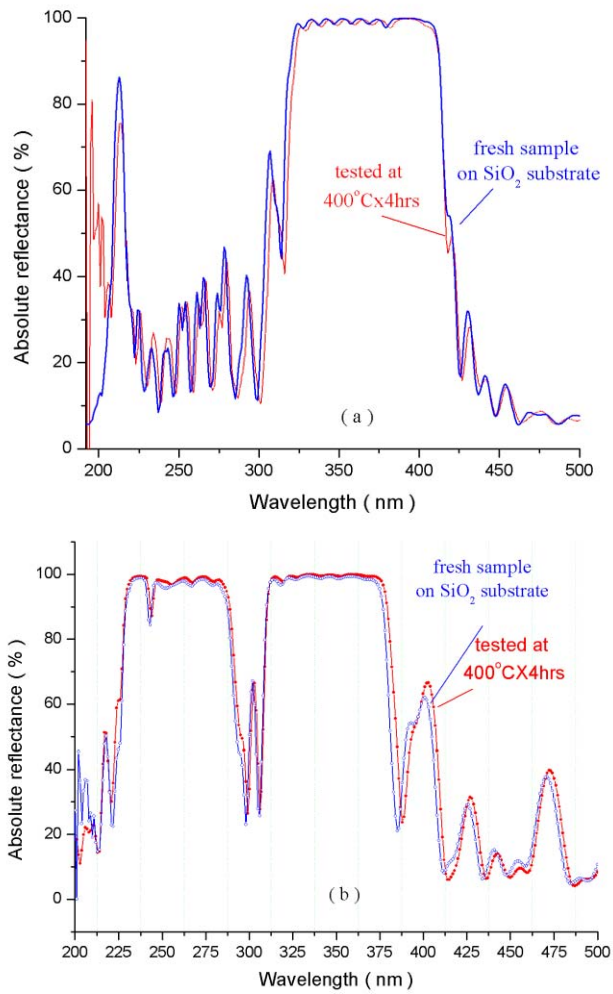

Figure 1: The spectral performances of the broadband (a) and dual-band (b) SR-FEL mirror with heating condition at 400°C×4hrs and without for the fresh samples. They are measured with varian-cary-5000 spectrophotometer.

Dual-band Mirror Coatings at 355nm/248nm

In the Figure 1 was also shown the spectra of the absolute reflectance for the dual-central wavelength mirror coatings at 355nm/248nm on fused silica substrate. The absolute reflectance higher than 99.00% is listed in Table 3. From these experimental data, it can be seen that, for the mirror coatings after heating condition, all the characteristics of the first band at 355nm is similar to that in Fig.1. It has a perfect shape. At the central wavelength 355nm, the absolute reflectance and wavelength-tunable range are R=99.69% and Δλ(R>99.00%)=373nm-314nm=59nm; Relative to the experimental data (R` and Δλ) in the Fig.1 for the fresh sample without heating treatment, the average increase of the absolute reflectance and wavelength-tunable range are ΔR= 0.73% and Δλ*=26nm, defined as above.

In the second band at 248nm for the sample with heating condition, the absolute reflectance is less than 99.00% at most of the wavelengths. The reflectance at 248nm central wavelength is only R(248nm)=98.21%. Only in the wavelength ranges of (275-272)nm and (240-234)nm, the absolute reflectance is higher than that 99.00% and Δλ(R≥99.00%)= (275-272)nm+(240-234) nm=9nm. At most of the wavelengths, the absolute reflectance is ranged from 98.00% to 99.20%, its corresponding wavelength-tunable range is Δλ(R≥98.00%) =33nm. Relative the optical spectrum of the fresh mirror coatings without heating treatment, its average increase of the absolute reflectance and wavelength bandwidth are ΔR(R≥98.00%)=1.04% and Δλ*(R≥98.00%)=9nm.

Table 2: The absolute reflectance and wavelength-tunable range of the SR-FEL broadband mirror at 355nm

λ/nm	406	405	401	400
R/%	99.02	99.10	99.55	99.67
R`/%	97.89	98.02	99.01	99.25
λ/nm	341	333	332	331
R/%	99.73	99.67	99.64	99.38
R`/%	98.65	99.02	98.53	97.73
Δλ/nm	Δλ (R>99.00%)=406nm–331nm=75nm, Δλ`(R`>99.00%)=401nm–333nm=68nm			

Table 3: The absolute reflectance and wavelength-tunable range of the SR-FEL mirror at 355nm/248nm.

λ/nm	373	364	363	355	330
R%	99.17	99.73	99.79	99.69	99.46
R`/%	97.54	98.83	99.01	99.14	99.04
λ/nm	323	322	316	314	283
R%	99.30	98.97	99.09	99.07	98.22
R`/%	98.87	98.77	97.81	98.39	96.45
Δλ/nm	Δλ(R>99.0%)=(373-314) nm=59nm,				
	Δλ`(R`>99.0%)=(363-330) nm=33nm				
λ/nm	275	272	271	270	248
R/%	99.19	99.12	98.8 79	98.49	98.21
R`/%	98.16	98.42	98.19	97.88	97.01
λ/nm	241	240	234	233	232
R%	98.83	99.17	99.12	98.82	98.09
R`/%	93.61	98.11	98.53	97.98	96.72
Δλ/nm	Δλ (R>98.0%) = (283-259)+(241-232)=33nm Δλ`(R`>98.0%) = (275-271)+(240-234)=10nm				

In additional, the highest reflectance is up to 99.19% at 275nm. The shortest wavelength with reflectance R≥99.00% is at 234nm. The shortest wavelength with reflectance R≥98.00% is at 232nm, its reflectance is 98.09%. The spectral breaking at 244nm may be induced by the bandwidth narrowing in the DUV region. Thus, it's necessary to improve the spectral continuity at 244nm further.

From the experimental results for tow types of the mirror coatings, we can get the following conclusion. (1) Heating condition to the fresh mirror coatings has an evident influence on increasing mirror's absolute reflectance and expanding spectral bandwidth. It implies that absorption coefficient of the mirror coatings have reduced after heating treatment. It's very important to develop the RS-FEL mirror toward the shorter wavelength and higher power output. (2) These resonator mirrors have get the designed absolute reflectance and spectral bandwidth. Thus, it can be used as the SR-FEL resonator mirror.

CONCLUSION

Today's experimental results show that it's possible to develop the SR-FEL cavity mirror with an absolute reflectance higher than 99.00% and wavelength-tunable range from 10nm to 75nm in the UV/DUV region. It is very effective to develop the SR-FEL mirror coatings with a compound optical design, a combined deposition technologies of electron beams evaporation and IBS, oxygen-leaked method, and heating treatment.

ACKNOWLEDGEMENTS

The research work is supported by the natural science foundation of China (NSFC) with the project No. 10475081. The authors gratefully thank NSFC for her support.

REFERENCES

[1] Patrick G. O'Shea and Henry P. Freund, "Free-Electron Laser: Status and Applications", Science, 292(2001) 1853-1858.

[2] S. V. Milton, E. Gluskin, N. D. Arnold, et al, "Exponential Gain and Staturation of a Self-

Amplified Spontaneous Emission Free-electron Laser", Science, 292(2001) 2037-2045.
[3] L. H. Yu, M. Babzien, I. Ben-Zvi, et al, "High-Gain Harmonic-Generation Free-Electron Laser", Science, 289(2000) 932-934.
[4] Jialin XIE, "Current FEL Development in China", Proc. 2nd Asian Particle Accelerator Conf., Beijing, China, 2001, 215-220.
[5] B. C. Zhang, K. Zhao, J. K. Hao, et al, "High Average Current Superconducting Accelerator At Peking University", Proc. 2nd Asian Particle Accelerator Conf., Beijing, China, 2001, 97-99.
[6] CHEN Nian, HE Duohui, LI Ge, at el, "General design of coherent harmonic generation storage-ring free-electron laser of NSRL", Nucl. Techn., 27(2004) 405-408, (in Chinese).
[7] D. NUTARELLI, D. Garzella, E. Renault, et al, "Super ACO FEL Oscillation at 300nm", Nucl. Instr. And Meth.. A 445(2000) 143-148.
[8] St. Gunster, A. Gatto, M. Trovo, et al, "VUV Optics Development for the ELETTRA Storage Ring FEL", Proc. 2004FEL Conf., 2004, 233-236.
[9] K. Yamada, N. Sei, H. Ohgaki, et al, "Characteristics of the NIJI-IV UV-VUV FEL System-Toward Lasing Down to 150nm Using a Compact Storage Ring", Nucl. Instr. And Meth.. A 475(2001) 205-210.
[10] Vladimir N. Litvinenko, Seong Hee Park, et al, "Operation of the OK-4/Duke Storage Ring FEL below 200nm", Nucl. Instr. And Meth.. A475 (2001) 195-204.
[11] M. Hosaka, S. Koda, M. Katoh, et al, "Recent Progress of the UVSOR", Proc. 2th Asian Particle Accelerator Conf., Beijing, CHINA 2001.
[12] A Gatto, J. Heber, N. Kaiser, et al, "High-performance UV/VUV optics for the storage ring FEL at ELETTRA", Nucl. Instr. And Meth.. A483 (2002) 357-362.
[13] GAO Huailin, WANG Naiyan and SHAN Yusheng, "Experimental Investigation on the Resonator mirror of the SR-FEL and ICF KrF Laser", High Energy Physics and Nuclear Physics, 29(2005)99-103, (in Chinese).
[14] Ralph Berggren and James D. Boyer, "Optics Technology for KrF laser", Inertial Confinement Fusion at Los Alamos, Progress Since 1985, Vol.I, Chapter VII, 1989, 1-8.
[15] F. Rainer, D. Milan and W. H. Lowdermilk, "Laser damage thresholds of thin film optical coatings at 248nm", NBS Special Publication, 638(1981) 339-343.
[16] GAO Huailin, SHAN Yusheng and WANG Naiyan, "Research on the UV Dielectric Coatings with High Damage Threshold", Chinese J. Laser, B6(1997) 229-237.
[17] Arthur H. Guenther, "Optical Damage: Boulder and Beyond", Lasers & Optronics, Oct.,1989, 57-62.
[18] Stephen R. FOLTYN and Brian NEWNAM, "Ultraviolet damage resistance of dielectric reflectors under multiple-shot irradiation", IEEE J. QE, 17(1981) 2092-20.

THE RESEARCH OF FIR-FEL IN CAEP

Xingfan Yang#, Ming Li, Xiao Jin, Weihua Li, Zhou Xu
Institute of Applied Electronics, CAEP, China.

Abstract

The research of FIR-FEL has been undertaken about 10 years in CAEP (China Academy of Engineering Physics) and first lasing at center wavelength 115 μm was observed in March 2005. The facility consists of RF-gun, alpha magnet, L-band SW accelerator, beam transport line, wiggler, optical cavity and measurement system. At present, a high brightness photo cathode RF-gun is commissioning, the cathode material is Cs2Te and the quadruple light is used. This injector will be used in the FIR-FEL project in the second half of this year. In this paper, the design consideration, the system layout and experiment results are introduced.

INTRODUCTION

The research work of FIR-FEL was started in 1997 in CAEP. In 1999 the 30MeV RF SW electron linac was built, the linac consists three accelerating sections, the resonant frequency is about 1.3GHz, a 1+1/2cell thermionic RF-gun was used as the injector. When doing the FIR-FEL, only the first accelerating section(ACC1) was used, the electron energy is about 6.5MeV~7MeV. The FIR-FEL facility consists of RF-gun, alpha magnet, ACC1, beam transport line, wiggler, optical cavity and measurement system (shown in Fig.1). Based on this facility the first lasing was observed in March 2005 and the center wavelength was 115 μm. As one important direction of FEL the high average power FEL was proposed. Two key technology of high average power FEL are the high brightness photo-cathode injector and the SRF ERL. The high brightness photo-cathode RF-gun injector was studied in our Lab in 1999 and the first photo-cathode injector with 2+1/2cell was operated in 2000.In order to study the SRF technology, cooperative with the Peking University, we built a superconducting cavity. This cavity includes a single cell (the frequency is 1.3GHz). This cavity was tested in our Lab in 2000, the energy gain is about 0.6MeV.

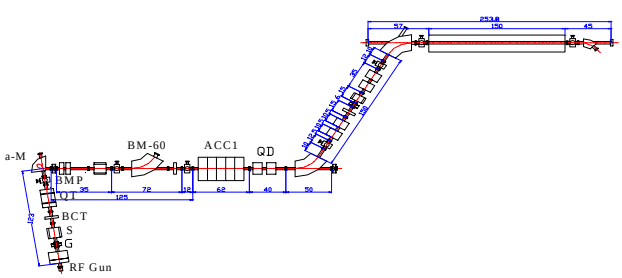

Fig.1: the schematic of the FIR-FEL facility.

#xingfan_y@caep.ac.cn

THERMIONIC CATHODE RF GUN INJECTOR

The study of FEL needs the high brightness electron beam with small energy spread. The beam quality is mainly determined by the injector. The development of high-brightness electron sources has been a challenging project for many years. RF gun is one kind of high brightness electron source which developed for the purpose of FEL research in 1984[1]. It has high electric field. The electron was accelerated to the light speed in a short distance, so the space charge effect has been reduced efficiently and easy to get the small emittance. There are two kinds of RF guns, one is the thermionic cathode RF-gun, the other is photo-cathode RF gun. The work of thermionic RF gun in our Lab is introduced in this section and the photo-cathode RF gun will be introduced in the next section. The advantages of thermionic cathode RF gun are the simple construction, operating reliability and low cost, it acts as an important role in the research of FEL especially at the beginning and it has been studied in detail. We built thermionic RF-gun as the injector for the 30MeV linac. The drawback of this kind of injector is the relative larger energy spread aroused by the wide capture phase and electron back bombardment. In order to decrease the electron back bombardment and obtain good quality electron beam, several guns with different structure have been built and experimented in our Lab. The SUPERFISH and PARMELA codes were used for the accelerating structure design. The ring cathode RF gun was tested also, but the experiment result was not good. Finally the 1+1/4cell gun was selected (shown in Fig.2), the electric field on the axis was measured using network analyser (shown in Fig.3). It was built in 2004(shown in Fig.4), the cathode material is LaB6, the diameter is 5mm and the electron energy of this injector is about 1.5MeV. Using this injector, the FIR-FEL stimulated emission was observed.

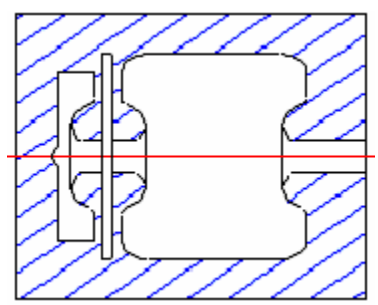

Fig.2: the schematic of the thermionic cathode injector.

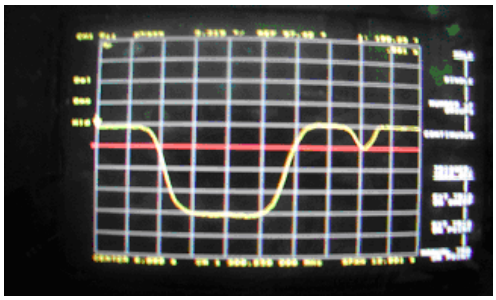

Fig.3: the electric field on the axis.

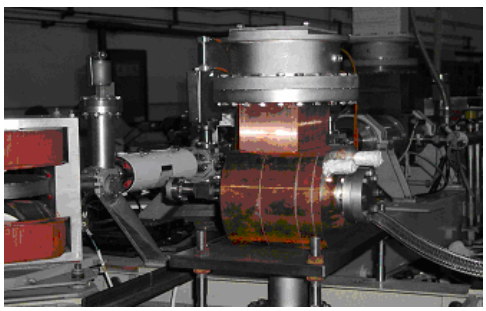

Fig.4: the thermionic cathode injector.

PHOTO-CATHODE RF GUN INJECTOR

The photo-cathode RF gun injector developed from 1985[2], comparing with the thermionic cathode RF-gun injector, the photo-cathode RF-gun is more adaptive to the research of FEL, it is easy to get the short pulse with high current and small energy spread. We started to study the photo-cathode RF-gun in 1999, and the first one was buil in 2000, the electron energy is about 3MeV. In order to develop the 3μm~8μm FEL, the second photo-cathode RF-gun with 4+1/2cell was studied in 2004(schematic was shown in Fig.5, the frequency is 1.3GHz), so the tota electron energy(including the injector and three accelerating sections) is about 37MeV. The electric field on the axis was measured using network analyser (shown in Fig.6). It was built in 2005(shown in Fig.7), the focusing solenoid and compensated solenoid were used This injector is commissioning at present.

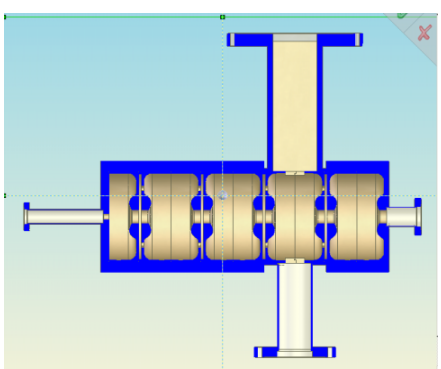

Fig.5: the schematic of the photo-cathode injector.

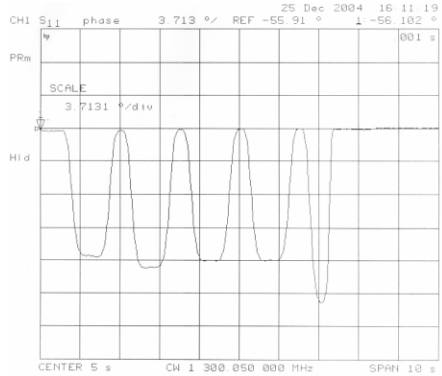

Fig.6: the electric field on the axis.

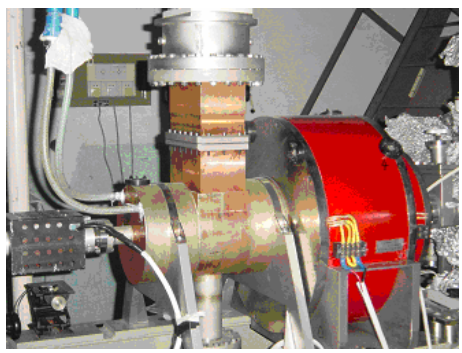

Fig.7: the 4+1/2cell photo-cathode injector.

The cathode material is Cs2Te and the quadruple light is used. The quantum efficiency is about 1%, the electron energy is 7MeV. The cathode-driving laser system(shown in Fig.8) of the RF photoinjector include the mode-locked oscillator(from Time-Bandwidth), diode-pumned amplifier and FHG (fourth harmonic generation). The average power of the oscillator is 10W , the timing jitter is 0.56ps, the width is 11.9ps at a repetition rate 54.167MHz . Micropulse energies is 3 μ J of 266nm light.

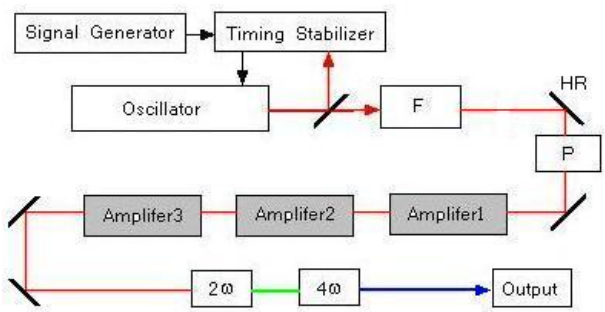

Fig.8: Optical Schematic of the cathode-driving laser system F, the Flady isolator.P, pockel .HR, high reflector.

THE WIGGLER

The Wiggler is one of the most important components for FEL and it is the region where the relative electron and the radiation field will interact. It's performance, such as the peak field, good field aperture etc. will determine

the FEL gain when we calculate the relative electron performance. A NdFeB-FeCoV hybrid wiggler has been designed and built for CFEL. More than 10mm good aperture and as high as 3235 Gs peak field were achieved with a 18 mm gap (shown in Fig.9). The trace simulation for a single electron showed that the center offset was less than 0.1 mm, the electron trajectory was simulated(shown in Fig.10), and the ratio of the small signal gain versus the ideal small signal gain was more than 98 percent. Recently, we've observed the resonance light in the 115 um FIR-FEL experimental study which used this wiggler.

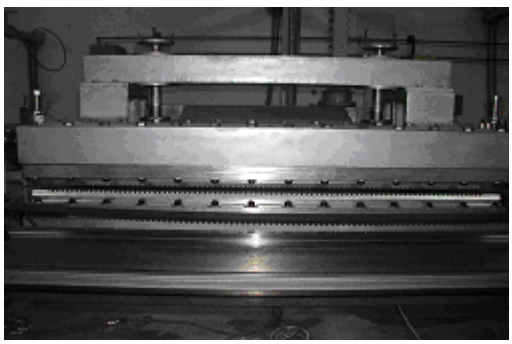

Fig.9: the wiggler.

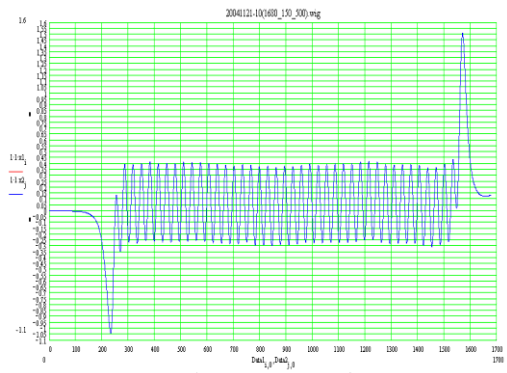

Fig.10: simulation trajectory of the electron in the wiggler.

THE STUDY OF SRF TECHNOLOGY

In order to get the high average FEL power, the high average electron beam power should be provided first, and the machine should be operated in the CW condition thus the SRF is required. SRF ERL technology is the practical way to obtain the high average power FEL and proved by JLAB[3]. Cooperate with the Peking University, we built a facility to study the SRF technology, (shown in Fig.11), at this facility the 2+1/2cell photo-cathode injector was used. The high average power FEL was proposed and we will begin to build the SRF ERL machine in the next years.

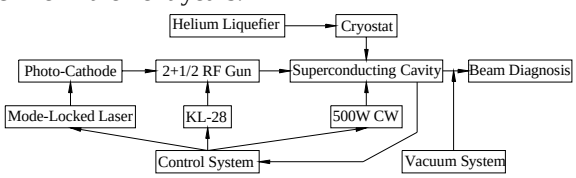

Fig.11: the schematic of the SRF test facility.

THE FIR FEL EXPERIMENT

The parameters of the FIR-FEL facility is shown in table 1.The macro-pulse current is measured by BCT and the beam currents are measured at the different position of the beam line, shown in Fig.12. The width of the micro-pulse is measured by the streak camera. The microwave power of the injector and ACC1 are provided by a klystron with 10MW. The stimulated signal is obtained in the March 2005, shown in Fig.13 and the spectrum of the stimulated signal is measured using grating analyser, shown in Fig.14, the center of the spectrum is 115μm, the width of spectrum is about 1%.

Table 1: parameters of the FIR-FEL facility

Energy 6.5MeV	Normalized emittance 20π mm·mrad
Macro-pulse current 130mA	Number of wiggler periods 44
Macro-pulse width 4μs	Period length 32mm
Micro-pulse current 4A	Wiggler gap 18mm
Micro-pulse width 25ps	Magnetic field 3250Gs
Energy spread 1%	Optical cavity length 2536mm

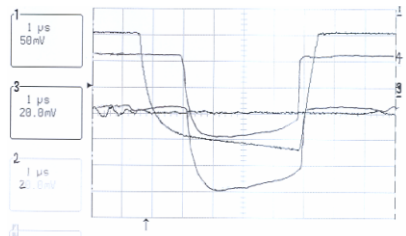

Fig.12: the beam current at the different position on the beam line, measured with BCT.

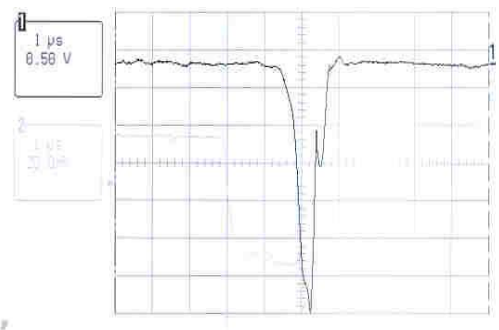

Fig.13: the FEL stimulated emission signal.

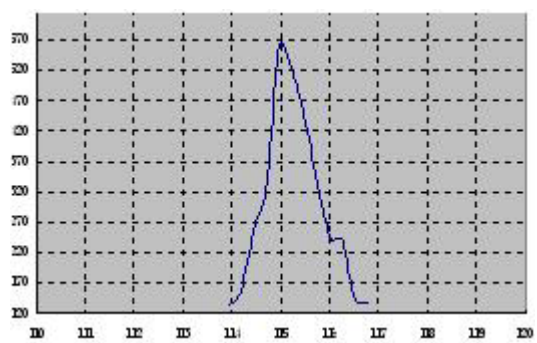

Fig.14: the spectrum of the stimulated signal.

CONCLUSION

We have made great efforts in the research of FIR-FEL, and obtained the stimulated emission in 2005. The thermionic-cathode and photo-cathode RF gun injectors have been built. The high power FEL project was proposed and a single cell superconducting facility was built and tested. The next step we will build the SRF energy recovery Linac.

REFERENCES

[1] A. Westenshop, J.M.J. Madey, “Microwave Electron Gun”, Laser and Particle Beam, 1984, 2(2), p223.

[2] C.H. Lee etc IEEE Trans Nucl Sci NS-225 1985, p3045.

[3] S. Benson, D. Douglas, M. Shinn, etc, “High Power Lasing in the IR Upgrade FEL at JEFFERSON LAB” Proceeding of FEL2004, p229-232.

DEVELOPMENT OF POWERFUL FEMS OF X, KA AND W BANDS FOR PHYSICAL AND INDUSTRIAL APPLICATIONS*

N. Ginzburg, N. Peskov, M. Petelin, Institute of Applied Physics RAS, N.Novgorod, Russia
A. Kaminsky, S. Sedykh, Joint Institute for Nuclear Research, Dubna, Russia
M. Einat, The College of Judea and Samaria, Ariel, Israel
A. Gover, Y. Socol, Tel-Aviv University, Israel
J. Lucas, The University of Liverpool, UK.

Abstract

The possibility to develop powerful FEMs capable for physical and industrial applications is being studied at Tel-Aviv University, IAP RAS, JINR and The University of Liverpool within the framework of the INTAS collaboration project. Present paper summarizes the progress in three successful FEM experiments: (1) Electrostatic-accelerator driven 70-130 GHz Tandem-FEM with kW-level pulse power (Tel-Aviv University); (2) Linac-driven 30-GHz FEM with pulse RF power of ~ 20 MW (JINR + IAP RAS); (3) Sub-relativistic e-beam industrial FEM tunable over X-band with output power up 1 kW (The University of Liverpool).

INTRODUCTION

Free electron masers (FEMs) are among the main sources of powerful microwave pulses from X to W-bands. Interest to such sources is caused by the large number of potential physical and industrial applications, requiring a wide variety of the radiation parameters. For example a new generation of the accelerators (SLAC, CERN etc.) requires sources of ~100 MW pulse power at 30-38 GHz with a narrow spectrum. Material processing stations require kW-level average power. Spectroscopic and imaging experiments as well as biological experiments, require lower power but fine control and tuning of the radiation spectrum.

Presently there are no ready industrial RF sources with parameters necessary for the applications mentioned above. Investigations carrying out in collaboration between aforementioned Institutes are aimed to partially fill up the gap with FEMs from X to W bands for different applications including testing components of high gradient accelerators and material processing. Present paper is devoted to the progress in the development of FEMs and their applications.

70-130 GHz TANDEM FEM

The Israeli FEM [1] resonator was re-designed in order to reduce the overall round-trip losses and achieve control on the radiation output-coupling. In its new configuration, the resonator consists of overmoded corrugated rectangular waveguide and two radiation mode splitters, separating the high-energy e-beam from the laser radiation. The electron input splitter is based on Talbot effect in an overmoded rectangular waveguide. The radiation out-coupling is done in the output splitter. It is based on novel design and it combines Talbot effect between two parallel plates with free space propagation, and focusing by two curved cylindrical mirrors in a confocal imaging scheme. The waveguide and the splitters were tested experimentally, showing improved performance in comparison with the former resonator. The measured unloaded Q-factor of the new version is increased by a factor of ~ 3, attaining up to Q = 25 000. Accordingly, the round-trip losses are ~ 23%. Rotating grids control the radiation out-coupling allowing wide variation for maximization of the radiation output power and extraction efficiency.

Additional R&D work was aimed on increasing FEM power by boosting the electron beam energy after the radiation build-up. A fine control of the electron beam energy during the radiation pulse is designed to compensate the small energy degradation during the pulse. Also, a controlled ramp (up or down) in the electron energy during the pulse will be applicable as well. We compared the theoretical estimations of the output power in the presence of electron energy change during the pulse, to the obtained experimental results. Two models, showing good agreement between them and with the existing data, were compared: low-gain analytical model based on the pendulum equation, and rigorous 3D FEM interaction model solved numerically. Another expected result of the design is to further extend the pulse duration with stable conditions and to obtain improved coherency.

30 GHz JINR-IAP FEM

The FEM-oscillator has been developed in Ka-band during last few years in a collaboration between JINR (Dubna) and IAP RAS (Nizhny Novgorod) [2]. These experiments aim to develop a pulsed power microwave source for testing behaviour of materials in high-Q structures under the influence of RF-pulses. Information about the life-time of different metals in strong RF-fields would be beneficial, in particular, when designing high-gradient accelerating structures for future linear colliders [3]. Such application requires a high power RF-source with a narrow frequency bandwidth. In addition, the

*This work is partially supported by INTAS (grant # 03-51-5319) and Russian RFBR (grants # 04-02-17118, # 05-02-16833, # 05-02-17036)

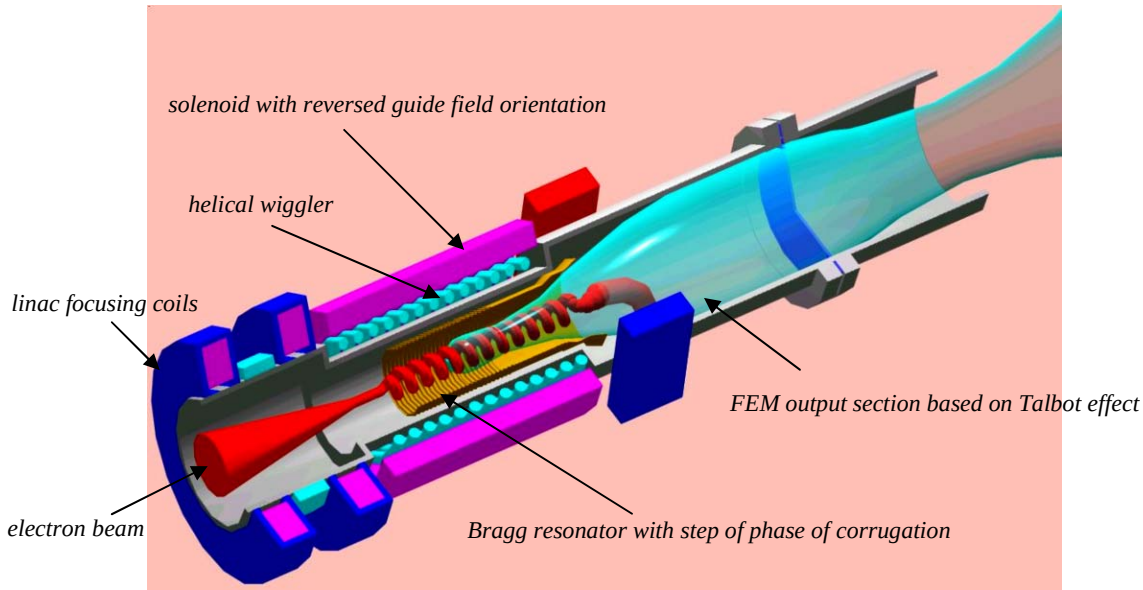

Figure 1: Schematic diagram of the JINR-IAP FEM.

radiation frequency should be exactly matched to the operating frequency of the accelerating structure, and therefore precise frequency tuning is essential for such a generator.

A schematic diagram of the JINR-IAP FEM experiments is shown in Fig.1. The induction linac LIU-3000 (JINR), which generates a 0.8 MeV / 200 A / 250 ns electron beam with a repetition rate of 1 Hz, drives the FEM-oscillator. Transverse velocity in the magnetically guided beam is pumped in a helical wiggler of 6 cm period. The main advantages of developed FEM is the use of a reversed guide field, which provides high-quality beam formation in the tapered wiggler section with a low sensitivity to the initial beam spread, alongside with Bragg resonator having a step of phase of corrugation, which possesses high electrodynamical mode selection. As a result, stabile single-mode operation with high electron efficiency was achieved in the FEM. At the present stage, the FEM generates 20 MW / 200 ns pulses at 30 GHz with the spectrum width of 6 - 10 MHz (Fig.2).

Precise tuning of the oscillation frequency of the FEM was performed by inserting short sections of smooth waveguide between the two Bragg structures. If the phase shift between the Bragg structures is varied from 0 to 2π the frequency of the fundamental eigenmode moves from the lower to the higher edge of the Bragg zone. It is important to note that only one high-Q eigenmode exists inside the Bragg zone at any value of phase shift, i.e. the high selective properties of the resonator are maintained over a sufficiently wide frequency band. For a phase shift equal to π the frequency of nearly 30 GHz was measured. In the experiments frequency tuning was achieved over a range of 6%, the spectrum width in all regimes of oscillations did not exceed 0.1% (Fig.3).

The test facility to study surface heating effects at 30 GHz, which was constructed based on the FEM source [4], is shown in Fig.4. The experimental set-up includes a two-mirror confocal transmission line and mode

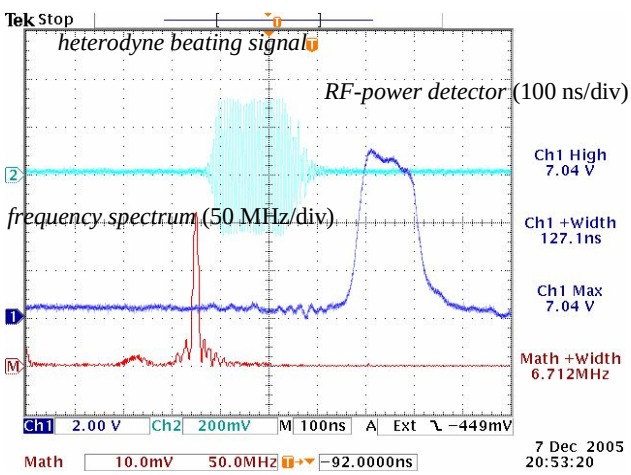

Figure 2: Typical oscilloscope traces of the RF-pulse generated by 30 GHz JINR-IAP FEM.

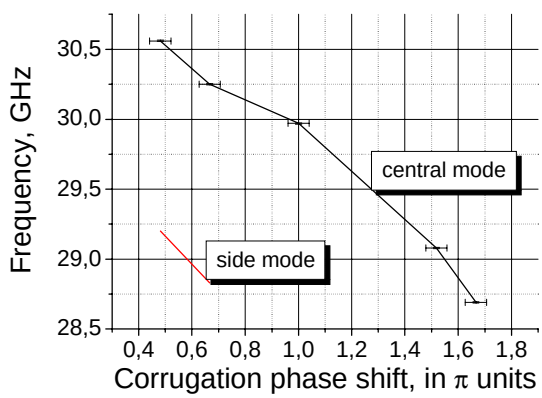

Figure 3: Measured dependence of the FEM oscillation frequency on the value of the phase shift of corrugation between the Bragg structures.

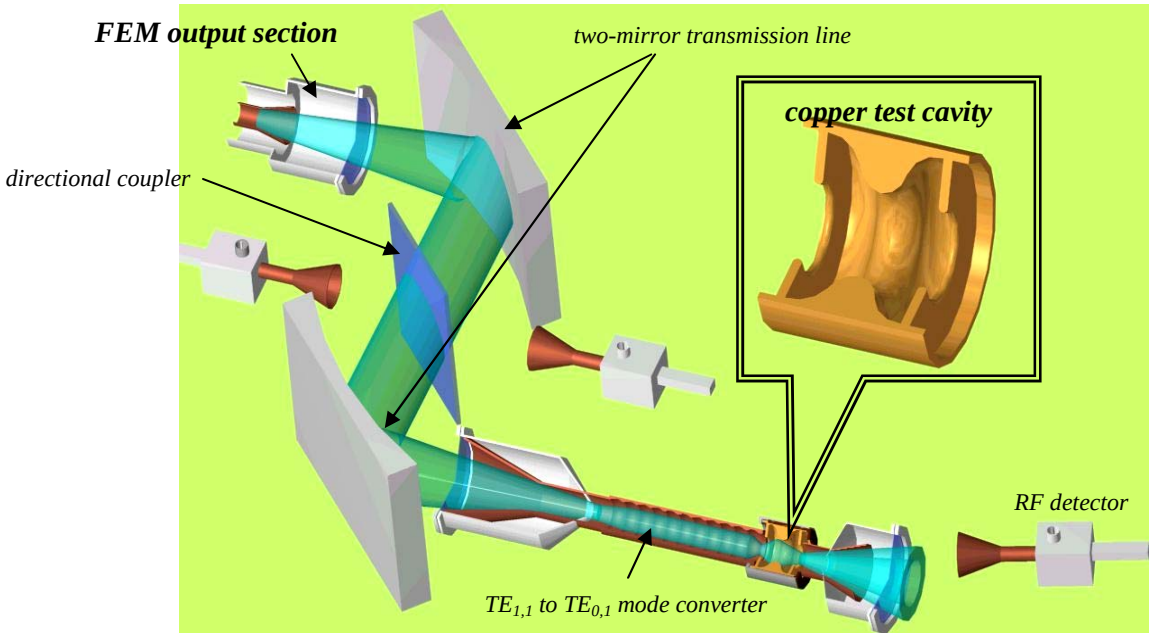

Figure 4: Schematic diagram of the test facility for studying surface heating effects based on JINR-IAP FEM.

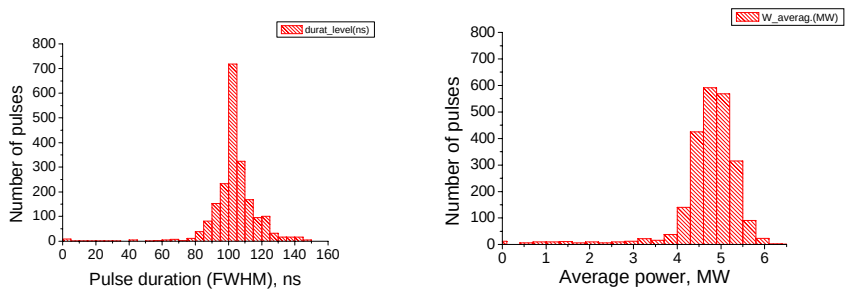

Figure 5: Statistic distributions of pulse duration and RF-power after the test cavity in the series of 10^4 pulses.

converters to transport the RF-power from the FEM to the test cavity. A special copper cavity operating with $TE_{0,1,1}$ mode and having Q-factor ~ 1500 was designed to model temperature regime in a high-Q accelerating structure of the CLIC project. The profile of the cavity surface was optimized to enhance the RF magnetic field in a certain zone and provide needed temperature rise during each RF-pulse. The resonant frequency of the cavities is also mechanically tuned to coincide with the frequency of the FEM source. A directional coupler is included to control both the incident and reflected powers. After a certain number of pulses the Q-factor of the cavity would be monitored using a network analyzer to detect early signs of surface damage. "Cold" tests of all components of the experimental set up were carried out and demonstrated good agreement with designed parameters.

Simulations carried out demonstrate principal ability of the FEM to be used for the aforementioned application. Results of the first experiments also proved possibility of the FEM to operate at the high-Q load. When frequency of the test-cavity was tuned to the FEM generation frequency it was observed that during the RF-pulse the reflected signal decreased and the test-cavity became transparent. As a result, accumulation of the RF-power in the load was achieved. At the present stage the effect of the copper surface degradation at 30 GHz was studied in the statistics of 10^5 pulses (Fig.5) at the temperature rise of 50 °C during each RF-pulse. The test cavity providing temperature rise at the certain zone up to 150 °C was designed and the experiments with the statistics of 10^6 pulses, which are important for design of CLIC collider components (CERN), are in progress currently.

REFERENCES

[1] A.Abramovich, M.Canter, A.Gover, e.a., Phys. Rev. Lett. 82 (1999) 5257.

[2] N.S.Ginzburg, A.K.Kaminsky, N.Yu.Peskov, e.a., Phys. Rev. Lett. 84 (2000) 3574.

[3] I.Wilson, CLIC Note 52, Oct. 1987.

[4] A.K.Kaminsky, A.V.Elzhov, I.N.Ivanov, e.a., Proc. of the 22nd Int. FEL Conf., Durham, USA, 2000, p.II-41.

A FEL AMPLIFIER BASED ON PLANAR BRAGG WAVEGUIDES*

Ginzburg N.S. #, Malkin A.M., Rozental R.M., IAP RAS, Nizhny Novgorod, Russia,
Dorfman K.E., Department of Physics, Texas A&M University, College Station, USA

Abstract

We study a new version of FEL amplifier on the base of wide sheet electron beams. We suggest using a transverse open Bragg structures which can provide radiation waveguiding with simultaneous effective mode selection (filtration). Theory of transverse current FEL amplifier based on planar Bragg waveguides is considered.

INTRODUCTION

A planar periodic Bragg structure can be used not only as resonant elements of FEL oscillators [1-3] but as selective waveguides in different new schemes of FEL amplifiers. Open Bragg waveguide where wave propagates in the direction transverse to the lattice vector (Fig.1) can provide high selectivity over the transverse coordinate when its size essentially exceeds wavelength. In a transverse current amplifier scheme it is beneficial to use a grating with a step of corrugation, which results in the existence of a single low dissipative mode located near defect. The sheet electron beam moves across the waveguide to be resonant to one of partial waves forming the operating mode. Another way is a traditional travelling wave amplifier scheme where electron beam moves along waveguide axis. To increase effective size of operating mode one ca use a structure with regular longitudinal corrugation that couples two partial waves propagating at some angle to the axis to the wave propagating directly along the axis. This wave, which in moving reference frame is transformed into a cut off mode, is excited by the electrons. Analysis shows rather high gain and efficiency of the novel schemes with simultaneous discrimination of parasitic modes.

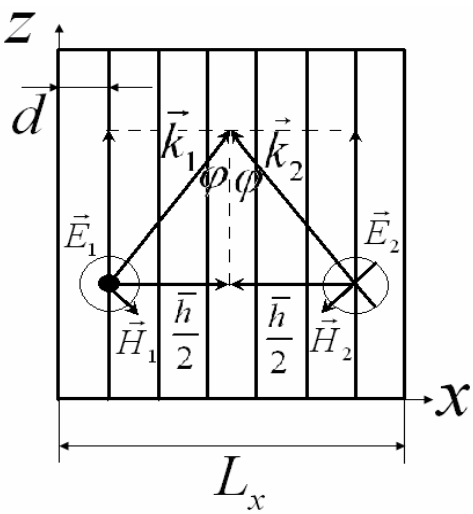

Figure 1: The diagram showing the coupling of waves on the Bragg lattice.

*Work supported by RFBR grants 06-02-17129-a and 05-02-17036-a and the Dynasty foundation.
#ginzburg@appl.sci-nnov.ru

This paper is organized as follows: in the Sect.1 we study wave propagation in the Bragg waveguide with a step of corrugation to find the mode spectrum of this structure. In the Sect.2 we investigate the model of the transverse current FEL amplifier. In Conclusion we briefly overview another scheme of Bragg amplifier based on coupling of some higher mode of the planar waveguide and two *TEM* modes.

EIGENMODES OF THE OPEN PLANAR BRAGG WAVEGUIDE WITH A STEP OF CORRUGATION

We consider a planar waveguide (Fig.4) with weakly corrugated walls

$$l = l_0 \cos(\bar{h}x) \qquad (1)$$

where $2\,l_0$ is the depth of corrugation. Assuming that lattice vector $\bar{h} = \frac{2\pi}{d}$, (d is the period of corrugation) is directed in x direction. The coupling exists for *TEM* waves with x- and z- wavenumbers satisfying Bragg resonance condition (see Fig.1)

$$h_{z1} = h_{z2} = h;\ h_{x1} = -h_{x2} = \bar{h}/2$$

We assume that the deflection of the waveguide surface $l(x)$ is much less than the wavelength λ and the corrugation period d: $l_0 << \lambda, d$. In this case perturbation of waveguide plates can be treated by using the equivalent surface magnetic current [4]. We seek the electric and magnetic fields as the linear combination of two TEM modes of a corresponding regular waveguide (Fig.5):

$$\vec{E} = \mathrm{Re}\left[\left(A_1(x,z)\vec{E}_1^{\,0}e^{i\frac{\bar{h}}{2}x} + A_2(x,z)\vec{E}_2^{\,0}e^{-i\frac{\bar{h}}{2}x}\right)\exp(i\omega t - ihz)\right],$$

$$\vec{H} = \mathrm{Re}\left[\left(A_1(x,z)\vec{H}_1^{\,0}e^{i\frac{\bar{h}}{2}x} + A_2(x,z)\vec{H}_2^{\,0}e^{-i\frac{\bar{h}}{2}x}\right)\exp(i\omega t - ihz)\right]$$

Slowly varying (in the wavelength scale) partial waves amplitudes, $A_{1,2}(x,z)$ satisfy the coupling equations:

$$\frac{h}{k}\frac{\partial A_{1,2}}{\partial z} \mp \frac{\bar{h}}{2k}\frac{\partial A_{1,2}}{\partial x} + i\alpha A_{2,1} = 0 \qquad (2)$$

where

$$\alpha = \frac{l_0}{4a_0}\frac{\bar{h}^2}{2k}$$

is the coupling parameter (a_0 is the distance between plates), $h = \sqrt{k^2 - (h/2)^2}, k = 2\pi/\lambda$. If we introduce an angle φ between the partial wave propagation directions ($\sin\varphi = \frac{\bar{h}}{2k}$), the coupling parameter can be represented as

$$\alpha = \frac{l}{4a_0}\bar{h}\sin\varphi \cdot$$

The maximum value of the coupling parameter takes place when the frequency tends to the cutoff frequency and the wave vectors of the two partial waves are counter directional $\left(\varphi = \frac{\pi}{2}\right)$. The coupling parameter and the angle φ tend to zero while the frequency shift from the cutoff increases. By seeking seek the solution of the eqs.(2) as $A_{1,2}\exp(igx + i\Gamma z)$, we have the dispersion equation for the unbounded grating

$$\left(\tfrac{\bar{h}}{2}g\right)^2 = (k\Gamma)^2 - (k\alpha)^2 \qquad (3)$$

where g and Γ are small amendment to the transverse and longitudinal wavenumbers $g << \bar{h}/2,\ \Gamma << h_0$.

The defect of corrugation in the middle of the waveguide can be entered as a $\pi/2$ phase step of the waveguide corrugation (1) which leads to the change of the sign of α in (2) at the point $x = L_x/2$:

$$\alpha = \alpha(x) = \begin{cases} +|\alpha|, & x < L_x/2 \\ -|\alpha|, & x > L_x/2 \end{cases}$$

Using the coupled waves equations (2) one can find the eigenmodes of an open in x direction planar Bragg waveguide with width L_x. In this case the boundary conditions for partial waves correspond to the absence of reflections and can be presented as follows:

$$A_1(0) = A_2(L_x) = 0 \cdot$$

Taking (2) into account and using the fields continuity condition on the step of corrugation, the characteristic equation for the bounded grating can be presented in a form similar to the theory of Bragg resonators [2]:

$$2\alpha^2 = \left[\Gamma^2 - \Gamma\left(g\tfrac{\bar{h}}{2k}\right)\right]\exp(igL_x) + \left[\Gamma^2 + \Gamma\left(g\tfrac{\bar{h}}{2k}\right)\right]\exp(-igL_x) \qquad (4)$$

Equations (3),(4) can be solved approximately in the assumption of strong wave coupling ($\alpha L_x >> 1$). The spectrum of longitudinal wavenumbers consists of the single mode at the exact Bragg resonance ($\mathrm{Re}\,\Gamma = 0$) (which would be treated as "0"th mode):

$$\begin{cases} g_0 = \pm i\alpha\dfrac{2k}{\bar{h}} \\ \mathrm{Re}\,\Gamma_0 = 0 \\ \mathrm{Im}\,\Gamma_0 = -2\alpha\dfrac{k}{h}\exp\left(-\alpha\dfrac{2k}{\bar{h}}L_x\right) \end{cases} \qquad (5)$$

and a set of higher modes:

$$\begin{cases} g_N = 2\dfrac{\pi N}{L_x} - i2\dfrac{\pi N}{\alpha L_x^2}\dfrac{\bar{h}}{2k} \\ \mathrm{Re}\,\Gamma_N = \alpha\dfrac{k}{h}\dfrac{N}{|N|}\left(1 + 2\left(\dfrac{\pi N}{\alpha L_x}\dfrac{\bar{h}}{2k}\right)^2\right) \\ \mathrm{Im}\,\Gamma_N = -\alpha\dfrac{k}{h}4\dfrac{(\pi N)^2}{(\alpha L_x)^3}\left(\dfrac{\bar{h}}{2k}\right)^3 \end{cases} \qquad (6)$$

where $N = \pm1, \pm2, \pm3...$ are the mode numbers.

Fig. 2 demonstrates the dispersion diagrams for the different mode numbers and the diffraction losses curves via the frequency shift from the cutoff $\Omega = \frac{2k}{\bar{h}} - 1$.

It should be noted that expressions (5,6) diverge at $h \to 0$, while the frequency tends to the cutoff. These formally infinite diffraction losses appear when the applicability conditions of perturbation theory fail to fulfill. Nevertheless for practical use of Bragg waveguides it is interesting situation of rather large wave group velocities corresponding to large detuning of radiation frequency from the cutoff (Bragg frequency) where expressions (5),6) are non-divergent.

For $N>0$ the transverse structure of the N^{th} waveguide mode represents the distribution close to a standing wave with sine wave envelope having $|N|$ half-periods on the length L_x (Fig.3a), while the lowest mode distribution is localized near the defect and has the exponential transverse structure (Fig.3b).

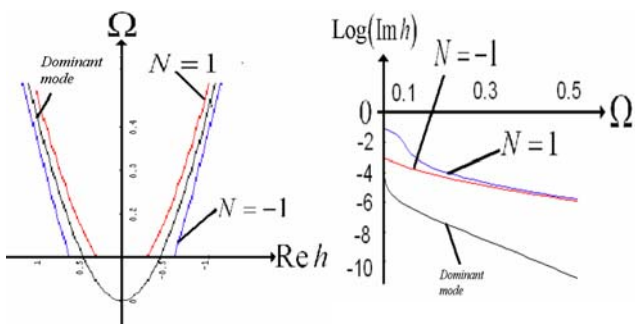

Figure 2: Dispersion diagrams for different mode numbers (left) and diffraction losses curves via the frequency shift (right).

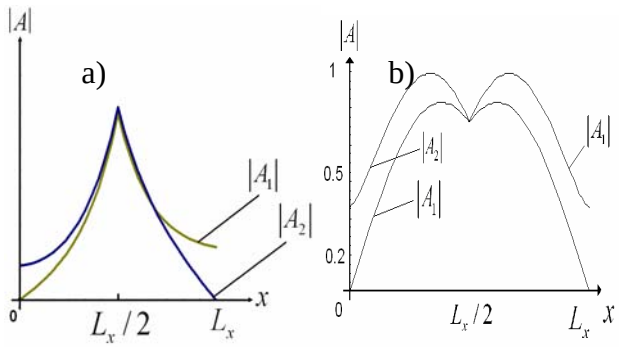

Figure 3: Transverse structure of modes with *N=0* (a) and *N=1* (b).

Diffraction losses of this mode (Im Γ) are proportional to $\exp(-\left|2k\alpha L_x/\bar{h}\right|)$ and are very small at large L_x, while the high order modes have significantly greater decrements (they decrease as $1/L_x^3$) than the dominant mode decrement. Thus, such wide structures can be used for highly selective waveguiding.

TRANSVERSE CURRENT FEL AMPLIFIER

Transverse current amplifier schemes are well known in microwave electronics. In case of a rectilinear electron beams such type of interaction can be realized by means of oblique corrugation of slow wave structure [5]. In case of curves beams the synchronous interaction can be realized in smooth electrodynamical systems. One of the problems arising in such systems is distortion of the transverse field structure by the electron beam [6, 7]. This problem can be solved by means of using the open waveguides based on Bragg structures which provides high selectivity over the transverse mode index.

We consider a thin over the *y* coordinate sheet electron beam moving in the undulator field and in the uniform guiding magnet field $\vec{H}_0 = H_0\vec{\xi}_0$ (the directions of the coordinates and ξ are shown in the Fig.4). The beam is injected into the waveguide in the direction corresponding to the direction of propagation of the one of the coupled *TEM* waves in the waveguide described in the previous section and it is synchronous to this mode.

We consider the electron-wave interaction in the case of the undulator synchronism assuming the bounce frequency Ω is far from cyclotron synchronism with electrons:

$$\left|\omega - h\nu_{II} - \omega_H\right|T >> 2\pi, \quad \left|\Omega - \omega_H\right|T >> 2\pi,$$

where $\omega_{H0} = eH_0/m_0c\gamma_0$ is a cyclotron frequency, ν_{II} is the longitudinal velocity of electrons, $\gamma_0 = \left(1 - v^2/c^2\right)^{-1/2}$ is relativistic factor, T is characteristic time of interaction. We also consider the ultra relativistic case $\gamma_0 >> 1$.

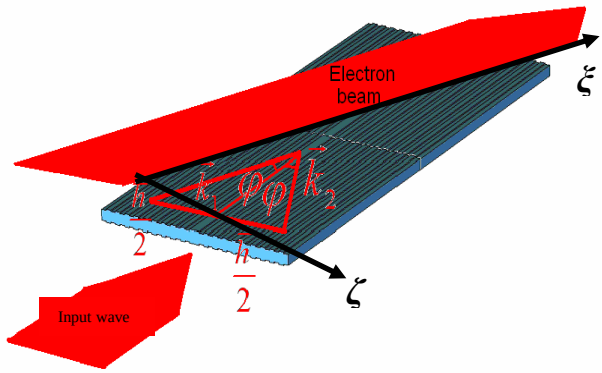

Figure 4: The scheme of a FEL amplifier with transverse current.

The process of monochromatic signal amplification in the transverse current FEL scheme can be described by the equations similar to the nonstationary equations of traditional FEL with 1D Bragg resonator [2] with time variable replaced by spatial one. These equations describe the formation of transverse structure of the fields together with their longitudinal structure

$$\begin{cases} \dfrac{h}{k}\dfrac{\partial a_1}{\partial \hat{z}} + \dfrac{\bar{h}}{2k}\dfrac{\partial a_1}{\partial \hat{x}} - i\delta a_1 + i\alpha a_2 = \dfrac{1}{\pi}\displaystyle\int_0^{2\pi} e^{-i\theta}d\theta_0 \\ \dfrac{h}{k}\dfrac{\partial a_2}{\partial \hat{z}} - \dfrac{\bar{h}}{2k}\dfrac{\partial a_2}{\partial \hat{x}} - i\delta a_2 + i\alpha a_1 = 0 \\ \left(\dfrac{h}{k}\dfrac{\partial}{\partial \hat{z}} + \dfrac{\bar{h}}{2k}\dfrac{\partial}{\partial \hat{x}}\right)^2 \theta = \mathrm{Re}\left(a_1 e^{i\theta}\right) \end{cases} \tag{7}$$

Here the normalizations, variables and parameters are defined as follows: $\hat{x}, \hat{z} = Ckx, Ckz$, $\hat{\alpha} = \alpha/(Ck)$, $a_{1,2} = eK\mu A_{1,2}/C^2$, θ is electron phase, C is Pierce parameter, μ is bunching parameter, K is electron-wave coupling parameter, δ is normalized synchronism detuning.

If the input signal is a *TEM* wave packet entering the system under the angle corresponding to the direction of propagation of the partial wave A_1, then the boundary conditions for (7) take the form

$$\begin{aligned} &\frac{d\theta}{dX}\Big|_{X=0} = 0,\ \theta\big|_{X=0} = \theta_0 \in [0, 2\pi), \\ &a_1\big|_{Z=0} = a_0,\ a_1\big|_{X=0} = 0,\ a_2\big|_{X=L_x} = 0 \end{aligned} \tag{8}$$

Results of direct numerical simulation of (7-8) are presented in Fig.5. In the Fig 5a the dependence of the amplification coefficient

$$\Gamma = \frac{\int_0^{L_x}\left(\left|A_1(X)\right|^2 + \left|A_2(X)\right|^2\right)dX}{\int_0^{L_x}\left|A_{ex}(X)\right|^2 dX}$$

on the longitudinal coordinate is depicted.

We can estimate the parameters of such system for an 8mm FEL basing that can be realized on the base of U2 high current accelerator at BINP RAS, Novosibirsk (width of the beam is ~150 cm, energy of electrons 1 MeV, $\gamma_0 = 3$, current density $j_0 = 1kA/cm$). We

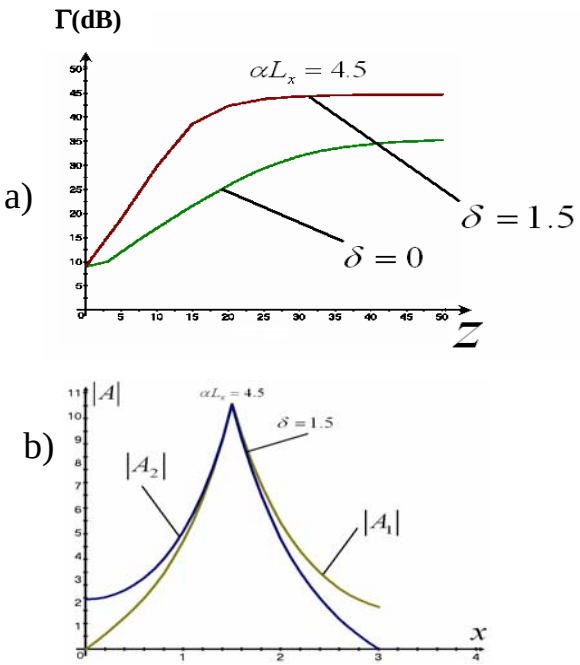

Figure 5: a) Dependence of the gain on the longitudinal coordinate, b) transverse structure of the fields.

assume the undulator period $d_u = 8cm$, undulator field amplitude $H_u = 2kOe$, guiding magnetic field $H_0 = 10kOe$, $a_0 = 1cm$ (the Pierce parameter is $C = 0.01$). At the following parameters of Bragg waveguide $l_0 = 0.4mm$, $d = 1mm$, $L_x = 50cm$, $L_z = 160cm$, $\varphi = 18^0$ one can get the gain up to 40 dB.

CONCLUSION

Another variant of using of an open Bragg structure for provision of higher selectivity in a FEL amplifier can be based on coupling between two TEM waves $A_{\pm}$ propagating at some angle to the axis and the wave *B* with a higher *y*-index propagating directly along the system axis. The latter wave is synchronous to the beam propagating directly along the axis, while the former waves provide the synchronization of radiation over the *x* coordinate. The coupling is provided by the regular corrugation with the following Bragg resonance conditions $\bar{h} = 2h_x$, where h_x is the transverse wavenumber of *TEM* modes. This interaction is described by the following equations.

$$\frac{\partial A_{\pm}}{\partial Z} \pm \frac{\partial A_{\pm}}{\partial X} = i\alpha B$$

$$\frac{\partial B}{\partial Z} + \frac{i}{2}\frac{\partial^2 B}{\partial Z^2} = -i\alpha(A_+ + A_-) + J$$

These equations are similar to those describing the excitation of the FEL oscillator based on coupling of the propagating and the trapped waves (see [10]) with excitation factor removed into the equations for the higher mode. Preliminary estimations show that in this case multiplication coefficient also should be rather high.

It should be noted in conclusion that the considered in section 1 system with defect of periodicity can be treated as a simple realization of photonic bandgap structures [8, 9]. Advantage of these Bragg waveguides is their compatibility with powerful sheet electron beam transportation system.

REFERENCES

[1] A. Yariv, Introduction to optical electronics (1976)

[2] V.L. Bratman , G.G. Denisov, N.S. Ginzburg, M.I. Petelin IEEE J. of Quant. Electr., v.9 E-19, N3, p.282 (1983)

[3] N.S. Ginzburg, A.S. Sergeev, N.Yu. Peskov, et al., IEEE Transactons on Plasma Science, Vol. 24, No. 3, pp. 770-780. (1996)

[4] N.F. Kovalev, I.M. Orlova, M.I. Petelin, Izv.Vuzov Radiofizika Vol.11 N.5 1968, p. 783.

[5] D.A.Dann, W.A.Harman, L.M.Field, G.S.Kino, Proc. IRE, 1956, p.879.

[6] Zhurahovsky A.V., Radiotehnika i electronika, 1969, p.8 (in Russian)

[7] Bykov Yu.V., Gaponov A.V., Petelin M.I., Izv. Vuzov Radiofizika, 1974, p.1219 (in Russian).

[8] R.J. Temkin, J.R. Sirigiri, K.E. Kreischer, et al., Phys. Rev. Lett., Vol. 86, p.5628 (2001)

[9] E. Yablonovitch, T.J.Gmitter, and K.M. Leung, Phys. Rev. Lett. Vol. 67, p.2295 (1991)

[10] N.S.Ginzburg, A.M.Malkin, N.Yu.Peskov, et al., Phys. Rev. ST Accel. Beams 8, 040705 (2005)

GENERATION OF NARROW BAND SHORT MM WAVE SUPERRADIANCE PULSES IN A NON-UNIFORM PLANAR WAVEGUIDE*

N. Ginzburg, R. Rozental#, A. Sergeev, I. Zotova, IAP RAS, N. Novgorod, Russia.

Abstract

A method for suppressing of spurious transverse modes excitation in the process of supperradiance from intense electron bunch is described. Such method based on the use of the waveguide with variable geometry (in the case of planar waveguide it is distance between plates). In such waveguide phase velocities of the different modes varied over longitudinal coordinate. For given waveguide profile variations are increased with increasing transverse mode indexes. As a result modes with large Brillouin angles (including near cut-off modes) which are responsible for low frequency radiation suppress more effectively than modes with small Brillouin angles. For the case of planar geometry this effect demonstrated both in the frame of the averaged equations and the full PIC-simulations.

INTRODUCTION

Recently significant progress was achieved in production of ultrashort pulses in millimeter wave band based on supperradiance from intense electron bunch [1-3]. One of the problems for advance generators based on such mechanisms in shorter (first of all sub-mm) wave bands is the spectrum broadening caused by the simultaneous excitation by an electron bunch several waveguide modes in oversized waveguide. For example at the fig.1 the dispersion diagram of the 1 MeV electron beam propagating through the planar waveguide with 1 cm gap is shown. Electron beam interacts simultaneously with three propagating modes (the interaction at the cut-off frequency with the TE_1 mode could be neglected): with TE_2 mode at the frequency of about 50 GHz, with TE_1 mode at the frequency of about 150 GHz and with the fundamental TEM mode at the frequency of about 200 GHz.

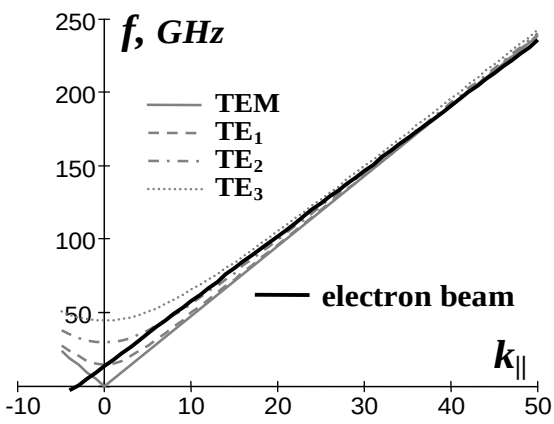

Figure 1: Dispersion diagram of the 1 MeV electron beam and planar waveguide with 1 cm gap.

To suppress spurious interaction we suggest using the non-uniform waveguide with tapered radius (cylindrical geometry) or distance between plates (planar geometry). In such a waveguide the phase velocities of the different modes varied over longitudinal coordinate. For given waveguide profile variations are increased with increasing transverse mode indexes. As a result modes with large Brillouin angles (including near cut-off modes) which are responsible for low frequency radiation suppress more effectively than modes with small Brillouin angles. In planar waveguide situation is even more preferable because phase velocity of fundamental TEM mode is totally independent on the distance between plates.

BASIC MODEL

Let us assume, that a sheet electron beam with initial velocity $\vec{v}_0 = v_0\vec{z}$ passes through a planar undulator with period *d* and homogeneous magnetic field with strength $\vec{H}_0$ in a planar waveguide with gap between plates *b* (Fig.2). We also assume that the system is infinite over the *y*-axis and the electron beam excites the TE_n-mode of a planar waveguide with *n* variations over the transverse coordinate *x*. Vector-potentials of the periodic undulator field (subscript *u*) and operating mode (subscript *s*) may be presented as

$$\vec{A}_u = \mathrm{Re}\{A_u ch(k_u x)\exp(ik_u z)\vec{y}\},$$
$$\vec{A}_s = \mathrm{Re}\{A_s(x,z)\exp(i\omega t - ik_\| z)\vec{x}\}$$

where $A_s(x,z)$ is the slowly-varying amplitude of the synchronous wave, $k_u = 2\pi/d$. The reference frequency ω was chosen to be the frequency at exact undulator synchronism $\omega - k_\| v_\| \approx \Omega$, where $k_\|^2 = k^2 - k_\perp^2$, $k = \omega/c$, $k_\perp = n\pi/b$, $\Omega = k_u v_\|$ is the bounce-frequency.

Using the independent variables

$$\zeta = \frac{kCZ}{\beta_\|^3\gamma_0^2},\ \tau = \frac{kC(t - z/v_\|)}{\beta_\|^3\gamma_0^2(1/v_\| - 1/v_{gr})}$$

superradiance process can be described by the following equations:

$$\frac{\partial a}{\partial\zeta} + \frac{\partial a}{\partial\tau} = f(\tau)\int_0^{2\pi} e^{-i\theta}d\theta_0$$
$$\frac{\partial u}{\partial\zeta} = \mathrm{Re}\{ae^{i\theta}\} \quad \frac{\partial\theta}{\partial\zeta} = u - \Delta \qquad (1)$$

with the boundary conditions

$$a|_{\tau=0} = a_0,\ a|_{\zeta=0} = 0,\ u|_{\zeta=0} = 0,$$
$$\theta|_{\zeta=0} = \theta_0 + r\cos(\theta_0),\ \theta_0 \in [0,2\pi)$$

*Work supported by Russian Fund for Fundamental Researches, grant 05-02-17553

#rrz@appl.sci-nnov.ru

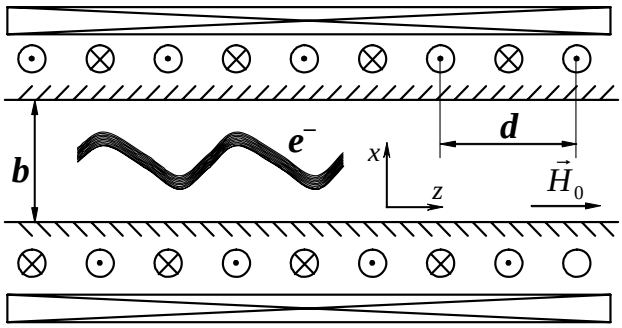

Figure 2: Scheme of the basic model.

The following dimensionless variables have been used:

$$a = \frac{eA_s}{2mc^2}\frac{eA_u}{2mc^2}\frac{\beta_\parallel^3 k_u c}{C^2}\left(\frac{1}{\Omega-\omega_H}-\frac{1}{\Omega+\omega_H}\right)$$

is the wave amplitude, $\theta = \omega t - (k_\parallel + k_u)z$ is the electron phase with the respect to the synchronous wave, $u = C^{-1}(1-\gamma/\gamma_0)$ is the relative electron energy,

$$C = \frac{eI}{mc^3}\frac{c\gamma_0}{4\pi N_s}\left[\frac{eA_u}{2mc^2}\beta_\parallel^3 k_u c\left(\frac{1}{\Omega-\omega_H}-\frac{1}{\Omega+\omega_H}\right)\right]^2$$

is the Pierce parameter, ω_H is the cyclotron frequency, I is the electron beam current, N_s is the norm of the operating wave,

$$\Delta = \frac{\beta_\parallel^3\gamma_0^2}{C}\left(\frac{k_\parallel + k_u}{k}-\frac{1}{\beta_\parallel}\right)$$

is the mismatch from the undulator synchronism, $f(\tau)=1$, $\tau\in[0,T]$, where T is the normalized duration of the electron bunch.

Let is consider the influence of the variation of the mismatch of the undulator synchronism over the longitudinal coordinate on the superradiance process. We choose the simplest linear dependence: $\Delta(\zeta)=\Delta_0\,\zeta/L-\Delta_0$. Fig.3 demonstrates the results of the simulation of Eqs. (1) for $L=T=30$ in the case of non-dispersive wave ($\Delta_0=0$, which corresponds to excitation TEM mode) and wave with dispersion ($\Delta_0=-1$, which corresponds to excitation TE_1 mode). In the first case we see formation of powerful superradaince spike. In the second case output radiation is practically suppressed.

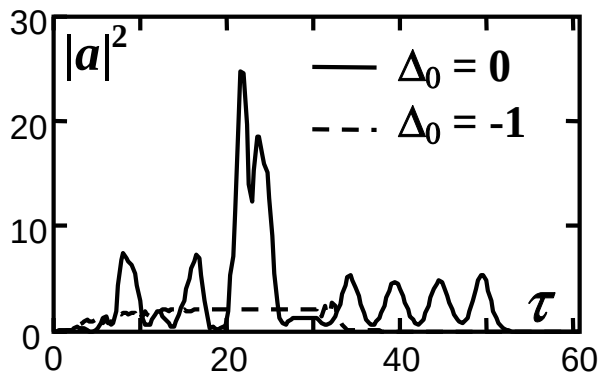

Figure 3: Simulation of averaged equations: output signal in case of uniform ($\Delta_0 = 0$) and non-uniform waveguide ($\Delta_0 = -1$).

PIC-SIMULATIONS

The 2-D version of the PIC-code KARAT was used for additional simulations. The 110 cm length planar waveguide was excited by the 1 MeV, 100 A/cm, 600 ps electron bunch which was transported through the periodic undulator with period 2 cm and 2 kOe strength and guiding magnetic field with strength of 22 kOe (Fig.4a). For regular waveguide simulation showed that the spectrum of the output signal includes three main frequencies (Fig.4c), which correspond to the simultaneous excitation of the TEM, TE_1 and TE_2 modes.

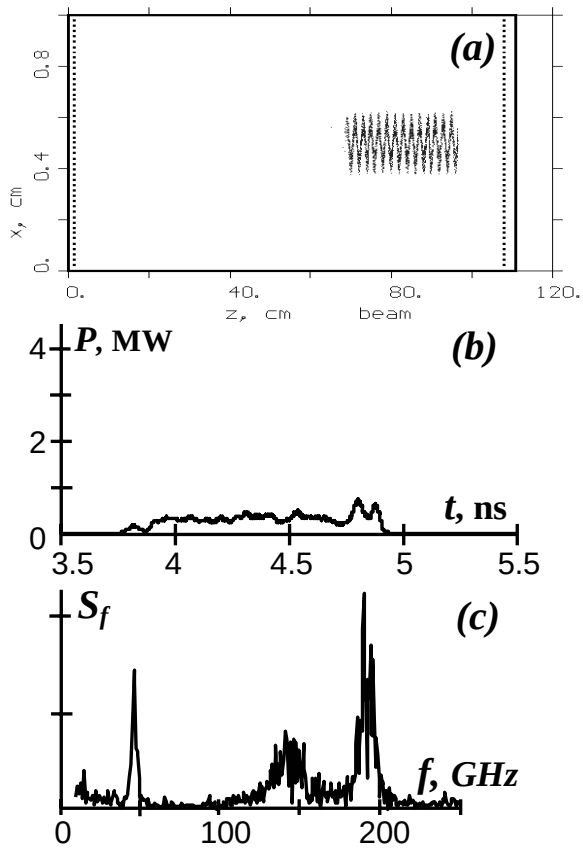

Figure 4: PIC-simulations of superradiance in the uniform oversized waveguide: *(a)* is the geometry of interaction space (solid lines denotes the ideal conductor, dash lines marked the boundary of the microwave absorption layers); *(b)* is the output signal and *(c)* is the spectrum of output radiation.

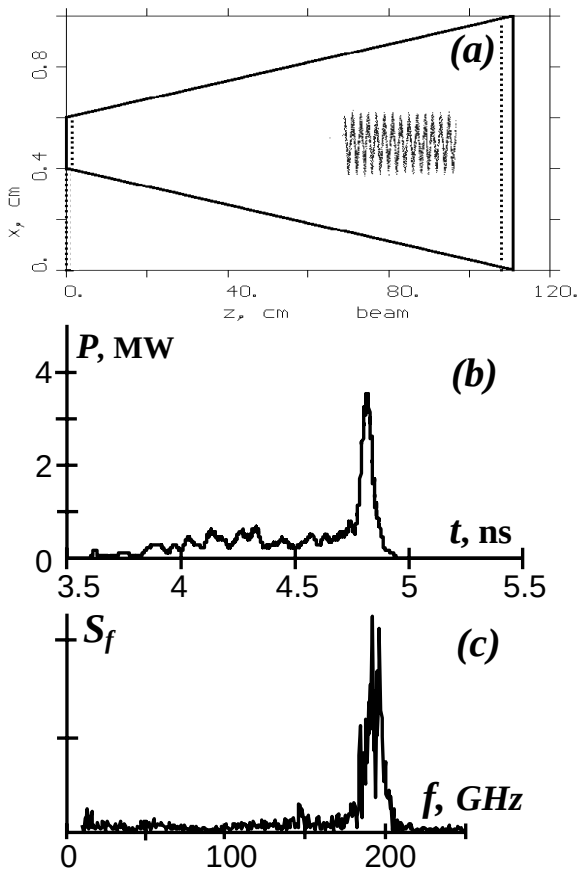

Figure 5: PIC-simulations of superradiance in the uniform oversized waveguide: *(a)* is the geometry of interaction space; *(b)* is the output signal and *(c)* is the spectrum of output radiation.

Fig.5 demonstrated the results of simulation of superradiance in the waveguide with linearly increased gap between plates from 0.2 to 1 cm (fig.5a). In this case all spurious modes were suppressed and the output radiation includes one powerful spike (fig.5b). As a result the spectrum of output radiation is concentrated near the operating frequency of 200 GHz corresponding to excitation fundamental TEM mode (fig.5c).

CONCLUSION

A method of suppressing excitation of spurious modes in the process of supperradiance from intense electron bunch in the planar oversized waveguide is considered. The simulations of the averaged equations and PIC-simulations were carried out and it was shown that in the planar waveguide with linearly increasing gap between plates the SR pulse associated with excitation of single transverse mode could be obtained.

REFERENCES

[1] Ginzburg N.S, et al., Nucl.Instr.Meth.Phys.Res., 1999, A429(1), 94.

[2] N.S.Ginzburg, et al., Opt.Comm., 2000, 175(1-3), 139.

[3] A.G.Reutova, et al. , JETP Lett., 2005, 82(5), 263.

GENERATION OF SUPERRADIANT PULSES BY BACKSCATTERING OF PUMPING WAVE ON THE INTENSE ELECTRON BUNCH*

V. Belousov, G. Denisov, N. Ginzburg, A. Sergeev, I. Zotova#, IAP RAS, N.Novgorod, Russia
A. Reutova, M. Ulmaskulov, A. Sharypov, V. Shpak, S. Shunailov, M. Yalandin, IEP RAS, Ekaterinburg, Russia.

Abstract

At the first time the generation of superradiance pulses in the process of stimulated backscattering of powerful pump wave by intense electron bunch (250 keV, 1 кA, 600 ps) has been observed experimentally. Using a relativistic 38 GHz BWO as a pump wave source, the short 200 ps superradiance pulses of scattered radiation with peak power ~1 MW were obtained. Due to the Doppler up-shift, in the spectrum of scattered radiation high frequency 150 GHz component was presented

INTRODUCTION

Recently a significant progress was achieved in the generation of subnanosecond pulses in the millimeter and centimeter wave bands utilizing the cyclotron and Cherenkov mechanisms of superradiance (SR) of electron bunches [1-3]. The maximal peak power in the case of Cherenkov SR exceeded gigawatt level [3]. This paper is devoted to the novel mechanism of superradiance in the case of the stimulated backscattering of powerful pump wave by intense electron bunch. In this situation, due to the Doppler up-shift effect the radiation frequency can significantly exceed the frequency of the pump wave:

$$\omega_s = \omega_i \frac{1+V_{||}/V_{ph.i}}{1-V_{||}/V_{ph.s}}, \qquad (1)$$

where $V_{||}$ is the translational electron velocity, $V_{ph.i,s}$ are the phase velocities of the pump wave (index *i*) and the scattered wave (index *s*). If the radiation of powerful laser undergoes backscattering at the electron beam with energy about 1-2 MeV the frequency of scattered radiation will belong to ultraviolet band. In the case when the pump wave is generated by relativistic microwave generator (for example BWO) it is possible to produce radiation at the short millimeter and submillimeter wave bands. In this paper we present a basic theoretical description of the superradiance regime of stimulated backscattering. The results of theoretical consideration are confirmed by the first experimental observation of above SR mechanism.

BASIC MODEL

Let us consider the backscattering of the powerful pump wave by the hollow electron bunch with injection radius R_b and duration Δt_b that moves through a cylindrical waveguide with radius *R* along homogeneous guiding magnetic field $\mathbf{H_0} = H_0\mathbf{z_0}$. Under assumption of the fixed pump wave amplitude, the generation of short single pulse of scattered radiation (SR pulse) can be described by the nonstationary equation for scattering signal amplitude A_s and the averaged equations for electrons' motion in the field of combination wave:

$$\frac{\partial a_s}{\partial\zeta}+\frac{\partial a_s}{\partial\tau} = if(\tau)a_i g\frac{I}{\pi}\int_0^{2\pi} e^{-i\theta}d\theta_0$$
$$\frac{\partial^2\theta}{\partial\zeta^2} = \mu\, Im\left\{a_s a_i\, g e^{-i\theta}\right\} \qquad (2)$$

Here $\zeta=\omega_c z/c$, $\tau=\omega_c c\left(t-z/V_{||}\right)\left(1/V_{gr}-1/V_{||}\right)^{-1}$, $a_{i,s}=eA_{i,s}/2m_0\gamma c^2$ are the dimensionless amplitudes of pump and scattered waves, $\theta=\omega_c t-k_c z$ is the electrons phase with respect to the combination wave, $\omega_c=\omega_s-\omega_i$, $k_c=h_s+h_i$, $h_{i,s}$ are the longitudinal pump and scattered wave numbers, $\mu=\gamma_0^{-2}\beta_{||}^{-3}$, $I=\left(eJ_0/mc^3\right)\cdot\left(2\gamma_0 h_s k_c R^2 N_s\right)^{-1}$, J_0 is the electron current, N_S is the norm of the scattered wave. Factor

$$g = J_{n_i-1}\left(k_{\perp i}R_b\right)J_{n_s-1}\left(k_{\perp s}R_b\right)\Omega/\left(\Omega-\omega_H\right) \qquad (3)$$

describes the increase of oscillation velocity of electrons near the cyclotron resonance, $\omega_H=eH_0/m_0c\gamma_0$ is the gyrofrequency, $\Omega=\omega_i+h_iV_{||}$ is the bounce frequency, $k_{\perp i,s}$ is the transverse wave number, $J_n(x)$ is the Bessel function, $n_{i,s}$ are the azimuth indices of the waveguide modes. Function $f(\tau)$ defines the profile of electron current with normalized duration $\tau_b=\Delta t_b\omega_c c\left(1/V_{gr}-1/V_{||}\right)^{-1}$.

Equations (2) describe the joint combinational action of the pump and the scattered waves on the electrons. Such an action leads to selfbunching that starts from small initial density perturbations. As a result the amplitude of scattered wave grows. In the absence of external feedback the synchronization of radiation from different parts of extended electron bunch is provided by slippage of the scattered wave with respect to electrons due to a difference between the electron velocity and the electromagnetic wave group velocity. As a result the scattered wave radiates in the form of a single short pulse, as is shown in Fig.1. The parameters of simulation are chosen in accordance with the performed experiment. The pump wave with 100 MW power and 38 GHz frequency has the transverse structure of the TE_{11} mode. This wave

*Work supported by Russian Fund for Fundamental Researches, grant 05-02-17553
#zotova@appl.sci-nnov.ru

undergoes the backscattering by the 250 keV, 1 kA, 200 ps electron bunch guided in 24 kG magnetic field. According to the simulation the duration of the scattered SR pulse is about 50 ps with peak power ~25 MW. According to waveguide dispersion the scattered wave frequency should be about 150 GHz.

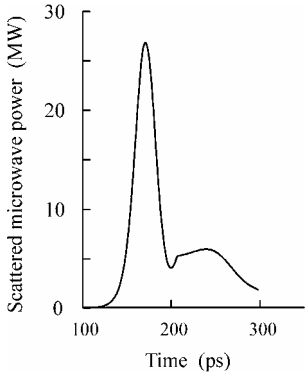

Figure 1: Superradiance pulse of scattered radiation.

KARAT PIC-CODE SIMULATIONS

The possibility of the observation SR in the process of backscattering has been tested also using the particle-in-cell (PIC) code KARAT. In simulation we used the simplified two-dimensional axial symmetric model of the scattering. The pump wave with frequency 38 GHz and power 100 MW represents the TE_{01} wave in contrast to the experimental situation. The guiding magnetic field was 28 kG.

As it is seen from Fig.2 scattered radiation has the form of the short pulse with the duration less than 100-200 ps and peak power about 3 MW. The radiation spectrum has a component with frequency about 150 GHz. Nevertheless the spectrum of radiation is rather wide. It may be explained by the dispersion of electron velocities as well as by excitation of several waveguide modes. Above factors also may result to the reduction of the peak power in comparison with the model described above.

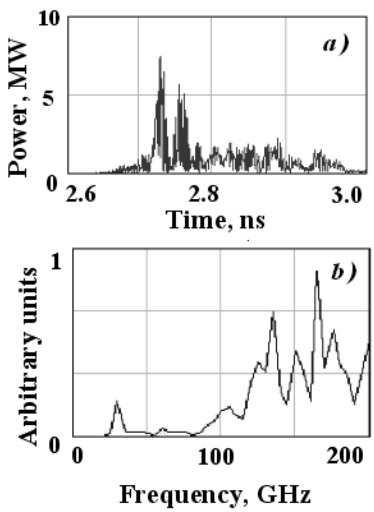

Figure 2: Results of KARAT PIC code simulations: (a) scattered SR pulse, (b) spectrum of SR pulse

EXPERIMENTAL SET-UP

Experiments on the observation of the stimulated backscattering in the superradiance regime were carried out at Institute of Electrophysics (Ekaterinburg, Russia) based on two synchronized nanosecond and subnanosecond high-current RADAN-303 accelerators [4-5]. The 4 ns electron beam from the first accelerator was used to drive the low frequency pump wave generator. The pump wave undergoes backscattering with frequency up-conversion on the subnanosecond electron bunch produced by the second accelerator. The general view of experimental set-up is shown in Fig.3.

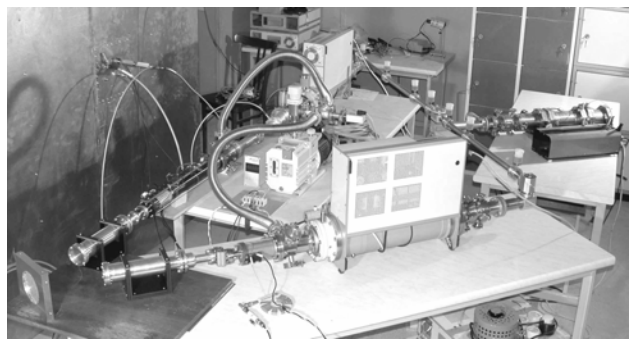

Figure 3: Experimental set-up

In experiments the pump wave was generated by relativistic BWO with operating frequency 38 GHz. For transmission of the pump wave to the scattering section a specially designed quasioptical mirror has been used. The mirror possessed the high reflectivity 95% at the pump wave frequency 38 GHz. The partial transparency of the mirror for the scattered radiation at frequencies above 60 GHz was provided by the mesh of holes with diameter of 3 mm having a step of 4 mm.

EXPERIMENTAL RESULTS

Oscilloscope trace of the 4 ns, 100 MW pump wave pulse with duration is shown in Fig.4a. In absence of subnanosecond electron bunch, the signal from BWO registered by detector installed after quasioptical mirror is shown in Fig.4b. This signal is caused by parasitic high-frequency radiation from the pump wave generator at the harmonics of operating frequency. Presence of such harmonics in a spectrum of the pump wave is confirmed by the direct simulation based on PIC-code KARAT.

In the scattering section with 30 cm length the low frequency pump wave underwent stimulated backscattering by the high current relativistic subnanosecond bunch (250 keV, 1 кA, 600 ps). It is important to note that in absence of the pump wave the background noise radiation of electron bunch was below the threshold sensitivity of a microwave detector. When the pump wave generator was switched on, the short powerful pulse could be observed, as is shown in Fig.4c. This pulse has rather short duration (about 200 ps) and can be interpreted as a superradiance pulse. SR pulses were observed in a large area of magnetic field detuning.

The maximal peak power was obtained for field strength 20-25 kG when the magnetic field strongly affects the amplitude of electron oscillations.

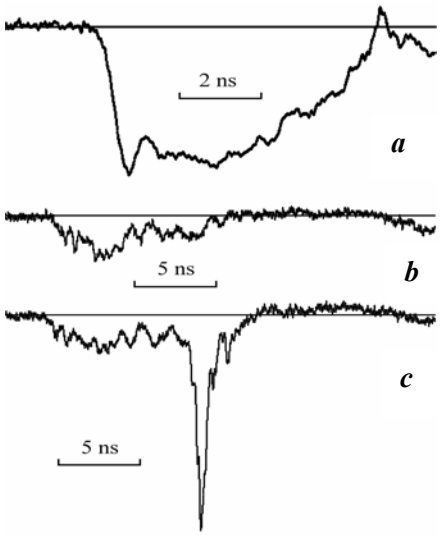

Figure 4: (a) Pulse of the pump wave. (b) High frequency component of BWO radiation in the absence of electron e-bunch registered by detector after quasioptical mirror. (c) Superradiance pulse caused by backscattering of pump wave by electron bunch.

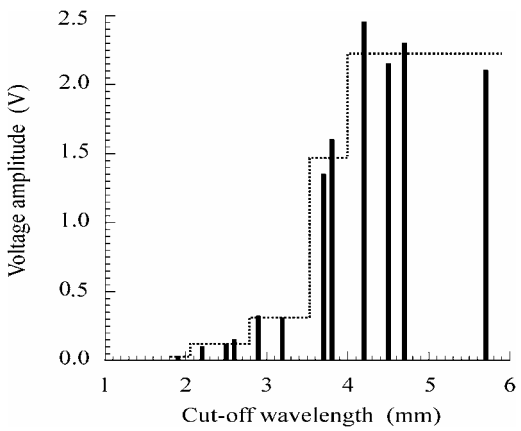

Figure 5: Spectrum measurements. Relative amplitudes of detector signal after filters with different cut-off frequencies.

To analyze the radiation spectrum a set of cut-off waveguides was used. Amplitudes of detector signals after filters with different cut-off frequencies are shown in Fig.5. Locations of vertical lines correspond to the cut-off wavelengths of different filters and the lengths of lines are proportional to the signals registered by the detector. Obviously the jumps of dashed line characterize the content of different spectrum components in the scattered radiation. The main components of radiation concentrate at the interval within wavelength $3.5 \div 4.2$ mm. But at the same time there are high frequency components with wavelength around 2 mm, which is rather close to the calculated one. However it should be noted that detector sensitivity decreases with frequency. So the real fall of intensity of high frequency components should be less than detector indications shown in Fig.4. A rather wide spectrum of scattered radiation can be explained by the spread of electron velocities in the real electron bunch as well as by excitation of several waveguide modes. Integral (over frequency spectrum) peak power of SR pulse amounts up to 1 MW. It was estimated basing on the power level indicated by microwave detector taking into account the aperture of the reception antenna, the distance from a radiator and the width of the radiation pattern.

CONCLUSION

As a result of the experiments the effect of generation of short electromagnetic pulses was observed in the process of stimulated backscattering of the powerful pump wave by the intense electron bunch. Scattered radiation had the form of ultrashort pulse with peak power of 1 MW and duration of 200 ps. Due to the Doppler frequency up-conversion the spectrum of scattered radiation included the frequencies up to 150 GHz that exceeded the pump wave frequency in several times. This process can be interpreted as a superradiance of electron bunch since the radiation of the short pulse occurs in the absence of external high frequency signal and in the absence of external cavity and correspondingly cannot be attributed to traditional amplification or oscillation regimes. Due to the development of selfbunching inside the extended electron bunch the peak power of scattered signal significantly exceeds the power of the spontaneous radiation of electrons in the pump wave and the duration of scattered pulse was essentially shorter than the duration of the background noise.

REFERENCES

[1] N. Ginzburg, I. Zotova, A. Sergeev, I. Konoplev, A. Phelps, A. Cross, S. Cook, V. Shpak, M. Yalandin, S. Shunailov and M. Ulmaskulov, Phys. Rev. Letters, 78(12) (1997) 2365.

[2] N. Ginzburg, Yu. Novozhilova, I. Zotova, A. Sergeev, N. Peskov, A. Phelps, A. Cross, V. Shpak, M. Yalandin, S. Shunailov and M. Ulmaskulov, Phys.Rev.E, 60(3) (1999) 3297.

[3] S. Korovin, G. Mesyats, V. Rostov, M. Ulmaskulov, K. Sharypov, V. Shpak, S. Shunailov and M. Yalandin, Technical Phys. Lett., 30 (2) (2004) 117.

[4] V. Shpak, S. Shunailov., M. Ulmasculov and M. Yalandin In Digest of the 12th IEEE Int. Pulsed Power Conf., USA,1999, 2, 1472

[5] G. Mesyats, S. Korovin, V. Rostov, V. Shpak and M. Yalandin. Proc. of the IEEE, 92 (7) (2004) 1166.

OPTIMIZATION OF THE INJECTION SYSTEM FOR MICROTRON-BASED TERAHERTZ FEL*

Grigory M. Kazakevich#, Viatcheslav M. Pavlov##, Gennady I. Kuznetsov, BINP, Novosibirsk, 630090, Russia,
Young Uk Jeong, Seong Hee Park, and Byung Cheol Lee, KAERI, Taejon, 305-600, South Korea.

Abstract

A compact widely-tunable microtron-based terahertz Free Electron Laser (FEL) has been developed and during last few years operates for users. The laboratory-size, stable facility at the macro-pulse power of tens of W is attractive for application in research laboratories and universities. Reliability in operation and stability of such microtron-based FEL is determined generally by the microtron injection system. Main parameters of the injection system were studied on the base of 2-D tracking considering the frequency drift of the accelerating cavity as a result of variation of the beam loading caused by cathode overheating due to back bombardment with non-resonance electrons. The obtained results show that the injection system based on a thermionic single crystal LaB_6 2.5 mm-in diameter emitter provides operation of the microtron-based FEL with standard deviation of the macro-pulse lasing power less than 10% during long-time work. Experimental check of the FEL during more than five years confirmed stable and reliable operation of the microtron-based FEL with the macro-pulse power of tens of W in the terahertz range.

INTRODUCTION

The injection system of the accelerator intended to drive the terahertz FEL has to provide a suitable bunch current with appropriate transverse parameters of the beam. The qualities are well matched in the system using the classical high-current microtron with an internal injection. In this case the acceleration starts in a high-gradient electric field that allows getting small beam emittance; the multi-turn motion of the electrons through the accelerating gap in the cavity provides good bunching of the beam. Worth to note that such system is simple and inexpensive in manufacturing but some drift of the beam loading during the macro-pulse is inherent to the system. The drift makes worse the intrapulse bunch repetition rate stability and the FEL operation as well because of the effective fluctuation of the FEL optical resonator length, detuning the resonator. The primordial source of the drift is a pulse overheating of the cathode emitting surface caused by back-streaming electrons.

*Work was supported in frames of the BINP-KAERI scientific collaboration and with Korea Research Foundation Grant (KRF-2004-042-C00053)
Corresponding author. Current affiliation:
FNAL, Batavia, IL 60510, U.S.A.
E-mail: gkazakevitch@yahoo.com (G.M. Kazakevich)
Current affiliation: University of Strathclyde, Glasgow, G4 0NG, UK.

To minimize the effect we optimized design and parameters of the microtron injecting system to operate with minimal acceptable cathode diameter. In this case the simplest and cheapest RF system employing the magnetron generator stabilized through the backward wave reflected from the accelerating cavity provides stable operation of the widely-tunable terahertz FEL based on the classical S-band microtron, [1]. For the optimization we calculated the accelerating cavity frequency drift caused by intrapulse variation of the beam loading as a function of the cathode diameter. The calculation was done for I-type injection, [2], basing on 2-D tracking in the microtron median plane. Comparison of the calculation with measured detuning curves of the FEL optical resonator showed that a single crystal LaB_6 emitter with diameter of 2.5 mm at a minimal acceptable detuning of the magnetron and the accelerating cavity can provide operation of the widely-tunable terahertz FEL with radiated macro-pulse power tens of W at a suitable stability and life time. Operation of the terahertz FEL during more than five years demonstrates that the optimized microtron injection system employing the thermionic cathode operating at the temperature of 1900^0 K at the strength of the electric field of > 10 MV/m provides reliable operation of the terahertz FEL. Results of simulations and measurements are presented and discussed in the article.

ANALYSIS OF THE EMISSION CURRENT IN THE MICROTRON WITH INTERNAL INJECTION

At operation of the high-current microtron with the internal injection the main part of electrons is emitted in non-resonance phases. The electrons could not reach the extracting channel, but they are participating in the process of acceleration and mainly hitting the cavity walls; a number of them hit the emitting surface making the back bombardment of the cathode. As was shown in [3], the back bombardment results in the pulse overheating of the emitting surface. This causes an additional emission including emission in resonance phases, thus the electron beam loading the cavity becomes increasing in time domain due to enhancement of number of synchronous electrons and non- synchronous as well.

To consider the effect of the back-streaming electrons hitting the cathode and increasing because of that the loading of the accelerating cavity we calculated the cathode overheats using 1-D analytic expression of the heat conduction along the emitter axis, [4]:

$$\Delta T^0(t_m) = \frac{P_{bs0}}{\pi \cdot r_C^2} \cdot \frac{1}{k_C} \cdot \sqrt{\frac{4\chi \cdot t_m}{\pi}}, \qquad (1)$$

where: k_C is thermal conductivity, χ is thermal diffusivity coefficient, r_C is the cathode radius, and t_m is the pulse duration of the emission current in the microtron. The average power of the electrons heating the emitter per the RF period, $P_{bs}(T)$, was calculated using expression:

$$P_{bs}(T) = \frac{1}{2\pi} \cdot \int_{\varphi_{bs}} \left[2\pi \cdot \int_0^{r_C} i_C(T,r,\varphi) \cdot \varepsilon(r,\varphi) \cdot r\, dr \right] d\varphi, \qquad (2)$$

where: $\varepsilon(r,\varphi)$ is the energy of back-streaming electron emitted in point with a coordinate r and with an initial phase φ, the average value of ε is approximately of 8.9 keV; $i_C(T,r,\varphi)$ is the emission current density of LaB_6 single crystal emitter depending on emitting radius r and initial phase φ; the term was calculated considering Schottky effect through the expression:

$$i_C(T,r,\varphi) = AT^2 \cdot \exp\left[\frac{-e\phi_C + 3.79 \cdot 10^{-4} \cdot \sqrt{E_{CS}(r,\varphi) \cdot 10^4}}{k \cdot T} \right], \qquad (3)$$

where $A = 73$ A / grad^2·cm^2 and $e\phi_C = 2.66$ eV are the Richardson constant and the work function for LaB_6, respectively, k is the Boltzmann constant and T is the emitter temperature in Kelvin deg; $E_{CS}(r,\varphi)$ is the electric field strength at the emitting surface with an initial phase φ. For cylindrical accelerating cavity employed in the microtron the E_{010} mode electric field strength was calculated for the emitting surface deepened relatively the cavity cover surface by d_C = 0.5 mm and emitter located in the center of the cathode hole, made in the cavity cover. The hole radius r_H is 2 mm; coordinate of the emitter center R_C is 30 mm. The $E_{CS}(r,\varphi)$ values were calculated using the expression:

$$E_{CS}(r,\varphi) = E_0 \cdot J_0(k_0 \cdot R_C) \cdot \cos(\varphi) \cdot \frac{J_0(k_r \cdot r)}{\mathrm{ch}(k_z \cdot d_C)}. \qquad (4)$$

Here: $E_0 \approx$ 35.53 MV/m is maximal field on the cavity axis corresponding to the microtron optimal regime, $k_0 = 2\pi/\lambda_0$, $k_r = \chi_{01}/r_H$, J_0 is the first kind Bessel function, $\chi_{01} = 2.405$ is the first square of Bessel function and $k_Z = \sqrt{k_r^2 - k_0^2}$.

Calculated maximal value of the current density at the emitter temperature of 1900^0 K is: $i_{C\max} = i_C(1900^0\ \mathrm{K}, 0, 0) \approx$ 49.5 A / cm^2. At this temperature the developed thermionic cathode with a single-crystal LaB_6 emitter, [3], has a life time approximately of 1000 h. The initial value of the emission cathode current was calculated using following expression, [3], for several values of the cathode diameter:

$$I_C(T) = \frac{1}{2\pi} \cdot \int_0^{2\pi} \left[2\pi \cdot \int_0^{r_C} i_C(T,r,\varphi) \cdot r\, dr \right] d\varphi. \qquad (5)$$

To calculate the loading current of the accelerating cavity we performed tracking of the electrons in the microtron using 2-D Lorentz equation in the median plane. The E_{010} mode electric and magnetic components of the cavity accelerating field and the permanent microtron magnetic field were considered. The electrons hitting the cavity walls (inside or outside the cavity) were non-participating in the tracking. The 2-D Lorentz equations were integrated up to last (12-th) orbit. The tracking in the microtron was done for several values of cathode diameter and the microtron parameter $Eps = E_0/cB$, where: B - is the value of the microtron permanent magnetic field (for our microtron the optimal value of $B =$ 0.1065 T).

Results of calculation of the cathode overheats vs. the cathode diameter for the microtron operating condition at the initial emitter temperature of 1900^0 K for several values of *Eps* parameter and the emission macro-pulse current having duration of 6 μs are presented in Fig 1. The values of k_C and of χ for LaB_6 at the high temperature were taken from [5].

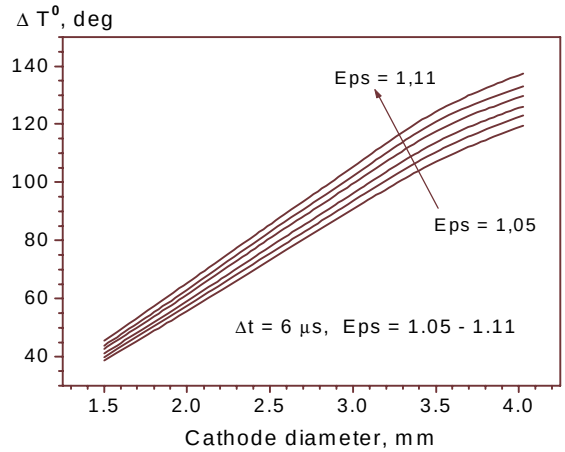

Fig. 1. Cathode overheats caused by back-streaming electrons during 6 μs macro-pulse vs. cathode diameter at the initial temperature of 1900^0 K. The arrow shows variation of the parameter Eps.

Note that we did not consider the heat losses caused by thermo-conductivity of the emitter holder and radiation of heat from the emitter. Because of that the $\Delta T°$ values and the overheating effects are overestimated.

Calculated values of the initial emission current at the initial temperature of 1900^0 K vs. the cathode diameter are plotted in Fig. 2.

Calculated values of the final emission current increased because of the overheating through the electron back-stream during the 6 μs- macro-pulse are plotted in this figure as well.

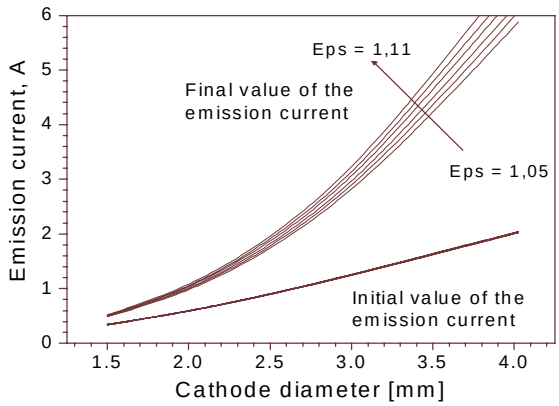

Fig. 2. Initial and final values of the emission current vs. cathode diameter at the initial emitter temperature of 1900^0 K and the macro-pulse duration of 6 μs. The arrow shows variation of the parameter *Eps*.

ESTIMATIONS OF THE FREQUENCY DRIFT IN A HIGH-CURRENT MICROTRON WITH INTERNAL INJECTION

Obtained data allow calculating the intrapulse variation of the accelerating cavity beam loading; that results in frequency drift of the cavity. Performing 2-D tracking of the electrons we calculated velocities of the electrons as well. That allowed us to determine the amplitude and phase of the fist harmonic cavity loading current. Note that the used method allows considering the cavity loading through all accelerated particles, synchronous and non-synchronous as well.

The highest possible frequency drift of the accelerating cavity caused by variation of the beam loading was calculated using following expression, [6]:

$$\Delta F \approx \frac{1}{2\pi} \cdot \frac{\eta_{e0} \cdot \omega_{0C}}{2Q_{0C}} \cdot \tan\varphi_W \cdot \left(1 - \frac{I_F}{I_0}\right), \qquad (6)$$

where: I_0 - initial emission current at the temperature of 1900^0 K, I_F - final value of the emission current increased because of additional heating of emitting surface through back-streaming electrons during 6 μs macro-pulse, Q_{0C} = 9800 is the accelerating cavity wall quality factor (measured value), ω_{0C} is the circular eigen frequency of the cavity, η_{e0} is the initial beam loading coefficient, and φ_W is the phase of the cavity loading current.

The value of η_e is determined as a ratio of the beam power P_e and the cavity wall loss power P_C:

$$\eta_e = \frac{P_e}{P_C} = \frac{[I \cdot V_C \cdot W \cdot \cos(\varphi_W)]}{\left[\frac{V_C^2}{R_{sh}}\right]} = \frac{R_{sh} \cdot I}{V_C} \cdot W \cdot \cos(\varphi_W). \qquad (7)$$

Here: R_{sh} = 1.08 MOhm is the effective shunt impedance of the accelerating cavity, I - is the averaged emission macro-pulse current, W and φ_W are dimensionless first harmonic current amplitude and the harmonic phase, respectively, depending on the cavity voltage amplitude, V_C. (V_C is equal to 0.586 MV for $Eps = 1.08$). The value of V_C is a constant (in steady-state); the values of W and φ_W are constants as well.

Note that using 2-D tracking without consideration of the vertical motion of the electrons causes overestimation of the contribution of the synchronous electrons in the beam loading; for the contribution of the non-synchronous electrons the 2-D tracking gives some underestimation.

From the tracking we determined the values of W and φ_W for various values of *Eps* parameter. For optimal value of *Eps* =1.08, W =2.607, φ_W =20.9º, and for I ≈1.07 A the calculated beam loading coefficient $\eta_e \approx$ 4.8. The value is higher by 10-20% than obtained from the measurements because of overestimation of the accelerated current as was noted above. Fig. 3 shows calculated maximal estimation for the frequency drift caused by overheating of the emitting surface with the electron back-stream vs. the cathode diameter.

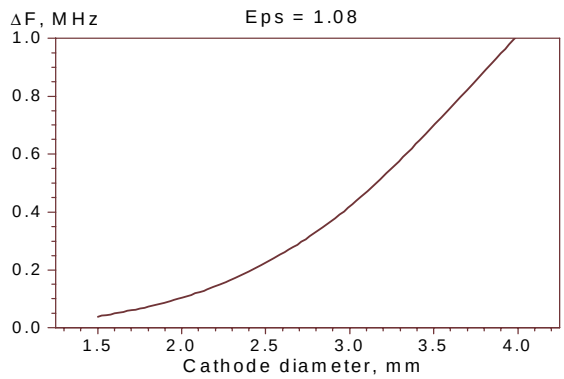

Fig. 3. The cavity frequency drift caused by overheating of the electron emitter with the electron back stream vs. cathode diameters at the initial emitter temperature of 1900^0 K and the value of *Eps* parameter of 1.08.

EFFECT OF THE FREQUENCY DRIFT ON THE TERAHERTZ FEL OPERATION

The described drift of the frequency of the accelerating cavity makes worse stability of the bunch repetition rate because of the stabilizing feedback through reflected wave coming to magnetron. Additional contribution in the bunch repetition rate instability causes increase of the magnetron current during the macro-pulse at a finite value of the frequency stabilization coefficient. The intrapulse increase of the magnetron current and the magnetron

power, respectively, is used to keep constant accelerating voltage and accelerated current at increase of the cavity loading, [1]. Both contributions result in the bunch repetition rate deviation during the macro-pulse; that effectively leads to intrapulse detuning of the FEL optical resonator.

Our terahertz FEL optical resonator, confocal free-space mode in horizontal plane and waveguide mode in vertical plane, was formed with two cylindrical mirrors mounted on the ends of a rectangular waveguide; one of the mirrors has a coupling hole to extract the FEL radiation.

The distance D between the mirrors was chosen using the expression:

$$D = 52 \cdot \frac{\lambda_b}{2} = 52 \cdot \frac{c}{2 \cdot F_b}, \qquad (8)$$

were: λ_b is the wavelength of the accelerating voltage, c is light velocity, F_b is the bunch repetition rate equal to the accelerating cavity frequency. For $F_b \approx 2.801$ GHz, $\lambda_b = \frac{c}{F_b} \approx 10.703$ cm. From expression (8) follows: $|\Delta D| = 26\lambda_b \cdot \frac{\Delta F_b}{F_b}$. I.e. for the optical resonator variation of the bunch repetition rate by 1 MHz approximately corresponds (in a signal level) to the detuning by 1 mm. Measured FEL optical resonator detuning curve at the lasing wavelengths of 113 μm is shown in Fig. 4.

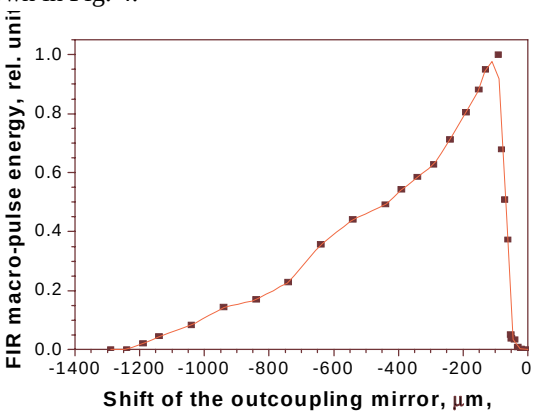

Fig. 4. Detuning curve of the FEL optical resonator measured at the wavelengths of 113 μm.

The measurements were done employing developed cathode assembly based on 2.5 mm-in diameter single crystal, face (100), LaB_6 emitter, operating at the initial temperature of ≈ 1900^0 K. The microtron operating parameters were chosen to provide the intrapulse bunch repetition rate deviations ≤ 0.25 MHz; that was measured using heterodyne method, [7]. At the measurements the microtron provided the beam current of 40 mA at the undulator entrance. The detuning of the FEL optical resonator was done by precise motion of the outcoupling mirror through a stepping motor.

The Fig. 4 curve shows that detuning by 0.2-0.25 mm, corresponding to variation in bunch repetition rate by 0.2-0.25 MHz, decreases the FEL macro-pulse energy by few tens of percents. The value can be used as an upper limit of the intrapulse bunch repetition rate deviations for the microtron intended driving the terahertz FEL. Considering curve plotted in Fig. 3, this points to a necessity in limitation of the emitter size though the emitter with larger diameter provides higher accelerated current at the same life time of the cathode.

Optimal diameter of 2.5 mm of the single crystal LaB_6 emitter for the microtron-terahertz FEL injector was chosen as a compromise considering requirements of reliable operation of the microtron and stable operation of the terahertz FEL. With the emitter at the microtron regime optimized for long-life operation of the cathode we obtained radiated macro-pulse lasing power of 40-50 W in the wavelength range of 100-200 μm. The measurements were done using calibrated pyro-electric detector measuring the lasing macro-pulse energy and the wide-band Schottky barrier detector measuring the lasing macro-pulse shape and the pulse width.

The thermionic cathodes with such emitters at optimized regime of the microtron have life time approximately of 1000 h, providing operation of the widely-tunable terahertz FEL with standard deviation of the lasing macro-pulse energy less than 10% during long-time work, [3].

SUMMARY

Effect of the back-streaming electrons bombarding the emitting surface of the thermionic cathode in a classical microtron with the internal injection on the lasing of the microtron-based FEL was analyzed. The results allow choosing the optimal size of the microtron thermionic cathode to provide stable and reliable operation of the microtron-based widely-tunable terahertz FEL with the macro-pulse lasing power few tens of W.

REFERENCES

[1]. G. M. Kazakevitch, Y. U. Jeong, V. M. Pavlov, B. C. Lee, NIM A 528 (2004) 115-119.
[2]. S. P. Kapitza and V. N. Melekhin, The Microtron London. Harwood, 1978.
[3]. G. M. Kazakevich, G. I. Kuznetsov, V. M. Pavlov, Y. U. Jeong, S. H. Park, and B. C. Lee "Injection system for microtron-based Terahertz FEL" Proceedings of the 27th International FEL Conference, JACoW / eConf C0508213.
[4] L. D. Landau and E. M. Lifshitz, in Course of Theoretical Physics ("Nauka" (In Russian), Moscow, (1986), Vol. **6**, Fluid Mechanics, p. 288-289.
[5] Takaho Tanaka, J. Phys. C **7**, L177-L180 (1974).
[6] E. L. Kosarev. Ph.D. Thesis, Inst. of Phys. Problems, Moscow, 1971, (in Russian).
[7] G. M. Kazakevitch, Y. U. Jeong, B. C. Lee, J. Lee, NIM A 483 (2002), 331-335.

FEL-OSCILLATOR SIMULATIONS WITH GENESIS 1.3

J.G. Karssenberg, P.J.M. van der Slot*, J.W.J. Verschuur, I.V. Volokhine † K.-J. Boller
Laser Physics and Non-Linear Optics Group, University of Twente
PO Box 217, 7500 AE Enschede, The Netherlands

Abstract

Modeling free-electron laser (FEL) oscillators requires calculation of both the light-beam interaction within the undulator and the propagation of the light outside the undulator. We present a paraxial Optical Propagation Code (OPC) based on the Spectral Method and Fresnel Diffraction Integral, which in combination with Genesis 1.3 can be used to perform either steady-state or time-dependent FEL oscillator simulations. A flexible scripting interface is used both to describe the optical resonator and to control the codes for propagation and amplification. OPC enables modeling of complex resonator designs that may include hard-edge elements (apertures) or hole-coupled mirrors with arbitrary shapes. Some capabilities of OPC are illustrated using the FELIX system as an example.

INTRODUCTION

Free-electron laser (FEL) oscillators are complex devices. They require simulation of both the amplification of the radiation field within the undulator and the propagation of the radiation field through the resonator, to correctly predict the spectral and spatial properties of the output of the laser. These properties are very important for the design of user experiments.

To date, several codes exist that can simulate an FEL amplifier or oscillator (see, e.g., [1]). However, the well-established Genesis 1.3 FEL code [2] is primarily used for FEL amplifier or SASE simulations. In this paper we present an optical propagation code (OPC) that works together with Genesis 1.3 to simulate FEL resonators. The full functionality of Genesis 1.3 is maintained and simulation of FEL oscillators can be done both in steady-state and time-dependent modes.

To propagate the radiation field between optical and gain elements, we have implemented three related paraxial methods: the Spectral Method [3], the Fresnel Diffraction Integral Method [4] and a modified Fresnel Diffraction Integral Method. The latter is based on the normal Fresnel Diffraction Integral, however, it includes the ABCD matrix of the optical system between input and output plane [5]. The radiation field produced by Genesis 1.3 at the undulator's exit is propagated using one of these methods to the first optical element. Then the action of that particular optical element is applied to the wave and one of the propagation methods is again used to propagate the wave to the next optical element. This procedure is repeated until the undulator's entrance is reached. Note that propagation through a cascaded set of optical elements can be done in a single step if this set can be represented by a single overall ABCD matrix and using the Modified Fresnel Diffraction Integral for the propagation.

We have chosen to separate the optical propagation model from the FEL simulation model for two main reasons. First, the optical propagation model can be used with different gain models and is, in principle, not limited to FELs. Second, the propagation model can then also be used to propagate the field outside the resonator and determine the field distribution, for example, in the far field or in a user area that can be located at a considerable distance from the laser in the case of FELs. The optical propagation code is available for download [10].

In the remainder of this paper, we first describe briefly the different propagation methods, then the OPC code and end with an example illustrating the capabilities of the combination of the OPC code with Genesis 1.3.

PARAXIAL OPTICAL PROPAGATION

By applying a Fourier transform over the transverse coordinates, the paraxial wave equation can be written as [5]:

$$(k_x^2 + k_y^2)\tilde{u} - 2ik\frac{\partial \tilde{u}}{\partial z} = 0, \tag{1}$$

where

$$\tilde{u}(k_x, k_y, z) = \int_{-\infty}^{\infty}\int_{-\infty}^{\infty} u(x, y, z)e^{-i(k_x x + k_y y)}\mathrm{d}x\mathrm{d}y \tag{2}$$

is the Fourier transform of the complex wave amplitude $u(x, y, z)$. Given a known optical field $u_0(x, y)$ at $z = 0$, the optical field after a propagation over a distance z can be obtained from eq. 1:

$$\tilde{u}(k_x, k_y, z) = \tilde{u}_0(k_x, k_y)e^{-i\frac{2z}{k}(k_x^2+k_y^2)}. \tag{3}$$

The propagation method described by eq. 3 is known as the Spectral Method and consists of applying the spatial Fourier transform eq. (2) to the input plane, propagate the field over a distance z (eq. 3) and applying the Inverse Fourier Transform to $\tilde{u}(k_x, k_y, z)$. This Inverse Fourier Transform is similar to eq. 2 with the roles of $\tilde{u}$, k_x and k_y interchanged with those of u, x and y, respectively, and a factor $1/4\pi^2$ added.

* p.j.m.vanderslot@tnw.utwente.nl
† Current address: Philips Research, High Tech Campus 34, 5656 AE Eindhoven, The Netherlands

It can be shown that paraxial wave propagation over a distance $z = L$ through a cascaded optical system can be realized in a single step using the elements of the overall ABCD matrix in Huygens' Integral for propagation [5]. If we use the following transform to remove the spherical portion of the wave at the input plane [5]:

$$v_0(\xi', \eta') \equiv \sqrt{a_1 a_3} u_0(\xi, \eta) e^{-i\frac{\pi(A_x - M_x)\xi^2}{B_x \lambda}} e^{-i\frac{\pi(A_y - M_y)\eta^2}{B_y \lambda}} \quad (4)$$

and at the output plane:

$$v(x', y') \equiv \sqrt{a_2 a_4} u(x, y, L) e^{+i\frac{\pi(D_x - M_x^{-1})x^2}{B_x \lambda}} e^{+i\frac{\pi(D_y - M_y^{-1})y^2}{B_y \lambda}}, \quad (5)$$

where $x' = a_1 x$, $\xi' = a_2 \xi$, $y' = a_3 x$, $\eta' = a_4 \eta$, and $A_{x(y)} \dots D_{x(y)}$ are the ABCD matrix coefficients for the x- and y direction respectively, then Huygens' Integral can be written as a modified Fresnel Diffraction Integral:

$$v(x', y') = i\sqrt{N_{c,x} N_{c,y}} \times \int_{-1}^{1}\int_{-1}^{1} K(x', y', \xi', \eta') v_0(\xi', \eta') \mathrm{d}\xi' \mathrm{d}\eta', \quad (6)$$

where the kernel K is given by

$$K(x', y', \xi', \eta') = e^{-i\pi N_{c,x}(x' - \xi')^2} e^{-i\pi N_{c,y}(y' - \eta')^2}, \quad (7)$$

and the equivalent collimated Fresnel numbers $N_{c,x(y)}$ are given by

$$N_{c,x(y)} = \frac{M_{x(y)} a_{1(3)}^2}{B_{x(y)} \lambda}. \quad (8)$$

The arbitrary scaling factors $a_{1..4}$ in eqs. 4-5 define two magnification factors $M_{x(y)} = a_{2(4)}/a_{1(3)}$, if they correspond to either the size of a hard aperture or a size sufficiently large that the field is just negligible outside the area covered by that size. Note that for free-space propagation $A = D$ =1, C =0 and $B = L = z$, and using $M_x = M_y$ =1, reduces eqs. 6-8 to the normal Fresnel Diffraction Integral.

Both the Spectral and the Modified Fresnel propagation methods are implemented using Fast Fourier Transforms and therefor their computation time scales as $N^2 log_2(N^2)$ for a $N \times N$ grid. For an equal grid, the Spectral method is the faster of the two because it requires less operations [6]. However, care has to be taken with the Spectral Method that the field remains zero at the border of the grid to avoid artificial reflections. The Modified Fresnel Diffraction Integral has the advantage that propagation through an optical system, described be a single overall ABCD matrix, is obtained in a single step. Another advantage is that the scaling applied to this method allows a magnification factor for the grid so that the mesh size in the input plane does not have to be the same as the mesh size in the output plane.

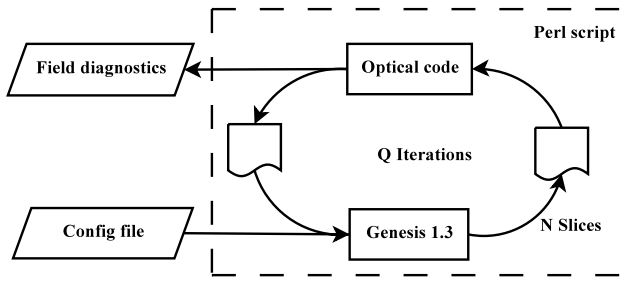

Figure 1: Flowchart of the simulation loop.

IMPLEMENTATION

Simulation of an FEL oscillator requires simulation of both the gain within the undulator and the propagation of the radiation through the remaining part of the resonator, that may contain multiple optical components. Genesis 1.3 [2] is used to propagate the optical wave through the undulator and calculate the amplification of the wave. The OPC receives the optical output from Genesis 1.3, and propagates it from optical element to optical element using one of the methods described above, until the undulator's entrance is reached and the next round trip can start. If a cascaded set of optical elements can be described by a single ABCD matrix, then propagation through the cascaded set can be done in a single step using the Modified Fresnel Diffraction Integral. Output can be produced at various positions, and by the optical elements, which is of advantage for beam diagnostics and for designing suitable optics for a further propagation of the output beam.

While the actual simulation algorithms are written in FORTRAN, the Perl scripting language is used to both control the program flow and define the resonator geometry. Fig. 1 shows schematically the program flow. The advantage of using a script to control the program instead of a config file is that it gives the user a lot of freedom to create complex models. Table 1 gives an example of a script for simulation of the FELIX system [7].

This example script contains all essential elements needed to simulate the FELIX system. The first three lines are headers needed to load a library. Then two objects are created, one that corresponds to the genesis program (l.5) and one that corresponds to the optical propagation code (l.6). The genesis object requires the standard configuration file for Genesis 1.3 as input. A Perl script function is provided that gives the user complete control over the parameters in the configuration file. This allows, for example, the use of a Gaussian seed for Genesis 1.3 in the first round trip and the resonator feedback as input for Genesis 1.3 in consecutive round trips.

To define the optical propagation through the resonator, the optics object (l.6) accepts a simple script that describes the propagation methods and optical components used (l.7-16). The available propagation methods are described above, and the optical components so far include diaphragms, square apertures, curved mirrors and thin

Table 1: Example script for simulating the FELIX FEL oscillator.

```
01:  #!/usr/bin/perl
02:  use lib './lib';
03:  use Physics::OPC;
04:
05:  $genesis = genesis('./felix.itdp.in');
06:  $optics  = optics( "
07:      fresnel z=1.062
08:      mirror  r=3 R=98%   # Downstream mirror
09:      fresnel z=5.89
10:      hole    r=0.0015 (    # Out-coupling
11:           dump var=output
12:           fresnel z=1       # Far field distance
13:           dump var=far  )
14:      mirror  r=4 R=98%   # Upstream mirror
15:      dump  var=reflected
16:      fresnel  z=2.358 "   );
17:
18:  for $i (1 .. 75) {
19:      run  $genesis;
20:      run  $optics;
21:      move $output   => "output.$i.dfl";
22:      move $far      => "far.$i.dfl";
23:      move $reflected => "reflected.$i.dfl";
24:      move $field    => "entrance.$i.dfl";
25:  }
```

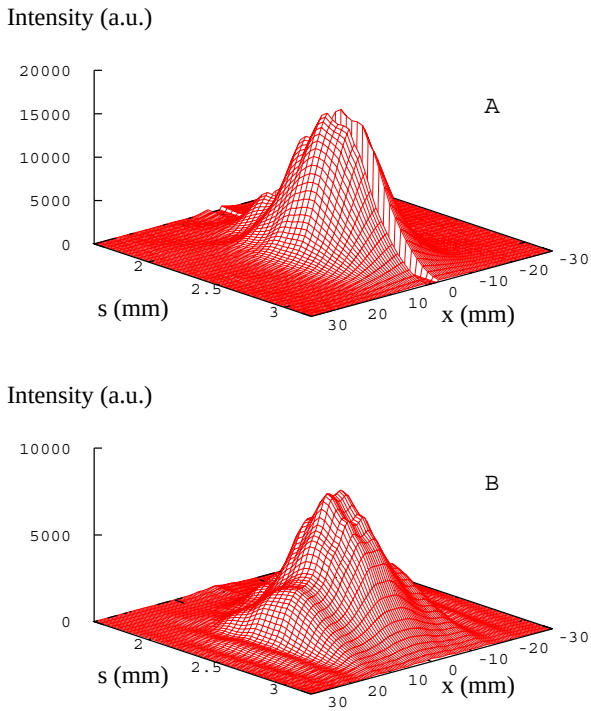

Figure 2: Radiation intensity just after reflection on the upstream mirror (A) and just before the undulator's entrance (B) as a function of the horizontal cross-section (at y=0) and the position within the optical micro pulse s after 75 round trips and for ΔL=-1.5λ.

lenses. Each optical component is defined by a set of parameters, for example the downstream mirror (l.8) for FELIX has a curvature ('r') of 3 m and a reflectivity ('R') of 98 %. Other possible parameters for a mirror are absorption ('A'), transmittance ('T'), offset ('xoff' and 'yoff'), and a small tilt ('xr' and 'yr'). The optical propagation starts with propagation over a distance z=1.062 m from the undulator's exit to the downstream mirror using the Fresnel Diffraction Integral (l.7). Then the downstream mirror is defined (l.8). After the downstream mirror the wave is propagated to the upstream mirror, again using the Fresnel Diffraction Integral (l.9). In FELIX, the output beam is extracted through a hole in the upstream mirror. In the model the "hole" component (l.10) is processed before the actual mirror component (l.14). The hole component creates two waves, one that is transmitted through the hole, and one that corresponds to the part outside the hole that remains within the resonator. In this case, the transmitted beam corresponds to the radiation extracted from the resonator. The output beam is propagated over a distance sufficiently large to be in the far field (l.11-13). At l.14 the script continues with the part outside the hole and this is reflected by the upstream mirror. The combination of the "hole" and "mirror" commands represent the upstream mirror with the hole. The resonator is closed by propagation from the upstream mirror to the undulator's entrance (l.16). The "dump" commands indicate positions where output is produced for further analysis.

The last part of the Perl script is the actual simulation loop where we run the two programs consecutively and save binary dumps (l.21-34) for each round trip at varies positions defined in the optical configuration. The binary files used by the propagation code have the same format as the field files produced by Genesis 1.3, so existing analysis tools can be re-used. Utilities to extract plain text data from these files are included with the OPC code. Using plotting tools such as Gnuplot, the user can create all kinds of views to analyze the optical pulse.

In steady-state mode Genesis 1.3 produces one field distribution, i.e., a single slice, as output, which is then processed by the propagation code. Genesis 1.3 can also run in time-dependent mode, which includes slippage effects. In this mode Genesis 1.3 produces a set of slices representing the radiation pulse as output. In time-dependent mode, the propagation code will process all slices produced by Genesis 1.3 consecutively. Each slice is propagated using the center wavelength of the optical pulse, which is valid only for a narrow bandwidth of the optical pulse. The slowly varying amplitude and phase approximation used by Genesis 1.3 limits the maximum bandwidth of the pulse. Furthermore, an analysis by Dattoli et.al. showed that the relative bandwidth is limit to about 10^{-3} to 10^{-2} for typical parameters of VUV, UV and IR FELs [8].

EXAMPLE

The script shown in Table 1 is used to illustrate some of the capabilities of the OPC code. The script describes the resonator for the FELIX system [7]. The script produces four binary dump files for each iteration (that is, for each round trip). The first gives the field distribution just outside the outcouple mirror (l.21), l.23 gives the field distribution just after reflection at the upstream mirror containing the hole for extraction of the radiation, and l.24 gives the distribution at the entrance of the undulator. The far-field distribution (l.22) will not be used here. It should be noted that the same script is used for both steady-state and time-dependent simulations, the only changes required are made in the genesis configuration file.

We performed a time-dependent simulation of the FELIX system. The horizontal cross-section (at y=0) of the radiation intensity just after reflection on the upstream mirror and just before the undulator's entrance are shown in Fig. 2 as a function the horizontal position x and the position s within the optical micro pulse after 75 round trips and for a cavity detuning ΔL=-1.5λ. This figure clearly shows the effect of the hole in the mirror (Fig. 2A) on the radiation profile and how this profile has changed when propagated to the undulator's entrance (Fig. 2B), that shows a near maximum on-axis intensity. Note that the broad radiation profile at the undulator's entrance may be clipped by the electron beam transport tube. Although not present in the current script, this can be included by adding a diaphragm component just after propagation to the undulator's entrance (l.16) in Table 1.

If we integrate the intensity over the cross-section of the optical pulse, we obtain the micro-pulse optical power as a function of the position s within the micro-pulse. This is shown in Fig. 3 as a function of the round-trip number. The oscillation in the micro-pulse optical power as a function of time (=round trip #) is known as the so called limit-cycle oscillations [9]. It is more clearly visible in the total micro-pulse energy that is shown in Fig. 4 for three different values of the cavity detuning ΔL.

CONCLUSION

We have developed an Optical Propagation Code that propagates an arbitrary radiation wave, in the paraxial approximation, through a complex optical system. In combination with a code to simulate the gain medium, such as Genesis 1.3 in case of FELs, this optical code can be used to model the output of a laser oscillator. The use of a flexible scripting interface allows a user to create both simple and complex resonator configurations. The OPC package is available for download at our website[10].

REFERENCES

[1] S. Biedron, Y. Chae, R. Dejus, B. Faatz, H. Freund, S. Milton, H.-D. Nuhn, and S. Reiche, Nucl. Instrum. Methods Phys. Res. A, Accel. Spectrom. Detect. Assoc. Equip. **A445**, 110 (2000).

[2] S. Reiche, *pbpl.physics.ucla.edu/ reiche*.

[3] E. Sziklas and A. Siegman, Appl. Opt. **14**, 1874 (1975).

[4] H.A. Hause, "Waves and fields in optoelectronics," 1984, Prentice-Hall, Englewood Cliffs.

[5] A.E. Siegman, "Lasers," 1986, University Science Books, Mill Valley.

[6] I.V. Volokhine, "Design and Numerical Analysis of TUE-FEL II", Ph.D. thesis, 2003 University of Twente.

[7] D. Oepts, A. van der Meer, and P. van Amersfoort, Infrared Phys. Technol. **36**, 297 (1995).

[8] G. Dattoli, H. Fang, L. Giannessi, M. Richetta, A. Torre, and R. Caloi, Nucl. Instrum. Methods Phys. Res. A, Accel. Spectrom. Detect. Assoc. Equip. **A285**, 108 (1989).

[9] D. Jaroszynski, R.J. Bakker, D. Oepts, A.F.G. van der Meer, and P.W. van Amersfoort, Nucl. Instrum. Methods Phys. Res. A, Accel. Spectrom. Detect. Assoc. Equip. **A331**, 52 (1993).

[10] OPC design team, *lf.tnw.utwente.nl/opc.html*.

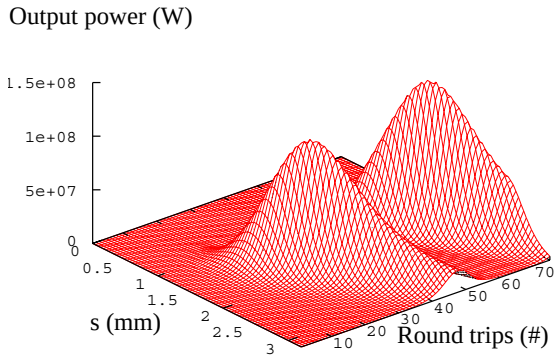

Figure 3: Micro pulse optical power as a function of both the position s within the pulse and the round trip number for a detuning ΔL=-1.5λ.

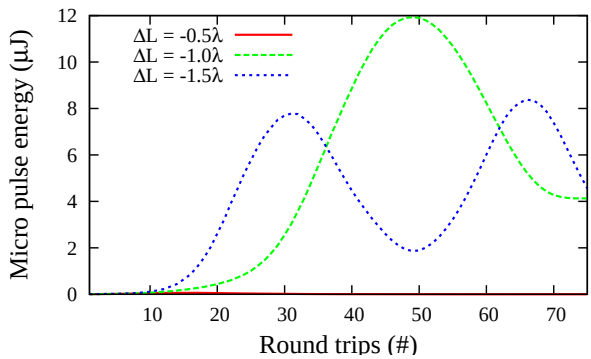

Figure 4: Total energy of the micro pulse as a function of round-trip number for a detuning ΔL of -0.5λ, -1λ and -1.5λ respectively.

COMMISSIONING OF S-BAND RF GUN AND LINAC FOR THE MARK-III FEL FACILITY AT DUKE UNIVERSITY

Y. Kim*, J. Gustavsson, P. Wang, G. Swift, M. Emamian, S. Hartman, P. Wallace, and G. Edwards
Free Electron Laser Laboratory, Duke University, Durham, NC 27708-0319, USA

Abstract

At the Free Electron Laser (FEL) Laboratory of Duke University, there is an S-band linac based Mark III FEL facility which can supply coherent FEL photon in the infrared wavelength range. To supply high quality electron beams and to have excellent pulse structure, we installed an S-band RF gun with a Lanthanum Hexaboride (LaB_6) single crystal cathode for the Mark III FEL facility in 2005. Its longest macropulse length is about 6 μs, and maximum repetition rates of a macropulse and a micropulse are 15 Hz and 2856 MHz, respectively. Therefore we can generate about 17142 bunches within a bunch train and about 257142 bunches within one second by the S-band gun. In this paper, we describe recent commissioning experiences of our newly installed S-band RF gun and linac for the Mark III FEL facility.

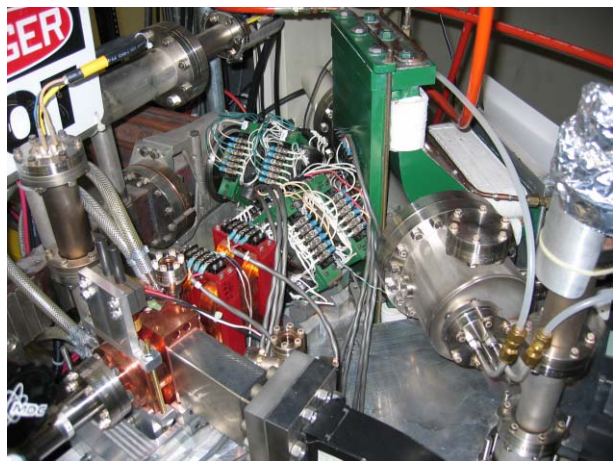

Figure 1: Photograph around the newly installed gun.

INTRODUCTION

The Mark III FEL is a wavelength-tunable light source facility which can generate coherent and ultra-bright FEL photon beams in the infrared wavelength range. Originally, the Mark III FEL facility was operated at Stanford University, then it was moved to Duke University in 1989 [1]. After relocating to Duke University, we had upgraded several machine components of the Mark III FEL facility [2], [3]. Recently, many FEL facilities started to use the laser driven RF photoinjector to generate high quality electron beams with a high peak current and a low transverse emittance. However, the laser driven RF photoinjector has a limitation to generate a good micropulse structure due to a low repetition rate of the gun driving laser. Since many users working for biophysical and biomedical science request high repetition rate of FEL photon beams, we have used an S-band thermionic RF gun with a LaB_6 cathode to supply excellent micropulse and macropulse structures [4]. After successful operation for several years, in 2003, we had met a strong back bombardment problem which caused malfunction of our gun [2], [5]. Therefore we re-installed a new S-band thermionic RF gun in 2005 to generate stable FEL photon beams continuously. In this paper, we describe our commissioning experiences of the new S-band RF gun and linac for the Mark III FEL facility.

LAYOUT OF GUN AND LINAC

The geometry and parameters of the newly installed gun are almost the same as those of our original gun. Its original shape and parameters can be found in reference [6] and [7]. In our new gun, we modified geometry of a deflection magnet and shifted its core position to backward by 3.175 mm for easy fabrication. Photograph around the new gun and layout of the Mark III FEL facility are shown in Figs. 1 and 2. And its main accelerator parameters are summarized in Table 1 where all emittances are estimated from ASTRA and ELEGANT simulations. As shown in Figs. 1 and 2, at the upstream of the gun cavity, there is the deflection magnet which bends electron beam orbit vertically to reduce the back bombardment on the LaB_6 cathode surface. At the downstream of the gun cavity, there are two vertical correctors to compensate vertically bended beam orbit which is intentionally generated by the deflection magnet. After those correctors, there is a quadrupole doublet (GQ1 and GQ2) and the first gun toroid (T1) to measure electron beam current in a macropulse or bunch train. Then electron beams are transferred to an α-magnet [8]. Since horizontal dispersion is not zero in the α-magnet, electron with a higher energy takes an outer or longer path, and electron with a lower energy takes an inner or shorter path in the α-magnet. In that manner, bunch length is compressed by the combined function of the nonzero momentum compaction factor R_{56} and nonzero energy spread in the α-magnet [6]. Since horizontal beam size becomes larger in the α-magnet due to nonzero dispersion as shown in Fig. 2, we chop tail or head part of electron beams by lower and higher energy filters to control beam energy spread, beam energy, and transverse emittance. Only electron beams which can go through two energy filters are transferred to linac [6]. Additionally, to supply macropulse with a frequency of 1 Hz,

* E-Mail : yjkim@FEL.DUKE.edu

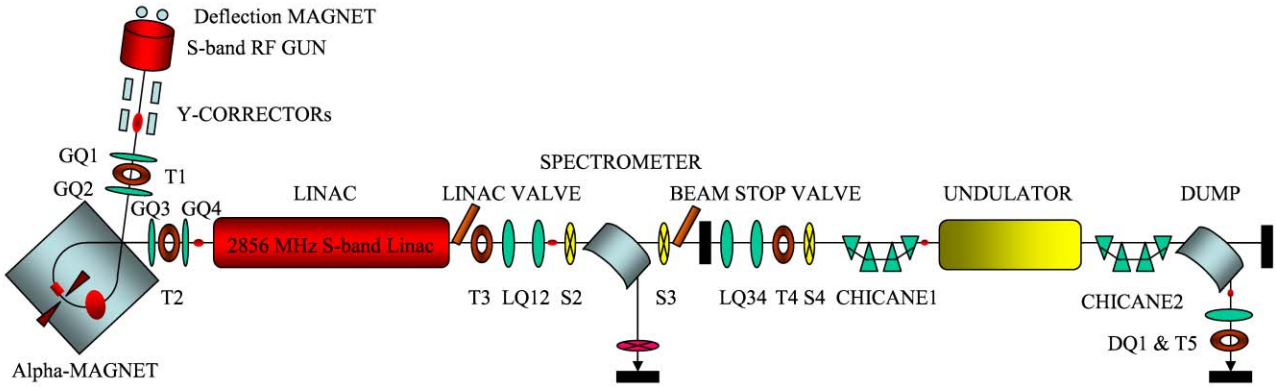

Figure 2: Layout of Mark III FEL Facility.

Table 1: Accelerator parameters of the Mark III FEL.

Parameter	Unit	Value
RF frequency of gun and linac	MHz	2856
number of gun cell	cell	1
cathode diameter	mm	1.75
cathode operation temperature	K	~ 1800
cathode energy spread	eV	~ 0.4
cathode work function	eV	2.69
cathode heater power	W	~ 11
operating vacuum in gun	Torr	$< 10^{-7}$
single bunch charge	nC	0.14
macropulse current at gun exit	mA	~ 400
macropulse current at α-magnet exit	mA	~ 180
klystron power	MW	30
gun forward RF power	MW	~ 1.8
max gradient on cathode	MV/m	~ 30
cavity cooling water temperature	deg	32.2
total beam energy at gun exit	MeV	~ 1.6
total beam energy at linac exit	MeV	$25 - 45$
beam energy spread at linac exit	%	0.3
peak current at linac exit	A	$15 - 45$
thermal emittance at cathode	μm	~ 0.35
projected emittance at linac exit	μm	~ 5
slice emittance at linac exit	μm	~ 1
macropulse length at linac exit	μs	$2 - 6$
max macropulse rate	Hz	15
micropulse length at linac exit	ps	$0.5 - 3$
micropulse rate	MHz	2856

there is a 11.5 kV kicker in the α-magnet. In this case, only one macropulse is transferred to linac in one second, and all other macropulses are dumped in the α-magnet by the kicker [6].

After the α-magnet, beams are focused by the second quadrupole doublet (GQ3 and GQ4). There are two toroids (T2 and T3) to measure beam current at the downstream of the α-magnet and linac. By accelerating electron beams with a 3 m long S-band accelerator, beam energy is increased up to about 45 MeV, and bunch length is more compressed to about 0.5 ps by the bunch compressor (CHICANE1). By optimizing two quadrupole doublets (LQ12 and LQ34) and steerers at the downstream of linac, we can get a beam waist in undulator which is helpful to increase interaction between electron beams and spontaneous emitted photon beams. After making the interaction to induce the microbunching in electron beams and lasing, electron beams are sent to the beam dump.

COMMISSIONING EXPERIENCES

To reduce space charge effects which increase transverse emittance and bunch length, we have to accelerate electron beams quickly in the gun cavity. By sending about 2 MW RF power to the gun cavity, electron beams can be accelerated to about 1.6 MeV in the gun. However, we could not send such a high power at the beginning stage of our commissioning due to too strong waveguide bangs, arcs, and poor vacuum at the gun region. Hence, first of all, we had to reduce gun reflected RF power by matching the resonance frequency of gun cavity with a driving RF frequency. By optimizing temperature of cavity cooling water, position of a gun cavity tuner, and position of the LaB_6 cathode, we could change volume of the gun cavity slightly, and we could get a best matched point which gives a minimum reflected RF power and the best beam emittance as shown in Fig. 3 [6]. Here the left means the head region of macropulse, and a large reflected RF power at the tail region was generated by a resonance frequency shift which was induced by the increased back bombardment and beam loading effect along the macropulse [5]. After reducing reflected power, by increasing gun forward power and macropulse length gently, we performed continuous gun cavity RF conditioning until we could get a stable vacuum status in gun region. Since gun reflected power is changed as forward RF power and macropulse length are increased, we had to re-optimize gun reflected RF power at a higher power and a longer macropulse. After performing continuous RF conditioning for three months, we

could obtain required basic beam parameters for the Mark III FEL operation, and vacuum at gun region was also stabilized as shown in Fig. 5. Here macropulse length is about 6 μs, the maximum beam current in the macropulse is about 400 mA at T1, and its maximum beam current at T2 is about 180 mA as shown in Figs. 3 and 4.

Although we optimized the deflection magnet to reduce the back bombardment on the cathode surface, we could not avoid the problem completely when macropulse length was longer than about 2 μs and beam current at T1 was higher than about 200 mA. Therefore, as shown in Figs. 3 and 4, beam current at T1 was continuously increased along the macropulse, and a large spike was generated at the tail region of the reflected power due to the resonance frequency shift. Generally, electron emission rate from a thermionic cathode becomes higher as the gradient on the cathode surface is increased. This increased current density J_s can be described by the well-known Schottky equation which is given by

$$J_s = A \cdot T^2 \exp\left[-(\Phi - e\sqrt{eE_c/(4\pi\epsilon_0)})/kT\right], \quad (1)$$

where $A = 120\,\mathrm{A/(cm^2 \cdot K^2)}$ is the Richardson constant, T is the cathode temperature, $\Phi = 2.69$ eV is the work function of the LaB_6 cathode, $k = 8.62 \times 10^{-5}$ eV/K is the Boltzmann constant, and E_c is the external electric field on the cathode surface [6], [9]. Therefore there are two ways to obtain a higher beam current at T1. One way is increasing RF forward power while keeping cathode temperature at a low value. The other way is increasing cathode temperature while keeping RF forward power at a low value. According to our experience, the latter way was useful to reduce the back bombardment along the macropulse. Hence during commissioning, we operated our gun with a high cathode temperature of about 1800 K.

After considering beam loading effect and the higher beam current at the tail region, we had to send more higher RF forward power along the macropulse to get a uniform energy distribution. If gun reflected power is close to unbalanced shape as shown Fig. 3(top left), head and tail parts in the macropulse are chopped by two energy filters in the α-magnet, and pulse length after the magnet became shorter. Therefore we optimized reflected and forward power signals to have a good linearity along the macropulse as shown in Fig. 3(bottom left) and (bottom right). From the information on position of the lower energy filter and magnetic field of the α-magnet, we could estimate total electron beam energy E at the gun exit which is given by

$$E\,[\mathrm{MeV}] \simeq 0.511\sqrt{1 + (0.205 \cdot I_\alpha[\mathrm{A}])^2}\,, \quad (2)$$

where I_α is the current of a power supply for the α-magnet, and the lower energy filter is located at 16 mm. By scanning I_α and monitoring T2 signal, we could estimate the lowest and the highest beam energies as well as energy spread in the macropulse, which are useful for us to keep reproducibility of gun RF amplitude and phase. Since peak current and beam loss along linac were sensitive to I_α, a

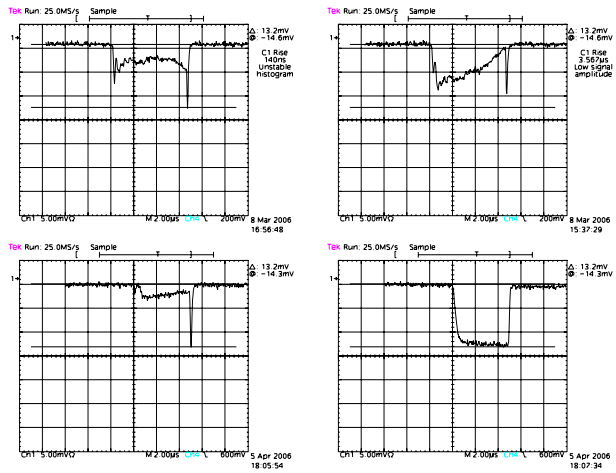

Figure 3: Signal of gun reflected RF power when reflected power are unbalanced at head and tail parts (top left), when head part has a high reflected power (top right), when reflected power is minimum and its slope along macropulse is optimized (bottom left), and signal of forward RF power when reflected power is optimized (bottom right).

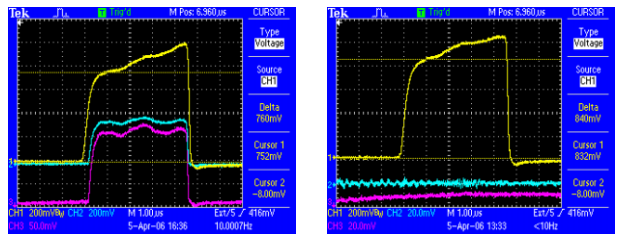

Figure 4: (left) signals of the first gun toroid (yellow), the second gun toroid (cyan), and linac toroid (magenta) when beam transmission from gun to linac and back bombardment along macropulse are optimized, (right) signal of the first gun toroid when there is no transmission in the α-magnet. Here calibration factors for T1, T2, and T3 are 0.4 A/V, 0.4 A/V, and 1.0 A/V, respectively.

fine tuning of I_α was also needed to get a lasing. After optimizing gun reflected power, quadrupoles, correctors, and the α-magnet properly, we could get about 45% transmission and a flat current distribution at the downstream of the α-magnet as shown in Fig. 4(left). If beam energy is too low or I_α is too high, we could not get any beam transmission at the α-magnet as shown in Fig. 4(right).

To optimize beam orbit and optics at gun and linac regions, we used signals from three radiation monitors which are distributed along linac. Although those signals were low during 1 Hz operation, they were significantly increased during 10 Hz operation as shown in Fig. 6. Due to the excellent pulse structures, those loss level were very high when beam orbit and optics at gun and linac region were slightly changed from a golden orbit and optics which give the minimum radiation loss and the best emittance for lasing. Therefore, we had to optimize all quadrupoles, steerers, and the α-magnet carefully to reduce those loss.

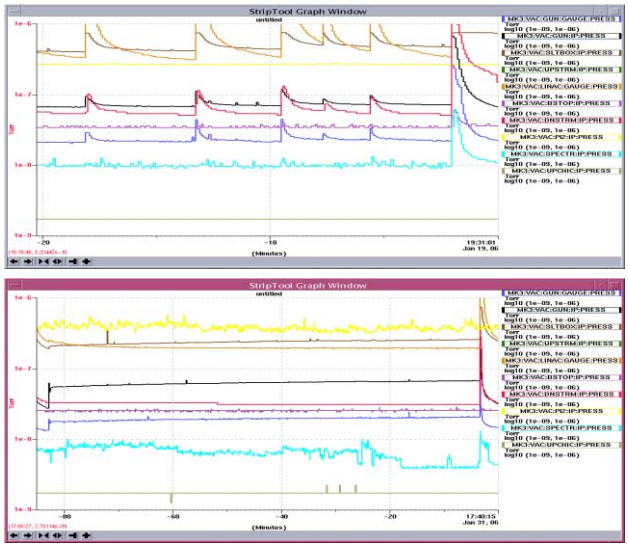

Figure 5: (top) spiky vacuum status on January 19, 2006 when gun generated 400 mA at T1 for the first time, (bottom) stabilized vacuum status on January 31, 2006 when gun generated 400 mA at T1 without any vacuum interlock for about 80 minutes.

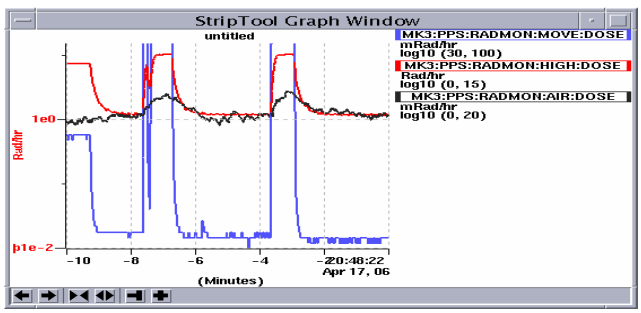

Figure 6: Signals of three radiation monitors along linac during 1 Hz and 10 Hz operations.

FUTURE UPGRADE PLANS

We are under developing and considering following upgrade plans to improve performance of the Mark III gun and linac. First of all, to keep electron beam current constant and to reduce the strong back bombardment problem, we need a real time cathode temperature monitoring system. By installing an infrared temperature detector and by giving a feedback to the power supply of a cathode heater, we can keep cathode temperature and beam current constant. And to remove the back bombardment problem completely, we are also under operating the other RF gun with the photoemission mode by shooting a Continuum Minilite-II Nd:YAG laser on the LaB_6 cathode surface [10]. Since the thermal emittance of the LaB_6 cathode is about 0.35 μm for a diameter of 1.75 mm, and quantum efficiency is about 0.05% at 266 nm, to improve transverse emittance, peak current, and energy spread more, we would like to use a high-class laser such an Nd:YLF laser whose the rms pulse length is about 4.4 ps, energy per a micropulse is about 1 μJ, and the maximum micropulse repetition rate is 9 MHz [11], [12]. This photoemission mode operation will be certainly helpful to increase the peak power of our Mark III FEL facility. Normally, electron beam quality and FEL performance are significantly changed even though RF amplitude and phase of gun and linac are slightly changed. Therefore we would like to develop a real time RF monitoring system to get a stable and reproducible FEL operation. And we want to develop an optical fiber based on-line beam loss monitor to stabilize beam orbit around undulator, which is certainly helpful to keep continuous and stable interaction between electron beams and spontaneous emitted photon beams in undulator. At the moment, we do not have a direct diagnostic tool to measure bunch length of about 0.5 ps long electron beam. To measure bunch length directly and to optimize FEL performance, we would like to install a small S-band deflection cavity in the near future. To control bunch length or peak current easily and to reduce geometrical wakefields and coherent synchrotron radiation, we are under developing a new bunch compressor with four electromagnetic dipoles. Now we are also under developing an emittance measurement system with a Flea digital camera of the Point Grey Research [13].

SUMMARY

By performing gun cavity RF conditioning for three months, we could get a stable vacuum status and required basic beam parameters. After optimizing reflected power, toroid signals, radiation loss along linac, and focusing around undulator, in January, 2006, we could send electron beams to the beam dump successfully. Since we could get a strong signal from a power meter in April, 2006, it is certain that our new gun and linac were optimized properly to generate FEL photon beams from our undulator. Authors thank to M. Pentico, O. Oakley, V. Rathbone, S. Huang, V. Popov, S. Mikhailov, and Y. Wu for their helpful comments and contributions for Mark III recommissioning project.

REFERENCES

[1] S. V. Benson *et al.*, Nucl. Instr. and Meth. A **296** (1990) 110.
[2] G.A. Barnett *et al.*, Nucl. Instr. and Meth. A **375** (1996) 97.
[3] I. Pinayev *et al.*, in *Proc. PAC2001*, 2001.
[4] G. S. Edwards *et al.*, Rev. Sci. Instrum. **74** (2003) 3207.
[5] Toshiteru Kii *et al.*, Nucl. Instr. and Meth. A **475** (2001) 588.
[6] G. A. Westenskow *et al.*, HEPL Tech. Note TN-86-1, 1986.
[7] C. B. McKee, Ph.D. dissertation, Duke University, 1994.
[8] Harald A. Enge, Rev. Sci. Instrum. **34** (1963) 385.
[9] Yu Song, IEEE J. Quantum Electronics **27** (1991) 898.
[10] J. G. Neumann *et al.*, Rev. Sci. Instrum. **76** (2005) 033303.
[11] J. M. Lafferty, J. Appl. Phys. **22** (1951) 299.
[12] S. Schreiber, in *Proc. FEL200*5, 2005.
[13] http://www.ptgrey.com/products/flea/.

BRIGHT ELECTRON BEAMS AND SMITH-PURCELL FREE-ELECTRON LASERS

Charles H. Boulware#, Heather L. Andrews, Jonathan D. Jarvis, Charles A. Brau
Department of Physics & Astronomy, Vanderbilt University, Nashville, TN 37235, U.S.A.

Abstract

We present further developments to the theory of Smith-Purcell free-electron lasers [1] (SPFELs) and characterization of a blunt needle cathode electron source in use to test the theory. The theory of SPFELs has been refined to include the effects of resistive losses on the evanescent surface wave supported by the grating and reflections of the wave from the ends of the grating. Losses are included directly in the grating dispersion relation and the reflections appear in the boundary conditions for the growing wave. Based on earlier work in sharp needle cathodes [2,3], an yttrium metal blunt needle cathode has been developed for the purpose of driving a SPFEL device. Space charge expansion of the beam in the transverse direction and aberration in the electron optics place limitations on the useful beam that can be generated. Both experimental and simple analytical characterizations of these limitations are presented and considered in light of the requirements of the SPFEL.

SPFEL THEORY

Smith-Purcell (SP) radiation is generated when an electron beam passes close to a grating. The virtual photons of the field of the electrons are scattered by the grating, and the wavelength λ_{SP} observed at an angle θ is

$$\lambda_{SP} = \frac{L}{|m|}\left(\frac{1}{\beta} - \cos\theta\right) \quad (1)$$

where L is the grating period, m is the diffraction order, βc is the electron velocity, and c is the speed of light. The angular spectral fluence of this radiation is described by several authors [4,5,6]. The intensity of the SP radiation falls off exponentially with the distance between the beam and the grating, with a characteristic length

$$h = \frac{\beta\gamma\lambda_{SP}}{4\pi} \quad (2)$$

where γ is the Lorentz factor for the electron beam [6].

When the electron beam current over the grating is sufficiently high, the interaction between the electrons and the fields above the grating becomes nonlinear, and the electrons become bunched. Periodic bunching of the electron beam intensifies the SP spectrum coherently [7]. Nonlinear emission with increasing beam current has been observed at Dartmouth College using a modified scanning electron microscope as a beam source [8,9].

The interaction between the electron beam and the fields above the grating is significant only for a grating surface wave whose phase velocity is equal to the electron velocity. The dispersion relation for a lamellar grating without external mirrors has been calculated by matching the boundary conditions for fields inside the grooves of the grating to a set of Floquet modes above the grating [10].

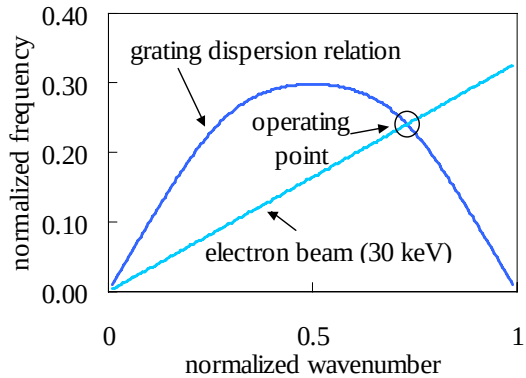

Figure 1. Grating dispersion relation showing synchronous solution

The electron beam is synchronous with a single evanescent mode of the grating, as shown in Fig. 1. The evanescent mode does not itself radiate except by scattering at the ends of the grating, and the wavelength of the mode is always longer than the lowest-order SP band. The SP radiation spectrum is coherently enhanced, however, at harmonics of the bunching frequency dictated by the wavelength of the synchronous evanescent wave.

The group velocity (the slope of the dispersion relation) at the synchronous point can be positive or negative, depending on the electron beam energy. The energy flow in the evanescent wave, therefore, can be copropagating or counterpropagating with respect to the electron beam. At high electron energy, the energy flow is copropagating, and the device operates on a convective instability as does a traveling wave tube amplifier. At low electron energy, the energy flow is counterpropagating and the device operates on an absolute instability in the manner of a backward wave oscillator. In the oscillator case, feedback is provided by the backward moving wave even in the absence of mirrors. At some intermediate energy, the synchronous point on the dispersion relation coincides with the Bragg point, where the group velocity v_g vanishes.

#charles.h.boulware@vanderbilt.edu

EFFECT OF LOSSES

The gain coefficient for the evanescent wave in either the amplifier or oscillator regime can be calculated by expanding the grating dispersion relation around the synchronous point. A dimensionless expression for this expansion (without losses) is

$$\left(\delta\omega - v_g\delta k\right)\left(\delta\omega - \beta c\delta k\right)^2 = \Delta \qquad (3)$$

where $\delta\omega$ is the frequency deviation from the synchronous point, v_g is the group velocity, δk is the wavenumber deviation, and

$$\Delta = \frac{\omega_p^2 G}{\gamma^3} \qquad (4)$$

where G is a constant that depends on the grating profile. The gain coefficient of the device varies as $\left|v_g\right|^{-1/3}$, which diverges near the Bragg point. However, the resistive losses in the grating have an attenuation coefficient that varies as $\left|v_g\right|^{-1}$, which diverges at the same point [1].

Resistive losses also introduce a real phase change. To see this, we consider a short section of grating as a resonant cavity by imagining perfect reflectors at each end. Small resistive losses in the grating surface then introduce a frequency shift given by

$$\delta\omega = -\frac{\langle Q\rangle}{2\langle U\rangle}(1+i) \qquad (5)$$

where $i=\sqrt{-1}$, Q is the power loss into the grating resistance, U the energy density in the surface wave, and the angled brackets represent averages over one period of the grating and one cycle of the wave [11]. The correct dispersion relation with losses is therefore

$$\left(\delta\omega - v_g\delta k + \frac{\omega_0}{2Q_c}(1+i)\right)\left(\delta\omega - \beta c\delta k\right)^2 = \Delta \qquad (6)$$

EFFECT OF REFLECTIONS

Equation 6 admits three solutions: a grating structure wave and so-called fast and slow space-charge waves. The three waves are locked together in frequency to form a single mode, but have slightly different wavenumbers and correspond to very different plasma dielectric susceptibilities. Interference allows the waves to satisfy boundary conditions at the ends of the grating. At the upstream end of the grating, the electron beam enters with uniform distributions of both density and velocity. In the absence of reflections, the electric field vanishes at the downstream end. These three boundary conditions are

$$\sum_{j=1}^{3}\frac{A_j}{\left(\delta\omega - \beta c\delta k_j\right)^2} = 0 \qquad (7)$$

$$\sum_{j=1}^{3}\frac{A_j}{\delta\omega - \beta c\delta k_j} = 0 \qquad (8)$$

$$\sum_{j=1}^{3} A_j e^{i\delta k_j Z} = 0 \qquad (9)$$

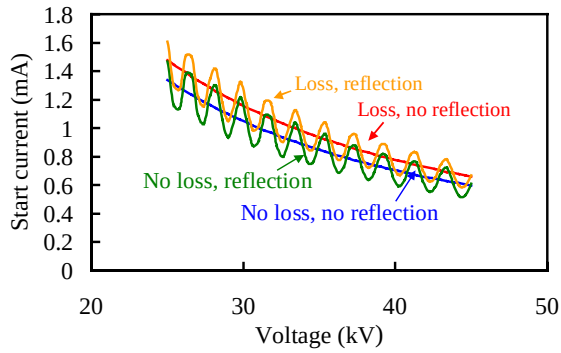

Figure 2. Effect of reflections on the start current as a function of beam voltage

where the index j represents the three different solutions of the dispersion relation expansion, A_j is the relative amplitude of the three waves, and Z is the length of the grating [1].

These boundary conditions can be refined to include reflections from the ends of the grating and losses in the reflected wave. When this is done, the last boundary condition becomes

$$\sum_{j=1}^{3}\left(e^{-i\delta_j Z} - Re^{i\delta_0 Z}\right) = 0 \qquad (10)$$

where

$$\delta_j = \frac{\delta\omega}{\beta c} - \delta k_j, \qquad (11)$$

$$\delta_0 = \frac{\beta+\beta_g}{\beta\beta_g c}\delta\omega + \frac{\beta+\beta_g}{\beta-\beta_g}\nu(1+i), \qquad (12)$$

R is the (complex) round-trip reflection coefficient, and $\nu = \langle U\rangle / 2v_g\langle Q\rangle$ is the empty grating loss coefficient. The boundary conditions are solved with the dispersion relation as a constraint. The effect of the reflection coefficient is to increase or decrease the computed growth rate according to whether the phase shift on reflection leads to constructive or deconstructive interference with the backward waves. The start condition for oscillation is that the growth rate, the imaginary part of the frequency, be positive. Details on the calculation of reflection at the grating ends and the inclusion of losses in the grating dispersion relation can be found elsewhere [12].

The condition for oscillation can be expressed as a start current. Figure 2 shows start current as a function of voltage for the parameters of the Dartmouth experiments [8]. The interference effects resulting from a nonzero reflection coefficient are clearly observed. The observed start current is on the order of 1 mA, in agreement with the experiments. However, the two-dimensional theory described here should underestimate the start current. We expect the diffraction width of the mode on the grating to be on the order of $\sqrt{Z_g/k} \approx 1\,\text{mm}$, where Z_g is the gain length of the evanescent wave, and k is the wavenumber at the operating point. This width is much greater than

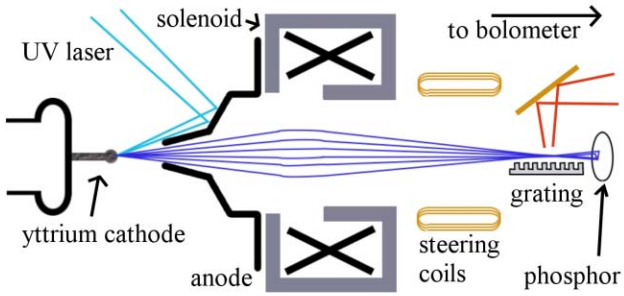

Figure 3. Schematic of electron source and focusing/steering magnets

the transverse size of the electron beam, thus reducing the effective interaction and raising the start current.

BLUNT NEEDLE CATHODES

The short vertical coupling length h between the electron beam and the grating makes necessary a high-brightness electron source for a SPFEL device. Sharp needle cathodes made of tungsten have been investigated as high-brightness electron sources [2,3]. The photoelectric quantum efficiency of photoemission from the tungsten metal is enhanced by several orders of magnitude at the high surface electric fields (up to 10^{10} V/m) that can be obtained at the 1 μm-radius tip of a chemically etched tungsten needle. At these fields, the Schottky effect reduces the barrier for electron emission by as much as 2.5 eV. The electron beams created from these sharp tips are highly divergent and difficult to focus.

A less divergent electron beam can be obtained from a blunt needle cathode with a tip radius on the order of 1 mm. The surface field is reduced to 10^7 V/m, but the loss in quantum efficiency can be mitigated by changing the needle material from tungsten to yttrium. Yttrium has a lower work function than tungsten (2.9 eV compared to 4.5 eV), so a reduction of the barrier by the Schottky effect is not necessary to enhance the quantum efficiency. At 10^7 V/m, for example, the Schottky effect is only 0.1 eV, but the effective work function of an yttrium cathode is similar to a tungsten cathode at 10^9 V/m.

The needle-cathode device at Vanderbilt University uses an yttrium cathode with a ≈ 700 μm radius spherical tip at the end of a 10 mm long square rod. Removal of adsorbate molecules from the yttrium surface is critically important to the quantum efficiency of the cathode. We use electron bombardment to raise the surface of the metal to its melting point (1800 K) for several seconds to produce a clean, smooth surface. The partially-covered cathode is held at a positive potential of 2-3 kV, and bombarding electrons are provided by a tungsten ion gauge filament positioned close to the cathode. The heating process is unstable when both the filament and the cathode tip are hot. Yttrium deposited on the tungsten filament lowers its work function, increasing the thermionic emission.

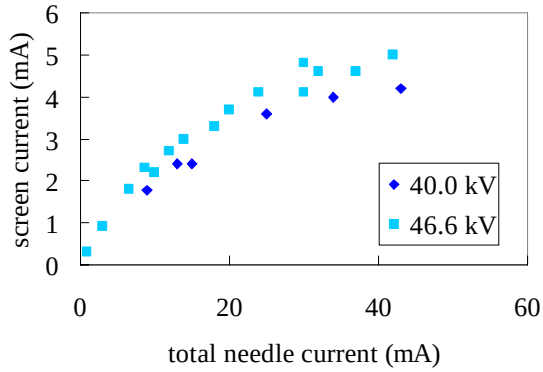

Figure 4. Current detected at the phosphor screen as a function of total needle current

After cleaning, the cathode is illuminated with a quintupled Nd:YAG laser (4-ns pulses at 20 Hz, <1 μJ per pulse, 5.9 eV per photon). Peak currents of 50 mA are produced reliably, corresponding to a QE of ~10^{-3}. The laser is focused on the cathode with a spot radius of 20 μm to give a current density at the source of $J_e \approx 10^7$ A/m^2. For an electron temperature $T_e \approx 1$ eV, the normalized brightness of the source is

$$B_N = \frac{m_e c^2 J_e}{2\pi k_B T_e} \approx 10^{12} \text{ A/m}^2\text{-steradian} \qquad (13)$$

where m_e is the electron mass and k_B is the Boltzmann constant [13].

A schematic of the experiment is shown in Fig. 3. A conical anode allows the ultraviolet laser light to enter the chamber from the side and be reflected by a mirror to the needle tip. The electron beam is focused by a 500-turn solenoid in an iron yoke designed to minimize the effective needle-lens distance, and therefore, the size of the beam in the lens. Steering coils direct the beam past an aluminum grating to a phosphor screen, which also serves as a Faraday cup. A fused quartz window above the grating allows millimeter-wave radiation to be collected by a He-cooled InSb bolometer. SP radiation above the bolometer noise level has yet to be detected.

The usable beam current from the needle cathode is limited by the fraction of the beam that can be collected and focused. Space-charge forces play a significant role in the divergence of the beam at the source, and the usable beam current increases sublinearly with total needle current at high laser intensities, as shown in Fig. 4. The importance of the space-charge effect is somewhat less at higher accelerating voltages. At 60 kV, with laser power at the needle damage threshold, 5 mA (about 10%) of the total beam current reaches the phosphor screen.

The spot size of the electron beam at the grating can be affected by aberration in the solenoid focusing magnet, beam emittance, and space charge at the beam focus [13]. The generalized perveance for a uniform round beam is

$$K = \frac{2I}{\beta^3 \gamma^3 I_0} \qquad (14)$$

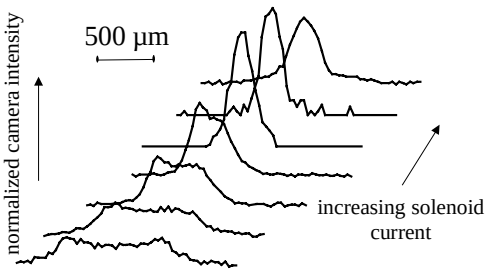

Figure 5. Transverse beam profiles show the effect of spherical aberration upstream of the electron focus

where I is the current in the beam, $I_0 = 4\pi\varepsilon_0 m_e c^3 / q_e$, ε_0 is the vacuum permittivity, and q_e is the electron charge. In terms of the generalized perveance, the space-charge dominated beam radius is

$$r = Ae^{\frac{-\alpha^2}{2K}} \tag{15}$$

where A is the beam aperture at the lens and α is the convergence angle. The space-charge limitation on the focal spot for the Vanderbilt device is less than 1 μm.

The calculated brightness of the yttrium blunt needle source corresponds to an emittance of $\varepsilon \approx 10^{-7}$ m for 5 mA current at the grating. The limitation posed by the emittance on the spot size at the focal point is

$$r = \frac{\varepsilon}{\alpha} \tag{16}$$

which corresponds to a 10 μm spot above the grating.

The limitation on the spot size resulting from spherical aberration in the focusing solenoid is independent of the beam current. Expanding the magnetic field near the axis and keeping terms up to third order in the transverse distance from the axis gives a radial dependence on the focal length of the solenoid (spherical aberration)

$$\frac{1}{f} = \frac{q_e^2}{4m_e^2\beta^2c^2}\left[\int_{-\infty}^{\infty} B_z^2 dz + \frac{5r^2}{8}\int_{-\infty}^{\infty}\left(\frac{dB_z}{dz}\right)^2 dz\right] \tag{17}$$

where B_z is the axial magnetic field and r is the transverse distance from the axis. The dependence of focal length on the transverse position of electrons entering the solenoid produces a spot size (at the circle of least confusion) of

$$r = \frac{5q_e^2}{128m_e^2\beta^2c^2} f_0 A^3 \int_{-\infty}^{\infty}\left(\frac{dB_z}{dz}\right)^2 dz \tag{18}$$

where f_0 is the paraxial focus of the lens. The aberration-limited spot size varies with the cube of the aperture size at the final lens. For the Vanderbilt experiment, this spot size is 125 μm at 60 kV and represents the dominant contribution to the radius of the beam at the circle of least confusion.

The size of the electron beam is measured by scanning the beam across a knife edge or by analyzing images of the phosphor screen. Images of the screen are captured with a CCD camera and provide differential current density across the beam. By changing the solenoid field strength, the beam is scanned through its focus. The effects of spherical aberration are observed clearly as an intense beam edge upstream of the electron focus. Several transverse current profiles at different lens strengths appear in Fig. 5. The measured radius at the beam waist is 200 μm, dominated by spherical aberration.

CONCLUSIONS

Detailed effects of losses and reflections have been incorporated into the theory of SPFELs. The modified dispersion relation for the grating evanescent wave gives both the attenuation and phase shift due to resistive losses. The effects of reflection at the grating ends are accounted for in the boundary conditions on the three waves that comprise the grating mode. The start current calculated in this way agrees with the Dartmouth experiments, though the two-dimensional treatment neglects diffraction of the evanescent mode in the transverse direction, which should increase the start current.

Experiments are underway using the yttrium cathode device at Vanderbilt to drive the oscillator-regime operation of a SPFEL. Spherical aberration limits the spot size of the electron beam in the Vanderbilt device, reducing the effective current interacting with the evanescent wave. Aperturing the beam to reduce spherical aberration also reduces the fraction of total needle current to the grating.

REFERENCES

[1] H. L. Andrews, C. H. Boulware, C. A. Brau, and J. D. Jarvis, Phys. Rev. ST-AB **8**, 050703 (2005).
[2] C. Hernandez Garcia and C .A. Brau, Nucl. Inst. Meth. Phys. **A483**, 273 (2002).
[3] C.H. Boulware and C.A. Brau, Free Electron Lasers 2002, K.-J. Kim, S.V. Milton, E. Gluskin (eds.), Elsevier Science B.V., II-47 (2003).
[4] P.M. van den Berg and T.H. Tan, J. Opt. Soc. Am. **64**, 325 (1974).
[5] L. Schaechter, *Beam-Wave Interaction in Periodic and Quasi-Periodic Structures* (Springer-Verlag, Berlin, 1996).
[6] Y. Shibata *et al*., Phys. Rev. E **57**, 1061 (1998).
[7] H. L. Andrews, C. H. Boulware, C. A. Brau, and J. D. Jarvis, Phys. Rev. ST-AB **8**, 110702 (2005).
[8] J. Urata *et al*., Phys. Rev. Lett. **80**, 516 (1998).
[9] A. Bakhtyari, J.E. Walsh, and J.H. Brownell, Phys. Rev. E **65**, 066503 (2002).
[10] H. L. Andrews and C. A. Brau, Phys. Rev. ST-AB **7**, 070701 (2004).
[11] J. D. Jackson, *Classical Electrodynamics*, 3rd edition (Wiley, New York, 1999), p. 374.
[12] H. L. Andrews, C. H. Boulware, C. A. Brau, J. T. Donohue, J. Gardelle, and J. D. Jarvis, submitted manuscript.
[13] J. D. Lawson, *The Physics of Charged Particle Beams, Clarendon Press*, Oxford, 1988.

EMITTANCE COMPENSATION OF SUPERCONDUCTING GUN AND LINAC SYSTEM FOR BEAMS WITH LARGE CHROMATIC VARIANCE

B. Buckley, Cornell University, Ithaca, NY 14853, USA
D. Kayran, V. N. Litvinenko,
Collider Accelerator Department, Brookhaven National Laboratory, Upton, NY 11973, USA*

Abstract

Among the methods of emittance compensation for a superconducting rf gun and linac system include utilizing a solenoid and drift space after the gun to achieve a specific beam envelope with zero beam divergence before entrance into the linac. Studies on this method have assumed minimal energy spread in the beam. However, in cases where chromatic effects cannot be ignored this one solenoid emittance compensation technique is inadequate. Proposed is a new method of emittance compensation utilizing two solenoids in order to minimize emittance in beams with large energy spread. We present a theoretical basis for the new technique along with a computer optimized configuration. The results are compared with previous methods of emittance compensation.

INTRODUCTION

First introduced by Carlsen [1] and expanded upon theoretically by Serafini and Rosenzweig [2] is a scheme for emittance compensation for an rf gun and linac system that uses a solenoid magnetic field to compensate for space charge defocusing. Chang et al. [3] extended the method for systems with a superconducting gun for which the solenoid must be placed outside the gun. Such studies and further experiments have achieved good emittance compensation results for beams with little energy spread [4].

Touched upon by Chang et al. are the effects on emittance caused by varying energy along the bunch. Energy dependence in solenoid focusing, space charge defocusing and linac ponderomotive focusing leads to emittance increases when large energy spread in the bunch is present. Previous studies have laid the foundation for cancelling out chromatic effects at the linac entrance [3]. However, there are other important chromatic effects that should be looked into.

In this paper we study the chromatic effects of the solenoid focusing and space charge defocusing. We introduce a method for compensating for emittance increases caused by these effects by adding a second solenoid. The mechanism of this emittance compensation scheme is studied with analysis of the beam through the system. The relationship between the placement and strengths of the two solenoids is studied theoretically and compared to a computer optimized setup. Finally, this two solenoid method is compared to the one solenoid method by running Parmela [5] simulations with both setups and comparing final normalized emittance values. We find that the two solenoid method is superior to the one solenoid method at minimizing emittance at the exit of the linac.

* Work performed under the auspices of the U.S. Department of Energy

EMITTANCE COMPENSATION

The essence of the emittance compensation method described in detail in Ref [2] involves focusing the diverging beam immediately after the gun with a solenoid and reaching a point of zero convergence after a drift space at which point the beam enters the linac. The solenoid field must be of a certain strength in order to have the beam enter the linac at the invariant envelope of the linac. This envelope is given by:

$$\hat{\sigma} = \left(\frac{2}{\gamma'}\right)\cdot\sqrt{\frac{I}{3I_A\gamma}} \tag{1}$$

where I_A= 17,054 A is the Alfven current, I is the current in the beam, and γ' is the average accelerating gradient of the linac. Entering at this envelope with zero divergence, the beam will exit the linac with zero divergence and with an envelope satisfying Eq. (1).

Chromatic Effects

Chromaticity comes into play in the energy dependence of the solenoid, space charge and linac focusing. As previously stated, we will not focus on the latter in this paper.

The envelope equation for a cylindrical space charge dominated beam through a focusing element, in this case a solenoid, is given by [2]:

$$\sigma'' = -\alpha_S\sigma + \frac{Q\beta c}{2I_A\sigma_z(\gamma\beta)^3\sigma} + \frac{\varepsilon_n^2}{(\gamma\beta)^2\sigma^3} \tag{2}$$

where ε_n is the normalized emittance and α_S is the solenoid focusing strength

$$\alpha_S = \left(\frac{eB}{2\gamma\beta mc}\right)^2 \tag{3}$$

where e is the charge of electron and B is the magnetic field of the solenoid. From the dependence on γ in each of these terms one can see that slices along the bunch with different energies will transform differently through the solenoid-drift space element.

ANALYSIS OF PHASE SPACE ANGLE

To illustrate these chromatic effects on the emittance we take a look at the transformation of the phase space angle

$$\theta = \frac{\sigma'}{\sigma} \tag{4}$$

through the solenoid and drift space elements.

Through Solenoid

In this analysis we will assume a small solenoid length in which no change in σ occurs, focusing only on the first term on the right hand side of Eq. (2). Taking the integral and dividing by σ we achieve

$$\Delta\theta = -\alpha_s L \tag{5}$$

with L the length of the solenoid.

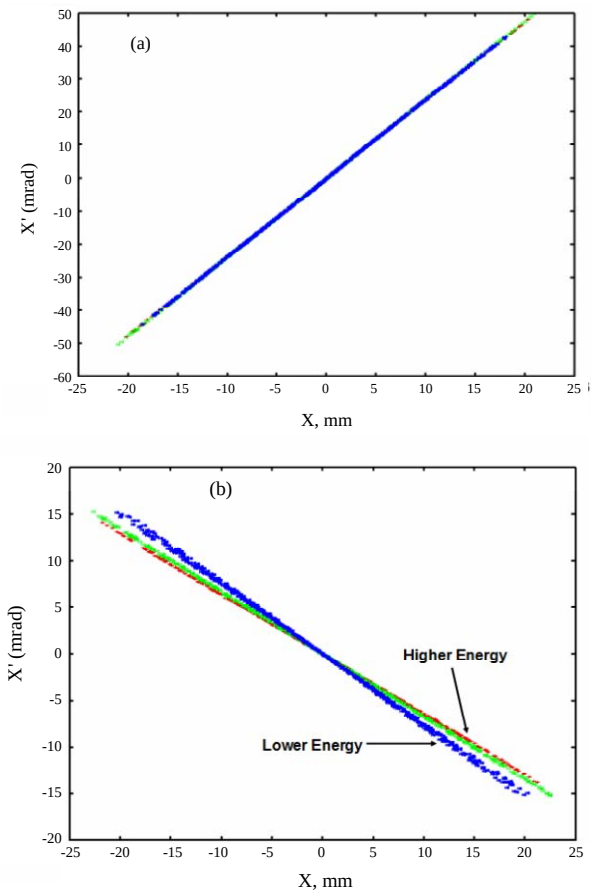

Figure 1: Phase space plots of three different slices of varying energy. Average energy of 2.5 MeV, energy spread of 3% and a total charge of 5nC, one of the possibilities for the RHIC e-cooling project at Brookhaven National Laboratory [6]. (a) Slices aligned before solenoid, immediately after gun. (b) Slices misaligned after solenoid focusing.

From Eq. (3) the dependence on energy is clear. Figures 1(a) and 1(b) illustrate the effect on the phase space distributions of three slices of varying energy. After the solenoid the phase space slices are no longer aligned leading to a rise in projected emittance.

Through Drift Space

For beam parameters typical for BNL's ERL injector (Q ~ 1 nC, γ ~ 5, $\sigma_z \sim \sigma$ ~ 1cm, and a normalized slice emittance of ε_n ~1 mm·mrad) the ratio between third and second terms on the right of Eq. 2 is very low: $I_A\sigma_z\gamma\varepsilon_n^2/Qc\sigma^2 \sim 5\cdot10^{-5}$. Hence, only the second term on the right side of the envelope equation is necessary:

$$\sigma'' = \frac{P}{\sigma}; \tag{6}$$

$$P = \frac{Q\beta c}{2I_A\sigma_z(\gamma\beta)^3} \tag{7}$$

with P being the perveance, a function of energy. Near the waist, the envelope can be approximated by a parabola [7]:

$$\sigma \cong \sigma_w + \frac{P(z-z_w)^2}{2\sigma_w} \tag{8}$$

with divergence of

$$\sigma' \cong \frac{P(z-z_w)}{\sigma_w} \quad . \tag{9}$$

Dividing the two we obtain a phase space angle of

$$\theta \cong \frac{2P(z-z_w)}{2\sigma_w{}^2 + P(z-z_w)^2} \quad . \tag{10}$$

The envelope at the waist is given by integrating the differential equation of Eq. 6 to obtain the equivalent first order differential equation and rearranging to achieve

$$\sigma_w = \sigma_i e^{-\frac{\sigma_i'^2}{2P}} \quad . \tag{11}$$

The position at the waist is found by taking the equivalent integral equation of Eq. 6 and using a polynomial approximate solution [3]:

$$z_w \cong \frac{\sigma_i}{\sqrt{P}}\left(.009165+.95449\frac{\sigma_i'}{\sqrt{P}}+.21824\frac{\sigma'^2{}_i}{P}\right) . \quad (12)$$

From these equations we are able to analyze how the spread in the phase space angle varies through the solenoid and drift space. In Fig. 2 we plot the difference in angle between the head and tail slices of the same bunch from Fig. 1, the head having a higher energy than the tail.

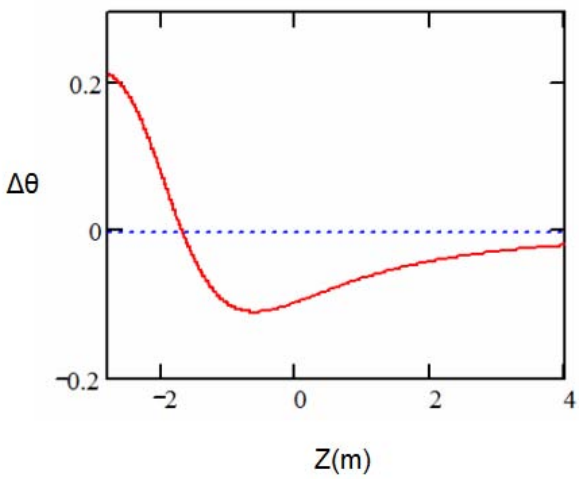

Figure 2: Difference between higher energy and lower energy slices in bunch immediately after solenoid. The beam waist occurs at z = 0 meters. The calculations and plots were done with Mathcad [8].

The plot begins after the solenoid at the maximum spread in angle and continues through drift space. We see that the slices align before z=0, the waist position, and are thus misaligned at the waist. This leads to a non-optimized emittance before entrance into the linac.

What one notices is that since the lower energy slices rotate past the higher energy slices it would be possible to use a second solenoid to realign the slices in phase space. The above equations allow one to calculate the spread in θ after an arbitrary distance and thus the relationship between the solenoid strengths of the first and second solenoids and the distance between them, which would result in realignment of the phase space slices.

OPTIMIZATION

A two solenoid, rf gun and linac system was optimized for lowest normalized emittance by optimizing position and field strengths of the two solenoids and position of the linac. Plots of normalized emittance and envelope can be found in Fig. 3 where they are compared to the same plots for a non-optimized one solenoid setup. The one solenoid configuration is set up following the invariant envelope method [2]. Since it is not optimized, looking at final emittances does not make for a definitive comparison. Instead, the plots serve to illustrate the overall advantage the two solenoid method has over the invariant envelope one solenoid method when dealing with large energy variation.

The optimized magnetic fields of the first and second solenoids and drift length between them are respectively 854 Gauss, 607 Gauss and 333.9 cm. To test the accuracy of the above equations describing the alignment of phase space slices we use them to calculate the magnetic field of the second solenoid, which would realign the phase space slices with all other optimized parameters unchanged. We obtain a theoretical magnetic field strength of roughly 520 Gauss for the second solenoid. This is significantly lower than the optimized value above. However, when comparing standard deviations in θ with 500 slices we find that the theoretical value has a lower spread in θ, .0846 inverse meters, than does the optimized value, .0897 inverse meters. This should not come as a surprise as the theoretical calculation minimized spread in θ after the second solenoid while the optimized value minimized normalized emittance after the linac, not necessarily minimizing spread in θ. What the comparison of spread in θ does is validate the accuracy of our theoretical approach, even if it should not be used as the exact value when attempting to minimize emittance.

DISCUSSION AND CONCLUSION

We have introduced a new method of emittance compensation that has advantages compared with previous methods using one solenoid in minimizing emittance of beams with significant energy spread. Our theoretical analysis of the transformations of phase space angle due to solenoid focusing and space charge defocusing has proven to be accurate and may serve as a basis for future analysis into this new emittance compensation scheme.

Further studies however must be undertaken in order to gain a better understanding of this new method. Firstly, alignment of sliced phase space angles is not the only parameter affecting total normalized emittance. Individual sliced emittances must also be minimized along with spread in slices and the two might not be simultaneously minimized. Studies into optimizing spread in θ after the linac have resulted in increases in normalized emittance.

Another aspect that should be looked into further are the chromatic effects of the linac focusing. As seen in Fig. 3, for the optimized two solenoid set up the beam does not enter the linac at the waist as is deemed necessary in previous one solenoid methods. Instead the beam enters at a significant convergence. Non-linearities

in the linac focusing due to this convergent entrance perhaps might be playing a large role in minimizing individual sliced emittances. Efforts at moving the linac further from the second solenoid have not resulted in lower values of normalized emittance.

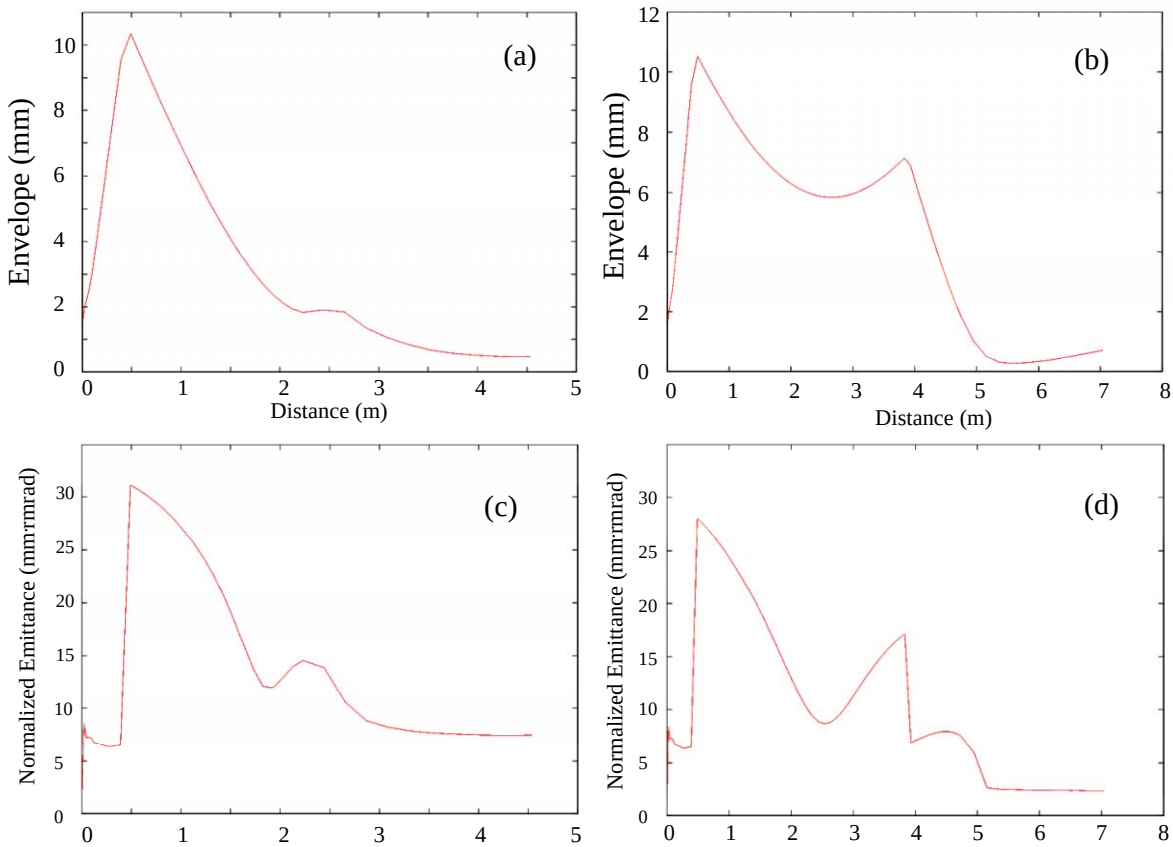

Figure 3: Comparison of one solenoid and two solenoid methods: Electron beam envelope with one solenoid (a) and two solenoids (b). (c) Normalized projected emittance with one solenoid (c) and two solenoids (d).

REFERENCES

[1] B. Carlsen, "New Photoelectric Injector Design for the Los Alamos National Laboratory XUV FEL Accelerator", NIM A285 (1989) 313-319.

[2] L. Serafini and J. B. Rosenzweig, "Envelope Analysis of Intense Relativistic Quasilaminar Beams in RF Photoinjectors: A Theory of Emittance Compensation", Phys. Rev. E 47, 2031 (1993).

[3] X. Chang, I. Ben Zvi, and J. Kewisch, "Emittance Compensation of Compact Superconducting Guns and Booster Linac System", PRST-AB 9, 044201 (2006).

[4] X. Qui, K Batchelor, I Ben-Zvi, and X-J Wang, "Demonstration of Emittance Compensation through the Measurement of the Slice Emittance of a 10-ps Electron Bunch", Phys. Rev. Lett. 76, 3723-3726 (1996).

[5] L. M. Young, Los Alamos National Laboratory Report No. LA-UR-96-1835 (revised 2001).

[6] V. Parkhomchuk and I. Ben-Zvi, Brookhaven National Laboratory Report No. C-A/AP/47, 2001.

[7] M. Reisner, Theory and Design of Charged Particle Beams (John Wiley and Sons, New York, 1994), p. 201

[8] Mathcad 2000, Reference Manual, MathSoft Inc., 101 Main Street Cambridge, Ma 02142, USA

FREE ELECTRON LASER STUDY OF FREE CARBON CLUSTERS

C. Spezzani*, E. Allaria, M. Coreno, F. Curbis, B. Diviacco, G. De Ninno, L. Romanzin, S. Tileva, M. Trovò, Sincrotrone Trieste, Strada Statale 14 - km 163.5, 34012 Basovizza, Trieste ITALY

M. Amati, G. Bongiorno, C. Lenardi, T. Mazza, P. Milani, T.A. Mostefaoui, P. Piseri, L. Ravagnan, Dipartimento di Fisica and CIMAINA, Università degli Studi di Milano, I-20133 Milano, ITALY.

Abstract

UV absorption from carbon nanoparticles is a very interesting astrophysical topic. The prominent hump centred at 217.5 nm is the most dominant feature in the interstellar extinction curve and also the most controversial and a long-standing problem in astrophysics. At the University of Milano an experimental set-up based on a Pulsed Microplasma Cluster Source has been developed for the investigation of free clusters at the Elettra Gas Phase beamline. The cluster source produces very intense cluster beams with tunable size distribution. The design of the apparatus is extended with a chamber for gas phase reaction (water vapour, CO, H_2...) providing a unique opportunity to study the gas phase properties of carbonaceous particles in different environments.

We plan to investigate Resonant Raman scattering of free carbon particles tuning the high brilliance UV/VIS storage ring FEL of ELETTRA across the region of 217.5 nm where the UV absorption hump in astrophysical data is observed and where a number of electronic transitions exist for variable size linear carbon chains.

INTRODUCTION

Since its discovery by Stecher (1965), the ultraviolet extinction curve feature observed at 217.5 nm has been attributed to π-electron plasmon absorption or π-π * band transitions in small graphite particles or amorphous carbon grains. Despite the early assignment to carbonaceous material, the exact physical nature of the carrier is still unknown and strongly debated. One peculiar behaviour of the 217.5 hump is the constancy of its spectral position regardless of the choice of the astronomical object under observation [1]. On the other hand, the peak position of the bump predicted for graphite particles is quite sensitive to grain size, shape and adsorbate coatings, which is inconsistent with the observations.

Many different models have been proposed to explain the experimental observation and many different attempts have been made to reproduce in laboratory an adequate prototype for cosmic dust [2,3,4]. Experiments conducted on hydrogenated carbon nanoparticles isolated in noble gas matrix pointed out the relevance not only of particle shape and size but also of their chemical environment [1]. Other observations indicate that the presence of an ice mantel surrounding the carbon particles strongly influence their UV optical response [3]. Other authors have succeeded in synthesizing carbon aggregates that show optical constants fitting quite well the extinction curve [4, 5], but, the adopted methods don't match very well with the environment conditions where carbon grains in the intergalactic medium are expected to form.

Actual models of dust astrophysics lack of experimental data about carbon dust in gas phase, their optical proprieties, mass distribution, reactivity and of course their absorption of the UV light in the 217 nm region. In order to attempt a meaningful reproduction, at the laboratory scale, of this astrophysical system it is important to study carbon clusters in isolated condition, as a function of their dimension and chemical environment. Recently the potential of optical spectroscopy in free jet expansion for experiments on astrophysically relevant species has been demonstrated [6].

Resonant Raman Scattering (RRS) is a powerful technique for the characterization of such a system. It combines the sensitivity to vibrational properties of carbon structures relevant for astrophysics like carbyne [7, 8] with a selective transfer of energy when the exciting photons are tuned at the energy corresponding to a given resonance, increasing in this way the scattering cross-section.

We present here an experimental setup for a RRS study of free carbon clusters which make use of the storage ring Free Electron Laser (SRFEL) radiation.

EXPERIMENTAL SETUP

This section quickly reviews the experimental setup that we are developing at ELETTRA in the framework of the collaboration between the CIMAINA of Milan University and the SRFEL group of ELETTRA, Trieste.

CESyRA

CESyRA (Cluster Experiments with Synchrotron RAdiation) [9] is a research project of the CIMAINA focused on free cluster spectroscopy with the high intensity UV and soft X-ray light from the ELETTRA synchrotron radiation facility.

* e-mail: carlo.spezzani@elettra.trieste.it

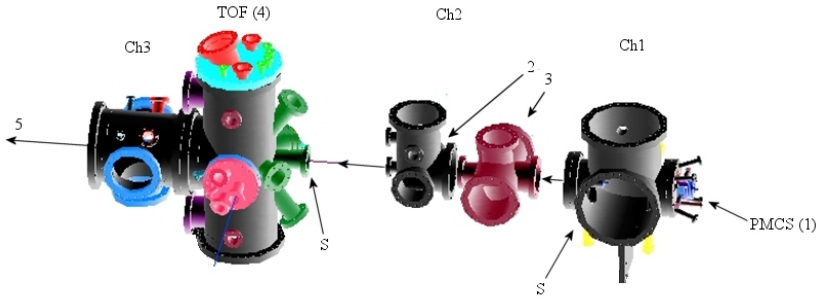

Fig. 1: Main elements of CESyRA apparatus: (Ch1) expansion chamber, (Ch2) deposition and gas exposure chamber, (Ch3) TOF, (1) PMCS, (2) manipulator, (3) gas line, (4) TOF, (5) to dumping chamber and quartz microbalance.

The experiments are implemented in a UHV compatible supersonic cluster beams apparatus. The main constituents of the system are sketched in figure 1. Briefly, it consists of three differentially pumped, high-vacuum chambers (Ch1, Ch2 and Ch3) separated by two skimmers (S). Heart of CESyRA apparatus is the Pulsed Microplasma Cluster Source (PMCS) [10,11], developed at the Molecular Beam and Nanocrystalline Materials Laboratory in Milano, which is able to deliver highly collimated and intense seeded beams of clusters from refractory materials (typical deposition rate for carbon: 100 μm/h at 500 mm source-substrate distance, ~ 0.8 cm^2 covered area). The PMCS is based on target ablation obtained by He plasma sputtering: a pulse of He flux is directed against a target by means of a valve driven by an electromagnet (opening time of about 300 μs). The gas is then ionized by a pulsed discharge fired between the target rod (cathode) and the anode. The sputtered particles are carried through an aerodynamic lens system by the He flow and the mixture eventually undergoes a supersonic expansion into a high vacuum chamber. In order to prevent the formation of holes on the cathode rod and to reduce the need for source maintenance, since the ablation is extremely localized, the target rod is maintained in rotation during source operation (see figure 2). The clusters are emitted in pulses that propagate at a speed of about 1000 m/s and that last typically 15 ms. Lighter aggregates are mostly located at the head of the pulse while the heavier ones at the tail.

The PMCS is located outside vacuum and communicates through the nozzle with the expansion chamber (Ch1). The beam passes through a skimmer that, due to particle focusing on the beam axis [12], efficiently separates the clusters from the carrier gas. In the second chamber a gas cell is installed to allow gas exposure of the free particles in the beam (3). A diaphragm separates the second from the third chamber (2) to produce differential vacuum and finally the beam is directed into an interaction chamber where a short linear time of flight (TOF) mass spectrometer is mounted perpendicularly to the plane formed by the intersection of the light and cluster beams (4). A sample manipulator is mounted, in order to intercept the beam and thus to allow cluster deposition onto a substrate. Finally, the beam is dumped onto a quartz microbalance (5) that monitors the cluster flux.

The SRFEL of ELETTRA

The CESyRA setup has primarily been thought for application with synchrotron radiation on refractory materials in gas phase, demonstrating for the first time the possibility of performing XAS measurements on free Ti nanoparticles [13]. However, for this particular application on carbon clusters, the requirements on the light source that has to be used make the SRFEL of Elettra [14] the best candidate for our objective. To probe the cluster beam in gas phase, we need a very high flux of photon with a wavelength that can be precisely tuned around 217.5 nm (5.7 eV). In this respect, the Elettra SRFEL can produce a very bright monochromatic beam that can be directed into the interaction volume by means of few optical elements, minimizing the photon flux losses due to radiation transport.

The maximum average lasing power that can be achieved using a SRFEL is limited by the heating of the electron beam induced by the laser onset [15, 16]. The increase of the electron-beam energy spread is indeed responsible for the diminution of the optical gain while, at

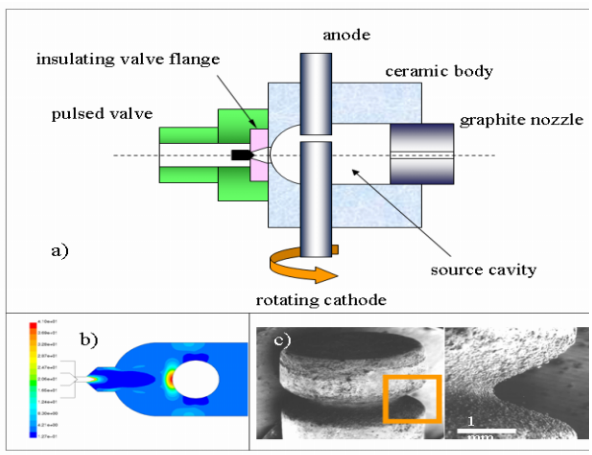

Fig. 2: a) schematic diagram of the PMCS source; b) pressure contour plot of He jet inside the PMCS cavity (see ref [11]); c) scanning electron microscope micrographs of the cathode region eroded by the plasma. The cathode is continuously rotated in order to prevent the formation of holes. A very smooth and precise trace formed by plasma erosion is clearly distinguishable.

saturation, the latter reaches the level of the optical cavity losses. However, for applications requiring a high peak power, the FEL power can be ‘‘concentrated’’ into a series of giant pulses, applying the so-called Q-switching regime. In this case, the peak power is considerably enhanced (one to few orders of magnitude) while the average power is only slightly reduced [17]. To operate the SRFEL in Q-switching, we apply a modulation on the radiofrequency (RF) that drives the electron bunches in the storage ring (figure 3a) [18]. The giant pulses that we obtain are typically 100 μs long (figure 3c). The development of a giant pulse introduce a quite big energy spread that implies a recovery time for the dumping of the electron beam of the order of 10~100 ms. For this reason Q-switching is normally operated at a repetition rate of few Hz (figure 3a and 3b). In RRS experiment setup, the RF modulation is triggered after a variable delay by the opening of the He valve in the clusters source. Adjusting the delay we are able to probe, with the highest power available, different parts of the cluster pulse and therefore sample cluster populations with different average size.

In order to probe the clusters with the Raman scattering in the spectral region of interest, we use mirrors for the FEL optical cavity especially designed for that wavelength. The interferential coating has been prepared at the Laser Zentrum Hannover.

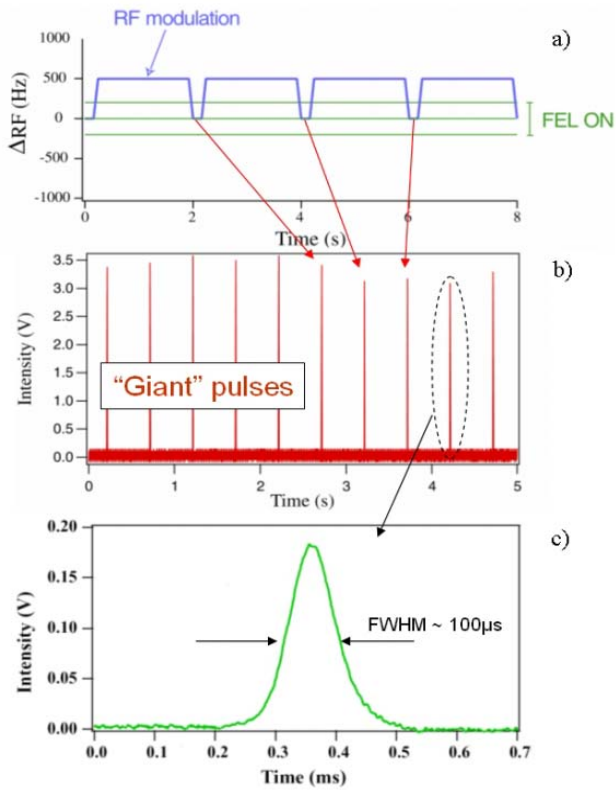

Fig. 3. Q-switching of the SRFEL: a) the RF modulation can be triggered by the opening of the He valve of the clusters source, b) development of a sequence of giant pulses, c) detail of a giant pulse: typical duration is 100 μs.

PRELIMINARY TESTS AND FUTURE DEVELOPMENT

The CESyRA system is in the experimental hall of ELETTRA since May 2006 for the long term project approved on the Gas Phase beamline [9,13,19]. When the chamber is not in use for this project it is available for the preparation of the RRS experiment.

In Raman spectroscopy, one of the most frequently encountered problems is related to the presence of the elastic background. Since the Raman cross section is typically 4-5 orders of magnitude smaller then the elastic one (Thomson scattering), the Raman signal risks to be submerged by the tails of the elastic peak. Moreover, in our setup, the interaction volume is in vacuum, separated from the spectrometer and the SRFEL by quartz view-ports. This introduces an additional source of scattered light that further decreases the "peak to background" ratio. The first step in the preparation of the Raman experiment has been the measurement of a total scattering yield, i.e. the collected light signal regardless of its spectral distribution, in order to evaluate the relevance of the background and to assess the interaction between the clusters and the radiation. For this purpose, we used a photomultiplier tube (PMT) to detect the photons that are collected by a small quartz lens focusing in the interaction volume about 5 mm far from the PMCS nozzle, where the cluster density is close to the maximum. When the setup will be optimized, the PMT will be replaced with a spectrometer.

Since now, few hours have been dedicated to optimize the experimental setup. FEL light at 217.5 nm has been generated with a very good stability. We expect to extract a power of few tenth of mW in free-run mode that should correspond to a flux of 10^{17}~10^{18} ph/s in the Q-switching regime. The FEL light has been used to perform the alignment of the chamber as well as some preliminary tests aimed at optimizing the Raman setup. The light was focused on the cluster beam by means of a lens located outside the chamber and one mirror in vacuum at 45º that deflect the light in the vertical direction. A second mirror at 45º was used to extract the light from the chamber. The focus of the collecting lens was placed at the intersection of the laser and clusters beams, so that the collection was done in the direction perpendicular to both of them. A multichannel time to digital conversion board has been used to record the detected events keeping track of their delay with respect to the opening of the valve. The full range temporal window of detection is 20 ms, with a time resolution of 82 ps. The acquisition software allows integration over an undefined number of consecutive pulses. To obtain a good background subtraction despite the possible drifts in laser and cluster source operation, the measurements have been done alternating acquisition of pulses with and without clusters; this was obtained by firing the vaporization discharge in the PMCS every second gas pulse only. Typical integration time was 5 min at a repetition rate of 5 Hz that corresponds to acquisition

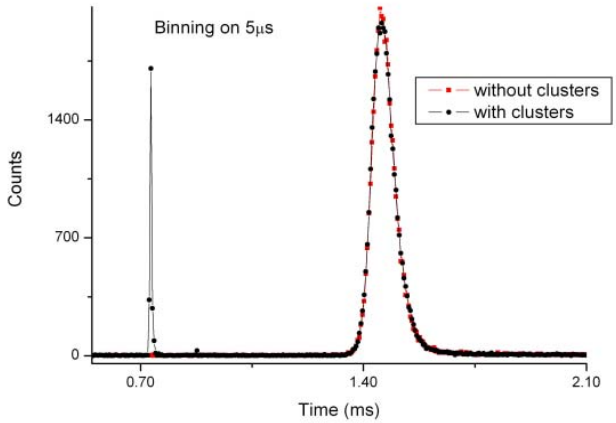

Fig. 4: Acquisition with PMT of the scattered intensity. Black line (circles) SRFEL pulse plus clusters pulse. Red line (square) SRFEL pulse with only the carrier gas (notice the absence of the HV discharge noise).

of about 750 laser pulses with clusters in the beam and 750 without clusters.

Figure 4 shows an example of detected events for an acquisition obtained setting a nominal delay of 1.2 ms between the He valve and the RF modulation. The peak at 1.45 ms corresponds to the photon counts collected under the giant pulses of the SRFEL. The black line with circles is associated to the pulses with clusters and the red one (squares) without clusters. The sharp spike at 0.73 ms is due to electrical noise introduced by the HV discharge in the PMCS and thus occurs only in the pulses where the generation of clusters is on; excluding this instrumental effect, no significant differences were measurable between the two curves at any delay. An expanded view of the peak at 1.45 ms (figure 5) shows that photon counts are detected with a time structure that closely follows the microtemporal structure of the FEL radiation. The fact that the detection rate is of the order of one photon count per micropulse indicates that the intensity of light scattered inside the chamber by the optical elements is hindering the signal of interest as the detector is probably saturated by background counts.

Those preliminary results show the importance of screening the detector from the intensity scattered by the optical elements. At present, we are developing a new optical scheme to minimize this source of background that certainly would prevent the detection of the weak Raman signal. We are also implementing a Nd:YAG table top laser that, even if not tunable at the proper wavelength, will be helpful for off-line preparation of the experiment with the SRFEL.

Considering the small number of shifts that for the moment have been dedicated to the experiment, we can be optimistic for the future developments. The CESyRA apparatus and the SRFEL reveal to be stable enough for the acquisition of data with good statistic.

We acknowledge the storage ring control group of Elettra for collaboration and Stefan Günster of LZH (Hanover) for the realization of FEL optics.

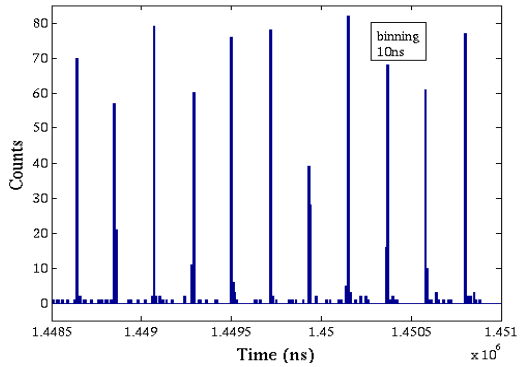

Figure 5: Expanded view of the microtemporal structure of photon count peak under FEL giant pulse in the Q-switch mode.

REFERENCES

[1] M. Schnaiter, et al., Astr. J. 498:486-496, 1998.

[2] W. Kraetschmer, Astrophysics and Space Science 128:93-99, 1986.

[3] D.C.B. Whittet, et al. Astr. J. 602:291-297, 2004.

[4] W.W. Duley and S. Lazarev, Astr. J., 612:L33-L35, 2004.

[5] Manish Chhowalla, et al., Phys. Rev. Lett. 90:155505, 2003.

[6] T. Motylewsky, et at., Astrophys. J. 531:312-320, 2000.

[7] L. Ravagnan, et al., Phys. Rev. Lett. 89:285506, 2002.

[8] L. Ravagnan, *"Synthesis and Characterization of Carbynoid Structures in Cluster Assembled Carbon Films"*, PhD thesis (2005).

[9] C. Lenardi, et al., Elettra Highlights 2003-2004, 92.

[10] E. Barborini, et al., J. Phys. D 32:L105-L109, 1999.

[11] H. Vahedi Tafreshi, et al. J. Nanosci. Nanotechnol. 6:1140-1149, 2006.

[12] P. Piseri, H. Vahedi Tafreshi, P. Milani Curr. Op. Solid St. Mater. Sci. 8:195-202, 2004.

[13] P Piseri, et al., New J. Phys. 8:136, 2006.

[14] R.P. Walker, et al., Nuclear Instruments and Methods in Physics Research A, 429: 179–184, 1999.

[15] N.A. Vinokurov, et al., preprint INP77.59 Novosibirsk, (unpublished) 1977.

[16] A. Renieri, Il Nuovo Cimento 35:161, 1979.

[17] I.V. Pinayev, et al., Nucl. Instr. and Meth. A 475:222, 2001. proceedings.

[18] G. De Ninno, et al., Nuclear Instruments and Methods in Physics Research A, 528:278–282, 2004.

[19] K.C. Prince, et al., J. Sync. Rad. 5:565, 1998.

FREE ELECTRON LASER PULSE CONTROL BY ACOUSTO- OPTIC MODULATORS

Taizou Kanai*, Sachiko Yoshihashi-Suzuki, Kunio Awazu, Institute of Free Electron Laser, Graduate School of Engineering, Osaka University, Japan

Abstract

The free electron laser (FEL) at Osaka University can be continuously varied over a range from 5.0 to 20.0 μm when using the 30 MeV electron beam. The FEL has a double pulse structure. The structure consists of a train of macropulses with a pulse width of 15 μs, and each macropulse contains a train of 330 micropulses with a pulse width of 5 ps. The FEL's tunability and short pulse make possible new medical applications, such as investigating protein dynamics and ablating soft tissues. Precise control of the micropulse train is essential for FEL medical applications because macropulses of long pulse duration lead to undesirable thermal effects. An FEL pulse control system, using an acousto-optic modulator (AOM), was developed to investigate the non-thermal effects of FEL on living tissues. This system provides efficiency (~ 65%) and a fast switching speed (> 200 ns), and we predict that FEL will serve as a novel tool in many new applications.

INTRODUCTION

The free electron laser (FEL) at Osaka University is a pulsed, tunable infrared source. It is designed to work in the region from 5 to 20 μm at an average power of up to 50 mW. The FEL applications research is broadly interdisciplinary, including measurements of investigation of protein dynamics, the ablation of soft tissues and narrow band-gap materials [1-4].

An electron beam of 30 MeV energy is the laser gain medium for the FEL. It is accelerated with a linear, pulsed RF accelerator. This leads to the pulsed beam current and complex temporal intensity profile of the emitted IR light as shown in Fig.1. The accelerated electron pulses have up to 20 μs duration and each of them generates one optical "macropulse" have duration of 15 μs. The mode locked pulse or "micropulse" have duration of approximately 5 ps with 44.8 ns spacing between pulses. For many FEL application 15 μs duration of the macropulse leads to undesirable thermal effects or obscures signals from fast optical process. The FEL user community has identified the need for selecting the number of micropulse. The switching device to achieve this should have the following properties;

(1) Operating wavelength of 5 to 12 μm;
(2) Variable pulse duration between 500 nanoseconds and the full macropulse length, with fast rise and fall times;
(3) High efficiency;
(4) Easy pulse duration adjustment; and
(5) Portability between different experimental stations.

An acousto-optic modulator (AOM) has therefore been chosen as the best solution for the Osaka University FEL system. Section 2 describes the principles of AOMs and pulse control systems. Section 3 details the performance evaluations of the pulse control system, and Section 4 reports the results of these evaluations.

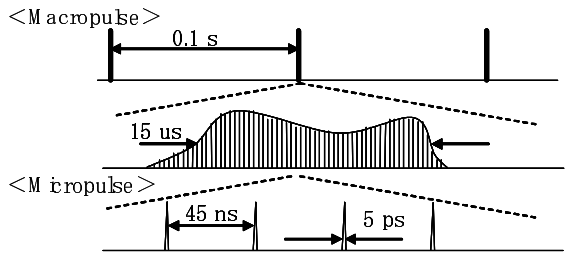

Figure 1: Pulse structure of FEL.

MATERIALS AND METHODS

The principle of an Acousto Optic Modulator

An AOM is a device that allows control of the power, frequency, or spatial direction of a laser beam using an electrical drive signal. It is based on the acousto-optic effect, i.e., refractive index modification by the oscillating mechanical pressure of a sound wave. The geometry of the input and output laser beams relative to the acoustic column is shown in Figure 2. An AOM's key element is a transparent crystal (or a piece of glass) through which the light propagates. A piezoelectric transducer attached to the crystal is used to excite a high-frequency sound wave. Light can then be diffracted at the periodic refractive index grating generated by the sound wave. The scattered beam has a slightly modified optical frequency (increased or decreased by the frequency of the sound wave) and a slightly different direction. The frequency and direction of the scattered beam can be controlled via the frequency of the sound wave, while the acoustic power allows control of the optical power. For sufficiently high acoustic power and to align the input laser beam for a true Bragg input angle, more than 70% of the optical power can be diffracted as the first order beam. When a supersonic wave intercepts the incident beam, the AOM generates a first order beam. Therefore, the rise time of first order beam depends on the diameter of the incident beam and the speed of the supersonic wave. The rise time of the first order beam is given by equation (1). The following

* kanai@fel.eng.osaka-u.ac.jp

equation describes the time required before the primary light output rises from 10% to 90% [5].

$$TR = S/ (v*1.56), \quad (1)$$

where:

TR = Rise time of first order beam,
S = Diameter of incident beam,
V = Speed of supersonic wave,
1.56 = correction factor.

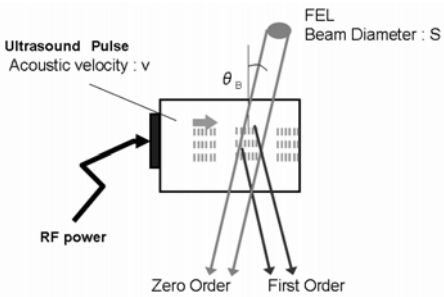

Figure 2: Principles of an AOM.

Pulse control system design

The diameter of the original FEL is about 50 mm Φ. To control the high efficiency/high speed pulse, it is necessary to incident para-parallel/diameter of very small beam into AOM. A schematic diagram of an FEL pulse control system is shown in Figure 4. The FEL beam (50 mm Φ) diameter was reduced in size to 1.5 mm Φ by two mirrors with either long (radius of curvature = 385 mm) or short (radius of curvature =50.0 mm) focal lengths. Table 1 shows the specifications of a standard AOM (AGM-402A1, IntraAction Corp).

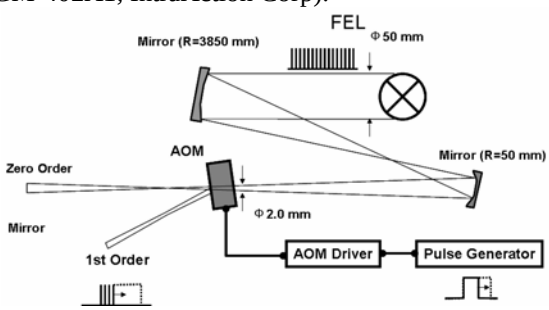

Figure 3: Experimental setup for pulse control.

Table 1: Specifications of Ge-AOM

Optical Wavelength	@10.6 µm
Acousto-optic Material	Single Crystal Germanium
Acoustic Velocity	5.5 mm/µsec
RF Center Frequency *	40 MHz
Optical Insertion Loss	<7 %
Optical Power Capability	25 Watts
Laser Polarization	Parallel to Base
Rise Time (diameter)	116 nsec (1 mm)
Bragg Angle	38.5 mrad
Beam Separation	77 mrad
Diffraction Efficiency	<70 %

*Other frequency available

PERFORMANCE EVALUATIONS

The laser damage threshold for Ge was determined empirically for the FEL. Surface damage occurred at 20 mW of average power, less than 1.5 mm Φ beam diameter, and 6.3 µm wavelength. The absorption by Ge does not change significantly between 6 and 12 µm. Our experimental setup is shown in Figure 5. The FEL enters the AOM at a diameter of 1.5 mm Φ and the pulse duration is controlled by adding a supersonic wave pulse to the AOM. First order beam is detected by infrared detector (MCT; VIGO Systems, R005). MCT signal is recorded by an oscilloscope (LeCroy, WaveMaster 8000).

RESULTS 1

Wavelength-dependence of pulse control system

The wavelength dependence of the pulse control system is shown in Figure 4, Input/picked FEL average power vs. wavelength in the range from 5.4 to 12 µm.

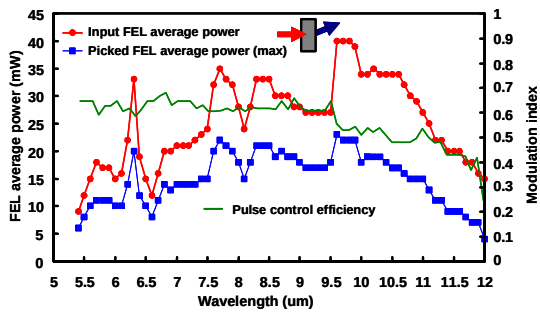

Figure 4:Wavelength-dependance of pulse control system.

Measurement of first order FEL

The MCT signal of the FEL first order beam is shown in Figure5. This pulse control system can control the FEL pulse width in the range of 10 micropulses (>200 ns) to the full macropulse (15 µs). A 630 ns first order FEL is produced by a control signal of 500 ns, a 360 ns first order FEL is produced by a control signal of 200 ns. Based on these results, the rise/fall time of this pulse control system is about 100 ns. This result aligns closely with the theoretical value derived from equation (1).

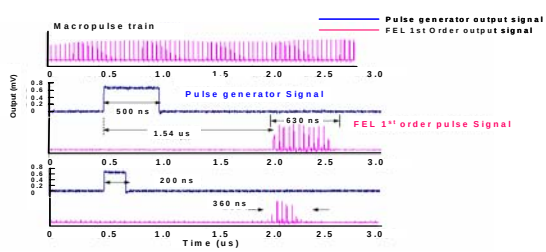

Figure 5: The pulse structure of the picked FEL.

EXPEREMENT

In case of FEL irradiation to gelatin, interaction arrives at depth of 2mm, at the maximum. However, Photo penetration depth = 3 μm. Interaction extends to much deeper from the region where light can arrive at. It is thought that this reaction depends on a shock wave.

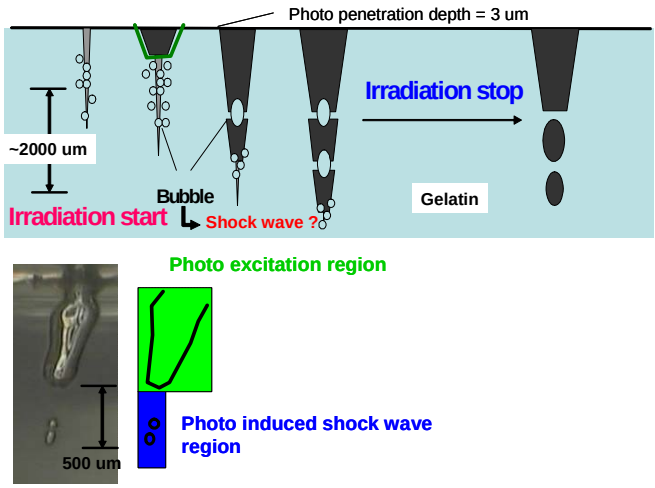

Figure 6: The process of gratin cut.

Experiment setup

Experiment setup for proof experiment of pulse control effect is shown in Fig 7. In this experiment, change of a shock wave is estimated by an image analysis and wave pattern analysis.

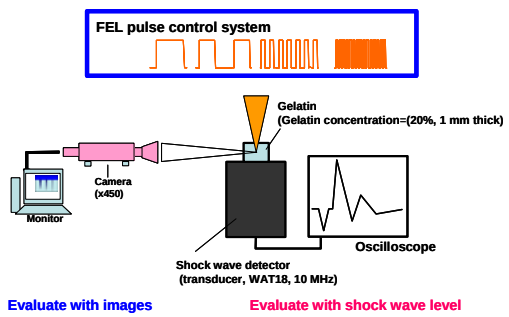

Figure 7: Experiment setup for proof experiment of pulse control effect.

RESULTS 2

A difference of a level of shock wave by a difference of pulse structure is shown in Figure8. Figure 9 illustrates the maximum shock wave level (peak to peak)/ maximum shock wave arrival depth (image analysis) vs. FEL pulse width. From these results, the same tendency was seen in an analysis result by an image and an analysis result by a wave pattern. A shock wave grows up to 1-2 μs and reaches saturation afterwards.

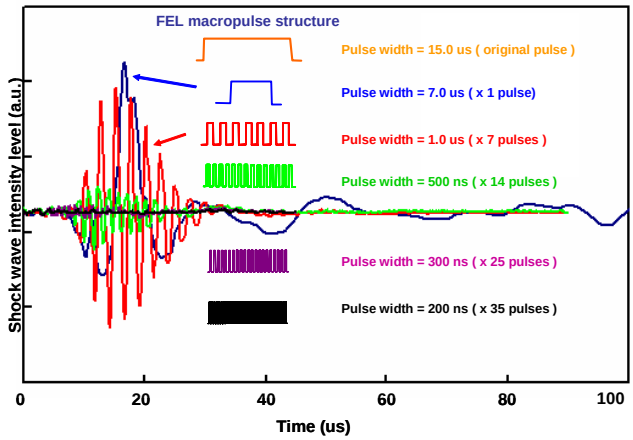

Figure 8: A difference of a level of shock wave by a difference of pulse structure.

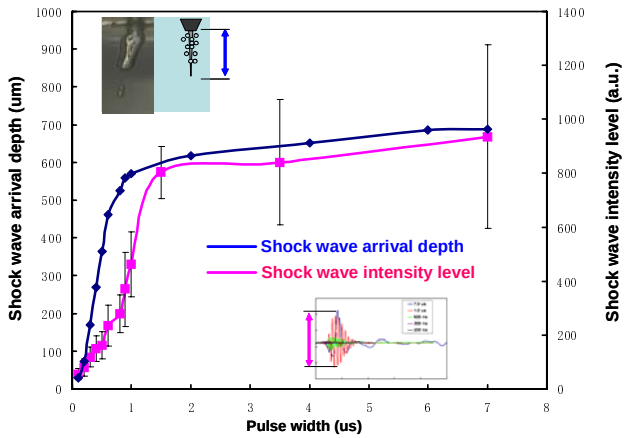

Figure 9: A difference of shock wave by a difference of pulse structure.

CONCLUSIONS

FEL pulse control system using an AOM was developed in order to investigate of non-thermal effect between the FEL and living tissue. With a time scale of 200 ns ~ 15 μs, this system provides the efficiency of ~65 % and a fast switching speed.

From results of pulse control effect proof experiment, the same tendency was seen in an analysis result by an image and an analysis result by a wave pattern. A shock wave grows up to 1-2 μs and reaches saturation afterwards. This system made it possible to control a shock wave by controlling a thing of pulse structure.

Picking out a single micropulse is impossible using this device with a time scale from 200 ns to 15 μs; it is, however, a very successful pulse control technique.

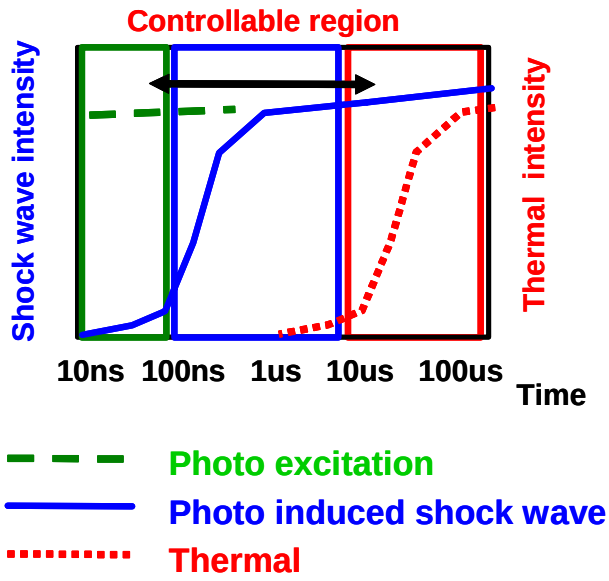

Figure 10: Controllable region by pulse control system.

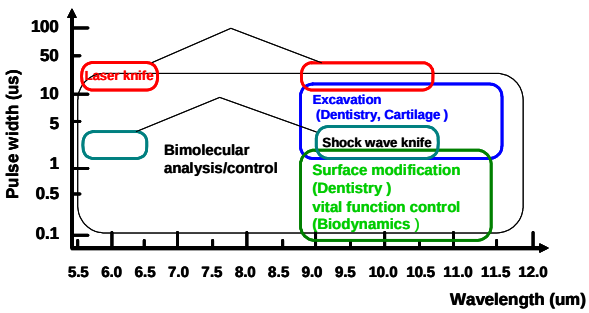

Figure 11: New regions that FEL can apply.

DISCUSSIONS

Using this system, the pulse width becomes the third parameter of the FEL system, in addition to the two conventional irradiation parameters of wavelength and power density. This system allows more precise FEL-biomolecular interactions, and was thereby able to produce a new irradiation effect of FEL that was not previously available (Figure 11). Improvement of the pulse control system (higher speed, higher power density) affords more selective excitation of biomolecules on a pico- and nanosecond time scale. In addition, by using FEL as the excitation light, we can introduce the picosecond time resolution vibration minute light method to the field of chemistry and biology.

REFERENCES

[1] GS. Edwards, D. Evertson, W. Gabella, TL. King, J. Kozub, M. Memdenhall, J. Shen, RH. Traeger: IEEE J. Sel. Top. Quantum Elec. Vol.2 (1998), p.810
[2] K. Awazu, A. Nagai, K. Aizawa, The Reveiew of Laser Engineering. Vol.26, No.5 (1998), p.369
[3] K. Awazu, The Reveiew of Laser Engineering.Vol.28, No.5 (2000), p.291
[4] Klaus Becker, J. Bruce Johnson, Gleen Edwards, Rev. Sci. Instrum. Vol.26, No.5 (1998), p.1496
[5] Mike Hillier: Acousto Optic Tuneable Filters Basic Theory And Design Considerations, Isomet corporation (1998)

ABSOLUTE AND CONVECTIVE INSTABILITY OF SMITH-PURCELL FREE ELECTRON LASER

D. Li#, K. Imasaki, ILT, 2-6 yamada-oka, suita, Osaka 565-0871, Japan
Z. Yang, UEST, Chengdu, 610054, P.R.China
Gun-Sik Park, SNU, Seoul 151-747, Korea
S. Miyamoto, S. Amano, T. Mochizuki, LASTI, 3-1-2 Koto, Kamigori, Hyogo 678-1205, Japan.

Abstract

The effect of dissipative loss in the grating surface on the Smith-Purcell free-electron laser is investigated with the help of a two-dimensional particle-in-cell simulation. The simulation model supposes an open aluminium grating driven by a continuous electron beam. With the present parameters, it has been shown that such a device can oscillate on both the convective and absolute instability when ignoring the surface-loss. The growth rate is found to be dependent of the beam energy, and it decreases when the surface-loss is involved. The results are compared with the recent theory.

INTRODUCTION

As a promising alternative in the development of a compact, tuneable and powerful THz source, the Smith-Purcell free-electron laser (SP-FEL) has attracted many attentions in recent years [1-5]. The SP-FEL can be realized on the configuration of an open grating [6-10], which is different from the conventional configuration, "orotron" or "ledatron" [11,12].

When an electron passes close to the surface of the grating, it not only emits Smith-Purcell radiation, but also excites the evanescent wave [13,14]. The evanescent wave, with the frequency below the lowest frequency of the Smith-Purcell radiation, travels along the grating and undergoes partial diffraction and partial reflection at both ends of the grating. The diffraction potion is radiative in the free space and can be utilized. The dispersion relation of the evanescent wave, as shown in Fig. 1, is similar to the backward-wave oscillators (BWOs) and traveling-wave tubes (TWTs), since the grating could be regarded as a kind of slow-wave structure. The frequency of the evanescent wave is determined from the intersection point of the dispersion curve and the beam line, as shown in Fig. 1, meaning that the beam velocity is synchronous with the phase velocity of the wave. The group velocity can be positive, negative or zero. When the interaction happens in the positive group velocity, the wave and the beam moves in the same direction. Such an interaction induces convective instability, and the device operates in the manner of TWTs [15]. When the group velocity is negative, the wave and the beam moves in the opposite direction. In this case, the interaction leads to absolute instability, and the device can operate without external feedback, like BWOs [15].

The case of absolute instability has been much addressed [6-9]. Andrews and co-workers predicated that there is possibility for device to start oscillation based on the convective instability, since the wave reflects at both ends of the grating, playing the role of external feedback [15]. In this paper, we address on the oscillation induced by absolute and convective instability, respectively, with the help of a two-dimensional particle-in-cell code, MAGIC [16], a code for simulating processes involving interactions between space charge and electromagnetic fields. The simulation is performed with and without involving the surface-loss of the grating, respectively, to demonstrate the effect of the loss on the operation of the device.

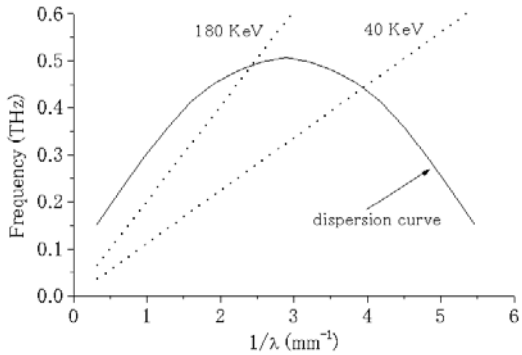

Figure 1: Dispersion relation for our grating.

SIMULATION DESCRIPTION

The simulation geometry is shown in Fig. 2. A grating with rectangular form is set in the centre of the bottom of the simulation box. The surface of the grating is assumed to consist of conductor whose grooves are

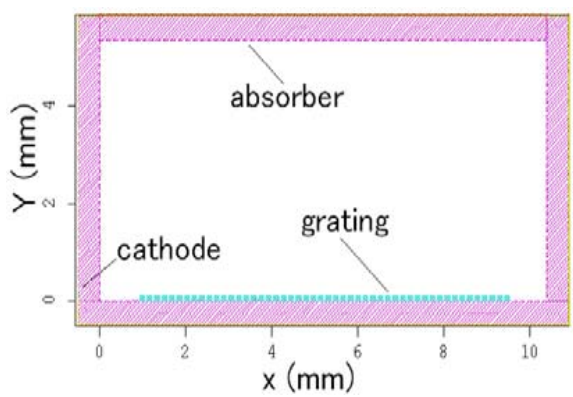

Figure 2: Simulation geometry.

#dazhi_li@hotmail.com

parallel and uniform in the *z* direction. We use a sheet electron beam with thickness of 24 μ m, and place its edge 34 μ m above the top of the grating. It is a perfect laminar beam produced by the MAGIC algorithm and is generated from a cathode located at the left boundary of the simulation box. The electron-wave interaction and radiation propagation happen in the vacuum area, which is enclosed by a special region (called *free-space* in MAGIC language), where the incident electromagnetic waves and electrons can be absorbed. The whole simulation area is divided into a mesh with rectangle cells of small size (δ x=17.3 μ m, δ y=17.3 μ m) in the region of beam propagation and grating, and large size (δ x=17.3 μ m, δ y=51.9 μ m) in the rest of the region. The Cartesian coordinate system is adopted with the origin at the centre of the grating. Since it is a two-dimensional simulation, it assumes that all fields and currents are independent of the z coordinate. And it should be noted that the current value mentioned in this paper represents the current per meter in the z direction.

The main parameters of the grating and electron beam are summarized in table 1. The electron beam

Table 1 Main parameters for simulation

Grating period	L=173 μ m
Groove width	w=62 μ m
Groove depth	d=100 μ m
Period number	N=50
Electron beam energy	E=40 ~140 KeV
Beam current	I=648A/m
Beam thickness	σ =24 μ m
Beam-grating distance	δ =34 μ m
External magnetic field	B_x=2T

energy will be varied in the following simulation. The external magnetic field is used in order to ensure stable beam propagation above the grating. It should be noted that some parameters of the grating and electrons, such as period length, groove depth and width, and electron's energy, used in our simulation are the same as those in Dartmouth experiment [1]. Consequently the radiation occurs in the THz regime. However, the grating length in our simulation is shorter than the one used in Dartmouth

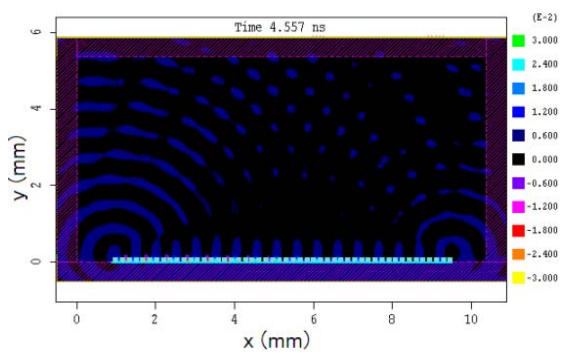

Figure 3: Contour plot of Bz for the case of 50 KeV electron beam.

experiment because of the limited capacity of our computers. In addition, the form of the beam is different, since we use a sheet beam and the experiment used a round beam.

As to the diagnostics, MAGIC allows us to observe a variety of physical quantities such as electromagnetic fields as functions of time and space, power outflow, and electron phase-space trajectories [16]. We can set the relevant detectors anywhere in the simulation area.

SIMULATION RESULTS

Ignoring Surface-loss

We first perform the simulation at the ignorance of the surface loss, i.e., the grating is supposed to be perfect conductor. The choice of beam energy spans the regions of absolute and convective instability. According to the theory of Andrews and Brau, the beam line intersects the point of zero group velocity, called Bragg condition, with the energy of 125 keV[15]. Fig.3 and 4 show the contour plot of B_z and energy modulation for the beam energy of 50 keV, at the time of 4.703 ns. In this case, the device operates on the absolute instability, and the energy modulation tells that the oscillation happens. If the beam energy is 140 keV, the device operates on the convective instability. From Fig. 5 we understand that the ends of the grating reflect the wave, and therefore provide feedback.

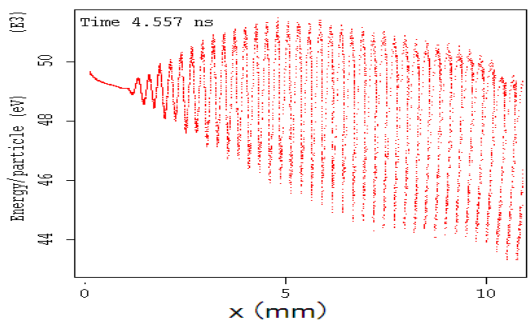

Figure 4: Energy modulation for the case of 50 keV eelectron beam.

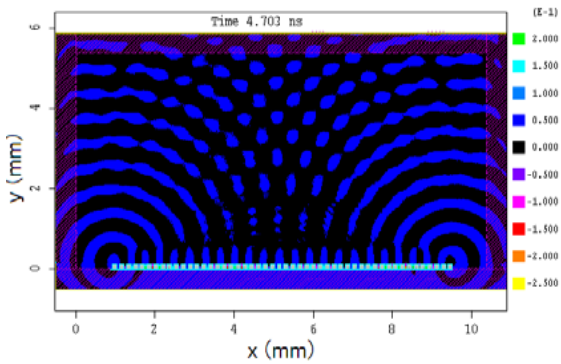

Figure 5: Contour plot of B_z for the case of 140 KeV electron beam.

The reflected waves form the interference pattern. Fig. 6 illustrates the modulation of the energy, meaning that the

device oscillates. The electric field component of the evanescent wave is observed near the grating surface, as examples, simulation results for some chosen energies are given in Fig.7. It is seen that the evolution of the

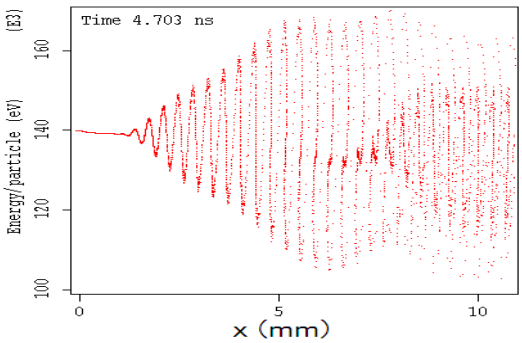

Figure 6: Energy modulation for the case of 140 keV electron beam.

amplitude of the electric field component in the x direction shows the exponential growth for all chosen energy, which means the device can oscillate by both absolute and convective instability, even at the Bragg condition. We noticed that when the beam energy is 125 KeV or more, the curves illustrate several sharp decreases as the amplitude growing.

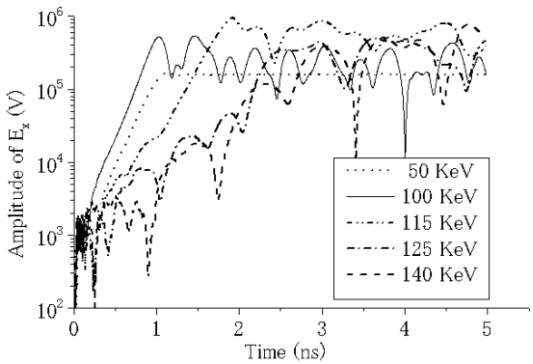

Figure 7: Evolution of amplitude of E^x with respect to time.

Involving Surface-loss

To be more practical, the grating should not be perfect conductor and it has loss in the surface. In this paper, we consider aluminium grating, which has the conductivity of 3.72×10^7 mhos/m. With involving the surface-loss, the evolution of the electric field amplitude corresponding to Fig.7 is as shown in Fig.8. It is understood that only the curves for 50KeV, 100KeV and 115KeV (operating on absolute instability) demonstrate the exponential growth, while for the case of 140KeV electron beam (operating on convective instability) the oscillation refuses starting. Further analysis of the simulation data shows that with the present parameters the device can only oscillate on the absolute instability. Comparing with Fig.7, the curve of 50KeV comes to saturation ahead of the curve of 100KeV in Fig. 8, which means the effect of surface loss strongly depends on the beam energy.

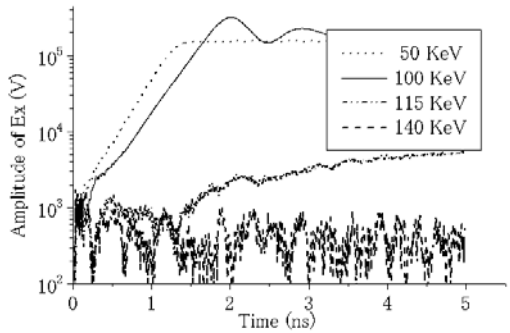

Figure 8: Evolution of amplitude of Ex with respect to time.

Growth rate

The growth rate of the evanescent wave can be derived from the simulation data. From the plot of amplitude of $E_x(t)$ vs t we can extract the slope of the linear envelop, which is the imaginary part of the frequency, Im(ω) [9]. Plenty of simulations are carried out with the variation of electron beam energy, and the growth rate for the particular energy is acquired by the way described above. The dependency of growth rate on beam energy is illustrated in Fig.9, for the cases of with and without surface loss, respectively. It has been shown that, the growth rate decreases when the surface-loss is involved. With the present parameters, the maximum growth rate appears at the energy of ~65 KeV for the case of with surface loss, then it goes down quickly to zero before the Bragg condition. That is the reason that the device can only operate on the absolute instability. If we expect the device oscillate at the convective instability, much higher current of electron beam is required to get the net gain. Also plotted in Fig.9 are the theoretical results from the recent theory [17], which show about two times larger than the simulation results.

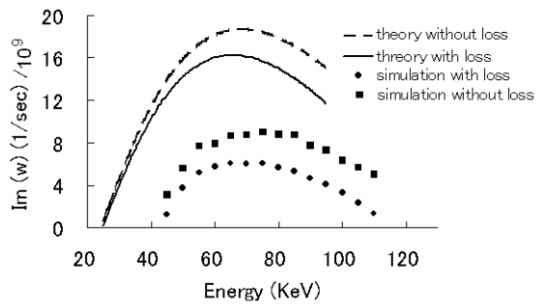

Figure 9: Growth rate with respect to beam energy.

CONCLUSION

The operation of a SP-FEL on absolute and convective instability is discussed in this paper. We demonstrate that the ends of the grating can provide the external feedback, which is possible to make the device oscillate at the

convective instability. The surface-loss will decrease the growth rate, especially in the region of convective instability. The growth rate drops down to zero before the Bragg condition with the present parameters. Higher beam current is predicted to provide the net gain if we expect the device to oscillate on the convective instability when the practical metal, such as aluminium, is used to make the grating.

ACKNOWLEDGMENTS

The authors gratefully acknowledge helpful discussions with Charles Brau and Heather Andrews.

REFERENCES

[1] J. Urata, M. Goldstein, M. F. Kimmitt, A. Naumov, C. Platt, and J. E. Walsh, Phys. Rev. Lett. **80**, 516 (1998).
[2] A. Bakhtyari, J. E. Walsh and J. H. Brownell, Phys. Rev. E **65**, 066503 (2002).
[3] L. Schachter and A. Ron, Phys. Rev. A **40**, 876 (1989).
[4] S.E.Korbly, A.S. Kesar, J.R.Sirigiri and R.J.Temkin, Phys. Rev. Lett. **94**, 054803, (2005).
[5] K. –J. Kim and S. –B. Song, Nucl. Instrum. Methods Phys. Res., sect. A **475**, 158 (2001).
[6] H. L. Andrews and C. A. Brau, Phys. Rev. ST Accel. Beams **7**, 070701 (2004).
[7] H.L.Andrews, C.H.Boulware, C.A.Brau and J.D.Jarvis, Phys. Rev. ST Accel. Beams **8**, 110720 (2005).
[8] V. Kumar and K.-J. Kim, Phys. Rev. E 73, 026501 (2006).
[9] J.T.Donohue and J.Gardelle, Phys. Rev. ST-AB, **8**, 060702 (2005).
[10] J.T.Donohue and J.Gardelle, Phys. Rev. ST-AB, **9**, 060701 (2006).
[11] R. P. Leavitt, D. E. Wortman, and C. A. Morrison, Appl. Phys. Lett. 35, 363(1979)
[12] K. Mizuno, S. Ono and Y. Shibata, IEEE Trans. Electron devices, ED-20, 749 (1973)
[13] D.Li, Z. Yang,K.Imasaki and Gun-sik Park, Phys. Rev. ST-AB **9**, 040701 (2006)
[14] D.Li, K.Imasaki , Z. Yang and Gun-sik Park, Appl. Phys. Lett. 88, 201501 (2006)
[15] H.L.Andrews, C.H.Boulware, , and J.D.Jarvis, Phys. Rev. ST Accel. Beams **8**, 050703 (2005).
[16] L. Ludeking, The MAGIC user's manual.
[17] C.A.Brau (private communication).

SUPERRADIANT SMITH-PURCELL RADIATION IN THE TERAHERTZ-WAVE REGION FROM BUNCHED ELECTRON BEAMS*

Zongjun Shi#, Ziqiang Yang, Zheng Liang, Institute of High Energy Electronic, University of Electronic Science and Technology of China, Sichuan, Chengdu, 610054, P. R. China
D.Li, K.Imasaki, Institute for Laser Technology, 2-6 Yamada-oka, Suita, Osaka 565-0871, Japan

Abstract

This paper presents an analysis of a possible method of producing the bunches and obtaining the coherent THz radiation. With the help of a two-dimensional particle-in-cell (PIC) simulation, the simulation proposes a model with two sections consisting of a square-toothed grating with a flat conducting roof above it and an open grating. In the first section, an initially continuous beam interacting with TM modes is bunched by using an external signal. In the second section, the coherent THz radiation is produced by the well bunched beam interacting with the open grating. The strongest radiation is at 120^0 and at frequency 266.5GHz.

INTRODUCTION

In recent years, there is a substantial interest in development of coherent radiation sources, especially to the coherent THz radiation. An important source of radiation in the THz region is Smith-Purcell(SP) radiation[1].

It is well known that the SP radiation may occur at angles θ measured from the direction of the electron beam and order *n* such that $\lambda = L(1/\beta - \cos\theta)/|n|$, where *L* is the grating period, βc the electron velocity, and c the speed of light. The coherent SP radiation has been observed in the THz region from experiments. One example is the Dartmouth experiments [2] with an initially continuous beam. The other is the MIT experiments [3] using the beam already bunched when it reaches the grating. The bunched beam from a linac operating at 17.14Ghz delivers pulses of duration 1ps. Quite recently, the PIC code simulations related to the coherent and superradiant SP radiation are performed by Li et al [4], Donohue and Gardelle, respectively [5,6]. In their simulations, the Dartmouth experiment and MIT experiment have been presented. These simulations are able to clearly observe coherent SP radiation at harmonics of imposed bunching frequency. Those results support the viewpoint of Andrews and Brau [7]. In the theoretical side, Kumar and Kim have performed a detailed 2D analysis in which the SP free-electron laser is treated as a BWO [8]. And a thorough discussion of the radiation emitted by prebunched beams has been given recently by Gover [9].

We know it is necessary for generating coherent SP radiation that the bunches are short comparing with the radiation wavelength. However, for the short electron bunches high quality electron accelerator which is expensive is needed. The bunches are unstable both in time and along the grating for the bunching of the initially continuous beam by an evanescent wave that is operating in backward wave region.

In this paper, with the help of a two-dimensional PIC simulation we discuss and analyze a new method of making the bunches and obtaining the coherent THz radiation. The simulation proposes a model with two sections consisting of a square-toothed grating with a flat conducting roof above it and an open grating. In the first section, an initially continuous beam interacting with TM modes is bunched by using an outer incoming signal. The electron-wave interaction is operating in the travelling-wave region, which resembles a Cerenkov amplifier. Due to the Mechanism for TWT, the bunches are relative stable compared with what is operating in backward wave region. In the second section, the coherent THz radiation is produced by the well bunched beam interacting with the open grating.

DETAILS OF THE NUMBER ANALYSIS

Geometry and parameters of the simulation

The simulations are carried out using the PIC code CHIPIC[10]. It is a finite-difference, time-domain code for simulating plasma physics process. Our simulations use a 2D PIC code in this paper. The geometry is given in Fig. 1. The basic structure consists of a grating bounded above by a roof and an open grating .The surface of the grating and the roof are assumed to consist of a perfect conductor whose rectangular groove are parallel and uniform in the z direction. A sheet electron beam propagates along the x-direction. It is a perfect beam produced from a small cathode located at the left boundary of the simulation. The drive signal is also

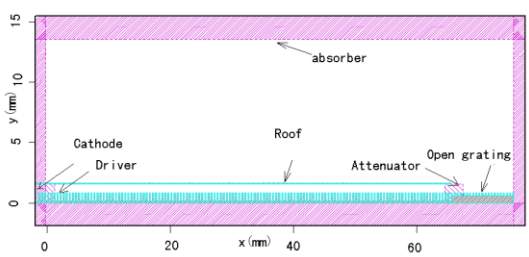

Figure 1. Simulation geometry.

*Work supported by National Nature Science Foundation of P.R.China (60571020),#shizongjun@163.com

Table 1. Parameters of the simulations

Parameters	First section	Second section
Beam energy	120 kV	
Current	200 A	
Beam thick	0.4 mm	0.4mm
Beam -grating distance	0.1 mm	0.1mm
Grating period	0.5mm	0.5mm
Grating groove depth	0.625mm	0.2mm
Grating groove width	0.25mm	0.3mm
Number of period	135	20
External magnetic field	2T	
Drive signal	2kW	
Mesh size	$(50um)^2$	$(50um)^2$

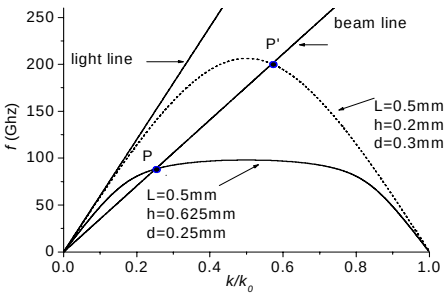

Figure 2.Dispersion relation for the grating

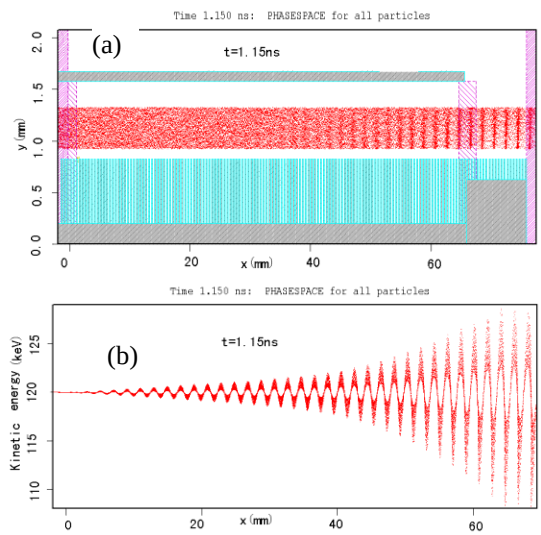

Figure 3. Phase-space distribution (a) density of electrons in the x-y plane at 1.15ns.Bunching is evident.(b) kinetic energy-*x* density at the same time

imposed on the left, which provides a 2kW power to the device. The beam-wave interaction and radiation propagation happen in the vacuum box. The boundary is enclosed with absorbers. At the end of the first section, there is an attenuator, which prevents most of the electromagnetic wave reaching the second section from perturbing the bunching and interpreting the coherent radiation. The grating parameters we choose have a period L=500*um*, a width of slots d=0.25*mm*, and a depth h=0.625 *mm*. The distance from the tops of the teeth to the roof is 0.75 *mm*. We assume a beam voltage of 120kV, a current of 200A, a beam thickness of 0.4mm, and beam-grating distance 0.1*mm*, external magnetic field B_x=2T. The main parameters of the grating and electron beam are summarized in Table 1.

Description of our idea

In fig. 2, the solid line shows the lowest order TM mode dispersion relation for the grating with a roof, and the dash line for open grating. Due to the choice of parameters, the lowest-order TM mode will be resonant with the beam in the neighborhood of 90-100GHz. At the operating point P, the group velocity is positive, which means electron-wave interacts at the traveling-wave region, as in the traveling-wave tube (TWT). The working process of the device is explained as follows. By using an initial injected signal with frequency 88.5GHz, the electron beam interacts with TM mode electromagnetic wave through the first section, and gets density bunching. The bunching wavelength will be the same as the spatial wavelength of the operating point P .In the second section in order to clearly observe coherent SP radiation at harmonics of the bunching frequency, we varied the parameters of the grating. In fig.2, the point P' is the operating point. Then the operating point frequency of the evanescent wave is different from the bunching frequency.

Through the second passage, which also acts a drift tube, the well bunched beam interacts with the grating, and the coherent radiation is produced.

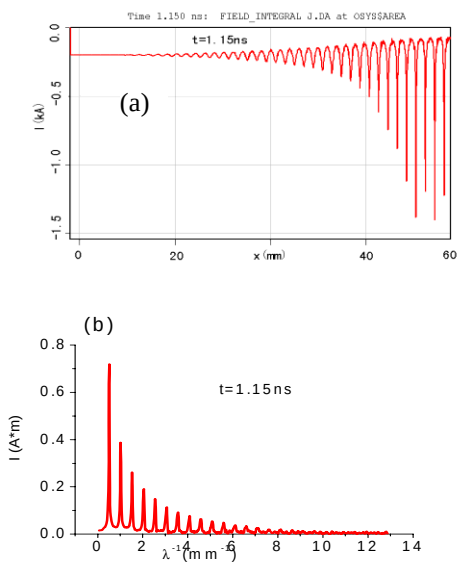

Figure 4. Space dependence of current (a) current I(x), (b) corresponding FFT.

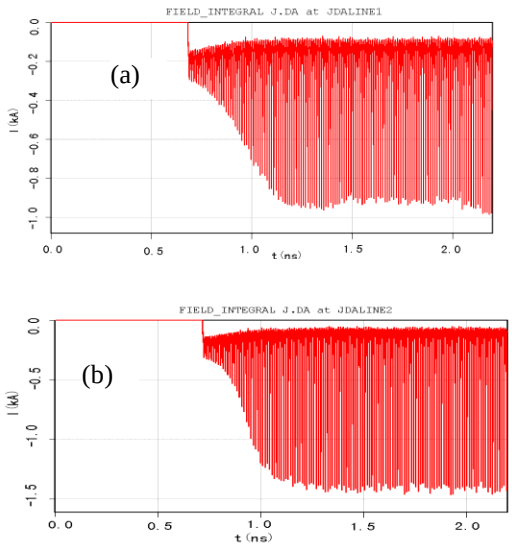

Figure 5. (Color) Current as a function of time: (a) at end of the first section .(b) at the center of the open grating .

SIMULATIONS RESULTS

Electron bunching

In this simulation, the main goal of the first section is not gaining the maximum output power of the beam-wave interaction, but obtaining the well stable bunches. Hence, by using of an outer injected wave, choosing a reasonable period numbers, an initial continuous beam travels through the first section and gets velocity modulation and density bunching, then passes through the open grating and the stable bunches are generated. The bunching can be clearly observed as a function of both space and time. In fig.3, we observe the beam bunching: phase-space plots at time 1.15ns and energy modulation of the electron .We note that the mean energy loss is about 5keV of the beam energy. The spatial modulation of the current displayed in fig.4 increases with *x*, and the period of the modulation is 1.94*mm*. The beam is well bunched at the downstream of the first of passage. We note that the bunching is relative stable along the open grating. In fig.4 (b) shows the bunching is nonlinear when it becomes strong. In fig.5 the beam current is a function of time, for locations at the end of the first of the passage and the center of the open grating. One clearly sees the bunching current is stable in time after time about 1ns. This is an advantage compared to the bunching of the initially continuous beam by an evanescent wave that is operating in backward wave region. In fig.5(b), the bunching current shows the beam is well bunched at the center of the open grating compared with that at the downstream of the grating with roof displayed in fig.5(a). It shows that the open grating also resembles a drift tube.

Coherent terahertz radiation

Here we analyze the radiation from the periodic bunching interacting with the open grating. The results of the simulation are given in fig.6, and three radiations are clearly observation. It has be shown that the dominant radiation is with the frequency of third harmonic of bunching wave, 88.5GHz peaked at the angle of about 120 deg which corresponds to the SP radiation angle. While the other two radiation are with the frequency of the fourth and fifth harmonics ,respectively, and also corresponds to the SP radiation angle. From the contour plot of fig.7 we can observe that the dominant third harmonic radiates at the angle of about 120^0, in agreement with that shown in fig.6.Of course, due to the interacting of the beam-wave which reduces the value of the particle velocity, the discrepancy appears somehow for the simulation data for the radiation angle compared to the theoretical value.

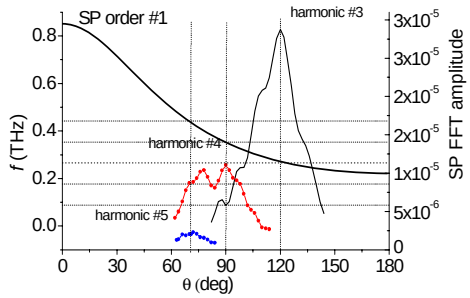

Figure 6. Radiation frequency and the peak of FFT amplitude of B_z as a function of angle, detected at the distance 10.58*mm* from the grating center.

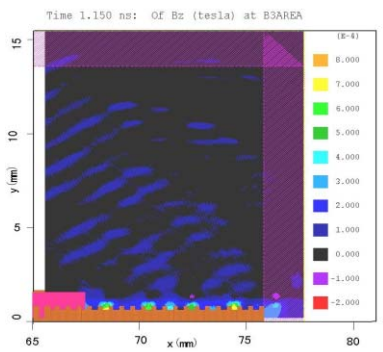

Figure 7. (Color) Contour plot of B_z for coherent radiation

CONCLUSIONS

We have presented results of the coherent THz radiation through the simulations of electron bunching of continuous beam interacting with an open grating. The results show that the bunching is stable in time and along the grating. The strongest radiation is at 120^0 and at frequency 266.5GHz at the simulation parameters. The coherent radiations are emitted at frequencies that are integer multiples of the bunching frequency, and at the corresponding SP angle.

REFERENCES

[1] S.J.Smith,E.M.Purcell. “Visible light from localized surface charges moving across a grating”.*Phys. Rev*. 1953， **92**（15）:1069

[2] J. Urata，M.Goldstein ,M.F. Kimmitt *et al*.. “Super radiation Smith-Purcell emission” .Phys. Rev. Lett., 1998,**80**(3): 516~519

[3] S.E.Korbly,A.S.Kesar,J.R.Sirigiri et al.. “Observation of frequency-Locked coherent terahertz Smith-Purcell radiation”. Phys.Rev.Lett.2005,94(5):054803-1~4.

[4] D. Li, Z. Yang, K. Imasaki, and Gun-sik Park. “Particle-in-cell simulation of coherent and superradiant SP radiation” .Phys. Rev. ST Accel. Beams **9** 040701 (2006). [5] J.T. Donohue and J. Gardelle. “Simulation of Smith-Purcell radiation using a particle-in-cell code”.Phys.Rev. ST Accel. Beams **8**,060702 (2005).

[6] J.T. Donohue and J. Gardelle.“Simulation of Smith-Purcell terahertz radiation using a particle-in-cell code”.Phys.Rev. ST Accel. Beams **9**,060701 (2006).

[7] H.L. Andrews, *et al*.. “superradiant emission of Smith -Purcell radiation”. Phys. Rev. ST Accel. Beams **8**,110702 (2005).

[8] Vinit Kumar and Kwang-Je Kim. “Analysis of Smith-Purcell free-electron lasers”Phys. Rev. E 73.020501(2006)

[9]A.Gover and Dyunin. “Superradiant and stimulated superradiant emission in prebunched electron-beam radiators”. Phys. Rev. ST Accel. Beams *I* 2005,**8**(3):030701-1~15

[10]Di Jun ,Zhu Da-jun ,and Liu Sheng-gang ,*et al*.. “Electronmagnetic field Algorith of the chipic code”.

STUDY ON SUPERRADIANT SMITH-PURCELL RADIATION

D. Li#, K. Imasaki, ILT, 2-6 yamada-oka, suita, Osaka 565-0871, Japan
Z. Yang, UESTC, Chengdu, 610054, P.R.China
Gun-Sik Park, SNU, Seoul 151-747, Korea
S. Miyamoto, S. Amano, T. Mochizuki, LASTI, 3-1-2 Koto, Kamigori, Hyogo 678-1205, Japan.

Abstract

An analysis of superradiant Smith-Purcell radiation is carried out with the help of performing a three-dimensional simulation in GHz regime using a particle-in-cell code. The simulation model supposes a rectangular grating with limited length and width, to be driven by a single electron bunch, a train of periodic bunches and a continuous beam, respectively. Besides the Smith-Purcell radiation, the evanescent wave is clearly observed, which holds the frequency lower than the allowed minimum Smith-Purcell frequency. It is also shown that the superradiant radiations excited by periodic bunches are emitted at higher harmonics of the bunching frequency and at the corresponding Smith-Purcell angles. The distributions of the radiation intensity are presented and compared with a recently proposed theory. The "start current" for a continuous beam to make the device start oscillation is addressed as well.

INTRODUCTION

The superradiant Smith-Purcell (SP) radiation has attracted many attentions since Urata and co-workers observed this phenomenon in their experiments [1,2]. It is a promising alternative in the development of a compact, tuneable and high power THz sources. To better understand the physics of the superradiant SP radiation is necessary for improving the performance of such kinds of devices.

It is known that the SP radiation is emitted as an electron passes close to the surface of a periodic metallic grating [3]. The wavelength λ of the radiation observed at the angle θ measured from the direction of electron beam is given by

$$\frac{\lambda}{d} = \frac{1}{|n|}\left(\frac{1}{\beta} - \cos\theta\right), \qquad (1)$$

where d is the grating period, βc the electron velocity, c the speed of light, and n the order of the reflection from the grating. The incoherent SP radiation has been analysed in many ways, such as diffraction theory, integral equation method and induced surface current model [4-8]. The experimentally observed superradiant effect is regarded as the result of the appearance of periodic electron bunches. Several theories have been proposed to reveal the physics of the superradiant phenomenon [9-13], and a three-dimensional simulation is supposed to be necessary.

#dazhi_li@hotmail.com

In this paper, we perform a three-dimensional particle-in-cell simulation for the coherent and superradiant SP radiation using MAGIC [14], a code for simulating processes involving interactions between space charge and electromagnetic fields.

SIMULATION MODEL

The simulation model involving a rectangular grating and a cylindrical electron beam is shown in Fig. 1, where d is the periodic length, s the groove width, h the groove depth and w the width of the grating. The main parameters are summarized in table 1, and we note that the grating period, groove width and depth and initial electron's energy are same as those in Ref. [15]. The length of the grating is set differently for particular simulation case, which will be mentioned lately. The grating, assumed to be a perfect conductor, is set in the

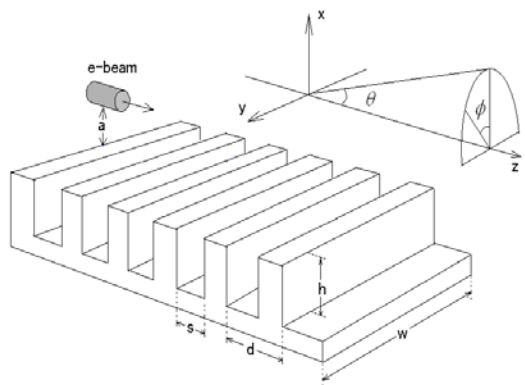

Figure 1: Three-dimensional simulation model of grating and electron beam.

centre of the bottom of a vacuum box, which is bounded by an absorption region. A perfect laminar beam produced from a cathode moves in the z-axis. The simulation area is divided into mesh with rectangular cell of very small size in the region of beam propagation and large in the rest.

Table I: Main Parameters for Simulation

Electron beam energy (injection)	E=100 keV
Beam radius	r=2.5 mm
Beam-grating distance	a=2 mm
Grating period	d=2 cm
Grating groove depth	h=1 cm
Grating groove width	s=1 cm
Grating width	w=10 cm

SIMULATION RESULTS

Single Bunch

We first perform the simulation of a single electron bunch. The grating is arranged to be 10 periods. The bunch length is chosen as 0.1 ps with the current of 1A. It is short compared to the radiation wavelength, so the radiation is coherent. In our simulation we focus on the first order SP radiation since the high orders are not evident. Fig. 2(a) illustrates the temporal behaviour of B_y, detected at the point of $\theta = 120^o$, $\phi = 0^o$. We notice that the SP radiation pulse consists of 10 periods and is separated in time from the evanescent wave. The corresponding FFT is given in Fig. 2(b), where one can find two clear peaks. The one peaked at 6.5 GHz is the SP radiation, while the other at 4.5 GHz is the evanescent wave. Not like the SP radiation, the evanescent wave frequency is angle independent. The dependency of the SP frequency and the amplitude of B_y on the angle θ is as shown in Fig. 3, observed at the same distance 36.35 cm to the centre of the grating. For comparison, we also plot the analytical result calculated from the theory of Andrews and co-workers [16]. It is seen that the simulation data for the SP radiation frequency agrees well to the theoretical curve as θ over 90°, somehow the discrepancy appears for the rest. Our best guess is that the detector is not far enough for far-field detection. We also see that the maximum amplitude of B_y appears at 125°. There are slight differences between the analytical and simulation results, which might be due to the fact that we use a broad electron beam that nearly reaches the grating, whereas they use a narrow electron beam model. In Fig.4, we give the distribution of field amplitude with respect to the azimuthal angle ϕ. The observation angle cannot vary in a large range due to the limit of the simulation geometry. The distribution shows maximum at the centre point $\phi = 0$ for cases of $\theta = 130^o$ and $\theta = 80^o$, but minimum for $\theta = 50^o$.

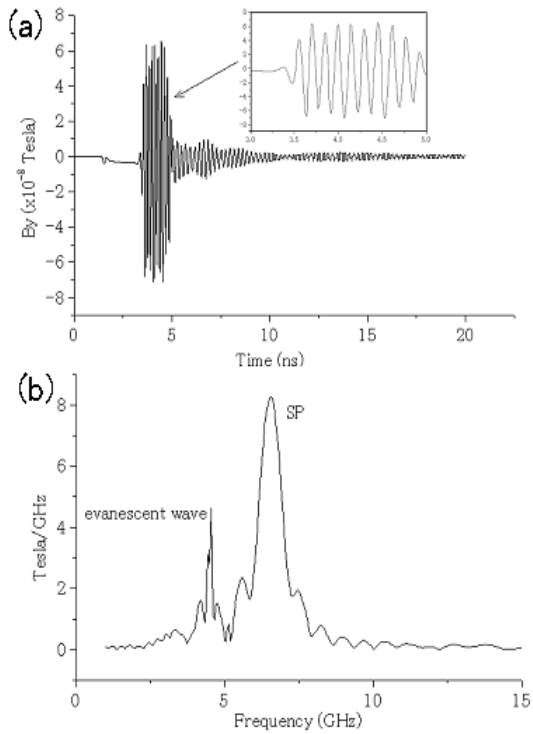

Figure 2: Time signal of B_y (a), and its corresponding FFT (b).

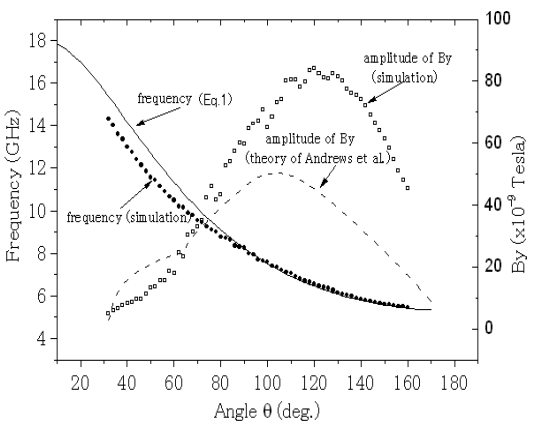

Figure 3: Distribution of SP frequency and its By amplitude.

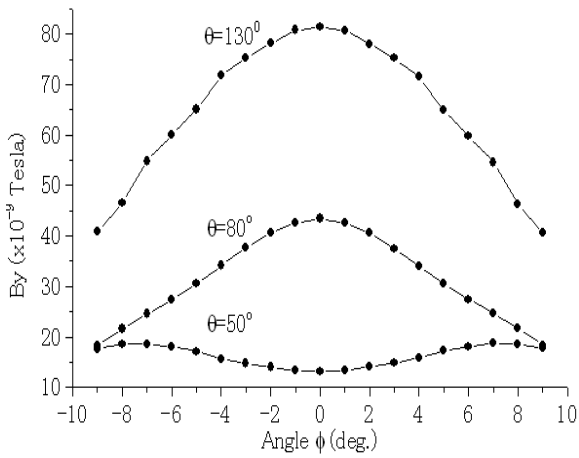

Figure 4: The dependency of By amplitude on azimuthal angle.

Periodic Bunches

In all radiation sources using an intense electron beam, the mechanism leading to superradiance is beam bunching. The spectral intensity of the radiation is enhanced at the bunching frequency and its harmonics. Recently Korbly and co-workers have carried out a SP experiment at MIT with using a pre-bunched electron beam [17]. When certain conditions are satisfied, a continuous beam can be bunched by the interaction with the evanescent wave, which has been discussed by Donohue and Gardelle [15]. In order to demonstrate the properties of superradiant radiation more clearly, we avoid the problem of bunching from an initially continuous beam. Instead, we generate a train of bunches to drive the grating.

The repetition frequency of bunches is chosen as 3 GHz, and the parameters for grating length and each single bunch are same to those mentioned earlier. Within the time of code running, 30 bunches are generated and enter the simulation area. From the FFT of the temporal behaviour observed by B_y detectors we know that the radiation focused on three frequencies, the second, third and forth harmonic of bunching frequency, as shown in

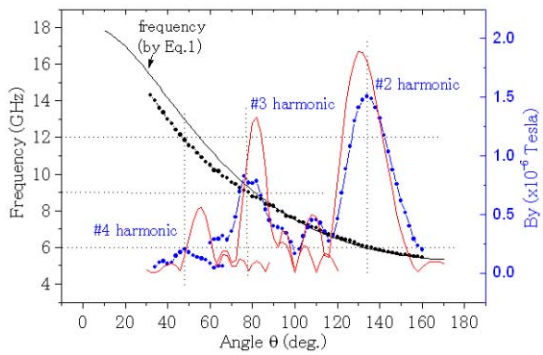

Figure 5: Distribution of superradiant SP radiation frequency and its B_y amplitude. The dotted blue line is the simulation results, and the red line the analytical result multiplied by 10.

Fig. 5. The dominant radiation is the second harmonic peaked at the angle 134°, which corresponds to Eq. 1. Also plotted In Fig. 5, is the analytical result according to Ref. [16], and we find the differences are smaller than one order of magnitude. Another evidence to show the fact that the radiations emit only at certain angles can be found in the contour plot of B_y, as shown in Fig. 6, where the second harmonic radiation is observed to radiate at the angle of about 134°, corresponding to what is shown in Fig. 5. These results strongly support the viewpoint of Andrews and co-workers.

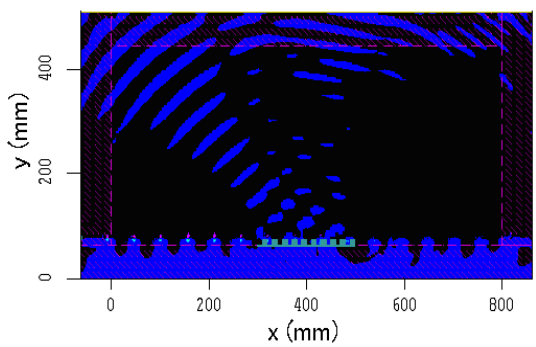

Figure 6: Contour plots of B_y.

Continuous beam

From the theoretical analysis in Ref. [15], we know that the beam line intersects the dispersion curve at a point representing a backward wave, which means the device operates in the mode of backward-wave oscillator (BWOs). Such a device is possible to start to oscillate without external feedback. When the beam current of an originally continuous beam is high enough to get the net gain, the beam will be bunched by the enhanced evanescent wave and the oscillation starts. The bunched beam consequently excites the superradiant SP radiation as discussed early. The value of the current starting the oscillation is called "start current", which needs careful analysis. In this section, we concentrate on determining the "start current" by three-dimensional simulation.

Considering the limit of the capacity of our computers, a grating consisting of 46 periods was employed in this simulation. The electron beam from the cathode is continuously generated, and an external magnetic field of 2T is introduced to prevent the beam from diverging. We vary the beam current and observe the amplitude of E_x of the evanescent wave. The appearance of exponential growth of E_x means that the oscillation happens.

The simulation results are given in Fig. 7. It is shown that, the electric field shows no growth when the current is lower than 0.4 A, while it shows evident growth as the current is above 0.5 A. And the radiation can reach saturation if the current is higher that 0.6 A. From Fig. 7, we can roughly estimate that the "start current" is ~0.5 A. The precise value can be reached if more simulations are performed.

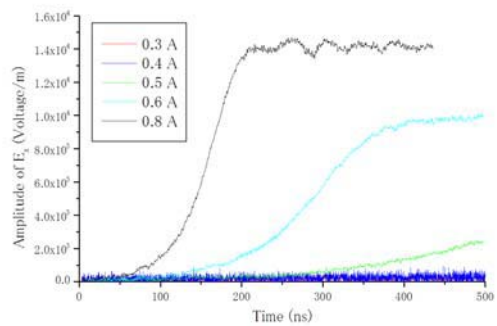

Figure 7: Evolution of amplitude of E_x.

CONCLUSION

In conclusion, we have studied the coherent and superradiant SP radiation through the three-dimensional simulation of an open grating system driven by different modes of electron beam. The single bunch simulation helps us to distinguish the true SP radiation from the evanescent wave. They are different in both frequency characteristics and generation mechanism. The amplitude of the SP radiation is angle dependent. The strongest radiation appears at 125° at the present parameters. The supperandiant effect is demonstrated with the simulation of a pre-bunched beam. We provide powerful evidence showing that the superradiant radiations are emitted at frequencies that are integer multiples of the bunching frequency, and at the corresponding SP direction. The simulation of an originally continuous beam determines the "start current" for the present parameters.

ACKNOLOWEDGEMENTS

The authors gratefully acknowledge helpful discussions with Charles Brau, John Donohue, and Heather Andrews.

REFERENCES

[1] J. Urata, M. Goldstein, M. F. Kimmitt, A. Naumov, C. Platt, and J. E. Walsh, Phys. Rev. Lett. **80**, 516 (1998).

[2] A. Bakhtyari, J. E. Walsh and J. H. Brownell, Phys. Rev. E **65**, 066503 (2002).

[3] S. J. Smith and E. M. Purcell, Phys. Rev. **92**, 1069 (1953).

[4] P. M. van den Berg, J. Opt. Soc. Am. **63**, 689 (1973).

[5] P. M. van den Berg and T. H. Tan, J. Opt. Soc. Am. **64**, 325 (1974).

[6] Y. Takaura and O. Haeberle, Phys. Rev. E 61,4441 (2000).

[7] J. Walsh, K. Woods and S.Yeager, Nucl. Instrum. Methods Phys. Res. A **341**, 277 (1994).

[8] Y. Shibata, S. Hasebe, K. Ishi, S. Ono, M. Ikezawa, T. Nakazato, M. Oyamada, S. Urasawa, T. Takahashi, T. Matsuyama, K. Kobayashi, and Y. Fujita, Phys. Rev. E **57**, 1061 (1998).

[9] L. Schachter and A. Ron, Phys. Rev. A **40**, 876 (1989).

[10] K. –J. Kim and S. –B. Song, Nucl. Instrum. Methods Phys. Res., sect. A **475**, 158 (2001).

[11] H. L. Andrews and C. A. Brau, Phys. Rev. ST Accel. Beams **7**, 070701 (2004).

[12] H.L.Andrews, C.H.Boulware, C.A.Brau and J.D.Jarvis, Phys. Rev. ST Accel. Beams **8**, 050703 (2005).

[13] V. Kumar and K.-J. Kim, Phys. Rev. E 73, 026501 (2006).

[14] D. Smithe and T.M. Abu-Elfadi, Comput. Phys. Commun. 106, **95** (1997).

[15] J.T.Donohue and J.Gardelle, Phys. Rev. ST-AB, **8**, 060702 (2005).

[16] H.L.Andrews, C.H.Boulware, C.A.Brau and J.D.Jarvis, Phys. Rev. ST Accel. Beams **8**, 110720 (2005).

[17] S.E.Korbly, A.S. Kesar, J.R.Sirigiri and R.J.Temkin, Phys. Rev. Lett. **94**, 054803, (2005).

FUTURE FEL STUDIES AT THE VISA EXPERIMENT IN THE SASE AND SEEDED MODES*

G. Andonian, M. Dunning, A. Murokh, C. Pellegrini, S. Reiche, J. Rosenzweig,
UCLA, Los Angeles, CA 90095, USA
M. Babzien, I. Ben-Zvi, V. Yakimenko, BNL, Upton, NY 11973, USA.

Abstract

The VISA (Visible to Infrared SASE Amplifier) experiment at BNL (Brookhaven National Laboratory) has previously demonstrated saturation at 840 nm in 2001. Further SASE studies, in 2003, have demonstrated an anomalously large bandwidth spread of the FEL spectrum due to off-angle emissions. This paper disseminates the current and future program of the VISA experiments at BNL. This includes a study of a seeded FEL, using a 1 micron YAG laser as a seed, and the accompanying diagnostics to characterize the radiation. Diagnostics include the double differential spectrometer, a mode converter to investigate the orbital angular momentum of light in the FEL, and an optical pepper-pot for coherence measurements. Start-to-end simulations, which are reliabily used for experimental modeling, are presented.

INTRODUCTION

The advent of the X-ray free electron laser (FEL) is on the horizon [1, 2]. The creation and diagnosis of ultra-short pulses is of great importance to the FEL community. The generation of femtosecond long, Ångstrom wavelength radiation will open doors to a myriad of scientific endeavors at ultra-short time scales [3].

The VISA program was developed to investigate properties of a high gain self amplified spontaneoous emission (SASE) free electron laser. A proposal to obtain ultra-short pulses [4], by manipulating frequency chirped FEL output, is the inspiration for the VISA II experiment. The frequency chirped radiation produced from an undulator is monochromatized and is used to seed a second undulator. The ultimate goal of the VISA II project is to operate the high gain SASE FEL with a large electron beam chirp.

The current mode of operations expands on this goal by utilizing the optimized capabilities of the facilities employed. Under these conditions, the VISA FEL operates in the seeded mode, using a 1 micron YAG laser as the seed. The experimental mission of the seeded FEL is to investigate high gain radiation properties with studies focusing on the far-field angular distribution and coherence of the radiation.

*This work supported by Dept. of Energy Contract no. DE-FG-98ER45693, and Office of Naval Research no. N000140210911

THE VISA EXPERIMENTAL PROGRAM

VISA I

The VISA project is hosted by the Accelerator Test Facility (ATF) of Brookhaven National Laboratory (BNL). The experimental layout is described in detail in Ref. [5] (Fig. 1 shows a schematic). The VISA I project succesfully demonstrated saturation of a SASE FEL within a 4 meter undulator at 840 nm. The high peak current, a result of nonlinear electron bunch compressoin along the dispersive line of the transport, was ultimately responsible for the observed high gain lasing. A start-to-end simulation suite of codes, PARMELA [6], ELEGANT [7], and GENESIS 1.3 [8], modeled the beam dynamics in the gun, transport and undulator, respectively. SASE FEL properties, such as pulse energy, profile, and angular distribution were computed with GENESIS. The complete characterization of the SASE FEL properties included gain lengths, spectra, energies, angular distributions and observation of nonlinear harmonics, and was successfully benchmarked against the simulation suite [9].

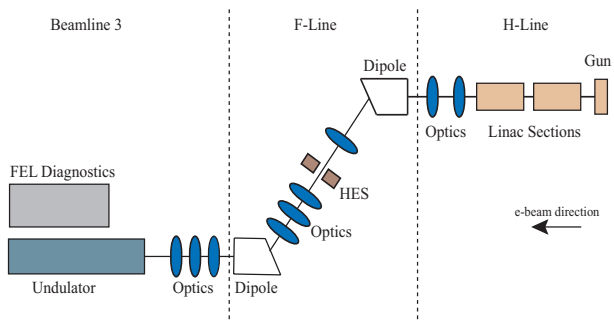

Figure 1: Layout of the ATF beam transport (not to scale). The VISA undulator is located along Beamline 3 after the 20 degree dogleg.

VISA IB

Subsequent measurements at VISA, informally referred to as VISA IB, also took place at the ATF in 2003. An anomolously large bandwidth, up to 15% full width, was observed at high gain (Fig. 2), accompanied by atypical far-field angular radiation patterns.

The electron beam (330 pC, 1.7% energy spread) was subjected to the same nonlinear bunch compression mechanism as in VISA I, except with a much higher degree of compression and thus a higher peak current. The SASE

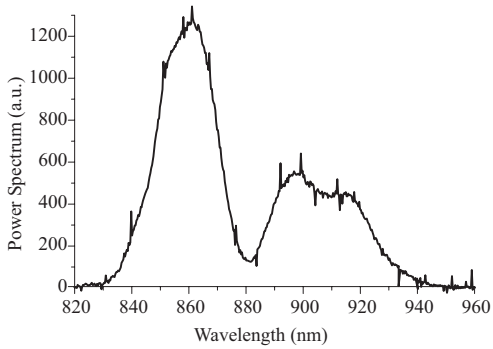

Figure 2: Sample shot of observed SASE FEL spectrum displays an anomalously large bandwidth.

FEL output (2 μJ average energy), was extremely stable and insensitive to RF and laser timing jitter. The spectrum is notable for a characteristic double peak structure, accompanied by a mean bandwidth value of 12% full width (greater than 100 nm), as seen in Fig. 2.

GENESIS simulations reproduced the features of the radiation (large bandwidth and double spiked structure). After transport, the electron beam displayed a highly nonlinear longitudinal phase space. The secondary spike was due to amplification of an off-axis mode. The mode was excited by the non-ideal centroid and envelope motion of the beam through the undulator's quadrupole focusing lattice. The lasing core of the beam was mismatched to the undulator focusing lattice yielding significant excursions in beam size in both transverse planes. Additional transverse motion causes a red-shift in the radiated wavelength and amplification of the off-axis modes [10].

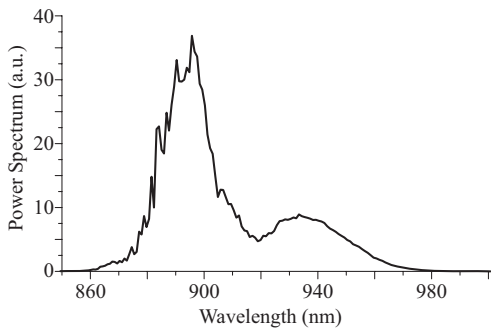

Figure 3: SASE FEL power spectrum obtained from GENESIS. The large bandwidth and the double hump feature observed in measurements were reproduced with simulations.

Double Differential Spectrometer The double differential spectrometer is diagnostic developed to unfold the relationships between frequency and angle of the FEL radiation. A slice of the FEL ouput is passed through graduated slits, then focused onto a set gratings (1200 in^{-1}). The resulting image displays the photon beam with frequency along one axis, and transverse angle along the other axis, and is a direct study of the intensity of the beam presented in the familiar form, $\frac{d^2I}{d\omega d\theta_y}$.

Raw data from a preliminary prototype of this diagnostic is presented in Fig. 4. The overall parabolic structure of the beam, from red shifting, in (θ, ω) space is evident, with even richer multi-mode patterns also present. Upgraded GENESIS post-processing tools were used to further understand this data and indeed displayed the parabolic structures along with the presence of higher order modes.

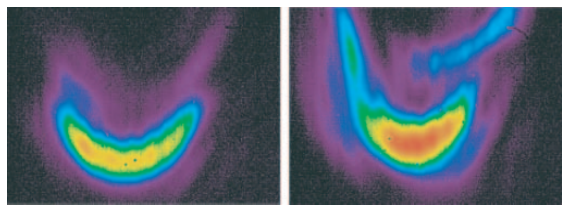

Figure 4: The parabolic structure (left) is evident in the images from the double differential spectrometer, where the angle is represented along the horizontal axis and the frequency along the vertical. Richer structures have also been observed (right).

Far-field Angular Distribution This far-field angular distribution measurement was made by propagating the output radiation, without optical focusing, to a screen located 3 m (10 Z_R) downstream. Observed patterns were hollow in nature, like previous VISA results, except more pronounced in angle (with spiral shaped patterns accompanying the hollow modes). The helicity of this patterns will be studied via a mode converter.

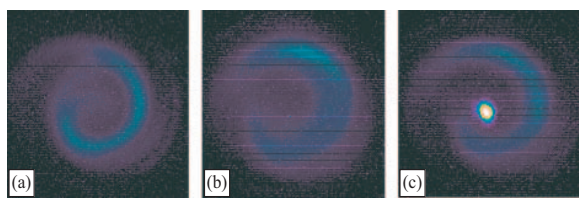

Figure 5: Far-field angular distribution profiles display an atypical spirality and helicity (a,b); superimposed with a reference alignment laser (c).

Chirped Beam FEL

The goal of the VISA II experiment is to inject a linearly chirped electron beam into the undulator to produce frequency chirped SASE FEL radiation. The bunch compression mechanism facilitates high-gain lasing, however, it restricts the management of beam properties through transport. Preservation of the electron beam chirp applied at the linac will be accomplished by the manipulation of nonlinear longitudinal compression by the addition of sextupole magnets placed at high horizontal dispersion points. The sextupoles will mitigate second order effects, particularly by diminishing the T_{566} element, of the transport matrix, to a negligible value [11]. Three sextupoles have been installed and commissioned at the ATF.

Frequency Resolved Optical Gating A frequency resolved optical gating (FROG) [12] system will be used to measure the frequency chirped, short pulse radiation. This method was successfully used elsewhere, to measure both the amplitude and phase of the radiation [13].

The frequency resolution of the FROG spectrogram is a concern at the VISA experiment. The diagnostic system is constrained by the doubling crystal and can not adequately resolve the radiation expected from the VISA II FEL. The thick lens must be replaced by a thin lens to increase the resolution; a dedicated spectrometer must be added to compensate for the loss of functionality of the thin lens. The CCD camera (several megapixel) must be able to cover a large range of wavelengths to resolve the observed bandwidth.

GENESIS outputs for the chirped beam case show a clear effect for idealized beam shapes and have been analyzed for varying degrees of chirp. Indeed, the inversion algorithm is robust enough to handle other exotic shapes and patterns which have been simulated and reconstructed via the commercial FROG software (Femtosoft) for the VISA II experiment. Fig. 6 shows an example of a spectrogram obtained from GENESIS for the running conditions of the VISA II FEL. This structure shows the complex nature of the FEL pulse, which is expected to contain several spikes. This longitudinal pulse profile was retrieved when the spectrogram was analyzed with the FROG reconstruction algorithm.

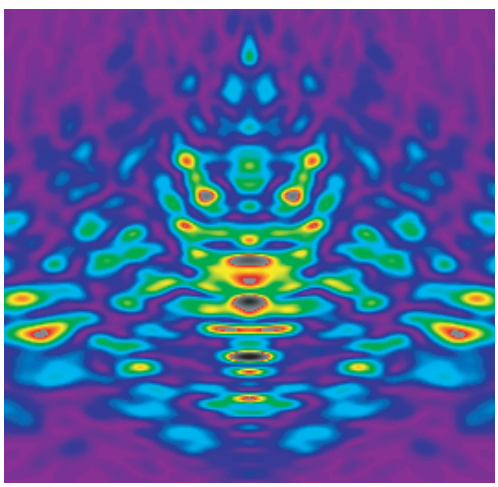

Figure 6: Spectrogram (with frequency along the vertical axis and time delay along the horizontal) of the expected radiation from the VISA II experiment. Further processing of this spectrogram has yielded the longitudinal profile of the pulse used in simulations.

Mode Converter The investigation of hollow mode and spiral shaped far-field angular radiation patterns at VISA is conducted with the introduction of a diagnostic mode converter. The mode converter is designed to transform light with planar polarization to circular polarization, and vice versa [14]. The $\pi/2$ mode converter is constructed of two cylindrical lenses, separated by a distance of $d = \sqrt{2}f$, and the resultant light will have distinct observable properties. This data will yield insight into the underpinnings of the unusual angular distribution patterns observed throughout the tenure of the VISA program. The cylindrical lenses for the mode converter have been setup and will be placed in the diagnostic station downstream of the undulator.

Polarizer The VISA project will also examine the study of coherent transition undulator radiation [15], the radiation emitted by the electron bunch as it passes through the entrance and exit of the undulator, due to the change in longitudinal velocity. Theoretically, the radiation is radially polarized, describing yet another possible explanation for the helicity of the observed far-field patterns from the planar undulator at VISA. The quantization of this effect requires minimal alteration of already existing diagnostics with the addition of grid polarizers to determine the polarization of the radiation. The effects of coherent transition radiation, from the electron beam striking a metal mirror, will have to be addressed (by the placement of a kicker magnet) before useful data is recovered from this measurement.

SEEDED FEL MEASUREMENTS

The results of the far-field angular distribution patterns at the VISA experiment have motivated further studies of the FEL in the seeded regime. The seeding pulse (a 1 micron YAG laser) will establish transverse and longitudinal coherence of the FEL (low bandwidth, high brightness). Such a radiation source will provide a short Rayleigh length FEL beam.

Further motivation for seeded FEL studies arises from controlling and managing the high power FEL in the far-field. Increasing the emission angles will decrease the intensity in the far-field (hollow modes) which will be technically useful in delivering high power radiation with minimal damage to sensitive optical elements.

The proposed experiment involves the VISA undulator with the ATF YAG laser as a seed. The YAG laser (1064 nm) serves as the drive laser for the photoelectron beam at the ATF and some its energy is transported to the experimental hall for deposition into the VISA undulator. A longitudinal delay line is currently being used to ensure adequate timing overlap with the electron beam and seed laser. The electron beam energy for the seeded FEL operations is lowered to 61 MeV to account for the higher wavelength operations

The experiments that will be carried out revolve around the detuning parameter of the FEL. Start-to-end simulations have been conducted for ideal and virtual particle sets. The results of the far-field angular distribution patters are presented in Fig. 7. It is apparent that detuning the electron beam indeed changes the angles and produces hollow

modes in the far-field. The power gain curves derived from GENESIS simulations (Fig. 8) have also been studied.

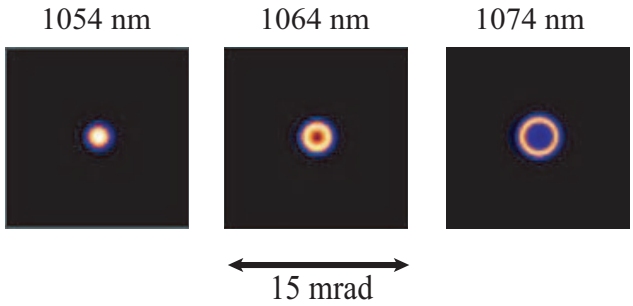

Figure 7: GENESIS simulation of the far-field angular distribution patterns of the seeded FEL for different values of detuning (1064 nm is the nominal wavelength).

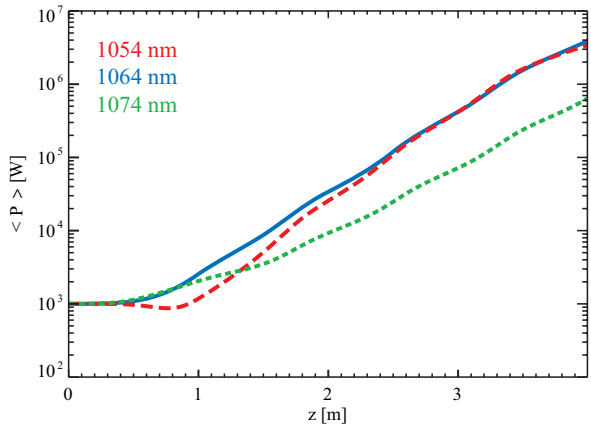

Figure 8: Power gain curves (GENESIS simulations) for varying detuning parameters.

Transverse Coherence

Transverse, or spatial coherence is an important figure of merit of any FEL. The transverse coherence for the seeded FEL will be verified with an arrangement of slits, by performing variations on the classical Young double-slit experiment. The FEL radiation diffracts at the slits, and the transverse coherence is calculated by measuring the ratio of the sum and difference of the maximum and minimum observed intensities [16]. Since the transverse coherence is a function of longitudinal position, it is measured at different positions downstream of the undulator exit. Several variations of slits have been fabricated for the transverse coherence study, including double-slits of various widths and spacings, crossed-slits, circular apertures of differing diameter, and a pepper-pot pattern of circular apertures. The use of these slits will be expanded after the seeded FEL experiment to also encompass SASE coherence measurements. The pepper-pot pattern is of particular interest because the emitted radiation from the uncorrected chirped-beam FEL experiments yielded intensity distributions with radial (helical) characteristics that provoke further investigation.

REFERENCES

[1] M. Cornacchia *et al.*, Linac Coherent Light Source Design Study Report no. SLAC-521 (1998)

[2] TESLA-FEL, Deutsches Elektronen Synchrotron 2001-05 (2001)

[3] R. Neutze *et al.*, Nature **406**, 752 (2000)

[4] C. Schroeder *et al.*, J. Opt. Soc. Am. B **19**, 1782 (2002)

[5] A. Murokh *et al.*, Phys. Rev. E **67**, 066501 (2003)

[6] L.M. Young, J.H. Billen, Los Alamos National Laboratory Report No. LA-UR-96-1835 (rev. 2000)

[7] M. Borland, Advanced Photon Source LS-287 (2000)

[8] S. Reiche, Nucl. Instrum. Methods A **429**, 243 (1999)

[9] A. Tremaine *et al.*, Phys. Rev. Lett. **88**, 204801 (2002)

[10] G. Andonian *et al.*, Phys. Rev. Lett. **95**, 054801 (2005)

[11] J. England *et al.*, Phys. Rev. ST Accel. Beams **8**, 012801 (2005)

[12] R. Trebino, *Frequency Resolved Optical Gating*, Kluwer Academic Publishers (2000)

[13] Y. Li *et al.*, Phys. Rev. Lett. **89**, 234801 (2002)

[14] M.W. Beijersbergen *et al.*, Optics Comm. **96**, 123-132 (1993)

[15] S. Reiche *et al.*, Procedings of the 2004 FEL Conference, 193-196, Trieste, Italy.

[16] R. Ischebeck, et al., Nuc. Inst. and Meth. in Phys. Res. A **507**, 175, 2003.

MAGNETIC CHICANE RADIATION STUDIES AT THE BNL ATF*

M. Dunning, G. Andonian, A.M. Cook, E. Hemsing, A. Murokh, S. Reiche, J. Rosenzweig,
D. Schiller, Particle Beam Physics Laboratory, Department of Physics and Astronomy, UCLA,
Los Angeles, CA 90095, USA
M. Babzien, K. Kusche, V. Yakimenko, Accelerator Test Facility, Brookhaven National Laboratory
Upton, NY 11973, USA.

Abstract

Radiation emitted by relativistic electrons traversing the magnetic eld gradients of a chicane bunch compressor has been studied in an attempt to characterize coherent edge radiation (CER). The studies performed at the Accelerator Test Facility (ATF) at Brookhaven National Laboratory (BNL) include frequency spectrum, angular distribution, and polarization measurements. A reconstruction of the longitudinal charge pro le from the measured spectrum shows that the bunch has been compressed to approximately 30 μm FWHM, with a peak current exceeding 1.5 kA. Measurements of radiation from the short pulses are compared to predictions from `QUINDI`, a new simulation code developed at UCLA to model the radiation.

INTRODUCTION

The chicane compressor studies are a collaboration with the Particle Beam Physics Laboratory (PBPL) at UCLA and the ATF, the user facility which hosts the experiment. The chicane was designed to compress the electron beam to yield the high peak current necessary to drive a self-ampli ed spontaneous emission free electron laser (SASE FEL) to saturation [1] and to expand the ATF core capabilities. Recent experiments have focused on the creation of very short electron beam pulses ($\sim$30 μm), and measurements of CER and coherent synchrotron radiation (CSR) emitted by such short bunches. The correlation between these radiative effects and microbunching instabilities are under investigation, as are other parasitic effects of the radiation. These are signi cant issues for larger projects, such as the Linac Coherent Light Source (LCLS), which will employ similar devices and diagnostics for the production of short duration pulses. CER has also been shown to be a bright source of infrared radiation, which makes it well-suited for certain types of microscopy and spectroscopy [2].

* Work supported by DOE grant DE-FG02-98ER45693 and NSF grant PHY-0355048.

EXPERIMENT DESCRIPTION

Chicane Compressor

The chicane compressor is currently installed along the high-energy line (H-line) of the ATF. The operating beam energy is 60-61 MeV for the present chicane radiation studies. The compressor consists of four dipole magnets oriented in a chicane layout, as in Fig. 1.

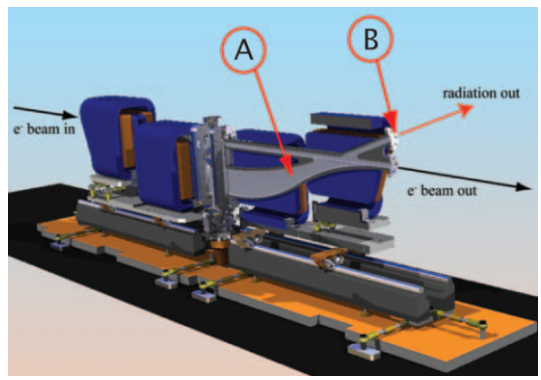

Figure 1: A rendering of the four dipole chicane compressor. The cutaway view shows the approximate radiation source between the third and fourth dipoles (A) and the radiation extraction port (B).

The chicane features a dedicated radiation extraction port that enables viewing of the region (Fig. 1A) which extends through the downstream edge of the third magnet to the upstream edge of the fourth magnet. The rectangular exit port (Fig. 1B) has transverse dimensions of 26 mm $\times$ 11 mm, with the longer dimension in the bend plane [3].

Table 1: Chicane design parameters

Parameter	Value	Units
B-Field	2015	Gauss
Bend Angle	20	deg
Geometric Length	41	cm
Magnet Gap	2.1	cm

Terahertz Radiation Transport

Radiation exits the chicane compressor through a fused silica vacuum window located on the extraction port (Fig. 1B). The radiation is guided with three adjustable mirrors (gold-coated) and a translatable Picarin lens, through metallic pipes (56 mm diameter) to an external diagnostic station. The entire length of the radiation transport line is approximately 7 m. The Picarin lens is positioned one focal length (1.25 m) from the approximate radiation source (between the third and fourth dipoles) to achieve a point-to-parallel transport con guration.

Diagnostic Station

The diagnostic station located at the end of the radiation transport is designed to be modular for versatility. It consists of focusing/turning mirrors, two individual l-ter wheels containing room temperature and cryogenically cooled lters, a wire grid polarizer, an iris on a two-dimensional translation stage, a silicon bolometer, and a Michelson-type interferometer.

Silicon Bolometer

In order to characterize the chicane radiation, a cryogenically cooled silicon bolometer (IR Labs model HDL-5) is employed. The bolometer is cooled with liquid helium and has a built in lter wheel, loaded with cut-on lters (long-pass) with wavelengths of 13, 27, 45, 103, and 285 μm. The detector element incorporates a Winston Cone collector, protected by a wedged polyethylene window (that provides an additional cut-on wavelength of 13 μm) [4].

Interferometer

The radiation spectrum is measured at the output of a Michelson-type interferometer as a function of bolometer voltage. The interferometer is optimized for the 15 μm to 1 mm wavelength range, and has a translatable mirror along one orthogonal leg with 1 μm spatial resolution [5].

CHICANE RADIATION OVERVIEW

Radiation exiting the chicane contains features of both synchrotron and edge radiation due to the measurement position and the magnet geometry. For electrons emitting under the same radiation process, the far- eld intensity distribution is expressed as

$$\mathscr{I}(\omega) = \mathscr{I}_0(\omega)[N_e + N_e(N_e - 1)F(\omega)], \qquad (1)$$

where $\mathscr{I}_0(\omega)$ is the single electron intensity distribution and $F(\omega)$ is the bunch form factor. For wavelengths longer than the bunch length ($\sim$ 30 μm), each type of radiation is coherently enhanced by a factor of N_e, the number of electrons in a bunch. Typically, $N_e \sim 10^9$ for the present ATF running parameters.

The edge radiation emitted from electrons entering and exiting the edges of bend magnets is expected to have greater intensity at longer wavelengths than synchrotron radiation [6]. The characteristics of CER also depend on the topology of the eld gradient. In the *zero-edge length model* [7], the eld of the bending magnet is approximated by a step function. The resultant radiation is radially polarized, with a cylindrically symmetric spatial distribution characterized by a null on the straight section axis and maxima at $\theta \sim 1/\gamma$, analogous to transition radiation. Analytic nite edge length models result in complicated expressions, requiring numerical calculations [8].

Simulations

Start-to-end simulations for the experiment were conducted with `PARMELA` [9] for the electron beam dynamics in the accelerating modules. The code `QUINDI` was used for the beam transport and radiation studies.

`QUINDI` is a parallel-computing code speci cally developed to model the emitted radiation from electron bunches within the ATF chicane. The program avoids the sequential approach of a magnetic lattice, relying instead on an object-driven description of magnetic elements. The observed radiation eld is calculated on a user-de ned plane based on the acceleration eld of the Liénard-Wiechert potentials.

MEASUREMENTS AND ANALYSIS

Frequency Spectrum

Spectral measurements of the emitted chicane radiation were conducted at the ATF. Interferograms were obtained from scans with the Michelson-type interferometer to provide information about the spectral content. This data was used to reconstruct the longitudinal charge distribution of the beam.

Interferometer signal amplitudes from the output of the silicon bolometer were recorded for N shots per mirror position. An averaged, normalized interferogram with the corresponding measured electron beam charge is shown in Fig. 2(a). Each point on the interferogram records the mean value and the error bars depict the standard deviation.

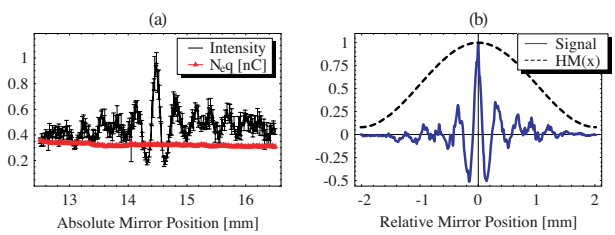

Figure 2: (a) Normalized, averaged signal amplitudes from interferometer scans of chicane radiation. (b) Apodized signal via a Hamming function.

For an accurate spectral reconstruction with a Discrete Inverse Fourier Transform (DIFT), the non-zero offset of the interferogram is removed and the signal is multiplied by an apodization function. Fig. 2(b)

shows the results of apodization by a Hamming function $\mathrm{HM}(x) = 0.54 + 0.46\cos(\frac{\pi x}{a})$, where $2a = 4$ mm is the length of the interferometer scan centered on the maximum peak. This standard procedure removes arti cial low-frequency components and corrects for the spurious tails that arise from the nite sum in the DIFT [10],

$$\tilde{I}_k = \frac{1}{n}\mathrm{Re}\sum_{j=1}^{n} I_j e^{2\pi i(k-1)(j-1)/n}, \qquad (2)$$

where n is the number of equally spaced interferometer mirror positions recorded over a nite distance $[ct_{min}, ct_{max}]$. This yields $n/2$ non-repeating intensity values, I_k, up to the maximum frequency, where I_j is the j^{th} intensity point in the modi ed interferogram.

Fig. 3(a) displays the resulting spectrum of the apodized signal. The peak at $f_{peak} \approx 0.5$ THz coincides with the dominant frequency given by results from QUINDI simulations.

Kramers-Kronig Reconstruction

The forward far- eld radiation intensity spectrum produced by the bunch is given by Eq. 1, where the longitudinal form factor $F(\omega)$ is

$$F(\omega) = \left| \int \hat{\rho}(z) e^{i\omega z/c} dz \right|^2, \qquad (3)$$

with $\hat{\rho}(z) = \rho(z)/N_e q$, the normalized longitudinal charge density. Following a minimal-phase reconstruction technique, a discretized Kramers-Kronig relation is used to extract $\hat{\rho}(z)$ [11].

The minimal phase is

$$\psi(\omega_i) = \frac{2\omega_i}{\pi}\sum_{j\neq i}^{N_{max}} \frac{\ln[\xi(\omega_j)/\xi(\omega_i)]}{\omega_j^2 - \omega_i^2}\Delta\omega, \qquad (4)$$

where $\xi^2(\omega_i) = F(\omega_i)$, and $\Delta\omega$ is the resolution from the spectrum. The normalized pro le $\hat{\rho}(z)$ then has the form

$$\hat{\rho}(z) = \frac{1}{\pi c}\sum_{i=0}^{N_{max}} \xi(\omega_i)\cos\left[\psi(\omega_i) - \frac{\omega_i z}{c}\right]\Delta\omega. \qquad (5)$$

The bunch distribution is calculated from the form factor, determined by tting well-behaved asymptotes to the measured normalized spectrum. Results of this reconstruction are shown in Fig. 3(b). The values for current are scaled to the average measured charge of $N_e q \approx 330$ pC. Due to experimental limitations (discussed below) and numerical tting of the form factor, this reconstruction technique is useful as an approximation of the true bunch distribution. Nevertheless, the reconstructed pro le shows general agreement with predictions from PARMELA simulations in the overall structure of the asymmetric bunch and the compressed head of ~ 30 μm FWHM.

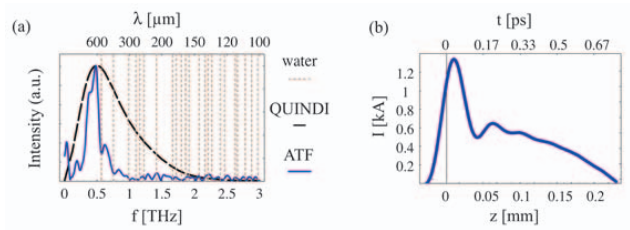

Figure 3: (a) Spectra from apodized interferogram and from simulation. Prominent water absorption frequencies are shown as vertical dotted lines. (b) Minimal phase Kramers-Kronig bunch reconstruction for the measured spectrum.

Limitations on Spectral Analysis

The simulated and measured spectra show that the radiation is dominated by frequencies below 1.5 THz, however, several experimental factors contribute to spectral l-tering which affect the measured frequency distribution and the longitudinal bunch reconstruction. The primary experimental artifact near the dominant frequency band is the selective ltering from water absorption (due to high levels of humidity encountered through the radiation transport on the dates of data acquisition). This effect is exempli ed by strong absorption troughs located near $f = 0.57$ and 0.75 THz. Signi cant absorption frequencies are plotted in Fig. 3(a) for a 7 m travel path [12]. The spectrum is also affected by the radiation transport line, which acts as a high pass lter due to its inherent nite apertures and acceptance angles. Further, the fused silica vacuum port window maintains a transmission coef cient that slowly decreases for frequencies greater than 0.3 THz, but rapidly approaches zero for frequencies greater than 6 THz.

Polarization

The transverse radiation pro le and polarization were measured in an effort to observe the distinctions between CER and CSR. Fig. 4 shows the measured intensity (normalized to maximum) as a function of polarizer rotation angle. The wire grid polarizer was mounted at the end of the transport and rotated in 15° increments, and the focused signal intensity was measured with the bolometer. The linearly polarized component of radiation (sinusoidal) is consistent with that expected from synchrotron radiation. The non-linearly polarized component, which introduces a vertical offset, is a clear signature of edge radiation. Analytic studies show that pure synchrotron radiation would give a ratio of approximately 7:1 between the maximum and minimum signal [13], while the observed ratio is approximately 4:1. QUINDI results are consistent with the measured data (Fig. 4).

Transverse Spatial Distribution

The transverse far- eld spatial intensity distribution of the emitted radiation was measured by scanning a small iris

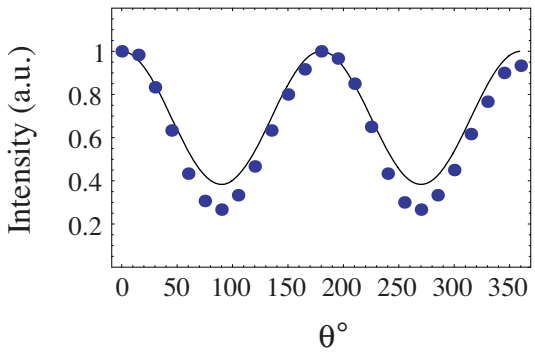

Figure 4: Normalized polarization intensity of the chicane radiation. Solid line is from QUINDI, dots are measured at the bolometer. The zero angle is arbitrary.

(3 mm diameter) in a 19 mm × 23 mm rectangular array of discrete points (Δd =3.8 mm). The iris was scanned across the transport tube exit and the signal was focused into the bolometer. Iris scans were performed for varying radiation polarizations with the aforementioned wire-grid polarizer (Fig. 5).

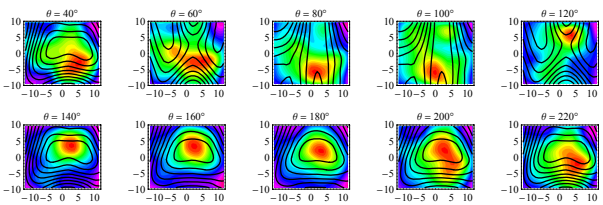

Figure 5: Interpolated far- eld radiation intensity distributions for 20 degree polarizer angle increments, with results from QUINDI simulations (contours) overlayed for comparison. The x and y scales have units of mm.

CONCLUSION

The chicane radiation studies at the ATF display telling signatures of edge radiation. The transverse spatial distributions show patterns consistent with simulations, namely strong peaks shifting into multiple peaks for varying degrees of polarization with identi able nulls in the distribution on-axis. The non linearly polarized component of radiation observed as an offset to the sinusoidal signal in the overall polarization curve is a clear indication of the actuality of prominent edge radiation.

Future plans to improve the measurements include radiation transport modi cations such as replacement of the fused silica chicane radiation port window with a diamond or z-cut crystalline quartz window; this will greatly improve the spectral range of the measurements. In addition, enclosing and ushing the transport line with dry nitrogen will mitigate the effects of water absorption lines in the measured spectrum. Also, a Czerny-Turner type monochromator is currently being built in order to more ef ciently resolve the chicane radiation spectrum.

REFERENCES

[1] G. Andonian, *et al.*, *Proceedings of the 2003 Particle Accelerator Conference*, 944, 2003.

[2] T. E. May, R. A. Bosch, and R. L. Julian, *Proceedings of the 1999 Particle Accelerator Conference*, 2394, 1999.

[3] R. Agustsson, *UCLA M.S. Thesis* (2003).

[4] http://www.irlabs.com/.

[5] http://www.radiabeam.com/.

[6] O. V. Chubar and N. V. Smolyakov, *J. Optics (Paris)* **24**, 117 (1993).

[7] R. A. Bosch, *Il Nuovo Cimento* **20D**, 483 (1998).

[8] O. V. Chubar and N. V. Smolyakov, *Proceedings of the 1993 Particle Accelerator Conference*, 1626, 1993.

[9] E. Colby, *UCLA PhD Thesis*, FERMILAB-THESIS-1997-03 (FNAL, 1997).

[10] J. F. Rabolt and R. Bellar, *Applied Spectroscopy* **35**, 132, 1981.

[11] R. Lai and A.J. Sievers, *Phys. Rev. E* **50**, 5 (1994).

[12] P.U. Jepsen, *private communication.*

[13] J.D. Jackson, *Classical Electrodynamics*, John Wiley and Sons, New York, 1999.

BEAM PICKUP DESIGNS SUITED FOR AN OPTICAL SAMPLING TECHNIQUE

K. Hacker, F. Loehl, H. Schlarb DESY, Hamburg, Germany

Abstract

The beam arrival-time monitor and large horizontal aperture chicane BPM at FLASH are important tools to stabilize the arrival-time of the beam at the end of the linac. The pickups for these monitors will be paired with a front-end that samples the zero-crossing of the transient through the use of electro-optical modulators (EOMs) and sub-picosecond-long laser pulses delivered by the master-laser oscillator (MLO). The design of pickups for this front-end requires the consideration of the transient shape as well as the amplitude. Simulations and oscilloscope traces for pickups that use or will use the EOM based phase measurement and the expected limitations of each pickup are presented. In particular, a method to reduce the beam position sensitivity of the beam arrival-time pickup, the potential resolution of a button pickup arrival-time measurement, and the design for a 5 μm resolution BPM with a 10 cm horizontal aperture are described.

INTRODUCTION

A beam arrival-time stability of 30 fs (~10 μm at v=c) is desired for pump-probe experiments and is mandatory for laser-based electron beam manipulation at FLASH and the XFEL [1]. With the accelerating LLRF goal energy stability of 10^{-4} at FLASH, the transverse position jitter in the dispersive section of the first chicane becomes 34.5 μm and results in a longitudinal position jitter of 18 μm. A monitor for a feedback system should be able to measure the beam energy by a factor of three better than the desired energy stability of $5*10^{-5}$ and this means that the resolution for a beam position measurement in the chicane must be better than 6 μm and a longitudinal time-of-flight path-length measurement should resolve 3 μm.

A longitudinal time-of-flight energy measurement can be made with two beam arrival-time monitors: one before and one after the chicane, but a chicane BPM energy measurement has an advantage given by the ratio of the R_{16} to the R_{56} terms. In the case of the first bunch compressor for the XFEL, this advantage in the required sensitivity of the monitor is a factor of six.

The arrival-time monitor and the chicane BPM can distinguish the energy jitter that results from injector timing jitter from the energy jitter caused by the acceleration RF phase and amplitude jitter. A bunch length monitor and the chicane BPM can distinguish the RF amplitude jitter from the RF phase jitter. BPMs before the chicane can be used to remove incoming orbit jitter from the chicane BPM's energy measurement.

The pickup transients for these energy measurements will be paired with the sub-picosecond pulses from the master laser oscillator (MLO) from the timing and synchronization system to sample the zero crossing of the beam transient through an electro-optical modulator (EOM). The beam arrival-time monitor installed in the tunnel, a perpendicularly mounted stripline to be installed in the dispersive section of the chicane in October 2006, and button-style pickups are analyzed with Microwave Studio simulations and compared to measured oscilloscope traces with regard to their suitability for the EOM phase measurement technique. The front-ends for beam transient pickups typically filter the transient down to 2 GHz or less and utilize the ringing or amplitude of the signal to get the desired beam information, but this EOM front-end works at 10 GHz or more and samples the zero-crossing, so attention must be paid to the transient shape.

EOM PHASE MEASUREMENT

Test Bench

To date, 30 fs resolution has been achieved with the EOM phase measurement and a limited but not combined output of the ring shaped arrival-time monitor pickup [2]. It utilizes a short optical pulse (< 1 ps) from a master laser oscillator that is locked to the 1.3 GHz reference of the machine. The light pulse travels via fiber optics through an electro-optical modulator (EOM) which encodes the amplitude information of an RF pulse into the laser pulse energy. Essentially, the laser pulse samples the beam transient. The modulated laser pulse is then detected with a 50 MHz bandwidth photo diode and read out by a 100 MHz, 12bit ADC that is clocked with the laser pulse at twice the repetition rate of the laser.

Since changes in the RF pulse arrival-time produce a change in laser intensity, the measurement is limited by the steepness of the RF signal slope and the precision of the laser amplitude detection. Slope changes can distort the measurement, so a feedback is used to maintain the measurement at the zero-crossing. The slope at the zero crossing for the 30 femtosecond resolution measurement was 250 mV/ps and the single-shot noise with which the laser pulse intensity was detected was 0.3%. Shot-noise of spontaneous emission from the laser is a suspected noise source, but as of yet there is no conclusion.

Future Applications

It is anticipated that for each pickup output, the transient signal will be split for a low-resolution (large range) phase measurement and a high-resolution (small range) phase measurement. A delay-line will use the low-resolution measurement to put the high-resolution measurement in range. The phase measurement is given by the position of this delay-line plus the fine

measurement given by the laser amplitude. This delay line must have sub-micrometer resolution over 10 cm and be adjusted between macro-pulses (10 Hz) in order to keep the system measuring the beam transient at the zero crossing, thereby reducing the systematic errors of slope variation.

The EOM setup will be standardized and duplicated several times for use with two or more beam arrival-time pickups and two large horizontal aperture chicane BPMs.

PICKUP DESIGN

Beam transient pickups for the EOM phase measurement must produce a steep slope for sampling of the zero-crossing with a picosecond-long laser pulse to give maximum resolution. They must also have a minimum of ringing so that the transient of a bunch that comes earlier is not detected. The bunch spacing will be 200 ns for the XFEL. A steep slope requires the high bandwidth and voltage that are produced by short bunches and pickups with a large area exposed to the beam. Bunches that are longer than ~25 ps (RMS) will have reduced resolution because the slope of the transient becomes less steep (e.g. 50% for 25 ps) for longer bunches. Minimal ringing can be achieved through tapering from the pickup to the feedthrough.

Position Monitor

The design utilizes a cylindrical pickup within a cylindrically shaped vacuum chamber channel that lies over and perpendicular to the path of the electron beam (see Fig. 1) [3]. It was originally proposed by [4]. When the electron beam travels beneath this pickup, short electrical pulses travel to opposite ends. The arrival-times of the pulses are then measured with the EOM technique and used to determine the position of the electron beam.

In Fig. 1, the perpendicularly mounted stripline is depicted in 3-D as well as in cross-section.

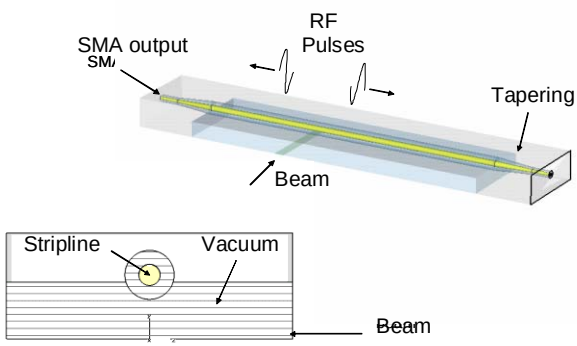

Figure 1: Perpendicularly-mounted stripline BPM pickup.

In the 3-D depiction, only the upper-half of the BPM is shown, since the lower-half is identical. The beam is represented by a thick line underneath the stripline. The central piece of the stripline is tapered on both ends from a 3 mm diameter to an SMA sized connector pin. The vacuum feedthroughs to SMA connectors are at the ends of the stripline.

Standard stripline designs do not have tapering from the pickup to the feedthrough, but instead have a larger radius pickup connected at a sharp angle to a smaller SMA connector sized feedthrough. The tapered design was chosen because in simulation it transmits 20% more signal amplitude and has 80% less ringing amplitude compared to the non-tapered design.

In a Microwave Studio simulation, a 50 GHz bandwidth (FWHM) Gaussian pulse was applied to the monopole mode of a waveguide port in order to simulate the electron beam. The output signals of the SMA connector ports were scaled according to a 1 nC electron bunch charge (Fig. 2).

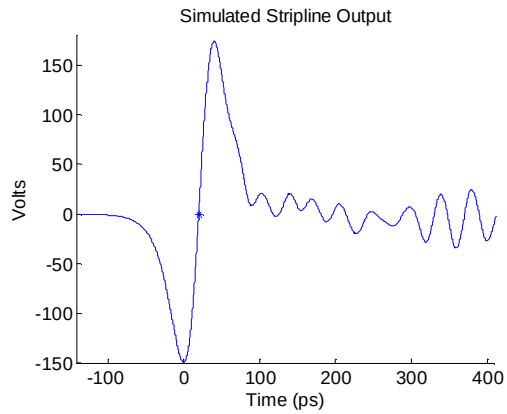

Figure 4: Simulated stripline output with a marker at the sampling location. The slope at the marker is 10 V/ps.

A similar simulation for an existing pickup also predicted such a high voltage, and when the pickup output was measured in the tunnel, the results matched the simulation within a few volts. The transient without a long cable is most interesting because the EOM front-end will be installed in the tunnel within a temperature stabilized enclosure, thus minimizing cable lengths and temperature dependent signal drifts.

The BPM's horizontal response is linear over the entire horizontal aperture and is insensitive to small changes in the beam shape. Vertical position changes and charge changes influence the amplitude of the signal but not the phase. The average of two outputs' phase measurements can also be used to measure the beam arrival-time, as long as the energy spread is constant. Alternatively, if the electron beam arrival-time is known, the energy spread can be measured through changes in the sum of the BPM outputs' phase measurements with a projected sensitivity of 1.5 fs/μm (Fig. 3), but this is only possible when the beam width is larger than the length.

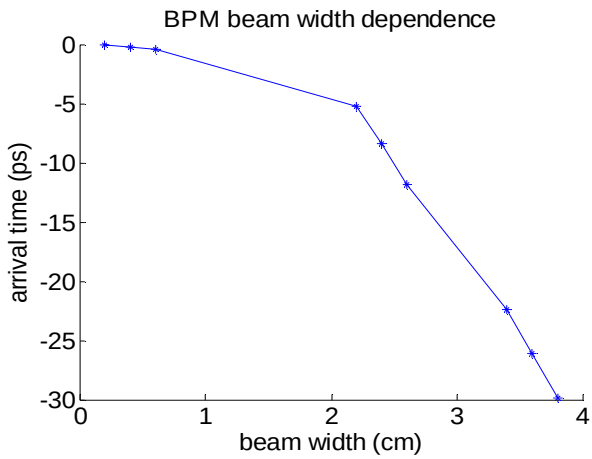

Figure 3: Energy spread measurement with BPM.

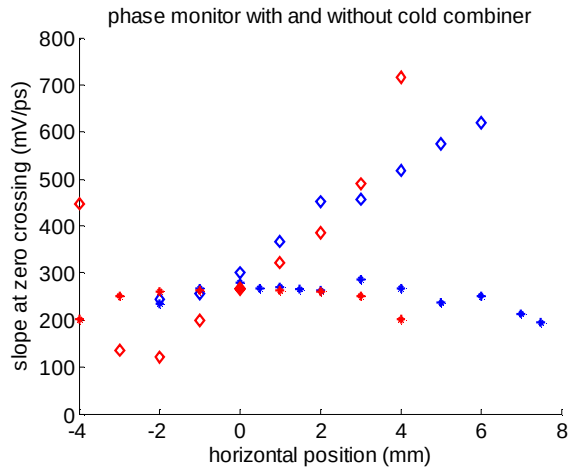

Figure 3: Slope at zero-crossing of arrival-time pickup with (star) and without (diamond) combiner. Simulation (red) and oscilloscope (blue) results are shown.

An important thing to note about pickup transients is that a measurement of the zero-crossing gives the RMS value of the beam position, in the case of the transverse stripline, or, in the case of the beam arrival-time monitor, it gives the RMS value of the arrival-time. This is different from measurements with devices that can measure the peak intensity of an electron distribution, such as synchrotron light monitors and electro-optical sampling. For non-linear, inhomogeneous compression schemes the RMS value and the peak value can differ, but for linear, homogeneous compression, they should be one and the same. About 30 fs difference between the peak and RMS values has been measured for the current compression scheme. The 3rd harmonic cavity will be installed in summer 2007 to linearize the compression.

Arrival-time Monitor

The arrival-time monitor pickup is a ring electrode in a thick flange with two SMA feedthrough sized pins attached to the ring in the horizontal plane. The frequency response of the ring shows a notch at 5 GHz which corresponds to a quarter-length of the ring circumference, implying that the beam does not couple strongly to the second harmonic of the ring. A position dependence of the output signals is therefore seen through a beat between the fundamental and third harmonic of the ring. This problem reflects the original intended use of the pickup in a lower-resolution RF down-mixing phase measurement that was not affected by the transient shape. For the EOM phase measurement the two outputs were combined to remove this effect (Fig. 3). The, so called, cold-combiner that was designed for a toroid-based charge measurement crossed the output pins of the SMA connectors in a circular void and terminated one of the arms of the cross with 50 Ohms [4].

The output from the monitor was measured with an 8 GHz bandwidth oscilloscope and simulated with a Gaussian 'beam' in Microwave Studio. Simulation and oscilloscope results agree well when cable, bandwidth, and combiner attenuation are taken into account (Figs. 3 and 4).

Button Pickups

Button pickups are installed in a few locations in the FLASH linac. Their output amplitude is proportional to the button size and distance from the beam and it can be comparable to that observed from the ring shaped pickup. Buttons can be more desirable than the ring electrode due to the lack of a notch in the frequency response that causes zero crossing changes with beam position changes. No detectable change of the transient zero crossing occurs for beam position changes. Buttons also produce a steeper, very linear slope with a lower peak-to-peak voltage.

Measurements of the beam transient with button pickups at FLASH were conducted with an 8 GHz bandwidth oscilloscope inside the tunnel and steep slopes of 1-2 V/ps were observed. The large changes in the slope due to beam position changes make the challenge of measuring on the zero crossing more critical. If the slope changes prove to be unworkable, a combiner could again be used.

The main problem with the pickups that were measured was that the signal was still ringing 200 ns after the transient with an amplitude that was 0.7% of the peak voltage. This would be a problem for the 200 ns XFEL bunch spacing because 10 fs resolution requires almost 10 times less ringing amplitude (Fig. 5).

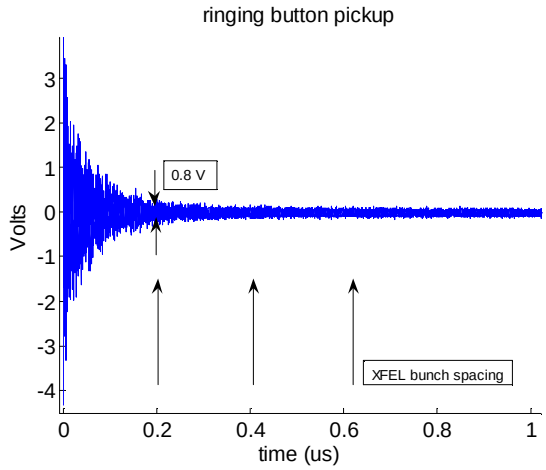

Figure 5: Ringing of button pickup with 120 Volt peak to peak transient. The ringing must be smaller than 10 mV by the time a new bunch comes for a 10 fs resolution phase measurement.

A few button pickup designs were simulated to look for ways to reduce or characterize the sources of the ringing. It was noted that for a large amplitude output, the pickup pin needed to be long or have a large button attached to it. For a long pin or a large cylindrical button, the transient amplitude was good, but the ratio between the transient amplitude and the ringing was bad. For a short pin without a button, there was practically no ringing, but the transient amplitude was insufficient (Fig. 6). More work needs to be done to understand and optimize the design.

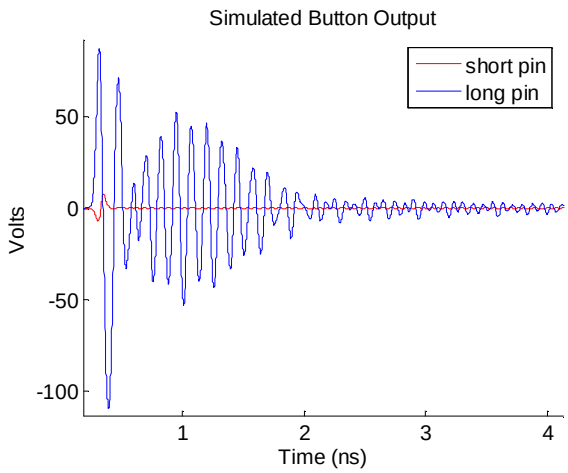

Figure 5: Button pickup with a long or short pickup pin. The long pin is more like a pickup in a cavity BPM.

EOM DAMAGE

The EOMs in the front-end are damaged by high voltages and care must be taken to preserve the steep slope of the transient while protecting the electronics from high voltage. Following a voltage surge through the arrival-time pickup caused by electron beam spray or incidence, the EOM's Lithium Niobate crystal was rendered opaque to the laser light. No limiter was in place and the damage occurred over less than a minute.

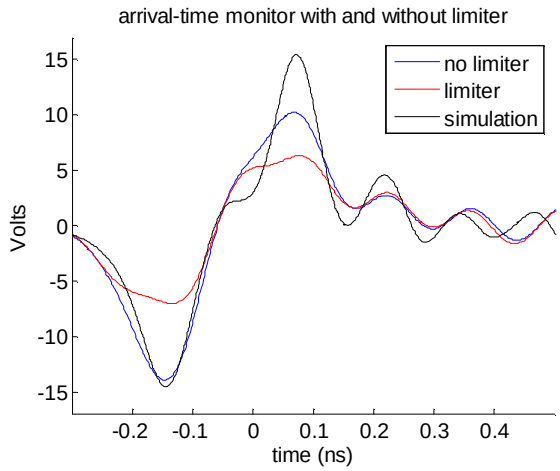

Figure 7: Limited and combined ring output from oscilloscope measurement and simulation including attenuation and dispersion from the cable, splitter, and combiner.

The Agilent N9355C 26.5 GHz bandwidth limiter that was in place throughout most tests of the EOM setup (Fig. 7) appeared to protect the EOM crystal from standard beam operation. With the limiter in place, even extreme off axis kicks from the transverse deflecting cavity upstream did not appear to damage the EOM. A conclusive study of the long-term effects of high voltage with the limiter has not, however, been done. The temperature dependent drifts of the limiter have also not been studied and are of interest even though the component will be used in a temperature controlled enclosure in the tunnel. It has also not bee used, long-term, in the tunnel, where 120 Volts peak to peak have been measured from the combined ring pickup.

SUMMARY

- EOM technique makes high resolution phase measurements possible.
- Optimal pickups for the EOM technique must maximize the slope and minimize ringing and transient distortions.
- EOMs must be protected from high voltage.

REFERENCES

[1] X-FEL Technical Design Report Sect. 4.8 2006.
[2] F. Loehl et. al., "Beam Arrival-time Monitor", EPAC'06, Edinburgh, June 2006.
[3] K. Hacker et. al., "BPM with Large Horizontal Aperture", EPAC'06, Edinburgh, June 2006.
[4] Manfred Wendt, personal communication.

DESIGN OF AN XUV FEL DRIVEN BY THE LASER-PLASMA ACCELERATOR AT THE LBNL LOASIS FACILITY*

C. B. Schroeder, W. M. Fawley, E. Esarey, W. P. Leemans
Lawrence Berkeley National Laboratory, Berkeley, CA 94720, USA

Abstract

We present a design for a compact FEL source of ultra-fast, high-peak flux, soft x-ray pulses employing a high-current, GeV-energy electron beam from the existing laser-plasma accelerator at the LBNL LOASIS laser facility. The proposed ultra-fast source would be intrinsically temporally synchronized to the drive laser pulse, enabling pump-probe studies in ultra-fast science with pulse lengths of tens of fs. Owing both to the high current ($\sim$10 kA) and reasonable charge/pulse ($\sim$0.1–0.5 nC) of the laser-plasma-accelerated electron beams, saturated output fluxes are potentially $10^{13} - 10^{14}$ photons/pulse. We examine devices based both on SASE and high-harmonic generated input seeds to give improved coherence and reduced undulator length, presenting both analytic scalings and numerical simulation results for expected FEL performance. A successful source would result in a new class of compact laser-driven FELs in which a conventional RF accelerator is replaced by a GeV-class laser-plasma accelerator whose active acceleration region is only a few cm in length.

INTRODUCTION

Recent advances in laser-plasma-based accelerators have demonstrated generation of low energy spread, $\sim$100 MeV electron beams [1]. These experiments used an ultra-intense $\sim 10^{19}$ W/cm^2 laser pulse focused on a gas jet, with typical length of a few millimeters, to generate plasma waves with accelerating fields on the order of 100 GV/m. By using a gas-filled discharge capillary for creating a plasma channel, the laser-plasma interaction length can be extended to a few centimeters, resulting in high-quality GeV electron beams [2]. In addition, the electron bunches emerging from a laser-plasma accelerator have naturally short durations (tens of fs) [3], and are intrinsically synchronized to the short-pulse laser driver, making such a source ideal for ultra-fast pump-probe applications. These laser-plasma accelerator experimental results [1, 2] open the possibility of a new class of compact, high-peak flux, x-ray free-electron laser (FEL) in which the conventional radio-frequency (RF) accelerator (10–100 m length) is replaced by a GeV-class laser-plasma accelerator (several cm length), in principle greatly reducing the size and cost of such light sources [4].

In this paper we discuss the design of an XUV FEL driven by the existing laser-plasma accelerator at the LOASIS laser facility at LBNL.

* Work supported by the U.S. Department of Energy under Contract No. DE-AC02-05CH11231.

LASER-PLASMA ACCELERATOR

The LOASIS Laboratory at LBNL presently produces ultra-short ($<$50 fs), relativistic electron bunches with high charge ($\gtrsim$100 pC/bunch) via a laser-plasma interaction. The bunches are generated by a laser wakefield accelerator (LWFA): radiation pressure from a short pulse, intense laser excites high-field plasma waves (wakefields) that accelerate electrons [5]. The LWFA at LBNL uses a 10 Hz, Ti:Sapphire laser system to focus ultra-short ($\sim$30 fs) laser pulses of relativistic intensity ($>10^{18}$ W/cm^2) into a plasma channel. GeV-energy electron beams have been demonstrated [2] using the LBNL 100 TW-class laser system and a gas-filled capillary discharge waveguide [6] for plasma channel production, which allows for low plasma densities ($\sim 10^{18}$ cm^{-3}) and long ($\sim$cm) laser-plasma interaction lengths. These LWFA-produced electron beams are high current ($\sim$10 kA) and ultra-short ($<$50 fs), properties which are attractive as an input beam for an FEL generating ultra-short x-rays.

In recent experiments using the plasma-channel-guided LWFA at LBNL, a 18-TW, 72-fs laser (25 μm focused spot size) is guided in capillary waveguide (which generates a plasma channel via a discharge in the hydrogen filled capillary), producing 0.5 GeV with 5% RMS *projected* relative energy spread, 2.0 mrad RMS divergence, and 50 pC of charge [2]. Experimental results using 2 J of laser energy have produced 1-nC electron beams at 0.5 GeV. At present, *slice* energy spread σ_γ measurements of the electron beam have not been performed, but simulation results [7] predict that the slice energy spread is an order of magnitude smaller than the projected value.

FEL DESIGN

We consider interaction of the LWFA-generated 0.5-GeV electron beam in a conventional magnetostatic undulator. For this study we will consider the LWFA electron beam and undulator parameters listed in Table 1; the latter correspond to the existing "THUNDER" device (see Ref. [8] for a detailed description), which provisionally will be transferred to LBNL from Boeing in late 2006. THUNDER contains 220 periods divided into ten 50-cm sections, each separated by a 4-cm diagnostic and steering space. The maximum RMS undulator strength parameter is $a_u = K/\sqrt{2} \simeq 1.31$ ($\approx$1.0 T peak magnetic field) which may be tapered section by section. Wiggle-plane

focusing is provided by a canted pole configuration with the expected matched beta-function $k_\beta^{-1} \approx 3.6\,\mathrm{m}$ for the peak field and 0.5-GeV beam. Conventional magnetic optics will transport the electron beam from the laser-plasma accelerator to the undulator. Note that there could be non-trivial beam transport issues concerning the required degree of achromaticity and preservation of pulse duration (*i.e.*, peak current). At 0.5 GeV, the beam is sufficiently "stiff" that pulse lengthening via drift will be small; for example, a 5% energy chirp results in less than 1 fs of pulse lengthening over a transport distance of a few meters.

Table 1: Electron Beam, Undulator and HHG Source Parameters

LWFA electron beam:	
Beam energy, γmc^2	0.5 GeV
Peak current, I	5 kA
Charge, Q	0.1 nC
Bunch duration (FWHM), τ_b	20 fs
Energy spread (RMS, slice), σ_γ/γ	0.25%
Normalized transverse emittance	1 mm mrad
Undulator:	
Undulator type	planar
Undulator period, λ_u	2.18 cm
Peak magnetic field	1.02 T
Undulator parameter (peak), K	1.85
Magnetic gap	4.8 mm
Beta-function, k_β^{-1}	3.6 m
HHG seed:	
HHG radiation wavelength	31 nm
Coherent HHG radiation power	15 MW
HHG pulse duration	20 fs

FEL PERFORMANCE

We consider two modes of FEL operation: self-amplified spontaneous emission (SASE) and seeding by a high-harmonic generation (HHG) source. Results from FLASH at DESY [9] and SSCS at Spring-8 [10], operating in the XUV wavelength regime, have confirmed the applicability of the basic SASE physics at XUV wavelengths. Existing laboratory HHG sources have demonstrated production of ultra-short (tens of fs) coherent soft x-ray (*e.g.*, 31 nm, 26th harmonic of a 0.8 μm drive laser) pulses with 0.3 μJ of energy (see, *e.g.*, Ref. [11]). HHG seeding has significant advantages over the simpler SASE mode of operation as it will provide improved temporal coherence and a much reduced power saturation length.

The resonant wavelength for the beam and undulator parameters of Table 1 is $\lambda = \lambda_u(1 + K^2/2)/(2\gamma^2) \simeq 31$ nm (40-eV photons), while the matched electron beam size in the undulator is 60 μm. The FEL parameter is $\rho \approx 5 \times 10^{-3}$ and the ideal 1D (*i.e.*, no emittance, energy spread, or diffraction effects) exponential power gain length is $L_{1D} = \lambda_u/(4\pi\sqrt{3}\rho) \simeq 0.19\,\mathrm{m}$. Including these non-ideal effects via the Xie gain length formula [12] can increase the gain length (L_g) 1.5–3 fold compared to the ideal 1D gain length, depending upon the assumed value of σ_γ. For the parameters of Table 1, the 3D gain length is $L_g \approx 0.3\,\mathrm{m}$. Figure 1 displays contours of gain length as a function of peak current I and relative energy spread σ_γ/γ. If one presumes empirically that the product $I\sigma_\gamma$ remains constant, one sees that it is best to operate at relatively large currents. However, consideration of slippage effects over the full THUNDER undulator ($\tau_s = \lambda N_u/c \approx 24$ fs) suggests that reducing the electron beam pulse duration τ_b below τ_s will have diminishing returns. Hence, we believe peak currents of $I \sim 2.5$–10 kA for a bunch charge of $Q \approx 100$ pC is the likely region of interest. Space charge effects will not degrade the FEL performance in this high-current regime provided $(\lambda_u/\lambda_p)^2/\gamma^3 \ll (2\rho)^2$ (*i.e.*, the characteristic wavelength of the space charge oscillation in the lab frame is much greater than the FEL gain length), where λ_p is the plasma wavelength of the electron beam. This condition is satisfied for the parameters of Table 1.

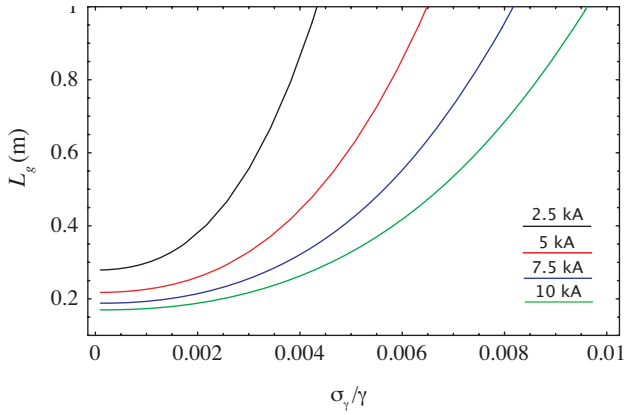

Figure 1: Exponential gain length as a function of incoherent energy spread for various electron beam currents as determined from the Xie [12] empirical fitting function.

We performed a series of time-independent GINGER [13] simulations to examine in detail the predicted FEL output from such a device, examining both the SASE and HHG-seeded cases. We adopted electron beam and undulator parameters as given in Table 1 with the exception that we also considered 7.5-kA peak current (150 pC charge) SASE and HHG-seeded cases and a 10-kA peak current (200 pC charge) SASE case, in addition to the nominal 5-kA HHG-seeded FEL. The simulations used a parabolic temporal profile for the electron beam; the details (*i.e.*, the sub-20 fs structure) of the actual experimental electron beam profile have not been measured. All the SASE results presented here are from one single simulation run for each of the two currents. Note that an ensemble average over many different runs, each with a different initial shot noise presentation would give smoother profiles for $P(t)$ and $P(\omega)$.

Figure 2 shows the maximum power for the HHG-seeded case (FEL in amplifier mode with 15 MW initial HHG

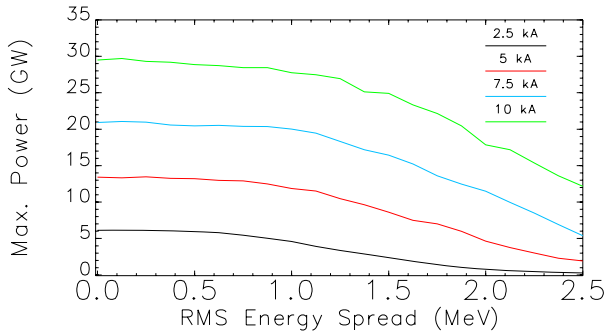

Figure 2: Predicted (GINGER calculations) maximum power in amplifier mode (with 15 MW initial HHG seed) over the THUNDER undulator (5 m) as a function of initial incoherent energy spread for various beam currents.

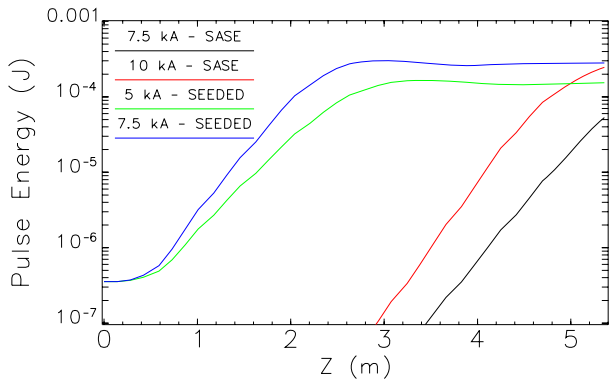

Figure 3: Predicted (GINGER calculations) radiation pulse energies as a function of undulator length z for both SASE and HHG-seeded cases.

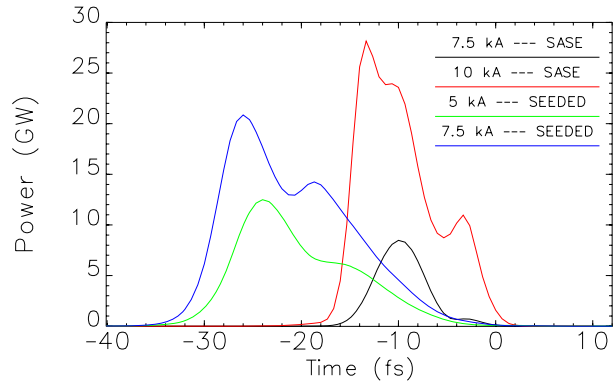

Figure 4: Predicted (GINGER calculations) output power temporal profiles for the cases associated with Fig. 3. The electron beam center is at $t = 0$.

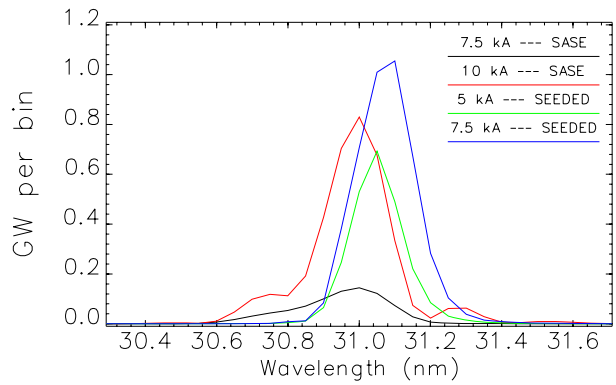

Figure 5: Predicted (GINGER calculations) output spectra at the 31-nm wavelength fundamental for the various SASE and seeded cases. Each bin is 64.6 meV wide while 1 GW is equivalent to 1.0×10^{13} photons.

seed) versus initial incoherent RMS energy spread for several beam currents. As the figure shows, for the nominal beam current (5 kA), greater than 10 GW of power can be achieved provided the RMS energy spread is $\lesssim$1.25 MeV ($\sigma_\gamma/\gamma \lesssim 0.25\%$).

Figure 3 displays time-integrated radiation pulse energies as a function of undulator length z; for reference, 1 μJ of energy corresponds to 1.5×10^{11} photons at 40 eV. The SASE results show a strong current dependence that is attributable to the sensitivity of L_g to current in this short-pulse regime with normalized σ_γ comparable to ρ. One sees in Fig. 3 that the 7.5-kA SASE case is about a gain length away from saturation, while the 10-kA SASE case reaches saturation. Given that we presumed idealized Gaussian transverse distributions with no offsets, tilts, *etc.*, additional current and charge might be required to reach full saturation with the assumed energy spread of 1.25 MeV. Earlier saturation in z might also be achieved by employing additional focusing (by adding focusing optics between the THUNDER undulator sections) thereby reducing the beta-function. Saturation is achieved in <3-m distance for the HHG-seeded cases.

Figure 4 shows output power temporal radiation profiles; one sees that the radiation pulse remains temporally close to the electron beam (whose center is at $t = 0$) when compared with slippage ($\tau_s \approx 24$ fs). Since the electron beam duration τ_b is only a few times the steady-state coherence length $c\tau_c \equiv \lambda/(4\pi\rho_{3D})$, the output profile is dominated by a single longitudinal mode, which results in spectral purity (at the price of reduced gain). This is apparent also in Fig 5 which shows quite clean power spectra for all cases except the 10-kA SASE run where there appear to be weak "sidebands" to either side of the central line; we expect ensemble average over many shots would likely show a simple Gaussian shape whose width would be slightly wider than this specific run.

For the HHG-seeded cases shown in Figs. 3, 4, and 5 we presumed an input seed with a 20-fs FWHM Gaussian temporal profile and peak power of 15 MW. The results indicate significantly improved performance of the HHG-seeded FEL, compared to the SASE cases (*e.g.*, compare the 7.5-kA cases). As seen in Fig. 3, saturation occurs before 3 m in the undulator, and peak powers exceeding 10 GW appear possible with FWHM durations ~15 fs (Fig. 4). Despite the early saturation, both HHG-seeded cases (5 kA and 7.5 kA) show essentially single mode spectral output with inverse normalized bandwidths (RMS) for the on-axis far field of $\omega/\Delta\omega \approx 500$ and autocorrelation times $\sim$ 12 fs. Predicted third harmonic power (due to

Table 2: FEL Performance

Radiation wavelength, λ	31 nm
Resonant photon energy	40 eV
FEL parameter, ρ	5×10^{-3}
3D Gain length	0.3 m
Slippage length	7.2 μm
Spontaneous radiation power	4 kW
Steady-state saturation power	12 GW
Photon/pulse (at saturation)	3×10^{13}
Peak brightness[a] (at saturation)	2×10^{16}
Saturation length (HHG-seeded, 5 kA)	2.4 m
Saturation length (SASE, 10 kA)	5 m

[a] photons/pulse/mm^2/mrad^2/0.1%BW

the nonlinear harmonic microbunching associated with the strong fundamental bunching) is about 0.4% and 0.8% of the fundamental for the 5-kA and 7.5-kA cases, respectively. The normalized spectral bandwidths for the third harmonic are narrower than the fundamental by slightly more than a factor of two; one expects less than the theoretical maximum of three due to the variation in temporal microbunching fraction [*i.e.*, the third-harmonic bunching parameter $b_3(t)$ has a narrower pulse shape than the fundamental $b_1(t)$]. Despite the much lower photon/pulse value of the third harmonic radiation, it may, nonetheless, be of interest for certain experiments.

DISCUSSION AND CONCLUSIONS

Recent advances in laser-plasma-based accelerator experiments [1, 2], and, in particular, the demonstration of high quality GeV electron beams [2], have enabled the possibility of a new class of compact laser-driven FELs in which the conventional RF accelerator is replaced by a cm-scale laser-plasma accelerator, greatly reducing the size and cost of the FEL. The natural short bunch length of the laser-plasma accelerator (tens of fs), and the intrinsic temporal synchronization between the short-pulse laser generating the electron beam and the FEL radiation, make the laser-driven FEL an ideal source for ultra-fast pump-probe applications. As discussed above, seeding of the FEL by an HHG source (generated from the same LWFA drive laser, and, therefore, temporally synchronized with the electron beam) has significant advantages over the simpler SASE mode of operation. The coherent amplification of the HHG source in the FEL leads to reduced undulator length and improved longitudinal coherence.

In this paper we have discussed the design of a XUV FEL employing the 0.5 GeV laser-plasma-generated electron beam produced at the LOASIS laser facility at LBNL. Table 2 shows the expected FEL performance employing a 31-nm HHG seed assuming the input parameters given in Table 1. Presuming a reasonably small incoherent energy spread of 1.25 MeV, a 15 MW HHG input seed provides sufficient initial power for the FEL to reach saturation in a few meters using the THUNDER undulator. For SASE, higher currents (*e.g.*, 10 kA) are needed to reach saturation in the 5 m undulator distance. The proposed HHG-seeded FEL, using the existing 0.5 GeV-LWFA at LBNL and the THUNDER undulator would capable of producing ultra-short ($\sim$15 fs) XUV (40 eV) pulses with $>10^{13}$ photons/pulse. The predicted third harmonic emission would be ~ 2.5 orders of magnitude less. A key beam parameter is the actual incoherent (*i.e.*, slice) energy spread. Values much above 1.25 MeV (0.25%) would require peak currents $\geq$ 10 kA for saturation to occur within the THUNDER undulator.

REFERENCES

[1] S. P. D. Mangles *et al.*, Nature 431 (2004) 535; C. G. R. Geddes *et al.*, *ibid.* 431 (2004) 538; J. Faure *et al.*, *ibid.* 431 (2004) 541.

[2] W. P. Leemans *et al.*, Nature Phys. 2 (2006) 696.

[3] J. van Tilborg *et al.*, Phys. Rev. Lett. 96 (2006) 014801.

[4] D. A. Jaroszynski *et al.*, Phil. Trans. R. Soc. A 364 (2006) 689.

[5] E. Esarey *et al.*, IEEE Trans. Plasma Sci. 24 (1996) 252.

[6] D. J. Spence and S. M. Hooker, Phys. Rev. E 63 (2001) 015401.

[7] C. G. R. Geddes *et al.*, Phys. Plasmas 12 (2005) 056709.

[8] K. E. Robinson, D. C. Quimby and J. M. Slater, IEEE J. Quantum Electron. QE-23, (1987) 1497.

[9] V. Ayvazyan *et al.*, Eur. Phys. J. D 37 (2006) 297.

[10] T. Shintake, "First Lasing at SCSS", Paper MOAAU04, these proceedings.

[11] E. Takahashi *et al.*, Phys. Rev. E 66 (2002) 021802(R).

[12] M. Xie, Nucl. Instrum. Methods Phys. Res. A445 (2000) 59.

[13] W. M. Fawley, LBNL Technical Report No. LBNL-49625 (2002); see also paper MOPPH073, these proceedings.

COMPARATIVE STUDY OF DIGITAL AND ANALOG SYNCHRONIZATION TECHNIQUES FOR LASERS IN ACCELERATORS

Axel Winter, Universität Hamburg, Hamburg, Germany,
Wojtek Jalmuzna, Warsaw University, Warsaw, Poland.

Abstract

Pulsed laser systems play an important role in present and future light sources. These lasers need to be synchronized very precisely to the accelerator RF. One approach is using an analog controller, which offers low-noise performance and has been demonstrated to achieve sub-50 fs stability. A digital controller based on a high-performance FPGA offers more flexibility, for instance the possibility to implement notch filters to evade the limitations by resonances of the piezo crystal used to adjust the laser cavity length. This paper presents results obtained with both approaches.

INTRODUCTION

A mode-locked laser serves as an ultra-stable laser master oscillator (LMO) for the proposed optical synchronization system for the European XFEL, which will be tested at the FEL facility FLASH [1]. Fiber lasers are well suited to realize such an optical master oscillator, because of the ease of coupling to the fiber distribution system, their excellent long-term stability, and the well-developed and mature components that are available at the optical communications wavelength of 1550 nm. A detailed description of the laser master oscillator can be found elsewhere [3]. Erbium-doped fiber lasers exhibit an extremely low phase noise at high offset frequencies making these lasers competitive with the best low-noise microwave oscillators around. Environmental effects like microphonics and vibrations cause excessive low-frequency phase noise, which can be significantly reduced by phase-locking the fiber laser to a ultra-low noise reference oscillator. Due to the extremely high upper state life time of erbium (1 ms), noise for frequencies above 1 kHz, due to for instance the pump laser, is suppressed.

SETUP OF THE LMO SYSTEM

A schematic of the setup of the LMO system is shown in Figure 1. Two fiber lasers run at a repetition rate of 54 MHz, which is the 24th subharmonic of the accelerator RF frequency of 1.3 GHz. Part of the laser pulse train is detected using a high-bandwidth photodiode. In frequency domain, the ultrashort pulses consist of harmonics of the repetition rate with equal energy and a spacing of the repetition frequency. Using a bandpass filter of appropriate

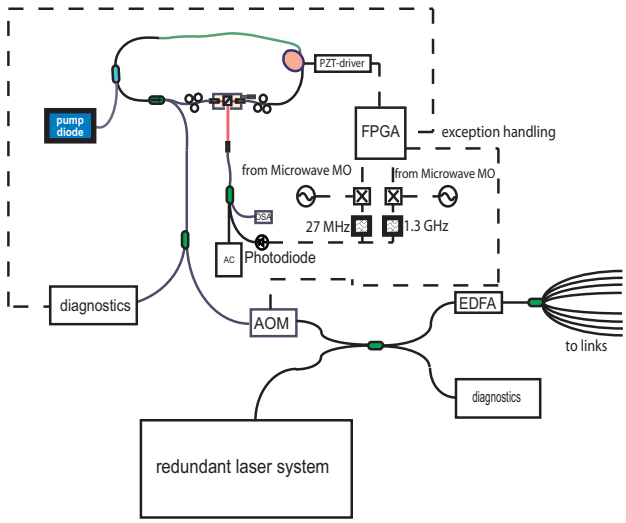

Figure 1: Schematic of the proposed FLASH LMO system.

bandwidth, the 23rd harmonic is selected and amplified to a level of around 5 dbm. The reference signal comes from a low phase noise RF oscillator at 1.3 GHz. Both signals are fed to a analog double-balanced diode ring mixer. The resulting error signal is now amplified by the loop filter, which is either a digital or analog proportional-integral controller. The proportional and integral part are in parallel, so the advantages of an integrator at low frequencies can be obtained without compromising the phase margin at higher frequencies. After being amplified to higher voltage levels to fit the range of piezo crystals, the signal is fed to a piezo-based fiber stretcher, onto which a substantial part of the optical fiber making up the laser cavity is wound. This adjusts the repetition rate of the LMO.

To achieve the required uptime of the LMO system, it is built redundant. Both lasers run continuously and should one of the lasers fail, the backup unit will take over. To enable an ultra-low residual jitter performance, the highest possible comparison frequency is selected which is 1.3 GHz in our case. This however leaves 24 possible positions where the PLL can catch. If the phase-lock of a failed unit is reestablished, it cannot be guaranteed that the laser pulse position is identical to the one of the backup laser which is now seeding the synchronization system. The solution to this problem is the introduction of a second PLL into the system. It runs at a comparison frequency which

is equal to the repetition rate of the LMO. This leaves only one zero-crossings where the PLL can catch per revolution of the laser pulse inside the cavity. The lower frequency PLL catches first and thus selects the phase of the laser pulse. Once the lock is established, the second PLL running at 1.3 GHz will take over.

There are two fundamental approaches which can be considered for the controller of this system. One choice is to use a conventional analog controller. It has been shown, that excellent synchronization performance can be achieved using such a system [4]. The limits of an analog controller lie in the flexibility it can offer. It is very difficult to realize more complex transfer functions than that of a simple PI controller. One aspect of where this is helpful is the implementation of a notch-filter to counteract the effects of the resonance of the piezo crystal in the fiber stretcher to obtain a higher gain in the PLL. Furthermore the switching of two PLL's is significantly easier using a digital controller which will be described in the next section.

DIGITAL CONTROLLER

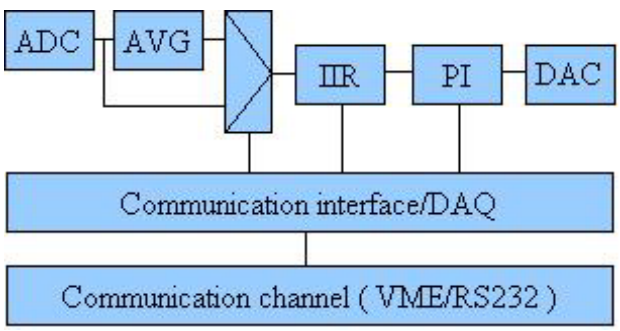

Figure 2: Schematic of the digital controller architecture.

The digital PI controller was implemented using an in-house developed controller board for the low-level RF control, called SIMCON 3.1[5]. The application utilizes the Virtex 2 Pro FPGA, located on the controller. The internal structure of the controller is shown on Figure 2. The digital controller offers the same functionality as its analog pendant, namely a parallel PI-controller with an optional second order infinite impulse response low-pass filter. The error signal from the double balanced mixer is sampled with a sampling frequency of 50 MHz. Then the data is decimated to provide one valid sample every 1 μs. Optionally averaging of 50 samples of the error signal can be used to reduce the ADC noise. The controller transfer function is applied to the resulting digital signal which is then converted with a DAC and fed to the piezo driver. For diagnostic purposes, a flexible data acquisition system was used. It saves 16 signals over 64 ms (64000 samples of each signal) to the external SRAM memory of the SIMCON controller. Two forms of communication were were implemented: a VME interface and an RS232 serial link.

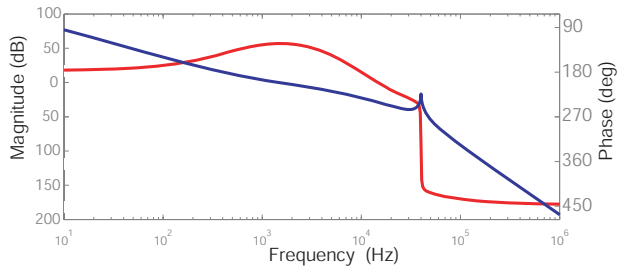

Figure 3: Bode Plot of the open loop transfer function (magnitude - blue, phase - red).

All the controller's parameters can be set with MATLAB software using a channel independent interface [6].

CONTROLLER TYPE AND SIMULATION

The feedback acts on the cavity length through the piezo which stretches the optical fiber. Care has to be taken not to disrupt the laser dynamics through introduced birefringence which occurs if the fiber is bent. The fiber stretcher is constructed such that bending is avoided and only the length of the fiber is varied by the piezo. Hence laser dynamics will to first order not be influenced and the laser will in terms of phase act as an integrator with the transfer function $G_l = \frac{k_l}{s}$, where k_l is the gain of the piezo inside the laser cavity (in our case is 0.35 $\frac{Hz}{V}$). Mechanical resonances of the piezo have to be considered (~ 40 kHz), which can be modeled by a harmonic oscillator. This yields a transfer function of $G_{piezo} = \frac{(2\cdot\pi\cdot f_{res})^2}{s^2+4\pi\gamma f_{res}\cdot s+(2\pi f_{res})^2}$ which ultimately limits the achievable gain of the PLL. A linear response is assumed for the phase detector around the locking point, which is valid for analog mixers around the zerocrossing, i.e. $\Delta\phi = 0, \pi, 2\pi \ldots$. The controller consists of a PI-controller ($G_{PI} = K_P + \frac{K_I}{s}$) and an optional low pass filter with a corner frequency of $f_{lp} = 10$ kHz.
The simulated open loop transfer function is shown in figure 3. The unity gain bandwidth is at 1 kHz which is in good agreement with the experimental results. It can be seen from Figure 5, that the phase noise spectra of the locked laser and reference oscillator start deviating just above 3 kHz which is the point of unity gain.

RESULTS

The first step to compare the performance of the two systems was to lock one LMO to a 1.3 GHz reference and evaluate the residual jitter. Figure 4 shows the power spectral density of the error signal when the system is locked for both analog and digital controller. The integration of these signal yields the respective residual jitter for either the analog or the digital controller. It amounts to 74 fs for the analog controller and 107 fs for the digital controller, both in a bandwidth from 1 Hz to 112 kHz. The difference in performance of the two controllers is almost entirely due

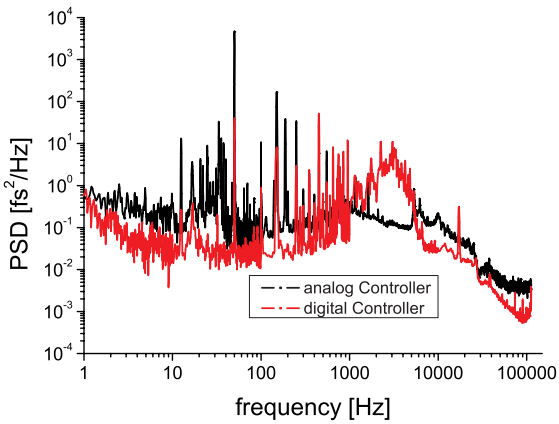

Figure 4: Power spectral density of the closed-loop error signal for both analog (black) and digital (red) controllers.

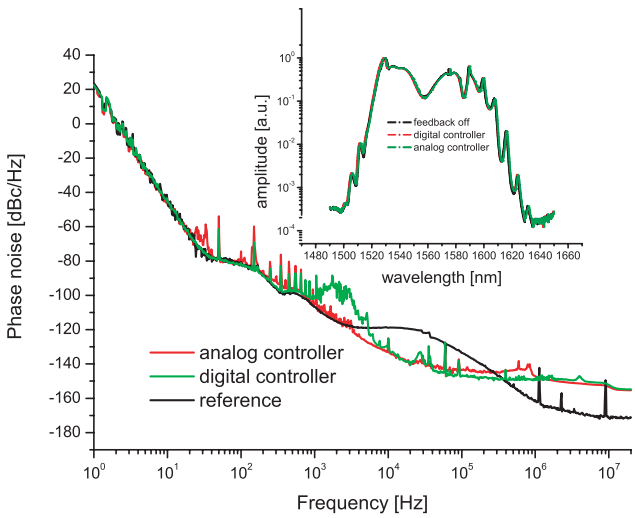

Figure 5: Phase noise for the locked fiber laser with both analog (red) and digital (green) controllers and the reference (black). Insert: Optical spectrum of the fiber laser without feedback (black), with digital controller (red) and analog controller (green).

to the PLL peaking of the digital controller. This is due to a slightly higher proportional gain which limits the phase margin of the system and leads to the power spectral density increase around 2 kHz. Reducing the proportional gain will yield a comparable result to the analog controller. It should be noted, that a significant part of the jitter in the digital controller is due to the 50 Hz line. The magnitude of this perturbation does not change with proportional and integral gain settings of the controller, making a crosstalk from the power supply to the DAC a likely candidate for the cause. It can possibly be improved in the next redesign of the digital controller board. An advantage of the digital controller is the possibility to average the ADC data. The sampling rate of the ADC is a lot higher than needed for the regulation (60 MHz), so an average was employed reducing the sampling rate to 1 MHz. This reduces the uncorrelated noise of the ADC by a factor of almost 8.

It is important, that the activated PLL does not increase the phase noise at higher offset frequencies. The measured phase noise with and without feedbacks is depicted in figure 5. There is no significant increase in the high frequency phase noise when locking with either system.

A further important issue is the possible change of the optical properties of the laser pulses due to the phase locking. The insert to Figure 5 shows the optical spectrum of the fiber laser without any feedback and with either controller. No significant change was observed for either feedback option.

CONCLUSION AND OUTLOOK

An optical master oscillator system requires a precise phase-lock of the fiber lasers to an external RF clock. This can be achieved by either using a digital or an analog controller. The measured performance for either system was comparable. No significant differences in the high frequency phase noise or the optical spectrum could be observed. This indicates that the more flexible approach using an FPGA as a digital loop filter is feasible without compromising the locking performance.

REFERENCES

[1] J. W. Kim et. al., “Large scale timing distribution and RF-synchronization for FEL facilities,” FEL Conference 2004, Trieste, Italy, 2004.

[2] J. Kim, F. X. Kärtner, and M. H. Perrott, “Femtosecond synchronization of radio frequency signals with optical pulse trains,” Opt. Lett. **29**, 2076-2078 (2004).

[3] A. Winter et. al., “Towards high-performance optical master oscillators for energy recovery linacs,” Nucl. Inst. Meth. A **557**, 299-304 (2006).

[4] A. Winter et. al., “Femtosecond Synchronisation of Ultrashort Pulse Lasers to a Microwave RF Clock,” Proceedings of the PAC 2005, Knoxville, TN.

[5] W. Giergusiewicz et. al., “Low latency control board for LLRF system SIMCON 3.1,” Proc. of SPIE Vol. 5948, (2005).

[6] J. Szewinski et. al., “Software for Development and Communication with FPGA Based Hardware”, TESLA Report 2005-16.

FIRST TOLERANCE STUDIES FOR THE 4GLS FEL SOURCES

D.J. Dunning, N.R. Thompson, J.A. Clarke and D.J. Scott, ASTeC, CCLRC Daresbury Laboratory
B.W.J. McNeil, SUPA, Department of Physics, University of Strathclyde, Glasgow, UK.

Abstract

The Conceptual Design Report for the 4th Generation Light Source (4GLS) at Daresbury Laboratory in the UK was published in Spring 2006 [1]. 4GLS features three distinct FEL designs, each operating in a different wavelength range: an externally seeded amplifier operating in the photon energy range 8-100eV (XUV-FEL); a regenerative amplifier FEL operating over 3-10eV (VUV-FEL); an FEL oscillator operating from 2.5-200μm (IR-FEL). Preliminary results of tolerance studies for the FEL designs are presented. In particular, the effects of the relative timing offset between the seed pulse of the XUV-FEL and the electron bunch, as well as the effects of electron bunch timing jitter in the VUV-FEL, are presented.

INTRODUCTION

4GLS is a 4th Generation Light Source proposed by CCLRC Daresbury Laboratory in the United Kingdom to meet the needs of the 'low photon energy' community. The 4GLS facility will combine energy recovery linac (ERL) and FEL technologies. This paper summarises the results of first tolerance studies for the XUV-FEL and the VUV-FEL. For the XUV-FEL, Genesis 1.3 [2] has been used to simulate the effects of a temporal offset between the electron bunch and the seed. For the VUV-FEL simulations, a one-dimensional, time-dependent FEL oscillator code which includes the effects of electron bunch arrival time jitter has been used.

The XUV-FEL design [3] consists of an undulator system directly seeded by a tuneable HHG laser source. It is capable of generating short, tuneable, high-brightness pulses of 8-100 eV photons with peak output powers of ~2-8 GW and typical FWHM pulse length < 50 fs. The FEL undulator consists of a lattice of undulator modules separated by beam focusing elements and diagnostics. The first eight undulator modules of the FEL will be planar, while the final five will be of APPLE-II design in order to produce variably elliptical polarised radiation.

The VUV-FEL [4] is a regenerative-amplifier-type FEL (RAFEL) [5] designed to deliver intense sub-ps pulses of tuneable coherent radiation in the photon energy range 3–10eV. A hole-outcoupled low-Q cavity using robust low reflectivity optics provides sufficient feedback to allow high gain type FEL saturation after only a few cavity round-trips. In its standard operating mode the VUV-FEL will generate temporally coherent photon beams with peak power ~500 MW and FWHM pulse lengths of ~170 fs. Cavity length adjustment may allow superradiant operation with enhanced peak powers of ~3 GW and FWHM pulse lengths of ~25 fs. These figures are the maximum values across the full wavelength range.

To enable variable polarisation, APPLE-II type undulator sections are employed throughout with a strong FODO focussing lattice and beam diagnostics distributed between sections.

XUV-FEL SIMULATIONS

100 eV Pulse Amplifier Lasing

A simulation of the XUV-FEL operating at 100 eV is performed, using the CDR parameters for the case of seed/electron bunch synchronism. The full set of planar and variable undulator modules are used with the APPLE-II undulators set to helical mode so that circularly polarised radiation is generated. Figure 1 shows the seed pulse of peak power P = 30kW and duration 30 fs FWHM. Also plotted is the electron beam current of peak current I_{pk} = 1.5kA and duration 626 fs (188μm) FWHM.

At the end of the FEL a peak saturated power of $P_{pk} \approx$ 2.4 GW is shown in Figure 2. A 'clean' central seeded region upon a noisier pedestal is seen. The pedestal is the pre-saturation SASE - as the shot noise power is only a few tens of watts, the seed power of 30 kW saturates first.

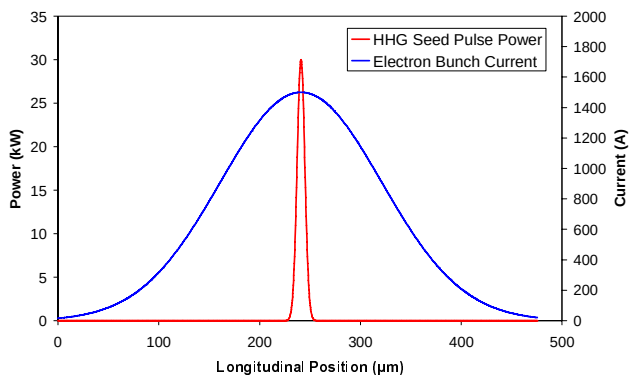

Figure 1. Input HHG seed power and electron bunch current as a function of longitudinal position.

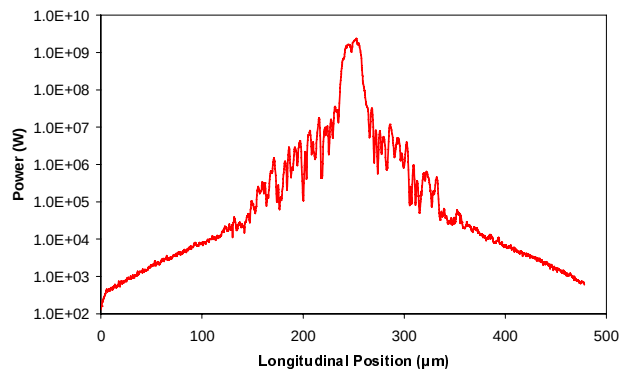

Figure 2. Radiation power at the exit of the XUV-FEL showing peak power $P_{pk} \approx$ 2.4 GW.

100eV Pulse Amplifier Lasing with Offset Seed

The above results are for synchronism between the peak HHG power and the peak of the electron bunch current. However, there may be an inherent noise associated with the arrival time of each bunch which results in a relative timing offset of magnitude Δt. Simulations have been carried out in which Δt is varied, as in Figure 3 (top). Also shown (bottom) is the radiation power at the end of the FEL, with the synchronous seed case for comparison. For seed offset of Δt = 100 fs, the peak power is reduced from 2.4 GW to 1.7 GW.

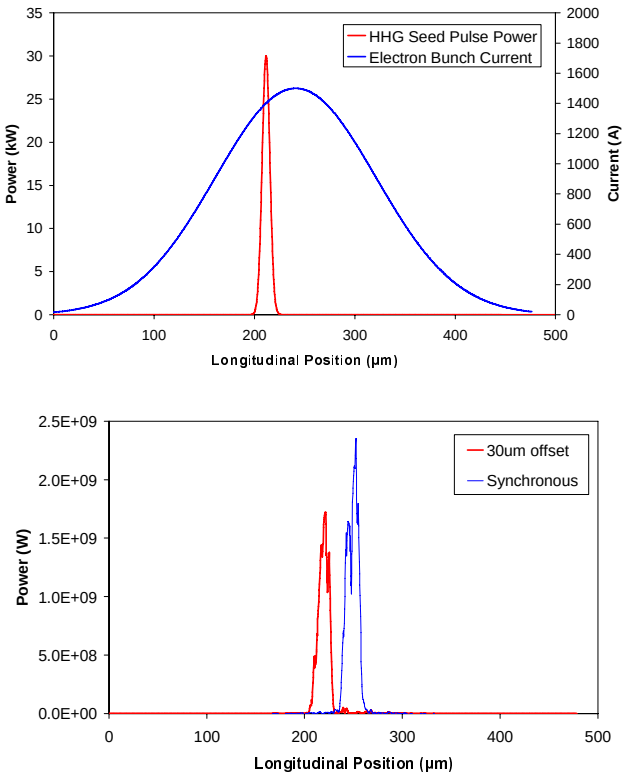

Figure 3. (Top) Seed offset by 100 fs (30 μm) behind the electron pulse and (bottom) radiation power at the end of the FEL for the offset case (red) and synchronous case (blue).

The offset, Δt, was varied between ± 250 fs and results of peak power against offset plotted in Figure 4. These results suggest that electron bunch offset should be limited to approximately ± 45 fs for peak output power to lie within 90% of the synchronous peak power P_{pk}.

From Figure 4, it is noted that the peak output power at the end of the FEL is higher for a negative Δt (seed pulse arriving behind the electron bunch) than for a positive offset of the same magnitude.

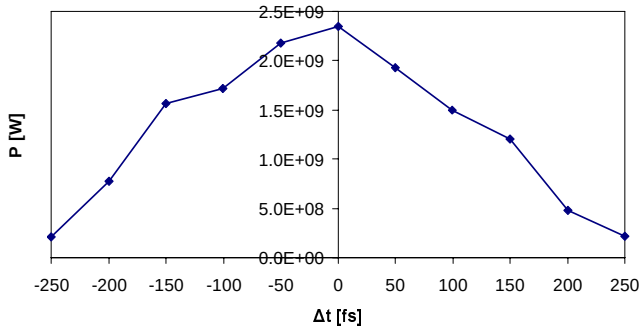

Figure 4. The effect of an offset Δt from electron/seed pulse synchronism upon the peak output power at the end of the FEL, for 100 eV operation.

Comparison with FEL design formulae

The Xie design formulae [6] have been used to estimate the effects of timing offset on the saturation power. This has been done by correlating the timing offset Δt with the beam current via the relation:

$$I(\Delta t) = I_{pk} \exp\left(-\frac{(\Delta t)^2}{2\sigma_e^2}\right).$$

This was carried out for the planar modules only. In Figure 5 these results are compared with the results of Genesis simulations which are seen to yield a slightly more stringent restriction on Δt.

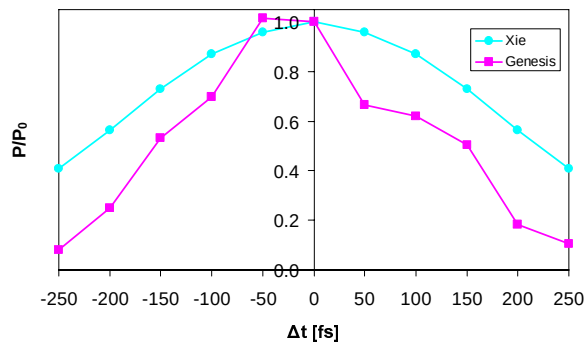

Figure 5. Simulations of the effect of an offset Δt from electron/seed pulse synchronism upon the peak power at the end of the FEL. The results are scaled with respect to their synchronous values at Δt = 0.

VUV-FEL SIMULATIONS

A one-dimensional, time-dependent FEL oscillator code (FELO [7]) has been used. The code includes the ability to model a temporal jitter in the electron bunch arrival into the FEL cavity (this effect is simulated by adding a jitter to the cavity length).

The simulated output power and pulse width variation with cavity length detuning is shown in Figure 6 for 10eV operation in planar mode. For cavity length detuning of 18μm, the pulse width is at a maximum. Typical pulse shape evolution with cavity pass number is shown in Figure 7. These simulations replicate start-up from shot-

noise, with the output pulse typically developing to saturation over 10-15 passes.

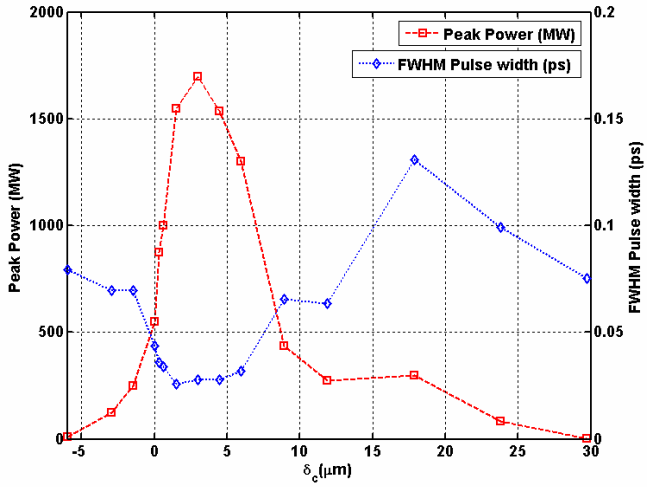

Figure 6. Plots of peak power and pulse width against cavity length detuning (δ_c) for simulations of the VUV-FEL operating at 10eV in planar mode.

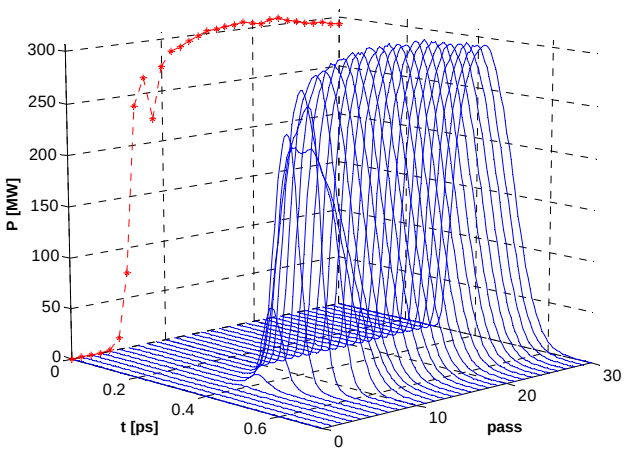

Figure 7. FELO simulation of the VUV-FEL at 10eV and cavity length detuning of 18μm with zero electron bunch arrival time jitter. The red points show the peak intensity of the pulse at each pass.

Simulations with Electron Bunch Time Jitter

In Figure 8 the variation of pulse shapes for different cavity pass numbers are plotted for three different electron bunch arrival time jitter values. Increasing jitter shows increasing variation of the pulse shape with pass number. The pulse shape remains approximately Gaussian for the cases where jitter $\leq \pm$ 80 fs. For the greater jitter value of ± 120 fs, the output pulse is seen to have a less stable shape.

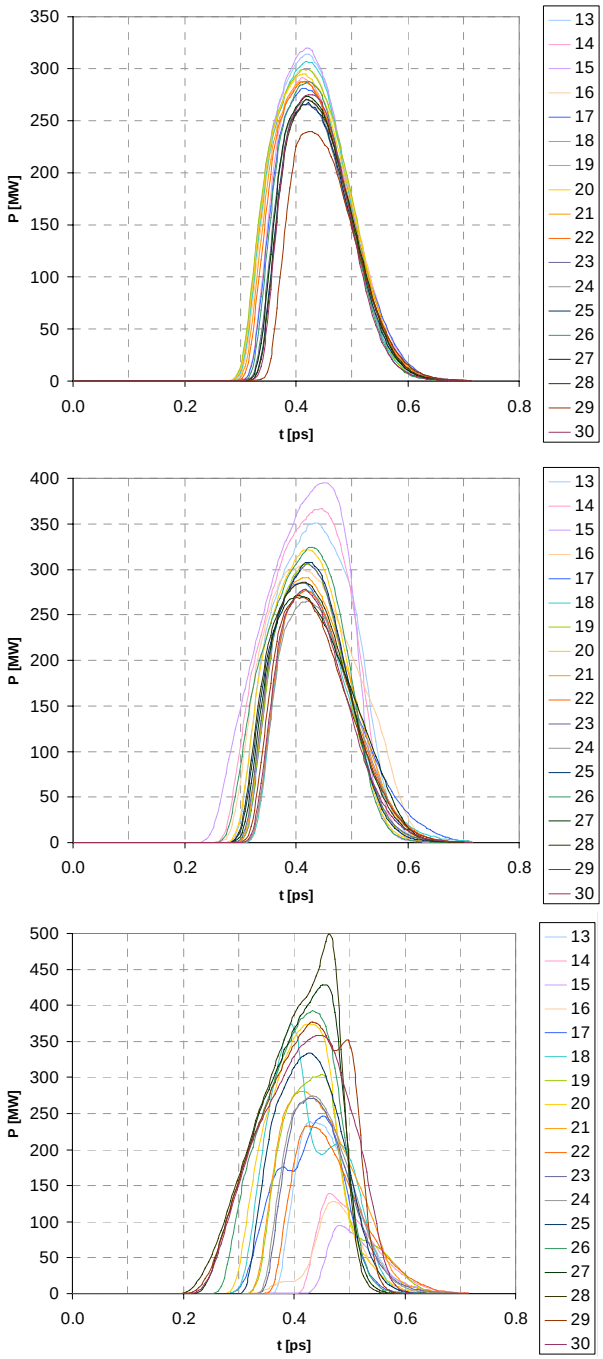

Figure 8. Variation of pulse shape with cavity pass number for electron bunch arrival time jitters of ± 40 fs (top), ± 80fs (middle) and ± 120 fs (bottom). Only passes 13 to 30 are shown. Increasing the temporal jitter shows increasing variation of the pulse shape.

Analysis of output power

Due to shot noise, repeat runs from the same input data yield slight variations in output. For jitter = 0, five runs were carried out and an average peak power was plotted as shown in Figure 9.

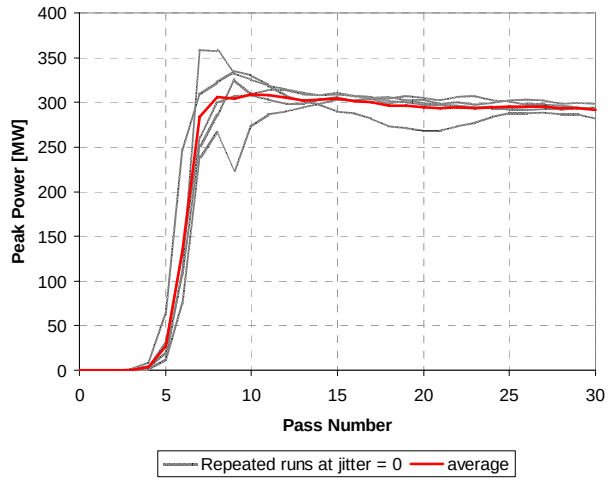

Figure 9. Peak power of pulse with pass for repeated runs at jitter = 0. The variation between different runs is due to the effect of shot noise only.

Repeated runs were carried out for different jitter values and the RMS variations from this average (at saturation) were calculated and are presented in Table 1.

Table 1. Variation of saturation power for different values of electron bunch arrival time jitter.

Jitter (fs)	Saturation Power (MW)
± 0.0	300 ± 2.5%
± 20	300 ± 4.1%
± 40	300 ± 6.0%
± 80	300 ± 8.0%
± 120	300 ± 18.8%

For the case of maximum jitter where the pulse shape remains approximately Gaussian (jitter = ± 80 fs), the output power at saturation is ~300MW ± 8%. The evolution of pulse shape with pass is shown for jitter of ± 80 fs in Figure 10.

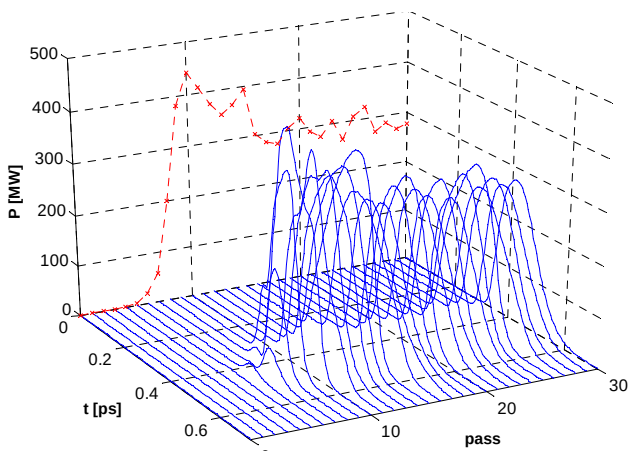

Figure 10. FELO simulation of the VUV-FEL at 10eV for cavity length detuning of 18μm with jitter of ±80 fs. The red points show the peak intensity of the pulse at each pass.

Short-pulse operation of the VUV-FEL

For a cavity length detuning of 1.5μm, operation is in superradiant mode, peak output power is near maximum and the pulse width is at a minimum (see Figure 6). Simulations using the FELO code show that at this cavity length detuning, it is possible for the side-spikes to develop into the peak with maximum power [8]. The evolution of the pulse where electron bunch arrival time jitter = ± 40 fs is shown in Figure 11.

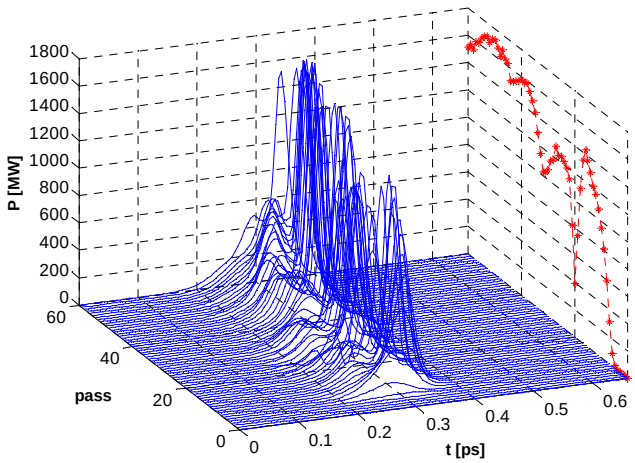

Figure 11. Pulse shape evolution for short-pulse operation with electron bunch arrival time jitter of ± 40 fs.

CONCLUSION

First tolerance studies for the 4GLS XUV-FEL and VUV-FEL have been carried out. For the XUV-FEL, increased offset between seed and electron pulse has been shown to decrease saturation power. For the VUV-FEL electron bunch arrival time jitter has been shown to result in increased instability in the shape of the output optical pulse. It has been concluded that for the XUV-FEL, temporal electron bunch offset should be limited to approximately ± 45 fs for output power to be within 90% of optimum. For the VUV-FEL, jitter should be limited to approximately ± 80 fs for approximate Gaussian output with peak power within ± 8 % of optimum.

REFERENCES

[1] 4GLS Conceptual Design Report, Council for the Central Laboratory of the Research Councils, UK (2006), available from: http://www.4gls.ac.uk/documents.htm#CDR
[2] S. Reiche, Nucl. Inst. Meth. Phys. Res. A, 429, 243, (1999)
[3] B.W.J. McNeil et al, 'The Conceptual Design of the 4GLS XUV-FEL', these proc.
[4] N.R. Thompson et al, 'A 3D Model of the 4GLS VUV-FEL Conceptual Design Including Improved Modelling of the Optical Feedback Cavity', these proc.
[5] B. W. J. McNeil, IEEE J. of Quantum Electron., 26, 1124 (1990)
[6] Ming Xie, Proc of 1995 Part. Accel. Conf., (1996) p183.
[7] B.W.J. McNeil et al, 'FELO, a one dimensional time-dependent FEL oscillator code', these proc.
[8] D.J. Dunning, 'Results of simulations varying the electron bunch arrival time jitter for the 4GLS VUV-FEL', Internal Report fgls-upcdr-rpt-0013, 2006.

PHASE NOISE COMPARISON OF SHORT PULSE LASER SYSTEMS

S. Zhang, S. Benson, J. Hansknecht, D. Hardy, G. Neil, and M. Shinn
TJNAF, Newport News, VA23606, USA.

Abstract

This paper describes phase noise measurements of several different laser systems that have completely different gain media and configurations including a multi-kW free-electron laser. We will focus on state-of-the-art short pulse lasers, especially drive lasers for photocathode injectors. Phase noise comparison of the FEL drive laser, electron beam and FEL laser output also will be presented.

INTRODUCTION

The stability of the drive laser plays a very important role in the performance of photogun-based accelerators and free-electron lasers (FELs). With the increasing demand for shorter wavelengths (including XFEL) and shorter pulse duration (sub-50 fs), phase noise and timing jitter issues are drawing more and more attention. Over the past decade, short pulse lasers technology has seen dramatic advancement due to the rapid development of solid-state materials and high power semiconductor laser diodes. Some state-of-the-art femtosecond lasers have shown superior performance in terms of both amplitude and phase stability. These lasers provide a unique opportunity to overcome challenges in the development of the next generation accelerator light sources.

The photogun drive laser is used to extract the electron beam that provides the gain medium for numerous FELs worldwide. Drive laser instabilities will limit high power FEL operation. Of all the instabilities associated with short pulse high repetition rate lasers, timing jitter appears to be the most important and most difficult to control. In this paper, we present phase noise and timing jitter measurements of several different lasers that can be used to drive photoguns. We believe a comparison of these lasers provides valuable information about the pros and cons of each system in their specific applications.

METHOD AND SETUP

Phase noise is a drive laser quantity that is often discussed. Phase noise is a direct representation of the timing jitter of a mode-locked laser system. Timing jitter can be quantified by measuring the phase noise. There are two basic methods widely used to measure the phase noise (and timing jitter) of optical pulse trains; a) the Phase Detector Technique (PDT) and, b) the Power Spectral Density Technique (PSDT) [1]. The PSDT provides better precision and was used for all of the measurements described below. The measurement requires a fast photodiode and a spectrum analyzer. In this case the timing jitter of the mode-locked or gain-switched optical pulse train is determined by measuring the phase noise spectral density.

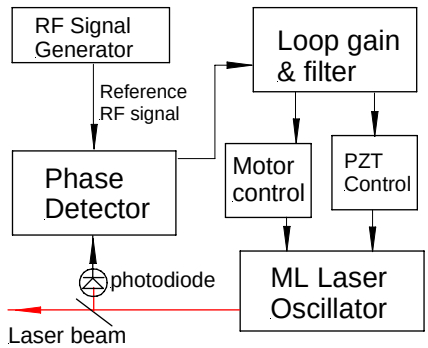

Fig.1. Schematic of a generic phase locking system.

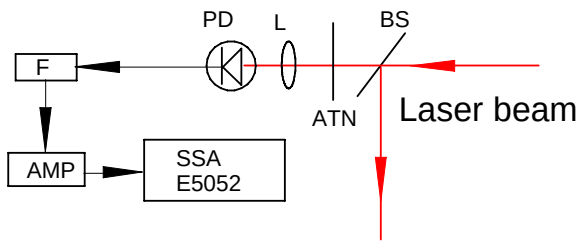

Fig.2. Schematic of the timing jitter measurement setup. BS, beam splitter. ATN, attenuator. L, lens. PD, photo-diode. F, RF filter. AMP, RF amplifier.

Fig.1 shows the basic principle of a generic phase-locking system used by many lasers. The laser phase error is detected and corrected by the RF feedback loop. The measurement setup is shown in Fig.2. The detectors used in the experiment were fast photo-diodes with bandwidth between 2 to 20 GHz. A Signal Source Analyzer (SSA, Agilent E5052A) was used for the phase noise and timing jitter data acquisition. This instrument presents faster speed and better precision compared with some other spectrum analyzers. The phase noise is usually measured at 1.497 GHz, the 20th harmonic of the 74.85 MHz laser pulse frequency in order to minimize the laser amplitude noise. The 1.497GHz signal was filtered out using an RF filter and amplified by a low noise RF amplifier before being fed into the SSA. For higher repetition rates, it was sometimes difficult to perform the measurement at the 20th harmonic. The noise added to the measurement from the RF amplifiers and filters was determined to be negligible.

DIFFERENT LASER SYSTEMS

Flash-lamp-pumped Active Mode-locked Laser

The first laser system tested was a frequency doubled CW mode-locked Nd:YLF laser pumped by flash lamps

(Coherent Antares laser made in early 90's). It has served as the drive laser for the photocathode injector at the JLab FEL facility for more than ten years. We studied the stability of this laser in the past [2]. Here we will focus on the phase noise characteristics. The laser has a folded cavity design and intracavity acousto-optic modulator (AOM) for mode-locking. The AOM can be driven with RF supplied by the laser power supply (internal RF) or with RF from the accelerator (external RF). The laser phase is monitored and controlled by the RF control module. A fast photodiode detects the optical pulses signal from the infrared light leaking through the high reflector. Unlike most other laser systems that use active laser cavity length adjustment to minimize the phase noise, the RF to the acoustic mode-locker on this laser is tuned to compensate the phase change. To detect the phase error and complete the phase loop, the 20th harmonic of the laser frequency (74.85 MHz) is filtered out, amplified and sent to an RF control module.

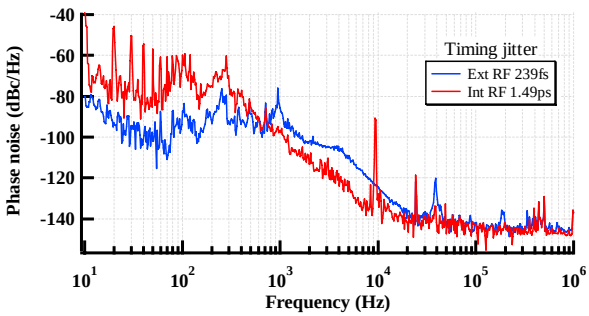

(a)

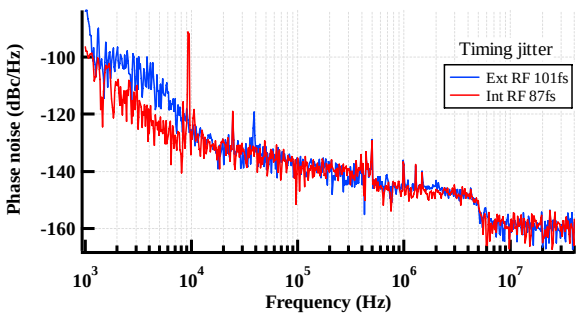

(b)

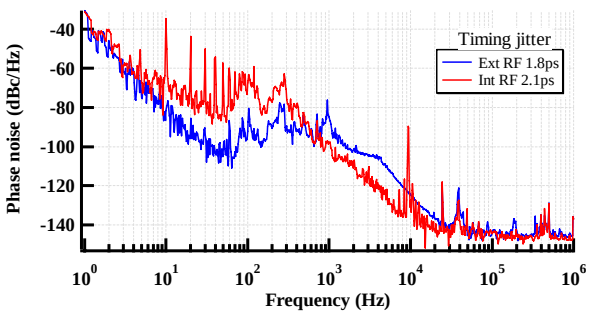

(c)

Fig.3. Phase noise spectral density plots of flash-lamped pumped Antares Nd:YLF laser at different offset frequency. (a)10 Hz~1 MHz. (b)1 kHz~40 MHz, and (c)1 Hz~1 MHz. As explained in the text, Ext and Int refer to external RF and internal RF, respectively.

From the results shown in Fig.3, the excellent performance is primarily due to the fact that the laser cavity was designed to have a particularly stable length: all components are mounted to an Invar rod to reduce temperature dependence. In addition, the phase control loop associated with the RF reference signal is very important, as can be seen by comparing the two RF sources, internal and external. The laser performs significantly better when using RF supplied by the accelerator, with timing jitter five times less compared to that obtained with RF supplied by the power supply. Most of the phase noise comes from the lower frequency band below a few hundred Hz. There are always more noises below 10Hz and the feedback loop does little to reduce them (Fig.3(c)). Usually a flash-lamp pumped laser tends to have noticeably higher phase noise than those pumped by diodes. But this measurement clearly indicates that the phase noise of a flash-lamp pumped system can be controlled to a very low level.

SESAM Mode-locked Laser

The SESAM mode-locked Nd:YVO_4 laser serves as the master oscillator, providing seed pulses for a multi-stage amplifier that provides over 50 W average power at 1.064 um and 25 W at 532 nm. This Maser-Oscillator-Power-Amplifier (MOPA) system will be used to drive a 100mA photoinjector. A detailed system description can be found in another paper [3]. The passively mode-locked Nd:YVO_4 laser is diode-pumped and produces over 500 mW at 1064 nm with 74.85 MHz pulse repetition rate and 25 ps pulses (Time-Bandwidth Product, GE100). It uses a semiconductor saturable-absorber mirror (SESAM) to initiate mode-locking. The laser cavity length is actively stabilized and the phase of the optical pulse train can be locked to an external RF reference signal.

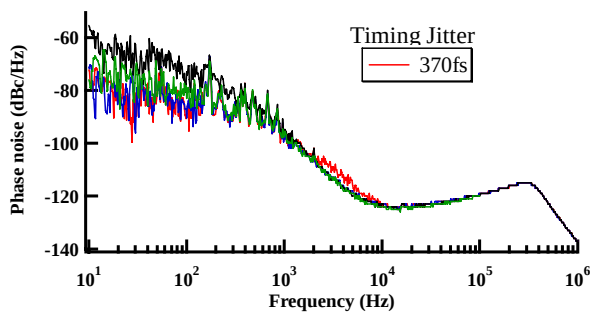

Fig.4. GE100 laser phase noise spectral density plots obtained over few minute time period. Mostly, the timing jitter is less than 400 fs but occasionally larger values are obtained.

When the laser cavity is optimized, it runs very well with timing jitter around 300 fs. Random fluctuations can be seen from time to time, which may be caused by environmental disturbances. Phase noise spectral density plots for this laser are shown in Figure 4. These plots were obtained over a few minutes and mostly timing jitter

is less than 400 fs but occasionally values surge over 500fs. We also intentionally unlocked the cavity length feedback loop. This has a profound affect, with timing jitter increasing to 4 ps (Fig.5). The overall timing jitter also depends highly on the laser cavity alignment and optimization. Timing jitter values can exceed 1ps in the case of poorly aligned cavity.

Phase noise measurements were also made downstream of the power amplifier section of this laser system. The Master oscillator (MO) seed light from the passively mode-locked Nd:YVO_4 laser passes through four Nd:YVO_4 amplifiers, with total output power at 1.064 um greater than 50 W. As expected, the diode-pumped amplifiers do not add much noise to the system (Fig.6). The added noises are most likely from the environment.

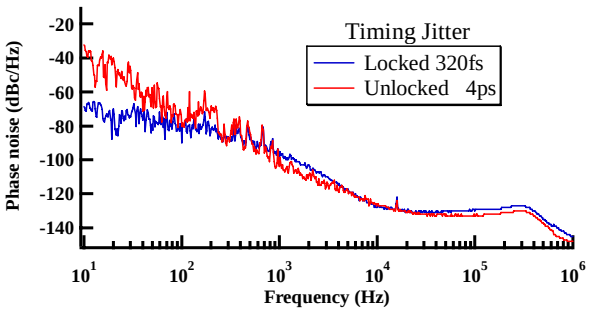

Fig.5. GE100 laser phase noise spectral density plots with laser cavity length feedback loop open and closed.

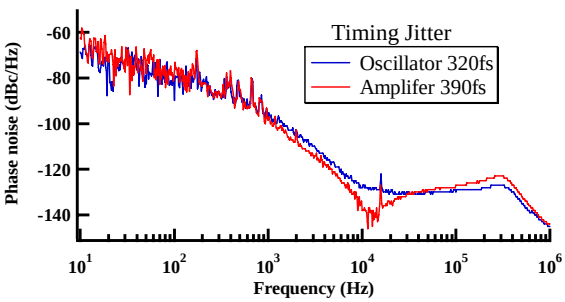

Fig.6. MOPA laser: GE100 laser and multistage power amplifier. Phase noise spectral density plots comparing MO and MOPA signals.

KLM Ti:sapphire Laser

Widely used fs-pulse Ti:sapphire lasers rely on self-mode-locking (KLM), a passive technique that relies on Kerr lensing within the Ti-sapphire crystal and a gain aperture effect that provides more gain for shorter pulses. These lasers are broadly tunable and can generate extremely short pulses because of the exceptionally broad gain bandwidth of the lasing medium.

Phase noise measurements were carried out using a Spectra Physics Kerr mode-locked Ti:sapphire laser (Tsunami, 100fs, 1W at 800nm) pumped by a frequency-doubled and diode pumped Nd:YVO_4 laser (Millennia, CW 10 W at 532 nm). The laser has a phase-locking unit that detects and corrects the laser phase by adjusting the cavity length with a pico-motor and PZT attached to the high reflector (HR) end mirror. A photodiode picks up the laser signal from a beam splitter and the phase is compared to the reference RF to create a phase error signal. The pulse repetition rate is 74.85 MHz, the same as for measurements with other laser systems. Phase noise spectral density plots are shown in Fig.7 for measurements at two different times. As with the SESAM mode-locked laser, phase noise was closely related to cavity alignment and optimization. The timing jitter was observed to jump up and down, but mostly values stay within a range between 200 and 400 fs (Fig. 8). When the feedback loop was turned OFF, timing jitter values surge upward by a factor of ten.

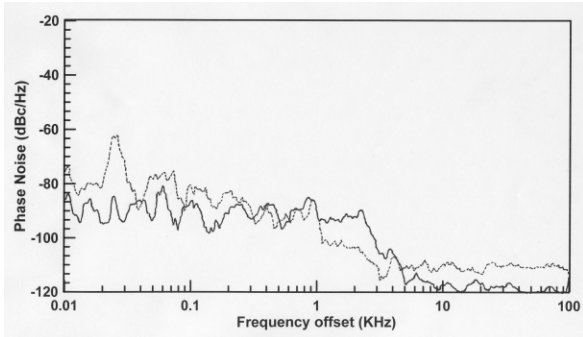

Fig.7. Tsunami laser phase noise spectral density plots at two different times.

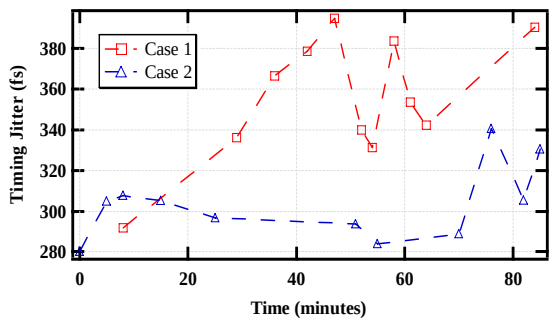

Fig.8. Tsunami laser. Timing jitter versus time. The square and the triangle stand for the data taken at two separate times.

The Tsunami laser uses an intracavity AOM to initiate and stabilize mode-locking. We investigated the influence of the AOM on timing jitter by making phase noise measurements with the AOM on and off. Measurements indicate that the AOM does not introduce additional instability. This confirms that AOM only helps to start the KLM process and set the fundamental frequency for the feedback loop to lock the cavity length. Once the cavity is optimized and loop is closed, AOM is not needed.

Gain-switched Diode Laser

Gain-switched diode lasers have a number of advantages over mode-locked lasers such as simplicity,

good stability and low cost. They also provide a wide range of pulse repetition rates independent of laser cavity length. While there is no doubt about amplitude stability, we did an investigation of phase noise performance. The laser system consists of a sub-milli-watt gain-switched InGaAs laser at 1.56 um and a fiber amplifier to boost the power to a level suitable for the measurement. Gain-switching at frequencies below 100 MHz produces longer optical pulses with tails, so a step-recovery diode (SRD) was used to improve the temporal profiles of the laser pulses. There is no cavity length adjustment for this system.

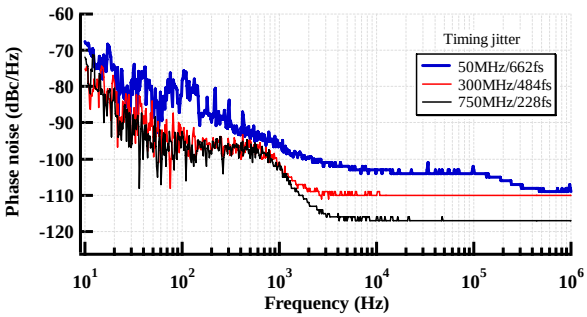

Fig.9. Phase noise spectral density plot and timing jitters of gain-switched diode laser and fiber amplifier at three different repetition rates.

Phase noise spectral density plots for the gain-switched diode laser at three pulse repetition rates are shown in Figure 9. The timing jitter increases inversely with the pulse frequency. At the lowest frequency 50 MHz, the timing jitter is larger than lasers mentioned previously. Note for the 50 MHz case, the phase noise at frequencies > 1 kHz is noticeably higher. The RF generator used here is the same as the previous lasers. The possible contribution to the noise is poor impedance matching at the SRD and driving circuits. The signal from the SRD shows different waveforms as the RF frequency and power changes. It requires a good balance between these parameters including the near threshold DC bias. Further work is needed to improve the performance before they can be adapted into the FELs.

High Power FEL

So far we have only talked about lasers with cavity lengths of 1.5 m or shorter. We also studied the phase noise properties of the high power JLab FEL, with output power over 1kW (pulse-width about 200 fs and wavelength 1.6 um). The FEL laser cavity is composed of two mirrors separated by 32 m. The mirrors sit inside vacuum chambers: the laser cavity length can be tuned over 1 cm with resolution sub-micron but there is no active cavity length control.

Phase noise measurements were made under different FEL operating conditions. Results are presented in Fig.10, together with the noise spectrum of the Antares drive laser. The FEL timing jitter is on the same level as other lasers, even operating without cavity length stabilization. The phase noise rises dramatically at all off-set frequencies, especially at the higher bands. If we look at the electron bunches in the wiggler region, they actually appear to be very quiet (timing jitter less than 60 fs). The phase noise actually gets suppressed compared to the drive laser. The two curves in Fig.10 for FEL were taken at two different times to show the random fluctuation during the same machine operation. In view of the exceptionally long FEL laser cavity length, the FEL output is remarkably stable. However, this measurement suggests that the FEL phase noise could be reduced using feedback mentioned in earlier sections.

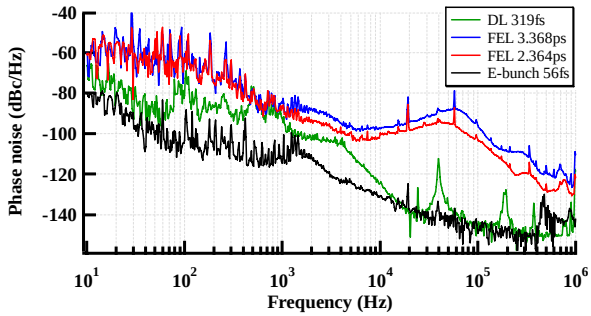

Fig.10. FEL phase noise spectra. The carrier frequency is 1.49 GHz. Laser frequency is 9.37 MHz. Lasing wavelength is 1.6 um. DL, drive laser. E-bunch, electron bunches.

SUMMARY

We have presented the phase noise characteristics of several lasers that can be used to drive GaAs photoguns. The performance of each laser depends on the phase locking mechanism. Active cavity length adjustment remarkably reduces the phase noise. The overall phase noise appears unrelated to the optical pulse length. The flash-lamp-pumped system does not necessarily have to be noisier. Diode-pumped amplifiers present very minor noise addition to the seed pulse. The gain-switched laser is good for repetition rates over 100 MHz but needs improvement to be used at sub-hundred MHz band.

ACKNOWLEDGMENT

The authors would like to thank M. Poelker for reviewing and extensive editing. This work is supported by the Office of Naval Research, the Joint Technology Office, the Commonwealth of Virginia, the Air Force Research Laboratory, and by DOE Contract DE-AC05-84ER40150.

REFERENCES

[1] D. von der Linde, Appl. Phys. B **39**,201 (1986).
[2] S. V. Benson, M. Shinn, 16th IEEE Particle Accelerator Conference (PAC 95) and International Conference on High-energy Accelerators (IUPAP), Dallas, Texas, May 1995. PAC, vol. 2(1052-1054).
[3] S. Zhang, S. Benson, et al., in Proceedings of the 27th International FEL Conference, SLAC, CA, August, 2005, pp. 351-354.

A MECHANICAL SHUTTER TO SELECT SINGLE BUNCH TRAINS AT THE FLASH FACILITY AT DESY

Martin Bräuer, now at SIEMENS Medical Solutions, 91052 Erlangen, Germany
Ulrich Hahn, and Sven Toleikis, Deutsches Elektronen-Synchrotron DESY, 22603 Hamburg, Germany.

Abstract

A fast mechanical shutter to select single photon bunch trains of the free electron laser FLASH is described. FLASH is installed at the Deutsches Elektronen-Synchrotron DESY in Hamburg and is based on superconducting linear accelerator technology. The accelerator provides bunch-trains with a repetition rate between 5 and 10 Hz. This time interval of down to 100 ms makes it possible to use a mechanical shutter system to select single bunch-trains for sample excitation.

A programmable logic controller (PLC) is used to steer a servo system based on an electronically commutated (EC) low-voltage motor. To select a bunch-train, the motor is started at the time when one train passes the station. During the following 100 ms, the cylinder is turned by 180°, leading to a movement of the shutter by 48 mm to the fully open position, thus allowing the passage of the following bunch-train. During the next 100 ms the rotation is continued to the 360° position, thus blocking the next bunch-train by pushing the shutter back to the fully closed position.

INTRODUCTION

Since 2005 the first FEL user facility for soft X-ray coherent light experiments FLASH is in operation at DESY [1]. The facility consists of a superconducting accelerator in combination with a 30 m long undulator producing highly intense (~GW) and extremely short (~10 fs) photon pulses. The superconducting linear accelerator creates and accelerates bunch-trains with up to 7200 bunches within 800 µs (at 10 Hz).

The experimental hall of the user facility is located approximately 30 m behind the last dipole magnet which separates the electron and the photon beam. The photon beam transport system delivers the FEL radiation under ultra high vacuum conditions to the five different end stations, which can be used alternatively.

The photon pulses energies are generated with an average energy of 10 µJ. Solid state samples irradiated in normal incidence are easily destroyed when the photons are focused to a spot size of ~20 µm. To study such damage processes it is important for FEL users to control the irradiation process. The 5 to 10 Hz repetition rate of the bunch trains allows the use of a mechanical shutter to select single bunch trains for sample irradiation.

The fast mechanical shutter is installed in the shared part of the first three beamlines. Figure 1 shows the shutter installed in the beamline system.

The fast shutter consists of a glassy carbon [2] shutter blade with a thickness of 4 mm. The blade motion is generated by a special linear drive developed for fast wire scanners for FEL electron beam diagnostics [3, 4]. The shutter covers the beam aperture of 20 mm.

In this paper, we report on the technical layout of the fast shutter, and first experimental results of a time-resolved damage and ablation measurement are presented.

TECHNICAL LAYOUT

Mechanical Set Up

Figure 2 shows the mechanical design of the fast shutter. The central part is the glassy carbon blade connected to the linear drive unit. Glassy carbon is chosen because of its low density of 1.6 g/cm^3 combined with high mechanical stability, good reflectivity in the spectral

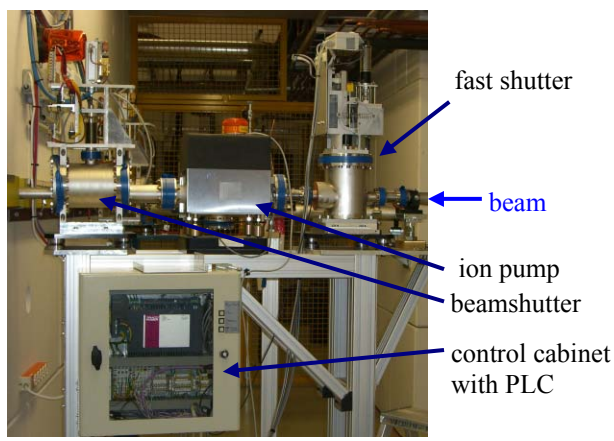

Figure 1: The fast shutter installed in the FLASH beam-line system

range of the FEL and the thermal robustness of carbon. The fast shutter has to be operated under ultra high vacuum conditions. As linear vacuum feed through a welded bellow is used. An incremental length gauge for position detection is connected to the linear drive. The essential features of the fast shutter are the stroke of 48 mm combined with a maximum shutter speed of 1 m/s in the linear velocity range of 24 mm. The speed is needed to shorten the opening and closing times into the ms range. The movement of the shutter blade is based on a slot winding cylinder (see Fig. 2 + 3) transforming the rotation of the servo motor into a linear motion [3, 4].

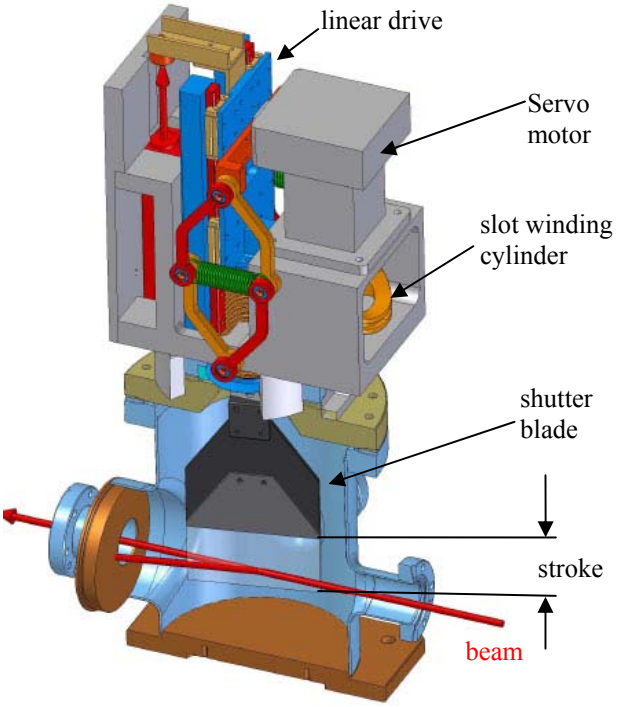

Figure 2: The mechanical layout of the fast shutter.

The cam of the slot winding cylinder uses the transfer function of a Bestehorn-sinuide (see Fig. 3):

$$S = s_0 \left[\omega t - (1/2\pi)\sin(2\pi\omega t)\right]$$
$$0 \le \omega t \le 1$$

where S is the stroke of the run up and down phase, s_0 the maximal stroke of 24 mm and ωt the normalized transmission angle. The region ωt = 0 until ωt = 1/2 represents the run up phase while ωt = 1/2 until ωt = 1 describes the run down phase. The speed and acceleration is given by

$$S' = s_0\,\omega\left[1 - \cos(2\pi\omega t)\right]$$

$$S'' = s_0\,\omega^2\,2\pi\sin(2\pi\omega t)$$
$$0 \le \omega t \le 1$$

At a stroke of 0mm the shutter is totally closed. The start up range between 0 and 12 mm accelerates the shutter to the opening speed of 0,36m/sec. Between 12 and 36 mm the shutter blade releases the photon beam aperture of 20mm. In the range from 36 to 48 mm the shutter blade changes the moving direction. When the blade transfers this range the photon bunch train can pass the shutter. Figure 3 shows the stroke, speed and acceleration of the blade during one turn, assuming that the shaft is rotating with constant speed.

The motor is connected to the slot-winding cylinder with a gearing-ratio of 15:1. For 10Hz operation, rotation speeds of the shaft of 450rpm and accelerations of 6750rpm/s are needed.

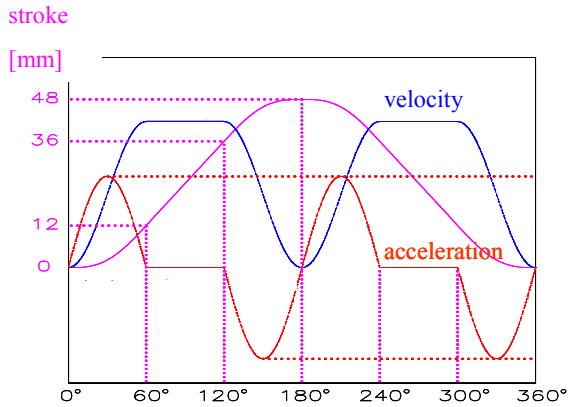

Figure 3: The transfer functions of the slot winding cylinder (Bestehorn sinuide).

Electronic Set Up

The electrical setup of the fast shutter is shown in Fig. 4. The central part is a PLC-controller with IO-Modules [5]. The controller acts on a servo system via a field-bus (CAN open [6]). The servo system consists of the servo controller/amplifier, the motor and two integrated feedback systems [7]. These components alone allow the

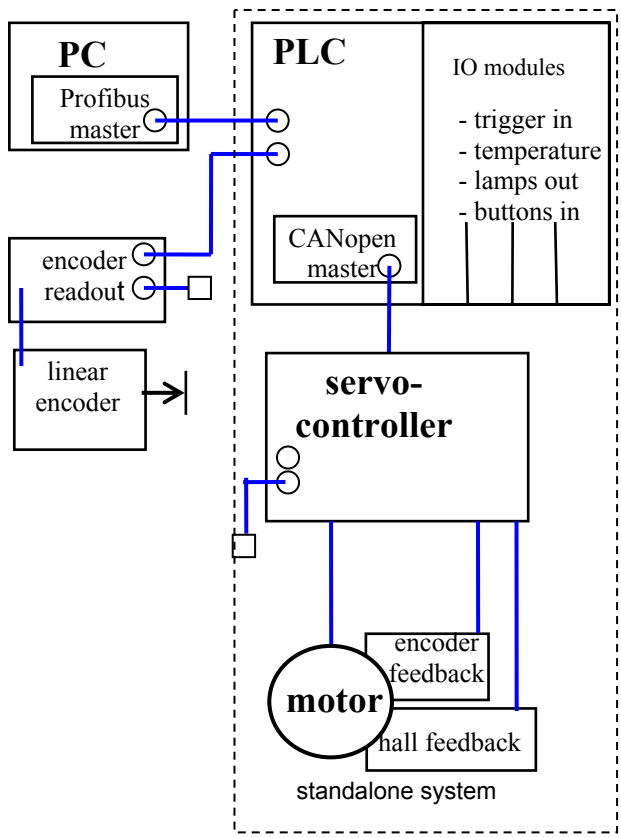

Figure 4: Layout of the electronic set-up.

operation of the fast shutter. In addition a PC, housing a Profibus-master card, was connected to the PLC. With the PC the parameterization and programming can be performed. Furthermore a Profibus-interface to read out the linear gauge is connected to the Profibus line. The linear gauge can only be accessed by the PC and be used for an independent feedback of the shutter position for diagnostics. All major components are described in the following.

All electronics parts are standard components from the general automation market. They are contained in a standard compartment, as shown in Fig. 1. Most space is occupied by the power supplies and the terminals to route the various electrical signals.

The PLC controller is programmed and parameterised from an external PC, but operating in a standalone mode afterwards. The cycle time for the SPS program was chosen to run at 3ms, which means that the whole program is running within 3ms under any condition while sampling inputs and setting outputs. The controller acts as a client on the Profibus and reactions to Profibus commands can be programmed. This allows the control from a master PLC in our case running on the PC. The connection to the beamline interlock system can be routed via this bus.

For the CANopen subsystem, the controller acts as a master. The CANopen subsystem is running with the cycle time of the PLC, allowing a fast reaction on events. Inputs and outputs are provided by appropriate IO-modules. Most important inputs are the user commands, generated by output cards of the FLASH experimental control system, by button states and the bunch signal. The bunch signal, derived from the FLASH-timing, announces the arrival of a photon bunch. This signal is stretched to 10 ms to be detected by the PLC.

The servo system uses an electronic commutated motor. While the controller/amplifier is connected to 48V DC, the motor is provided with two sinusoidal voltages to its static coils. The rotating permanent magnet follows the generated current. In contrast to a stepper-motor, the rotor position is measured by hall-elements to determine the absolute position of the magnet. To reach the ultimate precision for the velocity and position-control loops, an additional incremental encoder is attached to the motor shaft.

The controller firmware enables the user to work with the three nested servo-loops (current, velocity and position) in an easy way. Parameters are determined by an automatic tool and are stored together with further application specific data on the internal flash memory. Due to the CANopen standard, devices of various vendors can be mixed and exchanged, securing investments over the coming years.

In contrast to stepper-motors, the servo system can use a much larger speed-torque parameter space due to the active regulation.

Operational Principle

The shutter can be opened and closed by electrical signals, i.e. generated by buttons. The user commands are routed by the FLASH-control system via output-cards to 5V inputs of the PLC. Status information is transferred from the PLC via 5V terminals and input-cards to the user.

The states of the shutter are: ‘open’, ‘close’, ‘single shot’, ‘synchronized shot’ and ‘home’.

The home-mode is needed to orient the controller after power up. The shutter is driven to the open position until a precision switch mounted close to the open position is triggered.

All other movements are always executed synchronously to the bunch-trains.

After an open or close signal, the next following bunch-train-clock is waited for. When the PLC detects a rising edge on the bunch-signal, the motor is commanded to perform a 180ºrotation of the cylinder. This is thus changing the state of the shutter from closed to open or vice-versa.

After the detection of a single-shot signal, the procedure is executed in the same way but initiating a 360º turn of the cylinder. The timing of the later procedure is depicted in Fig. 5.

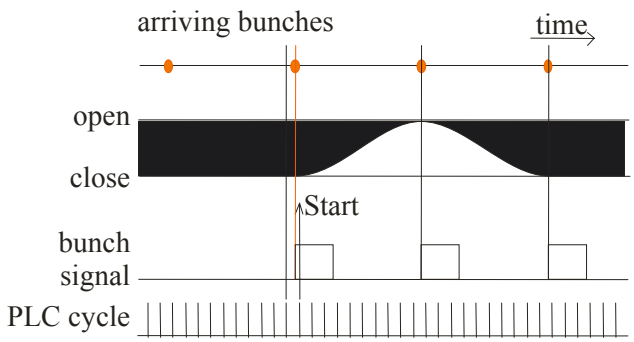

Figure 5: Timing scheme of the synchronous movements.

The synchronised move allows to trigger a single shot on an external 5V or TTL signal, generated by users instrumentation.

Since the bunch-train-frequency of FLASH can be adjusted by the operation-crew, a part of the PLC-software evaluates the frequency of detected bunch signals and automatically adjusts the appropriate velocity and acceleration values.

FIRST EXPERIMENTS

One of the first experiments that used the fast mechanical shutter at FLASH was a time-resolved damage and ablation measurement [8]. The aim of this experiment was to study the interaction of ultra short FEL pulses in the VUV wavelength range with solid state surfaces at moderate irradiation intensities ($I=10^{11}$-10^{14}

W/cm²). The irradiation with ultra short VUV pulses permits a high degree of electronic excitation but essentially without any non-linearity. In addition, the increased absorption depth for some materials helps to minimize the influence of transport effects, e.g., carrier diffusion and heat conduction. Therefore, ultra short VUV pulses allow the preparation of rather well defined excitation conditions in relatively large sample volumes as compared to femto second optical pulses. To directly study the dynamics of ultra fast VUV-induced phase transitions and ablation, time-resolved measurements of the optical reflectivity have been performed in a VUV pump - optical probe configuration. The VUV pulse (λ=32 nm) is used for sample excitation and a delayed visible probe pulse (λ=532 nm) serves as illumination in an optical microscope. This allows to follow the reflectivity evolution of the VUV irradiated surfaces with both temporal and spatial resolution.

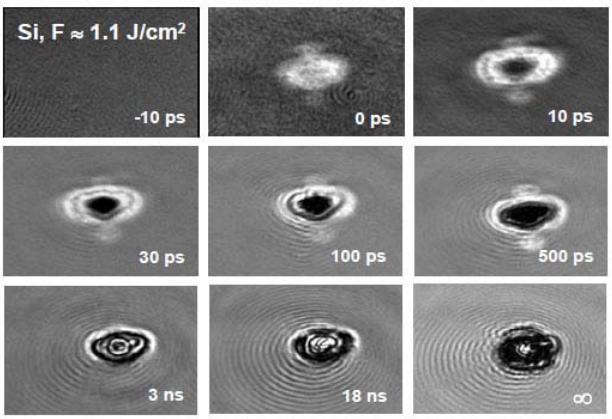

Figure 6: Surface of Si-wafer after irradiation with a <50 fs FLASH pulse (λ=32 nm) with a fluence of 1 J/cm². Frame size is 120 x 80 µm².

During the measurement FLASH was running in a single bunch operating mode having only one bunch in the bunch train. The mechanical shutter allowed the irradiation of the samples with exactly one ultra short VUV pulse of known intensity which was measured with a gas monitor detector system [9]. After irradiation the sample is moved to a new non-irradiated position and the reflectivity of the optical pulse is then measured at a different time delay. Figure 6 shows a sequence of time-resolved snapshots obtained on a bulk silicon sample for an excitation fluence of ~ 1 J/cm².

At early time (10 ps) a pronounced increase of the reflectivity is observed which can be attributed to a solid-liquid phase transition of the material. Although the temporal resolution was limited by the probe pulse duration to about 10 ps, this transition is most likely of electronic nature and occurs on sub-ps time-scales. Already after 10 ps the decrease of the reflectivity in the centre of the spot, where the fluence is highest, marks the onset of ablation. However, even after 18 ns ablation has not come to an end and the irradiated surface has not reached its final state.

The main goal of this measurement at FLASH was to establish the experimental technique and to obtain a first overview of the dynamics of the induced processes. Further measurements with enhanced temporal (<100 fs) and spatial resolution will follow which would provide a more detailed picture of these processes. Compared with femto second optical excitation distinct differences in the material response have been observed that are attributed to the larger absorption depths of the VUV radiation and the absence of non-linearity.

CONCLUSIONS

On the basis of existing wire scanner technology a fast shutter has been implemented in the FLASH beamline system. This allows users to choose single bunch trains with a repetition frequency of up to 10 Hz. First experimental results show the benefit of the fast shutter.

REFERENCES

[1] V. Ayvazyan, et al., "First operation of a Free-Electron Laser generating GW power radiation at 32 nm wavelength", Eur. Phys. J. D 37, (2006), 297-303

[2] Glassy carbon, SIGRADUR®, HTW Hochtemperatur Werkstoffe GmbH, Germany

[3] H. J. Grabosch, U. Hahn, M. Sachwitz, and H. Thom, „Wire Scanner System for Undulator Section of VUV-FEL at DESY", MEDSI-2004, Proceedings – 04 – 31

[4] P. Castro, U. Hahn, O. Hensler, S. Karstensen, M. Sachwitz and H. Thom, "Wire scanner system for FLASH at DESY", to be published

[5] BX3100 controller, Beckhoff Industrie Elektronik, 33415 Verl, Germany.

[6] CANopen, Controller Area Network, Can in Automation group, 91058 Erlangen, Germany.

[7] Servo system with EPOS 70/10 controller/amplifier and an EC-max 40 Motor with HEDL5540 Encoder by Maxon Motor AG, CH-6072, Switzerland.

[8] K. Sokolowski-Tinten, et al., to be published

[9] A.A. Sorokin, et. al., "Gas-Monitor Detector for Intense and Pulsed VUV/EUV Free-Electron Laser Radiation", Proceedings SRI2003, San Francisco, AIP Conf. Proc.705 (2004), 557-560

COMMISSIONING OF A NEW EMITTANCE MEASUREMENT SYSTEM AT PITZ*

L. Staykov†, J. Bähr, H.J. Grabosch, S. Khodyachykh, S. Korepanov, M. Krasilnikov, A. Oppelt, B. Petrosyan, F. Stephan, DESY, 15738 Zeuthen, Germany
J. Rönsch, Hamburg University, 22761 Hamburg, Germany
G. Asova, I. Tsakov, INRNE-BAS, 1407 Sofia, Bulgaria.

Abstract

The goal of the Photo Injector Test facility in Zeuthen (PITZ) is to test and optimize high brightness electron sources suitable for FEL's like FLASH and the European XFEL. Such sources are characterized by very low emittance at high bunch charge. The new Emittance Measurement SYstem (EMSY) described in this paper uses YAG and OTR screens to measure the transverse beam size and thin Tungsten slits to measure the divergence of the beam. It has been optimized to measure emittance for a beam of 1 nC in the energy range 5 - 30 MeV. The new EMSY was developed in a cooperation between DESY Zeuthen and the Institute for Nuclear Research and Nuclear Energy (INRNE) in Sofia. It was installed in the PITZ tunnel in the beginning of June and commissioning and first measurements are ongoing.

INTRODUCTION

The Photo Injector Test Facility at DESY in Zeuthen (PITZ) was built to test and to optimize electron sources which are capable for SASE FEL operation. The main PITZ components are a photocathode laser, an L-band RF gun and space charge compensating solenoids. A major upgrade on the existing PITZ facility is ongoing since last year [1]. This upgrade includes the installation of an additional accelerating RF booster cavity and various diagnostics elements. The laser system was also upgraded in the last year, by improving the transverse imaging to the photo cathode (see [2]) and the overall stability. One of the goals of the facility is to study and optimize the conditions for the conservation of emittance compensated electron beam with short pulse length and low transverse emittance [3, 4]. Extended optimization of the photoinjector with ASTRA [5] showed that transverse emittance smaller than 1 mm.mrad at 1 nC charge can be reached (fig. 1). The Emittance Measurement SYstem used at PITZ was upgraded for better performance in the extended momentum range [6]. Three of such devices were produced by the HITECH HEP Group in INRNE Sofia and are already installed in the PITZ tunnel. In this paper details about the new EMSY as well as first experience from the commissioning are given.

* This work has partly been supported by the European Community, Contract Number RII3-CT-2004-506008, and by the 'Impuls- und Vernetzungsfonds' of the Helmholtz Association, contract number VH-FZ-005.

† Presenting author, e-mail: lazaraza@ifh.de

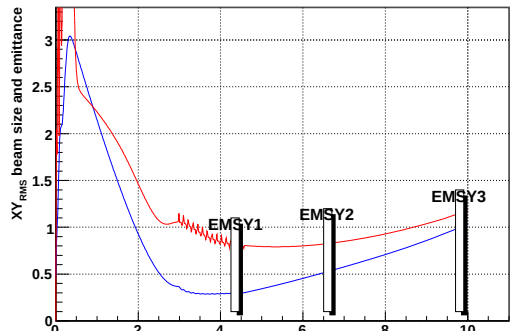

Figure 1: ASTRA simulation of the rms beam size in mm (blue) and normalized emittance in mm·mrad (red). The charge is 1 nC; accelerating gradient at the gun is 60 MV/m, phase of maximum energy gain; the focusing solenoid is at 385 A; the gradient of the booster cavity is 28.9 MV/m, phase of maximum energy gain.

PITZ SETUP

A detailed layout of the current PITZ setup is shown on Fig. 2. The electrons are produced in the RF gun (on the right hand side) and transported through the low energy diagnostic section, further acceleration up to the maximum of 30 MeV is given in the booster cavity after which the high energy diagnostic section is installed.

The low and high energy diagnostic sections consist of different view screens, BPM's, charge measurement devices and longitudinal phase space diagnostics. The charge per bunch can be monitored non-destructively at four positions along the beamline using Integrated Current Transformers (ICT's). The beam momentum and momentum spread are measured at two dispersive dipole arms, one in the low energy section and one after the booster cavity. The low energy dispersive dipole is also equipped with a streak camera readout providing full knowledge about the longitudinal phase space distribution (see [7]). Three EMSY's are located after the booster cavity in positions 4.3, 6.6 and 9.8 m from the cathode.
For the transverse phase space characterization we rely on YAG and OTR screens and the so called slit scan technique [8]. For this technique the uncorrelated local divergence is estimated by cutting the electron beam into thin slices and measuring their size on a screen after a drift. The so called sheared normalized RMS emittance is then calculated us-

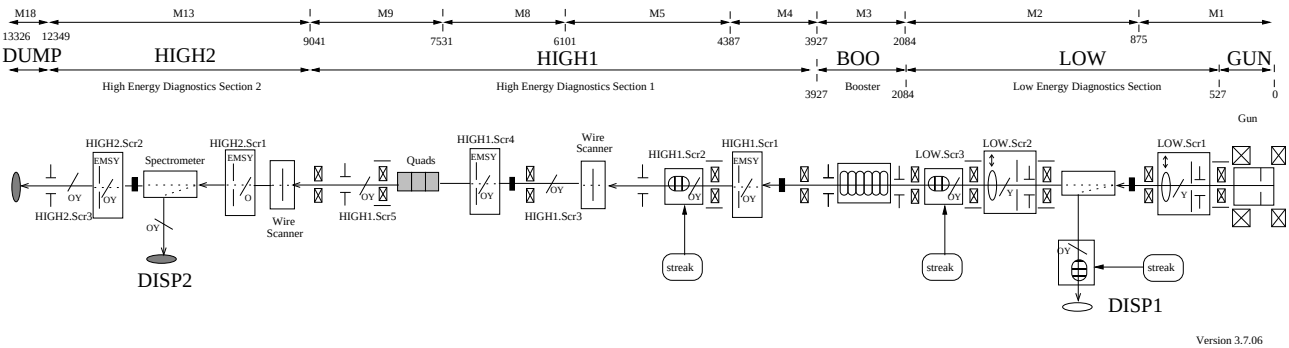

Figure 2: Layout of PITZ.

ing the following definition (1) taken from [8]:

$$\varepsilon_n = \beta\gamma \cdot \sqrt{\langle x^2 \rangle \cdot \langle x'^2 \rangle}. \quad (1)$$

Here $\langle x^2 \rangle$ and $\langle x'^2 \rangle$ are the second moments of the distribution of the electrons in the so called trace phase space where $x' = \sqrt{\langle p_x^2/p_z^2 \rangle}$ represents the divergence of the beam. The RMS beam size is measured on an OTR or YAG screen at the position of the slits along the beam axis. The uncorrelated divergence is obtained by analyzing the profiles of the beamlets produced from the slits which drift some distance L_d downstream where the spatial distribution of the beamlets corresponds to the local uncorrelated divergence, x' can be derived from the size of the beamlet using the formula in Eq. 2.

$$x' = \frac{\sqrt{\langle x_b^2 \rangle}}{L_d}. \quad (2)$$

Here x_b is the RMS size of the beamlet on the screen after distance L_d. The $\beta\gamma$ is measured using a dispersive arm after EMSY.

THE NEW EMITTANCE MEASUREMENT SYSTEM

EMSY consists of two orthogonal actuators (Fig. 3) which can be inserted separately to penetrate the beam in order to take images or to cut beamlets in the beam transverse planes. The actuators are driven into the beam line with stepper motors and positioned with precision better than 10 μm, their angular orientation with respect to the electron beam can be adjusted during the measurement again using stepper motors. Each actuator is equipped with an YAG or OTR screen for measurement of the transverse RMS beam size $\sqrt{\langle x^2 \rangle}$ and a single slit mask for estimation of the local divergence, multi slit masks are in production and will be mounted on the actuators in the next shutdown period. The design of the system enables us to measure the beam transverse parameters expected in PITZ with uncertainty less than 10 % (see [6]).

During the design the following considerations were taken into account:

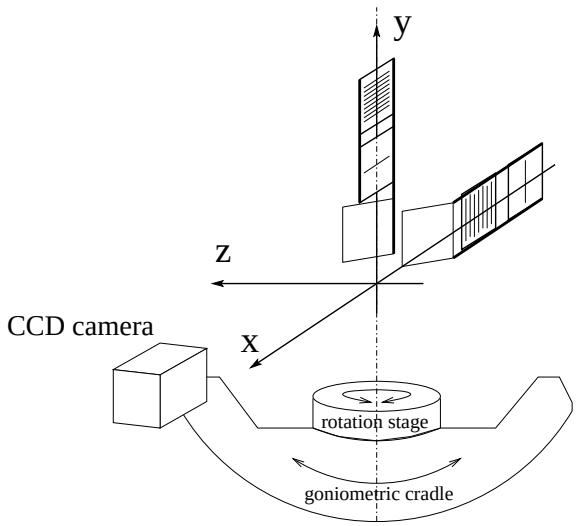

Figure 3: Layout of EMSY.

- The slit opening must be small enough to produce emittance and not space charge dominated beamlets, but still large enough to provide good transmission.
- The contribution of the initial beamlet size to the measured one at the screen of observation must be as small as possible.
- The distance betwen the slit mask and the screen must be big enough to resolve small beam divergence. But still short enough to prevent the space charge forces to degrade the beamlet and the overlapping of different beamlets from the multi slit mask.
- The mask thickness must be large enough to scatter the residual electrons from the beam in order to produce an uniform background for the beamlets measurements and still it must be thin enough provide sufficient acceptance angle.

The design of the slits was made using the above considerations, and GEANT4 [9] simulations for transport of the electrons through the masks and to assess the performance of the YAG screens to be used. Slits are made from 1 mm thick Tungsten with 10 μm slit opening, the slits of the multi slit mask are separated with 0.3 mm. The screens are made from 0.3 silica waffers coated with YAG powder

or with Al (for the OTR screens). The YAG screens are placed at 90 degrees with respect to the electron beam and an Al coated silicon mirror is used to direct the light to the CCD chip, the OTR screens are with 45 degrees orientation. Both the screens are observed with 8 bit CCD camera. It was found from the beam dynamics simulations, that in some cases 8 bit camera cannot provide the desired sensitivity, therefore 12 bit cameras are ordered and are soon to be installed. On fig. 4 a scan of the position of the slit trough the beam is shown, a good signal from the camera is obtained (blue line), with red the RMS beamlet size is plotted.

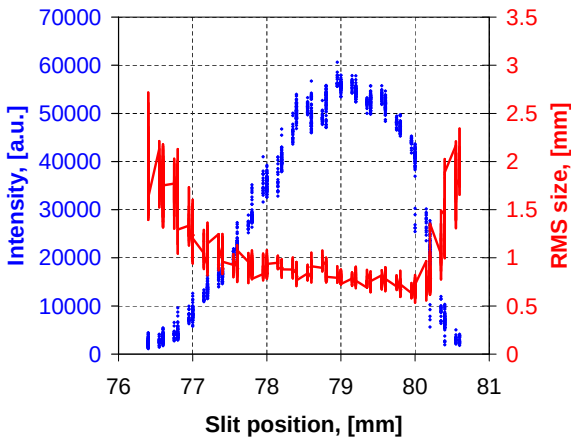

Figure 4: Scan with the 10 μm slit.

Further optimization of the readout can be made by adjusting the angular orientation of the slit, as can be seen in fig. 5. The slit at position 79 mm in fig. 4 was selected for the angular optimization, improvement of the intensity of the signal from the camera is seen (blue dots) as well as stable reading for the beamlet size (red line) in the angular range -10 to +8 mrad, for larger angular deviations lower signal transmission takes place as well as additional effects such as scattering of the electrons from the inner surface of the slit, etc.

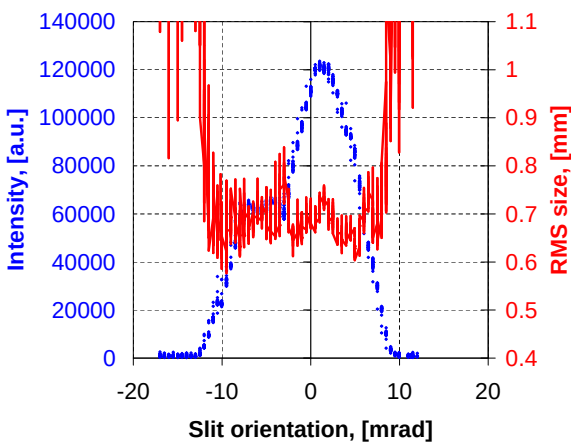

Figure 5: Scan of the angular orientation of 10 μm slit.

CONCLUSIONS

The 10 μm slits can provide sufficient signal for beamlet measurements with proper angular orientation. The emittance measurement system in PITZ is installed and commissioned. All the component from the system are tested and ready for use.

ACKNOWLEDGMENT

We would like to thank to Evstati Apostolov, Hristo Yotov and Luchezar Yotov from INRNE for the precise construction and Alexander Donat, Hartmut L¨udecke and Jochen Bienge from DESY Zeuthen for their outstanding support on the mounting and aligning the devices in the PITZ tunnel.

REFERENCES

[1] A. Oppelt, “Status of the PITZ facility upgrade”, LINAC 2006.

[2] J. B¨ahr et al., “Upgrades of the Laser Beam-line at PITZ”, FEL’05.

[3] M. Krasilnikov et al., “Recent developments at PITZ”, PAC’05, May 2005, Tennesy USA.

[4] L. Serafi ni, J. Rosenzweig, “Envelope analisys of intense relativistic quasilaminar beams in rf photoinjectors: A theory of emittance compensation”, Phys. Rev. E, Vol. 55, 1997.

[5] K. Floetmann,ASTRA,http://www.desy.de/˜mpyflo

[6] L. Staykov et al., “Design Optimization of an Emittance Measurement System at PITZ”, DIPAC’05.

[7] J. R¨onsch et al., “Investigations of the Longitudinal Phase Space at PITZ”, EPAC’06.

[8] V. Miltchev, “Investigations on the transverse phase space at a photo injector for minimized emittance”, PhD thesis.

[9] GEANT collaboration, CERN/LHCC 98-44, GEANT4: “An Object Oriented Toolkit for Simulation in HEP”; see also website: http//wwwinfo.cern.ch/asd/geant4/geant4.html

SIMULATION OF MIRROR DISTORTION IN FREE-ELECTRON LASER OSCILLATORS*

H.P. Freund#, Science Applications International Corp., McLean, VA 22102, U.S.A.
M. Shinn and S.V. Benson, Thomas Jefferson National Accelerator Facility, Newport News, VA 23606, U.S.A.

Abstract

Thermal distortions in high-average power FEL cavity mirrors can alter mode quality and degrade performance. We address these issues by developing simulation tools, and then benchmarking the simulation against observations on the 10 kW-Upgrade experiment at the Thomas Jefferson National Accelerator Facility in Newport News, VA. The modelling and simulation will rely on the MEDUSA code, which is a three-dimensional FEL simulation code that is capable of treating both amplifiers and oscillators in both the steady-state and time-dependent regimes. MEDUSA employs a Gaussian modal expansion, and treats oscillators by decomposing the modal representation at the exit of the wiggler into the vacuum Gaussian modes of the resonator and then analytically determining the propagation of these vacuum resonator modes through the resonator back to the entrance of the wiggler in synchronism with the next electron bunch. Knowledge of the power loading on the mirrors allows us to model the mode distortions using Zernike polynomials, and this technique will be incorporated into MEDUSA.

INTRODUCTION

Thermal distortions in cavity mirrors in high-average power FELs can alter mode quality and negatively impact performance; hence, it is important to predict the character and magnitude of the distortions and to be able to model their effect on FEL performance. To this end, we address these key issues by developing modelling and simulation tools that can accomplish these goals, and then benchmarking the simulation against observations on the 10 kW-upgrade experiment [1] at the Thomas Jefferson national accelerator facility in Newport News, VA (henceforth referred to as Jefferson Laboratory). The facility is undergoing continual upgrades; in particular, a new permanent magnet wiggler has been installed that will be used in comparing the experimental and simulation results (see Table 1). The modelling and simulation will rely on the MEDUSA code [2,3], which is a three-dimensional FEL simulation code that is capable of treating both amplifiers and oscillators in both the steady-state and time-dependent regimes. MEDUSA employs a Gaussian modal expansion, and treats oscillators by decomposing the modal representation at the exit of the wiggler into the vacuum Gaussian modes of the resonator and then analytically determining the propagation of these vacuum resonator modes through the resonator back to the entrance of the wiggler in synchronism with the next electron bunch. Knowledge of the power loading on the mirrors allows us to model the mode distortions using Zernike polynomials [4], and this technique will be incorporated into MEDUSA.

In this paper, we report on the progress to date in this activity. The first step is to compare MEDUSA predictions with the observed performance of the experiment at low duty factor where mirror distortions are unimportant. We then go on to determine the effects of the so-called first order properties, which include changes in the Rayleigh range and shifts in the position of the mode waist. Higher order distortions such as coma, astigmatism, and spherical aberration, collectively known as third-order aberrations, will be incorporated in the future. The organization of the paper is as follows. In the second Section we discuss the formulation used in MEDUSA. A description of the experiment is given in the third Section, and of the numerical results in fourth Section. A summary and discussion is given in the fifth Section.

THE NUMERICAL FORMULATION

The MEDUSA code [2,3] employs a three-dimensional formulation that includes the slippage of the radiation relative to the electron beam. MEDUSA can model both helical and planar wiggler geometry and treats the electromagnetic field as a superposition of either Gauss-Hermite or Gauss-Laguerre modes in the slowly-varying amplitude approximation, where

$$\delta\mathbf{A}(\boldsymbol{x},t)=\hat{\boldsymbol{e}}_x\sum_{l,n} e_{l,n}(x,y)\left[\delta A^{(1)}_{l,n}\cos\varphi(x,t) + \delta A^{(2)}_{l,n}\sin\varphi(x,t)\right], \quad (1)$$

where "l" and "n" are transverse mode numbers, "h" is the harmonic number, $e_{l,n,h} = \exp(-r^2/w_h^2)H_l(\sqrt{2}x/w_h)H_n(\sqrt{2}y/w_h)$, H_l is the Hermite polynomial of order l, and w_h is the spot size, $\varphi_h = h(k_0z - \omega_0t) + \alpha_h r^2/w_h^2$ ($k_0 = \omega_0/c$). We assume that $\delta A^{(1,2)}_{l,n,h}$, w_h, and α_h, vary slowly in z and t. The dynamical equations are

$$\left(\frac{d}{dz}+\frac{w_h'}{w_h}\right)\begin{pmatrix}\delta a^{(1)}_{l,n,h}\\ \delta a^{(2)}_{l,n,h}\end{pmatrix} + K_{l,n,h}\begin{pmatrix}\delta a^{(2)}_{l,n,h}\\ -\delta a^{(1)}_{l,n,h}\end{pmatrix} = \begin{pmatrix}s^{(1)}_{l,n,h}\\ s^{(2)}_{l,n,h}\end{pmatrix}, \quad (2)$$

where $\delta a^{(1,2)}_{l,n,h} = e\delta A^{(1,2)}_{l,n,h}/m_ec^2$, $d/dz = \partial/\partial z + c^{-1}\partial/\partial t$, the "prime" superscript denotes the total z-derivative,

$$K_{l,n,h} = (l+n+1)\left(\alpha_h\frac{w_h'}{w_h} - \frac{\alpha_h'}{2} - \frac{1+\alpha_h^2}{hk_0w_h^2}\right), \quad (3)$$

*Work supported by the Joint Technology Office.
#henry.p.freund@saic.com

$$\begin{pmatrix} s^{(1)}_{l,n,h} \\ s^{(2)}_{l,n,h} \end{pmatrix} = \frac{2\omega_b^2}{h\omega_0 c}\frac{F_{l,n}}{w_h^2}\left\langle \frac{v_x}{|v_z|} e_{l,n,h} \begin{pmatrix} \cos\varphi_h \\ -\sin\varphi_h \end{pmatrix} \right\rangle , \quad (4)$$

where $\omega_b(z,t)^2 = 4\pi e^2 n_b(z,t)/m_e$ for a beam density n_b, and $F_{l,n} = [2^{l+n}l!n!]^{-1}$, and <(…)> describes an average over the complete 6-D phase space. The spot size and radius of curvature for each harmonic component are given by

$$w_h' = \frac{2\alpha_h}{hk_0 w_h} - w_h Y_h \ , \quad (5)$$

$$\frac{\alpha_h'}{2} = \frac{1+\alpha_h^2}{hk_0 w_h^2} - \left(X_h + \alpha_h Y_h\right) \ . \quad (6)$$

These equations constitute the source-dependent expansion [5], which is a self-consistent adaptive eigenmode representation that tracks the optical guiding of the mode based upon the interaction with the electron beam. The field equations are integrated simultaneously with the complete three-dimensional Lorentz force equations for an ensemble of electrons. No wiggler-average orbit approximation is used so that the spatial step size must be small enough to resolve the wiggler motion.

Table 1: Nominal experimental parameters

ELECTRON BEAM	
Energy	115 MeV
Peak Current	310-370 A
Normalized Emittance	9 mm-mrad/7 mm-mrad
Energy Spread	0.35%
Bunch Length	380-420 fsec
Bunch Charge	79 pC
Initial Beam Size	257 microns/212 microns
Twiss-α Parameter	1.25
WIGGLER	
Amplitude	3.746 kG
Period	5.5 cm
Length	30 periods/1.65 m
OPTICAL MODE	
Wavelength	1.57 microns
Rayleigh Range	1.5 (±0.30) m
Mode Waist Position	1.03 (±0.05) m

THE JEFFERSON LAB EXPERIMENT

The Jefferson Lab IR-Upgrade FEL operates an energy recovery accelerator with a high power FEL wiggler and resonator. The electron beam consists of a core distribution and a halo distribution. The charge, emittance, and peak current are of that core beam. The wiggler is very well characterized and is essentially ideal. The optical resonator is nearly concentric, and consists of a high reflector at the upstream end and a transmissive element at the downstream end that out-couples approximately 10% of the power. The Rayleigh range can be varied in the experiment by changing the radius of curvature of the high reflector. However, the cavity is slightly astigmatic and can lead to a difference between the Rayleigh range in the two axes. The uncertainty in the Rayleigh range is about 20%. The measured gain and efficiency are 70±5% and 1.6±0.1% respectively.

The nominal parameters for the experiment that are used in simulation are given in Table 1. Observe that the normalized emittances and beam dimensions shown in the table refer to the wiggle-plane and the plane transverse to the wiggler-plane respectively. In addition, the Twiss-α parameter shown corresponds to a beam that is focused to a waist near the center of the wiggler. The estimate of the Rayleigh range and the location of the mode waist contain some uncertainty, and the values given are the best estimate at the present time. In particular, we note that the mode waist is located about 15 cm downstream from the wiggler center.

NUMERICAL RESULTS

As we mentioned previously, our first goal is to determine whether MEDUSA is in substantial agreement with the experiment when distortion is absent or minimal. This is the case when the experiment operates at low average powers (*i.e.*, low duty factors), where a single pass gain of the order of 65-75% is measured for a peak current of 310 A and a bunch length of 380 fsec.

The parameters shown in Table 1 are the nominal experimental parameters, and we note that the optical waist is located about 15 cm downstream from the wiggler center. The experiment was optimized by focusing the electron beam to a waist near the center of the wiggler, which provides an optimal match to the resonator mode. This was also found in simulation, and is obtained for a Twiss-α parameter of 1.25 in simulation. The single pass gain found using MEDUSA operating in steady-state mode for these parameters is of the order of 400%. However, the slippage time through the wiggler for this experiment is of the order of 160 fsec, which is a substantial fraction of the bunch length. Hence, slippage is important and can be expected to substantially reduce the single pass gain with respect to steady-state predictions.

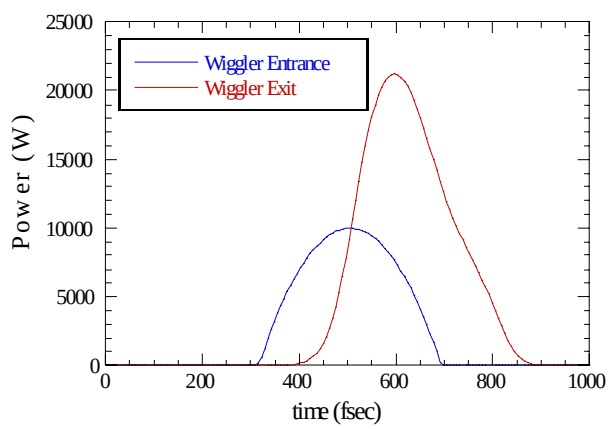

Figure 1: Plot of the power versus time through the pulse at the wiggler entrance and exit.

The slippage of the electromagnetic pulse through the wiggler is illustrated in Fig. 1 where we plot the pulse shapes at the entrance and exit from the wiggler. It is evident from the figure that while the pulse is assumed symmetric at the entrance to the wiggler, it has slipped by at least half the total pulse length over the course of the wiggler. Amplification of the peak power over the pulse has shrunk from the value of 400% found in steady-state simulation to just over 100% when slippage is included. However, in the time-dependent simulation, gain must be calculated based on the overall energy of the pulse, not the peak power. To this end, we plot the amplification of the total pulse energy through the wiggler in Fig. 2. The incident energy is 2.53 nJ and the energy at the output is 4.68 nJ yielding a single pass gain of about 84%. Given the uncertainties in the measured parameters, this represents reasonable agreement with the experiment. For example, there is a 20% uncertainty in the measurement of the Rayleigh range that would result in a reduction of the predicted gain to 73%.

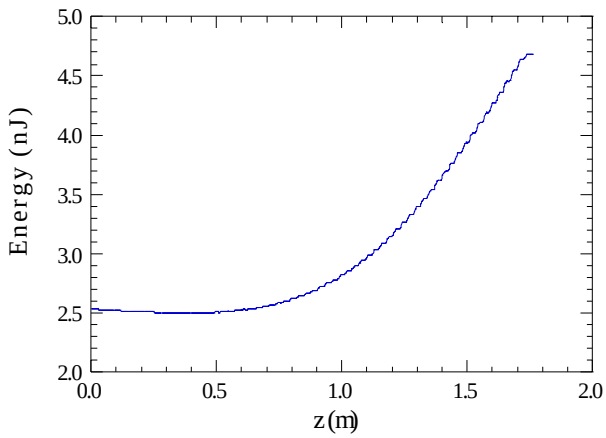

Figure 2: Plot of the amplification of the total pulse energy through the wiggler.

The lowest order mirror distortions involve variations in both the location of the optical waist and the Rayleigh range. In order to study the effects of these distortions, we (1) varied the position of the optical waist while holding the Rayleigh range fixed at 1.5 m, and (2) varied the Rayleigh range for an optical waist that is located at the wiggler center optical and 30 cm downstream from the wiggler center. These results are shown in Figs. 3 and 4 respectively. Figure 3 indicates that, for these parameters, the FEL gain is maximized when the optical waist is located about 20 cm upstream from the wiggler center, in contrast to the actual location that is 15 cm downstream from the wiggler center. Observe that we show the gain variation with Rayleigh range in Fig. 4 for an optical waist that is wiggler-centered and shifted downstream from the wiggler center by 30 cm. However, the optical waist is located 15 cm downstream from the wiggler center, and the actual location was used in the simulations shown in Figs. 1-3. We chose to use the larger displacement in Fig. 4 to better illustrate the performance sensitivity to these parameters, and the actual variation with Rayleigh range in the experiment is between these two lines. It is clear from Fig. 4 that the single pass gain would be larger if the Rayleigh range were smaller, and the optimal Rayleigh range found in simulation varies from about 0.5 m for a wiggler-centered resonator mode to 0.6 m when the mode waist is located 30 cm downstream from the wiggler center. The advantages that accrue from using a short Rayleigh range resonator were first pointed out by W. Colson and his collaborators [6]. The results shown in Figs. 3 and 4 indicate that were mirror distortions to either decrease the Rayleigh range or shift the mode waist upstream, then the single pass gain and FEL performance may actually be enhanced. Whether such an effect can actually be allowed for in the design of a high power FEL oscillator is currently under consideration.

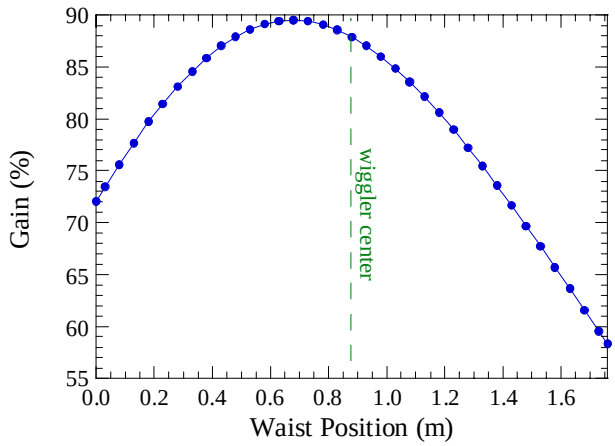

Figure 3: Variation of the single pass gain with the position of the optical waist.

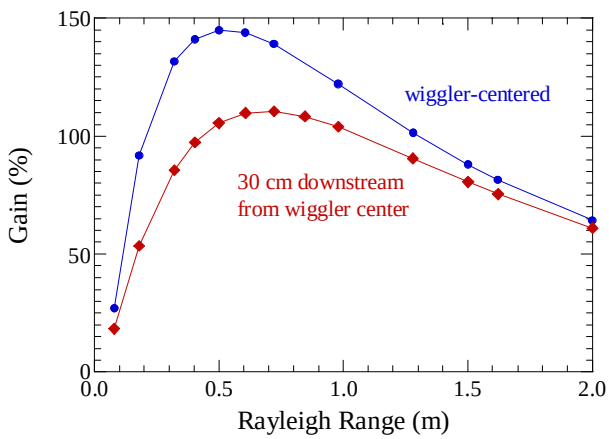

Figure 4: Variation of the single pass gain with the Rayleigh range.

SUMMARY AND DISCUSSION

In this paper we report on the initial work involved in a study of the effect of mirror distortions on the performance of a high power FEL oscillator using the MEDUSA simulation code. To this end, we first undertook to validate MEDUSA for low power (and duty factor) operation where mirror distortion was small. In this case MEDUSA predicted a single pass gain of 84%, which is in reasonable agreement with the measured range of 65-75% given the experimental uncertainties in the Rayleigh range, location of the optical waist, astigmatism in the resonator, and uncertainties related to the electron beam distribution. Experimentally, one derives the mode waist and position from the radii of curvatures (ROC) of the cavity mirrors. Repeated measurements set this uncertainty at ±5 cm. In turn, this creates a 20% uncertainty in the value of the Rayleigh range, but a relatively small (±5 cm) change in the waist position. There are also uncertainties associated with the electron beam parameters, especially those associated with the longitudinal distribution. Simulations indicate that the predicted gain is very sensitive to uncertainties of this magnitude. For example, a 20% uncertainty in the Rayleigh range and a ±5 cm uncertainty in the optical waist position can lead to a variation in the predicted gain of between 71% - 96%. As a consequence, the simulation is in substantial agreement with the experiment. Given the agreement between the simulation and experiment, we then undertook to investigate the variation in performance versus the Rayleigh range and the location of the optical waist. We found that the small signal gain would be substantially larger for much smaller Rayleigh ranges and for an optical waist located upstream from the wiggler center.

Future work will involve the inclusion of higher order mirror perturbations mentioned earlier, as well as validation of the harmonic generation predictions of MEDUSA.

REFERENCES

[1] G. Neil *et al.*, Nucl. Instrum. Meth. A557 (2006) 9.

[2] H.P. Freund, S.G. Biedron, and S.V. Milton, IEEE J. Quantum Electron. 36 (2000) 275.

[3] H.P. Freund, Phys. Rev. ST-AB 8 (2005) 110701.

[4] S.V. Benson *et al.*, Nucl. Instrum. Meth. A407 (1998) 401.

[5] P.A. Sprangle, A. Ting, and C.M. Tang, Phys. Rev. A 36 (1987) 2773.

[6] D.W. Small, R.K. Wong, W.B. Colson, and R.L. Armistead, Nucl. Instrum. Meth. A393, 262 (1997).

GENERATION AND CHARACTERIZATION OF THE MICROBUNCHED BEAMS IN THE RANGE FROM 0.3 TO 500 FEMTOSECONDS

V. E. Yakimenko, M. Babzien, K. P. Kusche, Brookhaven National Lab., Upton, NY 11973, U.S.A,
X. Ding, University of Southern California, CA 90089, U.S.A,
E. Kallos, P. Muggli UCLA, Los Angeles, CA 90095, U.S.A,
W. D. Kimura, STI Optronics, Inc., Bellevue, WA 98004, U.S.A,
F. Zhou, Stanford Linear Accelerator Center, Stanford, CA 94025, U.S.A.

Abstract

The recent results include formation and measurement of the micro bunch structures of the different time scales. Double beam structure produced and characterized at 100 fs – 0.5 ps range using beam splitting during compression in the magnetic chicane – "dog leg" arrangement. Arbitrary number of 10-50 femtoseconds micro bunches are sliced out of 5 ps long beam using wire mesh. CSR interferometer is used for detailed characterization of the beams in the two techniques above. 0.3 fs bunches are produced by IFEL and characterized by spectral measurements of the multiple harmonics. Presentation covers experimental results at Brookhaven Accelerator Test Facility.

INTRODUCTION

Three distinct experimental methods are discussed in this paper in the following 3 chapters. The first one discusses measurements of micro bunched beams generated with CO2 laser in the IFEL wiggler. Comparison of the coherent transition radiation CTR power in multiple harmonic leads to much more precise information about micro bunch length. The second part of the paper discuses generation of micro bunched beams that are not seeded with laser. Wire mesh targets were shaping the beam in the dispersive region and converting correlation between energy and time into current time modulation. Tunable spacing is the result of this technique. We used an interferometer to characterize these beams. The last chapter of this paper discusses controllable beam break up into two beam structure. The two beam formation happens during its compression in the magnetic chicane – dog-leg combination. Effects of the space charge and CTR are very important and stabilize the process contrarily to initial expectations. We used interferometer and plasma wakefield capillary to characterize two 100 fs bunches formed in this process.

CHARACTERIZATION OF SUBMICRON MICROBUNCHES PRODUCED BY IFEL WITH CTR IN MULTIPLE HARMONICS

We collect the coherent transition radiation (CTR) emitted when the microbunches traverse two 1μm thin titanium metal foils in order to diagnose the quality of the microbunching of the IFEL modulated electron beam. CTR is emitted because the electric fields of the electrons in the beam displace violently the free electrons in the metal surfaces, which in turn radiate due to the acceleration they suffer.

The first metal foil is placed perpendicularly to the beam direction of propagation and serves the purpose of blocking the CO2 radiation previously used at the IFEL interaction that could interfere with the CTR signal. The second foil is placed at 45° with respect to the direction of propagation and emits radiation out of the beamline. The sum of the radiation emitted from both foils is collected.

The spectrum of the CTR radiation contains information about the geometry of the electron beam. The on axis spectrum is proportional to the amplitude squared of the Fourier transform of the beam and shown on figure 1.

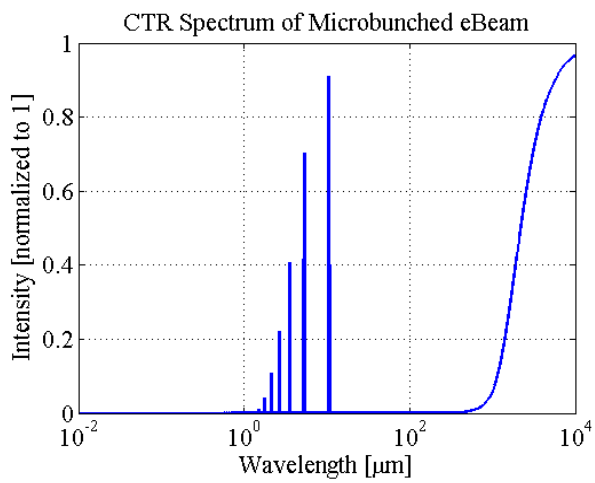

Figure 1. The spectrum of the CTR emitted when the microbunched electron beam passes through a metal foil.

The geometry of the electron beam is uniquely mapped into its CTR spectrum. The low frequency (long wavelength) radiation on the right corresponds to the envelope of the beam. In other wavelengths the radiation in general adds out of phase except at the harmonics of the separation wavelength λ_0=10.6μm between the microbunches.

Finally and most importantly, the amplitudes of these harmonics are modulated by the Fourier transform of each microbunch. The existence of radiation at each harmonic is a strong indication for the periodicity of the microbunch train. Also, the energy radiated at each harmonic depends

on the shape of each microbunch, hence it provides a direct way of estimating its width, which is assumed to be Gaussian in this case.

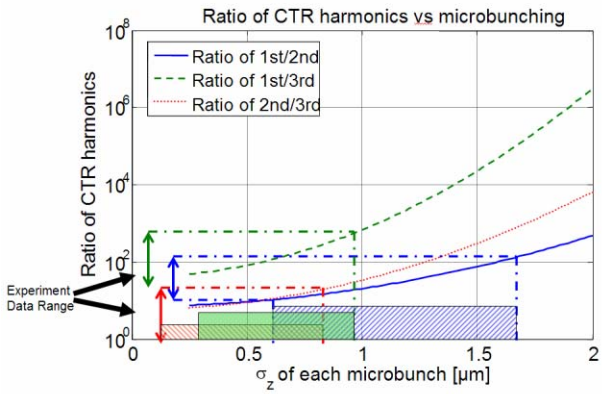

Figure 2. The ratios of the energies radiated at each of the harmonics as a function of microbunch width. The 3 data sets agree at the region around σ_z=0.7μm .

In order to collect the CTR, a cold detector sensitive between 3μm-20μm wavelengths is used. Furthermore, narrow Gaussian bandpass filters with roughly 5% FWHM transmission bandwidth were used to isolate the radiation of the first, second and third harmonic, in successive measurements. After recording about 100 events at a roughly constant IFEL laser pulse energy (within a factor of 2) at all three harmonics, we calculated the three possible ratios of the harmonics signals. The data range for each ratio is shown on the vertical axis on figure 2.

Using prediction for small angles and after accounting for the response of the detector and the filters calibrated with the black body source, we calculated the expected theoretical ratio between the energy radiated under each of the harmonics as a function of the microbunches' widths. These three predicted ratios also are plotted in figure 2. It shows that the measured rations indicate a width of σ_z=0.7μm for each microbunch. Although the microbunch width was inferred using CTR [1] and staged laser accelerator [2] before, this is its first direct measurement that also utilizes information from different harmonics.

In order to confirm the 10.6μm separation between the microbunches the IFEL laser was tuned at 10.2μm, while still using the same narrow 10.6μm filter to detect the CTR. In that case the signal recorded was at least 100 times less than when the IFEL was driven at 10.6μm and very close to the noise level of the detector, thus confirming the periodicity of the bunching at the laser's wavelength only.

TUNABLE MICROBUNCH TRAIN

The microbunched beam described above offers stable, well defined by spacing the laser. It is a disadvantage if the laser in not easily available in the range that is needed. We attempted to use a periodic wire mask installed at the dispersive region of the beam transport to generate microbunches with the spacing that is determined by the target period. The idea is very simple: a beam is chirped in the linac and therefore energy-time correlation is introduced. The target is installed in the location where dispersion is large while betatron size in the plane of the dispersion is smaller then target period. This effectively creates time-current modulation. We use 125-500μm diameter wire to make targets. Low emittance 50 MeV beam is effectively scattered by this wire. The photograph of the taget is shown on figure 3.

Figure 3. Photograph of the wire target for adjustable microbunch beam generation.

One can clearly see modulation in of current vs energy on the electron beam energy spectrometer. It is even possible to see unintentional defect of the target "double wire" approximately in the middle of the beam.

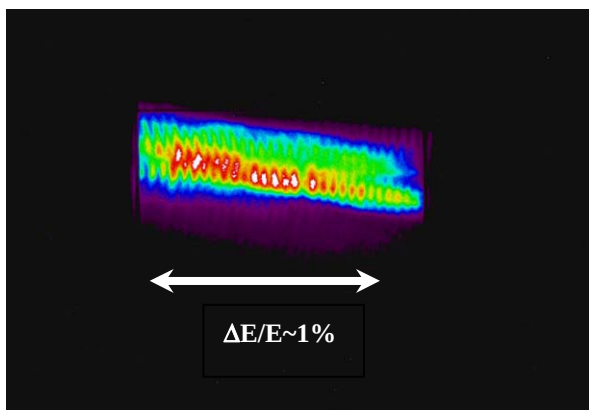

Figure 4. Image from the beam energy spectrometer. It shows 15 microbunches stretched over ~1% energy chirp induced on the beam.

The translation of the microbunch spacing from target period naturally depends on the chirp and dispersion value at the target location. We operated with a set of parameters where it is adjustable 10: target with 250 μm period will generate microbunches spaced by 25 μm. We use a pair of installed before target sextupole magnets to linearize or chirp the spacing between micro bunches. High energy slit opening that controls energy spread envelope of the beam can be used to select arbitrary number of microbunches. The demagnification can be

adjusted by change of dispersion, beam chirp or target rotation.

CTR interferometer [4] was used to measure modulation in time. Our attempt to measure individual microbunches with the period of ~25-30 μm did not produce the expected result due to cutoff of the window transmission around 30 μm. The signal strength on the detector increased considerably for the modulated beam. The interference showed expected envelope of the beam Interference curve was triangular that translates to the "square' beam envelope. (Tails of the beam were cat by high energy slip.)

We detected individual bunches with correct periodicity after switching to the 1mm target and retuning transport line for 1:5 demagnification. Interferogram is shown on figure 5.

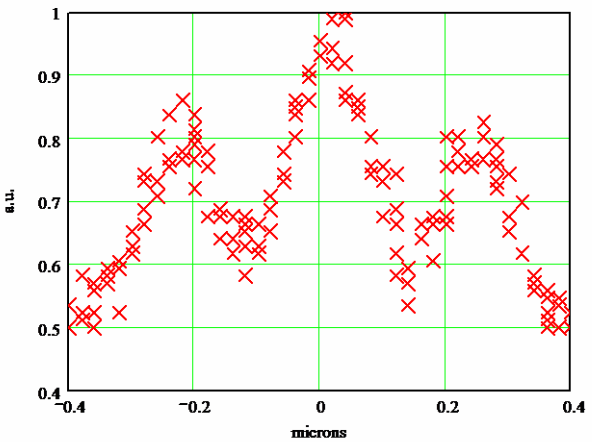

Figure 5. Interferogram of the microbunched beam generated with the periodic wire target.

SUBPICOSECOND DOUBLE ELECTRON BUNCH GENERATION

As part of these efforts towards improving beam for various experiments related to advanced accelerator research, a chicane, designed and built by UCLA [1], was installed on the linac downstream of the RF accelerating structures. The chicane was designed to provide approximately 30 times compression of the incoming electron bunch. Figure 6 is a diagram of the chicane.

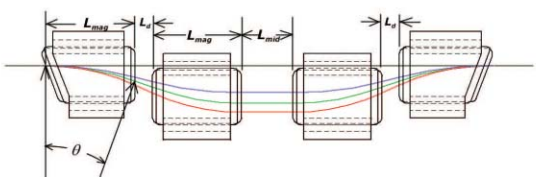

Figure 6. Diagram of ATF chicane.

It was discovered that when compressing the electron bunch from the linac that the beam breaks up into two distinct bunches with subpicosecond compressed bunch lengths. It does this in a consistent and reliable manner. Unlike most of other facilities that are utilizing a chicane for pulse compression, the ATF does not have a subsequent RF acceleration section downstream of the chicane, which can be used to compensate for residual energy chirp on the electron beam (e-beam) exiting the chicane. Not being able to use a downstream acceleration section was one reason the double-bunch formation process was possible.

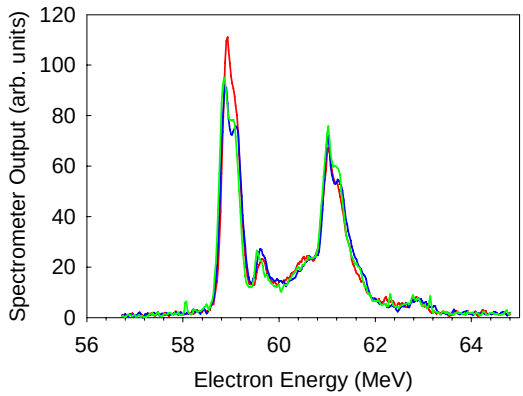

Figure 7. Energy spectrums of double-bunch e-beam. Three spectrums taken many minutes apart demonstrating stability of the double-bunch formation process

Figure 7 shows energy spectrums of the double-bunch beam. It shows two bunches separated in energy by 1.8 MeV. It is an overlay of three shots taken many minutes apart. The good reproducibility of the spectrums indicates the energy distribution and positions are very stable.

A coherent transition radiation (CTR) interferometer was used to characterize the compressed e-beam. The CTR emission is in the THz range. An autocorrelation of the CTR signal is obtained by scanning the translation mirror shown in Figure 8

Analysis of this autocorrelation signal yields information about the e-beam bunch characteristics [4].

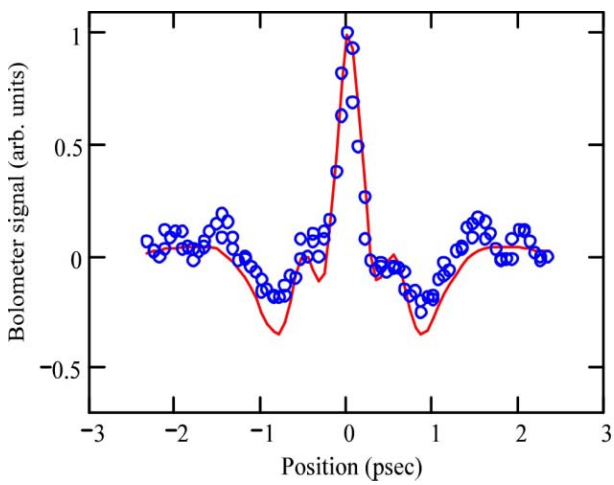

Figure 8: Example of raw data from CTR interferometer (circles) and the curve fits to the data (solid line) calculated from the autocorrelation integral [2]. "Bumps" around +- 0.5 ps indicate double bunch spacing.

For a single bunch, the curve fit of the autocorrelation integral with the data requires selecting values for the bunch length and the cut-off frequency of the detection

system, where we have assumed a Gaussian bunch shape. In particular, the width of the central peak of the autocorrelation signal is primarily affected by the bunch length. The shape of the curve on either side of the peak is mostly affected by the cut-off frequency.

For a double e-beam bunch, there are five free parameters in the autocorrelation integral. We were able to characterize each bunch individually using CTR and beam charge monitor. Single bunch data was obtained by using the high-energy slit located downstream of the chicane to block one of the bunches (either the low-E or high-E bunch). Individual bunch data for each bunch of the double bunches permits reducing the number of free parameters to one, i.e., the time delay between the two bunches. For the example shown in Figure 8, the single-bunch CTR data indicates the lengths of the two bunches is 144 and 90 fs, the cut-off frequency is 1.7 THz, and the second bunch has 60% of the charge in the first bunch. Hence, for the curve fit shown in Figure 8, we find the time delay between the bunches is 500 fs.

Results of simulations with Elegant [5] confirmed our hypothesis that double beam structure is cased by the combination of nonlinear energy chirp and different sign of compression in the chicane and dog leg. Self induced beam wakes narrowed energy spread in the beam and let to complete separation.

ACKNOWLEDGMENTS

The authors wish to thank Samer Banna and ATF staff for contributions to the experiments. This work was supported by the U.S. Department of Energy, Grant Nos. DE-FG02-04ER41294, DE-AC02-98CH10886, DE-FG03-92ER40695, and DE-FG02-92ER40745

REFERENCES

[1] Liu, Y. et al., Phys. Rev. Lett. 80, 4418–4421 (1998).
[2] Kimura, W. D., et al., Phys. Rev. Lett. 92, 054801 (2004).
[3] R. B. Agustsson, UCLA, M.S. thesis, 2004.
[4] A. Murokh, et al., Nucl. Inst. Meth. Phys. Res., A 410, 452 (1998).
[5] M. Borland, “User’s Manual for elegant,” available on-line at http://www.aps.anl.gov/asd/oag/manuals/elegantver14.1/elegant.html.

DESIGN OF A LONG WAVELENGTH FEL FOR EXPERIMENTS UNDER HIGH MAGNETIC FIELDS

Wim J. van der Zande#, Th. Rasing, J.C. Maan, A.P.M. Kentgens and F.J.M. Harren,
Institute for Molecules and Materials, Radboud University Nijmegen, PO Box 9010, 6500 GL Nijmegen, The Netherlands.

Abstract

At the University of Nijmegen, a novel collaboration has been established that combines a number of spectroscopic laboratories. These laboratories form a centre for advanced spectroscopy and constitute the spectroscopic department of the (Research) Institute for Molecules and Materials combining physical and chemical techniques. As part of the spectroscopic centre, a long-wavelength far-infrared free electron laser (FIR-FEL) operating between 100 μm/3 THz and 1.5 mm/200 GHz will be designed and constucted in the coming years. The FIR-light should facilitate new experiments in the existing high field magnet laboratory (HFML), a large European Rerearch Infrastructure and in the NMR pavillion equipped with NMR instrumentation operating up to 800 MHz, especially for dynamic nuclear polarization technology.

THE NIJMEGEN CENTRE FOR ADVANCED SPECTROSCOPY

The Insitute of Molecules and Materials at the University of Nijmegen houses a number of spectroscopic laboratories. These laboratories combine laser spectroscopy in the European Trace Gas Facility [1], scanning probe technology, employing various forms of scanning tunneling and atomic force microscopic techniques [2], nucelar magnetic resonance (NMR) laboratory [3] and the high field magnet laboratory (HFML) [4]. Existing collaborations between the various laboratories have resulted in experimetns ranging from a 1.277 GHz NMR spectrometer built in a 30 Tesla Bittter magnet to NMR on a chip employing force microscopy to detect the radiofrequency absorption, and experiments exploiting diamagnetism to neutralize gravity in near-zero-gravity experiments inside strong magnetic fields.

In respons to a call from the Netherlands Government named the National Programme for Investments in Large Scale Facilities [5], we have proposed to strengthen existing facilities and to develop two novel instuments, a 45 Tesla Hybrid magnet and a Free Electron Laser operating in the far infrared (FIR).

The frequency window between the microwave region on the low photon-energy side and the infrared radiation on the high photon-energy side is called Far Infrared or THz regime. This energy regime knows many applications and radiation sources with different characteristics are rapidly developed. We believe that at present the most powerful and versatile THz radiation source is a free electron laser. We have proposed the construction of a THz-FEL optimized for the demands of advanced material research in combination with high magnetic fields and for advanced studies of molecular and macromolecular systems. The design aims at generating light between 100 μm and 1.5 mm with a spectral bandwidth of $\Delta\lambda/\lambda<510^{-5}$ while maintaining intensities of the order of 100 Watt during pulses of minimum duration 10 μs and maintaining the possibility of pump-probe experiments at a 10 to 30 picoseconds time resolution. The science driver that resulted in the success of our proposal has been the ambition to bring material research a significant step forward by performing saturation experiments and pulse-echo experiments in magnetic fields above 30 Tesla. In these fields, the relatively high-energy excitations reduce the interference of thermal effects while studying material properties. The total proposal encompassing a 40-45 Tesla hybrid magnet, the FEL and received about 26 M€ (excluding building costs, including some exploitation funds). As the FEL will be a part of an operational large scale facility, and as experience in free electron lasers is still small in Nijmegen, some design specifications will be made conservatively.

SCIENCE DRIVERS AND EXPERIMENTAL LIMITATIONS.

The science call carried the intention to fortify in the Netherlands the number of large scale facilities. It was realized that the Netherlands could not play a sufficiently large role as host country for important international facilities and international researchers. In many other countries the relative number of facilities was found to be significantly larger. In our proposal, we express the ambition that the University of Nijmegen may host many scientific guests using scanning probe techniques, the laser laboratory, and the high field magnets (using the THz radiation source), NMR or the FEL in its own right as versatile spectroscopic light source. The specifications defined above have been formed in collaboration with the FOM Institute Rijnhuizen, which hosts FELIX (free electron laser for infrared experiments). The FELIX staff will not only provide a lot of experience and advice but also forms an example for the management of a highly successful FEL facility. The spectral range chosen for the proposed FIR-FEL complements that of FELIX

#w.vanderzande@science.ru.nl

purposefully to optimize the collaboration between the two facilities.

An ideal laser source is easily tuneable in the THz regime, has a flexible pulse structure allowing pump-probe experiments, as well as bandwidth limited in the case of long macro-pulses, and is (quasi-) continuous with an average power of about 1 kWatt. Although the physics does not pose fundamental restrictions, the relative inefficiency of the FEL principle, without energy recovery, and more importantly, technological limitations in the creation of high intensity, relativistic electron beams requires choices optimizing specific aspects.

.

Science Drivers

In the following three of the science drivers are identified. An important group of experiments study the spectroscopy and dynamics in solid state materials by observing pulse-echo's following electron spin excitations or cyclotron resonances in magnetic fields. Depending on the effective mass of the electron, FIR-radiation near 1 THz is required in a magnetic field around 35 T. Saturation of these transitions in the form of excitation by a $\pi/2$ pulse within about 100 ns requires powers of about 100 Watt with a bandwidth of $\Delta\lambda/\lambda \approx 2\ 10^{-5}$. Pulse-echo experiments further require the possibility to shape pulses and delay pulses. Atypical experiment requires three of even more of these pulses within a few μs separated at arbitrary time delays ranging from tens of nanoseconds to one microsecond. Hence, we require laser pulses with about 10 μs duration that can be transformed by fast mirrors into the requested pulse train.

A second group of experiments is the use of FIR radiation to saturate electron spin transitions within an NMR instrument. By exploiting the coupling between the electron spin with nearby nuclear spin, the saturation of the electron spin population may be transferred to the nuclear spin. This process is called dynamic nuclear polarization (DNP). Although in principle DNP can enhance the sensitivity of NMR by a factor of more than 10^4, technological and system specific hurdles are enormous for a realization with a wide scope of applications. For DNP, the need for a high absolute duty cycle for FIR radiation may establish the largest obstacle for FEL technology to be optimally applicable.

In the first two examples, large magnetic fields play an important role. A third science driver makes optimal use of the flexibility to change the wavelength of a FEL continuously. A research program is anticipated on molecular spectroscopy of bio-organic molecules, biomemetics (analogues of bio molecules), and smart organic molecules often inspired on biological systems. Characterization of the THz response may not only provide spectroscopic information on the structure of these molecules but also on slow intra- and intermolecular motions related to their functionality.

Technological Choices.

The anticipated design for the FIR-FEL is based on experiments performed with the FELIX instrument in The Netherlands. FELIX is a short-pulse Free-Electron Laser operating in the IR from 5 to 250 μm. The spectral width of the output ranges from 0.5 to 7% depending on the frequency. The overall duty cycle is small with a repetition rate up to 10 macro-pulses per second of a maximum duration of 10 μs each. Each individual macro-pulse consists of up to a few thousand micro-pulses each consisting of tens of optical cycles, implying duration of a few picoseconds for each micro-pulse.

In terms of the macro-pulse structure, the duty cycle of FELIX is about $5\ 10^{-5}$ with an average output power of about 1 Watt, implying an average power of 20 kWatt during the macro-pulse. The maximum power in the picoseconds micro-pulses is another three orders higher. From here, we will describe the design for the Nijmegen FIR-FEL. The pulse structure will be similar to the one of FELIX and has the form of a low repetition rate 10 – 15 μs macro pulse structure. The macro pulse will consist of micro pulses with a fixed repetition rate in the range from 1 to 3 GHz. The special property that we aim for is that *all micropulses have a very well defined phase relation.* It is of interest to note that a narrow bandwidth using this mechanism has been one of the original design ambitions of FELIX. Oepts and Colson [6] presented the initial ideas of phase locking otherwise independent micropulses. Also Madey and coworkers started around this time [7,8]. Initial measurements at FELIX were performed by Bakker, Oepts van der Meer and co-workers [9,10], followed by Weits, Oepts and coworkers [11,12]. This research resulted in an experimental scheme to create a pulse train of phase locked light pulses. These authors observed significant phase stability between the micropulses and drew favourable conclusions regarding the bandwidth that may be achieved using external filtering using interferometers.

It is required to have a large number of optical pulses circulating simultaneously in the normally very large FEL cavity (more than 40 pulses in a cavity with an effective length of about 10 meter). As the optical pulses are generated from electron pulses moving at nearly the speed of light, an extra (optical) system has to couple the optical phases in this train of light pulses. An interferometer inside the cavity ensures that photons from a single electron bunch will affect the coherence of the light generated from many electron bunches injected later. The resulting pulse train of coherent and phase coupled micropulses constitutes a frequency comb with narrow FIR lines spaced with the repetition rate of the electron pulses (by the 1 to 3 GHz rf frequency) . These narrow lines have a width that is determined by the quality of the interferometer and by the magnitude of the interpulse phase-coherence. Each line in the frequency comb further consists of one or more longitudinal modes of the large FEL laser cavity, separated by 0.001 cm^{-1} for a 10 m

cavity. To achieve really a single longitudinal frequency output, filtering of one interferometer mode outside of the laser cavity is required. This filtering reduces the average power of the macro pulse by factor of at least 50 depending on the quality of the filtering process.

At FELIX experiments have been performed at a fixed wavelength near λ=69 μm, achieving a spectral resolution of $2\ 10^{-5}$ using a Fox-Smith type interferometer. Other groups have simulated and employed Michelson type interferometers in the FEL cavity for the same purpose. [9,10] The above specifications have resulted in the expectation that a dedicated design for a FIR-FEL could provide near single mode lasing at the average power of 100 Watt during a macro pulse even when starting with a short pulse FEL instrument. It is realized that it will require a careful design to establish continuous tuning in such a FEL as the timing structure of the RF electron accelerator system and the RF frequency generates strongly preferred absolute frequencies.

DISCUSSION

Many of the specifications related to the science drivers discussed above suggest designing a quasi CW-FEL such as the high quality UCSB FIR FEL operating at the University of Santa Barbara. This long-wavelength output of the FIR-FEL in Santa Barbara combines many of the characteristics required for the experiments planned at high magnetic fields. In fact, the power output of a CW–FEL can be of the order of 1 – 6 kWatt during the macro pulse clearly exceeding the expectations of a pulsed frequency comb FIR FEL as suggested above. The ambition of the Israeli FEL project to improve on the UCSB FEL design such that an *average* power of kWatt may become feasible implying a near CW operation with very high duty cycle while maintaining a large wavelength range seems to bring very difficult experiments such as DNP in NMR experiments more feasible.

At this moment, the extra possibilities to use a pulsed FEL for strongly non-linear experiments employing the very high micro pulse peak powers and to use the FEL for time resolved experiments with 10- 30 picoseconds time-resolution has resulted in the decision to study the possibilities of a pulsed frequency comb type FIR-FEL. The planning of the project involves in the upcoming 18 months design studies and detailed planning of the construction phase of the FEL. Lasing and the opening of a user facility along the lines of the present very successful FELIX facility are foreseen in about five and a half years from now.

ACKNOWLEDGMENTS.

WJvdZ wants to express his gratitude to Dick Oepts, Lex van der Meer and the rest of the staff at the FOM Institute for Plasma physics for the many discussions and support while preparing the proposal and in preparing the design phase of the proposed FEL.

REFERENCES

[1] http://www.ru.nl/tracegasfacility/
[2] http://www.ru.nl/nanolab/
[3] http://www.ru.nl/physchem/solid_state_nmr/
[4] http://www.hfml.kun.nl/
[5] //nwo.nl/nwohome.nsf/pages/NWOP_6GFARR_Eng
[6] D. Oepts and W.B. Colson, IEEE J. of Quantum Electron., 26 (1990) 723
[7] E.B. Szarmes, E.D. Madden, and J.M. Madey, J. Opt Soc. Am. B, 13 (1996) 452
[8] E.B. Szarmes and J.M. Madey, IEEE J. of Quantum Electron., 29 (1993) 452
[9] D. Oepts, A.F.G. van der Meer, R.J.Bakker, and P.W. Amersfoort, Phys. Rev. Letters, 70 (1993) 3255
[10] D. Oepts, R.J.Bakker, D.A. Jaroszynski, A.F.G. van der Meer, and P.W. Amersfoort, Nucl. Instr. And Meth., A331 (1993) 42
[11] H.H. Weits, A.F.G. van der Meer, D. Oepts, and Meisong Ding, Nucl. Instr. And Meth., A393 (1997) 61
[12] H.H. Weits, Thesis, Technical University Eindhoven, 1998

THE ROSSENDORF IR-FEL ELBE

P. Michel, H. Buettig, F. Gabriel, M. Helm, U. Lehnert, Ch. Schneider, R. Schurig, W. Seidel, D. Stehr, J. Teichert, S. Winnerl, R. Wuensch
Forschungszentrum Rossendorf, Germany.

Abstract

The radiation source ELBE is the central research facility in the Forschungszentrum Rossendorf. The machine is based on a 40 MeV superconducting RF Linac which can be operated up to 1 mA in cw mode. After commissioning the Bremsstrahlung and the X-ray facilities in 2002 and 2003, respectively, and the first lasing of the mid-IR FEL (3-22 µm) in 2004 about 7000 hours user beamtime have been provided. At present a second FEL for long IR waves (20-150 µm) using a partial waveguide is under commissioning. First lasing was demonstrated on August 21-st, 2006. Besides in-house users particularly the IR beam is available to external users in the FELBE (FEL@ELBE) program which is a part of the EU funded integrated activity on synchrotron and free electron laser science. In this contribution the fundamental features of the ELBE IR FEL's and the operational experiences which were collected during two years of FEL user operation are described. Future projects like the combination of the new High Magnetic Field lab with the ELBE-IR beams will open up unique experimental possibilities.

INTRODUCTION

In the Forschungszentrum Rossendorf in Dresden, Germany, the superconducting electron accelerator ELBE (Electron Linac with high Brilliance and low Emittance) has come into user operation in 2002. ELBE accelerates electrons to energies up to 40 MeV with an average beam current of 1 mA in quasi continuous wave (cw) mode. The electron linac [1] serves as a driver to generate several kinds of secondary radiation and particle beams, which are FEL-Infrared Radiation for a very large field of applications reaching from semiconductor physics to biology, MeV Bremsstrahlung for nuclear (astro) physics, monochromatic hard-X-ray channelling radiation for radiobiological experiments, and in near future also neutrons and positrons for studies in nuclear reactor science and materials research. The kind and characteristics of the produced secondary beams at ELBE are in accordance with the scientific profile and the experimental requirements of the Forschungszentrum Rossendorf. For a layout of the ELBE building see Fig. 1.

ELECTRON LINAC

A driver for these different kinds of secondary radiation must be characterized by a high average beam current and a small transverse and longitudinal emittance. For this reason only a superconducting high frequency accelerator was taken into consideration. Low energy electron bunches are produced in a grid-pulsed thermionic gun operating at 250 keV DC voltage. It delivers pulses with a bunch charge up to 77 pC at 13 MHz repetition rate and about 450 ps length. The transverse emittance in this case is about 10 mm mrad caused by the electric-field deformation close to the grid [2]. To generate beams with smaller emittance values the grid can be pulsed with 260 MHz at drastically reduced bunch charge. In combination with phase space cutting using apertures, emittance values below 2 mm mrad can be achieved in this regime. For reduced average power, macro bunching is possible as well, yielding 100 µs or longer macro pulses at a < 25 Hz repetition rate. Pulse compression down to 10 ps which is necessary for injection into the 1.3 GHz RF accelerator is done by a two-stage RF bunch compressor operating at 260 MHz and 1.3 GHz, respectively.

The two main accelerator stages are based on two 9-cell RF cavities which were developed for the TESLA project at DESY [3] and are kept at 2 K using superfluid helium delivered by a commercial helium liquefier (Linde). The cavities are individually driven by 10 kW CPI klystron amplifiers. The RF couplers consist of a double-window arrangement and a door-knob shaped adapter for RF transmission from rectangular waveguides to co-axial cavity coupler antenna. The vacuum windows are rectangular plastic windows at room-temperature level and circular ceramic windows cooled by liquid nitrogen. The maximum acceleration field gradients of the cavities exceed 10 MV/m. In practice only 9-9.5 MV/m are accomplished limited by cavity heat loading and field emission. Taking into account that the total acceleration energy is reduced by nearly two MeV due to the capture of low-beta electrons in the first accelerator stage, the maximum total energy is about 36 MeV in practice. To achieve higher acceleration field the RF can be pulsed up to a duty cycle of 1:2. Maximum energy of about 50 MeV can be obtained at a duty cycle of 1:10. A magnetic bunch compressor with adjustable R_{56} < 500 mm is located between the acceleration modules and serves, together with the RF phase of the accelerator cavities, to modify the longitudinal phase space configuration. The electron beam parameters at ELBE will be considerably improved by replacing the thermionic DC gun by a superconducting RF photo gun [4] which is planned for 2007.

FREE ELECTRON LASERS

To cover the required wavelength range two FELs are required. The calculated ranges for both FELs are shown

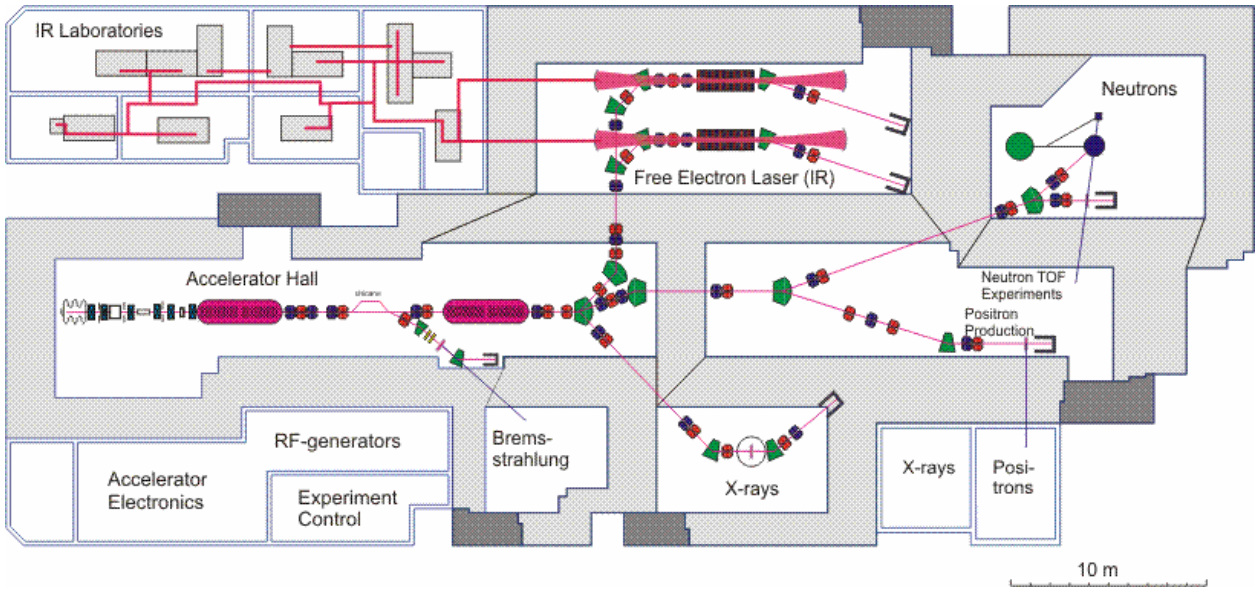

Figure 1: Layout of the Radiation Source ELBE

in Fig. 2. The U27 FEL consists of two 34-pole sections with individually adjustable gaps. The undulator period is 27.3 mm and the magnet material is NdFeB (hybrid type). The distance between the two sections is adjustable for phase matching. The gaps can be varied independently from 13.8 mm to 21 mm corresponding to K_{rms}= 0.7 to 0.3. To optimize the extraction ratio over the whole wavelength range mirrors with different outcoupling hole sizes (1.5, 2, 3, and 4 mm in diameter) are used. The mirrors are made of gold coated copper.

The U100 FEL for the far infrared range is based on a SmCo hybrid undulator which consists of 38 magnet periods each 100 mm long. The K_{rms} can be adjusted from

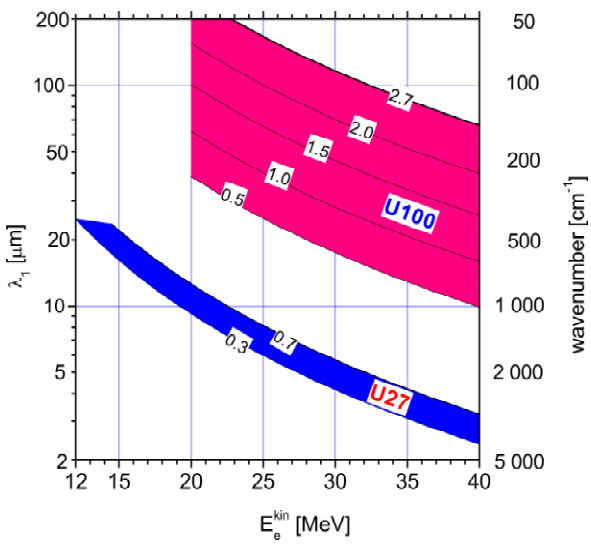

Fig.2: Wavelength ranges of the U27 and the U100 FELs at ELBE as a function of the electron kinetic energy calculated for the indicated values of the undulator parameter K_{rms}.

0.3 to 2.7 which corresponds to gaps of 85 to 24 mm. It is also equipped with interchangeable outcoupling mirrors (hole diameter 2, 4.5 and 7 mm). To obtain high enough magnetic fields in the undulator the gap and consequently the optical mode has to be sufficiently small. To fulfill this requirement the U100 FEL is equipped with a partial parallel-plate waveguide 10 mm wide. The horizontal size is wide enough to allow free propagation. The waveguide spans from the undulator entrance to the downstream mirror. In the remaining part of the optical cavity the optical mode propagates freely. Mirrors are toroidal on the free propagation side (6.33 m and 3.61 m curvature) and cylindrical (6.33 m curvature) on the waveguide side. They are also made of copper with gold coating.

OPTICAL USER LABS

Experiments are performed in the IR user labs, that are shown in the upper left corner of the sketch of Fig. 1. A lot of ancillary equipment is provided, most importantly a number of table-top optical sources like femtosecond Ti:sapphire lasers and a ps Nd:YAG laser which can be synchronized with the FEL to better than a picosecond. The labs are specially equipped for imaging of thin films on surfaces by polarization-modulation IR reflection-absorption spectroscopy and time resolved femtosecond (pump-probe) experiments. Scattering scanning-near-field optical microscopy (SNOM) has been performed as well, There is one user lab with permission for handling of radioactive substances which allows IR spectroscopy on radioactive samples.

The IR beams coming from U27 or U100 both enter a common beam path at the diagnostic station shown in Fig. 3. Most of its components are designed for remotely controlled operation. A scraper mirror is used to outcouple a certain fraction of the main beam for

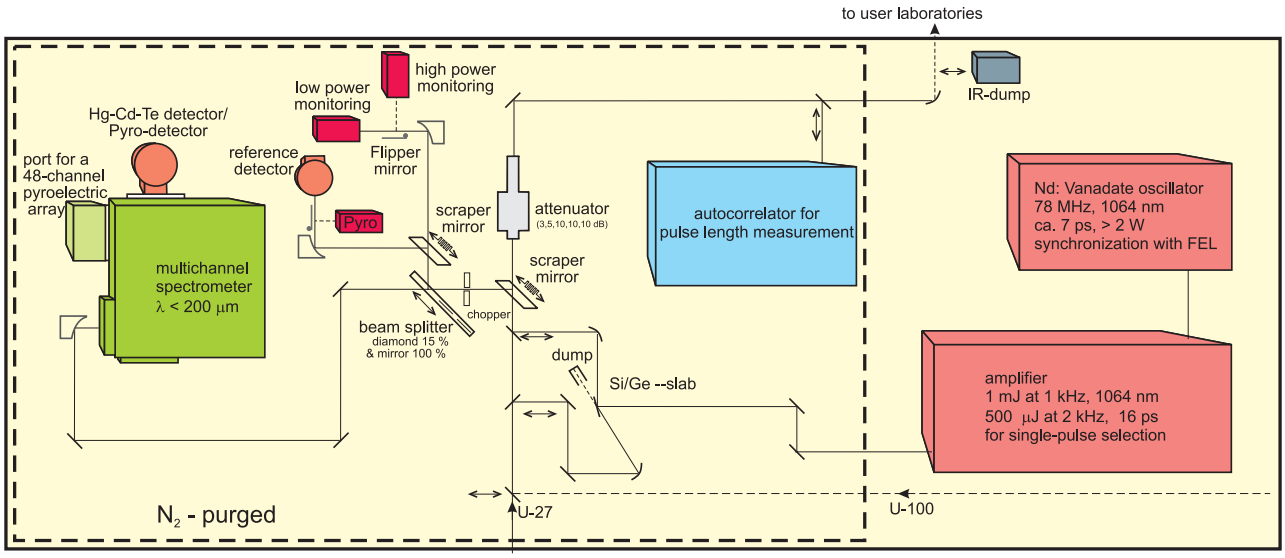

Fig 3. Layout of the diagnostic station for the IR beam.

diagnostic purposes. It can be directed either to an MCT detector which is used to monitor the start up of the laser and its temporal structure and which also acts as a reference detector for experiments or to one out of two power meters. Several MCT detectors are available with preamplifier bandwidth ranging up to 20 MHz enabling us to detect individual micro pulses. For very long wavelengths or measurements with extremely high sensitivity a Ge-Ga detector can be set up. Via a beam splitter part of the diagnostic beam can be sent through a wide-range spectrometer. To cope with CW operation of the FEL a chopper is included in the diagnostic beam path which is synchronized to the macro pulse in pulsed-mode operation. The main beam path to the user laboratories first contains a remotely controlled attenuator. A non-collinear background-free autocorrelator can be used to characterize the optical pulse duration. For experiments requiring lower repetition rates than the 13 MHz round-trip time of the optical resonators a semiconductor plasma switch driven by a Nd:YAG laser amplifier at 1 kHz rate can be used as pulse picker. The optical beamline to the user laboratories is designed for less that 15% transmission loss between 3 and 150 µm wavelength. The typical horizontal polarization is conserved but can be switched if necessary.

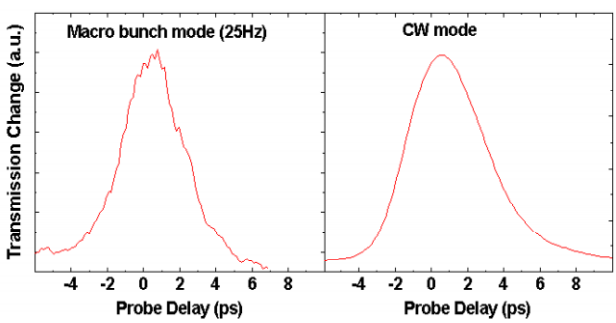

Fig 4. Transient transmission change measured with the pump-probe technique in accelerator macro pulsed mode (left) and in cw mode (right). Both pulses (15.8 µm) are generated by the FEL.

Proposals for FEL experiments are evaluated and selected in a peer-review system. Under the name FELBE the facility is a member of the EC funded "Integrating Activity on Synchrotron and Free Electron Laser Science (IA-SFS)" which comprises most synchrotron and FEL facilities in Europe and provides financial support to users from the EC and associated states. Up to now 12 experiments have been running at the ELBE FEL facility.

OPERATIONAL EXPERIENCES

First lasing of the U27 FEL was achieved in May 2004 [5]. Immediately after commissioning routine user operation was started. Up to now more than 1300 hours for user FEL experiments were delivered. The availability of the machine in 2006 has been higher than 90 %. The following parameters are achieved in practice: Laser radiation from 3.4 to 22 µm was generated. The outcoupled beam power depends strongly on the wavelength range. Low average power (<5 W) was observed in the ranges shorter than 5 and longer than 13 µm. In the range in between up to 25 W power could be extracted. In the region above 20 µm the outcoupled power is smaller than 1 W and finding stable conditions for lasing is difficult due to the high diffraction and aperture losses in the undulator vacuum chamber. The IR pulse duration can be varied by detuning the optical cavity. At 11 µm, which was an often required wavelength for user experiments, it could be adjusted from 0.9 to 3.4 ps. It could be shown by comparing autocorrelation traces with optical spectra that the pulses are bandwidth limited. By many of the FEL users high average power implying cw operation is required. Apart

from the higher measuring rate and the associated better signal to noise ratio a clearly higher stability of the laser at cw operation was observed. Reasons for this observation are the continuous loading of the superconducting RF cavities and the continuous laser operation. Fluctuations due to build up of the laser into saturation can be avoided. Fig. 3 demonstrates the improved quality of the experimental data in cw mode. It shows a typical time resolved transmission traces measured by the pump-probe-technique in macro pulse mode (left) and cw mode (right). The measurements were done in the framework of an experiment to study electron dynamics in superlattices [6].

OUTLOOK

First lasing of the U100 FEL was demonstrated on August, 21-st, a few days before the FEL2006 conference. Now the actually available wavelength range and the parameters of the IR beam have to be determined. Then the extended wavelength range will immediately be made available to the user experiments.

In the near future the beams of the two FELs will be delivered into the new High Magnetic Field Lab Dresden (HLD) [7] which was built recently in immediate vicinity to the ELBE building. The HLD will provide magnetic-field pulses in the 60-100 Tesla range with 1000-10 ms pulse duration, thus opening the way for many new spectroscopic investigations, in particular in solid state and semiconductor physics. For these investigations also time resolved experiments are envisaged. The challenge here is to obtain a complete time-delay scan during the time of one magnetic field pulse. Recently we have demonstrated the measurement of an FEL interferometric autocorrelation trace within 25 ms [8]. In general, no synchronization of the FEL with magnetic field pulses is needed, since the FEL runs continuously at 13 MHz in cw mode which means that about 10^5 FEL pulses overlap with one 10 ms-magnetic field pulse. This should provide excellent measurement conditions.

ACKNOWLEDGEMENT

The authors thank Todd Smith from HEPL Stanford University and A.F.G. van der Meer from FELIX Nieuwegein for her useful help and advice. Furthermore we thank the engineering stuff of the Forschungszentrum Rossendorf for the successful cooperation.

REFERENCES

[1] F.Gabriel et al., NIM B 161-163 (2000), 1143-1147.
[2] J. Teichert et al., Proceedings of the 6th International Computational Accelerator Physics Conference, Darmstadt, Germany, 2000.
[3] TESLA Test Facility Linac – Design Report (Ed. D.A. Edwards), DESY print TESLA 95-01.
[4] J.Teichert et al., Proceedings of the 2005 FEL Conference, p. 534-537, Stanford, USA.
[5] P.Michel et al., Proceedings of the 2004 FEL Conference, p. 8-18, Trieste, Italy.
[6] D. Stehr et al., Appl. Phys. Lett. **88** 151108 (2006)
[7] http://www.fz-rossendorf.de/HLD
[8] H. Schneider et al., Appl. Phys. Lett. **89** (2006), in print.

STATUS OF THE NOVOSIBIRSK HIGH POWER TERAHERTZ FEL*

N.A. Vinokurov#, N.G. Gavrilov B.A. Knyazev, E.I. Kolobanov, V.V. Kotenkov, V.V. Kubarev, G.N. Kulipanov, A.N. Matveenko, L.E. Medvedev, S.V. Miginsky, L.A. Mironenko, A.D. Oreshkov, V.K. Ovchar, V.M. Popik, T.V. Salikova, M.A. Scheglov, S.S. Serednyakov, O.A. Shevchenko, A.N. Skrinsky, V.G. Tcheskidov, Budker INP, Novosibirsk, Russia.

Abstract

The first stage of Novosibirsk high power free electron laser (FEL) was commissioned in 2003. It is based on the normal conducting CW energy recovery linac (ERL). Now the FEL provides electromagnetic radiation in the wavelength range 120 - 230 micron. The maximum average power is 400 W. The minimum measured linewidth is 0.3%, which is close to the Fourier-transform limit. Four user stations are in operation now. Manufacturing of the second stage of the FEL (based on the four-turn ERL) is in progress.

INTRODUCTION

A new source of terahertz radiation was commissioned recently in Novosibirsk. [1]. It is CW FEL based on an accelerator–recuperator, or an energy recovery linac (ERL). It differs from other ERL-based FELs [2, 3] in the low frequency non-superconducting RF cavities and longer wavelength operation range. Full-scale Novosibirsk free electron laser is to be based on the four-orbit 40 MeV electron accelerator-recuperator (see Fig. 1). It is to generate radiation in the range from 5 micrometer to 0.24 mm [4, 5].

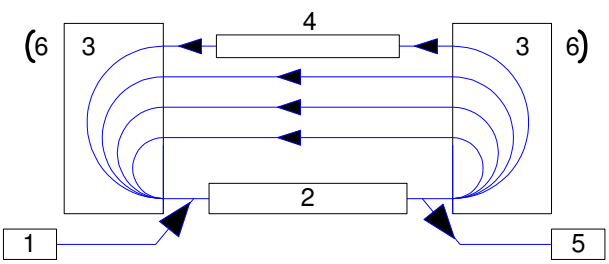

Figure 1: Scheme of the accelerator-recuperator based FEL. 1 - injector, 2 - accelerating RF structure, 3 - 180-degree bends, 4 – undulator, 5 – beam dump, 6 – mirrors of the optical resonator.

ACCELERATOR-RECUPERATOR

The first stage of the machine contains a full-scale RF system, but has only one orbit. Layout of the accelerator–recuperator is shown in Fig. 2. The 2 MeV electron beam from an injector passes through the accelerating structure, acquiring the 12 MeV energy, and comes to the FEL, installed in the straight section. After interaction with radiation in the FEL the beam passes once more through the accelerating structure, returning the power, and comes to the beam dump at the injection energy. Main parameters of the accelerator are listed in Table 1.

Table 1: Accelerator parameters (first stage)

RF frequency, MHz	180
Number of RF cavities	16
Amplitude of accelerating voltage at one cavity, MV	0.7
Injection energy, MeV	2
Final electron energy, MeV	12
Maximum bunch repetition rate, MHz	22.5
Maximum average current, mA	20
Beam emitance, mm·mrad	2
Final electron energy spread, FWHM, %	0.2
Final electron bunch length, ns	0.1
Final peak electron current, A	10

The electron source is the 300 keV DC gun with gridded cathode. Maximum charge per bunch is 1.7 nC.

FEL

The FEL is installed in a long straight section of a single-orbit accelerator-recuperator. It consists of two undulators, a magnetic buncher, and optical resonator. Both electromagnetic planar undulators are identical. The length of an undulator is 4 m, period is 120 mm, the gap is 80 mm, and deflection parameter K is up to 1.2. The buncher is simply a three-pole electromagnetic wiggler. It is necessary to optimize the relative phasing of undulators and is used now at low longitudinal dispersion $N_d < 1$.

Both laser resonator mirrors are spherical, 15 m curvature radius, made of the gold-plated copper, and water-cooled [6]. In the center of each mirror there is a hole. It serves for mirror alignment (using the He-Ne laser beam) and output of small amount of radiation. The distance between mirrors is 26.6 m. The forward mirror has the hole with the diameter 3.5 mm, and the rear one - with the diameter 8 mm (See Fig.3). The calculated transparency of the mirror with the 8-mm hole, at the wavelength 150 micron, is 1.5%. At this wavelength the measured round-trip loss are near 7%. The output radiation passes through two windows, which separated the FEL and accelerator vacuum from the atmosphere. After the forward mirror the additional iris and the normal-incidence quartz window are installed. After the rear one there is a diamond window, tilted at the Brewster angle.

* The work was partially supported by SB RAS grant N174/06 and by grant №2.1.1.3846 of Russian Ministry of Science and Education.
# vinokurov@inp.nsk.su

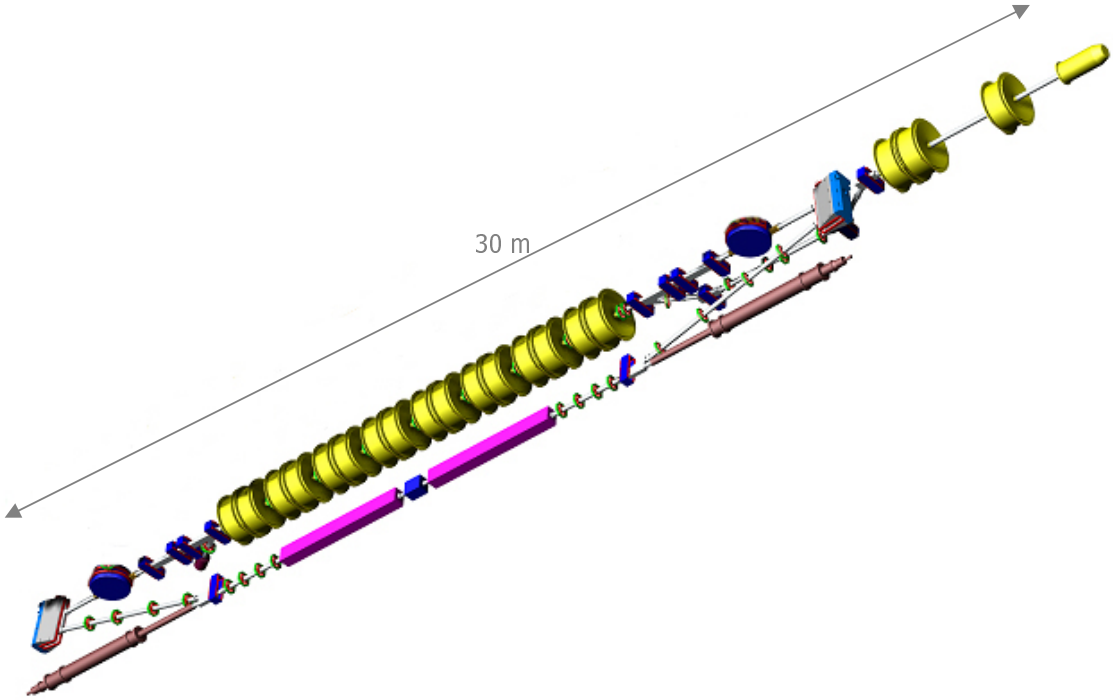

Figure 2: Scheme of the first stage of the Novosibirsk terahertz FEL. The loop lies in the vertical.

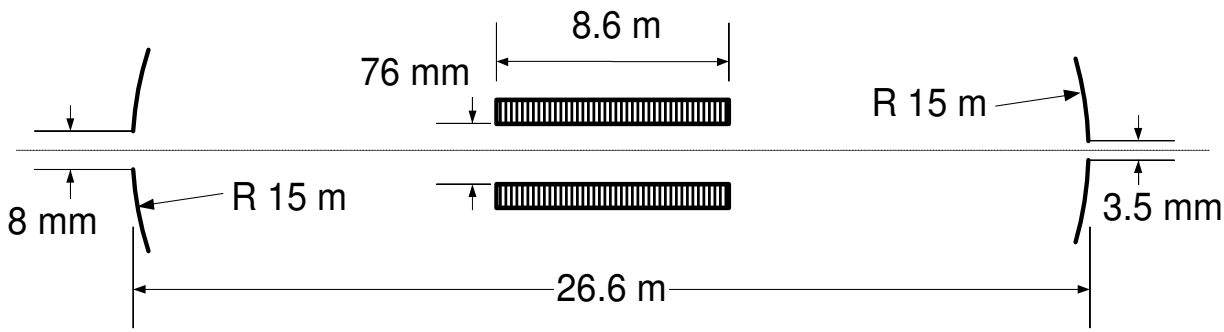

Figure 3: Scheme of the optical resonator.

RADIATION STUDY

The first measurements of radiation parameters were reported before [1].

Instead of the fine tuning of the optical resonator length we tuned the RF frequency. The tuning curve is shown in Fig. 4. The preliminary simulation results [7] demonstrated a reasonable agreement with measured data. The experimental curve is wider, which may be explained by the shortening of the optical resonator due to mirror heating.

The average radiation power, passed through the hole at the rear mirror, was about 400 W. Taking into account the 7% loss, one get approximately 2 kW of power, extracted from the electron beam. The electron beam power was 200 kW. Therefore an electron efficiency is about 1%. The radiation parameters are listed in Table 2.

Table 2: The radiation parameters

Wavelength, mm	0.12...0.23
Minimum relative linewidth, FWHM	0.003
Pulse length, FWHM, ns	0.05
Peak power, MW	1
Repetition rate, MHz	11.2
Maximum average power, kW	0.4

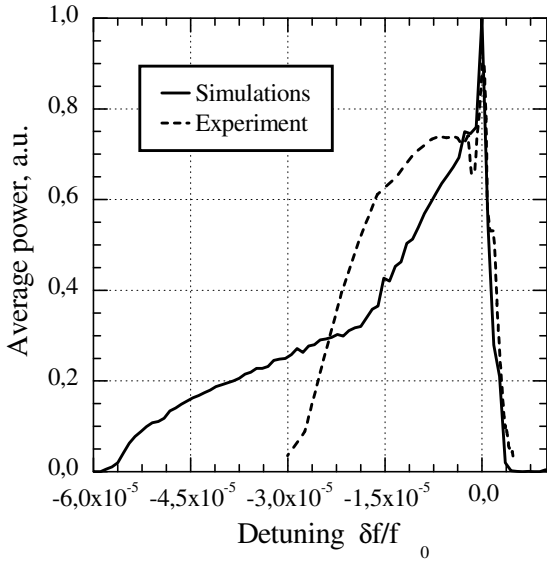

Figure 4: Dependence of the average power on the RF frequency detuning.

BEAMLINE AND USER STATIONS

To transmit the radiation from the rear mirror hole to user stations, the beamline from the accelerator hall to the user hall was built. As the diffractional angular divergence $1.22 \cdot \lambda/D = 0.03$ (for 200 micron) is high, the spherical mirror is used to transform the radiation beam to almost parallel one. The incidence angle is only 7 degrees, therefore astigmatism is negligible (see Fig. 5).

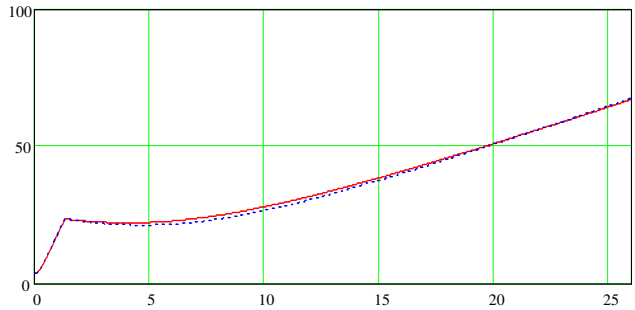

Figure 5: Calculated size of equivalent Gaussian beam (mm) vs. distance along the beamline (m).

Other 5 mirrors are flat. The beamline is filled by dry nitrogen. It is separated from the accelerator vacuum by the diamond window, and from the air by the polyethylene window. After installation of nitrogen dryer we obtained almost complete transparency of the beamline.

Now radiation may be delivered to 5 stations. Two of them are used for measurement of radiation spectrum, and other three – for users. In particular, the terahertz ablation of DNA and other biologically relevant molecules was performed [8]. It was shown, that transfer from surface occurred without molecular destruction.

FURTHER DEVELOPMENTS

We plan to increase further the output power. The electron gun upgrade for the increase of the average

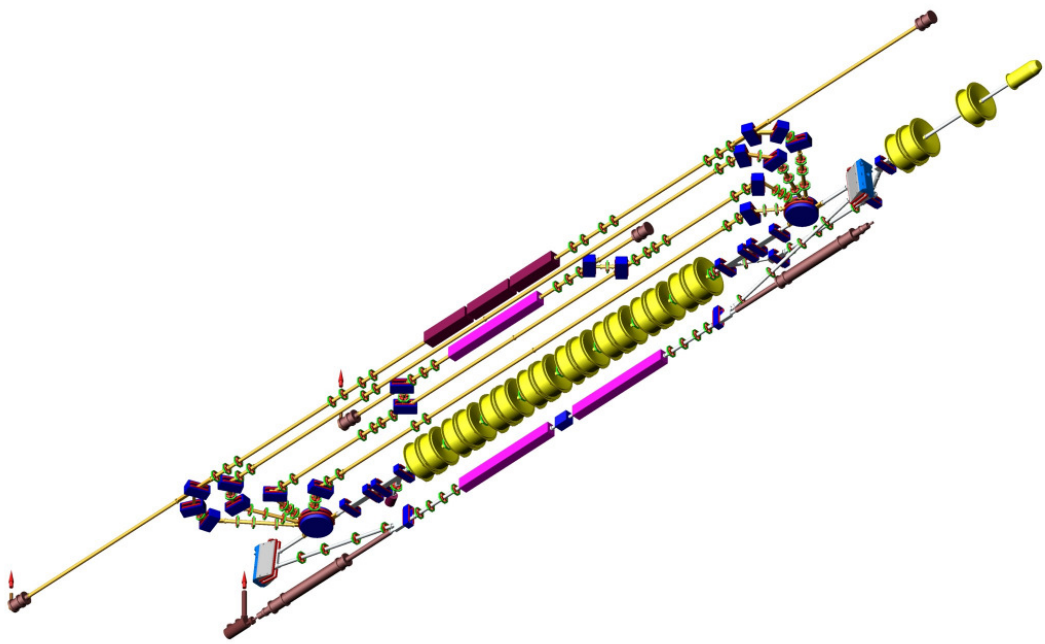

Figure 6: Scheme of the second stage of the Novosibirsk terahertz FEL. The terahertz FEL orbit lies in the vertical plain. Other four orbits lie in the horizontal one.

current up to 0.1 A is in progress.

The design and manufacturing of the full-scale four-turn ERL is underway. An artistic view of the machine is shown in Fig. 6. The existing orbit with the terahertz FEL lies in the vertical plane. The new four turns are in the horizontal one. One FEL is installed at the fourth orbit (40 MeV energy), and the second one at the bypass of the second orbit (20 MeV energy).

REFERENCES

[1] E. A. Antokhin et al. NIM A528 (2004) p.15-18.
[2] G.R. Neil et al. Phys. Rev. Lett. 84 (2000), p. 662.
[3] E.J. Minehara. NIM A483, p. 8, 2002.
[4] N.G. Gavrilov et al. IEEE J. Quantum Electron., QE-27, p. 2626, 1991.
[5] V.P.Bolotin et al. Proc. of FEL-2000, Durham, USA, p. II-37 (2000).
[6] Kubarev V.V., Persov B.Z., Vinokurov N.A., Davidov A.V. NIM A528 (2004), No. ½, p. 199-202.
[7] O.A. Shevchenko, A.V. Kuzmin, N.A. Vinokurov. NIM A543 (2005), No. 1, p. 114-117.
[8] A. K. Petrov et al., Russian Dokl. Acad. Nauk, v. 404 (2005), No. 5, p. 1 – 3.

FEL ACTIVITIES IN INDIA

S. Krishnagopal*, B. Biswas, S. Chouksey, S. K. Gupta, U. Kale, A. Kumar, V. Kumar, S. Lal, P. Mehta, P. Nerpagar, K. K. Pant, RRCAT, Indore, India.

Abstract

We are building a Compact Ultrafast TErahertz Free-Electron Laser (CUTE-FEL), designed to lase from 50 – 100 μm. The FEL will be driven by a 10-15 MeV electron beam from a Plane-Wave Transformer (PWT) linac. The undulator is a 5 cm period, 2.5 m long PPM planar undulator. We present details of the FEL design and the present status of activities. We also present very preliminary plans for a short-wavelength SASE FEL in India.

INTRODUCTION

FEL activity in India is presently restricted to the Raja Ramanna Centre for Advanced Technology, Indore, where a terahertz FEL is under construction. Earlier, however, there was some activity at Pune University, where a 26 mm period, 39 cm long pure permanent magnet undulator was built and characterized [1]. At the Institute for Plasma Research, Ahmedabad, there was interest in FELs for plasma heating and diagnostics. A 50 period electromagnet undulator was developed, a 300 keV sheet electron beam from a Tesla transformer was transmitted through this undulator, and spontaneous emission was observed [2].

In this paper we focus on ongoing activities at RRCAT, and present briefly our plans for the future.

THE CUTE-FEL PROJECT

The terahertz is a relatively unexplored part of the electromagnetic spectrum, and there is presently substantial interest in terahertz sources. For an FEL the terahertz is attractive because the long wavelength allows for higher gain, and reduces the requirements on the beam current and quality. A THz FEL is therefore a good green-field FEL project.

The Compact Ultrafast TErahertz FEL (CUTE-FEL) project aims to lase between 50-100 μm. The layout of the beamline is shown in Figure 1. The main parameters of the FEL are given in Table 1.

The electron source is a thermionic electron gun, that will provide 90 kV, 1 nC, 1 ns (FWHM) electron pulses at 36.62 MHz. The design normalized rms beam emittance is 5π mm-mrad, and the rms energy spread will be better than 1%. This gun is under procurement. In the meantime we continue experiments with a 40 kV, 2 μs, triode gun that was built by another group in RRCAT [3].

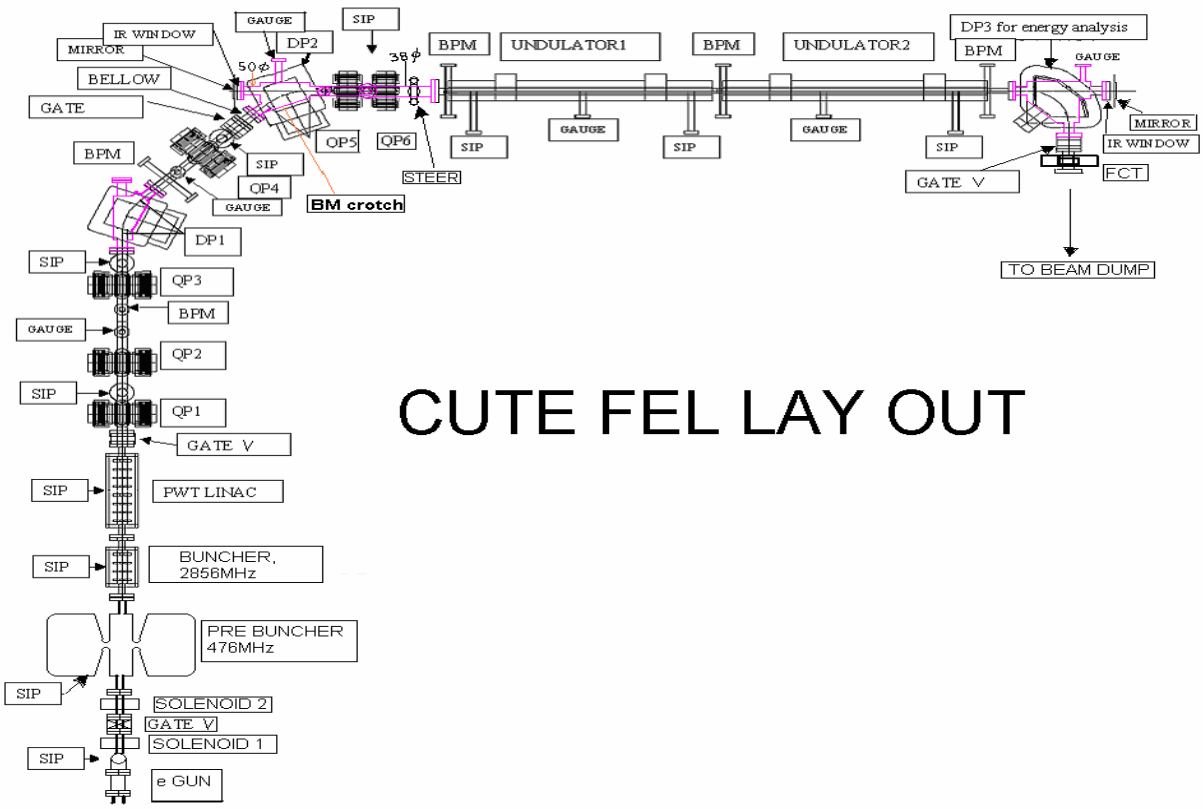

Figure 1: Beam-transport line for the CUTE-FEL.

*skrishna@cat.ernet.in

The electrons from the gun will be bunched in a 476 MHz pre-buncher, which has been designed by us and is presently being fabricated. The design is a standard re-entrant pillbox cavity, and will compress the beam by a factor of around 18.

The buncher at 2856 MHz will be a 4-cell Plane Wave Transformer (PWT) structure, and the linac itself will comprise up to two 8-cell structures to go to a maximum energy of 15 MeV. More details on the PWT structure, which we have developed ourselves, are given in a later section.

Table 1: Main parameters of the CUTE-FEL

Parameter	**Value**	**Unit**
Energy	10-15	MeV
Peak current	20	A
Micro-pulse	20 @ 36.62	ps @ MHz
Macro-pulse	8 @ 10	μs @ Hz
Und. period	5	cm
Und. length	2.5	m
Und. param.	0.8	
Wavelength	50-100	μm

The undulator is a standard Halbach configuration, planar PPM undulator, using NdFeB magnets. It has a period of 5 cm and a total length of 2.5 m. We have performed detailed design simulations using the code TDAOSC [4] AND GENESIS 1.3 [5]. In order to make the FEL compact, we have tried to keep the optical cavity as short as possible – it is only 4.1 m long. The resonator is near-concentric, to provide good mode stability.

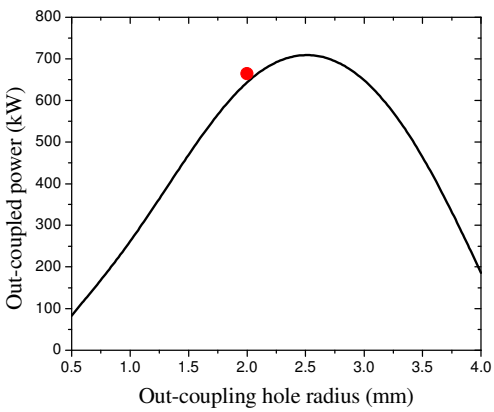

Figure 2: Optimisation curve for the size of the out-coupling hole.

Radiation is out-coupled through a hole at the centre of one of the gold-plated copper mirrors. The optimal hole radius, to maximize the out-coupled power while maintaining a good mode profile, was determined to be 2 mm (see Fig. 2). For our design we get a peak out-coupled power of around 0.5 MW. The small-signal gain is 88%, while the round-trip loss is 15%.

Figure 3 shows the variation of the FEL beam size down the undulator. At the entrance and exit of the undulator the maximum 1/e beam radius is around 5 mm. Note that the matched rms vertical beam size of the electron beam within the undulator is 0.8 mm.

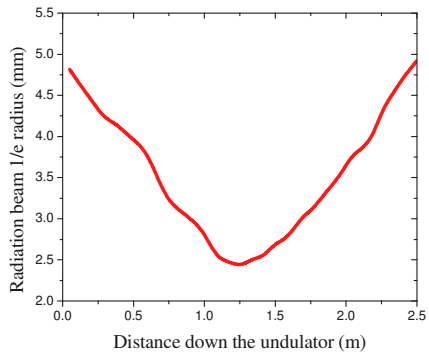

Figure 3: Size of the radiation beam as a function of distance down the undulator.

UNDULATOR

The 5 cm period, 2.5 m long PPM undulator has been constructed [6] in two equal segments of 25 periods each (Fig. 4). The undulator gap can be varied from 20-100 mm. The magnets are made of NdFeB, each 12.5 x 12.5 x 50 mm^3 in size. Individual magnets were characterized, and their arrangement in the undulator determined using a global optimisation (simulated annealing) algorithm. Field measurement of the assembled undulator segments was done using a three-axis Hall probe (Senis GmbH), with a spatial resolution of 0.1 mm.

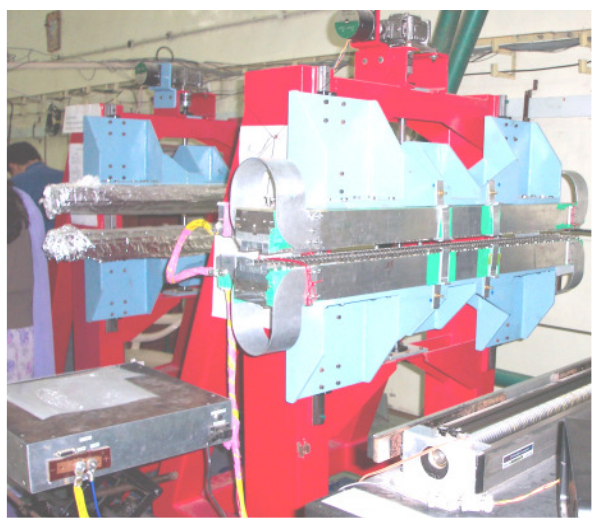

Figure 4: A view of the two undulator segments, each of length 1.25 m.

A summary of the measurements is given in Table 2. It can be seen that almost all the parameters are within the design specification. Our initial measurements showed that the beam trajectory through U25.2 had a degree of drift. To correct this we built a corrector coil that gives a

small, 0.77 G, vertical field. With this correction the trajectory straightens out to within acceptable limits (Fig. 5). Further improvements can be done by shimming the magnets.

Table 2: Design and measured parameters of the two undulator segments

Parameter	Design value	U25.1 measured	U25.2 measured
Error in peak field	< 1%	0.9%	0.7%
Error in period	< 100 μm	82 μm	85 μm
rms phase-shake	< 5°	2°	2°
Beam wander	< 1	1.14	0.33

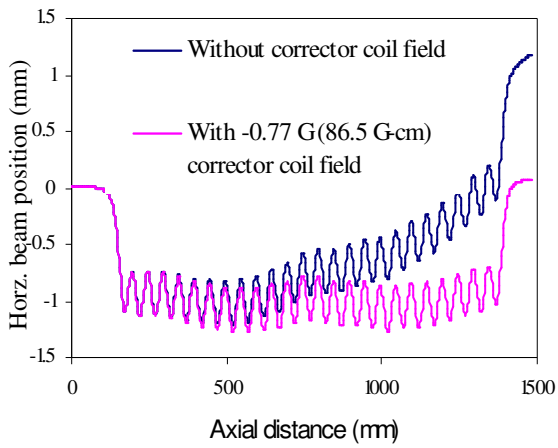

Figure 5: Electron beam trajectory through the undulator, with and without the corrector coil.

PWT LINAC

A major challenge has been the indigenous development of the linear accelerator technology. We also chose to build a rather unconventional structure – the plane wave transformer (PWT) linac [6]. This is a much more open structure, with strong coupling between the cells – and consequently with reduced fabrication tolerances. The only PWT linac working in the world is at UCLA [7], where it is routinely used, mainly for FEL applications.

After building a number of prototypes and ascending a steep learning curve, we now have a four-cell, 21 cm long structure, PWT3 (Fig. 6) that has been fabricated to the required tolerances (30 μm) and surface finish (0.2 μm CLA), which can hold UHV ($1x10^{-8}$ torr), resonates at the desired frequency of 2856 MHz, and has a loaded Q of 8,000.

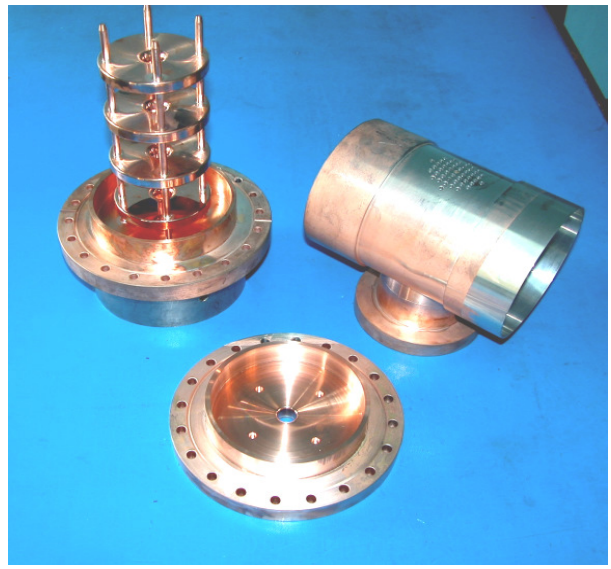

Figure 6: Components of the 4-cell PWT linac structure.

We have injected beam from a 40 kV thermionic electron gun into this structure, and have accelerated it to an energy of 3.5 MeV, corresponding to an accelerating gradient of around 25 MV/m. We also have ready a second 4-cell structure, PWT4, and are presently in the midst of fabricating an 8-cell PWT structure.

S-BAND PHOTOINJECTOR

Independent of the CUTE-FEL project, we have also been developing an S-band photoinjector, keeping in mind the requirements of short-wavelength FELs [8]. Our gun is based on the standard BNL/SLAC/UCLA Gun 4 design. We have performed extensive electromagnetic and beam dynamics design simulations using SUPERFISH, GDFIDL and PARMELA. We have also studied the injection of beam from the gun into a PWT linac structure.

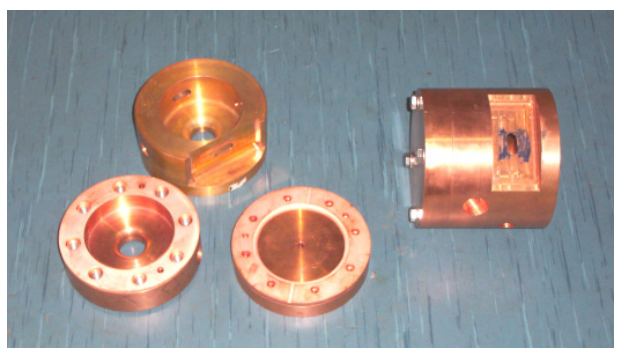

Figure 7: Components of the ETP Cu prototypes of the photocathode RF gun.

We have built a number of prototypes, of ETP and OFE copper, to qualify machining and brazing issues (Fig. 7). We have also built a number of aluminium prototypes for cold tests and for tuning the gun. We have developed a two-step tuning procedure to get the desired gun parameters – resonant frequency of the π-mode at 2856

MHz, β = 1 and field balance of unity, directly, without empirical tuning of the gun during cold-tests (Fig. 8). We have now given an order to an Indian vendor for fabricating four photocathode guns.

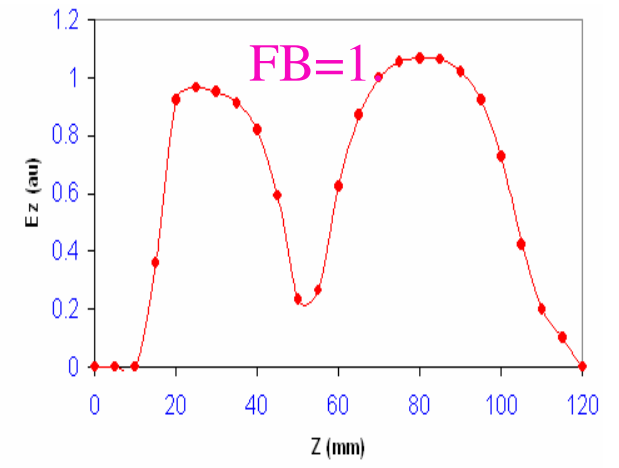

Figure 8: Bead-pull of a tuned Al prototype photocathode gun.

FUTURE PLANS

While we are presently focused on getting the CUTE-FEL lasing, some thought is also being given to future FEL activities in the country.

Table 3: Preliminary proposal of a 3-stage roadmap for the FEL programme in India

	Stage I	**Stage II**	**Stage III**
Wavelength (nm)	1,000	10	0.1
Energy (GeV)	0.1	1	10
Norm. emitt. (mm-mrad)	5	3	1
Undulator period (mm)	50	30	30
Undulator length (m)	5	30	100
Undulator param. 'K'	1	1.5	3
Peak current (A)	0.1	2	4
Pulse structure (fs @ Hz)	1,500 @ 50	150 @ 50	75 @ ??
Accel. Tech.	Norm. cond.	Norm. cond.	???

A joint Indo-French Workshop on FELs, was held in Goa, India, in March 2006. The consensus that emerged from this Workshop, especially from the Indian users who participated, was that a phased approach towards short-wavelength FELs, perhaps ultimately culminating in an XFEL, was highly desirable. To this end a preliminary three-stage roadmap has been proposed, summarized in Table 3.

There is already substantial interest amongst the user community in the country, particularly in materials science, for an IR-FEL facility (Stage I of the proposed roadmap). Another user workshop is planned to be held later this year.

CONCLUSIONS

A terahertz FEL, the CUTE-FEL, is in an advanced stage of construction at RRCAT. We have developed a PWT linac injector for the FEL, and have accelerated beam to 3.5 MeV in a 4-cell structure. We have built a 5 cm period, 2.5 m long PPM undulator. We are also in the final stages of development of an S-band photoinjector. Based on this foundation, and on interest shown by the user community, we expect a rapid expansion in the FEL activities in India in the coming years, starting with an IR-FEL facility, and perhaps continuing towards an XFEL in the future.

ACKNOWLEDGEMENTS

We thank Dr. R. V. Nandedkar and Dr. V. C. Sahni for their constant support and encouragement. We also thank a large number of colleagues, too numerous to be listed, for their support and contribution to the CUTE-FEL project.

REFERENCES

[1] V. B. Asgekar et al., Jap J Appl Phys, **37**, 3563, (1998).

[2] A. V. Ravi Kumar at al., IEEE Trans. Plasma Sci. **26**, 556 (1998).

[3] S. Mahadevan et al., Nucl. Instr. And Method **A**, **496**, 26 (2003).

[4] S. Krishnagopal et al., Nucl. Instr. And Meth. **A 318**, 661 (1992).

[5] http://pbpl.physics.ucla.edu/~reiche/index.html

[6] B. Biswas et al., InPAC'05, Kolkata, March 2005, p. 89.

[7] A. Kumar, K. K. Pant, S. Krishnagopal, Phys. Rev. ST Accel. Beams, **5**, 00033501 (2002).

[8] R. Zhang, Ph. D. Dissertation, UCLA, 1997.

[9] A. Kumar, K. K. Pant, S. Krishnagopal, Phys. Rev. ST Accel. Beams, **5**, 103501 (2002).

OUTPUT BANDWIDTH EFFECTS IN SEEDED, HARMONIC CASCADE FELS

W.M. Fawley, G. Penn, A. Zholents, LBNL, Berkeley, California

Abstract

A number of laboratories are studying and/or proposing seeded Harmonic Cascade (HC) FELs as a means both to reach soft x-ray output wavelengths and to provide a degree of longitudinal coherence much greater than that normally possible with SASE devices. While theoretically the output bandwidth of a HC FEL can approach the transform limit given a high quality input seed of reasonable power, there appear to be a number of practical considerations that in many cases can increase the output bandwidth many-fold. In particular, designs that employ dispersive sections following modulator sections in order to increase the amount of coherent harmonic microbunching, can be very sensitive to temporal variations in the electron beam energy, resulting in an output wavelength chirp. Unwanted microbunching induced by the combination of longitudinal space charge instability growth in the linac and CSR in compression sections also can lead to variations in the output radiation phase and amplitude, thus increasing the bandwidth. We give some semi-analytical results for the predicted bandwidth increase for HC configurations and also some detailed numerical simulation results.[1]

PAPER NOT AVAILABLE

[1]Work supported in part by the US DOE under Contract no. DE-AC02-05CH11231.

FOURIER OPTICS TREATMENT OF CLASSICAL RELATIVISTIC ELECTRODYNAMICS

G. Geloni*, E. Saldin, E. Schneidmiller and M. Yurkov,
Deutsches Elektronen-Synchrotron (DESY), Hamburg, Germany.

Abstract

We coupled Synchrotron Radiation (SR) theory with laser beam optics. In the space-frequency domain SR beams are described by solutions of the paraxial wave equation. They appear as laser beams with transverse size much larger than the wavelength. In practical situations (e.g. undulators, bends), SR beams exhibit a virtual source, similar to the waist of a laser-beam, strictly related with the inverse Fourier transform of the far-field distribution. The Fresnel formula can be used to propagate the field distribution from the waist to anywhere in space. The general theory of SR in the near-zone developed in this paper is illustrated for the special cases of undulator radiation, edge radiation and transition undulator radiation (TUR). By solving the inverse problem for the electric field we find analytical expressions for near-field distributions in terms of far-field data. A more detailed explanation of this subject is provided in [1].

INTRODUCTION

In previous works we developed a formalism ideally suited for analysis of SR problems, where we took advantage of Fourier Optics ideas [1]. Fourier Optics provides an extremely successful approach which revolutionized the treatment of wave optics problems and, in particular, laser beam optics problems. The use of Fourier Optics led us to establish basic foundations for the treatment of SR fields in terms of laser beam optics. Radiation from an ultra-relativistic electron can be interpreted as radiation from a virtual source producing a laser-like beam. The virtual source is regarded as the analogous of the waist for a laser beam, and often exhibits a plane wavefront. In this case it is specified, for any given polarization component, by a real-valued amplitude distribution of field. The laser-like representation of SR is intimately connected with the ultra-relativistic nature of the electron beam. In particular, paraxial approximation always applies. Then, free space basically acts as a spatial Fourier transformation, and the far-zone field is, aside for a phase factor, the Fourier transform of the field at any position z down the beamline. It is also, aside for a phase factor, the Fourier transform of the virtual source. Once the field at the virtual source is known, the field at other longitudinal positions, both in the far and in the near zone up to distances to the sources comparable with the radiation wavelength, can be obtained with the help of the Fresnel propagation formula. This means that the near-zone field can be calculated from the knowledge of the far-zone field, that is possible because the paraxial approximation applies. The knowledge of the far-zone field completely specifies, through the Fresnel integral, the near-zone field as well. In the case when the electron generating the field is not ultra-relativistic, though, the paraxial approximation cannot be applied. Typically, the wavelength is comparable with the radiation formation length, and it is impossible to reconstruct the near-field distribution from the knowledge of the far-field pattern [2]. An arbitrary SR source is equivalent to several virtual sources inserted between the edges of each magnetic device. This provides conceptual insight of SR sources and should facilitate their design and analysis. In fact, since the analysis of SR sources can be reduced to that of laser-like sources, it follows that any result, method of analysis or design and any algorithm specifically developed for laser beam optics (e.g. the code ZEMAX, see [1]) is also applicable to SR sources. We first apply our method to undulator radiation around resonance. We find the field distribution of the virtual source with the help of the far-zone field distribution and we propagate to any distance of interest. Similarly, we treat edge radiation [1], studying the emission from a setup composed by a straight section and two (upstream and downstream) bends. We derive an expression for the field from a straight section that is valid at arbitrary observation position. Due to the superposition principle, this expression can be used as building block for more complicated setups. We use this idea to analyze a TUR setup consisting of an undulator preceded and followed by straight sections and bends (upstream and downstream). The first study on TUR constituted a theoretical basis for many other studies [1], dealing both with theoretical and experimental issues. More recently, TUR has been given consideration in the framework of large XFEL projects. A method was also proposed [1] to obtain intense infrared/visible light pulses naturally synchronized to x-ray pulses from the LCLS XFEL by means of Coherent TUR. In view of these applications, there is a need to extend the knowledge of TUR to the near zone. We address it here.

FAR-FIELD DATA INVERSE PROBLEM

We represent the electric field in time domain $\vec{E}(\vec{r},t)$ as a time-dependent function of an observation point located at position $\vec{r} = \vec{r}_\perp + z\vec{z}$. In free-space, the field $\vec{E}(\vec{r},t)$ satisfies the source-free wave equation. For monochromatic waves of angular frequency ω the wave amplitude has the form $\vec{E}_\perp(z,\vec{r}_\perp,t) = \vec{\tilde{E}}_\perp(z,\vec{r}_\perp)\exp[-i\omega t]+C.C.$, where the frequency ω is related to the wavelength λ by

* gianluca.aldo.geloni@desy.de

$\omega/c = 2\pi/\lambda$, and $\vec{\tilde{E}}_\perp$ describes the variation of the wave amplitude in the transverse direction. $\vec{\tilde{E}}_\perp$ actually represents the amplitude of the electric field in the space-frequency domain. We assume that the ultra-relativistic approximation is satisfied, that is always the case for SR setups. In this case the paraxial approximation applies [1]. This implies a slowly varying envelope of the field with respect to the wavelength. We therefore introduce $\vec{\tilde{E}}_\perp = \vec{\tilde{E}}_\perp \exp[-i\omega z/c]$. In paraxial approximation and in free space, $\vec{\tilde{E}}_\perp$ obeys the paraxial wave equation along any fixed polarization component, that is $[{\nabla_\perp}^2 + (2i\omega/c)\partial_z]\widetilde{E}_\perp = 0$, where derivatives in the Laplacian operator ${\nabla_\perp}^2$ are taken with respect to the transverse coordinates. Solving this equation with given initial conditions at z gives

$$\widetilde{E}_\perp = \frac{i\omega}{2\pi c(z_o - z)} \int d\vec{r'} \widetilde{E}_\perp(z, \vec{r'}) \exp\left[\frac{i\omega \left|\vec{r}_{o\perp} - \vec{r'}\right|^2}{2c(z_o - z)}\right] \tag{1}$$

where the integral is performed over the transverse plane. A propagation equation for $\mathrm{F}(z, \vec{u}) = \int d\vec{r'}_\perp \widetilde{E}_\perp(z, \vec{r'}_\perp) \exp[i\vec{r'}_\perp \cdot \vec{u}]$, that is the spatial Fourier transform of the field, reads instead:

$$\mathrm{F}(z, \vec{u}) = \mathrm{F}(z_s, \vec{u}) \exp\left[-\frac{ic|\vec{u}|^2(z - z_s)}{2\omega}\right], \tag{2}$$

where z_s is identified with the position of a virtual source. Identification of the position $z_s = 0$ with a virtual source position is always possible, but not always convenient (although often it is). From Eq. (1) and Eq. (2) a relation follows between the far-zone field distribution, dependent on the observation angle $\vec{\theta}$, and the field distribution at the virtual source position z_s:

$$\widetilde{E}_\perp(z_s, \vec{r}_\perp) = \frac{i\omega z_o}{2\pi c} \int d\vec{\theta} \exp\left[-\frac{i\omega|\vec{\theta}|^2}{2c}(z_o + z_s)\right] \times \widetilde{E}_\perp(\vec{\theta}) \exp\left[\frac{i\omega}{c}\vec{r}_\perp \cdot \vec{\theta}\right]. \tag{3}$$

Finally, the transverse components of the envelope of the far field can be written as [1]:

$$\vec{\tilde{E}}_\perp = -\frac{i\omega e}{c^2 z_o} \int_{-\infty}^{\infty} dz' \exp[i\Phi_T] \left[\left(\frac{v_x(z')}{c} - \frac{x_o}{z_o}\right)\vec{x} + \left(\frac{v_y(z')}{c} - \frac{y_o}{z_o}\right)\vec{y}\right], \tag{4}$$

where the total phase Φ_T is

$$\Phi_T = \omega\left[\frac{s(z')}{v} - \frac{z'}{c}\right] + \omega\left(\frac{1}{z_o} + \frac{z'}{z_o^2}\right) \times \frac{[x_o - x'(z')]^2 + [y_o - y'(z')]^2}{2c} \tag{5}$$

and the charge of the electron is $(-e)$. Eq. (4) can be obtained starting directly with Maxwell's equations in the space-frequency domain. Here $v_x(z')$ and $v_y(z')$ are the horizontal and the vertical components of the transverse velocity of the electron, while $x'(z')$ and $y'(z')$ specify the transverse position of the electron as a function of the longitudinal position. Finally, we defined the curvilinear abscissa $s(z') = vt'(z')$, v being the modulus of the velocity of the electron. Eq. (4) can be used to characterize the far field from an electron moving on any trajectory as long as the ultra-relativistic approximation is satisfied. Then, once the far field is known, Eq. (3) can be used to calculate the field distribution at the virtual source. Finally, Eq. (1) solves the propagation problem at any observation position z_o. Note that part of the phase in Eq. (5) compensates with the phase in $|\vec{\theta}|^2$ in Eq. (3) at $z_s = 0$. If Eq. (4) describes a field with a spherical wavefront with center at $z = 0$, such compensation is complete. The centrum of the spherical wavefront is a privileged point, and the plane at $z = 0$ exhibits a plane wavefront. This explains why the choice $z_s = 0$ is often privileged with respect to others.

DISCUSSION

It makes sense to ask what is the range of observation positions where our algorithm applies, and what is the accuracy of our result in this range. We show that the paraxial approximation holds with good accuracy up to observation positions such that its distance d from the electromagnetic sources in the space-frequency domain, when $d \gg \lambda$. To do so, we compare results from the paraxial treatment with results without the help of the paraxial approximation. The paraxial equation must then be replaced with Helmholtz equation $c^2\nabla^2\vec{\tilde{E}} + \omega^2\vec{\tilde{E}} = 4\pi c^2\vec{\nabla}\bar{\rho} - 4\pi i\omega\vec{\tilde{j}}$, $\bar{\rho}(\vec{r}, \omega)$ and $\vec{\tilde{j}}(\vec{r}, \omega)$ being the Fourier transform of the charge density $\rho(\vec{r}, t) = -e\delta(\vec{r} - \vec{r'}(t))$ and of the current density $\vec{j}(\vec{r}, t) = -e\vec{v}(t)\delta(\vec{r} - \vec{r'}(t))$. Application of the proper Green's function yields:

$$\vec{\tilde{E}}(\vec{r_o}, \omega) = -\frac{i\omega e}{c} \int_{-\infty}^{\infty} dz' \frac{1}{v_z(z')} \left[\frac{\vec{\beta} - \vec{n}}{|\vec{r_o} - \vec{r'}(z')|} - \frac{ic}{\omega}\frac{\vec{n}}{|\vec{r_o} - \vec{r'}(z')|^2}\right] \exp\left\{i\omega\left[\left(\frac{s(z')}{v} - \frac{z'}{c}\right) + \left(\frac{|\vec{r_o} - \vec{r'}(z')|}{c} - \frac{z_o - z'}{c}\right)\right]\right\}. \tag{6}$$

Eq. (6) is an exact solution of Maxwell's equations with boundary conditions at infinity. The exactness of Eq. (6) allows us to control the accuracy of the paraxial approximation. A conservative estimate shows that when $d \gtrsim L_f$ this accuracy is of order $c/(\omega L_f)$, but quickly decreases as $L_f \gg d \gg c/\omega$ remaining, *at least*, of order of $c/(\omega d)$.

The integrand term scaling as $1/R^2$ (with $R = |\vec{r_o} - \vec{r'}(z')|$) can be dropped in Eq. (6) whenever $d \gg \lambda$. This is always the case in paraxial approximation. Note that the inverse field problem cannot be solved without application of the paraxial approximation. In this case we should solve the homogeneous Helmholtz equation with boundary conditions constituted by the knowledge of the field on a open surface (for example, a transverse plane) and additionally, Rayleigh-Sommerfeld radiation condition at infinity (separately for all polarization components). This is not enough to reconstruct the field at any position in space. However, if the paraxial approximation is applicable, the inverse field problem has a unique and stable solution. We recognize a few observation zones of interest. **Far zone.** d is such that $\vec{n} = \text{const.}$ **Formation zone.** Defined by $d \lesssim L_f$. **Radiation zone.** The field can be interpreted as radiation. $\mathbf{1/R}$**−zone .** The term in $1/R^2$ can be neglected in Eq. (6). **Reconstruction zone.** The inverse problem based on far-field data can be solved.

In all generality, from Eq. (6) follows that the $1/R-$zone always coincide with the reconstruction zone. Any system of interest is characterized by a size a, a formation length L_f and the radiation wavelength λ. In the case of ultra-relativistic systems $a \gtrsim L_f \gg \lambda$. Then, the near zone is defined by $d \lesssim a$, the formation zone by $d \lesssim L_f$, the radiation zone, the reconstruction zone and the $1/R-$zone by $d \gg (c/\omega)$. Ultra-relativistic cases present an increased level of complexity with respect to others. This complexity is at the origin of several misconceptions. Usually textbooks do not follow a direct derivation of Eq. (6). They start with the solution of Maxwell's equation in the space-time domain, the Lienard-Wiechert fields, and they apply a Fourier transformation:

$$\vec{\tilde{E}}(\vec{r}_o,\omega) = -e\int_{-\infty}^{\infty} dt' \left\{ \frac{\vec{n}-\vec{\beta}}{\gamma^2(1-\vec{n}\cdot\vec{\beta})^2 R(t')^2} + \frac{\vec{n}\times[(\vec{n}-\vec{\beta})\times\dot{\vec{\beta}}]}{c(1-\vec{n}\cdot\vec{\beta})^2 R(t')} \right\} \exp\left[i\omega\left(t' + \frac{R(t')}{c}\right)\right] \quad (7)$$

where $\dot{\vec{\beta}} = \dot{\vec{v}}/c$. Inspecting Eq. (7) it looks paradoxical that the near field, including velocity and acceleration terms, can be characterized starting from the far zone, including acceleration term only. However, the magnitude of terms in $1/R^2$ and $1/R$ in Eq. (7) does not depend on λ, while that of terms in $1/R$ and $1/R^2$ in Eq. (6) does. Eq. (6) and Eq. (7) are equivalent, as can be shown by addition of the full derivative $d\Phi(t')/dt'$ of a properly chosen $\Phi(t')$ function to the integrand of Eq. (7) (and using $t' = z'/v_z(z')$). Addition of different full derivatives yields an infinite number of equivalent representations for the field, and physical sense can be ascribed to the integral only. The terms in $1/R$ and in $1/R^2$ in Eq. (6) appear as a combination of the terms in $1/R$ (acceleration term) and $1/R^2$ (velocity term) in Eq. (7). They differ from each other. As a result, there are contributions to the radiation from the velocity part in Eq. (7). The presentation in Eq. (6) is most interesting because the magnitude of the $1/R^2$-term in Eq. (6) can be directly compared with the magnitude of the $1/R$-term inside the sign of integral, that is related to the $1/R$-zone and to the reconstruction zone. If one forgets about this fact one would incorrectly conclude that far-field data cannot be used to reconstruct the field in the near-zone.

UNDULATOR LASER-LIKE SOURCE

Let us apply our algorithm in the case of undulator radiation at resonance, i.e. $\omega/(2\gamma^2 c)(1 + K^2/2) = 2\pi/\lambda_w$. Here λ_w is the undulator period, and $K = \lambda_w e H_w/(2\pi m_e c^2)$, m_e being the electron mass and H_w being the maximum of the magnetic field produced by the undulator on the z axis. Position $z = 0$ is in the undulator center. A well-known, axis-symmetric expression for the distribution of the first harmonic field $\widetilde{E}_\perp(z_o,\theta)$ from a planar undulator in the far-zone as a function of the observation angle θ is

$$\widetilde{E}_\perp = -\frac{K\omega e L_w}{c^2 z_o \gamma} A_{JJ} \exp\left[i\frac{\omega z_o}{2c}\theta^2\right] \text{sinc}\left[\frac{\omega L_w \theta^2}{4c}\right], \quad (8)$$

where the field is polarized in the horizontal direction, $L_w = \lambda_w N_w$ is the undulator length, N_w the number of undulator periods and $A_{JJ} = J_o[K^2/(4+2K^2)] - J_1[K^2/(4+2K^2)]$, J_n being the n-th order Bessel function of the first kind. Eq. (8) describes a field with spherical wavefront centered at $z = 0$. Eq. (3) yields the field distribution at the virtual source (also axis-symmetric) [1]:

$$\widetilde{E}_\perp(0, r_\perp) = i\frac{K\omega e}{c^2\gamma} A_{JJ}\left[\pi - 2\text{Si}\left(\frac{\omega r_\perp^2}{L_w c}\right)\right], \quad (9)$$

Si$(\cdot)$ being the sin integral function and $r_\perp$ the distance from the z axis on the virtual-source plane. In laser physics, the waist is in the center of the optical cavity and the Rayleigh length is related to the resonator geometrical factor. Our virtual source is in the center of the undulator and the Rayleigh length is related to L_w. In both cases we have a plane phase front, and the transverse dimension of the waist is much larger than λ. Also, the phase of the wavefront in Eq. (9) is shifted of $-\pi/2$ with respect to the wavefront in the far zone in analogy with the Guoy phase shift. Eq. (1) gives the field at arbitrary observation position z_o:

$$\widetilde{E}_\perp = \frac{K\omega e A_{JJ}}{c^2\gamma} \times \left[\text{Ei}\left(\frac{i\omega r_\perp^2}{2z_o c - L_w c}\right) - \text{Ei}\left(\frac{i\omega r_\perp^2}{2z_o c + L_w c}\right)\right] \quad (10)$$

Ei$(\cdot)$ being the exponential integral function. The field singularity at $z_o = L_w/2$ and $r_\perp = 0$ is related with the use of the resonant approximation. Introducing normalized units $\vec{\hat{r}} = \sqrt{\omega/(L_w c)}\vec{r}_\perp$, $\vec{\hat{\theta}} = \sqrt{\omega L_w/c}\vec{\theta}$ and $\hat{z} = z/L_w$ we obtain the intensity profile at the virtual source

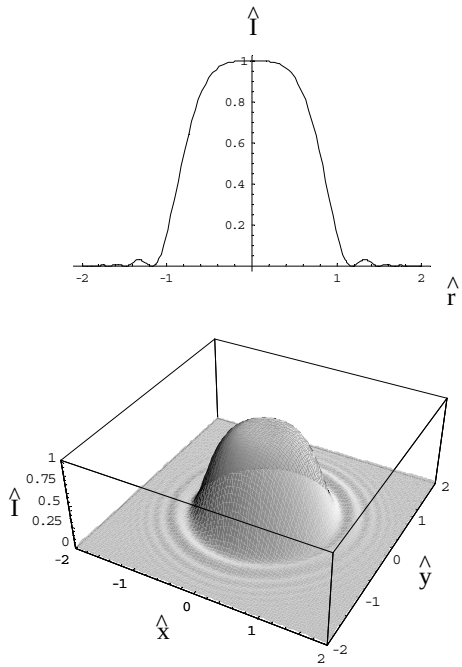

Figure 1: Intensity pattern $\hat{I}$ at the virtual source.

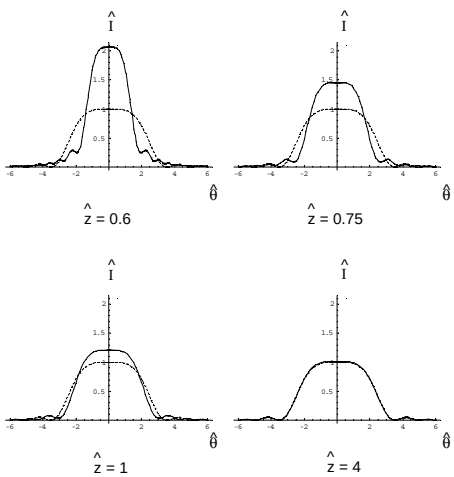

Figure 2: Evolution of the intensity profile as in Eq. (12) (solid lines) compared with far field asymptotic (dashed lines).

$$\hat{I}(0,\hat{r}_\perp) = \frac{1}{\pi^2}\left[\pi - 2\mathrm{Si}\left(\hat{r}_\perp^2\right)\right]^2 , \qquad (11)$$

and at any distance $\hat{z}_o$, both in the near and in the far zone:

$$\hat{I}\left(\hat{z}_o,\hat{\theta}\right) = \hat{z}_o^2\left|\mathrm{Ei}\left(\frac{i\hat{z}_o^2\hat{\theta}^2}{2\hat{z}_o-1}\right) - \mathrm{Ei}\left(\frac{i\hat{z}_o^2\hat{\theta}^2}{2\hat{z}_o+1}\right)\right|^2 , \qquad (12)$$

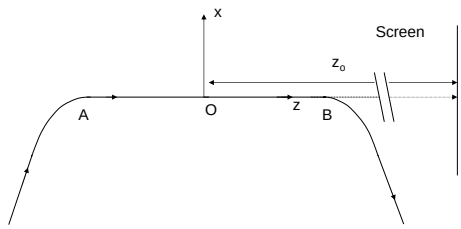

Figure 3: Edge radiation geometry.

where $\hat{\theta} = \hat{r}_\perp/\hat{z}_o$. $\hat{I}$ at the virtual source is plotted in Fig. 1. The evolution of the intensity profile for different z_o, Eq. (12), is given in fig. 2. A virtual source can be used as an input for wavefront propagation codes (as ZEMAX , PHASE, SRW [1]), allowing for the presence of complicate optics, likewise it has been used as an input to Eq. (1) for free-space propagation. Spontaneous SR from an electron beam can be treated as an incoherent collection of laser-like beams with different offsets and deflections (summing up the intensities), while if the electron beam is distributed coherently, radiation can be described as a coherent collection of laser-like beams.

EDGE RADIATION

We consider the system depicted in Fig. 3. An electron enters the setup via a bending magnet, passes through a straight section (segment AB) and exits the setup via another bend. Edge radiation (see references in [1]) is collected at a distance z_o from the center of the straight section. The trajectory and, therefore, the space integration in Eq. (4) consists of the two bends b_1 and b_2, and of the straight section AB. Let L be the length of AB. Points A and B are thus located at $z_A = -L/2$ and $z_B = L/2$. In general, one should sum the contribution due to the straight section to that from the bends. In some cases the presence of the bending magnets can be ignored as if they had zero length, and what may be called "zero-length switchers approximation" applies. Magnets act like switchers: the first magnet switches the radiation harmonic on, the second switches it off. Switchers may have different physical realizations, depending on the setup. There is no limitation to the length of the switcher. The only common feature between different switchers is that the switching process depends exponentially on the distance from the beginning of the process. Since electrodynamics is a linear theory, when the straight-section contribution cannot be considered a good approximation to the total field, it can still be considered as a fundamental building block for a more complicated setup. This justify our choice to deal with the straight-section contribution to the field only. It is interesting to discuss when the field due to switchers is negligible in our study-case. For $L \gg \gamma^2(c/\omega)$, the formation length for the straight section is $\gamma^2(c/\omega)$, while the formation length for the bend is $((c/\omega)\rho^2)^{1/3}$, ρ being the radius

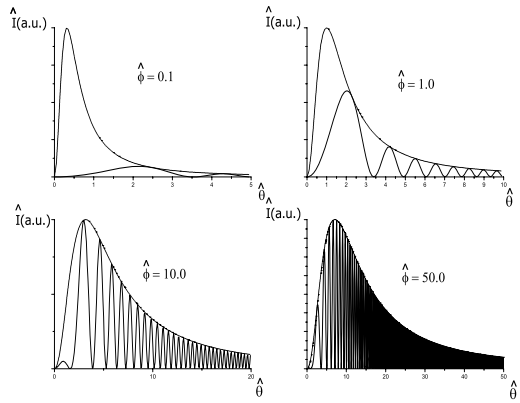

Figure 4: Directivity diagram (solid lines) of the radiation from the setup in Fig. 3 and envelope of the directivity diagram (dotted lines).

of the bend. Let the ratio between the latter and the former be $\epsilon^2 = (\lambda_c/\lambda)^{2/3} \ll 1$, where $\lambda_c = 4\pi\rho/(3\gamma^3)$ is the critical wavelength for SR and $\lambda \gg \lambda_c$, as we are interested in edge radiation. The distance $d_c = \epsilon\gamma^2(\omega/c)$ turns out to constitute an extra characteristic-length for our system. When $d \ll d_c$, the straight section contribution dominates the bending magnet one for $r_\perp > \epsilon\gamma(\omega/c)$, while for other values of $r_\perp$ the two contributions are comparable. When $d \sim d_c$ the zero-length switcher approximation cannot be used. When $d \gg d_c$ we the straight section contribution dominates for $0 < r_\perp \ll ((\omega/c)^2\rho)^{1/3}$, the characteristic size of the radiation being $\epsilon((\omega/c)^2\rho)^{1/3}$. Finally, when $d \gg \gamma^2(\omega/c)$, the straight section contribution dominates for $0 < \theta \ll ((\omega/c)/\rho)^{1/3}$, the characteristic angle of the radiation being $\epsilon((\omega/c)/\rho)^{1/3}$.

Far field pattern of edge radiation

Field contribution calculated along the straight section. Accounting for the geometry in Fig. 3 we have $s(z') = z'$ for $z_A < z' < z_B$. Use of Eq. (4) yields the field contribution from the straight section AB:

$$\vec{\tilde{E}}_{AB} = \frac{i\omega eL}{c^2 z_o} \exp\left[\frac{i\omega\theta^2 z_o}{2c}\right] \vec{\theta}\, \mathrm{sinc}\left[\frac{\omega L}{4c}\left(\theta^2 + \frac{1}{\gamma^2}\right)\right] . \tag{13}$$

Eq. (13) is describes a spherical wave and explicitly depends on L. The formation length L_{fs} for the straight section AB can be written as $L_{\mathrm{fs}} \sim \min[\gamma^2(c/\omega), L]$. The far-zone asymptotic is independent of such value and always valid at observation positions $z_o \gg L$.

Energy spectrum of radiation. With the help of normalized quantities $\hat{\vec{\theta}} = \sqrt{\omega L/c}\vec{\theta}$ and $\hat{\phi} = \omega L/(\gamma^2 c)$ we may write the directivity diagram $\hat{I}$ of the radiation as $\hat{I} \sim \hat{\theta}^2\ \mathrm{sinc}^2[(\hat{\theta}^2 + \hat{\phi})/4]$. This is plotted in Fig. 4 for several values of $\hat{\phi}$ as a function of the normalized angle $\hat{\theta}$. The natural angular unit is evidently $(2\pi L/\lambda)^{-1/2}$.

There are two asymptotic cases for the problem parameter $\hat{\phi}$: $\hat{\phi} \ll 1$ and $\hat{\phi} \gg 1$. The behavior of the far-field emission is well-known in literature [1]. We take this as the starting point for investigations based on Fourier Optics.

Method of virtual sources

Edge radiation as a field from a single virtual source. Eq. (3) and Eq. (13) yield the virtual source $\vec{\tilde{E}}(0, \vec{r}_\perp)$:

$$\vec{\tilde{E}} = -\frac{eL\omega^2}{2\pi c^3} \int d\vec{\theta}\vec{\theta}\mathrm{sinc}\left[\frac{L\omega}{4c}\left(\theta^2 + \frac{1}{\gamma^2}\right)\right] \exp\left[\frac{i\omega\vec{\theta}\cdot\vec{r}_\perp}{c}\right] \tag{14}$$

The Fourier transform in Eq. (14) is difficult to calculate analytically in full generality. An analytic expression for the field amplitude at the virtual source for $\hat{\phi} \ll 1$ reads:

$$\vec{\tilde{E}}(0, \vec{r}_\perp) = \frac{4\omega e}{c^2 L}\vec{r}_\perp \mathrm{sinc}\left(\frac{\omega}{Lc}\left|\vec{r}_\perp\right|^2\right) . \tag{15}$$

For any value of $\hat{\phi}$, Eq. (15) explicitly depends on L, as the far-field emission does. Using $\hat{\vec{r}} = \sqrt{\omega/(Lc)}\vec{r}_\perp$ the intensity pattern of the virtual source is $\hat{I}(\hat{r}) \sim \hat{r}^2\mathrm{sinc}^2(\hat{r}^2)$ and is plotted in Fig. 5. The Fresnel formula yields the field in the near and the far zone for $\hat{\phi} \ll 1$

$$\vec{\tilde{E}} = -\frac{2e}{c}\frac{\vec{r}_\perp}{r_\perp^2} \exp\left[i\frac{\omega r_\perp^2}{2cz_o}\right] \left\{\exp\left[\frac{-i\omega r_\perp^2}{2cz_o(1+2z_o/L)}\right] - \exp\left[\frac{i\omega r_\perp^2}{2cz_o(-1+2z_o/L)}\right]\right\} , \tag{16}$$

where the singular behavior at $\vec{r}_\perp = 0$ and $z_o \longrightarrow L/2$ cannot be resolved within the paraxial approximation. The intensity profile associated with Eq. (16) is

$$\hat{I} = \frac{1}{\hat{\theta}^2}\left|\left[\exp\left(\frac{-i\hat{\theta}^2\hat{z}_o}{2(1+2\hat{z}_o)}\right) - \exp\left(\frac{i\hat{\theta}^2\hat{z}_o}{2(-1+2\hat{z}_o)}\right)\right]\right|^2 , \tag{17}$$

where $\hat{\theta} = \hat{r}_o/\hat{z}_o$ and $\hat{z}_o = z_o/L$. A comparison between intensity profiles at different observation points $\hat{z}_o$ is plotted in Fig. 6. When condition $\hat{\phi} \ll 1$, studied until now, is not satisfied, the integral in Eq. (14) can be calculated numerically. The intensity distribution for the virtual source at $\hat{\phi} = 0.1$, $\hat{\phi} = 1$, $\hat{\phi} = 10$ and $\hat{\phi} = 50$ are plotted in Fig. 7. An enlarged plot of the case $\hat{\phi} = 50$ is given in Fig. 8. Fine structures are now evident, consistently with Fig. 4 for the far zone. Once the field at the virtual source is specified for any value of $\hat{\phi}$, Fourier Optics can be used to propagate it. However, we prefer to use an alternative way to solve the field propagation problem for any value of $\hat{\phi}$, capable of giving a better physical insight at $\hat{\phi} \gg 1$.

Edge radiation as a superposition of the field from two virtual sources. The far field in Eq. (13) can be written as $\vec{\tilde{E}}(z_o, \vec{\theta}) = \vec{\tilde{E}}_1(z_o, \vec{\theta}) + \vec{\tilde{E}}_2(z_o, \hat{\theta})$, where

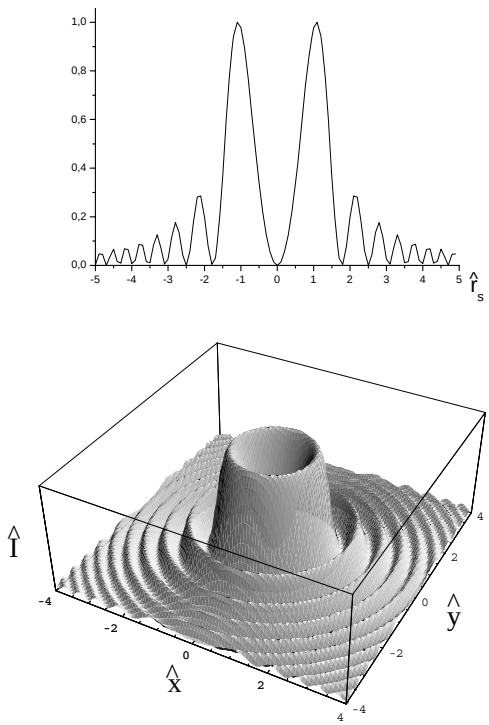

Figure 5: Intensity distribution of the virtual source, $\hat{I}$.

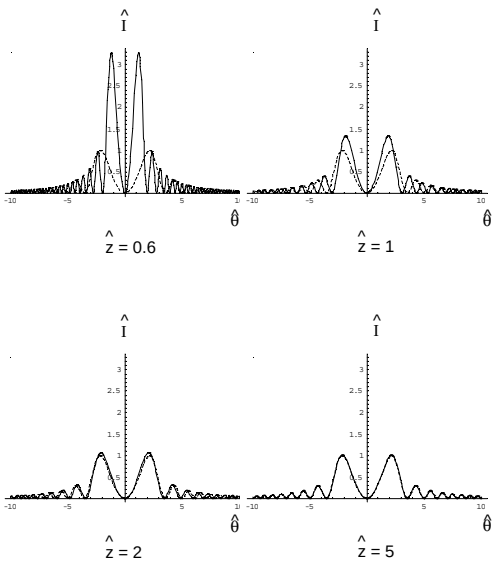

Figure 6: Evolution of the intensity profile for edge radiation for $\hat{\phi} \ll 1$ at different observation distances (solid lines) compared to the far-zone intensity (dashed lines).

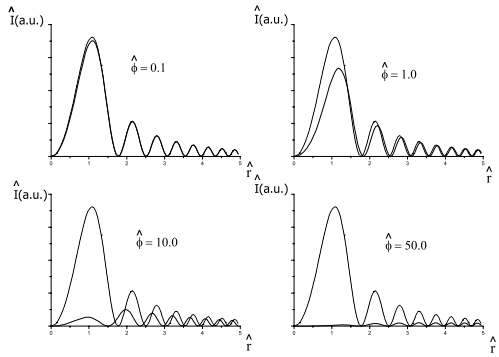

Figure 7: Intensity profiles of the virtual source for different values of $\hat{\phi}$ (solid lines) compared with the case $\hat{\phi} \ll 1$ (dotted lines).

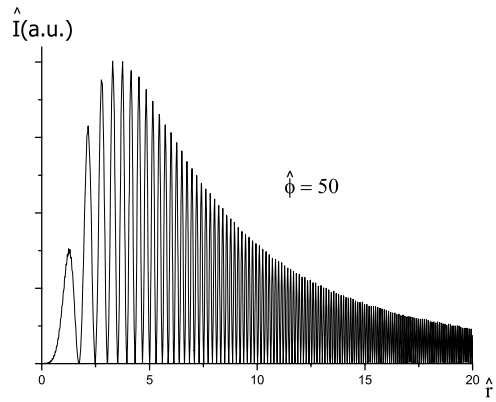

Figure 8: Intensity pattern at the virtual source for $\hat{\phi} = 50$.

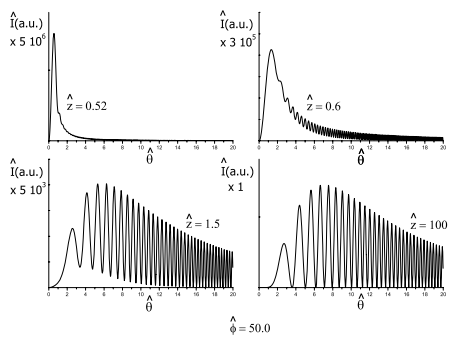

Figure 9: Edge radiation intensity profile at $\hat{\phi} = 50$ for different observation distances.

$$\vec{\tilde{E}}_{1,2}\left(\hat{z}_o,\vec{\hat{\theta}}\right)=\pm\frac{2e\vec{\theta}}{cz_o(\theta^2+1/\gamma^2)}$$
$$\times\exp\left[\pm\frac{i\omega L}{4c\gamma^2}\right]\exp\left[\frac{i\omega L\theta^2}{2c}\left(\frac{z_o}{L}\pm\frac{1}{2}\right)\right]. \quad (18)$$

The two terms $\vec{\tilde{E}}_1$ and $\vec{\tilde{E}}_2$ represent two spherical waves centered at $z_{s1}=L/2$ and $z_{s2}=-L/2$, corresponding to two virtual sources. Their field distribution is given by

$$\vec{\tilde{E}}\left(\pm\frac{L}{2},\vec{r}_\perp\right)=\mp\frac{2ie\omega}{c^2\gamma}\exp\left[\pm\frac{i\omega L}{4c\gamma^2}\right]\frac{\vec{r}_\perp}{r_\perp}K_1\left(\frac{\omega r_\perp}{c\gamma}\right), \quad (19)$$

where $K_1(\cdot)$ is the modified Bessel function of the first order. It should be noted that Eq. (19) is identical to the well-known frequency-domain expression for the transverse component of the field from an ultra-relativistic electron moving in uniform motion. Both far zone field and the field at the virtual sources exhibit dependence on L through phase factors only. Application of the Fresnel formula allows to calculate the field at any distance z_o in frees space. Using the definition $\vec{\hat{\theta}}=\vec{\hat{r}}_o/\hat{z}_o$ we obtain $\hat{I}\sim|A_1+A_2|^2$, where

$$A_{1,2}=\mp\frac{\vec{\hat{\theta}}}{\hat{\theta}}\frac{2i\sqrt{\hat{\phi}}\exp\left[\pm i\hat{\phi}/4\right]}{\hat{z}_o\mp\frac{1}{2}}\exp\left[\frac{i\hat{\theta}^2\hat{z}_o^2}{2\left(\hat{z}_o\mp\frac{1}{2}\right)}\right]$$
$$\times\int_0^\infty d\xi\xi K_1(\sqrt{\hat{\phi}}\xi)J_1\left[\frac{\hat{\theta}\xi\hat{z}_o}{\hat{z}_o\mp\frac{1}{2}}\right]\exp\left[\frac{i\xi^2}{2\left(\hat{z}_o\mp\frac{1}{2}\right)}\right] \quad (20)$$

In Fig. 9 we plotted results for the field propagation for the case $\hat{\phi}=50$. Radiation profiles are shown as a function of $\hat{\theta}$ at $\hat{z}_o=0.52$, $\hat{z}_o=0.6$, $\hat{z}_o=1.5$ and $\hat{z}_o=100.0$. Let us discuss the two limiting cases for $\hat{\phi}\ll1$ and for $\hat{\phi}\gg1$. Consider first $\hat{\phi}\ll1$. The field at any observation distance is given by Eq. (16). There are only two observation zones of interest. **Far zone,** in the limit for $\hat{z}_o\gg1$ and **Near zone,** when $\hat{z}_o\lesssim1$. From Eq. (16), the total field results from the interference of the two virtual sources. The transverse size of these sources is $\gamma(c/\omega)$, independently of L. In the center of the setup instead, the virtual source has a dimension $\sqrt{(c/\omega)L}$ (see Eq. (16)). The source in the center of the setup is much smaller than those at the edge, as the two sources at the edges interfere in the center of the setup. Consider now the case $\hat{\phi}\gg1$. Let $d_{1,2}=z_o\mp L/2$ be the distances of the observer from the edges. One can recognize four regions of interest, that are more naturally discussed in the two-source picture. **Two-edge radiation. Far zone.** When $d_{1,2}\gg L$ we are summing far field contributions from the two edge sources, see Fig. 9 for $\hat{z}_o=100$. **Two-edge radiation. Near zone.** When $d_{1,2}\sim L$ both contributions from the sources are important, but d_1 and d_2 become sensibly different, see Fig. 9 for $\hat{z}_o=1.5$. **Single-edge radiation. Far zone.** When $\gamma^2(c/\omega)\ll d_1\ll L$ the contribution due to the near edge is dominant, see Fig. 9 for $\hat{z}_o=0.6$. **Single-edge radiation. Near zone.** When $0\ll d_1\lesssim\gamma^2(c/\omega)$ we have the near-field contribution from a single edge, and the intensity distribution tends to reproduce the behavior of the square modulus of Eq. (19). See Fig. 9 for $\hat{z}_o=0.52$.

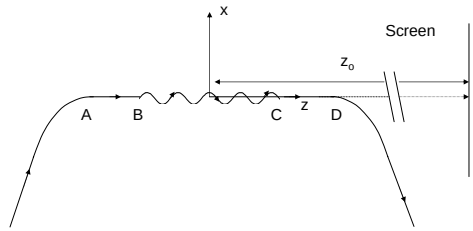

Figure 10: TUR geometry.

TRANSITION UNDULATOR RADIATION

Consider the system in Fig. 10. An electron enters the setup via a bending magnet, passes through a straight section AB, an undulator BC, and another straight section CD. Finally, it exits the setup via another bend. TUR (see references in [1]) is collected at a distance z_o from the origin of the reference system, located in the middle of the undulator. As before we ignore the presence of the bending magnets having already discussed the applicability of the "zero-length switcher approximation".

Far field pattern calculations

Field contribution from the undulator. We first consider the contribution $\vec{\tilde{E}}_u$ from the undulator. We assume a planar undulator and we introduce the longitudinal Lorentz factor $\gamma_z=\gamma/(\sqrt{1+K^2/2})$. Frequencies of interest are $\omega\ll2\gamma_z^2ck_w$ (with $k_w=2\pi/\lambda_w$). As a result one obtains

$$\vec{\tilde{E}}_u=\frac{i\omega e}{c^2z_o}\int_{z_B}^{z_C}dz'\exp\left[i\Phi_{BC}\right](\theta_x\vec{x}+\theta_y\vec{y}) \quad (21)$$

with

$$\Phi_u=\omega\left[\frac{\theta_x^2+\theta_y^2}{2c}z_o+\frac{z'}{2c}\left(\frac{1}{\gamma_z^2}+\theta_x^2+\theta_y^2\right)\right]. \quad (22)$$

Field contribution from the straight sections. The field contribution from a straight section has been dealt with in the previous Section. Accounting for the proper phase shift, one obtains the contributions $\vec{\tilde{E}}_1$ from AB and $\vec{\tilde{E}}_2$ from CD:

$$\vec{\tilde{E}}_{(1,2)}=\frac{i\omega e}{c^2z_o}\int_{z_{(A,C)}}^{z_{(B,D)}}dz'\exp\left[i\Phi_{(1,2)}\right](\theta_x\vec{x}+\theta_y\vec{y}) \quad (23)$$

where $\Phi_{(1,2)}$ in Eq. (23) is given by

$$\Phi_{(1,2)} = \omega\left[\frac{\theta^2}{2c}z_o - \frac{L_w}{4c\gamma_z^2} + \frac{L_w}{4c\gamma^2} + \frac{z'}{2c}\left(\frac{1}{\gamma^2}+\theta^2\right)\right]. \quad (24)$$

Total field and energy spectrum of radiation. The contributions from the segments AB, BC and CD are:

$$\vec{\tilde{E}}_{(1,2)} = \frac{i\omega e L_{(1,2)}}{c^2 z_o}\vec{\theta}\mathrm{sinc}\left[\frac{\omega L_{(1,2)}}{4c}\left(\frac{1}{\gamma^2}+\theta^2\right)\right] \times \exp\left[\frac{i\omega\theta^2 z_o}{2c}\right]\exp\left[-\frac{i\omega L_w}{4c}\left(\frac{1}{\gamma_z^2}+\theta^2\right)\right] \times \exp\left[\mp\frac{i\omega L_{(1,2)}}{4c}\left(\frac{1}{\gamma^2}+\theta^2\right)\right], \quad (25)$$

$$\vec{\tilde{E}}_u = \frac{i\omega e L_w}{c^2 z_o}\vec{\theta}\mathrm{sinc}\left[\frac{\omega L_w}{4c}\left(\frac{1}{\gamma_z^2}+\theta^2\right)\right]\exp\left[\frac{i\omega\theta^2 z_o}{2c}\right] \quad (26)$$

The total field produced by the setup is obtained by summing up these contributions. The resulting energy density of radiation is known in literature [1].

Virtual source specification. Field propagation.

Eq. (25) and Eq. (26) can be interpreted as far field radiation from separate virtual sources with plane wavefronts, located at $z_{s1} = -L_w/2 - L_1/2$, $z_{su} = 0$ and $z_{s2} = L_w/2 + L_2/2$ and characterized by

$$\vec{\tilde{E}}_{s(1,2)} = -\frac{\omega^2 e L_{(1,2)}}{2\pi c^3}\exp\left[\mp\frac{i\omega}{4c}\left(\frac{L_w}{\gamma_z^2}+\frac{L_{(1,2)}}{\gamma^2}\right)\right] \times \int d\vec{\theta}\vec{\theta}\mathrm{sinc}\left[\frac{\omega L_{(1,2)}}{4c}\left(\theta^2+\frac{1}{\gamma^2}\right)\right]\exp\left[\frac{i\omega}{c}\vec{\theta}\cdot\vec{r}_\perp\right], \quad (27)$$

$$\vec{\tilde{E}}_{su} = -\frac{\omega^2 e L_w}{2\pi c^3} \times \int d\vec{\theta}\,\vec{\theta}\,\mathrm{sinc}\left[\frac{\omega L_w}{4c}\left(\theta^2+\frac{1}{\gamma_z^2}\right)\right]\exp\left[\frac{i\omega}{c}\vec{\theta}\cdot\vec{r}_\perp\right]. \quad (28)$$

L_1, L_2 and L_w can assume different values. γ and γ_z are also different. We prescribe the same normalization for all quantities: $\vec{\hat{\theta}} = \sqrt{\omega L_{\mathrm{tot}}/c}\vec{\theta}$, $\hat{\phi} = \omega L_{\mathrm{tot}}/(\gamma^2 c)$ and $\vec{\hat{r}}_\perp = \sqrt{\omega/(L_{\mathrm{tot}}c)}\vec{r}_\perp$. Then, we introduce parameters $\hat{L}_1 = L_1/L_{\mathrm{tot}}$, $\hat{L}_2 = L_2/L_{\mathrm{tot}}$, $\hat{L}_w = L_w/L_{\mathrm{tot}}$ and $\hat{\phi}_w = (\gamma^2/\gamma_z^2)\hat{\phi}$. Finally, we define $\hat{z}_s = z_s/L_{\mathrm{tot}}$. One may check that, in the limit for $\hat{\phi} \ll 1$ and $\hat{\phi}_w \ll 1$ one obtains the same results as for edge radiation from a single straight section. A second region of interest in the parameter space that can be dealt with analytically is for $\hat{\phi} \ll 1$ and $\hat{\phi}_w \gg 1$. In this limit, the contribution from the undulator can be neglected, because the $\mathrm{sinc}(\cdot)$ is strongly suppressed. Then, $\vec{\hat{E}}(\hat{z}_{su}, \vec{\hat{r}}_s) \simeq 0$, where $\vec{\tilde{E}} = (\omega e/c^2)\vec{\hat{E}}$. The surviving virtual sources are:

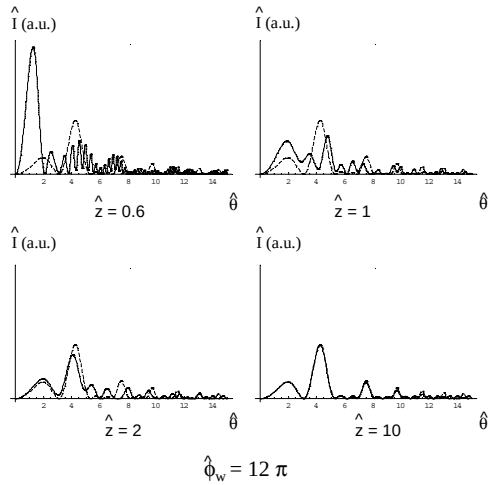

Figure 11: Evolution of the intensity profile for TUR for $\hat{\phi}_w = 12\pi$ (solid lines) and comparison with far-zone intensity (dashed lines).

$$\vec{\hat{E}}_{s(1,2)} = \frac{4\vec{\hat{r}}_\perp}{\hat{L}_{(1,2)}}\exp\left[-\frac{i\hat{L}_w\hat{\phi}_w}{4}\right]\mathrm{sinc}\left(\left|\vec{\hat{r}}_\perp\right|^2/\hat{L}_1\right). \quad (29)$$

Eq. (29) describes virtual sources characterized by plane wavefronts. Use of the Fresnel propagation formula, Eq. (1) allows reconstruction of the field in the near and in the far zone. The two surviving contributions to the field are:

$$\vec{\hat{E}}_{(1,2)} = -\frac{4\vec{\hat{r}}_\perp}{\hat{r}_\perp^2}\exp\left[\mp\frac{i\hat{L}_w\hat{\phi}_w}{4}+\frac{i\hat{r}_\perp^2}{2(\hat{z}_o-\hat{z}_{s(1,2)})}\right] \times\left\{\exp\left[-\frac{i\hat{L}_1\hat{r}_\perp^2}{2(\hat{z}_o-\hat{z}_{s(1,2)})(\hat{L}_{(1,2)}+2\hat{z}_o-2\hat{z}_{s(1,2)})}\right] -\exp\left[\frac{i\hat{L}_{(1,2)}\hat{r}_\perp^2}{2(\hat{z}_o-\hat{z}_{s(1,2)})(-\hat{L}_{(1,2)}+2\hat{z}_o-2\hat{z}_{s(1,2)})}\right]\right\} \quad (30)$$

Eq. (30) solves the propagation problem for the near and the far field when $\hat{\phi} \ll 1$ and $\hat{\phi}_w \gg 1$. The intensity pattern is obtained by summing up contributions in Eq. (30) and taking square modulus of the sum. To give an example we study the case $L_1 = L_2 = L_w = L_{\mathrm{tot}}/3$. The intensity pattern periodically depends on $\hat{\phi}_w \gg 1$ with a period 12π. For illustration, in Fig. 11 we plot the intensity profile for $\hat{\phi}_w = 12\pi$ at different distances $\hat{z}_o$ and we compare these profiles with the far field asymptote.

REFERENCES

[1] References and a more detailed description of this subject are included in: G. Geloni, E. Saldin, E. Schneidmiller and M. Yurkov, DESY 06-127 (2006), downloadable at http://arxiv.org/abs/physics/0608145.

[2] It is not so if near and formation zone do not coincide.

A SCALLOPED ELECTRON BEAM FREE-ELECTRON LASER *

D.C. Nguyen#, Los Alamos National Laboratory, Los Alamos, NM 87545, U.S.A.
H.P. Freund, Science Applications International Corp., McLean, VA 22102, U.S.A.
W.B. Colson, Naval Postgraduate School, Monterey, CA 93943, U.S.A.

Abstract

Typical high-gain FEL amplifiers employ an electron beam that is "matched" to the wiggler so that the envelope remains constant throughout the wiggler. This paper describes a novel approach in which the electron envelope undergoes scalloping motion along the wiggler because the beams are deliberately mismatched at the wiggler entrance. We present an analysis of the electron scalloping motion and the FEL interaction with a scalloped electron beam. Using MEDUSA simulations, we show the advantages of the scalloped-beam FEL and the properties of the radiation beam it produces.

INTRODUCTION

In high-gain FEL amplifiers, the electron beam radius plays a crucial role in determining the FEL interaction strength. Most FEL amplifiers use a tightly focused electron beam to enhance the FEL interaction, i.e. both the FEL gain and saturated power increase with smaller electron beam radius. A typical FEL employs electron beams that are "matched" to the wiggler so that the envelope remains constant throughout the wiggler. Since the matched beam radius is proportional to $\sqrt{\varepsilon_n}$, a small beam radius requires a small normalized rms emittance.

The use of external magnets to focus the electron beam to a radius smaller than allowed by the normalized rms emittance in order to pinch the optical beam was first suggested by Sprangle *et al*. [1]. In this paper, we suggest the use of natural betatron motion in a weak focusing wiggler, to refocus the electron beam periodically in the wiggler, resulting in pinching near the wiggler exit (Fig. 1). It is possible to select a combination of input laser power and wiggler length such that the FEL saturates near the second waist. Optical guiding causes the radiation beam to follow the electron beam's motion, resulting in pinching of the radiation beam near the exit [2].

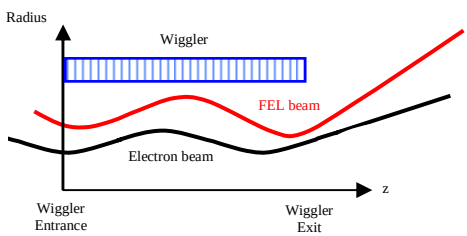

Figure 1: Illustration of a scalloped electron beam FEL with a uniform wiggler.

*Work supported by the Office of Naval Research and the High-Energy Laser Joint Technology Office. Author email: dcnguyen@lanl.gov

THEORY

The evolution of the rms radius σ of a relativistic, axi-symmetric beam with equal transverse emittance and equal two-plane focusing can be written as follow

$$\frac{d^2\sigma}{dz^2} = -k_\beta^2\sigma + \frac{2I}{\gamma^3 I_A \sigma} + \frac{\varepsilon_n^{\,2}}{\gamma^2\sigma^3}, \tag{1}$$

where k_β is the betatron wavenumber, I the peak current, I_A the Alfven current, γ the relativistic factor, and ε_n the normalized rms emittance. Under steady-state condition, the emittance-dominated rms matched beam radius is

$$\sigma_0 = \sqrt{\frac{\sqrt{2}\varepsilon_n}{k_w a_w}}. \tag{2}$$

Using a first order perturbation analysis of Eq. (1) we can show that

$$\sigma = \sigma_0 - \delta_0 \sin(k_\Sigma z) \tag{3}$$

where $\delta_0 = (\sigma_0 - \sigma_{min})$ is the initial deviation from the matched radius, and k_Σ, the scalloping wavenumber, as given by

$$k_\Sigma = 2k_\beta\sqrt{1 - \frac{I}{I_A}\frac{1}{\gamma^2 k_\beta \varepsilon_n}} \tag{4}$$

The power gain length in a high-gain FEL amplifier scales with the electron beam radius as follow [3]

$$L_G = \frac{\gamma}{\sqrt{3}}\left(\frac{I_A}{a_w^2 f_B^2 k_w I}\right)^{1/3}\sigma^{2/3}\left(1+\Lambda_{3D}\right) \tag{5}$$

where f_B is the difference in Bessel functions, and Λ_{3D} is the three-dimensional effect. Since the electron beam radius varies slowly with distance, the FEL power gain length also varies along the wiggler. The saturated power scales inversely with electron beam radius.

$$P_s = \frac{1}{\gamma}\left(\frac{a_w f_B}{2\sqrt{2}k_w\sigma}\right)^{2/3}\left(\frac{I}{I_A}\right)^{1/3}\frac{P_{beam}}{\left(1+\Lambda_{3D}\right)^2} \tag{6}$$

where P_{beam} is the electron beam power. The scalloped beam FEL performance depends on how the electron beam is focused in the wiggler and the scalloping period. We look at two cases: 1) the electron beam waist is focused near the entrance, and 2) the waist is the centre of the wiggler. In the first case, the electron comes to second waist near the wiggler exit and the FEL output power, which scales inversely with radius, is at a maximum. In the second case, the beam radius is largest near the wiggler exit and the output power is at a minimum [4].

SIMULATION

Table I summarizes the FEL and beam parameters used in the MEDUSA simulations. These parameters are chosen for a 1.06-micron wavelength where high-power seed lasers exist. The wiggler is a conventional permanent-magnet design with parabolic pole faces to provide equal two-plane, sextupole focusing. Alternatively, the magnets can be notched to approximate sextupole focusing [5]. We chose an input power of 10^6 W (1 μJ pulse energy and 1 ps FWHM, for instance) to achieve saturation in about 2 m of wiggler length with a matched electron beam. For the scalloped beam FEL, the saturation length is 2.6 m. The scalloping period is about 2 m so the second waist of the electron beam envelope is near the exit of the wiggler in both cases. The effects of using matched- and scalloped-beams in the two-stage wiggler are illustrated in Figs. 2 and 3. The power reaches a maximum of 0.84 GW in the matched case, and 1.03 GW in the scalloped case. The extraction efficiency increases correspondingly from the usual 1% to 1.27%. The only drawback is a 30% increase in the wiggler length required to reach saturation.

Table 1: MEDUSA simulation parameters and results.

Parameters	**Values**
Beam Energy	80.8 MeV
Peak Current	1000 A
Emittance	10 mm-mrad
Energy Spread	0.25%
Wiggler Period	2.18 cm
Wiggler Peak Magnetic Field	8.247 kG
rms Wiggler Parameter	1.187
Wiggler Length	2.6 m
Matched Beam Radius	0.27 mm
Scalloped Beam Minimum Radius	0.16 mm
Scalloping Period	2.05 m
Wavelength	1.058 μ
Peak Injected Power	1 MW
Injected Radiation Waist	0.305 mm
Matched Beam Peak Power	0.84 GW
Matched Beam Efficiency	1.0%
Matched Beam Saturation Length	1.96 m
Scalloped Beam Peak Power	1.03 GW
Scalloped Beam Efficiency	1.27%
Scalloped Beam Saturation Length	2.6 m

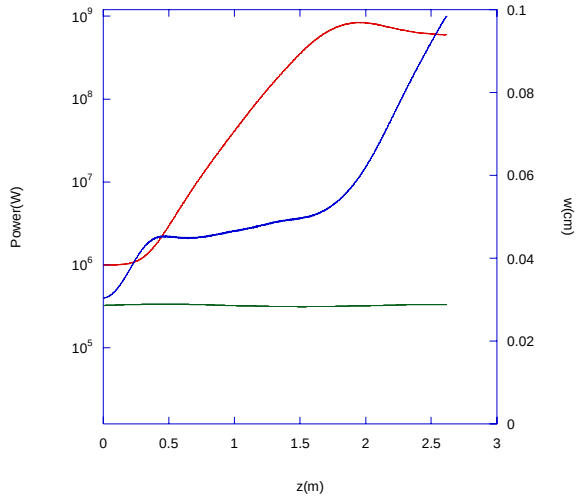

Figure 2: FEL power (red), optical beam radius (blue), and electron beam radius (green) for the matched case.

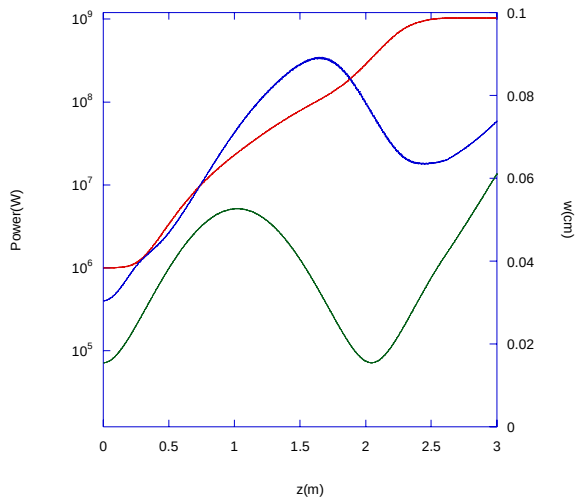

Figure 3: FEL power (red), optical beam radius (blue), and electron beam radius (green) for the scalloped case.

It is noteworthy that the lethargy region is reduced in the scalloped beam FEL as a result of high gain (short gain length) at the wiggler entrance. In the middle of the wiggler, exponential gain is reduced and the reduction in optical guiding causes the radiation beam to expand rapidly. At saturation, the scalloped beam optical waist is larger than the matched beam case. Thus, scalloping the electron beam in a uniform wiggler does not pinch the optical beam to a smaller radius. To significantly pinch the optical beam, we need additional optical guiding, for instance with the addition of a step-taper wiggler.

For seeded FEL amplifiers, it is advantageous to tune the input wavelength while keeping the electron beam energy constant in order to find where the power is maximized. In the matched beam case, the FEL output power increases toward larger detuning, namely longer wavelength at a fixed electron beam energy (or higher electron beam energy at a fixed wavelength) and then drops sharply. In the scalloped beam case, the FEL output power decreases rapidly on both side and the detuning bandwidth is narrower. This is a result of lower FEL gain due to the scalloped electron beam, but the FEL saturated power is higher than the matched beam case.

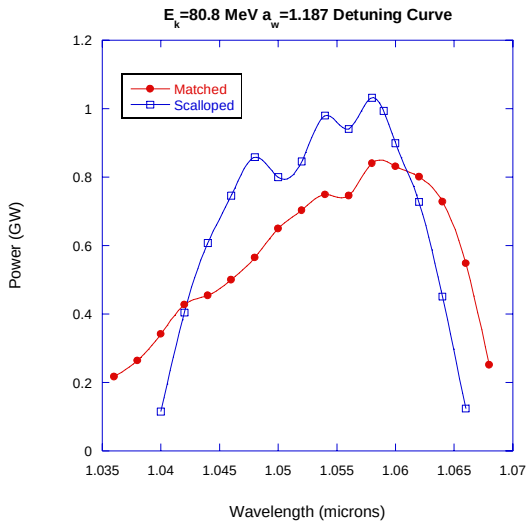

Figure 4: Detuning curves for the matched (red) and scalloped (blue) electron beam FEL.

We also study scalloped beam FEL with a step-taper wiggler to increase the extraction efficiency (Fig. 5). The step-taper starts at z = 1.92 m and the magnetic field is reduced to 8.032 kG while the period remains the same. The FEL peak power grows to 1.45 GW, corresponding to 1.8% efficiency (Fig. 6). The optical beam is pinched to a 0.3 mm radius in the second wiggler segment, compared to a 0.6 mm radius of the uniform wiggler. The optical divergence angle is increased from 0.8 to 1.6 mrad.

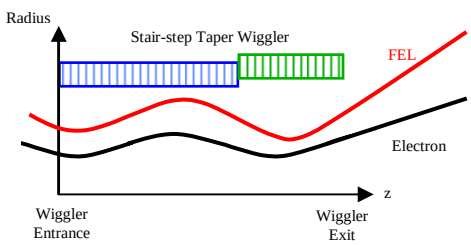

Figure 5: Illustration of a scalloped beam FEL with a step-tapered wiggler.

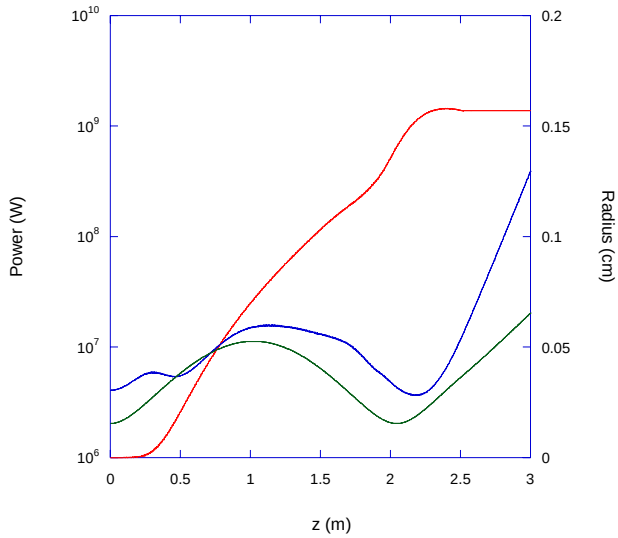

Figure 6: FEL power (red), optical beam radius (blue), and electron beam radius (green) for scalloped beam FEL with a step-tapered wiggler.

SUMMARY AND DISCUSSION

We have studied a new kind of FEL interaction in which the electron beam's envelope undergoes scalloping motion and the exponential gain varies along the wiggler length. For maximum power, the optimum approach is to focus the electron beam near the wiggler entrance and chose a wiggler length that is slightly longer than the scalloping period so that the second waist occurs near saturation. The smaller electron beam radius at saturation increases the saturated power of a uniform wiggler. The scalloped beam FEL detuning spectrum is narrower than the matched beam case. This is indicative of a lower net gain for the scalloped beam FEL.

As a result of this study, we conclude that the use of a scalloped-beam is advantageous even at the expense of a longer wiggler length to reach saturation. In addition, the combination of scalloped electron beams and a step-tapered wiggler can double the output power, and thus the FEL efficiency. The radiation beam is also pinched near the exit and expands rapidly afterward, thereby reducing the risk of damaging optics intercepting the FEL beam.

REFERENCES

[1] P. Sprangle, B. Hafizi, and J.R. Penano, IEEE J. Quantum Electron. 40 (2004) 1739.

[2] D.C. Nguyen, H.P. Freund, and W. Colson, Phys. Rev. ST-AB 9 (2006) 050703.

[3] M. Xie, Proceedings of the IEEE Particle Accelerator Conference, 1995, V.1, 183-185.

[4] P.P. Crooker et al., these Proceedings, paper MOPPH075.

[5] C. Fortgang, Nucl. Instrum. Meth. A393 (1997) 385.

INFLUENCE OF OPTICAL FEEDBACK ON THE COHERENCE PROPERTIES OF FEL OSCILLATORS

S. Bielawski, PhLAM/CERCLA, Villeneuve d'Ascq Cedex;
M.-E. Couprie, CEA, Gif-sur-Yvette;
M. Hosaka, M. Katoh, A. Mochihashi, UVSOR, Okazaki;
C. Szwaj, PhLAM/CERCLA, Villeneuve d'Ascq Cedex

Abstract

When detuned, the output of a FEL oscillator is dominated by a transient amplification of the spontaneous emission noise (SE). Here, we show that FEL oscillators in this situation appear to display a strong sensitivity to optical feedback. From a Dattoli-Elleaume type modeling, we show that a very small amount of reinjected power (typically $\ll 1 \cdot 10^{-8}$ in the case of the UVSOR SR-FEL) modifies dramatically the FEL operation. In particular, we demonstrate experimentally and numerically a strong spectral narrowing, correlated with a disappearance of the laser pulse microstructures. This is also accompanied by a suppression of SR-FEL instabilities for a wide range of parameters (half of the detuning curve). These topics (strong amplification of SE noise, and control using tiny reinjection), are of course more general. We propose a theoretical approach of these questions, using in particular the concept of convective instabilities.

PAPER NOT AVAILABLE

SPACE-FREQUENCY MODEL OF ULTRA WIDE-BAND INTERACTIONS IN FREE-ELECTRON LASERS

Y. Pinhasi*, Yu. Lurie, and A. Yahalom
The College of Judea and Samaria, Ariel, Israel.

Abstract

The principle of operation of intense radiation devices such as microwave tubes, free-electron lasers (FELs) and masers, is based on a distributed interaction between an electron beam and radiation. We developed a three-dimensional, space-frequency theory for the analysis and simulation of radiation excitation and propagation in electron devices and free-electron lasers operating in an ultra wide range of frequencies. The total electromagnetic field is presented in the frequency domain as an expansion in terms of cavity eigen-modes. The mutual interaction between the electron beam and the field is fully described by coupled equations, expressing the evolution of mode amplitudes and electron beam dynamics. The approach is applied in a numerical particle code WB3D, simulating wide band interactions in free-electron lasers operating in the linear and non-linear regimes. The code is used to study the statistical and spectral characteristics of multimode radiation generation in a free-electron laser, operating in various operational parameters. The theory is demonstrated also in the case of "grazing", resulting in a wide-band interaction between the electron beam and the radiation.

INTRODUCTION

In this paper we continue development of the previously stated space-frequency, 3D model, which describes broad-band phenomena occurring in electron devices, masers and FELs [1, 2, 3, 4]. In the model, the total electromagnetic field is presented in the frequency domain in terms of transverse eigen-modes of the cavity, in which the field is excited and propagates. A set of coupled excitation equations, describing the evolution of each transverse mode, is solved self-consistently with beam dynamics equations.

This coupled-mode model is employed in a three-dimensional numerical simulation code WB3D (see [1, 2] for the details). In the present work, the code is used to study the statistical and spectral characteristics of multimode radiation generation in a free-electron laser, operating in various operational parameters. The theory is demonstrated also in the case of "grazing", when the group velocity of the radiation mode is equal to the axial velocity of the electrons, resulting in a wide-band interaction between the electron beam and the generated radiation.

* *e*-mail: yosip@eng.tau.ac.il

THE MODEL

In the frequency domain the total electromagnetic field can be expanded in terms of transverse eigenmodes of the medium in which it is excited and propagates (see [1, 2] for the details). The perpendicular component of the electric and magnetic fields are given in any cross-section as a linear superposition of a complete set of transverse electric filed $\widetilde{\mathcal{E}}_{q\perp}(x,y)$ and magnetic field $\widetilde{\mathcal{H}}_{q\perp}(x,y)$ eigenmodes:

$$\widetilde{\mathbf{E}}_{\perp}(\mathbf{r},f) = \sum_{q} C_q(z,f)\, e^{+jk_{z_q}z}\, \widetilde{\mathcal{E}}_{q\perp}(x,y) \quad (1)$$

$$\widetilde{\mathbf{H}}_{\perp}(\mathbf{r},f) = \sum_{q} C_q(z,f)\, e^{+jk_{z_q}z}\, \widetilde{\mathcal{H}}_{q\perp}(x,y) \quad (2)$$

here $C_q(z,f)$ is amplitude of the mode q, that may be found from the excitation equations:

$$\frac{d}{dz}C_q(z,f) = \frac{1}{\mathcal{N}_q}\sum_i Q_i \left\{ \frac{\mathbf{v}_{\perp i}}{v_{z_i}}\widetilde{\mathcal{E}}^*_{q\perp}(x_i,y_i) + \widetilde{\mathcal{E}}^*_{q_z}(x_i,y_i) \right\} e^{j[\omega t_{z_i} - k_{z_q} z]} \quad (3)$$

Spectral energy distribution of the electromagnetic field is defined in the model as a sum of energy spectrum of the excited modes:

$$\frac{d\mathcal{W}(z)}{df} = \sum_q \frac{1}{2}|C_q(z,f)|^2\, \Re\{\mathcal{N}_q\} \quad (4)$$

MULTIMODE SUPER-RADIANT EMISSION

To demonstrate the utilization of the model, we present a study of super-radiant emission in a waveguide-based, pulsed beam free-electron maser (FEM), with operational parameters are given in Table 1. Such FEM is expected to operate at millimeter and sub-millimeter (THz) wavelengths. When a FEL utilizes a waveguide, the axial wavenumber of transverse mode q follows the dispersion relation:

$$k_{z_q}(f) = \frac{2\pi}{c}\sqrt{f^2 - f_{co_q}^2} \quad (5)$$

where $f_{co_q} = \frac{c}{2\pi}k_{\perp q}$ is the cut-off frequency of the mode. In synchronism with that mode, the dispersion relation for

Table 1: Operational parameters of millimeter and sub-millimeter wave free-electron maser.

Accelerator	
Electron beam energy:	E_k=1÷6 MeV
Electron beam current:	I_0=1 A
Electron beam pulse duration:	T=0.1 pSec
Wiggler	
Magnetic induction:	B_w=2000 G
Period:	λ_w=5 cm
Number of periods:	N_w=20
Waveguide	
Rectangular waveguide:	15×7.5 mm
mode	Cut-off frequency
TE_{01}	20.0 GHz
TE_{21} , TM_{21}	28.3 GHz
TE_{41} , TM_{41}	44.7 GHz
TE_{03}	60.0 GHz

the electron beam is given by

$$k_{z_q}(f) = \frac{2\pi f}{v_{z0}} + k_w \qquad (6)$$

where v_{z0} is the average velocity of the accelerated electrons and $k_w = \frac{2\pi}{\lambda_w}$ (λ_w is the wiggler's period). The corresponding curves of synchronism frequency vs. beam energy for the FEM are shown in Fig. 1. Only waveguide modes which have in their field profile components that interacts efficiently with the wiggling electrons are shown. Table 2 summarizes several examined cases resulted from Eq. (6) in the multi-transverse mode operational regime. For each transverse mode q, the acceleration energy E_k can be set to excite two frequencies corresponding to the "slow" ($v_{g_q} < v_{z0}$) and "fast" ($v_{g_q} > v_{z0}$) synchronism frequencies or to the special case of "grazing", where $v_{g_q} = v_{z0}$ and a single synchronism frequency is obtained. Here

$$v_{g_q} = 2\pi \frac{df}{dk_{z_q}} = \frac{c^2}{2\pi f} k_{z_q}(f) \qquad (7)$$

is the group velocity of the excited mode q.

The effect of super-radiance emerges when the duration of the electron beam pulse is much less then the period of the electromagnetic waves expected to be excited at synchronism frequencies according to Table 2. The waveguide and e-beam dispersion curves when the acceleration energy is $E_k = 2$ MeV are shown in Fig. 2. In this case a single waveguide mode TE_{01} is excited at two separated synchronism frequencies ("slow" and "fast") 46.1 GHz and 149.5 GHz, respectively. The spectral density of energy flux calculated with the code WB3D is shown in Fig. 3a. The spectrum peaks at the two synchronism frequencies with main lobe bandwidth of $\Delta f_{1,2} \approx \frac{1}{\tau_{sp_{1,2}}}$, where $\tau_{sp_{1,2}} \approx N_w \lambda_w \left| \frac{1}{v_{z_0}} - \frac{1}{v_{g_{1,2}}} \right|$ is the slippage time. The corresponding temporal wave-packet (shown in Fig. 3b) consist of two "slow" and "fast" pulses with durations equal to the slippage times modulating carriers at their respective synchronism frequencies. Lowering the beam energy to $E_k \approx 1.62$ MeV, results in grazing between the e-beam and the waveguide dispersion curves at a single synchronism frequency 69.6 GHz. The spectrum in the case of grazing, as well as the corresponding temporal wavepacket are shown in Fig. 4.

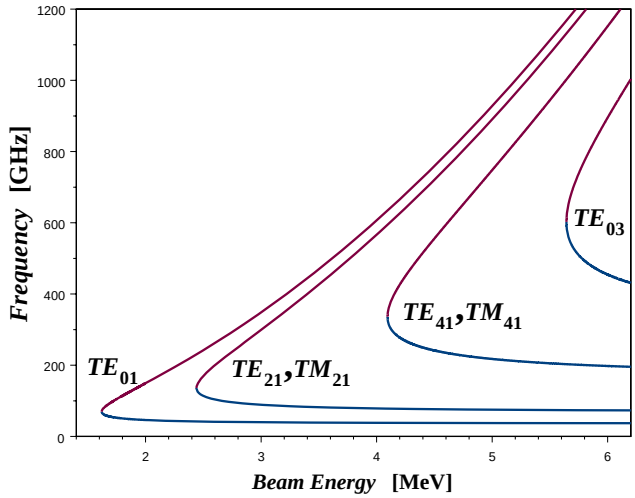

Figure 1: Energy dependence of the dispersion solutions.

As the acceleration energy is increased, transverse modes of higher orders are being excited simultaneously (in addition to the mode TE_{01}) extending the radiation spectrum over a wide rage of frequencies from few tens of GHz to more then THz. Fig. 5 shows the energy spectral densities of the excited waveguide modes as the beam energy is increased.

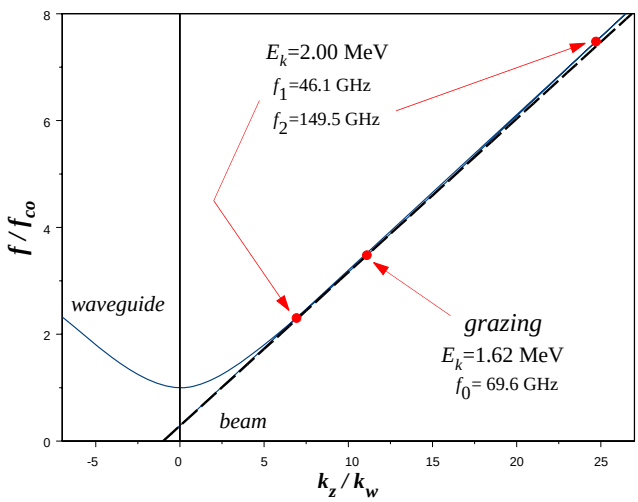

Figure 2: Dispersion solutions for TE_{01} transverse mode for $E_k = 2$ MeV.

Table 2: Synchronism frequencies for several beam energies.

Beam Energy	Synchronism frequencies [GHz]			
[MeV]	TE_{01}	TE_{21},TM_{21}	TE_{41},TM_{41}	TE_{03}
1.62	69.6 (grazing)	—	—	—
2.00	46.1 , 149.5	—	—	—
2.44	42.0 , 230.5	136.2 (grazing)	—	—
3.00	39.8 , 348.4	88.9 , 299.3	—	—
4.09	38.2 , 632.9	78.1 , 592.9	336.1 (grazing)	—
5.00	37.5 , 927.8	75.0 , 890.3	217.5 , 747.8	—
5.60	37.3 , 1151.0	73.9 , 1114.5	203.6 , 984.8	602.6 (grazing)

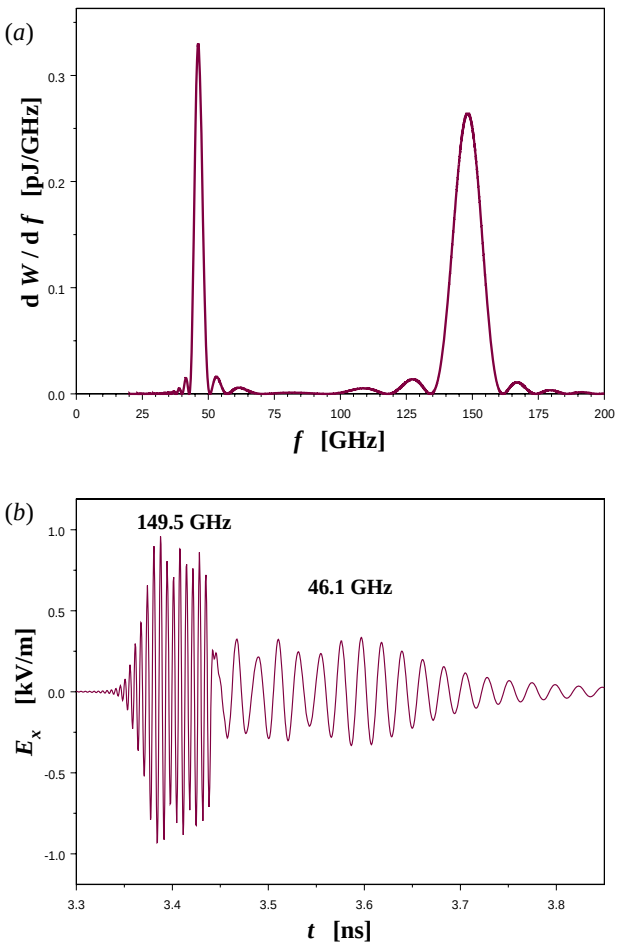

Figure 3: Super-radiant emission from an ultra short bunch when the beam energy is E_k=2 MeV and a single TE_{01} mode is excited: (a) Energy spectrum, and (b) temporal wavepacket.

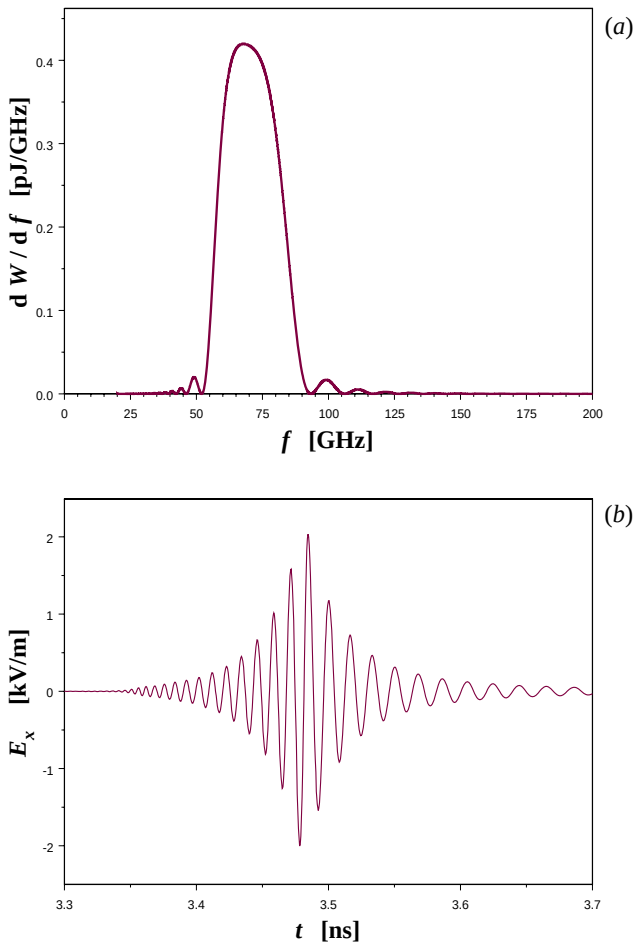

Figure 4: That of Fig. 3, but at grazing condition for mode TE_{01} (the beam energy is $E_k \approx 1.62$ MeV).

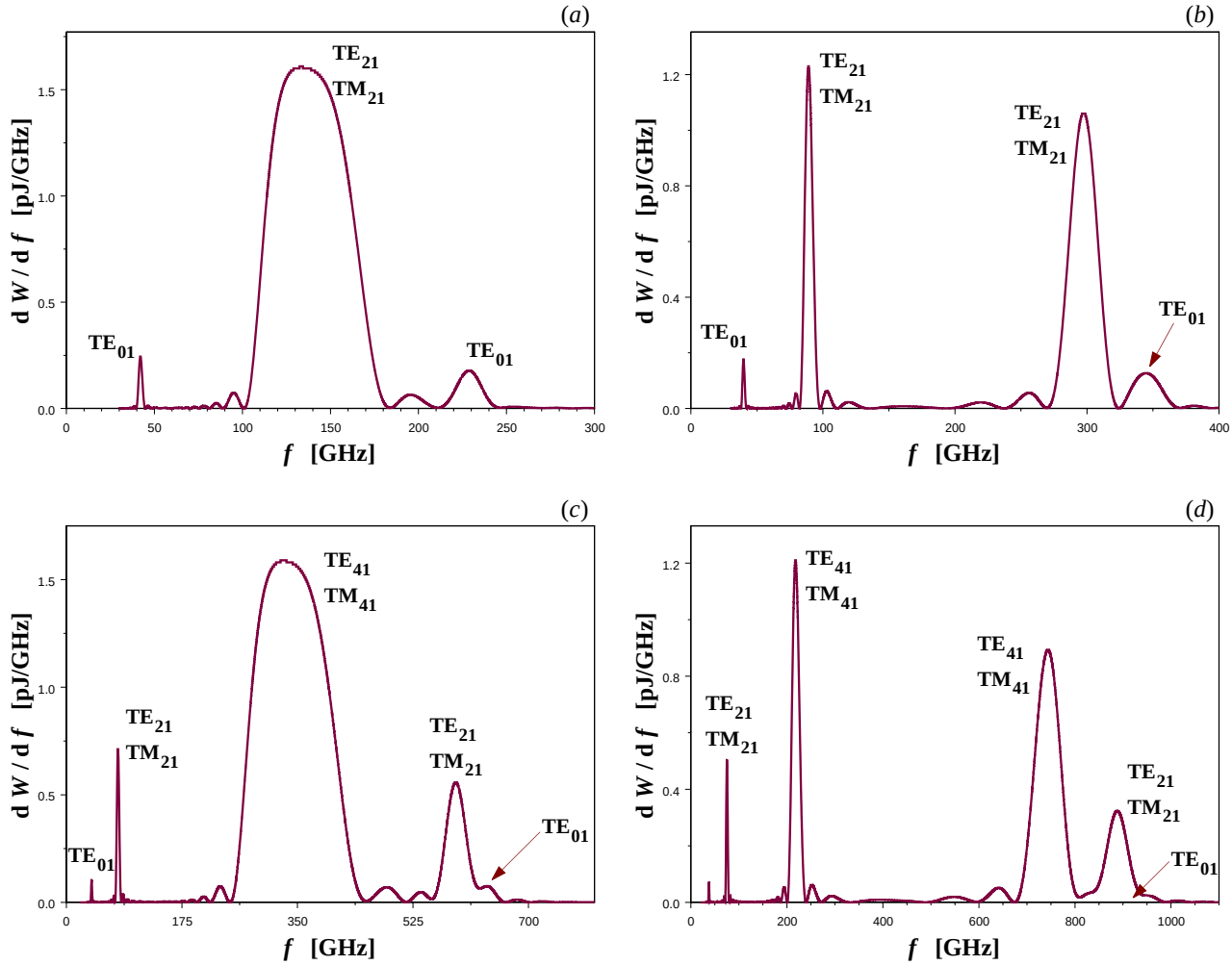

Figure 5: Energy spectra for different acceleration energies: (a) $E_k = 2.44$ MeV (grazing in the TE_{21},TM_{21} modes); (b) $E_k = 3.00$ MeV; (c) $E_k = 4.09$ MeV (grazing in the TE_{41},TM_{41} modes); (d) $E_k = 5.00$ MeV.

CONCLUSIONS

The presented coupled-mode theory, formulated in the frequency domain, enables development of a three-dimensional model, which can accurately describe wide-band interactions between radiation and electron beam in electron devices and free-electron lasers. Space-frequency solution of the electromagnetic equations considers dispersive effects arising from the resonator and gain medium. Such effects play a role also in the special case of grazing, and can not be accurately treated in approximated space-time approaches. We also note that our space-frequency model described here, also facilitates the consideration of statistical features of the electron beam and the excited radiation, enabling simulation of the interaction of a free-electron laser operating in the linear and non-linear regimes.

REFERENCES

[1] Y. Pinhasi, Yu. Lurie and A. Yahalom, Nucl. Instr. and Meth. in Phys. Res. A, **475**, 147 (2001).

[2] Y. Pinhasi, Yu. Lurie, A. Yahalom, and A. Abramovich, Nucl. Instr. Meth. Phys. Res. A, **483**, 510 (2002).

[3] Y. Pinhasi, Yu. Lurie, A. Yahalom, Phys. Rev. E **71**, 036503 (2005).

[4] Y. Pinhasi and Yu. Lurie, Phys. Rev. E **65**, 026501 (2002).

PARAMETRIC OPTIMIZATION OF A X-RAY FEL BASED ON A THOMSON SOURCE*

L. Serafini, A. R. Rossi, V. Petrillo, C. Maroli, A. Bacci, INFN-Milano, Milano, Italy
M. Ferrario, INFN-LNF, Frascati, Italy.

Abstract

We present a study based on a parametric optimization of a Thomson Source operated in FEL mode. This deals with the proposed scheme to use a high intensity laser pulse colliding with a high brightness electron beam of low to medium energy (around 10 MeV). Electrons undulating in the incoming laser field may emit radiation in a FEL coherent mode as far as some conditions are satisfied. A set of simple analytical formulas taking into account 3D effects is derived, in order to express these conditions in terms of three free parameters, namely the wavelength of the colliding laser pulse, the amplitude of the ripples in the time profile of the laser field, and the peak current carried by the electron beam. A few examples of possible operating points are compared with results of 3D numerical simulations, showing the FEL coherent emission of X-rays in the 0.1 to 5 nm range with tens of MeV high brightness electron beams colliding with high intensity ps-long laser beams carrying pulse energies of about 10 J.

INTRODUCTION

It has been recognized by several authors in the past [1,5] that the interaction between a high brightness electron beam and a counterpropagating - head-on colliding - high intensity laser pulse could lead to coherent emission of radiation, in the direction of the electron beam motion, according to a FEL-like mechanism driven by a collective instability that induces exponential growth of the radiation intensity. This coherent part of the emitted radiation overlaps with the spontaneous incoherent radiation generated by the Thomson back-scattering effect. Only recently, however, detailed 3D simulations[6] able to model the FEL collective instability showed the potential existence of this effect under particular conditions of electron beam emittance and current as well as laser field amplitude in the focal region, where the interaction between the two beams occurs. In this paper we derive a set of practical analytical formulas describing the existence of operating conditions in the dynamical range of the system where 3D effects can be mitigated so to allow the onset of the FEL instability, hence the generation of coherent radiation in a SASE-FEL emission mode.

Generally speaking, the situation is at all similar to a conventional SASE-FEL based on a magnetostatic undulator through which the electron beam propagates: the magnetostatic field of the undulator is replaced by the e.m. field of the incoming laser pulse, which causes the electrons to wiggle while they propagate through the pulse. Since the laser field is a classical description of a flux of real photons (to be compared with virtual photons for the case of a magnetostatic undulator), the resonance relationship for a Thomson source is at all similar to the FEL resonance apart for a factor 4 in the denominator.

$$\lambda_R = \frac{\lambda}{4\gamma^2}\left(1 + a_0^2 + \gamma^2\vartheta^2\right) \qquad (1)$$

where λ is the wavelength of the colliding laser pulse, γ the kinetic energy of the electron beam (expressed in terms of its dimensionless relativistic factor), λ_R the wavelength of the forward emitted radiation (within a small angle ϑ around the electron beam propagation axis) and a_0 is the laser parameter (dimensionless amplitude of the vector potential associated to the laser field), given by

$$a_0 = 8.5 \cdot 10^{-6}\frac{\lambda\sqrt{P}}{R_0} \qquad (2)$$

where R_0 is the laser focal spot size and P the peak power in the laser pulse (in TW).

The interaction between the electron beam and the laser pulse is assumed to take place in a drift space where no external forces (focusing or deflecting) act on the two beams, which are tightly focused by their individual final focus lens systems, taking them down to micron-size focal spots. Under the assumption that the laser pulse has a uniform transverse intensity profile of hard edge radius R_0 in the focus position, we can neglect ponderomotive transverse effects on the electron trajectories[7].

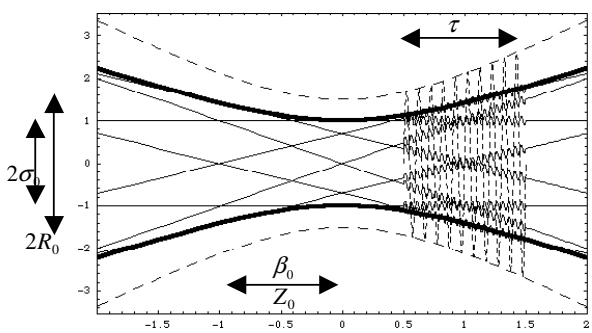

Figure 1: Electron orbits in the focal region (intersecting thin solid lines). Electron beam envelope (bold solid lines) and laser beam envelope (dashed lines) are also shown. Electrons are moving to the right, laser pulse (duration τ) is moving to the left.

As depicted in Fig.1, electrons cross the focus area traveling on rectilinear orbits: when they traverse the laser field their secular trajectories remain rectilinear, with a superimposed slightly wiggling motion.

PARAMETER DEFINITIONS

We break-up the set of parameters describing the whole system into three groups, one for each of the three interacting beams: the electron beam, the colliding laser beam and the emitted FEL radiation beam, respectivley.

The system is described by 11 main free parameters: 4 parameters for the electron beam, summarized in Table 1, 5 parameters for the laser beam, summarized in Table 2, and 2 parameters for the FEL radiation beam, summarized in Table 3. Note that units indicated in the tables are just the ones used for simplicity in the final set of formulas: all intermediate calculations are performed in standard MKS units.

Table 1: Electron Beam parameters

Energy γ	Current I [A]	Focal spot σ_0 [μm]	Emittance ε_n [μm]

There are some other additional parameters which represents ancillary quantities useful for handling the system of conditions relating the 11 main free parameters. These are: the electron beam beta-function in the focus, β_0 , which is defined by the usual relation

$$\sigma_0 = \sqrt{\frac{\varepsilon_n \beta_0}{\gamma}} \qquad (3)$$

the electron bunch rms length, σ_z , and the electron beam rms relative energy spread $\frac{\Delta\gamma}{\gamma}$. These last two quantities do not enter in the derivation of the final set of formulas: they are only used for an afterward check on additional ancillary conditions.

Table 2: Laser parameters

Wavelength λ [μm]	Power P [TW]	Pulse length τ [ps]	Focal spot R_0 [μm]	Intensity ripples Δ [%]

Additional parameters for the laser beam are the Rayleigh range Z_0 , given by

$$Z_0 = \frac{4\pi R_0^{\,2}}{\lambda} \qquad (4)$$

and the laser pulse energy, defined by $U = P\tau$. Note that the definition of the laser ripple parameter Δ is

$$\Delta \equiv \frac{\Delta a_0}{a_0} \qquad (5)$$

which represents the fluctuations of laser field amplitude along the pulse, which is assumed to have (at $\Delta = 0$) an ideal flat-top time profile.

Table 3: FEL radiation parameters

Wavelength λ_R [Å]	FEL parameter ρ

Additional parameters for the FEL radiation beam are the gain length, $L_g = \frac{\lambda}{4\pi\rho}$, and the quantum parameter, $\overline{\rho} = \rho\frac{\gamma\lambda_R}{\lambda_C}$ (with $\lambda_C = 0.024$ Å). As discussed elsewhere[8], as far as $\overline{\rho} \geq 0.5$ quantum effects are negligible ant the system can be described by means of classical FEL-like equations[6].

CONDITIONS FOR FEL EMISSION

Let us now analyze what are the conditions to be satisfied by the 11 main parameters (γ, I, σ_0, ε_n, λ, P, τ, R_0, Δ, λ_R, ρ) in order to operate the Thomson source as a Free Electron Laser.

The FEL resonance condition

$$\lambda_R = \frac{\lambda}{4\gamma^2}\left(1 + a_0^2\right) \qquad (C.1)$$

The definition of the FEL parameter

$$\rho = \frac{10^{-2}}{\gamma}\sqrt[3]{I\lambda^4 P/\sigma_0^4} \qquad (C.2)$$

Two conditions for optimal geometrical beam overlap of the envelopes of the two colliding beams: the first one is to ensure that the electrons will observe transversally constant undulator field

$$R_0 \geq 2\sigma_0 \qquad (C.3)$$

and the second one is to minimize the hour-glass effect in the collision of the two beams

$$c\tau \leq 2Z_0 \qquad (C.4)$$

Note that we will further check that the condition

$\beta_0 \geq Z_0$ is satisfied (assuring that the electron beam envelope is contained within the laser beam envelope). However, this condition is not explicitely used in order to simplify the following derivation.

We want of course that the interaction between the two beams, *i.e.* the equivalent undulator length, be longer than the FEL saturation length, which is typically set at 10 times the gain length. Hence

$$c\tau \geq 10 L_g \qquad \text{(C.5)}$$

Now we must take into account how 3D effects and non-uniformities in the laser filed (which is our undulator field) may affect the FEL instability, avoiding inhomogeneous broadening effects of the gain bandwidth that may damp the onset of the FEL exponential instability. We know that the gain bandwidth of a SASE FEL is set by $\Delta\lambda_R / \lambda_R = 2\rho$. This implies that 3D and non-uniformity effects must produce bandwidth broadening smaller than 2ρ .

For a Fourier trasnform limited laser pulse the spectrum line width is $\frac{\Delta\lambda}{\lambda} = \frac{\lambda}{c\tau}$, therefore $\frac{\Delta\lambda_R}{\lambda_R} = \frac{\Delta\lambda}{\lambda} = \frac{\lambda}{c\tau}$, hence the condition

$$c\tau \geq \frac{\lambda}{2\rho} \qquad \text{(C.6)}$$

The FEL frequency broadening due to fluctuations in the undulator field amplitude, in our case represented by Δ, is given by $\frac{\Delta\lambda_R}{\lambda_R} = \frac{2a_0^2}{1+a_0^2}\Delta$, which in turns implies

$$\Delta \leq \rho \frac{1+a_0^2}{a_0^2} \qquad \text{(C.7)}$$

The transverse motion of the electrons in the focal region, which is mainly determined by the electron beam emittance, produces a random distribution of the angle ϑ in the resonance relationship reported in eq.1, which in turns induces a broadening of the FEL bandwidth. As extensively discussed elsewhere[6,9], the limitation on this random angle can be casted in terms of an upper limit on the emittance. This criterion is generally known as Kim-Pellegrini criterion: it has been generalized in ref.6 to the expression

$$\varepsilon_n \leq \sqrt{\frac{Z_R}{L_G}} \frac{\lambda_R \gamma}{2\pi} \qquad \text{(C.8)}$$

whewre Z_R is the Rayleigh range of the emitted FEL radiation, $Z_R = \frac{4\pi R_0^{\,2}}{\lambda_R}$.

FINAL SET OF FORMULAS

In order to simplify the derivation of a solution for the system of equations (C.1-C.8) we assume equalities for all the conditions instead of inequalities: this will allow to derive the minimum condition that 8 parameters have to fulfill, expressed as functions of three free parameters. We choose as free parameters the laser wavelength λ, the electron beam current I and the laser ripple parameter Δ.

The electron beam parameters must obey:

$$\varepsilon_n = 0.18\lambda \ \text{(F.1)} \ ; \quad \gamma = 0.05 \sqrt[3]{\frac{I}{\Delta^2}} \ \text{(F.2)}$$

$$\sigma_0 = 0.21\lambda/\sqrt{\Delta} \ \text{(F.3)} \ ; \quad \beta_0 = 0.009\lambda \sqrt[3]{\frac{I}{\Delta^5}} \ \text{(F.4)}$$

the ancillary condition $\beta_0 \geq Z_0$, as anticipated, is respected if $I > 576\ \Delta^2$, which is easily satisfied, since Δ assumes values definitely lower than 0.1, while the beam curent I has expected values in excess of several hundreds Amps. Note that the additional condition $\Delta\gamma/\gamma \leq \rho$ has to be satisfied, though it was not explicitely considered in the derivation.

The laser parameters must obey:

$$P = 0.0018/\Delta \ \text{(F.5)} \ ; \quad U = 18.6\lambda/\Delta^2 \ \text{(F.6)} \ ;$$

$$a_0 = 1. \ \text{(F.7)} \ ; \quad \tau = 1.1 \cdot 10^{-8}\lambda/\Delta \ \text{(F.8)} \ ;$$

$$Z_0 = 1.6\lambda/\Delta \ \text{(F.9)}$$

The FEL radiation is characterized by:

$$\lambda_R = 200\lambda \sqrt[3]{\frac{\Delta^4}{I^2}} \ \text{(F.10)} \ ; \quad \rho = 0.25\Delta \ \text{(F.11)} \ ;$$

$$L_G = 0.32\lambda/\Delta \ \text{(F.12)} \ ; \quad \overline{\rho} = 10^{12}\lambda \sqrt[3]{\frac{\Delta^5}{I}} \ \text{(F.13)}$$

EXAMPLES

A relevant example is for the case of a CPA Ti:Sa laser system, which is nowadays capable of delivering fs to ps long pulses carrying energies in excess of a J, focused down to micron-size spots. In this case, setting $\lambda = 0.8\ \mu\text{m}$, the formula set (F.1-F.13) reduces to the following (expressing Δ in units of %):

$$\varepsilon_n = 0.14\ \mu\text{m} \ ; \ \gamma = 1.08 \sqrt[3]{\frac{I}{\Delta^2}} \ ; \ \sigma_0 = \frac{1.4}{\sqrt{\Delta}}\ \mu\text{m}$$

$$\beta_0 = \frac{0.015}{\Delta}\sqrt[3]{\frac{I}{\Delta^2}}\ [\mathrm{mm}]\ ;\ P = \frac{0.18}{\Delta}\ [\mathrm{TW}]\ ;$$
$$U = \frac{0.15}{\Delta^2}[\mathrm{J}]\ ;\ \tau = \frac{0.85}{\Delta}\ [\mathrm{ps}]\ ;\ Z_0 = \frac{0.13}{\Delta}\ [\mathrm{mm}]\ ;$$
$$\lambda_R = 3436\Delta\sqrt[3]{\frac{\Delta}{I^2}}\ [\text{Å}]\ ;\ \rho = 2.5\cdot 10^{-3}\Delta\ ;$$
$$L_G = \frac{26}{\Delta}\ [\mu\mathrm{m}]\ ;\ \bar{\rho} = 386\Delta\sqrt[3]{\frac{\Delta^2}{I}}\ .$$

We take into account now two specific examples, one in the classical SASE-FEL regime, the other in the quantum regime: all parameters now depend only on the beam current and the laser ripple parameter.

1) we set $\Delta = 0.15\ \%\ ;\ I = 1500\ A$: we find

$$\varepsilon_n = 0.14\ \mu\mathrm{m}\ ;\ \gamma = 44\ ;\ \sigma_0 = 3.7\ \mu\mathrm{m}\ ;$$
$$\beta_0 = 4.1\ \mathrm{mm}\ ;\ P = 1.2\ \mathrm{TW}\ ;\ U = 6.6\ \mathrm{J}\ ;$$
$$\tau = 5.6\ \mathrm{ps}\ ;\ Z_0 = 0.85\ \mathrm{mm}\ ;\ \lambda_R = 2.1\ \text{Å}\ ;$$
$$\rho = 4.\cdot 10^{-4}\ ;\ L_G = 159\ \mu\mathrm{m}\ ;\ \bar{\rho} = 1.4\ .$$

2) we set $\Delta = 0.05\ \%\ ;\ I = 2500\ A$: we find

$$\varepsilon_n = 0.14\ \mu\mathrm{m}\ ;\ \gamma = 108\ ;\ \sigma_0 = 6.4\ \mu\mathrm{m}\ ;$$
$$\beta_0 = 30\ \mathrm{mm}\ ;\ P = 3.5\ \mathrm{TW}\ ;\ U = 60\ \mathrm{J}\ ;$$
$$\tau = 17\ \mathrm{ps}\ ;\ Z_0 = 2.5\ \mathrm{mm}\ ;\ \lambda_R = 0.35\ \text{Å}\ ;$$
$$\rho = 1.2\cdot 10^{-4}\ ;\ L_G = 531\ \mu\mathrm{m}\ ;\ \bar{\rho} = 0.2\ .$$

The paremeter values predicted for case 1), which is in the calssical regime, are in agreement with the results of 3D simulations reported in ref.6,9, where a 15 MeV electron beam carrying 1.5 kA of current, focused down to 10 μm rms focal spot size, was considered colliding with a Ti:Sa pulse with $a_0 = 0.8$, and a 20 μm spot size, which corresponds to a power of 5.5 TW. The saturation of the FEL instability is reached, for an emittance of 0.44 μm, at 4 ps of laser pulse length, implying the need of 22 J of laser pulse energy and an effective gain length of about 120 μm. The radiation wavelength was 3.64 Å. Since these simulations were performed before deriving the set of formulas reported in this paper, the agreement is only on a general frame. More detailed comparisons between this set of formulas, that are meant to drive the initial choice of parameters for the simulations, and the simulation results, will be the subject of a future work.

As a last remark we report here the results of 1D simulations (performed with a code described elsewhere[10]) evaluating the effects of laser ripples on the growth of the FEL instability, taking same laser and electron beam parameters as for the previously mentioned 3D simulations. The laser amplitude modulation was taken as $\Delta\sin\left(k_{fluct}z + ct\right)$. The FEL saturation intensity is plotted as a function of ω_{fluct}/ω_L ($\omega_L \equiv 2\pi c/\lambda$) for different values of the laser ripple parameter Δ.

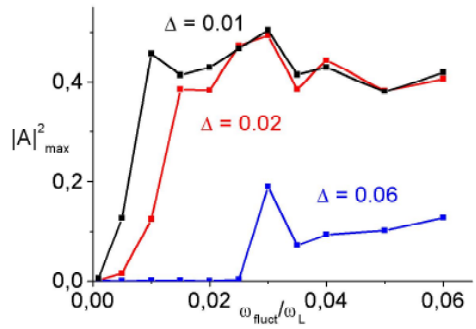

Figure 2: Saturation intensity in presence of laser ripples.

It is clearly visible in Fig.2 how the FEL instability is damped, *i.e.* the exponential growth is no longer attained, when Δ assumes values greater than a few percent, for almost any value of the modulation scale length k_{fluct}. Also, the system seems to tolerate laser amplitude modulations occurring on a scale much shorter than the gain length, as indicated by the fact that the saturation intensity goes to zero for any value of Δ when the scale of the laser modulation gets close to gain length, *i.e.* when $L_G/\lambda = \omega_{fluct}/\omega_L = 1/4\pi\rho = 0.0055$.

REFERENCES

[1] J. Gea-Banacloche, G.T. Moore, R.R. Schlicher, M.O. Scully, and H. Walther, IEEE Journ. of Quantum Electron., **QE-23**, 1558 (1987).

[2] B.G. Danly, G. Bekefi, R.C. Davidson, R.J. Temkin, T.M. Tran, and J.S. Wurtele, IEEE Journ. of Quantum Electron., **QE-23**, 103(1987).

[3] J.C. Gallardo, R.C. Fernow, R. Palmer, and C. Pellegrini, IEEE Journ. of Quantum Electron. **QE-24**, 1557 (1988).

[4] C.B. Schroeder, C. Pellegrini, and P. Chen, Phys. Rev. E **64**, 056502 (2001).

[5] R. Bonifacio *et al.*, FEL-2005 Proceedings, SLAC-R-791, JACoW / eConf C0508213, 71 (2005).

[6] A. Bacci, M.Ferrario, C. Maroli, V. Petrillo, L. Serafini, PRST-AB **9** (2006) 060704.

[7] L. Serafini, *AIP CP* **335**, 666 (1995).

[8] R. Bonifacio *et al.*, Nucl. Instr. and Methods, **A 543**, 645 (2005).

[9] A. Bacci *et al.*, X-Ray Generation with a FEL based on an Optical Wiggler, this conference.

[10] A.Bacci *et al.*, "Collective effects in the Thomson back-scattering between a laser pulse and a relativistic electron beam" EPJAP (in print).

APPLE UNDULATORS FOR HGHG-FELS

J. Bahrdt, BESSY, Berlin, Germany.

Abstract

Cascaded HGHG-FEL facilities have been proposed by several groups. In these machines the beam characteristics of the initial seeding laser like coherence, short time structure and small bandwidth are transformed to shorter wavelengths where seeding lasers are not available. The first stages are equipped with planar devices. For full polarization control the last amplifier and the final radiator can be realized as APPLE devices. The specific demands on the polarizing devices as compared to planar hybrid devices are discussed for the example of the proposed BESSY HE-FEL to be operated at 1nm. The field optimization procedure requires specific strategies. An improvement of the magnetic material is helpful in this context. The small good field region implies tight geometrical tolerances. Gap and phase dependent focussing effects have to be compensated. Other important issues are the complexity of the control system and the radiation protection system.

INTRODUCTION

FEL facilities are powerful sources for ultra short pulses and longitudinally and transversely coherent radiation in the soft X-ray and X-ray regime. Three X-ray FELs based on the SASE principle are currently under construction [1-3].

In the soft X-ray regime various seeding schemes have been proposed and realized which improve the spectral characteristics and the time structure. A cascaded HGHG FEL [4,5] starts with the coherent radiation of a high power Ti:Sapphire laser which interacts with the electron beam in a modulator. In a dispersive section the energy modulation is converted to a spatial modulation. The following radiator takes advantage of the higher orders of the electron beam bunching producing a seed for the next stage. Several stages can be cascaded achieving frequencies down to 1nm.

The number of stages can be reduced if the seed wavelength of the first stage is already in the few 10s nm regime which can be accomplished using the HHG process [6].

Only the light of the last radiator will be delivered to the experiment. All other undulator modules serve to provide a sufficient bunching of the electron beam in the last stage. For simplification all these modules can be realized as planar devices though they might be slightly longer than helical devices. The last radiator has to provide the full flexibility concerning the polarization control. APPLE type structures are suitable for this purpose. In this paper we concentrate on the design of APPLE undulators to be used as final radiators. We discuss the technical challenges and their solutions. For illustration we will apply the parameters of the proposed BESSY Soft X-Ray FEL.

The tolerances for HGHG and SASE FEL undulators are similar for comparable photon energies. The complexity of a HGHG undulator system is, however, higher. A 200m SASE undulator consists of 40 identical 5m modules whereas a cascaded FEL can be composed of 18 modules with 9 different lengths and 5 different period lengths (BESSY HE-FEL). This affects the concept of series production and modularity, the control system and the operation.

In contrast to an X-ray FEL undulator system the undulator focussing is an important issue for soft X-ray systems (in particular for polarizing devices) because the electron energies are generally lower.

MAGNETIC STRUCTURE

APPLE undulators provide the highest fields among all variably polarizing insertion devices. A single pass FEL permits the installation of a circular beam pipe without performance loss. In this geometry additional magnetic material can be arranged at the side of the vacuum chamber. Additionally, the angle of magnetization can be rotated by 45° (APPLE III [7]). The demagnetizing fields are slightly higher for an APPLE III than for an APPLE II (figure 1). The magnetic stability can be recovered with another magnet grade and the field gain is still about a factor of 1.4 as compared to an APPLE II [7].

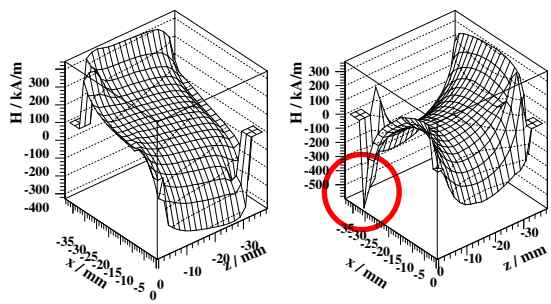

Figure 1: Difference of reverse fields between APPLE III and APPLE II design for the example of the planned BESSY UE50 (LE- and ME-FEL). Left: A-magnet (long. magnetized), right: B-magnet (vert. magnetized).

Today APPLE undulators can be built with the same field quality as planar devices using specific sorting and shimming techniques. At BESSY the magnets of the APPLE undulators are characterized individually with respect to the dipole moment (automated Helmholtz coil) and the inhomogeneities (stretched wire system). The data are used in a simulated annealing code which

minimizes the phase errors and reduces the multipoles by a factor of 5-10 as compared to an unsorted structure [8]. The field quality of devices consisting of 1000 magnets can be predicted with an accuracy of about 1.5 Gm (figure 2).

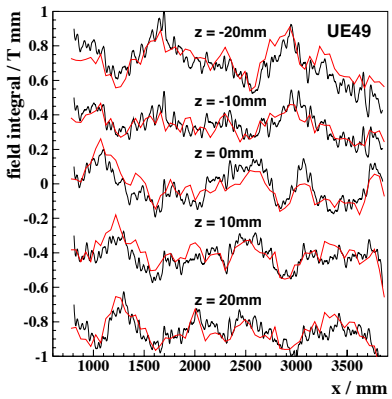

Figure 2: Prediction from single block characterization (red) and Hall probe measurements (black) of the BESSY UE49 field integrals at five transverse positions.

The field properties are optimized with various techniques:

- trajectories: block movements
- shift dependent terms: Fe-shims
- shift independent terms: permanent magnet arrays at both ends of the devices.
- dynamic multipoles: Fe-shims

Details can be found in [8,9,10]. The required magnet quality of FEL undulators can be achieved with state of the art techniques which can, however, be rather time consuming and are not suitable for a series production.

MAGNET MATERIAL

The new FEL facilities will consist of many undulator segments with totally 10.000s of individual magnets. Today, permanent magnets have typical remanence and angle errors in the order of 1-2% and 1-2°, respectively, where the distributions within one batch can be significantly narrower. The inhomogeneities are important as well and determine the field quality at small gaps. In principle, the required magnet field performance can be achieved with a detailed characterization of the magnets, sorting and shimming. The production process can, however, significantly be simplified if the magnet quality can be improved.

Triggered by the need for high quality magnets for the European X-Ray FEL at DESY and the BESSY Soft X-Ray FEL a BMBF funded joint collaboration between DESY, BESSY and Vacuumschmelze has started. The collaboration has the goal to reduce remanence and angle errors by a factor of 5-10 and to improve the block homogeneity. At a certain level the quality is determined by the geometrical tolerances of the blocks and hence, these tolerances have to be reduced to a level of 10µm. Magnet measurement equipment built at BESSY and DESY has been shipped to the magnet manufacturer who will use the machines to optimize the production process. BESSY provides a stretched wire system for the characterization of block inhomogeneities whereas DESY has built an automated Helmholtz coil system.

The north south effect (field difference between two opposite sides of a block) is not a useful quantity in particular for APPLE devices where the electron beam is located close to a magnet corner. Block inhomgeneities can be determined by cutting the magnet into slices and measuring the slices in a Helmholtz coil. Results are shown in figure 3 where a systematic variation of the magnetization angle over the position inside the magnet is plotted. The systematic trend can be minimized with an appropriate setting of the production parameters.

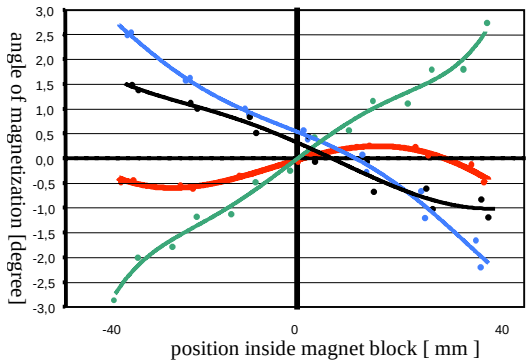

Figure 3: Variation of the magnetization angle inside four individual magnet blocks. The blocks have been produced with different production parameters (by courtesy of Vacuumschmelze, Hanau).

The magnet cutting and the characterization of the slices is time consuming. Similar information can be gathered with the new stretched wire setup in a much shorter time from the complete magnet. The magnet is moved with respect to a single wire in a distance of 5-10mm and induced voltages are measured (figure 4). Measurements from different sides give the information on the magnetization distribution inside the magnet.

Since the measurements are done in a strong field gradient a good positioning accuracy is essential. Temperature stabilized linear motors with absolute encoders and air bearings allow for fast and precise movements. Fe shieldings around the motors reduce the electrical noise.

Figure 4: Stretched wire system for the measurement of magnet block inhomogeneities.

Figure 5 shows a reproducibility of 3.0e-4 Tmm for magnets with the magnetization vector parallel to the wire (A-magnets) and 1.5e-3Tmm for magnets with an orientation perpendicular to the wire (B-magnets). In case of the B-magnets the measurement noise is dominated by a contribution which is proportional to the main signal. A positioning accuracy <4.0µm and a temperature stability of <0.2° is needed to bring the electrical noise to this level.

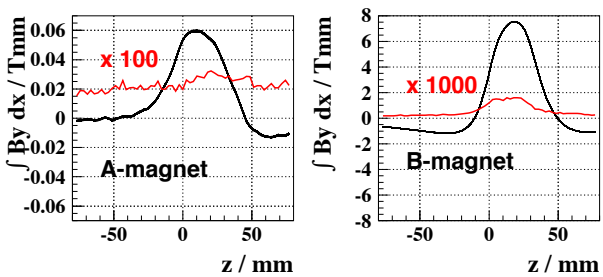

Figure 5: Reproducibilities of the stretched wire system. One hundred blocks of both types have been measured (black) and sigma values (red) have been determined. The distance to the single wire is 10mm and the block dimensions are 40x40x28mm^3.

TOLERANCES

The tolerances for HGHG and SASE FELs are different from those of storage ring IDs. A good overlap between the photon and electron beam ($\Delta x \leq 0.1 \times (\sigma_{eelctron}, \sigma_{photon})$) defines the maximum trajectory walk off. For a Pierce parameter of 0.001 (BESSY HE-FEL) a maximum variation in the K-parameter of $\pm 5 \times 10^{-4}$ can be tolerated ($\Delta E < 0.16$ x bandwidth). This defines the following tolerances: The temperature dependence of the magnet remanence of 0.0011 / °C requires a temperature stability $\Delta T \leq \pm 0.1$°C. The gap positioning accuracy must be $\Delta gap \leq \pm 1$µm and the transverse alignment tolerance has to be $\Delta x \leq \pm 40$µm. The largest contribution to $\Delta K / K$ is attributed to the transverse alignment error (see below). The phase error due to energy spread dominates the total phase error if

$$\Delta\Phi_{rms} \leq \frac{\sigma_\gamma}{\gamma}\frac{1}{\rho\sqrt{3}}$$

Assuming an energy spread of 2×10^{-4} the tolerance for the phase error of the magnetic field is $\Delta\Phi_{rms} < 6.6°$ for the BESSY HE-FEL. Apart from quadrupole terms (see later in this paper) static or dynamic multipoles are less important for single pass devices.

The trajectory errors can be measured and minimized with state of the art measurement and shimming techniques. Phase errors below 5° can be achieved even for the complicated APPLE II design without explicit phase shimming as demonstrated for the six BESSY APPLE II devices. A gap positioning accuracy of ±1.5µm has already been achieved [7] (see also next chapter). In the following, we will concentrate on the challenging transverse alignment tolerances.

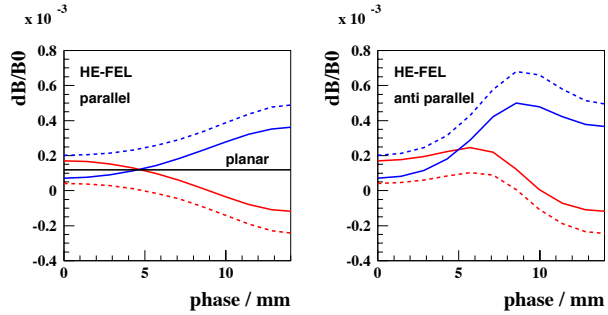

Figure 6: Relative field variation 0.1mm horizontal (red) and vertical (blue) off axis for APPLE III (solid) and APPLE II (dashed) undulator operating in the parallel (left) and antiparallel (right) mode.

The good field region of an APPLE device is significantly reduced as compared to a planar device (figure 6) though it is larger for the APPLE III design as compared to the APPLE II.

In figure 7 the transverse charge distribution of the BESSY FEL electron beam is compared to the field variations in various operation modes. For a maximum transverse displacement of 40µm more than 2σ of the electron beam are within $\Delta K / K < 5 \times 10^{-4}$.

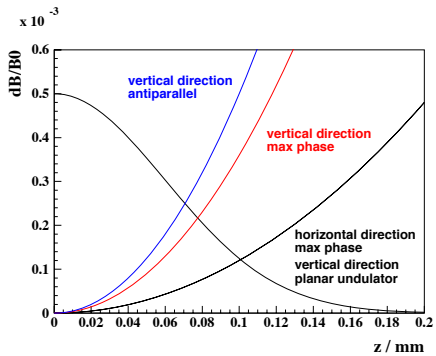

Figure 7: Averaged transverse size of the BESSY FEL electron beam compared to the field roll off for various operation modes.

Figure 8 shows all possible girder misalignments. They are classified as follows:

1. No circle: this movement is uncritical.
2. Black circle: the motion can be minimized with a stiff support structure. The motion is not driven by any force.
3. Blue circle: the movements are well controlled with a closed loop servo system.
4. Red dotted circle: The movement shifts the field amplitude and the center of the good field region. It shows up for antiparallel motion where longitudinal and transverse forces between the upper and lower magnet girders are present.
5. Red circle: The movement enhances $\Delta K / K$. It shows up for antiparallel motion.

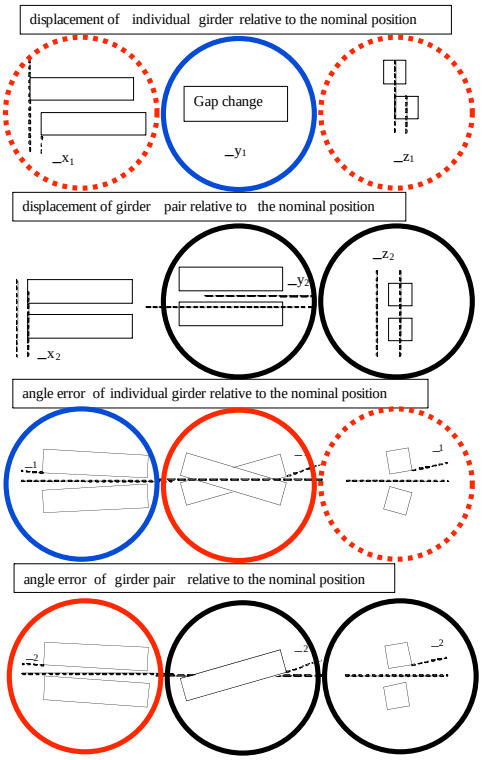

Figure 8: Classification of geometrical tolerances.

SUPPORT AND DRIVE SYSTEM

The tolerances discussed in the previous section define the mechanical design of the support and drive system.

Gap Accuracy

The gap setting has to be done with a closed loop servo system which uses a direct gap reading. The encoders have to be located in a vertical line with the electron beam to avoid Abbe's comparator error [7] (figure 9). Differential thermal expansion coefficients of the support structure (Fe) and the magnet girders and the measurement system (Al) result in a temperature dependent gap error of only 1.1µm/°C for the system described in [7] and can be ignored if compared to the thermal variation of the magnet material remanence.

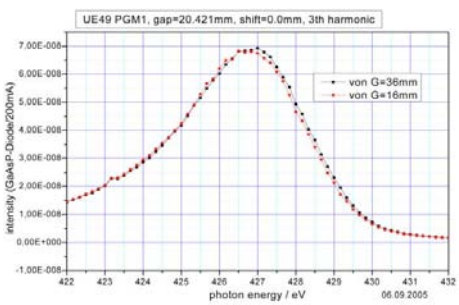

Figure 9: Approaching the third harmonic of the BESSY UE49 from two different directions results in a very small energy shift which corresponds to a gap error of only ±1µm. The device employs the new measurement system described in [7].

In principle an APPLE II type final amplifier of a HGHG cascade can be realized as a fixed gap device. The energy and polarization tuning can be performed by magnet row movements [11]. The BESSY final amplifiers will be of the APPLE III type. In this case the gap drive is necessary to install and remove the modules from the beam pipe without breaking the vacuum.

The magnets are assembled onto Aluminum girders with a length of up to 4m. They are gimbal-mounted to permit a tapering and to cope with the different thermal expansion coefficient of the Fe-support structure. The straightness of the assembling surfaces of such girders can be within ±8µm resulting in a gap variation of only ±15µm (figure 10). This remaining gap variation can be reduced to ±6µm using appropriate mechanical shims under the magnet holders.

The bending of the magnet girder can be minimized by choosing appropriate locations for the support. The bending can be further reduced by more than one order of magnitude with four supports instead of two using two crossbars inside the magnet girders. This has been demostrated for the BESSY undulators UE46, UE49 and UE112.

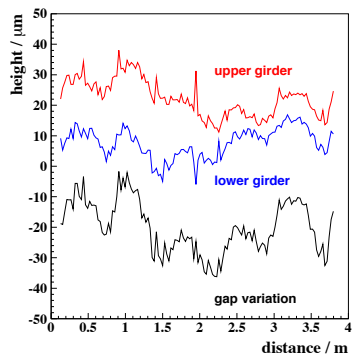

Figure 10: Straightness of upper and lower UE112 magnet girder and corresponding gap variations.

Bearings

In antiparallel mode strong longitudinal and transverse forces between the upper and lower magnet girder show up. The transverse forces can be supported with transverse flexible joints connecting the girders to the support structure. These joints have to permit a longitudinal motion (thermal expansion) and an intentional longitudinal taper of the girders.

The longitudinal forces produce a torque around the vertical axis and around the horizontal (transverse) axis where the strength depends on the location of the joints that keep the girders longitudinally in place. As a result the girders rotate and ΔK / K on axis is enhanced. The transverse motion can be kept within the acceptable limits with stiff joints between the girders and the support structure. The vertical parallel inclination of the girders can principally be compensated using four motors for the gap drive. Such a drive system can also compensate for the residual transverse girder crossing via a deliberate inclination of the girders. This concept implicates however a complication of the control system

and the gap measurement arrangement. Another solution is the positioning of the longitudinal fixed bearing vertically at the height of the magnets and longitudinally close to the drive system for the row phase. This arrangement eliminates any torque around the transverse axis (figure 11) and hence, any girder inclination or girder bending.

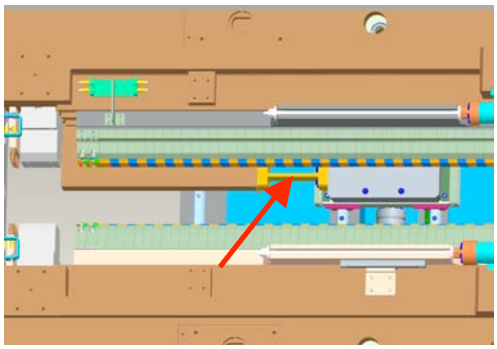

Figure 11: The vertical location of the longitudinal bearing (red arrow) is chosen such that there is no torque around the transverse axis.

Support Structure

The support structure of an APPLE undulator operating in the antiparallel mode has to cope with the strong longitudinal and transverse forces which are absent in a planar or elliptical device.

The support structure can be either a welded structure or a cast structure. The latter one has several advantages:

- The structure can be made extremely stiff without additional effort because literally any shape can be realized.
- A bionic optimization can be applied where material is added at locations with large stress and removed at locations of low stress (figure 12).
- The complete support structure can be cast and milled as a single piece.
- The procedure is suitable for series production since wooden forms can be used for many casts. Modular forms can be adapted to different undulator lengths.

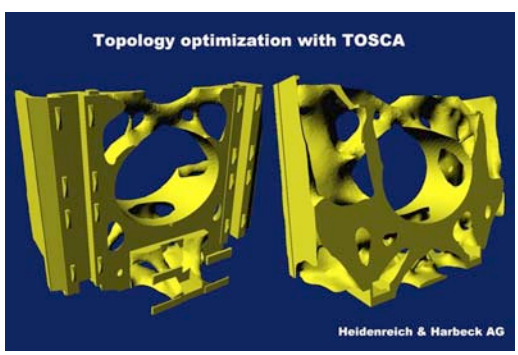

Figure 12: Bionic optimization of the support structure of the BESSY UE112 undulator (by courtesy of Heidenreich und Harbeck AG).

All BESSY undulators are based on cast iron structures. The last APPLE device (UE112) has a single piece support structure (figure 13) which significantly simplifies the assembling procedure.

Figure 13: The support structure of the 4m long UE112 is made from a single piece of cast Fe.

Alignment

The magnet centers of all final amplifier modules have to be aligned with an accuracy of ±40µm with respect to each other (assuming APPLE type devices). This can not be accomplished with standard alignment tools. Beam based alignment techniques have to be applied instead. For this purpose the modules have to be assembled onto moveable supports with an accuracy of 10µm.

UNDULATOR FOCUSSING

An undulator is a series of alternating dipole magnets which shows an edge focusing. Planar devices focus in the vertical direction. This second order effect can not be described with normal 2-dimensional multipoles. Polarizing devices show also a horizontal defocusing under certain operating conditions which results in an additional focusing in the vertical plane. For Halbach fields the focusing strength in the horizontal plane is given by:

$$K_x = \frac{2 \cdot e^2}{(\gamma mc)^2} k_{x-eff}{}^2 \cdot k^2 \cdot \sum_{n=1}^{\infty} (B_{xn}^2 + B_{yn}^2)$$

$$k_{x-eff}{}^2 = \sum_{n=1}^{\infty} \frac{B_{xn}{}^2 \cdot k_{xxn}{}^2 / n! + B_{yn}{}^2 \cdot k_{xyn}{}^2 / n!}{B_{xn}{}^2 / n! + B_{yn}{}^2 / n!}$$

and similar for the vertical plane (summation over the Fourier components *n*). The focusing strength in the antiparallel mode can not be described in this compact form since the fields are not of the Halbach type.

These effects influence the beam size and it has to be considered whether the transverse overlap between the electron beam and the photon beam is still maintained. Figure 14 shows the variation of the horizontal and vertical beam size for the BESSY HE-FEL. The values change by more than a factor of two which is not acceptable. For the BESSY ME- and the LE- FEL the effects are larger by factors of 9 and 45, respectively,

due to the larger period length and larger field (ME- and LE-FEL) and the lower beam energy (LE-FEL). Obviously, additional quadrupoles are essential to keep the beam size within acceptable limits and they have to be adapted during gap drive and row phasing.

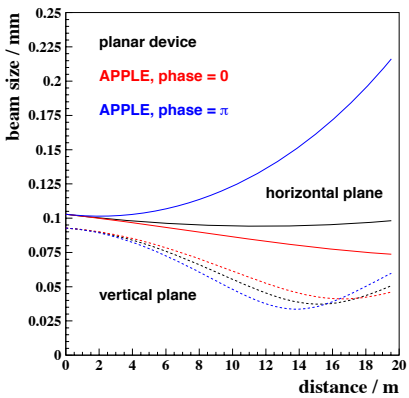

Figure 14: Horizontal (solid) and vertical (dotted) beamsize within the final amplifier of the BESSY HE-FEL at smallest gap without additional quadrupoles. The data are given for different operation modes of an APPLE III device and for a planar device.

MOTION CONTROL

A cascaded HGHG FEL requires a sophisticated motion control system. Each HGHG stage consists of a modulator and a radiator (maybe several submodules), steerer to compensate residual dipole errors, quadrupoles for tune compensation and phase adapting units between the modules. Between two stages fresh bunch dispersive sections are installed. All components have to be driven in synchronism. Reproducibility is essential and can be realized with closed loop servo systems for motion control, permanent magnet phase adapting units and quadrupoles and air coils to avoid hysteresis effects.

In the following we describe the BESSY system as one possible solution. Other hardware and software concepts are also possible.

Figure 15 shows the control system of a single undulator, the BESSY UE112, which can be adapted to the FEL requirements. The undulator control program runs on a VME-bus based computer called IOC. It is a reliable system and many interface cards are available on the market. The user interface does not run on the IOC but on an independent workstation, which communicates with the IOC via ethernet. In principle, one IOC can control all modules (modulator, radiator, etc.) of one HGHG stage. Four of these systems are required for the BESSY four stages HE-FEL. A fifth IOC operates as a master to synchronize the individual IOCs.

A PLC is useful for a low level safety control of the system checking parameters like air pressure (needed for the brakes), inclination of magnet girders, hard and software limit switches etc.

EPICS is used as a robust and reliable software framework for the undulator control software. All sources are available and it is actively developed in many research laboratories. Many drivers have been written. Useful tools are available such as an archiver for the process variables or a network protocol for the distribution of the process variables. GUIs can be easily built with a “point and click” tool.

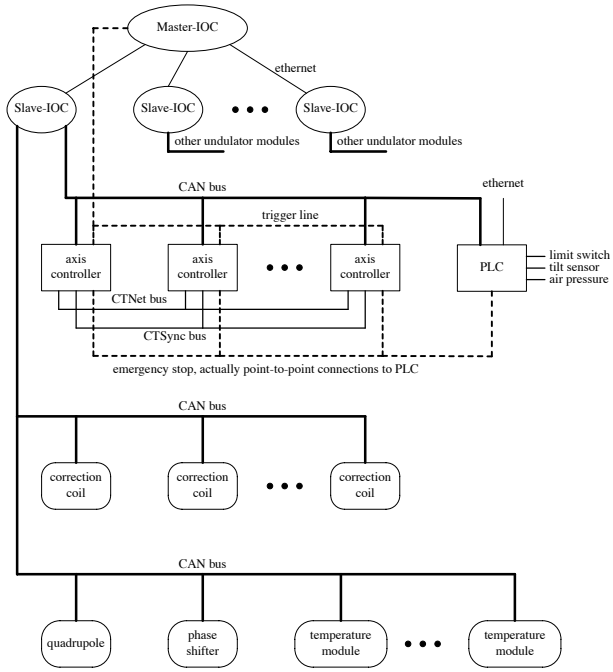

Figure 15: Control system of the BESSY UE112.

Each motor has its own detached motor controller which is connected to the IOC via CAN bus. Absolute linear encoders simplify reference procedures. Modern motor controllers as used for the UE112 can operate several tasks with different priorities. User defined parameters can be stored permanently in the controller and can even be modified during motor movement. The motor controllers can communicate among each other and with the IOC via CTNet (ruggedized version of ARCNet) and a synchronization between the modules can be realized via CTSynch.

BEAM PROTECTION SYSTEM

The electron beam can cause a demagnetization of the undulator magnets if it propagates severely off axis [12-14]. The electrons produce a shower of secondary electrons and photons in the vacuum chamber which may deposit energy into the magnets. Detailed experiments have been done to study the influence of various parameters on the process like the geometry, material, working point of the magnets, temperature etc. [15]. A reduced dose (electron energy > 20MeV) of 70 kGy produces already a remanence loss of 1% in a typical magnet material with a coercivity of 1800 kA/m [16].

For the layout of a beam protection system the maximum beam charge which may be dumped into the vacuum chamber without loss of performance has to be

determined. In the following we discuss the consequences on the spontaneous radiation spectrum. Simulations for the impact on the stimulated radiation will be done in the future using GENESIS. Two scenarios have been studied where the electron beam hits the vacuum chamber under grazing angles of 1mrad and 0.1mrad, respectively. Due to the small vacuum apertures larger angles are unlikely. Monte Carlo simulations with GEANT [17] have been done for both cases. The deposited charge was 300.000 nC. The magnets have been subdivided into 5x5 (1mrad case) and 7x7 (0.1mrad case) segments (figure 16). Doses have been evaluated for each of the segments.

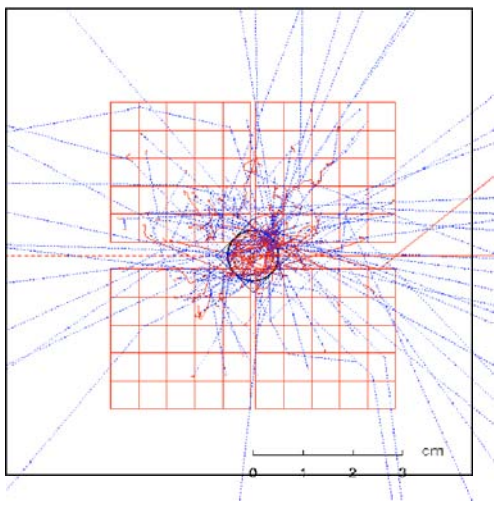

Figure 16: Monte Carlo simulations with GEANT. The geometry for the BESSY HE-FEL with APPLE III magnets (red) and a circular vacuum pipe (blue) has been used. Secondary electrons (red) and photons (blue) are plotted as well.

In the 1mrad case a maximum reduced dose of 700kGy has been detected close to the vacuum pipe. This corresponds to a maximum demagnetization of 10%. Based on the doses in each magnet segment the corresponding remanences have been evaluated. Then, the undulator on axis field has been derived from the contributions of all segments (totally about 70.000 segments). The field reduction close to the point of interaction is 1.6% (figure 17).

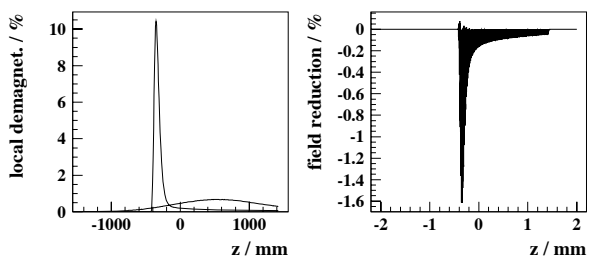

Figure 17: Maximum demagnetization of magnet segments (left) for 1mrad and 0.1mrad angle of incidence and field variation (right) for 1mrad.

In the 0.1mrad case the region of interaction is spread out over more periods and the local degradation is much lower. Since the magnet degradation extends over several periods the trajectory errors are negligible even for the 1mrad case (figure 18). The averaged phase error introduced in this case is 7° (figure 18) which results in a shift of the first harmonic and a splitting of the fifth harmonic (figure 19).

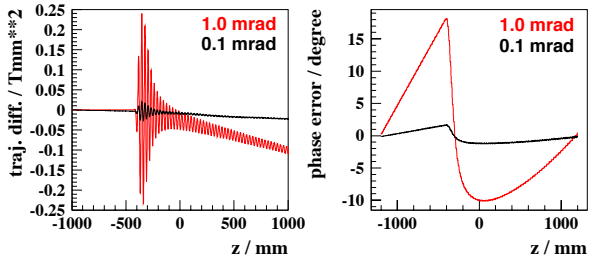

Figure 18: Trajectory errors for angles of incidence of 0.1mrad and 1mrad (left) and phase errors for both cases.

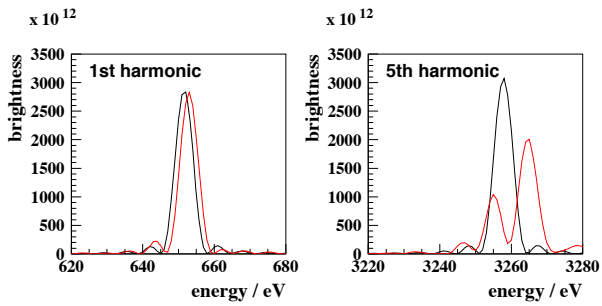

Figure 19: Spectra of the first (left) and fifth (right) harmonic for the unperturbed case (black) and the degraded magnets (red).

Even if the undulator is used only at the first harmonic the spectral shift has to be avoided. The simulations show that a deposited charge of 30.000nC (1mrad) shifts the first harmonic by only $\Delta E/E=2x10^{-4}$ which is acceptable.

The simulations show that a collimating system for the off axis particles as well as for the off energy particles is essential for a safe operation. The dog-leg collimator for the planned BESSY Soft X-Ray FEL collimates the beam transversally to ±30σ and energetically to 5%.

Fibre monitors are needed for several purposes: i) A fast interlock system which can switch off the gun laser has to be triggered, ii) information on the total deposited dose is required to estimate the lifetime of the magnets, iii) information on the longitudinal distribution of the deposited radiation helps to detect the hot spots. Two types of fast monitors have been tested at FLASH: i) Cerenkov monitors [18] and ii) fibres for optical time domain reflectometry used in power-meter mode [19]. The latter ones can be used also for spatially resolved measurements. Fibre Bragg gratings can be used as high dose radiation sensors on the scale of many kGy [20].

They provide also information on the spatial distribution of the dose.

CONCLUSION

Various technological aspects for using APPLE undulators in HGHG FELs have been discussed. Experiences gained with APPLE undulators at 3rd generation light sources have been extrapolated and strategies to meet the tight tolerances of HGHG FEL insertion devices have been proposed.

New concepts for the magnet field optimization, for the motion control, for a new support structure and for radiation dose monitoring have already been tested and will be further improved at a 3rd generation facility.

ACKNOWLEDGEMENT

The author thanks M. Scheer for doing the GEANT simulations and H.-J. Bäcker, W. Frentrup, A. Gaupp, S. Gottschlich, G. Pfeiffer, B. Schulz for many fruitful discussions.

REFERENCES

[1] TESLA-Technical Design Report, TESLA X-FEL, Technical Design Report, 2002-9, 2002.

[2] Linac Coherent Light Source (LCLS), Conceptual Design Report, SLAC-R-593, 2002.

[3] T. Shintake, Nucl. Instr. and Meth. in Phys. Res. A, 507 (2003) pp 382-397.

[4] L. H. Yu, Nucl. Instr. and Meth. in Phys. Res. A, 483 (2002) pp 493-498.

[5] X. J. Wang et al., Proceedings of the 26th International FEL Conference, Trieste, Italy, 2004, pp 209-211.
C. Bochetta et al., Proceedings of the 27th International FEL Conference, Stanford, CA, 2005, pp 632-685.
The BESSY Soft X-ray Free Electron Laser, Technical Design Report March 2004, eds.: D. Krämer, E. Jaeschke, W. Eberhardt, ISBN 3-9809534-08, BESSY, Berlin (2004).
J. Bahrdt et al., Proceedings of the EPAC 2006, Edinburgh, Scotland, pp 59-61.
M.-E. Cuprie et al., Proceedings of the 27th International FEL Conference, Stanford, CA, 2005, pp 55-58.
A. Andersson et al., Proceedings of the 26th International FEL Conference, Trieste, Italy, 2004, pp 190-192.
D. Wang et al., Proceedings of 2005 PAC, Knoxville, Tennessee, pp 1961-1963.
J. Wu, Z. Huang, Proceedings of the 27th International FEL Conference, Stanford, CA, 2005, ppxx.
J. Qi-ka et al., Proceedings of the 26th International FEL Conference, Trieste, Italy, 2004, pp 494-497.

[6] O. Tscherbakoff et al., Proceedings of the EPAC 2006, Edinburgh, Scotland, pp 47-49.
G. Lambert et al., Proceedings of the EPAC 2006, Edinburgh, Scotland, pp 44-46.
J. A. Clarke, Proceedings of the EPAC 2006, Edinburgh, Scotland, pp 181-183.
Gullens et al., Proceedings of the EPAC 2006, Edinburgh, Scotland, pp 142-144.

[7] J. Bahrdt et al., Proceedings of the 26th International FEL Conference, Trieste, Italy, 2004, pp 610-613.

[8] J. Bahrdt et al., Nucl. Instr. and Meth. in Phys. Res. A, 516 (2004) pp 575-585.

[9] J. Bahrdt et al., Proceedings of the International Conference on Synchrotron Radiation Instrumentation, Daegu, Korea, 2006.

[10] J. Bahrdt, G. Wüstefeld, Proceedings of the EPAC 2006, Edinburgh, Scotland, pp 3562-3564.

[11] T. Schmidt et al., Proceedings of the International Conference on Synchrotron Radiation Instrumentation, Daegu, Korea, 2006.

[12] P. Colomp, T. Oddolaye, P. Elleaume, "Partial Demagnetization of ID6 and Dose Measurements on Certain Ids", Machine Technical Note 1-1996/ID, 1996.

[13] M. Petra et al., Nucl. Instr. and Meth. in Phys. Res. A, 507 (2003) pp 422-425.

[14] P. Colomp, T. Oddolaye, P. Elleaume, "Demagnetization of Permanent Magnets to 180 MeV Electron Beam", Technical Report ESRF/MARCH-ID/93-09, European Synchrotron Radiation Facility, ESRF March 1993.

[15] T. Bizen, T. Tanaka, Y. Asano, D.E. Kim, J.S. Bak, H.S. Lee, H. Kitamaru, Nucl. Instr. and Meth. in Phys. Res. A 467-468 (2001) pp185-189.
M. Marechal, T. Shintake, SRI2003, Conference Proceedings, AIP 705, (2004) pp 282-285.

[16] H. Schlarb, "Collimation System for the VUV Free-Electron-Laser at the TESLA Test Facility", Thesis Work, Universität Hamburg, DESY-THESIS-2001-055, Nov. 2001.

[17] GEANT, Detector Description and Simulation Tool, Computing and Networks Division, CERN Geneva Switzerland.

[18] E. Janata, M. Körfer, H. Schlarb, Nucl. Instr. and Meth. in Phys. Res. A 253 (2004) 256-261.

[19] H. Henschel, J. Kuhnhenn, M. Körfer, F. Wulf , Nucl. Instr. and Meth. in Phys. Res. A, 507 (2003) pp 422-425.

[20] K. Krebber, H. Henschel, U. Weinhand, „Fibre Bragg Gratings as high dose radiation sensors", Meas. Sci. Technol. 17 (2006) pp 1-8.

ELECTRON BEAM ALIGNMENT STRATEGY IN THE LCLS UNDULATORS*

H.-D. Nuhn#, P.J. Emma, G.L. Gassner, C.M. LeCocq, F. Peters, R.E. Ruland, Stanford Linear Accelerator Center, 2575 Sand Hill Road, Menlo Park, CA 94025, U.S.A.

Abstract

The x-ray FEL process puts very tight tolerances on the straightness of the electron beam trajectory (2 μm rms) through the LCLS undulator system. Tight but less stringent tolerances of 80 μm rms vertical and 140 μm rms horizontally are to be met for the placement of the individual undulator segments with respect to the beam axis. The tolerances for electron beam straightness can only be met through beam-based alignment (BBA) based on electron energy variations. Conventional alignment will set the start conditions for BBA. Precision-fiducialization of components mounted on remotely adjustable girders and the use of beam-finder wires (BFW) will satisfy placement tolerances. Girder movement due to ground motion and temperature changes will be monitored continuously by an alignment monitoring system (ADS) and remotely corrected. This stabilization of components as well as the monitoring and correction of the electron beam trajectory based on BPMs and correctors will increase the time between BBA applications. Undulator segments will be periodically removed from the undulator Hall and measured to monitor radiation damage and other effects that might degrade undulator tuning.

Table 1: LCLS undulator parameters

Parameter	symbol	value	unit
min. fundamental wavelength	λ_r	1.5	Å
undulator period length	λ_u	3.0	cm
nom. undulator parameter	K	3.5	
peak field	B_{pk}	1.25	T
undulator segment length	L_s	3.4	m
number of segments	N_s	33	
full undulator length	L_s	132	m
nom. undulator full pole gap	g	6.8	mm
long break length	L_l	0.898	m
short break length	L_s	0.470	m
number of quadrupoles	N_Q	33	
number of BPMs	N_{BPM}	33+3	

INTRODUCTION

The undulator system for the Linac Coherent Light Source (LCLS), under construction at the Stanford Linear Accelerator Center (SLAC), is comprised of 33 identical 3.4-m-long undulator segments, separated from each other by short and long breaks. Every third break is long. The space provided by these breaks is used to place devices for controlling and monitoring the electron beam. A parameter summary is given in Table 1.

COMPONENT DESCRIPTION

The components relevant to the SASE (self-amplified spontaneous emission) lasing process in the LCLS undulator system include

- Undulator Segments
- Segment Slide Supports
- Quadrupoles
- Beam Position Monitor (BPM) System
- Girder Motion Supports
- Beam Finder Wire (BFW) Devices
- Fixed Girder Supports
- Vacuum chamber
- Alignment Diagnostic System (ADS) Sensors
- Temperature Sensors
- Air Temperature Stabilization

A brief description for each of these components is provided in this section

Undulator Segments

The undulator segments [1] are fixed-gap permanent magnet planar undulators with a period length of 3 cm and a nominal K value of about 3.5, and are mounted inside a 3.4-m-long Ti strongback of circular cross section. The undulator gap is arranged such that the electron wiggle motion is in the horizontal plane. The upper and lower pole face planes are canted with respect to each other by an angle of 4.5-mrad, which makes the K value dependent on the electron beam's horizontal position in addition to its dependence on the vertical position for the regular planar undulator. Each undulator will be operated at a different effective K value to compensate for energy losses during the radiation process and to optimize the SASE process. The magnetic axis, i.e., the ideal average beam trajectory, through the undulator segment will be determined during the tuning of the device and fiducialized to tooling balls on the device body. Undulator magnet tuning will be done in the Magnet Measurement Facility (MMF), which has been specially built for this purpose.

Segment Slide Supports

Each undulator segment is mounted on two parallel horizontal slides that allow remotely controlled repositioning of the segment relative to the electron beam and a full translation to a 'removed' position at 8 cm.

* Work by U.S. Department of Energy contract DE-AC02-76SF00515
# nuhn@slac.stanford.edu

Quadrupoles

The quadruple magnets in the LCLS undulator system are arranged in a FODO lattice. They are designed to operate with an integrated quadrupole field gradient of 3 T over the entire LCLS operational energy range between 4.3 GeV to 13.6 GeV. Each quadrupole magnet has dipole correction coils integrated into its design to provide independently controllable horizontal and vertical dipole fields superimposed on the quadrupole fields.

The quadrupole magnets are based on electromagnetic technology, each with its own power supply, and their integrated gradient can be changed in the range between 0 T and 4 T. By varying the gradient, the quadrupoles can be used to measure the transverse distance of the electron beam trajectory from the magnetic center of the quadrupoles, which is fiducialized to the magnetic center of the upstream undulator segment. This enables control of the alignment of the electron beam to the magnetic axis of the undulator segment at its down stream end, where the quadrupole magnet is located. The electromagnetic technology also provides the options of modifying the focusing optics.

Beam Position Monitor (BPM) System

The electron beam position monitor system uses RF cavity BPMs. It has been demonstrated that this type of BPM can provide relative beam position information at better than 1 μm resolution in the 0.2-1 nC charge range, at which the LCLS electron bunches will be operated. Their circular cavity body, machined to have a well-defined mechanical center, will be used in the alignment of this component. One BPM is located just downstream of each quadrupole magnet. An additional 3 BPMs of the same type are mounted upstream of the first segment to monitor the horizontal and vertical launch position and angle of the electron beam.

Girder Motion Supports

Each undulator segment and its beamline components are mounted on a remotely moveable support structure, called a girder [2]. The remote motion is controlled through cam shafts [3] and allows changing the horizontal and vertical position as well as yaw, pitch, and roll of the girders. The components mounted on each of the 33 identical girders include an upstream Beam Finder Wire (BFW) device, two horizontal slides supporting one undulator segment, a downstream quadrupole magnet, an RF cavity BPM, and a Cerenkov radiation detector, as well as the supports for the vacuum chamber throughout the girder, and the mounting plates for the Alignment Diagnostic System (ADS) sensors. The BFW device, the undulator segment, and the quadrupole are fiducialized in the MMF. The complete girder assembly will initially be aligned on the Coordinate Measurement Machine (CMM), which has been specially designed for that purpose. The undulator segment is mountable on and removable from the girder with the vacuum chamber in place and without compromising the alignment of the vacuum chamber. Segments will be swapped on the girder for magnetic measurements and will be interchangeable without the need for renewed CMM alignment.

Beam Finder Wire (BFW) Devices

The BFW device is a special wire scanner [4], with only two positions for the horizontal and vertical wire pair: the wires will be either in a well reproducible “in”-position, in which they can be brought in collision with the electron beam, or they will be in a “park”-position, where they won’t affect the electron beam. The locations of the wires in the “in” position will be fiducialized to tooling balls mounted on the device body.

Each BFW device enables control of the alignment of the electron beam at its up-stream end. After all quadrupoles are aligned using BBA (see below), the girder can then be moved to bring the wires of the BFW device into collision with the beam, which will complete the alignment of the undulator segments relative to the beam axis. The BFW device will provide a means to accomplish a beam-based undulator segment alignment from the control room without the need for tunnel access. The BFW device is only needed for occasional verifications. The alignment can be achieved at even tighter tolerance levels using portable Hydrostatic Leveling System (portable HLS) and portable Wire Position Monitor (portable WPM) devices without the need for the electron beam to be present [5]. The use of these devices requires, however, extended tunnel access and will be used prior to the beam–based commissioning process. It is expected that the ADS (see below) will be used to monitor the girder positions from then on.

Although not their primary purpose, the BFW wires will also provide transverse beam profile and rms size information. This functionality will be preserved as long as the wire diameter is not larger than about twice the rms beam width. With an rms beam width of 36 μm, a maximum wire diameter of 40 μm is a reasonable upper limit and the choice of a Carbon wire will adequately limit beam loss on the downstream undulators [6]. The transverse position of the wires will be monitored with the cam mover readback system and also, at sub-micron resolution but at a slower rate, with the ADS. Local BPMs can also be used to measure and compensate for any shot-by-shot trajectory jitter during the scan.

Fixed Girder Supports

Each girder is supported by two thermally isolated, sand-filled pillars, with manual adjustments at the top (Figure 4), which allow pre-alignment of the cam movers.

Vacuum chamber

The vacuum chamber of the LCLS undulator system has a 5 mm×12.5 mm rectangular inner cross section through the undulator segments and circular (both 8 mm and 10 mm diameter) cross sections in the breaks. The interaction of the electron beam with the vacuum chamber generates longitudinal and transverse wakefields. The amplitude of the latter is limited by keeping the beam at the center of the chamber with a ±200 μm tolerance. The

vacuum chamber will not be moved when the undulator segment is horizontally repositioned on the slides.

Alignment Diagnostic System (ADS) Sensors

The alignment of the girders will be continuously monitored by the ADS, which is a combination of a Wire Position Monitor (WPM) system and a Hydrostatic Leveling System (HLS), both permanently installed. There are four sensors for each of the two subsystems mounted on each girder, two each close to either end of the undulator segment. The sensors are supported by a mounting plate. The HLS is most sensitive to vertical positioning, while the WPM is best for horizontal positioning.

Temperature Sensors

The temperature will be monitored at several control points on girder components, at girder supports, and at the mounting plates of the ADS sensors.

Air Temperature Stabilization

The temperature of the LCLS undulator tunnel is controlled by a constantly flowing, thermally regulated, air stream [7]. The air enters upstream of the first girder and is blown through the 170-m-long tunnel in downstream direction. Temperature monitoring is done at the entrance point. As the air travels through the tunnel it is expected to pickup heat from the tunnel equipment at a rate of less than 50 W/m. The system is designed such that the air temperature will stay in the range of 19.5º C-20.5º C at all times along the entire undulator system. The undulator *K* value has been measured to change by 0.015% over a temperature range of 0.28º C.

TOLERANCES AND ALIGNMENT STRATEGY OVERVIEW

The purpose of the undulator system is to enable the SASE process, which is based on the interaction between an electron bunch and its spontaneous undulator radiation.

For obtaining and maintaining high gain in the SASE process, it is important that the electron bunch is in good overlap with the radiation field and that the individual electrons maintain a well defined phase relationship with that field. The radiation field is initially produced in the first undulator segment and will proceed in a straight line, while the electron beam trajectory will deviate from a straight line in the presence of magnetic and electric fields. The ideal undulator magnetic field will generate tiny periodic deviations from the straight line, which are necessary for the SASE process; the first and second field integrals over each undulator segment are ideally zero. Problems arise from off-axis fields of misaligned quadrupoles and undulator segments, the earth's magnetic field [8], other environmental fields, as well as from errors in the undulator fields that create finite field integrals or increase the electrons' path lengths through the undulator. The primary mitigation tool includes tuning [9], (for undulator field errors and earth's magnetic field), and shielding, (for environmental fields as well as earth's magnetic field).

The remaining error-fields (off-axis fields in quadrupoles and undulator segments, remnants of undulator field errors, the earth's magnetic field, and the environmental field) will be corrected through beam based alignment, which compensates the net effect of these fields by adjusting the transverse positions of the quadrupoles, through girder motion and by adding small dipole correction fields through trim coil adjustments. This process will automatically take the largest error field source, (e.g., misaligned quadrupoles), out of the system by moving the centers of the quadrupole magnets to a *goal* position, close to a common straight line. The *goal* position will be slightly away from that line, just enough to compensate for other remaining error sources. Thus, the *goal* position of each quadrupole will be precisely defined through the BBA process, and will be deviating from the electron beam trajectory (beam axis, defined by BBA) by about 20 µm (rms), a calculated number based on error amplitude estimates.

Table 2: Alignment tolerances for component alignment on girders for the LCLS undulator system

	Value	**Unit**
Horizontal Alignment of Quadrupole and BPM to Segment (rms)	125	µm
Vertical Alignment of Quadrupole and BPM to Segment (rms)	60	µm
Horizontal Alignment of BFW to Segment (rms)	100	µm
Vertical Alignment of BFW to Segment (rms)	55	µm

For best FEL performance, the effective magnetic centers of all quadrupoles need to be within ±2 µm of their *goal* position in both the horizontal and vertical directions. Additionally, the magnetic axes of the undulator segments need to be aligned to the beam axis to an accuracy of 140 µm (rms) horizontally and 80 µm (rms) vertically.

Table 3: Alignment tolerances for girder alignment in the LCLS Undulator Hall

	Value	**Unit**
Initial rms uncorrelated x/y quadrupole alignment tolerance wrt straight line	125	µm
Longitudinal Girder alignment tolerance	±1	mm
Undulator Segment yaw tolerance (rms)	240	µrad
Undulator Segment pitch tolerance (rms)	80	µrad
Undulator Segment roll tolerance (rms)	1000	µrad

The precise alignment of the quadrupoles can only be achieved using a beam based alignment method (energy scan) while the relative alignment (see Table 2) of the

undulator segments to the quadrupoles and the BFW devices is aided by mounting the components on common, remotely movable girders (see above). The tolerances for the conventional alignment of the girders in the tunnel are reasonably achievable (see Table 3).

ALIGNMENT DIAGNOSTIC SYSTEM

The ADS continuously tracks changes in the transverse position, tilt, yaw, and roll of all girders to better than 1 µm [10]. This position information together with temperature measurements on the girders will be used to calculate the motion of the geometric centers for BPMs and quadrupoles to better than 2 µm (rms) with respect to the ADS sensors.

The information will be used between BBA applications to correct for girder/quadrupole position changes due to ground motion and temperature fluctuations and to correct the offset used in evaluating the BPM readings.

Wire Position Monitor (WPM) System

The WPM system is based on two 140-m-long stretched wires, running parallel to the beam line axis on one side of the Undulator as illustrated in Figure 1.

The wire position monitors are mounted to the girders kinematically, as shown in Figure 1. The vertical position of monitors has to be adjustable at different girders according to the wire sag of about 15 cm. Each girder will be equipped with four wire position monitors, two on each end. With this geometry, positions of each girder can be measured in horizontal and vertical direction with respect to both stretched wires. Pitch, roll and jaw of the girders will be calculated. Transverse position of quadrupoles can be determined within 0.5 µm (rms) by measurements of support temperatures within ±0.1 K.

As extensive test measurements have shown [11], the readout resolution of the WPM system is much better than 100 nm and instrument drifts are lower than 100 nm per day.

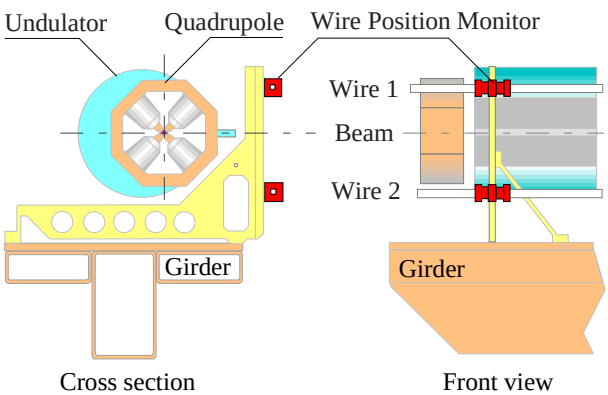

Figure 1: Functional cross section diagram of wire arrangements for the WPM system

Due to the unavoidable large sag of long wires, the uncertainty of the wires in vertical direction will be higher than one micrometer, which is the required design objective for the quadrupoles. Therefore, the vertical position of both wires will be correlated to the horizontal plain defined by the Hydrostatic Leveling System.

Hydrostatic Leveling System (HLS)

The HLS system is based on a system of water pipes also covering the entire 140-m-long undulator system.

Four sensors are mounted to the sides of each girder. The sensors are located at the same position as the WPM system sensors on each side of the girder.

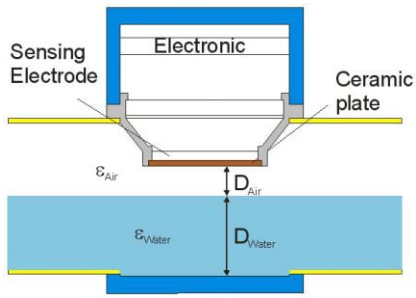

Figure 2: Functional cross section diagram of an HLS capacitive sensor

The system consists of two types of HLS sensors, which complement each other. One sensor type is based on capacitive measurements, which has the advantage of being widely used and having a lower purchase cost, see Figure 2. The repeatability of the sensor is 1 µm with an accuracy of 5 µm over the 5 mm measurement range. A disadvantage of this sensor type is that capacitive sensors drift by about 1 – 2 µm per month due to aging of electronic components. Ideally, the determination of the absolute distance between the sensing electrode and the water surface would require knowing the exact dielectric constants involved and the exact distance between the sensing electrode and the other electrode (vessel geometry). However, it is not possible to determine these values with sufficient accuracy to derive height readings directly from the capacitances of the sensors. Therefore, a calibration is performed by measuring the capacitance at different water levels and referring them to actual height readings.

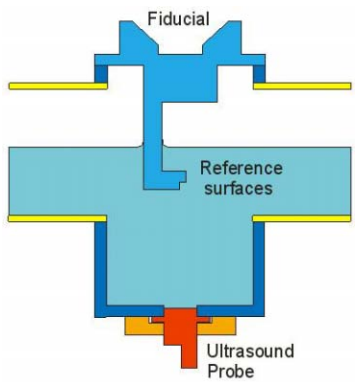

Figure 3: Functional cross section diagram of an HLS ultrasound sensor.

The second type of sensor is based on ultrasonic runtime measurements, see Figure 3. The measurements

are self calibrating and therefore no drifts are expected. The repeatability of the sensor is 1 µm with an accuracy of 5 µm over the 5 mm measurement range. The ultrasound sensors measure the runtime to the two reference surfaces of the probe and to the water surface. This provides information about the water level with respect to the external fiducial of the probe. The ultrasound sensors, once mounted to the girder, are measured with the CMM. They are used to set the height of the girder in the tunnel during the conventional alignment step. Since the ultrasound sensors provide actual height differences to the water surface they can be used to calibrate the capacitive sensors.

MONITORING ELEMENTS SUMMARY

Monitoring elements are used to detect girder position as well as electron beam position. The following list provides a summary:

- Hydrostatic Leveling System (HLS)
  - monitors *y*, pitch, and roll
- Wire Position Monitoring System (WPM) [11]
  - monitors *x*, (*y*), (pitch), yaw, and roll
- Temperature Sensors
  - in support of HLS/WPM readout corrections, undulator *K* corrections, and component motion interpretation
- Beam Position Monitors*
  - monitors *x* and *y* positions of the electron beam
- Quadrupoles*
  - can be used to measure *x* and *y* offsets of the electron beam with respect to the quadrupole center

ALIGNMENT CONTROLS

A number of manual (local) and remote adjustments are available for the alignment of the beamline components of the LCLS undulator system.

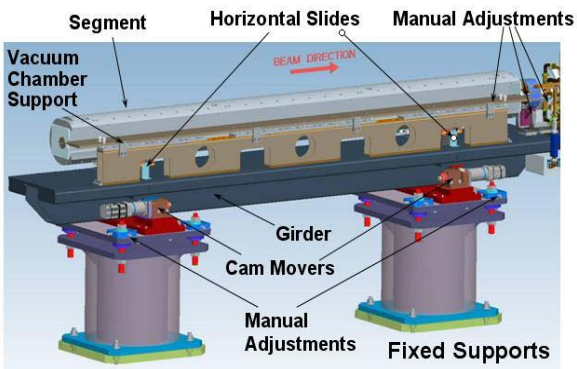

Figure 4: Undulator segment supports

Local Controls

Alignment of the cam supports is done using the manual adjustment controls on top of the support pedestals (see Figure 4). Relative alignment of girder components to the magnetic axes of the undulator segments (on the CMM) is done by using the manual adjustable supports of the quadrupole, BPM and BFW components, which provide a range of ±2 mm in the horizontal and vertical directions with a resolution of 2 µm. The height of the magnetic axes of the undulator segments above the segment supports is controlled by permanent shims created specially for the undulator after the tuning process and permanently bolted to its bottom. This makes all undulator segments interchangeable with each other.

Remote Controls

The transverse positions of the girders are (remotely) controlled based on cam mover technology

- during initial conventional alignment (see above)
- for quadrupole position control, i.e., beam steering during BBA.
- for BFW scans
- for compensation of ground motion effects etc.

The motion range is such that each quadrupole magnet can be moved ±0.7 mm in any transverse direction from its neutral position. The motion control allows moving a single quadrupole independently in the horizontal and vertical direction without affecting the adjacent quadrupoles and without introducing roll to the girder assembly. All girder components will be moved together when a quadrupole is repositioned so that the BFW device, the undulator segment, the quadrupole, the BPM and the vacuum chamber will stay aligned relative to each other. The horizontal position of the undulator segment is remotely controlled for

- field strength adjustment (change of *K*)
- reduction of radiation exposure during commissioning (full roll-out position),
- measurement of FEL gain as function of *z* (full roll-out position),
- measurement of *K* using spontaneous radiation from only two adjacent, interfering undulators [12].

CONVENTIONAL ALIGNMENT

The conventional alignment of the undulator system focuses on bringing the quadrupole magnets into a straight line at tolerances specified in Table 3.

To achieve this goal, the first step is to establish a monument network inside the undulator hall. This set of coordinates assigned to the network points serves as the representation of the coordinate system and is the basis for all component set-ups. In practice, the points are nests compatible with 1.5" spherical tooling. They can be equipped with SMRs (Spherically Mounted Retroreflectors) for laser tracker observations, or solid sphere based rods for leveling observations. Simulations have been made with a regular pattern of both floor and wall targets. Figure 5, below, represents the middle section of the undulator hall with the red rectangles representing quadrupoles. A floor point is installed in the

* Transverse Locations Tracked by HLS and WPM

middle of the tunnel at every other quadrupole location. The laser tracker positions are placed in front of the other quadrupoles with a staggered offset from the beamline. The tracker observations (purple lines) have a-priori standard deviations based on recent experiences and standard observation practices: 30 µm for the distances and an inverse function of the distance for the two angles (30 µm and 50 µm at one meter for the horizontal and the vertical, respectively). The weight of the leveling observations (green lines) is based on 50 µm as a-priori standard deviations.

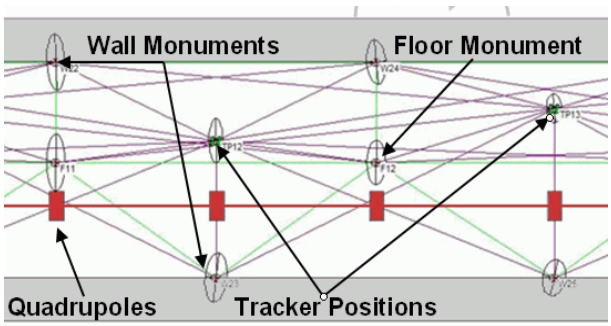

Figure 5: The undulator hall network, used in Simulation, is shown relative to quadrupole locations. Floor and wall monuments as well as tracker positions are shown. The largest semi-major axis of the error ellipses is below 50 µm.

Figure 5 shows the resulting error ellipse at 1 sigma for a free-net approach. All semi-major axes are below 50 µm. This free-net approach assumes that the location and orientation of the LCLS undulator coordinate system [13] has been established through the inclusion of a number of points known in the SLAC linac system.

Once the network is established, the points can be used for the markings on the floor, the alignment of the fixed support pillars and finally the pre-alignment of the girders. For all these tasks, total station set-ups are performed. A solid resection of the instrument, based on at least two floor monuments and three wall monuments, can guarantee the necessary requirement for point determination. Depending on the duration of the installation and the characteristics of the floor curing, an additional survey of the monument network will be observed to control and update the coordinates.

After the undulator segments are installed, a final mapping of all monuments and all fiducials is performed. The scenario for the laser tracker position and methodology is identical to the one used to derive the monument network. The fiducials of the girders, undulator segments, quadrupoles, BFW devices and HLS ultrasound sensors are observed from multiple laser tracker stations. Leveling observations between monuments and selected fiducials are added. The adjustment of all observations is again performed with a free-net approach. Finally the measurements with the laser tracker and the digital level are combined with the portable HLS and WPM observations. If moves are required, they can be checked by the ADS readings and do not require a full remapping of the undulator hall.

BEAM-BASED ALIGNMENT

The electron beam trajectory through the FEL undulator must be straight to a level of about 2 µm over one FEL gain length (~5 m). This level is difficult to achieve using standard component survey methods, and therefore requires a special electron Beam-Based-Alignment (BBA) algorithm [5] which samples undulator BPM readings at three different beam energies (13.6, 6.5, and 4.3 GeV). Changing the linac energy will require a change in many magnetic components upstream of the first undulator to keep the beam matched to the undulator optics, and to keep the horizontal and vertical position and angle of the trajectory at the entrance to the undulator independent of energy. The latter will be monitored by a set of three RF cavity BPMs located between the last quadrupole of the linac-to-undulator beam transport line and the first undulator segment. Detailed simulations have been made, which indicate that adequate beam-based alignment can be achieved if undulator quality and beam stability are within the tight tolerance specifications described here.

BBA will use quad motion and dipole trims for beam corrections. The BBA algorithm uses the off-axis field in the quadrupoles for trajectory correction. Changes are applied through cam-based girder motion, which will automatically align the quadrupoles in the process. Thus, the main source of the original trajectory errors, i.e., quadrupole misalignment, will be taken out by BBA. Secondary sources, such as undulator field errors, the earth's magnetic fields, and other environmental fields are expected to be small and will require slight off-center positioning of the quadrupoles to generate the required correction field on beam axis. The largest of these corrections can then be partially taken over by dipole trim correctors, which are integrated in the quadrupole design. Their range is equivalent to ±100 µm of quadrupole motion. The BPMs must have a relative position measurement resolution of <2 µm rms in order to achieve trajectory straightness adequate to support 1.5-Å FEL operations. This resolution definition implies that the BPM readback offsets (electrical or mechanical) must be stable to <2 µm over the one hour required to accumulate the BBA data.

TOLERANCE ZONES

A systematic plan for trajectory correction during operation has been developed based on tolerance zones and different levels of correction. This plan integrates the results of global tolerance studies, which predict an amount of FEL power loss as a function of the size of the errors, with a sequence of correction operations with increasing disruption to the FEL beam. Starting at the completion of a full BBA session, there will be continuous trajectory feedback systems running at 120 Hz, based on LTU (Linac-To-Undulator transport line) BPMs, and at 0.1 Hz, based on undulator BPMs,

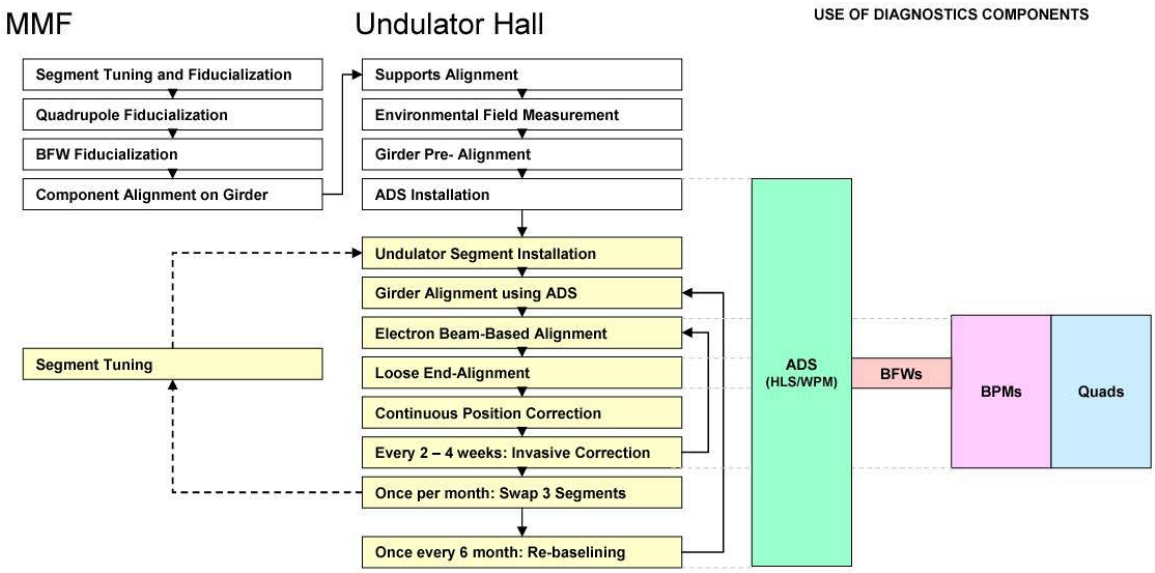

Figure 6: Alignment Function Diagram.

which are tracked by the ADS (Zone 1). Every few hours (Zone 2) small girder position corrections, based on ADS measurements, will keep the quadrupoles at their *goal* positions to restore most, but not all, of the beam power which is expected to sag by up to 10%. This can be done without disruption of the FEL beam. Once a day (Zone 3), re-adjustment of the FEL beam pointing direction may be done. Once a week or less (Zone 4), a full BBA session will be used to get back to the original tolerance zone, which will interrupt FEL beam delivery for less than an hour. Before the BBA is applied, the FEL power level is expected to drop by no more than 25%. Full BBA should fully restore the FEL power to the original level. At an interval of roughly once every six months (Zone 5), a cam mover may range-limit and a planned access will be used to reset cam blocks as necessary.

ALIGNMENT FUNCTION DIAGRAM

The main function block of the undulator alignment system is given in Figure 6. Alignment functions are performed in the Magnet Measurement Facility (MMF) and in the Undulator Hall (UH). Alignment tasks performed in the MMF include the tuning and fiducialization of the undulator segments as well as the fiducialization of the quadrupoles and the BFW devices. The components are then mounted on the girder and aligned. The alignment is checked on the CMM, which is also located in the MMF. The undulator segments are stored separately from the girders until they are installed in the UH. In preparation for the girder installation, fixed support pillars are installed in the UH and aligned. The girders are then installed and pre-aligned on the fixed support pillars after the environmental magnetic field has been measured and recorded along the entire undulator line. After installation of the ADS system, the continuous measurement and recording of the girder positions will start. The undulator segments are then mounted onto the horizontal slides on top of the girders, and the quadrupoles are aligned onto a straight line with conventional alignment. Then, portable WPM and HLS systems [14] will be used for a precise alignment of the undulator segments between neighboring quadrupole magnets.

Every few hours small girder position corrections based on ADS measurements will keep the quadrupoles at their goal position (which will be reset after BBA) to better than ±2 μm over a 1-hour period and to better than ±5 μm over a 24-hour period, in order to support BBA. The next alignment steps involve the electron beam. BBA based on BPMs and quadrupoles under observation of the ADS will be used to straighten the electron beam trajectory to the level required to achieve FEL gain. At this point, continuous position corrections based on BPM readings will start. The BPM readings will be corrected for any device motion, as reported by the ADS.

The BFW devices can now be used to check the alignment of the upstream end ('loose end') of the undulator segments.

Every 2-4 weeks, the procedure loops back to BBA (one iteration, rather than the initial three, may be sufficient), which requires interrupting beam delivery.

Once per month, three undulator segments will be swapped out of the tunnel and brought back to the MMF to be checked for detuning effects, such as radiation damage. At the same time, three of the six replacement undulator segments, which will have been prepared ahead of time, will be installed in the empty slots. As mentioned above, the undulator magnets are mechanically shimmed that the magnetic axis will come to lie in the same x, y location when placed onto a given girder. Every six months, when cam movers might have run out of range

due to the expected continuous ground motion, there will be a maintenance shutdown for re-baselining, i. e., realignment of the cam movers using the manual adjustments on top of the support pillars.

SUMMARY

The X-ray FEL demands very tight tolerances on magnetic field quality, electron beam straightness, and undulator segment alignment. These tolerances can be achieved through BBA procedures based on BPMs and quadrupoles (with energy scan) as well as BFW devices.

Relative component alignment to the required tolerances will be achieved through common girder mounting. Main tasks of the conventional alignment and motion systems are:

- Component fiducialization and alignment on girder
- Conventional alignment of girders in Undulator Hall as prerequisite for BBA.

The ADS measures and enables the correction of girder movement due to ground motion, temperature changes, and cam mover changes. A strategy is in place for using the monitor systems and the controls in order to establish and maintain a straight FEL trajectory.

ACKNOWLEDGEMENTS

It is a pleasure to acknowledge contributions by Argonne National Laboratory's LCLS team.

REFERENCES

[1] I. Vasserman, R. Dejus, P. Den Hartog, E. Moog, S. Sasaki, E. Trakhtenberg, and M. White, "LCLS Undulator Design Development." *FEL2004 Proceeding*, 2004.

[2] E. Trakhtenberg, J. Collins, P. Den Hartog, and M. White, "Design of a Prototype Precision Positioning System for the Undulators of the Linac Coherent Light Source." PAC2005 Proceedings, 2005.

[3] G. Bowden, P. Holik, S.R. Wagner, G. Heimlinger, and R. Settles, "Precision Magnet Movers for the Final Focus Test Beam." SLAC-PUB-95-6132, 1995.

[4] J. Wu, P. Emma and R.C. Field, "Preliminary Study on Electron Signal Detection for the Beam Finder Wire of the LCLS Undulator." LCLS-TN-06-7, 2006.

[5] P. Emma, H.-D. Nuhn, and R. Carr, "Beam Based Alignment for the LCLS FEL Undulator." Nucl. Instrum. Meth. **A**429:407-413, 1999.

[6] J. Welch, "Estimate of Undulator Magnet Damage Due to Beam Finder Wire Measurements." LCLS-TN-06-6, 2006.

[7] J. Welch, "Air Temperature in the Undulator Hall." LCLS-TN-06-2, 2006.

[8] K. Hacker, Z. Wolf, "Earth's Magnetic Field Measurements for the LCLS Undulators." LCLS-TN-05-4 , 2005.

[9] Z. Wolf, "Introduction to LCLS Undulator Tuning." SLAC-TN-05-043, 2004.

[10] J. Welch, "Ground Motion Expectations for the LCLS Undulator Hall." SLAC-TN-05-013, LCLS-TN-04-14, 2004.

[11] F. Peters, G. Gassner, and R. Ruland, "First Measurements and Results With a Stretched Wire Test Setup." LCLS-TN-05-7, 2005.

[12] J. Welch, et al., these FEL'06 proceedings.

[13] E. Bong, P. Emma, C. LeCocq, T. Montagne, and J. Welch, "LCLS Undulator Coordinate System." SLAC-TN-05-021, LCLS TN-03-8, 2004.

[14] G. Gassner, "Proposal for the Alignment of the 'Loose End'." LCLS-TN-06-11, 2006.

HOW TO OBTAIN HIGH QUALITY ELECTRON BUNCHES IN PRESENCE OF NORMAL CONDUCTING LINAC WAKEFIELDS

S. Di Mitri*, ELETTRA, Trieste, Italy

Abstract

The dynamics of electron beams involved in Free Electron Lasers (FELs) projects is an interplay between sources of 6-dimensional emittance dilution and methods of emittance preservation. Relatively long bunches are required for harmonic cascade seeded FELs in order to accommodate the timing jitter and the seed provided by the bunch itself at each stage of the cascade. A high quality is required from such electron beams (small transverse emittance and energy spread) together with a uniform distribution in time along the usable part of the bunch; non-linearity in the longitudinal phase space and in the transverse planes are also issues. A complex longitudinal phase space dynamics characterizes the study often in presence of by the Coherent Synchrotron Radiation (CSR) generated in magnetic compressors. This paper reviews specific problems related to the electron beam dynamics dominated by bunches of kA peak current and varying length (0.1 to 2 ps) in the presence of normal conducting linac wakefields. Methods implemented to minimize the 6-dimensonal phase space degradation are discussed. Results of high beam quality performance are illustrated with particles tracking codes.

INTRODUCTION

This paper describes the degrading effects on the electron beam performance of wake fields present in normal conducting linacs for single pass FELs; in particular: (i) geometrical wake fields in accelerating structures [1–4]; (ii) Coherent Synchrotron Radiation (CSR) [5–8]; (iii) Longitudinal Space Charge (LSC) [9–12]. Their impact on the electron beam quality is discussed in terms of the properties relevant for Spontaneous Emission Self Amplified (SASE) [13–15] and seeded [16–19] FELs.

All the mentioned wake fields couple the 6-dimensional particle dynamics by putting some conflicting constraints on the design of the beam delivery system dedicated to the formation of electron bunches. This paper reviews some strategies for the machine design to compensate the emittances growth and improve the beam quality. The conclusions demonstrate the validity of manipulation techniques to control the electrons 6-dimensional phase space to unprecedented levels.

*simone.dimitri@elettra.trieste.it

WAKE FIELDS AFFECTING THE ELECTRON BEAM QUALITY

In order to make the FEL process more efficient and the undulators chain reasonably short, the electron beam quality has to be characterised by high peak current, small transverse emittance, small energy spread. Due to the cooperative FEL process, priority is given to the slice beam quality.

Longitudinal phase space

Short range longitudinal wake fields generated by relatively short bunches with $\sigma_z << a$, being σ_z the bunch length and a the beam pipe radius, travelling into periodical structures induce a maximum FWHM relative energy loss [20]:

$$\frac{\Delta\gamma}{\gamma} = \frac{eW_0QL}{E_f} \qquad (1)$$

which is valid in the approximation $(\sigma_z / s_0)^{1/2} << 1$ with s_0 the characteristic parameter of the structure.

Assuming a linear energy gain in the linac, (1) shows that the impact of very long accelerators can be comparable to that of smaller machines. For example, the energy loss in the LCLS Linac 3 relative to the final average energy is about 0.5% [21], while that in the FERMI Linac 4 is 1.4% [22]. Off-crest acceleration is then needed to reduce the induced energy chirp below the FEL threshold and to re-establish the linearity in the longitudinal phase space.

With an appropriate positioning of the magnetic chicanes, longitudinal wake fields acting in the last part of the linac work for free to cancel the linear energy chirp required by the compression. In this way the chicane momentum compaction can be relaxed, thus reducing the influence of CSR, while using larger energy chirps.

Even after cancellation of the linear contribution, residual higher order energy chirps affect the final beam quality. A quadratic chirp $D(2) = d^2E/d^2z$ increases the correlated energy spread, thus reducing the SASE FEL gain. It also enlarges the bandwidth of a High Gain Harmonic Generation (HGHG) FEL to unwanted levels, corrupting the goal of producing a Fourier transform limited signal with narrow bandwidth of the order of few meV [23–25]. Figures 1–4 illustrate this topic comparing two cases with different values of the quadratic energy chirp.

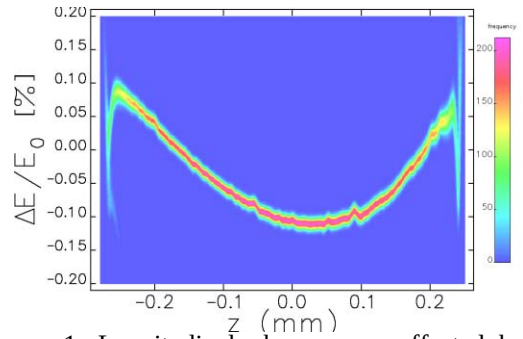

Figure 1. Longitudinal phase space affected by 0.9 MeV/ps^2 quadratic energy chirp.

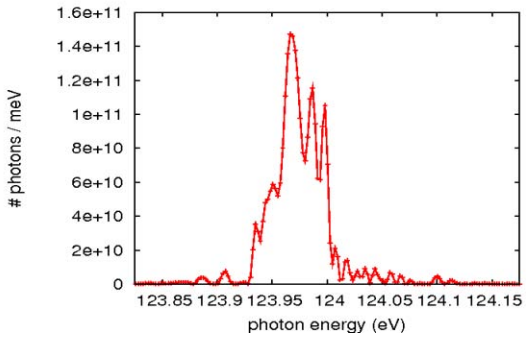

Figure 2. Spectral bandwidth of 40 meV FWHM generated by the electron bunch in Figure 1 through FERMI HGHG with fresh bunch technique at 10 nm.

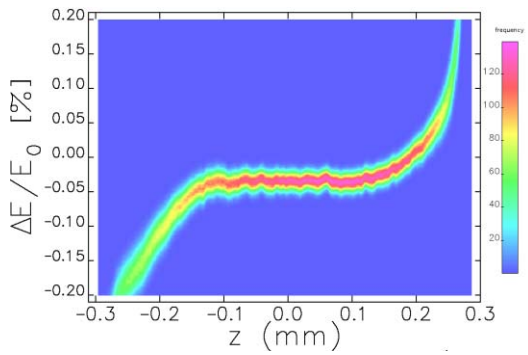

Figure 3. Longitudinal phase space affected by a reduced 0.5 MeV/ps^2 quadratic energy chirp.

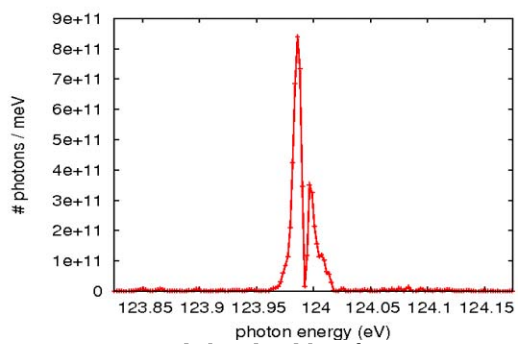

Figure 4. Spectral bandwidth of 10 meV FWHM generated by the electron bunch in Figure 3 through FERMI HGHG with fresh bunch technique at 10 nm.

Phase spaces and bandwidths were produced respectively by mean of Elegant [26] and Genesis [27].

The use of sextupoles [28] and of a high harmonic cavity [29–31] (also called "linearizer") to compensate the quadratic chirp is well-established. Nevertheless, it was also shown that a residual cubic chirp in the compression process can have a large impact on the final current profile [32].

Current profile

SASE FELs generally require a high peak current (kAs) in the bunch core, while HGHG FELs desire a uniform current distribution along the whole bunch, especially if based on fresh bunch injection technique. Even if with different purposes, both the first and the latter need a control of the final current distribution. A proper manipulation of the cubic energy chirp $D(3) = d^3E/d^3z$ is useful to maximize the current along the bunch and to avoid current spikes at the bunch edges. In fact, they are related to several dangerous effects: (i) introduce nonlinearity in the phase space (i.e., bifurcations); (ii) attract particles reducing the current in the bunch core; (iii) induce CSR instability at shorter wavelength than the bunch length; (iv) wake field excited by a leading edge spike may cause additional energy spread in the undulator vacuum chamber.

Transverse emittance

Apart from SC forces at low energy, slice emittance is directly affected by transverse CSR forces [6,33,34]. A coherent behaviour of the emitted radiation has been also observed at wavelength smaller than the bunch length [12,35]; due to the interplay of LSC and CSR on wavelengths which are a fraction of the bunch length, microbunching instability (μBI) [36–40] leads to phase space fragmentation and to slice emittance growth.

The projected emittance of high charge, short bunches is indirectly affected by CSR emitted on the scale of the bunch length [41–43]. Due to the absence of stochastic processes, the slices lateral offset can be cancelled through a $-I$ transport matrix between two identical dispersive regions [44].

The transverse wake field contributes to the projected emittance growth by mean of the induced beam break up (BBU) instability [45,46]. The coupling between the electron bunch and the wake field at a given energy can be estimated by mean of the following dimensionless parameter [47]:

$$\varepsilon_r = \frac{4\pi\varepsilon_0 W_0 l_b L^2 I_{pk}}{\gamma_i I_A} \qquad (2)$$

It multiplies the resonant term acting on the transverse motion of the slices centroid, thus it should be made as small as possible.

CUBIC ENERGY CHIRP

The sign of the cubic energy chirp in the photo-injector (PI) is mainly determined by the SC force and,

according to the present simulations, it is always negative for a flat-top charge distribution (bunch head on the left side of phase space) [48]. After the interaction with longitudinal wake fields, this sign is reversed at the entrance of the second compressor, enhancing the energy-position correlation of the bunch edges w.r.t the core. The edges are there over-compressed producing current spikes. On the contrary, a negative cubic chirp at the chicane provides under-compression of the edges. This mechanism is illustrated in Figure 5, where the longitudinal phase space and the corresponding current profile generated by LiTrack [49] are shown.

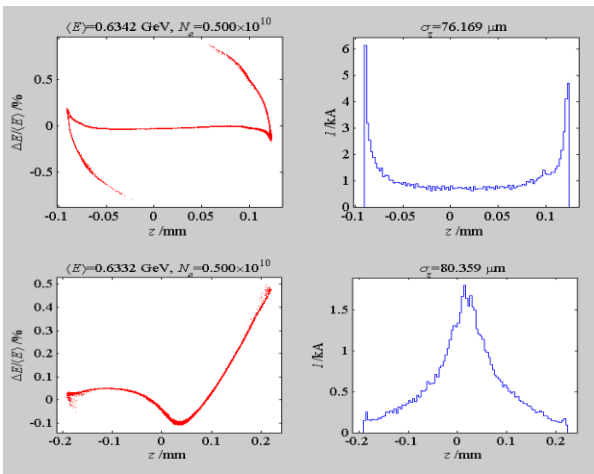

Figure 5. Longitudinal phase space (left) and current profile (right) at the end of the FERMI Linac. Cubic chirp at the PI is $-3.9\text{x}10^{-4}$ mm^{-3} at top and $8.1\text{x}10^{-4}$ mm^{-3} at bottom.

Voltage and phase of the high harmonic cavity allow to control the cubic chirp in the following transport line that is the final current profile. For a 1-stage compression the following parameters are defined: $k=2\pi/\lambda_{rf}$ is the RF wave number and λ_{rf} is the RF wavelength; U_0 is the voltage amplitude of a first linac accelerating on-crest; U_1 is the amplitude of a second linac with off-crest acceleration at phase ϕ_1 (referred to the crest of the RF wave); U_4 and ϕ_4 are the amplitude and phase of the 4-th harmonic cavity. Thus, the third derivative of the energy gain is:

$$U'''_{(s=0)} = -k^2 U'_{(s=0)} + + \frac{15}{4} k^3 \left(U_0 + U_1 \cos(\phi_1)\right) \tan(\phi_4) \quad (3)$$

The quadratic chirp is cancelled if:

$$U_4 = -\frac{U_0 + U_1 \cos(\phi_1)}{16 \cos(\phi_4)} \quad (4)$$

(3) and (4) define the space where parameters of the harmonic cavity can be moved in order to linearize the longitudinal phase space up to the 3rd order.

REVERSE TRACKING

Due to the complexity of the interplay of SC, longitudinal wake fields and higher order energy chirps, it is not obvious to control simultaneously longitudinal phase space and current profile. In addition, it was demonstrated [50] that the linearizer can be used to relax until an order of magnitude the sensitivities of the final beam properties to the linac phase and voltage. Unfortunately, this technique assumes a negligible effect of the cubic chirp on the longitudinal beam dynamics and considers it a free parameter.

The reverse tracking [32] suggests how to improve the global quality of the longitudinal phase space for a given configuration of the wake potential, eventually leaving the linearizer free to be moved for jitter purposes. It applies to ultra-relativistic particles and is based on the assumptions of no stochastic processes in the beam transport and of negligible energy loss from CSR. CSR with wavelength in the range of the bunch length can be neglected in presence of an appropriate shielding [32,51,52] of the vacuum chamber. Moreover, the induced energy loss is relatively small for long bunches.

Within these approximations, the equations of motion can be reversed and a unique solution exists. The density distribution obtained at the beginning of the linac will automatically compensate all the effects perturbing the beam dynamics in the forward tracking, like RF curvature, wake fields and higher order optics.

It is clear this method calls the beam shaping at the photo-cathode to be a fundamental contribution to the final beam quality. For the FERMI specific case [32], a final beam with a flat current profile and a linear phase space corresponds to an initial beam with a ramped current profile (see, Figure 6).

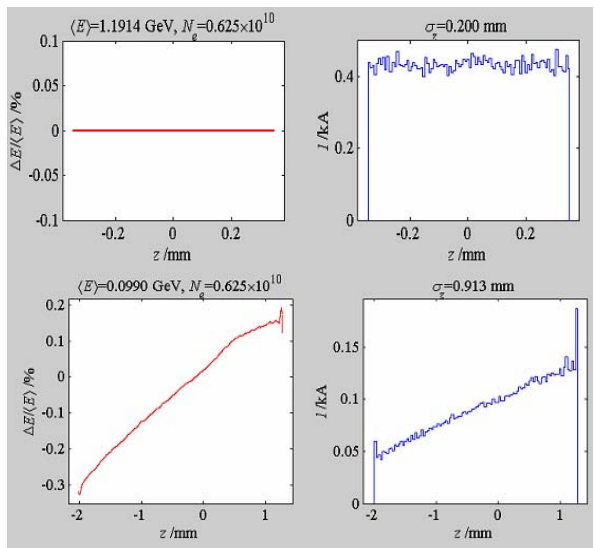

Figure 6. Top, electron beam desired at the undulators' entrance. Bottom, electron beam required at the PI end. LiTrack [49] output.

The approximate prediction of the reverse tracking was confirmed by the forward tracking, obtaining the phase space in Figure 3. In addition, it was proved that the convolution of the longitudinal wake function with

a ramped particle distribution results in a mostly linear wake potential (see, Figure 7), while an initial parabolic current profile brings nonlinear contributions to the phase space.

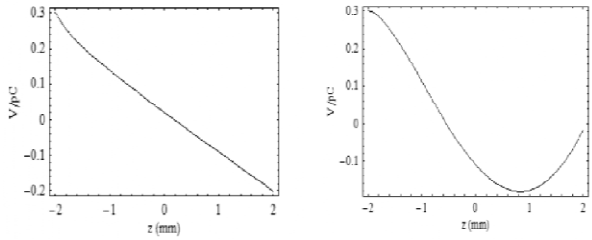

Figure 7. Longitudinal wake field generated in the FERMI Linac 4 resulting from the convolution of the wake function with a particles distribution characterized by a ramped current profile (left) and a parabolic one (right).

BEAM SHAPING AT THE PHOTO-INJECTOR

As discussed before, in presence of wake fields the initial electron density distribution plays an important role in formation of the electron bunches at the end of the accelerator [53–55]. As for the FERMI case, the LSC field at the cathode was investigated [56], since it is mainly responsible for blowing out the particles. Figure 8 shows the desired current profile at the cathode and the evolved charge distribution at the injector exit (at 100 MeV) for a 0.8 nC bunch.

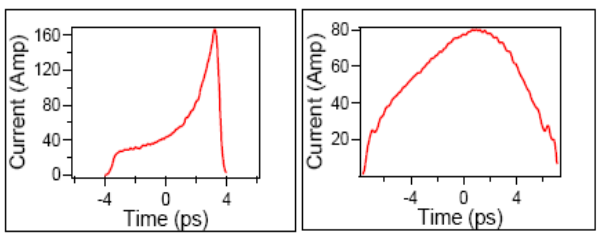

Figure 8. Ramped current distribution just after the cathode (left) and at the injector exit (right) for a 0.8 nC bunch.

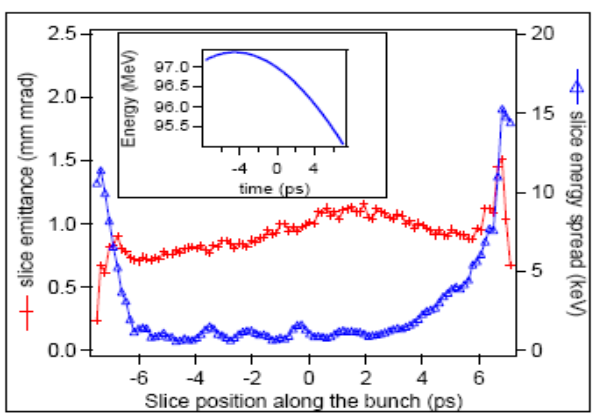

Figure 9. Slice emittance and slice energy spread along the bunch at the exit of the injector. $\varepsilon_{xn,80\%}$ = 1.2 mm mrad. Inside plot: longitudinal phase space including longitudinal wake fields. Head is on the left.

Since each longitudinal slice of the beam contains a differing amount of charge, each one evolves in a different way from the other. Thus, the so-called Ferrario's working point [57] can be only approximately adopted for the emittance compensation. Figure 9 shows the resulting slice emittance and the slice energy spread for the bunch in Figure 8 at the injector exit; results were produced through the GPT code [58].

BBU SUPPRESSION

BBU instability induces a lateral deviation of the bunch tail w.r.t. the head axis. The persistence of such oscillations tend to transform the temporal coordinate into the transversal one, thus inducing projected emittance dilution. A "banana" shape in the (t, x) and (t, y) plane is assumed by the electron bunch [59]; it makes a large part of the bunch travelling with a trajectory offset in the undulator. This fact reflects into an optical mismatch in the undulators and can also induce an effective K-value for the tailing particles different from the nominal one. The impact of a launching error of the bunch in an undulator for SASE FEL was studied and experimentally observed [60]. The off-axis motion in the device leads to power reduction and bandwidth enlargement because of the processes addressed above.

As for seeded FELs, if the bunch tail deviation is sufficiently larger than the beam size, it causes a missed overlap between the seeding laser and the bunch in the undulator, thus reducing the emitted photon pulse length and the peak power [61]. Figure 10 illustrates the horizontal banana shape exiting from the FERMI Linac (Elegant simulation) and a schematic of the seeding laser overlapping the beam.

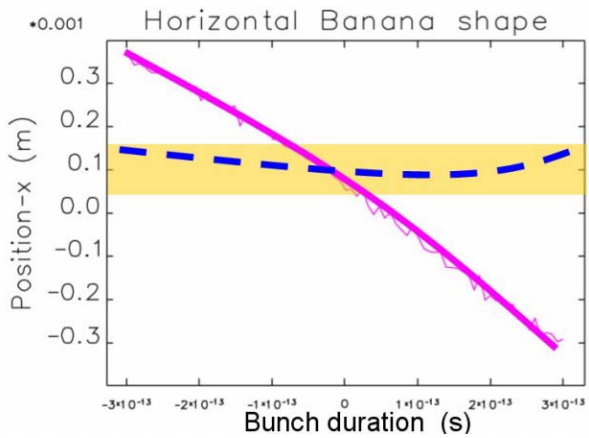

Figure 10. Horizontal banana shapes induced in the FERMI Linac. Bunch head is on the left. The solid curve shows a tail deviation 8 times larger than the 80 μm rms beam size. The dashed one corresponds to a different trajectory in the Linac for which the tail deviation is within the rms beam size. The superimposed rectangle sketches the seeding laser and points out its overlap with the bunch in the two cases.

Figure 11 represents the dependence of peak power and phase shift for the FERMI FEL-1 scheme at 40 nm on the off-axis displacement error of the electron bunch at the undulator entrance [61].

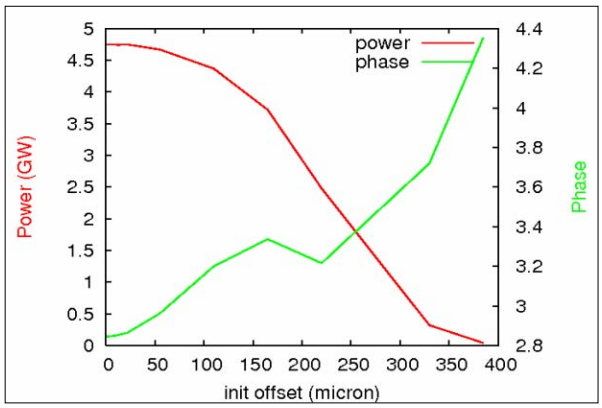

Figure 11. Effect of an off-axis displacement error of the electron bunch at the undulator entrance on peak power (decreasing with offset) and phase shift (increasing with offset) for FERMI FEL-1 HGHG scheme tuned at 40 nm. Seeding laser spot size is here assumed to be 210 μm.

In single pass FELs the BBU instability can be suppressed through trajectory bumps [59,62]. This technique looks for a "golden trajectory" for which all the kicks generated by the transverse wake field compensate each other and the banana shape is finally cancelled. Dashed curve in Figure 10 shows a compensated banana shape which maximizes the overlap with the seeding laser; the solid curve is the banana shape obtained in absence of bumps.

Since the bump is a local method of correction, it depends on the particular condition of operation at its location. For this reason, the sensitivity of the bump to the trajectory jitters has to be checked and made sufficiently small [59].

Reducing the average β-function along the linac is also useful since its square is proportional to the induced relative emittance growth [63]. On the other hand, in a FODO lattice the quadrupole strength $k \sim 1/\beta$ and the trajectory affected by errors $u_{err} \sim k\sqrt{\beta}$. Thus, lowering the β-function increases the sensitivity to the elements misalignment.

LOW CHARGE OPTION

The previous paragraphs describe techniques of electron beam manipulation in order to compensate the wake fields effects. Now a more general prescription of low charge beam production is exposed to minimize the wake fields once the compression factor, the final peak current and the final average energy are fixed.

The curves in Figure 12 represent the loss factor of a Gaussian charge distribution travelling in one accelerating structure of the FERMI Linac 4 vs. the rms bunch length; each curve is drawn for a given peak current (upper curve is at higher current), which is the parameter of interest for the FEL. Dots represent a 0.6 nC charged beam which is compressed twice (dots move from right to left) by a total factor of 15; triangles show the same dynamics for a 0.3 nC charged beam.

Due to the monotonic behaviour of the wake functions in the range of bunch length considered, a bunch with lower charge always suffers from a minor energy loss w.r.t. the higher charge option (look at the height of the yellow and orange bars). Obviously, for a fixed peak current a shorter bunch is required from the PI and will be provided at the end of the accelerator.

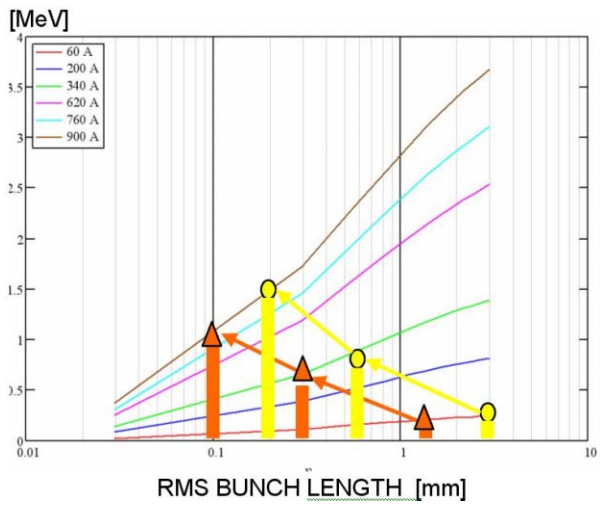

Figure 12. Loss factor in the FERMI Linac 4 accelerating structure vs. rms bunch length (a Gaussian charge distribution is assumed). Dots refer to the 0.6 nC electron bunch in a 2-stage linear compression (from right to left, the peak current increases as the bunch length decreases). Triangles refer to the 0.3 nC case.

Limitations to the shorter bunch length achievable are: (i) CSR instability; in the steady state approximation the induced rms energy spread $\sigma_{\delta,CSR} \sim I/\sigma_z^{1/3}$ [5]. This has an impact in terms of both energy modulation and brightness degradation [56]; (ii) timing jitter, especially for HGHG FELs with fresh bunch injection technique; the final bunch has to be sufficiently long in order to accommodate the timing jitter of the electron bunch w.r.t. the seeding laser.

A 0.2 nC low charge solution has been recently adopted by LCLS [64] instead of the 1.0 nC initially chosen; their dynamics is compared in Figure 13; there the low charge bunch shows an improvement in the longitudinal phase space linearity, a reduction of the current spikes at the bunch edges and a suppression of the BBU instability up to 10% of emittance growth. Reduction of the emittance from 1.2 to 0.85 mm mrad allows to obtain the same saturation length of the 1.0 nC case with a lower peak current (2.1 kA instead of 3.4 kA).

In some cases, a low charge option can also minimize the impact of CSR and SC forces on the

transverse emittance. For the TESLA-XFEL, a low charge working point [65] of 0.25 nC was found with a good compromise between the slice emittance growth, due to stronger CSR transverse forces at shorter bunch length, and the preservation of the projected emittance, which is no longer affected by the optical mismatch generated by SC forces at low energies.

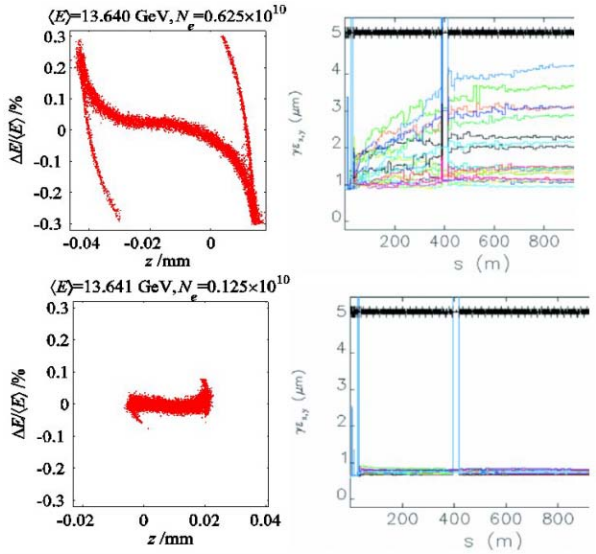

Figure 13. Longitudinal phase space (left plots) and transverse normalised projected emittance (right plots) in LCLS for the 1.0 nC charged bunch at top and for the 0.2 nC charged bunch at bottom.

LANDAU DAMPING

In the last 10 years microbunching instability (μBI) has been extensively studied and recently observed in experiments. The gain of the instability was calculated analytically in the 2-dimensional approximation [37,38]. Numerical solution was obtained including Landau damping from the beam finite emittance [39].

According to the linear theory, the longitudinal Landau damping can be made more effective by increasing the relative energy spread and the compression factor, like in a 1-stage compression. In fact, when adopting a 2-stage compression, analytical estimations confirmed by simulations demonstrate the fundamental role of the second compressor in the development of the μBI: it transforms all the LSC induced energy modulation accumulated in the upstream linac into density modulation; this effect sums to the enhancement of the density modulation already developed by the first compressor.

Figure 14 compares the spectral gain function of the 2-stage and of the 1-stage compression in the FERMI Linac [66]. The maximum of the instability gain is reduced by a factor 100 in the latter case.

The 1-stage compression is a pretty attractive solution but forces a very short bunch to travel along a large part of the linac; as a consequence, linearity of the longitudinal phase space is strongly affected by wake fields. This problem could be overcome by applying the reverse tracking to the single compression scheme [67].

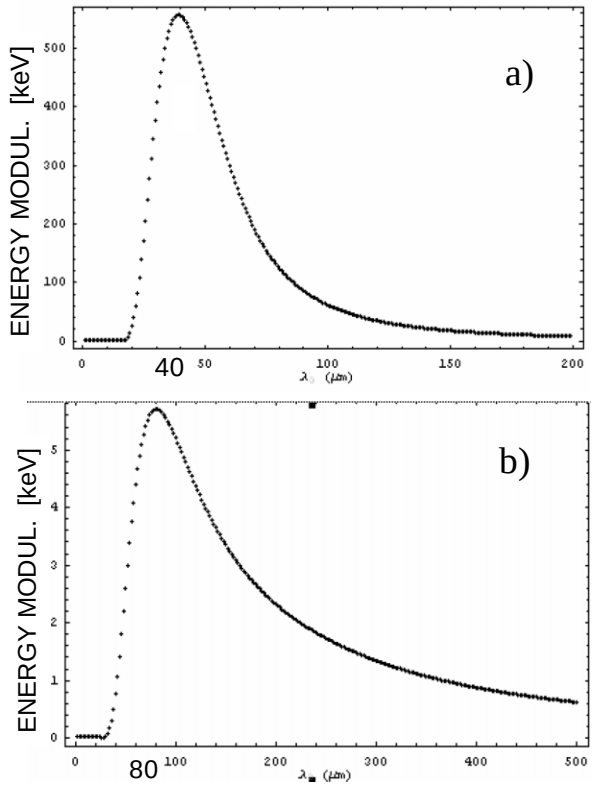

Figure 14. Spectral gain function of the microbunching instability in the FERMI Linac in case of double (a) and single (b) compression. Calculation is based on the 2-dimensional model for CSR and LSC in the linear approximation. μBI starts from realistic shot noise.

A 2-stage magnetic compression is generally associated with a laser heater at low energy for the reasons addressed above. This tool was proposed [9] to suppress the instability by increasing the relative energy spread just before the compression; on the other hand, its final value has to be still maintained below the FEL threshold. This is not obviously reached in low and medium energy machines and becomes more stringent for multi-stage harmonic cascade FELs.

Figure 15 shows the final slice energy spread as function of the energy spread induced by the laser heater in FERMI. μBI is supposed to start from shot noise in the initial density distribution. Figure 15 allows a comparison between the 2-dimensional analytical solution and the simulation of a Vlasov solver [68]. A Vlasov solver (see also [69]) avoids the problem of numerical noise in the simulation and automatically includes a nonlinear evolution of the instability which manifests itself in a folded phase space. This is not considered in the linear theory. Figure 15 shows a discrepancy in the results obtained with the two methods. Such studies, of general interest, are still in progress; the preliminary results indicate

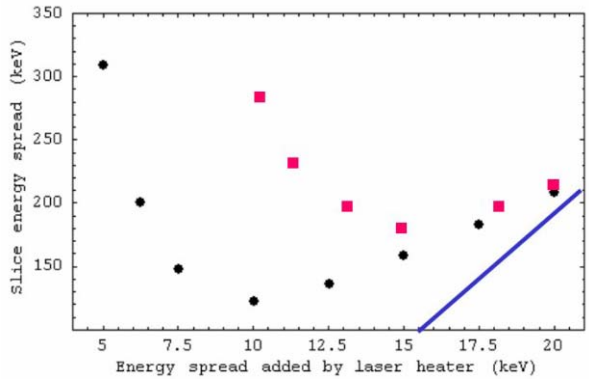

Figure 15. Rms slice energy spread in the final bunch for FERMI vs. the rms energy spread added by the laser heater at 100 MeV. Dots are the analytical prediction; squares are the results of the Vlasov solver. The solid line shows the expected energy spread in absence of any collective effect assuming a compression factor of 10 in linear approximation.

that the final prediction can often depend on details of the calculation.

CONCLUSIONS

The main effects on the electron beam quality by accelerating structures wake fields, CSR and LSC were reviewed in terms of the most relevant beam parameters for single pass FELs. This analysis points out the correlations between the 3 degrees of freedom of the electron dynamics in the accelerator generated by the wake fields.

A double magnetic compression results to be a suitable compromise to minimize instabilities induced by SC, longitudinal and transverse wake fields; at the same time, longitudinal wake field in the linac structures can be used to reduce the CSR effect in the second chicane.

Simultaneous control of the linearity in the longitudinal phase space and of the current profile can be achieved, under some approximations, by following the predictions of the reverse tracking. This technique forces the electron density distribution at the injector to cover an important role in formation of the electron bunches at the end of the accelerator. PI laser can be used to provide such suitable distribution for given wake potential; at the same time, special care has to be taken as for the emittance compensation scheme for unusual charge distributions exiting the photo-cathode.

A general prescription of low charge beam generation was investigated. Simulations demonstrate thatit brings several advantages in achieving a high beam quality; essentially, it reduces the effects of the accelerating structures wake fields, allows a compromise between slice and projected emittance growth, maximizes the current along the bunch.

Suppression of the microbunching instability was treated by mean of the single compression scheme, eventually joined with the reverse tracking, and of the laser heater. Implementation of the instability in 6-dimensional full s2e simulations is still work in progress. Nevertheless, recent results demonstrate the importance of shot noise as adriving term.

REFERENCES

[1] K. Bane, M. Sands, “Wakefields of very short bunches in an accelerating cavity”, SLAC-PUB-4441 (1987).
[2] K. Bane, “Short-range dipole wakefields in accelerating structures for the NLC”, SLAC-PUB-9663, LCC-0116 (2003).
[3] P. Craievich, T. Weiland, I. Zagorodnov, “The short-range wakefields in the BTW accelerating structure of the ELETTRA Linac, NIM A, **558**, 58 (2006).
[4] P. Craievich et al., “The accelerator design study for the FERMI FEL”, ST/F-TN-05/01 (2005).
[5] Y. Derbenev, J. Rossbach, E. Saldin, V. Shiltsev, “Microbunching radiative tail-head interaction”, TESLA-FEL 95-05 (1995).
[6] Y. Derbenev, V. Shiltsev, “Transverse effects of microbunch radiative interaction”, SLAC-PUB-7181 (1996).
[7] E. Saldin, E. Schneidmiller, M. Yurkov, “On the coherent radiation of an electron bunch moving in an arc of a circle”, NIM A, **398**, 373 (1997).
[8] M. Borland et al., NIM A, **483**, 268 (2002).
[9] E. L. Saldin, E. A. Schneidmiller, M. V. Yurkov, DESY Report No. TESLA_FEL-2003-02 (2003).
[10] T. Shaftan, Z. Huang, “Experimental characterization of a space charge induced modulation in high-brightness electron beam”, PRST-AB, **7**, 080702 (2004).
[11] K. Tian et al., “Experimental observation of longitudinal space-charge waves in intense electron beams”, PRST-AB, **9**, 014201 (2006).
[12] M. Huning, P. Piot, H. Schlarb, “Observation of longitudinal phase space fragmentation at the TESLA test facility free-electron laser”, NIM A, **475**, 348 (2001).
[13] S. Milton et al., Science **292**, 2307 (2001)
[14] C. Pellegrini, NIM A, **445**, 124 (2000).
[15] A. Tremaine et al., PRL **88**, 204801 (2002).
[16] R. Bonifacio, L. De Salvo Souza, E.T. Scharlemann, NIM A, **296**, 787 (1990).
[17] I. Ben-Zvi, K. M. Yang, L. H. Yu, NIM A, **318**, 726 (1992).
[18] L.H. Yu et al., Science, **289**, 932 (2000).
[19] G. Penn et al., Proc. of EPAC 2004, Lucern, Switzerland (2004).
[20] R. Gluckstern, PRD, **39**, 2780 (1989).
[21] “LCLS CDR”, SLAC-R-593 (2002).
[22] P. Craievich, S. Di Mitri, “Electron beam simulations for the FERMI project at Elettra”, Proc. of FEL 2004, Trieste, Italy.
[23] S. G. Biedron, S.V. Milton, and H.P. Freund, NIM A **475**, 401 (2001).

[24] T.Shaftan et al., Phys. Rev. E, **71**, 046501 (2005).
[25] W. Fawley, G. Penn, "Thoughts on Spectral Broadening Effects in FERMI and other FEL's Based upon Seeded Harmonic Generation", ST/F-TN-06/07 (2006).
[26] M. Borland, APS LS-287 (2000).
[27] http://corona.physics.ucla.edu/~reiche/
[28] R. England et al., PRST-AB, **8**, 012801 (2005).
[29] P. Emma, "X-band RF harmonic compensation scheme for linear bunch compression in the LCLS", LCLS-TN-01-1 (2001).
[30] K. Flottmann, T. Limberg, P. Piot, "Generation of ultrashort electron bunches by cancellation of nonlinear distorsions in the longitudinal phase space", TESLA FEL 2001-06.
[31] P. McIntosh et al., "Realization of an x-band rf system for LCLS", Proc. of PAC 2005, Knoxville, Tennessee
[32] A. Zholents et al., "Formation of electron bunches for harmonic cascade x-ray free electron lasers", Proc. of EPAC 2004, Edinburgh, Scotland, UK.
[33] R. Talman, "Novel relativistic effect important in accelerators", PRL, **56**, **14**, 1429 (1986).
[34] B. Carlsten, T. Raubenheimer, "Emittance growth of bunched beams in bends", PRE, **51**, **2**, 1453 (1995).
[35] T. Limberg, P. Piot, E. Schneidmiller, "An analysis of longitudinal phase space fragmentation at the TESLA test facility", NIM A, **475**, 353 (2001).
[36] M. Dohlus, A. Kabel, T. Limberg, "Uncorrelated emittance growth in the TTF-FEL bunch compression sections due to coherent synchrotron radiation and space charge forces", Proc. EPAC 1998, Stockholm, Sweden.
[37] E. Saldin, E. Schneidmiller, M. Yurkov, "Klystron instability of a relativistic electron beam in a bunch compressor", NIM A, **490**, 1 (2002).
[38] Z. Huang, K. Kim, "Formulas for coherent synchrotron radiation microbunching in a bunch compressor chicane", PRST-AB, **5**, 074401 (2002).
[39] S. Heifets, S. Krinsky, G. Stupakov, "Coeherent synchrotron radiation instability in a bunch compressor", PRST-AB, **5**, 064401 (2002).
[40] Z. Huang et al., "Suppression of microbunching instability in the linac coherent light source", PRST-AB, **7**, 074401 (2004).
[41] M. Dohlus, T. Limberg, "Emittance growth due to wake fields on curved bunch trajectories", NIM A, **393**, 494 (1997).
[42] P. Emma, R. Brinkmann, "Emittance dilution through coherent energy spread generation in bending systems", SLAC-PUB-7554 (1997).
[43] P. Emma, "Issues and challenges for short pulse radiation production", Proc. of EPAC 2004, Lucerne, Switzerland.
[44] D. Douglas, "Suppression and enhancement of CSR-driven emittance degradation in the IR-FEL driver", JLAB-TN-98-012 (1998).
[45] J. Delayen, PRST-AB, **6**, 084402 (2003).
[46] J. Delayen, PRST-AB, **7**, 074402 (2004).
[47] P. Craievich, S. Di Mitri, "Emittance growth due to short-range transverse wakefields in the FERMI linac", Proc. FEL 2005, SLAC, California, USA.
[48] G. Penco, private communications.
[49] K. Bane P. Emma, Proc. PAC 2005, Knoxville, Tennessee, (2005).
[50] M. Dohlus, T. Limberg, "Bunch compression stability dependence on RF parameters", Proc. of FEL 2005, SLAC, California.
[51] J. Nodvick, D. Saxon, "Suppression of coherent radiation by electrons in a synchrotron", PR, **96**, **1** (1954).
[52] R.Li, C.L. Bohn, J.J. Bisognano, Proc. Particle Accelerator Conference 1997, 1644 (1997).
[53] C. Limborg-Deprey, P. R. Bolton, LCLS-TN-04-16.
[54] C. Limborg-Deprey, Proc. of FEL 2005.
[55] H. Loos et al., Proc. of FEL 2005.
[56] S. Lidia, G. Penco, M. Trovo', "Optimization studies of the FERMI@Elettra photoinjetor", Proc. of EPAC 2006, Edinburgh, Scotland.
[57] M. Ferrario et al., SLAC-PUB-8400 (2000)
[58] S.B. Van der Geer et al., http://www.pulsar.nl/gpt/index/html.
[59] P. Craievich, S. Di Mitri, "Beam break-up instability in the FERMI@Elettra linac", Proc. of EPAC 2006, Edinburgh, Scotland, UK.
[60] G. Andonian et al., "Observation of anomalously large spectral bandwidth ina high-gain self-amplified spontaneous emission free-electron laser", PRL, **95**, 054801 (2005).
[61] G. De Ninno, W. Fawley, G. Penn, "Effect of Off-Axis Displacement Errors on FEL-1", ST/F-TN-06/01 (2006).
[62] P. Tenenbaum, SLAC-TN-04-038 (2004).
[63] K. Bane, Proc. of EPAC 2004, Lucerne, Switzerland.
[64] P. Emma et al., "An optimized low-charge configuration of the linac coherent light source", Proc. of PAC 2005, Knoxville, Tennessee.
[65] T. Limberg et al., "Optimized bunch compression system for the European xfel", proc. Of PAC 2005, Knoxville, Tennessee, USA.
[66] A. Zholents, ST/F-TN-05/15
[67] A. Zholents, private communications
[68] M. Venturini, R. Warnock, and A. Zholents, "Development of a 2D Vlasov Solver for Longitudinal Beam Dynamics in Single-Pass Systems", LBNL Report LBNL-60513.
[69] G. Bassi, J. A. Ellison, R. Warnock, "Progress on a Vlasov treatment of coherent synchrotron radiation from arbitrary planar orbits", Proc. of PAC 2005.

STAIR-STEP TAPERED WIGGLER FOR HIGH-EFFICIENCY FEL *

D.C. Nguyen#, Los Alamos National Laboratory, Los Alamos, NM 87545, U.S.A.
H.P. Freund, Science Applications International Corp., McLean, VA 22102, U.S.A.

Abstract

A concept of a high-efficiency wiggler called the stair-step tapered wiggler is presented. The stair-step tapered wiggler consists of several uniform wiggler segments with decreasing wiggler periods (or decreasing a_w). The relatively large bucket in each wiggler segment enables a substantial fraction of the electrons to be captured, resulting in high extraction efficiencies. The stair-step tapered wiggler provides other advantages, such as ease of fabrication and flexibility in the taper rate. Numerical simulations using MEDUSA will be presented to show the high-efficiency performance of a representative FEL with a stair-step tapered wiggler.

INTRODUCTION

The FEL is known for its wavelength tunability and scalability to high power. However, the extraction efficiency, defined as the FEL power divided by the electron beam power, can be low, with typical values around 1%. The low extraction efficiency increases the requirements for the electron beam's average power and puts stringent demands on the high-power RF systems driving the accelerators. One way to increase the extraction efficiency is through the use of tapered wigglers. Most tapered wigglers are continuous, *i.e.* the periods (λ_w) or dimensionless field (a_w) decreases continuously to maintain the resonance condition,

$$\gamma_R = \sqrt{\frac{\lambda_w}{2\lambda}\left(1+a_w^2\right)}\,, \tag{1}$$

where γ_R is the resonance Lorentz factor; and λ is the wavelength.

Continuously tapered wigglers are only optimized for a narrow range of input radiation intensities and wavelengths. For an oscillator FEL, extraction efficiencies as high as 4.6% inside the resonator have been achieved but the efficiency outside the optical cavity is not significantly higher than that of a uniform wiggler [1].

In this paper, we discuss a different concept of tapering to achieve high extraction efficiency using a series of uniform wigglers. Our approach is an extension of the compound wiggler [2], also known as the step-tapered wiggler [3]. In our approach, a long uniform wiggler is used to bunch the electrons longitudinally and a number of short uniform segments with decreasing the wiggler periods (Fig. 1) or increasing the gaps between the magnets (Fig. 2) are used to extract the energy from the electrons as they execute synchrotron oscillations inside the ponderomotive potentials.

*Work supported by the Office of Naval Research and the High-Energy Laser Joint Technology Office. Author email: dcnguyen@lanl.gov

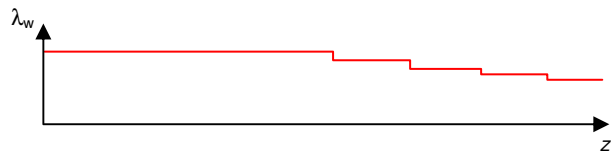

Figure 1: Plot of wiggler period versus z in a stair-step tapered wiggler with taper in wiggler period.

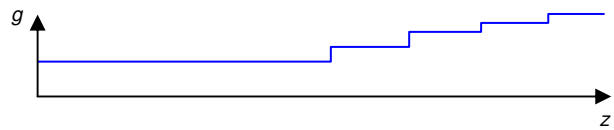

Figure 2: Plot of gaps between magnets versus z in a stair-step tapered wiggler with taper in magnetic field.

THEORY

In a uniform wiggler, the FEL extraction efficiency is the product of the capture efficiency (η_c) and the height of the bucket, as given by [4]

$$\eta = 2\eta_C\sqrt{\frac{a_w a_s}{1+a_w^2}}\quad, \tag{2}$$

where the term in the radical denotes the half-height of the bucket, and a_s the dimensionless optical field, is proportional to the square root of the optical intensity, I_s

$$a_s = \frac{e\lambda\sqrt{2Z_0 I_s}}{2\pi mc^2} \tag{3}$$

where e is electronic charge, Z_0 impedance of free space, m electron mass, and c speed of light.

As the electrons interact with the high optical intensity, they undergo synchrotron motion in the first uniform wiggler and, after becoming trapped, rotate to the bottom of the bucket. With a judicious combination of λ_w and a_w (see Eq. 1), the resonance energy of the next uniform wiggler segment can be lowered such that the electrons are at the top of the bucket of the new wiggler segment (Fig. 3). The electrons that are trapped in the bucket of the new segment now undergo synchrotron motion in this bucket to an even lower energy. The step-tapered wiggler efficiency is the sum of the first and second segments' efficiencies.

$$\eta = 2\eta_{C1}\sqrt{\frac{a_{w1}a_{s1}}{1+a_{w1}^2}} + 2\eta_{C2}\sqrt{\frac{a_{w2}a_{s2}}{1+a_{w2}^2}} \tag{4}$$

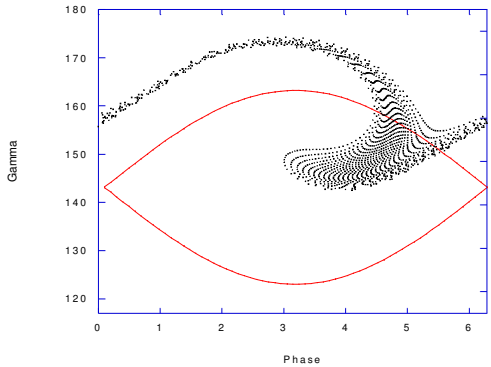

Figure 3: Longitudinal phase space of electrons at the transition between the first and second wiggler segment. The red line denotes the separatrix of the second wiggler.

The indices 1 and 2 in Eq. 4 correspond to the first two wigglers, respectively. The typical efficiency for a two-segment step tapered wiggler is twice that of a uniform wiggler, *i.e.* 2%. If there are n segments, then the efficiency can be increased n-fold. The limit in how far we can taper the wiggler is due to a steady reduction in the capture efficiency in each subsequent bucket, and in the induced energy spread. This is due to the non-adiabatic transitions from one segment to the next. However, since the bucket heights are large, it is possible to maintain high capture efficiency, and thus high extraction efficiency.

SIMULATION

We use the three-dimensional code MEDUSA [6,7] to model a seeded FEL amplifier with a stair-step tapered wiggler and a comparable linearly tapered wiggler. Table I summarizes the FEL and beam parameters used in the MEDUSA simulations. These parameters are chosen for a 1.05-micron wavelength where high-power seed lasers exist. Both wigglers are of a conventional permanent-magnet design with parabolic pole faces to provide equal two-plane, sextupole focusing. The first wiggler segment is the same for both linear and stair-step tapered wigglers. With an input power of 10^6 W (1 μJ pulse energy and 1 ps FWHM, for instance) the first wiggler saturates in 1.83 m. The subsequent wiggler segments are different for the two cases. For the linear taper, it has one 2.44-m long continuously tapered segment with a field taper rate of 0.48 kG per meter of wiggler length. For the stair-step taper, there are four short uniform wiggler segments, each with a smaller a_w. These wiggler segments can be short because the electrons are already bunched at the entrance of these segments. The pre-bunched electrons radiate power immediately and the electrons execute the synchrotron motion to the bottom of the bucket in each wiggler segment. For these simulations, the electron beam is matched in the wiggler. It is conceivable that a scalloped beam could be used to enhance the FEL interaction and/or to pinch the optical beam [5].

Table 1: MEDUSA simulation parameters and results.

Parameters	**Values**
Beam energy	80.8 MeV
Peak current	1000 A
Emittance	10 mm-mrad
Energy spread	0.25%
Wiggler period	2.18 cm
Wavelength	1.052 μ
First wiggler segment a_w	1.187
First wiggler segment length	1.831 m
Second wiggler segment a_w	1.159
Second wiggler segment length	0.698 m
Third wiggler segment a_w	1.116
Third wiggler segment length	0.567 m
Fourth wiggler segment a_w	1.058
Fourth wiggler segment length	0.523 m
Fifth wiggler segment a_w	1.007
Fifth wiggler segment length	0.654 m
Linear taper segment length	2.44 m
Linear taper rate	0.48 kG/m
Input power (peak)	1 MW
Stair-step taper output power (peak)	3.6 GW
Stair-step taper efficiency	4.5%
Linear taper output power (peak)	3.5 GW
Linear taper efficiency	4.4%

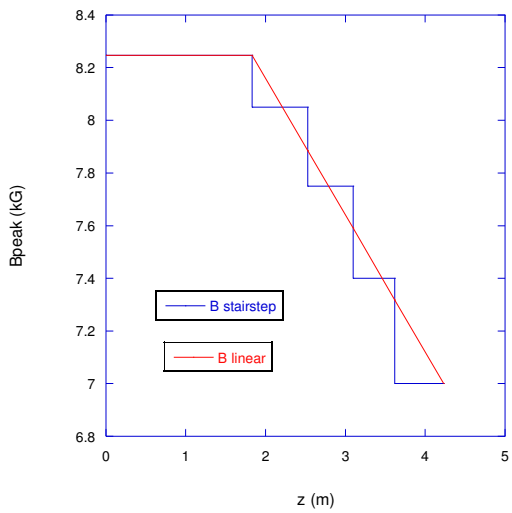

Figure 4: Plots of magnetic field versus distance along the wiggler for the linear (red) and stair-step (blue) tapered wigglers.

The MEDUSA simulation results are shown in Fig. 5. The stair-step and linear tapered wigglers achieve peak powers of 3.6 and 3.5 GW, respectively, corresponding to extraction efficiencies of 4.5% and 4.4%. While the FEL power grows continuously for the linear taper wiggler, the FEL power growth curve in the stair-step taper wiggler exhibit plateau regions in between segments. This is not due to a lack of wiggler magnets in the transition regions (there are no gaps in the stair-step wiggler). Rather, these plateaus are needed to rotate the electrons in the bucket so that they enter the next bucket in the correct phase of the synchrotron oscillation period. It is worth noting that the FEL peak power increase is approximately 0.7 GW per wiggler segment, and the extraction efficiency of the five-segment stair-step tapered wiggler is about 5 times that of the uniform wiggler.

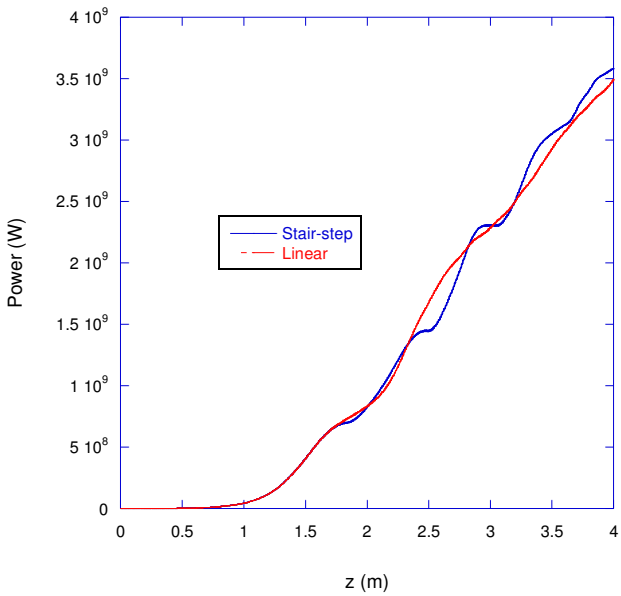

Figure 5: Plots of power versus distance for the linear (red) and stair-step (blue) tapered wigglers.

An important consideration in designing any high-efficiency wiggler is the energy spread in the electron beam exiting the wiggler. For energy recovery linac, it is necessary to minimize the energy spread of the spent electron beam so that one can transport the electron beam back through the linac for energy recovery. To this end, we plot the energy distributions of the electrons exiting the linear taper (red) and stair-step taper (blue) wigglers in Fig. 6. While the linear taper has a double-humped distribution with most electrons localized near the injected energy and maximum decelerated energy, the stair-step taper has electrons distributed in multiple peaks within the same energy bandwidth. The full energy spread for both tapered wigglers is 13%, three times the extraction efficiency of 4.5%. This energy spread is presently outside the 8% energy acceptance of the energy recovery linac [8]. However, we expect a reduction in electron energy spreads will be realized with further optimization of the stair-step tapered wiggler.

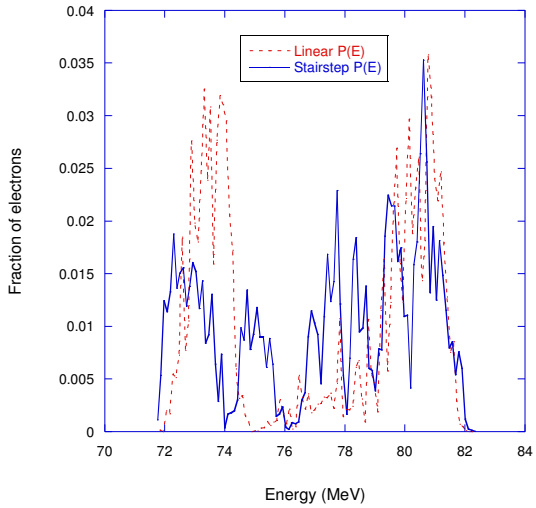

Figure 6: Energy distribution of electrons exiting the stair-step tapered wiggler.

SUMMARY

We have studied a different approach to high-efficiency wiggler called the stair-step tapered wiggler. The stair-step wiggler consists of uniform wigglers with decreasing magnetic fields (or wiggler periods) to extract power from a decelerated electron beam. MEDUSA simulations show the performance of the stair-step tapered wiggler is the same as that of a comparable linear tapered wiggler. For a representative example of an infrared FEL, the peak power (and extraction efficiency) that can achieved with a five-segment stair-step tapered wiggler is five times that of a uniform wiggler. The full energy spread of the electron beam exiting the stair-step wiggler is three times the extraction efficiency.

ACKNOWLEDGMENT

We thank Luca Giannessi for valuable assistance in programming a one-dimensional FEL code.

REFERENCES

[1] D. Feldman et al., Nucl. Instrum. Meth. A285 (1989) 11-16.

[2] R.W. Warren and D. Piovella, Nucl. Instrum. Meth. A304 (1991) 696.

[3] J. Blau *et al.*, Nucl. Instrum. Meth. A483 (2002) 148.

[4] C.A. Brau, Free Electron Lasers, Academic Press, Oxford (1990).

[5] D.C. Nguyen, H.P. Freund, and W. Colson, Phys. Rev. ST-AB 9 (2006) 050703.

[6] H.P. Freund, S.G. Biedron, and S.V. Milton, IEEE J. Quantum Electron. 36 (2000) 275.

[7] H.P. Freund, Phys. Rev. ST-AB 8 (2005) 110701.

[8] L. Merminga, D.R. Douglas and G.A. Krafft, Annu. Rev. Nucl. Part. Sci., 53 (2003) 387-429.

PRECISION MEASUREMENT OF THE UNDULATOR K PARAMETER USING SPONTANEOUS RADIATION *

J. Welch†, J. Arthur, P. Emma, J. Hastings, Z. Huang, H.-D. Nuhn, P. Stefan,
SLAC, Stanford, CA 94309, USA
R. Dejus, B. Yang, ANL, Argonne, IL 60439, USA
R. Bionta, LLNL, Livermore, CA 94550, USA.

Abstract

Obtaining precise values of the undulator parameter, K, is critical for producing high-gain FEL radiation. At the LCLS [1], where the FEL wavelength reaches down to 1.5 Å, the relative precision of K must satisfy $(\Delta K/K)_{rms} \lesssim 0.015\%$ over the full length of the undulator. Transverse misalignments, construction errors, radiation damage, and temperature variations all contribute to errors in the mean K values among the undulator segments. It is therefore important to develop some means to measure relative K values, after installation and alignment. We propose a method using the angle-integrated spontaneous radiation spectrum of two nearby undulator segments, and the natural shot-to-shot energy jitter of the electron beam. Simulation of this scheme is presented using both ideal and measured undulator fields. By 'leap-frogging' to different pairs of segments with extended separations we hope to confirm or correct the values of K, including proper tapering, over the entire 130-m long LCLS undulator.

INTRODUCTION

Several methods have been proposed to measure *in situ* undulator K differences by alternately comparing spontaneous radiation spectra from two undulator segments [2]. We are looking into the possibilities of using the combined radiation spectrum produced by two nearby segments.

The first harmonic peak of the on-axis spontaneous radiation energy spectrum from a single undulator has a bandwidth equal to the inverse of the number of periods. The combined radiation from two such undulators has a bandwidth that is narrower by a factor of two. Compared with a single undulator, combined undulators produce twice the number of photons in half the bandwidth, so the spectrum has four times the peak height and therefore eight times steeper slopes. Integrating the spectrum over angles about the beam axis produces a complication, since the off-axis undulator spectral peak shifts to lower energy. Such integration causes the low-energy edge to extend lower by an amount depending on the integration angle, but the high-energy edge will remain stationary, though the slope becomes somewhat less steep. Based on a far-field undulator radiation formula, angle-integrated spectra are calculated for one, and two identical undulators without any phase error between them, and shown in Figure 1.

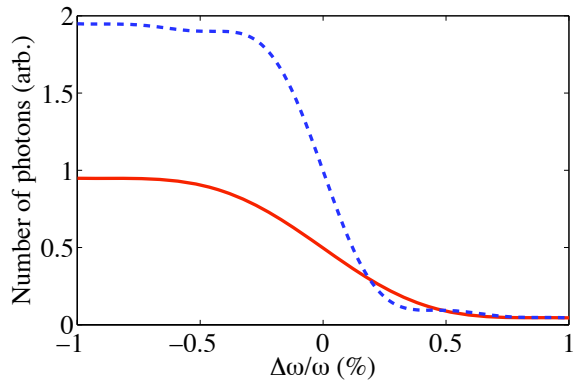

Figure 1: Angle-integrated spectra of a single undulator (solid-red) and two identical undulators (dashed-blue).

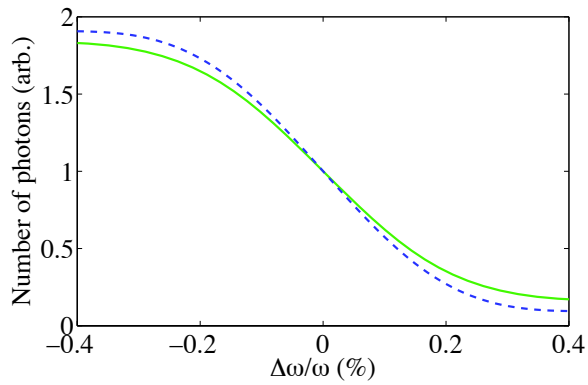

Figure 2: High-energy edge of spectrum for two cases: identical K (dashed-blue), and $\Delta K/K = +0.2\%$ (solid-green).

If the two undulators have different mean values of K, the slope of the high-energy spectrum edge will be reduced, depending on the relative difference, $\Delta K/K$. Figure 2 shows the high-energy edge of the angle-integrated spectrum of two undulators for two cases: identical K, and $\Delta K/K = +0.2\%$. As clearly shown, the slope of the high-energy edge of the spectrum is sensitive to the relative K differences of two adjacent undulators (phase errors will be addressed below). In this figure the left-right spectrum shift, $-\frac{K^2}{1+K^2/2}(\Delta K/K)$, has been subtracted off to allow

* This work is supported by the U.S. Department of Energy, contract DE-AC02-76SF00515, and was performed under the auspices of the U.S. Department of Energy, by University of California, Lawrence Livermore National Laboratory under Contract W-7405-Eng-48, in support of the LCLS project at SLAC.

† Welch@SLAC.Stanford.edu

more convenient comparison of the slopes at $\Delta\omega/\omega = 0$.

The LCLS undulator consists of 33 almost identical segments, each 3.4 m long. Each segment is provided with "roll-away" capability; and can be independently displaced up to 8 cm horizontally, effectively turning it 'off'. The segments are also constructed with a 4.5 mrad cant angle of the poles, which allows K-value adjustment by small horizontal displacements (about 1.5 mm per 0.1%), using the same "roll-away" mechanism. If the slope of the high-energy edge of the spectrum is measured with sufficient precision as a function of the horizontal displacement, (equivalent to scanning $\Delta K/K$), two undulator K values can be set equal within the required precision (0.015%), and this relative correction might be applied repetitively over the full 130-m undulator to adjacent, or nearly adjacent, segment pairs.

METHOD

The method proposed here requires retracting all but two adjacent, or nearly adjacent, undulator segments from the beamline so that all x-rays detected come only from the segments under test. The electron trajectory must then be brought to essentially beam-based alignment quality, so that the kinks in the trajectory between segments are less than 1μrad. Beam-based alignment is done by mechanically moving the quadrupoles to obtain a dispersion-free trajectory. The quadrupoles are mechanically tied to the undulator segments and both move together, so this step also insures that the undulator segments are brought vertically to within about 100 μm of the ideal position before starting.

On each machine pulse, a small portion of the x-ray spectrum is sampled in the region of the high-energy edge of the first harmonic, using a silicon crystal spectrometer, set for diffraction at a fixed Bragg angle from the (111) crystal planes. (The LCLS electron beam-angle jitter should be $< 1\mu$rad, which is small compared to the Darwin width of the crystal reflection.) As a result of the natural electron energy jitter ($\sim 0.1\%$ rms), the photon spectrum is randomly sampled. The electron energy jitter is measured on each pulse (see below) and the inferred photon energy shift is then associated with the detector data; the underlying spectrum is then reconstructed by plotting the detector data against the inferred photon spectrum shift.[1]

About 100 pulses will be needed to reconstruct a spectrum. After a spectrum is collected in this manner for a given arrangement of two adjacent undulator segments, the K value of the second undulator is changed by 0.05% by translating it $\Delta x = 0.75$ mm, and then a new spectrum is obtained. This process is repeated for 9 separate K values, ranging over about $\pm 0.2\%$.

The electron energy jitter is precisely measured by two beam position monitors (BPMs) located upstream of the undulator, at points of high horizontal momentum dispersion. The BPMs are separated in betatron phase advance by 2π and have opposite sign dispersion, such that the difference in their position readback values is proportional to the relative electron energy variation and completely insensitive to incoming betatron oscillations. With dispersion of ± 125 mm at each BPM, and a 5-μm rms single-pulse position resolution, the relative electron energy resolution is $(5\ \mu\text{m})/(125\ \text{mm})/\sqrt{2} \approx 3\times 10^{-5}$, and the corresponding photon energy resolution is twice this, or 6×10^{-5}.

Since the spectrum shifts towards $\Delta\omega/\omega > 0$ for $\Delta K/K < 0$ (see Fig. 3), the data tends to be poorly centered on the spectrum edge for $\Delta K/K \neq 0$. To improve resolution, we adjust the mean electron energy by $-\frac{K^2}{1+K^2/2}(\Delta K/K)$ for each new setting so that the energy always varies around the center of the edge. These small adjustments are possible using the BPM-based feedback loop, which maintains the desired average electron energy, but cannot remove the random pulse-to-pulse jitter.

The slope of each high-energy spectrum edge is found by fitting the data for each K value. The Δx at which the slope is steepest corresponds to equal K values in the two segments. At a 10 Hz machine rate, this process will require 90 seconds, plus the time required to translate the undulators nine times, for a total of about 4 minutes per undulator pair. A description of a simulation of this process, including realistic errors, follows.

SIMULATION

A simulation is performed using a computer-generated, two-undulator, spectrum integrated over all angles, at nine values of $\Delta K/K$: (-0.2% to $+0.2\%$ in steps of 0.05%). To simulate measured data, the perfect, computer-generated spectrum is sampled at random values of twice the electron energy error ($\Delta\omega/\omega = 2\Delta E/E$). The electron energy varies randomly in a Gaussian distribution with 0.1% rms. In practice, either the average electron beam energy or the Bragg angle can be adjusted to best center the data on the high-energy edge of the spectrum.

A cubic spline is used to interpolate the computer-generated spectrum for each randomly selected energy. An error of 6×10^{-5} rms is added to the photon energy to account for the BPM-based electron energy measurement resolution. An error is also added to the number of photons detected at that energy, assuming the bunch charge randomly varies from pulse to pulse, but a toroid charge monitor, capable of resolving the relative charge variation to within 0.5% rms, is used to normalize the data. In addition, the beam angle is assumed to vary by 0.5μrad rms (one-half the nominal rms beam divergence), adding another source of undetermined energy error based on small variations of the Bragg angle. Detector noise is also added assuming a noise level of 100 photons with respect to the the peak signal of 10^5 photons. And finally, a photon statistics error is included, which is proportional to the inverse square-root

[1] Electron energy loss from radiation is $\leq 0.005\%$ per segment and will be taken into account in setting the appropriate K values. Wakefield losses are expected to be even less. Both types of energy losses are ignored in the following discussion.

Table 1: Simulation parameters.

Parameter	symbol	value	unit
e^- energy	E_0	13.6	GeV
bunch charge	q	1.0	nC
undulator parameter	K_0	3.50	
fund. wavelength	λ_r	1.5	Å
Bragg spacing (111)	d	3.14	Å
Bragg angle (111)	θ	13.8	deg
rel. e^- energy jitter	$(\Delta E/E)_{rms}$	0.1	%
e^- energy meas. res.	$(\Delta E/E)_{res}$	0.003	%
bunch charge jitter	$(\Delta q/q)_{rms}$	2	%
charge meas. res.	$(\Delta q/q)_{res}$	0.5	%
e^- angle jitter	θ_{rms}	0.5	μrad
detector noise level	N_γ^{noise}	100	photons
peak signal	N_γ^{pk}	10^5	photons

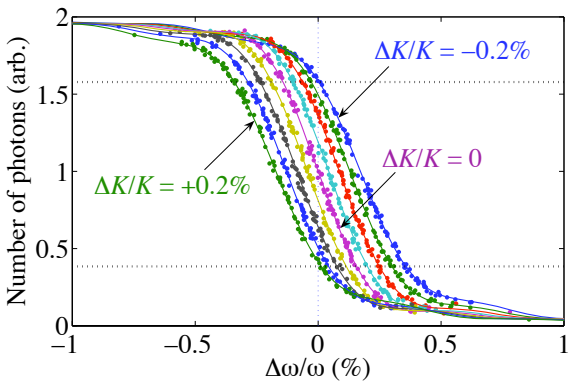

Figure 3: High-energy spectrum edge for each of nine values of $\Delta K/K$: (-0.2% to $+0.2\%$). Solid curves are perfect spectra and plot points are simulated noisy data.

of the number of photons detected in each pulse. Table 1 lists the simulation parameters.

Figure 3 shows the perfect, computer-generated spectrum for each of nine values of $\Delta K/K$ as solid curves, and the simulated, imperfect data as points randomly sampled on the frequency axis due to electron energy jitter. The scatter of the data points with respect to the curves is due to the various sources of error, such as BPM resolution, charge measurement resolution, unmeasured beam angle jitter, detector noise levels, and photon statistics, as described above.

The data shown in Fig. 3 must now be used to determine the slope of the high-energy spectrum edge for each value of $\Delta K/K$. The method used here is to fit the core of the data, which is between 15-20% below the signal peak and 15-20% above the signal minimum (see horizontal cut lines in Fig. 3), with a 3rd-order polynomial and solve for the steepest slope. The fitted polynomial form is

$$N = N_0 + a(\Delta\omega/\omega) + b(\Delta\omega/\omega)^2 + c(\Delta\omega/\omega)^3. \quad (1)$$

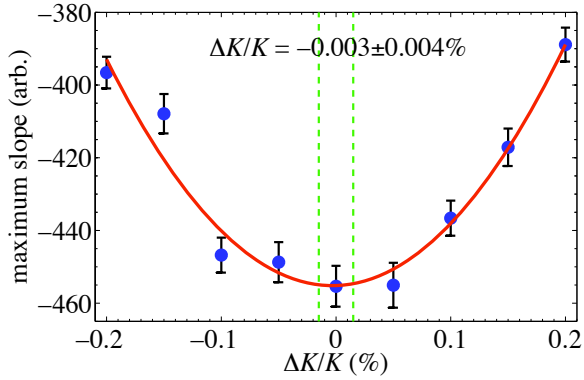

Figure 4: Maximum negative slope vs. $\Delta K/K$. Any $\Delta K/K$ error is resolved to within $\pm 0.004\%$. The goal of $|\Delta K/K| < 0.015\%$ is shown as vert. green lines.

This steepest slope (inflection point) on the cubic-fitted curve is then

$$\left(\frac{dN}{\Delta\omega/\omega}\right)_{max} = a - \frac{b^2}{3c}. \quad (2)$$

The nine determined steepest slopes of Eq. (2) are then plotted versus $\Delta K/K$, which is taken from the deliberate undulator displacements, Δx, and the known pole cant angle. The data is fitted to a simple parabolic curve in order to find the minimum. Figure 4 shows this plot where the steepest slope is found at $\Delta K/K = -0.003\%$, with a statistical error of $\pm 0.004\%$, well within the goal of 0.015%. The error bars are the propagated statistical errors, from the cubic fit, through each evaluation of Eq. (2).

Similar estimations are repeated for simulated radiation spectra using magnetic measurements from the real, imperfect prototype undulator. A systematic $\Delta K/K$ error of up to 0.008% is seen in this case, which is not fully understood, but is still within the required acceptance. It should be noted that the prototype is of lower magnetic quality than the first few production undulators.

In addition to statistical errors and imperfect undulators, the possibility also exists for a relative phase error between the two interfering undulators. Simulations were run for phase errors of 20 and 70 degrees. For reference, the maximum allowable net error within LCLS undulator specifications is 20 degrees. The 20 degree error has no significant impact on the result. The 70 degree error shown in Fig. 5, clearly affects the data, but the effect can be excluded from the fit if the lower data cut level is set no lower than 20%

DISCUSSION

Beam Angle and Alignment Systematics

There are two kinds of alignment errors that, when combined, can in principle lead to significant error in the measured $\Delta K/K$. One is a change in the electron beam angle

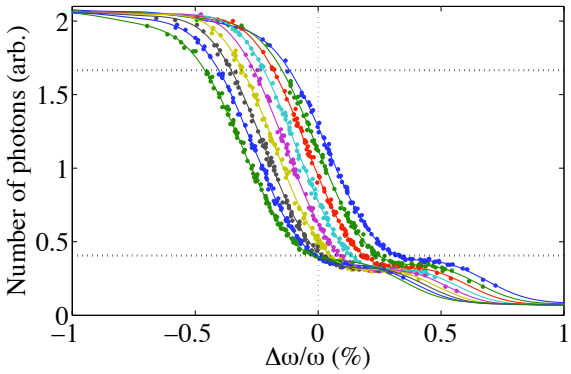

Figure 5: High-energy, two-undulator spectrum edge for 9 values of $\Delta K/K$ with a 70-degree relative phase error.

between segments (non-straightness). The other is a misalignment, with respect to the central ray of the beam, of the effective aperture (usually the vacuum chamber) which defines the angular distribution of photons detected.

Synchrotron radiation produced by undulator segments has a strong angle/energy correlation, whereby the spectrum is shifted to lower energy for finite angles between the central ray and the observation point. Theoretically, in the method presented above, the spectrum is integrated over all angles, so the measured spectrum should not change if there are alignment errors — all photons are collected. However, in practice the range of angular integration is limited by the vacuum chamber aperture, especially for the first segments, where there is only $\pm 20(32)$ μrad vertical(horizontal) acceptance, assuming a perfect chamber and a perfectly aligned beam.[2] The angle-energy correlation implies that, in part, the alignment of the aperture with respect to the central ray determines the spectrum of photons that pass through.

The FWHM angular spread for the resonant photon energy is $\pm 6.7\mu$rad. It is representative of the core angular size over which photons contribute to the high-energy edge of the spectrum. Figure 6 shows that beam angles of more than about ± 8 μrad will result in scraping ofthe core x-rays by the vacuum chamber. However, this situation will result in an error in the $\Delta K/K$ measurement only if there is also a change in beam angles between the segments being measured, because otherwise the effect would be the same for both segments.

We plan to avoid this error by using beam-based alignment, which will reduce the residual segment-to-segment angles to order 1μrad or less. In addition, we plan to check where the central ray is by scanning a 1 mm^2 'pinhole' aperture and finding the position that maximizes the average photon energy. If necessary, the beam orbit can be adjusted so that the central ray passes comfortably through the aperture so that no scraping of the core will occur.

[2]The angular acceptance of the detector, when properly aligned, is assumed to be larger than the angular acceptance of the vacuum chamber.

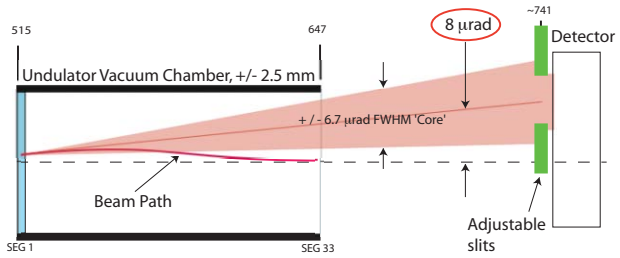

Figure 6: The 'core' synchtrotron radiation will start to scrape off on the vacuum chamber if the central angle is greater than 8 μrad.

Leap Frogging and Near Field Effects

The proposed method gives a measurement of the relative difference in K values between two nearby undulator segments. The complete undulator is composed of 33 segments and is 130 m long, with the last segment about 100 m from the detector. Simple pairwise measurement of adjacent segments builds up the expected error between the first and last segment by a factor of $\sqrt{33}$. By 'leap frogging' over two segments, only 11 measurements are needed to connect the first and last segments so the relative error between them would be $\sqrt{11}$ times more than the individual measurement error. If two segments are skipped, the phase difference that results from the missing segments can be adjusted using a closed orbit bump. Skipping more segments would tend to further reduce the error build-up. However, as the distance between the segments being measured increases, the possibility of significant electron trajectory angle errors increases as well. Also near-field effects can start to appear. The optimum strategy will become apparent during measurement.

In the theoretical model of the undulator segments, it is implicitly assumed that the observation angle from the beam to the detector is the same for the two segments, i.e., the detector is in the far-field of the spontaneous radiation. If the distance between segments is comparable with the distance to the detector, then the observation angles will be significantly different and the detector will see a red-shifted spectrum from the nearer segment. For the LCLS, segment spacing 10 m or less (roughly consistent with skipping over two segments) can be considered to be the far-field case.[3]

REFERENCES

[1] LCLS Conceptual Design Report, SLAC-R-593 (2002), http://www-ssrl.slac.stanford.edu/lcls/cdr/.

[2] www-ssrl.slac.stanford.edu/lcls/undulator/meetings/2005-11-14_bbkm_workshop/ The web page contains several relatively recent talks on the topic of *in situ* K measurement.

[3]Differences in angle of less than 1μrad have negligible effect on the the measured spectrum. If the integration of radiation from one segment is over ± 15 μrad then a difference in the integration angle of 1μrad for the other segment corresponds to a segment spacing on the order of 10 m or three segments.

TEMPORAL ANALYSIS AND SHAPE CONTROL OF UV HIGH ENERGY LASER PULSES FOR PHOTOINJECTORS*

D. Garzella†, O. Gobert, Ph. Hollander, F. Lepetit, M. Perdrix
Commissariat à l´Energie Atomique (CEA-France)
T. Oksenhendler
FASTLITE, Ecole Polytechnique, Palaiseau (France).

Abstract

This work shows a survey of the studies conceived for obtaining Ultraviolet, high energy laser pulses, totally controlled and characterized in shape, on the kHz, Chirped Pulse Amplification (CPA)-based Ti:Sa laser system PLFA at CEA-Saclay. The pulse shaping deals with the amplitude and phase control of the stretched laser pulses issued from an amplifier before entering the compressor and the tripling unit. The work presents the theoretical background and the proposed experimental setup, before showing the preliminary promising results.

INTRODUCTION

In order to generate high power, subpicosecond XUV radiation by following the classical Self Amplified Spontaneous Emission (SASE) scheme [1, 2] and/or seeded FELs [3, 4, 5, 6, 7], tight specifications on the electron bunch are required, noteworthy in terms of highly reduced emittance, both for achieving very short wavelength or high average power, thus high duty cycle continuous electron beams (repetition rates $\geq$ 1 kHz). Even though emittance compensation schemes [8] are used, or "RF-focusing" ones [9] for superconducting RF photo-injectors, for obtaining high brightness electron bunches, the laser pulses impinging onto the photocathode must meet special requirements not only in terms of wavelength and delivered energy per pulse. High repetition rate systems like the one retained for photo-injector operation at Arc-en-Ciel [10] will have to fulfil the following requirements:

- Up to 50 μJ pulse energy in the UV (following the cathode material work function, between 240 and 300 nm), for a 1 nC electron bunch production on a photocathode with $\rho \approx 0.1 - 1\%$ quantum efficiency (QE) (as in the case of the most commonly used semiconductor Cs_2Te). This calls, before a very highly efficient third harmonic generation, for laser amplifiers delivering at least 1 mJ in the IR (800 nm), and, for high repetition rates, on Chirped Pulse Amplified (CPA), Ti:Sa based systems.
- A final duration in the UV, before the cathode, between 5 and 20 ps [10].
- A precise measurement and control of longitudinal and transverse features (dimensions and shape) in order to prevent non-linear contribution to the emittance increase.

Indeed, it has been shown [11, 12] that in order to minimize the bunch emittance at the issue of the electron gun, temporally and spatially shaped UV pulses are needed to prevent non linear space charge forces and then minimize the electron emittance. Shaping techniques for ultrashort laser pulses (in the sub-ps range) are well known. In transverse space an homogeneous energy distribution with a circular symmetry is needed. This can be obtained by use of mask filters or deformable mirrors and lenses. In longitudinal space, shaping techniques are mostly based on the utilisation of spatial masks, in some cases by using programmable liquid crystals structures at the fourier plane of a $4f$ zero-dispersion line [13], or by using an Acousto-Optic Programmable Dispersive Filter (AOPDF), or DAZZLER [14]. Both techniques have been already used in the framework of accelerator and FEL studies [15, 16]. In the EUROFEL program framework, our goal is to obtain a few picosecond, 100 μJ laser pulses in the UV (266 nm) with a totally controlled and characterized longitudinal and transversal shape. This work presents the experimental setup and the main diagnostics designed to obtain every desired pulse shape from the "beer can" profile (corresponding to a cylindrical bunch in the 3D-space) to a parabolic one ("waterbag" bunch distribution) starting from the IR ultrashort pulse issued by the kHz, Chirped Pulse Amplification (CPA)-based Ti:Sa laser system PLFA (French acronym for Tunable Laser Femtosecond Platform) [17] at CEA-Saclay. The pulse manipulation is based on the amplitude and phase control of the stretched laser pulses issued from the amplifier, which is performed by the DAZZLER before entering the compressor and the tripling unit.

FEMTOSECOND LASER PULSES

Direct temporal manipulation of an ultrashort laser pulse is rather complicated. Thanks to Fourier Analysis, every temporal feature of a laser pulse has its corresponding one in the frequency domain. Thus, an ultrashort pulse in time space exhibits a very broadband spectrum (several tens of nm). The electric field $\widetilde{E}(\omega, \phi)$ can be described in terms of the spectral components of amplitude $E_0(\omega)$ and phase $\phi(\omega)$:

* This work has been supported by the EU Commission in the Sixth Framework Program, Contract No. 011935 - EUROFEL.
† david.garzella@cea.fr

$$\widetilde{E}(\omega,\phi) = E_0(\omega)\cdot e^{i(\omega_0 t+\phi(\omega))} \quad (1)$$

$$\phi(\omega) = \phi_0 + (\omega-\omega_0)\cdot\left.\frac{\delta\phi}{\delta\omega}\right|_{\omega_0} + \frac{(\omega-\omega_0)^2}{2}\cdot\left.\frac{\delta^2\phi}{\delta\omega^2}\right|_{\omega_0} \ldots + \frac{(\omega-\omega_0)^n}{n!}\cdot\left.\frac{\delta^n\phi}{\delta\omega^n}\right|_{\omega_0} \quad (2)$$

In the polynomial approximation of the phase term (eq. 2), the constant and the first order term coefficient, called respectively the "absolute" phase and the group delay, are not crucial for the propagation of the pulse, as they account respectively for the position of the peak amplitude of the field in the phase and the delay undertaken by the central frequency component $E_0(\omega_0)$ propagating between two reference planes [18]. The second-order term coefficient becomes extremely interesting for pulse manipulation as it accounts, for example, for the different response of the frequency components to the propagation of the pulse in a "dispersive" medium. Thus, an original transform-limited laser pulse will be stretched by a factor $\propto \left.\frac{\delta^2\phi}{\delta\omega^2}\right|_{\omega_0}$. Higher order terms account for symetric and antisymetric distortion terms of the pulse shape.

EXPERIMENT

Pulse Shaping Technique

The principle of the AOPDF [14] is based on the coupling between the laser pulse and an acoustic wave in a birefringent crystal. For IR laser pulses, around 800 nm, a TeO_2 crystal is cut in such a way that the acoustic wave energy and the optical waves energy travel along the same axis. The incident optical pulse polarized on the ordinary axis is diffracted by the Bragg grating made by the acoustic wave onto the extraordinary axis. Shaping the pulse is equivalent to programmming the associated suite of acoustic grating, so that the spectral amplitude and phase of the laser pulse is directly linked to the acoustic wave ones.

Target, Filter and Correction Loop

Defining a "target" pulse here means defining "target" spectral amplitude and phase. As the DAZZLER is a linear filter, the output optical pulse is the product of the input pulse by the filter response in the spectral domain:

$$\widetilde{E}_{out}(\omega,\phi) = \widetilde{E}_{in}(\omega,\phi)\cdot\widetilde{S}(\omega,\phi) \quad (3)$$

where $\widetilde{S}(\omega,\phi)$ is the filter response.

Therefore, knowing the input pulse, the target pulse is directly obtained by fitting the filter response (see fig. 1). The spectral amplitude and phase shapings can be separated as they are independently measured and controlled.

In practice, amplitude loop preceeds phase loop because of bandwidth limitation. The complete procedure can be described as the following steps:

1. The user builds the target amplitude and phase terms.
2. Amplitude loop:
   - Initial filter amplitude.
   - spectrum measurement.
   - Modification of the filter by dividing the "target" amplitude by the measured amplitude.
   - spectrum measurement ... loop until the measurement fits the "target".
3. Phase Loop: Analog process is made on the "target" phase.
4. Experimental amplitude and phase are acquired and an initial check in the time domain is made by IFT on the experimental data, thus retrieving the temporal duration and shape (fig. 2).

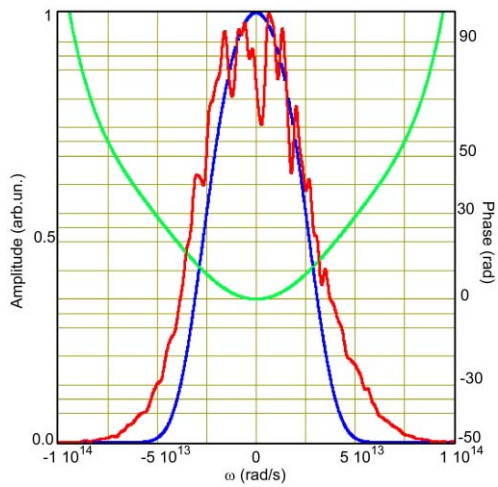

Figure 1: Blue curve : computed target spectral intensity; Red curve: experimental spectral intensity; Green curve: target spectral phase.

Spectral Interferometry

The crucial point in the laser pulse analysis is the retrieval of the spectral phase. Indeed, the spectrum intensity acquisition is not enough to characterise a non Fourier-limited pulse (i.e when its phase is not flat over all the spectral range). In our experiment, we want to measure the spectral phase on a single shot, simple, sensitive and extendable to UV range measurement. Spectral interferometry [21] between a reference pulse and the unknown pulse gives directly, through Fourier transform, access to the phase difference between these two pulses (cf. fig. 3). In our case, the reference pulse is the input pulse and the measurement confirms only the phase shaping. For complete phase shaping, the phase of the reference pulse is needed. As the reference pulse is close to Fourier transform pulse, any self-referenced measurement (SPIDER [19],

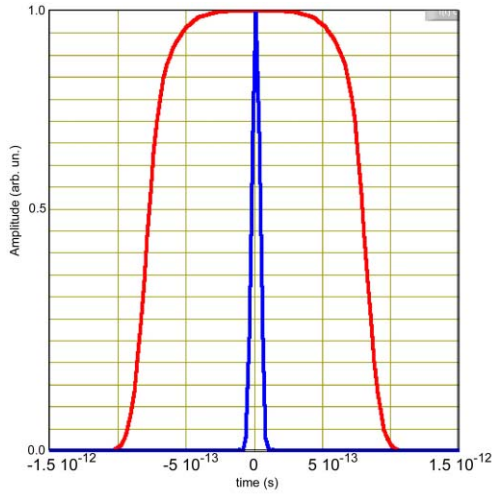

Figure 2: Blue curve : Fourier Limited laser pulse taking into account only the target spectral amplitude; Red curve: target temporal shape taking into account the target spectral phase.

FROG [20]...) is able to measure the residual phase of this pulse. This phase is then added to the measured one by spectral interferometry.

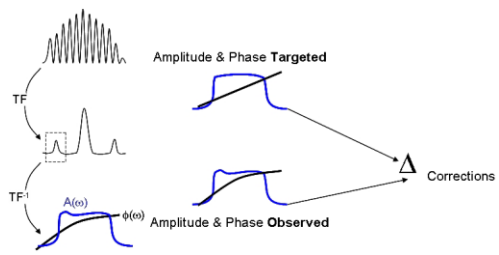

Figure 3: Layout of the Interferogram retrieving protocol.

Experimental Setup

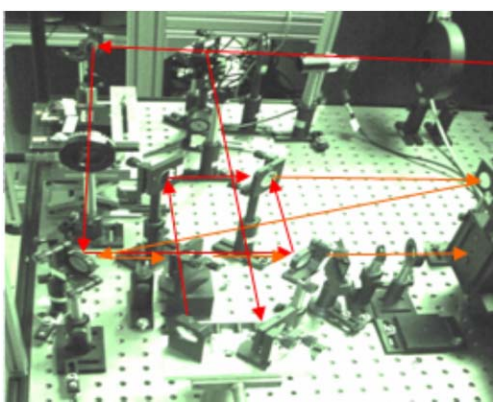

Figure 4: Experimental set-up for spectral interferometry. The red line shows the path for the two arms of the interferometer.

First studies are being performed on the laser facility LUCA (Tunable Ultra Short Laser) which delivers $50\ fs$ long, $800\ n$m laser pulses, with an energy of up to $100\ m$J, at a 20 Hz repetition rate. The pulse is split into the two arms of the interferometer (cf. fig. 4). On the first arm the laser passes through the acousto-optical device, thus undergoing a phase and/or amplitude manipulation. The second one travels through a delay line and it is then superposed on the first one. The two recombined beams enter the spectrometer where they interfere on the sensor. Single-shot interferograms are then collected on a personal computer. This latter also handles the transfer of the target or reference amplitude and phase files, as well as the associated reconstruction process. In practice the difficulty is to isolate the secondary lobe without information losses when the contrast is not very high. Also, to correctly recover the spectrum, a great care should be taken with the spectrometer calibration, and the signal processing to convert from the wavelength to the frequency space.

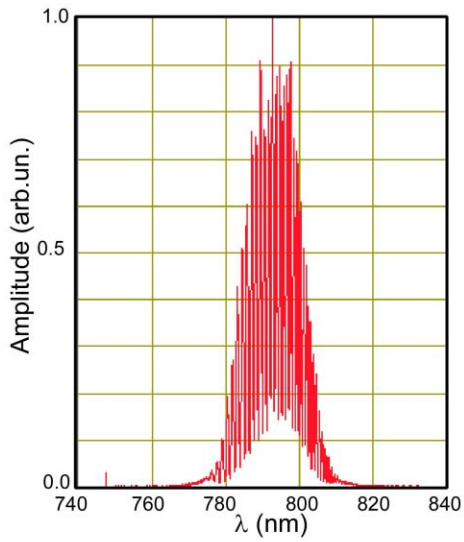

Figure 5: Typical interferogram acquired on the spectrometer.

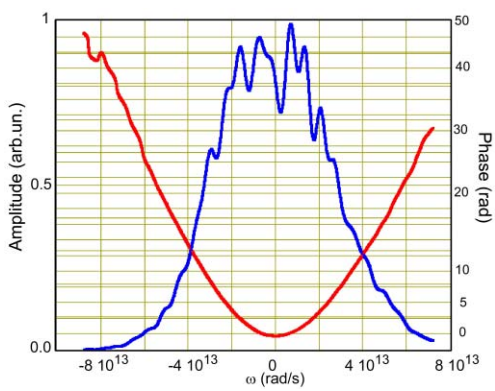

Figure 6: Retrieved Spectral Amplitude (blue curve) and Phase (red curve).

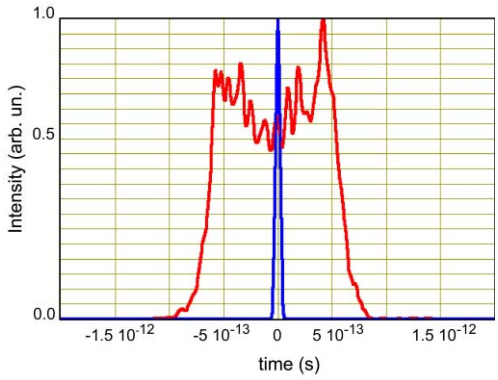

Figure 7: Temporal shape computed with IFT of the experimental data. Blue curve : Fourier Limited laser pulse taking into account only the target spectral amplitude; Red curve: with the target spectral phase.

PRELIMINARY RESULTS

The experiment has been implemented on the LUCA laser facility. Very low energy IR pulses ($\approx$ 10 μJ) have been processed up to now. The few obtained preliminary results are very encouraging. A first example for a rectangular laser shape has been performed. Fig. 6 shows the retrieved amplitude and spectral phase behaviours, this latter without the constant and first order terms, whereas in fig. 7 the computed temporal shape, obtained with only one iteration, highlights the difference between the gaussian shape pulse which is obtained when only the spectral amplitude is taken into account, and the rectangular shape, when the spectral phase is inserted. The obtained pulse has a duration of 1.3 ps $FWHM$, with leading and trailing edges lasting around 170 fs. In order to get rid of the observed modulation on the top of the pulse, a higher signal-to-noise ratio should be achieved, always in a single shot configuration.

CONCLUSIONS

The spectral interferometry setup has been implemented on LUCA. Future steps will deal with the improvement of the laser beam spatial profile, the completion of the corrective loop for several different longitudinal shapes, a big increase of the pulse energy injected in the Dazzler, up to 1 mJ before compression. Afterwards the grating compressor will be installed on the beamline, together with a third harmonic generation stage and a further prisms stretcher, in order to obtain shaped pulse in the UV at 266 nm, with an energy of several tens of μJ.

REFERENCES

[1] C. Pellegrini, "Design considerations for a SASE X-ray FEL", *Nucl. Inst. Meth.*, A475, (2001) 1-12.

[2] S. G. Biedron, S.V. Milton, H.P. Freund, "Modular approach to achieving the next-generation X-ray light source", *Nucl. Inst. Meth.*, A475, (2001) 401-406.

[3] F. Ciocci et al., "Design considerations on a high-power VUV FEL" *IEEE Jour. Quant. Elec.*,Vol. 31, No.7, July 1995, pp. 275-281.

[4] R. Bonifacio et al., "Generation of XUV light by resonant frequency tripling in a two-wiggler FEL amplifier"*Nucl. Inst. Meth.*, A293, (1990) pp.627-629.

[5] L. H. Yu et al., "High-Gain Harmonic-Generation Free-Electron Laser",*Science*, Vol. 289, 11 August 2000, pp.932-934.

[6] D. Garzella et al., "Using VUV high-order harmonics generated in gas as a seed for single pass FEL" *Nucl. Inst. Meth.* A528, August 2004, pp. 502-505.

[7] G. Lambert et al., "Seeding the FEL of the SCSS Phase 1 facility with the 13th laser harmonic of a Ti:Sa laser produced in Xe gas", *Proceedings FEL 2004*,Trieste, Italy, 29 August-3 September 2004, pp.155-158.

[8] L. Serafini and J.B. Rosenzweig, "Envelope analysis of intense relativistic quasilaminar beams in rf photoinjectors: A theory of emittance compensation", *Phys. Rev. E* 55 (1997) pp.7565-7590.

[9] M. Ferrario et al., An Ultra-High Brightness, High Duty Factor, Superconducting RF Photoinjector", *Proceedings of EPAC 2004*, Lucerne, June 2004, pp. 402-404.

[10] M. E. Couprie et al., "The ARC-EN-CIEL FEL proposal", these Proceedings.

[11] M. Ferrario et al., "Frontiers of RF Photoinjector", *Proceedings of PAC 2005*, Knoxville, USA, May 2005.

[12] C. Limborg-Deprey and P. R. Bolton, "Optimum electron distribution for space charge dominated beams in photoinjectors", *Nucl. Inst. Meth.* A557 (2006), p. 106-116.

[13] A. M. Weiner, "Femtosecond pulse shaping using spatial light modulators", *Rev.Scient. Inst.* Vol 71, No. 5, MAY 2000, pp. 1929-1960.

[14] F. Verluise et al., " Arbitrary Dispersion Control of ultrashort optical pulses with acoustic waves " *Jour. Opt. Soc. Am. B*, n 17 (2000), pp. 138-145.

[15] S. Cialdi and A. Boscolo,"A shaper for providing long laser target waveforms", *Nucl. Inst. Meth.*, A538, (2005) pp.1-7.

[16] C. Vicario et al.,"Preliminary results using an acousticooptic dispersive filter for laser pulse shaping", *SPARC Internal Note*, SPARC-LS-04/001, 15 January 2004.

[17] http://www-femtodrecam.cea.fr/

[18] I.A. Walmsley et al. "The role of dispersion in Ultrafast optics", *Rev.Scient. Inst.* Vol 72, No. 1, January 2001, pp. 1-29.

[19] C. Iaconis and I. A. Walmsley, Spectral phase Interferometry for direct electric-field reconstruction of ultrashort optical pulses, *Optics Letters* 23, pp. 792794 (1998).

[20] D.J. Kane and R. Trebino, "Characterization of arbitrary femtosecond pulses using frequency-resolved optical gating" *IEEE Jour. Quant. Elec.* 29 (2), February 1993 pp. 571-579.

[21] L. Lepetit et al., "Linear techniques of phase measurement by femtosecond spectral interferometry for applications in spectroscopy" *Opt. Lett.*, Vol. 12, No. 12, December 1995, pp. 2467-2474 and references therein.

CHARACTERISATION OF MICROPHONICS IN HOBICAT *

Oliver Kugeler, Wolfgang Anders, Jens Knobloch, Axel Neumann, Bessy GmbH, Berlin, Germany.

Abstract

The HoBiCaT test-facility at BESSY, which is designed for cryogenic testing of superconducting TESLA units has been equipped with a 9-cell TESLA-type cavity. Mechanical vibrations in the cryostat result in microphonic detuning of the cavity resonance. These microphonics have been characterized, and their sources analyzed, including the impact of operating conditions such as LHe pressure, cavity field and heater power. Furthermore, the mechanical transfer functions needed for the eventual compensation of the microphonics have been recorded.

INTRODUCTION

For CW operation of a superconducting, TESLA-type cavity microphonics represent the largest disturbance of the resonant frequency. In particular at a small bandwidth $\Delta f = \omega/Q_L$, according to the equation

$$\mathrm{P} \propto 1 + \frac{(\delta f)^2}{(\Delta f)^2} \qquad (1)$$

the microphonics δf lead to a significant increase of the generator power P, which is required to maintain a constant cavity field. Therefore it is highly desirable to minimize the microphonics. Measurements characterizing the microphonics and their impact on the cavity operation are presented below. The perspectives on possible countermeasures are described elsewhere [1].

MICROPHONICS MEASUREMENTS

Microphonics have been recorded in two different ways. In a first method, the RF-feedback signal, see Figure 1, is recorded over time. This is preferably done in open loop configuration, because obtaining a calibration factor is more straightforward here, than in closed loop configuration. A second method utilizes the sensor-actuator design of the piezo tuner to record the induced piezoelectric voltage over time. In this design, two high-voltage piezos are attached to the tuner, thus piezoelectric forces can be exercised on the cavity and measured simultaneously. The latter is only an indirect method, as the mechanical influence from cavity and tank on the frequency response does not necessarily lead to a linear relationship between cavity- and piezo position. The results presented here were solely obtained from the RF-feedback signal.

* Work funded by the European Commission in the Sixth Framework Program, contract No. 011935 EUROFEL.

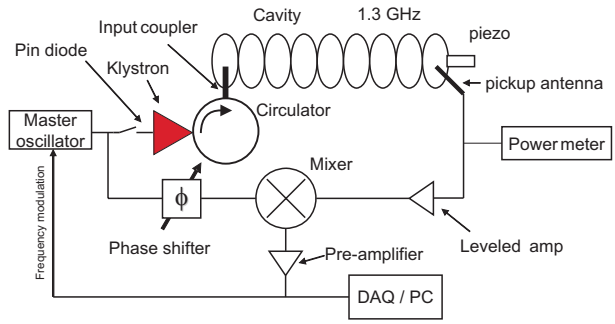

Figure 1: Phase-lock-loop used for cavity RF-measurements.

Calibration of RF-feedback signal

In order to interpret the voltage value from the RF-feedback in terms of a detuning frequency, a calibration factor has been determined. This was done by mechanically detuning the cavity with the piezo stack, which exhibited a detuning behavior of $\Delta\mathrm{f}/\Delta\mathrm{V}$ = 1.131 Hz/V. By varying the piezo voltage the cavity resonance was scanned open loop at a fixed master oscillator frequency over several bandwidths. The RF-feedback value varied by 0.84 V. Hence, all voltages could be easily interpreted as frequencies. This procedure is only possible because a leveled amplification is applied to the cavity pickup-signal. This ensures that the mixer output signal is solely dependent on the phase difference between master oscillator and cavity. Note that the frequency stability of the Rohde & Schwartz master oscillator at 1.3 GHz is better than 0.1 Hz.

Measurements at cryogenic temperatures

Microphonics have been measured at cryogenic temperatures. In Figure 2 the Fourier transform of a 30 second long measurement of the RF-feedback signal sampled at 5 kHz is depicted. An immediately identifiable feature is the constant signal of a turbo vacuum pump (18000 rpm) at 300 Hz. Furthermore, prominent features occur at 41 Hz, 90 Hz, and 170 Hz and are resonances of the cavity-tank-tuner system. The feature at 30 Hz is a so far unidentified source not related to any of the mechanical cavity resonances. It was further investigated whether the measured microphonics would change with the quality factor, or the bandwidth, respectively. For that purpose, the quality factor was varied over a wide range (a) by changing the coupler position and (b) by using a three stub tuner.

In Figure 3 the integrated microphonics frequency spectra taken at different values of $\mathrm{Q_L}$ are plotted. It can be seen that in general the RMS value of the microphonics in-

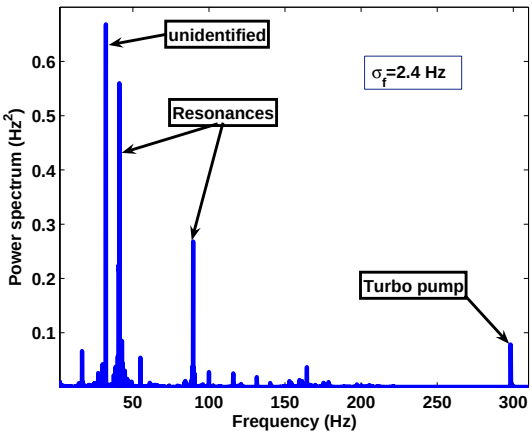

Figure 2: Microphonics in cavity measured open loop at 1.8 K.

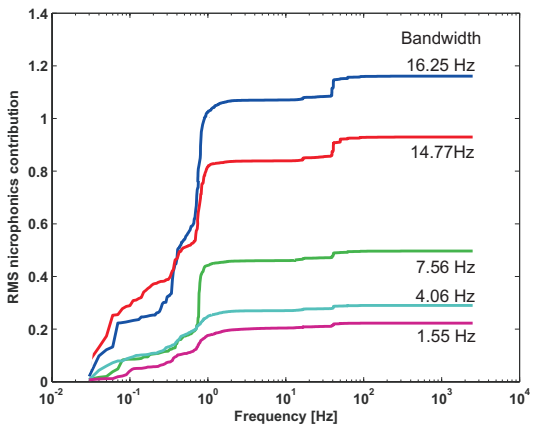

Figure 3: Integrated microphonics frequency spectra at different cavity bandwidths. The main contributions to the overall RMS value of the microphonics come from low microphonics frequencies (< 1 Hz). Microphonics increase with higher cavity bandwiths.

creases with the bandwidth, or in other words the cavity becomes less susceptible towards microphonics with increasing Q_L. It can also be seen that the largest contributions to the RMS-microphonics are at low frequencies.

Influence of cryogenics on the microphonics

The heavy machinery in our cryogenic system consists of a Sogevac SV200 Leybold pump and two pairs of Leybold SV1200 and RA7001 SO pumps. They operate at 24 Hz, 11.66 Hz, and 50 Hz, respectively. Note that these mechanical vibrations can not be found in the microphonics spectra which was also confirmed by slightly varying the pumping frequencies. This observation suggests that the decoupling of the pumps from the HoBiCaT facility is sufficient.

The main contribution to the microphonics was found to be

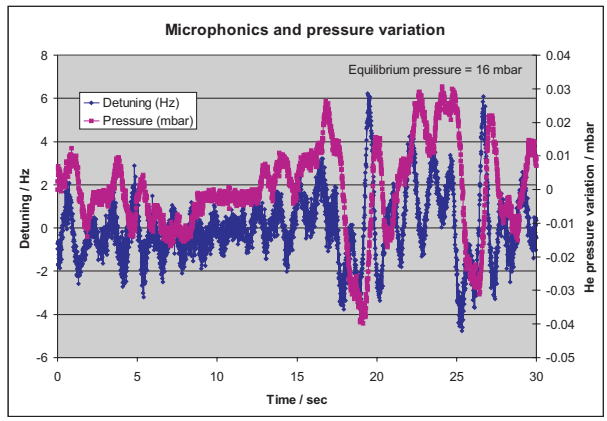

Figure 4: Microphonics and He-pressure difference.

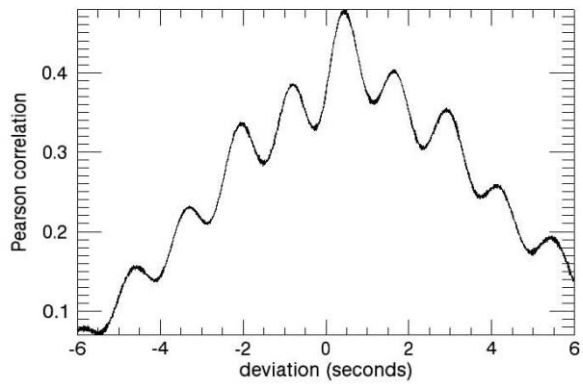

Figure 5: Pearson correlation between Helium bath pressure and microphonic detuning The 0.4 seconds offset is due to the preset sampling time of the pressure sensor. The occurrence of side maxima suggests, that there is some periodicity within the microphonics.

from within the cooling medium itself. A change in Helium pressure (measured with a Rosemount sensor) was measured to lead to a detuning of the resonant frequency of 55 Hz/mbar. Figure 4 shows the microphonics recorded over a period of 30 seconds in correlation with the He-bath pressure. In Figure 5 the Pearson correlation between the two signals is plotted. The maximum correlation occurs at an offset of 400 ms, which is due to the sampling time of the pressure sensor. This observation suggests, that a significant portion of the microphonics can be compensated with a feed forward system, provided fast and accurate pressure sensors are used. The microphonics created by the Helium heater, which is part of the cryogenic system and supports the Joule-Thomsen expansion of the cooling medium, were also investigated. In Figure 6 microphonics have been recorded as a direct fft from the RF feedback signal at different values of the heater power. It can be seen that different heater powers create significantly different microphonics spectra, suggesting that the heater itself is a source of microphonics.

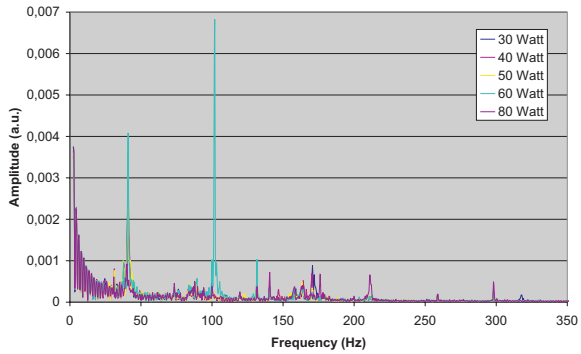

Figure 6: Influence of the heater power on the microphonics spectra

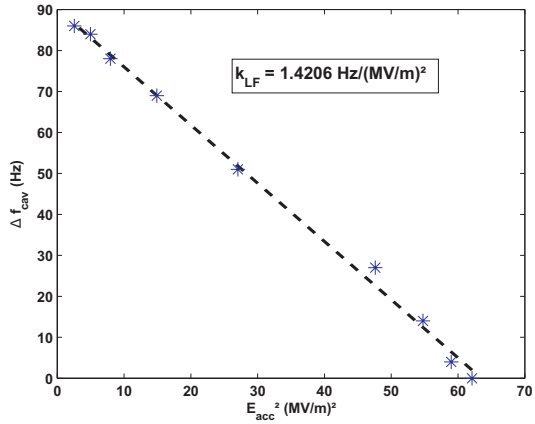

Figure 8: Lorentz Force Detuning vs. field gradient

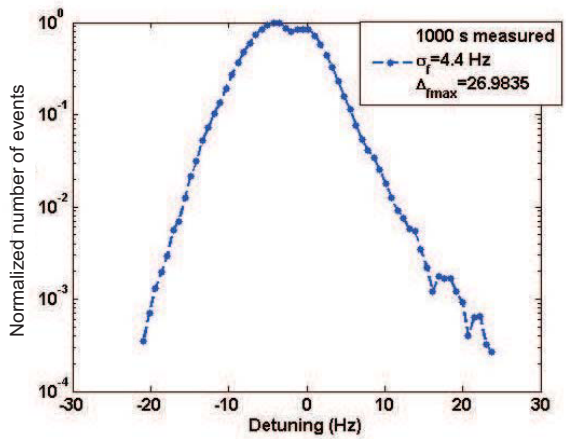

Figure 7: Long-time microphonics measurement.

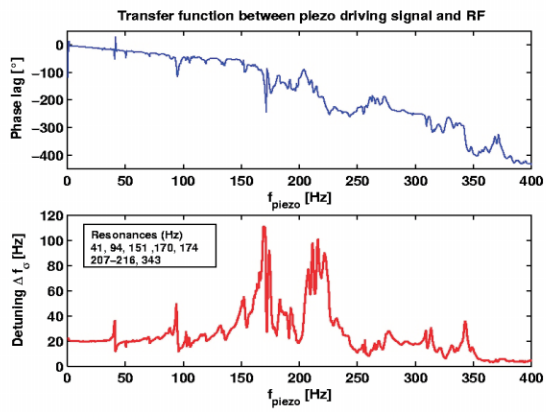

Figure 9: Transfer function of the cavity-tank-tuner system recorded over a frequency range of 0-400 Hz.

Long-time measurements of microphonics

As the RF-system has to be laid out to deal with the maximum possible microphonics detuning, several long-time microphonics measurements have been performed. From these measurements the probability for a certain detuning within a given time period could be determined. The measurement presented in Figure 7 is a histogram of measured detuning values. It was taken over 1000 seconds and gives a maximum detuning frequency of 26.8 Hz and a rms detuning of 4.4 Hz. A 24 hours+ measurement is planned, but has so far been postponed due to long time stability issues of the klystron.

Lorentz force detuning

The static response of our setup to Lorentz force detuning has also been measured. We have obtained a value of $k_{LF} = 1.42$ Hz/(MV/m)^2, see Figure 8, which is within the range of values of 1–2 Hz/(MV/m)^2 gained at DESY [2].

Transfer function

The reaction of the cavity resonance frequency on microphonic vibrations is determined by the mechanical eigenmodes of the tank-tuner-cavity system. Such Q-modes are measured via the transfer function. Here, the piezos are used to create sinusoidal vibration at distinct frequencies over a certain frequency range. The RF-feedback signal is recorded over time, yielding amplitude and phase information of the mechanical response, see Figure 9. Such modes arouse from transverse and longitudinal vibrations with respect to the cavity axis. Note, that only longitudinal symmetric stretch modes can be excited with the present piezo setup and thus only such modes can eventually be compensated. Numerical simulations by Luong et al. [3] suggest that these modes make up for the largest contribution to the detuning of the cavity.

Influence of passive cavity stabilizers

Titanium fixtures that can be attached between the cavity's stiffening rings and the helium tank have been developed by FZ Rossendorf and manufactured at AC-

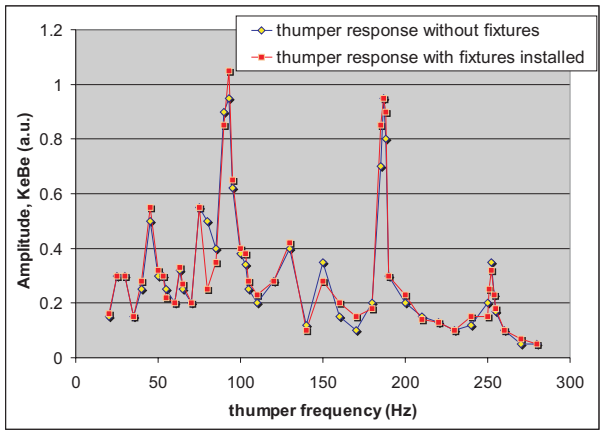

Figure 10: Integrated frequency response signal of cavity mounted in a He-tank (a) with and (b) without fixtures attached.

CEL. While they were originally intended for earthquake-protection, we have investigated to what extent they can dampen mechanical vibrations or shift resonances towards higher frequencies, and thus reduce the impact of microphonics. Room-temperature measurements were done at ACCEL with such a cavity. For the experiment, an acoustic thumper, operating between 30 Hz and 300 Hz, was attached to one end of the cavity (perpendicular to the cavity axis). The response was measured with KeBe inductive velocity meters attached at different positions of the tank. It was found that the fixtures contributed only marginally to a decrease of the microphonics response signal. As can be seen from Figure 10 the response function with and without fixtures is practically identical. The only significant deviation occurs at 80 Hz, but no significant microphonics were measured in HoBiCaT at this frequency.

OUTLOOK

The next step after characterization of microphonics is to take countermeasures to compensate them. Such a compensation does not have to be complete as even small improvements lower the required RF-power significantly. The correlation between He-pressure and low frequency microphonics suggests, that a feed-forward algorithm might be feasible. Such work is underway and will be presented soon. Also we are investigating adaptive feed forward compensation of higher frequency microphonics.

REFERENCES

[1] A. Neumann, et al., “Characterization of a Piezo-based Microphonics Compensation System at HoBiCaT”, EPAC’06, Edinburgh.

[2] H. Gassot, “Mechanical Stability Of The RF Superconducting Cavities”, Proceedings of EPAC 2002, Paris, 2002.

[3] M. Luong, et al., “Analysis of microphonic disturbances and simulation for feedback compensation”, Proceedings of EPAC’06, Edinburgh.

A HIGH AVERAGE POWER RF PHOTOINJECTOR GUN CAVITY DEVELOPED FOR THE BESSY SOFT X-RAY FEL*

F. Marhauser#, M. Dirsat, A. Meseck, D. Richter, V. Dürr, E. Weihreter,
BESSY, 12489 Berlin, Germany
G. Asova, J. Bähr, H.J. Grabosch, S. Khodyachykh, S. Korepanov, M. Krasilnikov, A. Oppelt,
B. Petrosyan, L. Staykov, F. Stephan, F. Tonisch, DESY, 15738 Zeuthen, Germany
O. Kalekin, Humboldt University, 12489 Berlin, Germany
J. Roensch, University of Hamburg, 22761 Hamburg, Germany.

Abstract

Based on the 1.3 GHz normal conducting RF photogun installed at the Free Electron Laser in Hamburg (FLASH) a new RF gun prototype with an optimized cooling layout has been developed at BESSY with the objective to operate in the 100 kW average power regime. This would significantly enhance the capability of present L-Band guns towards operation at higher accelerating fields or/and duty factors. High power RF-conditioning at the Photo Injector Test Facility at DESY in Zeuthen (PITZ) has recently been performed achieving 47 kW average power and an electric peak field of 53 MV/m in maximum respectively, so far only limited by power constraints of the RF-system. In this paper the RF-conditioning results and relevant simulation results are discussed. Tracking studies for the photoinjector including two linac modules and a subharmonic cavity section are presented.

INTRODUCTION

RF photoinjectors bear the potential to generate electron pulses of extraordinary high peak brightness suitable for future FELs and linear colliders. For the proposed BESSY Soft X-Ray FEL ("BESSY FEL") [1] with its superconducting CW driver linac a superconducting RF (SRF) gun would be the ideal electron source to deliver most flexible pulse pattern considering the manifold demands of experimental users. Superconducting guns are therefore a very active research area. For example, FZR, DESY, MBI and BESSY are collaborating to commission an SRF 1.3 GHz 3½-cell photoinjector gun cavity at FZR in 2007. Initially, this gun will accelerate 1 nC, but schemes have been identified and investigated that are capable of achieving slice emittances in the order of 1.5 π mm mrad at 2.5 nC bunch charge [2].

At present, though, normal conducting (NC) photoguns are more established and will therefore be used to commission the BESSY FEL. Still, a very high rep rate (1 kHz) is planned to approach CW operation. Later this NC gun can be replaced by an SRF gun. In particular much progress has been made by the PITZ collaboration which has developed a series of 1.3 GHz NC guns (1 ½ cells) characterized at the PITZ facility [3]. So far a minimum projected emittance of 1.6 π mm mrad (geometrical average of horizontal and vertical emittance) for a bunch charge of 1 nC could be demonstrated [4]. This system has also been operational at FLASH. Improvements at PITZ are expected by further optimizing the transverse and temporal profile of the photocathode laser, increasing the electric field at the photocathode to E_c = 60 MV/m and by utilizing a booster cavity, whereby the emittance conversation principle will be studied [5]. Beam operation hitherto was performed typically with E_c = 40-45 MV/m and a duty factor of 0.9 % (10 Hz RF pulse repetition rate) corresponding to an average power in the range of 30 kW. The European XFEL [6] and the proposed BESSY FEL however require even higher values to be achieved as listed in Table 1.

Table 1: Target parameters of NC RF guns as proposed for the European XFEL and the BESSY FEL at commissioning phase

Parameter	European XFEL	BESSY FEL
Frequency / GHz	1.3	
Number of cells (copper)	1½	
Bunch charge / nC	1	2.5
Single bunch rep. rate / MHz	5	1/3
RF pulse rep. rate / Hz	10	1000
Peak field / (MV/m)	60	40
Peak power* / MW	~6.5	~3
Beam pulse length** / μs	650 (max.)	6
Duty factor / %	~0.67	~2.5
Average power / kW	~44	~75
Beam parameters at undulator		
Trans. norm. slice emittance / π mm mrad	1.4	1.5
Max. beam energy / GeV	20	2.3

* depending on Q_0 (~23000), ** excluding RF rise/fall time (~20 μs)

Gun cavity thermal drifts as a source of severe phase and amplitude jitters may then become more apparent. Despite the progress of RF field stability control [7], one challenging task remains the mitigation of these drifts. Thus elaborate cooling concepts for the gun have to be

* This work has partly been supported by the European Community, contract numbers RII3-CT-2004-506008 (IA-SFS) and 011935 (EUROFEL) and by the "Impuls- und Venetzungsfonds" of the Helmholtz Association, contract number VH-FZ-005
# corresponding author: marhauser@bessy.de

considered. With respect to this issue a high average power 1 ½-cell RF gun cavity with an optimized cooling layout has been developed at BESSY ("BESSY Gun") as described below. A prototype of the cavity has been produced and thermal tests without photoemitted electrons were performed at PITZ. This gun also served as the basis for new beam dynamics simulations.

BESSY NC RF GUN CAVITY

A picture of the BESSY Gun and its outer water connections is shown in Fig. 1 (left), whereas the CAD model (right) reveals the inner cooling circuits. To provide sufficient water to the cavity a total number of 43 water inlets and outlets have been implemented with each water circuit separately addressable. Thus a sufficiently high water volume flow can be delivered to the cavity body and the water temperature rise within each meander can be kept rather low. Still emphasis has been placed on a simple conceptual design using drilled water holes of same dimensions throughout except in the iris aperture. Further details on the technical layout and cooling scheme can be found in [8].

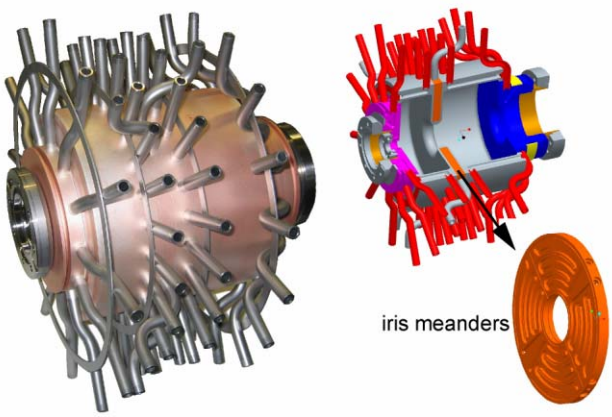

Figure 1: The copper 1 ½-cell BESSY Gun (photo left) with the outer water connections and the corresponding CAD model (right) revealing the inner water circuits.

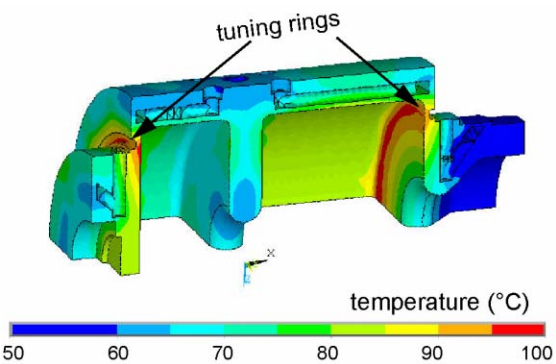

Figure 2: Temperature distribution in the BESSY Gun calculated at P_{ave} = 75 kW with T_{in} = 42°C for a quarter symmetric ANSYS model.

The cooling scheme was optimized with the help of thermal simulations using the FEA Code ANSYS [10]. Hence the BESSY Gun exhibits moderate temperatures (< 100°C) at an average power of P_{ave} = 75 kW, i.e. the nominal operation power for the BESSY FEL. As illustrated in Fig. 2 this has been achieved for a reasonable water inlet temperature of T_{in} = 42°C. Circular notches at each endplate ('tuning rings') have been implemented to ease a possible tuning effort. The reduced cooling efficiency at the tuning rings is taken into account for this prototype yielding the maximum local temperatures. Mechanical stresses however are not an issue [10].

As a feature the BESSY Gun was equipped with a small pickup port (Ø = 8mm) in the full cell implementing an antenna, loosely coupled to produce only a negligible field distortion. The antenna amplitude and phase information is beneficial for RF field stability control, critical for the overall jitter stability of the electron beam. Else - as practised at FLASH - the cavity field has to be artificially determined from the forward and reflected power signals of a directional waveguide coupler [7].

RF CONDITIONING

The first pulsed high power RF-conditioning tests of the BESSY Gun have been completed in May 2006 in the frame of the PITZ-collaboration. The conditioning test stand at PITZ is shown in Fig. 3. A 10 MW multi-beam klystron (MBK) was used to feed in the RF power to the gun via a standard DESY axially symmetric coupler. Due to the limited power capability of state-of-the-art RF vacuum windows the MBK output power is distributed into two separate WR650 waveguide arms. A T-combiner with two RF windows was flanged to the input coupler to add both RF-waves.

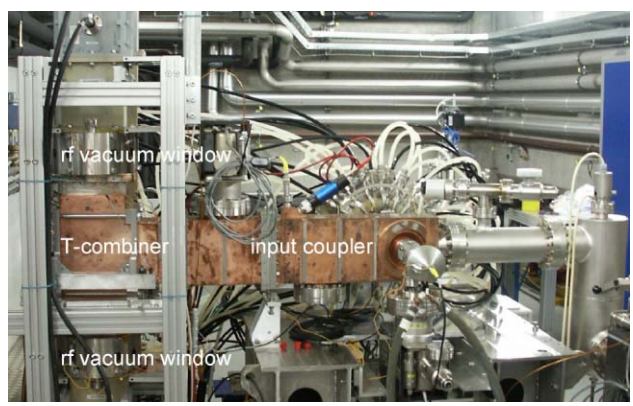

Figure 3: BESSY Gun on the conditioning test stand at PITZ. For conditioning no solenoids were installed.

After only 90 hours conditioning time -with a cavity vacuum interlock threshold of 10^{-7} mbar- a peak power of P_{peak} = 2.9 MW at t_{RF} = 100 µs was reached (P_{ave} = 2.9 kW) corresponding to a peak field of E_c = 40 MV/m as required for the BESSY FEL. It should

be noted, that prior to the installation at PITZ the integrity of the gun was checked at BESSY operating several days in CW mode at 10 kW, which might have been beneficial to achieve this rather rapid progress. Since the repetition rate of the low level RF-system at PITZ is limited to f_{rep} = 10 Hz, the average power could only be increased by operating with both the peak power and the pulse length far beyond the desired BESSY FEL specifications (see Table 1). This "thermal" conditioning was time consuming, particularly because of sparking in the waveguide arms of the klystron at peak power levels above 3 MW. Despite the constraints of the RF-system, conditioning could be carried out successfully to a maximum operable peak power of P_{peak} = 5 MW with t_{RF} = 540 µs corresponding to an electric field of E_c = 53 MV/m. The maximum average power of P_{ave} = 47 kW was reached at the maximum pulse length of t_{RF} = 1 ms with P_{peak} = 4.7 MW (E_c = 51 MV/m). Higher power levels and longer pulse lengths could not be reached because of operational limitations of the RF-system. However up to 47 kW average power no thermal or technical limitations attributable to the gun were encountered. The main RF-conditioning results are listed in Table 2.

Table 2: BESSY Gun RF-conditioning results at PITZ

Parameter	Achieved at limit of RF system	Desired	Unit
P_{ave}	47	75	kW
P_{peak}	4.7*	3	MW
E_c	51*	40	MV/m
t_{RF}	1000	25	µs
f_{rep}	10	1000	Hz
d.f.	1	2.5	%

* max. P_{peak} = 5 MW corresponding to E_c = 53 MV/m at t_{RF} = 540 µs

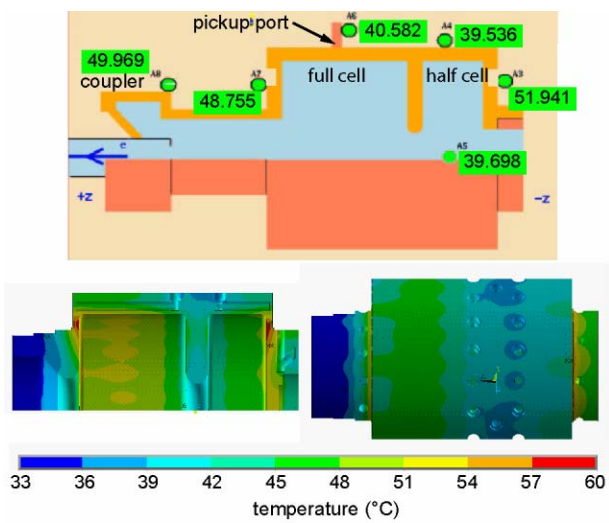

Figure 4: Measured (top) and simulated (bottom) gun temperatures when operating at P_{ave} = 40 kW and T_{in} = 27°C (P_{peak} = 4 MW, f_{rep} = 10 Hz, t_{RF} = 1 ms).

Fig. 4 (top) depicts a screen shot of the measured gun cavity temperatures using external PT100 sensors at distinctive locations (green dots). Here the temperatures are shown when operating at a thermal load of P_{ave} = 40 kW with an inlet water temperature of T_{in} = 27°C. At the bottom corresponding numerical results using ANSYS are plotted in good agreement with the monitored data. This is also true for the hot spots located at the tuning rings. At the antenna port no significant heat enhancement has been produced. The antenna port has been omitted in the calculation due to mesh size constraints.

To further check the reliability of numerical data, the frequency shift Δf caused by thermal deformation of the gun cavity has been measured at a constant inlet water temperature of 27°C when increasing the average power. Hereby the resonance was kept adjusting the master oscillator frequency to gain a reflected power below 1%. To evaluate Δf the resonance frequency at room temperature is taken as reference. In Fig. 5 the measured data are plotted as compared with numerical results. The latter have been computed by transferring the thermally deformed cavity profile given by ANSYS to Superfish [11]. This method has been extensively described in [12]. A linear drift in the order of Δf ~ -10 kHz/kW over the observed power regime at T_{in} = 27°C was obtained, consistent with the simulations.

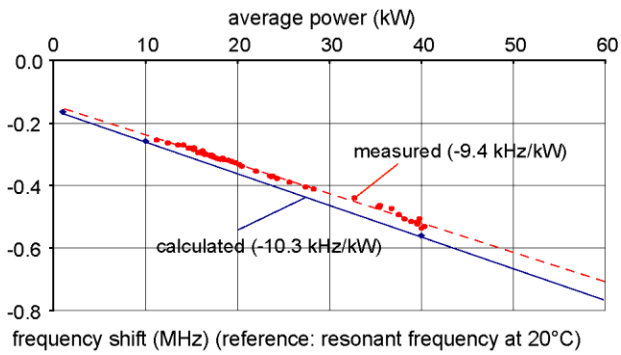

Figure 5: Thermal frequency drift in dependence on the average power as measured (red dots, f_{rep} = 10 Hz, t_{RF} = 1 ms) and calculated (blue line) both at T_{in} = 27°C.

BEAM DYNAMICS

Former beam dynamical studies using the accelerating field of the BESSY Gun as an input revealed that the photoinjector is able to deliver the required transverse slice emittances [10]. Further studies employing a multiparameter optimization with ASTRA [13] have been performed, the results being depicted in Figs. 6 and 7. Here 100000 macro particles have been tracked through the first two cryogenic linac modules comprising eight standard 1.3 GHz 9-cell TESLA-cavities. An intermediate section with quadrupoles as well as eight 9-cell 3.9 GHz cavities (under investigation at FERMILAB [14]) have

been implemented to linearize the longitudinal phase space serving the needs of the subsequent first bunch compressor. A thermal energy of 0.55 eV for electrons emitted from a Cs_2Te photocathode illuminated by a UV laser (262 nm) has been taken into account. For the laser a temporal profile of 38 ps (flat top) with 4 ps rise/fall time and a spot size of 3.3 mm have been chosen. Furthermore a peak field of E_c = 40 MV/m has been presumed, which already has been exceeded by the BESSY Gun during the high power tests. As mentioned above this value however is rather constrained by thermal considerations.

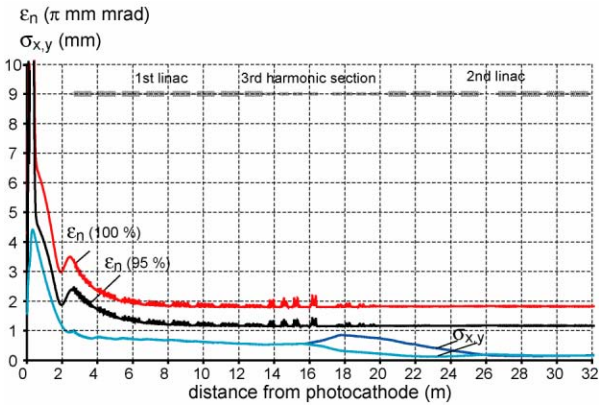

Figure 6: Evolution of the normalized transverse rms emittance ε_n (100% and 95% core emittance) and beam size $\sigma_{x,y}$ for a bunch charge of 2.5 nC up to the exit of the 2nd linac module.

For a bunch charge of 2.5 nC the normalized projected transverse emittance "frozen" at the exit of the second linac module (E_{kin} = 223 MeV) is 1.8 π mm mrad (1.2 π mm mrad for the 95% core emittance). At this point the slice emittance averaged over the whole bunch amounts to 1.5 π mm mrad fulfilling the design goal of the BESSY FEL.

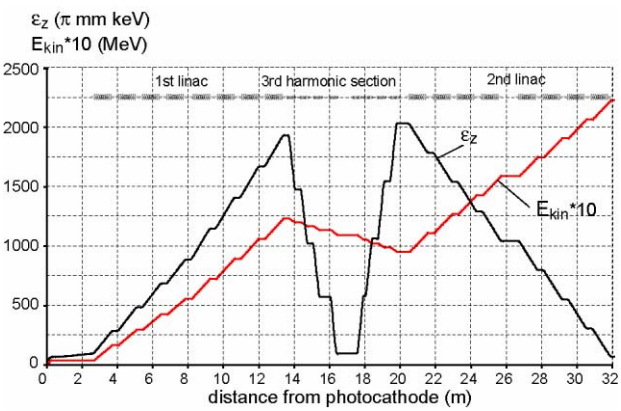

Figure 7: Evolution of the longitudinal rms emittance ε_z and average beam energy E_{kin} for a bunch charge of 2.5 nC up to the exit of the 2nd linac module.

The rms bunch length is 3.5 mm and a projected longitudinal rms emittance of 65 π keV mm has been obtained due to phase space linearization with the subharmonic cavity section (Fig. 7).

CONCLUSION

A high average power RF gun prototype developed at BESSY has been high power conditioned at the Photo Injector Test Facility at DESY in Zeuthen. The gun was tested up to an average power of 47 kW so far only limited by the maximum operable power of the RF-system. Similarly, the maximum electric field achieved at the cathode was 53 MV/m so far. All observations at present indicate that the gun is thermally stable at the desired power level of 75 kW or beyond. This is confirmed by corresponding thermal calculations. Operation of this prototype with photoemitted beams was not planned. However, new numerical tracking studies demonstrate that the gun is capable of producing the beam quality required for the BESSY FEL.

REFERENCES

[1] D. Krämer et al. (editors), "The BESSY Soft X-Ray Free Electron Laser", Technical Design Report, ISBN 3-9809534-0-8, BESSY, Berlin, 2004.
[2] D. Janssen at. al., "Progress of the Rossendorf SRF Gun Project", Proc. of the 2006 Europ. Acc. Conf., Edinburgh, Scotland, 2469.
[3] A. Oppelt et. al., "Tuning, Conditioning, and Dark Current Measurements of a New Gun Cavity at PITZ", these proceedings.
[4] F. Stephan, "Status and Perspectives of Photo Injector Developments for High Brightness Beams", Conf. on the Physics and Applications of High Brightness Beams, Erice, Italy, 2005.
[5] A. Oppelt et. al.,"Status of the PITZ Facility Upgrade", Proc. of the 2006 Lin. Acc. Conf., Knoxville, USA.
[6] M. Altarelli et al. (editors.), "The European X-Ray Free Electron Laser", Technical Design Report, ISBN 3-935702-17-5, DESY, Hamburg, July 2006.
[7] E. Vogel at. al.," FPGA Based RF Field Control at the Photo Cathode RF Gun of the DESY Vacuum Ultraviolet Free Electron Laser", Proc. of the 2006 Europ. Acc. Conf., Edinburgh, Scotland, 1456.
[8] F. Marhauser, "High Power Tests of a High Duty Cycle, High Repetition Rate RF Photoinjector Gun for the BESSY FEL", Proc. of the 2006 Europ. Acc. Conf., Edinburgh, Scotland, 68.
[9] www.ansys.com.
[10] F. Marhauser, "Photoinjector Studies for the BESSY Soft X-Ray FEL", Proc. of the 2004 Europ. Acc. Conf., Lucerne, Switzerland, 315.
[11] K. Halbach, R.F. Holsinger, Poisson Superfish, Particle Accelerators 7 (1976), page 213, distributed by the Los Alamos Accelerator Code Group (LAACG).
[12] F. Marhauser, "Finite Element Analyses for Photoinjector Gun Cavities", DESY Hamburg, January 2006, TESLA FEL-Report 2006-02.
[13] K. Flöttmann, http://www.desy.de/~mpyflo/.
[14] N. Solyak et. al, „The Progress in Developing Super-conducting Third Harmonic Cavities", Proc. of the 2006 Europ. Acc. Conf., Edinburgh, Scotland, 804.

PHOTOCATHODE LASER FOR THE SUPERCONDUCTING PHOTO INJECTOR AT THE FORSCHUNGSZENTRUM ROSSENDORF

Ingo Will#, Guido Klemz, Max-Born-Institute Berlin, Germany
Friedrich Staufenbiel, Jochen Teichert, Forschungszentrum Rossendorf, Germany.

Abstract

We report on the design of the photocathode laser for a superconducting RF gun, which is presently under development at the Forschungszentrum (FZ) Rossendorf. This laser is foreseen to drive the RF gun in CW mode with up to 1 nC bunch charge. It generates pulses of 12...14 ps duration with 500 kHz repetition rate and 0.8 µJ pulse energy at 263 nm wavelength. This should provide sufficient pulse energy for generation of bunches with 1 nC charge using caesium telluride photocathodes. Due to two active modelockers in the laser oscillator, the latter operates in tight synchronism to the RF master oscillator of the linac.

The laser consists of a short-pulse oscillator, a pulse picking Pockels cell, a regenerative amplifier and a wavelength conversion unit. The latter converts the infrared laser radiation to the ultra-violet (UV). This unit turns out to be a particularly critical element of such a photocathode laser driving a RF gun in CW mode.

INTRODUCTION

Photo injectors within RF guns are important for FELs, since they provide an efficient means for generating high-density electron bunches with low emittance. Most of the existing photo injectors are operated in pulsed or in burst mode.

At the FZ Rossendorf a superconducting RF gun is being developed [1], which needs an appropriate laser for illumination of the caesium telluride photocathode. This laser should deliver pulses of 500 kHz repetition rate at a wavelength within the range of 260 to 270 nm. The desired bunch charge of 1 nC demands a UV pulse energy in the order of 0.5 to 1 µJ. The present paper describes a first setup for a suitable laser system.

LAYOUT OF THE LASER

Fig. 1 shows the general scheme of the laser system, which consists of the following main building blocks:

- the laser oscillator,
- a pulse picker,
- a regenerative amplifier,
- a wavelength conversion stage.

The laser oscillator generates the initial picosecond seed pulses. Its Nd:YLF laser rod is pumped by two fiber-coupled laser diodes of 805 nm wavelength. Modelocking for generation of short picosecond pulses is accomplished by two active modelockers. One of them is a standard acousto-optic modelocker driven with a 27.08 MHz RF signal, while the second one is an electro-optical phase modulator for 1300 MHz. A detailed description how to operate several modelockers in a single cavity can be found in [2] and the references therein.

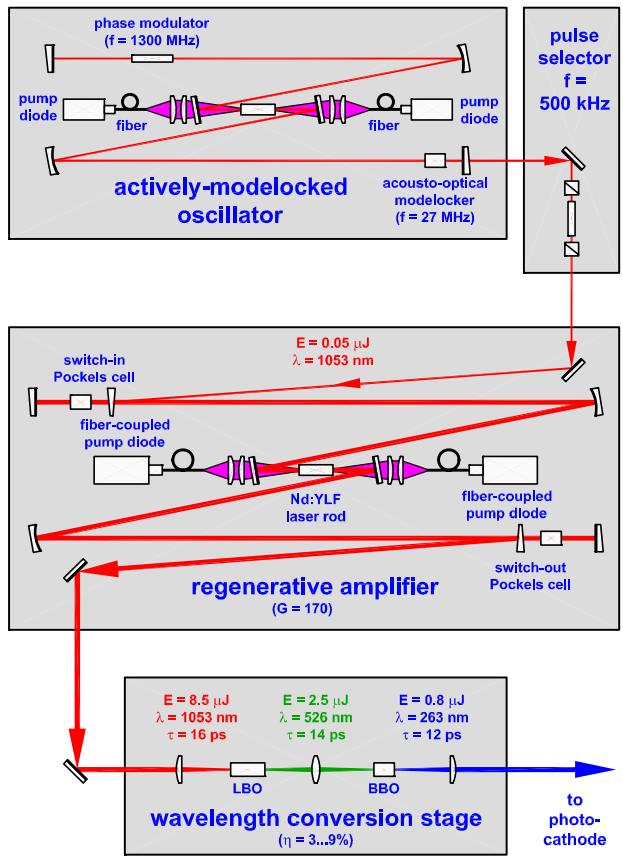

Figure 1: Optical scheme of the present photocathode laser.

The oscillator generates a CW pulse train of 54.16 MHz repetition rate and provides a single-pulse energy of 0.05 µJ. Since the signals for the active modelockers are derived from the electronic RF master oscillator of the gun, the laser pulses are synchronized with an accuracy of about 1 ps.

A subsequent electro-optic pulse selector reduces the high repetition rate of the pulses from the oscillator to the desired value of 500 kHz. This pulse train is further amplified by a regenerative amplifier (regen). The regen is based on a folded resonator with 25 ns round-trip time.

#will@mbi-berlin.de

In addition to the diode-pumped Nd:YLF laser rod, it contains two BBO Pockels cells. The first one switches the laser pulse from the oscillator into the cavity of the regen. Subsequently, this pulse performs 14 round trips in the resonator and is thereby amplified to an energy of 8.5 µJ.

THE WAVELENGTH CONVERTER

After switching the amplified pulses out of the resonator with the second Pockels cell, they are directed towards the wavelength conversion stage. This stage contains two consecutive nonlinear frequency doubling crystals that convert the infrared laser pulses of 1053 nm wavelength to the ultra-violet (263 nm wavelength).

The general scheme of this conversion unit is similar to the one used in the photocathode lasers of FLASH and PITZ. At first, a 12 mm long LBO crystal converts the pulses to green light. A further 8 mm long BBO crystal generates from this the UV output pulses

It turns out that both, the energy of the generated UV pulses as well as the profile of the UV beam depend in a highly sensitive way on the size of the beam waist in the BBO crystal. Tab. 1 as well as Fig. 1 show the results of appropriate measurements done for four different diameters of the beam in this crystal. Although the highest output energy of 0.83 µJ is achieved for the strongest focusing down to a diameter of 260 µm, this leads to a non-circular beam profile.

On the other hand, the most homogeneous output beam that largely maintains the original circular cross section is obtained when the beam diameter in the BBO crystal is larger. The optimum in this respect amounts to 703 µm. Unfortunately, this is accompanied by a drop of the laser intensity in that crystals by a factor of two, and only a smaller portion of the green light is converted to the UV. Since the conversion process is now operated far from saturation, the energy stability becomes much worse and we typically obtain a pulse energy between 2 and 4 µJ.

Table 1: Dependence of the resulting UV pulse energy on the focussing condition at the BBO crystal

Diameter of the beam waist [µm] in the BBO crystal	Measured output energy [µJ] of the UV pulses
260	0.83
352	0.71
527	0.49
703	0.45

Although the average power of the CW laser in comparison to the pulsed lasers at FLASH and SHARP (table 2) is significantly larger, its peak power is at least one order of magnitude less. This is reflected by the measured peak intensity in the UV. So, the above measurements show, that the present design of the wavelength converter cannot be used together with the photocathode laser for a CW gun without substantial modification.

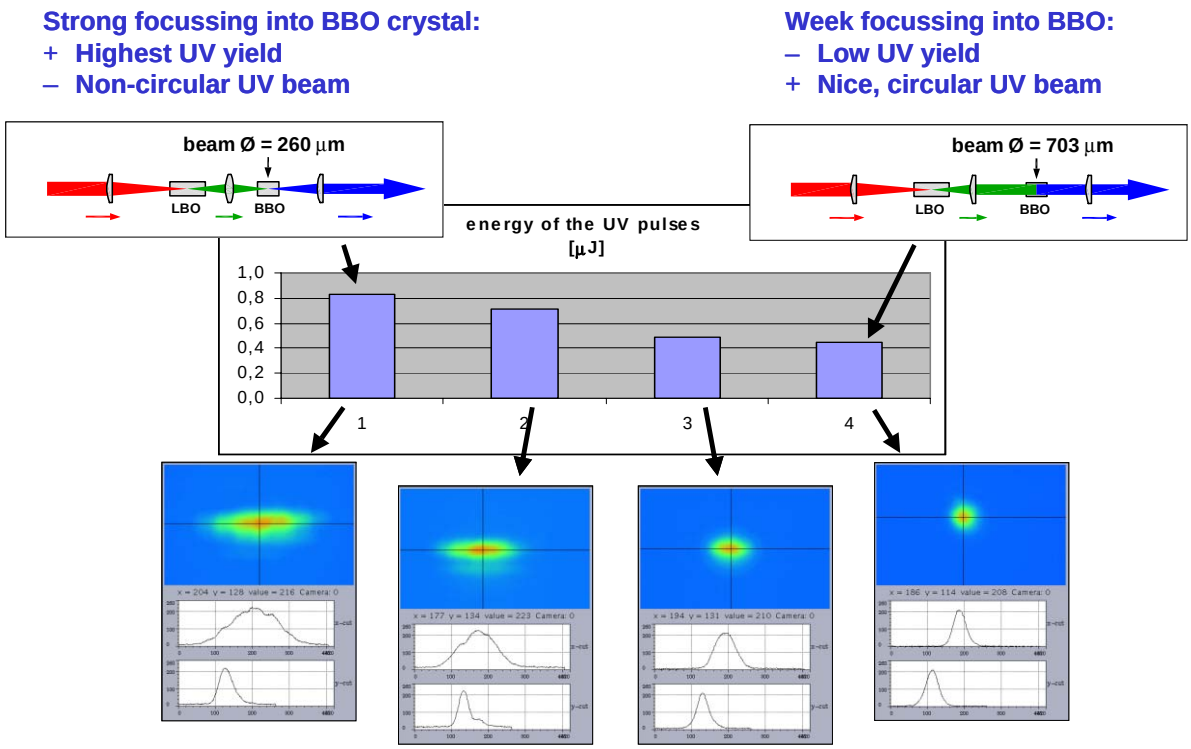

Figure 2: Intensity profile of the UV output at four different sizes of the focussed beam diameter in the BBO crystal (from left to right: 260, 352, 527 and 703 µm).

In order to still reach a reasonable conversion efficiency, the laser radiation must be stronger focused into the conversion crystals. This, in turn leads to a significant perturbation of the beam profile due to the limited acceptance angle as well as due to the walk-off between green and UV light in the BBO crystal.

Table 2: Comparison of the pulse parameters of the photocathode lasers at FLASH/PITZ and at the FZ Rossendorf

	FLASH, PITZ	**ELBE (f = 0.5 MHz)**	**ELBE (f = 13 MHz)**
pulses per s	$0.008 \cdot 10^6$	$0.5 \cdot 10^6$	$13 \cdot 10^6$
pulse energy (UV)	20 µJ	1 µJ	0.08 µJ
pulse duration	20 ps	20 ps	4 ps
average UV power	0.16 W	0.5 W	1 W
peak intensity (UV)	1	0.05	0.02

CONCLUSION AND OUTLOOK

From the above described measurements follows, that the photocathode lasers for RF guns in CW mode should be set up for the shortest pulse duration possible. This would yield better conversion efficiency to the UV at the same laser pulse energy. Since even sub-picosecond lasers with an average power larger than 10 W exist, the lower limit for the pulse duration is determined by space charge effects in the RF gun. Too short pulses however, will lead to an increased longitudinal emittance of the electron beam.

Further work is mainly required to develop an improved wavelength conversion unit to end up with reasonable conversion efficiency and simultaneously a nearly circular profile of the UV laser beam. A possible solution that is presently investigated at the MBI might be based on cylindrical lenses for focusing the beam differently in horizontal and vertical direction. Compensation of the walk-off between fundamental and harmonic wave that occurs in the crystals is another option.

ACKNOWLEDGEMENT

This work was supported by the German Ministry for Edjucation and Science, contract no. 05 ES4BM1/1 and 05ES4 BR1/8.

REFERENCES

[1] http://www.fz-rossendorf.de/pls/rois/Cms?pNid=604

[2] I. Will, G. Koss, I. Templin, The upgraded photocathode laser of the TESLA Test Facility, Nuclear Instruments and Methods in Physics research A 541 (2005), pp. 467-477.

1ST RF-MEASUREMENTS @ 3.5-CELL SRF-PHOTO-GUN CAVITY IN ROSSENDORF

A. Arnold#, H. Buettig, D. Jannsen, U. Lehnert, P. Michel, K. Moeller, P. Murcek, Ch. Schneider, R. Schurig, F. Staufenbiel, J. Teichert, R. Xiang, FZR, Dresden, Germany
A. Matheisen, B. v. d. Horst, DESY, Germany
J. Stephan, IKS, Dresden, Germany
W.-D. Lehmann, IfE, Dresden, Germany
T. Kamps, D. Lipka, F. Marhauser, BESSY, Berlin, Germany
V. Volkov, BINP, Novosibirsk, Russia

Abstract

At the Forschungszentrum Rossendorf the development and the setup of the 2nd superconducting radio frequency photo electron injector (SRF-Photo-Gun) is nearly completed. In this report we present the results of the cavity treatment. The warm tuning was carried out considering pre-stressing and the tuning range of both tuners (half cell and full cells). The optimal antenna length of the main coupler and both fundamental pickups were determined by practical external Q studies. Furthermore the characteristic tuning curves of the choke filter and both HOM filters were simulated, measured and tuned at the pi-mode frequency. The preparation (etching and rinsing) and the vertical cold test were done at DESY.

INTRODUCTION

For future FEL light sources and high energy linear accelerators a high current electron gun with high brilliance is absolutely essential. Thus, an innovative superconducting RF photo injector (SRF gun) is under development at the Forschungszentrum Rossendorf (ELBE), which is a collaboration of BESSY, DESY, MBI and FZR and supported by the European Community.

Table 1: rf cavity parameters calculated with MWS© normalized to 50MV/m peak axis field

stored energy U	***32.5 J***
quality factor Q_0	***1x10^10***
dissipated power P_c	***25.8 W***
geometry factor G	***241.9 Ω***
acceleration voltage V_{acc} acceleration gradient E_{acc}	***9.4 MV*** ***18.8 MV/m***
shunt impedance $R_a = V_{acc}^2 / 2P_c$	***1.72x10^12 Ω***
R_a/Q_0	***166.6 Ω***
E_{peak}/E_{acc}	***2.66***
B_{peak}/E_{acc}	***6.1 mT/(MV/m)***

This gun allows continuous wave operation at an energy of 9.4 MeV and an average current of 1 mA. It can generate short pulses and high-brightness electron beams, as known from the conventional photo-injectors. Moreover, the use of the superconducting cavity allows cw-mode operation and thus high average currents. Table 1 shows some simulated rf cavity parameters.

The current progress of this project is presented in [1]. This paper deals with the treatment of the cavity itself, one of the main parts of the SRF-Gun. Fig. 1 shows a schematic of its design which is described more in detail in [2].

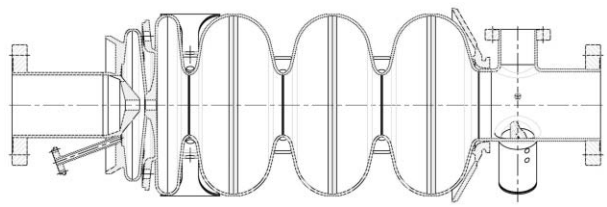

Fig. 1: cross section of the cavity design.

CAVITY WARM TUNING

In order to get the right field distribution and the accurate frequency at operation inside the cryostat, one has to consider different tuning parameters.

Table 2: evaluation of the estimated frequency @ 300K

operating frequency @ 2K	***1300.0 MHz***
cool down shrinking (measured @ ELBE)	*- 1.97 MHz*
50μm BCP @ DESY (simulated)	*+ 0.55 MHz*
pre-stressing half cell (measured)	*+ 0.10 MHz*
pre-stressing three TESLA cells (measured)	*+ 0.22 MHz*
required frequency @ 300K	***1298.9 MHz***

The correct frequency at room temperature mainly depends on cool down shrinking, additional chemical treatment and pre-stressing of both cavity tuners. These tuners permit an axial deformation of ±400μm and ±500μm for the half cell and the three TESLA cells, respectively. The induced frequency shifts have been taken into account. Thus, the estimated tuning frequency follows from Table 2.

Table 3: field detuning caused by pre-stressing half cell

	Gun Cell	TESLA1	TESLA2	End Cell
detuning axis field	***-7.3%***	***-1.8%***	***+1.4%***	***+3.1%***

#a.arnold@fz-rossendorf.de

A non-negligible detuning of the π-mode field, as shown in Table 3, is caused by pre-stressing of the half cell. This measurement has to be considered inversely by pre-tuning to obtain the right field profile in the cryostat.

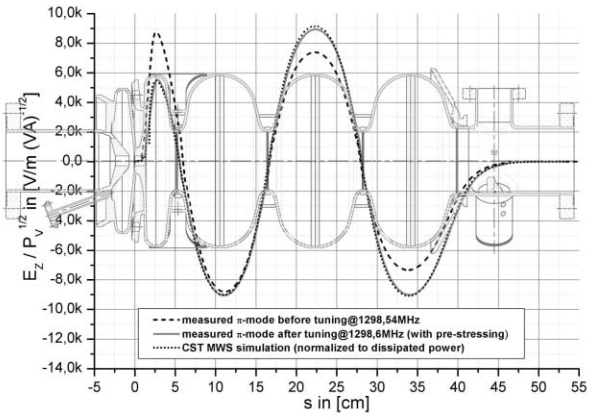

Fig. 2: measured vs. simulated π-mode field profiles before and after tuning.

Based on these target values, the tuning process was realized as presented in [3]. It succeeded in the measured field profile shown in Fig. 2 and met the calculated requirements.

EXT. Q STUDY MAIN-COUPLER

In order to maximize the rf power transfer from klystron to the electron beam, it is absolutely necessary to match the coupling. The applied Rossendorf main coupler is not adjustable, thus the antenna is optimized for maximum beam power with an external quality factor of:

$$Q_{ext} = \frac{Q_0}{1 + P_{beam}/P_C} = 2.7 \cdot 10^7 \qquad (1)$$

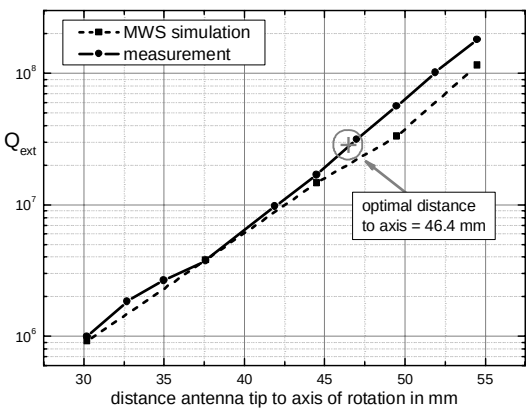

Fig. 3: external quality factor vs. antenna length.

The determination of the suitable distance between antenna tip and axis of rotation is done by an additional probe antenna added at the opposite side of the cavity at room temperature. As shown in equation 2 one has to measure incident and reflected power at the input port, the transmitted power at the main coupler as well as the unloaded quality factor of the cavity.

$$Q_{ext} = \frac{Q_0}{\beta_{ext}} \quad with \quad \beta_{ext} = \frac{P_t}{P_i - P_r - P_t} \qquad (2)$$

The results presented in Fig. 3, point to the best coupling at a distance of 46.4 mm from axis. An additional calculation, using the results of MWS©-simulations with different boundary conditions as shown in [4], gives a similar performance.

TUNING HOM-COUPLER

We use the welded DESY TTF II HOM-couplers. Due to the asymmetric design caused by the cathode and its cooling support, both couplers are welded to the coupler section at the end of the beam tube. To estimate the precision achieved by trap circuit tuning, we measured the external quality factor at the π-mode frequency versus tuning displacement and frequency shift. To prevent crosstalk it is necessary to place the input antenna probe at the opposite side of the HOM couplers. The result is presented in Fig. 4. It is obviously hard to get a better external quality factor than $Q_{ext}=10^{11}$. In that case less than 10% of the dissipated power is transmitted out of each HOM-coupler.

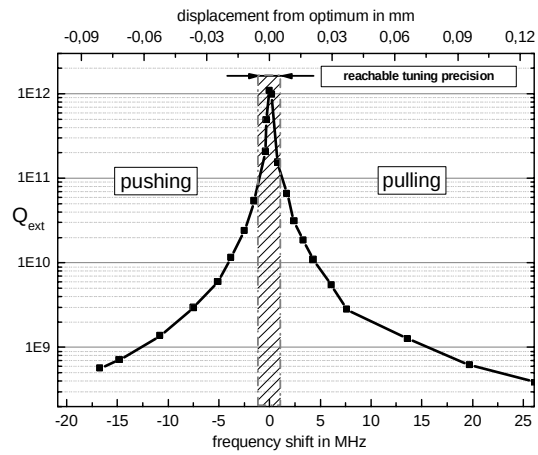

Fig. 4: external quality factor vs. detuning from best π-mode suppression.

TUNING CHOKEFILTER

The choke filter is situated next to the first gun cell and described more in detail in [5]. It prevents the leakage of RF power through the coaxial line out of the cavity which is caused by the cathode and its coupling to the gun cell. The filter is designed as a coaxial trap filter. Its band pass frequency will be adjusted during the assembling of the cryostat. To estimate the transmitted power, we measured

the external quality factor versus detuning of the choke cavity by crushing and stretching. For this purpose an antenna probe with the same diameter as the original cathode was used. Thus the power behind the choke filter depending on the dissipated power through the walls can be measured (Fig. 5).

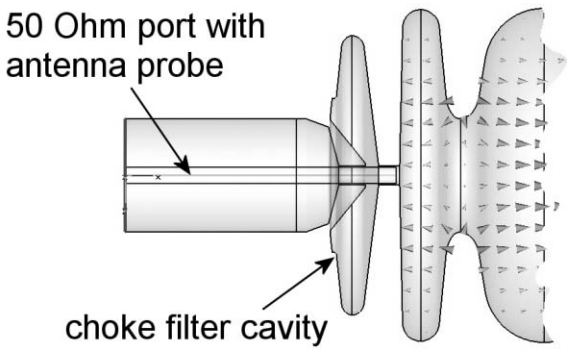

Fig. 5: assembly to measure π-mode suppression.

As a result one gets a tuning curve shown in Fig. 6. Because of mechanical tolerances during the assembling of the cryostat, it is hard to improve the accuracy better than ±100 microns. Within this range, the external quality factor is better than $Q_{ext}=10^{12}$ and the transmitted power behind the choke is less than 1% of the dissipated power. An additional MWS simulation yielded comparable results.

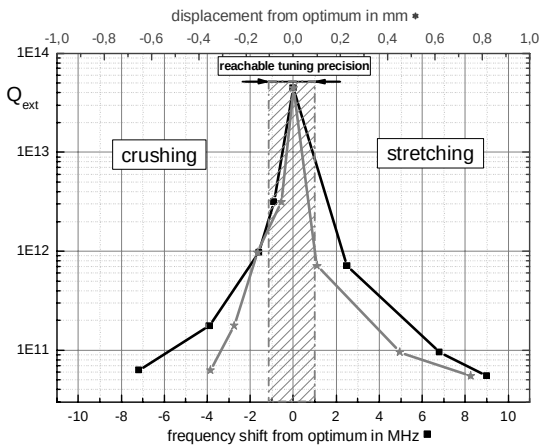

Fig. 6: external quality factor vs. choke filter detuning measured by frequency shift and deformation.

1ST VERTICAL COLD TEST

Following the tuning procedures the cavity was prepared at DESY Hamburg by buffered chemical polishing (40µm BCP) and high pressure rinsing (HPR). Afterwards the cavity was tested in a vertical cold test, as described in [6]. During the cool down from 4.4K to 1.6K the unloaded quality factor was measured at low rf power (Fig. 7). The illustrated surface resistance follows from eq. 3 and the numerical calculated geometry factor G.

$$R_S = \frac{G}{Q_0} \qquad with \qquad G = 241.9\Omega \tag{3}$$

$$R_S = A_S \bullet \omega^2 \bullet \frac{1}{T} e^{-\frac{\Delta}{k \bullet T}} + R_{res} \qquad \text{für} \qquad T < T_C / 2 \tag{4}$$

Based on the BCS-theory the surface resistance can also be calculated analytically. Fitting the measured data points by using eq. 4 leads to the following material parameters:

$$A_S = 2.42 \bullet 10^{-15} \frac{\Omega \bullet °K}{Hz^2} \quad ; \quad \Delta = 1.53 meV \quad ; \quad \underline{R_{res} = 3.43 n\Omega}$$

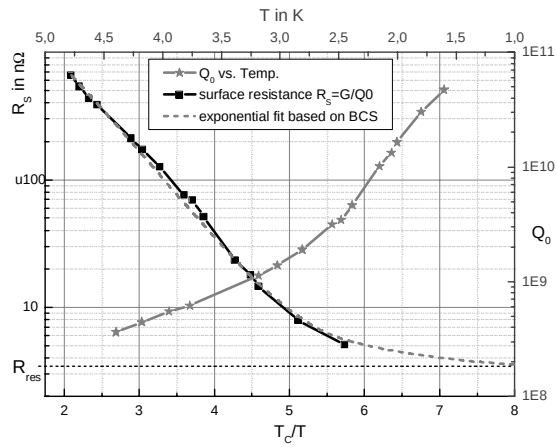

Fig. 7: surface resistance and unloaded quality factor versus temperature.

In view of the measured, unloaded high quality factor Q_0(@1.8K)=3x10^{10} and the calculated low residual resistance of R_{res}=3.4nΩ the preparation of the cavity proceeded well.

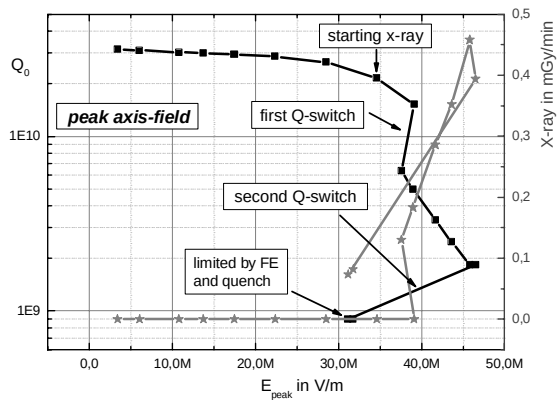

Fig. 8: Q_0 vs. peak axis field E_{peak} @1.8K.

Another matter of substantial interest is the Q vs. E chart. The corresponding measurement also takes place at DESY. In order to get comparable values, Q_0 is plotted versus peak axis field in the TESLA cells (design value

E_{peak}=50MV/m). Furthermore the radiation caused by field emitters is included into the same chart. As shown in Fig. 8 field emission started early and the quality factor decreases. Further increasing of rf power results in strong field emission and two Q-switches, which are probably caused by thermal breakdown at activated field emitters. After the second Q-switch the field was limited by quench. Especially the behaviour the Q-switches are most likely due to defects in the bulk niobium or to surface pollution. This might be induced by the hardly cleanable choke filter. Because of the narrow cathode feed through between choke filter and gun cell, direct cleaning of the filter cell wasn't feasible. Furthermore contaminated water runs out of it into the cavity which leads into polluted surface.

CONCLUSION

So far all measurements and tuning procedures yield acceptable results. In the next steps an improved HPR and BCP treatment will be established to achieve the designed peak field. Nevertheless the reached field of E_{peak}=39MV/m and the high quality factor of $Q_0=1.5x10^{10}$ demonstrates first of all the proper design of the gun cavity.

ACKNOWLEDGEMENT

This work is supported by the European Commission within the framework of the CARE project, EU contract number RII3-CT-2003-506395.

REFERENCES

[1] D. Janssen , et al., "progress of the Rossendorf SRF Gun project", proc. of EPAC 2006, Edinburgh, UK.

[2] J. Teichert, et al., "a superconducting photo-injector with a 3.5-cell cavity for the ELBE linac", proc. of EPAC 2004, Lucerne, Switzerland.

[3] A. Arnold, et al., "field profile measurements of the 3½ cell SRF Gun", proc. SRF Workshop, Ithaca, USA, 2005.

[4] P. Balleyguier: "External Q studies for APTT SC-Cavity Couplers", CEA/DPTA, Bruyères-le-Châtel, France.

[5] P. v. Stein, internal report, FZR-227, Forschungs-zentrum Rossendorf, 1998.

[6] Jens Knobloch: Basic Concepts of Measurements Made on Superconducting RF Cavities, Laboratory of Nuclear Studies, Cornell University, August 1991.

HIGH PEAK CURRENT DESIGN OF A SUPERCONDUCTING CAVITY FOR A SRF PHOTOINJECTOR

D. Janssen, FZ-Rossendorf, Dresden, Germany, F. Marhauser, BESSY, Berlin, Germany
V. Volkov, BINP, Novosibirsk, Russia.

Abstract

A 1.5-cell cavity for a superconducting RF gun has been designed and a magnetic RF mode for emittance compensation is applied. For a peak current of 125A a transverse emittance of 1.8 mm mrad has been obtained.

INTRODUCTION

In collaboration between BESSY, DESY, FZR, MBI and BINP a 3½-cell superconducting RF electron gun is under development. The status of the project and the progress obtained is reported on this conference. The motivation for the design of a new gun cavity is the proposed FEL project at BESSY. This FEL requires a bunch charge of 2.5 nC with transverse slice emittances around 1.5 π mm mrad. In the following we will discuss the design of a 1½-cell cavity with a frequency of 520 MHz for the accelerating mode (TM mode) and 1560 MHz for the magnetic mode (TE mode). The design of a 1½ cell superconducting cavity with a frequency of 1.3 GHz has been also reported in [5].

DESIGN CONSIDERATION USING THE PILLBOX MODEL

In order to find some general rules for the cavity design, we will discuss a simple pillbox model, where the frequencies and RF fields are known analytically.

Figures of merit

In order to avoid a quench of the cavity, the maximum magnetic field on the cavity surface should be clear below 180 mT. Otherwise an optimal beam dynamics needs large electric and magnetic fields on the cavity axis. So the expressions

$$F_{nml}^{TM} = \left| \frac{Ez_{nml}^{\max}(r=0)}{Bs_{nml}^{\max}} \right|, F_{0ml}^{TE} = \left| \frac{Bz_{0ml}^{\max}(r=0)}{Bs_{0ml}^{\max}} \right|$$

$F_{0ml}^{TM}\ [\frac{MV/m}{mT}]$	m = 1	m = 2	m = 3
l = 0	0.587	0.587	0.587
l = 1	0.351	0.502	0.543

are essential parameters for the quality of the cavity. For a pillbox with length L and radius R one obtains:

Table 1: Figures of merit of the TM mode for R = L

From the first table follows, that at the surface limit of 180 mT the pillbox has an accelerating field of 105 MV/m! Therefore our cavity design should be as close as possible to the pillbox geometry. The main difference between a pillbox and a realistic cavity cell is the beam tube. In order to minimize the influence of the beam tube on the RF field of the cavity cell, the ratio of the cell to the tube radius should be large. The lower limit of the beam tube radius is fixed by wake field effects of the bunch charge. Therefore the cell radius should be as large as possible. This radius is inversely proportional to the cell frequency, so we fix the frequency of the TM mode to 520 MHz, which is the TESLA frequency divided by 2.5.

Table 2: Figures of merit of the TE mode for

$$\mathrm{R/L} \geq J_1^{\max}\pi l / \left(J_0(q_m) q_m \right),\ J_1(q_m) = 0$$

F_{0ml}^{TE}	m = 1	m = 2	m = 3
l = 1	2.48	3.33	4.00

The second table shows that the axial magnetic field is enhanced when increasing the radial node number for a given surface field. Therefore a high frequency TE mode should be preferred.

Third order effects

The power expansion of radial RF field components with respect to the radius r starts with a linear term and is followed by third order terms. These third order terms produce an increase of the transverse beam emittance. In the pillbox cavity for the TM modes with l = 0 the third order terms are zero. For the magnetic TE modes the ratio of the third order term divided by the first order term is given by

$$\frac{\left(Bz''' + \frac{\omega^2}{c^2} Bz' \right)}{Bz'} = \left(\frac{q_m}{R} \right)^2 \qquad (1)$$

Therefore the nonlinear effects increase quadratic with increasing node number m of the TE mode and decreasing radius R of the cavity cell. From this point of view the gun should work at the lowest TE mode frequency.

Comparison of the TE mode with a static magnetic field

Neglecting terms in r^2 in the equation of motion for an electron in the RF field of the TE mode the following equations are obtained:

$$\varphi' = -\frac{eB_z}{2m\gamma}, \quad r'' = -\frac{e^2}{4\gamma^2} B_z^2 r \qquad (2)$$

These are the same equations as in the static magnetic field. Assuming $\beta \approx 1$ we can replace the time

dependence in the RF field by z/c and calculate the focal distance of the corresponding magnetic lenses.

$$\frac{1}{f} = \frac{e^2}{4m^2c^2\gamma^2}\int_{-\infty}^{\infty} B_z{}^2 dz\,, \quad B_z = b(z)\sin(\omega\frac{z}{c}+\varphi_0) \qquad (3)$$

In this case the focal distance is a function of the phase φ_0 of the TE mode. For the case of a pillbox cavity we obtain:

$$\frac{1}{f} = \frac{e^2}{4m^2c^2\beta^2\gamma^2}\frac{L}{\pi}B_0^2\left(\frac{\pi}{4}+\sin(\alpha\pi)\frac{\cos(\alpha\pi+2\varphi_0)}{4\alpha(\alpha^2-1)}\right)$$

$$\alpha = \sqrt{\left(\frac{q_m L}{\pi R}\right)^2+1} \qquad (4)$$

For α = 2,3, … the focal distance is independent of φ_o and for α =1/2 , 3/2, …. we have the maximal phase dependence. These limiting cases can be realized numerically also for realistic cell geometry.

The emittance compensation in a RF gun is based on the focussing of electrons inside a magnetic field. Therefore the quotient of cell radius and cell length defines the phase dependence of the focal distance and the phase dependence of the emittance.

CAVITY DESIGN AND RF FIELDS

As mentioned in the first section, the TM mode frequency of our gun cavity is 520 MHz. At this frequency the beam energy of a 1½-cell cavity with E_{peak} = 30MV/m is already greater 10 MeV. The cell radii are determined by the TM frequency and the field amplitudes on the cavity axis. We place the TE mode in the second cell. After this the phase slippage of the TM mode and the TE mode frequency define the width of the cells. As discussed in the previous section, the TE frequency can be defined by different arguments. In this calculation the frequency of 1560 MHz is used. This mode has the radial node number m = 2 and the field ratio $Bz_{max}(r=0)/Bs_{max}$ is 2.69. Furthermore, the integer value of the TE/TM frequency ratio allows the operation of the RF gun with the same TE - phase φ_o for each bunch. In this

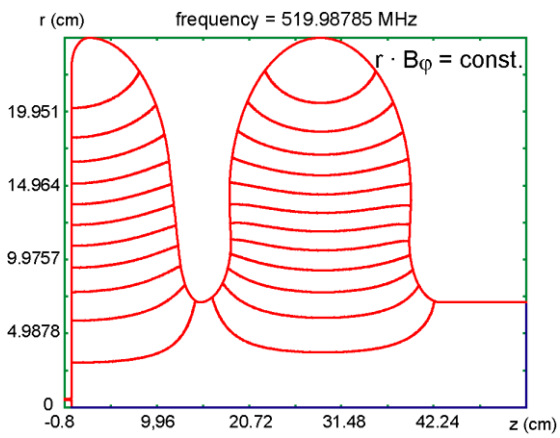

Figure 1: Cavity shape and electric field distribution of the TM mode.

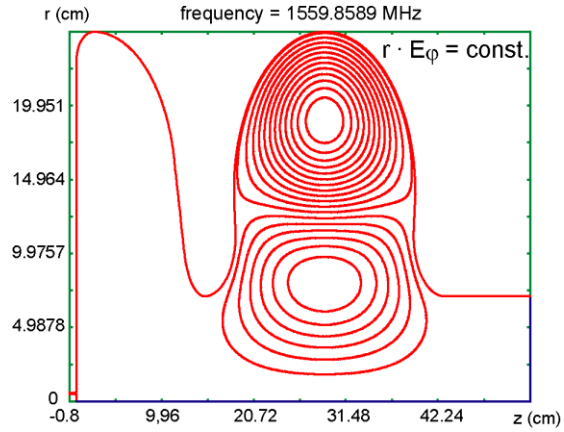

Figure 2: Cavity shape and magnetic field distribution of the TE mode.

case it is meaningful to minimize the emittance with respect to this phase. The cell geometry and the field distribution of the gun are given in Fig.1 and Fig. 2 respectively.

Fig. 3 shows the fields on the cavity axis.

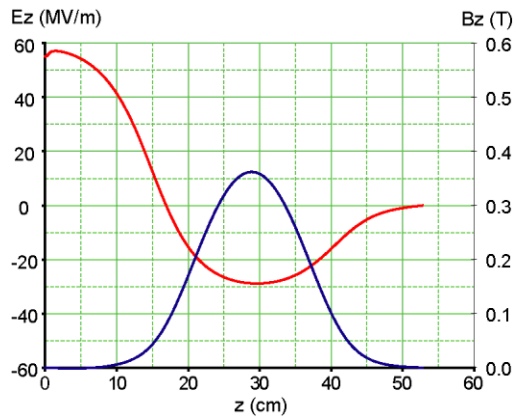

Figure 3: Axis fields of the cavity.

FIELD AMPLITUDES

The magnetic surface fields of the TM and the TE mode are perpendicular to each other. Therefore we have to evaluate the vector sum of both surface fields to compute the limiting field. Table 3 lists the maximal field limits used in the calculations. They are clearly below the critical limit. In Fig.4 the two surface fields and the sum of both fields are shown.

Table 3: Maximum axial and surface field values

field	unit	value
Ez_{max}	MV/m	57
Bz_{max}	mT	363
Bs_{max}(TM)	mT	130
Bs_{max}(TE)	mT	118
Bs_{max}	mT	130

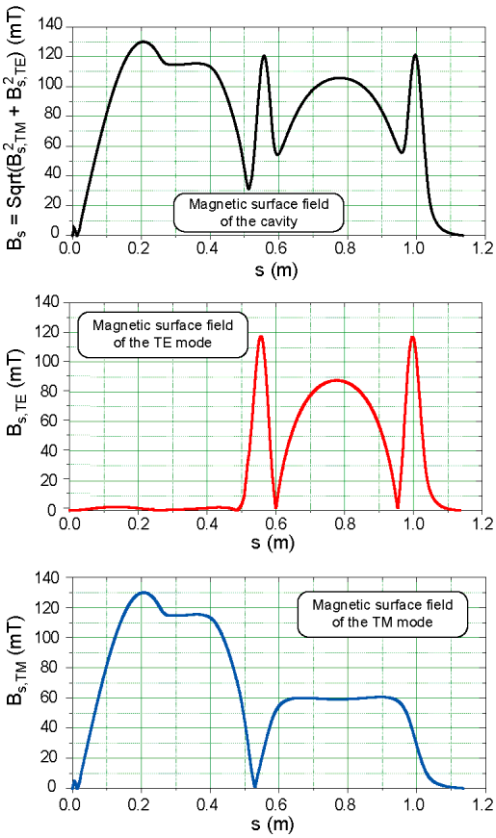

Figure 4: Magnetic surface fields in dependence on the surface coordinate s, $Bs = \sqrt{(Bs_TM)^2 + (Bs_TE)^2}$.

LASER PULSE SHAPE AND THERMAL EMITTANCE

In a RF photo cathode gun the laser pulse determines the bunch shape at the cathode. In the present calculations a temporal flat top laser pulse profile up to L_t = 40 ps and a rise and fall time of 2 ps have been used. The radial distribution is uniform. At a laser wavelength of 260 nm the electrons leave the cathode with a thermal energy of 1 eV isotropically in the whole space. This seems to be a set of realistic parameters [1].

RESULTS OF TRACKING CALCULATIONS

Tracking studies using ASTRA [2] have been performed for the gun cavity followed by a drift space and a booster linac section comprising 3 x 4 1.3 GHz standard 9-cell TESLA cavities to investigate emittance conservation. A Simplex routine has been utilized for a multi-parameter optimization. Hereby the transverse emittance at the linac exit has been minimized by varying the laser spot size at a given laser pulse length L_t and the operational parameters of the RF gun (TM and TE mode) and booster cavities with E_{acc} = 20 MV/m in maximum for the latter. To reduce the computation time four TESLA-cavities have been combined to one section. Typically for 1 nC bunch charge the reasonable laser pulse length is in the order of L_t =20 ps regarding space charge effects arising just at the cathode. To mitigate the enhanced space charge at 2.5 nC the laser pulse length could be further increased sacrificing some longitudinal emittance. First without the booster linac we have studied the behaviour for L_t = 20 ps resulting in a minimum transverse emittance of ~1.8 π mm mrad at a distance of ~5.3 m behind the photocathode for Bz_{max} = 363 mT as shown in Fig. 5.

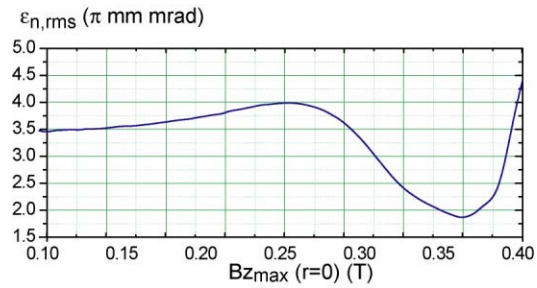

Figure 5: Dependence of the projected transverse emittance on the axial TE mode amplitude (position behind cathode z = 5.3 m, laser spot radius 1.25mm).

With these settings however one operates apart from the usual emittance compensation in the drift. Thus when including the booster we observed that the beam can not be matched according to the so-called invariant envelope (I.E.) [3]. Instead the beam is strongly focussed within the linac due to RF-focussing and without measures tends to extend behind the focal point.

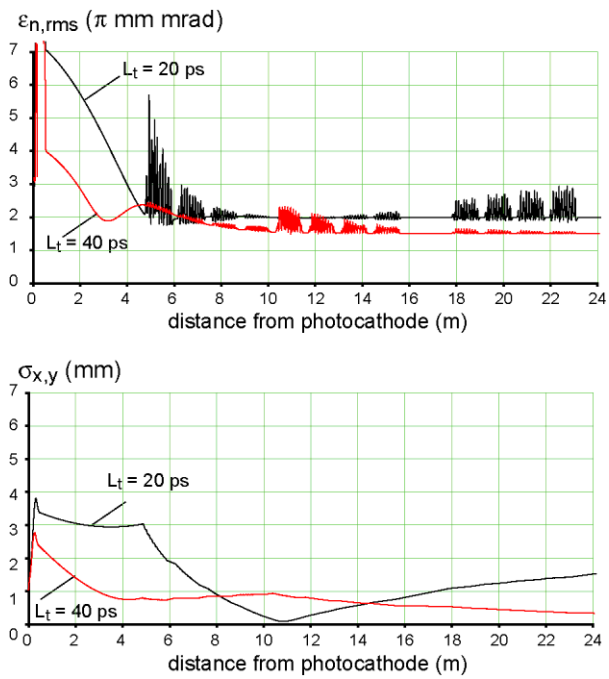

Figure 6: Evolution of the projected transverse rms emittance (top) and rms beam size (bottom) through the linac for L_t = 20 and 40 ps respectively (30000 particles).

The projected emittance can not be further minimized but rather stays constant. This is illustrated in Fig. 6 showing the evolution of the projected transverse rms emittance (top) and rms beam size (bottom) for L_t = 20. However the projected emittance is largely deluted by mismatched fringe particles which are responsible for the oscillations of the projected emittance within the linac cavities. Actually the slice emittance as the figure of merit amounts to only 1.1 π mm mrad in average.

We then tried to match the beam to the booster by following more closely the I.E.. This necessitates to adjust the electric field of the gun according to Bz_{max} to balance the repelling and focussing forces. Thus a typical emittance compensation accompanied by an emittance oscillation with a double emittance minimum in the drift [4] can be produced. Holding the I.E. criterion in this mode of operation the minimum projected emittance obtained for L_t =20 ps however is rather large (~4 π mm mrad). Moreover the accelerating fields in the first TESLA-cavities would be in the order of E_{acc} = 40 MV/m. However, the situation relaxes once the pulse length is further increased. This has been done using L_t =40 ps in a next step as shown in Fig. 6 as well. Here a projected transverse emittance of only 1.5 π mm mrad is achieved. As more particles follow the I.E., the average slice emittance is ~1.4 π mm mrad only marginally below the projected emittance.

Table 4 and 5 summarizes the optimized parameter settings and achieved results at the booster exit (z = 24m) for L_t = 20ps and L_t = 40ps respectively. Albeit the results are not regarded as an overall optimum yet, the required specifications of the BESSY FEL can be well fulfilled.

Table 4: Parameter settings for the photocathode laser, RF gun (TM and TE mode) and booster cavities respectively

parameter settings	unit	value	
laser			
flat top	ps	20	40
rise/fall time	ps	2	2
spot radius	mm	1.2	1.35
thermal energy	eV	1	1
thermal emittance	π mm mrad	0.69	0.77
RF gun			
gun TM field (max.)	MV/m	54.8	54.6
beam energy	MeV	9.8	9.7
magnetic TE field (max.)	mT	354	360
peak surface field	mT	128	127
booster cavities			
acc. field (cavities #1-4)	MV/m	10.5	7.5
acc. field (cavities #5-8)	MV/m	19.9	20
acc. field (cavities #9-12)	MV/m	17.6	17.4

Table 5: Achieved beam parameters with a bunch charge of 2.5 nC at the exit of the booster linac (z = 24m)

achieved parameters	unit	value	
laser pulse length (z = 0)	**ps**	**20**	**40**
normalized transverse projected rms emitttance	π mm mrad	2	1.5
average slice emittance	**π mm mrad**	**1.1**	**1.35**
trans. rms beam size	mm	1.45	0.37
long. rms beam size	mm	2.7	3.6
average kinetic energy	MeV	218	204
long. rms emittance	keV mm	1438	3250
correlated energy spread	keV	129	305

DISCUSSION AND SUMMARY

For two different lengths of the laser pulse it has been shown, that the design parameter of the injector for the BESSY FEL can be obtained, using a 1½-cell superconducting RF gun. In the calculation a maximal surface field of 130 mT has been assumed. This value corresponds to accelerating field strength of ~28MV/m in a TESLA cavity. For cavity frequencies in the order of 1.3 GHz this value is standard, but the frequency of the accelerating mode in the gun cavity is 520 MHz. For this frequency the maximal surface field, which can be obtained, is an open question.

In the present calculation the cathode has a flat surface, which is inside of the back wall of the cavity. In this simple arrangement we have near the cathode no focussing RF forces and possible wake fields from the cavity surface are absent.

In analogy to [6] we plan to place a Cs_2Te cathode into the superconducting cavity. For this material and λ_{laser} = 260 nm a quantum efficiency of 5% is realistic. In this case the bunch charge of 2.5 nC demands a laser pulse energy of 0.24 μJ.

ACKNOWLEDGMENT

The authors thanks Dirk Lipka (BESSY), Klaus Floettmann (DESY) and the members of the SRF gun project group for many helpful discussions.

REFERENCES

[1] I. Will, MBI Berlin, private communication.
[2] K. Flöttmann, http://www.desy.de/~mpyflo/.
[3] L. Serafini, J. B. Rosenzweig, Phys. Rev. E, Vol. 55, June 1996, 7565.
[4] M. Ferrario et. al., SLAC-PUB 8400, March 2000.
[5] J.Sekutowicz et al., Phys. Rev. ST Accel. Beams 8, 010701 (2005).
[6] D.Janssen et al., Nucl. Instr. and Meth. A507 (2003) 34.

CRYOMODULE AND TUNING SYSTEM OF THE SUPERCONDUCTING RF PHOTO-INJECTOR*

J. Teichert#, A. Arnold, H. Buettig , R. Hempel, D. Janssen, U. Lehnert, P. Michel, K. Moeller, P. Murcek, C. Schneider, R. Schurig, F. Staufenbiel, R. Xiang, FZ Rossendorf, Dresden, Germany,
T. Kamps, D. Lipka, BESSY, Berlin, Germany, J. Stephan, IKS, Dresden, Germany,
W.-D. Lehmann, SGE, Dresden, Germany, G. Klemz, I. Will, MBI, Berlin, Germany.

Abstract

The designs and a report on the progress in construction and testing of the cryomodule and the tuning system for the SRF gun are presented. The SRF gun project, a collaboration of BESSY, DESY, MBI and FZR, aims at the installation of a CW photo injector at the ELBE linac. The cryostat consists of a stainless steel vacuum vessel, a warm magnetic shield, a liquid N cooled thermal shield, and a He tank with two-phase supply tube. A heater pot in the He input port will be used for He level control. The 10 kW power coupler is adopted from the ELBE module. A cooling and support system for the NC photo cathode has been developed and tested. It allows the adjustment of the cathode with respect to the cavity from outside. The cryomodule will be connected with the 220 W He refrigerator of ELBE and will operate at 1.8 to 2 K. The static thermal loss is expected to be less than 20 W.

Two tuners will be installed for separate tuning of the three TESLA cells and the half-cell. The tuners are dual spindle-lever systems with step motors and low-vibration gears outside the cryostat. Functionality, tuning range and accuracy have been tested in cryogenic environment.

INTRODUCTION

Superconducting radio frequency (SRF) acceleration technology is well established for electron linacs with considerable progress in acceleration gradient during the last years [1]. The adequate SRF photo-injector was already proposed in 1988 [2], but up to now such an injector has not been operated at an accelerator. As electron sources for SRF electron linacs, DC photo-injectors or thermionic injectors are in use for CW operation or normal-conducting RF photoinjectors in pulsed mode. The RF photo-injectors deliver electron beams of highest quality (short bunch length and low transverse emittance at high bunch charge). Its combination with a superconducting cavity would further allow CW operation. After a successful proof-of-principle experiment with a half-cell cavity [3] a project for a SRF photo injector has been launched in 2004. The goal of this project, carried out in a collaboration of BESSY, DESY, MBI and FZR, is to build a fully functioning SRF photo-injector for the ELBE accelerator. Beside the significant beam quality improvement, the operation at ELBE will allow long term studies of important issues of SRF injectors like low-temperature operation and lifetime of photo cathodes, or cavity quality degradation.

The design parameters of the SRF gun are presented in Table 1. The gun will be operated in three modes: the standard ELBE FEL mode with 77 pC and 13 MHz pulse repetition, the high charge mode for neutron physics at ELBE and ERL studies (1 nC, 1 MHz), and the BESSY FEL mode (2.5 nC, 1 kHz). A UV driver laser system for these three operation modes is under development [4]. Beam parameter studies will be performed with a new diagnostic beam line [5]. The ELBE mode is determined by the two existing far infrared FELs which need 13 MHz bunch repetition rate, as well as the maximum average current of the ELBE accelerator. The high charge mode is essential for neutron physics experiments planned at ELBE where time-of-flight measurements require 1 µs pulse spacing without average current reduction. At the same time, 1 nC is a typical bunch charge for new FEL projects and state-of-the-art normal conducting RF photo injectors (e.g. FLASH at DESY) where the beam parameter should be measured and compared. It is planned to study and optimize different emittance compensation methods proposed for SRF guns, like a downstream magnetic solenoid, RF focusing with a backtracked and properly shaped photocathode, and RF focusing with an additional TE mode [6] in a future upgrade. For the soft x-ray BESSY FEL project [7] a bunch charge of 2.5 nC is envisaged and the SRF gun will be evaluated with respect to future application.

CRYOMODULE

The basic design for the SRF gun cryomodule was adopted from the ELBE cryomodule [8] which contains two 1.3 GHz TESLA cavities and is developed for CW operation with 10 MeV per cavity at a beam current up to 1 mA. ELBE modules are in routine operation since 2001 at FZ Rossendorf and wide experience has gained for these modules. The SRF gun cryomodule contains one 3½ cell cavity which consists of a half-cell with the normal-conducting cathode in it and three acceleration cells with TESLA shape [9]. The envisaged acceleration gradient of this cavity is 18.8 MV/m which corresponds to a

* We acknowledge the support of the European Community-Research Infrastructure Activity under the FP6 "Structuring the European Research Area" programme (CARE, contract number RII3-CT-2003-506395) and the support of the German Federal Ministry of Education and Research grant 05 ES4BR1/8.
#j.teichert@fz-rossendorf.de

maximum axial peak field of 50 MV/m in the TESLA cells. The geometry constant is 240 Ω and R/Q is 165 Ω. For $Q_0 = 1x10^{10}$ and the gradient mentioned above a RF power dissipation of 26 W is expected.

Table 1: Gun design parameters and expected beam values for the planned operation modes

	ELBE mode	**high charge mode**	**BESSY-FEL**
RF frequency	1.3 GHz		
beam energy	9.5 MeV		
Operation	CW		
drive laser	262 nm		
Photocathode	Cs_2Te		
quantum efficiency	>1 %		>2.5 %
average current	1 mA		2.5 µA
pulse length	5 ps	20 ps	50 ps
Repetition rate	13 MHz	[1MHz	1 kHz
bunch charge	77 pC	1 nC	2.5 nC
transverse emittance	1.5 µm	2.5 µm	3.0 µm

Fig. 1 shows a section view of the SRF gun cryomodule. The stainless steel vacuum vessel has a cylindrical shape with 1.3 m length and 0.75 m diameter. The vessel has flat plates on both sides and is designed as short as possible in order to get a minimum length of the transfer rod for cathode exchange, and on the beam line side it is planned to install a solenoid magnet for emittance compensation as close as possible. The He port and the N_2 port are on top on the right hand side. The refrigerator delivers 4.5 K helium to the valve box, about 5 m before the cryomodule. There is the Joule-Thompson valve for expansion. From the port the He flows through a heater pot and the two-phase supply tube into the chimney of the He tank. For the cooling of the thermal shield, liquid nitrogen is used. The 70 K shield consists of a cylindrical Al sheet welded to two circular tubes filled with N_2. The liquid N_2 tank in the upper part of the module must be refilled after about 5 h from an outside dewar. The liquid N_2 is also used for the cooling of the photo cathode stem. The photo emission layer, which is Cs_2Te, and the Cu cathode stem are normal conducting. The heat load from the RF field into these parts, estimated to be between 10 and 20 W, burdens the liquid N_2 bath.

The cavity is passively protected against ambient magnetic fields by means of a µ-metal shield, placed between the 80 K shield and the vacuum vessel. The shield is fabricated and its suppression of the earth magnetic field was measured. The results are shown in Fig. 2. In the region where the Nb cavitiy will be placed, the residual magnetic field is below 1 µT which is the limit during the cool-down [9].

The He tank is made of titanium. Three stainless steel bellows are integrated for the two tuning systems and for the manually tuned choke filter cell. The ten thin titanium spokes support the He tank and allow the adjustment of the cavity position. The spokes end in micrometer drives and vibration dampers attached to the vacuum vessel. The main power coupler is the 10 kW CW coupler of the ELBE module. It contains a conical cold ceramic window at 70 K in its coaxial part. The warm REXOLITE window is in the waveguide.

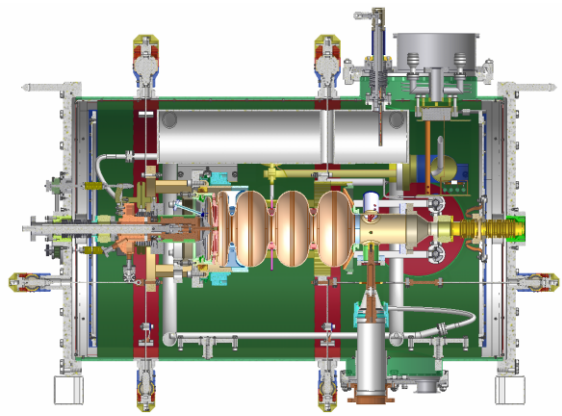

Figure 1: Cut drawing of the SRF gun cryostat.

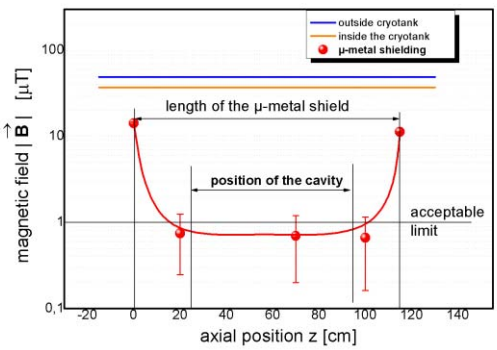

Figure 2: Measurement of the earth magnet field suppression by the µ-metal shield.

From outside it is also possible to move the cathode support and cooling system which allows the adjustment of the photo cathode with respect to the cavity. For that reason, three rotation feed-throughs exist in the backside plate of the vacuum vessel. Fig. 3 shows the design of that system.

The main sources for the static heat leak are the coaxial tube of the power coupler, the beamline vacuum tube and the vacuum tube for the cathode exchange system (both DN40), and the rotational drives of the two tuners. For all these subsystems the design is similar to the ELBE cryostat. Thus nearly the same static heat leak of less than 20 W can be expected.

The SRF gun will be installed in parallel to the existing thermionic injector of the ELBE accelerator. The cryostat will be connected with the existing 220 W He refrigerator. A new helium transfer line with valve box was assembled and tested in January 2006. Its design allows the connection of the SRF gun cryostat without warming up the other two ELBE cryomodules. The cryostat can be operated down to 1.8 K but the standard

operation temperature at ELBE is 2 K (31 mbar). In the ELBE helium cooling system, the pressure stabilization is performed with cold compressors located in the cool box of the helium refrigerator. It will be performed for all three cryostats together based on a pressure value in one module. During operation of the two ELBE modules, it turned out that the common pressure stabilization worked well for constant liquid helium flux to the modules. In order to realize that, the total heat power from the electrical heater in the module and the RF power dissipation was hold constant by means of a feed-forward control.

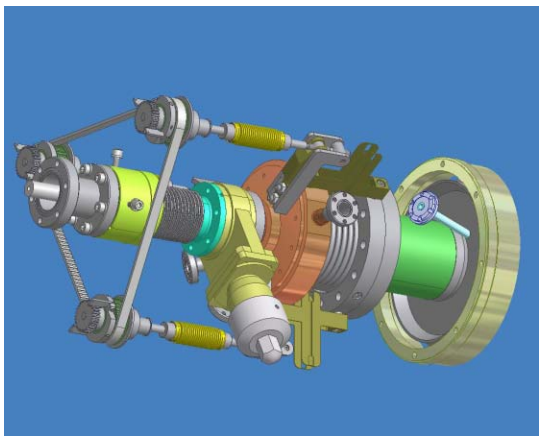

Figure 3: The cathode alignment system.

TUNING SYSTEMS

For the SRF gun cavity a frequency tuning is needed for the choke filter, the half-cell and the three TESLA cells. The bandwidth of choke filter is comparably large. Therefore a tuning during assembling in the warm stage is sufficient. For the accelerating cells tuning is required during operation. The half-cell on one hand and the three TESLA cells on the other essentially differ in their mechanical properties, especially in their stiffness. Therefore it was decided to use two separate tuning systems, one for the half-cell and one for the three TESLA cells in common.

The tuner design is adopted from the ELBE cryomodule dual spindle-lever tuning system [8]. Main objectives are a sufficiently large tuning range, high resolution, a hysteresis-free and linear operation, long life time and low cryogenic loss. But the requirements are less restrictive than for tuners in high-energy SRF linacs: Due to CW operation a fast tuning for the compensation of Lorentz force detuning (LFD) with piezoelectric actuators is not needed. This applies to active microphonics compensation too, since for a bandwidth of about 100 Hz and a moderate acceleration gradient up to about 20 MV/m, passive methods for microphonics reduction are sufficient. Costs per unit and compactness are less important too. On the other hand, the two tuners for the SRF gun cavity have required a sophisticated mechanical design due to many mechanical and cryogenic constraints and the insufficient clearance at cathode side of the cavity and the He tank. At the end, the ELBE tuner design was modified essentially.

The tuner mechanism consists of a spindle with partly left-hand thread and right-hand thread and two levers. Via the threads and the lever system the rotational motion is transformed into a longitudinal motion performing the length variation of the half-cell and the TESLA cells, respectively. The use of two levers ensures that no axial force is present on the spindle. The bearing point of the leverage system has no rotational parts. It consists of two flexible links as it is shown in Fig. 4. The advantage is the lack of any hysteresis due to friction effects and bearing clearance. The third flexible link is connected with a moving bolt which transfers the force to the parts of the He tank joint to the end plates of the half-cell or the TESLA cells. To allow the movement the He tank has two bellows.

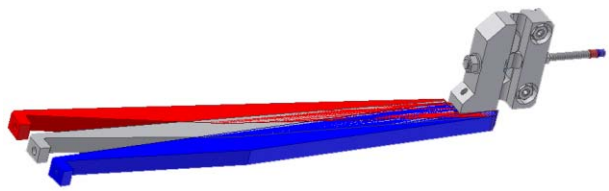

Figure 4: Lever and flexible link of the tuner.

The step motor driving the tuner spindle is outside the vacuum vessel. The fixed point is between the half-cell and the first full cell where the star-like arranged plates of the cavity are welded with the He tank. The motor motion is transmitted by rotation feed-throughs and a two-stage bellows coupling (the 70 K point is in between) to the spindle of the tuning system. The bellows compensate the shrinking offset and reduce the heat conduction. Both tuning systems have the same design. They differ in the lever lengths only.

The frequency constants $\Delta f/dL$ of the SRF gun cavity were measured with the help of the warm tuning machine developed at FZR [10]. The measurement results are 254 kHz/mm for the half-cell and 449 kHz/mm for the three TESLA cells. These values belong to the change of the π mode frequency of the whole cavity, where the three TESLA cells were unchanged in the first case, and the half-cell in the second. Simple numerical estimations with SUPERFISH assuming a smoothly and homogeneous change of the surface contour give 674 kHz/mm for the half-cell and 625 kHz/mm for the TESLA cell tuning. The large difference for the half-cell seems to be an effect of the low stiffness of the end disk or of other weak areas having low influence on the frequency.

For operating tests and parameter measurements a test bench for the designed tuning system was built up. This test bench consists of the liquid nitrogen dewar, the leverage of the tuner, a spring packet to simulate the cavity, and the equipment to produce the tuning force, to perform force and length measurements. The spring packet was variable in order to simulate the half-cell and the three TESLA cells, as well as to measure with

preload. For the three TESLA cells a spring constant of 9 kN/mm was taken [11]. The spring constant for the half-cell was assumed to be about three times higher. The preloads were varied between zero and 9 kN. In comparison to the final tuning systems the levers were made of aluminium instead of titanium and the tests were carried out with one lever only.

The results of the tuner test bench are summarized in Table 2. As expected, the tuning range became smaller with 5 kN preload due do the elastic behaviour of the flexible link of the tuner. The hysteresis measured is caused by the test bench mechanics itself. Fatigue effects were not found.

Table 2: Measurements of the tuning ranges in the tuner test bench

tuning range for 2° Lever range	half-cell tuner	TESLA cell tuner
without preload D = 0 N/mm	436 µm 416 kHz	450 µm 247 kHz
with 5000 N preload D = 9000 N/mm	218 µm 208 kHz	223 µm 122 kHz

Table 3 presents the properties of the two tuners for the SRF gun including the test bench results. The limit in the tuning range is given by the maximum bending of the flexible links of ± 1.5°. The expected tuning ranges are sufficient. By comparison, the tuning range in the ELBE modules is 230 kHz [8]. The overall tuner resolution given in the table are estimations taken from the ELBE system. A complete 3D view of the SRF gun tuners with parts of the He tank and the cavity is given in Fig. 5.

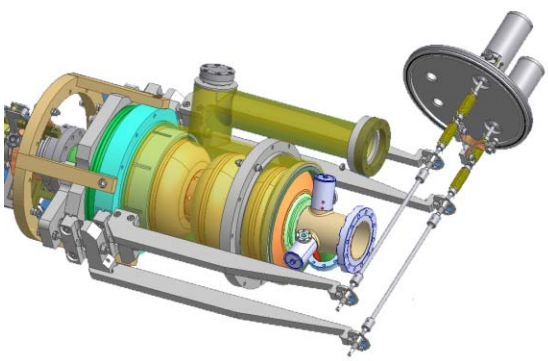

Fig. 5: The two tuners of the SRF gun.

SUMMARY AND OUTLOOK

In the paper the design and the parameters of the cryostat and the cavity tuning systems for the 3½ cell SRF gun are presented. Tests and parameter measurements of the tuners were carried out in a cryogenic test bench with sufficient results. At present, the different subsystems of the cryostat are being assembled und checked. In autumn, first vacuum and cryogenic test are planned. In parallel the treatment and measurement of the niobium cavity is carried out, following by the He tank welding. The commissioning is envisaged with the cool-down and RF tests beginning of 2007.

We would like to acknowledge the permanent support of the ELBE crew (FWL) and the staff of the technical departments (FWF) at FZ Rossendorf.

Table 3: Parameters of the SRF gun tuners

	half-cell tuner	TESLA cell tuner
lever length	630.6 mm	570.2 mm
leverage	50.4	44.2
lever range	33 mm 3.0°	30 mm 3.0°
tuning range	0.7 mm 204 kHz	0.7 mm 404 kHz
cavity frequency constants Δf/dL	178 kHz/mm	283 kHz/mm
mechanical drive step	0.70 nm/step	0.62 nm/step
frequency drive step	0.23 Hz/step	0.28 Hz/step
mechanical resolution	3 nm	
frequency resolution	1 Hz	
position of step-motors	warm, outside	

REFERENCES

[1] L. Lilje, et al., "High-Gradient Superconducting Radiofrequency Cavities for Particle Acceleration", Proc. of EPAC 2006, Edinburgh, UK, 2006, p. 2752.
[2] H. Piel, et al., FEL 1988, Jerusalem, Isreal, 1988.
[3] D. Janssen, et al., "First Operation of a Superconducting RF Gun", Nucl. Instr. and Meth. A 507 (2003) 314.
[4] I. Will, et al.," Photocathode Laser and its Beamline for the Superconducting Photoinjector at the Forschungszentrum Rossendorf", this conference.
[5] T. Kamps, et al.,"Diagnostics Beamline for the SRF Gun Project", Proc. of FEL 2005, Stanford, USA, 2005, p. 530.
[6] K. Floettmann, D. Janssen, V. Volkov, "Emittance Compensation in a Superconducting RF Gun with a Magnetic Mode", Phys. Rev. Special Topics, AB 7 (2004) 090702.
[7] "The BESSY Soft X-ray Free Electron Laser", TDR BESSY March 2004, eds.: D.Krämer, E. Jaeschke, W. Eberhardt, ISBN 3-9809534-0-8, Berlin (2004).
[8] J. Teichert, et al., "RF Status of Superconducting Module Development Suitable for CW Operation: ELBE Cryostats", Nucl. Instr. and Meth. A 557 (2006) 239.
[9] B. Aune, et al., "Superconducting TESLA Cavities", Phys. Rev. Special Topics, 3(2000) 092001.
[10] J. Teichert, et al., ".Progress of the Rossendorf SRF Gun Project", Proc. of FEL 2005, Stanford, USA, 2005, p. 534.
[11] C. Pagani et al., "Improvement of the Blade Tuner Design for Superconducting RF Cavities", Proc. of PAC 2005, Knoxville, USA, p. 3456.

DARK CURRENT COLLIMATION AND MODIFIED GUN GEOMETRY FOR THE EUROPEAN X-RAY FEL PROJECT

Jang-Hui Han* and Klaus Flöttmann, DESY, Hamburg, Germany

Abstract

An rf field of 60 MV/m will be applied at the L-band gun of the European X-ray FEL project. Such high rf gradient will allow to achieve a transverse emittance below 1 mm mrad for 1 nC electron bunches but will also produce a high dark current. The dark current generated in the gun shows a comparable dynamics as the electron beams because the same acceleration will be provided from the gun to the last acceleration module. The dark current from the gun might generate high radiation doses in the undulator and limit the long pulse operation of the SASE. To minimize dark current before the first acceleration module, a modified design of a gun cavity and collimator is investigated. The beam dynamics for minimal transverse emittance is optimized with the present and the new designed gun cavity and the resultant machine parameters are used to understand the dark current behavior.

INTRODUCTION

The Free Electron Laser in Hamburg (FLASH) gun operates with a max rf field of about 44 MV/m at cathode. The L-band Cu cavity with cylindrical symmetry is fed through the coaxial rf input coupler [1]. The photocathode is composed of a Mo cathode plug and a Cs_2Te film on the plug. The plug is a cylindrical rod with 16 mm diameter and the emissive film has typically 30 nm thickness and 5 mm diameter. The cathode has a high quantum efficiency (QE) of the order of 1%. Such high QE relaxes the requirement for the drive-laser producing photoelectrons from the cathode.

In August 2006, a long rf pulse of 800 μs has been applied into the gun cavity to produce 600 electron bunches per rf pulse. The number of bunches was limited only by the flat range of the rf pulse in the accelerator modules. In the near future, the bunch train will be expanded to fill out the rf pulse of the gun [2]. At the same time of the long rf pulse operation, the SASE lasing was also successfully achieved with the 600 bunches.

One critical factor limiting the long bunch train operation is the dark current generated in the gun cavity. At the exit of the gun, the dark current is 0.2 $\sim$ 0.3 mA. Simulations of dark current trajectories show that only the dark current emitted at the cathode area can escape from the gun cavity and flow downstream. The dark current starting at the cathode area is mostly released at an rf phase around 90°, i.e. when the rf field is maximum. At the FLASH gun, dark current starting at the cathode has a similar size as the election beams at the collimator position, 1.27 m downstream from the cathode (see Fig. 1). The inner ring-shape dark current seems to come from the boarder of the Cs_2Te film on the cathode plug [3]. The dark current has a larger radius at the emission position and obtains a lower kinetic energy through the gun than the beams. However, 1 nC beams are focused over a longer distance due to the space charge force and the higher momentum than the dark cur-

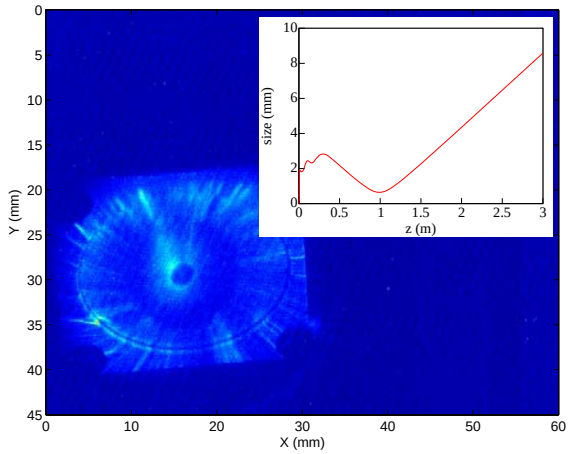

(a) Dark current image and simulation for the dark current from the cathode.

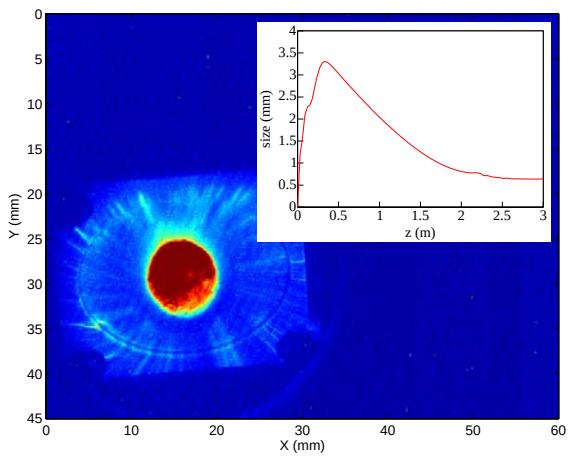

(b) Dark current and 1 nC beam image and beam simulation.

Figure 1: Dark current and beam images taken at the screen 1.27 m downstream from the cathode. Machine parameters for the nominal SASE operation are used. The simulations in the small boxes have been made with ASTRA [4]. A collimator is located at the same position as the screen. The dark current from the cathode has a similar size as the 1 nC bunch. Therefore, the dark current cannot be chopped with the collimator efficiently.

* jang.hui.han@desy.de

rent. With the influence of the focusing solenoid, the size of the dark current and the beams are similar at the collimator (see the simulations in Fig. 1).

For a better efficiency, the collimator should be located more downstream because the dark current is strongly overfocused. But, the collimator position is limited by the cryo tank of the first acceleration module. The dark current gets larger than beams as propagating downstream because the dark current has a lower momentum than the beams. This spreading dark current generates radiation doses at the accelerator modules, the bunch compressor and the other beamlines. After the first acceleration module, the dark current can get a kinetic energy of several tens MeV and possibly produce neutrons and γ rays especially at the first bunch compressor. Therefore, it is desirable to collimate the dark current before the first module. This situation is, however, significantly improved at the XFEL design parameters.

XFEL GUN

The XFEL gun will operate with 60 MV/m max rf field for a lower beam emittance and 700 μs rf pulse length for a long bunch train [5]. The dark current generated in the gun is an issue because the dark current might be very high due to the high rf field. Extrapolating the measured dark current level to gradients of 60 MV/m by means of the Fowler-Nordheim equation yields dark current levels in the mA range. This ignores conditioning effects. Moreover is a reduction of the dark current by improved cleaning techniques as dry-ice cleaning expected.

At FLASH a fraction of the dark current has a momentum as high as the electron beam [3]. As increasing the rf field in the gun cavity, the optimum emission phase for the highest momentum gain and the smallest transverse emittance is shifted toward 90° of the rf phase. At FLASH the optimum emission phase is about 38°. When 60 MV/m max field is applied to the FLASH gun cavity (type #1), the optimum emission phase will be shifted to 45°. This means that a larger fraction of the dark current emitted around 90° rf phase will overlap with the electron beam in the momentum spectrum.

In order to separate the momentum distribution of the dark current from the beam, the half cell of the gun cavity is elongated by 10 mm (type #2). The on-axis rf field profiles of the two cavity types are shown in Fig. 2. The rf field profile is calculated with SUPERFISH [6]. When the half cell is longer, the electrons have to start at an earlier rf phase to gain the most effective acceleration through the cavity. The dark current starting around 90° will be too late to be efficiently accelerated.

Beam dynamics

Machine parameters of the injector, including the gun and the first acceleration module, are optimized for a minimum emittance (Fig. 3 and Table 1). When the half cell is elongated, the optimum emission phase is shifted toward

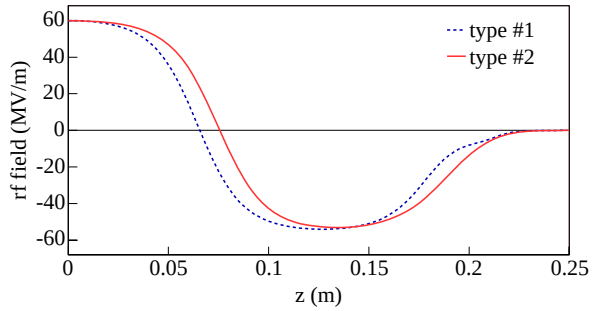

Figure 2: On-axis rf field profile for two gun types.

0°. For cavity type #1, the optimum emission phase is 45°, resulting in an rf field of 42 MV/m at cathode during emission. For cavity type #2, optimum emission phase is 31° and the rf field during emission is 31 MV/m.

In photocathode rf guns, a strong rf field suppresses the beam expansion due to the space charge forces during the emission of high charge density electron beams. Because the emission field is lower in gun type #2, the initial beam size at cathode need to be larger in order to reduce the space charge force.

The kinetic energy of the emitted electrons is assumed to be 0.55 keV and an isotropic emission is assumed according to Ref. [7]. The kinetic energy of electrons emitted from Cs_2Te cathode has been measured in laboratory condition with a very low electric field at cathode [8].

In a high rf field, a Cs_2Te cathode changes its surface properties and the kinetic energy of the emitted electrons increases with the field strength [9]. For the case of gun type #1, the kinetic energy of the emitted elec-

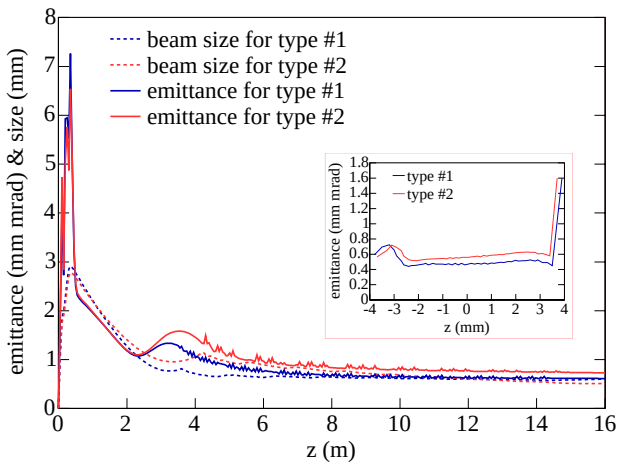

Figure 3: Rms beam size and normalized emittance evolution simulated with ASTRA. The simulation parameters are summarized in Table 1. The transverse slice emittances at z = 30 m are shown in the small box. The temporal profile of the electron bunches at z = 30 m is a hat-shape similar to the initial distribution of the bunch, i.e. the temporal profile of the drive-laser.

Table 1: Simulation parameters for two gun types.

Parameter	Type #1	Type #2
Initial distributions of electrons[a]		
transverse[b]	0.45 mm rms	0.55 mm rms
temporal (flat-top)	2 ps rise/fall and 20 ps fwhm	
thermal ε [c]	0.37 mm mrad	0.47 mm mrad
Gun		
max rf field		
at cathode	60 MV/m	60 MV/m
at full cell	54 MV/m	53 MV/m
emission phase	45°	31°
rf field at emission	42 MV/m	31 MV/m
max solenoid field	0.222 T at 0.28 m	0.226 T at 0.29 m
Accelerator[d]		
max rf field	20 MV/m	20 MV/m
start of 1st module	3.43 m	4.05 m
Simulation result[e]		
bunch charge	1 nC	1 nC
trans. projected ε	0.60 mm mrad	0.64 mm mrad
trans. slice ε [f]	0.47 mm mrad	0.56 mm mrad
bunch length	2.05 mm	1.95 mm
mean energy	90.1 MeV	90.4 MeV
energy spread	1.19 MeV rms	1.12 MeV rms
long. emittance	302 mm keV	262 mm keV

a This initial distribution is determined by controlling the three dimensional shape of the drive-laser at the cathode.
b Homogeneous distribution.
c Assuming the kinetic energy of emitted electrons to be 0.55 eV.
d Simulations include the acceleration with 8 $\times$ 9 cell TESLA type cavities.
e 200 000 macro particles are used for the tracking simulation with ASTRA.
f At the center of bunch.

trons is 0.738 eV according to the emission model in Ref. [9]. This kinetic energy rise and the field enhancement for photoemission increases the thermal emittance up to 0.59 mm mrad. For the case of gun type #2, the kinetic energy of the emitted electrons is 0.675 eV and the thermal emittance is estimated to 0.69 mm mrad.

Dark current

With the machine parameters obtained with the beam optimizations, dark current has been simulated (Fig. 4). For the two gun types, the same amount of dark current from the cathode is tracked with ASTRA. The inner structure of the cavities and beam pipe with 35 mm diameter is considered as aperture.

When machine parameters for the beam optimization are used, the amount of the surviving dark current to the entrance of the first acceleration module is below 40% for gun type #2 compared to the gun type #1 case. The overlapping of the momentum distribution with the beam is significantly reduced, which is of great benefit for the dark current collimator.

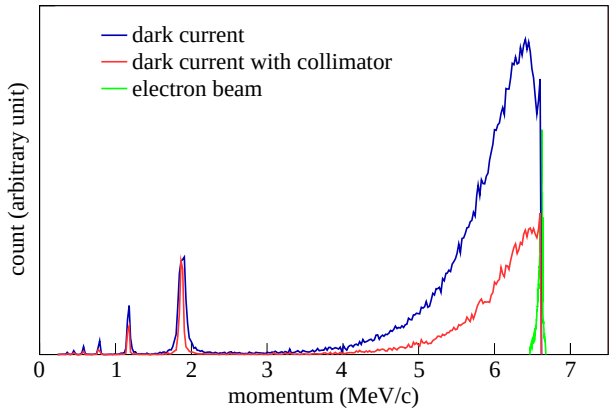

(a) Gun type #1.

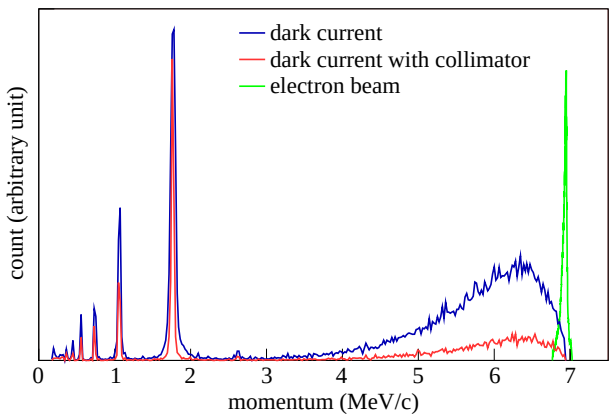

(b) Gun type #2.

Figure 4: Simulated momentum spectra of dark current and 1 nC beam. The machine parameters for the beam optimization are used. The dark current surviving to the entrance of the first acceleration module is shown. Because the emission phase of dark current is higher that the optimum emission phase, some part of the dark current stays in the gun cavity for several rf cycles. When the dark current finally escape from the gun cavity, the dark current can have certain definite momentum, appeared as spikes. The dark current reduction by the geometrical collimator is shown as well.

COLLIMATION IN THE GUN SECTION

In the gun section, two kinds of collimators can be used. The first one is a geometrical collimator for different transverse sizes (Fig. 5). Dark current with lower momentum is strongly overfocused by the solenoid field which is optimized for the beam focusing. The overfocused dark current is lost at the beam pipe. If a circular collimator is inserted inside the pipe, the dark current with larger transverse size can be cut out. Due to the cryo tank, a possible last position

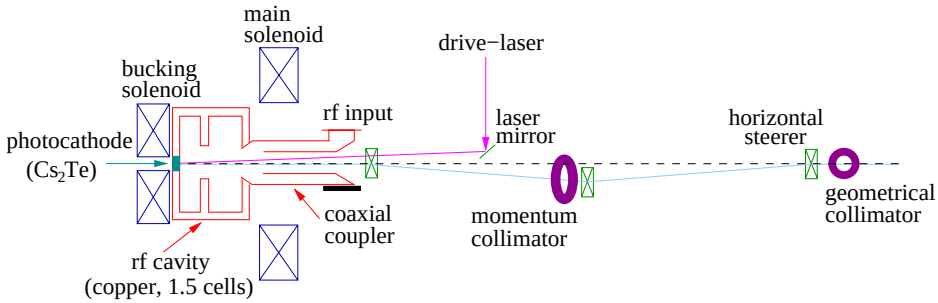

Figure 5: Schematic of gun section. The light blue line shows the reference path of beams. The circular shape collimator chops the dark current with larger transverse size. The elliptical shape collimator uses a difference in the momentum distributions of beams and dark current. The first horizontal steerer projects the momentum distributions of beams and dark current to the horizontal axis.

of the collimators is 1.2 m upstream from the entrance of the first acceleration module. For gun type #1, the position for the collimator is at 2.2 m. At that position, the electron beam size is 1.13 mm rms (Fig. 3) and a collimator with 10 mm diameter can be applied. With this collimator, the dark current from the gun can be reduced by 66%. For gun type #2, the position for the collimator is 2.8 m. The electron beam size will be 1.03 mm rms and a collimator with 10 mm diameter can be applied. With this collimator, the dark current current from the gun can be reduced by more than 70%. Taking into account the high losses at the beam pipe for gun type #2, the dark current behind the circular collimator is only 30% for type #2 compared to type #1.

The second possibility is a momentum collimator. This collimator is combined with a series of steerers and possibly has an elliptical shape with the major axis in the horizontal direction. If the first steerer kicks the beam and the dark current, the dark current with lower momentum is deflected more and can be chopped with a collimator. The minor axis length of the inner ellipsoid is determined by the beam size and the major axis length is determined by the beam size and the momentum distribution at the collimator position. When the dark current lower than 6.2 MeV/c, i.e. 10% lower than the mean momentum of the beam, is cut out with the elliptical collimator, again 75% of the dark current is possibly reduced for gun type #2. For gun type #1, 35% of the dark current is possibly reduced when the dark current lower than 5.9 MeV/c, again 10% of the mean momentum of the beam, is cut out.

The momentum collimator can be used to block the dark current from the acceleration modules which might have a momentum of several tens or even hundreds MeV/c. When the high energy dark current hits the Cs_2Te cathode, the emissive film might be seriously damaged.

CONCLUSION

The XFEL gun requires an rf field as high as 60 MV/m for 1 nC bunches with an transverse emittance below 1 mm mrad. But, such high rf field might generate very high dark current. With elonging the half cell length of the gun cavity, the dark current can be separated from the beam in the momentum spectrum. Collimators can be efficiently used to chop the dark current with lower momentum before the first acceleration module.

ACKNOWLEDGMENTS

The authors thank M. Krasilnikov and F. Stephan for helpful discussions.

REFERENCES

[1] B. Dwersteg, K. Flöttmann, J. Sekutowicz and Ch. Stolzenburg, “RF gun design for the TESLA VUV Free Electron Laser”, Nucl. Instr. and Meth. A **393** (1997) p. 93.

[2] S. Schreiber, private communication.

[3] J.-H. Han *et al.*, “Dark current and multipacting in the photocathode rf gun at PITZ”, in *Proceedings of the 2005 PAC*, p. 895.

[4] `http://www.desy.de/~mpyflo/`.

[5] `http://xfel.desy.de/`.

[6] J. H. Billen and L. M. Young, Poisson Superfish, LA-UR-96-1834.

[7] K. Flöttmann, “Note on the thermal emittance of electrons emitted by cesium telluride photo cathodes”, TESLA FEL Reports 1997-01, 1997.

[8] D. Sertore *et al.*, “Cesium telluride and metals photoelectron thermal emittance measurements using a time-of-flight spectrometer”, in *Proceedings of the 2004 EPAC*, p. 408.

[9] J.-H. Han, “Dynamics of Electron Beam and Dark Current in Photocathode RF Guns”, PhD thesis, University Hamburg, 2005.

IMPACT OF THE CATHODE ROUGHNESS ON THE EMITTANCE OF AN ELECTRON BEAM

M. Krasilnikov*, DESY, Zeuthen, Germany.

Abstract

An RF photo injector for the European XFEL should produce electron beams with normalized transverse emittance under 1 mm mrad. In order to achieve this high performance of the electron source the electric field at the photo cathode has to be increased up to 60 MV/m. The emittance budget of the optimized XFEL photo injector contains a significant part of thermal (intrinsic) emittance. A roughness of the cathode could lead to an additional uncorrelated divergence of the emitted electrons and therefore to an increased thermal emittance. The cathode roughness has been modelled using an analytical approximation and numerical simulations. The influence of the roughness parameters and the increase of the electric field have been studied.

INTRODUCTION

The main goal of the Photo Injector Test facility in Zeuthen (PITZ, [1]) is to optimize electron sources for FEL injectors, including already existing (FLASH) and future (XFEL) facilities. Increasing the maximum gradient at the photo cathode in the rf gun from 40 MV/m to 60 MV/m is one of the main improvements towards XFEL requirements. This implies (with taking into account an optimum launch rf phase) an increasing of the electric field at the photo cathode at the moment of the emission from 24 MV/m to 42 MV/m. The improved normalized beam emittance in the injector is expected to be under 1 mm mrad. Besides earlier suppressing of the space charge effect in the rf gun the gradient increase also leads to a significant increase of the contribution of initial (thermal) emittance in the total emittance budget.

The cathode roughness increases the intrinsic divergence of the emitted electron bunch. A model with a periodical roughness of the cathode is applied to study the geometrical emission effect in dependence on roughness parameters. A single bump model is used to study the impact of the applied electric field on the initial emittance.

THE MODEL OF THE PERIODIC SURFACE ROUGHNESS

2D model, normal emission only

Consider a cathode surface given by the formula

$$z = h\cos(kx)\ , \tag{1}$$

where $2h$ is the roughness depth and $\lambda = 2\pi / k$ is the roughness period along the cathode surface. Let's consider first the case of the emission normal to the cathode surface, so $\varphi = 0$ (Figure 1a), what implies zero thermal emittance from the non-perturbed (no roughness) cathode.

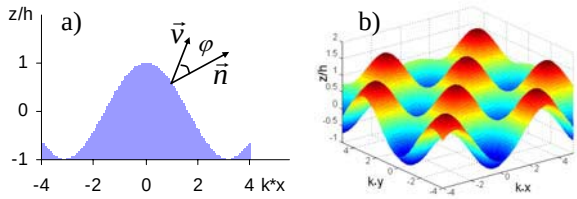

Figure 1: Periodic roughness, 2D (a) and 3D (b) models.

Transverse component of the electron velocity is

$$v_x = v_0 \frac{\xi \sin(kx)}{\sqrt{1+\xi^2 \sin^2(kx)}}, \tag{2}$$

where $\xi = kh$, v_0 is velocity of the emitted electron. After corresponding integration over the roughness period one can obtain an expression for the emittance induced by the rough cathode surface

$$\varepsilon_x^{2D} = \sigma_x \cdot \sqrt{\langle p_x^2 \rangle} \approx 2\sigma_x \sqrt{\frac{eE_0}{mc^2} h \cdot \left(1 - \frac{1}{\sqrt{1+\xi^2}}\right)}, \tag{3}$$

where σ_x is an rms electron beam size at the cathode, $p_x = \frac{v_x / c}{\sqrt{1 - v_0^2 / c^2}}$ is the normalized transverse momentum and E_0 is the electric field at the cathode at the moment of the emission.

3D model, normal emission only

A cathode surface with periodic roughness is given

$$z = h\cos(kx)\cos(ky)\,, \tag{4}$$

where $x - y$ isotropy is assumed (Figure 1b). Transverse component of the electron emission velocity:

$$v_x = v_0 \frac{\xi \sin(kx)\cos(ky)}{\sqrt{1+\xi^2\left(\sin^2(kx)\cos^2(ky) + \cos^2(kx)\sin^2(ky)\right)}}. \tag{5}$$

Transverse emittance induced by 3D rough cathode surface (4) is

$$\varepsilon_x^{3D} = \sigma_x \cdot \sqrt{\langle p_x^2 \rangle} \approx 2\sigma_x \sqrt{\frac{eE_0}{mc^2} h \cdot I(\xi)}, \tag{6}$$

where

$$I(\xi) = \frac{\xi^2}{4\pi^2} \int_{-\pi}^{\pi} dX \int_{-\pi}^{\pi} \frac{\sin^2 X \cos^2 Y}{1+\xi^2\left(\sin^2 X \cos^2 Y + \cos^2 X \sin^2 Y\right)} dY.$$

One can show, that for the for same roughness parameters the emittance ε_x^{3D} is in a factor $\sim\sqrt{2}$ smaller than 2D one, because the effective roughness depth ($\sim hI(\xi)$) in

*mikhail.krasilnikov@desy.de

the 3D case is smaller. A ratio $\varepsilon_x^{3D} / \varepsilon_x^{2D}$ is shown in Figure 2 as a function of the roughness parameter ξ.

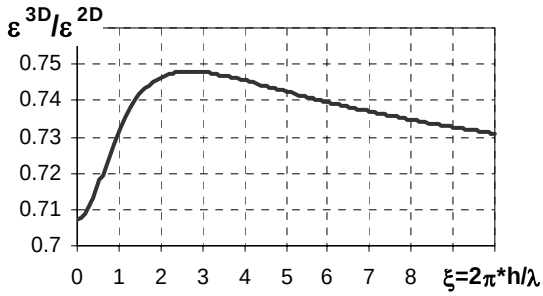

Figure 2: Emittance from 3D surface (4) compared to 2D case (1) vs. roughness parameter $\xi = 2\pi h / \lambda$.

2D model with emission distribution

In the case of nonzero non-perturbed thermal emittance there is an emission in a finite angle φ, as it happens i.e. by emission from the Cs2Te photo cathode. Using approach described in [2], one assumes that electrons are emitted isotropically in a cone with an angle $\varphi_m = \arccos\sqrt{E_A / E_k}$ with respect to the local surface normal, where E_A is the electron affinity of the emitting material and E_k is the electron kinetic energy. For the Cs2Te photo cathode $E_A \approx 0.2eV$, by a applying driving laser with 262 nm wavelength $E_k \approx 0.75eV$. This model yields a formula for the thermal emittance of the smooth cathode (no roughness assumed) [2]:

$$\varepsilon_x^{th,0} = \sigma_x \sqrt{\frac{2E_k}{mc^2}} \cdot \sqrt{\frac{2+\cos^3\varphi_m - 3\cos\varphi_m}{6(1-\cos\varphi_m)}}. \qquad (7)$$

Within an applied roughness model (1) a transverse momentum of the electron emitted at angle φ to the local normal is given

$$p_x = \sqrt{\frac{2E_k}{mc^2}} \cdot (\sin\varphi\cos\theta\cos\alpha + \cos\varphi\sin\alpha), \qquad (8)$$

where θ is a local azimuth angle, $\alpha(x)$ is a rough surface slope obtained from (1):

$$\tan\alpha = -\xi \sin kx. \qquad (9)$$

Applying triple integration to p_x^2 over $\varphi \in [0;\varphi_m]$, $\theta \in [0;\pi]$ and over the roughness period [3] yields a formula for the thermal emittance from the periodic rough surface:

$$\varepsilon_x^{th,rough} = \sigma_x \sqrt{\frac{2E_k}{mc^2}} \times \qquad (10)$$
$$\times \sqrt{\frac{(2+\cos^3\varphi_m - 3\cos\varphi_m)\cos\alpha_m + 2(1-\cos^3\varphi_m)(1-\cos\alpha_m)}{6(1-\cos\varphi_m)}},$$

where $\cos\alpha_m = 1/\sqrt{1+\xi^2}$. Obviously, that in the absence of the roughness ($\alpha_m = 0$) the formula (10) is reduced to the expression (7).

Thermal emittance growth $\left(\varepsilon_x^{th,rough} / \varepsilon_x^{th,0} - 1\right)$ due to the cathode roughness is shown in Figure 3. From this plot thermal emittance growth <30% corresponds to the cathode roughness with $\lambda > 5h$, for 10% growth $\lambda > 12h$ is required. Preliminary cathode plug roughness measurements performed at INFN LASA (Milano) [4] showed that photo cathodes presently used at PITZ have roughness with $\sigma \sim 10nm$. In order to keep the thermal emittance growth under 10% it is necessary to provide a roughness period over 100 nm.

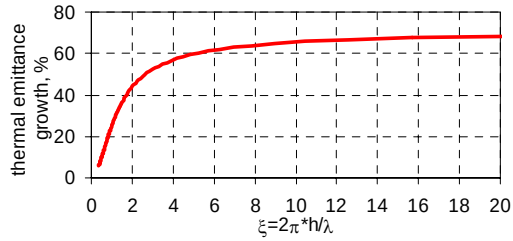

Figure 3: Thermal emittance growth vs. roughness parameter $\xi = 2\pi h / \lambda$. Ideal Cs2Te cathode parameters $E_A = 0.2eV$, $E_k = 0.75eV$ have been assumed [2].

In practical case the electron affinity is affected by many factors. It is well known that the quantum efficiency (QE) of the photo cathodes decreases with operation time; electron affinity increase due to the change of the cathode surface status is one of the possible mechanisms explaining QE degradation. On the other hand an applied rf field lowers the electron affinity due to the Schottky effect [5]. The electron affinity can be modelled as [6]:

$$E_A = \kappa E_{A,0} - \sqrt{\frac{e^3}{4\pi\varepsilon_0}\beta_{ph}E_0}, \qquad (11)$$

where κ is responsible for the increase with a time of the initial affinity $E_{A,0}$, β_{ph} is a field enhancement factor for photoemission, which partially can include also a surface roughness effect. A thermal emittance growth as a function of roughness period and electron affinity is shown in Figure 4 with a contour plot.

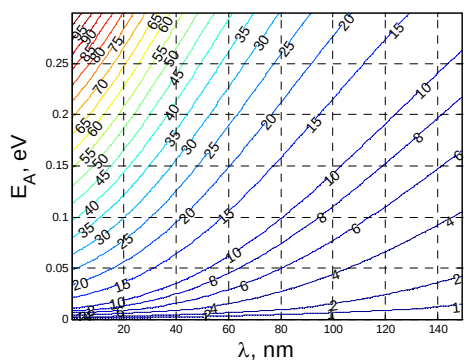

Figure 4: Thermal emittance growth $\left(\varepsilon_x^{th,rough} / \varepsilon_x^{th,0} - 1\right)$ given in % as a function of roughness period and electron affinity. For this plot $h = 10nm$, $E_k = 0.75eV$ is assumed.

DEPENDENCE ON ELECTRIC FIELD

In order to study the dependence of the initial emittance on the electric field during emission a model of single bump can be used. A two-dimensional model of the bump is described in [7]:

$$\frac{z}{b} = \sqrt{1 + \frac{a^2}{b^2 + x^2}} - 1, \qquad (12)$$

where parameters a and b are constants depending on roughness depth and width. Typical bump shapes are shown in Figure 5.

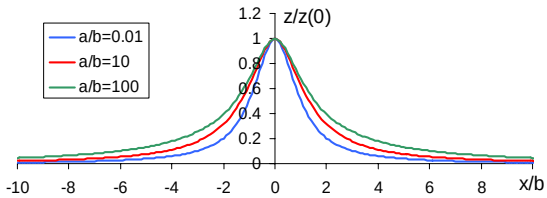

Figure 5: Rough cathode surface: single bump model (10). Upper curve corresponds to $a/b = 100$.

The choice of equation (12) for the rough cathode surface is motivated by the simple conformal transformation

$$\zeta = u + iw = \sqrt{(x + iz + ib)^2 + a^2} - ib, \qquad (13)$$

which maps the electric field of a plane capacitor onto the field of the surface (12). An analytical expression for the electric field can be obtained from the corresponding conformal transformation

$$E_x + iE_z = \frac{-iE_o \cdot [x - i(y + b)]}{\sqrt{[x - i(y + b)]^2 + a^2}}. \qquad (14)$$

The electric field lines are shown in Figure 6.

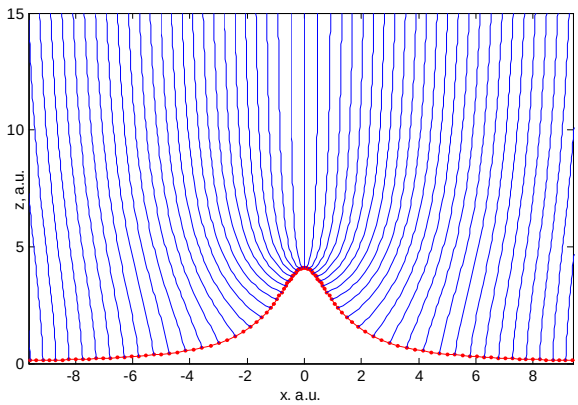

Figure 6: Electric field lines of the bump (10).

Once the electric field magnitude E_o and the bump parameters a and b are specified, the field profile is determined from (14) and particle position (x, z) and momentum (p_x, p_z) can be numerically integrated in time according to

$$\frac{d}{d(ct)}\begin{pmatrix} p_x/(mc) \\ p_z/(mc) \end{pmatrix} = \frac{e}{mc^2}\begin{pmatrix} E_x \\ E_z \end{pmatrix}$$
$$\frac{d}{d(ct)}\begin{pmatrix} x \\ z \end{pmatrix} = \frac{1}{\sqrt{1 + p_x^2 + p_z^2}}\begin{pmatrix} p_x \\ p_z \end{pmatrix}, \qquad (15)$$

with initial conditions:

$$x_n(t=0) = x_{n0}; \quad z_n(t=0) = z_{n0};$$
$$p_{xn}(t=0) = 0; \quad p_{zn}(t=0) = 0. \qquad (16)$$

Parameter u from (13) characterizes the location on the surface from which an electron is emitted ($w = 0$):

$$x_{n0} = \frac{u_n b}{z_n + b}; \quad u_n = n \cdot u_N / N; \quad n = 1...N$$
$$z_{n0} = -b + \sqrt{\frac{a^2 + b^2 - u_n^2 + \sqrt{(u_n^2 - a^2 - b^2) + 4u_n^2 a^2}}{2}}. \qquad (17)$$

The last emission location u_N can be defined from the condition:

$$z_N = 0.01 \cdot z(0) = 0.01 \cdot \left(\sqrt{a^2 + b^2} - b\right) \qquad (18)$$

It should be noticed that within this approach the space charge effect is neglected.

Shown in Figure 7 are typical numerical results of the local electron divergence $p_x/(mc)$ as a function of the emission parameter u/u_N at the moment in time when electrons reach the region of homogeneous field. At this z-position the electric field varies along x-axis not more than by 1%, it means that the field at this distance from the cathode does not "feel" the rough surface.

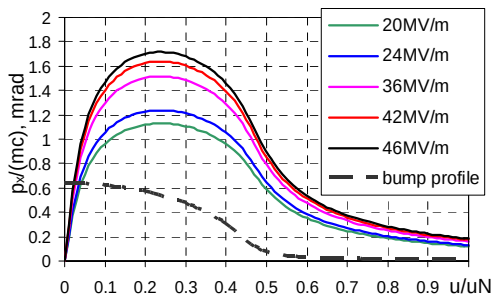

Figure 7: Local divergence as a function of u/u_N for various E_0. Roughness parameters: depth $h \approx 20nm$, width $\lambda = 10nm$ ($a = 21.52nm; b = 1.57nm$).

An estimation of the emittance growth due to the increase of the applied electric field could be done based on the analysis of the electron divergence for various roughness parameters. Emittance growth as a function of the applied electric field in comparison to the case of $E_0 = 24MV/m$ is shown in Figure 8. Relative emittance growth for various bump widths λ has a slope of about $2\%/(MV/m)$, so field increase up to $42MV/m$ results in a ~30% emittance growth.

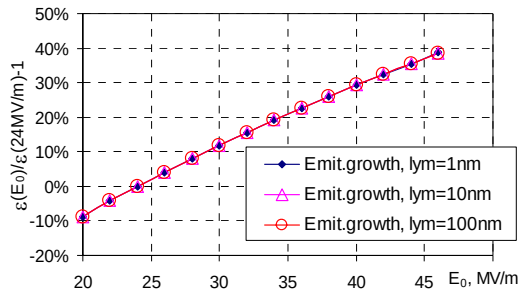

Figure 8: Emittance growth as a function of the electric field, compared to the emittance at $E_0 = 24MV/m$.

Simulations based on the assumption of the neglecting the space charge effect have been performed. Modelling the space charge limited emission from the bumpy cathode surface in the steady state regime [7] showed that the space charge may reduce the deterioration effect of the surface roughness. But from the other hand the cathode roughness may result also in additional density non-homogeneity of the emitted electron beam, which could lead to degradation of the beam quality.

CONCLUSIONS AND OUTLOOK

The photo cathode roughness contributes to the initial emittance of the electron beam. Several models of the cathode rough surface have been used to estimate the effect of the thermal emittance growth. Thermal emittance growth induced by the cathode roughness has been studied for different roughness parameters, including photo emission issues from a Cs2Te photo cathode.

Since one of the main improvement steps toward XFEL requirements is an increase of the maximum rf gun gradient from 40 to 60 MV/m, the impact of increasing the field at the cathode has been studied. The model of single bump has demonstrated that the increase of the electric field at the cathode could result in a ~30% growth of the roughness contribution to the initial thermal emittance.

Studies on the role of the space charge effect during emission from rough cathode as well as more detailed measurements of the cathode roughness have to be performed in order to improve the understanding of the thermal emittance features.

ACKNOWLEDGMENTS

I would like to thank K.Floettmann, F.Stephan and PITZ members for helpful discussions.

REFERENCES

[1] A. Oppelt et al., “Status and first results from the upgraded PITZ facility”, FEL 2005, Stanford, Aug.2005.
[2] K. Floettmann, “Note on the thermal emittance of electrons emitted by Cesium Telluride photo cathodes”, TESLA FEL Reports 1997-01, 1997.
[3] J. Schmerge, private communication.
[4] D. Sertore, private communication.
[5] R.Gomer, “Field emission and field ionization”, American Institute of Physics, New York, 1993.
[6] J.-H. Han, “Dynamics of electron beam and dark current in phototcathode rf guns”, PhD thesis, Hamburg University, 2005.
[7] Y. Lau, “Effects of cathode roughness on the quality of electron beams”, J. Appl. Phys 61(1), Jan. 1987.

FIRST EXPERIENCE WITH THE MACHINE PROTECTION SYSTEM OF FLASH

L. Fröhlich*, University of Hamburg and DESY, Hamburg, Germany
A. Hamdi, M. Luong, J. Novo, CEA-Saclay, Gif-sur-Yvette, France
M. Görler, P. Göttlicher, D. Nölle, D. Pugachov, H. Schlarb, S. Schreiber,
M. Staack, M. Werner, DESY, Hamburg, Germany

Abstract

The linac-based free electron laser facility FLASH[1] at DESY Hamburg is designed to transport electron beams with high average power of more than 50 kW. To protect the machine from serious damage passive and active systems have been installed. This paper concentrates on the fast active machine protection system (MPS), that stops the production of new bunches if hazardous machine conditions are detected. Furthermore, the results from the commissioning of the fast beam interlock system are presented that has for the first time allowed to operate the accelerator with macropulses of up to 600 bunches.

INTRODUCTION

The FLASH linac currently employs 40 superconducting 9-cell cavities distributed over five cryogenic modules to accelerate an electron beam to an energy of up to 700 MeV. The beam is guided through an undulator of approximately 30 m length to initiate a free electron laser (FEL) process based on the SASE principle. The facility is now alternating between blocks of accelerator development and user operation, supplying experimentators with pulsed radiation of high brilliance in the XUV wavelength range between 13 and 50 nm. [1]

As typical for superconducting linacs, the transported bunches are grouped in macropulses or bunch trains. The viable rf pulse length limits the length of a bunch train to 800 µs. With the standard bunch frequency of 1 MHz and a macropulse repetition rate of 5 Hz, the power delivered to the beam dump amounts to ∼3 kW. If the future option for high duty cycle operation with 9 MHz/10 Hz is realized, this figure increases above 50 kW. Even on partial loss of the beam along the linac, the induced heat load and radiation can cause substantial damage to accelerator components. Therefore, an active protection system is required to ensure safe operation of the machine.

MPS ORGANIZATION

The machine protection system of the FLASH linac is a substantially enhanced version of the system used in phase 1 of the TESLA Test Facility [2]. Since the description of the basic design in [3], the operational experience gained during the commissioning of FLASH has led to a number of changes that will be discussed in the following.

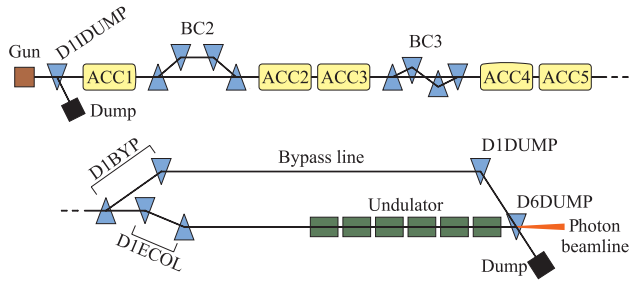

Figure 1: Schematic of the FLASH linac. The depicted elements include the five acceleration modules *ACCn*, the two bunch compressors *BCn*, and the main dipole magnets.

Detection Schemes

The detection of beam and darkcurrent losses in the linac is based on two independent approaches. The FPGA-controlled *Toroid Protection System* [4] measures the transmission by comparing the readings from charge monitors (toroids) in the injector and dump part of the machine, and generates alarms within less than 110 ns if one of several configurable thresholds is exceeded.

The second system for fault detection is constituted by a set of 51 photomultipliers and 18 secondary emission multipliers distributed along the machine. These *beam loss monitors* (BLMs) provide a bunch-resolved online display of electromagnetic shower intensities (Fig. 2). VME-based alarm generators with a reaction time far below 1 µs check whether user-defined thresholds for one or multiple bunches, or for the integrated signal are exceeded. They also generate an alarm on failure of the high voltage supply, or if a misconfiguration has been detected.

As the permanent magnets of the undulator are susceptiple to radiation, close monitoring of beam losses is required to avoid degradation of the field quality. Therefore, the undulator section features the highest concentration of BLMs in the whole machine, with 26 monitors currently in place and another 12 to be installed until the end of the year.

Response to alarms

The purpose of any MPS is to detect situations which may lead to damage of components, and to take appro-

* lars.froehlich@desy.de

[1] Since April 2006, FLASH—Free Electron Laser in Hamburg—is the new name for the VUV-FEL, part of the TESLA Test Facility TTF.

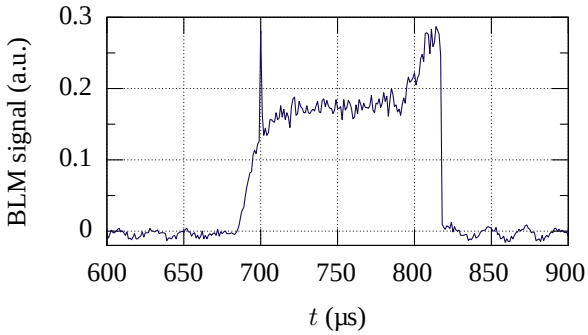

Figure 2: Signal from a beam loss monitor behind the collimation section. At $t = 700$ µs, a part of one single bunch is lost. The losses visible from 690–820 µs are caused by darkcurrent from the gun.

priate counter-measures. These potentially harmful conditions can be classified into three main categories:

Fast Since the loss of a complete macropulse may already present a substantial hazard, a fast system must stop the production of bunches within the train, i.e. on a time scale of few µs.

Intermediate For the major part of potential dangers, a reaction between two macropulses is sufficient. Since the time constants of all magnets employed at FLASH are of the order of tens of milliseconds or more, the failure of power supplies falls into this category.

Slow Even if moderate losses of darkcurrent or of few bunches do not pose an immediate threat, they contribute to the deposited radiation dose, and may thus cause damage over time scales of minutes or days. This issue is of special importance for the undulator.

To guarantee an appropriate response to events on any of these timescales, the FLASH MPS uses two independent subsystems: A network of *Beam Interlock Concentrators* for fast events, and a programmable logic control—the *Beam Interlock System*—for intermediate and slow events.

Beam Interlock Concentrators (BICs)

The function of the BIC modules is simply a fast logical OR concentrating 16 alarm inputs to two outputs within a processing time of ∼50 ns, with a configurable mask that allows to suppress any of the input channels. Ten modules are currently in use, connected in a tree-like fashion as illustrated in Fig. 3. Most of the input channels are used by the 69 BLM alarm signals, but also the TPS, the cavity quench detection, and a fast vacuum shutter are connected. When any of the inputs show an alarm, the top-level BICs will switch off the injector laser to suppress the production of new bunches in the gun, and cut the first acceleration module off from rf power as a precaution against further transport of darkcurrent.

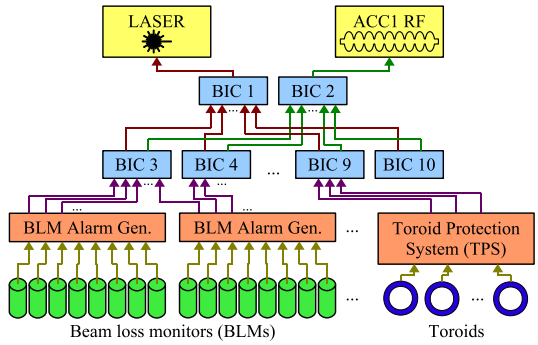

Figure 3: Organization of *beam interlock concentrators*. BIC 3–10 collect alarms from various alarm generators and relay them to BIC 1–2, which switch off the photoinjector laser and the rf power of the first acceleration module.

Measurements have confirmed that the reaction time of the BIC system to beam losses is below 4 µs. This time is dominated by cable delays, and it means that up to three more bunches enter the machine after detection of the loss at the standard bunch frequency of 1 MHz.

Beam Interlock System (BIS)

While the BIC system has been designed to guarantee minimum response time to fast events, the emphasis for the *Beam Interlock System* has been placed on flexibility. The programmable logic control continuously monitors the status of critical components like magnet power supplies, screens, collimators, and valves. It also checks the flow of cooling water, and the compliance to temperature limits.

From the status of the main dipole magnets and of several valves, the BIS deduces an *operation mode* defining the basic beam path through the machine according to Tab. 1. As a simple protective measure, no beam is allowed if there is no valid operation mode.

Furthermore, the BIS selects one of three *beam modes* as shown in Tab. 2. Besides defining the maximum allowed number of bunches per macropulse, the beam mode also determines whether the fast protection via the BIC system is active. This policy allows the operation under charge loss as long as only few bunches per macropulse are needed, which is necessary for tuning and for experiments using the beam. While the operator can choose between short and long mode, the BIS will automatically reduce to short or single mode if obstacles like screens are moved into the beam path, or if other conditions are met.

Apart from these general safety features, attempts have been made to limit the radiation dose deposited in the undulator with a special BIS routine. Due to the dense placement of BLMs in the undulator section, there is considerable overlap in their geometrical acceptances, and electromagnetic showers are usually observed on more than one monitor. The *BIS-BLM protection* takes advantage of this by counting the number of simultaneous BLM alarms in

Table 1: List of *operation modes* with the required valve and dipole magnet settings, and the maximum allowed beam mode.

operation mode	*conditions*	*beam mode*
Gun	gun valve open, ACC1 valve closed, D1IDUMP off	short
Analysis	gun valve open, ACC1 valve closed, D1IDUMP on	long
Bypass	all valves open, D1BYP on, D1DUMP on, D6DUMP off	long
FEL	all valves open, D1BYP off, D1ECOL on, D6DUMP on	long

Table 2: List of *beam modes* with the maximum allowed number of bunches per macropulse.

beam mode	*nr. of bunches*	*BIC system*
Single	2	disabled
Short	30	disabled
Long	no limit	active

the section. If 2 alarms are pending over 120 s, 4 over 30 s, or 8 over 5 s, the beam is stopped and has to be restarted manually via the control system. To allow tuning, the tolerances of this routine can be increased for 30 minutes.

Figure 4 shows the average dose rates in the first two undulator segments measured with thermoluminescence dosimeters [5]. Since the activation of the BIS-BLM protection in September 2005, the dose rates have been predominantly below 10 Gy/day, indicating that—together with an overall improved understanding of orbit and optics—the requirement of avoiding beam stops has led to a reduction of losses.

OPERATION WITH LONG MACROPULSES

The commissioning of MPS components relevant for long pulse operation has been completed in August 2006. The increase of the gun rf pulse length from 70 to 800 µs led to the expected rise of darkcurrent losses in the bunch compressors and in the collimation section by about an order of magnitude. By successive optimization of orbit and optics, the beam losses could be reduced to a minimum, and operation of the FEL with 600 bunches per macropulse was possible with minimal interference of the BIC system. At an average energy of 20 µJ per photon pulse, the output power during the test run has reached about 60 mW.

Imperfections of the rf regulation constitute the main problem in setting up a stable transmission of long macropulses. Due to poorly compensated beam loading or transient behavior at the beginning of the rf pulse, the bunches at the head of the macropulse can experience amplitudes and phases of the accelerating field that deviate significantly from the designated values. For the first bunch, an energy deviation of 0.6 % with respect to the last bunches of a 300 µs long macropulse has been measured after the first acceleration module. This effectively enlarges the total phase space occupied by the macropulse and thus reduces the tolerance for jitter and drifts.

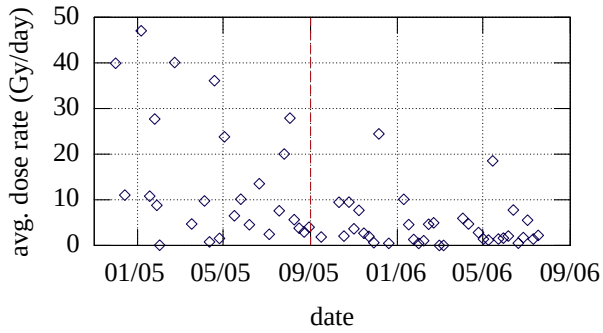

Figure 4: Average dose rates measured in the first two undulator segments.

CONCLUSION AND OUTLOOK

The FLASH machine protection system reliably prevents damage of the accelerator due to beam losses, with the total downtime of the linac caused by MPS failures and misconfigurations amounting to only few hours. It is also successful in limiting the slow accumulation of radiation dose in the undulator.

While the number of bunches per macropulse has been limited to 30 during past accelerator runs, the recent commissioning of the beam interlock concentrator system with reaction times in the microsecond range now allows to operate the machine with bunch trains of up to 800 pulses. We expect that future user experiments will benefit highly from the improved duty cycle.

ACKNOWLEDGEMENTS

We wish to thank all members of the operation crew for their outstanding commitment and support. The assistance of the controls and low-level rf groups is greatly appreciated.

REFERENCES

[1] V. Ayvazyan, et al., “First operation of a free-electron laser generating GW power radiation at 32 nm wavelength”. Eur. Phys. J. D, 37:297–303, November 2006.

[2] H. Schlarb, et al., “Expansion of the fast linac protection system for high duty cycle operation at the TESLA Test Facility”. EPAC’02, pp. 1966–1968. Paris, France, June 2002.

[3] D. Nölle, et al., “The beam inhibit system for TTF II”. DIPAC’03, pp. 62–64. Mainz, Germany, 2003.

[4] A. Hamdi, et al., “VHDL design and simulation of a fast beam loss interlock for TTF2”. EPAC’04, pp. 2020–2022. Lucerne, Switzerland, 2004.

[5] T. Vielitz, Hasylab, Hamburg, private communication.

EXPERIENCE WITH THE PHOTOINJECTOR LASER AT FLASH

S. Schreiber,*, M. Görler, K. Klose, M. Staack, L. Fröhlich, DESY, Hamburg, Germany
I. Will, I. Templin, MBI, Berlin, Germany

Abstract

The photoinjector laser system of FLASH is a key element for the generation of high quality electron beams required for a stable and reliable operation of the facility. FLASH is the VUV and soft X-ray FEL user facility at DESY. FLASH is based on superconducting accelerating structures allowing to accelerate electron bunch trains of a length of up to 800 μs with a repetition rate of 10 Hz. Based on the standard 1 MHz pattern, the laser provides to some extend a flexible bunch train structure. We report on operational issues and on the performance of the laser system and its integration into the machine protection system.

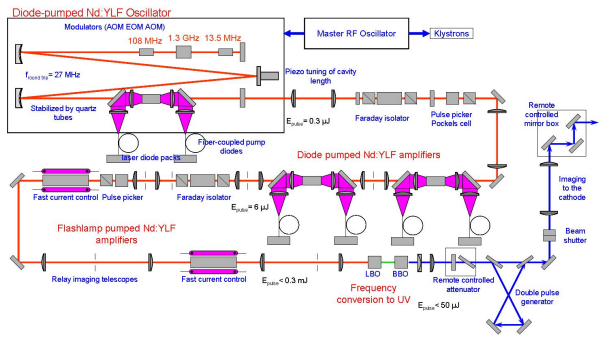

Figure 1: Schematic overview of the laser system.

INTRODUCTION

FLASH is a free electron laser user facility at DESY providing laser-like radiation from the VUV to the soft X-ray wavelength regime.[1, 2] SASE free electron lasers require an excellent beam quality, which is achieved with an injector based on a laser driven rf gun.[3] The electron beam is accelerated with TESLA superconducting modules.

A high quantum efficiency photocathode [4] together with a synchronized mode-locked laser system is used to generate the electron beam structure typical for superconducting accelerators: some thousand bunches in a millisecond long rf pulse. High quantum efficiency cathodes allow to use a laser system with moderate average power in the Watt range.

The user facility FLASH has been realized by upgrading the TESLA Test Facility (TTF) phase 1 FEL to phase 2.[5] The TTF phase 1 laser system [6] has also been upgraded to a partially diode pumped system as described in [7].

In this report we describe the running experience with the laser system and its integration into the machine protection system of FLASH.

OVERVIEW OF THE LASER BASED ELECTRON SOURCE

The FLASH electron source is based on a laser driven L-band 1+1/2-cell rf gun operated with a 5 MW 1.3 GHz klystron. The rf pulse length is up to 900 μs, the repetition rate 5 Hz, up to 10 Hz are possible.

The electron beam is generated by photoemission with a Cs_2Te photocathode. With a forward rf power of 3.2 MW a gradient of 42 MV/m on the cathode surface is achieved on crest. High gradient on the cathode surface is required to preserve excellent beam quality. The cathode exhibit a high quantum efficiency in the range between 1 and 5 % for UV laser light. The charge per bunch required is 1 nC which translates into a laser pulse energy of not more then 0.5 μJ per pulse. The design of the laser accounted for a QE of 0.5 % only, a bunch frequency of 9 MHz within the train and an overhead by a factor of 4. With a conversion efficiency of 15 % from the IR to UV this asks for an average power of 2 W in the infrared.

THE LASER SYSTEM

The laser design is based on a pulsed master oscillator with subsequent amplification stages. Details of the system layout are described in [7], a schematic overview shows Fig. 1.

The laser material chosen is Nd:YLF, lasing at a wavelength of 1047 nm. The material has together with a high gain a long upper-state lifetime of 480 μs, and exhibits only a weak thermal lensing. This makes it suitable to produce pulse trains with milliseconds length. The oscillator and preamplifers are end-pumped with laser diodes emitting at 805 nm with a maximum power of 32 W. The two main amplifiers are flashlamp pumped.

The Pulse Train Oscillator

The pulse train oscillator (PTO) runs at 27 MHz synchronized to the master rf of the accelerator. It is a pulsed osciallator with the advantage of a much higher single pulse energy of 300 nJ as compared to typical cw oscillators. The master provides reference rf signals in the frequency of the accelerator of 1.3 GHz and its harmonics 108, 27, and 9 MHz. The synchronization to the rf is achieved using two

* siegfried.schreiber@desy.de

Figure 2: As an example, the air temperature measured at the laser over a period of 3 days. The temperature reading is within ± 0.02°C.

acousto-optic modulators running at $27/2 = 13.5$ MHz and 108 MHz resp., and an additional electro-optic modulator powered with the amplified 1.3 GHz reference. The latter provides synchronization to the required 1 ps level. The oscillator length is stabilized against temperature drifts with two quartz rods. Quartz has a low temperature coefficient of expansion of $0.6{\cdot}10^{-6}$ m/°C. At the same time, the temperature of the laser room is stabilized to ± 0.02 °C (Fig. 2). Both measures provide the bases for an excellent phase stabilization of the laser pulses with respect to the rf. An active fast feedback loop could be omitted, only a slow feedback acting on the resonator length is implemented.

The phase jitter of the laser pulses in respect to the rf can be estimated using the phase scan technique. The phase stability measured with this technique depends also on the performance of the gun rf amplitude and phase regulation system and therefore only gives an upper limit. The measurement results an rms phase jitter of 0.14 °in respect to 1.3 GHz rf.[8] This translates in an timing stability of the laser pulses of better than 300 fs rms.

Amplification

Selected pulses of the 27 MHz output of the PTO is amplified with a chain of linear amplifiers, also based on Nd:YLF, diode and flashlamp pumped.

A Pockels cell based pulse picker before amplification runs at 1 MHz forming a pulse train with a length of 1.5 ms. With the present high voltage driver (4 kV), up to 3 MHz is possible. The train is amplified by two diode pumped single pass amplifiers from 0.3 to 6 μJ per micro pulse.

A second pulse picker before the last amplification stage has two functions. The diode pumped amplifiers produce a transient at the beginning of the pulse train. The second pulse picker choses the flat part of the train. The second aim is to give the operator or user of the laser the possibility to remote control the number of pulses and to a certain extend the bunch pattern. Details will be described later in this report.

The final amplification to 300 μJ per pulse is performed by two flashlamp pumped amplifiers. They have already been used at the phase 1 laser system. They provide a power over the pulse train of about 300 W or an average power of up to 3 W for 10 Hz repetition rate.

The pump diode lasers are running since their installation for more than 20.000 h without any visible degradation. The flashlamp life time is between 1 to $5{\cdot}10^7$ shots and are routinely replaced every 40 days.

The infrared radiation (1047 nm) is doubled twice with an LBO and a BBO crystal to the UV (262 nm). The energy stability of a single micro pulse is between 1 and 2 % rms. However, to maintain this stability, a frequent fine tuning of the BBO phase matching angle is required.

Transport Beamline

A variable attenuator consisting out of a Brewster angle polarizer together with a remotely rotatable half wave plate. It allows to adjust the laser pulse energy according to the electron beam charge required. It is also used for a slow charge feedback to compensate slow drifts in electron charge.

Spent beams at various locations (PTO, Pockels cell, LBO, attenuator) are measured with fast photodiodes and recorded with a 1 MHz ADC giving additional information to the operator.

A double pulse generator can be switched into the beamline doubling each micro pulse with a variable distance of some nanoseconds in order to accelerate double bunches in close-by rf buckets. Refer to [9] for details.

In addition, the laser beam can be directed remotely to a joulemeter to measure its energy. It is frequently used for quantum efficiency measurements. The laser pulse can also be directed to a fast streak camera (Hamamatsu FESCA 200) to measure its longitudinal pulse structure. The pulse length in the UV is measured frequently and is stable at 4.4 ± 0.1 ps sigma.

The UV beam is transported from the laser hut to the rf gun. The beamline has a length of 10 m. It is protected with tubes against dust and air turbulences. The beamline needs five dielectric mirrors with a coating optimized for 262 nm. A remote controlled mirror box allows true linear steering of the beam along the cathode. The last mirror in the vacuum chamber guides the beam to the cathode. It is manufactured of solid aluminum. Its surface is diamond turned and has a good optical flatness and a reasonable reflectivity of 90 %. We have chosen a solid metal mirror for two reasons. Dielectric mirrors charge up when hit by darkcurrent. Charging and discharging leads to cracks on the mirror surface and influences the electron beam trajectory. Secondly, experiments supported by simulations have shown, that the beam emittance is also effected.[10]

The laser beam transport is based on the relay imaging technique together with spatial filtering. A hard edge aperture downstream of the diode pumped amplifiers is consecutively imaged to the flashlamp pumped laser heads, to the doubling crystals and finally to the cathode. This results in a quasi flat laser pulse on the cathode which is further sharpened by a hard edge iris aperture close to the gun. The magnification of the telescope system is about 10 re-

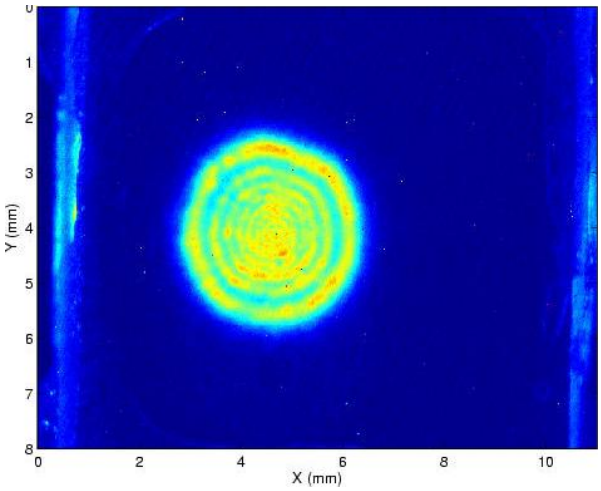

Figure 3: Laser beam profile measured with a Ce:YAG crystal at the 'virtual cathode'. A large laser spot (diameter 1 to 1.5 cm) is seen through an iris of 3 mm in diameter. Although interference fringes show up, the pointing stability is much improved.

Table 1: Laser parameters. Most parameters are adjustable and are set according to the requirements for the specific experiment.

parameter	value
laser material	Nd:YLF
wavelength after conversion	262 nm
output structure	pulsed trains
train repetition rate	5 or 10 Hz
train length	up to 800 μs *
micro pulse spacing	0.33 us to 800 μs *
micro pulse longitudinal shape	gaussian
micro pulse length	4.4$\pm$0.1 ps (sigma)
transverse profile	flat, with fringes
transverse size on cathode	3 mm diam.*
	*adjustable

sulting in a large beam size of about 1 cm in diameter. The iris is remote controlled and is usually adjusted to a diameter of 3 mm cutting a large portion of the laser beam. This results in a roughly flat transverse profile. In addition and most important, these measures reduce the pointing jitter by a large amount and contributes to the stability of the electron source. However, interference fringes created by the hard edge aperture could not been completely avoided. The modulation is about 20 %. An upgrade is foreseen to reduce the modulation (see [11]).

A so called virtual cathode is used to set-up and control the transverse laser beam shape. A remote controlled mirror directs the laser beam onto a Ce:YAG crystal mounted at a distance identical to the cathode position. Figure 3 shows an image of the laser beam on the virtual cathode.

Table 1 summarizes the main laser parameters.

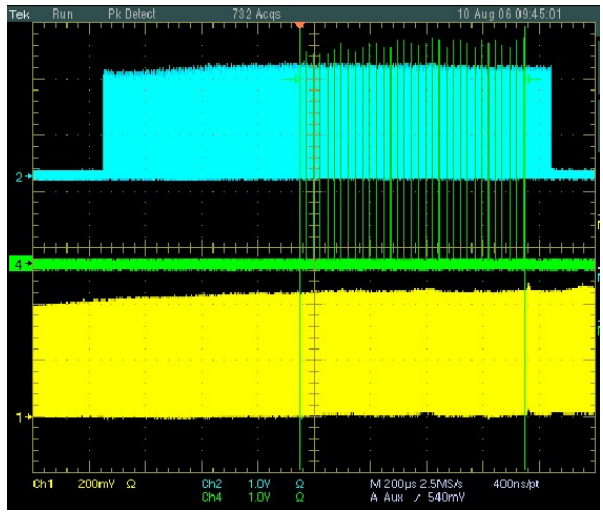

Figure 4: Scope screen shot of a 40 kHz pulse train (green trace, Nb. 4). In addition, the central part of the 27 MHz train of the oscillator (PTO) (yellow, nb 1), and the 1 MHz pulse train after the diode pumped preamplifiers (cyan, nb. 2) are shown.

BUNCH TRAIN PATTERN AND MACHINE PROTECTION

Experiments with FEL radiation often require different electron bunch train pattern. The laser can provide to a certain extend a flexible bunch train pattern chosen by the operator.

We use the Pockels cell based pulse pickers to vary the pattern of the laser pulse train. The Pockels cells may run for 1.5 ms with a rate of up to 3 MHz, pulsed with up to 10 Hz.

An FPGA based controller has been developed. It takes as an input the 9 MHz rf signal from the master oscillator and the 5 Hz or 10 Hz trigger from the control system. The controller produces the trigger gates which go to the Pockels cell drivers. The FPGA allows a flexible control on the number of pulses and the repetition rate, for example in addition to the standard 1 MHz, 250 kHz, 100 kHz, 10 kHz, and others are possible. As an example, Fig. 4 shows a scope screen shot of a 40 kHz pulse train.

The controller also serves as an interface to the machine protection system (MPS).[12] Three beam modes are defined: a single pulse, short pulse, and a long pulse mode. These modes are a machine safety measure, for instance only single bunches are allowed when screens are inserted in the high energy part of the accelerator. Depending on the mode, the controller limits the number of laser pulses picked by the second Pockels cell, independent of the operator request. It also receives a fast beam stop signal from the MPS, for instance when losses grow within a pulse train. The stop signal suppresses further triggers to the pulse pickers. The reaction is immediate within some tens of nanoseconds.

For a safe operation of the laser, important operating

conditions are surveyed by an SPS based system. For instance, the system issues warnings and interlocks on overtemperature, water flow interruptions and so on. The overall system is controlled with a VME-crate based cpu integrated into the FLASH control system providing an interface to the operators. The cpu reads important laser parameters and drives for instance flashlamps, slow feedbacks on a shot to shot bases.

CONCLUSION

The photoinjector laser system has been upgraded by partially replacing flashlamp pumped laser heads by diode pumped heads. The upgraded system has been put into operation at FLASH in February 2004 and providing beam since then (for more than 20.000 h). The stability and reliability of the system is satisfactory, maintenance a routine task. An FPGA based controller allows to drive the pulse pickers with a variable pulse pattern and serves at the same time as an interface to the machine protection system. The laser is integrated into the FLASH control system providing informations about the status of the system and various remote control options.

ACKNOWLEDGMENT

We like to thank our colleagues from the FLASH controls group for their support, mainly B. Petrosyan for the interface to the doocs control system, J. Thomas and O. Hensler for the motor drivers. We also thank M. Werner for many fruitful discussions and his valuable help on the implementing of the FPGA controller, and O. Grimm for his kind help with the streak camera.

REFERENCES

[1] V. Ayvazian *et al.*, Eur. Phys. J. **D 37**, 297 (2006).

[2] S. Schreiber, "First lasing at 32-nm of the VUV-FEL at DESY," eConf **C0508213**, MOOB002 (2005),
Presented at the 27th International Free Electron Laser Conference (FEL 2005), Stanford, California, 22-26 August 2005.

[3] S. Schreiber, eConf **C0508213** (2005) THPP038 [arXiv:/]
Presented at the 27th International Free Electron Laser Conference (FEL 2005), Stanford, California, 22-26 August 2005.

[4] D. Sertore, P. Michelato, L. Monaco, A. Bonucci, J. H. Han and S. Schreiber, PAC-2005-MOPB009 *Prepared for Particle Accelerator Conference (PAC 05), Knoxville, Tennessee, 16-20 May 2005.*

[5] "SASE FEL at the TESLA Facility, Phase 2," DESY-TESLA-FEL-2002-01.

[6] S. Schreiber, D. Sertore, I. Will, A. Liero and W. Sandner, Nucl. Instrum. Meth. A **445** (2000) 427.

[7] I. Will, G. Koss and I. Templin, Nucl. Instrum. Meth. A **541** (2005) 467.

[8] E. Vogel, W. Koprek, P. Pucyk, EPAC-2006-TUPCH189, Proceedings of EPAC 2006, Edinburgh, UK, 26-30 June 2006.

[9] O. Grimm, K. Klose and S. Schreiber, EPAC-2006-THPCH150, Proceedings of EPAC 2006, Edinburgh, UK, 26-30 June 2006.

[10] M. Krasilnikov *et al.*, DESY-M-04-03U *Prepared for 9th European Particle Accelerator Conference (EPAC 2004), Lucerne, Switzerland, 5-9 Jul 2004.*

[11] M. V. Hartrott *et al.*, eConf **C0508213** (2005) MOPP034 [arXiv:/]
Presented at the 27th International Free Electron Laser Conference (FEL 2005), Stanford, California, 22-26 August 2005.

[12] L. Fröhlich *et al.*, "First Experience with the Machine Protections System of FLASH", FEL-2006-THPPH016, these proceedings.

SINGLE-SHOT LONGITUDINAL DIAGNOSTICS WITH THZ RADIATION AT THE FREE-ELECTRON LASER FLASH

H. Delsim-Hashemi, J. Rossbach, P. Schmüser , Univ. Hamburg, Germany
O. Grimm, H. Schlarb , B. Schmidt, DESY, Hamburg, Germany
A.F.G. van der Meer, FOM, Nieuwegein, The Netherlands.

Abstract

The longitudinal charge distribution in the electron bunches has a strong impact on the lasing process in a Free-Electron Laser based on the principle of Self Amplified Spontaneous Emission of radiation. For the ultraviolet and soft X ray FEL FLASH at DESY, structures in the range of ten to hundred micrometers play a crucial role. The investigation of the longitudinal charge distribution in the electron bunches on a bunch-by-bunch basis is an important issue for optimizing the bunch compression and improving the performance of the machine. This paper introduces a new tool for longitudinal diagnostics based on THz spectroscopy of coherent radiation. A novel spectrometer has been designed which permits to analyze the radiation of single electron bunches in a broad spectral range and with high resolution. Preliminary measurements with this spectrometer are presented.

INTRODUCTION

FEL facilities in the VUV and X-ray regime require kA peak currents which are usually achieved by several stages of bunch compression. The longitudinal charge distribution of the compressed bunches has to be measured with high precision in order to fine-tune the off-crest phase in the accelerating section preceding the magnetic bunch compressor chicanes and to optimize the SASE performance. The existing interferometers operate in the scanning mode and determine the average pulse shape of many thousand bunches. They are intrinsically unable to yield information on single bunches. The new single-shot spectrometer uses diffraction gratings as dispersive elements and an array of pyro-electric detectors with multi-channel readout. Exploratory measurements with the first stage, containing thirty channels will be presented.

GRATING SPECTROMETER

The coherent radiation of the compressed bunches subjected to a radiation process in the FLASH linac covers a wide wavelength spectrum from the millimeter range down to a few micrometers. Diffraction gratings are well suited to disperse broad-band radiation to different detection channels. The principles of grating based spectrometers as tools for longitudinal diagnostic are described in reference [1]. These principles are applied in several devices that are described in [2] and [3] or will be explained in this paper.

Advanced bunch compression monitor

As it is described in reference [3], a multi stage reflectance blazed grating spectrometer is used to study bunch compression versus machine parameters. In the following comes an example. It is known that the off-crest phase φ in the first acceleration module ACC1 has a strong influence on the longitudinal bunch profile that is obtained when the bunches have passed the two magnetic chicanes. Empirically it is found that the SASE efficiency depends very critically on φ and reaches its maximum at $\varphi \approx -5^\circ$ to -6°. A phase scan around this value is shown in Fig.1. The signal of the gas monitor detector (GMD), measuring the pulse energy of the FEL light, exhibits a pronounced maximum at $\varphi = -5.7^\circ$ with a width of $\pm 0.2^\circ$. The coherent transition radiation intensities in various wavelength channels are also plotted in Fig.1. The remarkable observation is that the intensity for short wavelengths (20 to 75 μm) exhibits a strong peak in the region of maximum SASE intensity while the intensity of long wavelengths has a monotonic increase towards more negative phase.

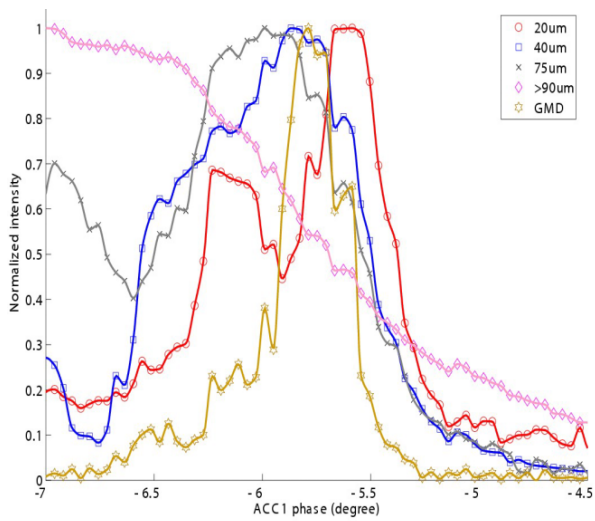

Figure 1: Amplitude of the SASE FEL signal as a function of the off-crest phase φ in the first acceleration module. Also the intensity of coherent transition radiation for wavelengths of $20 \pm 1 \mu m$, $40 \pm 2 \mu m$, $75 \pm 4 \mu m$ and for $\lambda > 90 \mu m$ is shown. Distributions are individually normalized to a maximum value of 1.

Spectrograph

Here a single shot spectrometer that gives the ultra broadband spectra of coherent radiation on a shot to shot basis is called spectrograph. As it was described in [1] a spectrograph is composed of three main components, one that disperses the polychromatic radiation, one that focuses the dispersed radiation to spatially different coordinates dependent on wavelength without mix-up and the detector system. The first two issues were covered and explored in [2] and [3]. The most new achievement is the development of a fast 30 channel detection system based on pyro-electric sensors, Fig. 2.

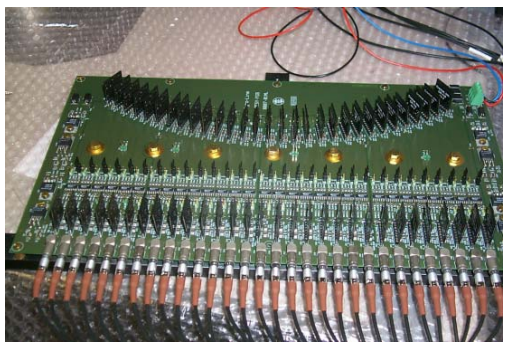

Figure 2: The 30 channel pyro line detector is equipped with fast read out electronics and pyro sensors with broadband smooth response function. The sensitivity is about 300 pJ (5 times noise level) for 1μm < λ < 1mm, [4].

Two types of single stage spectrographs based on Transmission Grating (TG) and Reflectance Blazed Grating (RBG) have been successfully tested.

A TG base spectrograph can cover a rather large range of wavelengths in a single stage. It should be noticed that with a single stage TG spectrograph we will cover the entire interesting wavelength range from 50 to 300 μm, with only two stages the spectra up to 1.8 mm could be derived, Fig. 3. Fig. 4 shows a sequence of 600 subsequent single shot spectra.

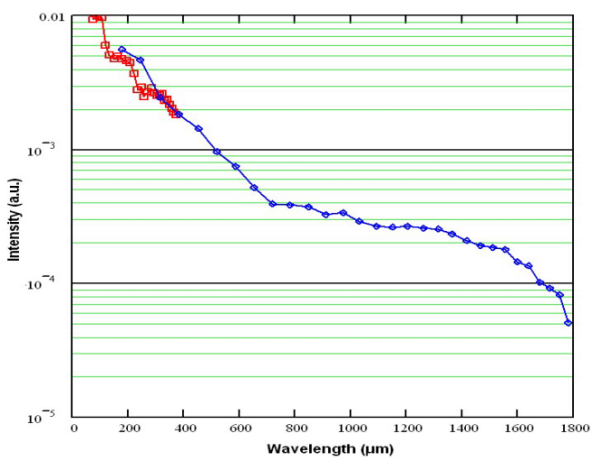

Figure 3: The averaged combined spectra recorded by stages with 2.5 and 0.5 line per mm.

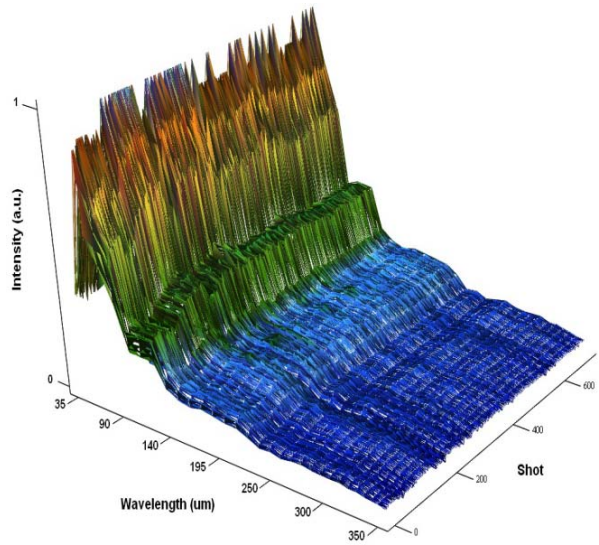

Figure 4: Recorded spectra by using a transmission grating with 2.5 lines per mm.

Reflectance blazed grating have a limited free spectral range of about a factor of two but offer much better resolution and efficiency and can be staged [1]. From the previous studies it is clear that the most relevant part of the spectra for the FLASH machine operation in SASE mode is about 10 to 100 μm. One of the measured spectra in this regime is shown in Fig.5. A combined plot of measured spectra on different regions, averaged over many shots, is shown in Fig. 6.

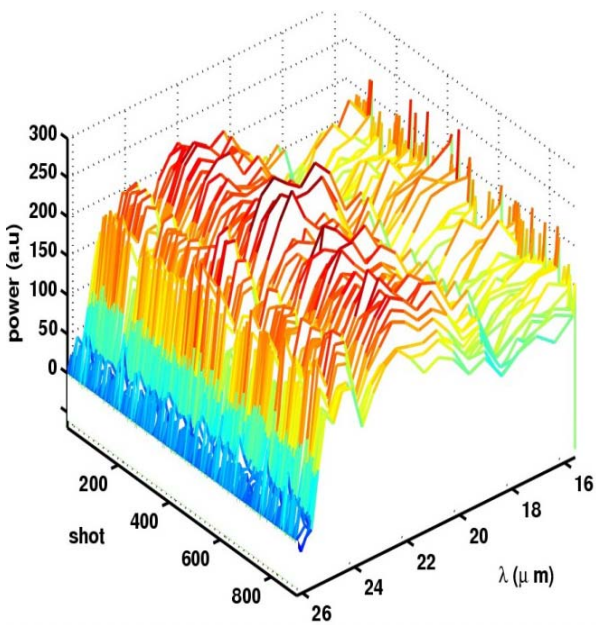

Figure 5: About 900 subsequent shots measured with reflectance grating of 50 lines per mm during SASE operation.

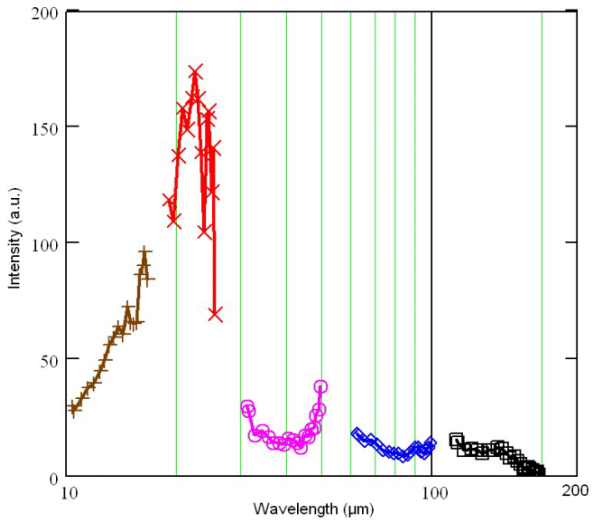

Figure 6: The averaged combined spectra recorded by different RBGs. Full coverage of interesting range of the spectra for FLASH electron bunches requires 5 stages of RBG base spectrograph.

Fig. 7 shows a series of single shot spectra in the wavelength range from 30 to 50 μm recorded while the phase of first accelerating module was changed by ~10 degrees. The spectra shows a very pronounced peak at the phase of operation for optimum SASE.

CONCLUSION

We have demonstrated that single-shot wavelength-selective spectroscopy of coherent radiation is possible. The described spectrograph can give, on a shot to shot basis, information on very short structures of the electron bunches which is not possible by other techniques and can be used for fast feedback systems.

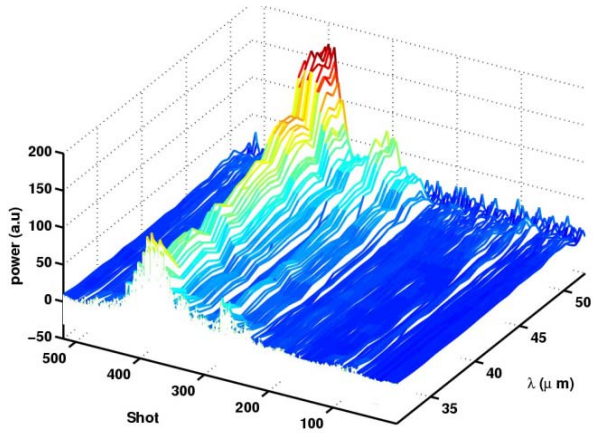

Figure 7: Plotted is the variation of the spectra in one of the stages of reflectance blazed grating spectrograph (with 25 lines per mm) when phase of the first accelerating module changed over ~10 degrees. The peak coherent radiation intensity corresponds to operational condition for optimum SASE.

REFERENCES

[1] H. Delsim-Hashemi et. al., Broadband single shot spectrometer, Proceedings FEL2005.
[2] H. Delsim-Hashemi et. al., Single-shot longitudinal diagnostics with THz radiation, Proceedings FLS2006.
[3] H. Delsim-Hashemi et. al., Bunch compression monitor, Proceedings EPAC2006.
[4] B. Schmidt and H. Delsim-Hashemi, to be published.

INVESTIGATIONS OF THE LONGITUDINAL BEAM PROPERTIES AT THE PHOTOINJECTOR TEST FACILITY IN ZEUTHEN*

J. Rönsch†, J. Rossbach, Hamburg University, 22761 Hamburg, Germany
G. Asova, J. Bähr, H.-J. Grabosch, S. Khodyachykh, S. Korepanov, M. Krasilnikov,
A. Oppelt, B. Petrosyan, S. Riemann, L. Staykov, F. Stephan, DESY, 15738 Zeuthen, Germany
D. Lipka, D. Richter, F. Marhauser BESSY, 12489 Berlin, Germany
A. Onuchin, Budker Institut of Nuclear Physics, Novosibirsk 630090, Russia.

Abstract

The goal of the Photoinjector Test Facility at DESY in Zeuthen (PITZ) is to test and optimise electron guns for FELs like FLASH and X-FEL at DESY in Hamburg. In 2005 the setup was extended by a booster cavity. In order to measure longitudinal and transverse properties of the beam with a momentum in the range between 4 to 40 MeV/c, a viewport after the booster cavity has been developed. It contains several radiators. One of them is Silica aerogel used as Cherenkov radiator for the measurement of the longitudinal electron distribution with a streak camera. Design considerations are presented in this paper.

INTRODUCTION

The main goal of PITZ is the test and optimization of L-Band RF photo injectors for Free-Electron Lasers (FELs). The demands on this photo injector are long bunch trains with short bunches, a charge of about 1 nC and small emittances. The linac based FEL at FLASH incorporates a 1.5 cell RF gun capable of producing a high charge density, followed by an acceleration section and a magnetic bunch compressor. For an effective bunch compression detailed studies of the longitudinal phase space after the gun and its evolution behind the booster cavity have to be performed. The new screen station (HIGH1.Scr2) is planed to be placed about 5 m downstream of the photocathode and about 1.5 m downstream of the exit of the booster cavity in the PITZ2 setup [1] as shown in Figure1.

In the past, PITZ made good experience by using the full cone of a Cherenkov radiator for bunch length measurements after the gun [2]. It will be discussed whether a copy of screen station LOW.Scr3 can be used and which modifications are necessary.

SCREEN STATION FOR BUNCH LENGTH MEASUREMENTS

Screen station LOW.Scr3 was designed for an electron energy of about 5 MeV. It contains a YAG screen to determine transverse properties using a TV camera, three radiators (aerogel, an optical transition radiator (OTR), quartz), whose light is transported to the streak camera [3] and a tapered empty tube, for beam passage without wakefield production. The Silica aerogel (refractive index $n = 1.03$, thickness $th = 2$ mm) is used as a Cherenkov radiator and the pulse length is measured using an optical transmission line [4] and a streak camera.

The new screen station (HIGH1.Scr2) and its elements should be designed for electron energies in the range of 4 up to 40 MeV, so it can be used even if the booster cavity is off. Planed elements are: a YAG-screen and an OTR for the determination of the transverse beam size and position of the electron beam using a TV camera, Silica aerogel and a further OTR for bunch length measurements as well as an empty tube.

Screen Dimensions

For higher energies the beam size becomes smaller, but when the booster cavity is turned off the beam size increases. Simulations of transverse beam size at the position of HIGH1.Scr2 were made to clarify the needed dimensions. Figure 2 (a) shows the simulated transverse beam size at a gun and booster phase with maximum energy gain for different solenoid currents, when the booster is turned on. The smallest transverse beam size could be reached for about 260 A. In Figure 2 (b) the simulated transverse beam distribution are shown for 260 A and a gun and booster phase with maximum energy gain.

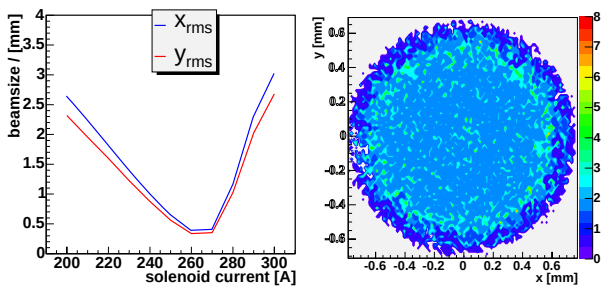

(a) (b)

Figure 2: Simulations of the electron beam size as a function of the solenoid current (a) and transverse beam properties at the screen station (b) for a gun and booster phase with maximum energy gain and a flat-top longitudinal laser distribution at 1 nC.

* This work has partly been supported by the European Community, contract numbers RII3-CT-2004-506008 and 011935, and by the 'Impuls- und Vernetzungsfonds' of the Helmholtz Association, contract number VH-FZ-005.

† jroensch@ifh.de

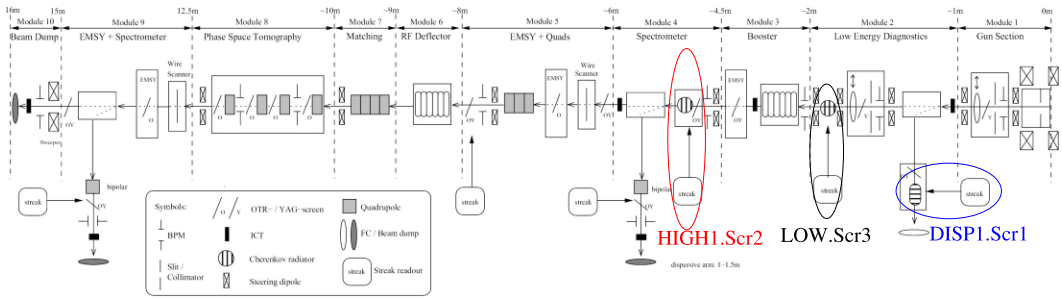

Figure 1: Planed setup of PITZ2. The screen station HIGH1.Scr2, LOW.Scr3 and DISP1.Scr1 are marked.

Results of simulations of the beam dynamics, when the booster is off are shown in Figure 3. In this case the beam size is almost 10 times higher than with the booster cavity turned on.

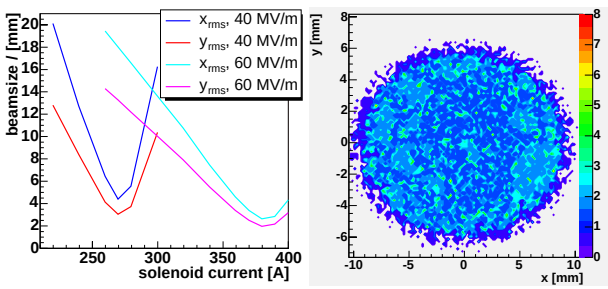

(a) (b)

Figure 3: Simulated transverse electron beam size as a function of the solenoid current for 40MV/m and 60MV/m gradient (a) and transverse beam properties at the screen station (b) for a gradient of 40MV/m in the gun and a phase with maximum energy gain, a flat-top longitudinal laser distribution at 1 nC, when the booster is turned off.

For measurements using the booster the beam size could be very small, therefore both OTRs will have an effective size of 20 mm × 20 mm. Using an OTR at an angle of 45° with respect to the beam direction, backward radiation is emitted at 90° regarding the beam direction. A thin plate (about 300 μm) will be used as OTR, because of its better optical quality and resistance compared to a thin foil. Two different types of OTR screens are in use at FLASH [5]:

- 350 um thick polished silicon (Si)
- 350 um thick Si with an aluminium (Al) coating

The Si has a better thermal resistance than Al, and therefore the pure Si screen stands a higher charge density (i.e small beam with high charge) than Si coated with Al. On the other hand the Al emits about 2-3 times more photons than polished Si, i.e. the light yield is much better. That is why we decided to use the Al coated Si plates.

Since there are no quadrupoles planed before this screen station there is no possibility to reduce the beam size in the case the booster is off. To catch the whole beam even when the booster is off the effective size of the YAG screen should have the dimension size as the beam tube (diameter = 35 mm).

Bunch Length Measurement

The temporal resolution of the Silica aerogel used at LOW.Scr3 was calculated to be 0.12 ps at a beam momentum of 4.5 MeV/c [6]. This value is very small compared to the resolution of the optical transmission line. The temporal resolution of the optical transmission line was determined with 1.15 ps when using an optical transmission filter of 550 nm with a bandwidth of 10 nm [7]. The bunch length measurements were typically done for a streak camera slit width of 100 μm. The temporal resolution of a 100 μm slit was determined with about 1.75 ps for the streak camera used at PITZ [2]. The resolution of the streak camera C5680 is denoted by the producer with 2 ps FWHM [3]. Therefore it is useful to increase the thickness of the Silica aerogel in order to increase the number of photons, so one could reduce the slit width or the number of pulses used for a measurement. The initial idea was to use Silica aerogel with an index of refraction $n = 1.03$ and a thickness of 5 mm. Cherenkov light is emitted under a certain angle depending on the average refractive index of the radiator (n) and the electron energy. It leaves the radiator following Snells law. Figure 4(a) shows the emission angle of Cherenkov radiators with three different indices of refraction. For low energies the angle changes strongly with the energy, but at higher energies it stays constant. Aerogel with $n = 1.03$ has an emission angle of up to $14.3°$ at an electron beam momentum of 40 MeV/c, but the acceptance angle of the optical system from the screen station to the streak camera is only $\pm 11.8°$. Using an aerogel with $n = 1.03$ it is impossible to collected the whole Cherenkov cone.

In contrast to Cherenkov radiator the optical transition radiator emits the light within a certain angular distribution. The angular distribution of transition radiation depends on the particle energy and the angle of incident [8]. In Figure 4,(b) the angular distribution for a beam momentum of 40 MeV/c and 5 MeV/c electrons are shown. At 40 MeV/c beam momentum most of the light is emitted within a small angle. At smaller energies it becomes impossible to collect

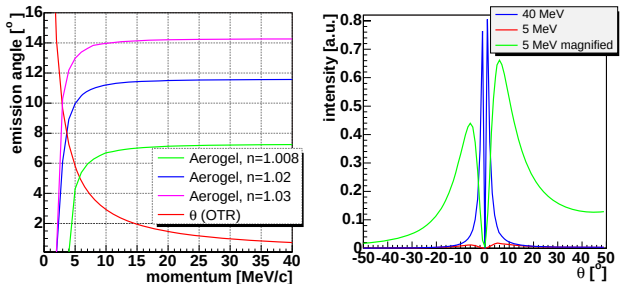

(a) (b)

Figure 4: The emission angle of OTR and the Silica aerogel radiators with different reflective indices as a function of the electron momentum (a) and the angular distribution of optical transition radiation produced by 40 MeV and 5 MeV electrons (b).

all the light by the used optical system. The red curve in Figure 4 (a) shows the angle with the highest number of emitted photons.

An aerogel with $n = 1.02$ and $th = 7$ mm (as well as $n = 1.008$ and $th = 15$ mm) would lead to about the same temporal resolution as an aerogel with $n = 1.03$ and a thickness of $th = 5$mm, but the number of photons is lower, as shown in Figure 5.

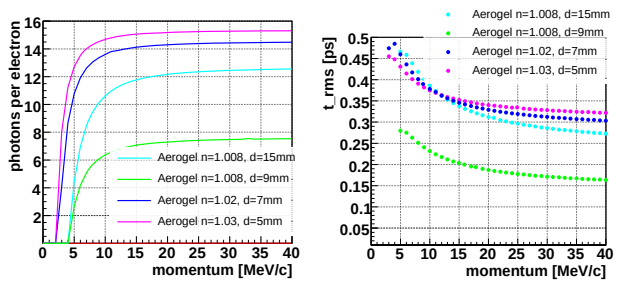

(a) (b)

Figure 5: Number of photons (a) and resolution (b) of Silica aerogels with different indices of refraction and thickness's as a function of the energy.

By mechanical reason the maximum usable thickness is 9 mm. The Budker Institut of Nuclear Physics (Novosibirsk) is producing Silica aerogel for PITZ, but only Silica aerogel with $n = 1.008$, 1.03 and 1.05 are produced by default. A production of Silica aerogel with $n = 1.02$ would take a lot of effort. So we will start to use aerogel with n = 1.008 and 9 mm, which can be replaced later. The main disadvantage of the refractive index $n = 1.008$ is that the lower limit for the production of Cherenkov light is at about 4 MeV/c and the photon yield changes strongly within the beam momentum range from 4 to 6 MeV/c. The advantage is that the Cherenkov light of bigger transverse distributions can be transported and small misalignments of the optical transmission line does not lead to losses. The number of photons produced by aerogel at 40 MeV/c is still a factor of a few hundred higher compared to OTR.

LONGITUDINAL PHASE SPACE MEASUREMENTS

The longitudinal phase space after the gun at DISP1.Scr1 (shown in Figure1) and its projection were measured for different phases of the gun. In order to compare simulated (Fig.6 second row) and measured (Fig.6 first row) longitudinal phase space the simulated one was tracked through the dipole using matrix formalism. The vertical scale was converted into momentum scale after the correction of M_{56} [9] by shearing the distribution (Fig.6 third row). Matrix element M_{56} describes the influence of the dipole on the longitudinal distribution due to different particle momenta. The measured momentum distribution fits very well with the distribution traced through the dipole (Fig.6 fourth row). Also the longitudinal distribution (Fig.6 fifth row) shows a rather good agreement. It is difficult to find similarities with in the longitudinal phase space. The longitudinal phase space changes completely after tracing the particle though the dipole. In [10] it will be shown, how to design a dipole magnet in order to minimize this problem. Beside the influence of the dipole magnet the optical transmission line and the streak camera itself have an influence onto the resolution as described in [7].

CONCLUSION

A screen station to measure longitudinal and transverse beam properties in the momentum range from 4 to 40 MeV/c was designed. One of the radiator is Silica aerogel used as Cherenkov radiator for the measurement of the longitudinal electron distribution with a streak camera. Even at 40 MeV/c Silica aerogel produces a higher photon yield than OTR. Longitudinal phase space studies and improvements of the system are ongoing.

ACKNOWLEDGMENT

We would like to thank Lap Van Vu (DESY Zeuthen) for the technical design and J. Kolbe for useful discussions and hints concerning the design and construction.

REFERENCES

[1] A. Oppelt, PITZ2 Elements and Coordinates, http://www-zeuthen.desy.de/∼apohl/pitz2/PITZ2-Schema.jpg (11.08.2006).

[2] D. Lipka, "Investigations about the longitudinal phase space at a photo injector for minimized emittance", PhD Thesis 2004 Humboldt University Berlin.

[3] Hamamatsu, "Test report C5680-21, Serial No. 040168".

[4] J. Bähr, D. Lipka, H. Lüdecke, "Optical transmission line for streak camera measurement at PITZ", Dipac Mainz 2003.

[5] K.Honkavaara private communication.

[6] D. Lipka et al, "Silica aerogel radiators for bunch length measurements", Nuclear Instruments and Methods in Physics Research A 538 (2005) 597?607.

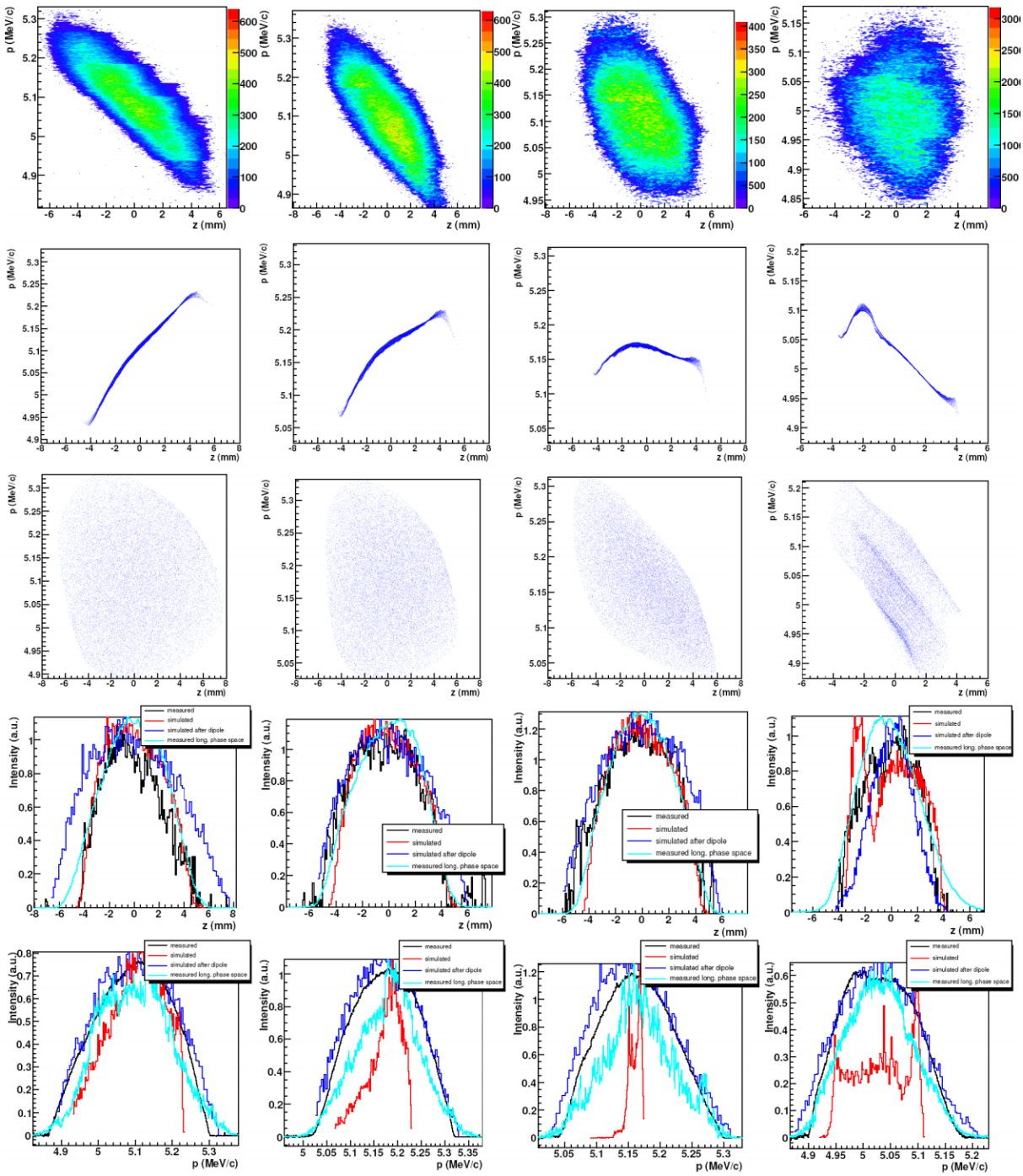

Figure 6: Measurement (1st row) and simulation (2nd row) of the longitudinal phase space. The simulation was traced through the dipole to show the expected distribution. The projections of the three distributions were compared to the direct bunch length measurement (4th row) and momentum measurement (5th row). Black line is direct measurement, red simulation, cyan projection of the phase space measurement and blue projection of the traced distribution. The results were shown for gun phase with maximum energy gain +10 °, +0°, -10° and -25° (from left to right).

[7] J. Rönsch et al, "Investigations of the longitudinal phase space at PITZ", EPAC Edinburgh 2006.

[8] K.Honkavaara, "Considerations of streak camera measurements for Photoinjector Test Facility (PITZ) in DESY Zeuthen", note, July 2000.

[9] D. C. Carey, K. L. Brown, F. Rothacker, "Third-Order TRANSPORT with MAD Input", FERMILAB-PUB-98/310.

[10] S. Khodyachykh et al., Design of the Multipurpose Dispersive Section at PITZ, contribution THPPH020, FEL 2006.

DESIGN OF MULTIPURPOSE DISPERSIVE SECTION AT PITZ*

S. Khodyachykh†, J. Bähr, M. Krasilnikov, A. Oppelt, L. Staykov, F. Stephan,
DESY, Zeuthen, Germany,
T. Garvey, LAL, Orsay, France, D. Lipk, BESSY GmbH, Berlin, Germany,
J. Rönsch, University of Hamburg, Hamburg, Germany.

Abstract

A detailed knowledge of the parameters of a high-brightness electron beam is of major importance for evaluating the performance of a free electron laser using the beam. Therefore, a full characterization of the beam parameters is required during the commissioning of RF photo injectors. As one important contribution to fulfill this task, a multi-purpose high energy dispersive arm (HEDA1) for electron energies up to 40 MeV is presently under construction at the Photo Injector Test Facility at DESY in Zeuthen (PITZ). The dispersive section is designed such that it will combine the functionality of 1) an electron spectrometer, 2) a device for characterization of the longitudinal phase space, and 3) a transverse slice emittance measuring system. The HEDA1 consists of a 180° dipole magnet (C-Bend), followed by removable slit, a quadrupole magnet, and a screen station with a read-out for the streak camera. Design considerations and the detailed lay out of the high-energy dispersive section are presented.

INTRODUCTION

The Photo-Injector Test Facility at DESY in Zeuthen (PITZ) is an electron accelerator which was built by Deutsches Elektronen-Synchrotron (DESY) in collaboration with international partners with the goal to develop and to optimize high brightness electron sources suitable for SASE FEL operation.

The PITZ facility consists of a 1.5 cell L-band RF gun, a photo-cathode laser system, a normal-conducting booster cavity and a diagnostic section. Being an operational machine showing pioneering results in achieving of high-charge low-emittance electron beams for electron bunch trains [1], PITZ is still under development. The beam line which has a present length of about 13 meters will be extended up to about 21 meters within the next two years. Many additional diagnostics components will be added to the present layout. Together with the deflecting cavity [2], the phase space tomography module [3] and the second high-energy dispersive arm (HEDA2), HEDA1 will extend the existing diagnostics system of the photo injector. The scope of the present paper is the multi-purpose high energy dispersive arm (HEDA1). The dispersive section is designed to combine the functionality of (i) an electron spectrometer, (ii) a device for characterization of the longitudinal phase space, and (iii) a transverse slice emittance measuring system.

* This work has partly been supported by the European Community, contracts RII3-CT-2004-506008 and 011935, and by the 'Impuls- und Vernetzungsfonds' of the Helmholtz Association, contract VH-FZ-005.

† sergiy.khodyachykh@desy.de

SETUP

The layout of the dispersive section HEDA1 is schematically shown in Fig 1.

The heart of the dispersive section is a 180° dipole magnet having the bending radius of 300 mm. The bending radius has been chosen as a compromise between the space requirements and momentum resolution on the one hand and the ability of the spectrometer to operate within the large range of gun and booster parameters. Being deflected in vertical plane, the electron beam enters the dispersive arm which goes below the main beam line parallel to it. The dispersive arm includes a pumping port combined with a removable slit mask, a quadrupole magnet Q_1 for the slice emittance measurements, a drift space of 600 mm followed by two screen stations (for simplicity only one is shown) and by a beam dump. For measuring of the bunch charge an integrating current transformer (ICT) is foreseen between the two screen stations (not shown).

For the reasons described in the following sections additional components which contribute to the measurements at HEDA are located in the main beam line. These are the quadrupole magnet Q_2 and the screen station S_2 placed up- and downstream to the dipole magnet D, respectively.

The main advantage of the 180-degree spectrometer is the simplicity to reconstruct the momentum distribution [4]. One uses the screen S_2 in the straight section and measures the contribution from the transverse beam size and divergence, which can be de-convoluted with the measured spectrum to obtain the pure momentum distribution. This can be illustrated by comparing of the transport matrix M_D (describing the transport of the electron beam between the position of the quadrupole magnet Q_2 and the screen S_1) with the matrix M_S which corresponds to the drift between Q_2 and the screen S_2. The matrices in thin lens approximation have the form

$$M_D = \begin{pmatrix} -1 & -l_1 - l_2 & 2\rho \\ 0 & -1 & 0 \\ 0 & 0 & 1 \end{pmatrix}$$

$$M_S = \begin{pmatrix} 1 & l_1 + l_2 & 0 \\ 0 & 1 & 0 \\ 0 & 0 & 1 \end{pmatrix} \qquad (1)$$

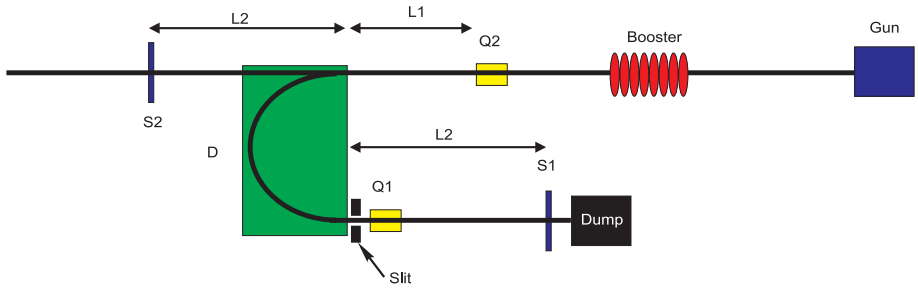

Figure 1: Simplified layout of PITZ with the first high energy dispersive section.

where ρ is the bending radius of the dipole magnet and lengths l_1 and l_2 are defined in Fig 1.

The transverse coordinates of the i-th electron can be described by a vector $\vec{y}_i = (y_i, y_i', p_i/\langle p \rangle)^T$, where y_i is the transverse position, y_i' is the divergency and $p_i/\langle p \rangle$ is the relative momentum. Assuming the electron with the coordinate y_0 is transported through the spectrometer it will get the transverse coordinate on the screen S_1 which is described by the first component of vector $\vec{y}_1 = M_D \vec{y}_0$. The shift of the particle with respect to the reference trajectory is thus defined not only by the relative momentum of the particle, but also by it initial transverse offset and divergency. To exclude these two contributions one uses the measurements on the screen S_2 where only initial coordinate and initial divergency define the position of the particle (compare M_{11} and M_{12} elements of matrices in Eq.1). Moreover, by focusing the beam on the screen S_2 with the help of the quadrupole magnet Q_2 one can control the resolution of the momentum measurement.

Beam momentum and momentum spread depends strongly on the machine parameters. It is very sensitive to the RF phases of the gun and of the booster. Because of the large dispersion of the dipole magnet the spot sizes on the screen S_1 are expected to be very large, especially in cases of far off-crest RF phases. Figure 2 shows the dependence of the vertical beam size on the screen S_1 as a two dimensional function of the gun and booster phases. The aperture of the quadrupole magnet Q_1 (80 mm) defines the transversal acceptance of the dispersive section. Thus, using HEDA1 measurements within the range of $-35...35°$ of booster phases will be possible in single shot. For larger off-crest phases a scan of dipole current will be used.

LONGITUDINAL PHASE SPACE

Very important information for the understanding of the photo-injector can be gained by studying the electron distribution in the longitudinal phase space, when the electron momentum is measured as a function of its longitudinal position within the bunch. For this purpose one of the screen stations will be equipped with an aerogel screen used as a Cherenkov radiator and a read-out for the streak-camera.

Figure 3 (a) shows the results of numerical simulation of the longitudinal phase space using the code ASTRA [7] at the entrance of the dipole magnet. The particles were tracked through the dipole using the matrix formalism, similar to that described in previous section, but using 6×6 transport matrix. The longitudinal phase space reconstructed on the screen S_1 of the dispersive section after the drift having the length of a 1 m is shown in Fig. 3 (b). A correction of the influence from the matrix element M_{56} [6] was applied in Fig. 3 (c). Figure 3 (d) shows the momentum distribution as a projection of Fig. 3 (a) in red and 3 (c) in blue.

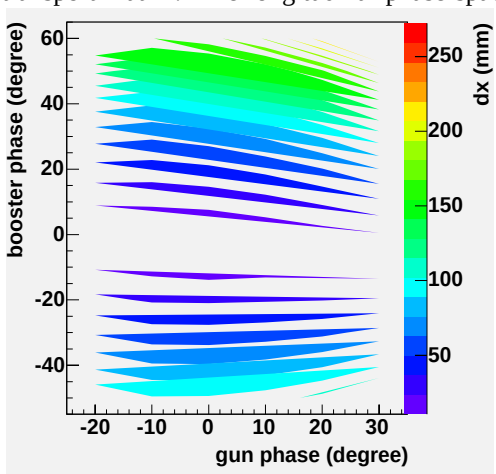

Figure 2: The total beam size in dispersive plane on screen S_1 as a function of gun and booster phases.

A comparison of the initial and the reconstructed values of mean momentum $\langle p \rangle$, momentum spread p_{rms} and longitudinal emittance ϵ_l are shownin table 1. The

Table 1:Initial and reconstructed values of mean momentum, momentum spread and longitudinal emittance.

	$< p >$ (MeV)	p_{rms} (keV)	ϵ_l (π keV mm)
(a)	18.3111	36.6	75.99
(c)	18.3109	49.0	105.08
$(a-c)/a$	-0.0009%	33.8%	38.3%

results in Fig. 3 and table 1 were done without quadrupole. These results could be improved by applying deconvolution with known beam size at S_2. However, this procedure unnecessary complicates data analysis comparing to the method discussed below.

The simulations were repeated using a quadrupole triplet 4.5 m downstream the photocathode in order to focus the

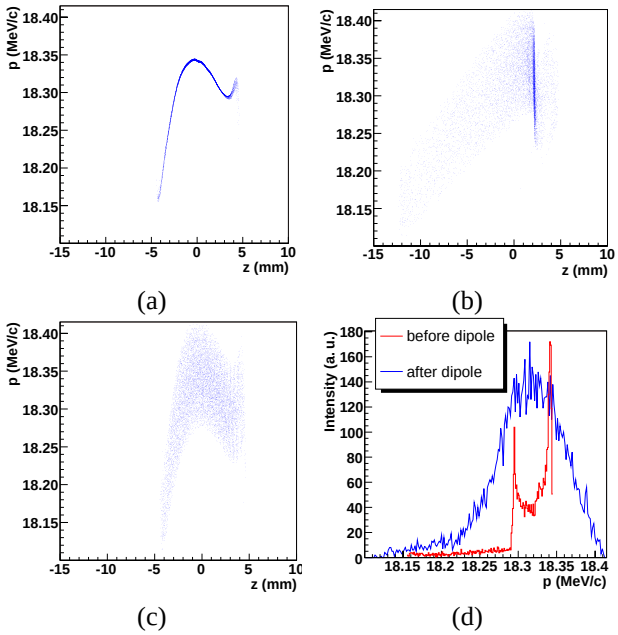

Figure 3: Longitudinal phase space obtained with the quadrupole magnet Q_2 being off: longitudinal phase space (a), reconstructed longitudinal phase space at S_1 (b), reconstructed longitudinal phase space at S_1 after correction of M_{56} (c), momentum distribution (d).

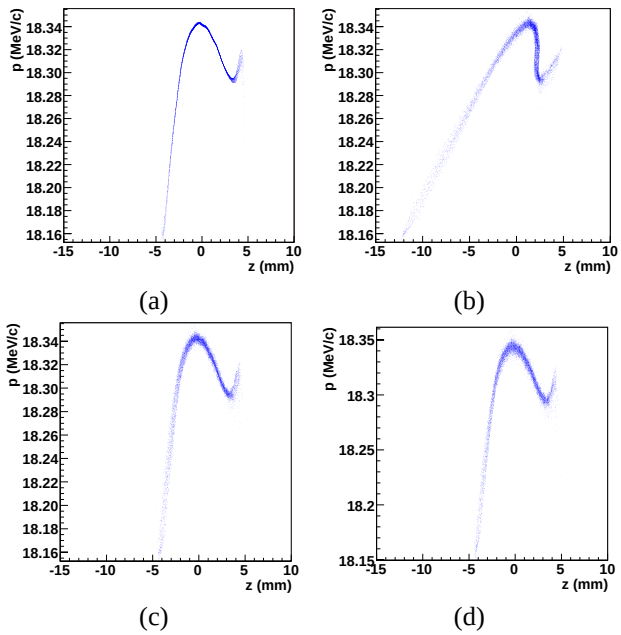

Figure 4: Longitudinal phase space obtained with the quadrupole triplet placed on the position of Q_2 being on: longitudinal phase space (a), reconstructed longitudinal phase space at S_1 (b), reconstructed longitudinal phase space at S_1 after correction of M_{56} (c). For a comparison reconstructed longitudinal phase space at S_1 [as (c)] but with a single quadrupole instead of a triplet.

beam onto screen S_1 (at position 6.5 m). The results are shown in figure 4 and table 2.

Table 2: Initial and reconstructed values using a quadrupole triplett

	p_{mean} (MeV)	p_{rms} (keV)	ϵ_l (π keV mm)
(a)	18.3105	36.54	75.72
(c)	18.3104	36.59	76.11
$(a-c)/a$	-0.0005%	0.16%	0.5%

The use of a quadrupole triplet brings a remarkable improvement to the measurements of the longitudinal phase space. Both, the longitudinal phase space and the momentum distribution are reproduced with very good agreement. The differences between the simulated and reconstructed values of the momentum spread and longitudinal emittance reduces by using of the triplet from about 35% down to less than one per cent.

In order to save some space in the main beamline, we studied the possibility to exchange the quadrupole triplet with a single quadrupole magnet. Indeed such replacement almost does not decrease the accuracy of the longitudinal phase-space reconstruction. Figure 5 shows a comparison of the momentum measurements. The differences between the simulated and reconstructed mean momentum, momentum spread and longitudinal phase space are still within 1 %.

TRANSVERSE SLICE EMITTANCE MEASUREMENTS

The functionality of the HEDA can be enhanced with a setup that allows us to measure the transverse emittance of the electron beam at different longitudinal positions along the bunch. The so called slice emittance is providing better understanding of the physics of a photoinjector, particulary the emittance compensation and conservation principles. It is also an important parameter for the SASE FELs since the slice emittance and slice peak current define the gain of the SASE FEL process. Using proper phasing of the booster cavity we can obtain linear correlation between the momentum and longitudinal distribution of the electrons in

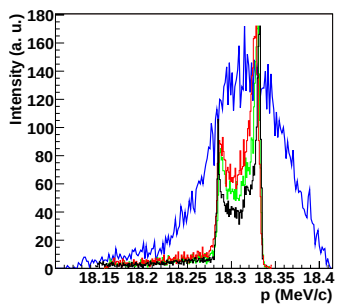

Figure 5: Simulated momentum distribution (black) compared to its reconstruction in the dispersive arm with the single quadrupole Q_2 (red), quadrupole triplet (green) and without quadrupole (blue).

the bunch. Afterwards one applies the standard quadrupole scan technique and measures the emittance for different momentum/time slices of the bunch.

A setup similar to that in [8] will be implemented. A slit at the dipole exit selects the necessary slice from the energy chirped beam. This slice is scanned with the quadrupole Q_1 focusing in a plane orthogonal to the dispersion plane of the dipole, the beam distribution will be observed on screen S_1. Due to the short distance between the quadrupole and the screen the beam size tends to become very small during the scan. For the correction of this the quadrupole magnet Q_2 with fixed strength placed before the dipole will be used (see Fig.1). The experimental setup was simulated with

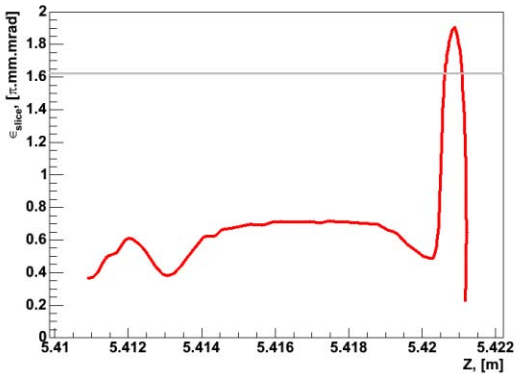

Figure 6: Slice emittance distribution at the dipole entrance. The solid line gives the value for the projected emittance.

ASTRA [7] in attempt to verify the technique and to optimize the setup. For the simulations presented here, a gun gradient of 60 MV/m and a phase of maximum acceleration in the gun, the current in the main solenoid was 385 A, and a booster phase of +70 degrees were chosen. This corresponds to a projected emittance of $1.6\ mm \cdot mrad$ (see Fig. 6), a mean momentum of 17 MeV/c and an RMS momentum spread of 1.4 MeV/c.

The electron bunch was separated in ten longitudinal slices which were scanned with ten different quadrupole strengths. The distribution is fited to a quadratic equation (2) where the corresponding beam parameters are obtained.

$$\langle x_s^2 \rangle = M_{11}^2 \cdot \langle x_0^2 \rangle + 2 \cdot M_{11} M_{12} \langle x_0 \cdot x_0' \rangle + M_{22}^2 \cdot \langle x_0'^2 \rangle \quad (2)$$

Here $\langle x_s^2 \rangle$ is the beam size coresponding to the particular strength of the quadrupole magnet, M_{11}, M_{12} and M_{22} are the elements of the transport matrix, functions of the quadrupole strength, $\langle x_0^2 \rangle$, $\langle x_0 \cdot x_0^{'} \rangle$ and $\langle x_0^{'2} \rangle$ are the initial beam parameters that need to be found. The corresponding value for the emittance then is calculated using Eq. 3.

$$\varepsilon_n = \beta\gamma \cdot \sqrt{\langle x_0^2 \rangle \cdot \langle x_0'^2 \rangle - \langle x_0 \cdot x_0' \rangle^2}. \quad (3)$$

Here $\langle x_0^2 \rangle$ and $\langle x_0'^2 \rangle$ are the rms dimensions of the beam in the so-called trace phase space and $\langle x_0 \cdot x_0' \rangle$ is the correlation between both.

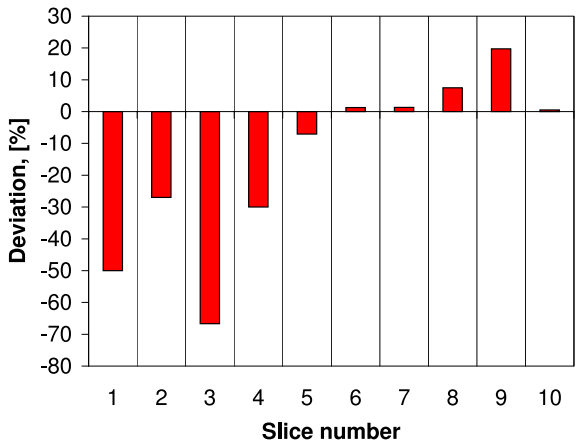

Figure 7: Deviation between the result from the simulated measurement and the slice emittance distribution obtained with ASTRA.

Figure 7 shows the deviation between the result from the simulated measurement and the slice emittance distribution obtained with ASTRA. The average deviation is 21 % but for some slices it can reach up to 66 %. Further improvement of the measuring accuracy can be reached by taking into account the space charge during the reconstruction.

ACKNOWLEDGEMENTS

Besides the funding agencies mentioned on the first page of the present paper the authors would like to thank S. Riemann, H.-J. Grabosch (both DESY) for valuable discussions. Without brilliant ideas of our engineers the realization of this work would not be thinkable.

REFERENCES

[1] F. Stephan, Status and perspectives of photo injector developments for high brightness beams, proceedings of teh workshop on the Physics and Applications of High Brightness Electron Beams. Erice, Italy, 2005.

[2] S. Korepanov et al., Design Consideration of the RF Deflector to Optimize the Photo Injector for PITZ, Proceedings of the FEL2006, Contribution THPPH021.

[3] D.J. Holder et al., A phase space tomography diagnostic for PITZ, Proceedings of EPAC 2006.

[4] D. Lipka, Spectrometer design for the SRF Gun, BESSY Note SRFgun-BESSY-003-12-2004, 2005.

[5] D. Lipka et al, Silica aerogel radiators for bunch length measurements, Nucl. Instr. Meth. A 538 (2005) 597.

[6] J. Rönsch et al., Measurement of the longitudinal phase space at the photo injector test facility at DESY in Zeuthen (PITZ), Proceedings of DIPAC 2005, Lyon.

[7] K.Floetmann, ASTRA, http://www.desy.de/ mpyflo.

[8] X. Qiu et al., Demonstration of emittance compensation through the measurement of the slice emittance of a 10 picosecond electron bunch, Phys. Rev. Let. 76 No. 20 (1996) 3723.

DESIGN CONSIDERATION OF THE RF DEFLECTOR TO OPTIMIZE THE PHOTO INJECTOR AT PITZ*

S. Korepanov#, S. Khodyachykh, M. Krasilnikov, A. Oppelt, F. Stephan, DESY-Zeuthen, Germany
V. Paramonov, INR, Moscow, Russia.

Abstract

In order to optimize photo injector for Free Electron Laser (FEL) applications, a detailed characterization of the longitudinal and transverse phase space of the electron beam provided by the Photo Injector Test Facility at DESY in Zeuthen (PITZ) is required. In the paper we present design considerations of the RF deflecting cavity for transverse slice emittance and longitudinal phase space measurements.

INTRODUCTION

The main research goal of PITZ is the development of electron sources with minimized transverse emittance [1]. The current setup at PITZ permits us to measure transverse emittance averaged along a bunch using the Emittance Measurement System (EMSY) [2]. With the use of an RF deflector it is possible to analyse the slice transverse emittance. Adding a dispersive arm the longitudinal beam phase space can be completely re-constructed.

At PITZ2 the application of an RF deflector is planned. The deflector position is about 9 m from the gun. The next 3.5 m space is taken by a tomography module, which will be used for transverse phase space measurements. At about 15.5 m a spectrometer based on dipole magnet is positioned.

In Fig. 1 the effect of the RF deflector is illustrated: the RF deflector voltage is null in the longitudinal centre of the bunch and gives a linear transverse deflection to the bunch itself. The maximum displacement of the edge slice Y_B can be estimated by the expression

$$Y_b = \frac{\pi \cdot f_{RF} \cdot L \cdot L_B \cdot V_\perp}{c \cdot E / e}\ , \qquad (1)$$

where f_{RF} is the frequency of the deflecting voltage, $V_\perp$ is the peak transverse voltage, L – drift space after the deflector, and E is the beam energy in eV units [3].

The resolution length L_{res} can be estimated as the bunch length L_B divided by the number of slices N_{slices} which can be resolved at the screen. And the number of the slices is Y_B divided to transverse beam size σ_B.

$$L_{res} = \frac{L_B}{N_{slices}} = \frac{L_B \cdot \sigma_B}{Y_B} = \frac{\sigma_B \cdot c \cdot E / e}{\pi \cdot f_{RF} \cdot L \cdot V_\perp} \qquad (2)$$

* This work has been partly supported by the European Community, contracts RII3-CT-2004-506008 and 011935, and by the 'Impuls- und Vernetzungsfonds' of the Helmholtz Association, contract VH-FZ-005
# sergey.korepanov@desy.de

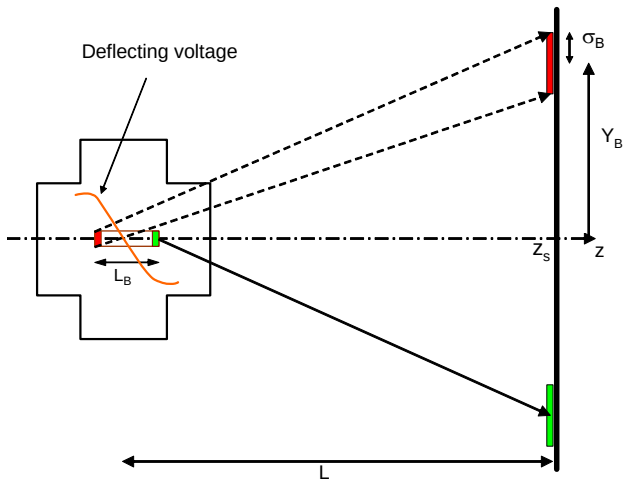

Figure 1. The principle of the RF deflector work.

For the prospect beam parameters at PITZ2 (Table 1) the possible resolution length is limited by the transverse size of the screen (< 36 mm) and minimum transverse beam size (σ_B ~ 1.6 mm). That gives the maximum number of the slices about 20 and the longitudinal resolution length about 0.4 mm (1.3 ps).

Table 1. PITZ2 beam parameters.

bunch charge	1 nC
max. long. momentum	32 MeV/c
min. norm. emittance (rms)	< 1 π mm mrad
transverse beam size on screen in tomography module, rms (full)	< 0.4 (1.6) mm
full longitudinal beam size	8 mm (27 ps)
pulse frequency	1-9 MHz
repetition rate	10 Hz

RF DEFLECTORS

For PITZ2 diagnostics we have reviewed three kinds of RF deflectors. Two of them are steady wave resonators and one is a travelling wave cavity. We analyzed electron beam parameters after passing the cavity and compared the results for the different deflectors.

Steady wave cavities

We have chosen the well known cavity which is a disk loaded waveguide [3]. It has five cylindrical cells. We scaled it to the frequency 1.3 GHz, Fig.2a. This cavity

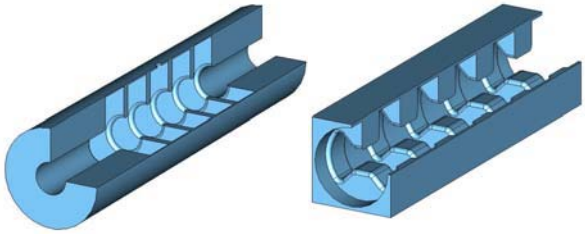

a) b)

Figure 2. General view of “classical” cavity (a) and “Paramonov” cavity (b).

operates with TM11 mode. Another steady wave cavity is a new one designed by V. Paramonov. The shape of the structure is shown in Fig.2b. It operates in TE11 mode. More details about this cavity are given in [4].

Travelling wave cavity

The third cavity is based on LOLA-IV - transverse deflecting cavity [5], Fig.3. We have adapted it for our beam: scaled it from 2.856 GHZ to 1.3 GHZ and changed length from 3.6 m to 0.7 m. It has 9 cells and two additional cells for coupler and load.

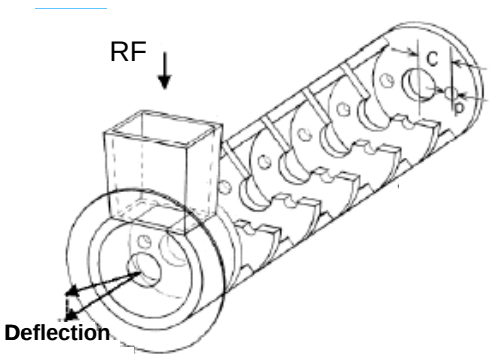

Figure 3. Travelling wave cavity based on LOLA-IV.

In the Table 2 we compare the deflector parameters for two operations regimes - to analyse the longitudinal phase space at a distance of about 6 m from the deflector in the dispersive arm and – to observe the beam at the first screen in tomography module at a distance of ~ 2 m from the deflector. In the table Q is unloaded quality factor, “Field build up” is the time which field needs to reaches about 99% of there maximum value [5].

Table 2. Deflector parameters.

	Classic cavity		“Paramonov” cavity		Travelling wave cavity	
Frequency GHz	1.3	1.3	1.3	1.3	1.3	1.3
Distance, m	2	6	2	6	2	6
$V_{\perp}$, MV	1.8	0.6	1.8	0.6	1.8	0.6
Q	21000	21000	15000	15000	19000	19000
P_{RF}, MW Field	2	0.12	0.17	0.02	9.1	1.01
build up, μs	~20	~20	~20	~20	~0.2	~0.2

BEAM DYNAMICS

Beam dynamics simulations have been performed for comparing the cavities presented above. For our simulations we use a beam with the parameters: average energy 32 MeV, energy dispersion 140 keV, transverse beam size about 0.7 mm, transverse emittance - 0.9 π mm mrad. The beam is passing through the deflector and is observed at the points of screens positions in the tomography module and in the dispersive section after the dipole.

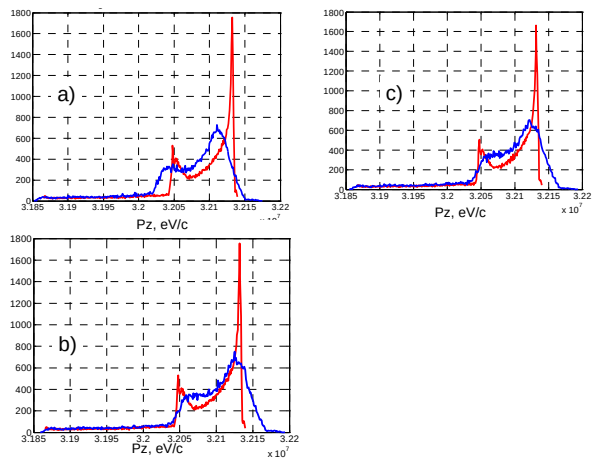

Figure 4. Longitudinal momentum distribution. Red line corresponds to the initial distribution (before deflector).Blue line is the distribution for the beam passed through a)“classic” cavity, b) “Paramonov” cavity, c) traveling wave cavity.

For correct longitudinal phase space measurements in the dispersive arm we have to minimize distortion of the longitudinal momentum distribution during passing the deflector. We compared the longitudinal momentum distribution on the dispersive arm screen for the different deflectors. In Fig.4 momentum distributions for the three variants of the deflectors are compared with the initial momentum distribution (before deflector). One can not see large difference between these three cases. The estimated resolution of the method is about 25keV/c. This value we can roughly resolve from the presented distributions. The rise or fall edge in the initial momentum distribution is about a few keV. They are transformed to the edges with the width of about 25 keV.

The transverse slice emittance measurements require high similarity of the initial longitudinal charge distribution to the transverse charge distribution (along deflecting direction) after deflector. This requires a lineal dependence of the deflecting voltage to the position inside the bunch. The requirement is provided by a quite large RF wave length (230 mm) in the cavities in comparison with the bunch length (8 mm). Beside that the cavity has to generate a minimum distortion in the transverse

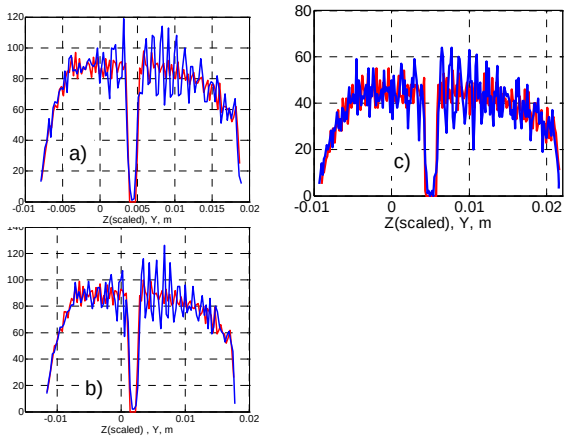

Figure 5. Charge distributions.
Red line corresponds to the initial longitudinal distribution (before deflector). Blue line is the transverse distribution in the deflected direction for the beam passed through a) "classic" cavity, b) "Paramonov" cavity, c) traveling wave cavity.

direction (perpendicular to deflected direction). This is necessary for correct emittance measurements. In Fig.5 we compare the longitudinal charge distribution of the initial beam and transverse charge distribution for the beam passed through deflecting cavity. We add a special gap (0.4mm) in the initial distribution in our simulations. That helps us to estimate the resolution length by observing the gap in the transverse distribution of the

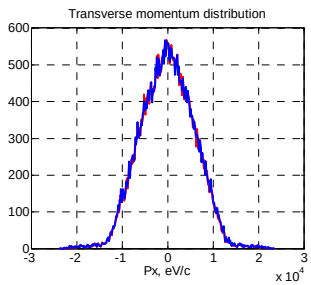

Figure 6. Transverse momentum distribution (perpendicular to deflect direction). Red line – initial distribution (before deflector), blue line – distribution for the beam passed through traveling wave cavity

deflected bunch. One can see that all cavities provide transverse bunch charge profile (corresponds to deflected direction) similar to the initial longitudinal charge profile. Because of the 100 % degree of the modulation in the final distribution we can estimate that the resolution length for these measurements is about the gap width (0.4 mm). The transverse momentum distributions (perpendicular to deflection direction) practically are not changed in the deflector. An example of the transverse momentum distribution before and after the deflector is shown on Fig.6 for the travelling wave cavity. The simulations show minimal influence from the deflectors to transverse beam parameters (perpendicular to deflection direction).

DISSCUSION OF THE RESULTS

All presented cavities can be used for the beam phase space analysis. We have considered their advantages and disadvantages. The main differences are between steady wave and travelling wave cavities. The first one request less RF power (see Table 2) and is easy in control. But the travelling wave cavity gives us a possibility to analyse a single bunch in a bunch train. We plan to work with the beam bunch repetition frequency up to 9 MHz (period ~0.11 μs). Because of short filling time in travelling wave cavity (0.2 μs) we can "take" a single bunch and direct it to a screen and distort 1-2 other pulses in the train only. This possibility is important for the analysis of the beam parameters fluctuation in the train from bunch to bunch. Also we can make the beam monitoring during tuning the beam. We decided to use the travelling wave cavity in combination with the tomography module for the possibility to analyse single bunches.

DIAGNOSTIC COMPLEX FOR LONGITUDINAL SLICE TRANSVERSE EMITTANCE MEASUREMENTS

The layout of the prospect system for slice emittance measurements is shown in Fig.7. It contains a deflecting cavity, a tomography module and four kickers. The beam is matched by quadrupoles on the entrance of the tomography section so that α and β functions are periodically repeated from screen to screen [6]. That permits us to analyse the beam more easily. The bunch deflected in the RF cavity in vertical direction is deflected by the kicker in horizontal direction to the screens. The screens are located off axis. The kicker pulse duration is less 100 ns with rise(fall) time about 10 ns. That permits to observe deflected bunches only. The few bunches which are distorted in deflecting cavity by the rising or falling RF field don't hit the screens and are lost in the beam line. All other bunches are passing through the tomography module and accepted at the beam dump.

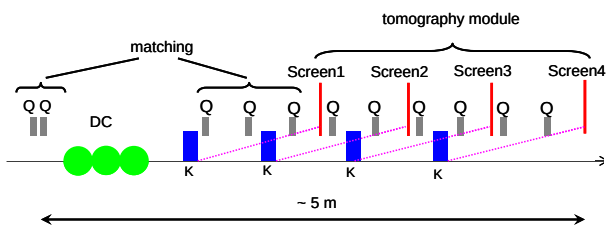

Figure 7. Prospect diagnostic for longitudinal slice emittance measurements.
Q – quadruple; K – kicker; DC – deflecting cavity

The layout of diagnostics for longitudinal beam phase space measurements is shown in Fig.8. After tomography module downstream we plan to set dispersive section. The distance between the deflector and the screen in the dispersive arm is about 6 m. Bunches are deflected by a dipole magnet and are analysed on the screen. During the

dispersive arm operation the magnets in the tomography module will be off.

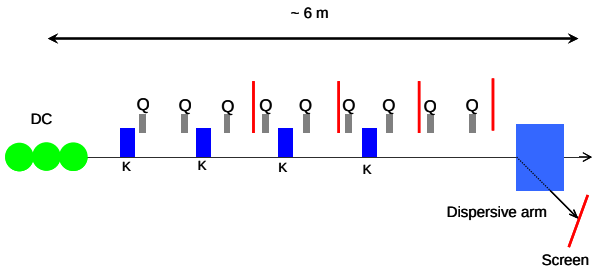

Figure 8. Prospect diagnostics for longitudinal beam phase space measurements.

CONCLUSION

The deflectors reviewed in this paper satisfy the requirements for the beam diagnostic at PITZ2. We consider to use the travelling deflecting cavity due to its additional possibility to analyse single bunches in a bunch train. We expect the possibility to measure transverse slice emittance with ~20 slices in the tomography module. For longitudinal phase space measurements in the dispersive arm we estimate the resolution as ~25 keV/c.

The authors would like to thank D.J. Holder and B.D. Muratori for their work under the tomography module analysing.

REFERENCES

[1] F.Stephan, D.Kraemer, I.Will and A.Novokhatski, Proc. FEL2k, Durham, USA, August 2000

[2] V.Miltchev et al., “Transverse Emittance Measurements at the Photo Injector Test Facility at DESY Zeuthen (PITZ)”, DIPAC, 2003

[3] D.Alesini, C.Vaccarezza, “Longitudinal and transverse phase space characterization”, SPARC-RF-03/003, INFN/LNF, Frascati, 2003

[4] V.Paramonov, et. al. “Effrctive standing-wave RF structure for charged-particle deflector”, LINAC, 2006, (to be published)

[5] O.H.Altenmueller, et.al., “Investigations of traveling – wave separator s for the Stanford two-mile linear accelerator”, The rev. of Sci. instr., Vol.35(4), 1964

[6] D.J.Holder, et. al., “A phase space tomography diagnostic for PITZ”, EPAC2006, Edinburgh, UK

TUNING, CONDITIONING, AND DARK CURRENT MEASUREMENTS OF A NEW GUN CAVITY AT PITZ*

A.Oppelt†, K.Abrahamyan, O.Aldrian, G.Asova, J.Bähr, G.Dimitrov, H.-J.Grabosch, L.Hakobyan, J.Ivanisenko, S.Khodyachykh, S.Korepanov, M.Krasilnikov, B.Petrosyan, R.Spesyvtsev, L.Staykov, F.Stephan, F.Tonisch, DESY, 15738 Zeuthen, Germany
F.Marhauser, D.Richter, E.Weihreter, BESSY, 12487 Berlin, Germany
K.Flöttmann, J.H.Han, C.Martens, R.Meyer, V.Miltchev, DESY, 22603 Hamburg, Germany
O.Kalekin, Humboldt University, 12489 Berlin, Germany
P.Michelato, L.Monaco, D.Sertore, INFN Milano, 20090 Segrate, Italy
J.Rönsch, University of Hamburg, 22761 Hamburg, Germany.

Abstract

In December 2005, a new gun cavity for the Photo Injector Test Facility at DESY in Zeuthen (PITZ) was tuned with the help of a specially designed tuning device. The tuning procedure and its results as well as RF measurements will be presented. Meanwhile, the cavity was installed in the PITZ facility and conditioned. Dark current measurements with different cathodes were performed and are described. Comparisons to former measurements are made.

INTRODUCTION

The photo injector test facility at DESY in Zeuthen (PITZ) was built in order to test and optimize electron sources for Free Electron Lasers and Linear Colliders. One of the main tasks is to prepare gun cavities for subsequent use at FLASH and XFEL. Up to now, three gun cavities have been built by DESY and another one is in production. They are designed for a peak power of 4.5 MW and an average heat load of 50 kW [1]. In order to reach higher power levels, two further guns with improved cooling will be built towards the end of 2006.

After the production of the first gun cavity, prototype No.1, a water-to-vacuum leak was found. It was figured out that the used copper did not fulfill the specifications. The leak was repaired with a kind of glue, but an installation at FLASH was not recommended. Therefore, this gun was used for high power tests at PITZ after the commissioning of a 10 MW multi beam klystron in June 2005 [2]. The conditioning towards higher peak and average power ended suddenly with the break-up of the old water-to-vacuum leak which appeared at a gradient of about 57 MV/m [3]. Meanwhile, the cavity was again repaired and is available for further tests.

Frequency measurements after the gun production showed a frequency difference from the goal frequency of 1.3 GHz (detuning) of 615 kHz, see Table 1. This detuning is caused by the brazing and cannot be calculated. Thus, the gun was mechanically tuned and the dimensions of the cells have been corrected in the design of the next gun cavity.

Gun cavity prototype No.2 was nevertheless showing a large detuning, probably due to the different copper quality. The gun was used in the PITZ1 phase until Nov.2003 and was installed at FLASH after a complete characterization at PITZ [4] where it is in operation since February 2004.

Table 1: RF measurements results of all three existing DESY cavities before tuning. The detuning was calculated for an operation temperature of 43°C under vacuum (measurement at 23°C in air).

Gun cavity prototype No.	1	2	3.1
Frequency detuning (kHz)	616	1207	632
Field flatness E_{half}/E_{full}	0.90	0.97	0.94
Mode spacing 0-π-mode (MHz)	5.3	5.2	5.2

The third gun cavity (prototype No.3.1) has been built in 2003. In order to avoid the complicated tuning procedure that was necessary for the previous guns, the cell's dimensions have been corrected again. In addition, the gun has special tuning knobs that allow modifying the resonance

Figure 1: Photograph of gun cavity prototype No.3.1.

* This work has partly been supported by the European Community, contract numbers RII3-CT-2004-506008 (IA-SFS) and 011935 (EUROFEL), and by the 'Impuls- und Vernetzungsfonds' of the Helmholtz Association, contract number VH-FZ-005.

† presenting author: anne.oppelt@desy.de

frequency by up to 300 kHz. However, after some first rf measurements of the resonance frequency in September 2004, it became clear that the tuning knobs cannot be used: the measured detuning was too large (Table 1).

TUNING OF THE NEW GUN CAVITY

In order to shift the frequency and to correct the field profile, a new tuning device has been developed. It consists of a stable girder on which the gun is placed, and two tools for deforming the cavity walls: a tuning stamp for pushing the cathode wall at the cathode plane, and a tuning clamp for pulling the coupler-facing wall of the full cell. For frequency measurements a small tapered coupler has been built by BESSY. Thus the system became much easier to handle compared to the large and heavy coaxial coupler used in the beamline installation. A bead pull setup for field profil measurements can be easily mounted to the tuning device. Figure 2 shows a photograph of the complete setup.

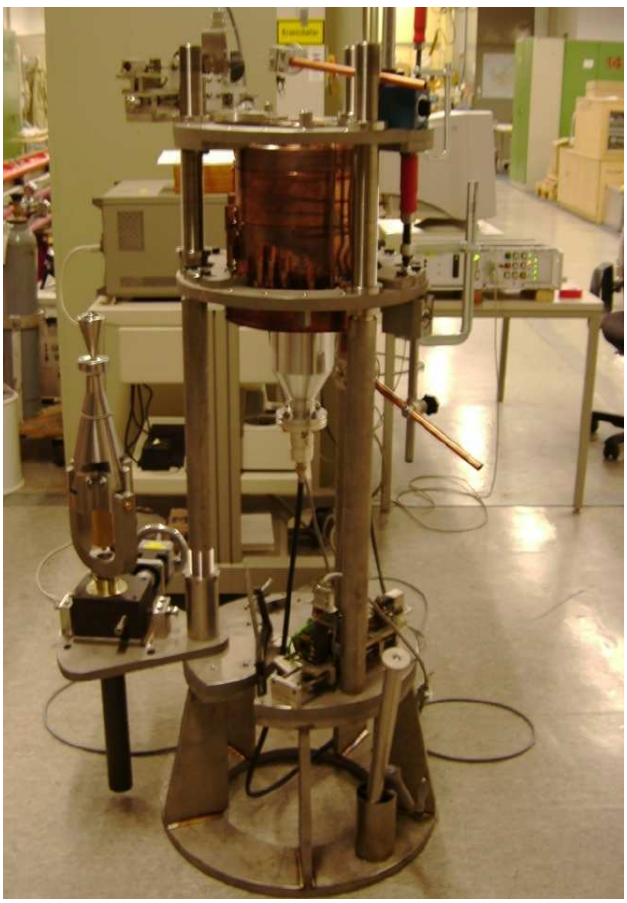

Figure 2: Photograph of the tuning device with the gun cavity, the BESSY test coupler, the bead pull setup, and the tuning tools: the clamp (mounted) and the stamp.

In November 2005, the new tuning device was used for the first time. Gun cavity No.3.1 was tuned in several consequent steps. Each time the cavity walls were pushed or pulled some ten microns and the deformation was surveyed. The use of the tuning tools left partly visible signatures in the material, but mostly not to recognize when touching. Figure 3 shows an example of the marks from both tuning tools.

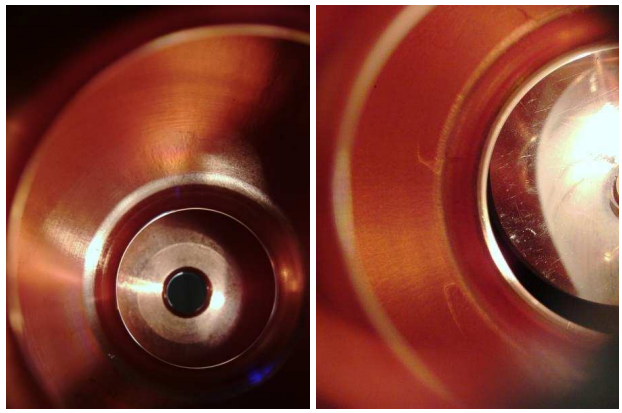

Figure 3: Marks in the copper material from the tuning stamp (left; a circular mark around the cathode hole) and from the tuning clamp (right; two imprints in the coupler-side wall).

As result of the tuning, the resonance frequency is reached at the design operation temperature of $54°$C, while the field flatness E_{half}/E_{full} was measured to be about 1.06, see Figure 4. This means, the field at the cathode is 6% higher than in the full cell. According to simulations, this is a good compromise between high average accelerating

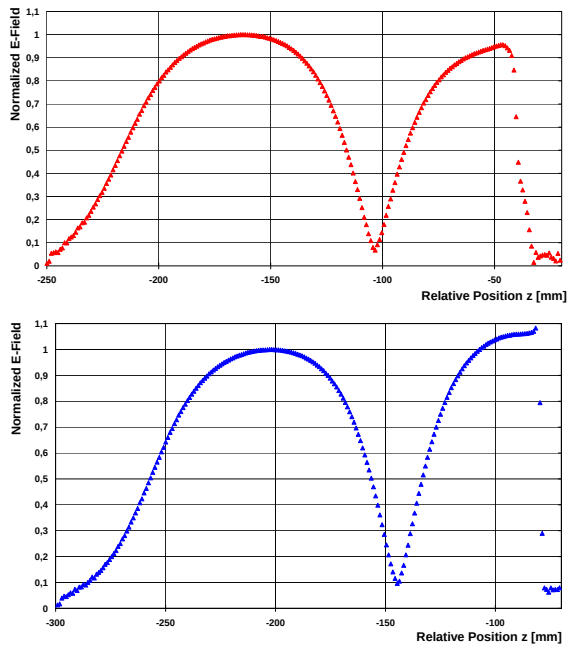

Figure 4: Field distribution in the gun before (top) and after (bottom) tuning. The cathode field is finally 6% higher than the field in the full cell.

gradient and maximum gradient at the cathode for space charge compensation. The quality factor of the cavity was also determined: Q_0= 24200.
Using the new tuning device, the tuning procedure was very smooth and comfortable. Therefore, it was decided to do a re-tuning of cavity No.1 which was tuned in 2001 for an operation temperature of 35°C. But during the high power tests in 2005 it was found that the lower temperature limit of the cooling water system limits the reachable average power at such a low operation temperature. The goal of the tuning was thus to increase the operation temperature. As a result of the re-tuning, an operation temperature of 50°C was obtained while keeping the field flatness constant at a value of about 1.05.

DARK CURRENT STUDIES

After the tuning, the new gun cavity was installed in the PITZ beamline and conditioned up to the full FLASH specifications: 3.5 MW peak power, 900 μs pulse duration, and 10 Hz repetition rate, corresponding to an average power of 31.5 kW [3].
Extensive dark current studies started in April 2006 and continued during the summer. The measurements were done for one Cs_2Te cathode (used for beam operation in 2005 and 2006), and for four Mo cathodes (with optical polished surface, used for gun conditioning). One of the Mo cathodes (cathode 80.1) has a hole pattern on its surface [5]. It was foreseen to serve for dark current generation studies but the corresponding pattern was not found in the dark current images. An example of such an image is displayed in Figure 5: it shows the YAG screen signal of dark current emitted by this specially prepared cathode 80.1.

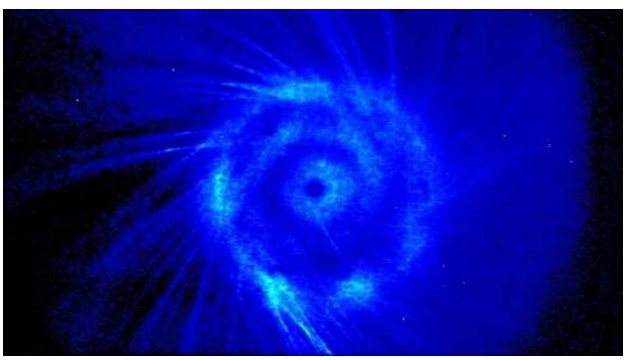

Figure 5: Dark current from cathode 80.1 on a YAG screen.

Figure 6 displays a photograph of the cathode 80.1 as well as a picture of cathode 58.1 (Cs_2Te).
Figure 7 shows the measured dark current level without solenoid magnets ($I_{main} = I_{bucking} = 0$ A) as function of the gradient at the cathode for two different guns: cavity prototype No.2 (data from 2002) and cavity prototype No.3.1 (data from 2006). For each gun, one distribution is shown for Mo and one for Cs_2Te. The dark current level

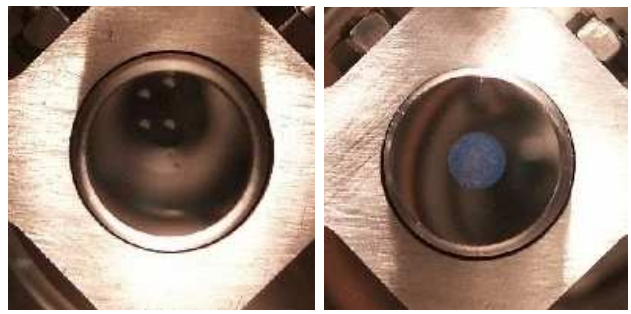

Figure 6: Topview of two of cathodes in the cathode chamber: Mo cathode 80.1 with the special hole pattern (left) and Cs_2Te cathode 58.1 (right).

produced 2002 without magnets is higher than the currently measured level. In order to understand the origin of this difference - the cavity or the photo cathodes or both - more detailed studies are necessary. One possible reason is a difference in the emitted dark current spectrum, as presented in [3]. At fixed magnet settings it can lead to a different effective aperture (due to the gun itself, the coupler, and the following beamline) and thus to a different detected dark current level downstream the gun.

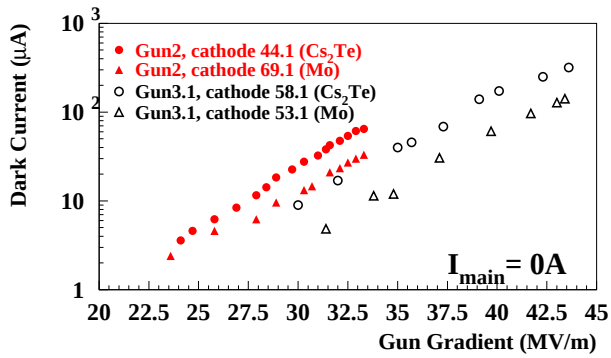

Figure 7: Dark current without solenoids produced with two gun cavities for different cathodes at PITZ.

Dark current measurements at different gradients have been performed as function of the currents in the main and the bucking solenoids. Examples for such 2D dark current measurements are shown in Figure 8: the dark current emitted by cathode 75.1 (Mo) was recorded for all combinations of I_{main} and $I_{bucking}$ at three different gradients.
Taking the maximum entry in such a 2D dark current distribution, one obtains the maximum dark current level emitted by a certain cathode at a defined gradient. Figure 9 shows the resulting distribution for gun cavity No.3.1 with cathode 53.1 (Mo) and cathode 58.1 (Cs_2Te). In addition to the data from 2006, an old result from the PITZ1 phase (spring 2003) when using gun cavity No.2 is drawn for comparison. The level of the emitted dark current is approximately equal, at least for the Cs_2Te cathode.
Finally, the maximum dark current of all Mo cathodes used in gun cavity No.3.1 is shown in Figure 10. The maxi-

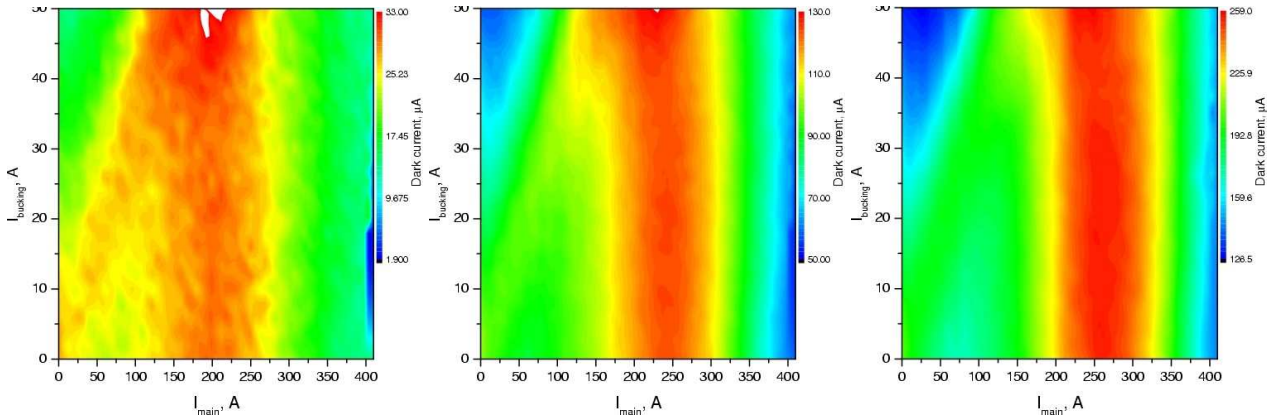

Figure 8: 2D scans of dark current emitted by Mo cathode 75.1 for all combinations of I_{main} and $I_{bucking}$ at different gradients: 35 MV/m, 40 MV/m, and 3543 MV/m (from left to right). Note the different color coded scale.

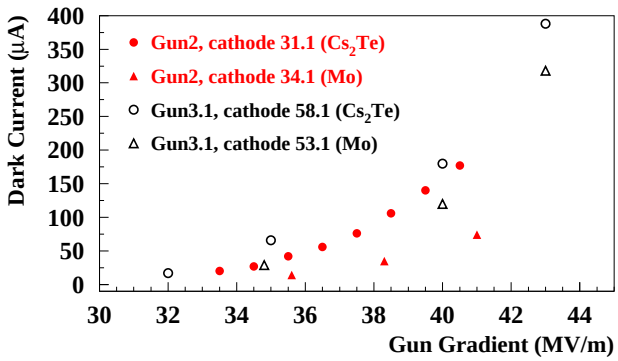

Figure 9: Maximum emitted dark current with two gun cavities for different cathodes.

mum amount of dark current is comparable for the analyzed cathodes, even if the emitted spectrum was different, as reported in [3].

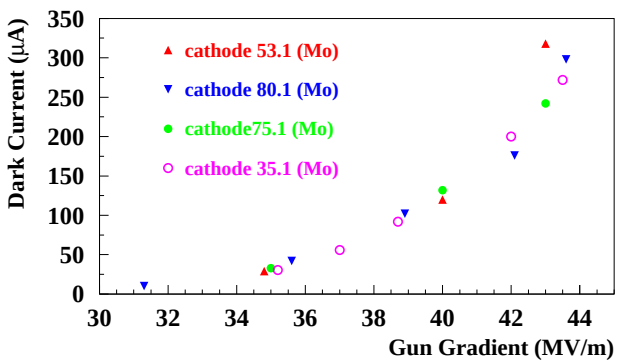

Figure 10: Maximum emitted dark current from the Mo cathodes used in gun cavity No.3.1.

From all dark current studies done with the new gun cavity it can be concluded that this cavity produces about the same amount of dark current as the former used cavity (prototype No.2). This means that there is no influence on the dark current from the tuning marks which have been produced by using the new tuning device. Therefore, the device can be also used for the tuning of further new cavities which are planned to be used at PITZ.

Nevertheless, the dark current level produced by the cathodes needs to be further decreased. In order to do so, more detailed studies of the dark current emission are necessary as well as improvements on the photo cathodes themselves.

SUMMARY AND OUTLOOK

A new gun cavity (prototype No.3.1) has been built, tuned, and commissioned at PITZ. The results of the tuning and extensive dark current measurements have been presented in this paper. Comparisons with formerly taken data was done. The gun is currently used for beam measurements at PITZ. After its full characterization, it will be dismounted from the beamline in autumn 2006 in order to be available as spare gun for the FLASH user facility. For PITZ, a new gun is currently in preparation (prototype No.3.2).

REFERENCES

[1] K.Flöttmann et al., RF gun design for the TESLA VUV Free Electron Laser, NIM A 393 (1997) 93-95.

[2] A.Oppelt et al., Status and first results from the upgraded PITZ facility, FEL 2005, Stanford, Aug.2005.

[3] A.Oppelt et al., Status of the PITZ facility upgrade, LINAC 2006, Knoxville, Aug.2006.

[4] F.Stephan et al., Recent results and perspectives of the low emittance photo injector at PITZ, FEL 2004, Trieste, Sept.2004.

[5] L.Monaco et al., dark current investigations of FLASH and PITZ RF guns, EPAC 2006, Edinburgh, June 2006.

DESIGN OF THE CAVITY BPM FOR FERMI@ELETTRA

P. Craievich*, D. Castronovo, M. Ferianis, ELETTRA, Trieste, Italy
M. Poggi, Laboratori Nazionali di Legnaro, INFN, Legnaro, Italy

Abstract

High resolution Beam Position Monitors (BPM) are fundamental diagnostics for a seeded FEL, like FERMI@ELETTRA, as they allow to measure the electron beam trajectory non destructively and on a shot-by shot basis. Cavity BPMs provide the required sub-micrometer resolution relying on the excitation of the TM_{110} dipole mode when the beam passes through the cavity off axis. For the seeded FEL FERMI, we adopted a pair of cavity BPMs located upstream the modulating undulator to measure the electron beam trajectory at the sub-micrometer level. In this paper we first discuss the requirements for such a cavity BPM including those for the beam based alignment. The scaling from an X-band design to the final C-band design is presented. The resolution to stay below one micrometer has been cross-checked, both analytically and numerically. The losses of the common mode TM_{010} have been also checked, leading to the final dimensions which keep the losses at the level of the X-band cavity BPM.

INTRODUCTION

An accurate measurement of the transverse beam position is an important issue throughout all the machine; in the undulator sections, the position and angle of the electron beam at the entrance is a fundamental parameter to be measured in order to match it to the seed laser trajectory to maximise the interaction, laser to beam. In order to provide the required single shot resolution for the position measurement two cavity BPMs have been adopted in front of the modulator. According to the FERMI layout based on two undulator sections (FEL-1 and FEL-2), two pairs of cavity BPMs will be located in front of each FEL. The design of this cavity BPM is based on a previous development [1, 2]. It is a resonant pill-box cavity where the information on beam position is encoded in the amplitude and phase variations of the dipole mode (TM_{110}) with beam transverse position, as measured on the two ports located on opposite sides of the cavity. A scaling from X-band to C-band of cavity BPM has been performed. We evaluated by means of analytical and numerical models that the resolution at C-band remains below 1 micron. In the scaling process we paid attention at the losses in the common mode: the new dimensions have been set to get same losses as for the X-band common mode. Using previous analysis we have fixed geometrical dimensions for a 3-D model of the cavity BPM and coupling waveguide used to extract the signals excited by electron bunch. Here we present results of the simulations obtained by means of Microwave Studio 3-D code [3].

* paolo.craievich@elettra.trieste.it

BACKGROUND

The cavity BPM is essentially a pill-box cavity; the analytical formulas for a cylindrical cavity with circular section without beam pipe are an upper limit to estimate beam losses and RF parameters. From a theoretical point of view the energy losses experienced by a charge q when passing through a cavity are: $\Delta U_{110} = q^2 k_{110} x^2$ and $\Delta U_{010} = q^2 k_{010}$ for TM_{110} and TM_{010} modes respectively. The loss factors are defined as $k_{110} = (\omega_{110}/2)(R/Q)_{110}$ and $k_{010} = (\omega_{010}/2)(R/Q)_{010}$. ω_{110} and ω_{010} are the resonant frequencies of dipole and monopole modes. The ratio R over Q is defined for the two modes as:

$$\left(\frac{R}{Q}\right)_{110} = \frac{|V_z(x)|^2_{110}}{x^2 2\omega_{110} U_{110}} \tag{1}$$

$$\left(\frac{R}{Q}\right)_{010} = \frac{|V_z(x)|^2_{010}}{2\omega_{010} U_{010}} \tag{2}$$

where $|V_z(x)|^2_{110}$ and $|V_z(x)|^2_{010}$ are the squared voltages for each mode seen by a charge particle when it flies along the longitudinal axis at some offset x (x=0 for monopole). U_{110} and U_{010} are stored energy in cavity for the TM_{110} and TM_{010} modes respectively. The ratio R over Q of a given mode can be also theoretically computed for a cavity without beam pipe.

Dipole mode TM_{110}

$$\left(\frac{R}{Q}\right)_{110} = \frac{2L J_1(\frac{a_{11}}{b}x)^2 T^2}{\pi \epsilon_0 \omega_{110} b^2 J_0(a_{11})^2 x^2} \tag{3}$$

where L is cavity gap, b is the cavity radius, ϵ_0 is the permeability of the vacuum, J_0 is the 0^{th} order Bessel function of the 1^{st} kind, J_1 is the 1^{st} order Bessel function of the 1^{st} kind, with its first zero $a_{11} = 3.832$ and T is the transit time factor defined by:

$$T = \frac{sin\left(\frac{\omega_{110} L}{2c_0}\right)}{\frac{\omega_{110} L}{2c_0}} \tag{4}$$

being c_0 the speed of light. It is worthwhile to mention that for small x, $J_1(\frac{a_{11}}{b}x) \approx \frac{a_{11}}{2b}x$; furthermore R over Q and also k_{110} become independent from x. The loss factor k_{110}, as a function of the cavity gap L and of the resonant frequency of TM_{110}, is plotted in figure 1. In general for a small cavity gap, the transit time factor T is almost equal to 1, but from figure 1 we can see that in the X-band range

and with a cavity gap longer than 15mm, approximately, there is a reduction of the loss factor due to influence of T.

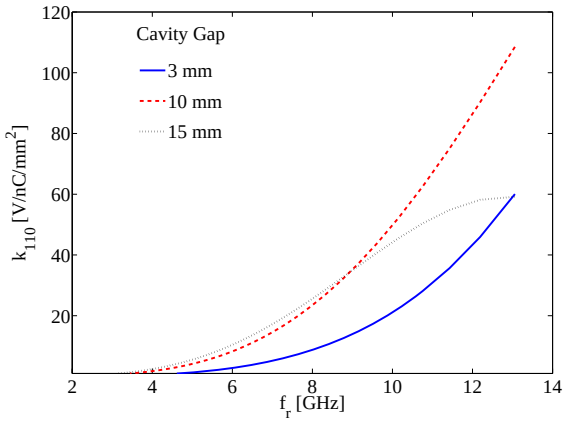

Figure 1: Loss factor of the dipole mode TM_{110} versus cavity gap L and resonant frequency.

Monopole mode TM_{010}

$$\left(\frac{R}{Q}\right)_{010} = \frac{LJ_0(\frac{a_{01}}{b}x)^2T^2}{\pi\epsilon_0\omega_{010}b^2J_1(a_{01})^2} \quad (5)$$

where $a_{01} = 2.405$ is the first zero of the Bessel function J_0 and T defined as above. For the monopole mode the R over Q is calculated on longitudinal axis (x=0) where $J_0(\frac{a_{01}}{b}x) = 1$. The loss factor k_{010} as a function of cavity gap L and resonant frequency of TM_{010} is shown in figure 2. The energy lost in the TM_{010} mode produces undesirable wake fields and has to be minimized in the design. We can see from figure 2 that, using a lower resonant frequency, we can increase cavity gap L without increasing the value of the loss factor.

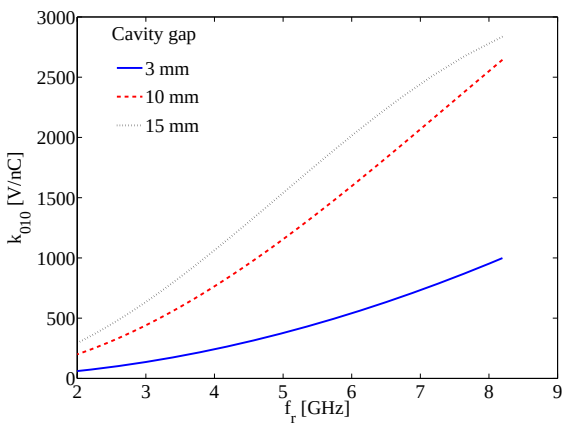

Figure 2: Loss factor of the monopole mode TM_{010} versus cavity gap L and resonant frequency.

BPM RESOLUTION

As presented in [1, 2] it is possible to design the coupling waveguide to selectively couple out to the TM_{110} mode but not the TM_{010} mode. Without the contamination of the monopole mode, the intrinsic BPM resolution is limited by the signal to thermal noise ratio of the system. For a given coupling coefficient, the external signal voltage on matched impedance Z_0 for a charge q is:

$$V_{ext} = q\sqrt{Z_0\frac{\omega_{110}}{Q_{ext}}k_{110}}\ x \quad (6)$$

The thermal noise voltage of the BPM is given by $N = \sqrt{Z_0kT_k\Delta f}$ where k is the Boltzmann's constant, T_k the temperature in Kelvin and $\Delta f = f_{110}/Q_{ext}$ is the bandwidth. The upper limit of resolution can be achieved when the external signal V_{ext} is equal to the thermal noise N for:

$$x_{min} = \frac{1}{q}\sqrt{\frac{kT_k}{2\pi k_{110}}} \quad (7)$$

Assuming a charge $q = 0.8nC$ and $T_k = 300K$, in figure 3 we plot the BPM resolution with respect to the resolution at X-band as a function of resonant frequency of dipole mode TM_{110}. As a reference case for an X-band design we have assumed a pill-box cavity without beam pipe, with gap length $L = 3mm$ and cavity radius $b = 14.7mm$. In table 1 we report the parameters for the X-band cavity used as reference.

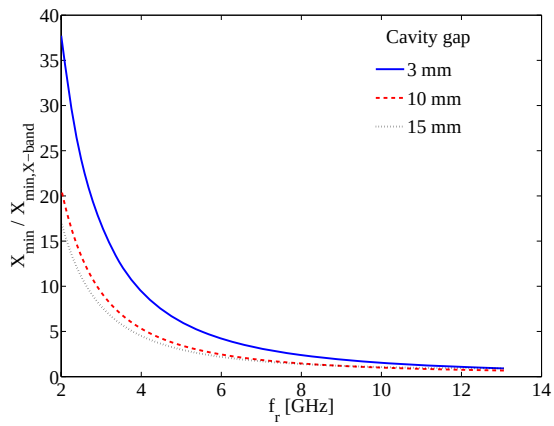

Figure 3: Resolution of the cavity BPM with respect to the resolution of an X-band cavity BPM versus its resonant frequency.

Table 1: Loss factors and resonant frequencies for X-band cavity BPM without beam pipe used as reference.

f_{110} $[GHz]$	k_{110} $[V/nC/mm^2]$	x_{min} $[nm]$	f_{010} $[GHz]$	k_{010} $[V/nC]$
12.4	49.7	0.14	7.8	907.6

SCALING OF THE CAVITY BPM

At X-band frequencies the mechanical tolerances are more stringent than at lower frequencies. Considering also the requirement on the minimum beam pipe radius, being equal to about $10mm$ in the undulator region, we have explored the achievable performance adopting a scaling at frequencies lower than X-band. In fact, dipole mode TM_{110} will be coupled away into the beam pipe if its resonant frequency is higher than the lowest cut-off frequency of the beam pipe. Assuming a beam pipe radius of $10mm$, the beam pipe cut-off frequencies are: $8.8GHz$ and $11.5GHz$, respectively for the TE_{11} and TM_{01} circular waveguide modes. Considering the available C-band hardware together with the above motivations, a resonant frequency of $6GHz$ (C-band) for the cavity BPM (radius cavity $b = 30.4mm$) has been selected. From figure 3, we can see that the resolution at C-band is still within an acceptable range. Looking at figures 2 we can increase the cavity gap up to about $L = 10mm$ without increasing losses in TM_{010} mode if compared to the losses in the X-band cavity. Assuming a charge $q = 0.8nC$, at room temperature, in table 2 are reported the parameters for C-band BPM cavity.

Table 2: Loss factors and resonant frequencies for C-band BPM cavity without beam pipe (cavity radius $b = 30.4mm$ and gap length $L = 10mm$).

f_{110} $[GHz]$	k_{110} $[V/nC/mm^2]$	x_{min} $[nm]$	f_{010} $[GHz]$	k_{010} $[V/nC]$
6.0	8.3	0.35	3.8	684.9

C-BAND CAVITY BPM

Preliminary numerical simulations by means of CST MWS[3] were done on a 3-D model with beam pipe to have a comparison with previous analytical treatments. For 3-D model we have adopted the following dimensions: $b = 30.4mm$, $L = 10mm$ and beam pipe radius $a = 10mm$. Table 3 shows results from analytical and numerical calculations and we can observe that the analytical one without beam pipe is a good estimation of cavity BPM with beam pipe for both dipole and monopole modes. We have adopted as waveguide the commercially available standard WR137 with internal dimensions of $34.85 \times 15.80mm^2$. To couple this waveguide to the cavity we have left unchanged the width while we have used a transition to 6mm for the height. This standard works in the frequency range of 5.85-8.20 GHz thus we have fixed the resonant frequency at 6.5GHz decreasing the radius of the cavity to 26.4mm. Figure 4 shows the 3-D model of the C-band cavity BPM where we can observe the waveguide transition to the standard WR137.

The external voltage in eq. 6 depends on $Q_{ext} = Q_0/\beta$ where β is the coupling coefficient and $Q_0 = 8530$ is the

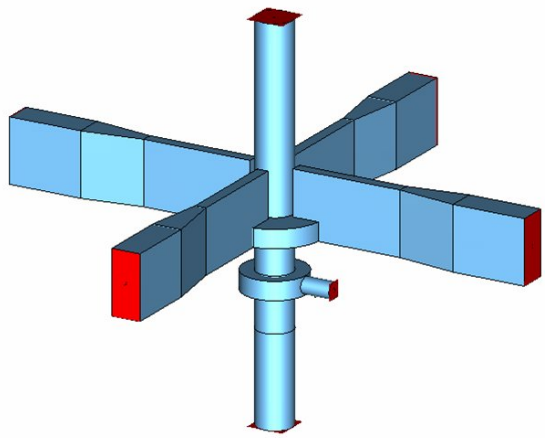

Figure 4: C-band cavity BPM with its four coupling waveguides and reference cavity.

Table 3: Comparison between numerical obtained by means of CST MWS and analytical results for C-band BPM.

	analytical	numerical	unit
f_{110}	6.0	5.7	$[GHz]$
$(R/Q)_{110}$	0.44	0.39	$[\Omega/mm^2]$
k_{110}	8.3	7.0	$[V/nC/mm^2]$
Q_0		8400	
f_{010}	3.8	4.0	$[GHz]$
k_{010}	685	523	$[V/nC]$

unloaded Q factor of the cavity with new dimensions. Figure 5 shows the dipole Q_{ext} as a function of the distance between beam axis and bottom of the waveguide.

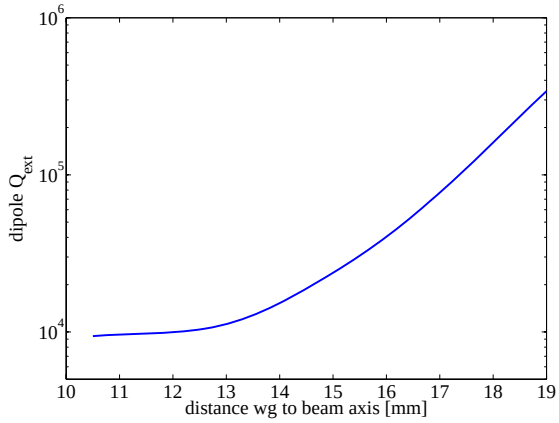

Figure 5: Q_{ext} of the dipole mode as a function of distance of the bottom of waveguide to beam axis.

The waveguide is always under coupled to the cavity and for distance below 13 mm the Q_{ext} remains about constant. We have fixed the distance between waveguide and beam axis at 12 mm thus $\beta = 0.1$ and $Q_{ext} = 10500$. In this

situation we only have a loss of 0.9 dB in the external voltage with respect to a critical coupling $\beta = 1$. In figure 4 the reference cavity is also indicated. The cavity will be used to provide the reference signal in the RF electronics and is designed to resonate at 6.5 GHz approximately with TM_{010} mode. The external coupling is foreseen by means of an antenna placed on the cavity lateral side.

A prototype C-band cavity BPM is being designed and cold test are foreseen. Table 4 shows dimensional and RF parameters of the C-band and reference cavity prototypes. From the mechanical point of view, we are faced with some challenges. First of all the required machining tolerance was fixed to $\pm 10\mu m$ for cavities, waveguides and their relative positioning. An important item is to decide how to build the BPM and reference cavities from bulk copper. One idea is to divide in two parts the whole geometry along the longitudinal symmetrical plane. The first part consists of half cavity together with waveguides, as shown in figure 6 [4], and second part consists of the other half cavity without waveguides. Both parts will be milled with the profile of the cavity and waveguides and subsequently the beam pipes, cavity and waveguides are brazed together. So the challenge concerns the brazing process and in particular to find the best brazing material. During the process it is important not to pollute the copper nor to deform the construct. This last item must be investigated through additional numerical simulations.

Table 4: Collections of the dimensional and RF parameters of the C-band cavity BPM and reference cavity.

C-band cavity BPM	
Cavity gap	$10mm$
Cavity radius	$26.4mm$
Beam pipe radius	$10mm$
Coupling WG	$34.85 \times 6mm^2$
Distance WG to beam axis	$12mm$
WG standard	WR137
Resonant frequency	$6.5GHz$
Unloaded Q factor	8530
External Q	10500
Coupling coefficient	0.1
Reference cavity	
Cavity gap	$10mm$
Cavity radius	$17.6mm$

CONCLUSION

In this paper we have explored a possible scaling of the cavity BPM presented in [1, 2]. For our considerations, we have used a model of a pill-box without beam pipe and have shown that a scaling from X-band to C-band frequencies is possible without loss of resolution. In addition, we have done simulations on a 3-D model to validate the analytical treatment and we have analyzed the position of the coupling waveguide to the cavity. These studies have allowed fixing dimensional parameters for a C-band prototype of the cavity BPM.

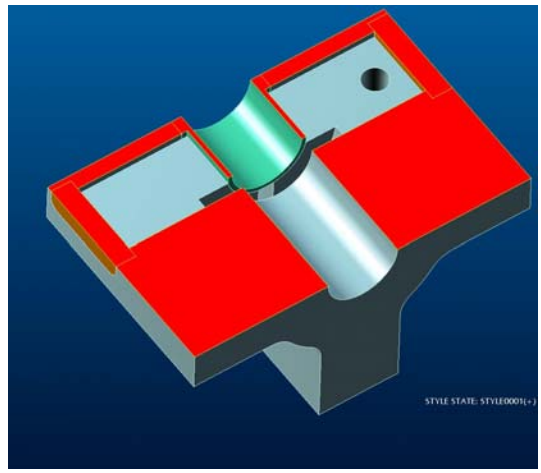

Figure 6: Preliminary technical drawing of the cavity BPM [4].

REFERENCES

[1] R. Johnson et al., "Cavity BPMs for NLC", BIW 2002, Upton, NY, May 2002.

[2] Z. Li et al., "An X-band Cavity for a high precision beam position monitor", DIPAC 2003, Mainz, Germany, May 2003.

[3] CST Microwave Studio, http://www.cst.de.

[4] Cinel Strumenti Scientifici, http://www.cinel.com.

DESIGN OF A TWO-STAGE LASER PULSE SHAPING SYSTEM FOR FEL PHOTOINJECTORS*

M. B. Danailov, A. Demidovich, R. Ivanov (ELETTRA, Basovizza, Trieste).

Abstract

This paper presents an approach for photoinjector laser pulse shaping which combines the two main pulse shaping techniques, namely acousto-optic dispersive filter (DAZZLER) and Fourier-based 4-f system. The DAZZLER is inserted between the seed mode-locked oscillator and the amplifier and is used for preliminary shaping in the infrared, while the final pulse shape and duration are determined by a 4-f dispersive system positioned after the harmonic conversion to UV.

INTRODUCTION

Temporal pulse shaping is one of the most important requirements to photoinjector lasers needed in the majority of FEL projects. The laser pulses commonly requested for excitation of the photocathode are in the UV (around 260 nm) and have flat-top shape of duration in the 5-10 ps range. Recently, more complex pulse shapes like ramps have been shown to be advantageous and proposed for implementation [1,3], indicating that the pulse shaping scheme must offer flexibility in generating different shapes. In principle, there are two main ultrashort pulse shaping techniques, namely 4-f type Fourie shaping [4] and acousto-optic dispersive modulator (DAZZLER) based [5] shaping. As it will be shown below, the use of one of these only is unlikely to allow reaching the required performance. The main complication comes from the fact, that the pulse shape is needed in the UV, and the required pulse energy is quite high, while pulse shaping is easy to do at low pulse energy in the IR. In the paper we describe a hybrid scheme proposed for the FERMI photoinjector, which utilizes both methods, one in the infrared and the other in UV. The paper starts with brief introduction to the ultrashort pulse shaping basics and notation, which is important for understanding the analysis and results presented later on. The specific problems related to photoinjector laser pulse shaping and the proposed optical scheme are discussed in the next section, followed by simulations and preliminary experimental results of flat-top and increasing ramp pulse generation.

PULSE SHAPING BASICS

As mentioned above, there are different laser pulse shapes that can be used to optimize the photoinjector (and overall FEL) performance. Here we will mostly refer to two of them, namely flat-top and increasing ramp, however the techniques used allow in principle to generate any desired pulse shape. To make the discussion of the pulse shaping schemes clearer, we will very briefly introduce some basics of the pulse shaping theory.

Assuming that the light field can be factorized into spatial and time dependent part, the electric field of the latter can be written as:

$$E(t)=1/2\ [I(t)]^{1/2}\ exp\{i[\omega_0 t-\varphi(t)]\}+ \text{c.c.}\ , \qquad (1)$$

where ω_0 is the central frequency , $I(t)^{1/2}$ and $\varphi(t)$ are the time dependent temporal amplitude and phase. For simplicity in the following equations the c.c. part will be omitted. The quantity

$$E(t)= I(t)^{1/2}\ exp[-i\varphi(t)] \qquad (2)$$

is referred to as the complex amplitude in the time domain. In the frequency domain, the pulse field can be represented in a similar manner:

$$E(\omega)=1/2\ [S(\omega)]^{1/2}\ exp[-i\psi(\omega)]\ , \qquad (3)$$

where $S(\omega)$ is the spectral intensity of the light pulse. As it is known, the time and frequency domain field representations are linked by a Fourier transform relation:

$$E(t)=(1/2\pi)\int_{-\infty}^{\infty} E(\omega)exp\ (i\omega t)\ d\omega \qquad (4).$$

Most of the known methods for shaping of ultrashort pulses are based on this relation, they implement manipulation of the spectral amplitude or phase (or both) of the pulse, which in turn leads to the required modulation in the time domain. The output pulse shape is given by the convolution of the input pulse and the impulse response function of the modulating function:

$$E_{out}(t)=\int_{-\infty}^{\infty} E_{in}(t`)h(t-t`)\ dt`\ , \qquad (5)$$

where h(t) can be calculated from its complex frequency transfer function by:

$$h(t)=(1/2\pi)\int_{-\infty}^{\infty} M(\omega)exp\ (i\omega t)\ d\omega. \qquad (6)$$

The complex transmission function $M(\omega)$ can be presented as:

$$M(\omega)=[M_I(\omega)]^{1/2}\ exp[-i\Phi(\omega)]\ \ , \qquad (7)$$

and the phase transmission is commonly expanded in Taylor series :

$$\Phi(\omega)=\Phi(\omega_0)+\Phi^{(1)}\Delta\omega+(1/2!)\Phi^{(2)}\Delta\omega^2+ +(1/3!)\Phi^{(3)}\Delta\omega^3+\ldots \qquad (8)$$

* This work has been partially supported by the EU Commission in the Sixth Framework Program, Contract No. 011935 EUROFEL

where $\Phi^{(i)}$ is the i-th derivative of the phase evaluated at ω_0 and are usually called i-th order dispersion. While the first and second terms in (9) represent only a constant and an overall time shift of the pulse, the third and higher order terms may lead to significant pulse shape changes even if the spectral amplitude $[M_I(\omega)]^{1/2}$ remains constant. In principle, if one could design a frequency filter with a prescribed optical frequency transmission function, any desired pulse shape (with temporal resolution limited by the inverse bandwidth of the input pulse $E_{in}(t)$) can be generated. In reality, it is quite difficult to produce optical filters with complex frequency transmission functions defined with high precision. As will be shown later, some specific shapes, like flat-tops, however, can be produced by use of interference filter.

The first technique which solves in a general way the pulse shaping has been known for more than a decade [4] : the spectral components of the input pulse are spatially separated by a dispersive element (e.g. diffraction grating) , and then manipulated in the spatial domain by using a modulator with spatially dependent transmission, placed in the Fourier (focal) plane of a lens, as shown on Fig.1. A second lens and grating recollimated the pulse spectral components, so the output pulse has again a spatially independent pulse shape that can be calculated using Eq.6. By proper choice of the modulator the technique allows to use both amplitude and phase modulation. It is worth noting that large second order phase terms (i.e large linear chirp) can be produced even without the use of modulator in this scheme, by just shifting the grating with respect to the focal plane of the lens.

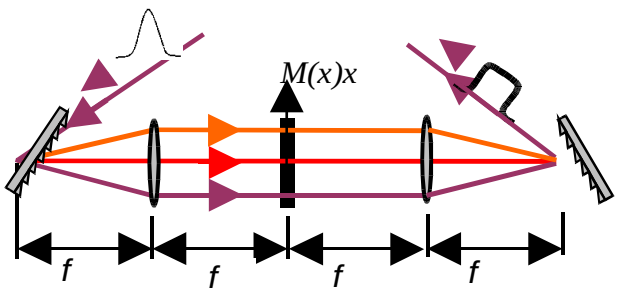

Figure 1: 4-f Fourier shaping system

A newer and very powerful technique for pulse shaping is the so called DAZZLER introduced by P.Tournois [5] and commercially available from Fastlite (France). In this method, also based on Eq.6, the spectral components are not separated spatially, the optical pulse travels in an acousto-optic modulator where a longitudinal acoustic wave is present. By shaping the acoustic wave frequency and amplitude, the spectral components of the optical pulse are diffracted out of the crystal at different positions (and therefore with different delay) and with different efficiency. In this way, the deviated part of the incoming pulse can be time modulated with very good precision.

DISCUSSION

The basic gun laser specs in the case of Copper photocathode are relatively well agreed. It is usually accepted that about 0.5 mJ of pulse energy in the UV (wavelength around 260 nm) has to be provided in order to obtain about 1 nC of charge.

Both techniques presented above allow in principle to obtain pulses with the required shape for the photoinjector. When flat-top is concerned, some experimental results with Dazzler have been presented in [6].The Dazzler has the obvious advantage of flexibility and compactness. It is provided with computer control allowing both amplitude and phase modulation. However, it has the following limitations:

- wavelength resolution of the high resolution model is about 0.3 nm. For this reason the bandwidth of the input pulse should be about 10 nm or higher in order to obtain high fidelity amplitude shaping;
-if a single pass is used, the maximum second order dispersion that can be provided by the Dazzler allows to generate pulses of up to 4 ps, which is not enough in most cases. A two pass geometry can be used for having ~10 ps long pulses, however in this case the insertion loss , even at maximum diffraction efficiency, is above 90% which does not seem to be practical;
-the Dazzler can be used only in IR. Fastlite announced recently a UV version, however it is not suitable for the task considered here (allowed power levels and wavelength resolution can not be met)
- maximum peak power limitation in the IR does not allow to use the Dazzler after the amplifier. For this reason it has to be placed between the seed oscillator and laser amplifier.

On the other hand, the 4-f based shaping can be used directly in UV, if a proper modulator is found. At present, the only available option is a piezo-deformable mirror [7] with a dielectric coating. Liquid crystal modulators like are only available down to 350 nm, which is not enough for our photoinjector case. There are two main limitations to be taken into account:

- the use of deformable mirror allows to obtain only phase modulation
- the obtainable phase curvature is limited by the limit of about 8 micron for maximum mirror deformation, so the deformable mirror alone will not be enough for obtaining large phase gradients, it can rather be used as a tool for compensating slow phase curvature errors.

PROPOSED LAYOUT

Fig.2 presents a layout of the hybrid shaping setup proposed for the FERMI photoinjector. Input seed pulses with a bandwidth of about 12 nm at 780 nm are generated by a mode-locked Ti:Sapphire laser. The IR pulse shaping is done by a DAZZLER inserted before the amplifier stages. The Dazzler is implemented primarily for producing the desired spectral amplitude shape (e.g. super-gaussian like) , and in addition for compensation of

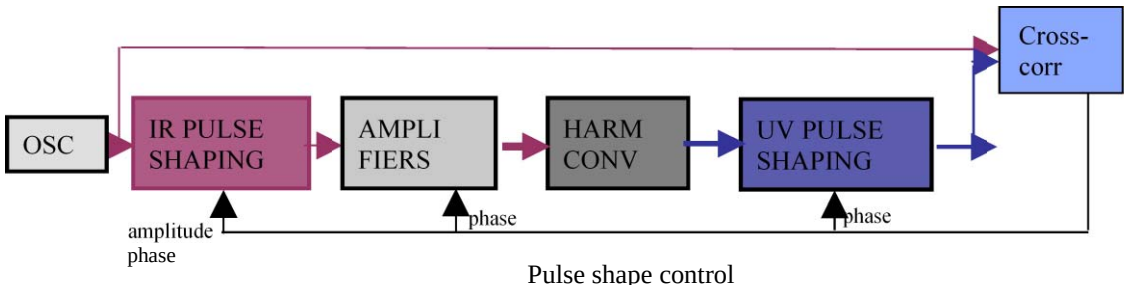

Figure 2: Proposed two-step shaping setup

third-order phase distortions due to the grating compressor of the amplifier. Usually this compressor is used for exact compensation of the chirp introduced by the stretcher. In our scheme it is also used for adding a second order dispersion by detuning with respect to maximum compression point. In this way, the pulse duration at the entrance at the harmonic generation crystals can be adjusted to an optimum value which allows to have high enough harmonic efficiency while still keeping high order nonlinear effects (e.g. self-phase modulation) at low. Such a safe peak power level is reported to be in the order of 10-20 GW/cm^2 for BBO. We note that our approach gives an additional degree of freedom for adjusting this level.

The final pulse duration and shape is then controlled by a dispersion based system working in the UV. Two version of this system are under consideration. The simpler one is just a two-pass grating stretcher used for adding a second-order phase needed to obtain the exact pulse duration (see the simulation later on). This version will be used in case the DAZZLER alone allows good enough compensation of all phase distortions. If it appears that an additional high order spectral phase compensation is needed after the harmonic generation, the UV shaping will include also a deformable mirror in a modified 4-f arrangement.

In order to illustrate better the described scheme, on Figs.3 and 4 we present the results of a simple simulation

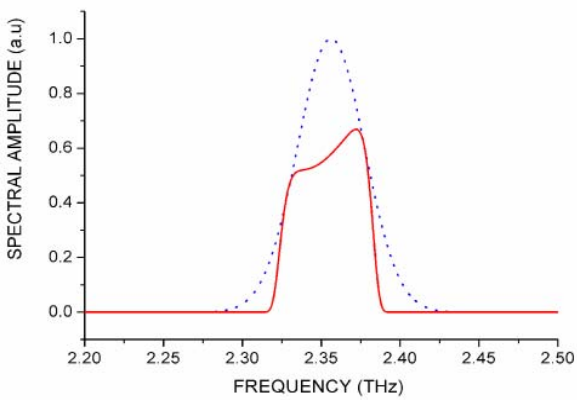

Figure 3: Input spectrum for the simulation (blue dots) and modulated spectrum after Dazzler (red solid line).

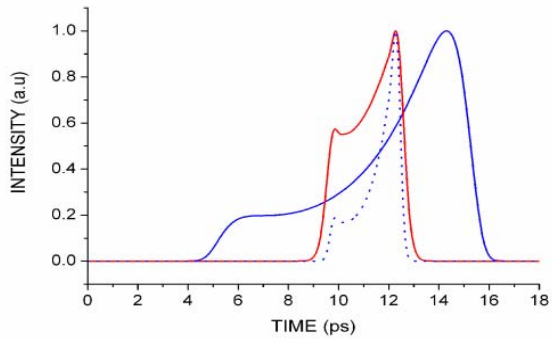

Figure 4: Pulse profiles after compressor in the IR(red solid line), after THG (blue dots), after UV stretcher (blue solid).

of pulseshaping which generates the pulse shape (increasing ramp) requested for the FERMI 'long bunch case' [3].

The simulation is done starting with a transform-limited Gaussian pulse at 800 nm having 12 nm of FWHM bandwidth (dashed blue line on Fig.3). The spectrum shown in red line is obtained after amplitude filtering by the Dazzler. In addition, it is assumed that the latter completely compensates the residual third-order dispersion of the system. The pulse shape shown by blue line on Fig.4 corresponds to the amplifier output, where a second order dispersion of about 60000 fs^2 has been introduced by detuning the compressor. Assuming that the third harmonic generation is performed in sufficiently thin BBO crystals , so GVM and spectral acceptance effects can be neglected, the UV pulse shape (dashed blue line) is proportional to the third power of the IR one. The final shape and duration, shown by solid blue line are obtained by adding only an additional second order dispersion from the UV grating stretcher. We note that this stretcher will inevitably add also a third order dispersion term on the order of 100 000 fs^3 , which is in principle possible to compensate in advance by the Dazzler, so it has not been taken into account into the above presented simulation. As mentioned above, in case the DAZZLER compensation is not sufficient the odd dispersion terms will be cancelled by the use of deformable mirror.

PRELIMINARY EXPERIMENTAL RESULTS

Most of the components of the above presented setup have already been tested at Elettra. Here we will briefly summarise some of the results. The DAZZLER has been installed and tested using a femtosecond Ti:Sapphire oscillator at 780 nm. On Figure 5, two typical flattop pulse shapes are presented: phase only polynomial modulation (blue line) and amplitude super-gaussian modulation. In both cases, the pulses were additionally stretched by the use of grating stretcher. The pulse measurement is done by cross-correlating the shaped pulse with a part of the input 100 fs long pulse.

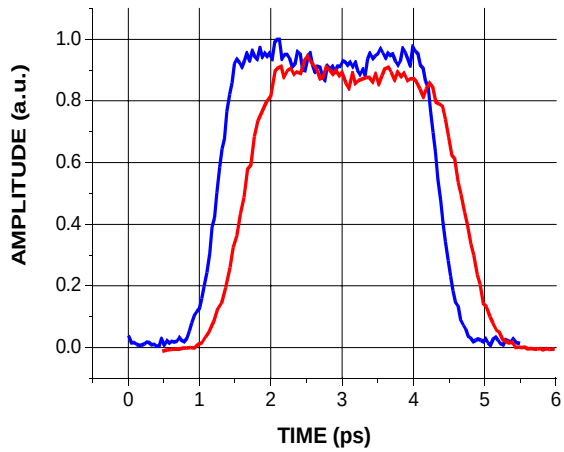

Figure 5: Flat-top pulses generated by the Dazzler; blue line: phase modulation, red line: amplitude modulation

It is important to mention here that the fact that amplitude filtering plus stretcher added second order dispersion works well indicates a simpler method. The amplitude filtering can be performed by the use of an interference filter. Indeed, we demonstrated this by the use of a commercial filter (Spectrogon), centered at 780 nm. There

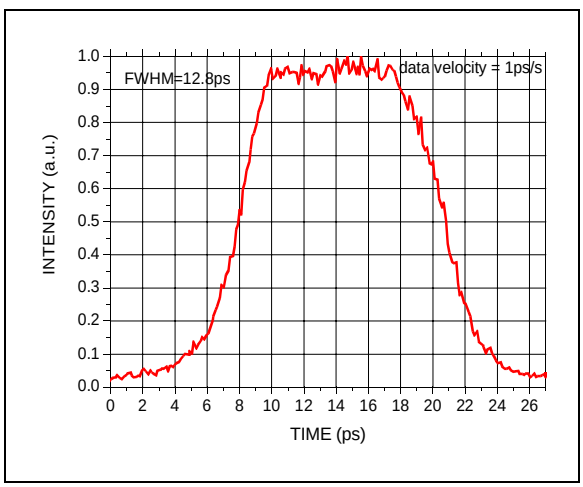

Figure 6: Flat-top pulse generated by the use of interference filter as an amplitude filter.

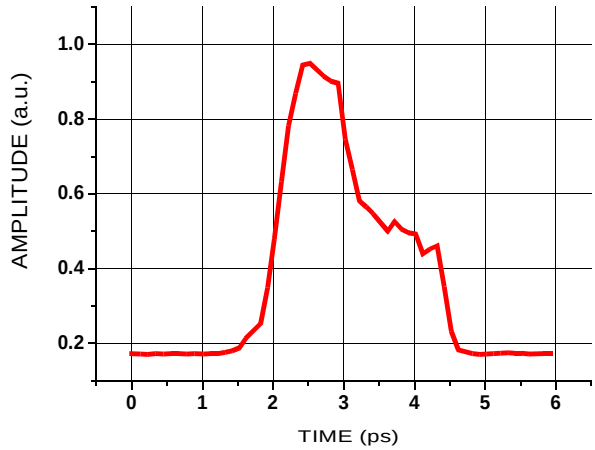

Figure 7: Increasing ramp generated by the Dazzler with pure amplitude modulation

is some freedom to detune the filter transmission curve position and shape by tilting and to obtain a nearly perfect super-Gaussian spectrum. As a result, after stretching , a flat-top pulse can also be obtained, as shown on Fig.6.The price to pay for the simplicity is that there is no control on phase, this might not be a problem if the UV part contains the deformable mirror.

On Fig. 7 we show a ramp type pulse profile [3] obtained on the same setup by using the Dazzler in amplitude modulation mode. We note that the cross-correlator scanning in this setup was starting from the back of the pulse, so the pulse front is on the right of graph and the ramp is increasing, as requested.

CONCLUSIONS

The setup described above is in principle capable of producing arbitrary pulse shapes in UV, especially in the version containing deformable mirror. The two basic techniques have been already tested at low power at Elettra, and a high energy version including the UV part is to be completed and tested in a few months time. There is still some freedom to choose the exact system and laser pulse parameters in order to obtain the required shapes with high fidelity.

REFERENCES

[1] C. Limborg-Deprey, Proc.27th FEL Conf.(2005), 418.
[2] O.J. Luiten, M.J. Van der Wiel, 27th FEL Conf.(2005) ,paper WEOB003.
[3] G.Penco et al, Proc.EPAC 2006, to be published
[4] A. M. Weiner, J. P. Heritage, E. M. Kirschner, J. Opt. Soc. Am. B **5**, (1988). 1563
[5] P. Tournois, Opt. Comm. 140 (1997), p.245 .
[6] C.Vicario et al, Proc.EPAC 2004, p.1300
[7] J.Gardino-Mejia et al, JOSA B 21 (2004), 833.

RAMPING LONGITUDINAL DISTRIBUTION STUDIES FOR THE FERMI@ELETTRA INJECTOR

G. Penco*, M.Trovò, Sincrotrone Trieste, Trieste, Italy
Steven M. Lidia, LBNL, Berkeley, California, USA.

Abstract

In the FERMI Linac optimization studies it comes out the request to have at the exit of the photoinjector a linear ramp in the current distribution along the bunch as alternative option with respect to the flat-top. This requirement is translated in the photoinjector optimization in a big issue. In fact the longitudinal bunch profile at the exit of the photoinjector is affected by the strong non linearity of the space charge fields at the cathode and in the drift between the gun and the first booster. The knowledge of the space charge fields at the cathode plays in important role in finding the optimum driven laser pulse shape. At this purpose an analytical description of the space charge fields produced by a bunch with an arbitrary current distribution at the cathode is provided. Space charge codes (GPT [1] and ASTRA [2]) have been used to evaluate the evolution of several ramping profiles from the cathode to the entrance of the first booster and the results are presented in this paper.

INTRODUCTION

In the optimization of the high brightness RF photoinjector a great effort is usually spent to produce an electron bunch as much as possible uniformly charged distributed. This is a precise requirement coming from the optimization of the emittance compensation in the injector and in the bunch transport through the linac, especially in presence of bunch compressors. By the other hand it has been demonstrated that the strong non-linearity of the linac sections longitudinal wakefields can be compensated by providing at the exit of the photoinjector a linear ramping electrons distribution instead of a flat top [3]. This requirement translates to the photoinjector optimization as a large perturbation due to the strong nonlinearity of the space charge fields at the cathode and in the drift between the gun and the first booster. To produce a ramped current bunch, a special initial profile has to be found that evolves along the injector to produce the final desired shape.

LONGITUDINAL SPACE CHARGE FIELD ON AXIS

In order to solve this problem, the longitudinal space charge fields on axis at the cathode was investigated, since it is mainly responsible for blowing out the particles, especially in case of high peak current. In case of a uniformly charged bunch the longitudinal space charge field on axis, inside and outside the bunch, at a distance z from the bunch tail is given by the following equation [4]:

$$E_z^{SC}(z) = \frac{Q}{2\pi\epsilon_0 R^2} H(z) \tag{1}$$

where H(z) is

$$H(z) = \sqrt{\left(1-\frac{z}{L}\right)^2 + \left(\frac{R}{\gamma L}\right)^2} - \sqrt{\left(\frac{z}{L}\right)^2 + \left(\frac{R}{\gamma L}\right)^2} - \left|1-\frac{z}{L}\right| + \left|\frac{z}{L}\right| \tag{2}$$

and Q is the total bunch charge, L the bunch length, R the bunch radius. For simplicity $\gamma = 1$ is assumed.
As example the figure 1 shows the field $E_z^{SC}(z)$ versus z (normalized with respect to the bunch length L) for a nominal 1nC bunch, with a radius of 1mm and a bunch length of 3mm. The flat-top current distribution at the cathode is

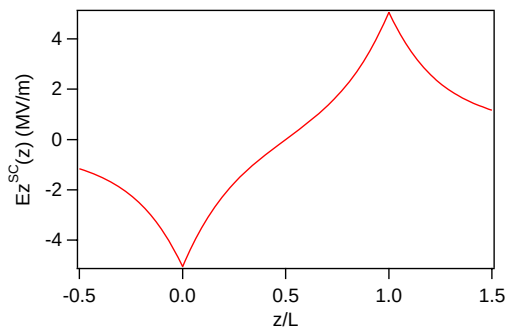

Figure 1: Longitudinal space charge field on axis of a bunch just extracted from the cathode; Q=1nC, R=1mm, L=3mm

deformed by this space charge field into a parabolic distribution after several centimeters, suggesting that a linear current distribution would suffer a strong degradation before entering into the relativistic regime. Thus the drive laser pulse should be shaped according to a non-linear distribution pattern. Eq.(1) has been generalized for an arbitrary longitudinal current density distribution $\rho(z)$ at the cathode [5], obtaining:

$$E_z^{SC}(z) = \int_0^L dz' \frac{\rho(z')}{2\epsilon_0}\left[\frac{z'-z}{\sqrt{(z'-z)^2+R^2}} - \frac{|z'-z|}{z'-z}\right] \tag{3}$$

* giuseppe.penco@elettra.trieste.it

Eq.(3) represents a useful analytical instrument to quickly predict the evolution and distortion of an arbitrary current profile. For example figure 2 shows the longitudinal space charge field on axis inside a bunch with respectively a linear and a quadratic ramping in the current distribution (image charge not included). Electrons in the high charge density region are pushed backwards during the bunch propagation because of the strong repulsive electric field and this modifies the starting bunch profile.

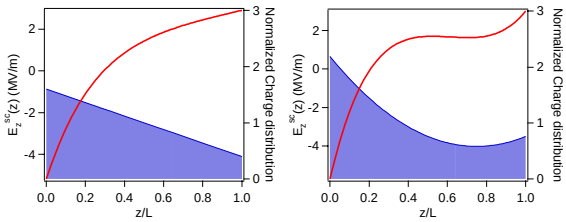

(a) (b)

Figure 2: Longitudinal space charge field on axis of a linear (a) and parabolic (b) ramping charged bunch just extracted from the cathode having different radius; Q=1nC, L=3mm. Cathode plate is in z=0.

Figure 2a shows that a linear ramp charge distribution samples an almost quadratic longitudinal space charge field (Figure 2a). Thus one can easily expect a large deterioration of the initial ramping current profile while propagating through the injector. Multiparticles codes trackings of linear ramp profiles similar to figure 2a have confirmed the expectation and figure 3 shows the bunch current profile at the exit of the injector: the initial linear ramp has been destroyed and the bunch presents a parabolic-like charge distribution.

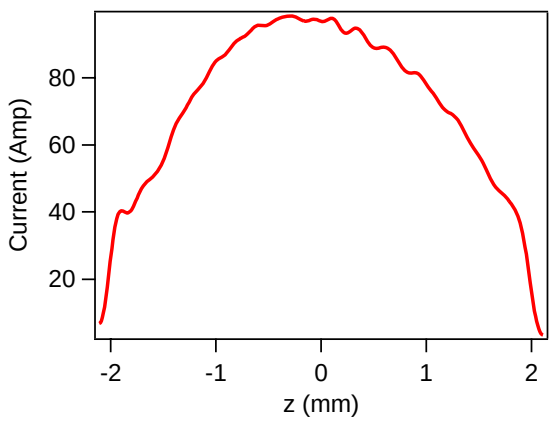

Figure 3: Resulting profile at the exit of the injector in case of an 800pC-bunch with a linear ramp at the cathode.

Also a quadratic ramp, like Figure 2b, is strongly modified during the transport between the cathode and the first booster section, but the linearity of the space charge field at least in the middle of the bunch helps in preserving the linear ramp in about 70% of the bunch (see Figure 4).

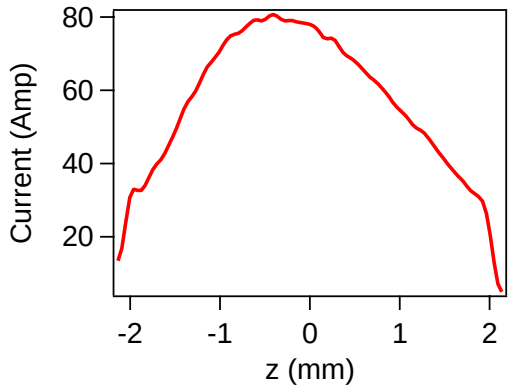

Figure 4: Resulting profile at the exit of the injector in case of an 800pC-bunch with a quadratic ramp at the cathode as Figure 2b.

Several initial current distributions have been studied in order to find the best one which linearizes as much as possible the space charge field experienced by electrons within the bunch and which evolves into the desired longitudinal profile. A fourth-degree polynomial distribution (see Figure 5) has been found to be an interesting solution that offers flexibility in compensating the high orders contributions of the space charge field and that increases the bunch fraction sampling a linear space charge field.

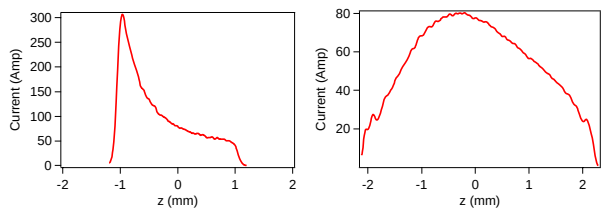

(a) (b)

Figure 5: A fourth-degree polynomial distribution at the cathode (a) and at the end of the photoinjector (b).

The current distribution plotted in Figure 5a has been considered as the baseline ramping distribution for the medium bunch case assuming a large efficiency in the laser pulse shaping process [6]. However in a conservative scenario even a quadratic distribution could be used without severe drawbacks.

A large charge density close to the cathode surface increases the image charge field and this should be considered in the generation of a ramping charge distribution. The effect of the image charge at the cathode can be easily included by adding the field $E_z^{SC}(-z)$ to the formula 3.
As example the space charge field with and without the image charges effects in case of a parabolic ramping charged bunch is shown in figure 6: the electrons close to the cathode sample a space charge field two times the value obtained without considering the image charges. In the optimization process and in the multiparticles trackings the

image charge effects have been included.

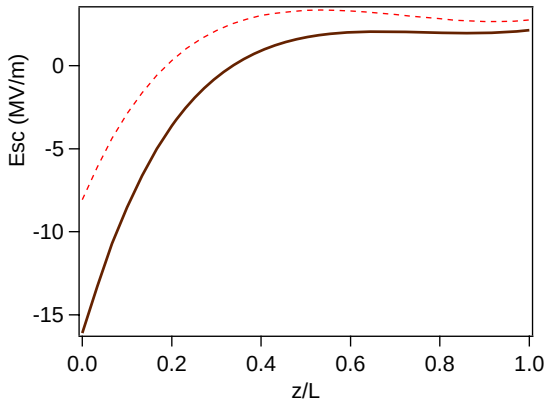

Figure 6: Comparison between the Longitudinal space charge field on axis with (continuous line) and without (dashed line) the image charges effects; Q=1nC, L=3mm

EMITTANCE COMPENSATION AND OPTICS MATCHING ISSUES

Because of the non-uniform charge distribution of the ramping regime, it is very difficult to find an injector parameter set-up that completely satisfies the invariant envelope equation, performing perfect emittance compensation for all slices. Since each slice contains a different amount of charge, each slice evolves in a particular and unique way in the gun-booster drift when the injector parameters are fixed. In order to minimize the projected emittance at the end of the injector an average parameters setting should be found, taking in account also the slice parameters behavior along the bunch. Studies were carried on by tracking several initial laser shapes with GPT and ASTRA. A crucial role has been played by the coefficients of the quadratic ramp chosen at the cathode. For example an attractive solution is to consider a quadratic profile with "double peaks", as showed in figure 7a. The small peak electrons are pushed forwards by the space charge field and this partially compensates the backwards spreading of the high peak electrons, increasing the linearity and the width of the ramping fraction of the bunch (figure 7b). In addition the head of the bunch presents a hard edge, instead of a smoothing falling edge. By the other hand, finding the optimum focusing condition is an issue in this case. In fact in order to compensate the emittance contribution of the high charge fraction of the bunch, the solenoid strength has been increased, leading to an overfocusing of the bunch core and head, as showed in the top view of figure 8.

Figure 9 shows the slice analysis concerning the emittance and the Twiss parameters for this case. The overfocused electrons in the middle of the bunch have even a higher slice emittance, around 1.4mm mrad. This ovefocusing has consequences also in the optics parameters: Twiss parameters suffer a very large oscillation slice by

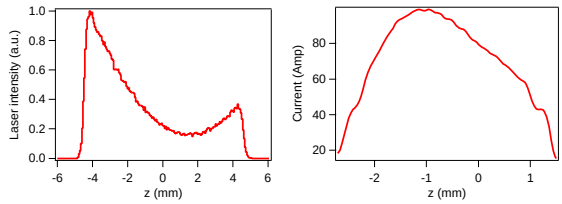

Figure 7: The "double peaks" charge distribution at the cathode (a) and at the end of the potoinjector (b).

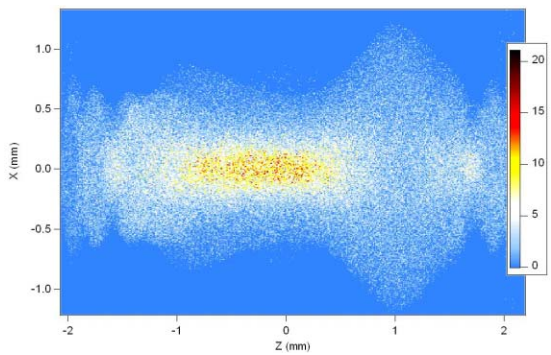

Figure 8: Top view of the evolved "double peaks" option. The initial charge distribution is translated into a transversal charge density.

slice. These modulations in α and β affect not only the matching with the linac optics, but they can be even sources of microbunching instabilities when the bunch propagates through the chicanes, leading finally to enlarge the bandwidth of the FEL output radiation [7]. A different result is

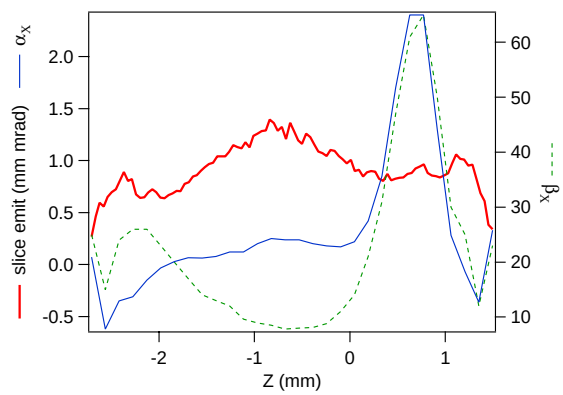

Figure 9: Slice analysis of the emittance, α_X and β_X parameters for the double peaks solution.

obtained starting with a profile similar to figure 5a, which presents at the end of the injector a trasversal distribution showed in figure 10. The slice analysis have been performed as well and the results are reported in figure 11. In this case the slice emittance has a ramping behavior very similar to the ramp in the charge distribution, and no bunch

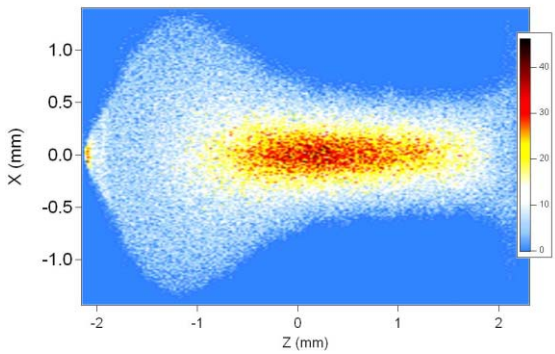

Figure 10: Top view of the evolved profile of figure 5a.

fraction is overfocused. By the way in correspondence of the high charge density the space charge field leads to increase the transversal dimension, as showed in the plot inside of figure 11. Also the slice β and α functions are very high in correspondence to the high charge density, but they are quite constant in the remainder bunch fraction and this constitutes a great improvement for the linac matching

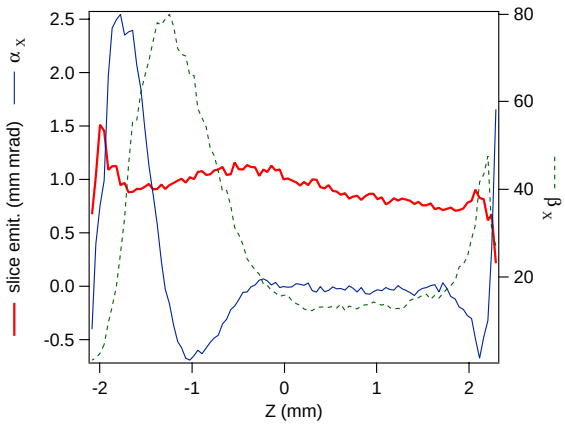

Figure 11: Slice analysis of the emittance, α_X and β_X parameters for the propagated bunch of figure 5a.

CONCLUSION

The linac requirement to have a bunch with a linear current ramp at the injector exit has been translated in studying the best current distribution at the cathode that evolves in the desired profile. An analytical description of the longitudinal space charge field on axis helps in predicting the evolution of an arbitrary current ramp before running the multiparticles space-charge codes. A quadratic current ramp at the cathode constitutes a good option to have at the end of the injector a reasonable large ramping bunch fraction.
Emittance compensation scheme has been showed to be an issue since each slice evolves in an unique way. Optimization of the injector parameters has to aim not only to minimize the projected emittance, but also to avoid overfocusing and slice emittance blowing-up, paying attention also to the behavior of the slice optics parameters. In fact tracking results have revealed that large modulation of the slice α and β functions can be an issue in the bunch propagation through the linac chicanes. Finally great attention has to be paid in the choice of the coefficients of the quadratic ramp, in order to reach the best compromise between the achievement of the linear ramp at the end of the injector and emittance and optics functions slice behavior.

REFERENCES

[1] S.B. Van der Geer et al.,"General Particle tracer Overview", http://www.pulsar.nl/gpt/index/html.

[2] K. Flöttman, ASTRA User's Manual, *https://www.desy.de/˜mpyflo/Astra_dokumentation*.

[3] A.Zholents at al., "Study of the electron beam dynamics in the FERMI@ELETTRA linac", Proc. of the EPAC 2006 Conf., Edimburgh (GB).

[4] M.Ferrario et alter, "HOMDYN Study for the LCLS RF Photo-Injector", LCLS-TN-00-04.

[5] G. Penco, "Longitudinal Space Charge Field at the Cathode In Case of a Non Uniform Bunch", ST/F-TN-06/03 (2006).

[6] M.Trovò, G.Penco, S.Lidia, "Further Studies in the FERMI@elettra photoinjector optimization", this conference.

[7] S. di Mitri and E. Allaria, private communication.

FURTHER STUDIES IN THE FERMI@ELETTRA PHOTOINJECTOR OPTIMIZATION

M. Trovò*, G. Penco, Sincrotrone Trieste, Trieste, Italy
S. M. Lidia, LBNL, Berkeley, California

Abstract

In the framework of the FERMI@elettra project we are presently studying an electron beam configuration satisfying the bunch energy distribution requirements coming from the FEL photon production system. The multi-particle tracking results concerning the photoinjector, which include the RF gun and the first two accelerating sections, are presented in this paper. We describe two possible electron bunch configurations which satisfy the FEL operation modes. Both injector configurations match the linac requirements for a 'ramped' current profile at the exit of the photoinjector. Sensitivity studies and time and energy jitter estimations are presented for both cases.

INTRODUCTION

Several configurations of the electron bunch delivered to the undulator chain by the linac accelerator have been considered in the optimization study process for the FERMI@elettra project. After considerations of performance optimization in the remainder of the FERMI linac [1], a new type of laser excitation at the photocathode, consisting in a ramped current distribution, is proposed. In particular, the linac studies show that the accelerating structure wakefield and chicane CSR effects require an initial electron beam distribution with a quasi-linear head-tail ramp in the instantaneous current in order to produce a 'flat-flat' beam profile (i.e. uniform in current and energy) at the entrance of the FEL undulators. This linac requirement translates to photoinjector in the problem of finding a special laser shape that extracts from the cathode a bunch that evolves along the gun machine section (mainly a drift at low energy), producing the desired output profile. In this paper two possible 'ramped' bunch solutions are presented. These two FERMI photoinjector configurations are suitable for the machine operation in the so called medium and long bunch modes [2].

PHOTOINJECTOR CONFIGURATIONS

For the FERMI@elettra project two machine operating modes are proposed that provide at the undulator entrance two different bunches in term of length and peak current [3]. These two mode require the gun to provide two different beams, presented in Table 1. To produce a quasi-linear head-tail current ramp in the bunch an unconventional shape of the laser pulse has to be introduced. In the simulations performed so far a transverse cylindrical distribution (top hat with 1mm edge radius) has been used while a time-varying intensity is used to produce the variation in instantaneous current along the bunch. This particular shaping is achievable with the appropriate design of the drive laser optical system [4].

Table 1: Main beam parameters required at the exit of injector in the two studied configurations.

Parameters	Medium	Long
E	95 MeV	95 MeV
Q	800 pC	1 nC
I_{peak} A	80 A	100 A
L_b (FWHM)	8 ps	10 ps
$\epsilon_{proj.}$	$<$1.5 μ m	1.5 μm
ϵ_{slice}	$<$1.0 μm	$<$1.0 μm
σ_E (uncorr.)	$<$2 keV	$<$2 keV

Medium bunch case

The first case (so called medium bunch case) requires from the photoinjector a bunch charge of 800pC and a current profile, in the ramped part, with a length of about 8ps.

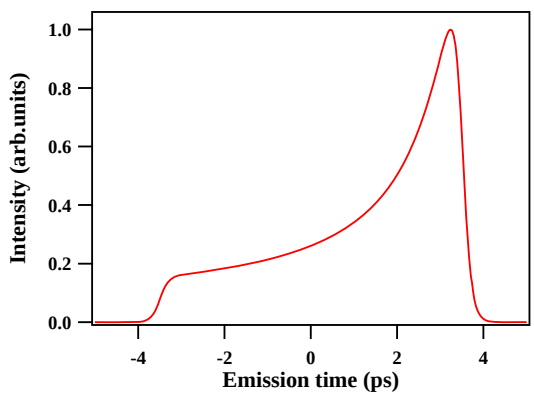

Figure 1: Longitudinal laser pulse shape: temporal intensity modulation.

Figure 1 shows the shape chosen for laser pulse intensity [2]. The curve is a Fermi-edge (with 7ps FWHM, 0.5ps of rise/fall time) multiplied by a polynomial ($0.26 + 0.05 \cdot t + 0.012 \cdot t^2 + 0.008 \cdot t^3 + 0.0019 \cdot t^4$). A bunch generated

* mauro.trovo@elettra.trieste.it

by such a laser pulse propagates in the FERMI Gun machine section producing the output current profile shown in Figure 2.

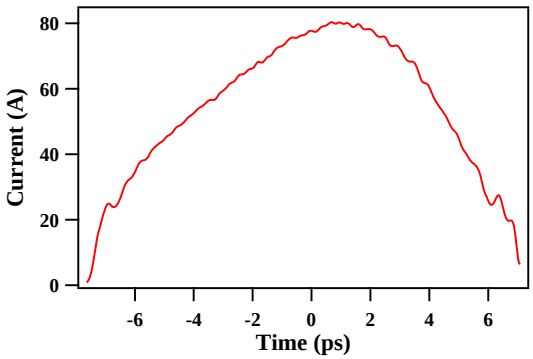

Figure 2: Current profile of the output bunch (head on the left).

Because of the highly non-linear charge distribution of the ramped profile, it is difficult to find an injector parameter configuration that completely satisfies the invariant envelope equation, performing perfect emittance compensation for all slices. Since each slice contains a different amount of charge, it evolves in a particular and unique way in the gun drift. Thus an average setting has been found that minimizes the projected emittance at the exit of the photoinjector (see Figure 3), which reaches 1.39 mm mrad. In the core 80% of the bunch particles the emittance is reduced to 1.21 mm mrad.

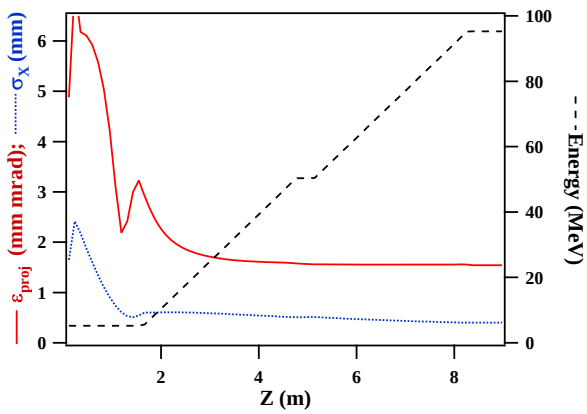

Figure 3: Transverse normalized emittance, radial spot dimension and energy along the photoinjector beamline for the medium bunch regime.

The slice analysis of the bunch at the injector exit, see Figure 4, shows that the slice emittance is affected by the current ramp and presents an head-tail increase from 0.7 up to 1.1 mm mrad.

Long bunch case

The second, or "long bunch", case represents the configuration with higher bunch charge (1 nC) and longer drive

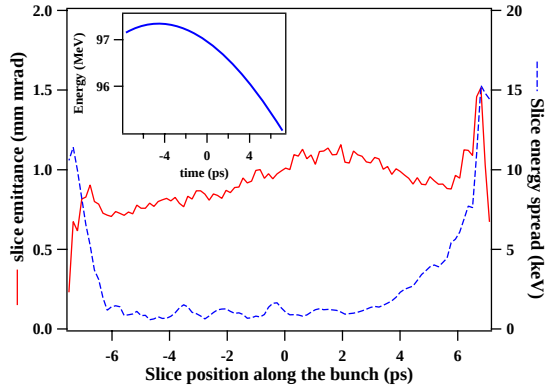

Figure 4: Slice emittance and slice energy spread at the injector exit for the medium bunch case calculated at the exit of the photoinjector machine section. Plot inside: Longitudinal phase space. Bunch head is to the left.

laser pulse. Figure 5 shows the laser shape chosen for the long case. The curve has FWHM of 10ps and the slope is driven by polynomial as $35 + 10 \cdot t + 1.5 \cdot t^2$. The output current profile is also shown and it reaches a peak current of 100 A. The useful bunch part (from head to the current drop) is about 10ps and this satisfies the linac requirements (Table 1).

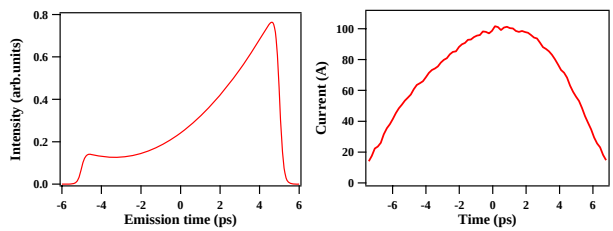

Figure 5: Longitudinal laser pulse shape: temporal intensity modulation on the left. Output current profile on the right.

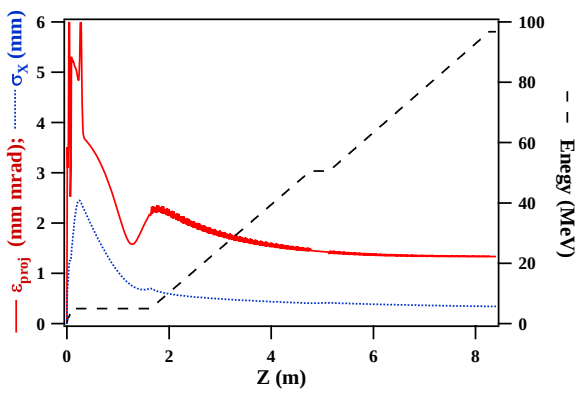

Figure 6: Transverse normalized emittance, radial spot dimension and energy along the photoinjector beamline for the long bunch regime.

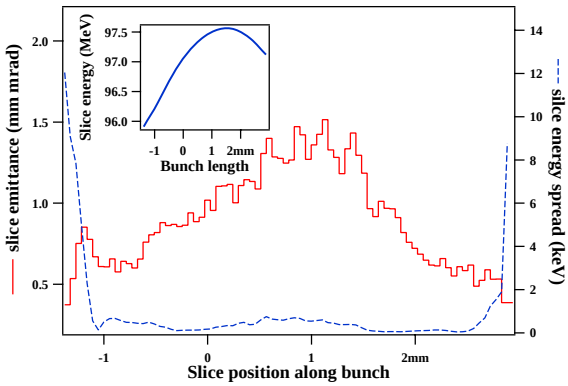

Figure 7: Slice emittance and slice energy spread at the injector exit for the long bunch case calculated at the exit of the photoinjector machine section. Plot inside: Longitudinal phase space. Bunch head is to the left.

Figure 6 shows the evolution of the transverse beam emittance, spot size and beam energy in this case. A final projected emittance of 1.33 mm mrad is achieved. Similarly to the medium bunch case The slice emittance also presents an head-tail ramp (see Figure 7).

SENSITIVITY AND JITTER STUDIES

The time of flight, the energy, the energy spread and the emittance at the end of the injector have been identified as the main output parameters whose shot to shot variation should be quantified, as well the slice properties of the bunch. To identify the main sources of variation for each of these, a single-parameter sensitivity study has been performed for the two cases, with results shown in Table 2. The time of flight is sensitive to gun parameters, while the emittance is more effected by a solenoid variation.

By randomly sampling each injector parameter within a specified tolerance range fixed by present technology (see Table 3), one thousand injector cases have been tracked (with 50000 particles), obtaining a statistical evaluation of the expected jitter. Results are presented in Table 4. Figures 8 and 9 show the jitter distributions for the emittance and the time of flight and their histograms. The gun solenoid has been neglected in this analysis due to the high stability (10^{-5}) provided by DC power supplies. The bunch time of flight jitter is about 300 fs at the injector exit and, linked to the energy jitter, it is propagated through the whole machine [5]. This effect becames an issue in the synchronization in the undulators between bunch and a short seed laser.

In order to consider the optical matching between the injector and the linac, an analysis of the jitter in the Twiss parameters has been also carried out on the same ensemble of bunches. The results are reported in Table 4. The average α_x and β_x are respectively -0.09 and 18m for the medium case (0.77 and 21m for the long), but the jittered outputs are spread out with a standard deviation respectively of 0.15

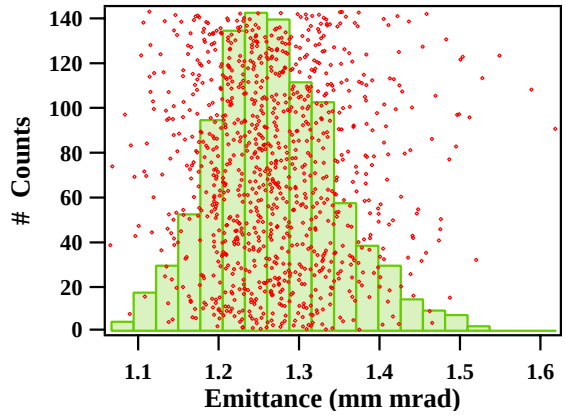

Figure 8: Projected transverse emittance jitter at the injector exit obtained by randomly sampling input injector parameters.

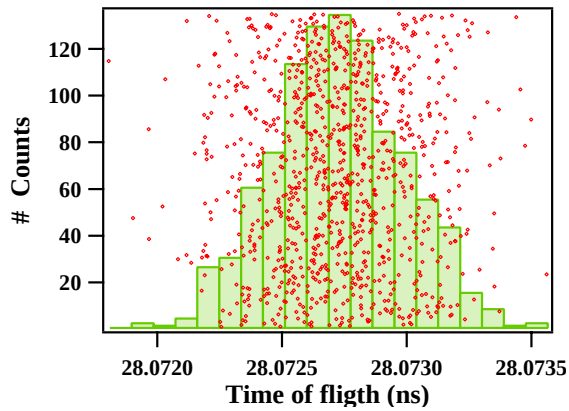

Figure 9: Electron bunch time of flight jitter at the injector exit obtained by randomly sampling input injector parameters.

and 2.1m (0.26 and 6.3m for the long case). This should be taken into account for the finalization of the optics matching.

Parameters	Tolerances
RF injection phase	0.1 deg
Laser time jitter	200 fs
Gun Eacc	0.25%
SOA Eacc	0.25 %
SOA RF phase	0.1 deg
Charge	4%
Laser spot size	4%
Laser pulse length (FWHM)	5%

Table 3: Tolerance budget for the injector parameters.

Further analysis

A further analysis of the injector output bunches from the jitter simulations has been implemented. Polynomial fittings of the longitudinal phase space and current bunch

Table 2: Minimum parameters variation, for the medium bunch and long bunch (in parentheses) cases, providing a fixed variation of the outputs, indicated in brackets in the first row. The average slice emittance $< \epsilon_{slice} >$ is calculated over all the slices. n/s = not sensitive.

Parameters (variation)	ΔI **(1%)**	ΔT **(100fs)**	σ_E**(10keV)**	$\Delta E/E$ **(0.1%)**	ϵ_{proj} **(10%)**	$< \epsilon_{slice} >$ **(10%)**
$Gun\ B_{sol}$ (%)	1.5 (2.2)	$>$ 10 (10)	1.1 (5)	n/s (n/s)	0.2 (0.8)	2 (1.2)
$Gun\ E_{acc}$ (%)	0.47 (0.6)	0.13 (0.15)	0.12 (0.17)	0.96 (1.6)	0.33 (0.5)	4.3 (0.9)
$Gun\ RFphase$ (deg)	0.65 (1.0)	2.8 (0.3)	0.8 (0.28)	3.8 (1.8)	0.5 (2.9)	4.8 (4.6)
$SOA\ E_{acc}$ (%)	20 (n/s)	2.0 (2.0)	3.9 (1.1)	0.21 (0.2)	n/s (n/s)	n/s (n/s)
$SOA\ RFphase$ (deg)	6.2 (n/s)	n/s (n/s)	0.1 (0.22)	1.9 (0.7)	n/s (n/s)	n/s (n/s)

Table 4: Simulation results of the output jitter for the medium and long bunch cases.

Output parameter	**RMS jitter medium**	**RMS jitter long**
Arrival Time (fs)	351	266
Peak Current (%)	2.4	3.3
Energy (%)	0.17	0.17
σ_E (keV)	42	24
Emittance$_x$ (%)	13.1	6.3
α_x	0.15	0.26
β_x (m)	2.1	6.3

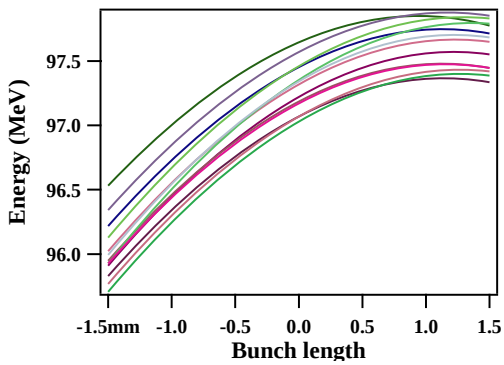

Figure 10: Twelve polynomial curve fits (fourth order), randomly sampled in the thousands performed, of the longitudinal phase spaces of bunches simulated for the long case. Bunch head is on the left.

profile have been performed for each simulated case. Figure 10 shows twelve fourth order polynomial curve fits of the longitudinal phase spaces of the bunches simulated for the long case, while Figure 11 shows the current profile cases. The curves show the synchronous bunch core (3mm) while the bunch tails are neglected.

After fitting all simulation results, a statistical analysis of the fit coefficients has been performed [6]. These statistical characterization can be used to reconstruct analytically the injector output particle distribution with respect to the jitter.

CONCLUSION

Injector optimization of the medium and long bunch ramped cases have been described. The ramped current distributions have been presented as possible interesting so-

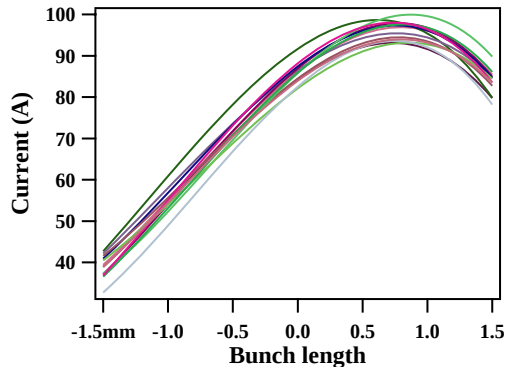

Figure 11: Twelve polynomial curve fits (fourth order), randomly sampled in the thousands performed, of the current profile of bunches simulated for the long ramped case. Bunch head is on the left.

lutions for the FERMI@elettra FEL operation with respect to the "standard" flat-top distribution despite the slight projected emittance increase. The jitter studies have shown that time jitter remains a critical parameter for seeded machine FELs and it will drive the future improvements in the performance of the laser and RF systems.

REFERENCES

[1] A. Zholents et al., "Study of the electron beam dynamics in the FERMI@ELETTRA linac", Proc. EPAC 2006, Edinburgh, UK.

[2] G. Penco et al., "Optimization Studies of the FERMI@ELETTRA Photoinjector", Proc. EPAC 2006, Edinburgh, UK.

[3] S. D. Mitri, "How to obtain high quality electron bunches in presence of normal conductiong Linac Wakefields", Proc. this conferece.

[4] M. B. Danailov et al., "Design of a Two-Stage Laser Pulse Shaping System for FEL Photoinjectors", Proc. this conferece.

[5] P. Craievich et al., "Jitter Studies for the FERMI@ELETTRA Linac", Proc. EPAC 2006, Edinburgh, UK.

[6] G. Penco, M. Trovò and S. Lidia, *Technical Note* ST/F-TN-06/11.

THE DIAGNOSTICS OF THE FERMI@ELETTRA BUNCH COMPRESSORS

M. Veronese*, S. Di Mitri, M. Ferianis, Sincrotrone Trieste, Trieste, Italy

Abstract

Bunch compressors (BC) are key components of the seeded FEL FERMI@ELETTRA. A complete set up of non destructive diagnostics is foreseen to provide the required stability for the production of sub-psec electron bunches. Main task of these diagnostics is to provide the error signals to the feedback systems used to stabilize the energy and the peak current of the electron bunch which are crucial parameters for optimum FEL operation. The different operation regimes foreseen for FERMI [1] call for a flexible set-up, for both the bunch compressors and the associated diagnostics. In this paper we present the adopted diagnostics for the measurement of position, energy and energy spread; both "energy" BPM, in between bunch compressors (BC), and optical transition radiation (OTR) screen plus wire scanner have been adopted. The design of a relative bunch length monitor needed for the determination of the optimal compression and for peak current stabilization is presented as well. The scheme is based on non-invasive techniques, namely the detection of the coherent synchrotron radiation (CSR) from the last bending of the BC plus the coherent diffraction radiation (CDR) from a downstream slit. Finally, a technique for the bunch phase measurement is presented.

INTRODUCTION

The FERMI FEL, presently under construction at the Elettra Laboratory, is based on a seeded HGHG scheme. Two FEL undulator chains FEL1 and FEL2 are foreseen according to the needs of the FERMI scientific community, to lase in two adiacent UV spectral regions (100-40nm and 40-10nm) with different pulse lengths. The FERMI layout has been described in detail in [1], its main parameters are presented in Table 1. High charge (~nC) electron bunches are produced in a RF photo-injector, with bunch length (L_B) of about 10psec$_{FWHM}$. The acceleration is provided by normal conducting S-band RF structures and the bunch compression is achieved by two magnetic chicanes. Up to now, two main bunch regimes have been studied: the "medium bunch" (L_B=600fs$_{FWHM}$) optimized for the FEL1 operation and the "long bunch" (L_B=1.4ps$_{FWHM}$) which is best suited for FEL2. High quality beams (low emittance, low energy spread, high current stability and high energy stability) are needed to obtain high quality FEL output radiation. Non-standard diagnostics and instrumentation suitable to fully characterize and monitor the beam during the machine operation have to be developed according to the specific beam parameters and machine requirements.

*E-mail: marco.veronese@elettra.trieste.it

Table 1: Fermi@Elettra parameters

Parameter	**FEL 1 (medium bunch)**	**FEL 2 (long bunch)**
Wavelength	100-40 nm	40-10 nm
Electron Beam Energy	1.2 GeV	1.2 GeV
Bunch Charge	0.8 nC	1 nC
Peak Current	800 A	500 A
Bunch Length (FWHM)	600 fs	1400 fs
Energy Spread (slice)	100 KeV	100 KeV
Norm. emittance (slice)	1.5 mm mrad	1.5 mm mrad
Repetition Rate	10-50 Hz	50 Hz
Photon Pulse Length (FWHM)	≤ 100fs	~ 1000 fs

BUNCH COMPRESSORS

Bunch compressors are used to produce high peak current electron bunches needed to obtain GW peak power FEL radiation generation. Several aspects have to be considered to avoid beam quality degradation (e.g. CSR induced emittance dilution). In particular, the stabilisation of the peak current and the energy in the chicane are needed to guarantee the long term stability of the FEL output [2]. The bunch compression is obtained with two magnetic chicanes located at the nominal energies of 220 MeV (BC1) and 600 MeV (BC2) respectively. This design allows for both single and double compression schemes, with a total compression factor ranging from 2 up to about 100 [3].

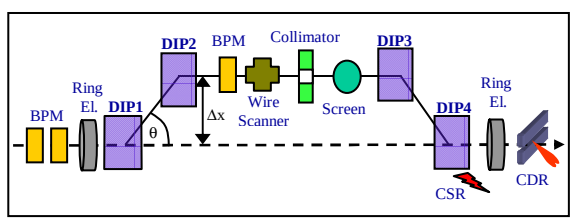

Figure 1: Bunch Compressor Diagnostics layout.

The conceptual scheme is the same for BC1 and BC2, but some components are adapted according to the different bunch parameters. In Fig. 1 the bunch compressor scheme is sketched together with the foreseen diagnostics. The main parameters of BCs for a double compression scheme are summarized in Table 2.

Table 2: Fermi bunch compressors parameters.

Parameter	BC1	BC2
Number of magnets	4	4
Magnetic length	0.5 m	0.5 m
Distance DIP1-DIP2	2.5 m	2.5 m
Distance DIP2-DIP3	1 m	1 m
Distance DIP3-DIP4	2.5 m	2.5 m
Nominal DIP angular range	66.8 :77.2 mrad	53.1:77.5 mrad
Commis. DIP angular range	50 : 80 mrad	50 : 80 mrad
Linac phases ranges	L1=-42° : -20°	L1=-42° : -20° L2,3=-20° : -10°

From Table 2 it can be seen that even if the bending angles are quite small they span over a wide relative range [3]. This fact, together with the dispersion and the energy spread, has a deep impact on the electron beam parameters in the chicanes (see Table 3) and on their measurement.

Table 3: Main beam parameters at BC1 and BC2.

Parameter	BC1	BC2
Energy Range	220 : 260 MeV	580 : 615 MeV
Rel. En. Spread	2.3 : 2.7 %	0.97 : 1.05 %
Beta (β_x)	16 m (z=31 m)	23 m (z=98 m)
Dispersion (D_x)	0.165 : 0.255 m	0.155 : 0.24 m
Transverse displacement (Δx)	0.165 : 0.255 m	0.155 : 0.24 m
Energy Spread Beam size $\pm 3\sigma$	28 : 44 mm	10 : 15 mm
Betatron Beam size $\pm 3\sigma$	1.4 mm	2.0 mm

In particular, in the area between DIP2 and DIP3, where all diagnostics will be located, the beam size is expected to be dominated by the dispersion.

DIAGNOSTICS

We will now discuss the diagnostics according to the measured parameter: energy, energy spread, bunch arrival time, relative bunch length.

Energy Measurement

The transverse displacement of the beam centroid (Δx of Fig.1) spans, for the BC1 and BC2 ranges, over approximately 100mm. If we consider building the BCs with a wide vacuum chamber, then for that chamber a width of at least 150mm is needed to allocate the wide electron beam ($\pm 3\sigma$ beam size of 35mm) and its displacements. Taking in account a beam transversely centred at Δx=200 mm, the rms energy stability required by the FEL ($\Delta E/E$=0.1%) will translate in terms of rm displacement variations to 200 μm (at nominal BC1 operating conditions). To correctly operate the feedback system, the resolution of the position measurement has to be at least four times better than the value we want to stabilize within, which means that a single shot resolution of 50 μm is needed. This is a very tough value to be met on a 150mm chamber width and with a beam size of 35mm. Therefore, we plan to put the second and the third dipoles of the chicanes and all the related diagnostics on a transverse high precision translator stage. This will allow us to reduce the vacuum chamber transverse size to about 60 mm and thus to use an "energy BPM". Another possible approach to the problem has been proposed at DESY; it is based on the measurement of the relative time difference between two pulses generated in a transverse strip-line arrangement [4]. Its applicability to Fermi will be evaluated in the near future.

Energy Spread Measurement

The energy spread is a crucial parameter for the machine operation and it has to be carefully monitored. It will be measured by means of a wire-scanner on multi shot basis and by an OTR screen plus a CCD camera, shot by shot. Both techniques are destructive and the measurements will be performed during the commissioning and, periodically, during the operation to check the long term stability of the energy spread. As depicted in Fig. 1, in between the wire-scanner and the OTR screen, we plan to install a collimator. With this geometry the energy spread of the beam can be measured upstream and downstream of the collimator and its effect can be followed step by step. The energy spread can be directly extracted from the measurement of the transverse size of the beam since the dispersion in the middle of the chicane is known and dominates the beam size. The needed resolution is different for the two bunch compressors. For BC1 the minimum $\delta E/E$ is 2.3% which will reflect in a 28 mm beam size ($\pm 3\sigma$ beam). The needed relative resolution is estimated to be 2%, which means 0.56 mm, in terms of spatial resolution. For BC2 the energy spread will be smaller and it will have a small operation range. Then for a 0.95% $\delta E/E$ will reflect in a $\pm 3\sigma$ beam size of 10 mm and to appreciate the changes in energy spread we will need to have a 1% relative resolution which means 100 microns spatial resolution. This resolution level can be achieved with an OTR screen plus a CCD detector, higher resolutions will be achieved by the wire-scanners [5].

Bunch Arrival Time Measurement

The bunch arrival time measurement will be provided by a new kind of diagnostics. The concept has been proposed at DESY [6] and will make use of the optical pulses from the ultra stable timing distribution system [7] to measure

the bunch arrival time relative to the optical clock pulse. This technique is non-destructive and it has shown so far a resolution better than 100fs. Two devices, one at the entrance and one at the exit of each chicane, will be installed. The signal from the device at the entrance of BC1 will provide a direct measure of the total initial jitter from the injector.

$$\Sigma_f^2 = \left(\frac{r_{56}}{c_0}\frac{\sigma_A}{A}\right)^2 + \left(\frac{C-1}{C}\right)^2\left(\frac{\sigma_\phi}{c_0 k_{RF}}\right)^2 + \left(\frac{1}{C}\right)^2\Sigma_i^2 \quad (1)$$

As can be seen from Eq. 1 the coupled measurement of the jitter at the entrance and at the exit of the chicane initial will give us the RF contribution of the timing jitter.

Relative Bunch Length Measurement

The needs for peak current stabilisation push to develop a non-destructive relative bunch length monitor, so that its signal can be fed to the feedbacks systems that will keep the peak current stability acting on the phases of the RF accelerating sections. For this purpose we will develop power monitors based on the detection of coherent synchrotron radiation (CSR) [8] and coherent diffraction radiation (CDR) [9]. We plan to implement a redundant system based on the detection of the CSR emitted from the last dipole of the chicanes and on the detection of the CDR emitted from a slit placed downstream the chicane.

Coherent radiation is emitted from short electron bunches, in the case of a Gaussian bunch where σ_z is the sigma of the distribution, it is emitted at wavelengths longer than roughly $2\pi\sigma_z$. For electron bunches with psec and sub-psec duration the coherent emission is in the mm/sub-mm wavelength spectral range. An overview of the related physics can be found in [10]. The CSR spectral angular distribution of a N-electrons bunch can be related to the spectral angular distribution of a single electron as shown in Eq. 2.

$$\left.\frac{d^2I}{dvd\Omega}\right|_{N-el.} = \left[N + N(N-1)\left|F(\rho(t))\right|^2\right]\left.\frac{d^2I}{dvd\Omega}\right|_{1-el.} \quad (2)$$

Where F(ρ(z)) is the Fourier transform of the longitudinal normalized bunch distribution ρ(t). From Eq. 2 we can see that the total N-electron CSR angular distribution is the sum of the incoherent synchrotron radiation of N electrons ($\propto$ N) and a coherently enhanced term ($\propto$ N^2). The frequency behaviour of the coherently enhanced term depends on the square of the Fourier Transform of ρ(t). As the bunch gets shorter the F(ρ) get spectrally broader and the emitted power increases. To evaluate the emission properties (spectral distribution and intensity) we have computed the CSR spectra angular distribution in two steps. In the first we have calculated F(ρ), by means of the FFT of the bunch profile coming from Elegant simulations (shown in Fig. 2). In the second, to calculate the single electron spectral-angular distribution, since the circular motion approximation is not sufficient in our case, we have used a numerical code written by O.Grimm at DESY.

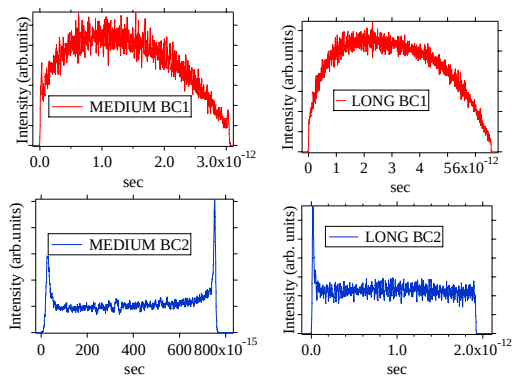

Figure 2: Longitudinal electron distributions at BC1 exit (red) and BC2 exit (blue) for the "medium bunch" (left) and the "long bunch" (right).

The code implements a full Liénardt-Wiechert potential formalism, and makes a tracking of a single electron through an arbitrary magnetic field. In the calculation both velocity and acceleration terms are included as well as the finite dimensions of the dipoles, the contributions of both 3rd and 4th bending magnets and the shielding effects of the vacuum chamber walls (in a parallel perfectly conducting planes approximation). Some results of these simulations are shown in Fig.3 for the CSR emission from the last bending magnet of BC1 for the "medium bunch" and in Fig.4 for the "long bunch" case. Plotted are the angle integrated spectral intensity distributions, for a detector (30x30 mm) placed 150 mm downstream the last bending of BC1 and normal to the edge radiation direction centred 25 mm away from the straight beam path.

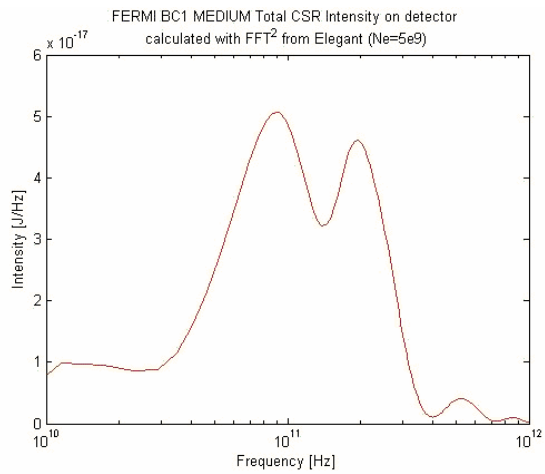

Figure 3: Expected spectral distribution of the radiation extracted from the 4th dipole of BC1 for the "medium bunch.

These results suggest that, for the CSR emitted from the bunch compressors of FERMI the Gaussian bunch plus circular motion approximations [8] might not be sufficient. They also indicated that the choice of the

frequency range for the detectors has to be done with special care for narrowband detectors. Moreover considering both BC1 and BC2 the core of CSR emission is in a critical spectral region (between 10GHz and 1THz) for the detectors.

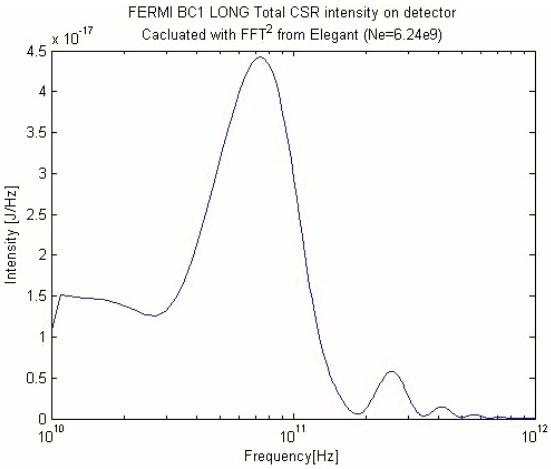

Figure 4: Expected spectral distribution of the radiation extracted from the 4th dipole of BC1 for the "long bunch".

In this region the detection of CSR can be done by RF diodes or pyrodetectors. The diodes have higher sensitivity in the sub-THz range, but are limited at about 600GHz while pyrodetectors offer a wider operation range starting from about 150GHz. We plan to use the pyrodetectors for their flexibility and ease of use, but RF diodes may be employed especially for the case of "long" bunch in BC1. The total energy per pulse emitted in the spectral range from 10 GHz to 1THz is of about 10μJ for the "medium bunch" and of about 4μJ for the "long bunch". In the spectral range of the pyrodetector (e.g. Coherent/Molectron P4-42) the energy per pulse is respectively of 1.5μJ and 0.3μJ. In this case a simple estimate gives us a sensitivity of 0.04% sufficient to fulfil the 2% of the feedback requirements (to obtain 10% current stability). Other factors should also be considered: the efficiency of the radiation collection, the absorption and reflection from air and from the vacuum window.

A second coherent radiation source, a CDR source (e.g. an OTR screen with a small aperture) will be installed immediately downstream the bunch compressors. It is meant to add redundancy to the CSR system. We have performed some calculations to evaluate its application to FERMI diagnostics. Our calculation started from the CDR description given in [11] for a relativistic electron beam. Here γ is the Lorentz factor of the electrons passing through a hole of radius "b" in a circular screen of radius "a". It is worth saying that the infinite screen approximation is satisfied if $a > \lambda\gamma$. For FERMI BC1 "medium" bunch we can consider: λ=3 mm and γ=430 then the condition becomes a > 1.3 m. This shows that a large screen and a large detector angular acceptance are desirable to avoid low frequency intensity suppression. On the other hand a compromise has to be found to meet space requirements. This led us to choose a screen radius "a" of 60 mm and an angular acceptance of 0.2 rad. The effect of the hole radius has to be considered, for CDR emission, the smaller the hole radius is, the better. On the other side the higher is the radius, the smaller is the impact of the CDR emitter on the beam dynamics. CDR Spectral distributions calculated with a rectangular distribution approximation of the longitudinal bunch profile are shown in Fig. 5 for two extreme cases: BC1 "long bunch" and of BC2 medium bunch for different values of the hole radius.

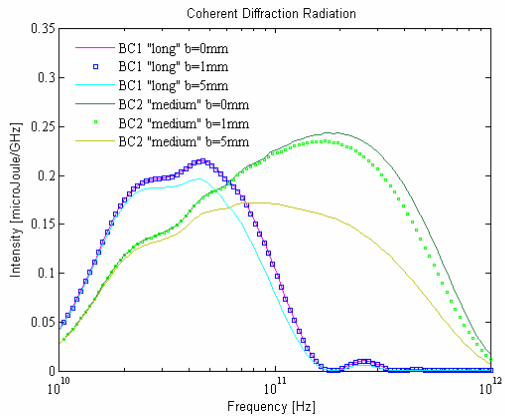

Figure 5: CDR spectral distributions for "medium bunch" at the exit of BC2 and the "long bunch" at the exit of BC1 for values of b=0, 1, 5 mm.

The calculation indicates that, for the "long" bunch at BC1 a quite large hole can be used without loosing too much in intensity, while the hole size effect is more important in the case of the "medium" bunch in BC2.

ACKNOWLEDGMENTS

We would like to thank O.Grimm for providing his code, P. Craievich, M. Cornacchia, M. Dunnig, J. Travish, J. Wu and P. Krejcik for fruitful discussions. And F. Rossi for his help with Matlab simulations. This work has been partially supported by the EU Commission in the Sixth Framework Program, Contract No. 011935 – EUROFEL.

REFERENCES

[1] M. Cornacchia, *et al.* EPAC 06, 145, (2006).
[2] J. Wu, *et al.* PAC 05, 1156, (2005).
[3] S. Di Mitri, ELETTRA, ST/F-TN-06/09, (2006).
[4] K. Hacker, *et al.* EPAC 06, 1043, (2006).
[5] K. Wittenburg, Tesla Report 2000-18 (2000).
[6] F. Loehl, *et al.* EPAC 06, 2781, (2006).
[7] M. Ferianis, *et al.* FEL 05, 134, (2005).
[8] J. Wu, *et al.* PAC 05, 428, (2005).
[9] E.Chiadroni, *et al.* EPAC 06, 1127, (2006).
[10] O. Grimm, EPAC 06, 1040, (2006).
[11] S. Casalbuoni, *et al.* TESLA Report 2005-15 (2005).

MAIN HIGH VOLTAGE SOLID STATE GYROTRON POWER SUPPLY 60kV / 80A *

G. Taddia, M. Pretelli#, L. Rinaldi, V. Rossi, L. Sita, O.C.E.M. SpA, San Giorgio di Piano, Italy
T. Bonicelli, P.L. Mondino, EFDA CSU Garching, Germany
D. Fasel, EPFL/CRPP Lausanne, Switzerland
R. Claesen, M. Santinelli, ENEA Frascati, Italy.

Abstract

This paper will describe the preliminary design of a 4.8 MW Main High Voltage Power Supply, rated 60kV/80A, especially conceived to supply the voltage between Cathode and Collector of a Gyrotron. A full solid state technology, named SWM (Stair-Way Modulation) for the full scale Electron Cyclotron (EC) Test Facility at CRPP, Lausanne. The ITER EC system may also make use of a similar system, in alternative to the present baseline design based on naturally commutated thyristor converters and series high voltages solid state switches. The 60kV output is reached by adding more than 120 high voltage modules in series connection, with ad hoc control criteria to allow a regulation at full performances in the range of 45kV-60kV, a square wave modulation and a fast switch-off in less than 10us.Components choices and simulations of the system will be highlighted in order to demonstrate the fulfilments of the technical specification before the manufacturing stage. This solution can be extended to several applications in the High Voltage domain and is aimed to enhance the reliability, decrease costs, provide redundancy, plug-in modularity, component de-rating and component standardization.

INTRODUCTION

The ITER Heating and Current Drive (H&CD) system, includes the installation of an Electron Cyclotron system based on CPD type Gyrotrons (170GHz). This type of RF sources requires two power supplies, one Main High Voltage Power Supply (MHVPS) between cathode and collector (typically V = 50 ÷ 60kV, 80A) and an Acceleration Power Supply, which, with the MHVPS, establishes the voltage between body and cathode, typically 80 ÷ 100 kV. The modulation frequency specified in the ITER reference design is 1 kHz but in the developments on-going in Europe, 5 kHz are considered for the stabilization of Neoclassical Tearing Modes (NTM). The continuous developments of solid state devices, available for both higher voltages and higher switching frequencies, have highlighted several advantages of the fully static solutions which could conveniently replace the more traditional systems based on vacuum tubes (e.g. tetrodes). On the basis of the above considerations, OCEM has performed a conceptual study of a Solid State Body Power Supply (BPS) [1] for ENEA Frascati, with support from EFDA. The first fully solid state BPS has now been completed [2] and installed at ENEA Frascati. For the new EC Test Facility in Lausanne, EFDA is now procuring, on behalf of European Commission, both power supplies (MHVPS and BPS). The results of a competitive tendering showed that the above described modular topology was economically convenient beside yielding some important technical advantages.

*Work supported by European Fusion Development Agreement
#physics@ocem.com

OUTLINE SPECIFICATIONS

The performance specifications are listed in Table 1:

Table 1: Main Performance Specifications

Description	**Value**
Duty Cycle	8 / 24 hours
AC input Voltage	20kV / 50Hz (±10%)
Nominal Output Voltage	-60 kV DC
Output Voltage range	-1 kVDC < V_{DC} < -60kVDC regulation at full performances -45kV to –60kV
Nominal Output Current	80 A
Modulation freq.(ON/OFF)	5kHz
Output Voltage Accuracy: Static Reproducibility Dynamic transient Ripple	 <± 1% of V_{DC} nominal <± 0.5% of V_{DC} nominal <± 1500V <± 2%@600Hz, <±0.5% for higher frequencies
Voltage Settling time	<15us
Shutdown time	<10us
Max Energy delivered to the load in case of arc	10J
Protection Transm. delay	<1us
Measurement Accuracy Voltage Current	 +/-0.1% in DC +/-0.2% at 10kHz +/-0.3% at 50kHz <± 1% of nom. value
Measurement Bandwidth	≥500kHz

MHVPS TOPOLOGY

The preliminary design of the MHVPS is based on a series connection of elementary power modules which do not require direct series connection of semiconductors. Each module, is provided with its own DC power supply so that the voltage is evenly shared during normal operation. The total output voltage is hence controlled by the number of switched-on modules in quantization steps of voltage. This topology, together with an ad hoc control strategy developed by OCEM, the Multi Pulse Width Modulation (MPWM), has been named Stair-Way Modulation (SWM). This type of modulation has the advantage of an averaged power distribution among all the modules, with a consequent minor stress of the main transformers. Also the achievement of a high bandwidth is not related to the increasing of the switching frequency of only a few modules. In a SWM system the maximum switching frequency of each module remains equal to all the modules. This leads to reach a very high value of bandwidth, according to the constraints due to the particular specifications. The overall system also foresees a level of modularity in a redundant and fault tolerant configuration. Hence, in case of fault of a single module, the faulty module can be easily excluded from the main circuit, ensuring continuous operation.

The MHVPS consists mainly of the following blocks:

- **Input circuit breaker** with a protection relay, to connect the P.S. to the medium voltage grid (20kV, 50Hz, three-phase) through a soft start equipment.
- **Multi Secondary Transformer system**, to adapt the input voltage from the grid to the voltage required by the downstream parts, with the proper insulation level.
- **Power modules** in series connection, to transform the 50 Hz supply voltage from the transformer system in a regulated DC voltage.
- **Control electronics**, to provide regulation, protection and interface.

The main parts of the MHVPS are described in the following subsections.

Multi Secondary Transformer System

Due to the design constraints (mainly the 120kVdc insulation voltage, the reduced available space on the installation site and the requested very low harmonic content in the input current) the transformer system is based on two cast-resin transformers, made of several secondary, each feeding one power module.

The secondary coupling of these two transformers is either of the star type or of the delta type, in order to obtain an overall primary current from the grid with low harmonics. Finally, soft-start devices are integrated between the transformers and the main grid.

Power Modules

The general scheme diagram of the power module is shown in Figure 1.

The switched-on power modules, controlled by a modulation index, determine the total output voltage. By using this technique and a proper switching strategy, the modulation can be performed in order to obtain the

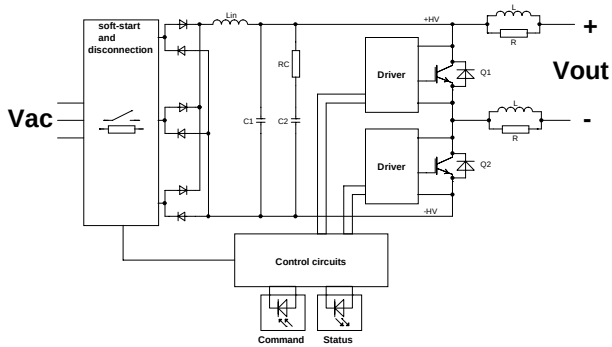

Figure 1: General schematic of a Power Module.

desired value of output voltage within the specification requirements. The Module is ON when the switch Q2 is closed and Q1 is open; a voltage step of -Vdc is added to the total output voltage. The Module is OFF when the switch Q2 is open and Q1 is closed; the module is bypassed. The two switches Q1 and Q2 must be never ON simultaneously. Using this structure it is relatively simple to perform a fast switch-off: there is enough time to simultaneously open the series switches (Q2) of each module, and then to close all the parallel switches (Q1); this operation can be very fast, in the order of 2-3 us.

Each module has an output L-R filter, which is a portion of the total output filter seen by the load. The filter has been conceived for:

- smoothing the output voltage ripple;
- limiting the di/dt and the peak current during the arc;
- obtaining a correctly damped overall system;

Calculations show that in order to minimize the energy delivered to the system it is necessary to consider an additional resistor of some ohms (4 ohms) in series with the load; this will permit to dissipate a portion of the energy before that this energy is delivered to the Gyrotron. The module is designed for an output voltage of 560V. This leads to a series connection of more than 120 modules with the consequence of a relatively high complexity of transformer and cabling. However the components mounted on each module can be low voltage devices, with an advantage in terms of cost and availability. Moreover, each stair of voltage is lower than the allowable peak to peak ripple, leading to have an additional degree of freedom in the dimensioning of the output filter.

Control Electronics

The control electronics has been designed to perform the following functions:

- measurement of the output voltage and current;
- regulation: to keep the output voltage at the desired value and within the allowed fluctuations;

- protection: to guarantee an effective protection in case of internal faults or external overloads;
- interface: to communicate with the main control system and to allow the local or remote command of the power supply.

The user interface, data log and Ethernet connections are based on commercially available electronics, with custom designed software. The regulation system (fully digital, based on an high performance FPGA card) determines the number of modules that must be ON in each time interval, providing a proper "rotation" in the module sequence. This allows to equally share the stresses among the modules. During commutations, with a proper modulation strategy for the semiconductor switches, the switching frequency seen by the load is equal to the frequency of the single module multiplied by the number of modules. This allows an high output switching frequency (seen by the load) with the advantage of a relatively low switching frequency seen by the components of the modules.

In steady state, when the output voltage is between an acceptable range around the set value, the algorithm foresees a lock modulation input that stops the switching of the modules and the rotation. This prevents an unnecessary power dissipation.

Components Choice

After a careful market inspection, the main standard components have been chosen. The IGBTs is a V_{CES}=1200V / I_C=140A @80°C (I_C=200A @25°C) device based on the SPT technology which offers a good compromise between the V_{CE_ON} and the switching speed (switching losses). The size of the IGBT was chosen also looking at its overload behaviour: it has a short circuit capability of 1000 pulses at ten times I_C and self limiting current capability to $6 \cdot I_C$. The IGBT driver choice was made looking firstly to its delays which are extremely small. The input DC filter topology is an LC-parallel damped filter. The damping is chosen to avoid excessive over-voltages during power connection or load disconnection and to limit the filter peak output impedance to less then 0.5 Ohm.

PRELIMINARY SIMULATIONS RESULTS

The preliminary simulations for the MHVPS have been performed by considering the overall system which will be installed in Lausanne and which include the CPD Gyrotron, the BPS and MHVPS in order to verify the adequate compatibility of the MHVPS to the already designed BPS now under construction.

The model of the whole system has been developed using Pspice and Matlab/Simulink. Figure 2 shows the step up of the whole system simulation (with Simulink): the ramp up of the MHVPS current and voltage are shown in the first and third rows respectively. In the second row the switch-on of the BPS is simulated. This leads to the increase of the Body to Cathode Voltage up to the maximum value 100kV, as shown in the fourth row.

In Figure 3 it is sketched how the MHVPS and the overall system behave during the required 5kHz modulation. The first two rows show the commands given to the BPS and MHVPS for starting the modulation; both power supplies start modulating as specified, and the voltage patterns can be observed in rows 3 (BPS) and 4 (MHVPS). The total output voltage between Body and Cathode is the result shown in row 5 (100kV peak). Last row is the MHVPS current which shows a promising behaviour of the overall system during the 5kHz modulation.

Finally, Figure 4 reports a simulation of the overall system in case of an arc between Cathode and Collector. The arc is simulated by adding in the Simulink model a voltage generator of 100V. At 200 us the arc occurs and Body to Cathode voltage collapses by leading to an increase of the amount of charge in the Gyrotron (fifth row). The 0,1 limit value depicted in the fifth row, represents the amount of charge delivered to the load and, considering an arc voltage of 100V, corresponds to the maximum value of energy that could be delivered as per technical specification (10 Joules). However it can be

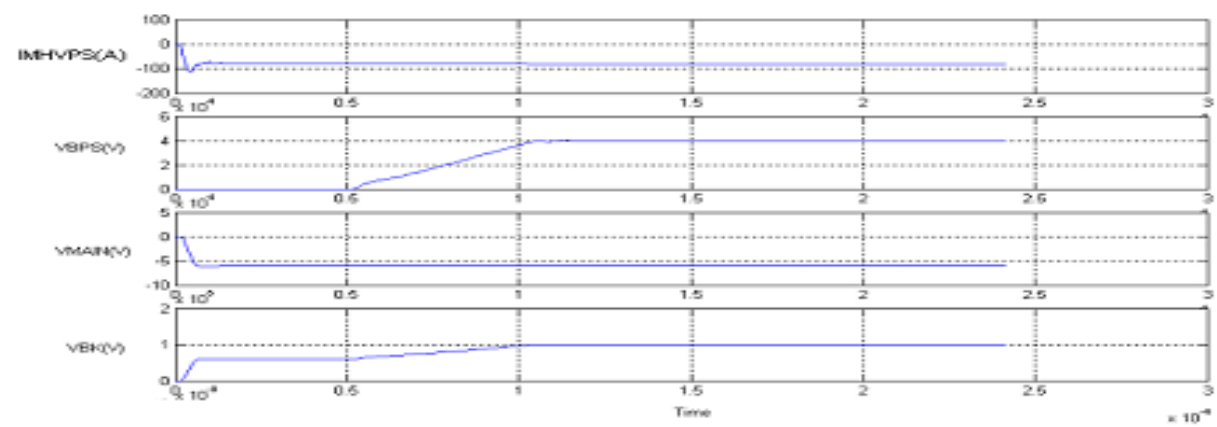

Figure 2: Simulation of the Step up of the whole system (MHVPS+BPS+Gyrotron)

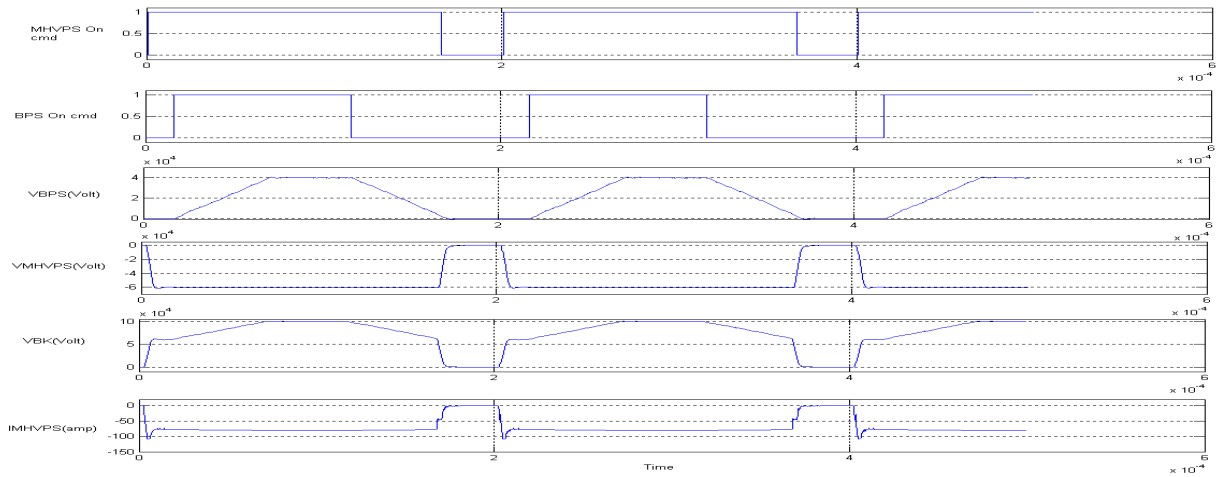

Figure 3: Simulation of the 5kHz Modulation

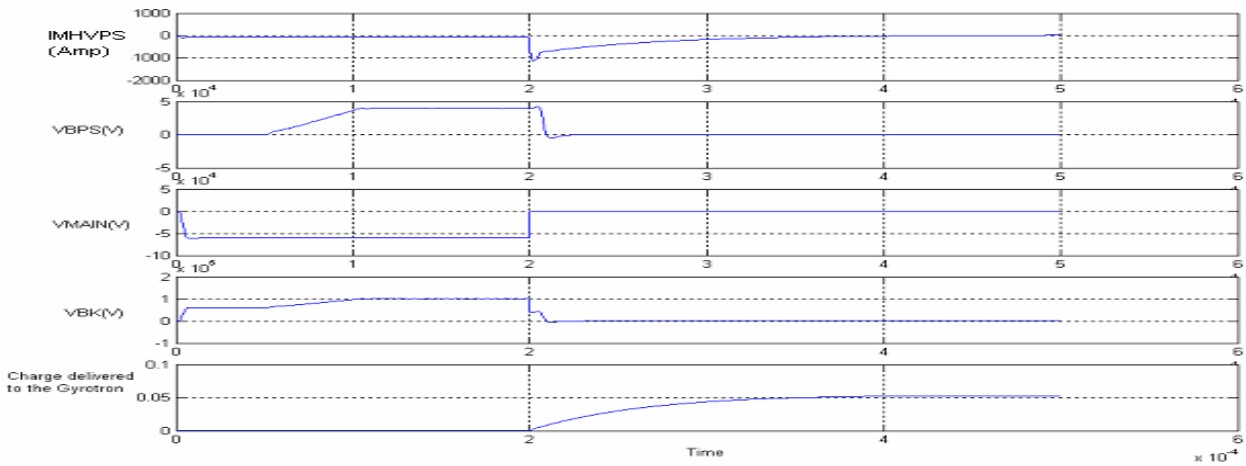

Figure 4: Simulation of the Step up of the whole system with an arc between K-C at 200us

CONCLUSIONS

This paper has described the preliminary design of a 4.8 MW Main High Voltage Power Supply, rated 60kV/80A, especially conceived to supply the voltage between Cathode and Collector of a Gyrotron. This topology has been chosen for the EC Test Facility at CRPP, Lausanne (CH). Similar systems could be adopted for ITER, which includes the installation of an Electron Cyclotron system based on CPD type Gyrotrons (170GHz) in alternative to the present baseline design.

The first simulations have demonstrated the correct behaviour of the MHVPS not only as a stand alone modulator but as part of a complete system which will be installed in Lausanne, and which include the MHVPS, the BPS and the CPD Gyrotron. Three main situations have been depicted in the simulation sketches: the step-up and the steady state, the 5kHz ON/OFF modulation and the behaviour of the system in case of an arc between Cathode and Collector. The first results are very encouraging and the design phase can enter into a further final detail before entering the manufacturing stage. The installation of the overall system in Lausanne is foreseen to be starting by September 2007.

REFERENCES

[1] T. Bonicelli et alia, “High Frequency/High Voltage Solid State Body Power Supplies for CPD Gyrotrons”, SOFT’02, Helsinki, September 2002, p. 543-548.

[2] G. Taddia et alia, “High Voltage Solid State Gyrotron Body Power Supply”, 14th Joint Workshop on Electron Cyclotron Resonance Heating, Santorini, May 2006, p 95.

COMMISSIONING OF THE SPARC PHOTO-INJECTOR*

M. Bellaveglia, D. Alesini, S. Bertolucci, M. E. Biagini, R. Boni, M. Boscolo,
M. Castellano, E. Chiadroni, A. Clozza, L. Cultrera, G. Di Pirro, A. Drago, A. Esposito,
M. Ferrario, L. Ficcadenti, D. Filippetto, V. Fusco, G. Gatti, A. Gallo, A. Ghigo,
S. Guiducci, M. Incurvati, C. Ligi, M. Migliorati, A. Mostacci, L. Palumbo,
L. Pellegrino, M. Preger, R. Ricci, C. Sanelli, F. Sgamma, B. Spataro,
F. Tazzioli, C. Vaccarezza, M. Vescovi, C. Vicario (INFN/LNF);
A. Bacci, I. Boscolo, F. Broggi, S. Cialdi, D. Giove, M. Mauri,
A. Rossi, L. Serafini (INFN/Milano);
M. Mattioli, P. Musumeci, M. Petrarca (INFN/Roma1);
L. Catani, A. Cianchi, S. Tazzari (INFN/Roma2);
A. Perrone (INFN /Lecce);
L. Giannessi, M. Quattromini, A. Renieri, C. Ronsivalle (ENEA/FIS);
J. Rosenzweig (UCLA)

Abstract

The SPARC project [1] is born to perform R&D activity headed to realize SASE-FEL experiments at $500nm$ and higher harmonic generation. The project foresees the realization of a high brightness photo-injector able to produce a $150 \div 200MeV$ electron beam to drive FEL process inside a dedicated $12m$ long undulator. The machine is going to be assembled at LNF and its final configuration is made up of an RF gun, driven by a Ti:Sa laser, injecting into three SLAC type accelerating sections. Nowadays we are working in a photo-injector test phase, aiming to characterize the main hardware components and to investigate the behavior of the e-beam dynamics in the first meters of drift. To do this we utilize the emittance-meter, a home designed diagnostic device placed just after the RF gun, able to move 1.2 meters along the longitudinal axis to measure beam parameters. In this paper we report a more accurate description of the project, the status of the single systems constituting the machine and the most important results we obtained in the e-meter phase.

INTRODUCTION

The commissioning of the SPARC photo-injector is started at Frascati INFN laboratories and we are operating in a gun test phase, before installing the accelerating sections. In this phase, laser, radiofrequency, timing, control system and beam diagnostics are installed and working in the SPARC bunker. We performed a characterization of the beam at the gun exit with the home-designed movable emittance-meter [2] and a spectrometer. A picture of the hardware installed in the bunker is reported in figure 1. The most significant results are reported in table 1 that shows the two investigated main beam configurations.

* Work supported by the EU Commission in the 6th FP, contract no. 011935 EUROFEL and contract no. RII3-CT-2003-506395 CARE.

Table 1: Main beam configurations

	Low charge	**High charge**
Charge	$200pC$	$900pC$
Emittance	$0.8mm\ mrad$	$2.2mm\ mrad$
Energy	$5.65MeV$	$5.55MeV$
Energy spread	1%	2.6%
Pulse length	$8ps$	$12ps$

PHOTO-INJECTOR STATUS

In the following paragraphs we will give a short description of the main systems constituting the machine.

Figure 1: Picture taken in the SPARC bunker

RF and timing system

The SPARC RF system is mainly constituted by two RF chains and its scheme is reported in figure 2 together with the synchronization system layout [3]. The power sources, shown in figure 3(a), are the 45 MW peak, 2856 MHz klystrons TH2128C. The klystron n.1 presently feeds only the RF gun with $3\mu sec$ pulses and it is designed to feed also one accelerating section via a $3dB$ waveguide coupler and an RF deflecting cavity for beam diagnostic purposes.

The RF gun, reported in figure 3(b), was successfully conditioned without relevant problems and we fed into it more than $10MW$ of RF power that corresponds to an

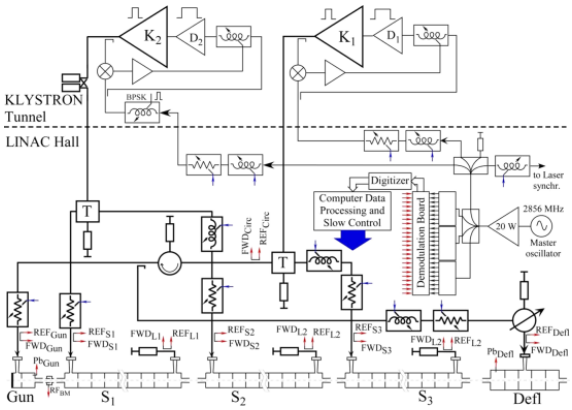

Figure 2: RF system layout

(a) (b)

Figure 3: Installed RF hardware: (a) modulators and klystrons and (b) RF gun

accelerating electric field of about $120 MV/m$. Klystron n. 2 and its waveguide distribution lines are now under test and they will feed two high gradient accelerating sections through an energy compressor that allows to obtain a $60 MW$ - $0.8 \mu sec$ RF pulse.

The timing distribution system is installed and it provides the $79.33 MHz$ reference to lock the laser system to the RF oscillator using a home-designed frequency divider board. It also furnish the $10 Hz$ repetition rate signal to the machine, synchronous with the external line and to the $2856 MHz$ internal distribution.

The synchronization diagnostic is working with good and stable performances and the time jitter from each location of the machine (relative to the main oscillator) is displayed in the control room monitors. Also an RF phase feedback system was implemented to correct slow drifts due to temperature. The observed time jitter of the accelerating field inside the gun is $250 fs_{RMS}$ and the laser oscillator time jitter is $350 fs_{RMS}$.

Laser system

Beam dynamics simulations defined the SPARC laser system [4] specs in order to obtain $2 mm\ mrad$ emittance at $100 A$. The laser is a $10 Hz$ CPA Ti:SA, TW system produced by Coherent. At the laser exit a THG and an UV stretcher produce the required wavelength ($266 nm$) and pulse duration ($2 \div 10 ps$). To manipulate the time profile an acousto-optic programmable dispersive filter is installed before the amplifier.

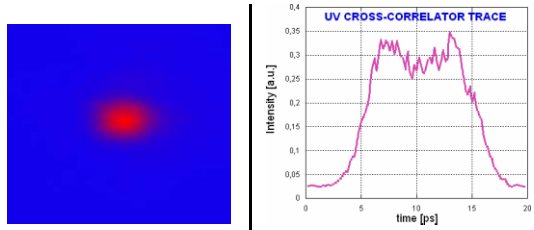

(a) (b)

Figure 4: (a) transverse laser spot on the cathode and (b) UV pulse longitudinal shape

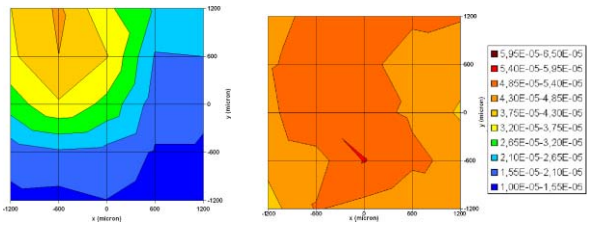

Figure 5: Cathode QE before (left) and after (right) laser cleaning

The pulse profile is flat in time and gaussian in transverse plane (with $1 mm$ spot size) and an image of the spot is shown in figure 4(a). We are using a cross-correlator to investigate the longitudinal behavior of the UV pulse and a typical observed shape is reported in figure 4(b). The optical transfer line is designed to increase the pointing stability, to easily change the spot dimension and to compensate the $72°$ incidence distortions.

A laser cleaning on the cathode was performed and it has given good results, increasing the quantum efficiency from $3.75 \cdot 10^{-5}$ to $6 \cdot 10^{-5}$ and improving the emission uniformity as can be seen in figure 5.

Control system

The control system is perfectly working and it is ready to be extended to the SPARC full configuration. The SPARC main server with a RHEL3 operating system, is in a LTSP configuration so that the consoles are identical diskless workstations. The photo-injector device drivers are installed in industrial PCs placed in the bunker. The layout of figure 6 report the SPARC protected $1 Gbit/s$ LAN architecture. Two machines form a connecting bridge from the front-end industrial PCs to the control room consoles:

- the data server: it accepts a request of information from the consoles and send them the data read from the proper industrial PC. The data can be software variables (that identify the controlled devices), sampled signals, images or information about the status of the computer itself;

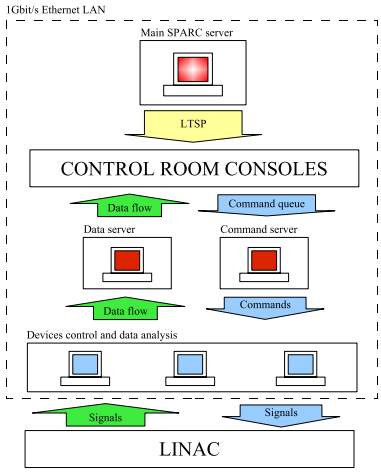

Figure 6: Control system architecture

- the command server: it elaborates the queue coming from the consoles and, once identified legal commands, it delivers them to the front-end PCs to control the photo-injector devices.

Diagnostics

Beam diagnostic devices are placed along the photo-injector as shown in figure 7 and reported in table 2. The main diagnostic tool is the home-designed emittance-meter, able to move $1.2m$ along the longitudinal axis and to study the first meters of beam propagation, where space charge effects and plasma oscillations dominate the electron dynamics.

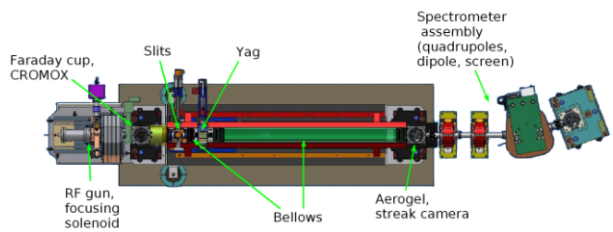

Figure 7: Photo-injector actual layout

Table 2: Diagnostic elements

Distance from cathode [cm]	Device	Measurement
60	Faraday cup, CROMOX screen	charge, beam centering
$85 \div 200$	E-meter (slits, YAG screen, CCD)	emittance, beam envelope and parameters
220	aerogel + streak camera	beam duration
$250 \div 300$	FODO cell, dipole	beam conditioning before spectrometer
$250 \div 300$	spectrometer (Yag + CCD)	energy and energy spread
350	BCM	beam charge

An exhaustive description of the measurements taken using these items is given in the next section.

BEAM MEASUREMENTS

Charge vs phase

First of all we report the charge relative to the gun RF phase measurement (phase scan) that allow us to choose day by day the optimal phase for the electron extraction and to collect information about the accelerating gradient and the quantum efficiency. Moreover this kind of measurement permit us to obtain a rough estimation of the beam duration. Picture 8 report some phase scans performed in different photo-injector working points.

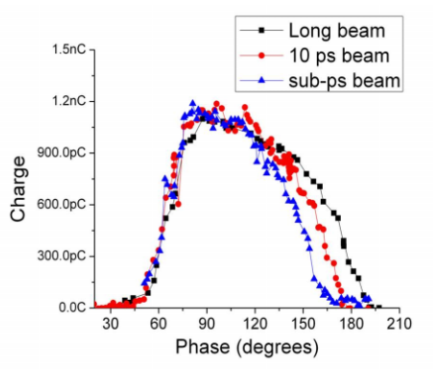

Figure 8: Charge vs phase in three different beam configurations

Energy and energy spread

A spectrometer and its transport line (constituted by a FODO cell) are placed at the end of the diagnostics chain to measure energy and energy spread. We performed these measurements in low and high charge configurations as function of the launching phase as shown in figure 9. The difference both in maximum energy and energy spread between the low and high charge case are due to longitudinal space charge effects (including the image charge at the cathode) and to the wakefield effects in the long bellows.

The presence of the emittance-meter allowed us to perform some special energy spread measurements inserting a slit in the bunch orbit and selecting a beam slice in different longitudinal locations. In fact, as shown in picture 10, we 'froze' the beam evolution under the longitudinal space charge and wakefield effects at different points along the beamline.

Bunch length

A longitudinal diagnostic, based on Cherenkov radiation produced by the beam passing through a $5mm$ thick aerogel slab with index of refraction $n = 1.017$, was installed with the main purpose of studying the photo-injector response to hundreds femtosecond long laser pulses created

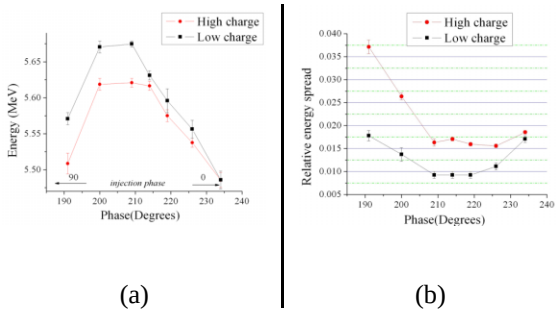

Figure 9: Energy (a) and energy spread (b) for low and high bunch charge

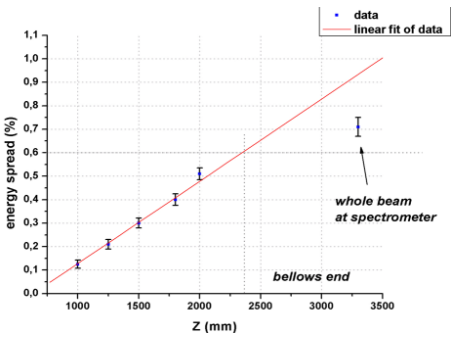

Figure 10: 'Slit' energy spread

by the Ti:Sa laser system [5]. A field-lens narrow band filtering optical system delivers the Cherenkov light to the entrance slit of a $2ps$ resolution Hamamatsu streak camera enabling pulse length measurements (see figure 11).

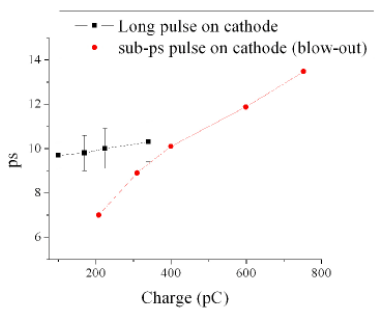

Figure 11: Bunch length measurements with streak camera

Transverse dynamics

Using the emittance-meter we were able to characterize the emittance as function of the longitudinal coordinate and to observe clear indications of emittance oscillations driven by space charge forces in the drift downstream of the RF gun, in agreement to what expected from our theoretical model and numerical simulations. Figure 12 reports two set of measurements compared with numerical simulation. The algorithm used to calculate the emittance was designed also to reconstruct the phase space and good results were achieved (see figure 13).

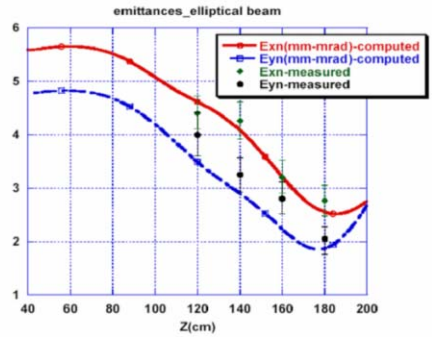

Figure 12: Emittance measurement with relative simulated curves

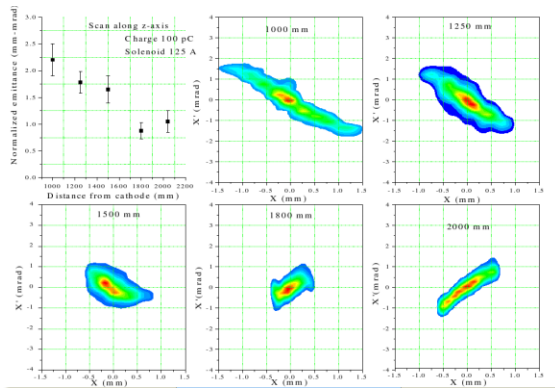

Figure 13: Phase space reconstruction

CONCLUSIONS

The SPARC photo-injector commissioning was started and a good characterization of the electron beam at the exit of the gun has been performed with the emittance-meter. In particular measurements show that the beam brightness required to drive a SASE-FEL experiment was achieved. The linac installation phase will begin at the end of this summer with the commissioning of the accelerating sections and the second RF power line. Moreover it is planned to use a SPARC-like system as photo-injector for the future SPARX X-ray FEL experiment [6].

REFERENCES

[1] D.Alesini et al., IEEE Cat. N. 05CH37623C, (2005) 1327.

[2] L. Catani et al., 'Operational experience with the emittance-meter at SPARC', these proceedings.

[3] A. Gallo et al., 'The SPARC RF Synchronization System', PAC'05 proceedings, Knoxville, May 2005, p. 1024.

[4] C. Vicario et al., 'Commissioning of the Laser System for SPARC Photoinjector', EPAC'06 proceedings, Edinburgh, June 2006.

[5] M. P. Dunning et al., 'Optimum beam creation in photoinjectors using space-charge expansion', these proceedings.

[6] D. Alesini et al., 'Status of the SPARX FEL project', EPAC'06 proceedings, Edinburgh, June 2006.

FREE ELECTRON LASER TRIGGERED PHOTO-CATHODE

E. Sabia, A. Dipace, ENEA, C.R. Portici (Napoli), Italy
G. Dattoli, ENEA, C.R. Frascati (Roma), Italy.

Abstract

The possibility of realizing a FEL triggered photocathode has been proposed long time ago and the advantages have been pointed out. In these devices the FEL can be exploited to extract electrons from a photocathode to provide a high quality e-beam. The device becomes even more appealing if photo-thermoionic cathodes can be exploited in two different phases. In the first the electrons are extracted from the cathode working as thermoionic and are used to drive a FEL oscillator, the FEL light is then used to flash the cathode which operates as a photo thermal assisted device. We comment on the possibility of using FEL triggered photocathodes to produce high quality e-beams for SASE or oscillator FEL devices. The use of the same e-beam driving the photocathode and the FEL makes the system naturally free of any synchronization problem arising when an external laser is used. Examples of interplay between the generation of electron and optical bursts are also investigated.

INTRODUCTION

In previous investigations it has been shown that FEL radiation can be exploited to trigger a photocathode gun [1], [2]. In this paper an extension to an "hybrid device" has been considered: in such a device, sketched in Fig. 1,2 a thermoionic gun produces an e-beam driving a FEL oscillator, the FEL radiation can be backward sent to illuminate the thermoionic cathode in order to exploit a different operating regime, i.e., a thermally assisted photoemission. Such a feedback mechanism, with a proper choice of the parameters, can enhance the e-beam brightness despite a modest increase of the transverse emittance.

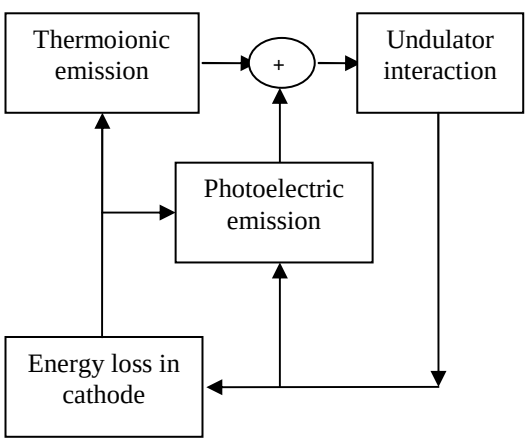

Fig. 1: Block diagram of "hybrid FEL oscillator".

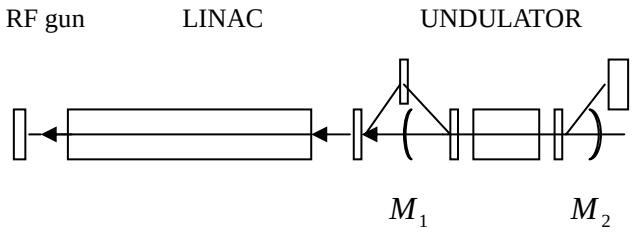

Fig.2: Layout of the "hybrid FEL oscillator".

In this paper we will consider a thermal dispenser cathode [3], with good photoelectric quantum efficiency, initially operating in the thermoionic mode and heated at a sufficient temperature in order to have enough e-beam current to allow FEL operation, radiation is then feed back to the cathode to switch it on the photo-assisted mode.

THEORETICAL MODEL

Under a number of assumptions and proper approximations that will be explained in the following, a semi-analytical model has been developed to take into account the interplay among the oscillator intra-cavity radiation growth, the temperature rise due the photonic incident energy loss in the cathode material and the electron current extracted. It has already been shown that the round-trip evolution of a FEL oscillator can be written as [4]:

$$I_n = I_0 \frac{[(1-\eta_{cl})(1+G)]^n}{1+\frac{I_0}{I_E}[[(1-\eta_{cl})(1+G)]^n-1]} \qquad (1)$$

where n is the round trip number, G the maximum small signal gain, η_{cl} the total cavity losses, I_0 the initial seed and I_E the intra-cavity equilibrium intensity given by

$$I_E = \left(\sqrt{2}+1\right)\left(\sqrt{\frac{1-\eta_{cl}}{\eta_{cl}}G}-1\right)\frac{1}{2Ng_0}P_e \qquad (2)$$

with N being the number of undulator periods, g_0 the small gain coefficient and P_e the e-beam power.

In the previous relations (1) and (2), the quantities I_0, g_0, G, P_e are no longer constant but, due to the feed-back mechanism, they are updated at each round trip.

The temperature rise due to the photonic incident energy loss in the cathode can be evaluated using the Anisimov heat equations [5], [6] which relate the electron to the lattice temperature. As suggested in [3], for time scale characteristic of laser pulse in the range 1ps-1ns, a steady state approximation of the Anisimov equation can be considered, which implies that the electron and lattice temperature are equal. Moreover, under the assumption of a laser pulse with a uniform spatial profile and a constant power of duration τ (microbunch duration) [7], at a power level such that neither melting nor vaporization occure, and by considering the heat to be generated at the surface of the cathode, we get:

$$\Delta T = \frac{(1-\eta-R)I_\lambda \tau}{\sqrt{2\kappa\rho c_v \tau}} \tag{3}$$

where η is the photoelectric quantum efficiency, κ, ρ, c_v are the thermal conductivity, the density and the specific heat of the cathode material respectively, R the cathode reflectance, τ the laser micro-pulse duration, I_λ the power laser density to the cathode.

The electron current density extracted from the cathode, using the Richardson approximation, can be obtained as a sum of 2 contributions: one proportional to the laser intensity, the other to the Richardson-Laue-Dushmann current density for thermoionic emission [3]:

$$J = (1-R)\left(\frac{e}{h\nu}\right) I_\lambda \left(\frac{U((h\nu-\phi)/kT)}{U(\mu/kT)}\right) + J_{RLD} \tag{4}$$

$$J_{RLD} = AT^2 e^{-\phi/kT} \tag{5}$$

where A is the Richardson constant, R the cathode reflectance, $h\nu$ the incident photon energy, k the Boltzmann constant, T the electrons temperature, μ the chemical potential, $\phi = \Phi - \sqrt{4QF}$ the barrier height, Φ the cathode work function, $\sqrt{4QF}$ the Schottky barrier lowering due to the image charge Q, F the product of the electric field gradient between cathode and anode and the electron charge and finally U is the Fowler-DuBridge function [8], [9].

It may be argued that since the cathode is operated as thermoionic and photocathode there is a detrimental effect due to the increase of beam emittance (both transverse and longitudinal). The emittance increase can be estimated following the recent analysis by Bazarov and Sinclair [10]. In their scaling law the transverse emittance is related to the extracted charge and bunch length :

$$\varepsilon\,[\text{mm mrad}] = q\,[\text{nC}] \cdot \left(0.73 + \frac{0.15}{\sigma_z^{\,2.3}[mm]}\right) \tag{6}$$

where q is the photoelectric extracted charge and σ_z is the length of the bunch.

We can estimate the amount of emittance increase by relating it to the illuminating power. An example of the relevant behaviour is given in Fig. 3.

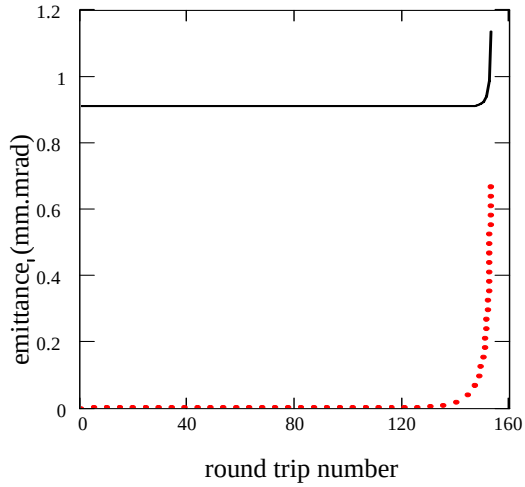

Fig.3: Emittance increase vs. round trip number (in red the photoelectric contribution, see Eq. 6, in black the total emittance) [mm mrad].

It is evident that with increasing number of reflections the emittance grows (we have assumed quadratic composition for the different emittance contributions) but the increase of current is larger and the net effect is an increase of the e-beam brightness. We must however not exceed the reflections to avoid effects of power overloading which may create a too large emittance degradation as shown in Fig. 4. It may also be argued that the Bazarov-Sinclair scaling holds for an optimized system and therefore the previous estimation may be optimistic.

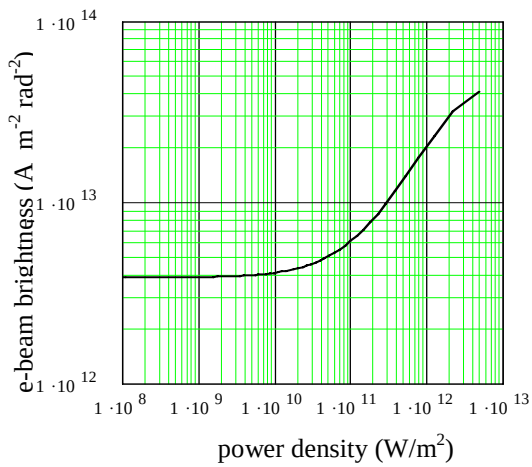

Fig. 4: e-beam brightness [A m^{-2} rad^{-2}] vs. power density [W m^{-2}]

RESULTS AND DISCUSSION

A preliminary analysis of the device has been developed using the parameters listed in Table 1 and 2

Table 1: FEL oscillator

λ	laser wavelength	500 nm
λ_u	undulator wavelength	2.8 cm
N	number of undulator periods	100
γ	e-beam energy	305.8
σ_ε	relative energy spread	10^{-3}
r	e-beam radius	$8.9\ 10^{-3}$ m
I_0	Input seed	1 W/cm^2
τ	e-beam micropulse duration	3 ps
τ_M	e-beam macropulse duration	10 μs
n	round trip number	153
δ	distance between RF gun and mirror M_1 (see Fig. 2)	20 m
L_c	resonator cavity length	10 m
η_{cl}	total cavity losses	4%
T_1	mirror M_1 transmissivity	2%

Table 2: Dispenser cathode characteristics

Sc_2O_3 in matrix of W		
Φ_w	work function	1.8 eV
ϕ	effective barrier height	1.68 eV
d	inter-electrode distance	1 cm
κ	thermal conductivity	1.78 W/cm°K
ρ	density	19.3 g/cm^3
c_v	specific heat	0.13 J/g°K
T_{in}	temperature operation before first illumination	1300 °K

The example we have considered is a FEL oscillator in which the distance between the cathode and the first semitransparent mirror M_1 (see Fig. 2) is 2 times the length L_c of the resonator cavity. The system is designed in such a way that for the first 3 round trips the intra-cavity radiation grows according to the Eq. 1 with constant parameters (I_0 , g_0, G , P_e), then Eqs. 1, 2, 3, 4 and 5 are fully coupled.

In our example we have considered 153 round trips which ensure, as already remarked

- Increase of the bunch current.
- Increase of the e-beam brightness despite a modest increase of the transverse emittance (this last point deserves however a dedicate analysis including the contributions from the longitudinal and transverse shapes of the optical bunch).

In Fig. 5, 6 and 7 the time evolution of cathode temperature, e-beam current density and laser intensity are shown respectively.

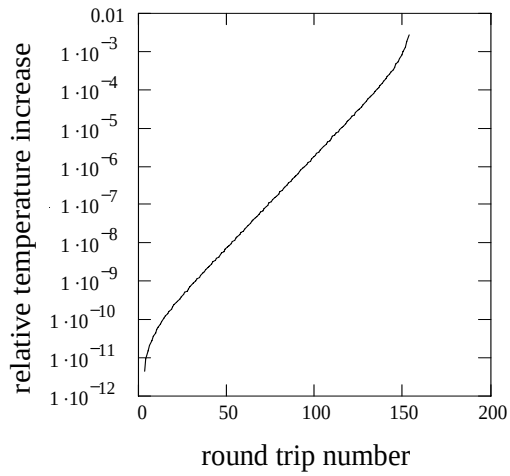

Fig. 5: Relative temperature increase vs. round trip number.

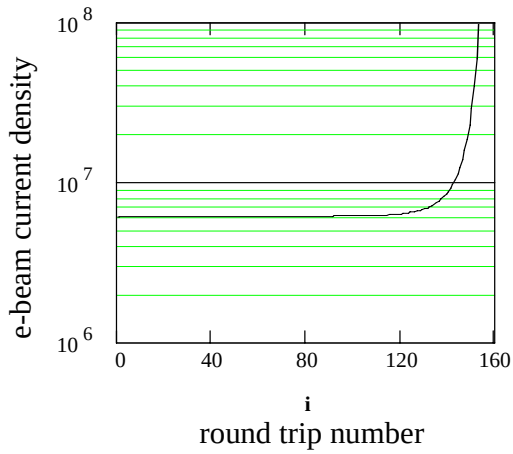

Fig. 6: E-beam current density [A m^{-2}] vs. round trip number.

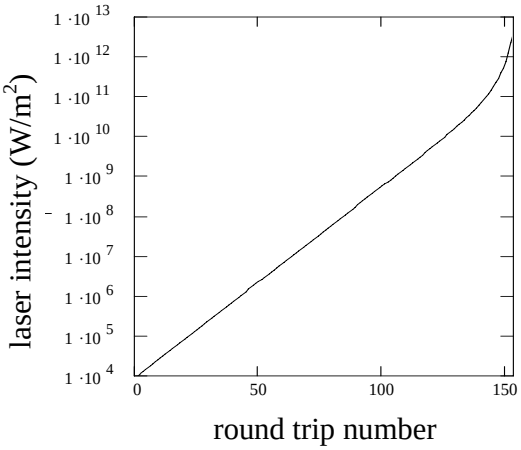

Fig. 7: Laser intensity [W m^{-2}] vs. round trip number.

CONCLUSIONS

A different possibility has been discussed in a previous paper [11] in which a hybrid SASE FEL has been considered: the radiation inside the undulator may be collected with a mirror (if we consider radiation in the visible) and sent back to the cathode. This has not a feed back on the radiation and it is just an external passive device. We must underline that for this device the radiation grows from the noise and the optical spectrum may be dominated by spikes and energy fluctuations, thus inducing dangerous effects which may strongly affect the quality of the e-beam itself. On the contrary, the use of the resonator cavity, acting as an active feed back on the optical field, may eliminate all the problems due to the shot noise, and the length of the optical pulse can also be easily controlled as well as other problems due to the transverse distribution.

It is worth noting that the technique we have considered can be exploited for higher harmonics of the radiation. It is indeed well known that along with the fundamental higher order harmonics are generated in the optical cavity. The harmonic power is not stored in the cavity but it is emitted shot after shot. The harmonic radiation too can be exploited to irradiate the cathode. This different operation will be more deeply examined in a forthcoming investigation.

REFERENCES

[1] G. Dattoli, L. Giannessi, and L. Serafini, J. Appl. Phys., 93,1 (2003).
[2] G. Dattoli, L. Giannessi, A. Renieri, A. Marino, and L. Serafini, Appl. Phys. B: Photophys. Laser Chem. B55, 446 (1992).
[3] K.L. Jensen, D.W. Feldman, M. Virgo, P.G. O'Shea, Phys. Rev. Special Topics, 6, 083501 (2003).
[4] G. Dattoli and P.L. Ottaviani, Opt. Commun. 204, 283 (2002).
[5] S.I. Anisimov, B.L. Kapeliovich, T.L. Perelman, Zh. Eksp. Teor. Fiz., 66,776 (1974) (Engl. Transl. 1974 Sov. Phys.-JETP,39,375).
[6] N.A. Papadogiannis, S.D. Moustaizis, J.P. Girardeau-Montaut, J. Phys. D: Appl. Phys. 30,2389 (1997).
[7] J.H. Bechtel, J. Appl. Phys., 46, 1585 (1975).
[8] R.H. Fowler, Phys. Rev. 38,45 (1931).
[9] L.E. DuBridge, Phys. Rev., 43,727 (1933).
[10] I.V. Bazarov and C.K. Sinclair, Phys. Rev. Special Topics-Accelerators and Beams 8, 03402-1 (2005).
[11] E. Sabia, G. Dattoli, A. Dipace and G. Messina, submitted to J. Appl. Phys.

SUB-PICO-SECOND TRIGGER SYSTEM FOR THE SCSS PROTOTYPE ACCELERATOR

Yuji Otake[A)], Hirokazu Maesaka [A)], Takashi Ohshima [B)], Naoyasu Hosoda[B)],
Toru Fukui [B)], Toru Ohata [B)], Tumoru Shintake [Ä)]

[A)] RIKEN, Harima Institute 1-1-1 Kouto, Sayo-tyou, Sayo-gun, Hyogo, 679-5148, Japan
[B)] Japan Synchrotron Radiation Research Institute (JASRI/SPring-8)
1-1-1 Kouto, Sayo-tyou, Sayo-gun, Hyogo, 679-5198, Japan.

Abstract

To verify the feasibility of X-FEL using an 8 GeV linac, the 250 MeV SCSS prototype accelerator was built at SPring-8. A sub-pico-second time jitter was set as a development target for the timing system of the prototype accelerator, because of its beam pulse width of several pico-seconds. This jitter value had a possibility to be achieved by the present technology. In accordance with the target, we developed a very low-noise reference signal source that generates 238 MHz and 5712 MHz RF signals for acceleration, a master trigger VME module having output pulses synchronized to 238 MHz, and a trigger delay VME module synchronized to 5712 MHz. The time jitters of the delay module are less than 700 fs, and the SSB noise of the 5712 MHz reference signal source is less than -120 dBc at 1 kHz offset. These values are sufficient for our present requirement. A beam energy variation of 0.06% was achieved by the timing system. The beam stability based on AM noise theory in the FEL linac is discussed based on the above data.

INTRODUCTION

The SASE (Self Amplified Spontaneous Emission) X-FEL project at RIKEN HARIMA Institute is now under way.[1] The important component of the project is an accelerator, having an energy of 8 GeV, which comprises a 500 kV thermonic electron gun, a 238 MHz sub-harmonic buncher, a 476 MHz booster, a 2856 MHz booster and 2856 MHz accelerating structures, 5712 MHz accelerating structures with an accelerator field of 32 MV/m, and in-vacuum undulators. To evaluate the feasibility of X-FEL, a 250 MeV prototype accelerator, including the main key elements of the above-mentioned linac (not a full number of the elements), at SPring-8 was constructed by November, 2005, and is under beam testing to generate SASE VUV-FEL.

To generate a stable VUV laser in the prototype linac, an accelerated electron beam with a pulse width of less than 1 ps should pass through an orbit within one hundred micrometers for the undulator section having a length of 12 m.[2] The energy stability of the beam is in the order of 10^{-4}, and the timing jitter of the trigger pulses to accelerator instruments is less than 1 ps were required to archive the orbit and the stable beam pulse width in a bunch compressor, which means the constant peak current of the beam to generate stable laser light. Therefore, we employed a timing jitter and a drift of less than 1ps, as development targets. This is because the beam energy variation of 10^{-4} corresponded to a phase change of about 1 deg. (about 500 fs) in 5712 MHz RF acceleration at the crest point. For the present, in the case of the prototype accelerator, these targets are sufficient for generating and amplifying 60 nm light with about a 1 ps pulse width. In accordance with the targets, we have developed the timing system of the prototype accelerator as shown in Fig. 1. In this system, the final time jitters and drift of the accelerated electron beams, which are directly connected to the energy variation, are decided by the synchronization accuracy of the trigger delay, and the SSB noise of RF instruments, such as a signal source. The long-term drift of the timing is reduced by a feedback control. Therefore, to decrease the SSB noise and to realize a less than 1ps time jitter were set as the main purposes of our instrument development to make the system. This paper describes how to realize these purposes.

TIMMING CONTROL SYSTEM

System Configuration

The configuration of the timing system of the SCSS prototype accelerator is shown in Fig. 1. The timing system comprises a master trigger VME module synchronized to a 238 MHz RF signal and also synchronized to a commercial AC of 60 Hz, a very low-noise signal oscillator to generate 238 and 5712 MHz RF signals as a time reference, a 10 W RF amplifier to amplify the RF signals for signal transmissions, RF signal distributors, a trigger transmission system using 100 Ω differential cables with LVDS (Low Voltage Differential Signaling), and trigger delay VME modules synchronized to both acceleration RF signals of 238 MHz and 5712 MHz.

Master Trigger VME Module

The circuit configuration of the master trigger VME module is shown in Fig. 1. The module comprises a FPGA including 24-bit counters of eight channels, which are driven by a 238 MHz clock signal. The output pulse is also resynchronized by a fast flip/flop working by the 238 MHz clock to reduce the time jitters. The main function of the modules is to generate a trigger pulse train from 1 Hz to 60 Hz for activating the accelerator components, such as the klystron modulators. The pulses are also synchronized to a commercial AC line, and distributed to the components.

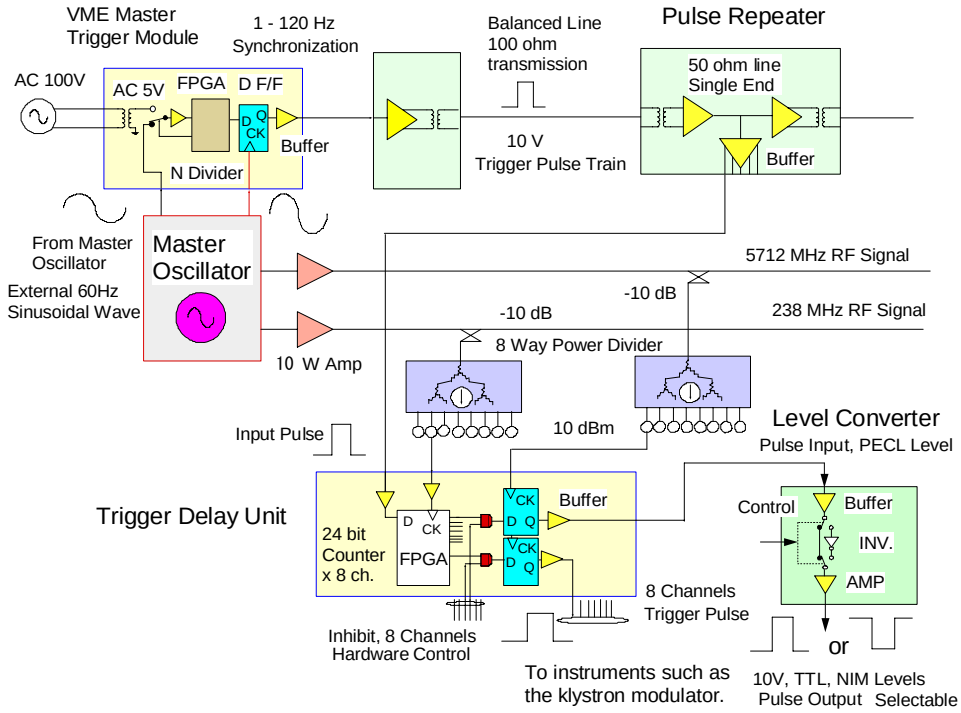

Fig. 1. Trigger system of the SCSS prototype accelerator.

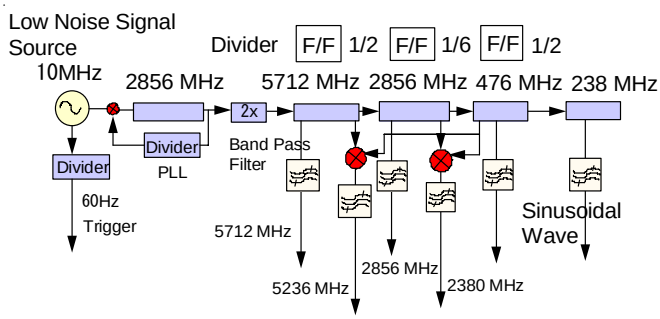

Fig. 2. Circuit diagram of the master oscillator. The signal source uses frequency dividing, a very low-noise power supply and the PLL connection between the 10 MHz and 2856 MHz sources to achieve a low noise.

Master Oscillator

The master oscillator, which generates 238, 476, 2380, 2856, 5236, and 5712 MHz stable RF signals, is a time reference source. The circuit configuration of the oscillator is shown in Fig. 2. It comprises a very stable reference generator (stability of 10^{-11}) of 10 MHz, which has a low-noise characteristic in the frequency region below 1 kHz measured from 10 MHz, a 2856 MHz signal generator having a low noise characteristic in the frequency region over 1 kHz measured from 2856 MHz, a frequency doubler instrument to make 5712 MHz from 2856 MHz, and frequency dividers to generate the above-mentioned frequency signals. Both low-noise signal generators are connected by a PLL (Phase Locked Loop) circuit to make the very low SSB (Single Side Band) power noise over the whole frequency range, as shown in Fig. 3. The noise level is -140 dBc at 1 MHz measured from 2856 MHz. The most important feature is that the signal source uses the frequency-dividing method, a very low-noise power supply (-150 dBV), and the above-mentioned PLL connection. The other important function is to decrease the effect of the environmental temperature around the master oscillator. For achieving this function, a temperature controller using a heater to eliminate the temperature variation within +/- 0.1 ^{o}K was employed.

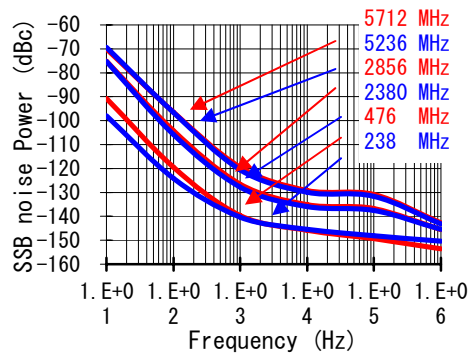

Fig. 3. SSB noise power spectrum of the master oscillator. The decreasing noise level at individual frequencies is proportional to the dividing ratio.

Differential trigger pulse transmission system

Our trigger system employs a trigger-pulse repeater including the function of a differential trigger pulse transmission of LVDS to reduce the influence of noise. The twisted-pair cable to transmit LVDS has a characteristic impedance of 100 Ω to easily adapt to the usual 50 Ω circuit without any signal reflection. The temperature dependence of its electrical length is about 100 ppm, which does not exceed quarter wavelengths of

238 MHz under the conditions of the usual temperature variation for a day and a length of several ten meters used in the prototype accelerator. The repeater, as shown in Fig. 1, can interconnect between the other two repeaters separated by more than 10 m. One port of the repeater is input from the previous repeater, and the other port is output to the following repeater. The repeater also has a function to distribute 8 trigger pulses of LVPECL (Low Voltage Positive Emitter Couple Logic) from the master trigger module to the trigger delay VME modules.

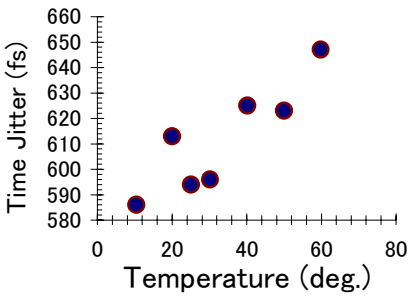

Fig. 4. Measurement result of the time jitters of the trigger delay unit. The jitters (rms) are less than 1ps, which satisfies our requirement. The temperature dependence of the jitter is very low.

Trigger delay unit

The trigger delay unit is the main instrument of our trigger system, and the VME module, as shown in Fig. 1. The circuit of the module comprises a FPGA having 8 counters with 24 bits driven by the 238 MHz RF signal, fast flip/flops, and a temperature controller using a heater to stabilize the temperature of the flip/flips circuit within +/- 0.1 ^{o}K. The output pulses of the FPGA are resynchronized by fast flip/flops working by the 5712 MHz signal to realize sub-picosecond time jitters referred to the acceleration RF. The outputs of the delay unit have a voltage level of LVPECL to decrease jitters. A jitters measurement used to evaluate the module was carried out; Fig. 4 shows the result of the measurement to a 5712 MHz signal dependent on the temperatures. The result shows that the jitters are about 700 fs (rms). In addition, a delay time change of the unit dependent on the temperature was about 400 fs/ ^{o}K (rms).

Level converter

The accelerator comprises many instruments, equipping such various trigger voltage levels as TTL, NIM, and 10V, for historical reasons. However, the output of the delay unit is LVPECL. Therefore we developed an eight-channel level converter to change from the output voltage level of the delay unit to the input levels of the instruments (Fig. 1).

RF distribution and 10 W RF amplifier

To drive the VME modules related to the trigger system (Fig. 1), the RF signals generated with the master oscillator must be transmitted. This signal transmission guarantees synchronization of the whole accelerator system to achieve the stable generation of FEL light. Phase-stabilized RF cables having an electrical length variation of 5 ppm/^{o}K were employed to transmit such signals as 5712 MHz for about more than 20 m. By considering the RF loss of the cables, RF amplifiers, having PLL, ALC and 10 W outputs were used. The amplifier was cooled by water to stabilize the temperature within +/- 0.5 ^{o}K. For distributing many RF signals of about 1 mW to drive the trigger instruments, RF distributors handling the 238 MHz and 5712 MHz signals were developed. The phase variation of the distributor dependent on the temperature was decreased by such design work as choosing an RF divider with a low thermal effect. The thermal phase variation of the amplifier and the distributor were 0.8 deg./^{o}K and 0.28 deg./^{o}K at 5712 MHz without PLL.

SUMMARY AND DISCUSSION

In the SCSS prototype accelerator, we finally obtained a fruitful result: a beam energy stability of less than 0.06 % at the exit of the S-band accelerating structure (at 50 MeV). This accelerated beam almost stably drove a SASE of 53 nm in the undulator section. The measured time jitter of the accelerated beams to the acceleration RF, which was directly connected to the energy variation, was less than 340 fs (rms). The measured jitter of the delay unit was about 700 fs (rms). These jitter values satisfied our requirement.

These jitters were mainly determined by the rise time of a pulse of the synchronization clock for the delay unit and the SSB noise of the RF signal. To realize the sub-pico-second jitters, we employed a clock signal of 5712 MHz, and very low-noise signal sources of 238 MHz and 5712 MHz.

The influence of the SSB noise on the beam energy variation and the time jitters of the beams is not very clear. Therefore, we want to discuss the verification of the SSB noise effect to the beam energy stability in the prototype accelerator. The effect, that is the time-domain voltage variations, of the SSB noise to an RF pulse in an accelerating structure is calculated by integrating the SSB noise amplitude for a certain frequency band width.[5] In general, a carrier signal including SSB noise is expressed, as shown in Fig. 5-A, and as the rotating vector of the noise at the top end of the carrier wave vector. The AM and FM modulations generated by the SSB noise are an equivalent. To calculate the energy variation of the beam caused by the amplitude and phase variation on a CW RF signal, the integration span on the frequency axis of the SSB noise graph is from less than 1 Hz to several more figures of the frequency corresponding the filling time of an accelerating cavity. If this integration span is applied to the calculation in the case of our accelerator with the 5712 MHz RF pulse of 2 μs (f_p = 0.5 MHz) width, the time-domain noise level on the pulse increases by more about 7 digits compared to the noise level of -140 dB at f_p in Fig. 3. In this calculation, the voltage variation on the

pulse is near 0.1%. This value should be over estimated, if the other noises generated by the accelerator components are taken into account of. We can not explain the present beam energy stability of 0.06%. For these reasons, the frequency span of the integration should be limited to the case of pulsed RF acceleration.

In this paper, we do not consider a beam energy variation below a reputation frequency of 60 Hz in our accelerator, because it can be eliminated by feedback control. Here, we consider the SSB noise components around f_p, which do not change the base level of the RF pulse, and only change the amplitude of the pulse. This SSB noise effect to the beam energy change is assumed as shown in Fig. 5. In the case of the frequency components over f_p, (Fig. 5-C), the effects of the noise, which is expressed as odd functions (f_{h2} ---) mixed on the RF pulse, are cancelled by integration of the accelerating force, when the beam passes through in the accelerating structure. However, the even components ($f_{h1,}$ f_{h3} --- f_{hn}), like Fig. 5-C, are not cancelled, and have an influence on the energy variation, which is inversely proportional to the frequency. In the lower frequency components, measured from the RF pulse frequency, f_p, the effect of the noise components to the pulse decreases in proportion to the frequency, because of a constant pulse width. The slope of the amplitude variation of individual frequency components ($f_{l1,}$ f_{l3} ---- f_{ln}) of the noise within the pulse width decreases in proportion to the frequency, as shown in Fig. 5-B.

The integration of the SSB noise to estimate the effect, *N(t)*, to the beam energy variation could have a factor of 1/2, which corresponds to the influence of the even functions, and the weight functions reflecting the above mentioned frequency dependence. By an assumption based on the above-mentioned discussion, we can consider the flowing equations. In the case of a higher frequency, *f*, than f_p, the equation is

$$N(t) = \int \frac{1}{2} w(f) N_{SSB}(f) df \qquad f \geq f_p . \qquad 1)$$

At a frequency lower than f_p, the equation is

$$N(t) = \int w(1/f) N_{SSB}(f) df \qquad f < f_p . \qquad 2)$$

The equations are integrating the SSB noise, $N_{SSB}(f)$, times the weight functions, *w(f* or *1/f)*, having a linear peak shape like Fig. 5-D. For describing the above-mentioned method by another way, we can also consider applying the square window function (RF pulse) in a time-domain to the SSB noise, to calculate FFT.[6]

The RF amplitude and phase variations in the accelerating structure of the prototype accelerator were estimated by integrating the 5712 MHz noise spectrum of Fig. 3 with the weigh functions described in Fig. 5-D. The result of the integration for a frequency span between 1 Hz and 1 MHz was that the amplitude variation was 0.01% and the phase variation was 0.06 deg (about 30 fs). These values were ten-times smaller than the values that were integrated without the weight functions. From these results, we can explain the 0.06% energy variation of the prototype accelerator with the noise caused by the other components by using the above-mentioned method. The 30 fs time variation is enough for our requirement.

REFERENCES

[1] SCSS X-FEL Conceptual Design Report, 2005.
[2] Dr. T. Tanaka, private communications.
[3] M. Cohlus et al., Bunch Compression Stability Dependence on RF Parameters, Proc. The 27th FEL conf., 250-253, USA, 2005.
[4] SCSS X-FEL Conceptual Design Report, pp 81-89,2005.
[5] S. Goldman, Frequency Analysis, Modulation and Noise, DOVER, pp 211-215, 1967.
[6] T. Koshikawa, Introduction of Signal Analysis, Kindai Kagakusya pp25-30, 2001, in Japanese.

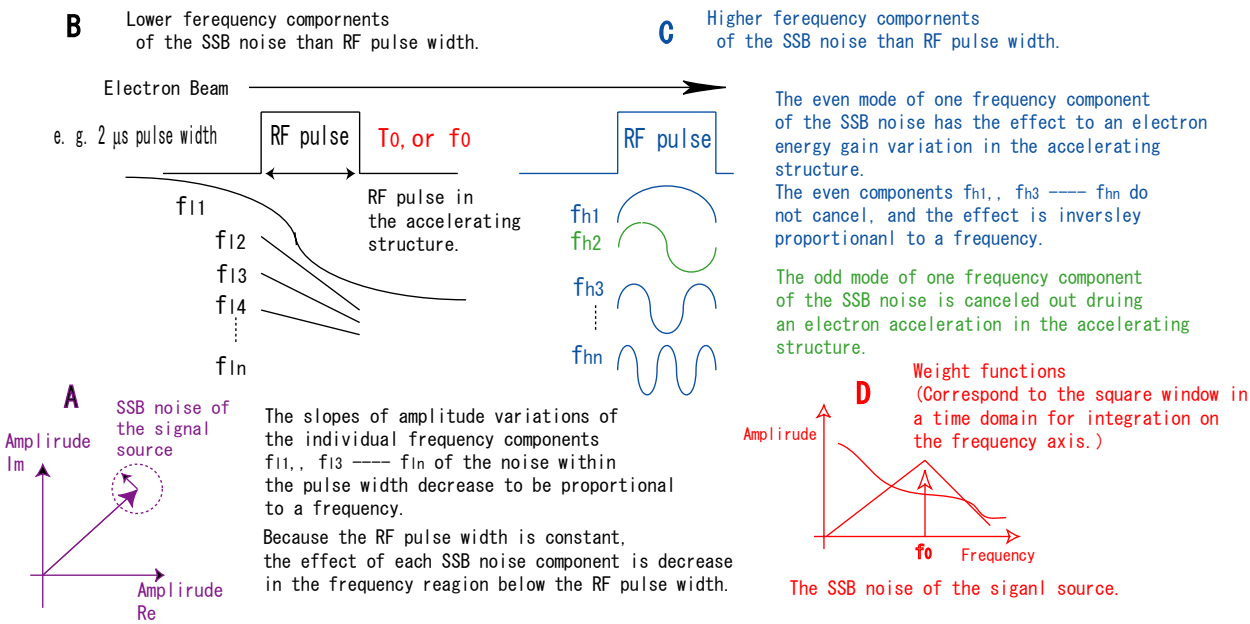

Fig. 5. SSB noise effect on the RF pulse in the accelerating structure.

LASER PULSE LENGTH DEPENDENCE OF BEAM EMITTANCE OF PHOTOCATHODE RFGUN

H. Dewa, T. Asaka, H. Hanaki, T. Kobayashi, A. Mizuno, S. Suzuki, T. Taniuchi, H. Tomizawa, and K. Yanagida, SPring-8, 1-1-1 Kouto, Sayo-cho, Sayo-gun, Hyogo-ken 679-5198, Japan

Abstract

Laser pulse length and laser shape should be optimized to minimize the beam emittance of photo-cathode RF-gun. A 3-D particle tracking simulation predicted the smallest beam emittance could be obtained with the square laser pulse length of about 20 ps. To examine the effect of the laser pulse length to beam emittance, the square laser pulse of 10 and 20 ps was generated with laser pulse stacking of 2.5-ps micro pulses and each beam emittance was measured at the low beam charge of 0.4 nC/pulse. The measured beam emittance was not significantly different each other.

Then beam emittance was measured at the higher beam charge of 1.0 nC/pulse. The minimum beam emittance with 20-ps laser pulse was 2.3 πmmmrad with 0.8mm x 1.0 mm elliptical laser profile. Although we also tried to measure the beam emittance with 10-ps laser pulse, the beam charge of 1.0 nC could not be generated at the same laser spot size due to probably space charge limit. The measured beam emittance for 20-ps laser pulse was smaller than the minimum beam emittance 3.0 πmmmrad for 10-ps laser pulse measured under different laser condition, especially micro pulse of 1.0 ps and laser spot diameter of ø 1.0 mm.

Although we could not compare the laser pulse 10 ps and 20 ps at the equivalent conditions in high charge region, these experimental results would indicate at least the possibility of using long laser pulse about 20 ps to minimize the beam emittance for beam charge around 1.0 nC.

INTRODUCTION

The electron source for several XFEL projects [1-3] requires very low emittance beam as low as 1 πmmmrad. To minimize the beam emittance of a photocathode RF-gun, the laser pulse shape should be optimized three-dimensionally. The transverse shape could be modified with a microlens array [4] or a deformable mirror (DM) [5]. As well as the transverse shape, the longitudinal shape can be also modified with a spatial light modulator [5,6] or pulse stacker described in this paper. Beam emittance of 1.2 πmmmrad for 1 nC/pulse has already realized by J. Yang et. al. with square 9-ps laser pulse [6].

So far, we demonstrated transverse shape optimization and low emittance beam generation of 1.7 πmmmrad at the electron charge of 0.1 nC [5]. The beam emittance at high charge was, however, much larger, because the laser pulse length is too short (5 ps) and the diameter was 1mm (top hat) and therefore the charge density was too high.

#dewa@spring8.or.jp

In this paper, we tested longer laser pulse of 10-ps and 20-ps square generated with laser pulse stacker to get low emittance in high charge region. Three stages of pulse stacking generated 20-ps pulse from eight micro pulses. The purpose introducing longer laser pulse is to keep the laser beam size small but decrease the charge density. The small beam size contributes to decreasing the initial emittance, and small charge density to the space charge effect. Therefore, long laser pulse is effective especially in high charge region. A 3-D particle tracking simulation predicted smaller beam emittance could be obtained with the laser pulse length of about 20 ps at 1nC/pulse as shown in Fig. 1. It also predicted electron bunch length can keep around 10 ps with both 10 and 20-ps laser pulse length due to bunch length compression in the RF cavity.

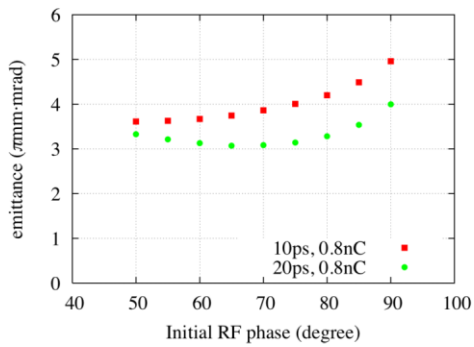

Figure 1: Beam emittance of the photo cathode RF gun for 10 and 20-ps laser square pulse length calculated with a 3-D particle tracking simulation. In the calculation, the laser spot diameter was 1.6 mm (top hat) and the maximum electric field on the cathode was 135 MV/m.

LASER PULSE STACKING

Pulse stacker is composed of sets of half-wave plates and polarizing beam splitter cubes. The fully s-polarised pulse laser is rotated to 45 degrees polarised pulse with a half-wave plate. It is divided into an s-polarized pulse and p-polarised one with a polarizing beam splitter. The p-polarized pulse is delayed with an optical delay line and then combined with the s-polarized pulse after another polarized beam splitter. Finally, as shown in Fig. 2, the laser pulse of 2.5 ps was stacked with optical delay at each stage to generate longer square pulse. With three stages, we can obtain 20-ps square pulse.

The polarizing beam splitter cubes used in the first and second stage is optical contact type (produced by Showa Optronics) considering the high power density of the UV laser. The polarizing beam splitter used in the third stage is bonded with optical cement, because the power density

is lower at the stage. The diagram of the optical system is shown in Fig. 3.

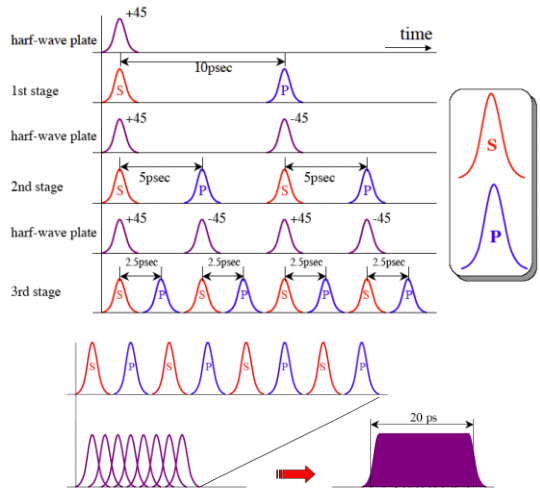

Figure 2: Timing chart of pulse stacking

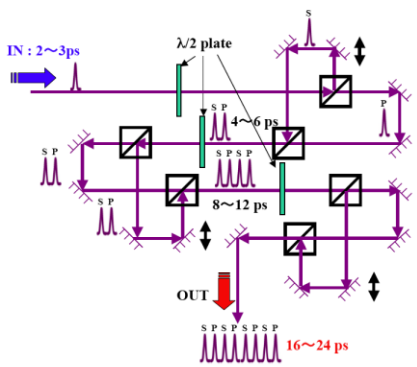

Figure 3: Optical system of laser pulse stacker (three stages)

PULSE LENGTH CONTROL

Finding the origins of optical delay lines

To generate long pulse without any timing gap or overlap, origins of the optical delay lines must determined with a precision less than 1 ps. The origin is defined here as the position of micrometer in the delay line such that the s-polarization and p-polarization pulses reach the cathode at the same time. The way that determines the origin is as follows. The energy of the electron pulse was measured for two laser pulses divided by each stage of the pulse stacker. The energy of the electron beam is measured as beam position on a profile monitor after a bending magnet downstream the RF-gun cavity. To eliminate the positioning jitter and short time drift, the beam positions were measured for 5000 times. The micrometer for p-polarized pulse was tuned as these two electron beam pulses come to the same position on the profile monitor after 3-5 times iterations. The timing precision of the origin was about 0.5 ps estimated from the position jitter distribution.

Setting of optical delay lines

After setting the origins of three micrometers, the position of these micrometers are determined by simple calculation. For example, if the pulse length is 20 ps, the micrometer positions are set as follows,

Position for 1st stage: origin - 1.5mm
Position for 2nd stage: origin - 0.75mm
Position for 3rd stage: origin - 0.375mm.

The stacked laser pulse was finally checked by the beam energy distribution on the profile monitor with illuminating all eight micro pulses. The energy distribution of the beam is shown in Fig. 4. At an optimum phase (85 degree), the beam focuses on the profile monitor. When RF phase is 44 degree, the energy dispersion was made purposely larger to evaluate stacking pulse structure. The uniformity is not ideal but there are not any gaps and strong hot spot in the distribution. Therefore, the eight micro pulses are thought to be stacked properly. The incomplete uniformity mainly comes from the insufficient flatness of energy among the laser micro pulses.

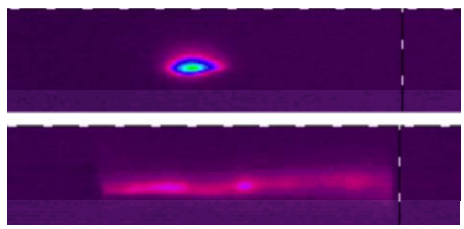

Figure 4: The energy distribution on the profile monitor for the 20-ps laser square pulse at different RF phase. Top: RF phase at 85 degree (3.52 MeV @center), Bottom: RF phase at 44 deg (3.29MeV @center)

The information of the pulse length of the micro pulse can be also obtained from this measurement. When the micro pulse was around 1.5 - 2.0 ps, five strong spots were observed on the profile monitor as shown in Fig. 5. These spots come from overlapping on the edges of two micro pulses. Not all energy spots are seen on the profile monitor, because of small screen. The number of the spot was found to be totally seven when the RF phase was moved.

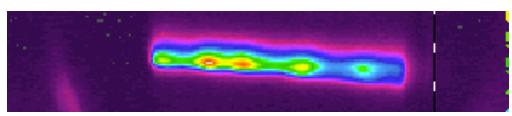

Figure 5: The energy distribution on the profile monitor for the 20-ps laser pulse, when the micro pulse is around 1.5 -2.0 ps.

Simulation results of the energy distribution for micro pulse lengths of 1.5 ps and 2.5 ps are shown in Fig. 6.

There are seven spots for the case of 1.5 ps, while there is not any strong spot for the case of 2.5 ps.

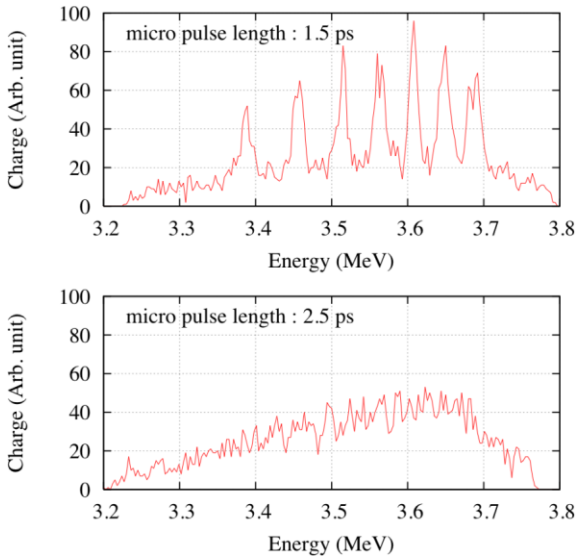

Figure 6: Simulated of the energy distribution for micro pulse length of 1.5 ps (Top) and 2.5 ps (Bottom).

BEAM EXPERIMENTS

Laser distribution and electron beam charge

The laser pulse energy of eight (20 ps) and four (10 ps) micro pulses was tuned by the angle of half-wave plates to get the beam charge of 0.4 nC and energy flatness. The results are shown in Fig. 7.

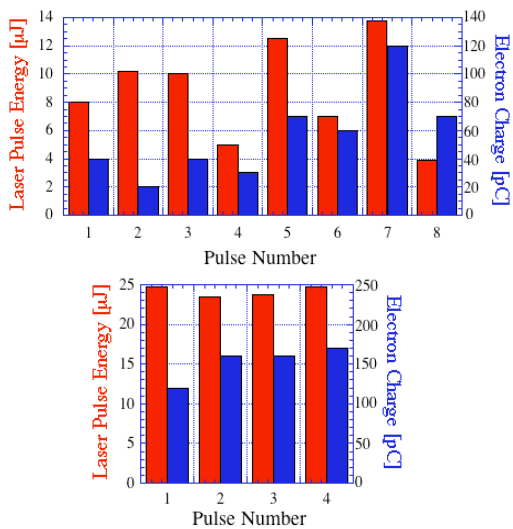

Figure 7: The laser pulse energy and electron beam charge of micro pulse for 20-ps (Top), and 10-ps pulse structure (Bottom).

The 20-ps pulse was generated with pulse stacker of three stages, and 10 ps with first two stages. The energy flatness for 20 ps is worse than 10 ps. The polarizing beam splitter of the third stage could not divide the two pulses ideally because it is bonded with optical cement and the energy loss of p-polarization pulse is larger at higher intensity.

There is a difference in total pulse energy to get the same charge of 0.4 nC; 70.4 μJ for 20 ps and 96.6 μJ for 10 ps. This is due to both of the Schottky effect and space charge limit. These effects is not theoretically calculated but can be understand from the facts that four micro pulses in 10-ps pulse individually generate increasing charge of 0.12, 0.16, 0.16, 0.17 nC, but generate only 0.4 nC with all four pulse at the same time.

Setup of Beam emittance measurements

The electron beam generated from the RF gun was accelerated to 26 MeV with a 3m-long accelerating structure. The beam emittance was measured with quad scan downstream the accelerating structure [7].

When we operate quad scan to measure the beam emittance, the beam size must be measured at the resolution of the order of 10 μm. To realize the fine resolution, we adopted a profile monitor with a thin screen and high resolution CCD camera. The screen is an alumina fluorescence sheet (Desmarquest AF995) with the thickness of 0.05 mm. The CCD camera is 1.3-mega pixels camera (SONY XCD-SX910). It has a 1/2-inch CCD chip with 1280(H) x 960 (V) pixels, and each pixel size is 4.65 x 4.65 μm^2. To get a large depth of field, we used a telecentric lens of 1/4 magnification. The estimated resolution of the image is about 20-30 μm. Only center quadrupole magnet of the triplet quadruple magnet was used to focus the beam on the screen with quad scan. The setup of the quad scan measurement is shown in Fig. 8.

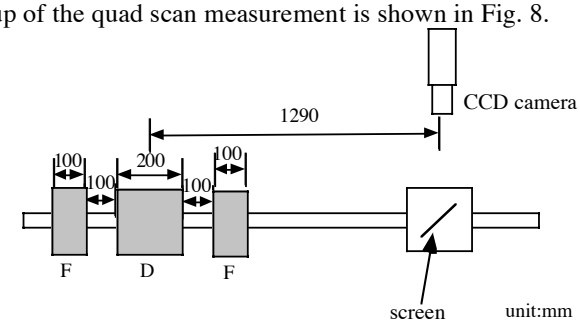

Figure 8: Setup of quad-scan measurement.

The emittance measurement was automatically executed in about 5 minutes if the measurement points were less than 15. The automatic measurement system was programmed with Labview 7.1 and Vision developing module (National Instruments Co.).

Beam emittance measurements

Beam emittance for 10 and 20-ps laser pulse was measured in low charge region of 0.4 nC/pulse. The current of solenoid coils were optimized to get minimum beam emittance. The laser shape was elliptical (0.8 mm (H) x 1.0 mm (V)). In this experiment, the optimization of DM could not executed because the CCD of laser profiler

was damaged. The results of the quad scan are shown in Fig. 9. The emittance of both beam were almost same, 3.2 πmmmrad for 20 ps and 3.3 πmmmrad for 10 ps.

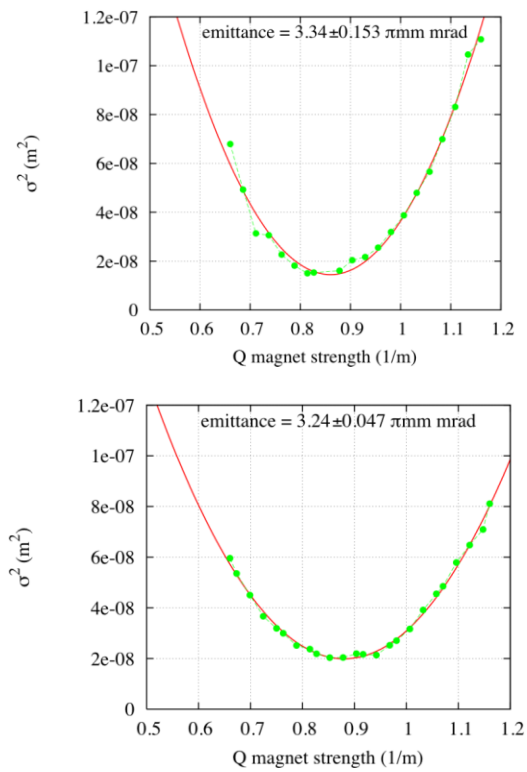

Figure 9: Measured beam emittance for 10-ps and 20-ps laser pulse at the beam charge of 0.4 nC/pulse.

Next, the beam emittance was measured in case of high current beam. The beam current of 1.0 nC was generated for 20-ps pulse but only 0.6 nC beam current could be generated for 10-ps pulse at the same laser spot size, though the laser power was high enough. It may be due to space charge limit. After further optimizing parameters such as solenoid current, RF phase and half-wave plates, the measured minimum emittance of the beam for 20-ps laser pulse was 2.3 πmmmrad as shown in Fig.10.

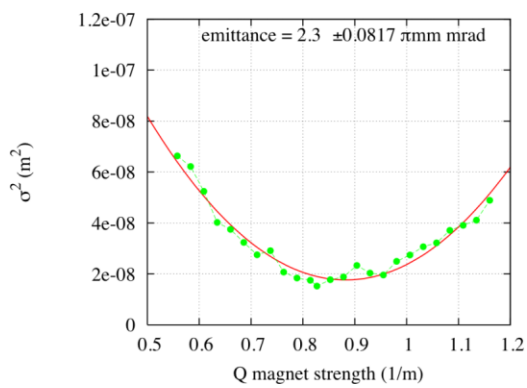

Figure 10: Measured beam emittance for 20-ps laser pulse at the beam charge of 1.0 nC/pulse.

DISCUSSION

Long laser pulse of 20 ps generated with a pulse stacker was tested, and low emittance beam of 2.3 πmmmrad was generated successfully without optimization of laser transverse profile with DM. No large difference was found between 10 ps and 20 ps in the low charge region. It is very important that the beam current for 10 ps could not reach 0.7 nC if the laser beam size was small even if the laser pulse energy was increased high. This effect may limit the initial emittance of the beam in high charge region. Long laser pulse of 20 ps is thought to have an advantage in generating high charge with small initial beam size.

Of course, the pulse charge of 1nC could be generated if the laser spot size was large enough. However, the measured beam emittance for 20-ps laser pulse was smaller than the minimum beam emittance 3.0 πmmmrad for 10-ps laser pulse at 1.0 nC/pulse measured under different conditions of micro pulse length at 1 ps and laser profile modified with DM to a flat circle of ø1.0 mm [8].

The possibility of 20-ps laser pulse to get low emittance has been confirmed by these results. Next, the splitter cube of the third stage in pulse stacker will be exchanged to that bonded with optical contact. Then micro laser pulses should be tuned to get flat longitudinal distribution of electron beam. Further experiments to pursue smaller beam emittance will be planed with simultaneous transverse and longitudinal laser profile optimization.

REFERENCES

[1] "Linac Coherent Light Source (LCLS) Conceptual Design Report", SLAC-R-593, April 2002.

[2] "TESLA Technical Design Report, PART V, The X-Ray Free Electron Laser", ed. G. Materlik and Th.Tschentscher, March 2001.

[3] "SCSS X-FEL Conceptual Design Report, RIKEN, May 2005.

[4] H. Tomizawa et. al., "Reduction of electron-beam emittance with shaping both spatial and temporal profiles of UV laser light source for photo-cathode RF gun", Proceedings of EPAC 2002, Paris, June 2002, pp. 1819-1821.

[5] H. Tomizawa et. al., "Status of SPring-8 photocathode RF gun for future light sources", Proceedings FEL2005, Stanford, August 2005, pp138-141.

[6] J. Yang et. al., "Low-emittance electron-beam generation with laser pulse shaping in photocathode radio-frequency gun", J. Appl. Phys. Vol 92, pp. 1608-1612.

[7] H. Dewa et. al., "Photocathode RF gun designed a single cell cavity", Proceedings of EPAC 2004, Lucern, July 2004, pp. 411-413.

[8] H. Tomizawa et. al., "Automatic minimization of electron beam emittance with three-dimensionally shaping laser pulse for a light source of rf gun", Proc. of the 2nd Annual Meeting of Particle Accelerator Society of Japan, Sendai, Japan, 2-4 August 2006, (2006) pp. 16, (in Japanese).

DESIGN STUDY ON HIGH- TC SUPERCONDUCTING MICRO-UNDULATOR

T. Kii, H. Zen, N. Okawachi, M. Nakano, K. Masuda, H. Ohgaki, K. Yoshikawa, T. Yamazaki.
Institute of Advanced Energy, Kyoto University, Uji, Japan.

Abstract

Design study on a new type of high critical temperature (T_C) superconducting micro-undulator was carried out. In this work, we introduce staggered array type micro-undulator using high T_C superconducting material. Transverse magnetic field was measured with $YBa_2Cu_3O_7$ bulk superconductors at 77 K. The maximum transverse magnetic field strength was about 0.5 mT, when longitudinal magnetic field of the strength in the range of 2 mT to 15 mT was applied.

INTRODUCTION

A micro-undulator or short period undulator will be a useful device for a compact FEL device and/or a short wavelength FEL.

When a high energy electron beam moves in the periodic magnetic field, resonant wavelength emitted from the undulator λ_R is written by following well-known equations.

$$\lambda_R \cong \frac{\lambda_u}{2\gamma^2}\left(1+\frac{K^2}{2}\right) \qquad (1)$$

$$K = \frac{e \cdot B_0 \cdot \lambda_u}{2\pi \cdot m_0 c} \approx 93.36 B_0 \cdot \lambda_u \qquad (2)$$

Here, λ_u is the undulator period and γ is Lorentz factor, K is the undulator parameter, e is the charge of the electron, B_0 is the maximum transverse magnetic field strength of the undulator, m_0 is the electron mass and c is the speed of light. To obtain shorter wavelength radiation, undulator period should be short or electron energy should be high. Thus, if the λ_u is limited, high energy electron beam is required for short wavelength FEL such as X-FEL. In other word, if a short period undulator realizes, high energy electron is not required. Moreover since the FEL gain increases as the number of period of undulator increases, the short period undulator will have advantage.

However, if we need K=1 for short period undulator of 5 mm, B_0 should be almost 2 T. Thus, to realize micro undulator or short period undulator, strong transverse magnetic field is required.

#kii@iae.kyoto-u.ac.jp

HIGH TC SUPERCONDUCTING UNDULATOR

Design of high T_C superconducting undulator

To obtain transverse periodic magnetic field in a short period, we introduce following micro-undulator as shown in Fig. 1.

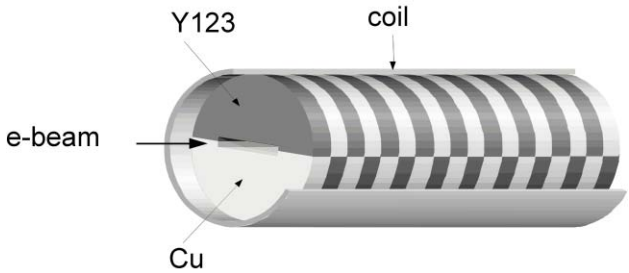

Fig. 1. Conceptual drawing of the high T_C SC undulator.

High Tc bulk superconducting materials are stacked in the solenoid. First, these superconducting pieces are cooled down below the critical temperature T_C. Then, a solenoid field is applied. As a result, density modulation of the magnetic field is produced, and thus the periodic transverse magnetic field is generated on the electron beam axis. To realize shorter period, in vacuum structure is planned. If we can control the magnetic field precisely, extreme good electron beam confinement can be realized [1].

If a perfect Meissner state is kept in a high magnetic field strength of several T, excellent performance will be realized. Unfortunately, Meissner region is typically limited below the lower critical field of several hundred mT, but superconductivity is left up to the higher critical field of 100 T. Thus we tried to measure the transverse magnetic field above lower critical field.

Expected performance

We have estimated performance of the undulator for following applications.

1) Compact IR device
2) Ultra short wavelength FEL
3) THz device

If such short period undulator with high transverse magnetic field is applied for 1) compact IR FEL device, required electron energy will be less than 15 MeV as shown in Fig. 2. Therefore a very compact IR system can be designed.

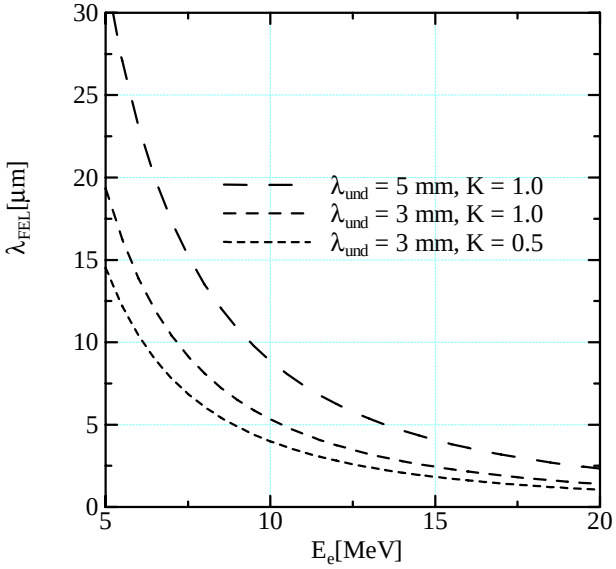

Fig. 2. Expected wavelength for short period undulator with several tenth MeV electron beam.

For application to 2) ultra short wavelength FEL, the device is also fascinating as shown in Fig. 3. The FEL wavelength of 1 Å will be achieved with 3 GeV electron beam. It is expected that the whole system could be compact, because the length of the undulator and the accelerator will be shortened compared to present configurations of such X-FEL systems.

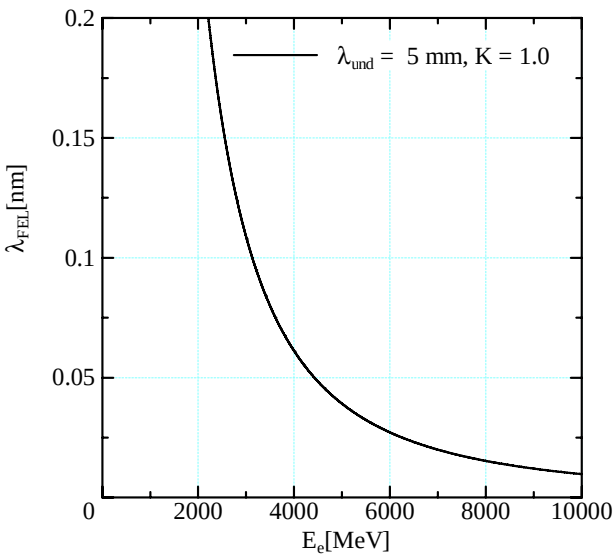

Fig.3. Expected wavelength for GeV class electron beam.

A simple configuration consisted of an electron injector and the proposed micro-undulator will provide 3) the THz radiation as shown in Fig. 4. This system could generate an intense THz radiation with a variety of operation mode, in CW, because we can use a CW electron injector.

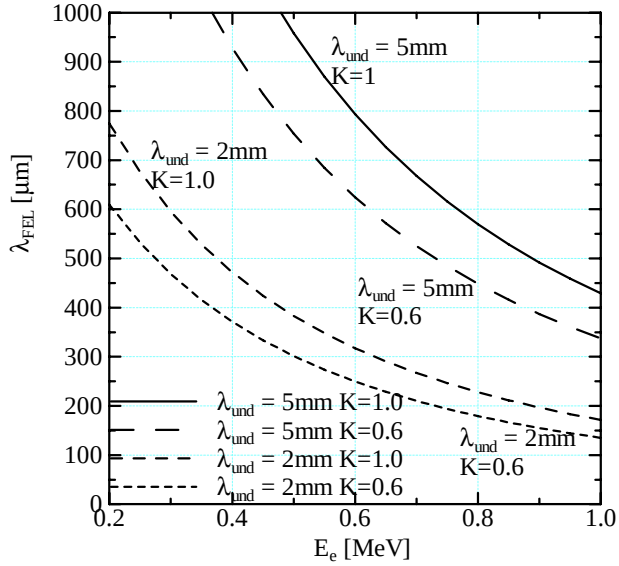

Fig. 4. Expected wavelength for THz device.

EXPERIMENT

To confirm the proposed micro-undulator, a preliminary experiment has been performed. In this work, $YBa_2Cu_3O_7$ (YBCO) ceramic was selected as the high T_C superconducting materials, because it is easy to obtain, and Tc is higher than the boiling point of liquid nitrogen. Presintered YBCO powder made by Furuuchi Chemical Corporation was used for sample fabrication. Test peaces were made as following. The powder was pressed into disks and sintered in an oxygen-containing atmosphere for 12 hours at a temperature of 900° C, and annealed for 48 hours at a temperature of 500° C. Diameter of the test pieces was 27 mm and thickness was 2.5 mm. Superconductivity of the test pieces were checked by the Meisner effect and pinning effect using small permanent magnet on the cooled test material. Schematic drawing of the superconducting test piece is shown in Fig. 6.

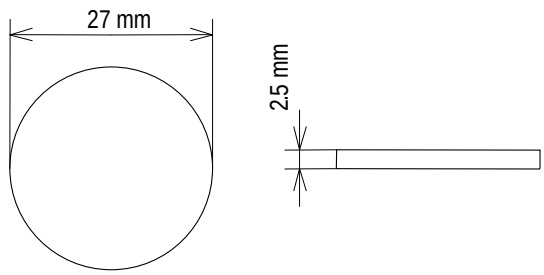

Fig. 5 Schematic drawing of the YBCO test piece.

Transverse magnetic field produced by the cooled ceramics was measured with a dipole magnet and a 3-Channel Gaussmeter Model 460, manufactured by Lake Shore Cryotronics, inc. Experimental setup is shown in Fig. 6.

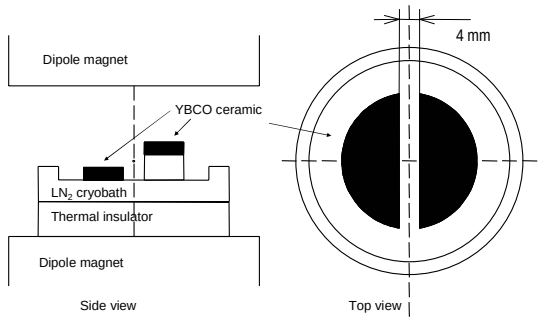

Fig. 6 Experimental setup.

Test piece was cut into two 'D shapes' for the transverse magnetic field measurement. The test pieces were cooled down to 77 K in a LN_2 cryobath. After cooled down below the critical temperature, they were moved into the gap of the dipole magnet. Longitudinal magnetic field of the strength in the range of 2 mT to 15 mT was applied. The magnetic field strength was measured using a Hall probe. The measured strength was about 0.5 mT, and did not depend on the amplitude of the longitudinal magnetic field.

DISCUSSION

Transverse magnetic field was successfully generated with YBCO test pieces, but the magnitude was very small. Let us discuss on the small transverse magnetic field strength. Although the upper critical field strength for the YBCO is high, the lower critical field is about 1 mT. Thus, the magnetic vortex lines penetrate into the superconductors. As a result the enough transverse magnetic field was not produced.

To overcome this problem, strong pinning center should be introduced. Then the penetration of the vortex lines would be suppressed. Doping of Praseodymd[2] is planned to introduce pinning center and increase critical current density.

Although, zero-field cooling is introduced in this work, filed cooling is also considerable to produce transverse magnetic field. If the each superconducting pieces with strong pinning center are cooled in the strong solenoid field, each pieces work as strong permanent magnet of several T after the solenoid field is turned off. Such strong permanent magnet would increase the performance of hybrid staggered undulator [3]. Although the peak field depends on the trapped magnetic field by the superconducting pieces, recently typical trapped field is greater than 2T [4], thus the peak field of greater than 1T is expected.

ACKNOWLEDGEMENT

This work was supported by the Grant-in-Aid for Young Scientists (A) by the Ministry of Education, Culture, Sports, Science and Technology of Japan.

REFERENCES

[1] J. Kitagaki, et al, "A design study on electron beam confinement in a staggered array undulator based on a 3D code", Nucl. Instr. Meth. A475 (2001) 613-616.

[2] T. Harada; K. Yoshida, "The effects of Pr-doping on the critical current density in $YBa_2Cu_3O_{7-\delta}$", Physica C: Superconductivity and Its Applications 383 (2002) 48-54.

[3] S. Sasaki, "The possibility for a short-period hybrid staggered undulator", Proceedings of 2005 Particle Accelerator Conference, Knoxville, Tennessee (2005) 982-984.

[4] M. Morita, et al, "Development of Oxide Superconductors - High T_c Bulk Superconductor, QMG, and Its Magnetic Applications -", Nippon Steel Technical Report No. 93 January 2006 (2006) 18-23.

DESIGN STUDY OF RF TRIODE STRUCTURE FOR THE KU-FEL THERMIONIC RF GUN

K. Masuda[#], K. Kusukame, T. Shiiyama, H. Zen, T. Kii, H. Ohgaki, K. Yoshikawa, T. Yamazaki,
Institute of Advanced Energy, Kyoto Univ., Gokasho, Uji, Kyoto 611-0011, Japan

Abstract

A coaxial rf cavity with a thermionic cathode on its inner rod has been designed to be adopted in a 4.5-cell rf gun in order to minimize the inherent back-bombardment of electrons onto the cathode. Dependences of the back-bombardment power and the output beam properties on the axial mounting position of the coaxial cavity have been studied using a 2-dimensional simulation code. With an optimal mounting position and phase of ~90 kW rf input fed into the coaxial cavity have shown significant reduction of back-bombardment power of over 80 %. It has also shown a lower longitudinal emittance and a higher peak current of the output beam than the conventional rf gun, while the transverse emittance degradation is reasonably acceptable.

INTRODUCTION

Thermionic rf guns have advantages against photocathode ones, such as low cost, high micropulse repetition rate (high averaged current), and easy operation, which make them well suited for FELs. They however suffer from back-bombardment of electrons onto the thermionic cathode which eventually leads to an output beam energy drop and limits the macropulse duration [1-3]. The back-bombardment effect is seen significant in the 4.5-cell rf gun (Fig. 1 and Table 1) for the KU-FEL linac because of its original design, i.e. a high coupling coefficient, large number of cells, small aperture between the cells. Some countermeasures are applied, such as the use of transverse magnetic fields [4,5] and the temporal control of the rf input for compensating time-varying beam-loading [6-8] with limited successes. The macropulse duration achieved so far is 4 μsec at most for a limited beam output of ~80 mA [8], while a longer duration and a higher current would be desired for the FEL operation.

Numerical studies so far have suggested that the rf triode structure could potentially reduce the back-bombardment power drastically (~80 - 99%) [9,10].

Especially the use of a metal grid for the rf cutoff has shown numerically over 99% reductions of the back-bombardment power without degradation in the output beam properties, by simulations on neglect of the beam scattering by the grid [10,11]. In this work, we investigated an rf triode without a grid for comparison, since the use of a grid is practically undesirable unless it is necessary in terms of the back-bombardment reduction and/or the output beam characteristics.

Also, though the beam properties at the 1.6-cell [9] and the half-cell [10] exits have shown reasonably acceptable degradations or rather enhancements, the beam extraction phase from the rf triode should be considered in adopting it to the 4.5-cell gun, because an off-crest beam injection to the successive cells would lead to a degradation in the output beam transverse emittance due to an increased rf contribution to the emittance growth. In this work, we investigated both the input rf phase and axial mounting position of the coaxial cavity with respect to the main accelerating cells.

[#]masuda@iae.kyoto-u.ac.jp

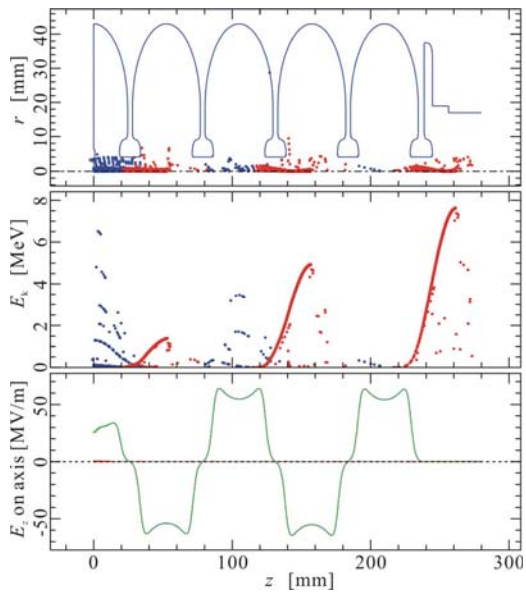

Figure 1: A simulation snapshot showing electrons' radial positions and energies along the longitudinal position, and the on-axis cavity field. The blue dots indicate back-streaming electrons. A 2mm ϕ thermionic cathode with a 30 A/cm^2 current density is located at z = 0, and the cavity voltage is 10 MV to yield 7.6 MeV output.

Table 1: Beam properties by the simulation on neglect of the back-bombardment effect. Only the electrons within an output beam energy spread of $\Delta E_k/E_{k,max}$ = 3 % are taken into account.

at the gun exit	
charge, ΔQ	29.00 pC
peak current, I_{peak}	10.00 A
normalized rms emittance, $\varepsilon_{r,n}$	1.20 π mm mrad
longitudinal rms emittance, ε_z	37.00 psec keV
at the 1st cell exit	
energy spread, $\Delta E_{k1}/E_{k1,max}$	6.60 %
charge, ΔQ_1	29.00 pC
peak current, $I_{1,peak}$	10.40 A
normalized rms emittance, $\varepsilon_{r1,n}$	0.53 π mm mrad
longitudinal rms emittance, ε_{z1}	1.80 psec keV

COAXIAL CAVITY DESIGN

Figure 2 shows the coaxial cavity geometry to be installed in the rf gun instead of the conventional cathode, and the fundamental (2856 MHz) eigenmode pattern by a 2-dimensinal eigenmode solver [12]. The outer radius is limited up to ~15 mm due to the cathode mount geometry in the rf gun. We set it as the maximum, 15 mm to minimize the coupling coefficient, β, between the coaxial cavity and the backside coaxial waveguide from which an rf power is to be fed. The rf cutoff is ensured by a drift tube of 4 mm in diameter and 5 mm in length between the coaxial cavity and the successive half cell.

Figure 3 shows particles' snapshots by a 2-dimensional particle-in-cell simulation code [13] for three different coaxial inner rod geometries on which the same thermionic cathode (2 mmϕ, 30 A/cm^2) as is used in the conventional diode rf gun shown in Fig. 1. The code can reproduce the required rf input, P_{in}, for a given rf voltage, V_0, taking into account the beam-loading effect [3,13].

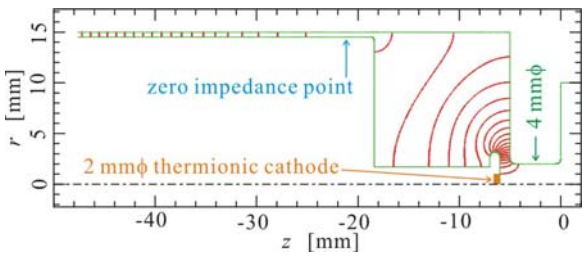

Figure 2: An eigenmode pattern in a coaxial cavity with a thermionic cathode on its inner rod, to replace the cathode in the conventional diode rf gun.

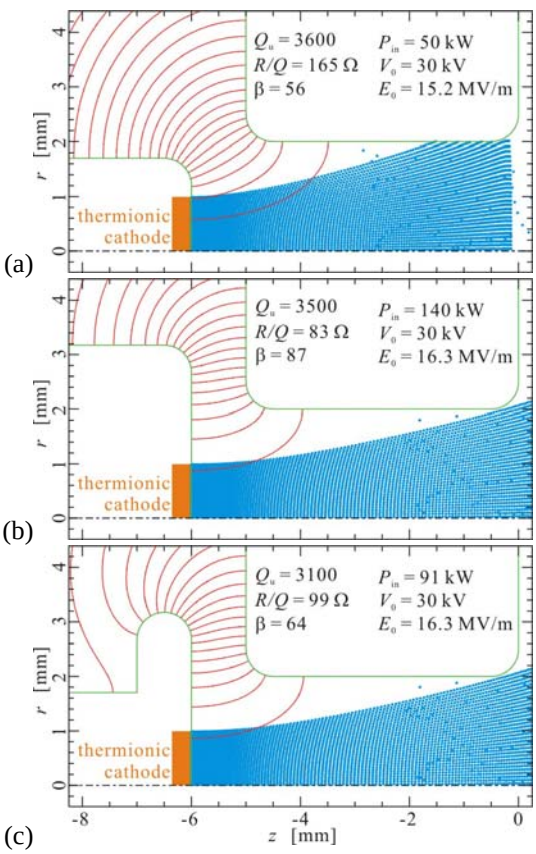

Figure 3: Eigenmode patterns and particle snapshots in the coaxial cavity, comparing three different geometrical designs of the coaxial inner rod. Peak electric field strengths on the cathode (E_0), and required rf input (P_{in}) are shown for a fixed peak cavity voltage, V_0 = 30 kV.

In the design (a), the beam tends to hit the drift tube due to radial forces by both the rf and the space charge. The geometry (b) shows a good beam transport because of a reduced radial rf field, while at the same time the larger inner rod diameter increases β, leading to a higher P_{in} requirement for a fixed V_0. Finally, the design refinement in (c) meets both the requirements, showing a good beam transport and an acceptably high field with a moderate P_{in} below 100 kW, the maximum available power in our experiments scheduled in the near futere.

BACKBOMBARDMENT AND BEAM PROPETIES BY THE TRIODE RF GUN

In the simulations in the triode rf gun, we varied the axial mounting position, z_0, of the coaxial cavity with respect to the main accelerating cells in the 4.5-cell rf gun (see Fig. 4), as well as the rf voltage, V_0, and phase, $\Delta\phi_{01}$, in the coaxial cavity. The cavity voltage in the main accelerating 4.5 cells is fixed as 10 MV throughout.

As seen in Fig. 4, the 1st half cell geometry is slightly changed as the z_0 varies, so that its resonant frequency, quality factor and shunt impedance remain unchanged.

The back-bombardment effect is neglected, i.e. the cavity voltages and the cathode current density are kept constant until periodically steady-state solutions.

Back-Bombardment Power and Beam Properties at the First Cell Exit

Figure 5 and 6 show back-bombardment power onto the 2 mmϕ cathode, P_{back}, bunch charge, ΔQ_1, and transverse normalized rms emittance $\varepsilon_{r1,n}$ at the 1st half cell exit. For comparisons, they are normalized by those in the conventional diode rf gun listed in Table 1. Electrons

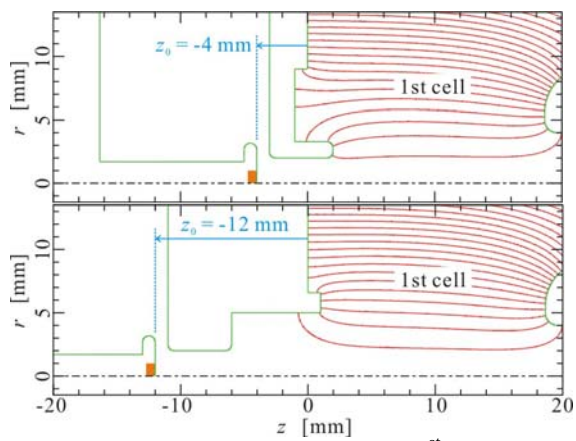

Figure 4: Eigenmode patterns of the 1st cell for two different mounting positions (z_0) of the coaxial cavity. In the conventional diode rf gun (see Fig. 1 and Table 1) the cathode is located at z = 0.

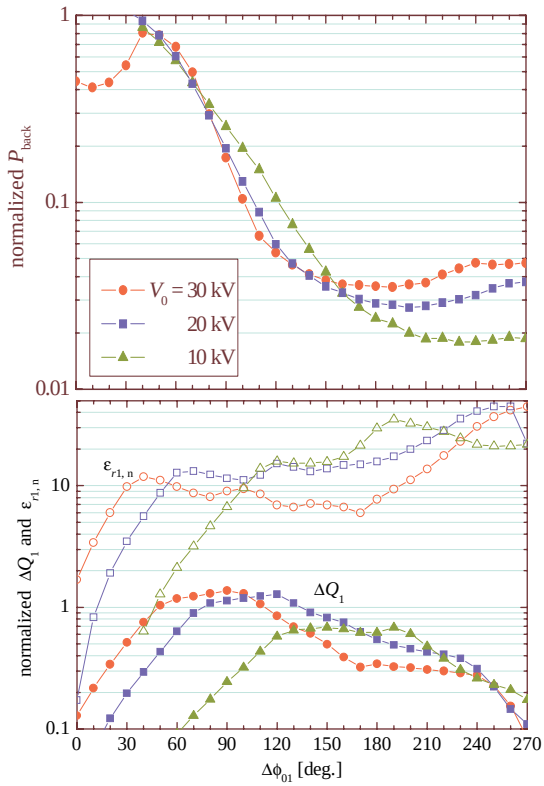

Figure 5: Back-bombardment power (P_{back}), bunch charge and transverse normalized rms emittance at the 1st cell exit (ΔQ_1 and $\varepsilon_{r1,n}$) divided by those in the conventional diode rf gun (see Table 1), as functions of $\Delta\phi_{01}$ and V_0 for z_0 = -4 mm.

within an energy spread of $\Delta E_{k1}/E_{k1,max}$ = 6.6 % are taken in account in the ΔQ_1 and $\varepsilon_{r1,n}$, since they are found contribute to an acceptable output beam energy spread of $\Delta E_k/E_{k,max}$ = 3 % for the case of the conventional diode rf gun shown in Fig. 1 and Table 1.

As seen in Fig. 5, a lower V_0 results in a lower ΔQ_1 and larger $\varepsilon_{r1,n}$ without significant reduction of P_{back}. Thus V_0 is fixed as the maximum, 30 kV hereafter.

In comparison with the use of a metal grid instead for the rf cutoff [10], the existence of zero-field region in between the cathode and the 1st half cell is found result in higher P_{back}, while the reduction of P_{back} by the present rf triode is still significant.

In Fig. 6, regardless of the phase control by z_0, $\phi_{1,head}$ is found far ahead of the crest for $\Delta\phi_{01}$'s where the P_{back} reduction is over 90 % (called operational mode (I) hereafter).

At a lower $\Delta\phi_{01}$, however, a local minimum of P_{back} is found, which is seen to reach 80 % reduction for z_0 = –6, –8 and –10, and is also seen to shift in terms of $\Delta\phi_{01}$ as z_0 decreases. Thus P_{back} at $\phi_{1,head}$ = 1 π rad (crest) decreases with decreasing z_0 as shown in Fig. 7. This operational mode (II) is not seen in the grid-based rf triode [10], which corresponds virtually to z_0 = ~ –1 mm.

Note that, in the conventional rf gun, $\phi_{1,head}$ is 0.94 π rad, slightly ahead of the crest as shown in Fig. 6, because the rf voltage and corresponding output energy of 7.6 MeV is higher than the nominal value of 5 MeV. Nevertheless we usually operate the gun at a higher energy, since it results in a lower beam emittance.

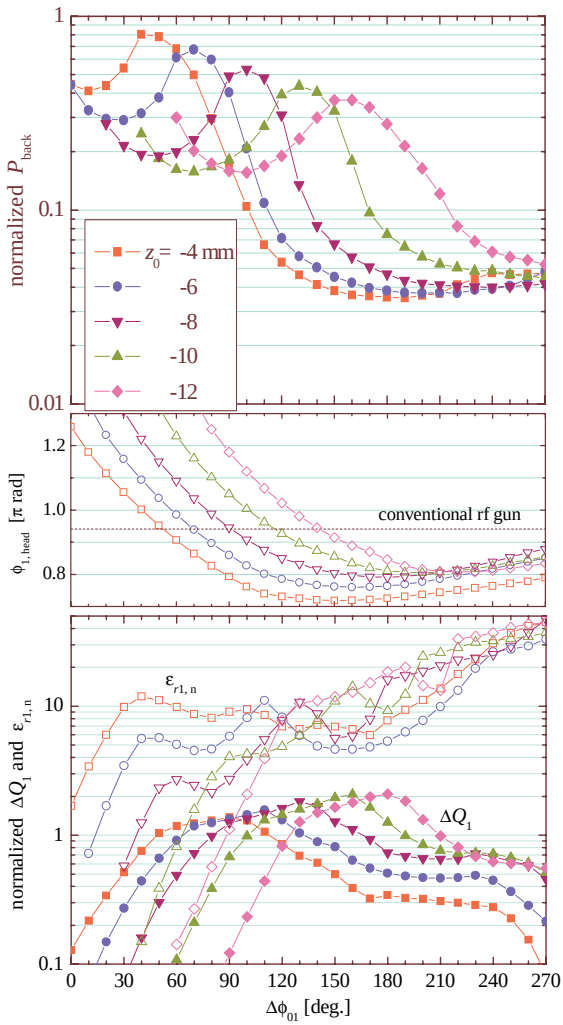

Figure 6: P_{back}, ΔQ_1 and $\varepsilon_{r1,n}$ divided by those in the conventional diode rf gun, and bunch head phase through the 1st cell exit ($\phi_{1,head}$), as functions of $\Delta\phi_{01}$ and z_0 for V_0 = 30 kV.

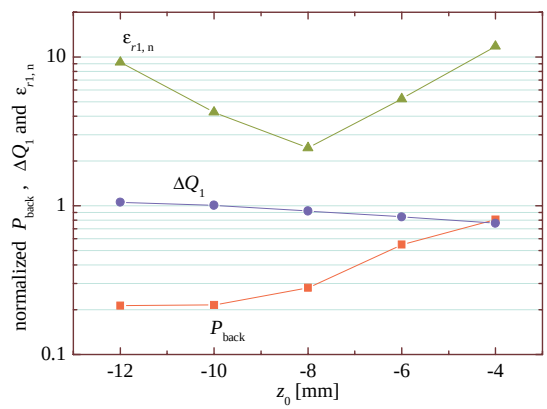

Figure 7: P_{back}, ΔQ_1 and $\varepsilon_{r1,n}$ divided by those in the conventional diode rf gun for $\Delta\phi_{01}$ where $\phi_{1,head}$ = 1 π rad, as functions of z_0 for V_0 = 30 kV.

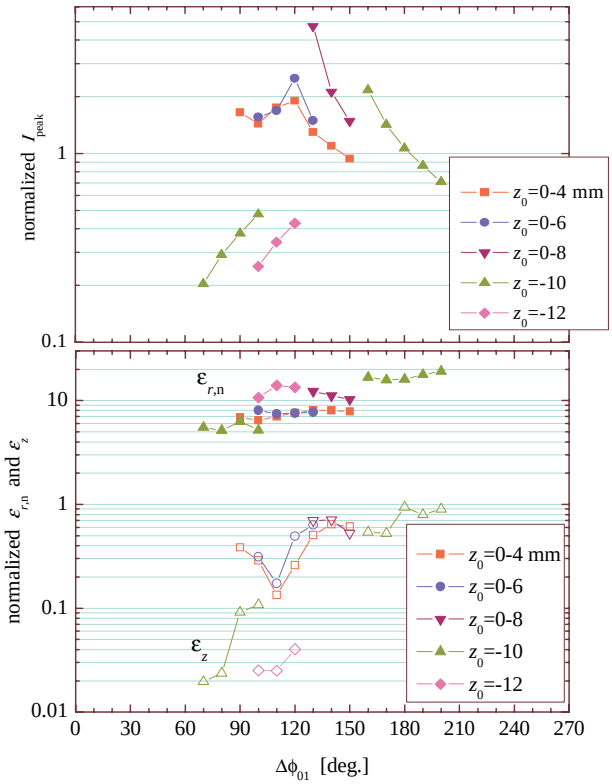

Figure 8: Dependences of the output beam properties on $\Delta\phi_{01}$ and z_0.

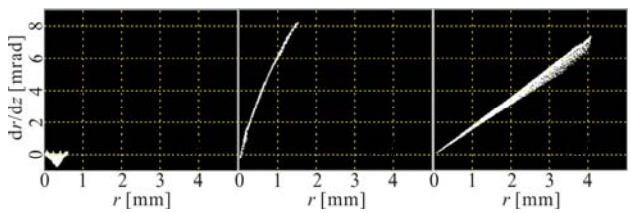

Figure 9: Transverse phase space distributions of the output beams by (a) the conventional diode gun, the triode gun with (b) z_0 = –10 mm, $\Delta\phi_{01}$ = 100 deg. (mode (II)), and (c) z_0 = –6 mm, $\Delta\phi_{01}$ = 120 deg (mode(I)).

Table 2: Comparisons of back-bombardment powers and output beams' properties between the conventional diode and the triode rf guns.

	P_{back} [kW]	I_{peak} [A]	$\varepsilon_{r,n}$ [π mm mrad]	ε_z [psec keV]
conventional diode rf gun	21.0	10.0	1.2	37.0
z_0 = –10 mm, $\Delta\phi_{01}$ = 100 deg.	04.3	04.9	6.3	04.0
z_0 = 0–6 mm, $\Delta\phi_{01}$ = 120 deg.	01.6	26.0	9.1	18.0

Output Beam Properties

Figure 8 shows output beam properties for $\Delta\phi_{01}$'s and z_0's where the reduction of P_{back} is found over 80 % in Fig. 6, in both modes (I) and (II). Figure 9 and Table 2 show the output beams at optimal $\Delta\phi_{01}$'s and z_0's in terms of $I_{peak}/e_{r,n}^2$ for the modes (I) and (II), together with the output by the conventional diode rf gun.

The off-crest beam injection in the mode (I) is found to result in larger emittances than the mode (II) in exchange of higher peak currents. It should be noted that the mode (I) greatly reduces the rf contribution to the transverse emittance growth, i.e. the beam is obviously seen narrow in the phase space in Fig. 9(b), because of the optimal beam injection phase into the 2nd full cell. In comparison with the conventional rf gun, though the rf contribution is seen much reduced in the mode (II), transverse emittance is rather degraded by the radial rf field nonlinear to the radial position, i.e. the phase space distribution is seen bent much in Fig. 9(b). In the longitudinal emittance, improvements are seen in both modes (I) and (II).

CONCLUSIONS

The present rf triode structure has shown significant reductions of the back-bombardment power, and reduced longitudinal emittances and enhanced peak currents of the output beam. The optimal axial position of the coaxial cavity with respect to the main cells has shown a greatly reduced rf contribution to the transverse emittance growth by controlling the beam longitudinally with respect to the rf. Transversely, however, the present design yields a larger beam radius, eventually leading to a transverse emittance growth due to the contribution by the nonlinear radial rf fields. Though the transverse emittance degradation is reasonably acceptable, the wehnelt configuration and/or optimal control of the rf voltages should be considered in order to induce radial beam focusing to minimize the output transverse emittance.

REFERENCES

[1] C.B. McKee, et al., Nuclear Instruments and Methods in Physics Research A **304** (1991) 386.
[2] T. Kii, et al., Nuclear Instruments and Methods in Physics Research A **475** (2001) 588.
[3] K.Masuda, et al., Nuclear Instruments and Methods in Physics Research A **483** (2002) 315.
[4] T. Kii, et al., Proc. 9th Intnl. Conf. Synchrotron Radiation Instrumentation, May 2006, in press.
[5] C.B. McKee, et al., Nuclear Instruments and Methods in Physics Research A **296** (1990) 716.
[6] T. Kii, et al., Nuclear Instruments and Methods in Physics Research A **507** (2003) 340.
[7] F. Li, et al., Nuclear Instruments and Methods in Physics Research A **407** (1998) 332.
[8] T. Kii, et al., Proc. FEL2005 (2006) 584.
[9] K. Kanno, et al., Japanese Journal of Applied Physics **41**-1 (2002) 62.
[10] K. Masuda, et al., Proc. FEL2005 (2006) 588.
[11] K. Kusukame, master thesis Kyoto Univ., 2006 (in Japanese).
[12] K. Masuda, et al., IEEE Transaction on Microwave Theory and Techniques **46**-8 (1998) 1180.
[13] K.Masuda, Ph,D. thesis Kyoto Univ, 1997.

MAGNETIC FIELD MEASUREMENT OF UNDULATOR IN KU-FEL

M. Nakano, N. Okawachi, H. Zen, T. Kii, K. Masuda, H. Ohgaki#, K. Yoshikawa, T. Yamazaki
Institute of Advanced Energy, Kyoto University, Gokasyo, Uji, 611-011, Japan.

Abstract

An FEL system (KU-FEL) covering wavelengths from 4 to 13 μm is under construction at Institute of Advanced Energy, Kyoto University. The magnetic field of the undulator in KU-FEL has been measured. Measured magnetic field showed demagnetization in the downstream part of the undulator. By using the measured data, we have estimated the optimal parameters of both the electron beam and the optical cavity to enhance the FEL gains for the first lasing. In this optimized condition, though FEL gains decreased by a few % but, FEL powers were not much decreased, compared with those for the design field. Saturated FEL in 6-12 μm is expected from the recent studies in the macropulse width of the electron beam from the RF gun.

INTRODUCTION

KU-FEL system for bio/chemical researches in 4-13μm is under construction [1]. Figure 1 shows a schematic view of the system. The system consists of a 4.5 cell thermionic RF gun, a 3-m accelerator tube, a Halbach type undulator and an optical cavity. The RF gun and the accelerator tube have been installed and accelerated an electron beam up to 40 MeV. The undulator and the optical cavity will be installed within this year.

In parallel with the construction, in order to estimate the high FEL gains for the first lasing, we have optimized parameters of electron beam and optical cavity based on original design parameters of our undulator (shown in Table 1) [2]. However, demagnetization was anticipated since the undulator had been used for lasing experiments under the cooperation of FELI and University of Tokyo [3]. Then, we measured the magnetic field of the undulator. By using the date, we have optimized parameters of electron beams and the optical cavity and calculated realistic FEL gains and powers.

MEASUREMENT OF MAGNETIC FIELD

The magnetic field of the undulator was measured in vertical and horizontal direction, using a Hall probe manufactured by F. W. BELL. The probe was driven by moving stage that run on a stepping motor (Fig. 2) and was moved on the central axis of the undulator by 1 mm step. Specification of the measurement device is shown in Table 2. Figure 3 shows the measured magnetic field of the undulator. The undulator error (shown in Fig. 4) is

#ohgaki@iae.kyoto-u.ac.jp

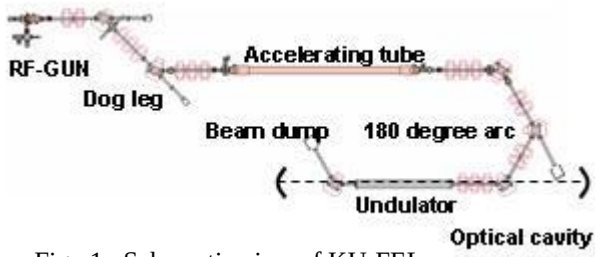

Fig. 1 . Schematic view of KU-FEL.

Table 1: Parameters of the original designed undulator of KU-FEL

Length	1.6 m
Period	40 mm
Number of period	40
Gap	26 - 45 mm
Maximum magnetic field	0.25 - 0.045 T
K-value	0.95 - 0.17

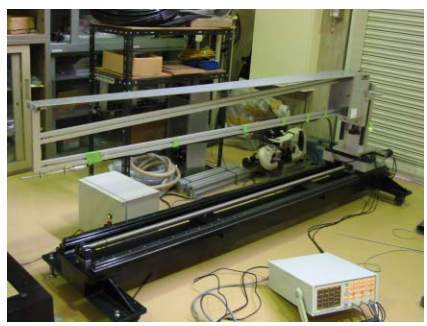

Fig. 2: Measurement device for magnetic field.

Table 2: Specification of measurement device

Moving stage	
Motor	Stepping motor
Resolution	0.01 mm
Operation range	2 m
Gauss meter	
Resolution	0.10%
Stability of temperature	0.040 %/K

defined by following : $Error = 1- B_{p,exp}/B_{p,ideal}$, where $B_{p,exp}$ is the peak magnetic induction from fitting the measured date to sinusoidal function and $B_{p,ideal}$ is the peak value of the design magnetic field. Thus, the error is positive when there is demagnetization. The initial and end peak of the measured magnetic field of the undulator

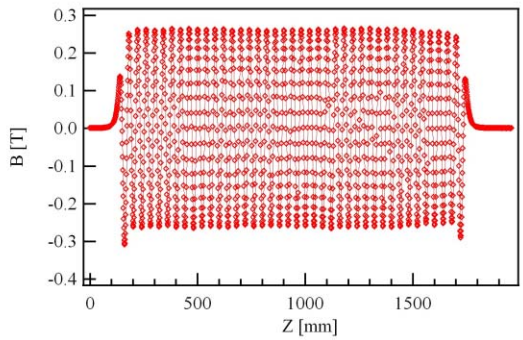

Fig. 3: Measured magnetic field of the along the central undulator axis.

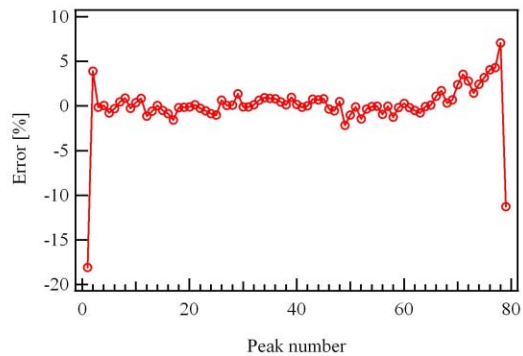

Fig. 4: Undulator error as a function of peak number.

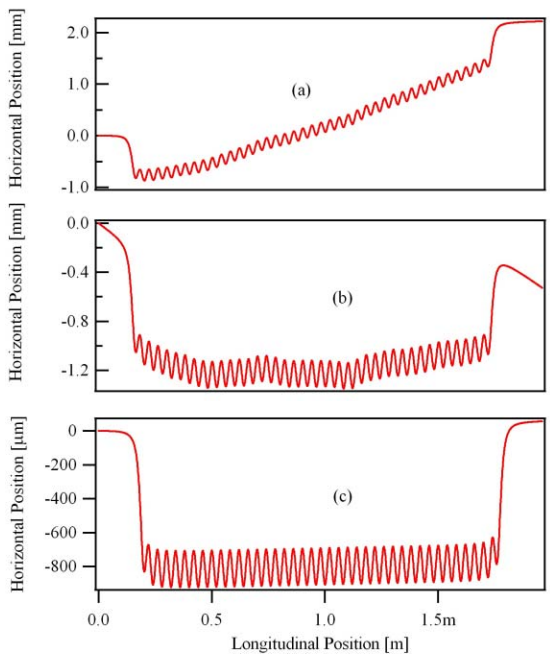

Fig. 5: (a) and (b) is horizontal trajectories calculated from the measurement without and with deflection at the entrance of the undulator, respectively. (c) is a horizontal trajectory calculated from the design.

is not considered as peak number: the number of peak field is 79. Figure 3 and Fig. 4 clearly show a demagnetization in the downstream part, peak number 70-78 in Fig.4. The gap is narrower (25.5 mm) than the original design, because we have modified the undulator in order to make the gap variable. Thus, the maximum value of peak magnetic field and K-value are 0.26 T and 0.99, respectively.

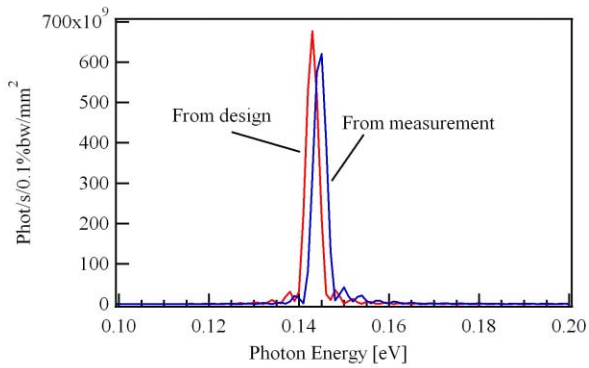

Fig. 6: Calculated spectrum of spontaneous radiation.

BEAM TRAJECTORY AND SPONTANEOUS RADIATION

Evaluation of beam trajectory and spontaneous radiation is an effective method to verify the measurement of the magnetic field. At first, We calculated electron beam trajectories at 30 MeV with the measured magnetic field and the designed field by using SRW [4]. Vertical displacement of the electron beam in the undulator shown in Fig. 5 (a) is 2 mm so that overlap between electron beam and laser is too poor. In order to compensate this, we are going to set a steering magnet before the undulator. The beam trajectory thus deflected at an angle of 1.4 mrad is shown Fig. 5 (b). Figure 5 (c) shows a beam trajectory calculated from the designed field. Fig 6 shows calculated spectra of spontaneous radiations. The radiation intensity calculated from the measured magnetic field is reduced by 9 %, and the spectrum is shifted to longer wavelength and shows asymmetric distribution, compared with that from the design field.

FEL GAIN CALCULATION

We previously reported on FEL gains based on designed magnetic field of undulator (Table 1) [2]. On the other hand, by using the measured magnetic field instead of the designed one, FEL gains have been recalculated to estimate realistic gains, which will be compared in the following.

The axial symmetric 3D code TDA3D [5] was used to calculate FEL gain and saturation. In addition, the undulator period was forced to be 39. This is because the number of peak magnetic field for TDA3D is defined as double of the undulator period while the undulator period in KU-FEL is 39.5.

At the 180-degree arc between the accelerator tube and the undulator shown Fig. 1, we can control the electron beam parameters for the optimization. Among the

Table 3: Fixed parameters of electron beam

Peak current	40 A
Normalized emmitance in x	11 πmm-mrad
Normalized emmitance in y	10 πmm-mrad
Energy spread	0.50%

Table 4: The optimized beam parameters

Beam energy (MeV)	25	30	35
Beam size in x (mm)	0.65	0.60	0.55
Beam size in y (mm)	0.33	0.36	0.36
Twiss parameter α_x	1.9	2.0	1.9
Twiss parameter α_y	0	0	0

Table 5: Optimized optical parameters

Beam energy (MeV)	25	30	35
Rayleigh range	0.40 m		
Beam waist position	0.60 m		
Wavelength (mm)	12.3	8.6	6.3
Out coupling (%)	4.0	2.5	0.8
Diffraction loss (%)	5.6	6.0	7.0
Total loss (%)	9.6	8.5	7.8

electron beam parameters, a peak current, a transverse emittance, and an energy spread, which are evaluated by PARMELA [6], are fixed (Table 3) during the calculation. The other electron beam parameters, electron beam sizes and Twiss parameters, are optimized to obtain the maximum FEL gains in three electron beam energies, 25, 30, 35 MeV. Electron beam sizes are RMS values. Twiss parameter α_y is set to zero due to the natural focusing of the undulator field. Table 4 shows the beam parameters optimized to the measured magnetic field of the undulator.

Optimization of the parameters of the optical cavity is also essential to enhance the FEL gains. We also optimized the optical parameters, Rayleigh range and beam waist position, for three electron beam energies. Table 5 shows the optimized optical parameters. The optical cavity of the KU-FEL system has been designed taking into account the diffraction loss and the out coupling. The laser field is assumed to be the Gaussian in the calculation optical loss. The out coupling hole is 1 mmϕ located at the upstream mirror. As the result, the curvature of upstream mirror is calculated to be 2.58 m and that of downstream mirror is 1.92 m. Table 5 also shows the diffraction loss and out coupling of the designed optical cavity. From the setup condition of the optical cavity, shown in Fig. 7, the beam waist position is not at the center of the undulator but is shifted to upstream in order to reduce the diffraction loss at upstream chamber (30 mmϕ). FEL gains with optimization of both of electron beam and of optical cavity are shown in Table 6. The realistic FEL gains are lower by a few % than those based on the design magnetic field distribution.

By using the above optimized conditions, we have estimated the evolution of the FEL power with the

Table 6: Comparison of the optimized FEL gains of the measurement with those of the design

Beam energy (MeV)	25	30	35
Gain of design undulator (%)	89	65	49
Gain of real undulator (%)	87	64	49

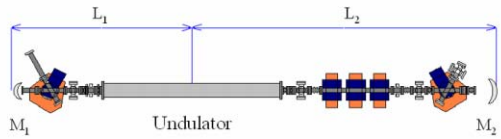

Fig. 7: Undulator and optical cavity in KU-FEL. L_1 is 1.605 m, L_2 is 2.70 m, R_1 (the curvature of M_1) is 1.92 m, and R_2 is 2.58 m.

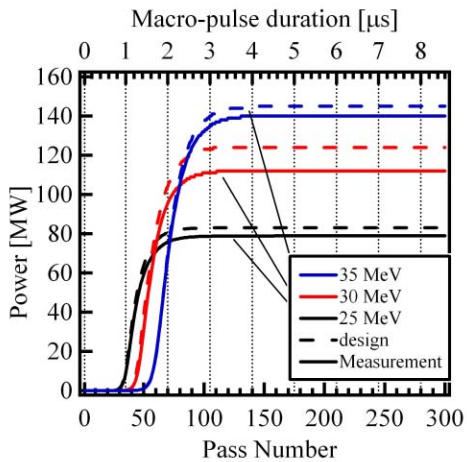

Fig. 8: FEL power as a function of pass number in each beam energy.

TDA3D modified to take into account the successive development of the laser power after round-trip. The optical loss is subtracted from the FEL gain in each pass. Figure 8 shows that FEL power from the measured magnetic field decreases by about 5 %.Then the numbers of round-trips necessary for saturation increase by about round-trips to reach gain saturation by 0.2 μm, compared with those from the design ones.

The injector in KU-FEL is a thermionic RF gun which have a disadvantage of back bombardment, so that macropulse duration has been restricted to 4 μs. However, since we have estimated macropulse duration is up to 8 μs [7], FEL saturation in each energy is expected.

SUMMARY

The measurement of the magnetic field of the KU-FEL undulator has been carried out. The electron beam trajectory in the undulator and the spontaneous radiation have been evaluated with measured magnetic field. The beam displacement is about 2 mm for 30 MeV electron beam. However, it can be reduced to 0.2 mm with a steering magnet placed just before the undulator. By using the measured magnetic field, the beam parameters and the

optical parameters were optimized to obtain the maximum FEL gain. Calculation of FEL gain and FEL gain saturation have been performed. Although FEL gains show a few % decrease and thus the times to reach FEL saturations with the measured magnetic field are slightly longer than these with the design field, FEL saturation is expected in the wavelength region of from 6 to 12 μm.

REFERENCES

[1] T. Yamazaki, et al., Proc. Free Electron Laser Conf. 2001 (2002) II–13.

[2] T. Fukui, et al, Proc. Free Electron Laser 2005 (2006).

[3] E. Nishimura, et al., Nucl. Instrum. Methods, A341(1994) 39.

[4] O. Chubar, et al., Proc. of EPAC98, p.1177, 1998.

[5] J.S. Wurtele T.M. Tran. Computer Physics Comm., Vol.54, p.263, 1989.

[6] L. M. Young, James H. Billen : LA-UR-96-1835 (2002).

[7] N. Ohkawachi, et al., “Production of electron beam with constant energy by controlling input power into a thermionic RF gun”, in these proceedings.

PRODUCTION OF ELECTRON BEAM WITH CONSTANT ENERGY BY CONTROLLING INPUT POWER INTO A THERMIONIC RF GUN

N. Okawachi, M. Nakano, H. Zen, T. Kii#, K. Masuda, H. Ohgaki, K. Yoshikawa, T. Yamazaki,
Institute of Advanced Energy, Kyoto University, Uji, Japan

Abstract

A thermionic RF gun is compact and economical, but it is difficult to produce electron beam of pulse width longer than a few μsec with constant energy owing to inherent back-bombardment effect. In this work we tried to keep beam energy constant in macro pulse duration by feeding modulated RF power. We also tried to perform transient analysis with equivalent circuit taking into account the back-bombardment effect in macro pulse duration in the cases of the W cathode and the LaB_6 cathode. We found that the degradation of the peak energy could be kept below 100 keV in the macro pulse duration of 8.0 μsec and 8.2 μsec, respectively.

INTRODUCTION

It is necessary for the development of an FEL to improve the source of electron beam, and a thermionic RF gun is suitable for a compact and economical FEL system. However a back-bombardment effect degrades the beam energy during the macro pulse. In a previous work, we reported the preliminary result of improvement of a thermionic RF gun [1]. In this work we tried to reduce beam energy degradation due to the back-bombardment effect by feeding modulated RF power into a thermionic RF gun. In addition, we have performed a self-consistent transient analysis which took into account the back-bombardment effect during macro pulse duration by using an equivalent circuit model and a thermal conduction.

EXPERIMENTAL SETUP

Fig.1 shows the experimental setup. The cathode is of 6-mm diameter made of porous tungsten impregnated with barium. RF power fed into the RF gun is controlled by remotely adjusting the reactors in the pulse forming network (PFN) with stepping motors. This experiment was performed varying the beam current drawn from the RF gun and input RF power in both the cases a flat input RF and a modulated RF waveform power.

The profiles of the electron beam current were measured with current transformer (CT) and Faraday cup (FC). The energy spectrum of the electron beam was analyzed with a bending magnet, beam slit and CT.

#kii@iae.kyoto-u.ac.jp

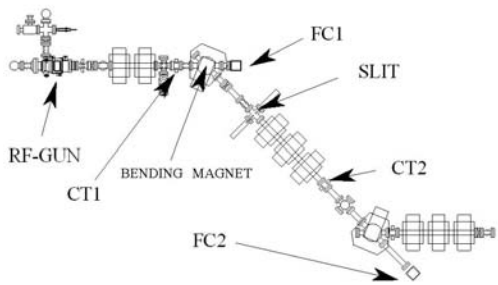

Figure 1: Experimental setup.

METHOD OF ANALYSIS

Back-bombardment effect depends on both the cavity voltage in the RF gun and the cathode current density. We performed a transient analysis in the RF gun taking into account the time evolution of the beam loading depending on the cavity voltage and the cathode current density by using an equivalent circuit model and a thermal conduction model. The beam loading was calculated from the cavity voltage and the cathode current density which was calculated from the thermal conduction in the cathode taking into account the stopping power of the back streaming electron in the cathode.

Analysis of the cathode current density

The energy distribution of the back-streaming electrons was calculated by using the results of the particle simulation code PARMELA [2]. From this result the heat quantity given to the cathode by the back streaming electron with various energy was calculated. In this calculation we assumed that the cathode consisted of thin 2000 disks.

In order to evaluate the effect of the back streaming electrons on the time evolution of the cathode temperature, we used following quasi empirical formula of the TIO [3]:

$$R = \frac{a_1}{\rho}\left\{\frac{\ln\left[1+a_2(\gamma-1)\right]}{a_2} - \frac{a_3(\gamma-1)}{1+a_4(\gamma-1)^{a5}}\right\} \qquad (1)$$

$$a_1 = 2.335A/Z^{1.209} \qquad a_2 = 1.78\times10^{-4}Z$$

$$a_3 = 0.9891 - (3.01\times10^{-4}Z)$$

$$a_4 = 1.468 - (1.180\times10^{-2}Z)$$

$$a_5 = 1.232/Z^{0.109} \qquad \gamma = (E + m_0c^2)/m_0c^2$$

where, R is the stopping range of the electron in m, A is the mass number of the absorber material, Z is the atomic number of it, E is the kinetic energy of electrons in MeV, ρ is the density of the absorber material in kg/m^3. Equation (1) is applicable to the 0.3 keV – 30 MeV electrons. With this equation, stopping power dE_b/dz was obtained. Here, we used the values of ρ = 19250 kg/m^3, A = 183.85, Z = 74 assuming that the cathode material was made of W alone..

The time evolution of the temperature was calculated in each disks of the cathode, and the time evolution of the cathode temperature was calculated by using the equation below,

$$c\rho V\frac{\partial T}{\partial t} = \lambda\frac{\partial^2 T}{\partial z^2} + Q_b(z,t) \qquad (2)$$

where, c is the specific heat, ρ is the density, V is the volume, T is the temperature, λ is the thermal conductivity of the cathode, z is the distance from the cathode surface, $Q_b(z, t)$ is the heat quantity from the back streaming electrons. Here, we used the values of c = 130 J/kg/K, λ = 174 W/m/K.

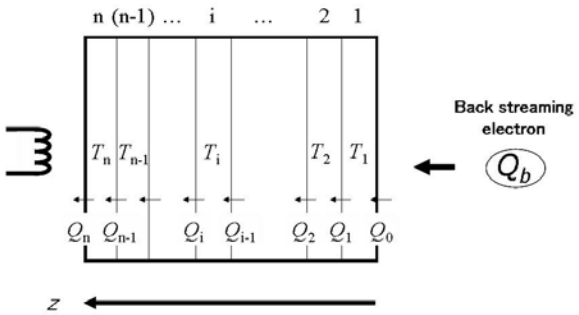

Figure 2: Thermal conduction model.

The cathode current density was obtained from the time evolution of the cathode temperature calculated above. The relationship between the cathode temperature and the cathode current density used in this analysis was obtained by the results of the cathode performance test of Heat Wave Labs, Inc.

Analysis of the cavity voltage in the RF gun

The cavity voltage in the RF gun and the reflecting RF power were calculated with the equivalent circuit model shown in Fig. 3. In this circuit, the RF power source was expressed by a source i_g, the RF gun was expressed by LCG resonant circuit, and the beam loading was expressed by an admittance Y_b. The conductance and the susceptance of the electron beam were calculated from the cavity voltage and the cathode current density by using the particle simulation code KUBLAI [4]. Thus the beam loading was calculated.

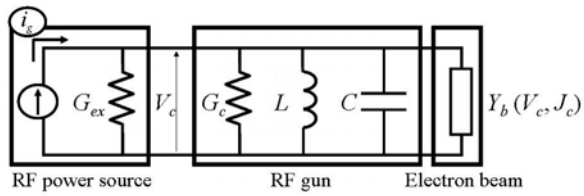

Figure 3: Equivalent circuit model.

RESULT

Experimental result

We have succeeded to keep the peak energy of the electron beam constant in 4 μsec by feeding a modulated RF power into a RF gun. Fig. 4 shows the flat RF power waveform and the modulated RF power waveform fed into a RF gun. Fig. 5 shows the beam current waveform whose peak energy is 8.6 MeV at CT2. Fig. 6 shows the time evolution of the peak energy in macro pulse duration.

As shown in Fig. 5 feeding modulated RF power into a RF gun was an effective way to extend the macro pulse duration and to increase the beam current. As shown in Fig. 6 the beam energy which had been degraded in the latter part of the macro pulse duration was kept constant by feeding modulated RF power.

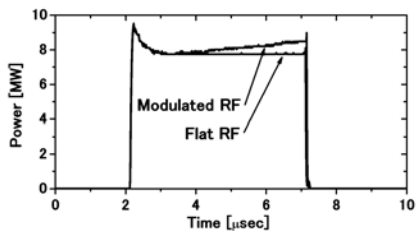

Figure 4: Input RF power waveform.

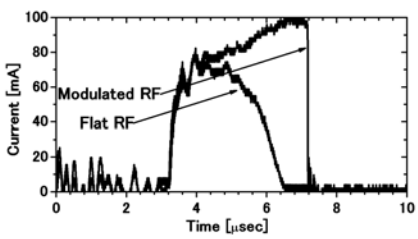

Figure 5: Beam current waveform.

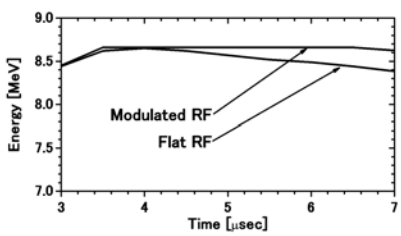

Figure 6: Peak energy @ CT2.

Result of calculation

In order to confirm the validity of calculation model, experimental and calculated reflecting RF power waveforms were compared. Fig.7 shows the measured and reproduced reflecting RF power waveform when a flat RF power was fed. Fig. 8 shows them when a modulated RF power was fed. Experimental and calculation results agree very well.

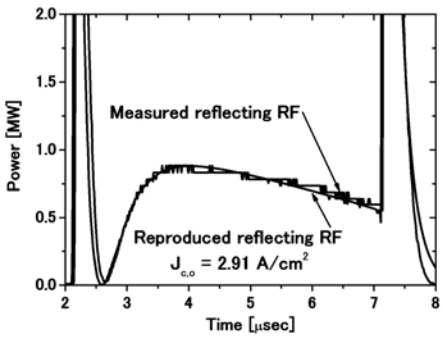

Figure 7: Reflecting RF power waveform.

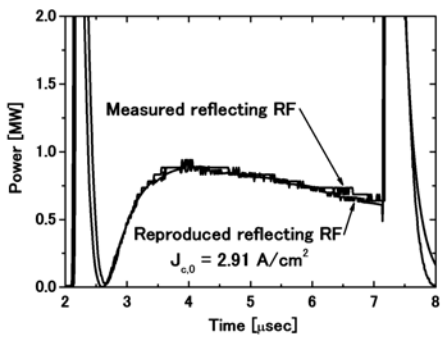

Figure 8: Reflecting RF power waveform.

As shown in Fig. 9, there was a relationship between the cavity voltage (V_c) and the peak energy of the electron beam (E), and the peak energy could be kept constant by keeping the cavity voltage constant.

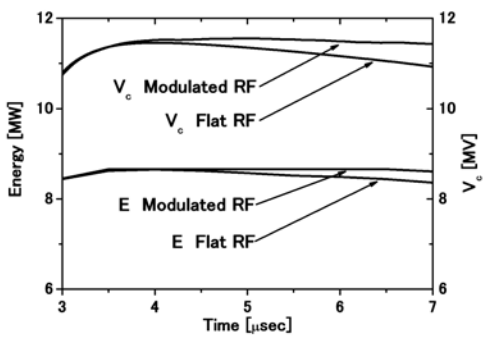

Figure 9: Time evolution of the cavity voltage and the peak energy.

We estimated how long time the peak energy of the electron beam could be kept constant by using our KU-FEL 4.5 cell RF gun. The calculation was performed in both cases of W cathode and LaB_6 cathode. We used the value of ρ = 4700 kg/m^3, A = 94.75, Z = 40, c = 122 J/kg/K, λ = 147 W/m/K and the relationship between the cathode temperature and the cathode current density was obtained by the results of the cathode performance test of KIMBALL PHYSICS INC, in the case of LaB_6 cathode.

Fig. 10 shows the time evolution of the cavity voltage of W and LaB_6 when a flat RF power was fed, respectively. The degradation of the cavity voltage of LaB_6 was a little smaller than that of W.

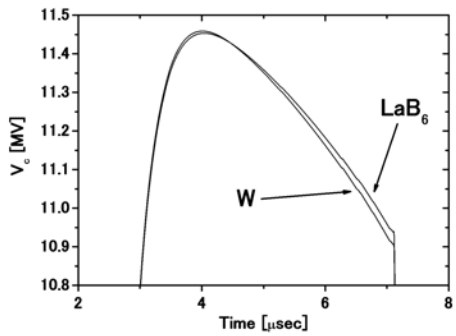

Figure 10: Comparison of W with LaB_6.

Fig. 11 and Fig. 12 show the time evolutions of the cavity voltage when an optimized modulated RF power was fed. The input RF power was 8 MW at the beginning of the macro pulse and the controlled range was 1.6 MW and the initial current density was 2.28 A/cm^2 in each calculations. We found that the degradation of the peak energy could be kept below 100 keV in the macro pulse duration of 8.0 μsec when the cathode was W, 8.2 μsec when the cathode was LaB_6.

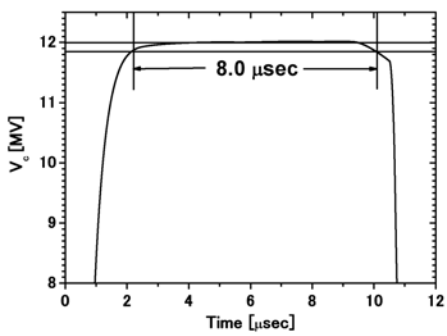

Figure 11: Expected time evolution of the cavity voltage (W).

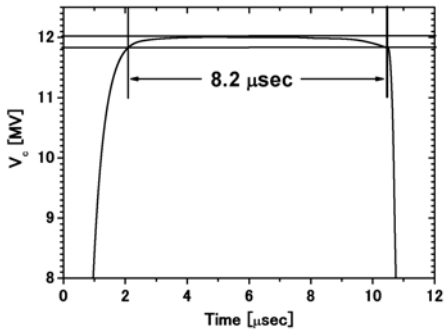

Figure 12: Expected time evolution of the cavity voltage (LaB_6).

SUMMARY

It was confirmed in experiment that feeding modulated RF power into a RF gun was effective on the reduction of the degradation of the beam energy.

By the calculation in this work, the experimental results were reproduced well. Moreover, the degradation of the peak energy of the electron beam could be kept below 100 keV in the macro pulse duration of 8.0 μsec when the cathode was W, 8.2 μsec when the cathode was LaB_6.

REFERENCES

[1] T. Kii, et al, Proceedings of the 27th International Free Electron Laser conference, (2005) pp584-587.

[2] L. M. Young, James H. Billen : LA-UR-96-1835 (2002).

[3] M. J. Berger and S. M. Seltzer, STOPPING POWER AND RANGES OF ELECTRONS AND POSITRONS (2nd Ed.),NBSIR (1982).

[4] K. Masuda, Development of numerical simulation code and application to Klystron efficiency enhancement, Ph. D Thesis, Kyoto University, (1998).

EXPERIMENTAL STUDY ON EFFECT OF ENERGY DISTRIBUTION ON TRANSVERSE PHASE SPACE TOMOGRAPHY

H. Zen#, H. Ohgaki, K. Masuda, T. Kii, T. Shiiyama, S. Sasaki, N. Okawachi, M. Nakano, K. Yoshikawa, T. Yamazaki
Institute of Advanced Energy, Kyoto University, Gokasho, Uji, Kyoto, 611-0011, Japan.

Abstract

Effect of energy distribution of electron beam on transverse phase space distroiion obtained by the use of tomographic method is described. Experimental phase space distribution of electron beam with low energy-tail has weak and scattered halo, which does not appear in the case of the beam without the tail. The result is consistent with the result of previous simulations. An iterative elliptical analysis is proposed to extract the beam parameters of main component from distorted phase space image. It was shown in simulation that the method could extract the beam parameters of main component from distorted image. And then, the method was applied to experimental results. As the results, the vertical and horizontal emittances at the upstream and downstream of energy filter are agreed well.

INTRODUCTION

It is indispensable to measure not only emittances but also phase space distributions of electron beams to evaluate and optimize the performance of electron guns. Transverse phase space tomography [1] is powerful method especially for non-Gaussian beam, because the method directly reconstructs the phase space distribution of electron beams. However, the assumption of mono-energy is essential for the method. Thermionic rf guns inherently produce electron beams which have large energy spread (about 10 to 15 percent) and low energy tail, and the energy distribution distorts measured phase space distribution obtained by tomographic method.

We have evaluated the effect of energy distribution on the tomographic method by numerical simulations [2]. It was found that the signals of low energetic electrons are reconstructed as weak and scattered signals on wide region of reconstructed phase spaces, and those signals lead to large errors in beam parameters. On the other hand, it was also found that the energy spread of main component have no large effect on the method even if the energy spread is 15 percent.

The effect was evaluated by comparison of the reconstructed image from the upstream and that from the downstream of an energy filtering section. Furthermore for the beam just after the gun, we introduced an elliptical analysis to remove the effect of low energy tail in order to obtain correct beam parameters at the gun exit by the tomographic method.

EXPERIMENTAL SETUP

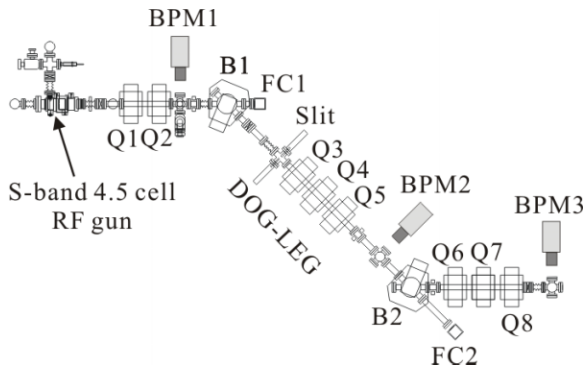

Figure 1: Experimental arrangement.

Figure 1 shows the experimental setup. A dispenser cathode of disk shape with 6 mm diameter is mounted in the first half cell of our 4.5 cell RF gun. To reduce back-streaming electrons [3], transverse magnetic field was applied with a dipole magnet located just before the rf gun [4]. The beam profile monitor (BPM) consist of a fluorescence screen (Cr doped Al_2O_3) and a CCD camera, and its spatial resolution is 0.05 mm.

Dog-leg section in Fig. 1, which consisted of two dipole magnets, a slit, and a quadrupole triplet, worked as an energy filter and its energy resolution is about 5 percent.

The quadrupole magnet 1 (Q1) and the BPM1 are used to measure the phase space distributions at the upstream of the energy filter, and the Q6 and BPM3 are used to measure them at the downstream.

Beam parameters in the experiments are shown in Table 1, and the energy distribution obtained with bending magnet 1 (B1) and Faraday cup 2 (FC2) is shown in Fig. 2. Unfortunately signals of FC2 of low energy tail (less than 7 MeV) were too weak to be separated from the electric noise. However, the existence of low energy tail has been predicted in the previous simulation for our rf gun [2].

For tomographic reconstruction, we used ordered-subset expectation maximization algorithm [5] whose advantage is that there is no artefact on reconstructed images.

#heishun@iae.kyoto-u.ac.jp

Table 1: Beam parameters in experiments

	@ BPM1	@ BPM3
Macro pulse duration	1.6 μ sec	1 μ sec
Total charge	300 nC	100 nC
Charge per bunch	66 pC	35 pC
Peak Energy	9.2 MeV	

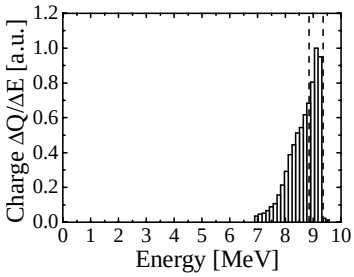

Figure 2: Measured energy spectrum of the electron beam at the exit of gun (dashed lines indicate the energy acceptance of dog-leg section).

RESULTS OF EXPERIMENT

The results of experiments are shown in Fig. 3 and 4. Before reconstruct the Q1 result, background signals were subtracted. At the Q1 entrance horizontal and vertical normalized emittances are evaluated as 82 and 44 π mm mrad, respectively, while those are 12 and 6.9 π mm mrad at the Q6 entrance.

There are weak and scattered signals in Fig. 3 where the electron beam had a low energy tail, while such signals are not seen in Fig. 4. It is consistent with previous numerical studies that the phase space distributions for the beam with low energy tail are severely distorted.

In Fig. 3, the region between dashed lines indicates where electrons can exist and the region is calculated from aperture of the gun exit (4 mm in diameter) and the distance between the gun exit and Q1 (27.5 cm). The signals in outside of the region are miss-reconstructed signals due to difference from assumed energy at least.

Therefore, it was shown in experiment that the signals from low energy tail are reconstructed as weak and scattered signals. We can not obtain correct phase space distributions by using tomographic method if low energy tail is contained in an electron beam.

REMOVAL OF LOW ENERGY SIGNALS

Amount of low energy electrons produced by a thermionic rf gun is much fewer than amount of electrons included in main component, and low energy electrons are reconstructed wider and weaker than true distribution. So intensity of low energy electrons on reconstructed phase space is much weaker than intensity of electrons included in main component. However, the emittance calculation is strongly affected by the tail. Therefore, we need to remove the weak signals which are originated from low energy electrons to obtain correct beam parameters by the tomographic method.

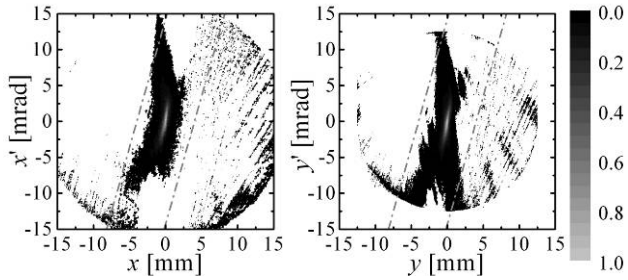

(a) (b)

Figure 3: Phase space distributions at the entrance of Q1 (dashed lines indicate the regions where electrons can exist and are calculated from experimental geometry). (a) Horizontal and, (b) vertical.

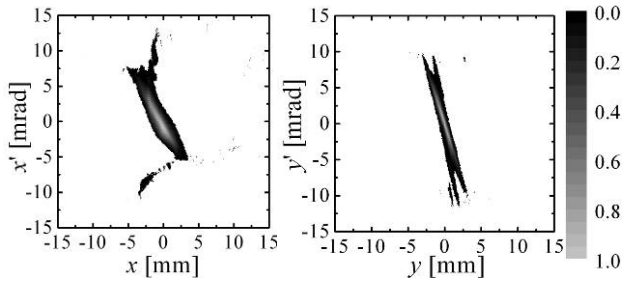

(a) (b)

Figure 4: Phase space distributions at the entrance of Q6 measured by tomographic method, (a) Horizontal and (b) vertical.

Procedure of Iterative Elliptical Analysis

To remove the weak signals produced by low energy electrons automatically, we introduced an iterative elliptical analysis (IEA) [6]. The procedure is:

I : Calculate $\langle x^2 \rangle$, $\langle x'^2 \rangle$ and $\langle xx' \rangle$ from reconstructed phase space distribution.

II : Draw ellipse defined by Eq. 1 on reconstructed phase space.

$$\langle x'^2 \rangle x^2 + 2\langle xx' \rangle xx' + \langle x^2 \rangle x'^2 = 9\varepsilon^2 \quad (1)$$

Eq. (1) represents the 99 percent ellipse of Gaussian distributions.

III: Calculate $\langle x^2 \rangle$, $\langle x'^2 \rangle$ and $\langle xx' \rangle$ from reconstructed phase space distribution only in the ellipse.

IV : In the same way with step II and III, draw ellipse using newly calculated $\langle x^2 \rangle$, $\langle x'^2 \rangle$ and $\langle xx' \rangle$ in step

V : Repeat step III and IV until $\langle x^2 \rangle$, $\langle x'^2 \rangle$ and $\langle xx' \rangle$ sufficiently converge.

Simulation of Iterative Elliptical Analysis

Reliability of IEA was examined by using numerical simulation. We gave the Gaussian-shaped phase space distribution with the energy distribution shown in Fig. 5 as original distribution and simulated the experiment of tomographic method. In this simulation, space charge effect was neglected, since it was not significant for our thermionic rf gun. As the result of the simulation, a distorted phase space distribution was reconstructed (Fig. 6). Although weak and scattered signals exist in the figure,

strong signals in the center are looked similar to the original phase space distribution (Fig.5).

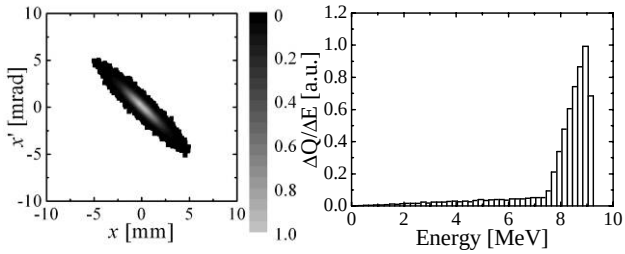

(a) (b)

Figure 5: Original distribution of numerical simulation, (a) phase space distribution (normalized emittance = 3.3 π mm mrad, α = 2.9 and β = 3.1 m), (b) energy spectrum.

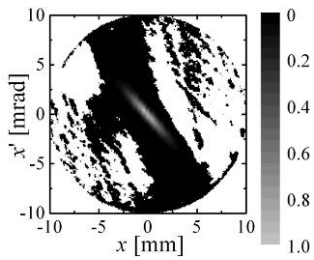

Figure 6: A result of numerical simulation (normalized emittance = 10 π mm mrad, α = 1.5 and β = 1.4 m).

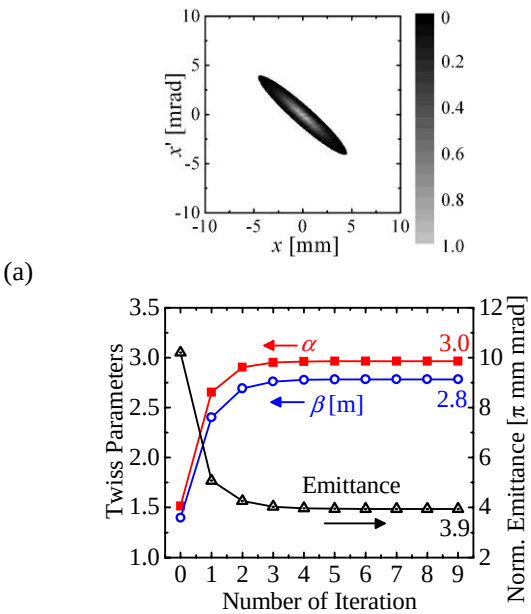

(a)

(b)

Figure 7: Result of IEA applied to simulation result, (a) phase space distribution (normalized emittance = 3.9 π mm mrad, α = 3.0 and β = 2.8 m), (b) convergence of emittance and Twiss parameters.

The result of IEA applied to the Fig.6 is shown in Fig. 7. The normalized emittance and Twiss parameters gradually converged to 3.9 π mm mrad, α = 3.0 and β = 2.8 m, respectively as iteration number increased. The beam parameters of original distribution were normalized emittance = 3.3π mm mrad, α = 2.9 and β = 2.8 m. Since each error in beam parameters is less than 20 percent, this method is reliable.

Application of IEA to Experimental Result

IEA was applied to experimental results at the entrance of Q1 and the results are shown in Fig. 8. A center core of reconstructed phase space distribution was successfully obtained and beam parameters sufficiently converged. As results of application of IEA, measured horizontal and vertical emittances were 5.4 and 4.7 π mm mrad, respectively.

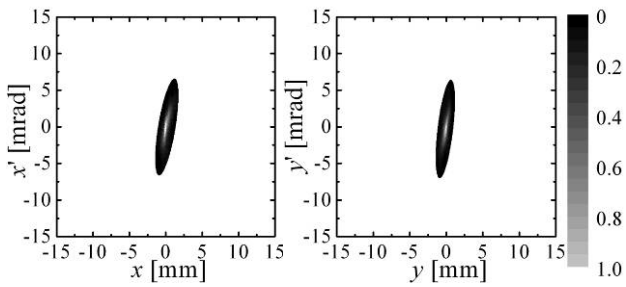

(a) (b)

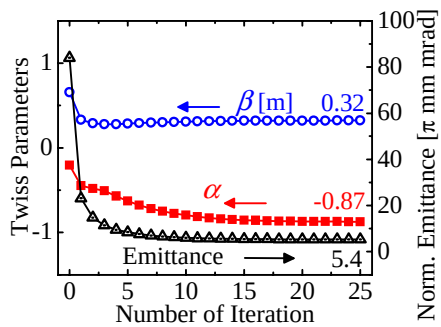

(c)

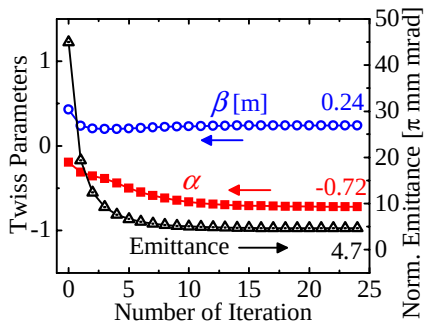

(d)

Figure 8: Results of IEA applied to experimental results. (a) Horizontal phase space distribution of horizontal direction. (b) Vertical phase space distribution. (c) and (d) convergence of horizontal and vertical beam parameters, respectively.

The IEA was also applied to experimental results at the Q6 entrance and measured emittances of horizontal and vertical directions at the Q6 entrance were 7.4 and 4.3 π mm mrad, respectively. Measured emittances of vertical direction at the Q1 and Q6 entrance agreed well. However, emittances of horizontal direction did not agree well. The reason of this disagreement was the non-zero horizontal dispersion in the Dog-leg section.

Reliability and an ability of IEA were confirmed both in simulation and experiment. We are now planning to do more experiments under various conditions of the gun in order to evaluate the accuracy of IEA quantitatively. Comparison of transverse phase space distribution with the slit methods will be useful, since the methods are not suffered from energy distribution.

SUMMARY

To study the effect of energy distribution to transverse phase space tomography, experimental results at the upstream and downstream of the energy filter were compared. As the result, the low energy electrons are reconstructed as weak and scattered signals, which are predicted by previous numerical investigation.

To remove the signals from low energy electrons, IEA was introduced and examined. By a numerical simulation, the validity of the analysis was shown. IEA was applied to experimental results at the upstream of energy filter and compared with the experimental results at the downstream of the filter. The emittances of vertical direction at the upstream and downstream of energy filter agreed well, although horizontal ones were not due to non zero horizontal dispersion in the Dog-leg section. Consequently, reliability and an ability of IEA were shown both in simulation and in experiment.

REFERENCES

[1] C.B.McKee, et al., NIM A358, 1995, p.264.
[2] H.Zen, et al., Proc. of FEL2005, 2006, p.592.
[3] T.Kii, et al., Proc. of FEL2005, 2006, p.584.
[4] T.Kii, et al., NIM A507, 2003, p.340.
[5] H.M. Hudson, et al., *IEEE. Trans. Med. Imaging*, **13**, 1994, p.601.
[6] H.Zen, et al, "Transverse phase space measurement using tomographic method", conference proceedings of SRI2006, in press.

STUDY ON FOCUSING PROPERTY OF NEW TYPE WIGGLER AND SASE-FEL EXPERIMENT AT THE ISIR, OSAKA UNIVERSITY

S. Kashiwagi#, R. Kato, Y. Kon, T. Igo, G. Isoyama,
Institute of Scientific and Industrial Research, Osaka University, Ibaraki, Osaka 567-0047, Japan
S. Yamamoto*, K. Tsuchiya and H. Sasaki
Institute of Materials Structure Science, KEK, Tsukuba, Ibaraki 305-0801, Japan
*School of Advanced Sciences, The Graduate University for Advanced Studies,
Tsukuba, Ibaraki 305-0801, Japan.

Abstract

We have developed a new type of wiggler based on the edge-focusing wiggler for free electron laser (FEL) and self-amplified spontaneous emission (SASE) in the infrared region at the Institute of Scientific and Industrial Research (ISIR), Osaka University. The strong focusing (SF) scheme is adopted for the new wiggler in order to keep the beam size small along whole the wiggler. The wiggler consists of four FODO cells for double focusing. A gain length and SASE output power for the strong focusing wiggler were numerically estimated using the 1D FEL model and Genesis code. Measuring the electron beam size in the wiggler at different wiggler gaps performed the experimental study on focusing property of the new type wiggler. We are conducting experiments to generate SASE in the infrared region and to measure its characteristics, using the strong focusing wiggler and a high intensity single bunch electron beam. We have measured the wavelength spectrum of SASE in the wavelength region between 220 and 50 μm using a grating monochromator and a Ge:Ga detector. The second harmonic and the third harmonic peaks of SASE were also observed in the spectrum measurement.

INTRODUCTION

We are conducting experiments of FEL and SASE with a high intensity electron beam in the infrared region at ISIR L-band linear accelerator, Osaka University. While the beam experiment are performing, we have developed a new type wiggler, named the edge-focusing (EF) wiggler, which produces the strong transverse focusing field incorporated with the normal wiggler field [1]. To demonstrate its principle and evaluate the performance, the first model wiggler has been fabricated. It is experimentally confirmed that a field gradient of 1.0 T/m is realized along the beam axis in the EF wiggler. The details of the model wiggler were reported in previous conference [2-3]. The EF scheme has been applied to the wiggler being used for FEL and SASE in the far-infrared region at the ISIR L-band linear accelerator, to make the gain length of SASE shorter by keeping the beam size small along whole the wiggler. Before replacing of the wiggler, the wiggler was a conventional Halbach-type wiggler and we changed its magnet parts with new ones. We, therefore, hold the wiggler parameters same as before. In order to meet a wide range of the electron beam energy and the wiggler gap, we adopt the strong focusing scheme using the EF wiggler. Focusing and defocusing elements are composed of permanent magnet blocks with the edge angle and they are alternately inserted in magnet arrays of the wiggler. The strong focusing wiggler has been fabricated and the magnetic field has been measured at KEK. In June 2005, the strong focusing wiggler installed to the FEL system at ISIR L-band linear accelerator [4].

After the installation of the strong focusing wiggler, we resumed to conduct the experiment to generate SASE in the far-infrared region. In the beam experiments, a focusing property of the strong focusing wiggler is also studied by measuring the beam sizes using screen monitors in the wiggler at different gaps.

STRONG FOCUSING WIGGLER

In this section, the developed strong focusing wiggler is described shortly. The edge-focusing wiggler is basically a Halbach type wiggler made only of permanent magnet blocks, but their shapes are not rectangular parallelepipeds. The field gradient on the permanent magnet with edge is approximately proportional to the edge angle ϕ and hence the focusing force can be easily adjusted with the edge angle. A polarity of the field gradient can be decided by choosing positive or negative angle of edge against to beam trajectory. In the strong focusing scheme, the electron beam is focused alternatively in the vertical and the horizontal directions to obtain focusing in the both directions using a sequence of focusing and defocusing elements separated by drift spaces, which is called the FODO lattice. Parameters of the FODO lattice were optimized to meet the requirements of our experiment and the parameters of the strong focusing wiggler are listed in Table 1. The permanent magnet used is NdFeB (NEOMAX-38VH, NEOMAX Co.) with Br = 1.22 T and the peak magnetic field of the EF wiggler is 0.39 T at the minimum gap of 30 mm. The number of FODO cells in the wiggler is four and the cell length is 0.48 m. The number of cells is a factor of the number of wiggler periods, 32. Focusing elements are single wiggler periods with the edge angle of +5° and defocusing ones are those with –5°, and they are

#shigeruk@sanken.osaka-u.ac.jp

Table 1: Main parameters of the SF wiggler

Block sizes	90x20x15 mm^3
Magnet materials (Coating)	Nd-Fe-B (TiN)
Period length	60 mm
Number of periods	32 periods
Total length	1.938 m
Peak magnetic field	0.39 T (gap 30mm)
Number of FODO cells	4 cells
Length of FODO cell	0.48 m
Edge angle	±5 °
Field gradient	±3.2 T/m

separated by 3 normal wiggler periods. Longitudinally magnetized blocks are added at both ends of the strong focusing wiggler in order to compensate for the horizontal shift of the oscillatory beam orbit due to the fringing magnetic field at the ends. Thus the total length of the SF wiggler is 1.938 m.

In the field measurement, the peak magnetic field was 0.392 T and peak magnitude of field gradient at focusing and defocusing elements was about 3.2 T/m at the wiggler gap of 30 mm. The results of measurements were good agreement with the numerical calculations.

NUMERICAL ESTIMATION

Beam focusing of the strong focusing wiggler

The envelope of beam sizes in horizontal and vertical direction for the strong focusing wiggler and a planar wiggler were calculated with an electron beam of 10 MeV, a normalized emittance of 150π mm mrad in transverse directions and a peak wiggler field of 0.392 T. Figure 1 shows the calculated beam envelopes and the solid line and dashed line show the strong focusing wiggler and the planer wiggler, respectively. In the horizontal direction, the beam envelope of the strong focusing wiggler alternatively changes along the wiggler and the average beam size (σ) in the wiggler much smaller than that of the planar wiggler. On the other hand, the vertical beam sizes for the both type of wigglers are almost same. The FODO lattice of the strong focusing wiggler slightly distorted due to the natural focusing of the wiggler. The average beam size for the strong focusing wiggler (σ_{SF}) and the planar wiggler (σ_{PL}) are 1.41 mm and 1.69 mm respectively, when the average beam size in the wiggler assumed to be $\sqrt{\sigma_{horizontal} \cdot \sigma_{vertical}}$. Transverse charge density of the beam, which is a square of the average beam size, in that of the strong focusing is about 30% higher than that of the planar wiggler. The gain length (L_g) for each wiggler is estimated from the above average beam sizes by 1D FEL model using Eq. 1.

$$L_g = \frac{\lambda_u}{4\sqrt{3}\pi \cdot \rho} \quad (1)$$

where λ_u and ρ are period length of the wiggler and FEL parameter. Here, the bunch charge and the length of the electron beam are assumed to 30 nC and 30 ps (FWHM),

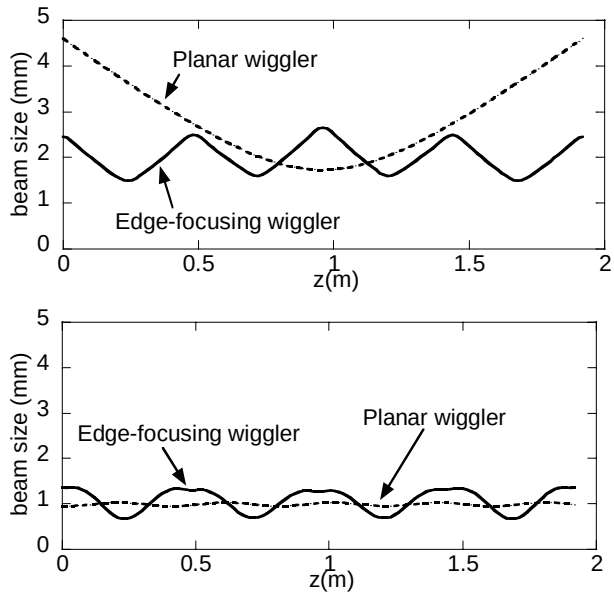

Figure 1: The envelopes of beam size in horizontal (upper) and vertical (down) directions for the strong focusing wiggler and a planar wiggler.

corresponds to the peak current of 1.0 kA. The derived the gain length of the strong focusing wiggler and the planar wiggler are 0.152 m and 0.163 m respectively, therefore the gain length of the strong focusing wiggler is about 7% shorter than that of the planar wiggler. From the difference of the gain length, it can expect 2 times large gain of FEL can be obtained by using the strong focusing wiggler.

SASE output power

SASE output power of the strong focusing wiggler and the planar wiggler are estimated using Genesis code [5]. The beam parameters of electron beam are same in above calculations. Figure 2 shows SASE radiation power along the wigglers. In this figure, the red and the blue lines are SASE radiation power of the strong focusing wiggler and the planar wiggler, respectively. At 10MeV, the beam size is kept small in the strong-focus wiggler and the SASE power of strong focusing wiggler is 5~6 times higher than that of planar wiggler.

BEAM EXPERIMENT

The beam experiment was conducting using the L-band linear accelerator at ISIR, Osaka University. ISIR L-band linac consists of an electron gun, three-stage sub-harmonic buncher (SHB) system, pre-buncher, buncher, 3m-long accelerating structure and the experimental beam lines. The electron beam with peak current of 17 A and a pulse duration of 5 ns was produced with a thermionic gun. The electron beam was injected into the SHB system composed of two 1/12 and one 1/6 SHB cavities for the accelerating frequency of 1.3 GHz to generate a high intensity single bunch beam, and then it was accelerated to 10.3 MeV in the linac. The electron beam was

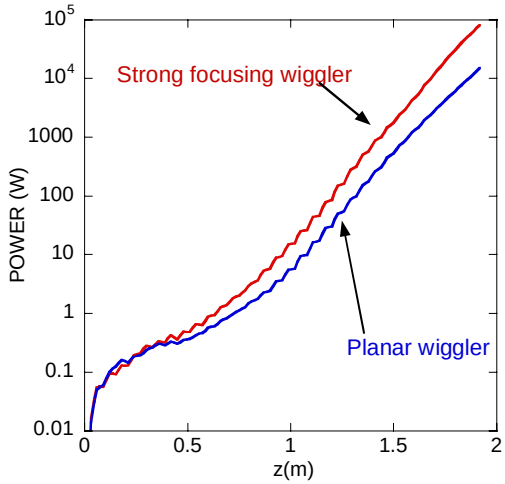

Figure 2: SASE radiation power along the wiggler. (Red line: Strong focusing wiggler, Blue line: Planar wiggler).

transported to the strong focusing wiggler via the achromatic beam transport line as shown in Fig. 3. The peak magnetic field and K-value of the strong focusing wiggler were 0.353 T and 1.4 at the wiggler gap of 32 mm. Twiss parameter and the emittance were measured using a quadrupole scan technique with a 100 μm thickness phosphor screen monitor at the exit of the accelerating structure. The normalized transverse beam emittance was ~170π mm mrad with a bunch charge of 30 nC and an energy spread of 3.0 % (FWHM). The beam injection condition and an orbit of electron beam were tuned using quadrupole magnets and steering coils at the beam transport line for FEL experiment. The unnecessary energy part of the electron beam was collimated by an energy-slit located at the dispersion section of the transport line and the energy width of the slit was about 2 %. Therefore, the net charge per bunch passing through the wiggler was about 20 nC. The experimental arrangement is shown schematically in Fig. 3. SASE radiation by the single bunch beam passing through the wiggler was reflected with a mirror (MP1) at downstream, and led to a far-infrared monochromator in the measurement room via an optical transport line. The optical transport line and the monochromator were evacuated together with a rotary vacuum pump. The low vacuum in the optical transport line and the high vacuum in the beam transport line were separated by a 0.2 mm thick, 20 mm in diameter synthetic diamond window, denoted by W1 in Fig. 3. The monochromator is a cross Czerny-Tuner type with a plane reflective grating, whose braze wavelength is 112.5 μm. The monochromator can be used in the wavelength region from 50 to over 240 μm. The wevelength resolution of the monochromator is almost constant over the range and approximately 1.5 μm for a slit width of 6 mm. The monochromatized light was detected with a Ge:Ga photo-conductive detector cooled with liquid-helium.

EXPERIMENTAL RESULT

Beam size measurement in the wiggler

We measured the transverse beam size in the wiggler using three screen monitors, denoted by F3, F4 and F5 in Fig. 3, at different wiggler gap with 10.3 MeV electron beam. In Fig. 4, the solid circles with the solid lines show horizontal beam size and the open circles with the dashed lines show vertical beam on each screen monitors at different wiggler gap from 30 to 50 mm. The horizontal beam sizes on the all screens slightly change; but they were almost constant at different wiggler gap. The vertical beam size on the F4 and F5 periodically change at different wiggler gap. It seems that the variation of the vertical beam sizes come from the changing of the natural focusing, which is strongly depend on the magnetic field strength of the wiggler. The strength of natural focusing is proportional to the square of the peak magnetic field and

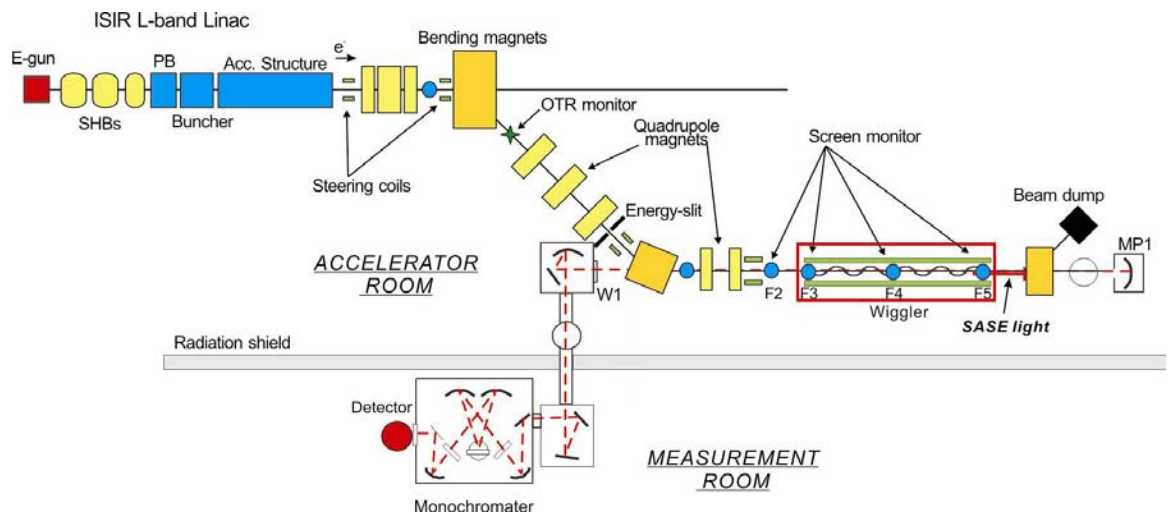

Figure 3: Schematic layout of the ISIR L-band linac and the FEL system. SASE radiation is deriver to the grating monochromator and Ge:Ga detector using optical mirrors.

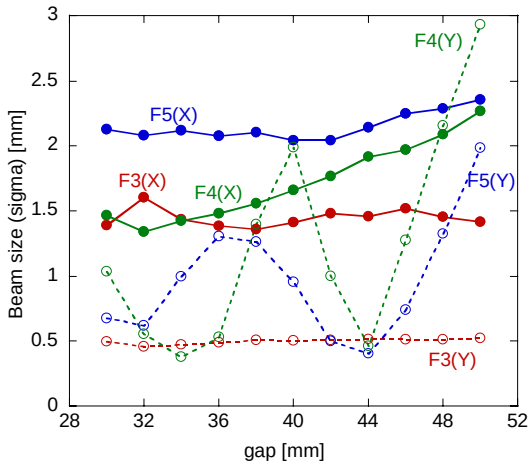

Figure 4: Measured horizontal (X) and vertical (Y) beam size using three screen monitors, denoted by F3, F4 and F5 in Fig. 3.

the strength of the edge focusing is only proportional to the peak magnetic field in the simple model of the wiggler composed of alternating bending magnets with the edge angle. Furthermore, as reported previous FEL conference [4], we have observed the peak field decreases to one-third with wiggler gap from 30 to 50 mm, whereas the field gradient decreases only by 56 % in the magnetic field measurement. The field gradient of the edge-focusing wiggler is kept at different wiggler gap. At this condition of electron beam, the natural focusing is strong and the edge focusing effect cannot be observed clearly. The measurement results were compared with the calculated beam size in the wiggler. In vertical direction, the periodically variation of beam sizes are large different, since the electron beam was injected into wiggler with not matching conditions. We will continue the study on the focusing property of the strong focusing wiggler at different condition of electron beam energy using the beam profile monitors.

Result of SASE spectrum measurement

Figure 5 shows a wavelength spectrum of SASE in the wavelength range from 50 to 240 μm with 1μm step. The closed dots and the error bar show the average values of intensities and a standard deviation, respectively, of five highest intensities in thirty successive optical pulses for each wavelength. As reported in Ref. [6], the total sensitivity of the measurement system, including the sensitivity of the detector, the efficiency of the monochromator, the transmission efficiency of the optical transport line, was calibrated over the wavelength range from 50 to 200 μm using a blackbody radiator. We have not measured the sensitivity of the measurement system above 200 μm. In Fig.5, the plotted intensities are, therefore, signal intensities from the detector and the intensities at different wavelengths are not calibrated. Although the second and the third harmonic peaks are comparable in signal intensity to the fundamental one due to the higher sensitivity of the measurement system around 100 μm wavelength, the fundamental peak is actually strongest. The intensity ratios of the second and the third harmonic peak to the fundamental one are roughly estimated from the extrapolation from the previous calibration data to be 1/35 and 1/10, respectively.

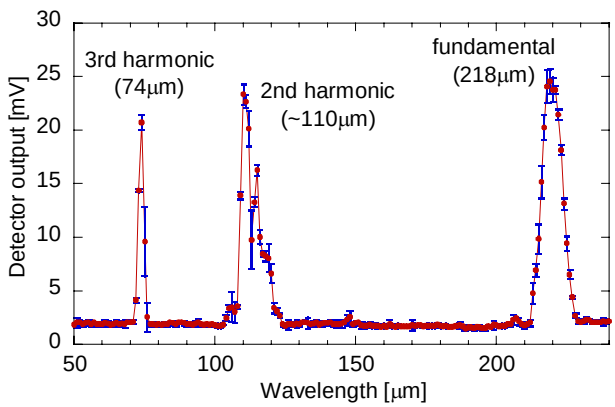

Figure 5: Wavelength spectrum of SASE in the wavelength range from 50 to 220 μm.

The measured spectral width of the fundamental peak was about 1.75 %, which is slightly smaller than those predicted value (1.9 %) by the 1D FEL model (Eq. 2).

$$dw = \sqrt{\frac{9\rho}{2\pi\sqrt{3}\cdot N_w}} \qquad (2)$$

We can expect that the FEL parameter (ρ) in the actual experiment is smaller than the predicted one due to that the Twiss parameter of the electron beam are different with matching condition at the entrance of the wiggler and the beam size is larger than optimum one. We will conduct to study on SASE about the spectral width and the angular distribution of the higher-harmonics and the statistically fluctuation of SASE output power.

ACKNOWLEDGEMENTS

The authors would like to thank Messrs. S. Suemine and T. Yamamoto for the help of accelerator operation. This research was partly supported by the Joint Development Research at the High Energy Accelerator Research Organization (KEK), 2006-15, 2006 and The Ministry of Education, Culture, Sports, Science and Technology (MEXT), Grant-in-Aid and for Young Scientists (B), 17740144, 2005-2006.

REFERENCES

[1] G. Isoyama et al., Nucl. Instr. and Meth. A 507 (2003) 234
[2] S. Kashiwagi et al., Nucl. Instr. and Meth. A 528 (2004) 203
[3] S. Kashiwagi et al., Proceedings of the 2004 FEL Conference (2004) pp458-461.
[4] S. Kashiwagi et al., Proceedings of 27th International FEL Conference (2005) pp199-202
[5] http://pbpl.physics.ucla.edu/~reiche/index.html
[6] R. Kato et al., Nucl. Instr. and Meth. A 507 (2003) 409-412.

LONGITUDINAL PHASE-SPACE MEASUREMENTS OF A HIGH-BRIGHTNESS SINGLE-BUNCH BEAM

R. Kato#, S. Kashiwagi, T. Igo, Y. Kon, G. Isoyama
ISIR, Osaka University, Ibaraki, Osaka 567-0047, Japan

Abstract

A measurement system of the longitudinal phase-space distribution of electrons using the combination of an optical transition radiation profile monitor and a streak camera are currently under development at ISIR, Osaka University. The energy spectrum is measured using transition radiation in a preliminary experiment. It is found that the OTR monitor has a higher momentum resolution than the momentum analyzer system usually used.

INTRODUCTION

We are conducting experimental studies on Self-Amplified Spontaneous Emission (SASE) in the infrared region using the L-band linac at the Institute of Scientific and Industrial Research (ISIR), Osaka University [1-3]. The performance of SASE-FEL strongly depends on beam parameters, such as a longitudinal beam profile, bunch charge, the transverse emittance and an energy profile. A correlation between longitudinal positions of electrons in a bunch and their energies has a crucial effect on the temporal evolution of the optical pulse of SASE. Several types of methods are extensively under study to evaluate the longitudinal phase-space profile of the electron beam [4-7]. Among them, a combination of Cherenkov radiation and a streak camera was used in Ref. 5 and a combination of synchrotron radiation and a streak camera in Ref. 7.

In order to measure the electron distribution in the longitudinal phase-space, we use a combination of an optical transition radiation (OTR) monitor and a streak camera together with a bending magnet. Since the bending magnet produces momentum dispersion in the electron beam, electrons diverge in the horizontal direction. The OTR radiator is placed in the lower course of the beam line from the bending magnet and it works as a converter from electrons to photons. The horizontal intensity distribution of photons is proportional to the momentum distribution of electrons, provided that the beam size of the electron beam due to the transverse emittance is negligibly small compared with the momentum distribution. By means of an appropriate optical system, the intensity distribution of photons on the OTR radiator can be focused on the horizontal slit of the streak camera. When the temporal sweep of the camera is turned on, a streak image reproduces the electron distribution on the longitudinal phase-space.

Advantages of using OTR are as follows: (1) the radiator is a simple metallic plate or foil, which produce no vacuum degradation by irradiation, (2) since the emission process is a very rapid phenomenon at a flat surface, the temporal resolution is expected to be high, (3) the number of photons is proportional to the incident electron number without intensity saturation. Furthermore, if a very thin organic film vapour-deposited with metal is used as an OTR radiator, a quasi-non-destructive monitor will be realized [8].

Compared with Cherenkov radiation or synchrotron radiation, on the other hand, the intensity of transition radiation is lower and the photon yield in the visible region is of the order of 10^{-2} photons per incident electron [9]. The L-band linac, however, can produce a high-intensity single-bunch beam typically with charge of 30 nC, so that a detectable number of photons is expected.

We recently began the feasibility study of the longitudinal phase-space monitor with OTR. In this contribution, we will present preliminary experimental results of the energy spectrum measurements with OTR.

PROPERTIES OF TRANSITION RADIATION

Transition radiation is produced by relativistic charged particles when they traverse the boundary surface of two media with different dielectric constants. When a charged particle of the velocity βc, energy γ and charge e passes across a metallic surface in a vacuum, the radiation energy per unit solid angle dΩ and unit frequency dω is given by [10]:

$$\frac{d^2W}{d\omega d\Omega} = R\frac{e^2}{4\pi^2 c}\frac{\sin^2\theta}{(1-\beta\cos\theta)^2}, \qquad (1)$$

where R is the reflection coefficient of the metal and θ the angle of emitted photons with respect to the electron

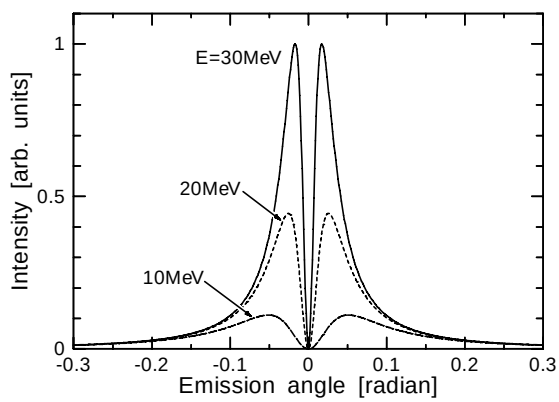

Figure 1: Angular distribution of the transition radiation.

#kato@sanken.osaka-u.ac.jp

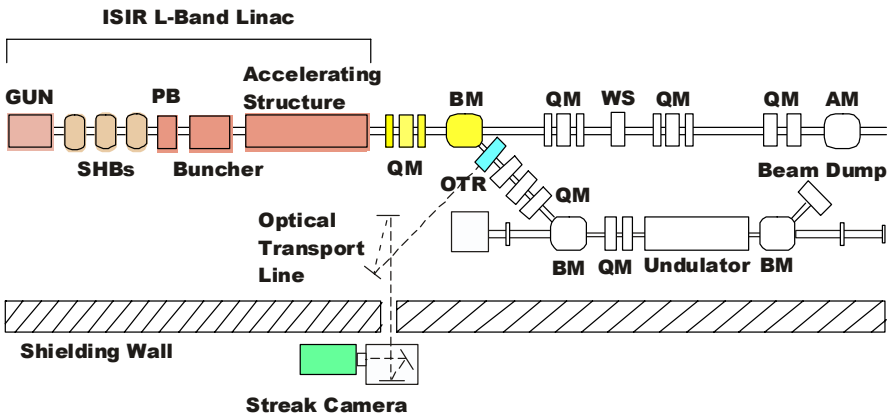

Figure 2: Schematic layout of the ISIR L-band Linac and FEL beam line. GUN: Electron gun, SHBs: Sub-harmonic Bunchers, BM: Bending magnet, QM: Q-magnet, AM: Analyser magnet, WS: Wire Scanner Monitor.

beam axis for the forward radiation and the direction of specular reflection for the backward. The angular distributions of the emitted radiation for electron energies obtained with our linac are shown in Figure 1. The emission angle of the maximum intensity is expressed by

$$\theta \cong \frac{1}{\gamma}. \qquad (2)$$

The peak intensity of transition radiation for 10 MeV energy is one-tenth of that for 30 MeV, and the emission angle for 10 MeV increases three times wider than that for 30 MeV. We, therefore, have to broaden the acceptance angle of the photon detection system in order to make use of the transition radiation as a longitudinal phase space monitor for lower energy electrons.

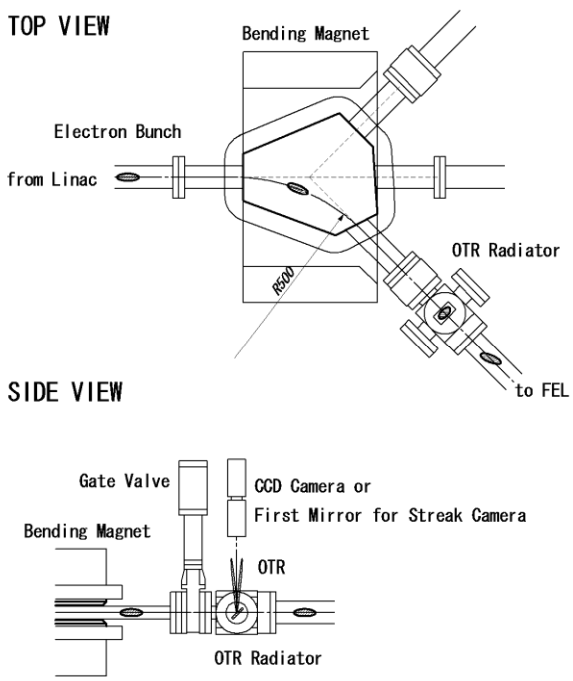

Figure 3: Configuration of the OTR radiator.

EXPERIMENTAL SETUP

Figure 2 shows a schematic layout of the L-band linac. The linac is equipped with a three-stage sub-harmonic buncher (SHB) system composed of two 1/12 and one 1/6 SHBs in order to produce an intense single-bunch beam with charge up to 91 nC/bunch. For single-bunch operation, the electron beam with a peak current up to 28 A (typically 18 A in our experiments) and a duration of 5 ns is injected from a thermionic gun (EIMAC, YU-156) into the SHB system. After being compressed to a single-bunch, the electron beam is accelerated to 10 – 30 MeV in the 1.3 GHz accelerating tube. The electron beam is transported via an achromatic beam transport line to the wiggler for the FEL system.

The OTR radiator, which converts electrons to photons, is placed at a position 320 mm downstream from the first bending magnet as shown in Figure 3. The screen is an aluminium plate having sizes of $55 \times 40 \times 1.6$ mm^3, and it is tilted vertically by an angle of 45° with respect to the

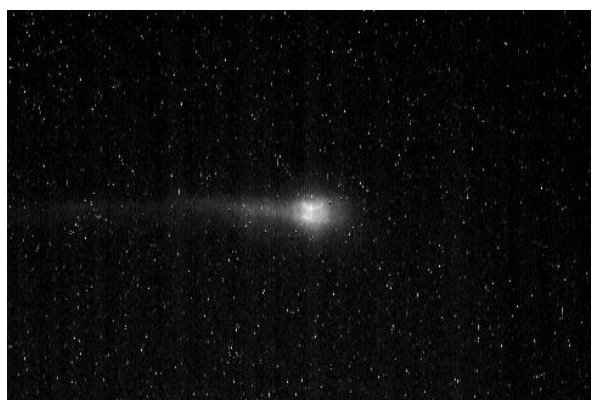

Figure 4: The OTR image of the beam profile measured using a CCD camera. The horizontal direction is the bending orbital plane of the electron beam. Left side of the image is lower momentum one.

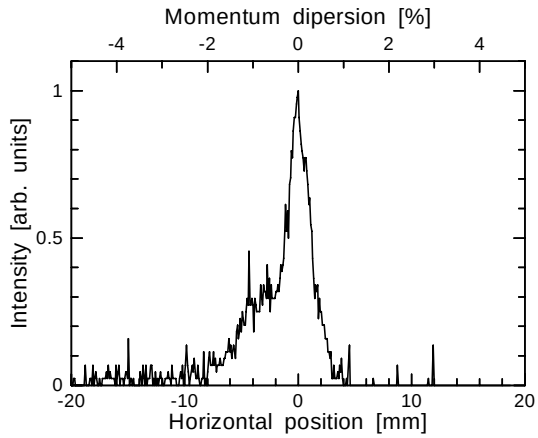

Figure 5: Momentum profile of the electron bunch obtained by integrating the OTR image in a vertical.

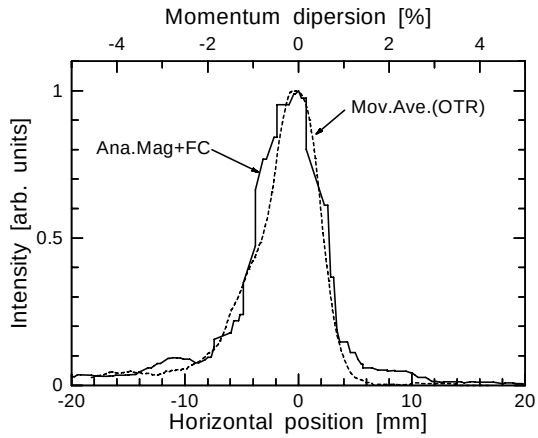

Figure 6: Momentum profiles of the electron bunch. The solid line is the momentum profile measured with an analyzer magnet and a faraday-cup current monitor. The dashed line is the profile obtained by moving average of the OTR profile within a ± 0.5 % width.

bending orbital plane, so that backward transition radiation is emitted in the vertical plane. The first mirror of the optical transport system is a concave mirror and it is placed the focal length away from center of the radiator, so that OTR image on the radiator, which diverges in the horizontal direction, is mostly included in the depth of field of the first mirror.

At first we have used a CCD camera, instead of the streak camera, for directly observing the OTR image. The camera (TAKEX, FC300M) is a progressive shutter camera and works with 659(H) × 494(V) pixels in 1/3 inch. A macro lens (Canon, J6X11) with a lens aperture of 40 mm was used for focusing. The camera was placed at a distance of 210 mm from the OTR radiator. In this configuration, an acceptance angle is approximately ± 0.1 radians, which is sufficient to capture the radiation emitted by the 20 – 30 MeV electrons.

EXPERIMENTAL RESULTS

An experiment is conducted with a single-bunch electron beam of 26.6 MeV energy. The normalized emittances are 165 π mm mrad in the horizontal direction and 160 π mm mrad in the vertical direction. A measured OTR image is shown in Figure 4. The horizontal and the vertical scales are 0.085 mm/pixel. Figure 5 shows the momentum profile of the electron bunch obtained by integrating the image in a vertical. Since dispersion function η is 0.4 m at the position of the OTR radiator, momentum resolution of the measurement system is estimated to be 0.02 %/pixel. Using the resolution, the momentum spread of the OTR profile was evaluated to be 0.4 % (full-width half-maximum). Figure 6 shows a momentum profile measured with a momentum analyzer magnet and a faraday-cup current monitor. The spectrum width of the profile is 1.6 %. The dashed line in Figure 6 shows the profile obtained by moving average of the OTR profile within a ± 0.5 % width. Since the both profiles have a similar width, the resolution of the analyzer magnet slit is estimated approximately to be 1 %. It turns out that the OTR monitor has a higher momentum resolution than the momentum analyzer system usually used.

SUMMARY

In order to measure the longitudinal phase-space profile of the electron beam, we are developing the measurement system consisted of an OTR radiator, a bending magnet and a streak camera. As a preliminary experiment, the momentum spectrum is obtained from the OTR profile, and the momentum resolution of the new system is evaluated. We are now preparing for the longitudinal phase-space measurement experiments.

ACKNOWLEDGEMENTS

The authors express their sincere thanks to Mr. T. Yamamoto for his technical contribution and Mr. S. Suemine for his support of linac operation. This research is partially supported by Japan Society for the Promotion of Science (JSPS), Grant-in-Aid for Scientific Research (C), 18540273, 2006.

REFERENCES

[1] R. Kato et al, Nucl. Instr. and Meth. in Phys. Res. A 445 (2000) 164.

[2] R. Kato et al, Nucl. Instr. and Meth. in Phys. Res. A 475 (2001) 334.

[3] R. Kato et al, Nucl. Instr. and Meth. in Phys. Res. A 483 (2002) 46.

[4] A. Doria et al., Nucl. Instr. and Meth. in Phys. Res. A 475, (2001) 296.

[5] J. Rönsch et al, “Longitudinal Phase Space Studies at PITZ”, FEL’05, Stanford, August 2005, p.552, http://www.jacow.org.

[6] H. Loos et al, “Experimental Studies of Temporal Electron Beam Shaping at the DUV-FEL Accelerator”, FEL’05, Stanford, August 2005, p.632, http://www.jacow.org.

[7] S. Zhang et al, “Temporal Characterization of Electron Beam Bunches with a Fast Streak Camera at the JLab FEL Facility”, FEL’05, Stanford, August 2005, p.640, http://www.jacow.org.

[8] T. Asaka et al, "Development of the quasi-non-destructive beam screen monitor", 27th Linear Accelerator Meeting in Japan, (2002).

[9] L. Wartski et al, IEEE. Trans. Nucl. Sci. NS-20 (1973) 544.

[10] M. Jablonka et al, “Beam Diagnostics Using Transition Radiation Produced By A 100 MeV Electron Beam”, PAC’91, San Francisco, May 1991, p.1534.

A COMPACT LOW EMITTANCE DC GUN EMPLOYING SINGLE CRYSTAL CATHODE OF LaB_6*

K. Kasamsook#, K. Nanbu, M. Kawai ,K. Akiyama, F. Hinode, T. Muto , T. Tanaka, M. Yasuda, H. Hama
Laboratory of Nuclear Science, Tohoku University,
1-2-1 Mikamine, Taihaku-ku, Sendai 982-0826, Japan

Abstract

Development of an electron gun capable of producing low emittance is in the interests of further applications of high brightness electron beam such as Smith-Purcell FEL [1] for example. A prominent point of this DC gun is that operation high voltage is very low (50 kV). Since a higher beam current of the macropulse is required in general, a cathode should have higher current density, while the smaller size of the cathode is preferred for lower emittance. Consequently we have chosen single crystal LaB_6 as the cathode, which can provide higher current with good homogeneity emission. Some numerical calculations have also been performed. There are some good agreement in calculated results between them. Numerical calculations show a normalized rms emittance is expected to be less than 5 π mm mrad. A state-of-the-art electron source will possibly open new scientific opportunities in the many fields.

INTRODUCTION

Nowadays, the demand for high-brightness electron gun has increased dramatically to achieve many applications in the field of electron beam technolygy. The low emittance DC electron gun at LNS is one of the candidates. This DC electron gun has no grid which would degrade beam emittance. The cathode is made of materials with the low work function, and heated to 1700 - 1900 K for producing electrons. We have employed the cathode voltage of -50 kV with respect to grounded anode and variable pulse duration from 1 to 5 μsec. This low voltage choice can make the entire system to compact. The schematic diagram of DC gun power supply is shown in Fig.1. In spite of such low voltage, the emittance can be reduced to very small because of a very short distance between the cathode and the anode. In order to produce low emittance beam, the cathode size should be small, so that the higher current density is required. Such high current density can be realized by some cathode materials such as single crystal LaB_6 [2] or CeB_6 [3].The design parameters and the drawing of the low emittance DC electron gun are shown in Table 1 and Fig.2, respectively.

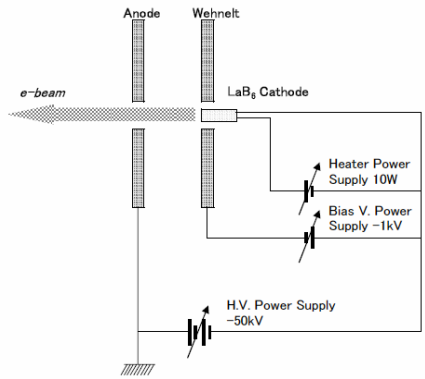

Figure 1: The schematic diagram of DC gun power supply.

Table 1: Design parameters of electron gun.

Beam energy	50 keV (Max.)
Peak current	>300 mA
Pulse width (FWHM)	1-5 μsec
Repetition rate	300 pps (Max.)
Normalized emittance	<10 π mm mrad.
Normalized thermal emittance	0.25 π mm mrad* *theoretical
Cathode diameter	1.75 mm.

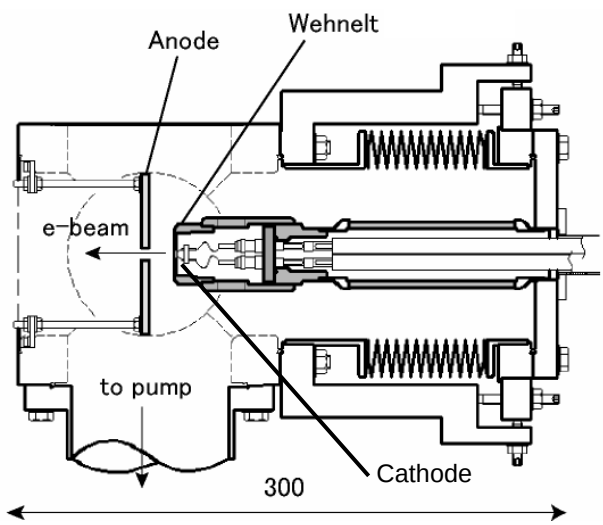

Figure 2: The low emittance DC electron gun.

*Work supported by KEK grant for accelerator science.
#kasam@lns.tohoku.ac.jp

THE LOW EMITTANCE DC GUN

LaB_6 cathode

The normalized rms thermal emittance of electrons emitted from a hot cathode is followed by equation (1):

$$\varepsilon_{\mathrm{n,rms}} = \frac{r_c}{2}\sqrt{\frac{k_B T}{m_o c^2}} \quad , \tag{1}$$

where r_C is the cathode radius, k_B is Boltzman's constant, m_0 is electron rest mass and T is the cathode absolute temperature. From the above relation, in order to obtain the small emittance less than 1 π mm mrad required for an example, the X-ray FEL application, the diameter of the cathode must be in the range of a few mm. On the other hand, high emission density (~12 A/cm^2) is required to produce a several hundred miliampere peak current from the small surface. The LaB_6 or CeB_6 can emit such an intense current over long lifetimes. A single crystal is preferable for obtaining low emittance because of its extremely flat surface with low porosity after surface material evaporation. The emission density is more uniform because the crystal orientation is the same over the whole surface. In recent years, single crystal LaB_6 cathodes are widely used for scanning electron microscope (SEM) and superior stability has been demonstrated. So, we decided to use a single-crystal LaB_6 cathode with a flat crystal surface shown in Fig.3. The diameter of our LaB_6 cathode is 1.75 mm. The 300 mA peak current will be produced when the cathode is heated to ~1900 K at vacuum level of 10^{-8} torr or better. The theoretical thermal normalized emittance is 0.25 π mm mrad.

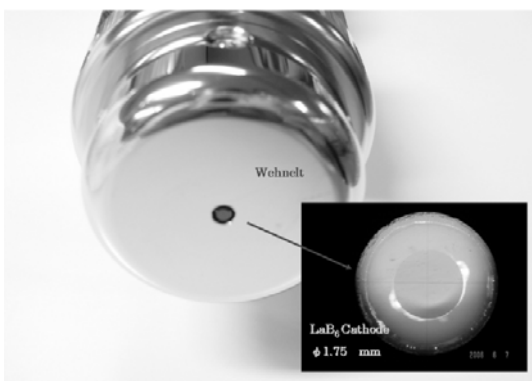

Figure 3: The assembly of single-crystal LaB_6 cathode.

High-voltage power supply

A high voltage DC thermionic gun uses a heated cathode to produce electrons, which are then initially accelerated with a DC pulse voltage. A low energy electron gun high-voltage power supply was developed for 0~-50 kV with 300 mA a peak current, a pulse width of 1-5 μsec, and pulse droop 0.1%, respectively. The wehnelt voltage can be adjusted from 0~-1 kV. In addition, a floating bias voltage can be applied between the cathode and the wehnelt to optimize the electric field for achieving the lowest emittance. In the case of the heater power supply, we use 1 V_{dc} and 12 A maximum current to feed the LaB_6 cathode.

The high-voltage power supply was tested by loading at an electron gun system to generate an electron beam.The beam current was measured by the Faraday plate. The cathode was heated up to ~1800 K and the current, 200 mA, was measured in the test chamber by applying 10 W of heater power. So, one of reasons to achieve peak current, 300 mA, is that we have to increase the absolute temperature of the cathode. Up to now, the cathode has been operated for 1000 hours without failure. Fig. 4 shows the measurement waveform of the accelerating voltage and beam current.

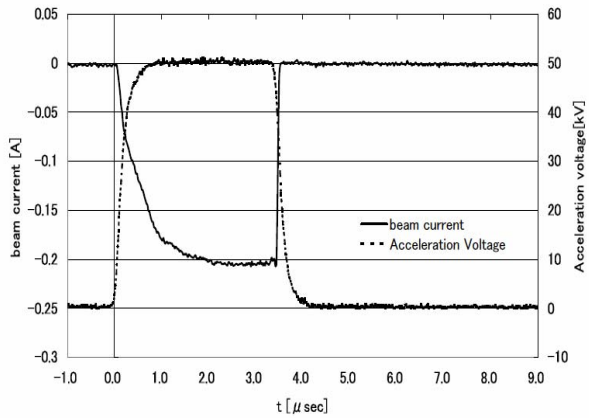

Figure 4: The measurement waveform of the accelerating voltage and beam current.

NUMERICAL CALCULATION RESULTS

We performed a computer simulation using 2 dimensional simulation code [KUAD2 v2.21] developed by Kyoto University [4,5] for 50 keV, 300 mA beam current and 15 mm cathode-anode distance in simple model. As shown in Fig.5, the beam trajectories diverge too much including the emittance growth due to space charge, which would result in a rapid increase in beam spot size. Nevertheless, the normalized emittance from the anode exit still has a small value (4 π mm mrad) at the longitudinal position far from the anode. Fig.6 shows the macro-particle distribution and the phase space distribution at the position 200 mm from the cathode. In addition, the simulation result shows electric field near the cathode surface is very sensitive to the emittance growth, which means the mechanical positioning of the cathode is very important. So we need special bias voltage between cathode and wehnelt to manipulate the electric field around cathode surface. On the other hand, we developed the 3 dimensional self-developed code 3-D FDTD [6] and compared with 2 dimensional simulation code. The trend of position dependence of the emittance is good agreement between them, and both of them still result in the small value of normalized emittance. The result of electron beam extraction and normalized emittance is shown in Fig.7, and the macro-particle

distribution and phase space distribution at the end point are shown in Fig.8.

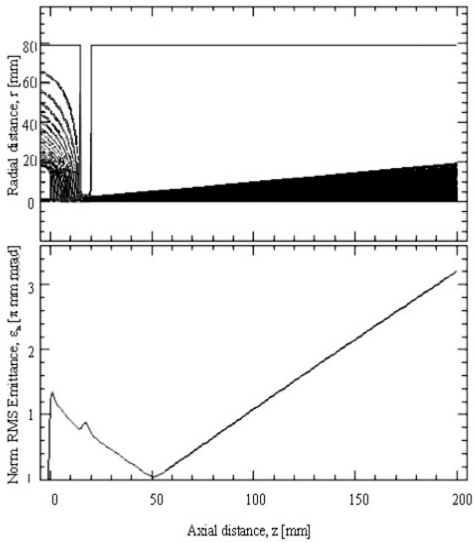

Figure 5: An electron beam extraction and normalized emittance of 300 mA in a DC gun according to a simulation with KUAD2.

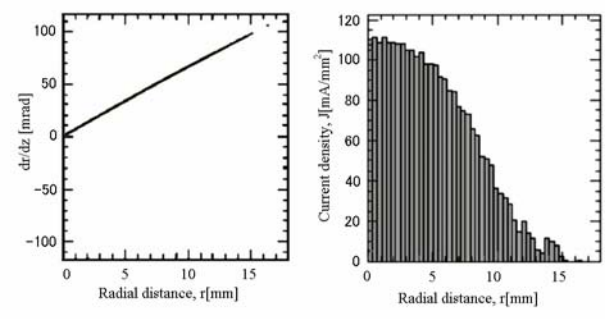

Figure 6: The macro-particle distribution and phase space distribution at the position 200 mm from cathode according to a simulation with KUAD2.

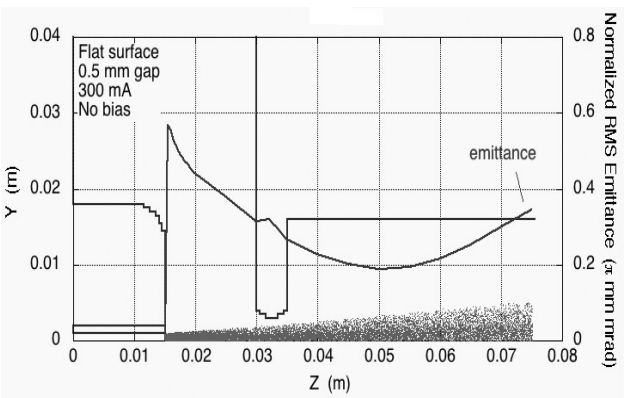

Figure 7: An electron beam extraction and normalized emittance of 300 mA in a DC gun according to a simulation with 3D FDTD.

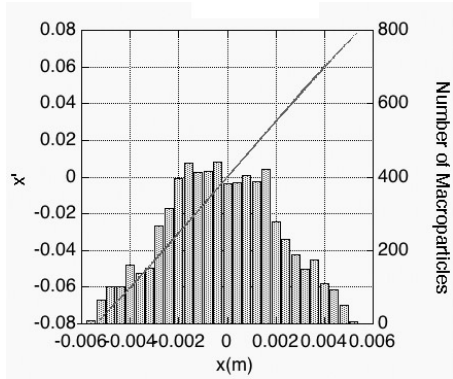

Figure 8: The macro-particle distribution and phase space distribution at the end point according to a simulation with 3D FDTD.

In another result of the 3D FDTD simulation, we applied bias voltage between wehnelt and cathode to manipulate the electric field around the cathode surface as shown in Fig.9. At the low bias voltage, a little focussing action, therefore, the emittance is gradually grow and become smoothly when the bias voltage was increased from 200 V to 400 V. The minimum point of emittance was shifted backward to cathode side by increasing of special bias voltage. At the high bias voltage, the negative field from wehnelt predominates and deflects the electron beam away from anode, so the 600 V case shows the over correction of emittance. This result shows that we can manipulate the equipotential line near the cathode surface by adjusting the special bias voltage to optimize the extracted beam emittance.

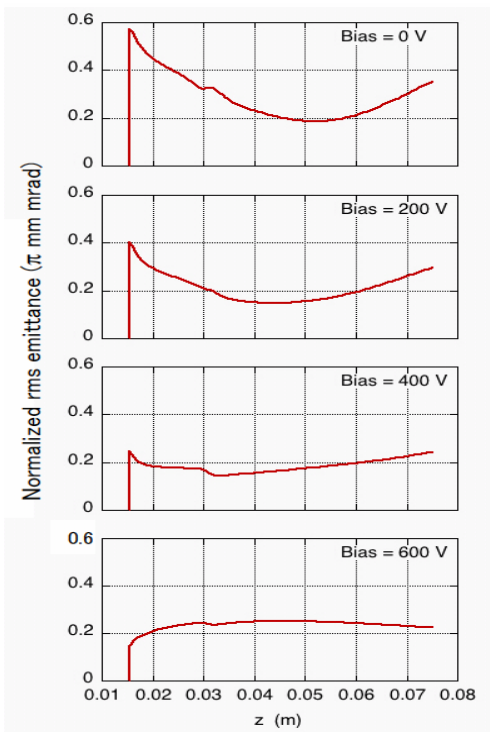

Figure 9: The bias voltage dependence of normalized emittance.

SUMMARY

Presently the DC gun has been examined on a test stand, and characteristics of the extracted beam from the gun are measured. Some numerical calculations have also been performed using 2 dimensional code and 3 dimensional self-developped code. There are some good agreement in calculated results between them. Moreover, both of them show the small value of normalized emittance. So that, the beam transportation after the gun should be carefully designed to keep such small emittance and utilize the beam. We can also apply special bias voltage to manipulate the electric field near the cathode surface.

ACKNOWLEDGEMENT

This work was supported by the KEK grant for related university accelerator science and the authors would like to thanks Prof. Kai Masuda for his 2 dimensional code calculation and the discussions.

REFERENCES

[1] K. Kim et al., Nucl. Instr. And Meth. A 475 (2001) 158.
[2] H. Kobayashi et al., Emittance Mearsurement for High-Brightness Electron Guns, 1992 Linear Accelerator Conf., Ottawa, Canada, August 1992.
[3] K. Togawa et al.,"CeB_6 Electron Gun for the Soft X-ray FEL Project at Spring-8",FEL2003, Tsukuba, Japan, September 2003.
[4] K. Masuda, private communication.
[5] K. Masuda, Development of Numerical Simulation Codes and Application to Klystron Efficiency Enhancement ,Ph.D thesis , Kyoto University(1997).
[6] H. Hama, et al., Nucl. Instr. And Meth. A 528 (2004) 371.

STABLE RF PHASE INSENSITIVE TO THE MODULATOR VOLTAGE FLUCTUATION OF THE C-BAND MAIN LINAC FOR SCSS XFEL

Jong-Seok Oh[1, 2, #], Takahiro Inagaki[1], Katsutoshi Shirasawa[1], Toru Hara[1], Tsumoru Shintake[1]
[1]RIKEN Harima Institute, [2]PAL/POSTECH.

Abstract

The SCSS (SPring-8 Compact SASE Source) XFEL [1] requires extremely stable RF system in both amplitude and phase. The pulse-to-pulse fluctuation of RF output is mainly caused by modulation of the klystron beam-voltage pulse, which is directly governed by the charging stability of a klystron modulator. During R&D study on beam stability, we found a special operation point, where the beam energy gain is insensitive to the modulator voltage fluctuation. This phase can cancel out the both fluctuations and provide constant accelerating field. The stable phase depends on the klystron parameters such as the length of drift tube, operating voltage, efficiency. It is about +9° in case of the C-band main linac for SCSS XFEL. The bunch length after bunch compressor is so short that additional longitudinal energy spread due to the RF curvature is about 5% of the one caused by the longitudinal wake field. The particle energy is high enough so that longitudinal defocusing is negligible. The reduction of beam energy due to off-crest acceleration is less than 2%. This paper shows the analytical relation of the stable phase. ELEGANT [2] simulation shows no appreciable degradation of the slice parameters.

INTRODUCTION

The stability of the beam acceleration is determined by the fluctuation of both RF power and phase that are mainly caused by the modulation of a klystron voltage pulse, which is directly governed by the PFN (pulse forming network) charging stability of a modulator. Therefore, it is useful to define the sensitivities of the RF parameters such as klystron voltage, RF phase and RF power by its relative stabilities to the one of a charging voltage. This paper analyzes the sensitivities of RF parameters and beam energy, and shows a special operation point, where the beam energy gain is insensitive to the modulator voltage fluctuation.

In general, off-crest acceleration makes the beam energy more fluctuate. However, at certain phase, it is possible for this fluctuation to be same as the one due to power fluctuation with opposite polarity in the falling slope with respect to beam. This phase is preferable to get the stable beam energy even under the voltage fluctuation of the klystron. This paper shows the analytical relation of the stable phase and experimental verification.

The longitudinal profile of a bunch has to be managed to fit the SASE requirements. Energy spread, slice emittance and peak current are analytically evaluated and compared with numerical results obtained by ELEGANT simulation.

#jsoh@postech.ac.kr

RF SENSITIVITY

The klystron voltage is directly determined by the PFN charging voltage in a modulator. The sensitivity of a klystron voltage defined by

$$s_V = \left(\frac{dV_K}{V_K}\right) / \left(\frac{dV_O}{V_O}\right) = \left(1+\frac{Z_{PFN}}{Z_K}\right) / \left(1+1.5\frac{Z_{PFN}}{Z_K}\right) \quad (1)$$

is obtained by using the Ohm's law

$$V_O = V_K + Z_{PFN} \times I_K \ , \quad (2)$$

and the klystron beam current

$$I_K = k\, V_\kappa^{1.5} \quad (3)$$

where V_o is a PFN charging voltage, V_K is a klystron voltage, Z_{PFN} is PFN impedance, k is a klystron perveance, Z_k is klystron impedance. At the nominal klystron voltage where the impedance is matched, the typical sensitivity of a klystron voltage becomes 0.8.

The RF phase ϕ_{RF} from a klystron [3]

$$\phi_{RF} = \phi_o - 2\pi\, f\, t_{transit} = \phi_o - 2\pi\left(\frac{c}{\lambda_{RF}}\right)\left(\frac{L_{KLY}}{v}\right) \quad (4)$$

is delayed from a driving input RF phase ϕ_o by the transit time $t_{transit}$ of a drift length L_{KLY} between the input cavity and the output cavity of the klystron with an electron velocity v where λ_{RF} is a wavelength in a free-space, c is the speed of light in vacuum. Therefore, the RF phase fluctuation of a klystron is

$$\left(\frac{d\phi_{RF}}{2\pi}\right) / \left(\frac{dV_K}{V_K}\right) = \left(\frac{L_{KLY}}{\lambda_{RF}}\right)\left(\gamma^2-1\right)^{-1.5}\left(\gamma-1\right) \quad (5)$$

where γ is the Lorentz factor of the electron. And the sensitivity of the RF phase is

$$s_\phi = \left(\frac{d\phi_{RF}}{2\pi}\right) / \left(\frac{dV_O}{V_O}\right) \approx \left(\frac{L_{KLY}}{\lambda_{RF}}\right)\left(\gamma^2-1\right)^{-1.5}\left(\gamma-1\right) \times s_V \ . \quad (6)$$

The typical sensitivity of the RF phase at 350 kV is 1.26 for a C-band klystron.

The RF power P_{RF} of a klystron is given by

$$P_{RF} = \eta\, I_K V_K = \eta\, k V_K^{2.5} \quad (7)$$

where η is the RF conversion efficiency of a klystron. Therefore, the RF power fluctuation of a klystron is

$$\left(\frac{dP_{RF}}{P_{RF}}\right) / \left(\frac{dV_K}{V_K}\right) = \left(\frac{d\eta}{\eta}\right) / \left(\frac{dV_K}{V_K}\right) + \left(\frac{dk}{k}\right) / \left(\frac{dV_K}{V_K}\right) + 2.5 \ . \quad (8)$$

Figure 1 shows the calculated relative variation of RF power, efficiency and perveance due to the klystron voltage fluctuation of the C-band klystron (Toshiba E3746A). The perveance dependency is relatively so small that it is neglected in the sensitivity of the RF power

$$s_P = \left(\frac{dP_{RF}}{P_{RF}}\right) / \left(\frac{dV_O}{V_O}\right) \approx s_\eta + 2.5\, s_V \qquad (9)$$

where s_η is the sensitivity of efficiency given by

$$s_\eta = (d\eta/\eta)/(dV_o/V_o) \quad . \qquad (10)$$

The efficiency variation of a klystron at low voltage has large effect on the sensitivity of RF power. The typical sensitivity of the RF power at 350 kV is 2.4 for the C-band klystron.

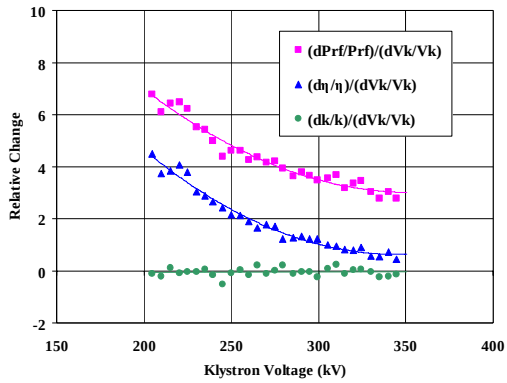

Figure 1: Relative variation of RF power (P_{rf}), efficiency (η), and perveance (k) of a C-band klystron.

ENERGY SENSITIVITY

The energy gain of an accelerating unit is

$$E \propto \sqrt{P_{RF}}\cos\phi_{RF} \quad . \qquad (11)$$

Thus, its relative fluctuation by a klystron is

$$\frac{dE}{E} = 0.5 \times \left(\frac{dP_{RF}}{P_{RF}}\right) - (2\pi \times \tan\phi_{RF}) \left(\frac{d\phi_{RF}}{2\pi}\right) \quad . \qquad (12)$$

Using Egs. (6) and (9), the sensitivity of energy gain is

$$s_E = \left(\frac{dE}{E}\right) / \left(\frac{dV_O}{V_O}\right) = 0.5\, s_\eta + 1.25\, s_V - 2\pi \tan\phi_{RF}\; s_\phi \,. \qquad (13)$$

Figure 2 shows the relative energy gain of C-band units as a function of operating RF phase with charging voltage variations at the klystron voltage of 350 kV. On a certain RF phase of the falling slope with respect to beam, which is marked by the circle in the figure, the amplitude is somewhat constant because the both fluctuations are cancelled out, which provides constant accelerating field. The energy gain is insensitive to the modulator voltage fluctuation around the stable phase satisfying following condition

$$\tan\phi_{RF} = \left(\frac{1}{2\pi\, s_\phi}\right)(0.5\, s_\eta + 1.25\, s_V) \quad . \qquad (14)$$

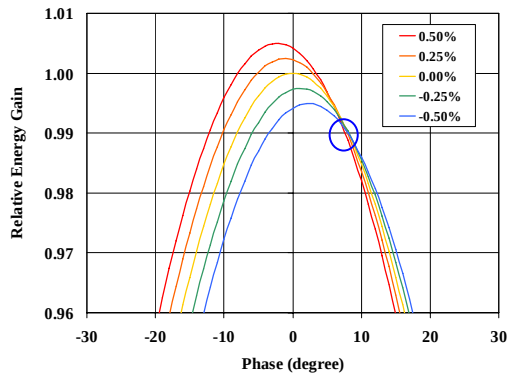

Figure 2: Relative energy gain vs. RF phase with charging voltage variations at the klystron voltage of 350 with a C-band klystron. The stable phase is +7.2° at 350 kV level.

Figure 3 shows the sensitivity of energy gain for the crest phase and the off-crest phase. The typical sensitivity of the energy gain at 350 kV is 1.2 for a C-band unit. The energy gain is insensitive over wide range of klystron voltage at the off-crest phase of +9°. A little large angle than +7.2° provides better sensitivity for wide operating range below 350 kV. The loss of energy gain by the off-crest acceleration is 1.2%.

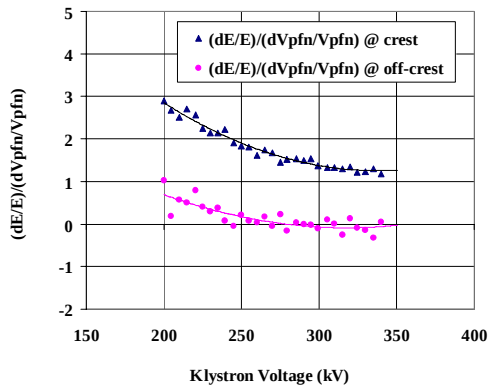

Figure 3: Relative variations of energy gain due to the fluctuation of the PFN charging voltage for crest phase and off-crest phase of +9°.

Including the effect of relative phase jitter σ_ϕ between injected beams and C-band RF at an arbitrary phase, the sensitivity of energy gain becomes

$$s_E^2 = \left(0.5\, s_\eta + 1.25\, s_V - 2\pi \tan\phi_{RF}\, s_\phi\right)^2 + \left(2\pi \tan\phi_{RF}\right)^2 \left(\frac{\sigma_\phi}{2\pi}\right)^2 / \left(\frac{dV_o}{V_o}\right)^2 \quad . \qquad (15)$$

EXPERIMENTS

The SCSS prototype accelerator has a C-band main linac after an S-band unit of an injector [4]. The main linac has two RF sources and increases the beam energy from 50 MeV to 250 MeV. The beam energy fluctuation is measured for different RF phases by the screen monitor located at the middle of a chicane having a dispersion of

150 mm. Figure 4 shows the measured beam energy fluctuation of the C-band main linac. The beam energy stability at crest for two C-band units is 0.34% (6σ); the stability of energy gain per unit is 0.59% (6σ). The energy fluctuation is sensitive to the operating phase and also is asymmetric with respect to the crest phase. The energy fluctuation at the off-crest phase of +10° is reduced to 50% level of the one at crest acceleration.

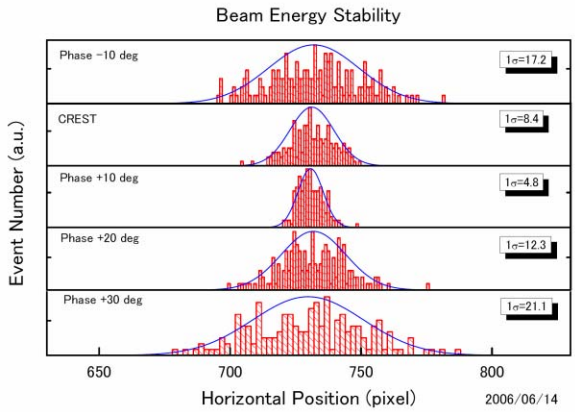

Figure 4: Beam energy fluctuation vs. RF phase of C-band main linac of SCSS prototype accelerator (0.01 mm/pixel).

Figure 5 shows the stability trend of energy gain per C-band unit normalized by the one at crest phase:

$$\left(\frac{dE}{E}\right)^2 / \left(\frac{dE}{E}\right)^2_{crest} = \left(1 - \frac{2\pi \tan\phi_{RF} s_\phi}{0.5 s_\eta + 1.25 s_V}\right)^2 + (2\pi \tan\phi_{RF})^2 \left(\frac{\sigma_\phi}{2\pi}\right)^2 / \left(\frac{dE}{E}\right)^2_{crest} \quad . \tag{16}$$

Each curve has different relative phase jitter normalized by the energy stability at crest, $(\sigma_\phi/(2\pi))/(dE/E)_{crest}$. For example, with 0.2% energy stability at crest, 50% normalized phase jitter corresponds to 0.1% relative phase jitter that is equivalent to 0.36°. Measured data (C-band 060614) in Figure 5 agree to the case of 50% normalized relative phase jitter. It means that the phase jitter is about 1.1° that corresponds to the timing jitter of 0.52-ps at C-band frequency.

At the off-crest phase satisfying Eq. (14), the energy stability becomes

$$\left(\frac{dE}{E}\right) = \left(\frac{0.5 s_\eta + 1.25 s_V}{s_\phi}\right)\left(\frac{\sigma_\phi}{2\pi}\right) \quad . \tag{17}$$

Then, it becomes ~ $\sigma_\phi/(2\pi)$ at 350 kV. Therefore, the total energy stability is directly determined by the phase jitter.

Measured data (C-band 060614) indicate that the minimum fluctuation of the beam energy is located at about +8° from the crest as expected. The fluctuation at this phase is limited by the phase jitter. The different set of measured data (C-band 060711) shows that the normalized relative phase jitter is increased to 100%, which is identified later to be caused by the instability of a maser RF oscillator.

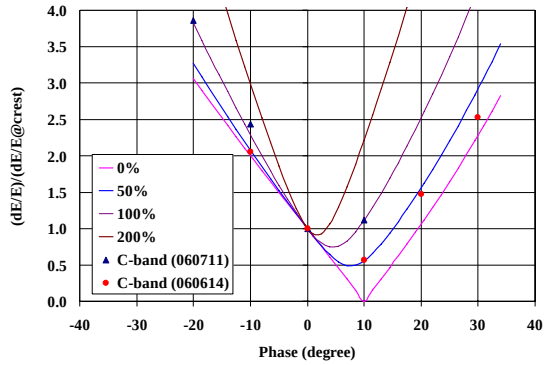

Figure 5: Stability of energy gain per C-band unit normalized by the one at crest phase for relative phase jitter of 0%, 50%, and 100%.

BEAM QUALITIES

The geometry of a C-band accelerating structure with iris radius *a*, cavity radius *b*, gap length *g*, and cavity period L_{cell} is shown in Figure 6. The short-range wakefield of the structure is evaluated by the K. Bane's formula [5]

$$W(s) = \frac{Z_o c}{\pi a^2} \exp(-\sqrt{s / s_{oo}}) \tag{18}$$

where

$$s_{oo} = \frac{g}{8}\left(\frac{a}{\alpha(g_{cell}/L_{cell})L_{cell}}\right)^2 \quad , \tag{19}$$

and

$$\alpha(\gamma) = 1 - 0.4648\sqrt{\gamma} - 0.0704\gamma \quad , \tag{20}$$

and $Z_o = 120\pi$ [Ω].

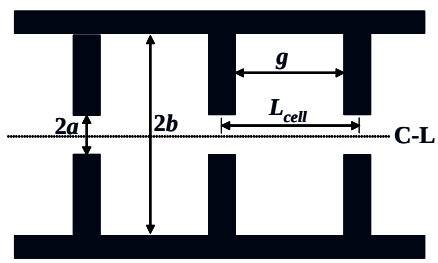

Figure 6: The geometry of a C-band accelerating structure: a = 7.6 mm, b = 21.2 mm, g = 15.2 mm, and L_{cell} = 19.682 mm.

With structure parameters of a C-band unit, s_{oo} = 982 μm, and $W(0)$ = 0.623 kV/pC/m. This paper uses the beam parameters given in the "Optimization of Parameters" of the 6-GeV SCSS CDR [1] where the accelerating gradient is 34.0 MV/m after the second bunch compressor BC2. The compressed bunch length *s* after BC2 is 24 μm. It is so short that the wakefield over the bunch is close to $W(0)$, then the longitudinal energy spread of a bunch due to the short-range wakefield with a bunch charge Q over a total accelerator length L is approximately

$$\Delta W \approx -eQW(0)L \quad . \tag{21}$$

There are 25 accelerator modules in the C-band main linac of the SCSS 6-GeV machine. Each module has 4 units of 1.8-m long structures. Therefore, total accelerating length is 180 and the longitudinal energy spread becomes -44.6 MeV. Considering the effect of finite bunch length, it is -40.1 MeV. The net change of head-tail energy spread through the C-band linac obtained by ELEGANT code is – 41.3 MeV as shown in Figure 7.

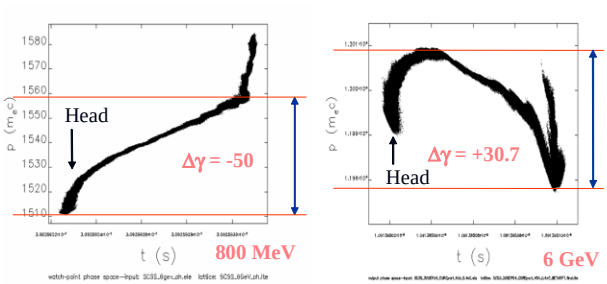

Figure 7: Structural wake effect on the longitudinal energy profile of a bunch (left: 800-MeV beam at the inlet of C-band main linac, right: 6-GeV beam after C-band main linac, bunch head at left side).

There is energy gain difference ΔW_{RF} between the head electron and the tail electron of a bunch, which is caused by the phase difference of RF fields along the bunch.

$$\Delta W_{RF} = \Delta[eEL\cos\phi] \cong -eEL\sin\phi_o\Delta\phi \tag{22}$$

where e is electronic charge, E is peak accelerating field. In case of 6-GeV SCSS design, eEL = 5200 MeV, and $\Delta\phi$ = 0.164° for s = 24 μm. Therefore, the energy spread due to the RF fields becomes -2.33 MeV for the off-crest phase of ϕ_o = +9°. This energy spread is 5.81% of the one caused by wakefield. The ELEGANT simulation shows the difference of -1.53 MeV as shown in Figure 8.

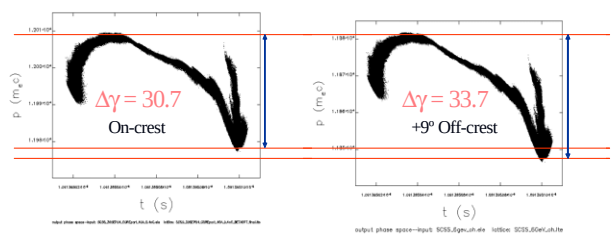

Figure 8: Comparison of longitudinal energy profile of a bunch for the on-crest acceleration (left) and +9° off-crest acceleration (right).

The slice parameters such as slice emittance and peak current are dominant governing parameters of SASE process. We have to keep the slice parameters as good as possible. It is confirmed that there is no appreciable degradation of slice parameters for off-crest acceleration as shown in Figure 9.

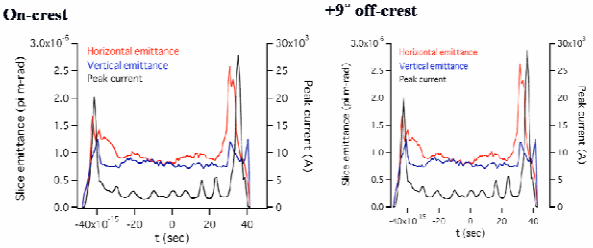

Figure 9: Horizontal slice emittance (top), vertical slice emittance (middle), and peak current (bottom) profile of a bunch (left: on-crest acceleration, right: +9° off-crest acceleration).

SUMMARY AND DISCUSSION

The SCSS XFEL is a challenging machine that requires extremely stable RF system. Therefore, it is critical issue to realize stable RF system for both phase and amplitude to provide stable XFEL. The phase-dependent stability characteristics are in detail analyzed and examined. It is confirmed that the off-crest phase of around +9° provides better stability in case of the C-band main linac for SCSS XFEL if phase jitter is small. The low-level RF control has to provide better stability than the one of a klystron modulator for this scheme to be effective. The reduction of beam energy due to off-crest acceleration is about 1%.

The additional longitudinal energy spread due to the RF curvature is about 5% of the one caused by the longitudinal wake field and there is no appreciable degradation of the slice parameters.

The RF unit for a velocity buncher or a bunch compressor is more sensitive to the RF fluctuation because of the off-crest operation to provide a necessary energy chirp. For example, the energy fluctuation is more than 4 times higher than the crest one at the typical off crest phase of -40° for SCSS accelerating units between BC1 and BC2.

REFERENCES

[1] http://www-xfel.spring8.or.jp
[2] M. Borland, “ELEGANT” LS-287, ANL, Argonne, IL 60439, USA.
[3] Linear Accelerators, P. M. Lapostolle and A. L. Septier, editors, North Holland Publishing Company, p322 (1970).
[4] T. Hara, “Electron Beam Simulations on the SCSS Accelerator,” the 26th International Free Electron Laser Conference, Italy, 2004.
[5] K. L. F. Bane, “Short-Range Dipole Wakefields in Accelerating Structures for the NLC,” SLAC-PUB-9663, LCC-0116, 2003.

ANALYSIS OF INVERTER CHARGING WAVEFORM FOR ULTRA STABLE SCSS MODULATOR

Jong-Seok Oh[1, 2, #], Takahiro Inagaki[1], Katsutoshi Shirasawa[1], Tsumoru Shintake[1]
[1]RIKEN Harima Institute, [2]PAL/POSTECH.

Abstract

The SCSS (SPring-8 Compact SASE Source) XFEL [1] requires ultra stable RF sources. The SCSS smart modulator driving a klystron RF source uses an inverter charging system. Therefore, the stability of RF sources is directly determined by the one of inverter power supplies. The regulation and the stability of an inverter depend on not only the structure of inverter topology but also the fidelity of a signal monitoring. For better stability, we need stable and adequate monitoring of a charging voltage. The charging waveform is composed of a net PFN (pulse forming network) voltage and ripple components that is related to the system-dependent circuit parameters. This ripple is proportional to the ratio of the PFN capacitance to the stray capacitance of a pulse transformer and a klystron load. We can manipulate the feedback signal with suitable filtering but it is shown that the charging stability depends on the way of signal conditioning also. The long-term drift has to be minimized by the temperature stabilization of the probe and feedback circuits.

INTRODUCTION

The SCSS XFEL uses normal conducting technology for beam acceleration, in which pulse-to-pulse power fluctuation in RF-system dominates beam stability. The RF output is mainly fluctuating due to the pulse-to-pulse variation of a klystron voltage that is determined by the PFN charging voltage of a modulator. The inverter is responsible to the RF stability because it charges the PFN capacitor. In order to stabilize the charging level, we need a clean and stable signal for the PFN voltage. There are not only pulse forming network capacitors but also protective series resistors and distributed reactive components of a pulse transformer and a klystron load in the charging path. Therefore, the charging waveform becomes somewhat complicated. The understanding of the charging waveform and the proper conditioning of feedback signal is necessary to realize an ultra stable charging performance. This paper shows the detail analysis of the charging waveform of SCSS modulators and the stability dependency on the signal conditioning.

SCSS MODULATOR

Figure 1 shows the circuit topology and its charging waveform for inverter charging scheme using a constant current source. This scheme is compared with the ones of the traditional resonant charging scheme using a constant voltage source. The inverter topology provides high reliability: a thyratron switch is safely turned off because next charging schedule is digitally controllable, it is inherently fail-safe system under short-circuit condition due to the current limit feature of a constant current power supply. In addition, it is naturally compact by using a high frequency inverter. Also it has other attractive features: expandability, easy maintenance, and flexible control interface [2]. These features are well matched to the next generation modulator for SCSS XFEL facility.

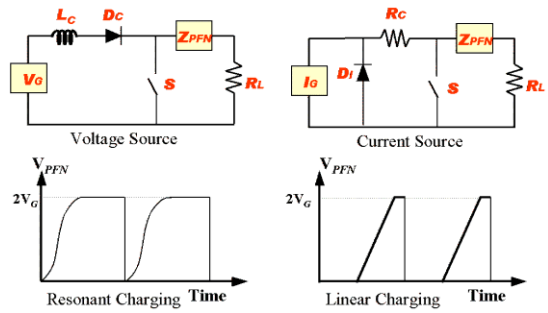

Figure 1: Basic circuits and charging waveforms of a voltage source and a current source power supply.

Figure 2 shows the simplified circuit diagram of SCSS modulator that consists of a PFN, a thyratron switch, a pulse transformer, and an inverter power supply as a PFN charging unit. The inverse voltage is limited by a tail circuit absorbing the magnetic energy stored in the pulse transformer. The main specifications are as follows; 114-MW peak power, 30-kW average power, 60-pulse per second, 3.8-μs pulse width, 1:16 step-up ratio, 350-kV peak voltage (secondary side) [3].

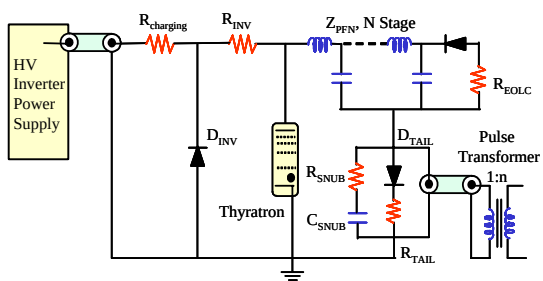

Figure 2: Simplified circuit diagram of SCSS modulator.

Figure 3 shows detailed charging waveforms of a C-band modulator (C_{PFN} = 0.4 μF) around the charging level of 38 kV. The average increment of charging step ΔV_{PFN} is about 100 V with a switching frequency f of 34.6 kHz; therefore, the average charging current I_{dc} is 1.38 A at this charging level according to the following equation.

$$I_{dc} = C_{PFN} \Delta V_{PFN} f \qquad (1)$$

#jsoh@postech.ac.kr

The charging voltage is not rising smoothly and monotonically but includes high-frequency spikes. The magnitude of spikes is larger than the increment of charging level for each switching cycle. The voltage waveform at the pulse transformer secondary shown in the figure has similar oscillating pattern. Therefore, it is expected that the spike is made by the circuit components connected in parallel to the pulse transformer. The noisy spikes seem to be harmful for the feedback circuit to correctly compare the charging level with a reference level.

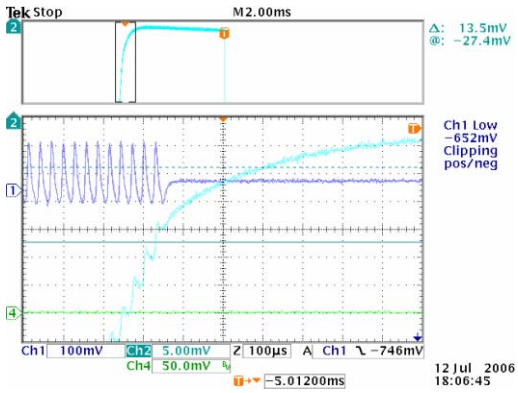

Figure 3: Waveforms of charging buckets (Upper box: charging voltage waveform, Lower box: expanded view of square box marked on the upper box for pulse transformer secondary voltage (upper curve, 1.18 kV/div) and PFN charging voltage (lower curve, 100 V/div), Horizontal: 100 µs/div)

ANALYSIS OF CHARGING WAVEFORM

In order to analyze the circuit response of charging current, it is useful to know the Fourier components of charging current. The inverter output is a full-wave rectified current as shown in Figure 4.

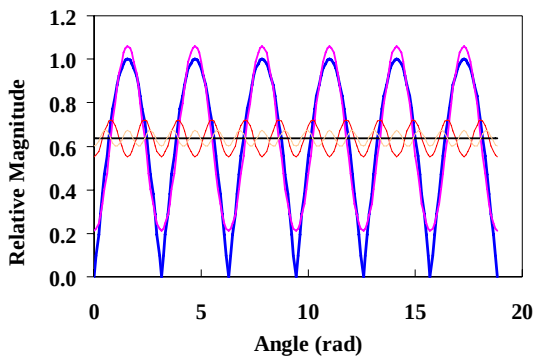

Figure 4: Full-wave rectified current (thick blue line) and Fourier series.

It has an average value of I_{dc} and higher frequency components I_{ac}. The average current is 2/π of a peak value I_{peak}. The second harmonic current is dominant and it is 4/(3π) of the peak value according to Eq. (2). Therefore, the magnitude of second harmonic current is 66.7% of the average charging current; I_{ac} = (2/3) I_{dc}.

$$\frac{I_{ac}}{I_{peak}} = -\frac{4}{\pi}\sum_{n=2}^{\infty}\frac{\cos n\omega t}{(n+1)(n-1)} \quad (n = even\ only)$$
$$= -\frac{4}{\pi}[\frac{1}{3}\cos 2\omega t + \frac{1}{15}\cos 4\omega t + \ldots] \approx -\frac{4}{3\pi}\cos 2\omega t \qquad (2)$$

The output current from an inverter power supply, I, has to flow through the series impedances of R_1, R_2, Z_{PFN}, and Z_L in the equivalent charging circuit shown in Figure 5. The charging current flows through the complicated load impedance network Z_L. The spike voltage is generated by oscillation caused by the total stray capacitance and the magnetizing inductance of a pulse transformer.

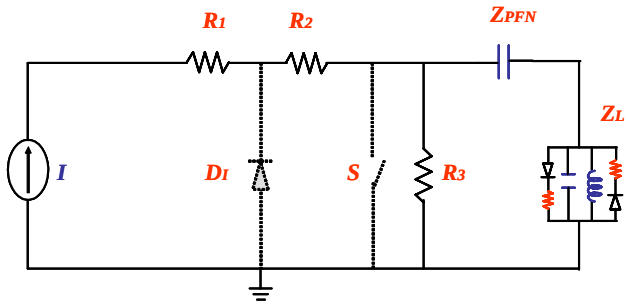

Figure 5: Equivalent charging circuit.

To improve the present stability of SCSS modulators, it is planed to use an ultra stable inverter power supply that is operating in parallel with a main inverter. The concept and design example is described in Ref. [4]. This inverter has small charge per switching with higher switching frequency. The frequency response of the charging network of a SCSS modulator measured because of the possibility of a resonance, which distorts the charging waveform. Figure 6 shows the measured data and the calculated frequency response by the circuit model. The phase transition occurs at 40 kHz that is caused by the parallel resonance driven by the magnetizing inductance L_{mag} of a pulse transformer and total stray capacitance C_{stray} of a pulse transformer and a klystron load. Series resonance at higher frequency of Figure 6-(b) is driven by C_{stay} and a series inductance in the charging path.

The second harmonic current of a SCSS modulator is capacitive-coupled because its frequency is higher that 40 kHz. There is no resonance till 250 kHz and the gain is monotonically decreasing. Therefore, higher frequency is able to be applied without serious waveform distortion for a high precision inverter up to 100 kHz.

The ripple voltage, V_{ac} introduced by the second harmonic current through a stray capacitive impedance X_c (=2πfC_{stray}) is given by

$$V_{ac} = I_{ac}X_c = I_{dc}/(6\pi f C_{stray}) \ . \qquad (3)$$

The ripple factor defined by $2V_{ac}$ / ΔV_{PFN} is the relative magnitude of the ripple voltage to the increment of a charging voltage per one cycle of an inverter switching. By using Eq. (1) and (3), the ripple factor is

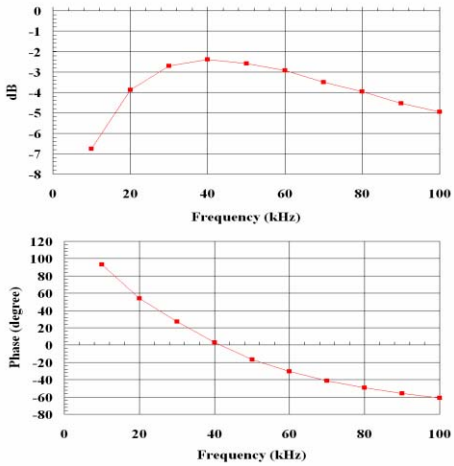

(a)

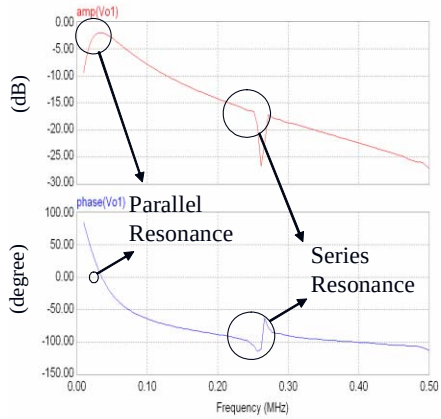

(b)

Figure 6: Frequency response of a charging network of a SCSS modulator: (a) measured data, (b) circuit simulation.

$$2V_{ac}/\Delta V_{PFN} = C_{PFN}/(3\pi C_{stray}) \quad . \tag{4}$$

Table 1 shows the summary of ripple voltage parameters for the SCSS modulator. In order to verify this evaluation, equivalent circuit analysis is performed.

Table 1: Ripple voltage parameters of charging waveform

PFN capacitance, C_{PFN}	0.4 μF
Average charging current, I_{dc}	1.58 A
Switching frequency, f	34.6 kHz
Increment of charging, ΔV_{PFN}	114.2 V
Stray capacitance, C_{stray}	25.9 nF
Ripple current, I_{ac}	1.05 A
Charging impedance, X_c	88.8 Ω
Ripple voltage, V_{ac}	93.2 V
Ripple factor, $2V_{ac}/\Delta V_{PFN}$	1.63

Figure 7 shows the simulated charging waveform with the conditions given in the Table 1. Figure 7(a) is the initial charging waveform. The net PFN voltage (VPFN-V_primary) is monotonically increasing but the PFN voltage (VPFN) has 100-V ripple with second harmonic frequency. It shows that the DC component I_{dc} is flowing through the magnetizing inductance of a pulse transformer (I_Lmag) and AC ripple current is mainly flowing through the stray capacitance (I_Cstray). Figure 7(b) is the charging waveform at the 38 kV level. The former half of the full-wave rectified current is gradually increasing to two-time large value than the initial one, and the latter half is gradually decreasing to zero. Accordingly, the diode in the tail circuit is turned on as the positive primary peak is increasing. At last, it becomes half-wave rectified waveform having a two times large peak current but the net average charging current is still same.

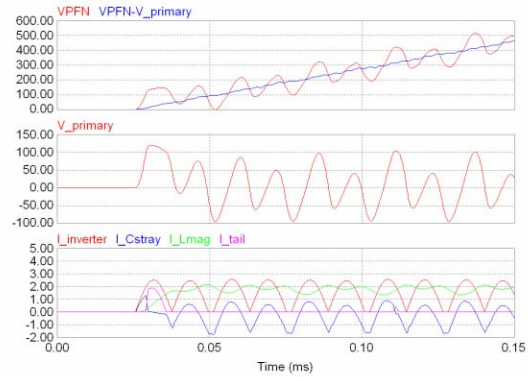

(a)

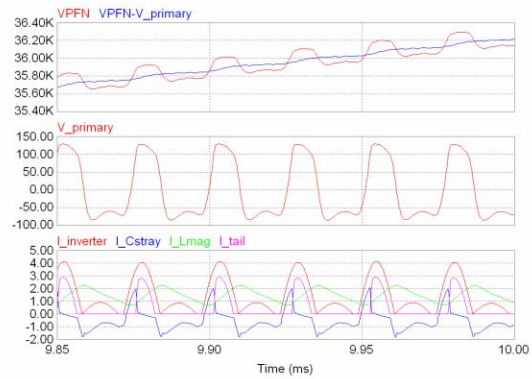

(b)

Figure 7: Simulated charging waveforms: "V_PFN" = PFN voltage from ground potential, "V_PFN - V_primary" = net PFN voltage: (a) initial charging waveform, (b) charging waveform around 36 kV.

The Fourier series of the higher harmonic for the half-wave rectified waveform depicted in Figure 8, is described by

$$\frac{I_{ac}}{I_{peak}} = \frac{1}{2}\sin\omega t - \frac{2}{\pi}\sum_{n=2}^{\infty}\frac{\cos n\omega t}{(n+1)(n-1)} \quad (n \text{ even only})$$
$$= \frac{1}{2}\sin\omega t - \frac{2}{\pi}\left[\frac{1}{3}\cos 2\omega t + \frac{1}{15}\cos 4\omega t + \ldots\right] \quad . \tag{5}$$

The dominant term now has same frequency as the switching one and its magnitude is 50% of the average

charging current that is similar to the one of dominant term for the full-wave rectified waveform. Therefore, its ripple has same magnitude as the one of full-wave mode.

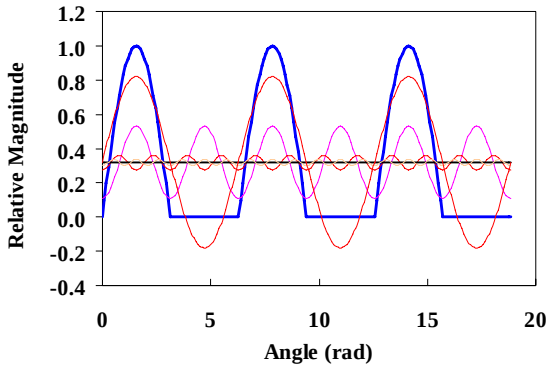

Figure 8: Half-wave rectified current (thick blue line) and Fourier series.

EFFECT OF SIGNAL FILTERING

The charging voltage is determined by the command reference. The reference level is compared with a feedback signal coming from a high voltage probe. Therefore, not only the reference level but also the feedback signal has to have high fidelity and stability. Figure 9 shows how improper conditioning of monitoring signal affect the charging stability under the reference level of 30 kV. The high frequency ripple on the rising slop of a feedback signal is well filtered out in the case (a); 1-kHz low pass filter. The charging voltage is regulated at the level higher than the reference one. Therefore, it is not able to correct the time dependent variation of the droop of top level. If the circuit has low frequency cut below 0.5 Hz, then, the actual PFN voltage is gradually rising even the comparator circuit is feeling the same level of feedback signal as shown in the case (b).

SUMMARY AND DISCUSSION

The SCSS modulator has many features fitting to the XFEL application, which are provided by adopting the inverter power supply that is one of governing factors for the stability of electron beams of SCSS linac. The ripple voltage superimposed on the PFN charging waveform is analyzed as a function of circuit parameters. It is found that the ripple factor is proportional to the ratio of the PFN capacitance to the stray capacitance. The conditioning of the feedback signal has large effect on the regulation of PFN voltage. The understanding of the charging waveform and the proper conditioning of feedback signal is essential to realize an ultra stable charging performance.

It is possible to measure the net differential voltage by using an additional probe that has equally calibrated and balanced for high frequency response.

The high voltage components of a probing system such as resistors and capacitors are temperature sensitive elements. The devices on the low level feedback circuits

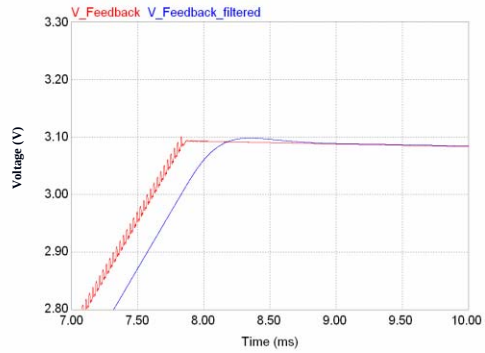

(a)

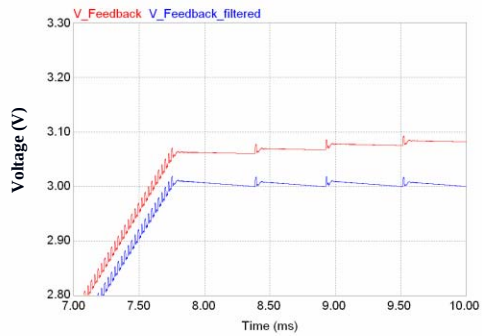

(b)

Figure 9: Regulation characteristic for different filtering of a feedback signal with high voltage probe attenuation of 1/10,000: (a) 1 kHz low pass filter, (b) 0.5 Hz high pass filter.

also have thermal drift. Therefore, it is essential to stabilize the temperature of the probe and feedback circuits to remove the long-term slow drift of beam energy.

REFERENCES

[1] http://www-xfel.spring8.or.jp
[2] J. S. Oh, et. al., “Development and Application of an Inverter Charging Supply to a Pulse Modulator,” the XXI International LINAC Conference, Korea, 2002.
[3] T. Inagaki, et. al., “High Power Test of the Compact, Oil-Filled Modulator for C-band Klystron,” the third Asian Particle Accelerator Conference, Korea, 2004.
[4] J. S. Oh, et. al., “Development of an Ultra Stable Klystron-Modulator for PAL XFEL,” the 27th International Free Electron Laser Conference, USA, 2005.

ELECTRO-OPTIC SAMPLING METHOD USING HIGH DC VOLTAGE APPLYING SETUP*

Yong-Woon Parc#, Changbum Kim, Jung Yun Huang, Jangho Park, Sung-Ju Park, In Soo Ko,

PAL, Pohang, Korea

Xiang Dao,
Department of Engineering Physics, Tsinghua University, Beijing, China.

Abstract

A RF photo-cathode (RF PC) gun with 1.6 cell cavity is installed at GTS(Gun Test Stand) being built at the Pohang Accelerator Laboratory (PAL). The short, intense, and low emittance electron beams are produced by the RF PC gun. For the successful construction of PAL-XFEL, the timing jitter and bunch length of the beam at the exit of the gun should be measured accurately. EOS (Electro-Optic Sampling) is a very promising method to measure the jitter without any interference with the electron beam. The spatially resolved method will be used in this experiment, which is a single shot measurement using cooled CCD carmera due to very low energy. Before the measurement with the beam at the exit of the gun, the calibration experiment is done with DC high voltage applying setup with 1mm thick ZnTe crystal. The broadening of our laser pulse by the ZnTe crystal will be measured with auto-correlation method to know the resolution limit in this experiment and to do data analysis properly. In this presentation, the result of calibration experiment will be presented with a description of the experiment in detail and simulation result for low energy beam.

INTRODUCTION

EOS (Electro Optic Sampling) method to measure short, intense electron beam which is essential to construct XFEL light source is developed greatly in last few year [1,2,3,4]. For the successful construction of XFEL light source, the monitoring of timing jitter of electron beam is crucial in online condition. The method can be used for monitoring the timing jitter of all section of the light source for example injector, bunch compressor, undulator sections. We are now trying to measure the electron beam at the injector part of XFEL to be constructed in PAL. A 2 MeV electron beam with a tunable bunch length and 0.2nC bunch charge has recently been realized at PAL[5,6].

* This work is supported by the KOSEF under the contract number R01-2006-000-11309-0 and also by the Ministry of Science and Technology.
#young1@postech.ac.kr

THEORY

The theory for the signal detection scheme of EOS is well described in ref[7], so we give only a short summary of it here.

Balanced detection scheme

The vertical and horizontal polarized part intensities of the incident laser to the ZnTe crystal is changed due to the birefringence of the crystal induced from the electron electric field. The analytic expression is in Eq.(1),(2)

$$\Gamma = \frac{\omega_0 d}{c}\left(n_h - n_v\right) = \frac{\pi d}{\lambda_0} n_0^3 r_{41} E_0 \qquad (1)$$

$$I_h - I_v = \left|\mathrm{E}_h\right|^2 - \left|\mathrm{E}_v\right|^2 = E_0^2 \sin\left(\Gamma\right) \qquad (2)$$

where the Γ is the relative phase shift between the two polarized parts of the laser field, and d is the crystal thickness.

Layout

In order to understand the theory for the signal detection scheme of EOS, the layout is described in detail in Fig. 1. The linearly polarzed laser experiences the birefringence in EO crystal due to electric field from the electron beam. The difference of the vertical and horizontal part of the laser field can be measured with quarter wave plate and Wollaston prism with sine function proportionality as mention in above section.

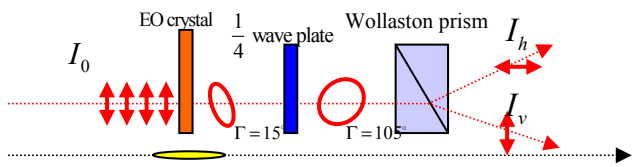

Figure 1: Layout of Electro-optic sampling

DC SETUP EXPERIMENT

To test the EO crystal response to the electric field strength, we made a high DC voltage applying setup. The result is shown in Fig. 2.

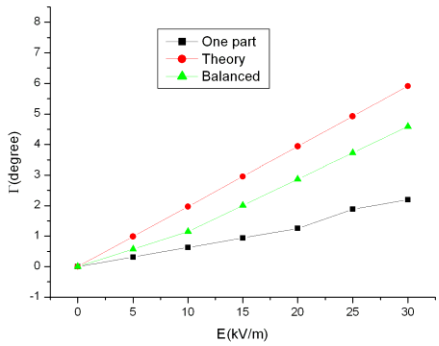

Figure 2: The response of the ZnTe crystal in DC electric field. The circle(red line) is theory, the triangle(green line) is balanced detected result and the square(black line) is measured result from the vertical part of the laser using single photodiode

The result showed that the crystal which thickness is 3.2 mm used in this experiment followed the theory well.

SIMULATION

Simulation method for Thz propagation

The ZnTe crystal showed frequency dependent refractive index which is propotional to the electric field called Pockel effect. The electric field profile due to the electron longitudinal profile is Fourier transformed to know the response of the electric field inside the crystal. We know the speed of each Fourier component in the crystal, which make us possible to reconstruct the field profile passing through the crystal. The field profile is shown in Fig. 3 with time domain representation.

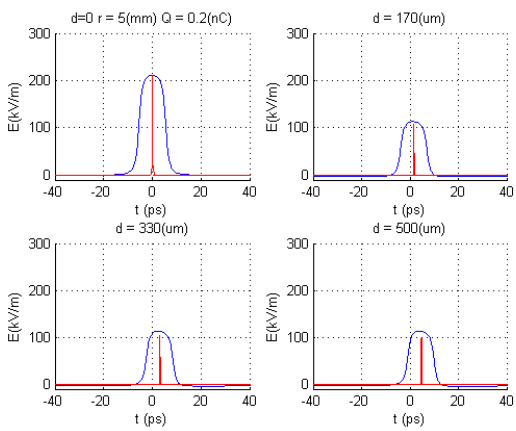

Figure 3: Electric field propagation in the crystal. The blue line showed the electric field strength, the red line showed the laser pulse. The r is the distance between the laser and electron beam and d is the thickness of the crystal.

Ring approximation of electron beam

The exact field profile of the electron beam is complicated to expressed in an analytic form. Instead of the exact field profile, we can use the ring approximation which has an exact solution which allowed the relativistic expression. The result showed that we can make almost exact field profile with only two terms, one is monopole term and the other is quadrupole term. The quadrupole term amplitude is very small compared to the monopole term. The Equation(3) showed the relativitic expression of the ring approximation.

$$E_r = \frac{q\gamma}{4\pi\varepsilon_0}\left[\frac{r}{\left(\gamma^2v^2t^2+r^2\right)^{3/2}} - \frac{a^2}{4}\left(\frac{2r}{\left(\gamma^2v^2t^2+r^2\right)^{5/2}} + \frac{5r\left(2\gamma^2v^2t^2-r^2\right)}{\left(\gamma^2v^2t^2+r^2\right)^{7/2}}\right)\right] \quad (3)$$

In the above equation, q is the charge of the electron beam and v is the velocity of the beam and r is the distance between the laser passing point and the electron beam. In Fig. 4, the green line shows the field profile in the free space and the blue line sowes it in the crystal which is smaller than free space case because of the reflection in the surface of the crystal due to the boundary condition of electro-magnetic theory.

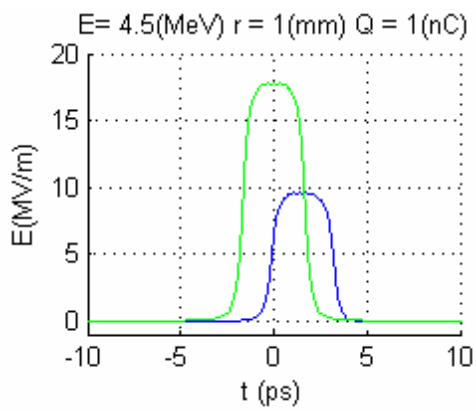

Figure 4: Electric field strength in free space (green) and in the crystal (blue).

Balanced signal

The laser pulse speed and the Thz radiation speed in the crystal is not same which makes the slippage between two pulse. In our simulation, we calculate the relative phase shift from the integral with 50 sections of the crystal.

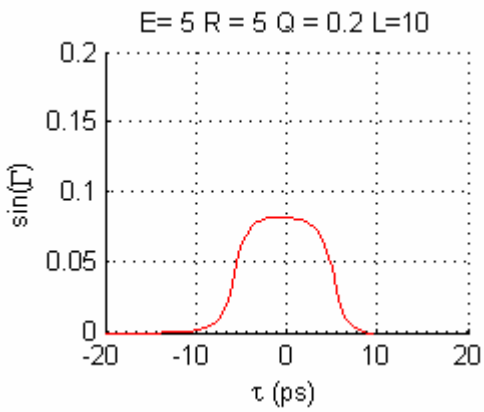

Figure 5: The simulated balanced signal of low energy beam which energy is 5MeV, beam charge is 0.2nC and the pulse length is 10ps uniform beam. R the distance between the laser and electron beam is 5mm. τ is the arrival time of the laser at the crystal compared to the electron beam.

The result showed that the low energy beam of the injector of XFEL can also be measured with EOS very successfully. The signal level is almost 1/10 of initial laser intensity incident in the crystal which is very easily detected using phtodiode or balanced detector.

LOW ENERGY BEAM DIAGNOSITICS

At present, we completely installed the EOS experiment setup in the GTS(Gun Test Stand) in PAL. The coarse timing of the arrival time of electron beam and laser beam at the crystal is solved with measurement of all path of the UV and IR laser and the distance between the gun cathode and electro optic crystal chamber. Belanced detector signal is observed easily in the oscillocope which is not saturated. We moved two mirrors in the path of 800nm laser beam to make time delay between electron beam and laser beam to find exact synchronization to see the change of the signal. The precision timing will be done very accurately with balanced detector. Sampling method is not appropiate to measure the bunchlength due to the electron arrival time jitter. Instead of the sampling method, the spatial method which is using the CCD carmera to take a picture of the laser gives a way to measure the bunch length and timing jitter simultaneously.

REFERENCES

[1] X. Yan et al., Phys. Rev. Lett. 85, p 3404 (2000).
[2] I. Wilke et al., Phys. Rev. Lett. 88, p 124801 (2002).
[3] G. Berden et al., phys. Rev.. Lett. 93, p 114802 (2003).
[4] A. L. Cavalieri et al., phys. Rev.. Lett. 94, p 114801 (2005).
[5] Jangho Park et al., to be appeared in FEL2006 (2006).
[6] Tae-Yeon Lee et al., to be appeared in FEL2006 (2006).
[7] M. Bruken et al., TESLS Report 2003-11, (2003).

PRELIMINARY MEASUREMENT OF EMITTANCE EVOLUTION USING EMITTANCE METER AT THE PAL*

Jangho Park#, Sung-Ju Park, Changbum Kim, Yong-Woon Parc, Jung Yun Huang, and In Soo Ko,
Pohang Accelerator Laboratory, POSTECH, Pohang 790-784, Korea
Xiang Dao, Department of Engineering Physics, Tsinghua University, Beijing 100084, China
X.J. Wang, NSLS, Brookhaven National Laboratory, Upton, NY 11973, USA.

Abstract

A high-brightness electron beam is emitted from a RF photocatoode gun with 1.6 cell cavity from October 2005 at the Pohang Accereator Laboratory (PAL). The project of 4th Generation Light Source (4GLS) with the Spontaneous Amplification Sponteneous Emission Free-electron Laser (SASE FEL) in the PAL is called Pohang Accereator Laboratory X-ray Free-electron Laser (PAL-XFEL). In order to success of the PAL-XFEL project, it is necessary to research the high-brightness electron beam at the injector. A emittance meter (E-Meter) is installed for the high-brightness research in GTS (Gun Test Stand). The measurement of transverse emittance and beam size profile along the longitudinal direction was done by the E-Meter. Precise measurement of the emittance profile will be provided with a powerful tool for the commissioning of the 4GLS injectors based on the emittance compensation principle. We are going to achieve this with the use of slit-based E-Meter that can be moved along the longitudinal direction. In this article, we present a preliminary measurement of the emittance evolution with the E-Meter for the commissioning of the photocathode RF gun.

INTRODUCTION

The Pohang Accelerator Laboratory X-ray Free Electron Laser (PAL X-FEL) is proposed with self amplifiered spontanous emision (SASE) lasging sheme that will use the final 3.7 GeV for the drive beam energy [1-2]. The performance of the PAL X-FEL in the 3.0 Angstrom regime is predicted on the capacity of 1 nC, 100 A beam at the end of the photoinjetor with transverse normalized rms emittance of 1.2 π mm mrad. For the low emittance beam, emittance compensation scheme is essential for the design and commitioning of the photoinjector.

In this paper, we review and report the emittance evolution in the beam drift region with emittance meter (E-Meter). This paper is composed of previous work on the subject of the emittance evolution measurements systems and the preliminary measuring of the beam emittance evolution of the photocathode rf gun. We then describe preliminary experimental result at the PAL where the slit based emittance measurement technique is used to measure the emittance evolution of the PC RF gun. The results of the experiment, which show that a possibility of the emittance evolution measurement found with the E-Meter, are compared with simulation.

*Work supported by the CHEP and the KOSEF (Project No.: R01-2006-000-11309-0) of Korea.
#wpjho@postech.ac.kr

EMITTANCE COMPENSATION

The emitance compensation is a technique used to reduce the normailzed rms emittance of the beam at the photoinjector. The emittance compensation typically involves two complementary stages: the rotation of phase space for each slice of the beam in the solenoid and the realignment of the slices and fast acceleration in the booster. Essentially, the principle of the emittance compensation by solenoid is the balance between the repulsive forces due to space-charge and external focusing forces. After the beam goes through the solenoid magnet region, the beam is blowed up by space-charge force if there is no booster linac [3-4]. Thus a booster is needed to fast accelrate the beam to a relatively high energy region at which the phase space is frozen and the beam is emittance dominated. To shift the second emittance minimum to the enterance of the booster where the beam is emittance dominated, Serafini and Ferrario suggested a matching condition [3-4] for properly matching the space-charge dominated beam from the gun to the booster,

$$\sigma' = 0, \qquad \gamma' = \frac{2}{\sigma}\sqrt{\frac{I_P}{2\,I_A\,\gamma}}, \tag{1}$$

where σ is the rms transverse spot size, I_P is peak current of the beam, I_A = 17 kA is the Alfven current. The booster matching point will be investigated by our experiments for optimizing the emittance compensation process i.e., by the emittance characterizations for various longitudinal position which will be performed with the Emittance-Meter using a slit based emittance measument technique. We use the rms emitance and the normalized rms emitance, defined by [5]

$$\varepsilon_{rms} = \sqrt{\langle x^2\rangle\langle x'^2\rangle - \langle xx'\rangle^2}, \qquad \varepsilon_{n,rms} = \beta\gamma\varepsilon_{rms}, \tag{2}$$

where β and $\gamma = 1/\sqrt{1-\beta^2}$ are the relativistic factors, the bracket denotes an average over the beam distribution at each location, the primes refer to axial derivatives, and

$\langle x^2 \rangle, \langle x'^2 \rangle$ are the second monents of the beam distribution.

A BNL GUN-IV type rf photo-cathode gun for far infra-red radiation (FIR) project is installed in the PAL. A resonant frequency of the gun cavity is 2856.0 MHz with 3.4 MHz mode separation. The photoelectron beam is emitted from the PC RF gun at the PAL since October 2005. The beam parameters are achieved 2.5 MeV beam energy with 2.5 % relative energy spread and 400 pC beam cahrge at the 30º laser injection phase. The emittance, the beam size, and the beam energy are simulated by the PARMELA code for the PAL XFEL injector with fullfilled emittance matching condition and the emittance compensation as shown in Fig. 1.

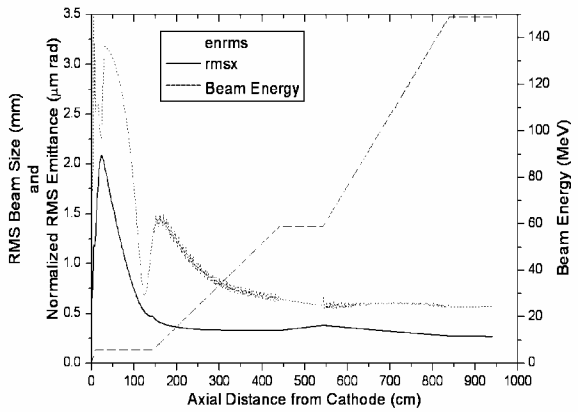

Figure 1. The beam size (solid line), the normalized rms emittance (dot line), and the beam energy (dash line) are simulated by PARMELA code for PAL-XFEL injector with fulfilled emittance matching condition.

EXPERIMENTAL SETUP

Our electron beam parameters are shown in Table1. The beam parameters depend on the laser parameters and rf power and phase.

Photocathode RF Gun and Basic Instruments

Figure. 2 shows the experimental setup with a 1.6 Cell photocathode S-band (2856 MHz) rf gun with 8 pancake-like solenoids. The PC rf gun was developed and constructed by collaboration of the BNL, KAIST, and PAL. The laser driven copper cathode rf gun consisted of 1.6 cell cavity with a half cell and a full cell. The half cell of the 1.6-cell rf gun is symmetrized by two laser ports which are rotated 45° from the waveguide, tuner, and pumping port in the full cell. The laser incident port, there is an angle of 67.5° between the laser propagation direction and the cathode normal vector, allows for ultra-violet (UV) laser to flash the cathode surface and to minimize the transmission loss. The gun is operated in pi-mode at S-band with multi-pole suppression achieved through cavity symmetrization. The coupling between the waveguide and the full cell is accomplished via the coupling slot on the full cell cavity. An electric coupling located between the half cell and full cell is utilized to couple rf power from the full cell to half cell. A home made klystron was proceeded to yield 80 MW at an rf pulse length of 1 μs of 2856 MHz. The klystron can be operated with maximum 60 Hz repetition rate at a 10MW rf power. The field gradient in the cavity was built by the rf power with 2856 MHz of 2 μs pulse width. The temperature of the cavity can be maintained by the precision cooling system for tuning the rf resonant condition. In order to reduce the space-charge induced emittance growth should be quickly accelerated in the gun. After the gun, a solenoid for the transverse emittance compensation is directly mounted with four ceramic key to prevent heat transmission. A steering magnet with maximum magnetic field of 80 Gauss is installed a space between inside the solenoid bore and outside the vacuum pipe. Immediately following the solenoid is an integrated current transformer (ICT) to measure the beam charge without beam dump.

After the ICT there was a screen to downstream for measurement and monitoring of the beam profile. The screen, which is about 15 μm layer of YAG:Ce doped on aluminium substrate of 100 μm thickness, is mounted on an aluminium holder at the 45° with respect to the beam axis. The position of the screen is 0.56 m from the cathode. A charged coupled device (CCD) camera to acquire of the electron beam image is synchronized to the electron beam for a shot-to-shot measurement. The spectrometer with a 60° sector dipole magnet for electron beam energy and the energy spread is located downstream of the screen.

Laser Systems

The laser system consists of an active mode-locked Ti:Sapphire oscillator, a regenerative amplifier, a second harmonic generator (SHG), a third harmonic generator (THG), and a custom designed UV stretcher system. The laser system for the rf PC gun is installed in a clean room which temperature stability is dynamically controlled within 0.5 °C for stable operation. The oscillator is operated at a frequency of 79.33 MHz by using a frequency divider (/36) with the master oscillator of 2856 MHz for the lock-to-clock between the master and laser oscillator. The oscillator output is phase-locked with a reference 79.33 MHz divided rf frequency by dynamically adjusting the cavity length of the oscillator with piezo mirror by lock-to-clock module. The timing jitter is measured to within an rms value of 130 fs using a phase detection method. The measured energy stability of the oscillator output using by infra-red (IR) power meter is 1 % peak to peak. From the oscillator, 105 fs width with a full width at half maximum (FWHM) value, 800 nm wavelength pulse is generated with 79.33 MHz repetition rate. These laser pulses come into the regenerative amplifier to amplify the pulse energy up to about 2.5 mJ with 1 kHz repetition rate. After the regenerative amplifier, the amplified laser pulse comes into the THG with a pair of frequency conversion non-linear crystals to obtain 266 nm UV light with maximum

laser energy of 250 μJ. The UV laser pulse still has an ultra short pulse width. An UV pulse stretcher with a pair of prisms is installed in order to stretch the pulse width of the UV laser to 10 ps FWHM. In addition, the UV pulse stretcher has a capability to change the pulse duration of the UV laser from 1 ps (FWHM) to 10 ps (FWHM). A cross correlator with a BBO crystal is installed in order to measure the pulse width at the UV region using cross correlation method.

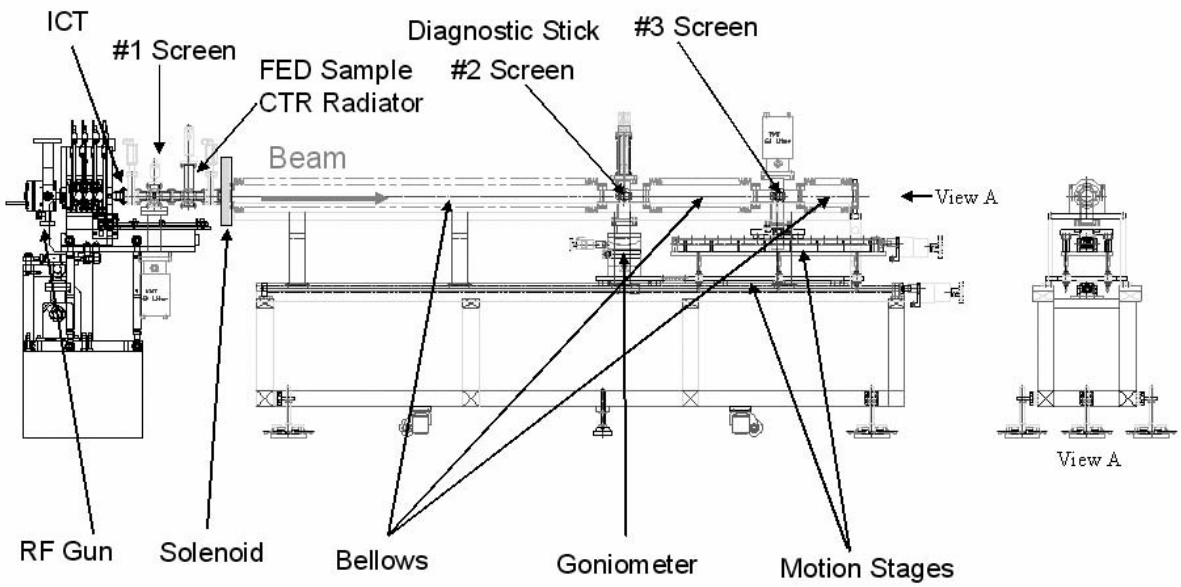

Figure 2: Schematic diagram of experimental setup of the gun test stand (GTS) for photo-injector developments of the PAL-XFEL.

Emittance Meter

We have designed the Emittance-Meter which has the movable slits chamber and screen chamber along the beam axis with bellows independently, which will be used to demonstrate the emittance evolution predicted by theory and simulation [3-4]. The transverse emittance evolution after solenoid magnet to compensate of the beam emittance along the beam axis can be measured by this Emittance-Meter. Designed Emittance-Meter was shown in Fig. 2, the left side part was the PC RF gun, and the right side part was the Emittance-Meter. The Emittance-Meter consisted of three long bellows, the slit plate chamber with the YAG screen to make beamlet and to measure the main beam size, at the downstream of the slit chamber YAG screen chamber to measure of the beamlet size. The long bellows is used for the transverse emittance measurement from 0.9 m to 2.1 m position measured from the cathode. The length of the bellows can be changed from 0.54 m to 1.54 m without vacuum breaking. The distance from pin-hole chamber to screen chamber can be moved along to the beam divergence. If the beam has a big divergence, the distance should be short and the other case it should be large to make an optimized image size at the screen. In the last part, we put another bellows to make the vacuum force balance in the front part bellows. We will check the position of the slit plate chamber and the screen chamber with CCD cameras and a long scale attached on the shelf. The slits are fabricated by high power Laser micro-drilling with 30 μm, 40 μm, and 50 μm silt widths in tungsten plate with 0.5 mm thickness. The plates in the Emittance-Meter are designed to be changeable at the specific experimental position with stepping motor. We can compare the emittance value to each slit width along to a space-charge dominance factor [6]. The sizes of the slit are determined by considering the signal to noise ratio (SNR) and the acceptance angle when the beam goes through the plate [7]. Also, very small size hole should be aligned on the beam axis for beam measurement, because if the hole is not aligned, the beam is dumped on the tungsten plate. We designed to realize an alignment technique with goniometric motion, rotary motion, and linear motion with high accuracy stepping motor. The single slit scanning method will be used in usually with x and y directional linear motion which method is needed precision moving control, however the analysis of the data files is easy [8].

.

THE PRELIMINARY MEASUREMENT OF TRANSVERSE EMITTANCE EVOLUTION

The transverse emittance evolution was measured by a pair of a singe slit with 30, 40, and 50 μm slit width and

an YAG screen downstream of the slit. The beamlet.is created by the slit plate, which is made by 0.5 mm tungsten plate. The beamlet distribution is then imaged on the screen downstream of the slit plate at a distance of 71 cm from the slit. The width of the beamlet has a connection with a measure of the width of the transverse momentum distribution at the slit. The beamlet yield the correlated beam divergence and the rms transverse divergence,

$$x_c' = < x - w > / L,$$

$$\sigma' = \sqrt{\frac{\langle x^2 \rangle}{L^2} - (x_c')^2},$$

where L is the distance between the slit and the YAG screen, x is the measured beamlet size on the screen, and w is the slit width. Here the average is performed over the distribution in the measured beamlet. The beamlet size

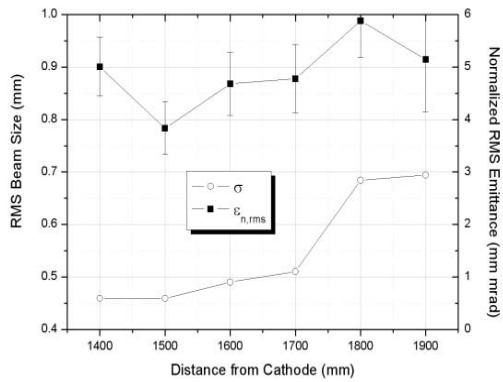

Figure 3: Preliminary measurement of the emittance evolution (solid circle) and the beam evolution (empty circle).

is measured about 10 times larger than the slit width to reduce the space-charge effect in the emittance measurement In generally, quad technique for beam emittance measurement was reported over-estimated due to the purely space-charge dominated region [refer insert]. The position of the slit from the cathode can be changed with stepping motor without vacuum break which of the least position of the slit is 1.4 m from the cathode. The distance between the slit and the YAG screen can be changed for optimizing of the beamlet measuring on the YAG screen.

The distance is 0.71 m between the slit chamber with the screen and the screen chamber for measuring of a beamlet size. The main beam size on the #2 screen at the slit chamber and beamlet size on the #3 screen at the screen chamber are measured by the synchronized CCD camera. From measured the beam size and the beamlet size the beam gradient is calculated which for the beam emitance calculation. The evolution of the beam emitance and beam size is shown in Fig.3.This experiment is performed with the condition of 2.0 MeV beam energy and 350 pC beam charge with 30º laser injection phase.

SUMMARY

The experimental measurement by the E-Meter is to measure the emittance evolution in the drift region for many experimental conditions to find optimized operating condition for our injector. We measure the first measurement of the emittance evolution at the drift region of the photo-injector. For better results of the emittance evolution, we need to improve data analysis methodology, and to automate data acquisition processes. For advanced experiments, we need to improve high energy (more than 5 MeV at the gun) beam experiment or normal laser incidence.

REFERENCE

[1] 4th Generation Light Source: *Conceptual Design Report*, Pohang Accelerator Laboratory (Nov. 2004).
[2] T.-Y. Lee et al., J. Korea Phys. Soc. **48** pp. 791-795 (2006).
[3] M. Ferrario et al., SLAC-PUB-8400, March 2000.
[4] L. Serafini, J.B. Rosenzweig, Nucl. Instrum. and Meth. A 311 (1992), 437.
[5] J. D. Lawson, *The Physics of Charged-Particle Beams*, 2nd ed., Oxford University Press (1988).
[6] S. G. Anderson and J. B. Rosenzweig ed. al., PRST-AB Vol 5, 014201 (2002).
[7] K. Flottmann, TESLA-FEL 96-09, May 1996.
[8] A. Cianchi, et al., Proceedings of EPAC 2004, Lucerne, Switzerland (2004).

BEAT-WAVE LASER-DRIVEN PHOTOINJECTOR FOR SUPERRADIANCE FREE-ELECTRON LASER

Yen-Chieh Huang, Han-Lung Chang, and An-Chung Chiang, National Tsinghua University, Taiwan.

Abstract

A periodically bunched electron beam is useful for generating electron superradiance. This paper studies the generation and acceleration of density-modulated electron beams from a photocathode electron gun driven by a laser beat wave. Computer simulation shows feasibility of accelerating and preserving the density-modulated electron beam in an accelerator.

INTRODUCTION

Radiation from relativistic electrons is important for generating THz and *x*-ray wavelengths at which solid-state laser sources are not readily available. The spectral brightness of electron radiation is strongly influenced by the electron bunch length relative to the radiation wavelength. When the electron bunch length is significantly shorter than the radiation wavelength, the radiation fields from all electrons are coherent and can be summed to a large value.

In a conventional free-electron laser (FEL) the optical feedbacks from resonator mirrors can help the electron bunching process during laser buildup. At short wavelengths a single-pass, mirrorless FEL generating self-amplified spontaneous emission (SASE) is the preferred mode of operation due to the scarce of mirror materials at deep UV and *x*-ray wavelengths. However, it usually takes a long undulator for a high-quality electron beam to form micro-bunches and reach the onset of the SASE mode. It is therefore desirable to invent an accelerator that generates a periodically bunched electron beam with an arbitrarily tunable bunch length and bunch frequency. Perviously Neumann *et al.* [1] used a comb filter to induce a few temporal ripples to the driver laser of a photocathode gun and observed coherently enhanced radiation at THz. In the paper, a laser beat wave with a tunable beat frequency is employed to induce a density-modulated photocurrent from the photocathode cathode of an electron gun. We study in this paper the acceleration of the density-modulated electron beam and the implementation of such a beat-wave laser system.

SUPERRADIANCE

Superradiance from relativistic electrons has been studied theoretically and experimentally in numerous papers. To facilitate subsequent discussions, we briefly review a few key concepts of superradiance based on Gover's work [2].

Regardless of the nature of the radiation device or scheme, let $(dW/d\omega)_1$ denote the spectral energy emitted from a single electron, where W is the radiation energy, ω is the angular frequency of the radiation, and subscript 1 denotes "a single electron". When a long stream of N electrons traverses a radiation device, the electrons radiate with all possible phases between 0 and 2π and the radiation has a spectral energy expressed by

$$(dW/d\omega)_{inc} = N(dW/d\omega)_1 , \qquad (1)$$

Eq. (1) is linearly proportional to the total number of electrons participating in the radiation process, because not all the radiation fields from the electrons are added up constructively. However, if N_b electrons are distributed in an infinitesimal time period, all the radiation fields from the electrons are in phase and summed up constructively, resulting in a total spectral energy equal to $N_b^2(dW/d\omega)_1$. This radiation process is dubbed as superradiant emission or superradiance. To account for a finite electron bunch length τ_b the total energy spectral density from an electron bunch is expressed by

$$(dW/d\omega)_{SR} = N_b^2(dW/d\omega)_1 M_b^2(\omega) , \qquad (2)$$

where $M_b(\omega)$ is the Fourier transform of the electron pulse-shape function with a unitary peak amplitude. Usually $M_b^2(\omega)$ has a characteristic width $\sim 1/\tau_b$ in the frequency domain. If there are N_{pb} electron "micro-bunches" repeating at a rate $\omega_{pb}/2\pi$ and there are N_b electrons in each micro-bunch, the total spectral energy from such an electron beam becomes

$$(dW/d\omega)_{SR,pb} = N_b^2 N_{pb}^2 (dW/d\omega)_1 M_b^2(\omega) M_{pb}^2(\omega) , \qquad (3)$$

where

$$M_{pb}^2(\omega) = \frac{\sin^2(N_{pb}\pi\omega/\omega_{pb})}{N_{pb}^2 \sin^2(\pi\omega/\omega_{pb})} \qquad (4)$$

is the coherent sum of the radiation fields from all the micro-bunches and has a unitary amplitude at the resonance frequencies (m = 1, 2, 3…). At $\omega = \omega_{pb}$, the spectral energy, Eq. (3), is enhanced by a factor equal to the number of electrons compared with that from an unbunched beam. Superradiance power has a quadratic dependence on a beam current, as can be seen from Eq. (2, 3); whereas the incoherent radiation power from a long-bunch beam is linearly proportional to a beam current, according to Eq. (1).

In Eq. (1), the spectral linewidth of the radiation from a long electron bunch is determined by the radiation bandwidth of a radiation device or a radiation scheme.

The superradiance linewidth from a short electron bunch, according to Eq. (2), is further modulated by $M_b^2(\omega)$. For a short electron bunch, $M_b^2(\omega)$ is usually a broadband curve. The coherent sum Eq. (4), however, has narrow spectral peaks at the frequencies $\omega = m\omega_{pb}$. Each resonant peak has a linewidth of ω_{pb}/N_{pb}. The superradiance linewidth from periodically bunched electrons can be greatly reduced for a large N_{pb}.

GENERATION OF LASER BEAT-WAVE BUNCHED BEAM

We illustrate in Fig. 1 the schematic of the proposed beat-wave bunched beam technique for producing and accelerating periodically bunched electrons with a variable bunch frequency. The idea is to use a laser beat wave to induce periodically density-modulated photoemission from the photocathode of an electron gun. The density-modulated photocurrent is then accelerated to some energy for generating superradiance in a downstream radiation device. The beat-wave laser system consists of wavelength-tunable lasers for generating laser beat waves with a variable beat frequency. If the desired electron bunch frequency is higher than the beat frequency available from a laser beat wave, one could in principle first generate an energy-chirped, density-modulated beam and compress it in a magnetic compressor to obtain a beam with a higher bunch frequency.

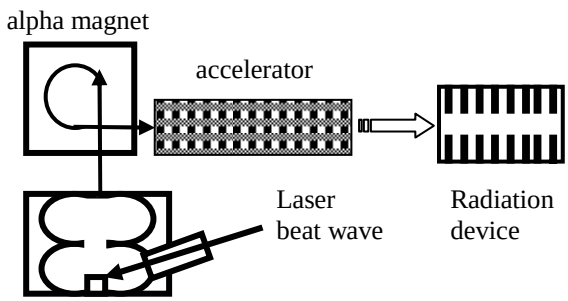

Figure 1: A laser beat wave excites a density-modulated photocurrent from a photocathode, which is subsequently accelerated to some energy for generating superradiance in a radiation device. An alpha magnetic could compress a density-modulated, energy-chirped beam to obtain a beam with a higher bunch frequency.

A laser beat wave can be generated from a superposition of two laser fields with a constant frequency offset. Assume that a beat-wave field is generated from the sum of two equal-amplitude laser fields with a frequency offset $\Delta\omega$. The instantaneous intensity of the beat wave is given by

$$I_{ins} = 4I_0 \cos^2[(\omega + \frac{\Delta\omega}{2})t] \cdot \cos^2(\frac{\Delta\omega}{2}t), \qquad (5)$$

where t is the time variable, I_0 is the average intensity of each laser component, and $\omega + \Delta\omega/2$ is the central frequency of the laser beat wave. A laser beat wave can also be generated from a superposition of several laser fields with a constant frequency shift $\Delta\omega$. For example, the coherent sum of the N_l equal-amplitude laser fields gives a time-averaged intensity

$$I_{avg} = N_l^2 I_0 \frac{\sin^2 \frac{N_l \Delta\omega}{2} t}{N_l^2 \sin^2 \frac{\Delta\omega}{2} t} . \qquad (6)$$

Eq. (6) shows laser beat pulses repeating at a frequency $\Delta\omega$ with a pulse width equal to $(2\pi/\Delta\omega)/N_l$. The beat pulses given in Eq. (6) are very useful for providing high-contrast density modulation to the photocurrent from a photocathode. By adjusting the number of interfering waves N_l one can adjust the beat-pulse width to optimize the modulation depth of the photocurrent emitted from a photocathode. In fact the locked-locked laser pulse commonly used for exciting a photocathode gun is a consequence of beating many longitudinal modes in a laser cavity with a beat frequency of ~100 MHz. To obtain a narrow beat pulse repeating at THz, one could, for example, use an intense laser to pump a Raman material with a THz Stokes shift and generate multiple Stokes waves beating at the Stoke shift. Of course, the shortest electron bunch that can be generated from photoemission depends on the temporal response of a specific cathode material. In view of the mechanism of a photoemission process, it is also preferred that all the beat-wave photons have photon energy higher than the work function of a cathode material.

ACCELERATION OF PERIODICALLY BUNCHED ELECTRONS

A major concern for the proposed bunching technology is whether particle acceleration following the density-modulated photoemission would smear out the periodic electron micro-bunches. In the following we conduct a feasibility study for accelerating ps and fs micro-bunches by using a space-charge tracking code ASTRA [3].

We first simulated the particle acceleration for the 1-1/2 cell SSRL electron gun [4] with twenty-five Gaussian electron bunches with 1-fs rms bunch length periodically emitted over 250-fs duration from the photocathode. The emitted charges have a uniform radial distribution on a 3-mm diameter cathode. Each micro-electron bunch contains 1 pC in a 10-fs time period. The total 25 pC charge was evenly divided into 12500 negatively charged macro-particles. The average current over the whole 250 fs duration is 100 A. With a peak acceleration field of 125 MV/m in the 2nd gun cell and an acceleration phase of 211.6°, Fig. 2 shows periodic density modulation of a 4-MeV beam with a characteristic period of 6 μm along the

axial distance (z_e) at the gun exit. The output pulse duration is stretched to 500 fs and thus the average beam current is reduced to 50 A. Since the 250-fs emission time only occupies a very small RF acceleration phase, we confirm in the ASTRA simulation that the space charge field is responsible for the pulse-length increase. Although the shortest possible electron bunch is limited by a cathode material, the above computer stimulation is just an illustration of preserving periodic fs electron bunches during particle acceleration. Whether generation of fs electron bunches from a certain cathode mateiral is practical or not, it is another subject of study in the future.

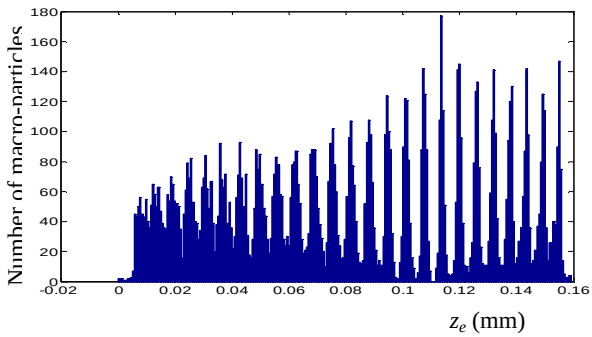

Figure 2: Histogram of the 4-MeV charges versus z at the exit of the SSRL gun with an input beam of twenty-five Gaussian bunches periodically emitted over 250 fs. The output beam distribution shows a good contrast in the density modulation.

A Smith-Purcell emitter driven by a keV, mA electron gun usually generates negligible radiation at THz. This proposed technique could be very useful for producing coherent radiation at THz frequencies from a miniature Smith-Purcell free-electron laser. Previously Ref. [5] reported Smith-Purcell superradiance, which was interpreted by Ref. [6] as coherent radiation from surface-mode induced electron bunching at the sub-harmonic of the Smith-Purcell radiation frequency. Up to date, no independent experiment can verify the superradiance claimed by Ref. [5]. A convenient approach is to produce electron bunches repeating at the radiation frequency directly from an electron source and generate wavelength tunable superradiance from a Smith-Purcell radiator. In our simulation, we emitted 50 Gaussian electron bunches each having a 0.2-ps rms bunch length from the photocathode of a 42 keV DC accelerator over a 50-ps time period. Each electron bunch contains 1 fC charge or 6.25×10^3 electrons, resulting 1 mA average current over the 50 ps macropulse. The electrons have a uniform radial distribution on the cathode with an rms radius of 0.3 mm. The electron gun has a length of 4.5 cm with 1-Tesla axial magnetic field for beam confinement. Figures 3(a) and (b) are the $M_b^2(\omega)M_{pb}^2(\omega)$ for the emitted electrons and the 42-keV output electrons, respectively. The accelerated electrons are slightly re-distributed due to the space charge force. Nonetheless the enhancement in the spectral power due to the periodic bunching is apparent at the harmonics of the bunching frequencies. For example, with 6.25×10^3 electrons/bunch and 1000 bunches over a 1 ns time, the spectral energy is coherently enhanced by almost 7 orders of magnitude at 1 THz.

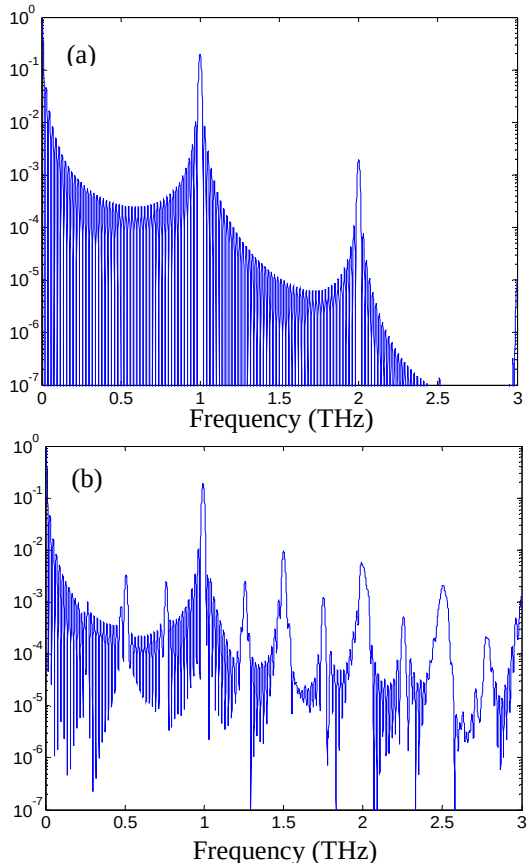

Figure 3: The $[M_b(\omega)M_{pb}(\omega)]^2$ of 50 electron bunches repeating at 1 THz (a) before and (b) after acceleration in a 40 keV DC electron gun. Spectral enhancement at the harmonics of 1 THz frequency is apparent.

FREQUENCY-TUNABLE BEAT-WAVE LASER SYSTEM

Although the laser beat wave can simply be obtained by overlapping two chirped pulses from the laser driver of a photocathode gun, the intensity contrast in the beat wave and the tunability in the beat frequency are not ideal [7]. We describe below one example of engineering a beat-wave UV laser system capable of generating mJ-level, 10-ps laser pulses near 260 nm with a tunable beat frequency range over 200 THz. Figure 4 shows the block diagram of the proposed beat-wave laser system, which consists of three major stages with a beat-wave seed source, a first-stage broadband pulsed amplifier and a second harmonic generator, and finally a frequency-tripled Ti:sapphire laser amplifier. The two seed lasers in the first stage are often used in optical communications. The Ti:sapphire laser amplifier and harmonic generators are commonly seen for driving a Cu photocathode gun. Specifically, one can starts with the beating of kHz-linewidth distributed-feedback (DFB) and frequency-tunable external-cavity

diode lasers (ECDL) near the optical-communication wavelength 1.5 μm. An Erbium-doped fiber amplifier (EDFA) following the DFB diode laser and ECDL boosts the beat-note power to ~100 mW. The CW beat signal can be further amplified in a pulsed optical parametric amplifier (OPA) pumped by, say, a diode-pumped mode-locked Nd:YVO_4 laser to generate ~10-ps beat-wave pulses with nJ pulse energy. After frequency doubling the beat-wave pulses in a second harmonic generator (SHG), the wavelengths of the beat wave will fall into the bandwidth of a Ti:sapphire amplifier. Therefore, the rest of the laser system can be a replication of the UV laser amplifier for driving a Cu photocathode gun. The proposed beat-wave laser system spares a mode-locked Ti:sapphire laser oscillator from a typical photocathode-gun laser driver. Instead, a user-friendly, directly diode-pumped mode-locked Nd:YVO4 is proposed for pumping the OPA to generate beat-wave pulses near the optical-communication wavelengths.

To produce the proposed Smith-Purcell superradiance, the mode-locked Nd laser can be replaced by an economic Q-switched Nd laser, and harmonic generators can directly follow the OPA to generate long-pulse UV laser.

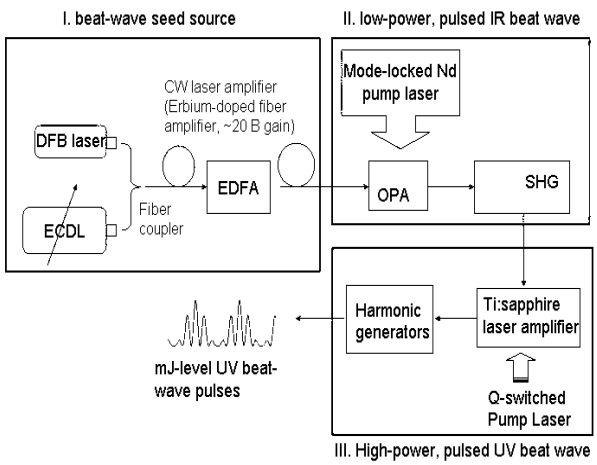

Figure 4: One example of a beat-wave laser system modified from a typical UV laser system for a Cu-photocathode gun.

The beat frequency of the laser system can be arbitrarily tuned by adjusting the wavelength of the ECDL or by plugging in assorted narrow-line telecommunication diode lasers with a wavelength range between 1.3 and 1.6 μm. Taking into account the successive harmonic generations leading to the 260 nm photons, one would expect a beat-frequency tuning range well over 240 THz.

SUMMARY

We have described a novel scheme for generating tunable periodic electron bunches for superradiance FEL. Specifically a laser beat wave is used to introduce density modulation to the photocurrent of a photocathode electron gun. The periodic electron bunches are subsequently accelerated to high energy in a particle accelerator. Computer simulations using the space-charge tracking code, ASTRA, showed feasibility of accelerating and preserving the density-modulated electron beam at both nonrelativistic and relativistic energies.

We have also described the implementation of a beat-wave laser system with a beat-frequency tuning range over 200 THz. The laser system adopts the state-of-the-art and yet economic photonics products often used in the optical-communication and laser industries. Real-time tuning on the beat frequency provides unprecedented flexibility to match the frequency of down-stream radiation devices.

The shortest electron-bunch length from the proposed beat-wave bunching technique could be limited by the beat-wave frequency or the response time of a cathode material. We proposed chirped-pulse compression in an alpha magnet to increase the bunch frequency. Knowing the potential problem of microbunching instability in the compression, we have planned a feasibility study in the near future.

The author is in debt to Michael Borland and Klaus Floettmann for advices on computer simulations. This work is supported by National Science Council under Contract 95-2112-M-007-027-MY2 and NTHU Frontier Research Initiatives under Project Code 95N2509E1.

REFERENCES

[1] J.G. Neumann, P.G. O'shea, D. Demske, W.S. Graves, B. Sheehy, H. Loos, and G.L. Carr, "Electron beam modulation by using a laser-driven photo-cathode" Nucl. Inst. Meth. Phys. Res. A **507**, 498 (2003).

[2] A. Gover, "Superradiance and stimulated-superradiant emission in prebunched electron-beam radiators. I. Formulation", Phys. Rev. ST AB, 8, 030701 (2005).

[3] K. Floettmann, ASTRA User Manual, http://www.desy.de/mpyflo/Astra_dokumentation.

[4] Y.C. Huang, H.C. Wang, R.H. Pantell, J. Feinstein, J.F. Schmerge, and J. Lewellen, "Electron Beam Characterization for a Far Infrared Free-electron Laser," IEEE J. Quantum Electronics, 31, 1637-41 (1995).

[5] J. Urata, M. Goldstein, M.F. Kimmitt, A. Naumov, C. Platt, and J.E. Walsh, "Superradiant Smith-Purcell Emission", Phy. Rev. **80**, 516 (1998).

[6] H.L. Andrews, C.H. Boulware, C.A. Brau, J.D. Jarvis, "Gain and coherent radiation from a Smith-Purcell free-electron laser," Proceedings FEL04, Trieste, Italy, p. 278 (http://www.JACoW.org).

[7] A.S. Weling, B.B. Hu, N.M. Froberg, D.H. Auston, "Generation of tunable narrow-band THz radiation from large aperture photoconducting antennas," Appl. Phys. Lett. 64, 137 (1994).

3-D LASER PULSE SHAPING FOR PHOTOINJECTOR DRIVE LASERS*

Yuelin Li#, ANL, Argonne, IL 60439, U.S.A.
Xiangyun Chang, BNL, Upton, NY 11973, U.S.A.

Abstract

In this paper we present a three-dimensional (3-D) laser pulse shaping scheme that can be applied for generating ellipsoidal electron bunches from a photoinjector. The 3-D shaping is realized through laser phase tailoring in combination with chromatic aberration in a focusing optics. Performance of an electron beam generated from such shaped laser pulses is compared with that of a uniforma ellipsoidal, a uniform cylindrical, and a Gaussian electron beam. PARMELA simulation shows the advantage of this shaped beam in both transverse and longitudinal performances.

INTRODUCTION

The emittance of an electron beam is governed by the emittance at its birth and the growth during its propagation. If the beam is only subjected to linear force, the latter can be fully recovered with proper beam compensation. It is well known that an ellipsoidal beam with uniform charge distribution has a linear space-charge force [1-3] and hence the most expected distribution for modern high-brightness beams. Recently, several researchers looked at practical ways of generating such ellipsoidal beams, including self-evolving [4], cold electron harvesting [5], and laser pulse manipulations including spectral masking, pulse stacking, and dynamic spatial filtering [6]. In-depth analysis shows that in practical situations, the ellipsoidal beams do generate beam with lower emittance than Gaussian and cylindrical beams [1, 6-8]. Applications for such high-brightness beams include next-generation light sources such as the Linac Coherent Light Source (LCLS), high-energy colliders such as the International Linear Collider, as well as energy-recovery linacs (ERLs).

LASER PULSE SHAPING

To generate an ellipsoidal beam directly from the photocathode, the laser pulse has to be shaped in 3-D. It is well known that the longitudinal laser pulse shape can be manipulated by controlling the phase space using techniques such as DAZZLER [9] or SLIM [10]. One essence of this phase modulation is to control the phase and amplitude at certain frequencies at the same time. In the meantime, we notice that the instant frequency of a laser pulse is related to the phase by $\omega(t) = \mathrm{d}\phi(t)/\mathrm{d}t$. This gives a way of actively controlling the focal size of the laser as a function of time using the chromatic aberration of a common lens, of which the focal length can be expressed as [11]

$$\frac{1}{f(\omega)} = [n(\omega)-1]\left(\frac{1}{R_1}-\frac{1}{R_1}\right), \quad (1)$$

where R_1 and R_2 are the radius of curvature of the first and second surface of the lens, respectively, and n is the frequency-dependent refractive index. Clearly, the time-dependent frequency can then be mapped onto a time-dependent focal length. For an observer at the focal plane at a nominal frequency ω_0, this is equivalent to a time-dependent defocusing of the beam of

$$\delta f(t) = -\frac{f_0}{n_0-1}\beta\delta\omega(t), \quad (2)$$

where we assume the frequency range is small and $\beta = dn/d\omega$ is constant. For a Gaussian beam this translates into a time-dependence of the beam size at the nominal focal plane,

$$w(t) = w_0\left[1+\left(\frac{\lambda_0\delta f(t)}{\pi w_0^2}\right)^2\right]^{1/2}. \quad (3)$$

Here, $w_0 = N\lambda_0/\pi$ is the beam waist at the nominal wavelength λ_0, and N is the numerical aperture. For $\delta f >> w_0$, we have asymptotically,

$$w(t) \cong \frac{|\delta f(t)|}{N}. \quad (3a)$$

To generate an ellipsoidal outline, the transverse beam size should be of the form:

$$w(t) = W\left[1-\left(\frac{t}{T}\right)^2\right]^{1/2}. \quad (4)$$

Here, W is the maximum transverse beam size at $t = 0$ and $2T$ is the laser pulse duration.

From Eqs. (3-4), we have

$$|\delta\omega(t)| = \Delta\omega\left[1-\left(\frac{t}{T}\right)^2\right]^{1/2}, \quad (5)$$

where $\Delta\omega = (n_0\text{-}1)NW/\beta f_0$ is the bandwidth of the pulse; hence the phase of the pulse is

$$\begin{aligned}\phi(t) &= \int[\omega(t)-\omega_0]dt \\ &= -\omega_0 t \pm \frac{\Delta\omega}{2}\left[t\left(1-\left(\frac{t}{T}\right)^2\right)+T\sin^{-1}\frac{t}{T}\right].\end{aligned} \quad (6)$$

To make the pulse intensity constant over time, i.e., $|A(t)|^2/w(t)^2 =$ constant, the amplitude of the pulse is thus

$$A(t) = A_0\left[1-\left(\frac{t}{T}\right)^2\right]^{1/2}. \quad (7)$$

With a transverse top-hat spatial profile, the field $E(t) = A(t)\exp[i\phi(t)]$ represents a 3-D ellipsoidal pulse at the nominal focal plane at λ_0. The time domain representation of the pulse and its spectrum are shown in Fig. 1.

* Work supported by U.S. Department of Energy, Office of Science, Office of Basic Energy Sciences under Contract No. W-31-109-ENG-38.
# ylli@aps.anl.gov

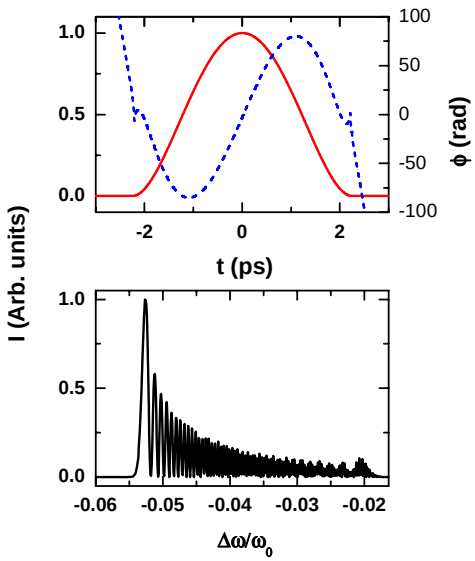

Figure 1: Laser pulse calculated using Eqs. (6) and (7). The intensity and phase in the time domain (top) and its spectrum (bottom).

Note that the above model used Gaussian beam geometrical optics, and the effects of group velocity delay (GVDE) and group velocity dispersion (GVDI) due to the varying thickness across the aperture of the lens are not included [11]. It does not take into account the wave property of the light. To evaluate the effects of GVDE and GVDI, we use the method elaborated by Kempe et al. [12] to calculate the temporal-spatial distribution of the pulse near the focus of a lens. The calculation assumes a collimated beam with top-hat intensity distribution for the input and was performed in the frequency domain. The final result was Fourier transformed into the time domain to give the laser intensity distribution at the focal plane as a function of time. Figure 2 shows one example of such a shaped pulse generate by sending a pulse in Fig. 1 though a zone plate (a zone plate has similar chromatic aberration as a lens).

Clearly, this shaped pulse differs from an ideal ellipsoid. It has substantial substructures. The deviation from an ideal ellipsoidal is not unexpected due to the group delay across the plate, which is the source for the distortion at the beginning and the end of the pulse. This has been studied theoretically and experimentally by a few authors and is an important effect in focusing short-duration, short-wavelength laser light [12].

The substructure is due to the fringes typical of the Fourier transform of a square waveform. As is shown below, those substructures seem to have minimum impact on the performance of the beam.

BEAM SIMULATION

To evaluate the performance of this shaped laser beam, preliminary simulations using PARMELA were performed and compared with other beam shapes for the following setting.

The simulation followed a setup for the design of the electron cooling ring injector for Relativistic Heavy Ion Collider [13]. The gun is a 1.5-cell rf gun at 703.75 MHz with maximum field on axis of 29.5 MV/m and maximum field on surface at 49.3 MV/m. The rf initial phase is set at 40 degrees. Beam distortion due to image charge is considered. The gun is followed with a drift space before entering a linac.

A series of simulations were performed using PARMELA. The simulations compared the performance of the 3-D laser pulse against three standard cases (see Table 1): c) a perfect ellipsoidal beam, d) a cylindrical beam, and e) a transversely uniform but longitudinally Gaussian beam. For the shaped beam, two cases were tested: a) without considering the substructures and b) with. The simulations use the parameters listed in Table 1. Both the longitudinal and the transverse emittances are compared at the exit of the gun. In total, 46,600 particles are used in each simulation, representing 0.15 nC of charge. The low charge is used due to the relatively low rf field in this setup.

The emittances as a function of the propagation distance are shown in Fig. 3. In general, the performances

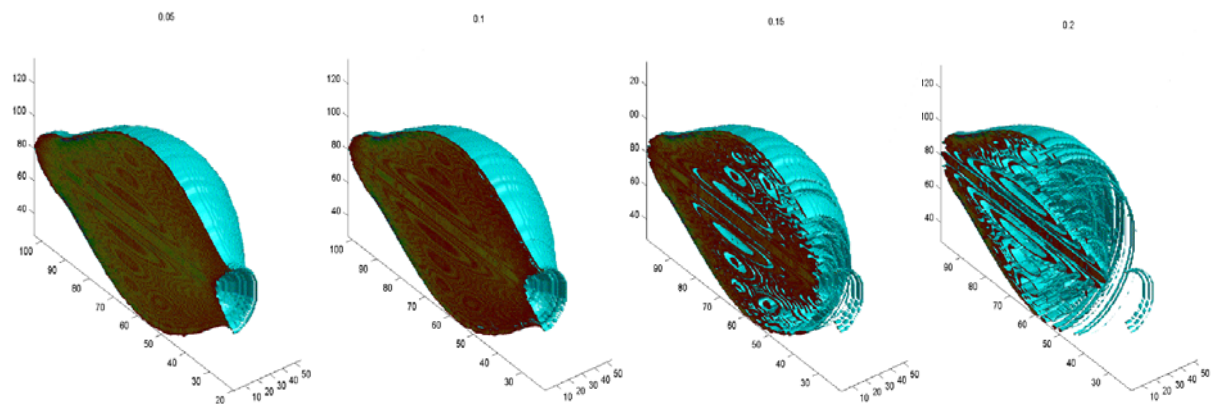

Figure 2: An ellipsoidal laser pulse. The isosurface plots show the structure at different laser intensities of 0.05, 0.1, 0.15, and 0.2. The pulse is generated using a zone plate with 20-mm diameter and 150-mm focal length at 249 nm. The pulse parameter is shown in Table 1, case b.

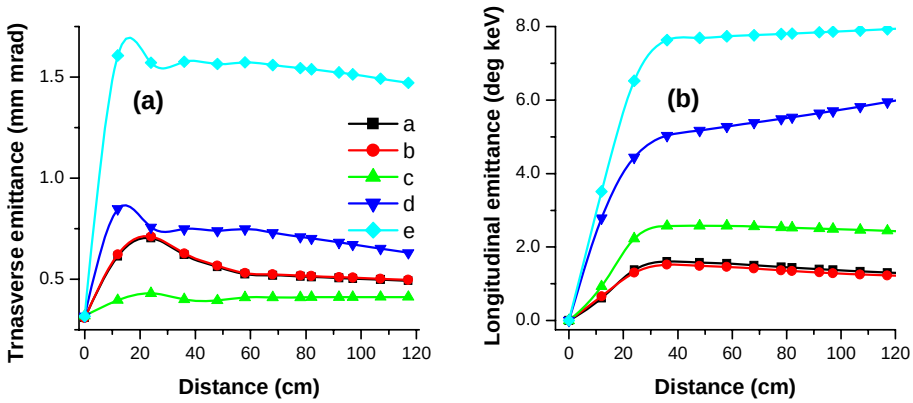

Figure 3: Transverse (a) and longitudinal (b) emittances as a function of propagation distance. The labels correspond to those in Table 1. Clearly, the shaped pulse has a better performance in comparison with those of the cylindrical and Gaussian form, even with the presence of the substructures shown in Fig. 2. The gun exit is located at 48 cm, followed a drift space.

Table 1. Initial Beam Conditions

	Length (ps)	Radius (mm)
a.Shaped, no substructure	17	1.28
b.Shaped, substructure	17	1.28
c. Ideal ellipsoid	18	1.28
d. Ideal cylinder	18	1.13
e. Ideal Gaussian	σ= 3.82, truncated at 9	1.13

of the shaped-pulse cases closely trail the performances of the ideal ellipsoidal beam in both longitudinal and transverse emittances. More remarkably, the substructure, as shown in Fig. 2, has almost no impact on the performance of the beam in this setup. It will be interesting to perform simulations with bending magnets, such as a chicane structure to evaluate the influence of coherence transition radiation, which is detrimental to cylindrical and Gaussian beams but has minimum impact on an ideal ellipsoidal beam. One simulation indicates that after accelerated to high beam energy, the ellipsoidal beam shape will be destroyed but the low emittance of the beam is preserved [8], making it favorable for application in free-electron lasers such as LCLS and ERLs.

SUMMARY

We described a scheme for generating an ellipsoidal laser pulse and performed preliminary simulations comparing the electron beam generated from this laser beam with an ideal ellipsoidal beam, a cylindrical beam, and a Gaussian beam. It is shown that although the beam generated still defers from an ideal ellipsoidal beam, it has clearly better performance than a cylindrical beam and a Gaussian beam in providing smaller transverse and longitudinal emittance. Further beam simulations are needed to investigate the coherent synchrotron radiation effect for setup relevant to LCLS and future ERLs.

REFERENCES

[1] F. Sacherer, IEEE Trans. Nucl. Sci. NS-**18**, 1105 (1971).
[2] I.M. Kapchinskij, V.V. Vladimirskij, Conference on High Energy Accelerators and Instrumentation, CERN, Geneva, 274 (1959).
[3] P.M. Lapostolle, IEEE Trans. Nucl. Sci. NS-**18**, 1101 (1971).
[4] O.J. Luiten, S.B. van der Geer, M.J. de Loos, F.B. Kiewiet, and M.J. van der Wiel, Phys. Rev. Lett **93**, 094802 (2004).
[5] B.J. Claessens, S.B. van der Geer, G.Taban, E.J.D. Vredenbregt, and O.J. Luiten, Phys. Rev. Lett **95**, 164801 (2005).
[6] C. Limborg-Deprey and P. Bolton, Nucl. Instrum. Methods A**557**, 106 (2006).
[7] J.B. Rosenzweig et al., Nucl. Instrum. Methods A**557**, 87 (2006).
[8] S.B. van der Geer, M.J. de Loos, T. van Oudheusden, W.P.E.M. op't Root, M.J. van der Wiel, and O.J. Luiten, Phys Rev. ST-AB **9**, 044203 (2006).
[9] P. Tournois, Opt. Commun. **140**, 245 (1997).
[10] A.M. Weiner, D.E. Leaird, J.S. Patel, and J.R. Wullert, Opt. Lett. **15**, 326 (1990).
[11] M. Born and E. Wolf, *Principles of Optics*, University Press, Cambridge, UK, 2003.
[12] M. Kempe, U. Stamm, B. Wilhelmi, and W. Rudolph, J. Opt. Soc. Am. B**9**, 1158 (1992).
[13] I. Ben-Zvi et al., Nucl. Instrum. Methods A**557**, 28 (2006).

LINAC COHERENT LIGHT SOURCE UNDULATOR RF BPM SYSTEM *

R. Lill, G. Waldschmidt, D. Walters, L. Morrison
Advanced Photon Source, Argonne National Laboratory, Argonne IL
S. Smith, T. Straumann, Z. Li, R. Johnson
Stanford Linear Accelerator Center, Sand Hill Road
Menlo Park, CA 94025 USA

Abstract

The Linac Coherent Light Source (LCLS) will be the world's first x-ray free-electron laser (FEL) when it becomes operational in 2009. The LCLS is currently in the construction phase. The beam position monitor (BPM) system planned for the LCLS undulator will incorporate a high-resolution X-band cavity BPM system described in this paper. The BPM system will provide high-resolution measurements of the electron beam trajectory on a pulse-to-pulse basis and over many shots. The X-band cavity BPM size, simple fabrication, and high resolution make it an ideal choice for LCLS beam position detection. We will discuss the system specifications, design, and prototype test results.

INTRODUCTION

The LCLS FEL will produce x-ray radiation over the 1.5-to 15-Angstrom wavelength range. To produce x-rays in this regime, the electron and photon beams within the 131-m-long undulator must be collinear to less than 10% of the transverse beam size (≈37 μm rms) over a minimum distance that is comparable to the FEL amplitude gain length (≈10 m) in order to achieve saturation [1,2]. To establish and maintain the electron beam trajectory, a high-resolution and stable BPM system has been designed. The requirements for the system are delineated in Table 1. The beam-position resolution and stability over 1-h and 24-h periods were the major design challenges for the BPM system. Other design considerations were physical size, centering accuracy, radiation hardness, and reproducibility.

The LCLS undulator hall will house 33 undulators. The BPMs will be located in the drift space between each undulator and at the upstream end of the first undulator for a total of 34 BPMs. There are also two BPMs placed in the Linac to Undulator (LTU) transport line. The BPM system must provide stable and repeatable beam position data for both planes on a pulse-to-pulse basis for up to a 120-Hz repetition rate. The BPMs are critical for beam-based alignment and operations.

*Work supported by U.S. Department of Energy, Office of Basic Energy Sciences, under Contract No. W-31-109-ENG-38.

Table 1. General system specifications.

Parameter	Specification	Conditions
Resolution	< 1 μm rms	0.2– 1.0 nC
Offset Stability	< +/- 1 μm rms	1 hour
Offset Stability	< +/- 3 μm rms	24 hours
Dynamic Range, Position	+/- 1mm	10mm diameter chamber
Dynamic Range, Intensity	0.2-1 nC	PC Gun (single bunch)
Gain Error	< +/- 10 %	+/- 1mm range

BPM SYSTEM OVERVEIW

The system proposed for the LCLS undulator features a high-resolution X-band cavity BPMs. Each BPM detector has a reference cavity and position cavity as shown in Fig. 1. The major sub-systems include the cavity BPM, receiver, and data acquisition components. The cavity BPM and downconverter will reside in the tunnel and the analog-to-digital converter (ADC) will be located in surface buildings.

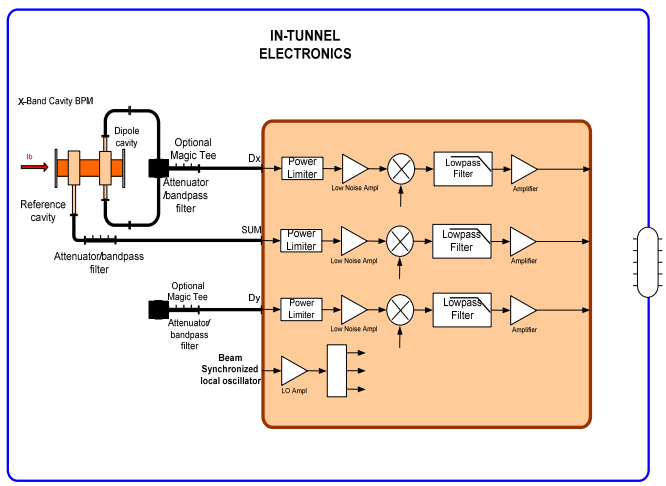

Figure 1: System block diagram.

X-BAND CAVITY DESIGN

The simplicity of fabrication and assembly of the X-band cavity BPM due to its cylindrical geometry make it our first choice for the LCLS undulator. The cavity BPM offers the advantage of being a small, compact detector that inherently reads zero when the beam is centered. Cavity BPMs show extremely good resolution and stability. The two-cavity BPM design shown in Fig. 2 illustrates the cross section of the detector. The beam passes through the monopole reference cavity, shown on the left, which excites the TM_{010} monopole mode signal at 11.384 GHz, proportional to the beam intensity or charge. The second cavity, 37 mm downstream through the 10 mm diameter beam pipe, is the TM_{110} dipole cavity shown at the far right. The output of the dipole cavity produces a signal that is dependent on the relative beam displacement r/r_{fix} shown in equation 1 [3]. Where R_s/Q is the normalized shunt impedance of the TM_{110} mode, Z is the output line impedance, Q_{ext} is the external quality factor and q is the charge. The voltage is linearly dependent on the offset and can be scaled.

$$V_{out} = \frac{\omega_0}{2}\sqrt{\frac{Z}{Q_{ext}}\left(\frac{R_s}{Q}\right)_{fix}}\,\frac{r}{r_{fix}}q \cdot \qquad (1)$$

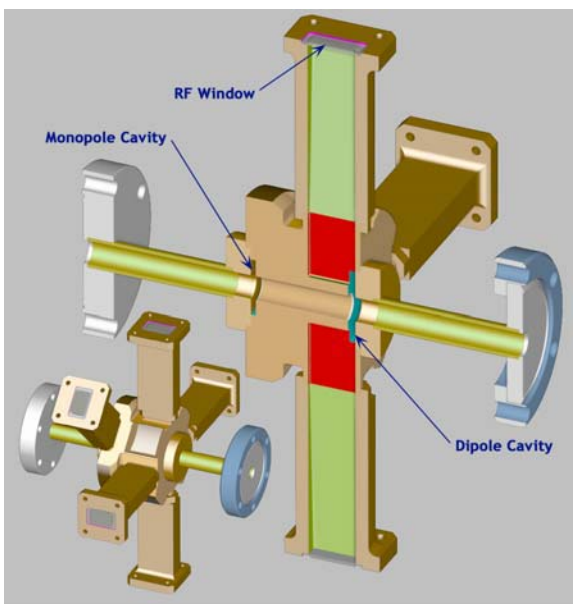

Figure 2: X-Band Cavity BPM Cross-Section.

The X-band cavity BPM inherently has the capability of resolving the beam position in the tens of nanometers, far exceeding the 1-micron resolution requirement indicated in Table 1. Equation 2 estimates the BPM thermal noise voltage output. Given the Bolzmann constant k, operating temperature T in Kelvin, impedance Z is 50 Ohms, the signal bandwidth B is about 2 MHz, and considering a system noise figure of 3 dB the minimum resolution would typically be less than 10 nm. The single-shot resolution will be limited by other processing and data acquisition electronic noise.

$$Vn \approx \sqrt{k \times T \times Z \times B} \qquad (2)$$

Horizontal and vertical position signals are generated from the two polarizations of the TM_{110} dipole mode. The polarized fields are coupled to four iris slots equally spaced around the cavity. The magnetic field of the dipole couples to the TM_{110} mode of the rectangular waveguide shown in Fig. 2. The distinctive modal patterns of the TM_{010} monopole and TM_{110} dipole modes make it possible to couple only to the dipole mode and reject the monopole mode. This selective coupling technique, pioneered by SLAC, has been incorporated in this design [4]. The iris couplers are precisely electrical discharge machined (EDM) into the solid copper block to ensured repeatable and accurate coupling. EDM provides the exceptional accuracy and repeatability that is critical for this device. This technique also ensures that the waveguide braze has little or no affect on the cavity performance from the migration of braze material. The two cavities are designed to operate at the same frequency and a small amount of tuning is provided for adjustment after brazing.

The outputs of the cavity are fed into 76-mm-long linear E-plane tapered waveguide transitions, which transform the cavity outputs (3 mm by 19.05 mm) to standard WR-75 waveguide (9.53 mm by 19.05 mm). The vacuum window shown in Fig. 3 is brazed into the WR75 waveguide flanges with a gold germanium filler alloy. The rf windows are made from glass fused onto a kovar base. The kovar is plated with nickel and then copper to facilitate brazing. The overall electrical performance of the transitions and windows together have a -20-db return loss with less than 0.2-dB insertion loss over a 200-MHz bandwidth centered at 11.384 GHz.

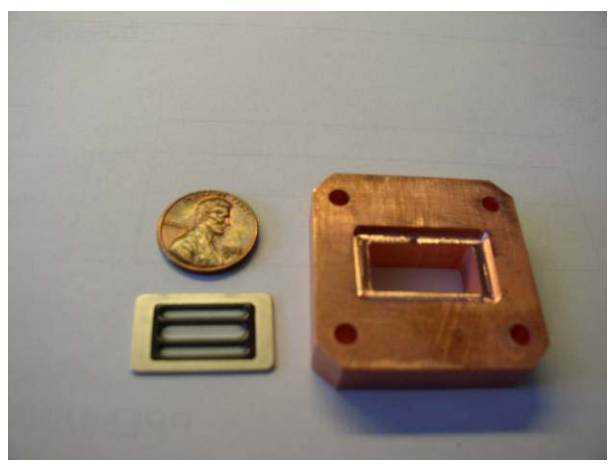

Figure 3: X-Band Cavity RF Window.

The BPM is a brazed assembly made up of the body, waveguide transitions, cavity end caps, rf windows, and end EVAC-type vacuum flanges. The 11.738-mm-radius monopole and 14.937-mm-radius dipole cavities are machined within a +0.000/-0.015-mm tolerance, with a surface finish of 0.1 μm (4 μin Ra) or better into a single piece of oxygen-free electronic copper. The machining tolerance deviation of +0.000/-0.015 mm will equate to a frequency increase of 7.5 MHz, which is within the system tuning capability. The final assembly is brazed in a vacuum furnace back-filled with dry hydrogen.

To facilitate installation alignment, the outer surface of the BPM body shown in Fig. 2 is machined to be concentric to the cavity to within 0.025 mm. This surface will be used as the fiducilization reference to align the BPM during installation.

There are two waveguide outputs for each plane on the dipole cavity. The output flanges are connected directly to the flexible WR75 waveguide shown in Fig. 4 to mechanically decouple any shock or vibration from the rest of the components. The waveguide provides an ideal transmission line for the X-band signals exhibiting very low loss and excellent radiation hardness. The original design concept incorporated optional magic tee power combiners at each pair of outputs on the dipole cavity. This effectively reduces the common mode noise generated by unwanted modes by about 20 db. It is expected that full compliance to the specification can be accomplished without the use of the combiner. This would facilitate the potential for using the unused or terminated ports for future diagnostics.

Each of the three inputs to the receiver is band limited by bandpass filters. The filters provide a 20-MHz bandwidth (-3 dB) centered at 11.384 GHz. The filters also provide a broadband -10 dB return loss match to the cavities. Out-of-band filtering of -60 db reduces unwanted modes from saturating the receiver input.

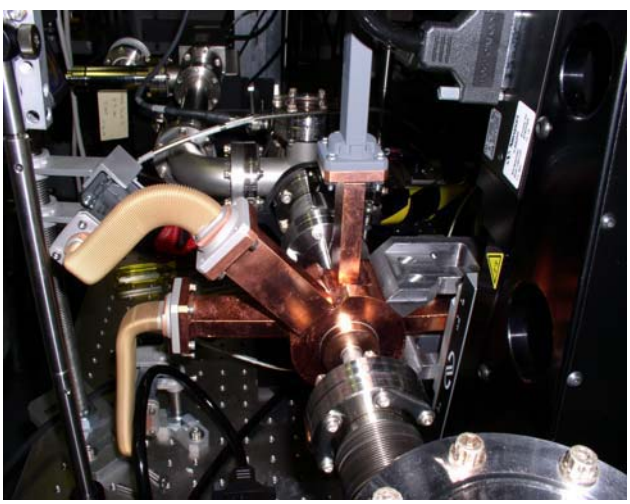

Figure 4: X-band cavity testing.

RECEIVER DESIGN

The receiver topology used is a single-stage three-channel heterodyne receiver shown in Fig. 1. The cavity BPM X-band signals are downconvertered to a 25- to 50-MHz intermediate frequency (IF) in the accelerator tunnel. The signals are first amplified in a low noise amplification (LNA) stage, then translated to a lower IF by mixing with a local oscillator (LO). The LO is a phase-locked dielectric resonate oscillator (PDRO) featuring low phase noise. One option is to lock the LO to the SLAC 119-MHz timing reference. This has the advantage of synchronizing the data with the beam. The other option would have the LO operate in a free-run mode. A single LO will drive all three channels and will be housed in the receiver chassis. The LNA is protected against high-power surges by a limiter that is rated at 50 W peak. After the X-band signals are down-converted, they are filtered and then amplified. The signals are then cabled out of the tunnel. The expected output of the receiver will be a bi-polar +/- 1-volt full-scale exponentially decaying sine wave between 175-260 ns (Q=2000-3000) in duration.

The receiver will be housed in an aluminum 3 in. high × 12 in. wide × 12 in. deep shielded enclosure. The unit will not dissipate more that 20 W and can be heat sunk. Special consideration is given to electro magnetic interference (EMI) susceptibility and emissions by using DC blocks on the inputs, EMI gaskets, feed through pins, and proper grounding. The receiver will be mounted in the tunnel below the undulator girder.

The data acquisition utilizes a commercially available ADC digitizer board. The ADC front end should have a minimum of 14-bit resolution and a sampling rate of 119 MSPS. The ADC clock will be synchronized to the frequency of the 119-MHz timing system of the SLAC linac. This will be considered the minimum requirement for the ADC and it is hoped that the performance requirement can be exceeded when the system is required.

The original plan for acquiring data for the prototype was to simply capture the exponentially decaying waveform and digitally peak detect the reference and position signals. The position and reference cavity IF signal data would then be fit to an exponential curve, with the position data being normalized to the reference.

Another processing algorithm being investigated is to digitally down-convert the IF signals. The raw digital waveform is multiplied point-by-point by a complex LO $e^{j\omega t}$ where ω is the IF frequency. A digital low-pass filter removes the 2ω component leaving a complex baseband signal. A quasi-Gaussian, symmetric, finite impulse response (FIR) digital filter is chosen to remove the 2ω product as well as out-of-band noise. The complex amplitude of the position signal is normalized by the reference cavity to remove bunch charge dependence (amplitude) and beam arrival time dependence (phase). Normalized phase and amplitude are converted to position via scaling and rotation by calibration data.

PROTOTYE RESULTS

Two X-band cavity BPMs have been prototyped and cold tested using a test fixture that precisely moves an $\lambda/4$ E probe driven by an Hp 8510 network analyzer that excites the cavity and then measures the response. Table 2 shows the predicted and measured results of a bolted-together prototype and brazed prototype. The monopole and dipole cavities were modeled using HFSS [5]. The difference of predicted vs. the measured frequency for the TM_{110} dipole mode was less than 0.2 % for both prototypes.

Table 2: Prototype cold test results.

Parameter (500 µm offset)	Predicted	Measured Prototype # 1 bolted end caps	Measured Prototype # 2 brazed end caps
Frequency TM_{010}	8.262 GHz	8.271 GHz	8.243 GHz
Coupling TM_{010}	-53 dB	-69 dB	-62 dB
Frequency TM_{110}	11.364 GHz	11.344 GHz	11.357 GHz
Coupling TM_{110}	-32 dB	-28 dB	-24 dB
Q (loaded) TM_{110}	2704	2086	2391
X/Y Isolation TM_{110}	-26 dB	-33 dB	-23 dB
Dipole to Monopole cavity Isolation	<-80 dB	<-85 dB	<-89 dB
Frequency TM_{020}	15.825 GHz	15.767 GHz	15.785 GHz
Coupling TM_{020}	-78 dB	-64 dB	-50 dB

The brazed prototype cavity BPM is presently installed in the Advanced Photon Source Injector Test Stand (ITS) shown in Fig. 4. The BPM is mounted on a precision 2-axis translation stage to test and calibrate the BPM. The ITS provides 1-nC single-bunch charge with bunch lengths 3-4 ps FWHM. The preliminary data shown in Table 3 indicates good correlation with the cold test and predicted values. An estimated voltage output of the dipole cavity was calculated to be 2.3 mV/µm/nC and the measured value was 1.22 mV/µm/nC. The current monitor used for this measurement has been recently recalibrated and the BPM output response will be re-measured.

Table 3. Prototype ITS test results.

Parameter	Predicted	Cold Test	ITS Test
Frequency	11.364 GHz	11.357 GHz	11.359 GHz
Loaded Q	2704	2391	2500
Isolation X/Y	-26 dB	-23 dB	-21 dB

CONCLUSIONS

X-band cavity BPM and receiver electronics have been designed and tested for micron-level resolution for eventual installation into the LCLS. Preliminary low-power test and beam test using the ITS have produced encouraging results in validating the design for achieving the stated goals. ITS testing is scheduled to continue to obtain valuable operational experience.

The second phase of testing will involve building three new BPMs and installing them at a fixed distance from each other in order to measure single-shot trajectories. The new BPMs will incorporate changes that will facilitate a small amount of cavity tuning. The BPMs will be installed in the APS LEUTL tunnel in October 2006. The testing objective is to provide a complete compliance table for the given specification given in Table 1. Beam conditions will be similar to the expected LCLS photo cathode beam. The prototype testing should be complete by early next year, followed by the production of 34 cavity BPMs.

ACKNOWLEDGMENTS

The authors would like to acknowledge Stephen Milton, John Carwardine, Glenn Decker, and Om Singh for many helpful discussions. The authors would also like to thank Randy Zabel for all his help with building and testing the prototypes.

REFERENCES

[1] R. Hettel, R. Carr, C. Field, and D. Martin, "Investigation of Beam Alignment Monitor Technologies for the LCLS FEL Undulator," BIW 98, Stanford CA, May 1998, p. 413.

[2] P. Emma, J. Wu, "Trajectory Stability modeling and Tolerances in the LCLS," EPAC 2006, Edinburgh, Scotland, June 2006.

[3] A.Liapine, www.hep.ucl.ac.uk/~**liapine**/part_one_**waveguides**_and_cavities.doc

[4] Z. Li, R. Johnson, S. Smith, T. Naito, J. Rifkin, "Cavity BPM with Dipole-Mode-Selective Coupler," PAC 03, Portland Oregon, May 2003.

[5] Ansoft HFSS, version 10.0, Ansoft Corporation, Pittsburgh, PA, USA, 2005.

NONINTERCEPTING BEAM SIZE AND POSITION MONITOR USING ODR FOR X-RAY FELS*

A.H. Lumpkin**, N.S. Sereno, W.J. Berg, D.W. Rule†, B.X. Yang, and C.-Y. Yao
Advanced Photon Source, Argonne National Laboratory, Argonne, IL 60439, U.S.A.
†Carderock Division, NSWC, West Bethesda, MD 20817 USA.

Abstract

Interest in nonintercepting (NI) beam size and position diagnostics between the undulators of x-ray free-electron lasers (XFELs) is driven by the requirement of beam-emittance matching and beam alignment, as well as by the need to minimize radiation damage to the undulator permanent magnets from scattered beam produced by the insertion of converter screens. For these reasons our investigations on optical diffraction radiation (ODR) as relative beam size and position diagnostics are particularly relevant to XFELs. We report the extensions of our studies at 7-GeV beam energy to aspects of the vertical and horizontal polarization components of the ODR near-field and far-field images. The near-field, vertically polarized data are particularly interesting because the vertical field lines at the metal more directly reflect the actual horizontal beam sizes. Although our experiments to date are with mm-scale beams and impact parameters of 1-2 mm, our analytical model indicates that this technique scales with beam size and has sensitivity at the 20- to 50-μm regime with an impact parameter, d = 5 times σ_y = 100 μm. This is the x-ray FEL intraundulator beam size regime.

INTRODUCTION

The interest in nonintercepting (NI) diagnostics for beam size and position in the undulators of x-ray free-electron lasers (XFELs) for beam match reasons is driven by the need to minimize the radiation damage to the undulator permanent magnets by scattering of beam by inserted converter screens. For such reasons our investigations on optical diffraction radiation (ODR) as NI relative beam size and position diagnostics [1-10] are particularly relevant. We reported initial experiments at FEL05 [11], and now we report the extensions of our studies at 7-GeV beam energy to aspects of the vertical and horizontal polarization components of the ODR near-field and far-field images. It appears that the near-field, vertically polarized data are particularly interesting. For our measurements of the beam size along the horizontal axis with a vertically displaced metal screen, the induced currents from the vertical field lines at the metal more directly reflect the actual beam size as revealed by scans of the upstream quadrupole fields. In addition, in our experimental configuration the vertical polarizer also rejects the strongest component of a weak background of visible-light optical synchrotron radiation (OSR) generated when the beam transits the horizontal bend dipole magnet that is 5.84-m upstream of the ODR station [12]. This same concept would be applicable to blocking the polarized visible undulator radiation co-propagating with the e-beam in an XFEL.

Although our experiments are with larger beams and impact parameters of 1-2 mm, our analytical model indicates that the technique scales with beam size and has sensitivity at the 20- to 50-μm regime with the impact parameter, d = 5 times σ_y = 100 μm. The beam size is similar to the 30-μm beam size in the XFEL intraundulator location. In addition, a direct comparison of the horizontal position readings of the nearby rf beam position monitor (BPM) and the ODR image centroid values during the scan of the upstream dipole current showed good agreement. The ODR data were also found to be very similar to an OTR image value during a similar dipole current scan. Our experimental results and some modeling results will be presented.

EXPERIMENTAL BACKGROUND

The Advanced Photon Source (APS) facility includes an injector complex with an rf thermionic cathode gun, an S-band linear accelerator, a particle accumulator ring (PAR) that damps the linac beam at 325 MeV, a booster injector synchrotron that ramps the energy from 0.325 GeV to 7 GeV in 220 ms, and the 7-GeV storage ring. At the exit of the booster, a dipole magnet allows direction of the beam to an alternate booster extraction beamline (BTX) that ends with a beam dump. This spur line has been used to develop our optical transition radiation (OTR) and our ODR diagnostics. The setup includes the upstream corrector magnets, two quadrupoles, and a dipole; and then, 5.8-m downstream the rf BPM (horizontal), the OTR/ODR imaging station, a localized beam-loss monitor based on a Cherenkov radiation detector, a Chromox beam-profiling screen, and the beam dump, as schematically shown in Fig. 1. An additional feature of the remote control of one strategic lens changes the optics from near-field to far-field imaging.

The ODR converter is a polished Al blade/mirror that is 1.5-mm thick, 30-mm wide, 30-mm tall, and it is mounted with its surface normal at 45º to the beam direction on a vertical stepper assembly. Its horizontal edge can be vertically positioned with an overall accuracy of ±10 μm over a span of 27.5 mm. The alignment of the optics with converter surface angle was done with an alignment laser placed on the surveyed beamline axis during an access

*Work supported by the U.S. Department of Energy, Office of Science, Office of Basic Energy Sciences, under Contract No. W-31-109-ENG-38.
**lumpkin@aps.anl.gov

period as described previously [12]. The near-field magnification resulted in calibration factors of 60-μm per pixel in x and 45-μm per pixel in y. Two 6-position filter wheels were used to select neutral density (ND) filters, bandpass filters, or two polarizers, which are oriented at 90 degrees to each other. The images are detected with a standard SONY charge-coupled device (CCD) camera, and the video is digitized with a MaxVideo MV200 digitizer interfaced to the Experimental Physics and Industrial Control Systems (EPICS) software architecture. The online image processing allows the selection of a region of interest, formation of the projected x and y profiles, and both a Gaussian fit to the profile and a numerical evaluation of the FWHM of the profile. The rms size is then the sigma of the Gaussian result or the estimated value found by dividing the numerically calculated FWHM by 2.35.

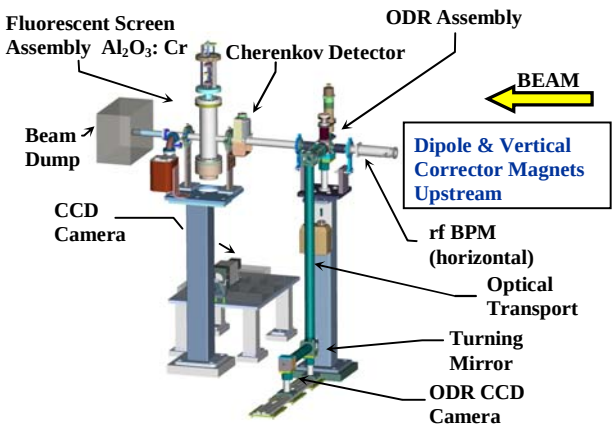

Figure 1: A Pro-E drawing of the OTR/ODR imaging station showing the rf BPM, the cube and stepper drive, the optical transport, the Cherenkov detector local loss monitor, and the Chromox profile monitor.

EXPERIMENTAL AND ANALYTICAL RESULTS

As mentioned in the previous section, the ODR profile results are referenced to complementary OTR profile results, and the image centroids are compared to the nearby, upstream rf BPM. The SDDS tools are used for the tracking of the process variables [13, 14].

The potential to monitor relative beam size has been discussed in our earlier papers [11, 12, 15]. However, in this case we now have the results of vertically polarized data. The OTR image profiles were first obtained by inserting the Al metal screen during a scan of the upstream AQ2 quadrupole field. This quadrupole strongly affects the horizontal beam size at our OTR/ODR station. Unfortunately, this is at a dispersive point in the lattice so we do not get emittance data cleanly from the quadrupole field scan. However, we do obtain a test of ODR as a relative beam size monitor. As seen in Fig. 2, the unpolarized, OTR-measured horizontal beam size varies from 2300 μm down to about 1300 μm. Results of both algorithms are shown, and they are seen to be in very good agreement because the beam shape is basically Gaussian when extracted from the 7-GeV booster synchrotron. Next, in Fig. 3, we show the observed vertically polarized ODR image profiles with an impact parameter of 1.25 mm during a similar quadruople field scan. The vertically polarized ODR horizontal image profiles track the beam size changes as seen qualitatively by the shape of the curve with AQ2 current. A direct comparison of the OTR and ODR is seen in the Fig. 4 combined plot of their fitted rms values. The ODR profiles are about 10% to 25% larger than the corresponding OTR profiles from the largest beam size to the smallest, respectively. The ratio of ODR/OTR for the size scan is next plotted in Fig. 5 to act as a lookup table for the beam-size monitor. As can be seen, at the minimum size of 1300 μm for the OTR, the ODR fit value is only 25% larger. This is much better than our factor of two results with unpolarized ODR observed on the same shift for this minimum beam focus and also reported at BIW06 [12]. The vertical polarization component would appear to be more reliable and direct in monitoring the actual beam size to better than 10% one has the ratio table or plot for these conditions.

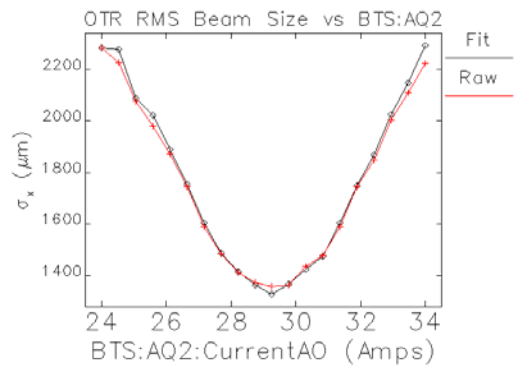

Figure 2: A plot of the OTR rms horizontal profile sizes for the upstream AQ2 quadrupole field scan. Both a Gaussian fit and a simple peak intensity to FWHM algorithm were used, which are in good agreement.

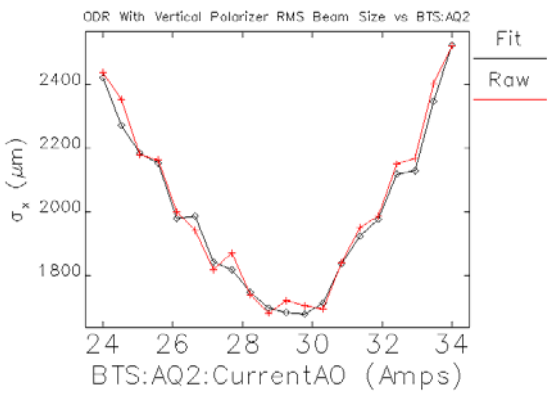

Figure 3: A plot of the vertically polarized ODR rms horizontal profile sizes for the upstream AQ2 quadrupole field scan. Both a Gaussian fit and a simple peak intensity to FWHM algorithm were used to measure image sizes, which are in good agreement.

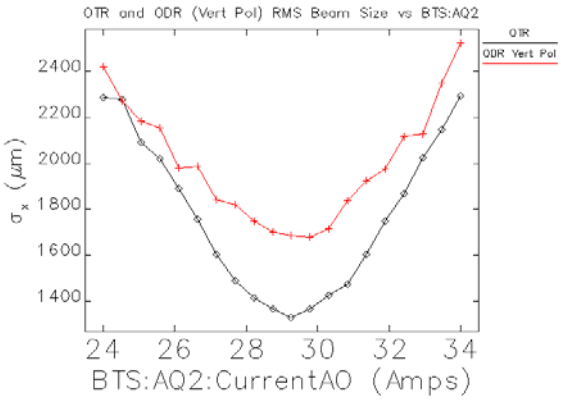

Figure 4: A direct comparison of the ODR (plus) and OTR (diamonds) Gaussian-fit horizontal profile size s during the quadrupole field scan. The vertically polarized ODR tracks the beam-size changes.

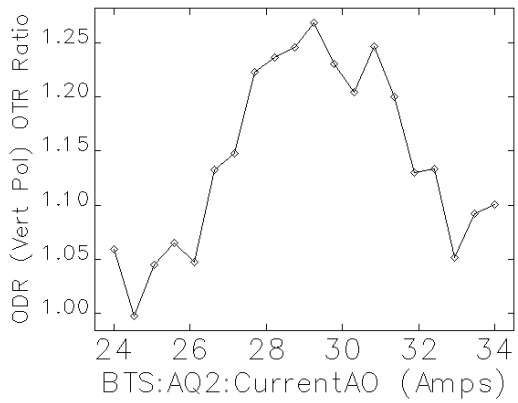

Figure 5: The ratio of ODR/OTR horizontal image sizes for different beam sizes during the AQ2 quadrupole scan. This ratio is noticeably smaller than for unpolarized data reported earlier.

In Fig. 6, we show the analytical results from our model described previously [11] for a beam size change of ±20% around the nominal σ_x=1300-μm value and the corresponding ODR image profile changes at the 1/e points in intensity. First, it is clear there is sensitivity to the beam-size changes that should be detectable in the camera images. Second, the HWHM values indicate an ODR profile of about 1.2 times the actual beam size as seen in the polarized data comparisons. These were done with a fixed σ_y = 200 μm. Initial vertical polarization effects have also been calculated, but further work is needed. The calculated ODR x width using the vertical polarization component was 20 to 50% narrower than that calculated using the horizontal component for d = 1000 and 2000 μm, respectively.

We also have calculated the sensitivity of ODR profiles to smaller beam sizes. In this case, we held the y size constant at 20 μm and varied the x-size from 20 to 50 μm using an impact parameter of 100 μm and beam energy of 7 GeV. In Fig. 7 it is clear that approximately a 25% increase in the ODR horizontal profile half width is calculated for the 50-μm beam size. Image processing should easily detect this change and use of polarization would improve the sensitivity. This should be a good match to monitoring beams of 30-μm size in the XFELs, subject to signal levels.

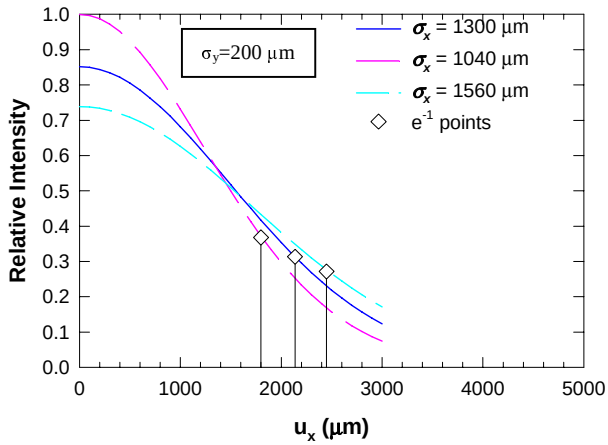

Figure 6: Analytical model results for the effects on the unpolarized ODR horizontal profiles for a variation of the beam size by ±20% around the 1300-μm value with d=1000 μm.

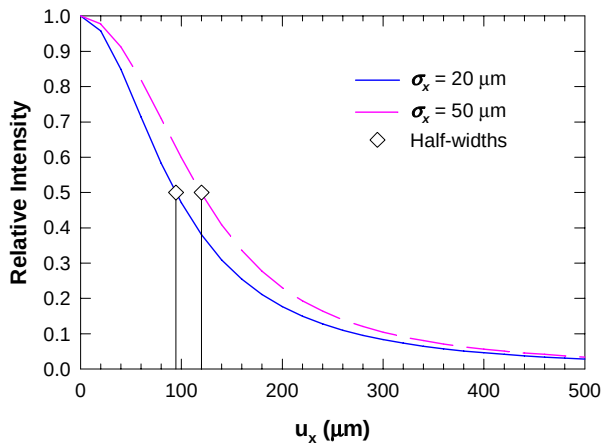

Figure 7: Analytical results for the change in unpolarized, horizontal ODR profiles for a change in beam size from 20 to 50 μm while holding the y value constant at 20 μm. The impact parameter is 100 μm for the 7-GeV beam. This is relevant to XFEL beam-size monitoring.

In addition, we repeated our relative beam position measurements first done with unpolarized ODR and compared to the rf BPM and OTR values [11]. In this case, we again used vertically polarized ODR with an impact parameter, d = 1.25 mm and a vertical size σ_y of 200 μm or less. The plot in Fig. 8 actually compares the centroid values from both OTR and ODR to the horizontal BPM readings. The OTR and ODR data overlap each other almost completely. This was done with the beam size σ_x = 1300 μm, the AQ2 quadrupole field set for the beam size minimum. Again, we believe the vertically polarized ODR component benefits the measurement sensitivity in the horizontal axis. Sensitivity at the 50- to

100-μm relative position level is attained. As in the case of beam size monitoring, for the much smaller beam and impact parameter in the XFEL case, we would expect much better position sensitivity (sub-10 μm) subject to signal level. Correspondingly, a vertical, single edge of a metal screen or aperture can be employed to obtain information on vertical position and beam size.

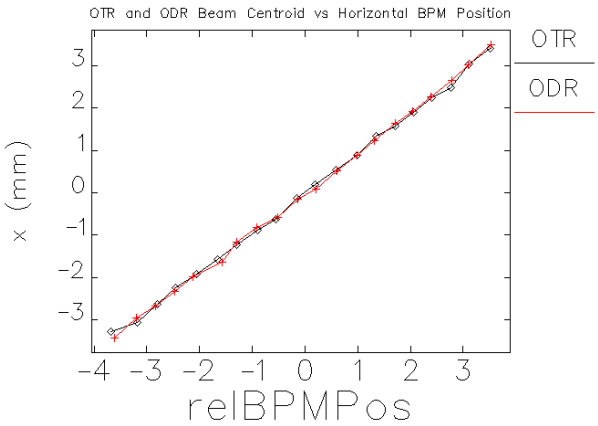

Figure 8: A plot of the OTR and ODR centroid value changes versus the nearby rf BPM values in mm during a scan of the upstream dipole current supply (and magnet fields). Horizontal position information can be reliably obtained from the vertically polarized ODR image centroids.

SUMMARY

In summary, we have extended our NI diagnostics techniques by evaluating the vertical and horizontal polarization components of near-field ODR images. As expected, the induced currents from the vertical field lines more directly represent the horizontal beam size in our configuration. Our results indicate that the tracking of relative beam size and position can be scaled down to address the potential needs of x-ray FELs. Complementary information on beam trajectory angle and beam divergence is being explored as well for higher average current beams.

ACKNOWLEDGMENTS

The authors acknowledge the support of Brian Rusthoven, Al Barcikowski, and Mike Bracken in the Mechanical Engineering Group, Joe Gagliano and Wayne Michalek in the Vacuum Group, Chuck Gold of the Diagnostics Group, and Bill Jansma and Horst Friedsam in the Survey Group for installation and resurvey, respectively, of the station in December 2005 and January 2006. The laser alignment proved to be a critical contribution to the new optics setup and the rotated BPM addressed the horizontal plane request.

REFERENCES

1. A.P. Kazantsev and G.I. Surdutovich, Sov. Phys. Sokl. **7**, 990 (1963).
2. M.L. Ter-Mikaelian, *High Energy Electromagnetic Processes in Condensed Media* (Wiley/Interscience, New York, 1972).
3. M. Castellano, Nucl. Instrum. Methods A **394**, 275 (1997).
4. Y. Shibata et al., Phys. Rev. E **52**, 678 (1995).
5. A.P. Potylitsyn, Nucl. Instrum. Methods B **145**, 169 (1998).
6. R.B. Fiorito, D.W. Rule, and W.D. Kimura, AIP Conf. Proc. **472**, 725 (1999); W.D. Kimura, R.B. Fiorito, and D.W. Rule, Proc. of the 1999 Particle Accelerator Conference, 487 (1999).
7. D.W. Rule, R.B. Fiorito, and W.D. Kimura, AIP Conf. Proc. **390**, 510 (1997).
8. R.B. Fiorito and D.W. Rule, Nucl. Instrum. Methods B **173**, 67 (2001).
9. T. Muto et al., Phys. Rev. Lett. 90(10) 104801-1 (2003).
10. P. Karataev et al., Phys. Rev. Lett. **93**, 244802 (2004).
11. A.H. Lumpkin et al., "Nonintercepting Electron Beam Diagnostics Based on Optical Diffraction Radiation for X-ray FELs," Proceedings of the International FEL05 Conference, Stanford, CA, Aug. 21-26, 2005, JACoW/eConfC0508213, p. 604.
12. A.H. Lumpkin et al., "Developments in OTR/ODR Imaging Techniques for 7-GeV Electron Beams at APS," submitted to Proceedings of BIW06, Batavia, Illinois, May 1-4, 2006.
13. L. Emery, M. Borland, H. Shang, R. Soliday, "User's Guide for SDDS-Compliant EPICS Toolkit Version 1.5," Advanced Photon Source, March 9, 2005.
14. H. Shang, Proc. of PAC2003, 3470 (2003).
15. A.H. Lumpkin et al., "Near-Field Imaging of Optical Diffraction Radiation Generated by a 7-GeV Electron Beam," submitted to Phys. Rev.

INITIAL SEARCH FOR 9-keV XTR FROM A 28-GeV BEAM AT SPPS*

A.H. Lumpkin, J.B. Hastings,** and D.W. Rule***
Advanced Photon Source, Argonne National Laboratory
Argonne, IL 60439 USA

Abstract

The potential to use x-ray transition radiation (XTR) as a beam diagnostic and coherent XTR (CXTR) as a gain diagnostic in an x-ray FEL was proposed previously. At that time we noted that the unique configuration of the SLAC Sub-picosecond Photon Source (SPPS) with its known x-ray wiggler source, a special three-element x-ray monochromator, x-ray transport line, and experimental end station with x-ray detectors made it an ideal location for an XTR feasibility experiment. Estimates of the XTR compared to the SPPS source strength were done, and initial experiments were performed in September 2005. Complementary measurements on optical transition radiation (OTR) far-field images from a 7-GeV beam are also discussed.

INTRODUCTION

The use of x-ray transition radiation (XTR) as a beam diagnostic and coherent XTR (CXTR) as a gain diagnostic in an x-ray free-electron laser (XFEL) was proposed previously at FEL04 [1]. There have been a number of experiments to develop XTR as a source of x-rays in the past at several laboratories using moderate beam energies of a few hundred MeV to GeV [2-6], but there have been no applications in the FEL world to date. Partly based on recent experiments with a 7-GeV beam with optical transition radiation (OTR) and far-field or focus-at-infinity imaging [7], we projected that there should also be useful diagnostic information in the XTR field. In addition, we wanted to evaluate how to measure CXTR in an XFEL at 1.5 Angstroms. We identified the configuration of the SLAC Sub-picosecond Photon Source (SPPS) [8] with its known x-ray wiggler source, a special three-element x-ray monochromator, x-ray transport line, and experimental end station with x-ray detectors as a large-scale and ideal location for an XTR feasibility experiment. It was also the closest setup to what one might encounter in an x-ray FEL such as the Linac Coherent Light Source (LCLS) with its capability of translating in the 3-m undulator segments one at a time in the 100-m string of magnetic structures [9].

A test of XTR intensity with respect to the x-rays emitted by the SPPS wiggler when a 28-GeV beam transited it was proposed. Estimates of the XTR were done, the experiment proposal was approved, and initial experiments were performed in September 2005.

EXPERIMENTAL BACKGROUND

The OTR experiments were performed at the Advanced Photon Source (APS) as described elsewhere [7], and the XTR experiments were performed at the SPPS. The SPPS has been a short-pulse x-ray facility since 2004 [8]. The 28-GeV electron beam with a charge of Q = 3 nC, an emittance of 35 π mm-mrad, and bunch length of 230 fs was transported to the Final Focus Test Beam (FFTB) facility from the main SLAC accelerator [10] and through the single, permanent magnet wiggler as shown schematically in Fig. 1. The SPPS source was tuned to 9 keV by adjusting the wiggler gap, and a three-element x-ray monochromator is used to direct the x-rays down a 50-m long beamline to the end station. In addition, as noted in the schematic, there are several OTR stations with 1-μm-thick Ti foil installed in support of the series of experiments on beam driven plasma Wakefield acceleration by M. Hogan and his collaborators [11]. These Ti foils were used to generate the forward XTR for the trial experiments. A dipole at the end of the electron beam beamline directed the electrons to a beam dump.

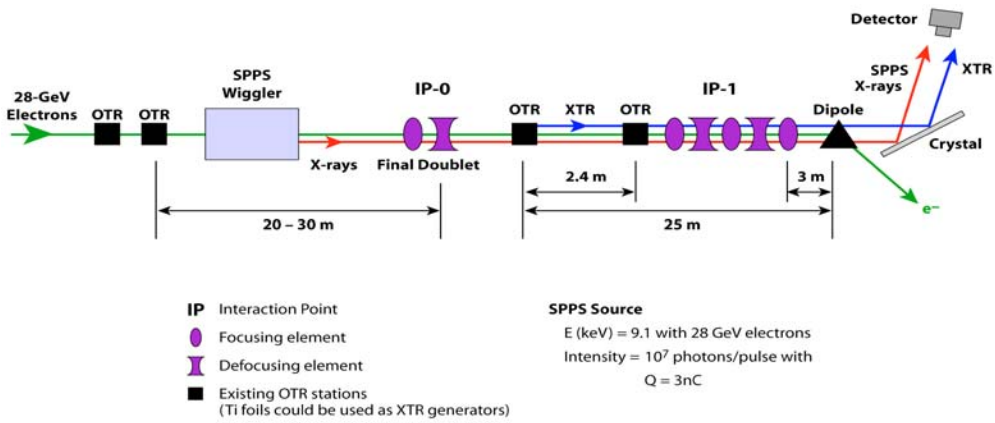

Figure 1: A schematic of the FFTB facility showing the beamline, SPPS wiggler, OTR stations, monochromator, and x-ray detectors.

*Work supported by the U.S. Department of Energy, Office of Science, Office of Basic Energy Sciences, under Contract No. W-31-109-ENG-38.
**SPPS/SLAC, Menlo Park, CA USA
***Carderock Division, NSCW, West Bethesda, MD USA

This dipole was the source of broadband x-ray synchrotron radiation (XSR) that also would be interacting with the three-element crystal monochromator. The three-element monochromator was adjusted to transport 9-keV x-rays from the wiggler using a series of x-ray detectors along the beamline.

At the end station an ANDOR x-ray CCD camera and Photonic Science X-Ray Eye intensified camera were used as the principle diagnostic components. The wiggler x-rays were also aligned based on a series of x-ray APDs along the beamline. The ANDOR camera is designed to be cooled to reduce read noise and dark current. Unfortunately on these particular experiments, a small vacuum leak in the camera prevented the final cool down, so we ran it at room temperature. The X-ray Eye was positioned about 1 meter downstream of the CCD camera and was used for initial wiggler beam and hence monochromator alignments. The attenuation of the SPPS source x-ray was done with various selections of Al foil thicknesses that were calculated to attenuate 9-keV x-rays by factors of up to 4000. At 10-keV x-ray energy the counts per detected photon was about 391, resulting in a dynamic range of 167. This assumed a 16-bit device and a gain of seven photoelectrons per count in the CCD.

Aspects of the possible eventual XTR application to LCLS are shown in Fig. 2. In the schematic the beam energy is 14 GeV and the OTR and XTR are generated by a thin foil (or foil stack). For OTR an off-axis mirror might be used, but for XTR an annular crystal would be used. The expected opening angle of the radiation cones in either case would be $1/\gamma$ = 35 μrad. For OTR an imaging system would be used, and for XTR the YAG:Ce converter plus lens and CCD camera might be employed. A far-field imaging experiment with lenses appears feasible for the OTR. This would be done in a manner similar to our recent 7-GeV beam work at APS [7].

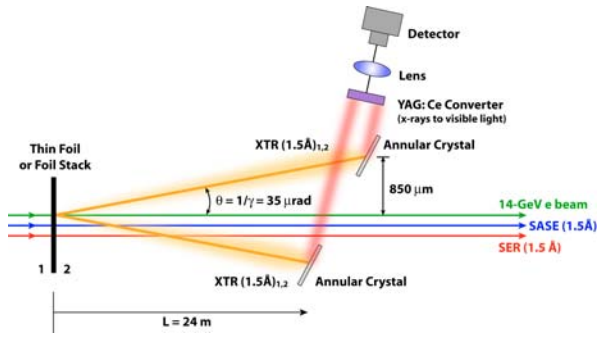

Figure 2: A schematic of the generation of XTR from a foil or foil stack from a 14-GeV beam and with competing wiggler x-rays or spontaneous emission in a SASE FEL.

EXPERIMENTAL RESULTS AND DISCUSSION

OTR Results at 7 GeV

As a point of reference, the results of complementary experiments on the 7-GeV beam at APS are included. In this case a single Al screen was used to generate the backward OTR. At this beam energy the expected OTR opening angle would be 70 μrad. This is within a factor of two of the angle in LCLS and of four in that for SPPS. In Fig. 3 we see the unpolarized, vertically polarized, and horizontally polarized images for the beam extracted from the booster synchrotron. For beam charges of 3 nC one could image these far-field angular distributions. The depth of the central minimum indicates the ensemble beam divergence is much smaller than 70 μrad, probably less than 10 μrad. An analytical model [12] was used to evaluate the expected profiles for different divergences. An example is shown in Fig. 4 for 3-μrad divergence.

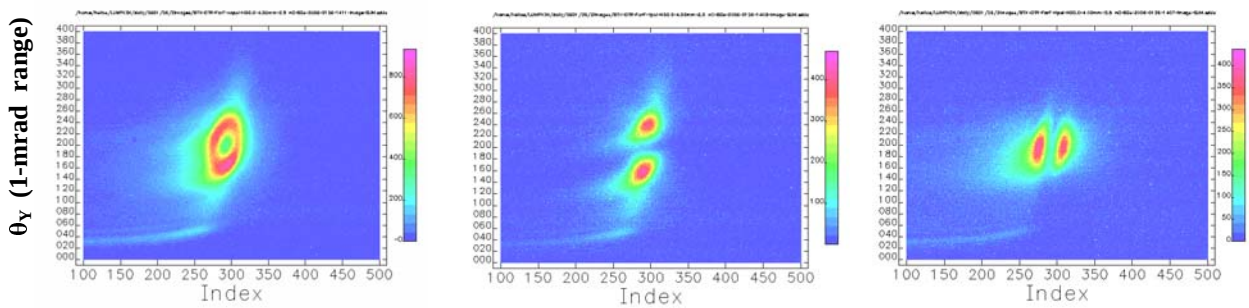

Figure 3: Example of far-field OTR images generated by a 7-GeV beam at APS; a) unpolarized, b) vertically polarized, and c) horizontally polarized.

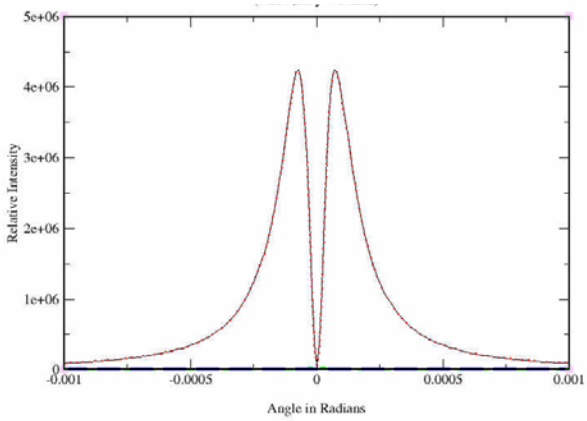

Figure 4: An analytical calculation of the OTR single foil angular distribution for a 7-GeV beam with 3-μrad divergence. The opening angle is ~70 μrad.

9-keV X-rays

In the case of the SPPS experiments we accepted the standard tuneup for 9-keV photons. The nominal intensity was projected to be 10^7 photons per 3 nC of charge. We had calculated the XTR yield from carbon foils as ~10^3 photons per 3 nC. The initial SPPS result is shown in Fig. 5 using the Al foil attenuation of 1000. The observed image corresponds to supported transport of 30×80 μrad^2. The three-element crystal monochromator is oriented in the horizontal plane with a spatial acceptance of about 1 mm, but subtends larger vertical angles. An example profile is shown in Fig. 6, indicating a vertical FWHM of about 20 μrad. In Fig. 7 we show the 9-keV x-ray image of the background XSR (attributed to the dipole upstream of the monochromator) obtained with the wiggler gap open and foils extracted. The gas nozzle from the experimental chamber just upstream of the x-ray CCD is actually inserted vertically from the top. It shadows the x-rays, and was seen in the horizontal axis because the CCD camera is rotated 90 degrees in the installation. The uniform stripe of the XSR from the vertically deflecting dipole is seen clearly. There is also a ghost image in the 10-shot average due to some camera trigger inconsistency.

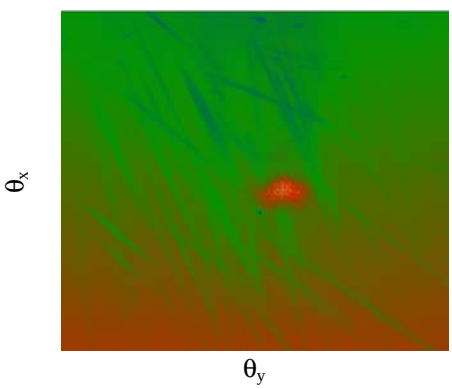

Figure 5: An x-ray CCD image of the SPPS 9-keV x-rays from the wiggler. The camera is rotated 90º so θ_y is along the image horizontal axis. The signal is attenuated by 1000.

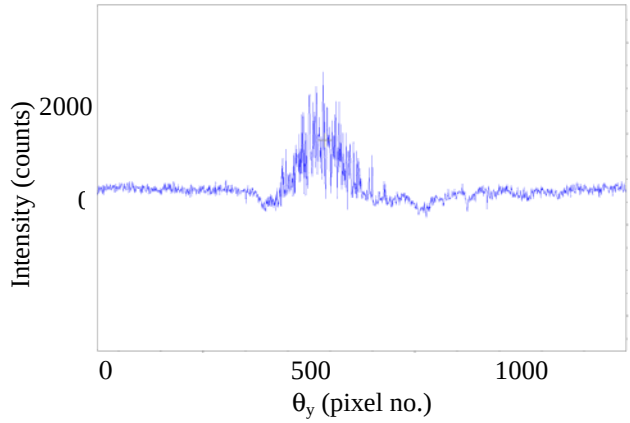

Figure 6: A vertical angular distribution profile from Fig. 5.

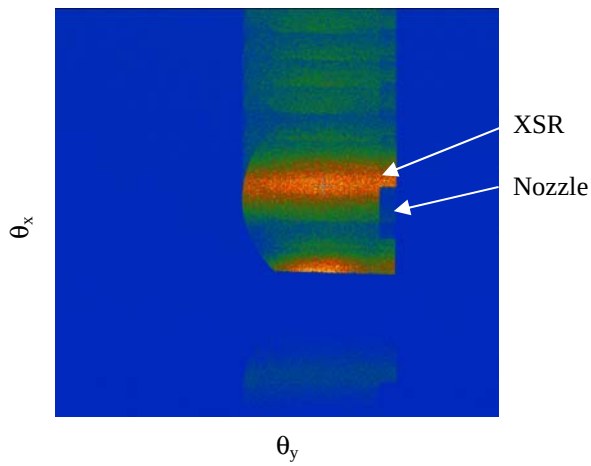

Figure 7: An x-ray CCD image of 9-keV XSR background coming down the beamline. The gas jet nozzle in a chamber upstream of the camera is shadowed. It is vertically insertable.

In Fig. 8 we show the observed x-ray image signal with all three foils inserted using a selected region of interest (ROI) with 4x4 pixel binning and with background subtraction of the signals with the wiggler gap open and all three foils out. This is a localized ROI pixel binning to improve statistics and camera sync. In Fig. 9 the profile in θ_y is shown. There is a hint of an annular shape, and the opening angles are marked on the profile as might be for the middle foil distance. Based on a calibration factor of 1.1 μrad per 4-pixel bin, the 18-μrad location is estimated for a foil at 80 m. In Fig. 10 a calculation for OTR from a 28-GeV beam is shown as a point of comparison for a divergence value of 5 μrad. The central minimum is deeper in the calculation than in the data profile.

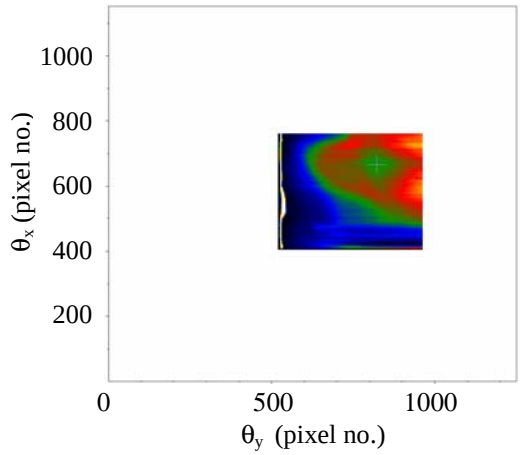

Figure 8: A background subtracted x-ray CCD ROI image of the 9-keV x-rays with three Ti foils inserted.

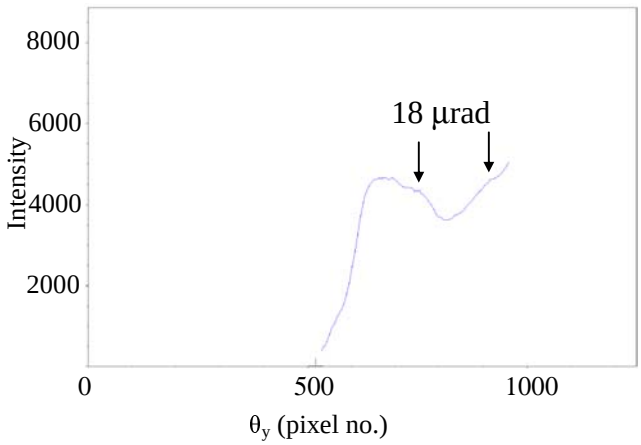

Figure 9: An x-ray CCD region of interest for the three XTR foils inserted case including background subtraction of the XSR source.

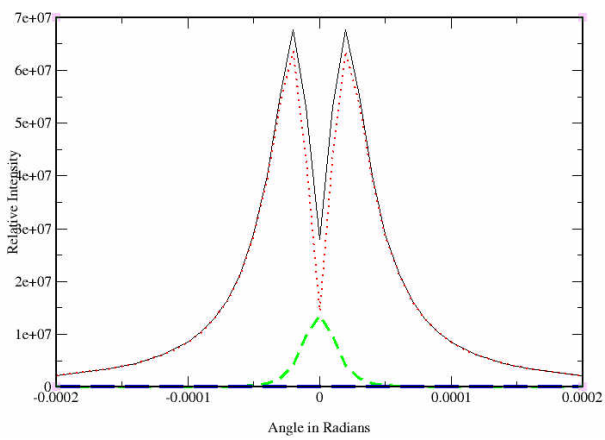

Figure 10: A calculation of the OTR angular distribution for a 28-GeV beam and 5-μrad divergence.

SUMMARY

In summary, we have shown the possibilities of OTR far-field imaging for a 7-GeV beam and report our initial attempts to extend such research to XTR from a 28-GeV beam. Due to the unfortunate event that the x-ray CCD camera could not be cooled during the XTR trials, the results are inconclusive. Certainly, XTR was generated by the Ti foils, but the unambiguous imaging of that radiation was problematical. The concept of a foil stack to enhance the XTR signal and the ability to actually cool the CCD were next on the agenda. The closing of the SPPS facility occurred before these experiments could be done, but the LCLS or SABER facilities at SLAC may provide a future opportunity to test the concepts.

ACKNOWLEDGMENTS

The authors acknowledge the assistance of Kelly Gaffney on the x-ray CCD, Aaron Lindenberg for borrowing the X-ray Eye, and the team of SPPS graduate students who rotated through the extended shifts at SLAC. They also thank Mark Hogan for use of the OTR stations in the FFTB.

REFERENCES

[1] A.H. Lumpkin, W.M. Fawley, and D.W. Rule, "A Concept for Z-dependent Microbunching Measurements with Coherent X-ray Transition Radiation in a SASE FEL," Proceedings of the 2004 FEL Conference, Trieste, Italy, Editors: Bakker, Giannessi, Marsi, and Walker, 515 (2005).

[2] A.N. Chu et al., J. Appl. Phys. **51** (3) 1290 (March 1980).

[3] Michael J. Moran, Nucl. Instrum. Methods **B24/25** 335 (1987).

[4] Michael J. Moran, Nucl. Instrum. Methods **B33**, 18 (1988).

[5] M.A. Piestrup et al., Phys. Rev. **A 45** (2) 1183 (1992).

[6] H. Backe et al., Z. Phyz. **A 349** 87 (1994).

[7] A.H. Lumpkin et al., "Developments in OTR/ODR Imaging Techniques for 7-GeV Electron Beams at APS," submitted to Proceedings of BIW06, Batavia, Illinois, May 1-4, 2006, AIP (in press).

[8] J.B. Hastings, "Sub-Picosecond Pulse Source: Recent Results," presented at PAC2005, Knoxville, Tennessee, TOPB002.

[9] R.M. Bionta, "Characterization of X-ray FEL Radiation," presented at FEL2005, Stanford, CA, THOB003.

[10] P. Emma et al., Proceedings of the PAC2003, 3129 (2003).

[11] M.J. Hogan et al., "Review of Beam-Driven Plasma Wakefield Experiments at SLAC," presented at PAC2005, Knoxville, Tennessee, TOPA002.

[12] D.W. Rule, code Singlef, transported to APS Unix system 1992.

MODELING AND MEASUREMENT OF μ-METAL SHIELDING EFFECT ON THE MAGNETIC PERFORMANCE OF AN LCLS UNDULATOR*

Shigemi Sasaki, Isaac B. Vasserman, Emil Trakhtenberg
APS/ANL, Argonne, IL 60439, USA.

Abstract

In a previous paper [1], we presented results showing that the Earth's field might have a significant effect on the Linac Coherent Light Source (LCLS) undulator performance due to a large concentration of the field by the undulator poles. Based on the result of model calculation, we decided to shield the Earth's field by surrounding the undulator backing structure with a 1-mm-thick μ-metal sheet.

First, the effect of the shield was modeled using the code RADIA. According to the calculation, the shielding factor of a "C-shape" μ-metal shield was better than a factor of eight. Second, we measured the Earth's field shielding effect without an undulator. In our measurement laboratory, the vertical component of the Earth's field was about 0.5 gauss. It was suppressed down to smaller than 0.1 gauss with the shield. After these background measurements, we examined the effect of the shield with an undulator in place. The measurement results show very good agreement with the model calculation.

INTRODUCTION

For the commissioning of the Linac Coherent Light Source (LCLS), beam-based alignment will be used to correct the offsets of quadrupoles and beam position monitors. This strategy works only when the field integrals in each undulator segment are small enough [2]. Undulator segments will be measured and tuned in the magnetic measurement facility (MMF) at the Stanford Linear Accelerator Center and then installed on the iron girders and moved to the LCLS tunnel. Several sources of errors are possible here. The first one is due to the difference of the Earth's field at the locations of MMF and tunnel. This difference is exaggerated by a concentration of the Earth's field by vanadium-permendur poles of the device. Another possible source of error is the existence of the magnetic elements, such as iron, used in the support system and other elements of the tunnel. Based on the computer simulations using a simple model in the RADIA code [3], we decided to use the μ-metal sheet to shield unwanted external field effect.

EARTH'S FIELD MODELING

As shown in our previous paper [1], a seven-period undulator model with a large surrounding solenoid was used for simulating the Earth's field effect. By using this simple model, we found that the averaged field concentration factor was about 2.4, i.e., a 0.5-gauss external vertical dipole field gave a 1.2-gauss dipole field in an undulator. The horizontal component of Earth's field was found to be well suppressed on the undulator axis.

Because a dipole field above 0.7 gauss in an undulator gives an electron trajectory excursion of more than 2 μm from the undulator axis, this unwanted field needs to be suppressed or corrected. Figure 1 shows the model used for the calculation of shielding effect of μ-metal. The B-H curve of CO-NETIC sheet [4] was assumed for the calculation.

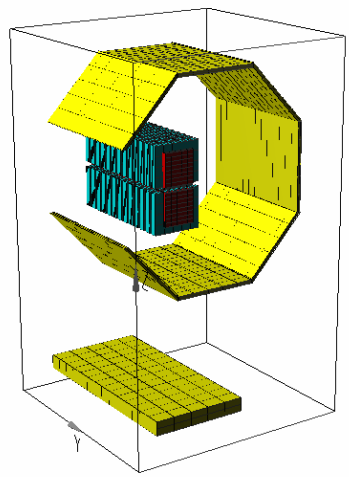

Figure 1: A μ-metal shield model used for the calculation.

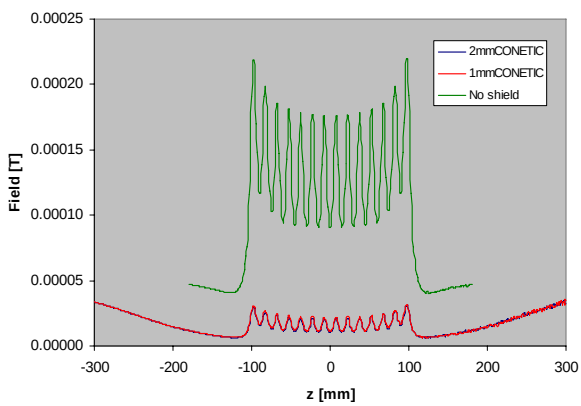

Figure 2: Summary of calculated results.

Figure 2 shows the summary of calculated results. The green curve represents the field change due to the 0.5-gauss external vertical field without a shield. In the central region, a field strength averaged over a half period is about 1.2 gauss. The red and blue curves are for 1-mm- and 2-mm-thick μ-metal shields, respectively. The

* Work supported by the U.S. Dept. of Energy, Office of Science, Office of Basic Energy Science, under Contract W-31-109-ENG-38.
# sasaki@aps.anl.gov

averaged field was 0.156 gauss for a 1-mm sheet and 0.147 gauss for a 2-mm sheet, respectively. Based on these calculations, we decided to use a 1-mm thick sheet for better cost performance. (A sheet with a double thickness provides only 6 % better shielding.)

From these results, we find that the concentration (enhancement) factor by the poles in an undulator is 2.4, and the suppression (damping) factor by the μ-metal shield is eight.

MEASURED RESULTS

The first and second articles of LCLS undulators were tuned in the magnetic measurement facility (MM1) at the Advanced Photon Source. Prior to the measurement, the background field along the measurement bench was measured with a moving coil. Figure 2 shows the Earth's field distribution along the z-axis.

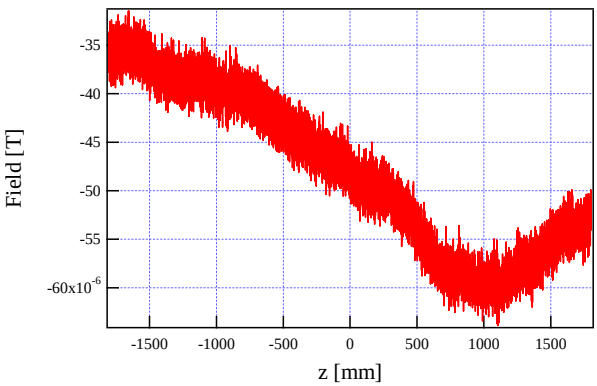

Figure 3: Earth's field distribution measured in MM1.

From this result, we can estimate the shielding effect by the μ-metal in an undulator based on the simulation result described in the previous section. Without the shield, the field, B_y, in an undulator due to the Earth's field is magnified by a factor of 2.4, i.e., $B_y = B_{EF} \times 2.4$. After applying the shield, the remaining field, B_{yrem}, is reduced by a factor of eight, i.e., $B_{yrem} = B_y/8$. Therefore, the signature of shield, B_{sig}, is: $B_{sig} = B_y - B_{yrem}$.

Figure 4 shows the signature of μ-metal shield. After measuring the undulator field without the shield, we can predict the field distribution with the shield by adding the shield signature to the raw data.

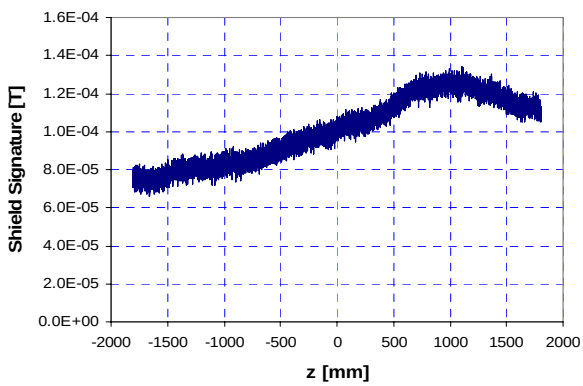

Figure 4: Signature of the μ-metal shield.

In Figure 5, the solid green curve is the second field integral of the raw data measured without the shield, and the blue broken curve is the prediction for after the shield is installed.

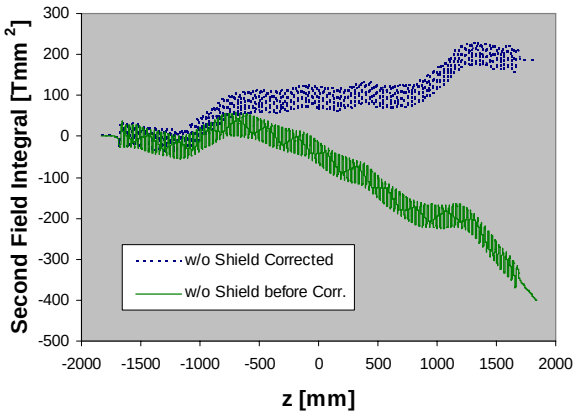

Figure 5: Second field integrals of raw data and corrected data.

Figure 6 shows the predicted second field integral and the integral measured after the shield was attached.

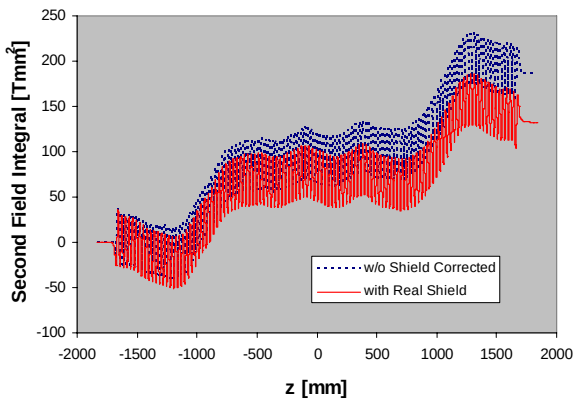

Figure 6: Second field integrals predicted from data without shield (blue broken line) and the data with the shield (red solid line), respectively.

The actual measured field data with the μ-metal shield is in good agreement with the corrected data based on simulation with a simple model.

DISCUSSION AND SUMMARY

In the example shown in this paper, we applied additional trajectory shims and phase shims to straighten the trajectory and to reduce the phase error after applying the μ-metal shield. Also, we corrected the first and second field integrals by applying appropriate shims at the entrance and the exit ends of undulator. Figure 7 shows the trajectory after the final tuning with the shield. The net kick (corresponding to the first integral) and the net displacement (corresponding to the second field integral) are well below the tolerances as shown. Also, the trajectory excursion in the undulator is well below the tolerances (2 μm).

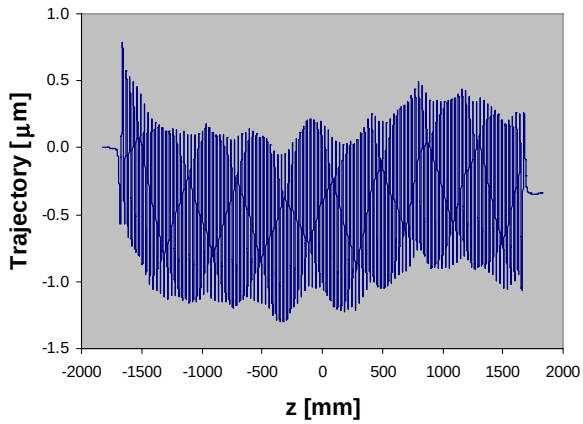

Figure 7: Trajectory of the first article undulator after final tuning.

In the example in this paper, we used the estimation procedures in a relatively early stage of the tuning process in order to demonstrate the effectiveness of this method. However, because the effectiveness of this method had been proven, we used it at the very end of the tuning process for the second article of LCLS undulators.

Here are the steps of the tuning procedures:

- Mechanically align an undulator to the Hall-probe measurement bench.
- Magnetically align the undulator axis to the Hall-probe.
- Set a proper gap by changing the thickness and/or the location of spacers (mechanical shims).
- Straighten the horizontal (x) trajectory by using trajectory shims.
- Minimize the phase errors by using phase shims.
- Straighten the vertical (y) trajectory.
- Apply shims to compensate multipoles.
- Apply μ-metal shield and do final measurements and tuning of field integrals.
- Do final fine tuning, if necessary.

REFERENCES

[1] S. Sasaki and I. B. Vasserman, Proceedings on 27th International Free Electron Laser Conference (FEL2005), Stanford, CA, August 2005.

[2] "Conceptual Design Report (CDR) for the Linac Coherent Light Source Project," SLAC-R-593, April 2002, http://www-ssrl.slac.stanford.edu/lcls/cdr .

[3] O. Chubar, P. Elleaume, J. Chavanne, J. Synchrotron Radiat. **5**, 481 (1998).

[4] http://www.magnetic-shield.com/ .

BEAM SPREADING AND EMITTANCE OSCILLATION OF AN INTENSE MAGNETIZED BEAM IN FREE SPACE*

Chun-xi Wang†, Kwang-Je Kim, ANL, Argonne, IL 60439, USA
Jack G. Zhang, IIT, Chicago, IL 60616,USA

Abstract

Intense beams with large angular momentum have important applications in electron cooling and in producing flat beams suitable for ultrafast x-ray generation, Smith-Purcell radiators, and possibly for a future linear collider. To gain a basic understanding of the influence of beam angular momentum in an otherwise space-charge-dominated beam, the behavior of such a beam in free space will be examined here, in particular, beam spreading due to space-charge force, as well as emittance oscillation. Drift space is an important part of a split photoinjector and plays a significant role in emitance compensation of a high-brightness photoinjector.

INTRODUCTION

By immersing the cathode in a magnetic field, beam with (large) angular momentum can be created and is referred to as "magnetized" beam. High-intensity magnetized beams have important applications in electron cooling and flat-beam generation. The emittance oscillation of a non-magnetized beam in the drift space of a split photoinjector has some generic properties such as the "double minimum" feature [1], which has been explained by space-charge induced beam spreadings of individual slices [2]. Here, we generalize the technique used in [2] to examine the influence of beam angular momentum on beam spreading and emittance oscillation in drift space.

For a round beam in an axisymmetric channel, the beam envelope is governed by the reduced beam envelope equation [3, 4]

$$\hat{\sigma}'' + \frac{\kappa}{\beta^2\gamma^2}\,\hat{\sigma} - \frac{\kappa_s}{\beta^2\gamma^2}\frac{1}{\hat{\sigma}} - \frac{\epsilon^2}{\hat{\sigma}^3} = 0. \qquad (1)$$

where $\hat{\sigma} = \sqrt{\beta\gamma}\,\sigma$ is the reduced envelope, κ represents the external focusing, and perveance $\kappa_s = I/2I_A$ gives the space-charge defocusing. Here, we consider uniform non-accelerating channels with constant κ and κ_s. In a drift space, $\kappa = 0$ and κ_s decreases somewhat due to longitudinal debunching, which will be ignored here. The emittance ϵ is conserved and may contain two parts: thermal emittance and angular momentum. Although angular momentum is correlated motion and intrinsically different from random thermal emittance, from the beam envelope evolution point of view, these two types of emittances make no difference. In high-brightness photoinjectors, the thermal emittance is sufficiently small such that a non-magnetized beam can be considered space-charge dominated. However, the existence of beam angular momentum qualitatively changed the property of the envelope equation by addding a significant emittance term. In the following, we present preliminary exploration of the effects of angular momentum. Because we will only consider non-accelerating beams, $\beta\gamma = 1$ is set in the following sections to simplify the notation. By the same token, we will use σ instead of $\hat{\sigma}$ for the reduced envelope as well.

* Work supported by U.S. Department of Energy, Office of Science, Office of Basic Energy Sciences, under Contract No. W-31-109-ENG-38.
† wangcx@aps.anl.gov; http://www.aps.anl.gov/~wangcx

BEAM SPREADING IN A UNIFORM NON-ACCELERATING CHANNEL

In a uniform non-accelerating channel, the coefficients in the beam envelope equation are all constants. The corresponding envelope Hamiltonian (with the setting $\beta\gamma = 1$)

$$H = \frac{p^2}{2} + \kappa\frac{\sigma^2}{2} - \kappa_s \ln(\sigma) + \frac{\varepsilon^2}{2\sigma^2} \qquad (2)$$

is a constant of motion, whose value can be expressed with the initial σ_0 and σ_0'. Thus, we have the first integral

$$\sigma'^2 + \kappa\sigma^2 - \kappa_s \ln\sigma^2 + \frac{\varepsilon^2}{\sigma^2} = \sigma_0'^2 + \kappa\sigma_0^2 - \kappa_s \ln\sigma_0^2 + \frac{\varepsilon^2}{\sigma_0^2}. \qquad (3)$$

The beam envelope is bounded by the potential well [4]. The lower bound is due to space-charge defocusing and emittance pressure. If any, the upper bound is due to external focusing. It reaches an extreme size σ_m at $\sigma' = 0$, which can be determined by

$$\sigma_0'^2 + \kappa\sigma_0^2 - \kappa_s \ln\sigma_0^2 + \frac{\varepsilon^2}{\sigma_0^2} = \kappa\sigma_m^2 - \kappa_s \ln\sigma_m^2 + \frac{\varepsilon^2}{\sigma_m^2}. \qquad (4)$$

Note that in drift space, i.e., without external focusing, $\sigma_m'' > 0$, there will be a beam waist for a converging beam. With external focusing, σ_m may be a minimum or maximum depending on the sign of σ_m''. From these equations, σ' can be solved as

$$\tilde{\sigma}' = \frac{\sigma'}{\sigma_m} = \pm\sqrt{\kappa\left(1-\tilde{\sigma}^2\right) + \frac{\kappa_s}{\sigma_m^2}\ln\tilde{\sigma}^2 + \frac{\varepsilon^2}{\sigma_m^4}\left(1-\frac{1}{\tilde{\sigma}^2}\right)}, \qquad (5)$$

where $\tilde{\sigma} \equiv \sigma/\sigma_m$. The sign depends on whether the beam is converging $(-)$ or diverging $(+)$. By integrating Eq. (5) we obtain the solution of the beam envelope as

$$s = \int_{\frac{\sigma_0}{\sigma_m}}^{1} \frac{\mathbf{sign}(\sigma_0')\,dx}{\sqrt{\kappa\left(1-x^2\right) + \frac{\kappa_s}{\sigma_m^2}\ln\left(x^2\right) + \frac{\varepsilon^2}{\sigma_m^4}\left(1-\frac{1}{x^2}\right)}} + \int_{1}^{\frac{\sigma}{\sigma_m}} \frac{\mathbf{sign}(\sigma')\,dx}{\sqrt{\kappa\left(1-x^2\right) + \frac{\kappa_s}{\sigma_m^2}\ln\left(x^2\right) + \frac{\varepsilon^2}{\sigma_m^4}\left(1-\frac{1}{x^2}\right)}}. \qquad (6)$$

This integral cannot be expressed with elementary functions. In the case $\kappa = \kappa_s = 0$, this integral yields the well-known hyperbola envelope for a bunch of free particles. For a space-charge dominated beam in free space ($\kappa = \epsilon = 0$), this integral yields the so-called universal beam-spreading curve for $\sigma/\sqrt{\kappa_s}$, which is independent of slice perveances. However, for a magnetized beam, there is a non-zero emittance term. Thus, the beam perveance can not be scaled away from the envelope equation. Therefore, beam spreading of a magnetized beam will have nontrivial dependence on beam perveance, and there is no universal beam-spreading curve anymore.

ENVELOPE EVOLUTIONS NEARBY A REFERENCE ENVELOPE

The relative motions of various beam slices are responsible for the variation of projected emittance in high-brightness photoinjectors. Thus, it is interesting to examine the evolution of envelopes nearby a reference envelope. Assuming small deviations, we expand a slice envelope around the reference envelope $(\bar{\sigma}, \bar{\sigma}')$ as

$$\begin{pmatrix} \sigma \\ \sigma' \end{pmatrix} = \begin{pmatrix} \bar{\sigma} \\ \bar{\sigma}' \end{pmatrix} + \sum_\alpha \begin{pmatrix} \partial_{q^\alpha}\bar{\sigma} \\ \partial_{q^\alpha}\bar{\sigma}' \end{pmatrix} \delta q^\alpha , \qquad (7)$$

where δq^α represents a small deviation in certain parameter q^α. Here, we consider the deviations in the initial values $\delta\sigma_0$ and $\delta\sigma_0'$, as well as the slice perveance $\delta\kappa_s$, assuming all slices have the same emittance and angular momentum.

To compute the partial derivatives with respect to σ_0, we take derivatives on both sides of Eq. (6) with respect to σ_0 and use Eq. (5) for simplification, which yields

$$0 = \frac{1}{\sigma'/\sigma_m}\partial_{\sigma_0}\frac{\sigma}{\sigma_m} - \frac{1}{\sigma_0'/\sigma_m}\partial_{\sigma_0}\frac{\sigma_0}{\sigma_m} + \frac{\partial_{\sigma_0}\sigma_m}{\sigma_m}F_x, \quad (8)$$

where F_x denotes the integral,

$$F_x = \int_{\frac{\sigma_0}{\sigma_m}}^{1} \frac{\mathbf{sign}(\sigma_0')\left[\frac{\kappa_s}{\sigma_m^2}\ln\left(x^2\right) + 2\frac{\varepsilon^2}{\sigma_m^4}\left(1-\frac{1}{x^2}\right)\right]dx}{\left[k\left(1-x^2\right) + \frac{\kappa_s}{\sigma_m^2}\ln\left(x^2\right) + \frac{\varepsilon^2}{\sigma_m^4}\left(1-\frac{1}{x^2}\right)\right]^{3/2}} + \int_{1}^{\frac{\sigma}{\sigma_m}} \frac{\mathbf{sign}(\sigma')\left[\frac{\kappa_s}{\sigma_m^2}\ln\left(x^2\right) + 2\frac{\varepsilon^2}{\sigma_m^4}\left(1-\frac{1}{x^2}\right)\right]dx}{\left[k\left(1-x^2\right) + \frac{\kappa_s}{\sigma_m^2}\ln\left(x^2\right) + \frac{\varepsilon^2}{\sigma_m^4}\left(1-\frac{1}{x^2}\right)\right]^{3/2}}.$$

Thus, $\partial_{\sigma_0}\sigma$ can be solved as

$$\partial_{\sigma_0}\sigma = \frac{\sigma'}{\sigma_0'} + \frac{\sigma'}{\sigma_m}\partial_{\sigma_0}\sigma_m\left(\frac{\sigma}{\sigma'} - \frac{\sigma_0}{\sigma_0'} - F_x\right), \qquad (9)$$

where $\partial_{\sigma_0}\sigma_m$ can be obtained by differentiating Eq. (4) as

$$\partial_{\sigma_0}\sigma_m = \frac{\kappa\sigma_0 - \kappa_s/\sigma_0 - \varepsilon^2/\sigma_0^3}{\kappa\sigma_m - \kappa_s/\sigma_m - \varepsilon^2/\sigma_m^3} = \frac{\sigma_0''}{\sigma_m''}, \qquad (10)$$

which is non-zero unless staying at equilibrium.

Similarly, taking derivatives on both sides of Eq. (6) with respect to σ_0' yields the derivative $\partial_{\sigma_0'}\sigma$. Combined with Eq. (9), they give the first two expressions in the following sets of four derivatives:

$$\partial_{\sigma_0}\sigma = \frac{1}{\sigma_0'}\left(\sigma' - \sigma_0''\partial_{\sigma_0'}\sigma\right), \qquad (11)$$

$$\partial_{\sigma_0'}\sigma = \frac{\sigma_0\sigma' - \sigma_0'\sigma}{\sigma_m\sigma_m''} + \frac{\sigma_0'\sigma'}{\sigma_m\sigma_m''}F_x, \qquad (12)$$

$$\partial_{\sigma_0}\sigma' = \frac{1}{\sigma_0'}\left(\sigma'' - \sigma_0''\partial_{\sigma_0'}\sigma'\right), \qquad (13)$$

$$\partial_{\sigma_0'}\sigma' = \frac{\sigma_0\sigma''}{\sigma_m\sigma_m''} - \frac{\sigma_0'(\sigma\sigma'' - \sigma_m\sigma_m'')}{\sigma_m''\sigma_m\sigma'} + \frac{\sigma_0'\sigma''}{\sigma_m\sigma_m''}F_x. \qquad (14)$$

The last two expressions can be obtained by differentiating the first two expressions with respect to s. Clearly, these derivatives have the initial values $\partial_{\sigma_0}\sigma(0) = \partial_{\sigma_0'}\sigma'(0) = 1$ and $\partial_{\sigma_0'}\sigma(0) = \partial_{\sigma_0}\sigma'(0) = 0$. In the special case $\kappa = 0$ and $\varepsilon = 0$, these expressions reduce to the simple results of Eqs. (16) and (18) in [2], and $F_x = s$. It is important to note that, for a space-charge dominated beam where the emittance term can be neglected, all these expressions are independent of slice perveance, with or without external focusing. This property may play a significant role in emittance compensation of high-brightness photoinjectors. However, for a magnetized beam, these expressions will depend on the perveance of the (reference) slice.

To evaluate the effect of small perveance variations, we compute $\partial_{\kappa_s}\sigma$ and $\partial_{\kappa_s}\sigma'$ similarly. Differentiating Eqs. (3) and (4) yield, respectively,

$$\partial_{\kappa_s}\sigma' = \frac{1}{\sigma'}\left(\ln\frac{\sigma}{\sigma_0} + \sigma''\partial_{\kappa_s}\sigma\right), \qquad (15)$$

$$\partial_{\kappa_s}\sigma_m = \frac{1}{\sigma_m''}\ln\frac{\sigma_0}{\sigma_m}. \qquad (16)$$

Differentiating Eq. (6) with the help of function F_x and the above expression for $\partial_{\kappa_s}\sigma_m$ gives

$$\partial_{\kappa_s}\sigma = \frac{\sigma'}{\sigma_m\sigma_m''}\left(\frac{\sigma}{\sigma'} - \frac{\sigma_0}{\sigma_0'} - F_x\right)\ln\frac{\sigma_0}{\sigma_m} + \frac{\sigma'}{2}F_s, \quad (17)$$

where the function F_s is defined the same as F_x except that $\kappa_s = 1$ and $\epsilon = 0$ are set in the numerators. (Thus, for a space-charge dominated beam, $F_x = \kappa_s F_s$.) The initial values of both $\partial_{\kappa_s}\sigma$ and $\partial_{\kappa_s}\sigma'$ are zero.

EMITTANCE OSCILLATION

From the envelope expressions in Eq. (7), assuming the various deviations from the reference envelope are uncorrelated, the emittance due to slice envelope variations can be calculated as [2]

$$\epsilon^{\mathrm{env}} \simeq \sqrt{\sum_\alpha W_{q^\alpha}^2\left(\overline{(\delta q^\alpha)^2}\Big/\,\overline{q^\alpha}^2\right)}, \qquad (18)$$

where

$$W_{q^\alpha} \equiv (\bar{\sigma}\partial_{q^\alpha}\bar{\sigma}' - \bar{\sigma}'\partial_{q^\alpha}\bar{\sigma})\,\overline{q^\alpha}. \quad (19)$$

Here, the bar over δq^α and q^α indicates averaging over the slices.

Inserting the above partial derivatives into Eq. (19), we have

$$W_\sigma = \bar{\sigma}_0\left[\frac{\bar{\sigma}\bar{\sigma}'' - \bar{\sigma}'^2}{\bar{\sigma}_0'}\left(1 - \frac{\bar{\sigma}_0''}{\bar{\sigma}'}\,\partial_{\sigma_0'}\bar{\sigma}\right) - \frac{\bar{\sigma}\bar{\sigma}_0''}{\bar{\sigma}'}\right], \quad (20)$$

$$W_{\sigma'} = \bar{\sigma}_0'\left[\frac{\bar{\sigma}\bar{\sigma}'' - \bar{\sigma}'^2}{\bar{\sigma}'}\,\partial_{\sigma_0'}\bar{\sigma} + \frac{\bar{\sigma}\bar{\sigma}_0'}{\bar{\sigma}'}\right]. \quad (21)$$

These expressions reduce to the special results of Eqs. (17) and (19) in [2]. Since $\partial_{\sigma_0'}\bar{\sigma}$ equals zero at the beginning, we have the initial values

$$W_\sigma(0) = -W_{\sigma'}(0) = -\bar{\sigma}_0\bar{\sigma}_0'. \quad (22)$$

To examine the extreme values of $W_\sigma(s)$ and $W_{\sigma'}(s)$, we take the s-derivative of these functions and have, after some algebra,

$$W_\sigma' = \bar{\sigma}_0\,\frac{\bar{\sigma}\bar{\sigma}''' - \bar{\sigma}'\bar{\sigma}''}{\bar{\sigma}_0'\bar{\sigma}'}\left(\bar{\sigma}' - \bar{\sigma}_0''\,\partial_{\sigma_0'}\bar{\sigma}\right), \quad (23)$$

$$W_{\sigma'}' = \bar{\sigma}_0'\,\frac{\bar{\sigma}\bar{\sigma}''' - \bar{\sigma}'\bar{\sigma}''}{\bar{\sigma}'}\,\partial_{\sigma_0'}\bar{\sigma}. \quad (24)$$

It is easy to see that the factor

$$\frac{\bar{\sigma}\bar{\sigma}''' - \bar{\sigma}'\bar{\sigma}''}{\sigma'} = -2\left[\frac{\kappa_s}{\sigma} + 2\frac{\varepsilon^2}{\sigma^3}\right] \neq 0,$$

thus W_σ reaches the extreme value of $-\bar{\sigma}_0\bar{\sigma}_0''\bar{\sigma}/\bar{\sigma}'$ when $\bar{\sigma}' = \bar{\sigma}_0''\,\partial_{\sigma_0'}\bar{\sigma}$, and $W_{\sigma'}$ reaches the extreme value of $\bar{\sigma}_0'^2\bar{\sigma}/\bar{\sigma}'$ when $\partial_{\sigma_0'}\bar{\sigma} = 0$. Using Eq. (12) and the condition for the extreme, we can further express the extreme values $W_\sigma^{\rm m}$ as

$$W_\sigma^{\rm m} = -\bar{\sigma}_0\bar{\sigma}_0''\frac{\bar{\sigma}}{\bar{\sigma}'} = \frac{\bar{\sigma}_0}{\bar{\sigma}_0'}\left(\bar{\sigma}_m\bar{\sigma}_m'' - \bar{\sigma}_0\bar{\sigma}_0''\right) - \bar{\sigma}_0\bar{\sigma}_0''F_x, \quad (25)$$

$$W_{\sigma'}^{\rm m} = \bar{\sigma}_0'^2\frac{\bar{\sigma}}{\bar{\sigma}'} = \bar{\sigma}_0\bar{\sigma}_0' + \bar{\sigma}_0'^2F_x \quad (26)$$

where F_x integrates up to the extreme point. However, it is not obvious that the condition for the extremes can be satisfied (except the trivial case $W_{\sigma'}' = \partial_{\sigma_0'}\bar{\sigma} = 0$ at the beginning).

From these expressions, a few general properties can be drawn about emittance oscillation. In particular, for a beam focused into a drift, $\bar{\sigma}_0' < 0$, $\bar{\sigma}_0'' > 0$, $\bar{\sigma}_m\bar{\sigma}_m'' - \bar{\sigma}_0\bar{\sigma}_0'' > 0$, thus $W_\sigma(0) > 0$ and $W_\sigma^m < 0$, which leads to emittance minimum when W_σ crosses zero, as discussed in [2]. Furthermore, $W_\sigma^m < 0$ requires $\bar{\sigma}' > 0$ at that location, thus the emittance maximum due to W_σ is always located after the beam waist where $\bar{\sigma}' = 0$.

Similarly, W_{κ_s} can be worked out as

$$W_{\kappa_s} = \bar{\kappa}_s\left[\frac{\bar{\sigma}}{\bar{\sigma}'}\ln\frac{\bar{\sigma}}{\bar{\sigma}_0} + \frac{\bar{\sigma}\bar{\sigma}'' - \bar{\sigma}'^2}{\bar{\sigma}'}\,\partial_{\kappa_s}\bar{\sigma}\right], \quad (27)$$

where $\partial_{\kappa_s}\bar{\sigma}$ is given by Eq. (17). Clearly, $W_{\kappa_s}(0) = 0$.

EFFECTS OF BEAM ANGULAR MOMENTUM

To see the influence of beam angular momentum on the beam envelope spreading of an individual slice and on the emittance oscillation of a bunch of slices, we plot a set of five figures showing the quantities σ, σ', W_σ, $W_{\sigma'}$, and W_{κ_s}, using the expressions given above. In each figure, the red curve shows the evolution of a space-charge dominated beam and the blue curve shows the same beam but with an angular momentum term 10 times larger than the space-charge term at the beam waist (2 mm). The other parameters are $\sigma_0 = 9\,mm$, $\sigma' = -9.5\,mrad$, $\beta\gamma = 12$, $\kappa_s = 0.05$, which are adopted from an optimized SPARC photoinjector design.

Through this example and the above analysis, we see that, qualitatively speaking, the basic behavior of beam spreading and emittance oscillation in drift space are not changed by the large angular momentum, although there are significant quantitative changes. For example, the beam waist becomes much larger and is reached much quicker. Also, the emittance oscillation amplitude gets larger, and so on. From this point of view, W_{κ_s} may be an exception because there is no zero crossing anymore for the blue curve.

However, emittance compensation for magnetized beam [5] may be significantly different from conventional space-charge dominated beam. For example, there is no invariant envelope solution for the envelope equation in a booster when there is a significant emittance term. Thus, the matching condition for space-charge dominated beam may not be appropriate any more. Furthermore, the ability to compensate emittance may be limited by the fact that beam perveance cannot be scaled away from the envelope equation of a magnetized beam.

CONCLUDING REMARK

We developed a technique to examine the beam spreading and emittance oscillation of a magnetized beam in free space. Clearly, the technique also applies to a beam with significant thermal emittance and/or in a uniform focusing channel (we have kept both focusing κ and emittance ϵ in all the expressions). In a focusing channel, a beam may reach both minimum and maximum size because it is bounded by a potential well. For example, a diverging beam reaches a maximum beam size in the focusing solenoid for emittance compensation. The emittance evolution in the solenoid can be described by the same expressions presented above. Much more work is needed to understand emittance compensation of a magnetized beam.

REFERENCES

[1] M. Ferrario, J.E. Clendenin, D.T. Palmer, J.B. Rosenzweig, L. Serafini, SLAC-PUB-8400 (2000).

[2] C.-x. Wang, "Emittance oscillation in the drift space of split photoinjectors," Proceedings of the 35nd Advanced ICFA

Beam Dynamics Workshop on Physics and Application of High-Brightness Electron Beam, October 2005.

[3] See, for example, J.D. Lawson, *The Physics of Charged Particle Beams*, 2nd ed. (Oxford University Press, New York, 1988).

[4] C.-x. Wang, Nucl. Instrum. Methods A**557**, 94 (2006).

[5] X. Chang, I. Ben-Zvi, J. Kewisch, BNL-73192-2004-CP.

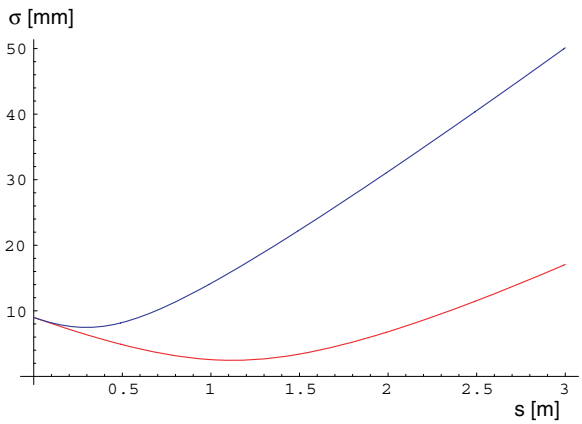

Figure 1: Reduced envelope in free space for space-charge dominated beam (red) and beam with large emittance (blue).

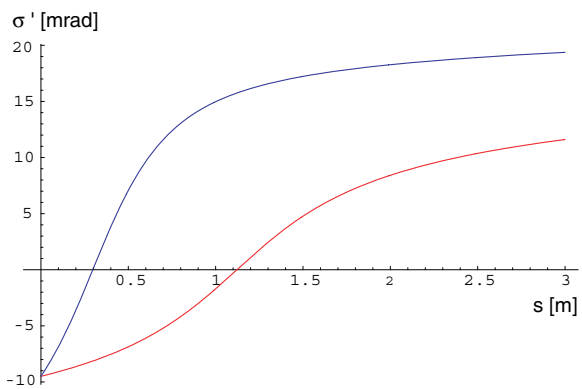

Figure 2: Reduced envelope slope in free space for space-charge dominated beam (red) and beam with large emittance (blue).

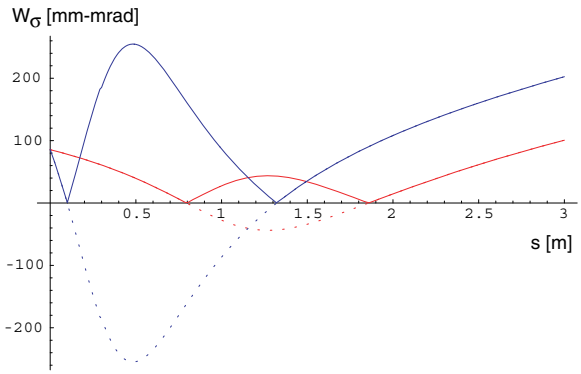

Figure 3: Emittance oscillation in free space due to initial slice envelope variation for space-charge dominated beam (red) and beam with large emittance (blue). The solid curves plot the absolute values.

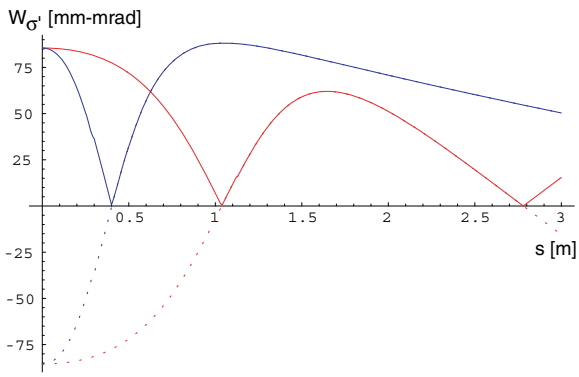

Figure 4: Emittance oscillation in free space due to initial slice slope variation for space-charge dominated beam (red) and beam with large emittance (blue). The solid curves plot the absolute values.

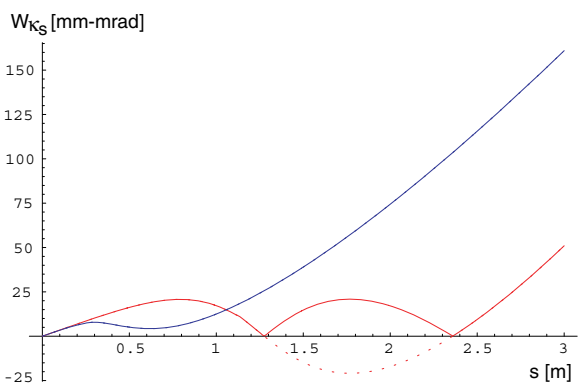

Figure 5: Emittance oscillation in free space due to slice perveance variation for space-charge dominated beam (red) and beam with large emittance (blue). The solid curves plot the absolute values.

ENERGY MODULATION OF THE ELECTRONS BY THE LASER FIELD IN THE WIGGLER MAGNET: ANALYSIS AND EXPERIMENT

A.A. Zholents #, LBNL, Berkeley, CA 94720, U.S.A.
K. Holldack, BESSY, 12489 Berlin, Germany.

Abstract

Energy modulation of the electron beam after the interaction with the laser field in the wiggler magnet can be calculated using interference of the laser field and the field of spontaneous emission in the far field region of wiggler radiation. Quite often this approach gives a deeper insight on the process than traditional calculations where the effect of the laser field on the electron energy is integrated along the electron trajectory in the wiggler. We demonstrate it by showing the agreement between the analytical model and the experiment involving wiggler scan measurements with large detuning from the FEL resonance producing more than one order of magnitude variations in the amplitude of the energy modulation. The high sensitivity was achieved using the THz radiation from a sub-mm dip in the electron density that energy modulated electrons leave behind while propagating along the storage ring lattice. All measurements were performed at the BESSY-II electron storage ring.

ENERGY MODULATION

The energy gain/loss obtained by the electron in the interaction with the laser field E_x polarized in the horizontal plane and co-propagating the planar wiggler magnet together with the electron in z direction can be found by solving the equation [1]:

$$\frac{d\gamma}{dz} = \frac{e}{mc} E_x \cdot \beta_x , \qquad (1)$$

where γ is the relativistic factor, $\beta_x = v_x / c$, where v_x is the horizontal velocity of the electron and c is the speed of light, e, m are the electron charge and mass, and

$$E_x = E_0 / \sqrt{1+(z/z_0)^2}\, \sin[k(z-ct)+\psi] e^{-\tau^2/4\sigma_\tau^2}, \qquad (2)$$

where k is the wave number of the laser field, $z_0 = ka_0^2/2$ is the Rayleigh length, a_0 is the waist size which is assumed to be in the center of the wiggler, $\psi = \psi_0 - \tan^{-1}(z/z_0)$, where ψ_0 is the phase of the wave at the beginning of the interaction with the electron at the entrance of the wiggler and σ_τ is the rms width of the laser pulse intensity.

For electron motion inside the wiggler one obtains:

$$\beta_x = -\frac{K}{\gamma}\sin(k_w z), \qquad \beta_z = \sqrt{1-\frac{1}{\gamma^2}-\beta_x^2} \approx 1-\frac{1}{2\gamma^2}\left(1+K^2/2\right)+\frac{K^2}{4\gamma^2}\cos(2k_w z) \qquad (3)$$

where $k_w = 2\pi/\lambda_w$ and λ_w is the wiggler period, $K = eB_0/k_w mc$, B_0 is the peak magnetic field and β_z is the normalized velocity along the wiggler, *i.e.*:

$$z(t) = c\int_0^t \beta_z(t')dt' \cong ct - \frac{1}{2\gamma^2}\left(1+\frac{K^2}{2}\right)ct + \frac{K^2}{8k_w\gamma^2}\sin(2k_w z) \qquad (4)$$

In what follows we consider on-axis electrons only. This assumption can be extended to all electrons in the electron bunch if the electron beam size $\sigma_{x,y} << a_0$. Then, using (1) and (3) we write:

$$\frac{d\gamma}{dz} = \frac{eE_0 K}{2mc^2\gamma\sqrt{1+(z/z_0)^2}}\{\cos(k(z-ct)+k_w z+\psi) - \cos(k(z-ct)-k_w z+\psi)\}e^{-\tau^2/4\sigma_\tau^2} \qquad (5)$$

It is further convenient to define the resonance electron energy, also called an FEL resonance energy, $\gamma_r^2 = \frac{k}{2k_w}\left(1+K^2/2\right)$ and assume a small energy spread $\Delta\gamma/\gamma_r$ such as to obtain:

$$k(z-ct) = -k_w z\frac{\gamma_r^2}{\gamma^2} - \frac{\xi}{2}\sin(2k_w z) \qquad (6)$$

with $\xi = K^2/(2+K^2)$. Using a generation function for Bessel functions [2] we found:

$$\cos\left[k_w z\left(1-(\gamma_r/\gamma)^2\right)-\xi/2\sin(2k_w z)+\psi\right]- \cos\left[k_w z\left(1+(\gamma_r/\gamma)^2\right)+\xi/2\sin(2k_w z)+\psi\right] \approx \left[J_0(\xi/2)-J_1(\xi/2)\right]\cos\left[k_w z\left(1-(\gamma_r/\gamma)^2\right)+\psi\right]$$

where in the last step we retain only slowly varying terms with $1-(\gamma_r/\gamma)^2 << 1$. Finally, using dimensionless variables in Eq. (6) [3]: $\hat{z} = z/L_w$, $\nu = N2\delta\gamma/\gamma_r$, and $q = L_w/z_0$, where L_w is the length of the wiggler with N periods, $\hat{\sigma}_\tau = \sigma_\tau/\tau_0$ and $\tau_0 = 2\pi N/kc$, one obtains:

$$\frac{d\gamma}{d\hat{z}} = \frac{eE_0 KL_w}{2mc^2\gamma}\{JJ\}\frac{\cos\left(2\pi\nu\hat{z}-\tan^{-1}(q\hat{z})+\psi_0\right)}{\sqrt{1+(q\hat{z})^2}}e^{-\hat{z}^2/4\hat{\sigma}_\tau^2} \qquad (7)$$

where definition $\{JJ\} = J_0(\xi/2)-J_1(\xi/2)$ is used following [4]. Introducing the laser pulse energy $A_L = \left(E_0^2/8\pi\right)\left(\pi a_0^2/2\right)\sqrt{2\pi}\sigma_\tau c$, Eq.(7) can be written as:

$$\left\langle\frac{d\gamma}{d\hat{z}}\right\rangle = \frac{2}{mc^2}\sqrt{A_L\alpha\hbar\omega_{0s}\frac{K^2}{2+K^2}}\{JJ\} \times \sqrt{\frac{2q}{(2\pi)^{1/2}\hat{\sigma}_\tau}}\frac{\cos\left(2\pi\nu\hat{z}-\tan^{-1}(q\hat{z})+\psi_0\right)}{\sqrt{1+(q\hat{z})^2}}e^{-\hat{z}^2/4\hat{\sigma}_\tau^2} \qquad (8)$$

where α is the fine structure constant, ω_{0s} is central frequencies of the field of spontaneous emission, and $\langle ... \rangle$

AAZholents@LBL.GOV

defines averaging over one wiggler period. By integrating Eq.(8) one obtains for the amplitude of the energy modulation:

$$\Delta\gamma(q,\nu,\hat{\sigma}_\tau) = \frac{2}{mc^2}\sqrt{A_L\alpha\hbar\omega_{0s}\frac{K^2}{2+K^2}}\{JJ\}f(q,\nu,\hat{\sigma}_\tau) \quad (9)$$

where:

$$f(q,\nu,\hat{\sigma}_\tau) = \sqrt{\frac{2q}{(2\pi)^{1/2}\hat{\sigma}_\tau}}\int_{-0.5}^{0.5}\frac{\cos\left(2\pi\nu\hat{z}-\tan^{-1}(q\hat{z})\right)}{\sqrt{1+(q\hat{z})^2}}e^{-\hat{z}^2/4\hat{\sigma}_\tau^2}d\hat{z}$$

Figure 1 shows plots of $f(q,\nu,\sigma_\tau)$ for various q and ν and $\hat{\sigma}_\tau$. Using the maximum value of $f(q=8,\nu=-0.7,\hat{\sigma}_\tau=0.25)$ =2.2, one finds:

$$\Delta\gamma_{\max} \cong \frac{2}{mc^2}\sqrt{5A_L\alpha\hbar\omega_{0s}\frac{K^2}{2+K^2}}\{JJ\} \quad (10)$$

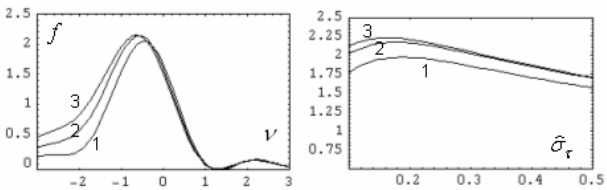

Figure 1. Function $f(q,\nu,\hat{\sigma}_\tau)$ for $\hat{\sigma}_\tau$=0.25 (left plot) and ν=-0.7 (right plot) and for q = 4, 6, and 8 (curves 1, 2, and 3).

Alternatively, the energy gain/loss obtained by the electron in the interaction with the laser field can be calculated considering the interference of the field of its spontaneous emission in the wiggler and the laser field. This technique takes it roots in a so-called acceleration theorem [5,6] declaring that the very existence of spontaneous emission is mandatory if the acceleration by the external field is employed in a linear order to this field. Following this idea and using Parseval's theorem, we write for the amplitude of the energy modulation:

$$mc^2\Delta\gamma_{\max} = 2\frac{\pi a_0^2 c}{16\pi}\int E_s(t)E_L^*(t)dt = 2\frac{\pi a_0^2 c}{16\pi}\int E_s(\omega)E_L^*(\omega)d\omega \quad (11)$$

where $E_s(\omega) = \sqrt{2/\pi}E_{0s}\sin\left((\omega-\omega_{0s})\tau_0/2\right)/(\omega-\omega_{0s})$ is Fourier component of the field of spontaneous emission, $E_L(\omega) = E_{0L}\sqrt{2}\sigma_\tau\cdot e^{-(\omega-\omega_{0L})^2\sigma_\tau^2}$ is a Fourier component of the laser field, and ω_{0L} is the central frequency of the laser field. Further defining the energy of spontaneous emission (see, also [3]):

$$A_S = \left(E_s^2/8\pi\right)\left(\pi a_0^2/2\right)\tau_0 c = 5\alpha\hbar\omega_{0s}\frac{K^2}{2+K^2}\{JJ\}^2 \quad (12)$$

radiating in the mode with a rms divergence of the intensity $\sigma'_R = \sqrt{2\lambda_s/\pi L_w}$, where $\lambda_s = 2\pi c/\omega_{0s}$, one can obtain from (11):

$$\Delta\gamma_{\max} \cong \frac{2}{mc^2}\sqrt{A_L A_s}\left\{\sqrt{\hat{\sigma}_\tau}\int e^{-4(x-x_{0L})^2\hat{\sigma}_\tau^2}\frac{\sin(x-x_{0s})}{(x-x_{0s})}dx\right\} \quad (13)$$

where we used substitution $x = \omega\tau_0/2$ and $x_{0s} = \omega_{0s}\tau_0/2$ and $x_{0L} = \omega_{0L}\tau_0/2$. The entire expression inside the figure bracket shows the overlapping of the spectra of the laser signal and the spectra of spontaneous emission signal. This expression is normalized in such a way that it is approximately one when $\omega_{0s} = \omega_{0L}$ and $\hat{\sigma}_\tau$=0.25 corresponding to the optimal condition of the maximum energy modulation found previously. Finally we note that in the case of a large detuning from the FEL resonance a contribution of the second term with $\sin(x+x_{0s})/(x+x_{0s})$ could be comparable to a contribution of the main term with $\sin(x-x_{0s})/(x-x_{0s})$ and, thus, should be added to the overlapping integral.

EXPERIMENT

The energy modulation of electrons by the laser field was measured as a function of the detuning of the central frequency of the electron spontaneous emission in the wiggler from the central frequency of the laser field. The experiment was conducted at BESSY-II synchrotron light source [7]. The laser operated at a fixed wavelength of 800 nm while wiggler detuning covered large range of frequencies with the wavelengths changing from 200 nm to 1000 nm, *i.e.* in the range greatly exceeding the bandwidth of the laser pulse. As an illustration, Figure 2 shows normalized spectra of the laser field and the field of the electron spontaneous emission in the wiggler for a single set point during this scan.

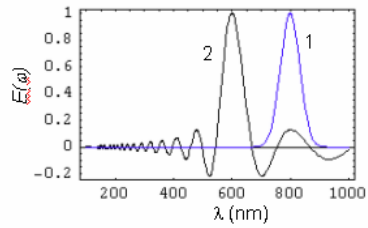

Figure 2. Spectra of the laser field (curve 1) and the field of spontaneous emission of electrons in the wiggler (curve 2).

Measurements of the energy modulation were performed indirectly using coherent THz radiation from a bending magnet 11 m downstream of the wiggler magnet. THz radiation was produced by the dip in the electron density distribution that energy modulated electrons leave behind after propagating the storage ring lattice with non-zero time-of-flight properties, a phenomena which is described elsewhere [8]. Use of the THz signal allowed us to obtain sufficient signal-to-noise ratio even with wiggler settings leading to very small amplitudes of the energy modulation. A typical example of THz spectra and the dip in the electron density distribution is shown in Figure 3.

The width and the magnitude of the dip are defined by the amplitude of the energy modulation of electrons and by time-of-flight parameters R_{51}, R_{52}, R_{56} of the lattice

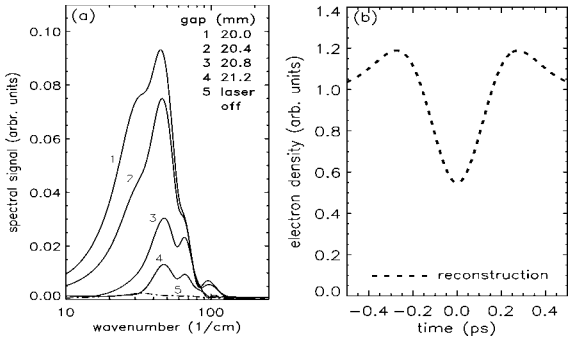

Figure 3. a) THz spectra for different wiggler gaps corresponding to different detunings near the FEL resonance, b) a dip in electron density determined from spectra measured at the FEL resonance and corrected for beamline transmission.

between the wiggler magnet and a source of the THz radiation. Figure 4 shows the magnitude of the dip calculated as a function of the amplitude of the energy modulation normalized on the relative energy spread of electrons σ_E. The following parameters were used: $\sigma_E = 10^{-3}$, R_{56}=-0.011 m, R_{51}= 5.5 10^{-5}, R_{52}= 0.53 m [9] , the electron beam size and angle in the wiggler magnet σ_x=320 μm and $\sigma_{x'}$ = 55 μrad.

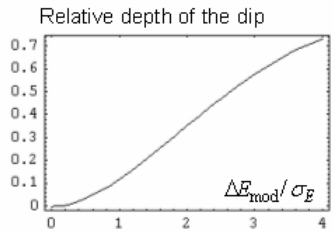

Figure 4. A relative magnitude of the dip as a function of the amplitude of the energy modulation ΔE_{mod}. The magnitude of one corresponds to 100% electron density modulation.

Variations in width and magnitude of the dip affect the THz signal, which was measured using an InSb-bolometer during the wiggler scan and plotted in Figure 5. Analyzing this measurement, we assumed that the THz signal is proportional to the square of the magnitude of the dip and that the magnitude of the dip itself is proportional to the amplitude of the energy modulation of electrons. We calculated the amplitude of the energy modulation using Eq. (13), which was, essentially, a calculation of the function $F(x_{0s}, x_{0L}, \hat{\sigma}_\tau)$, *i.e.* the overlapping area between two spectra shown in Figure 2. These calculations are more accurate than calculations using Eq. (9) because of the assumption of a small detuning used there does not work for a broad scan of the wiggler wavelength as used in the experiment.

The width of the dip defines the spectra of the emitted THz signal [8] and, therefore, indirectly impacts the measurement because of the spectral dependence of the detector and THz beamline transmission. We accounted for this effect using empirically defined coefficient 0.75 for calculated intensity of THz radiation when the amplitude of the energy modulation dropped below $\Delta E/\sigma_e$ <3. The other parameters used to obtain the fit were $N = 9.75$ (i.e. effective number of wiggler periods instead of 10 real periods), σ_τ = 45 fs and a floor level of 10^{-4} (defined in the units used in Figure 5) as given by incoherent synchrotron radiation from the regular bunch.

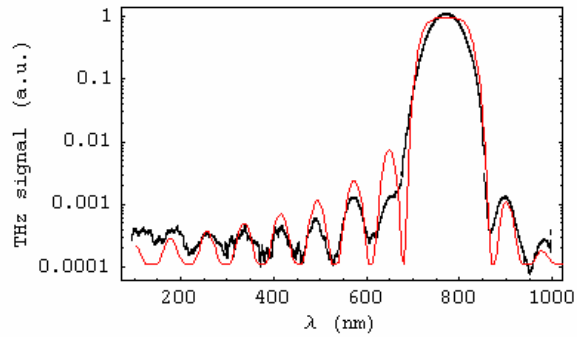

Figure 5. THz signal produced by the electron bunch with a dip in the electron density. The black curve shows the experimental result and the red curve the analytical fit.

CONCLUSION

Using a concept of the far field region we demonstrated that the energy modulation of electrons in the wiggler magnet by the laser light can be found by calculating the interference of the laser field and the field of the electron spontaneous emission in the far field region of the electron radiation in the wiggler. This allowed us to obtain a correct explanation for the measurements, where the wiggler detuning from the laser frequency covered a large range of frequencies exceeding the bandwidth of the laser field by many times.

Acknowledgement. A.Z. is grateful to M. Zolotorev for reading the manuscript and critical comments. K.H. is indebted to T. Quast, R. Mitzner, S. Khan and D.Ponwitz. This work was supported by U.S. DoE under Contract No: DE-AC03-76SF00098 and by the Bundesministerium für Bildung und Forschung and the Land Berlin.

REFERENCES

[1] J.B. Morphy, C. Pellegrini in: *Laser handbook,* vol 6, p.9, Elsvier Science Publisher, (1990).
[2] M. Abramovitz and I. Stegun, *Handbook of Math. Functions*, DOVER, New York, 1972, p.360;
[3] W.B. Colson, in: *Phys. of Quantum Electronic,* vol.5, p.157, Addison Wesley, (1978).
[4] K.-J. Kim, in: *AIP Conf. Proc., Am. Inst. Phys*., New York, p.565, (1989); LBNL/PUB-490, Rev.2, (2001).
[5] R. B. Palmer, in, *AIP Conf. Proc*. No. 335,edited by P. Schoessow, , AIP, NewYork, (1995)90.
[6] Z. Huang, G. Stupakov, M. Zolotorev, Phys. Rev. Spec. Topics Acc. and Beams, 7, (2004)011302.
[7] BESSY-II, http://www.bessy.de/
[8] J. Byrd *et.al.*, Phys. Rev. Lett., **96**, (2006)164801; K. Holldack *et.al.*, Phys. Rev. Lett., **96** (2006)054601.
[9] courtesy G. Wüstefeld.

CALCULATION OF THE BEAM FIELD IN THE LCLS BUNCH LENGTH MONITOR

G. Stupakov, Y. Ding and Z. Huang
Stanford Linear Accelerator Center, Stanford University, Stanford, CA 94309, USA.

Abstract

Maintaining a stable bunch length and peak current is a critical step for the reliable operation of a SASE based x-ray source. In the LCLS, relative bunch length monitors (BLM) right after both bunch compressors are proposed based on the coherent radiation generated by the short electron bunch. Due to its diagnostic setup, the standard far field synchrotron radiation formula and well-developed numerical codes do not apply for the analysis of the BLM performance. In this paper, we develop a calculation procedure to take into account the near field effect, the effect of a short bending magnet, and the diffraction effect of the radiation transport optics. We find the frequency response of the BLM after the first LCLS bunch compressor and discuss its expected performance.

INTRODUCTION

Maintaining a stable bunch length and peak current is a critical step for the reliable operation of a SASE based x-ray source. In the LCLS, relative bunch length monitors (BLM) right after both bunch compressors are proposed based on the coherent radiation generated by the short electron bunch [1]. A similar diagnostic device is used in the operation of the DESY VUV-FEL (FLASH) [2].

In the previous calculations of the beam radiation [1] standard formulae for the synchrotron radiation in the far field were used. However, due to the close proximity of the reflecting mirror to the magnet, applicability of these formulae is not fully justifiable. An additional factor which complicates the radiation pattern is the short length of the magnet comparable to the formation length of the radiation with the wavelength of the order of the bunch length. To the authors' knowledge, the available computer codes for calculation of the beam radiation (*e.g.*, the Synchrotron Radiation Workshop [3]) cannot be used for our case because the beam passes through the hole in the mirror.

It is a goal of this paper to calculate the electromagnetic field of an electron bunch which takes into account the near field effect, the effect of a short bending magnet, and the diffraction of the radiation caused by reflection from the mirror. We find the energy spectrum intercepted by the mirror in the first LCLS bunch compressor (BC1). We carry out these calculation assuming radiation in free space and neglecting the effect on the radiation of the conducting walls of the vacuum chamber.

We use Gaussian units throughout this paper.

FORMULATION OF THE PROBLEM

A simplified layout of the problem is presented in Fig. 1. The beam passes through a short magnet (e.g., the last dipole of the first LCLS bunch compressor or BC1) of length l_m with the bending radius ρ and propagates along a straight line. A reflective mirror of diameter D with a circular hole of diameter d is located at a distance L from the exit edge of the magnet. The mirror is tilted at 45° and sends the beam field to the detector at the right angle to the beam trajectory. To simplify the calculation we, however, assume that the mirror's plane is perpendicular to the beam orbit (that is, it reflects the radiation back toward the magnet) and calculate the fields incident on as well as reflected from the mirror. Such modification of the geometry does not loose any significant physical effects of the problem.

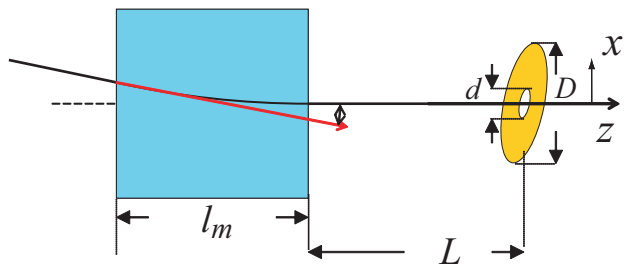

Figure 1: Layout of the bunch length monitor. The coordinate z is measured in the direction of beam propagation after the magnet with $z = 0$ at the exit edge of the magnet. The coordinate x is in the plane of the orbit, and the coordinate y is perpendicular to the plane.

We carried out calculations in the frequency domain. To calculate the Fourier component at frequency ω of the beam field on the surface of the mirror we used two approaches. In the first one, a standard expression for the electromagnetic field of an electron moving in free space was used (see, *e.g.*, [4])

$$\boldsymbol{E}(\boldsymbol{r},\omega) = \frac{e}{\gamma^2}\int_{-\infty}^{\infty} dt\, \frac{\boldsymbol{n}-\boldsymbol{\beta}}{R^2(1-\boldsymbol{n}\cdot\boldsymbol{\beta})^2} e^{i\omega(t+R/c)} + \frac{e}{c}\int_{-\infty}^{\infty} dt\, \frac{\boldsymbol{n}\times[(\boldsymbol{n}-\boldsymbol{\beta})\times\dot{\boldsymbol{\beta}}]}{R(1-\boldsymbol{n}\cdot\boldsymbol{\beta})^2} e^{i\omega(t+R/c)}. \quad (1)$$

Here R, $\boldsymbol{n}$, $\boldsymbol{\beta}$ and $\dot{\boldsymbol{\beta}}$ are functions of time t: $\boldsymbol{R}$ is the vector connecting the current position of the electron with the observation point $\boldsymbol{r}$, with $R = |\boldsymbol{R}|$, $\boldsymbol{n}$ is the unit vector directed along $\boldsymbol{R}$, $\boldsymbol{\beta}$ and $\dot{\boldsymbol{\beta}}$ are the velocity and acceleration

normalized by the speed of light, and $\gamma = (1-\beta^2)^{-1/2}$. The first term in Eq. (1) is usually referred to as the *velocity field*. Note that for a relativistic particle with $\gamma \gg 1$ the integrands in Eq. (1) have sharp narrow peaks in the direction for which $\boldsymbol{n}$ is parallel to $\boldsymbol{\beta}$ because in this direction the denominators $(1-\boldsymbol{n}\cdot\boldsymbol{\beta})^2 \sim 1/4\gamma^4$ become extremely small.

We remind the reader that the usual approximation for the *far zone* (FZ) is to neglect the velocity field and to take the limit $R \to \infty$:

$$\boldsymbol{E}_{\rm FZ}(\boldsymbol{r},\omega) \approx \frac{e}{cR}\int_{-\infty}^{\infty} dt\, \frac{\boldsymbol{n}\times[(\boldsymbol{n}-\boldsymbol{\beta})\times\dot{\boldsymbol{\beta}}]}{(1-\boldsymbol{n}\cdot\boldsymbol{\beta})^2} e^{i\omega(t+R/c)}\,.$$

In this expression, the value of R in front of the integral and the vector $\boldsymbol{n}$ are considered as constant but R in the exponential (and of course $\boldsymbol{\beta}$ and $\dot{\boldsymbol{\beta}}$) are functions of time. If one integrates this expression over a finite time interval from t_1 to t_2 the result is

$$\begin{aligned}\boldsymbol{E}_{\rm FZ}(\boldsymbol{r},\omega) = &-\frac{ie\omega}{cR}\int_{t_1}^{t_2} dt\, \boldsymbol{n}\times(\boldsymbol{n}\times\boldsymbol{\beta})e^{i\omega(t+R/c)} \\ &+ \frac{e}{cR}\frac{\boldsymbol{n}\times(\boldsymbol{n}\times\boldsymbol{\beta})}{1-\boldsymbol{n}\cdot\boldsymbol{\beta}}e^{i\omega(t+R/c)}\Big|_{t_2} \\ &- \frac{e}{cR}\frac{\boldsymbol{n}\times(\boldsymbol{n}\times\boldsymbol{\beta})}{1-\boldsymbol{n}\cdot\boldsymbol{\beta}}e^{i\omega(t+R/c)}\Big|_{t_1}\,.\end{aligned}$$

The last two terms are responsible for the *edge* radiation in the far zone [5].

We found advantageous for numerical calculations to use another expression for the electromagnetic field of a moving point charge [6]:

$$\boldsymbol{E}(\boldsymbol{r},\omega) = \frac{ie\omega}{c}\int_{-\infty}^{\infty}\frac{dt}{R}\left[\boldsymbol{\beta}-\boldsymbol{n}\left(1+ic/\omega R\right)\right]e^{i\omega(t+R/c)}\,. \quad (2)$$

This is the underlying equation used in the Synchrotron Radiation Workshop code [3]. Although this equation looks very different from Eq. (1), they give the same result for $\boldsymbol{E}(\boldsymbol{r},\omega)$. The derivation of Eq. (2) using Lienard-Wiechert potentials can be found in Ref. [7]. In passing, we note that neglecting the velocity field in Eq. (1) is not justified in our situations and yields very different numerical results as compared to Eq. (2).

To integrate Eq. (2) over the particle's orbit we split the integration path into three pieces. The first one is a straight line before the entrance to the magnet, the second one is an arc of a circular orbit inside the magnet, and the third one comprises the part of the trajectory after the exit from the magnet. The first two integrals were computed numerically using the Mathematica built in integration routine [8] (in the first integral the lower limit of integration $-\infty$ was replaced by a large negative number). A direct numerical integration of the third integral turns out be slow and poorly convergent because of a fast variation of the phase in the integrand. To improve the speed of calculation we used a method described in Ref. [7], which is valid in the limit of large values of γ. Although formally the integration in Eq. (2) is extended beyond the position of the mirror, the dominant contribution to the integral comes from the part of the trajectory located in front of the mirror.

RESULTS OF THE CALCULATIONS

The quantity $c|E(\boldsymbol{r},\omega)|^2/8\pi$ can be considered as an energy flow of the electromagnetic field. We calculated this quantity at the location of the mirror for various frequencies ω and integrated it over the mirror surface. The resulting quantity is a measure of the energy reflected by the mirror in a unit interval of frequencies.

To illustrate the distribution of the spectral energy in the plane of the mirror, we plot in Fig. 2 the quantity $|E|^2$ (in arbitrary units) in the mirror plane at the distance $L = 22$ cm for $\omega/c = 50$ cm^{-1}. We also assume that the γ factor for the beam is equal to 500, the bending radius of the magnet is 2.5 m, and the magnet length $l_m = 22$ cm. The plot

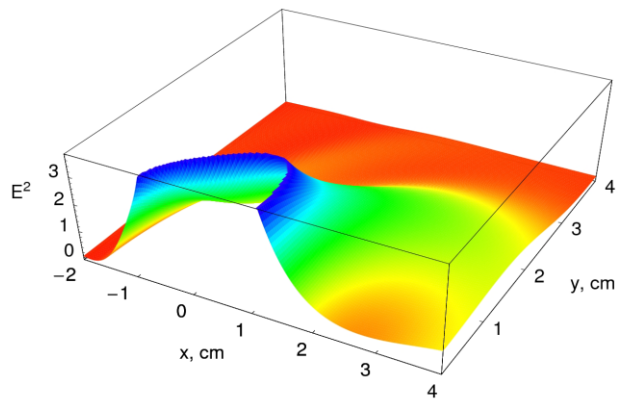

Figure 2: Square of the electric $|E|^2$ (in arbitrary units) in the observation plane x, y. The picture is symmetric with respect to the axis x. The color coding goes from red through yellow, green, and blue as the intensity increases.

is truncated at small distances close to the trajectory of the beam after the magnet ($x = y = 0$) because the field has a singularity at the trajectory. Since the reflecting mirror has a hole for the passage of the beam, the field from this region is not reflected by the mirror.

Fig. 3 shows the same field as in Fig. 2 projected onto the surface of the mirror. The mirror outer diameter $D = 7.6$ cm, and the diameter of the hole is $d = 1.5$ cm. Note a complicated pattern of the field on the surface of the mirror.

We calculated the spectral energy $S(k)$ intercepted by the mirror as a function of the wavenumber $k = \omega/c$, $S(k) \propto \int_{\rm mirror}|E(\boldsymbol{r},k/c)|^2 d^2r$. It is normalized in such a way that the total energy reflected by the mirror due to the passage of a bunch with the longitudinal charge distribution $\lambda(z)$ ($\int\lambda(z)dz = 1$) is given by

$$\mathcal{E} = \int_0^\infty dk S(k)F(k)\,, \quad (3)$$

where $F(k)$ is the form factor related to the shape of the

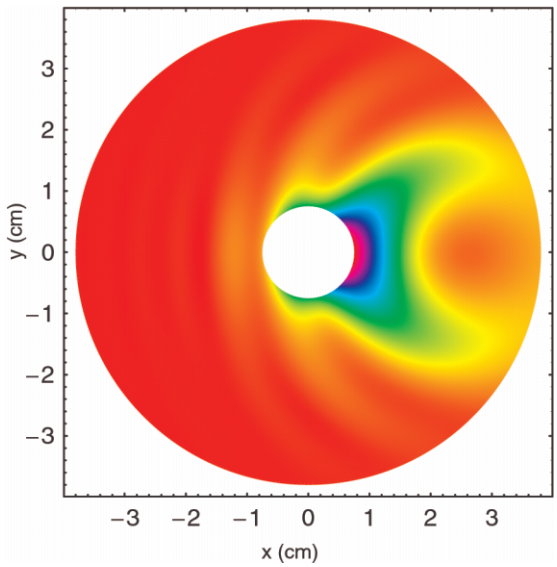

Figure 3: Distribution of the quantity $|E|^2$ on the surface of a round mirror. Shown is a hole at the center of the mirror for the beam passage.

electron bunch,

$$F(k) = \left| \int_{-\infty}^{\infty} \lambda(z) e^{ikz} dz \right|^2 . \qquad (4)$$

The plot of the function $S(k)$ for the geometry of the mirror shown above is shown in Fig. 4.

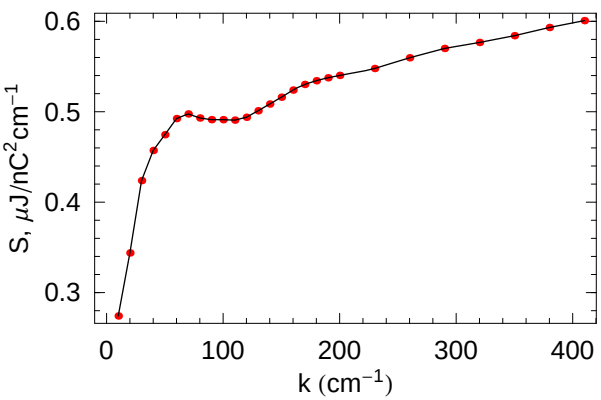

Figure 4: The spectral energy of the beam field intercepted by the mirror as a function of wavenumber $k = \omega/c$. The dots show the calculated values of S.

Using the calculated spectrum we computed the amount of energy intercepted by the mirror for various values of the bunch lengths, taking a parabolic bunch profile that is expected after BC1 [1]. This energy as a function of the compressed rms bunch length is shown in Fig. 5.

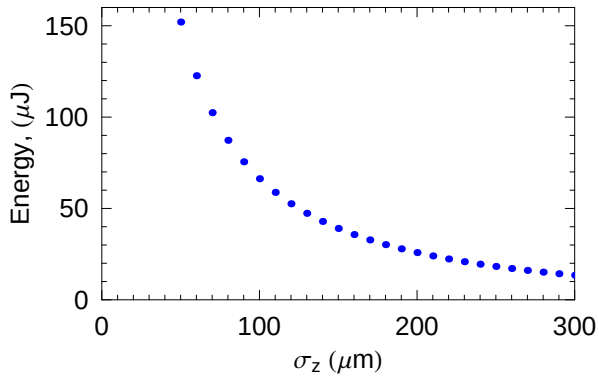

Figure 5: The reflected energy as a function of the compressed rms bunch length.

FIELD REFLECTED FROM THE MIRROR

To calculate the field reflected from the mirror, we use the vectorial diffraction theory as the wavelengths of interests (comparable to the bunch length) are much smaller than the size of the mirror [4]. The detector is assumed to be located far away from the mirror. Although there may be additional optical elements between the mirror and the detector, we neglect them here in order to illustrate the calculation method. According to the diffraction theory, the detected field is given by

$$\boldsymbol{E}_r = \frac{ie^{ikR_1}}{2\pi R_1} \boldsymbol{k} \times \int_{\text{mirror}} (\boldsymbol{n}_1 \times \boldsymbol{E}_s) e^{-i\boldsymbol{k}\cdot\boldsymbol{r}} d^2 r \,, \qquad (5)$$

where R_1 is the distance between the detector and the mirror, $\boldsymbol{E}_s$ is the induced field at the mirror, and $\boldsymbol{n}_1$ is the unit vector perpendicular to the mirror surface dS. The induced field is defined as follows. The total electric field on the surface of the mirror is the sum of the beam field $\boldsymbol{E}$ (calculated in the previous section) and the induced field $\boldsymbol{E}_s$. Due to the boundary condition on the metal surface, the tangential component of this sum should vanish, $\boldsymbol{n}_1 \times (\boldsymbol{E}_s + \boldsymbol{E})_{\text{mirrror}} = 0$, which gives

$$(\boldsymbol{n}_1 \times \boldsymbol{E}_s)_{\text{mirrror}} = -(\boldsymbol{n}_1 \times \boldsymbol{E})_{\text{mirrror}} \,. \qquad (6)$$

We will make the small angle approximation around the field propagation direction (for the mirror perpendicular to the beam orbit, the reflected field propagates in the direction opposite to the z axis). Using the cylindrical coordinate system r and ϕ in the mirror plane, we find the reflected field at the point with coordinates x and y in the detector plane as follows:

$$\boldsymbol{E}_r(x,y) = \frac{ike^{ikR_1}}{2\pi R_1} \int_{d/2}^{D/2} r dr \int_0^{2\pi} d\phi \boldsymbol{E}^{\text{tang}} \times \exp\left[-i\frac{kr}{R_1}(x\cos\phi + y\sin\phi) \right] , \qquad (7)$$

where the superscript "tang" indicates the component of the electric field tangent to the surface. Given the beam field $\boldsymbol{E}$ on the mirror as found in the previous section, we integrated Eq. (7) numerically to compute the detected signal. As a numerical example, Fig. 6 shows the reflected field intensity distribution at the distance $R_1 = 81$ cm from the mirror for $\omega/c = k = 50$ cm^{-1}. Note that the maximum of the field in the detector plane is shifted along the x coordinate. Equation (7) can be generalized to include a paraboloid mirror that focuses the radiation.

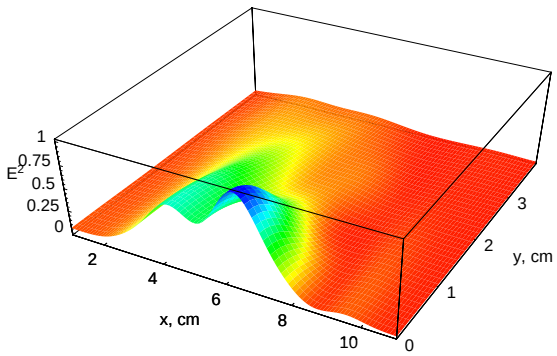

Figure 6: Square of the electric $|E|^2$ (in arbitrary units) in the detector plane x, y located 81 cm away from the mirror. The plot is symmetric with respect to the x axis.

CONCLUSION

We calculated the electromagnetic field intercepted and reflected by a metallic mirror for the geometry of the LCLS bunch length monitor. Unlike the previous calculations, we do not assume the far zone approximation for the radiation field. Our calculation takes into account the near field effect, the short length of the bending magnet (the so called "edge radiation" effect), and the diffraction of the radiation caused by reflection from the mirror.

Our calculations assume propagation of the beam in free space and neglect the effect on the radiation of the conducting walls of the vacuum chamber. In reality, those effects are not negligible, and our result should be considered as an approximation to the real spectrum.

ACKNOWLEDGMENT

We wish to thank P. Emma, H. Loos, and J. Wu for useful discussions. This work was supported by Department of Energy contract No. DE–AC02–76SF00515.

REFERENCES

[1] J. Wu, P. Emma, and Z. Huang, in *Proceedings of the 2005 Particle Accelerator Conference* (2005), p. 428.

[2] S. Casalbuoni, L. Fröhlich, O. Grimm, O. Peters, and J. Rossbach, in *Proceedings of the 2004 European Particle Accelerator Conference* (2004), p. 2586.

[3] O. Chubar and P. Elleaume, in *Proceedings of the 6th European Particle Accelerator Conference* (1998), p. 1177.

[4] J. D. Jackson, *Classical Electrodynamics* (Wiley, New York, 1999), 3rd ed.

[5] R. A. Bosch, Il Nuovo Cimento **20 D**, 483 (1998).

[6] O. V. Chubar, Rev. Sci. Instrum. **66 (2)**, 1872 (1995).

[7] G. Stupakov, Y. Ding, and Z. Huang, *Calculation of the beam field in the LCLS bunch length monitor*, Preprint SLAC-PUB-11890, SLAC (2006).

[8] S. Wolfram, *The Mathematica Book* (Wolfram Media/Cambridge University Press, 1999), 4th ed.

IN-SITU CLEANING OF METAL PHOTO-CATHODES IN RF GUNS

J.F. Schmerge, J.M. Castro, J.E. Clendenin, E.R. Colby, D.H. Dowell, S.M. Gierman, H. Loos, M. Nalls, and W.E. White, SLAC, Menlo Park, CA, U.S.A.

Abstract

Metal cathodes installed in rf guns typically exhibit much lower quantum efficiency than the theoretical limit. Experimenters often use some sort of in situ technique to "clean" the cathode to improve the QE. The most common technique is laser cleaning where the laser is focused to a small spot and scanned across the cathode surface. However, since the laser is operated near the damage threshold, it can also damage the cathode and increase the dark current. The QE also degrades over days and must be cleaned regularly. We are searching for a more robust cleaning technique that cleans the entire cathode surface simultaneously. In this paper we describe initial results using multiple techniques such as keV ion beams, glow discharge cleaning and back bombarding electrons. Results are quantified in terms of the change in QE and dark current.

INTRODUCTION

The LCLS RF gun requires fields up to 120 MV/m to achieve the desired emittance of 1 μm with 1 nC of charge in a 10 ps bunch. The high field requires the use of a Cu cathode to avoid breakdown at the cathode joint. The LCLS laser can produce 250 μJ of energy at 255 nm which will require a QE of 2 10^{-5} to generate 1 nC of charge. In the case of the Gun Test Facility (GTF) drive laser operating at 263 nm, the theoretical QE for a clean Cu surface using a 263 nm photon is 33 10^{-5} with a 100 MV/m rf field and 8.4 10^{-5} with no applied field [1]. However, experience with multiple cathodes at the GTF indicate the QE of Cu can vary from as low as 10^{-6} to nearly 10^{-4} at 100 MV/m. In addition the QE is not constant over the laser spot leading to increased emittance from the non-uniform space charge forces.

Our experience with laser cleaning [1] has convinced us to search for a better technique that cleans the entire surface simultaneously, does not increase the dark current and is easily repeatable. Here we report QE and dark current measurements before and after using multiple techniques intended to clean the metal surface and increase the QE.

IN-SITU TECHNIQUES AND RESULTS

One of the simplest proposed cleaning methods is to heat the entire gun and drive off any surface contaminants with thermal energy. This was motivated by a test where a small Cu sample was heated in a vacuum chamber to 230 C for 100 minutes which increased the QE over 2 orders of magnitude [2]. All four Cu cathodes installed at the GTF have been baked after installation to 200 C for several days, resulting in measured QEs that range from 10^{-6} to nearly 10^{-4} at 60 MV/m.

Ion Beam Cleaning

Previously we reported QE measurements on Cu samples before and after exposing the sample to a few keV ion beam [3]. The measured QE as a function of illumination wavelength with no applied field agreed very well with the theoretical Cu QE [4] after dosing the sample with up to 10 mC of charge. X-ray photoelectron spectroscopy (XPS) measurements showed the primary contaminant was carbon.

This ion gun could not be installed on the GTF gun due to interference with the gun solenoid. The SLAC Accelerator Research Department B (ARDB) rf gun is nearly identical to the GTF gun but with more clearance between the gun and solenoid. Thus the ion gun, model number ZMB7C from Micro Photonics Inc., was installed on the ARDB rf gun. The two rf guns have interchangeable cathode plates but the lasers operate at slightly different wavelength. The ARDB drive laser wavelength is 266 nm and the GTF wavelength is 263 nm.

The ion gun was installed on one of the two laser ports in the half cell as shown in Figure 1. The beam has a direct line of site to the cathode through an oval opening in the cavity side wall measuring 0.433" X 0.25" with approximately a 70° angle of incidence at the cathode. The beam size at the cathode is approximately 1 cm in diameter.

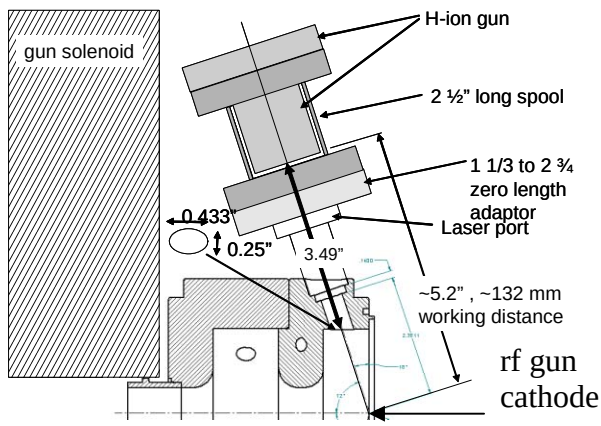

Figure 1: Layout of the ion gun and rf gun. The gun is installed on a laser port with a direct line of site to the cathode.

The QE was measured prior to the ion gun installation and was only 0.4 10^{-5} at 60 MV/m. The rf gun was vented using LN_2 tank boil-off and the ion gun installed. Before the ion gun was operated the QE was re-measured and found to have increased nearly an order of magnitude to 3 10^{-5}. The ion gun was then operated for 40 minutes at 2 keV and 2μA for a total integrated charge on the cathode of nearly 5 mC. After pumping out the hydrogen the QE was measured and found increased to 6 10^{-5} with no

increase in the dark current. The ion gun was operated for a second time for 2 hours at 4 μA for a total dose of 29 mC but the QE decreased back to 3 10^{-5}. An additional 7 mC dose (1 hour at 2 μA) did not change the QE. The dark current was not affected by the hydrogen ion beam.

Although the QE increased initially after the first hydrogen ion beam cleaning, the subsequent QE was unchanged at 3 10^{-5} at MV/m. This is significantly lower than the 10 10^{-5} measured on the Cu samples at the same wavelength with no applied field [3]. The most interesting result was the substantial increase in QE after the gun was vented. This was also observed at the GTF and will be discussed in the next section.

The hydrogen was replaced with Argon and the ion gun operated for 30 minutes at 2-2.5 keV between 1.5-3 μA for a total dose of 3 mC. The dark current was measured but the rf system failed before the QE could be measured. The total integrated dark current more than doubled from 1.6 nC prior to the Argon cleaning to 3.4 nC after cleaning with a peak field of 105 MV/m. The peak dark current in the macropulse went from 1.1 mA to 2.6 mA.

The poor results compared to the test samples may partially be explained due to misalignment of the ion gun and thus limited cleaning at the center of the cathode. The 70° angle of incidence of the ion beam relative to the rf gun cathode is 33° larger than tested on the Cu samples which may limit the effectiveness of the ion beam cleaning. It is also theorized that contaminants removed from other areas exposed to the ion beam migrate to the cathode instead of getting pumped out of the gun.

Glow Discharge Cleaning

Glow discharges are commonly used to clean vacuum vessels [5-6] and optical components [7]. A possible advantage of this technique over the ion beam is that it cleans the entire surface of the gun which should reduce migration of contaminants and improve the cathode lifetime. Glow discharges have also been used to clean Cu accelerator structures such as the AFEL linac [8], an eleven cell photo-injector/linac. There it was observed that the glow was largely confined to a single cell, but could be moved to different cells through small changes in the rf drive frequency used to excite the glow discharge.

This technique was implemented on the GTF gun using both hydrogen and an oxygen-helium mixture (90% He and 10% O_2). Gas can flow into the gun through either the half cell via the laser port or the full cell via the waveguide and is pumped out the beam exit port of the gun with a scroll pump. The discharge is started using an rf source connected to the waveguide. We have used both a 26 W CW rf source and a pulsed 1 kW rf source with 30 μs pulse length, 200 Hz repetition rate and 5 W average power. The rf frequency can be adjusted to control the location of the glow discharge as determined by a visual inspection. Exciting the glow at the π mode frequency of 2856 MHz confines the glow to the full cell and exciting the 0 mode at 2852.5 MHz confines the glow to the half cell. However, atoms can move between cells through the cell to cell coupling aperture.

The QE of the cathode was 0.5 10^{-5} at approximately 80 MV/m after the gun was vented with LN2 boil-off to install the leak valve used to introduce the gas. The first discharge was on for roughly 1 hour using hydrogen flowing into the full cell with an inlet pressure of approximately 300 mTorr. The discharge was excited with the CW rf source at 2856 MHz. The QE increased significantly to 6 10^{-5} and further increased to 8 10^{-5} after a second hour with the glow discharge. Then we switched to the 0 mode frequency of 2852.5 MHz with all other parameters constant and the QE dropped over one order of magnitude to 0.3 10^{-5}. Multiple glows at 2856 MHz at pressures ranging from 30-600 mTorr had no effect on the QE. This was an attempt to control the mean free path and thus the number of ions that reach the cathode from the glow discharge in the full cell.

We theorized that with the glow in the half cell we had actually added carbon to the surface possibly by migration of carbon from the stainless tubes attached to the laser ports on the half cell to the cathode. We introduced oxygen to the system which is expected to bond with the carbon forming CO or CO_2 and accelerate the removal rate of surface carbon [5,7]. After a glow with the oxygen and helium gas at a pressure of 200 mTorr with the CW rf source at 2856 MHz the QE dropped to 0.01 10^{-5} which is the lowest value we have ever observed. An identical glow discharge with hydrogen restored the QE to 0.3 10^{-5}. It appears the oxygen attached to the Cu surface instead of the carbon and the hydrogen glow discharge removed the oxygen. Apparently the hydrogen ions are not energetic enough to remove the carbon. We tried to increase the hydrogen ion's energy by exciting the hydrogen with the 1 kW pulsed rf source for one hour and the QE increased to 0.8 10^{-5}. However later glows with the pulsed rf source caused the QE to decrease.

In an attempt to flow more hydrogen through the half cell we installed a leak valve on the laser port and then flowed directly into the half cell instead of into the full cell from the waveguide. However, the QE decreased every time we glowed with the gas flowing into the half cell possibly indicating some sort of contamination introduced through this leak valve. We also repeated the glow at 2852.5 MHz with the hydrogen flowing into the half cell instead of the full cell. This time the QE had an insignificant change compared to the previous glow at 2852.5 MHz when the QE decreased over an order of magnitude. This seems to indicate the flow rate is an important parameter and may help remove contaminants instead of relocating them.

One interesting result was an increase in the QE nearly every time we vented the gun with LN_2 boil-off. In one case the QE increased from 0.08 10^{-5} to 1 10^{-5} after venting and in another case it increased from 0.3 10^{-5} to 2 10^{-5}. The QE would slowly decrease after every glow and then increase once the gun was vented. We theorize that a contaminant in the LN2 boil-off attaches to the surface and reduces the work function or modifies the surface

states to increase the QE [9]. Subsequent hydrogen glow discharges then remove this contaminant which reduces the QE but leave the primary contaminant, Which is assumed to be carbon, untouched. This "doping" of the surface was also observed on the ARDB cathode after venting the gun.

The dark current emitted from this cathode actually decreased during these tests. Prior to the glow discharge the total integrated dark current at a field of 95 MV/m was 250 pC with a peak current of 0.3 mA. The final charge was only 100 pC with a peak current of 0.1 mA. The Fowler-Nordheim field enhancement factor decreased from 120 to 90 but the emitting area increased nearly an order of magnitude. The dark current decrease occurred after the glow discharge at 2852.5 MHz.

Electron Bombardment of the Cathode Surface

The possibility of cleaning photo-cathodes with electrons was also investigated. A very simple method using electrons is possible by selecting a laser arrival time such that the electrons do not exit the gun but actually reverse direction and strike the cathode. These back bombarding electrons have been extensively studied in thermionic rf guns [10-11].

By adjusting the laser arrival time, the energy of the back bombarding electrons can be controlled as shown in Figure 2 where the energy of the electrons exiting the gun and those returning to the cathode are plotted as a function of laser phase for a peak field on axis of 95 MV/m. Electrons that reverse direction in the full cell are emitted at a laser phase between 93 and 117°. Electrons emitted at a phase greater than 119° reverse direction in the half cell and thus typically have lower energy at the cathode. Interestingly there are two narrow phase regions where the electrons actually reverse direction twice and finally exit the gun. This phenomenon is observed experimentally when the emitted charge versus laser phase is carefully measured. The emitted charge falls to zero around 115° and then a small peak reappears around 120°. Of course the exact phase where the charge turns on and off depends on the rf field amplitude and the laser pulse length.

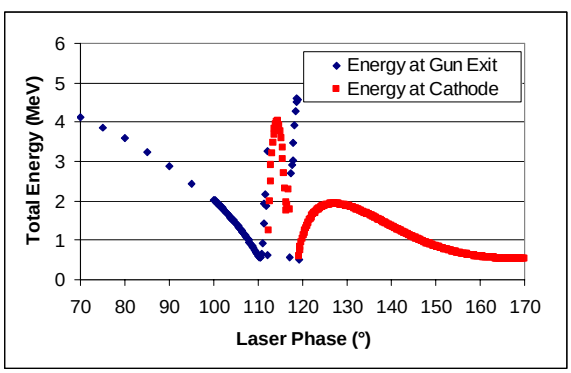

Figure 2: Simulation of the electron energy at the gun exit as a function of laser phase is plotted as diamonds. The squares show the energy of the electrons that return and strike the cathode.

Experiments were conducted with a Mg cathode and 3000 back-bombarding pulses with an estimated total charge of approximately 1 μC. The initial experiment used a laser phase of 140°, which should produce an electron with a kinetic energy of 0.85 MeV striking the cathode. No change in the QE was detected. The laser phase was adjusted to 160° and later to 125° corresponding to a kinetic energy of the bombarding electrons at the cathode of 0.076 MeV and 1.4 MeV. In all cases no measurable effect on the QE was observed. Back bombarding electrons also had no effect on the measured dark current.

The total dose of the electrons is over a factor of 1000 less than the ion beam dose and is possibly insufficient to produce a measurable effect on the QE. Plus the electron beam size may be larger when it returns to the cathode further limiting the total charge available for cleaning. The electrons may also penetrate too deep to remove surface contaminants.

CONCLUSIONS

Glow discharge cleaning appears to remove some surface contaminants without increasing the dark current. However, at least one contaminant, which is assumed to be carbon, was not removed but rather appears to have increased. Introduction of a small amount of water vapor may significantly improve the removal rate of surface carbon [7]. The hydrogen ion beam has the potential to remove all contaminants but the initial results showed no improvement in QE possibly due to misalignment of the ion beam or migration of contaminants. The electron beam bombardment had no effect on the QE or dark current possibly due to the low amount of charge per unit area incident on the cathode.

It is clear that additional diagnostics are necessary to understand the surface chemistry. We hope to add an RGA to the vacuum system to understand what species are present. Plus the surface contaminant coverage of the cathode should be measured using a technique such as XPS when the cathode is removed from the rf gun. It is important to understand which contaminants are present since this information can help determine what technique is best suited to remove them. In addition it is desirable to measure the QE versus wavelength to understand the contaminants effect on the emission process. The wavelength dependent QE gives detailed information regarding the work function and density of surface states.

Perhaps a combination of techniques such as heating, glow discharge, ion beams and doping will be required to produce a clean metal cathode with high QE. We will continue to study various cleaning techniques and the effect on the cathode QE, dark current and lifetime.

ACKNOWLEDGMENTS

We would like to acknowledge many helpful discussions and suggestions with R. Kirby and P. Pianetta at SLAC. Their surface science expertise has helped us

better understand the cleaning process and guided us in choosing experimental parameters. This work was supported by Department of Energy contract DE-AC02-76SF00515.

REFERENCES

[1] J.F. Schmerge et al., proceeding of the SPIE Free Electron Laser Challenges II at Photonics West, San Jose, CA, 1999.
[2] D. Palmer et al., SLAC-PUB-11355, 2005.
[3] D.H. Dowell et al., Proceedings of the 27th Int. FEL Conf., Stanford, CA, 2005.
[4] D.H. Dowell et al., PRST-AB **9**,063502(2006);, SLAC-PUB-11788, 2006.
[5] H.F. Dylla, J. Vac. Sci. Tech. A, 6, 1276, (1988).
[6] E.Hoyt et al, SLAC PUB-95-6990, 1995.
[7] E.D. Johnson et al, Rev. Sci. Instrum., 58, 1042, (1987).
[8] R.L. Sheffield et al., Nucl. Instrum. and Meth. A, 318, 282, (1992).
[9] Q. Yuan et al., J. Vac. Sci. Tech. B, 21, 2830, (2003).
[10] H. Liu, Nucl. Instrum. and Meth. A, 302, 535, (1991).
[11] C.B. McKee and J.M.J. Madey, Nucl. Instrum. and Meth. A, 296, 716, (1990).

BUNCH LENGTH MEASUREMENTS AT JLAB FEL

P. Evtushenko, J. Coleman, K. Jordan, J. Michael Klopf, G. Neil, G. P. Williams
Thomas Jefferson National Accelerator Facility 12000 Jefferson Avenue, Newport News, VA 23606, U.S.A.

Abstract

The JLab FEL is routinely operated with sub-picosecond bunches. The short bunch length is important for high gain of the FEL. Coherent transition radiation has been used for the bunch length measurements for many years [1]. This diagnostic can be used only in the pulsed beam mode. It is our goal to run the FEL with CW beam and a 74.85 MHz micropulse repetition rate, which, with the 135 pC nominal bunch charge corresponds to the beam average current of 10 mA. Hence it is very desirable to have the possibility of making bunch length measurements when running CW beam with any micropulse frequency. We use a Fourier transform infrared (FTIR) interferometer, which is essentially a Michelson interferometer, to measure the spectrum of the coherent synchrotron radiation generated in the last dipole of the magnetic bunch compressor upstream of the FEL wiggler. This noninvasive diagnostic provides bunch length measurements for CW beam operation at any micropulse frequency. We also compare the measurements made with the help of the FTIR interferometer with data obtained using the Martin-Puplett interferometer [1]. Results of the two diagnostics agree within 15 %. Here we present a description of the experimental setup, data evaluation procedure and results of the beam measurements.

INTRODUCTION AND MOTIVATION

The Jefferson Lab Free Electron Laser (FEL) facility is a superconducting rf (SRF) energy recovery linac based light source [2]. It is capable of running CW electron beam with an average current of up to 10 mA. The nominal bunch charge is 135 pC. The maximum possible micro-pulse frequency is 74.85 MHz, which is the 20th subharmonic of the fundamental (1497MHz) frequency of the linac. The micro-pulse frequency can be reduced by a factor of 2n, where n is an integer ranging from 1 to 8. Thus the accelerator can be operated at the nominal bunch charge but at the lower average beam current that is essential for the machine setup and tuning. Another set-up used for tuning up the machine is pulsed beam mode, where the beam consists of 250 μs long macro pulses coming with a repetition rate of 2, 10 or 60 Hz. The micro-pulse frequency within such a macro pulse is not more than ~4.68 MHz. Thus the average beam current in the pulse beam mode is kept very low and this beam mode can be used for invasive measurements of the beam properties.

A modified Martin-Puplett interferometer built by U. Happek [1] has been used for several years for the bunch length measurements at JLab FEL. The interferometer is used with the coherent transition radiation (CTR). To generate the CTR, a view screen made of 100 μm thin gold plated silicon wafer is inserted in to the beam. This diagnostic is invasive and can be used only in pulsed beam mode. The challenge of the bunch length diagnostic was to be able to measure the bunch length when running CW beam with average beam currents from 0.5 mA to 10 mA.

The coherent synchrotron radiation (CSR) can be used for the bunch length measurements the same way as the CTR. The longitudinal bunch compression is finalized by the magnetic bunch compression placed upstream of the wiggler. The bunch length at the wiggler is almost the same as at the exit of the bunch compressor. In fact the amount of the CSR generated in the last dipole of the bunch compressor is very high. A beam line was built to transport the CSR to one of the FEL user labs where it will be used for user experiments [3]. We use a rapid-scan Michelson interferometer with the CSR for the noninvasive bunch length measurements when running CW beam.

USING COHERENT RADIATION FOR BUNCH LENGTH MEASUREMENTS

The underlining principals of using coherent radiation produced by an electron bunch for the bunch length measurements have been described in detail many times in the literature [4]. Here is a short summary of the principals upon which the measurements with coherent transition radiation, as well as for the ones with coherent synchrotron radiation, are based. Consider an electron bunch consisting of N_e electrons generating transition radiation (TR) or synchrotron radiation (SR). For a wavelength shorter than the bunch length, the radiation power is proportional to N_e, since for every electron there is on average another electron radiating in an opposite phase, and so the coherence term is zero. Both TR and SR are very broadband. For a wavelength much longer than the bunch length, all electrons radiate almost in one phase and, since the phase difference is constant, the radiation is coherent and therefore the power of the radiation is proportional to N_e^2. There is a transition region where the spectral power density changes from N_e to N_e^2. The position of this transition depends on the bunch length. Hence measurements of the radiation spectrum, which would cover the transition region, contain information about the bunch length. Rigorously it is expressed as follows, spectral power density associated with the radiation of the entire bunch is

$$P_b(\omega) = P_S(\omega)\left[N_e + N_e(N_e - 1)\left|\tilde{f}_b(\omega)\right|^2 \right]$$

where $P_S(\omega)$ is the spectral density of a single electron radiation and $\left|\tilde{f}_b(\omega)\right|^2$ is the so-called longitudinal bunch form factor.

INTERFEROMETERS

The first device we use is a modified Martin-Puplett interferometer [1]. That is a step-scan device installed in the accelerator vault right next to the beam line. A lens made of polished Picarin is set in front of the interferometer and is used to transform the divergent TR into a nearly parallel beam going in to the interferometer. Wire grids made of 20 μm tungsten wire are used as the polarizing beam splitter and as the polarizer-analyzer. The period of the grid is 50 μm. A linear stage with a step motor is used to change the position of the movable mirror in the adjustable arm of the interferometer. An off-axis parabolic mirror is then used then to focus the radiation onto the input window of the Golay cell detector. Figure 1 shows an example of an interferogram measured with the interferometer and the corresponding spectrum, which, as will be explained later, is a Fourier transform of the interferogram.

Another interferometer, which we use for the measurements with the synchrotron light, is a rapid-scan device. This interferometer is commercially available from Thermo-Nicolet, and called a Nexus 670. The optical beam line used to transport the synchrotron radiation to the user lab is all reflective and is made of off-axis ellipsoidal and plane mirrors [3].

A synchrotron radiation opening angle of 150 milliradians is collected from the accelerator. The final beam is collimated into the Michelson using a 6" focal length off-axis paraboloid. For the measurements presented here we used a beam splitter made of silicon. For the measurements with the synchrotron radiation we used a PY55 detector in conjunction with a PAPY 1153 amplifier, both made by Goodrich [5]. One fundamental difference between the two interferometers is the determination of the path length difference. In the rapid-scan interferometer the path length is changed by a free running mirror, which moves with constant velocity during a scan. To measure the path difference in the interferometer there is one more interferometer built into it. The additional interferometer utilizes a HeNe laser, the fixed and the movable mirrors of the main interferometer and a beam splitter which is nested inside the main interferometer beam splitter. The detector for the HeNe laser light is placed at the output port of the interferometer. During the interferometer scan, the signal of the HeNe detector is a sine function with one period of the signal corresponding to a path length change of one wavelength of the HeNe laser, which is 632.8 nm. Thus the effective sampling frequency of the rapid-scan interferometer is much higher than the one of our step-scan interferometer. The frequency resolution of the measurements with a Michelson interferometer depends on the scan range and in our measurements is typically about 50 GHz.

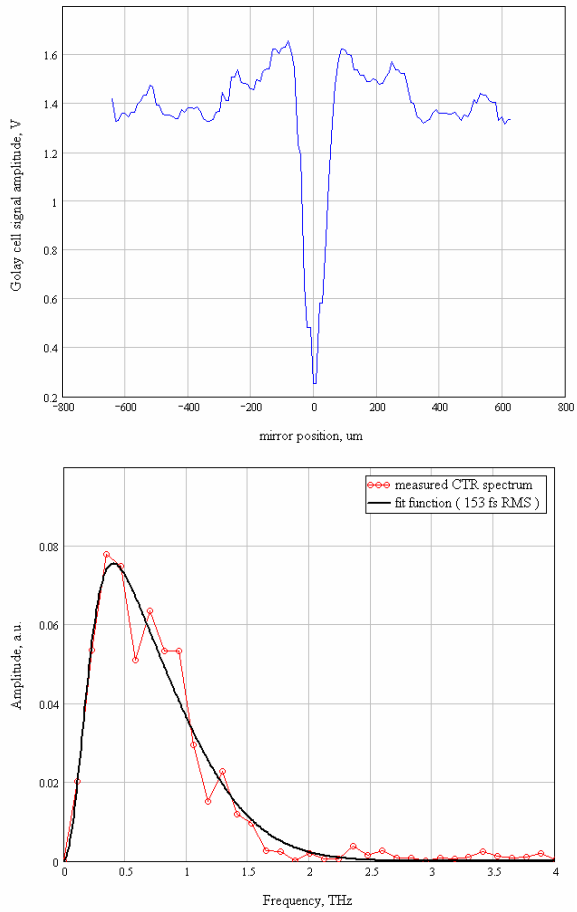

Figure 1: Interferogram measured with the modified Martin-Puplett interferometer and the corresponding spectrum.

In our measurements one scan of the rapid-scan interferometer takes about 2 seconds. Since both interferometers we use are essentially Michelson interferometers, the same data evaluation procedure for the bunch length reconstruction can be applied to the data obtained from either interferometer.

BUNCH LENGTH RECONSTRUCTION

We use the following data evaluation procedure for the bunch length estimation. The procedure is similar to the one described in [6]. According to the Wiener-Khintchine theorem [7], the autocorrelation function is the Fourier transform of the power spectrum. We use a Fast Fourier Transform (FFT) algorithm to calculate the powers spectrum from the interferogram since the data are discrete. The power spectrum defines uniquely the amplitude of the components of the frequency domain representation of the pulse. However, information about the relative phases of the different Fourier components is lost in the interferometric measurement. This is why a

direct pulse shape reconstruction from the power spectrum is not possible.

We assume a Gaussian shape of the bunch, with the RMS bunch length σ_t. The Fourier transform of the distribution function is also a Gaussian function. Thus we can write the Gaussian bunch power spectrum as $\tilde{P}(\omega) = C \cdot e^{-(\omega\sigma_t)^2}$, where C is a constant. In the measured power spectrum, the intensity is strongly reduced below a certain threshold frequency as shown in Fig. 1. The reduction of the spectral density is due to diffraction losses. The general Huygens' integral can be used to describe the diffraction losses [8]. Result of the integration of the general Huygens' integral is not an analytical function and is not very convenient to use for further data evaluation. We approximate the low frequency cut-off function with the following analytical function $F_{filter} = 1 - e^{-(\omega/\omega_0)^4}$, where ω_0 is the characteristic cut-off frequency. The product of the Gaussian power spectrum and the filter function is the modified power spectrum

$$f_{fit}(\omega) = \left(1 - e^{-(\omega/\omega_0)^4}\right) \cdot C \cdot e^{-(\omega\sigma_t)^2}.$$

Once the modified power spectrum is expressed as an analytical function it can be used as a fit function with the nonlinear least square fit (NLSF) to approximate a measured power spectrum. From such a fit we can obtain σ_t, which we define as the RMS bunch length. There are several options regarding the characteristic cut-off frequency ω_0. The best would be to have it measured, but such a measurement in the frequency range of the interests is very difficult. Another option, which we have used so far, is to add in the effects of ω_0 to the fit parameter and to make sure it stays consistent during the measurements.

EXPERIMENTAL RESULTS

The accelerator setup is always done in diagnostic mode with pulsed beam. In this mode the modified Martin-Puplett interferometer is used for the bunch length measurements. We routinely operate the machine with an RMS bunch length of about 150 fs. However, dependent on the machine setup we have been measuring RMS bunch lengths in the range from about 100 fs up to 200 fs RMS. That implies that we do indeed successfully reconstruct the bunch lengths from the interferometer measurements as was described in the previous section. Figure 1 shows an example of an interferogram measured with the step-scan interferometer, while the corresponding spectrum also shows the fit function, which is the result of the data evaluation. For this particular measurement the fit gives the RMS bunch length of 153 fs.

When the accelerator is set up we can run CW beam and use the rapid-scan interferometer. Our experience is that the results of the measurements with two interferometers agree to within about 15 %. It is very important that with the Michelson interferometer and synchrotron radiation we can do bunch length measurements as a function of the average beam current. Figure 2 shows spectra of the CSR measured at 0.31 mA, 0.62 mA, 1.25 mA and 2.5 mA of beam average current and the measured CTR spectrum measured with pulsed beam, all the measurements were done with the same machine setup. The figure also shows the corresponding fit functions and the resulting RMS bunch length. The measurements show that the bunch length is not changing when the average beam current is increased. This is what one would expect, since the average current is increased by increasing the pulse repetition rate, keeping the bunch charge constant. However, at present the FEL efficiency has been decreasing with beam current and one explanation would be that it is due to an increase in bunch length. These measurements are therefore critical in ruling this out.

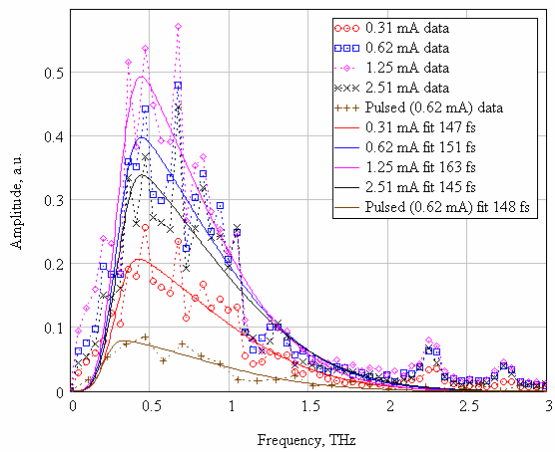

Figure 2: Spectra of the CSR measured at different average beam current with the CTR spectrum and the corresponding fit functions for bunch length reconstruction.

Another significant finding we have made is that the bunch length at the wiggler depends very strongly on the bunch charge. The bunch compression is normally optimized for the nominal bunch charge of 135 pC. When operating with much smaller bunch charge and without any changes in the machine setup, we have a much shorter bunch at the entrance to the linac. This results in a very small energy spread of the bunch at the exit of the linac. As a result, the M_{56} of the 180° bend and the chicane do not provide the same compression as for a bunch with nominal charge. As a result a bunch with a very small charge will be much longer at the wiggler than a nominal bunch. Figure 3.a shows measurements of the CSR spectrum of the nominal bunch, with an RMS bunch length of 129 fs, and that of a bunch with a very small charge where the RMS bunch length was measured to be 384 fs.

The rapid-scan interferometer provides more information than just a spectrum of CSR. Consider the interferometer scanning with the mirror velocity of 5mm/sec. Then the optical path length difference changes

at a rate of 10 mm/sec. If the incoming radiation has, for example, a wavelength of 1 mm it will result in a modulation of the signal at the detector at a frequency of 10 Hz.

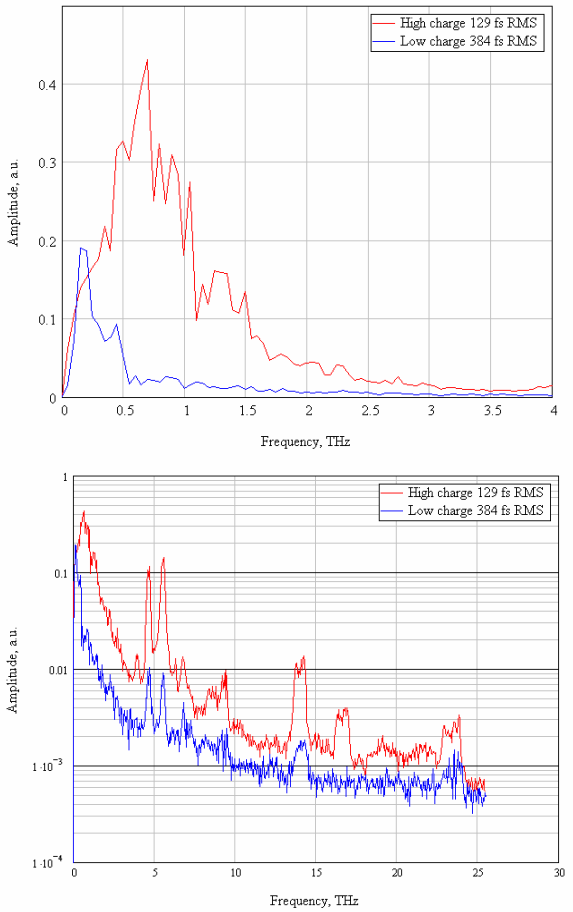

Figure 3: (a. top) spectra of the CSR measured at nominal bunch charge and much smaller bunch charge.;(b. bottom) the same data are shown on a logarithmic scale.

Thus different wavelengths measured by the interferometer be modulated at the detector at different frequencies. The frequency of the detector signal modulation is $f_M = 2v/\lambda$, where v is the velocity of the mirror during the scan and λ is the wavelength of the measured radiation. If the intensity of the incoming radiation is modulated, for instance due to a beam instability at some frequency, that will also result in modulation of the detector signal at that specific frequency. Hence the interferometer measurements also contain information about the beam stability. This technique has been used at numerous synchrotrons to diagnose and improve the beam stability [9]. Figure 3.b shows the data shown in Fig. 3.a on a logarithmic scale and over a bigger frequency span. The spectral power density peak at 4.69 THz corresponds to the radiation intensity modulation at 60 Hz; the next peak at 5.69 THz corresponds to the intensity modulation at 72.8 Hz and so on. We have yet to study in detail, the origin of all the observed beam modulations.

All the measured CSR spectra shown in Fig. 2 show local minima in the spectral power density, these are due to the water vapor absorption. This data corruption certainly reduces the accuracy of our bunch length reconstruction. To improve the setup we will switch to a newer Michelson interferometer operating in vacuum. It has been already demonstrated that such an interferometer can be operated in vacuum [10].

ACKNOWLEDGMENTS

We would like to thank S. Benson and D. Douglas for a numerous stimulating discussions and for operating the machine during measurements and systematic study of the interferometers.

This work supported by The Office of Naval Research the Joint Technology Office, NAVSEA PMS-405, the Air Force Research Laboratory, U.S. Army Night Vision Lab, the Commonwealth of Virginia, and by DOE Contract DE-AC05-84ER40150.

REFERENCES

[1] G. A. Krafft, P. Piot, K. Jordan, and J. Song, U. Happek and M. James, “Measuring and characterizing ultrashort bunches in the Jefferson Lab Free Electron Laser”, Proceedings of the EPAC98

[2] S. Benson, D. Douglas, M. Shinn, K. Beard, C. Behre, G. Biallas, J. Boyce, H. F. Dylla, R. Evans, A. Grippo, J. Gubeli, D. Hardy, C. Hernandez-Garcia, K. Jordan, L. Merminga, G. R. Neil, J. Preble, T. Siggins, R. Walker, G. P. Williams, B. Yunn, S. Zhang, H. Toyokawa, “High Power Lasing in the IR Upgrade FEL at Jefferson Lab”, Proceedings of the 2004 FEL Conference, Trieste, Italy, 229 (2004)

[3] S. Benson, D. R. Douglas, H. F. Dylla, J. Gubeli, K. Jordan, G. R. Neil, M. Shinn, S. Zhang and G.P. Williams, “High Power THz Generation from Sub-ps Bunches of Relativistic Electrons”, Mater. Res. Soc. Symp. Proc. 850, MM4.3.1 (2005)

[4] U. Happek, A.J. Sievers and E.B. Blum, Phys. Rev. Lett. 67, 2962 (1991)

[5] http://www.oss.goodrich.com/datasheets/oss/Goodrich_PAPY_DetectorPreamplifier.pdf

[6] A. Murokh, J.B. Rosenzweig, M. Hogan, H. Suk, G. Travish, and U. Happek, "Bunch Length Measurement of Picosecond Electron Beams from a Photoinjector using Coherent Transition Radiation", Nucl. Instr. Meth. A 410, 452 (1998)

[7] N. Wiener, Acta. Math. 55, 117, (1930)

[8] A. Siegman, Lasers, University Science Books, (1986)

[9] R. Biscardi, G. Ramirez and G.P. Williams, "Effects of RF Side-Bands on Spectral Reproducibility for Infrared Synchrotron Radiation", Rev. Sci. Instr. 66, 1856 (1995)

[10] P. Brierley, B. Badeau, P. Dumas, M. Smith, G. P. Williams, “Performance of a rapid-scan vacuum Michelson interferometer at the NSLS”, Review of Scientific Instruments 73, 1595-1598 (2002)

LONGITUDINAL PHASE SPACE CHARACTERIZATION OF ELECTRON BUNCHES AT THE JLAB FEL FACILITY

S. Zhang, S. Benson, D. Douglas, D. Hardy, G. Neil, and M. Shinn
TJNAF, Newport News, VA23606, USA

Abstract

We report longitudinal phase space measurements of short electron bunches at the 10kW Free-Electron Laser Facility at Jefferson Lab using broadband synchrotron radiation and a remotely controlled fast streak camera. Accurate measurements are possible because the optical transport system uses only reflective components that do not introduce dispersion. The evolution of longitudinal phase space of the electron beam can be observed in real time while phases of accelerator RF components are being adjusted. This fast and efficient diagnostic enhances the suite of machine setup tools available to JLab FEL operators and applies to other accelerators. The results for certain beam setups will be presented.

INTRODUCTION

High power Free-Electron Lasers (FELs) require very short electron bunches. The picosecond electron bunches produced by the DC high voltage GaAs photoguns must be accelerated and compressed to femto-second time scale using RF and magnetic compressors (for example, RF buncher cavities, off-crest acceleration, drift spaces and magnet chicanes). Setting and maintaining proper phase of the electron bunches with respect to the RF fields in the accelerating linac is critical for effective bunch compression and high power FEL operation. Longitudinal phase space (LPS) measurements provide extremely valuable correlated information between the temporal position of the electrons and their longitudinal momenta. Knowledge of LPS and perhaps more importantly, its evolution with time, helps during machine setup. We report a convenient and non-invasive means to monitor LPS in real-time using synchrotron radiation and a fast streak camera. This work builds upon work reported previously [1], and is part of an ongoing effort to enhance the diagnostic capabilities at the JLab 10KW FEL Facility. In this paper, we describe the measurement technique and discuss the results obtained under different beam setups.

SYSTEM DESCRIPTION

Figure 1 shows a schematic overview of the Jefferson Lab 10kW energy-recovery FEL facility which has been described in detail elsewhere [2]. Electron bunches from the gun are accelerated to 115MeV using a superconducting RF linac and turned 180 degree using a Bates-style arc magnet (ARC1) toward the FEL wiggler magnet located midway between the high-reflector and output-coupler mirrors. The electron beam then passes through a second 180 degree arc magnet for energy recovery through the linac.

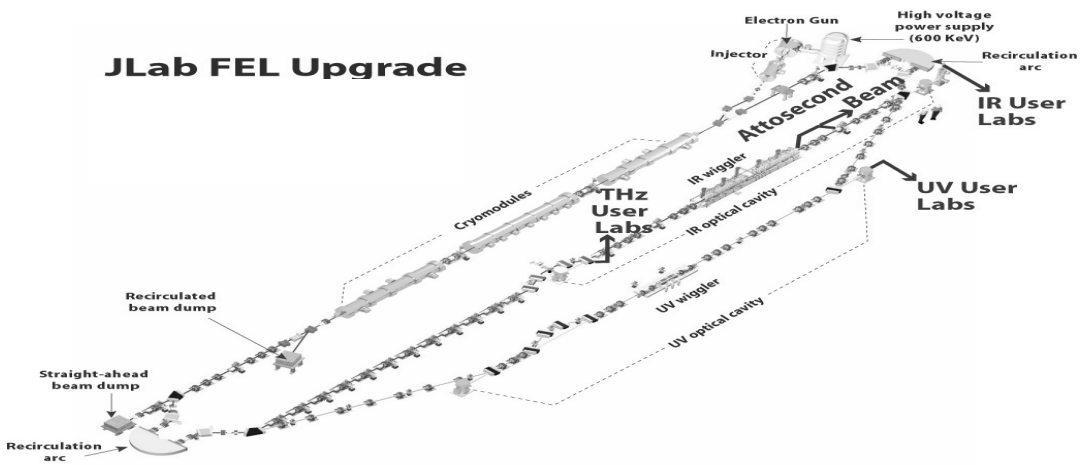

Figure 1: Layout of 10kW FEL facility at Jefferson Lab. The 1KW UV line is under construction. The linac consists of three cryo-modules. The ARC bending magnets are located at each end with ARC1 in the lower-left corner.

Managing the beam energy spread is critical for high current, high micro-bunch charge accelerator operation. In addition, it is particularly important to see how energy spread varies for the two states of accelerator operation: FEL on and off. As described in this paper, energy spread can be monitored non-invasively by monitoring the SR light emitted from the 180 degree bend magnets because electrons with lower energy

travel a shorter radial path compared to electrons with higher energy. By monitoring the emission profile of the SR light in the horizontal plane, one can measure the size of the electron beam and therefore the beam energy spread.

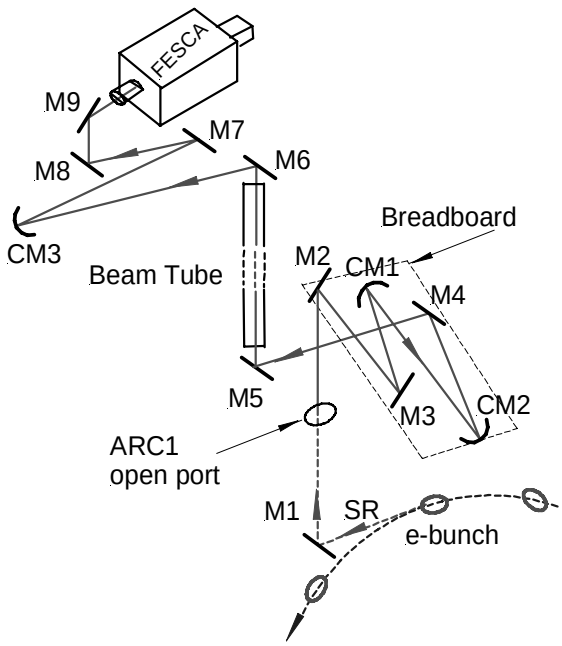

Figure 2: Schematic of the optical transport system (OTS). M, flat mirrors. CM, concave mirrors. Detailed description is given in the text.

For the measurement described here, SR light from the first 180 degree bend magnet (ARC1) was reflected upwards and out of the accelerator vault using an all-reflective optical transport system (Figure 2). The optical transport was designed to image-relay the bunch beam profile from outermost location of the beam orbit in ARC1 to the streak camera entrance slit. The SR light from the electron bunch is extremely broadband and it is important that transmission optics such as lenses are not used. Each mirror was coated with metallic coating to eliminate the dispersion effect. The three concave mirrors have radii of curvature of 200, 500 and 1000mm. Mirror M1 directs the SR beam from the bunch upwards through an open port to M2. The beam then reflects off several mirrors mounted on a small breadboard. The magnification can be adjusted by changing the distance between CM1 and CM2 in order to match the beam size to the camera cathode. The SR light propagates through a tube inserted into a penetration in the building floor. The final image at the streak camera was formed by the concave mirror CM3. A HeNe laser was available for rough pre-alignment of the system, but final alignment with SR light was time consuming, mostly because the distance between the bend magnet and the streak camera is long, more than 8m. Final optimization of the optical transport system was done with SR light during accelerator operations using several motorized mirrors.

The streak camera is a Hamamatsu Synchroscan FESCA system, the measured resolution is about 700fs. Having the streak camera outside the harmful environment of the accelerator vault is beneficial because sometimes local alignment of the camera must be performed, although data acquisition is completely remotely controlled.

MEASUREMENT AND DISCUSSION

Energy Calibration and Resolution

LPS measurements are presented on two-dimensional plots, showing energy spread along the temporal distribution of the electron bunch. Note however that what is actually measured is beam size versus the temporal distribution of the bunch. To convert beam size to energy requires calibration of the streak camera pixel display. This was accomplished using different beam energies and setups that provide minimum energy spread. Figure 3 shows five streak camera images for five different beam energies. The red curve is the initial energy set-point of 115MeV. The green (yellow) curve corresponds to higher (lower) with energy difference of 1.5%. The two peaks are separated by 391 pixels which yields a calibration factor of 0.00385% energy difference per pixel. Next, the pixel/energy resolution was studied using two energies separated by only 0.046%. The blue and pink peaks are separated by only 12 pixels but are clearly distinct. So the system resolution is definitely better than 0.05%.

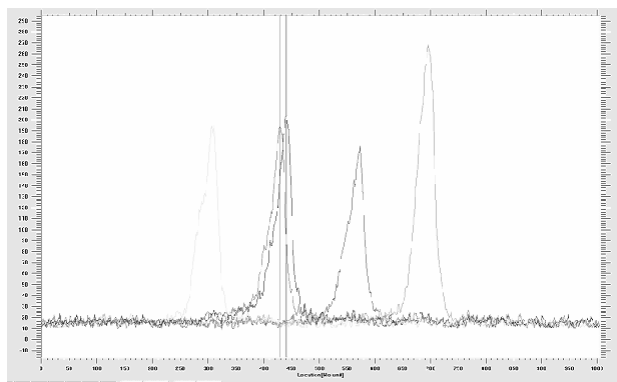

Figure 3. Streak camera images for five different beam energies. The yellow and green curves provide a calibration ratio, beam energy to pixel location. The pink and blue curves demonstrate the high degree of energy resolution of the system. The red curve is the nominal 115 MeV setpoint energy.

LPS vs. Linac Gang Phase

Production of high power FEL light requires off-crest operation of the accelerator. Deviations from this desired phase relationship may lead to reduced FEL output power. The phase relationship of the electron bunches relative to the linac gang phase can be quantified using LPS measurement and the SR light

streak camera. This is dramatically evident in Figure 4 which shows streak camera data for different linac RF gang phases relative to on-crest operation. Each picture represents a snap-shot of data presented live within the FEL control room while the accelerator was running.

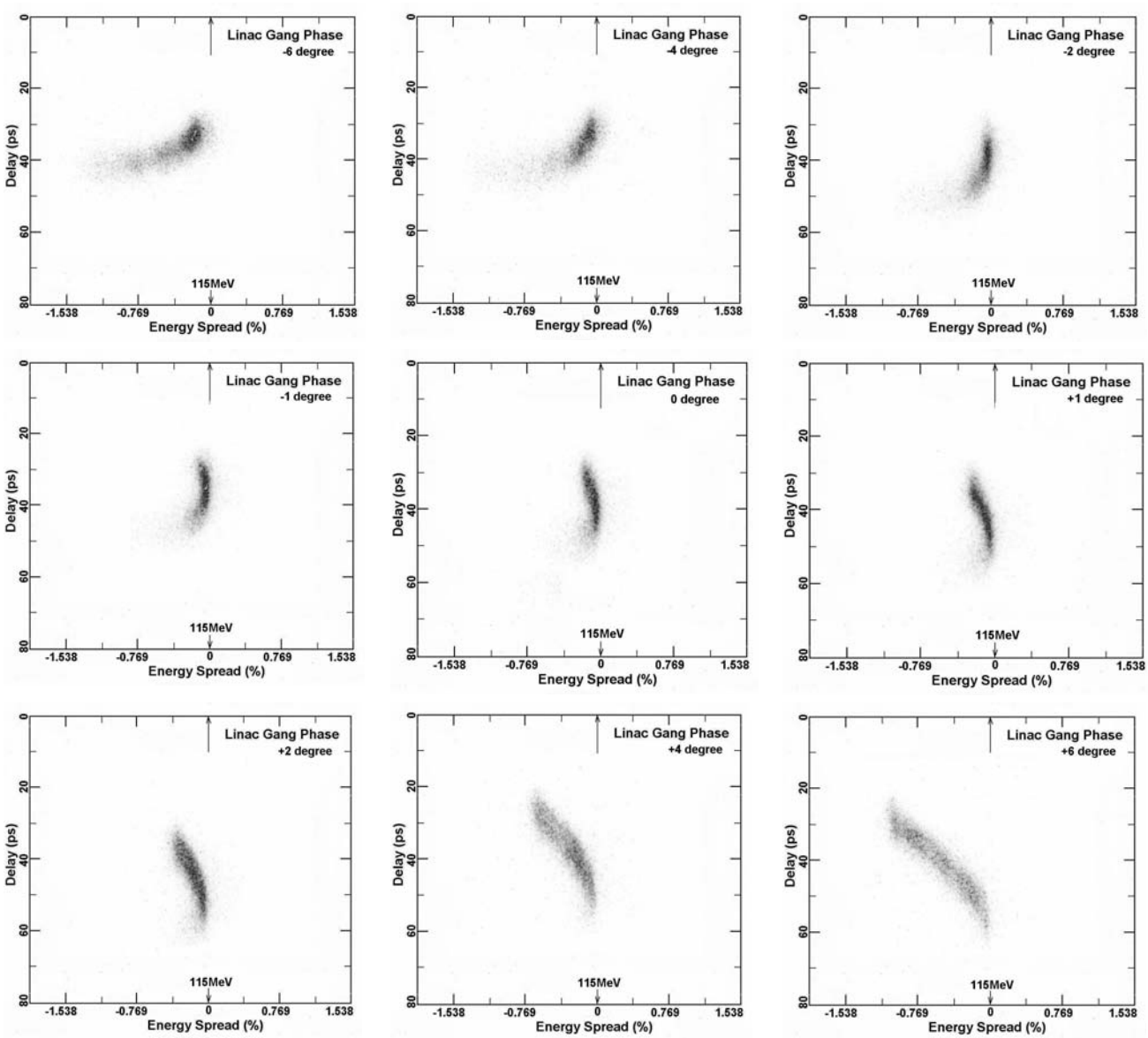

Figure 4: The LPS for different linac gang phase. Beam energy, 115MeV. Micro-pulse repetition rate: 9MHz. Macro-pulse, 1ms at 60Hz. Charge, 110pC per bunch.

From Fig.4, it is clear that the LPS can be quite different even if the bunches sit symmetrically on the two sides of the RF crest. This is the case when the phase angles are equal but have opposite signs. Apparently, a linear chirp and longer bunch length is obtained at 6 degree off-crest. At -6 degree off-crest, the bunch length becomes shorter but the shape is more like a banana, indicating high non-linearity. For on-crest operation, the bunches experience very little energy spread and the phase space is straight up with the least tilt.

LPS vs. Buncher Gradient

The whole injector of the JLab FEL facility consists of a high-voltage DC gun, a quarter cryo-unit followed by a transverse match section and an RF bunch compressor. The electron bunches from the photo-cathode initially have the same temporal length as the drive laser pulses but expand due to space charge effects. Passage through the quarter cryo-module also affects the electron bunch length. Optimum FEL operation requires the electron bunches be compressed before entering linac. We have observed that the

gradient of the buncher can affect the phase space of the electron bunches. To investigate this phenomenon, we did LPS streak camera measurements while changing the buncher gradient (Figure 5).

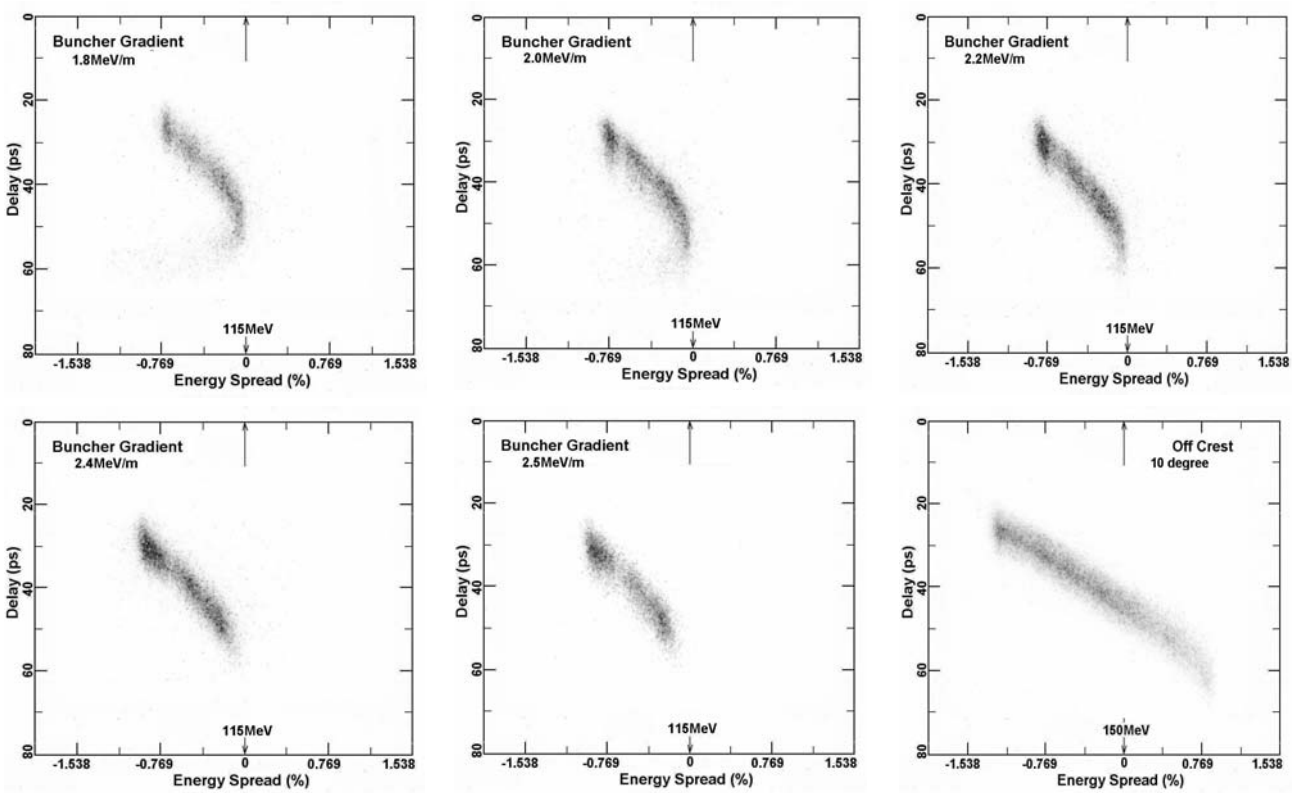

Figure 5: Longitudinal phase space for different buncher gradient. The beam energy, 115MeV. Micro-pulse repetition rate, 9MHz. Macro-pulse, 1ms at 60Hz. Charge, 110pC/bunch. The graph in lower right corner is explained in the text.

As the buncher gradient increases from low to high, the LPS trace gradually stretches out to become a linear chirp. The low energy head is basically preserved through the process while the curled tail disappears at 2.5MeV/m. The last graph in the lower right represents normal FEL operating condition. The excellent linear chirp can be seen across the whole 2.3% energy spread range.

A small part of the information at the two ends of the graph is lost, especially at low energy side of the plot. This is perhaps due to the limited energy window. This can be solved in the future by changing the optical demagnification at the expense of reduced resolution. We also used several band-pass filters with different bandwidth to see if there were dispersion effects induced in the optical transport. No difference was found with and without filters in the bean path, testament to the all-reflective nature of our design.

SUMMARY

We have established a diagnostic that provides real-time longitudinal phase space information without interruption to the accelerator operation. The longitudinal phase space was successfully measured with different linac gang phase and injector bunch gradient. The system was well calibrated with an energy resolution better than 0.05%. We are expecting to get better understanding on some important beam physics as we push toward high current beam and high power FEL on our facility in near future.

Acknowledgement

The authors would like to thank the FEL team, especially the I&C group. Thanks to M.Poelker for reviewing and extensive editing. This work is supported by the Office of Naval Research, Research, the Joint Technology Office, the Commonwealth of Virginia, the Air Force Research Laboratory, and by DOE Contract DE-AC05-84ER40150.

REFERENCES

[1] S. Zhang, et al., "Temporal Characterization of Electron Beam Bunches with a Fast Streak Camera at Jlab FEL Facility", FEL2005, SLAC, August 2005, p.640.

[2] D.Douglas, et al., "Driver Accelerator Design for the 10kW Upgrade for the JLAB IR FEL", LINAC2001, Monterey, CA 2001, p.867.

THE DEVELOPMENT AND APPLICATION OF A PHOTOEMISSION MODEL FOR CESIATED PHOTOCATHODE SURFACES

K. L. Jensen, J. E. Yater, J. L. Shaw, Naval Research Laboratory, Washington DC, 20375 USA
N. A. Moody, D. W. Feldman, P. G. O'Shea, University of Maryland, MD 20742, U.S.A.

Abstract

A theoretical photoemission model including thermal and field effects is presented. Particular attention is given to considering the impact of electron-electron and electron-lattice scattering and the development of an integrated absorption-transport-emission model developed to evaluate the moments of the electron emission distribution function. For the experimental conditions to which the theory is compared, there are no adjustable parameters. The performance of the model for the QE of bare metals and coated surfaces is discussed. A simple asymptotic model of emittance and brightness is given.[1]

INTRODUCTION

A high quantum efficiency (QE) photoemitter capable of in situ rejuvenation would fill a critical need in the development of high power FELs and linear accelerators. The demands placed on photocathode and drive-laser combinations by high power FELs are often both demanding and conflicting. Nano-Coulomb bunches in O(10) ps time scales require high quantum efficiency photocathodes, but such cathodes have traditionally degraded prematurely in vacuums characteristic of rf photoinjectors, whereas more rugged metal photocathodes require short wavelengths and therefore demand much of the drive lasers. The dispenser photocathode is intended to provide a rugged, low work function, long lived photocathode addressing these conflicting needs, and its development necessitated a validated photocathode model capable of analyzing data and predicting performance. A program to develop a controlled porosity dispenser (CPD) photocathode led to the creation and validation of a theoretical model that accounts for low work function surfaces from submonolayer coverage of alkali (and alkali earth) metals [i]. Efforts to extend and update that model have been in response to two needs: first, to provide theoretical support to an experimental CPD photocathode program by systematically studying cesiated surfaces, conventional sintered tungsten dispenser cathodes, and ultimately, custom engineered dispenser cathode; and second, to render the validated photoemission model in a form amenable to particle-in-cell (PIC) beam simulation codes [ii, iii] to predict performance of an rf injector gun using such a photocathode. Here the latest modifications to the model and its application are discussed.

Changes to the theoretical model are on two fronts. First, the scattering model affecting photoelectron excited transport to the surface has been revised. Second, the revisions motivated a moments-based emission model that is able to address cathode emittance. The beams of high power FEL's will be space charge dominated at some stage in the accelerator but especially in the gun. Non-uniform, transverse and temporal distributions affect emittance, and while the problem is of significant concern, predictive modeling efforts of device operation are compromised by the lack of adequate emission models in beam simulation codes. The photoemission models developed attempt to rectify the deficiency.

THE PHOTOEMISSION MODEL

Background

The photoemission model described in Ref. [i] represented quantum efficiency QE by

$$QE(T,F) = \frac{q}{\hbar\omega} F_\lambda(T)(1-R)P(\hbar\omega)$$
$$P(\hbar\omega) = \frac{U\left[\beta_T(\hbar\omega-\phi)\right]}{U\left[\beta_T\mu\right]} \qquad [1]$$

where $R(\omega)$ is the reflectivity of the surface, P is a probability of emission factor, U is the Fowler-Dubridge function, $\beta_T = 1/k_BT$ is the inverse temperature, ϕ is the barrier height above the Fermi level (work function minus Schottky barrier lowering factor, or $\Phi - \sqrt{4QF}$, where Q = 0.36 eV-nm and F is the product of electric field and electron charge). When coatings such as Cs are introduced, the work function Φ is dependent upon the degree of coverage θ in a manner predicted by Gyftopoulos-Levine theory. The scattering factor F_λ (not to be confused with field F) governs the probability that an electron will suffer a scattering event on its trajectory towards the surface and therefore be prevented from being photoemitted. It can be approximated by

$$F_\lambda \approx \frac{1}{\pi}\int_0^{\pi/2} \frac{\cos(\theta)}{\cos(\theta)+(\delta/l(E))} d\theta \qquad [2]$$

where δ is the laser penetration depth, and the length $l(E)$ is the product of the electron velocity and relaxation time (the notation has changed from Ref. [i])

Amending recent work in measuring the QE of cesiated surfaces and the prediction of the QE of bare metals, we have revised components of the QE model by first, utilizing models of the relaxation rates τ implicit in f_λ at the electron energy augmented by the photon energy, and second, using a moments-based approach that changes the probability of emission term P. It is the moments-based approach that allows for transverse energy and velocity expectation values to be determined, from which estimates of the emittance and brightness can be made.

[1] Support by *Joint Technology Office* & *Office of Naval Research*

Scattering Rates and Their Determination

The relaxation time is taken to be the sum of three components:

$$\tau^{-1} = \tau_{ee}^{-1} + \tau_{ac}^{-1} + \tau_{imp}^{-1} \quad [3]$$

where "*ee*" refers to electron-electron, "*ac*" refers to acoustic phonon, and "*imp*" to residual low temperature scattering due to impurities or defects. In the case of electron-electron scattering, the scattering rate is given by

$$\tau_{ee} = \frac{4\hbar K_s^2}{\alpha^2 \pi m c^2 (k_B T)^2} \left[\left(1 + \frac{E-\mu}{\pi k_B T} \right) \gamma\left(\frac{2k_F}{q_o} \right) \right]^{-1}$$

$$\gamma(x) = \frac{x^3}{4} \left(\tan^{-1} x + \frac{x}{1+x^2} - \frac{\tan^{-1}\left(x\sqrt{2+x^2} \right)}{\sqrt{2+x^2}} \right) \quad [4]$$

where K_s is the dielectric constant, α is the fine structure constant, k_F is the Fermi wave vector, and q_o is the Thomas-Fermi screening length [iv] (the form given here corrects coefficient errors that exist in Ref. [iv]). To leading order, the Thomas-Fermi factor is given by

$$q_o^2 = \frac{4\alpha m c}{\pi \hbar^2 K_s} \sqrt{2m\mu} \quad [5]$$

For acoustic scattering, the rate is given by [v]

$$\tau_{ac} = \frac{\pi \rho \hbar^3 v_s^2 \left(T_D / T \right)^5}{m k_B T k_F \Xi^2} \left(\int_0^{T_D/T} \frac{s^5 ds}{\left(e^s - 1 \right)\left(1 - e^{-s} \right)} \right)^{-1} \quad [6]$$

where Ξ is the magnitude of the deformation potential, T_D is the Debye temperture, v_s is the velocity of sound, and ρ is the density. The Debye Temperature is given by

$$T_D = \frac{\hbar v_s}{k_B} \left(6\pi^2 N r \right)^{1/3} \quad [7]$$

where N [#/cm^3] is the number density of the crystal, r is the (# of atoms / unit cell), and v_s is the sound velocity.

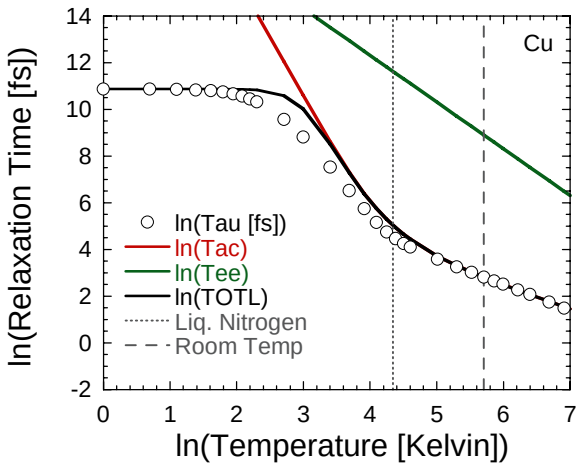

Figure 1: Determination of τ_{imp} and Ξ from thermal conductivity data from the literature.

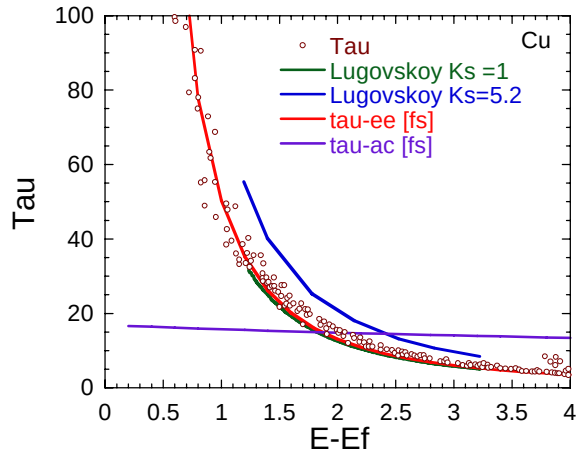

Figure 2: Determination of K_s from Monte Carlo simulations (red line) compared to parameters considered by Lugovskoy and Bray (green and blue)

Consequently, three parameters require an intricate simultaneous determination: τ_{imp}, K_s and Ξ. The values of τ_{imp} and Ξ are determined by low temperature thermal conductivity measurements after K_s is determined from Monte Carlo simulations in the literature [vi].

Comparison to Experiment

An example for Cu is shown in Figure 1 and 2. The procedure is reiterated for many metals, and in particular, for tungsten (W) and silver (Ag) which are the two cesiated metals experimentally examined [vii]. Parameters extracted from the literature become part of a library of material terms implicit in code and are not adjusted further. Comparisons of predictions of the resulting model with experimental data have been favorable for the cases of photoemission from copper [viii] and lead [ix] for a range of photon frequencies, as well as for other metals and particular frequencies discussed in the literature.

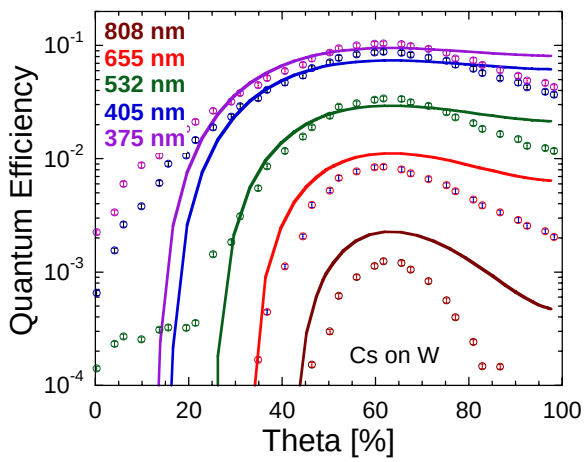

Figure 3: QE of Cs on W for low F and I_λ at 300 K versus fractional surface coverage (Ar-cleaned W). Symbols = experimental data; lines = theoretical model.

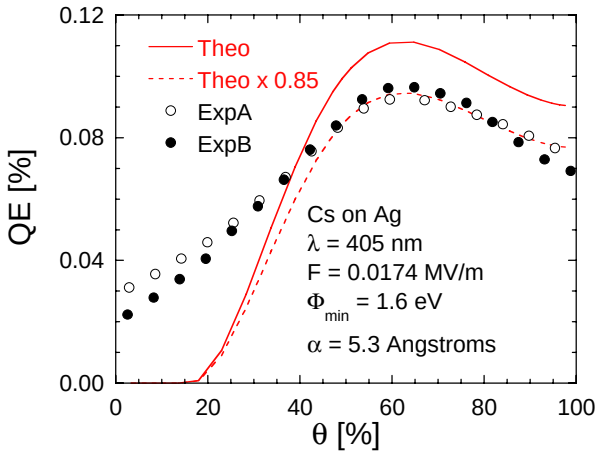

Figure 4: QE of Cs on Ag for conditions as in Fig. 3

Using the Gyftopoulos-Levine theory to relate the degree of surface coverage of Cesium on a bulk metal to the resulting work function [i], the prediction of QE for Cs on W and Cs on Ag was made and compared to experimental data. The results of that comparison are shown in Figures 3 and 4, respectively. The low coverage discrepancy shown in Fig. 4 is due to residual Cs on the surface from one experiment to the other. Issues of surface contamination led to investigations of cleaning using Ar ions, resulting in the better results for Cs on W shown in Fig. 3.

Origin Of Experimental-Theoretical Differences

The overall comparison between theory and experiment is shown to be remarkably good. Nevertheless, there are differences and an account of their probable origins is necessary. Theoretically, a simple nearly-free electron gas model is presumed, and so the significant complexities introduced by the density of states near the Fermi level are suppressed, and such complexities can matter for transition metals. Experimentally, in contrast to physical surfaces, the theoretical models are highly idealized. Cleaning is required to remove contaminants, and if due to sputtering, structure can be introduced. If the cathode is heated for cleaning, not all metals endure the necessary temperatures because of relatively low melting points (W can be strongly heated, whereas Ag cannot). Residual contamination can therefore remain in addition to what collects from an imperfect vacuum. Adsorbates often have higher work functions, *e.g.*, carbon-based contamination can induce local work functions of 5.5 eV. Assuming the surface is adequately cleaned, different exposed crystal faces can show markedly different work functions (*e.g.*, faces of Cu can vary by almost 0.8 eV): moreover, in Gyftopoulos-Levine theory, the exposed crystal plane affects the *f*-factor (see Ref. [i]: affects the number of Cs atoms per unit area) and which changes the shape of the QE hump: observations of the tungsten face, as shown in Figure 5, as well as considering other values of *f* suggest the generic (single) value chosen for *f* is not necessarily the optimal value when several faces are present.

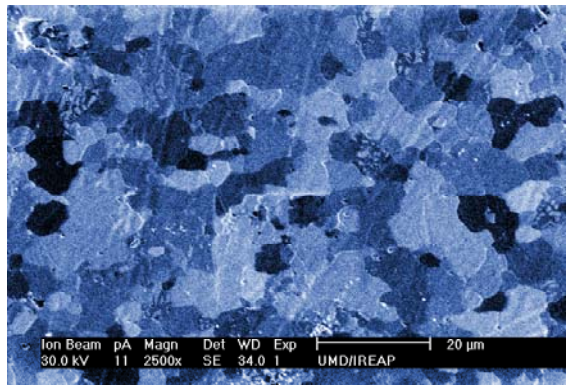

Figure 5: Image of sintered tungsten surface showing multiple crystal faces. Average grain size is O(10µm).

MOMENTS-BASED FORMULATION

The development of an energy-dependent relaxation time coincides with efforts to develop a modified emission probability model to replace Eq. [1], in which the energy of an incident electron affects its transmission probability *T(E)* over (or through for high fields) a barrier. By using a distribution function approach, parallel and transverse momentum expectation values are ascertained, the former used to evaluate the photoemission current, the latter to evaluated emittance (and both to evaluate brightness). Define the nth moment

$$M_n(x) = (2\pi)^{-3}\left(\frac{2m}{\mathrm{h}^2}\right)^{3/2}\int_0^\infty E^{1/2}dE\times$$

$$\int_0^{\pi/2}\sin\theta d\theta\left(\frac{2m}{\mathrm{h}^2}Ex^2\right)^{n/2}T\left\{(E+\mathrm{h}\omega)\cos^2\theta\right\}\times \qquad [8]$$

$$f_\lambda(\cos\theta, E+\mathrm{h}\omega)\,f_{FD}(E)\left\{1-f_{FD}(E+\mathrm{h}\omega)\right\}$$

where x = cos(θ) for parallel, and sin(θ) for transverse components. T is the transmission probability; f_λ is the integrand of F_λ, and the factor $f_{FD}(1\text{-}f_{FD})$ represents the probability that the initial state is occupied and the final state is not based on the Fermi Dirac distribution. The revised relaxation times are used in the determination of the f_λ factor. The inclusion of the transmission probability factor, and the impact on the integration limits it entails, generally results in current density estimates on the order of 30% less than the Modified Fowler-Dubridge approach, all other factors being equal. Methods to calculate Eq. [8] numerically rely on approximations to the transmission probability and models for the relaxation time in the scattering factor: below, however, an asymptotic case is considered so as to provide a simple model of emittance and brightness.

Under the Richardson approximation for the transmission coefficient and the zero-temperature approximation for the FD functions, the asymptotic expressions for the transverse (x = sinθ) moments are [x]

$$M_0 \approx \frac{1}{(2\pi)^2}\left[\frac{2m}{\hbar^2}\right]^{3/2}\frac{\mu^{1/2}(\hbar\omega-\phi)^2}{4(\mu+\phi)\left[p(\hbar\omega+\mu)+1\right]}$$
$$M_2 \approx \frac{2m\mu(\hbar\omega-\phi)}{3\hbar^2(\hbar\omega+\mu)}M_0 \qquad [9]$$

From the definition of the emittance [xi] as

$$\varepsilon_{n,rms}(z) = \frac{\hbar}{mc}\sqrt{\langle x^2\rangle\langle k_x^2\rangle - \langle xk_x\rangle^2} \qquad [10]$$

and following a derivation and approximations (uniform emission over a circular uniformly illuminated surface area) analogous to that leading to the widely-used thermal emittance relation

$$\varepsilon_{n,rms}(therm) = \rho_c / \left(4\beta_T mc^2\right)^{1/2} \qquad [11]$$

where ρ_c is the cathode radius and β_T is $1/k_BT$, it can be shown that $\varepsilon_{n,rms}(photo)$ is proportional to the illumination radius and the root of the 2nd and 0th moments, or

$$\varepsilon_{n,rms}(photo) \approx \frac{\rho_c}{2}\left[\frac{\mu(\hbar\omega-\phi)}{3mc^2(\hbar\omega+\mu)}\right]^{1/2}$$
$$\frac{B_n}{(1-R)I_\lambda A} \approx \frac{3qmc^2}{2\pi^2\mu^3\hbar\omega}\left(\frac{(\hbar\omega+\mu)(\hbar\omega-\phi)}{1+p(\mu+\hbar\omega)}\right) \qquad [12]$$

where B_n is the brightness [xii], R is the reflectivity, I_λ is the laser intensity per unit area, and A is the illuminated area. The brightness ratio in Eq. [12] is designed to forestall issues associated with reflectivity, laser particulars, and illumination area. Two observations are important: first, the emittance does not depend on the scattering factor to leading order (the brightness does through the p factor); second, the asymptotic form of B_n indicates that an optimal wavelength exits for which the brightness is maximized. The behavior of $\varepsilon_{n,rms}$ and B_n are shown in Figure 6.

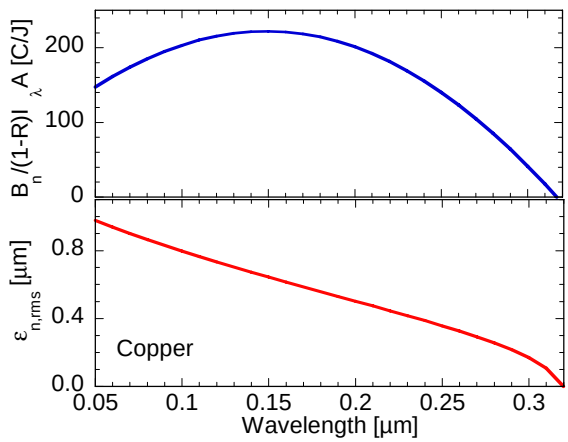

Figure 6: emittance and brightness ratio as a function of incident laser wavelength for copper parameters for conditions described in Ref. [viii].

Experimental values of emittance at 233 nm are approximately 50% larger than the theoretical value shown. The emittance of thermionic sources are generally within a factor of 2 larger than the theoretical estimate entailed by Eq. [11], and it is reasonable to presume similar explanations hold here: non-linear field components in the cavity, wakefields, non-uniformity of the illumination source (laser), thermal effects, quantum efficiency non-uniformity due to contamination or cathode structure, and space-charge effects occur for sufficiently high charge in the bunch, and likely some combination contribute to the theoretical-experimental differences between the simple asymptotic limit herein and experiment.

CONCLUSION

We have presented a revised photoemission model to account for theoretical-based scattering models and a moments-based approach for the evaluation of quantum efficiency. The revised scattering model enabled good agreement with experimental data of cesiated surfaces. The moments-based approach allowed for simple asymptotic expressions of emittance and brightness.

Acknowledgements

We gratefully acknowledge funding provided by the *Joint Technology Office* and the *Office of Naval Research*. In addition, we have benefited from interaction with many colleagues: in particular we thank (*alph*) C. Bohn, C. Brau, D. Dimitrov, D. Dowell, Y.Y. Lau, J. Lewellen, E. Nelson, J. Petillo, and J. Smedley.

REFERENCES

i K. L. Jensen, Donald W. Feldman, Nathan A. Moody, and Patrick G. O'Shea, Journal of Applied Physics 99, 124905 (2006).
ii J. J. Petillo, E. M. Nelson, J. F. DeFord, N. J. Dionne, B. Levush, *IEEE Trans. El. Dev.* **52**, 742 (2005).
iii D. A. Dimitrov, D. L. Bruhwiler, J. R. Cary, P. Messmer, P. Stoltz, K. L. Jensen, D. W. Feldman, P. G. O'Shea, *Conference Proceedings of the 27th Intl. Free Electron Laser Conference* (Stanford, CA, Aug. 21-25, 2005), paper TUPPE039.
iv A. V Lugovskoy, Igor Bray, *J. Phys. D: Appl. Phys.* **31** L78 (1998).
v Harald Ibach, Hans Lüth, *Sold State Physics* 2nd *Ed.*, (Springer-Verlag, Berlin, 1995).
vi F. Ladstädter, U. Hohenester, P. Puschnig, C. Ambrosch-Draxl, *Phys. Rev.* **B70**, 235125 (2004)
vii N. A. Moody, D. W. Feldman, P. G. O'Shea, K. L. Jensen, J. L. Shaw, J. E. Yater, (*Free Electron Laser Conference*, Berlin, Aug 27-Sep 1, 2006)
viii D. H. Dowell, F. K. King, R. E. Kirby, J. F. Schmerge, J. M. Smedley, *Phys. Rev. Spec. Top.*-AB 9, 063502 (2006)
ix Data from J. M. Smedley (*private communication*).
x K. L. Jensen, P. G. O'Shea, D. W. Feldman, N. A. Moody (*submitted to Appl. Phys. Letters*)
xi Patrick G. O'Shea, *Phys. Rev.* **E57**, 1801 (1998).
xii C. Brau, *Nucl. Inst. Meth. Phys. Res.* **A407**, 1 (1998).

EXPERIMENTAL PROGRESS TOWARD LOW WORKFUNCTION CONTROLLED POROSITY DISPENSER PHOTOCATHODES*

N. A. Moody#, D. W. Feldman, E. J. Montgomery, A. E. Balter, P. G. O'Shea,
U. of Maryland, College Park, MD, USA
K. L. Jensen, J. E. Yater, J. L. Shaw, Naval Research Laboratory, Washington DC, USA.

Abstract

Photoinjectors for accelerator applications require long-lived photoemitters with high quantum yield in the visible range. Multi-alkali cesium-based photocathodes are frequently used but suffer from short lifetime, due to loss of cesium. A novel dispenser cathode is proposed and demonstrated that provides controlled delivery of cesium to the cathode surface at <200°C. This method allows for *in situ* rejuvenation of the photoemitting surface and could dramatically extend the effective lifetime of many alkali-based high-efficiency photocathodes.

INTRODUCTION

Laser-switched photoemitters are a source of electrons for high current applications such as free electron lasers [1],[2][3]. Photoinjector systems consist of a drive laser producing short bunches of photons and an efficient photocathode, which converts photon bunches into electron beam pulses [4]. Development of both technologies is required, but the scope of this project is restricted to improvement of the photocathode. Most high-efficiency photocathodes employ cesium-based surface coatings to reduce work function and enable efficient electron emission in the visible range. Lifetime is severely limited by the loss of this delicate coating, which degrades rapidly in practical vacuum environments. More robust photocathodes exist, but have much lower efficiency, and place unrealistic demands on drive laser power and stability. A common figure of merit for photocathodes is quantum efficiency: the ratio of the number of photoemitted electrons to incident photons. It is related to photocurrent J_e and optical intensity I_λ according to:

$$QE = \frac{\hbar\omega}{q}\left(\frac{J_e}{I_\lambda}\right) = 1.2398\frac{J_e\left[\mathrm{A/cm^2}\right]}{I_\lambda[\mathrm{W/cm^2}]\lambda[\mu\mathrm{m}]} \quad (1)$$

This research proposes a novel dispenser concept that dramatically extends the lifetime of high QE cesium-based cathodes by continuously or periodically restoring the cesium surface monolayer during an *in situ* rejuvenation process. A prototype dispenser cathode was fabricated and tested for two modes of operation: continuous and periodic near-room temperature rejuvenation. The data are compared with a photoemission model of partially covered surfaces under design for integration with existing beam simulations.

*Work supported by Office of Naval Research, Joint Technology Office, and Directed Energy Professional Society
#nmoody@ieee.org

Overall performance suggests that this cesium-delivery mechanism can significantly enhance the efficiency and operational lifetime of a wide variety of present and future cesium-based photocathodes.

Dispenser Concept

A dominant degradation mechanism for high QE cesium-based cathodes is the loss of cesium either from a surface monolayer or a stoichiometric compound. Replenishing this layer with cesium continuously or periodically could restore cathode performance. Our concept of a cesium based dispenser photocathode involves three essential elements: a cesium reservoir, a photoemitting surface, and an interface between the two that controls the rate of cesium arrival. In this design, shown schematically in Figure 1, a small stainless steel cylinder contains a pellet of cesium chromate and titanium powders. A disk of made from 70% dense sintered tungsten (top) serves as both the photoemitting surface and the interface boundary [5]. During an initial heating process, the pellet breaks apart and releases elemental cesium, which diffuses through and across the sintered tungsten substrate to create a low workfunction photoemitting surface. This simple cesium-on-tungsten photocathode was used to characterize the behavior of the dispenser, but more complex cathodes such as cesium antimonide could also be built on the substrate.

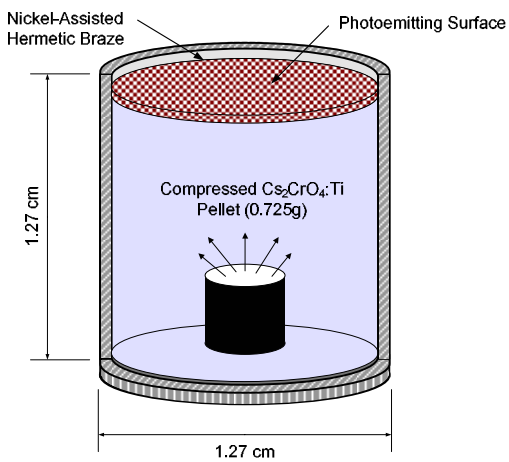

Figure 1: Schematic of Dispenser Cathode

Experimental Overview

In order to characterize the performance of the dispenser cathode, a detailed study of the photoemissive properties of cesium on tungsten was undertaken using the fabrication chamber shown in Figure 2.

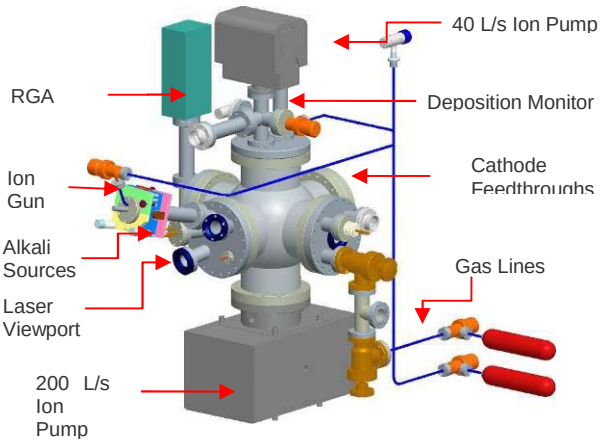

Figure 2: Vacuum Fabrication Chamber

Cesium was deposited externally using commercial sources onto a sintered tungsten disk identical to the one used to fabricate the dispenser cathode. QE was measured during deposition at several wavelengths as a function of cesium coverage, which was observed using a quartz crystal balance. Because cesium deposition occurred externally from an isotropic source, the resulting layer was assumed to be uniform. A characteristic curve was obtained whose shape and peak value depended upon the surface conditions of the cathode. Recall that for a dispenser cathode, cesium arrives at the surface through diffusion from within, so direct measurement of cesium coverage is not possible. Studying the effect of external, uniform deposition of cesium on tungsten, however, allows comparison of the dispenser's QE to that of a known system. This work is therefore divided in two parts: 1.) photoemission measurements of cesium on tungsten and 2.) characterization of the dispenser cathode.

Experimental Setup

Cesium is deposited onto the surface of a clean metal disk using SAES sources, while coverage is measured using an Inficon quartz crystal deposition monitor situated directly above the cathode. A circular anode biased at +186 volts is separated from the cathode by a distance of one centimeter. Photocurrent is measured across the anode-cathode gap using a Keithley 486 picoammeter. The entire circuit is isolated from the chamber and all connections are made using Triax to minimize noise and interference.

Five semiconductor CW lasers are sequentially shown onto the cathode while photocurrent, cesium coverage, laser intensity, background pressure, and cathode temperature are recorded using Labview. The lasers have output powers of 5mW with 2% stability at 355nm, 405nm, 532nm, 655, and 808nm. A Labview-controlled, motorized translation stage selectively positions a desired laser at the UHV chamber viewport, enabling QE measurement at multiple wavelengths during a single evaporation run. The laser spot is circular and expanded to a FWHM size of 1 cm.

Because a DC potential is used to extract charge from the cathode, ion back-bombardment occurs, where positively charged contaminants within the chamber accelerate toward and collide into the cathode, damaging and/or removing the surface layer of cesium [6]. Minimizing contaminants *during* evaporation is difficult because both the dispenser cathode and the cesium sources (having been exposed to atmosphere) contain trapped gases and traces of impurities that are emitted along with cesium. This effect is minimized by first outgassing the dispenser in a controlled manner at temperatures beneath that required to emit cesium.

EXPERIMENTAL RESULTS

Surface Metrology

The surface characteristics of sintered tungsten were studied in detail using optical, scanning electron, and focused ion beam microscopy. The porosity and thickness of the sintered disks used in the dispenser cathode were chosen such that extremes in either case were avoided. Figure 3 shows a side view of the sintered tungsten disk at 1000x magnification. Characteristic length scales of its polished surface were determined, including average pore diameter of 350nm, nearest-neighbor separation distance of 3.1μm, and average grain size of 4.8μm. The surface area each pore must coat with cesium was found on average to be 33.3μm^2 for uniform monolayer coverage. These lengths are significant because they estimate the surface diffusion length of cesium required to achieve complete coverage. Coverage uniformity is crucial because variation in the cesium surface coating causes similar variation in work function and electron emission.

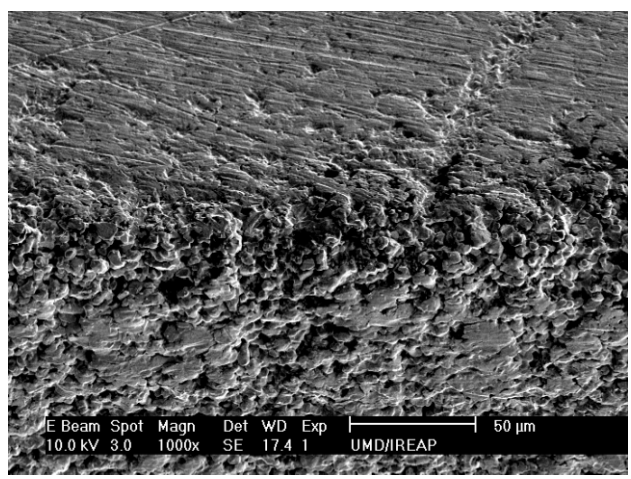

Figure 3: Side View of Dispenser Cathode

Cleaning Techniques

A standardized cleaning procedure using a 6.4keV ion argon beam was developed and shown to be remarkably effective in cleaning sintered tungsten. When cesium was deposited following the procedure, the effects of the treatment became apparent: a two-fold increase in QE with a peak QE of 0.11% in the UV, as shown in Figure 4.

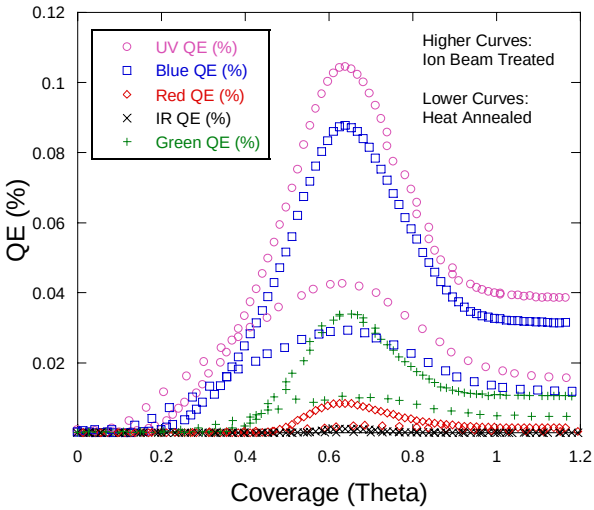

Figure 4: Effects of Ion Beam Cleaning

Coverage θ is reported in the above graph as a fraction of a monolayer, where $\theta = 0$ corresponds to bare tungsten and $\theta = 1$ is a full cesium monolayer. A single 45 minute treatment provided a 40mC dose of 6keV argon ions which was sufficient to produce apparent atomic cleanliness. This claim is justified because increasing the number of consecutive ion treatments and/or the energy of the ion beam did not produce further improvement in QE. Because cesium was deposited uniformly on an atomically clean surface, the QE of 0.11% can be said to be characteristic of a uniform, optimal cesium coating. This cleaning technique dramatically reduces the amount of time required to prepare a cathode for cesium deposition because it eliminates the need for a lengthy high temperature anneal.

Theory Comparison

The model used in this work is based upon the Fowler-DuBridge treatment of photoemission [6],[7] and follows the Gyftopolous-Levine approach of accounting for the effects of cesium coverage [9]. A distinguishing factor about the modified model is that an effort has been made to systematically reduce or eliminate unknowns, either by means of models or approximations, which were arbitrarily assigned or used as fit parameters in other treatments. The components of the model relevant to the experiments in this program are described in detail elsewhere [10]. Data describing the effect of surface cesium coverage on the work function and QE of metal photocathodes was compared to the model's predictions and found on average to be within 22% agreement, as shown in Figure 5. Similar agreement was found for cesium-on-silver and suggests that the theory is capable of predicting performance of metallic-based photocathodes. This experiment enables theory comparison for an important set of operation parameters: low drive laser intensity and low accelerating electric field. These parameters are typically much higher and are usually cited as reasons for drastic discrepancies between theory and experiment (e.g., laser heating, damage to cathode surface, etc.).

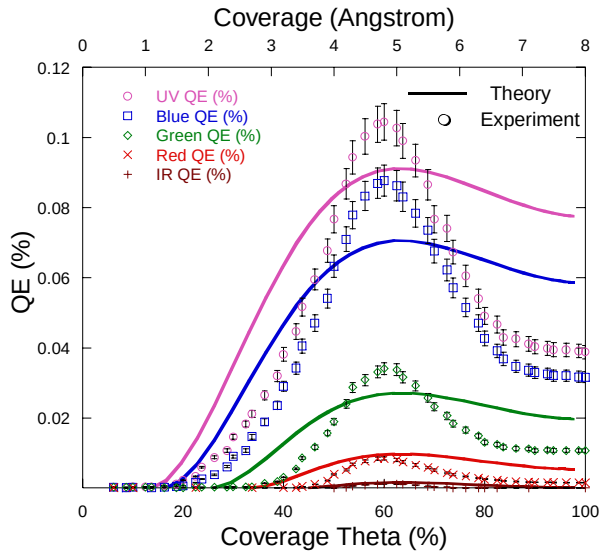

Figure 5: Comparison of Theory and Experiment

The inputs to the theory were simply generalized material parameters that could be widely applied to any number of different photocathodes.

Dispenser Cathode

The two basic procedures for operating the dispenser cathode are activation and rejuvenation. Activation occurs at higher temperatures and initiates a chemical reaction between the powders inside the cell, while rejuvenation occurs at much lower temperature and involves bringing atomic cesium to the surface in a controlled manner. Initial activation prepared the dispenser for use, as seen by the onset of photoemission at 425°C, followed by complete activation at 477°C, which produced a reduction in work function such that a large thermionic current was measured. Because of the elevated temperature, a significant amount of cesium was released throughout the chamber, producing up to a 50Å coating on an adjacent deposition monitor. This release is expected, however, and is not considered problematic because 1.) a large quantity of cesium remained within the dispenser following activation, and 2.) the activation procedure for a working dispenser cathode would most likely occur in a chamber separate from the actual electron gun (whose contamination with cesium would lead to field breakdown).

Following activation, the dispenser was allowed to cool and its 1/*e* lifetime was measured to be 5.2 days. After 65 hours of continuous operation, its QE decayed from its peak of 0.11% in UV to 0.06%. Complete rejuvenation was demonstrated when QE returned to its previous peak value of 0.11% upon heating to 140°C, as shown in Figure 6. Less than 3Å of cesium was deposited during this process, suggesting that *in situ* rehabilitation of the cathode is possible. Coverage at peak QE was indirectly measured to be about 64% using the relationship between cesium coverage and QE.

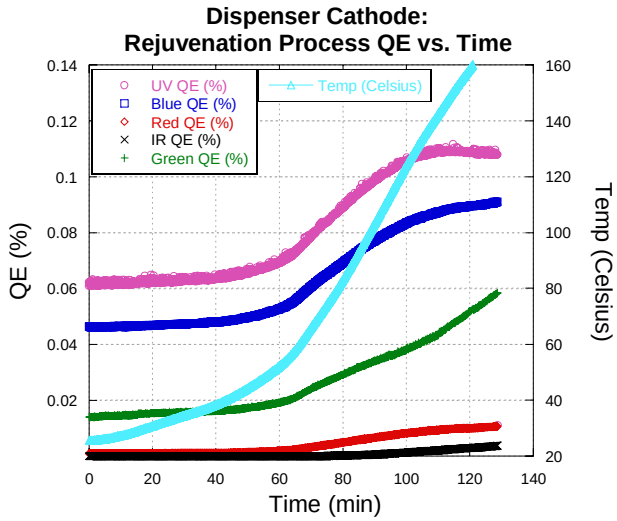

Figure 6: Rejuvenation of Cathode Surface

Two modes of cathode operation were demonstrated: periodic and continuous rejuvenation. For the continuous mode, temperature is held between 160-180°C, resulting in constant replenishment of the cesium layer. The 1/*e* effective (continuous duty cycle) lifetime in this mode was an astounding 47 days.

CONCLUSIONS

A prototype design for a near-room temperature dispenser cathode was proposed and demonstrated for the case of cesium-on-tungsten using commonly available components: thin-walled stainless steel and porous sintered tungsten. It is distinguished from other dispenser-type cathodes [11] by its low operating temperature, which makes it a good candidate technology where cathode thermal management is a concern. A method for conveniently integrating cesium chromate into the dispenser cell was demonstrated by forming the powder into a solid pellet under high pressure. The peak QE of the activated dispenser cathode, following an ion beam cleaning treatment, was 0.11%. This QE value was shown to correspond to that of a uniform, optimal cesium coating and suggests that the sintered tungsten interface facilitates uniform cesium coverage. This result suggests that the surface diffusion length of cesium across tungsten at temperatures ranging from 200-400°C is at least 5μm. The overall performance of the dispenser cathode suggests that its design could serve as a temperature-controlled cesium dispensing platform onto which a variety of high QE cesium-based photocathodes could be built.

REFERENCES

[1] P. G. O'Shea, H. P. Freund, Science **292**, 1853 (2001).
[2] D. H. Dowell, S. Z. Bethel, K. D. Friddell, Nucl. Instr. & Meth. in Phys. Res., A**356** 167 (1995).
[3] C. Travier, Nucl. Instr. & Meth. in Phys. Res. **A304**, 285 (1991).
[4] P. G. O'Shea, et. al., *Proc. Particle Accel. Conf.*, vol. 5, San Fran., May 6–9, 1991, pp. 2754–2756.
[5] Fabrication performed by B. Vancil, E-Beam Inc, Beaverton, OR.
[6] C. H. Garcia, C. A. Brau, Nucl. Instr. And Meth. in Phys. Res., A 475 (2001) 559-563.
[7] R. H. Fowler, Phys. Rev. 38, 45 (1931); L. A. DuBridge, Phys. Rev. 43, 727 (1933).
[8] J. H. Bechtel, W. L. Smith, and N. Bloembergen, Phys. Rev. B15, 4557 (1977).
[9] E. P. Gyftopolous and J. D. Levine, Jour. of App. Phys. **33**, 67 (1962).
[10] K. L. Jensen, D. W. Feldman, N. A. Moody, P. G. O'Shea, Jour. App. Phys., **99**, 1 (2006).
[11] R. E. Thomas, J. W. Gibson, G. A. Haas, and R. H. Abrams, IEEE Transactions on Electron Devices 37, 850 (1990).

OPTIMUM BEAM CREATION IN PHOTOINJECTORS USING SPACE-CHARGE EXPANSION*

J.B. Rosenzweig, A.M. Cook, M. Dunning, R.J. England
Particle Beam Physics Laboratory, Department of Physics and Astronomy
University of California Los Angeles, Los Angeles, CA 90095, USA

M. Bellaveglia, M. Boscolo, L. Catani, A. Cianchi, G. Di Pirro,
M. Ferrario, D. Filippetto, G. Gatti, P. Musumeci, L. Palumbo, C. Vicario
Istituto Nazionale di Fisica Nucleare, Laboratori Nazionale di Frascati
00044 Frascati (Roma), Italy

S. Jones
Jet Propulsion Laboratory, California Institue of Technology
4800 Oak Grove Drive, Pasadena, CA 91101, USA.

Abstract

It has recently been shown that by illuminating a photocathode with an ultra-short laser pulse of appropriate transverse profile, a uniform density, ellipsoidally shaped bunch is dynamically formed, which then has linear space-charge fields in all dimensions inside of the bunch. We study here this process, and its marriage to the standard emittance compensation scenario that is implemented in most modern photoinjectors. It is seen that the two processes are compatible, with simulations indicating that a very high brightness beam can be obtained. The scheme has produced stimulus for a series of experiments at the SPARC injector at Frascati in 2006-2007. An initial time-resolved experiment has been performed involving Cerenkov radiation produced at an aerogel. We discuss the results of this preliminary experiment, as well as plans for future experiments to resolve the ellipsoidal bunch shape at low energy. Future measurements at high energy based on fs resolution RF sweepers are discussed.

INTRODUCTION

In order to obtain the highest brightness electron beams from photoinjectors, it is most common to rely on the emittance compensation process [1]. Optimization of this process demands that the transverse fields be as uniform, and linear (in radius r) as possible. The existing studies of emittance compensation have, to that end, assumed use of a uniform density electron beam, having a cylindrical shape. However, this shape produces space-charge fields near the beam head and tail that have pronounced nonlinear dependencies on the spatial coordinates. These nonlinearities result in both transverse and longitudinal emittance growth.

It has been known for some time, however, that a uniform ellipsoidal density distribution yields space-charge fields that are linear in all dimensions [2]. Under such conditions, it is conceivable that one may obtain essentially emittance growth-free dynamics. How to produce such a distribution has, until recently, remained an unanswered question.

In 1997, Serafini proposed the dynamic creation of an ellipsoidal bunch by launching an ultra-short, radially shaped beam, which then evolves to achieve the desired longitudinal shape [3]. On the other had, it has recently been shown by Luiten, et al., that in obtaining the correct final ellipsoidal distribution, there is essentially no requirement on the shape of the initial laser pulse other than it be ultra-short (length τ_l much shorter than eventual beam length after space charge expansion) [4]. Thus such laser pulses are a natural, and technically achievable way of producing an ellipsoidally shaped, nearly uniform density beam.

As the beam dynamics just after photoemission are qualitatively different in the traditional emittance compensation scenario and in the Luiten-Serafini scheme, it is not immediately apparent that one may successfully combine the two. The UCLA-SPARC collaboration has recently shown [5] that this marriage is indeed possible; further, the combination of emittance compensation and dynamic creation of the ellipsoidal shaped beam produces results that in many ways are superior to those obtained in state-of-the-art designs. As the bunches that are produced are shorter than in standard cases, very high brightness beam creation is possible.

The basic idea behind the Luiten-Serafini scheme is simple: the beam profile expands and deforms longitudinally to produce, in the final state, a uniformly filled ellipsoid of charge. In the process, phase space rearrangements occur which degrade the emittances– especially in the longitudinal dimension. In order to understand this process, to specify experimental requirements, and to identify experimental signatures associated with the process, we have analyzed the dynamics of space-charge-dominated beam ex-

* Work supported by the US Dept. of Energy under grant DE-FG03-92ER40693, and the Italian Ministry.

pansion [5].

This analysis may be summarized in a few points:

First, the injected bunch surface charge density $\sigma_b = dQ_b/dA$ must not be too high, or image charge effects at the cathode distort the final pulse profile so that it is not ellipsoidal. This is quantified by the condition $\alpha \equiv 4\pi\sigma_b/E_0 << 1$.

Second, the beam must be much shorter than its eventual size in order to be able to ignore the details of the initial pulse profile. In practice, 300 fs laser pulses (typical of the limitations of the SPARC photocathode drive laser after conversion to UV) excite roughly the same length electron bunch, which expands to around 4 psec in our example cases. The pulse length after expansion is estimated as $L_b \approx 2\pi\sigma_b m_e c^2/E_0^2$.

The current density that is achieved after expansion is $J_z = eE_0^2/4\pi m_e c$, a constant dependent only on the applied electric field E_0. All beams become uniform in density. To achieve the desired ellipsoidal beam shape, one must choose the initial surface current density distribution correctly, which implies that $\sigma_b(r) = (3Q_b/2\pi a^2)\sqrt{1-(r/a)^2}$.

While the analysis of the beam dynamics is useful, the central issue of joining this regime with emittance compensation must be explored with simulations. The initial simulations begun in Ref. [5] that we have performed are in the context of the SPARC scenario, so that we may proceed directly to discussing the experimental tests of this new regime– now commonly known as the "blowout regime"– of the photoinjector there.

BLOWOUT REGIME WITH EMITTANCE COMPENSATION: GENERAL STUDY

We have performed initial UCLA PARMELA [6] simulations to explore joining the Serafini-Luiten scheme with the optimized emittance compensation working point of the SPARC injector at LNF. We assume that the gun (1.6 cell, 2856 MHz) and solenoid are the same, and run near to the standard conditions. Through trials, we have optimized the launch conditions of the beam. In order to have values of α which do not give excessive image charge effects, the beam charge is lowered and the beam radius is slightly enlarged. In the preliminary optimization, we launch a 0.33 nC beam with an initial longitudinal Gaussian distribution having $\sigma_t = 33$ fs beam, and a radial Gaussian with $\sigma_x = 0.77$ mm (cutoff at 1.8σ). The gun is run with a peak on-axis gradient of 120 MV/m; the beam is launched at 33 degrees forward of crest. This is a bit advanced in comparison to the nominal launch phase for a standard bunch, and serves to control the excessive beam energy spread after the gun. The emittance compensation solenoid is run with peak field $B_z = 2700$ G, which is slightly below the standard scenario, as the beam has slightly lower energy exiting the gun. We note that the peak value of α in our case is 0.11, as opposed to 0.42 in the LCLS design.

The formation of the quasi-ellipsoidal bunch is clearly

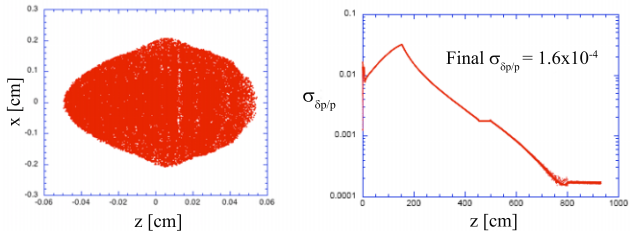

Figure 1: (left) PARMELA simulation results of electron bunch (x, z) distribution 133 cm from cathode (6.3 MeV energy), showing ellipsoidal beam boundary. (right) Evolution of $\sigma_{\delta p/p}$ in z for emittance compensation case, from PARMELA simulation.

shown in Fig. 1, which displays the bunch (x, z) distribution at a point 133 cm from the cathode, in the drift space after the gun and just preceding initial traveling wave linac section. Here the beam has 6.3 MeV mean energy, and its transverse dynamics are space charge-dominated. Thus one sees clearly the "inflated" ellipsoidal beam shape. The final bunch length is 1.3 mm full width, corresponding to a peak current of 105 A. Thus even with one-third of the charge, this scheme should produce a higher current than obtained in simulations of the standard design.

Two notable defects are seen in the beam shape in Fig. 1. The first is the extension of the half-ellipsoid in the trailing part of the bunch as compared with the initial half– an asymmetry caused by image charge effects. This non-ideal behavior in fact gives the limit on σ; when one attempts to launch a higher surface charge density, the bunch deformation from the desired symmetric ellipsoid produces poor emittance performance. The second notable feature is the existence of an anomalous ring at the outer radial edge of the beam. This part of the beam has low surface charge density and experiences radially fringing fields due to its edge location. Because of these effects, it does not experience enough longitudinal expansion to keep pace with the rest of the bunch, but instead has a moderate amount of radial expansion.

As the longitudinal space-charge during much of the acceleration is also linear, and total pulse length T is short, the longitudinal phase space is very compact. The evolution of the relative momentum spread $\sigma_{\delta p/p}$ in z is shown in Fig. 1. The final achieved RMS value is $\sigma_{\delta p/p} = 1.6 \cdot 10^{-4}$, which is an order of magnitude smaller than that obtained in the standard LCLS type (or SPARC type) design.

The evolution of the RMS transverse beam size σ_x , and the RMS normalized emittance $\epsilon_{n,x}$ are shown in Fig. 2. While the behavior of σ_x is similar in most respects to the standard design, with the beam approximately matched at linac entrance to the invariant envelope, the emittance behavior is not as familiar. In the standard LCLS design, $\epsilon_{n,x}$ achieves a minimum value in the post-gun drift, rising to a local maximum at injection into the linac. The focusing and adiabatic damping of the motion in the linac then produce a

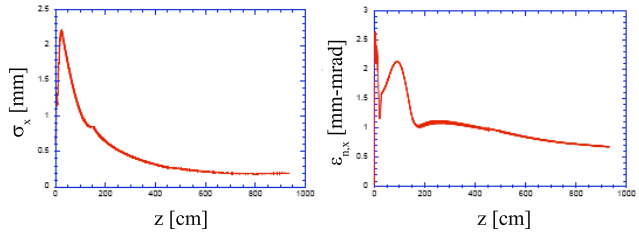

Figure 2: (left) The evolution of RMS transverse beam size σ_x for emittance compensation case, from PARMELA simulation. (right) Evolution of RMS normalized emittance $\epsilon_{n,x}$ for emittance compensation case.

monotonic decrease of $\epsilon_{n,x}$ in z. In our case, the transverse space-charge and thus the plasma/emittance oscillations do not "turn on" until after the longitudinal expansion is well underway, thus delaying the emittance minimum in Fig. 2 to occur inside of the linac. In order to produce faster emittance oscillations in the linac to strongly diminish $\epsilon_{n,x}$ before acceleration removes the plasma-dominated beam behavior, the solenoid field in the first linac section has been raised by 40% relative to the standard scenario. This ploy works well, as the final value (still slightly decreasing) of $\epsilon_{n,x}$ at the end of the second linac (84.5 MeV energy) is 0.68 mm-mrad. The thermal emittance at the cathode is 0.4 mm-mrad, and so the space-charge induced emittance is well compensated.

After acceleration to higher energy (84.5 MeV), the beam is not spacecharge dominated, and the (x, z) profile no longer ellipsoidal. Nonetheless, the beam has excellent emittance, and maintains a current profile with shape $I(t) \propto \sqrt{1-(2t/T)^2}$. With a high initial current, and low intrinsic energy spread, this beam may be compressed further, with very high final peak current achievable [7].

CONSIDERATIONS FOR SPARC EXPERIMENT

Laser and photocathode issues

Before discussing the planned electron beam measurements, we first review some experimental considerations specific to the use of such short lasers. First, we note that the laser pulse should be tailored, either by collimating and relay imaging, and that it must be quite short. In first measurements at SPARC, we have found, through cross-correlation measurements, that the UV pulse is difficult to make shorter than 300 fs using 3rd harmonic generation with noncollinear mixing in the conversion crystals. In order to obtain even this result, we must give up UV energy, going from 1.5 mJ to 0.2 mJ. While this energy is still adequate for obtaining 0.33 nC of charge using a metal cathode (Cu or Mg), to go shorter may be difficult. In order to check the effect of this extra pulse length on the scheme, we have performed simulations analogous to the original exploratory, indications are that the added length in the laser pulse does not affect the final electron beam configuration at this level.

The laser intensity needed for this scenario is a factor of 30-100 higher than in the LCLS case. The issue of laser damage at the cathode surface has been examined, and found based on previous experience at UCLA and at the BNL ATF to not be worrisome [7].

Experimental signatures and measurements

In the SPARC experiment, we plan first to image the beam (time-integrated) at low energy (5-7 MeV) in the region after the gun, using a YAG detector. For time resolved measurements we will first convert the beam spatial information to photons with a Cerenkov convertor. In order to have a manageably small angle of emission we use aerogel, which has a small index of refraction (n = 1.005-1.02). At 5 MeV the Cerenkov emission threshold is reached for $n = 1.005$; we may choose angles of emission from near zero at this threshold to up to 9 degrees with the aerogels that are presently in hand. The aerogels have been custom fabricated at the Jet Propulsion Laboratory.

Simulations consist of providing electrons (typically 40,000) from PARMELA to GEANT [8], which simulates the scattering of the electrons in the entrance foil and generates a collection of Cerenkov photons in the aerogel. The photon distributions that result are then passed to a *Mathematica* based, optical ray-tracing program, *Rayica*.

The streak camera at SPARC has 2 ps FWHM time resolution, which is on the border of resolution for the bunch length of interest. This will be handled in initial measurements by use of higher charges (above 1 nC), and thus longer beams, to test the longitudinal expansion dynamics of the beam. We thus must consider alternative schemes based on ultra-fast gating [7].

FIRST RESULTS

The first stage of experimentation on the blowout regime took place at INFN-LNF beginning at the end of March 2006. During commissioning of the SPARC RF photocathode gun, the UCLA-produced gun was conditioned quickly up to 11 MW, which produces 110 MV/m peak electric field, and a 5.7 MeV electron beam.

The laser was reconfigured for short pulses (less than 0.5 psec FWHM) and up to 1.6 nC of charge. The conditions for observing the dynamic creation of nearly uniformly filled ellipsoidal charge distributions were not quite present; in fact, the emittance was not of equivalent quality to that obtained in standard operation. Nevertheless, impressive first data was obtained.

Initial measurements of the longitudinal-transverse profile of the beam were made with aerogel with index $n = 1.008$, with the Cerenkov radiator placed 2.4 m away from the cathode, downstream of the slit-based emittance measurement system. Streak camera images were obtained using the transport system described in the previous section. Such a streak, after correction, is shown in Fig. 3.

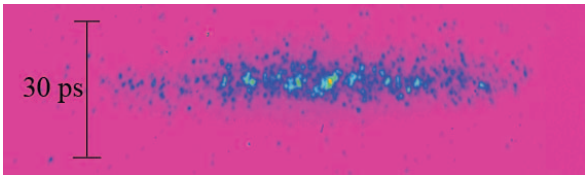

Figure 3: Streak image from SPARC experiment, after correction.

This image displays the profile obtained from a bunch with charge of 700 pC. A large charge is preferred in this case in order to discern information at a time scale longer over the streak camera resolution; the 700 pC case is expected to have expansion of approximately 7 psec FWHM, well in excess of this 2 psec FHWM resolution.

Streak images obtained in the highest temporal resolution mode are inherently noisy; this condition is required in order to avoid space-charge induced pulse distortion inside of the streak tube. Thus in order to extract information from single shots concerning the streak image– which should represent the beam density distribution in an (x, z) slice in the midplane of the bunch– we have adopted a maximum likelihood analysis to test for different assumed types of beam distributions.

The (x, z) slice distributions we have tested for consistency with the data include: (1) a bi-Gaussian (thermal-type) distribution; (2) a uniformly filled ellipse (assumed arising from a parent uniformly filled ellipsoid); and (3) a nearly uniformly filled ellipse with a tail, which we choose to represent as a Fermi-Dirac distribution.

As all of the distributions assumed have contours of constant density that are elliptical, a systematic statistical approach is possible, in which we look at the total integrated intensity inside of ellipses of size varying from zero area to an area covering the entire streak image. These ellipses are all required to have the same aspect ratio, which is given by the intensity profile itself, $R = \sigma_x / v_s \sigma_t$, where v_s is the streak velocity, and σ_t=3.45 psec for the streak in Fig. 3.

With these functions in hand, we can fit to the data given in the streak images to determine the likelihood that one of the assumed three profiles is more likely than the others. Such an exercise has been performed for the streak given in Fig. 3, with the results shown in Fig. 4. It can be seen the bi-Gaussian hypothesis can be rejected as the least likely model. While the uniformly filled ellipsoid gives a good fit near the distribution center, it is not very accurate at the edge, where one expects strong deviations in any case from this model. Finally, we note that the best fit obtained from the Fermi-Dirac model gives an excellent match to the data.

CONCLUSIONS

While the first measurements have established the soundness of the basic experimental approach, much more remains to be done. As of now, the SPARC injector is being modified to allow for near-axis (as opposed to 70 degree) injection. Additional improvements should also result from use of laser cleaning of the cathode. The SPARC injector will soon be completed with the addition of post-acceleration linacs and beam diagnostics (e.g. RF sweeper). In this fully mature experimental scheme, a complete test of the consistency of the Luiten-Serafini scheme with emittance compensation should be possible, using the large array of techniques described here. Further experiments will also emphasize the demonstration of high quality longitudinal phase space and concomitant low energy spread, as well as high compressibility.

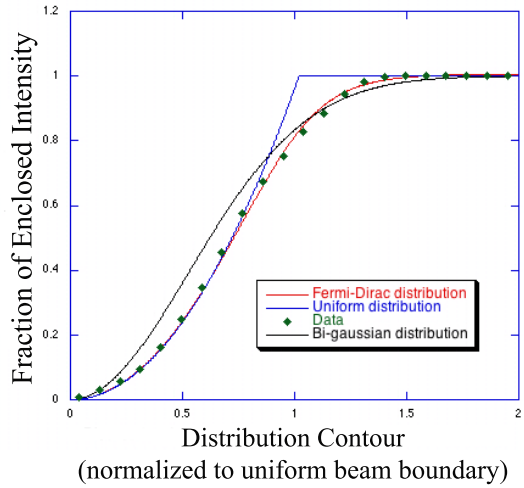

Figure 4: Analysis of streak data, with fraction of integrated intensity of data inside of elliptical contour shown. Best fit of data points to three models are shown: bi-gaussian distribution, uniform elliptical distribution, and Fermi-Dirac (uniform with tails) distribution.

ACKNOWLEDGEMENTS

The authors acknowledge useful interactions with Scott Anderson, Luca Giannessi, Marcello Quattromini, and Dirk Lipka.

REFERENCES

[1] L. Serafini and J.B. Rosenzweig, *Physical Review E* **55**, 7565 (1997).

[2] I.M. Kapchinskii and V.V. Vladimirskii, in *Proc. Int. Conf. High En. Accs.*, CERN, Geneva, 274, 1959.

[3] L. Serafini, *AIP Conf. Proc.* **413**, 321 (1997).

[4] O. J. Luiten, et al., *Phys. Rev. Lett.*, **93**, 094802-1 (2004).

[5] J. B. Rosenzweig, et al., *Nucl. Inst. and Meth. A*, **57** 87 (2006).

[6] E. Colby, *UCLA PhD Thesis*, FERMILAB-THESIS-1997-03 (FNAL, 1997).

[7] J.B. Rosenzweig, et al., *Proc. 2005 Phys. App. High Br. Beams*, Erice, 2006.

[8] S. Agostinelli, et al., *Nuc. Inst. and Meth. A* **506**, 250 (2003).

FREE ELECTRON LASERS IN 2006

W. B. Colson*, J. Blau, and A. Kampouridis
Physics Department, Naval Postgraduate School, Monterey CA 93943 USA

Abstract

Twenty-nine years after the first operation of the free electron laser (FEL) at Stanford University, there continue to be many important experiments, proposed experiments, and user facilities around the world. Properties of FELs operating in the infrared, visible, UV, and x-ray wavelength regimes are listed and discussed.

The following tables list existing (Table 1) and proposed (Table 2) relativistic free electron lasers (FELs) in 2006. A location or institution, followed by the FEL's name in parentheses, identifies each FEL; references are listed in Tables 3 and 4. Another good site for FEL references is http://sbfel3.ucsb.edu/www/vl_fel.html.

The first column of the table lists the operating wavelength λ, or wavelength range. The longer wavelengths are listed at the top with short x-ray wavelength FEL at the bottom of the table. The large range of operating wavelengths, seven orders of magnitude, indicates the flexible design characteristics of the FEL mechanism. In the second column, σ_z is the electron pulse length divided by the speed of light *c*, and ranges from almost CW to short sub-picosecond pulse time scales. The expected optical pulse length can be 3 to 5 times shorter or longer than the electron pulse depending on the optical cavity Q, the FEL desynchronism, and the FEL gain. The optical pulse can be up to 10 times shorter in the high-gain FEL amplifier. Also, if the FEL is in an electron storage-ring, the optical pulse is typically much shorter than the electron pulse. Most FEL oscillators produce an optical spectrum that is Fourier transform limited by the optical pulse length.

The electron beam energy E in MeV and peak current I in Amperes provided by the accelerator are listed in the third and fourth columns, respectively. The next three columns list the number of undulator periods N, the undulator wavelength λ_0, and the rms undulator parameter $K = eB\lambda_0/2\pi mc^2$ in cgs units, where e is the electron charge magnitude, B is the rms undulator field strength, and m is the electron mass. For an FEL klystron undulator, there are multiple undulator sections as listed in the N-column. Note that the range of values for N, λ_0, and K are much smaller than for the other parameters, indicating that most undulators are similar. Some exceptions are the long undulators containing many periods N that are being developed for the x-ray FEL amplifiers. Only a few of the FELs use the klystron undulator at present, and the rest use the conventional periodic undulator. Most of the undulators are configured to have linear polarization. The FEL resonance condition, $\lambda = \lambda_0(1+K^2)/2\gamma^2$ where γ is the relativistic Lorentz factor, provides a relationship that can be used to relate K to λ, E, and λ_0. The middle entry of the last column lists the accelerator type (RF for Radio Frequency Linear Accelerator, MA for Microtron Accelerator, SR for Storage Ring, EA for Electrostatic Accelerator), and the FEL type (A for FEL Amplifier, O for FEL Oscillator, S for SASE FEL, H for a high-gain high harmonic HGHG FEL). Most of the FELs are oscillators, but recent progress has resulted in short wavelength FELs using SASE (Stimulated Amplification of Spontaneous Emission) and high-gain harmonic generation (HGHG).

For the conventional undulator oscillator, the peak optical power can be estimated by the fraction of the electron beam peak power that spans the undulator spectral bandwidth, 1/(2N), or $P \approx EI/(8eN)$. For the FEL using a storage ring, the optical power causing saturation is substantially less than this estimate and depends on ring properties. For the high-gain FEL amplifier, the optical power at saturation can be substantially greater. The average FEL power is determined by the duty cycle, or spacing between the electron micropulses, and is typically many orders of magnitude lower than the peak power. The Jlab infrared FEL has now reached an average power of 10 kW with the recovery of the electron beam energy in superconducting accelerator cavities.

In the FEL oscillator, the optical mode that best couples to the electron beam in an undulator of length $L = N\lambda_0$ has Rayleigh length $z_0 \approx L/12^{1/2}$ and has a mode waist radius of $w_0 \approx N^{1/2}\gamma\lambda/\pi$. The FEL optical mode typically has more than 90% of the power in the fundamental mode described by these parameters.

This year the DESY FLASH FEL has reached the shortest wavelength ever for an FEL, $\lambda \approx 0.013$ μm. There are several other new lasings: Rossendorf (U-100) at $\lambda \approx$ 20-150 μm, RIKEN (SCSS Prototype) at $\lambda \approx 0.049$ μm, and BNL (SDL FEL) at $\lambda \approx 0.198$ μm. New FEL lasings are highlighted in bold in Table 1.

ACKNOWLEDGMENTS

The authors are grateful for support from ONR, NAVSEA, and the JTO.

* Corresponding Author: 831-656-2765, Colson@nps.edu

Table 1: Free Electron Lasers (2006)

EXISTING FELs	**λ(μm)**	**σ_z(ps)**	**E(MeV)**	**I(A)**	**N**	**λ_0(cm)**	**K(rms)**	
Italy (FEL-CAT)	760	15-20	1.8	5	16	2.5	0.75	RF,O
UCSB (mm FEL)	340	25000	6	2	42	7.1	0.7	EA,O
Novosibirsk (RTM)	120-230	70	12	10	2x33	12	0.71	RF,O
Korea (KAERI-FEL)	97-1200	25	4.3-6.5	0.5	80	2.5	1.0-1.6	MA,O
Osaka (ISIR,SASE)	70-220	20-30	11	1000	32	6	1.5	RF,S
Himeji (LEENA)	65-75	10	5.4	10	50	1.6	0.5	RF,O
UCSB (FIR FEL)	60	25000	6	2	150	2	0.1	EA,O
Osaka (ILE/ILT)	47	3	8	50	50	2	0.5	RF,O
Osaka (ISIR)	32-150	20-30	13-19	50	32	6	1.5	RF,O
Tokai (JAEA-FEL)	22	2.5-5	17	200	52	3.3	0.7	RF,O
Bruyeres (ELSA)	20	30	18	100	30	3	0.8	RF,O
Osaka (FELI4)	18-40	10	33	40	30	8	1.3-1.7	RF,O
UCLA-Kurchatov	16	3	13.5	80	40	1.5	1	RF,A
LANL (RAFEL)	15.5	15	17	300	200	2	0.9	RF,O
Stanford (FIREFLY)	15-80	1-5	15-32	14	25	6	1	RF,O
Rossendorf (U-100)	**15-150**	**0.3-10**	**15**	**240**	**38**	**10**	**2.7**	**RF,O**
UCLA-Kurchatov-LANL	12	5	18	170	100	2	0.7	RF,A
Beijing (BFEL)	5-20	4	30	15-20	50	3	1	RF,O
Dresden (ELBE)	3-22	1-10	34	30	2x34	2.73	0.3-0.7	RF,O
Korea (KAERI HP FEL)	3-20	10-20	20-40	30	30x2	3.5	0.5-0.8	RF,O
Jlab (IR upgrade)	0.7-10	0.1	120	400	29	5.5	3	RF,O
Darmstadt (FEL)	6-8	2	25-50	2.7	80	3.2	1	RF,O
BNL (HGHG)	5.3	6	40	120	60	3.3	1.44	RF,A
Osaka (iFEL1)	5.5	10	33.2	42	58	3.4	1	RF,O
Tokyo (KHI-FEL)	4-16	2	32-40	30	43	3.2	0.7-1.8	RF,O
Nieuwegein (FELIX)	3-250	1	50	50	38	6.5	1.8	RF,O
Duke (MARKIII)	2.7-6.5	3	31-41.5	20	47	2.3	1	RF,O
Stanford (SCAFEL)	3-13	0.5-12	22-45	10	72	3.1	0.8	RF,O
Orsay (CLIO)	3-53	0.1-3	21-50	80	38	5	1.4	RF,O
Vanderbilt (FELI)	2.0-9.8	0.7	43	50	52	2.3	1.3	RF,O
Osaka (iFEL2)	1.88	10	68	42	78	3.8	1	RF,O
Nihon (LEBRA)	0.9-6.5	<1	58-100	10-20	50	4.8	0.7-1.4	RF,O
UCLA-BNL (VISA)	0.8	0.5	70.9	250	220	1.8	1.2	RF,S
BNL (ATF)	0.6	6	50	100	70	0.88	0.4	RF,O
Duke (OK-5)	0.45	0.1-10	270-800	35	2x32	12	0-4.75	SR,O
Dortmund (FELICITAI)	0.42	50	450	90	17	25	2	SR,O
BNL (SDL FEL)	**0.2-1.0**	**0.5-1**	**100-250**	**300-400**	**256**	**3.9**	**0.8**	**RF,A,S,H**
Orsay (Super-ACO)	0.3-0.6	15	800	0.1	2x10	13	4.5	SR,O
Osaka (iFEL3)	0.3-0.7	5	155	60	67	4	1.4	RF,O
Okazaki (UVSOR)	0.2-0.6	6	607	10	2x9	11	2	SR,O
Tsukuba (NIJI-IV)	0.2-0.6	14	310	10	2x42	7.2	2	SR,O
Italy (ELETTRA)	0.2-0.4	28	1000	150	2x19	10	4.2	SR,O
Duke (OK-4)	0.193-2.1	0.1-10	1200	35	2x33	10	0-4.75	SR,O
ANL (APSFEL)	0.13	0.3	399	400	648	3.3	2.2	RF,S
RIKEN(SCSS Prototype)	**0.05**	**1**	**250**	**800**	**600**	**1.5**	**1.3**	**RF,S**
DESY (FLASH)	**0.013**	**0.025**	**700**	**2000**	**984**	**2.73**	**0.81**	**RF,S**

Table 2: Proposed Free Electron Lasers (2006)

PROPOSED FELs	$\lambda(\mu m)$	σ_z(ps)	E(MeV)	I(A)	N	λ_0(cm)	K(rms)	
Tokyo (FIR-FEL)	300-1000	5	10	30	25	7	1.5-3.4	RF,O
Netherlands (TEUFEL)	180	20	6	350	50	2.5	1	RF,O
Romania (NILPRP)	60	10	7	2	100	2	0.4	RF,O
Dresden (ELBE)	20-150	1-10	20-40	30	38	10	0.3-2.7	RF,O
Novosibirsk (RTM1)	5-100	10	50	20-100	3x33	6	2	RF,O
Daresbury (4GLS-IRFEL)	3-75	0.5-1	18-50	70	27	2.7	2	RF,O
Novosibirsk (RTM)	2-11	20	98	100	4x36	9	1.6	RF,O
Frascati (SPARC)	0.533	0.1	142	500	6x71	3	1.3	RF,S
Hawaii (FEL)	0.3-3	2	100	500	84	2.4	1.2	RF,O
Jlab (UV FEL)	0.25-1	0.2	160	270	60	3.3	1.3	RF,O
Harima (SUBARU)	0.2-10	26	1500	50	33,65	16,32	8	SR,O
Shanghai (SDUV-FEL)	0.5-0.088	1	300	400	400	2.5	1.025	RF,O
Daresbury (4GLS-VUV)	0.4-0.1	0.1-1	600	300	150	5	2	RF,O
Daresbury (4GLS-XUV)	0.1-0.01	0.1-1	750-950	1500	1000	4.5	1-3.5	RF,S
Frascati (COSA)	0.08	10	215	200	400	1.4	1	RF,O
DESY (FLASH)	0.006	0.17	1000	2500	981	2.73	0.9	RF,S
Italy (SPARX)	0.0015	0.1	2500	2500	1000	3	1.2	RF,S
BESSY (Soft X-ray)	0.0012	0.08	2300	3500	1450	2.75	0.9	RF,S
Trieste (FERMI)	0.001-0.1	0.1	1200	500-2500	1140	3.5	1.2	RF,S
Pohang (PAL X-FEL)	0.0003	0.1	3000	4000	6000	1.5	1.1	RF,S
MIT (Bates X-Ray FEL)	0.0003	0.05	4000	1000	1500	1.8	2	RF,S
SLAC (LCLS)	0.00015	0.07	14350	3400	3328	3	3.7	RF,S
DESY (XFEL)	0.0001	0.08	17500	5000	4700	3.6	3.2	RF,S
RIKEN (SPring8 SCSS)	0.0001	0.5	8000	2000	1500	1.5	1.3	RF,S

Table 3: References and Websites for Existing FELs

EXISTING FELs	Internet Site or Reference
ANL (APSFEL)	J. W. Lewellen et. al., NIM **A483**, 40 (2002).
Beijing (BFEL)	http://bfel.ihepa.ac.cn
BNL (SDL FEL)	http://www.nsls.bnl.gov/facility/Accelerator/DUVFEL
BNL (ATF)	K. Batchelor et. al., NIM **A318**, 159 (1992).
BNL (HGHG)	A. Doyuran et. al., NIM **A475**, 260 (2001).
BNL (VISA)	A. Tremaine et. al., NIM **A483**, 24 (2002).
Bruyeres (ELSA)	P. Guimbal et. al., NIM **A341**, 43 (1994).
Darmstadt (FEL)	http://linaxa.ikp.physik.tu-darmstadt.de/richter/fel
DESY(FLASH)	http://flash.desy.de
Dortmund (FELICITAI)	http://www.delta.uni-dortmund.de/pub/fel/FEL.html
Dresden (ELBE)	http://www.fz-rossendorf.de
Duke (MARKIII)	http://www.fel.duke.edu/lightsources/mk3.html
Duke (OK-4, OK-5)	http://www.fel.duke.edu
Himeji (LEENA)	http://www.lasti.himeji-tech.ac.jp/NS/LEENA/LEENA_HP.html
Italy (ELETTRA)	http://www.elettra.trieste.it/projects/euprog/fel
Italy (FEL-CAT)	A. Doria et. al, Phys. Rev. Lett. **80**, 2841 (1998).
Jlab (IR upgrade)	http://www.jlab.org/FEL
Korea (KAERI HP FEL)	http://www.kaeri.re.kr/fel/index.php
Korea (KAERI-FEL)	http://www.kaeri.re.kr/fel/index.php
LANL (RAFEL)	http://www.lanl.gov/orgs/ibdnew/usrfac/userfac03.html
Nieuwegein (FELIX)	http://www.rijnh.nl/n4/n3/f1234.htm
Nihon (LEBRA)	http://www.lebra.nihon-u.ac.jp
Novosibirsk (RTM)	http://www.inp.nsk.su
Okazaki (UVSOR)	http://uvsor-ntserver.ims.ac.jp
Orsay (CLIO)	http://www.lure.u-psud.fr/CLIO.HTM
Orsay (Super-ACO)	M. E. Couprie et. al., NIM **A407**, 215-220 (1998).
Osaka (FELI4)	T. Takii et. al., NIM **A407**, 21-25 (1998).
Osaka (iFEL1)	http://www.fel.eng.osaka-u.ac.jp/english/index_e.html
Osaka (iFEL2)	http://www.fel.eng.osaka-u.ac.jp/english/index_e.html
Osaka (iFEL3)	http://www.fel.eng.osaka-u.ac.jp/english/index_e.html
Osaka (ILE/ILT)	N. Ohigashi et. al., NIM **A375**, 469 (1996).
Osaka (ISIR)	http://www.ei.sanken.osaka-u.ac.jp
RIKEN(SCSS Prototype)	http://www-xfel.spring8.or.jp
Rossendorf (U-100)	http://www.fz-rossendorf.de
Stanford (FIREFLY)	K. W. Berryman and T. I. Smith, NIM **A375**, 6 (1996).
Stanford (SCAFEL)	H. A. Schwettman et. al., NIM **A375**, 662 (1996).
Tokai (JAEA-FEL)	R. Hajima et. al., NIM **A507**, 115 (2003).
Tokyo (KHI-FEL)	M. Yokoyama et. al., NIM **A475**, 38 (2001).
Tsukuba (NIJI-IV)	K.Yamada et. al., NIM **A475**, 205 (2001).
UCLA-Kurchatov	http://pbpl.physics.ucla.edu
UCLA-Kurchatov-LANL	http://pbpl.physics.ucla.edu
UCSB (FIR FEL)	http://sbfel3.ucsb.edu
UCSB (mm FEL)	http://sbfel3.ucsb.edu
Vanderbilt (FELI)	http://www.vanderbilt.edu/fel

Table 4: References for Proposed FELs

PROPOSED FELs	References for Proposed FELs
BESSY (Soft X-ray)	M. Abo-Bakr et. al., Nucl. Inst. and Meth. **A483**, 470 (2002); Tsukuba Mo-P-07,Mo-P-08,We-P-51 (Sept 2003).
Daresbury (4GLS)	M. W. Poole and B. W. J. McNeil, Nucl. Inst. and Meth. **A507**, 489 (2003).
DESY (XFEL)	http://xfel.desy.de
DESY (FLASH)	http://flash.desy.de
Dresden (ELBE)	http://www.fz-rossendorf.de
Dresden (ELBE)	P. Michel et. al., FEL2004 (2004) p. 8, http://www.JACoW.org.
Frascati (COSA)	F. Ciocci et. al., A. Torre, IEEE J.Q.E. **31**, 1242 (1995).
Frascati (SPARC)	A. Renieri et. al., Nucl. Inst. and Meth. **A507**, 507 (2003).
Harima (SUBARU)	S. Miyamoto et. al., Report of the Spring-8 International Workshop on 30 m Long Straight Sections, Kobe, Japan (August 9, 1997).
Italy (SPARX)	A. Renieri et. al., Nucl. Inst. and Meth. **A507**, 507 (2003).
Jlab (UV FEL)	S. Benson et. al., Nucl. Inst. and Meth. **A429**, 27-32 (1999).
MIT (Bates X-Ray FEL)	http://filburt.lns.mit.edu/xfel
Netherlands (TEUFEL)	J. I. M. Botman et. al., Nucl. Inst. and Meth. **A341**, 402 (1994).
Novosibirsk (RTM)	N. G. Gavrilov et. al., Status of Novosibirsk High Power FEL Project, SPIE Proceedings, vol. **2988**, 23 (1997); N. A. Vinokurov et. al., Nucl. Inst. and Meth. **A331**, 3 (1993).
Novosibirsk (RTM1)	V. P. Bolotin et. al., Nucl. Inst. and Meth. **A475**, II-37 (2001).
Pohang (PAL X-FEL)	pal.postech.ac.kr/kor
RIKEN (SPring8 SCSS)	T. Shintake et. al., Nucl. Inst. and Meth. A507, 382 (2003); http://www-xfel.spring8.or.jp
Rocketdyne/Hawaii (FEL)	R. J. Burke et al, Proc. SPIE: Laser Power Beaming, Los Angeles, Jan. 27-28, 1994, Vol **2121**.
Romania (NILPRP)	Proceedings of FEL 2006; www.jacow.org
Shanghai (SDUV-FEL)	Z. T. Zhao et. al, Nucl. Inst. and Meth. **A528**, 591 (2004).
SLAC (LCLS)	M. Cornacchia, Proc. SPIE 2998, 2-14 (1997); LCLS Design Study Report, SLAC R-521 (1998).
Tokyo (FIR-FEL)	H. Koike et. al., Nucl. Inst. and Meth. **A483**, II-15 (2002).
Trieste (FERMI)	C. J. Bocchetta et. al., Nucl. Inst. and Meth. **A507**, 484 (2003); Tsukuba We-P-53 (Sept 2003).

OVERVIEW ON DIAGNOSTICS FOR X- AND XUV-FEL

Bernhard Schmidt*, DESY, Germany.

Abstract

Controlling and optimizing the SASE process of X-FEL and XUV-FEL requires detailed knowledge and information about the parameters of the driving electron beam which are of critical influence on the laser performance. Due to the very high peak current, collective phenomena have to be carefully measured and controlled while integral (projected) parameters are of limited use. This necessitates the development of a variety of diagnostics tools to monitor the electron bunch parameters in detailedness beyond the capabilities of conventional systems. Longitudinal bunch structures can be derived from time domain methods like electro optic techniques or using transverse deflecting RF-structures, and from frequency domain methods using coherent radiation. The paper will report on recent developments with special emphasis on single shot and online monitoring capabilities in this field. Other topics will be new concepts and experience in measuring the projected and time-sliced emittance of the beam, high precision beam position monitors and sub-picosecond beam phase and arrival time monitor systems.

INTRODUCTION

Diagnostics for X- and XUV-FEL is a very wide subject and can not, even rudimentary, be covered in a short conference contribution. This paper therefore concentrates on certain areas which are especially demanding and where new developments can be reported. Photon diagnostics is a separate important issue but is completely omitted here.
Single pass FEL, as they are used for the production of X- and XUV radiation, are challenging machines in terms of beam quality and parameter control. On one side, the lasing process depends more or less exponentially on beam parameters like emittance and peak current, on the other side are these parameters subject to a delicate balance between concurrent externally steered and uncontrolled collective effects. Diagnostics has to measure and to control these beam parameters such that optimum FEL operation is achieved. The feedback between the diagnostic tools measuring the parameters and the steering of the machine spans all time scales from the very slow experienced human advice to ultra fast intra-bunch feedback on the microsecond scale. A region of special importance is the longitudinal phase space, since the FEL operation requires high peak currents with good transverse emittance. All the compression mechanisms used and proposed so far will achieve these conditions only for a fraction of the entire bunch charge and the longitudinal diagnostic has to be sensitive to the parameters of this specific fraction.

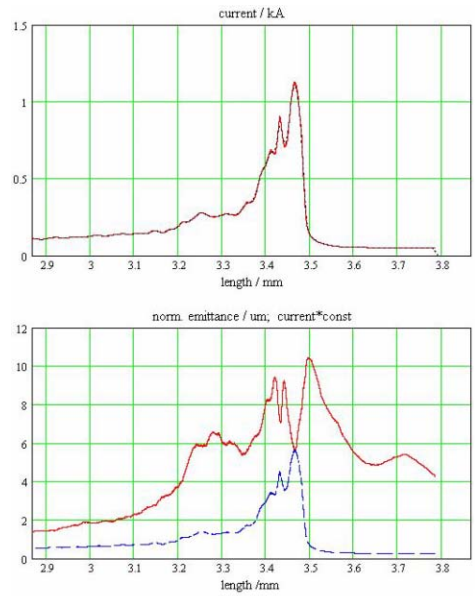

Figure 1: Simulated longitudinal bunch profile and emittance for a non-linear compressor scheme as used in FLASH. The influence of space charge effects and coherent synchrotron radiation on the bunch are included [1].

As an example, Fig. 1 shows the result of a comprehensive simulation of the longitudinal bunch profile and emittance for a non-linear compression scheme as used in FLASH [1]. Collective effects like space charge and coherent synchrotron radiation strongly influence the beam parameters and it becomes obvious, that projected values are of very limited use. Diagnostics has to reveal details of the bunch structure and to do so on a single bunch basis since the collective phenomena are of partially 'chaotic' behavior.

BEAM POSITION MONITORS

SASE FEL are single pass machines and thus the trajectory of the electrons is not stabilized due to periodic boundary conditions. It is subject to shot to shot fluctuations and requires meticulous monitoring along the full lengths of the linac. The requirements on accuracy in the injector and main linac sections are of the order a few tens of micrometer which can be achieved by conventional button or resonant strip-line BPMs which are numerously used as workhorses in existing storage rings. Much higher demands on accuracy have to be faced in the undulators. Ac-

* bernhard.schmidt@desy.de

cording to simulations[2][10] , stable SASE operation at X-ray wavelengths (1 $\mathring{A}$) requires a well defined trajectory which is reproduced with an accuracy of a few micron. This means that undulator BPMs have to work with sub-micrometer resolution and an overall mechanical stability at the same level. The requirements can be met by cavity BMPs which have demonstrated nanometer resolution during prototype studies for the ILC[13] . For LCLS, X-band BPMs are under development at ANL and SLAC[6] while for the European XFEL, C-band structures working at 4.38 GHz are foreseen[7]. These BPMs will be used in a fast intra-bunchtrain feedback system to correct the beam trajectory actively [8]. Besides the monitors itself, maintaining the required mechanical accuracy requires sophisticated alignment tools and procedures for the undulator section; an overview on the status of the plans for LCLS has been given during this conference[3].

Two specialties in the field of beam position monitors should be mentioned here since they comprise new concepts. One idea is to use the beam induced higher order modes (HOM) in super-conducting cavities to derive information on the beam trajectory. The complex amplitude of the various HO modes depends on the transverse location of the trajectory inside the cavities as well as on its inclination with respect to the cavity axis. Accurate measurement of the HOM amplitude pattern therefor allows to derive these values with an accuracy of a few micrometer and μrad. Test measurements at FLASH[9] have shown the feasibility of the method and impressive first results.

The second field to be mentioned are large aperture BPMs to measure the beam position and size inside the dispersive section of the bunch compressors. The aim is to derive accurate information on the mean energy and energy spread of the beam with single bunch resolution. The accuracy required on the transverse beam center is of the order 5 micron for an energy resolution of 10^{-4} while the width of the beam is of the order 50 - 100 mm. An interesting technique which has been studied recently proposes to measure the arrival time of the signals on both ends of a transverse stripline across the compressor beam pipe with an accuracy on the 10 fs scale[4]. The sum of left and right timing provides the information on the transverse center of the charge and thus the mean energy while the timing difference contains information about the width of the distribution and thus the energy spread. The method to derive timing signals from beam pick-ups with fs accuracy will be described in the next section. An alternative method to measure the transverse distribution in the bunch compressors has been successfully investigated at FLASH; it is based on high resolution imaging of the synchrotron radiation in the UV range produced in the bunch compressor dipoles [5].

ARRIVAL TIME (BEAM PHASE) MONITORS

Monitoring the performance of the machine and providing high precision 'time stamps' for the FEL users requires to measure the arrival time of the electron bunches in front of the undulators with fs accuracy. This is well above the capabilities of conventional RF methods and requires either specialized longitudinal diagnostics (see section on electro-optic methods) or a new type of beam phase monitors as proposed in ref.[11]. These monitors use the rather large beam induced signals from conventional button or ring pick-up electrodes to modulate the intensity of a probe laser pulse with electro-optic modulators (based on 'Periodically Poled Lithium Niobate' structures). These modulators combine a bandwidth of several GHz with high sensitivity and allow to detect the zero crossing of the signal with an accuracy of a few femtoseconds. A test set-up at FLASH has demonstrated very promising resolutions recently. Fig. 2 shows the measured time difference between two bunches of the same bunch train at FLASH. The combined effect of real time jitter and resolution of the phase monitor is of the order 50 fs. A potential drawback of the method is, that it measures strictly the 'center of charge' of the bunch and not the actually lasing part. Ideally, the probing laser of the phase monitor is part of an optical timing system of the machine which avoids any additional timing jitter due to RF synchronization.

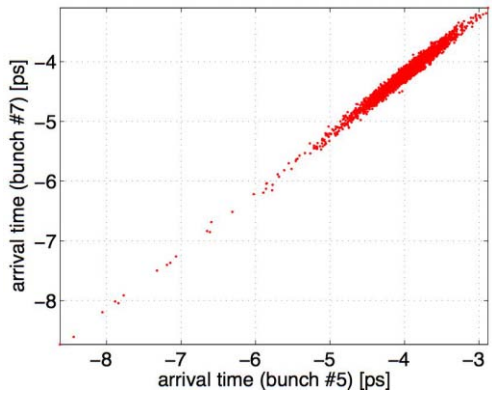

Figure 2: Time difference between two bunches of the same bunch train at FLASH, measured with a phase monitor using electro-optic detection of the zero crossing of a pick-up signal. The combined time jitter and monitor resolution is of the order 50 fs[12].

TRANSVERSE DEFLECTING STRUCTURES

Transverse deflection structures (TDS) are amongst the most powerful and developed tools to measure the phase space distribution of particle bunches. They have been developed at SLAC during the 60th[15] of the last century and used for both, beam separation and diagnostic purposes (e.g. [16]. Operating the deflecting structure close to the zero crossing of the RF, the bunches experience no net deflection but are streaked transversely. Adding a fast transverse kicker allows to send the streaked bunch to an off-

axis screen independent of the streak power. If the transverse deflecting structure is combined with a FODO section, quadrupol scans allows to investigate the slice emittance of the bunches. In combination with a dispersive section, the streaked bunch images the slice energy spread of the beam. All future XFEL projects foresee transverse deflecting structures for diagnostic purposes. In the case of the European XFEL, multiple pairs of TDS are foreseen to allow measurements in both transverse planes at different locations along the injector section. An overview can be found in ref. [17].

For operation at zero crossing, the transverse deflection at the screen Δy depends on the longitudinal position Δz with respect to the center as

$$\Delta y = \Delta z \frac{eV}{E_0} \frac{2\pi}{\lambda_{HF}} \sqrt{\beta_c \beta_s} sin(\Delta\psi) \qquad (1)$$

with V the total deflection Voltage of the cavity, E_0 the beam energy and $\Delta\psi$ the phase advance between cavity center and screen. It depends on both β-functions at the cavity and the screen and since the temporal resolution of the method is determined by the ratio of $\Delta y/\Delta z$ to the unstreaked transverse size of the beam, the optimal optics for the TDS operation demands large β_c and small β_s. This has to be foreseen during the design of the machine and is not necessarily coincident with the optimal optics for FEL operation.

An S-band TDS operating at 2,856 GHz from SLAC (LOLA IV cavity) has been installed at the FLASH linac and is routinely used for beam diagnostic measurements and to develop the TDS method further. At optimized conditions, a streak power of more than $1mm$ per $100fs$ can be achieved which for a nominal beam diameter of $200\mu m$ would lead to a resolution of about $20fs$ (RMS). Under normal FEL operation conditions, the resolution observed is slightly less. The image of a typical, well compressed bunch is shown in Fig. 3, the width of the charge spike at the bunch head is of the order $150fs$ (FWHM). Fig. 4 shows a bunch fragmented by space charge and CSR due to too high compression (notice the difference in time scale compared to Fig. 3).

Scanning quadrupols in front and after the TDS, the slice emittance of the bunches can be measured; a detailed report on recent results has been given at this conference[18]. If the streaked bunch passes a dispersive section in front of the observation screen, the slice energy spread of the bunch can be derived with high accuracy. The example shown in Fig. 5 demonstrates the complex structure of the longitudinal distribution and the strong coupling between ΔE and z. The bunch head clearly has two well separated peaks in phase-space which almost coincide longitudinally. Such observations are in good agreement with start-to-end simulations and emphasise the necessity of powerful diagnostics for a detailed understanding of the machine. The TDS method can be called semi-parasitic since the observed bunches are lost from the FEL process. The read-out speed is limited by the complex imaging required, the information can not be used for fast feed-back systems.

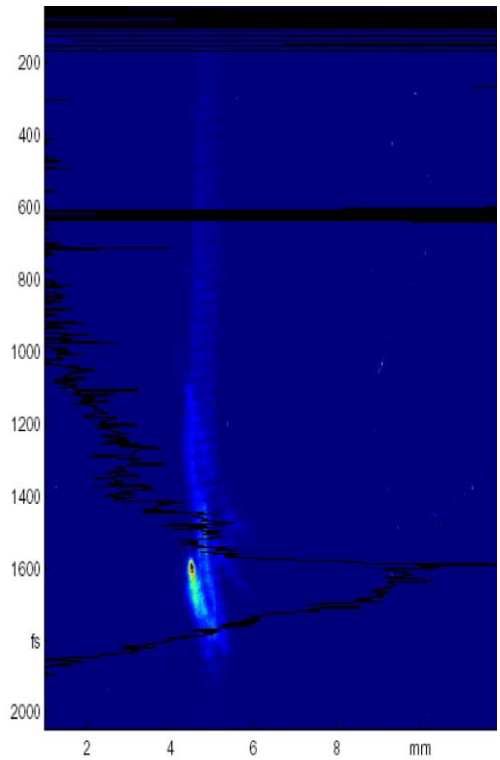

Figure 3: Image of a TDS streaked bunch at FLASH. The phase of the first accelerating module is set such to produce a well formed current peak[14].

ELECTRO OPTIC (EO) METHODS

The longitudinal charge profile of the bunches can be probed by detecting their relativistic Coulomb field by means of electro-optic crystals close to the beam trajectory. The optical properties (namely the birefringence) of the crystals is changed proportional to the electric field strength and the cumulative effect on a co-propagating short laser pulse can be detected. In this way, the temporal (longitudinal) structure of the bunch charge is impressed in a polarization modulation of the optical pulse. An overview on the different methods to decode this information is shown in Fig. 6. The scanning delay method is not single shot and can not be used if the temporal jitter of the mean time of the bunch is comparable or even larger than the length of the bunch. Single-shot EO bunch length measurements were pioneered at FELIX [20] with the spectral decoding method (EOSD), the more recently developed spatial decoding [22] and temporal decoding [23] techniques offer higher resolution at the price of enhanced complexity.

The spectral decoding method is of striking simplicity: the probing pulse is stretched to several ps by applying a linear chirp, that is a correlation between time and 'local' wavelength. The polarization modulation due to the EO effect is translated into an intensity modulation by a

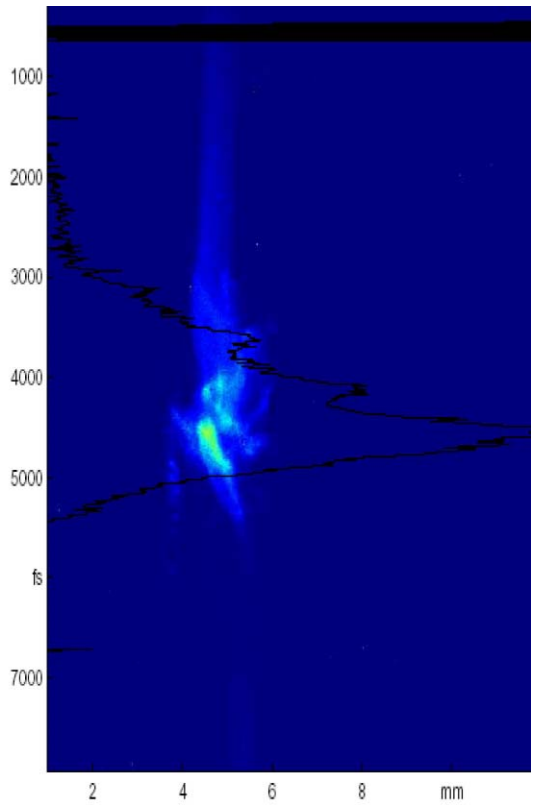

Figure 4: Image of a TDS streaked bunch at FLASH. The phase of the first accelerating module is set too much off-crest, the bunch is strongly distorted by space charge and CSR effects [14].

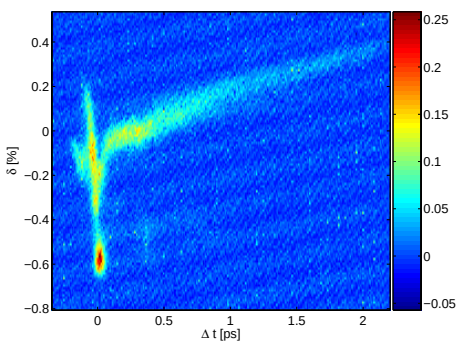

Figure 5: TDS streaked bunch with energy dispersion. The bunch head is contains two separated peaks, less than 100 fs apart and with an energy difference of 0.5 % [18].

set of crossed polarizers, the intensity as function of wavelength, measured with a conventional grating spectrometer, images the longitudinal charge profile. Unfortunately, the method has an intrinsic limitation: the amplitude modulation of the probe pulse creates unavoidably a spectral modulation which mixes with the linear chirp and thus spoils the 'decoding gauge'. For the very fast modulations (that is short pulses), this creates an apparent broadening of the

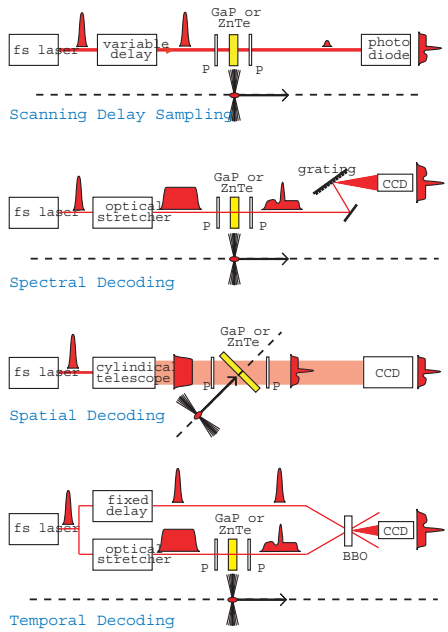

Figure 6: Overview on different methods to decode the temporal information form the laser pulse probing the EO crystal [19].

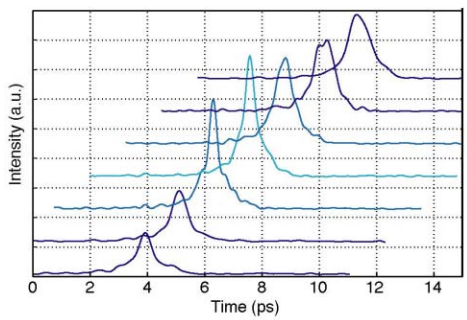

Figure 7: Single shot bunch profiles measured with electro-optic spatial decoding at the SLAC-FFTB using a ZnTe crystal [22].

pulse and even artificial temporal structures. For the typical optical wavelengths of 800 nm and a length of the chirped pulse of a few ps, structures shorter than about 200-300 fs (FWHM) can not be decoded correctly. Nevertheless, the centroid of the bunch can be detected with much higher accuracy (<50 fs) and coarse deterioration (double spikes etc.) can be easily detected. The method has the potential for further developments in the direction to become a routine on-line monitoring system. For that, the expensive and delicate Ti:Sa laser systems used so far have to be replaced by more robust devices (potentially fiber lasers). If the spectroscopy can be done by using a line camera with fast readout, multi-bunch capability can be envisaged for even the 200 ns bunch distance at the European XFEL.

Spatial decoding has been mainly developed at SLAC [22].

The spatially extended short probing laser pulse hits the EO crystal with non-perpendicular incidence, thus a spatial image of the crystal decodes the electric field a different points in time. The method has the great advantage to be free of the intrinsic limits of EOSD but relies on the spatial uniformity of the EO crystal which can be, especially for ZnTe, quite poor. It requires a quite complex optics and imaging system inside the accelerator tunnel but can operate with rather modest laser energy. Fig. 7 shows a result obtained at SLAC using a ZnTe crystal, the resolution of $270fs$ achieved is close to the limit for this material. At FLASH, a similar set up using GaP is installed and resolutions of the order $120fs$ have been demonstrated[21].

Temporal decoding is the most powerful and most complex EO method developed so far. The short laser pulse is split in two halves, one is chirped to a length covering the length of the electron bunch and passes the EO crystal in the beam line. The other one is kept short. The polarization modulation is transferred to an intensity modulation in the usual way, after that the probing pulse hits a non-linear crystal (SHG). There it is merged under a certain angle of inclination with the short 'gate' pulse from the same origin. In the SHG crystal, a second harmonic component is created proportional to the product of both laser intensities, leaving the crystal in a direction well separated from the two incoming components. The temporal information thus is decoded by optical cross correlation as shown in Fig. 8 schematically. Since a non-linear optical process is involved, the method requires much higher laser power (mJ) and thus a complex and expensive laser amplifier system. On the other hand, the method has demonstrated the best resolution so far. At an installation at FLASH, spike widths of the order 100 fs (FWHM) have been measured in good agreement with TDS data recorded simultaneously (Fig. 9).

Single-shot electro-optic diagnostic techniques are rather mature as experiments meanwhile but still in an infant state as routine operation tools. Since they are totally non-destructive and can be applied to any bunch, it is worthwhile to spend considerable efforts to overcome the technical problems to make them more robust an usable as continuously running monitoring tools. The development of optical synchronization systems makes them even more attractive, since they can be directly coupled to them by means of optical synchronization, avoiding any additional jitter introduced by RF components. They are ideal candidates to provide not only detailed information about the bunch structure online but as well to act as extremely precise bunch arrival time monitors and time stamp generators for pump-probe experiments.

COHERENT RADIATION DIAGNOSTICS

The relativistic electrons of the bunches radiate electromagnetic waves whenever their Coulomb field is subjected to changes: synchrotron radiation due to directional changes in the bending sections or transition and diffraction radiation if the field enters regions of changing dielectric

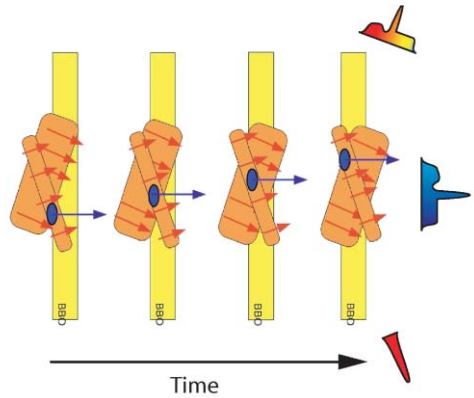

Figure 8: Temporal decoding of the intensity modulation of the probe pulse by spatial cross correlation in a second harmonic (SHG) crystal.

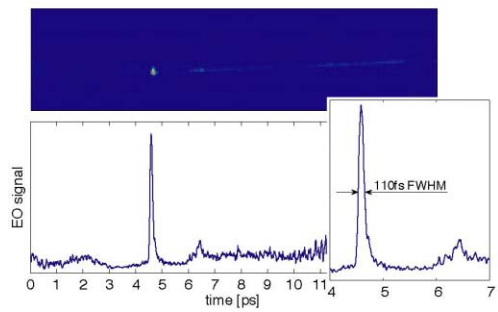

Figure 9: Longitudinal bunch profile measured at FLASH with the electro-optic temporal decoding technique using a 100μm thick GaP crystal [24].

properties. For wavelengths of the radiation longer than the distance of two electrons, these electrons radiate 'in phase' or coherently, the intensity of this coherent radiation scales with the square of the number of contributing electrons and can be a massive effect. More precisely, the radiated power per frequency interval can be written as

$$\frac{dU}{d\omega} \propto N^2 |F_{long}(\omega)|^2 T(\omega, \gamma, r_b, \Theta, source) \qquad (2)$$

with

$$F_{long}(\omega) = \int_{-\infty}^{\infty} \rho(t) exp(-i\omega t) dt \qquad (3)$$

F_{long} is the longitudinal form factor of the bunch, the Fourier transform of the longitudinal charge distribution and T summarizes all other, potentially complex, properties of the radiation source.

The most popular application of coherent radiation diagnostics is to measure a global intensity of the radiation integrating over a certain (normally large) range of frequencies and use the signal strength as an index for the shortness (the 'compression') of the bunch. It should be kept in mind that the information on the bunch length obtained that way is restricted to the wavelength range

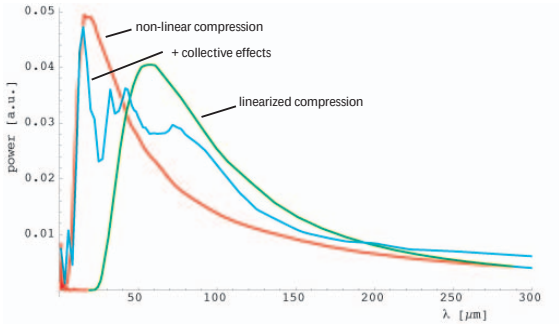

Figure 10: Simulated wavelength spectra of coherent transition radiation for two compression schemes without space charge and CSR effects and for an example of non-linear compression including space charge and CSR effect (data courtesy M. Dohlus).

covered by the radiation detector. If the coherent radiation intensity is observed spectrally resolved, information about the longitudinal form factor and thus the charge distribution can be obtained. For the typical bunch lengths between 10 fs and 100 fs contributing to the FEL process, the corresponding range of wavelengths is in the far infrared from 10 μm to 300 μm. As shown in Fig. 10, the wavelength spectra of coherent transition radiation from ideally compressed electron bunches strongly peak in the region below 200 μm, the position of the intensity maximum directly reflects the length of the current spike[1]. If the bunch is distorted by collective effects, the wavelength spectrum exhibits characteristic substructures which could be used to get information on the strength and nature of the collective phenomena. Despite the fact that a direct reconstruction of the bunch shape from radiation spectra is impossible due to the missing phase information, the wavelength spectra reveal sufficient information to act as 'fingerprints' of the longitudinal bunch structure.

The wavelength range of interest puts a few stringent boundary conditions to the experimental set up: conventional crystalline quartz windows are not transparent for wavelength shorter than about 80 μm and humid air absorbs below 300 μm even over short distances substantially. In consequence, the radiation has to be coupled out of the beam pipe by using a CVD diamond window and the entire coherent radiation set up has to be evacuated or flushed with a dry gas. Conventional IR spectrometers used so far in bunch length diagnostics are Michelson type interferometers measuring the autocorrelation function of the radiation. This method is intrinsically not single shot capable and the information has to be derived in a complex de-convolution process. Recently, a new type of spectrograph has been proposed[25] and assembled which is able to measure wavelength spectra over a sufficiently large range on a single shot basis. The central elements are gratings as dispersive elements and a multichannel detector with fast read out. In a first step, a set of reflective blazed

[1]For a Gaussian bunch, the position of the intensity maximum in wavelength space depends linearly on the temporal width of the bunch

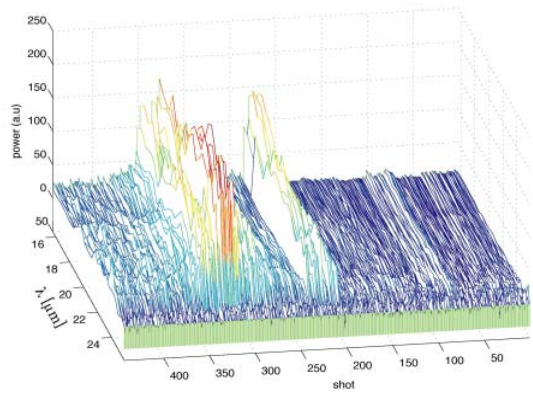

Figure 11: A set of successively recorded single shot spectra in the wavelength range 16-26 μm from coherent transition radiation at FLASH. While recording from right to left, the off-crest phase of the first accelerating module was scanned from zero to about -8 degrees.

gratings has been used to separate different wave length bands and to detect them with single element pyro-electric sensors. Such a device can be used as 'advanced bunch compression monitor' which is much more sensitive to the actually lasing part of the bunch than conventional integrating devices. It has been tested at the THz beam line[28] of FLASH using coherent transition radiation and proven capabilities. More details can be found in ref. [**?**].

The development of a 30 channel fast read out pyro-electric sensor at DESY[29] made it possible to record coherent radiation spectra for single shots online. The device has a sensitivity of about 300 pJ per channel (5σ noise-level) and is almost free of disturbing 'etalon' resonances in the sensitivity in the interesting wavelength range from 1 μm to $1mm$. For this, newly designed pyro-electric sensors have been developed together with industry. The device has been used together with transmission gratings and reflective gratings for fist online single-shot spectroscopy at the FLASH THz beamline[2]. As an example, Fig. 11 shows a set of successively recorded spectra in the range of 16-26 μm while the phase of the first accelerating module was scanned over 8 degrees[27]. Radiation in this wavelength range is produced in two (probably three) narrow regimes of the off-crest phase. One of them is usually used for FEL operation. In contrast to this, fig. 12 shows the equivalent scan for very short wavelengths between 5 μm and 8 μm. No such pronounced bands are seen, the intensity pattern fluctuates from shot to shot and the overall intensity increases with larger off-crest phase angles. This is a very clear indication for micro-bunching on a few femtosecond scale.

Single shot coherent spectroscopy has made a step forward but still to prove its benefits for bunch profile diagnostics and online monitoring. Transmission gratings

[2]The evacuated beamline images transition or diffraction radiation from an off-axis screen over a distance of 20m to outside the linac tunnel. A fast kicker is used to kick individual bunches to the screen, thus the measurements can run in parallel to normal FEL operation.

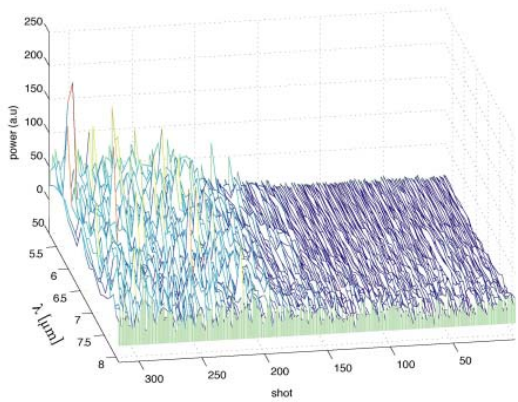

Figure 12: A set of successively recorded single shot spectra in the wavelength range 5-8 μm from coherent transition radiation at FLASH. While recording from right to left, the off-crest phase of the first accelerating module was scanned from zero to about -8 degrees.

offer a wider spectral range but can not reach the shortest wavelengths, reflective gratings span only about one octave in wavelength but have higher efficiency and are available down to the UV region. The natural next step is to 'stage' several reflective gratings with a final transmission grating to span the full range of interest simultaneously. Equipped with fast read-out, these devices can be used even for fast feedback systems.

SUMMARY

Diagnostics for XUV and XFEL requires a variety of new developments on various fields to cope with the very demanding challenges of these machines. Considerable progress has been made during the past years for beam position monitors and especially on the field of longitudinal phase space diagnostics and arrival time monitors. But most of the new methods are still not mature and more or less far from being applicable as routine online tool to control and steer the machine. This is a reach and challenging field for the next years. On top of this, even more sophisticated techniques like the "optical replica synthesizer" are on their way to be explored [30][31].

REFERENCES

[1] M. Dohlus, "Modeling of Space Charge and CSR Effects in Bunch Compressor Systems", Proceedings EPAC2006, MOPCH015.

[2] W. Decking, X-FEL Project Team at DESY, private communication.

[3] H.D. Nuhn, "Electron Beam Alignment Strategy in the LCLS Undulators", Proceedings FEL06, THBAU02.

[4] K.E.Hacker et al., "Large Aperture BPM for use in Dispersive Regions of Magnetic Chicanes", Proceedings FEL06, TUPPH054.

[5] C.Gerth, "On-line Energy Spread Measurements Using Synchrotron Radiation in the Bunch Compressors at FLASH", Proceedings FEL06, THPPH011.

[6] R.M.Lill et al., "Linac Coherent Light Source (LCLS) Undulator BPM System", FEL06, THPPH054.

[7] D. Noelle et al., "First Ideas for the XFEL BPM System", FEL06, THPPH014.

[8] B. Keil et al., "An Intra Bunch Train Feedback System for the European XFEL", Proceedings FLS06, WG521.

[9] J. Frisch et al.,"High Precision SC Cavity Alignment Diagnostics with HOM Measurements", Proceedings EPAC06, TUYPA02.

[10] J. Wu and P. Emma, "Trajectory Stability Modeling and Tolerances in the LCLS",Proceedings EPAC06, MOPCH049.

[11] F. Loehl et al. , "A Sub 100 fs Electron Bunch Arrival-time Monitor System for the VUV-FEL", Proceedings EPAC06, THOBFI01.

[12] F. Loehl , private communication.

[13] S. Walston et al., "Performance of a Nanometer Resolution BPM System", Proceedings EPAC06, TUPCH105.

[14] courtesy Holger Schlarb, DESY.

[15] O.H. Altenmueller, R.R. Larsen and G.A. Loew, "Investigation of Traveling-Wave Separators for the Stanford Two-Mile Linear Accelerator", The Review of Scientific Instruments, Vol. 35, Number 3, April 1964.

[16] R. Akre, L. Bentson, P. Emma and P. Krejcik, "Transverse RF Deflecting Structure or Bunch Length and Phase Space Diagnostics", Proceedings PAC 2001, p. 2353.

[17] C. Gerth, M.Roehrs and H. Schlarb, "Layout of the Diagnostic Sections for Emittance and Energy Spread Measurements at teh European XFEL", Proceedings FEL06, THPPH010.

[18] C. Gerth, M.Roehrs and H. Schlarb, "Investigations of the Longitudinal Electron Bunch Structure at the FLASH Linac with a transverse deflecting RF-Waveguide.", Proceedings FEL06, TUBAU06.

[19] S.P. Jamison et al., "Femtosecond bunch length measurements", Proceedings EPAC2006, TUYPA01.

[20] I. Willke et al., "Single-shot electron-beam bunch length measurements", Phys. Rev. Lett. 88, 124801, 2002.

[21] H. Schlarb et al., "Comparative Study of Bunch length and Arrival Time Measurements at FLASH", Proceedings EPAC2006, TUPCH024.

[22] A.L. Cavalieri et al., "Clocking Femtosecond X Rays", Phys. Rev. Lett. 94, 114801 (2005).

[23] G. Berden et al., "Electro-optic techniques with improved time resolution for realtime, nondestructive single-shot measurements of femtosecond electron bunch profiles", Phys. Rev. Lett. 93, 114802, 2004.

[24] B. Steffen at al. , "Single Shot Longitudinal Bunch Profile Measurements at FLASH using Electro-Optic Techniques", Proceedings EPAC2006, TUPCH026.

[25] H. Delsim-Hashemi et al., "Broadband Single Shot Spectrometer", Proceedings FEL2005, THPP029.

[26] H. Delsim-Hashemi et al., "Bunch Compression Monitor", Proceedings EPAC2006, MOPTH016.

[27] H. Delsim-Hashemi et al., ”Single-Shot Longitudinal Diagnostics with THz radiation at the Free-Electron Laser FLASH”, Proceedings FEL2006, THPPH018.

[28] S. Casalbuoni et al., ”Far-infrared transition and diffraction radiation Part II: the Thz beamline at the VUV-FEL linac”, TESLA FEL 2006-04.

[29] B. Schmidt et al. , ”A 30 channel pyro-electric line detector with MHz read out for mid and far infrared detection”, in preparation.

[30] E. Saldin et al. , ”A simple method for the determination of the structure of ultrashort relativistic electron bunches”, Nucl. Instr. Methods A 539, 499 (2005).

[31] P. van der Meulen et al. , ”Technical aspects of the Integration of the Optical Replica Synthesizer for the Diagnostics of Ultra-short Bunches into FLASH at DESY”, Proceedings FEL2006, TUBAU05.

LOW EMITTANCE INJECTOR AT SCSS

Hitoshi Tanaka*,A,B), Kazuaki Togawa[A)], Hitoshi Baba[A)], Toru Hara[A,B)], Atsushi Higashiya[A)], Takahiro Inagaki[A)], Hirokazu Maesaka[A)], Hiroshi Matsumoto[B,C)], Kazuyuki Onoe[A)], Yuji Otake[A)], Katsutoshi Shirasawa[A)], Takashi Tanaka[A,B)], Takanori Tanikawa[A)], Makina Yabashi[A,B)], Tsumoru Shintake[A)],

A) RIKEN/SPring-8, 1-1-1, Kouto, Sayo, Hyogo, 679-5148, Japan
B) JASRI/SPring-8, 1-1-1, Kouto, Sayo, Hyogo, 679-5198, Japan
C) KEK, 1-1, Oho, Tsukuba, Ibaraki, 305-0801, Japan.

Abstract

The SPring-8 compact SASE source (SCSS) project aims at SASE-based FEL at wavelength region of 1 angstrom. To generate a high quality electron beam, a low emittance injector comprising of a 500 kV pulsed electron gun, beam deflector and three-stage velocity bunching process has been investigated [1, 2]. To confirm beam performance of the injector, the SCSS prototype accelerator with the identical injector system was constructed [3]. Via beam tuning of the prototype accelerator over half a year, the first stage beam commissioning was completed successfully and SASE at wavelength of about 50 nm was observed in June 20th, 2006 [3]. The analysis of experimental SASE data predicts that essential beam quality, i.e., "effective electron beam brilliance" reaches to the target value, 200 $A/\pi^2 mm^2 \cdot mrad^2$. In this paper, we describe the injector design of the SCSS prototype accelerator and show the achieved beam performance.

INTRODUCTION

In order to achieve SASE-based x-ray FEL, normalized slice emittance of ~1 πmm.mrad is required with a high peak current of a few kA. For this purpose, it has been believed that a photo-cathode RF electron gun (RF-gun) based system is the most promising. The RF-gun based system has been thus adopted as the injector for the LCLS [4] and XFEL [5] projects.

In the SCSS project, we however took a different approach to this problem. A conventional technology-based injector, which comprises of a pulsed electron gun with a thermionic-cathode, a beam deflector and three-stage velocity bunching process was chosen [1, 2]. This choice is due to potentiality achieving simultaneously high stability and tunability, which are critically important for realization of "stable" x-ray FEL. This injector system is free from the dark current from the cathode, which could be a serious problem in the RF-gun based system.

In the SCSS injector system, basic functions on beam handling such as emission of electrons, beam pulse processing, beam acceleration and bunch compression are separated. Machine parameters in each function are thus adjustable independently, which assures wide tunability in operation. This is an advantage when compared to the RF-gun based system, where these functions are tightly coupled. Furthermore, the RF-gun based system has to use a state of the art laser system to extract electrons from the cathode, which may cause instability in the initial beam condition.

Although the SCSS injector system has an advantage on the electron beam stability and operation tunability, there remains the question whether "emittance conservation" through the injector is a sufficient level or not under the practical error condition. To reply this, in other words, to confirm beam performance of the injector and investigate hidden problems in operation, the SCSS prototype accelerator was constructed and has been tested.

OUTLINE OF INJECTOR SYETEM

Figure 1 shows the schematic view of the injector system of the SCSS prototype accelerator. Since the SCSS injector is basically the same as that of the prototype accelerator, we explain beam handling over the injector by using Fig. 1.

Electron beams are extracted from the single crystal CeB_6 cathode by a 500 kV pulse voltage (1 in Fig. 1) [6]. The repetition rate is 60 Hz at most and the electron pulse width is about 2 μsec. The theoretical thermal emittance is 0.4 πmm.mrad. The initial beam energy is 500 keV and peak current is 1 A.

The developed beam deflector (2 in Fig. 1) cuts out about 1 nsec short pulse from the extracted beam. Due to the fast rising and falling time of the deflector electric field, 1 nsec beam pulse has a beam tail of about 100 psec, in front of and behind the beam. The deflector has a collimator with a hole of which diameter is 5 mm and the beam is collimated into a cylindrical shape with a transversally hard edge.

Owing to the high beam energy of 500 keV, a conventional solenoid coil, which covers a wide beam path, is unnecessary. Instead of the solenoid, a special magnetic lens, where the solenoid coil is covered by an iron york, has been developed (3 in Fig. 1). This magnetic lens has two significant advantages: (1) Due to the localized focusing field, three functions, beam focusing, beam acceleration and bunch compression can be separated. (2) Due to the properly large aperture, nonlinear fringe fields are suppressed enough to avoid the

* E-mail: tanaka@spring8.or.jp

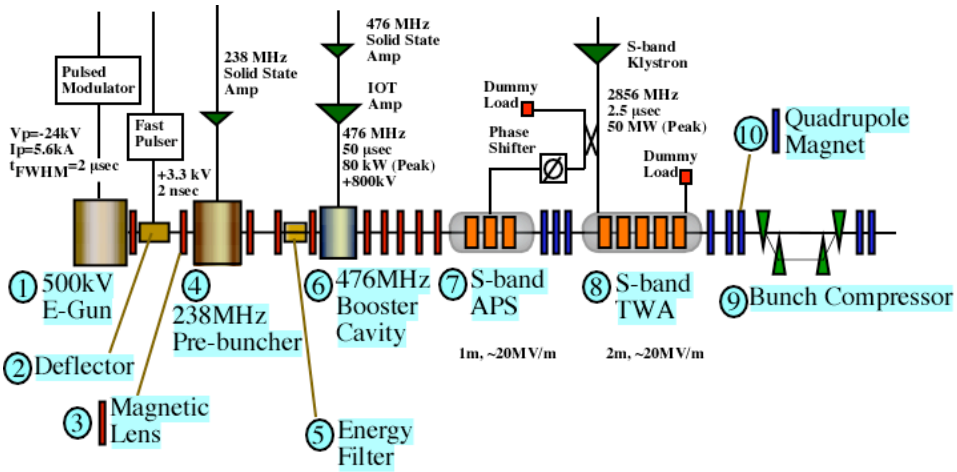

Fig. 1: Schematic drawing of SCSS injector system.

emittance growth. The former advantage is quite important for precise beam tuning.

The cylindrical beam with the pulse width of 1 nsec receives energy modulation, about 400 keV in a peak-to-peak value, in the 238 MHz pre-buncher (4 in Fig. 1). The energy modulated beam develops the density modulation when passing through a 1.6 m drift section. The energy filter (5 in Fig. 1) is now not used. In front of the booster, the average beam energy is ~0.43 MeV and the peak current reaches to 5 A (~200 ps). Then, in the 476 MHz booster cavity (6 in Fig. 1), the beam energy is boosted up to ~1 MeV to suppress the space charge effect and to linearlize the velocity gradient. In the velocity bunching process, both the voltage and phase of the two cavities are crucial for the bunching performance. Structures of both cavities were therefore carefully designed so that the frequency and gap-voltage are not sensitive against a vibration and temperature change. The peak current increases up to 50 A (~10 ps) while the 1 MeV electron beam flights over 1.3 m from the booster to the first S-band acceleration tube (7 in Fig. 1).

The energy of the electron beam is boosted by the two S-band accelerating tubes (7 and 8 in Fig. 1) up to ~41 MeV with the design bunching phase and up to~50 MeV with the crest phase. To suppress the emittance growth due to the symmetry-break of the first acceleration tube, APS structure was adopted. The velocity bunching process completes by the end of the first tube, where the peak current reaches to ~80 A (~6 ps).

Downstream of the first S-band accelerator tube, the beam energy is higher than 10 MeV and a quadrupole magnet (10 in Fig. 1) is used to focus the beam instead of the magnetic lens.

In the SCSS prototype accelerator, the beam is further compressed for SASE experiments by the bunch compressor, which comprises of four identical rectangular magnets (10 in Fig. 1). The deflecting angle is 0.1 rad and the maximum linear dispersion is about 110 mm. After the bunch compression, the peak current reaches to ~800 A (~0.7 ps).

The injector system is divided into three main parts, the electron gun, the beam deflector and three-stage velocity bunching process. Details of each part are described in the following three sections.

500 KV PULSED ELECTRON GUN

To constantly obtain low emittance electron beam with high beam current of 1~3 A, the electron gun was significantly improved from conventional electron guns. Table 1 lists the main electron gun parameters and Fig. 2 shows the CeB_6 cathode assembly (left) and the cathode being heated in the test chamber. The major improvements are:

- A small sized single crystal CeB_6, of which diameter is 3mm, was used as a cathode.
- The control grid was removed from the cathode, because the grid increases beam emittance by distorting the electric field.
- The gun voltage was raised up to 500 kV to suppress a space charge effect and remove troublesome solenoid coils.
- The cathode was stably heated up to high temperature as 1400~1600 deg.C by use of graphite heater.

Table 1: Gun Parameters

Beam Energy	500 keV
Peak Current	1~3A
Pulse Width (FWHM)	2 μsec
Repetition Rate	60 Hz
Cathode Temperature	1400~1600 deg.C
Cathode Diameter	3mm
Theoretical Thermal Emittance (rms)	0.4 πmm.mrad
Measured Normalized Emittance (rms, 90% particles)	0.6 πmm.mrad [7]

- The graphite sleeve surrounding the cathode was adopted to reduce beam halo.
- The flat Wehnelt was used as the anode to reduce emittance growth and to enlarge dynamic range of the peak current.

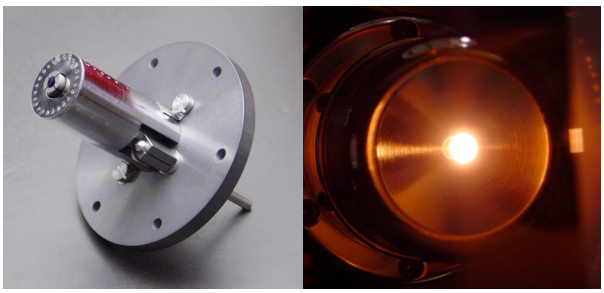

Fig. 2: Cathode assembly (left) and heated cathode (right).

BEAM DEFLECTOR

Since the control grid was removed from the developed electron gun to suppress beam emittance growth, beam deflector, which cuts out a 1nsec short pulse from the long one, is indispensable for the SCSS injector system. Figure 3 shows the principle of the beam deflector. The deflector comprises of two parallel electrode plates and one steering coil. The coil generates a DC magnetic field in the horizontal plane, which deflects the beam vertically and dumps it by using the narrow physical aperture as shown in the figure. The short pulsed electric field in the vertical plane, which cancels out the vertical kick by the DC magnetic field, achieves gating of ~1 nsec. The driving pulse has a fast rising and falling time, ~200 psec, which can generate a well-edged electron beam with a short tail. The flatness of the pulsed electric fields at the flat top determines the emittance degradation in the deflector. Hence, to achieve the sufficient field quality, impedance matching was fully considered in the design of the electric circuit and the parallel electrode plates including the casing chamber.

THREE-STAGE VELOCITY BUNCHING

The SCSS injector starts beam compression from the low beam energy of a 500 keV and reduces the bunch

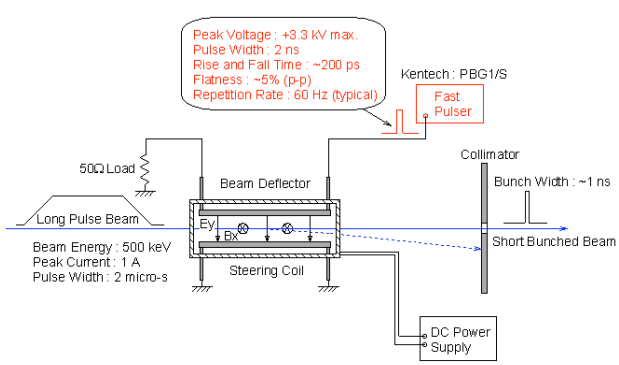

Fig. 3: Schematic drawing of beam deflector.

length by a several hundredth as the energy increases up to a few tens MeV. In the design of the SCSS injector, it is thus important to suppress emittance growth caused by a space charge force. On the other hand, the high compression ratio, higher than hundred, is required. Hence, handling of nonlinearity in the compression process is important.

Suppression of Emittance Growth

Assuming that the beam transverse shape is round and hard-edged and all electro-magnetic potentials are axial-symmetric, equation of motion under a space charge force is described in a cylindrical coordinate by [8]

$$r'' + \frac{\gamma'}{\beta^2\gamma} r' + \frac{\gamma''}{2\beta^2\gamma} r + \left(\frac{qB}{2m_0 c\beta\gamma}\right)^2 r - \left(\frac{p_\theta}{m_0 c\beta\gamma}\right)^2 \frac{1}{r^3} - \frac{2I}{(\beta\gamma)^3 I_A} \frac{r}{r_m^2} = 0, \quad (1)$$

where r, β, γ, B, p_θ, I, I_A and r_m are the electron radius, relative velocity, relative energy, longitudinal magnetic field, azimuthal momentum, peak current and Alfven current, respectively. The last term in L.H.S. shows the space charge force acting on the electron beam, suggesting that the guideline on the bunch compression is the ratio of γ^3. For example, when γ increases from 1 to 2, criterion on the compression ratio is $(2/1)^3=8$. This idea was first proposed by T. Shintake [1].

The bunch compression in the SCSS prototype accelerator however, apparently exceeds the above guideline and the simulation code, PARMELA predicts that the emittance growth is larger than that in 8-GeV SCSS. Because the injector parameters of the prototype accelerator were optimized not for SASE in wavelength region of 1 angstrom, but for in VUV region under the limited boundary condition, the peak current rather than the slice emittance was pursued. In the 8-GeV SCSS design, RF parameters, especially the RF voltage of 238 MHz pre-buncher will be re-optimized and the use of L-band accelerators instead of the S-band (7 and 8 in Fig. 1) is under investigation.

Nonlinearity Handling

To achieve the high compression ratio, suppression of nonlinearity in the bunch compression process, which originates from a RF voltage and velocity dependence on relative energy of the beam, is the key. For the simple system comprising of a RF potential, drift space and initially mono-energetic beam, the condition achieving the linear velocity distribution against time can be easily solved by neglecting a space charge force and expressed using only three parameters: an initial beam energy, peak RF voltage and RF phase. By using 500 keV and 209 kV as the initial beam energy and peak RF voltage of the pre-buncher, respectively, the linear distribution is obtained at about -125 deg. from the crest phase. Since the injector of the prototype accelerator has the 476 MHz booster cavity downstream of the pre-buncher, the condition for the

linear distribution becomes more complicated at the exit of the booster, i.e., it also depends on the booster parameters. Figure 4 shows the velocity distribution dependence on RF phase of the pre-buncher behind the booster, which was calculated with the injector parameters of the prototype accelerator. In this case the phase between -100 and -120 deg. is found to be optimum. In consideration of the experimental results obtained at the prototype accelerator, all the parameters relating to the three-stage velocity bunching process have been re-investigated.

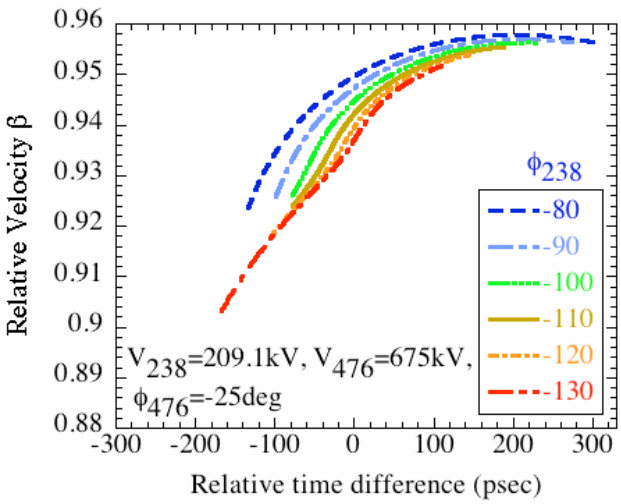

Fig. 4: Velocity distribution dependence on RF phase of the pre-buncher behind the booster calculated with the injector parameters of the prototype accelerator.

SCSS PROTOTYPE ACCELERATOR

The SCSS prototype accelerator comprises of the low emittance injector, bunch compressor with a magnetic chicane, C-band acceleration system, and two in-vacuum undulators as shown in Fig. 5. To verify the injector capability providing the high quality electron beam, the design target of the normalized slice emittance and peak current was set at 2 πmm.mrad and 800 A, respectively. Attainment of the target confirms that the beam performance for x-ray FEL is reachable by smooth extension of the prototype accelerator. And also, the target performance is enough for SASE lasing at wavelength of 40 ~ 60 nm.

Since both the injector and bunch compressor were already described in the previous sections (see Fig. 1), we start a brief explanation of the prototype accelerator from the C-band acceleration system. The system is divided into two acceleration units. Each unit has two 1.8 m-long choke-mode type traveling wave acceleration (TWA) tubes [9] driven by a 3/4π mode. Each unit has one 50MW C-band klystron. The RF power from the klystron is boosted up by a factor of 3.4 by the RF pulse compressor and equally fed to the two acceleration tubes. In the prototype accelerator, different compressors, SKIP [10] and SLED [11] were adopted for the first and second units, respectively, to compare the performance of the two compressors. The nominal accelerating field gradient is about 30 MV/m when the beam is accelerated at the crest phase and in this operating condition RF power fed to each acceleration tube is 46 MW on average of 300 nsec filling time.

The undulator part is divided into two identical in-vacuum undulators of 4.5 m. The permanent magnet material is NdFeB and magnet structure is a 45-deg. tilted Halbach type [12]. Minimum, nominal and fully opened gaps are 2, 3 and 25 mm, respectively. At the minimum (nominal) gap K-value reaches to about 1.8 (1.3) and the wavelength of the first harmonic is about 80 (60) nm with the beam energy of 250 MeV. The period length is 15 mm and the number of periods is 300 per undulator. To keep a small beam size in the horizontal plane, one focusing quadrupole locates between two undulators. In front of the first undulator, a magnet chicane is installed to protect the undulator permanent magnets from accidental electron bombardments and dark currents from the C-band accelerators.

The symbol "M" in Fig. 5 shows a chamber port for a usual beam profile measurement with fluorescence and optical transition radiation. In the beam tuning, these ports are also used to measure a longitudinal beam density distribution by using coherent transition radiation because evolution of the longitudinal distribution is quite important for setting RF parameters in the velocity bunching process. The symbol "S" shows a transverse beam slit to collimate the beam in energy and transverse space.

TUNING STRATEGY OF SCSS PROTOTYPE ACCELERATOR

In the beam tuning, the following points were well considered, because there is no diagnostics to measure the slice emittance directly.

(1) Suppression of slice emittance growth by a space charge force: Over-focusing of the beam causes the emittance growth by a space charge force and hence, it is important to tune the real beam envelope same as the calculation. To this end, initial condition of the real beam from the electron gun should be fixed. We made series of systematic measurements on the beam profiles by changing strengths of the plural magnetic lenses one by one without RF power of both the 238 MHz pre-buncher and 476 MHz booster. By analyzing the data, the virtual beam source was thus determined for the prototype accelerator.

(2) Suppression of slice emittance growth by over-bunching: RF voltage and phase were calibrated and set based on the real beam response for the pre-buncher, booster and S-band accelerators. As the beam response, dependences of the bunch compression on these two parameters were measured. The measurements were performed with the developed microwave spectrometer and the detection system combining the wide frequency band diode detector [13] with a high-pass mesh filter. For

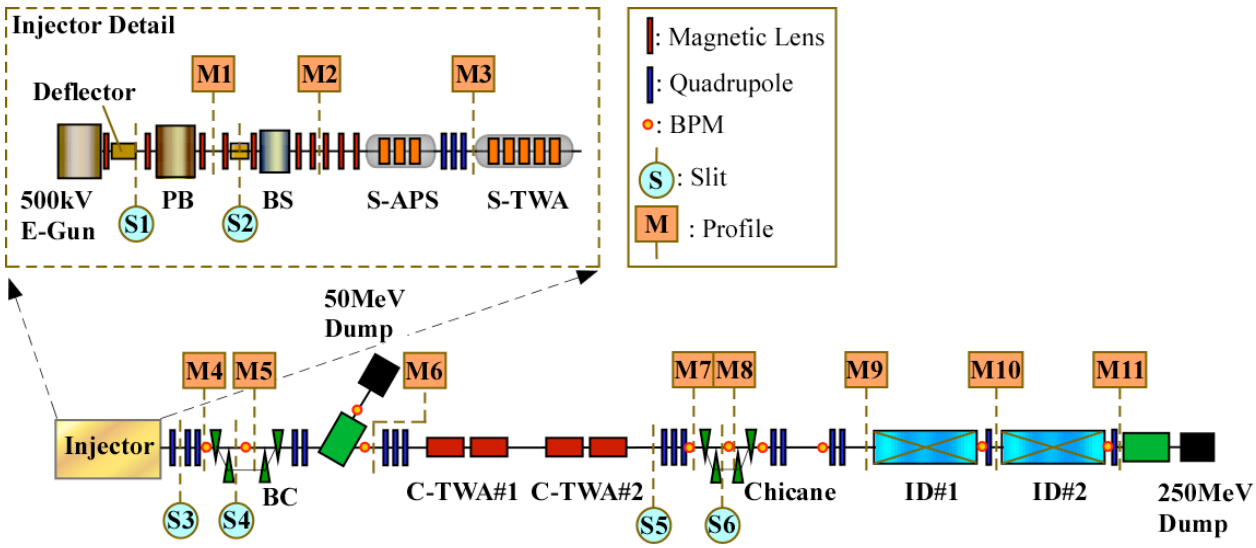

Fig. 5: Schematic drawing of SCSS prototype accelerator.

the crest phase detection, we used the following three methods depending on the condition; beam induced field method [14], the method based on the maximum beam transmission and the method based on the maximum displacement at the dispersive section.

(3) Suppression of slice emittance growth by nonlinear fields: Nonlinear fields at both fringes of the magnetic lenses and RF cavities increase the slice emittance. To suppress this growth, electron beam centering to each device is important. We centered the beam on each device by dithering, i.e., by observing the beam responses against the current and acceleration phase modulation.

(4) Confirmation of slice emittance: Condition of the transverse phase space was indirectly confirmed by comparing the measured data with the simulated ones. For the comparison, five beam profiles upstream of the C-band acceleration system and three kinds of projected emittance were used.

EXPERIMENTAL RESULTS OBTAINED AT SCSS PROTOTYPE ACCELERATOR

In this section, we summarize the obtained results, i.e., the projected emittance, bunch length, dark current, stability and electron beam brilliance.

Projected emittance

The projected emittance values were measured under the following three conditions: (1) 500 keV beam with the pulse-width of 1nsec after the beam deflector (M2 in Fig. 5), (2) 50 MeV beam accelerated at the crest phase of the S-band TWA tube (M6 in Fig. 5), and (3) 250 MeV beam accelerated at the bunching phase (crest -30 deg.) of the S-band TWA tube and at the crest phase of the C-band TWA tubes (M9 in Fig. 5). The emittance of condition (1) was estimated from the beam size and angular divergence measured by the horizontal slit scan. On the other hand, the emittance of the conditions (2) and (3) were estimated by a conventional Q-scan method. Table 2 lists the estimated emittance values together with the calculated ones. The measured emittance of the long pulse beam emitted from the electron gun is also shown. Comparing the emittance values with and without the deflector, we see that the emittance growth by the deflector is not significant. We also see that the estimated values have good agreement with the calculation at the beam energy of 50 and 250 MeV.

Fig. 6 shows the beam size dependences obtained by the Q-scan method at the beam energy of 50 MeV. Each point represents the average of 10 data. The solid and dashed lines represent the fitting curves of which form is determined by linear beam theory. Since scattering of 10 data is smaller than the radius of the plotted circles, it was neglected in the figure. The error bar represents 1σ of a fitting error. We see that the all data points over the wide range of the focusing strength are well fitted by the parabolic curve. These facts show that the electron beam is stable enough for this kind of measurement.

Bunch length

Bunch length was measured with a femto-second streak camera (Hamamatsu Photonics FESCA-200, temporal resolution of 200 fs). Cherenkov radiation from conically shaped BK7 glass was observed for the 41MeV electron beam and optical transition radiation (OTR) from an Au

Table 2: Estimation of normalized emittance

Beam Energy [MeV]	Norm.Emittance (ε_x, ε_y) [πmm.mrad]	Calculation (ε_x, ε_y) [πmm.mrad]
0.5(bef.deflector)	(0.6, -)	-
0.5(aft.deflector)	(1, -)	-
50	(3, 3)	(2.8, 2.6)
250	(4, 2)	(2.3, 2.3)

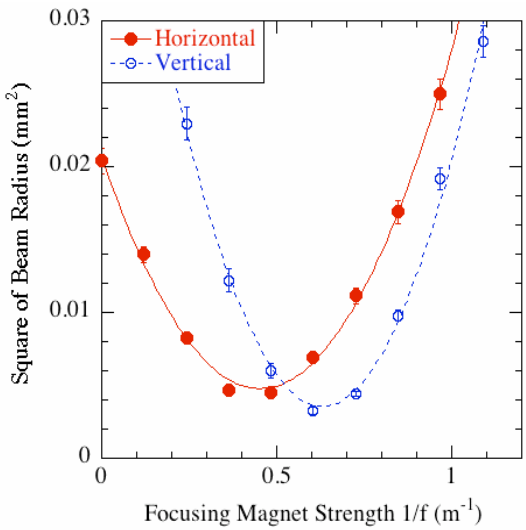

Fig. 6: Measured data by the Q-scan method at the beam energy of 50 MeV.

thin film was observed for the 250 MeV electron beam. The results are 5 psec (41 MeV) and 2 psec (250 MeV) in 1σ, which are much larger than the simulated bunch length of 1 psec. As causes of this discrepancy, we presently predict that the transverse beam size enlarges the pulse length of Cherenkov radiation. And also, in respect to measurement with OTR, we doubt that the optics including streak camera system enlarges the pulse length.

We measured bunch length with another method, where the pulse length of beam is converted to a systematic energy chirp by using a RF field gradient [15]. In our case, the second C-band acceleration unit (C-TWA#2 in Fig. 5) is operated at a zero-crossing phase to generate a systematic energy chirp. Beam density distribution

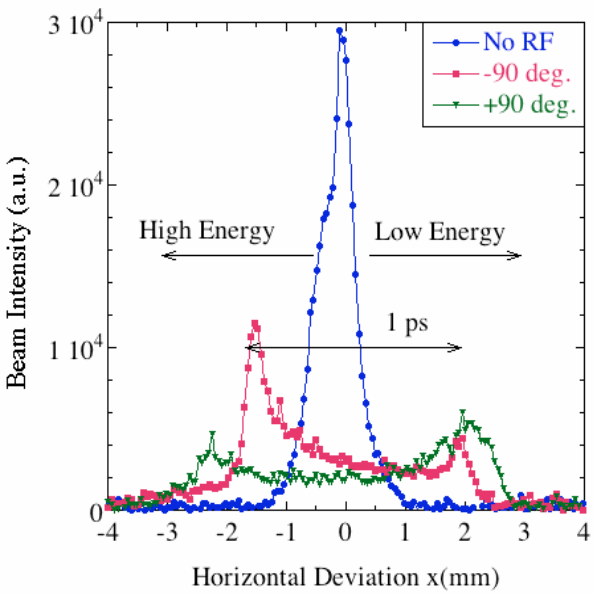

Fig. 7: Measured beam density profile projected on the horizontal plane with three different operating conditions.

projected to the horizontal plane is then observed with OTR from the Au thin film located in the middle of the chicane (M8 in Fig. 5). The linear dispersion at the OTR screen is about 150 mm. Figure 7 shows the measured density profiles under three different operating conditions of the second C-band unit, i.e., RF turned off and at the crest ± 90 deg. accelerating phase. By using the RF parameters and dispersion value, the full pulse width is estimated to be about 1.1 ps, which agrees well with the simulation.

Dark current

When the deflector is switched on, dark current downstream of the pre-buncher is invisible on a fluorescence screen of M1 in Fig. 5. It is true that the dark current from the electron gun is negligible for any beam tuning. Quantitative measurements are planned in next operation period after the summer shutdown.

Stability

Long-term stability of the electron beam or the prototype accelerator is the following. The standard SASE lasing is basically reproduced by reloading the nominal parameter set of the magnets and RF systems. At present, the SCSS prototype accelerator has not been operated continuously over a long period, but operated day by day. In 2 to 3 hr after the operation starts in the morning, we suffer the slow drifts of some parameters such as the high voltage of the electron gun, etc, which is so far adjusted manually. Introduction of slow feedback controls is thus under investigation.

With respect to short-term stability of the electron beam, the stability of the beam energy is 0.37 % in full-width downstream of the second C-band acceleration unit. This was estimated by using the shot-by-shot fluctuation of the horizontal position at M8 in Fig. 5. The beam orbit stability was measured by using the beam position monitor (BPM) [16] at the entrance of the first undulator, where no linear dispersion exists in the design. The horizontal and vertical orbit stabilities at this position are 13 and 21 μm in 1σ, respectively. These values are smaller than a fifth of the beam size.

With respect to lasing stability, the peak performance has not been achieved routinely. In order to maximize the laser amplification, slight tuning is needed for the pre-buncher phase, S-band TWA phase, position and width of the slits, S4 and S6 in Fig. 5. Figure 8 shows the shot-by-shot lasing stability measured by the photodiode (International Radiation Detectors Inc. SXUV100) in the VUV beamline [17]. The energy per pulse was measured by integrating the photogenerated charge of the photodiode. The lasing wavelength is about 60 nm and the repetition rate was 5 Hz. The data however were taken asynchronously at 3 Hz due to the reading speed of the temporary data acquisition system. We see that relatively strong lasing occurred in all shots over the period of measurement without any feedback correction.

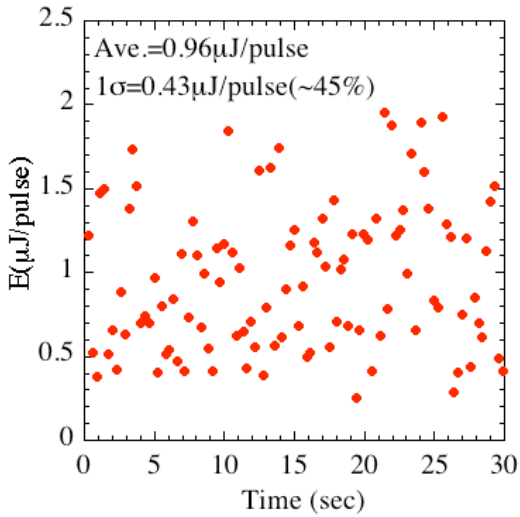

Fig. 8: Shot-by-shot stability of lasing. The beam energy is 250 MeV and the undulator gap is 3 mm.

Electron beam brilliance

Effective electron beam brilliance, the ratio of a peak current to 4-dimensional transverse phase space volume, is estimated by the following two approaches. One is to reproduce the measured dependence of the laser amplification on the peak current by using the 1-D model [18]. The other is to reproduce the measured dependence of the laser amplification on the K-value by using the 3-D simulation code, SIMPLEX [19].

(1) Estimation with 1-D model: The bunch current was controlled with the slit S4 in Fig. 5. Through the bunch length measurement with a systematic energy chirp, we confirmed that the local density peak in the bunch depends on the slit width of S4. Figure 9 shows the dependence measured by the photodiode in the VUV beamline. The filled circles and error bars represent the average and 1σ of 100 data, respectively. In this measurement, the gaps of both undulators were closed to 4 mm and the beam energy was accelerated up to the nominal energy, 250 MeV. Hence, the lasing wavelength is 49nm.

In the 1-D model, the total radiation intensity I is written by the sum of the spontaneous radiation intensity I_N and coherent radiation intensity I_L as

$$I = I_L + I_N = I_{L0}\exp\left(z/L_{1G}\right) + I_N, \qquad (2)$$

where z and L_{1G} represent the total length of the undulators and the 1-D gain length, respectively. Assuming that the horizontal normalized slice emittance is the same as the vertical one, L_{1G} is expressed by using the beam parameters as

$$L_{1G} = \frac{150.2}{\left(\frac{H}{\left\langle\beta_x^{1/2}\right\rangle\left\langle\beta_y^{1/2}\right\rangle}\right)^{1/3}}, \quad H = \frac{I_p}{\varepsilon_{ns}}. \qquad (3)$$

Here, ε_{ns} and I_p represent the normalized slice emittance and peak current, respectively. β_x and β_y are the horizontal and vertical betatron functions, respectively. The bracket < > represents the average of the inside parameter over the undulator length. First we determined the betatron functions experimentally. Then, we fitted the experimental data by using H as only a parameter in consideration with the dependence of Eq. (2) and (3) on the beam charge. The solid line in Fig. 9 shows the result, which agrees well with the experimental data. The ratio of I_p to ε_{ns}, namely H is estimated to be 480 A/πmm·mrad. Assuming that ε_{ns} is the design value, 2 πmm·mrad, the electron beam brilliance becomes 240 A/π^{2}mm^2·mrad^2.

(2) Estimation with 3-D model: Fixing the electron beam condition, we measured the dependence of the angular photon flux density on the K-value by changing the gap of the first undulator only. To extract the core photon beam, the horizontal acceptance was limited within ±100μm from the beam center by using the horizontal slit in the VUV beamline. Then, the horizontally narrow beam was monochromatized and detected by the CCD camera [17]. We further set a small window on the CCD image for limiting the bandwidth and the vertical acceptance. The angular photon flux density was finally obtained by integrating the intensities in the window. Figure 10 shows the measured dependence of the angular flux density on the K-value with the filled circles. Each data was taken by the integration time of 10sec, i.e., the integration of 50 data. The vertical axis represents the ratio of the flux density to that of the spontaneous radiation. The spontaneous radiation data were measured for each K-value by operating S-band TWA at the de-bunching phase.

Assuming that the normalized slice emittance and momentum spread are the design values, 2 πmm.mrad and 0.1 % (1σ), respectively, we simulated the

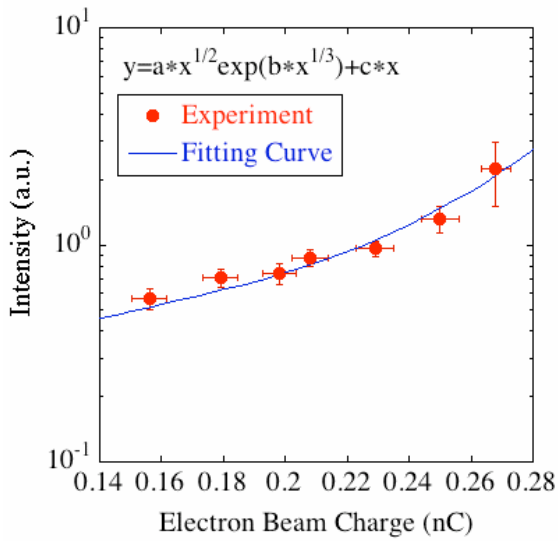

Fig. 9: Dependence of laser amplification on the beam charge.

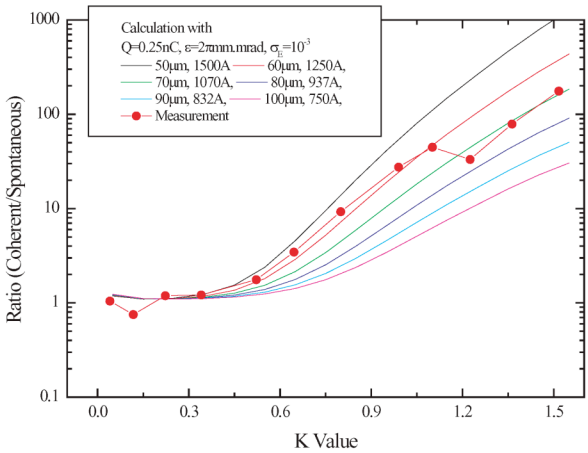

Fig. 10: Dependence of laser amplification on the K-value.

dependence on the K-value with SIMPLEX. Here, the peak current was used as a parameter. The solid lines in Fig. 10 show the results. By comparing the simulation and experimental data, we see that the experimental data locate between the two lines obtained with 1070A and 1250A. The electron beam brilliance is estimated to be 270 ~ 310 $A/\pi^2 mm^2 \cdot mrad^2$.

SUMMARY

The SCSS injector system was designed to achieve the stable and flexible beam operation satisfying the high beam quality required for SASE-based x-ray FEL. On the other hand, our design needs the bunch compression of relatively long electron beam in a low energy regime ranging from 500 keV to a few MeV, with suppressing the emittance growth due to a space charge force and non-linearity. This is quite challenging and there remains the question whether "emittance conservation" through the injector is a sufficient level or not under the practical error condition. To confirm beam performance of the injector, the SCSS prototype accelerator was constructed.

Owing to careful beam tuning based on the emittance conservation, SASE lasing in the wavelength ranging from 40 to 60nm has been stably obtained at the SCSS prototype accelerator. We analysed the reproducible SASE lasing data by the 1-D model and 3-D simulator. As a result, we found that electron beam brilliance is estimated to satisfy the design target, $200A/\pi^2 mm^2 \cdot mrad^2$.

This experimental result shows that PARMELA gives a good design guideline in our case and concludes that the beam performance for x-ray FEL is reachable by the smooth extension of the prototype accelerator.

REFERENCES

[1] T. Shintake et al., "SPring-8 Compact SASE Source (SCSS)", SPIE, Optics for Fourth-Generation X-Ray Sources, Bellingham, August 2001, p. 12.

[2] "SCSS X-FEL Conceptual Design Report", RIKEN/SPring-8, May 2005, Mikazuki, Japan, http://wwwxfel.spring8.or.jp/.

[3] T. Shintake, "Status of the SCSS Test Accelerator and XFEL Project in Japan", EPAC'06, Edinburgh, June 2006, p. 2741; http://www-xfel.spring8.or.jp/fist_lasing/FirstLasingofSCSS.html.

[4] "Linac Coherent Light Source (LCLS) Conceptual Design Report", SLAC-R-593, April 2002.

[5] "TESLA Technical Design Report, PART V, The X-ray Free Electron Laser", ed. G. Materlik and Th. Tschentscher, March 2001.

[6] K. Togawa et al., "CeB6 Electron Gun for the Soft X-ray FEL Project at SPring-8", NIMA, **528** (2004) 312.

[7] K. Togawa et al., "Emittance Measurement on the CeB_6 Electron Gun for the SPring-8 Compact SASE Source", FEL'04, Trieste, August 2004, p.351.

[8] M. Reiser, "Theory and Design of Charged Particle Beams", John Wiley & Sons, Inc., New York, 1994, p. 210.

[9] T. Shintake et al., "HOM-Free Linear Accelerating Structure for e+e- Linear Collider at C-band", PAC'95, Dallas, May 1995, p. 649.

[10] T. Sugimura et. al, "SKIP–A Pulse Compressor for SuperKEKB", LINAC'04, Lübeck, August 2004, p.754 (2004).

[11] T. Shintake et al., "A New RF Pulse-Compressor Using Multi-Cell Coupled-Cavity System", EPAC'96, Sitges, June 1996, p. 2146.

[12] T. Tanaka et al., "Development of the short-period undulator for the X-ray FEL project at SPring-8", SRI'03, San Francisco, August 2003, p. 227.

[13] International Radiation Detector Inc., http://www.ird-inc.com/.

[14] R. B. Neal, "The Stanford Two-Mile Accelerator-I", W. A. Benjamin, Inc., New York, 1968, p.383.

[15] L. Rivkin et al., "Bunch Lengthening in the SLC Damping Ring", EPAC'88, Rome, June 1988, p.634.

[16] T. Shintake, "Development of Nanometer Resolution RF-BPMs", HEACC'98, Dubna, October 1998, http://lcdev.kek.jp/Conf/HEACC98/133.PDF .

[17] M. Yabashi et al., in these proceedings.

[18] R. Bonifacio et al., "Collective Instabilities and High-Gain Regime in a Free Electron Laser", Opt. Commun., **50** (1984) 373.

[19] SIMPLEX was developed by Takashi Tanaka (RIKEN/SPring-8), http://radiant.harima.riken.jp/simplex/.

Operational Experience with the Emittance-Meter at SPARC*

L. Catani†, A. Cianchi, INFN-Roma Tor Vergata, Roma, Italy
C. Ronsivalle, ENEA C.R. Frascati, Roma, Italy
P. Musumeci, M. Petrarca, INFN-Roma, Roma, Italy
M. Bellaveglia, R. Boni, M. Boscolo, M. Castellano, E. Chiadroni, L. Cultrera, G. Di Pirro, A. Drago, M. Ferrario, D. Filippetto, V. Fusco, A. Gallo, G. Gatti, F. Tazzioli, C. Vaccarezza, M. Vescovi, C. Vicario, INFN-LNF, Frascati, Roma, Italy
M. Migliorati, L. Palumbo, University La Sapienza, Roma, Italy.

Abstract

We report the operational experience of the movable emittance meter at SPARC. It is based on the well-known technique of pepper pot measurements (1-D slits in our case) but, in addition, it allows moving the measuring device along the beam line from about 840 mm to 2200 mm from the cathode, following the emittance oscillations. More than a simple improvement over conventional, though non-trivial, beam diagnostic tools this device defines a new strategy for the characterization of high performance photo-injectors, providing a tool for detailed analysis of the beam dynamics, over a section of the accelerator where emittance compensation take place. With this device we planned to perform detailed and systematic studies on beam dynamics with particular attention to the transverse parameters as well as longitudinal.

INTRODUCTION

The aim of the SPARC [1] project is to promote R&D towards high brightness photo-injectors to drive a SASE-FEL experiment. The 150 MeV SPARC photo-injector consists of a 1.6 cell RF gun operated at S-band (2.856 GHz, of the BNL/UCLA/SLAC type) and high-peak field on the cathode incorporated metallic photo-cathode of 120 MV/m, generating a 5.6 MeV, 100 A (1 nC, 10 ps) beam.

The beam is then focused and matched into 3 SLAC-type accelerating sections, which boost its energy to 150-200 MeV. The first phase of the SPARC Project was dedicated to the beam RMS emittance measurement along the drift space following the RF gun, where the emittance compensation process occurs.

The complete characterization of the beam parameters at different distances from the cathode is important to define the injector settings optimizing emittance compensation and for code validation. For this measurement, a dedicated moveable (in z, z being the distance from the cathode, measured along the accelerator axis) emittance measurement device [3] (emittance-meter) is used allowing to measure the RMS emittance in the range from about z=86 cm to z=210 cm.

* This work has been partially supported by the EU Commission in the sixth framework program, contract no. 011935 EUROFEL-DS1.

† luciano.catani@roma2.infn.it

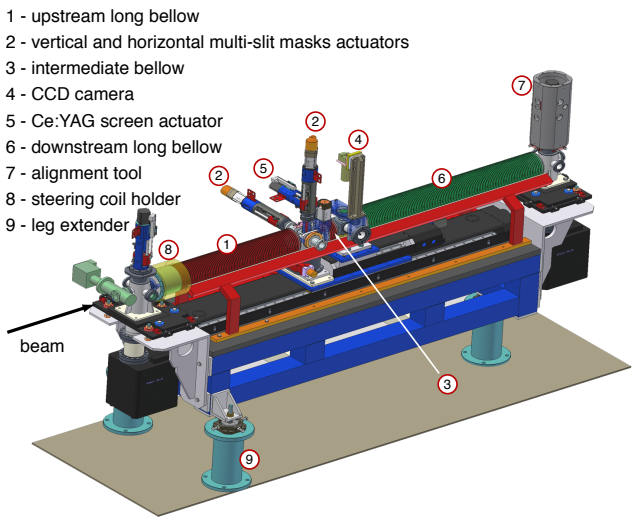

Figure 1: 3D mechanical drawing of the SPARC emittance-meter

The technique to measure the beam emittance and the phase space, in both the horizontal and vertical planes, makes use of a double system of horizontal and vertical slit masks [2]. Each mask consists of a slits array (7 slits, 50 μm width spaced of 500 μm, 2 mm thick) and two single slits, 50 and 100 μm width. The slits are realized by photo-chemical etching providing, compared to mechanical machining, higher precision and improved smoothness of slits edges. The multislits are used for single shot measurements, provided the beam size is large enough for an adequate beam sampling by the slit array. Alternatively, a single slit can be moved across the beam spot. In this case the accuracy of transverse sampling can be freely chosen adjusting the step between the different positions of the slit. This measurement is an integration over many pulses.

Linear actuators with stepper motors are used to control the insertion of the slits masks into the beamline. A differential encoder and a reference end switch guarantee reproducibility and accuracy of the movement to better than 2 μm, required for single-slit multi-shots measurements.

The projected cross-section of beamlets emerging from the slit-mask are measured by means of a downstream

Ce:YAG radiator. Because beam size and divergence depend on the longitudinal position, the slit to screen distance must be properly adjusted in order to optimize the accuracy of the beamlets profile measurement as the movable device is placed at different z. A bellow is therefore interposed between the slit mask and the screen, allowing their relative distance to be changed while keeping the masks at a fixed position with respect to the gun. This solution allows to set the length of drift between slit mask and the screen that best fits the different scenarios: converging beam, diverging beam, single or multi-slits. Refer to Fig.1 for a schematic drawing of the emittance meter.

Radiation emitted in the forward direction from the Ce:YAG crystal is collected by a 45 degrees mirror downstream from the radiator. The back face of the transparent crystal radiator is observed, thus minimizing degradation of the spatial resolution due to the depth of field of the optics.

Beam images are acquired using digital CCD cameras equipped with a 105mm "macro" type objective. The magnification of 0.66 gives a resolution of 15.4 μm per pixel.

Beam charge is measured by means of a Faraday cup, placed in a cross together with a chrome-oxide screen to image the beam at 60 cm from the cathode. This screen is also used to monitor the position of the laser spot on the cathode. The emittance-meter is followed by a magnetic spectrometer measuring the beam energy and energy spread

DETAILS ON MEASUREMENTS WITH THE MOVABLE EMITTANCE-METER

The movable emittance-meter was built to perform a detailed characterization of the SPARC photo-injector studying the beam dynamics as function of relevant parameters such as the solenoid field, the beam charge and size, the laser pulse length and its shape. Refer to [4] for more details.

Beam Envelope

Evolution of the bunch transverse size along the photo-injector is a important, though simple, measurement we regularly perform with the emittance-meter. It takes less than 5 minutes to complete the measurement consisting of continuously changing the z-position of the movable system between the upper and lower ends to grabb beam images at various position. These images are on-line processed to filter out the background noise and to calculate the RMS value of the beam size. In Fig.2 are shown results of measurements of the RMS beam size vs z for different values of the solenoid field at the gun. The measurement procedure is a completely automatic one-click operation of the control system.

At a glance we can guess the solenoid current that gives the waist in the required z position or, by comparing x and y envelopes curves, check for the causes that might produce beam envelope irregularities, laser or solenoid misalignment for instance. The different curves in Fig.2 show how the beam waist and its position in z are changed as consequence of the different solenoid currents.

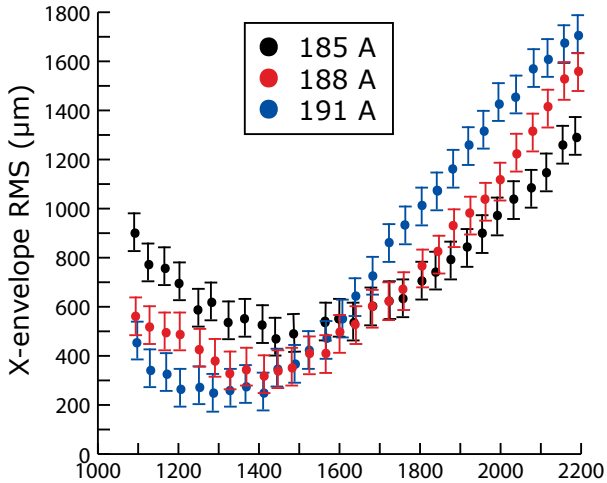

Figure 2: Envelope of the beam (x-plane) along z for different solenoid currents

Emittance

The emittance can be measured, in both x and y planes, at different positions along the emittance-meter. The beam size and its divergence are expected to change as the distance from the cathode changes: the beam is converging at the beginning of the emittance-meter and diverging in the second half. Different measurement strategies are then implemented to achieve the best accuracy of the emittance calculation algorithm.

When the beam is close to the waist, its size is small and the multi-slits mask is not suited because it produces a limited number of beamlets. The single-slits multi-shot measurement is also preferable in the region close to the end of the emittance-meter where the beam size is typically larger than the part of the mask covered by the slit-array and when the beam is strongly converging because profiles of beamlets produced by the multi-slits mask might overlap. Typical values of the sampling distance between the slit positions ranges from 110 μm to 380 μm. At least nine beamlets are always collected with the single slit. In all of the other conditions the multi-slits mask provides fast single-shot measurements, while the single-slit is preferred for accurate analysis.

It's worth mentioning that, for given beam conditions, results produced by both single-slit and multi-slit measurement have always been fully consistent. A simple check of results produced by the emittance calculation algorithm consists in comparing the RMS beam size at the slit-mask (measured by moving the screen at the longitudinal position of the slit-mask during emittance measurement) against the value of beam size estimated by the emittance calculation algorithm. We always obtained an excellent agreement between the two results.

Fig.3 shows an example of emittance measurements at different positions along the emittance-meter. In this case the beam charge was 700 pC and the energy 5.14 MeV with a longitudinal profile σ= 4.35 psec.

A typical emittance measurement with the single-slit mask consists of collecting 15 beam images for each slit position. The center of mass and RMS size of beamlets are calculated for each image and averaged. We verified that larger statistic doesn't significantly improve the accuracy of results. In details, from each beamlets image we calculate the projection on the axis, subtract the baseline, try gaussian fit to find the best position for the center of intensity distribution, reduce the number of the relevant points skipping these that are outside the 3 standard deviations from the centre and only on the remaining points we calculate the RMS parameters.

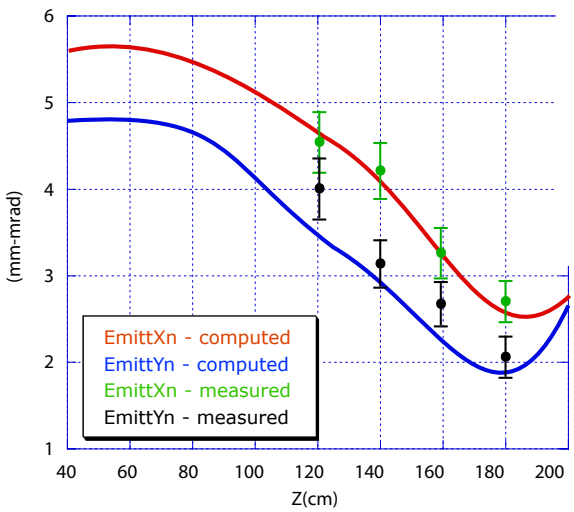

Figure 3: Emittance measurements along the e-meter

The high magnification optical system, the high efficiency YAG screen and a CCD with a remotely controlled gain always provide a good signal to noise ratio and large number of sampling point for every beamlet in all the conditions.

Transverse phase space

The measurement of RMS Twiss parameters and emittance with the single-slit mask allow, as a side-product, the reconstruction of the beam transverse phase space [5]. For each slit position, the beamlet profile on the screen yelds the divergence distribution of particles at the given x position, i.e. those emerging from the slit-mask. Interpolation of the different profiles produces the two dimensional x - x' distribution.

In Fig.4 we show the phase-space measured at different positions along the emittance-meter for a low charge (100 pC) beam. Clearly the beam is going through a focus evolving from convergent to divergent. On the other hand, as the photoinjector theory predicts, the evolution has many differences from that in a linear optics crossover. In a "standard" drift the particles being on the left (negative x) move to the right crossing the origin thus following the lines of motion of constant x. Here the particles that are on left at the beginning of the beamline stay on the left. They get close to the origin (both in x and x') without crossing it and after the laminar space charge dominated waist they move back (still negative x) changing the sign of their divergence

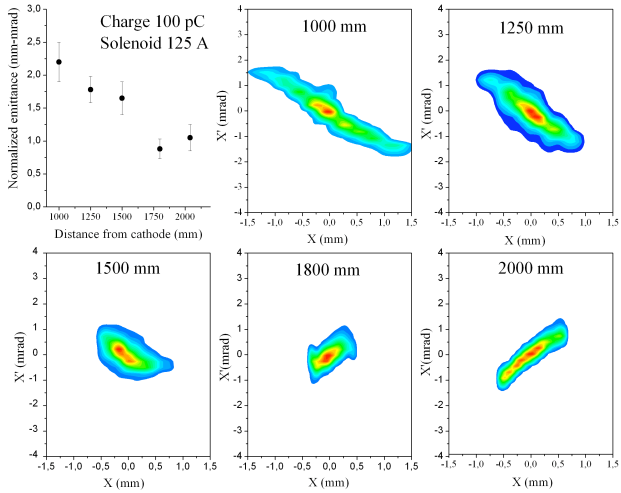

Figure 4: Phase space measure along the e-meter

subsectionBeam energy and energy spread

The e-meter gives also the possibility to investigate the longitudinal dynamics and correlation between transverse and longitudinal planes.

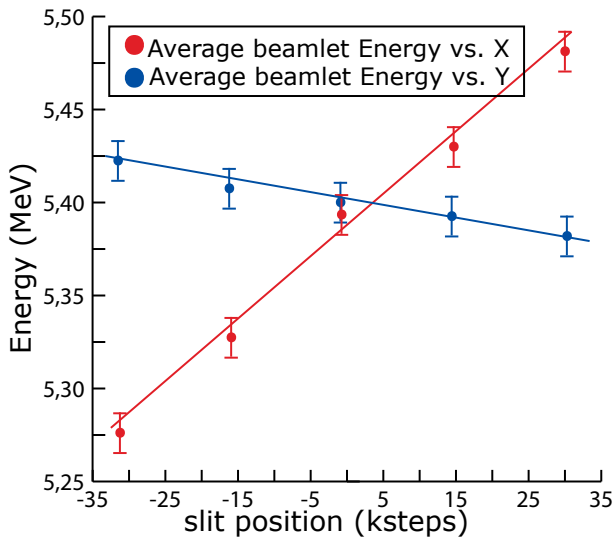

Figure 5: Beamlet energy vs transverse position

Moving the x or y single-slit across the beam and measuring the energy at the spectrometer gives evidence of a possible correlation between particles transverse position and their energy. The measurements in Fig.5 show a varia-

tion of beamlets mean energy when the position of the vertical single-slit is changed moving it across the beam in the horizontal direction. The correlation, clearly stronger in the x-direction, suggest as possible cause the non-normal incidence of the laser beam on the cathode in the y=0 plane.

As a final example of the extended diagnostic capabilities of the emittance-meter we report in Fig.6 the evolution of the energy spread measured for the central beamlet (i.e. with the vertical single-slit centered on the beam center of mass) as function of the position along z of the slit mask.

Note that all the points in the graph, except the last one representing the energy spread of the whole beam obtained removing the slit-mask from the beam path, correspond to positions within the high impedance bellows. Inside the long bellows the wakefields contribution to the energy spread adds to the longitudinal space charge effect and the energy spread grows faster. These effects significantly contribute to the energy spread up to the slit-mask while for the low charge beamlet the wakefields and space charge effect are practically negligible. As consequence an increasing energy spread is expected as the distance of the slit-mask from the cathode became larger. It is clearly confirmed by

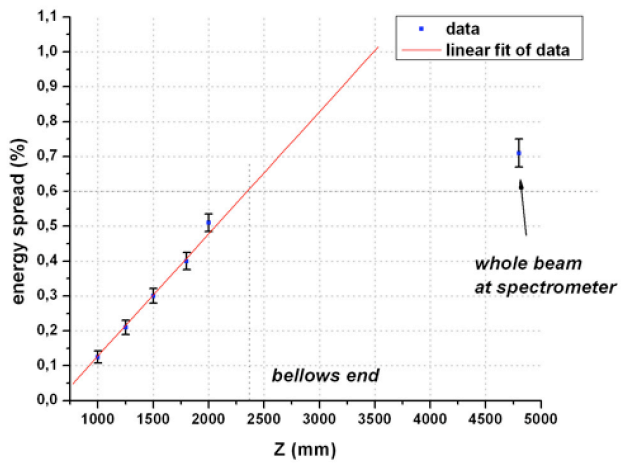

Figure 6: Contribution of bellows to energy spread is evidenced selecting a small portion of the beam with the singl-slit mask and moving it at different Z.

CONCLUSION

The final task of the SPARC photo-injector commissioning is to provide a complete sets of measurements (including transverse and longitudinal profiles of the laser) allowing a complete characterization of the beam dynamics by following the evolution of all the beam parameters.

As it appears from the previous paragraphs, beam dynamics in a photo-injector is a non trivial problem that critically depends on many variables. In systems equipped with a single (at a given longitudinal position) emittance diagnostic station, beamline parameters like solenoid strength or laser launching phase are varied to obtain emittance values that can be checked against those predicted by simulation codes. Unfortunately, the changing of a set-point is often hindering a cross-talk between different simulation parameters which so far has been taken into account somewhat externally (for example varying the gun phase affects the extracted charge, and varying the solenoid strength changes the quadrupole component effect).

The clear advantage in characterizing a photo-injector with the SPARC movable emittance-meter is that once the working point is set, a single simulation run generates results which reproduce the evolution of the experimental data (beamsize, emittance, energy spread) taken with the movable measurement device at the different positions along the beamline. In other words a single simulation run can be checked against a number of experimental points, not just a single one, all representing, or measured with, the same identical photo-injector working point.

Further work, more detailed and accurate measurements, is foreseen in order to approach such ambitious goal, fully understand the system, and validate the prediction capabilities of the modeling codes.

REFERENCES

[1] D. Alesini et al., Nucl. Instr. & Meth. In Phys. Res. A 507 (2003) 345-349C.

[2] M. Zhang, FERMILAB-TM-1988, Oct 1996.

[3] L.Catani et.al., Rev. Sci. Instrum. 77, 093301 (2006).

[4] M. Bellaveglia "Commissioning of SPARC Photoinjector", these Proceedings.

[5] S. G. Anderson et al. "Space-charge effects in high brightness electron beam emittance measurements", Phys. Rev. ST Accel. Beams 5, 014201 (2002).

HIGH CURRENT ELECTRON EMISSION FROM MICROSCOPIC TIPS

R. Ganter, R.J. Bakker, M. Dehler, J. Gobrecht, C. Gough, E. Kirk, S.C. Leemann, K. Li, M. Paraliev, M. Pedrozzi, F. Le Pimpec, J.-Y. Raguin, L. Rivkin, V. Schlott, H. Sehr, S. Tsujino, A. Wrulich, Paul Scherrer Institut, Villigen CH 5232, Switzerland.

Abstract

In order to find electron sources with low intrinsic emittance (< 5.10^{-8} m.rad) and high brigthness (B > 5.10^{13}A.m^{-2}.rad^{-2}), single tip field emitter as well as Field Emitter Arrays (FEAs) are investigated. By field emission very high current densities can be obtained (up to 10^{12}A.m^{-2}) from extremely small source sizes. Illumination of such field emitting sources by laser pulses (photo-field emission) gives in addition the possibility to pre-bunch the emission to very short pulse lengths. Maximum peak currents, measured from single tips of ZrC with a typical apex radius around one micrometer are presented. Voltage pulses of two nanoseconds duration and up to 50 kilovolts amplitude lead to field emission currents of several hundreds of milliamperes. By combining these electrical pulses with laser pulses, peak currents of several amperes were extracted from the tip apex. This high current emission mode is different from field emission or photo-field emission and has many similarities with the so-called explosive electron emission.

INTRODUCTION

Reducing the beam emittance while keeping high brightness is the most direct way to reduce cost and size of Free Electron Lasers (FELs). In linear accelerators, the parameters of the accelerated beam depend strongly on the performances of the electron gun. The beam emittance in the electron gun is ultimately limited by the intrinsic emittance at the electron source which can be expressed as follow [1,2]:

$$\varepsilon_{n,rms} = \frac{R}{2}\sqrt{\frac{2E_{kin}}{3mc^2}} \qquad (1)$$

where R is the beam radius in the case of a uniform radial distribution and E_{kin} is the mean transverse kinetic energy of emitted electrons (Maxwell energy distribution), m is the electron mass and c the speed of light. In order to reduce the thermal emittance one can either reduce the beam size (R) and/or the mean transverse kinetic energies (E_{kin}) of produced electrons. Field emitter arrays should be capable of producing electron beams with extremely low transverse kinetic energy due to a focusing electrode positioned just one micrometer after the emitting point [3-5]. A single tip electron source should also produce low emittance beam because of the extremely small emitting area (<1μm^2) [6]. Indeed, current densities as high as 10^{12} A.m^{-2} can be achieved by field emission [7]. In practice, the strong dependence of the field emitted current on the local field enhancement factor (down to nanometric scale) and on the local work function (which depends on contaminants, crystal orientation) makes this emission very difficult to control (breakdowns) and to stabilize (fluctuations). Laser illumination of field emission electron sources gave encouraging results in stabilising and increasing the total current emission [8]. If the regime of emission is dominated by photo-field emission, it should become possible to pre-bunch the emission down to 10-30ps with picosecond lasers while keeping high current densities.

LOW EMITTANCE GUN PROJECT

The goal of the Low Emittance Gun (LEG) Project [9] at Paul Scherrer Institute (PSI) is to produce electron bunches of 15ps rms duration with a normalized transverse emittance of 5.10^{-8}m.rad and a minimum peak current of 5.5A at an energy of 4 MeV (see also companion paper [10]). The requirement in peak current is already quite challenging for both FEAs and single tip cathodes. Furthermore, if the electron source is capable of reaching the targeted emittance then the acceleration of such a beam into the relativistic regime without emittance blow up remains very difficult. The LEG concept will combine diode and RF acceleration. A few millimeters gap will separate the electron source from the first radio frequency (RF) cavity. Voltage pulses of 0.5MV and 250ns duration will be applied across this diode gap at a repetition rate of 10Hz. The resulting high accelerating gradient should minimize the emittance growth caused by space charge forces. Comissioning of this high voltage pulser is under way at PSI [9]. After the diode gap the electron beam will enter the RF cavities. A two-frequencies RF cavity (1.5GHz and 4.5GHz) has been designed in order to obtain flat top acceleration waves which minimize the emittance dilution due to RF acceleration [11].

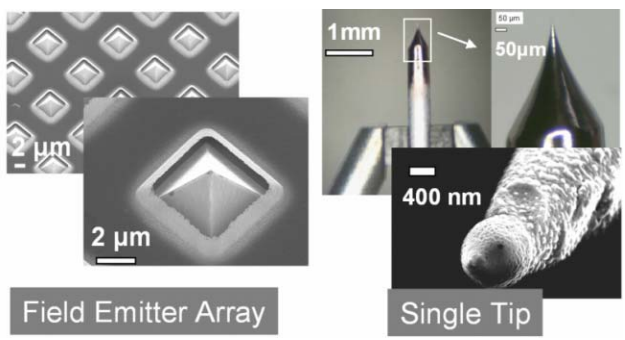

Figure 1: Field Emitter Array produced at PSI and single tip of ZrC from AP Tech Inc. .

The maximum peak current reached with commercial FEAs [12] was around 120 mA [8] for a one millimeter diameter array with 50000 tips. The main limitation comes from the non uniformity of the emission from tip to tip. The intrisic emittance of the same commercial single gated FEAs (no focusing grid) has recently been measured to be around 2.10^{-6}m.rad [13] for a one millimeter diameter cathode. Performances achieved with commercially available FEAs enabled us to better define the ideal FEA for LEG. PSI is currently developping an own production of FEAs based on a self aligned moulding technique. With this technology, pyramid shaped tips can be produced (see Fig. 1) which should better dissipate the heat and thus be able to carry more current. Since FEAs are still under development at PSI the rest of the paper will focus on single tip electron sources.

Single tips are produced by etching a wire which is then inserted in a so called Vogel mounting (see Fig. 1). This mounting allows current circulation and thus tip flash heating as well as field forming [14] of the apex. Metal carbides, like ZrC, are conductors with lower work functions (~ 3.5 eV) than commonly used W or Mo surfaces [15]. ZrC surfaces are also known to be more resistant against sputter damage and the threshold temperature for surface migration (~ 1500 K) is higher than for W or Mo surfaces [16]. We used commercially available ZrC tips from APTech Inc. [17] (McMinnville, USA). Field emission is always localised to small surface imperfections which have a smaller work function and / or a more favorable geometry for field enhancement so that current density goes rapidly to values as high as 10^{12} A/m^2 [7]. The consequence is a fast local heat up with an increased risk for a vacuum arc. The best way to limit the heat up is to emit during very short pulses and at low repetition rates. Nanosecond voltage pulses were applied to a ZrC tip in order to increase the emission current.

EXPERIMENTAL SETUP

Fig. 2 represents the experimental setup used to measure the emitted current from single tips of ZrC [17]. A fast pulser from the company FID GmbH delivering pulses up to 100 kV in amplitude and with 2ns duration (FWHM) at 10 Hz was connected to the tip. A special broad bandwidth (up to 1 GHz) coaxial vacuum feedthrough has been designed to feed the ZrC tip. The tip has a fairly large apex radius (r ~ 1 µm) and is positioned 1 mm behind an aluminium gate electrode (see inset in Fig. 2). The gate has a 2 mm diameter hole and is grounded. The faraday cup is also grounded and about 5 mm away from the tip apex on the same axis.

FIELD EMISSION FROM SINGLE TIPS

Fig. 3 represents the current pulses collected by the faraday cup when voltage pulses of amplitude V_{Tip} were applied to the tip.

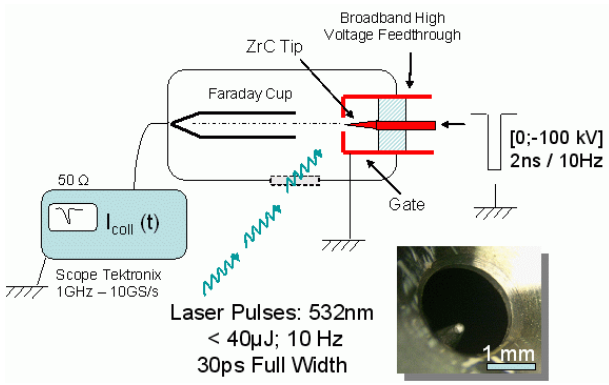

Figure 2: Experimental setup for pulsed field emission and photo-field emission tests.

Field emitted current starts to be detected at voltages around 20 kV (Fig. 3); peak currents as high as 460 mA were measured for applied voltages around 50kV. At this level of current, amplitude fluctuations became relevant (as illustrated by the two pulses at 51kV on Fig.3, left graph) and a monotonic decay of the amplitude was observed. Fluctuations usually indicate that the surface temperature became high enough to activate surface migration of contaminants which in turn change the field emission properties. At lower currents (Fig. 3, right graph), the emission was more stable and the current - voltage characteristics could be measured. These measurements are also represented in a Fowler-Nordheim (F-N) plot (Fig. 4, right graph). From the F-N plots, one can estimate the field enhancement factor β as well as the emitting area [18,19]. The local electric field F_{loc} at the tip apex is then defined as $F_{loc}= \beta.V_{Tip}$. A linear fit (see Fig. 4) of measured values gives $\beta \sim 2.10^5$ m^{-1} and an emitting area around S $\sim 10^4$ nm^2 (assuming a work function of 3.5eV for ZrC). This is consistent with a tip radius of 1 µm. With such a small emitting area and if we assume a divergence of sixty degrees [20] a rough estimate gives a normalized emittance less than 5.10^{-8}m.rad and a beam brightness around: B $\sim 10^{13}$ A.m^{-2}.rad^{-2}.

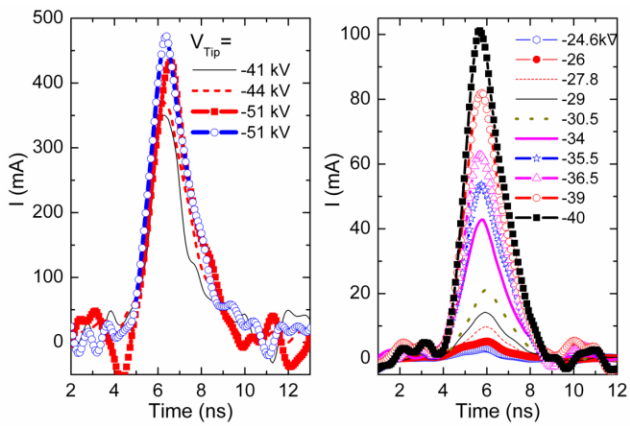

Figure 3: Current pulses collected on the faraday cup for different voltage pulse amplitudes V_{Tip}.

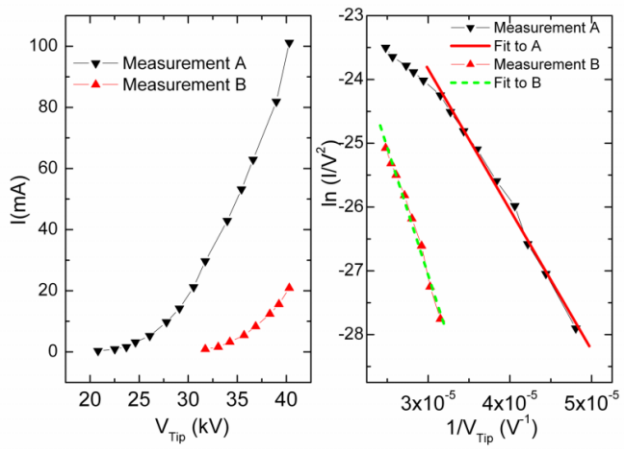

Figure 4: Current voltage characteristics acquired at 5 min interval (left) and Fowler-Nordheim representation of the same curves (right).

With the use of short (2ns) high voltage pulses at low repetition rate, it has been possible to limit the heat up of the tip and to increase the current that can be extracted from a ZrC tip up to 470 mA. For comparison, with a DC electric field, only currents below 10 µA could be safely extracted. However, these high current field emitted pulses revealed strong fluctuations in amplitude. The illumination of the tip with picosecond laser pulses should help to increase the stability and to reach higher peak currents.

LASER ASSISTED ELECTRON EMISSION

Laser assisted field emission [21] [22] is an interesting approach to combine the advantage of field emission (high brigthness) and laser photo-emission (stability, short time modulation). In the photo-field emission regime, the high electric field around the apex lowers the potential barrier of the crystal so that photoemission with large wavelength (λ>532nm) becomes possible and efficient. In previous experiments, similar ZrC tips were illuminated by laser pulses while a DC electric field was applied [8]. Peak currents as high as 580 mA were reached with 10ns long laser pulses of 532nm wavelength. Shorter laser pulses of 1ns (FWHM) at 1064nm produced photo-field current pulses of similar duration [23] suggesting the possibilty to pre-bunch the emission to even shorter levels. In consequence, we recently combined the voltage pulser presented in the first part of the paper with a picosecond laser from the company Time Bandwith Products (see Fig. 2).

The laser system provides 30 ps long laser pulses at 532 nm with a maximum energy per pulse of 40 µJ. The laser was focused on the tip apex with a lens positioned at the focal distance (200 mm) from the tip outside the vacuum chamber. Nanosecond voltage pulses were applied to a ZrC tip while laser pulses were illuminating the tip apex at a repetition rate of 10Hz. If emission is dominated by photo-field emission then the expected current pulse should be as short as 30 ps (FWHM). Unfortunately the bandwidth of our faraday cup (< 1GHz) limits the detection of such short current pulses. The incident laser energy per pulse can be varied between 1 and 40µJ. At low laser energy (<5 µJ/pulse) no change from the pure field emission mode was observed. Above 5 µJ, the current increased suddenly by one order of magnitude leading to the current pulses shown on Fig. 5.

Figure 5 represents the current pulses measured by the faraday cup when laser pulses (532 nm, 20 µJ, 10^8-10^9 W.cm^{-2}) were synchronised with the high voltage pulses for different voltage amplitude V_{Tip}. The collected peak current was as high as 5.5 A at a repetition rate of 10 Hz. The shape of the current pulse follows the applied voltage pulse (the satellite peak at t=3ns corresponds to a similar reflexion in the applied voltage). No significant jitter or amplitude variations were observed as it would be the case for vacuum breakdowns. No decay of the amplitude was observed after several hours of 10 Hz operation and pressure was stable around 10^{-8} mbar. This electron emission was probably not resulting from photo-field emission since it was lasting several nanoseconds. The dependence of the extracted current on laser energy (step like dependence) indicates that there is a threshold above which this large current emission is detected. This has much in common with the so called explosive electron emission (EEE) which is a kind of stable vacuum arc regime. EEE has been largely described by Mesyats [24] and Fursey [7,25]. EEE takes place when a large amount of energy is concentrated into a small volume (by joule effect or laser heating) which eventually explodes and generates a large flow of electrons together with other particles. The difference between this regime of EEE and normal vacuum arcs is the very good reproducibility and stability of the process. The quasi-stationary behaviour is based on the fact that at each explosion the surounding surface melts and some new micro protrusions (and nearly identical) arise which serve as new emitting centers.

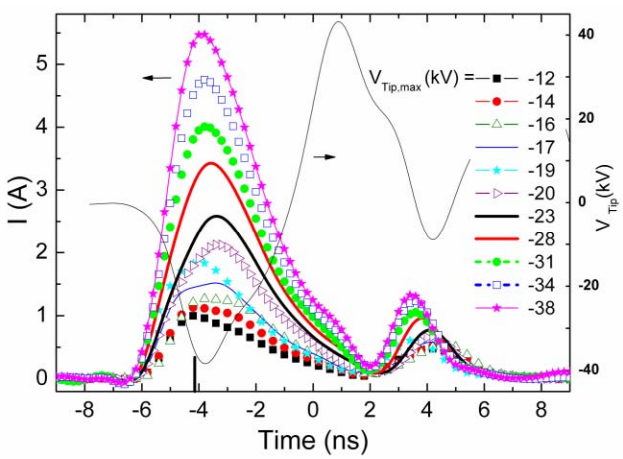

Figure 5: Current collected on the faraday cup when picosecond laser pulses were synchronised (at t ~ -4ns) with high voltage electrical pulses. One example of the voltage applied to the tip is also represented.

The current density during EEE can be extremely high usually above 10^{12} A.m^{-2} so that the size of the emitting center is small (around 1 μm). Further tests are required to better understand and estimate the interest of these large current pulses for a low emittance gun application.

CONCLUSION

Field emission naturally produces very large current density beam so that good performances in terms of beam emittance and beam brightness can be expected from a single tip. The consequence of large current density emission is a high risk of overheating with generation of vacuum arcs. For accelerator application field emission sources must provide a minimum peak current of several amperes. Pulsed field emission at low repetition rate showed that larger peak currents (from 10 μA in DC to almost 500 mA in pulsed mode) can be extracted from a single tip of ZrC. In order to reach LEG goals, photo-field emission is an attractive mechanism which allows time modulation with fast lasers. Preliminary tests of illumination of a tip with picosecond laser pulses while nanosecond voltage pulses are applied have been made. An interesting regime of electron emission (similar to explosive electron emission) delivering stable current pulses of several amperes has been observed. Further tests are still required to see if it has some relevance for a low emittance gun application.

REFERENCES

[1] S. Humphries, *Charged Particle Beams* (John Wiley & Sons, 1990).
[2] J. E. Clendenin *et al.*, NIM A **455,** 198-201 (2000).
[3] A. E. Candel, Ph. D. Thesis, ETHZ, 2005.
[4] A. E. Candel *et al.*, Nuclear Instruments and Method in Physics Research A **558,** 154-158 (2006).
[5] M. Dehler *et al.*, J. Vac. Sci. Technol. B **24,** 892-897 (2006).
[6] V. M. Zhukov *et al.*, Radioteckhnika i elektronika **10,** 2153-2162 (1988).
[7] G. Fursey, *Field Emission in Vacuum Microelectronics* (Plenum Publishers, New York, 2005).
[8] R. Ganter *et al.*, J. Vac. Sci. Technol. B **24,** 974-979 (2006).
[9] http://leg.web.psi.ch.
[10] R. J. Bakker, this Conference, 2006.
[11] J.-Y. Raguin *et al.*, in *Progress in the design of a two-frequency RF cavity for an ultra-low emittance pre-accelerated beam*, Proceedings of the EPAC06 Conference, Edinburgh, Scotland, 2006.
[12] http://www.sri.com/psd/microsys/.
[13] S. C. Leemann *et al.*, in *First measurement results at the LEG Project's 100 keV DC gun test stand* Proceedings of the EPAC06 Conference, Edinburgh, Scotland, 2006.
[14] B. Grishanov *et al.*, Radiotekhnika i Elektronika **23,** 575 (1978).
[15] W. A. Mackie *et al.*, J. Vac. Sci. Technol. B **12,** 722-726 (1994).
[16] F. M. Charbonnier *et al.*, J. Vac. Sci. Technol. B **19,** 1064-1072 (2001).
[17] http://www.a-p-tech.com/.
[18] W. Zhu, *Vacuum Microelectronics* (John Wiley & Sons, 2001).
[19] A. Brenac *et al.*, Revue Phys. Appl. **22,** 1819-1834 (1987).
[20] F. Charbonnier, Appl. Surf. Sci. **94/95,** 26-43 (1996).
[21] M. Boussoukaya *et al.*, Nucl. Instr. and Meth. A **279,** 405-409 (1989).
[22] C. H. Garcia *et al.*, Nucl. Instr. and Meth. A **483,** 273-276 (2002).
[23] R. Ganter *et al.*, Nuclear Instruments and Method in Physics Research A **In Press** (2006).
[24] G. A. Mesyats, Plasma Phys. Control. Fusion **47,** A109-a151 (2005).
[25] G. N. Fursey *et al.*, Applied Surface Science **215,** 286-290 (2003).

PHOTON OPTICS AT SCSS

M. Yabashi[1,2], T. Hirono[1,2], H. Kimura[1,2], H. Ohashi[1], S. Goto[1], S. Takahashi[1,2], K. Tamasaku[2], and T. Ishikawa[1,2]
[1] SPring-8/JASRI, Kouto 1-1-1, Sayo, Hyogo 671-5198, Japan
[2] SPring-8/RIKEN, Kouto 1-1-1, Sayo, Hyogo 671-5148, Japan.

Abstract

Vacuum ultraviolet (VUV) optics for the SCSS Prototype Accelerator (electron beam energy of $E_B = 250$ MeV) and X-ray optics for SCSS ($E_B = 8$ GeV) are summarized. The VUV optics have been designed for the diagnostics of the photon-beam properties in order to optimize the operation parameters of the accelerator. The system covers a radiation energy in the pulse from pJ to ≥ 10 μJ in the visible to VUV range. The first results were obtained during the commissioning period in the spring of 2006. In the latter part, R&D for x-ray free-electron laser (XFEL) optics at SPring-8 are introduced. Qualities of crystals, mirrors, and windows have been improved for coherent x-ray applications.

VUV OPTICS FOR SCSS PROTOTYPE ACCELERATOR

Introduction

The SCSS Prototype Accelerator [1] has been constructed for investigating fundamental performance of the accelerator system, which has been originally designed for the Japanese XFEL project, SCSS [2]. The Prototype machine is composed of a thermionic electron gun [3], an injector system, a main accelerator system with C-band linacs, and a couple of undulators. The undulators (with a period of 15 mm, a total period number of 600, and a minimum gap of 3 mm) produce VUV radiation with a wavelength range shorter than 60 nm at an electron beam energy of 250 MeV. Strong SASE radiation is emitted with the optimized operation conditions.

The photon diagnostics system has been constructed for the single-shot measurement of photon-beam properties such as spectrum, radiation energy, spatial profile. These parameters are crucial for studying accelerator conditions and for tuning SASE amplification. The system covers a wavelength range from visible (including a wavelength of 633 nm for the alignment with a He-Ne laser) to VUV light ($\geq$ 30 nm), and a radiation energy in the pulse from pJ (spontaneous radiation) to $\geq$10 μJ (SASE saturated radiation).

The system has been designed in the beginning of 2005, and installed during the summer construction period. The first beam of the visible light was observed in the end of November. After the replacement of some optical components, the system has been dedicated for the VUV diagnostics in the commissioning period from May to July of 2006. In particular, the first lasing was observed in June, 15th. After the first lasing, the beam tuning has been proceeded for optimizing SASE condition.

Design and Evaluation

General The schematic of the system is shown in Fig. 1. The components are placed on two granite tables, which are common designs to those used in the accelerator section. The beam pipes and components are evacuated with turbo-molecular pumps to a vacuum level of $\leq 10^{-6}$ Pa. Since the average power of the incident radiation is smaller than 1 mW at a maximum, cooling for optical components is unnecessary. A plane mirror (Au coating on a SiO_2 substrate for VUV; Al coating on a SiO_2 substrate for visible light) with a deflection angle of 170° is placed at the downstream of the first table for eliminating high-energy bremsstrahlung. A dispersive spectrometer, which is composed of an incident slit, a concave grating, and a charge-coupled device (CCD), is located in the second table. Several pneumatic actuators (indicated as monitors in Fig. 1) are prepared for inserting detectors, screens, and optical components in the beam path. At the upstream of the first table, a CCD camera and a movable plane mirror are installed for monitoring the He-Ne laser, which is used both for the alignment of the upstream components in the accelerator section and for this optical system.

Spectrometer The spectrometer is designed in a normal-incidence, constant-deviation geometry. The radius of the concave grating, the deflection angle, and the distance between the incident slit and the grating are $R = 922$ mm, $\gamma = 25°$, and $L_i = 1615$ mm, respectively. The wavelength λ focused in the center of the CCD is controlled by changing the incident angle of the grating, α, and the distance between the grating and the CCD, L_o, so as to satisfy the following equations simultaneously,

$$\frac{\cos^2\alpha}{L_i^2} + \frac{\cos^2(\alpha-\gamma)}{L_o^2} = \frac{\cos\alpha + \cos(\alpha-\gamma)}{R}, \quad (1)$$

and

$$\sin\alpha + \sin(\alpha-\gamma) = mN\lambda, \quad (2)$$

where m and N are the diffraction order and the line density of the grating, respectively. Two laminar gratings (Shimadzu Corp., Al coating with 600 lines/mm; Au coating with 2400 lines/mm) are prepared for covering longer ($\geq$ 100 nm) and shorter ($\leq$ 200 nm) wavelength region, respectively.

In the dispersed beam from the grating, different wavelengths are focused at different horizontal positions on the

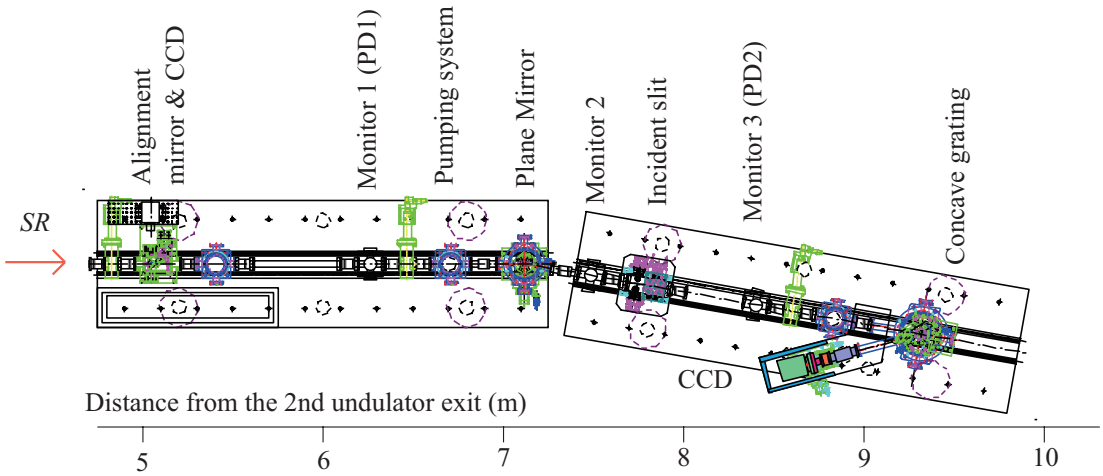

Figure 1: Layout of the optical system.

CCD. (Princeton Instruments Inc., PI-SX 400-1340B). The device, which has a back-illuminated sensor with electric cooling, covers from visible to the x-ray range. A pixel number and a pixel size are 1340 (h)×400 (v) and 20×20 μm^2, respectively. In the vertical direction, the concave grating simply works as a concave mirror. Thus, the vertical intensity distribution corresponds to a real image in the vicinity of the incident slit. An example of the spectrum image measured with the He lamp is shown in Fig. 2 (a).

The spectrum resolution is determined mainly from the following conditions: i) the line number in the illuminated area of the grating; ii) the spatial resolution of CCD; and iii) the aberration. Note that the incident beam to the slit is the quasi-plane wave, not focused as usual, because the plane mirror is used as a pre-optic. Thus the illuminated area on the grating is determined mainly by the beam divergence of the plane-wave diffraction at the slit.

Figure 3 shows calculated resolutions at a slit width of 100 μm and a detector resolution of 60 μm (3 pixels). The measured values using a helium lamp (He I, $\lambda = 58.43$ nm) and a mercury lamp (Hg I, $\lambda = 184.95$ and 253.65 nm) at the same slit width are also indicated in the figure. The measured results are mostly agreed with that calculated with the detector limitation. The resolution $\lambda/\Delta\lambda$ is grater than 1000 even at $\lambda = 58.4$ nm [see Fig. 2 (b)]. We note that a ray-trace calculation shows that the effect of the aberration is smaller than the other two factors. This result is supported by the experiment.

The spectrometer can be used for measuring a spatial profile at the slit position by switching the diffraction condition to the 0th order.

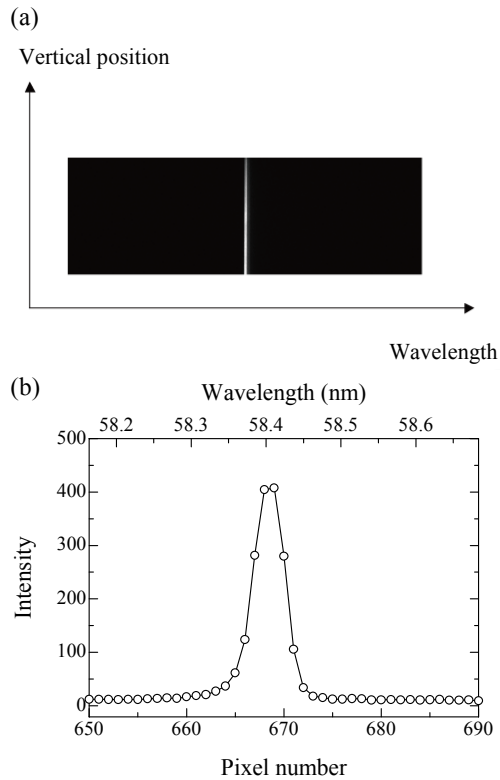

Figure 2: (a) Spectrum image measured with He lamp. The horizontal axis is the dispersive direction, where the right direction corresponds to longer wavelength. The vertical axis corresponds to the real image in the vicinity of the incident slit. (b) Intensity distribution along horizontal pixels, after the average over vertical pixels of (a). The upper axis shows the corresponding wavelength.

Intensity monitor Single-shot radiation intensities are measured with photodiodes, which are installed in the front of the mirror (PD1) and in the downstream of the slit (PD2). They are inserted to the beam axis by the remote control. The devices are designed for high-dose measurement (IRD Inc., SXUV100; SXUV100RPD [4]) with sensor sizes of 10x10 mm^2. The sensors are combined with a charge amplifier (PA-100) or with an oscilloscope. The gain of amplifier can be changed by a factor of 10^5. The signal is connected into the accelerator control system using an A/D

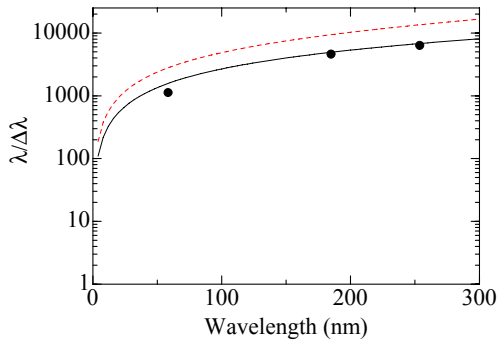

Figure 3: Resolution of spectrometer with a line density of grating of 2400 lines/mm. The dashed and solid lines are calculated results from the line number and the detector resolution, respectively. The solid circles are measured values.

converter.

Commissioning results

Spectrum Spectrum measurements for spontaneous and SASE radiations have been dedicated for tuning and evaluating the following conditions: i) optimization of electron-beam conditions including orbit, focusing, bunching condition, etc.; ii) tuning of undulators; iii) evaluation of the electron-beam density from SASE spectrum. In particular, the last [1].

The spectrum data are obtained typically with 100-shots accumulation for spontaneous light, and with single shot for SASE radiation. Figure 4 (a) shows a single-shot spectrum for SASE radiation at an electron charge of 0.24 nC, an undulator gap of 3 mm, and a slit width of 100 μm. The arc shape of the spectrum indicates that the wavelength tends to longer in the peripheral area, which is a similar phenomenon to the spontaneous radiation. The split into several lines are due to the fact that the beam is multimode. Figure 4 (b) shows a central, on-axis spectrum. The central wavelength is determined to be $\lambda = 59.0$ nm with a FWHM of $\Delta\lambda = 0.234$ nm.

The pulse length can be estimated from the spectrum. For example, if one assume that the pulse has a rectangular shape, the energy bandwidth ΔE and the pulse width Δt is represented as,

$$\Delta E \cdot \Delta t = 3.6 \ (\mathrm{eV} \cdot \mathrm{fs}), \qquad (3)$$

in the Fourier-limited pulse. In our case, $\Delta E = 0.083$ eV is simply deduced from the relationship $\Delta E/E = \Delta\lambda/\lambda$. Then the pulse width is estimated to be $\Delta t = 43$ fs.

Radiation intensity The radiation intensities measured with photodiodes are particularly used for quick optimization of the operation parameters such as electron-beam orbit, bunching condition, timing, beam collimation, alignment of undulators, etc.

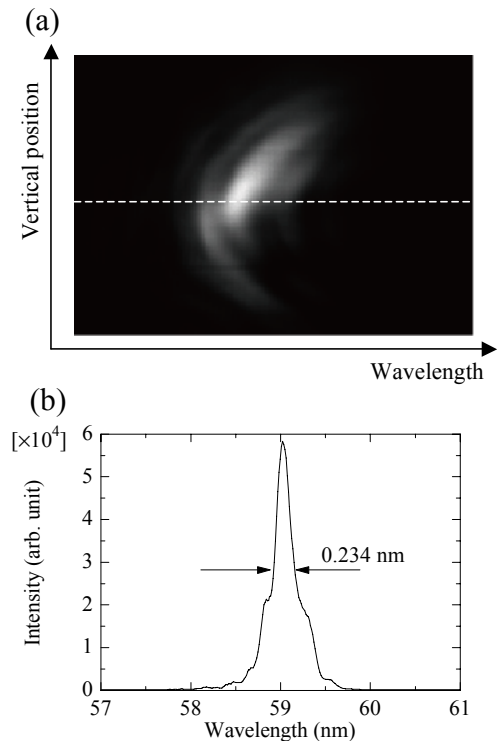

Figure 4: (a) Single-shot image of SASE radiation. (b) On-axis spectrum of (a) along the dased line.

The conversion from the output charge to the absolute intensity is necessary for evaluating SASE energy. At present, we use a catalog table [4] for refering the efficiency ($i.e.$, output charge of the detector per incident energy of the radiation pulse). However, it is desirable to determine the efficiency experimentally. For the purpose, we have tested a calibration method using the spontaneous radiation. First, the accelerator parameter is set to be debunching condition for producing only spontaneous radiation. Then the output charge per pulse is measured. The theoretical radiation energy to the detector is calculated using the sensor size and the distance to the detector. This partial energy has small dependences of machine parameters except the electron-beam energy and the charge. Thus the efficiency can be accurately obtained from the normalization of the measured charge by the calculated partial energy. The important point of the method is to choose moderate K parameter; the contamination of higher-order radiation is increased at a large K, while the dependence of the energy on K is too large at a small value. The optimized value is considered to be 0.2 to 0.7.

Figure 5 shows efficiencies of PD1 and PD2, measured with changing K parameter of the first undulator from 0.2 to 0.73. The catalog values are also indicated. The efficiency of PD1 is agreed with the catalog value within a 30 % deviation. Smaller values in PD2 are explained by the fact that PD2 is located in the downstream of the Au mirror, which has a reflectivity of ~ 80 %. Thus, it is plausible that the method can be applied to the quick check of

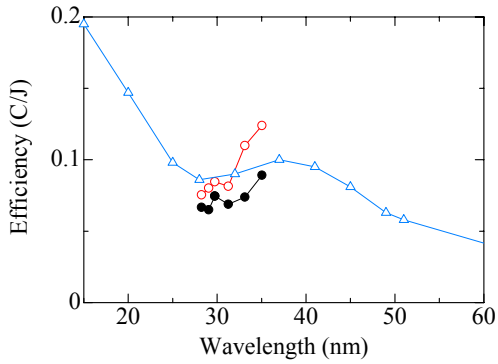

Figure 5: Detector efficiencies for PD1 (red open circles) and for PD2 (black closed circles). The blue open triangles show the catalog values.

the efficiency. We are planing to install thin-metal attenuators, because the present maximum energy, around 2 μJ, is nearly the saturation level of the detector. The above calibration method is effective even in this case. We note that the efficiencies in a wavelength range longer than 35 nm will be measured with low-energy operation of the accelerator.

Spatial profile and coherence The spatial profile at the slit position is measured using the 0th-order diffraction of the grating, where the grating simply works as a spherical mirror. Figure 6 (a) shows a single-shot image at a lasing condition only using the first undulator. The horizontal (vertical) width and divergence (in FWHMs) are determined to be 3.4 (3.9) mm and 240 (280) μrad, respectively, using a distance of 13.9 m from the undulator exit to the slit, as seen in Fig. 6 (b).

The spatial coherence is evaluated with a Young's double-slit experiment. The double slit with each width of 100 μm (height of 500 μm) and a central spacing of 400 μm were installed at the incident slit position. The grating was replaced with a plane mirror, and the diffraction image was recorded with the CCD, as shown in Fig. 7. The image with SASE radiation (single-shot detection) is compared to that at spontaneous radiation (100 shots). The former image has a higher visibility [Fig. 7 (c)], which indicate higher spatial coherence. We are planing to make more quantitative measurement using double slits with different spacings.

Extension for user experiment

In 2007, we are planning to start the operation dedicated for user experiments. A present plan for the extension is as follows: The experimental hall (about 12×8 m^2) is constructed at the outside of the accelerator tunnel. The beam transport channel is branched from the middle of the present diagnostic system. The beam is two-dimensionally collimated with double mirrors. A gas chamber with a differential pumping system is installed for a transparent, shot-by-shot monitor for the radiation intensity.

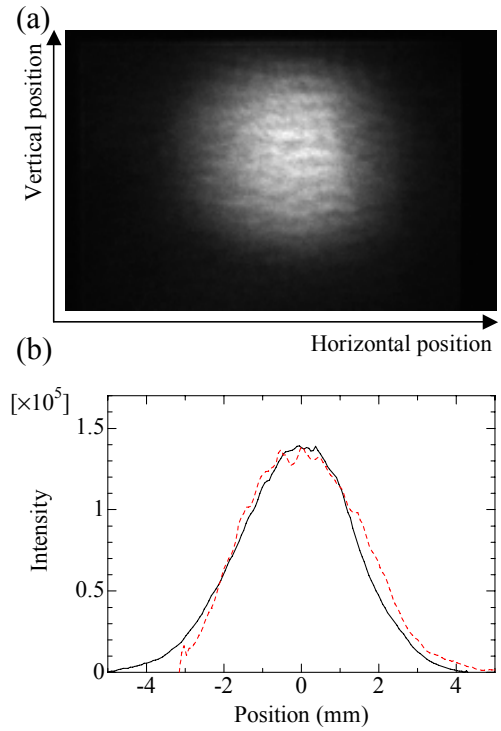

Figure 6: Spatial profile of SASE radiation (a), and its projections for horizontal (solid line) and the vertical (dashed line) axes (b).

X-RAY OPTICS FOR SCSS

Introduction

The principal missions of the optics in XFEL are i) to condition photon beam for user experiments, and ii) to diagnose radiation properties for the feedback to the accelerator. In this section, we will introduce R&D activities proceeded at SPring-8.

There are two technological challenges in XFEL optics. One is to suppress speckles possibly originating from imperfections of optical components under the coherent illumination. Both surface and bulk qualities should be strictly controlled.

The other is to keep the radiation dose below the melting limit [5, 6]. A simple solution is to extend the x-ray transport line for decreasing the energy density. However, in the SCSS case, the magnification of the beam area, when compared to that at the entrance of the beamline, is not larger than 10 because of small beam divergence (0.4 μrad at E=12.4 keV, for example) and the limited distance of $\sim$ 200 m. An alternative method is to use components made from light elements such as Be, B, C, etc. Figure 8 shows calculated doses for several materials that are placed normal to the incidence. The following beam parameters [2] are used for the calculation: the photon flux of 7.6×10^{11} photons/pls, the STD beam size at the source of 50 μmϕ, and the distance from the undulator exit of 100 m. The STD beam divergence is calculated from the diffrac-

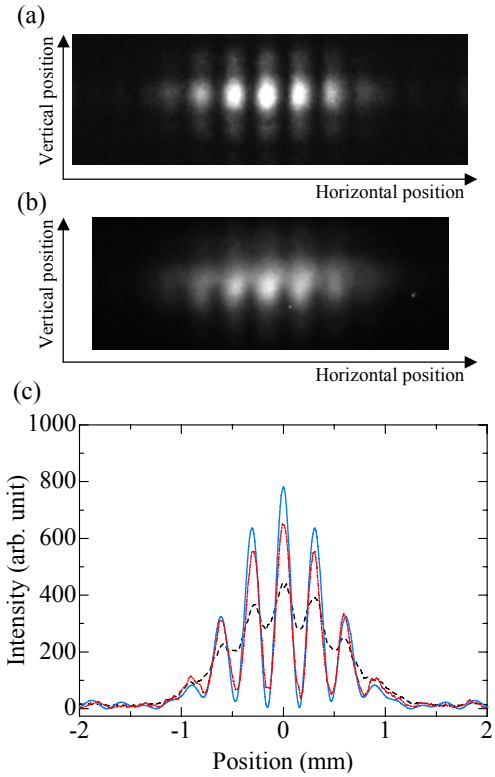

Figure 7: Young's double-slit experiment for SASE radiation with single shot (a), and for spontaneous radiation with 100 shots (b). The cross sections of the cental region at these conditions are shown in (c) as the red dot-dashed and black dashed line, respectively. A calculated result under the coherent illumination is also represented as a blue solid line.

tion limited condition for each photon energy. It is found that i) the doses of light materials (Be and C) have a margin to the threshold levels more than two-order of the magnitude, and ii) the dose of Si is still below the threshold, but iii) the dose of Cu is above threshold in the energy range higher than the K-absorption edge.

Crystals and windows

Crystal monochromator is used to set specific spectral window at SASE and spontaneous radiation. We have two candidates for crystal materials: Si and diamond. The energy resolutions ($\Delta E/E$) are 1×10^{-4} and 6×10^{-5} for Si (111) and Diamond (111) reflections, respectively.

Si is the most popular materials for monochromator crystal at the present synchrotron facilities, because of the availability of high-quality, large-volume ingots. Since the Bragg angle for (111) reflection at $E = 10$ keV is 11 degree, the dose per atom around this photon energy is decreased by a factor of 5, compared to the normal incidence case shown in Fig. 8. The ratio is further increased for higher photon energy ($i.e.$, lower Bragg angle). Thus, Si would be useful as XFEL monochromator above 10 keV. Crystal cooling is not a serious problem for SCSS. Because

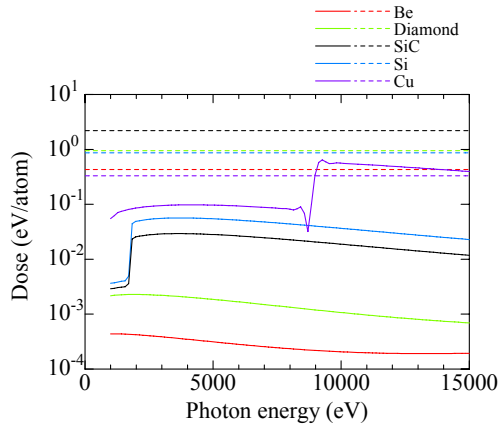

Figure 8: Energy dependence of dose for several materials. Solid lines are calculated values with SCSS beam parameters, while dashed lines are the threshold levels of melting limit.

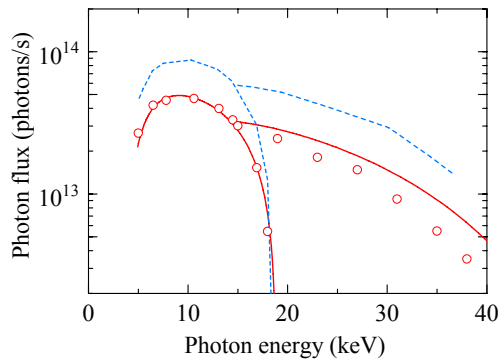

Figure 9: Photon flux of the monochromatic beam at SPring-8 undulator beamlines. The open circles and solid lines are measured and calculated values for diamond monochromator, respectively, and the dashed lines are measured values for cryogenically-cooled Si monochromator.

the average power is smaller than 100 mW, water cooling would be sufficient.

Diamond monochromator is the most promising when utilized under a higher dose. We have collaborated with Sumitomo Electric Industries Ltd. (SEI) to develop high-quality synthetic diamond in type IIa [7]. Recently, (111) crystal plates with relatively large sizes ($\sim 8 \times 4$ mm^2) are commercially available. We have tested performance of diamond double-crystal monochromator (DCM) at a SPring-8 undulator beamline. Two (111) diamonds crystals, which are attached to copper crystal holders using indium sheets, are cooled by water. Figure 9 shows the measured photon flux. Experimental results are well agreed with the theory in the energy range below 20 keV. Topographic studies showed a relationship between the surface condition and the image quality. It is necessary to develop surface polishing technique.

For windows, Be foils have been widely used at syn-

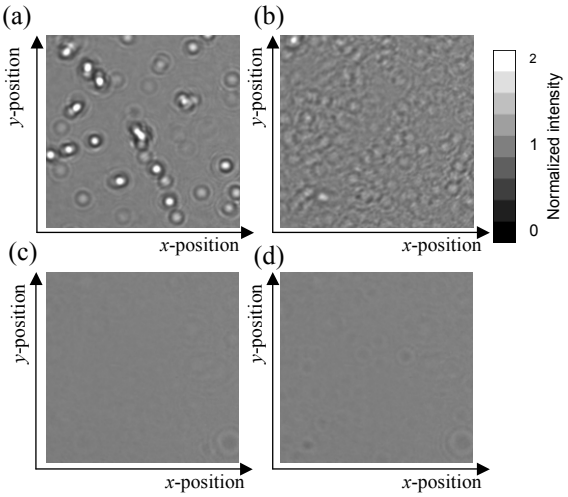

Figure 10: Transmission images of Be windows: Polished PF-60 (a), polished IF-1 (b), polished PVD (c), and Kapton foil (d). The photon energy is $E = 12.4$ keV. The beam areas are 300×300 μm^2. The distance between the sample to the camera is 1400 mm. The round spots commonly seen at the bottom-right corners of (c) and (d) are caused from a Kapton foil in the upstream of the system.

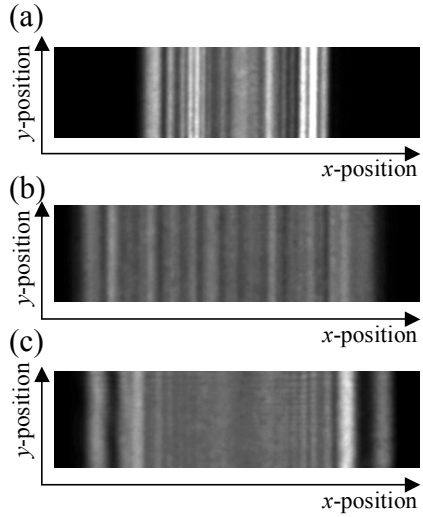

Figure 11: Reflection images of Si mirrors: Pre-machined surface (a), PCVM polished surface (b), and PCVM+EEM polished surface (c).

chrotron facilities owing to their low absorptions for x-rays. They are also promising candidates for XFEL windows from the viewpoint of the dose issue (see Fig. 8). However, it has been found that they produced speckles under coherent illumination. From the experiment at the 1 km beamline of SPring-8, it was found that the speckles in the conventional Be windows shown in Fig. 10 (a,b) are originated mainly from voids in the bulk [9]. To remove the voids, the physical vapor deposition (PVD) method has been tested. The surface of the PVD Be foil has been polished to decrease the surface roughness to be 0.05 μm. Finally, the image of a polished PVD Be shown in Fig. 10 (c) was found to be superior to that of a Kapton foil in (d) [10]. We note that Be will be useful for attenuators. Higher attenuation will be achieved using Si or SiC.

Mirror

Total-reflection mirrors are used for deflecting SASE radiation in order to eliminate high-energy bremsstrahlung. Focusing is another important function of the mirror. The surface quality is crucial for suppressing speckles under coherent illumination. From 2000, we have collaborated with Osaka University to realize high-quality mirrors. Special techniques of surface polishing have been developed: EEM (Elastic Emission Machining) and PCVM (Plasma Chemical Vaporization Machining) [11]. Figure 11 shows reflected images of Si mirrors measured at the 1 km beamline with a photon energy of $E = 20$ keV. The incident angles and the distance between the mirrors to the camera are set at 1.2 mrad and 966 mm, respectively. The intensity fluctuations observed with the pre-machined surface in Fig. 11 (a) are mostly suppressed with the PCVM+EEM polished mirror in (c). Thus, we can conclude that the mirror is available for conditioning coherent x-rays.

These machining techniques with combination of a new metrological method called the microstitching interferometry (MSI) [12] were applied to fabrication of aspherical mirrors for nano-focusing. A couple of Pt-coated mirrors are fabricated with figure accuracies of 2 nm (p-v). Two dimensional focusing down to 36×48 nm^2 has been achieved at $E = 15$ keV with the Kirkpatrick-Baez arrangement [13].

Another critical issue for the XFEL mirror is to choose appropriate surface material to suppress the dose under the melting limit [5]. Figure 12 shows the calculated doses and reflectivities for several materials. The beam parameters are as same as those used in Fig. 8 with a photon energy of $E = 12.4$ keV. It is found that C or SiC seems to be useful, while Si and Au are questionable. From the figure, the incident angles should be smaller than 2 mrad (0.14 degree). If we set an acceptance width to be 1 mm, the total length of the mirror should be larger than 500 mm. Thus, the next R&D issues for XFEL mirror fabrication are i) to study coating and polishing method for the light materials, and ii) to product large mirror with a sufficient figure accuracy. It is also important to establish technologies to protect the surface from contaminations or dusts, because small decrease of reflectivity can cause serious damage of the surface under the high-dose irradiation. Great care should be required in the design of the driving mechanism in order to keep an ultraclean environment.

Single-shot spectrometer

As shown in the previous section, the VUV single-shot spectrometer has played a central role for the radiation diagnostics. Development of similar instrument that works

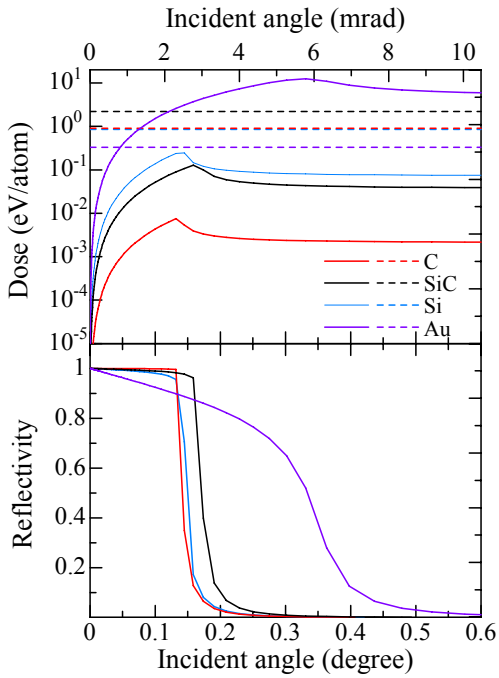

Figure 12: (above) Angular dependences of doses for the total reflection mirrors. Several materials are compared. Solid lines are calculated values with SCSS beam parameters, while dashed lines are the threshold levels of the melting limit. (below) Dependences of reflectivities.

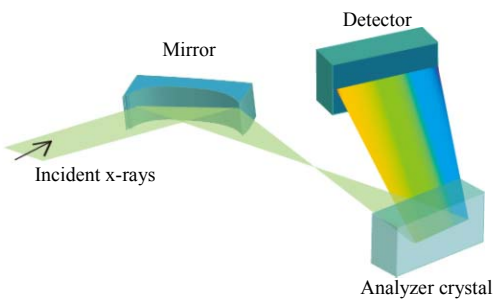

Figure 13: Setup for single-shot x-ray spectrometer.

in the x-ray region is crucial. Recently, we have developed such a spectrometer that combines a high-quality mirror and a Si flat crystal. The former is used to diverge the incident parallel beam, while the latter is to select specific energy according to the Bragg's law. As a result, the exit beam has an energy dispersion. The key point is again the figure accuracy of the mirror to suppress speckles. Using (555) reflection for the analyzer crystal, the energy resolution of the instrument has been measured to be 13.1 ± 1.9 meV at $E = 10$ keV with a full energy range of ~ 3 eV. Wider energy range can be easily obtained by changing diffraction plane to lower index [14].

SUMMARY

The VUV diagnostic system for the SCSS prototype accelerator has been constructed and successfully operated. At a lasing condition, a radiation energy in the pulse has been evaluated to be ~ 2 μJ. The pulse width is estimated to be shorter than 100 fs from the measurement of the energy spectrum. The double-slit experiment showed that higher spatial coherence is achieved at a lasing condition.

As XFEL optical components, we have developed high-quality diamonds, mirrors, and Be windows. A single-shot spectrometer for XFEL diagnostics has been tested and confirmed to have a high resolution of 1.3×10^{-6} at $E = 10$ keV.

ACKNOWLEDGEMENT

We thank all SCSS members for fruitful discussions and suggestions. We acknowledge Dr. Y. Takata (RIKEN), Dr. Y. Harada (RIKEN), and Dr. T. Tokushima (RIKEN) for their suggestions on designing the spectrometer, Dr. A. Higashiya (RIKEN), Dr. T. Matsushita (JASRI), Dr. Y. Tamenori (JASRI), and Dr. A. Sekiyama (Osaka Univ.) for their help in the calibration of the spectrometer, Mr. T. Kirimura (RIKEN) for the calibration of the photodiodes, Mr. M. Tanaka (JASRI), Mr. T. Irie (JASRI), and Mr. K. Onoe (ULVAC) for their activities in the installation of the VUV diagnostic system.

REFERENCES

[1] H. Tanaka et al., in these proceedings.

[2] "SCSS X-FEL Conceptual Design Report", RIKEN/SPring-8, May 2005, Mikazuki, Japan, http://www-xfel.spring8.or.jp/

[3] K. Togawa et al., "Emittance Measurement on the CeB_6 Electron Gun for the SPring-8 Compact SASE Source", FEL 2004 conf. proc. (2004) THBOC03.

[4] International Radiation Detector Inc., http://www.ird-inc.com/

[5] R. Tatchyn, "LCLS Optics: Technological Issues and Scientific Opportunities", SLAC-PUB-6064, SLAC, Stanford (1993).

[6] "Linac Coherent Light Source (LCLS) Conceptual Design Report", SLAC-R-593, SLAC, Stanford (2002).

[7] K. Tamasaku, T. Ueda, D. Miwa, and T. Ishikawa, "Goniometric and topographic characterization of synthetic IIa diamonds", J. Phys. D: Appl. Phys. **38** (2005) A61.

[8] M. Yabashi et al., "Diamond double-crystal monochromator for SPring-8 undulator beamlines", Proc. for SRI 2006 (in press).

[9] S. Goto, M. Yabashi, K. Tamasaku, S. Takahashi, and T. Ishikawa, "Characterization of Beryllium Windows using Coherent X-rays at 1-km Beamline", AIP conf. proc. **705** (2004) 405.

[10] S. Goto, M. Yabashi, K. Tamasaku, and T. Ishikawa, "Characterization of Beryllium Windows for Coherent X-ray Optics", Proc. for SRI 2006 (in press).

[11] Y. Mori et al., ”Development of plasma chemical vaporization machining and elastic emission machining systems for coherent X-ray optics”, Proc. SPIE, Vol. 4501 (2001) 30.

[12] K. Yamauchi et al., ”Microstitching interferometry for x-ray reflective optics”, Rev. Sci. Instrum. **74** (2003) 2894.

[13] H. Mimura et al., ”Hard X-ray Diffraction-Limited Nanofocusing with Kirkpatrick-Baes Mirrors”, Jpn. J. Appl. Phys., **44** (2005) L539.

[14] M. Yabashi et al., ”Single-shot spectrometry for x-ray free-electron laser”, Phys. Rev. Lett. **97** (2006) 084802.

X-RAY DETECTORS AT DESY

H. Graafsma, DESY, Hamburg

Abstract

The European X-ray Free Electron Laser to be constructed in Hamburg, presents interesting challenges for the X-ray detectors. Every pulse of the XFEL represents an entire experiment of its own, partly because of sample degradation or destruction, and partly because of pulse to pulse fluctuations. Therefore, a maximum amount of data has to be collected in a single shot. This means first of all that photon counting detectors cannot be used, instead one has to construct integrating detectors, still with single photon sensitivity. Secondly, since the strength of the European XFEL is a very flexible pulse structure with high repetition rates, fast framing times down to 200 ns (5 MHz) are required. I will present some of the requirements imposed by the science cases foreseen at the European XFEL, and some of the possible solutions under consideration, both at DESY and at other places in the world.

PAPER NOT AVAILABLE

WAVE-FRONT OBSERVATIONS AT FLASH

M. Kuhlmann, E. Plönjes, K. Tiedtke, S. Toleikis, HASYLAB at DESY, 22607 Hamburg, Germany
P. Zeitoun, J. Gautier, T. Lefrou, D. Douillet, ENSTA, 91761 Palaiseau cedex, France
P. Mercère, Synchrotron SOLEIL, 91192 Gif-sur-Yvette Cedex, France
G. Dovillaire, X. Levecq, S. Bucourt, Imagine Optic, 91400 Orsay, France
M. Fajardo, Centro de Física dos Plasmas, Instituto Superior Técnico,1049-001 Lisboa, Portugal.

Abstract

During the first year of user operation at the Free-Electron Laser in Hamburg (FLASH) wave-front measurements were recorded in the vacuum-ultraviolet region using a Hartmann sensor (by Imagine Optic). The Hartmann principle is based on a hole array, which divides the incoming beam into a large number of sub-rays monitored in intensity and position of individual spots. The identification of the local slope of the incident wave front makes the aberrations from a perfect spherical wave front visible. Ray tracing in upstream direction accesses the beam path especially the focal spot in size and position.

The intense and coherent vacuum-ultraviolet FEL beam leads to unique requirements for the wave-front sensor setup. We report an optimized setup to observe the metrology of flat and curved mirrors at FLASH beam lines. The use of wave-front measurements to provide reliable machine parameter is discussed.

The wave-front sensor proved to be a valuable tool to observe the FEL beam quality and the performance of optical elements, filters and diagnostic tools.

GENERAL

FEL beam characteristics

The here-introduced wave-front sensor is used as tool in the photon diagnostics at FLASH. A free electron laser beam shows specific characteristics which demand certain requirements for any diagnostic tool.

Based on the SASE principle all FEL features differ from shot to shot depending on the degree of saturation. At a high level of some µJ per pulse the FEL operates in an intensity regime of two orders of magnitude. The required adaptations in the wave-front sensor setup and the needed data statistics which can document the shot to shot changes are discussed in the following sections.

The wavelength regime of 13 nm to 60 nm is of no consequence for the achromatically wave-front sensor. The short pulse length of 10 – 50 fs and the variable rates of repetition will be a challenge if the wave-front sensor becomes an online diagnostic tool in the future.

Wave-front measurements

In the regime of visible light sensors based on the Hartmann respectively the Shack-Hartmann principle are of common use. Astigmatism, spherical aberration and coma are quantitatively determined. Aberrations of such kind are generally of lower amplitude in the extreme-ultra-violet or soft x-ray domain. For the first time Le Pape et al. used a wave-front sensor in the EUV regime. The experiment took place at a tabletop saturated soft-x-ray laser [1]. Here, the wave-front sensor shall be evaluated for

- FLASH beam line commissioning
- FEL characterisation
- Online diagnostics as part of user experiments

SETUP

Setup of the beam lines

Five beam lines are in operation mode for user experiments. At each an additional optical laser for pump-probe experiments is available. Figure 1 shows a scheme of the FLASH experimental hall. The beam lines discussed in the following are identified by the full-width-half-maximum (fwhm) beam size of their focal spot, considering the theoretical design parameters of the FEL. More than 10 switching or focusing mirrors are in use. Only one beam line can make use of the FEL beam at a time.

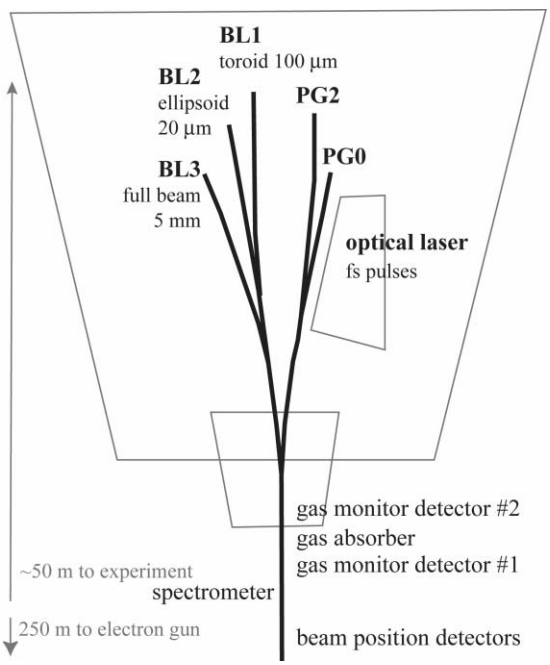

Figure 1: Scheme of the FLASH experimental hall and its beam lines. Some photon diagnostics tools are outlined along the FEL beam.

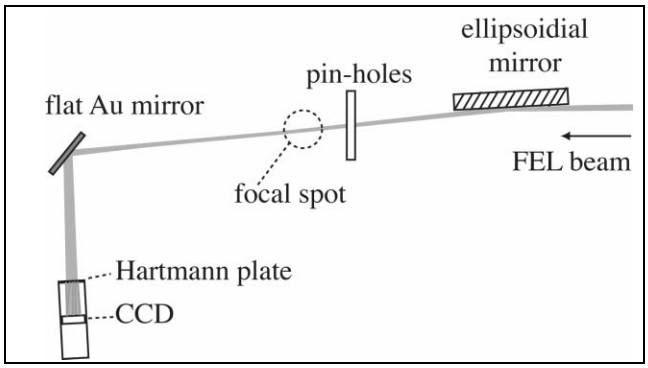

Figure 2: Setup for wave-front measurements at beam line BL2. The sensor is positioned 3.5 m behind the focal spot.

Up to now, the wave-front sensor was used at the beam lines BL1, 2, and 3. All are high intensity beam lines without a monochromator. Whereas at BL3 the unfocused FEL beam can be measured, BL1 and BL2 are designed to a focal spot size of approximately 100 µm and 20 µm, respectively. All switching and focusing mirrors working with an incident angle of 2 or 3 degree and have a carbon coating.

Setup of the wave-front sensor

A perfect spherical wave is compared with the actual beam to analyze its wave front. Therefore, both beams have to pass through a two dimensional array of holes (Hartmann plate) and are recorded under similar conditions on a CCD. Here, the Hartmann plate is made of nickel. It consists of 51 x 51 square holes each 110 µm in size and with a pitch of 387 µm. Therefore, the maximal field of view is 19.5 mm x 19.5 mm. The quadratic holes are tilted by 25° to prevent the long-range diffracted signal coming from one hole to interfere with the spot of the adjacent hole, generating an unpredictable error on data treatment. The sensor includes a direct CCD camera, PI-SX1300, with 1340 x 1300 pixels, each 20 µm in size. It is operated at –40° to minimize the noise level. In general, a zonal reconstruction is used to take as much pixels as possible into account [2]. To distinguish the contributions of higher order aberrations a modal reconstruction algorithm can be used, too. Imagine Optic provides the complete sensor.

Figure 2 is the sketch of a typical setup. The plotted example was build up at beam line BL2. The sensor is positioned in 3.5 m distance from the focal spot, more than the 2 m focal distance of the focusing ellipsoidal mirror. This allows for a full illumination of the sensor. A flat gold mirror placed in 45 degree absorbs 97% of the beam intensity at a wavelength of 32 nm. Currently, mirrors with gold, silver, and aluminium surfaces are used. The different mirrors are required to operate the sensor at different wavelengths and levels of intensity. Otherwise the camera pixels are generally saturated. Pinholes, generating a perfect spherical wave, can be moved in the beam to allow relative measurements. The sensor was calibrated using this setup in the direct beam without the additional mirror. Only than the FEL intensity was sufficient to illuminate the full field of view of the sensor. A pinhole 5 µm in diameter was used.

BEAM LINE COMMISSIONING

The spatial characterization of the wave front has important applications in discovering localized defects in beam line optics. The proposed intensities of FLASH forced the beam line design to work with grazing incidences of 2° to 4° for both switching and focusing mirrors. The FEL wavelength of 60 nm to 13.1 nm in the fundamental demands full vacuum and particle free equipment towards the experiment. The task is to prove the feasibility of the sensor for the use as commissioning tool at FLASH.

Documentation of the focal spot size

Beam line BL2 consists of two flat switching mirrors and one focusing ellipsoidal mirror. The design proposed a spot size of 20 µm at a focal distance of 2 m. Figure 3 shows the depth of focus reconstructed from wave-front measurements in October 05. Displayed are the full-width-half-maximum (fwhm) values of the beam size at distinguished positions relative to the calculated focal point. The focal spot is reconstructed to a fwhm-size of 31 µm x 31 µm, an error of ± 2 µm is given by the Gaussian fit of the reconstructed beam spot. A minor astigmatism can be seen in Figure 3 according the difference in horizontal and vertical minimal focal spot position. With further investigations this problem was imputed to a switching mirror and was eliminated by remounting the mirror.

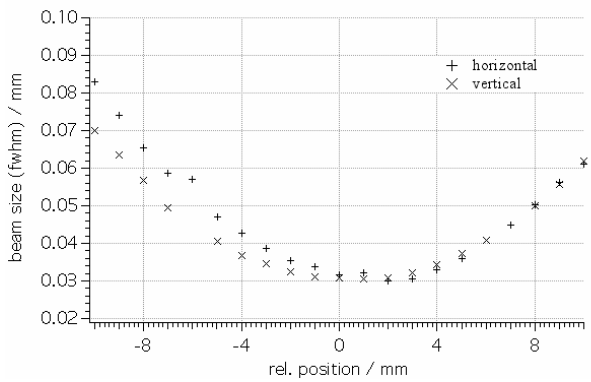

Figure 3: The depth of focus at beam line BL2 at a wavelength of 32 nm. Shown are fwhm values at distinguished distances from the measured focal position in vertical and horizontal direction. The minimal beam size is 31 µm x 31 µm (± 2 µm).

Nevertheless, the overall wave front here displayed in Figure 4 is of high quality. Displayed are absolute values of the difference to a perfect wave for each pixel. So the comparison of variable wavelengths of the FEL is possible. For wave-front analysis the generally used scaling in parts of lambda complicates the comparison and documentation of different measurements. The wave front can be characterized by the root-mean-square error rms=3nm and the peak-valley difference PV=19nm. The

wave front used for the calibration of the sensor was measured with rms=0.64nm and PV=4nm. Additional the position of the focal spot is recorded to allow for the shot to shot characteristic of the FEL. In the here shown early phase of the FEL operation an unstable beam correspond to a standard deviation of 4.5 µm in spot size.

The design values for the beam line parameters are not achieved up to now. The wave-front measurements verify that the situation is not origin in a misalignment or in manufacturing errors of the optics. Further measurements at the unfocused beam line BL3 explain the discrepancy by the observation of a large source size, see section FEL Characterization.

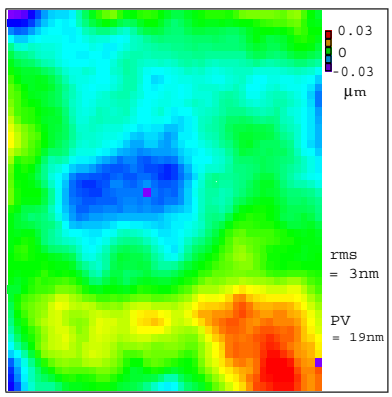

Figure 4: Full field of view (51 x 51 pixels) of a wave front. Displayed are the absolute discrepancies from a perfect wave front. The achieved result is close to the actual resolution limit of the used wave-front sensor.

Mirror alignment

A toroidal mirror with a focal length of 10 m is used at the beam line BL1. The critical alignment of the yaw angle is demonstrated in Figure 5. First the small field of view is obvious. Far from optimal for this kind of measurements it is due to the long focal distance of 10 m that we were forced to position the sensor only 2.55 m behind the focal spot, which leaves the here displayed beam size of ~3 mm. Image (a) shows a strong astigmatism. The overall ellipsoidal beam profile is narrow and tilted. The rms of 395 nm only documented the obvious misalignment. From image (a) to image (b) in Figure 5 the toroidal mirror was moved by 5 mrad in the direction of the yaw angle. A strong change in beam profile and shape took place. The beam profile is more of the true circle of the FEL itself but still tilted. The rms of the distortions is 70 nm, only. The centre of the beam stays at the same pixel position than before. From image (b) to image (c) the mirror was further moved by 5 mrad around the yaw angle. Closer to an optimal alignment the improvement is not as drastic as it had been before. The shape of the beam stays the same and only its diagonal becomes a perfect horizontal line. Therefore the centre of the beam moved by 5 pixels in x and in y direction. The wave front is of rms=50 nm. The detailed analysis of the best image (c) evaluated 73% of the distortions as astigmatism caused by a wrong position in the yaw angle direction, and 12% as coma, due to a minor misalignment in the roll angle orientation. Further alignments are planed in the future after improvements, concerning the field of view and some mirror mechanics, took place. The wave-front measurements proved the need of such upgrades at beam line BL1.

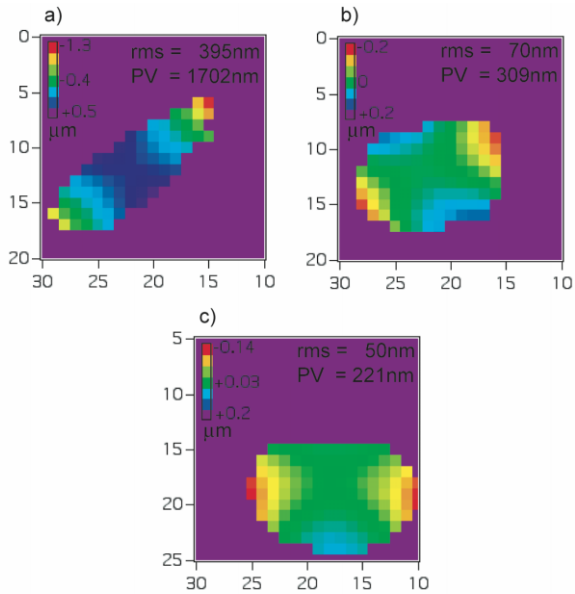

Figure 5: Wave front changes during the optimisation of the toroidal mirror in the direction of the yaw angle at beam line BL1. The scales are different for the images to identify the shape of each wave front. To document the position of the spot the illuminated pixels of the CCD are displayed, bottom and left. Between the images the mirror was tilted in the yaw direction by total 10 mrad.

Long-term documentation

In the last year the FLASH beam performance shown an incredible improvement. Especially the mean beam intensity increases by more than one order of magnitude. The long-term effects to the optical elements need to be observed. The highly sensitive wave-front measurements are excellent to show even slight damages to the carbon coating of the mirrors. No other diagnostic tool can provide us with such information during an operation mode of the FEL.

Filter performance

A FEL beam consists of higher harmonic parts. Less than 1% intensity of the fundamental can contribute in the third harmonic, the most intense higher harmonic. Nevertheless, orders up to the seventh harmonic were measured. The application of filters and filter systems is required to make detailed use of these lower wavelengths or to eliminate any ill effects for some experiments.

The standard used nitrogen gas absorber not influences the FEL wave front. This was checked during a FEL operation with a wavelength of 32 nm. The use of the absorber to a transmission of only 0.1% leaves the FEL wave front unchanged.

More critical is the use of solid filters, metal foils or crystalline membranes. A generally used thickness of such a filter is 200 nm. Up to now, no effect in this regime is recorded. To get a change in wave front an aluminium foil of > 2 μm had to be put in the beam. Even then, the wave front distortions are homogenous and of only 13 nm rms. Therefore, the effect to the optical geometry by creating a second source component is of more consequent for an experiment.

This result eased the wave front measurements itself in the future, as the still complicated reactions on changes in intensity can be countered with additional filters without questioning the achieved results.

FEL CHARACTERIZATION

FLASH is the first working FEL in the EUV and soft x-ray regime [3, 4]. Source size, shape, and position can vary on a shot to shot characteristic. The importance for most beam line optics has been pointed out in the section above. Here the characteristic of the FEL itself and any conclusions considering the machine operation is discussed. The task is to evaluate the resolution of the sensor for the requirements at FLASH.

A good wave front of 4 nm rms was recorded at the end of beam line BL3 with four flat mirrors along the regular beam path. Relative measurements to a beam origin in a 50 μm pinhole in front of these mirrors lead to a portion of 2 nm rms caused by the optics and of 2 nm rms origins in the incident FEL beam. In this regime the measurements are close to the limit of the sensor calibration. Further, the shot to shot variations of the FEL pulses were observed with the same magnitude. To allow an analysis of such a beam we are in need of a better calibration of the sensor.

Similar limits are recorded concerning the source size and distance. In general the realistic value of 82 m distance to the source is reproduced. Nevertheless, the current setup and software can produce errors of some meters for a focal spot in a distance of more than 80 m. This is unacceptable by at least one order of magnitude.

The beam size at the experimental station of BL3 in February 06 was 10 mm fwhm. In a situation of not fully reached the saturation level such a large beam size is not surprising. The standard deviation of the x- and y-position of the beam centre was 1.3 mm and 2.3 mm respectively, translated in an angle of ~24 μrad. These results match the theoretical parameters of a FEL just close to saturation [3].

A qualitative measurement of relevant machine parameter is not resolved with the current wave-front sensor setup. Improvements are foreseen: First an automatic alignment of some equipment parts is planed to minimize the sensor alignment time in respect to the limited beam time available. In this context the diffraction limit of the sensor design λ/120 at 13 nm [5] shall be reached at the FEL, too. Therefore a new and perfect calibration is required. Thinkable is the use of a different Hartmann plate or the development of a new sensor specialized for the different and progressed circumstances at a FEL facility like FLASH.

ONLINE IMPLEMENTATION

In contrast to other diagnostic tools the here-introduced sensor measured the wave front in a distance of some meters behind the focal spot. A use as online diagnostic is possible when the direct beam path is not blocked by the experiment itself, e.g. most experiments operating in the gas phase. Even if a target block the beam a verification of the FEL performance in between some measurements is useful.

Main problems are the intensity and geometric circumstances, which will be dictated by the experiment itself and not by the wave-front measurements anymore. As critical as these adaptations have been so far it is a challenge to provide a setup with even more flexibility.

CONCLUSION

The here reported measurements proved the feasibility of wave front observations under FEL conditions. The high sensitivity of the wave-front sensor is required for the high beam quality at FLASH. First order aberrations were recorded during first beam line commissioning. The ongoing improvement of the FLASH beam quality in stability, source size, and intensity as well as optimized optics alignment was documented during the last year. The non-invasive and remote sensor can be used as online tool to document the shot to shot characteristics of the FEL.

ACKNOWLEDGMENT

These measurements based upon the work of U. Hahn and the HASYLAB optics and vacuum groups. The commissioning is part of the FLASH team [3].

This work was supported by the European Community Research Infrastructure Action under the FP6 “Structuring the European Research Area” Programme through the Integrated Infrastructure Initiative “Integrating Activity on Synchrotron and Free Electron Laser Science”, contract number RII3-CT-2004-506008.

REFERENCES

[1] S. Le Pape, P. Zeitoun, M. Idir, P. Dhez, J. J. Rocca, M. Francois, Phys. Rev. Lett. vol. 88 (2002), p. 183901.

[2] W. H. Southwell et al., JOSA, vol. 70 (1980) p. 8

[3] V. Ayvazyan et al., Eur. Phys. J. D, vol. 37 (2006), p. 297.

[4] E. L. Saldin, E. A. Schneidmiller, M. V. Yurkov, DESY Print TESLA-FEL, 2004-06 (2004).

[5] P. Mercere, P. Zeitoun, M. Idir, S. Le Pape, D. Douillet, X. Levecq, g. Dovillaire, S. Bucourt, K. A. Goldberg, P. P. Naulleau, S. Rekawa, Optics Lett., vol. 28 (2003), p. 135.

A NEW GENERATION OF X-RAY OPTICS BASED ON PYROLYTIC GRAPHITE*

H. Legall, H. Stiel, Max-Born-Institute, Berlin, Germany
A. Antonov, I. Grigorieva, Optigraph GmbH, Berlin, Germany
V. Arkadiev, IAP e.V., Berlin, Germany
A. Bjeoumikhov, IfG GmbH, Berlin, Germany and A. Erko, BESSY GmbH, Berlin, Germany

Abstract

Highly Oriented Pyrolytic Graphite (HOPG) is a mosaic crystal, which consists of a large number of small nearly perfect crystallites. The unique structure of HOPG crystals enables them to be highly efficient in diffraction in an energy range between 2 keV up to several 10 keV. The mosaicity of the crystal is responsible for the dramatic increase of integral reflectivity in comparison to perfect crystals. Furthermore thin HOPG crystal films can be easily bent and exhibit a very high thermal conductivity making them interesting for application in experiments with high average power x-ray sources. For application in x-ray spectroscopy the achievable spectral resolution of the crystal optics is of particular interest. Recently performed measurements with very low foil thickness have revealed a spectral resolution of E/ΔE = 2900 in (004)-reflection. This is by far the highest spectral resolution reported for Pyrolytic Graphite (PG) crystals. The integral reflectivity of these films is still comparable to that of ideal Ge crystals. In this work we present new results concerning the energy resolution, integral reflectivity and application of thin bent Graphite films.

INTRODUCTION

Highly oriented pyrolytic graphite (HOPG) is an artificial graphite produced by thermal cracking of a hydrocarbon gas and deposition under low pressure and afterwards annealing the deposit under pressure [1]. In this way and after some further fabrication steps thin films of HOPG can be made with thickness of less than 10 μm. These films can be easily bent by mounting them adhesively on a mould of any shape [2].

Sectional topographical diffraction measurements have shown an arrangement of the small crystallites with some μm in size to larger mosaic blocks with some 100 μm in diameter and some 10 μm in thickness [3]. The angular distribution of the crystallites, with plane orientations off to the normal axis to the crystal surface, is called mosaic spread. The mosaic spread between the crystallites is much smaller than that between the mosaic blocks. The mosaic blocks again show a correlation in orientation and form larger crystal domains with some mm in size.

Because of its high thermal conductivity κ and low linear thermal expansion coefficient α in basal plane (cp. Table 1), which both are similar to those of diamond crystals, PG crystals could be interesting for many applications with regard to x-ray sources delivering high average x-ray power. Also the absorption thickness t_{abs} of HOPG is similar to that of diamond. Consequently less heat is absorbed in comparison to other crystals.

The diffraction properties influencing the energy resolution of PG films are determined by the mosaicity and the intrinsic width of Bragg reflection. Latter refers to the diffraction properties of the small crystallites and is called the Darwin width for nearly perfect crystals. It results from particle size and/or strain broadening. Mosaicity makes it possible that even for a fixed angle of incidence to the crystal surface, an energetic distribution of photons can be reflected, because each photon of this energetic distribution can find a crystallite plane at the right Bragg angle. The width of this energetic distribution depends on the mosaic spread. The mosaicity is also responsible for the dramatic increase of integrated reflectivity in comparison to perfect crystals in an energy range between 2 keV and several 10 keV [4]. The so-called mosaic-focusing, as shown in Fig. 1, which occurs in a 1:1 magnification geometry enhances further the intensity in the image plane.

In contrast to ideal crystals, in mosaic crystals the photon has to penetrate deeper into the crystal, before it finds a crystallite aligned well, from which it can be reflected. That means that the effective depth, from which diffraction in mosaic crystals occurs, is much larger compared to ideal crystals. Therefore the energy resolution can be strongly affected by the thickness of the Graphite films. Recently we have shown that very thin Graphite films can reveal energy resolutions and integral reflectivity comparable to Ge(111) [5].

Table 1: Thermal properties and absorption thickness at 8 keV for different crystals.

Material (hkl)	κ **[W/cm K]**	α **[/K x 10^{-6}]**	$\mathbf{t}_{abs}$ **[μm]**
Diamond(111)	21	0.8	250
Si(111)	1.25	2.33	8.7
Ge(111)	0.58	5.9	2.94
HOPG(002)			239
(parallel (002))	17	1	
(perpendicular)	8	20	
HOPG(004)			477

* Work supported by the German national program of supporting development, innovation and technology (ProFIT Programm zur Förderung von Forschung, Innovationen und Technologien, Land Berlin, #10126367) and the European found for regional development (EFRE).

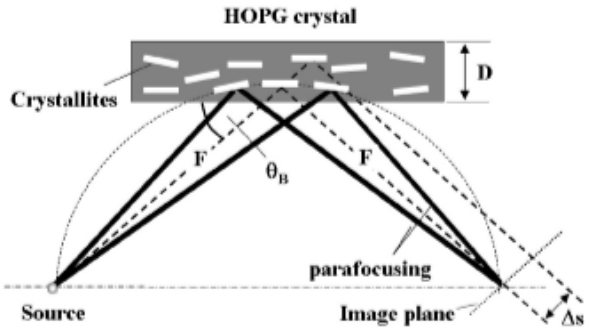

Figure 1: Diffraction properties of HOPG.

Because PG can be treated as an agglomeration of very small crystallites less strain is induced by bending the films and therefore no drastically changes of the diffraction properties determining the spectral energy resolution are expected and were measured up to now.

EXPERIMENTAL AND RESULTS

Samples

Two kind of HOPG crystals manufactured by Optigraph GmbH were investigated. Firstly, the well known "Highly Oriented Pyrolytic Graphite" (HOPG) crystal and secondly a new kind of HOPG crystal. This new material was already presented in [5]. Because the diffraction properties of the new material differ considerably from the well known HOPG it will be named by Optigraph henceforth "Highly Annealed Pyrolytic Graphite" (HAPG) to distinguish it from the commonly HOPG. This new kind of PG crystal is optimized for the application in x-ray spectroscopy by a modifed fabrication process. To get a comprehensive overview over the relationship between energy resolution and thickness in flat and bent geometry, crystals with different thickness were measured in (004)-reflection in both geometries. To realize precise variations in thickness the PG films were fabricated by stacking thin 10 - 15 μm thick PG films. The influence of the stacking on the energy resolution was investigated by measuring also thicker PG films consisting of only one sheet. The flat crystals were mounted on polished glass plates and the bent crystals were mounted on a cylindrical polished lens with radius 150 mm. The thickness of the investigated films was determined with an accuracy of $\pm$ 5 μm using a micrometer screw before mounting them on the moulds. It must be noted, that the measured thickness is an averaged value. That means, that the thickness can vary slightly for different sites of the crystal.

Experimental setup

The experimental setup is shown in Fig. 2. It consists of the HOPG crystals, an x-ray tube and a CCD camera. The x-ray source, which was used for the measurements, is a low power microfocus x-ray tube (IfG) with a source diameter of about 50 μm. Measurements were performed with the Cu K_α emission of a Cu anode at 8 keV. The spec-

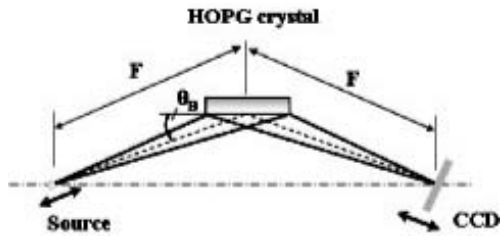

Figure 2: Experimental setup.

tra were collected with a 16-bit deep depletion CCD camera (Roper Scientific model PI-LCX 1300) with a quantum efficiency of about 50% at 8 keV. A thin (250 μm) Be window in front of the deep depletion CCD was used for vacuum sealing of the camera, so that a deep cooling (down to -50 °C) of the CCD was possible. The distance between source and crystal and between crystal and detector was F = 400 mm in each measurement. All measurements were carried out with the detector plane oriented perpendicularly to the reflected x-ray beam.

Results

In Fig. 3 selected images of the reflected Cu K_α emission are presented for both investigated PG crystals. In the upper image a 15 μm HAPG and in the lower image a 10 μm thick HOPG crystal in flat geometry is shown. As can be seen from the cross sections of the images in

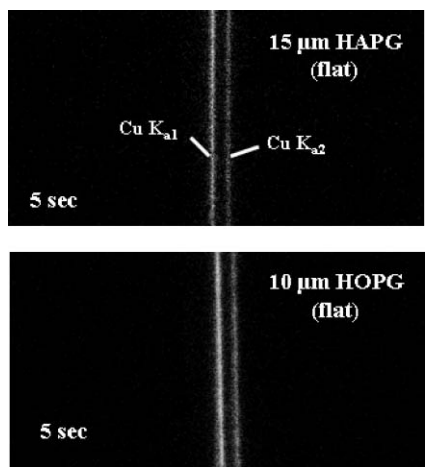

Figure 3: Recorded images of the reflected Cu K_α emission from a 15 μm thick HAPG and a 10 μm thick HOPG.

Fig. 4 the measured energy resolution of the flat HAPG crystal is better than that of the HOPG crystal with nearly same thickness. The energy resolution was determined by a convolution procedure as described in [5]. From the convolution procedure an energy resolution E/ΔE of 4100 was

found for the 15 μm flat HAPG and 3500 for the 10 μm flat HOPG. The reflection broadening due to crystal thickness, which is in the range of a single mosaic block, cannot explain the difference in energy resolution between both crystals. Therefore, the differences in energy resolution are more likely a broadening due to the flat geometry of the crystals. Latter gives rise to a focusing error in the image plane, because the alignment of the mosaic blocks in the basal plane deviates from a Rowland circle. These so-called flat focusing error increases with mosaicity (cp. [6]). Hence for the HAPG lower mosaic spread can be expected.

As mentioned above the 15 μm HAPG crystals are comparable to the 15 μm thick crystal which was presented in [5]. The energy resolution in Fig. 4 is higher because the distance F is larger. Taking the values for the energy resolution from [5] and comparing these values with the measured energy resolution at 400 mm distance a nearly linear increase of energy resolution over distance is observed.

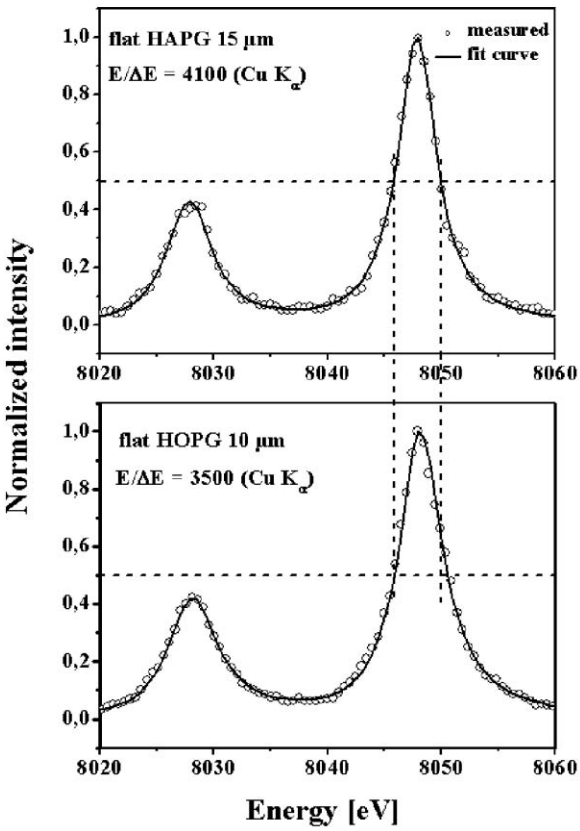

Figure 4: Cross sections of the recorded images in Fig. 3. The circles are measured points and the lines represents the fit curves of the convolution procedure.

As already reported in [5] the integral reflectivity of the 15 μm thick HAPG in (004)-reflection is similar to that of Ge(111) crystals. For the 10 μm HOPG the integral count rate on the CCD over the Cu K_α emission is by factor two higher than that of the 15 μm HAPG.

The energetic reflection bandwidth of these thin 15 μm HAPG films can be determined by rocking curve measurements. The measurements of the rocking curves were performed in (002)-reflection using a triple-crystal diffractometer at BESSY. In Fig. 5 the mosaic reflection and the intrinsic width of reflection of HAPG(002) are shown. The rocking curve width (FWHM) is 0,056 ° for the mosaic reflection and 27 arcsec for the intrinsic reflection. From the mosaic reflection the mosaic spread can be determined. To determine the mosaic spread from the measured rocking curves a reflectivity formula [7] derived from Zachariasen's treatment was used [8]. The best fit was obtained with a Lorentzian distribution and a mosaicity of 0.042 °. From the measured mosaic spread the energetic bandwidth can be calculated in both reflection orders.

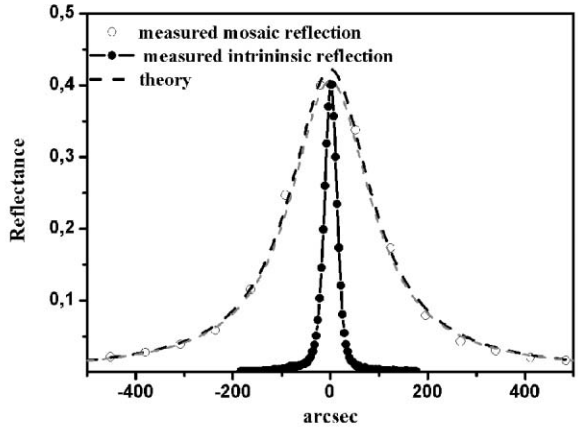

Figure 5: Measured rocking curves of a 15 μm thick HAPG crystal in (002)-reflection. The measurements of the rocking curves where performed using a triple-crystal diffractometer (BESSY).

To enhance the reflectivity the thickness of the HAPG films was increased. In Fig. 6 the images of a 40 μm thick

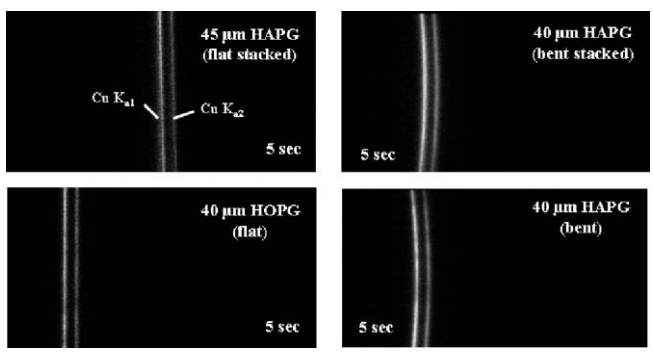

Figure 6: Recorded images of the reflected Cu K_α emission from a stacked 45 μm thick flat HAPG (upper left image), a 40 μm bent stacked HAPG (upper right image) and a 40 μm single sheet HAPG in flat (left lower image) and bent (right lower image) geometry.

HAPG single sheet and a stacked HAPG of same thickness are shown. Due to thickness broadening the energy resolution drops down to 3300 for both sheets. In contrast the integral count rate increases by a factor 4 for both 40 μm PG films in comparison to the 15 μm thick film. Also shown in Fig. 6 are bent HAPG crystals of same thickness. Bending these 40 μm thick HAPG crystals revealed fully different energy resolutions . While bending increases the energy resolution for the single sheet of HAPG as shown in Fig. 7, for the stacked bent HAPG the energy resolution drops down to 2300 (not shown). This result was surprisingly and indicates maybe changes in the mosaic structure by bending. In the case of the stacked HAPG an interaction between different layer has to be taken into account.

Finally, to enhance further the integral reflectivity accompanied with high energy resolution a 100 μm thick single HAPG sheet was investigated. The integral count rate increases further by a factor 2 and the energy resolution drops down to 2500 as can be seen in Fig. 7.

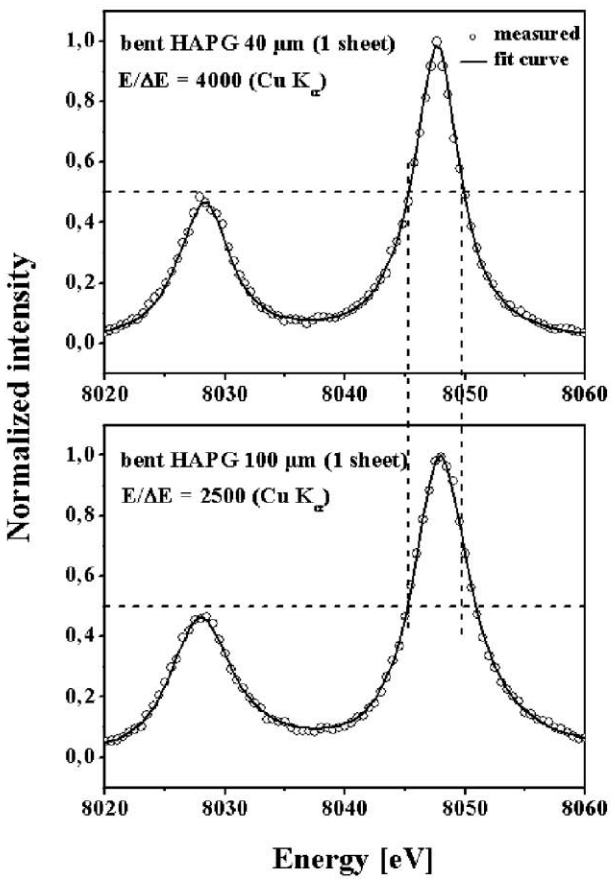

Figure 7: Cross sections of the recorded images in Fig. 6. The circles are measured points and the lines represents the fit curves of the convolution procedure.

CONCLUSION

High energy resolution can be obtained in (004)-reflection using very thin PG crystals. These high energy resolutions are accompanied with high integral reflectivity. As shown, bending single sheets of these very thin crystals seems not to decrease the energy resolutions.

Because of its good thermal properties PG could be interesting for many different applications based on high averaged x-ray sources, as e.g. the Free Electron Laser. A very promising application for PG crystals could be the single shot x-ray spectroscopy in an energy range between several keV up to several 10 keV. This can be done with PG because the mosaic spread enables to record a broad energy range with high energy resolution in a single shot.

REFERENCES

[1] A.W. Moore, "Chemistry and Physics of Carbon", Vol. 11, New York:Marcel Dekker (1973) 69-187.

[2] I.G. Grigorieva, A.A. Antonov, X-Ray Spectrometry 32(1) (2003) 64-68.

[3] M. Ohler, M. Sanchez del Rio, A. Tuffanelli, M. Gambaccini, A. Taibi, A. Fantini and G. Pareschiet, J. Appl. Cryst. 33 (2000) 1023-1030.

[4] A. K. Freund, A. Munkholm and S. Brennan, Proc. SPIE 2856 68–81.

[5] H. Legall, H. Stiel, V. Arkadiev, and A. A. Bjeoumikhov, Opt. Expr. 14 (2006) 4570-4576.

[6] G. E. Ice and C. Sparks , J.Nucl. Instrum. Methods A 291 (1990) 110-116.

[7] G.E. Bacon and Lowde R.D., Acta Cryst. 1 (1948) 303-314.

[8] W.H. Zachariasen, "Theory of X-Ray Diffraction in Crystals", New York:Dover (1945).

QUANTITATIVE DETECTION OF FEMTOSECOND X-RAY PULSES

Mathias Richter, Levent Cibik, Udo Kroth, Michael Krumrey, Hendrik Schoeppe,
Gerhard Ulm, PTB, Berlin;
Christian Blome, Ulf Jastrow, Jochen Schneider, Kai I. Tiedtke, Thomas Tschentscher, DESY, Hamburg;
Sergey Bobashev, IOFFE, St. Petersburg; Andrei Sorokin, PTB, Berlin, IOFFE, St. Petersburg;
Jerome Hastings, Rasmus Ischebeck, Stefan Moeller, SLAC, Menlo Park, California

Abstract

A detection system for femtosecond X-ray pulses has been developed within close cooperation between the Deutsche Elektronen-Synchrotron in Hamburg and the Physikalisch-Technische Bundeanstalt in Berlin. It is based on photoionization of Xenon gas and, hence, radiation hard. Photoions generated are extracted by an electric field and, in contrast to former devices developed for the vacuum-ultraviolet spectral range [1], detected by an amplifying open electron multiplier. Operation is performed at low gas pressure in the range between 0.1 and 0.01 Pa. Thus, the detector is almost transparent and may be used as a fast online monitor for quantitative and pulse-resolved determination of photon numbers and pulse energies of X-ray free electron lasers. After design and construction, a prototype has been successfully characterized and calibrated for photon energies from 4 to 10 keV in the PTB laboratory at the electron storage ring BESSY II in Berlin. First application has recently been realized in collaboration with the Linear Coherent Light Source at the Sub-Picosecond Pulse Source in Stanford with up to $1{\cdot}10^6$ photons per pulse detected at a photon energy of 9.4 keV.

PAPER NOT AVAILABLE

[1] M. Richter et al., Appl. Phys. Lett. 83, 2970-2972 (2003)

SCIENCE AT SINGLE PASS X-RAY FREE ELECTRON LASERS

J.R. Schneider, DESY, Hamburg

Abstract

Based on recent experience gained at the Free Electron Laser in Hamburg (FLASH) operating in the spectral range of the VUV, the first free electron laser user facility world wide, the requirements for successful experiments will be discussed. This includes the interplay between experimentalists on one and accelerator physicists and operators on the other hand, the need for various diagnostic tools, samples and sample environment, as well as the need for new approaches for data analysis

PAPER NOT AVAILABLE

ONE- AND TWO-COLOUR PHOTOIONIZATION EXPERIMENTS AT FLASH

M. Meyer, LIXAM, Orsay

Abstract

Photoionization processes induced by femtosecond extreme-ultraviolet (XUV) pulses of the Free Electron Laser in Hamburg (FLASH at DESY) were investigated in He, Ar, Kr and Xe by means of photoelectron spectroscopy. The well-known photoionization cross sections of rare gases enabled us to determine for each individual FEL pulse the importance of higher orders (0.5 - 1%) of the fundamental wavelength (32, 25 or 13.7 nm)[1]. In a second series of experiments, the FEL was combined with a synchronized optical laser of 12 ps or 120 fs temporal width. ATI (Above Threshold Ionization) processes induced by the optical laser are giving rise to 'sidebands' in the photoelectron spectrum. Their intensity exhibits a characteristic dependence on the relative time delay between both pulses and provides an inherent time marker for time-resolved pump-probe experiments. The results are in excellent agreement with theoretical predictions and allow a first analysis of two-colour ionization processes[2]. Finally, the temporal stability, i.e. the jitter of the FEL pulses with respect to the optical laser, was determined by measuring cross correlation curves with the ps- (523 nm) or the fs-laser (800 nm).

PAPER NOT AVAILABLE

[1] S. Düsterer et al., Opt. Lett. 31, 1750 (2006)
[2] M. Meyer et al., Phys. Rev. A (Rap. Comm.) submitted.

ULTRAFAST COHERENT DIFFRACTION IMAGING WITH X-RAY FREE-ELECTRON LASERS*

H. N. Chapman#, S. Bajt, A. Barty, W.H. Benner, M.J. Bogan, M. Frank, S.P. Hau-Riege, R.A. London, S. Marchesini, E. Spiller, A. Szöke, B.W. Woods, LLNL, Livermore, CA 94550, U.S.A.

J. Hajdu†, M. Bergh, F. Burmeister, C. Caleman, G. Huldt, F.R.N.C. Maia, M.M. Seibert, D. van der Spoel, U. Uppsala, S-75124 Uppsala, Sweden.

S. Boutet, K.O. Hodgson, SSRL, SLAC, Menlo Park, CA 94305, U.S.A.

D.A. Shapiro, CBST, UC Davis, Sacramento, CA 95817, U.S.A.

Abstract

The ultrafast pulses from X-ray free-electron lasers will enable imaging of non-periodic objects at near-atomic resolution [1]. These objects could include single molecules, protein complexes, or virus particles. The specimen would be completely destroyed by the pulse in a Coulomb explosion, but that destruction will only happen after the pulse. The scattering from the sample will give structural information about the undamaged object. There are many technical challenges in carrying out such experiments at an XFEL. We are addressing some of these challenges with experiments at the FLASH soft-X-ray FEL at DESY.

SINGLE PARTICLE IMAGING

The success of crystallography lies in its ability to overcome radiation damage by spreading the X-ray dose over many ($> 10^9$) identical copies of the molecule and by taking advantage of the strong signal that arises from the coherent superposition of X-rays within Bragg spots. However, by performing measurements with ultrashort pulses, we can apply crystallographic techniques to non-repetitive structures (including cells, viruses, and single macromolecules). The radiation dose required for such "diffraction imaging" will be orders of magnitude above the steady-state damage threshold of about 200–4000 photons/Å^2 (depending on sample size and wavelength) [2]. Even so, the high-angle (high-resolution) scattering from a single molecule will be extremely weak since, unlike diffraction from a crystal, there will be no coherent addition of scattering from many identical unit cells. We expect that the proposed XFELs will provide enough photons per pulse to give a measurable atomic-resolution signal.

Atomic-resolution imaging of biological objects with X-rays will necessarily be "lensless"; a diffraction pattern is recorded and a computer reconstruction algorithm performs the image formation step, replacing the role of a lens. Although the phase (wavefront) of the diffraction pattern is not recorded, it is possible to reconstruct the complex-valued image of a finite object from the far-field diffracted intensity. For single molecules and other non-periodic objects, the diffracted intensity is not confined to Bragg spots as it is for crystals. This allows an "oversampling" of the diffraction pattern, and the collection of information not accessible in a crystallographic experiment [3,4]. The "shrinkwrap" algorithm [5] is a particularly robust and practical method of using this information and performing 2D and 3D image reconstructions [6].

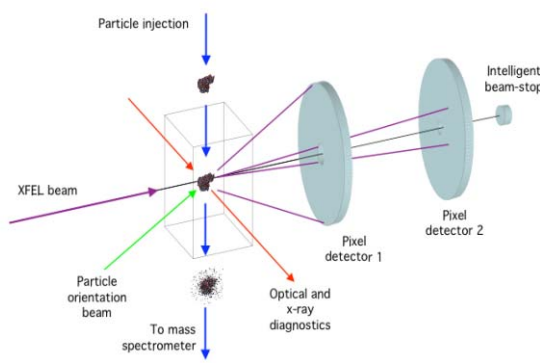

Figure 1: Schematic diagram of a single-particle diffraction imaging experiment at an XFEL.

*Work supported by U.S. Department of Energy (DOE) under Contract W-7405-Eng-48 to the University of California, Lawrence Livermore National Laboratory; the National Science Foundation Center for Biophotonics, University of California, Davis, under Cooperative Agreement PHY 0120999; The National Center for Electron Microscopy and the Advanced Light Source, Lawrence Berkeley Lab, under DOE Contract DE-AC02-05CH11231; Natural Sciences and Engineering Research Council of Canada; the U.S. Department of Energy Office of Science to the Stanford Linear Accelerator Center; the European Union (TUIXS); The Swedish Research Council; The Swedish Foundation for International Cooperation in Research and Higher Education; and The Swedish Foundation for Strategic Research.

#henry.chapman@llnl.gov
†janos.hajdu@xray.bmc.uu.se

A full 3D reconstruction can be achieved from diffraction patterns taken from many different orientations of the structure. With an XFEL, a complete data set will require identical copies of the object exposed to the beam one by one, which may be injected into the vacuum environment of the experiment and pass through the beam path at a random orientation. With identical samples it will possible to sort diffraction patterns to find those of similar orientation that can then be averaged. The averaging step will be important in order to improve the signal to noise ratio (SNR) and hence improve resolution. The critical step in the analysis becomes finding the minimum dose that is required not to image a particle, but to infer its orientation. Hence any method that can be employed to fix a particle's orientation, such as laser alignment [7,8] will have a big impact on the success of the technique.

A concept of the single-particle diffraction experiment is shown in Fig. 1. Some of the challenges we face to develop this technique include: understanding the interaction of the specimen and the FEL pulse to determine how short a pulse is required to overcome radiation damage; methods to focus X-ray FEL pulses to below 0.1 micron focal spots to achieve high intensity; development of high-dynamic range, low noise, and fast area detectors; methods of delivering purified samples into the beam without containers or substrates; handling the large data stream from the detectors and performing the classification and averaging of the diffraction data; and developing robust 3D imaging techniques.

RESOLUTION LIMITS

Radiation Damage

Radiation damage significantly limits the resolution of conventional imaging experiments. Damage is caused by energy deposited into the sample by the probes used for imaging (photons, electrons, neutrons, etc.). Cooling can slow down sample deterioration, but it cannot eliminate damage-induced sample movement *during* conventional measurements [9-12]. Ultra short x-ray pulses from X-ray free-electron lasers offer the possibility to extend the conventional damage limits, and will allow the imaging of non-crystalline biological (and other) materials. For proteins, simulations based on molecular dynamics (MD) [1, 13, 14], hydrodynamic [15, 21], and on plasma models [16] indicate that if very short (100 fs or less) and very intense x-ray pulses are available ($\geq 10^6$ photons/Å^2 on the sample), then a single scattering pattern could be recorded from a single protein molecule in the gas phase before radiation damage manifests itself and ultimately destroys the sample (Figure 2).

The hydrodynamic (HD) model can be computed fast on a computer, as compared with MD models. However, the MD models are potentially more accurate since they treat the microscopic atom-atom and atom-electron interactions in greater detail. The general approach at our laboratories is to use HD for simulations of the soft x-ray experiments at FLASH and to quickly explore new concepts for molecular imaging at XFELs, while developing an advanced MD model including electrons for more accurate simulations of the x-ray-molecule interaction for XFELs.

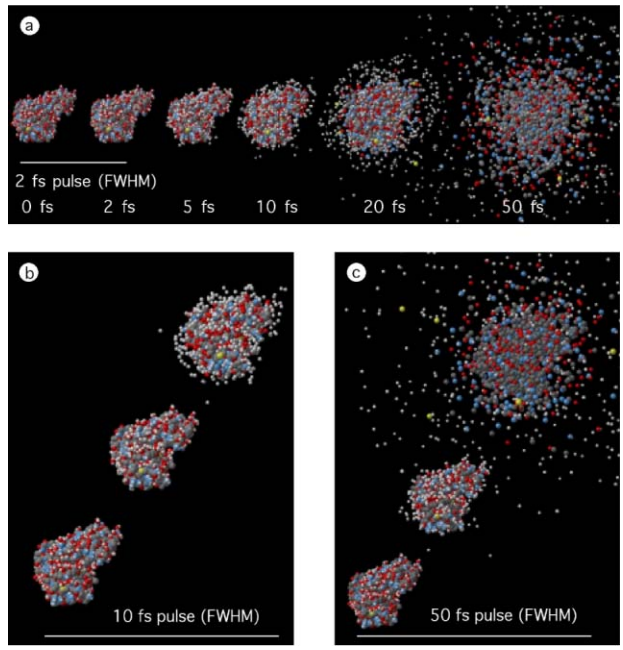

Figure 2: MD simulation of radiation-induced Coulomb explosion of a small protein (lysozyme). White balls: H, Gray: C, Blue: N, Red: O, Yellow: S. Integrated X-ray intensity: $3x10^{12}$ (12 keV) photons/100 nm diameter spot (corresponding to 3.8 x 10^8 photons/nm^2, or 3.8 x 10^6 photons/Å^2 on the sample) in all cases. (a) Protein exposed to a 2 fs FWHM X-ray pulse, and disintegration followed in time. The atomic positions in the first two structures (before and after the pulse) are practically identical at this pulse length due to an inertial delay in the explosion. (b) Lysozyme exposed to the same number of photons as in (a) but the pulse FWHM is now 10 fs. The images show the structure at the beginning, in the middle and near the end of the X-ray pulse. (c) Behaviour of the protein during a 50 fs FWHM X-ray pulse. It is also apparent from the figure that during the Coulomb explosion, hydrogen ions and highly ionised sulphurs are the first to escape the immediate vicinity of the protein (at 12 keV, the photoelectric cross section for sulphur is about fifty times larger than that for carbon). Based on Neutze at al. [1].

The basic assumption of the HD model is that the sample can be described by a liquid-like continuum of matter rather than considering individual atoms. This gives a simplified description of the average effects of x-ray material interaction and atomic motion, which then permits calculations even on very big samples. The model further assumes that the particle is spherically symmetric, reducing the mathematical model to one dimension plus time. The model assumes that the motion of the atoms within the molecule is solely in the radial direction. The electrons and the atoms are treated as separate, structureless, fluids that interact through the Coulomb

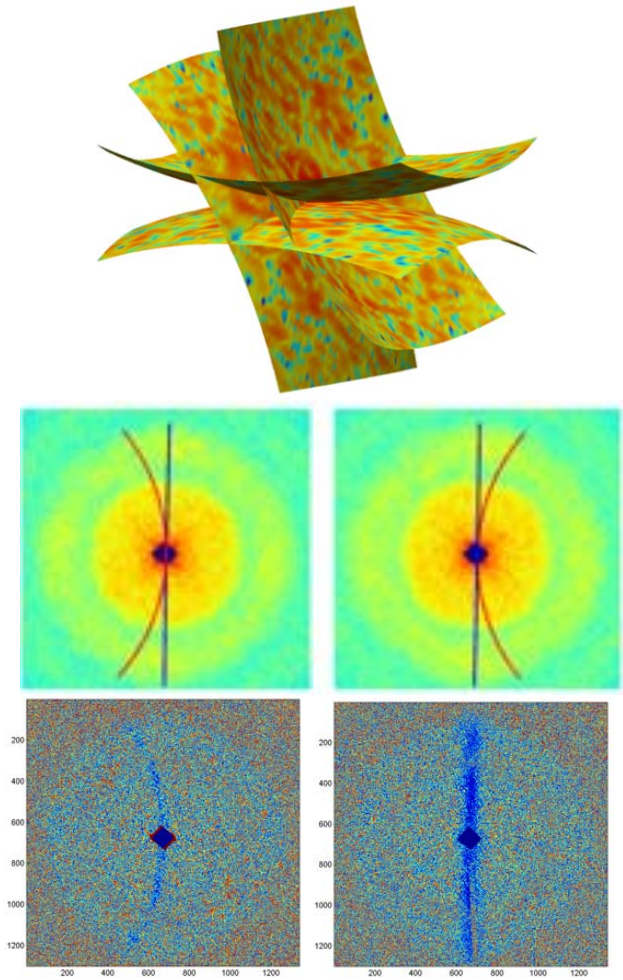

Figure 3: Intersection of two Ewald spheres with their centrosymmetric opposites. Centrosymmetry gives an extra intersect as there are *two* common arcs of intersection in *each* diffraction pattern (middle). The patterns in the middle show the expected arcs of intersections in two diffraction patterns from the experimental pyramid X-ray diffraction data set from Figure 10. Patterns at the bottom show these very lines of intersections when the experimentally obtained patterns are subtracted from each other pair wise (Huldt et al., in preparation).

force and ionization processes. The short-range electron-electron interactions are treated as a hydrodynamic pressure, and the long-range electron-electron and electron-ion Coulomb interactions are determined from the continuous net charge of the electrons and ions. In this model, all forces act radially. The model further assumes that the trapped electrons are thermalised among themselves, and that they are inertia free, so that they quickly relax to a force-free spatial equilibrium. Finally, the x-ray matter interaction, atomic ionization processes, and energy of the trapped electrons are described by time-dependent rate equations. The model shows that at later phases in an exposure, trapped electrons quickly relax in energy and position to form a cloud around the positive ions, leaving a neutral core and a positively charged outer shell (similar to Debye shielding). This layer is ejected first from the particle, and the Coulomb explosion proceeds from the outside in. A rarefaction wave propagates in from the surface at the sound speed, and hence the centre of the particle undergoes destruction later. In the inner core, there is hardly any ion motion but the high electron temperature leads to ionization and blurring of the electron density.

This behaviour has led to the proposal of a tamper as a sacrificial layer that will delay the onset of damage on the structure of interest [17]. The tamper may be a small water or helium drop that surrounds the molecule, and which has a total mass comparable to that of the molecule. Modern electrospray techniques can precisely control the amount of solvent left around the molecule and can be used to select an optimum layer thickness.

Sample reproducibility and orientation

Each particle (macromolecule) is exposed to the beam only once, and disintegrates at the end of this process. The diffraction pattern so recorded encodes a two-dimensional projection image of the sample (and this may provide sufficient information for some applications). Three-dimensional imaging requires more than one view from the sample. In addition, the signal-to-noise ratio of raw diffraction images will probably be insufficient for a high-resolution reconstruction, and it will be necessary to obtain a redundant data set so that averaging can enhance the signal. One could extend the depth of view from a single exposure by various holographic techniques based on external or internal reference beams, but a full three-dimensional reconstruction will most likely require *reproducible samples* exposed to the beam one-by one, and in different orientations. A "reproducible sample" (e.g. purified proteins) may contain heterogeneities, different subgroups of sample, and distinct conformers of the molecule. How reproducible is a "reproducible sample" and how well can we distinguish between similar and dissimilar structures will affect resolution through a B-factor-like component.

Conventional "single molecule" electron cryo-microscopy [18,19] faces similar challenges as those described here. The basic requirement for reconstruction and/or signal averaging from many diffraction images is the ability to tell whether two noisy diffraction patterns represent the same view of the sample or two different views [20]. Huldt *et al.* [20] have shown that a signal of less than one photon per pixel would be sufficient to correlate diffraction images of identical particles presenting the same view, assuming photon noise only. Correlation-based methods to average and orient large numbers of noisy, randomly oriented real-space images have been successfully developed in the electron microscopy community [18,19]. Diffraction patterns are first classified into classes of like-orientation so that they can be averaged to increase the signal relative to noise. The average signal per diffraction pattern at the highest

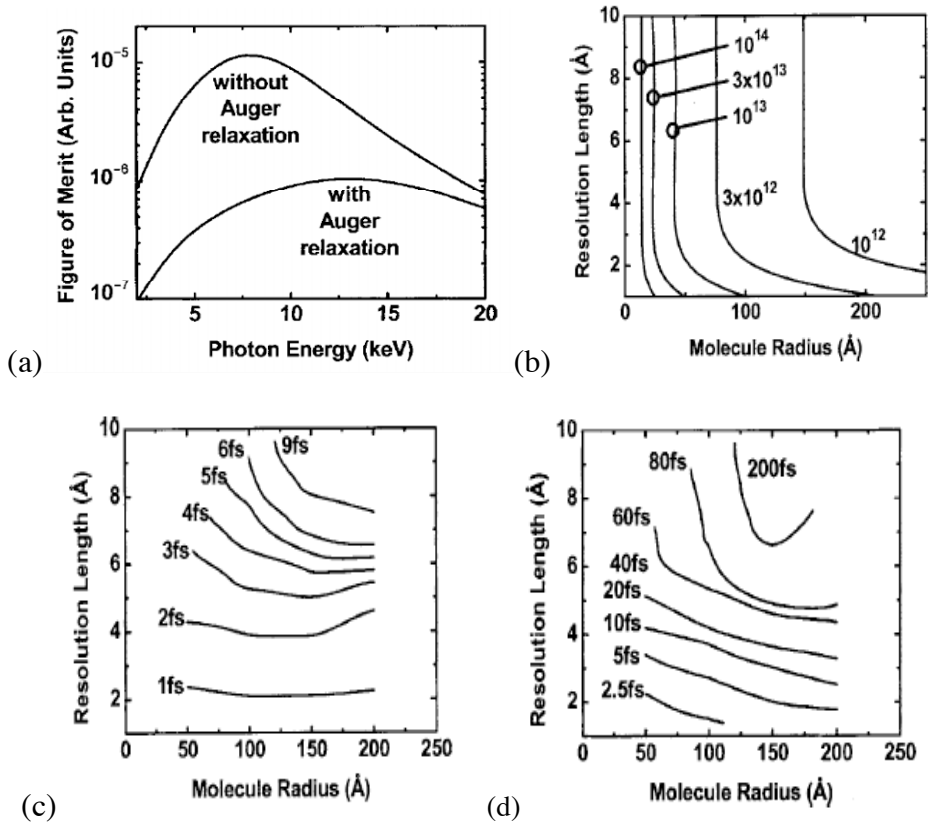

Figure 4: Resolution vs. radius for different X-ray fluences. (a) FOM for imaging conditions as a function of photon energy. (b) X-ray fluence requirements to classify two-dimensional diffraction patterns of biological molecules according to their orientation with 90% certainty. The curves are labeled with the X-ray fluence in units of photons in a 100 nm spot. (c) Plot of achievable resolution vs. molecule size for various pulse durations as limited by damage and classification. Atomic resolution imaging is achievable with pulse durations less than 5 fs and fluences greater than 10^{12} photons per 0.1 micron spot size. (d) Pulse duration requirements are significantly relaxed for samples that give 10 times larger scattering signal (e.g. viruses or nanocrystals) [21].

resolution, required for classification, is found to be much less than one photon per pixel, and an incident fluence of 10^8 ph/nm^2 is sufficient to achieve atomic resolution for particles greater than 15 nm radius [20].

Averaged diffraction patterns must be oriented with respect to each other in 3D Fourier space, which may be achieved by the method of common lines, a technique widely used in electron microscopy, where the micrographs represent planar sections through the center of the molecular transform. X-ray diffraction patterns are recorded on the Ewald sphere and so two patterns of different orientations will intersect along an arc in reciprocal space that passes through the zero spatial frequency. If the signal is strong enough for the line of intersection to be found in two averaged images, it will then be possible to establish the relative orientation of these patterns. We note that due to the curvature of the sections (especially at X-ray wavelengths), the common arc will provide a three-dimensional fix rather than a hinge-axis. Moreover, since the electron density of the object is real, its molecular transform exhibits centrosymmetry. This symmetry ensures that we obtain two independent repeats of the common lines in the two images. This feature provides redundancy for determining sample orientation, and is unique to diffraction patterns (Figure 3).

Resolution for reproducible particles

A combination of results from the hydrodynamic continuum model [15] with the diffraction pattern classification model of Huldt et al. [20] allows one to map out the landscape of imaging resolution, molecule size and pulse requirements [21]. The results are shown in Figure 4, which show that it will be possible to image single molecules at very high resolutions with very short pulse durations (atomic resolution with pulses less than about 5-10 fs).

First, the optimal photon energy for diffraction imaging was estimated by maximizing a figure of merit (FOM), defined as the ratio of signal minus noise to the radiation damage. As shown in Figure 4a, for pulses shorter than the Auger decay time (~10 fs for C), the optimum photon energy is 8 keV, and for longer pulses it is 13 keV, although the peak FOM is much smaller. Figure 4b shows

the required x-ray fluence versus image resolution length and particle radius, required to achieve a large enough diffraction signal to classify the patterns. Figure 4c shows the pulse length requirements for x-ray imaging biological molecules with 12 keV photons, assuming no pre-orientation of the molecules. When the fluence requirements are relaxed by orienting molecules with laser fields, using nanocrystals containing only a small number of molecules, or helical molecules, or icosahedral virus particles up to 10-20 times longer pulses can be tolerated, see Figure 4d.

IMAGE RECONSTRUCTION

A number of methods exist for recovering phases for objects that have a finite size, or "support". These include oversampling of continuous molecular transforms [4,22-25], holographic imaging methods [26-28], holographic data evaluation methods [29,30], classical methods of crystallography, and techniques for phase extension from lower resolution electron/X-ray cryo-microscopy images.

The past few years have seen the development of robust algorithms in solving the phase problem through oversampling the diffraction pattern, and this seems to be a most promising technique for the future. The 3D diffraction transform of a non-periodic particle is continuous. Only the diffraction amplitudes are sampled at discrete points by the pixellated detector and the process of classification. The measured diffraction intensities are proportional to the modulus squared of the Fourier transform of the wave exiting the object. On their own, these diffraction intensities are insufficient to back-transform to form an image in real space. That inversion requires knowledge of both the diffraction intensity and phase. If the diffraction pattern intensities are sampled finely enough, then it is possible to solve for the diffraction pattern phases [22,23]. The solution to this non-linear inversion problem is usually obtained iteratively by sequentially enforcing known constraints in reciprocal space and in real space. Specifically, in real space we assert that the image has zero scattering strength outside the area of the object's boundary (called its support) [23], whilst in reciprocal space the squared modulus of the Fourier transform of the image must equal the measured diffraction intensities. Such algorithms have now been used successfully for image reconstruction in X-ray diffraction experiments [4-6,31-34]. An example of a reconstructed 3D image is shown in Figure 5.

The algorithms usually require that the support of the object be known *a priori*, and the closer the support to the actual object boundary, the better the reconstruction. The algorithm called SHRINKWRAP successively refines an estimate of the support from a current estimate of the image [5]. This algorithm does not require the support to be known and is remarkably robust at finding the smallest image support that contains the majority of the image intensity.

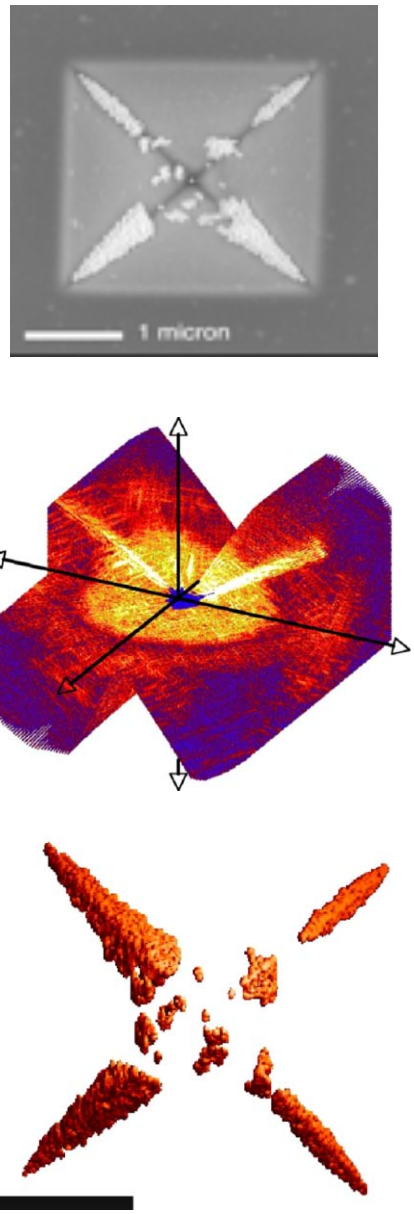

Figure 5: Coherent diffraction imaging and image reconstruction [6]. Three-dimensional diffraction data (middle) recorded from a test object (top), consisting of 50-nm diameter gold balls on a silicon-nitride pyramid-shaped membrane, at a wavelength of 1.6 nm, and a rendering of the *ab initio* 3D image (bottom) reconstructed from the diffraction intensities to a resolution of 10 nm. The diffraction data were obtained by rotating the specimen in 1° increments from -70° to +70°, and then interpolated onto a 1024^3-element array. A quadrant of the diffraction dataset has been removed for visualization in the central rendering of the 3D diffraction intensities. The gold balls seen in the rendering of the 3D reconstructed image on the right fill the inside edges of the silicon-nitride pyramid. The scale bar is 1 micron.

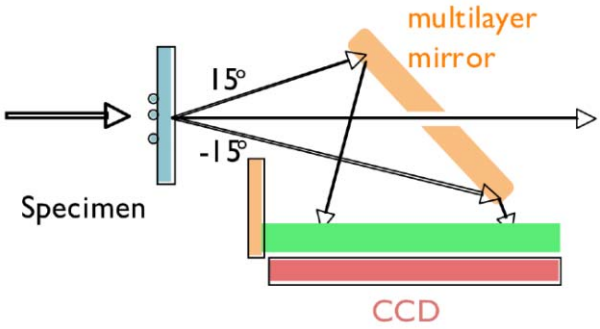

Figure 6: Schematic diagram of the diffraction camera for FLASH experiments, which uses a multilayer-coated mirror to reflect the diffraction pattern onto a CCD. The intense direct beam passes through a hole in the mirror.

EXPERIMENTS AT FLASH

Experiments were carried out at FLASH (Free-electron LASer at Hamburg, formerly known as the VUV-FEL). During the experiments the machine operated at a wavelength of 32 nm and in the ultrafast pulse mode of 25 ± 5 fs duration [36]. The pulses were focused to a 20 μm spot on the sample by an ellipsoidal mirror [37], achieving intensities up to about 10^{14} W/cm^2. We carried out experiments to demonstrate ultrafast coherent diffraction imaging and to study the interaction of matter with FEL pulses, in order to constrain our models to determine ultimate resolution limits with XFELs.

Our experiments at FLASH depend critically on being able to measure the forward scattering from samples with high sensitivity and low noise or parasitic scattering. The main experimental challenge was to prevent the direct beam from hitting the direct-detection CCD and to prevent out of band radiation (plasma emission from the sample) or non-sample scatter from obscuring the coherent diffraction signals. We solved these problems using a flat mirror oriented at 45° to the beam. The direct beam passes through a hole in the mirror whereas the diffracted beam is reflected from the mirror onto a bare CCD. The camera records diffraction angles between –15° to +15°, which requires a multilayer coating on the mirror that varies in layer spacing by a factor of two over a distance of only 28 mm (Bajt et al, in preparation). The multilayer coating was challenging because of the low absorption length of materials at 32 nm wavelength. We designed a coating consisting of three layers (Si, Mo, and B_4C), which simultaneously met the requirements of low stress, high reflectivity at 32 nm, and high reflectivity at the characterization wavelength of 0.154 nm. An advantage of the multilayer mirror is that it acts as a bandpass filter both for wavelength and direction. Plasma emission from the sample in the UV and visible ranges is rejected by the mirror. Stray light, from the scattering of beamline optics for example, hits the mirror at an angle that does not obey the Bragg law, and hence are also filtered out. Additionally, the mirror reflectivity diminishes smoothly to zero at the edge of the hole, due to roughness of the substrate at the edge. This "soft edge" reduces scatter from the hole.

We have performed several experiments using this apparatus, which will be reported on in forthcoming publications.

REFERENCES

[1] Neutze, R. Wouts, D. van der Spoel, E. Weckert, and J. Hajdu, "Potential for biomolecular imaging with femtoscond X-ray pulses," Nature 406 (2000) 752.

[2] D. Sayre and H.N. Chapman, "X-ray microscopy," Acta Cryst. A. 51 (1995) 237.

[3] D. Sayre, "Some implications of a theorem due to Shannon," Acta Cryst. 5, (1952) 843.

[4] J. Miao, P. Charalambous, J. Kirz and D. Sayre, "Extending the methodology of x-ray crystallography to allow imaging of micrometre-sized non-crystalline specimens," Nature 400 (1999) 342.

[5] S. Marchesini *et al.* "X-ray image reconstruction from a diffraction pattern alone," Phys. Rev. B 68 (2003), 140101.

[6] H.N. Chapman *et al.* "High-resolution ab initio Three-dimensional X-ray Diffraction Microscopy," J. Opt. Soc. Am. A 23 (2006) 1179.

[7] J.C.H. Spence and R. B. Doak, "Single molecule diffraction," Phys. Rev. Lett. 92 (2004) 198102.

[8] D. Starodub *et al.* "Damped and thermal motion of laser-aligned hydrated macromolecule beams for diffraction," J. Chem. Phys 123 (2005) 24430.

[9] R. Henderson, "Cryoprotection of protein crystals against radiation-damage in electron and X-ray diffraction," Proc. R. Soc. 241 (1990) 6.

[10] R. Henderson, "The potential and limitations of neutrons, electrons and X-rays for atomic resolution microscopy of unstained biological molecules," Quart. Rev. Biophys. 28 (1995) 171.

[11] C. Nave, "Radiation damage in protein crystallography," Rad. Phys. Chem. 45 (1995) 483.

[12] M.R. Howells *et al.*, "An assessment of the resolution limitation due to radiation-damage in x-ray diffraction microscopy," http://arxiv.org/physics/0502059

[13] Z. Jurek, G. Faigel, and M. Tegze, "Dynamics in a cluster under the influence of intense femtosecond hard x-ray pulses," Euro. Phys. J. D 29 (2004) 217.

[14] Z. Jurek, G. Oszlanyi and G. Faigel, "Imaging atom-clusters by hard x-ray free electron lasers," Europhys Lett., 65 (2005) 491.

[15] S.P. Hau-Riege, R.A London and A. Szöke, "Dynamics of X-Ray Irradiated Biological Molecules," Phys. Rev. E 69 (2004) 051906.

[16] M.Bergh, N. Timneanu and D. van der Spoel, "A Model for the Dynamics of a Water Cluster in an X-ray Free Electron Laser Beam," Phys. Rev. E 70 (2004) 051904.

[17] R.A. London, A. Szoke, and S.P. Hau-Riege, "A tamper to delay the motion of a sample during irradiation by short intense x-ray pulses," patent pending (2006).
[18] J. Frank, "Three-Dimensional Electron Microscopy of Macromolecular Assemblies," Academic Press, San Diego (1996).
[19] M. van Heel *et al.* "Single-particle electron cryo-microscopy: towards atomic resolution," Quart. Rev. Biophys. 33 (2000) 307.
[20] G. Huldt, A. Szöke and J. Hajdu, "Diffraction imaging of single particles and biomolecules," J. Struct. Biol. 144 (2003) 219.
[21] S.P. Hau-Riege, R.A. London, G. Huldt and H.N. Chapman, "Pulse requirements for x-ray diffraction imaging of single biological molecules," Phys. Rev. E 71 (2005) 061919.
[22] R.H.T. Bates, "Fourier phase problems are uniquely solvable in more than one dimension. 1. Underlying theory," Optik 61 (1982) 247.
[23] J.R. Fienup, "Phase retrieval algorithms-a comparison," Appl. Opt. 21 (1982) 2758.
[24] D. Sayre in Proceedings of the 1990 NATO Course, Erice (H. Schenk, ed.) (1991) p.353.
[25] A. Szöke, "Time-resolved holographic diffraction at atomic resolution," Chem. Phys. Letts. 313 (1999) 777.
[26] A. Szöke, "X-ray and electron holography using a local reference beam," in Short Wavelength Coherent Radiation: Generation and Application. Attwood, D. T. and Bokor, J. eds., American Institute of Physics Conference Proceedings No. 147, New York (1986).
[27] M. Tegze and G. Faigel, "Atomic-resolution X-ray holography," Europhys. Lett. 16 (1991) 41.
[28] M. Tegze and G. Faigel, "X-ray holography with atomic resolution," Nature 380 (1996) 49.
[29] A. Szöke, "Holographic methods in X-ray crystallography. 2. Detailed theory and connection to other methods of crystallography," Act. Cryst. A 49 (1993) 853.
[30] A. Szöke, H. Szöke and J.R. Somoza, "Holographic methods in X-ray crystallography 5. Multiple isomorphous replacement, multiple anomalous dispersion and non- crystallographic symmetry," Acta Cryst. A 53 (1997) 291.
[31] I.K. Robinson, I.A. Vartanyants, G.J. Williams, M.A. Pfeifer and J.A. Pitney, "Reconstruction of the shapes of gold nanocrystals using coherent x-ray diffraction," Phys. Rev. Lett., 87 (2001) 195505.
[32] H. He, S. Marchesini, M. Howells, U. Weierstall, G. Hembree, and J. C. H. Spence, "Experimental lensless soft-x-ray imaging using iterative algorithms: phasing diffuse scattering," Acta Cryst. A 59 (2003) 143.
[33] G. J. Williams, M. A. Pfeifer, I. A. Vartanyants, and I. K. Robinson, "Three-dimensional imaging of microstructure in Au nanocrystals," Phys. Rev. Lett. 90 (2003) 175501.
[34] J. Miao, T. Ishikawa, E. H. Anderson, and K. O. Hodgson, "Phase retrieval of diffraction patterns from noncrystalline samples using the oversampling method," Phys. Rev. B 67 (2003) 174104.
[35] D. Shapiro, P. Thibault, T. Beetz, V. Elser, M. Howells, C. Jacobsen, J. Kirz, E. Lima, H. Miao, A. M. Neimann, and D. Sayre, "Biological imaging by soft x-ray diffraction microscopy," Proc. Natl. Acad. Sci. U.S.A. 102 (2005) 15343.
[36] V. Ayvazyan *et al.,* "First operation of a free-electron laser generating GW power radiation at 32 nm wavelength," Eur. Phys. J. D 37 (2006) 297.
[37] K. Tiedtke *et al.*, "The SASE FEL at DESY: Photon Beam Diagnostics for the User Facility, *Proceedings SRI2003*, San Francisco, AIP Conf. Proc. 705 (2004) 588

THE PROPOSED EXPERIMENTAL PROGRAM AT LCLS

I. Lindau, MAX-lab, Lund;
R.W. Falcone, UCB, Berkeley, California

Abstract

I will discuss experiments planed for the LINAC Coherent Light Source, which is under construction at the Stanford Linear Accelerator Center. Experimental Teams have been organized, and construction of a range of instruments is underway. The science program currently includes atomic physics, femtochemistry, nanoscale dynamics in condensed matter physics, structural studies on single particles and biomolecules, and plasma and warm dense matter. New ideas for experiments continue to emerge.

PAPER NOT AVAILABLE